FAA CENTER OF EXCELLENCE FOR ALTERNATIVE JET FUELS & ENVIRONMENT

Annual Technical Report

2022

For the period

October 1, 2021 – September 30, 2022

Boston University
Georgia Institute of Technology
Massachusetts Institute of Technology
Missouri University of Science and Technology
Oregon State University
Pennsylvania State University
Purdue University
Stanford University
University of Dayton
University of Hawaii
University of Illinois
University of North Carolina
University of Pennsylvania
University of Tennessee
University of Washington
Washington State University

This work was funded by the US Federal Aviation Administration (FAA) Office of Environment and Energy as a part of ASCENT Project AJFE under FAA Award Number 13-C. Any opinions, findings, and conclusions or recommendations expressed in this material are those of the authors and do not necessarily reflect the views of the FAA or other ASCENT Sponsors.

Table of Contents

Overview

This report covers the period October 1, 2021, through September 30, 2022. The Center was established by the authority of FAA solicitation 13-C-AJFE-Solicitation. During that time the ASCENT team launched a new website, which can be viewed at ascent.aero. The next meeting(s) will be held during the months of April and May 2023.

Over the last year, the ASCENT team has made great strides in research, outreach, and education. The team's success includes the following:

- **64 active research projects*.**

The projects are divided into five main categories: tools, operations, noise, emissions, and alternative fuels, with cross-cutting research in aircraft technology innovation and supersonics. See the project category descriptions for more detail on each category and a summary of the projects. Funding for these projects comes from the FAA in partnership with Transport Canada.

*Note that projects 001, 059, 065 and 082 include several separately funded projects within a single project number. An individual report section is provided for each of these funded "sub-projects" and are titled Projects 001A-001E, 059A-059E, 065A-B and 082A-B.

- **181 publications, reports, and presentations by the ASCENT team.**

Each project report includes a list of publications, reports, and presentations. A comprehensive list of the publications, reports, and presentations for all projects is available in the publications index.

- **214 students participated in aviation research with the ASCENT team.**

ASCENT research projects were supported by 181 graduate students and 33 undergraduate students. Each project report includes the names and roles of the graduate and undergraduate students in the investigator's research. Students are selected by the investigators to participate in this research.

- **75 active industry partners involved in ASCENT.**

ASCENT's industry partners play an important role in the Center. Industry partners may contribute matching funds, participate on the Advisory Board, or both. Three new industry partners joined the Advisory Board in 2022. Advisory Board members provide insight into the view of stakeholders, advice on the activities and priorities of the Center's co-directors and ensure research will have practical application. The committee does not influence FAA policy. Industry partners also play a direct role in some of the research projects, providing matching funds, resources, and expertise to the project investigators.

Leadership

Dr. Michael Wolcott
Center Director and Technical Lead for Alternative Jet Fuels Research
Washington State University
(509) 335-6392, wolcott@wsu.edu

Dr. R. John Hansman
Center Co-Director and Technical Lead for Environmental Research
Massachusetts Institute of Technology
(617) 253-2271, rjhans@mit.edu

Dr. Jonathan Male
Assistant Vice Chancellor for Research and Director of National Laboratory Partnerships
Washington State University
jonathan.male@wsu.edu

Fabio Grandi
Acting Chief Scientific and Technical Advisor for Environment and Energy, Office of Environment and Energy
Federal Aviation Administration
fabio.grandi@faa.gov

Research Topics

Research projects within ASCENT are divided into five categories: alternative fuels, emissions, noise, operations, tools, aircraft technology innovation and supersonics. The list below includes all ASCENT funded research projects. This report includes research on active projects only. Reports for projects marked as COMPLETE are available on the ASCENT website at: https://ascent.aero/project/.

Alternative Fuels

The development of alternative jet fuels (AJFs) -- or sustainable aviation fuels (SAF) -- is of great interest to an array of aviation stakeholders, including aircraft and engine manufacturers and airlines. Alternative fuels that are produced from bio-based materials provide sustainable jet fuel alternatives that not only help alleviate environmental impacts from aviation emissions but can also create jobs in rural areas and lessen our reliance on foreign petroleum supplies.

Effective research and development, co-funded by the federal government and industry, enables SAF development by reducing the costs of producing renewable fuel. ASCENT research provides the scientific expertise and data to evaluate the environmental benefits associated with these sustainable fuels. ASCENT's collaborative R&D activities focuses on evaluating promising sustainable aviation fuel pathways to ensure environmental and social benefits, reduce technical uncertainties, inform aviation emission policies, and promote private sector investment in production.

Projects include:

- 001A-F - Alternative Jet Fuel Supply Chain Analysis
- 025 - National Jet Fuels Combustion Program – Area #1: Chemical Kinetics Combustion Experiments
- 026 - (COMPLETE) - National Jet Fuels Combustion Program – Area #2: Chemical Kinetics Model Development and Evaluation
- 027 - (COMPLETE) National Jet Fuels Combustion Program – Area #3: Advanced Combustion Tests
- 028 - (COMPLETE) National Jet Fuels Combustion Program – Area #4: Combustion Model Development and Evaluation
- 029A - National Jet Fuels Combustion Program – Area #5: Atomization Tests and Models
- 030 - (COMPLETE) National Jet Fuels Combustion Program – Area #6: Referee Swirl-Stabilized Combustor Evaluation/Support
- 031 - Alternative Jet Fuels Test and Evaluation
- 032 – (COMPLETE) - Worldwide LCA of GHG Emissions from Petroleum Jet
- 033 - Alternative Fuels Test Database Library
- 034 - (COMPLETE) National Jet Fuels Combustion Program – Area #7: Overall Program Integration and Analysis
- 052 - Comparative Assessment of Electrification Strategies for Aviation
- 065 - Fuel Testing Approaches for Rapid Jet Fuel Prescreening
- 066 - Evaluation of High Thermal Stability Fuels
- 067 - Impact of Fuel Heating on Combustion and Emissions
- 073 - Combustor Durability with Alternative Fuel Use
- 080 – Hydrogen and Power-to-Liquid (PtL) Concepts for SAF Production

Emissions

The demand for passenger and cargo air transportation has grown rapidly over the last several decades. According to the International Air Transport Association (IATA), in 2016 there were 3.8 billion air travelers, a number it predicts will rise to 7.2 billion passengers by 2035—a near doubling of current levels. This staggering growth is accompanied by airport expansions and increases in emissions from aircraft, ground services equipment, and vehicle traffic on and near airports. The increases in these activity-based emissions impact the air quality around airports, cumulatively contribute to global climate change, and can negatively affect human health.

ASCENT researchers are analyzing data and improving predictive models to understand the effects of aircraft and ground vehicle emissions, create and refine emission-based analytical techniques at both airport-specific and global scales, and assess how policy changes affect emissions and its impacts.

Projects include:

- 002 - (COMPLETE) Ambient Conditions Corrections for Non-Volatile PM Emissions Measurements
- 013 - (COMPLETE) - Micro-Physical Modeling & Analysis of ACCESS 2 Aviation Exhaust Observations

- 014 - (COMPLETE) - Analysis to Support the Development of an Aircraft CO2 Standard
- 018 - Community Measurement of Aviation Emission Contribution of Ambient Air Quality
- 019 - Development of Improved Aviation Emissions Dispersion Capabilities for AEDT
- 020 - (COMPLETE) - Development of NAS wide and Global Rapid Aviation Air Quality
- 021 - (COMPLETE) - Improving Climate Policy Analysis Tools
- 022 - Evaluation of FAA Climate Tools
- 024 - (COMPLETE) - Emissions Data Analysis for CLEEN, ACCESS, and Other Recent Tests
- 039 – (COMPLETE) - Naphthalene Removal Assessment
- 047 - Clean Sheet Supersonic Aircraft Engine Design and Performance
- 048 - Analysis to Support the Development of an Engine nvPM Emissions Standard
- 051 - Combustion Concepts for Next-Generation Aircraft Engines
- 052 - Comparative Assessment of Electrification Strategies for Aviation
- 058 - Improving Policy Analysis Tools to Evaluate Higher-Altitude Aircraft Operations
- 064 - Alternative Design Configurations to Meet Future Demand
- 067 - Impact of Fuel Heating on Combustion and Emissions
- 068 - Combustor Wall Cooling Concepts for Dirt Mitigation
- 069 - Transitioning a Research nvPM Mass Calibration Procedure to Operations
- 070 - Reduction of nvPM emissions via innovation in aero-engine fuel injector design
- 071 - Predictive Simulation of nvPM Emissions in Aircraft Combustors
- 074 - Low Emissions Pre-Mixed Combustion Technology for Supersonic Civil Transport
- 078 – Contrail Avoidance Decision Support and Evaluation
- 081 – Measurement and Prediction of Non-Volatile Particulate Matter (nvPM) Size and Number Emissions from SAF and Conventional Aviation Fuels
- 082 – Integrated Noise and Emissions CO_2 Standard Setting Analysis

Noise

ASCENT researchers work to understand all aspects of the aircraft operations that contribute to aviation's noise impact. They are working on understanding how aircraft and rotorcraft performance and operation affect noise generation and how they could be modified for mitigation measures. Research is also under way to look how noise propagates from the source to the ground and how it affects human health, wellbeing, and quality of life. This research will improve the modeling tools used to estimate the noise impacts from aviation operations and provide data to inform policy development as well as public engagement and education.

Projects include:

- 003 - Cardiovascular Disease and Aircraft Noise Exposure
- 004 - (COMPLETE) - Estimate of Noise Level Reduction
- 005 - (COMPLETE) - Noise Emission and Propagation Modeling
- 007 - (COMPLETE) - Civil, Supersonic Over Flight, Sonic Boom (Noise) Standards Development
- 008 – (COMPLETE) - Noise Outreach
- 009 - Geospatially Driven Noise Estimation Module
- 017 – (COMPLETE) -Pilot Study on Aircraft Noise and Sleep Disturbance
- 038 – Rotorcraft Noise Abatement Procedures Development
- 040 – Quantifying Uncertainties in Predicting Aircraft Noise in Real-world Situations
- 041 – Identification of Noise Acceptance Onset for Noise Certification Standards of Supersonic Airplane
- 042 – (COMPLETE) Acoustical Mode of Mach Cut-off
- 043 – Noise Power Distance Re-Evaluation
- 044 - Aircraft Noise Abatement Procedure Modeling and Validation
- 049 - Urban Air Mobility Noise Reduction Modeling
- 050 - Over-Wing Engine Placement Evaluation
- 053 - Validation of Low Exposure Noise Modeling by Open Source Data Management and Visualization Systems Integrated with AEDT
- 055 - Noise Generation and Propagation from Advanced Combustors
- 057 - Support for Supersonic Aircraft En-route Noise Efforts in ICAO CAEP
- 059A-E - Modeling and Measurements of Supersonic Civil Transport Jet Noise
- 061 – Noise Certification Streamlining
- 062 - Noise Model Validation for AEDT

- 063 - Parametric Noise Modeling for Boundary Layer Ingesting Propulsors
- 072 - Aircraft noise exposure and market outcomes in the US
- 075 - Improved Engine Fan Broadband Noise Prediction Capabilities
- 076 - Improved Open Rotor Noise Prediction Capabilities
- 079 – Novel Noise Liner Development Enabled by Advanced Manufacturing
- 082 – Integrated Noise and Emissions CO_2 Standard Setting Analysis

Operations

Aviation operations result in fuel burn, emissions, and noise impacts. The nature and scale of these effects depends on a number of related factors, including:

- Aircraft flight paths and profiles,
- Schedule and frequency of operations, and
- Aircraft fleet mix.

ASCENT research focuses on identifying and accelerating the implementation of operational concepts that will reduce aviation environmental impacts and/or improve energy efficiency while maintaining the efficiency of the National Airspace System. The research spans multiple phases of flights and targets all environmental impact areas.

Projects include:

- 006 - (COMPLETE) - Rotorcraft Noise Abatement Operating Conditions Modeling
- 015 - (COMPLETE) - Cruise Altitude and Speed Optimization
- 016 - (COMPLETE) - Airport Surface Movement Optimization
- 023 - Analytical Approach for Quantifying Noise from Advanced Operational Procedures
- 038 - Rotorcraft Noise Abatement Procedures Development
- 044 - Aircraft Noise Abatement Procedure Modeling and Validation
- 053 - Validation of Low Exposure Noise Modeling by Open Source Data Management and Visualization Systems Integrated with AEDT
- 077 - Measurements to Support Noise Certification for UAS/UAM Vehicles and Identify Noise Reduction Opportunities

Tools

The aviation system operation involves complex interactions between many different components when aircraft are on the ground, taking off, in the air, and when landing. Aviation system operations also require the understanding of how to optimize aviation activities, which is best done by implementing advanced modeling tools.

The Federal Aviation Administration's suite of modeling tools have been developed to characterize and quantify the interdependences of aviation-related noise and emissions, impacts on human health and welfare, and the costs and market impacts to industry and consumers under varying policies, technologies, operations, and market scenarios.

The ASCENT researchers are further developing and expanding the capabilities of these modeling tools in a variety of ways, from improving the way basic physical properties are represented and effectively modeled to how new technologies will enter the aircraft fleet and identifying the benefits of such technologies.

Projects include:

- 009 - Geospatially Driven Noise Estimation Module
- 010 - Aircraft Technology Modeling and Assessment
- 011 - (COMPLETE) - Rapid Fleet-wide Environmental Assessment Capability
- 012 - (COMPLETE) - Aircraft Design and Performance Assessment Tool Enhancement
- 035 - (COMPLETE) - Airline Flight Data Examination to Improve flight Performance Modeling
- 036 - (COMPLETE) - Parametric Uncertainty Assessment for AEDT2b
- 037 – CLEEN II Technology Modeling and Assessment
- 040 - (COMPLETE) - Quantifying Uncertainties in Predicting Aircraft Noise in Real-world Situations
- 043 - Noise Power Distance Re-Evaluation (NPD+C) to Include Airframe Noise in AEDT
- 045 – (COMPLETE) Takeoff/Climb Analysis to Support AEDT APM Development

- 046 – Surface Analysis to Support AEDT APM Development
- 049 - Urban Air Mobility Noise Reduction Modeling
- 053 - Validation of Low Exposure Noise Modeling by Open Source Data Management and Visualization Systems Integrated with AEDT
- 054 - AEDT Evaluation and Development Support
- 058 - Improving Policy Analysis Tools to Evaluate Higher-Altitude Aircraft Operations
- 060 - Analytical Methods for Expanding the AEDT Aircraft Fleet Database
- 062 - Noise Model Validation for AEDT
- 064 - Alternative Design Configurations to meet Future Demand

Aircraft Technology Innovation

The evolution of airframes and engines has resulted in modern designs that significantly reduce aviation fuel use, emissions and noise on a per-flight basis. ASCENT researchers conduct the analyses, modeling and testing required to demonstrate the viability of innovative airframe, engine and flight management technologies that reduce noise, emissions, and fuel burn. Future innovations will drive further improvements and the ASCENT research helps accelerate technology development.

Projects include:

- 010- Aircraft Technology Modeling and Assessment
- 037 - CLEEN II System Level Assessment
- 047 - Clean Sheet Supersonic Aircraft Engine Design and Performance
- 050 - Over-Wing Engine Placement Evaluation
- 051 - Combustion Concepts for Next-Generation Aircraft Engines
- 052 - Comparative Assessment of Electrification Strategies for Aviation
- 055 - Noise Generation and Propagation from Advanced Combustors
- 056 - Turbine Cooling through Additive Manufacturing
- 059 - Modeling and Measurements of Supersonic Civil Transport Jet Noise
- 063 - Parametric Noise Modeling for Boundary Layer Ingesting Propulsors
- 064 - Alternative Design Configurations to Meet Future Demand
- 066 - Evaluation of High Thermal Stability Fuels
- 067 - Impact of Fuel Heating on Combustion and Emissions
- 068 - Combustor Wall Cooling with Dirt Mitigation
- 070 - Reduction of nvPM emissions via innovation in aero-engine fuel injector design
- 071 - Predictive Simulation of Soot Emission in Aircraft combustors
- 074 - Low Emissions Pre-Mixed Combustion Technology for Supersonic Civil Transport
- 075 - Improved Engine Fan Broadband Noise Prediction Capabilities
- 076 - Improved Open Rotor Noise Prediction Capabilities
- 077 - Measurements to Support Noise Certification for UAS/UAM Vehicles and Identify Noise Reduction Opportunities

Supersonics

ASCENT supersonics research supports implementation of new technologies by advancing the understanding of the perception of sonic boom noise over a range of sonic boom levels, assessing Mach cut-off levels that will allow supersonic flight over land and furthering development of supersonic aircraft noise certification standards.

Projects include:

- 007 (COMPLETE) - Civil, Supersonic Over Flight, Sonic Boom (Noise) Standards Development
- 010- Aircraft Technology Modeling and Assessment
- 022 - Evaluation of FAA Climate Tools
- 041 - Identification of Noise Acceptance Onset for Noise Certification Standards of Supersonic Airplanes
- 042 - (COMPLETE) Acoustical Model of Mach Cut-off
- 047 - Clean Sheet Supersonic Aircraft Engine Design and Performance
- 057 - Support for Supersonic Aircraft Noise Efforts in ICAO CAEP
- 058 - Improving Policy Analysis Tools to Evaluate Aircraft Operations in the Stratosphere
- 059 - Jet Noise Modeling to Support Low Noise Supersonic Aircraft Technology Development
- 074 - Low Emissions Pre-Mixed Combustion Technology for Supersonic Civil Transport

Project 001(A) Alternative Jet Fuel Supply Chain Analysis

Washington State University

Project Lead Investigator

Michael P. Wolcott
Regents Professor
Department of Civil & Environmental Engineering
Washington State University
PO Box 642910
Pullman, WA 99164-2910
509-335-6392
wolcott@wsu.edu

University Participants

Washington State University

- P.I.s: Michael P. Wolcott, Regents Professor; Christina Sanders, Acting Director, Division of Governmental Studies and Services; Manuel Garcia-Perez, Professor; Xiao Zhang, Professor; and Ji Yun Lee, Assistant Professor
- FAA Award Number: 13-C-AJFE-WaSU-023, 026
- Period of Performance: October 1, 2021 to September 30, 2022
- Tasks:
    1. Prepare and assess design cases.
    2. Evaluate the most promising biorefinery concepts for alternative jet fuel (AJF) production.
    3. Supplement and maintain the current inventory of biorefinery infrastructures that are useful for the production of AJF, as identified in the conversion design cases.
    4. Perform a community social asset assessment.
    5. Refine and deploy facility siting tools to determine regional demand and to identify potential conversion sites to be used in regional analyses.
    6. Perform a refinery-to-wing stakeholder assessment.
    7. Conduct a supply chain analysis.
    8. Provide analytical support for regional Commercial Aviation Alternative Fuels Initiative (CAAFI) and U.S. Department of Agriculture (USDA) jet fuel projects.

Project Funding Level

This project has received $1,091,455 in FAA funding, $1,091,455 in matching funds, and state-committed graduate school contributions for four PhD students. Faculty time for Michael Wolcott, Manuel Garcia-Perez, and Xiao Zhang contributes to the cost share.

Investigation Team

- Michael Wolcott, WSU, Project Director/P.I. (Tasks 3,5,7,8)
- Christina Sanders, WSU, Co-Project Director/Co-P.I.
- Season Hoard, WSU, Co-Project Director/Co-P.I.
- Manuel Garcia-Perez, WSU, Co-Project Director/Co-P.I. (Tasks 1,2,7)
- Xiao Zhang, WSU, Co-Project Director/Co-P.I. (Tasks 1,2)
- Ji Yun Lee, WSU, Co-Project Director/Co-P.I.
- Michael Gaffney, WSU, Faculty (Tasks 4,6)
- Kristin Brandt, WSU, Staff Engineer
- Dane Camenzind, WSU, Staff Engineer
- Lina Pilar Martinez Valencia, WSU, Graduate Student/Postdoctoral Research Associate

- Anamaria Paiva, WSU, Graduate Student
- Kelly Nguyen, WSU, Graduate Student
- Jie Zhao, WSU, Graduate Student
- Fangjiao Ma, WSU, Graduate Student

Collaborating Researchers

- Burton English, University of Tennessee
- Edward Yu, University of Tennessee
- Scott Turn, University of Hawaii
- Florian Allroggen, Massachusetts Institute of Technology
- Kristin C. Lewis, Volpe Center

Project Overview

As part of an effort to realize an "aviation system in which air traffic will move safely, swiftly, efficiently, and seamlessly around the globe," the FAA set a series of goals and supporting outcomes, strategies, and performance metrics (Hileman et al., 2013). The goal entitled "Sustaining our Future" outlines several strategies collectively aimed at reducing the environmental and energy impacts of the aviation system. To achieve this goal, the FAA set an aspirational goal for the aviation industry to utilize one billion gallons of AJF by the year 2018. This goal was created according to economic, emissions, and overall feasibility perspectives (Richard, 2010; Staples et al., 2014). In the past year, the goals for U.S. AJF use have been updated with the Sustainable Aviation Fuel (SAF) Grand Challenge that by 2030 the United States will produce and use three billion gallons of AJF, with an increase to 35 billion gallons in 2050 with a minimum reduction of 50% in lifecycle greenhouse gases (White House, 2021).

Most approaches to supply chain analyses for AJF optimize feedstock-to-refinery and refinery-to-wing transportation logistics (Bond et al., 2014). One of the greatest barriers to large-scale AJF production is the high capital of greenfield facilities, which translates to risk in the investment community (Huber et al., 2007). The cost of cellulosic ethanol plants ranges from $10 to $13 per gallon capacity (Hileman & Stratton, 2014); moreover, the additional processing steps required to convert the intermediate to a drop-in AJF could increase this cost to more than $25 per gallon capacity (Hileman, 2014).

Motivated by the realities of converting these initial commercialization efforts into second-generation AJF, researchers have considered alternative conversion scenarios, including the transitioning of existing facilities (Brown, 2013). The conversion of existing refineries to produce renewable diesel and AJF is underway at both the Martinez and Rodeo refineries in California (Marathon, 2022; Phillips 66, 2022). Research on approaches for achieving the SAF Grand Challenge goals for AJF consumption has relied on "switching" scenarios, in which existing and planned capacities are used to produce drop-in fuel (Malina, 2012). These approaches require the identification of existing industrial assets, similar to refinery conversions, that can be targeted for future AJF production. Thus, siting becomes not only an exercise for optimizing feedstock transportation but also a necessary task for aligning this critical factor with the existing infrastructure, markets within regions, and the appropriate social capital for developing this new industry (Henrich et al., 2007; Seber et al., 2014).

To date, all published AJF supply chain analyses have been limited to stand-alone jet fuel production technologies that do not generate bioproducts. Hence, future studies must consider the potential techno-economic and environmental benefits of using the existing industrial infrastructure and the production of co-products with respect to the development of jet fuel production scenarios.

Design cases of stand-alone AJF production facilities will be used in supply chain evaluations. Social asset modeling is not well developed, and efforts are likely to be hampered by difficulties in quantifying social assets when compared with improved environmental performance or reductions in AJF costs, which may be better observed by optimizing economic and environmental constraints. However, the community characteristics of a potential site must be considered when determining preferred locations for a new biorefinery. Community resistance or enthusiasm for the AJF industry can strongly influence the success or failure of a facility (Martinkus et al., 2014; Rijkhoff et al., 2017). Thus, community social asset modeling efforts conducted within this project, such as those based on the Community Asset and Attribute Model (CAAM), will inform disciplinary applications and advances. Clearly, social factors can have substantial effects, either positive or negative, on project adoption and implementation, particularly in high-technology or energy-related projects (Lewis et al., 2012; Martinkus et al., 2012; Mueller et al., 2020). The consideration of social factors in site selection and implementation decisions can maximize positive social support and minimize opposition and social negatives, thereby substantially promoting the success

of a project. In this regard, the CAAM originally piloted in the Northwest Advanced Renewables Alliance project was designed to provide a quantitative rating of select social factors at the county level (Martinkus et al., 2014).

Focusing on regional supply chains, this research aims to identify the key barriers that must be overcome to meet AJF targets. We will address this overall goal by developing tools to support the AJF supply chain assessment performed at the Volpe Center. Our efforts will provide facility siting analyses that assess conversion design cases combined with regional supply chain assets and social capacity assessments for communities to act collectively toward development goals. Finally, a refinery-to-wing stakeholder assessment will support modeling and accounting of AJF distribution for downstream fuel logistics.

References

Bond, J. Q., Upadhye, A. A., Olcay, H., Tompsett, G. A., Jae, J., Xing, R., Alonso, D. M., Wang, D., Zhang, T., Kumar, R., Foster, A., Sen, S. M., Maravelias, C. T., Malina, R., Barrett, S. R. H., Lobo, R., Wyman, C. E., Dumesic, J. A., & Huber, G. W. (2014). Production of renewable jet fuel range alkanes and commodity chemicals from integrated catalytic processing of biomass. *Energy Environ. Sci.*, *7*(4), 1500–1523. https://doi.org/10.1039/C3EE43846E

Brown, N. (2013). *FAA Alternative Jet Fuel Activities*. Overview. Presented to: CLEEN Consortium.

Henrich, E. (2007). *The status of FZK concept of biomass gasification*. 2nd European Summer School on Renewable Motor Fuels. Warsaw, Poland.

Hileman, J. I., De la Rosa Blanco, E., Bonnefoy, P. A., & Carter, N. A. (2013). The carbon dioxide challenge facing aviation. *Progress in Aerospace Sciences*, *63*, 84–95. Doi: 10.1016/j.paerosci.2013.07.003

Hileman, J. I., & Stratton, R. W. (2014). Alternative jet fuel feasibility. *Transport Policy*, *34*, 52–62. Doi: 10.1016/j.tranpol.2014.02.018

Hileman, J. (2013). *Overview of FAA alternative jet fuel activities*. Presentation to the Biomass R&D Technical Advisory Committee, Washington DC.

Huber, G. W., & Corma, A. (2007). Synergies between bio- and oil refineries for the production of fuels from biomass. *Angewandte Chemie International Edition*, *46*(38), 7184–7201. Doi: 10.1002/anie.200604504

Lewis, K., Mitra, S., Xu, S., Tripp, L., Lau, M., Epstein, A., Fleming, G., & Roof, C. (2012). Alternative jet fuel scenario analysis report. Publication No. DOT/FAA/AEE/2011-05. (http://ntl.bts.gov/lib/46000/46500/46597/DOT-VNTSC-FAA-12-01.pdf) (Retrieved on 2014-07)

Malina, R. (2012). *HEFA and F-T jet fuel cost analyses*. Laboratory for Aviation and the Environment. MIT.

Marathon (2022). Martinez Renewable Fuels. https://www.marathonmartinezrenewables.com/

Martinkus, N., Kulkarni, A., Lovrich, N., Smith, P., Shi, W., Pierce, J., & Brown, S. (2012). *An Innovative Approach to Identify Regional Bioenergy Infrastructure Sites*. Proceedings of the 55th International Convention of Society of Wood Science and Technology, Beijing, China.

Martinkus, N., Shi, W., Lovrich, N., Pierce, J., Smith, P., & Wolcott, M. (2014). Integrating biogeophysical and social assets into biomass-to-alternative jet fuel supply chain siting decisions. *Biomass and Bioenergy*, *66*, 410-418.

Mueller, D., Hoard, S., Roemer, K., Sanders, C., & Rijkhoff, S. (2020). *Quantifying the Community Capitals Framework: Strategic Application of the Community Assets and Attributes Model*. Community Development.

Phillips 66 (2022). *San Francisco Refinery: The Evolution of Rodeo Renewed*. https://www.phillips66.com/refining/san-francisco-refinery/

Rijkhoff, S. A. M., Hoard, S. A., Gaffney, M. J., & Smith, P. M. (2017). Communities ready for takeoff Integrating social assets for biofuel site-selection modeling. *Politics and the Life Sciences: The Journal of the Association for Politics and the Life Sciences*, *36*(1), 14–26. PMID: 28884650

Richard, T.L. (2010). Challenges in scaling up alternative jet fuels infrastructure. Science, 329:793.

Seber, G., Malina, R., Pearlson, M. N., Olcay, H., Hileman, J. I., & Barrett, S. R. H. (2014). Environmental and economic assessment of producing hydroprocessed jet and diesel fuel from waste oils and tallow. *Biomass and Bioenergy*, *67*, 108–118. Doi: 10.1016/j.biombioe.2014.04.024

Staples, M. D., Malina, R., Olcay, H., Pearlson, M. N., Hileman, J. I., Boies, A., & Barrett, S. R. H. (2014). Lifecycle greenhouse gas footprint and minimum selling price of renewable diesel and jet fuel from fermentation and advanced fermentation production technologies. *Energy Environ. Sci.*, *7*(5), 1545–1554. Doi: 10.1039/C3EE43655A

White House (2021). FACT SHEET: Biden Administration Advances the Future of Sustainable Fuels in American Aviation. https://www.whitehouse.gov/briefing-room/statements-releases/2021/09/09/fact-sheet-biden-administration-advances-the-future-of-sustainable-fuels-in-american-aviation/

Task 1 - Prepare and Assess Design Cases

Washington State University

Objectives

In previous years, our team has worked toward completing reviews and final reports of design cases for six stand-alone AJF technologies (Table 1) and four relevant industries (sugarcane, pulp and paper, corn ethanol, and petroleum refineries). The status of each stand-alone AJF techno-economic analysis (TEA) and report is shown in Table 1. The results on pyrolysis and alcohol-to-jet (ATJ) pathways have been published in the referenced peer-reviewed journals. The work conducted from October 1, 2021 to September 30, 2022 focused on the following tasks:

1. Complete a detailed analysis of a "catalytic hydrothermolysis pathway for jet fuel production," including two publications.
2. Conduct a detailed analysis of a new AJF pathway for hydrothermal liquefaction (HTL) processing.
3. Conduct TEA on the integration of lignin co-product technologies in the ATJ pathway to determine the potential for reducing fuel costs.
4. Develop a new case report focusing on a technology review, an evaluation of lipid conversion processes (hydroprocessed esters and fatty acids [HEFA], catalytic hydrothermolysis [CH], SBI, Forge, Tyton, and decarboxylation), and new technologies for the production of alternative lipids (HTL and sugar-to-lipid).
5. Prepare manuscripts for publication.

Table 1. Evaluated stand-alone alternative jet fuel (AJF) technologies.

	Literature review and design report date	Publications	Techno-economic analysis (TEA) model
Pyrolysis	Literature review based on a design report, 138 pages (2017)	*Energy Fuel 33*, 4683, 2019; *Fuel Process Technology 195*, 106140, 2019	A standardized TEA is complete and available for use by university partners.
Alcohol-to-jet (ATJ)	Literature review based on a design report, 28 pages (2015)	*ChemSusChem 11*, 3728, 2018	A standardized TEA is complete and available for use by partners.
Synthetic kerosene and synthetic aromatic kerosene (SK-SKA)	Literature review based on a design report, 36 pages (2015)	Manuscript based on the case design report in preparation	This work was based on a Sasol process, on which we have not found any significant development since 2016. Because of a lack of adequate process information/data on SK-SKA production from renewable feedstock, we are not able to build a reliable TEA.
Direct sugar-to-hydrocarbon (DSHC)	Literature review based on a design report, 88 pages (2017)	*Biomass and Bioenergy 145:105942,* 2021	A standardized TEA is complete and available for use by partners.
Virent BioForming process	Literature review based on a design report, 46 pages (2015)	*Biomass and Bioenergy 145:105942,* 2021	A standardized TEA is complete and available for use by partners.
Catalytic hydrothermolysis (CH)	Literature review based on a design report, 35 pages (2018)	*Renewable and Sustainable Energy Reviews 115:111516,* 2021 *Data in Brief 39:107514,* 2021	A standardized TEA is complete and has been posted on the WSU repository.
Gasification Fischer Tropsch (GFT)	No literature review conducted	*Biomass and Bioenergy 145:105942,* 2021	A standardized TEA is complete and available for use by partners.
Microchannel GFT (microGFT)	No exhaustive literature review written; capital costs found in the open literature for microchannel FT deemed unreliable	Capital cost results deemed unreliable	A standardized microGFT TEA was completed; however, the cost information is considered unreliable.
Hydroprocessed esters and fatty acids (HEFA)	No literature review conducted	*Biomass and Bioenergy 145:105942,* 2021	A standardized TEA is complete and available for use by partners.

Research Approach

Background

We have conducted a detailed literature review and prepared design case reports on six AJF pathways, including pyrolysis, ATJ, synthetic kerosene, direct sugar-to-hydrocarbon (DSHC), Virent BioForming, and CH. We have also collected data from the literature to conduct TEAs for these pathways. The results from these design cases were applied in the development of supply chains and the identification of synergisms that may eventually lead to the construction of integrated AJF production systems that take advantage of the infrastructure in a given region. An analysis of the locations of existing infrastructure demonstrated that the United States can be divided into regions according to the dominant biomass. Thus, we believe that the generation of advanced biorefinery concepts focused on petroleum refineries, pulp and paper mills, sugarcane mills, and corn ethanol mills is a viable approach for evaluating the synergism among AJF pathways, existing infrastructure, and co-products. We can then compare the biorefinery concepts developed for each technology to identify the most promising approach, which can subsequently be used in supply chain analyses.

Stand-alone design case reports were generated by reviewing relevant research in the academic literature and public information provided by commercial entities developing the corresponding technology. The published manuscripts were subjected to an industrial expert review. The reports provide details regarding the processes involved in each conversion pathway and outline the technology readiness and particular barriers to implementation. Publicly available information regarding the commercial processes and research literature will provide a foundation of information to be used in modeling efforts. In cases lacking detailed process engineering information, new models will be built to estimate the parameters needed to complete assessments such as techno-economic modeling and supply chain modeling. Aspen Plus primarily generates process models and details, including mass balances, energy balances, energy requirements, and equipment size and cost. These results will also provide the basis for a comparative analysis of design cases, which will identify the key advantages and markets for each technology.

Each design case has the following components:

- Feedstock requirements
- Companies developing/commercializing the technology
- Current locations of units in the United States and worldwide
- Block and flow diagram of the technology
- Unit operations and process conditions (reactor type, separation unit type, catalysts, product yield, and jet fuel yield)
- Properties of the produced jet fuel
- Identification of potential intermediates
- Current and potential uses of wastes and effluents
- Developed co-products
- Potential methods for coprocessing intermediates, wastes, and co-products by using existing infrastructure (e.g., petroleum refineries or pulp and paper mills)
- Preliminary TEA
- Technological challenges and gaps

We have submitted technical reports and supplementary Microsoft Excel files with mass and energy balances and TEAs for the pathways listed below. Furthermore, we have conducted a strategic analysis to identify the overall weaknesses of the technologies under study. All files are available on shared drives for the Project 01 team members.

- Pyrolysis-bio-oil hydro-treatment concept (hydro-treated depolymerized cellulosic jet): The TEA is complete.
- ATJ: A manuscript with information on the mass and energy balances and the TEA has been published.
- Gasification Fischer Tropsch (GFT): Two design cases have been prepared for biomass gasification. The first case focuses on microreactors, and the second design case is applicable to technology based on larger, standard reactors (reviews on the TEAs for GFT and microGFT have been completed). However, the limited reliability of the microreactor capital costs hinders the value of the practical impact of our microreactor TEA study. The TEAs are available for use by partners.
- HEFA: A stochastic TEA was created in MATLAB and was confirmed to match the completed, deterministic TEA when the assumptions and costs match (deterministic TEA review completed). The TEA is now available for use.
- CH: The TEA is complete.

Major progress has been made on the analysis of corn ethanol, sugarcane, and petroleum refinery infrastructure that could support jet fuel production. A manuscript on the conversion of corn ethanol mills was published in *Biomass and Bioenergy*. Two additional manuscripts repurposing either sugarcane mills or petroleum refineries to reduce AJF production costs were also published.

We have worked with the Pacific Northwest National Laboratory and completed a case design report on HTL for AJF conversion.

A summary manuscript reviewing several lipid conversion pathways, including SBI, Forge, Tyton, decarboxylation, and coprocessing, entitled "Lipid and Bio-processing Technologies: An Insight into Bioconversion Potential of Process Intensification and Continuous Flow-Through Reaction (PICFTR), Lipid to Hydrocarbon (LTH) and TYTON Bioenergy" has been prepared.

Milestones

A Microsoft Excel file with TEAs for all AJF technologies has been completed, and design cases for the corn ethanol and sugarcane industries have been completed. A detailed analysis entitled "Catalytic Hydrothermolysis Pathway for Jet Fuel Production" has been completed, and a manuscript entitled "Jet Fuel Design Case: Hydrothermal Liquefaction Case Design Report" has been published. A summary report entitled "Lipid and Bio-processing Technologies: Process Intensification and Continuous Flow-Through Reaction (PICFTR), Lipid-to-Hydrocarbon (LTH), Tyton, Decarboxylation and Coprocessing" has been produced, and corresponding manuscripts have been prepared for publication.

Major Accomplishments

A manuscript entitled "Economic Analysis of Catalytic Hydrothermolysis Pathway for Jet Fuel Production" has been published in *Renewable and Sustainable Energy Reviews*, and a TEA dataset on the CH pathway for jet fuel production was published in *Data in Brief* in 2021. A manuscript reporting on a preliminary TEA of biorefinery lignin for fine chemical production was published in *Green Chemistry* in 2021. We have also updated two draft manuscripts: "Hydrothermal Liquefaction Case Design Report" and "Lipid and Bio-processing Technologies: An Insight into Bioconversion Potential of Process Intensification and Continuous Flow-Through Reaction (PICFTR), Lipid to Hydrocarbon (LTH) and TYTON Bioenergy." A manuscript entitled "Comparison of Techno-economic and Environmental Performance of Alternative Jet Fuel Production Technologies" has been prepared, reviewed, and updated in preparation for FAA review. We intend to submit these manuscripts to the FAA for review within the next four months. We are working on the construction of a TEA for lignin extraction and utilization in a biorefinery process (NREL, 2018).

We have assisted the International Civil Aviation Organization (ICAO), Committee on Aviation Environmental Protection through participation in the Fuel Task Group and the Long-Term Aspirational Goal task group. An Excel spreadsheet of publicly announced, global AJF producers has been updated, and work with ICAO for integrating the historical portion of these data with their database is ongoing. In addition, a separate U.S. database that does not include ICAO-specific assumptions and data is being maintained to assist in tracking progress toward meeting the SAF Grand Challenge goals.

Six Excel spreadsheet-based TEAs have been published on the WSU repository site to make these tools publicly available for analyses. These TEAs include HEFA, ATJ, FT with both solid and gaseous feedstocks, FT feedstock preparation, pyrolysis, and CH. The TEAs are being used by other ASCENT member universities and interested industry and government parties.

Data generated from the design cases have been made available to 01A partners to assist with supply chain analysis and techno-economic modeling by improving the conversion and cost figure database values. Evaluations of the effects of process variations in the chemical properties of the generated products are being used to provide insight into the challenges that will be faced when AJFs are blended into commercial jet fuel.

Publications

Peer-reviewed journal publications

Brandt, K., Camenzind, D., Zhu, J. Y., Latta, G., Gao, J., & Wolcott, M. (2022). Methodology for quantifying the impact of repurposing existing manufacturing facilities: Case study using pulp and paper facilities for sustainable aviation fuel production. *Biofuels, Bioproducts and Biorefining*, *16*(5), 1227–1239. https://doi.org/10.1002/bbb.2369

Brandt, K. L., Martinez-Valencia, L., & Wolcott, M. P. (2022). Cumulative impact of federal and state policy on minimum

selling price of sustainable aviation fuel. *Frontiers in Energy Research*, *10*, 828789. Doi: 10.3389/fenrg.2022.828789

Eswaran, S., Subramaniam, S., Geleynse, S., Brandt, K., Wolcott, M., & Zhang, X. (2021). Dataset for techno-economic analysis of catalytic hydrothermolysis pathway for jet fuel production. *Data in Brief*, *39*, 107514. Doi: 10.1016/j.dib.2021.107514

Eswaran, S., Subramaniam, S., Geleynse, S., Brandt, K., Wolcott, M., & Zhang, X. (2021). Techno-economic analysis of catalytic hydrothermolysis pathway for jet fuel production. *Renewable and Sustainable Energy Reviews*, *151*, 111516. Doi: 10.1016/j.rser.2021.111516

Ma, R., Sanyal, U., Olarte, M. V., Job, H. M., Swita, M. S., Jones, S. B., Meyer, P. A., Burton, S. D., Cort, J. R., Bowden, M. E., Chen, X., Wolcott, M. P., & Zhang, X. (2021). Role of peracetic acid on the disruption of lignin packing structure and its consequence on lignin depolymerisation. *Green Chemistry*, *23*(21), 8468–8479. Doi: 10.1039/D1GC02300D

Tanzil, A. H., Brandt, K., Wolcott, M., Zhang, X., & Garcia-Perez, M. (2021). Strategic assessment of sustainable aviation fuel production technologies: Yield improvement and cost reduction opportunities. *Biomass and Bioenergy*, *145*, 105942. Doi: 10.1016/j.biombioe.2020.105942

Outreach Efforts

During the preparation of design case reports, we have closely interacted with industrial companies, including Gevo, LanzaTech, Sky Energies, and Agrisoma (now NuSeed). These companies have also helped us review reports and draft manuscripts. Our results have been presented to the FAA and CAAFI. Six harmonized TEAs have been posted on the WSU Research Repository for public use. We have also made several presentations to graduate and undergraduate students.

- Wolcott, M., Brandt, K. SAF Grand Challenge A Path to 3-billion Gallons by 2030. SAF Summit & CAAFI Biennial General Meeting. (2022)
- Brandt, K; Tanzil, AH; Martinez-Valencia, L; Garcia-Perez, M; Wolcott, MP; Pyrolysis techno-economic analysis, v. 2.1. Washington State University (2022)
- Brandt, K; Wolcott, MP; Fischer Tropsch feedstock pre-processing techno-economic analysis, v. 2.1. Washington State University (2022)
- Brandt, K; Tanzil, AH; Martinez-Valencia, L; Garcia-Perez, M; Wolcott, MP; Fischer Tropsch techno-economic analysis, v. 2.1. Washington State University (2022)
- Brandt, K; Tanzil, AH; Martinez-Valencia, L; Garcia-Perez, M; Wolcott, MP; Hydroprocessed esters and fatty acids techno-economic analysis, v. 2.1. Washington State University (2022)
- Brandt, K; Geleynse, S; Martinez-Valencia, L; Zhang, X; Garcia-Perez, M; Wolcott, MP; Alcohol to jet techno-economic analysis, v. 2.1. Washington State University (2022)
- Brandt, K; Eswaran, S; Subramaniam, S; Zhang, X; Wolcott, MP; Catalytic hydrothermolysis techno-economic analysis, v. 2.1. Washington State University (2022)

Awards

None.

Student Involvement

Several graduate students (Sudha Eswaran, Kelly Nguyen, Abid Hossain Tanzil, Anamaria Paiva, and Lina Martinez) and one undergraduate student (Kitana Kaiphanliam) participated in the creation, editing, and updating of design cases for stand-alone AJF technologies, relevant existing infrastructure, and lignin co-products.

Plans for Next Period

We will focus on the following areas and plan to submit three to five manuscripts on lignin co-product analyses and AJF technology analyses. The following are the proposed manuscripts to be completed this project year:

1. Continue to support ICAO work through participation in the Committee on Aviation Environmental Protection's Fuel Task Group.
2. Lipid and Bio-processing Technologies: Process Intensification and Continuous Flow-Through Reaction (PICFTR), Lipid-to-Hydrocarbon (LTH), Tyton, Decarboxylation, and Coprocessing.
3. The Opportunity for Lignin Co-Products to Improve the Economics of Sustainable Aviation Fuel Production.

References

National Renewable Energy Laboratory. (2018). *Process Design and Economics for the Conversion of Lignocellulosic Biomass*

to Hydrocarbon Fuels and Coproducts: 2018 Biochemical Design Case Update (Publication No. NREL/TP-5100-71949). https://www.nrel.gov/docs/fy19osti/71949.pdf

Task 2 - Evaluate the Most Promising Biorefinery Concepts for AJF Production

Washington State University

Objectives

Continuation from previous years

We have completed our evaluation of biorefinery scenarios for AJF production using corn ethanol, sugarcane, and pulp and paper mills and petroleum refineries.

We will conduct detailed TEAs on the integration of lignin co-product technologies and the ATJ pathway to determine the potential for reducing fuel costs.

Research Approach

Background

In this task, we used the design cases for existing infrastructure, AJF production technology, and identified co-products to generate new biorefinery concepts for petroleum refineries, pulp and paper mills, sugarcane mills, and corn ethanol mills. The results from this effort will allow us to identify and select the most commercially feasible biorefinery concepts. Major technical gaps or barriers to the commercialization of each biorefinery concept will also be determined from the results of this study.

The integration of process technologies will be assessed with an approach similar to that for the stand-alone design cases. The integration concepts will be developed by pairing stand-alone cases with these concepts to evaluate the economic and environmental advantages of the integration approaches. Over this period, we have conducted detailed analyses of ATJ conversion and integration with pulp mill operations. We have also investigated the potential contribution of lignin co-products to the overall process economy.

A dry-grind corn ethanol mill with a capacity of 80 million gallons of ethanol per year was studied to evaluate potential biorefinery scenarios for AJF production. Similarly, we used a sugarcane mill with a sugarcane processing capacity of 12,444 million tons per day that produces raw sugar, molasses, surplus bagasse, and surplus electricity. The petroleum refinery used as the base case processes 120,000 barrels per day of crude oil. Five AJF technologies were studied: Virent's BioForming, ATJ, DSHC, fast pyrolysis, and GFT. A standardized methodology was adopted to compare the biorefinery concepts for a dry-grind corn ethanol mill, sugarcane mill, and petroleum refinery in several integration scenarios with six jet fuel production scenarios. For all cases, we estimated the minimum fuel selling price and greenhouse gas emissions.

A manuscript on the integration of ATJ technologies with pulp mill infrastructure was published. Three additional manuscripts were published with results for corn ethanol mills, sugarcane mills, and petroleum refineries.

Use a p-graph to generate and rank biorefinery concepts utilizing a database of SAF's technological pathways built from a data base of unitary operations created by our team.

Major Accomplishments

Building on the ATJ pathway analyses, we have analyzed the integration of the ATJ process within the pulp, corn ethanol, sugarcane, and petroleum refinery infrastructure. A manuscript entitled "Pulp Mill Integration with Alcohol-to-Jet Conversion Technology" has been published in *Fuel Processing Technology*. Economic models and life cycle assessments have been applied to select the most promising biorefinery concepts for corn ethanol, sugarcane, pulp and paper, and petroleum refineries. A manuscript on corn ethanol was published in *Biomass and Bioenergy*. A manuscript on integration with petroleum refineries was published in *Frontiers in Energy Research*, and a manuscript analyzing the integration of AJF with sugarcane mills was published in *Fuel*.

A manuscript entitled "Synthesis and Techno-Economic Analysis of Pyrolysis-Oil-Based Biorefineries Using P-Graph" was published in *Energy and Fuels.*

Publications

Peer-reviewed journal publications

Tanzil, A. H., Brandt, K., Zhang, X., Wolcott, M., Silva Lora, E. E., Stockle, C., & Garcia-Perez, M. (2022). Evaluation of bio -refinery alternatives to produce sustainable aviation fuels in a sugarcane mill. *Fuel*, *321*, 123992. doi: 10.1016/j.fuel.2022.123992

Tanzil, A. H., Brandt, K., Zhang, X., Wolcott, M., Stockle, C., & Garcia-Perez, M. (2021). Production of sustainable aviation fuels in petroleum refineries: Evaluation of new bio-refinery concepts. *Frontiers in Energy Research*, *9*, 735661. doi: 10.3389/fenrg.2021.735661

Tanzil, A. H., Zhang, X., Wolcott, M., Brandt, K., Stöckle, C., Murthy, G., & Garcia-Perez, M. (2021). Evaluation of dry corn ethanol bio-refinery concepts for the production of sustainable aviation fuel. *Biomass and Bioenergy*, *146*, 105937. doi: 10.1016/j.biombioe.2020.105937

Pinheiro Pires, A. P., Martinez-Valencia, L., Tanzil, A. H., Garcia-Perez, M., García-Ojeda, J. C., Bertok, B., Heckl, I., Argoti, A., & Friedler, F. (2021). Synthesis and techno-economic analysis of pyrolysis-oil-based biorefineries using p-graph. *Energy & Fuels*, *35*(16), 13159–13169. doi: 10.1021/acs.energyfuels.1c01299

Geleynse, S., Jiang, Z., Brandt, K., Garcia-Perez, M., Wolcott, M., & Zhang, X. (2020). Pulp mill integration with alcohol-to-jet conversion technology. *Fuel Processing Technology*, *201*, 106338. doi: 10.1016/j.fuproc.2020.106338

Outreach Efforts

None.

Awards

None.

Student Involvement

Graduate students (Senthil Subramaniam, Kelly Nguyen, Abid Hossain Tanzil, Lina Martinez Valencia, and Anamaria Paiva) have received training in this project. An undergraduate student, Kitana Kaiphanliam, funded under a National Science Foundation Research Experience for Undergraduates grant, assisted in building techno-economic models for co-product production scenarios.

Senthil Subramaniam, who has been supported by this project, graduated with a PhD degree from WSU (December 2020).

Kelly Nguyen, who has been supported by this grant, graduated with a Master's degree from WSU (May 2020).

Abid Hossain Tanzil submitted and defended a PhD dissertation during the fall 2020 semester.

Plans for Next Period

During the next period, Dr. Zhang's team will focus on lignin manuscripts and corresponding TEAs. Dr. Garcia-Perez's team will work to generate new biorefinery systems using p-graphs.

Task 3 - Supplement and Maintain the Current Inventory of Biorefinery Infrastructures that are Useful for AJF Production, as Identified in the Conversion Design Cases

Washington State University

Objective

This task requires periodic evaluation of the databases to add new facilities or update the status of closed facilities in each category to ensure that the geospatially specific assets are current.

Research Approach

The use of existing infrastructure assets is a key component of retrofit approaches for advances in this industry. To differentiate between the relative values of various options, the specific assets must be valued with respect to their potential use within a conversion pathway. Regional databases of industrial assets that might be utilized by a developing AJF industry

have been assessed on the national level. These baseline databases have been compiled from a variety of sources, including industry associations, universities, and news outlets. These databases will be expanded, refined, and validated as the conversion design cases indicate additional needs for regional analyses.

Milestones
National databases have been compiled, geolocated, validated, and shared for biodiesel, corn ethanol, energy pellet, pulp and paper, and sugar mill production. We have evaluated the databases as necessary to add new facilities or change the status of closed facilities in each category, to ensure that the geospatially specific assets are current.

The geospatial infrastructure data were converted for use in supply chain resiliency models. Tools were updated for transportation cost modeling, which should lead to future improvements.

Major Accomplishments
National databases have been compiled, validated, and shared with the 01A teams. All metadata are available for use in regional analyses.

Publications
None.

Outreach Efforts
None.

Awards
None.

Student Involvement
None.

Plans for Next Period
None.

Task 4 – Perform a Community Social Asset Assessment
Washington State University

Objective
The objective of this task is to update CAAM with available data and strategically apply it to additional U.S. regions.

Research Approach
Based on the Community Capitals Framework, we created the CAAM model, which provides quantitative indicators of four social assets: social, cultural, human, and political capital. The CAAM provides quantitative proxy measures of qualitative concepts for initial site-selection assessments. Variations of the model have been applied to the Pacific Northwest, Idaho, Montana, Colorado, and Wyoming. Manuscripts on applications of the CAAM have been published in *Community Development*, *Politics and Life Sciences*, *Biomass & Bioenergy*, and *Frontiers in Energy Research*. The CAAM model is being updated with current data with plans to apply it to other regions and contexts.

Milestone
CAAM benchmark measures have been applied to the Bioenergy Alliance Network of the Rockies (BANR) region.

Major Accomplishments
The collaboration with the BANR social science team and application of the CAAM to Colorado and Wyoming have been completed. These efforts resulted in a publication in *Frontiers in Energy Research*. Additionally, the CAAM team published a manuscript in *Frontiers in Energy Research* that reviews social science applications in sustainable aviation research.

Publications

Peer-reviewed journal publications

Boglioli, M., Mueller, D. W., Strauss, S., Hoard, S., Beeton, T. A., & Budowle, R. (2022). Searching for culture in "cultural capital": The case for a mixed methods approach to production facility siting. *Frontiers in Energy Research*, *9*, 772316. doi: 10.3389/fenrg.2021.772316

Anderson, B. J., Mueller, D. W., Hoard, S. A., Sanders, C. M., & Rijkhoff, S. A. M. (2022). Social science applications in sustainable aviation biofuels research: Opportunities, challenges, and advancements. *Frontiers in Energy Research*, *9*, 771849. doi: 10.3389/fenrg.2021.771849

Outreach Efforts

None.

Awards

None.

Student Involvement

None.

Plans for Next Period

We will update the CAAM with the latest U.S. data.

Task 5 - Refine and Deploy Facility Siting Tools to Determine Regional Demand and Potential Conversion Sites to be Used in Regional Analyses

Washington State University

Objective

This task's objective is to develop tools for siting potential conversion facilities. Two primary tools are needed for this task: a generalized tool to site initial locations that meet the needs of a specific conversion facility type and a second tool to select optimal conversion facility sites from the initial set of locations.

Research Approach

We began developing a geospatial siting pre-selection (GSP) tool in early 2019. This tool is a Python-based script that automates ArcGIS to produce points representing locations that suit the needs of a conversion facility. The GSP tool uses a combination of buffer and cost datasets. Buffer datasets ensure that a candidate is sited in proximity to the necessary infrastructure, such as roads, rails, and natural gas pipelines. Because the candidate set generated by using only buffers will be very large, cost datasets have been added to distinguish candidates from each other. Cost datasets represent geospatially variable costs including electricity, natural gas, and transportation. In early 2020, a graphic user interface was added to the GSP tool to make it more user-friendly. An additional script was developed in 2022 to model the transportation cost inputs for the GSP tool based on the local density of feedstock, the maximum feasible travel distance from the facility for feedstock collection, and regional road characteristics. This script also includes a rudimentary user interface.

The Many Step Transshipment Solver (MASTRS) is another Python-based script that models large supply chains across multiple levels by building and solving mixed-integer linear programming problems. The model starts with feedstock spread across many locations and then models the distribution and conversion of feedstock into biofuels and other co-products through multiple levels of intermediate facilities that may include temporary storage, pre-treatment, and fuel production, before new products are sent to their destinations. Intermediate facilities may include existing facilities or new candidate facilities that are generated by the GSP tool. The MASTRS output shows the flow of materials throughout the supply chain and the most cost-efficient capacities and locations for new facilities.

The modeling combination of GSP and MASTRS scripts has been implemented for several regional supply chains. MASTRS was first implemented with the Pacific Northwest oilseed-to-jet-fuel supply chain in 2018. Since 2019, GSP and MASTRS scripts have been used together for two supply chain models for both the production of jet fuel from forest residuals and

lumber production byproducts in the Pacific Northwest. The first supply chain model uses single-stage conversion at integrated biorefineries, and the second supply chain model is a multi-stage model with distributed pre-processing facilities.

Milestones
The GSP and MASTRS tools have undergone continual development to become more practical. Along with the expansion of tool capabilities, substantial improvements have been made regarding tool accessibility for new potential users.

Major Accomplishments
None.

Publications
None.

Outreach Efforts
None.

Awards
None.

Student Involvement
None.

Plans for Next Period
We plan to begin the process for publishing manuscripts that define the GSP and MASTRS tools. We will continue implementing the GSP and MASTRS tools in regional supply chain analyses and will complete the BANR supply chain analysis.

Task 6 - Perform a Refinery-to-Wing Stakeholder Assessment
Washington State University
The full report for this task is provided in the report for Award No. 13-C-AJFE-PSU-002.

Objective
We will extend the stakeholder assessment to a limited sample of informed stakeholders in the remaining sections of the country to provide insight into market and industry dynamics, with the aim of optimizing successful outcomes.

Research Approach
A national survey of airport management, fixed base operators, aviation fuel handlers, and relevant airlines to assess opinions on factors impacting the adoption and diffusion of AJF was completed in 2019. Unfortunately, low response rates impacted data collection and analysis.

Milestones
None.

Major Accomplishments
None.

Publications
None.

Outreach Efforts
None.

Awards
None.

Student Involvement
None.

Plans for Next Period
We plan to complete an updated publication based on national results.

Task 7 - Conduct a Supply Chain Analysis
Washington State University, Volpe

Objective
WSU and Volpe have each developed modeling tools that apply transshipment optimization to model the geospatial layout of developing supply chains. A comparison of these tools would be useful to identify the strengths and weaknesses of each.

The objective of Task 7 is to develop tools for supply chain risk and resilience assessment. To achieve this objective, WSU has developed a theoretical framework that assesses the resilience of a supply chain system subjected to various risk factors. In addition, by working closely with the Volpe Freight and Fuel Transportation Optimization Tool (FTOT) team, WSU has developed FTOT supply chain resilience (FTOT-SCR) tools.

Research Approach
Focusing on the use of woody-biomass-to-jet-fuel conversion via fast pyrolysis and the upgrading of a supply chain centered in the northern Rockies, a series of comparison studies was conducted by using optimization tools from Volpe and WSU. Each modeling approach was required to determine sites for new pyrolysis depots and upgrading refineries. Forest production data were provided by the land use and resource allocation (LURA) model from the University of Idaho. Pyrolysis depot locations were selected by candidate generation tools included in each approach, and existing petroleum refineries were used as candidates for upgrading refineries. Cities, ports, and airport hubs throughout the U.S. West Coast and Rocky Mountain regions were used as markets for road transportation fuel, bunker fuel, and jet fuel.

Probabilistic Wildfire Risk Assessment
A new probabilistic framework was proposed to quantitatively assess wildfire risk to a supply chain network. This framework provides rigorous probabilistic descriptions of wildfire ignition likelihood and growth, the interaction between supply chain components and wildfire, consequent component damage, and network-level performance reduction. The framework has been designed to systematically account for uncertainties throughout all phases of risk assessment. The framework first develops a wildfire occurrence estimation model by combining historical fire records with weather data and estimates the occurrence times and locations of fire ignitions through Monte Carlo simulation. The growths of all ignitions are then simulated based on weather conditions, topography, and fuel properties. For each simulated fire, the component-level physical damages and losses of functionalities are calculated based on vulnerability analyses and are subsequently incorporated into supply chain analysis to capture risk propagation throughout the network. In this manner, wildfire-caused supply chain disruptions can be quantified in terms of the post-wildfire unmet demand ratio, total supply chain cost, and total transportation time. This framework can be used as a planning tool to evaluate network performance subject to a set of what-if scenarios and assess the effect of pre- and post-wildfire risk mitigation measures.

Multi-Component Resilience Assessment
As part of this task, the team completed the development of a quantitative resilience assessment framework for a supply chain system exposed to multiple risk factors consisting of two stages: multi-risk assessment and multi-component resilience assessment. The first stage identifies the key risk factors that may affect supply chain performance over the planning horizon and combines their effects by generating a set of plausible scenarios. In the second stage, a new multi-component resilience index is proposed to measure (a) hazard-induced cumulative loss of functionality, (b) opportunity-induced cumulative gain of functionality, and (c) non-hazard-induced cumulative loss of functionality. The proposed resilience index is divided into these three measurable components to render each component more manageable and to facilitate decisions regarding the effective combination of various resilience-enhancing strategies. Finally, a hypothetical forest-residuals-to-SAF supply chain system in the Pacific Northwest region has been introduced to illustrate the proposed framework. This framework can provide

decision-makers with information on the key risk factors that should be mitigated to enhance supply chain resilience. Such information can be further used to determine cost-effective resilience-enhancing solutions.

Milestones

The team completed the development of both theoretical and FTOT tools for supply chain risk and resilience assessment. The FTOT-SCR tool is now available for use, and a manuscript detailing the theoretical procedure for this FTOT-SCR tool has been submitted. A manuscript on probabilistic wildfire risk assessment for a supply chain network was published in September 2022 in the *International Journal of Disaster Risk Reduction*.

Major Accomplishments

The WSU MASTRS and Volpe FTOT were compared for siting analyses in the BANR region. Similar and differing modeling assumptions were identified, and the appropriate model for a given objective was determined.

The team completed the development of both theoretical and FTOT tools for supply chain risk and resilience assessment.

Theoretical framework: The team presented the theoretical framework and a corresponding case study at the ASCENT meeting in February 2022 and submitted a manuscript on multi-component resilience assessment. A conference paper that applied this theoretical framework to a transportation network was presented at the *13th International Conference on Structural Safety and Reliability*, Shanghai, China (Zhao et al., 2022a).

FTOT tool: The FTOT-SCR tool has been released and is now available on a GitHub fork of the main FTOT-Public repository. Upon completion, the team presented this FTOT-SCR tool at the FTOT Users' Group meeting in April 2022. In addition, the team has utilized the FTOT-SCR tool in other studies and has published these findings (Zhao et al., 2022b)

The team completed the development of a probabilistic wildfire risk assessment framework for a supply chain network. A manuscript and conference paper were published as part of this subtask (Ma et al., 2022; Ma and Lee, 2022).

We published a review on the selection and cost estimation of commercially available equipment involved in the collection and adequation of feedstock. The publication includes aggregated information regarding equipment cost, energy consumption, efficiency, feedstock storage, and transportation systems. Five feedstock types for producing AJF were studied: (a) agricultural residues and grasses, (b) forest residues, (c) urban wood waste, (d) oilseeds, and (e) fats, oils, and greases.

Publications

Ma, F., Lee, J. Y., Camenzind, D., & Wolcott, M. (2022). Probabilistic Wildfire risk assessment methodology and evaluation of a supply chain network. *International Journal of Disaster Risk Reduction*, *82*, 103340. Doi: 10.1016/j.ijdrr.2022.103340

Ma, F., Lee, J.Y. (2022). "Probabilistic wildfire risk assessment for a supply chain system." *Proceedings of the 13th International Conference on Structural Safety and Reliability*, Shanghai, China, September 2022.

Martinez-Valencia, L., Camenzind, D., Wigmosta, M., Garcia-Perez, M., & Wolcott, M. (2021). Biomass supply chain equipment for renewable fuels production: A review. *Biomass and Bioenergy*, *148*, 106054. Doi: 10.1016/j.biombioe.2021.106054

Zhao, J., Lee, J.Y. (2022a). "Multi-component resilience assessment framework for transportation systems." *Proceedings of the 13th International Conference on Structural Safety and Reliability*, Shanghai, China, September 2022.

Zhao, J., & Lee, J. Y. (2022). Effect of connected and autonomous vehicles on supply chain performance. *Transportation Research Record: Journal of the Transportation Research Board*, 036119812211154. Doi: 10.1177/03611981221115425

Outreach Efforts

None.

Awards

None.

Student Involvement

Dane Camenzind, MS in Environmental Engineering, WSU, graduated in September 2019 and is currently employed by WSU as an operations research engineer.

Jie Zhao, PhD in Civil Engineering, WSU, graduated in August 2022 and is currently a postdoctoral scholar in the Department of Civil and Environmental Engineering at WSU.

Fangjiao Ma, PhD candidate in Civil Engineering, WSU, successfully passed his preliminary examination.

Plans for Next Period

We will utilize regional supply chain tools to assess forest residuals for SAF using pyrolysis methods, as described below for Task 8.

The team will complete the development of (a) a comprehensive machine-learning-assisted wildfire risk assessment tool for a supply chain network and (b) a robust, adaptive decision-making framework for a supply chain system. The team also plans to submit two manuscripts for publication.

Task 8 - Provide Analytical Support for Regional CAAFI and USDA Jet Fuel Projects

Washington State University

Objectives

We will develop a readiness-level tool to assess the status of regional SAF production projects and will use supply chain and stand-alone design cases to support the USDA BANR project in TEA and supply chain analysis. This regional Community Agricultural Project (CAP) focuses on the use of softwood forest salvage feedstock for fuels via a catalyzed pyrolysis conversion pathway.

We will assess the regional feedstock, conversion pathways and fuel minimum selling price (MSP) for SAF manufactured in the northwest United States. The aim of this work, requested by the Port of Seattle, is to determine whether the Seattle-Tacoma International Airport can attain its 10% SAF goal by using SAF manufactured in the region from regional feedstock.

Research Approach

We will develop readiness-level tools for regional projects to assess the status of developing fuel projects and to identify critical missing components. This tool will be similar in form to the CAAFI Feedstock and Fuel Readiness Levels tool and will be used to assist CAAFI in understanding the stage of development for projects of interest and to assess critical gaps. In addition, we will assist the regional USDA BANR team in deploying TEA and supply chain analysis for their project. This effort will focus on the use of softwood forest salvage feedstock in a thermochemical conversion process to produce fuels and co-products.

The facility siting tools discussed in Task 5, i.e., GSP and MASTRS, have been implemented for the BANR supply chain and Port of Seattle project. The most recent model runs included feedstock and markets in an 11-state region including the West Coast and intermountain regions. Feedstocks include forest residue from logging operations, mill residues from lumber production, and beetle-killed timber. The model results generated by MASTRS will help determine the relationships between facility location, fuel MSP, and conversion facility revenue.

The Port of Seattle project required a detailed feedstock survey for forest residuals, municipal solid waste, and lipids. Forest residuals were quantified with the LURA model for Oregon, Washington, Idaho, and Montana. Regional landfills were identified and located, scales were determined, and the remaining lifetimes were assessed to determine the most viable biorefinery location. The composition of municipal solid waste in the region was determined, as well as a method and the related costs for sorting the material to match the SAF conversion pathway. Lipids were separated into two major categories: (a) waste fats, oils, and greases and (b) vegetable oil. Each feedstock was quantified and then paired with a compatible SAF conversion pathway to determine the SAF MSP by using ASCENT-developed TEAs.

A financial model that uses a system dynamics approach was conceptualized and developed. The model analyzes the effects of policies on the financial performance of projects to produce SAF. This model can perform both deterministic and stochastic analyses. A case study was developed based on the production of SAF from municipal solid waste in the United States and the U.S. Northwest for regional deployment.

Milestones

We are making progress in the use of supply chain and stand-alone design cases to support the USDA BANR project in TEA and supply chain analysis. Additionally, we have supported the BANR team in creating TEAs for the technologies under consideration.

The Port of Seattle analysis and report have been completed, submitted, and presented.

A review entitled "Supply chain configuration of sustainable aviation fuel: review, challenges, and pathways for including environmental and social benefits" was published in *Renewable and Sustainable Energy Reviews*. A companion manuscript that analyzes the effect of policies that incentivize CO_2e reductions on the financial performance of AJF projects was submitted to the *Journal of Cleaner Production*.

Major Accomplishments

We have collaborated with the USDA BANR project team and attended their annual meeting to coordinate analyses. We currently await their completion of dead wood estimates to complete the supply chain analysis. Moreover, analyses with previous forest-residue data have been successfully modeled.

The Port of Seattle feedstock and SAF assessment was completed, presented to the Port of Seattle, and released to the public.

Publications

Peer-reviewed journal publications

Martinez-Valencia, L., Garcia-Perez, M., & Wolcott, M. P. (2021). Supply chain configuration of sustainable aviation fuel: Review, challenges, and pathways for including environmental and social benefits. *Renewable and Sustainable Energy Reviews*, *152*, 111680. doi: 10.1016/j.rser.2021.111680

Martinez-Valencia, L., Peterson, S. Brandt, K., King, A., Garcia-Perez, M., Wolcott, M. Impact of services on the supply chain configuration of sustainable aviation fuel: The case of CO_{2e} emission reduction in the U.S. (*Submitted to Journal of Cleaner Production*)

Outreach Efforts

Martinez, L., Brandt, K., Camenzind, D., Wolcott, M. ASCENT Supply Chain Tools. SAF Summit & CAAFI Biennial General Meeting. June 2, 2022.

Awards

None.

Student Involvement

Dane Camenzind, MS in Environmental Engineering, WSU, graduated in September 2019 and is currently employed by WSU as an operations research engineer.

Lina Martinez, PhD candidate in Biosystems Engineering, WSU graduated in April of 2022 and now works for WSU as a postdoctoral research associate.

Plans for Next Period

- Analysis of the BANR region is underway and will be completed in 2022.
- The Port of Seattle report will be adapted for peer-reviewed publication.

Project 001(B) Alternative Jet Fuel Supply Chain Analysis

University of Hawaii

Project Lead Investigator

Scott Q. Turn
Researcher
Hawaii Natural Energy Institute
University of Hawaii (UH)
1680 East-West Rd., POST 109; Honolulu, HI 96822
808-956-2346
sturn@hawaii.edu

University Participants

University of Hawaii
- P.I.: Scott Q. Turn, Researcher
- FAA Award Number: 13-C-AJFE-UH, Amendment 005
- Period of Performance: October 1, 2015 to August 4, 2021
- Task 1:
    1. Informing regional supply chains
    2. Identification of supply chain barriers in the Hawaiian Islands

University of Hawaii
- P.I.: Scott Q. Turn, Researcher
- FAA Award Number: 13-C-AJFE-UH, Amendment 007
- Period of Performance: October 1, 2016 to August 4, 2021
- Task 2:
    1. Informing regional supply chains
    2. Support of Indonesian alternative jet fuel supply initiatives

University of Hawaii
- P.I.: Scott Q. Turn, Researcher
- FAA Award Number: 13-C-AJFE-UH, Amendment 008
- Period of Performance: August 1, 2017 to August 4, 2021
- Task 3:
    1. National lipid supply availability analysis
    2. Hawaii regional project

University of Hawaii
- P.I.: Scott Q. Turn, Researcher
- FAA Award Number: 13-C-AJFE-UH, Amendment 011
- Period of Performance: May 31, 2019 to August 4, 2021
- Task 4: Hawaii regional project

University of Hawaii
- P.I.: Scott Q. Turn, Researcher
- FAA Award Number: 13-C-AJFE-UH, Amendment 013
- Period of Performance: June 5, 2020 to August 4, 2021
- Task 5: Hawaii regional project

University of Hawaii

- P.I.: Scott Q. Turn, Researcher
- FAA Award Number: 13-C-AJFE-UH, Amendment 017
- Period of Performance: October 1, 2021 to September 30, 2022
- Task 6: Hawaii regional project

Project Funding Level

Under **FAA Award Number 13-C-AJFE-UH, Amendment 005**, the Alternative Jet Fuel Supply Chain Analysis–Tropical Region Analysis project received $75,000 in funding from the FAA and cost-share funding of $75,000 from the State of Hawaii.

Under **FAA Award Number 13-C-AJFE-UH, Amendment 007**, the Alternative Jet Fuel Supply Chain Analysis–Tropical Region Analysis project received $100,000 in funding from the FAA, cost-share funding of $75,000 from the State of Hawaii, and $25,000 of in-kind cost match in the form of salary support for Scott Turn from UH.

Under **FAA Award Number 13-C-AJFE-UH, Amendment 008**, the Alternative Jet Fuel Supply Chain Analysis–Tropical Region Analysis project received $125,000 in funding from the FAA and cost-share funding of $125,000 from the State of Hawaii.

Under **FAA Award Number 13-C-AJFE-UH, Amendment 011**, the Alternative Jet Fuel Supply Chain Analysis–Tropical Region Analysis project received $200,000 in funding from the FAA and cost-share funding of $200,000 from the State of Hawaii.

Under **FAA Award Number 13-C-AJFE-UH, Amendment 013**, the Alternative Jet Fuel Supply Chain Analysis–Tropical Region Analysis project received $200,000 in funding from the FAA and cost-share funding of $200,000 from the State of Hawaii.

Under **FAA Award Number 13-C-AJFE-UH, Amendment 017**, the Alternative Jet Fuel Supply Chain Analysis–Tropical Region Analysis project received $100,000 in funding from the FAA and cost-share funding of $100,000 from the State of Hawaii.

Investigation Team

Lead

Scott Turn, University of Hawaii, P.I.

Other Lead Personnel

Tim Rials, Professor, and Burt English, Professor (University of Tennessee co-P.I.s)
Manuel Garcia-Perez, Professor (Washington State University [WSU] co-P.I.)
Kristin Lewis, Principal Technical Advisor (Volpe National Transportation Systems Center P.I.)
Michael Wolcott, Professor (WSU P.I.)
Lara Fowler, Professor (The Pennsylvania State University P.I.)

UH Investigation Team

Under **FAA Award Number 13-C-AJFE-UH, Amendment 005**, Task 1 and Task 2:
Dr. Scott Turn, Researcher, Hawaii Natural Energy Institute, UH
Dr. Trevor Morgan, Assistant Researcher, Hawaii Natural Energy Institute, UH
Dr. Richard Ogoshi, Assistant Researcher, Department of Tropical Plant and Soil Sciences, UH
Dr. Adel H. Youkhana, Junior Researcher, Department of Tropical Plant and Soil Sciences, UH

Under **FAA Award Number 13-C-AJFE-UH, Amendment 007**, Task 1 and Task 2:
Dr. Scott Turn, Researcher, Hawaii Natural Energy Institute, UH
Dr. Trevor Morgan, Assistant Researcher, Hawaii Natural Energy Institute, UH
Dr. Richard Ogoshi, Assistant Researcher, Department of Tropical Plant and Soil Sciences, UH
Dr. Adel H. Youkhana, Junior Researcher, Department of Tropical Plant and Soil Sciences, UH
Dr. Curtis Daehler, Professor, Department of Botany, UH

Ms. Sharon Chan, Junior Researcher, Hawaii Natural Energy Institute, UH
Mr. Gabriel Allen, Undergraduate Student, Biochemistry Department, UH

Under **FAA Award Number 13-C-AJFE-UH, Amendment 008**, Task 1 and Task 2:
Dr. Scott Turn, Researcher, Hawaii Natural Energy Institute, UH
Dr. Trevor Morgan, Assistant Researcher, Hawaii Natural Energy Institute, UH
Dr. Jinxia Fu, Assistant Researcher, Hawaii Natural Energy Institute, UH
Dr. Quang Vu Bach, Postdoctoral Fellow, Hawaii Natural Energy Institute, UH
Ms. Sabrina Summers, Undergraduate Student, Bioengineering Department, UH
Ms. Sarah Weber, Undergraduate Student, Molecular Biosciences and Biotechnology, UH
Mr. Taha Elwir, Undergraduate Student, Chemistry Department, UH

Under **FAA Award Number 13-C-AJFE-UH, Amendment 011**, Task 1:
Dr. Scott Turn, Researcher, Hawaii Natural Energy Institute, UH
Dr. Quang Vu Bach, Postdoctoral Fellow, Hawaii Natural Energy Institute, UH

Under **FAA Award Number 13-C-AJFE-UH, Amendment 013**, Task 1 and Task 2:
Dr. Scott Turn, Researcher, Hawaii Natural Energy Institute, UH
Ms. Sharon Chan, Junior Researcher, Hawaii Natural Energy Institute, UH

Under **FAA Award Number 13-C-AJFE-UH, Amendment 017**, Task 1:
Dr. Scott Turn, Researcher, Hawaii Natural Energy Institute, UH

Project Overview

Under **FAA Award Number 13-C-AJFE-UH, Amendment 005**, the research effort has two objectives. The first objective is to develop information on regional supply chains for use in creating scenarios of future alternative jet fuel (AJF) production in tropical regions. Outputs from this project may be used as inputs to regional supply chain analyses being developed by the FAA and Volpe Center. The second objective is to identify the key barriers in regional supply chains that must be overcome to produce substantial quantities of sustainable aviation fuel (SAF) in the Hawaiian Islands and similar tropical regions.

The **FAA Award Number 13-C-AJFE-UH, Amendment 005** project goals are to

- Review and summarize:
  - the available literature on biomass feedstocks for the tropics
  - the available literature on pretreatment and conversion technologies for tropical biomass feedstocks
  - the available literature on geographic information systems (GIS) datasets available for assessment of AJF production systems in the tropics
- Identify AJF supply chain barriers in the Hawaiian Islands

Under **FAA Award Number 13-C-AJFE-UH, Amendment 007**, the research effort has two objectives. The first objective is to develop information on regional supply chains for use in creating scenarios of future SAF production in tropical regions. Outputs from this project may be used as inputs to regional supply chain analyses being developed by the FAA and Volpe Center. This objective includes the development of fundamental property data for tropical biomass resources to support supply chain analysis. The second objective is to support the memorandum of understanding between the FAA and the Indonesian Directorate General of Civil Aviation (DGCA) to promote the development and use of sustainable alternative aviation fuels.

The **FAA Award Number 13-C-AJFE-UH, Amendment 007** project goals are to

- Support the Volpe Center and Commercial Aviation Alternative Fuels Initiative (CAAFI) Farm to Fly 2.0 supply chain analysis
- Use GIS-based estimates of fiber crop production potential to develop preliminary technical production estimates of jet fuel in Hawaii
- Develop fundamental property data for tropical biomass resources
- Transmit data and analysis results to other ASCENT Project 1 researchers to support the improvement of existing tools and best practices
- Support Indonesian SAF supply initiatives

Under **FAA Award Number 13-C-AJFE-UH, Amendment 008**, the research effort has two objectives. The first objective is to support a national lipid supply availability analysis that will inform industry development and guide policy. The second objective is to conduct a targeted supply chain analysis for a SAF production facility based on the Hawaii regional project.
The **FAA Award Number 13-C-AJFE-UH, Amendment 008** project goals are to

- Support ASCENT partners conducting the national lipid supply availability analysis by contributing information on tropical oilseed availability
- Evaluate supply chains for targeted waste streams and purpose-grown crops in Hawaii to a location in the principal industrial park on the island of Oahu

Under **FAA Award Number 13-C-AJFE-UH, Amendment 011**, the main objective of the research effort is to conduct bench-scale testing of tropical feedstocks for use in targeted supply chain analysis for a SAF production facility based on the Hawaii regional project initiated under Amendment 008.

The **FAA Award Number 13-C-AJFE-UH, Amendment 011** project goals are to

- Survey bench-scale systems available for relevant SAF conversion technology options
- Down-select from the available bench-scale systems to no more than two systems capable of conducting feedstock testing, and quantify product yields and contaminant concentrations
- Conduct bench-scale feedstock tests; quantify product yields, quality, and contaminant concentrations

The **FAA Award Number 13-C-AJFE-UH, Amendment 013** project goals are to

- Conduct tropical oil to SAF supply chain analysis
- Develop management strategies for elements present in construction and demolition waste that affect use in thermochemical-conversion-based SAF production pathways

The **FAA Award Number 13-C-AJFE-UH, Amendment 017** project goals are to

- Explore the impacts of HB2386 on waste management in Hawaii and potential for waste-based SAF production systems

Task 1.1 - Informing Regional Supply Chains

University of Hawaii

Objectives

This task included two activities: (a) reviewing the archival literature on existing tropical crops and potential new crops that could provide feedstocks for SAF production and (b) reviewing relevant pretreatment and conversion technology options, and experience with feedstocks identified in (a).

Research Approach

Activity 1

The archival literature was reviewed to construct an updated database of relevant citations for tropical crops; new potential energy crops were identified and added to the database. Available information on agronomic practices, crop rotation, and harvesting techniques was included. The database was shared to serve as a resource for the ASCENT Project 1 team and Volpe Center analyses of regional supply chains.

Activity 2

A database of relevant pretreatment and conversion technology options, and experience with potential tropical feedstock materials, was assembled from the archival literature and from existing Project 1 team shared resources. Of particular interest were inventories of material and energy flows associated with the pretreatment and conversion unit operations fundamental to the design of sustainable systems and the underlying analysis. Pairings of pretreatment and conversion technology options provided the starting point for the evaluation of tropical biorefineries that can be integrated into ASCENT Project 1 team and Volpe Center activities.

Milestones

Activity 1

- Identified a target list of databases to search for relevant literature

- Provided an interim report summarizing progress in the literature search

Activity 2

- Identified a target list of databases to search for relevant literature
- Provided an interim report summarizing progress in the literature search

Major Accomplishments

This work has been completed. A report was produced for each of the two activities, and the two reports were combined into a manuscript published in the journal *Energy & Fuels*.

Publications

Peer-reviewed journal publication

Morgan, T. J., Youkhana, A., Ogoshi, R., Turn, S. Q., & Garcia-Perez, M. (2019). Review of biomass resources and conversion technologies for alternative jet fuel production in Hawai'i and tropical regions. *Energy & Fuels, 33(4)*, 2699–2762. doi: 10.1021/acs.energyfuels.8b03001

Outreach Efforts

On February 21, 2018, the P.I. participated in a ThinkTech Hawaii broadcast focused on SAFs, with collaborators from WSU and CAAFI (https://www.youtube.com/watch?v=Ci4oWITPRKQ&feature=youtu.be).

Awards

None.

Student Involvement

None.

Plans for Next Period

None.

Task 1.2 - Identification of Supply Chain Barriers in the Hawaiian Islands

University of Hawaii

Objective

The objective of this task was to identify the key barriers in regional supply chains that must be overcome to produce substantial quantities of SAF in the Hawaiian Islands and similar tropical regions.

Research Approach

UH developed the Hawaii Bioenergy Master Plan for the State of Hawaii (http://www.hnei.hawaii.edu/wp-content/uploads/Hawaii-Bioenergy-Master-Plan.pdf), which was completed in 2009. In that plan, UH was tasked with determining whether Hawaii had the capability to produce 20% of land transportation fuels and 20% of electricity from bio-based resources. To this end, the plan included assessments of (a) land and water resources that could support biomass feedstock production, (b) potential biomass resources and their availability, (c) technology requirements, (d) infrastructure requirements to support logistics, (e) economic impacts, (f) environmental impacts, (g) availability of human capital, (h) permitting requirements, and (i) limitations to developing complete value chains for biomass-based energy systems. In keeping with the stakeholder-driven development of the Hawaii Bioenergy Master Plan, barriers to the development of regional supply chains for ASCENT were identified through interaction with key stakeholder groups. Green Initiative for Fuels Transition Pacific (GIFTPAC) meetings are held quarterly and attended by biofuel development interests in Hawaii, including representatives of large landowners, producers of first-generation biofuels, petroleum refiners, electric utilities, the State Energy Office, U.S. Pacific Command, biofuel entrepreneurs, county government officials, and UH. Additional stakeholders are invited as necessary to fill information and value chain gaps. These meetings serve as excellent opportunities to receive stakeholder input, identify barriers to supply chain development, and organize data collection efforts that span supply chain participants.

Milestones

- Introduced activities at the next regularly scheduled GIFTPAC meeting after contract execution
- Prepared an interim report outlining two tropical supply chain scenarios developed in consultation with the Project 1 team, with input from GIFTPAC participants

Major Accomplishments

This task has been completed. A stakeholder meeting was held and documented in a report submitted to the FAA. The stakeholders identified barriers to SAF production in Hawaii and ranked the barriers in order of importance as follows:

- Economic constraints (e.g., high costs of entry for production factors such as land) throughout the entire production chain
- Issues associated with access to capital, including high initial risks and uncertain return on investment
- Insufficient government support in the form of incentives and favorable policies to encourage long-term private investment
- Cost, availability, and competition for water
- SAF production technologies (emerging but not yet demonstrated to have full commercial viability)
- Insufficient or inadequate infrastructure (e.g., harbors, roads, fuel distribution infrastructure, irrigation systems) to support the entire production chain

Several of the barriers are also faced by other locations in the continental United States; however, those related to water and infrastructure are unique characteristics of an island state.

Publications

None.

Outreach Efforts

This activity engaged stakeholders to identify barriers to SAF production in Hawaii. Preparation included reviewing stakeholder lists from previous activities. Facilitators appropriate to the stakeholder group were retained. The stakeholder meeting included a presentation of the scope and goals of the larger ASCENT program and other aspects of the UH ASCENT project.

Awards

None.

Student Involvement

None.

Plans for Next Period

This task is complete, but stakeholder outreach activities will continue under other tasks, as outlined below.

References

hnei.hawaii.edu

Task 2.1 - Informing Regional Supply Chains

University of Hawaii

Objectives

Building on FY16 activities, additional supporting analysis will be conducted for proposed supply chains in Hawaii, including the following:

3.1
Support Volpe Center and CAAFI Farm to Fly 2.0 supply chain analysis.

3.2
Use GIS-based estimates of fiber crop production potential to develop preliminary technical production estimates of jet fuel in Hawaii.

3.3
Develop fundamental property data for tropical biomass resources.

3.4
Transmit data and analysis results to support the improvement of existing tools (e.g., POLYSYS; https://bioenergykdf.net/content/polysys).

Research Approach

Activity 3.2 has been conducted by using GIS data to identify areas suitable for purpose-grown crop production of feedstocks for SAF production in Hawaii. The approach has used GIS layers for land capability class (LCC), slope, and zoning as preliminary screens for suitability. Lands are classified by the Natural Resources Conservation Service with ratings from 1 to 6. LCCs from 1 to 3 are generally suitable for agricultural production; an LCC of 4 can be productive with proper management; and LCCs of 5 or 6 can support less intensive production and may be suitable for forestry. The slopes of terrains affect aspects of production, including mechanization and erodibility. An elevation GIS layer was used to derive a slope layer. Zoning layers were acquired from state and county GIS offices. Only agricultural zoning was deemed suitable for this analysis.

The EcoCrop model was used to develop yield models for the crops selected in Task 1, according to annual rainfall and mean minimum monthly temperature data. EcoCrop includes model parameters on sugarcane, bana grass, five species of eucalyptus, *Gliricidia*, *Leucaena*, pongamia, *Jatropha*, and sorghum. The parameters for sugarcane have been used to provide a base case assessment for comparison with historical sugarcane acreage and yield. Through sensitivity analysis, the model can be tuned to account for the differences between parameters developed from global sugar production and a century of production experience in Hawaii that has been refined through plant breeding to adapt sugarcane varieties to a wide variety of agro-ecosystems. The analysis has purposely avoided land-use conflict with food production by limiting suitability to areas capable of sustaining AJF feedstocks under rain-fed conditions. Areas suitable for SAF production that do not conflict with current agricultural land use (i.e., fallow land) have also been identified.

Pongamia (*Millettia pinnata*) was the initial focus of Activity 3.3. *Pongamia* is an oilseed-bearing, leguminous tree that has production potential in Hawaii and Florida. The tree produces pods containing oil-bearing seeds. Pods, oilseed cake, and oil were evaluated from trees growing on the island of Oahu. Fundamental measurements of chemical composition were conducted and reported. Torrefaction of pods as a coproduct in oil production has been conducted. Investigation of pretreatment methods to improve pod feedstock properties for thermochemical conversion applications has been completed.

Milestones

- Identified target opportunities to augment POLYSYS, the Alternative Fuel Transportation Optimization Tool (AFTOT; https://trid.trb.org/view/1376122), and conversion modules
- Reviewed previously developed GIS information layers for tropical fiber crops, and identify updating requirements
- Conducted preliminary estimates of SAF technical potential in Hawaii, according to previously developed GIS information layers

Major Accomplishments

The GIS-based analysis of SAF production potential is ongoing. The assessment of potential lands meeting the requirements for LCC, slope, and land-use zoning has been completed. The EcoCrop model was implemented to predict yield as a function of minimum mean monthly temperature and annual rainfall. This process identified potential SAF feedstock crops for land areas capable of supporting their production under both rain-fed and irrigated conditions. This analysis provided information necessary for determining cropping patterns and assessing transport costs to processing facility locations. The EcoCrop model's prediction of sugarcane potential was determined, and the results were compared with historical sugarcane acreage, both rain-fed and irrigated. EcoCrop's upper and lower values for temperature and rainfall that support optimal sugarcane production were varied to calibrate the prediction against historical acreage. The difference between the EcoCrop values and those representative of conditions in Hawaii is attributable to improvements due to plant breeding and unique combinations of environmental conditions, e.g., the relatively young volcanic soils present in high-rainfall areas on the island of Hawaii that enable high drainage rates and accommodate sugar production.

Calibration of the EcoCrop model by using historical sugarcane planted acreages was completed in 2018. This effort used a confusion matrix approach for validation (resulting in a kappa value >.4) and demonstrated that the mean annual temperature was a better indicator of environmental capability than the minimum mean monthly temperature recommended by the EcoCrop developers. This effort highlights the need to adapt models to local conditions. Model predictions for suitable cropping are being compared with current land uses to provide another indicator of agreement.

The GIS analysis of SAF feedstock production potential has been completed. Statewide working maps for each of the species have been summarized in a draft report currently undergoing internal review. This report will serve as the basis for a journal article publication.

Dr. Curtis Daehler (UH, Department of Botany) has completed a report assessing the invasiveness of *Pongamia*. Retrospective analyses have shown that predictive weed risk assessment systems correctly identify many major pest plants, but their predictions are not 100% accurate. The purpose of this study was to collect field observations of *Pongamia* planted around Oahu to identify direct evidence of *Pongamia* escaping from plantings and becoming an invasive weed. Seven field sites were visited in various environments across Oahu. Although some *Pongamia* seedlings were found in the vicinity of some *Pongamia* plantings, particularly in wetter, partly shaded environments, almost all observed seedlings were restricted to areas directly beneath the canopies of mother trees. This finding suggests a lack of effective seed dispersal away from *Pongamia* plantings. According to its current behavior in the field, *Pongamia* is not invasive or established outside of cultivation on Oahu. Because of its limited seed dispersal and low rates of seedling establishment beyond the canopy, the risk of *Pongamia* becoming invasive can be mitigated through monitoring and targeted control of any rare escapes in the vicinity of plantings. Because seeds and seed pods are water dispersed, future risks of *Pongamia* escape and unwanted spread could be minimized by avoiding planting at sites near flowing water, near areas exposed to tides, or on or near steep slopes. Vegetative spread by root suckers was not observed around plantings on Oahu; however, monitoring for vegetative spread around plantations is recommended; unwanted vegetative spread might become a concern in the future that could be addressed with localized mechanical or chemical control.

Pods, oilseed cake, and oil have been evaluated from a number of trees growing on the island of Oahu. TerViva, a company pursuing *Pongamia* commercialization, provided material from orchards on Oahu. Fundamental measurements of chemical composition were made for seeds, pods, extracted oil, and post-extraction seed material. Measured values included C, H, N, and S elemental composition; energy content; volatile matter, fixed carbon and ash content; and trace element composition. Oils were characterized for peroxide value, iodine value, fatty acid profile, free fatty acid content, flash point, density, viscosity, and phase transition temperatures. The chemical composition and fuel properties of the oilseed cake and the pod material were characterized. A manuscript summarizing the results of this effort has been published in the journal *ACS Omega*.

Coproduct evaluation of *Pongamia* pod feedstock for thermochemical conversion has been conducted. Evaluation included both untreated pods and pods pretreated by a torrefaction process to improve their properties. Torrefaction produces a material with improved grindability and storage stability, and diminished oxygen content and microbial availability. The effects of process conditions on feedstock properties relevant to thermochemical conversion technologies, proximate and ultimate composition, heating value, and Hardgrove grindability index were measured. The chemical structure, reactivity, and changes in elemental composition of the torrefied materials were also investigated. A manuscript summarizing the results of this effort has been published in the journal *Fuel*.

Pongamia seedpods are recognized as a potential feedstock for SAF production because of the relatively high oil content of the seeds. Pongamia pods are byproduct residues available after seed separation. Pods have high chlorine and potassium content that may be problematic in thermochemical energy conversion systems. Leaching experiments were performed to remove inorganic constituents of pods and thereby decrease the potential for fouling, slagging, and agglomeration. A manuscript summarizing the results of this effort has been published in the journal *Fuel*.

Aleurites moluccanus, commonly known as kukui and candlenut, is an oil-nut-bearing tree frequently found in the tropics. It is also the state tree of Hawaii. Nuts from a number of trees growing on the island of Oahu were collected, and the nut shell, oilseed cake, and oil components were fractionated and analyzed for common properties necessary for designing SAF production systems. A manuscript has been submitted to the journal *Biomass & Bioenergy*. Revisions are in process.

Publications

Peer-reviewed journal publications

Fu, J., Allen, G., Weber, S., Turn, S. Q., & Kusch, W. (2021). Water leaching for improving fuel properties of pongamia pod: Informing process design. *Fuel, 305,* 121480. doi:10.1016/j.fuel.2021.121480

Fu, J., Summers, S., Turn, S. Q., & Kusch, W. (2021). Upgraded pongamia pod via torrefaction for the production of bioenergy. *Fuel, 291,* 120260. doi:10.1016/j.fuel.2021.120260

Fu, J., Summers, S., Morgan, T. J., Turn, S. Q., & Kusch, W. (2021). Fuel properties of pongamia (*Milletia pinnata*) seeds and pods grown in Hawaii. *ACS Omega, 6,* 9222–9233. doi:10.1021/acsomega.1c00635

Written report

Chan, S., Ogoshi, R. & Turn, S. Feedstocks for sustainable jet fuel production: An assessment of land suitability in Hawaii. A draft report has been prepared and a draft manuscript is under preparation for publication.

Outreach Efforts

Outreach in this task has focused on interactions with TerViva, a startup company that has identified *Pongamia* germplasm production and marketing as the central focus of its business plan.

Chan, S., Ogoshi, R. & Turn, S. (2020, July 6-9). *Feedstocks for Sustainable Jet Fuel Production: An Assessment of Land Suitability in Hawaii* [Poster presentation]. European Biomass Conference and Exhibition. Virtual.

Fu, J., Summers, S. & Turn, S. "Upgraded *Millettia Pinnata* Pod via Torrefaction for the Production of Bioenergy in Hawaii" was presented orally at the 2020 Thermal & Catalytic Sciences Virtual Symposium.

Turn, S. (2019, December 3). *Regional Supply Chain Analysis for Alternative Jet Fuel Production in the Tropics* [Poster presentation]. Hawaii Aviation and Climate Action Summit, Honolulu, HI, United States.

Fu, J., Allen, G., Weber, S., Turn, S. Q., & Kusch, W. (2021, August 22-26). *Water Leaching for Improving Fuel Properties of Pongamia Pods* [Oral and virtual presentation]. 2021 Fall National Meeting of the American Chemical Society, Atlanta, GA, United States.

Fu, J., Summers, S. & Turn, S. "Upgraded *Millettia Pinnata* Pod via Torrefaction for the Production of Bioenergy in Hawaii" was presented virtually and orally at the 2021 Spring National Meeting of the American Chemical Society, April 5–16, 2021.

Fu, J., Weber, S. & Turn, S. "Comprehensive Characterization of Kukui Nuts for Bioenergy Production in Hawaii" was presented orally at the 2022 Fall American Chemical Society National Meeting & Exposition, Chicago, IL, August 21–25, 2022

Awards

The poster titled "Feedstocks for Sustainable Jet Fuel Production: An Assessment of Land Suitability in Hawaii," presented at the European Biomass Conference and Exhibition held virtually July 6–9, 2020, received the Best Visual Presentation Award.

Student Involvement

Three undergraduate students are involved in the project; their primary responsibility is processing and analyzing samples of biomass materials selected for evaluation as potential SAF feedstocks. The *Pongamia* torrefaction work was the focus of an Undergraduate Research Opportunity Program project for Sabrina Summers, a bioengineering and chemistry double major. The results of her work were presented at the fall 2019 American Chemical Society meeting in San Diego, California. The *Pongamia* pod leaching work was the focus of an Undergraduate Research Opportunity Program project for Gabriel Allen, a biochemistry major.

Plans for Next Period

The report summarizing the analysis of the GIS analysis of SAF feedstock production potential and a companion manuscript will be completed.

Statewide working maps for each of the feedstock species will be used as the basis for ongoing discussions with targeted stakeholder groups, including landowners and Natural Resources Conservation Service staff. Funding for planting and evaluating the more promising feedstock plants on UH experimental station land will be pursued in collaboration with stakeholders (e.g., TerViva).

Task 2.2 - Support of Indonesian Alternative Jet Fuel Supply Initiatives

University of Hawaii

Objectives

This task supports the memorandum of understanding between the FAA and the Indonesian DGCA to promote the development and use of sustainable alternative aviation fuels. Under the coordination of the FAA, efforts to establish points of contact and coordinate with Indonesian counterparts are ongoing.

Research Approach

The process will begin with working with the FAA to establish points of contact to coordinate efforts with Indonesian counterparts. The Indonesian Aviation Biofuels and Renewable Energy Task Force (ABRETF) members include Universitas Indonesia, Institut Teknologi Bandung, and Universitas Padjadjaran. A prioritized list of tasks will be developed in consultation with Indonesian counterparts, and data required to inform sustainability and supply analyses and potential sources of information will be identified. The information collected may include Indonesian jet fuel use and resources for SAF production, airport locations, and annual and monthly jet fuel consumption patterns. Characterization of sustainable biomass resources with potential for use in producing SAF supplies could include developing preliminary GIS mapping information of their locations and distributions, and preliminary estimates of their technical potential.

Milestones

- Identify points of contact at Indonesian universities participating in ABRETF
- Identify research needs and develop a project plan
- Develop data for potential projects

Major Accomplishments

The P.I. traveled to Jakarta in the first week of August 2017 and met with the following individuals:

- Cesar Velarde Catolfi-Salvoni (International Civil Aviation Organization)
- Dr. Wendy Aritenang (International Civil Aviation Organization)
- Dr. Ridwan Rachmat (Head of Research Collaboration, Indonesian Agency for Agricultural Research and Development)
- Sylvia Ayu Bethari (Head of Aviation Fuel Physical & Chemical Laboratory, Research and Development Centre for Oil and Gas Technology)
- Dr. Ina Winarni (Forest Product Research and Development Center, Ministry of Environment and Forestry)
- Dr. SD Sumbogo Murti (Center of Technology Energy Resources and Chemical Industry, Agency for the Assessment and Application of Technology)

The activities of the tropical supply chain analysis effort were presented to the group, and a general discussion followed. The conclusion from this introductory meeting was that the Indonesian counterparts would seek agreement on how to move forward with future cooperation.

The P.I. traveled to Jakarta and met with Dr. Wendy Aritenang of the International Civil Aviation Organization's Jakarta office. The same trip included meetings with renewable energy Researchers at Universitas Indonesia. After the meeting, Dr. Aritenang suggested several points of contact for future engagement: Frisda Panjaitan from the Palm Oil Research Institute, and Tatang Soerawidjaja, Tirto Prakoso Brodjonegoro, and Imam Reksowardojo from the Bandung Institute of Technology.

In October of 2022, the P.I. traveled to Jakarta and met with Dr. Wendy Aritenang in Jakarta. The following day, the P.I. and Dr. Aritenang traveled to Bandung to visit the Bandung Institute of Technology (ITB) and meet with faculty members Professor Adiwan Aritenang (Head Department of Regional Planning) and Professors Tatang Soerawidjaja, Tirto Prakoso Brodjonegoro, and Iman Reksowardojo from the Faculty of Industrial Technology. Ongoing UH ASCENT activities were presented, and the ITB researchers discussed their SAF-related research efforts.

Publications

None.

Outreach Efforts
Outreach efforts by the P.I. are described in the Major Accomplishments section above. In addition, the P.I. participated in the Asia Pacific Economic Cooperation event "Energy Transition toward Carbon Neutrality, APEC BCG Economy Thailand 2022: Tech to Biz" in Bangkok, and gave a presentation entitled "US Initiatives on Sustainable Aviation Fuel."

Awards
None.

Student Involvement
None.

Plans for Next Period
The P.I. will continue to develop the cooperative research agenda between UH and Indonesian universities through continued dialog with the FAA, the International Civil Aviation Organization, and the Indonesian DGCA. Travel to Southeast Asia for other projects is anticipated in 2023, and meetings and relationship building with researchers at Indonesian institutions will be continued. ITB faculty members have expressed interest in pursuing collaborative work. Planning for a regional workshop on SAF is in progress.

Task 3.1 - National Lipid Supply Availability Analysis
University of Hawaii

Objective
Activities under this task will support ASCENT partners working on a national lipid supply availability analysis by sharing data on tropical oilseed availability developed under previous years' activities.

Research Approach
This support will include estimates of *Pongamia* production capability in the state, in addition to assessments of waste cooking oil and tallow.

Milestones
Milestones will coincide with the schedule of the lead institution (WSU) for the national lipid supply analysis.

Major Accomplishments
Additional seeds and pods were collected from the *Pongamia* tree on the UH campus, Foster Botanical Garden, and Ke'ehi Lagoon Beach Park. Large quantities (tens of kilograms) of material were acquired from TerViva's plantings on Oahu's north shore for use in oil evaluation. Two oilseed presses were acquired, and safety documents were developed. Pods, oilseed cake, and oil were evaluated from a number of trees growing on the island of Oahu. Fundamental measurements of chemical composition were made for seeds, pods, extracted oil, and post-extraction seed material. Measured values included C, H, N, and S elemental composition; energy content; volatile matter, fixed carbon and ash content; and trace element composition. Oils were characterized for peroxide value, iodine value, fatty acid profile, free fatty acid content, flash point, density, viscosity, and phase transition temperatures. Development of coproducts from the pods and oilseed cake will be explored.

Areas in Hawaii with agricultural zoning suitable for rain-fed production of *Pongamia* have been identified. Conflicts with current agricultural land use have been identified.

Waste oil resources in Hawaii are estimated to be on the order of 2–3 million gallons per year, according to the de facto population, and are directed to biodiesel production.

Publications
Fu, J., Summers, S., Morgan, T. J., Turn, S. Q., & Kusch, W. (2021). Fuel properties of pongamia (*Milletia pinnata*) seeds and pods grown in Hawaii. *ACS Omega, 6*(13), 9222–9233. doi:10.1021/acsomega.1c00635

Outreach Efforts
Data were presented at the April 2019 ASCENT review meeting in Atlanta, Georgia.

Awards
None.

Student Involvement
Three undergraduate students—Sabrina Summers, Sarah Weber, and Taha Elwir—are involved in the project. Their primary responsibility is processing and analyzing samples of biomass materials selected for evaluation as potential SAF feedstocks.

Plans for Next Period
Characteristics and suitable production areas for additional oilseed crops in Hawaii will be assessed as needed. Information will be provided to the lead institution (WSU).

Task 3.2 - Hawaii Regional Project
University of Hawaii

Objectives
A supply chain based on fiber feedstocks transported to a conversion facility located at Campbell Industrial Park (CIP) on Oahu will be evaluated (Figure 1). CIP is the current site of two oil refineries. Construction and demolition (C&D) wood waste from the PVT Land Company's landfill could be the primary source of feedstock. Other sources will be evaluated from elsewhere on Oahu and from outer islands, including municipal solid waste streams from outer islands and mining of current stocks of waste-in-place. Waste streams and purpose-grown crops form the basis of a hub-and-spoke supply system, with the hub located on Oahu. Pipelines for jet fuel transport are in place from CIP to Daniel K. Inouye International Airport and the adjacent Joint Base Pearl Harbor/Hickam. Other coproduct offtakers for alternative diesel fuel include the Hawaiian Electric Company and several military bases, including Schofield Barracks (~50-MW alternative fuel-capable power plant under development) and Kaneohe Marine Corps Base. Hawaii Gas (a local gas utility) is also seeking alternative sources of methane if methane or feedstock suitable for methane production is available as a coproduct. Hawaii Gas currently offtakes feedstock (naphtha) from the refinery.

Figure 1. Possible locations of value chain participants for a fiber-based alternative jet fuel production facility located at Campbell Industrial Park, Oahu.

Research Approach

Task 3.2.G1. Analysis of feedstock-conversion-pathway efficiency, product slate (including coproducts), and maturation

Building on activities from previous years, additional supporting analysis will be conducted for proposed supply chains in Hawaii, as follows:

- 3.2.G1.1 Assess feedstock suitability for conversion processes (e.g., characterization, conversion efficiencies, and contaminants) [UH and WSU (Manuel Garcia-Perez)]
- 3.2.G1.2 Acquire data on feedstock size reduction, particle size of materials, and bulk densities [UH, WSU (Manuel Garcia-Perez)]
- 3.2.G1.3 Evaluate coproducts at every step of the supply chain [ASCENT Project 1 team]

Task 3.2.G2. Scoping of techno-economic analysis (TEA) issues

This task will determine the current TEA status of targeted SAF production technologies that use fiber feedstocks as production inputs [UH, WSU (Manuel Garcia-Perez), Purdue University (Wally Tyner)]

Task 3.2.G3. Screening-level greenhouse gas (GHG) life-cycle assessment (LCA)
This task will conduct screening-level GHG LCA on the proposed target supply chains and SAF conversion technologies.

Subtasks:
- 3.2.G3.1 Assess Massachusetts Institute of Technology (MIT) waste-based GHG LCA tools in the context of application to Hawaii [MIT (Mark Staples)]
- 3.2.G3.2 Assess requirements to link previously completed eucalyptus energy and GHG analysis to the edge of the plantation with available GHG LCA information for conversion technology options [MIT (Mark Staples), UH]
- 3.2.G3.3 Identify and fill information/data gaps

Task 3.2.G4. Identification of supply chain participants/partners
Subtasks:
- 3.2.G4.1 Define C&D landfill case
- 3.2.G4.2 Identify eucalyptus in existing plantations, landowners, leaseholders/feedstock producers, harvesting contractors, truckers, etc. [UH]
- 3.2.G4.3 Define other feedstock systems as identified [ASCENT Project 01 Team]

Task 3.2.G5. Develop an appropriate stakeholder engagement plan
Subtasks:
- 3.2.G5.1 Review stakeholder engagement methods and plans from past work to establish baseline methods [UH, WSU (Season Hoard)]
- 3.2.G5.2 Identify and update engagement strategies according to the updated Community Social Asset Modeling (CSAM)/Outreach support tool [UH, WSU (Season Hoard)]

Task 3.2.G6. Identify and engage stakeholders
Subtasks:
- 3.2.G6.1 Identify stakeholders along the value chain, and create a database based on value chain location [UH]
- 3.2.G6.2 Conduct a stakeholder meeting by using the instruments developed in Task 3.2.G5 [UH, WSU (Season Hoard)]
- 3.2.G6.3 Analyze stakeholder response and feedback to the process [UH, WSU (Season Hoard)]

Task 3.2.G7. Acquire transportation-network and other regional data needed for the Freight and Fuel Transportation Optimization Tool (FTOT) and other modeling efforts
Subtasks:
- 3.2.G7.1 Acquire necessary data to evaluate harbor capacities and current usage [UH, Volpe (Kristin Lewis), WSU (Michael Wolcott)]
- 3.2.G7.2 Acquire data on interisland transport practices [UH, Volpe (Kristin Lewis), WSU (Michael Wolcott)]

Task 3.2.G8. Evaluate infrastructure availability
Subtasks:
- 3.2.G8.1 Evaluate interisland shipping options and applicable regulation [UH, Volpe (Kristin Lewis), WSU (Michael Wolcott)]
- 3.2.G8.2 Evaluate transport or conveyance options from conversion location to end users, and applicable regulation. [UH, Volpe (Kristin Lewis), WSU (Michael Wolcott)]

Task 3.2.G9. Evaluate feedstock availability
Subtasks:
- 3.2.G9.1 Refine/ground truth prior evaluations of options for purpose-grown feedstock supply [UH]
- 3.2.G9.2 Conduct projections of future C&D waste supply and mining of waste-in-place on Oahu, municipal solid waste, and mining of waste-in-place on other islands [UH]

Task 3.2.G10. Develop a regional proposal
This task will use the information collected in Tasks 3.2.G1 through 3.2.G9 to develop a regional project proposal.

Milestone

One milestone is associated with each of the subtask activities identified in the Research Approach section above.

Major Accomplishments

Characteristics of the feedstock generated at the landfill have been determined and summarized in a draft publication.

The elemental compositions of feedstock materials have been used as the basis for equilibrium analysis of gasification systems using oxygen, steam, and steam–oxygen mixtures.

Material flows relevant to the screening-level GHG analysis of C&D waste as SAF feedstock have been assembled. Preliminary discussions of GHG analysis of C&D-based SAF systems with landfill operators have been initiated.

Plans for solid waste management from all counties in Hawaii have been used to provide a broader picture of the waste stream composition, diversion, and recycling practices, and planned uses.

Publications

Peer-reviewed journal publications

Bach, Q. V., Fu, J., & Turn, S. (2021). Construction and demolition waste-derived feedstock: fuel characterization of a potential resource for sustainable aviation fuels production. *Frontiers in Energy Research, 9,* 711808. doi: 10.3389/fenrg.2021.711808

Bach, Q. V. & Turn, S. Fate of arsenic and other inorganic elements during gasification of construction and demolition wastes – thermochemical equilibrium calculations. Draft manuscript in process.

Outreach Efforts

Results of the fuel sampling, fuel analyses, and gasification equilibrium analyses were presented at the October 2019 ThermoChemical Biomass 2019 Conference in Chicago, Illinois.

Information from this task was included in the talk "Regional Supply Chain Analysis for Alternative Jet Fuel Production in the Tropics" presented at the Hawaii Aviation and Climate Action Summit, December 3, 2019, at the Hawaii State Capitol.

Data acquired under this task were presented to the management of PVT Land Company and their consultants from Simonpietri Enterprises and T. R. Miles Technical Consultants, Inc.

"Construction and Demolition Waste as an Alternative Energy Source: Fuel Characterization and Ash Fusion Properties" was presented as a poster at the 2020 Thermal & Catalytic Sciences Virtual Symposium.

Discussion with Dr. Kristin Lewis and Volpe Center staff on the addition of Hawaii transportation infrastructure to the FTOT was initiated and deferred until a clearer definition of the system emerges.

As suggested by FAA management, UH worked with the Servicios y Estudios para la Navegación Aérea y la Seguridad Aeronáutica (SENASA) to identify a counterpart university in the Canary Islands, Spain. Universidad de la Laguna (ULL) was selected, and a memorandum of understanding was signed between UH and ULL. A nondisclosure agreement was subsequently signed among SENASA, ULL, UH, and the Spanish company Abengoa Energía, S.A. Regularly scheduled meetings have been held biannually with Professor Dr. Ricardo Guerrero Lemus from ULL to discuss common research themes.

Awards

None.

Student Involvement

Three undergraduate students—Sabrina Summers, Sarah Weber, and Taha Elwir—have been involved in sample preparation and in operating the laboratory analytical equipment used for sample analysis.

Plans for Next Period

Manuscripts covering the prediction of gasification product streams including contaminant concentrations will be completed and submitted. This manuscript awaits comparative data from the bench-scale gasification test underway at ThermoChem Recovery International facilities.

Work on the GHG analysis of C&D waste use for SAF production will be extended from the landfill to a point of use (to be determined) and interfaced with the system TEAs described by WSU.

Outreach to interested industries will be continued.

Task 4 - Hawaii Regional Project

University of Hawaii

Objective

This task builds upon the results from the previous years' work under the Hawaii regional project. The focus is on the data and analysis necessary to plan a project that uses C&D waste as feedstock for SAF production. The Task 4 objective is to use previous years' C&D feedstock characterization data and thermochemical equilibrium analysis to conduct bench-scale gasification tests, and to quantify the product gas yield, composition, and contaminant concentrations. These results will be compared with equilibrium prediction used to identify contaminants that must be addressed before end use and will provide the basis for designing contaminant control systems.

Research Approach

Bench-scale gasification tests will be conducted on samples of C&D wastes characterized in the earlier tasks, to measure product yields, identify contaminants, and investigate element partitioning between product phases.

Information gained from the tests will be used to identify opportunities to improve TEA, identify coproducts, inform supply chain participants and stakeholders, and identify necessary infrastructure improvements.

Milestones

- Identify and evaluate capabilities of experimental bench-scale facilities to gasifier tests
- Specify system performance parameters to be measured
- Specify techniques to sample and analyze contaminants
- Select and engage an experimental bench-scale facility for testing
- Prepare and ship feedstock from Hawaii to the experimental test facility
- Conduct tests, reduce data, and prepare a summary report of the results

Major Accomplishments

Operational measurements to be conducted as part of the bench-scale tests were summarized, and a test plan was developed; these were used as the basis for entertaining proposals for test services.

Through a competitively structured proposal process, ThermoChem Recovery International, Inc. was engaged to provide bench-scale test services for C&D waste feedstock and other opportunity fuels of relevance to Hawaii and the tropics.

A synthetic construction and demolition waste recipe was developed according to the results published in *Frontiers in Energy Research* (Bach et al., 2021). Component fractions in the recipe were determined with a least-squares approach to matching critical fuel characteristics, including volatile matter, fixed carbon, and ash content; higher heating value, and concentrations of the elements Na, Mg, Al, Si, P, S, Cl, K, Ca, Ti, Cr, Mn, Fe, Cu, Zn, As, Ru, and Pb. This recipe will enable a reproducible C&D waste fuel lot to be assembled and aid in decreasing test-to-test variability.

In November and December of 2021, tests were conducted in the bench-scale facility at the ThermoChem Recovery International facility in Durham, NC. After shakedown testing was completed, two subsequent tests were conducted: the first used *Leucaena leucocephela* stemwood, and the second used synthetic construction and demolition waste. ThermoChem Recovery International has provided a draft summary report for the *Leucaena* test, and revisions are in process.

Publications

Peer-reviewed journal publications

Bach, Q. V., Fu, J., & Turn, S. (2021). Construction and demolition waste-derived feedstock: fuel characterization of a potential resource for sustainable aviation fuels production. *Frontiers in Energy Research, 9,* 711808. doi: 10.3389/fenrg.2021.711808

Outreach Efforts
None.

Awards
None.

Student Involvement
None.

Plans for Next Period
During the next period, activities identified in the Research Approach section above will continue. The primary focus will be on conducting the bench-scale gasification tests, collecting and analyzing samples from the tests, and preparing reports and publications summarizing the results. The sequence of milestones identified above provides a roadmap of necessary subtasks.

Task 5 - Hawaii Regional Project
University of Hawaii

Objective
Subtask 5.1: Tropical oil to SAF supply chain analysis
The goal of subtask 5.1 is to develop a model for tropical oil supply chains for AJF and associated coproducts. Hawaii will be the initial focus, but the modeling tools will be developed for wider use in island settings.

Subtask 5.2: Contaminants in the gasification of C&D wastes
The goal of subtask 5.2 is to develop management strategies for elements present in C&D waste that affect its use as a feedstock for thermochemical conversion.

Research Approach
Subtask 5.1:
Prior ASCENT EcoCrop GIS modeling activities identified growing locations for *Pongamia*, kamani, croton, and *Jatropha*, according to suitable environmental conditions, geography, and zoning. If unavailable, primary data on the chemical and physical characteristics of these tropical oils and their coproducts (e.g., pods/shell and oilseed cake) were acquired. The project will use these earlier results as the basis for developing supply chain models for AJF production. Model results will identify feedstock production areas, and locations and scales of primary processing sites for shell and pod separation, oil extraction from seeds, and oil conversion to SAF. Potential sources of hydrogen from oilseed coproducts, other renewable resources, and fossil sources will be analyzed and included in the model. Options for points of production, SAF production technologies (e.g., ARA, SBI, or Forge), transportation strategies, and blend ratios at airports (or for specific end users, e.g., the military) across Hawaii will affect model outcomes and will be evaluated. Options for coproducts such as animal feeds and high-value materials will be evaluated and incorporated into the model decision-making. Criteria used to drive the model solution might include minimizing SAF production costs while meeting a minimum total production benchmark or minimum blending rate for annual state jet fuel consumption. Other criteria—such as system resiliency to extreme weather events and climate change, provision of environmental services, and stakeholder acceptability—will also be of importance and will be used to evaluate model solutions.

Subtask 5.2:
Thermochemical gasification of biorenewable resources is the initial conversion process for two entry points to AJF production: (a) synthesis gas (syngas) used in direct production of Fischer–Tropsch liquids, and/or (b) green/renewable hydrogen used in biorefineries for hydrotreating lipids or in existing petroleum refining activities for the production of hybrid jet fuel. Urban wood waste from C&D activities provides a reliable source of biorenewable material and requires a tipping fee for disposal—characteristics that enhance its attractiveness as feedstock. Negative aspects of C&D feedstock are its physical and chemical inhomogeneity. In the latter case, inorganic elements present in the feedstock can negatively influence the gasification process (e.g., corrosion of, or accumulation on, reactor working surfaces, bed material agglomeration, catalyst deactivation, or pollutant emissions). Using data generated from previous ASCENT Project 01 tasks, this project will assess methods for managing contaminants in C&D feedstocks. This project will be based on gasification systems proposed for the

production of syngas/Fischer–Tropsch liquids and green hydrogen. Technology options for contaminant removal or conversion to benign forms will be assessed at each step in the conversion process; that is, presorting at the waste generation site, sorting/diversion at the C&D waste intake facility, removal by physical/chemical/other methods before gasification, in situ reactor control methods, and gas cleanup. Technology options from existing process industries and from the scientific literature will be considered. Laboratory-scale testing of removal techniques will be conducted to provide a preliminary assessment of selected promising technology options. Integrated gasification process options and contaminant control options will be evaluated as complete systems to guide system design and enable system comparisons. Risks associated with the technology options will also be assessed to guide implementation and risk mitigation of the system as a whole. Impacts of processing scale (e.g., Mg waste/day) on selection of technology options will also be assessed.

Milestones

Subtask 5.1: Established a model framework for an oilseed-based SAF supply chain in an island setting, using the scenario of Hawaii

Subtask 5.2: Completed a review of options to manage contaminants along the supply chain; conduct bench-scale tests to confirm the efficacy of options

Major Accomplishments

On the basis of the *Pongamia* production areas identified by GIS analysis in Task 3 (described above), sites for processing *Pongamia* (pod and seed separation, oil extraction from seed) have been evaluated on each island. Candidate processing sites in the analysis included all locations with (a) industrial zoning and (b) lands with slope of less than 5%, a contiguous area of 50 acres, and agricultural zoning. A total transportation cost index was calculated for each candidate processing site, according to the *Pongamia* production estimates and the road distance from each production site to candidate processing sites.

Publications

None.

Outreach Efforts

None.

Awards

None.

Student Involvement

None.

Plans for Next Period

Subtask 5.1: Costs for *Pongamia* delivered to the processing site gate will be used with TEA spreadsheets (oilseed crushing, hydroprocessed esters and fatty acids, etc.) developed by WSU collaborators to provide estimates of SAF production costs according to supply chain scenario assumptions.

Subtask 5.2: A review of options to manage contaminants along the supply chain will be conducted. Results of the review and contaminant measurements from the bench-scale gasification tests in Task 4 will be used to target bench-scale contaminant control tests.

Task 6 - Hawaii Regional Project

University of Hawaii

Objective

Task activities in Year 6 will explore the impacts of Hawaii State Legislative Bill HB2386 on waste management and the potential for waste-based SAF production systems. HB2386 requires 0.5-mile buffer zones around waste and disposal facilities (including landfills), and restricts facilities from land with conservation-district zoning.

Research Approach
The goal of this task is to assess and evaluate the impacts of HB2386 on waste management strategies in Hawaii. HB2386 was disruptive to disposal practices for C&D waste on the island of Oahu, and its impacts are currently not fully understood. Task 6 seeks to collect updated waste generation data, understand how HAVE BEen2386 will affect current management strategies, and develop scenarios for waste-based SAF production under the new regulatory environment. The impacts of HB2386 on the capacity to perform landfill mining will also be considered. Preliminary assessment of restricted and unrestricted sites for waste and disposal facilities will be reviewed and refined as necessary. Preliminary impacts on GHGs and SAF technology choices will be explored.

Milestone
Impacts of removing or diminishing the role of an active C&D landfill as a supply chain participant will also be evaluated.

Major Accomplishments
None.

Publications
None.

Outreach Efforts
None.

Awards
None.

Student Involvement
None.

Plans for Next Period
A postdoctoral fellow will be recruited to work on this task, and analysis will begin.

Project 001(C) Alternative Jet Fuel Supply Chain Analysis

Purdue University

Project Lead Investigator

Farzad Taheripour
Research Professor
Department of Agricultural Economics
Purdue University
403 West State Street
West Lafayette, IN 47907-2056
765-494-4612
tfarzad@purdue.edu

University Participants

Purdue University

- P.I.: Farzad Taheripour, Research Professor
- FAA Award Number: 13-C-AJFE-PU, Amendments 25, 29, 34, 36, 41
- Period of Performance: October 1, 2021to September 30, 2022
- Tasks:
    1. Develop techno-economic models for relevant pathways and identify key stochastic variables to model for assessing risk in conversion pathways, which will lead to our capability to compare pathways, their expected economic cost, and the inherent uncertainty in each pathway (lead: Farzad Taheripour; supported by Chepeliev)
    2. Perform a life cycle analysis (LCA) of alternative jet fuel pathways in coordination with the International Civil Aviation Organization's Committee on Environmental Protection Fuels Task Group (ICAO CAEP FTG); work with the CAEP FTG life cycle assessment group on issues such as system boundaries, induced land use change (ILUC), LCA methodology, and pathway greenhouse gas emissions assessments (lead: Taheripour; supported by Sajedinia, Aguiar, and Malina [Hasselt University])
    3. Develop estimates of land use change (LUC)-associated emissions for alternative jet fuels for the ICAO CAEP FTG, in close relation to Task #2 (lead: Taheripour; supported by Sajedinia, Debadrita, Aguiar, and Chepeliev)
    4. Provide support for other ASCENT universities on alternative jet fuel policy analysis (lead: Taheripour)

Project Funding Level

- Amendment 3: $250,000
- Amendment 6: $110,000
- Amendment 10: $230,000
- Amendment 15: $373,750
- Amendment 19: $400,000
- Amendment 29: $400,000
- Amendment 36, 41: $523,000

Current cost sharing for this project year was provided by Sami Jauhiainen from Neste US, Inc.

Investigation Team

Purdue University

- Farzad Taheripour (P.I.), research professor, works on all tasks.

- EhsanReza Sajedinia, PhD student, Purdue University: Stochastic techno-economic analysis (TEA) and Global Trade Analysis Project (GTAP) ILUC analysis, works on all tasks.
- Omid Karami, postdoctoral fellow (joined the research team in August 2021), works on all tasks.

GTAP Center

Maksym Chepeliev, PhD, research associate (collaborating part-time on the project) works on all tasks.
Angel H. Aguiar, PhD, research associate (collaborating part-time on the project) works on all tasks.
Kundu Debadrita. PhD student, research assistant (collaborating part time on the project), works on task 3.

Project Overview

This project has followed four main components in this performance time period. The first component is focused on advancing TEA for aviation biofuel pathways. The second component is concentrated on life cycle and production potential analysis of alternative jet fuel pathways in coordination with the ICAO CAEP FTG. The third component also coordinates with the FTG, with a specific focus on estimating LUC-associated emissions for alternative jet fuels. The fourth component aims to provide support for the policy subgroup of the FTG by providing policy guidelines to facilitate expansions in using sustainable aviation fuels (SAFs). This task includes bridging existing TEAs for alternative jet fuels with partial and general equilibrium economic models to develop alternative scenarios for alternative jet fuels in the fuel mix used by the industry.

Task 1 - Develop Techno-economic Models for Relevant Pathways and Identify Key Stochastic Variables for Assessing Risk in Conversion Pathways

Purdue University

Objectives

This task aimed to develop TEAs for relevant pathways and identify key factors to model for assessing the feasibility of conversion pathways. This work will lead to our capability to compare pathways, their expected economic cost, and the inherent uncertainty in each pathway. This activity will help us to include new pathways in the GTAP-BIO model to assess their LUC impacts.

Research Approach

For each fuel pathway under evaluation, we collected the required data and developed the required analyses for both TEA and LCA to determine the cost structure of new pathways to be included in the GTAP-BIO model to support FTG tasks.

Milestones

Over this period, we continued to work on various analyses for various technologies at the global level. This research has been fully and successfully conducted. The results of these analyses helped to establish required cost structure of various global pathways to be used in the LUC assessments for Task 3.

Major Accomplishments

The following TEAs have been developed to support the inclusion of several new pathways in the GTAP-BIO database at the global level:

- Global value for soy oil hydroprocessed esters and fatty acids (HEFA) covering USA, Brazil, and Rest of South America;
- Global value for rapeseed oil HEFA covering Canada, EU27, Rest of Europe, and Commonwealth of Independent States;
- Global values for corn alcohol-to-jet (ATJ) and ethanol-to-jet (ETJ) covering USA, Brazil, Rest of South America, EU27, Rest of Europe, and Commonwealth of Independent States;
- Global values for sugarcane ATJ and ETJ and synthesized iso-paraffins (SIP) covering Brazil, Central America and Caribbean, Rest of South America, sub-Saharan Africa, India, Rest of South Asia, China, and Rest of Asia;
- Global value for sugar beet SIP covering USA, EU27, Rest of Europe, and Commonwealth of Independent States, Middle East and North Africa, and China;

- Global values for carinata and camelina oil HEFA covering USA, Canada, Brazil, Rest of South America, and European Union (ERU);
- Global values for miscanthus, switchgrass and poplar ATJ, ETJ, and Fischer-Tropsch (FT) covering USA, Brazil, and EU 27.

Publications

Peer-reviewed journal publications

Taheripour, F., Sajedinia, E., & Karami, O. (2022). Oilseed cover crops for sustainable aviation fuels production and reduction in greenhouse gas emissions through land use savings. Frontiers in Energy Research, 9(790421), 10. doi: 10.3389/fenrg.2021.790421

Outreach Efforts

Taheripour participated in ASCENT Advisory meetings in fall 2021 and spring 2022 and shared the findings of this research with the ASCENT community.

Awards

None.

Student Involvement

EhsanReza Sajedinia, current PhD student, Purdue University, full time assistantship (50%) for data collection and running simulations.

Plans for Next Period

We plan to work on TEAs to support calculation of LUC emissions associated with new SAF pathways. In particular, TEA of the use of renewable electricity for SAF production will be examined during the CAEP13 cycle to support FTG analyses.

Task 2 - LCA of Alternative Jet Fuel Pathways in Coordination with ICAO Alternative Fuels Task Force (AFTF) FTG

Purdue University

Objectives

- Provide required data and analysis to support the low-LUC-risk practices adopted by CAEP
- Provide required data and analysis to support the core LCA group with respect to ILUC for coprocessing of esters and fatty acids in petroleum refineries and other tasks as needed

Research Approach

This task incorporates many varied assignments and components. We followed standard approaches to support FTG subgroups including the core LCA, Technology Production Policy (TPP), Emission Reductions Accounting (ERA), and Sustainability subgroups. Using the GTAP-BIO model, we collected data and provided appropriate analyses to accomplish this task. Taheripour is co-chair of the FTG ILUC group. Taheripour collaborates with the LCA, TPP, ERA, and Sustainability subgroups of ICAO CAEP FTG.

Milestones

Taheripour participated in the CAEP12/FTG11 and CAEP13/FTG01 meetings and was involved in many of the tasks and document preparation activities for these meetings. He also responded to other subgroup requests for help and collaboration. He has led efforts in ILUC modeling and ILUC-related tasks associated with other subgroups. He continued to examine regional and global ILUC values for each SAF and led a set of efforts to define a methodology to calculate direct land use change (DLUC) to support the FTG activities.

Major Accomplishments

A methodology has been defined and finalized to calculate DLUC to be used within the Carbon Offsetting and Reduction Scheme for International Aviation (CORSIA) sustainability systems to evaluate the land use emissions of individual projects

that will be launched by economic operators for SAFs.

Publications

Written reports

International Civil Aviation Organization. (2022). CORSIA methodology for calculating actual life cycle emissions values, Section 8: CORSIA methodology for calculating direct land use change emissions values. https://www.icao.int/environmental-protection/CORSIA/Documents/CORSIA_Eligible_Fuels/ICAO%20document%2007%20-%20Methodology%20for%20Actual%20Life%20Cycle%20Emissions%20-%20June%202022.pdf

Outreach Efforts

Taheripour served as a member of the Committee on Current Methods for Life Cycle Analyses of Low-Carbon Transportation Fuels in the United States of the National Academy of Sciences, Engineering, and Medicine in 2021 and 2022. This committee has published the following comprehensive report on the LCA approach:

National Academies of Sciences, Engineering, and Medicine. 2022. Current Methods for Life-Cycle Analyses of Low-Carbon Transportation Fuels in the United States. Washington, DC: The National Academies Press. doi:10.17226/26402.

Taheripour attended the Commercial Aviation Alternative Fuels Initiative (CAAFI) Sustainable Aviation Fuels Summit & Biennial General Meeting Agenda (June 1-3, 2022) and updated the participants of this meeting regarding the efforts and findings of this research.

Taheripour attended the ASCENT Advisory Group meetings in fall 2021 and spring 2022 and discussed the findings of this task with members of this community.

Awards

None.

Student Involvement

EhsanReza Sajedinia, current PhD student, Purdue University, full time assistantship (50%) for data collection and running simulations.

Plans for Next Period

We will continue to support FTG subgroups, including the core LCA, TPP, and ERA subgroups, to accomplish the required LCAs for new SAF pathways. In addition, we will continue to develop required TEAs to include the cost structure of new SAF pathways in the GTAP-BIO database.

Task 3 - Develop Estimates of LUC-Associated Emissions for Alternative Jet Fuels for the ICAO FTG

Purdue University

Objectives

- Compute ILUC emissions of alternative jet fuels for use in CORSIA
- Improve the GTAP-BIO model and its database and make appropriate modifications to the agro-ecological zone emission factor model
- Define and implement a method to determine regional ILUC values and rank countries according to their LUC determinants

Research Approach

We modify, update, and use the GTAP-BIO model to produce ILUC estimates for the FTG. We also collaborate with the International Institute for Applied Systems Analysis and Hugo Valin to evaluate the outcomes of GTAP-BIO and GLOBIOM models. We collect data and develop new approaches to assess issues related to ILUC emissions due to the production of alternative jet fuels.

Milestones

We added several new pathways to the GTAP-BIO model and examined new regional ILUC values. We also developed a methodology for estimating global ILUC values and assessed ILUC values for numerous SAF pathways.

Major Accomplishments

The primary accomplishments in this task are based on the work progress of ICAO CAEP FTG. Some of the working papers and information papers that we have produced over this period are listed in this section and in the overall publication list at the end of this report.

Publications

Peer-reviewed journal publications

Busch, J., Amarjargal, O., Taheripour, F., Austin, K. G., Siregar, R. N., Koenig, K., & Hertel, T. W. (2022). Effects of demand-side restrictions on high-deforestation palm oil in Europe on deforestation and emissions in Indonesia. *Environmental Research Letters*, *17*(1), 014035. doi:10.1088/1748-9326/ac435e

Taheripour, F., Sajedinia, E., & Karami, O. (2022). Oilseed cover crops for sustainable aviation fuels production and reduction in greenhouse gas emissions through land use savings. *Frontiers in Energy Research*, *9*(790421), 10. doi: 10.3389/fenrg.2021.790421

Published conference proceedings

Taheripour F., Kwon H., Mueller S., Emery I., Karami O., and Sajedinia E. (2022). Biofuels induced land use change emissions: The role of implemented emissions factors in assessing terrestrial carbon fluxes. *Global Trade Analysis Project 25th Annual Conference and 2022 AAEA Annual Meeting*.

Written reports

Malina R., Prussi M. and Taheripour F. (2022). *Method for establishing lifecycle greenhouse gas emission factors for sustainable aviation fuels*. In 2022 Environmental Report: Innovation for a Green Transition, International Civil Aviation Organization, Montreal QC, Canada.

Several working papers and information papers have been produced based on our work for the AFTF/FTG. Working and information papers presented at FTG meetings include

- CAEP/12-FTG/11-WP/06 – "Revisions to methodology on Low Land Use Change (LUC) Risk Practices based on pilot applications", October 2021, Virtual
- CAEP/12-FTG/11-WP/09 – "Direct Land Use Change Emissions Methodology", October 2021, Virtual
- CAEP/12-FTG/11-WP/10 – "ILUC default values", October 2021, Virtual
- CAEP/12-FTG/11-IP/04 – "Foregone carbon sequestration accounting for Direct Land Use Change", October 2021, Virtual
- CAEP/12-FTG/11-IP/05 – "Updating the GTAP-BIO data base from 2011 reference year to 2014 reference year", October 2021, Virtual
- CAEP/12-FTG/11-FL/05 – "Proposal for carinata and camelina oil HEFA pathway characterization", October 2021, Virtual
- CAEP/13-FTG/01-WP/06 – "Approach to ILUC-Related CAEP/13 Work Plan Items", May 2022, Virtual

Outreach Efforts

Taheripour attended several meetings to present research outcomes on ILUC values, including:

- GTAP 25th Annual Conference on Global Economic Analysis, June 2022, Virtual
- AAEA Annual Meeting, Anaheim, California, July 31-August 2, 2022

Awards

None.

Student Involvement

EhsanReza Sajedinia, current PhD student, Purdue University, full time assistantship (50%) for data collection and running simulations.

Plans for Next Period

We will continue working with ICAO on ILUC emission estimates. In particular, we prepare to serve the FTG group during the CAEP13 cycle to accomplish the following tasks:

- Continue to carry out the computations of ILUC emissions associated with SAF production for requested world regions, for use in CORSIA
- Review the approach to ILUC in light of emerging scientific evidence and data
- Further examine assumptions in ILUC models, such as double cropping representation with a view to better reflect verified historical trends and market behavior
- Revisit the inclusion of foregone sequestration to the CORSIA DLUC methodology, based on the concrete certification experience and feedback from Sustainability Certification Schemes (SCSs)
- Develop pathway specifications for the pathways with negative ILUC emissions, to be verified by the SCSs during certification
- Monitor low-LUC-risk practices implemented for SAF production and incorporate lessons learned in the methodology, as appropriate
- Evaluate a potential inclusion of soil organic carbon and agricultural biomass sequestration at the project level, instead of the current approach that only accounts for changes in these sources as part of the ILUC
- Further explore the consequences of a potential inclusion of ILUC for biomass-derived process fuels (e.g., biomass used to generate electricity for the SAF conversion process)
- Develop sample calculations and/or methods for use in validating SCS tool calculations relating to LCA and DLUC to assist the Sustainability Certification Schemes Evaluation Group (SCSEG) in assessing SCS capabilities; this information could be made publicly available in the CORSIA supporting “LCA methodology” document

Task 4 - Provide Support for Other ASCENT Universities on Alternative Jet Fuels Policy Analysis

Purdue University

Objective

To provide support for the other ASCENT universities on alternative jet fuels policy analysis.

Research Approach

See Tasks 1, 2, and 3.

Milestone(s)

See Tasks 1, 2, and 3.

Major Accomplishments

See Tasks 1, 2, and 3.

Publications

None.

Outreach Efforts

None.

Awards

None.

Student Involvement

None.

Plans for Next Period

None.

Project 001(D) Alternative Jet Fuel Supply Chain Analysis

The Pennsylvania State University

Project Lead Investigator

Lara Fowler
Interim Chief Sustainability Officer, The Pennsylvania State University (Penn State)
Interim Director, Penn State Sustainability Institute
Professor of Teaching, Penn State Law
Affiliate Faculty, Penn State School of International Affairs
The Pennsylvania State University
103 Land & Water Research Building
University Park, PA 16802
814-865-4806
Lbf10@psu.edu

University Participants

The Pennsylvania State University

- P.I.: Lara Fowler, Interim Director, Penn State Sustainability Institute; Professor of Teaching, Penn State Law
- P.I.: Saurabh Bansal, Associate Professor of Supply Chain Management (through funding period ending January 31, 2022)
- P.I.: Anne Menefee, Assistant Professor of Energy and Mineral Engineering (starting with funding period beginning June 14, 2022)
- P.I.: Armen Kemanian, Professor of Production Systems and Modeling (starting with funding period beginning June 14, 2022)
- P.I.: Tom Richard, Professor of Agriculture and Biological Engineering (starting with funding period beginning June 14, 2022)
- Researcher: Ekrem Korkut, Legal Research Postdoctoral Associate
- FAA Award Number: 13-C-AJFE-PSU, RISK-INFORMED ALTERNATIVE JET FUEL (AJF)
- Periods of Performance: period A: August 1, 2017 to January 31, 2022; period B: June 14, 2022 to November 13, 2023
- Tasks:

Period A (August 1, 2017 to January 31, 2022)

1. 1.3.1: Risk–reward profit-sharing modeling for first facilities
   1.3.2: Additional quantification of risk and uncertainties in supply chains (foundational part of Task 1.3.1)
   1.3.3: Supply chain risk analysis tools for farmer adoption
   1.4.1: National survey of current and proposed state and federal programs that monetize ecosystem services
   1.4.3: Support of stakeholder engagement efforts

Period B (June 14, 2022 to November 13, 2023)

   1.1: Research on existing federal law and policy drivers
   1.2: Research on existing state and regional law and policy drivers
   1.3: Research on proposed legislation (federal and state)
   1.4: Research on other law/policy issues, as identified by the ASCENT 001 team
2. 2.1: Work with ASCENT 001 to identify stakeholder engagement opportunities
   2.2: Development of a list of potential stakeholders critical to discussion
   2.3: Development of agenda/materials for critical discussions; meeting facilitation as needed
3. 3.1: Work with ASCENT 001 team members to identify critical questions, and refine the scope of work related to carbon capture and sequestration (CCS)

3.2: Conduct literature review regarding CCS and its potential use in conjunction with alternative jet fuels (AJFs)
3.3: Draft a review manuscript examining opportunities to integrate CCS and AJF

4. 4.1: Work with ASCENT 01 team members to identify critical questions, and refine the scope of work related to soil organic carbon
4.2: Conduct literature review regarding soil organic carbon and its potential relation to AJF
4.3: Draft review manuscript examining opportunities for organic soil carbon and AJF.

Washington State University (WSU)

- Michael Wolcott, Regents Professor (for funding period from June 14, 2022 to November 13, 2023)
- Kristin Brandt, Staff Engineer (through funding period ending January 31, 2022)

University of Tennessee

- Tim Rials, Associate Dean of Agricultural Research (through funding period ending January 31, 2022)
- Burt English, Professor of Agricultural and Resource Economics (through funding period ending January 31, 2022)

Project Funding Level

FAA funding: $100,000 (for period B, June 14, 2022 to November 13, 2023)
Matching from Penn State: $100,000
Total funding: $200,000

Investigation Team

Period A (August 1, 2017 to January 31, 2022)
Task 1.3.1 (Bansal; supported by Brandt and English): Risk–reward profit-sharing modeling for first facilities
Task 1.3.2 (Bansal; supported by Brandt and English): Additional quantification of risk and uncertainties in supply chains (foundational part of Task 1.3.1)
Task 1.3.3 (Bansal; supported by Brandt and English): Supply chain risk analysis tools for farmer adoption
Task 1.4.1 (Fowler; supported by Korkut): National survey of current and proposed state and federal programs that monetize ecosystem services
Task 1.4.3 (Fowler; supported by Korkut): Support of stakeholder engagement efforts

Period B (June 14, 2022 to November 13, 2023)
Task 1.1 (Fowler, supported by Korkut): Research on existing federal law and policy drivers
Task 1.2 (Fowler, supported by Korkut): Research on existing state and regional law and policy drivers
Task 1.3 (Fowler, supported by Korkut): Research on proposed legislation (federal and state)
Task 1.4 (Fowler, supported by Korkut): Research on other law/policy issues, as identified by the ASCENT 001 team

Task 2.1 (Fowler, supported by Korkut): Work with ASCENT 001 to identify stakeholder engagement opportunities
Task 2.2 (Fowler, supported by Korkut): Development of a list of potential stakeholders critical to discussion
Task 2.3 (Fowler, supported by Korkut): Development of agenda/materials for critical discussions; meeting facilitation as needed

Task 3.1 (Menefee): Work with ASCENT 001 team members to identify critical questions, and refine the scope of work related to carbon capture and sequestration (CCS)
Task 3.2 (Menefee): Conduct literature review regarding CCS and its potential use in conjunction with alternative jet fuels (AJFs)
Task 3.3 (Menefee): Draft a review manuscript examining opportunities to integrate CCS and AJF

Task 4.1 (TBD, supported by Wolcott): Work with ASCENT 01 team members to identify critical questions, and refine the scope of work related to soil organic carbon
Task 4.2 (TBD, supported by Wolcott): Conduct literature review regarding soil organic carbon and its potential relation to AJF
Task 4.3 (TBD, supported by Wolcott): Draft review manuscript examining opportunities for organic soil carbon and AJF.

Project Overview

For the first period of performance (period A), this project focused on developing a qualitative and quantitative understanding of factors to help establish biofuel supply chains for AJFs. Although efforts are being made to establish these supply chains, many face challenges because of a lack of clarity regarding the incentives that stakeholders would require to engage in these supply chains and devote their resources to investing in the facilities required for these supply chains. To this end, this project has two goals:

1. Develop pro forma cash flows that represent the financial status of various participants in biofuel supply chains for AJFs, to inform a transparent risk-sharing tool
2. Understand the policy landscape in various parts of the United States to encourage AJF supply chains and identify additional policy initiatives that may be needed

During the second period of performance (period B), this project continues to focus on understanding the law and policy drivers associated with AJF, while expanding focus to include two new areas—CCS and organic soil carbon—and their potential linkages to AJF.

Period A, Task 1.3.1 - Risk–reward Profit-sharing Modeling for First Facilities

The Pennsylvania State University

Objective

Develop a transparent risk-sharing tool to provide all partners with an understanding of the cash flows and risks faced by all supply chain partners.

Research Approach

We first collected a large number of risk-sharing tools that have been proposed in the supply chain literature. Subsequently, we narrowed this list to 9–12 mechanisms. We created an Excel-based framework in which the cash flows of all supply chain partners are modeled on the basis of data from the techno-economic analyses developed by WSU. This framework incorporates the risk-sharing mechanisms.

Milestone

We developed Excel models for four realistic configurations by using data from techno-economic analysis models developed by WSU.

Major Accomplishments

We developed an Excel-based framework showing the cash flows of four key stakeholders in AJF supply chains: farmers, preprocessors, refineries, and airlines. The framework shows various risk-sharing contracts that each of the stakeholders could extend to others, as well as the financial burdens or opportunities associated with these mechanisms. The framework also shows the government's financial burden of supporting these mechanisms. The framework was developed for four levels of refinery capacity. Overall, this framework can be used as a decision support tool by various stakeholders to determine whether to engage in alternative jet biofuel supply chains and negotiate with one another.

Publications

We have provided the tool to the sponsor and will provide training on its use to the project sponsor upon request.

Outreach Efforts

Our tool has been presented and discussed at three ASCENT advisory committee meetings.

Awards

None.

Student Involvement

None.

Period A, Task 1.3.2 - Additional Quantification of Risk and Uncertainties in Supply Chains (Foundational Part of Task 1.3.1)

The Pennsylvania State University

Objective

Develop methods to rely on expert judgments to quantify uncertainties associated with biofuel supply chains.

Research Approach

We developed a new econometric approach to quantify the probability distributions of uncertain quantities, such as yield or demand, when an expert panel provides judgments regarding the most likely values. This approach exploits the well-known theory of generalized least squares in statistics for the context in which historical data are available to calibrate expert judgments or when these data are not available.

Milestones

We have described this method in two manuscripts. In the first manuscript, "Using Subjective Probability Distributions to Support Supply Chain Decisions for Innovative Agribusiness Products," we developed a two-stage procedure to calibrate expert judgments regarding the distribution of biofuel uncertainties, such as the uncertain yields of new varieties of oilseeds, demand, or selling price. In the first step of the procedure, we calibrated the expert judgments by using historical data. Specifically, we used prior judgments provided by experts and compared them with actual realizations (such as predicted yield versus actual yield) to determine the frequency with which each expert over- or underestimated the uncertainty, e.g., expert 1 underestimated the yield 60% of the time, whereas expert 2 underestimated the yield 90% of the time. In the second manuscript, "Optimal Aggregation of Individual Judgmental Forecasts to Support Decision Making in a R&D Program," we used this information to determine the optimal approach for aggregating the experts' judgments to determine the mean and standard deviation of the probability distributions. In this manuscript, we developed a new optimization protocol for determining the optimal acreage for growing specific crops by considering the estimated mean and standard deviation, as well as incorporating the variability in these estimates. This manuscript won two awards at a professional conference (INFORMS 2021) in November 2021 and in October 2022.

Major Accomplishments

Theoretical development and a numerical study have demonstrated the promise of this approach.

Publications

Peer-reviewed journal publications

Bansal, S., & Gutierrez, G. J. (2020). Estimating uncertainties using judgmental forecasts with expert heterogeneity. *Operations Research*, *68*(2), 363-380. doi: 10.1287/opre.2019.1938

Written reports

Bansal, S., & Wang, T. (2019). Using subjective probability distributions to support supply chain decisions for innovative agribusiness products. Report for the *Federal Aviation Administration*. https://s3.wp.wsu.edu/uploads/sites/2479/2021/05/ASCENT-Project-001D-attachment-1.pdf

Bansal, S., & Gutierrez, G. J. (2021). Optimal aggregation of individual judgmental forecasts to support decision making in a R&D program. Submitted to *Operations Research*. https://s3.wp.wsu.edu/uploads/sites/2479/2021/05/ASCENT-Project-001D-attachment-2.pdf

Outreach Efforts

None.

Awards

2021 Decision Analysis Practice Award - INFORMS, November 2021
2022 Decision Analysis Best Publication Award - INFORMS

Student Involvement

None.

Plans for Next Period
This work is now wrapped up so there are no plans for the next period.

Period A, Task 1.3.3 - Supply Chain Risk Analysis Tools for Farmer Adoption
The Pennsylvania State University

Objectives
Understand farmers' risk preferences over a long duration and how these preferences affect their decisions to grow crops that can support AJF supply chains.

Research Approach
We surveyed farmers to understand their risk preferences over extended durations. Specifically, we presented farmers with sample yield ranges over extended periods and asked them to estimate the lowest equivalent guaranteed yield that they would be willing to accept, given the uncertain yields. We used these responses to perform statistical analyses.

Milestones
We have completed the survey and have written a manuscript based on the survey.

Major Accomplishments
We compiled data from 43 farmers in central Pennsylvania regarding their preferences, given uncertain yields from their land. The results quantify the loss of value that farmers attribute to an uncertain yield. Results are reported for both 1-year and 10-year horizons. For the 10-year horizon, we also report results for an initial yield build-up, which often arises with most biofuel crops. The key takeaways from this study are as follows: (a) farmer valuations of a new crop decrease acutely as the uncertainty in yield increases, and (b) the initial build-up period of low yields can be a large deterrent that inhibits farmers from adopting new crops for the purpose of supporting biofuels.

Publications
A manuscript detailing this work has been written and provided to the sponsor.

Outreach Efforts
None.

Awards
None.

Student Involvement
None.

Plans for Next Period
This work is now wrapped up so there are no plans for the next period.

Period A, Task 1.4.1 - National Survey of Current and Proposed State and Federal Programs that Monetize Ecosystem Services
The Pennsylvania State University

Objectives
Conduct a survey and summarize current and proposed state and federal programs to monetize ecosystem services.

Research Approach

This task builds on and continues the work performed under ASCENT Project 001, Task 8.1, which focused on the biomass and water quality benefits to the Chesapeake Bay watershed. In previous years, we examined the biofuel law and policy landscape of the Pacific Northwest and Southeast regions, as well as the state of Hawaii. During this most recent time period for reporting (October 1, 2021 to September 30, 2022), we focused on federal biofuel law and policy, and how they have been affected by international drivers.

Milestones

Our research was previously circulated in three region-specific white papers. In addition, we developed a federal-level white paper in the list of tasks, which was subsequently published (see below).

Copies of these documents are available online:

- Western U.S. policy manuscript (with a focus on Washington state, last updated in 2019): Western US Bioenergy Law & Policy - Draft 5.docx
- Southeast policy manuscript (with a focus on Tennessee): Southeast Bioenergy Law & PolicyDraft3.docx
- Hawaii policy manuscript: Hawaiian Biofuel Law & Policy_v5.docx
- Federal-level white paper: 2021_01_08_SAF paper draft_ circulated for review_KCL_NB (1).docx

Major Accomplishments

In addition to developing the white papers described above, we adapted the federal-level white paper for publication (see below). We also provided a briefing and poster during the ASCENT fall meeting (October 2021). Additionally, P.I. Lara Fowler is involved in another project, funded by the USDA National Institute of Food and Agriculture, entitled "Consortium for Cultivating Human and Naturally Regenerative Enterprises" (USDA-NIFA Sustainable Agricultural Systems Award 2020-68012-31824), dubbed the "C-CHANGE" project. She has built upon her work in this ASCENT project to link to the regenerative agriculture work being pursued in C-CHANGE, including providing a briefing on second-generation biofuel law and policy.

Publications

Peer-reviewed journal publications

Korkut, E. & Fowler, L. B. (Nov. 2021). Regulatory and policy analysis of production, development and use of sustainable aviation fuels in the United States." *Frontiers in Energy Research*, *9,* 750514. doi:10.3389/fenrg.2021.750514.

Outreach Efforts

Presentations

- Fowler, L. B., & Lewis, K. (October 2021). Sustainable aviation fuel development: Law, policy and the blender's tax credit. Manuscript presented at the ASCENT Annual Meeting.

Awards

None.

Student Involvement

Ekrem Korkut graduated from the Penn State School of International Affairs in May 2021 and transitioned to working as a postdoctoral associate on this project (50% of his time; the other 50% is funded by another project).

Plans for Next Period

As noted above, we will continue adapting the existing white papers for publication. The next step again focuses on regional efforts. As needed, we will provide support to working groups under the sustainable aviation fuel (SAF) Grand Challenge. Of note, work on this task was delayed by the lack of a contract in the 4.5 months from February 1, 2022 to June 14, 2022.

Period A, Task 1.4.3 - Help Support Stakeholder Engagement Efforts

The Pennsylvania State University

Objective

Facilitate dialogue among producers, industry, government, and other affected stakeholders.

Research Approach

Our work under this objective has focused on stakeholder engagement and facilitation of effective dialogue to help bridge gaps among producers, industry, government, and other affected stakeholders. This role supports the needs of other team members.

Milestone

These efforts have supported stakeholder engagement efforts led by other teams, including but not limited to the regional partners identified in ASCENT Project 01, Tasks 3.1, 3.2, and 3.3.

Major Accomplishments

This set of tasks has been relatively limited, and no major accomplishments have been made to date. We have continued to participate in discussions and calls related to potential stakeholder engagement needs.

Publications

None.

Outreach Efforts

None.

Awards

None.

Student Involvement

None.

Plans for Next Period

Future work under this objective will include presenting to the project partners on facilitation skills and tactics. Additional support for regional projects will be offered as needed for facilitation and stakeholder engagement sessions as the regional projects move to the deployment stage. As needed, we will provide support to working groups under the SAF Grand Challenge.

Note: although the proposed contract period was intended to start on February 1, 2022, no contract was in place from February 1, 2022 to June 13, 2022, thus leaving a gap of approximately 4.5 months without funding.

Period B, Task 1- Law and Policy Research

The Pennsylvania State University

Objectives

Understand existing federal law and policy drivers affecting SAF, including participation by the United States in international discussions and agreements (Task 1.1); research existing state law and policy drivers (Task 1.2); research potential law and policy drivers as needed (Task 1.3); and explore other issues identified by the ASCENT 001 team as needed (Task 1.4).

Research Approach

Following up on publication of the *Frontiers in Energy* review of law and policy, we began research on the recently adopted Blender's Tax Credit and the potential Sustainable Skies Act. In addition, we updated our legal and policy research on different states' activities regarding SAF (including CA, OR, WA, and others).

Milestone
We engaged in team meetings and provided updates on legal research topics.

Major Accomplishments
We provided real-time analysis of pending federal legislation (the Inflation Reduction Act) at the request of Project Manager Nate Brown. In addition, we researched and shared information related to pending Securities and Exchange Commission rulemaking on greenhouse-gas-emissions accounting.

Publications
We are exploring possibilities for another formal publication.

Outreach Efforts
Our research has been discussed through several presentations:

- Fowler, L. B., & Korkut, E. (December 2022). ASCENT 001 Team Briefing on pending Securities and Exchange Commission Greenhouse Gas Emission rules.
- Fowler, L. B. (October 2022). Briefing to Volvo Corporation on Opportunities Related to the Renewable Fuel Standard and SAF.
- Fowler, L. B., & Korkut, E. (July 2022). Update on State Legal and Regulatory Opportunities for SAF. ASCENT 001 Project Meeting.
- Fowler, L. B. (June 2022). Legal and Regulatory Drivers of Sustainable Aviation Fuel. Global Council for Science and the Environment.

Awards
None.

Student Involvement
None.

Plans for Next Period
We will continue to work with the ASCENT 001 Team to identify potential law and policy concerns and opportunities. How SAF and renewable natural gas might be developed in synergistic ways is another question that we are exploring.

Period B, Task 2 - Support Stakeholder Engagement Efforts
The Pennsylvania State University

Objective
Facilitate dialogue among producers, industry, government, and other affected stakeholders.

Research Approach
Our work under this objective has focused on stakeholder engagement and facilitation of effective dialogue to help bridge gaps among producers, industry, government, and other affected stakeholders. This role supports the needs of other team members.

Milestone
These efforts have supported stakeholder engagement efforts led by other teams, including but not limited to the regional partners identified in ASCENT Project 001.

Major Accomplishments
This set of tasks has been relatively limited, and no major accomplishments have been made to date. We have continued to participate in discussions and calls related to potential stakeholder engagement needs.

Publications
None.

Outreach Efforts
None.

Awards
None.

Student Involvement
None.

Plans for Next Period
Future work under this objective will include presenting to the project partners on facilitation skills and tactics. Additional support for regional projects will be offered as needed for facilitation and stakeholder engagement sessions as the regional projects move to the deployment stage. As needed, we will provide support to working groups under the SAF Grand Challenge.

Period B, Task 3 - Carbon Capture and Sequestration
The Pennsylvania State University

Objective
Understand how CCS could be integrated with sustainable aviation fuel development.

Research Approach
The new area of research involves a technical focus on integration of CCS with liquid fuel production and examination of soil organic carbon. For this task, Dr. Anne Menefee will focus on the technical viability and sustainability of integrating liquid fuel production with CCS. Her research is broadly focused on decarbonization of the energy sector; she has extensive experience specifically in carbon sequestration. Across scales, her research ranges from exploring fundamental geochemical–geomechanical feedback in stressed fracture systems that are targeted by subsurface sequestration operations to evaluating the system-level environmental impacts of emerging technologies that can both curb net emissions and be self-sustaining in the market. Most relevantly, she has worked on life-cycle and techno-economic assessments of subsurface technologies for carbon sequestration and waste management in the energy sector.

Milestone
This work has recently started.

Major Accomplishments
None.

Publications
None.

Outreach Efforts
None.

Awards
None.

Student Involvement
None.

Plans for Next Period
Because approval for this work was delayed, this work has just started. Additional consultation with the ASCENT 001 Team is needed regarding the proposed and potential next steps. This technical work should support implementation of the SAF Grand Challenge, the International Civil Aviation Organization Committee on Aviation Environmental Protection, and/or both.

Period B, Task 4 - Organic Soil Carbon
The Pennsylvania State University

Objective
Understand how organic soil carbon might be integrated with sustainable aviation fuel development.

Research Approach
This is another new area of research identified by the ASCENT 001 team. As part of the request on this topic, we identified Dr. Armen R. Kemanian to join the ASCENT 001 Team. The research approach for this task will involve identifying critical questions and refining the scope of work (Task 4.1); conducting a literature review (Task 4.2); and drafting a review manuscript analyzing the opportunities to link organic soil carbon and SAF (Task 4.3).

Milestone
This work has recently started. Dr. Kemanian provided an initial presentation of ideas to think about during the August 25, 2022 ASCENT 001 team meeting.

Major Accomplishments
None.

Publications
None.

Outreach Efforts
Presentation, ASCENT 001 Team (August 2022): “Agroecosystem Productivity and Carbon Intensity when Producing Aviation Fuel: Amplifying Opportunities and Taming Trade-offs.”

Awards
None.

Student Involvement
None.

Plans for Next Period
Because approval for this work was delayed, this work has just started. Additional consultation with the ASCENT 001 Team is needed regarding the proposed and potential next steps. As with the technical work associated with CCS, this technical work should support implementation of the SAF Grand Challenge, the International Civil Aviation Organization Committee on Aviation Environmental Protection, and/or both.

Project 001(E) Alternative Jet Fuel Supply Chain Analysis

University of Tennessee

Project Lead Investigator

Timothy Rials
Professor and Director
Center for Renewable Carbon
University of Tennessee (UT)
2506 Jacob Dr., Knoxville, TN 37996
865-946-1130
trials@utk.edu

University Participants

University of Tennessee

- P.I.: T. Edward Yu, Professor
- FAA Award Number: 13-C-AJFE-UTenn, Amendments 09, 11, 13, 15, 17
- Period of Performance: October 1, 2021 to September 30, 2022
- Tasks:
    1. Assess and inventory regional forest and agricultural biomass feedstock options
    2. Develop national lipid availability analysis as feedstock for SAF
    3. Lay the groundwork for supplying lipid and/or biomass for SAF production in Tennessee and the Southeastern United States
    4. Perform biorefinery infrastructure assessment and siting (supporting role)

Project Funding Level

Total estimated project funding: $1,375,000 (total 6-year funding)/$800,000 (this year)
Total federal and non-federal funds: $1,375,000 (total 6-year funding)/$1,375,000 (this year)
The UT Institute of Agriculture, in support of the project, provided faculty salary. Additional non-federal support was derived from contributions from the stakeholder group.

Investigation Team

- Timothy Rials, Project Director (P.D.)/P.I. (UT) (Task 3)
- T. Edward Yu, co-P.D./P.I. (UT) (Tasks 1,2,4)
- Burton English, Faculty (UT) (Tasks 1-4)
- Kim Jensen, Faculty (UT) (Task 2)
- Jim Larson, Faculty (UT) (Task 2)
- Carlos Trejo-Pech, Faculty (UT) (Task 1)
- David Hughes, Faculty (UT) (Task 3)
- Jada Thompson, Faculty (UT) (Task 1)
- Tongtong Lee, Master's Graduate Student (UT) (Task 2)

Project Overview

UT will lead the feedstock production (Task 1) component of the project. This component targets the need to assess and inventory regional forest and agricultural biomass feedstock options and delineate the sustainability impacts associated with various feedstock choices, including land-use effects. UT will lead the national lipid supply availability analysis, using POLYSYS to develop information on the potential impacts and feasibility of using lipids to supply aviation fuel. The team at UT will facilitate regional deployment/production of jet fuel by laying the groundwork and developing a regional proposal for deployment. Additionally, UT will support activities in Task 3 with information and insights regarding feedstocks, along

with potential regional demand centers for aviation fuels and coproducts, and information on current supply chain infrastructure, as required.

Major goals include the following:

1. Develop a rotation-based oilseed crop scenario and evaluate potential with POLYSYS
2. Reevaluate the production potential of biomass feedstocks and evaluate potential with POLYSYS
3. Develop a database on infrastructure for the Southeast United States
4. Continue monthly meetings with Central Appalachia stakeholders
5. Initiate aviation fuel supply chain studies in the Southeast by using pine and oilseeds
6. Continue with sustainability work for both goals 1 and 4

Task 1 - Assess and Inventory Regional Forest and Agricultural Biomass Feedstock Options

University of Tennessee

Objectives

1. Complete the economic viability analysis for switchgrass, short-rotation woody crops, crop residues, forest residues, and cover crops
2. Assist in risk–reward profit-sharing modeling by providing information from past work on cellulosic supply chains to Pennsylvania State University (PSU)
3. Develop new supply curves for both lignocellulosic and oilseed feedstock for sustainable aviation fuel (SAF). Because the markets for lignocellulosic biomass (LCB) feedstock, i.e., grasses, short-rotation woody crops, and agricultural residues, are currently not well established, evaluation of the feasibility of supplying those LCB feedstocks is important. The production, harvesting, and storage costs of the feedstocks are included in the assessment. A variety of potential crop and biomass sources will be considered in the feedstock path, including the following:

   Oilseed crops: potentially including pennycress (*Thlaspi arvense*), camelina (*Camelina sativa*), and carinata (*Brassica carinata*) as "cover crops"

   Perennial grasses: switchgrass (*Panicum virgatum*), miscanthus (*Miscanthus sinensis*), and energy cane (*Saccharum complex*)

   Short-rotation woody crops: poplar (*Populus* species), willow (*Salix* species), loblolly pine (*Pinus taeda*), and sweetgum (*Liquidambar styraciflua*)

   Agricultural residue: wheat straw, corn stover, and other agricultural residues

   Forest residue: forest residue
4. Evaluate the potential economic impacts of a mature SAF industry on regional, state, and national economies.

Research Approach

POLYSYS was used to estimate and assess the supply and availability of these feedstock options at the regional and national levels, and different feedstock farm-gate prices. County-level estimates of all-live total woody biomass, as well as average annual growth, removals, and mortality, were obtained from the Forest Inventory and Analysis Database. Mill residue data were not incorporated because most of that material already has a market. The Forest Sustainable and Economic Analysis Model (ForSEAM) will be used to estimate and predict forest residues. Forest residue encompasses removal of logging residues, thinnings, and unmerchantable trees. Forest residues exclude any logs from areas defined as supplying sawtimber but do include the logging residues that occur from sawtimber harvest. ForSEAM uses U.S. Forest Service Forest Inventory and Analysis data to project timber supply according to the demand projections from the U.S. Global Forest Product Model module of the Global Forest Product Model. Specific tasks related to this objective are outlined below. Estimates from 2020 through 2047 are made. The potential supply analysis is based on 2045 projections, although little difference exists in the national numbers between 2025 and 2045.

Two sets of POLYSYS scenarios were analyzed:

- The initial set examined the quantity of agricultural residues coming from traditional plantings from corn, sorghum, oats, barley, wheat, soybeans, cotton, and rice, along with the contributions of dedicated herbaceous energy crops and short-rotation woody crops at farm-gate prices of $30 to $80 per ton in $5 increments.

Currently, the analysis has focused on $40, $60, and $80 per ton. Analysis has been extended to $90, $100, and $110 per ton.

- A second scenario focused on oilseeds as "cover crops." This analysis allowed for areas where corn and/or cotton and soybeans were historically grown to add a crop between the row crop and soybeans. The analysis assumed a 6.5% decrease in soybean yield if the region switched from corn (or cotton)/soybeans to corn (or cotton)/cover crop/soybean rotations. The data generated in these runs provided results for Task 2.

The UT Department of Agricultural & Resource Economics models supply chains for liquid and/or electricity-generating technologies currently in use or forthcoming for the bio/renewable-energy industry by using the input–output model IMPLAN. The approach for ethanol, biodiesel, and liquid fuels includes the establishment and production of the feedstock, the transportation of the feedstock to the plant gate, and the one-time investment and annual operating of the facility that converts the feedstock to a biofuel. This modeling approach may also include the preprocessing and storage of feedstocks at depots. Also included in the supply chain analyses are the labor/salary requirements for these activities, renewable identification numbers (RINs) and credits attributable to the conversion facility, and land-use changes for growing the feedstock. Recent modeling has centered on the supply chain for liquid fuels by using the 179 economic areas of the Bureau of Economic Analysis (BEA) as modeling regions (Figure 1). The data layers necessary to estimate the economic impacts are contained in the Renewable Energy Economic Analysis Layers (REEAL) modeling system.

IMPLAN (version 3.0, using basic data for 2018) contains an input–output model based on county-level data that can be used to estimate the supply chain economic impacts of the bio/renewable-energy industry. Data are aggregated to BEA economic areas and then converted to BEA input–output models to measure changes in economic activity. As with all input–output models, IMPLAN describes the buying and selling of products and the resulting transfer of money among various industries and institutions within a BEA. Output from the model provides descriptive measures of the economy, including total industry output (the value of all sales), employment, labor income, value added, and state/local taxes for 546 industries in each BEA.[1] Each BEA IMPLAN model provides estimates of multiplier-based impacts (e.g., how siting a conversion facility will affect the rest of the BEA economy). In analysis of the impacts of the supply chain activities, the indirect multiplier effect (i.e., the impact on the supply chain part of the economy in this case) is also included. Multipliers are based on the assumption that as consumers and institutions increase expenditures, demand increases for products made by local industries, which in turn make new purchases from other local industries, and so forth. Stated another way, the multipliers in the model measure the response of the entire BEA economy to a set of changes in production for liquid fuel technologies currently located within the region and/or forthcoming for the bio/renewable-energy industry. The analysis uses IMPLAN's available local purchase percentage (LPP) option, which affects the direct impact value applied to the multipliers. Instead of a 100% direct expenditure value (i.e., electricity, water, construction, manufacturing, or waste management) applied to the BEA multipliers, the value reflects the BEA's actual purchases. The analysis is achieved with Analysis by Parts, through splitting the inputs purchased into the industries that receive the purchase and their corresponding impacts. The total impact is the aggregation of all the parts. Each part represents an industry that provides input into the industry under consideration. In addition, labor impacts and the impacts of changes in proprietor income are included.

[1] Total industry output is defined as the annual dollar value of goods and services that an industry produces. Employment represents total wage and salary employees, as well as self-employed people in a region, for both full- and part-time workers. Labor income consists of employee compensation and proprietor income. Total value added is defined as all income to workers paid by employers (employee compensation); self-employed income (proprietor income); interests, rents, royalties, dividends, and profit payments; and excise and sales taxes paid by individuals to businesses. State/local taxes comprise sales tax, property taxes, motor vehicle license taxes, and other taxes.

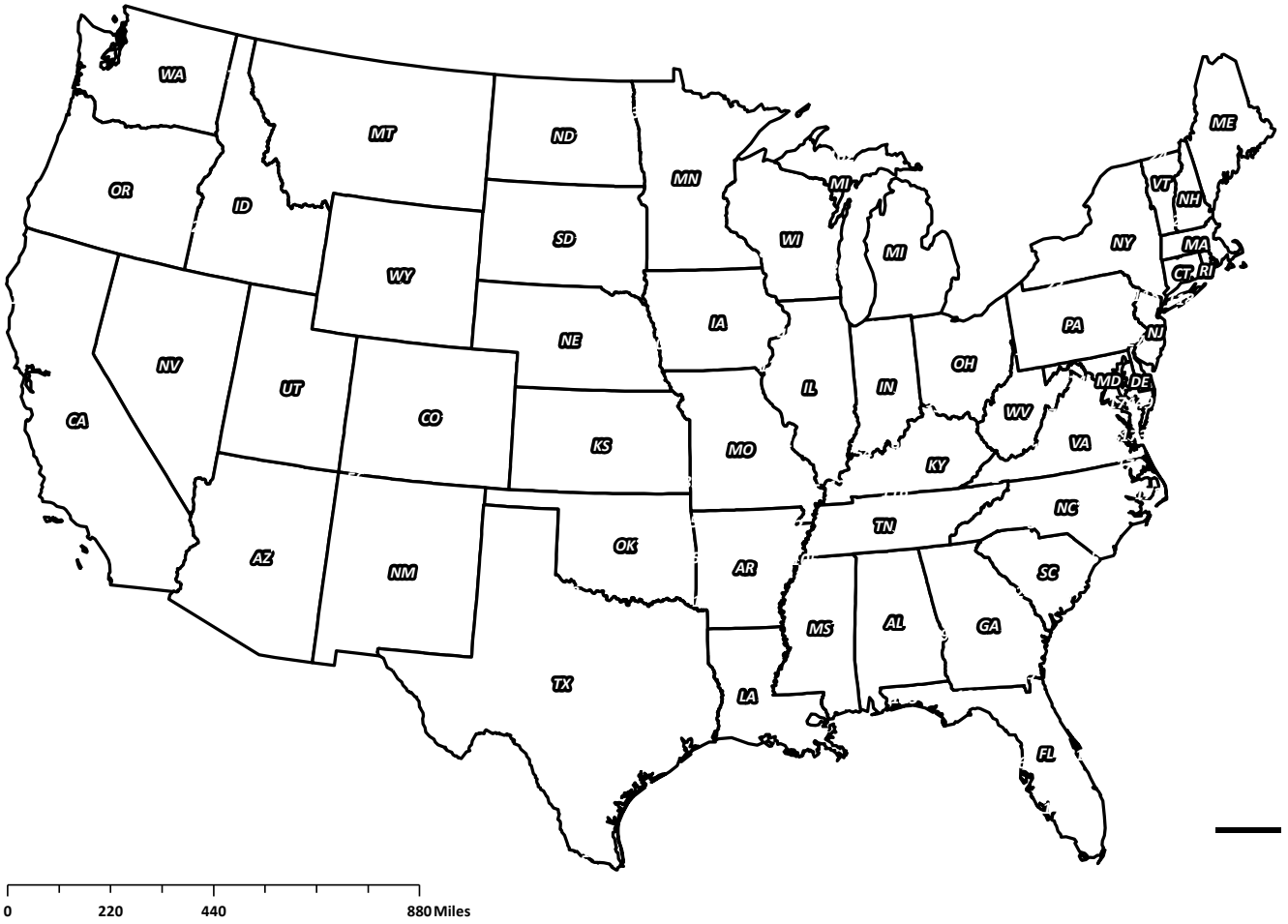

Figure 1. Bureau of Economic Analysis economic areas for input-output analysis modeling.

An example scenario is presented to show modeling capabilities. The conversion technology is a gasification Fischer-Tropsch biorefinery with a feedstock input of 545,000 tons per year of forest residue in Central Appalachia. The distance for a logging road for the feedstock is less than 1 mile. The biorefinery is expected to produce SAF, diesel, and naphtha. An estimated 1.1 million tons of forest residue is required at 10% moisture content. If work is conducted for 330 days per year and 10 hours per day, an estimated 16 or 17 trucks must be emptied every hour (or one truck every 4 minutes) if a truckload comprises 20 tons of chips (longer trailers could haul 22.5 tons of chips and could unload 14 or 15 trucks per hour). Based on the techno-economic analysis (TEA) information, for the Central Appalachia region, three biorefineries could be sited, each producing 545,000 dry short tons or 495,000 dry metric tons per year. Each biorefinery could produce 12.6 million gallons of SAF, 10.7 million gallons of diesel, and 6.2 million gallons of naphtha. Gross revenues for fuel are estimated at $425.0 million, with RINs contributing an additional $52.0 million. The break-even plant-gate fuel prices, when RINs and 12.2% return on investment are assumed, are $4.90 per gallon for SAF, $5.05 per gallon for diesel, and $4.26 per gallon for naphtha. In addition, a blender's fee of $1 to $2 per gallon for SAF fuel might be available, thus further decreasing the costs. Current legislation includes a blender's fee of $2 per gallon for biodiesel and $1 per gallon for gasoline.

According to IMPLAN-estimated economic impacts, the annual economic impact to Central Appalachia if three biorefineries were established is $1.2 billion, on the basis of an investment of $1.7 billion. Leakages occur as investment dollars leave the region; according to the regional local purchase coefficients (i.e., LPPs), the total amount is $500 million. Thus, the economic activity is $2.1 billion, with a multiplier of 1.7. In other words, for every 1 million dollars spent, an additional $0.7 million in economic activity is generated in the regional economy. The estimated gross regional product is $1.0 billion, and nearly 14,000 jobs are created during the construction period of the biorefineries, thus resulting in $700 million in labor income with multiplier effects.

Milestones

- Generated data have been passed on to the ASCENT 1 database for hardwood and softwood forest residues in the Southeast United States for two sustainability scenarios.
- A pine pathway for the Southeast United States was developed, and the potential that exists within the region was evaluated by using an ASCENT cellulosic pathway.
- A pennycress and crush facility spreadsheet was delivered to PSU for use in risk–reward profit-sharing modeling.
- Economic multipliers were developed for Fischer–Tropsch synthetic paraffinic kerosene, by using forest residues as the feedstock, and producing SAF and naphtha.

Major Accomplishments

Recent modeling emphasis has centered on the supply chain for liquid fuels by using the Bureau of Economic Analysis's 179 economic trading areas as modeling regions. These various data layers, which are necessary to estimate the economic impact, are contained in UT's REEAL modeling system. This analysis provides an example scenario to demonstrate REEAL's modeling capabilities. The conversion technology modeled is a gasification Fischer–Tropsch biorefinery with feedstock input of 495,000 metric tons per year of forest residue transported to a logging road that is less than 1 mile in distance. The biorefinery is expected to produce SAF, diesel, and naphtha. An estimated 1 million tons of forest residue is required at 50% moisture content. On the basis of a TEA developed by ASCENT and the quantity of hardwood residues available in the Central Appalachian region, three biorefineries could be sited, each utilizing 495,000 dry metric tons per year. The feedstock cost at the biorefinery gate is shown in Figure 2.

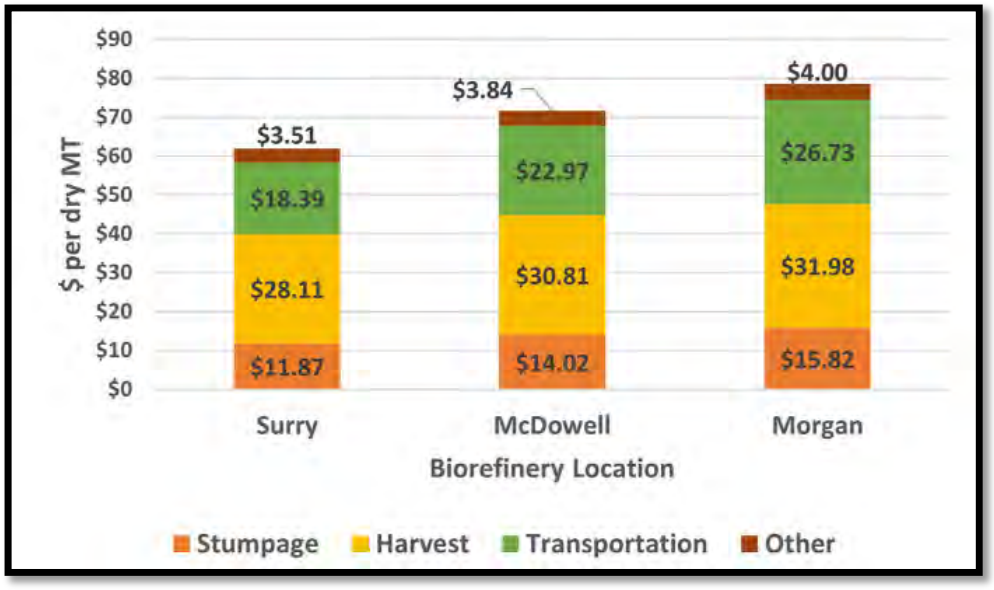

Figure 2. Costs of delivered feedstocks per dry metric ton for each of the biorefineries.

Each biorefinery could produce 47.5 million liters of SAF, 40.3 million liters of diesel, and 23.6 million liters of naphtha. The annual gross revenue for fuel required for the biorefineries to break even is estimated at $193.7 million per biorefinery. The break-even plant gate fuel prices, if RINs and 12.2% return on investment are assumed, are $1.12 per liter for SAF, $1.15 per

liter for diesel, and $0.97 per liter for naphtha. On the basis of IMPLAN, with an input–output model and an investment of $1.7 billion, the estimated economic annual impact to the Central Appalachian region if the three biorefineries are sited exceeds half a billion dollars. Leakages occur as investment dollars leaving the region; according to the region's local purchase coefficients (i.e., LPPs), the total is $500 million. This results in an estimated $2.67 billion in economic activity with a multiplier of 1.7; i.e., for every million dollars spent, an additional $0.7 million in economic activity is generated in the regional economy. Gross regional product is estimated at $1.28 billion, and employment of nearly 1,200 jobs is created during the construction period of the biorefineries, thereby resulting in $700 million in labor income with multiplier effects. The economic activity for the feedstock operations (harvesting and chipping) is estimated at slightly more than $16.8 million, thus resulting in an additional $30 million economic impact. The stumpage and additional profit from the harvesting of forest residues result in $40 million flowing directly to the resource and logging operation owners. Their subsequent expenditures result in a total economic activity increase of $71.4 million. These operations create an estimated 103 direct jobs, for a total of 195 with multiplier effects. Direct feedstock transportation expenditures exceeding $36.7 million provide an estimated increase in economic activity of almost $68 million, accounting for the multiplier effects (Figure 3).

Item causing the impact	Multiplier	Direct	Total
—	—	Million $	
Biorefineries			
Investment:	—	—	—
Economic activity	1.68	$1,589.5	$2,671.9
Gross regional product	1.76	$725.5	$1,277.5
Employment (jobs)	1.64	11,265	18,429
Annual operations:	—	—	—
Economic activity excluding salaries	1.68	$198.8	$333.2
Salary	1.98	$17.7	$35.2
Annual economic activity generated	—	$216.5	$368.3
Gross regional product	1.61	$128.6	$206.6
Feedstock operations			
Annual operations:	—	—	—
Feedstock to landing:	—	—	—
Economic activity excluding salaries	1.79	$11.1	$19.9
Salary	1.76	$5.7	$10.1
Resource and logging operation owners	—	$40.2	$71.4
Annual economic activity generated	1.78	$57.1	$101.3
Gross regional product	1.55	$12.7	$19.8
Feedstock transportation:	—	—	—
Economic activity	1.85	$36.7	$67.8
Gross regional product	1.80	$20.3	$36.5

Figure 3. Economic activity generated by the three biorefinery industries.

A preliminary analysis for the SAF Grand Challenge was initiated. Several goals were examined by using crop residues, dedicated energy crops, and forest residues as feedstocks for the GTP pathway. Waste streams from human consumption were not included, nor was oilseed production. The analysis included four scenarios of meeting 25%, 50%, 75%, and 100% of the SAF Grand Challenge target with these feedstocks.

The impacts on agricultural prices (Figure 4a) were evaluated, along with changes in land use (Figure 4b). Pressure on commodity prices for the grains decreased slightly over all alternative scenarios, with prices remaining the same for other program crops. Corn acreage increased as demand for stover for SAF production increased. Meeting the 2030 market did not substantially affect the crop markets. Figure 4c summarizes the main source of biomass feedstock over time to meet the 100% SAF Grand Challenge target. Corn stover serves as the major source (47%) of biomass feedstock, followed by wood residues (39%) and switchgrass (34%), in 2045.

	Change from baseline (2030)							
Crop price	25% target		50% target		75% target		100% target	
	$	%	$	%	$	%	$	%
Corn ($/bu)	−0.06	−1.64%	−0.06	−1.64%	−0.06	−1.64%	−0.06	−1.64%
Grain sorghum ($/bu)	−0.01	−0.29%	−0.01	−0.29%	−0.01	−0.29%	−0.01	−0.29%
Oats ($/bu)	−0.02	−0.67%	−0.02	−0.67%	−0.02	−0.67%	−0.02	−0.67%
Barley ($/bu)	−0.01	−0.22%	−0.01	−0.22%	−0.01	−0.22%	−0.01	−0.22%
Wheat ($/bu)	0.00	0.00%	0.00	0.00%	0.00	0.00%	0.00	0.00%
Soybeans ($/bu)	0.08	0.84%	0.08	0.84%	0.08	0.84%	0.08	0.84%
Cotton ($/lb)	0.00	0.00%	0.00	0.00%	0.00	0.00%	0.00	0.00%
Rice ($/cwt)	0.00	0.00%	0.00	0.00%	0.00	0.00%	0.00	0.00%
Hay ($/ton)	0.00	0.00%	0.00	0.00%	0.00	0.00%	0.00	0.00%

Figure 4a. Change in commodity prices with respect to the baseline solution under the SAF Grand Challenge.

Harvested land	Change from baseline (2030) 25% target		50% target		75% target		100% target	
	Million acres	%	Million acres	%	Million acres	%	Million acres	%
Corn	0.33	0.40%	0.33	0.40%	0.33	0.40%	0.33	0.40%
Grain sorghum	0.01	0.19%	0.01	0.19%	0.01	0.19%	0.01	0.19%
Oats	−0.01	−1.11%	−0.01	−1.11%	−0.01	−1.11%	−0.01	−1.11%
Barley	−0.01	−0.42%	−0.01	−0.42%	−0.01	−0.42%	−0.01	−0.42%
Wheat	−0.04	−0.10%	−0.04	−0.10%	−0.04	−0.10%	−0.04	−0.10%
Soybeans	−0.27	−0.32%	−0.27	−0.32%	−0.27	−0.32%	−0.27	−0.32%
Cotton	0.00	0.00%	0.00	0.00%	0.00	0.00%	0.00	0.00%
Rice	0.00	0.00%	0.00	0.00%	0.00	0.00%	0.00	0.00%
Hay	0.00	0.00%	0.00	0.00%	0.00	0.00%	0.00	0.00%

Figure 4b. Change in land use with respect to the baseline solution under the SAF Grand Challenge.

Biomass	2030	2035	2040	2045
Stover (mil.dt)	140.4	143.3	151.9	168.7
Straw (mil.dt)	0	0	12	17.4
Switchgrass (mil.dt)	0	0	39.7	121.8
Miscanthus (mil.dt)	0	0	5.3	79.7
Wood residues (mil.dt)	20.1	21.8	67.7	137.7
Willows (mil.dt)	0	0	0	0.8

Figure 4c. The biomass feedstock for the SAF Grand Challenge.

Publications

Peer-reviewed journal publications

Burton, C., English, R., Menard, J., & Wilson, B. (2022). The Economic Impact of a Renewable Biofuels/Energy Industry Supply Chain Using the Renewable Energy Economic Analysis Layers Modeling System, *Frontiers in Energy Research*, *10*:3389. doi: 10.3389/fenrg.2022.780795

Sharma, B.2, T.E. Yu, B.C. English, and C.N. Boyer. 2021. Economic Analysis of Developing a Sustainable Aviation Fuel Supply Chain Incorporating with Carbon Credits: A Case Study of the Memphis International Airport. *Frontiers in Energy Research*, *9*:802. doi: 10.3389/fenrg.2021.775389.

Trejo-Pech, C. J., Larson, J. A., English, B. C., & Yu, T. E. (2021). Biofuel discount rates and stochastic techno-economic analysis for a prospective Pennycress (Thlaspi arvense L.) sustainable aviation fuel supply chain. *Frontiers in Energy Research*, *9*:867. doi: 10.3389/fenrg.2021.770479

Outreach Efforts

The UT Institute of Agriculture and the Commercial Aviation Alternative Fuels Initiative have partnered to identify sites with optimal woody biomass and essential supply chain infrastructure, because these factors present challenges for processors with limited resources to conduct site assessments with sufficient detail to attract investment capital. The initial attempt will highlight the availability of woody biomass in the region and thereby extend its potential utilization. Analysis has been initiated for DRAX Group and USA BioEnergy.

Awards

None.

Student Involvement

Plans for Next Period

- Develop a forest harvest model
- Complete several manuscripts
- Continue our work on the forest sector
- Continue our work on the stochastic analysis focusing on pennycress feasibility in the Southeast United States
- Continue to work on the Memphis airport region analysis using camelina and pennycress as feedstocks
- Work on feedstock sustainability issues
- Continue working with stakeholders

Task 2 - Develop National Lipid Supply Availability Analysis

University of Tennessee

Objective

The UT team will complete the national lipid supply availability analysis by using POLYSYS to develop information on the potential impacts and feasibility of using lipids to supply aviation fuel.

Research Approach

POLYSYS was used to estimate and assess the supply and availability of these feedstock options at the regional and national levels. This U.S. agricultural sector model forecasts changes in commodity prices and net farm income over time. Analysis requires consistency among the crops. Budgets have been reevaluated for pennycress, camelina, and carinata for consistent assumptions, where possible. These budgets have been uploaded into the PSU BOX platform and sent to Washington State University, and are available at https://arec.tennessee.edu/. Yields have been compared with literature sources and are available at https://arec.tennessee.edu/.

Milestone

The potential oilseed cover crops and SAF production have been estimated and will be included in a manuscript.

Major Accomplishments

1. Consistent assumptions regarding the prices of inputs were reviewed, and budgets were updated. POLYSIS was updated with the changes.
2. The pennycress spreadsheet incorporating risk into the analysis was completed and is still under review.
3. The assumptions among the three oilseed crops were compared, and we have attempted to develop spreadsheets containing similar price data and other assumptions.
4. Analysis was run in POLYSYS by assuming on-farm prices of $0.05 to $0.20 per pound. Supplies of the oilseed were estimated and impacts to the national and rural economies are being estimated.

Figure 5 shows the potential production areas of the three oilseed cover crops—pennycress, carinata and camelina—under two scenarios: (a) corn/oilseed/soybeans and (b) cotton/oilseed/soybeans. The major production concentrates in the north-central region or Corn Belt. Figure 6 presents the total oilseed cover crop production, given the six external price levels. On the basis of the oilseed production, the potentially production of SAF and co-products under the six oilseed price levels was determined (Figure 7). At $0.11 per pound, 54 billion pounds of oilseed could be produced and converted to nearly 5 million short tons of oil, and eventually make 0.75 billion gallons of SAF plus other renewable fuels, if 20 facilities generating hydrotreated esters and fatty acids are operated, 259,000 short tons would be required annually. At the highest price level ($0.20/lb), 75 billion pounds of seed could be produced and could make 1 billion gallons of SAF, thereby meeting one-third of the 2030 target. Among those three oilseeds, the primary cover crop is pennycress (77%), followed by camelina (17%) and carinata (6%).

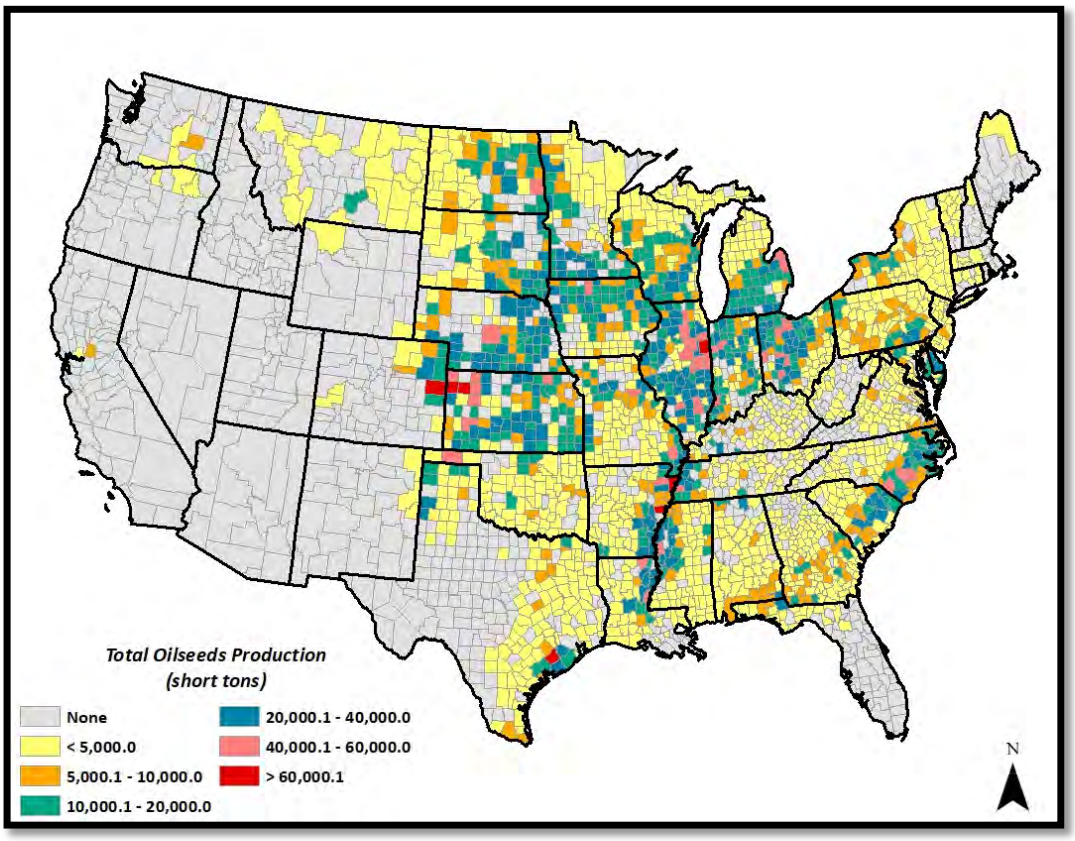

Figure 5. Total production of three oilseed cover crops in the United States.

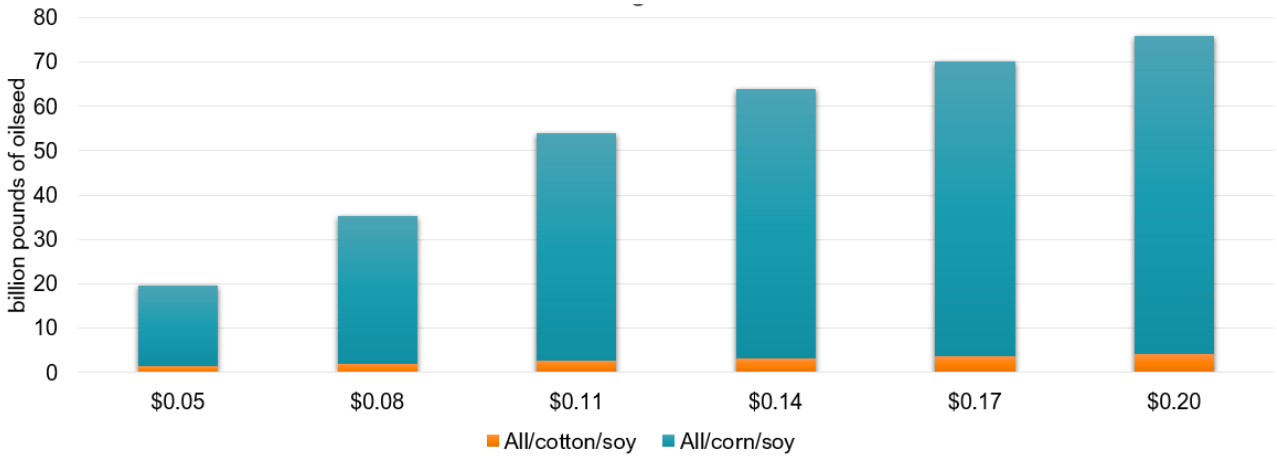

Figure 6. Total production of three oilseed cover crops under various external prices.

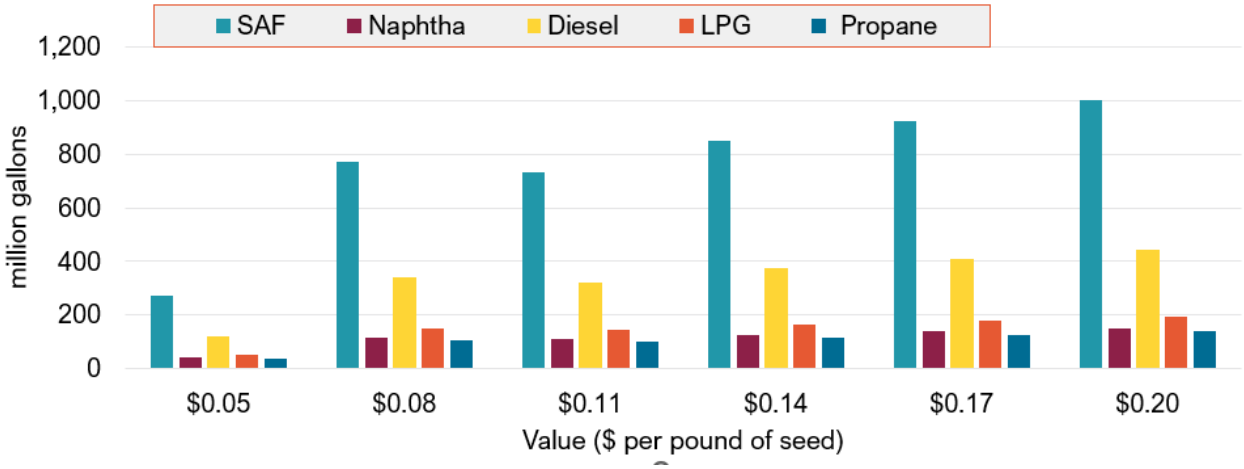

Figure 7. Total SAF and co-products derived from three oilseed cover crops under various external prices.

Publications
See Task 1 above for publications.

Outreach Efforts
None.

Awards
None.

Student Involvement
Alan Robertson examined the impacts of fertilizer on switchgrass yield and ash content, and evaluated the biorefinery's desired level of fertilizer application.
Tongtong Li was included in the project to develop the stochastic budget model for pennycress.

Plans for Next Period
We plan to produce a manuscript based on the analysis.

Task 3 - Lay the Groundwork for Supplying Lipid and/or Biomass for SAF Production in Tennessee and the Southeast United States
University of Tennessee

Objectives
The team at UT will facilitate regional deployment/production of renewable jet fuel by completing the groundwork phase of the regional oilseed feedstock-to-biofuel pathway and developing a proposal for regional deployment in the Southeastern United States and in Central Appalachia, thus leading to the development of SAF Regional Deployment Plans for the Southeast and Appalachia.

Research Approach
- The approach is as in Task 1, but is focused on small areas such as Central Appalachia, Memphis, and Nashville.
- Softwood analysis is focused on the Southeast, and findings were provided in last year's report.

- A seed trial for oilseed cover crops was developed with funding from UT seed money; we will incorporate findings in this report for the first year under subproject 2.

Central Appalachia: second year of a multi-year project
The project was initiated at the start of the COVID-19 pandemic and was subsequently rearranged to reflect laboratory closures and travel restrictions.

The research approach was somewhat modified to reflect these changes. A hardwood forest residue layer was developed for BioFLAME and the Freight and Fuel Transportation Optimization Tool (FTOT) (Figures 7 and 8). An initial FTOT analysis has been run, and adjustments to the analysis are underway.

A stakeholder group has been formed and has met multiple times. Typically, the meeting occurs on the second Thursday of each month.

A summary of the work accomplishments under the subcontract with the Center for Natural Capital to assist in the Central Appalachia area is provided below. Item 8 has been cancelled because of the funding decrease for 2021–2022. In addition, the Center continues to play an active and vital role in stakeholder meetings even though the funding for the project covered the initial year, and future years were not funded. Initial-year funding was extended for a second year through a no-cost extension.

1. Form an expert advisory board
    a. Develop an invitee list of potential advisory board members
    b. Hold Zoom calls and obtain input regarding stakeholder invitees
2. Group formed
    a. Monthly calls held
3. Monthly calls
    a. Advise the expert advisory board regarding the needs of the airline industry
    b. Identify and engage consultants with substantial experience in airline industry fuels
4. Assemble a stakeholder cabinet
5. Assist UT in identifying potential brown and green field locations
6. Review and comment on UT's determination of the ability and willingness of forest landowners, agricultural producers, and reclaimed mine landowners to make land available for feedstock production
7. Procure and deliver to UT 50–60 different hybrid poplar samples in chipped form from Powell Project Travel to Powell River Project, with assistance from Virginia Tech; collect samples; cut pieces of hybrid poplar and return them to Rapidan, Virginia, for processing into chips
    a. A total of 110 pounds of hybrid poplar tree trunks only (without stems and leaves) have been procured and delivered to UT.
    b. Samples have been collected and processed; boles of hybrid poplar have been cut and sent to UT for analysis.
8. Assist Don Hodges and his students in procuring hardwood forest residue samples from ongoing logging activities in the region by identifying current logging operations
9. Form a task force to prepare proposals to fund follow-on work
    a. A group of energy-related companies has been compiled, and contacts are being made to solicit interest in building a biorefinery in the region. One company has prepared a high-level proposal to install wood pyrolysis systems to break down feedstock and deliver it to a biorefinery.
10. Make considerable efforts to reach out to other related projects in the region
    a. The most notable project is MASBIO based at West Virginia University. The MASBIO leadership took the lead on a proposal to the U.S. Department of Commerce.

The team initiated a workforce analysis for the Appalachian region. The goal is to assess the nature of the demand for workers (quantity and quality) that a wood-based biofuel processing facility would have on a regional economy, and the ability and willingness of workers in the area to meet this demand, by using BEA region 66 as an example. To assess the former, the level of employment required by the biofuel firm (IMPLAN sector 163) is translated into a set of demand for specific workers by occupation. Occupations are then translated into a set of skill sets via IMPLAN's analysis of O*NET skills by occupation analysis. To assess the latter, we estimate changes in the local workforce to determine candidates likely to seek employment. Major changes in employment by economic sector are translated into occupational changes and then skill

changes by using the IMPLAN-O*NET analysis. A weighted average is then used to provide a supply of workers by skill set; the skill sets in turn are compared with those likely to be sought in prospective workers at the biofuel firm.

As shown in Table 1, in terms of the skill characteristic ability, workers assumed to be regional job seekers do not necessarily have the skills sought by the biofuel processing firm. Attributes that show a "good" match in terms of worker demand (IMPLAN sector 163) and supply (job seekers) include oral comprehension and expression, deductive reasoning, and inductive reasoning. However, attributes such as written comprehension, written expression, and originality are relatively important to the biofuel firm, but the ability of job seekers to supply such attributes may be lacking. Across all 52 ability attributes that we examined, a Wilcoxon test statistic (646.5) indicated a significant difference in rank (alpha = .01 level) indicating a possible mismatch between the skills desired by the firm and the ability of the available regional workforce to readily supply such skills.

Table 1. Ability as an example: Biofuel firm's (sector 163) vs. regional job seekers' rank of attribute importance (more than 52 attributes) with respect to worker skills.

Ability category	IMPLAN sector 163	Job seekers
Oral comprehension	1	1
Written comprehension	**2**	**20**
Oral expression	3	3
Written expression	**4**	**26**
Fluency of ideas	**5**	**29**
Originality	**6**	**31**
Problem sensitivity	7	4
Deductive reasoning	8	8
Inductive reasoning	9	10
Information ordering	10	6

Note: Underlining indicates a close match, and bold denotes a possible mismatch, between the demand for worker skills and the ability of local workers to provide such skills.

The hybrid poplar samples were evaluated by the Center of Renewable Carbon's lab headed by Niki Labbe. Collaborating with a hardwood National Institute for Food and Agriculture project, the laboratory characterized the feedstock performance and conversion potential of Central Appalachia region hardwood forest thinnings, harvest residuals, and short-rotation woody crops from university experimental plots and reclaimed surface mine lands, and the invasive species that have colonized formerly mined lands; in addition, their locations and costs were defined. Hardwood residue biomass was collected from various locations and preprocessed (drying and size reduction) for near-infrared data collection and wet-chemistry analysis.

Major Accomplishments

- The Nashville modeling work using cover crop oilseeds has been completed. The next step will be to develop a regional deployment plan after risk and uncertainty are evaluated.
- The Memphis modeling work has been initiated, but analysis has not begun. Analysis will be initiated during the second quarter of 2023.
- The Central Appalachian Project has a regular stakeholder group meeting and held its initial workshop online to discuss state and national incentives for SAF development in the region.

Publications

None.

Outreach Efforts
None.

Awards
None.

Student Involvement
None.

Plans for Next Period (Year)
- Complete the Central Appalachian Regional Deployment Plan
- Continue to work on the Nashville Regional Deployment Plan
- Continue to work on the Southeast Regional Deployment Plan
- Continue to work on the Memphis Regional Deployment Plan

Task 4 - Biorefinery Infrastructure and Siting (Supporting Role)
University of Tennessee

Objective
Provide feedstock support to other members of ASCENT as requested.

Research Approach
This task involves providing necessary input through research efforts by using feedstock tools developed before or as part of this project. The approach will vary as questions arise from other universities. We have received two requests, which were met this year: a request from PSU regarding the cost of feedstock production and a request from FTOT for information on feedstock availability in the Central Appalachian region. We also discussed the potential of assisting the University of Hawaii with economic analysis of the Hawaii feedstock and conversion effort.

Milestones
- Delivered the feedstock spreadsheets on oilseeds
- Developed a hybrid poplar spreadsheet, which is under review
- Worked with WSU in TEA assessment

Major Accomplishments
See Tasks 1 and 3 above.

Publications
None.

Outreach Efforts
None.

Awards
None.

Student Involvement
None.

Plans for Next Period
- Enhance economic indicator analysis
- Review feedstock spreadsheets, and make them available online

Project 001(F) Alternative Jet Fuel Supply Chain Analysis

Massachusetts Institute of Technology

Project Lead Investigators

Steven R. H. Barrett
Professor of Aeronautics and Astronautics
Director, Laboratory for Aviation and the Environment
Massachusetts Institute of Technology
77 Massachusetts Ave, Building 33-207, Cambridge, MA 02139
617-253-2727
sbarrett@mit.edu

Dr. Raymond L. Speth
Principal Research Scientist
Laboratory for Aviation and the Environment
Massachusetts Institute of Technology
77 Massachusetts Ave, Building 33-322, Cambridge, MA 02139
617-253-1516
speth@mit.edu

Dr. Florian Allroggen
Executive Director Aerospace Climate & Sustainability; Research Scientist
Laboratory for Aviation and the Environment
Massachusetts Institute of Technology
77 Massachusetts Ave, Building 33-115A, Cambridge, MA 02139
617-715-4472
fallrogg@mit.edu

University Participants

Massachusetts Institute of Technology (MIT)

- P.I.: Professor Steven R. H. Barrett; co-P.I.s: Dr. Florian Allroggen, Dr. Raymond Speth
- FAA Award Number: 13-C-AJFE-MIT, Amendment Nos. 003, 012, 016, 028, 033, 040, 048, 055, 058, 067, 082, 088, and 096
- Period of Performance: August 1, 2014 to September 19, 2023
- Tasks (for reporting period October 1, 2021 to September 30, 2022):
    1. Support U.S. participation in the International Civil Aviation Organization Committee on Aviation Environmental Protection (ICAO CAEP) to enable appropriate crediting of the use of sustainable aviation fuels (SAFs) under the Carbon Offsetting and Reduction Scheme for International Aviation (CORSIA)
    2. Support U.S. participation in the ICAO CAEP by performing core life-cycle analysis (CLCA) to establish default values for use under CORSIA
    3. Contribute to the development of the fuel production assessment for CORSIA-eligible fuels
    4. Develop methods for probabilistic life-cycle analyses and techno-economic analyses in the context of assessing U.S.-based SAF production
    5. Support knowledge sharing and coordination across all ASCENT Project 01 universities working on SAF supply-chain analyses

Hasselt University (UHasselt, through subaward from MIT)

- P.I.: Professor Robert Malina
- Period of Performance: September 1, 2016 to August 31, 2023
- Tasks (for reporting period October 1, 2021 to September 30, 2022):

1. Support and provide leadership for U.S. participation in ICAO CAEP to enable appropriate crediting of the use of SAFs under CORSIA, particularly as it relates to feedstock classification and pathway definitions
2. Support U.S. participation in ICAO CAEP by performing CLCA to establish default values for use under CORSIA
3. Contribute to the development of fuel production assessment for CORSIA-eligible fuels

Project Funding Level

This project received $4,035,000 in FAA funding and $4,035,000 in matching funds. The sources of the match are approximately $632,000 from MIT, plus third-party in-kind contributions of $809,000 from Byogy Renewables, Inc.; $1,038,000 from Oliver Wyman Group; $1,155,000 from NuFuels, LLC; and $401,000 from Savion Aerospace Corporation. Funding is reported for the entire period of performance indicated above.

Investigation Team

Principal Investigator:	Prof. Steven Barrett (MIT) (all MIT tasks)
Principal Investigator (UHasselt Subaward):	Prof. Robert Malina (UHasselt) (all UHasselt tasks)
Co-Principal Investigator:	Dr. Florian Allroggen (MIT) (all MIT tasks)
	Dr. Raymond Speth (MIT) (Task 4)
Co-Investigators:	Dr. Sergey Paltsev (MIT) (Task 3)
	Dr. Jennifer Morris (MIT) (Task 3)
Postdoctoral Associates:	Christoph Falter (MIT) (Task 3)
	Freddy Navarro Pineda (UHasselt) (all UHasselt tasks)
Research Specialist:	Matthew Pearlson (MIT) (Tasks 2 and 4)
Graduate Research Assistants:	Tae Joong Park (MIT) (Task 1, 2 and 4)
	Sarah Demsky (MIT) (Task 4)

Project Overview

The overall objectives of ASCENT Project 01 (A01) are to (a) derive information on regional supply chains to explore scenarios for future SAF production and (b) identify supply-chain-related obstacles to commercial-scale production in the near term and to larger-scale adoption in the longer term. For the reporting period, the MIT/UHasselt team contributed to these goals by (a) providing leadership in the International Civil Aviation Organization Committee for Aviation Environmental Protection (ICAO CAEP) CLCA Task Group of the Fuels Task Group (FTG), which is mandated to calculate life-cycle greenhouse gas (GHG) emissions associated with the use of SAF, (b) performing core life-cycle GHG emissions analyses to enable the inclusion of additional SAF pathways under CORSIA or verify CLCA values calculated by other institutions, (c) contributing to SAF availability assessments, (d) analyzing U.S.-produced SAF potential and their life-cycle emissions and costs, including options to further reduce the environmental footprint of SAFs, and (e) contributing to knowledge transfer in the ASCENT 01 team.

Task 1 - Support and Provide Leadership for U.S. Participation in ICAO CAEP to Enable Appropriate Crediting of the Use of SAFs under CORSIA, Particularly as it Relates to Feedstock Classification and Pathway Definitions

Massachusetts Institute of Technology
Hasselt University

Objectives

The overall objective of this task is to provide leadership for, and support to, the FAA in its engagement with the ICAO CAEP FTG (during CAEP/12 and CAEP/13). The specific focus of the work during this reporting period was (a) to support preparation of FTG papers for submission to the CAEP/12 meeting; (b) to help define the FTG work program for CAEP/13; (c) to update feedstock classifications and the list of pathways to be considered for CLCA; and (d) to provide guidance on the inclusion of power-to-liquid (PtL) fuels in CORSIA.

Research Approach

To achieve the goals outlined above, the team continued to co-lead the CLCA Task Group of the FTG. Prof. Malina acted as a co-lead. This role ensures that Prof. Malina remains a focal point of CLCA research, so that specific research tasks can be guided efficiently and effectively. The following research has been conducted in support of the leadership role:

Prepare for CAEP/12 and define the work program for CAEP/13

The UHasselt and MIT worked closely with the FAA and other FTG members to (a) prepare FTG input to the CAEP/12 meeting and (b) to define and review the work program for the CAEP/13 cycle. The main goal of the team was to ensure that the tasks reflect the current state of the art in SAF research, are in line with existing methods and concepts of FTG, and are defined sufficiently.

Update feedstocks and pathways

The UHasselt and MIT team worked with the CLCA subgroup to update and prioritize the list of feedstock-to-fuel pathways, and to assign lead modeling groups for each of the pathways that were set to be the priority. The team also provided support to FTG regarding feedstock classification, including guidance for CORSIA-approved sustainability certification schemes. Guidance has been made publicly available through CORSIA online ("Frequently Asked Questions," 2023). Finally, the team worked with other FTG experts in agreeing upon a definition for PtL fuels (see below).

Guidance on including PtL fuels

During CAEP/13, FTG was tasked with developing an actual-value method for PtL fuels. The MIT and UHasselt team are co-leading this effort through collaboration among the CLCA, Sustainability, and induced land-use change (ILUC) subgroups within FTG. During the reporting period, the team worked toward capturing a range of potential conversion technologies which use electricity as a significant input (Figure 1). The definition covers not only "pure PtL" pathways, which use hydrogen made from low-carbon electricity and CO_2 captured from the atmosphere or from industrial point sources, but also more conventional SAF production pathways using hydrogen from electrolysis.

Because electricity is a major input in the production of CORSIA-eligible fuels, its characteristics must be assessed. Most importantly, the source of electricity can substantially influence the life-cycle GHG emissions of the fuel (Figure 2). At the same time, electricity produced from low-carbon and high-carbon sources cannot physically be distinguished, particularly if the fuel production facility is connected to an electricity grid fed by multiple sources. Therefore, an approach for tracing the electricity used for fuel production is required. In addition, electric power generation, particularly from low-carbon sources, can be intermittent, thus prompting questions regarding how electricity sourcing or storage strategies can meet the demand of a fuel production process at a particular time, despite meeting annual average electricity requirements (Figure 3). Finally, because electricity is used in substantial quantities for SAF production, concerns regarding competing uses of electricity and a need for load balancing must be considered.

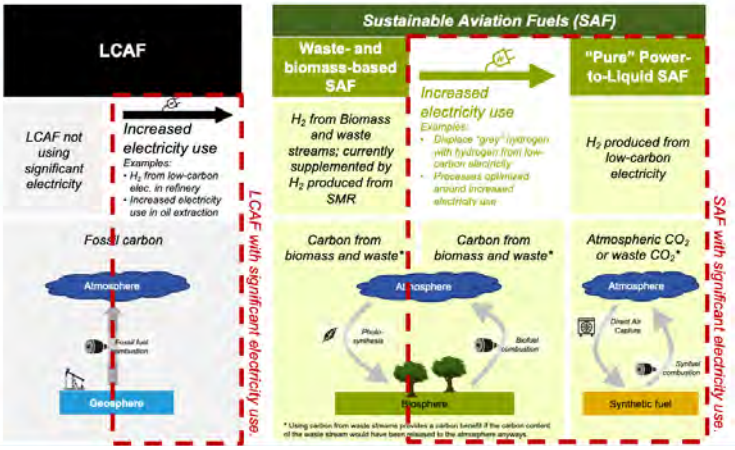

Figure 1. Production of CORSIA-eligible fuels using significant electricity inputs.

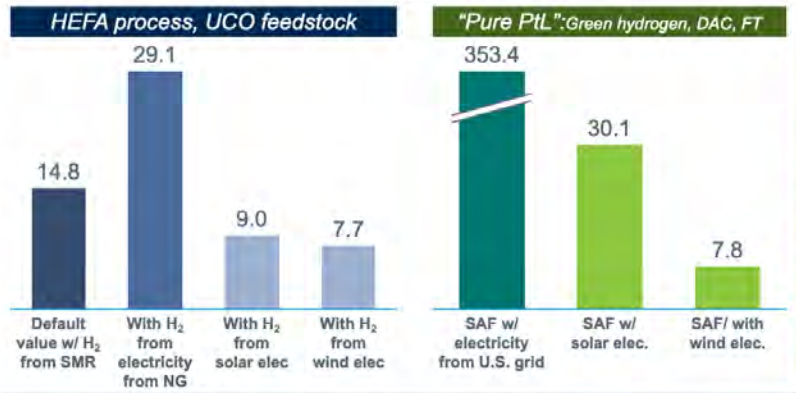

Figure 2. Electricity-based SAF production using a hydroprocessed esters and fatty acids (HEFA) pathway with used cooking oil (UCO) (left) or a "pure PtL" pathway using electrolytic hydrogen, CO_2 from direct air capture and Fischer–Tropsch conversion (right). Different hydrogen sources include steam methane reforming (SMR) and electrolytic hydrogen using different electricity sources, including natural gas (NG), solar photovoltaic, and wind electricity.

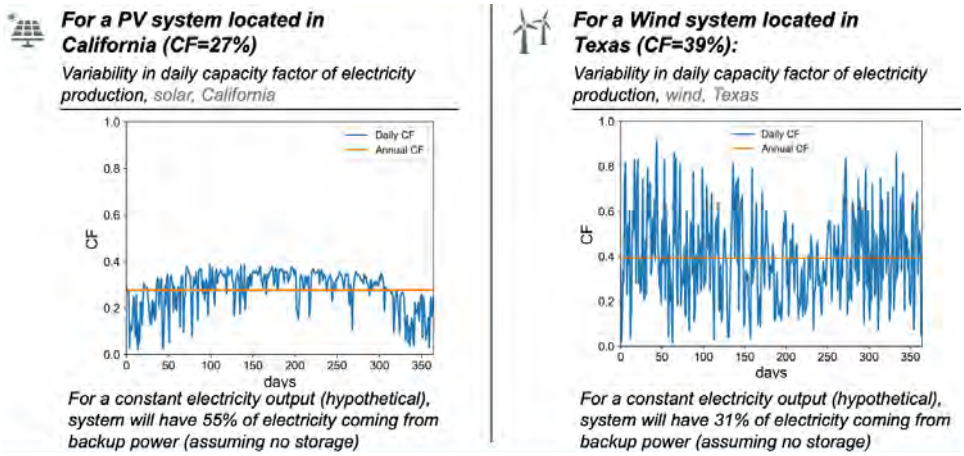

Figure 3. Impact of intermittency in solar- and wind-based electricity production on electricity availability in Texas and California. CF is the capacity factor, which reflects the availability of electricity.

Milestones

UHasselt and MIT have brought forward analyses to support progress in the areas outlined above. The results have been presented to FTG during FTG meetings and numerous subgroup and expert meetings. Most importantly, UHasselt and MIT experts participated in, and contributed to, numerous FTG meetings, including CAEP12_FTG/11 (October 2021), CAEP13_FTG/01 (May 2022), and CAEP13_FTG/02 (October 2022) (see manuscripts below).

Major Accomplishments

The MIT and UHasselt team accomplished the following under this task:

1. As co-lead of the FTG CLCA Task Group, Prof. Malina drafted CLCA progress reports for FTG meetings, where CLCA topics were discussed. In addition, Prof. Malina co-led several Task Group meetings.
2. The team helped shape preparation of the CAEP/12 meeting and contributed to the preparation of the CAEP/13 work program for FTG.
3. The MIT team led the development of CORSIA life-cycle analysis (LCA) methods for fuels requiring significant electricity input. The team worked with technical experts on identifying the fuel pathways, which rely on electricity input. Furthermore, the key issues for analysis have been identified, and further work has been scoped accordingly.

Publications

CAEP/12-FTG/11-WP/05. Summary of the work on the core LCA group since FTG/03, October 2021.
CAEP/13-FTG/01-WP/04: Core LCA approach for the tasks of the CAEP/13 cycle, May 2022.
CAEP/13-FTG/02-WP/03: Summary of the progress of the core LCA subgroup on Task S.06 and S.17, October 2022.
CAEP/13-FTG/02-WP/04: Proposed path forward on CORSIA eligible fuels (CEF) using significant electricity inputs, October 2022.
CAEP/13-FTG/02-WP/14: Actual value method for CORSIA eligible fuels (CEF) using Significant electricity inputs, October 2022.
CAEP/13-FTG/02-FL/02: Core LCA pathway discussions, October 2022.
CAEP/13-FTG/02-FL/03: Flowchart threshold, October 2022.

Outreach Efforts

Progress on these tasks was communicated during weekly briefing calls with the FAA and other U.S.-delegation members to FTG, as well as during numerous FTG teleconferences between meetings. In addition, UHasselt and MIT experts participated in, and contributed to, FTG meetings, including CAEP12_FTG/11 (October 2021), CAEP13_FTG/01 (May 2022), and CAEP13_FTG/02 (October 2022).

Student Involvement

During this reporting period, the MIT graduate student involved in this task was TJ Park.

Plans for Next Period

In the coming year, the MIT/UHasselt ASCENT Project 01 team will continue its work in FTG. Default CLCA values will be calculated and proposed for additional pathways. Prof. Malina will continue to lead the CLCA Task Group. A particular focus will be on helping to develop the actual-value method for calculating the LCA values for fuels requiring substantial electricity inputs. Close collaboration with technical experts in the ILUC and Sustainability subgroups will be pursued.

References

Frequently asked questions. (n.d.). Retrieved February 7, 2023, from https://www.icao.int/environmental-protection/CORSIA/Pages/CORSIA-FAQs.aspx

Task 2 - Support U.S. Participation in ICAO CAEP by Performing CLCA to Establish Default Values for Use Under CORSIA

Massachusetts Institute of Technology
Hasselt University

Objective

During the CAEP/11 and CAEP/12 cycle, the MIT ASCENT Project 1 team took leadership in applying the agreed-upon CLCA method to establish default CLCA values for CORSIA-eligible fuels. However, the list of pathways is not exhaustive, and further CLCA analysis is required to enable the inclusion of SAF technologies nearing commercialization. During the current reporting period, the team supported (a) an in-depth analysis of the impact of biomass-based process fuels on default CLCA values; and (b) initial analyses toward the establishment of CLCA values for Fischer–Tropsch co-processing of lipid bio-feedstocks, catalytic thermolysis, and hydroprocessed hydrocarbon (HC)–hydroprocessed esters and fatty acids (HEFA)–synthetic paraffinic kerosene (SPK).

Research Approach

Analysis of the impacts of biomass-based process fuels on CLCA values

The GHG-emission mitigation potential of the inclusion of biomass-based energy to meet the heat and power requirements of SAF conversion was explored. For this purpose, the team modeled the GHG emissions associated with heat and electricity production in a range of SAF conversion stages. For the replacement scenarios, the life-cycle inventory for the cultivation and transportation of poplar was used, with emissions from the combustion of poplar taken from the Greenhouse gases, Regulated Emissions, and Energy use in Technologies (GREET) model. Although the emissions do not depend on how the resulting energy from the biomass combustion is harnessed, they are adjusted according to conversion efficiencies. Heat generation and power generation were assumed to have 90% and 40% efficiency, respectively, thus depicting scenarios using

highly efficient technologies. Biomass-based heat and energy production was then implemented with SAF conversion processes by using the CORSIA calculation tool based on GREET v2.8 (2019). The electricity required in other stages of SAF production was assumed to be provided by the grid with a GHG-emission intensity factor equal to that for the United States. In total, four energy scenarios were defined, representing the different combinations for integrating biomass-based energy into the SAF conversion process (Table 1). The first scenario represents the current baseline and does not consider any inclusion of biomass-based energy. In contrast, Scenario 4 represents the full inclusion of biomass-based energy to meet power and heat requirements. Scenarios 2 and 3 capture biomass-based heat or electricity use, respectively.

Table 1. Definition of the short-term SAF production scenarios.

Energy scenario	Use of electricity from the grid	Use of natural gas	Remarks
1	Yes	Yes	Reference scenario (default LCA values without ILUC)
2	No	Yes	Effect of natural gas
3	Yes	No	Effect of electricity from the grid
4	No	No	Combined biomass-based energy integration

The avoided GHG emissions associated with the inclusion of biomass-based energy into the conversion stage are shown in Table 2. Because the Fischer-Tropsch (FT) and Synthesized Isoparaffins (SIP) pathways are self-sufficient in terms of energy requirements, they are not affected by the inclusion of biomass-based energy. For all other pathways, the GHG mitigation potential of the inclusion of the biomass-based electricity is <3 g CO_{2e}/MJ_{SAF}, with the exception of ethanol alcohol-to-jet (ATJ)- or isobutanol ATJ-based SAF production using corn grain (GHG mitigation potential of 6–7 g CO_{2e}/MJ_{SAF}). In comparison, the GHG-emission reduction potential of biomass-based heat production is high for almost all SAF production pathways, reaching 30 g CO_{2e}/MJ_{SAF}.

Table 2. Avoided GHG emissions due to the inclusion of biomass-based energy in the SAF conversion stage. Data are in g CO_2e/MJ_{SAF}.

	Fossil energy source	1	2	3	4
	Electricity				
	Natural gas				
Pathway	Feedstock				
HEFA	*Brassica carinata*	0.00	1.40	7.13	8.53
	Corn oil	0.00	0.50	4.66	5.16
	Palm fatty acid distillate	0.00	1.00	5.60	6.60
	Palm oil	0.00	0.87	4.70	5.57
	Rapeseed/canola	0.00	1.45	7.60	9.05
	Soybean	0.00	1.53	7.67	9.19
	Tallow	0.00	0.60	6.97	7.58
	Used cooking oil (UCO)	0.00	0.60	6.97	7.58
Ethanol ATJ	Agricultural residues	0.00	2.96	19.37	22.34
	Corn grain	0.00	6.78	24.03	30.81
	Forest residues	0.00	2.57	14.13	16.71
	Miscanthus	0.00	2.57	11.59	14.16
	Switchgrass	0.00	2.57	11.59	14.16
	Sugarcane	0.00	0.00	0.00	0.00
Isobutanol ATJ	Agricultural residues	0.00	0.01	5.87	5.88
	Corn grain	0.00	6.18	20.84	27.01
	Forest residues	0.00	0.01	3.04	3.05
	Miscanthus	0.00	0.58	9.89	10.47
	Sugarcane	0.00	0.00	1.33	1.33
	Switchgrass	0.00	0.02	9.31	9.32
FTJ	Corn Stover	0.00	0.00	0.00	0.00
	Forest residues	0.00	0.00	0.00	0.00
	Miscanthus	0.00	0.00	0.00	0.00
	MSW	0.00	0.00	0.00	0.00
	Switchgrass	0.00	0.00	0.00	0.00
	Wheat Straw	0.00	0.00	0.00	0.00
SIP	Sugarcane	0.00	0.00	0.00	0.00
	Sugarbeet	0.00	0.00	0.00	0.00

Evaluation of Fischer–Tropsch co-processing, catalytic thermolysis, and HC-HEFA-SPK
Work has been initiated to obtain the necessary data for the modeling of these pathways from producers. For the catalytic hydrothermolysis pathway, a first-order LCA was conducted.

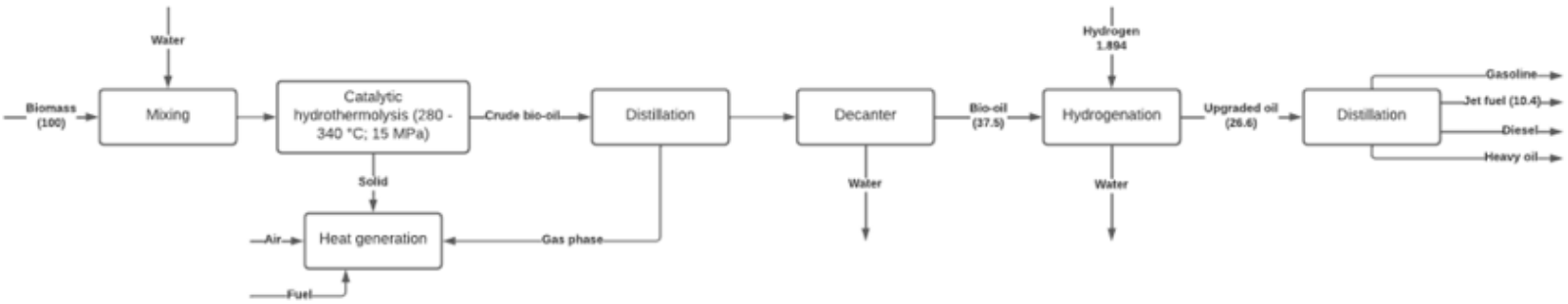

Figure 4. Flowchart of the catalytic hydrothermolysis pathway.

As shown in Figure 4, the catalytic hydrothermolysis pathway transforms biomass into bio-oil by using hot pressurized water (at 280–340°C and 15 MPa). Publicly available data are limited regarding the mass and energy balances of the process. The life-cycle GHG emissions of SAF production via catalytic hydrothermolysis have been estimated to fall between 17 and 43 g CO_2eq/MJ_{SAF}.

Milestones

The work described above has been documented in working papers and information papers submitted to FTG. Furthermore, the team discussed the work outlined above with various technical experts. UHasselt and MIT experts participated in, and contributed to, the FTG meetings held during the reporting period, including CAEP12_FTG/11 (October 2021), CAEP13_FTG/01 (May 2022), and CAEP13_FTG/02 (October 2022).

Major Accomplishments

The MIT and UHasselt team accomplished the following under this task:

1. The team finished a comprehensive assessment of the quantitative impact of the inclusion of process biomass fuels on life-cycle GHG emissions of different SAFs.
2. The team developed a first assessment of new pathways to be considered for CLCA analysis in the future.
3. The team published a journal publication on the CORSIA default values (see below).

Publications

Peer-reviewed journal publications

Prussi, M., Lee, U., Wang, M., Malina, R., Valin, H., Taheripour, F., Velarde, C., Staples, M. D., Lonza, L., & Hileman, J. I. (2021). CORSIA: The first internationally adopted approach to calculate life-cycle GHG emissions for aviation fuels. *Renewable and Sustainable Energy Reviews*, *150*, 111398. doi: 10.1016/j.rser.2021.111398

Written reports

CAEP/12-FTG/11-WP/05. Summary of the work on the core LCA group since FTG/03, October 2021.
CAEP/13-FTG/01-WP/04: Core LCA approach for the tasks of the CAEP/13 cycle, May 2022.

Outreach Efforts

Progress on these tasks was communicated during weekly briefing calls with the FAA and other U.S.-delegation members to FTG, as well as during numerous FTG teleconferences between meetings. In addition, UHasselt and MIT experts participated in, and contributed to, FTG meetings, specifically CAEP12_FTG/11 (October 2021), CAEP13_FTG/01 (May 2022), and CAEP13_FTG/02 (October 2022). Professor Malina also presented the default CLCA values at the 2022 FAA AEC Emissions Roadmap meeting in May 2022.

Plans for Next Period

The team will continue to perform attributional CLCA to establish default values for use under CORSIA. More specifically, the team expects to support efforts to determine CLCA values for mixed animal fat HEFA, mixed animal fat co-processing, and FT co-processing. The team will also conduct a comprehensive local sensitivity analysis to understand the sensitivity of the CLCA default values to changes in input parameters. This process will guide FTG in defining requirements for different types of SAF to qualify under a certain default value.

Task 3 - Contribute to the Development of the Fuel Production Assessment for CORSIA-eligible Fuels

Hasselt University
Massachusetts Institute of Technology

Objective

The team aimed to contribute to the development of the fuel production assessment for CORSIA-eligible fuels to the year 2035, on the basis of detailed information gathered in a fuel production database. The data were further extrapolated to the year 2050. During the reporting period, the team worked jointly with researchers from Washington State University to finalize fuel production estimates for the long-term aspirational goal (LTAG) report, including the availability of fuels from biomass and waste streams, as well as waste CO_2 sources and atmospheric CO_2 (direct air capture). For the latter pathways, detailed modeling was developed under ASCENT Project 52.

Research Approach

The research team maintains a short-term projection database of publicly available production announcements from companies planning to produce SAFs over the next 5 years. Using this database, and a set of criteria and assumptions, the team modeled a short-term SAF production ramp-up under five production scenarios (low, moderate, high, high+, and max). These scenarios differed with respect to the types of companies included, the maturity of the production plans, and the assumptions concerning product slate and the success rates of the announced production plans. The resulting ramp-ups from each scenario were taken as a starting point to forecast SAF production to 2035, assuming a diffusional approach, which was then extended to 2050. For fuels that leverage waste CO_2 sources from industrial installations and from direct air capture, electricity-based SAF production via the Fischer–Tropsch process with hydrogen produced from low-carbon electricity via electrolysis was considered. The availability of renewable electricity and CO_2 sources are modeled as factors limiting the availability of these SAFs.

The scenarios were combined to obtain insights into the scale-up curves for SAF production. The results (Figure 5) indicate that, even in the most favorable scenarios, neither biofuels nor PtL alone could fully displace conventional jet fuel by 2050. In contrast, a combination of both technologies would enable full replacement by 2045 (in the most optimistic case). Regarding total emissions, using either technology alone would leave the aviation industry with annual emissions of at least 300 Mt/year because of limited scale-up potentials and residual emissions. A combination of both fuel pathways with emphasis on PtL production could minimize emissions. We note that the combined potential of biofuels and PtL exceeds the maximum jet fuel demand in 2050 under the moderate and high scenarios. If preference were given to biomass-based SAFs (covering the remaining volumes with PtL-based SAFs), the net emissions would reach 265–709 Mt CO_2eq. In contrast, if preference were given to PtL-based SAFs, the net emissions would reach 218–350 Mt CO_2eq.

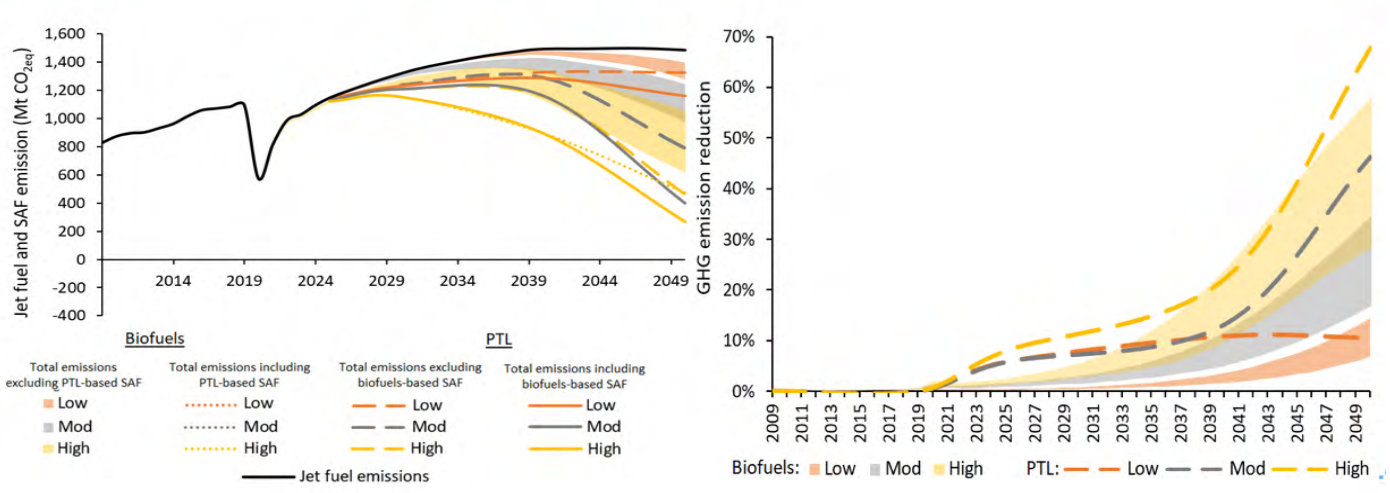

Figure 5. GHG emissions of the aviation industry (left) using SAFs, and SAF decarbonization potential (right) under the analyzed scenarios.

Milestone

Both the SAF production scenarios and the fuel production scenarios for fuels produced from waste CO_2 and atmospheric CO_2 provide the scientific basis for the fuel availability assessments under LTAG.

Major Accomplishments

The team developed comprehensive scenarios of future availability of SAFs and provided the data as input to LTAG. The results were included in the LTAG report.

Publications

Written reports

ICAO (2022). *Report on the Feasibility of a Long-term Aspirational Goal (LTAG) for International Civil Aviation CO_2 Emission Reductions*. https://www.icao.int/environmental-protection/LTAG/Pages/LTAGreport.aspx

Outreach Efforts

Progress on these tasks was communicated during weekly briefing calls with the FAA and other U.S.-delegation members to FTG, as well as during numerous FTG and LTAG teleconferences. Results have been included in the LTAG report and are regularly presented as part of the results.

Plans for Next Period

The team will continue to update scenarios and projections as needed.

Task 4 - Develop Methods for Probabilistic Life-cycle Analyses and Probabilistic Techno-economic Analyses of SAFs

Massachusetts Institute of Technology

Objective

Analysis of the potential for U.S.-based SAF production

Work conducted under this project in previous reporting periods has shown that the availability of biomass may limit biomass-based SAF production in the United States. During the current reporting period, the team aimed to understand pathways for increasing SAF supply, including expanding land use for biomass production, rerouting existing biomass production, and decoupling SAF production from bioenergy supply through PtL pathways. The rerouting of biomass

production was specifically considered for ethanol. As electric cars are adopted in the United States, the demand for ethanol from the road sector is expected to decrease, thereby offering additional potential for SAF production.

Analysis of approaches for reducing the carbon footprint of U.S.-based SAF production
Under the SAF Grand Challenge, the minimum reduction in life-cycle GHG emissions for SAF volumes to be counted against the goals of the challenge is a 50% (89 gCO_2e/MJ to 44.5 gCO_2e/MJ) (DOE, 2022). As shown in the current CORSIA default life-cycle emissions assessments, many fuels might not meet this target (Figure 6). The team analyzed potential levers for reducing the life-cycle GHG emissions of different pathways and worked toward understanding the maximum decarbonization potential of SAFs while considering process innovation. Such an analysis not only is important for the SAF Grand Challenge but also supports the long-term ambitions of the aviation sector to reach net-zero CO_2 emissions.

Research Approach

Analysis of potentials of U.S.-based SAF production
Previous studies performed by this team have shown that the United States might not be able to produce sufficient biomass for meeting 2035 U.S. jet fuel demand with bio-based SAFs through expanding agricultural land use, because of limited land availability and suitability. During this reporting period, the team analyzed whether additional pastureland conversion could mitigate these concerns. According to the analysis, approximately 40% of existing pastureland in the United States would need to be converted to cropland to produce sufficient energy crops. Such a conversion is possible under aggressive assumptions for pastureland requirements.

Another approach for meeting the demand could rely on rerouting ethanol from road transportation into SAF production. In the most optimistic biomass availability scenario, an additional 10.5 billion gallons of ethanol would be needed to meet 2035 jet fuel demand. In 2021, the United States produced a total of approximately 17.5 billion gallons of ethanol; therefore, approximately 60% of the total ethanol production would be needed to close the gap in SAF production.

The team also assessed how PtL-based SAFs could help increase SAF supply. According to a preliminary assessment assuming current technology, the cost of such a scenario would be very high. However, future process innovation could make such a strategy more realistic.

Analysis of approaches for reducing the carbon footprint of U.S.-based SAF production
Because the SAF Grand Challenge focuses on the United States, the team initially analyzed SAF production by using feedstocks grown in North America, specifically soybean, rapeseed/canola, camelina, carinata (*Brassica carinata*), and corn. Figure 6 shows the considered pathways as well as their associated CLCA, ILUC, and total life-cycle emissions (LSf) CO_2e values published under the CORSIA default values. As shown, SAFs from HEFA soybean and rapeseed, and from ATJ and ethanol-to-jet (ETJ) corn grain currently may not qualify for the SAF Grand Challenge target of 44.5 gCO_2e/MJ. SAFs from HEFA camelina and carinata already meet the SAF Grand Challenge target because of negative ILUC values. Similarly, HEFA corn has an ILUC value of zero, because the corn oil from DDGS is considered a by-product (ICAO, 2022B). We note that the default values presented here reflect default assumptions; individual producers might have implemented innovations to reduce the life-cycle GHG emissions of their processes.

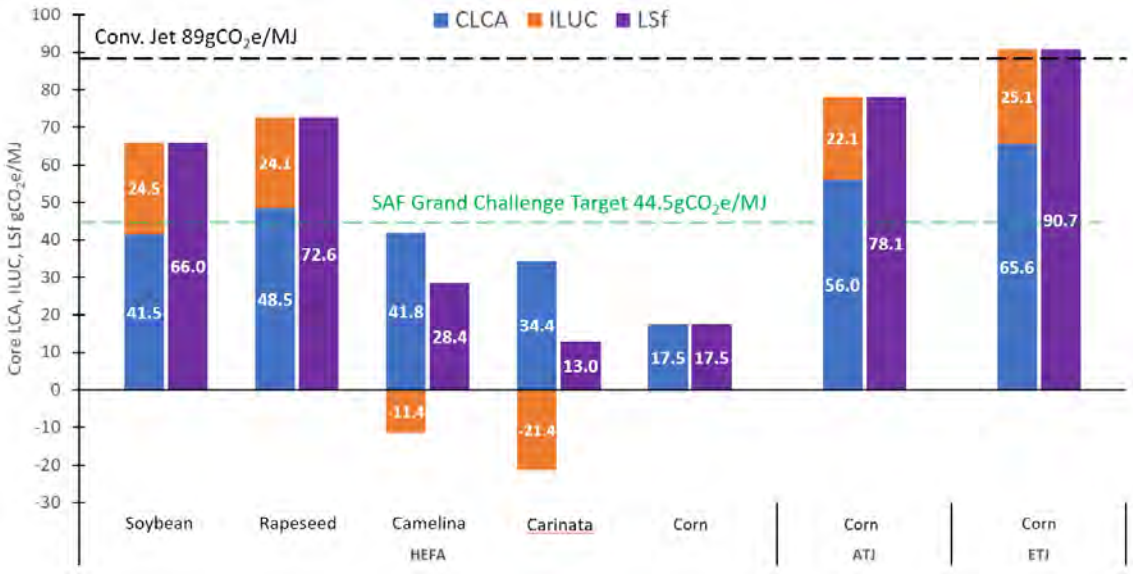

Figure 6. CORSIA default values for CLCA, ILUC, and LSf for HEFA, ATJ, and ETJ fuels from North American agricultural feedstocks. Note that individual producers might have introduced process innovations to reduce life-cycle GHG emissions.

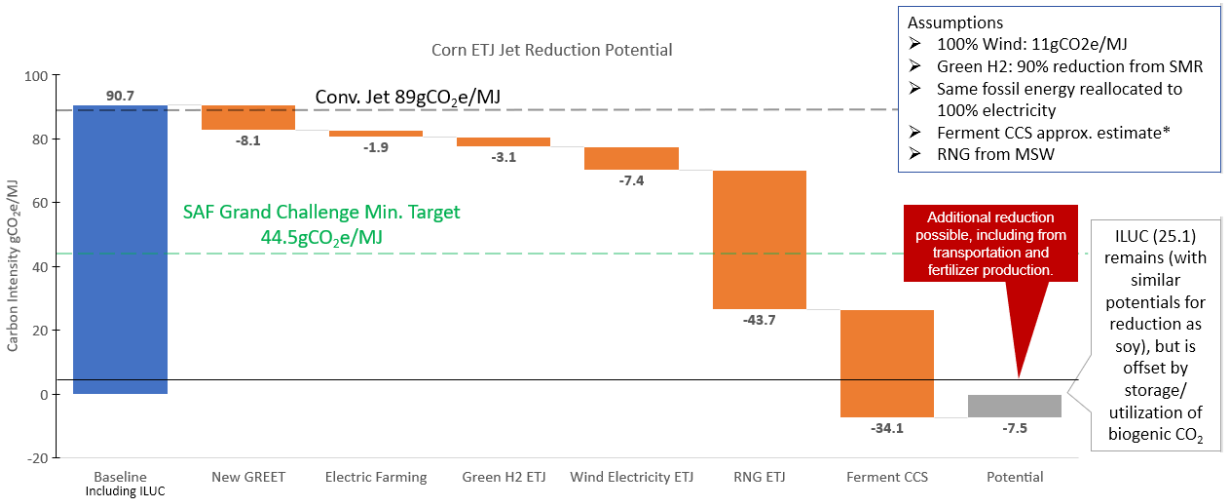

Figure 7. Corn grain ethanol-to-jet potential CO_2 reductions from the current CORSIA LSf value.

The team then analyzed how the soybean- and corn-based processes could be optimized to reduce GHG emissions. The corn grain ETJ process and the HEFA soybean process were considered for that purpose.

Through detailed analysis, the following approaches for GHG emissions savings were identified for the corn ETJ process (Figure 7):

1. Natural gas combustion: The default values for the corn ETJ process were calculated with GREET 2011. Assuming improved technology, lower emission factors for natural gas handling and combustion (Argonne National Laboratory, 2022) can be used, thus leading to an emissions saving of 8.1 gCO_2e/MJ.
2. Electric farming: If all fossil fuel use in farming is replaced with electric energy (e.g., electric tractors), a 1.9 gCO_2e/MJ reduction can be achieved if the electricity is sourced from 100% wind energy (emissions factor of 11 gCO_2e/MJ).

3. Hydrogen use: If all H_2 used in the fuel conversion process is sourced from electrolysis using 100% wind electricity (instead of steam methane reformation), a 3.1 gCO_2e/MJ life-cycle GHG emissions reduction can be achieved.
4. Electricity use: If the U.S. grid electricity used in the fuel conversion step is replaced by 100% wind electricity, 7.4 gCO_2e/MJ can be eliminated from the life-cycle GHG emissions.
5. Heat production: If all fossil natural gas use in the fuel conversion stage is replaced with renewable natural gas sourced from municipal solid waste, a savings of 43.7 gCO_2e/MJ is achievable.
6. Carbon capture: If biogenic CO_2 emissions from the ethanol fermentation step is captured and permanently stored, the life-cycle GHG emissions of the fuel can be reduced by 34.1 gCO_2e/MJ reduction (Spaeth, 2021).

Together, if all these measures are implemented, the corn ETJ process could be brought to negative life-cycle GHG emissions at −7.5 gCO_2e/MJ of SAF. Further reductions could be achieved, for example by including green fertilizer, by decarbonizing feedstock and fuel transportation, or by applying agricultural practices that decrease ILUC emissions. These reductions would allow SAFs from the ETJ process to not only meet the SAF Grand Challenge qualification target but also be compatible with the aviation sector's long-term decarbonization ambitions.

A similar analysis was conducted for the HEFA soybean process (Figure 8). The analysis shows that the LSf value of the process could be reduced to 35.9 gCO_2e/MJ (including ILUC), thereby meeting the SAF Grand Challenge qualification target. Again, additional reductions would be possible from green fertilizer, decarbonized transport of feedstock and fuel, and low land use change farming practices. However, the emissions reductions of this process are inherently limited, partly because of the emissions associated with the growing cycle of the soybean plant itself.

Figure 8. HEFA soybean SAF potential CO_2 reductions from the current CORSIA LSf value.

Milestone

A baseline analysis has been completed and is being prepared for publication in the scientific literature. The SAF Grand challenge analysis of life-cycle emissions has been completed.

Major Accomplishments

First presentation of results and discussion with stakeholders.

Publications

None.

Outreach Efforts
MIT presented the work under this task to the ASCENT 1 Team meeting in May 2022 and to the ASCENT Fall meeting in October 2022.

Student Involvement
The MIT graduate students involved in this task were Sarah Demsky and TJ Park.

Plans for Next Period
MIT will continue to apply and refine the regional stochastic modeling, specifically focusing on PtL as well as cover crops and double-cropping. In addition, together with WSU, MIT will assess the costs of optimized SAF production pathways.

References
Argonne National Laboratory. (2022). *GREET Aviation Module.* https://greet.es.anl.gov/greet_aviation

ICAO. (2022). *CORSIA Default Life Cycle Emissions Values for CORSIA Eligible Fuels.* https://www.icao.int/environmental-protection/CORSIA/Documents/CORSIA_Eligible_Fuels/ICAO%20document%2006%20-%20Default%20Life%20Cycle%20Emissions%20-%20June%202022.pdf

ICAO. (2022). *CORSIA Eligible Fuels – Life Cycle Assessment Methodology (CORSIA Supporting Document).* https://www.icao.int/environmental-protection/CORSIA/Documents/CORSIA_Eligible_Fuels/CORSIA_Supporting_Document_CORSIA%20Eligible%20Fuels_LCA_Methodology_V5.pdf

Kelso, W. (2021). *Cost optimization of us sustainable aviation fuel supply chain under different policy constraints* [Thesis, Massachusetts Institute of Technology]. https://dspace.mit.edu/handle/1721.1/140169

Office of Energy Efficiency & Renewable Energy. (2022). *Sustainable Aviation Fuel Grand Challenge.* https://www.energy.gov/eere/bioenergy/sustainable-aviation-fuel-grand-challenge.

Spaeth, J. (2021). *Sustainable aviation fuels from low-carbon ethanol production.* Energy.gov. Retrieved May 20, 2022, from https://www.energy.gov/eere/bioenergy/articles/sustainable-aviation-fuels-low-carbon-ethanol-production

Task 5 - Support Coordination of All A01 Universities' Work on SAF Supply Chain Analyses
Massachusetts Institute of Technology

Objective
The objective of this task is to provide support for coordination of all ASCENT Project 1 (A01) universities' work on SAF supply chain analysis. The sharing of methods and results decreases the replication of A01 universities' work on similar topics.

Research Approach
The MIT A01 team performed several functions to accomplish this task. Specifically, the team:
- Participated in the bi-weekly A01 coordination teleconferences, which served as a venue to discuss progress in various grant tasks and learn about the activities of other ASCENT universities, and also presented current research on co-processing to the A01 universities
- Contributed to efforts for developing a special journal issue on SAFs, based on the research conducted under A01

Milestone
The MIT ASCENT A01 team presented current research to other ASCENT universities.

Major Accomplishments
The major accomplishments associated with this task include participation in bi-weekly A01 coordination teleconferences; presentation of current research to other ASCENT universities; and contribution to the development of a journal special issue.

Publications
None.

Outreach Efforts
See above.

Awards
None.

Student Involvement
None.

Plans for Next Period
Continued engagement in bi-weekly teleconferences and other events to disseminate MIT's A01 work.

Project 002 Ambient Condition Corrections for Nonvolatile Particulate Matter Emissions Measurements

Missouri University of Science and Technology, Aerodyne Research Inc., and Honeywell

Project Lead Investigator

Philip D. Whitefield
Professor Emeritus of Chemistry
[Department of Chemistry]
Missouri University of Science and Technology
400 W 11th Street, Rolla, MO 65409
573-465-7876
pwhite@mst.edu

University Participants

Missouri University of Science and Technology (MS&T)

- P.I.: Philip D. Whitefield, Professor Emeritus of Chemistry
- FAA Award Number: 13-C-AJFE-MST, Amendments 002, 003, 005, 008, 010, 012, and 019
- Period of Performance: September 18, 2014 to June 30, 2023
- Task:
    1. Collect nonvolatile particulate matter (nvPM) data in a combustor rig to assess ambient effects on nvPM emissions

Project Funding Level

Project	Funding	Matching	Source
13-C-AJFE-MST-002	$1,288,836.34	$1,288,836.34	EMPA letter
	$284,613.66	$284,613.66	Transport Canada
13-C-AJFE-MST-003	$500,000.00	$500,000.00	EMPA letter
13-C-AJFE-MST 005	$500,000.00	$500,000.00	EMPA letter
13-C-AJFE-MST-008	$579,234.00	$579,234.00	EMPA letter
13-C-AJFE-MST-010	$725,500.00	$725,500.00	EMPA letter
13-C-AJFE-MST-012	$1,217,221.00	$1,217,221.00	EMPA letter
13-C-AJFE-MST-019	$521,246.00	$521,246.00	GE letter

Investigation Team

- Professor Philip Whitefield, P.I., Missouri University of Science and Technology (Task 1)
- Steven Achterberg, Research Technician, Missouri University of Science and Technology (Task 1)
- Max Trueblood, Research Technician, Missouri University of Science and Technology (Task 1)
- Dr. Richard Miake-Lye, Subcontractor, Aerodyne Research, Inc. (Task 1)
- Rudy Dudebout, Subcontractor, Honeywell Aerospace (Task 1)
- Paul Yankowich, Subcontractor, Honeywell Aerospace (Task 1)

Project Overview

During this reporting period, the MS&T/Aerodyne team collaborated with Honeywell to collect and interpret nvPM data for a combustor rig to assess ambient effects on nvPM emissions.

Task 1 - Collect nvPM Data in a Combustor Rig to Assess Ambient Effects on nvPM Emissions

Missouri University of Science and Technology

Objectives

The nvPM emissions from aircraft engines are affected by changing inlet conditions. A combustor rig test provides the most flexibility for quantifying the impact of changing conditions on nvPM emissions and developing methods for use in inventory modeling. The MS&T/Aerodyne team has worked with Honeywell to conduct combustor rig tests, collect nvPM mass and number emissions data, and perform data analysis to determine predictive emissions index models and nvPM ambient corrections.

Research Approach

Research Goals

- Define and assemble a standardized nvPM measurement system that will include the same Mobile Measurement System used to sample nvPM from 25 Honeywell HTF7350 production engines in 2017
- Design and fabricate the nvPM emission rakes and combustor rig adaptive hardware required to enable nvPM and gaseous emissions data to be acquired from Honeywell's existing HTF7000 Combustor Test Rig
- Perform four combustor rig tests with Jet A and three alternative fuels
- Vary combustor test conditions (derived from engine cycle performance analysis, covering a range of engine ambient inlet conditions on the ground and at altitude), and measure nvPM emissions
- Analyze data to inform performance-based nvPM emissions modeling for all altitudes

Summary of the Jet A data set for the Honeywell HTF7000 Combustor Rig Measurements

Six different temperature points (idle to 100% thrust) were studied as a function of corrected flow, fuel/air ratio, and pressures. One-factor-at-a-time perturbations enabled exponents to be calculated for each control variable. Facility constraints limited the measurements to approximately half of the 100% Landing and Take Off (LTO) full engine pressure. EIm, nvPM number (EI#), NO_x, CO, Unburned Hydrocarbons (UHC) and smoke numbers were gathered, and the following correlating parameters were evaluated: Combustor inlet pressure (P_3), combustor inlet temperature (T_3), combustor primary zone, equivalence ratio (ϕ_{PZ}), and combustor referred flow (correlates with pressure drop). Other parameters also assessed were exit temperature (T_4), overall fuel/air ratio, residence time, and primary zone temperatures. Best-fit functions were developed for both EIm and EI#.

$$EIm = 6.14 \times \left(\frac{W_{3c}}{W_{3c,\,100\%}}\right)^{(-30*e^{-0.5*\delta_3})} \times {\delta_3}^{(\varphi_{PZ})^{3.2}} \times (\varphi_{PZ})^{(-12.6*(\varphi_{PZ}-0.97)*(\delta_3)^{\,0.35})}$$

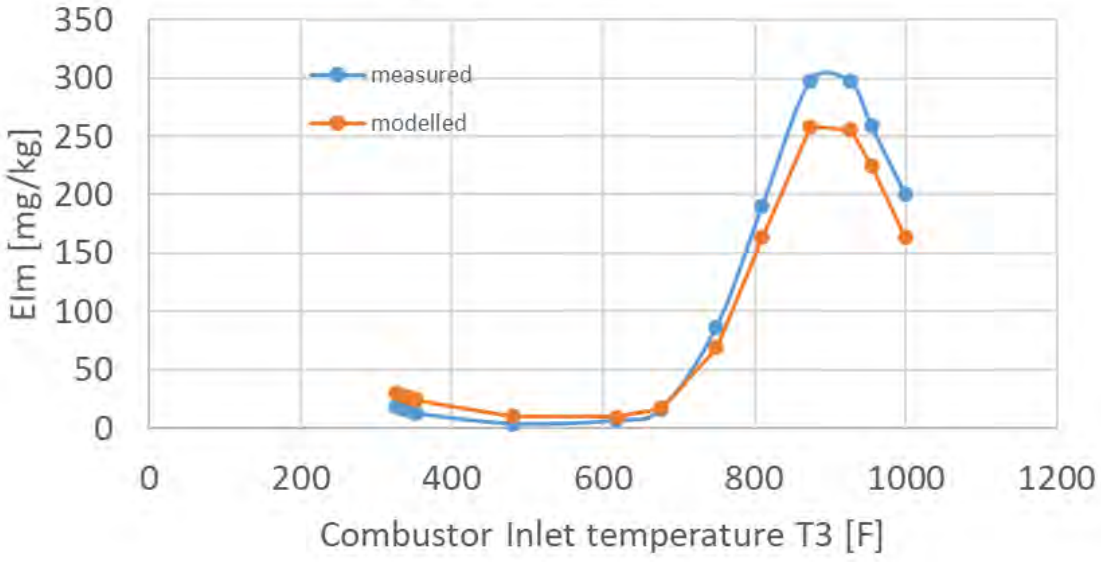

$$EI\# = 1.8025 \times 10^{15} \times \left(\frac{w_{3c}}{w_{3c,100\%}}\right)^{(-5*e^{-0.2*\delta_3})} \times e^{0.1083\times\delta_3} \times {\theta_3}^{-2.17} \times e^{-\left(\frac{(\ln(\varphi_{PZ})-0.06)^2}{2\times 0.22^2}\right.}$$

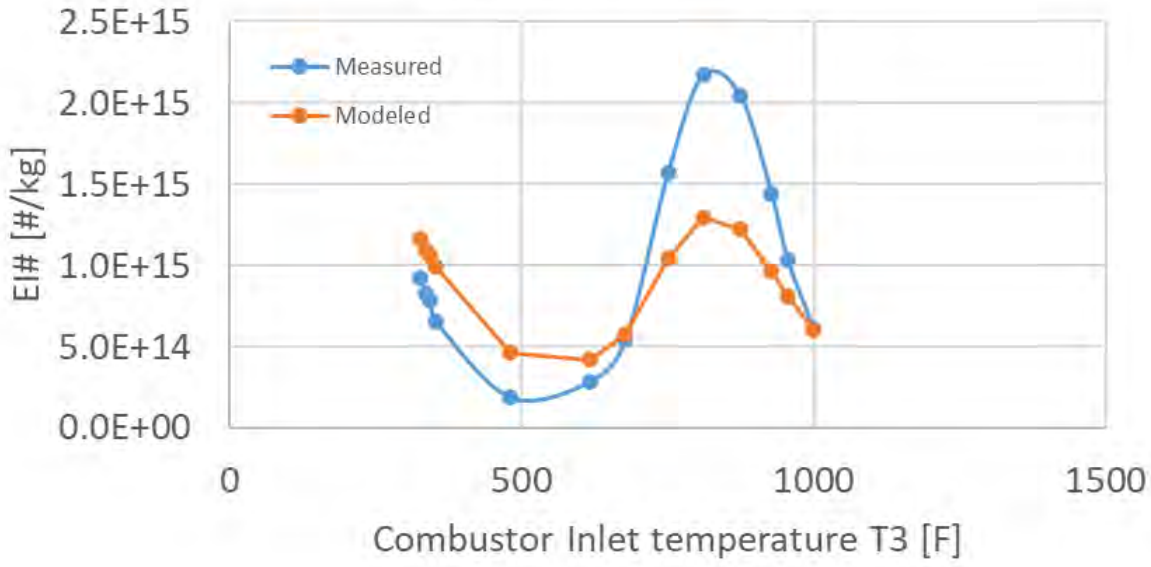

Conclusions

- Mass and number-based emission indices (EIm and EI#) nvPM models have been developed that have good predictive capability, including capturing non-monotonic behaviors.
- The model also appears to capture trends observed in various different Turbofan engines that could be associated with design and operating conditions.

Milestones

A rig test matrix has been devised and executed for burning exclusively Jet A. Detailed data analysis has been performed during this reporting period. An outstanding dataset has been acquired, albeit under the constraints of the ongoing pandemic protocol restrictions. The entire North American Reference System could not be deployed, because of travel restrictions associated with the pandemic protocol; however, critical nvPM size measurement capabilities (Cambustion DMS500) were deployed, and their operation was monitored remotely, thus yielding a synchronized size dataset. Analysis of the size data has been completed.

Major Accomplishments

- Honeywell and the MS&T/Aerodyne team have assembled two standardized nvPM emissions measurement systems.
- Honeywell has completed the design and fabrication of rakes and adaptive rig hardware required to enable nvPM emissions measurements in the HTF7000 Combustor Test Rig.
- The calibrations required for the Honeywell and North American Reference System nvPM measurement systems expired. Thus, these instruments have undergone recalibration.
- Specifically, data for six different temperature points ranging from idle to 100% thrust with associated variations in corrected flow, fuel air ratio, and pressures were studied with Jet A as the candidate fuel. Facility pressure limitations resulted in a pressure limit of approximately half of the 100% landing and takeoff full-engine pressure. The reported mass-based emissions index (EIm) and noise-based emissions index data were corrected for thermophoretic loss. A summary of the data interpretation to date is given below.

Publications

Published conference proceedings

Re-Examination of Engine-to-Engine PM Emissions variability using an ARP Reference Sampling and Measurement System. Presented at ASCENT Advisory Board Meeting in Alexandria VA 5 April 2022.

ASCENT Project 002: to characterize the non-volatile Particulate Matter (nvPM) emissions and develop predictive emission functions for a series of conventional and synthetic alternative jet fuels. Presented at the Coordinating Research Council (CRC) Aviation Meeting Properties and Emissions" session May 5th 2022.

Outreach Efforts

- Results were presented at the Coordinating Research Council Aviation meeting, May 2022.
- A non-disclosure agreement has been established between Honeywell and the research team led by Prof. Raymond Speath at MIT, and the data sets arising from the measurements described in this report have been shared between Honeywell and MIT.

Awards

None.

Student Involvement

No graduate students were employed in this task; however, four undergraduate research assistants (Dominic Torre, Zachary Alton, Aleck Barchenski, and Zachary Achterberg) were employed in pretest activities, including individual component testing and calibration and data reduction and interpretation.

Plans for Next Period

- Re-install and perform a shake-down test of the nvPM combustor rig measurement system with rig in the test cell
- Conduct a rig test with Jet A and three sustainable aviation fuel blends (phase II)

Project 003 Cardiovascular Disease and Aircraft Noise Exposure

Boston University

Project Lead Investigator

Junenette L. Peters
Associate Professor
Department of Environmental Health
Boston University School of Public Health
715 Albany St., T4W, Boston, MA 02118
617-358-2552
petersj@bu.edu

University Participants

Boston University (BU)

- P.I.s: Prof. Jonathan Levy (university P.I.), Prof. Junenette Peters (project P.I.)
- FAA Award Number: 13-C-AJFE-BU-016
- Period of Performance: October 1, 2021 to September 30, 2022

Massachusetts Institute of Technology (MIT)

- Sub-P.I. and co-P.I.: Prof. R. John Hansman (sub-P.I.), Dr. Florian Allroggen (sub-co-P.I.)

Tasks (performance period)

Related to 2018 FAA Reauthorization, Section 189, Tasks 1–3:

1. Present results of analysis of hypertension and aircraft noise exposure based on the day–night average sound level (DNL) metric, and generate new results on exposure to nighttime noise
2. For supporting analysis
   a. Write up and publish final results of supporting analysis of sociodemographic patterning of aircraft noise exposure
   b. Generate final results and write up supporting analyses of trends in aircraft noise exposure
3. Generate final results and write up analysis of sleep quantity and quality, and aircraft noise exposure
4. Generate final results on cardiovascular disease (CVD) and aircraft noise exposure
5. Generate preliminary results on intermediate risk marker (adiposity) and aircraft noise exposure

Related to 2018 FAA Reauthorization, Section 189, Tasks 4 and 5:

6. Develop a model for measuring changes in business activities attributable to aircraft noise exposure, prototype a model city, and include an assessment comparing a change in the visibility of aircraft due to a change in aircraft flight paths

Related to 2018 FAA Reauthorization, Section 189, all tasks:

7. Draft a report on the study results for policy-makers

Project Funding Level

Total funding (3-year funding): $1,729,286
Matching funds: $1,729,286
Sources of matching funds: Nonfederal donors to the Nurses' Health Study (NHS), Health Professional Follow-up Study (HPFS), and Women's Health Initiative (WHI) cohorts

Investigation Team

Junenette Peters, P.I., Boston University
Dr. Peters is responsible for directing all aspects of the proposed study, including study coordination, design and analysis plans, and co-investigator meetings.

Jonathan Levy, Boston University
Dr. Levy will participate in noise exposure assessment and provide expertise in the areas of predictive modeling and air pollution.

Francine Laden, Jaime Hart, and Susan Redline, Harvard Medical School/Brigham and Women's Hospital
Dr. Laden is our NHS and HPFS sponsor for this ancillary study. Dr. Hart will assign aircraft noise exposures to the geocoded address history coordinates of each cohort member. Dr. Laden and Dr. Hart will also assist in documenting data from the NHS and HPFS, on the basis of their previous experience in research on air pollution and chronic disease outcomes in these cohorts, and in performing appropriate analyses of hypertension and cardiovascular outcomes. Dr. Redline will lead efforts related to noise and sleep disturbance in the NHS and WHI.

John Hansman and Florian Allroggen, Massachusetts Institute of Technology
Dr. Hansman will participate in the economic impact assessment and will provide expertise on analytical approaches for quantifying noise. Dr. Allroggen will perform an economic impact assessment based on his expertise in analyzing the societal costs and benefits of aviation.

Project Overview

Exposure to aircraft noise has been described as "the most readily perceived environmental impact of aviation" in communities surrounding airports (Wolfe et al., 2014). Exposure to aircraft noise has been associated with physiological responses and psychological reactions (Bluhm & Eriksson, 2011; Hatfield et al., 2001) including sleep disturbances, sleep-disordered breathing, nervousness, and annoyance (Hatfield et al., 2001; Rosenlund et al., 2001). Recent literature, primarily from European studies, has provided evidence of a relationship between aircraft noise and self-reported hypertension (Rosenlund et al., 2001), elevated blood pressure (Evrard et al., 2017; Haralabidis et al., 2008; Haralabidis et al., 2011; Jarup et al., 2008; Matsui et al., 2004), antihypertensive medication use (Bluhm & Eriksson, 2011; Floud et al., 2011; Franssen et al., 2004; Greiser et al., 2007), and the incidence of hypertension (Dimakopoulou et al., 2017; Eriksson et al., 2010). However, the extent to which aircraft noise exposure increases the risk of adverse health outcomes is not well understood. Impacts related to annoyance have been empirically studied with the stated preference approach (Bristow et al., 2015) and the revealed preference approach, which often relies on analyses of transaction prices for residential properties (Almer et al., 2017; Kopsch, 2016; Wadud, 2013). Although the impacts of aircraft noise on individuals are well understood, little evidence has been presented regarding the impact of aircraft noise exposure on businesses in communities located beneath flight paths. Section 189 of the FAA Reauthorization Act of 2018 (Pub. L. 115–254) calls for a study on the potential health and economic impacts attributable to aircraft overflight noise.

The goal of this ongoing project is to examine the potential health impacts attributable to noise exposure resulting from aircraft flights; this project leverages ongoing work within ASCENT to respond to Section 189. This study aims to assess the potential associations between aircraft noise exposure and outcomes such as sleep disturbance and elevated blood pressure. The study will leverage existing collaborations with well-recognized and respected studies that have followed more than 250,000 participants through courses of their lives to understand factors that affect health. These studies include the NHS and HPFS. Furthermore, this work is aligned with a concluded National Institutes of Health-funded effort that examined these associations in the WHI. The research team is leveraging aircraft noise data for 90 U.S. airports from 1995 to 2015, generated with the Aviation Environmental Design Tool; these data are being linked to demographic, lifestyle, and health data for the participants in long-term health studies. These studies provide considerable geographic coverage of the United States, including all geographic areas specified in Section 189.

This work also responds to the aspect of Section 189 calling for the study of economic harm or benefits for businesses located in communities underneath regular flight paths. The study involves a first-of-its-kind empirical assessment of the economic impacts on businesses located beneath flight paths at selected U.S. airports. These impacts are expected to be driven by (a) potential positive economic impacts related to the airport and its connectivity, and (b) environmental impacts such as noise, which may decrease the revenue and productivity of businesses beneath flight paths. The team proposed to

evaluate whether such impacts can be empirically identified while considering economic outcome metrics such as the gross domestic product (GDP), employment, and revenue.

The overall aims for the 3-year project as it relates to the provisions of Section 189 are as follows:

- Perform Tasks 1–3 [*Sec. 189. (b)(1–3)*]: Potential health impacts attributable to aircraft overflight noise
  - Investigate the relationship between aircraft noise exposure and the incidence of hypertension in the NHS and HPFS, accounting for other individual- and area-level risk factors
  - Investigate the relationship between aircraft noise exposure and the incidence of CVD in the NHS and HPFS cohorts, and determine whether sufficient data exist to demonstrate a causal relationship
  - Determine whether a relationship exists between annual average aircraft noise exposure and general sleep length and quality in the NHS and the Growing Up Today Study (GUTS), and report whether sufficient data exist to demonstrate a causal relationship
  - Evaluate the potential relationship between residing under a flight path and measures of disturbed sleep in the WHI WHISPER sub-study
- Perform Task 6 [*Sec. 189. (b)(4–5)*]: Potential economic impacts attributable to aircraft overflight noise
  - Model noise exposure before and after the introduction of area navigation (RNAV) procedures, on the basis of FAA flight trajectory data
  - Combine noise data with yearly county-level data from the Bureau of Economic Analysis (e.g., GDP, employment) and with city-level statistics for the years 2007, 2012, and 2017 from the Economic Census (e.g., revenue and employment)
  - Compare economic outcomes through state-of-the-art econometric approaches while controlling for regional and national economic trends
  - Evaluate whether the spatial resolution of the available data can substantially influence the study results
  - New task [*Sec. 189. (b)(4)*]: Assess the relationship between a perceived increase in aircraft noise and increases in visibility of aircraft, in collaboration with ASCENT 72
- Perform Task 7: Draft report on study results for policy-makers

Task 1 - Present Final Results of Analyses of Average Aircraft Noise and Hypertension, and Generate Results on Nighttime Noise and Hypertension

Boston University, Harvard University

Objective

The aim of this task is to present the final results of analyses of aircraft noise (DNL) and hypertension, and generate preliminary results of analyses of aircraft noise (nighttime equivalent sound levels [L_{night}]) and hypertension.

Research Approach

We intersected modeled noise exposure surfaces for 1995, 2000, 2005, 2010, and 2015 with the geocoded addresses of the participants over the follow-up period. We selected a large set of a priori variables to be examined as confounders and/or effect modifiers, and used time-varying Cox proportional hazards models to estimate the hypertension risk associated with time-varying aircraft noise exposure, while adjusting for both fixed and time-varying covariates. We also performed sensitivity analyses to address potential biases.

Milestones

- Present findings at the 182nd Meeting of the Acoustical Society of America (ASA) (May 2022)
- Generate preliminary results on aircraft noise (L_{night}) and hypertension

Major Accomplishments

- Generated tables comparing results from our study on aircraft noise (DNL) and hypertension in the NHS/NHSII for presentations (Figure 1)
- Presented research on aircraft noise (DNL) and hypertension at the ASA meeting
- Generated preliminary results on aircraft noise (L_{night}) and hypertension

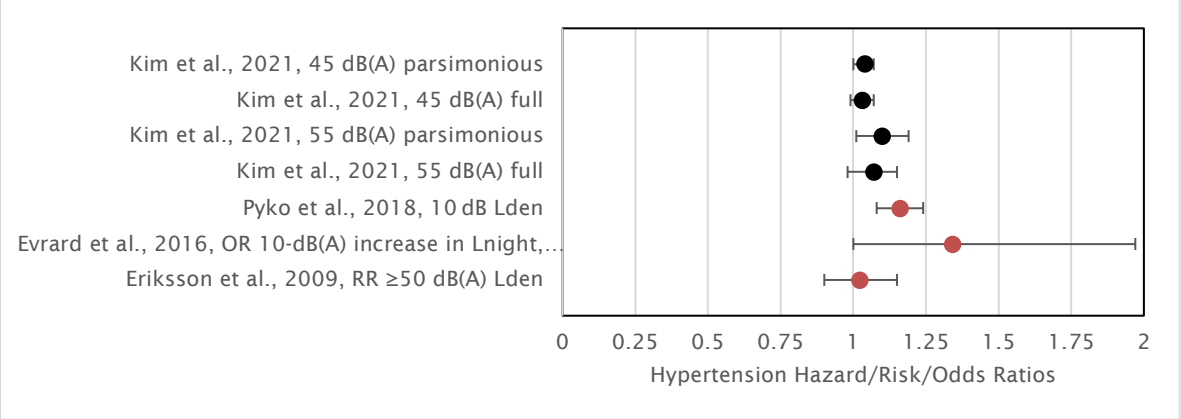

[1]Parsimonious model: adjusted for age, calendar year, race, physical activity, smoking status, alcohol use, dietary approaches to stop hypertension (DASH), spouse's educational attainment, neighborhood-level socioeconomic status, and region of residence.
[2]Fully adjusted model: adjusted for age, calendar year, race, physical activity, smoking status, alcohol use, DASH, spouse's education attainment, neighborhood-level socioeconomic status, region of residence, menopausal status, family history of hypertension, and body mass index (BMI).

Figure 1. Hazard, risk, or odds ratios (95% confidence intervals) for studies evaluating the association between aircraft noise and hypertension, comparing our Nurses' Health Studies (Kim et al., 2021) with previous studies.

Interpretation of our results (Kim et al., 2021) using the DNL 55-dB cut point as an example
In the combined parsimonious model, participants in NHS and NHS II exposed to levels ≥ DNL 55 dB had a 10% greater risk of hypertension than participants exposed to levels < DNL 55 dB, with a 95% confidence interval (CI) of 1% to 19%. In the combined fully adjusted model, participants exposed to ≥ DNL 55 dB had a 6% greater risk (95% CI: −2%, 15%) than unexposed individuals. The hazard ratios were relatively stable across the sensitivity analyses, including after controlling for air pollution. The findings suggested that smoking modifies the relationship between noise and hypertension.

Task 2 - For Supporting Analyses, (a) Write up and Publish Final Results on Sociodemographic Patterning of Aircraft Noise Exposure and (b) Generate Final Results on Trends in Aircraft Noise Exposure

Boston University

Objective

The aim of this task is to understand changes in exposure that will facilitate the interpretation of time-varying exposure measures in noise-health analyses and to understand the sociodemographic patterning of noise exposure that may confound or modify potential associations between noise and health.

Research Approach

For (a) (sociodemographic patterning), we described the characteristics of populations exposed to aviation noise by race/ethnicity and income/education, by using data from the U.S. Census Bureau and American Community Survey for 2010. We then performed univariate and multivariable hierarchical and multinomial analyses. For (b) (noise trend), we overlaid noise contours for 2000, 2005, 2010, and 2015 with census block data from the U.S. Census Bureau and American Community Surveys for 2000, 2010, and 2015 in a geographic information system to estimate population changes within noise levels. We used group-based trajectory modeling to statistically identify fairly homogeneous clusters of airports, that follow similar changes in outcomes over time. We used linear fixed-effects models to estimate changes in the sizes of exposure areas according to airport clusters for DNL values ≥65 dB and ≥45 dB and L_{night} value ≥45 dB.

Milestones

- Publish supporting analyses characterizing aircraft noise trends and sociodemographic patterns of exposure to aviation noise

- Perform supporting analyses characterizing population changes within noise levels over time (noise trends)
- Submit manuscript reporting results on trends in aircraft noise exposure

Major Accomplishments

- We overlaid noise contours for 2000, 2005, 2010, and 2015 and census block data from the U.S. Census Bureau and American Community Surveys for 2000, 2010, and 2015.
- We determined social patterning of aircraft noise exposure by race/ethnicity and income/education for 2010 using univariate and multivariable analysis (multinomial, mixed effects, hybrid, and Bayesian approaches) at three DNL cut points: 45 dB, 55 dB, and 65 dB, Overall, across multiple airports, block groups with larger Hispanic populations and higher proportions of residents with only high school education had higher odds of exposure. However, substantial heterogeneity was observed across airports.
- We evaluated the sociodemographic patterns of exposure to aircraft noise over time (1995–2015).
- We evaluated geographic and airport characteristics as predictors of patterns of exposed area over time. We found that non-monotonic trends in noise contour areas over time among our sample of 90 U.S. airports by airport characteristics peaked in 2000, then generally decreased until 2010, and subsequently increased from 2010 to 2015. Using group-based trajectory modeling at three cut points—DNL 45 dB and 65 dB, and L_{night} 45 dB—we identified four distinct trajectory groups of airports that shared underlying airport characteristics (Figure 2 for 45 dB for (a) DNL and (b) L_{night}). We also found that populations who identified as White or non-Hispanic/Latino had the highest counts of exposure, yet underrepresented groups (e.g., Hispanic, Black/African American, Asian, etc.) carried a disproportionate burden of exposure among their respective sub-populations.

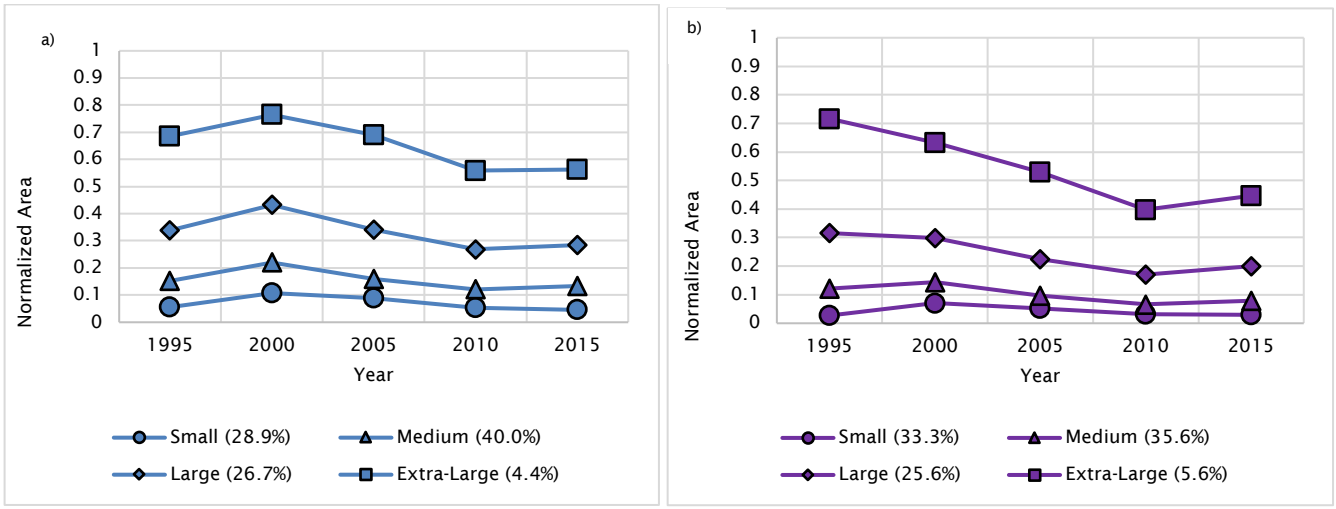

Figure 2. Trends in noise contour areas by clustering of airport types using group-based trajectories for (a) DNL ≥45 dB(A) and (b) L_{night} ≥45 dB(A).

Task 3 - Generate Final Results and Write Up Analysis of Sleep Quantity and Quality, and Aircraft Noise Exposure

Boston University, Harvard University

Objective

The aim of this task is to generate final results of analyses of aircraft noise (DNL and L_{night}) and nighttime equivalent sound levels, and identified sleep outcomes.

Research Approach

We intersected modeled nighttime noise exposure surfaces for 1995, 2000, 2005, 2010, and 2015 with the geocoded addresses of the participants over the follow-up period (first in NHS [original]). We selected a large set of a priori variables

to be examined as confounders and/or effect modifiers, used generalized estimating equations to estimate the odds from repeated measures of sleep insufficiency over multiple survey years, and used conditional logistic regression models of sleep quality to estimate the odds for the one survey year.

Milestone

- Obtain final results of analysis of DNL and nighttime aircraft noise, and sleep quantity and sleep quality in NHS (original)

Major Accomplishments

- Produced descriptive statistics of sleep measures and numbers of individuals exposed for each measure in NHS
- Determined relevant confounders and effect modifiers
- Performed final analysis of noise, and sleep quantity (insufficiency) and sleep quality.
- Drafted manuscript reporting the results of analysis of aircraft noise and sleep
- Gained all Harvard/Brigham and Women's Channing Division manuscript approvals including undergoing scientific, program, and technical review; submitted manuscript for FAA review
- Submitted the manuscript to a peer-reviewed journal
- Responded to journal reviewer comments; awaiting journal decision

Table 1. Odds ratio of the relationship between L_{night} ≥45 vs. <45 dB and repeated measures of sleep insufficiency and a one-time measure of poor sleep quality.

Model	Sleep insufficiency	Poor sleep quality
L_{night} ≥45 vs. <45 dB	**OR (95% CI)**	**OR (95% CI)**
Model 1: crude[a]	1.34 (1.17, 1.53)	0.94 (0.72, 1.21)
Model 2: adjusted[b]	1.27 (1.11, 1.45)	0.91 (0.70, 1.18)
Model 3; adjusted + ambient environmental[c]	1.23 (1.07, 1.41)	0.91 (0.70, 1.18)

OR, odds ratio; CI, confidence interval.
Models were adjusted for (a) age; (b) other demographics, behaviors, and comorbidities were added; (c) ambient environmental factors were added: particulate matter ≤2.5 microns ($PM_{2.5}$), greenness (normalized difference vegetation index, NDVI), and light at night.

Interpretation using L_{night} 45 dB as an example
In Model 3, participants in NHS exposed to L_{night} ≥45 had 23% greater odds of sleep insufficiency than participants exposed to L_{night} <45, with a 95% confidence interval of 7% to 41%. In addition, in Model 3, participants exposed to L_{night} ≥45 had 9% lower odds of poor sleep quality than participants exposed to L_{night} <45, with a 95% confidence interval of −30% to 18%.

Task 4 - Generate Final Results in Analyses of Cardiovascular Disease and Aircraft Noise

Boston University, Harvard University

Objective

The aim of this task is to perform final analysis of the potential relationship between CVD and aircraft noise.

Research Approach

We designed the statistical analysis and selected a large set of a priori variables to be examined as confounders and/or effect modifiers. We compiled appropriate data sets and conducted descriptive statistics analysis. We are using time-varying Cox proportional hazards models to estimate the CVD risk associated with time-varying aircraft noise exposure.

Milestones

- Obtain final results of analysis of aircraft noise and CVD

- Present at the 51st International Congress and Exposition in Noise Control Engineering (Inter-Noise 2022) (August 2022)
- Present at the 34th Annual Conference of the International Society of Environmental Epidemiology (ISEE) (September 2022)

Major Accomplishments

- Determined relevant confounders and effect modifiers
- Performed final analyses of noise and CVD and mortality
- Drafted manuscript reporting the results of analysis of aircraft noise, and CVD and mortality
- Presented research at the Inter-Noise Congress
- Presented research at the ISEE Conference

Table 2. Hazard ratios (95% confidence intervals) for associations between aircraft noise exposure (DNL) and cardiovascular disease in NHS and NHSII, meta-analyzed.

DNL (dB)	Cases	Person-time	Basic	Parsimonious	Fully adjusted
≥50	317	122,642	1.01 (0.90, 1.13)	1.00 (0.89, 1.12)	0.97 (0.87, 1.09)
<50	4,212	1,583,635	Ref.	Ref.	Ref.
Continuous, per 10 dB	4,529	1,706,278	0.99 (0.84, 1.18)	0.98 (0.83, 1.16)	0.97 (0.82, 1.15)

Basic model: adjusted for age and calendar year.
Parsimonious model: adjusted for age, calendar year, race/ethnicity, marital status, spouse's educational attainment, neighborhood socioeconomic status score, region of residence, fine particulate matter ($PM_{2.5}$), and population density.
Fully adjusted model: adjusted for age, calendar year, race/ethnicity, marital status, spouse's education attainment, neighborhood socioeconomic status score, region of residence, $PM_{2.5}$, population density, physical activity, smoking status, alcohol use, diet, menopausal status, and family history of cardiovascular disease.

Interpretation using DNL 50 dB as an example
In the crude models comparing exposure to DNL ≥50 dB, participants in NHS/NHSII exposed to DNL ≥50 dB had a 1% greater risk of CVD than participants exposed to DNL <50 dB, with a 95% confidence interval of −10% to 13%. In the fully adjusted model, participants exposed to DNL ≥50 dB had a 3% lower risk of CVD than participants exposed to DNL <50 dB, with a 95% confidence interval of −13% to 9%.

Task 5 - Develop an Analysis Plan and Generate Preliminary Results of Analyses of Aircraft Noise and the Intermediate Risk Marker of Adiposity

Boston University, Harvard University

Objective

The aim of this task is to develop an analysis plan and generate preliminary results of analyses of aircraft noise and an intermediate risk marker (adiposity, a measure of cardiometabolic disease).

Research Approach

We developed an analysis plan for studying adiposity and aircraft noise, and obtained approval from the NHS and HPFS oversight committees. We designed the statistical analysis and selected a large set of a priori variables to be examined as confounders and/or effect modifiers. We compiled appropriate data sets and performed descriptive statistics analysis. We are using generalized estimating equations to estimate the relationship between aircraft noise and longitudinal, repeated measures of adiposity (body mass index [BMI], waist circumference, and waist/hip ratio).

Milestones

- Produce preliminary results of analysis of aircraft noise and adiposity
- Present at the International Society of Environmental Epidemiology 2022 meeting (September 2022)

Major Accomplishments

- Developed an analysis plan
- Obtained approval from NHS/HPFS oversight committees
- Produced descriptive statistics of sleep measures and numbers of participants exposed for each measure in NHS
- Determined relevant confounders and effect modifiers
- Performed preliminary analysis of noise in relation to adiposity (results for three ordinal categories of BMI of 18.5–24 [reference], 25–29, and ≥30 kg/m^2 in Figure 3)
- Presented research at the ISEE Conference

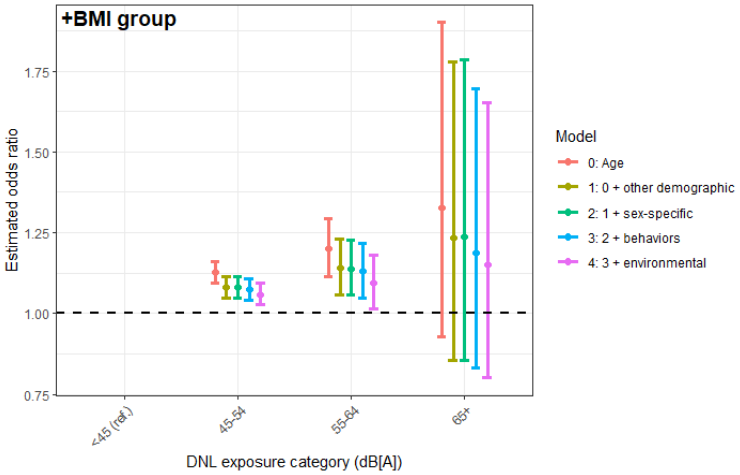

0: age; 1: 0 + demographics: region, race, individual socioeconomic status; 2: 1 + sex-specific: parity, menopausal status, hormone therapy; 3: 2+ behaviors: smoking status, alcohol use, diet quality, physical activity; 4: 3 + environmental: neighborhood SES, greenness, environmental noise, light at night.

Figure 3. Odds of increasing BMI groups (reference 18.5–24 kg/m^2) relative to increasing exposure group (reference DNL <45 dB); increasing BMI with increasing noise.

Task 6 - Develop a Model for Measuring Changes in Business Activities Attributable to Aircraft Noise Exposure, Prototype a Model City, and Include an Assessment Comparing a Change in the Visibility of Aircraft due to a Change in Aircraft Flight Paths

Massachusetts Institute of Technology

Objective

The long-term goal of Task 6 is to conduct an assessment of the economic impacts of aircraft noise exposure on businesses located underneath flight paths at selected U.S. airports. This goal is achieved through the following objectives:

1. Collect data on noise exposure changes over the past decade (e.g., owing to the introduction of new runways or performance-based navigation (PBN) procedures)
2. Combine noise data with yearly county-level data from the Bureau of Economic Analysis (e.g., GDP and employment), with city-level statistics from the Economic Census (e.g., revenue and employment), and/or with high-resolution business data from business databases
3. Compare economic outcomes while controlling for regional and national economic trends
4. Evaluate whether the spatial resolution of the available data can influence the results

In addition, the MIT team is working to understand how changes in flight paths might have changed aircraft visibility.

Objectives 1–4 were met during previous reporting periods. During the current reporting period, the team worked on the visibility analysis and focused on documenting results in a draft report for policy-makers.

Research Approach

The economic impact of noise exposure changes was studied for Boston Logan Airport and Chicago O'Hare Airport. The methods focused on the difference-in-difference approach, which was applied to identify differences between changes in business trends before and after exogenous noise exposure changes, i.e., the introduction of PBN procedures at Boston Logan Airport and the opening of new runway infrastructure at Chicago O'Hare Airport. Details can be found in previous reports.

During the current reporting period, the team developed a method to gain insights into whether the implementation of PBN procedures at Boston Logan Airport changed the frequency of aircraft sightings on the ground. For this purpose, the MIT team used flight track data from 2010 and 2017 to compare aircraft visibility on peak runway operation days for 33L departures, 27L departures, and 4R arrivals. An aircraft is assumed to be visible if it is above a visibility line of 45° from the ground (Figure 4). Consequently, the team obtains a grid of observation points on the ground, which can subsequently be aggregated to determine the number of aircraft visible that day from each grid location.

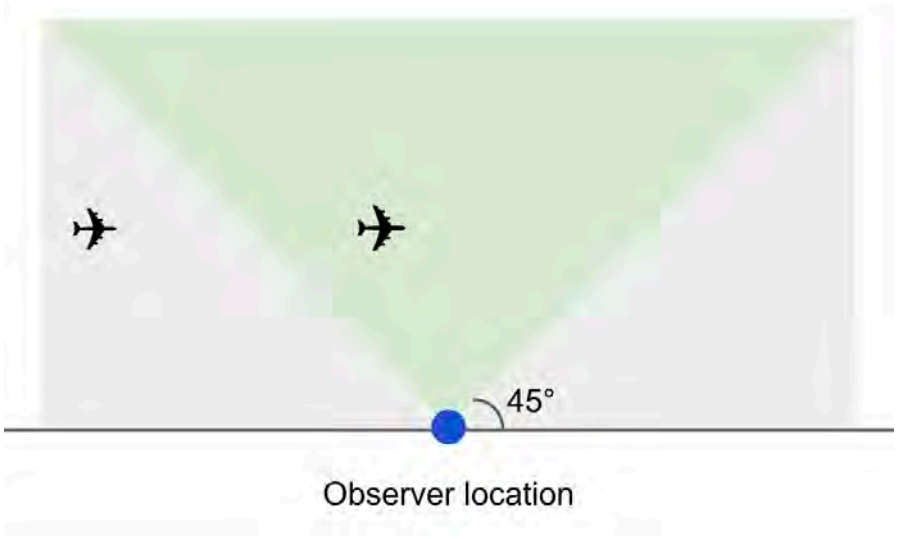

Figure 4. Visibility analysis approach. Aircraft in the green area are assumed to be visible from the observer location (blue dot). In the scenario depicted above, the aircraft on the far left is not visible, whereas the second aircraft in the center is visible.

Milestone

- Perform initial visibility analysis based on Boston Logan Airport

Major Accomplishments

- Perform visibility analysis to incorporate results of the project for policy-makers and the public

Task 7 - Draft a Report on the Study Results for Policy-makers

Boston University, Massachusetts Institute of Technology, Harvard University

Objective

The aim of this task is to develop a report of overall study results in response to Section 189 for policy makers.

Milestone

- Generate an initial first-draft report of overall study results in response to Section 189 for policy-makers

Major Accomplishments

- Drafted report summarizing the overall study results as it relates to Section 189

Publications

Simon, M. C., Hart, J. E., Levy, J. I., VoPham, T., Malwitz, A., Nguyen. D. D., Bozigar, M., Cupples, L. A., James, P., Laden, F., & Peters, J. L. (2022). Sociodemographic patterns of exposure to civil aircraft noise in the United States. *Environmental Health Perspectives, 130(2).* https://doi.org/10.1289/EHP9307

Bullock, C. (2021). Aviation effects on local business: Mapping community impact and policy strategies for noise remediation. [S.M. thesis.] Massachusetts Institute of Technology]. https://hdl.handle.net/1721.1/138966

Kim, C. S., Grady, S. T., Hart, J. E., Laden, F., VoPham, T., Nguyen, D. D., Manson, J. E., James, P., Forman, J. P., Rexrode, K. M., Levy, J. I., & Peters, J. L. (2021). Long-term aircraft noise exposure and risk of hypertension in the Nurses' Health Studies. *Environmental Research, 112195*. https://doi.org/10.1016/j.envres.2021.112195

Outreach Efforts

Presented on current progress orally during the ASCENT Spring Meeting (April 5–7, 2022).

Presented on "Associations Between Aircraft Noise Exposure and Adiposity in the U.S.-based Prospective Nurses' Health Studies" at the International Society for Environmental Epidemiology (ISEE) Conference on September 18–21, 2022.

Presented on "Associations Between Residential Exposure to Aircraft Noise, Cardiovascular Disease, and All-Cause Mortality in the Nurses' Health Studies" at the ISEE Conference on September 18–22, 2022.

Presented on "Long-term Aircraft Noise Exposure and Incident Cardiovascular Disease in National U.S. Cohort Studies" at Inter-Noise 2022 on August 21–24, 2022.

Presented on "Long-Term Aircraft Noise Exposure and Incident Hypertension in National U.S. Cohort Studies" at the 182nd Meeting of the ASA, May 23–27, 2022.

Awards

None

Student Involvement

The dissertation of Chloe Kim (doctoral graduate, BU) included the development and implementation of statistical analyses of noise and hypertension risk. Chloe Kim graduated in the fall of 2019 and is currently working for the Environmental Science, Policy, and Research Institute.

The dissertation of Daniel Nguyen (doctoral graduate, BU) included a characterization of the temporal trends in aviation noise surrounding U.S. airports. Daniel Nguyen graduated in the spring of 2022 and is currently working for the Centers for Disease Control and Prevention.

The dissertation of Stephanie Grady (doctoral candidate, BU) includes the development and running of statistical analyses on noise and cardiovascular event risk. Stephanie also worked with Chloe Kim on noise and hypertension risk.

The thesis of Carson Bullock (master's student, MIT) included conducting economic impact analysis. Carson graduated in the summer of 2021.

The thesis of Zhishen Wang (master's student, MIT) includes the visibility analysis.

Plans for Next Period

(October 1, 2022 to September 30, 2023)
Ongoing analyses, Tasks 1–5

- Complete analyses to estimate the risk of CVD events associated with aircraft noise exposure
- Complete analyses to evaluate the relationship between noise and sleep
- Continue analyses to evaluate the risk of hypertension associated with nighttime aircraft noise exposure
- Continue analyses to evaluate the relationship between noise and measures of adiposity
- Verify, document, and publish results

Related to 2018 FAA Reauthorization, Section 189, Tasks 6 and 7

- Complete aircraft visibility analyses and verify results for inclusion in the Section 189 report
- Document results for policy-makers in iterative drafts and a final report

Related to FAA's Office of Environment and Energy Roadmap

- Start processes related to adding noise to an additional cohort, and explore other health outcomes (e.g., mental health)

References

Allroggen, F., & Malina, R. (2014). Do the regional growth effects of air transport differ among airports? *Journal of Air Transport Management, 37*, 1–4. https://doi.org/10.1016/j.jairtraman.2013.11.007

Brueckner, J. K. (2003). Airline traffic and urban economic development. *Urban Studies. 40(8)*,1455–1469. https://doi.org/10.1080/0042098032000094388

Campante, F., & Yanagizawa-Drott, D. (2018). Long-range growth: Economic development in the global network of air links. *Quarterly Journal of Economics, 133(3)*, 1395–1458. https://doi.org/10.1093/qje/qjx050

Lakshmanan, T. R. (2011). The broader economic consequences of transport infrastructure investments. *Journal of Transport Geography, 19(1)*, 1–12. https://doi.org/10.1016/j.jtrangeo.2010.01.00

Project Overview References

Almer, C., Boes, S., & Nuesch, S. (2017). Adjustments in the housing market after an environmental shock: Evidence from a large-scale change in aircraft noise exposure. *Oxford Economic Papers, 69(4)*, 918–938.

Bluhm, G., & Eriksson, C. (2011). Cardiovascular effects of environmental noise: Research in Sweden. *Noise and Health, 13(52)*, 212–216. doi: 10.4103/1463-1741.80152

Bristow, A. L., Wardman, M., & Chintakayala, V. P. K. (2015). International meta-analysis of stated preference studies of transportation noise nuisance. *Transportation, 42(1)*, 71–100. https://doi.org/10.1007/s11116-014-9527-4

Dimakopoulou, K., Koutentakis, K., Papageorgiou, I., Kasdagli, M. I., Haralabidis, A. S., Sourtzi, P., Samoli, E., Houthuijs, D., Swart, W., Hansell, A. L., & Katsouyanni, K. (2017). Is aircraft noise exposure associated with cardiovascular disease and hypertension? Results from a cohort study in Athens, Greece. *Occupational and Environmental Medicine, 74(11)*, 830–837. http://dx.doi.org/10.1136/oemed-2016-104180

Eriksson, C., Bluhm, G., Hilding, A., Ostenson, C. G., & Pershagen, G. (2010). Aircraft noise and incidence of hypertension--gender specific effects. *Environmental Research, 110(8)*, 764–772. https://doi.org/10.1016/j.envres.2010.09.001

Evrard, A. S., Lefevre, M., Champelovier, P., Lambert, J., & Laumon, B. (2017). Does aircraft noise exposure increase the risk of hypertension in the population living near airports in France? *Occupational and Environmental Medicine, 74(2)*, 123–129. http://dx.doi.org/10.1136/oemed-2016-103648

Floud, S., Vigna-Taglianti, F., Hansell, A., Blangiardo, M., Houthuijs, D., Breugelmans, O., Cadum, E., Babisch, W., Selander, J., Pershagen, G., Antoniotti, M. C., Pisani, S., Dimakopoulou, K., Haralabidis, A. S., Velonakis, V., Jarup, L., & HYENA Study Team. (2011). Medication use in relation to noise from aircraft and road traffic in six European countries: Results of the HYENA study. *Occupational and Environmental Medicine, 68(7)*, 518–524. http://dx.doi.org/10.1136/oem.2010.058586

Franssen, E. A., van Wiechen, C. M., Nagelkerke, N. J., & Lebret, E. (2004). Aircraft noise around a large international airport and its impact on general health and medication use. *Occupational and Environmental Medicine. 61(5)*, 405–413. doi: 10.1136/oem.2002.005488

Greiser, E., Greiser, C., & Janhsen, K. (2007).Night-time aircraft noise increases prevalence of prescriptions of antihypertensive and cardiovascular drugs irrespective of social class—the Cologne-Bonn Airport study. *Journal of Public Health, 15,* 327-337. https://doi.org/10.1007/s10389-007-0137-xHaralabidis, A. S., Dimakopoulou, K., Vigna-Taglianti, F., Giampaolo, M., Borgini, A., Dudley, M. L., Pershagen, G., Bluhm, G., Houthuijs, D., Babisch, W., Velonakis, M., Katsouyanni, K., Jarup, L., & HYENA Consortium. (2008). Acute effects of night-time noise exposure

on blood pressure in populations living near airports. *European Heart Journal, 29(5)*, 658–664. https://doi.org/10.1093/eurheartj/ehn013

Haralabidis, A. S., Dimakopoulou, K., Velonaki, V, Barbaglia, G., Mussin, M., Giampaolo, M., Selander, J., Pershagen, G., Dudley, M. L., Babisch, W., Swart, W., Katsouyanni, K., Jarup, L., & HYENA Consortium. (2011). Can exposure to noise affect the 24 h blood pressure profile? Results from the HYENA study. *Journal of Epidemiology and Community Health, 65(6)*, 535–541. http://dx.doi.org/10.1136/jech.2009.102954

Hatfield, J., Job, R., Carter, N. L., Peploe, P., Taylor, R., & Morrell, S. (2001). The influence of psychological factors on self-reported physiological effects of noise. *Noise and Health, 3(10)*, 1–13.

Jarup, L., Babisch, W., Houthuijs, D., Pershagen, G., Katsouyanni, K., Cadum, E., Dudley, M. L., Savigny, P., Seiffert, I., Swart, W., Breugelmans, O., Bluhm, G., Selander, J., Haralabidis, A., Dimakopoulou, K., Sourtzi, P., Velonakis, M., Vigna-Taglianti, F., & HYENA Study Team. (2008). Hypertension and exposure to noise near airports: The HYENA study. *Environmental Health Perspectives, 116(3)*, 329–333. https://doi.org/10.1289/ehp.10775

Kopsch, F. (2016). The cost of aircraft noise - does it differ from road noise? A meta-analysis. *Journal of Air Transport Management, 57*, 138–142. doi: 10.1016/j.jairtraman.2016.05.011Matsui, T., Uehara, T., Miyakita, T., Hiramatsu, K., Yasutaka, O., & Yamamoto, T. (2004). The Okinawa study: Effects of chronic aircraft noise on blood pressure and some other physiological indices. *Journal of Sound and Vibration, 277,* 469–470. doi: 10.1016/j.jsv.2004.03.007

Pyko A., Lind T., Mitkovskaya N., Ögren M., Östenson C.-G., Wallas A., et al. (2018). Transportation noise and incidence of hypertension. *International Journal of Hygiene and Environmental Health, 221*, 1133–1141. https://doi.org/10.1016/j.ijheh.2018.06.005

Rosenlund, M., Berglind, N., Pershagen, G., Jarup, L., & Bluhm, G. (2001). Increased prevalence of hypertension in a population exposed to aircraft noise. *Occupational and Environmental Medicine, 58(12)*, 769–773. http://dx.doi.org/10.1136/oem.58.12.769

Wolfe, P. J., Yim, S. H. L., Lee, G., Ashok, A., Barrett, S. R. H., & Waitz, I. A. (2014). Near-airport distribution of the environmental costs of aviation. *Transport Policy, 34*, 102–108. https://doi.org/10.1016/j.tranpol.2014.02.023

Project 009 Geospatially Driven Noise Estimation Module

Georgia Institute of Technology

Project Lead Investigators

P.I.: Professor Dimitri N. Mavris
Director, Aerospace Systems Design Laboratory
School of Aerospace Engineering
Georgia Institute of Technology
Phone: (404) 894-1557
Fax: (404) 894-6596
Email: dimitri.mavris@ae.gatech.edu

Co-P.I.: Dr. Holger Pfaender
Aerospace Systems Design Laboratory
School of Aerospace Engineering
Georgia Institute of Technology
Phone: (404) 385-2779
Fax: (404) 894-6596
Email: holger.pfaender@ae.gatech.edu

University Participants

Georgia Institute of Technology

- P.I.s: Dr. Dimitri Mavris, Dr. Holger Pfaender
- FAA Award Number: 13-C-AJFE-GIT-059
- Period of Performance: October 1, 2021 to September 30, 2022
- Tasks:
    1. Literature review and evaluation of geographic information systems (GIS) software
    2. Investigation of emerging computational technologies
    3. Collaboration with the unmanned aircraft system (UAS) computation module development team
    4. Noise computation engine integration

Project Funding Level

Georgia Institute of Technology has received $249,999 in funding for this project. Georgia Institute of Technology has agreed to a total of $83,333 in matching funds. This total includes salaries for the project director, research engineers, and graduate research assistants and for computing, financial, and administrative support, including meeting arrangements. The institute has also agreed to provide tuition remission for students whose tuition is paid via state funds.

Investigation Team

Georgia Institute of Technology

- P.I.: Dimitri Mavris
- Co-Investigator: Holger Pfaender
- Graduate Students: Joaquin Matticoli, Deepika Singla, Xi Wang, Hugues Chardin, Aroua Gharbi, Martin Delage
- Postdoctoral Fellow: Raphael Gautier

Project Overview

Context and Motivation

The UAS market is expected to grow rapidly in coming years, with projections estimating the civil UAS market at $121 billion in the next decade [0]. Multiple operators are currently developing and testing various concepts of operations that fall within the umbrella of urban air mobility (UAM), with the two main use cases being drone delivery and e-taxi operations. Similar to traditional aircraft operations, these novel concepts are expected to influence the environment in which they operate, particularly regarding noise. In the same way that noise assessments of terminal operations are carried out today for commercial aviation, noise assessments of UAM operations are expected to be necessary in the future.

Problem Definition

UAM operations bring unique requirements. First, UAM operations are expected to be denser than current general or commercial aviation operations, possibly by orders of magnitude. Thus, noise assessment methods should be able to handle such large vehicle densities. Second, the vehicles are expected to be smaller and therefore quieter, e.g., small drones for deliveries or helicopter-sized vehicles for e-taxi applications, but these vehicles are also expected to benefit from novel electric propulsion systems. As a result, the noise footprint of such vehicles is expected to be more localized. Therefore, noise exposure levels should be estimated with sufficient resolution. Third, instead of primarily following fixed trajectories dictated by approach and departure routes around airports, UAM vehicles are expected to operate point-to-point within populated areas. Departure and arrival locations are expected to vary from day to day: delivery drones may depart from warehouses or mobile staging locations and deliver goods to different customers each day, and e-taxis may pick up and drop off customers throughout an urban area. Thus, noise assessment methods should be sufficiently flexible to accommodate changing flight paths, and the resulting noise assessments should account for corresponding variability.

Research Objectives

In view of these requirements, the methods used to perform noise assessments in terminal areas, such as the Aviation Environmental Design Tool (AEDT), are not fully suitable for UAM assessments: these methods are usually limited to studies of relatively low-density operations around airports, with vehicles following pre-defined ground tracks. Thus, there is a need for the development of new noise assessment capabilities tailored to UAM operations, which is the focus of this project.

Research Approach

Research efforts supporting the development of a UAS noise assessment tool have been broken down into four tasks.

First, GIS capabilities are expected to play a major part in the development of this tool, as the scenarios under consideration, as well as the resulting noise metrics, are to be visualized and overlayed on the geographical area of study. Therefore, Task 1 focuses on a literature review and evaluation of GIS software.

Second, the complexity of assessing noise in the context of UAM use cases, as discussed in the previous section, calls for the investigation of emerging technologies in multiple computational domains. The size of these problems and the flexibility needed to analyze a wide variety of operational scenarios require the introduction of recent innovations to address the challenges discussed previously. This is the focus of Task 2.

This research was conducted in collaboration with other entities, starting with Mississippi State University (MSU) and followed by subsequent collaborations, which are presented under the umbrella of Task 3.

Finally, Task 4 focuses on the integration of all components investigated or provided by other tasks into the actual UAS noise assessment engine. Technical details pertaining to the implementation, as well as preliminary results on benchmark test cases, are presented in this section.

Task 1 - Literature Review and Evaluation of GIS Software

Georgia Institute of Technology

Task 1 Contents

1.1. Objective

This task aims to identify the leading open-source GIS software using preset evaluation criteria.

1.2. Research Approach

This review focused on open-source options. For an adequate evaluation of the options, six criteria were set forth:

1. Data import: Ability to read shape files with different formats of input geometrical data as well as rasterized (gridded) data
2. Data storage: Capability to store geospatial data in either shape/vector formats or as rasterized data
3. Geometric calculations: Ability to convert to and from a Cartesian coordinate system and other Earth model coordinates and ability to compute polygon areas and lengths as well as unions and subtractions
4. Geospatial calculations: Ability to perform calculations on given vector or raster data and to draw contour plots
5. Display: Ability to print raw or processed geospatial data as various map displays and to enable standard desktop and web applications
6. Map data: Capability to display results with relation to landmasses, political boundaries such as states and counties, and roads and buildings

In addition to evaluating software, we also investigated GIS applications to examine the option of creating a stand-alone, customized library or component.

1.3. GIS Libraries

1.3.1. QGIS

QGIS is a user-friendly open-source GIS written in C++. The latest version is 3.24 (released in February 2022). QGIS runs on Linux, Unix, Mac OSX, Windows, and Android and supports numerous vector, raster, and database formats and functionalities. Apart from built-in functionalities, QGIS allows users to install and create their own plug-ins. New applications can also be created in QGIS through C++ and Python languages. Screenshots of QGIS are shown in Figure 1.

Figure 1. Screenshots of QGIS.

Evaluation Criteria

1. Data import: Imports shape files such as GPX, GPS, DXF, DWG, and OpenStreetMap, as well as raster files
2. Data storage: Stores geospatial data in vector and raster formats
3. Geometric calculations: Supports Cartesian (x, y), polar (length, angle), and projected (x-north, y-east) calculations; calculates length or area of geometrical features; and provides overlay, union, and difference between areas
4. Geospatial calculations: Creates a vector contour map from an elevation raster and carries out raster-to-vector conversion
5. Display: Can provide web mapping with QGIS2Web; can publish data on the internet using a webserver with the University of Minnesota MapServer or GeoServer installed
6. Map data: Displays geospatial data such as countries, states, and counties as well as roads

1.3.2. OpenJUMP

OpenJUMP is a Java-based open-source GIS (latest version: 2.0, released in March 2022). OpenJUMP works on Windows, Linux, and Mac platforms with Java 1.7 or later. OpenJUMP's features include reading and writing vector formats, displaying geospatial data, and executing geometric calculations. Additional plug-ins for more capabilities are also available. OpenJUMP is distributed under the GNU General Public License version 2. Screenshots of OpenJUMP are shown in Figure 2.

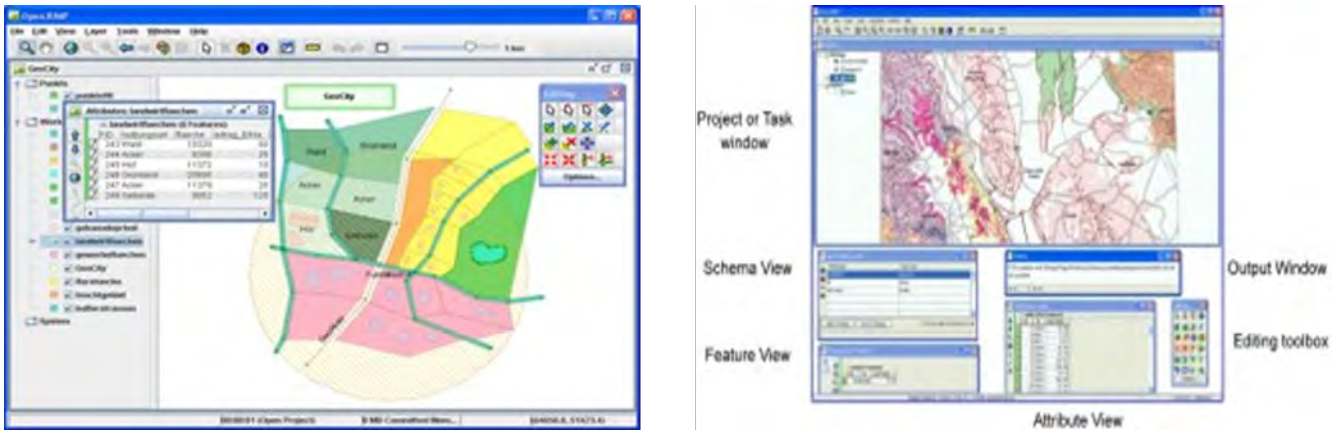

Figure 2. Screenshots of OpenJUMP.

Evaluation Criteria

1. Data import: Imports shape and raster files
2. Data storage: Stores geospatial data in vector and raster formats
3. Geometric calculations: Supports coordinate reference system (CRS) (Cartesian [x, y, z], geographic [longitude, latitude, height], and projected [x-north, y-east]) conversions; provides a CRS transformation tool (PROJ4); calculates length or area of geometrical features; provides overlay, union, and subtraction
4. Geospatial calculations: Provides conversion between desired file formats (raster-to-vector conversion); does NOT provide contour plots
5. Display: Does NOT provide a web application
6. Map data: Displays geospatial data such as countries, states, and counties as well as roads

1.3.3. SAGA (System for Automated Geoscientific Analyses)

SAGA is an open-source cross-platform GIS software written in C++ (latest version: 2.0, released in June 2007). SAGA can be run on Windows, Linux, FreeBSD, and Mac (OS X). SAGA provides multiple libraries for GIS calculations: digital terrain analysis, image segmentation, fire spreading analysis and simulation, etc. In addition to these libraries, SAGA allows the scripting of custom models through the command line interface (CLI) and Python interface. Screenshots of SAGA are shown in Figure 3.

Evaluation Criteria

1. Data import: Imports shape and raster files
2. Data storage: Stores geospatial data in vector and raster formats
3. Geometric calculations: Supports geographic coordinate system (latitude, longitude) and Universal Transverse Mercator (UTM) calculations; computes polygon areas or lengths
4. Geospatial calculations: Performs raster-to-vector conversions and can create contour lines
5. Display: Displays data as histograms and scatter plots
6. Map data: Enables visualization of spatial data as cartographic maps; can also import maps from Web Map Service and OpenStreetMap.

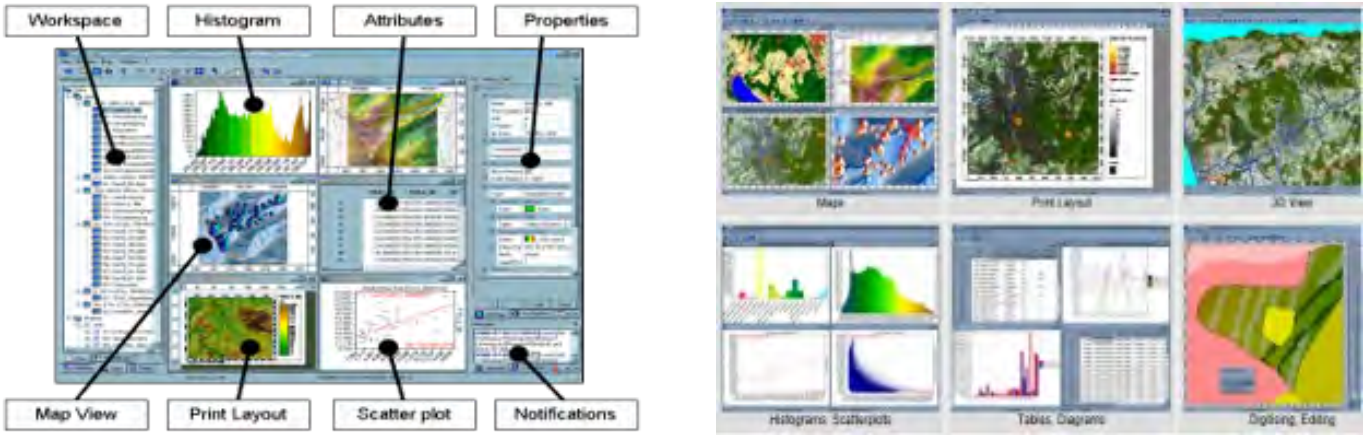

Figure 3. Screenshots of SAGA.

1.3.4. Deck.gl

Deck.gl is a WebGL visualization framework for large datasets (latest version: 8.7.3, released in March 2022). Deck.gl allows the user to map data (JavaScript Object Notation [JSON] objects, CSV) into a stack of layers. These layers can be imported directly from a catalog or built by the user.

Evaluation Criteria

1. Data import: Reads shape files and CSV/GeoJSON files
2. Data storage: Can store geospatial data as vector or shape files
3. Geometric calculations: Supports geographic coordinate system (latitude, longitude) using Web Mercator; does NOT calculate polygon areas or lengths
4. Geospatial calculations: Does not convert raster data to vector data; can create contour lines for a given threshold and cell size
5. Display: Offers an architecture for packaging advanced WebGL-based visualizations; enables users to rapid obtain impressive visual results with limited effort
6. Map data: Easily displays geospatial data with relation to roads and buildings

1.3.5. Kepler.gl

Kepler.gl is an open-source geospatial analysis tool for large-scale datasets (version 2.5.5). The most recent update was made in September 2021. A user interface was created to facilitate the process of saving a map to back-end storage, and a graphics processing unit (GPU) data filter was added, with the ability to create polygon filters in the user interface.

Evaluation Criteria

1. Data import: Can read CSV/GeoJSON files and Kepler.gl's sample datasets; must convert shape files to a GeoJSON file to be consumable by kepler.gl
2. Data storage: Cannot store geospatial data as vector or shape files
3. Geometric calculations: Supports geographic coordinate system (latitude, longitude) using Web Mercator; does NOT calculate polygon areas or lengths
4. Geospatial calculations: Does not convert raster data to vector data; can create contour lines
5. Display: Offers an architecture for packaging advanced WebGL-based visualizations and can easily handle the sample data to visualize
6. Map data: Easily displays geospatial data with relation to roads and buildings

1.3.6. Geographic Resources Analysis Support System (GRASS) GIS

GRASS is an open-source Java-based software for vector and raster geospatial data management, geoprocessing, spatial modeling, and visualization. GRASS has compatibilities with QGIS, meaning that QGIS can run some features of GRASS GIS as a plug-in. Already developed add-ons are available, along with the capability to develop additional add-ons. The latest version (8.0, released in March 2022) has an improved graphical user interface (GUI) and Python scripting. GRASS provides rapid linking of external raster files and spatiotemporal data analysis with an improved internal data structure. A vector attribute update was also found with Python syntax. A screenshot of GRASS GIS is shown in Figure 4.

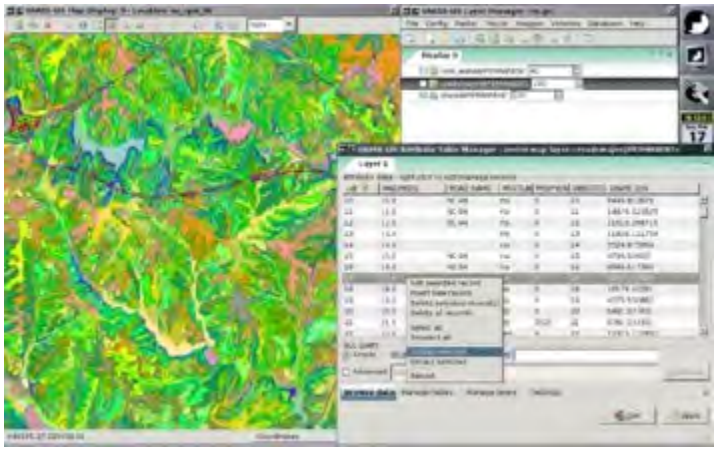

Figure 4. Screenshot of Grass GIS.

Evaluation Criteria

1. Data import: Imports vector and raster files
2. Data storage: Stores geospatial data in vector and raster formats
3. Geometric calculations: Supports CRS (Cartesian [x, y, z] and geographic [longitude, latitude, height]) conversions; provides a CRS transformation tool (PROJ4); calculates length or area of geometrical features; provides overlay, union, and subtraction
4. Geospatial calculations: Provides conversion between desired file formats (raster-to-vector conversion); creates contour lines
5. Display: Provides a Web Mapping Service and graphics display monitor that can be controlled from the command line; can display frames on the user's graphic monitor
6. Map data: Displays geospatial data such as countries and states by using Inkspace

1.3.7. gvSIG

gvSIG is an open-source GIS written in 2021 that runs on Windows, Linux, and Mac platforms. A screenshot of gvSIG is shown in Figure 5.

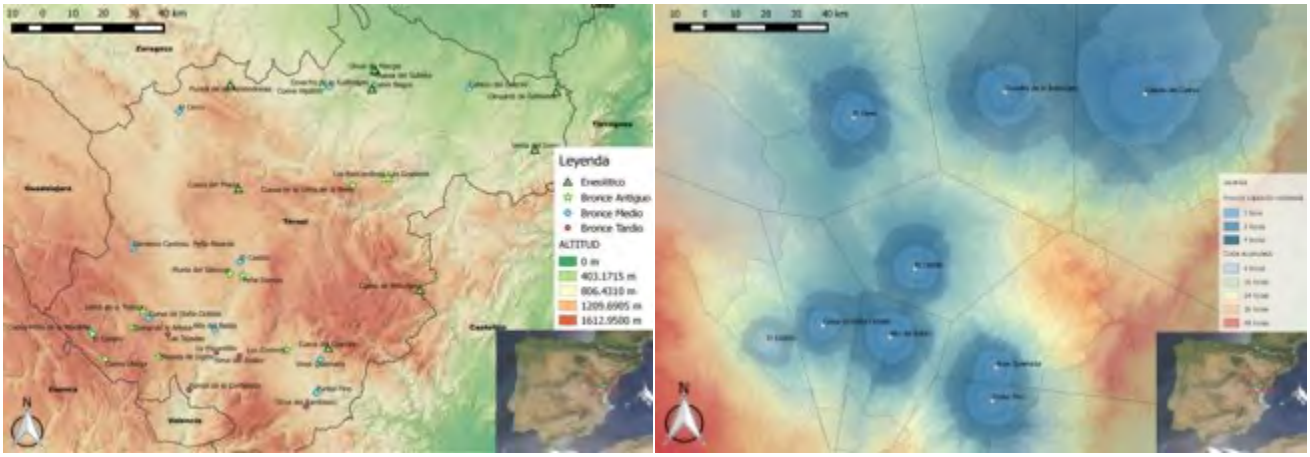

Figure 5. Screenshot of gvSIG.

Evaluation Criteria

1. Data import: Can import shape and raster files
2. Data storage: Can store geospatial data in vector and raster formats
3. Geometric calculations: Supports geographic coordinate system (latitude, longitude) using Web Mercator; does NOT calculate polygon areas or lengths; supports CRS (Cartesian [x, y, z] and geographic [longitude, latitude, height]) coordinates; provides a CRS transformation tool (PROJ4); calculates length or area of geometrical features; provides overlay, union, and subtraction
4. Geospatial calculations: Can convert other file types to the desired file format; does NOT produce contour plots
5. Display: Does NOT provide a web application
6. Map data: Displays geospatial data such as countries and states by using Inkspace

1.3.8. MapWindow GIS

MapWindow GIS is an open-source GIS written in C++ programming language using optimal features from the .NET framework v4/4.5. MapWindow runs on Windows (latest version: 5.3.0, released in 2019), as shown in Figure 6. This version was compiled using VS2017. The new version supports tiles from a local file system and provides extendable snapping events. MapWindow was licensed under the Mozilla Public License.

Evaluation Criteria

1. Data import: Can import shape and raster files
2. Data storage: Can store geospatial data in vector and raster formats
3. Geometric calculations: Supports geographic coordinate system (latitude, longitude) and UTM calculations; can calculate length or area of geometrical features
4. Geospatial calculations: Can convert other file types to the desired file format; does NOT produce contour plots
5. Display: Allows multi-threaded HTTP tile loading
6. Map data: Displays geospatial data such as countries and states by using Inkspace

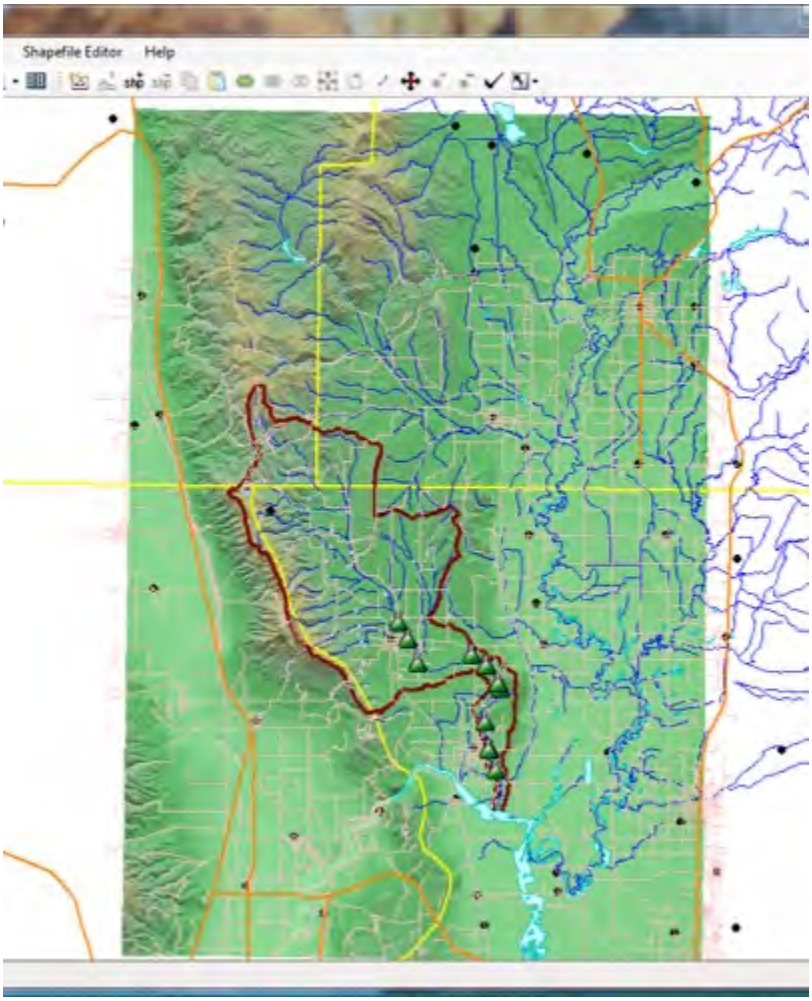

Figure 6. Screenshot of MapWindow GIS.

1.3.9. GeoPandas

GeoPandas is an open-source project developed in Python to provide a useful library for working with geospatial data, as shown in Figure 7. GeoPandas can run on distributions of Linux and Windows. This software primarily uses the Python packages pandas (as a base for its data storage), shapely (to manipulate the shapes stored in the advanced database), Fiona (for file access), and Descartes and matplotlib (for data visualization). GeoPandas is most adept at displaying discrete sections of data in a geospatial visualization. It is limited in its ability to display graphics outside of the Python environment and does not support conversion to the desired raster/vector formats. The last update was made in 2021, which improved the software from v0.5.0 to v0.10.2 and corrected the regression in the overlay and plotting.

Evaluation Criteria

1. Data import: Reads almost any vector-based spatial data format
2. Data storage: Stores geospatial data in vector and raster formats
3. Geometric calculations: Supports CRS calculations; cannot calculate the length or area of geometrical features; has overlay functions, such as intersections between two or more areas, union (merges the areas of one layer to one single area), difference (A-B areas), and polygons

4. Geospatial calculations: Does not convert to any desired file formats (no raster-to-vector formats); does not provide a contour plot function
5. Map data: Uses various map projections using the Python library Cartopy
6. Display: Does not provide a web application; provides a good representation in three-dimensional (3D) color space using matplotlib

Figure 7. GeoPandas can overlay processed geospatial data over existing maps.

1.3.10. WorldWind

WorldWind is an open-source virtual 3D globe visualization application programming interface (API) developed by NASA in partnership with the European Space Agency. WorldWind is written in both Java (for desktop and Android devices) and JavaScript (for web applications). After its development was suspended in 2019, it was restarted in August 2020. WorldWind can import a variety of input files with geospatial data, stores the data in both raster and vector formats, provides sufficient geometric and geospatial calculations, and produces good visualizations with comprehensive map data. WorldWind finds its application in unmanned aerial vehicle imagery, where such vehicles can provide continuous monitoring of an active fire, with higher resolution and more frequent updates. WorldWind was licensed under NASA Open-Source Agreement Version 1.3. Screenshots of WorldWind are shown in Figure 8.

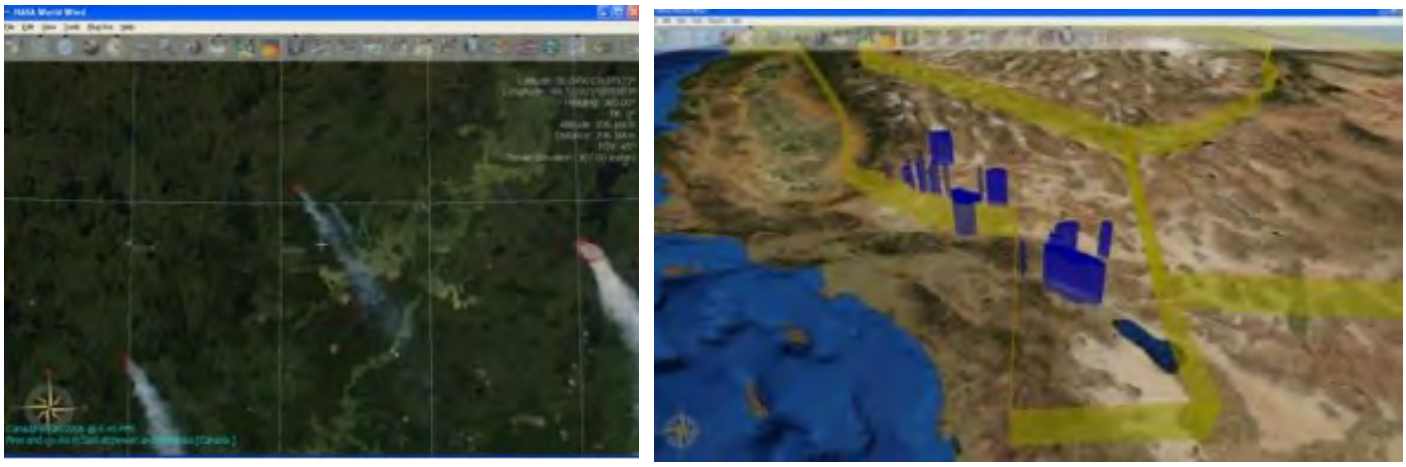

Figure 8. Screenshots of WorldWind.

Evaluation Criteria

1. Data import: Imports shape files, KML, VPF, GML, GeoJSON, GeoRSS, GPX, NMEA, etc.
2. Data storage: Stores geospatial data in vector and raster formats
3. Geometric calculations: Supports geographic coordinate system (latitude, longitude), UTM, and Military Grid Reference System calculations; can draw and measure distance and area across a terrain
4. Geospatial calculations: Displays contour lines on surface terrain at a specified elevation
5. Map data: Provides visual representations of scalar values, such as noise, over a grid of geographic positions; can visualize the results on web and Android platforms
6. Display: Displays geospatial data divided into country, state, and city

1.3.11. Overall Evaluation

An overall evaluation of all of the investigated libraries is provided in Table 1. QGIS seems to surpass the other libraries with respect to our defined metrics.

Table 1. Comparison of different libraries.

	Intuitive GUI	Compatibility	Statistical Analyses	Data Import	Data Storage	Geometrical Calculations	Geospatial Calculations	Map Data	Display	Total
QGIS	3	5	3	5	5	5	5	5	4	40
OpenJUMP	3	4	1	5	5	5	3	5	2	33
SAGA	3	3	4	5	5	4	5	5	4	38
Deck.gl	4	3	1	5	5	3	3	5	5	34
Kepler.gl	4	5	1	1	1	3	3	5	5	28
GRASS	4	3	1	5	5	4	5	5	4	36
gvSIG	3	4	1	5	5	4	3	5	2	32
MapWindow	3	4	1	5	5	3	3	4	2	30
GeoPandas	2	*4*	1	5	5	4	1	2	2	26
WorldWind	5	*5*	1	5	5	4	4	5	5	39

1.4. GIS Applications

GIS applications can be broadly classified in two categories: desktop and web-based applications.

WebGIS applications use web technologies to display and communicate geospatial information to an end user. There are five common elements in every WebGIS application:

1. A web application: The interface used by the client, which has tools for visualizing, analyzing, and interacting with geographic information and can be run on a web browser or a GPS-enabled device
2. Digital base maps: The geographical context for the application (e.g., transportation, topography, imagery, etc.)
3. Operational layers: The layers used in order for the results of an operation to be displayed (e.g., observations, sensor feeds, query results, analytic results, etc.)
4. Tasks and tools: Tools to perform operations beyond mapping
5. Geodatabase(s): Container of geographical data, which can consist of geodatabases, shape files, tabular databases, computer-aided design files, etc.

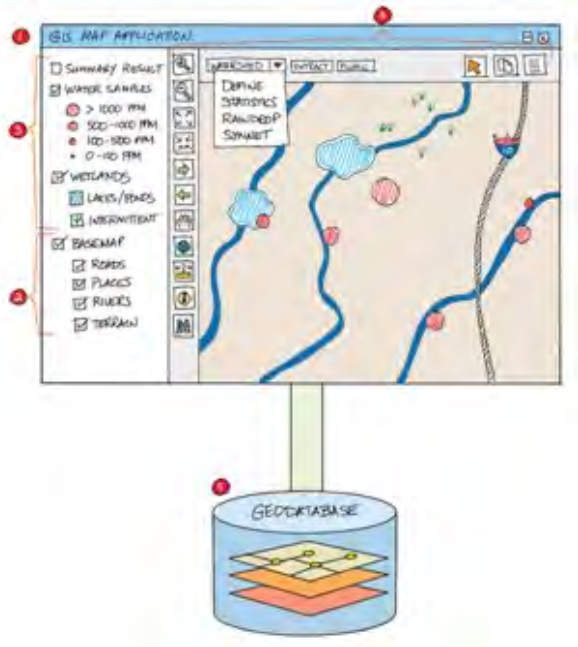

Figure 9. Sketch of a Web geographic information system application.

WebGIS applications come with multiple advantages as well as limitations. Table 2 presents a non-exhaustive list of these advantages and limitations.

Table 2. Advantages and disadvantages of Web geographic information systems (WebGISs).

Advantages of WebGIS	Drawbacks of WebGIS
• Provides a broader reach for customers compared **with** a traditional desktop application • Better cross-platform capability with the different web browsers that can be used • Easy to use for customers with different levels of GIS expertise • Extendable to cloud services, hence allowing manipulation and use of big GIS data • Lower cost to entry (most libraries and tools are open-source with good community support) • Allows real-time analysis	• Harder to build (developers need to have a good knowledge of multiple scripting languages to build the app [Python, JavaScript, html, etc.]) • Data security may depend on a third party • Application may need to be hosted outside of the organization

Our team has started a dialogue with the AEDT development team regarding which GIS functionalities will be required to be able to integrate the UAS noise engine with the AEDT in the future.

Task 2 - Investigation of Emerging Computational Technologies

Georgia Institute of Technology

Task 2 Contents

2.1. Task 2 Overview

2.1.1. Context and Motivation

As explained in the project's overview, assessing noise exposure for UASs brings unique requirements that existing frameworks do not meet. Namely, three primary abilities are needed: (a) the ability to analyze scenarios involving large volumes of flights, (b) the ability to cover large areas with small resolution, and (c) the ability to account for sources of uncertainty related to the evolving UAS concepts of operation. Thus, there is a need for the development of a new analysis capability that can fulfill these requirements.

2.1.2. Problem Definition

Although the actual estimation of noise exposure levels plays a central role in noise assessment tools, many other peripheral functions are also needed: inputs must be read and pre-processed, computations must be implemented in such a way that they meet the requirements listed in the previous section, and a visualization of the operational scenario and noise assessment results must be provided in a manner that is intuitive to the user. Each of these functionalities requires a substantial development effort and can leverage specific computational technologies.

2.1.3. Research Objectives

In this task, we aim to investigate the emerging technologies that could be used to implement the variety of functions to be performed by the noise assessment tool. In particular, we are seeking technologies that are compatible with the stringent requirements related to UAS operations.

2.1.4. Research Approach

For this task, the following areas of emerging technologies were identified and investigated. Figure 10 presents a partial depiction of these areas and the associated technologies.

First, GIS visualization techniques were investigated. Within the noise assessment tool, these techniques are used to visualize the defined operational scenarios, such as the flights included in the scenario, as well as the analysis results, in the form of noise levels mapped over a pre-defined geographical area.

Second, parallel computation approaches were investigated to address the problem of performing noise computations with large problem sizes encountered due to 1) the large flight volumes in UAM scenarios, 2) the low resolution and large areas needed to effectively cover populated areas, and 3) the small time discretization needed to properly assess noise exposure.

Third, data pre- and post-processing approaches were investigated, as working with geographical data usually requires many transformations, such as clipping to the analysis area or converting from one CRS to another.

Fourth, motivated by the need to speed up noise computations in order to enable faster uncertainty quantification, we investigated running the noise engine on a GPU.

Finally, we developed the capability to run the noise engine on cloud-based platforms, specifically AWS, since this approach allows us to scale noise computations for a large number of workers and large amounts of total memory, enabling the analysis of problems whose size would be prohibitively large to execute on a single machine.

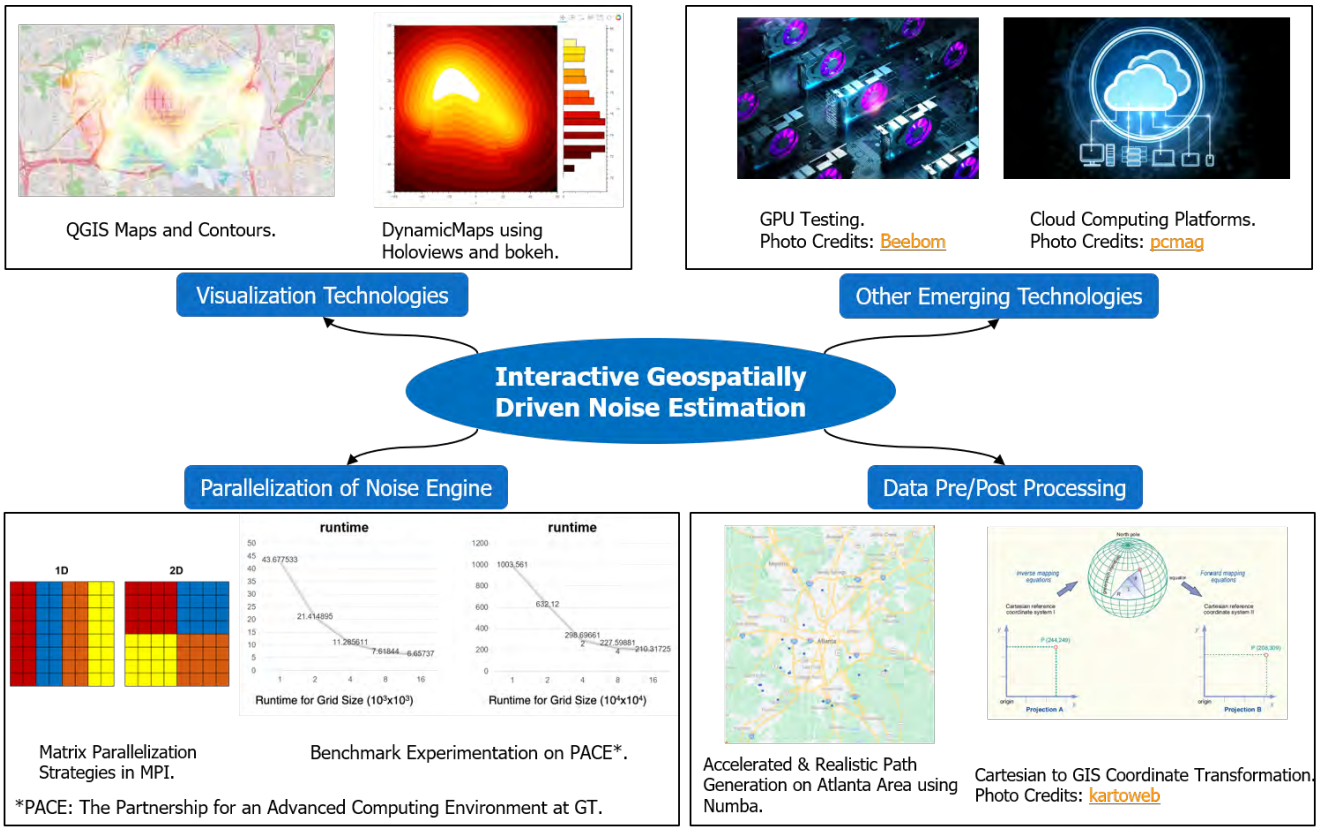

Figure 10. Visual summary of the emerging technologies under investigation. GIS: geographic information system; GPU: graphics processing unit; GT: Georgia Institute of Technology; MPI: message passing interface.

2.2. GIS Visualization Technologies

The team focused on technologies that provide interactive visualizations of large data on maps, which narrowed the choices to QGIS and interfaces based on Python or JavaScript. Working with large datasets on QGIS requires the use of an Structured Query Language (SQL) plug-in as a conduit for data communication. Furthermore, the GUI aspect of QGIS limits the interactive capabilities that can be achieved.

Therefore, the focus was directed to JavaScript and Python libraries and interfaces, including the D3 library for JavaScript and Bokeh for Python. Bokeh emerged as the preferable choice, as it builds on JavaScript visualizations without the need to explicitly use JavaScript. Furthermore, with this library, it is possible to code both the front-end and back-end of a web application using Python.

2.3. Parallel Computing Technologies

Parallel computing technologies are critical for calculations that involve large grids. These grids can be expressed as matrices and hence take advantage of their regular structures for the partition of computation tasks.

The team initiated their analysis by exploring the standards for parallel programming via the message passing interface (MPI) implemented on different libraries, such as OpenMPI, MPICH, and MVAPICH. As the noise computation engine is built from common mathematical and computational operations, OpenMPI was selected for its portability and its ability to support most existing platforms.

Parallel algorithms for matrix computations have been well documented in the literature. Typically, the data are partitioned either along one axis of the matrix or both, as shown in Figure 11. These algorithms are usually designed with considerations of the communication overhead and the computation cost for individual processors.

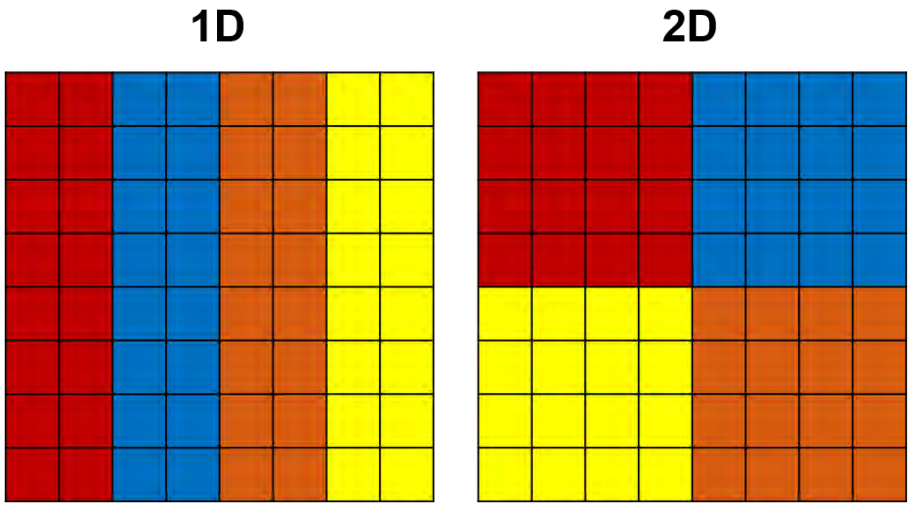

Figure 11. Common partition strategies for matrix computations.

The noise engine can be viewed as a large, dense matrix problem in which the calculations for each element do not depend on its neighbors. Instead, these calculations depend on the path of the noise source, which can be modeled as a vector. Hence, the partition strategies shown are theoretically the same, where the main challenge is to manage the data communicated. In addition to communicating the path data to each partition, the engine needs to collect the results and send them to the visualization tool.

These considerations prompted us to examine the input/output (IO) operations in parallel, as shown in Figure 12. There are three main approaches for parallel IO operations, as briefly defined below:

- Non-parallel: A central unit is uniquely responsible for the IO operations.
- Independent Parallel: Each process writes to a separate file.
- Cooperative Parallel: All processors collaboratively write in one file.

The main advantages and drawbacks for each approach are summarized in Table 3. Although the cooperative parallel approach has the potential to achieve the best performance, it is limited in the file types that can be used and may result in a performance that is worse than that of the sequential algorithm. Therefore, we did not select a cooperative parallel IO approach; instead, the choice will depend on other characteristics of the overall noise module.

Table 3. Parallel input/output (IO) operations.

Parallel IO Approach	Advantages	Drawbacks
Non-Parallel	• Easy to code	• Poor performance (worse than sequential)
Independent Parallel	• Easy to parallelize • No inter-process communication	• Generates many small files to manage
Cooperative Parallel	• Performance can be great • Only one file is needed	• More complex to code • Depends on implementations of concurrent updates in file types, which are rare

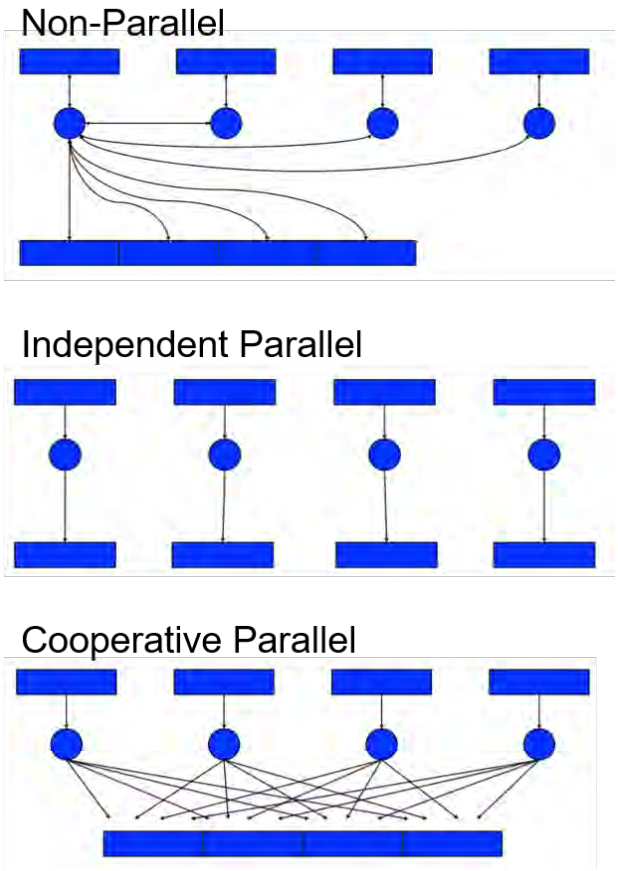

Figure 12. Input/output operations in a message passing interface.

Source: William Gropp, Introduction to MPI I/O

The analysis of parallel IO approaches led to the need to examine the file formats used in parallel as well. Three major categories of file formats are listed in Table 4, along with their major benefits and drawbacks.

- ASCII
- Binary
- Standard scientific libraries (HDF5, NetCDF, etc.)

Table 4. Benefits and drawbacks of file formats.

File Format	Advantages	Drawbacks
ASCII	• Human-readable • Portable	• Requires a larger amount of storage • Costlier for read/write operations
Binary	• Efficient storage • Less costly for read/write operations	• Needs formatting to read
Standard scientific libraries	• Allows data portability across platforms • Data stored in binary form • Includes data description	• Has a risk of corruption

This analysis was conducted with a gridded data format in mind. Instances of these files that are encoded in binary format are relatively straightforward to create and manage in parallel because the MPI writes to binary format by default. Instances that use ASCII characters are more difficult to use, however, because a binary–ASCII conversion is needed for formatting.

To showcase the runtime difference between ASCII files and binary files, a test case was run with a fixed problem size and a variable number of processors (p). The test used the independent parallel approach to eliminate the need for a central unit that collects the results. Figure 13 illustrates the runtimes of text file problems and binary problems for 2–16 processors. The "runtime no IO" scenario was included in Figure 13 as a baseline to showcase the cost of communication due to the IO operations. As expected, for a fixed problem, the runtime decreased as the number of processors increased; however, the difference between runtimes with respect to the file formats is quite apparent.

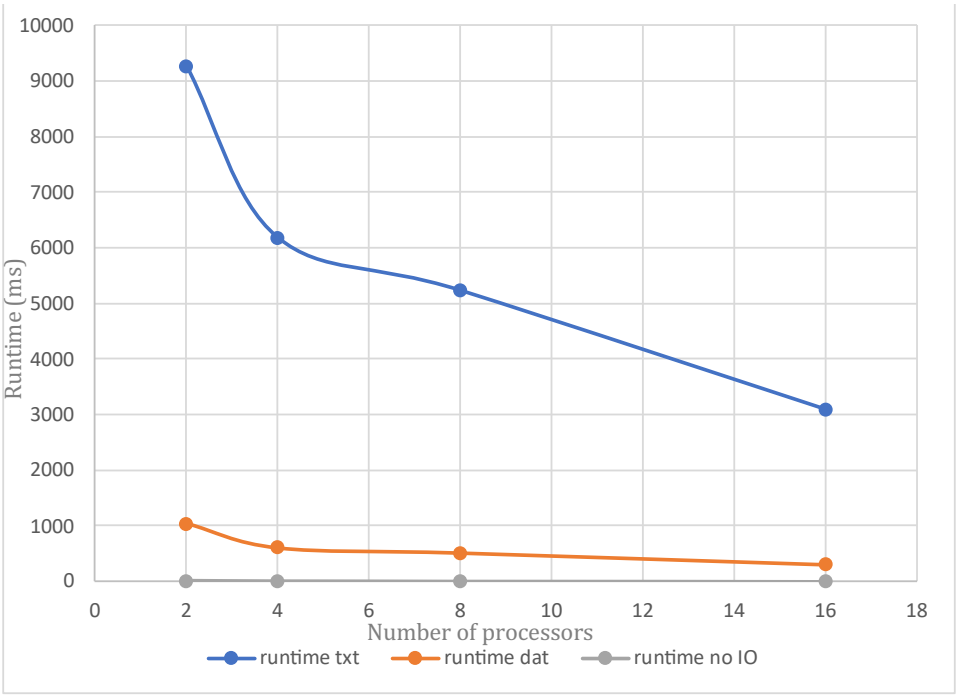

Figure 13. Runtime vs. number of processors for different input/output (IO) formats.

Furthermore, for any format used, storage space will be needed to contain the data, as shown in Figure 14, which reveals an exponential growth in size as the grid becomes finer. This test case reveals that the available memory of the hardware used will play an important role in the calculation of large grids.

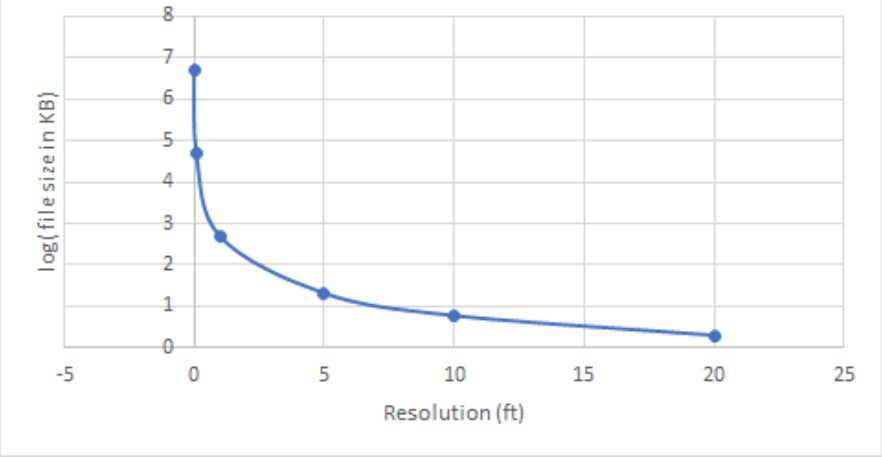

Figure 14. Log(file size in kB) vs. resolution (ft).

The choice of programming language is another important aspect to consider in this investigation. Programming languages such as C and C++ combined with MPI libraries are the primary choice of many high-performance computing (HPC) practitioners, as they have some access to low-level machine language, which results in good performance for parallel computations. However, the main challenge in using these languages is the integration with interactive GIS visualization tools. Higher-level languages such as MATLAB and Python provide these libraries with much less scripting and easier integration, but this comes at the expense of speed in running parallel code. In particular, MATLAB requires the setup of a virtual network computing session prior to launching any calculations. Python, despite being slower than C/C++, emerged as an adequate choice for the noise module, as it is better equipped to facilitate large interactive GIS visualizations without greatly sacrificing speed for this particular application while still being able to act as a wrapper for rapid C/C++ implementations of the computational code.

2.4. Data Processing Technologies

The team investigated libraries for processing GIS data. As the investigation of visualization techniques favored the use of Python to code the application, libraries such as GeoPandas and GeoTIFF were explored to assess their compatibility with the goals of this project.

The GeoPandas library brings the powerful functionalities of pandas to geospatial operations. The GeoTIFF format allows the embedding of geospatial data into images. GeoPandas is more suited to work with vector data whereas GeoTIFF supports both raster and vector formats. Each of these libraries has its own merits and utilizations and can be used in the noise calculation engine. The final choice will depend on the data pipeline from the computation to the visualization and the data conversions needed in this process.

2.5. Support for GPU-Backed Computations and Scaling Study

2.5.1. Context and Motivation

The ability to account for variability in operations, as well as other sources of uncertainty emanating from currently unknown parameters, is one of the main requirements for the UAS noise assessment tool. Indeed, the need for this ability is one of the reasons why existing tools are not adapted for UAS use cases and why the development of a new capability is needed.

Once sources of uncertainty have been characterized and quantified, Monte-Carlo simulations are a priori the preferred option for propagating the impact of those uncertainty sources to system-level responses of interest. Monte-Carlo simulations are preferred because, among the multiple options available to propagate uncertainty, running full Monte-Carlo simulations (a) usually does not require any additional assumptions regarding the nature of the uncertainty sources or the system model and (b) gives access to full probability distributions for system-level responses, which can be used to estimate any statistical quantity related to these responses. In contrast, approximate uncertainty propagation methods (a) may require

uncertainty sources and the system model to behave a certain way to produce valid results and (b) may only approximate a few statistics, such as the mean of the responses.
In the case of UAM operations, the nature of uncertainty sources (e.g., vehicles may depart and arrive in different locations, the number of flights may vary), as well as the nature of the system model, does not immediately appear to be prone to an approximation method; therefore, a full Monte-Carlo simulation will be conducted. Applying approximate uncertainty quantification on this problem will be the topic of future research.

2.5.2. Problem Definition

An initial Monte-Carlo study was carried out using the initial Dask implementation of the noise assessment tool running on a central processing unit (CPU). The setup and results of this study are discussed under Task 4. One of the main observations was the long runtime required to carry out the study: it took several weeks to complete the study, despite the use of Georgia Tech's HPC environment. This motivated the exploration of methods to speed up the execution of the noise engine.

Multiple options are available for speeding up the execution of the computer code: applying surrogate modeling and running the code on GPUs were considered as options. In the context of uncertainty propagation, a surrogate would need to take the uncertain parameters as inputs and output the system-level quantities of interest. Because of the nature of the problem and the sources of uncertainty, building such a surrogate is not immediately possible: it requires multiple steps, which were beyond the scope of this project. Instead, this will be the topic of future research.

In contrast, attempting to run the code on a GPU falls within the scope of this project, under the exploration of emerging computational technologies, and does not require a fundamental change in the computational setup. Moreover, the ability to execute the noise computations on a GPU is fully compatible with other ways of speeding up execution, such as surrogate models, as this would allow training data to be produced more rapidly.

2.5.3. Research Objective

The research objective of this subtask was to measure the benefits of running noise computations on a GPU instead of a CPU. This subtask first required that the noise computations be implemented in such a way that they can run on a GPU. Then, two studies were carried out. First, the CPU and GPU runtimes were compared to confirm the benefits brought by the GPU in terms of runtime: because the runtime on a CPU is high, this first study was conducted on relatively small problems. Second, to estimate the ability of GPU-backed computations to handle larger problems, a scaling study was performed, in which the evolution of GPU runtime was estimated as a function of the problem size. Along with runtime, memory requirements also become a challenge for large problems; thus, the memory requirements were estimated.

2.5.4. Technical Approach

Dask is a framework for executing parallel processing across many machines, while presenting the user with simple and familiar storage and computational approaches. Internally, Dask includes optimization routines that optimize the flow of code and data across machines. Because Dask's GPU capabilities presented limitations, Google's JAX, another computational framework, was selected to run the noise engine on a GPU. JAX is a cutting-edge computational framework developed at Google that combines XLA, the computational back-end behind TensorFlow, with other tools such as autodiff for automatic differentiation, all while keeping the same simple API as numpy, Python's de facto standard library for numerical computations. JAX allows one to re-use the exact same code to run on a GPU instead of a CPU when available.

As discussed previously, runtime and memory use are the two metrics on which we focus to 1) compare CPU and GPU implementation and 2) study GPU scaling. In our case, runtime is simply measured using wall-clock time: the time instants before and after the computations are recorded, and their difference yields the elapsed wall-clock time. Care was taken to ensure that computations were actually carried out within the measured time interval: Dask, among others, implements the concept of "lazy evaluation," in which expressions may not be actually evaluated until the result is accessed.

Measuring memory use is more challenging, as it depends on the back-end (CPU or GPU). For the CPU, we could not find a way to directly measure the amount of memory used by specific processes. This step is more difficult with Dask because multiple processes may be spawned to handle computations. As a work-around, the total memory use is recorded before computations are started and then continuously updated at regular intervals while the computations are running, and only the maximum system memory use is retained. Memory use is estimated by the difference between maximum memory use during computations and the pre-computation system memory use. This estimation assumes that the difference in memory usage can be solely attributed to the noise assessment computations and that other mechanisms, such as memory swapping

to disk, do not occur. To avoid swapping, the problem dimensions considered when performing the computations on the CPU were kept relatively small.

Measuring GPU usage was not possible via JAX's built-in functions, as a mismatch was observed between actual GPU memory usage and the value returned by JAX's helper functions. As a consequence, we applied the same approach used for the CPU, except that CUDA-specific commands were issued when polling the GPU memory usage.

As explained previously, the first step of this study was to compare CPU and GPU runtimes. For completeness, the original Dask back-end was also considered in the comparison, both with and without atmospheric absorption improvements (as briefly discussed under Task 4). We varied the problem size by varying the resolution of the square analysis grid. CPU runs were executed locally on a PC equipped with an Intel Core (i7-9700 CPU and 16 GB of RAM). GPU runs were executed on nodes of Georgia Tech's PACE (Partnership for an Advanced Computing Environment) cluster equipped with a Tesla V100 (32 GB) GPU.

In the second step, we focused on GPU runs only. Multiple dimensions of the problem were varied to obtain a wide range of problem size. We varied the resolution, as in the first part of the study, and the number and maximum length of the trajectories. In the current implementation, trajectories are handled sequentially, while for a given trajectory, the complete grid as well as all of the trajectory's time steps are simultaneously computed. Thus, we expect all of those dimensions to influence the runtime, while memory use should not be affected by the number of trajectories, since they are treated sequentially.

To increase the maximum allowable GPU memory use, and therefore the maximum size of the problems under consideration, a dual-GPU implementation was developed. This dual-GPU implementation took advantage of the fact that Georgia Tech's PACE cluster offers some nodes with two GPUs, totaling 64 GB of GPU memory. In the current implementation, the analysis grid on which noise exposure levels are computed is split into two regions: the first half is processed on one GPU while the second half is processed on the second GPU. Because all analysis points are independent, this approach does not introduce communication overhead.

2.5.5. Results

Error! Reference source not found. Figure 15 depicts the evolution of t he runtime duration in seconds as a function of the analysis grid resolution for four cases: the original Dask implementation with and without atmospheric absorption, JAX (CPU), and JAX running on a GPU. Here, a log scale is used for the duration on the y-axis. We observe that JAX on a GPU is faster than CPU-based computations by approximately two orders of magnitude: running the same code on a GPU instead of a CPU allows a 100-fold speed-up. This gain is significant, especially when considering the many cases that need to be run as part of an uncertain propagation study using Monte-Carlo simulations.

The differences between the different CPU implementations can be justified as follows. First, neglecting atmospheric absorption consistently reduces runtime across the considered grid resolutions, compared with the Dask version of the noise engine that accounts for atmospheric absorption. We found that the CPU JAX version of the code initially runs faster than its Dask counterpart for small resolutions, but appears to match the Dask implementation for higher resolutions. We hypothesize that this result is due to the overhead introduced by Dask when setting up its scheduler and workers: while this overhead is significant for low-resolution grids that can be rapidly analyzed, it becomes negligible compared with the actual cost of computations once the resolution increases sufficiently.

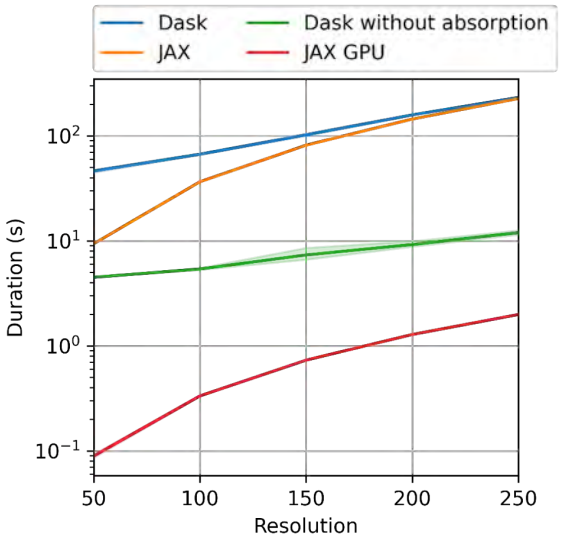

Figure 15. Runtime comparison between different implementations of the noise model. GPU: graphics processing unit.

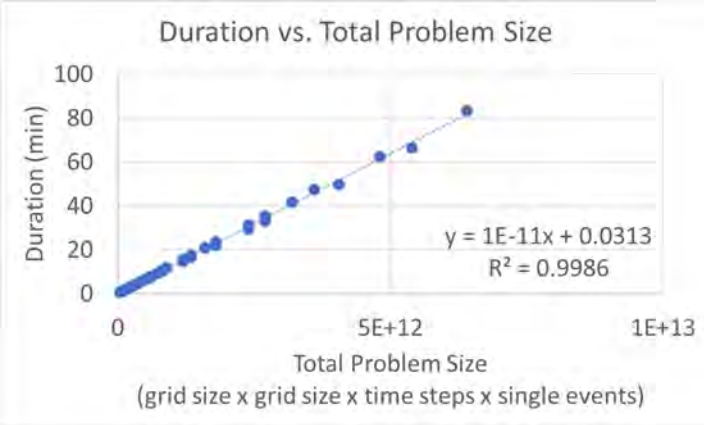

Figure 16. Scaling of the runtime of the graphics processing unit (GPU) implementation.

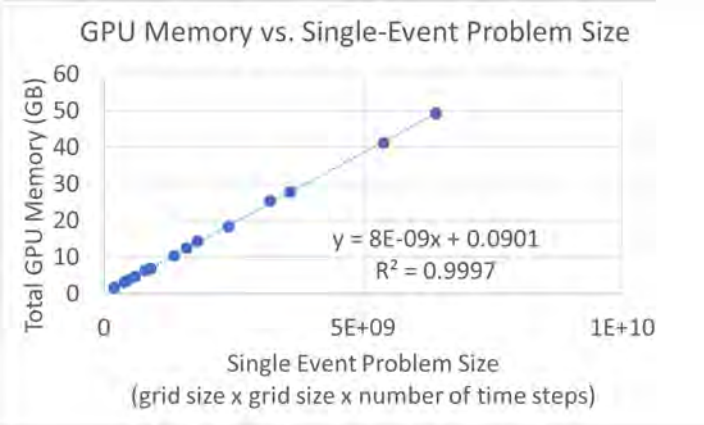

Figure 17. Scaling of the memory use of the graphics processing unit (GPU) implementation.

Figures 16 and 17 depict (a) the evolution of the runtime duration as a function of the total problem size and (b) GPU memory as a function of the single-event problem size, respectively. As discussed previously, while the total problem size encompasses all dimensions of the problem, including the number of trajectories (referred to as single events here), the single-event problem size corresponds to the problem size for a given trajectory. As expected, the duration depends on the total problem size, whereas the total GPU memory depends on the single-event problem size because trajectories are processed sequentially by the current implementation. In both cases, linear regression confirms a linear dependence.

These graphs can be used to estimate the runtime and GPU memory use when running a new case: the total and single-event problem sizes can be computed from the individual problem dimensions, and the linear formulae provided here can be used to obtain a runtime and memory use estimate. In practical applications, this information can be used to estimate the total duration of, for example, a Monte-Carlo simulation or to ensure that the memory use will not exceed the available GPU memory.

2.5.6. Conclusions

The two studies carried out in this section confirm the benefits brought by GPU computation. Thanks to the JAX framework, the same code can be used on a CPU for local development and testing and then on a GPU when additional speed is needed. These benefits are substantial: a 100-fold speed-up was observed when the same code ran on a GPU instead of a CPU. In the Task 4 Section, we will see that this enables us to run a Monte-Carlo simulation in a couple hours, when it would have taken weeks if ran on a CPU.

2.6. Cloud-Based Computations on AWS

2.6.1. Context and Motivation

Among emerging technologies suitable for use in the development of the UAS noise assessment tool, cloud-based options were retained because they enable a flexible selection of the amount of computational resources allocated to solving a problem. For example, when using Dask paired with AWS Elastic Compute Cloud (EC2), the user can choose the number and characteristics of workers across which computations are distributed: each worker will be executed within a dynamically spawn AWS instance with its own resources, and individual instance resources can be selected based on AWS' offerings. This flexibility allows us to tackle a wide spectrum of problem sizes: from the small problems encountered, for example, when developing and debugging the noise engine to the larger problems encountered when running a full-fledged noise assessment on a large urban area.

2.6.2. Problem Definition and Research Objective

While executing the noise engine on AWS EC2 is made easier by using Dask as a computational framework, the level of maturity of these frameworks still does not allow for a plug-and-play experience. Multiple hurdles had to be overcome in

order to successfully run noise computations in the cloud. In this section, we document the required steps, in order to ease the process for future users and developers of the tool.

Because ASDL does not have specific resources allocated to AWS EC2, this development effort was carried out using Amazon's free-tier instances, which have limited computational power and system memory (a single virtual CPU and 1 GB of RAM). Therefore, it was not possible to demonstrate the ability to run large problems in the cloud; instead, the objective was to develop a proof-of-concept end-to-end workflow using a simplistic scenario (small grid and very few flights). Scaling to larger problems should not raise additional technical hurdles, but should simply require the allocation of additional resources, which can be easily done by the user via simple configuration parameters.

2.6.3. Technical Details

The content of this section is very detailed: at the time of implementation, such details are needed in order to benefit from the advantages of cloud-based computations.

Initial Setup Steps

The following steps can be followed to setup AWS. Depending on the organizational setup, some steps may be skipped or require different actions. For example, instead of creating a root account and using it to create a lower-privilege account, a lower-privilege account may need to be directly requested from the administrators of the organizational AWS EC2 account.

1. If not already available, create an AWS root account.
2. Create a lower-privilege account. For the security policy, allow programmatic access to EC2 only, "AmazonEC2FullAccess." More details on how to create a user can be found in AWS' documentation.
3. Install and configure AWS CLI on the client machine. Use "pip install awscli" to install the CLI tool, followed by "aws configure" to proceed with the initial configuration. This step requires the user's AWS access key ID as well as their secret access key.
4. Install the dask_cloudprovider library for AWS using "pip install dask_cloudprovider[aws]."
5. The cryptography package is also needed and can be installed via "pip install cryptography."

More details are available in Dask's documentation.

Disable TLS Certificates

Dask automatically provisions AWS EC2 instances by sending a script via the AWS API. The size of this script is limited to 16 kB. However, Dask's configuration often exceeds 16 kB, mainly due to the transmission of self-signed TLS certificates used to secure cluster communications. This is a known Dask limitation discussed in the project's issue tracker:

- https://github.com/dask/dask-cloudprovider/issues/249
- https://github.com/dask/distributed/pull/4465

The proposed solution is to not use TLS certificates. This is achieved by instantiating the Dask cluster by setting the security keyword argument to False:

```
cluster = EC2Cluster(env_vars=credentials, security=False)
```

As a result, for example, the Dask dashboard is not available through https, only http. Additional steps can be taken to properly secure the dashboard if served from a publicly accessible server.

More details on the user-provided setup scripts for creating AWS EC2 instances can be found in AWS EC2's documentation:

- https://docs.aws.amazon.com/AWSEC2/latest/UserGuide/ec2-instance-metadata.html
- https://docs.aws.amazon.com/AWSEC2/latest/UserGuide/instancedata-add-user-data.html

Python and Package Versions

Other errors may arise when using Python 3.9/3.10, and the solution is to use Python version 3.8 or earlier. The relevant tracked issue is located at https://github.com/dask/dask-cloudprovider/issues/359.

We must ensure that package versions match between client and EC2 instances that are automatically set up by Dask. Dask issues a warning when versions mismatch. This is important, as class instances created on EC2 using one version are serialized and sent back to the client, which may not be able to deserialize them.

Debugging the AWS EC2 Workers

Debugging is difficult due to the fact that the workers are ephemeral EC2 instances. Workers are automatically terminated by Dask when an error is encountered. The only output that can be easily accessed after EC2 instances are terminated is the system log. Dask can be configured to log to the system log. The steps to achieve this are documented in the Dask and Python logging library documentations:

- https://docs.dask.org/en/stable/how-to/debug.html?highlight=logging#logs
- https://docs.Python.org/3/library/logging.handlers.html

Manually Copying Scripts to Workers and Manually Configuring Workers' Python Environments

All of the additional scripts called from the main script used to launch the Dask instance (such as library files not installed through pip) need to be manually copied to the workers (EC2 instances) using `client.upload_file()`. Likewise, Python environments local to the workers also need to be manually set up, using Dask's PipInstall "worker plug-in."

2.6.5. Conclusions

A proof of concept was developed to illustrate how the noise assessment tool can run in the cloud. Because of the limited resources available to the team, a problem of very limited size was considered. This effort allowed us to gauge the ease of using Dask's cloud functionalities: although the capability to run a computation with minimal changes to the initial Dask implementation exists, the experience is not yet seamless. Hopefully, the documentation provided here will help streamline the use of Dask in the cloud.

Task 3 - Collaboration with the UAS Computation Module Development Team

Georgia Institute of Technology

Task 3 Contents

3.1. MSU Collaboration

3.1.1. Objective

In this task, we collaborated with the UAS computation module development team at MSU to explore ways in which both teams can effectively exchange data and ideas.

3.1.2. Research Approach

The ASCENT9 team met with the team working on the eCommerce project at MSU on a bi-weekly basis. Led by Dr. Adrian Sescu, this team provided demand data and a data generator to create random UAS paths. The teams discussed the simulation of noise footprints from a notional UAS delivery network in the Memphis area. The ASCENT9 team shared an early version of the noise engine calculation with the MSU team.

The eCommerce project revolved around emerging UAS networks and their implications in national airspace system integration. The project's case study is an analysis of an Amazon UAS delivery network using ground support. The MSU team collected data for warehouses in the greater Memphis area along with the residential addresses served by these warehouses. Trucks were placed in the area to reduce the flight time of the UASs and to help with last-mile delivery. These warehouses are shown in Figure 18. Multiple scenarios were considered in this study:

- 8 drones per warehouse and 4 drones per truck (1,132 drones)
- 12 drones per warehouse and 6 drones per truck (1,698 drones)
- 16 drones per warehouse and 8 drones per truck (2,264 drones)
- 24 drones per warehouse and 12 drones per truck (3,396 drones)

- 32 drones per warehouse and 16 drones per truck (4,528 drones)
- 55 drones per warehouse and 50 drones per truck (12,305 drones)

The ASCENT9 team shared an early version of the noise engine developed under Task 4 with the MSU team, who verified that they were able to run the noise engine on their systems.

The ASCENT9 team used the first scenario to test the noise engine with variable grid precision. These trajectories are shown in Figures 18 and 19. The trajectories span an area of approximately 40 miles, with each trajectory's length varying between 3,000 and 8,000 ft.

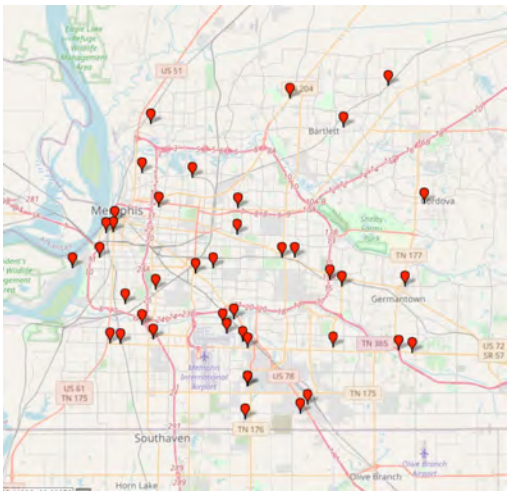

Figure 18. Warehouses in the Memphis, TN area.

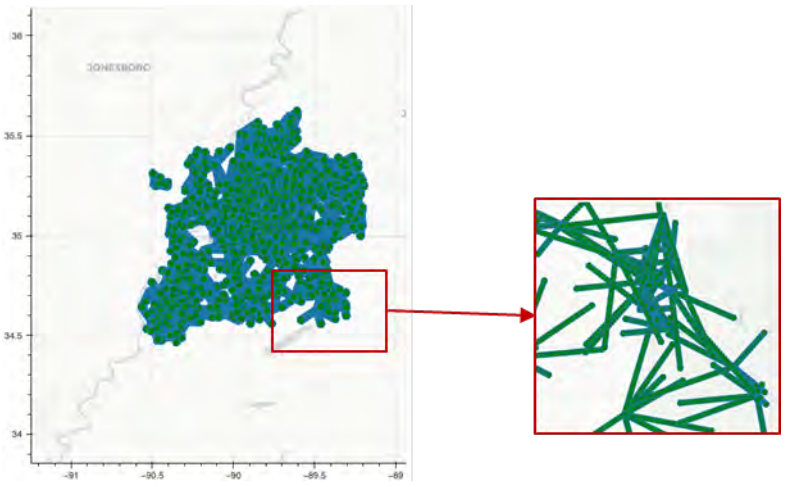

Figure 19. Random trajectories provided by Mississippi State University.

3.2. Volpe Collaboration

In addition to collaborating with MSU, the ASCENT9 team collaborated with the Volpe Research Center to acquire national transportation noise data. These data consist of combined gridded road, aviation, and railroad noise for the entire United States provided in A-weighted 24-hr exposure levels. These data are used as background noise that is added to the noise calculated by the engine module. A cropped overview of these data for the greater Memphis area is shown in Figure 20.

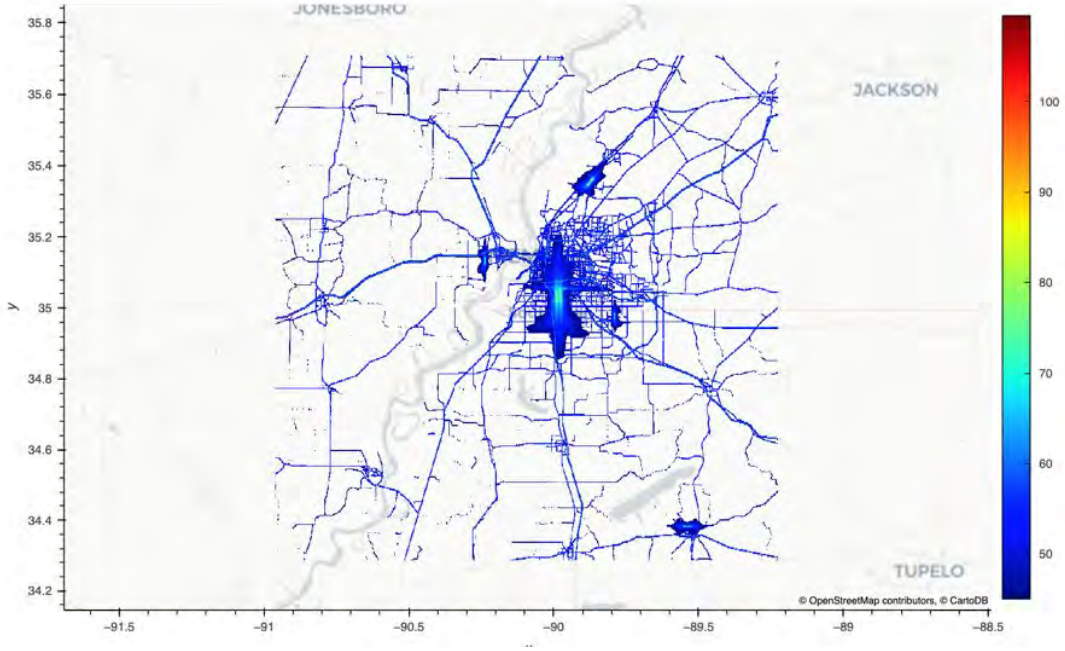

Figure 20. National transportation noise data for the greater Memphis area.

3.3. PACE Collaboration

In addition to these external collaborations, this research was also supported in part through research cyber-infrastructure resources and services provided by PACE at the Georgia Institute of Technology. This computing environment consists of a large computing cluster that was used to develop and test the noise engine under Task 4. This cluster was also used to conduct experiments and help tune various parameters and aspects of how the noise engine is executed in parallel. For example, parameters range from the number of computing nodes to the amount of memory per node and the number of parallel processes per node.

3.4. Improvements to MSU's Trajectory Generation Code

After the MSU collaboration ended, the initial trajectory generation code was reworked. In addition to introducing a more efficient implementation and increased flexibility, the code was broken down into multiple logical steps that relate to different phases of the workflow, as presented in the Task 4 Section.

Prior to the proper noise computations, the first step consists of creating tuples of staging locations, delivery locations, and vehicles. In general, these locations are the start and end points of a flight. For example, if different use cases are considered, such as for an e-taxi, these locations would map to pick-up and drop-off locations. The generation of these so-called "pairings" is dictated by the concept of operations, and these pairings are then used as input for the actual noise assessment. Currently, the implementation of this step is simple because only straight trajectories are considered, with either hover, cruise climb, or cruise flight segments. This logic could be made more complex in the future in order to accommodate new concepts of operations. Here, this logic is separated because it is independent from the noise computations and can therefore be developed in parallel, as long as the data interface between these two steps of the workflow is properly maintained.

In the second step, the definitions of the flights, or flight segments, are discretized in time. We have included this step as part of the preliminary analysis because the need for time discretization is purely an artifact of the current analysis method. If another analysis method was to directly take in flight segments as inputs instead of vehicle locations, then the flight segments would not need to be discretized.

This split also has the advantage of allowing for a more compact representation of a scenario, i.e., a set of daily flights.

Among other improvements, the vehicle attributes are now provided externally and stored in a CSV file instead of being hard-coded.

Task 4 - Noise Computation Engine Integration

Georgia Institute of Technology

Task 4 Contents

4.1. Task Overview

The motivation for developing a noise assessment tool specific to UASs was presented in the previous sections, and the previous tasks aimed at investigating the building blocks for this tool. Once promising technologies have been identified for the application components, they must be integrated within a coherent and easy-to-use tool: this is the purpose of Task 4.

The following sections are organized chronologically: an initial implementation was developed and used to carry out an initial benchmark study and an initial Monte-Carlo study. Then, a consequent refactor of the code was undertaken to improve both the internal code structure and the user interface. The refactor was intended to make it easier to work with and extend the codebase. This latest iteration was used to study the effect of interactions between trajectories. Finally, a new uncertainty propagation study is discussed, in which we took advantage of the speed-up brought by the GPU implementation discussed and studied in the Task 2 Section.

4.2. Initial Noise Computation Engine Implementation

The investigation conducted in Task 2 led to the identification of adequate tools to build a high-performance, interactive, GIS-based noise module for UASs. A Python web application was set to be built with the ability to run either locally or in a distributed setting provided by the HPC infrastructure of Georgia Tech PACE. As Python was already determined to be the programming language for this module, different libraries enabling parallel matrix computation and large interactive visualization were explored. The selection process resulted in four libraries, as shown in Figure 21.

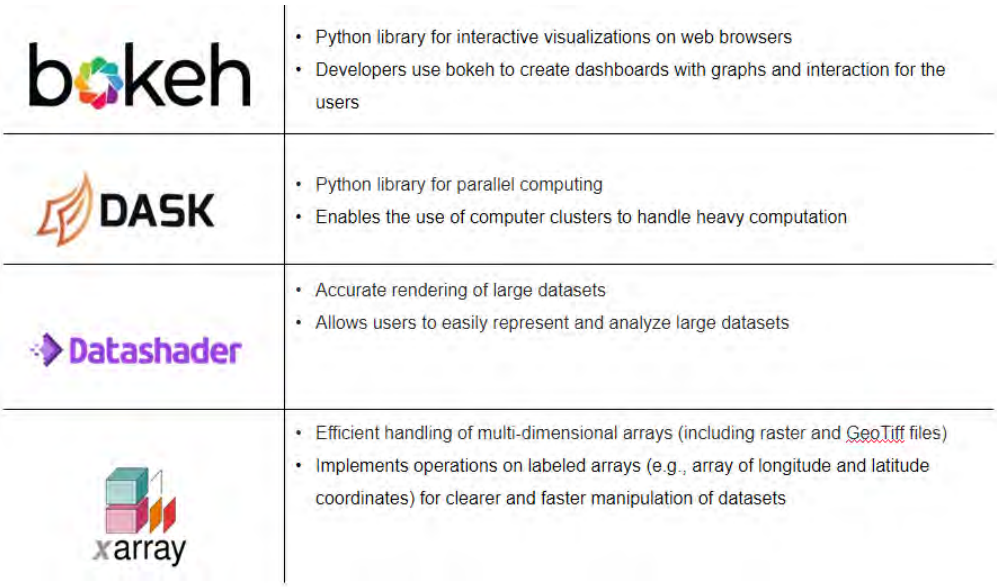

Figure 21. Enabling capabilities for the unmanned aircraft system (UAS) noise engine prototype.

Before showcasing the architecture of the web application, we discuss the structure of the Python object for the grid. Noise metrics are built on the distances between the grid and the path of the noise source. In other words, for each point in the path, its distance to every point in the grid must be calculated. This information can be stored as a 3D matrix, where the third dimension matches the number of points in the path. A notional sketch of this structure is shown in Figure 22. This choice benefits from the highly optimized methods of numpy, a Python library for multi-dimensional arrays.

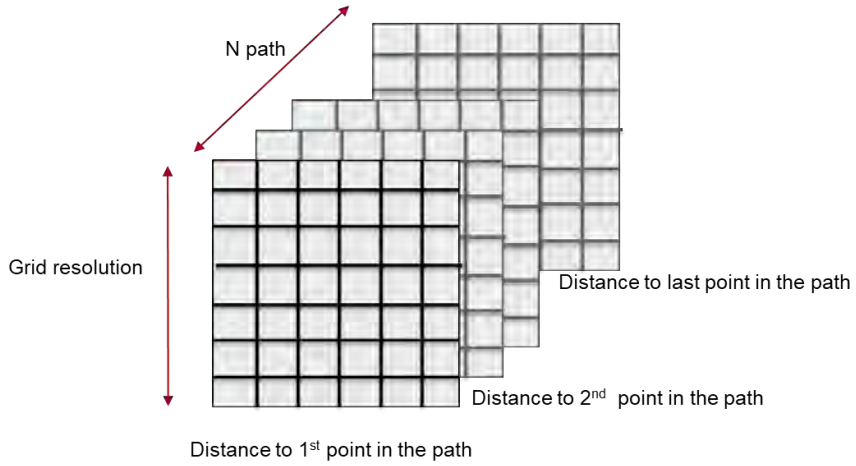

Figure 22. Notional structure of the noise module object.

The UAS prototype must demonstrate the calculation and visualization of two types of noise metrics: peak metrics and exposure metrics. The individual steps to calculate each metric are presented in Figure 23.

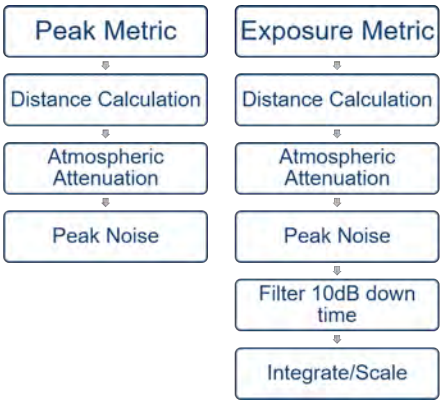

Figure 23. Steps for calculating peak and exposure noise metrics.

The parallel execution of the noise engine is carried out using the Dask library, with the following implementation steps:

1. Define computational steps as operations on generic datasets.
2. Prepare datasets.
3. Define computational resources.
4. Launch the dynamic scheduler and map/apply operations on the datasets.
5. Collect results.

The computational resources are defined by the hardware available for parallel computation, which is characterized by the number of cores or workers and the available memory per core. In addition to allowing parallel computations on single machines, Dask supports cluster schedulers such as PBS and Slurm and is supported by AWS.

The dynamic scheduler is one of the most powerful features of Dask, as it handles data partitioning and calculations without much user interference. This scheduler creates an optimized directed acyclic task graph to transfer data and apply computations using the given resources. An example of such a task graph is shown in Figure 24. This graph corresponds to a peak metric event calculation using 10 workers.

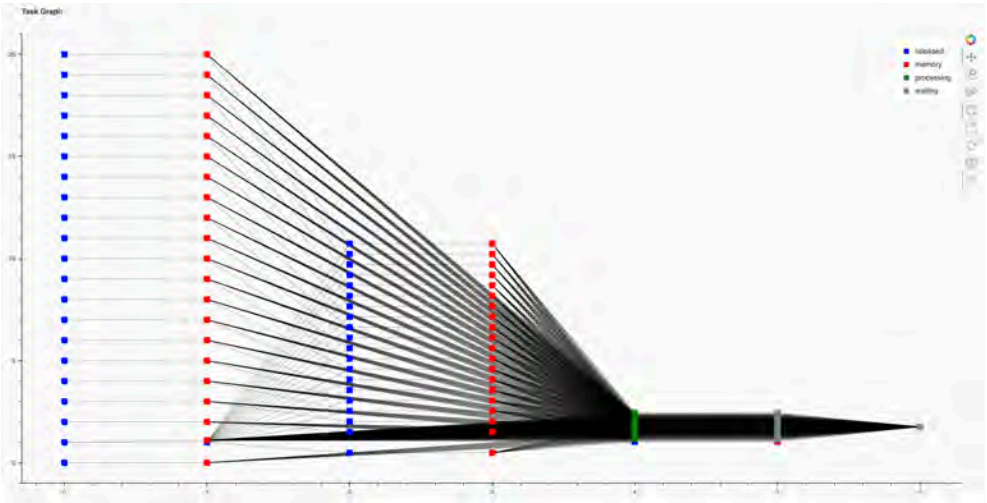

Figure 24. Task graph generated by Dask's dynamic scheduler.

The generic implementation steps on Dask are illustrated in Figure 25, where the client refers to the web browser used to visualize the noise contours.

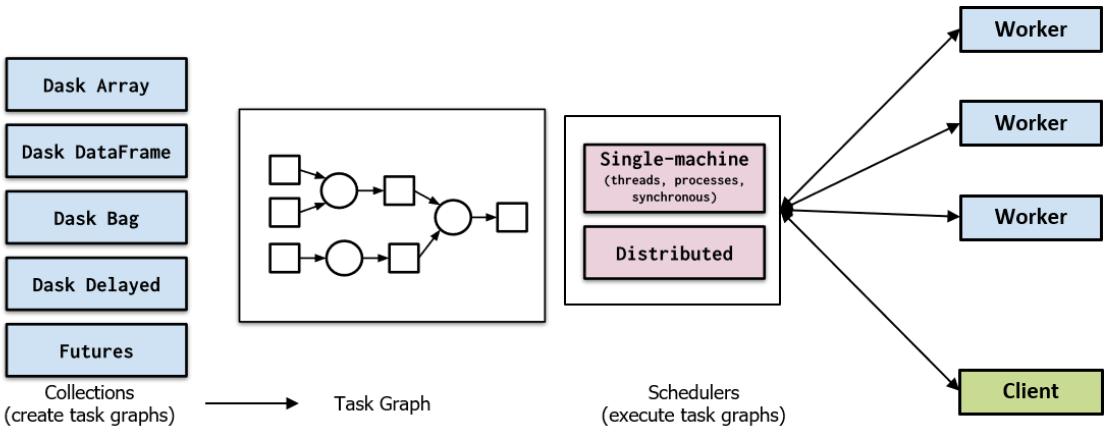

Figure 25. Implementation steps in Dask.

To visualize these contours on the browser, the Dask data objects need to undergo packaging operations using xarray and datashader. There is a limitation on the number of points a browser can support; therefore, datashader is used to allow the data to be sampled and visualized in a meaningful way. Datashader objects are integrated in Bokeh, but they do not support Dask arrays. Xarray was used to wrap the Dask objects for use within datashader. This data pipeline is illustrated in Figure 26.

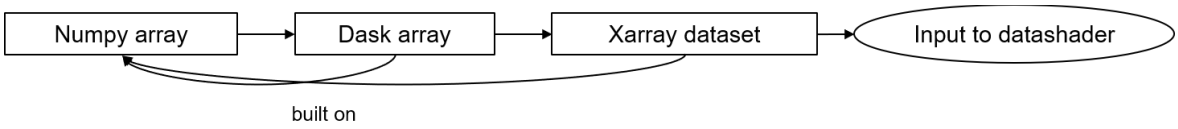

Figure 26. The data pipeline from Dask to Bokeh.

The overall architecture of the UAS noise calculation prototype is displayed in Figure 27. The noise contours are calculated and stored on the PACE distributed cluster. For visualization, Bokeh requests a portion of the data that is aggregated and projected using datashader. This step requires continuous communication between the Dask scheduler and the workers writing the data that have been bypassed to files. Alternatively, a central file could be created to collect the results; however, this comes with a high communication cost that must be considered. The data are accessible from the Bokeh server through secure ssh tunneling to the PACE interface. This is a major advantage of web applications over desktop applications, as it provides broader cross-platform access for clients.

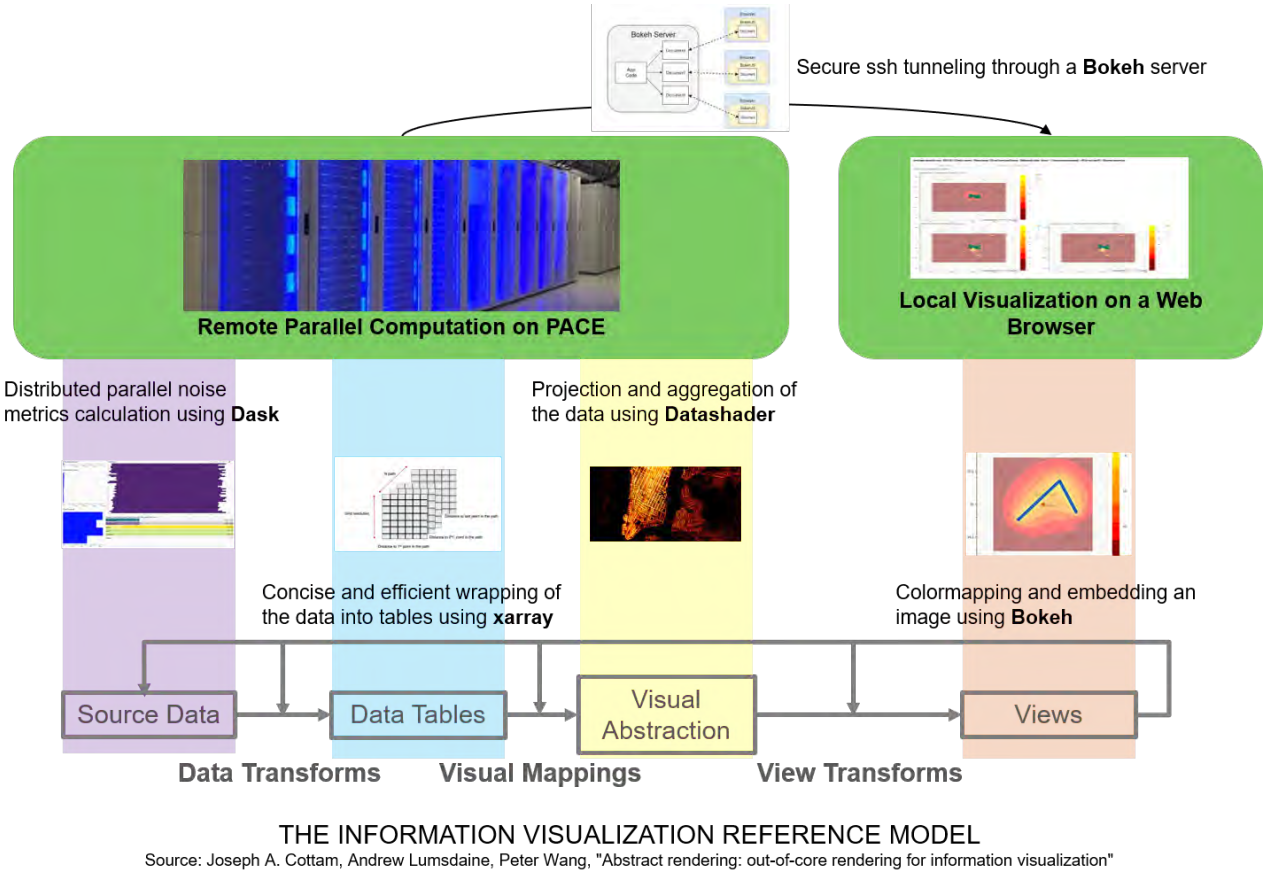

Figure 27. Overview of the noise module. PACE: Partnership for an Advanced Computing Environment.

4.3. Initial Benchmark Demonstration

This benchmark study aimed to simulate the noise footprint from a notional UAS delivery network in the greater Memphis area. In this study, 40 warehouses serving approximately 30,000 residential addresses were considered. Trucks that serve as UAS staging platforms are positioned near some neighborhoods, which reduces UAS range requirements and reduces delivery times. For this study, 8 UASs per warehouse were considered, with 4 UASs per truck and a total of 1,132 total flights. The paths for these flights are shown in Figure 28.

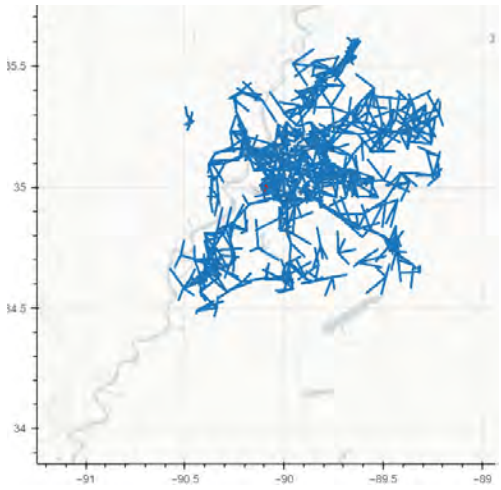

Figure 28. Flight paths in the benchmark study.

The national transportation noise map was used as background to supplement the engine's computations. The contours of this background noise are shown in Figure 29. The cumulative L_{Aeq} noise contours generated uniquely from UAS activities are displayed in Figures 30 and 31. The effect of UAS activity on the existing noise in the greater Memphis area is shown in Figure 32.

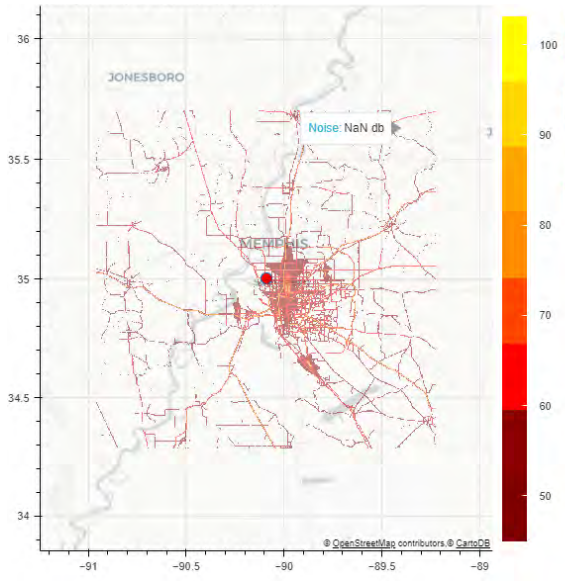

Figure 29. National transportation noise map of the greater Memphis area.

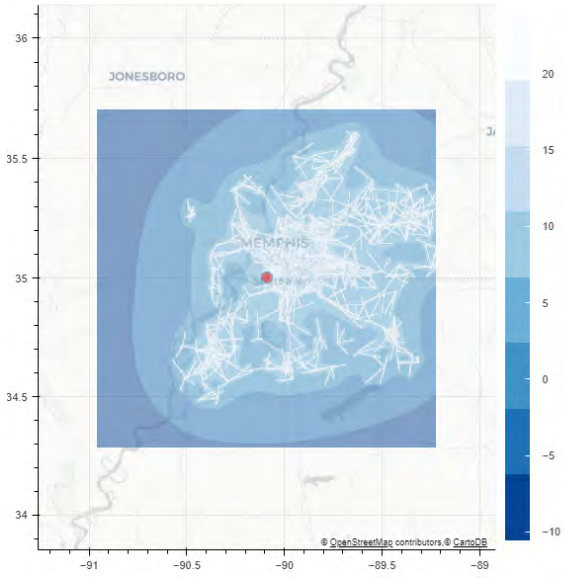

Figure 30. Computed unmanned aircraft system (UAS) noise ($L_{Aeq,24hr}$).

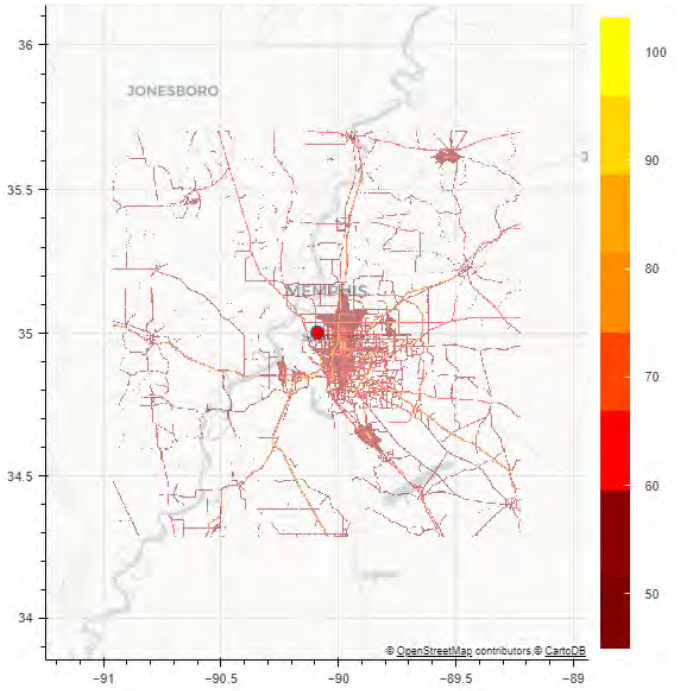

Figure 31. Combined noise ($L_{Aeq,24hr}$).

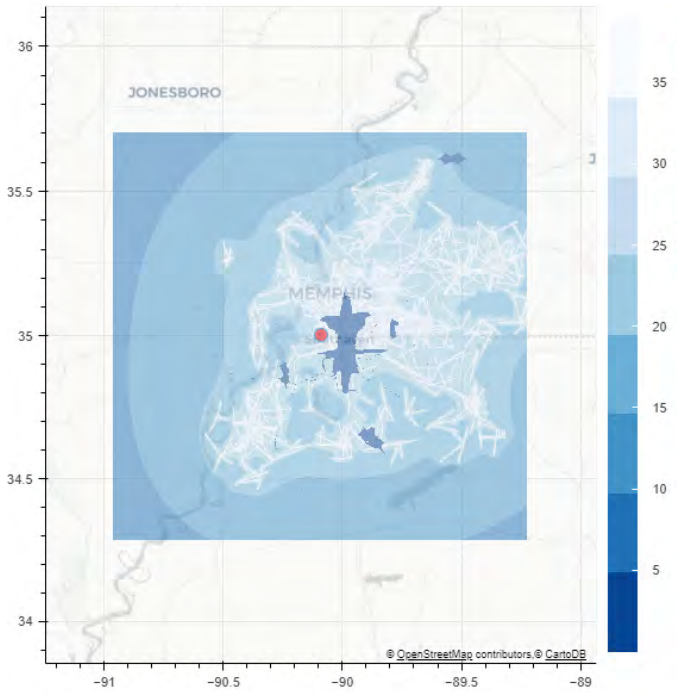

Figure 32. Change in $L_{Aeq,24hr}$.

The $L_{A,max}$ value for UAS noise with the interactive demo is illustrated in Figures 33 and 34. This figure indicates the potential difference in noise impacts across areas with high noise exposure levels compared with areas that currently have limited noise exposure levels. A large difference is found between exposure and peak metrics. The interaction can be better understood by including the background noise.

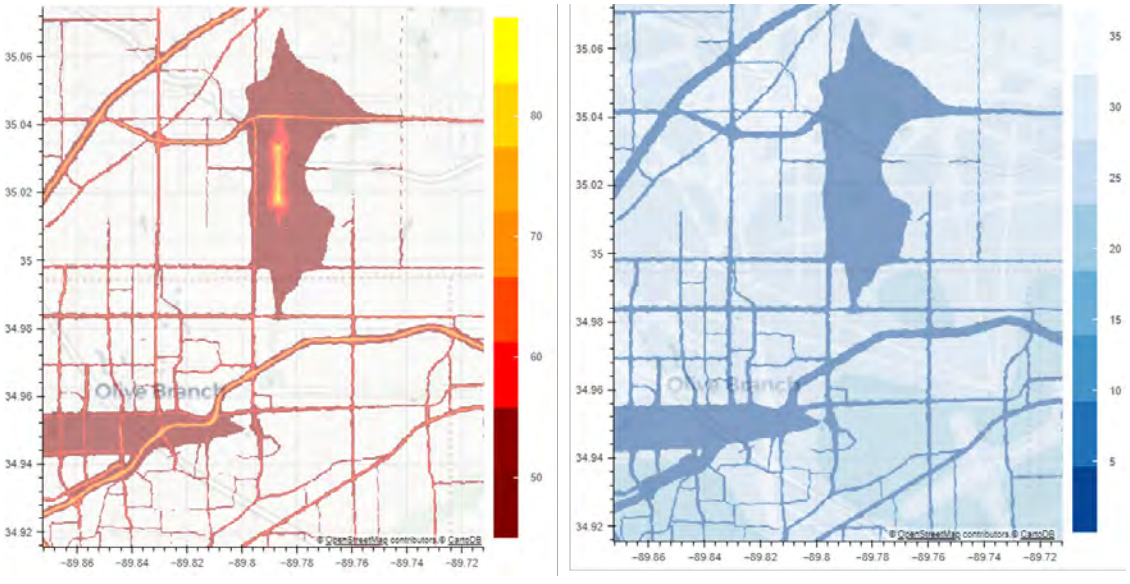

Figure 33. Combined noise $L_{Aeq,24h}$ (left) and change in $L_{Aeq,24h}$ (right).

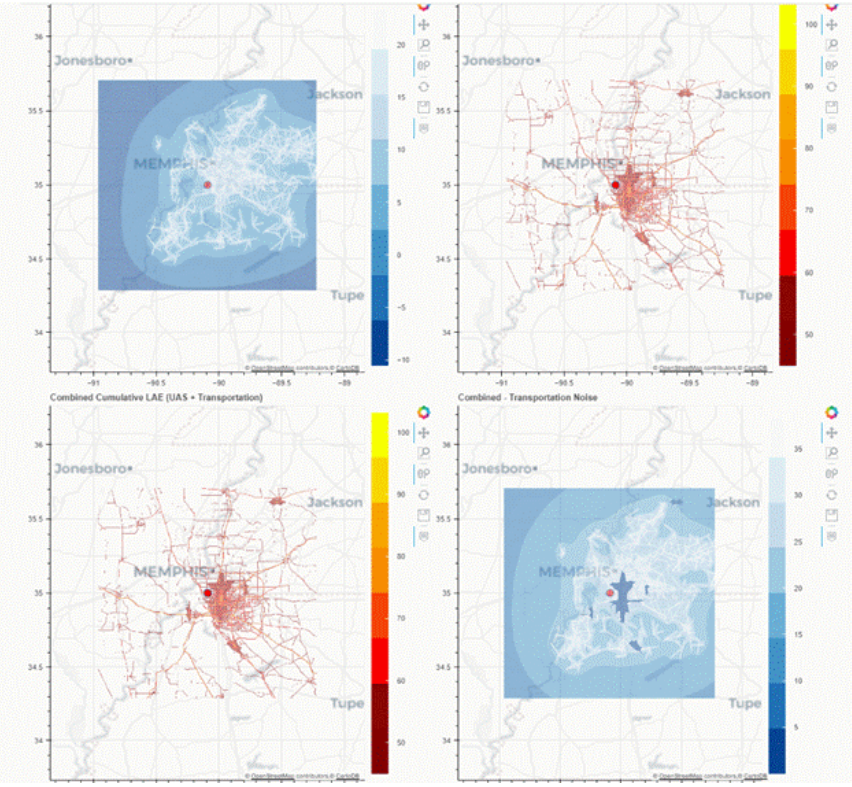

Figure 34. Interactive demo.

4.4. Initial Monte-Carlo Study

Because UAS operations are stochastic in nature, individual flight trajectories for each day depend on daily orders and demand, as shown in Figure 35. In some cases, staging locations can also vary. The operator strategy applied to the trajectory planning can also include noise dispersion and altitude constraints to minimize the noise. The annual average day metrics are not capable of capturing daily changes.

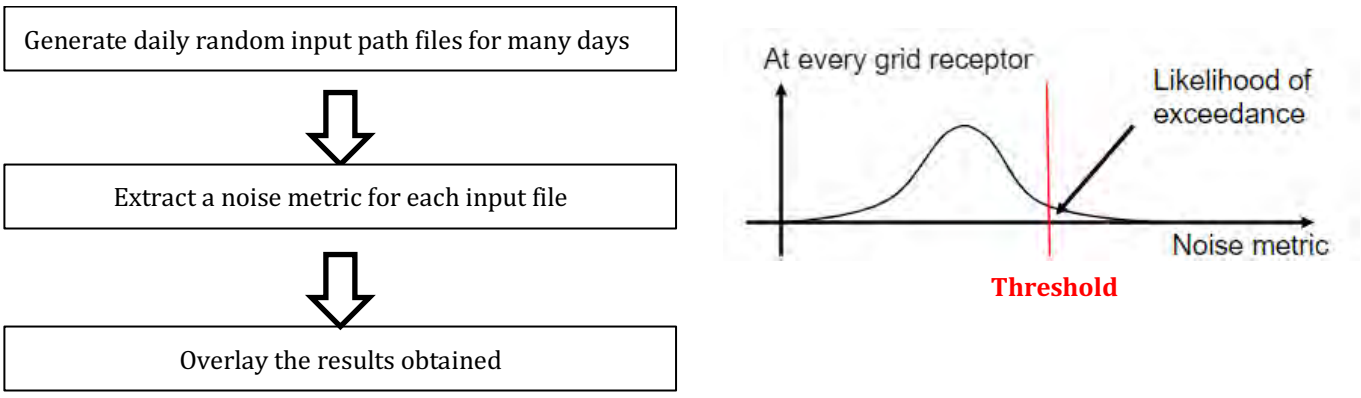

Figure 35. Notional workflow for a probabilistic approach to noise assessment.

A question arises: what is the likelihood of exceeding some threshold on any given day and how many locations will exceed this threshold? We first attempted to answer this question using a Monte-Carlo simulation; however, this process is computationally expensive. The goal of this probabilistic assessment is to obtain the likelihood of exceedance contour. The first attempt included 100 daily deliveries for 3,800 days on a coarse grid (250k points). The CPU time included 10,000 simulated days and resulted in collecting multiple noise metrics at the same time. To a first-order approximation, the delivery noise distribution was based on the address/population distribution.

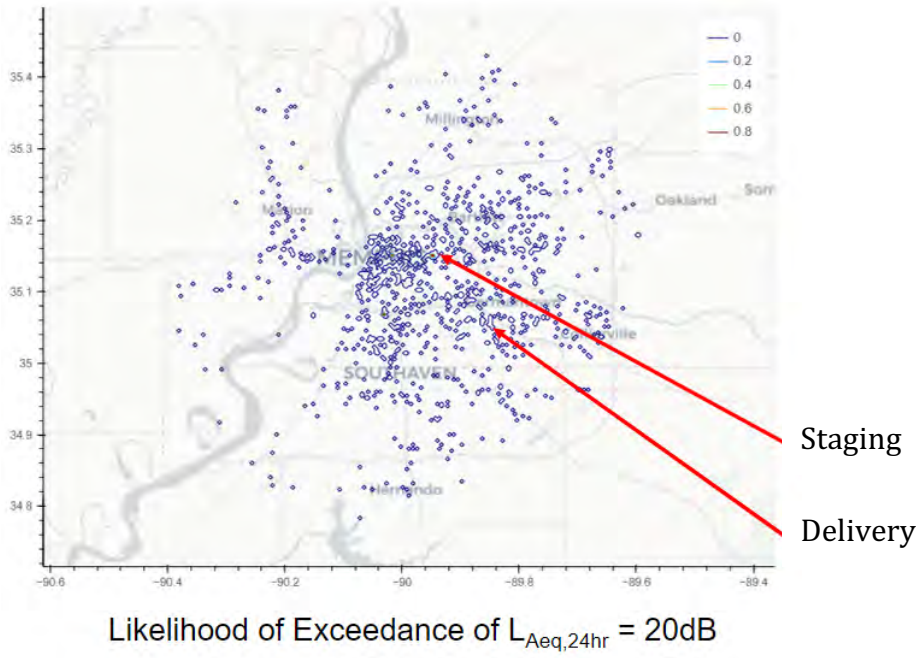

Figure 36. Likelihood of exceedance for $L_{Aeq,24hr}$ = 20 dB.

The choice of metric and threshold has a significant impact on the observed results, as demonstrated in Figure 37, which shows the likelihood of exceedance when L_{Amax} is increased from 20 dB to 50 dB.

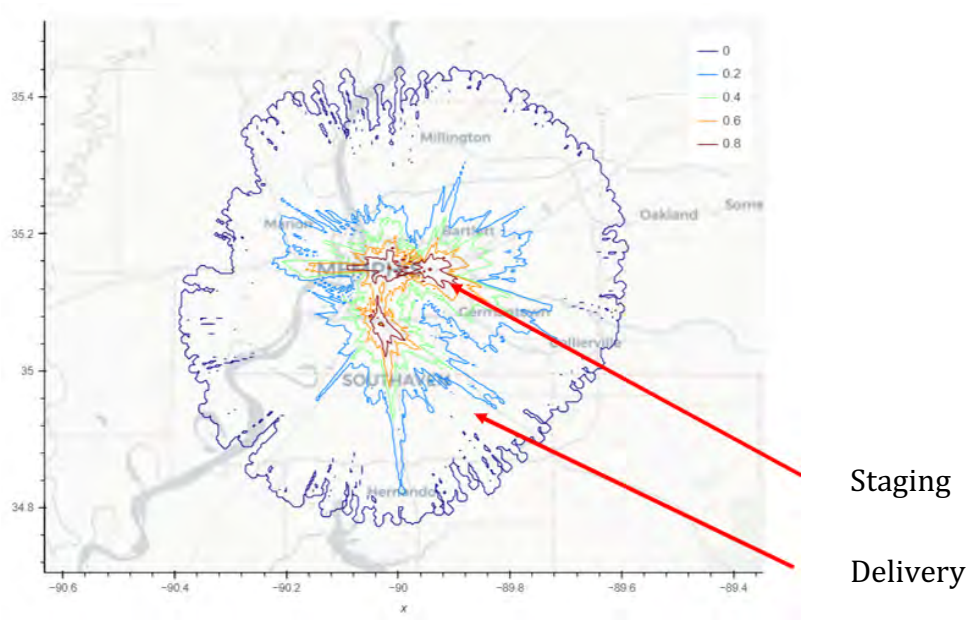

Figure 37. Likelihood of exceedance for L_{Amax} = 50 dB.

4.5. Implementation of the SAE5534 Atmospheric Absorption Model

The team implemented the atmospheric absorption losses defined in SAE ARP5543. This implementation provides a more realistic method of atmospheric sound absorption than the very simplified method used at the beginning of this project. This approach also builds on earlier standards, such as ARP866A, and allows the modeling of noise absorption to be sensitive to humidity and temperature, as expected. The current implementation works as a function that replaces the simplistic distance scaling. This function is also included in the Dask implementation as a function that utilizes parallel execution. The JAX implementation serves as the basis of a GPU shader function. While there is some penalty in the execution speed in both cases, the current implementation appears to work reasonably well. The team also worked to ensure accuracy in the implementation by comparing the implementation's output to the reference data supplied in ARP5543. In addition, the team compared the current implementation with AEDT's implementation. Both comparisons yielded only minor differences attributable to floating point precision and rounding differences.

4.6. Workflow Definition and Code Refactor

4.6.1. Workflow Definition

The analysis workflow was formalized in order to drive the development of the new GUI. The resulting workflow is depicted in Figure 38. In the first step, all of the inputs to the analysis are specified and/or loaded; this step includes defining the analysis area, generating or retrieving trajectories, and loading the background transportation noise. In the second step, analysis settings are provided by the user, and the proper noise assessment is executed. Finally, the results are visualized.

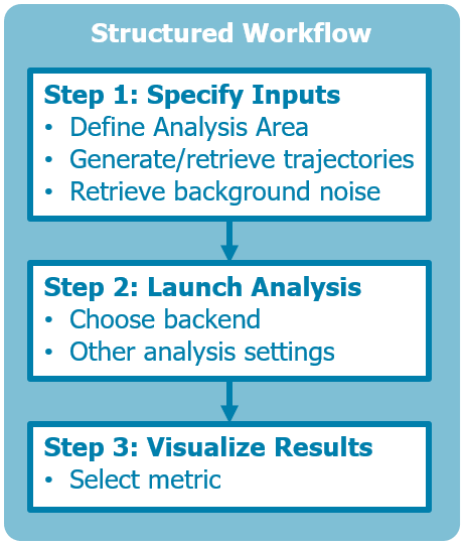

Figure 38. New structured workflow.

4.6.2. Code Refactor

A code refactor was undertaken to make the codebase more modular. By modular, we mean, for example, logically splitting the code between the GUI-related parts and the analysis-related parts. Within the part of the code devoted to the GUI, modularity means defining clear interfaces between components. For example, the map displayed in the main noise assessment tool can now easily be reused within Jupyter notebooks in the context of a stand-alone study.

Many new features were developed, including the ability to display more operational scenario details (staging and delivery locations, flights, etc.), the inclusion of multiple input panels allowing the user to specify analysis inputs (instead of hard-coded values), and an integrated display of all output metrics on a single map.

As mentioned in the Task 2 Section, the trajectory generation was also enhanced, with more flexibility in defining new vehicles and their noise characteristics.

4.6.3. Upgraded GUI

The upgraded GUI is shown in Figure 39. Similar to most GIS software, the map occupies most of the screen. On the left-hand side, a tab-divided panel contains all of the controls necessary to follow the workflow defined in the previous section.

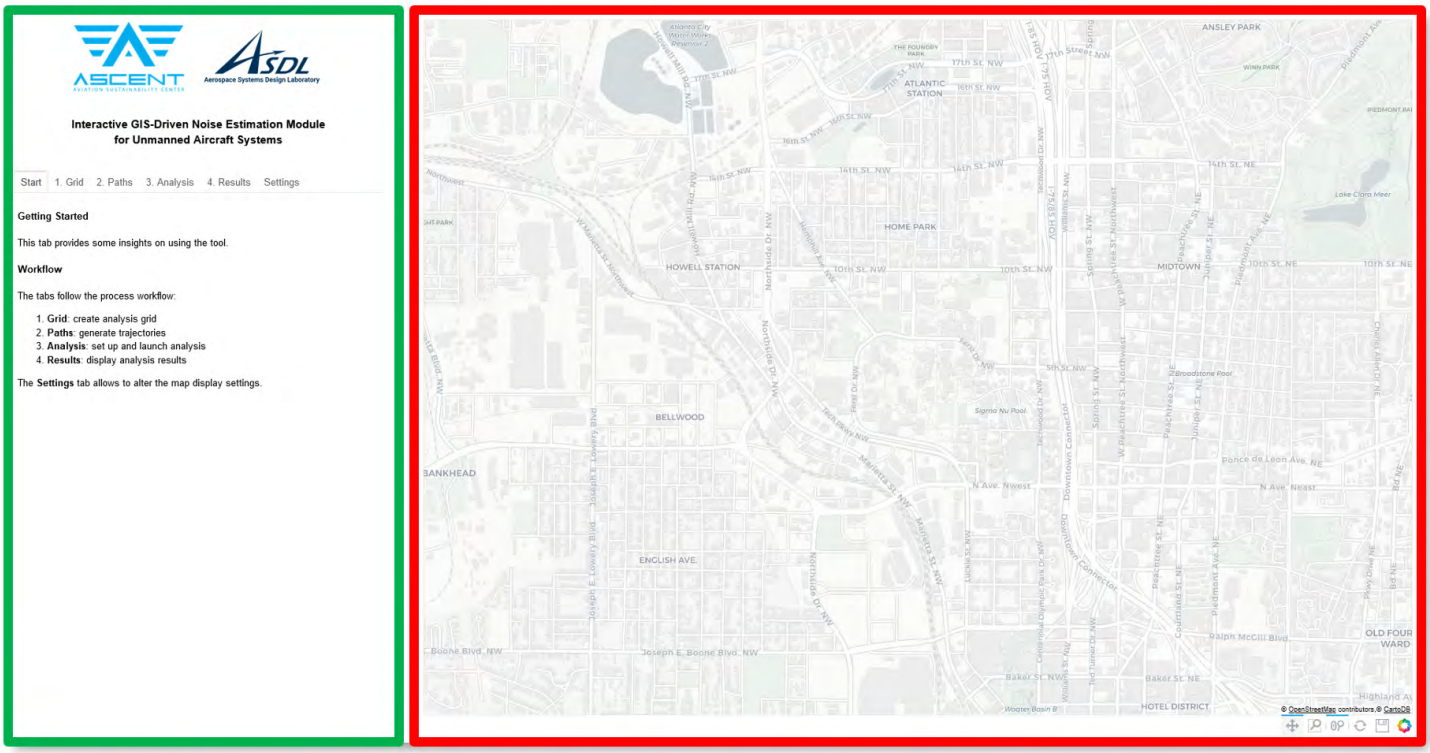

Figure 39a. Annotated screenshot of the new graphic user interface. The left-hand side (shown in a green box for emphasis) displays the control panel, featuring tab-based navigation. The visualization map occupies the remaining space on the right-hand side (shown in a red box for emphasis).

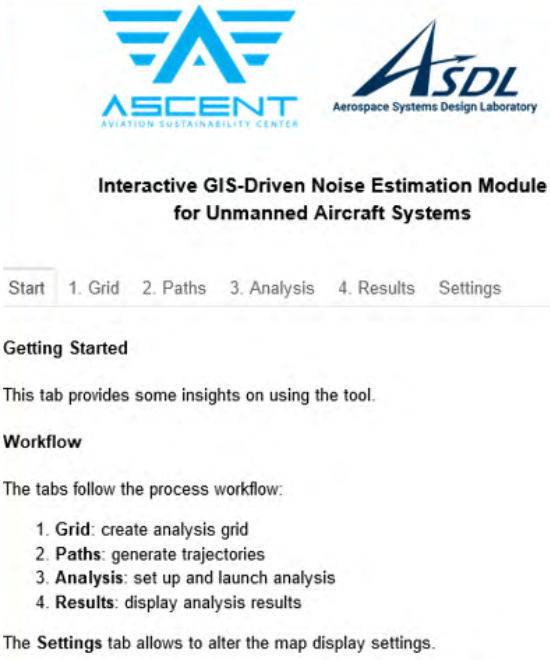

Figure 39b. Screenshot of the control panel of the new graphic user interface.

4.7. Study of Interactions Between Trajectories

4.7.1. Motivation and Objective

In the current implementation of the noise engine, trajectories are processed separately. Therefore, the combined impact of two flights at the same geographical location (i.e., the same virtual microphone) is not considered. To assess the validity of this simplification in the context of the operational scenarios under consideration, we conducted a study to quantify the discrepancy introduced by this approach.

Instead of using a full operational scenario to characterize the discrepancy, we focused on a smaller test case, and we proceeded in two steps. First, using two vehicles, we illustrated the error that results when the two vehicles are considered independently. We then generalized this error to a larger number of vehicles: because of the simple noise model being used, the error could be computed analytically as a function of the vehicle number. This first part of the study allowed us to identify the types of situations in which the error was significant, namely, when multiple vehicles were simultaneously close to a microphone location. Then, in a second step, we sought to determine the frequency at which such situations occurred in the considered operational scenarios.

More specifically, we aimed to assess the impact of computing the $L_{A,max}$ metric by considering all vehicles independently, rather than summing the individual sound intensities of nearby vehicles at every microphone location. We focused on the $L_{A,max}$ metric because this is the only metric of interest that is affected by an independent treatment of trajectories. The other metrics result from a time integration, making the concurrency of events irrelevant to their final computed value.

The following simplifications were made compared with the usual noise assessment setup:

- The analysis grid consists of a single microphone.
- All vehicles had the same noise level at 100 ft (65 dBA).
- All vehicles flew at the same altitude/z-coordinate (100 ft).
- Each vehicle was located at a set distance from the microphone in the horizontal x-y plane.

4.7.2. Two Vehicles with Varying Distance from the Microphone

We considered two vehicles and varied their respective distances, d_1 and d_2, to the microphone in the x-y plane (same altitude, same source noise level). As shown in Figure 40, the difference in the two metrics approaches zero when the vehicles are far from each other (one has a significantly higher contribution than the other; therefore, taking the maximum of the two noise levels becomes a good approximation). When the two vehicles are located at the same distance from the microphone, the intensity is underestimated by 1/2 when the maximum is used instead of the sum of intensities, and accordingly, the difference between the two noise level metrics is $10\log(2) = 3.01$.

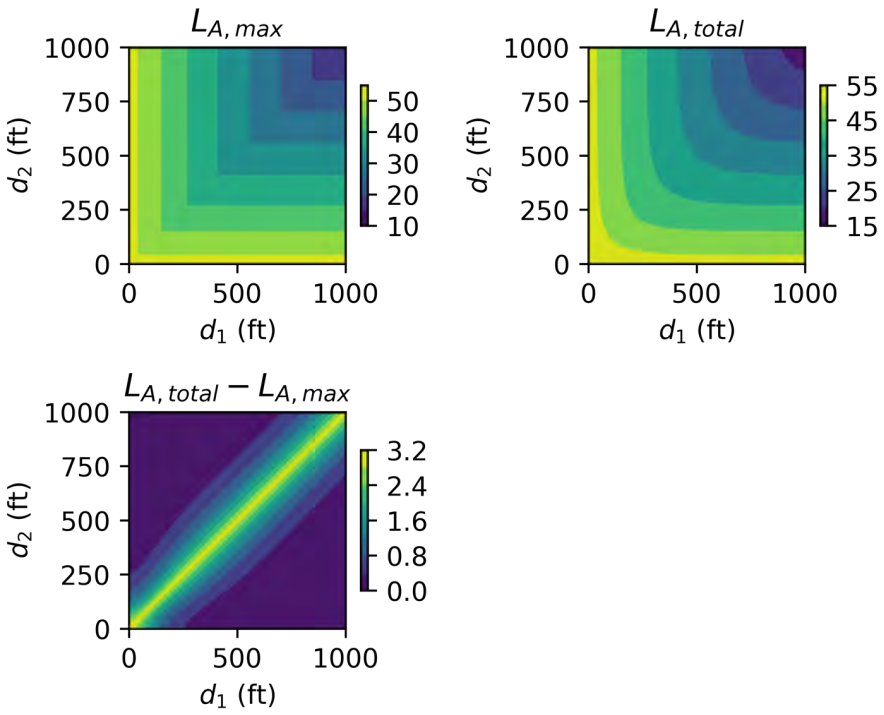

Figure 40. Evolution of $L_{A,max}$ (upper left), $L_{A,total}$ (upper right), and the difference between these two quantities (lower left).

4.7.3. Varying the Number of Vehicles

We varied the number of vehicles from 2 to 100. All vehicles were assumed to be at an altitude of 100 ft and a distance of 1,000 ft from the microphone. These assumptions correspond to the diagonal of the previously shown plots, i.e., the situation in which the difference between the two metrics is the largest.

In the previous section, the noise level was underestimated by $10\log(2)$ because we were considering two vehicles. Here, we expect the difference to be $10\log(N_{vehicles})$, which is confirmed in Figure 41.

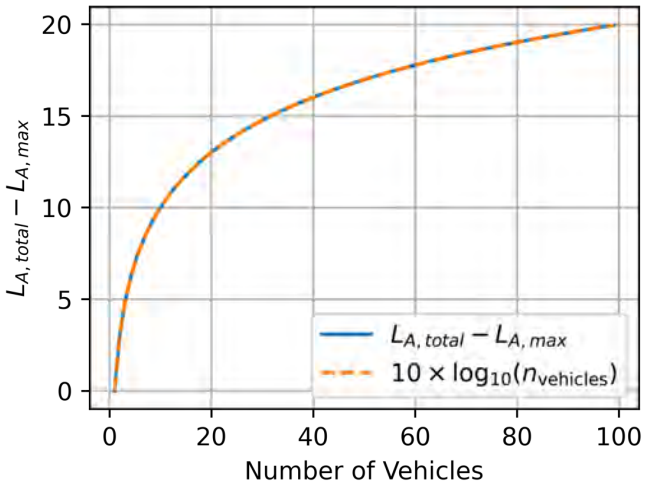

Figure 41. Evolution of the approximation error.

4.7.4. Assessing Situations in which Multiple Vehicles are Simultaneously Close to a Geographical Location

In the previous sections, we assessed situations in which multiple vehicles are simultaneously located within a relatively close distance to a given geographic location. We sought to verify whether such a situation would arise in a drone delivery scenario. In the following, we applied a fixed time window for the simulation (e.g., 1 hr).

Within this time window, a fixed number of vehicles depart and proceed to deliver packages. The departure times were chosen such as to be uniformly distributed within the time window. Delivery trips that would exceed the time window were truncated.

We plotted the duration during which more than a certain threshold number of vehicles are within a certain threshold distance (measured in feet) of the grid point. Here, we set the threshold number of vehicles to 2 or 5 and the threshold distance to 100, 500, or 1,000 ft. The total number of vehicles in the simulation was set to 100, 500, or 1,000 vehicles.

These results correspond to situations in which the value of $L_{A,max}$ may significantly differ based on the method of computation.

Creating the Flight Schedule

We created a flight schedule and stored it in a 3D array whose dimensions are (a) the number of time steps, (b) the total number of vehicles in the simulations, and (c) four data values. The last dimension, which has a size of 4, contains the (x, y, z) coordinates of the vehicle and the noise level at 100 ft. In the present study, the vehicle's noise level is not used since we only focus on distances. Here, we keep the number of 1-s-long time steps fixed to 3,600 (1 hr), but we vary the total number of vehicles departing within that flight window.

Counting the Number of Nearby Flights

To obtain a quantity that can be easily represented on a map, for each location on the grid, we counted the number of time steps in which the threshold number of vehicles was exceeded within the threshold distance. Both the threshold distance and the threshold number of vehicles were varied.

Results

We used Texas data as an example, where the locations and vehicle noise values are loosely based on the Noise Assessment for Wing Aviation [8], with two warehouses used as staging locations for the drones. Results are shown for the different threshold values in Figures 42–44.

Observations and Conclusions

In Figures 42–44, we observe the following:

- As we increase the distance threshold, the number of time steps for which the condition is met increases: there are more situations in which vehicles are within a 500-ft radius of a grid point than situations in which they are located within 100 ft.
- As we increase the threshold number of vehicles, the number of time steps in which the condition is met decreases: there are fewer situations in which five vehicles are within a given distance of a grid point than situations in which only two vehicles are within this distance.
- As the total number of vehicles simulated within the 1-hr time window increases, the number of time steps in which multiple vehicles can be found within a given distance of a grid point increases. As the vehicle concentration increases, it becomes easier to find situations in which multiple vehicles are simultaneously within a given distance of a grid point.
- There are two main grid points for which many vehicles may be found simultaneously, corresponding to the two warehouses from which vehicles depart.

These observations match our expectations: the zones of high traffic correspond to the neighborhoods of the staging locations. When the total number of vehicles remains relatively low, there are few situations in which two or more vehicles are found simultaneously near a grid point, and these situations occur only when the radius is set to 500 or 1,000 ft. These correspond to situations in which the sound levels would be relatively low because of the relatively high distance, and the noise would need to be summed for fewer than five vehicles.

As the number of vehicles increases, such situations become more common, and more than five or more vehicles may be found within the threshold distances used in this study. However, such occurrences are relatively rare and are concentrated at locations from which the vehicles depart. For 1,000 vehicles departing within a 1-hr time window, we begin to observe ray-shaped zones, for which multiple vehicles may be present within a given distance. However, this level of traffic most likely exceeds realistic levels (a rate of 1,000 departures per hour corresponds to a departure every 3.6 s). Moreover, if such a high density of traffic was needed, more staging locations would most likely be used, therefore reducing the noise impact at each of the staging locations.

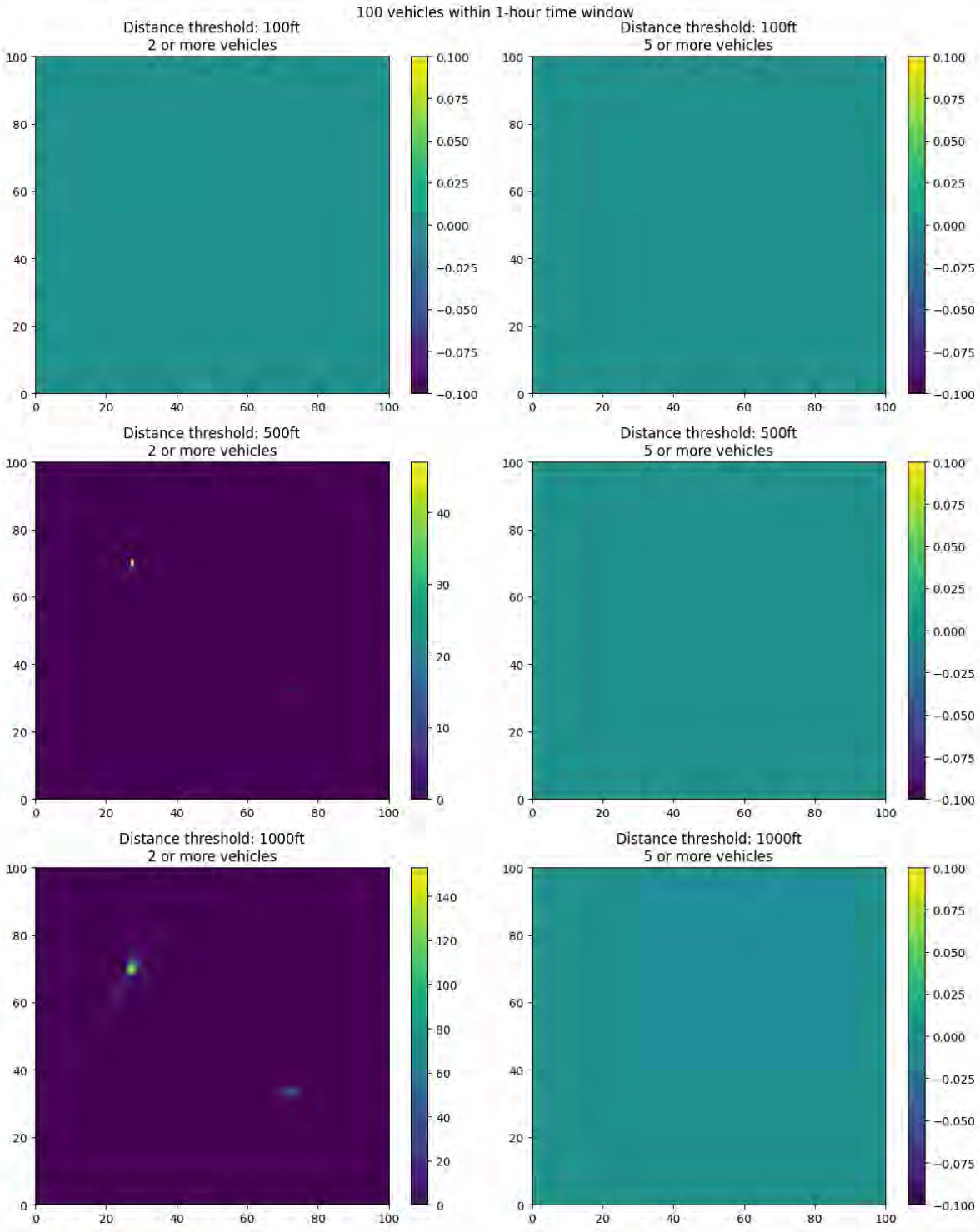

Figure 42. Number of occurrences in which the number of vehicles simultaneously flying within a certain threshold distance of a location in the study area exceeds a threshold number of vehicles. Results are shown for the least dense scenario: 100 vehicles within a 1-hr time window.

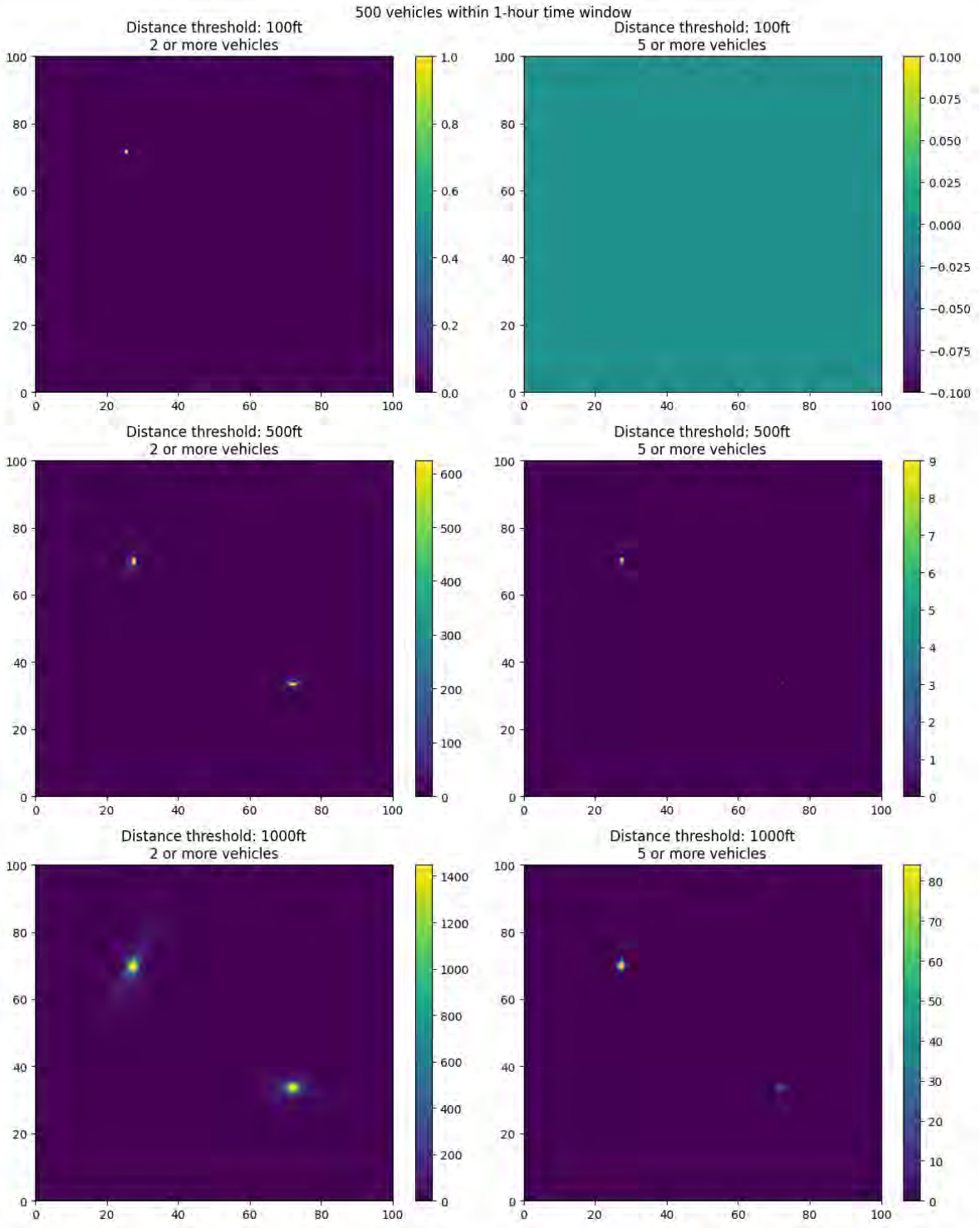

Figure 43. Number of occurrences in which the number of vehicles simultaneously flying within a certain threshold distance of a location in the study area exceeds a threshold number of vehicles. Results are shown for the least dense scenario: 500 vehicles within a 1-hr time window.

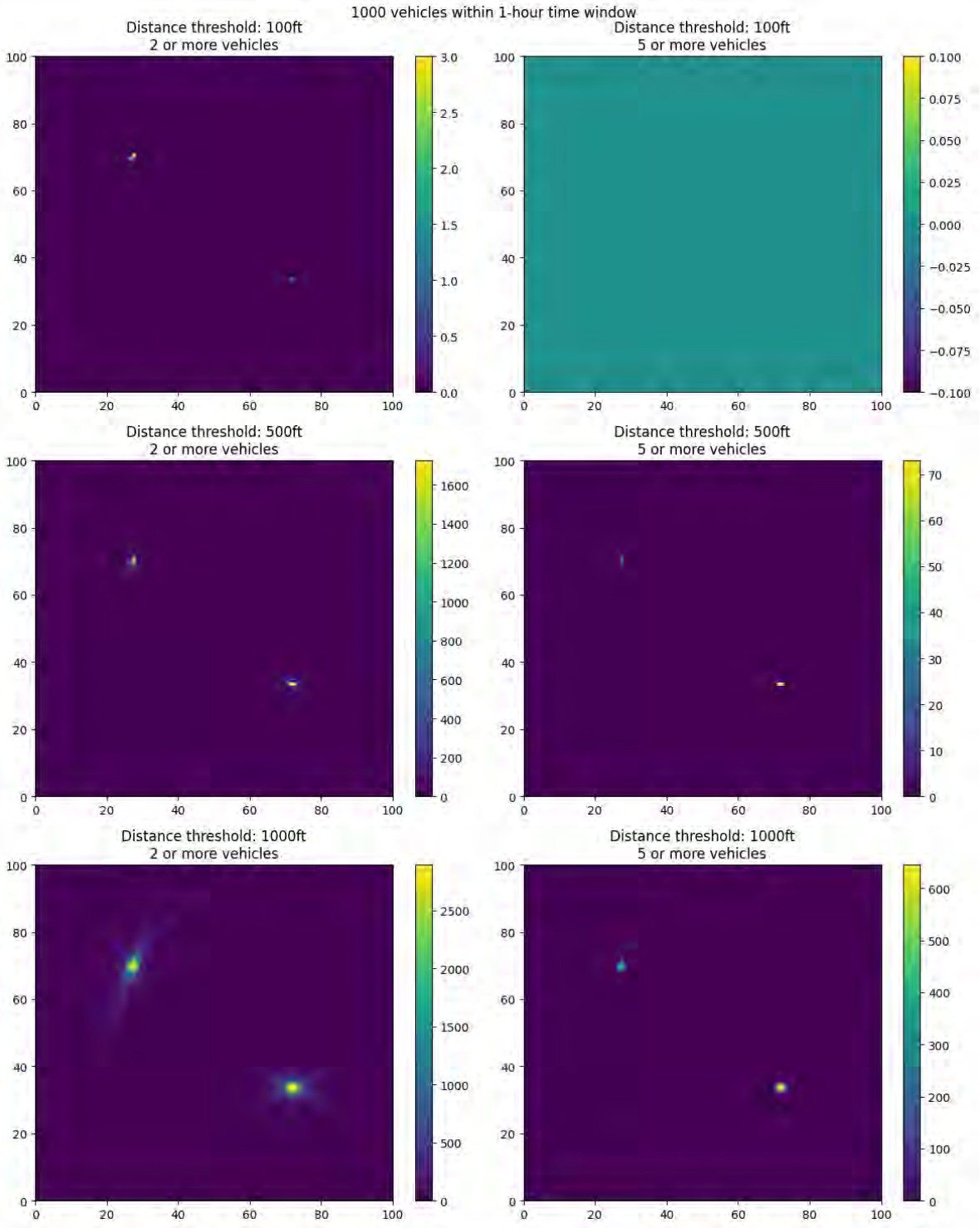

Figure 44. Number of occurrences in which the number of vehicles simultaneously flying within a certain threshold distance of a location in the study area exceeds a threshold number of vehicles. Results are shown for the least dense scenario: 1,000 vehicles within a 1-hr time window.

4.8. Uncertainty Propagation Leveraging GPU

4.8.1. Motivation and Objective

UAS operations are subject to multiple sources of variability, including the following:

- Daily individual flight trajectories are dependent on orders/demand.
- Staging locations may change day to day (e.g., when trucks are used for staging drones).
- Operator strategies for trajectory planning may include noise dispersion and altitude constraints to minimize noise.

Thus, UAS operations should be modeled as a stochastic process, as annual average day metrics do not capture daily changes. Instead of seeking deterministic measures of noise exposure, we aim to estimate the likelihood of exceedance for some threshold on any given day across the study area. In mathematical terms, we consider $P(L_{A,max} \geq X\ dBA)$, the probability that $L_{A,max}$ will exceed $X\ dBA$. Results are depicted as contours on a map of the study area, with the level X being varied, therefore leading to different contour plots for each value of X. This study is the second attempt at a Monte-Carlo simulation, which takes advantage of the GPU speed-up.

4.8.2. Setup

The study area covers the urban region of Memphis, TN, representing a 60 x 60 mile square. Delivery drones may depart from 1 of 41 warehouses, and delivery locations are uniformly sampled from residential locations within the study area. The resolution of the analysis grid is 1,056 cells in each direction: as a result, the sides of the square cells measure approximately 300 ft. In the considered operational scenario, 500 deliveries are performed per day, and the simulation is repeated for 10,000 days. The only source of variability considered in this study is the day-to-day variability of the flights.

Compared with the first Monte-Carlo study, the grid is approximately 4 times larger, and there are approximately 5 times more flights per day, resulting in an overall 20-fold-larger problem size.

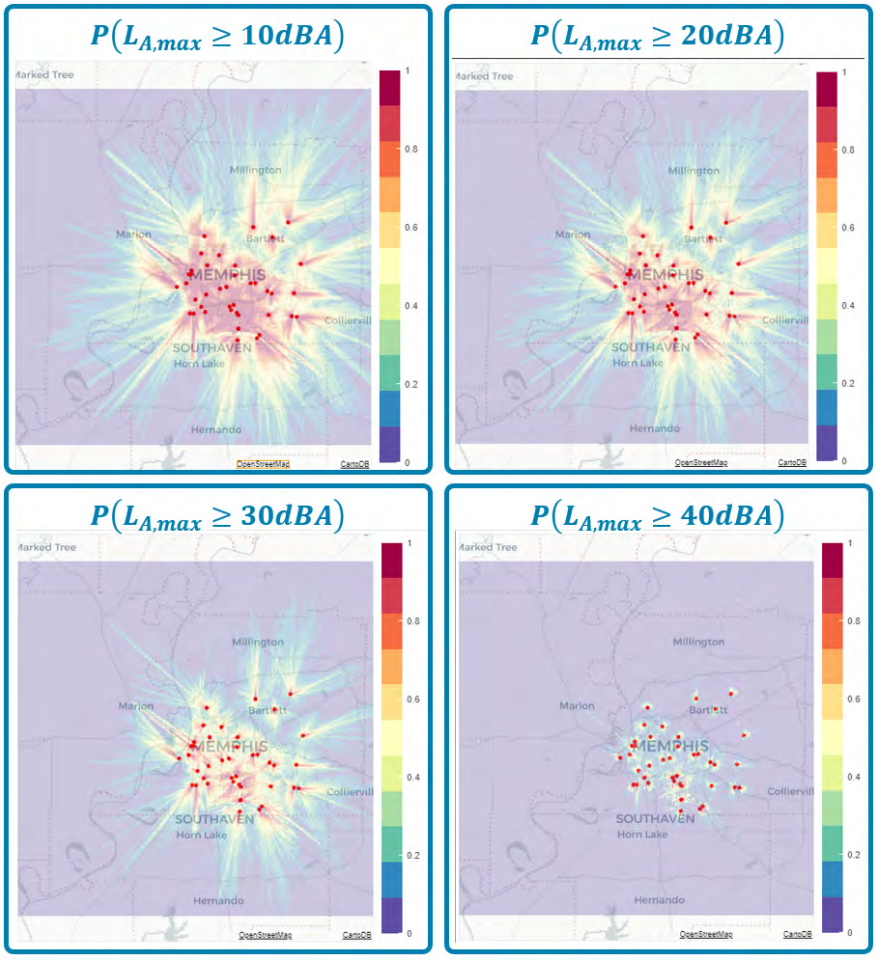

Figure 45. Results of the graphics processing unit (GPU) Monte-Carlo simulation. Contour plots denote the probability that $L_{A,max}$ exceeds a threshold level. Threshold levels were varied at 10, 20, 30, and 40 dBA.

4.8.3. Results and Conclusions

The results of this study are shown in Figure 45. As discussed previously, each plot corresponds to a different noise exposure level threshold: 10, 20, 30, or 40 dBA. Warehouses are shown as red dots. We observe that the high-probability area shrinks as the threshold increases, consistent with expectations. The geographical areas with a high probability of exceeding 40 dBA are concentrated near the staging locations.

The full Monte-Carlo simulation was completed in approximately 7 hr by using 50 GPUs from Georgia Tech's PACE cluster. Each run takes approximately 2 min to complete. This runtime is orders of magnitude shorter

than the first Monte-Carlo attempt that was run on a CPU (hours instead of weeks), thus confirming the benefits achieved when running the noise engine on GPUs.

Milestone

The team delivered a recommendation for an updated GIS system to the FAA and members of the AEDT development team.

Major Accomplishments

The team presented an initial prototype of the UAS noise engine with an interactive display while running on a parallel computing cluster to the FAA.

Publications

None

Outreach Efforts

The team engaged in outreach and coordination with the ASSURE Center of Excellence team and their work at MSU. The team also collaborated with the Volpe Center and participated in the NASA UAM Noise Technical Working Groups.

Awards

None

Student Involvement

The Georgia Institute of Technology student team consists of three graduate research assistants. At the beginning of the project, all graduate research assistants engaged in the GIS background research. The team is now divided to tackle the different aspects and implementation of the noise engine, novel computational technology testing, and the creation of benchmark studies that serve as a test bed for testing the computational scaling of different approaches.

Plans for Next Period

In the next reporting period, we plan to complete the current work plan and perform more testing with emerging computational technologies on a defined sample problem. After further discussion with the FAA, the team will look to support the FAA in potential applications of the UAS noise engine and to transfer the UAS noise engine to the FAA.

References

Aftomis, M. J., Berger, M. J. & Alonso, J. J. (2006). *Applications of a Cartesian mesh boundary-layer approach for complex configurations* [Meeting presentation]. 44th AIAA Aerospace Sciences Meeting, Reno NV, United States.

Gropp, W. (n.d.). Introduction to MPI I/O [CS 598, Lecture Notes]. University of Illinois, Urbana-Champaign, IL, United States.

The Office of Spatial Analysis and Visualization at the Bureau of Transportation Statistics, U.S. Department of Transportation

Bokeh Development Team. (2018). *Bokeh: Python library for interactive visualization*. http://www.Bokeh.pydata.org

Dask Development Team. (2016). *Dask: Library for dynamic task scheduling*. https://dask.org

Cottam, J. A, Lumsdaine, A., & Wang, P. (2014). Abstract rendering: Out-of-core rendering for information visualization. *Proc. SPIE 9017, Visualization and Data Analysis 90170K*. https://doi.org/10.1117/12.2041200

Teal Group (2022). *2021/2022 Civil UAS Market Forecast*.

HMMH (2021). *Noise assessment for wing aviation proposed package delivery operations in Frisco and Little Elm, Texas*. (HMMH Report No. 309990.003-2.)

Project 010 Aircraft Technology Modeling and Assessment

Georgia Institute of Technology and Purdue University

Project Lead Investigators

Dimitri Mavris (PI)
Regents Professor
School of Aerospace Engineering
Georgia Institute of Technology
Mail Stop 0150
Atlanta, GA 30332-0150
404-894-1557
dimitri.mavris@ae.gatech.edu

William Crossley (PI)
Professor
School of Aeronautics and Astronautics
Purdue University
701 W. Stadium Ave
West Lafayette, IN 47907-2045
765-496-2872
crossley@purdue.edu

Jimmy Tai (Co-PI)
Senior Research Engineer
School of Aerospace Engineering
Georgia Institute of Technology
Mail Stop 0150
Atlanta, GA 30332-0150
404-894-0197
jimmy.tai@ae.gatech.edu

Daniel DeLaurentis (Co-PI)
Professor
School of Aeronautics and Astronautics
Purdue University
701 W. Stadium Ave
West Lafayette, IN 47907-2045
765-494-0694
ddelaure@purdue.edu

University Participants

Georgia Institute of Technology

- PI(s): Dr. Dimitri Mavris (PI), Dr. Jimmy Tai (Co-PI)
- FAA Award Numbers: 13-C-AJFE-GIT-006, 13-C-AJFE-GIT-012, 13-C-AJFE-GIT-022, 13-C-AJFE-GIT-031, 13-C-AJFE-GIT-37, 13-C-AJFE-GIT-041, 13-C-AJFE-GIT-50, 13-C-AJFE-GIT-52, 13-C-AJFE-GIT-56, 13-C-AJFE-GIT-76, 13-C-AJFE-GIT-94
- Period of Performance: September 1, 2021 to August 31, 2022

Purdue University

- PI(s): Dr. William A. Crossley (PI), Dr. Daniel DeLaurentis (Co-PI)
- FAA Award Numbers: 13-C-AJFE-PU-004, 13-C-AJFE-PU-008, 13-C-AJFE-PU-013, 13-C-AJFE-PU-018, 13-C-AJFE-PU-026, 13-C-AJFE-PU-032, 13-C-AJFE-PU-035, 13-C-AJFE-PU-044, 13-C-AJFE-PU-047
- Period of Performance: September 1, 2021 to August 31, 2023

Project Funding Level

The project is funded by the FAA at the following levels: Georgia Institute of Technology: $700,000; Purdue University is continuing on a no-cost extension. Cost-sharing details are below:

The Georgia Institute of Technology has agreed to a total of $700,000 in matching funds. This total includes in-kind cost-sharing from Boom Supersonics; salaries for the project director, research engineers, and graduate research assistants (GRAs); and funding for computing, financial, and administrative support, including meeting arrangements. The institute has also agreed to provide tuition remission for the students, paid by state funds.

The most recent FAA funding to Purdue University for this project was a total of $225,000. Purdue provides matching support through salary support for the faculty PIs, and through salary support and tuition and fee waivers for one of the GRAs working on this project. OAG Aviation Worldwide Limited also provided in-kind cost-sharing to the Purdue team. The total of this matching is $225,000.

Investigation Team

Georgia Institute of Technology

- PI: Dimitri Mavris
- Co-investigator: Jimmy Tai
- Vehicle modeling technical leads (Research Faculty): Jai Ahuja, Christian Perron, Chung Lee, Brennan Stewart
- Fleet modeling technical lead (Research Faculty): Holger Pfaender
- AEDT modeling technical leads (Research Faculty): Dushhyanth Rajaram, Michelle Kirby, Ameya Behere
- Graduate students: Nikhil Iyengar, Barbara Sampaio, Edan Baltman, Joao De Azevedo, Jiajie (Terry) Wen, Ted Vlady, Zayne Roohi and Srikanth Tindivanam Varadharajan

Purdue University

- PI: William Crossley
- Co-investigator: Daniel DeLaurentis
- Research faculty: Muharrem Mane
- Graduate students: Samarth Jain, Suzanne Swaine, Tien-Yueh Fung, Boning Yang, and Katelin Zichittella

Project Overview

Georgia Institute of Technology (Georgia Tech) and Purdue University have partnered to investigate the future demand for supersonic air travel and the environmental impact of supersonic transports (SSTs). In the context of this research, environmental impacts include direct carbon dioxide (CO_2) emissions, noise, and fuel consumption. The research is conducted as a collaborative effort to leverage the capabilities and knowledge available from the multiple entities that make up the ASCENT university partners and advisory committee. The primary objective of this research project is to support the FAA in modeling and assessing the potential future evolution of the next-generation supersonic aircraft fleet. The research in this project consists of five integrated focus areas: (a) establishing fleet assumptions and performing demand assessment (completed last year); (b) performing preliminary SST environmental impact prediction (ongoing); (c) developing modeling approaches to model SSTs within the FAA Aviation Environmental Design Tool (AEDT); (d) performing vehicle and fleet assessments of potential future supersonic aircraft; and (e) performing physics based modeling of SSTs and performing conceptual design using the Framework for Advanced Supersonic Transport (FASST).

To better understand the potential demand for supersonic air travel, the team developed a parametric airline operating-cost model to explore the sensitivities of key vehicle, operational, and cost parameters on the required yield that an airline would need to target for ticket prices on potential new supersonic aircraft. The current model, however, assumes fixed parameters for key vehicle metrics, which can be changed but do not include sensitivities to key vehicle design choices such as vehicle

size, design cruise Mach number, and maximum range. This task will examine the implications of the physical and technical dependencies on airline operational cost. Through the vehicle performance sensitivities, such as passenger capacity and design cruise Mach number, the combined "sweet spot," i.e., the most profitable vehicle for an airline to operate, can be determined. To accomplish this goal, the existing vehicle models created in the prior year will be utilized and supplemented with the additional vehicles proposed in this period of performance. These vehicles together will serve as the foundation to create credible sensitivities regarding parameters such as vehicle size and design cruise Mach number. These sensitivities will then be embedded in the airline operating-cost estimation model and used to explore the combined vehicle and airline operational space to identify the most economically feasible type of supersonic vehicle.

In an independent complementary approach, to consider the demand and routes for supersonic aircraft, the Purdue team developed a ticket pricing model for possible future supersonic aircraft that relies on the "as-offered" fares, before the novel coronavirus (COVID-19) pandemic, for business-class and first-class tickets on routes expected to have passenger demand for supersonic aircraft. Via an approach considering the number of passengers potentially demanding fares at business class or above on a city-pair route, the distance of that city-pair route, an adjustment to increase the over-water distance of the route where the aircraft can fly supersonically to allow for the shortest trip time, and the range capability of a low-fidelity modeled medium SST (55-passenger capacity) to fly that route with the shortest trip time, the Purdue team identified a network among 257 airports that could potentially allow for supersonic aircraft service in a network of routes with at least one end (i.e., the origin or destination) in the United States (US).

Work undertaken this year included expanding the US-touching network to a worldwide network. This change to a worldwide network required the identification of a global fleet of aircraft (type and number of aircraft) as well as the passenger demand on each route. By providing these potential routes as input to the Fleet-Level Environmental Evaluation Tool (FLEET) simulation, the allocation problem in FLEET then determines which routes would be profitable for the airline to offer supersonic transportation and how many supersonic aircraft would operate on these routes, providing a prediction of which routes might have supersonic aircraft use and the number of supersonic flights operated on those routes at dates in the future. Because of the evolution of the existing fleet of subsonic aircraft and changes to the cost-estimation module of NASA's FLight Optimization System (FLOPS), the Purdue team developed an acquisition and operating cost model that is used to estimate these costs for all aircraft modeled in FLEET. During this year's efforts, the Purdue team also began work to adapt FLEET to analyze the operations and environmental emissions of business jet operations. This task entails estimating travel demand of business jet aircraft, the fleet size and mix that serve that demand, the worldwide network of operations, and the development of the resource allocation model that estimates the optimal utilization of aircraft to satisfy travel demand.

One major accomplishment of the project during the performance period is the preliminary results for the design of a 65-passenger SST cruising at Mach 1.7 for 4,250 nmi. The preliminary results are arrived at through computational fluid dynamics (CFD)-based vehicle shape optimization, engine cycle modeling using Numerical Propulsion System Simulation (NPSS), and noise modeling using NASA's Aircraft Noise Prediction Program (ANOPP), and mission analysis and detailed takeoff and landing analysis that incorporates variable noise reduction system (VNRS) using FLOPS. These modeling approaches and programs are all integrated into FASST, which allowed Georgia Tech to generate interdependency results between fuel burn (or maximum takeoff weight [MTOW]) and certification cumulative noise levels (in EPNdB; effective perceived noise in decibels). The other major accomplishment is Georgia Tech's support of the environmental assessment (EA) study of Greensboro airport in order for a potential supersonic airframe manufacturer to perform flight tests. The EA study required Georgia Tech to model a generic transport SST that is representative of the potential supersonic airframer's concept except with marginal noise characteristics (small cumulative noise margin). The rationale is to account for noise at the current limiting, highest-noise case (bounded within the existing subsonic, Stage 5 noise certification limits of compliance) so that developmental SST configurations operated at or below this upper MTOW can be built, tested, and refined to these noise goals. Georgia Tech generated all the necessary performance attributes and imported them into AEDT to generate noise contours for Greensboro. Both the vehicle performance and AEDT databases are provided to the FAA, who in turn worked with Greensboro airport to perform the actual environmental assessment. The final major accomplishment during the period of performance is the development of a methodology to construct regression models to be used in the full-flight simulation for FAA's AEDT. The current method is to rely on a base of aircraft data (BADA) databases; however, there is currently no BADA database for supersonic transports. Georgia Tech has successfully developed a regression methodology to predict fuel burn, net thrust, and drag coefficient values over the entire span of mission.

Purdue used its FLEET tool to produce initial estimates of the fleet-level impact of future supersonic aircraft operating on the worldwide network. The SSTs required for these fleet-level analyses were provided by the Georgia Tech vehicle modeling tasks with FASST, to maintain consistent aircraft modeling throughout the project. The studies provide a glimpse into future

supersonic air travel by using physics-based models of supersonic vehicle performance. Future work should build on current estimates to conduct more detailed vehicle and fleet performance.

Project Introduction

Georgia Tech and Purdue partnered to investigate the effects of supersonic aircraft on the future environmental impacts of aviation. Impacts assessed at the fleet level include direct CO_2 emissions and fuel consumption. The research is conducted as a collaborative effort to leverage capabilities and knowledge available from the multiple entities that make up the ASCENT university partners and advisory committee. The primary objective of this research project is to support the FAA in modeling and assessing the potential future evolution of the next-generation supersonic aircraft fleet.

Milestones

Georgia Tech had three milestones for this year of performance:

1. Generate interdependency results showing trades between fuel burn and cumulative noise levels
2. Support FAA in an EA using FASST and AEDT
3. Provide FASST SST descriptions and characteristics in Microsoft PowerPoint format

For Purdue, the proposal covering this year of performance included several milestones:

1. Update the aircraft cost coefficients
2. Expand the FLEET route network to include global routes
3. Analysis of alternate SST aircraft concepts
4. Develop a FLEET-like model to analyze business jet operations

Previously, the aircraft cost information needed for FLEET simulations, including the acquisition and operating costs, were generated using the cost module in FLOPSv8. The cost module is no longer available in FLOPSv9, which both Purdue and Georgia Tech are using for vehicle sizing and performance estimation, so a new cost model with similar functionality was needed and developed during this year's effort.

To increase the utility of FLEET and the insights that can be gained by analyzing the introduction of an SST into the fleet, the Purdue team expanded the network of operations from the US-touching network to a global network. The airports in the network are still the original 257 airports, but the routes among them in the FLEET network now include all global routes with regularly scheduled service. This update to FLEET also included the identification of the worldwide size and mix of aircraft used by airlines to provide service and meet passenger demand.

Finally, the team began work to enable the analysis of environmental emissions and impact of a supersonic business jet on operations. This entails the creation of a FLEET-like tool that mirrors the analysis of airline operations but is adapted to capture the features of business jet operations.

Major Accomplishments

Major accomplishments of the project during the period of performance include the generation of preliminary results for the design of a 65-passenger SST cruising at Mach 1.7 for 4,250 nmi, with interdependency results between fuel burn (or maximum takeoff weight) and certification cumulative noise levels (in EPNdB). These results were obtained through CFD based aerodynamic shape optimization of the aircraft geometry, NPSS engine modeling, noise modeling in ANOPP, and mission analysis coupled with detailed takeoff and landing analysis incorporating VNRS through FLOPS.

In addition, Georgia Tech supported the EA study of the Greensboro airport in order for a potential supersonic airframe manufacturer to perform flight tests. This was accomplished by modeling a generic SST representative of the potential supersonic airframer's concept except with a small cumulative noise margin Georgia Tech generated all the necessary performance attributes and imported them into AEDT to generate noise contours for Greensboro, shared these databases with the FAA, , who in turn worked with Greensboro airport to perform the actual environmental assessment. Lastly, Georgia Tech developed a methodology to construct regression models to be used in the full-flight simulation for FAA's AEDT, sidestepping the current way of relying on BADA databases, which do not even exist for supersonic transports. As such, this methodology can now predict fuel burn, net thrust, and drag coefficient values over an entire mission flight envelope.

One major accomplishment of the Purdue team during this year's effort was the successful expansion of the network of operations from 1,149 US-touching routes among 257 airports to 5,503 worldwide routes; this increases the analytical capability of FLEET and enables a more comprehensive assessment of the impact of supersonic transportation on the environment. The updated FLEET models can identify routes on which an SST can provide profit to airline operations and the associated environmental emissions. Because of the available data, this update also moved the FLEET baseline year of analysis from 2005 to 2011. With the addition of more historical data, which includes the impact of COVID-19 on airline operations and travel demand in 2020 and 2021, the demand and emissions projections until 2050 are more realistic.

Task 1 - SST Aerodynamic Modeling

Georgia Institute of Technology

Objectives

There are two primary objectives of the SST aerodynamic modeling task:

- Aerodynamic shape optimization of the SST outer mold line (OML) for a given cruise Mach number (for a fixed planform area and wing capture area)
- Generation of parametric drag polars for the optimized vehicle that capture aerodynamic performance across the entire flight envelope as a function of wing planform area and inlet capture area

Research Approach

Analysis Workflow

A general analysis process was developed to obtain the aerodynamic performance of multiple aircraft designs. This process was then automated with Python and implemented by using Georgia Tech's high-performance computing facilities. Because the analysis workflow was automated and easily parallelizable, many designs could be analyzed at once. Hundreds of aerodynamic analyses could be completed in a matter of hours, allowing for rapid evaluation of designs and generation of drag polars.

Starting from a set of design variables, the first step was to generate a computer-aided design (CAD) representation of the aircraft geometry. This process was done using Engineering Sketch Pad (ESP), a lightweight, open-source CAD tool developed by MIT [1]. ESP allows users to easily script generation of complex geometries and to expose design parameters. Therefore, changing global parameters, such as the sweep angle or taper ratio, would automatically and seamlessly scale and reposition the different sections of the wing. After a new geometry was defined, it was then saved to a generic CAD file (the EGADS format in the current workflow) and tessellated for later use in CFD analysis.

The OML is tailored to maximize lift/drag (L/D) at the design cruise Mach number as a surrogate to minimize mission fuel burn. The optimization is broken down into three stages: two initial phases focusing on the fuselage and vertical tail (VT) design, and one main stage focusing on the wing planform optimization. Both inviscid (Euler) and Reynolds-Averaged Navier-Stokes (RANS) CFD analyses are used in a multi-fidelity optimization approach to reduce design time and cost. NASA's Cart3D [2] is the inviscid solver used and Siemens' STAR-CCM+ [3] is the RANS solver used. The following sections detail each airframe design phase.

Fuselage Design

Using the number of passengers set by requirements, the fuselage design, in terms of minimum cabin length and width requirements, is constrained by the cabin layout. While slender fuselages are preferable for supersonic cruise performance, care must be taken to avoid an excessively long body, as takeoff rotation constraints necessitate longer and thus heavier landing gears. Once the cabin layout is frozen, additional refinements are conducted on the fuselage nose and tail cone sections, in terms of length and cross-sectional radius, to optimize for cruise L/D. During this fuselage design process, the wing planform is frozen. A design of experiments (DoE) is developed, with the length of the nose, length of the tail, and cross-sectional radii for various stations of the fuselage as independent variables. CART3D with a single-pass viscous correction is used for the aerodynamic analysis. The results from this DoE are used to train a neural network surrogate, which in turn is used to optimize the vehicle for cruise L/D. The resulting fuselage design is then frozen and used in the wing optimization stage.

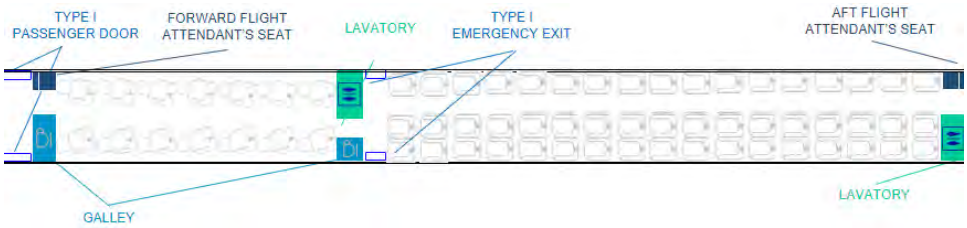

Figure 1. Cabin layout for a 65-passenger aircraft.

Vertical Tail Design

The VT is designed primarily based on two critical Federal Aviation Regulations (FAR): §25.147 for directional control under two-engine inoperative (2EI) conditions and §25.237 for crosswind requirements. Directional stability is analyzed using first-order principles and semi-empirical relations, rather than CFD. Design variables considered are wing planform area, aspect ratio, taper ratio, leading edge sweep, and thickness to chord. The goal is to find the smallest VT planform area that satisfied the requirements for the furthest feasible VT location relative to the wing. A symmetric biconvex airfoil is used, with a thickness-to-chord ratio (t/c) fixed to a value that ensures an adequate cross-sectional thickness for the rudder actuators but is small enough to not penalize supersonic cruise performance. The rudder chord length to mean aerodynamic chord fraction is set to 0.35.

Wing Planform Design

Since the aerodynamic performance of the vehicle is strongly dependent on the wing planform, most of the optimization effort is focused on this component. As such, RANS CFD is used to analyze the performance of each design perturbation. The wing is defined by two sections, inboard and outboard, and five airfoil profiles. Global variables like taper ratio, aspect ratio, sweep, and dihedral apply to the entire wing, whereas the delta variables control the difference between the inboard and outboard sections. The wing break location variable determines the spanwise extent of the inboard section relative to the outboard, for a fixed total span. Biconvex airfoils are used to define the wing, with twist and camber being part of the design space. The maximum camber is limited to half the specified t/c ratio.

Given the dimensionality of the problem and the cost of each function call, there is a need to be strategic about how this optimization exercise is carried out. As such, a gradient-free active subspace approach is first used to reduce the dimensionality of the design space using less expensive inviscid CFD. Then, adaptive sampling is performed in this reduced design space with RANS simulations to improve the L/D. A high-level overview of this process is shown in Figure 2. The goal of the active subspace method [4] is to reduce the high-dimensional input space of some function to a lower-dimensional subspace, the so-called active subspace. For instance, given a function $f(\mathbf{x})$, where $\mathbf{x} \in \mathbb{R}^d$ is a high-dimensional input vector, the following approximation is made:

$$f(\mathbf{x}) \approx g(\mathbf{z}) = g(\mathbf{W}^T\mathbf{x}) \tag{1}$$

where $g(\mathbf{z})$ is an approximate predictor of $f(\mathbf{x})$, and $\mathbf{W} \in \mathbb{R}^{d\times k}$ is a projection matrix that maps the inputs $\mathbf{x}$ to a low-dimensional representation $\mathbf{z} \in \mathbb{R}^k$, which are referred to as the active variables with $k < d$. In other words, the active subspace method aggregates potentially many design variables into a few modes that best capture the variability of the output. As a result, optimization with respect to the active variables is more efficient because the size of the design space is exponentially reduced. Fitting a surrogate to predict the output of interest is also made easier as the active subspace alleviates the infamous "curse of dimensionality." The main difficulty of the active subspace method is in finding the matrix $\mathbf{W}$ that best approximates the variability of $f(\mathbf{x})$. Although most dimensionality reduction methods are unsupervised, the active subspace is a supervised approach. This implies that the reduction of the input spaces is not based on the similarity between design vectors; rather, it is informed by the functional dependence between the input and the output spaces.

The classical active subspace approach for dimensionality reduction proposed by Constantine relies on gradient information of the objective function, which can be challenging to obtain. Gradient-free approaches have been proposed in the literature [5, 6, 7], but these methods require extensive sampling of the objective function, which can be costly in scenarios where the objective is being evaluated by high-fidelity codes like RANS solvers. To counter this drawback, Mufti et al. [8] have proposed a gradient-free and multi-fidelity approach whereby a lower fidelity and relatively cheaper code, in this case Cart3D, is used to extract an approximation of the RANS active subspace. The requirement for this approach is an initial DoE that samples the design space. Each case in this DoE is evaluated in Cart3D and L/D is recorded. The proposed multi-fidelity

approach is then applied to obtain a reduced representation of the design variables based on the lower fidelity results. Although the inviscid L/D results from Cart3D are not as accurate as those obtained with RANS, both tend to have similar behaviors. Therefore, it is reasonable to assume that an active subspace computed using inviscid results is a good representation of the corresponding subspace that would be obtained with RANS results. Mufti et al. have demonstrated that this assumption holds for the design of transonic airfoils and wings. Although using lower fidelity results to compute the active subspace has drawbacks and does reduce the accuracy of the method, it also significantly reduces the cost of computing the active subspace. For the purposes of this work, this tradeoff between accuracy and computational cost is considered acceptable.

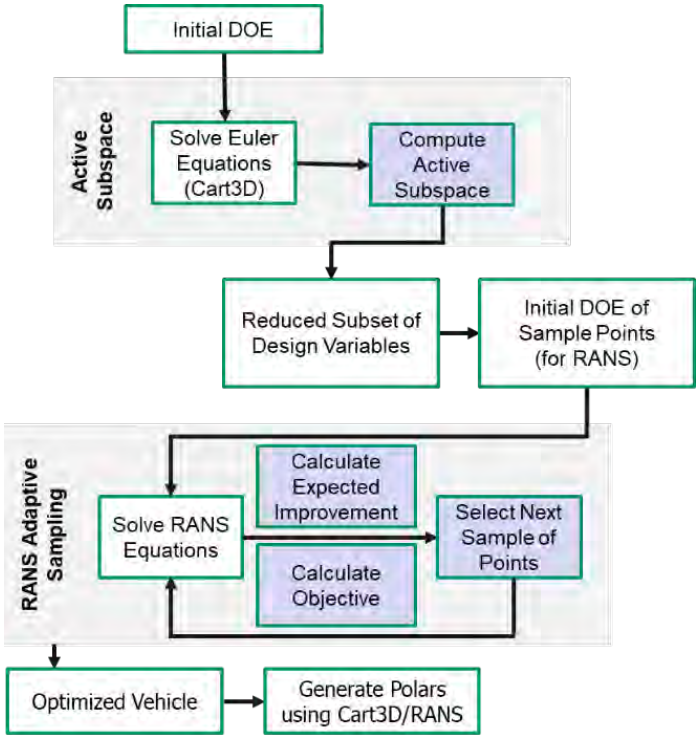

Figure 2. Aerodynamic optimization process. DOE, design of experiments; RANS, Reynolds-Averaged Navier-Stokes.

Once the reduced representation of the design variables is determined, the RANS optimization process begins. The objective function is maximized through an adaptive sampling approach, using the efficient global optimization (EGO) method [9]. To start the process, a warm-start DoE is run to train a Kriging surrogate model. The Kriging model not only provides a prediction of the objective function at nonsampled points, but it also provides an estimate for the model prediction uncertainty between two sampled points. These two ingredients are used in the EGO method to balance "exploration" vs "exploitation" of the design space. In the current context, "exploration" refers to sampling in regions where model uncertainty is high, and "exploitation" denotes sampling in regions close to the optimum. After the initial warm-start DoE and model training, a small number of candidate points are selected that maximize the "expected improvement" criterion of the objective function. These samples are then evaluated in RANS, the Kriging model is retrained, the expected improvement is recomputed, and the process repeats until a user-defined stopping condition is met. In this fashion, the aerodynamic performance of the vehicle is improved iteratively. The sample size of the warm-start DoE and the number of additional samples required is dependent on the dimension of the design space and, as such, the active subspace dimensionality reduction in the previous step is critical for minimizing the overall design time and cost.

Note that for some vehicles, the optimization process would converge on a wing design with an excessive sweep and aspect ratio. The resulting vehicle would then have a large wing weight during the system analysis, which would severely hinder mission performance. This is because the wing planform design is purely aerodynamic and lacks any structural consideration. To circumvent this issue, an upper limit on wing weight has been added to the adaptive sampling approach. As a result, the

EGO algorithm searches for new samples that maximize the expected improvement of the objective while having a high probability of meeting the wing weight constraint following the process described in [10]. For this purpose, the wing weight is estimated from a given planform using the FLOPS weight equations [11]. From these weight estimates, an additional Kriging model is trained, which is then used to predict the likelihood of a new design to satisfy the weight constraint. Figure 3 shows an example of a design optimized without and without the wing weight constraint.

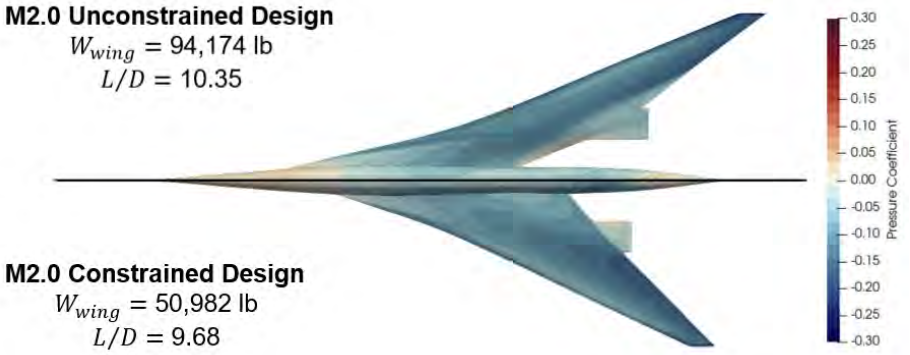

Figure 3. Comparison between an unconstrained and a wing weight–constrained optimum. W_{wing}, wing weight; L/D, lift-to-drag ratio.

Drag Polar Generation for Optimized Vehicle

Once the vehicle with the highest cruise L/D is obtained, to enable mission analysis, drag polars for every point in the operating envelope are generated in the form of a table with Mach, altitude, lift coefficient (C_L), and drag coefficient (C_D) as the columns. Generating a drag polar that covers the entire envelope is quite costly to perform solely with RANS CFD. Therefore, a hybrid approach is used, as shown in Figure 4. First, the less expensive Cart3D is used to generate a set of "baseline polars" for all Mach number and angle-of-attack (AoA) combinations. Note that since Cart3D is an inviscid solver, altitude is not an input because it only impacts viscous forces. RANS CFD is then used to sample a subset of the low-fidelity flight conditions. In this case, a total of 15 RANS samples are considered. The flight conditions for these RANS cases were chosen strategically to minimize the root mean square error of the surrogate model and the number of high-fidelity cases required to achieve that. Because altitude was not a consideration for the low-fidelity CFD, random values were assigned to each RANS sample in a way that spread them out uniformly in the expected range of Reynolds number. These viscous results are then used to calibrate the inviscid polars to account for viscous effects. This is achieved using hierarchical Kriging [12], which is a type of multi-fidelity surrogate model. In this situation, the low-fidelity data are the numerous Cart3D results and the high-fidelity samples are the few RANS CFD solutions.

Parametric Drag Polars Capturing Impacts of Changing Wing Planform Area and Inlet Capture Area

Aerodynamic optimization is conducted for a fixed-wing planform area and inlet capture area. However, as part of vehicle sizing and mission analysis, both the engine size and wing planform area are allowed to scale. To account for the impacts of these changes on the aerodynamic performance of the vehicle, it is desirable to have a set of drag polars that are a function of these design variables. This objective is efficiently achieved through a proper orthogonal decomposition (POD) reduced-order model (ROM).

A parametric ROM approximates the prediction of a function by mapping an *m*-dimensional input vector to a *d*-dimensional output vector. Unlike a conventional surrogate model, the quantity being predicted is a high-dimensional vector. The development of parametric drag polars at a high level is illustrated in Figure 5 and mostly follows the work shown in [13], where a similar approach was used for a parametric engine deck. The main steps are as follows: First, a DoE is created to sample the design space spanned by wing planform area and inlet capture area. A total of 10 samples are defined with unique combinations of the two design variables. The nacelle length is correlated with the inlet capture area and is thus a fallout. A multi-fidelity mission drag polar is generated for each of the samples in the DoE using the process outlined in the preceding section. These drag polars are then used as observations to train the ROM. Once the modes and coefficients for the POD model are obtained, a radial basis function is used as the interpolating mechanism for the POD coefficients such that drag polars can be predicted at previously unseen values of the design variables.

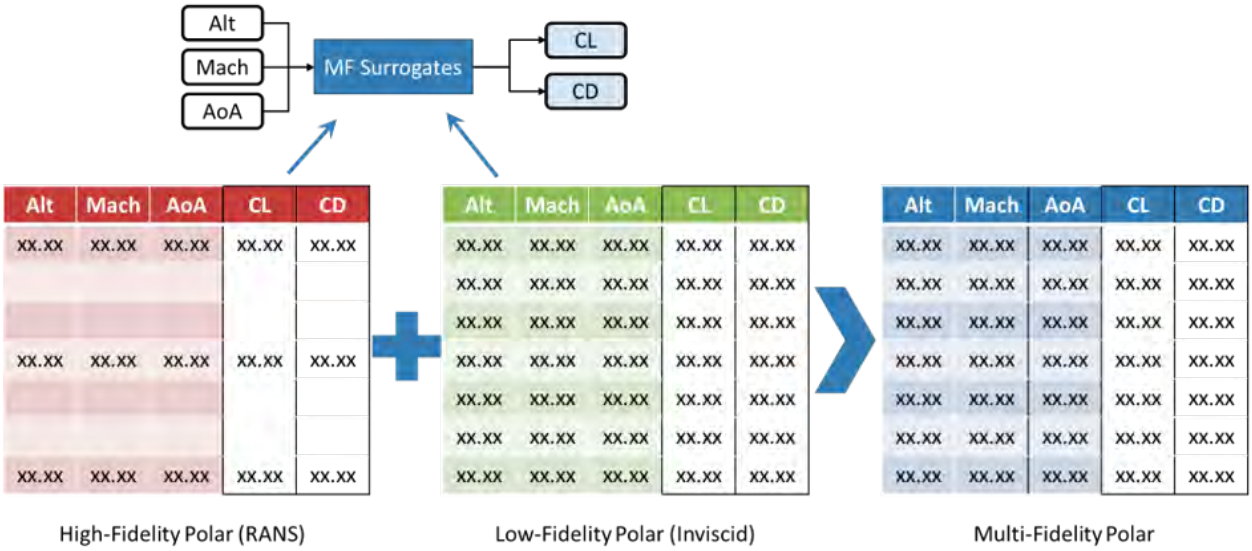

Figure 4. Schematic depicting multi-fidelity drag polar generation process. Alt, altitude; AoA, angle of attack; MF, multi-fidelity; CL, lift coefficient; CD, drag coefficient.

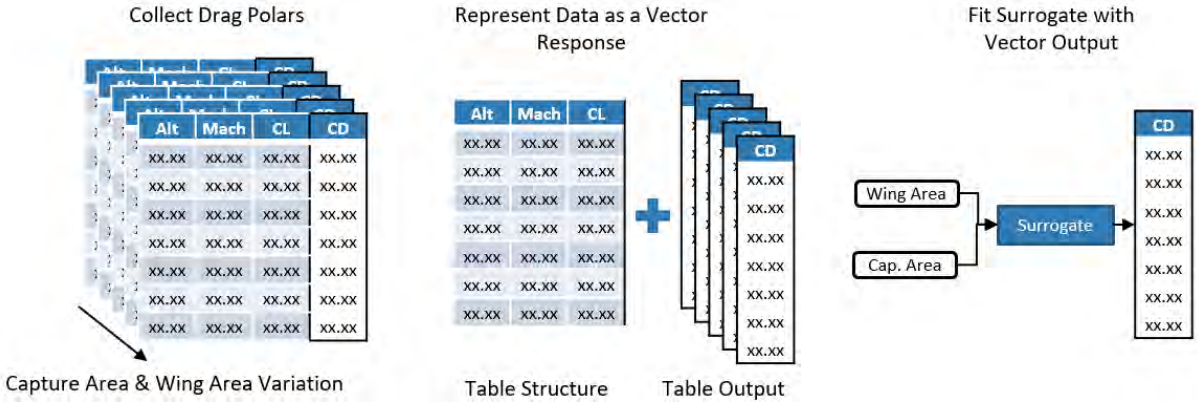

Figure 5. Schematic demonstrating the construction of the parametric drag polars. Alt, altitude; CL, lift coefficient; CD, drag coefficient.

Results

Fuselage Design

Table 1 shows the variables and ranges for the fuselage OML DoE. Figure 6 shows the L/D trends against each of the design variables at the design point that maximizes cruise L/D. Analysis of the DoE results through the surrogate model reveals a plateau in L/D for the nose length variable and a natural maximum for the tail length. The radius at the start of the cabin, the radius at two-thirds cabin length, and the radius at the end of the cabin have a peak cruise L/D at the minimum allowed value due to the cabin constraint. The radius at one-third cabin length does not have a peak cruise L/D at the minimum radius, and instead has a maximum cruise L/D at 1.2 times the minimal allowed radius. The radius at the midpoint of the tail does have a peak L/D at the upper bound of the design range.

Table 1. Fuselage outer mold line design of experiments.

Parameter	Min Value	Max Value	Parameter	Min Value	Max Value
Nose length	200 in	1,200 in	Radius at 1/3 of cabin length	54 in	81 in
Cabin length	1,122 in	1,122 in	Radius at 2/3 of cabin length	54 in	81 in
Tail length	200 in	1,200 in	Radius at end of cabin	54 in	81 in
Radius at start of cabin	54 in	81 in	Radius at midpoint of tail	12.5 in	37.5 in

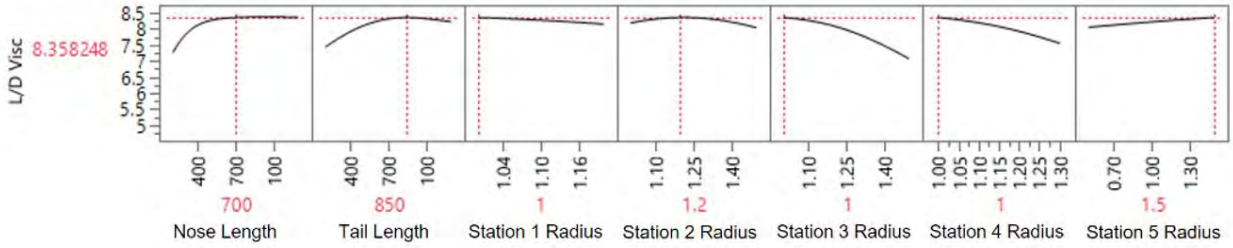

Figure 6. Profiler of fuselage design of experiment surrogate model.

Vertical Tail Design

The chosen VT planform area is 375 ft², which requires a 28° rudder deflection under two-engine inoperative (2EI) conditions defined by FAR §25.147. This deflection is 2° lower than the assumed reasonable limit of 30° and thus provides a buffer. Figure 7 shows the rudder deflection required as a function of VT planform area to maintain a straight heading under 2EI conditions (left), along with the rudder deflection required as a function of crosswind speed (right). The sub-figure on the right in Figure 7 shows that to satisfy FAR §25.237, a rudder deflection of approximately 15° at 25 kts crosswinds is needed, which is well below the assumed limit of 30°. Table 2 presents a summary of the final VT design parameters.

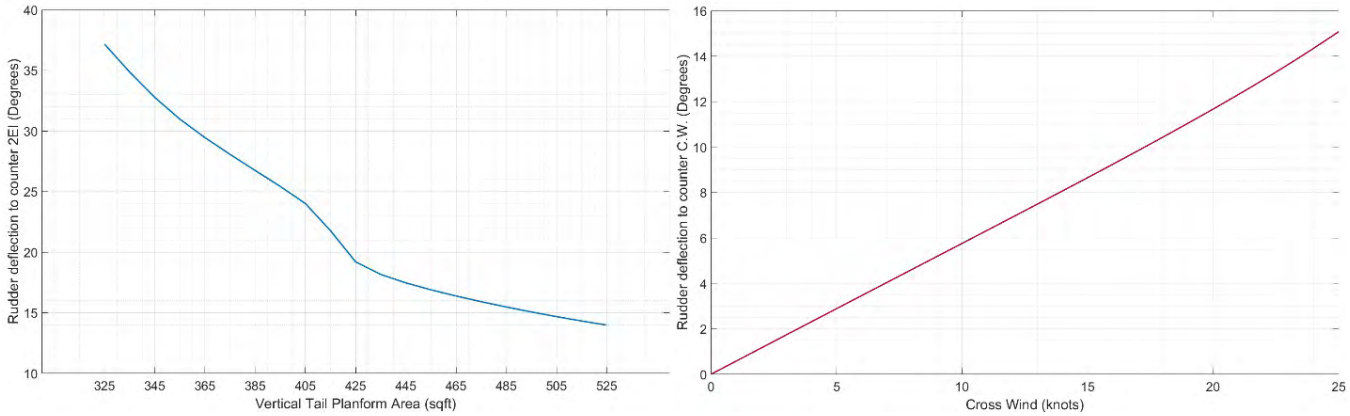

Figure 7. Rudder deflection required to counter yaw from two-engine inoperative (2EI; left) and crosswind (C.W.; right) conditions.

Table 2. Vertical tail design parameters.

Vertical Tail Parameter	Value
Planform area (ft^2)	375
Aspect ratio	1.5
Taper ratio	0.25
Leading edge sweep (degrees)	45
Thickness to chord (average)	0.04

Mach 1.7 Vehicle Wing Design

For this study, the planform area of the wing is fixed at 5,125 ft^2. In total, there are 18 geometric variables (Table 3) with angle of attack being the 19th design variable. One hundred warm-start cases are executed to sample the design space initially, followed by an additional 100 adaptive samples. The adaptive sampling is stopped when the expected improvement in L/D is on the order of 0.01. Figure 8 shows the distribution of L/D over the warm-start and adaptive samples. As depicted in this figure, the majority of the adaptive sampling cases (blue and purple) have L/D values between 9 and 10 at cruise. Some adaptive samples with lower L/D (between 5 and 9) correspond to early points in the adaptive sampling; i.e., during the "exploration phase" of the optimization.

Table 3. Wing design variables and bounds.

Parameter	Lower Bound	Upper Bound	Parameter	Lower Bound	Upper Bound
Overall taper	0.1	0.3	Delta c/4 sweep break [deg]	-20	0
Overall AR	2.25	4	Section 1 (twist, max camber)	[0, 0%]	[1.5, 0.5(t/c)]
Overall c/4 sweep [deg]	40	60	Section 2 (twist, max camber)	[-5, 0%]	[5, 0.5(t/c)]
Overall dihedral [deg]	-5	5	Section 3 (twist, max camber)	[-5, 0%]	[5, 0.5(t/c)]
Delta taper break	0	0.3	Section 4 (twist, max camber)	[-5, 0%]	[5, 0.5(t/c)]
Delta dihedral break [deg]	-5	5	Section 5 (twist, max camber)	[-5, 0%]	[5, 0.5(t/c)]
Wing break location	0.3	0.6			

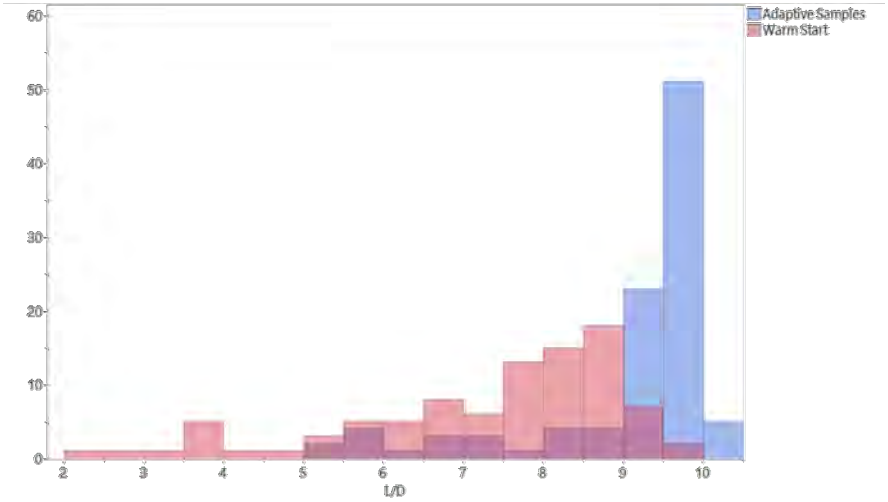

Figure 8. Distribution of lift to drag (L/D) over warm-start and adaptive sampling.

Figure 9 shows a comparison of baseline and optimized wing planforms with the design variable values compared in Table 4. The major differences in the optimized vehicle relative to the baseline are the larger sweep, an inboard shift in the wing

break location, and a change in the twist distribution and camber of the wing. The highest L/D for this vehicle at cruise is 10.16 for a C_L of 0.156, which is a 9.25% improvement over the baseline vehicle peak L/D, which occurs at a C_L of 0.146.

Table 4. Comparison of baseline and optimized wing design variables.

Parameter	Baseline	Optimized	Parameter	Baseline	Optimized
Overall taper	0.1	0.109	Delta dihedral break [deg]	0	0.08
Overall AR	2.5	2.519	Section 1 (twist, max camber)	[0, 0%]	[0.77, 0.92%]
Overall c/4 sweep [deg]	52.5	61.65	Section 2 (twist, max camber)	[0, 0%]	[0.93, 0.34%]
Overall dihedral [deg]	0	-0.62	Section 3 (twist, max camber)	[0, 0%]	[1.44, 0.53%]
Delta taper break	0.2	0.138	Section 4 (twist, max camber)	[0, 0%]	[-2.23, 0.56%]
Delta c/4 sweep break [deg]	-10	-11.60	Section 5 (twist, max camber)	[0, 0%]	[-0.76, 0.42%]
Wing break location	0.45	0.347			

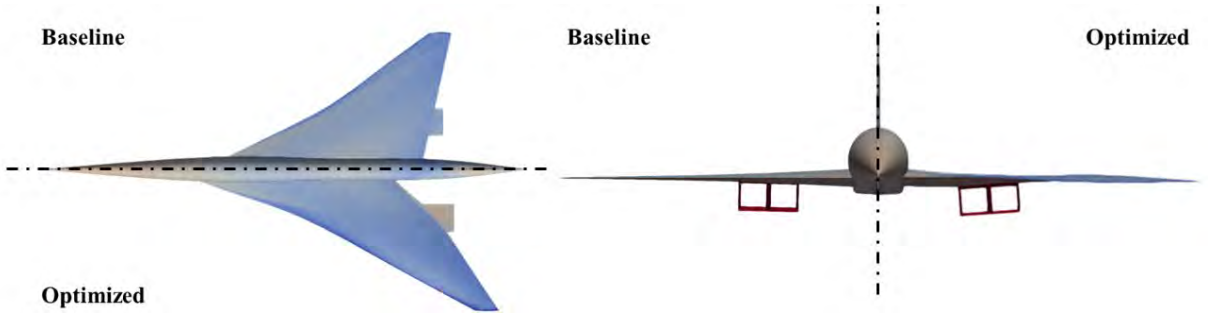

Figure 9. Comparison of baseline and optimized wing planforms.

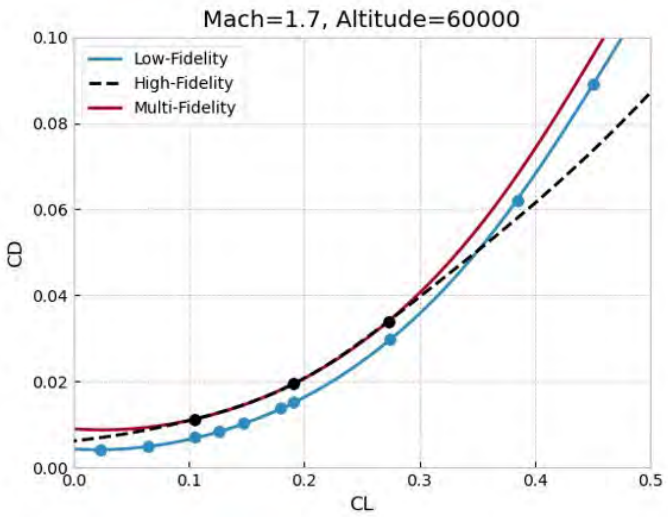

Figure 10. Multi-fidelity drag polar at cruise conditions. CL, lift coefficient; CD, drag coefficient.

Figure 10 shows the multi-fidelity drag polar at cruise conditions for the optimized vehicle. Black points represent the three RANS samples at this flight condition. The high-fidelity curve in this figure shows the drag polar that would have resulted if only the RANS data points were used to fit the surrogate and to extrapolate to the entire flight envelope. Likewise, the blue points are the inviscid data from Cart3D, and the blue low-fidelity curve represents the drag polar obtained from the low-

fidelity data only. The red multi-fidelity curve thus depicts the final drag polar for this vehicle, generated by the multi-fidelity surrogate using both inviscid and RANS data. The effect of the multi-fidelity surrogate can be summarized by an upward shift of the inviscid drag polar, which can be attributed to the effect of friction drag.

Mach 2.0 Vehicle Wing Design

The design of the Mach 2.0 vehicle closely follows the approach described previously for the Mach 1.7 vehicle. The same variable listed in Table 34 was used, 100 warm-start cases were initially generated, and roughly 100 additional cases were adaptively generated until the expected improvement was below a given threshold. However, to accommodate the higher cruise Mach number, the wing sweep bounds were shifted by 10˚; i.e., the lower and upper bounds were 50˚ and 70˚, respectively. Also, the optimization of the Mach 2.0 was performed with a constraint on the estimated wing weight. This is because an unconstrained optimization would produce a wing planform with an unreasonably high wing weight. A wing weight upper limit of 53,000 lbs was assumed based on the estimated wing weight of the Mach 1.7 vehicle.

The table below lists the optimized design parameters of the Mach 2.0 aircraft with a wing weight constraint. Many of the parameter values are similar to those of the Mach 1.7 design, with the sweep being noticeably larger, as expected for the higher cruise Mach number. The highest L/D at cruise, among the feasible designs, was 9.68 at a C_L of 0.156. This aerodynamic performance is 4.72% smaller than the Mach 1.7 optimum, which is explained by the higher design cruise speed. Note that this is still higher than the maximum L/D of the baseline. Figure 11 provides a comparison of the Mach 1.7 and 2.0 optima.

Parameter	Baseline	Optimized	Parameter	Baseline	Optimized
Overall taper	0.1	0.098	Delta dihedral break [deg]	0	0.24
Overall AR	2.5	2.607	Section 1 (twist, max camber)	[0, 0%]	[0.86, 0.98%]
Overall c/4 sweep [deg]	52.5	63.63	Section 2 (twist, max camber)	[0, 0%]	[1.30, 0.62%]
Overall dihedral [deg]	0	-0.914	Section 3 (twist, max camber)	[0, 0%]	[0.19, 1.05%]
Delta taper break	0.2	0.199	Section 4 (twist, max camber)	[0, 0%]	[-1.84, 0.86%]
Delta c/4 sweep break [deg]	-10	-7.838	Section 5 (twist, max camber)	[0, 0%]	[-0.74, 0.41%]
Wing break location	0.45	0.347			

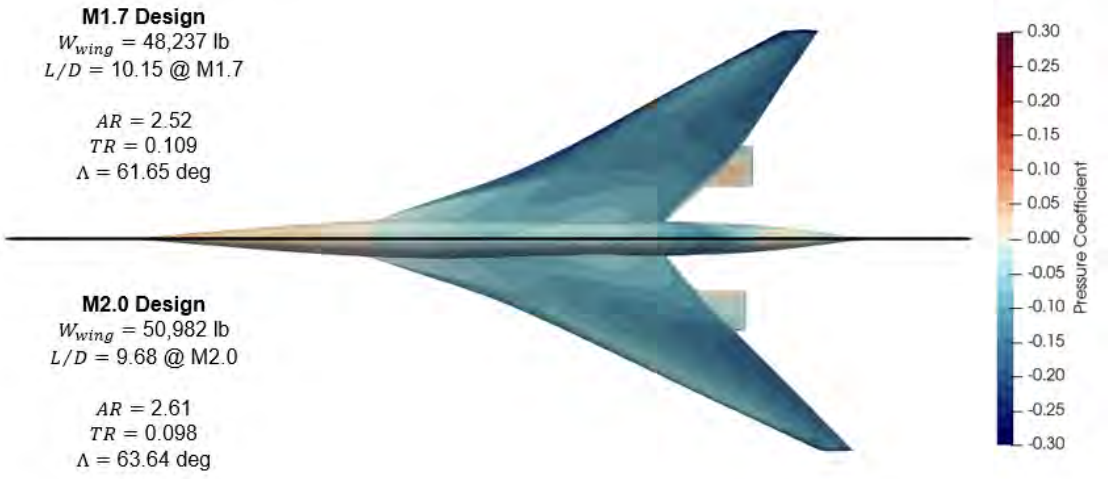

Figure 11. Comparison of the Mach 1.7 and 2.0 optima. W_{wing}, wing weight; L/D, lift-to-drag ratio; AR, aspect ratio; TR, taper ratio; Λ, wing quarter chord sweep.

Task2 - SST Propulsion System Modeling

Georgia Institute of Technology

Objectives

The propulsion system plays an important role on performance metrics, such as fuel burn, gross weight, and takeoff field length, and in environmental metrics, such as noise and emissions. As such, the objective of the propulsion system modeling was to develop the capability to analyze and predict the necessary data to model those metrics of interest. The developed model needed to provide thrust and fuel flow as a function of Mach number, altitude, and throttle setting. Engine dimensions needed to be predicted and provided to aerodynamic analysis to assess aircraft drag. The engine weight needed to be predicted as part of the overall aircraft empty weight. Additionally, the propulsion analysis must provide the necessary information to model the noise produced by the engine.

Research Approach

Much of the details for the propulsion model were described in the last report [14]. As a brief summary, the propulsion system models a mixed-flow turbofan (MFTF) engine cycle. The engine cycle performance is modeled using Numerical Propulsion System Simulation (NPSS), and the dimensions, flowpath and weight are modeled using Weight Analysis of Turbine Engines (WATE++). This report focuses on changes applied to the propulsion model over the last year. For further details on the propulsion model, the reader is directed to the report from previous years and an AIAA article [21].

Propulsion Performance: Model

Several updates have been made to the propulsion cycle model. The pressure losses in ducts were previously set as constant values. This was updated so that the duct losses now scale with the square of corrected airflow in the duct, as described by Walsh [15]. The mixer loss model was also updated to better account for losses due to mixing as the flow conditions at the mixer change with flight condition, throttle, and variable nozzle throat. This is important for the noise power-management, which will be explained in the Off-Design Analysis section. The mixer loss model is based on the works of Frost [16] and Zola [17] and accounts for momentum losses due to unequal total pressures on the bypass and core side, friction losses in the chute of the mixer, and incomplete mixing losses. The turbine mean-line analysis was updated to ensure a 50% reaction design. This was done to ensure consistency with the efficiency correlations used. The number of stages for all turbomachinery can be adjusted to ensure reasonable work-coefficients (i.e., pressure ratio per stage). Since part of the mean-line analysis allows varying the design speed of the shafts and the radii of the turbomachinery, the stresses on the blades can change. To ensure that the allowable metal temperature used in the cooling flow model was appropriate to the blade stresses experienced, a turbine creep life model was implemented that uses a Larson-Miller correlation to estimate the creep life of the blades, given the metal temperature and predicted stress on the blades.

Propulsion Performance: On-Design Sizing

Engine cycle analysis previously used throttle ratio, the ratio of design turbine inlet temperature to maximum turbine inlet temperature, as a means of varying the theta-break, the Mach number at which the engine becomes temperature limited. However, with the turbine-creep life analysis setting a reasonable blade temperature, it was desirable to vary the maximum (max) turbine inlet temperature to trade cooling-flow penalties with the performance benefits of a higher turbine inlet temperature. This meant that for a given range of throttle ratio, the range of design turbine inlet temperature would shift with max turbine inlet temperature. Additionally, it was possible to set a throttle ratio that would place the theta-break at a higher Mach number than cruise. Because the point of picking a theta-break is to control the thrust lapse at cruise, it was decided to size the cycle such that design turbine inlet temperature was varied to target a desired corrected fan speed (i.e. thrust lapse) at top-of-climb when operating the top-of-climb turbine inlet temperature at maximum turbine inlet temperature. This ensures that both the max turbine inlet temperature and the thrust lapse at top-of-climb can be varied in a manner that ensures a more reasonable range of top-of-climb thrust lapse. This process is enabled by the multi-design point setup which allows perturbing design point parameters to meet targets at other flight conditions.

Propulsion Performance: Off-Design Analysis

In the last report, we detailed two different power-management schemes that utilize the fuel flow and a variable nozzle throat control. The first was an efficiency approach, used throughout the majority of the flight, by holding a peak efficiency line on the fan as the thrust was reduced. The second method favored noise when reducing thrust and is used only for landing and takeoff (LTO) noise analysis. This works by initially decreasing thrust along the 100% speed line of the fan, resulting in constant airflow and a greater reduction in fan pressure ratio and therefore jet velocity. This approach results in significantly more airflow in the bypass duct, which increases the Mach number and extraction ratio at the mixer. The mixer

model described above enables capturing the performance losses as a result of using this power-management scheme. The noise power-management approach has been further improved by favoring lower fan speed over lower fan pressure ratio at low thrust. This was done to favor a reduction in fan noise, which is dominant during the lower thrust used at approach. The fan operating point is always constrained by limits on the mechanical actuation of the nozzle throat as well as stall margin limits.

Propulsion Weight

As mentioned earlier, the stress predicted by the flowpath model is used to determine the turbine rotor blade creep life, which enables setting a reasonable allowable metal temperature. This in turn allows varying the maximum allowable turbine inlet temperature, which affects the amount of cooling air required to maintain the desired metal temperature. Additionally, noise results showed a significant reduction in noise from the fan rotor-stator spacing variable. To avoid exploiting the benefits of increasing rotor-stator spacing, the flowpath model is updated to reflect the increases in the length and weight of the engine. Additionally, an efficiency penalty is imposed on the fan to reflect the pressure losses that would occur in the extended distance between the rotor and stator due to both end wall friction losses and rotor wake mixing.

Results

The propulsion system modeling described in this section supports the design space exploration described and explained in Task 5. The results shown in Table 5 and Table 6 are the propulsion cycle performance and geometry and weight for the selected design discussed in Task 5.

Table 5. Engine performance for current selected design.

Engine Metric	Aerodynamic design point M1.2/39kft/ISA	Top-of-Climb M1.7/55kft/ISA	Takeoff M0.3/SL/ISA+18F
Fan pressure ratio	2.17	1.92	2.17
Bypass ratio	3.21	3.58	3.21
Overall pressure ratio	25.49	20.77	25.42
Compressor exit temperature (T3) [R]	1,357	1,540	1,460
Burner exit temperature (T4) [R]	3,173	3,536	3,360
Turbine inlet temperature (T41) [R]	3,083	3,436	3,266
Corrected airflow at the fan face [lbm/s]	908.8	839.3	919.3
Percent of design corrected fan speed	100.0	94.5	100.0
Thrust [lbf]	10,415.6	6,757	32,143
Thrust specific fuel consumption TSFC $\left[\frac{lbm}{lbf \cdot h}\right]$	0.847	1.029	0.642
Nozzle pressure ratio	4.58	7.71	1.99
Jet velocity [ft/s]	2,003	2,396	1,481

Table 6. Engine geometry and weight for current selected design.

Engine Geometry Variable	Value
Fan diameter [in]	67.2
Inlet capture area [in^2]	3,401
Engine pod length [in]	438
Engine pod weight [lb]	11,464

Task 3 - Mission Analysis

Georgia Institute of Technology

Objectives

The objective of mission analysis was to synthesize and size the supersonic transport for a specified design mission. The top-level requirement for sizing the current SST was to cruise at Mach 1.7 carrying 65 passengers for 4,250 nmi.

Research Approach

As with previous work, Georgia Tech researchers leveraged the Framework for Advanced Supersonic Transports (FASST) modeling and simulation (M&S) environment to model the supersonic vehicles for this task. This framework is based on the Environmental Design Space (EDS). The goals of EDS and FASST are the same: to provide a modeling and simulation environment that enables tradeoffs and interdependencies among aircraft system-level metrics. The difference is that EDS was designed for subsonic aircraft; therefore, modifications were implemented to enable the modeling and simulation of supersonic aircraft. In the case of FASST, the system-level metrics of highest interest are the vehicle weight, design mission fuel burn, and LTO certification noise. The flow diagram for the FASST environment (Figure 12) shows the inputs, outputs, and interconnections between each discipline's analysis module in the modeling and simulation environment.

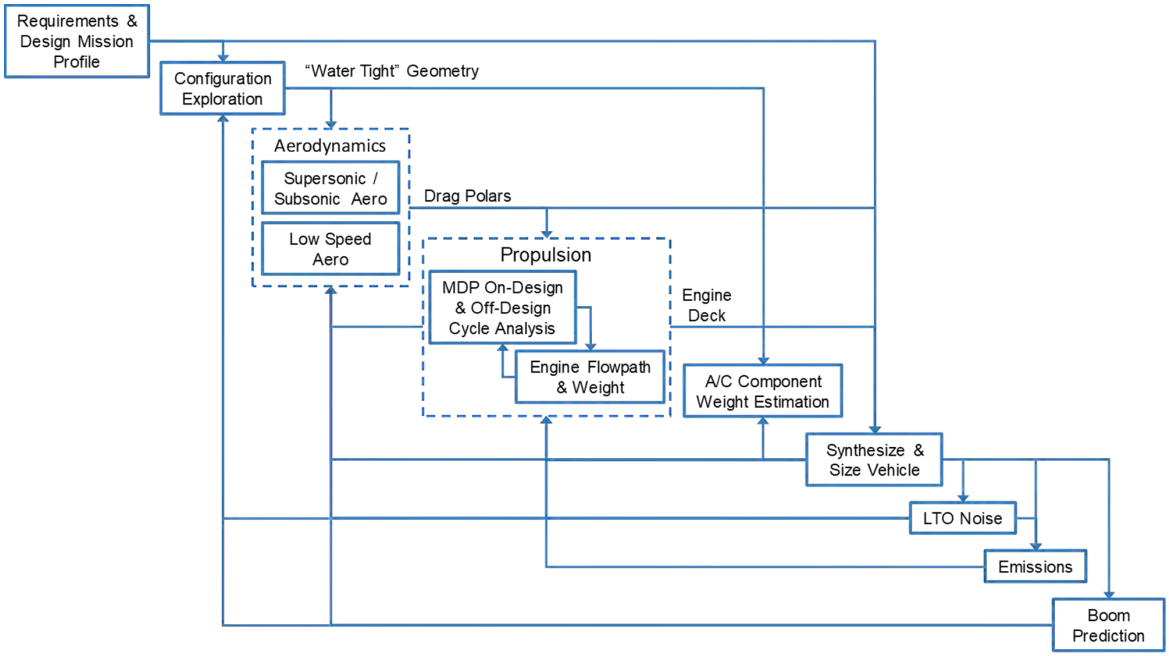

Figure 12. Framework for Advanced Supersonic Transport (FASST) flow diagram.

The requirements and design mission were specified by the research team and outlined in the following sections. Some of the high-level requirements were the number of passengers (65), the design Mach number (1.7), and the design mission range (4,250 nmi). The configuration exploration and aerodynamics drag polar generation are performed in a local setting, outside of FASST, and are described in Task 1. The resulting drag polars are fed into the mission analysis and vehicle sizing module. The engine cycle modeling is performed in NPSS, and flowpath and weight estimation is conducted with WATE. The engine architecture is a mixed-flow turbofan. The propulsion system modeling, discussed in Task 2, provides an engine deck, engine weight and engine dimensions to the mission analysis and vehicle sizing module. For the vehicle mission analysis and sizing, FLOPS is used. FLOPS uses the inputs of engine deck, drag polar, and other vehicle configuration parameters to estimate the overall empty weight of the aircraft. FLOPS then iterates on the vehicle gross weight to complete the mission prescribed by the designer. FLOPS also scales the engine thrust and wing area to produce the designer specified wing-loading and thrust-loading. If the engine is scaled in FLOPS, it is subsequently rescaled in the engine analysis to obtain an updated engine performance and weight. This iteration continues until the engine no longer requires scaling. After sizing, the vehicle is analyzed through a series of off-design missions.

Reference 18 offers more description of the mission segments within FLOPS; they are climb, cruise, refueling, payload releases, accelerations, turns, hold, and descent [18]. Many of these mission segments are developed for modeling military aircraft. The mission segments used for this study are climb, cruise, loiter, and descent, and the performance of each segment is done using a step integration method to compute fuel burn, elapsed time, distance covered, and changes in speed and altitude. The mission profile used for this study is shown in Figure 13. Also shown in Figure 13 is the reserve mission that is flown to compute reserve fuel. The reserve fuel has an additional safety margin of 5% of total trip fuel.

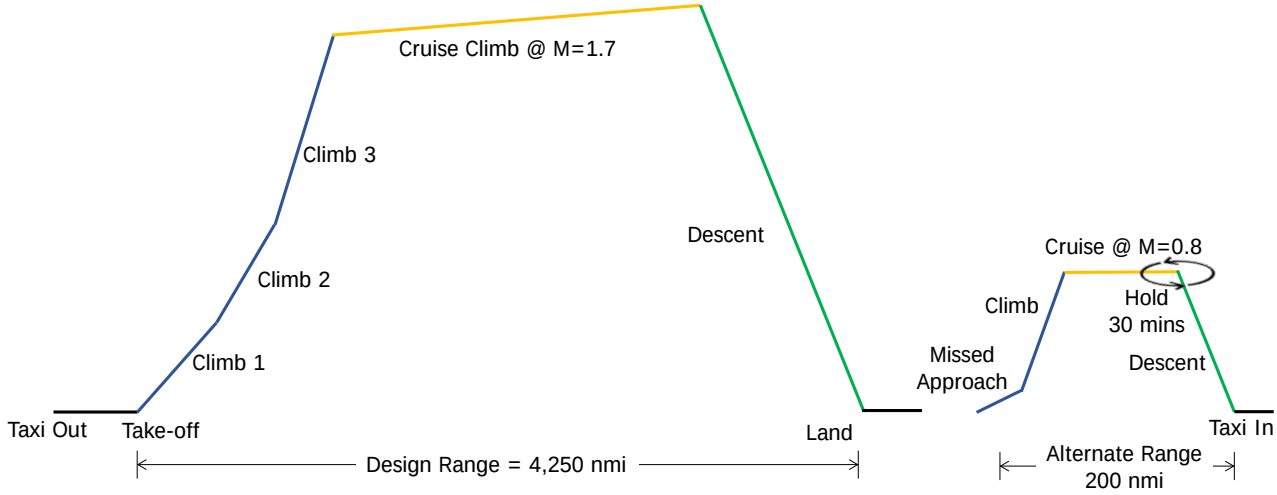

Figure 13. Mission profile for 65-passenger, M1.7 supersonic transport.

For the climb segment, FLOPS offers users a choice of providing a climb profile or it may be optimized by the program. The latter option is used for this sizing exercise. More specifically, the optimization option of minimum fuel to climb (as opposed to minimum time to climb or minimum time to distance) is chosen for the climb optimization. For this climb optimization, FLOPS divides the climb into a series of energy steps. Within each energy step, the combination of speed and altitude that maximizes the objective—in this case, inverse of minimum fuel—is determined.

For the cruise segment, FLOPS has several options for suboptimization, and they are optimum altitude, optimum Mach number, or both to achieve max specific range or minimum fuel flow, fixed Mach number and altitude, fixed altitude and constant lift coefficient, and maximum Mach number for either fixed altitude or optimum altitude. For the 65-passenger Mach 1.7 SST, the option of fixed Mach number/optimum altitude for specific range is chosen.

For the descent segment, FLOPS offers three options: prescribed profile, at constant lift coefficient, or at maximum L/D. For the SST of interest, the descent is flown with maximum L/D.

Although not part of the synthesis and sizing process, the detailed takeoff and landing module of FLOPS is used in order to provide detailed information on the takeoff and landing trajectories for the LTO noise analysis. The LTO noise prediction is discussed in the next task (Task 4 - LTO Noise Modeling).

Finally, to synthesize and size the supersonic transport, FLOPS requires the following information:

- Geometry definition of the optimized shape configuration from Task 1: Aerodynamics
- Parametric high speed drag polars from Task 1: SST Aerodynamics Modeling
- Landing and takeoff drag polars also from Task 1: SST Aerodynamics Modeling
- Engine deck, engine weight, and max nacelle diameter and length from generated from Task 2: SST Propulsion System Modeling
- Aircraft component weights from FLOPS internal empirical weight equations based on vehicle gross weight and geometric information provided
- Two major vehicle scaling parameters, wing loading (W/S) and thrust to weight (T/W) ratio, are varied with each mission analysis execution to satisfy balanced field length and approach speed constraints while minimizing take-off gross weight.

Results

The mission analysis result for the Mach 1.7 SST carrying 65 passengers for 4,250 nmi (excluding reserve mission) is listed below and depicted in Figure 14:

- Takeoff: Mach = 0–0.30 at altitude of 0 ft
- Subsonic climb: M = 0.30–0.95; altitude changing from 0 ft to 25,000 ft
- Transonic supersonic climb: M = 0.95–1.4; altitude changing from 25,000 ft to 30,000 ft
- Supersonic climb: M = 1.4–1.7; altitude changing from 30,000 ft to 47,910 ft
- Cruise climb: constant cruise M = 1.7; altitude changing from 47,910 ft to 54,771 ft
- Descent: deceleration from M = 1.7–0.30; altitude decreasing from 54,771 ft to 0 ft

The reserve mission results are as follows:

- Reserve fuel available: 28,139 lb (includes 5% of fuel used in main mission)
- Total hold time: 30 min
- Climb: from 0 to 30,000 ft, with Mach increasing up to 0.88
- Cruise: 30,000 ft at M = 0.88

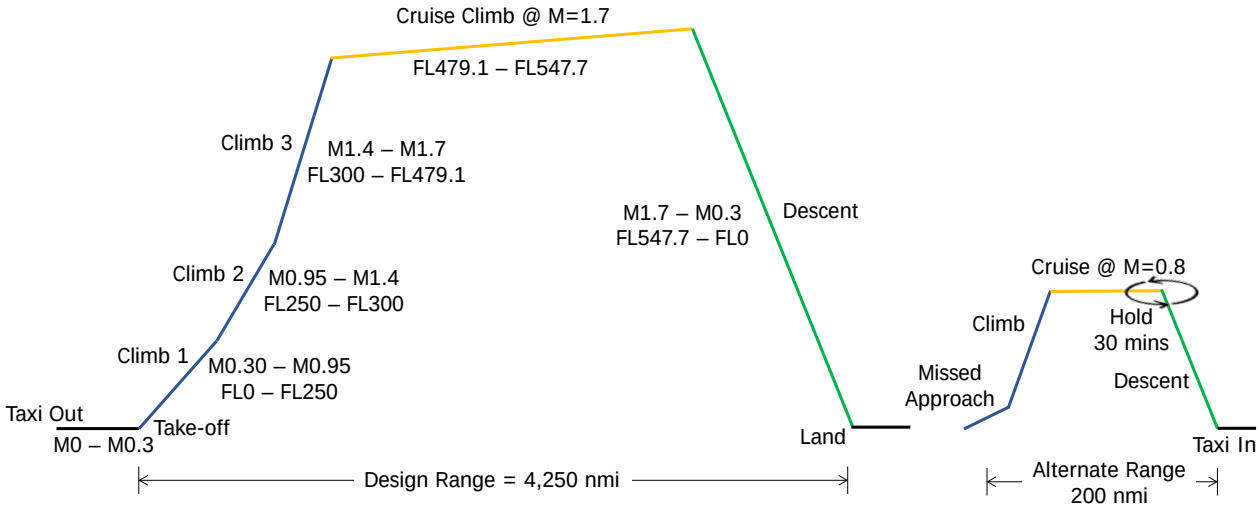

Figure 14. Mission profile for medium supersonic transport.

Task 4 - LTO Noise Modeling

Georgia Institute of Technology

Objective

The objective of this task was to study the impact of different takeoff trajectories and noise assessments for LTO noise. Alongside the team's traditional VNRS trajectory and its associate variables, the Georgia Tech group took upon the modeling of noise abatement departure procedures (NADP) set forth by NASA and ICAO, again with respective associated trajectory variables. Furthermore, in the interest of quantifying noise reduction benefits both close to and distant from the aerodrome, the team considered a new metric based on integrated sound exposure level (SEL).

Research Approach

As for many tasks developed by the Georgia Tech team in the context of supersonic aircraft, the modeling and simulation was performed in the FASST. Within this framework, once the configuration is properly modeled, the code uses FLOPS' detailed takeoff and landing module to calculate the takeoff trajectory. This information, along with many other engine and aircraft modeling parameters, is then passed on to ANOPP, which is also developed by NASA. The focus of this task is, therefore, to study the impact of the variables that control the takeoff trajectory on the noise assessment for a particular configuration. In essence, while this work is "nested" in the overarching design space exploration, the trajectory variables can be varied with no sizing impact to the configuration being studied.

The previously mentioned VNRS consists of a series of pilot-initiated and automatic (i.e., no pilot control) changes to engine and airframe configurations during a takeoff run to help reduce noise. In addition to the VNRS trajectory, two NADP trajectories, identified as ICAO-A and ICAO-B, have been implemented into the off-design analysis to explore other potential takeoff procedures. The ICAO-A trajectory is meant to minimize noise near the aerodrome and the ICAO-B trajectory is meant to minimize noise farther away from the aerodrome. To better illustrate each takeoff procedure, Table 7 presents a rundown of each of the options. Also, it is worth pointing out that the programmed high lift devices (PHLD) mentioned in Table 7 consist of a flap deflection schedule optimized for the aerodynamic efficiency for the required lift at each point in the takeoff trajectory, which is controlled by the flight management system. On a similar note, the programmed thrust lapse rate (PLR) is used differently by the VNRS and NADP procedures. In the former, it is an automatic thrust reduction controlled by FADEC and implemented immediately after the aircraft clears the obstacle during takeoff; in the latter, it is used as the engine cutback setting. Finally, the various highlighted aspects of each takeoff procedure are variables in our DoE that control aspects of the trajectory.

Table 7. Trajectories breakdown.

	VNRS	NADP-1 (ICAO-A)	NADP-2 (ICAO-B)
Takeoff start	Initiate the takeoff run with a specified power reserve (VARTH)		
After the obstacle	Reduce power to specified lapse (PLR), engage PHLD schedule and adopt a constant flight path (GFIX) and fly up to specified altitude (HSTOP_1)	Maintain current flight setting and fly up to specified altitude (HSTOP_1a)	Keep current thrust setting constant, adopt a constant flight path (GFIX_1b) and fly up to specified speed (VSTOP_1b)
	Transition to constant thrust and constant speed and fly up to specified altitude (HSTOP_2)		Engage PHLD schedule and fly up to specified speed (VSTOP_2b)
Pilot-initiated cutback	Cutback engine setting set automatically by FLOPS	Cutback engine setting set by the PLR variable in the next step	
		Transition to constant thrust and speed, reduce power to specified lapse (PLR) and fly up to specified altitude (HSTOP_2a)	Transition to constant thrust and speed, reduce power to specified lapse (PLR) and fly up to specified altitude (HSTOP_3b)
		Transition to constant thrust and flight path (GFIX_3a) and fly up to specified speed (VSTOP_3a)	Transition to constant thrust and flight path (GFIX_4b) and fly up to specified speed (VSTOP_4b)
		Adopt a constant flight path (GFIX_4a), engage the high lift devices schedule and fly up to specified speed (VSTOP_4a)	
Final segment	Fly off the aerodrome (50,000 ft distance from break release) with the previous settings		

As previously stated, the noise assessment for each aircraft configuration is done using NASA's ANOPP program. In performing these assessments, some assumptions were made in selecting and using different ANOPP modules. Table 8 presents a breakdown of the ANOPP input file structure and the rationale applicable to each module or section.

Table 8. Modules used in aeroacoustics analysis.

Component	ANOPP Module	Acronym	Rationale
Trajectory	Source Flyover Module	SFO	Considered separate trajectories (prescribed by FLOPS) for the sideline and the cutback/approach noises assessments – the difference being that the sideline trajectory did not include a cutback section after the second segment acceleration – and both cases used a VNRS takeoff trajectory
Airframe	Fink's Airframe Noise Module	FNKAFM	Standard module to predict the broadband noise from the dominant components of the airframe and based on a method developed by Fink for the FAA
Jet	Single Stream Circular Jet Noise Module	SGLJET	The single stream jet mixing noise was calculated with a methodology based on SAE ARP 876 as this is known to be the best representation of the current nozzle type
Fan	Heidmann Fan Noise Module	HDNFAN	The fan inlet and discharge noises were assessed separately for their tone and broadband contributions using a methodology based on correlations to model and full-scale test data
Treatment	Fan Noise Treatment Module	TREAT	Given that the chosen fan module assumes that the inlet and discharge ducts are without acoustic treatment, the attenuation spectra are applied to separate predictions of the inlet and aft radiated source noise produced by the source noise module and a total attenuated fan noise prediction is produced
Combustor	Combustion Noise Module	GECOR	The combustor noise was predicted with a methodology developed by General Electric, and later adopted by the SAE A-21 Committee
Shielding	Wing Module	WING	Used to compute the geometric effects of wing shielding or reflection on the propagation of engine noise (depending on the engine placement/configuration)

Finally, the key metric of merit for the LTO analysis for design/cycle selection is certification EPNL (effective perceived noise level), Georgia Tech has been starting to explore the potential for alternative noise metrics that better account for the whole noise footprint of the aircraft. While the most obvious means to do this would be to measure the noise footprint as predicted by AEDT, Georgia Tech currently does not have an automatic FAAST to AEDT pipeline, which would be needed to include AEDT results in our design space studies. For this reason, a new noise metric was considered where SEL was integrated along the flight path. Potentially this could be a more holistic method of comparing takeoff noise impacts, as opposed to only examining the three certification points, and better minimize noise footprints in a region of interest. By using this metric in combination with the ICAO-A and ICAO-B takeoff procedures, the Georgia Tech team plans to explore whether our current design space exploration procedure is optimizing for certification noise to the detriment of the overall noise footprint.

Results

Certification noise is a key metric for the design space exploration in described in Task 5, and the procedures described in this section allow the Georgia Tech team to analyze how this metric varies across the design space.

Task 5 - Design Space Exploration

Georgia Institute of Technology

Objective

The objective of this task was to explore a large design space of engine, airframe, and operational parameters to assess the interdependencies of fuel burn and LTO noise. In conceptual design, the final performance and environmental impact of a given vehicle is unknown. A key task in conceptual design is to parameterize the vehicle model such that different vehicle designs can be generated and evaluated. Doing so allows an assessment of how different parameters affect the metrics of interest and what the tradeoff between metrics looks like. By understanding these tradeoffs in the context of current regulatory limits, it enables designers to better understand how to design vehicles to meet current regulations and it allows policy makers an understanding of the implications of modifying current regulatory limits.

Research Approach

All the modeling elements described above and in previous reports are part of a modeling and simulation environmental called FASST. FASST was used as the model to map alternatives to objectives. Alternatives were determined from a design of experiments, which included engine cycle, engine flowpath, thrust-loading, wing-loading, and LTO operational parameters. The engine cycle parameters include fan pressure ratio, overall pressure ratio, design turbine inlet temperature, max turbine inlet temperature, and extraction ratio (i.e., bypass ratio). The engine flowpath parameters include variables such as hub-tip ratio, tip Mach number, specific flow, etc. The LTO operational parameters include takeoff thrust setting, programmed lapse rate, second segment flight path angle, fixed-speed transition altitude, and cutback altitude. The design space exploration for the airframe geometry was done separately and described above in Task 1. From the available parameters, a DoE was used to generate alternatives. The design included a fractional factorial design and a random uniform sampling of several thousand additional designs. This was done as more sophisticated space-filling designs would take too long to generate given the number of designs desired. Additionally, the run time of FASST is fairly short and FASST can be distributed across ~1,700 cores using HTCondor [19]. The results are analyzed and plotted using JMP v16 [20], and ranges are refined for subsequent analysis as needed.

Results

Interim results of this work resulted in paper published at AIAA Aviation 2022; interested readers are encouraged to consult that paper [21]. This section will focus on the current status of results, which includes several model updates since the publication of that paper. These results pertain to a 65-passenger aircraft designed for a Mach 1.7 cruise and a range of 4,250 nmi. The results shown in Figure 15 demonstrate the type of results that can be obtained using FASST. The Pareto front is shown in pink and the currently selected design in green. These results are preliminary and require refining design variables ranges, as mentioned earlier, to fully resolve the Pareto front. Currently the Pareto front is not a smooth curve and appears to be missing designs at the lower noise margin. As such, additional runs will be performed to better resolve these trends. In identifying the Pareto front shown below, various constraints were imposed. These included limits on the takeoff and landing field lengths, approach speed, turbine creep life, and turbomachinery loading, as well as ensuring that each of the individual noise margins meets Chapter 14 requirements.

Additionally, obtaining these results involved increasing the empirical weight factors in FLOPS by 10%. There remains uncertainty in the applicability of current empirical correlations for a commercial supersonic transport. Although various items such as fuselage are expected to be greater due to the larger pressure differential at the higher cruise altitude and the higher dynamic pressure experienced by the airframe as a whole, there remains uncertainty as to what the weight of different parts of the aircraft will be. This will ultimately affect the results of the tradeoff shown below.

The results shown below are for a vehicle designed to cruise at Mach 1.7. In addition to the Mach 1.7 aircraft, a Mach 2.0 and Mach 1.4 vehicle will be evaluated in order to demonstrate how the interdependency shifts with Mach number. As Mach number is perhaps the most important design variable for a supersonic aircraft, it is important for policy makers to understand the implications of changing Mach number on this interdependency. Similarly, the upcoming results will inform designers when selecting the cruise Mach number for a vehicle.

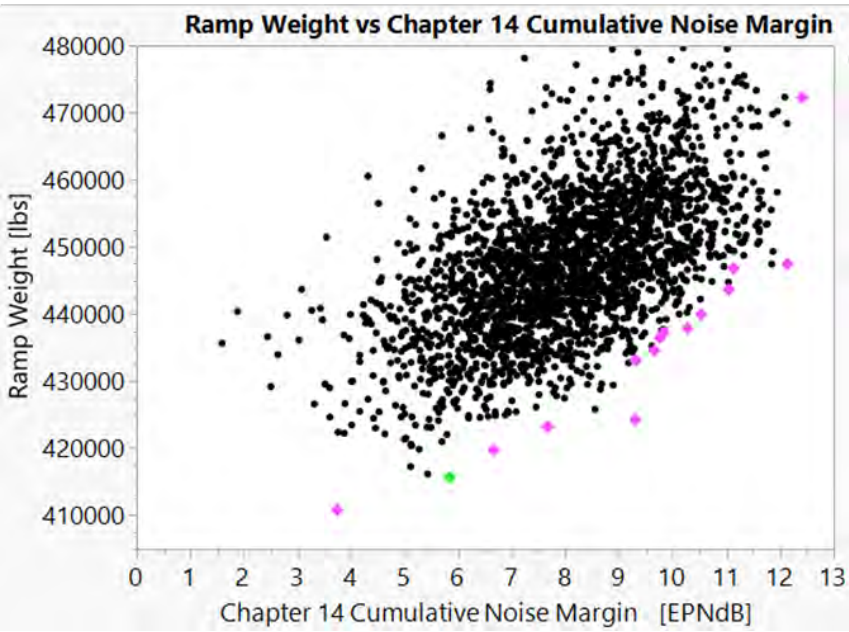

Figure 15. Pareto front of ramp weight vs noise margin.

Task 6 - SST Modeling in AEDT

Georgia Institute of Technology

Objective

The primary objective of this task is to propose a methodology for the construction of models to predict fuel burn, net thrust, and the drag coefficient value over the entire span of missions that a given SST will be performing and to support the implementation of full-flight modeling capability for SSTs in AEDT. A sample data package for the NASA Supersonic Technology Concept Aeroplanes (STCA) concept has been sent to FAA subject matter experts to kick-off the implementation efforts in AEDT on a set of four origin-destination (OD) pairs.

Research Approach

The technical approach for this section of the report is organized into propulsion data and aerodynamic data regression subsections. Also note that the propulsion and aerodynamic data used in this task are from a different SST discussed in Tasks 1 to 5 due to their availability.

Propulsion

To generate coefficients for net thrust and fuel consumption for each SST concept, the engine deck data are regressed using a fifth-order least squares linear regression through JMP. In this case, net thrust and fuel flow are both regressed against static pressure ratio, total temperature ratio, Mach number, and power code (δ_s, θ_t, M, and PC, respectively). This results in two regression equations with 31 coefficients (the unknowns) plus the intercept. For the sake of simplicity and efficient implementation within AEDT, note that both net thrust and fuel flow have the same regression equation form.

Because it is not possible to obtain a good fit for the whole engine deck data using one regression equation, boxes of different Mach number, altitude, and power code interval combinations are designated in such a way that the union of the set of boxes encapsulates the design mission and other notional missions for the specific SST concept in question. The data from the engine deck are then filtered according to these boxes, and the regression exercise explained above is employed for each box, resulting in two regression equations, one for net thrust and one for fuel flow, for each designated box. Shown in Figure 16 is the box selection for the 55-passenger M 1.8 SST concept, with the box selection for the ascent phase of the design mission in green and the descent phase in blue. In this case, 7 boxes would result in 14 equations. Also note that

the box selection is unique for each SST concept, because each concept has a different design mission. A concept with a higher cruise speed and altitude might require more boxes to be defined to obtain good regression results than would a concept with lower cruise speed and altitude.

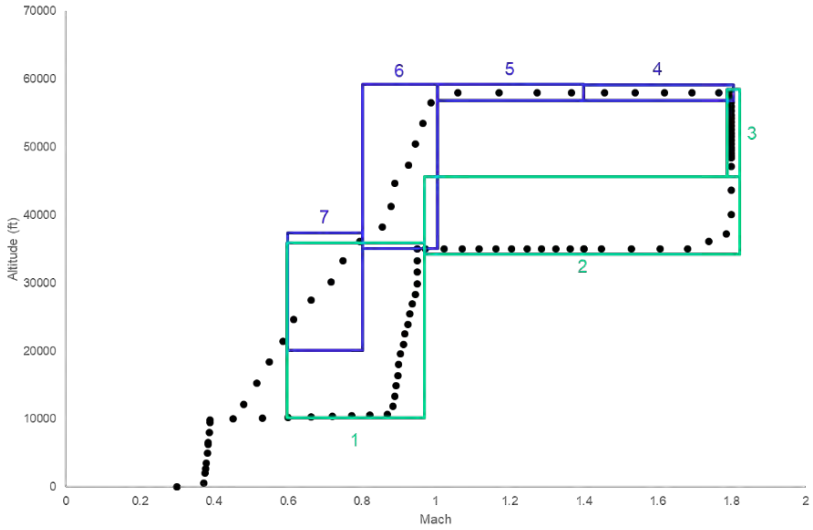

Figure 16. Propulsion box selection for 55-passenger M1.8 supersonic transport concept.

To evaluate the goodness of fits for each box, the values for predicted value for net thrust and fuel flow that can be obtained using the regression equations and the values for net thrust and fuel flow from the concept engine deck are used to calculate percent error. Probability density function distributions are then constructed using JMP to visualize the error for each box individually. A standard deviation of less than 1, a mean equal to 0, and percent error values lower than 4% at the 97.5% and 2.5% quantiles are all signs of a good regression. An example of these percent error distributions is shown in Figure 17.

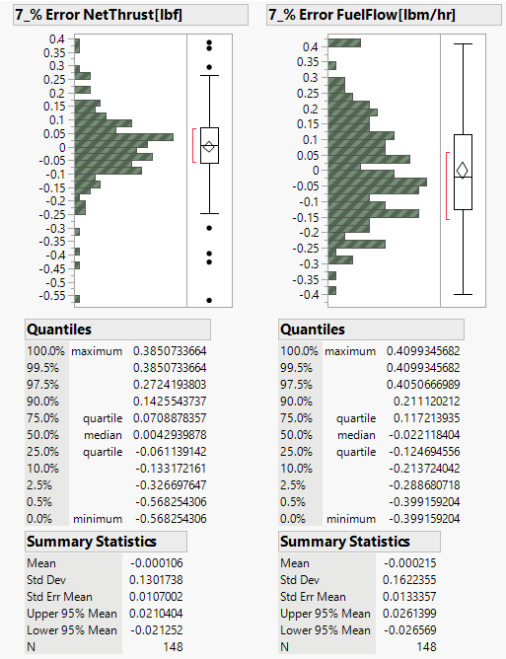

Figure 17. Percent error distribution example.

After obtaining a promising set of regressions for a particular concept, the next step is to validate them against the concept's design mission and off-design mission data generated using FLOPS. This will be explained in more detail in the validation section below.

Aerodynamics

To generate coefficients for the regression of the coefficient of drag for each SST concept, the design team provides raw FLOPS data that contain cardinal values of Mach number, C_L, altitude, and their corresponding C_D. The strategy that is exploited is to first regress the drag coefficient on those cardinal values using a stepwise fit before conducting a quadratic interpolation. By using this strategy with fewer C_L cardinal values, introducing Mach number as a cardinal value, and empowering the quadratic interpolation rather than the stepwise regression, the results were much better (errors ranged between -1.4% and 1.8%). Hence, the team decided to exploit this strategy for all future aero regressions using the latter strategy with fewer C_L.

JMP is exploited to perform the stepwise regression of the drag coefficient on Mach number, altitude, and C_L number. Because the behavior of the drag coefficient is quite different between subsonic, transonic, and supersonic phases, three different boxes are usually created and regressed against. The set of cardinal values to be chosen should always encompass the design mission in order to avoid extrapolation. Figure 18 shows an example of a supersonic regime equation obtained with the stepwise fit analysis.

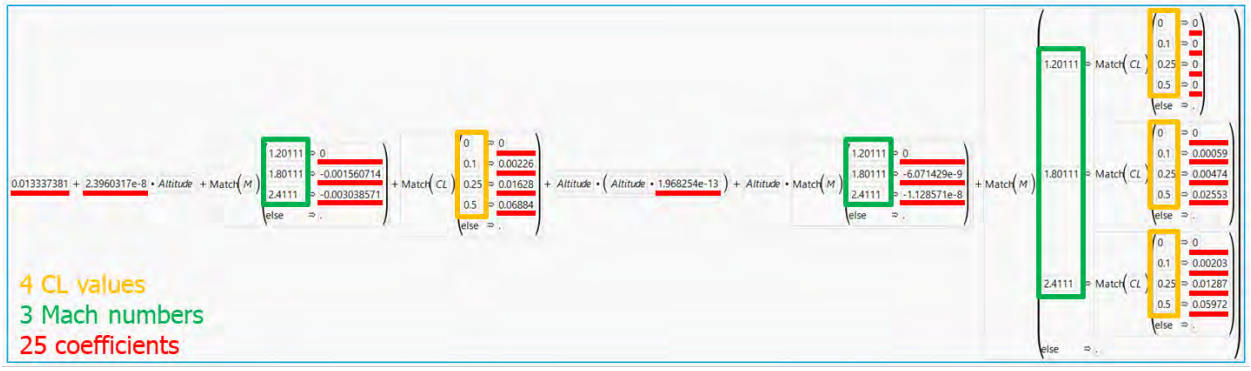

Figure 18. Form of the equation yielded by the stepwise fit on the cardinal values of Mach number (green) and lift coefficient (C_L; yellow) and a continuous altitude.

The design mission to which the validation is performed does not have specific cardinal values: Mach number, altitude, and C_L number are continuous. To enable predictive power for any input combination that is in between the original cardinal values of the inputs, a custom-made Python script was developed to perform a quadratic interpolation. The quadratic interpolation has the following form (see Figure 19):

$$C_D = a_1 + a_2 h + a_3 h^2 + b_1 + b_2 h + c_1 + d_1$$

$$b_1 = \begin{cases} b_{1,1}, & if M = M_1 \\ b_{1,2}, & if M = M_2 \\ b_{1,3}, & if M = M_3 \end{cases} \qquad b_2 = \begin{cases} b_{2,1}, & if M = M_1 \\ b_{2,2}, & if M = M_2 \\ b_{2,3}, & if M = M_3 \end{cases}$$

$$c_1 = \begin{cases} c_{1,1}, & if C_L = C_{L,1} \\ c_{1,2}, & if C_L = C_{L,2} \\ c_{1,3}, & if C_L = C_{L,3} \\ c_{1,4}, & if C_L = C_{L,4} \end{cases} \qquad d_1 = \begin{cases} d_{1,1,1}, & if M = M_1 \text{ and } C_L = C_{L,1} \\ d_{1,2,1}, & if M = M_2 \text{ and } C_L = C_{L,1} \\ \vdots & \\ d_{1,3,4}, & if M = M_3 \text{ and } C_L = C_{L,4} \end{cases}$$

Figure 19. Form of the quadratic interpolation.

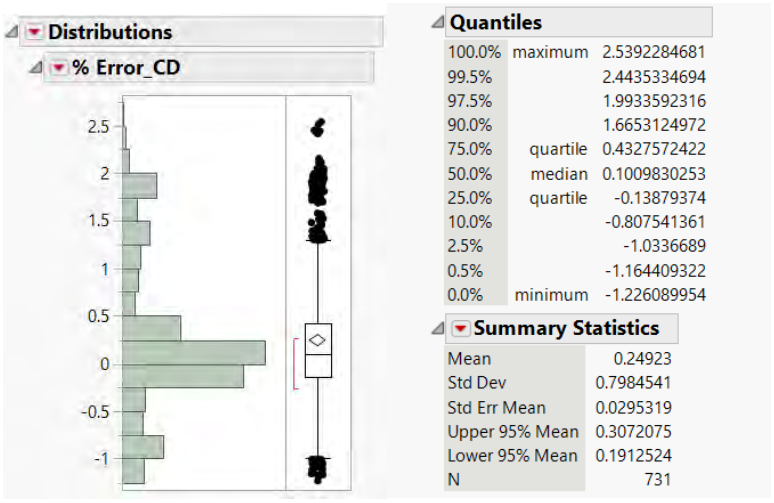

Figure 20. Total drag coefficient (C_D) error distribution example.

Figure 20 shows an example of total C_D error distribution after the quadratic interpolation has been conducted. Boxes are evaluated on their own at first, and then the total error distribution is evaluated. Once the fit is satisfactory, the design mission comes in and is considered as the validation set. This will be discussed in the next section.

Validation and Implementation in AEDT

The validation exercise consists of using the propulsion and aerodynamic regressions to obtain values for thrust, fuel flow, and drag coefficient for the SST concept's design mission and off-design mission data generated through FLOPS, and to compare the predicted values to the actual values from that data by calculating percent error and constructing probability density function distributions to visualize the results. To perform this exercise in a quick and efficient manner, a Python script was created that takes the propulsion and aerodynamic regression equations, as well as the data from the FLOPS mission, as inputs and calculates the percent error between the predicted regression outputs and the actual FLOPS outputs for net thrust and fuel flow. A flow chart that outlays how the validation process works and how the Python script was developed is shown in Figure 21.

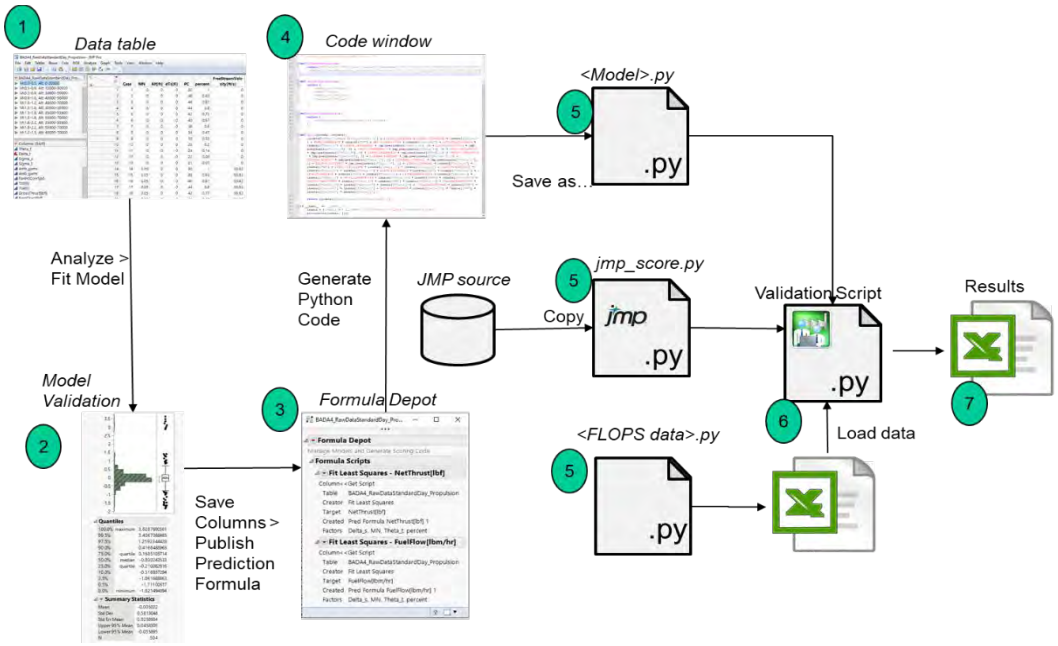

Figure 21. Validation process flowchart.

Since the FLOPS mission data does not contain values for static pressure ratio and total temperature ratio, atmospheric models must be incorporated into the code in order to calculate these values as functions of altitude and Mach number. Note that different models were used for the troposphere (altitude <36,089 ft) and stratosphere (altitude >36,089 ft) portions of the mission data to account for the differences in how static pressure ratio and total temperature ratio behave between the two regimes. The box selection used for the propulsion and aerodynamic regressions is also incorporated into the script, and the script automatically uses the corresponding regression equation for the segments of the mission data that fall into the designated boxes.

Assumptions That May Affect Modeling

The following assumptions about the atmosphere model, specifically for total temperature ratio and static pressure ratio, are made during the regression. The equations to compute the static pressure ratio are as follows:

$$\delta_s = \frac{P}{P_0} = (1 - 2.25577 * 10^{-5} * h)^{5.25588} \qquad \text{for altitudes below 11 km}$$

with P_0 = normal pressure at sea level (standard day) = 101,325 Pa

$$\delta_s = \frac{P}{P_0} = 1 + \frac{L_b}{T_0}.(h - h_b)^{-\frac{g_0 M}{R.L_b}} \qquad \text{for altitudes above 11 km}$$

where

- P_0 = normal pressure at sea level (standard day) = 101,325 Pa
- T_0 = standard temperature at sea level [K]
- L_b = standard temperature lapse rate = −0.0065 [K/m]
- h = height above sea level [m]
- h_b = height at the bottom of atmospheric layer [m]
- R = universal gas constant = 8.31432 [N·m/mol·K]
- g_0 = gravitational acceleration constant = 9.80665 [m/s²]
- M = molar mass of Earth's air = 0.0289644 [kg/mol]

The equations to compute the static temperature ratio are as follows:

$$\frac{T}{T_0} = \delta_s^{\frac{L_b * R}{g}}$$ for altitudes below 11 km

where

- δ_s = static pressure ratio
- T_0 = standard temperature at sea level [K]
- L_b = standard temperature lapse rate [K/m]
- R = universal gas constant = 8.31432 [N·m/mol·K]

For altitudes above 11 km, the static temperature ratio is assumed constant:

$$\frac{T}{T_0} = \frac{216.5}{288} = 0.751736$$ for altitudes above 11 km

Using the appropriate static temperature ratio, the total temperature ratio is computed as follows:

$$\theta_t = \frac{T_t}{T_0} = \frac{T}{T_0} * (1 + 0.5 * (\gamma - 1) * M^2)$$

where

- γ = ratio of specific heats for a calorically perfect gas and has a constant value of 1.4
- M = Mach number
- T = static temperature at a given altitude [K]
- T_t = total temperature [K]

Input Data Format

For the first cut of the full-flight SST implementation in AEDT, the off-design missions for the NASA STCA are categorized into three classes: purely subsonic, purely supersonic, and mixed missions, and an OD pair was chosen for each of the categories. Table 9 lists the OD pairs and their airport (APT) IDs.

Table 9. Origin–destination pairs.

Mission Type	Departure APT	Departure APT ID	Arrival APT	Arrival APT ID
Purely Subsonic	VNUKOVO (Moscow)	11276	COTE D AZUR (Nice)	6052
Purely Supersonic	TETERBORO (Teterboro)	30540	FARNBOROUGH (Farnborough Military)	6570
Mixed	TETERBORO (Teterboro)	30540	BENITO JUAREZ INTL (Mexico City)	9457

The process for the off-design mission has two steps: ground tracking and route writing. Figure 22 depicts the flowchart that outlines this process.

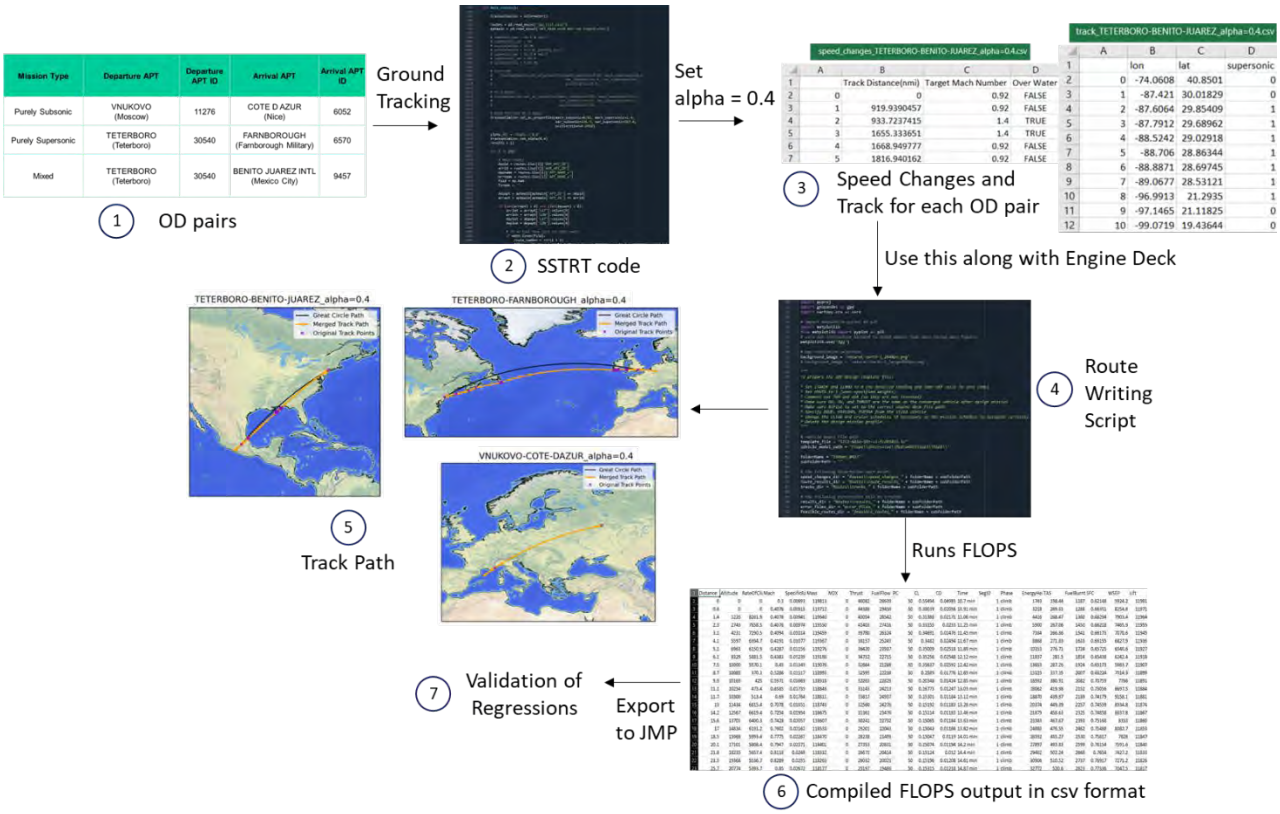

Figure 22. Off-design mission flowchart. OD, origin–destination; FLOPS, Flight Optimization System.

Validation of the Approach

Due to huge discrepancy between the predicted fuel burn by the model based on the engine deck compared with that given by FLOPS 8.11, a cumulative fuel burn sanity check has been performed on the A320neo. The results of this sanity check are shown below. The missions that were used to generate this will later be flown in AEDT, and the team will be able to finish the validation phase stating how accurate the proposed model is compared to the current AEDT model for subsonic aircraft.

Table 8. Propulsion validation.

Box	Actual Fuel Burn (lbm)	Predicted Fuel Burn (lbm)	% Error
Cruise/climb	33,563.56	33,322.35	0.719
Descent	515.53	514.66	0.168
TOTAL	34,079.09	33,837.01	0.710

Results

The JMP table generated from FLOPS output is used to validate the previously generated propulsion and aero regressions. The box definitions for these regressions are modified to reduce the % error based on the updated FLOPS data. Figure 23 and Figure 24 depict the modified box definitions for the propulsion and aero regressions, respectively. Table 10 and Table 11 tabulate the validation of the regression fits against the FLOPS outputs for propulsion and aero, respectively.

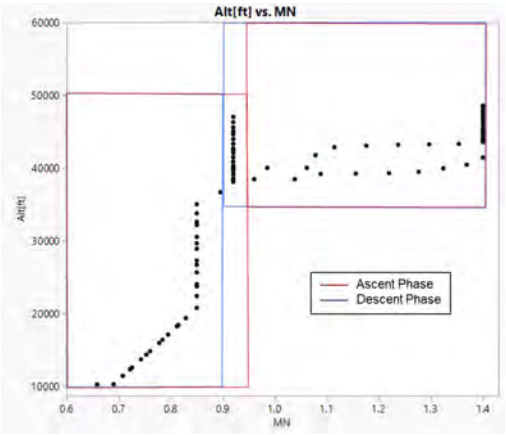

Figure 23. Propulsion box definition – NASA Supersonic Technology Concept Aeroplanes (STCA).

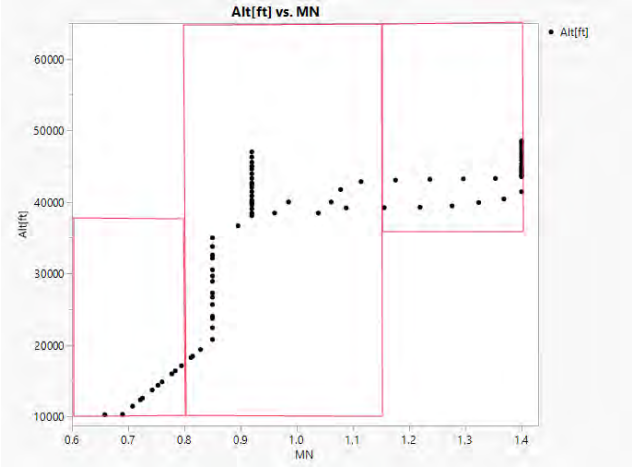

Figure 24. Aero box definition – NASA Supersonic Technology Concept Aeroplanes (STCA).

Table 10. Propulsion validation.

Box	Points per Box Training / Validation	Net Thrust				Fuel Flow			
		Training		Validation		Training		Validation	
		Mean	Std dev	Mean	Std dev	Mean	Std dev	Mean	Std dev
1	5,184 /119	-0.0070%	0.8786	-9.0027%	2.3982	0.0016%	0.5750	-9.9362%	1.5499
2	3,213 /40	0.0073%	1.2741	-5.8857%	3.6125	0.0047%	1.1494	-6.8557%	3.0681
3	1,020 /12	-0.0216%	1.2524			-0.0051%	0.5378	-0.9303%	1.0227
4	1,134 /48	0.0009%	0.4347			-0.0005%	0.2891	-4.3352%	1.3507

Table 11. Aero validation.

Mode	Points/Box	Training		Validation	
		Mean	Std dev	Mean	Std dev
Subsonic	72 / 36	0.0000%	0.0246	4.9182%	0.3294
Transonic	144 / 138	-0.0002%	0.1159	3.7639%	2.3807
Supersonic	84 / 33	0.0000%	0.0113	4.6703%	0.3037

The final data package consisting of the JMP table with the predicted formula of the net thrust, fuel flow rate, and C_D for each of the boxes have been provided to the FAA. The prediction formula can be exploited in diverse programming languages such as Python, C++, etc. to aid the implementation efforts in AEDT. Henceforth, the work will focus on supporting the implementation of the SST models and eventually developing full-flight modeling capability in AEDT.

Task 7 - Environmental Assessment Process

Georgia Institute of Technology

Objectives

The Georgia Tech team was tasked with supporting the EA of the planned SST testing by Boom Supersonic at Greensboro Airport. The process used by Georgia Tech to support this effort entailed the development of a generic SST that would be comparable to the planned Boom aircraft. Using the Georgia Tech FAAST tool, a design space exploration produced a field of aircraft that could be down-selected to a final configuration that met both Boom and FAA requirements for a notional SST to be used in the analysis for the EA. After the final vehicle was selected, acoustic analysis produced a set of noise power distance (NPD) curves, and trajectory analysis produced a set of fixed-point trajectories; both were imported into AEDT to produce a notional aircraft for use by the independent consultant hired by the FAA to conduct the EA.

Research Approach

Using the design process described previously in this report, the Georgia Tech team produced a field of potential configurations that could be used as the generic SST for the Greensboro EA as shown in Figure 25, which displays the filtered design space in terms of the MTOW over the Chapter 14 noise margin. Although Georgia Tech was able to generate a vehicle with up to ~7 dB margin to Chapter 14, the FAA requested that the Georgia Tech team select a vehicle with minimal noise margin to Chapter 14. The purpose of this was to analyze a more conservative vehicle in terms of noise performance, in case the test vehicle for the Greensboro airport underperformed Boom's predictions for noise margin. This would mean that the EA would be conducted using worse-than-expected noise emissions to provide a buffer for uncertainty in regards to the noise performance of this novel concept. The characteristics of the final down-selected vehicle are shown below in Table 12.

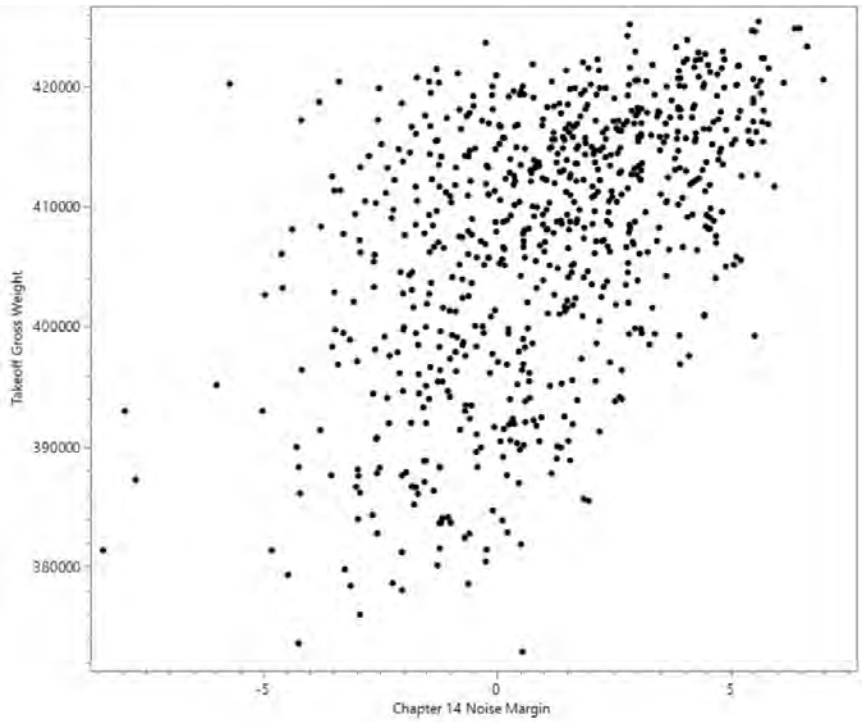

Figure 25. Design space exploration used for environmental assessment vehicle down-selection.

Table 12. Generic supersonic transport (SST) characteristics.

	Unit	Value
MTOW	Lbf	412,815
FPR (ADP, M1.2/39K)	Ratio	1.925
HPCPR (ADP, M1.2/39K)	Ratio	12.13
BPR (ADP, M1.2/39K)	Ratio	4.2429
Corrected mass flow @ fan face (ADP, M1.2/39K)	Lbm/s	1,108.04
Jet velocity	ft/s	1,168.37
TWR	Ratio	0.3366
WSR	Psf	88.498
Cutback noise	EPNdB	96.01
Approach noise	EPNdB	98.99
Sideline noise	EPNdB	92.83
Cumulative noise	EPNdB	287.83
Cutback margin	EPNdB	4.86
Approach margin	EPNdB	3.61
Sideline margin	EPNdB	6.34
Cumulative margin	EPNdB	0.81
Design range	nmi	4250
Far TOFL (OEO)	Ft	10,943.3
Landing field length	Ft	10,742.47

With a generic SST selected, three types of analysis are required in order to proceed with AEDT simulations: a weight-range study, fixed-point trajectory generation, and NPD generation. A requirement for AEDT is to define the stage length of a trajectory (since stage length serves as a proxy for aircraft takeoff weight in AEDT) and, because the test vehicle for the Greensboro airport currently plans to operate at 80% of its MTOW, it was necessary to ensure that one of the stage lengths defined in AEDT aligned with this MTOW percent. A weight-range study was conducted to discover the range that would correspond with the 80% MTOW target, and the results from this study are shown below in Table 13. This study revealed that a range of 2,422 nmi would correspond to the 80% MTOW target; therefore, stage length 4 was selected to represent this range in AEDT to serve as the proxy for the 80% MTOW configuration in AEDT, and the fixed-point trajectory for takeoff generated for AEDT was simulated with this takeoff weight in FLOPS. The output from the FLOPS simulation was selectively sampled to capture the shape of key aircraft trajectory parameters (altitude, ground track distance, thrust, and speed), while reducing the total number of data points required to ease database entry of the trajectory into AEDT. After this sampling of the FLOPS output was completed, a table consisting of horizontal distance relative to brake release, true airspeed (kts), altitude above field elevation (ft), and net corrected total thrust per engine (lbf) was compiled. All of these metrics are shown below in Figure 26. Similarly, this process was conducted for the approach trajectory for the aircraft's maximum landing weight. The trajectory information given to AEDT for approach is shown below in Figure 27.

Table 13. Generic supersonic transport stage length chart.

Stage Length	Range Interval (nmi)	Representative Range (nmi)	Weight (lb)	% Max Takeoff Weight
1	0-500	400	264,738	0.641
2	500-1,000	850	278,147.2	0.674
3	1,000-1,500	1,350	293,832.4	0.712
4	1,500-2,500	2,422	330,347.4	0.800
5	2,500-3,500	3,200	359,738.2	0.871
6	3,500-4,500	4,200	401,545.2	0.973

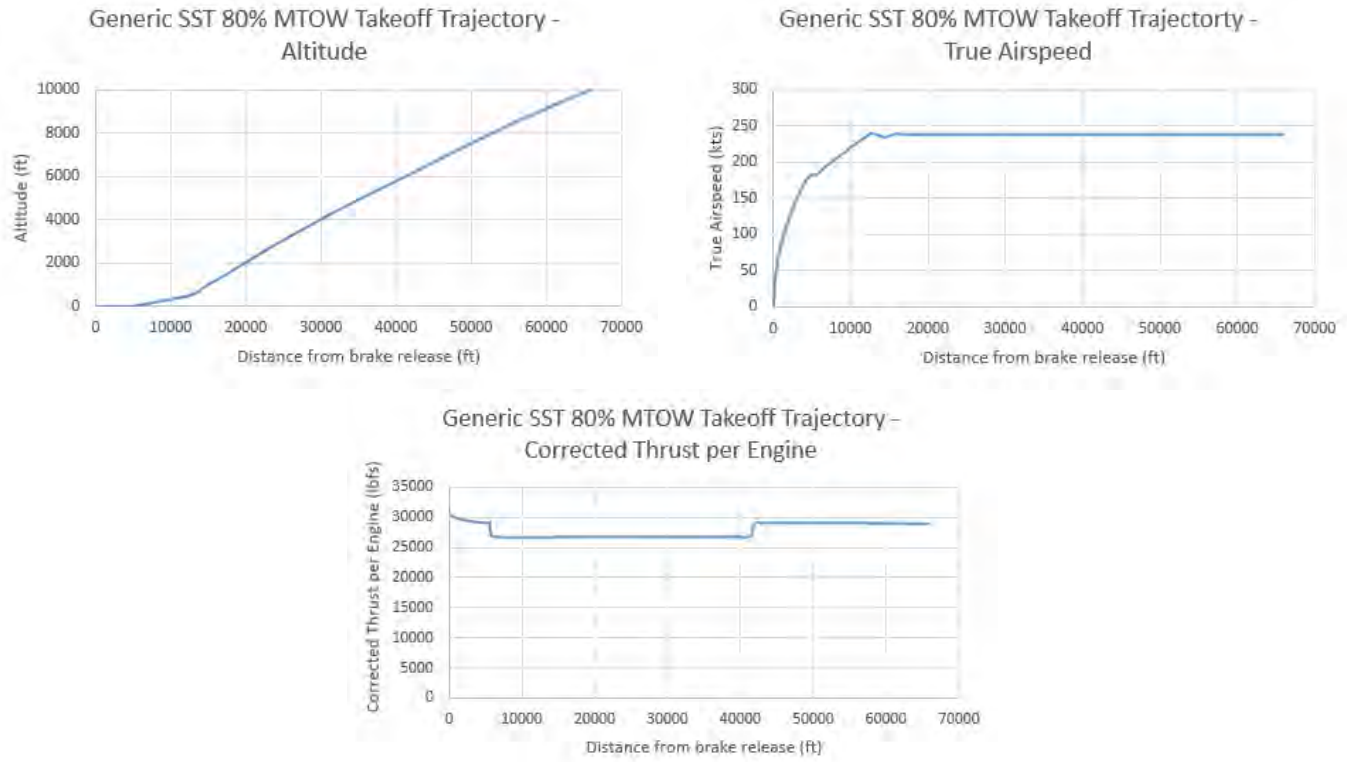

Figure 26. Generic supersonic transport (SST) 80% maximum takeoff weight (MTOW) takeoff trajectory.

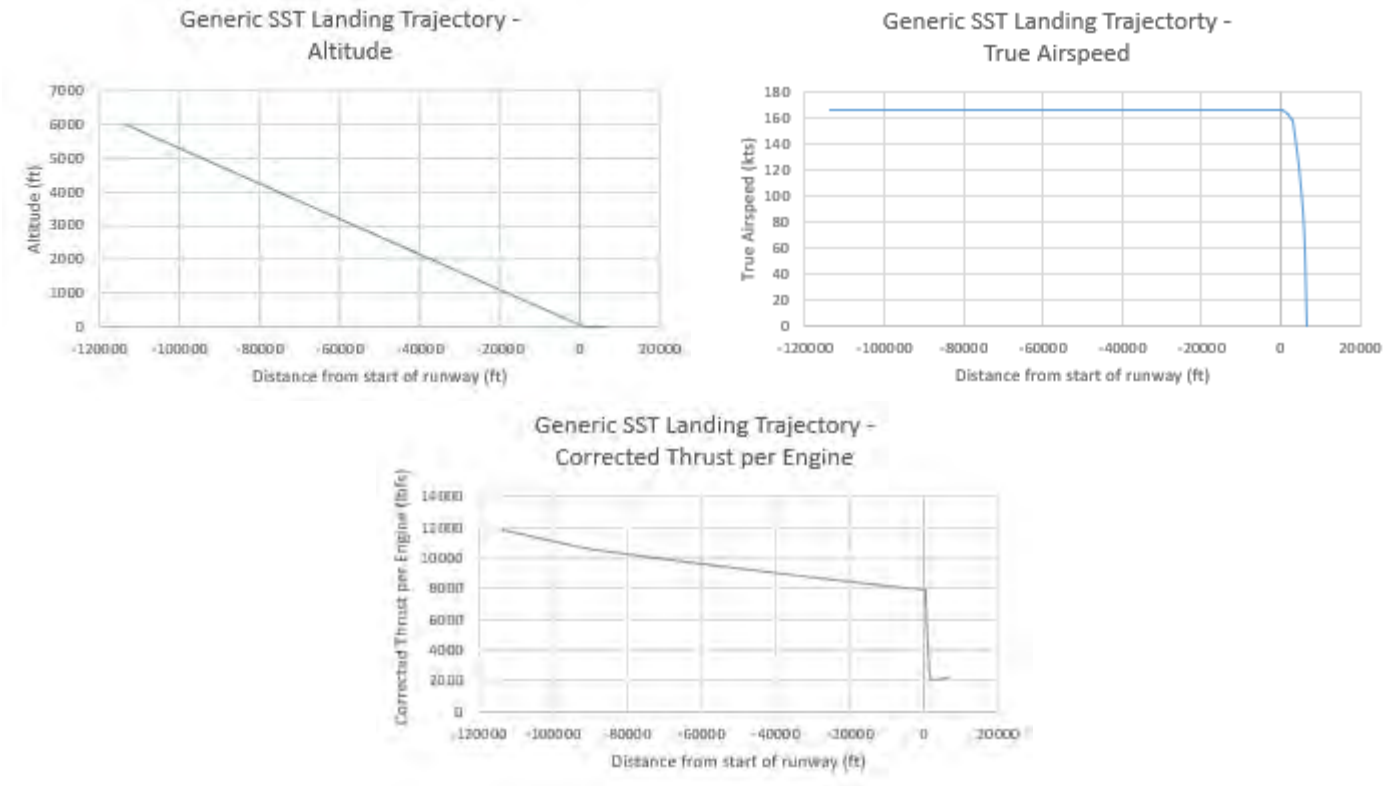

Figure 27. Generic supersonic transport (SST) landing trajectory.

NPD curves are a set of measurements from a single observer resulting from a series of steady level flyovers at various altitudes and throttle settings. NPD curves are expressed as four noise metrics: EPNL, SEL, maximum sound level (LAMAX), and perceived noise level tone-corrected maximum (PNLTM). The metrics that are used in this study will primarily be EPNL and SEL. The EPNL NPDs will be used in AEDT to verify that when the certification trajectory is simulated in AEDT, the predictions from AEDT for certification EPNL are within 1 dB of the ANOPP predictions to check consistency between the models. The SEL NPDs will be used to generation SEL noise contours, which will be one of the critical inputs when computing the area exposed to 65 dB day-night average sound level (DNL), one of the key parameters for the EA. NPDs along with the trajectories are included together in the dataset released to the FAA.

The other set of information the Georgia Tech team released to the FAA is an AEDT database updated to include the generic SST. The generic SST was included in the AEDT database by modifying an existing 777-200 aircraft file. Using the 777-200 ANP aircraft definition as a template, the NDPs, the fixed-point trajectories, and some key metadata information was updated to the values specified in the dataset described previously. Once this data had been updated, an AEDT model of the approach and takeoff certification trajectories was conducted, the purpose of which was to test whether the AEDT simulation predicted certification ENPL within the tolerance of 1 dB of the ANOPP predictions. The results are shown below in Table 14, indicating that there was agreement between the ANOPP and AEDT predictions.

Table 14. ANOPP and AEDT effective perceived noise level (EPNL) prediction comparisons (in EPNdBs).

	ANOPP	AEDT	Delta
Approach	98.99	98.93	0.06
Flyover/Cutback	96.01	95.49	-0.52
Sideline	92.83	92.02	-0.81

Results

The Georgia Tech team is supporting the Greensboro EA by providing aircraft trajectories, NPDs, and the AEDT database. The EA is ongoing at the time of writing; therefore, the Georgia Tech team will be refraining from publishing NPD dataset and SEL contour predictions. The Georgia Tech team intends to publish the team's findings once the ongoing FAA study has been completed.

Task 8 - Purdue Fleet Analysis

Purdue University

Objective

The Purdue team pursued four subtasks as a part of the fleet analysis task. During this year, the Purdue team developed cost estimation models for the acquisition and operating cost of the subsonic aircraft models, expanded the network of airline operations from the US-touching network to a global network, created simple sizing and performance models for alternate supersonic aircraft, and developed a demonstration model for the estimation of operations and emissions of business jet aircraft.

Subtask 1: Acquisition and Operating Cost Estimation Models

Previously, the aircraft cost information needed for FLEET simulations, including the acquisition and operating costs, were generated using the cost module of FLOPSv8. The cost module is no longer available in FLOPSv9, and a new cost model with similar functionality was needed. The cost model needs to provide the costs information needed for FLEET, so the team named this the FLEET cost function (FCF). The FCF categorizes the cost items in exactly the same categories needed as inputs to FLEET:

- Acquisition cost,
- Direct operational cost (DOC, which includes flight and crew cost, maintenance cost, aircraft servicing cost, and insurance cost), and
- Indirect operational cost (IOC, which includes ground property and equipment cost, passenger service cost, and other costs not directly related to flight service).

Note that, while the fuel cost is usually considered part of the DOC, FLEET considers this separately to study the impact of future fuel prices and/or prices for alternative or sustainable jet fuels. Therefore, fuel cost is external to FCF.

To build the FCF, four well-known cost models were used. For the acquisition cost, FCF uses a modified RAND DAPCA IV model from Raymer [22]. For operational costs, FCF uses a mixed model combining the Liebeck model [23], the ATA model [24], and a model originally developed by Johnson for FLOPS [25]. Although the different cost models mentioned have different baseline dollar years, all costs in the final version of FCF are converted to 2011 US dollars (USD) to reflect the newest starting year in the worldwide version of FLEET using a Consumer Price Index (CPI) inflation calculator from U.S. Bureau of Labor Statistics [26]. If the desired starting year of FLEET simulation is different from 2011, the CPI factor will need to be changed accordingly for all cost components. Using the CPI adjustment is straightforward and the information is readily available; not all aircraft-related costs will follow the CPI.

Acquisition Cost Model

A modified version of RAND's DAPCA IV model from Raymer's "Aircraft Design: A Conceptual Approach" (sixth edition) provided the acquisition cost estimation, and some calibration of this used previous FLOPS results and real-world data. Raymer's version of the DAPCA model was modified and converted to 2011 USD values. The DAPCA model mainly uses empty weight, maximum velocity, and the number of aircraft to be produced in five years as variables to determine the acquisition cost, among a few other variables that have less effect on the result. Because empty weight and maximum velocity are aircraft parameters that are an input (maximum velocity) and an output (empty weight) of the aircraft sizing code, the number of aircraft to be produced in five years (Q) is the variable to adjust in order to calibrate the acquisition price. The models and acquisition prices used for calibration appear in Table 15, based on the available FLOPS aircraft models previously tested. The historical acquisition price is mainly from Boeing's website [27], credible sources such as Jane's [28], and aircraft industry enthusiast websites such as https://aerocorner.com/aircraft [29]. For calibration, the acquisition price of the aircraft is assumed to be the same as the advertised or published value. Note that the listed price from those sources may be different from the actual price airline companies pay to the manufacturer, because there are almost always additional deals made

between manufacturers and airlines to bring the acquisition price lower than the listed or advertised price. Details of these discounts and actual sale prices are not publicly available.

Table 15. Aircraft models used for acquisition cost calibration.

Regional Jet	**ERJ 145**	**CRJ 200**	**CRJ 700**	**CRJ 900**
Acquisition cost [million 2005 USD]	20.68	24.00	32.10	32.00
Single-Aisle	**B737-300**	**B737-700**	**B737-800**	**B757-200**
Acquisition cost [million 2005 USD]	37.90	56.50	67.75	81.60
Twin-Aisle	**B767-200ER**	**B777-200LR**	**B747-400**	**A330-200**
Acquisition cost [million 2005 USD]	113.23	220.50	220.75	143.30

After testing and calibrations, a different value of Q is assigned to aircrafts of different sizes: for aircraft less than 100 seats in a two-class layout (regional airliner), Q is equal to 375; for aircraft larger than 100 seats but less than 200 seats in a two-class layout (single-aisle airliner), Q is equal to 210; and for aircraft larger than 200 seats in a two-class layout (widebody airliner), Q is equal to 165. The resulting acquisition price for the historical aircraft models in Table 15 is as shown in Figure 28.

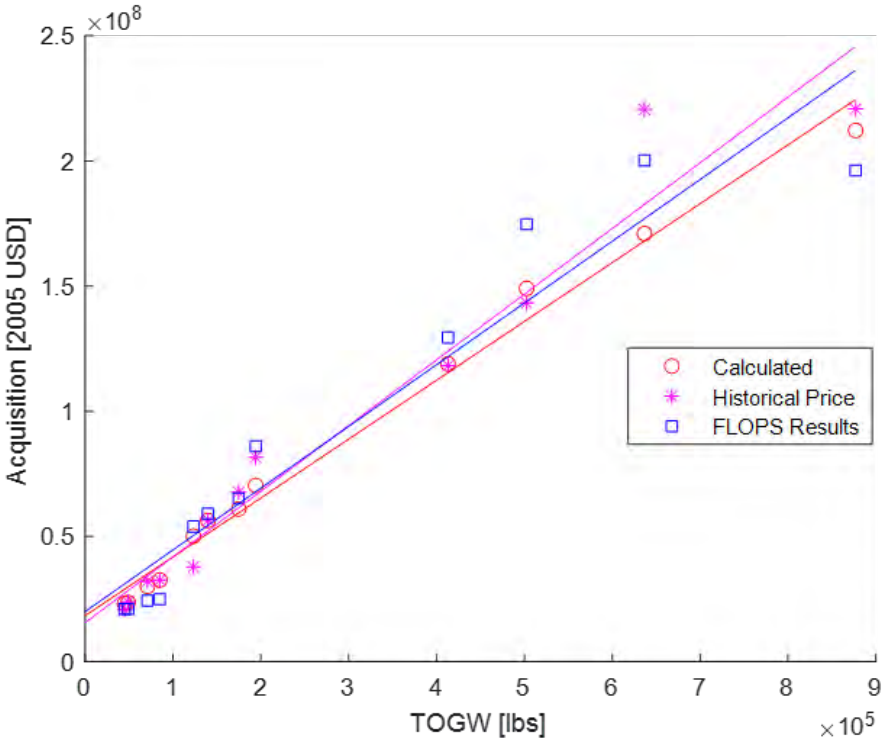

Figure 28. Acquisition prices for the historical aircraft models. FLOPS, FLight Optimization System; TOGW, takeoff gross weight.

Direct Operating Cost Model

The operational cost model is built with various models to have operational costs with a similar trend and scale as the previous operational costs predicted by FLOPSv8 with the limited input information. The Liebeck model [23] calculates the maintenance costs and pilot costs; the ATA model [24] calculates the insurance costs; and Johnson's model [25] calculates

the servicing costs and IOC. Note that, in theory, Johnson's model should produce the same cost results or at least a similar trend compared with the current operational cost inputs to FLEET, which were generated by the cost module in the previous FLOPSv8. However, upon testing, the costs generated from FLOPSv8 do not always have a similar trend to the original version of Johnson's model. Sometimes, Johnson's model requires a significant number of additional inputs that the sizing code no longer uses and default input values that might have been used in the FLOPSv8 implementation were unknown to the Purdue team. As a result, the cost model for some cost components was chosen to be from Liebeck or ATA, which are well-known aircraft cost estimation methods.

The operational costs are calibrated using the previous results from FLOPSv8 to the same scale, because calibrating the costs to have the same trend is extremely difficult without knowing the equations used. The 2011 Bureau of Transportation Statistics (BTS) database Air Carrier Financial Report (Form 41) data [30] was used as a guideline to determine if the pilot salary, maintenance cost, and insurance cost estimations are reasonable.

The resulting operational costs have a similar scale and proportions to the previous cost input for FLEET. Figure 29 presents the resulted DOC (including fuel cost) and IOC for a Boeing 737-800 aircraft on a 2,950 nmi mission with the same payload and fuel burn/fuel cost. For the previous result from FLOPS, the total DOC (without fuel) is $8,495, and the total IOC is $22,252; for the result from FCF, the total DOC (without fuel) is $9,144, and the total IOC is $19,365, which has a total operational cost 7.3% lower. Notice that the difference in the resulting operational costs is model- and mission-dependent (i.e., the overall operational cost might end up being higher for some models but lower for other models on the same route), and the overall average difference in the operational costs is lower than 5%.

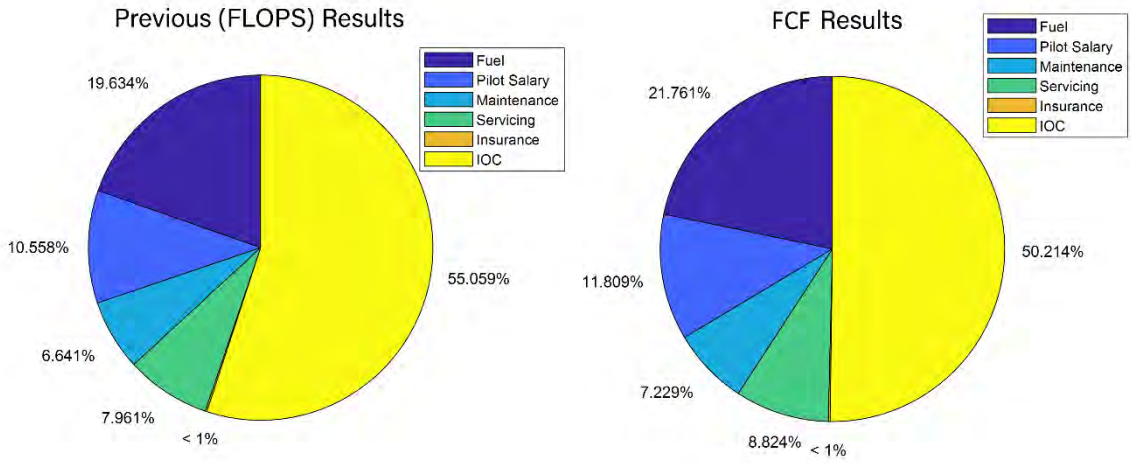

Figure 29. Operational cost for Boeing 737-800 at a 2,960 nmi mission. FLOPS, FLight Optimization System; FCF, FLEET cost function; IOC, indirect operating costs.

Subtask 2: Expand FLEET Route Network

Overview of Worldwide Demand Data and Representation

To extend FLEET's capability to provide supersonic and subsonic aircraft allocation data on global routes (in addition to those present in the previous FLEET network of "US-touching" routes), the Purdue team updated FLEET's route network to a worldwide route network. The global fleet demand data were obtained from the Official Airline Guide (OAG) Traffic Analyser [36]. The data were extracted from the OAG Traffic Analyser for years 2011 to 2020; OAG did not have relevant global fleet demand data available for any year earlier than 2011. Based on this global data availability, the team decided to move the initial year of FLEET simulation from 2005 to 2011 and update the initial network, passenger demand, and fleet composition accordingly.

In 2019 (and all subsequent years), there are 5,317 routes in the FLEET network that connect a subset of WWLMINET 257 airports. Comparing this with the previous "US-touching" route network in FLEET, this is a 170% increase in the number of

routes, increasing from 1,974 routes (US-touching only) to 5,317 routes (worldwide). Figure 30 compares the worldwide route network with the US-touching only network, visually highlighting the increased routes in the new network.

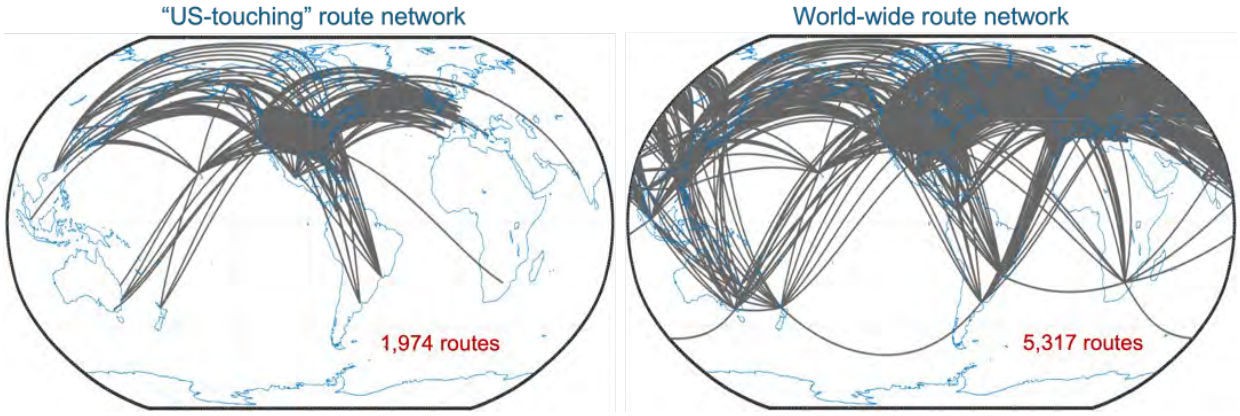

Figure 30. Comparing the worldwide route network with the existing US-touching route network in FLEET.

Estimation of Fleet Size and Mix for Worldwide Operations

The methods to determine the 2011 initial global fleet composition are similar to the methods described in Moolchandani's thesis [31] to obtain the 2005 initial US fleet. However, the methods have been adapted accordingly with expansion to include a global fleet instead of just the US fleet. BTS data of the 2011 US fleet was the primary source to determine the detailed fleet composition. Boeing's 2012-2031 Current Market Outlook Report [32] (hereafter called Boeing's) and Oliver Wyman's 2017 Global Fleet & MRO Market Forecast Summary [33] (hereafter called OW's) were used as the primary sources to determine the global fleet size in 2011. The resulting 2011 initial global fleet is shown below in Table 16. Details about the worldwide fleet geographic regions, representative model, how the initial fleet divided into representative-in-class and best-in-class models based on age, and the average age for each model is available at the end.

Table 16. 2011 Initial global fleet. RIC, representative-in-class; BIC, best-in-class.

	Africa		Middle East		Asia Pac		Latin America		North America		CIS		Europe		World	
	RIC	BIC	RIC	BIC	RIC	BIC	RIC	BIC	RIC	BIC	RIC	BIC	RIC	BIC	RIC	BIC
Class 1	20	230	0	40	40	370	20	220	140	1370	20	190	50	480	290	2900
Class 2	10	140	0	20	20	230	10	140	70	850	10	120	20	300	140	1800
Class 3	90	150	90	140	680	1080	220	350	830	1320	160	250	640	1010	2710	4300
Class 4	50	110	50	100	370	770	120	240	450	930	90	180	340	710	1470	3040
Class 5	20	50	90	200	200	470	10	30	150	360	20	50	120	280	610	1440
Class 6	10	30	30	140	60	300	0	10	40	210	10	30	30	160	180	880
Total	200	710	260	640	1370	3220	380	990	1680	5040	310	820	1200	2940	5400	14360
	910		900		4590		1370		6720		1130		4140		19760	

Regions in the Global Fleet Network

As shown in Table 16, the 2011 initial global fleet divides the global fleet into seven regions: Africa, Middle East, Asia Pacific, Latin America, North America, Commonwealth of Independent States (CIS; East Europe), and Europe. This follows the same geographic regions as in Boeing's. Although FLEET is not able to utilize any of this detailed information during allocation, it may beneficial for future FLEET works when FLEET is capable of allocating aircraft separately in each geographic region. Figure 31 from Boeing's below shows the mapping of each region.

Figure 31, Global fleet regions.

Classification Method and Representative Models of Aircraft

Because detailed global fleet data were not widely available, the 2011 BTS data of the US fleet composition are used to determine the classification method and the representative models of aircraft operating in the new 2011 worldwide network. It is assumed that the model and age of aircraft in the US fleet is representative of the fleet in the rest of the world. This assumption may not be perfect, but given the available data, it is deemed adequate for the purposes of this work. The 2011 worldwide network is represented by 14 aircraft models, divided into six classes based on seat capacity, and then into representative-in-class (RIC), best-in-class (BIC), and new-in-class (NIC) based on the average age of the aircraft according to the BTS data. The previous classification and representative models in 2005 US-touching FLEET network are shown below in Table 17 as the starting point of the work.

Table 17. 2011 Classification of aircraft classes for US-touching network.

Class	Seats	Representative-in-Class	Best-in-Class	New-in-Class
Class 1	20 – 50	Canadair RJ200/RJ440	Embraer ERJ145	Aircraft X1
Class 2	51 – 99	Canadair RJ700	Embraer 170	Aircraft X2
Class 3	100 – 149	Boeing 737-300	Boeing 737-700	CS100
Class 4	150 – 199	Boeing 757-200	Boeing 737-800	Purdue ASAT
Class 5	200 – 299	Boeing 767-300	Airbus A330-200	Boeing 787
Class 6	300+	Boeing 747-400	Boeing 777-200ER	Aircraft X6

A few adjustments are made to the previous table. Previously, RIC were models with the greatest number of aircraft in the fleet; BIC were the models with the most recent service entry date; and NIC were models in development that will enter service in 2015. In the 2005 baseline year for the US-touching network version of FLEET, this classification made sense and could be a good indication of the average age and technology age of the models, where the RIC has older average age and technology age than the BIC (and NIC would be the newest in the fleet when entering service). In the BTS 2011 data, we found that for many aircraft seat classes, the models with the greatest number of aircraft in the fleet were no longer the "oldest" model. As a result, in the 2011 worldwide network, the RIC was the model with an average age >10 years; BIC were the models with an average age <10 years; and NIC were still the models that entered service in 2015. Note that for different classes, the dividing ages for RIC and BIC are different; more details will be shown in the later Age Distribution section.

As in the 2005 US-touching fleet, the six seat-capacity classes can roughly represent the different sizes of aircraft: Class 1 and 2 are generally regional jet/turboprop aircraft; Class 3 and 4 are generally single-aisle/narrow-body aircraft; and Class 5 and 6 are generally double-aisle/widebody aircraft. The six seat-capacity classes in the 2011 worldwide fleet were the same

as in 2005 US-touching fleet, except in Class 5 and Class 6. In the 2005 US-touching fleet, Class 5 has 200-299 seats, and Class 6 has more than 300 seats. In the 2011 worldwide fleet, Class 5 has 200-279 seats, and Class 6 has more than 280 seats. This change is primarily made to divide some large twin-aisle airliners (such as the Boeing 777 and Airbus A350) into Class 6 instead of Class 5. Based on the manufacturers' information, those large twin-aisle airliners can carry more than 300 passengers in two-class or even three-class configurations. As a result, they should be able to be classified as Class 6 aircraft in the 2005 US-touching network. However, in the 2011 BTS data, the researcher found that most of the Boeing 777s in the US operators had a seating capacity of around 290. The US operators configured the aircraft into a three-class configuration and potentially gave larger space for each seat to provide a better experience for transcontinental flights. The resulting representative models of each class are shown below in Table 18. Each model was the one with the greatest number of aircraft in the BTS data that fell into the specific seat-capacity range and average age range. Note the Class 1 will be discontinued in new and future-in-class models.

Table 18. Representative models and classification of 2011 worldwide fleet.

Class	Seats	Representative-in-Class	Best-in-Class	New-in-Class	Future-in-Class
Class 1	20-50	Saab 340B	CRJ-200	-	-
Class 2	51-99	ATR 72	CRJ-700	Gen 1 DD RJ (2020)	Gen 2 DD RJ (2030)
Class 3	100-149	MD 80	Boeing 737-700	Gen 1 DD SA (2017)	Gen 2 DD SA (2035)
Class 4	150-199	Boeing 757-200	Airbus A320-200	Gen 1 DD STA (2025)	Gen 2 DD STA (2040)
Class 5	200-279	Boeing 767-200	Airbus A330	Gen 1 DD LTA (2020)	Gen 2 DD LTA (2030)
Class 6	280+	Boeing 747-400	Boeing 777-200	Gen 1 DD VLA (2025)	Gen 2 DD VLA (2040)

Age Distribution

Because detailed global fleet information is not available to the team, an assumption was made that the global fleet in 2011 has the same class-wise age distribution as in the 2011 BTS data for the US fleet. This assumption may not be very accurate in some regions such as Asia and the Middle East. The fleets in those regions will likely be younger than the US fleets because airline fleets in those regions have grown rapidly in recent years and massive numbers of new aircraft were acquired. The resultant age distribution for each class is shown in Figure 32, with different presentation of the age distribution for each class.

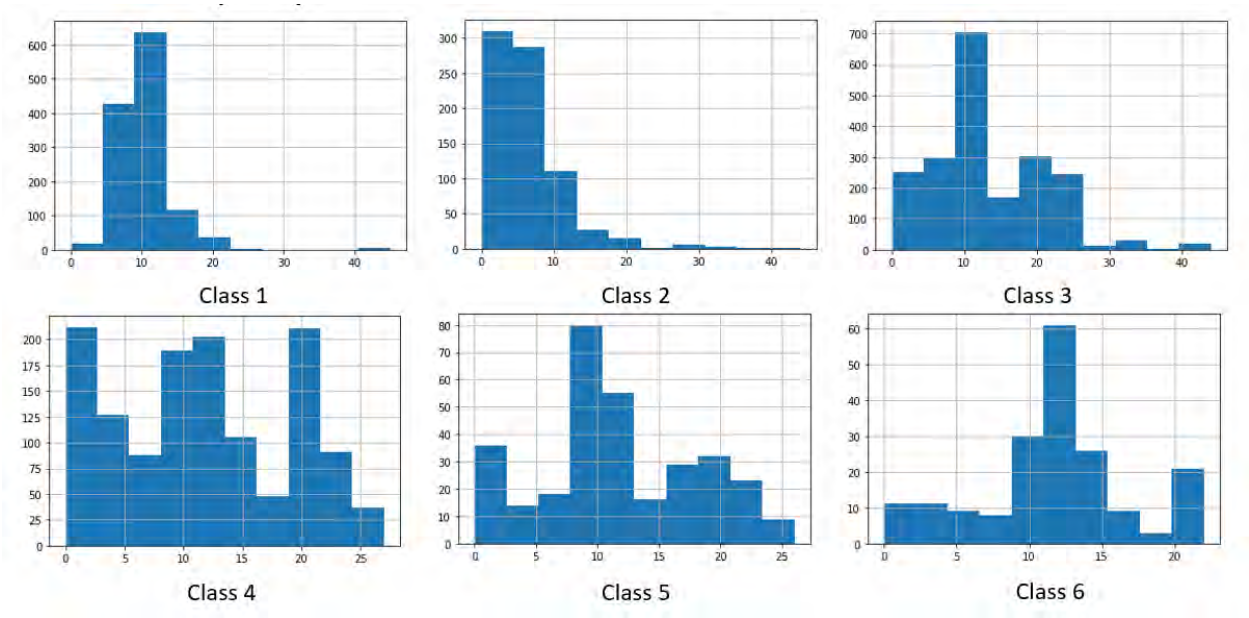

Figure 32. Age distribution (x-axis; years) in Bureau of Transportation Statistics (BTS) 2011 data for each class.

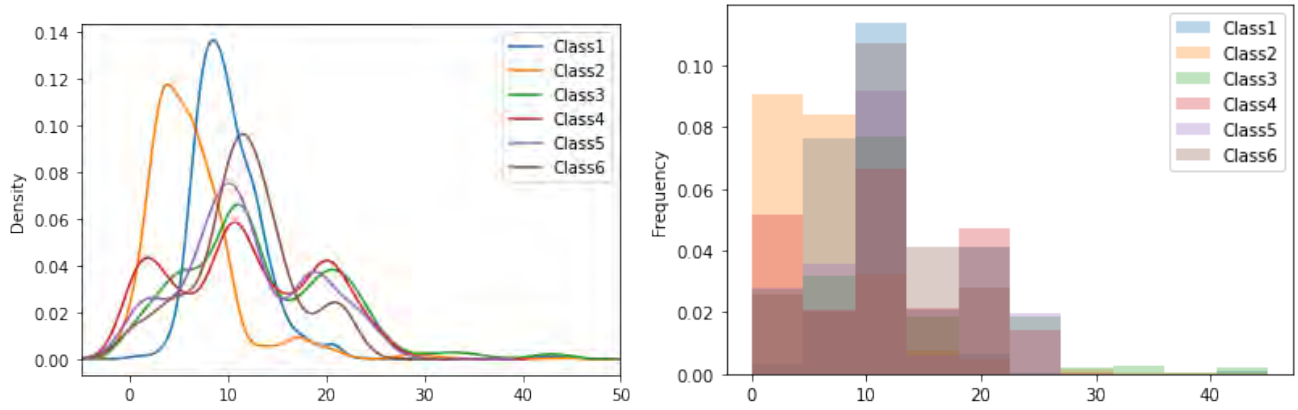

Figure 33. Age distribution in Bureau of Transportation Statistics (BTS) 2011 data for each class in percentage. Notice that the x-axis of the two plots is the age of the aircraft in years.

As the above figures show, the different classes have different age distributions. This indicates that the different classes of the fleet have very different age compositions and possibly very different technology age distributions. As a result, dividing the entire fleets to RIC and BIC based on only a single common factor seems unreasonable. Hence, we divided the average age for the RIC and BIC modes according to the BTS 2011 US fleet data, as shown below in Table 19. We can confirm that dividing ages were reasonable, as each average age for RIC and BIC lies around the peaks, as shown in Figure 33.

Table 19. 2011 US initial fleet divided into representative-in-class (RIC) and best-in-class (BIC).

Class	Dividing Age	RIC Mean Age	BIC Mean Age
Class 1	14	18.37	9.37
Class 2	12	19.39	5.30
Class 3	13	21.74	8.17
Class 4	15	20.43	7.40
Class 5	15	20.13	8.26
Class 6	15	19.52	9.87

FLEET Allocation Results for Worldwide Operations (Subsonic Only)

The results shown here consider the previously developed "Current Trends Best Guess" (CTBG) scenario (presented in previous annual report [34]) as the baseline scenario, utilizing the subsonic-only CTBG results on both the US-touching network and the new worldwide network for comparing and analyzing. Note the CTBG scenario presented here *does not* include the impact of the COVID-19 pandemic on air travel demand and is referred to as "baseline (no COVID)" scenario in later parts of this section. The FLEET simulations using the worldwide network ran from year 2011 to 2050. Figure 34a compares the normalized fleet-level CO_2 emissions considering a worldwide network (depicted by the solid red line) with the CO_2 emissions considering a US-touching only network (depicted by the solid blue line). As expected, the CO_2 emissions considering a worldwide network are always higher than those from the US-touching network due to the increased network size; in 2050, total CO_2 emissions for the worldwide network simulation are about 2.7 times higher than for the US-touching network. This increase in emissions is proportional to the increase in the network size (the number of routes increased from 1,974 to 5,317, an almost 2.7-fold increase), as the aircraft models used in the simulation are the same for the two route networks.

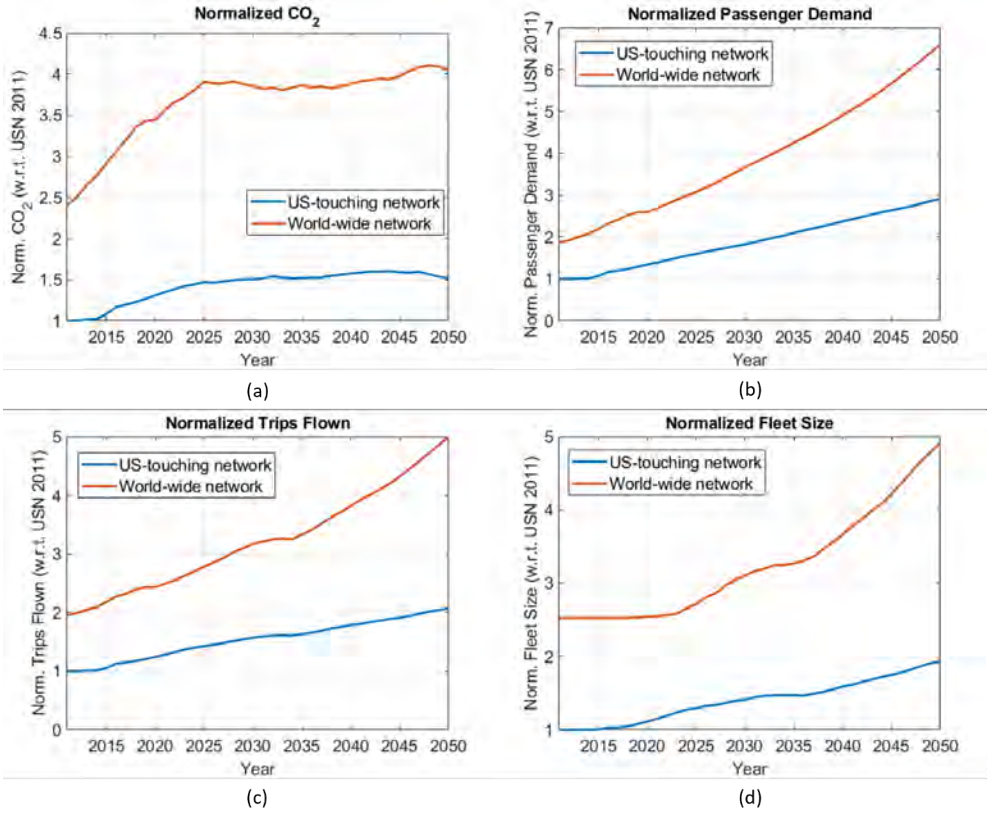

Figure 34. Normalized CO_2 emissions (a), normalized passenger demand (b), normalized trips flown (c), and normalized fleet size (d) for the worldwide network and US-touching network.

Similarly, Figure 34b compares the passenger demand in FLEET considering a worldwide network (depicted by the solid red line) with the passenger demand considering a US-touching only network (depicted by the solid blue line). The passenger demand for the worldwide network grows considerably faster than that of the US-touching network, which is consistent with what the team observed from the passenger demand data. Figure 34c and Figure 34d, respectively, show the increase in the number of trips flown and the fleet size when FLEET models a worldwide route network.

FLEET Allocation Results for Worldwide Operations (Simultaneous Subsonic and Supersonic)

In order to analyze worldwide airline operations that include the entry in service of a supersonic aircraft, the research team modified and update FLEET to (1) ingest the worldwide demand and fleet characteristics, and (2) solve the resource allocation problem while considering the introduction of the supersonic aircraft. Assuming an entry-in-service date of 2024 for the SST concept and using the demand evolution assumptions described in previous reports leads to the projected travel demand and associated emissions shown in Figure 35. These are initial estimates of the impact of introducing a 55-passenger, Mach 2.2 cruise number SST; at the time of this report, additional work is underway to assess the quality of these results.

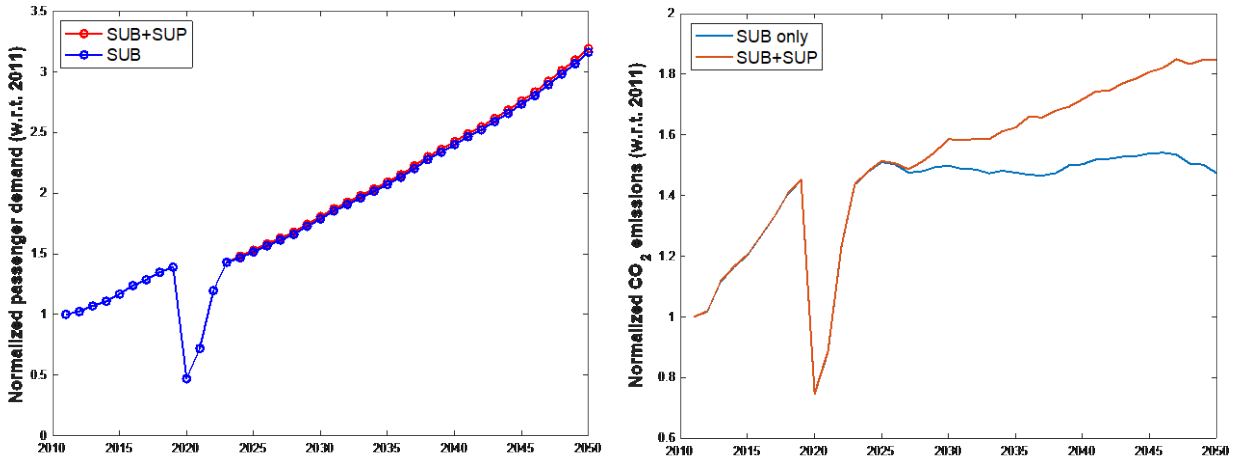

Figure 35. Initial estimates of travel demand and associated emissions, normalized to 2011 levels.

Travel demand reflects historical data until 2019, a steep drop associated with early estimates of air travel demand decrease associated with the COVID-19 pandemic, and then makes assumptions about a potential recovery scenario following COVID-19. As discussed earlier, we assume that up to 5% of travel demand can be served by the SST. As Figure 35 (right) shows, the emissions contributions of SSTs are considerable. In fact, a ~37% increase in 2050 emissions levels is due to the SST. The combination of high fuel burn and low passenger capacity of this aircraft concept results in this estimation. This contribution to emissions is even more clear when observing the emission levels that each aircraft class and technology group contribute. Figure 36 (left) presents the normalized emissions that each aircraft class contributes to total emission levels and Figure 36 (right) presents the contribution grouped by technology (RIC: representative-in-class aircraft; BIC: best-in-class aircraft; NIC: new-in-class aircraft; FIC: future-in-class aircraft; SST: supersonic transport).

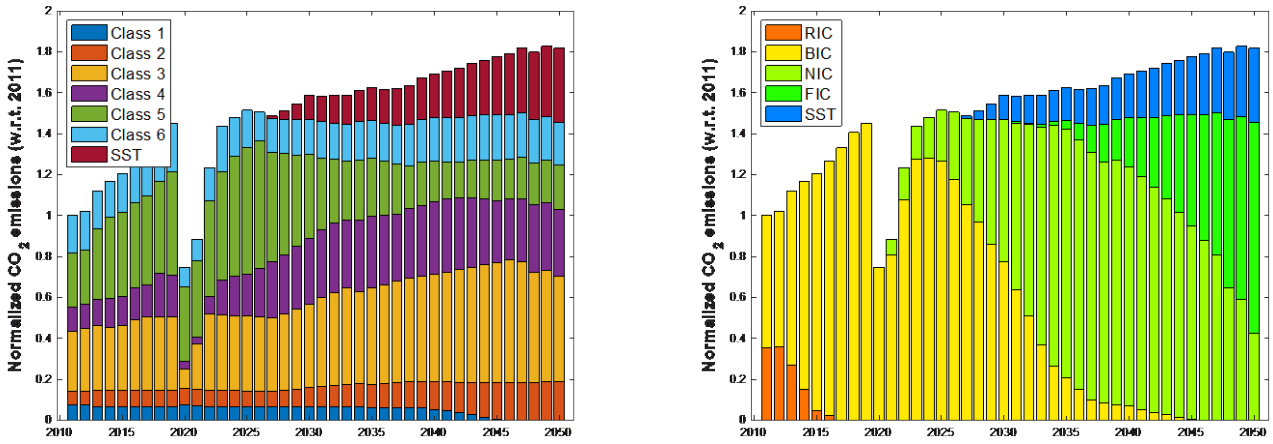

Figure 36. Emissions contribution of aircraft fleets and technology groups. RIC, representative-in-class aircraft; BIC, best-in-class aircraft; NIC, new-in-class aircraft; FIC, future-in-class aircraft; SST, supersonic transport.

Even as demand continues to grow (passenger trip demand is roughly 3.2 times larger in 2050 than in 2011), the introduction of more fuel-efficient subsonic aircraft manages to maintain 2025 emission levels. However, the introduction and use of the SST results in an overall increase in emission levels with respect to the 2011 baseline in these initial results. Future work will investigate the impact that alternate demand evolution scenarios, SST fuel-burn assumptions, and even alternate SST concepts have on the expected emissions and environmental impact of aviation.

Subtask 3: Analysis of Alternate SST Concepts

Simple SST Sizing Approach (Placeholder 2.0)

In previous work, the authors utilized a 55-seat "placeholder" commercial supersonic aircraft model to identify potential supersonic routes in a US-touching route network; the placeholder model was based on Boom's Overture concept with an over-water supersonic cruise speed of Mach 2.2 and an over-land subsonic cruise speed of Mach 0.95. The authors use the "placeholder" notation because these aircraft models were used only for identifying potential supersonic routes and have been replaced in FLEET simulations by higher-fidelity supersonic aircraft models. These higher-fidelity models were developed by colleagues at Georgia Tech. The maximum range of the placeholder aircraft was designated to be 4,500 nmi. The L/D ratio and the specific fuel consumption (SFC) value for sizing the placeholder supersonic aircraft were based on some improvements over Concorde's values. For performance calculations, the over-land segment was assumed to be equally split at each end of the over-water segment. In reality, the over-land segment is airport pair- and route-dependent (e.g., for one airport pair, the origin might be close to the ocean and the destination further inland; the return flight on this pair would have the opposite), so a higher-resolution representation of the routes for aircraft performance calculations will lead to different fuel burn characteristics for each direction on each route.

For this work, the authors develop an updated version of the placeholder commercial supersonic aircraft model, dubbed the "placeholder v2.0" aircraft model. The L/D ratio and SFC value for the placeholder v2.0 model are based on the higher-fidelity supersonic aircraft models developed by our colleagues at Georgia Tech. Additionally, the placeholder v2.0 model takes into account the higher-resolution representation of the routes for aircraft performance calculations, allowing it to reflect the difference in fuel burn (and the aircraft range capability) for each direction on each route.

This work includes different size and speed supersonic aircraft in the FLEET simulations. The set includes 55-seat, 75-seat, and 100-seat supersonic aircraft operating at multiple supersonic cruise speeds.

Table 20. Alternate supersonic transport concepts (developed by Georgia Tech).

Vehicle Seating Capacity	Supersonic Cruise Mach Number		
55 passengers	1.8	2.0	2.2
75 passengers	2.2	2.2	2.2
100 passengers	1.6	1.8	2.0

Each combination of seat capacity and cruise speed leads to a different aircraft configuration, with the higher-fidelity models provided by our colleagues at Georgia Tech. This leads to a total of seven aircraft available for implementation in FLEET. The authors adapt the placeholder v2.0 aircraft model to depict all seven aircraft and identify potential supersonic routes for each aircraft type.

Supersonic Flight Path Calculations

Previous work relied on a simplistic method of flight path calculation, whereas the distance flown is calculated from the great circle path distance. The over-land and over-water distances were calculated by dividing the total distance by given fixed over-water percentages. The work presented in this paper uses a polygon approach to calculate accurate over-water distances, whereas the intersection between the flight path and the coastline separates over-land and over-water segments. The block time is then simply calculated by dividing segment distance by over-land or over-water airspeed. This approach also takes into account the differences in fuel burn when flying in different directions on the same route, i.e., when flying from A to B and B to A.

The block time for each origin destination pair is calculated as follows:

1. Calculate the great circle path between the origin airport and the destination airport of a route.
2. Deviate the midpoint by $\pm 7^{\circ}$ with 1° intervals along the direction perpendicular to the heading at midpoint.
3. Separated each route by land-water intersections into k segments.
4. Calculate the distances of each segment and record the sum of over-water distances.
5. Calculate block time of each route option.
6. Find the minimum block time path for both forward and return directions.

The block time calculation follows the equation below, where k is the total number of segments within the route, d_k is the distance of segment k, and V_k is the airspeed at that segment. Because all supersonic operations are restricted to over-water, aircraft fly at $V_{supersonic}$ on over-water segments and at $V_{subsonic}$ on over-land segments.

$$block\ time = \sum_{k=1}^{N} \frac{d_k}{V_k}$$
$$V_k = V_{supersonic}\ (k \subset over\text{-}water\ segment)$$
$$V_k = V_{subsonic}\ (k \subset over\text{-}land\ segment)$$

All available nonstop routes are found by filtering all routes by range. To extend flight range, a search algorithm finds all available fuel stops along the path for each OD pair. The routes with fuel stops are again filtered based on the design range of "placeholder v2.0" aircraft.

Identification of SST-Eligible Routes – Nonstop Routes

Nonstop supersonic routes—like the example route, LAX–TPE, shown in Figure 37—are shorter than 4,500 nmi and do not require a fuel stop (shown in the figure, midpoints are deviated by $\pm 7^{\circ}$ with 1° increments). The green lines represent the deviated routes and the red triangles represent midpoints of each route. As shown in the figure, the top route path has more overlap with land, which would increase block time. In this case, the bottom route path has the least block time, and it is the best route for the example in consideration.

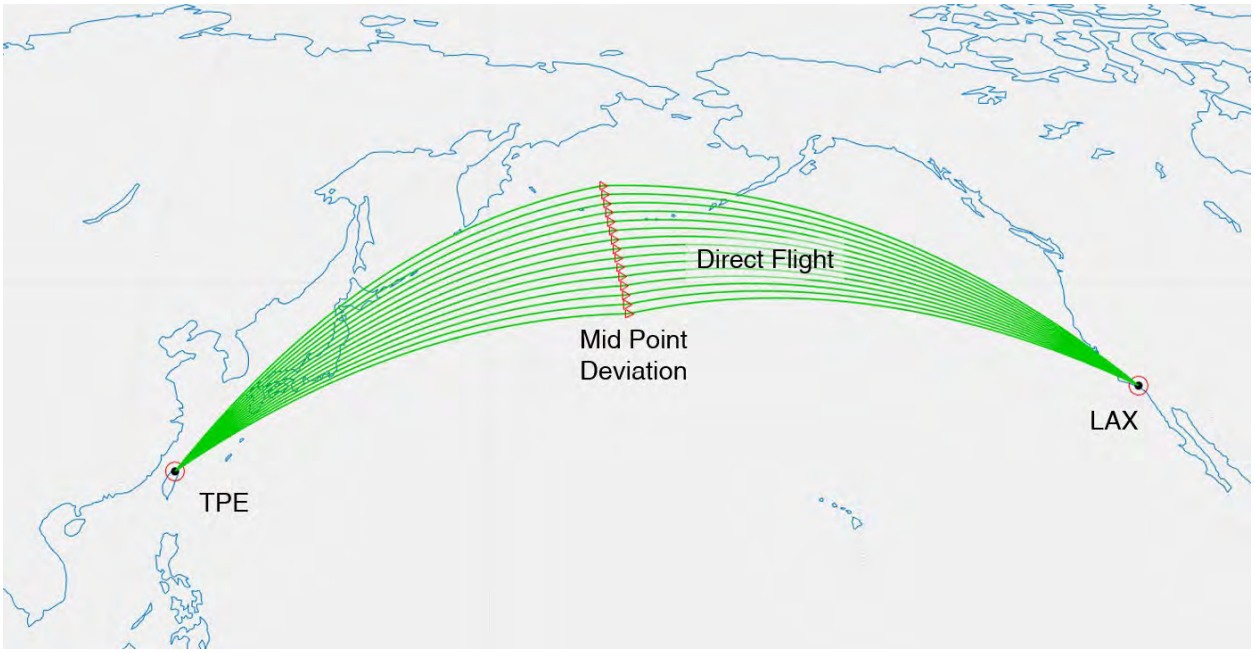

Figure 37. Example supersonic route (LAX–TPE) that does not require a fuel stop.

Identification of SST-Eligible Routes – Routes With Fuel Stops
Earlier, the fuel stop options for routes longer than 4,500 nmi only included Honolulu, Hawaii (HNL) and Anchorage, Alaska (ANC) for cross-Pacific routes, and Shannon, Ireland (SNN); Keflavik, Iceland (KEF); Oslo, Norway (OSL); and San Juan, Puerto Rico (SJU) for cross-Atlantic routes. This approach was valid only for the US-touching route network and required manual inputs to select the appropriate fuel stop. To capture fuel stops for all global routes, an automated area-search method is developed and implemented. For each OD pair, a search area is placed on the great circle path between them. All airports within the area would be captured as potential fuel stops. To avoid the case where the supersonic aircraft lands for a fuel stop immediately after takeoff, a circular search area is placed at the route's midpoint to ensure airports in the vicinity of the origin or the destination are not captured. The diameter of the search area is set to 35° spherical arc to include maximum possible fuel stop options; the arc size was based on trial and error.

With each fuel stop, a deviation process similar to nonstop supersonic routes is implemented for both segments and both directions to find the minimum block time path of each path. In the case shown in Figure 38, HNL and ANC are selected as fuel stop options for the LAX–TPE route. The gray routes shown in the figure depict the deviated routes with fuel stops, whereas the red triangles depict the midpoints for each deviated route; the red route path represents the path with minimum block time.

The fuel required to fly any such route is calculated by modeling both segments of the route, accounting for the departure and arrival of each segment, and the block time accounts for the extra time required to land and take off at the fuel stop airport.

Higher-Resolution Supersonic Aircraft Modeling and Routing
The computational models of the 55-seat, 75-seat, and 100-seat supersonic aircraft for this study are developed by colleagues at Georgia Tech. These models provide mission performance characteristics, including fuel consumption and block time, for the supersonic aircraft to operate on routes in the FLEET network. Because the supersonic aircraft can only operate at supersonic speed over water, the ground path of the flight to optimize a combination of fuel consumption and block time can deviate significantly from typical subsonic aircraft routes. For consistency in the ASCENT project, the studies presented here also use flight path ground tracks generated by teammates at Georgia Tech.

The Purdue team considers two generations of supersonic aircraft with entry-into-service (EIS) dates of 2025 (generation 1) and 2038 (generation 2). The generation 2 supersonic aircraft show a 10% improvement in fuel burn with no change in aircraft noise or sonic boom characteristics.

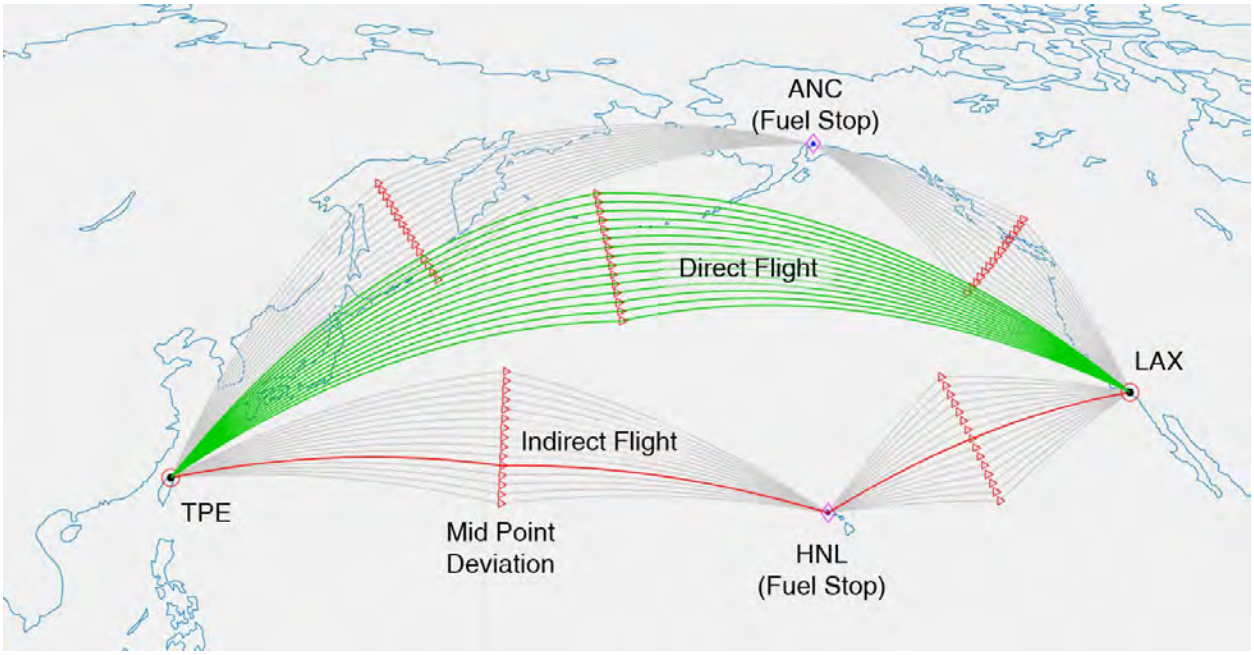

Figure 38. Example supersonic route that requires a fuel stop.

The detailed supersonic routing developed by Georgia Tech works to identify the optimum supersonic route path by solving an optimization problem to minimize a weighted sum "cost to the goal" objective function. The goal here is to minimize a combination of block time and block fuel values for flying supersonic aircraft on a supersonic route. This approach essentially finds a supersonic route path that is a tradeoff between the time optimal-only route and fuel optimal-only supersonic route path. A simplistic representation of this approach is:

$$weightedsum_{objective} = \alpha * \frac{BlockFuel}{BlockFuel_{min}} + (1-\alpha) * \frac{BlockTime}{BlockTime_{min}}$$

Current work uses α = 0.4 as the recommended value for the weighted sum supersonic routing (based on various supersonic routing tests conducted by our partners at Georgia Tech). The authors use FLOPSv9 to "fly" the detailed supersonic aircraft models on the weighted sum routes, conducting separate FLOPS runs for each direction of a supersonic route; the team observed different block fuel values (and in some cases, block time) when flying the detailed notional supersonic aircraft in different directions on a supersonic route.

Subtask 4: FLEET for Business Jet Operations

To increase the value and utility of FLEET in assessing the environmental impact of aviation beyond airline operations, the Purdue Team began work to expand FLEET to model and analyze business jet operations. The goal of this effort is to create a baseline modeling capability that can be expanded and improved in its fidelity in possible follow-on work. Developing FLEET-B entails four efforts:

- Modeling of business jet travel demand
- Representation and modeling of business jet fleet of aircraft
- Modeling of business jet resource allocation
- Evolution of business jet operations (fleet of aircraft and demand)

Business Jet Travel Demand

Data provided by the Common Operations Database (COD) for 2018 [35] represents worldwide travel on business jets for 2018. The data contain the operations of 11,214 companies; however, only a small fraction of these companies provide the most and somewhat regular service. For the purpose of this work, we define regular service by a company if four or more daily trips are flown. With this assumption, only 2% of the companies (217) flew more than four daily trips and provided 50% of business jet travel in 2018.

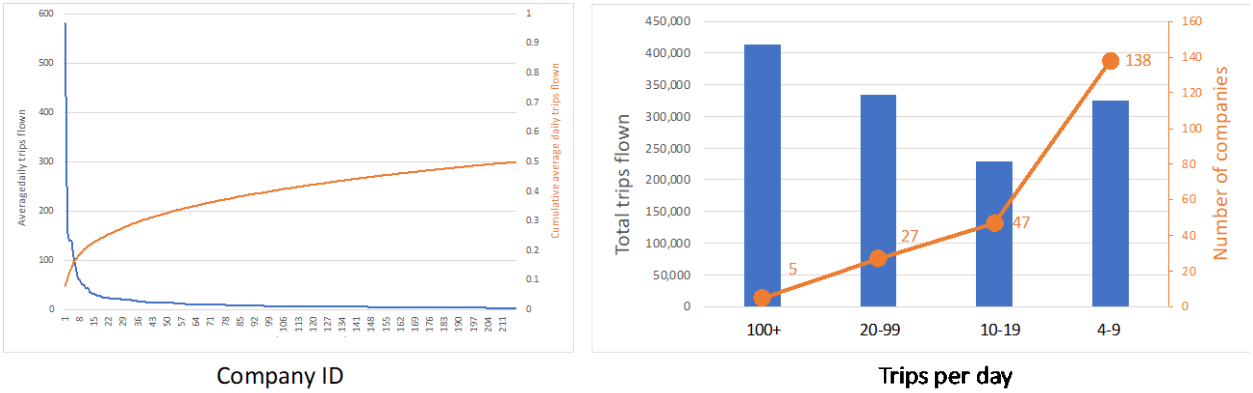

Figure 39. Companies providing business jet services in 2018.

Furthermore, less than half of these 217 companies had a high level of operation, reaching more than 10 daily trips (Figure 39, right). Fractional operators NetJets, Privaira, and Bombardier Jet Solutions were the companies providing most of the activity in 2018. The other companies were a mix of fractional, charter, air taxi, and corporate operators. The activity of these operators consisted of ~1.3 million trips between ~160,000 city-pairs among 4,417 airports.

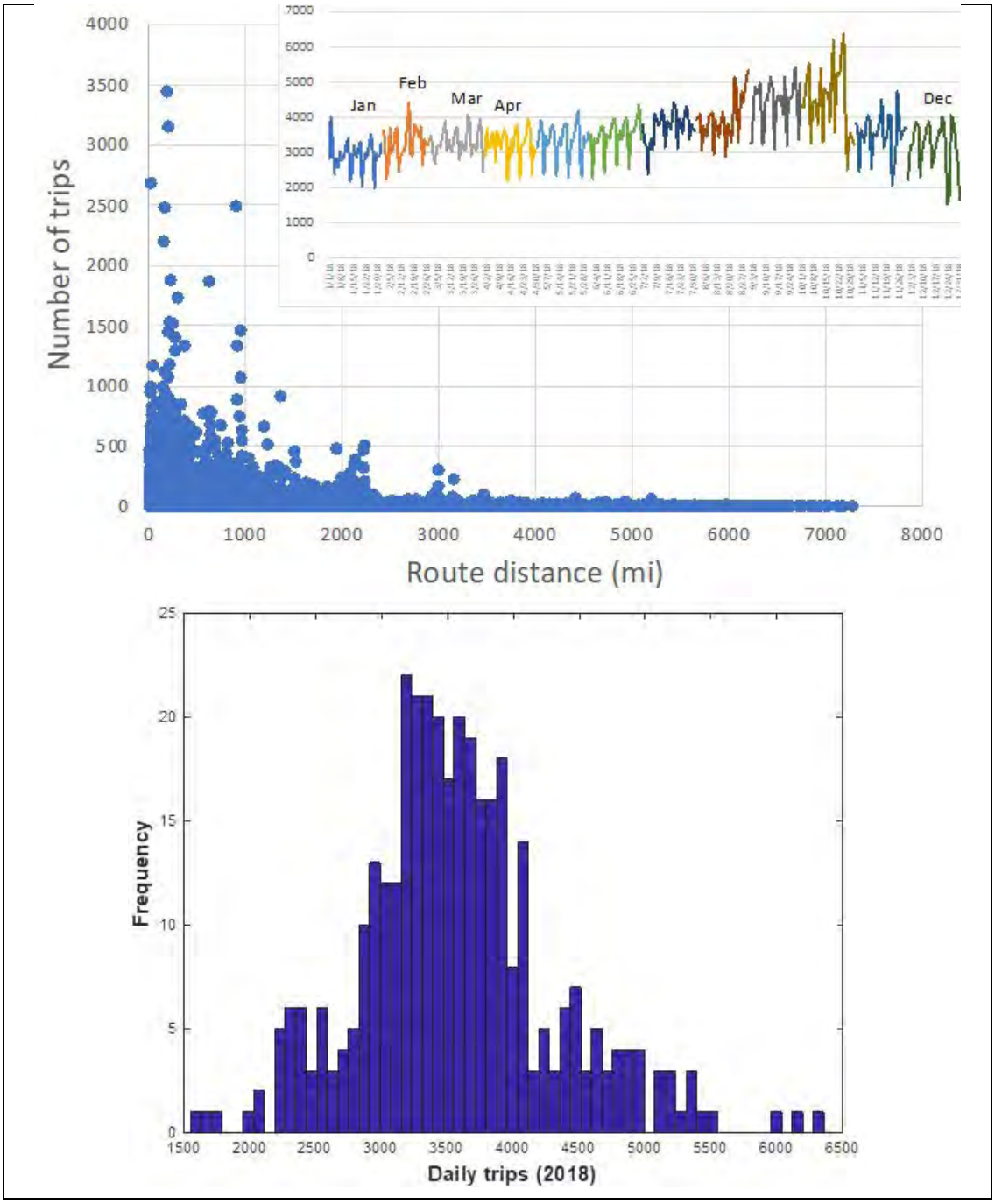

Figure 40. Trip distribution of business jet travel; top: number of trips and route distance; bottom: daily trip distribution.

Directly applying the current resource allocation model in FLEET to represent and analyze the level of operations presented here is infeasible. Because the combined number of airports, city-pairs, and trips is too large for the model to generate a solution in any reasonable time, we group the daily trips into 50-mile bins. This generates a total of 146 route-bins for the

city-pair distances between 0 and 7,300 miles. This assumption greatly reduces and simplifies the allocation model, but it retains the ability to estimate the number of aircraft required to meet all trip demand and their emissions. However, this approach eliminates the ability to capture the number of operations at any given airport, because any given route-distance bin contains many different city-pairs and airports.

Aircraft Fleet Size and Mix

The data provided by COD also contains information about the type of aircraft used to provide the service for each company. The aircraft are also grouped into categories based on their size and range. Table 21 presents these groups of aircraft, exemplars for each, and the fraction of aircraft in the fleet.

Table 21. Aircraft flown by business jet operators.

Aircraft type ID	Aircraft Category	Exemplars
B1	BJ 1.5 Very Light Jet	Embraer 500, Citation M2, etc.
B2	BJ 2.0 Light Jet	Beechjet 400, Citation V, Premier I, etc.
B3	BJ 3.0 Light Jet	Citation XLS, Lear 60, Lear 45
B4	BJ 3.5 Light Jet	Citation Sovereign, Falcon 50, Hawker 800
B5	BJ 4.0 Medium	Challenger 300, Hawker 1000, Citation X
B6	BJ 5.0 Medium	Falcon 2000, Challenger 604
B7	BJ 6.0 Large	G450, G5000, Falcon 900EX
B8	BJ 7.0 Large	Falcon 7X, Global 6000, Falcon 8X
	BJ 7.5 Large	G650
	BJ 8.0 Corporate	B737-700, A319-100
	BJ 8.5 Corporate Very Large	B777-200, B787-8

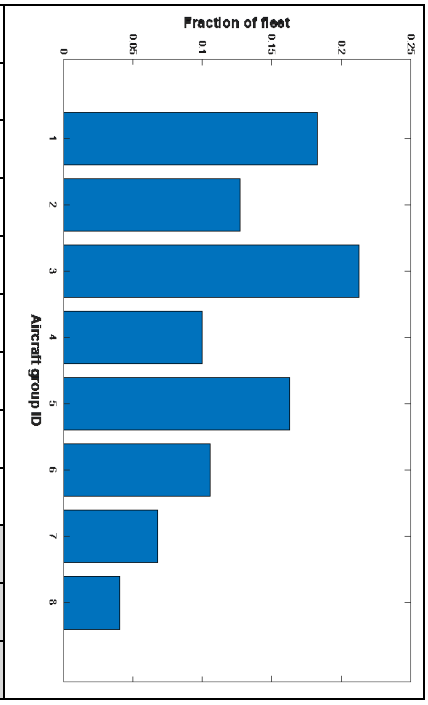

Because the number and operations of category 7.5, 8.0, and 8.5 were very small, they are included in aircraft type ID B8 in this study. Most of the service is provided by group B1, followed by group B3, and then B2. Figure 41 shows the daily trip distribution for each of these groups of aircraft. This will be the basis for the trip demand on which the aircraft allocation problem will be solved.

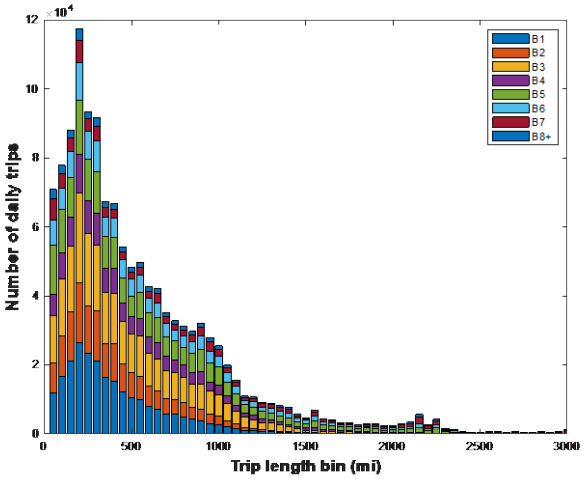

Figure 41. Daily trip distribution by aircraft group.

To allocate aircraft properly to satisfy demand, the FLEET tool requires information about each aircraft's performance and cost. For the analysis of airline operations, the team has developed FLOPS models that provide performance and cost estimations. Similar models are needed to fully develop FLEET into FLEET-B. However, for the purposes of this current effort (to demonstrate the utility of a business jet version of FLEET), we estimate the cost to operate each group of aircraft by using historical data. Figure 42 presents the available cost information as a function of aircraft range and the DOC of each group of aircraft based on the exemplar aircraft in each group. The three sets of data fits shown here are based on different aircraft speeds, and the fit selected to estimate the aircraft cost is the one that most closely approximates the performance of the exemplar aircraft.

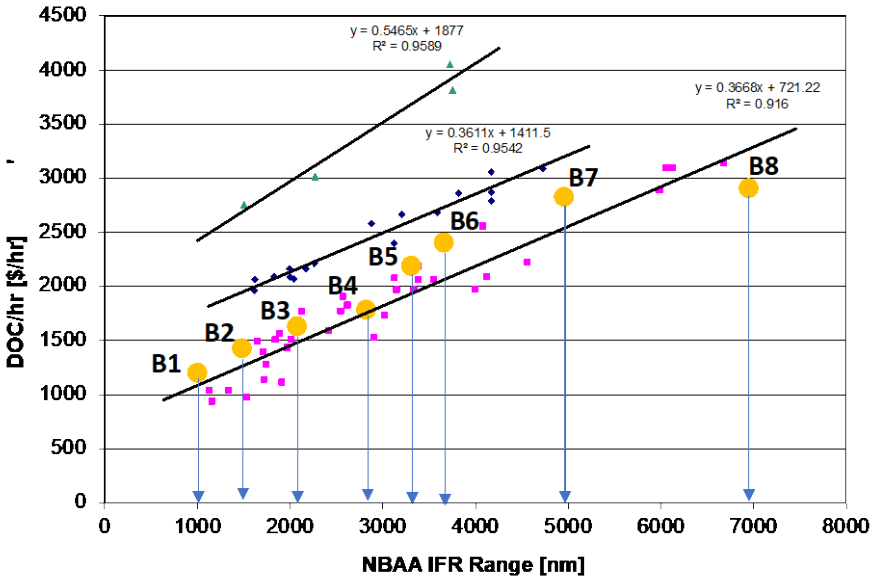

Figure 42. Direct operating cost (DOC) of aircraft considered in study. NBAA IFR, National Business Aviation Association instrument flight rules.

With this information at hand, the input parameters for the resource allocation model are complete. We note that the goal of this effort is to demonstrate the utility of the analysis and create a foundation upon which to refine the model with more accurate aircraft performance parameters, demand information, and fleet and demand evolution in the future.

Resource Allocation Model

Business jet operations, and the companies that provide this type of service, are different from airline operations. While both provide a transportation service, business jet operations are governed less by a need to fulfill passenger-based travel and more by trip-based travel. In other words, the primary goal of business jet operations is to satisfy trip demand and not necessarily passenger demand. For corporate operators, for example, the decision to acquire an aircraft with a given passenger capacity dictates the number of passengers that can be carried on a given trip, and the only decision during operations is whether to use the aircraft or not. Similarly, fractional share owners decide the type of aircraft in which they want to own a share based on its performance characteristics, then only decide when and where to fly within those constraints. The daily decisions of a fractional operator center on how to allocate aircraft to meet the trip demand of specific owners in the least costly manner, not how to fill seats on the aircraft.

If a supersonic business jet (SSBJ) is considered as an addition to the fleet of aircraft, the decision on how to use that aircraft would be similar. Because the primary benefit of an SSBJ is the reduction in travel time, the allocation model would need to accommodate and account for this. Based on this type of operation and decision-making, we define the following decision variables and parameters:

Sets:
c = company type (fractional, charter, air taxi, corporate)
k = aircraft type
j = route
Variables:
$trips_{c,k,j}$ = number of trips flown by company c on aircraft k and route j
$trips_{c,s,j}$ = number of trips flown by company c on SST aircraft s and route j
$aircraft\_hours_{c,k}$ = number of aircraft-hours flown by company c on aircraft k
$fleet\_used_{c,k}$ = number of aircraft used by company c of type k
Parameters:
$C_{c,k,j}$ = cost for company c to fly aircraft type k on route j
$dem_{c,k,j}$ = number of trips of company c aircraft type k on route j
$fleet_{c,k}$ = fleet size (number of aircraft) for company c of type k
$AA_{c,k}$ = aircraft availability for company c of type k
$OH_{c,k}$ = operational hours for company c of type k
$BH_{c,k,j}$ = block time of company c for aircraft type k on route j
$MH_{c,k,j}$ = maintenance of company c hour for aircraft type k on route j
$DH_{c,k,j}$ = deadhead hours of company c hour for aircraft type k on route j
t_c = aircraft turnaround time for company c
$(tt_{sub})_{c,j}$ = average travel time of subsonic aircraft operated by company c on route j
$(tt_{sup})_{c,j}$ = travel time of supersonic aircraft operated by company c on route j
$(value\ of\ time)_c$ = value of travel time for customers of company c

We formulate the resource allocation of business jet operations as follows:

$$Min \quad \left(\sum_{c=1}^{C} \sum_{k=1}^{K} \sum_{j=1}^{J} trips_{c,k,j} C_{c,k,j} - \sum_{c=1}^{C} \sum_{j=1}^{J} savings_{c,j} \right) + M \sum_{c=1}^{C} \sum_{k=1}^{K} fleet_{used}{}_{c,k} \qquad (1)$$

where

$$savings_{c,j} = \left[(tt_{sub})_{c,j} - (tt_{sup})_{c,j} \right] \times (value\ of\ time)_c \qquad (2)$$

Subject to

$$trips_{c,k\prime,j} + trips_{c,s,j} \geq dem_{c,k,j} \quad \forall (k' + s) \in k \tag{3}$$

$$\sum_{j=1}^{J} trip_{c,k,j}\left(BH_{c,k,j} + DH_{c,k,j} + MH_{c,k,j} + t_c\right) = aircraft\_hours_{c,k} \tag{4}$$

$$aircraft\_hours_{c,k} \leq fleet\_used_{c,k} \cdot AA_{c,k} \cdot OH_{c,k} \tag{5}$$

$$fleet\_used_{c,k} \leq fleet_{c,k} \tag{6}$$

The objective function (Eq 1) aims to minimize the cost of satisfying the trip demand while also minimizing the number of aircraft used, captured here by the big-M quantity. The cost to fly the demanded trips accounts for the value of travel time and the expected travel time savings when the value of travel time is taken into consideration (represented by Eq 2). The constraints represented by Equation 3 ensure that the number of trips flown on subsonic and supersonic aircraft satisfy all demanded trips on each aircraft type, for each company, and on each route. Equation 4 calculates the number of aircraft-hours required to fly all trips for each aircraft type and company when taking into consideration block hours flown and deadhead time (repositioning flights that do not carry passengers, maintenance time, and turnaround time). Constraints in Eq 5 ensure that we capture the aircraft availability ($AA_{c,k}$) and the number of operational hours that the company has available to satisfy daily demand ($OH_{c,k}$). This last parameter is designed to capture the different types of operations and scheduling requirements of different companies and business models. For example, the daily travel demand of a corporate operator is very different from that of a fractional operator. A corporate operator may only have two trips in a given day, but those trips happen at the same time, which means that they may require two aircraft to satisfy demand. A fractional operator, on the other hand, may have 10 trips in a day, but if they occur in two-hour intervals and are less than 1-hour trips, then the company may only need 2 to 5 aircraft to satisfy that demand. For the purposes of this demonstration model, we make assumptions about these parameters and will research possible data sources to obtain more realistic values and values that accurately estimate and capture the operational tempo of different operators. Finally, the constraints in Equation 6 ensure that the number of aircraft required to satisfy all demand (when accounting for the operational realities of the company) does not exceed the available fleet size.

Results

Solving the above allocation problem for daily demand and the aircraft models described earlier is relatively fast. Because the number of routes is only 146, GAMS and its algorithms are able to generate a solution in a few seconds. We solve the allocation model for each day of operations and are able to generate statistics of the results. Figure 43 presents these results when only subsonic aircraft are considered and when we assume that there is only one company satisfying all travel demand.

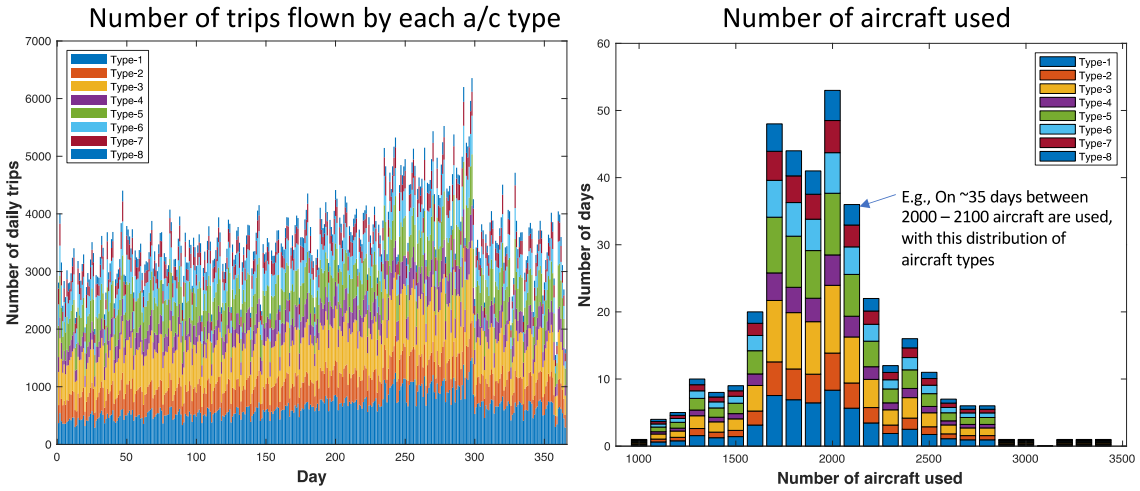

Figure 43. Aircraft allocation results assuming single-operator and subsonic-only aircraft to demonstrate potential capability of the FLEET-B simulation.

Recall that demand is specified for each route and for each aircraft type; therefore, the decision made by the resource allocation model is to identify the number of aircraft required to satisfy demand. The ability to analyze each day of operation makes possible the identification of the distribution of the number of aircraft that are needed to satisfy demand. Figure 43 (right) clearly displays these results by providing the number of days that a given number of aircraft is required. For example, on 35 days of the year, between 2,000 and 2,100 aircraft are used to satisfy all demand. An interesting implication of this type of result is that it is clear how the fleet size for a given operator may be driven not by the average number of operations but by the busiest day. The simplicity of the allocation model (only 146 binned routes) facilitates this analysis and observation.

When introducing the supersonic aircraft to the available fleet of aircraft, it is necessary to include its speed and cost in the allocation model. Figure 44 (left) provides an overview of the difference in travel time that an SSBJ can offer compared to subsonic aircraft, and Figure 44 (right) provides a similar comparison for the cost. We assume here that for trip distances less than 600 mi, a supersonic aircraft would not be able to get up to supersonic speeds, hence the similar block time for those distances.

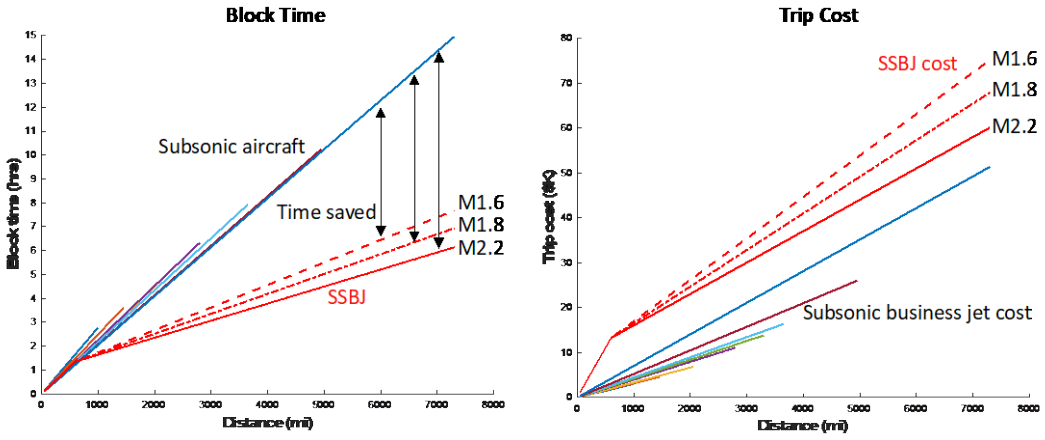

Figure 44. Block time and trip cost of subsonic and supersonic business jets (SSBJ).

Because the advantage of SSBJ is in the travel time savings, and as shown in the description of the resource allocation model, we include this travel benefit in the model by defining an effective trip cost that reduces the cost to operate the aircraft by the value of travel time savings (Eq 2). Figure 45 presents the effect of this adjustment on the trip cost when different values of travel time are considered.

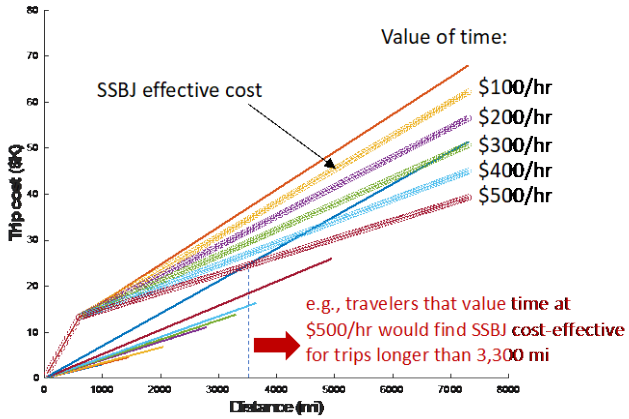

Figure 45. Trip cost when accounting for value of travel time savings. SSBJ, supersonic business jet.

For example, for those travelers who value time at $500/hr or more, trips longer than 3,300 mi would be considered cost effective, and the effective trip cost would be less than the trip cost if flown on a subsonic aircraft. By using these data and by making the supersonic aircraft an option for any trip and a substitute for any aircraft type, the allocation model is able to determine on which routes the use of an SSBJ would be cost effective when all components of travel time (block time, turnaround time) and operational requirements (maintenance time, repositioning time) are considered. We highlight that no assumptions are made a priori about the routes on which an SSBJ would be available. It is the allocation model that determines the routes on which an SSBJ is cost effective.

Therefore, when accounting for the value of travel time savings and including the SSBJ aircraft in the allocation model, it is possible to identify which routes could see supersonic service. Figure 46 (left) presents the number of trips that are flown on each route-bin by an SSBJ that is able to cruise at M1.6 for values of time of $500/hr, $400/hr, and $300/hr; Figure 46 (right) shows the total number of trips that would be flown for SSBJ of M1.6, M1.8, and M2.2 as a function of the value of travel time.

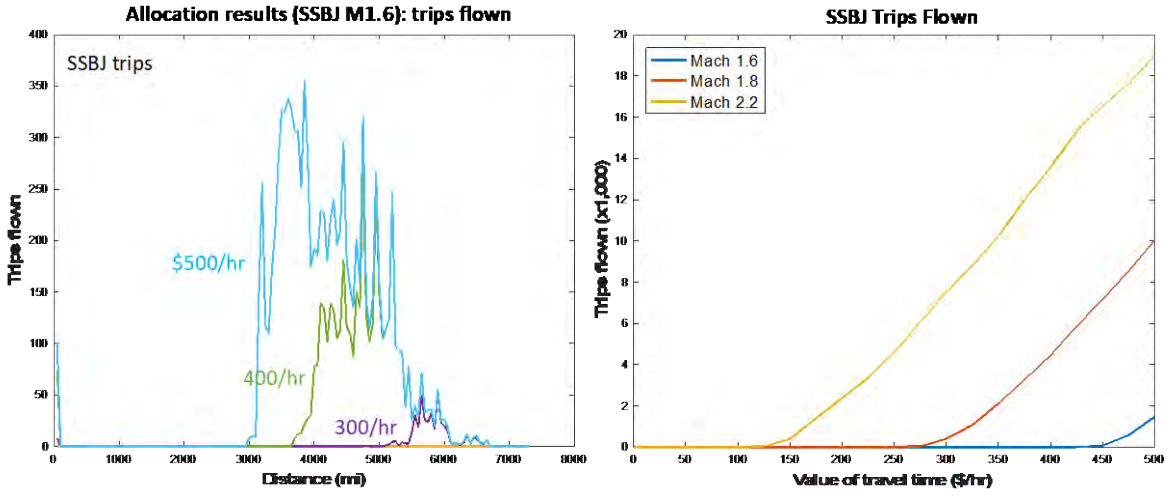

Figure 46. Level of service provided for varying values of travel time. SSBJ, supersonic business jet.

As expected, when the value of time is large, SSBJ travel time savings are sufficient to offset the trip cost. As the value of travel time increases, the number of trips flown also increases. Furthermore, the faster the SSBJ, the greater the travel time savings, and therefore the larger the number of trips flown on the SSBJ. Although several simplifying assumptions are made here to demonstrate the viability of this type of analysis, the model shows that it is possible to capture the possible decision-making of business jet operators and to account for the benefits of supersonic travel.

Future Work
Further work on this task will entail improving the fidelity of the subsonic and supersonic aircraft models to generate better approximation of ownership and operating costs. Refinement of the operational model of the various types of business jet operators is another area of improvement that will increase the fidelity of the analysis. Identifying meaningful assumptions about the daily operating hours of each operator will enable the model to more accurately estimate the number of aircraft required to satisfy demand. While the estimation of fuel burn, environmental emissions, and number of operations at a given airport would not be affected by this, the ability to estimate the degree of penetration of supersonic aircraft in the fleet mix and the evolution of new aircraft and associated aircraft technologies will require more accurate information.

Outreach Efforts
During this period of performance, the Georgia Tech team published the following:

Baltman, E., Tai, J. C., Ahuja, J., Stewart, B., Perron, C., De Azevedo, J., Vlady, T. R., & Mavris, D. N. (2022). A Methodology for Determining the Interdependence of Fuel Burn and LTO Noise of a Commercial Supersonic Transport. AIAA AVIATION 2022 Forum, 1–16. https://doi.org/10.2514/6.2022-4110

During this period of research, the Purdue team published the following:

Yang, B., Mane, M., and Crossley, W. (2022). An Approach to Evaluate Fleet Level CO2 Impact of Introducing Liquid-Hydrogen Aircraft to a World-Wide Network, AIAA Aviation Forum 2022, https://doi.org/10.2514/6.2022-3313

Jain, S., H. Chao, M. Mane, W. A. Crossley and D. A. DeLaurentis. (2021). Estimating the Reduction in Future Fleet-Level CO2 Emissions From Sustainable Aviation Fuel, Frontiers in Energy Research, Nov 2021, doi: 10.3389/fenrg.2021.771705

Awards
None.

Student Involvement
The Purdue team included four graduate students during this year's effort, all of whom have been conducting tasks in support of the project. Samarth Jain finished his PhD studies, Suzanne Swaine continued her MS work, Fung Tien-Yueh continued his PhD work, Boning Yang finished his MS work and graduated.

The GT team also included the following graduate students during this year's effort: Nikhil Iyengar, Barbara Sampaio, Edan Baltman, Joao De Azevedo, Jiajie (Terry) Wen, Ted Vlady, Zayne Roohi and Srikanth Tindivanam Varadharajan

The GT team also trained one undergraduate student, Madeleine Graham, in matters related to CFD and optimization using the 65 pax Mach 1.7 baseline configuration as a starting point

Plans for Next Period
Georgia Tech
The plan for the next period of performance is to apply the improved design methodology presented in the current report to a wider set of supersonic vehicles. Specifically, the same process previously used for a 65-passenger SST vehicle with a cruise speed of Mach 1.7, will be applied to a similarly sized vehicle, but with a cruise speed of Mach 2.0. The Georgia Tech team will also examine an SST vehicle designed for a lower cruise speed of Mach 1.4, still with a 65-passenger capacity. Finally, a supersonic business jet with an 8-passenger capacity and a cruise speed of Mach 1.4 will be investigated. This last vehicle will notably be designed with only two engines due to its smaller scale, unlike the 4 engines configuration used for the other SST aircraft. The fuel burn and the LTO noise for each of the proposed configurations will be captured and

compared, allowing us to investigate the interdependence of both metrics with more granularity. The analysis of these SST vehicles will also be performed with an updated demand forecast.

References

[1] Haimes, R., & Dannenhoffer, J. F. (2013, June 24-27). *The engineering sketch pad: A solid-modeling, feature-based, web-enabled system for building parametric geometry* [Conference presentation]. 21st AIAA Computational Fluid Dynamics Conference, San Diego, CA. https://doi.org/10.2514/6.2013-3073

[2] NASA Advanced Supercomputing Division, (n.d.) *Cart3D Documentation* https://www.nas.nasa.gov/publications/software/docs/cart3d/

[3] Siemens. (n.d.) *Simcenter STAR-CCM+*. https://www.plm.automation.siemens.com/global/en/products/simcenter/STAR-CCM.html

[4] Constantine, P. G., Dow, E., & Wang, Q. (2014). Active subspace methods in theory and practice: Applications to Kriging surfaces. *SIAM Journal on Scientific Computing., 36(4)*, 1500–1524. https://doi.org/10.1137/130916138

[5] Tripathy, R., Bilionis, I., & Gonzalez, M. (2016). Gaussian processes with built-in dimensionality reduction: Applications to high-dimensional uncertainty propagation. *Journal of Computational Physics, (321),*191–223. https://doi.org/10.1016/j.jcp.2016.05.039

[6] Seshadri, P., Yuchi, S., & Parks, G. T. (2019). Dimension reduction via Gaussian ridge functions. *SIAM-ASA Journal on Uncertainty Quantification, (7)4*, 1301–1322. https://doi.org/10.1137/18M1168571

[7] Gautier, R., Pandita, P., Ghosh, S., & Mavris, D. (2021). A fully Bayesian gradient-free supervised dimension reduction method using Gaussian processes. *International Journal for Uncertainty Quantification, 12(2)*,1–32.

[8] Mulfti, B., Chen, M., Perron, C., & Mavris, D. N. (2022). *A multi-fidelity approximation of the active subspace method for surrogate models with high-dimensional inputs* [Conference presentation]. AIAA Aviation Forum, Chicago, IL. https://doi.org/10.2514/6.2022-3488

[9] Jones, D. R., Schonlau, M., & Welch, W. J. (1998). Efficient global optimization of expensive black-box functions. *Journal of Global Optimization, 13(4)*, 455–492. https://doi.org/10.1023/A:1008306431147

[10] Forrester, A. I. J., & Keane, A. J. (2009). Recent advances in surrogate-based optimization. *Progress in Aerospace Sciences, 45(1–3)*, 50–79. https://doi.org/10.1016/j.paerosci.2008.11.001

[11] Wells, D. P., Horvath, B. L., & Mccullers, L. A. (2017). *The flight optimization system weights estimation method*. NASA/TM–2017–219627

[12] Han, Z.-H., and Görtz, S. (2012). Hierarchical Kriging model for variable-fidelity surrogate modeling. *AIAA Journal, 50*, 1885–1896. https://doi.org/10.2514/1.J051354

[13] Lee, K., Nam, T., Perullo, C., & Mavris, D. N. (2011). Reduced-order modeling of a high-fidelity propulsion system simulation. *AIAA Journal, 49(8)*. https://doi.org/10.2514/1.J050887

[14] Mavris, D., Crossley, W., Tai, J., & Delaurentis, D. (2019). *Project 010 aircraft technology modeling and assessment*. https://s3.wp.wsu.edu/uploads/sites/2479/2020/05/ASCENT-Project-010-2019-Annual-Report.pdf

[15] Walsh, P., Gas turbine performance

[16] Frost, T., (1966) *Practical bypass mixing systems for fan jet aero engines.* https://www.cambridge.org/core/journals/aeronautical-quarterly/article/practical-bypass-mixing-systems-for-fan-jet-aero-engines/8C316D80FD32E17F8A9A656A1DC6EFEA

[17] Zola, C., (2000) *Advanced propulsion system studies in high speed research.* https://ntrs.nasa.gov/citations/20000057336

[18] McCullers, A. (1984). *Recent experiences in multidisciplinary analysis and optimization, Part 1*, NASA-CP-2327-PT-1, 395–412.

[19] Computing with HTCondor. (n.d.) https://research.cs.wisc.edu/htcondor/

[20] SAS Institute Inc. JMP®, Version 16. https://www.jmp.com/en_us/events/mastering/topics/new-in-jmp16-and-jmp-pro16.html

[21] Baltman, E. M., Tai, J. C., Ahuja, J., Stewart, B., Perron, C., Azevedo, J. H. De, Vlady, T., & Mavris, D. N. (2022). A methodology for determining the interdependence of fuel burn and LTO noise of a commercial supersonic transport. *AIAA Aviation Forum*. https://doi.org/https://doi.org/10.2514/6.2022-4110

[22] Raymer, D. P. (2018). *Aircraft design: a conceptual approach, Sixth Edition*. American Institute of Aeronautics and Astronautics, Inc.

[23] Liebeck, R. H., Andrastek, D. A., Chau, J., Girvin, R., Lyon, R., Rawdon, B. K., Scott, P. W., & Wright, R. A. (1995). Advanced subsonic airplane design and economic studies. *Tech. Rep.* 19950017884. https://ntrs.nasa.gov/citations/19950017884

[24] Air Transportation Association of America, (1967). Standard method of estimating comparative direct operating costs of turbine powered transport airplanes. *Tech. Rep.* https://docplayer.net/39861253-Standard-method-of-estimating-comparative-direct-operating-costs-of-turbine-powered-transportairplanes.html

[25] Johnson, V. S. (1989). *Life cycle cost in the conceptual design of subsonic commercial aircraft*. [Ph.D. dissertation]. University of Kansas.

[26] U.S. Bureau of Labor Statistics. *Cpi inflation calculator*. https://www.bls.gov/data/inflation_calculator.htm

[27] Boeing Commercial. *About Boeing commercial airplanes*. https: //www.boeing.com/company/about-bca/

[28] Jane's Information Group. *Jane's all the world's aircraft*. https: //www.janes.com/publications/

[29] AeroCorner. *Archives: Aircraft*. https://aerocorner.com/aircraft

[30] U.S. Department of Transportation, Bureau of Transportation Statistics. (n.d.) *Air carrier financial reports (form 41 financial data)*. [Online database]. https://www.transtats.bts.gov/databases.asp?Z1qr_VQ=E&Z1qr_Qr5p=N8vn6v10&f7owrp6_VQF=D

[31] Moolchandani, K. (2012). *Impact of environmental constraints and aircraft technology on airline fleet composition*. [Master's thesis]. Purdue University.

[32] Boeing. *Boeing current market outlook 2012–2031*. http://libraryonline.erau.edu/online-full-text/books-online/Boeing_Current_Market_Outlook_2012.pdf

[33] Wyman, O. *Oliver Wyman global fleet & MRO market forecast summary 2017-2027*. https://www.oliverwyman.com/our-expertise/insights/2017/feb/2017-2027-fleet-mro-forecast.html.

[34] Mavris, D., Delaurentis, D., Crossley, W., & Alonso, J. J. (2017). *Project 10 aircraft technology modeling and assessment: Phase I report*. https://ascent.aero/project/aircraft-technology-modeling-and-assessment/ https://s3.wp.wsu.edu/uploads/sites/192/2017/10/ASCENT_P10_2017_PhaseI_Final_Report.pdf

[35] Federal Aviation Administration, EUROCONTROL, ICAO's Committee on Aviation Environmental Protection (CAEP), U.S. Department of Transportation's Volpe Center, Common Operations Database (COD). (2018).

[36] Official Airline Guide. (n.d.) *Traffic Analyser.* https://www.oag.com/traffic-analyzer

Project 018 Community Measurements of Aviation Emission Contributions to Ambient Air Quality

Boston University School of Public Health

Project Lead Investigator

Kevin J. Lane
Assistant Professor
Department of Environmental Health
Boston University School of Public Health
715 Albany St. T4W
Boston, MA 02118
617-414-8457
klane@bu.edu

University Participants

Boston University School of Public Health (BUSPH)

- PI(s): Kevin J. Lane, assistant professor; Jonathan I. Levy, professor and associate chair
- FAA Award Number: 13-C-AJFE-BU, Amendment 7
- Period of Performance: September 30, 2021 to August 30, 2022
- Task(s):
    - **Task 1:** Continue long-term mobile and stationary monitoring sites in communities within 5 km of Logan International Airport to assess spatial and temporal variation in aviation source contributions in greater Boston area communities. ASCENT Project 19 will support us in evaluation of current sites and new sites for the new monitoring phase.
    - **Task 2:** Incorporate NO_2 and SO_2 federal equivalency methods (FEM) and/or federal reference methods (FRM) at monitoring sites to inform our understanding of aviation contributions to community air pollution relative to background sources.
    - **Task 3:** Establish a new monitoring site within close proximity to the airport fence line to better characterize the contribution from ground-based aviation emissions, supported by ASCENT Project 19 in decision-making for monitor siting.
    - **Task 4:** Compile from FAA essential flight activity and meteorological covariates needed for regression modeling under Project 18 and dispersion modeling under Project 19 using a data-sharing platform. Share data with University of North Carolina (UNC) in the prescribed formats over required averaging times, including both measured concentrations and, when available, estimated aviation-attributable concentrations for the validation of the dispersion model developed in the ASCENT 19 project.
    - **Task 5:** Apply regression modeling techniques to monitoring data previously collected under Project 18 to determine the contributions of aviation sources to ultrafine particles (UFPs) and NO_2 concentrations, while developing and refining the analytical approaches to be applied to data collected, including SO_2 within this expanded campaign. These outputs would allow for comparisons between atmospheric dispersion models developed by ASCENT Project 19 and aviation-attributable concentrations determined from regression models from Project 18.

Project Funding Level

FAA provided $549,000 in funding. Matching funds were provided by a non-federal donor to the Women's Health Initiative cohort studies as cost-sharing support to Boston University through Project 3.

Investigation Team

- ASCENT BUSPH director and Project 18 co-investigator: Jonathan I. Levy, ScD (professor of environmental health, chair of the Department of Environmental Health, BUSPH). Dr. Levy is the Boston University PI for ASCENT. He initiated ASCENT Project 18 and serves as the director of BUSPH ASCENT research.
- ASCENT Project 18 PI: Kevin J. Lane, PhD (assistant professor of environmental health, Department of Environmental Health, BUSPH). Dr. Lane joined the Project 18 team in July 2017. Dr. Lane has expertise in the assessment of UFP exposure, geographic information systems, statistical modeling of large datasets, and cardiovascular health outcomes associated with air pollution exposure. He has contributed to study design and data analysis strategies and, as of October 1, 2017, has taken over the primary responsibility for project execution. Dr. Lane also contributes to the manuscripts and reports produced.
- Tufts University associate professor John Durant, PhD. Dr. Durant oversees the Tufts Air Pollution Monitoring Laboratory (TAPL) team, leads the development of field study design, and contributes to scientific manuscript preparation.
- Tufts University research professor Neelakshi Hudda, PhD. Dr. Hudda joined the Project 18 team in September 2020 and is managing the TAPL team and the mobility data analysis, field study design and implementation, and scientific manuscript preparation.
- BUSPH assistant professor Dr. Prasad Patil. Dr Patil is a machine learning and regression modeling expert who is assisting Dr. Lane with modeling of the 2017–2019 UFP data.
- Graduate student: Sean Mueller is a doctoral student at BUSPH and has been analyzing aviation-related particle number concentration (PNC) during COVID-19.
- Postdoctoral research associate: Dr. Tiffany Duhl at Tufts University is managing mobile monitoring and analyzing the mobile PNC and fast-scanning mobility particle sizer (FMPS) size distribution data.
- Research assistants: Flannery Black-Ingersoll and Breanna van Loenen at Boston University are supporting analysis of mobile monitoring and stationary monitoring data.
- Undergraduate students: Olivia Moore, Isabelle Woollacott, and Lily Sandholm at Tufts University are working on the mobile monitoring platform and helping to clean the air pollution data.

Project Overview

The primary goal of this project was to conduct a new air pollution monitoring campaign beneath flight paths to and from Boston Logan International Airport, using a protocol specifically designed to determine the magnitude and spatial distribution of UFPs in the vicinity of arrival flight paths. Data were collected to assess whether aircraft emissions, particularly arrival emissions, significantly contribute to UFP concentrations at appreciable distances from the airport. Task 1 builds upon the previous air pollution monitoring performed under ASCENT Project 18 with the introduction of two new stationary monitoring sites. Tasks 2 and 3 specifically leverage the infrastructure previously developed for our field campaign and enable measurements that address a broader set of research questions than those evaluated in the previous monitoring year, with additional data collection for UFP size distributions and a new air pollutant (NO/NO_2). These tasks provide a strong foundation for Tasks 4 and 5, which increases the potential for future collaborative efforts with Project 19, in which we interpret and apply the collected measurements to inform ongoing dispersion modeling efforts at UNC and regression modeling at BUSPH.

We have continued our monitoring campaign to collect and analyze community air pollution measurements to determine the contributions of in-flight arrival and departure aircraft to ground-based concentrations. Previous studies have not had the monitoring infrastructure and real-time flight activity data necessary to determine how much of the measured pollution arises from aviation sources. We have used state-of-the-art air pollution monitoring technology that can measure different air pollutants every 1–5 s. Stationary sites have been established at varying distances from flight paths for Boston Logan International Airport, with measurements collected across multiple seasons. We have also employed a mobile monitoring system (electric vehicle) outfitted with the same monitoring equipment to drive throughout these communities to better characterize geographic variations in air pollution. Statistical analyses will compare the stationary and mobile measurements with flight activity data from the FAA and meteorology to determine aircraft contributions to ground measurements. We will compare these source attribution estimates with comparable outputs from atmospheric dispersion models.

A summary of the current project methods and data collection is included below to describe the continued application of Project 18 data, including bivariate statistical analysis and multiple regression model development conducted under Task 5.

Task 1 - Continue Long-Term Mobile and Stationary Monitoring Sites in Communities Within 5 km of Logan International Airport to Assess Spatial and Temporal Variation in Aviation Source Contributions in Greater Boston Area Communities

Boston University School of Public Health

Objective(s)

The objective of this task is to determine whether aircraft emissions, particularly in-flight arrival and departure emissions, contribute significantly to ground-level UFP concentrations at variable distances from the airport. To achieve this objective during the 2021–2022 period, we have continued to implement a monitoring approach that allows us to characterize both continuous long-term temporal trends in aviation-derived UFPs as well as higher-resolution spatial characterization of UFPs and other air pollutants in near-airport communities. Under the current project, we are collaborating with Drs. John Durant and Neelakshi Hudda and their team at Tufts University to deploy a mobile monitoring platform concurrent with our stationary monitoring under this task, which allows us to efficiently monitor more communities near Logan Airport in less time and with a limited number of monitoring devices. New to our scope of work in 2021–2022, we added adaptive mobile monitoring to delineate and characterize the impacts of landing and takeoff (LTO) and airport emissions in neighborhoods downwind of Logan Airport and to increase the spatial characterization of air pollutant measurements in these neighborhoods.

Research Approach

An air pollution monitoring campaign is underway that includes both stationary and mobile measurements. There are four stationary monitoring locations situated at varying distances from the airport and proximal to the main arrival/departure flight paths for Boston Logan Airport (Figure 1). These sites were specifically chosen to isolate the contributions of in-flight aircraft, excluding locations close to major roadways or other significant sources of combustion. PNC (a proxy for UFP) monitoring instruments were deployed at each monitoring site; two sites also include measurements of nitrogen oxides (NO_x), and one site includes measurement of black carbon (BC).

Additionally, real-time measurements of air pollutants are being acquired with the TAPL, a mobile platform equipped with fast-response instruments for monitoring gas- and particle-phase pollutants that facilitates the collection of reliable and robust data. The TAPL is an electric vehicle (2017 Chevrolet Bolt) equipped with instruments powered by six 12-V marine deep cycle batteries, which are connected in series to a 2-kW inverter/charger (Xantrex 2000). Individual measurements are matched to location by 1-s-interval global positioning system (GPS) readings. The TAPL monitoring setup is currently outfitted with a combination of air pollution monitors, including a condensation particle counter (CPC) to measure UFP (model 3775, 4–1,000 nm; TSI, Shoreview, MN), an aethalometer to measure BC (model AE-33, Magee Scientific, Berkeley, CA), and a CO_2/water vapor analyzer (model LI-840A, LI-COR Environmental, Lincoln, NE). Direct absorption measurements of nitrogen dioxide (NO_2) are obtained via cavity attenuated phase shift (CAPS) spectroscopy (model CAPS NO_2, Aerodyne Research Inc., Billerica, MA). The TAPL is shown in Figure 3, with a description of the monitoring devices given in Table 1.

Stationary Field Monitoring

We have collected air pollution data at a single site in Chelsea since April 2020, allowing us to capture nearly the entire COVID-19 time period with a full mobile and stationary monitoring launch that began in September 2020. UFP data have also been collected from three other long-term monitoring sites in Revere (starting September 2020), South Boston (starting May 2021), and Winthrop (starting January 2021), allowing for a comparison of PNC results within our monitored communities. Each monitoring site is located more than 200 m from major roadways and intersections and is near the arrival and takeoff locations on runways 4/22 or 9). The map in Figure 1 indicates the locations of the stationary monitoring sites in relation to the airport.

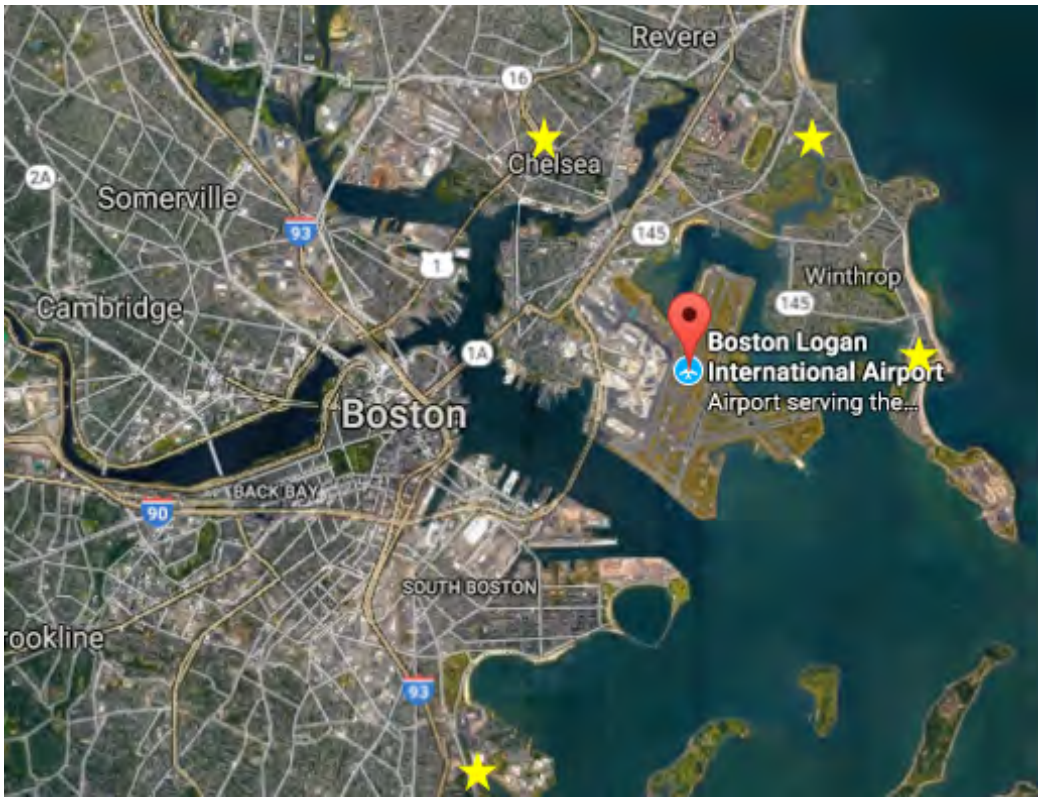

Figure 1. Stationary sites (yellow stars) for the 2020–2021 monitoring campaign.

Each stationary site is outfitted with a climate-controlled enclosure that allows for year-round sampling. Monitoring sites have a combination of UFP (TSI CPC or TSI FMPS), $NO/NO_2/NO_x$ (2B Technologies), and BC (Magee Scientific AE22) monitors. An example of the box setup with climate control is shown in Figure 2.

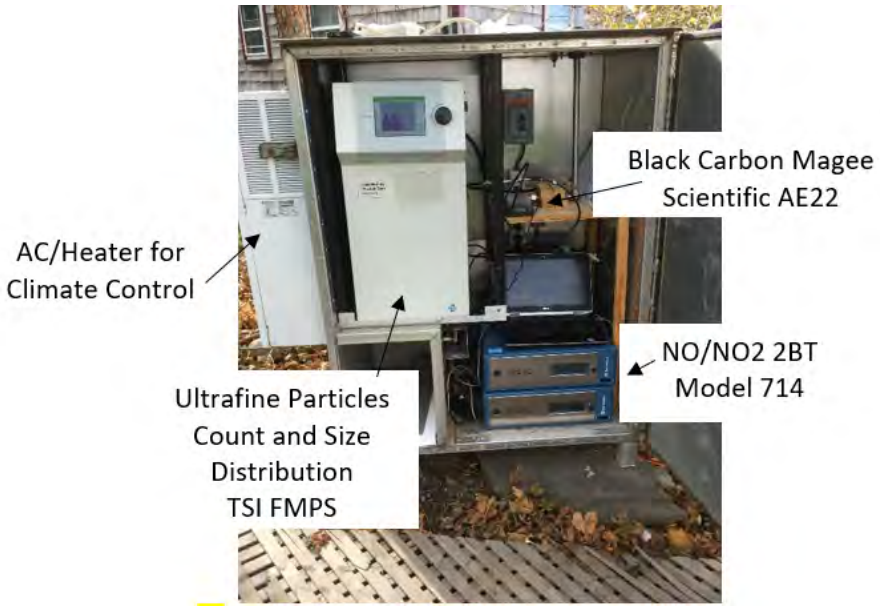

Figure 2. Long-term air pollution monitoring box at Winthrop, Massachusetts.

The monitoring enclosures are equipped with the following monitoring equipment:

- **Chelsea**
  - UFP – TSI CPC
  - NO/NO_2 – 2B Technologies
- **Revere**
  - UFP – TSI CPC
- **Winthrop**
  - UFP – TSI FMPS
  - NO/NO_2 – 2B Technologies
  - BC – Magee micro-aethalometer
- **South Boston**
  - UFP – TSI FMPS

Mobile Monitoring: TAPL Instruments

The monitoring instruments used in the TAPL are listed in Table 1. Measurements are acquired every 1 second to 1 minute. All instruments were factory-calibrated by the equipment manufacturers prior to the start of the campaign. Quality assessment (QA) measures were performed before each monitoring run, including a flow rate and zero-concentration check and instrument clock resets to the National Institute of Standards and Technology. Periodic side-by-side tests of the instruments are also performed as part of the QA process to determine instrument-specific measurement differences before data analysis.

Figure 3. Exterior and interior images of the Tufts Air Pollution Monitoring Laboratory (TAPL).

Table 1. Air pollution monitoring equipment in the Tufts Air Pollution Monitoring Laboratory (TAPL) used for this study.

Instrument	Parameter measured	Instrument flow rate (L/min)	Response time	Detection limit, sensitivity
TSI CPC (butanol-based) model 3775	UFP count, 4 nm–1 μm	1.5	< 9 s for 95% response	4 nm, < 0.01 particles/cm^3
TSI CPC (water-based) model 3783	UFP count, 7 nm–3 μm	3	< 3 s for 95% response	7 nm, < 0.01 particles/cm^3
Aerodyne CAPS NO_2	NO_2	0.85	8 s	0.3 ppb, < 0.1ppb
Magee Scientific aethalometer AE-33	BC	5	< 60 s	Proportional to time base and sample flow rate settings: approximately 0.03 μg/m^3 at 1 min, 5 L/min
LI-COR LI 840-A	CO_2/H_2O	~1	1 s	CO_2: 0 ppm, <1 ppm H_2O: 0 mmol/mol, <0.01 mmol/mol
Garmin GPSMAP 76CSx	GPS location	N/A	1 s	3 m

Data Acquisition and Data Processing

Data from the instruments are recorded in real time on a laptop in the TAPL. After each monitoring day, the data files are screened and collated in a master database. Air pollution measurements are matched to location by 1-s-interval GPS readings. The database then goes through a QA and quality check process, where the data are screened for errors flagged by instruments and quality criteria developed by the research team. Both the raw data and QA-processed database are stored on a secure server.

Monitoring Routes

Two monitoring routes that encompass the communities impacted by the most commonly used runways at Logan were developed: (1) a route to the north (north route) that includes all or parts of the communities of Winthrop, Revere, Chelsea, East Boston, and Lynn located 1–4 miles from the airport, and (2) a route to the south (south route) that includes all or parts of the communities of South Boston, Dorchester, and Quincy located 1–6 miles from the airport. The routes are shown in Figure 4. Criteria applied in determining the routes included (1) coverage of communities in proximity to the airport, (2) coverage under main flight paths, (3) spacing of transects underneath flight paths such that spatial gradients of air pollutants can be assessed over a large area, (4) ability to perform measurements on multiple transects in an area within a relatively

short period of time (1-2 hr) to capture both spatial and temporal changes in aviation impacts within the study area, and (5) ability to cover the entire route within the period associated with peak and off-peak flight activity periods (3-4 hr).

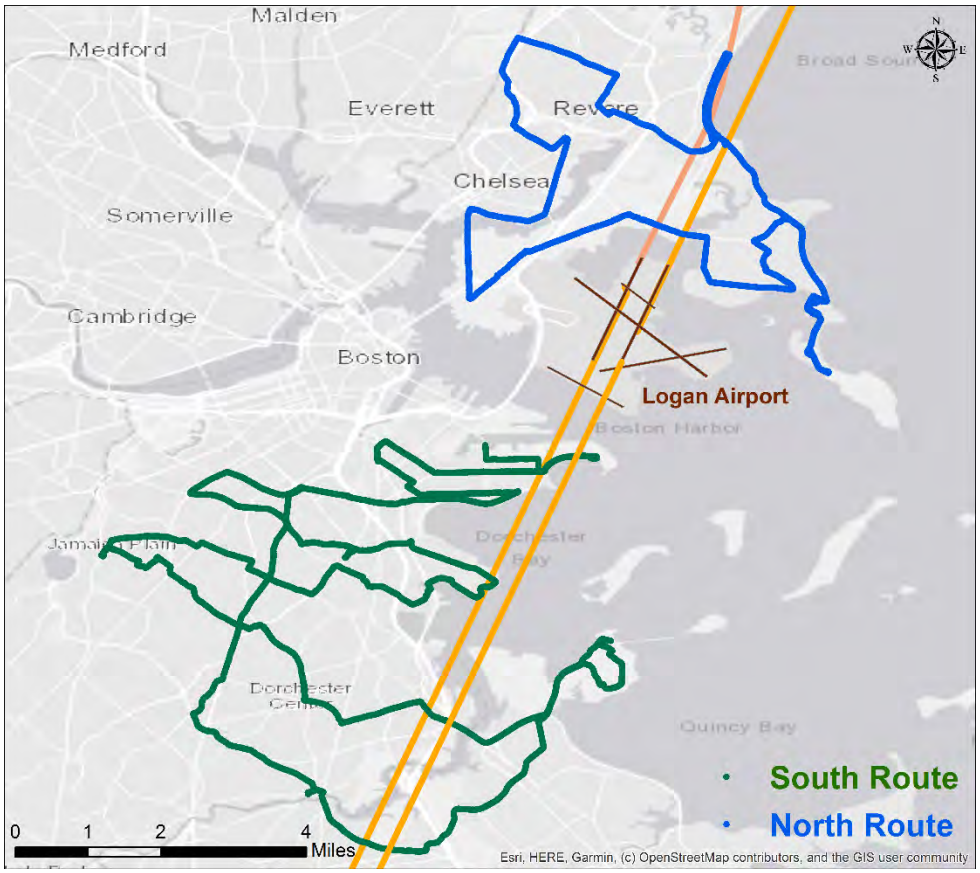

Figure 4. Map showing the north and south monitoring routes, the airport, and typical flight trajectories for arrivals on multiple runways at Logan Airport.

Beginning in May 2022, "adaptive" sampling routes were developed to complement the north and south routes. The spatial coverage of the adaptive routes is determined on a day-to-day basis based on observed and predicted wind direction and runway usage. As opposed to the routine routes, the adaptive routes cover a smaller geographic area but have a higher spatial resolution (Figure 5). The adaptive routes are selected based on the regions within the study domain expected to lie downwind of the airport on a given sampling day and are monitored to delineate and characterize impacts from LTO activities within neighborhoods downwind of Logan Airport.

Figure 5. Map showing an example of an adaptively selected route, the airport, and the prevailing wind direction observed during sampling.

Monitoring Schedule

Measurements are collected under a variety of meteorological and airport-activity conditions. We have adopted a purposeful, flexible monitoring approach rather than a rigid, repetitive schedule. The advantage of this approach is that it allows us to capture a much wider range of meteorological and airport-activity conditions and to thereby more fully characterize the main factors that influence aviation-related pollutant concentrations in the two study areas. The following criteria are being used to guide the monitoring schedule:

1. Maximal coverage of the periods of the day associated with peak and off-peak flight activity,
2. Coverage of the periods of the day associated with predictable diurnal variations in air pollution due to changes in meteorological factors (e.g., temperature, mixing height, onshore and offshore winds),
3. Coverage of the seasonal wind patterns (we are aiming to reasonably mimic the natural distribution [two-thirds westerly flow vs. one-third easterly flow] that is prevalent in the research area and are scheduling the monitoring runs to cover different wind speed/direction combinations),
4. Coverage of various temperature regimes (e.g., seasonal and diurnal), and
5. Coverage of various active runway configurations.

Mobile Monitoring Protocol

During the 2021–2022 period, mobile monitoring has continued, but at a lower frequency and with increased emphasis on delineating and characterizing impacts in communities downwind of the airport. The decision of where and when to monitor is based on weather, current flight activity patterns, and arrivals and takeoffs for the day of sampling. Route selection is being designed to maximize variations in meteorology and LTO activity over a community to inform regression modeling. The standard operating procedure for preparation of a mobile monitoring route (see Figure 6) begins with (a) checking weather conditions including wind direction and speed are used by Massport, (b) checking a real-time flight tracker to identify flight paths and which communities are being flown over, (3) preparing monitoring equipment and driving to the starting point of the route, and (4) driving the route and subsequently downloading data. Data are cleaned weekly and integrated with the stationary monitoring data platform at BUSPH.

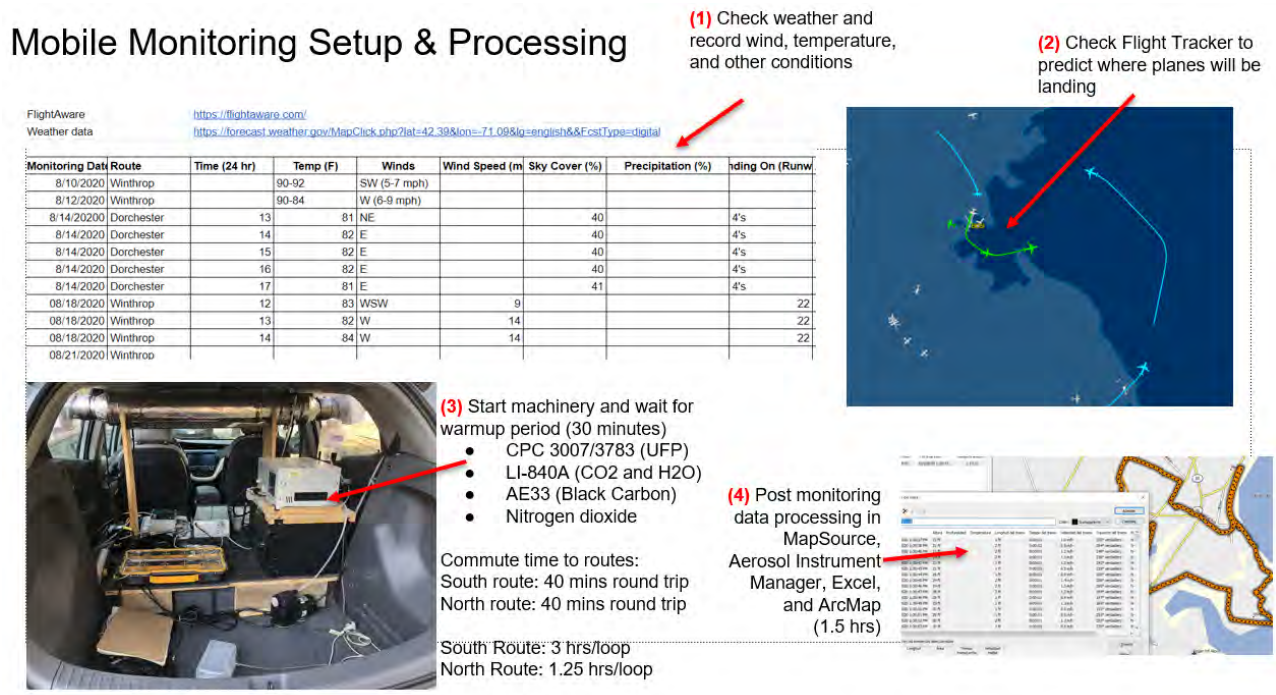

Monitoring Dat	Route	Time (24 hr)	Temp (F)	Winds	Wind Speed (m	Sky Cover (%)	Precipitation (%)	nding On (Runw
8/10/2020	Winthrop		90-92	SW (5-7 mph)				
8/12/2020	Winthrop		90-84	W (6-9 mph)				
8/14/20200	Dorchester	13	81	NE		40		4's
8/14/2020	Dorchester	14	82	E		40		4's
8/14/2020	Dorchester	15	82	E		40		4's
8/14/2020	Dorchester	16	82	E		40		4's
8/14/2020	Dorchester	17	81	E		41		4's
08/18/2020	Winthrop	12	83	WSW	9			22
08/18/2020	Winthrop	13	82	W	14			22
08/18/2020	Winthrop	14	84	W	14			22
08/21/2020	Winthrop							

Figure 6. Standard operating procedure for mobile monitoring route preparation.

Major Accomplishments

As of October 2, 2022, we have completed two full years of ambient stationary monitoring and have implemented QA and quality control (QC) procedures on the data. Field tests and side-by-side comparisons are periodically performed to compare CPCs for low and high air pollution scenarios and include recently factory-calibrated instruments. These tests will continue to be conducted every six months or when a monitor requires factory recalibration. Data from the stationary monitors have been compiled and merged with meteorological data. Figure 7 provides a polar plot for two of our stationary monitoring locations as an example of the UFP data being collected. Although formal statistical analyses are still underway, we observe meaningful variation in the PNC as a function of times of day with limited LTO activity (top panels) versus regular LTO activity (bottom panels), with higher PNC levels corresponding to times with regular flight activity and when the dominant wind direction is from the airport. Regression analysis with flight activity needs to be conducted to better understand the contributions from aviation activities (e.g., LTO vs taxiing and ground transport vehicles).

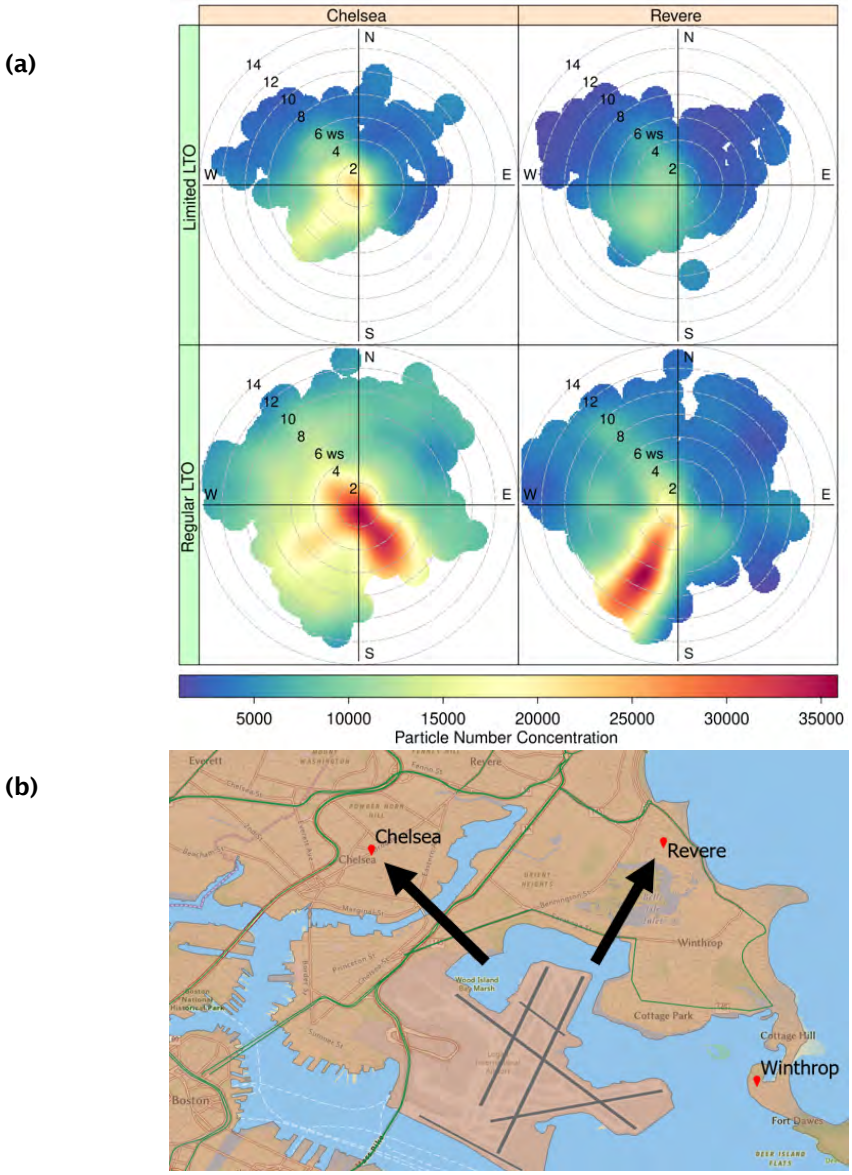

Figure 7. (a) Polar plot of particle number concentration at Chelsea (left) and Revere (right) stationary monitoring locations as a function of limited LTO activity (top) and regular LTO activity (bottom) and wind direction; and **(b)** area map showing Chelsea and Revere monitoring sites relative to Logan Airport, with black arrows indicating when each site was downwind of Logan.

Mobile monitoring has been performed representing a wide variation of meteorology and ramp-up of aviation activities following COVID-19. Table 2 provides a breakdown of the number of days sampled during different months of the year after the full launch of the simultaneous mobile and stationary monitoring platform.

Table 2. Number of mobile monitoring sampling runs by month and year.

Mobile Monitoring Runs: South Route

Year	Dec-Feb	Mar-May	Jun-Aug	Sept-Nov
2020			2	5
2021	16	21	16	8
2022	9	10	2	6
Total	**25**	**31**	**20**	**19**

Mobile Monitoring Runs: North Route

Year	Dec-Feb	Mar-May	Jun-Aug	Sept-Nov
2020			4	15
2021	18	23	16	9
2022	10	11	7	
Total	**28**	**34**	**27**	**24**

Comparison of Meteorology During Stationary and Mobile Monitoring

We aim to capture the meteorology in a representative manner in both our mobile and stationary monitoring campaigns. The wind rose plots in Figure 8 show the wind speed and wind direction distribution for (a) average daily wind speed and direction at Logan Airport, (b) mobile monitoring average wind speed and direction by sample days, and (c) mobile monitoring average wind speed and direction by sample hour. Moving forward, mobile monitoring will be conducted purposefully to address any gaps in meteorology representativeness (e.g., southwest winds).

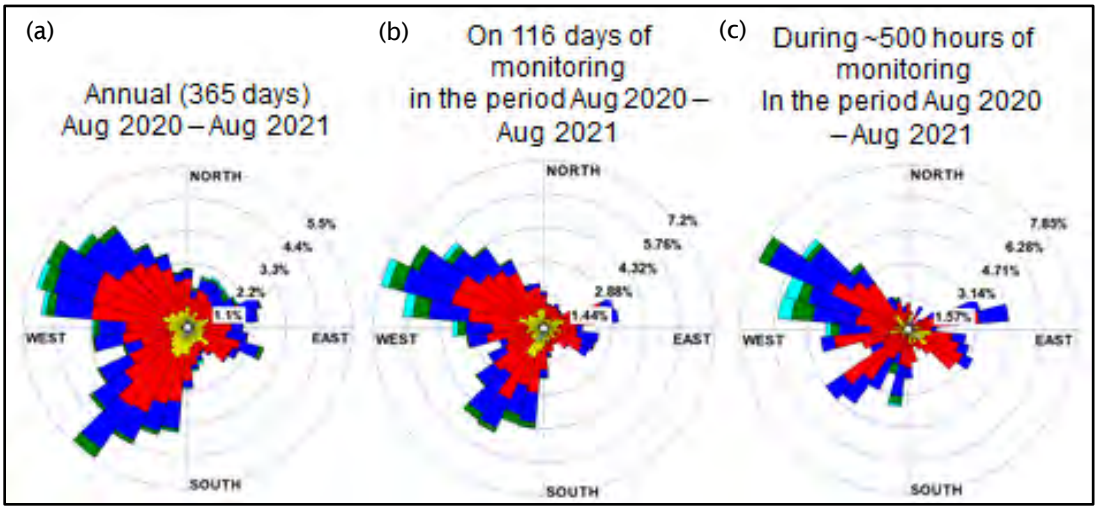

Figure 8. Comparison of long-term stationary and mobile monitoring data meteorology by days and hours.

Mobile Monitoring Maps

Figure 9 presents PNC data from our mobile monitoring routes with consistent prevailing winds throughout the sampling period that would allow for a descriptive understanding of the meteorological impacts on PNC distribution. In Figure 9, maps A and B were obtained from the northern portion of the study area and include a map of the routine monitoring route case (Fig. 9a; map A) and an adaptive monitoring route case (Fig. 9b; map B). In map A, the stationary platforms for Revere, Winthrop, and Chelsea are downwind, upwind, and upwind of Logan Airport, respectively. Also shown in map A is a time series plot of UFP measurements collected by the mobile platform and the three stationary sites in the northern portion of the study area. The time series indicates excellent agreement between TAPL-derived measurements and all three stationary platform measurements during times when TAPL was nearby each of the three sites (boxes 1, 2, and 5, respectively). The map also indicates additional UFP hotspots indicative of both aviation (box 3) and non-aviation (box 4) sources. Flight trajectory data for arriving (red airplanes) and departing (blue airplanes) flights are also shown. In Fig. 9b, an example of an adaptively selected mobile monitoring route is shown under conditions of easterly winds when the East Boston portion of the study domain would be expected to be downwind of airport emissions. In this example, adaptive high-spatial-resolution mobile monitoring was performed in areas both downwind and not downwind of the airport in order to confirm the absence of aviation-driven UFP increases in neighborhoods outside of the downwind region. This map illustrates the utility of the adaptive monitoring approach in delineating the downwind region of the study area and providing high-spatial-resolution characterization of the spatial extent and magnitude of impacts.

(a)

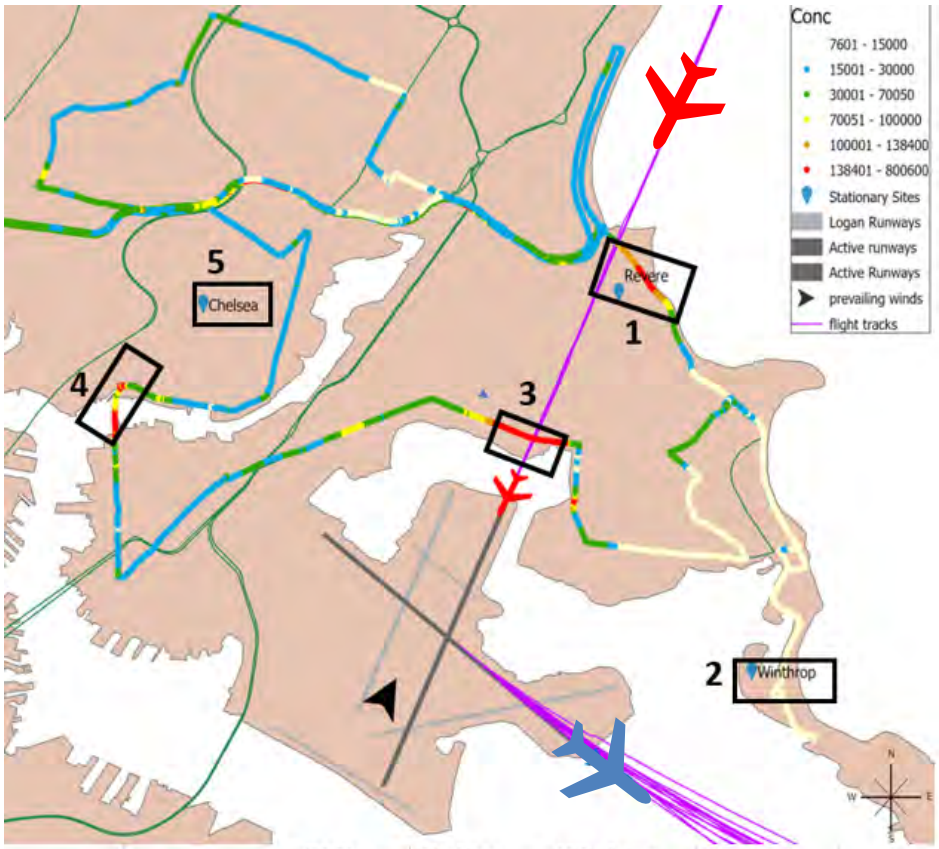
Conc
7601 - 15000
15001 - 30000
30001 - 70050
70051 - 100000
100001 - 138400
138401 - 800600
Stationary Sites
Logan Runways
Active runways
Active Runways
prevailing winds
flight tracks
Chelsea
Revere
Winthrop
1
2
3
4
5

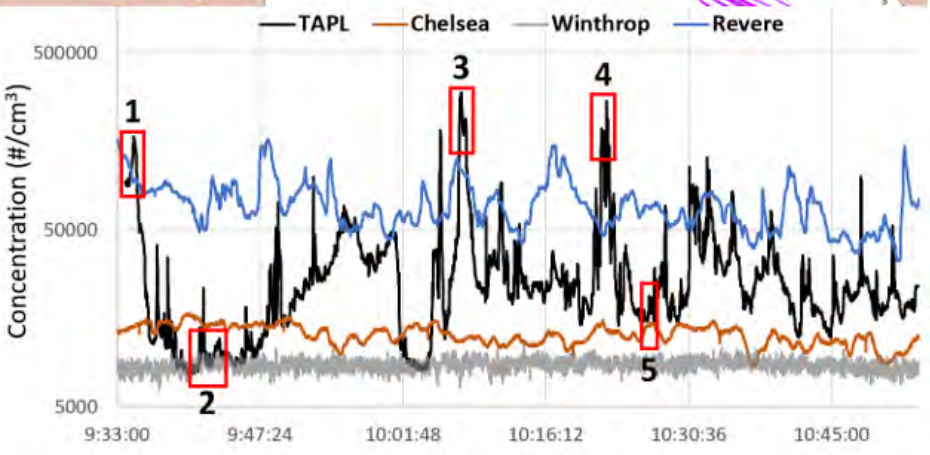
TAPL
Chelsea
Winthrop
Revere
Concentration (#/cm³)
500000
50000
5000
9:33:00
9:47:24
10:01:48
10:16:12
10:30:36
10:45:00
1
2
3
4
5

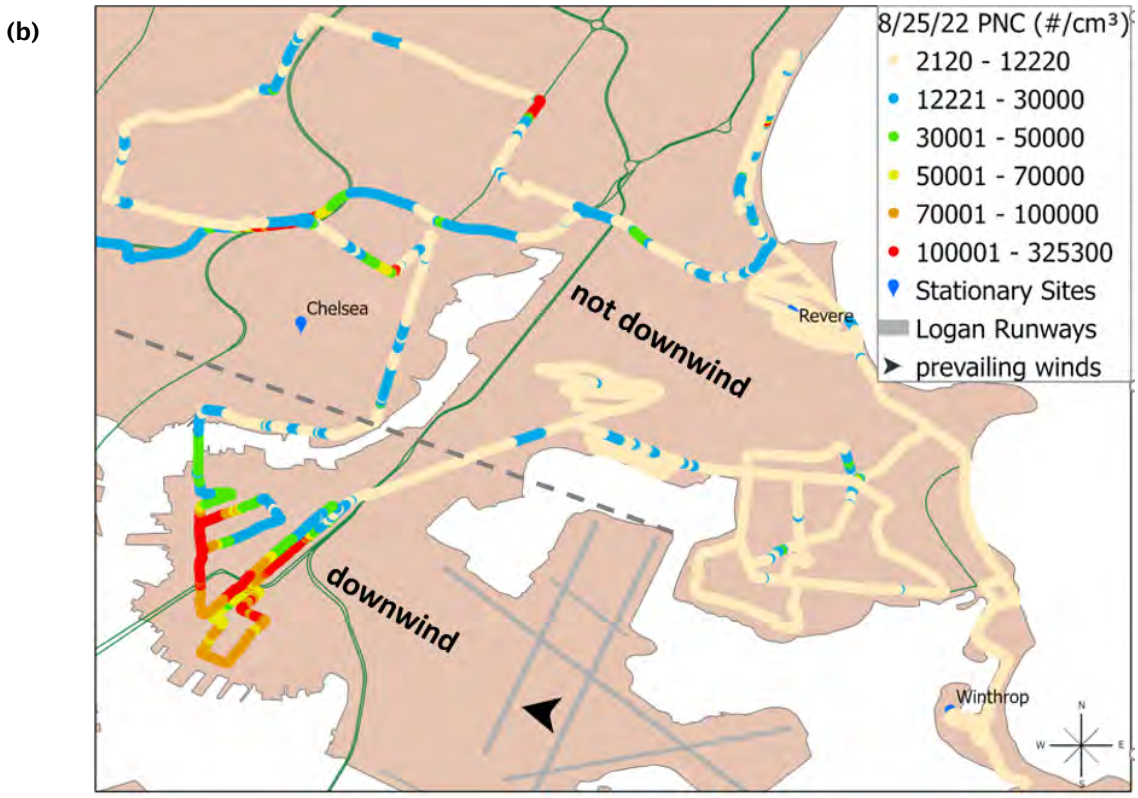

Figure 9. Mobile monitoring particle number concentration (PNC) maps showing routine **(a)** and adaptive **(b)** routes in the northern portion of the study area.

Milestone(s)

In addition to our major accomplishments, we have also completed the following milestones:

- Obtained permission to continue monitoring at each stationary site
- Completed annual manufacturer cleaning and calibration of the CPCs and FMPS, and performed a side-by-side PNC calibration
- Designed and implemented monitoring routes and protocols to integrate mobile monitoring for community measurements of aviation-related UFPs, including adaptively selected routes for more detailed characterization of aviation impacts on downwind communities
- Compiled data for wind rose plotting and for inclusion in UFP regression modeling
- Characterized differences in typical UFP concentrations in downwind and nondownwind locations within the study area as a function of observed variations in drivers of UFP variability (e.g., temperature, wind speed, time of day)

Publications

None.

Outreach Efforts

None.

Awards

None.

Student Involvement

Sean Mueller, a doctoral student involved in this study, has been analyzing descriptive statistics of the stationary monitoring data. Olivia Moore, Isabelle Woollacott, and Lily Sandholm, undergraduate students at Tufts University, have been assisting with the collection and processing of stationary site monitoring data. Research associate Dr. Tiffany Duhl is leading the mobile monitoring and data processing effort.

Plans for Next Period

As proposed tasks for the next study period (October 1, 2022 to September 30, 2023), we will continue monitoring at our stationary sites and will add NO_2 and SO_2 to our monitoring efforts. Validation and refinement of aviation-specific air pollution dispersion models require (1) the collection of monitoring data, (2) the use of federal reference methods and/or federal equivalency methods, and (3) the application of statistical approaches for source attribution. In addition, we will continue mobile monitoring, with an increased emphasis on adaptive monitoring as well as characterizing spatial variations in NO_2.

Task 2 - Incorporate NO_2 and SO_2 Federal Equivalency Methods and/or Federal Reference Methods at Monitoring Sites to Inform Our Understanding of Aviation Contributions to Community Air Pollution Relative to Background Sources

Boston University School of Public Health

Objective(s)

In this task, we aimed to incorporate FEM and/or FRM established by the Environmental Protection Agency for surveillance and monitoring of NO_2 and SO_2 at the Chelsea and Winthrop monitoring sites using the 2B Technologies model 405 nm NO_2/NO/NO_x monitor.

Research Approach

We deployed two 2B Technologies model 405 nm NO_2/NO/NO_x monitors at the stationary monitoring platforms in Chelsea and Winthrop. Two devices, referred to as instrument A and instrument B, were placed at each site and began collecting data on June 10, 2021. Device malfunctions necessitated that we pause collection in December 2021; however, these errors have since been resolved and collection began again on May 20, 2022. These instruments collect NO_2 samples (in ppb) at 5-s intervals. These data were downloaded at regular intervals from the devices and combined with meteorology data from Boston Logan Airport, sourced from the Automated Surface Observing System. Regression analysis was conducted to determine the impacts of seasonality and weather events on NO_2/NO/NO_x contributions from aviation sources.

Milestone(s)

The core milestones for Task 2 include incorporating NO_2 and SO_2 concentrations into our monitoring campaign, deploying the NO_2 monitoring instruments in the field, troubleshooting and ultimately resolving device malfunctions in the field, and conducting preliminary analyses of these data.

Major Accomplishments

We successfully integrated monitoring of NO_2/NO/NO_x and SO_2 into our Year 2021–2022 monitoring campaign.

The 2B Technologies model 405 nm NO_2/NO/NO_x monitor measures NO through selective conversion using the highly selective reaction of NO with ozone. NO_2 is measured directly by absorbance, using a folded cell with corner mirrors to produce a long absorbance path of ~2 m to improve sensitivity. NO_x is calculated by adding NO and NO_2. Measurements are collected at 5-s sampling intervals.

Preliminary analysis shows a relationship between seasonality and NO_2/NO_x concentrations; this relationship was not observed with NO. Figures 10a and 10b below illustrate this relationship.

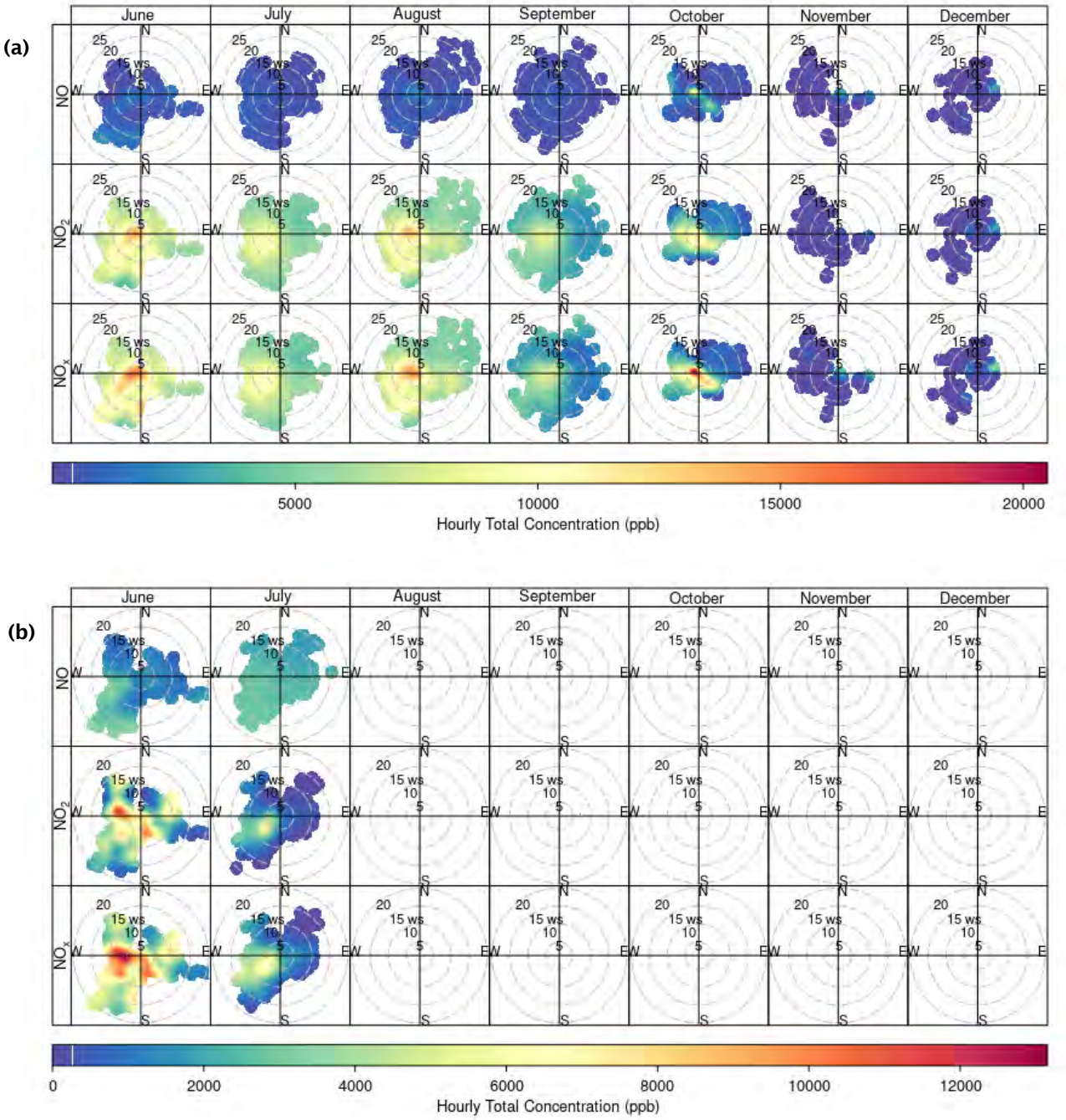

Figure 10. Polar plots showing $NO/NO_2/NO_x$ concentrations from June 2021 to December 2021 from **(a)** instrument A, and **(b)** instrument B .

Publications

None.

Outreach Efforts
None.

Awards
None.

Student Involvement
None.

Plans for Next Period
We have purchased two NO_2 and SO_2 analyzers and will be launching these at our new sites to collect data as outlined in Task 3.

Task 3 - Establish a New Monitoring Site Close to the Airport Fenceline to Better Characterize the Contribution From Ground-Based Aviation Emissions, Supported by ASCENT Project 19 in Decision-Making for Monitor Siting
Boston University School of Public Health

Objective(s)
We have focused on designing an air pollution monitoring study that will enable us to identify contributions from arriving aircraft to ambient air pollution in a near-airport setting. The objective of this task is to determine the impact of aircraft emissions, particularly in-flight arrival and departure emissions, to ground-level UFP concentrations at stationary monitoring sites located within 0.25 to 0.5 miles of the airport.

Research Approach
Two additional stationary monitoring sites (Figures 11a and 11b) have been systematically selected, considering distances from the airport and laterally from each flight path and excluding locations close to major roadways or other significant sources of combustion. These sites are complementary to our existing stationary monitoring sites and were specifically chosen to be close to Boston Logan Airport in order to isolate the contributions of in-flight aircraft (as illustrated in Figure 12) and to characterize the spatial gradient of pollutant concentrations as a function of distance to Logan Airport. PNC (a proxy for UFP) monitoring instruments will be established at each monitoring site as well as instruments for monitoring nitrogen oxides and (at one location) sulfur dioxide.

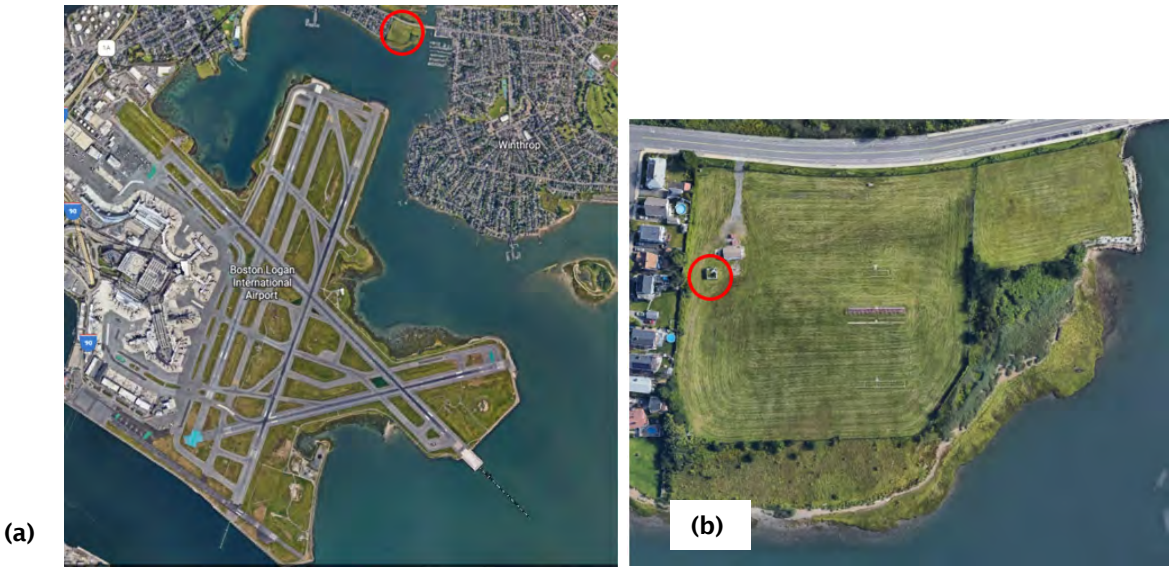

Figure 11 (a) and **(b).** Locations of stationary site on Saratoga St. FAA/Massport site in Winthrop, Massachusetts.

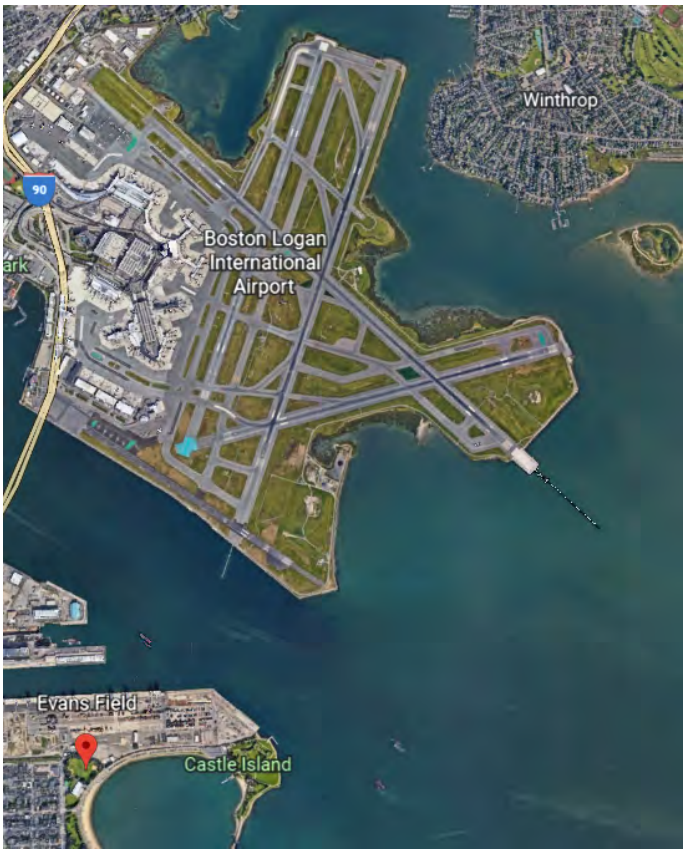

Figure 12. Location of stationary site (red pin) on Department of Conservation and Recreation property site in South Boston, Massachusetts.

Milestone(s)
The appropriate research permit applications have been submitted to property owners, including the Massachusetts Department of Conservation and Recreation, Massport, and FAA. Weatherproof instrument boxes have been built and are being fitted with gas- and particle-phase instruments in anticipation of immediate deployment once the necessary permits have been obtained.

Publications
None.

Outreach Efforts
None.

Awards
None.

Student Involvement
Sean Mueller, PhD student at Boston University

Plans for Next Period
We will complete the approval process and furnish these new sites with proper equipment to begin active air monitoring. With these data, we will attempt to isolate aviation-specific PNC patterns at these new sites for comparison to existing data capture and analysis.

Task 4 - Compile from FAA Essential Flight Activity and Meteorological Covariates Needed for Regression Modeling Under Project 18 and Dispersion Modeling Under ASCENT Project 19 Using a Data-Sharing Platform
Boston University School of Public Health

Objective(s)
We are currently analyzing data from the 2017 stationary site monitoring campaign to provide insight regarding the ability of statistical analyses of real-time UFP concentration measurements to capture arrival aircraft source contributions to UFPs, providing a roadmap for future investigations. Thus far, our analyses indicate that we can explain significant variability in UFPs across multiple monitoring sites, with statistically significant terms for aviation flight activity as well as meteorology and other site attributes. We are also examining the contribution of aviation activity to UFP concentrations in communities. This task includes the concurrent collection of UFP concentrations at multiple sites, with sites selected specifically for the purpose of aircraft source attribution, the application of insight about detailed flight activity tracks, and the use of statistical methods to separate the aviation signal from other sources of UFPs.

Research Approach
A new data repository system has been created to house the ASCENT 18 project data. It was created using a strict folder and file structure as well as metadata guidelines so that raw, in process, and cleaned project data are well organized, easy to maneuver between, and intuitive to use for new project team members. This data repository also includes the relevant cleaning code used to prepare, aggregate, and summarize the data so that there is a record of all cleaning processes archived with the data sources themselves. This will aid in and speed future data sharing, manuscript writing, and analyses needs for the project team. This data repository is housed on the Boston University Shared Computing Cluster (SCC), a supercomputing environment with both immense storage capacity and substantial computational power. The co-location of data and code and the integration with the analysis platform allows ASCENT 18 team members to actively collaborate on analyses in a single environment. This system functions as an integrated data storage, collaborative computing, and data-sharing platform for our ASCENT 18 data and analyses.

Total PNC data collected from the ASCENT 18 stationary monitoring programs around Boston Logan have been completely prepared, cleaned, aggregated, merged with relevant meteorological data, and summarized for the seven stationary monitoring sites active in 2017. Team members are currently working to accomplish the same for all total PNC and NO_2 data collected at our four current stationary monitoring sites for all recent years until the ongoing collection in 2022.

ASCENT 18 project team has continued to share data, code, and other analysis resources with the ASCENT 19 team by adding members to the aforementioned SCC environment. Specifically, ASCENT 18 has prepared and shared all of our cleaned PNC data from the seven stationary monitoring sites located around Boston Logan Airport active in 2017, already merged with relevant meteorological data aligned and summarized at an hourly resolution. We have also shared all of the highly resolved flight data from both the FAA Performance Data Analysis and Reporting System (PDARS) and Terminal Radar Approach Contol (TRACON) systems for Boston Logan Airport, which encompass data for the years 2017, 2020, 2021, and 2022. Last, we have made available several spatial GIS shapefiles, including the spatial location of all retired and new monitoring sites and the footprint of all Boston Logan runways.

Milestone and Major Accomplishments
A new data storage organization system for ASCENT 18 project data was created and implemented to support data archival, data sharing, and collaborative analyses.

Members of the ASCENT 19 team have been added to the ASCENT 18 data platform to facilitate the easy sharing of project data to support both teams' goals.

Publications
None.

Outreach Efforts
None.

Awards
None.

Student Involvement
Sean Mueller, PhD student at Boston University

Plans for Next Period
We will continue to obtain and compile flight activity, meteorology and air pollution data and compile into formats to support the ongoing work of ASCENT Projects 18 and 19.

Task 5 - Apply Regression Modeling Techniques to Monitoring Data Previously Collected Under Project 18 to Determine the Contributions of Aviation Sources to UFP and NO_2 Concentrations
Boston University School of Public Health

Objective(s)
We conducted a monitoring campaign to inform an aviation source attribution analysis as an expansion of the regression model development. In our 2021 report, we presented a preliminary analysis of the impact of the COVID-19 pandemic's mobility restrictions on ambient PNC to evaluate time trends and contributions from various transportation sources. In this year's report, we present our published analysis and present preliminary analysis on regression model development. Our goals are as follows:

1. Utilize the pandemic natural experiment to understand the impact of emissions reduction of transportation sources on ambient PNC in a near-airport setting.
2. Conduct machine learning regression to predict mean PNC and evaluate important feature classes for model prediction.

Research Approach

Utilizing air pollution, flight activity, and meteorological data collected across multiple monitoring campaign years under ASCENT Project 18, we developed insights as part of our ongoing analyses of stationary site monitoring data collected during our initial 2017 monitoring campaign through June 2021 by using the differential emissions profiles during the pandemic in primary UFP sources (i.e., roads and aviation) to inform source attribution. We began by analyzing concentrations as a function of wind conditions and flight activity to help inform the structure and form of subsequent regression models. The contributions of aircraft to ambient UFP concentrations were examined by comparing measurements obtained before the COVID-19 state of emergency (SOE) declaration in Massachusetts (before April 2020), during the COVID-19 SOE (April to June 2020), and after the SOE (July 2020 to June 2021). To control for seasonality and meteorology in the dataset, we performed a stratified analysis (comparing April to June across the three time periods). The results of this work were used to inform the formation of a machine learning regression model to predict and apportion ambient PNC. Machine learning regression models were also trained and assessed across monitoring sites to study variation in prediction and apportionment and to improve model generalizability.

Milestones

- Published the natural experiment emissions reduction impact manuscript in *Environmental Science and Technology Letters*
- Completed regression modeling analysis of aviation-related contributions to community-level UFPs and presented our findings at conferences
- Drafted two additional manuscripts for submission on generalized regression modeling of aviation-related UFPs and machine learning regression modeling of UFPs
- Presented multi-site machine learning methods at 2022 Joint Statistical Meetings

Major Accomplishments

Stationary Monitor Analysis of the COVID-19 Lockdown Period by Wind Direction

Here, we present select results of the analysis of the monthly distribution of PNC compared with changes in source activity levels before and during the COVID-19 lockdown. Figure 13 identifies the Chelsea monitoring site in relation to the airport. The Chelsea site is located approximately 3 miles north of Logan International Airport.

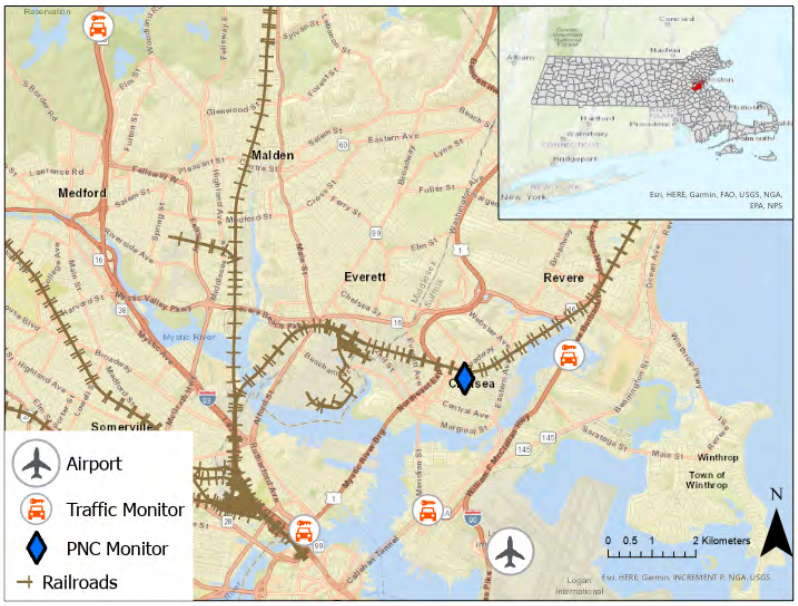

Figure 13. Map of the Chelsea monitoring site.

We have leveraged a set of UFP measurements in a community near a major airport across multiple years to evaluate time trends and contributions from transportation sources to analyze PNC patterns before and during the COVID-19 pandemic to ascertain changes in transportation sector contributions. We utilized high-temporal-resolution data, including wind speed and wind direction data, to discern impacts from aviation activity, an intermittent but impactful UFP source. Data collected prior to August 2017 were recorded at 30-s averaging periods, with subsequent data recorded at 1-s averages. Processed data were aggregated to hourly resolution (n = 41,904 hr) and merged with flight activity (landings, takeoffs, and sum of LTO), meteorological data, and MADT. Data were classified into impact sector or nonimpact sector depending on whether the hourly average wind direction positioned the site downwind of the airport. Impact sector was defined as 135° to 175° based on the azimuth angle of the site to the widest span of runways. Figure 14 presents a comparison of data analyzed during the study period, showing substantial reductions in both vehicle and flight activity during the pandemic period.

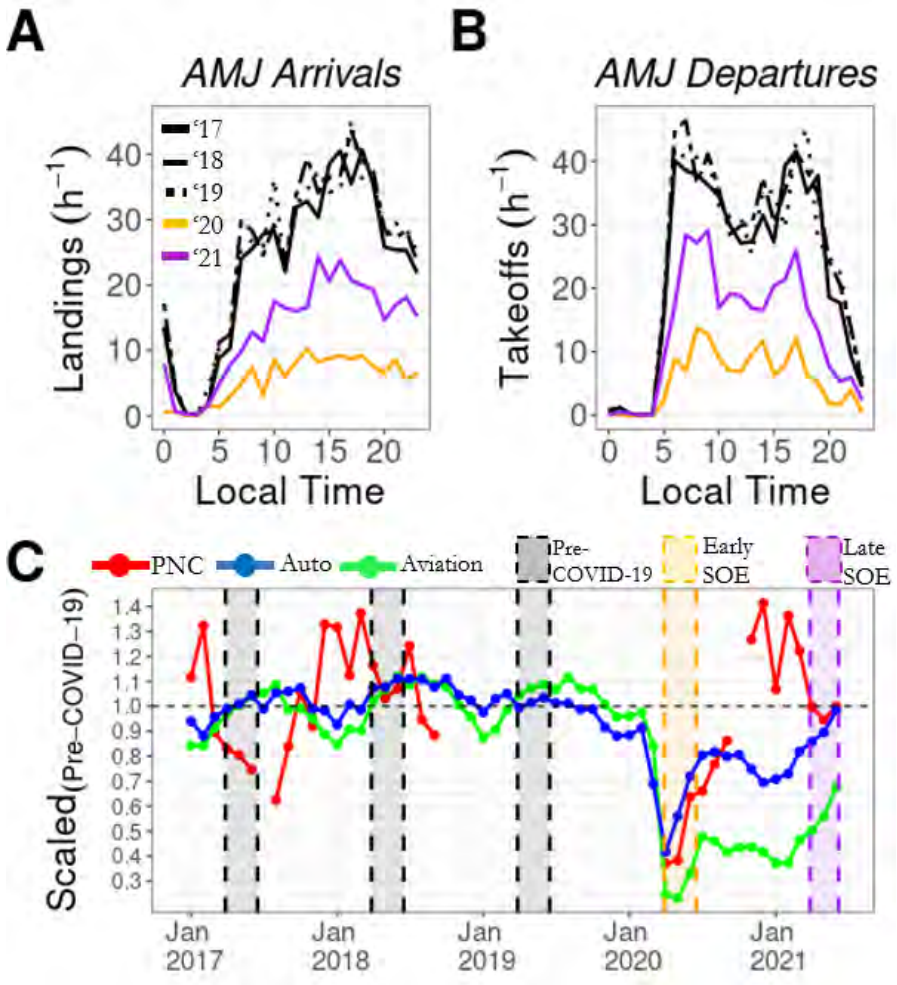

Figure 14. Landings and takeoffs per hour for (A) arrivals and (B) departures at Logan Airport from 2017 to 2021 for the months of April, May, and June (AMJ). (C) Time series for particle number concentration (PNC; particles/cm^3) for all wind directions, automobile traffic at US 1 Boston Tobin (AET15, monthly average daily traffic), and combined landings and takeoffs (operations h^{-1}) scaled by pre-pandemic mean (before March 10, 2020). Points represent the monthly average of the pre-pandemic mean scaled value per respective time series. Highlighted boxes within the dotted lines represent the time periods selected for analysis, AMJ 2017–2019 (black), AMJ 2020 (orange), AMJ 2021 (purple). Adapted from Mueller et al. (2022). SOE, state of emergency.

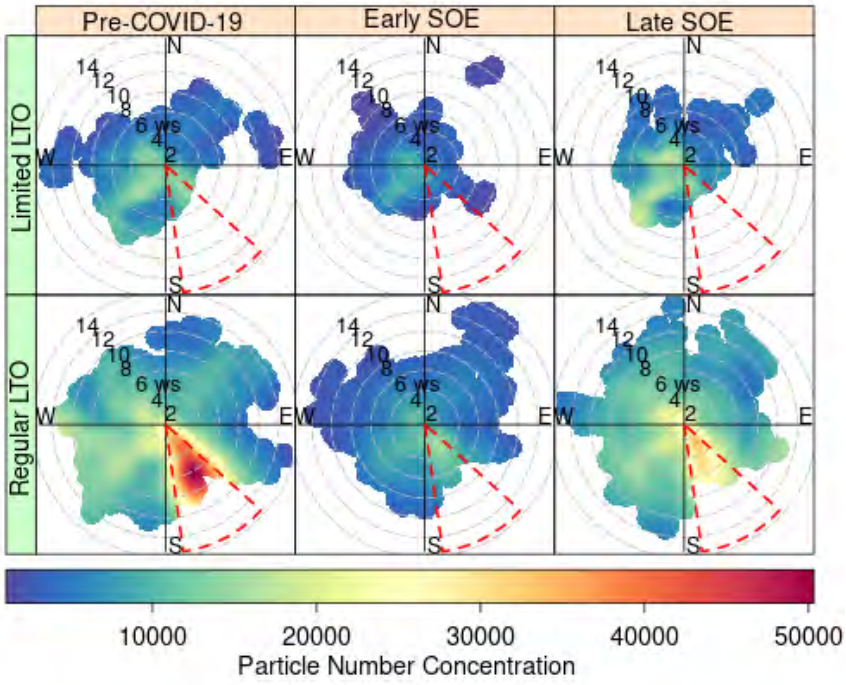

Figure 15. Polar plots showing the interactions between the hourly mean particle number concentration (PNC; particles/cm^3) during April, May, and June (AMJ), wind speed (ms^{-1}), and wind direction. Columns subset data by pre-pandemic levels (mean AMJ of 2017 and 2018), in the early months of the Massachusetts state of emergency (SOE) (AMJ 2020), and a year later (AMJ 2021), and rows subset by periods of limited landing and takeoff (LTO) (0100–0400) and regular LTO (0500–0000). Dotted red lines represent winds from the aviation impact sector. Variations in plot shape are a function of wind speed and wind direction, whereas variations in color are a function of PNC. Adapted from Mueller et al. (2022).

Although formal statistical analyses are still underway, we can observe in Figure 15 lower PNC values for April–August in 2020 compared with 2017 or 2018. Regression analysis with flight activity needs to be conducted to examine the contributions from aviation activity versus other sources during the pandemic.

To quantify the change in air pollution and transportation sector activity during the pandemic, we compared during-pandemic data to pre-pandemic data on a month-by-month basis to control for seasonal variations between the three time periods. The dramatic decrease in transportation sector activity in response to the COVID-19 pandemic provided a natural experiment by which we could better understand the emissions reduction impact of transportation sources on ambient PNC in a near-airport setting. During the early months of the COVID-19 pandemic, we observed that PNC was dramatically reduced (48% on average, for all wind directions) near an international airport and that daytime PNC was similar to pre-pandemic PNC during nighttime hours with no flight activity. In addition, we observed that mean PNC mirrored automobile ground traffic volume patterns throughout the pandemic, but under wind conditions that placed the monitor downwind from the airport, mean PNC more closely followed flight activity volume patterns. The fact that the two predominant source types in a near-airport setting had different activity profiles and different associations with wind speed and direction allowed us to better differentiate their relative impacts on ambient PNC. Although the highest PNC was observed when the site was downwind from the airport throughout the study period, the difference between downwind and non-downwind PNC was negligible during the early SOE, providing a sharp contrast to clearly indicate airport contributions under aviation impact sector winds.

To explicitly quantify the effect of aviation operations on ambient UFP while controlling for other important variables informed from our descriptive analysis (meteorology, automobile traffic, etc.), we are building regression models using machine learning algorithms. Machine learning methods provide strong UFP predictive capabilities compared with traditional

regression approaches but have not been used to characterize aviation contributions to UFP. Preliminary analysis of the association between aircraft arrivals and departures, respectively, with ambient UFP concentrations shows that the relationship is complex and nonlinear (Figure 16).

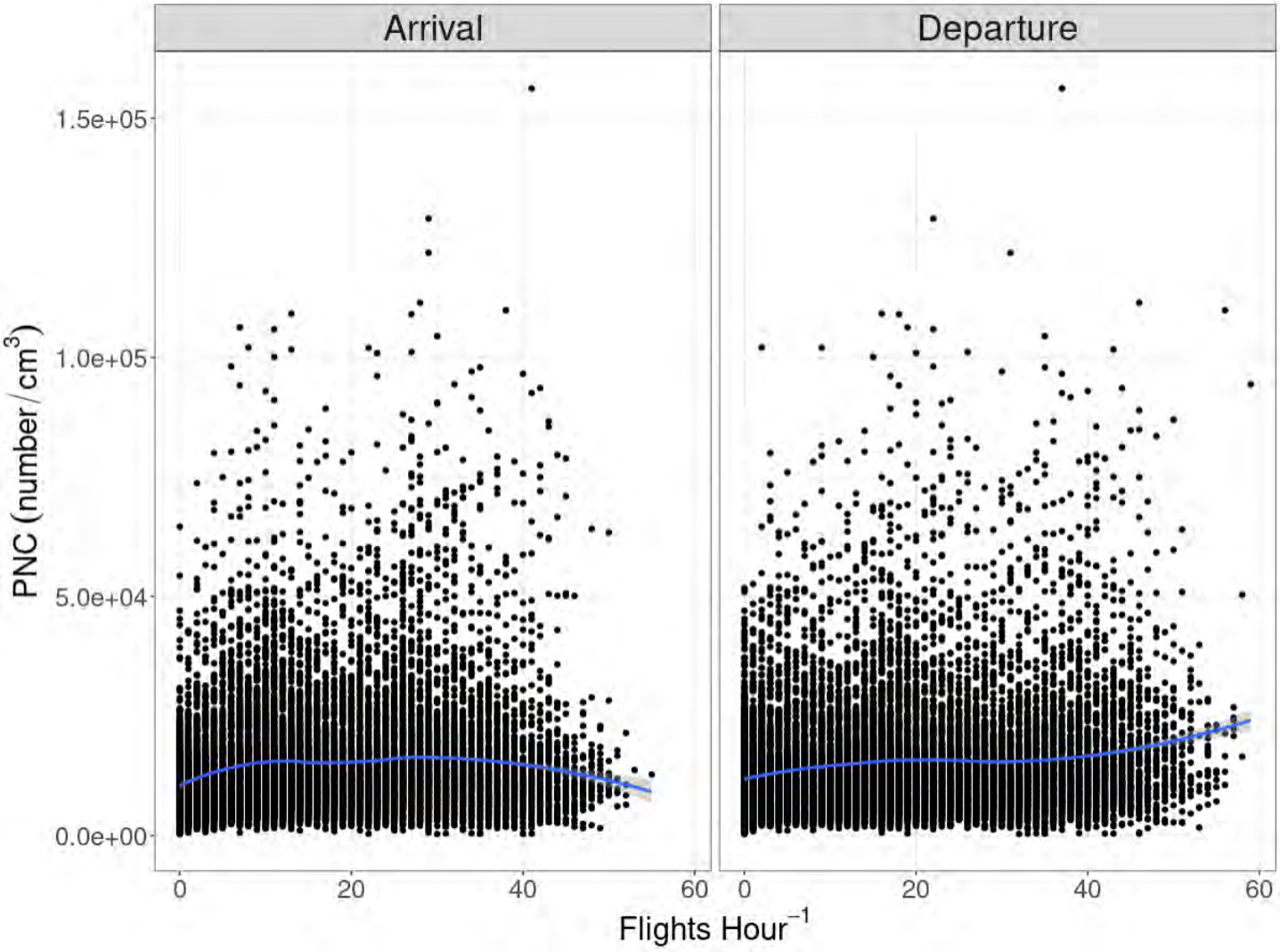

Figure 16. Preliminary analysis of association between landing and takeoff operations on ambient particle number concentration (PNC).

Given that the relationship between aircraft operations and ambient UFP is nonlinear and our COVID-19 analysis showed that interactions between predictor variables exist (e.g., wind speed and wind direction), we need a model that can handle many predictor variables and has no underlying distributional assumptions. We therefore chose to model ambient UFP as a function of meteorology, flight activity, and automobile traffic with the random forest algorithm. The random forest machine learning algorithm is an ensemble method that uses bootstrapped aggregated decision trees to predict ambient UFP from a combination of predictor variables. In brief, the method builds a series of decision trees from the data where, at each decision tree split, only a random sample of predictors are allowed to be chosen for the next split (hence, the "random" in the random forest algorithm). The effect of the random predictor feature in the method is that it prevents overfitting and thus improves predictive performance. Approximately 15,000 hours of UFP measurements from January 2017 to June 2021 were regressed against 26 predictor variables, with 75% of the dataset training the model via the random forest algorithm and 25% used for

testing the model. The model was trained with 10-fold cross validation repeated three times. Preliminary models indicate that UFP can be predicted from transportation activity and meteorology (R^2 = 0.40–0.60, root mean square error = 6,000–8,000 particles/cm^3). The most important predictor of UFP before the pandemic was whether the site was downwind of the airport (Figure 17). In pre-pandemic models that only considered time periods when the monitoring site was downwind of the airport, flight activity was the most important predictor of UFP. In contrast, for the COVID-19 period, being downwind of the airport and flight activity had less explanatory power, with UFP concentrations best explained by meteorology.

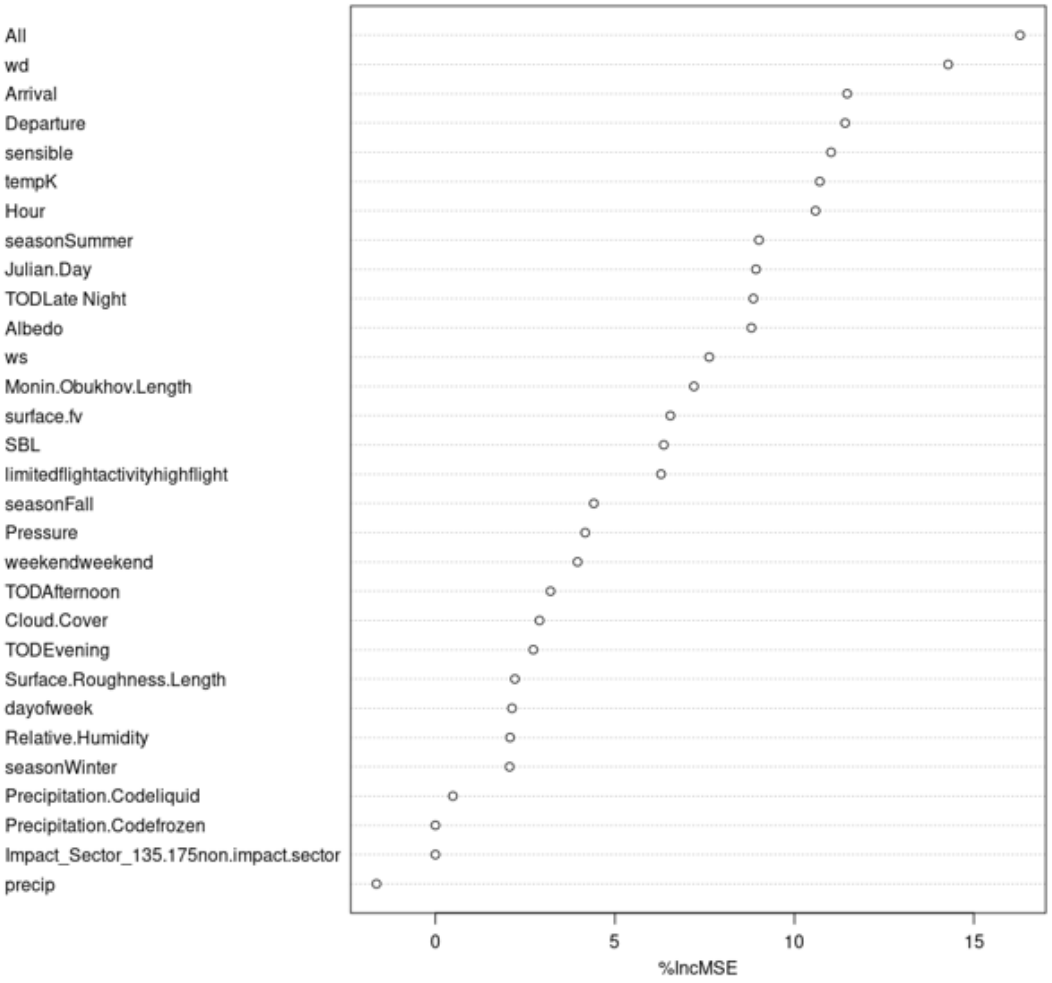

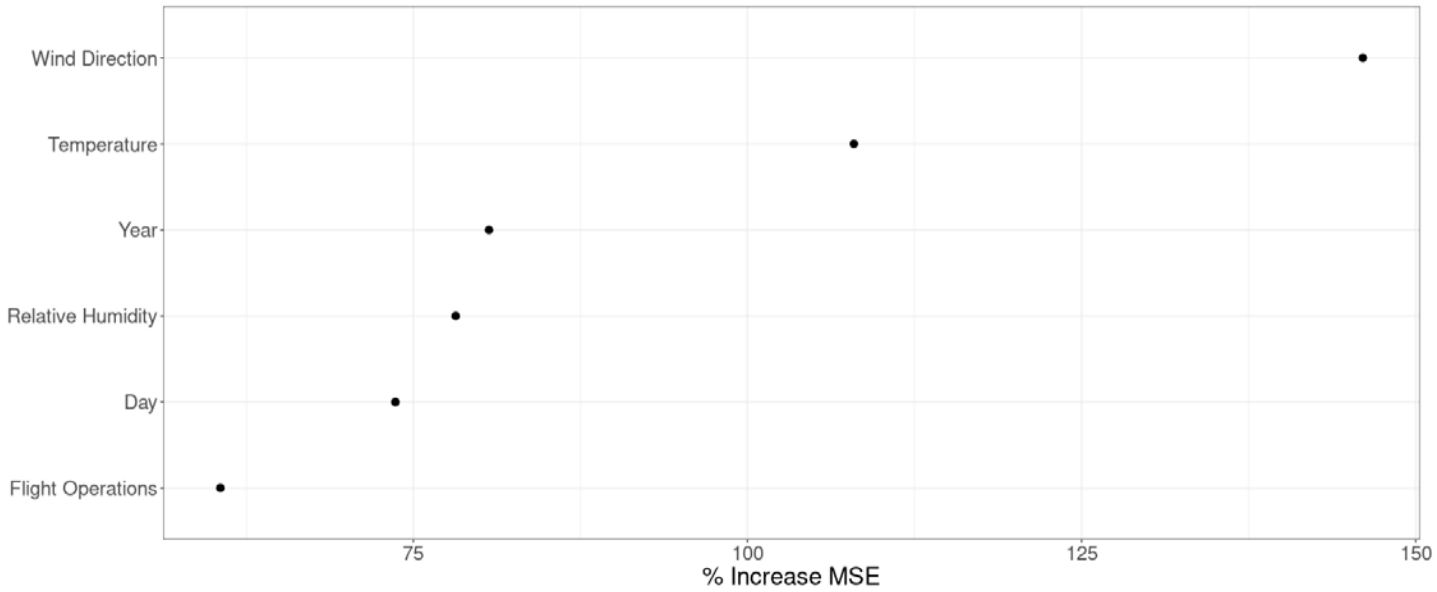

Figure 17. Variable importance plot for the machine learning regression model predicting ambient ultrafine particles from transportation activity and meteorology. A higher percent increase in mean square error (MSE) when the variable is removed indicates the variable's relative importance in the output prediction. The plot shows the six most important variables in model prediction. The variable "Flight Operations" is the summation of flight takeoffs and landings per hour.

Multi-Site UFP Modeling

Our data collection program includes stationary UFP monitoring at a number of sites distributed along Logan flightpaths (Figure 18.1). This configuration allows for two avenues of investigation: understanding how associations between UFP concentrations and meteorological/flight activity data vary across sites, and developing UFP prediction models that better generalize to out-of-site measurements.

Variation in Predictor Associations Across Sites

We analyzed hourly UFP concentration measurements at four distinct monitoring sites ("cdc," "dcr," "fb," "um") from April to October 2017. Figure 18.2 shows the time courses of these measurements, where the color of each point indicates how many other sites also recorded a measurement at that hour. Although merging data across all four sites would give us a nearly complete picture of UFP concentrations across this time period, we observe significant variation in average heights of signals due to distance from airport and flightpath, and we note that merging the data would not adequately take advantage of repeated measurements across sites.

We first trained a random forest model on the merged data to obtain a rough picture of which predictors of UFP were strongly associated with concentration levels. We included meteorological measurements such as average dry bulb temperature, wind speed/direction, and station pressure (among others), as well as flight activity summaries indicating the number of arrivals and departures at that hour and aggregated flight altitude information. The most predictive variables were then included in simple linear regressions conducted at each site. Figure 18.3 displays the coefficient estimates for each variable across each model (left panel includes intercept, right panel suppresses intercept). We find that the effects of some variables stay consistent across sites, whereas others (station pressure, wind speed) have differing magnitudes and directions of association from site to site. This suggests that a model trained on data in a single site (1) may not be portable to other regions, and (2) may not provide a complete and accurate picture of the impact of a given predictor variable.

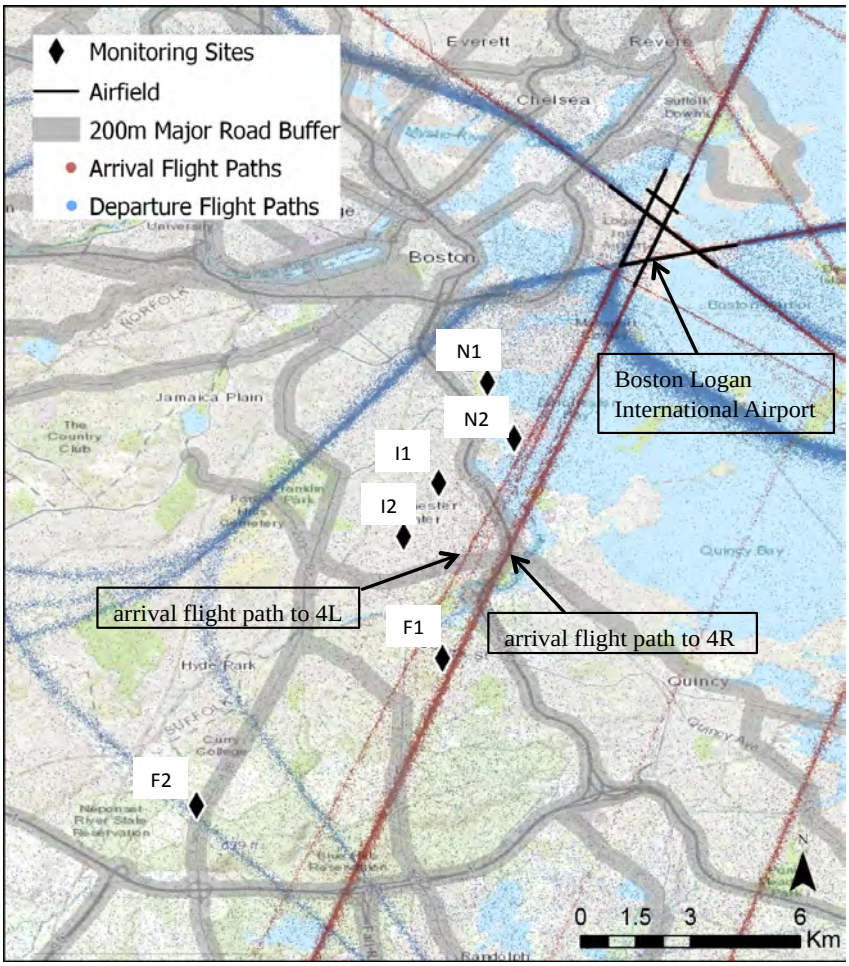

Figure 18.1. Positioning of near (N1, N2), intermediate (I1, I2), and far (F1, F2) stationary monitoring sites along Logan flightpaths.

Figure 18.2. Hourly concentrations of ultrafine particles (UFP) across four monitoring sites (dcr, um, fb, cdc) from April to October 2017. Color indicates how many sites have a measurement at that hour.

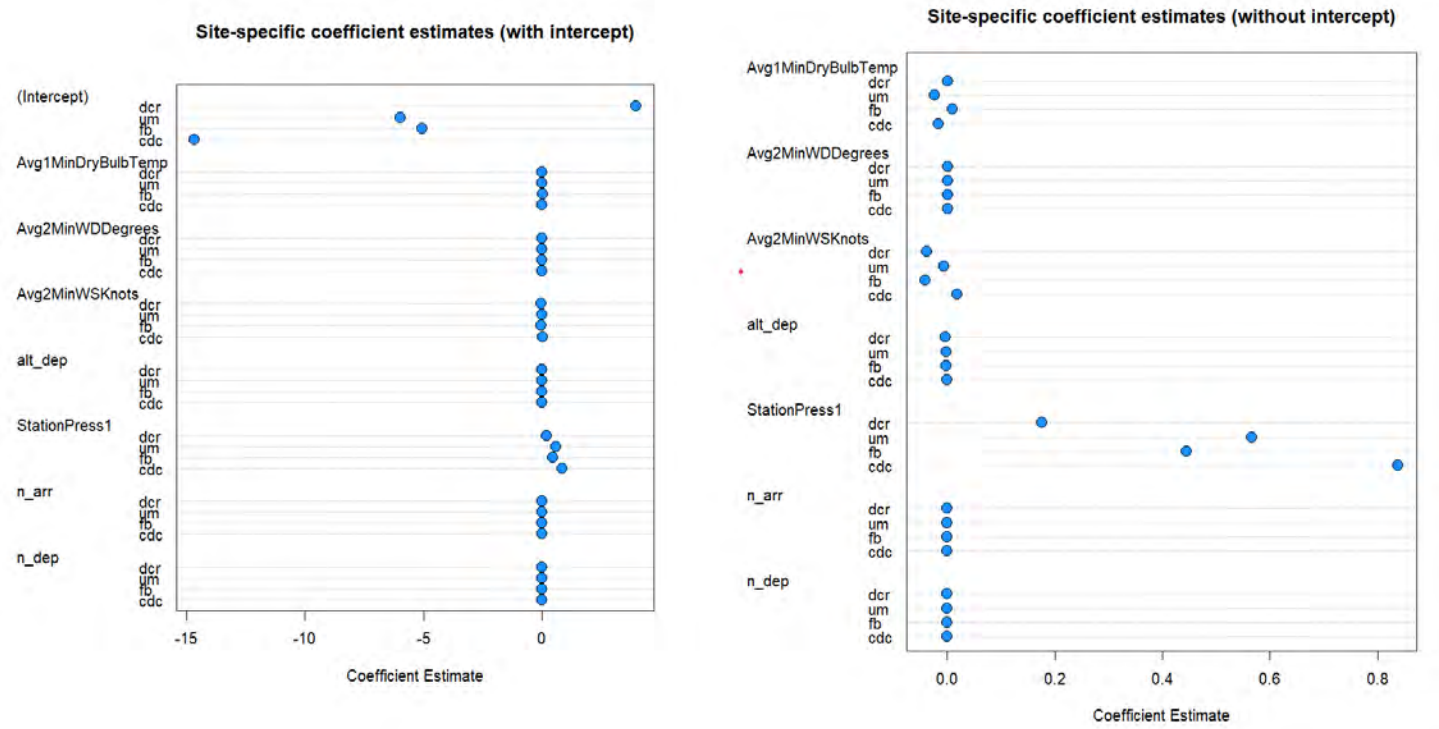

Figure 18.3. Site-specific regression coefficient estimates for most predictive variables. The coefficient value for each variable is plotted for each of the four sites (dcr, um, fb, cdc).

Multi-Site Prediction Models

Given our insights regarding the variability of associations across sites, we examined a number of different strategies for building a predictive random forest model for UFP that better generalizes to potential regions where monitoring is not possible. We studied the benefits and disadvantages of (1) applying a model trained on single-site data with the best performance metrics, (2) merging all site data together and training a single model, and (3) averaging predictions from all single-site models. For (3), we considered (a) simple averaging, (b) stacking (a technique where regression of predicted values on actual values is used to determine model averaging weights), (c) weighting based on geodesic distance, and (d) composing the weights from (b) and (c). Figure 19 compares these approaches on the four sites, where one site is held out at a time and models are trained/combined on the other three. We display the log root mean square error (RMSE) ratio between each method and the merging strategy (2) that maximizes the sample size of the model training dataset. Any point that falls below the dashed line indicates that the given method outperformed merging. Generally, we found that model averaging techniques (3b) and (3d) performed well. These findings suggest that model averaging approaches that leverage multiple sites' worth of data collection may generalize better to unknown locations, although there is significant additional analysis regarding stacking approaches, sample sizes, and cross-site data standardization left to be done.

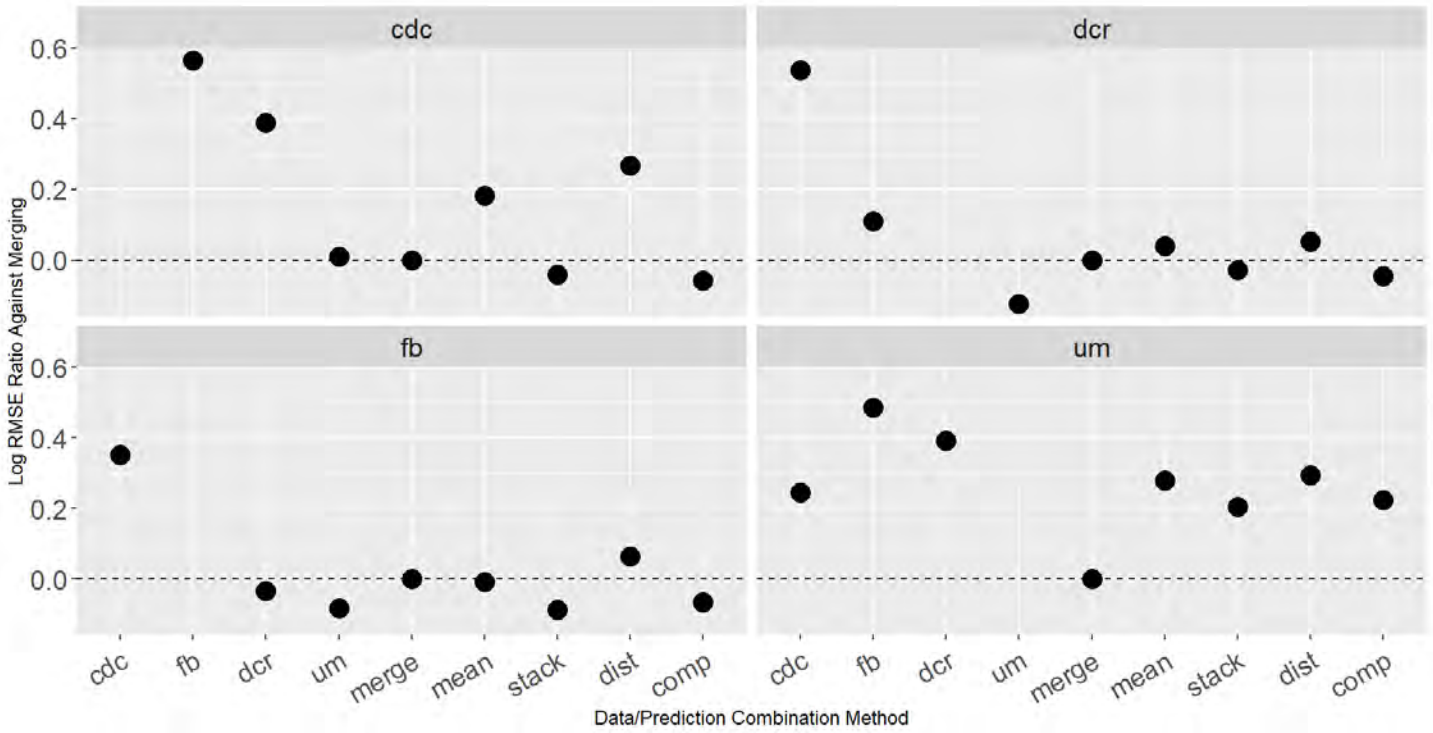

Figure 19. Comparison of log root mean square error (RMSE) ratio between each ultrafine particle (UFP) random forest modeling technique and merging. Each point below the dashed line indicates that the given method has a lower RMSE than merging. "cdc"/"fb"/"dcr"/"um" – single models trained at each site; "merge" – merging all site data together and training a single model; "mean" – averaging predictions from single-site models; "stack" – averaging using stacking weights; "dist" – averaging using distance-based weighting; "comp" – composite weight from stacking and distance-based weighting.

Publications

Mueller, S. C., Hudda, N., Levy, J. I., Durant, J. L., Patil, P., Lee, N. F., Weiss, I., Tatro, T., Duhl, T., & Lane, K. (2022). Changes in ultrafine particle concentrations near a major airport following reduced transportation activity during the COVID-19 pandemic. *Environmental Science & Technology Letters 9(9)*, 706–711. https://doi.10.1021/acs.estlett.2c00322

Outreach Efforts

Patil, P., Mueller, S., Hudda, N., Durant, J., Levy, J. I., Lane, K. J. (2022). *Combining multi-site UFP concentration models using stacking and location weighting*. [Meeting presentation.] 2022 Joint Statistical Meetings, Washington, DC, United States.

Awards

None.

Student Involvement

Sean Mueller, a doctoral student at BUSPH, has been involved in field monitoring, data cleaning, and manuscript preparation for the COVID-19 UFP analysis, and conducting preliminary regression modeling using machine learning algorithms.

Plans for Next Period

We will continue to test machine learning algorithms to find the most suitable algorithm for predicting ambient UFP at our measurement sites. We will evaluate these models through standard techniques (Pearson's R, R^2, RMSE). The preliminary machine learning models were developed using only one measurement site; however, we plan to develop regression models

for our other sites, as well as a generalizable model for all sites. Furthermore, we plan to explore autocorrelation in our data, fitting various lagged terms and autocorrelation structures to our models to improve performance. Ultimately, the best predictive model can provide the best insights as to which predictor variables provide the most contribution to modeled output, allowing for source apportion. We will also continue to examine variability of contribution across sites and its impact on source apportionment analysis, as well as study more sophisticated techniques for multi-site data combination and joint modeling/model averaging.

Project 019 Development of Aviation Air Quality Tools for Airshed-Specific Impact Assessment: Air Quality Modeling

University of North Carolina at Chapel Hill

Project Lead Investigator

Saravanan Arunachalam, Ph.D.
Research Professor
Institute for the Environment
University of North Carolina at Chapel Hill
100 Europa Drive, Suite 490
Chapel Hill, NC 27517
919-966-2126
sarav@email.unc.edu

University Participants

University of North Carolina at Chapel Hill (UNC)

- PI: Saravanan Arunachalam, research professor and deputy director
- FAA Award Number: 13-C-AJFE-UNC Amendments 1-18
- Period of Performance: October 1, 2021 to September 30, 2022
- Tasks: Development of new aircraft dispersion model (ADM)

Project Funding Level

FAA provided $650,000 in funding. EU-AVIATOR provided matching cost-share.

Investigation Team

Saravanan Arunachalam (PI)
Chowdhury Moniruzzaman (postdoctoral fellow #1)
Gavendra Pandey (postdoctoral fellow #2)
Ramarao Mandavilli (postdoctoral fellow #3)
Christos Efstathiou (emissions modeler)
Praful Dodda (graduate student #1)
Hyeongseok "Darby" Kim (graduate student #2)
Brian Naess (GIS specialist)
Consultant: Dr. Akula Venkatram, University of California at Riverside

Project Overview

Aviation is predicted to grow steadily in upcoming years;[1] thus, a variety of aviation environmental policies will be required to meet emission reduction goals in aviation-related air quality and health impacts. Tools are needed to rapidly assess the implications of alternative policies for an evolving population and atmosphere. In the context of the International Civil Aviation Organization (ICAO)'s Committee on Aviation Environmental Protection (CAEP), additional approaches are required to determine the implications of global aviation emissions.

The overall objective of this project is to develop a new aircraft-specific dispersion model and continue the development and implementation of tools, both domestically and internationally, to allow for an assessment of year-to-year changes in significant health outcomes. These tools must be acceptable to the FAA (in the context of Destination 2025) and/or other

[1] Boeing Commercial Airplane Market Analysis, 2010.

decision-makers. More importantly, this new model must have the capability to address the 1-hour form of the NO_2 National Ambient Air Quality Standard (NAAQS) in the United States, as well as support National Environmental Policy Act (NEPA) and/or NAAQS analyses that may be needed by airports. The developed methods must also rapidly provide output in order to support a variety of "what if" analyses and other investigations. While the tools for use within and outside the United States need not be identical, several goals are desirable for both cases:

- Enable the assessment of premature mortality and morbidity risks due to aviation-attributable particulate matter (PM) having diameter up to 2.5 μm ($PM_{2.5}$), ozone, and other pollutants known to exert significant health impacts;
- Capture airport-specific health impacts at regional and local scales;
- Account for the impact of landing/take-off (LTO) versus non-LTO emissions, including a separation of effects;
- Allow for an assessment of a wide range of aircraft emission scenarios, including differential growth rates and emission indices;
- Account for changes in nonaviation emissions;
- Allow for assessments of sensitivity to meteorology;
- Provide domestic and global results;
- Include quantified uncertainties and differences with respect to Environmental Protection Agency (EPA) practices, which are to be minimized when scientifically appropriate; and
- Be computationally efficient such that tools can be used in time-sensitive rapid turnaround contexts and for uncertainty quantification.

During this period of performance, the University of North Carolina at Chapel Hill's Institute for the Environment (UNC-IE) team performed work on the two tasks below:

Task 1 - Develop and Evaluate a New Dispersion Model for Aircraft Sources

University of North Carolina at Chapel Hill

Objectives

The FAA's Aviation Environmental Design Tool (AEDT) is currently coupled with the U.S. EPA's AERMOD dispersion model for modeling aircraft sources and is the required regulatory model in the United States for modeling airport-level aircraft operations during LTO cycles.

Recent studies have shown several limitations in the use of AERMOD for modeling aircraft sources. The Airport Modeling Advisory Committee (AMAC) developed a series of recommendations in 2011 to improve modeling jet exhaust. Since then, Airport Cooperative Research Program (ACRP) project 02-08 developed a guidance for airport operators on conducting measurement and modeling for air quality at airports, published in ACRP Report 70 (Kim et al., 2012). This study conducted a measurement and modeling study at Washington Dulles International Airport (IAD). Since then, ACRP project 02-58 developed a final report ACRP Report 171 (Arunachalam et al., 2017a) for providing dispersion modeling guidance for airport operators for local air quality and health. This study applied four different dispersion models—AERMOD, CALPUFF, SCICHEM, and the U.K.'s ADMS-Airport—for the Los Angeles International Airport (LAX) and compared modeled predictions with high-resolution measurements taken during the Los Angeles Air Quality Source Apportionment Study (AQSAS). All of these reports identified several limitations with AERMOD and developed a series of recommendations for improving dispersion modeling of aircraft emissions for airport-level air quality.

UNC recently developed the C-AIRPORT dispersion model for application to LAX (Arunachalam et al., 2017b). Initially, C-AIRPORT was designed to be part of the C-TOOLS series of community-scale, web-based modeling systems. The objective of C-TOOLS was to create a web-based interface to model multiple source types for short-term or long-term pollutant concentration averages and perform various "what if" scenarios that assess the changes in air quality at local scales due to changes in inputs. C-AIRPORT used a line source–based approach to model aircraft sources, based upon the C-LINE modeling system (Barzyk et al., 2015), and preliminary evaluation of the algorithms against LAX AQSAS was conducted.

Under the previous year's funding, UNC completed development of a modeling framework that addresses known limitations from the above tasks and proposed a viable and suitable approach for modeling pollutants from aircraft sources. The primary objective of this plan was to demonstrate that a robust, improved pollutant dispersion model for aircraft can be developed for U.S. regulatory compliance purposes. The proposed new model will disperse pollutants from aircraft sources in a more

technically and scientifically advanced manner (compared with current AERMOD capabilities), with the ultimate goal of becoming a potential U.S. regulatory compliance tool, based on future discussions between FAA and EPA. This plan will include an itemized list of known limitations along with a corresponding proposed developmental approach with recommendations to address them.

As part of the proposed ASCENT research under this task, we will continue to implement the plan with specific focus on four broad areas, over a period of 2 years. We give a very high-level summary here, because the actual specifics of this implementation are described in previous documents and reports that were independently developed earlier.

Our approach is to ensure that the new model will be "robust" and based on the state-of-science on physical and chemical processes and the associated algorithms.

1) **Source Characterization**
   Existing approaches in AEDT/AERMOD treat aircraft sources as an area source segment. In ongoing work, we are moving away from that approach to treat aircraft sources as line segments, as described in Arunachalam et al. (2019). We are currently adapting new high-resolution aircraft movement data from a research version of AEDT for an airport for use in the new dispersion model last year. We will finalize the approach with a streamlined tool for data processing in the dispersion model, and this will be tested and verified for implementation in AEDT.
2) **Physical Processes**
   We will go beyond the initial implementation last year, with specific new focus on the following:
   i. Treatment of dispersion under low wind conditions and assessment of effects of atmospheric stability
   ii. Treatment of dry and wet deposition
   iii. Exploration of additional options for aircraft exhaust plume rise such as the fluid mechanical entrainment (FEM) model that was scoped out in the ACRP report 171, where four new options can be implemented and evaluated:
      a. An empirical model for plume rise and initial dispersion based on LIDAR (light detection and ranging) measurements at LAX (Wayson et al., 2004),
      b. An FEM based on the average ground roll speed along the runway,
      c. An FEM as a function of the ground roll speed or distance down the runway (i.e., a different plume rise for each AERMOD area source, which is a function of runway distance), and
      d. An FEM based both on distance and time as independent variables describing the plume.
   iv. Incorporation of aircraft downwash effects
   v. Treatment of complex terrain and building downwash
3) **Chemical Processes**
   - We will go beyond the initial implementation last year, with specific new focus on the following:
     i. Note that the 1-hr form of the NO_2 NAAQS is a critical issue for air quality around U.S. airports, with several modeling studies showing overestimates of these compared to observations. It is important that the new model performs adequately to capture this short-term form of the NO_2 NAAQS.
     ii. New detailed chemical mechanism for NO_2 including the generic reaction set (GRS) (Valencia et al., 2017; Venkatram et al., 1994) or other,
     iii. Condensed version of the aerosol treatment as included in CMAQ and SCICHEM and described in Chowdhury et al. (2015)
4) **Model Evaluation**
   - Ongoing model evaluation involved evaluating model predictions using only measurements from the LAX AQSAS for winter 2012. We will now look at developing and testing the model for other case studies, including the following:
     i. LAX AQSAS for summer 2012.
     ii. One of three airports (Copenhagen, Madrid, and Zurich) with measurements being undertaken as part of the EU-AVIATOR project (see https://aviatorproject.eu/). We will rely on the AVIATOR team to provide emissions inventories for the chosen airport. If emissions inventories are not directly available for use, we will obtain airport operations data for the campaign period and develop an inventory using AEDT.
     iii. New measurements from ASCENT 18 investigators at Boston Logan International Airport (BOS). *This is new collaboration that will help focus on both designing the monitoring campaign to assist in obtaining valuable data to characterize aircraft emissions impacts on air quality and*

developing the ADM, as well as in source attribution of the measured fields to the aircraft or other source types.

- Model evaluation will focus on the model's ability to capture the behavior of the plume related to aircraft sources during LTO cycles at an airport, while comparing with observations that are available, and identifying strengths and weaknesses compared to another existing model.
- In collaborating with Boston University (BU), we will rely on BU to perform appropriate clean-up and quality assurance/quality control (QA/QC) of observation data before using it in our model evaluation routines. We will also work closely with BU to ensure appropriate and careful interpretation of the data. UNC and BU have collaborated extensively on similar projects in the past, and we expect to have robust model measurement and modeling assessment from the BOS study.

5) **Prepare AEDT Emissions Inventories**
   - To support this task, we will obtain aircraft operations data from the FAA and use the latest public version of AEDT to create BOS-specific airport-level emissions inventory corresponding to the measurement campaign period.

Task 2 – Develop and Evaluate a Multiscale WRF-SMOKE-CMAQ Model Application for BOS Focused on UFP

University of North Carolina at Chapel Hill

Objectives

In this task, we will collaborate with ASCENT 18 investigators at BU with a specific focus on modeling BOS at multiple spatial scales and perform intercomparison of the measurement and modeling with a focus on ultrafine particulate matter, mass and number concentrations, due to aircraft emissions. Using airport-specific inventories (see additional discussion below), we previously started to explore the use of two modeling approaches: CMAQ and the SCICHEM model. The SCICHEM model incorporates complete gas, aqueous, and aerosol phase chemistry within a state-of-the-science Gaussian puff model SCIPUFF (Second-order Closure Integrated Puff; Chowdhury et al., 2015). Since SCICHEM uses the same aerosol treatment as CMAQ but is able to characterize aircraft impacts at very fine scales around the airport, a key project outcome is the ability to improve aircraft-attributable PM on prior estimates. Note that because SCICHEM only predicts PM mass concentrations, we will develop post-processing routines to convert PM mass to particle number concentration (PNC) using the same approach as in CMAQ before model validation. Also, SCICHEM has not been used to predict PNC to date; therefore, this will be a new direction in research.

During spring and summer of 2017, ASCENT 18 investigators made multiple measurements of ultrafine particles (UFP) and black carbon at various locations south and west of BOS. Since then, an entire year of data on both UFP and black carbon have been collected for 2018. We will collaborate with BU to obtain these measurements to perform intercomparison against model outputs.

To support this modeling study, we will explore the use of obtaining BOS-specific airport-level emissions inventories from AEDT for 2018 from Massport, the public authority that manages BOS. If not available during the proposed period of performance, we will use existing AEDT-based full-flight aircraft inventories from one of the global-scale 2018 inventories that FAA/Volpe may have and extract BOS operations during LTO phases to support this assessment.

In this task, we will create a 12/4/1-km nested application of the Weather Research Forecast (WRF)–Sparse Matrix Operator Kernel Emissions (SMOKE)–CMAQ modeling system for two seasons (summer and winter) and simulate two emissions scenarios:

- Background emissions from all sources except BOS
- Background + BOS airport emissions during LTO cycles

Next, we will perform multiple sensitivity simulations with CMAQ v5.3 base and v5.3 augmented with the new nucleation mode described by Murphy et al. (2017). Specifically, this study adds a third mode in addition to the Aitken and Accumulation modes that have been historically used in all CMAQ applications to date.

The emissions inventories for nonaviation sectors for this application will rely on the EPA's National Emissions Inventories (NEI) for the year 2018 (if available) or projected from the NEI-2017. The meteorological fields will be downscaled from NASA's Modern-Era Retrospective Analysis for Research and Applications (MERRA) v2 (Reinecker et al., 2011).

The base CMAQ model application will be configured as follows:

a) Aircraft emissions from AEDT processed through AEDTProc;
b) Background emissions from NEI processed through SMOKE v3.6;
c) Meteorology from MERRA downscaled with WRF v3.8;
d) Lightning NOx;
e) Inline photolysis; and
f) Latest version of CMAQ (v5.32) but enhanced with the new aircraft-specific emissions module as described in Huang et al. (2017).

The initial and boundary conditions for the outermost grid (12 km) will be downscaled from CMAQ applied at the Northern Hemisphere at the 108-km resolution. The subsequent 4 km and 1 km grids will be nested down appropriately from the immediate outer grid as is standard practice.

After the model application has been developed and evaluated, UNC will obtain 2017–2018 field observations from the ASCENT 18 team at BU and perform model measurement comparisons. Previously in 2017, BU captured measurements at five fixed-site locations on the arrival path of aircraft at BOS. We will collaborate with BU on this task and compare regression and dispersion model-based assessments of UFP from BOS. As can be seen above, this is a collaborative effort with the ASCENT 18 investigators that will require constant exchange of information and sharing results throughout the period of performance, which will lead to an integrated measurement and modeling-based assessment of UFP due to aircraft emissions at BOS.

Research Approach

In this research, we describe progress made on the two tasks.

Task 1: Develop and Evaluate a New Dispersion Model for Aircraft Sources

1. Source Characterization

1.1 Aircraft Source Characterization in AERMOD

Modeling aircraft dispersion near the surface is challenging because aircraft are dynamic mobile sources that emit pollutants at varying rates depending on the operating mode. In 2005, the U.S. EPA adopted AERMOD, the most recent version of short-range steady-state atmospheric dispersion model for air quality regulatory purposes. AERMOD (v04300) was promulgated into EDMS (Emissions and Dispersion Modeling System; Martin, 2006) by the U.S. EPA in 2006, and EDMS was replaced by the FAA's AEDT (FAA, 2014) in May 2015, despite the fact that AERMOD was not designed to model elevated mobile sources. The representation of mobile sources, such as motor vehicles and the aircraft LTO cycle, has traditionally consisted of a series of AREA or VOLUME sources placed at various heights, and recently AERMOD (v21112) included an option to model on-road mobile sources as LINE segments. The publicly released version of FAA's AEDTv3e models aircraft emissions as a series of AREA source segments. This new version also has a key feature that allows users to model aircraft sources, both fixed wing and rotorcraft, as a series of VOLUME sources. Here we describe an evaluation of AERMOD predictions when modeling aircraft sources as AREA vs. VOLUME sources, along with a detailed comparison of spatial-temporal patterns in emissions.

The case study for this evaluation is LAX. We used datasets from the summer campaign (July 18 to August 28, 2012) from the LAX AQSAS (Arunachalam et al., 2017a; Tetra Tech, 2013).

We summarize below the various comparisons that we performed to quantify emissions estimates when using the AREA-and VOLUME-based treatments, and then the AERMOD-based concentration predictions of SO_2 for these two treatments.

1.1.1 Emissions and Source Parameter Comparisons

Based on the height and LTO cycle, we divided all AERMOD sources into the following five categories: AIRG620M (at height 619.2 m), AIRL620M (at height less than 619.2 m), GATE (at height 1.5 m), RUNWAY (at height 12 m lying on runways), and

TAXI (at height 12 m).

We compared the number of sources on AREA and VOLUME treatment files and found that the VOLUME source treatment file has a large number of sources at each category defined above except the GATE sources. The source characterization of GATE sources is similar in both files as AREA-POLYGON. In the VOLUME source file, the number of TAXI sources was13 times greater compared with the AREA source file (Table 1). The reason for the higher number of VOLUME TAXI sources is because for AREA sources, each TAXI link is assigned as a single AREA source (as a rectangle), but for VOLUME sources, each TAXI link is divided into 20 × 20 squares (Figure 1). However, the number of RUNWAY and airborne sources increased, respectively, by 38% and 41% in the VOLUME treatment file compared with the AREA treatment file (Table 1).

Irrespective of the greater number of sources in the VOLUME source treatment file, the SO_2 emissions (ton/period) were identical in both files for all five categories (Table 1). The average hourly total emissions in both the files were also identical at each hour for each category (Figure 2). The total average hourly emission for all five categories is high at around 16 g/s at hour 14 and lowest at hour 4 in both files (Figure 3).

Source parameters are given in Table 2 for both source treatments. The initial vertical dispersion parameter (σ_{z_0}) for all VOLUME sources is increased from 4.1 m (AREA source treatment) to 14 m. GATE source characterization is similar to AREA-POLYGON in both source files, and σ_{z_0} is 3 m for these sources (Table 2). The main reason behind the change in initial vertical dispersion parameter here is that the VOLUME sources are broken out by airframe-engine type and mode to allow for different initial dispersion parameters for each combination.

Table 1. Quantitative comparison of AREA and VOLUME source treatment files.

Source Group	Release Height (m)	Number of Sources in Each File		SOx Emissions (ton/period)	
		AREA	VOLUME	AREA	VOLUME
AIRG620M	Hs = 619.2 m	19,013	26,296	11.91	11.91
AIRL620M	Hs <619.2 m	4,729	7,142	5.81	5.81
RUNWAY	12 m	2,593	3,569	6.00	6.00
TAXI	12 m	248	3,320	14.01	14.01
GATE	1.5 m	21	21	1.19	1.19
Total	All	26,604	40,348	38.92	38.92

Table 2. Source parameters at each category in AREA and VOLUME source treatment files.

Source Group	Release Height (m)	AREA				VOLUME	
		Length (m)	Width (m)	Angle (°)	$\sigma_{z_0}(m)$	$\sigma_{y_0}(m)$	$\sigma_{z_0}(m)$
AIRG620M	Hs = 619.2 m	200	200	0	4.1	46.51	14
AIRL620M	Hs < 619.2 m	200	200	0	4.1	46.51	14
RUNWAY	12 m	20	20	0	4.1	4.65	14
TAXI	12 m	22.86	variable	variable	4.1	4.65	14
GATE	1.5 m	AREA-POLYGON			3	AREA-POLYGON	3

(a) AREA Treatment (TAXI)

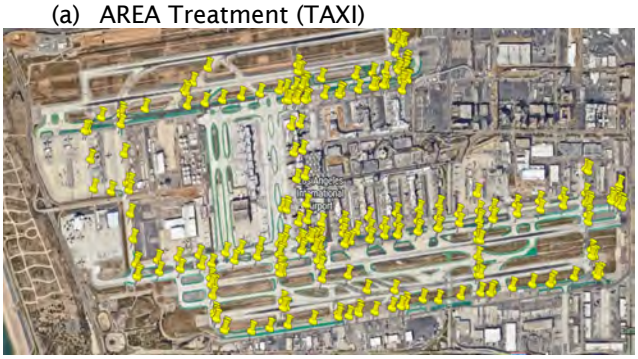

(b) VOLUME Treatment (TAXI)

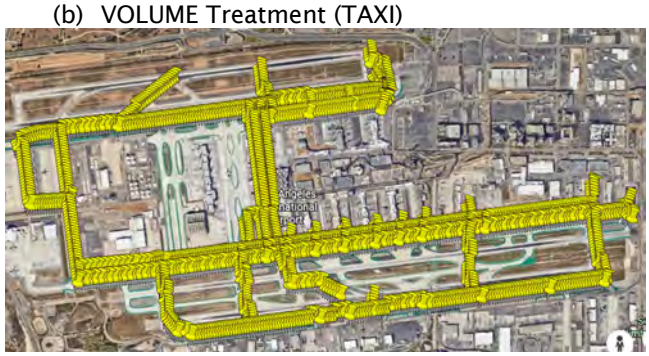

Figure 1. TAXI source locations in (a) AREA and (b) VOLUME source treatment files.

(a) AREA Source Treatment

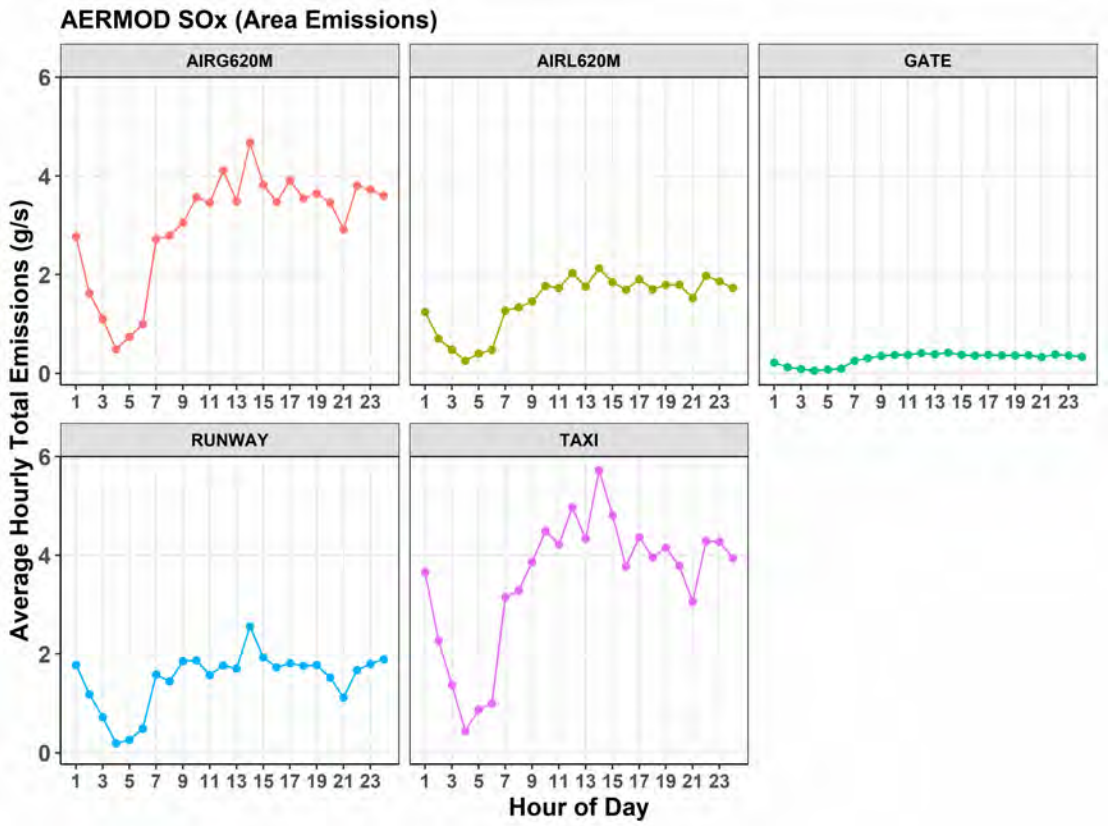

(b) VOLUME Source Treatment

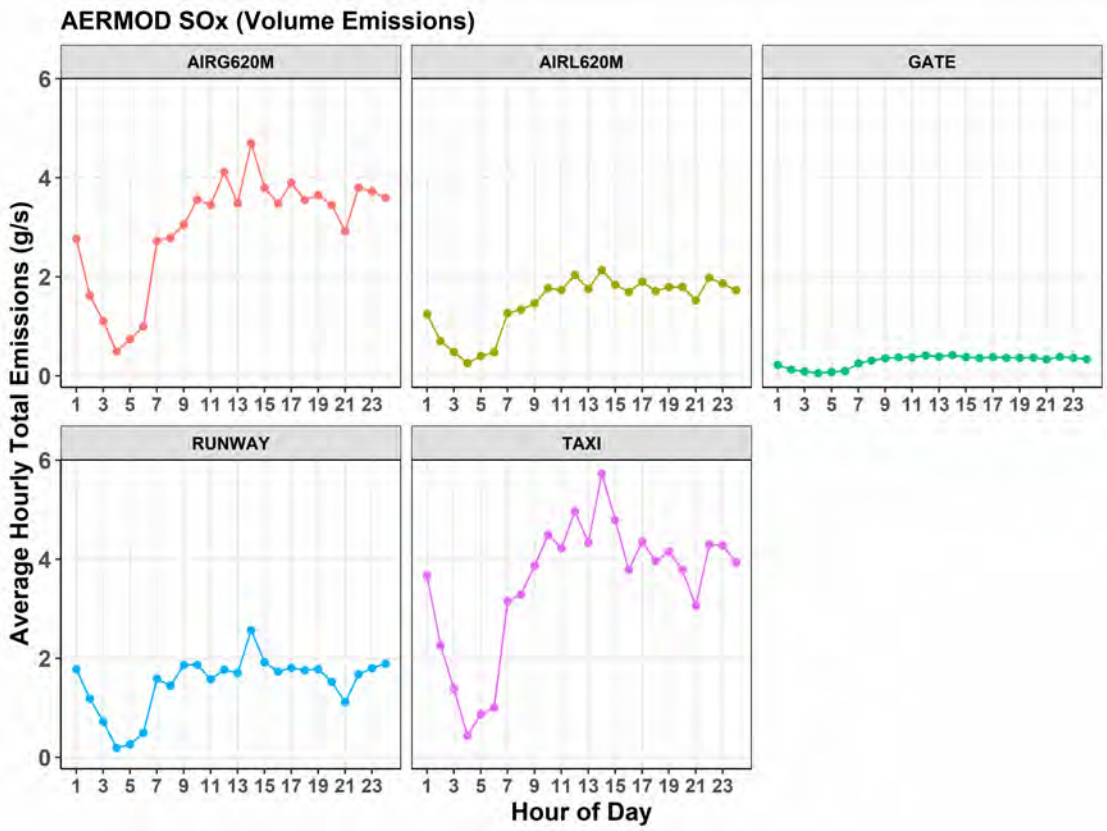

Figure 2. Average hourly total emissions at each hour in (a) AREA and (b) VOLUME treatment files for all five categories (AIRG620M, AIRL620M, GATE, RUNWAY, and TAXI).

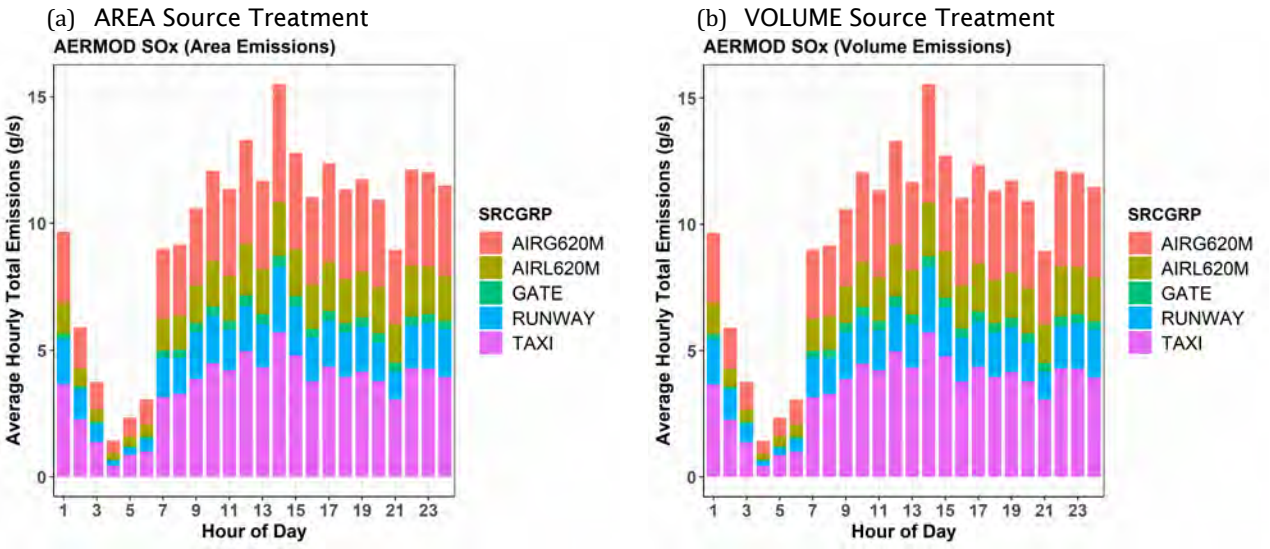

Figure 3. Average hourly total emissions at each hour in (a) AREA and (b) VOLUME treatment files for all five categories (AIRG620M, AIRL620M, GATE, RUNWAY, and TAXI).

1.1.2 Concentration Comparisons Using AERMOD (V21112):

To compare model performance using both source treatment files, we utilized the AERMOD (v21112) dispersion model and ran the model for aircraft sources only using the existing summer meteorological files for LAX. For the modeled concentration comparison using both files, we used the diurnal and quantile-quantile (Q-Q) distribution plots with a few EPA-recommended statistical parameters such as FAC2 (factor of 2 to the observation), FB (fractional bias [standard in diurnal plot and based on top 26 robust highest concentrations in QQ plot; Cox and Tikvart, 1990]), R (correlation coefficient), and PR (peak ratio; the ratio of highest modeled concentration to highest observed concentration) at four core sites, namely Air Quality (AQ), Community North (CN), Community South (CS), and Community East (CE) of LAX.

At all four core sites in the diurnal plots, neither source file was able to predict the concentration close to observation. There was high over-prediction in the morning at AQ and CS, and high over-prediction in the late evening at CN, CS, and CE sites (Figure 4a). However, both source treatment files had similar characteristic features at all four core sites (Figure 4a). There was a slight improvement in all statistical measures using the VOLUME source treatment (Figure 4a).

In Q-Q plots at all four sites, the higher concentrations declined slightly, and lower concentrations increased and came close to FAC2 lines using the VOLUME source treatment compared to the AREA source treatment (Figure 4b). In quantitative terms, the FB was improved using VOLUME source treatment (Figure 4b).

1.1.3 Sensitivity Analysis Based on Initial Vertical Dispersion Parameter

In addition, we performed a sensitivity analysis based on the initial vertical dispersion parameters (σ_{z_0}) in both source treatment files:

a) Changed the σ_{z_0} values from 4.1 m to 14 m for all surface, airborne, and taxi sources in AREA source file.
b) Changed the σ_{z_0} values from 14 m to 4.1 m for all the surface, airborne, and taxi sources in VOLUME source file.

In this sensitivity analysis, when we increased σ_{z_0} from 4.1 m to 14 m in the AEDT-generated AERMOD AREA source treatment file, we found that the modeled higher concentrations declined slightly; we can easily see this from the change in FB values (Figure 5b). In contrast, when we decreased σ_{z_0} from 14 m to 4.1 m in the AEDT-generated VOLUME source treatment file, there was a slight increase in FB that suggested an increase in the modeled concentration (Figure 6b). However, in both sensitivity analyses, the diurnal characteristic features did not change after an increase or decrease in σ_{z_0} values, except for a slight change at high concentrations, which can be seen by the change in FB values (Figures 5a and 6a).

Overall, we found better performance by VOLUME source treatment. However, from this improved performance arose the following two questions, which are addressed in the next section:

a) Is improved performance due to the increase in the number of sources in VOLUME source treatment?
b) Is improved performance due to the source characterization (meander component in VOLUME source)?

1.1.4 Conversion of AREA to VOLUME and VOLUME to AREA (UNC)

To check the above-mentioned concerns, we converted the AEDT-generated AREA and VOLUME source files into VOLUME and AREA source files. This was done by converting the emissions and taking the appropriate source parameters as per Table 2 for each source. At UNC using an R script, we converted AEDT-generated AREA and VOLUME source input files into VOLUME and AREA source files. The main key findings from this conversion analysis are as follows:

a) AREA to VOLUME/VOLUME to AREA conversion showed that AERMOD predictions are better when using VOLUME source treatment (Figures 7 and 8).

b) As the number of sources is the same after each conversion, all improvements in model predictions were shown to be due to the VOLUME source treatment (Figures 7 and 8).

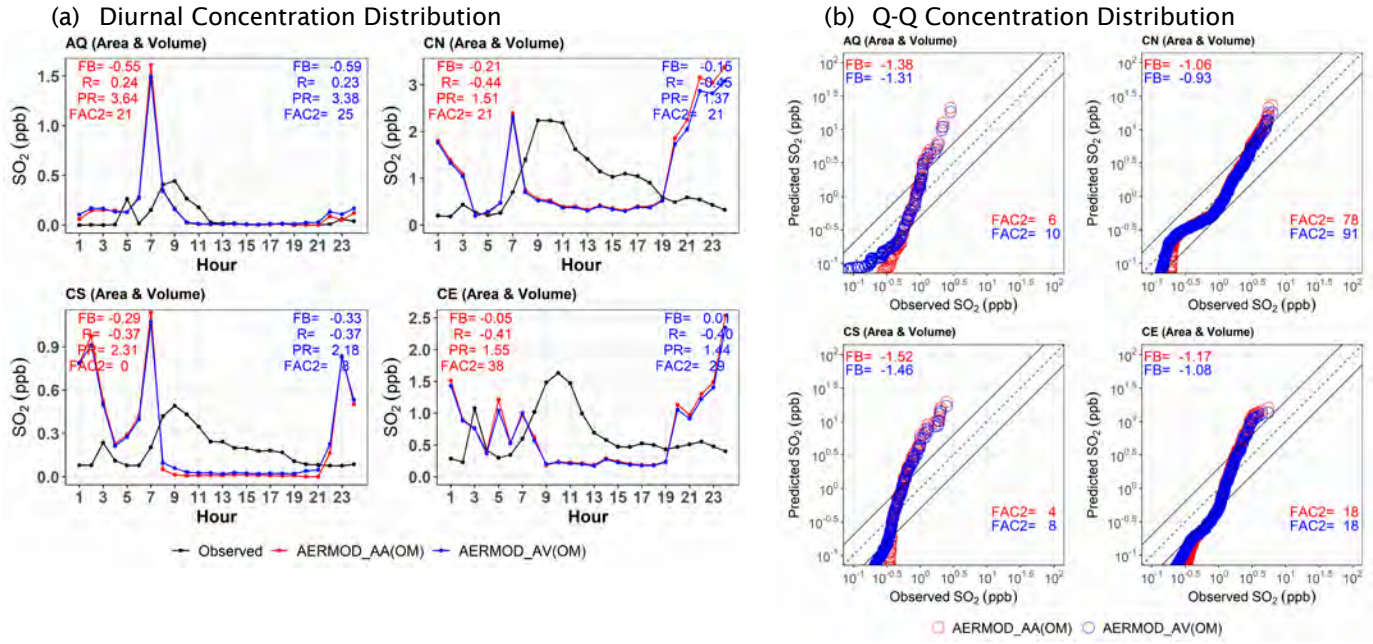

Figure 4. (a) Diurnal variability in observed and modeled SO_2 concentrations, (b) quantile-quantile (Q-Q) concentration distribution between observed and modeled SO_2 concentrations files at all four core sites (AQ, CN, CS, and CE) using AEDT-generated AREA and VOLUME source treatment. OM, original meteorology; AA, AEDT-generated AREA source file; and AV, AEDT-generated VOLUME source file.

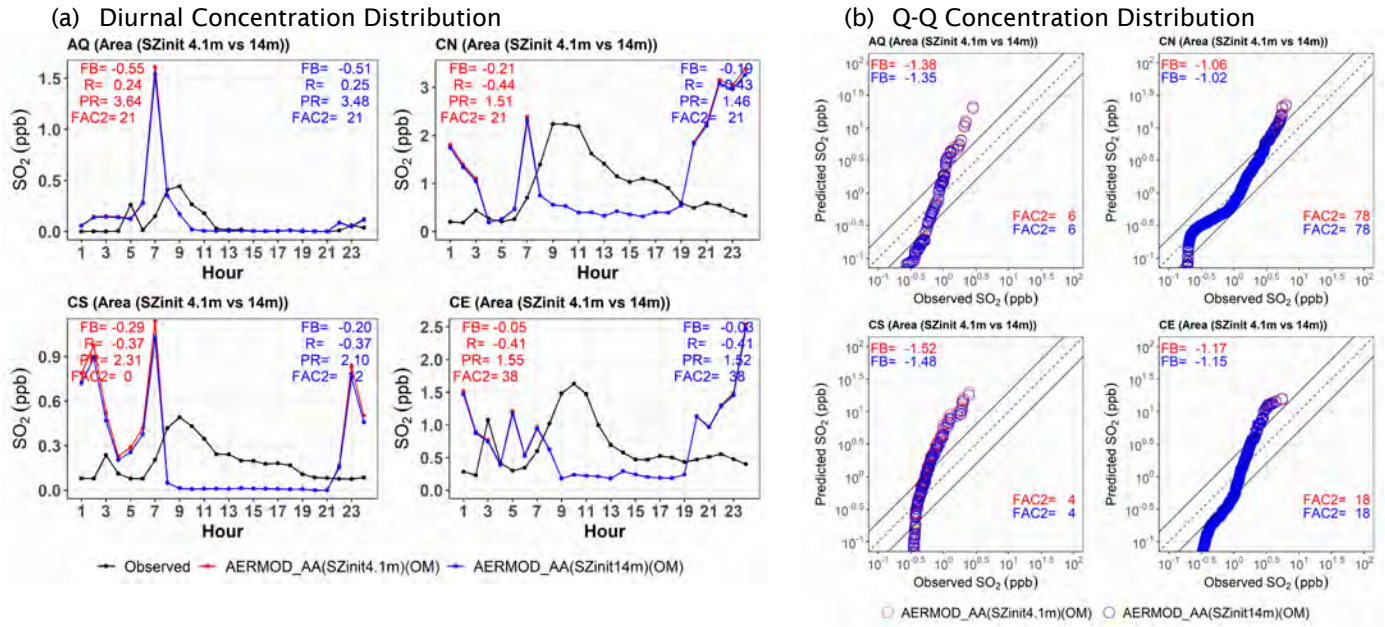

Figure 5. (a) Diurnal variability in observed and modeled SO_2 concentrations, (b) quantile-quantile (Q-Q) concentration distribution between observed and modeled SO_2 concentrations files at all four core sites (AQ, CN, CS, and CE) using AEDT-generated AREA source treatment. OM, original meteorology; AA, AEDT-generated AREA source file; SZinit, initial vertical dispersion parameter (σ_{z_0}).

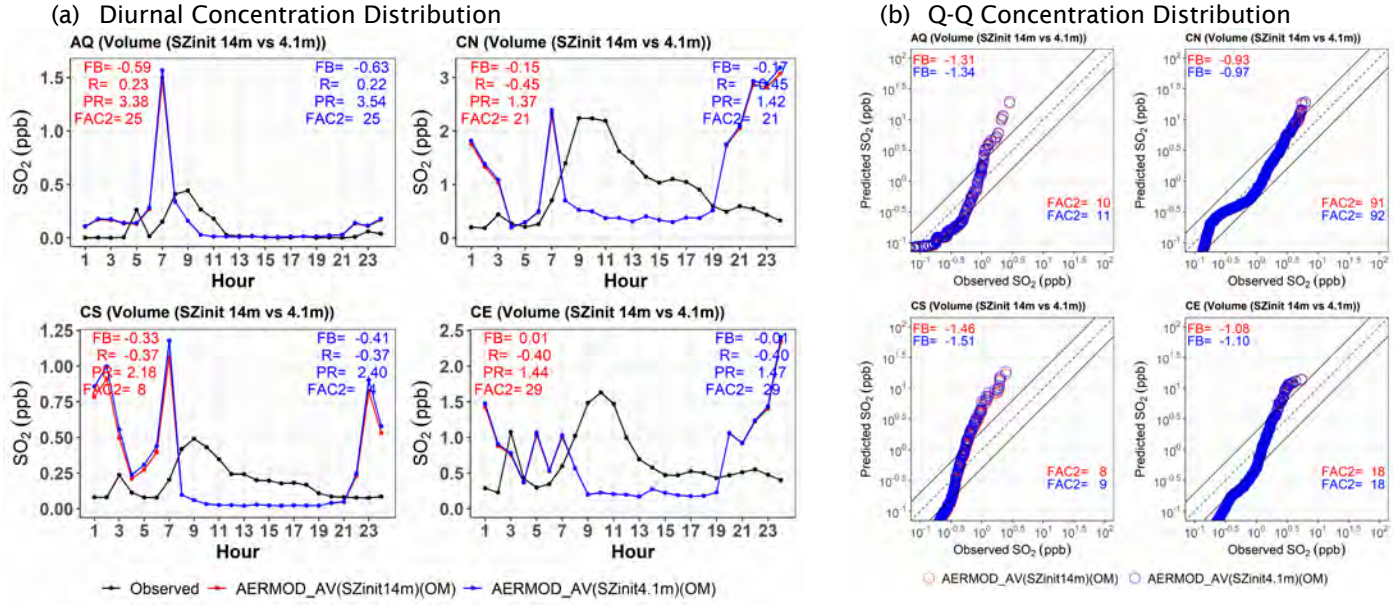

Figure 6. (a) Diurnal variability in observed and modeled SO_2 concentrations, (b) quantile-quantile (Q-Q) concentration distribution between observed and modeled SO_2 concentrations files at all four core sites (AQ, CN, CS, and CE) using AEDT-generated VOLUME source treatment. OM, original meteorology; AV, AEDT-generated VOLUME source file; SZinit, initial vertical dispersion parameter (σ_{z_0}).

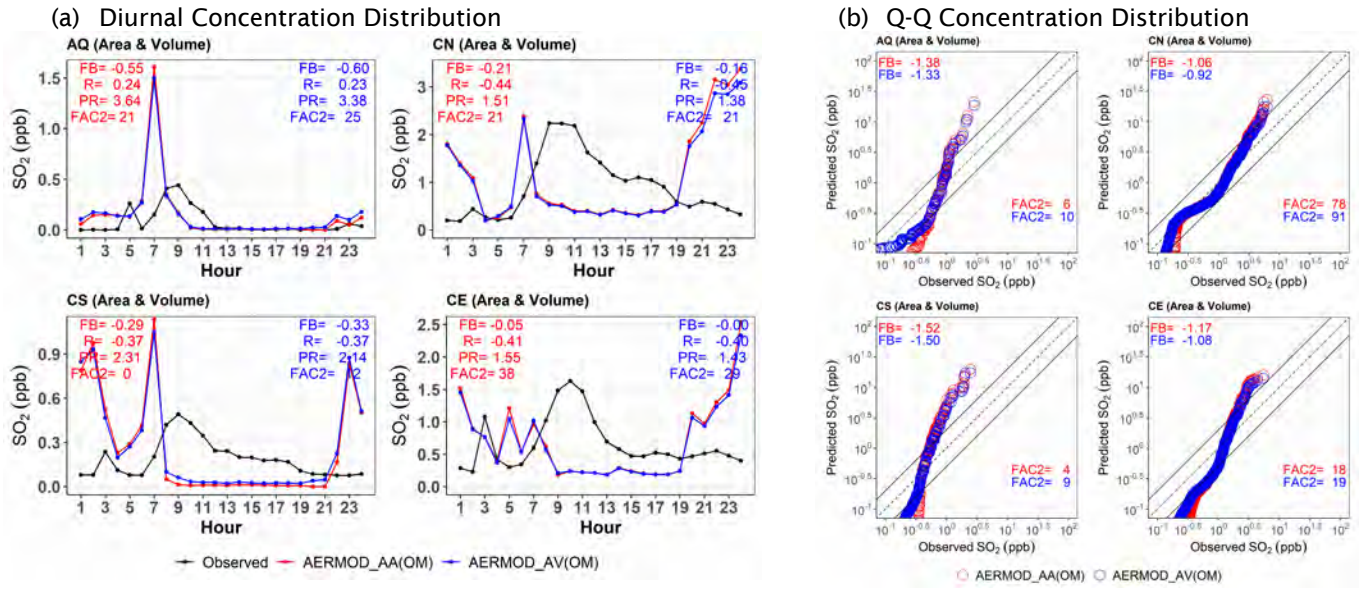

Figure 7. (a) Diurnal variability in observed and modeled SO_2 concentrations, (b) quantile-quantile (Q-Q) concentration distribution between observed and modeled SO_2 concentrations files at all four core sites (AQ, CN, CS, and CE) using AEDT-generated AREA source treatment and UNC-converted VOLUME source treatment file from AEDT-generated AREA source file. OM, original meteorology; AA, AEDT-generated AREA source file; AV, UNC-converted VOLUME source file.

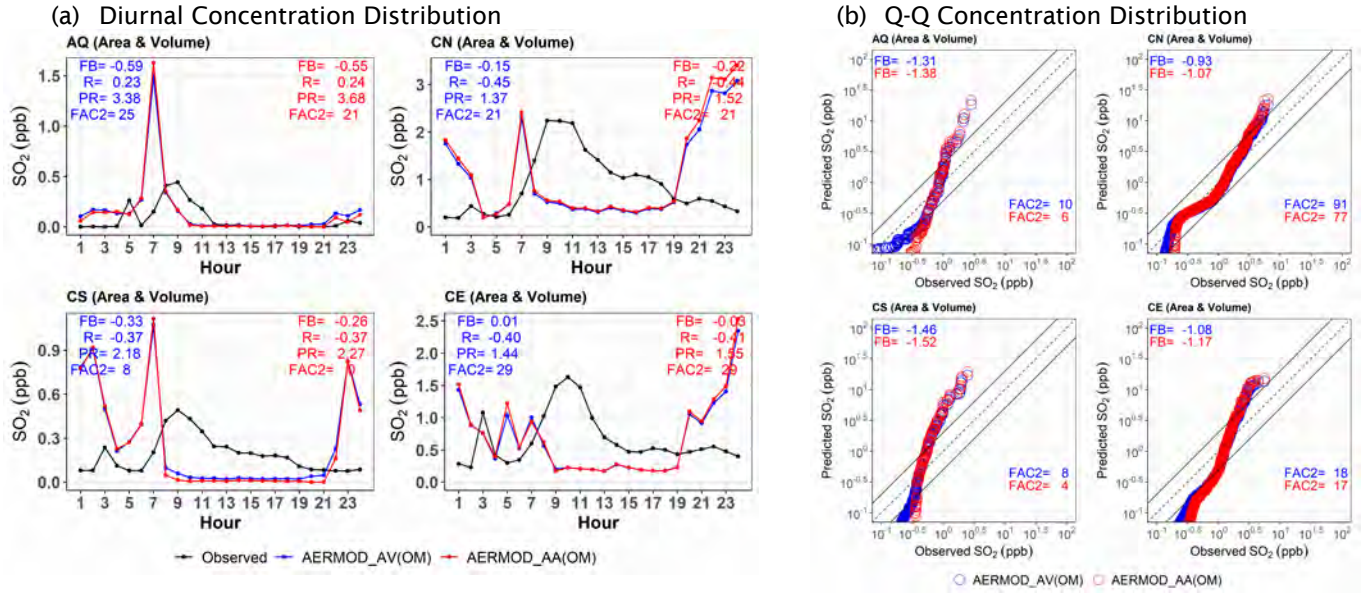

Figure 8. (a) Diurnal variability in observed and modeled SO_2 concentrations, (b) quantile-quantile (Q-Q) concentration distribution between observed and modeled SO_2 concentrations files at all four core sites (AQ, CN, CS, and CE) using AEDT-generated VOLUME source treatment and UNC-converted AREA source treatment file from AEDT-generated VOLUME source file. OM, original meteorology; AV, AEDT-generated VOLUME source file; AA, UNC-converted AREA source file.

1.1.5 Summary

Here, we found that VOLUME source treatment had a greater number of sources than AREA source treatment. Irrespective of the greater number of VOLUME sources, emissions were identical at each mode in both treatment files. The key finding is that AERMOD model predictions improved slightly for higher concentrations and significantly for lower concentrations through VOLUME source treatment. In quantitative terms, VOLUME source treatment has less FB (based on robust highest concentrations (RHC)). Hence, VOLUME source treatment is slightly better than AREA. To check this, we performed sensitivity analyses based on the increase/decrease in initial vertical dispersion parameter and conversion from AREA/VOLUME to VOLUME/AREA. At each conversion, the number of sources did not change, and the overall results suggest that all improvements at the lower end of model predictions were due to the meander component of VOLUME source, and that improvements at higher concentrations were due to the increase in the initial vertical dispersion parameter (σ_{z_0}) from 4.1 m to 14 m. However, all sensitivities suggest that VOLUME source treatment was better than AREA source treatment.

1.2 AEDT2ADM Tool

A Python-based emission processor called "AEDT2ADM" has been developed that can produce emission files of the new ADM and AERMOD dispersion models using the AEDT's flight segment data. We have updated the emission processor and evaluated the flight segment data of both AEDT winter and summer 2012 files.

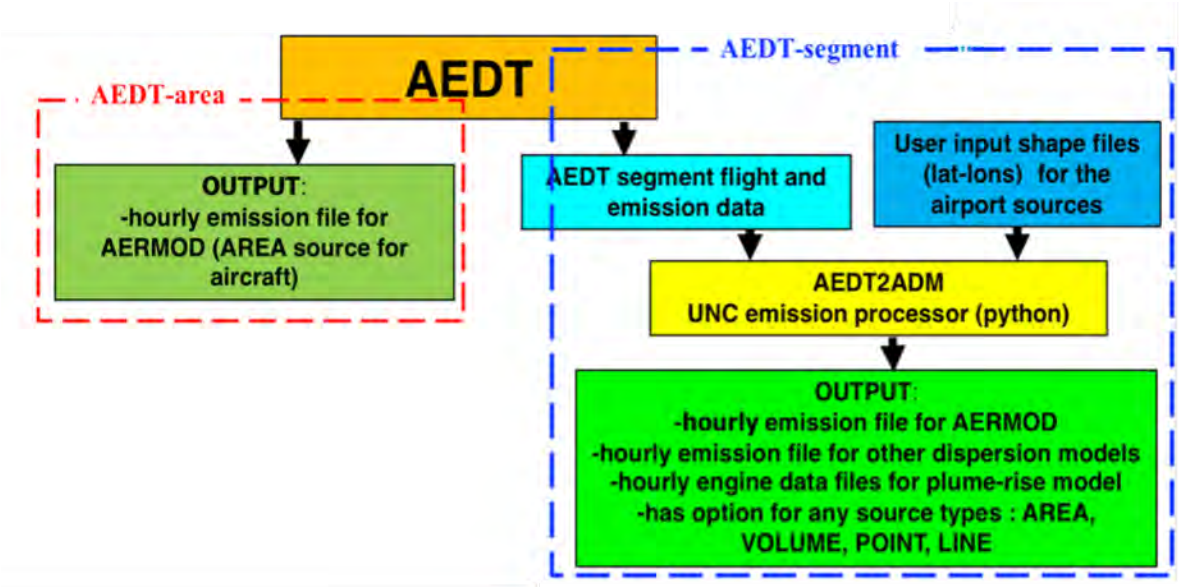

Figure 9: The schematic of input/output data flow off AEDT2ADM emission processor.

1.2.1 Update of the AEDT2ADM Emission Processor

The AEDT2ADM emission processor has been updated to include multiple new features since the last version reported in UNC's ASCENT 2021 annual report. The new updates are described below as follows:

a) We cleaned the 2021 version AEDT2ADM code and put this whole package into a private GitHub repository and shared it with FAA. Now, the AEDT2ADM emission processor has been updated and it can produce emission input files of ADM as well as AERMOD models for all species present in the AEDT-segment files for each day for the entire time period in a single run. From Figure 9, we can see how this processor works to generate AERMOD- and ADM-ready input files.

b) In the 2021 version, we updated the spatial resolution capability of the surface sources based on users' specific latitude and longitude of runways and gateways. In the current 2022 version, we updated the spatial resolution of airborne sources. Previously, there were only 144 fixed airborne point sources based on nine fixed layers; this new airborne source methodology starts with the extent of the ground sources and user-provided latitude/longitude

sources of the full domain to create an inverted pyramid grid with increasing grid-cell sizes. This allows ADM to use the same number of sources for all days of a modeling run (Figure 10 and Table 3).

c) We added new functionality to generate gridded surface source files as well as emission and engine parameter files for an additional feature within ADM. With this additional feature, ADM can use a simple short-range gridded dispersion model, which could be better in low and variable wind dispersion cases.

d) AEDT2ADM is also updated to generate the engine parameters files for ADM. Winter AEDT-segment data do not include taxi speed so we have used the average summer season taxi speed to calculate aircraft speed. Negative thrust values in the AEDT-segment data are replaced by 7% of maximum thrust while aggregating hourly data for ADM inputs.

e) Apart from the above AEDT2ADM updates, we reported several issues in the FAA/Volpe-provided segment and AERMOD-ready input files for LAX. All issues are summarized in each month's report.

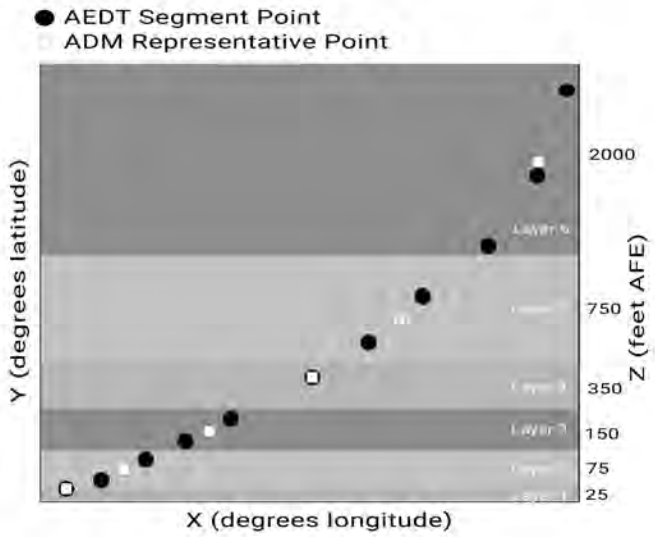

Figure 10. Schematic of new airborne source methodology.

Table 3. Layer-wise airborne source distribution based on grid sizes.

Layer	Grid Size (m)	Top of Layer (ft)	Number of sources
1	250	50	612
2	350	100	1,152
3	575	200	903
4	975	500	578
5	1,600	1,000	338
6	2,000	3,000	512
		Sources	4,095
		Sources with directions	8,190

2. Physical Processes

2.1 Aircraft's Plume Rise Algorithm Development and Implementation in AERMOD

In view of the incompleteness of the dispersion models used in aircraft dispersion modeling, we have developed a plume rise algorithm for turbojet and shaft-based aircraft engines. In the 2021 UNC ASCENT report, we mentioned only the simple algorithm to calculate plume rise for turbojet engines. We have now substantially updated this algorithm and developed a new algorithm for shaft-based engines for surface and airborne aircraft sources. It builds upon our current understanding of plume rise of emissions from stationary point sources and can be readily incorporated into AERMOD or the new ADM.

The buoyancy parameter, F_b, that governs plume rise from a point source is associated with energy output from an aircraft engine. The buoyancy parameter, F_b, of the exhaust plume is given by the following expression (Briggs, 1965):

$$F_b = \frac{g}{T_a} v_e r_0^2 (T_e - T_a), \quad (1)$$

where v_e and T_e are the velocity and temperature, respectively, of the exhaust plume, T_a is the ambient temperature, and g is the acceleration due to gravity. The plume rise, h_{pb}, associated with a buoyant release from a point source in a neutral atmosphere is given by (Briggs, 1965)

$$h_{pb} = \left(\left(\frac{r_0}{\beta} \right)^3 + \frac{3}{2\beta^2} \frac{F_b}{U_{eff}^3} x^2 \right)^{1/3} - \left(\frac{r_0}{\beta} \right), \quad (2)$$

where $\beta = 0.6$ is an entrainment constant, x is the effective distance between the source and receptor, U_{eff} is the effective velocity within the plume, and r_0 is the initial radius of the plume.

Generally, there are two types of engines in aircraft: jet/gas turbine and piston engines (Figure 11). Here, we have divided all engine types into two categories to calculate the plume rise. The first category is based on the known bypass ratio (turbojet and turbofan engines), and the second one does not have a known bypass ratio (turboprop, turboshaft, and piston engines).

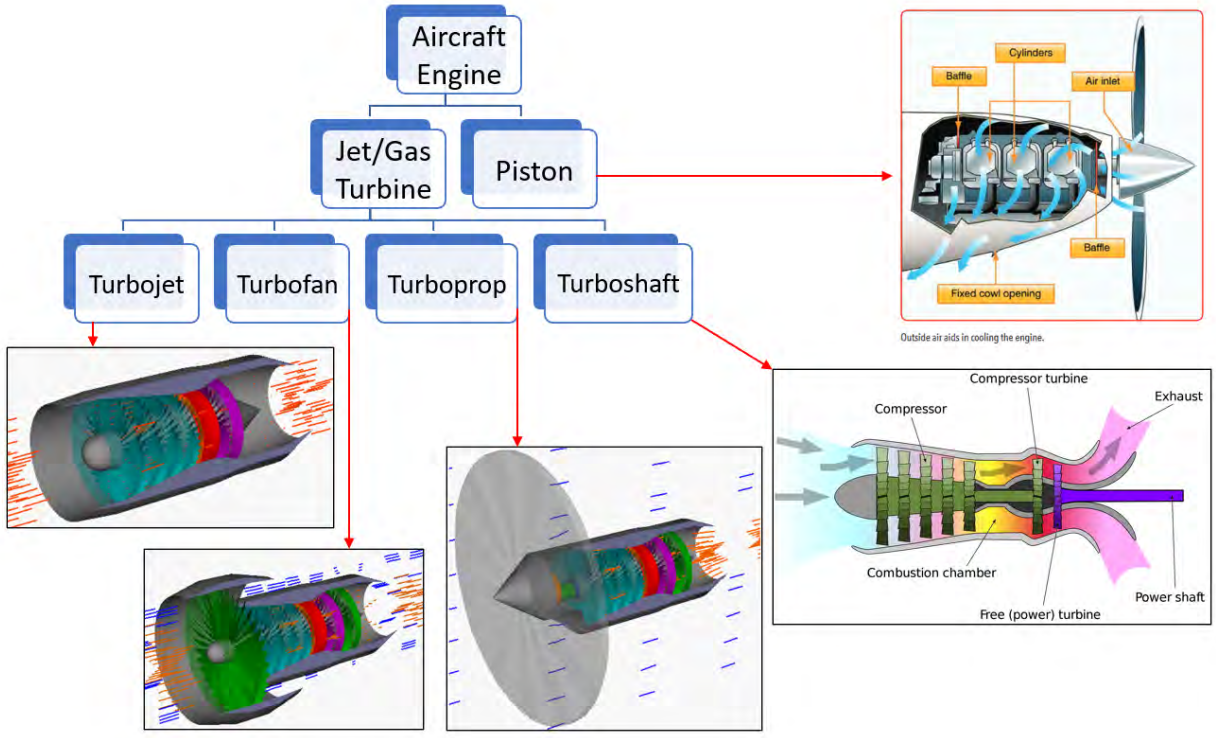

Figure 11. Aircraft engine types and working (Source: NASA).

2.1.1 Category 1

This category consists of two jet/gas turbine engines such as turbojet and turbofan engines. When the aircraft is moving, air enters the engine at the speed of the aircraft relative to the aircraft. A fraction of the incoming air is directed into the core, where it is first compressed, then enters the combustion where the injected fuel increases the temperature of the gases, which then drives a gas turbine. The gas turbine generates enough power to drive the compressor and the fan. The core flow is then exhausted through a nozzle. Figure 11 shows the operation of a modern turbofan/turbojet engine. Most of the air entering the engine "bypasses" the core as it is driven toward the exit by the fan at the entrance. The mass flow rate of the bypass air is several times that of the core air; the ratio of the two mass flow rates is known as the bypass ratio, which we denote here by $bypr$. The bypass ratio of modern turbofan engines is >5. The exiting air is a mixture of core air and bypass air, and the average velocity of the two streams is much smaller than that of the core air. Low-bypass turbofans are commonly used in fighter jet engines and have ratios in the 0.30 to 0.50 range, whereas modern high-bypass engines may have a ratio as high as 9 or 10.

The thrust of the engine is the product of the total mass flow rate and the difference between the inlet and exit velocities. As we will see, the power associated with propulsion is maximized by bringing the exit velocity of the exhaust gases as close as possible to the inlet velocity and, at the same time, increasing the mass flow rate through the engine. This is achieved through as large a bypass ratio as possible, which requires making the fan as large as possible.

The ratio of the mass of air entering the core to that of the fuel injected into the combustion chamber is known as the air-fuel ratio, denoted here by AF. Although the stoichiometric AF ratio is about 15, it is maintained at values >45 to ensure that the temperature of the gases exiting the combustion chamber is below that required for the integrity of the turbine blades. The ratio of the mass flow rate of air plus fuel, $\dot{m}$, to that of the fuel, $\dot{m}_f$, is approximately $AF(1+bypr)$, which is >200 for most aircraft engines. Therefore, the mass flow rate through the engine is essentially that of air. We now have the background to relate the buoyancy parameter to the characteristics of an aircraft engine.

2.1.1.1 Computing the Buoyancy Parameter From Engine Characteristics

The exhaust gas velocity and temperature required in Equation (1) to compute the buoyancy parameter are not available for jet/gas turbine engines. Thus, it is necessary to estimate the buoyancy parameter using variables used to characterize jet engines. These variables are the engine thrust, *T*, the aircraft velocity, v_a, fuel burn rate, $\dot{m}_f$, the air-fuel ratio, *AF*, and the bypass ratio, *bypr*. We show below how these variables are used to estimate the buoyancy parameter, which can be written in terms of Q_e, the thermal power added to the air passing through the engine:

$$F_b = \frac{g}{T_a}\frac{Q_e}{\pi\rho_e C_p}, \tag{3}$$

where ρ_e is the exhaust density, and C_p is the specific heat of the exhaust gases, which is mostly air.

We can derive an expression for Q_e by writing the energy balance:

$$\dot{m}_f H_f = \frac{\dot{m}}{2}(v_e^2 - v_a^2) + Q_e, \tag{4}$$

where $\dot{m}_f$ is the fuel consumption rate, and H_f is the heating value of the fuel. Equation (4) states that the power supplied by the fuel (left-hand side) is the sum of the increase in kinetic power and thermal power added to the air passing through the engine. Rearranging the equation gives

$$Q_e = \dot{m}_f H_f \left(1 - \frac{\frac{\dot{m}}{2}(v_e^2 - v_a^2)}{\dot{m}_f H_f}\right). \tag{5}$$

The second term within the parentheses on the right-hand side is the thermal efficiency, defined by

$$\eta_t = \frac{\frac{\dot{m}}{2}(v_e^2 - v_a^2)}{\dot{m}_f H_f}, \tag{6}$$

which can be expressed in terms of the thrust, T, and the exhaust velocity, v_e, of the gases from the engine

$$T = \dot{m}(v_e - v_a), \tag{7}$$

where v_e is the exhaust velocity, v_a is the aircraft velocity, and $\dot{m}$ is the mass flow rate of air plus fuel. Substituting Equation (7) in (6) yields

$$\eta_t = \frac{T(v_e + v_a)/2}{\dot{m}_f H_f} = \frac{T v_{avg}}{\dot{m}_f H_f}, \tag{8}$$

where the average velocity, $v_{avg} = (v_e + v_a)/2$. Thermal efficiency can be written in terms of overall efficiency, η_o, and the propulsive efficiency, η_p.

The overall efficiency η_o, is the ratio of the propulsive power, Tv_a, to the power derived from the fuel:

$$\eta_o = \frac{Tv_a}{\dot{m}_f H_f}. \tag{9}$$

The propulsive efficiency, η_p, is the ratio of the propulsive power to the power associated with kinetic energy imparted by the engine:

$$\eta_p = \frac{Tv_a}{\dot{m}(v_e^2 - v_a^2)/2} = \frac{\dot{m}(v_e - v_a)v_a}{\dot{m}(v_e - v_a)v_{avg}} = \frac{v_a}{v_{avg}}. \tag{10}$$

Substituting Equations (9) and (10) into Equation (8) results in

$$\eta_t = \frac{\eta_o}{\eta_p} \text{ and}$$
$$\eta_o = \eta_t \eta_p. \tag{11}$$

We see that calculation of thermal efficiency, η_t, requires an estimate of the exhaust velocity, v_e, which can be obtained from Equation (7):

$$v_e = v_a + \frac{T}{\dot{m}}, \tag{12}$$

and the total mass flow rate, $\dot{m}$, is related to the fuel burn rate, $\dot{m}_f$, through

$$\dot{m} = \dot{m}_f AF(1 + bypr), \tag{13}$$

where AF is the air-fuel ratio, and $bypr$ is the engine bypass ratio.

Then, the preceding equations allows us to compute the buoyancy parameter, F_b, from

$$F_b = \frac{g}{T_a} \frac{\dot{m}_f H_f (1 - \eta_t)}{\pi \rho_e C_p}, \tag{14}$$

where the exit density, ρ_e, is computed from the energy conservation equation and the equation of state,

$$T_e = T_a + \frac{Q_e}{\dot{m} C_p}$$
$$\rho_e = \frac{p_a}{R_a T_e}, \tag{15}$$

where T_e is the average temperature of the exhaust gases, p_a is the ambient pressure, and R_a is the gas constant of air. We see that the inputs required to compute F_b are the thrust, T, the aircraft velocity, v_a, the fuel burn rate, $\dot{m}_f$, the air-fuel ratio, AF, and the engine bypass ratio, $bypr$.

2.1.2 Category 2

This category has two jet/gas turbine engines such as turboprops and turboshaft, and it consists of a third type: piston engines. These engines do not have known bypass ratios.

Turboprops extract virtually all the kinetic energy and a larger portion of the thermal energy via expansion turbines to drive the propeller, whereas turbofans utilize an expansion nozzle to create high-speed exhaust (thrust) (Figure 11). For turboprops, very little thrust is produced by the exhaust directly (2%-3% of total thrust output); the propeller does the work of converting heat to thrust via a gearbox driven by the expansion turbine. It can be useful to think of turboprops as unducted turbofans in some sense, where the propeller is the first fan in the compressor section. However, it should be noted that there is no actual bypass air for a turboprop engine. This analogy breaks down in a mechanical sense but is useful in the aerodynamic and thermodynamic sense. The ideal turboprop would convert all the exhaust's energy into mechanical work to drive the propeller.

The turboshaft engine is another common type of jet/gas turbine engine. It delivers power to a shaft that drives something other than a propeller. The biggest difference between a turbojet and turboshaft engine is that on a turboshaft engine, most

of the energy produced by the expanding gases is used to drive a turbine rather than produce thrust. Many helicopters use a turboshaft gas turbine engine. In addition, turboshaft engines are widely used as auxiliary power units on large aircraft. Turboshaft engines and piston engines do not have a known bypass ratio. We could calculate a bypass ratio for a given engine/propeller configuration, but because manufacturers can install propellers of arbitrary diameter and blade count on a particular engine, we cannot know this value as a function of the engine itself. We could potentially determine a bypass ratio for a particular application (i.e., a propeller or rotor of a known diameter) of a turboshaft engine used on a helicopter by assigning the "bypass" air transported through that known propeller or rotor.

2.1.2.1 Computing the Buoyancy Parameter From Engine Characteristics

In a turboshaft engine, the propeller is driven by a gas turbine. The air passing through the propeller is not heated, so the hot exhaust from the turbine constitutes the primary source of buoyancy. The heat ejected by the turbine can be estimated if the compression ratio of the compressor in the turbine, *CR*,[2] is specified. The compression ratio is the ratio of the stagnation pressures at the outlet and inlet of the compressor.

For an ideal turbine, *CR*, determines the thermal efficiency of the turbine, which is given by

$$\eta_t = 1 - \frac{1}{\alpha_1}$$
$$\alpha_1 = CR^{\frac{k-1}{k}}, \quad (16)$$

where $k = \frac{C_p}{C_v} = 1.4$ is the ratio of the specific heats of air at constant pressure and volume. Then, the power transferred to the propeller is $W = \dot{m}_f H_f \eta_t$ and the heat rejected is

$$Q_e = \dot{m}_f H_f (1 - \eta_t) = \frac{\dot{m}_f H_f}{\alpha_1}, \quad (17)$$

where H_f is the heating value of the fuel, and $\dot{m}_f$is the fuel rate.

The temperature of the exhaust is seen to be

$$T_e = T_a + \frac{H_f}{\alpha_1 C_p AF}, \quad (18)$$

where AF is the air-fuel ratio. This temperature is used to compute the density assuming that the pressure is ambient, p_a,

$$\rho_e = \frac{p_a}{R_a T_e}. \quad (19)$$

This density is used in the formula for the buoyancy parameter equation 3.

The formulation for the buoyancy parameter of the exhaust of a piston engine is similar to that of a turbine. Here the compression is defined in terms of volumes of the fuel-air mixture before and after compression in the engine. The ideal thermal efficiency is given by

$$\eta_t = 1 - \frac{1}{\beta_1}$$
$$\beta_1 = CR^{k-1}. \quad (20)$$

The exhaust temperature used to compute exhaust density becomes

$$T_e = T_a + \frac{H_f}{\beta_1 C_v AF}, \quad (21)$$

where $C_v = C_p/k$ is the specific heat of air at constant volume. Equations (17), (19), and (3) also hold for piston engines, given Equations (20) and (21).

If the power output of the engine is available, we can estimate the thermal efficiency directly as

$$\eta_t = \frac{p_s P_r}{\dot{m}_f H_f}, \quad (22)$$

where p_s is the power setting and P_r is the rated power. Then, the rejected heat, Q_e, is simply

$$Q_e = (1 - \eta_t)\dot{m}_f H_f, \quad (23)$$

[2] UNC needs CR (if applicable) otherwise related power by engine type as input from AEDT from plume rise calculations

as in Equation (17).

The exit temperature, T_e, required to compute the exit density ρ_e(equation 19), is estimated from

$$T_e = T_a + \frac{(1-\eta_t)H_f}{C_p AF}. \quad (24)$$

Now we can calculate the buoyancy parameter F_b from Equation (3).

Note: If we can obtain the rated power directly as an input, there is no need for compression ratio (*CR*) or thermal efficiency as inputs for this category because the related power and power setting are used to calculate the thermal efficiency in Equation (22). Now, we need only one extra column of related power (kilowatt) rather than earlier implemented six engine parameter columns in the AERMOD's HRE file, whereas the power setting values can be used on the basis of air-fuel ratio (AFR) column (Table 1) (Wayson et al., 2009).

Table 4. Representative air-fuel ratios (AFR) by power setting (Wayson et al., 2009).

Mode	Power Setting (%)	AFR
Idle	7	106
Approach	30	83
Climb-out	85	51
Take-off	100	45

Once the buoyancy parameter, F_b, for any category described above is computed, estimating buoyant plume rise from Equation (1) is straightforward.

Exhaust gases exit from jet/gas turbine engines with large horizontal momentum (only for category 1; category 2 does not have the momentum part) and buoyancy. We have a limited understanding of the behavior of such plumes in the atmosphere. The model formulated by Barrett et al. (2013) includes the combined effects of plume buoyancy and horizontal momentum. However, the model has not been evaluated sufficiently to warrant adopting it in preference to the simpler approach, in which total plume rise is the sum of plume rises associated with momentum and buoyancy; the advantage of this approach is that it reduces to well-worn formulations when either buoyancy or horizontal momentum can be neglected. Here we assume that plume buoyancy and momentum act independently, as in Yamartino & Donald (1979), but we allow interaction between these processes as described below.

2.1.3 Accounting for Jet Momentum (Category 1)

We assume that the horizontal momentum is conserved as the radius of the horizontal plume grows with distance from a stationary point within the area source. For a top-hat profile of velocity within the plume, the momentum balance can be written as

$$\rho_p U_p (U_p - U_a)\pi r^2 = T, \quad (25)$$

where U_p is the velocity inside the plume *relative to a stationary observer*, U_a is the ambient velocity at the level of the plume, and ρ_p is the plume density. The initial momentum flow inside the plume is the thrust, T, exerted by the engine on the air. A version of this equation is derived in Appendix A1 of Arunachalam et al. (2017a).

As in Barrett et al. (2013), we assume that the radius of the jet exhaust grows linearly with distance from a point within the area source:

$$r = \alpha x + r_0, \quad (26)$$

where $\alpha = 0.1$ is an entrainment constant, and r_0 is the radius of the engine exhaust. This estimate of the radius of the plume allows us to calculate the velocity of air, U_p, inside the plume from Equation (22):

$$U_p = U_a \left[0.5 + 0.5\left(1 + \frac{4T}{\pi r^2 \rho U_a^2}\right)^{1/2}\right]. \quad (27)$$

The radius of the momentum plume is taken to grow until the difference between the plume and ambient velocities is comparable to the standard deviation of the ambient horizontal velocity fluctuations, $\sigma_u = 2.0u_*$, where u_* is the surface friction velocity. Then, the maximum plume radius is given by the relationship

$$T = \pi \rho_a r_m^2 (U_a + \sigma_u)\sigma_u, \quad (28)$$

where U_a is evaluated at $z = r_m$, and ρ_a is the ambient density. Then, r_m is given by

$$r_m = \left(\frac{T}{\pi\rho_a(U_a+\sigma_u)\sigma_u}\right)^{1/2}. \quad (29)$$

The plume rise associated with momentum, h_{pm}, is taken to be the radius of the plume

$$h_{pm} = \begin{cases} r_0 + \alpha x, & x \le x_m \\ r_m, & x > x_m \end{cases} \quad (30)$$

where x_m is the distance at which the radius reaches its maximum value:

$$x_m = \frac{(r_m - r_0)}{\alpha}. \quad (31)$$

The effect of buoyancy is treated by assuming that it acts independently on the expanding jet plume.

2.1.4 Plume Rise Due to Buoyancy

We estimate plume rise associated with buoyancy using the formulation applicable to point releases in a neutral atmosphere (Briggs, 1965):

$$h_{pb} = \left(\left(\frac{R}{\beta}\right)^3 + \frac{3}{2\beta^2}\frac{F_b}{U_{eff}^3}x^2\right)^{1/3} - \left(\frac{R}{\beta}\right), \quad (32)$$

where $\beta = 0.6$ is an entrainment constant, x is the effective distance between the area source and receptor, and U_{eff} is the effective velocity, which is taken to be the maximum of the velocity in the jet, U_p, and the ambient velocity at plume height, U_a.

Buoyant plume rise interacts with that associated with horizontal momentum through the initial radius, R, in Equation (32). It is taken to be the average value of the radius of the momentum plume between 0 and x to account for the impact of momentum on the initial radius of the buoyant plume,

$$R = \frac{1}{x}\int_0^x r(x)\,dx, \quad (33)$$

which yields

$$R = \begin{cases} r_0 + \alpha x/2, & x \le x_m \\ \frac{x_m}{x}\left(r_0 + \frac{\alpha x_m}{2}\right) + r_m\left(1 - \frac{x_m}{x}\right), & x > x_m \end{cases} \quad (34)$$

The buoyancy parameter, F_b, is computed using the equations described previously. Equation (32) has to be solved iteratively because wind speed at plume height is not known a priori.

The total plume rise is then

$$h_p = h_{pb} + h_{pm}, \quad (35)$$

where the second term on the right-hand side is the plume rise associated with the momentum jet, given by Equation (30) only for category 1; for category 2, it is almost negligible or zero.

2.1.5 Buoyancy Flux and Plume Rise Results

In this section, we present the results of buoyancy flux and plume rise for one day of summer 2012 (July 1, 2012) at LAX. For this day, there was no climb-out source up to 22 m height. All engine parameters were taken from the sample AERMOD HRE plume rise files, which UNC obtained from Volpe.

2.1.5.1 Buoyancy Flux

Here, we plot the buoyancy flux with respect to fuel burn rate; the color bar represents the thrust for surface and airborne sources for both types of aircraft engines (Figures 12 and 13).

2.1.5.1.1 Surface Aircraft Sources

Here, we calculated the buoyancy flux for all sources having 12 m height, especially all surface take-off sources only (surface aircraft sources) in all 24 hours of a day for both types of engines. We found that turbofan engines have much larger buoyancy flux than shaft-based engines and that the number of shaft-based engines is less compared to turbofan engines (Figure 12). Overall, the higher the fuel burn rate, the higher the buoyancy flux.

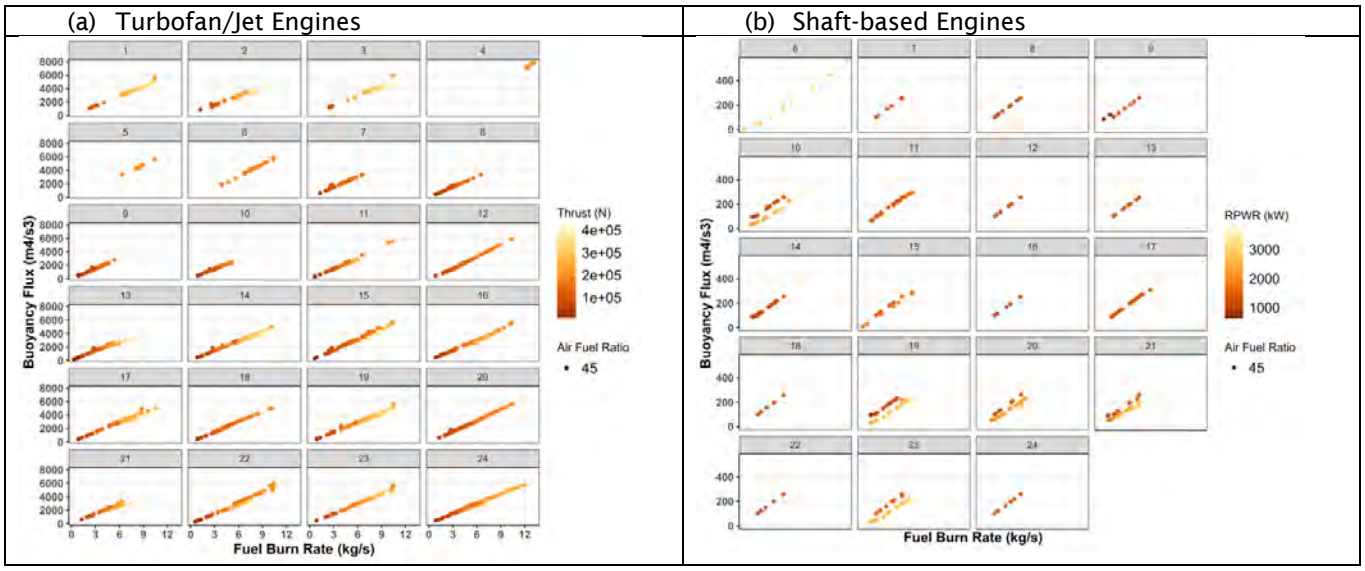

Figure 12. Buoyancy flux with respect to fuel burn rate for (a) turbofan, and (b) shaft-based aircraft engines for surface sources at 12 m height.

2.1.5.1.2 Airborne Aircraft Sources

Here, we show the buoyancy flux for airborne sources at 22 m height only and found that turbofan engines have higher buoyancy flux than shaft-based engines at each hour (Figure 13).

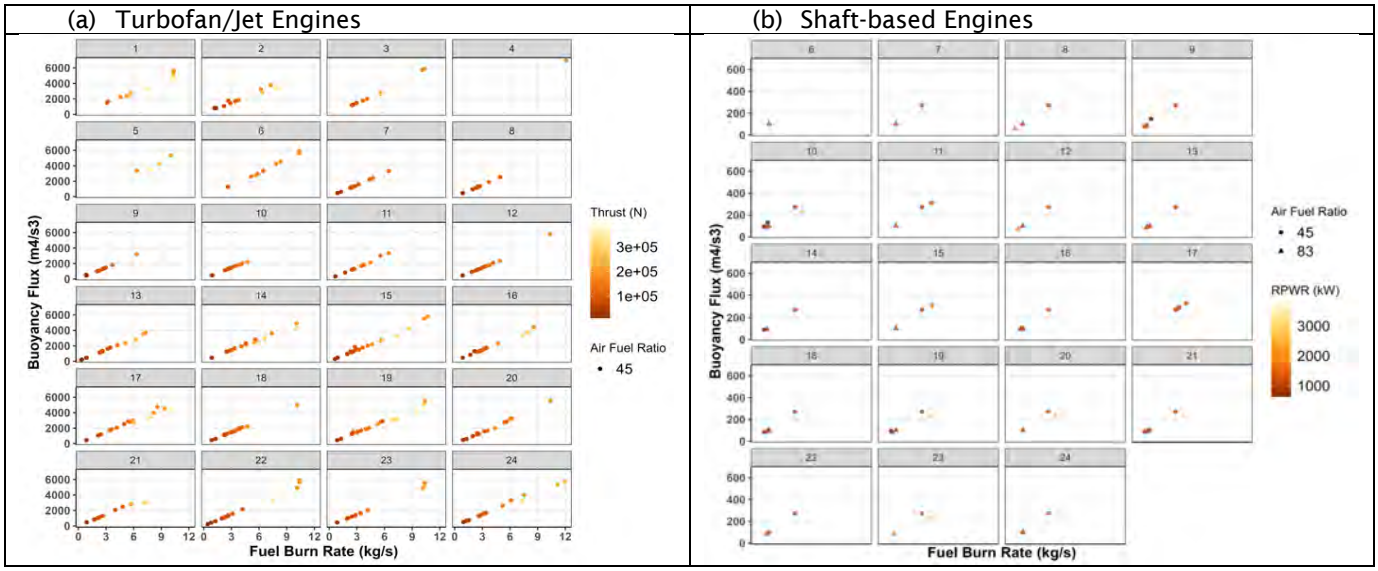

Figure 13. Buoyancy flux with respect to fuel burn rate for (a) turbofan, and (b) shaft-based aircraft engines for airborne sources at 22 m height.

2.1.5.2 Plume Rise

Here, we calculate the plume rise at 100 m downwind from the sources for both type of engines at each mode (Figures 14 and 15).

2.1.5.2.1 Surface Aircraft Sources

For surface sources, the maximum plume rise at 100 m downwind distance is about 30 m for turbofan/jet engines and around 120 m for shaft-based engines.

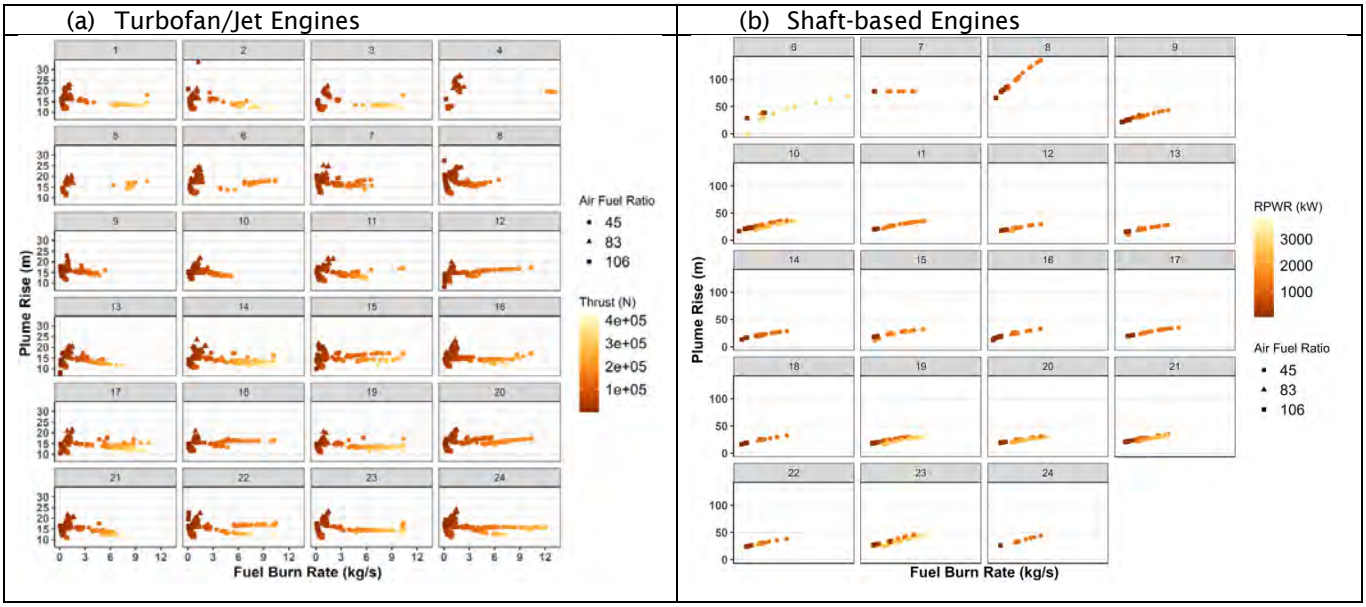

Figure 14. Plume rise with respect to fuel burn rate for (a) turbofan, and (b) shaft-based aircraft engines for airborne sources at 12 m height at each landing/take-off (LTO) mode.

2.1.5.2.2 Airborne Aircraft Sources

For airborne sources, the maximum plume rise at 100 m downwind distance was about 180 m for turbofan/jet engines and around 150 m for shaft-based engines.

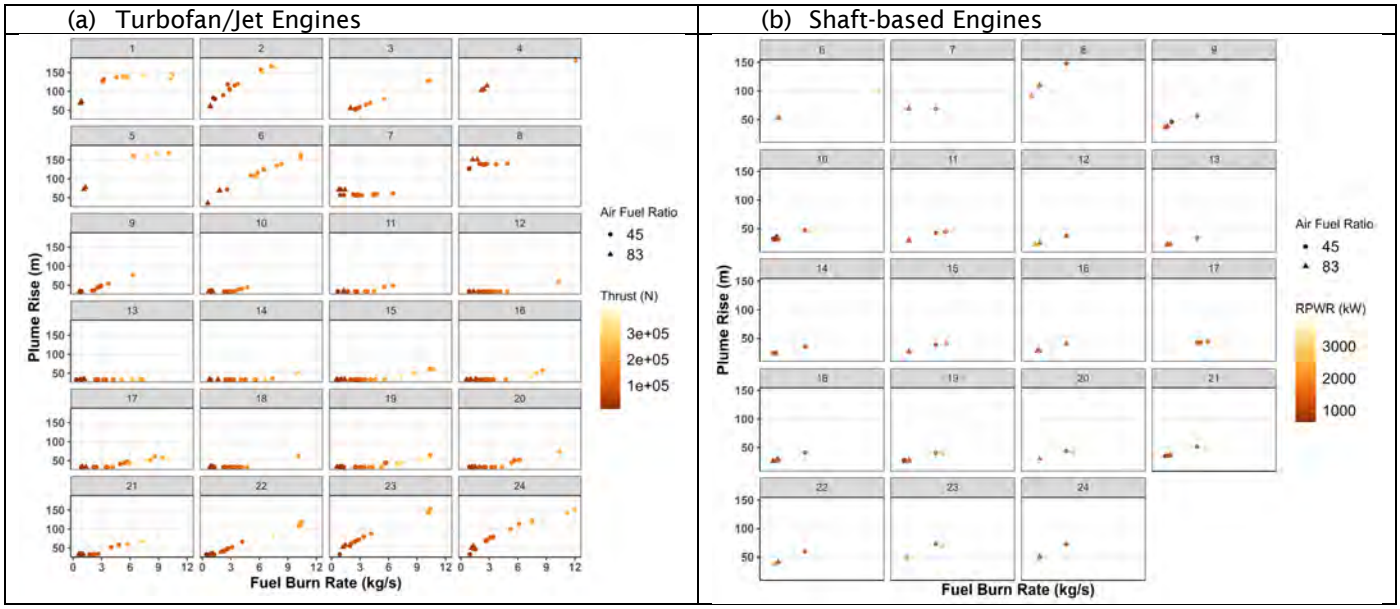

Figure 15. Plume rise with respect to fuel burn rate for (a) turbofan, and (b) shaft-based aircraft engines for airborne sources at 22 m height at each landing/take-off (LTO) mode.

2.1.6 Meteorological Modifications in AERMET-Generated Output Files

Modeling dispersion of aircraft-related sources poses challenges because of the large number and variety of airport sources, which include aircraft, ground operation vehicles, and traffic in and out of the airport, most of which are mobile. Emissions from aircraft sources are transient, buoyant, and occur at different heights from the ground. Quantifying these emissions and modeling the governing processes is challenging. An added complexity occurs when the airport is situated near a shoreline, where meteorological conditions are far from being spatially uniform. These features that characterize the dispersion of airport emissions are being incorporated into the AERMOD model in this work. This work examines the impact of shoreline meteorology and urban effects on dispersion by comparing model estimates of SO_2 with corresponding measurements made during a field study conducted at LAX during winter and summer of 2012 at the four core sites (AQ, CN, CE, and CS) as part of the LAX AQSAS. We modified the output from AERMOD's meteorological preprocessor AERMET to account for (a) the formation of the internal boundary layer that is formed when stable air from the ocean flows onto the warmer land surface of the airport, and (b) urban roughness effects on winds flowing from Los Angeles, east of the airport. Simulations with unmodified AERMET yielded concentrations that were substantially higher than the concentrations at AQ and CS and much lower than those at CN and CE. Model performance improved when AERMOD used modified meteorology. The fraction of model estimates within a factor of 2 of the observations (FAC2) improved from 0 to 31% at the CS and CE sites by up to 50% in winter season, whereas in summer, FAC2 improved only at the CE site. The ratio of robust highest modeled value to measured value improved from 7.72 to 2.78 and from 4.92 to 1.94, respectively, in winter and summer seasons. Overall, in the morning and late evening hours, concentrations are decreasing with modified met (Figure 16).

This meteorological modification work has been accepted for publication in the *Atmospheric Environment* journal.

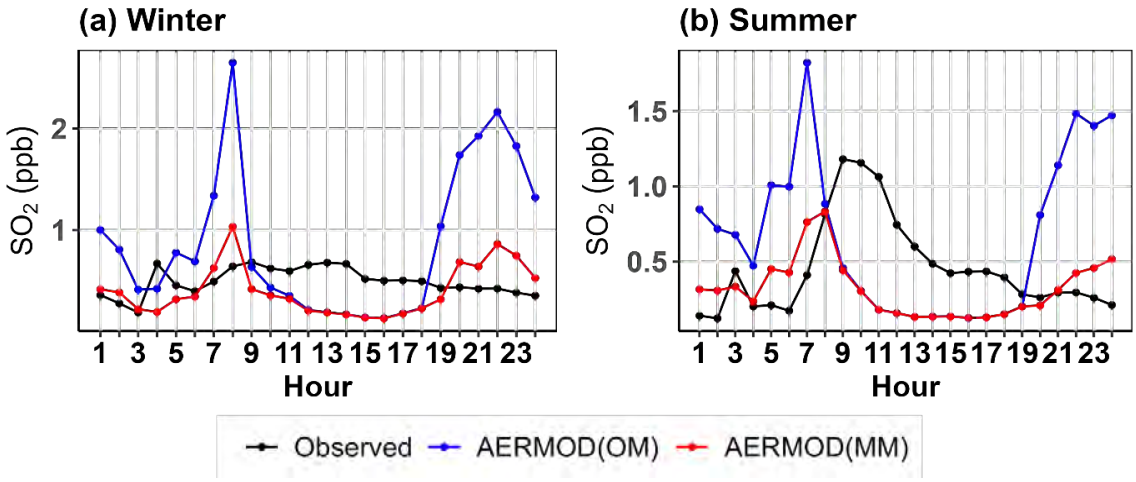

Figure 16. Diurnal variation of SO_2 concentrations averaged over the four sites and experimental periods.

3. Chemical Processes

AERMOD greatly underpredicted the NO_2 concentrations using all its chemistry schemes, which was due to the lack of chemical reactions. More detailed chemistry schemes can improve the estimation of NO_2 concentrations. ADM is a decoupled model, where the dispersion module first estimates the NOx and volatile organic compound (VOC) concentrations at each of the receptors along with "Age," the time it takes to reach the receptor from the source. ADM chemistry uses these concentrations as initial concentrations and Age as time to solve differential chemistry equations for NO_2 and PM. Addition of VOC speciation using Wilkerson et al. (2010) did not greatly improve the NO_2 concentrations.

In ADM, NO_x-NO_2 conversion can be modeled using four different schemes: ozone limiting method (OLM) based on Cole and Summerhays (1979), travel time method (TTM) based on AERMOD's travel time reaction method (TTRM), generic reaction set (GRS) based on Venkatram et al. (1994), and ambient ratio method (ARM) based on AERMOD's ARM2. Although NO_2 contributions by LTO operations at each receptor are estimated for both summer and winter periods, only summer results are used for model evaluation.

Model performance was compared against observations after adding the NO_x concentrations from AERMOD (with non-LTO emissions) to ADM-dispersion outputs. OLM performed slightly better than the other three schemes, followed by TTRM, GRS, and ARM. The ADM results for NO_2 concentrations contributed by LTO operations can be seen in Figure 17. To evaluate model performance, the ADM results from all operations near LAX can be seen in Figure 18, and the evaluation metrics for different schemes can be found in Table 5.

Diurnal Concentration Distribution

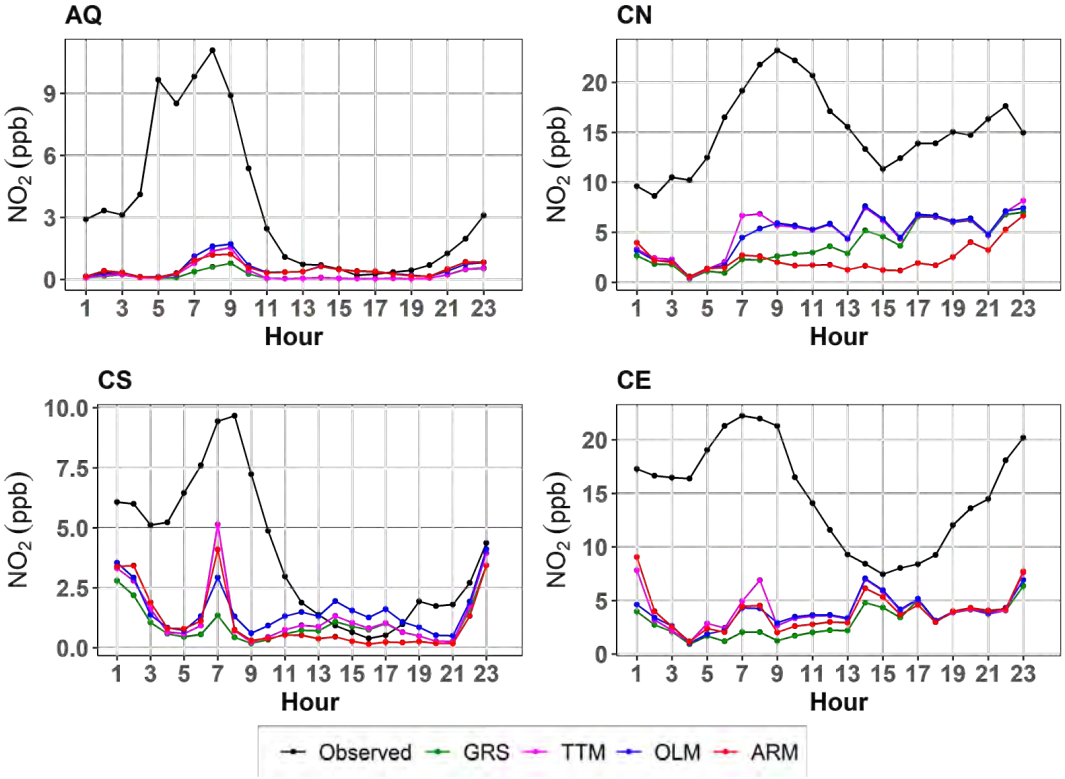

Figure 17. Diurnal variability in observed and modeled NO_2 concentrations for the summer period at all four core sites (AQ, CN, CS, and CE) contributed by the landing/take-off (LTO) operations at LAX. GRS, generic reaction set; TTM, travel time method; OLM, ozone limiting method; ARM, ambient ratio method.

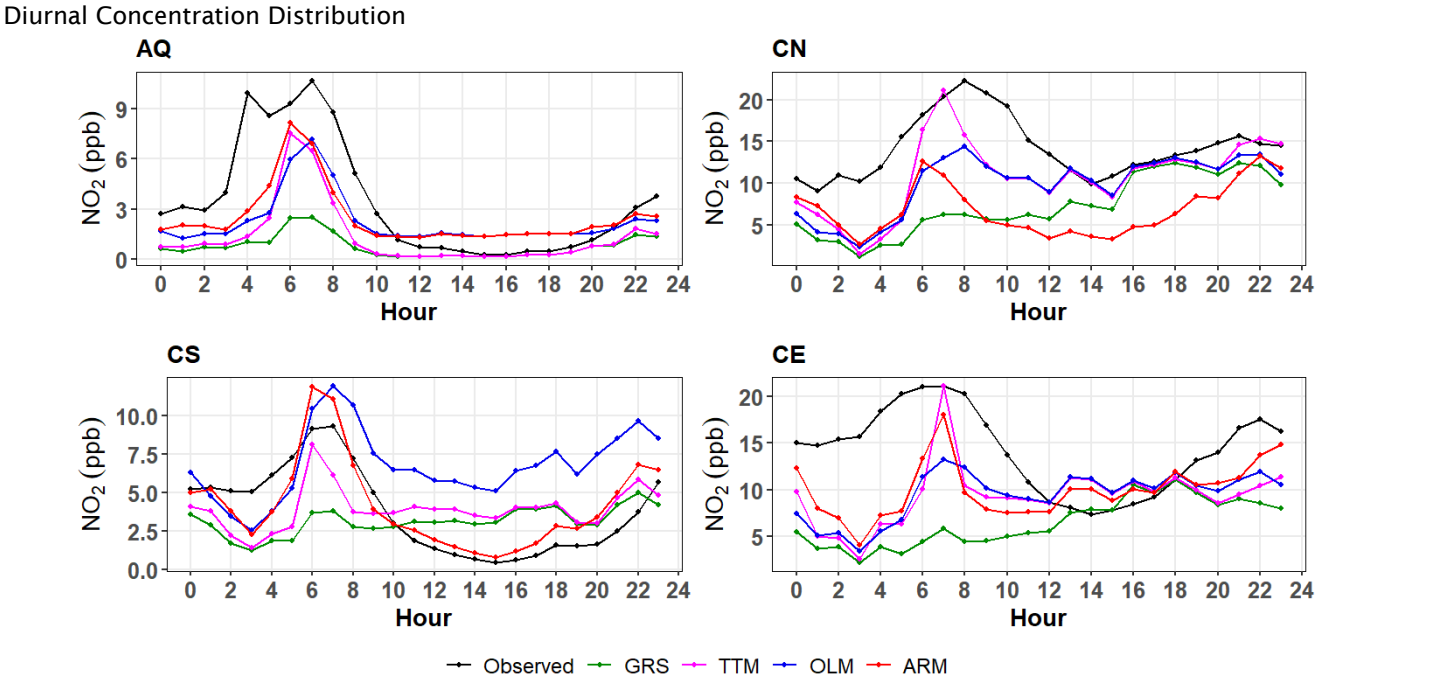

Figure 18. Diurnal variability in observed and modeled NO_2 concentrations for summer period at all four core sites (AQ, CN, CS, and CE) contributed by the landing/take-off (LTO) operations modeled by LAX and the rest of the emissions modeled by AERMOD. The evaluation metrics for each of these schemes can be found in Table 5. GRS, generic reaction set; TTM, travel time method; OLM, ozone limiting method; ARM, ambient ratio method.

Table 5. Evaluation metrics for different ADM chemistry schemes. GRS, generic reaction set; TTM, travel time method; OLM, ozone limiting method; ARM, ambient ratio method[3].

	FAC2	R2	FB	IOA	AFB_RHC
GRS	0.33	0.44	0.68	0.56	0.38
TTM	0.39	0.49	0.33	0.59	-0.9
OLM	0.45	0.47	0.22	0.59	0.31
ARM	0.48	0.37	0.44	0.57	-0.62

From the results, CN and CE were the most affected among the four sites due to aircraft LTO operations. ADM estimated that LTO operations contributed, on average, 4.90 and 3.54 ppb/hour of NO_2 at the sites CN and CE, respectively. These values are comparable with those of Carslaw et al. (2006); they estimated upper limit of NO_2 contribution as 7.98, 3.51, 3.46, 2.23, 1.06, 0.8, and 0.8 ppb at seven receptors using 2001–2004 data.

We also coded for modified GRS (MGRS) based on Venkatram et al. (1997) but are still determining the initial concentrations for other chemical compounds involved in this scheme. Initial results for MGRS can be seen in Figure 19, where the initial concentrations of compounds other than NO and NO_2 are assumed as ROC1 = 0.5*ROG; AROM=0.5*ROG; TERP=0; aH2O2=0; RNO3=0; OH=10; SO4=0; HNO3=0; y1_OC=0; y2_OC=0; SO2=0. The underestimation of NO_2 could be due to lower VOC concentrations or due to the conversion of NO_2 to HNO_3. [ROC: Reactive Organic Compounds; ROG: Reactive Organic Gases;

[3] FAC2: Factor of two; R2: R-squared; FB: Fractional Bias; IOA: Index of Agreement; AFB_RHC: Fractional Bias for Robust Highest Concentrations

AROM: Aromatics; TERP: Terpenes; H2O2: Hydrogen Peroxide; RNO3: Radical Nitrate; SO4: Sulfate; HNO3: Nitric Acid; OC: Organic Carbon; SO2: Sulfur dioxide; NO; Nitrogen oxide; NO2: Nitrogen dioxide]

Diurnal Concentration Distribution

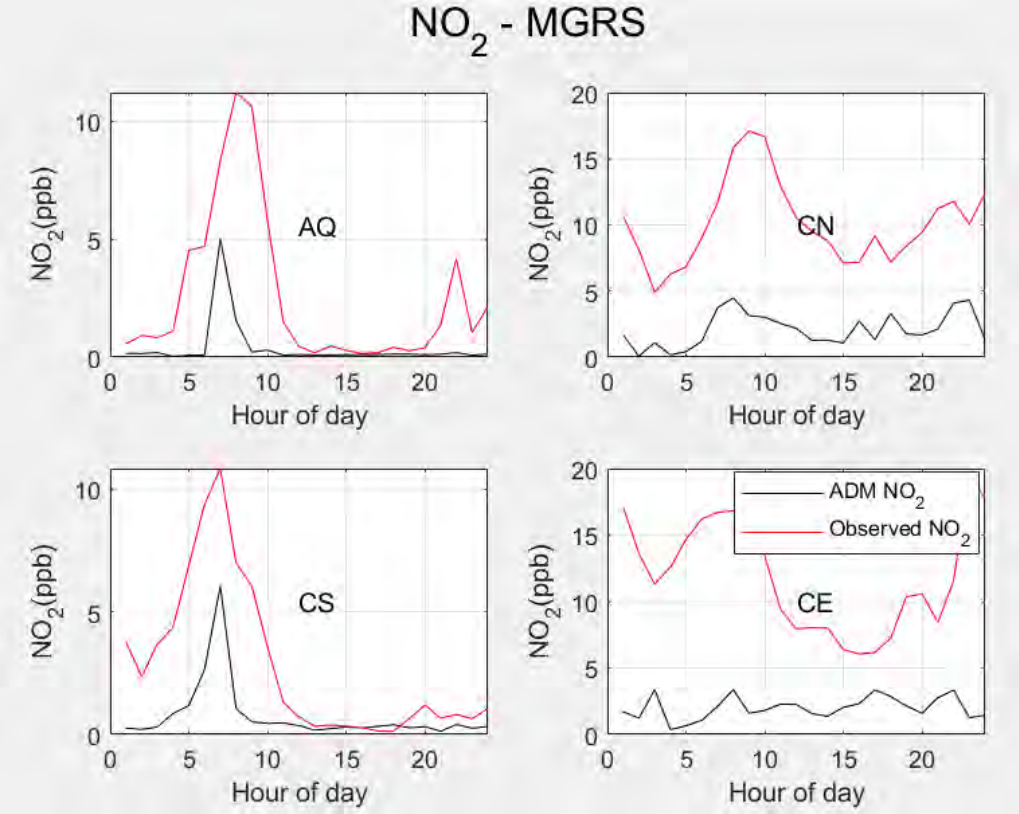

Figure 19. Diurnal variability in observed and modeled NO_2 concentrations for the first 5 days of summer at the four core sites (AQ, CN, CS, and CE) contributed by landing/take-off (LTO) operations at LAX.

4. Model Evaluation

4.1 ADM Evaluation With and Without Plume Rise

The newly developed ADM was evaluated using the SO_2 measurements from the Los Angeles AQSAS for both seasons (winter and summer of 2012). In the past year, we updated the ADM and added some additional features, including meander for low wind dispersion. Here, we present only the diurnal concentration distributions for both seasons. We found that the higher concentrations decreased and came close to the diurnal observed concentrations at all four core sites (AQ, CN, CS, and CE) using the plume rise algorithm and the meander algorithm with ADM in both seasons of 2012 (Figure 20). However, here, we modeled only the aircraft emissions.

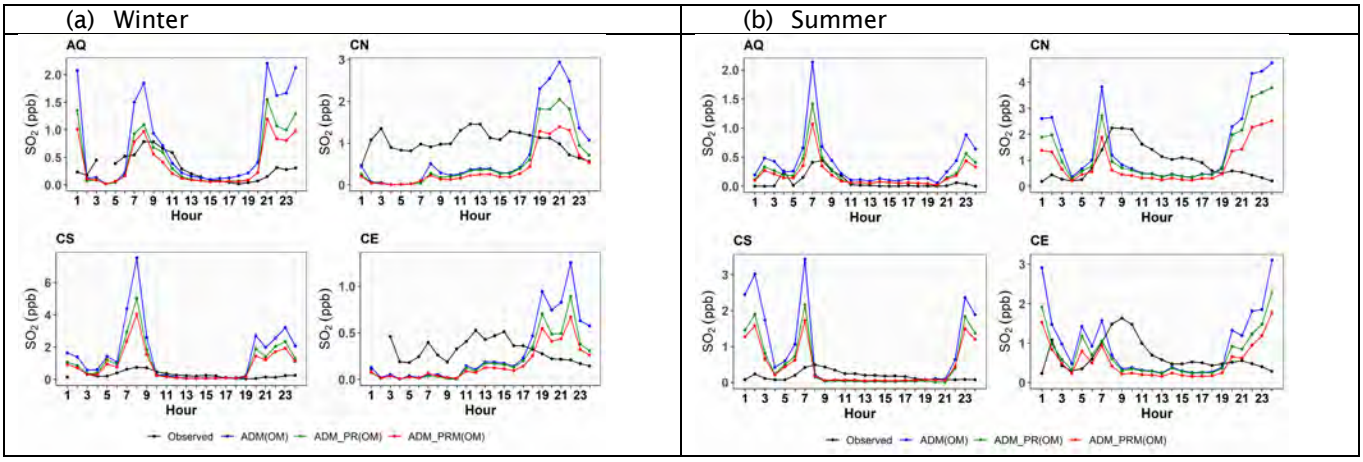

Figure 20. Diurnal variation of SO_2 concentrations at the four core sites (AQ, CN, CS, and CE).

4.2 AERMOD Evaluation With and Without Plume Rise for Both Source Types (AREA and VOLUME)

We evaluated updated AERMOD having plume rise using NOx observed concentrations for both source types only in summer of 2012. Here, we used only the emissions from aircraft sources. We found that the high concentrations decreased substantially for source types with plume rise (Figures 21 and 22).

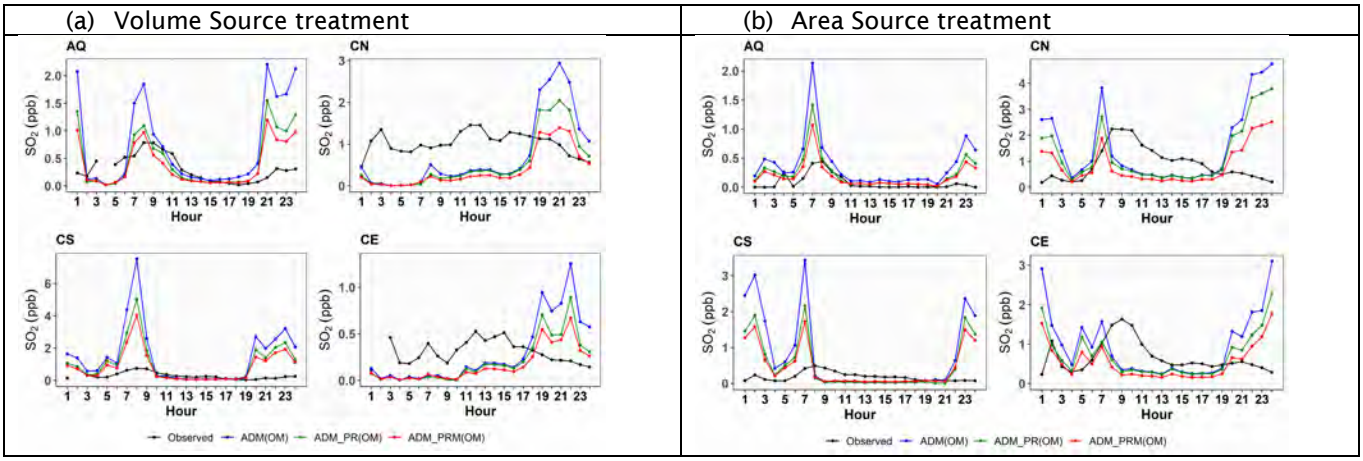

Figure 21. Diurnal variation of NO_x modeled and observed concentrations at the four core sites (AQ, CN, CS, and CE).

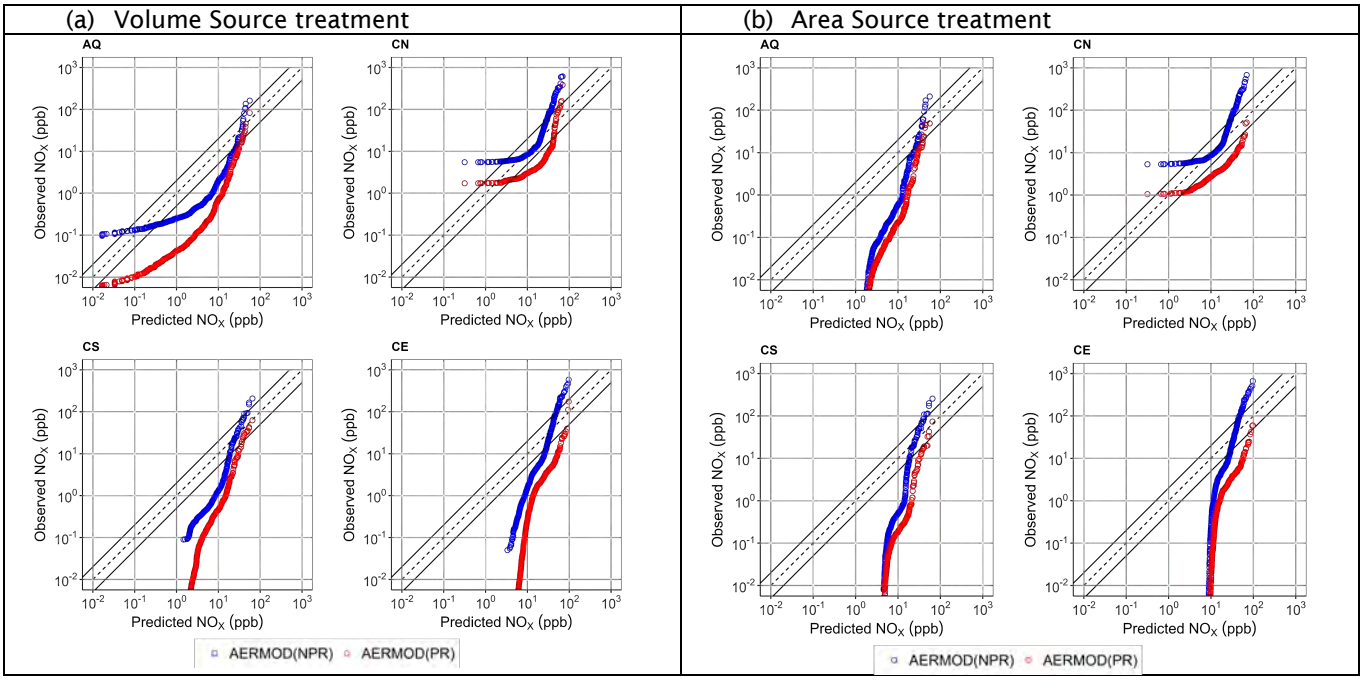

Figure 22. Quantile-quantile (QQ) distribution of NO_x modeled concentrations with respect to observed concentrations at the four core sites (AQ, CN, CS, and CE).

5. Preparing AEDT Emissions Inventories

UNC was involved in all AEDT updates to generate the AERMOD-ready inputs for aircraft plume rise. For this, UNC developed a plume rise algorithm for both types of aircraft engines (turbofan/jet and shaft-based engines). During this development, we found that the jet engine's buoyancy flux computation, the heat rejection term became negative. To overcome this, UNC developed another method to compute heat rejection for turbofan/jet engines, which is based on the Mach number but as per the Volpe team, this algorithm was not working for high bypass ratio. After this, we agreed to use the first algorithm, which gives negative heat rejection for inconsistent fuel burn rate and thrust values. We are now ignoring records with negative heat rejection hours/sources. Based on the plume rise parameters file exchange and analysis of those files, UNC performed many statistical analyses of the algorithm and files. UNC also developed two different approaches to compute the buoyancy flux for shaft-based engines, one based on the compression ratio and the other on the rated power. The first method was not applicable to introduce within AEDT, as compression ratio was not available. Based on this work, the Volpe team updated the AEDT model to generate AERMOD-ready input files as well as files for AEDT2ADM.

Task 2: Develop and Evaluate a Multiscale WRF-SMOKE-CMAQ Model Application for BOS Focused on UFP

1. CMAQ Application for BOS

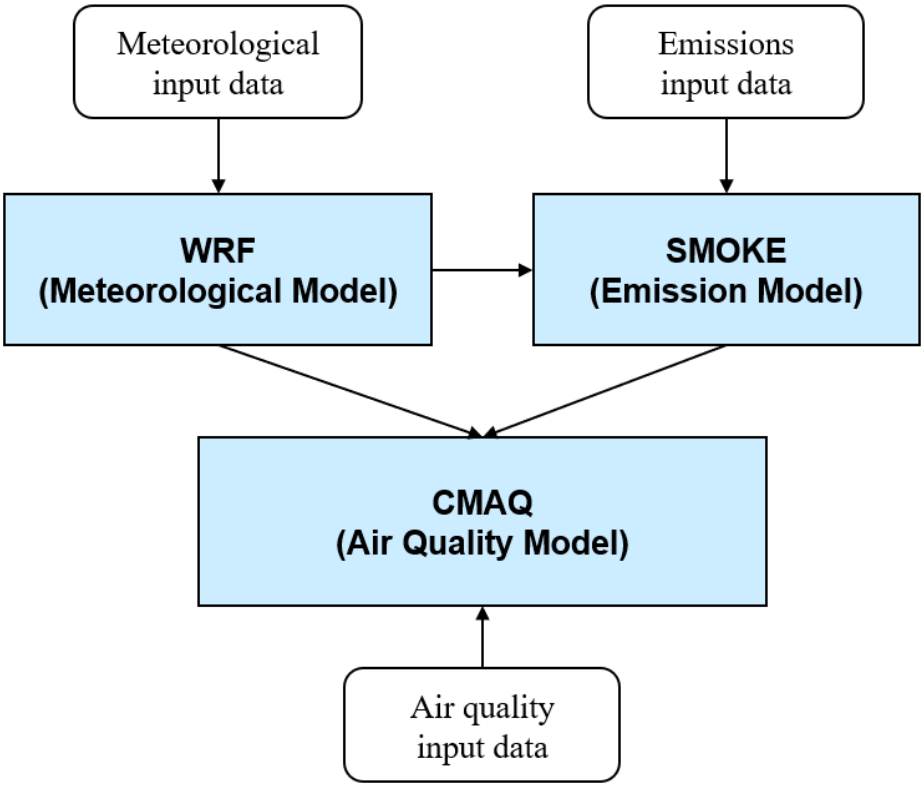

Figure 23. Weather Research and Forecasting–Sparse Matrix Operator Kernel Emissions–Community Multiscale Air Quality Model (WRF-SMOKE-CMAQ) modeling system.

1.1 Weather Research and Forecasting (WRF)
Weather Research and Forecasting (WRF) was developed by the National Center for Atmospheric Research (NCAR) and the National Center for Environmental Prediction (NCEP) in the National Oceanic and Atmospheric Administration (NOAA). It is a meteorological model using fully compressible non-integer equations, and the horizontal grid utilizes the Arakawa-c grid system and uses the hydrostatic barometric pressure vertical coordinates based on topography. The WRF modeling software consists of a dynamic processing module (ARW solver) including preprocessing, bidirectional and unidirectional nesting, and various post-processing programs.

1.2 Community Multiscale Air Quality Model (CMAQ)
The CMAQ modeling system is currently widely used in various fields by many researchers worldwide. The preprocessors of CMAQ are ICON (Initial CONditions processor), which is an initial condition generation module, BCON (Boundary CONditions processor), which is a boundary condition generation module, MCIP (Meteorology-Chemistry Interface Processor), which is in charge of preprocessing meteorological data, and a chemical transport module, which is composed of CCTM (Chemical Transport Model). Using the results derived through the preprocessing module as input data, CCTM numerically calculates the 3D advection diffusion equation to calculate the concentration of pollutants in space every hour. At this time, horizontal and vertical advection, horizontal and vertical diffusion, deposition, and gaseous chemical reactions, etc. applied to the law of conservation of mass in the advection process are considered.

1.3 Comparison of Base-NEI 2017 (2017 National Emission Inventory [NEI]) and No-Airport (NEI Without Airport Emission)

CMAQ was used to evaluate the impact of airport emissions with configuration in Table 6 for winter (January) and summer (July) 2017.

Table 6. CMAQ v5.3.3 model configuration.

	Domain 1	Domain 2	Domain 3
Horizontal Grid	459 × 299 (12US2)	102 × 108	126 × 141
Resolution (km)	12 km × 12 km	4 km × 4 km	1.33 km × 1.33 km
Vertical Grid	35 Layers		
CMAQ Chemical Option	· Carbon Bond 6 r3 · AERO 6 non-volatile POA (6th generation CMAQ aerosol module)		
SMOKE Input Data	· NEI 2017 Emission		
Modeling Period	January 1-31, 2017	July 1-31, 2017	
	2-week spin-up in Dec 2016	2-week spin-up in June 2017	

1.4 $PM_{2.5}$ Monthly Average

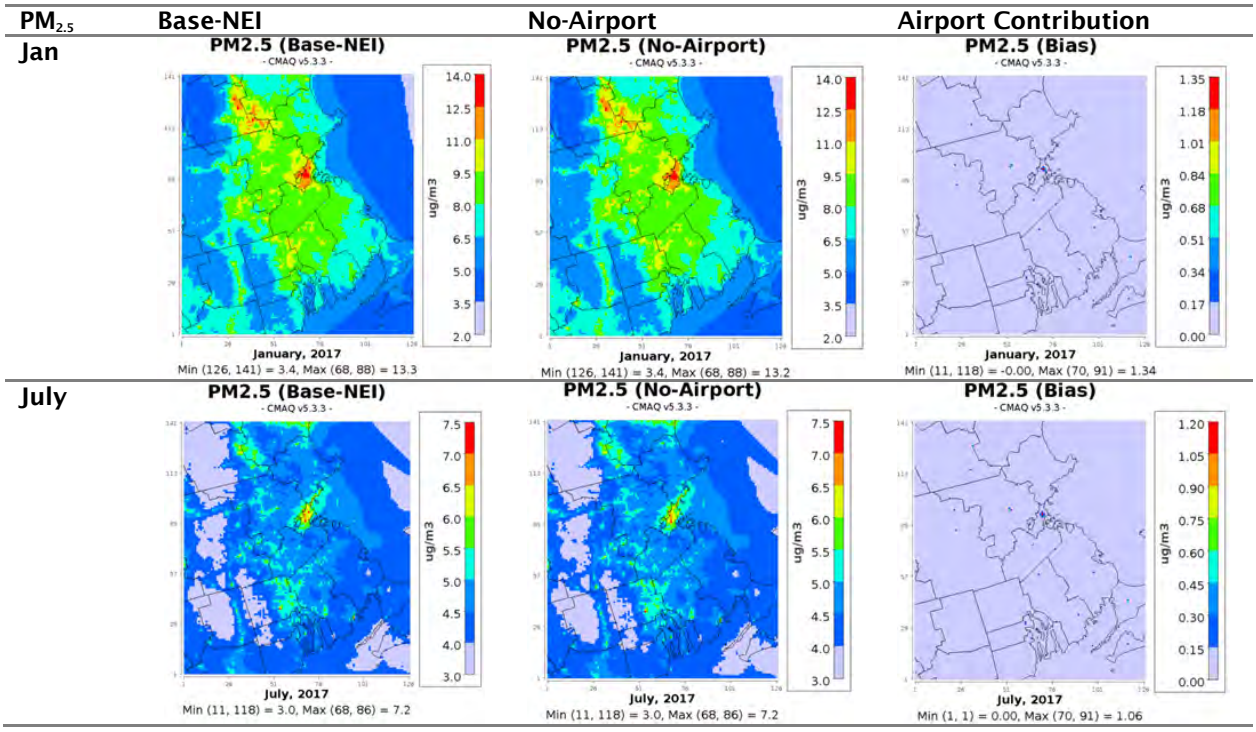

Figure 24. Comparing Base-NEI and No-Airport with $PM_{2.5}$ (monthly average) for January and July (1.33 km × 1.33 km).

CMAQ modeling of $PM_{2.5}$ monthly average concentration for January 2017 demonstrated a 10.7% reduction in $PM_{2.5}$ concentration (from 12.5 to 11.2 μg/m^3) at Airport grid-cell (70, 91), showing the maximum reduction. For July 2017, although the absolute concentration reduction and maximum concentration were low, the 15.1% reduction in $PM_{2.5}$ (from 7.0 to 6.0 μg/m^3) showed that the contribution of airport emission to $PM_{2.5}$ was higher in July than in January.

1.5 Maximum Daily Average 8-Hour O_3 Monthly Average

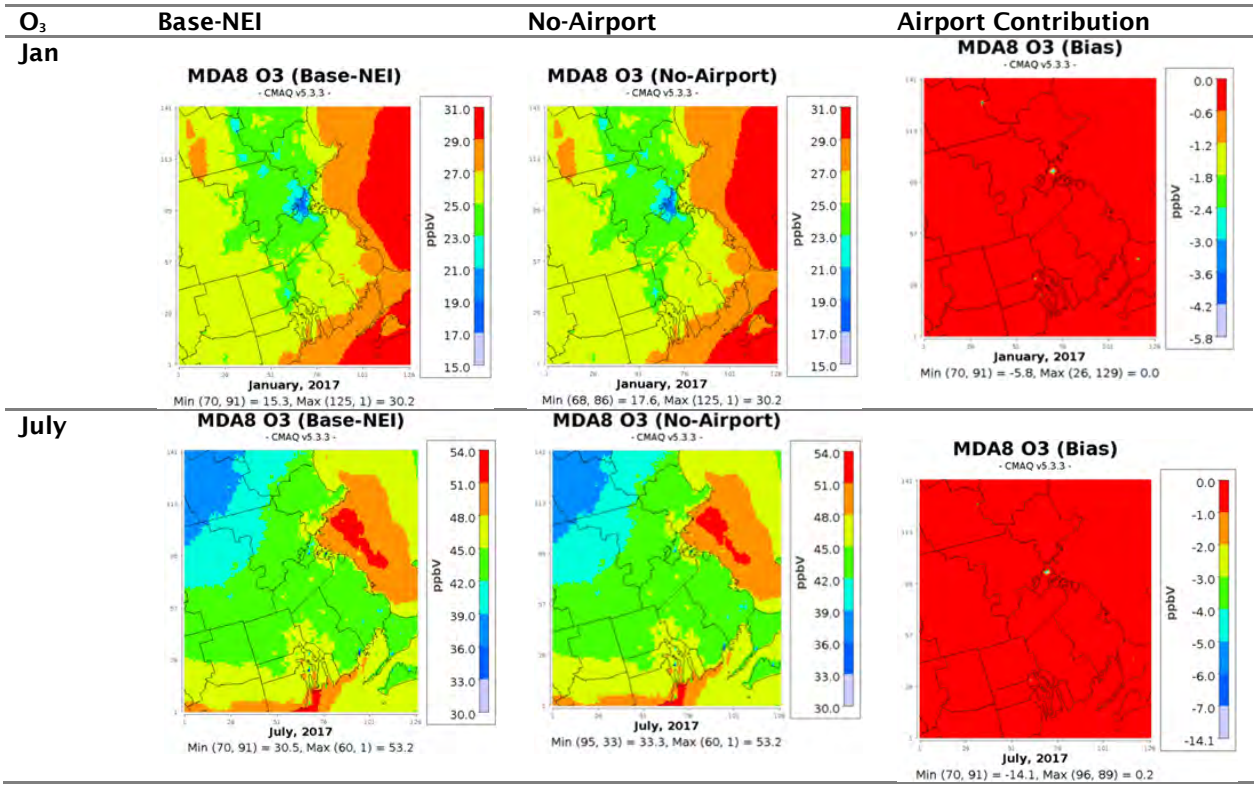

Figure 25. Comparing Base-NEI and No-Airport with O_3 (maximum daily average 8-hour) for January and July (1.33 km × 1.33 km).

In contrast, monthly average of O_3 maximum daily average 8-hour (MDA8 O_3) for January 2017 demonstrated a 37.9% increase in $PM_{2.5}$ concentration (from 15.3 to 21.1 ppb) at Airport grid-cell (70, 91), showing the maximum differences. For July 2017, $PM_{2.5}$ increased 46.2% (from 30.5 to 44.6 ppb), showing that the contribution of airport emission to O_3 (as shown by $PM_{2.5}$ concentration) was higher in July than in January.

1.6 NO_2 Monthly Average by Time

NO_2	Base-NEI	No-Airport	Bias
Jan	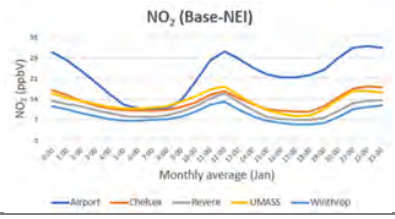	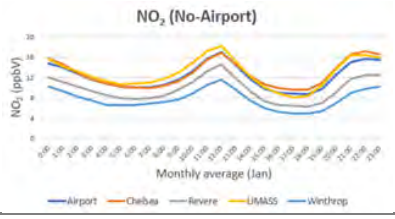	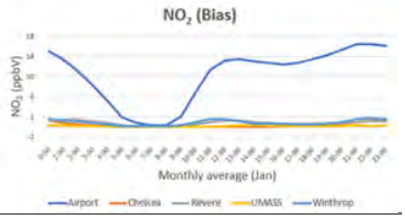
July	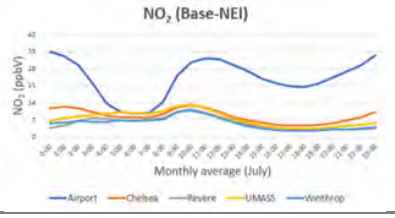	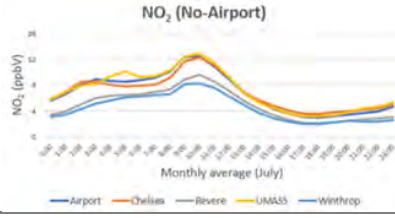	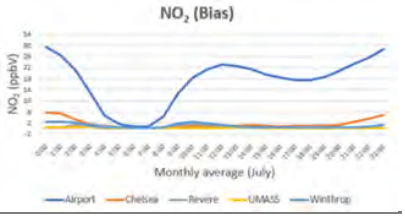

Figure 26. Comparing Base-NEI and No-Airport with NO_2 (monthly average each time) for January and July with airport and four monitoring sites.

In the Base-NEI scenario, NO_2 monthly average concentration by time for January (from 10.4 to 32.0) and July 2017 (from 9.4 to 35.0) showed that NO_2 concentration was highest at the airport except from 5:00 to 7:00 AM because of aircraft activities. In the No-Airport scenarios, however, airports with four monitoring sites, which were the near airport, showed a similar pattern of NO_2 concentrations.

2. Computing Exceedance in the Boston Domain

The Clean Air Act requires EPA to set NAAQS for six principal pollutants ("criteria" air pollutants) that can be harmful to public health and the environment. Units of measure for the standards are parts per million (ppm) by volume, parts per billion (ppb) by volume, and micrograms per cubic meter of air (μg/m^3). CMAQ results are post-processed to evaluate the contribution of airport for criteria pollutants based on NAAQS analyses. Therefore, we computed exceedances in the Boston area (1.33 km domain) by scenarios with different pollutants ($PM_{2.5}$, O_3, and NO_2) for January and July.

2.1. Daily $PM_{2.5}$

In January, 840 grid-cells in the Base-NEI scenario and 822 grid-cells in the No-Airport scenario exceeded 25 μg/m^3 of $PM_{2.5}$, a difference of 18 grid-cells near airports; no grid-cell exceeded more than twice. The number of grid-cells exceeding 30 μg/m^3 of $PM_{2.5}$ was 80 in the Base-NEI scenario and 75 in the No-Airport scenario, a difference of 5 grid-cells, near Manchester-Boston Regional Airport. Even though the highest monthly average $PM_{2.5}$ occurred near BOS, a greater number of exceedances were found near Manchester-Boston Regional Airport. No grid-cells showed $PM_{2.5}$ exceedances of more than 35 μg/m^3. In July, 22 grid-cells exceeded the 25 μg/m^3 of $PM_{2.5}$ concentration in the Base-NEI and No-Airport scenarios (Table 7 and Figure A1).

Table 7. The number of daily $PM_{2.5}$ exceedances in Boston domain by scenario.

Daily $PM_{2.5}$ Scenarios	Exceeded 25 µg/m³	Exceeded 30 µg/m³	Exceeded 35 µg/m³
Base-NEI (Jan)	840	80	7
Base-NEI (Jul)	22	0	0
No-Airport (Jan)	822	75	7
No-Airport (Jul)	22	0	0

2.2 Annual $PM_{2.5}$

A total of 233 grid-cells in the Base-NEI scenario and 221 grid-cells in No-Airport scenario exceeded 8 µg/m³ of $PM_{2.5}$, with eight of these 12 grid-cells near airports. Two and one grid-cells, respectively, exceeded 10 µg/m³ of $PM_{2.5}$ in the Base-NEI and No-Airport scenarios; the only difference was at BOS. No grid-cell showed annual $PM_{2.5}$ exceedances of more than 12 µg/m³ (Table 8 and Figure A2).

Table 8. The number of annual $PM_{2.5}$ exceedances in the Boston domain by scenario.

Annual $PM_{2.5}$ Scenarios	Exceeded 8 µg/m³	Exceeded 10 µg/m³	Exceeded 12 µg/m³
Base-NEI (Jan + Jul)	233	2	0
No-Airport (Jan + Jul)	221	1	0

2.3. Ozone (O_3)

In January, no grid-cells showed O_3 exceedances at any standard (60, 65 70 ppb). In contrast, the July O_3 concentration exceeded 60 ppb at 29,166 grid-cells in the Base-NEI scenario and 28,946 in the No-Airport scenario, showing differences mainly on the East and South coastline. Some grid-cells exceeded 60 ppb on 14 of 31 days. Although the number of grid-cells exceeding 65 ppb decreased by more than half relative to 60 ppb, more than 12,000 grid-cells exceeded 65 ppb in both scenarios. More than 4,684 grid-cells exceeded the O_3 standard (70 ppb) in the Base-NEI scenario. The number exceeding 70 ppb increased near Boston airport (Table 9 and Figure A3).

Table 9. The number of maximum daily average (MDA) 8-hour O_3 exceedances in the Boston domain by scenario.

MDA O_3 Scenarios	Exceeded 60 ppb	Exceeded 65 ppb	Exceeded 70 ppb
Base-NEI (Jan)	0	0	0
Base-NEI (Jul)	29,166	12,508	4684
No-Airport (Jan)	0	0	0
No-Airport (Jul)	28,946	12,324	4638

2.4. Nitrogen Dioxide (NO_2)

A greater number of grid-cells exceeding 5 ppb and 10 ppb were found in the Base-NEI compared with the No-Airport scenario in January and July. The only grid-cells exceeding 20 ppb were for BOS in January and July. No grid-cells exceeded the NO_2 NAAQS standard (53 ppb).

Table 10. The number of NO_2 exceedances in the Boston domain by scenario.

Daily NO_2 Scenarios	Exceeded 5 ppb	Exceeded 10 ppb	Exceeded 20 ppb	Exceeded 53 ppb
Base-NEI (Jan)	4,392	129	1	0
Base-NEI (Jul)	148	15	1	0
No-Airport (Jan)	4,328	122	0	0
No-Airport (Jul)	131	10	0	0

2.5. Particle Number Concentration (PNC)

The ultrafine particle number concentration (UFPNC) was computed based on error function approximation (Jiang et al., 2006; Meng & Seinfeld, 1994). The diameter for UFP in this research was between 7 nm and 100 nm. The UFPNC is the sum of Aitken mode and accumulation mode with their diameter and standard deviation.

Table 11. Calculation of UFP number concentrations.

Variable	Value or Equation
Low diameter cut (LDC)	7 nm
Upper diameter cut (UDC)	100 nm
Aitken mode	
ERF1 Aitken [a, b]	ERF((LOG(LDC) - LOG(DGATKN_WET))/(SQRT * LOG(STDEVATKN)))
ERF2 Aitken	ERF((LOG(UDC) - LOG(DGATKN_WET))/(SQRT * LOG(STDEVATKN)))
fUFP Aitken	0.5*(ERF2_ATKN – ERF1_ATKN)
Aitken UFP number Conc.	NUMATKN * fUFP_ATKN
Accumulation mode	
ERF1_ACC	ERF((LOG(LDC) - LOG(DGACC_WET))/(SQRT * LOG(STDEVACC)))
ERF2_ACC	ERF((LOG(UDC) - LOG(DGACC_WET))/(SQRT * LOG(STDEVACC)))
fUFP_ACC	0.5*(ERF2_ACC – ERF1_ACC)
ACC. UFP number Conc.	NUMATKN * fUFP_ACC
UFP Number	UFP_ATKN + UFP_ACC

[a] ERF, error function approximation (Meng & Seinfeld, 1994), [b] ERF1, ERF2 (Jiang et al., 2006).

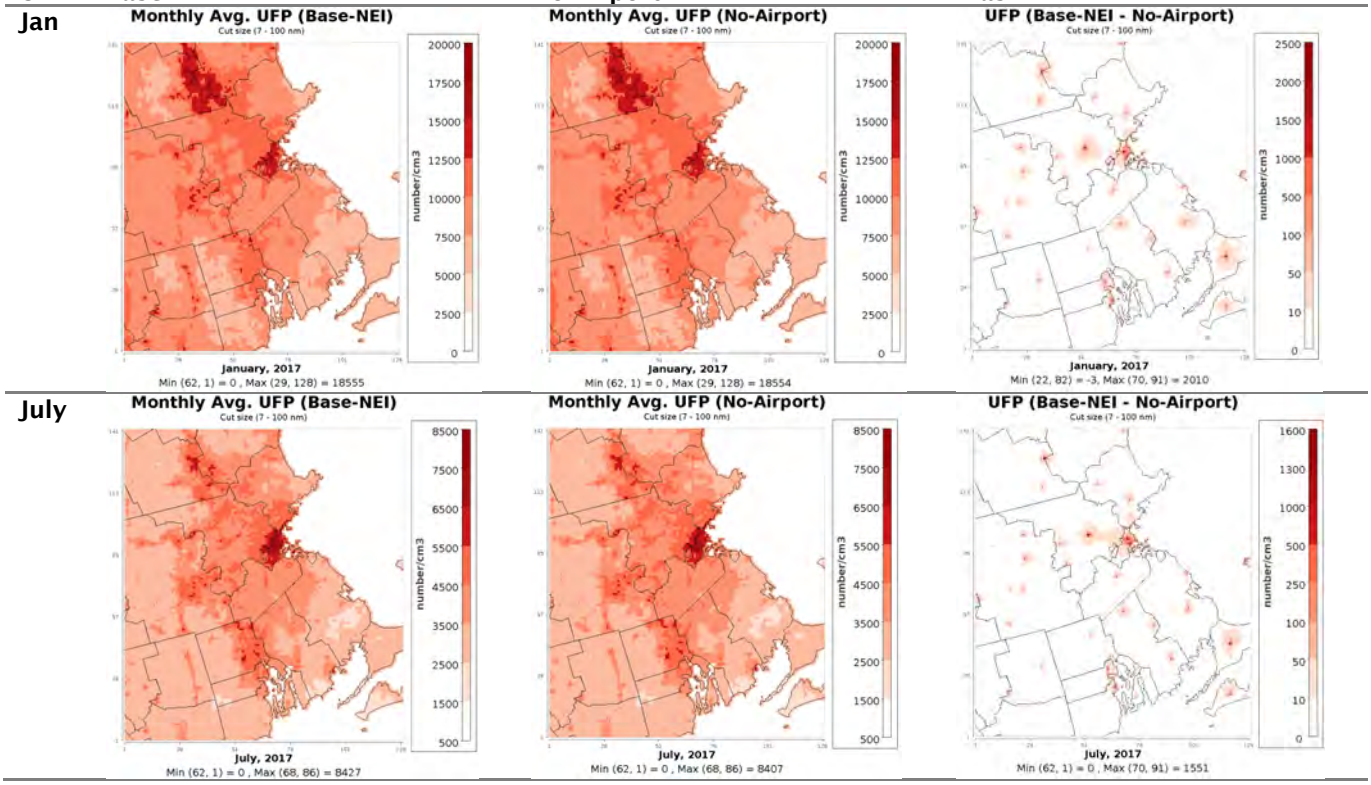

Figure 27. Comparing Base-NEI and No-Airport scenarios with UFP (monthly average) for January and July (1.33 km × 1.33 km).

The monthly average of UFPNC for January 2017 demonstrated that UFPNC decreased by 12.8% (from 15,611 to 13,601 number/cm^3) at airport grid-cell (70, 91) when airport emissions were removed, the maximum reduction. For July 2017, although the absolute concentration reduction and maximum concentration were low, the 19.0% reduction in UFPNC (from 8,157 to 6,606 number/cm^3) showed that the contribution of airport emissions to UFP was higher in July than in January. The contribution of airport emissions to UFP (12.8%, 19.0%) was higher than that to $PM_{2.5}$ (10.7%, 15.1%) for January and July, respectively.

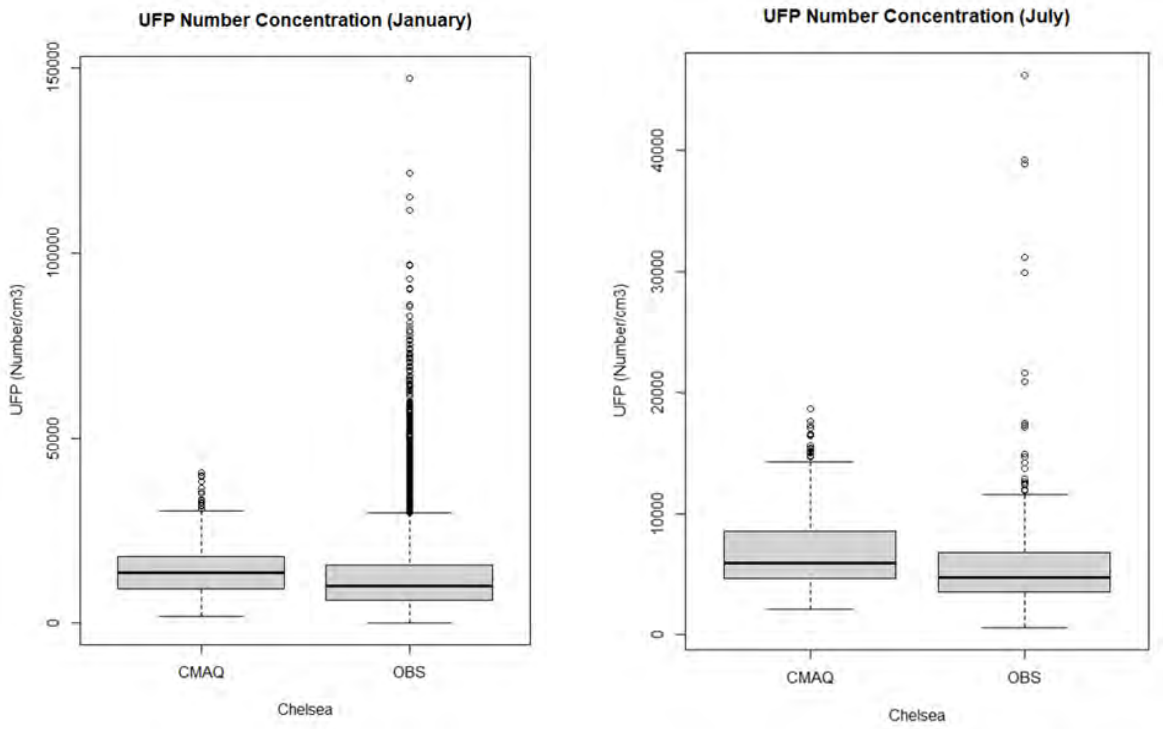

Figure 28. Comparison of CMAQ (Base-NEI) and Observation (OBS) boxplots at Chelsea in January and July.

CMAQ overpredicted the median of observed UFP distribution by 9% for January and by 23% for July but underestimated the 95th percentile by 37% for January and by 3% for July at Chelsea. Furthermore, CMAQ (40,734 number/cm^3) underpredicted the UFPNC by more than half compared with observations (81,101 number/cm^3) at maximum for January. In July, UFPNC showed the same pattern of underprediction between CMAQ (18,683 number/cm^3) and observation (46,230 number/cm^3).

3. Development of AEDT-Based Inventories for BOS

After identifying the basic requirements to run AEDT-3e, we acquired a new desktop server meeting those requirements. We had technical difficulties adding the server to the UNC system and obtaining administrative rights (which are necessary to install AEDT). We successfully installed and ran AEDT-3e for the current IAD Dulles study to obtain dispersion results for NO_2 concentrations at the receptors. The results from the run can be seen in Figure 29.

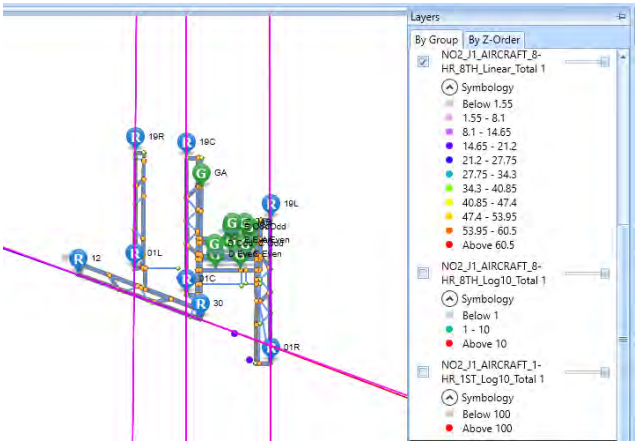

Figure 29. IAD Dulles Airport layout with NO_2 concentrations (in ppb) at the receptors.

Along with the BOS-AEDT study, we are also working on the LAX-AEDT summer 2012 study to replicate the results. SQL-Express could not load a database >10 GB, so we reinstalled AEDT on SQL-Eval 2017 to run the LAX-AEDT test case. The setup for this study can be seen in Figure 30. For AEDT-LAX data, we were able to create seasonal average emission reports.

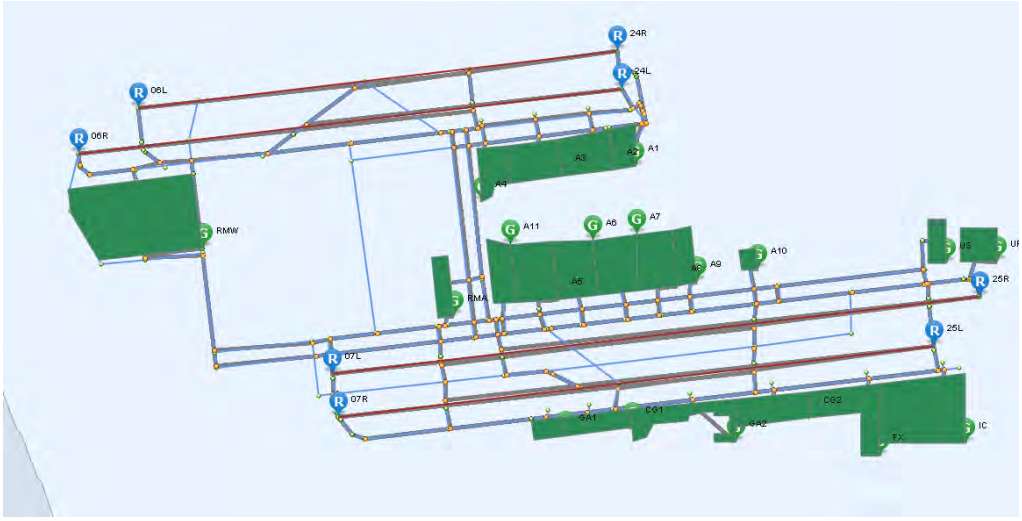

Figure 30. LAX airport layout for summer 2012 study.

We listed the data needed as inputs to run the BOS-AEDT study for 2017. Initially, we only obtained hourly averaged aircraft operational data from BU but later received Performance Data Analysis and Reporting System (PDARS) data. After analyzing it, we highlighted the data gaps for the BOS-AEDT study, which can be found in Appendix Table A1.

Milestones

We submitted drafts of the following documents to the FAA:

- Design document for ADM
- Version 2 of ADM
- Scoping plume Rise treatment document for AEDT/AERMOD plume rise implementation

We also shared the updated AERMOD plume rise implemented version with EPA/FAA.

Major Accomplishments

- Updated design document detailing features that will go into the new ADM
- Developed a scoping document on plume rise treatment with a focus on AERMOD
- Developed a final version of plume rise treatment
- Implemented plume rise in AERMOD and delivered it to the EPA/FAA
- Drafted papers on plume rise algorithm and AREA vs VOLUME source comparison and evaluation of AERMOD at LAX AQSAS

Publications

- Pandey, G., Venkatram, A., & Arunachalam, S. (2022). Evaluating AERMOD with measurements from a major U.S. airport located on a shoreline. *Atmospheric Environment, 294, 119506*. doi:10.1016/j.atmosenv.2022.119506

Outreach Efforts

We presented the ADM work in multiple arenas, including the CMAS 2021 conference held in Chapel Hill (November 2021), the AEC Roadmap meeting held in Washington, DC (May 2022), and the 21st HARMO conference held in Aveiro, Portugal (September 2022).

Awards

None.

Student Involvement

Praful Dodda and Hyeongseok "Darby" Kim are PhD students involved in developing ADM chemistry and the Boston case study, respectively.

Plans for Next Period

- Finalize plume rise implementation in AERMOD and finalize manuscript for submission
- Finalize AEDT data for Boston case study and redo CMAQ modeling using AEDT data for Boston
- Finalize ADM development and evaluate both ADM and AERMOD with LAX AQSAS data

References

Arunachalam, S., Valencia, A., Woody, M., Snyder, M., Huang, J., Weil, J., Soucacos, P., & Webb, S. (2017a). *Dispersion modeling guidance for airports addressing local air quality concerns.* Transportation Research Board Airport Cooperative Research Program (ACRP) Research Report 179. http://nap.edu/24881

Arunachalam, S., V. Isakov, T. Barzyk, A. Venkatram, J. Weil, B. Naess, A. Valencia, C. Seppanen, J. Brandmeyer (2017b). C-AIRPORT: A New Web-based Air Quality Model for Community-Scale Assessments around Airports, *In Proceedings of the 18th International Conference on Harmonisation within Atmospheric Dispersion Modelling for Regulatory Purposes*, Bologna, Italy, October 2017.

Arunachalam, S., B. Naess, C. Seppanen, A. Valencia, J. Brandmeyer, A. Venkatram, J. Weil, V. Isakov, T. Barzyk *(2019).* A new bottom-up emissions estimation approach for aircraft sources in support of air quality modeling for community-scale assessments around airports, *International J. Environ. Pollution*, 65(123):43 - 58, (2019). https://doi.org/10.1504/IJEP.2019.101832.

Barrett, S. R. H., Britter, R. E., & Waitz, I. A. (2013). Impact of aircraft plume dynamics on airport local air quality. *Atmospheric Environment, 74*, 247–258. doi:10.1016/j.atmosenv.2013.03.061

Barzyk, T.M., V. Isakov, S. Arunachalam, A. Venkatram, R. Cook, B. Naess (**2015**). A Near-Road Modeling System for Community-Scale Assessments of Mobile-Source Air Toxics: The Community Line Source (C-LINE) Modeling System, *Environ. Model. Software,* 66:46-56.

Briggs, G. A. (1965). A plume rise model compared with observations. *Journal of Air Pollution Control Association, 15*, 433–438. doi:10.1080/00022470.1965.10468404

Carslaw, D., Beevers, S., Ropkins, K., Bell, M., 2006. Detecting and quantifying aircraft and other on-airport contributions to ambient nitrogen oxides in the vicinity of a large international airport. Atmos. Environ. 40, 5424–5434. doi:10.1016/j.atmosenv.2006.04.062

Chowdhury, B.; Karamchandani, P.; Sykes, R.; Henn, D.; Knipping, E. Reactive puff model SCICHEM: Model enhancement and performance studies. Atmos. Environ. 2015, 117, 242−258.

Cimorelli, A. J., Perry, S. G., Venkatram, A., Weil, J., Paine, R., Wilson, R. B., Lee, R. F., Peters, E. D., & Brode, R. W. (2005). AERMOD: A dispersion model for industrial source applications. Part I: general model formulation and boundary layer characterization. *Journal of Applied Meteorology 44*, 682–693.

Cole, H. S., & Summerhays, J. E. (1979). A Review of Techniques Available for Estimating Short-Term NO_2 concentrations. *Journal of the Air Pollution Control Association*, *29*(8), 812–817. https://doi.org/10.1080/00022470.1979.10470866

Cox, W. M., & Tikvart, J. A. (1990). A statistical procedure for determining the best performing air quality simulation model. *Atmos. Environ. Part A, Gen. Top. 24*, 2387–2395.

Federal Aviation Administration. (2014). *Aviation environmental design tool (AEDT).* https://aedt.faa.gov/

Huang, J., P. Vennam, F.S. Binkowski, B. Murphy and S. Arunachalam (2017). A Nationwide Assessment of Particle Number Concentrations from Commercial Aircraft Emissions in the U.S., *Presented at the 36th Annual Conference of the American Association for Aerosol Research*, Raleigh, NC, October 2017.

Jiang, W., S. Smyth, É. Giroux, H. Roth, and D. Yin, "Differences between CMAQ fine mode particle and PM2.5 concentrations and their impact on model performance evaluation in the lower Fraser valley," Atmos. Environ., vol. 40, no. 26 (2006) : 4973–4985.

Kim, B., J. Rachami, D. Robinson, B. Robinette, K. Nakada, S. Arunachalam, N. Davis, B.H. Baek. U. Shankar, K. Talgo, D. Yang, A. Hanna, R. Wayson, G. Noel, S.S. Cliff, Y. Zhao, P. Hope and P. Kumar (2012). "Guidance for Quantifying the Contribution of Airport Emissions to Local Air Quality", Transportation Research Board Airport Cooperative Research Program (ACRP) Report 71, Washington, D.C. Available at: http://onlinepubs.trb.org/onlinepubs/acrp/acrp_rpt_071.pdf

Martin, A. (2006). *Verification of FAA's emissions and dispersion modeling system (EDMS).* University of Central Florida, Orlando, Florida.

Meng, Z. and J. H. Seinfeld, "On the Source of the Submicrometer Droplet Mode of Urban and Regional Aerosols," Aerosol Sci. Technol., vol. 20, no. 3 (1994): 253–265.

Murphy, B.; F.S. Binkowski; E. WInijkul; T. Olenius; M. Alvarado; I. Rippinen; M. Woody and H.O.T. Pye (2017). Quantifying Primary and Secondary Ultrafine Particle Contributions in the U.S. with CMAQ-NPF, *Presented at the 36th Annual Conference of the American Association of Aerosol Research*, Raleigh, NC, October 2017.

Rienecker, M. M.; Suarez, M. J.; Gelaro, R.; Todling, R.; Bacmeister, J.; Liu, E.; Bosilovich, M. G.; Schubert, S. D.; Takacs, L.; Kim, G. K.; et al. MERRA: NASA's modern-era retrospective analysis for research and applications. *J. Clim.* **2011**, *24* (14), 3624–3648.

Tetra Tech, Inc. (2013). *LAX air quality and source apportionment study*, Los Angeles World Airports.

Tetra Tech, Inc., 2013. LAX Air Quality and Source Apportionment Study. Los Angeles World Airports. Available at: http://www.lawa.org/airQualityStudy.aspx?id=7716.

Valencia, A., S. Arunachalam, D. Heist, D. Carruthers, and A. Venkatram (**2018**). Development and Evaluation of the R-LINE Model Algorithms to Account for Chemical Transformation in the Near-road Environment, *Transp. Res. Part D: Transp. Environ.,* 59, 464 – 477.

Venkatram, A., Karamchandani, P., Pai, P., Goldstein, R., 1994. The development and application of a simplified ozone modeling system (SOMS). *Atmos. Environ.* 28(22), 3665–3678. http://dx.doi.org/10.1016/1352-2310(94)00190-V .

Venkatram, A., Karamchandani, P., Pai, P., Sloane, C., Saxena, P., & Goldstein, R. (1997). The Development of a Model to Examine Source-Receptor Relationships for Visibility on the Colorado Plateau. *Journal of the Air & Waste Management Association*, *47*(3), 286–301. https://doi.org/10.1080/10473289.1997.10464453

Wayson, R. L., Fleming, G. G., & Iovinelli, R. (2009). Methodology to estimate particulate matter emissions from certified commercial aircraft engines. *Journal of the Air & Waste Management Association, 59(1)*, 91–100. https://doi.10.3155/1047-3289.59.1.91

Wayson, R.L., Fleming, G.G., Kim, B., Eberhard, W.L., Brewer, W.A., 2004. Final report: the use of LIDAR to characterize aircraft initial plume characteristics (No. FAA-AEE-04-01; DTS-34-FA34T-LR3;). FAA.

Wilkerson, J. T.; Jacobson, M. Z.; Malwitz, A.; Balasubramanian, S.; Wayson, R.; Fleming, G.; Naiman, A. D.; Lele, S. K. Analysis of emission data from global commercial aviation: 2004 and 2006. *Atmos. Chem. Phys.* **2010**, *10*, 6391–6408.

Yamartino, R. J., & Donald M. R. (1979). Updated model assessment of pollution at major U.S. airports. *Journal of the Air Pollution Control Association, 29(2)*, 128–132. https://doi.10.1080/00022470.1979.10470767

Appendix A: Exceedance Computation Using CMAQ Results

$PM_{2.5}$ (Jan)	Base-NEI	No-Airport	Base-NEI - No-Airport
25 µg/m³	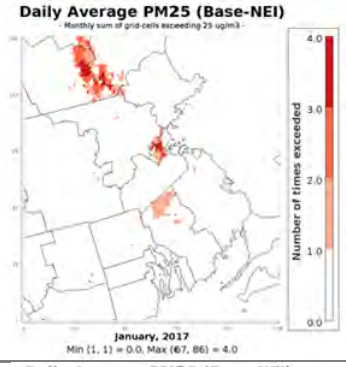	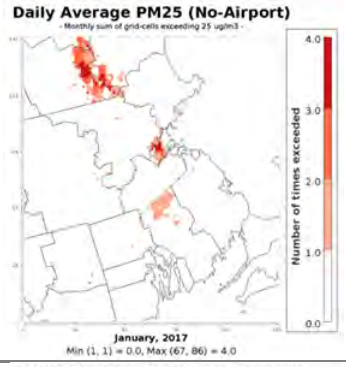	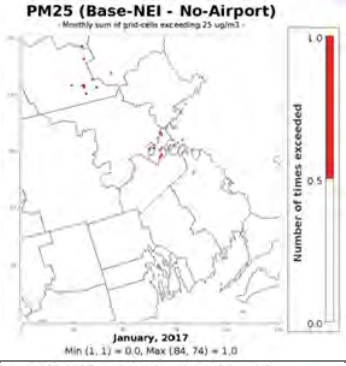
30 µg/m³	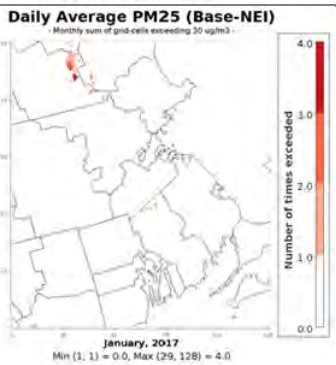	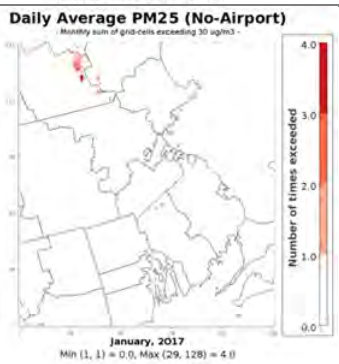	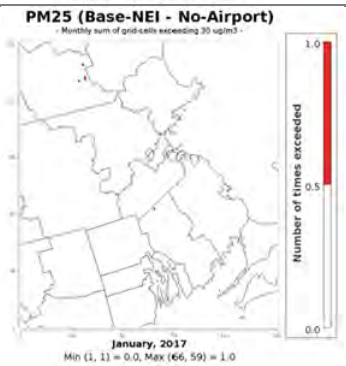
35 µg/m³	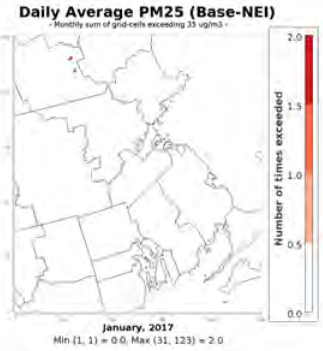	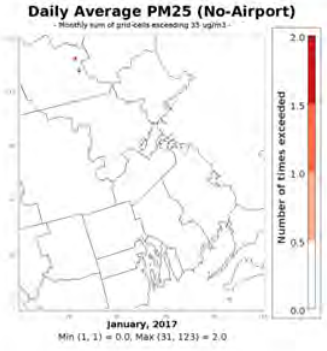	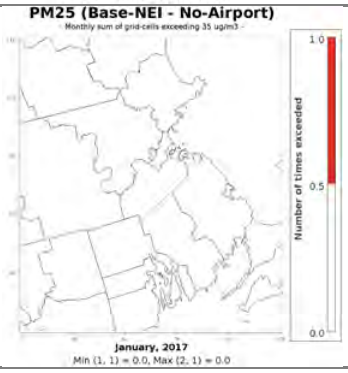

Figure A1. Comparing daily $PM_{2.5}$ sum by concentration (25-35 µg/m³) at all grid-cells for January.

$PM_{2.5}$ Annual	Base-NEI	No-Airport	Base-NEI - No-Airport
8 µg/m³	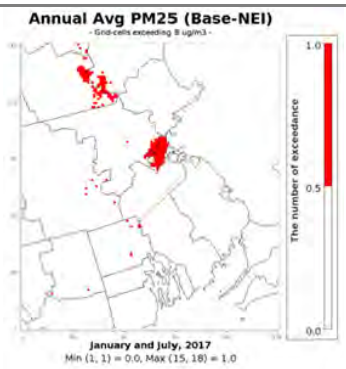	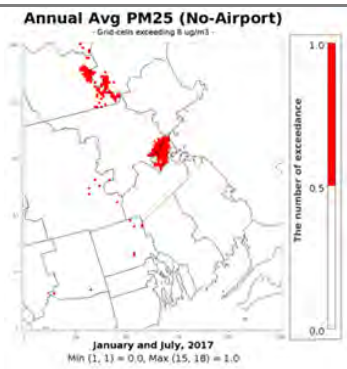	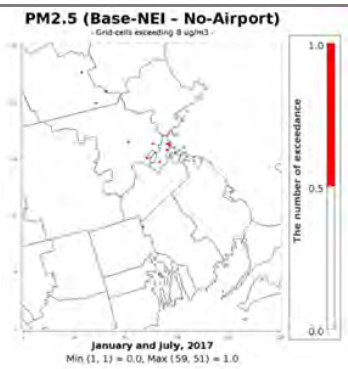
10 µg/m³	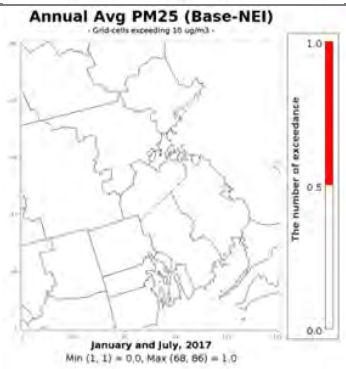	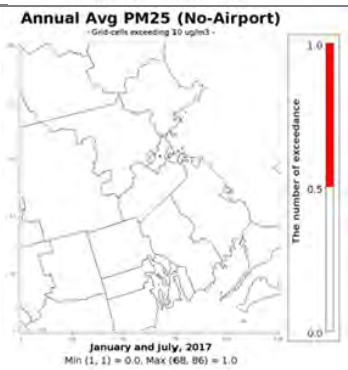	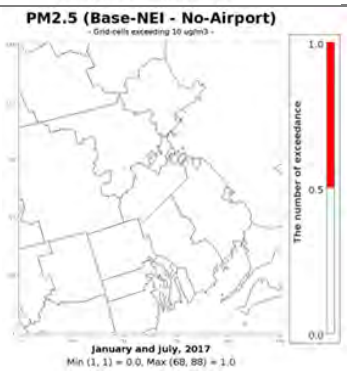

Figure A2. Comparing annual $PM_{2.5}$ average (January + July average) by concentration (8-10 µg/m³) at all grid-cells.

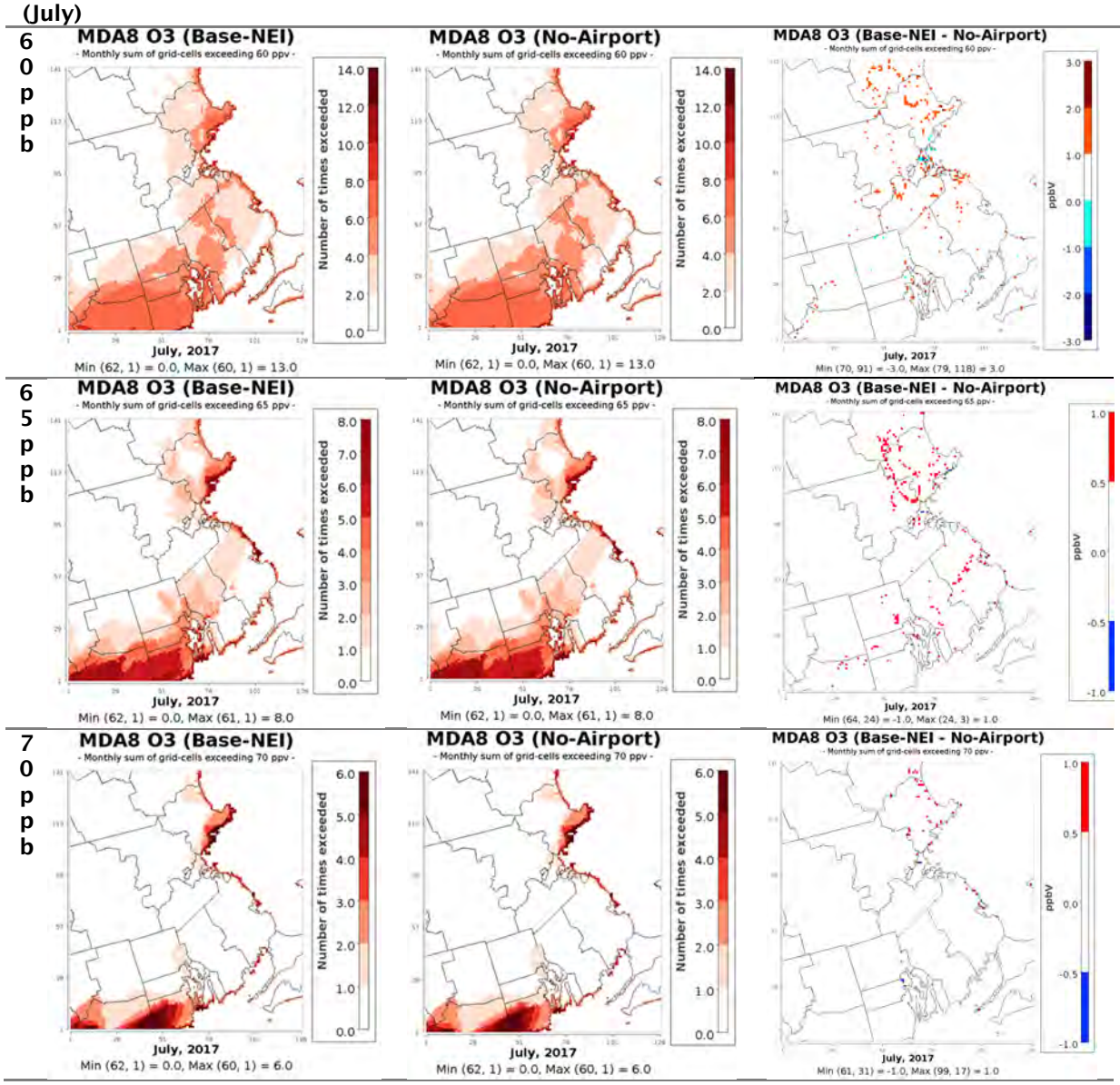

Figure A3. Comparing maximum daily average 8-hour O_3 each day by concentration (60-70 ppb) at land grid-cells for July.

Table A1. Summary of issues related to AEDT data for BOS airport study.

Color code for data availability according to the user-manual and BU's PDARS data

Available in BU's data or optional information	Can be created from BU's data or a recommended option	Can't be created from BU's data

Color code for data importance:

Recommended	Required

Data availability for aircraft operation csv input file columns (needed unless specified in Comments column):

Column Name	Description	Notes	Data Availability	Comments
AirOp_UserID	User-defined operation ID		Can be created from BU's data	Required. Input file requirements by operation type for schedule-based operations
AcType	ICAO/IATA aircraft type (used to map aircraft types to an engine) e.g., B738	Can be found in AEDT equipment tab, Equipment: Aircraft data grid, Airframe Model column	Can be created from BU's data and Appendix (shared by BU)	Required
AirframeModel	Airframe model name e.g., Boeing 737-800 Series	Can be found in AEDT equipment tab	Can be created from BU's data and Appendix (shared by BU)	Required
EngineCode	Engine ID, e.g., 203	Can be found in AEDT equipment tab	Can be created from BU's data and Appendix (shared by BU)	Required
EquipID	Equipment ID	Can be found in AEDT equipment tab	Can't be created from BU's data	Not needed if we have data for either of the combinations of AirframeModel and EngineCode or AcType and EngineCode
OpType	Operation type (A) Arrival, (D) Departure, (T) Touch and Go, (F) Circuit, (V) Overflight, (5) Runway to Runway (great circle)		Can't be created from BU's data	Required
OpCount	Operation count	This value can represent an average annual day, distinct operation count (i.e., 1), or annual number of operations	Can't be created from BU's data	Required
OpTime	Operation time	e.g., 2010-01-06 08:24:00.000	Can be created from BU's data	Required

DepApt	Departure airport ICAO code	Can be found in the Airports tab, Add Existing Airport dialog	Can be created from BU's data	Required for departures
ArrApt	Arrival airport ICAO code	Can be found in the Airports tab, Add Existing Airport dialog	Can be created from BU's data	Required for arrivals
DepRwyEnd Name	Departure runway end name e.g., 10L	This runway end must exist in the study prior to importing	Can't be created from BU's data	Required for departures
ArrRwyEnd Name	Arrival runway end name e.g., 10L	This runway end must exist in the study prior to importing	Can't be created from BU's data	Required for arrivals
ProfileID	Aircraft's profile ID e.g., 253	If not provided, the Profile Name will be used in conjunction with the stage length to determine the profile	Can't be created from BU's data	Optional
ProfileName	Name of flight performance profile e.g., STANDARD, ICAO_A, ICAO_B	If both the profile ID and profile name are unspecified, STANDARD is assumed	Can't be created from BU's data	Recommended
TrackName	Track name from the tracks input file or an existing track name	Track name is option for operational profile-based operations.	Can't be created from BU's data	Optional
StageLength	Stage length 1-9 or M		Can't be created from BU's data	Recommended
TaxiOut_Sec	Taxi-out time in seconds		Can't be created from BU's data	Optional
TaxiIn_Sec	Taxi-in time in seconds		Can't be created from BU's data	Optional
ArrGatrName	Arrival gate name	This gate must exist in the study prior to importing	Can't be created from BU's data	Required
QuarterHourly ProfileName	Name of quarter-hourly operational profile	Used to define a profile-based operation When defining profile-based operations, all three profile types must be defined (quarter hour, daily, and monthly) and the operational profiles must exist in the study prior to importing	Can't be created from BU's data	Required for Profile-based operations
DailyProfile Name	Name of daily operational profile	Used to define a profile-based operation When defining profile-based operations, all three profile types must be defined (quarter hour, daily, and monthly) and the operational profiles must exist in the study prior to importing	Can't be created from BU's data	Required for Profile-based operations

MonthlyProfile Name	Name of daily operational profile	Used to define a profile-based operation When defining profile-based operations, all three profile types must be defined (quarter hour, daily, and monthly) and the operational profiles must exist in the study prior to importing	Can't be created from BU's data	Required for profile-based operations

Data availability for tracks csv input file columns (needed):

Column Name	Description	Notes	Data Availability	Comments
APT_CODE	Airport Code		Can be created	Required
RWY_END_NAME	Runway end name	Runway end must exist in the study prior to importing. Not required for overflight tracks	Can be created	Required
TRACK_NAME	Track name	Track names in the study must be unique	Can be created	Required
TRACK_TYPE	Track type		Can be created	Required
OP_TYPE	Operation type		Can't be created from BU's data	Required
RUNWAY_END_DELTA_ DISTANCE	Delta distance from nominal start-roll or touch down point	Typically set to 0	Can be created	Required
AIRCRAFT_TYPE	0 for fixed wing, 1 for helicopter		Can be created from BU's data	Required
VECTOR_COURSE_AT_ HELIPAD	Direction for helicopter operations		Can't be created from BU's data	Required
SUBTRRACK_NUM	Sub-track number		Can't be created from BU's data	Required
PCT_DISPERSION	Percent of flights dispersed to the sub-track		Can't be created from BU's data	Required
SEGMENT_NUM	Number of the current segment		Can't be created from BU's data	Required
SEGMENT_TYPE	Segment type		Can't be created from BU's data	Required
PARAM_1	Point-type track: latitude (in deg) Vector-type track: angle in distance/radius (in feet)		Can be created from BU's data	Required
PARAM_2	Point-type track: longitude (in deg) Vector-type track: angle in distance/radius (in feet)		Can be created from BU's data	Required

Project 022 Evaluation of FAA Climate Tools: Aviation Portfolio Management Tool (APMT)

University of Illinois at Urbana-Champaign

Project Lead Investigator

Dr. Donald Wuebbles
Emeritus Professor
Department of Atmospheric Sciences
University of Illinois
105 S. Gregory Street
Urbana, IL 61801
217-244-1568
wuebbles@illinois.edu

University Participants

University of Illinois at Urbana-Champaign

- P.I.: Dr. Donald Wuebbles (FAA Award 13-C-AJFE-UI-029)
- Period of Performance: October 1, 2021 to September 30, 2022 (project started February 5, 2020)
- Tasks:
    1. Examine potential environmental effects of possible fleets of supersonic aircraft, particularly on ozone and climate
    2. Support and perform analyses for the International Civil Aviation Organization (ICAO) Impact Sciences Group (ISG)

Project Funding Level

Support from the FAA over this time period was approximately $70,000. An additional approximately $70,000 in matching support was provided by the University of Illinois at Urbana-Champaign.

Investigation Team

Dr. Donald Wuebbles: oversee project
Dr. Jun Zhang (graduate student; graduated in the fall of 2021): conduct studies and perform analyses using the Community Earth System Model (CESM) Whole Atmosphere Community Climate Model (WACCM), a three-dimensional atmospheric-climate-chemistry model.
Dr. Dharmendra Singh (postdoctoral associate): conduct studies and perform analyses using the CESM WACCM.

Project Overview

This project uses state-of-the-art modeling and technical knowledge to analyze the potential global environmental effects of aircraft and to conduct analyses that underpin the development of analytical tools for assessing costs-and benefits, to inform decision-making regarding technology development. The studies rely on state-of-the-art models of the Earth system that can provide useful scientific input for consideration by decision-makers. The analyses in the project will aid in decision-making by translating complex models into simpler tools for use in cost–benefit analyses. Specific project goals include (a) evaluation of potential environmental effects of assumed fleets of supersonic commercial and business jet aircraft, to compare their benefits in terms of decreased air-travel time; (b) when needed, science-based evaluation of analytical tools used by the FAA; (c) development of ideas and concepts for the next-generation treatment of aviation effects on the Earth system; and (d) updated evaluation and analyses of the science of aviation effects on atmospheric composition. The accomplishments for this year fit within these overall objectives.

Task 1 - High-Speed Civil Transport Aircraft and Their Potential Effects on Ozone and Climate

University of Illinois at Urbana-Champaign

Objective

To quantify the costs and benefits of using advanced aircraft and engine technologies, the FAA uses tools that are underpinned by state-of-the-art technical knowledge. These tools are used to inform decision-making by providing the benefits and costs of various options that could enable technology development. The overall objective of this project is to enhance understanding of the relationships between subsonic or proposed supersonic aircraft and the atmospheric state, and the development and evaluation of the capabilities, limitations, and uncertainties of metrics and simple models (e.g., the Aviation Portfolio Management Tool), to assist decision-makers. Interest in developing commercial supersonic transport aircraft has been renewed because of the increased overall demand by the public for air travel, aspirations for more intercontinental travel, and the desire for shorter flight times. Various companies and academic institutions have been actively considering the designs of such supersonic aircraft. As these new designs are developed, the environmental impacts of these realistic fleets on ozone and climate have required exploration. This study examines one such proposed supersonic fleet developed by scientists and engineers at the Georgia Institute of Technology (Georgia Tech) that is projected to fly at Mach 2.2, corresponding to cruise altitudes of 17–20 km, which would burn 122.32 Tg of fuel each year and emit 1.78 Tg of nitrogen oxides (NO_x) annually.

Research Approach

The CESM2/WACCM6 model was used to conduct the numerical experiments. This state-of-the-art coupled chemistry–climate model includes comprehensive troposphere–stratosphere–mesosphere–lower thermosphere chemistry from the Earth's surface to approximately 140 km. We also used the PORT (Parallel Offline Radiation Tool) model, a configuration of the Community Atmosphere Model in the CESM, which runs the radiative transfer code offline for derivations of the radiative forcing on climate.

Results and Discussion

With the Georgia Tech emission scenario for a new proposed fleet of supersonic aircraft, our study investigated the potential atmospheric impacts of this realistic near-term supersonic design. We used the state-of-the-art whole-atmospheric-chemistry climate model WACCM with the latest specified dynamics scheme to assess the impacts on atmospheric ozone and non-CO_2 and non-contrail climate forcing of this near-future supersonic aircraft fleet, whose target entry into service is in approximately 2030–2035. This new proposed supersonic fleet is projected to fly at Mach 2.2 and 17–20 km altitude, to burn 122.32 Tg of fuel each year, and to emit 1.78 Tg NO_x. The aircraft designs and emission scenarios proposed in this study are quite different from those in a study by Eastham et al. (2022) for a different supersonic fleet. Eastham et al. proposed a fleet of supersonic aircraft flying at Mach 1.6 and 15–17 km altitude, burning 19 Tg of fuel each year, and emitting 170 Gg NO_x. The fuel burn and NO_x emissions projected in our study are approximately 6 and 10 times larger than the projections in Eastham et al. (2022), respectively.

As shown in Figure 1, we found that the proposed fleet of supersonic aircraft is predicted to cause a 0.74% decrease in global column ozone, which is approximately 2 Dobson units of global ozone depletion, equivalent to as much as 20% of the total impact of chlorofluorocarbon emissions at their peak. This ozone depletion is attributable primarily to the large amounts of NO_x released into the atmosphere from supersonic aircraft, whereas the impacts of water vapor and SO_2 on the ozone column are relatively smaller. The maximum ozone loss occurs in the northern hemisphere tropics in the fall season, with an approximately 1.4% regional decrease in the total column ozone. The ozone decrease calculated in our study is more than 10 times higher than the estimate from Eastham et al. (2022), who calculated a decrease of 0.046% in global column ozone. This number is consistent with the NO_x emissions used in our study and by Eastham et al. (2022).

We assessed the ozone increase in the upper troposphere and lower stratosphere, and the ozone decrease in the middle to the upper stratosphere. The mechanisms of ozone change at different latitudes have been explored. In the tropics, the ozone increase is attributed to smog chemistry production and total odd-oxygen production; at the middle latitude, the combination of smog chemistry production, total odd-oxygen production, and decreased ozone loss from the HO_x–O_x cycle are responsible for the ozone increase. In the polar region, the decreased HO_x–O_x loss rate plays a relatively more important role.

To determine the climate impact of this proposed fleet of supersonic aircraft, we estimated the stratospheric-adjusted radiative forcing (Figure 2) from changes in atmospheric concentrations of ozone (59.5 mW/m^2), water vapor (10.1 mW/m^2), black carbon (−3.9 mW/m^2), and sulfate aerosols (−20.3 mW/m^2), thus resulting in a net non-CO_2, non-contrail forcing of 45.4 mW/m^2, indicating an overall warming effect. In contrast, Eastham et al. (2022) estimated a net radiative forcing from non-CO_2, non-contrail forcing of −3.5 mW/m^2, varying from −3.0 to −3.9 mW/m^2 year to year, thereby indicating an overall cooling effect.

The atmospheric impacts of any proposed fleet of supersonic aircraft must be fully examined and understood before these aircraft are placed into operation. Some assumptions made in this study might contribute to uncertainties in the resultant effects on ozone and climate. For example, the background atmosphere was assumed to be under volcanic clean conditions in the 2035 time period. Ozone depletion might be more substantially affected if emissions were to occur on a background of a major volcanic eruption and the background atmosphere influence on heterogeneous chemistry. We did not consider plume chemistry in this study, which may be important in the initial plume if compared with the well-mixed case in short time intervals. The dynamic effects due to local heating by black carbon and ozone changes are also not included but may substantially influence ozone and climate for supersonic aviation.

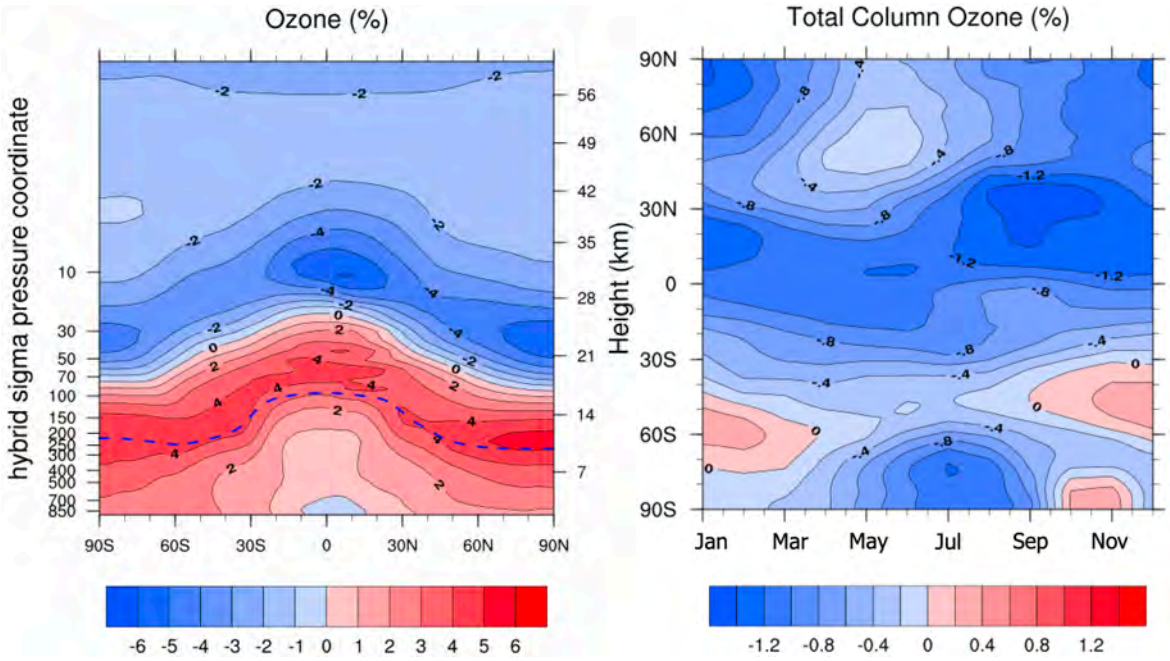

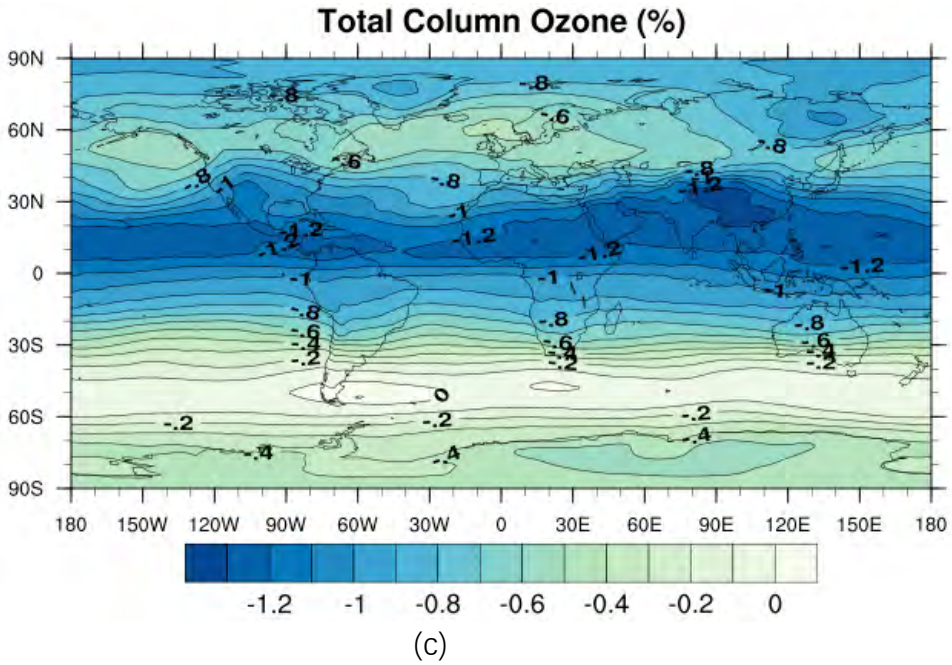

Figure 1. For the assumed supersonic aircraft fleet emissions, (a) the simulated annual and zonal mean perturbations (%) in atmospheric ozone concentration at steady state, (b) seasonal dependence of the calculated change in the total column ozone (%), and (c) annual average change in the total column ozone distribution (%).

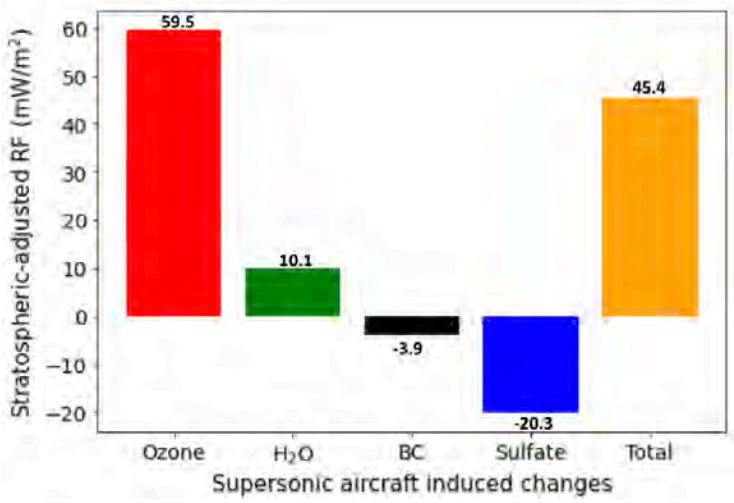

Figure 2. Annual and global average changes in stratospheric-adjusted radiative forcing (mW/m^2) at the tropopause for supersonic aircraft induced changes in ozone, H_2O, black carbon, and sulfate.

We also have received emissions for two different supersonic commercial aircraft designs and associated mature fleets from the Massachusetts Institute of Technology (MIT). We are currently translating these emissions onto our model grid and including those emissions in the climate-chemistry WACCM model, and we will be running the scenarios in separate studies for the two aircraft designs. The aim of this task is to compare our analyses with those from the MIT model and to develop a joint journal manuscript. Runs for these analyses are expected to start soon.

Milestones

- A journal manuscript has been submitted to the journal *Earth's Future*, on the basis of the Georgia Tech proposed supersonic transport (SST) commercial aircraft.
- An article on the future of travel and tourism, including a discussion of aviation and possible development of supersonic aircraft, has been published.
- Emissions received from MIT for its proposed fleet of SSTs are being translated onto our model grid as a prelude to the model runs for these scenarios.

Publications

Wuebbles, D. J. (2022). The future of travel and tourism in the changing climate. *International Affairs Forum, 14(1*), 18–13.
Zhang, J., Wuebbles, D., Kinnison, D., Pfaender, J. H., Tilmes, S., & Davis, N. (2022). Potential impacts on ozone and climate from a proposed fleet of supersonic aircraft. [Manuscript submitted for publication.] *Earth's Future*.

Task 2 - Support and Analyses for the International Civil Aviation Organization Impact Sciences Group

University of Illinois at Urbana-Champaign

Objectives

A series of analyses conducted last year resulted in reports for ICAO relating to the environmental impacts of aviation.

Research Approach

The University of Illinois at Urbana-Champaign, particularly through Dr. Wuebbles, has contributed to three of the reports for ICAO, one of which was led by Dr. Wuebbles.

Results and Discussion

The three reports for ICAO to which the University of Illinois at Urbana-Champaign contributed are described below.

1. Assessment of the Impact of Airport Emissions on Local Levels of NO_x and Human Health; Impacts of Cruise Emissions of NO_x on Human Health; Impacts of Cruise NO_x on Climate

Dr. Wuebbles was a contributing author to this report.

According to the current view, aviation NO_x emissions over the 1940–2018 period have contributed to a net warming of the climate system. However, the uncertainty associated with the estimates of the net climate forcing remains high. A recent study has suggested that the net climate impact of aviation NO_x might switch to net cooling, depending on future background atmospheric composition, future aircraft emissions, or the consideration of new processes or refined parameterizations. The estimated impacts of NO_x emissions on the climate system relative to other forcing agents are dependent on the choice of the climate metric and the time horizon considered. In response to the important challenges due to climate change, several studies have focused on how to reduce the climate impact of aviation through changing flight operations. In the case of NO_x, lowered flight altitudes may provide a possible mitigation option for reducing the NO_x climate impact at the cost of increased CO_2.

Aircraft ground operations and the landing and takeoff cycle emit various gaseous and particulate pollutants or their precursors, thus affecting human health. Aircraft landing and takeoff emissions contribute to premature mortality around major airports. At the local scale, NO_2 health impacts have been shown to outweigh $PM_{2.5}$ health impacts. Most NO_x emissions from aviation do not occur near the ground, and more than 90% occur above 3,000 ft. Those emissions still contribute to the background levels of O_3 and thus to the O_3 at ground level. Similarly, cruise emissions could potentially be an important source of surface-level particulate matter globally and an important cause of aviation-related premature mortality.

The options for controlling aviation NO_x are limited, and are countered by the international growth in commercial aviation and by the mandate to increase engine energy efficiency by increasing engine core temperatures. Historically, continued reductions in NO_x have tended to increase fuel burn and the resulting emissions of CO_2—the primary gas of concern regarding

climate change. Thus, a trade-off arises between reducing impacts on climate, due primarily to CO_2, and reducing the impacts on air quality from NO_x.

2. Allowed Emission of Carbon Dioxide for Limiting Global Mean Temperature Increases to 1.5 or 2 ˚C

Dr. Wuebbles wrote major sections of this report. The ICAO Committee on Aviation Environmental Projection Long Term Aspirational Goal Task Group (LTAG-TG), during the process of developing the scenarios for aviation CO_2, requested the following from the ISG:

> "ISG should examine the literature and summarize the amount of carbon dioxide (a.k.a. carbon budget) that can be released into the atmosphere while limiting the increase in global mean temperature to 1.5 and 2 degrees Celsius. These carbon budgets can then be compared against the aviation CO_2 scenarios being developed by LTAG-TG. The ISG should also capture the latest information on the impacts of non-CO_2 aviation emissions such that decision-makers understand the relative impact of aviation CO_2 emissions and the non-CO_2 emissions on the climate."

This report addresses the above request from the LTAG-TG.
The aim of this report is to examine and summarize the understanding of the amount of CO_2, in terms of the number of gigatons of CO_2 ($GtCO_2$) that could still be emitted into the atmosphere by human activities if the amount of climate change, in terms of the global mean surface temperature increase, is to be limited to either 1.5 or 2 ˚C over pre-industrial levels. The Paris Agreement sets a long-term temperature goal of: "holding the increase in the global average temperature to well below 2 ˚C above pre-industrial levels and pursuing efforts to limit the temperature increase to 1.5 ˚C above pre-industrial levels, recognizing that this would significantly reduce the risks and impacts of climate change" (Article 2.1 (a)) (as discussed later, this statement is often interpreted as starting with the period from 1850 to 1900, when adequate global temperature records became available). Although CO_2 is the main driver of human-induced long-term climate change, approximately one third of the current changes in climate relate to non-CO_2 emissions of other gases and particles emitted by human activities (Smith et al., 2020). We will start by considering these allowed emissions only in terms of CO_2 and will include assumptions regarding the contributions of non-CO_2 effects.

The amount of allowable remaining carbon emissions—the "remaining carbon budget"—to limit global warming to 1.5 or 2 ˚C over pre-industrial levels from all anthropogenic sources is provided in this report, according to the Intergovernmental Panel on Climate Change (2021). The remaining amounts of carbon emissions from January 1, 2020 are estimated to be 500 and 1,350 $GtCO_2$ for 1.5 and 2 ˚C limits, respectively, for a 50% probability, and 400 and 1,150 $GtCO_2$ limits, respectively, for a 67% probability of limiting temperature increases to 1.5 and 2 ˚C. The assumptions underlying these estimates are described, along with updates on the current level of global warming. Non-CO_2 effects (e.g., largely from methane, nitrous oxide, and fluorinated gases) are included in the above estimates and introduce an uncertainty in the allowed CO_2 emissions for a given temperature limit, and the probability of staying at or below this limit. The total aviation forcing effect was approximately 3.5% of the total anthropogenic climate forcing in 2011. Aviation non-CO_2 climate effects are currently estimated to be approximately two thirds of the total aviation forcing, according to historical data, although future projections are uncertain.

3. Understanding the Potential Environmental Impacts from Supersonic Aircraft: An Update

Dr. Wuebbles led the team writing this report and wrote major sections of the report.

Increasing demand for air travel, the aspiration for more intercontinental travel, and the desire for shorter flight times have all contributed to renewed interest in the potential development of civil aircraft that fly at supersonic speeds. Consequently, various governments and companies worldwide have been reconsidering the development of supersonic aircraft for the business jet and commercial airline markets. Fleets of hundreds to thousands of these supersonic business jets and/or SST aircraft would probably be necessary to make their development economically feasible. This report is aimed at providing an update on the understanding of the noise and the environmental concerns relating to emissions, and the resulting impacts on climate and ozone, associated with the substantial use of such aircraft. A short summary of the history of these environmental concerns is described below.

Interest in the potential development of commercial and civil aircraft that fly at supersonic speeds has been renewed. Noise and emissions impacts were first extensively studied in the 1970s, then again in the 1990s and early 2000s. Consequently, a need exists to update understanding of the potential impacts of noise and the environmental concerns relating to

emissions, particularly the resulting affects ozone and climate. SST fleets of differently sized aircraft using conventional fuels are being considered, extending from business jets to larger aircraft that can transport hundreds of passengers. Scientists are now undertaking new studies using state-of-the-art models of global atmospheric chemistry and physics to understand the potential effects on stratospheric ozone and the radiative forcing of climate associated with SST fleets. These studies set the stage for the next generation of analyses of potential environmental effects from supersonic aircraft that are under consideration for development. Along with the emissions of long-lived CO_2, the radiative forcing of climate in turn depends on the spatial changes in concentrations of water vapor, O_3, CH_4 (primarily because of feedback from the emissions of NO_x and water vapor), and particles (both inorganic and organic aerosols). The emissions from the fleet of aircraft particularly depend on the fleet size, flight characteristics, Mach speed, cruise altitude, fleet fuel use at cruise, NO_x emission index, and assumptions regarding sulfur in the fuel and soot emissions. For projections of the number and type of aircraft currently under evaluation for SST fleets, a 1% change in globally averaged total ozone over the next two to three decades is likely, and whether the change is positive or negative will depend on specific fleet parameters. The climate effects are also likely to be small, resulting in generally much less than a 0.03 ˚C change in globally averaged surface temperature (the total effect will also depend on whether sustainable aviation fuels are used). Substantial progress has been made in modeling and mitigating the effects of sonic booms from supersonic flight. Ongoing research to assess the impact on the public has indicated that future low-boom supersonic aircraft designs will create quieter sonic "thumps" that are much less irritating than conventional sonic booms. Nonetheless, further studies are necessary to fully evaluate the noise effects for specific aircraft.

Major Accomplishments

- Three reports were well received by the ICAO.
- Dr. Wuebbles gave a major presentation to the ICAO during the summer of 2022 about the potential environmental effects of supersonic commercial aircraft.

Milestones

Analyses have been completed, and reports have been published.

Publications

Hauglustaine, D. R., Miake-Lye, C., Arunachalam, S., Barrett, S. R. H., Fahey, D. W., Fuglestvedt, J. S., Madden, P., Skowron, A., van Velthoven, P., & Wuebbles, D. J. (2022). *Assessment of the impact of airport emissions on local levels of NO_x and human health; impacts of cruise emissions of NO_x on human health; impacts of cruise NO_x on climate*. International Civil Aviation Organization (ICAO). The United Nations, Montreal.

Jacob, S. D., Lee, D. S., Wuebbles, D. J., Fuglesvedt, J. S., Johansson, D., Fahey, D. W., Hauglustaine, D., Sausen, R., van Velthoven, P. J. F., & Barrett, S. R. H. (2022). *Allowed emission of carbon dioxide for limiting global mean temperature increases to 1.5 or 2˚C.* International Civil Aviation Organization (ICAO). The United Nations, Montreal.

Wuebbles, D. J., Baughcum, S., Barrett, S., Catalano, F., Fahey, D. W., Madden, P., Rhodes, D., Skowron, A., & Sparrow, V. (2022). *Understanding the potential environmental impacts from supersonic aircraft: An update*. International Civil Aviation Organization (ICAO). The United Nations, Montreal.

Additional Information and Future Efforts

Outreach Efforts

Presentations at ASCENT meetings
Presentations to ICAO
Presentations at the SPARC (Stratosphere-troposphere Processes And their Role in Climate) conference and at the AGU (American Geophysical Union) annual meeting

Biweekly meetings with project manager
ICAO ISG meetings (monthly) for Dr. Wuebbles

Student Involvement

Former graduate student Jun Zhang (now a postdoctoral associate at the National Center for Atmospheric Research (NCAR) was primarily responsible for the analyses and modeling studies within the project, and for leading the initial preparation of the project reports. A new postdoctoral associate, Dr. Dharmendra Singh, is currently performing the newest studies. He is

working with another team member, postdoctoral associate Dr. Swarnali Sanyal, as he learns to perform the modeling runs required.

Plans for Next Period

- Complete studies based on the emission inventories developed by ASCENT Project 10 to consider specific designs of SSTs from MIT, and compare those results to model analyses performed by MIT for the same scenario plus their similar analyses of the Georgia Tech SST fleet. Publish journal article.
- Use the results from this study to inform the development of the Aviation Portfolio Management Tool–Impacts Climate (APMT-IC) for supersonic impacts (ASCENT Project 58).
- Initiate new projects for the ICAO ISG (new meetings expected to start after January 1, 2023).

References

Eastham, S. D., Fritz, T., Sanz-Morère, I., Prashanth, P., Allroggen, F., Prinn, R. G., ... Barrett, S. R. (2022). Impacts of a near-future supersonic aircraft fleet on atmospheric composition and climate. *Environmental Science: Atmospheres.* https://doi.10.1039/D1EA00081K

Hauglustaine, D. R., Miake-Lye, C., Arunachalam, S., Barrett, S. R. H., Fahey, D. W., Fuglestvedt, J. S., Madden, P., Skowron, A., van Velthoven, P., & Wuebbles, D. J. (2022). *Assessment of the impact of airport emissions on local levels of NO_x and human health; impacts of cruise emissions of NO_x on human health; impacts of cruise NO_x on climate.* International Civil Aviation Organization (ICAO). The United Nations, Montreal.

Jacob, S. D., Lee, D. S., Wuebbles, D. J., Fuglesvedt, J. S., Johansson, D., Fahey, D. W., Hauglustaine, D., Sausen, R., van Velthoven, P. J. F., & Barrett, S. R. H. (2022). *Allowed emission of carbon dioxide for limiting global mean temperature increases to 1.5 or 2˚C.* International Civil Aviation Organization (ICAO). The United Nations, Montreal.

Smith C. J., Kramer R. J., Myhre G., Alterskjær K., Collins W., Sima A., Boucher O., Dufresne J.-L., Nabat P., Michou M., Yukimoto S., Cole J., Paynter D., Shiogama H., O'Connor F. M., Robertson E., Wiltshire A., Andrews T., Hannay C., Miller R.L., Nazarenko L., Kirkevåg A., Olivié D., Fiedler S., Pincus R and P. M. (2020) Effective radiative forcing and adjustments in CMIP6 models. *Atmos. Chem. Phys.* 20, no. 16, 9591-9618, doi:10.5194/acp-20-9591-2020.

Wuebbles, D. J., Baughcum, S., Barrett, S., Catalano, F., Fahey, D. W., Madden, P., Rhodes, D., Skowron, A., & Sparrow, V. (2022). *Understanding the potential environmental impacts from supersonic aircraft: An update.* International Civil Aviation Organization (ICAO). The United Nations, Montreal.

Wuebbles, D. J. (2022). The future of travel and tourism in the changing climate. *International Affairs Forum, 14(1),* 18–13.

Zhang, J., Wuebbles, D., Kinnison, D., Pfaender, J. H., Tilmes, S., & Davis, N. (2022). Potential impacts on ozone and climate from a proposed fleet of supersonic aircraft. [Manuscript submitted for publication.] *Earth's Future.*

Project 023 Analytical Approach for Quantifying Noise from Advanced Operational Procedures

Massachusetts Institute of Technology

Project Lead Investigator

R. John Hansman
T. Wilson Professor of Aeronautics & Astronautics
Department of Aeronautics & Astronautics
Massachusetts Institute of Technology
Room 33-303
77 Massachusetts Ave, Cambridge, MA 02139
617-253-2271
rjhans@mit.edu

University Participants

Massachusetts Institute of Technology

- P.I.: R. John Hansman
- FAA Award Number: 13-C-AJFE-MIT, Amendment Nos. 008, 015, 022, 031, 046, and 051
- Period of Performance: October 1, 2021 to September 30, 2022
- Tasks:
    1. Document and disseminate key lessons learned from the process of designing new noise-reducing flight procedures for Boston Logan Airport.
    2. Identify and document system constraints affecting the design of advanced flight procedures that limit the available solution space for noise abatement through operational means.
    3. Identify approaches for mitigating flight procedure constraints and expanding opportunities for noise abatement through novel flight procedure implementations.

Project Funding Level

The FAA provided $860,000 in funding, and matching funds totaling $860,000 were provided by the Massachusetts Institute of Technology (MIT) (approximately $80,000) and the Massachusetts Port Authority (Massport) (approximately $780,000).

Investigation Team

- Professor R. John Hansman (P.I.)
- Sandro Salgueiro (graduate student)
- Clement Li (graduate student)
- Zhishen Wang (graduate student)
- Kevin Zimmer (graduate student)

Project Overview

In this project, the team is evaluating the noise reduction potential of advanced operational procedures in the terminal (arrival and departure) phases of flight. The noise impact of these procedures is not well understood or modeled in current environmental analysis tools, presenting an opportunity for further research to facilitate air traffic management system modernization. The project leverages a noise analysis framework previously developed at MIT under ASCENT Project 23 to evaluate a variety of sample procedures. In conjunction, this project contributes to the memorandum of understanding between the FAA and Massport to identify, analyze, and recommend procedure modifications at Boston Logan International Airport (hereafter, Boston Logan Airport).

Task 1 - Document and Disseminate Key Lessons Learned from the Process of Designing New Noise-Reducing Flight Procedures for Boston Logan Airport

Massachusetts Institute of Technology

Objectives

This task involves the analysis of key lessons learned from the five-year process of working with FAA, airport, and community stakeholders to create a new set of noise-reducing flight procedures for Boston Logan Airport. Areas of further analysis and documentation will include community communication (including the choice of noise metrics), common types of community requests, operational stakeholder roles and interactions, the role of design tools (e.g., TARGETS), the influence of key stakeholders in the acceptable solution space, and the identification of barriers to more advanced procedure concepts (continuing into Task 2).

This task aims to produce documentation that can be used to inform future efforts in the National Airspace System related to the design of flight procedures for noise abatement.

Research Approach

- Documented lessons learned from Block 1 and Block 2, focusing on parsing findings to the extent that they can provide useful information for future flight procedure design projects. Block 1 included flight procedures that provided clear noise benefits and had low technical barriers. Block 2 included procedures with noise re-distribution and higher technical barriers.

Major Accomplishments

- Documented a set of lessons learned from the Boston project, classified as general observations (identified low-noise procedure options, flight procedure constraints, collaboration with operational stakeholders, community interactions) and specific observations (RNAV vs. RNP considerations, VI-CF vs. VA-DF considerations, modifications to initial departure segments causing downstream procedure changes, merging and spacing, dispersion, charting constraints, and modifications of vertical profiles)
- Presented a document on lessons learned to a group of key FAA and Massport stakeholders on April 1, 2022 in a virtual meeting organized by the FAA's Office of Environment and Energy (AEE).

Task 2 - Identify and Document System Constraints Affecting the Design of Advanced Flight Procedures that Limit the Available Solution Space for Noise Abatement through Operational Means

Massachusetts Institute of Technology

Objectives

This task involves the identification and documentation of existing system constraints that impose limitations on the design of flight procedures. This work includes analyzing and decomposing identified key constraints in order to understand the parameters and assumptions driving them, as well as their impact on flight procedure design and operation. Key areas to be analyzed include constraints related to aircraft operations and operation of the air traffic control system. These constraint areas ultimately impose limitations on the feasible geometry and operation of flight procedures, although currently no documentation exists on their interactions or net impact on system performance.

Research Approach

- Based on an initial set of flight procedure constraints identified through the Boston project, develop an initial structure for classifying constraints.
- Develop a framework and identify key data/material needed for an effective and systematic identification of constraints during flight procedure design efforts.
- Develop methods for communicating flight procedure constraints across different stakeholder groups (e.g., air traffic stakeholders, airline stakeholders, communities).

Major Accomplishments

- Identified an initial key set of flight procedure constraints based on our experience at Boston Logan Airport
- Based on an initial set of constraints, developed a structure to classify flight procedure constraints as terrain clearance constraints, air traffic control structure constraints, flyability constraints, and operational stakeholder acceptance constraints
- Developed methods to illustrate and communicate constraints using three-dimensional visualization software, which can be helpful in establishing a common understanding of the flight procedure solution space among stakeholders involved in flight procedure design
- Presented work on constraint identification and visualization at the FAA Technical Center in Atlantic City, NJ; currently preparing an AIAA paper on this topic

Task 3 - Identify Approaches for Mitigating Flight Procedure Constraints and Expanding Opportunities for Noise Abatement through Novel Flight Procedure Implementations

Massachusetts Institute of Technology

Objectives

This task will use the documentation and results from Task 2 to assess potential pathways for relaxing key constraints limiting procedure design flexibility. This work will include the identification of technology limitations related to current technology performance, where new technology, decision support tools, or procedures could represent feasible mechanisms for increasing flexibility in procedure design and operation. The objective of this task is to ultimately produce recommendations for changes that could lead to an expanded solution space for advanced noise-reducing procedures.

Research Approach

- Based on lessons learned from the Boston project as well as the literature, identify low-noise procedure concepts that have previously been deemed infeasible due to technical reasons.
- Identify and classify technical factors contributing to the infeasibility of low-noise procedure concepts.
- Identify potential enablers of low-noise concepts previously deemed infeasible, including new navigation capabilities, procedure types, safety analysis methods, risk mitigation strategies, and merging and spacing tools.

Major Accomplishments

- Completed a survey of past and current merging and spacing methods that could enable fixed-path low-noise approach procedures and delayed deceleration approaches
- Completed a survey of existing safety analysis methodologies used to reduce the minimum separation between flight procedures and to enable more flexibility in flight procedure design
- Began an investigation of refinements for safety analysis methodologies that could lead to more accurate risk assessments for flight procedures and enable higher flexibility in low-noise flight procedure design

Publications

(2017). Hansman, R. J., Jensen, L., Huynh, J., O'Neill, G., Yu, A., *Block 1 procedure recommendations for Logan Airport community noise reduction*. http://hdl.handle.net/1721.1/114038

Thomas, J, & Hansman, J. (2019). Framework for analyzing aircraft community noise impacts of advanced operational flight procedures. *Journal of Aircraft*, 6(4). https://doi.org/10.2514/1.C035100

Thomas, J., Yu, A., Li, C., Toscano, P., & Hansman, R.J. (2019, June 17-21). *Advanced operational procedure design concepts for noise abatement*. [Seminar presentation.] Thirteenth USA/Europe Air Traffic Management Research and Development Seminar, Vienna, Austria.

Yu, A., & Hansman, R.J. (2019, January 7-11). *Approach for representing the aircraft noise impacts of concentrated flight tracks*. [Conference presentation.] AIAA Aviation Forum, Dallas Texas, United States.

Salgueiro, S., Thomas, J., Li, C., & Hansman, R. J. (2021, January 11-21). *Operational noise abatement through control of climb profile on departure*. [Conference presentation.] AIAA SciTech Forum

(2021). Hansman, R. J., Salgueiro, S., Huynh, J., Li, C., Jansson, M., Mahseredjian, A., Zimmer, K., *Block 2 procedure recommendations for Logan Airport community noise reduction*. https://hdl.handle.net/1721.1/131242

Outreach Efforts

- September 27, 2017: Poster to the ASCENT Advisory Board
- December 5, 2017: Call with Boeing to discuss procedure noise impact validity
- March 16, 2018: Discussion with Minneapolis-St. Paul (MSP) Airport about metrics
- April 4, 2018: Poster to the ASCENT Advisory Board
- May 7, 2018: Presentation to the FAA 7100.41 PBN Working Group
- June 24, 2018: Discussion with air traffic controllers about dispersion concepts
- July 23, 2018: Briefing at the FAA Joint University Program research update meeting
- October 9, 2018: Poster to the ASCENT Advisory Board
- November 8, 2018: Presentation to the Airline Industry Consortium
- March 3, 2019: Presentation at the Aviation Noise and Emissions Symposium
- October 15, 2019: Presentation to the ASCENT Advisory Board
- November 12, 2019: Presentation to the Airline Industry Consortium
- May 21, 2020: Meeting with operational stakeholders from the FAA 7100.41 process to discuss Block 2 concepts
- September 23, 2021: Public hearing to present Block 2 procedure recommendations for Boston Logan Airport
- Numerous community meetings
- Numerous briefings to politicians representing eastern Massachusetts (local, state, and federal)
- Briefing to the FAA Management Advisory Council
- In-person outreach and collaboration with Massport, an operator at Boston Logan Airport, and an ASCENT Advisory Board member
- April 1, 2022: Presentation of a summary of lessons learned from the Boston project to an audience of FAA, Massport, and HMMH stakeholders
- August 16, 2022: Presentation of work on flight procedure constraints at the FAA Technical Center in Atlantic City, NJ as part of the Joint University Program
- September 20–21, 2022: 7100.41 Working Group meeting at the Boston TRACON; presentation to air traffic and airline stakeholders on flight procedures proposed for Boston Logan Airport as part of Block 2; received approval for all presented procedures for further implementation work

Awards

2018 Department of Transportation/FAA Centers of Excellence Outstanding Student of the Year Award to Jacqueline Thomas
2021 Massachusetts Port Authority Logan Stars Award to the MIT International Center for Air Transportation research group

Student Involvement

Graduate students have been involved in all aspects of this research in terms of analysis, documentation, and presentation.

Plans for Next Period

The next phase of this project will focus on the continuation of Tasks 2 and 3, in which a framework for identifying and understanding flight procedure constraints during procedure design projects will continue to be developed. We expect to conclude this task within the next year.

Project 025 Shock Tube Studies of the Kinetics of Jet Fuels

Stanford University

Project Lead Investigator

Ronald K. Hanson
Woodard Professor
Mechanical Engineering Department
Stanford University
452 Escondido Mall
Stanford, California 94305
650-723-6850
rkhanson@stanford.edu

University Participants

Stanford University

- P.I.: Prof. Ronald K. Hanson
- FAA Award Number: 13-C-AJFE-SU-027
- Period of Performance: October 1, 2021 to September 30, 2022
- Task:
    1. Chemical kinetics combustion experiments.

Project Funding Level

2021–2022: $200,000 from the FAA, with 1:1 matching funds of $200,000 from Stanford University

Investigation Team

- Prof. Ronald K. Hanson, P.I., research direction
- Alison Ferris, Research Scientist, research management
- Vivek Boddapati, Graduate Student, research assistance

Project Overview

The eighth year of this program has focused on developing and refining strategies for the accurate prediction of jet fuel properties (chemical and physical) and composition. To achieve this goal, the research focused on two areas: new spectroscopic measurements of infrared (IR) spectra of jet fuels and neat hydrocarbons, and correlation of the physical and combustion properties of these fuels with their infrared spectral features. The results of the IR spectral analysis work will be used to establish the strong sensitivity of jet fuels' physical and chemical properties to their molecular structure, with the ultimate goal of developing a rapid pre-screening approach, requiring minimal fuel volume, to streamline the testing and certification process of alternative jet fuels.

Task 1 - Chemical Kinetics Combustion Experiments

Stanford University

Objectives

This work is aimed at developing fuel prescreening tools based on the IR absorption cross-section measurements of jet fuels and their constituent molecules. Specific fuel analysis objectives include developing effective strategies for correlating (a) chemical, physical, and combustion properties, and (b) functional group and molecular species composition of jet fuels with their IR spectra.

Research Approach

An important goal of the current research is to characterize jet fuel composition and properties based on the fuel's mid-IR absorption spectrum, measured using a Fourier transform IR (FTIR) spectrometer. Over the past 3 years, a database of spectroscopic measurements and property data for a variety of jet fuels and jet fuel components has been acquired. Using this database, we have developed correlations between the spectroscopic properties of jet fuels with fuel composition and with important physical/combustion properties, such as initial boiling point (IBP), density, derived cetane number (DCN), and ignition delay time (IDT). Here, we present an overview of the two research areas (expansion of the FTIR spectrum/fuel property training dataset and IR fuel analysis), along with experimental and modeling results obtained over the past year.

Expansion of the FTIR spectrum and fuel property training dataset:

An FTIR instrument (Nicolet 6700) and heated cell are used to measure the mid-IR spectra of gas-phase fuel samples. Analysis of gas-phase samples enables the detection of sharp spectral features, and even individual absorption transitions, which can in turn be directly linked to the structural characteristics of fuel molecules. This work focuses on analysis of mid-IR absorption spectra, because of the strong sensitivity of this spectral region to hydrocarbon bonding. Work in the previous year of the program focused on extending the spectral range to cover the full 2- to 15- μm region, in contrast to the 3.4- μm region used in the initial work. This process helped us capture additional features corresponding to cycloparaffins and aromatic compounds, which are often important constituents of jet fuels.

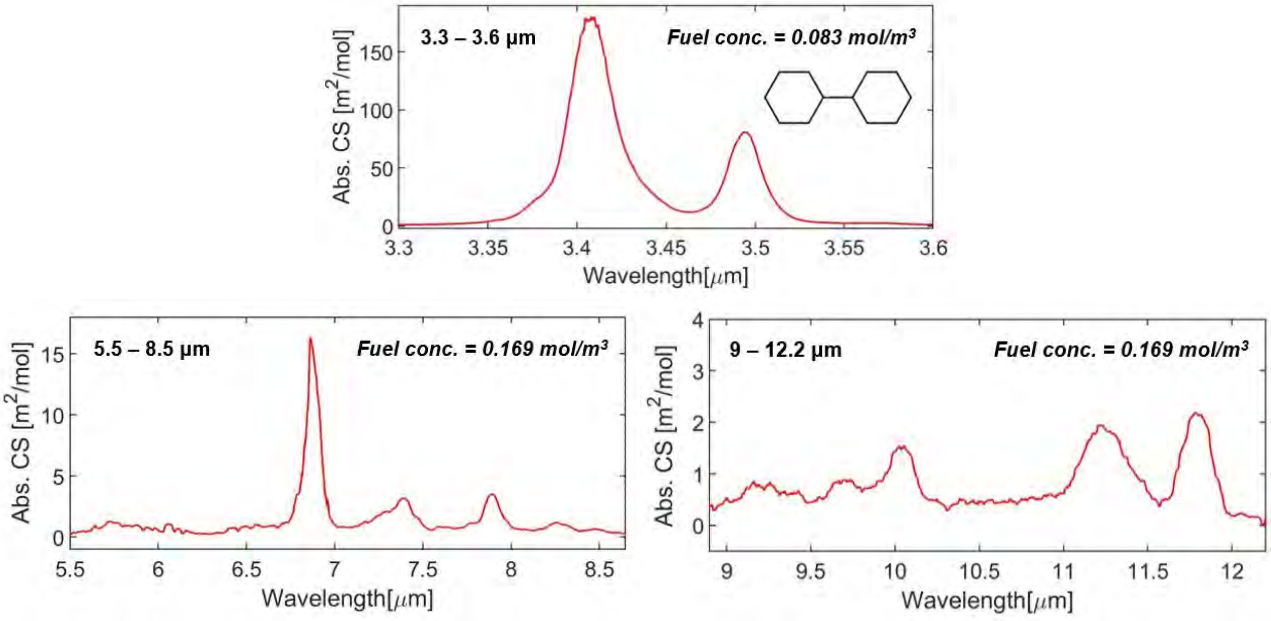

Figure 1. Measured 2- to 15- μm spectrum of bicyclohexane: strong features in the 3.3- to 3.6- μm region, captured with low fuel concentration (top); relatively weaker features in the 5.5- to 8.5- μm region (bottom left) and the 9- to 12.2- μm region (bottom right), captured with high fuel concentration.

Using the modified FTIR spectrometer facility at Stanford, we measured the spectra of additional neat hydrocarbons belonging to molecular classes relevant to jet fuels (isoparaffins, cycloparaffins, and aromatic compounds) at a temperature of 150 °C and added them to our database of FTIR spectra. These hydrocarbons are butylcyclohexane, bicyclohexane, tetralin, pentamethylheptane, trans-decalin, 2-methylhexane, 2-methylheptane, 3,3-dimethylpentane, and 2,2,3-trimethylbutane. Multiple fuel concentrations were used during the measurement of each fuel to capture the weaker absorption features with a high signal-to-noise ratio. An example measurement of bicyclohexane is shown in Figure 1, in which the three panels represent regions with important spectral features.

The dataset was further expanded through the addition of FTIR spectra and property data of blends of neat hydrocarbons. The 2- to 15- μm FTIR spectra of hydrocarbon blends were calculated as the mole-fraction-weighted sum of the spectra of the individual components. Overall, five categories of hydrocarbon blends were added to the training dataset. These categories are as follows:

- BF: 14 two- to three-component blends of *n*-decane, isooctane, and toluene (from the literature)
- Won: 10 binary blends of *n*-dodecane/*n*-decane and toluene (from the literature)
- CB (cycloparaffin blends): 9 binary blends of methylcyclohexane and *n*-butylcyclohexane
- MB (multi-class blends): 70 four-component blends of *n*-dodecane, isooctane, *n*-butylcyclohexane, and *n*-propylbenzene
- AG: 43 three- to five-component blends of *n*-heptane, isooctane, *n*-hexadecane, cyclopentane, and toluene (from the literature)

The addition of these hydrocarbon blends has increased the size of the training dataset to 228 fuels, thus representing a substantial improvement over the dataset size of 81 fuels in the previous year.

The physical/chemical properties of the above-mentioned hydrocarbon blends were either sourced from property measurements reported in the literature, or estimated from the individual components' property values through various property blending correlations as follows:

- Molecular weight (MW): mole fraction-weighted sum
- H/C ratio: ratio of H and C numbers obtained from the mole-fraction-weighted sum
- Net heat of combustion (NHC): mass-fraction-weighted sum
- Density: volume fraction-weighted sum
- Flash point: nonlinear correlation based on volume fractions (from the literature)
- Freezing point: nonlinear correlation based on volume fractions (from the literature)
- Kinematic viscosity (KV): nonlinear correlation based on volume fractions (from the literature)
- Threshold sooting index (TSI): linear correlation based on mole fractions (from the literature)

The use of these blending correlations has enabled us to directly populate the training dataset, thereby circumventing the need for property data measurements.

Five new, candidate Sustainable Aviation Fuel (SAF) samples were recently acquired from other ASCENT members (Steve Zabarnick). These fuels show considerable differences in their molecular class distribution, as detailed in Table 1. A brief description of these five SAFs is provided below.

- POSF 14080: synthetic jet fuel processed from biomass; manufactured by Swedish Biofuels
- POSF 14314: synthetic jet fuel processed from biomass; manufactured by Swedish Biofuels
- POSF 14113: bio-sourced isoparaffinic jet fuel; manufactured by Global Bioenergies
- POSF 13350: synthesized aromatic kerosene; manufactured by Virent
- POSF 14197: biojet fuel; manufactured by the Council of Scientific and Industrial Research-Indian Institute of Petroleum (CSIR-IIP)

Table 1. Molecular class distributions of the five new SAF samples, according to gas chromatography (GCxGC) analysis.

Molecular class	Weight % (GCxGC)				
	14080 (Swedish Biofuels)	14113 (Global Bioenergies)	14314 (Swedish Biofuels)	13350 (Virent)	14197 (CSIR)
n-paraffins	1.40	0.03	1.16	0.03	18.68
isoparaffins	83.13	99.34	56.95	0.19	63.00
cycloparaffins	8.68	0.22	28.22	2.04	12.05
aromatics	6.78	<0.01	13.66	97.73	6.32

The 2- to 15- μm FTIR spectra of these five SAF samples were measured. Figure 2 shows a comparison of the spectra of these five fuels in the 3.4- μm region. The differences in fuel composition result in clear differences in spectral features. As seen in Figure 2, the magnitude of the -CH_3 asymmetric stretch feature increases, and the -CH_2 asymmetric stretch feature grows weaker with increasing isoparaffin content. Owing to its high aromatic content, POSF 13350 shows a distinct aromatic -CH stretch feature, which is absent in the spectra of the other four fuels. These spectral differences follow the expected trend based on the compositions determined through gas chromatography (GCxGC), and demonstrate the strong sensitivity of the FTIR spectra to fuel composition, a crucial aspect for developing accurate property prediction strategies.

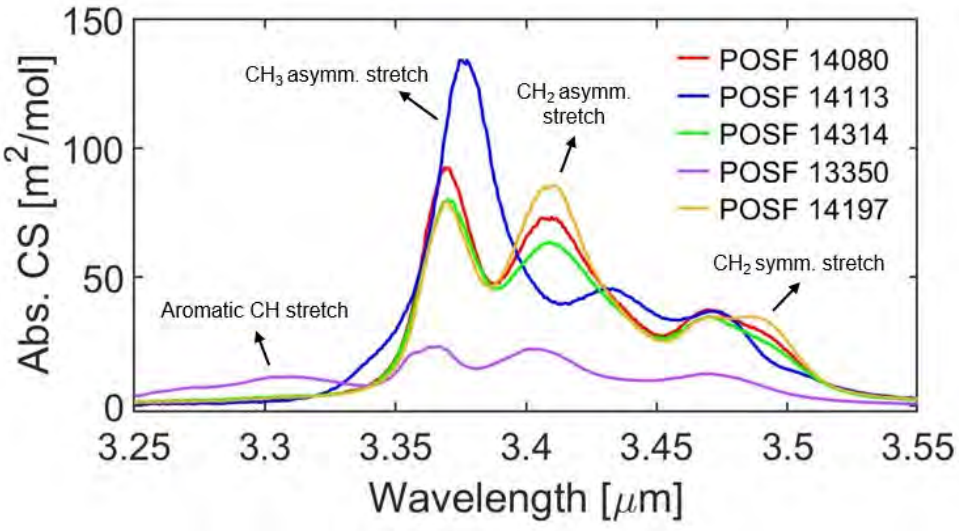

Figure 2. The FTIR spectra of five SAF samples in the 3.4- μm region.

IR fuel analysis:
Over the past 3 years of this program, four strategies (Strategies 1-4) were developed for estimating physical and chemical properties, functional group fractions, and molecular species constituents of fuels directly from mid-IR spectra. In the previous year, two of these developed strategies (Strategies 1 and 4) were further refined to improve their predictive performance. In the current year of this program, Strategy 1 models were trained for different properties by using the expanded training dataset, and these updated models were used to make property predictions on an SAF sample provided by Prof. Josh Heyne (ASCENT P65). The methodology of Strategy 1, along with some results are discussed below.

The first iteration of Strategy 1 implemented cross-validated linear models with Lasso regularization to correlate the FTIR spectra from 3,300 to 3,500 nm with a fuel's physical and chemical properties. Although these preliminary models showed good prediction accuracy for *n*-paraffins and isoparaffins, they had higher property prediction error for aromatics. To improve the performance of these models, we modified the training dataset to include the full 2- to 15- μm FTIR spectra of fuels.

Furthermore, the models were modified to use Elastic-Net regularization instead of Lasso regulation, thereby enabling the selection of optimal model parameters for each property during training. For implementation, a grid search was first performed to choose the combination of model parameters resulting in the minimum cross-validation error, which was then used to train the final model for each property.

As discussed in the previous section, the training dataset was also augmented by addition of the FTIR spectra and property data of blends of neat hydrocarbons, thereby increasing the total dataset size from 81 fuels to 228 fuels. The modified model parameter optimization Strategy, along with the expanded training data, improved the predictive performance of Strategy 1 models for various physical/chemical properties.

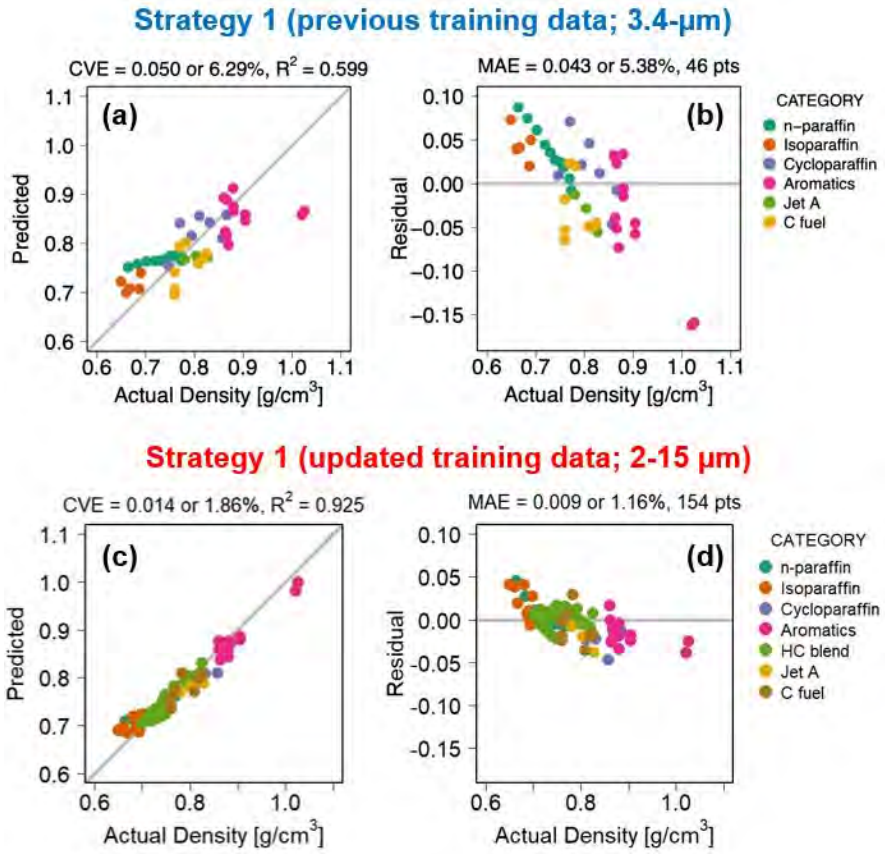

Figure 3. Strategy 1 model performance on training data: (a) predicted density and (b) residuals, on the basis of the previous dataset (3.4-μm region, without hydrocarbon blends); (c) predicted density and (d) residuals, on the basis of the updated dataset (2- to 15- μm region, with added hydrocarbon blends).

Figure 3 shows the predictive performance of the Strategy 1 model for density on the training dataset fuels, comparing the model trained on the previous dataset (3.4-μm region spectra, without hydrocarbon blends) with that trained on the updated dataset (2- to 15- μm spectra, with added hydrocarbon blends). These plots indicate that the updated Strategy 1 model fits the data much better than the previous model. The previous model shows poor prediction for aromatics in particular, which do not have distinctive absorption features in the 3.4-μm region. The predictive performance of each model is evaluated according to three metrics: the cross-validation error (CVE, indicative of future predictive performance), the mean absolute error of prediction (MAE), and the R^2 value (measure of goodness of fit). The updated model shows a reduction in CVE by a factor of 3.6, and a reduction by nearly a factor of 5 in the MAE as compared with the previous model. The updated model also has a substantially higher R^2 value, thus indicating a better fit to the training data. Similar performance improvement was observed for all properties considered.

The previous and updated Strategy 1 models were also used to make property predictions on unseen test data. This step is often a crucial component in assessing the performance of machine learning models. The test data considered here are three volumetric blends of A2 (distillate jet fuel) and C1 (synthetic, alcohol-to-jet fuel). Table 2 shows the density predictions of the previous and updated Strategy 1 models for the three test fuel blends. This table clearly shows that the updated model performs better on the test data, achieving an error reduction on the order of 60%-90%, as compared with the previous model for density.

Table 2. Predictive performance of the previous and updated Strategy 1 models on test data (A2/C1 jet fuel blends).

Property	Fuel blend (% vol.)	Actual	Previous dataset (3.4-μm)		Updated dataset (2-15 μm)	
			Predicted	Error (%)	Predicted	Error (%)
Density [g/cm^3]	80% A2 / 20% C1	0.795	0.763	-4.05	0.783	-1.52
	50% A2 / 50% C1	0.781	0.744	-4.80	0.774	-0.92
	20% A2 / 80% C1	0.768	0.722	-5.97	0.764	-0.55

The Strategy 1 models were finally used to predict the properties of an SAF sample provided by Prof. Josh Heyne (ASCENT P65). The measured 2- to 15- μm FTIR spectrum of this fuel indicated that cycloparaffins were major constituents of the fuel. The predictions of both the previous and updated Strategy 1 models, along with the reference property values are shown in Table 3. The reduction in prediction error of the updated model on the SAF sample, with respect to the previous model, further highlights the impact of the extended spectral range as well as the larger training dataset size on the predictive performance. The updated Strategy 1 predictions closely match the reference values for most properties. However, the relatively higher prediction error in the case of MW, DCN, and IBP indicate that scope exists for improving the IR analysis strategies through use of nonlinear regression techniques.

Table 3. Strategy 1 property predictions of the SAF sample obtained from Prof. Josh Heyne (ASCENT P65).

Property	3.4-μm region model		2-15 μm region model		Reference values
	Predicted	CVE (%)	Predicted	CVE (%)	
MW (g/mol)	108.4	8.99	150	2.83	**140**
H/C ratio	1.48	6.88	1.98	1.71	**2.00**
NHC (MJ/kg)	43.0	0.88	43.5	0.25	**43.7**
DCN	7.81	15.59	24.8	11.20	**18**
Density @ 20℃ (g/cm^3)	0.861	6.29	0.817	1.46	**0.821**
IBP (℃)	118	18.93	154	14.31	**179.8**
TSI	41.2	33.01	12.4	7.59	**10.8**

Overall, the IR analysis results obtained over the past year by using the extended wavelength range and the expanded training dataset show improved predictive performance over that of the spectral analysis strategies developed in the previous years of this work. These strategies enable accurate prediction of the physical and chemical properties of alternative jet fuels directly based on their infrared spectra.

Milestones

Major milestones included regular reporting of experimental results and analysis at the Fall and Spring ASCENT meetings (October 2021 and April 2022), and presentation of results at the 39th International Symposium on Combustion (July 2022, Vancouver, British Columbia).

Major Accomplishments

During the eighth year of this program, major advances were made in several areas:

- The 2- to 15- um FTIR spectra of butylcyclohexane, bicyclohexane, tetralin, pentamethylheptane, trans-decalin, 2-methylhexane, 2-methylheptane, 3,3-dimethylpentane, and 2,2,3-trimethylbutane were measured and added to the training dataset.
- The 2- to 15- um FTIR spectra of blends of neat hydrocarbons were calculated using linear addition of the individual components' spectra and were added to the training dataset, thus increasing the sample size from 81 fuels to 228 fuels.
- Property blending correlations were used to estimate the molecular weight, H/C ratio, net heat of combustion, density, flash point, freezing point, kinematic viscosity, and threshold sooting index of these hydrocarbon blends.
- Strategy 1 models were trained for these properties by using the expanded dataset (228 fuels). The models trained on the expanded dataset showed an improvement in prediction accuracy over that of the earlier models trained on the limited dataset (81 fuels).
- Strategy 1 models were used to predict properties of an SAF sample provided by Prof. Josh Heyne (ASCENT P65): molecular weight, H/C ratio, net heat of combustion, derived cetane number, density, initial boiling point, and threshold sooting index. The models trained on the 2- to 15- um FTIR spectra showed improvement in prediction accuracy over that of the models trained on just the 3.4-um region.
- The 2- to 15- um FTIR spectra of five new SAF samples (procured from Swedish Biofuels, Global Bioenergies, Virent, and the Council of Scientific and Industrial Research) were measured. Property predictions are forthcoming.

Publications

Peer-reviewed journal publications

Boddapati, V., Ferris, A. M., Hanson, R. K. (2022), "On the use of extended-wavelength FTIR spectra for the prediction of combustion properties of jet fuels and their constituent species," *Proceedings of the Combustion Institute 39*. https://doi.org/10.1016/j.proci.2022.08.041

Outreach Efforts

Our IR fuel analysis work was presented at the Virtual Fall ASCENT Advisory Board Meeting (October 26–28, 2021), and at the Spring ASCENT Advisory Board Meeting (April 5–7, 2022). Research was also presented at the 39th International Symposium on Combustion (July 24–29, 2022) in Vancouver, British Columbia.

Awards

None.

Student Involvement

Graduate students are actively involved in the acquisition and analysis of all experimental data. Vivek Boddapati (current graduate student) performed the IR spectral analysis/fuel prescreening. Alison Ferris (current research scientist) has additionally contributed to the project through research management and report writing.

Plans for Next Period

In the next period, we plan to:

- Revisit Strategy 3 models (principal component analysis plus support vector regression) to better capture nonlinear spectrum-property relationships and compare their performance with the linear Strategy 1 models.
- Use the updated Strategy 1 models to make property predictions for the five new SAF samples and compare the predictions against the actual property values.
- Review other fuel property prediction methods (e.g., GCxGC, near IR, etc.) reported in the literature; compare prediction accuracies with those attainable with our FTIR method.
- Continue measuring the 2- to 15- um spectra of relevant neat hydrocarbons, conventional jet fuels, and SAFs.
- Explore batch distillation of multi-component fuels as a potential way to isolate molecular classes with weaker spectral features (e.g., cycloparaffins, aromatics, etc.) and possibly identify strategies to make more accurate property predictions based on the FTIR spectra of individual distillate fractions.

Project 31 Alternative Jet Fuel Test and Evaluation

University of Dayton Research Institute

Project Lead Investigator

Steven Zabarnick, PhD
Division Head, Fuels and Combustion
University of Dayton Research Institute
300 College Park
Dayton, OH 45469-0043
937-255-3549
Steven.Zabarnick@udri.udayton.edu

University Participants

University of Dayton Research Institute (UDRI)

- P.I.: Steven Zabarnick, Division Head
- FAA Award Number: 13-C-AJFE-UD
- Overall Period of Performance: April 8, 2015 to September 30, 2022
- Tasks:
  - Period of Performance: April 8, 2015 to March 14, 2016; Amendment No. 006
    1. Evaluate the performance of candidate alternative fuels via the ASTM D4054 approval process
  - Period of Performance: August 13, 2015 to August 31, 2016; Amendment No. 007
    2. Evaluate the performance of candidate alternative fuels via the ASTM D4054 approval process
  - Period of Performance: August 5, 2016 to August 31, 2017; Amendment No. 012
    3. Manage the evaluation and testing of candidate alternative fuels
  - Period of Performance: July 31, 2017 to August 31, 2019; Amendment No. 016
    4. Manage the evaluation and testing of candidate alternative fuels
  - Period of Performance: August 30, 2018 to August 31, 2019; Amendment No. 021
    5. Manage the evaluation and testing of candidate alternative fuels
  - Period of Performance: Extended period of performance end from September 10, 2019 to September 9, 2020; Amendment No. 023
  - Period of Performance: February 5, 2020 to February 4, 2021; Amendment No. 25
    6. Manage the evaluation and testing of candidate alternative fuels
  - Period of Performance: Extended period of performance end from September 9, 2019 to September 9, 2021; Amendment No. 028.
  - Period of Performance: February 4, 2021 to February 5, 2022; Amendment No. 32
    7. Manage the evaluation and testing of candidate alternative fuels
  - Period of Performance: August 10, 2021 to February 10, 2022; Amendment No. 33
    - No cost extension (Amendment 33 is not task specific)
  - Period of Performance: October 1, 2021 to September 30, 2022; Amendment No. 38
  - Period of Performance: October 1, 2022 to September 30, 2023; Amendment No. 43

Project Funding Level

Amendment No. 006	$309,885
Amendment No. 007	$99,739
Amendment No. 012	$693,928
Amendment No. 016	$999,512
Amendment No. 021	$199,966
Amendment No. 025	$1,926,434

Amendment No. 032	$1,049,700
Amendment No. 038	$499,784
Amendment No. 043	$1,499,940
Total	**$7,278,888**

In-kind cost sharing has been obtained from the following organizations:

Organization	Amount	Year
LanzaTech	$55,801	2015
LanzaTech	$381,451	2016
UDRI	$43,672	2016
Neste	$327,000	2017
Boeing	$2,365,338	2017
Shell	$280,000	2019
IHI	$1,150,328	2019
Shell	$325,000	2020
Global Bioenergies	$6,875,900	2021
Global Bioenergies	$290,000	2021
Total	**$12,094,490**	

Investigation Team

- Steven Zabarnick, P.I., new candidate-fuel qualification and certification
- Richard Striebich, Researcher, fuel chemical analysis and composition
- Linda Shafer, Researcher, fuel chemical analysis and composition
- John Graham, Researcher, fuel seal swell and material compatibility
- Zachary West, Researcher, fuel property evaluation
- Rhonda Cook, Technician, fuel property testing
- Sam Tanner, Technician, fuel sampling and shipping
- Carlie Anderson, Researcher, fuel chemical analysis
- Brandon Brown, Researcher, fuel chemical analysis
- Marlin Vangsness, Researcher, fuel chemical analysis
- Megan Pike, Researcher, fuel seal swell and material compatibility

Project Overview

Alternative jet fuels offer the potential benefits of reduced global environmental impacts, greater national energy security, and stabilized fuel costs for the aviation industry. The FAA is committed to the advancement of “drop-in” alternative fuels. The successful adoption of alternative fuels requires approval for use by the aviation community, followed by large-scale production of fuel that is cost competitive and meets the safety standards for conventional jet fuel. Alternative jet fuels must undergo rigorous testing to become qualified for use and to be incorporated into ASTM International specifications.

Cost-effective, coordinated performance testing capability (in accordance with ASTM D4054) is needed to support the evaluation of promising alternative jet fuels. The objective of this project is to provide the necessary capability to support fuel testing and evaluation of novel alternative jet fuels.

The proposed program should provide the following capabilities:

- Identify alternative jet fuels, including blends with conventional jet fuel, with the potential to be economically viable and to support FAA’s NextGen environmental goals for testing
- Perform engine, component, rig, or laboratory tests, or any combination thereof, to evaluate the performance of alternative jet fuels in accordance with ASTM International standard practice D4054
- Identify and conduct unique testing, beyond that defined in ASTM International standard practice D4054, to support the evaluation of alternative jet fuels for inclusion in ASTM International jet fuel specifications
- Obtain baseline and alternative jet fuel data to assess any effects of an alternative jet fuel on aircraft performance, maintenance requirements, and reliability

- Coordinate efforts with activities sponsored by the Department of Defense and/or other governmental parties that may be supporting relevant work
- Report relevant performance data for the alternative fuels tested, including quantified effects of the alternative fuel on aircraft and/or engine performance and on air-quality emissions relative to conventional jet fuel; share reported data with the FAA National Jet Fuel Combustion Program, the broader community (e.g., ASTM International), and the ASCENT COE Program 33 "Alternative Fuels Test Database Library."

Tasks 1 and 2 - Evaluate the Performance of Candidate Alternative Fuels via the ASTM D4054 Approval Process, and Manage the Evaluation and Testing of Candidate Alternative Fuels

University of Dayton Research Institute

Objective

Cost-effective, coordinated performance testing capability (in accordance with ASTM D4054) is needed to support the evaluation of promising alternative jet fuels. The objective of this project is to provide the capability necessary to support either (a) the evaluation of to-be-determined alternative fuels selected in coordination with the FAA or (b) a fuel testing and evaluation project with specific alternative fuels in mind.

Research Approach

The intent of this program is to provide the capability needed to perform specification and fit-for-purpose evaluations of candidate alternative fuels, with the aim of providing a path through the ASTM D4054 approval process. The UDRI team can perform many of these evaluations and is prepared to work with other organizations, such as the Southwest Research Institute (SwRI) and engine original equipment manufacturers (OEMs), with unique test capabilities, as needed. These assessments include additional engine, auxiliary power unit (APU), component, and rig evaluations. The UDRI testing capabilities include efforts at the laboratories of the Fuels Branch of the Air Force Research Laboratory and at our campus laboratory facilities.

The following lists provide examples of the evaluations that can be provided by UDRI:

Tier 1

1. Thermal stability (quartz crystal microbalance)
2. Freeze point (ASTM D5972)
3. Distillation (ASTM D86)
4. Hydrocarbon range (ASTM D6379 and D2425)
5. Heat of combustion (ASTM D4809)
6. Density, API gravity (ASTM D4052)
7. Flash point (ASTM D93)
8. Aromatics (ASTM D1319)

Tier 2

1. Color, Saybolt (ASTM D156 or D6045)
2. Total acid number (ASTM D3242)
3. Aromatics (ASTM D1319 and D6379)
4. Sulfur (ASTM D2622)
5. Sulfur mercaptan (ASTM D3227)
6. Distillation temperature (ASTM D86)
7. Flash point (ASTM D56, D93, or D3828)
8. Density (ASTM D1298 or D4052)
9. Freezing point (ASTM D2386, D5972, D7153, or D7154)
10. Viscosity at −20 °C (ASTM D445)
11. Net heat of combustion (ASTM D4809)
12. Hydrogen content (ASTM D3343 or D3701)
13. Smoke point (ASTM D1322)

14. Naphthalenes (ASTM D1840)
15. Calculated cetane index (ASTM D976 or D4737)
16. Copper strip corrosion (ASTM D130)
17. Existent gum (ASTM D381)
18. Particulate matter (ASTM D2276 or D5452)
19. Filtration time (MIL-DTL-83133F Appendix B)
20. Water reaction interface rating (ASTM D1094)
21. Electrical conductivity (ASTM D624)
22. Thermal oxidation stability (ASTM D3241)

Extended physical and chemical characterization

1. Lubricity evaluation: ball-on-cylinder lubricity evaluator (BOCLE) test (ASTM D5001)
2. Evaluation of low-temperature properties: scanning Brookfield viscosity
3. Detection, quantification, and/or identification of polar species, as necessary
4. Detection, quantification, and/or identification of dissolved metals, as necessary
5. Initial material compatibility evaluation: optical dilatometry and partition coefficient measurements to determine the fuel-effected swell and fuel solvency in three O-ring materials (nitrile, fluorosilicone, and fluorocarbon) and as many as two additional fuel system materials
6. Experimental thermal stability evaluation: quartz crystal microbalance to measure thermal deposition tendencies and oxidation profiles at elevated temperatures
7. Evaluation of viscosity versus temperature: ASTM D445 to determine the fuel viscosity at 40 °C and −40 °C, to assess the viscosity variation with temperature

In addition to the above physical and chemical fuel evaluation capabilities, UDRI has extensive experience in evaluating microbial growth in petroleum-derived and alternative fuels. These evaluations include standard laboratory culturing and colony counting methods, as well as advanced techniques, such as quantitative polymerase chain reaction (QPCR) and metagenomic sequencing. These methods enable quantitative measurements of microbial growth rates in candidate alternative fuels for comparison with petroleum fuels.

UDRI also has extensive experience in the evaluation of elastomer degradation upon exposure to candidate alternative fuels. Various methods are used to evaluate seal swell and O-ring fixture leakage, including optical dilatometry, sealing pressure measurements, fuel partitioning into the elastomer, and the use of a pressurized temperature-controlled O-ring test device.

Moreover, UDRI can perform fuel–material compatibility testing by using the D4054 procedures for fuel soak testing, postexposure nonmetallic and metallic material testing, and surface and microstructural evaluation. The 68 “short-list” materials and the 255 materials on the complete list can be tested.

Milestone(s)

The schedule for this project is dependent on the receipt of alternative fuel candidates for testing. As candidate fuels are received, a testing schedule will be established via coordination with the FAA and collaborators. Our existing relationships with these organizations will help expedite this process.

Major Accomplishments

Shell IH^2 testing

Discussions with Shell on their IH^2 fuel and process (hydropyrolysis and hydrotreating of woody biomass, municipal solid waste (MSW), and agriculture residue) began in 2017 and proceeded through 2018. In January 2019, samples of their CPK-0 (zero aromatics) fuel were received by the Clearinghouse for testing. Testing proceeded at UDRI and SwRI through the spring of 2019, and a draft research report was produced in the summer. In October 2019, initial warm lean blowout (LBO) testing of the CPK-0 fuel blends was performed in the referee combustor. We await the production of larger quantities of IH^2 fuel for additional cold LBO and ignition studies in the referee rig. In addition, a Phase 1 research report was presented to the OEM committee in June 2020, with the anticipation of OEM APU and engine combustor sector testing in 2022. Feedback from the OEM committee resulted in additional testing being performed. The unusually high cycloparaffin content (>95%) of this fuel will dictate the need for additional Tier 3 testing. Because of the fuel’s excellent performance in the referee rig, the extent of additional testing may be limited. OEM feedback from the Phase 1 research report was provided to Shell, and plans are

being made to perform combustion testing via CLEEN 3 and this ASCENT project. Unfortunately, delays in acquiring sufficient fuel from Shell have resulted in delaying the planned APU and combustor sector testing to 2023.

Global BioEnergies (GBE)
Tier 1 and 2 testing of GBE Rewofuel has been completed. The feedstock is wood residue, and jet fuel is produced via isobutylene oligomerization. The isobutylene is produced via a genetically modified organism. During the year, a Phase 1 research report was completed and submitted to the OEM committee for review. The OEM committee provided their review and comments. GBE responded to these comments, and additional testing was performed. Because no major OEM issues were identified with the report, GBE has submitted the fuel to an ASTM ballot.

Swedish Biofuels
Tier 1 and 2 testing of the Swedish Biofuels alcohol-to-jet fuel has been completed. The feedstock consists of a variety of mixtures of alcohols. The research report has been completed and reviewed by the OEM committee. An ASTM ballot will be submitted soon.

CSIR-IIP
CSIR-IIP has developed a single-step process to convert lipids (plant-derived oil and animal-derived fats) into hydrocarbons containing aromatic compounds. A single sample of the fuel was received, and Tier 1 and 2 testing has been completed. We are awaiting receipt of an additional fuel sample.

Revo
The Revo fuel is a hydroprocessed esters and fatty acids HEFA-type fuel containing a higher level of cycloparaffins. Initial testing has been completed, and we are awaiting an additional sample for further evaluation.

Virent SAK
Virent SAK is an aromatics-only stream produced from a sugar feedstock. The OEM committee has recommended that this candidate be reevaluated as a blend with petroleum jet fuel. A test plan has been created, the fuel has been received, and testing will commence soon.

OMV
The OMV ReOil candidate is produced from waste plastics via pyrolysis. The OEM committee has approved this fuel for entry to the Fast Track process after reviewing initial fuel property and composition data. An initial fuel sample has been received, and testing will commence soon.

Publications

Written reports

ASTM International. (2019). *Modification of ASTM D1655: Co-processing of Fischer-Tropsch feedstocks with petroleum hydrocarbons for jet production using hydrotreating and hydrocracking.* (Modification of Report No. ASTM D1655).

(2019). *Evaluation of synthesized paraffinic kerosene from algal oil extracted from botryococcus braunii (IHI Bb-SPK).* (Report No. D4054).

ASTM International. (2020). *Standard specification for aviation turbine fuels*. Report No. ASTM D1655-20. https://astm.org/d1655-20.html

(2022). *Evaluation of Global Bioenergies' isobutene derived synthetic paraffinic kerosene (IBN-SPK).* (Research Report D02 - WK71952).

(2022). *Evaluation of alcohol-to-jet synthetic kerosene with aromatics (ATJ-SKA) fuels and blends*. (Research Report).

Outreach Efforts

Presentations on Project 31 activities were given at the April 2022 and October 2022 ASCENT virtual meetings. Meetings were held with the OEM team, FAA, fuel producers, and others at numerous virtual (generally two per month) FAA/OEM meetings.

Awards

None

Student Involvement
None

Plans for Next Period
We are awaiting the receipt of larger quantities of the Shell IH² fuel for further evaluation, which will include cold LBO testing, ignition testing, APU cold start and ignition evaluation, and engine OEM sector evaluation. We will be conducting future testing of the CSIR-IIP, Revo, OMV, and Virent SAK fuels. We will continue discussions with new fuel producers, and we expect new candidates to enter the process in the coming months.

Tasks 3 and 4 - Manage the Evaluation and Testing of Candidate Alternative Fuels
University of Dayton Research Institute

Objective
The objective of this work is to manage the evaluation and testing of candidate alternative jet fuels in accordance with ASTM International standard practice D4054 (Figure 1).

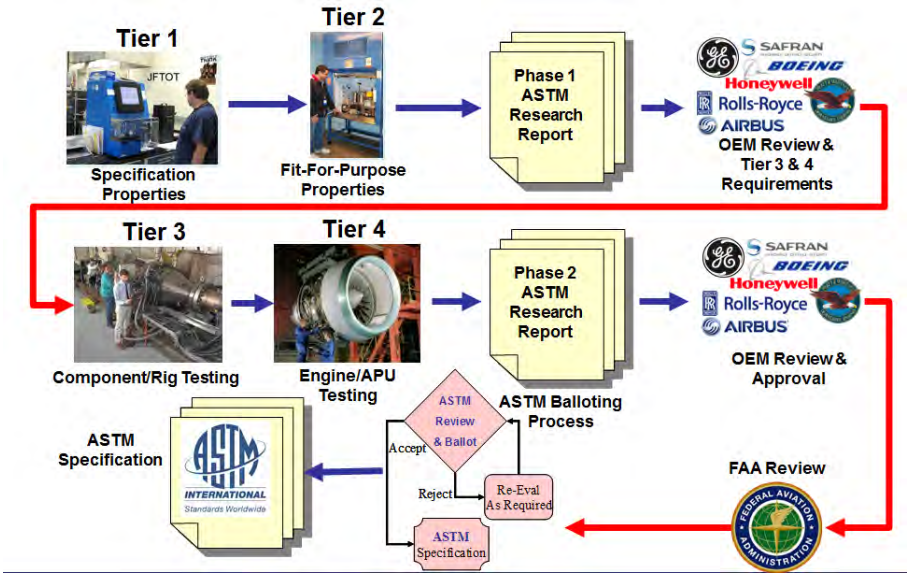

Figure 1. ASTM D4054 qualification process.

Research Approach
UDRI will subcontract with other research organizations, testing laboratories, and/or OEMs to conduct the following tasks in support of the evaluation and ASTM specification development for alternative jet fuels. The purpose of this project is to manage and coordinate the D4054 evaluation process (illustrated in Figure 2) to facilitate the transition of alternative fuels to commercial use.

Subtask 1: general support
- Develop and make available a D4054 process guide describing logistical procedures for the handling of test fuels, documentation requirements, test report issuance and delivery, and contact information, to provide clear instructions for candidate-fuel producers entering the ASTM D4054 process

Subtask 2: phase 1 support
- Coordinate the handling of Phase 1 candidate test fuel samples for Tier 1 and 2 testing

- Review process descriptions provided by the fuel producer to determine the acceptability for incorporation into the Phase 1 research report
- Review test data from Tier 1 and 2 testing to determine acceptability for incorporation into the Phase 1 research report
- Issue and deliver a Phase 1 research report to OEMs
- In conjunction with the fuel producer, review and respond to comments regarding the Phase 1 research report, as submitted by the OEMs
- Conduct additional Tier 1 or 2 testing in response to OEM comments, as required
- Review and consolidate OEM requirements for D4054 Tier 3 and 4 testing, as submitted by the OEMs
- Deliver consolidated D4054 Tier 3 and 4 testing requirements to the fuel producer

Subtask 3: phase 2 support

- Coordinate the funding and scheduling of D4054 Tier 3 and 4 testing with OEMs and other test facilities
- Coordinate the handling of Phase 2 candidate test fuel samples for Tier 3 and 4 testing
- Review test data from Tier 3 and 4 testing to determine acceptability for incorporation into the Phase 2 research report
- Issue and deliver the Phase 2 research report to OEMs
- In conjunction with the fuel producer, review and respond to comments submitted by OEMs regarding the Phase 2 research report
- Conduct additional Tier 3 or 4 testing in response to OEM comments, as required
- Issue and deliver Phase 2 research report addenda reporting the additional Tier 3 or 4 test results, as required

Subtask 4: OEM review meetings

- Schedule periodic OEM meetings to review the testing status and the research report evaluations
- Identify suitable meeting venues and support equipment
- Develop agendas and coordinate with attendees for participation in these meetings
- Record meeting minutes, including agreements, commitments, and other action items
- Issue and distribute meeting minutes to all attendees

Subtask 5: single-laboratory GCxGC method documentation

- Document UDRI GCxGC methods for hydrocarbon type analysis
- Develop reference materials for the creation of GCxGC hydrocarbon type templates
- Measure single-laboratory precision of the GCxGC methods

Subtask 6: multi-laboratory GCxGC method documentation

- Validate the precision of GCxGC methods across multiple laboratories
- Identify alternative GCxGC methods, including column selection and order, and modulation techniques
- Perform a correlation study to determine the agreement among laboratories, methods, and hardware choices

Milestone(s)

The schedule for this project is dependent on the receipt of alternative fuel candidates for testing. As candidate fuels are received, a testing schedule will be established via coordination with the FAA and collaborators. Our existing relationships with these organizations will help expedite this process. Figure 3 shows a Gantt chart schedule for the testing and approval of candidate fuels that are either currently under evaluation or will soon enter the evaluation process.

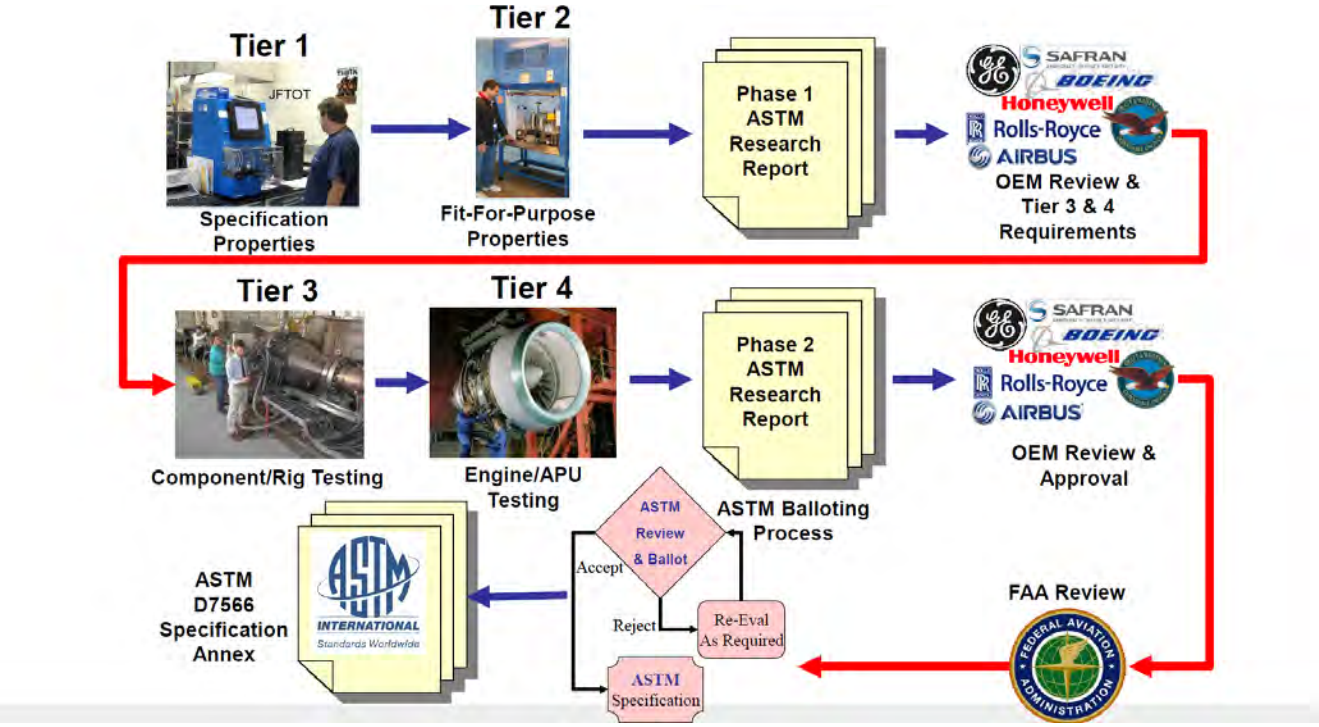

Figure 2. D4054 evaluation process.

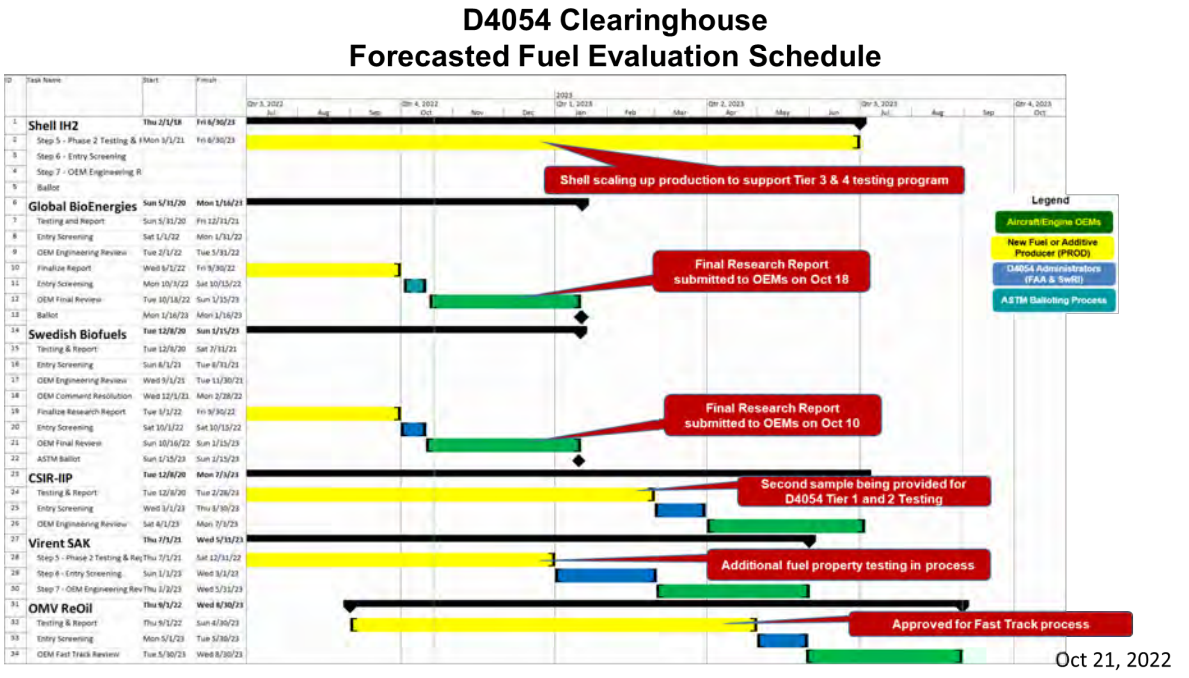

Figure 3. Schedule for fuel evaluations.

Major Accomplishments

GCxGC precision: intra- and interlaboratory comparisons
To investigate the precision of GCxGC hydrocarbon type analyses, we assessed a single fuel over several years with a single instrument (intralaboratory comparison). We also compared two different GCxGC systems: flow modulation with a nonpolar initial column and a polar secondary column versus thermal modulation with a polar initial column and a nonpolar secondary column. We also compared measurements between two laboratories (UDRI/Air Force Research Laboratory versus NASA Glenn) for multiple fuels with the same instrument type and column configuration. In addition, we have recently compared measurements among multiple laboratories using several different GCxGC systems and methods.

A report describing these results has been drafted and submitted to the FAA for comments (UDR-TR-2021-159). This report details the following:

- 2.0 Phase 1 results: single-laboratory GCxGC method documentation
  - 2.1 Methods and documents describing UDRI methods
  - 2.2 Development of reference materials
  - 2.3 Single-laboratory precision
- 3.0 Phase 2 results: multi-laboratory GCxGC method documentation
  - 3.1 Precision validation of normal phase GCxGC, flow modulation with an outside laboratory (reproducibility)
  - 3.2 Identification of alternative methods
  - 3.3 Correlation study

Most recently, the GCxGC precision results were reported at the September 2022 IASH meeting in Dresden, Germany. A proceedings manuscript is being prepared.

CAAC
The Chinese government has approached the FAA/OEM committee with a request to evaluate two jet fuel additives for approval for use. These include a static dissipator additive (SDA) and a corrosion inhibitor/lubricity improver (CI/LI) additive. These additives have been received, and the testing has been completed on the SDA additive; testing of the CI/LI will be completed very soon. Review of the SDA results has resulted in the OEM committee recommending additional testing, which will begin soon.

ICP-MS
Recent observations of inconsistent results for the dissolved metals concentrations in fuel evaluated in the Clearinghouse have prompted an evaluation of these analyses. In particular, the phosphorus results have been an issue during ongoing evaluations. UDRI acquired an ICP-MS system and is in the process of developing improved methods for analyses of metals. We will soon be reporting our results on the development of these methods.

OEM committee coordination
The ongoing efforts in ASTM OEM committee coordination continued during this period. These efforts involve coordinating the engine and airframer OEM meetings, which have typically occurred in concert with the biannual ASTM Committee D02 sessions and at the annual U.K. Ministry of Defense Aviation Fuels Committee meeting in London. During travel restrictions due to the COVID-19 pandemic, these meetings have been occurring virtually and more frequently, once or twice per month. SwRI continues to receive funding to aid in coordinating the OEM meetings, and in communicating with the OEMs for discussions and research report reviews of new candidate alternative jet fuels. In addition, a Gantt schedule is updated monthly; this schedule shows a queue of candidate fuels, and the completed and expected schedules as these fuels move through the ASTM D4054 process of testing, review, balloting, and approval. A recent version of this schedule is shown in Figure 3. In support of the ongoing OEM committee coordination, subcontracts with Boeing, GE Aviation, Honeywell, Rolls Royce, Pratt & Whitney, and SwRI have been extended to our ASCENT grant end date of September 30, 2023.

Publications

Written reports

(2018). *UDRI Method FC-M-101: Flow modulation GCxGC for hydrocarbon type analysis of conventional and alternative aviation fuels*. (Report No. UDR-TR-2018-40).

(2018). *UDRI Method FC-M-102: Identification and quantification of polar species in conventional and alternative aviation fuel using SPE-GCxGC*. (Report No. UDR-TR-2018-41).

(2020). *Evaluation of integrated hydropyrolysis and hydroconversion (IH²®) cycloparaffinic kerosene (CPK-0).* (Report No. D4054).
(2019). *Evaluation of synthesized paraffinic kerosene from algal oil extracted from Botryococcus braunii (IHI Bb-SPK).* (Fast Track Research Report).
(2021). *Alternative jet fuel evaluation and specification development support: GCxGC methods draft report.* (Report No. UDR-TR-2021-159).
(2022). *Evaluation of Global Bioenergies' isobutene derived synthetic paraffinic kerosene (IBN-SPK).* (Research Report D02 - WK71952).
(2022). *Evaluation of alcohol-to-jet synthetic kerosene with aromatics (ATJ-SKA) fuels and blends.* (Research Report).

Outreach Efforts

Presentations on Project 31 activities were given at the April 2022 and October 2022 ASCENT virtual meetings. Meetings were held with the OEM team, FAA, fuel producers, and other attendees at numerous virtual FAA/OEM meetings (generally two per month). We have also met with multiple candidate-fuel producers, including Global Bioenergies, OMV, CSIR-IIP, Revo, Par Hawaii Refining, BioWright, Greenfield Global, ExxonMobil, Uzbekistan GTL, Vertimass, Green Lizard, Virent, Swedish Biofuels, Deutsche Energie-Angentur, Zero Petroleum, Licella, and Varo Energy.

Awards

None

Student Involvement

None

Plans for Next Period

We plan to continue coordination of the OEM committee reviews. We will continue to hold both in-person and virtual OEM committee meetings.

Project 033 Alternative Jet Fuels Test Database (AJFTD) Library (2022)

University of Illinois Urbana-Champaign

Project Lead Investigator

Tonghun Lee
Professor
Mechanical Science & Engineering
University of Illinois at Urbana-Champaign
1206 W. Green St.
Urbana, IL 61801
517-290-8005
tonghun@illinois.edu

University Participants

University of Illinois at Urbana-Champaign

- P.I.: Tonghun Lee, Professor
- FAA Award Number: 13-C-AJFE-UI-038
- Period of Performance: October 1, 2021 to September 30, 2022
- Tasks:
    1. Online database development with JETSCREEN, ALIGHT, NewJET, and domestic airport connection
    2. Machine-learning-based online analysis

Project Funding Level

FAA funding level: $150,000
Cost sharing: Software license support from Reaction Design (ANSYS)

Investigation Team

- Tonghun Lee (Professor, University of Illinois at Urbana-Champaign): overall research supervision
- Alex Solecki (Graduate Student, University of Illinois at Urbana-Champaign): database development
- Ji Hun Oh (Graduate Student, University of Illinois at Urbana-Champaign): machine-learning-based analysis

Project Overview

This study seeks to develop a comprehensive and foundational database of current and emerging alternative jet fuels by integrating relevant pre-existing jet fuel data into a common archive that can support scientific research, enhance operational safety, and provide guidelines for the design and certification of new jet fuels. In light of the September 2021 White House statement on advancing the future of sustainable aviation fuels (SAFs) in America, the database now has even greater potential for serving the national agenda. In previous years of this project, efforts focused on the integration and analysis of pre-existing jet fuel data from various government agencies and individual research groups. In 2020, we converted all the compiled data to a new nonstructured query language (NoSQL) format by using a JavaScript object notation (JSON) schema, thus allowing the data to be analyzed in a flexible manner by using various programming languages. To this end, we have launched the second generation of our online database, the National Alternative Jet Fuels Test Database (AJFTD), which uses the new nonrelational database structure. This version is equipped with interactive analysis functions for users, and flexible methods for plotting and downloading data. In the previous year, we extended this effort to incorporate advanced machine learning algorithms into the analysis process. Additionally, we have integrated our database with the database assembled by the European JETSCREEN program. In the future, data acquisition from domestic and international airports will help further develop the database and support its use as a repository for all SAF-related property and test data.

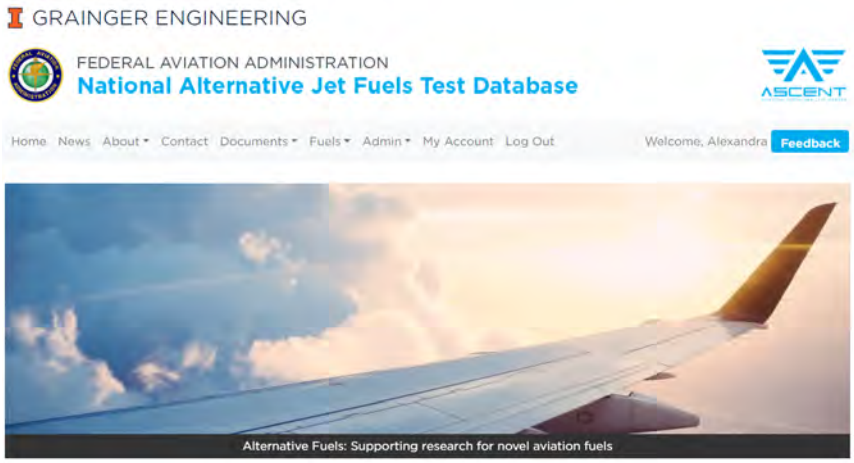

Figure 1. Alternative Jet Fuels Test Database homepage.

We hope that the database will, one day, serve not only as a comprehensive and centralized knowledgebase used by the jet fuel research community, but also as a resource to enhance global operation efficiency and safety. Future efforts will include linking real-time fuel usage and certification data from domestic and international airports. Connecting our database with ongoing European projects, such as ALIGHT and NewJET, will help create avenues for future database development in this area. Given the prolific diversification of new alternative jet fuels expected in the near future, the ability to track critical fuel properties and test data from both research and operation perspectives will be highly valuable for the future of commercial aviation. Furthermore, increasing the breadth of data categories available on the database, from fuel data to global usage trends, will make the database relevant to a greater audience. We hope that ongoing website development and an improved user interface will also allow the general public to engage with high-level information regarding SAFs, thereby increasing the general public's knowledge and awareness of SAFs, and further supporting the national visibility of sustainable aviation.

Task 1 - Database Development: ALIGHT, NewJET, and Domestic Airport Connection

University of Illinois at Urbana-Champaign

Objectives

The main objective of this task is to upgrade and debug the generation II online AJFTD functions and link the database to the European ALIGHT and NewJET programs. The generation II database was designed by using a new architecture based on a NoSQL data format that allows for flexible analysis and scaling. This format can accommodate various data types that can be easily accessed by any common programming language, and basic analysis functions have been built directly into the web interface. Additionally, substantial effort has been made in the past year to improve the data organization and retrieval process for both website administrators and standard users. Ensuring that all users can efficiently locate and collect all relevant data samples for their purposes is the main objective for future website adjustments and improvements. The main Task 1 objectives are as follows:

- Detail data type, frequency, and sharing methods with the ALIGHT program led by Copenhagen Airport and the NewJET program led by the University of Birmingham
- Establish methods for acquiring real-time airport fuels data from domestic U.S. airports, beginning with Chicago O'Hare International Airport

Research Approach

Generation II Database Debugging and Upgrade

The current generation II version of the web interface for the AJFTD maintains most of the functional features present in the originally developed database. Much like generation I, generation II is an HTML-oriented program built on a layer of metadata,

which supports search functions for users. The tree structure applied to organize the data folders in the first database has been retained in the second version, thereby allowing users to access the data in a similar manner. The main difference is that an additional inner core houses the JSON files, where the test data reside. Currently, the database has grown to house more than 25,000 separate fuel records.

The catalog of data currently available in the database is assembled primarily from four separate sources. The fuels with POSF (Air Force Research Laboratory fuel database code) number designations were added from the internal database maintained by the Air Force Research Laboratory at the Wright Patterson Air Force Base. The second dataset was obtained from the Petroleum Quality Information System (PQIS) reports of the Naval Air Systems Command and corresponds to a compilation of fuel data geared primarily toward government use. The third set was provided by Metron Aviation, which compiled fuel properties from samples collected at airports through a previous ASCENT project. The dataset resulting from this study has proven valuable by showing the landscape of fuels currently used in commercial aviation and will guide our future efforts focused on capturing this type of data in real time. The final dataset was obtained from the National Jet Fuel Combustion Program within ASCENT.

After the launch of the generation II database, substantial changes have been made to fix bugs and upgrade various aspects of the database. Some of the key changes to the database are summarized below.

- Efforts have been made to convert the JSON format on the database to a CSV format for select files to enable machine-learning-based analysis, which will be addressed further in Task 2. The actual files that are stored will use the NoSQL JSON format, which is conducive to maintaining a flexible database. However, certain parts of the data that are to be analyzed using machine learning will need to be converted to CSV format, for which multiple Python-based machine learning scripts are available. In the future, a process may be necessary to automate this conversion in real time.

- Online viewing of 2D gas chromatography (GCxGC) data has been made available to users. The scripts that process data uploads have been revised to properly process the section containing GCxGC data and now present this information on the web portal. This is an important development, because it is the first of many upcoming improvements to the user interface that will allow users to engage with data on the website itself in a comprehensive and high-level fashion before downloading and processing raw files.

- The “Documents” categories have been updated to reflect a wider range of document categories (now available under “Documents” → ”Browse by Category”) including ASCENT reports for relevant alternative jet fuel projects and recent literature relating alternative jet fuels to flight and laboratory tests on emissions, contrails, etc.

- With an emphasis this year on the optimization of the data retrieval process, the acquisition of firsthand user feedback was a priority. A feedback portal has been added and is present on every page on the AJFTD to provide users with a quick and optionally anonymous method for reporting technical issues, usage concerns, questions, or all other feedback regarding the usage or content of the database. This option is presented in addition to existing contact information supplied under the “Contact” and “About” → ”Directory” tabs.

- In prior website versions, the differences between the “Fuels” and “Documents” tabs were ambiguous, and the information was searchable under either or both tabs. To clarify the purposes of these two pages, an “About” page has been added to the “Documents” drop-down menu detailing the searchable results. Additionally, the “Fuels” page has been converted to a “Fuels” drop-down menu with a similar “About” page detailing the contents of the “Search Fuels” page, and how to navigate this page by using available filters and keywords.

- Similarly to the above point, various small changes and clarifications have been made to other drop-down categories such as changing “Categories” under the “Documents” drop-down to “Browse by Category,” and inserting scroll-over buttons on pages such as “Search Fuels” for expanding upon the functionalities and intended uses of various interface features.

- Fuel data are organized and searchable under the “Fuels” tab according to various filter categories and keywords. However, many of these keywords and filters previously yielded either incomplete lists of results or results that were erroneously tagged or keyed. The issue was found to arise from several thousand JSON files that were unlabeled or erroneously labeled in various metadata categories (e.g., “fuel type” or “origin”). Python scripts have been written to comb through all database JSON files (>25,000) and retag them with the proper metadata categories. Fuel records for blends of multiple fuel types have been retagged with each blend component separated by a forward slash. In all cases, when a blend contains at least

one conventional and at least one alternative fuel, the alternative fuel is listed first. If the blend comprises two alternative fuels, they are ordered alphabetically. If the blend contains only conventional fuels, the fuels are ordered alphabetically. This process was undertaken to eliminate ambiguity regarding the contents of the previously implemented "Blend" fuel type, to assist in efficient record retrieval. All retagged files have been reuploaded and are now searchable on the website.

- As displayed in Figure 2, the "Search Fuels" page now includes new filters for searching by fuel records containing data under certain compositions and property data categories (for searching for all results containing, for example, GCxGC data and/or flash point values). This functionality was inspired by increasing use of the database for generating datasets for training and testing models that map composition to properties; building such models would require quick filtering of all fuel records containing relevant data.

- An additional metadata category, "Fuel Class," has been created to support future development of a tool for quickly comparing a given fuel sample to all other fuel samples in a given category. Such a category may be an existing metadata category, such as "Fuel Type" or "Origin," or the new category "Fuel Class." This category aims to organize all fuel samples by more qualitative descriptions, sorting fuels into five main categories: Alternative Fuels, Blends, Conventional Fuels, Engineered Fuels, or Sustainable Aviation Fuels. Tagging fuels with these colloquial descriptions is intended to assist in higher-level engagement with fuel comparisons and data that are not restricted to a single fuel type; users may want to see how their fuel record compares with those of all previously approved SAFs, for example. This mass-comparison feature has not yet been fully developed; however, the "Fuel Class" metadata category is a preemptive development for supporting such a feature on a large scale and making the data on the website more accessible to a wider variety of users with various degrees of domain knowledge. We note that the "Sustainable Aviation Fuel" fuel class category is likely to be converted to "ASTM Approved Blendstocks" or some equivalent, because of the ambiguity surrounding the term "Sustainable Aviation Fuel" in the jet fuel market. A "Fuel Class" page will also be included under the "Fuels" drop-down menu; similarly to the "Fuel Type" page, it will clarify the distinctions made by website administrators.

- Website compare features have been updated to include the ability to compare multiple new composition categories including GCxGC data for various fuels (Figure 3). A 100% bar chart breaking down chemical family representation in the fuel sample is now displayed below the detailed composition bar chart, which separates a sample by chemical family and carbon number. This functionality is included for enhancing quick comparison between fuel samples by category as well as carbon number distribution. These bar charts also retain functionalities, such as the zoom, scroll-over detail, and on/off toggle, present on the complete composition bar chart. These comparisons can be exported similarly to other comparison results.

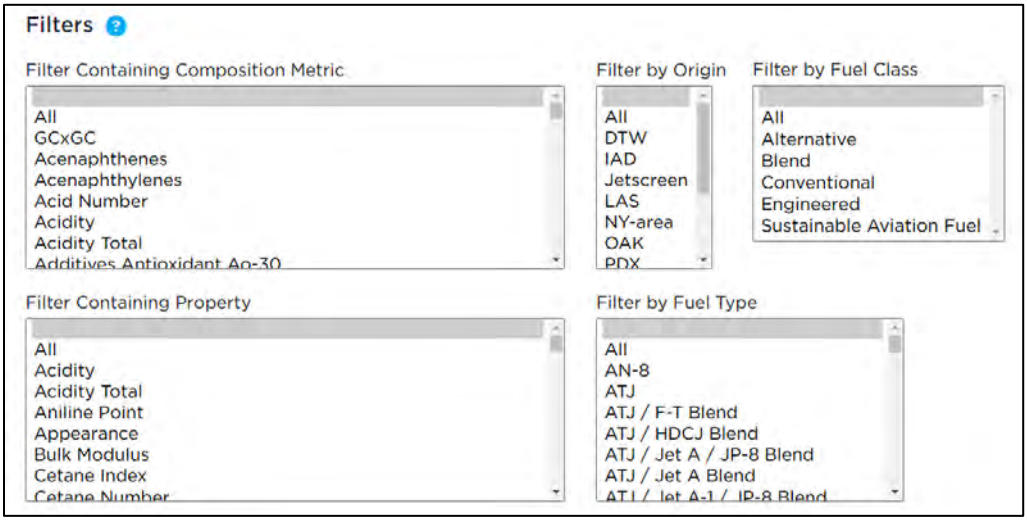

Figure 2. Updated fuel search bar filters and cleaned data sub-categories.

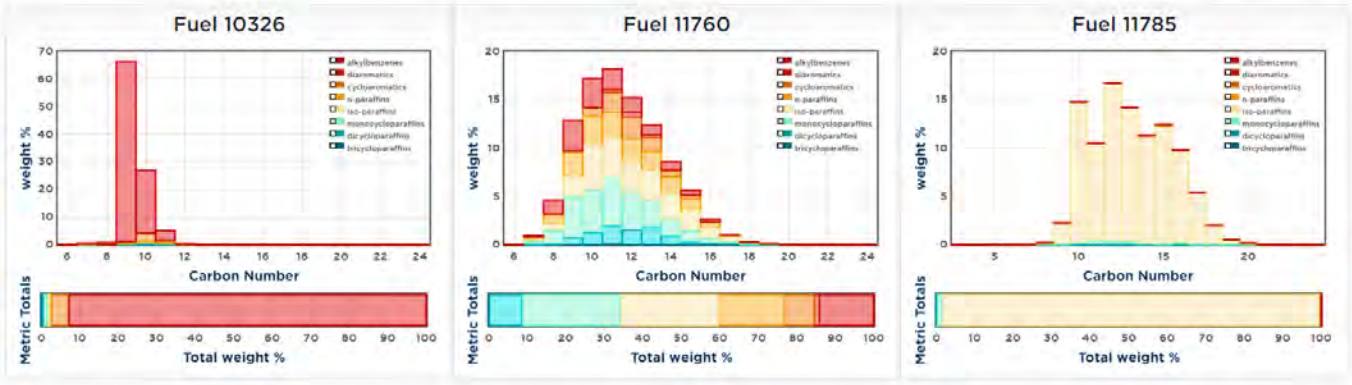

Figure 3. "Compare" functionality for GCxGC compositional data for various fuel samples.

Integration of the Database with JETSCREEN, ALIGHT, and NewJET

In 2020, we completed the integration of our database with the European JETSCREEN program. The JETSCREEN program was initiated (a) to provide fuel producers, air framers, and aero-engine and fuel system original equipment manufacturers with knowledge-based screening tools for fuels and (b) to produce a similar database that could be linked with ours. We first started discussing a potential merger with the JETSCREEN database in 2018, after which we started methodically synchronizing the data structure so that a merger would be possible. After extensive beta testing, the two databases were first linked in Spring of 2020. Data sharing between AJFTD and JETSCREEN ended in 2020 when the JETSCREEN project was completed and archived.

After the completion of JETSCREEN, AJFTD will continue to acquire new data through connection with the new European programs ALIGHT and NewJET. ALIGHT is a program aimed at assessing and improving the supply chain, integration, and use of SAFs and smart energy solutions through examining and optimizing operations at Copenhagen Airport. NewJET is a research program headed by the University of Birmingham, which is aimed at improving pathways for production of new SAFs. A similar data sharing structure is likely to be used to connect these programs with AJFTD, as was used with JETSCREEN; the process is outlined in Figure 4.

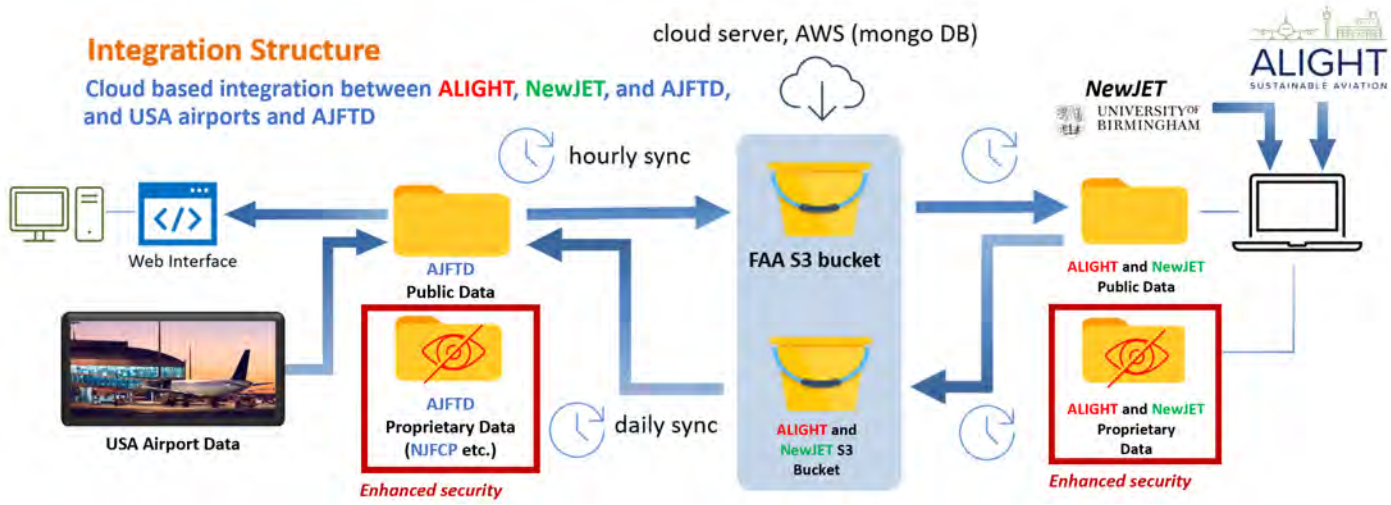

Figure 4. Plans for future data sharing with the European sustainable aviation programs ALIGHT and NewJET.

The JETSCREEN integration process helped streamline a data sharing method that ensures frequently updated and well-secured data flow between two projects; thus, this method of data sharing will probably also be used in future integration

with the aforementioned ALIGHT and NewJET programs. Previously, the JETSCREEN and FAA databases were joined by a common cloud storage. Amazon Web Services was selected as the server to store the shared data, mainly because of its affiliation with the University of Illinois. S3 buckets (Amazon database structure) were created for both FAA and JETSCREEN to share their JSON files. Each could pull files from the other's folder, but read and write access was granted for only the owners of the bucket. The FAA data were shared to its S3 bucket via altjetfuels.illinois.edu. All public FAA data on the website had an option to be shared with JETSCREEN, and this option could be toggled by administrators. The website synchronized hourly with the bucket to upload newly shared data. No proprietary data were shared to the FAA S3 bucket. Any files uploaded to the FAA bucket could be viewed and downloaded by JETSCREEN. For downloading new JETSFCREEN data to the website, a script ran daily to verify JETSCREEN's S3 bucket for newly shared data. Any new files were then downloaded to our local database and could be accessed by users.

The completion of the JETSCREEN database integration process was a monumental first step in linking many other fuel databases worldwide. From this joint effort between FAA and JETSCREEN, we established a foundation for data sharing that can be used again with other programs, such as ALIGHT and NewJET. The ultimate goal of international database integration is to help monitor and evaluate fuels used in the international airspace and paint an accurate picture of how the fuel composition and usage trends are changing with time. As new fuels are integrated into the global supply chain, a means to keep track of their properties will become critical. Such an interconnected database will ensure provision of the most representative information needed for research and certification of new SAFs. The impacts of database integration are outlined in Figure 5.

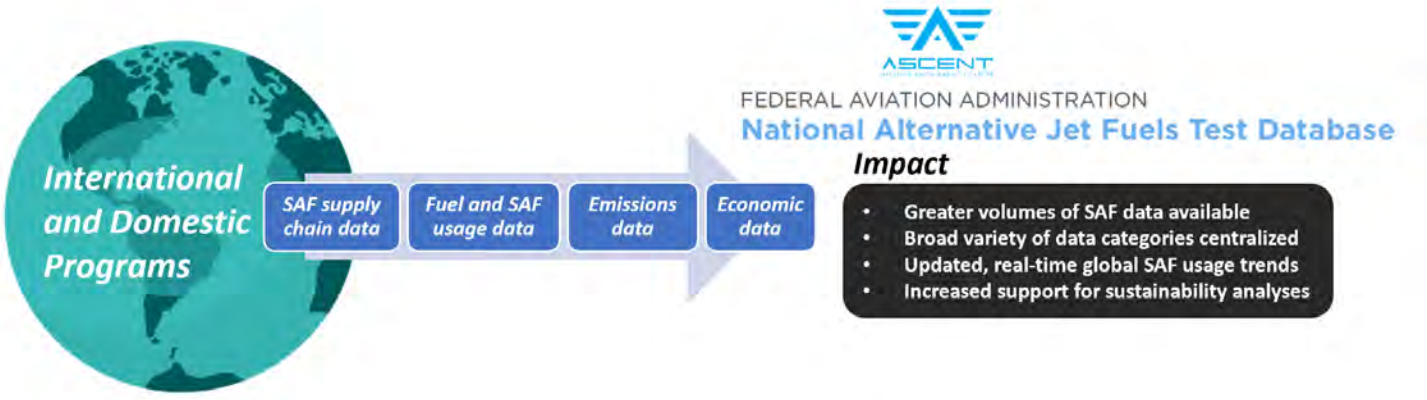

Figure 5. Plan to expand AJFTD's available data categories through data sharing with domestic airports, and the current international SAF projects ALIGHT and NewJET.

National motivation to achieve a more sustainable and emission-free aviation sector grew in the fall of 2021, with the announcement of the Sustainable Aviation Fuel Grand Challenge at a White House event. This initiative outlined a governmental approach for supporting SAF research, development, and implementation. As the topic gains national visibility, the platform for further development of the AJFTD is also growing.

In the past year, we have ramped up efforts to intercept fuel data from Chicago O'Hare International Airport. Efforts have included a variety of industry players including representatives from airlines, such as United Airlines, fuel testing facilities such as Nobil Petroleum Testing, and the FAA itself, among others. This effort requires extensive coordination at all levels of the aviation fuel industry, to acquire and formalize proper permissions for collection and publication of fuel data. Real-time acquisition of fuel data from the ground level on site at actual airports will be pivotal for converting the database from a static archive to a regularly updated monitoring tool for fuel trends in commercial aircraft. As alternative fuel deployment and incorporation into the supply chain accelerate, this data pipeline could serve as a crucial tool for measurement of the extent of the impact of blending on the compositions and properties of the fuel actively being used in commercial aircraft. The implications of such a tool are as diverse as supply chain analysis and the generation of fuel composition property datasets, as outlined in Figure 6.

This effort is expected to lay a foundation for achieving the sustainability targets set by both the U.S. (Sustainable Aviation Fuel Grand Challenge) and global community (Renewable Energy Directive II of the EU and the Paris agreement) by providing the data and analytic tools for sustainable pathways toward zero-emission airport operation through the integration of SAFs.

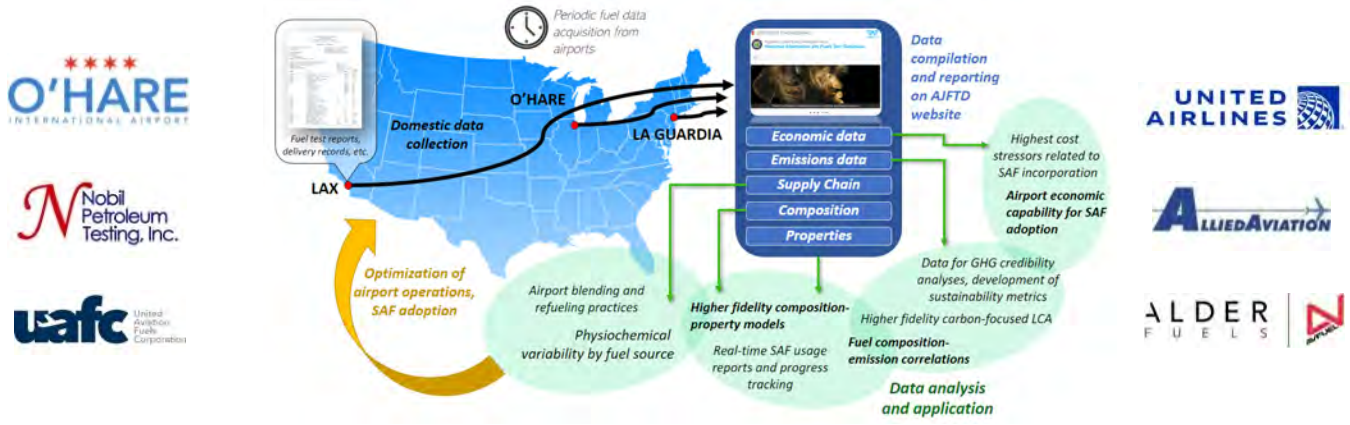

Figure 6. Domestic airport data collection scheme, publication, and potential effects.

Future efforts to broaden data sources for fuel data available on the website will include connection of our database with other ASCENT projects, including a newly piloted World Fuel Survey, which will largely replicate the global data collection process for the 2006 Coordinating Research Council's World Fuel Survey. This connection will provide a substantial source for the development of a dataset of recent, regionally representative conventional jet fuels' physical and chemical properties.

Milestones

3 months

- Debugging and optimization of the data structure in the generation II database
- Keyword fixes and resolution of search bar bugs
- Initial communication with Chicago O'Hare International Airport, United Airlines, Alder Fuels, and other industry partners

6 months

- Data cleaning commenced; all major JSON file bugs identified, and plan for scrubbing drafted
- New document sections live online
- User feedback tools built

9 months

- Python scrips completed for JSON editing; files cleaned and uploaded to website
- New search filters published to production site; troubleshooting complete
- Mission statement and formally documented plan for airport data collection finalized

12 months

- New interactive viewing features for comparing fuels finalized and published
- Communication with FAA contacts on next steps for airport data collection

Major Accomplishments

Initiation of Domestic Airport, ALIGHT, and NewJET Connections

Correspondence with relevant contacts for the aforementioned programs has been initiated and plans to proceed with international program integration are in place. These three connections will serve as new sources for acquiring greater amounts of fuel data, as well as the expansion of the data categories available on the database to categories such as usage and emissions data. Continued international collaboration will increase the long-term potential for support and data sharing with other international programs as they are formed. Connection with domestic airports will also support the long-term

reliability of in-country data acquisition, if consistent avenues for data sharing are built and maintained, thus providing the database with the most up-to-date and relevant information available.

Modifications to the Generation II Online Database
The usability of the web interface is paramount to the purpose of the website. Data retrieval was addressed through the reconstruction of the search method on the backend site through frequent collaboration with the University of Illinois' web developer. The 25,000+ data files themselves were scanned, modified, and rewritten through various automated Python codes for eliminating redundancies, clarifying categories, and fixing tags and names in the fuel data and metadata categories. The modified files were then reuploaded to the website, and changes are reflected in updated search filter categories visible on the "Search Fuels" page. Search results now yield complete results and do not contain erroneously called fuel records.

Publication

Peer-reviewed journal publications
Oldani, A. L., Solecki, A. E., & Lee, T. (2022). Evaluation of physicochemical variability of sustainable aviation fuels. *Frontiers in Energy Research*, *10*, 1052267. doi: 10.3389/fenrg.2022.1052267

Outreach Efforts

The database has been made accessible through https://altjetfuels.illinois.edu/.

Awards

None.

Student Involvement

This project was conducted primarily by two graduate students (Alex Solecki and Ji Hun Oh).

Plans for Next Period

In the next period, the focus will be on ramping up progress in data collection from the aforementioned data sources: domestic airports, ALIGHT, and NewJET. In addition, pending the award of the project, the next World Fuel Survey will yield data in the coming years that will also be integrated into the database. Collaboration with all involved parties will ensure that the data are treated and represented properly online, and that all proprietary information is protected on both ends of the data sharing pipeline.

Additional efforts anticipated to improve the functional and aesthetic features of the database are summarized below.

- User interface and online analysis tools: The last year focused mainly on optimizing data retrieval and ensuring that the data currently available on the website are being called properly on the basis of relevant search filters and keywords. Moving forward, we will focus on user-driven interaction with the data after retrieval and will build a series of features to allow further first-level analysis of data. For example, a mass-compare function will be able to quickly build graphs and charts to compare the composition or properties of a single or group of fuel samples to all other samples in a relevant category, such as all samples of fuel type Jet A or all samples of fuel class SAF. These features will not only encourage use of the website but also make meaningful interaction with the data available to a wider audience.

- Domestic and international data collection: The focus of the next period will be to begin actual data transfer among Chicago O'Hare International Airport, ALIGHT, and NewJET. Because of the nature of fuel test data from on-site testing at domestic airports, some delays may occur in determining the proper contacts with authority to grant permissions to such data. This process remains underway, and we expect further progress in the coming months. Currently, no substantial obstacles prevent data sharing between Project 33 and the European ALIGHT and NewJET projects, and progress on these fronts is anticipated to be achieved soon in the next period.

Task 2 - Machine-Learning-Based Analysis

University of Illinois at Urbana-Champaign

Objectives

The main objective of this task was to develop advanced analysis methods based on machine learning algorithms for analysis of the data in the alternative jet fuel database. The effort is inspired by the notion that the intricate relations between properties of fuels and their chemical compositions are critical, but may be beyond the complexity that can be addressed in routine, classical, regression-based analysis. The effort becomes increasingly important as new analysis techniques, such as GCxGC, provide large amounts of data that are difficult to process with simple analytical algorithms. Machine learning can provide a means for the most advanced analysis to be applied to our current data, and this analysis should become even more powerful as the size and diversity of the data grow in the future. Previous work has verified the efficacy of artificial neural networks in modeling the complex and obscure correlations between jet fuels' chemical composition or structure and physicochemical properties. The next step of this task is to exploit neural networks and deep learning methods to address realistic challenges in SAF databases. Specifically, the major goals are as follows:

- Identify real-world challenges in the analyses of jet fuel, specifically SAFs and datasets
- Devise deep-learning-based strategies for addressing these challenges
- Perform composition–property modeling by using GCxGC and advanced machine learning techniques
- Specify the degree of uncertainty in such models and how to mitigate them

Research Approach

Data-driven Modeling and Uncertainty Quantification

In previous years, the machine learning applications focused on in this context were centered primarily around how to obtain a better predictive model for the properties of a given fuel, on the basis of its detailed chemical composition, typically obtained through a chemical separation method, such as GCxGC. However, higher predictive uncertainty was seen for alternative jet fuels than conventional fuels. To understand why, and to report on the required actions needed to decrease such uncertainty for future models, an uncertainty classification and quantification study was conducted. This study attempted to decompose two main sources of uncertainty, epistemic and aleatoric uncertainty, and compare the relative effects of each on the predictive uncertainty in alternative fuel data.

There are two main categories of uncertainty relevant to modeling inaccuracies. The first, epistemic uncertainty, also referred to as model uncertainty, arises when a model is given insufficient training data to learn the patterns present in the dataset and accurately map input to output. This issue is particularly relevant in composition–property modeling for SAFs, because only extremely limited datasets are available for newer fuels, in contrast to conventional fuels. Consequently, machine learning models can predict the properties for conventional fuels quite well, yet they perform poorly on SAFs. The other source of uncertainty is aleatoric uncertainty, also known as data uncertainty, which can arise from various events, such as low-resolution input data; inaccurate measurement techniques for the collection of model input data; and stochastic events, such as ignition delay, that introduce unresolvable noise into the model. Figure 7 outlines the process of building composition–property models, and the locations of epistemic and aleatoric uncertainty in the process.

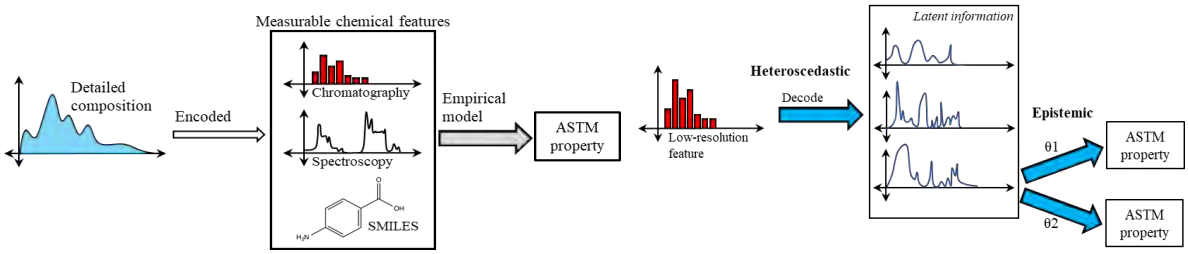

Figure 7. Schematic of SAF modeling, and epistemic and heteroscedastic uncertainties in this study.

To study the respective effects of each individual uncertainty type on the final model prediction for SAFs, we ran two separate computational tests, wherein epistemic and aleatoric uncertainty were induced artificially into the model, and the resulting uncertainty was calculated. To test epistemic uncertainty, we used three datasets with increasing SAF representation—and

thus, theoretically, decreasing epistemic uncertainty—to build three separate probabilistic machine learning models. The performance of each model on the same test set of fuels was compared quantitatively. Figure 8 shows the test set of fuels used to assess the performance of each consecutive model; the black bars show data for the proxy fuels, thus demonstrating the qualitative chemical similarity of the proxy fuels introduced into each consecutive model compared with the test set fuel that the proxy fuel is meant to resemble. The test set was deliberately selected to be highly chemically diverse, to serve as a good indicator of model performance.

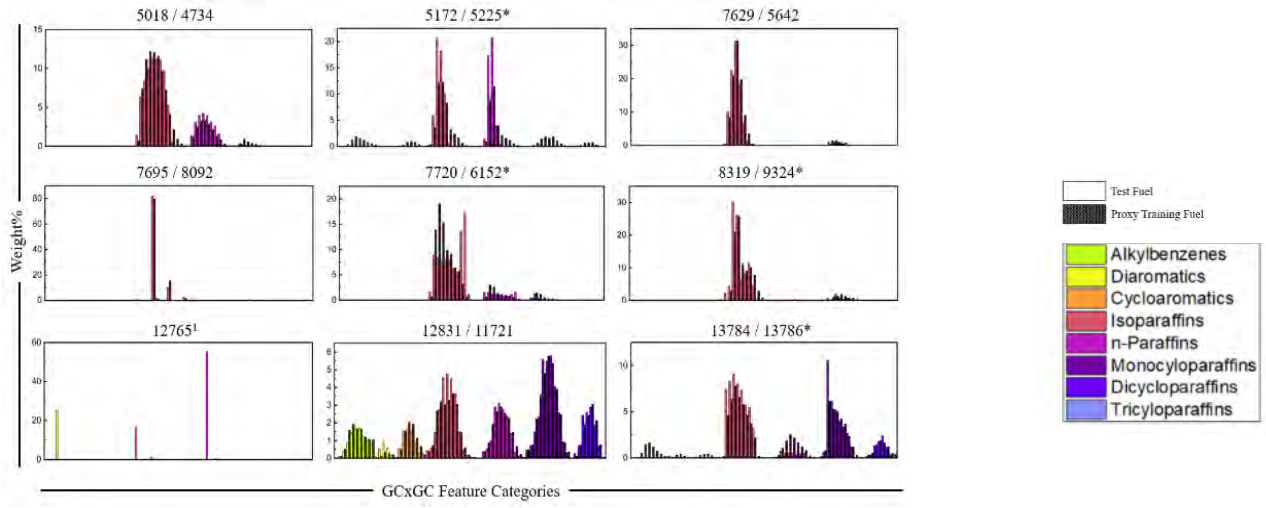

Figure 8. Summary of the test sample F68, juxtaposed with its proxy (black solid lines), with the exception of POSF 127651. Pseudo-proxies are marked with an asterisk.

In this study, we were able to obtain quantitative results for the varying performance of each model on the same test set. Figure 9 represents the probability density functions for the predicted flash point values for each test set fuel according to each of the three machine learning models. The vertical lines represent the true value (experimental). In almost all cases, we were able to establish the anticipated result: the most diverse training set—D3, in blue—showed a shift in the peak of the probability density function closest to the actual value. In most cases, we observed that the distribution of the probability density function was narrower with increasing dataset diversity, thus translating to higher confidence in the predicted value at a higher accuracy.

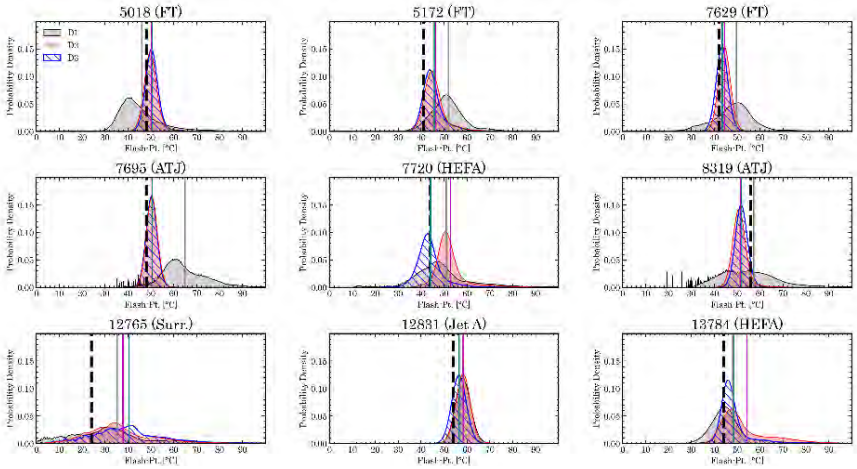

Figure 9. Predicted probability density functions using eBNN (explanation based neural network) with five hidden layers, trained on F68 and D1–D3.

The heteroscedastic (aleatoric) uncertainty was tested by artificially inducing lower-resolution data into a dataset with minimal epistemic uncertainty (one trained on only Jet A fuel, the most abundant fuel type), by summing the weight percentages in each subcategory of the 68 original GCxGC features in their respective chemical families. Through this process, and training two separate probabilistic models—one with 68 features and one with 8 compressed features—we observed a noticeable increase in uncertainty after feature compression (Figure 10). This uncertainty, indicated by the variance of the resulting predictions on the test samples, was then decomposed according to the law of total variance into its epistemic uncertainty and aleatoric uncertainty.

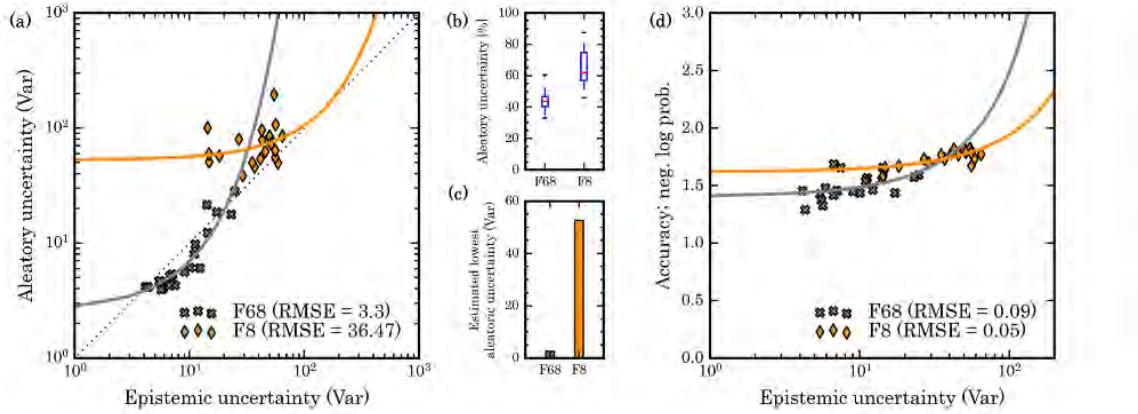

Figure 10. Uncertainty decomposition of POSF 12831, Jet A. (a) Epistemic versus heteroscedastic uncertainty. (b) Relative ratio (%) of heteroscedastic uncertainty of F68 and F8. (c) Minimum heteroscedasticity, estimated by the exponential fit of F68 and F8. (d) Accuracy (negative log probability of truth) versus epistemic uncertainty.

The results underscore the importance of generating and centralizing a more extensive dataset for SAFs for decreasing the uncertainty and thus increasing the confidence of predictive models for low-volume fuel prescreening. After sufficient data are generated and compiled, the bottleneck then becomes the resolution and subsequent reliability of the input and output data themselves. This bottleneck can be overcome through higher-fidelity laboratory testing and new experimental methods, such as vacuum ultraviolet radiation, which may potentially resolve the composition of single isomers within a given GCxGC bin.

Milestones

3 months

- Formalization of machine learning implementation plan

6 months

- Establishment of scripts and algorithms for implementation of machine learning
- Organization of target data from the database for implementation of machine learning

9 months

- Implementation and optimization of machine learning algorithms

12 months

- Finalization of all machine learning tasks for publication

Major Accomplishments

In the past year, work was undertaken to address the substantial issue of uncertainty in machine learning applications in this field of study. Outstanding obstacles were identified with respect to any future work in reducing uncertainties in the prescreening phases of new fuel certification. Machine learning applications such as these will be critical to advancing the prescreening and optimization process for new alternative jet fuels in the commercial sector. Neural networks were used to investigate confidence levels under various data circumstances to better understand their potential.

Publication

Peer-reviewed journal publications

Oh, J., Oldani, A., Lee, T., & Shafer, L. (2022, January 3). Deep neural networks for assessing sustainable jet fuels from two-dimensional gas chromatography. *Aerospace Research Central, AIAA 2022-0228*. doi: 10.2514/6.2022-0228

Outreach Efforts

The database has been made accessible through https://altjetfuels.illinois.edu/.

Awards

None.

Student Involvement

This project was conducted primarily by two graduate students (Ji Hun Oh and Alex Solecki).

Plans for Next Period

Moving forward, we anticipate that the machine learning component of this project will make up a less substantial portion of the efforts on this project. The focus will turn toward the development of the database and data collection, and the presentation of data from U.S. airports and international programs. Progress made to this point in the Machine Learning subtask will serve as a foundation for future case work on an “as-seen-fit” basis (see “Plans for Next Period” from Task 1).

Project 037 CLEEN II System-Level Assessment

Georgia Institute of Technology

Project Lead Investigator

Dimitri Mavris
Regents Professor
School of Aerospace Engineering
Georgia Institute of Technology
Mail Stop 0150
Atlanta, GA 30332-0150
404-894-1557
dimitri.mavris@ae.gatech.edu

University Participants

Georgia Institute of Technology

- P.I.s: Dr. Dimitri Mavris (P.I.), Dr. Jimmy Tai (Co-P.I.), Dr. Joshua Brooks (Co-P.I.)
- FAA Award Number: 13-C-AJFE-GIT-055
- Period of Performance: October 1, 2021 to September 30, 2022
- Tasks:
  1. Establish Working Relationships with CLEEN III Contractors
  2. Model Aircraft Technologies and Advanced Configurations
  3. Finalize CLEEN II Analysis

Project Funding Level

The FAA provided $250,000 in funding to the Georgia Institute of Technology (GT).

GT has agreed to a total of $250,000 in matching funds. This total includes salaries for the project director and research engineers, as well as funding for computing, financial, and administrative support, including meeting arrangements. GT has also agreed to provide tuition remission for students, paid from state funds.

Investigation Team

- Professor Dimitri Mavris – P.I., GT (Tasks 1-3)
- Jimmy Tai - Co-Investigator, GT (Tasks 1-3)
- Joshua Brooks - Program Manager, GT (Tasks 1-3)
- Holger Pfaender - Fleet Modeling Technical Lead, GT (Tasks 1-3)
- Brennan Stewart - Noise Modeling Technical Lead, GT (Tasks 1-3)
- Joao De Azevedo, Madelyn Focaracci, Sebastian Seubert, Krutik Desai, Mitchell Mu, and Martina Tehubijuluw – Students, GT (Tasks 1-3)

Project Overview

The objective of this research project is to support the FAA by independently modeling and assessing the technologies that are being developed under the Continuous Lower Energy, Emissions and Noise (CLEEN) II and CLEEN III programs. This work will involve direct coordination and data sharing with CLEEN-funded companies in order to accurately model the environmental benefits of these technologies at the vehicle and fleet levels.

GT was previously selected to perform all system-level assessments for the CLEEN program under PARTNER Project 36 and ASCENT Project 10. As a result, GT is in a unique position from both technical and programmatic standpoints to continue the system-level assessments for CLEEN II. From a technical perspective, GT has significantly enhanced the Environmental

Design Space (EDS) over the past 5 years to incorporate advanced, adaptive, and operational technologies targeting fuel burn, noise, and emissions. EDS has been successfully applied to all CLEEN I contractor technologies including the following: GE's open rotor, twin annular premixing swirler (TAPS) II combustor, Flight Management System (FMS)-Engine, and FMS-Airframe; Pratt & Whitney's geared fan; Boeing's adaptive trailing edge and ceramic matrix composite nozzle; Honeywell's hot section cooling and materials; and Rolls-Royce's turbine cooling technologies. GT has also gained extensive experience in communicating system-level modeling requirements to industry engineers and translating impacts to fleet-level fuel burn, noise, and emission assessments. This broad technical knowledge base covering detailed aircraft and engine design as well as high-level benefit assessments places GT in a unique position to assess CLEEN II technologies.

Because the ultimate goal of this work is to conduct fleet-level assessments for aircraft representative of future "in-service" systems, GT will need to create system-level EDS models using a combination of both CLEEN II and other public domain N+1 and N+2 technologies. The outcomes of the technology and fleet assumption-setting workshops conducted under ASCENT Project 10 are being used for this effort. Non-CLEEN II technologies for consideration, along with potential future fleet scenarios, will help to bound the impact of CLEEN II on future fleet fuel burn, emissions, and noise.

Because the FAA will also be performing a portion of the EDS technology modeling work, periodic (i.e., weekly) EDS training sessions were provided to the FAA during the period of performance. The training provided the requisite skill set for using EDS. In the prior year of this project, GT continued modeling activities with Collins, Honeywell, Boeing, and Pratt & Whitney. This modeling process included validation of underlying EDS models, information and data exchange necessary to model the individual technologies, and related EDS modeling activities. In addition, GT has assisted the FAA with in-house EDS modeling. This process has increased the number of FAA personnel performing EDS system-level assessment modeling.

Next year's work will focus on moving toward the end of the project, with the completion of vehicle- and fleet-level assessments for CLEEN II. These efforts will include final technology modeling details for each CLEEN II industry contractor, the generation of vehicle-level assessments of fuel burn, emissions, and noise compared with current best-in-class values, and fleet-level estimates of fuel burn, emissions, and noise, including community noise impact estimates for a standard representative airport. Individual technology impacts to the vehicle airframe and engine will not be reported to preserve contractor confidentiality. Quantifying this impact will provide an understanding of the number of increased operations per day that CLEEN II technologies enable without worsening the surrounding community's noise exposure. Although airports in the United States are not generally noise-constrained, some European airports have a limited capacity to meet noise constraints. Understanding the impact of technologies on future U.S. fleets will be critical to quantifying the interaction between economic growth (i.e., increased flight operations at a given airport) and community noise impacts.

GT has completed most of the technology modeling to date. Remaining items include updating technology models by using the most recent data from contractors and conducting a final fleet assessment. The table in the Milestones section shows the current status of the technology modeling. Where work remains, a brief description is provided after the table.

Milestones
The major milestones and planned completion dates from the previous year are listed in the table below:

Task No.	Milestone	Planned Completion Dates
Task 1	Attend CLEEN II Contractor Kick-off Meetings	8/31/2022
Task 2.1	Identify Required EDS Modeling Enhancements	8/31/2022
Task 2.2	Develop CLEEN II 5-Year System Modeling Roadmaps for Each Contractor	8/31/2022
Task 3	Document EDS Modeling Approaches	8/31/2022

Major Accomplishments

- The modeling for Boeing's compact nacelle acoustic system is complete.
- The modeling for Collin Aerospace's zoned liner is complete.
- The modeling for Rolls-Royce's advanced rich-quench-lean (RQL) combustor is complete.
- The modeling for Pratt & Whitney's compressor and turbine aero-efficiency technologies is complete.

- The modeling for Honeywell's blade outer air seal system is complete.
- The modeling for Honeywell's compact combustor is complete.
- The modeling effort for Honeywell's advanced high-pressure compressor system, a late-addition CLEEN II+ technology, is ongoing.
- The modeling effort for Honeywell's engine acoustic system, a late-addition CLEEN II+ technology, is ongoing.
- An updated fleet fuel burn assessment is complete.
- A preliminary fleet landing and take-off (LTO) nitrogen oxide (NOx) assessment is complete.
- A preliminary fleet noise assessment is currently underway.

Task 1 - Establish Working Relationships with CLEEN III Contractors

Georgia Institute of Technology

Objective

Working relationships will need to be established between GT and CLEEN III contractors in order to facilitate the GT CLEEN III system level modeling (SLM) effort.

Research Approach

Working relationships with CLEEN III contractors have been largely established through GT's participation at contractor kick-off meetings held in the second half of 2021 and CLEEN consortia meetings held throughout 2022. Where necessary, non-disclosure agreements are standing for all CLEEN III contractors.

Milestones

SLM kickoff calls with all CLEEN III contractors.

Major Accomplishments

N/A

Publications

N/A

Outreach Efforts

N/A

Awards

N/A

Student Involvement

Six graduate students are currently receiving funding from this effort.

Plans for Next Period

N/A

Task 2 - Model Aircraft Technologies and Advanced Configurations

Georgia Institute of Technology

Objective

To estimate the impact of CLEEN-relevant technologies at the vehicle system level, each technology must be modeled regarding their impact on aircraft fuel burn, noise, and emissions using EDS.

Research Approach

GT was previously selected to perform all system-level assessments for the CLEEN program under ASCENT Project 10. Because the ultimate goal of this work is to conduct fleet-level assessments for aircraft representative of future "in-service" systems, GT will need to create system-level EDS models using a combination of both CLEEN II and other public domain N+1 and N+2 technologies. Vehicle system-level modeling for all relevant CLEEN II technologies will be performed using EDS.

Table 1 presents an update on the vehicle system-level modeling efforts regarding each of the CLEEN II-relevant technologies.

Table 1. Update on CLEEN II technology modeling.

Contractor	Technology/Model Impact Area	Initial Modeling Discussions Held with Contractor?	Modeling Underway	Percentage Complete
Aurora (Double Bubble Fuselage)	D8 configuration	✓	✓	100%
Boeing	Structurally efficient wing	✓	✓	100%
	Compact nacelle	✓	✓	100%
	Compact nacelle (noise liner)	✓	✓	100%
Delta/MDS/America's Phenix	Leading-edge protective fan blade coating	✓	✓	100%
GE	Twin annular premixing swirler (TAPS) III low-NOx combustor	✓	✓	100%
	More Electric Systems and Technologies for Aircraft in the Next Generation (MESTANG)	✓	✓	100%
	Flight Management System (FMS)	✓	✓	100%
Honeywell	Compact combustor	✓	✓	100%
	Advanced acoustic fan rotor/liner	✓	✓	50%
	Advanced high-pressure compressor	✓	✓	75%
	Turbine blade outer air seal	✓	✓	100%
Pratt & Whitney	Compressor and turbine aero-efficiency technologies	✓	✓	100%
Collins/Rohr/United Technologies Aerospace Systems	Slim nacelle	✓	✓	100%
	Noise liner technologies	✓	✓	100%
Rolls-Royce	Advanced rich–quench–lean (RQL) low-NOx combustor	✓	✓	100%

Remaining Modeling Work

- Honeywell advanced high-pressure compressor
  - The GT modeling approach has been presented to the contractor and has been approved for capturing the impact of this technology.
  - Engine modeling to match Honeywell's baseline engine is currently underway to best enable the assessments of Honeywell's engine technologies.
  - Result generation is underway.
- Honeywell advanced acoustic fan rotor/liner
  - Preliminary modeling is underway. Preliminary modeling results will be shown to Honeywell in Q1 of 2023.

Table 2 presents the list of technologies currently included in the system-level modeling effort regarding each of the CLEEN III technologies. Efforts are underway to capture the impact of these technologies. The team is working with the respective CLEEN contractors, as data become available.

Table 2. Introduction to CLEEN III technology modeling.

Modeling Planned: 08/01/22–07/31/23

Contractor	Technology/Model Impact Area	Fuel Burn	NOx	Noise	Testing Complete
Boeing	Quiet Landing Gear			X	2023
	Quiet High-Lift System			X	2023
	Advanced Inlet	X		X	2024
	Intelligent Operations	X		X	2024
Collins	Large Cell Novel Core Exhaust			X	2026
Delta/MDS/America's Phenix	Fan Leading-Edge Protective Coating	X			2023
GE	More Electric Systems and Technologies for Aircraft in the Next Generation (MESTANG) III	X			2023
	Open Fan	X		X	2024
GE	Advanced Thermal Management	X			2024
	Hybrid Electric Integrated Generation	X			2024
	Combustor Technology	X	X		2024
	Advanced Acoustics			X	2024
Honeywell	High-Pressure Core – Seals/Materials	X			2024
	High-Pressure Core – Combustor		X		2024
	High-Pressure Core – Acoustic SBV			X	2024
	Highly Efficient Fan - Performance	X			2024
	Highly Efficient Fan – Acoustic			X	2024

	Compact Low-Pressure Turbine – Blading	X			2024
	Compact Low-Pressure Turbine – Acoustics			X	2024
Pratt & Whitney	Fan Noise Technologies			X	2023
	Fan Performance Technologies	X			2023
	Combustor – Swirlers			X	2024
	Combustor – Cooling Technologies	X			2024
	Combustor – Low Pattern Factor	X			2024
	Combustor – NOx Reduction		X		2024
Safran	Short Inlet			X	2025
Rolls-Royce	Advanced Centrifugal Stage	X			2024

Milestones
Completion of modeling effort for each CLEEN III technology.

Major Accomplishments
N/A

Publications
N/A

Outreach Efforts
N/A

Awards
N/A

Student Involvement
Six graduate students are currently receiving funding from this effort.

Plans for Next Period
Continue modeling each of the CLEEN III technologies.

Task 3 - Finalize CLEEN II Analysis
Georgia Institute of Technology

Objective
The objective of this task is to evaluate the impact of CLEEN-relevant technologies as propagated forward into the U.S. civil fleet of domestic and international departing aircraft, with a specific focus on the impact of CLEEN technologies on fleet-level noise, fuel burn, and NOx emissions.

Research Approach

Vehicle system-level modeling for all relevant CLEEN II technologies will be performed using EDS. Fleet benefit assessments for aircraft fleet fuel burn, NOx, and noise through the year 2050 will be performed using the information delivered by the vehicle system-level modeling effort alongside fleet replacement matrices, technology integration scenarios, and projected aviation demand schedules.

Updated Fuel Burn Assessment

GT and the FAA have updated the preliminary fleet-level fuel burn assessment from 2021. This update includes the results of an audit of the previously presented study, with the objective of ensuring traceability of all relevant technology impacts and repeatability of the fleet benefit assessment. Technologies in the fuel burn assessment update include the following:

- All relevant CLEEN I technologies
- Aurora double bubble (fuselage weight reduction)
- Boeing structurally efficient wing
- Boeing compact nacelle
- Delta/MDS/America's Phenix leading-edge protective coating
- GE MESTANG
- GE FMS
- GE TAPS III low-NOx combustor
- Honeywell turbine blade outer air seal
- Honeywell compact combustor
- Pratt & Whitney compressor and turbine aero-efficiency technologies
- Collins slim nacelle
- Collins noise liner technologies
- Rolls-Royce advanced RQL low-NOx combustor

The fuel burn assessment update does not represent the entire set of CLEEN II technologies. Moreover, this analysis only includes domestic U.S. flights and U.S. departures, which may represent lower growth rates than a more global analysis. The applied fleet analysis definition and underlying assumptions have remained consistent throughout the CLEEN program.

Figure 1 displays the percentage fuel savings relative to the evolutionary scenario projected by the CLEEN fleet fuel burn assessment. The individual contributions of the CLEEN program phases are isolated based on the technology integration scenarios defined in this work.

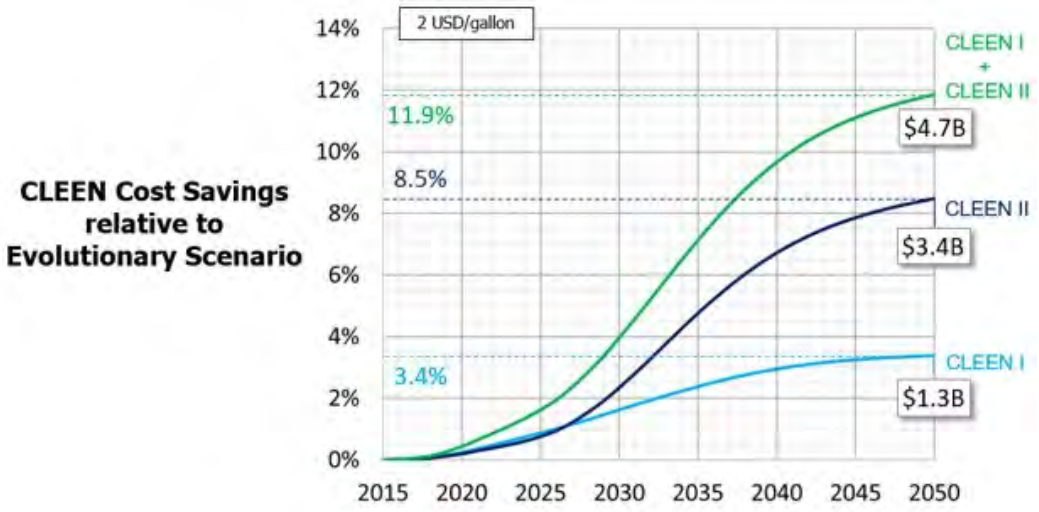

Note: Not all technologies are modeled/included at this time.

Note: CLEEN II contributions are shown as an annual (not cumulative) benefit.

Note: Results assume a constant fuel cost of 2 USD/gallon.

Figure 1. Preliminary fuel burn assessment: savings relative to the CLEEN evolutionary scenario (updated).

According to the analysis presented above, the technologies that have matured in the first 5-year phase of CLEEN will reduce U.S. fleet-wide fuel burn by 1.6% by the year 2030 and 3.4% by 2050 relative to the evolutionary scenario, thus providing a cumulative savings of 11.6 billion gallons of jet fuel. The CO_2 savings are the equivalent of taking 977,000 cars off the road in the years 2020–2050.

This preliminary analysis projects that the technologies matured in the CLEEN II program will reduce fuel consumption by 2.4% by 2030 and 8.5% by 2050 relative to the evolutionary scenario, thus bringing the contribution of CLEEN I and II to a fuel burn reduction of 11.9% in the fleet by 2050.

Cumulatively, the CLEEN I and II programs are estimated to save 36.1 billion gallons of fuel by 2050, resulting in a savings of approximately 72.2 billion dollars for airlines and a reduction in CO_2 emissions of approximately 420 million metric tons. These CO_2 reductions are equivalent to removing 3.03 million cars from the road in the years 2020–2050.

Preliminary LTO NOx Assessment

GT presented a preliminary LTO NOx emission assessment in Spring 2022. This fleet assessment is identical to the fleet fuel burn assessment of the considered fleet replacement matrices, demand forecast, technology integration scenarios, and scope of domestic flights with international departures. Among the existing collection of fuel burn technologies, the following CLEEN combustor technologies are represented:

- GE TAPS II (GT model)
- GE TAPS III
- Rolls-Royce RQL combustor
- Honeywell compact combustor

In-house modeling was performed at GT for which cases in which contractor models were unavailable and for the integration, baseline, and vehicles of each relevant fixed technology. The GT modeling approach, a P3T3 method, relied on correlations linking the emission index for NOx production of an individual combustor to the conditions of the core flow entering the combustor (DuBois, D., & Paynter, G. C., 2006). The boundary conditions defining this relation for each of the four LTO cycle points, i.e., take-off, climb-out, approach, and idle, are defined by the aircraft emission databank of the International Civil Aviation Organization and GT in-house engine models (ICAO, n.d.).

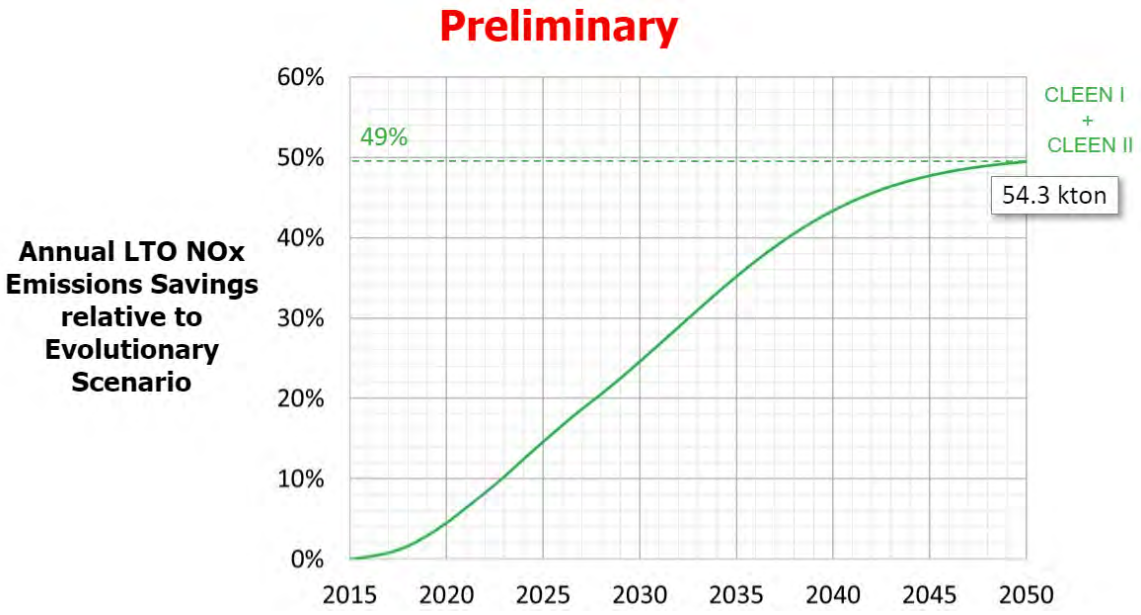

Note: Not all technologies are modeled/included at this time.

Note: CLEEN II contributions are shown as an annual (not cumulative) benefit.

Figure 2. Preliminary lift/take-off (LTO) NOx fleet emission assessment: reduction relative to the CLEEN evolutionary scenario.

According to the fleet emission analysis performed above, the technologies matured in the CLEEN program will reduce U.S. fleet-wide NOx emissions in the LTO cycle by 24.6% by the year 2030 and 49.4% by 2050 relative to the evolutionary scenario, thus providing a cumulative reduction of 997 kton LTO NOx.

The fleet-level noise benefit assessment of CLEEN II is underway. Results are expected to be complete in early 2023.

Milestones
Completion of CLEEN II fleet noise, fuel burn, and NOx emissions assessment.

Major Accomplishments
N/A

Publications
None.

Outreach Efforts
- CLEEN consortium presentation and panel participation.

Awards
None.

Student Involvement
Six graduate students are currently receiving funding from this effort.

Plans for Next Period

Future work will focus on completing technology modeling and updating fleet analysis assessments for the remaining technologies. The next period will also include the transition of efforts toward the incoming CLEEN III initiative.

This transition will include an update to the current fleet assessment assumptions regarding the exercised demand forecast, replacement matrix, technology integration scenarios, and baseline vehicles.

This work will also support attendance at CLEEN consortium meetings and contractor preliminary and detailed design reviews to identify any updates required for the technology models developed in prior years.

References

DuBois, D., & Paynter, G. C. (2006). *"Fuel flow method2" for estimating aircraft emissions*. 2006-01-1987. doi: 10.4271/2006-01-1987

ICAO. (n.d). *ICAO Aircraft Emissions Databank*. https://www.easa.europa.eu/en/domains/environment/icao-aircraft-engine-emissions-databank

Project 038 Rotorcraft Noise Abatement Procedure Development

The Pennsylvania State University, Continuum Dynamics, Inc.

Project Lead Investigator

Kenneth S. Brentner
Professor of Aerospace Engineering
Department of Aerospace Engineering
The Pennsylvania State University
233 Hammond Building
University Park, PA
814-865-6433
ksbrentner@psu.edu

University Participants

The Pennsylvania State University (Penn State)

- P.I.: Kenneth S. Brentner, Professor of Aerospace Engineering
- FAA Award Number: 13-C_AJFE-PSU-038, Amendment No. 81
- Period of Performance: October 1, 2021 to September 30, 2022
- Tasks (during this period):
  23. Complete evaluation of noise abatement procedure effectiveness by helicopter class, using 2017 and 2019 flight test data
  24. Investigate the modeling of shrouded rotor noise
  25. Continue effort to develop helicopter noise abatement flight procedures
  26. Develop documentation and training materials for the noise prediction system (NPS)

Project Funding Level

FAA funding $150,000; Continuum Dynamics, Inc. (CDI) with points of contact Daniel A. Wachspress and Mrunali Botre, will provide $75,000 of cost sharing in the form of a 1-year license for the Comprehensive Hierarchical Aeromechanics Rotorcraft Model (CHARM) rotorcraft comprehensive analysis software to the FAA or its designee.

Investigation Team

- Kenneth S. Brentner, P.I., Penn State; acoustic prediction lead on all tasks
- Joseph F. Horn, co-P.I., Penn State; flight simulation lead, support for all tasks
- Daniel A. Wachspress, co-P.I., CDI; rotor loads, wake integration, and CHARM coupling
- Mrunali Botre, co-P.I., CDI; support for rotor loads, wake integration, and CHARM coupling
- Lauren Weist (August 2021 through August 2022) and Sagar Peddanarappagari (from August 2022), Graduate Research Assistants, Penn State; establishing new aircraft models, developing simulations for new helicopter types, performing acoustic predictions, and developing flight abatement procedures

Project Overview

Rotorcraft noise consists of several components, including rotor noise, engine noise, and gearbox and transmission noise. Rotor noise is typically the dominant component of rotorcraft noise to which the community is exposed upon takeoff and landing, and along the flight path of the helicopter. Rotor noise arises from multiple noise sources, including thickness noise and loading noise (the combination of these two is known as rotational noise), blade-vortex interaction (BVI) noise, high-speed impulsive (HSI) noise, and broadband noise. Each noise source has its own unique directivity pattern around the helicopter. Furthermore, aerodynamic interactions among rotors, interactions between the airframe wake and a rotor, and

unsteady time-dependent loading generated during maneuvers typically substantially increase loading noise. The combination of all potential rotor noise sources makes the prediction of rotorcraft noise highly complex, although not all noise sources are present at any given time in the flight (e.g., BVI noise usually occurs during descent, and HSI noise occurs only during high-speed forward flight).

In ASCENT Project 6, "Rotorcraft Noise Abatement Operating Conditions Modeling," the project team coupled a MATLAB-based flight simulation code with CHARM and PSU-WOPWOP to perform rotorcraft noise prediction. This NPS was used to develop noise abatement procedures through computational and analytical modeling. Although this NPS cannot predict engine noise or HSI noise, it was thoroughly validated via a comparison between predicted noise levels for a Bell 430 aircraft and flight test data (Snider et al., AHS Forum, 2013) for several observer positions and operating conditions.

In previous work for ASCENT Project 38, representative helicopters were recommended for noise abatement procedure development. These helicopters were selected to enable determination of whether noise abatement procedures could be developed for various categories of helicopters (two-blade light, four-blade light, two-blade medium, etc.) or whether aircraft-specific design considerations would be required. Aircraft models were established for the following aircraft: Bell 430, Sikorsky S-76C+ and S-76D, Bell 407 and 206L, Airbus EC130 and AS350, and Robinson R66 and R44. Predictions were made before the 2017 FAA/NASA noise abatement flight test to provide guidance for the flight test. After the flight test, a comparison of *A*-weighted sound pressure level time histories and sound exposure level contour plots revealed a problem in the broadband noise prediction, which was subsequently corrected. Initial validation comparisons demonstrated that the simulations were within several dBA of the flight test data; however, some discrepancies in the simulations (simplifications) remained, thus requiring a detailed examination. Work was also performed on the NPS, including modifying PSU-WOPWOP to output plots of the maximum dBA, as plotted in the flight test. Further work was conducted to enhance the postprocessing of noise data to enable a direct comparison with flight test data. Detailed analysis of the noise components and noise sources was performed for several helicopters in the 2017 FAA/NASA flight test. Further enhancements were added to compute moving averages and devise strategies for window overlapping in the post proposing of predicted noise data. In the cases studied, de-Dopplerization (used in flight test data processing) and moving observers (used in noise predictions to eliminate Doppler effects) were demonstrated to be effectively equivalent (typically within 0.5 dB or less).

In the previous year, a comparison of the effectiveness of noise abatement procedures by helicopter class was performed by using the 2017 and 2019 flight test data. In particular the Bell 205, 206, and 407 aircraft were compared for various flight conditions in the flight tests. In the predictions, the Pegg broadband noise prediction did not work as well for some aircraft, and a simple scaling of the broadband noise was considered as a potential correction. Unfortunately, no clear relationship for the scaling among aircraft was observed. In addition, an analysis of the 2019 FAA/NASA flight test was performed by comparison of prediction and experimental data for 3° and 4.5° descents, and left and right turns at different bank angles (25° and 45°, respectively) for two aircraft (Bell 205 and Sikorsky S-76D). Planning to implement coupling between the Penn State noise predictions system and Volpe's Advanced Acoustics Model software and to preliminarily develop of a noise optimized trajectory generator was also part of the previous year's accomplishments.

The objective of this continuing project is to reduce the need for flight testing of each rotorcraft of interest for continued development of low-noise operating procedures. Current guidelines provided to pilots and operators in the Fly Neighborly guide are based on recommendations from manufacturers, but this guidance is not required and is often not provided. Other methods for developing noise abatement procedures at the FAA and NASA are empirical, on the basis of previous flight measurements of specific aircraft. The tasks described below will enable analyses of new flight procedures and noise analysis strategies through computations alone. This year's efforts included detailed analyses and investigation of the 2017 and 2019 FAA/NASA noise abatement flight tests, along with documentation and training materials to enable the FAA to use the tools more effectively, and a configuration study to evaluate the differences in noise for light vs. heavy two- and four-bladed vehicles.

Task 23 - Complete Evaluation of Noise Abatement Procedure Effectiveness by Helicopter Class, Using 2017 and 2019 flight Test Data

The Pennsylvania State University

Objectives

The objective of this task (Task 8.1 in the 2021–2022 proposal) is to perform detailed noise prediction of noise abatement procedures executed in the 2017 and 2019 FAA/NASA noise abatement flight tests (with an emphasis on the 2019 flight test), with the goal of explaining the how the noise abatement was achieved or why the procedures did not work as expected. This project extension includes plans to complete predictions and analysis for more aircraft from the 2019 flight test (particularly the Leonardo AW139 and to a lesser extent the Airbus Dauphin). Thickness, loading, and broadband noise from both the main and tail rotors will be predicted to determine the relative importance of noise sources for these aircraft compared with the lighter aircraft in the 2017 flight test. Variations in flight procedures may also be predicted to assess the "robustness" of the abatement procedures to variations. This evaluation is expected to lead to better noise abatement procedures and perhaps even procedures tailored to helicopter models.

Research Approach

The NPS developed in ASCENT Projects 6 and 38 was used and updated as necessary. The noise prediction was performed with the coupled rotorcraft NPSs PSUHeloSim flight simulator, CHARM comprehensive rotorcraft model, and PSU-WOPWOP noise prediction code. The PSU-WOPWOP code was also used to process the flight test data to ensure that all postprocessing of acoustic pressure was the same for both the flight test and predictions. The flight test data were examined, data from similar or different runs were compared, and the predicted results were compared to investigate the details of the noise for the flight procedures flown. This investigation was also able to identify the primary and secondary noise sources involved in each flight procedure and clarify how noise abatement was achieved (thus potentially leading to generalized procedures for other helicopter categories, weights, etc.). In this task, the focus was on understanding the noise measured in the flight test by comparing different runs and examining the predicted noise components in the NPS simulation. Furthermore, although validation of the NPS was performed previously, validation continues during the evaluation of flight procedures and the comparison of predictions with flight test data.

The modeling of the aircraft in the noise predictions was approximate: several key parameters were based on open sources and engineering judgement. For example, because several details of the S-76D aircraft were unavailable, the parameters from an earlier version of the S-76 were used, with some changes to account for likely changes in the S-76D model.

Milestones

The milestones for this task include (a) updating and correcting the helicopter models for aircraft from the 2017 and 2019 flight tests, (b) studying flight test noise measurements for similar flight conditions for the same aircraft, and for nominally same flight conditions for different aircraft, and (c) using the NPS to identify the primary sources of noise during flight maneuvers.

Major Accomplishments

In the assessment of the flight test aircraft under study, we determined that the flight test data for the Leonardo AW139 and Airbus Dauphin were relatively more limited and had greater uncertainty. Therefore, for the 2019 flight test evaluation, the focus was switched to the S-76 and Bell 205, which were compared with the Bell 407 and 206. The S-76 and Bell 407 have four-bladed main rotors, and the Bell 205 and Bell 206 have two-bladed main rotors.

Throughout the year, several bug fixes to the codes and corrections of the PSUHeloSim and CHARM helicopter models were made. One identified bug was that the PSU-WOPWOP coordinate transformation files that PSUHeloSim output for pitch and roll and pitch were swapped, thus resulting in small but non-negligible changes in the noise (particularly for turns) with the corrections. Similarly, in the helicopter models, the *Z*-force was not in the correct direction in descent cases for some models, and the vehicle weight was too high for the Bell 205 and 407. In addition, the rotation directions of the main rotors were reversed. Such setup problems sometimes cause only small errors that are not easily identified in the predictions. The effects of all these changes are shown in Figure 1. Of note, the velocities, forces (with *Z*-forces highlighted), and flight path angles (FPAs) are changed for each aircraft. In the new results (Figure 1b), the *Z*-force magnitude is not typically much closer to the weight of the aircraft (differences arise because of aircraft pitch, etc.) than observed in the original computations shown in Figure 1a. This finding was not the case for the original results; therefore, we performed a detailed examination of the setup

to determine the source of the discrepancies. Some concerns remain that the Bell 205 model may still have some problems, but none have been identified. All noise predictions for these vehicles have been rerun to use the new models.

S76-D	
Weight (lbs)	10,687
X velocity (ft/s)	87.72
Y velocity (ft/s)	-1.22
Z velocity (ft/s)	-13.79
X force	1036.83
Y force	-46.31
Z force	-9916.79
FPA	-8.93

Bell 407	
Weight (lbs)	3824
X velocity (ft/s)	106.07
Y velocity (ft/s)	4.93
Z velocity (ft/s)	-11.88
X force	1672.94
Y force	865.04
Z force	-12197.77
FPA	-6.39

Bell 205	
Weight (lbs)	7460
X velocity (ft/s)	119.66
Y velocity (ft/s)	0.82
Z velocity (ft/s)	-19.30
X force	-685.59
Y force	292.44
Z force	7063.89
FPA	-9.16

Bell 206	
Weight (lbs)	3462
X velocity (ft/s)	113.57
Y velocity (ft/s)	2.37
Z velocity (ft/s)	-18.96
X force	-1298.70
Y force	22.26
Z force	-6010.18
FPA	-9.48

(a) Velocity, forces, and FPAs computed by using the original (incorrect in some cases) aircraft models

S76-D	
Weight (lbs)	10,687
X velocity (ft/s)	114.72
Y velocity (ft/s)	2.38
Z velocity (ft/s)	-17.33
X force	855.99
Y force	117.63
Z force	-9514.66
FPA	-8.50

Bell 407	
Weight (lbs)	3824
X velocity (ft/s)	104.55
Y velocity (ft/s)	-3.20
Z velocity (ft/s)	-17.41
X force	383.95
Y force	14.11
Z force	-3748.99
FPA	-9.46

Bell 205	
Weight (lbs)	7460
X velocity (ft/s)	116.84
Y velocity (ft/s)	-0.09
Z velocity (ft/s)	-18.72
X force	-551.95
Y force	185.35
Z force	5836.37
FPA	-9.10

Bell 206	
Weight (lbs)	3462
X velocity (ft/s)	105.24
Y velocity (ft/s)	-0.88
Z velocity (ft/s)	-18.23
X force	-513.39
Y force	81.38
Z force	-3423.31
FPA	-9.86

(b) Results from the new (corrected) aircraft models

Figure 1. Comparison of velocity, forces, and flight path angles (FPAs) for old and new aircraft models.

In another major accomplishment, four helicopters flown in the flight tests—S-76D, Bell 407, Bell 205, and Bell 206 (shown in Figure 2)—were compared. Predictions for each were made by using approximately the same flight path of the helicopter in the flight test, but the weights used were slightly different from the final values described in the previous paragraph. Although our goal was to analyze the same approach trajectory for all aircraft, our secondary goals were for the flight condition to have steady forward and vertical velocity, no turns, and very small to no accelerations. The flight conditions selected to compare these vehicles comprised a -9° FPA and flight velocity of 60 knots for all vehicles. Figures 3–5 show the components of the noise for each of the four aircraft on a hemisphere below the rotors. The thickness noise, which has the smallest contribution to the total noise for each helicopter, is shown in Figure 3. The grid lines in Figure 3 are equally spaced lines of azimuth and elevation; Ψ is the azimuth angle around the vehicle; and $\Psi = 0^{\circ}$ downstream, and $\Psi = 90^{\circ}$ is on the advancing side of the main rotor. The Bell 407 thickness noise is much lower than that of the other aircraft, but it has the smallest chord and thickness. Table 1 shows the relevant parameters for thickness noise for each aircraft. The Bell 407 has a smaller chord and thinner blade, but these differences alone were not expected to lead to the substantially lower thickness noise in Figure 3; hence, further investigation of this result may be warranted.

S-76D

Weight	10,690 lb
Number of blades	4
MR Radius	22 ft
Rotation speed	32.83 rad/s
TR number of blades	4

Bell 205

Weight	7,460 lb
Number of blades	2
MR Radius	24 ft
Rotation speed	33.93 rad/s
TR number of blades	2

Bell 407

Weight	3,600 lb
Number of blades	4
MR Radius	17.5 ft
Rotation speed	43.25 rad/s
TR number of blades	2

Bell 206

Weight	3,300 lb
Number of blades	2
MR Radius	16.67 ft
Rotation speed	41.26 rad/s
TR number of blades	2

Figure 2. Helicopters compared in the study of noise components.

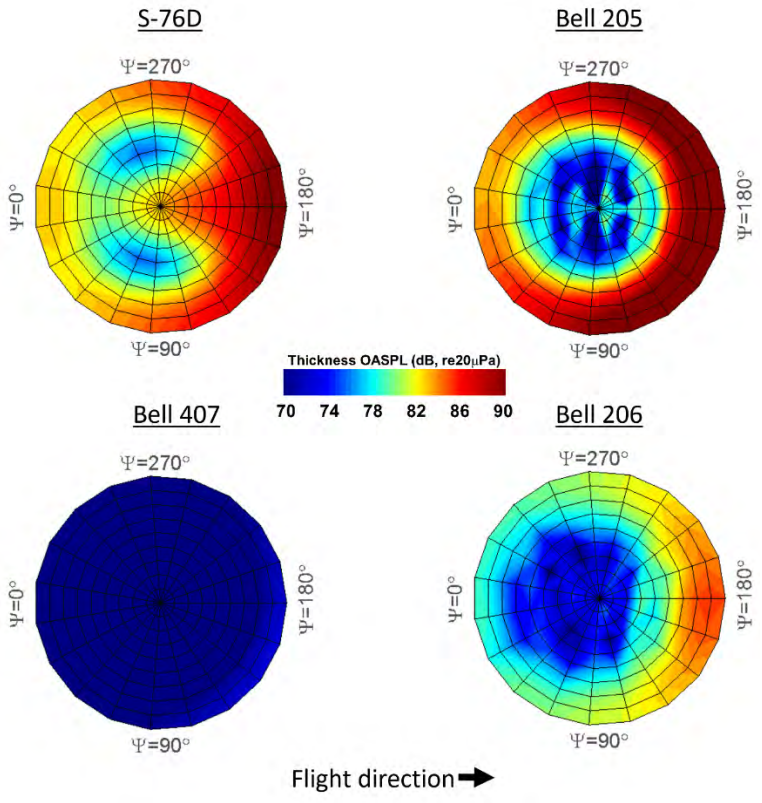

Figure 3. Comparison of thickness noise for the S-76, Bell 205, Bell 407, and Bell 206 helicopters. Radial distance is the elevation angle from the rotor plane to directly underneath the helicopter; Ψ is the azimuth angle around the vehicle, with $\Psi = 0°$ downstream, and $\Psi = 90°$ on the advancing side of the main rotor.

Table 1. Parameters relevant to thickness noise.

Vehicle	Blade thickness	Chord	MR Radius	Tip speed
S-76	0.12 ft	1.29 ft	22.0 ft	722 ft/s
Bell 407	0.11 ft	0.90 ft	17.5 ft	757 ft/s
Bell 205	0.21 ft	1.75 ft	24.0 ft	814 ft/s
Bell 206	0.12 ft	1.00 ft	16.7 ft	688 ft/s

The Pegg broadband noise prediction for each aircraft is shown in Figure 4. In last year's work, we determined that the broadband noise prediction accuracy depends on the aircraft and can show significant error. Correction of this error may be beyond the scope of this project, but for most helicopters in this flight condition, the broadband noise is not the dominant noise source (comparison of Figures 3–5). The broadband noise predicted for the Bell 206 is the highest among all vehicles, because this aircraft falls in a different segment of the Pegg empirical equation. Thus, this finding is likely to be incorrect, and the model may need to be adjusted (and validated) to achieve correction. Beyond this anomaly, the two heavier aircraft, the Sikorsky S-76 and the Bell 205, have higher levels of broadband noise, probably because, in addition to their weight, they have higher tip speeds and larger blade areas.

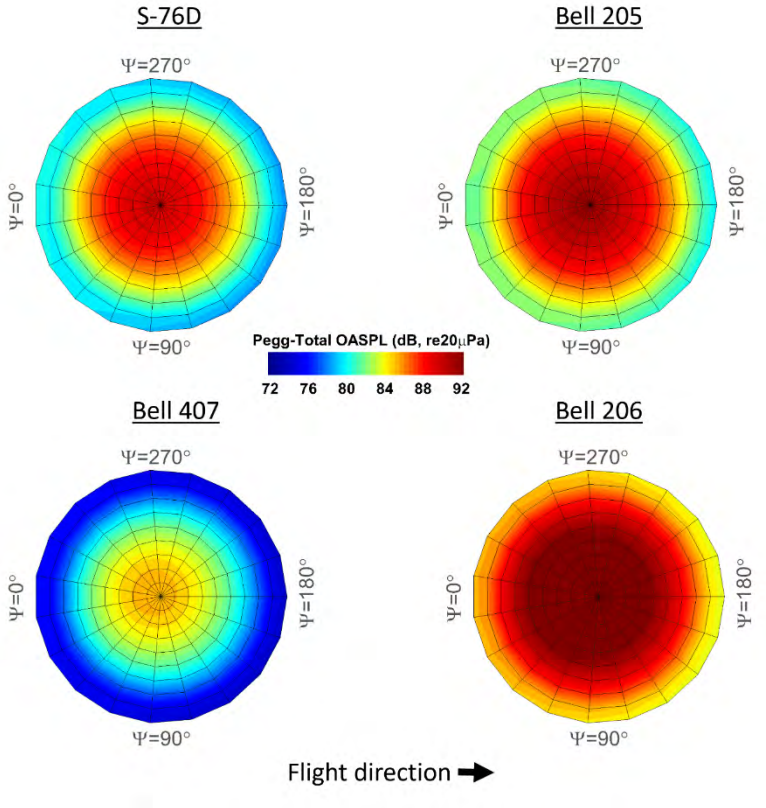

Figure 4. Comparison of Pegg broadband noise for the S-76, Bell 205, Bell 407, and Bell 206 helicopters. Radial distance is the elevation angle from the rotor plane to directly underneath the helicopter.

Finally, the loading noise predictions for each of the four aircraft are shown in Figure 5. The loading noise is the most dominant source (~10 dB higher than the others) under this flight condition for all aircraft (comparison of Figs. 3–5). The Sikorsky S-76 and Bell 205 have the highest levels, as might be expected for the heavier aircraft. The Bell 407 has substantially less loading noise than the other helicopters (approximately the same as the broadband noise), whereas the lightest helicopter, the Bell 206, has quite high loading noise levels in this flight condition. This difference is thought to be related to the number of blades in the main rotor (two for the Bell 206 and four for the Bell 407) and the occurrence of BVI noise (the loading for the Bell 407 does not show evidence of BVI loading, whereas the Bell 206 does appear to be experiencing BVI).

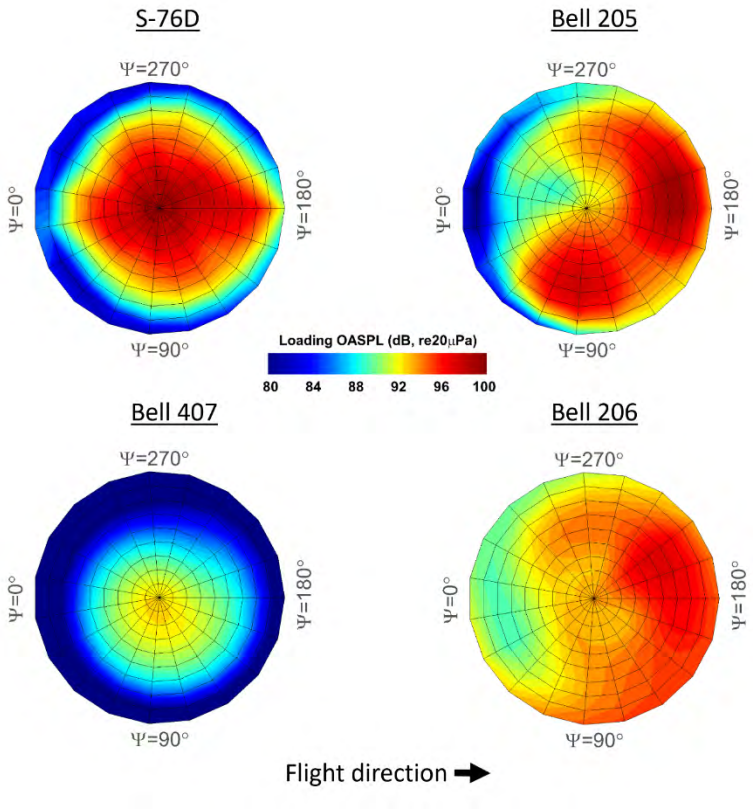

Figure 5. Comparison of loading noise for the S-76, Bell 205, Bell 407, and Bell 206 helicopters. Radial distance is the elevation angle from the rotor plane to directly underneath the helicopter.

Some additional conclusions of this task (not just those shown to date) are as follows: (a) the number of blades in the main rotor is a strong indicator of noise; (b) two-bladed rotors are louder than four-bladed rotors; and (c) lighter vehicles are generally quieter than heavier vehicles (but not always). Although not shown here, detailed studies have indicated that the changes in trajectory due to external perturbations that occur in flight tests result in differences in noise, which are sometimes significant. Furthermore, the nominal or desired flight trajectory is not always achieved.

To compare the results in another way, we analyzed the predicted results from the end of last year's effort in more detail this year. The noise from each aircraft during a flyover is shown in Figure 6. Of note, for the four-bladed main rotor cases, the Bell 407 has comparable peak noise levels to those of the Sikorsky S-76, although the weight of the S-76 is nearly three times that of the Bell 407. Thus, weight alone is not a factor determining helicopter noise. The noise of the two-bladed helicopters shows a similar trend, although the peak noise of both helicopters with two-bladed main rotors is higher than that of the four-bladed main rotor vehicles. Figure 7 shows that the broadband noise is responsible for the peak levels for both two-bladed and four-bladed main rotor helicopters in this case. Given that the Pegg model does not agree as well for heavier aircraft, the findings suggest that the comparison of the total noise curves must be interpreted with caution, but the

thickness and loading noise components should be reliable. In follow up work, a comparison of the flyover noise from the flight test data for the same observer location should be made for the four vehicles, perhaps with scaling of the flyover altitude to eliminate differences in the flight test data among different aircraft.

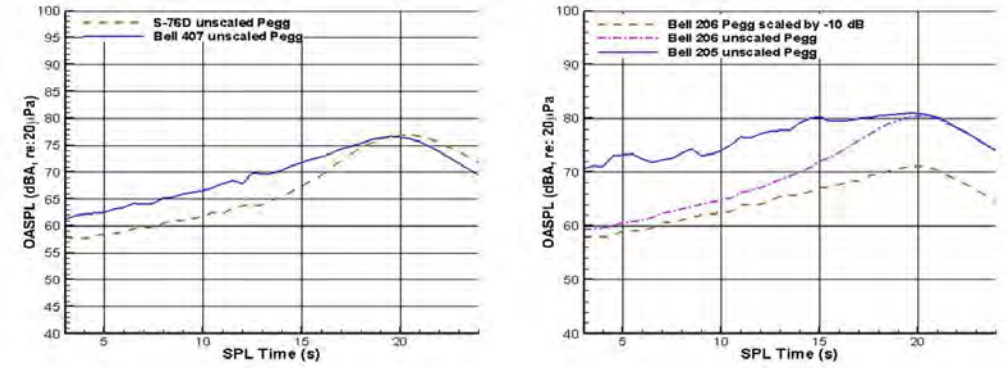

Figure 6. *A*-weighted overall sound pressure level (OASPL) of total noise vs. time for four-bladed main rotor aircraft. Left: four-bladed main rotor aircraft; right: two-bladed main rotor aircraft. (Please ignore the Bell 206 Pegg scaled by −10 dB curve.)

Four-bladed main rotor aircraft

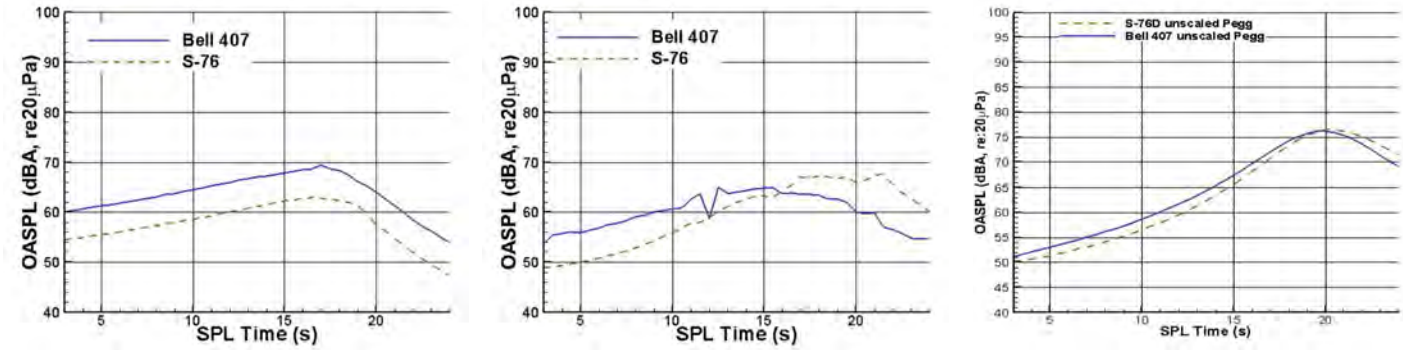

(a) Thickness noise (b) Loading noise (c) Broadband noise - Pegg model

Two-bladed main rotor aircraft

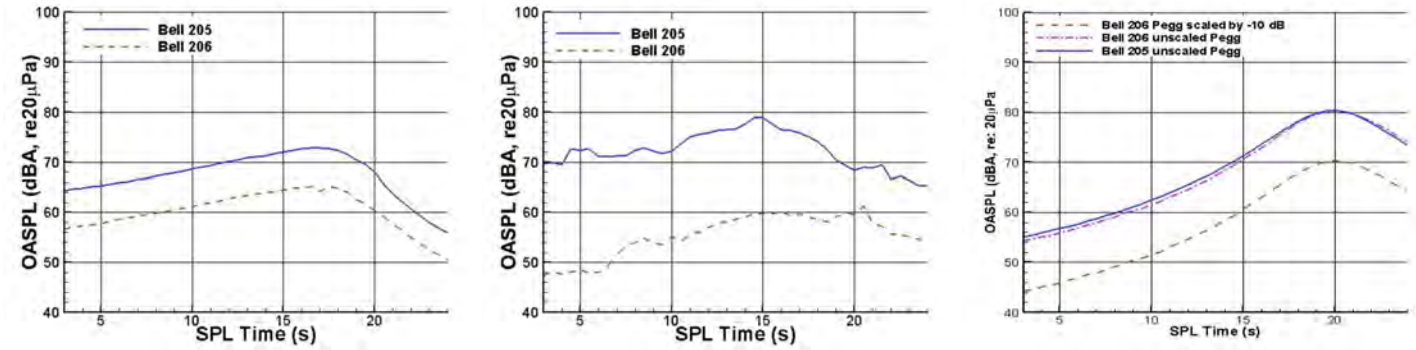

(d) Thickness noise (e) Loading noise (f) Broadband noise - Pegg model

Figure 7. *A*-weighted overall sound pressure level (OASPL) of noise components vs. time for the four flight test aircraft.

In a final comparison for Task 23 in this report, Figure 8 shows the loading noise predicted for the Sikorsky S-76 and the Bell 407, both with four-bladed main rotors, but with the main rotor and tail rotor noise separated. For the S-76, the tail rotor noise is higher than the main rotor noise (until approximately 12 seconds), and then the noise is comparable until the aircraft passes overhead, and the tail rotor noise decays rapidly. For the Bell 407, the tail rotor noise is significantly lower throughout but comes closer to the main rotor loading noise after approximately 18 seconds.

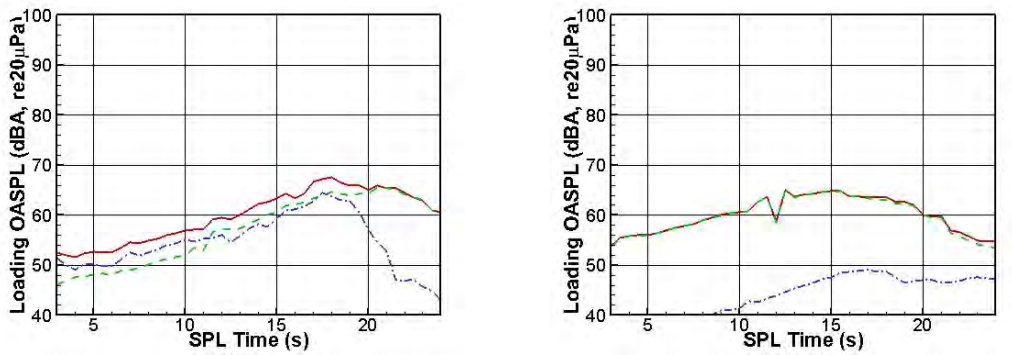

(a) S-76 (b) Bell 407

Figure 8. Predictions for loading noise for the S-76 (medium weight) and Bell 407 (light weight) aircraft, both with four-bladed main rotors. – – – – main rotor, – ▪ – ▪ – tail rotor, ——— all rotors.

A detailed analysis of the configuration study can be found in Lauren Weist's M.S. thesis (Weist, 2022).

Publications

Weist, L. (2022). *Helicopter Noise Modeling with Varying Fidelity Prediction Systems* [Master's thesis, The Pennsylvania State University].

Outreach Efforts

None.

Awards

None.

Student Involvement

Lauren Weist, a graduate assistant who finished her master's degree at Penn State in August 2022, generated predictions for the Bell 407, Bell 206, Bell 205, and S-76.

Plans for Next Period

During the next period, the focus will be on studying and resolving deficiencies in noise prediction of 2017 and 2019 flight test data. These deficiencies include overprediction of noise as the aircraft approaches, underprediction of peak noise as the aircraft is overhead, and overprediction again as the aircraft is downrange. Broadband noise appears to be a source of problems in the predictions, and simple scaling of the broadband noise is not sufficient to match the experiment through the entire maneuver, nor is it generalizable to different aircraft. Scattering of the tail rotor noise by the fuselage may also occur as the aircraft approaches the observer. These issues and others will be studied, and new models will be proposed to address these issues. This effort will be led by Penn State with limited support for aircraft modeling from to investigate potential problems with the current system modeling.

References

Weist, L. (2022). *Helicopter Noise Modeling with Varying Fidelity Prediction Systems* [Master's thesis, The Pennsylvania State University].

Task 24 - Investigate the Modeling of Shrouded Rotor Noise

The Pennsylvania State University

Objective

The goal of this task (Task 8.2 in the 2021–2022 proposal) is to develop a simplified method to approximately calculate the shrouded rotor noise so that the noise can be properly included in aircraft procedure assessment and noise abatement procedure development.

Research Approach

The approach to develop noise prediction for a shrouded rotor antitorque device is to use simple modeling to provide a "correction" to the rotor noise of the shrouded rotor. Two items will be considered, (a) increased thrust on the rotor to account for the extra trust produced due to the shroud, and (b) increased thrust on the rotor to "mimic" the noise radiated by the fluctuating pressure on the shroud due to the rotor. Introduction of phase lag into the effective shroud noise may be appropriate. In addition to this simplest approach, another option would be to use CHARM to provide the unsteady pressure field on the shroud and use it to predict the noise on the shroud with PSU-WOPWOP. The Airbus EC130 (2017 FAA/NASA noise abatement flight test) and, to a lesser extent, the Airbus Dauphin (2019 FAA/NASA noise abatement flight test) can be used to understand how the noise from the shrouded rotor (Fenestron) differs from that of a similar isolated rotor, and then to use the measured noise from these aircraft to validate the various models developed for the shrouded rotor noise.

Milestones

The milestones for this task include (a) developing a complete model and implementation strategy for the approaches described in the "Research Approach" section; (b) fixing the EC 130 model for the NPS so that the shrouded rotor model can be implemented and tested; (c) comparing noise prediction of the isolated EC 130 Fenestron rotor (but as part of the complete aircraft) for comparison with the EC 130 flight test data; and (d) implementing and testing the proposed shrouded rotor models for the EC 130 Fenestron (shroud and rotor), for comparison with the flight test data.

Major Accomplishments

Work was initiated to start developing a modeling strategy and to update the EC 130 helicopter model in the Penn State NPS. Unfortunately, little progress has been made in the effort by graduating student Lauren Weist, because she was required to learn the NPS, and her efforts were focused on Tasks 23 and 25 over the year (she worked on Project 38 for only 1 year). Sagar Peddanarappagari, a new M.S. student, joined Project 38 in August 2022 and has restarted this effort. Currently, Penn State is awaiting shrouded rotor data already generated by CDI.

Publications

None.

Outreach Efforts

None.

Awards

None.

Student Involvement

Lauren Weist, a graduate assistant at Penn State, began an initial investigation into the shrouded rotor noise problem. Sagar Peddanarappagari has joined the project as a graduate assistant to restart this task.

Plans for Next Period

The noise directivity of the Airbus EC130 and the Airbus Dauphin will be studied, because these aircraft are equipped with shrouded rotor antitorque devices (Fenestron). Basic ideas on how to model the shrouded rotor noise have been developed, but in the next year, these models will be more fully developed and implemented in the Penn State NPS. Although simple modifications to the rotor loads for the shrouded rotor will be examined, the primary approach planned is based on work conducted by CDI for rotor–structure interactions (rods and cones) (Botre et al., 2022) and older work modeling the shroud with a panel method. Investigations into correcting for compressibility effects (propagation delay) are also planned. This

work is unlikely to be able to directly predict the noise from high-tip speed fans and longer ducts, but that capability will also be needed in the future (beyond the next year).

References

Botre, M., Wachspress, D., Brentner, K., & Gan, Z. F. T. (2022). *Aeroacoustic Prediction and Validation of Variable RPM Rotors and Rotor-Airframe Interactions for Advanced Air Mobility Applications.* Paper presented at 78th Vertical Flight Society Annual Forum and Technology Display, FORUM 2022, Fort Worth, Texas, United States.

Task 25 - Continue Effort to Develop Helicopter Noise Abatement Flight Procedures

The Pennsylvania State University

Objective

The objective of this task (Task 8.3 in the 2021–2022 proposal) is to contribute to the development of a wider range of noise abatement procedures. Depending on the type of helicopter, the type of operation, and the location of noise-sensitive areas, certain noise abatement procedures may be more effective than others in specific scenarios. The NPS can identify the physical mechanisms of effective noise abatement procedures, because it is based on first-principles methods, thus providing insight into how procedures can be tailored to specific conditions to reduce noise. In addition, the flight simulation system may be used to assess the level of difficulty for a pilot to perform a noise abatement procedure or the level of automation required to assist a pilot, including the sensitivity of the procedure to inevitable variations from the desired procedure.

Research Approach

After the validation of noise predictions with 2019 FAA/NASA flight test data (Task 18 last year and Task 23 this year), the prediction system was validated for multiple maneuvers. With the validated NPS (even with known limitations), various maneuvers can be simulated to evaluate the noise abatement effectiveness of different maneuvers. The focus this year was on investigating the effects of variations between the executed flight procedure and the nominal or desired flight procedures. This process yields information that can be used to determine the robustness of noise abatement procedures.

Milestones

The milestones for this task include (a) examining flight test runs for nominally the same flight conditions, flown by the same pilot in the same aircraft, and comparing the effects of the variation on the noise; (b) studying the aeroacoustic impact of longitudinal and vertical acceleration; and (c) exploring the small changes in FPA and rates of change in FPA in flight tests relative to the desired nominal FPA requested.

Major Accomplishments

With the Penn State NPS, coupled flight simulation (PSUHeloSim), CHARM, and noise prediction code (PSU-WOPWOP), we examined the S-76D helicopter noise variation during approach maneuvers. The study consisted of parametric sweep of both the longitudinal acceleration and time rate of change in FPA. The findings indicated that longitudinal acceleration variation has very little effect on the loading noise (<1 dB) and causes no change in thickness and broadband noise (Pegg model). The FPA rate, in contrast, has a larger effect on the noise. For a thrust change of approximately 700 lb, introduced in ±1˚/s FPA rate increments, the loading noise varies by approximately 3 dB. For an FPA change of 3˚ at a rate of ±1˚/s FPA change, the loading noise varies by up to 6 dB.

Another accomplishment was studying the flight test data to determine the typical variability across multiple runs of the same requested (nominal) flight condition. For example, Figure 9 shows the flight path (x, y, z as a function of time) and the velocities in the x, y, z directions for two different runs with the Sikorsky S-76D aircraft, as compared with the nominal flight path. In this comparison, substantial differences were observed between runs. The pilots in the flight test were professional pilots, but not pilots normally accustomed to flight testing. The longitudinal velocity deviations from the nominal ranged from 20 to more than 30 ft/s (about 12 to 18 kts), with as much as 65 ft/s (38 kts) between runs. The requested flight condition was a 4.5˚ descent, and differences as high as 30 ft/s (18 kts) were observed between runs in the lateral direction and approximately 10 ft/s (6 kts) in the vertical direction. Furthermore, some cases flown were steadier than others. The effects of such variations on the maximum dBA level (on a hemisphere moving with the vehicle) are shown in Figure 10, where the nominal case is on the left, and the two flight test runs are shown in the middle and the right. All maximum dBA

plots are predictions, but the two flight test runs used the flight path measured in the flight tests (predictions were used to fully populate the hemisphere; substantially less microphone data was measured during the test). Figure 10 shows substantial differences in maximum dBA (5 dBA or more) among the three cases, in both amplitude and directivity.

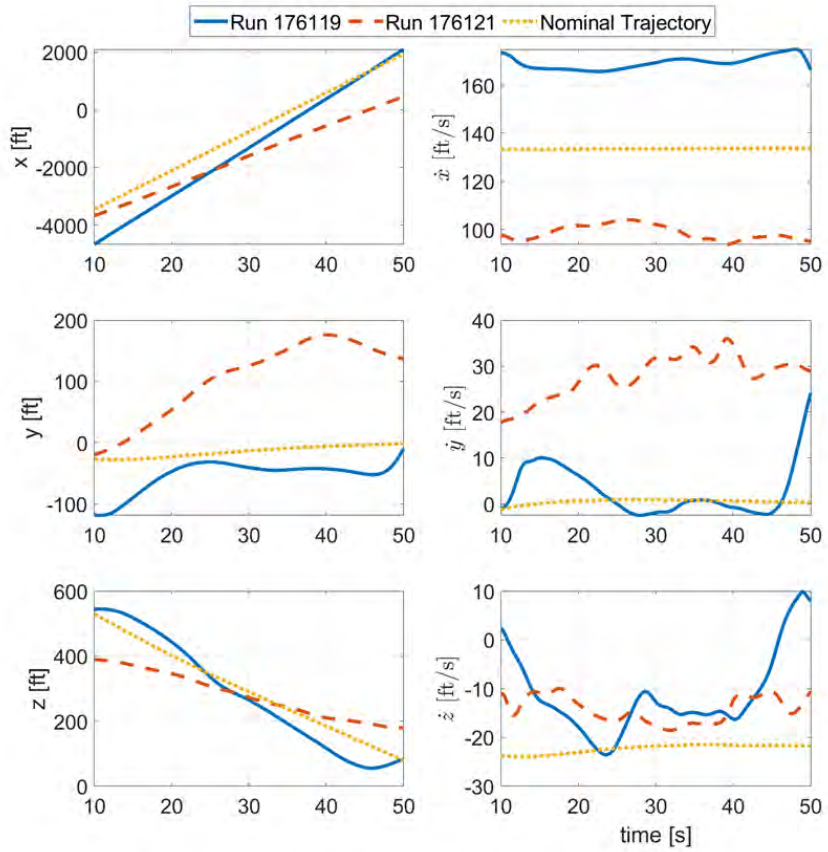

Figure 9. Position and velocity for S-76 with nominal 100 kts, 4.5˚ descent. Runs 176119 and 176121 were the actual position and velocity of two runs in which the pilots were requested to fly the nominal flight path.

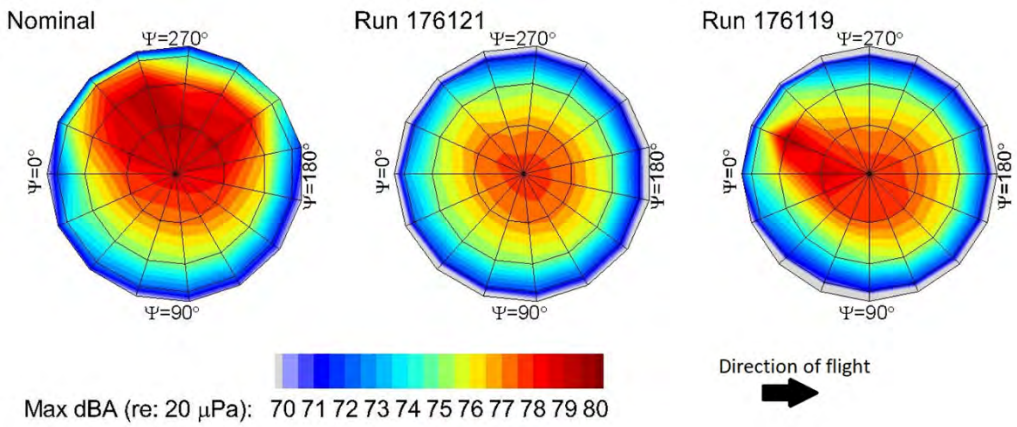

Figure 10. Predicted max dBA levels on a hemisphere for S-76 with nominal 100 kts, 4.5˚ descent, and predictions with an approximation for the actual flight path for the same 100 kts, 4.5˚ descent for two different flight test runs.

To further investigate the importance of variations from the nominal flight condition as the flight progresses, we plotted the vehicle position, velocities, FPA γ, and time rate of change in the FPA $\dot{\gamma}$ as a function of time for the S-76D in a 6˚ descent condition (Figures 11 and 12). The three colored bands indicate three different time segments (25.0–25.5 s, 27.5–28.0 s, and 29.0–29.5 s), which are compared in Figure 13. These three time segments were chosen to have negative, positive, and nominally zero $\dot{\gamma}$ values. Figure 13 shows the overall sound pressure levels for the baseline and flight test flight profiles, along with the difference between (on the right) for each time segment. For the time segment $t = 25$s, where $\dot{\gamma} \approx -1^{\circ}$/s, large differences (up to 6 dB) are observed between the baseline and flight test predictions, whereas less difference is observed for time segment $t = 27.5$, where $\dot{\gamma} \approx 1^{\circ}$/s, and for time segment $t = 29$, where $\dot{\gamma} \approx 0^{\circ}$/s; the differences are as great as 4 dB. These findings indicate that in actual flight, the noise levels might vary as much as 6–8 dB, and any noise abatement procedure should probably reduce the noise beyond that range to be considered fully effective in practice. This conclusion must be studied further by comparison with more flight test runs. More detailed analysis of this study and others can be found in Zachos et al. (2022) and Weist (2022).

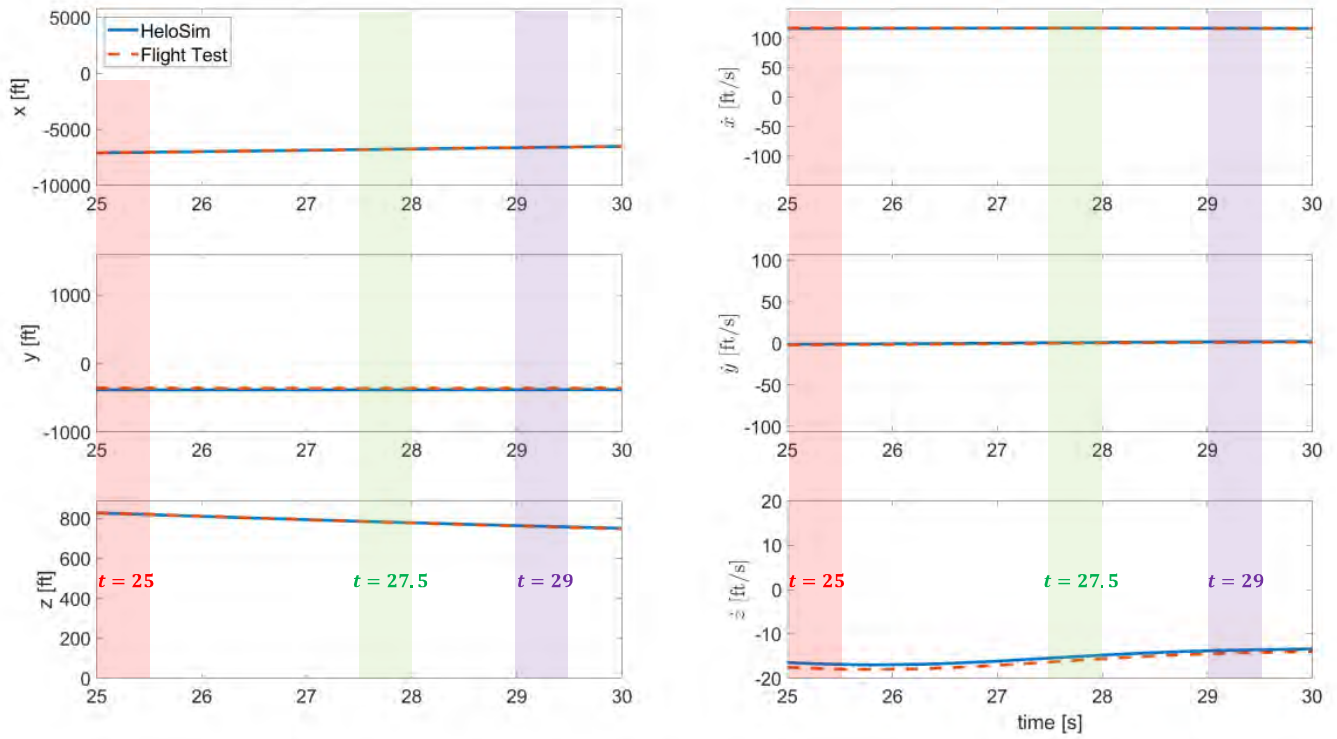

Figure 11. Comparison of predicted (HeloSim) and measured (flight test) position (left) and velocity (right) during part of an S-76D flyover. Three different periods, indicated by $t = 25, t = 27.5$, and $t = 29$ seconds, are compared in Figure 13.

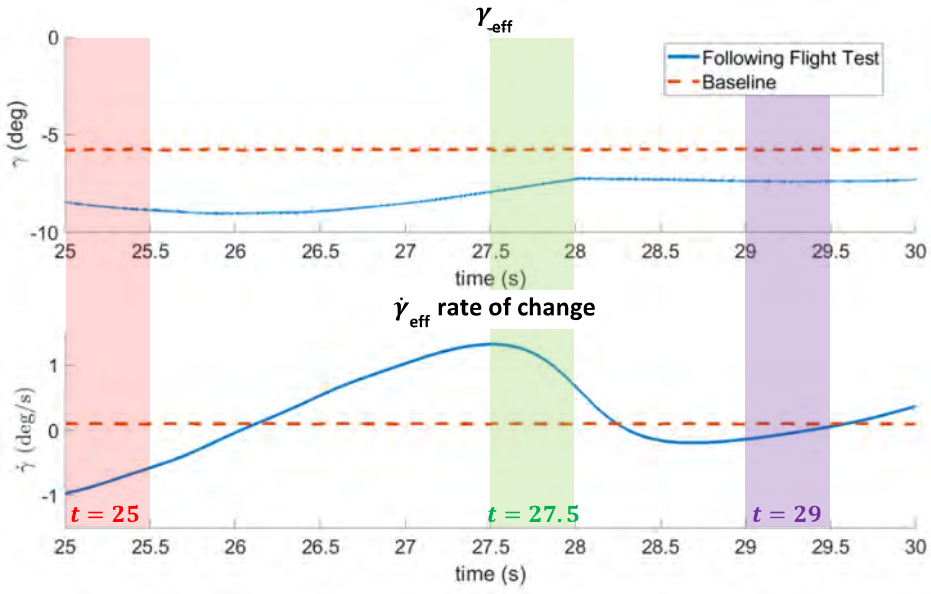

Figure 12. Comparison of the effective descent rate γ_{eff} (top) and rate of change in the effective descent rate $\dot{\gamma}_{eff}$ (bottom) for following flight test and baseline trajectories. Three different periods, indicated by $t = 25, t = 27.5$, and $t = 29$ seconds, are compared in Figure 13.

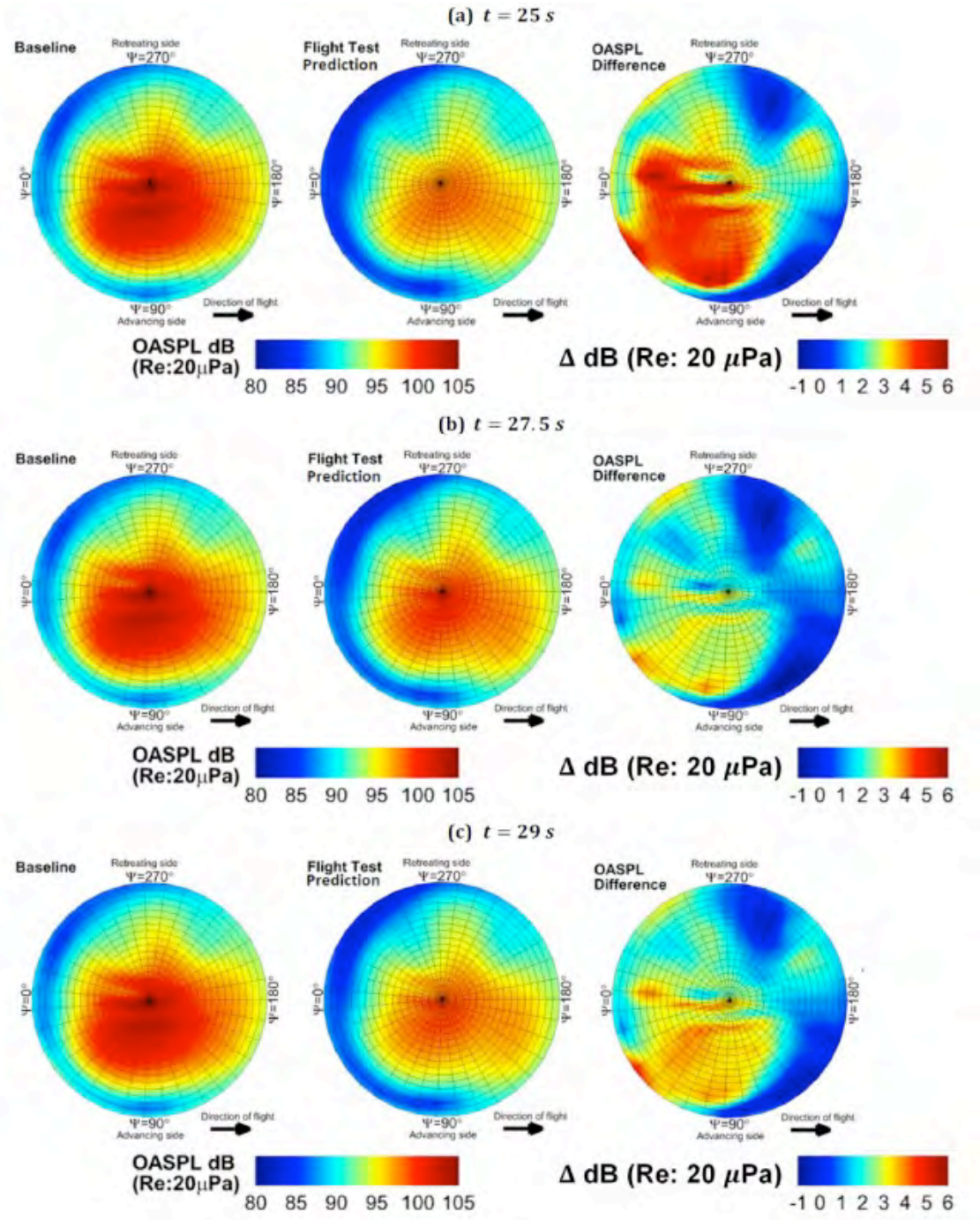

Figure 13. Comparison of predicted OASPL for following flight test and baseline trajectories (left and middle columns) and the difference in OASPL between the two predictions (right column). Three different periods, indicated by (a) $t = 25$, (b) $t = 27.5$, and (c) $t = 29$ seconds, are compared.

Publications

Published conference proceedings

Weist, L. (2022). *Helicopter Noise Modeling with Varying Fidelity Prediction Systems* [Master's thesis, The Pennsylvania State University].

Zachos, D. R., Weist, L., Brentner, K. S., & Greenwood, E. (2022). *Variation in Helicopter Noise During Approach Maneuvers*. Paper presented at 78th Vertical Flight Society Annual Forum and Technology Display, FORUM 2022, Fort Worth, Texas, United States.

Outreach Efforts

None.

Awards

None.

Student Involvement

Lauren Weist, a graduate assistant who completed her master's degree at Penn State in August 2022, compared and selected flight test runs, generated predictions, and analyzed the results.

Plans for Next Period

The Penn State NPS will be enhanced to correct for some of the current deficiencies, and then will be tested and demonstrated in helicopter noise abatement procedures. For some cases studied this year, more analysis of the flight test data should be performed and compared with the predictions from this year. This work should then be applied to provide the information to enhance noise abatement procedures.

References:

Weist, L. (2022). *Helicopter Noise Modeling with Varying Fidelity Prediction Systems* [Master's thesis, The Pennsylvania State University].

Zachos, D. R., Weist, L., Brentner, K. S., & Greenwood, E. (2022). *Variation in Helicopter Noise During Approach Maneuvers*. Paper presented at 78th Vertical Flight Society Annual Forum and Technology Display, FORUM 2022, Fort Worth, Texas, United States.

Task 26 - Develop Documentation and Training Materials for the Noise Prediction System

The Pennsylvania State University

Objective

The objective of this task (Task 8.4 in the 2021–2022 proposal) is to develop documentation and training material for the Penn State NPS. This documentation will help new users use this very complex system and generate simulations.

Research Approach

The Penn State NPS was developed to predict noise for various helicopters in many different maneuvers through previous work in ASCENT Project 6 and ASCENT Project 38. The system has been validated against 2017 and 2019 FAA/NASA flight test data. Individual components of the system have their own documentation, and a draft document describes on how to install the PSUHeloSim/CHARM/PSU-WOPWOP software to start using the system. In this project, the remaining documentation of how to run the system—specifically how to run the different tools as a unified system—is needed. Furthermore, training materials are needed for self-learning or to serve as reference material for a training course. The goal is to transfer this technology to the FAA, and this documentation will be essential for seamless setup utilization for new users.

Milestone

Setup documentation has been developed for internal Penn State use and has been demonstrated to be useful for new students. This document will be further developed for external use with corresponding software repositories. Further development of training materials was delayed for several reasons: (a) Because Volpe did not have the resources to interact with Penn State for implementation or training during the past year, the documentation was not viewed as urgent; (b) we plan to start using the DEPSim software used in Project 49 for helicopters in the future, and this shift will require substantial changes to any documentation and training materials; and (c) the graduate student working on the project was not able to make substantial progress in this task, mainly because of reasons (a) and (b).

Major Accomplishments

All steps required for the setup and operation of the Penn State NPS have been compiled into a document for internal use, which has proven valuable in setup for new students.

Publications

None

Outreach Efforts

None

Awards

None

Student Involvement

Lauren Weist, a graduate assistant at Penn State, worked on the documentation that was developed.

Plans for Next Period

Documentation and sample cases have been developed in previous work in Project 38 but are not ready for external users or training. Given the increasing interest and maturity of the current system, a set of documentation and example cases will be prepared for use at Volpe and the Tech Center first. Collaboration is desired to provide feedback for improving the documentation, training materials, and example cases. The task will also help transfer this technology to both the FAA and industrial partners.

Project 043 Noise-Power-Distance Reevaluation

Georgia Institute of Technology

Project Lead Investigator

Dimitri Mavris
Regents Professor
School of Aerospace Engineering
Georgia Institute of Technology
Mail Stop 0150
Atlanta, GA 30332-0150
404-894-1557
dimitri.mavris@ae.gatech.edu

University Participants

Georgia Institute of Technology (GT)

- P.I.s: Dr. Dimitri Mavris (P.I.) and Dr. Michelle Kirby (co-P.I.)
- FAA Award Number: 13-C-AJFE-GIT-075 and 095
- Period of Performance: August 11, 2020 to December 31, 2022
- Tasks:
    1. Development and testing of the noise-power-distance+ configuration ((NPD+C) correction function (CF)
    2. Engagement with Original Equipment Manufacturers (OEMs) for Validation of the NPD+C Approach with Real Data
    3. Noise Validation Efforts with Noise Monitoring Data at the San Francisco Airport
    4. Rescoping of the Problem to Focus on NPD Corrections at Low-Thrust Values

Project Funding Level

This project is funded at the following levels: GT, $200,000. In addition, $200,000 in matching funds has been provided through in-kind contributions from a major airline. This total includes salaries for the project director, research engineers, and graduate research assistants, as well as funding for computing, and financial and administrative support, including meeting arrangements. The institute has also agreed to provide tuition remission for students whose tuition is paid via state funds.

Investigation Team

- Dimitri Mavris, P.I., GT
- Michelle Kirby, Co-Investigator, GT
- Dushhyanth Rajaram, Research Faculty, GT
- Ameya Behere, Graduate Student, GT

Project Overview

The standard technique for evaluating fleet noise is to estimate the flight procedure source noise by using noise-power-distance (NPD) curves. Noise calculations within the Aviation Environmental Design Tool (AEDT) rely on NPD curves provided by aircraft manufacturers. This dataset reflects representative aircraft categories at set power levels and aircraft configurations. Noise levels are obtained as a function of slant distance via spherical spreading through a standard atmosphere, and other correction factors are applied to obtain the desired sound field metrics at the location of the receiver. The current NPD model does not consider the aircraft configuration (e.g., flap settings) or alternative flight procedures being implemented. These factors are important, because the noise characteristics of an aircraft depend on the thrust, aircraft speed, and airframe configuration, among other contributing factors such as ambient conditions. The outcome of this

research is an approach based on the suggested NPD+C format, which will enable more accurate noise predictions because of its inclusion of aircraft configuration and speed changes.

Task 1 - Refinement of the Final NPD+C Correction Functions

Georgia Institute of Technology

Objectives

The objective of this task is to create a CF to correct the baseline NPD for an aircraft class to match a given flight configuration, incorporating flight velocity (FV), flap deflection angle (FDA), and gear setting (gear).

Research Approach

Overview

Before a CF was created, several categories of commercial transportation aircraft were identified according to their payload capacity. Ultimately, four categories were identified: 50, 150, 210, and 300 passenger (pax) categories. Fitting the NPD CF involved four steps. The first was the aircraft class definition, in which the bypass ratios, overall pressure ratios, and rated thrusts (i.e., sea-level static thrust) were collected for a given aircraft class. Next, these values were used to create a series of engine variants for the aircraft class and were evaluated with the EDS software to generate engine state tables for use in the Aircraft Noise Prediction Program (ANOPP). The final step of this process was to fit a model to these data, so that the difference between a given configuration and a baseline condition could be predicted. The model itself would be a function of both engine parameters and aircraft configuration, i.e., *fcn* (bypass ratio, overall pressure ratio, sea-level static thrust, FDA, FV, gear). This process is shown in the left column of Figure 1. A general form of the CF equation can be found in which *a, b, c, d,* and *e* are constants, and the remaining terms are cross-products, raised to powers (up to the fifth power) and multiplied by constants.

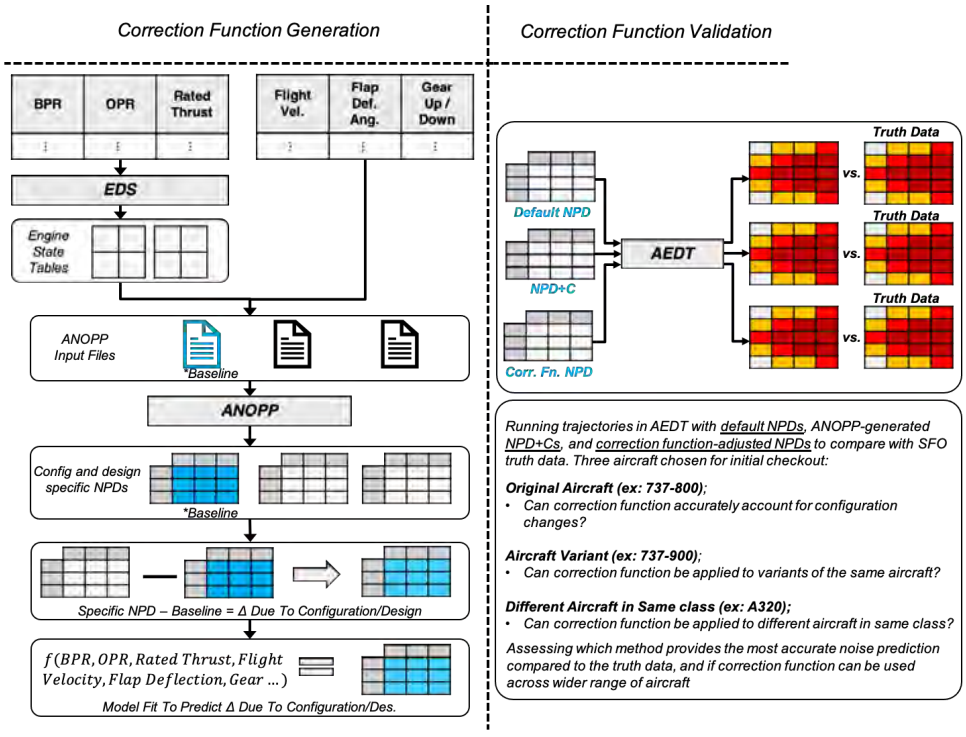

Figure 1. CF generation and validation processes.

Milestone(s)
None.

Major Accomplishments
None.

Publications
None.

Outreach Efforts
None.

Awards
None.

Student Involvement
Ameya Behere

Plans for Next Period
Continue efforts of task under Project 54.

Task 2 - Engagement with Original Equipment Manufacturers (OEMs) for Validation of the NPD+C Approach with Real Data
Georgia Institute of Technology

Objectives
The objective of this task is to engage with OEMs to potentially validate GT's CF approach to correcting the baseline NPD by using real aircraft data. Given a specific aircraft, the idea is to have an OEM provide NPD data for a variety of flight configurations, incorporating FV, FDA, and gear, and to compare the trends in the real data against predictions made by GT's correction functions.

Research Approach
Boeing agreed to engage with GT to provide limited NPD+C data for a variety of configurations for a Boeing 737-8 type aircraft. Subsequently, GT invoked the CFs for a 737-8 type aircraft by fixing the engine-level parameters to the baselines of the 737-8, as confirmed by Boeing for a specific engine–airframe combination. Values of NPD+C were computed for the exact configurations for which Boeing provided data. Subsequently, a one-to-one comparison was made between NPD corrections predicted by the CFs and the data provided by Boeing. Broadly, the trends did not unequivocally match across the entire dataset. On further investigation, we found that the potential reasons for the mismatch were likely to be due to differences in the underlying truth model (ANOPP by GT and an in-house proprietary program by Boeing) used to generate the NPD data. Moreover, Boeing noted that, because they are not typically required to generate NPD+C data for a large variety of aircraft configurations, they rely on many simplifying assumptions to speed up the analysis and decrease the computational cost. The high-fidelity analyses and actual noise measurements are exclusively relied upon to meet certification requirements. Consequently, any validation effort with GT's approach would not be likely to scale to entire fleets of aircraft.

Milestones
1. Noted that differences in underlying assumptions between truth models are likely to lead to mismatches in trends when data from OEMs are compared with predictions from GT's NPD+C correction functions
2. Noted that, given how OEMs generate limited data for varying aircraft configurations, the validation efforts will be difficult to scale across multiple aircraft

Major Accomplishments

1. Successfully engaged with Boeing in validating the NPD+C approach

Publications

None.

Outreach Efforts

Engagement of airframe manufacturers

Awards

None.

Student Involvement

Ameya Behere

Plans for Next Period

None.

Task 3 - Noise Validation Efforts with Noise Monitoring Data at the San Francisco Airport

Georgia Institute of Technology

Objective

The objective of this task is to validate the NPD+C approach by comparing modeled noise metric values to a real-world data source. The real-world data in this case come from two sources: the San Francisco airport (SFO) noise monitoring program and GT's airline partner.

Research Approach

The data from SFO consist of noise values, along with metadata including date and time, measured at several noise monitor locations. The airline data consist of flight operational quality assurance (FOQA) parameters recorded at a high sampling frequency. These two data sources were correlated so that each flight could be linked to its observed noise impact. After down-selecting flights to be modeled at the SFO airport, we developed four modeling cases for each flight. Across all four modeling cases, the ground track from the FOQA data was used. Additionally, the airport-averaged weather was used for all four cases. These cases differed in their use of the flight profiles and whether they used the default NPD in AEDT or the NPD+C approach:

1. AEDT standard arrival profile with default NPD
2. FOQA fixed-point profile with default NPD
3. AEDT standard arrival profile with NPD+C
4. FOQA fixed-point profile with NPD+C

The modeled noise metrics for all four cases were obtained and compared with the measured noise values from SFO's noise monitoring program. This comparison should indicate the accuracy of using the NPD+C instead of the default NPD. Because the NPD+C is currently being re-scoped and re-developed, this task is currently paused.

Major Accomplishments

1. Development of a process to model NPD+C in AEDT
2. Preliminary analysis of NPD+C modeled noise results from AEDT and comparison to real-world noise monitoring data

Publications

None.

Outreach Efforts
None.

Awards
None.

Student Involvement
Ameya Behere

Plans for Next Period
None.

Task 4 - Rescoping of the Problem to Focus on NPD Corrections at Low-Thrust Values
Georgia Institute of Technology

Objectives
1. Setup of ANOPP to run at low-thrust values, i.e., lower than the typical 7% thrust
2. Generation of NPD data for three aircraft in the low-thrust regime for a variety of configurations

Research Approach
The learning from the validation efforts with Boeing made GT re-focus its approach to NPD+C corrections at low-thrust values to enhance AEDT's interpolation capabilities, specifically at low-thrust values during approach. GT will continue to seek validation data, which are very challenging to find.

GT recently successfully generated new sets of NPD data for three specific aircraft, one each in the regional jet, single aisle, and twin aisle classes. Of note, the engine-level parameters were set to the baseline values for the respective aircraft. Subsequently, NPD data were generated through ANOPP with the process outlined above under Task 1 for thrust fractions, i.e., thrust levels of 3%, 7%, 9%, and 11% for a range of flap deflection angles, approach speeds, and landing gear configurations. Of note, having the engine cycle converge at thrust values lower than 7% was challenging. GT devoted substantial effort to setting up ANOPP to run at thrust values as low as 3%. Below 3% thrust, the engine cycle did not converge.

GT is currently in the process of generating the NPD+C correction functions for these low-thrust cases.

Milestones
- Developed correction functions across vehicle classes
- Validated the approach with OEM data and any potential sources of noise monitoring data

Major Accomplishments
Correction factors were refined and finalized for a range of vehicle classes and compared with OEM data and real-world noise monitoring data.

Publications
None.

Outreach Efforts
A21
Manufacturers

Awards
None.

Student Involvement

Ameya Behere

Plans for Next Period

- ASCENT Project 43 has been sunset, and all further efforts will be rolled under the Project 54 umbrella, specifically:
  - Continue engagement of the manufacturers to obtain "fit-for-purpose" application of the correction function within AEDT
  - Compare noise contours against "truth data" in the form of real-world noise observations for aircraft of the same class
  - Finalize implementation plan to AEDT
  - Complete an airport-level study to determine the impact on the day–night average sound level contours

References

AEDT. (2016). Aircraft Environmental Design Tool (2.c) [Computer software]. FAA, Washington, DC.

ANOPP. (1998). Aircraft noise prediction program (1.0) [Computer software]. NASA, Langley, VA.

Aratani, L. (2018, August 9). D.C. residents suffer major setback in fight over plane noise from National Airport. *Washington Post*. https://www.washingtonpost.com/news/dr-gridlock/wp/2018/08/09/d-c-residents-suffer-major-setback-in-fight-over-plane-noise-from-national-airport/.

Federal Aviation Administration (FAA). (Retrieved December 2019) *Aircraft noise issues*. United States Department of Transportation.

Page, J. A., Hobbs, C. M., Plotkin, K. J., Stusnick, E., & Shepherd, K. P. (2000). *Validation of aircraft noise prediction models at low levels of exposure* (Report No. CR-2000-210112). National Aeronautics and Space Administration.

Plotkin, K. J., Page, J. A., Gurovich, Y., & Hobbs, C. M. (2013). *Detailed weather and terrain analysis for aircraft noise modeling* (Report No. 13-01). John A. Volpe National Transportation Systems Center.

Raymer, D. P. (2006). *Aircraft design: A conceptual approach* (4th ed.). AIAA, Reston, VA.

John A. Volpe National Transportation Systems Center. (2008). *Integrated Noise Model (INM) version 7.0 technical manual* (Report No. FAA-AEE-08-01).

Federal Aviation Administration. (2016). *Aviation Environmental Design Tool (AEDT) (2c) technical manual* (Report No. DOT-VNTSC-FAA-16-11).

John A. Volpe National Transportation Systems Center. (2017). *Aviation Environmental Design Tool (AEDT) (2d) technical manual* (Report No. DOT-VNTSC-FAA-17-16).

Project 044 Aircraft Noise Abatement Procedure Modeling and Validation

Massachusetts Institute of Technology

Project Lead Investigator

R. John Hansman
T. Wilson Professor of Aeronautics & Astronautics
Department of Aeronautics & Astronautics
Massachusetts Institute of Technology
Room 33-303
77 Massachusetts Ave
Cambridge, MA 02139
617-253-2271
rjhans@mit.edu

University Participants

Massachusetts Institute of Technology (MIT)

- P.I.: Professor R. John Hansman
- FAA Award Number: 13-C-AJFE-MIT, Amendment Nos. 050, 057, and 073
- Period of Performance: September 1, 2018 to September 30, 2023
- Tasks:
    1. Evaluate general approaches to aircraft noise validation
    2. Develop validation approach options
    3. Develop flight test plans
    4. Perform initial experimental runs on targets of opportunity
    5. Evaluate experimental results and implications for advanced operational flight procedure noise modeling and low-noise procedures

University of California, Irvine (UCI; sub-award from MIT)

- P.I.: Professor Jacqueline Huynh
- Award Number: MIT Subaward Purchase Order No. S5171-PO 523807
- Period of Performance: September 1, 2020 to September 30, 2023
- Tasks:
    1. Evaluate general approaches to aircraft noise validation
    2. Develop validation approach options
    3. Develop flight test plans
    4. Perform initial experimental runs on targets of opportunity
    5. Evaluate experimental results and implications for advanced operational flight procedure noise modeling and low-noise procedures

Project Funding Level

The FAA provided $720,000 in funding. A total of $720,000 in matching funds was provided, approximately $125,000 from MIT and $595,000 from the Massachusetts Port Authority.

Investigation Team

- Professor R. John Hansman – P.I., MIT (Tasks 1-5)
- Professor Jacqueline Huynh – P.I., UCI (Tasks 1-5)

- Clement Li - graduate student, MIT (Tasks 1-5)
- Sandro Salgueiro - graduate student, MIT (Tasks 1-5)
- Ara Mahseredjian - graduate student, MIT (Tasks 1-5)

Project Overview

This project uses empirical noise data to develop validation methods from noise and flight surveillance datasets and improve existing noise models. Field measurements of aircraft noise on approach and departure have historically shown significant variation (on the order of 10 dB), which have traditionally been attributed to factors such as varied power settings, aircraft configuration differences, and propagation effects. Recent analyses in this and other ASCENT projects have attempted to account for these factors but have been constrained by limited detailed flight data. This project explores approaches to combine emerging sources of flight data from flight data recorders and other sources such as Automatic Dependent Surveillance-Broadcast (ADS-B) with current and emerging networks of ground noise monitors, to validate or improve aircraft noise models and to validate proposed noise abatement procedures. The rise of data mining techniques has substantially enabled new insights and modeling capabilities based on the use of large datasets without requiring full a priori knowledge of all relevant physics. The development of advanced data mining approaches applied to noise modeling is expected to provide insight into aircraft noise prediction for refining or validating noise models, and developing strategies for noise mitigation, through either new aircraft technologies or operational changes. Furthermore, improved noise modeling capabilities would enable more informed decision-making for stakeholders considering the options and consequences of operational or technological changes, thus facilitating the minimization of noise impacts on communities. Because noise is becoming an increasingly important factor in operational decisions regarding airports in the National Airspace System, an accurate understanding of noise impacts is necessary to minimize unnecessary disruptions to, or inefficiencies in, National Airspace System operations.

Task 1 - Evaluate General Approaches to Aircraft Noise Validation

Massachusetts Institute of Technology
University of California, Irvine

Objectives

This goal of this task is to evaluate the different options for validation of the Aircraft Noise Prediction Program (ANOPP) source component models and to confirm noise reductions from proposed low-noise procedures. Approaches to experimental design were considered, including dedicated engineering flight trials involving parametric sweeps of velocity and aircraft configuration at various power conditions. This process would involve collaborating with airline operators, who would need to be willing to fly trials of procedures, and air traffic control, which would need to approve the procedures. A ground measurement system would need to be in place under the departure tracks.

Potential monitoring approaches will also be considered, including distributed microphone arrays or single microphone installations, as well as potential phased-array microphone configurations. In addition, alternative flight data sources will be obtained, either through airline sources or through available surveillance data. Sources of noise data from existing and emerging noise monitoring systems will be identified. Boston Logan International Airport (BOS) has agreed to provide data, and additional airports will be approached to participate in the effort. Emerging open-source and community noise monitoring systems such as those being developed under ASCENT Project 53 will also be investigated. Opportunities for collaboration will be explored, with a focus on providing correlated flight data and noise datasets.

This task will use a systems approach and will explore options with potential collaborators regarding experimental opportunities to validate research concepts.

Research Approach

- Evaluate the different options for validation of the ANOPP source component models, and confirm any noise reductions from proposed procedures
- Identify potential existing data sources for noise validation
- Model aircraft flight profiles by using existing surveillance (e.g., ADS-B or Airport Surface Detection Equipment, Model-X) data to generate noise estimates (Readily available surveillance data are easier and less expensive to acquire than Flight Data Recorder (FDR) data and dedicated flight tests.)
- Evaluate flight profiles to understand why some procedures are quieter than others

Milestones

- Identified Seattle–Tacoma International Airport (SEA) and Boston Logan International Airport (BOS) noise monitor networks as potential sources of noise data for validation.
- Identified the OpenSky surveillance database as a potential source of flight procedure data for noise validation.

Major Accomplishments

- Approach and departure ADS-B and noise monitoring data were collected for 2 months at Seattle–Tacoma International Airport (SEA).
- A framework was developed to generate flight profiles by using raw ADS-B and atmospheric data. Noise monitor recordings were correlated with ADS-B data.
- Flight profiles were generated from raw ADS-B data for various departures and arrivals at SEA. Flight profiles were used to identify factors potentially significantly contributing to noise measurement variation.
- Quieter flyover cases were analyzed, and trends in aircraft altitude, airspeed, and lateral position were identified.
- Sources of weather data as a function of altitude were identified to make atmospheric absorption corrections for noise modeling validation.

Publications

Published conference proceedings

Jensen, L., Thomas, J., Brooks, C., Brenner, M., & Hansman, R. J. (2017). *Analytical approach for quantifying noise from advanced operational procedures* [Presentation]. European Air Traffic Management Research and Development Seminar. Seattle, Washington.

Reynolds, T., Sandberg, M., Thomas, J., & Hansman, R. J. (2016). *Delayed deceleration approach noise assessment* [Presentation]. 16th AIAA Aviation Technology, Integration, and Operations Conference, Washington, DC.

Salgueiro, S., Thomas, J., Li., C. & Hansman, R. J. (2021). *Operational noise abatement through control of climb profile on departure* [Presentation]. AIAA Scitech 2021 Forum, Washington, DC. https://doi.org/10.2514/6.2021-0007.

Salgueiro, S., Huynh, J., Li., C. & Hansman, R. J. (2022). *Aircraft Takeoff and Landing Weight Estimation from Surveillance Data* [Presentation]. AIAA Scitech 2022 Forum, San Diego, CA. doi: 10.2514/6.2022-1307.

Thomas, J., Jensen, l., Brooks, C., Brenner, M., & Hansman, R. J. (2017). *Investigation of aircraft approach and departure velocity profiles on community noise* [Presentation]. AIAA Aviation 2017 Forum, Grapevine, TX.

Thomas, J., Yu, A., Li., C., Maddens Toscano, P., & Hansman, R. J. (2019). *Advanced operational procedure design concepts for noise abatement* [Presentation]. 13th USA/Europe Air Traffic Management Research and Development Seminar, Vienna, Austria.

Thomas, J., Yu, A., Li, C., Toscano, P., & Hansman, R. J. (2019). *Advanced operational procedure design concepts for noise abatement* [Presentation]. 13th USA/Europe Air Traffic Management Research and Development Seminar, Vienna, Austria.

Thomas, J., & Hansman, R. J. (2020). *Modeling and assessment of delayed deceleration approaches for community noise reduction* [Presentation]. AIAA Aviation Forum, Dallas, TX.

Yu, A., & Hansman, R. J. (2019). *Approach for representing the aircraft noise impacts of concentrated flight tracks* [Presentation]. AIAA Aviation Forum 2019, Dallas, TX. doi: 10.2514/6.2019-3186

Written reports

Jensen, L. & Hansman, R. J. (2018). *Data-driven flight procedure simulation and noise analysis in a large-scale air transportation system* (Report No. ICAT-2018-02). Massachusetts Institute of Technology, Cambridge, MA.

Jensen, L., O'Neill, G., Thomas, J., Yu, A., & Hansman, R. J. (2018). *Block 1 procedure recommendations for Logan Airport community noise reduction* (Report No. ICAT-2017-08). Massachusetts Institute of Technology, Cambridge, MA.

Thomas, J., & Hansman, R. J. (2017). *Modeling performance and noise of advanced operational procedures for current and future aircraft* [S. M. thesis, Massachusetts Institute of Technology]. DSPace@MIT. https://dspace.mit.edu/handle/1721.1/108937

Thomas, J., & Hansman, R. J. (2020). *Systems Analysis of Community Noise Impacts of Advanced Flight Procedures for Conventional and Hybrid Electric Aircraft* [Ph.D. thesis, Massachusetts Institute of Technology]. DSpace@MIT. https://dspace.mit.edu/handle/1721.1/125995

Thomas, J., & Hansman, R. J. (2020). *Evaluation of the impact of transport jet aircraft approach and departure speed on community noise* (Report No. ICAT-2020-03). Massachusetts Institute of Technology, Cambridge, MA.

Yu, A., & Hansman, R. J. (2019). *Aircraft noise modeling of dispersed flight tracks and metrics for assessing impacts* [S. M.

thesis, Massachusetts Institute of Technology]. DSpace@MIT. https://hdl.handle.net/1721.1/122382

Mahseredjian, A., Huynh, J., & Hansman, R. J. (2022). *A Data-Driven Approach to Departure and Arrival Noise Abatement Flight Procedure Development* [S. M. thesis, Massachusetts Institute of Technology]. DSpace@MIT. https://hdl.handle.net/1721.1/144311

Outreach Efforts

- September 28, 2021: presentation to Stanford
- Collaborated with Port of Seattle to obtain noise data for arrivals and departures over several months
- Biweekly teleconferences and meetings with FAA Technical Monitors
- In-person outreach and collaboration with Massport, operator of BOS, and ASCENT Advisory Board members
- Presentations at the biannual ASCENT Advisory Board meetings

Awards

None

Student Involvement

Graduate students have been involved in all aspects of this research in terms of analysis, documentation, and presentation.

Plans for Next Period

The next phase of the project will continue outreach to other projects using noise monitor data in airport noise validation research.

Task 2 – Develop Validation Approach Options

Massachusetts Institute of Technology

Objectives

On the basis of the results of Task 1 and initial discussions with potential collaborators (measurement experts, model developers, manufacturers, operators, and test locations), one or more validation options will be identified. Targets of opportunity will be explored in which noise measurements may supplement other planned flight trials. For each option, the potential advantages and disadvantages will be identified, and preliminary flight test plans will be developed in coordination with the identified collaborators and in consultation with subject-matter experts such as NASA. Potential advantages include the willingness of operators or collaborators to participate and provide test resources, including aircraft and measurement systems. Other factors include measurement system resolution and the discrimination of noise sources. Timing and location may also be considered. On the basis of this analysis, recommendations for the next steps will be made.

Research Approach

- Identify methods to correct variations in modeled noise due to flap setting, aircraft weight, and ambient atmospheric conditions; apply these methods to approaches at BOS and SEA
- Acquire ADS-B data from the OpenSky Network and atmospheric data from NOAA High-Resolution Rapid Refresh; use these data to estimate weight from true airspeed and atmospheric attenuation from relative humidity
- Model noise at various flap configurations to identify the noise impact of high-lift devices

Milestones

- Noise was modeled at various flap configuration settings for several approach procedures.
- Developed method to relate OpenSky surveillance operational data to atmospheric data and noise monitor data at particular time stamps.

Major Accomplishments

- Demonstrated the impacts of aircraft configuration and relative humidity on modeled and measured noise over noise monitors of interest at SEA
- Developed a data-driven approach to understanding departure noise as a function of various operational, weather, and carrier factors

- Presented data driven approach results at the 2022 InterNoise conference and in a 2022 Journal of Aircraft manuscript
- Demonstrated the noise benefit of delayed-deceleration approaches using empirical data; analyzed flyovers of various monitors at BOS and SEA, and demonstrated a correlation between the fastest flyovers, flying at indicated airspeeds consistent with clean or almost-clean flap configurations, and the quietest noise monitor recordings

Publications

Peer-reviewed journal publications

Thomas, J., & Hansman, R. J. (2019). Framework for analyzing aircraft community noise impacts of advanced operational flight procedures. *Journal of Aircraft*, *6*(4), 1407-1417. doi: 10.2514/1.C035100

Huynh, J., Mahseredjian, A., & Hansman, R. J. (2022). Delayed Deceleration Approach Noise Impact and Modeling Validation. *Journal of Aircraft*, *59*(4), 992-1004. doi:10.2514/1.C036631

Published conference proceedings

Mahseredjian, A., Thomas, J., & Hansman, R. J. (2021). *Advanced procedure noise model validation using airport noise monitor networks* [Presentation]. Inter-Noise 2021, Washington, DC. doi: 10.3397/IN-2021-2842.

Mahseredjian, A., Huynh, J., & Hansman, R. J. (2022). *Analysis of community departure noise exposure variation using airport noise monitor networks and operational ADS-B data* [Presentation]. Inter-Noise 2022, Glasgow, Scotland.

Outreach Efforts

- Biweekly teleconferences and meetings with FAA Technical Monitors
- In-person outreach and collaboration with Massport, operator of BOS, and ASCENT Advisory Board members
- Presentations at the biannual ASCENT Advisory Board meetings

Awards

None

Student Involvement

Graduate students have been involved in all aspects of this research in terms of analysis, documentation, and presentation.

Plans for Next Period

The next phase will involve determining additional methods and data for evaluating aircraft noise variation, such as procedure type (RNAV versus ILS approaches, for example).

Task 3 - Develop Flight Test Plans

Massachusetts Institute of Technology
University of California Irvine

Objectives

For the recommended validation options identified in Task 2, detailed flight test plans will be developed. Flight test plans for dedicated engineering flights would involve detailed planning of the speed, configuration, and thrust of each trial. Test plans for flight trials in collaboration with airline operators would focus on documenting the flown profiles to analyze the associated data measurements. Opportunity exists in both types of trials to validate not only the expected effects of aircraft speed versus noise in the analysis models but also the expected noise impacts of procedures, including delayed deceleration approaches, steeper approaches, and continuous approaches.

Research Approach

- Develop flight test plans, where appropriate, for the validation of low-noise procedures
- Collaborate with airline operators and industry to determine appropriate data collection for trial flight tests

Milestones

- Sought partnerships with operators for FDR data (MIT was unable to obtain FDR data because of operator restrictions on the sharing of flight data.)

Major Accomplishments

- Determined that validation for low-noise flight procedures, such as the delayed deceleration approach, can be performed by using available surveillance and noise monitoring data, if reasonable assumptions regarding the weight, flap and slat configuration, and atmospheric attenuation are made
- Examined additional lower-noise departure procedures in 2 months of noise monitoring data from SEA

Publications

None

Outreach Efforts

- Biweekly teleconferences and meetings with FAA Technical Monitors
- In-person outreach and collaboration with Massport, operator of BOS, and ASCENT Advisory Board members
- Presentations at the biannual ASCENT Advisory Board meetings

Awards

None

Student Involvement

Graduate students have been involved in all aspects of this research in terms of analysis, documentation, and presentation.

Plans for Next Period

The next phase of this project will evaluate the departure and arrival noise of various aircraft at SEA from a full year of noise monitor recordings from Boeing 737-800, Airbus A320, and Boeing 777 flights.

Task 4 - Initial Experimental Runs on Targets of Opportunity

Massachusetts Institute of Technology
University of California Irvine

Objective

If targets of opportunity are identified in Task 2 that would occur within the period of performance of this proposed research, initial experimental runs will be conducted after consultation with the FAA Office of Environment and Energy and other relevant parties.

Research Approach

- Document procedural recommendations to enable flight trials
- Meet with airline technical pilots and representatives from aircraft manufacturers to discuss operational constraints and test opportunities
- Develop test plans and protocols for potential flight trials
- Develop test plans and protocols for potential noise measurement campaigns
    - Specific flight test locations
    - Operational field measurements

Milestones

- Conventional and delayed deceleration approach procedures were observed in surveillance data at BOS and SEA and were identified as sufficient for noise analysis instead of dedicated flight test plans.

Major Accomplishments

- Instead of using dedicated flight test plans, approach flights from the surveillance data were grouped by altitude and analyzed with varied speed, configuration, and thrust. The noise monitor readings from these flights were then compared. For departures, measured noise levels versus weight, thrust, speed, altitude, weather factors, and airlines were examined in 2D correlations.
- For approach procedures, flights for which the speeds were more likely to have been in the clean configuration when they flew over the monitors were shown to correlate with lower recorded noise levels than flights that were more likely to have been in a dirty configuration when they flew over the monitors.
- For departure procedures, aircraft that achieved higher altitudes early in the flight profiles were found to correlate with lower measured noise levels.

Publications

Peer-reviewed journal publications

Thomas, J., & Hansman, R. J. (2021). Modeling of delayed deceleration approaches for community noise reduction. *Journal of Air Transportation, 29*(3), 127-136. doi: 10.2514/1.D0237

Outreach Efforts

- Biweekly teleconferences and meetings with FAA Technical Monitors
- In-person outreach and collaboration with Massport, operator of BOS, and ASCENT Advisory Board members
- Presentations at the biannual ASCENT Advisory Board meetings

Awards

- 2021, 2020 AIAA Air Transportation Systems Best Student Paper Award “Modeling, Assessment, and Flight Demonstration of Delayed Deceleration Approaches for Community Noise Reduction” (AIAA-2020-2874) by Jacqueline L. Thomas and R. John Hansman

Student Involvement

Graduate students have been involved in all aspects of this research in terms of analysis, documentation, and presentation.

Plans for Next Period

In the next phase, the validation approaches developed in the previous phase applied to one year’s worth of noise measurements and operations data will be assessed. A main goal of the upcoming work is to understand the causes of variation in both measured departure and arrival noise. The approach to understanding noise level variation uses a data-driven analysis framework for examining the impacts of various operational, weather, and airline factors on noise levels. Flight profiles and noise models will be generated for these cases of interest. Different data-mining approaches such as multivariate correlations, clustering, and machine learning will be applied to the data to examine trends in variables affecting aircraft noise, including those due to aircraft weight, thrust, distance to monitor, airspeed, ambient atmospheric conditions, and compounding factors.

Task 5 - Evaluate Experimental Results and Implications for Advanced Operational Flight Procedure Noise Modeling and Low-Noise Procedures

Massachusetts Institute of Technology
University of California Irvine

Objectives

Contingent on data availability from Task 4 or other data identified as part of the experimental approach and discussions with collaborators, this task, in coordination with NASA, will involve the following:

- Evaluating Advanced Operational Flight Procedure Noise Modeling relative to experimental results
- Identifying discrepancies requiring correction
- Determining whether the results and data are sufficient to improve discrepancies, or whether continued validation and testing are required

The implications for Advanced Operational Flight Procedure Noise Modeling from the data will be evaluated.

Validation of procedures, such as delayed deceleration approaches, will also create opportunities for the development of further low-noise procedures.

Research Approach

- Treat noise monitoring data from SEA and BOS as experimental data, which could serve as a benchmark for comparison against ANOPP component-based noise models
- Model departure noise for various departures from SEA, and identify the characteristics of the quietest departures; determine whether learning could be applied to future departure noise abatement procedure designs

Milestones

- Noise monitor recordings versus modeled results were determined to be acceptable approaches for comparing measured noise data to noise models when weather factors and operational factors were taken into account.

Major Accomplishments

- Noise models demonstrated similar trends to monitor recordings for approach procedures when proper assumptions regarding flap configuration were made. Both speed and configuration were shown to influence the noise model results.
- Aircraft weight and thrust levels were shown to influence the noise modeling results for approach procedures.
- Aircraft altitude and thrust levels were found to have the strongest correlations with measured noise for the procedures examined.
- Weather factors such as relative humidity, temperature, and wind magnitude and direction were found to have some correlations, albeit weaker, with the measured noise levels on departure.

Publications

Published conference proceedings

Thomas, J., Mahseredjian, A., & Hansman, R. J. (2021). *Delayed deceleration approach procedure noise modeling validation using noise measurements and radar data* [Paper presentation]. AIAA Aviation 2021 Forum, Virtual Meeting. doi: 10.2514/6.2021-2135.

Outreach Efforts

- Biweekly teleconferences and meetings with FAA Technical Monitors
- In-person outreach and collaboration with Massport, operator of BOS, and ASCENT Advisory Board members
- Presentations at the biannual ASCENT Advisory Board meetings

Awards

- 2018 Department of Transportation/FAA COE Outstanding Student of the Year Award to Jacqueline Thomas

Student Involvement

Graduate students have been involved in all aspects of this research in terms of analysis, documentation, and presentation.

Plans for Next Period

The next phase of this project will evaluate how different variables identified in the previous tasks influence aircraft noise and will inform the design of future advanced flight procedures intended to reduce aircraft noise.

Project 046 Surface Analysis to Support AEDT Aircraft Performance Model (APM) Development

Massachusetts Institute of Technology and Massachusetts Institute of Technology Lincoln Laboratory

Project Lead Investigator

Hamsa Balakrishnan
William E. Leonhard (1940) Professor of Aeronautics and Astronautics
Massachusetts Institute of Technology
77 Massachusetts Ave., 33-328
Cambridge, MA 02139
617-253-6101
hamsa@mit.edu

University Participants

Massachusetts Institute of Technology (MIT)

- P.I.: Prof. Hamsa Balakrishnan
- FAA Award Number: 13-C-AJFE-MIT, Amendment Nos. 021, 035, 044, 047, 063, 068, 077, and 092
- Period of Performance: July 7, 2016 to February 13, 2023
- Task:
    1. AIR: Fuel Flow Rates for Jet-Powered Commercial Aircraft Taxi Operations

MIT Lincoln Laboratory (via internal university allocation from MIT Main Campus)

- P.I.: Dr. Thomas G. Reynolds
- Award Number: Cost Object No. 1276191
- Period of Performance: Sept 1, 2019 to February 13, 2023
- Task:
    1. Develop SAE International Aerospace Information Report (AIR) "Fuel Flow Rates for Jet-Powered Commercial Aircraft Taxi Operations" to document recommendations from ASCENT46 project.

Project Funding Level

This project received $700,000 in FAA funding and $700,000 in matching funds from MIT.

Investigation Team

- Prof. Hamsa Balakrishnan, co-P.I. – MIT (Task 1)
- Dr. Tom Reynolds, co-P.I. - MIT Lincoln Laboratory (Task 1)

Project Overview

The AIR document summarizes prior empirical findings to recommend a modified baseline fuel flow rate model for jet-powered commercial aircraft during taxi operations on the airport surface that better reflects operational values (Chati, 2018; Clemons et al., 2018). Existing standard modeling approaches have been found to significantly overestimate the taxi fuel flow rate; therefore, application of a modified multiplicative factor to these existing approaches is recommended to make them more accurate. Results from the analysis of operational flight data have been reported, which form the basis for the modeling enhancements being recommended.

Task 1 – Develop AIR document "Fuel Flow Rates for Jet-Powered Commercial Aircraft Taxi Operations"

Massachusetts Institute of Technology
Massachusetts Institute of Technology Lincoln Laboratory

Objectives

The objective of this research project is to identify and evaluate methods for improving airport taxi performance modeling in the Aviation Environmental Design Tool (AEDT) to better reflect actual operations (Clemons et al., 2018). This objective is being met through the analysis of relevant data sources, including surface surveillance (Airport Surface Detection Equipment, ASDE-X), Aviation System Performance Metrics taxi time, Flight Data Recorder (FDR), and air quality monitoring datasets. Prior phases of the ASCENT46 project have identified first-order enhancements to the AEDT Aircraft Performance Model for surface operations. Specific improvement areas include enhanced baseline taxi fuel flow models; improved taxi times at different airports; and estimation of pre-taxi engine and auxiliary power unit fuel burn, and a detailed assessment of surface operations and associated air quality impacts at Los Angeles International Airport, because of the extensive data availability at that location. These enhancements were described in prior reports. Recently, we have documented our work on enhanced taxi fuel flow models in an SAE Aerospace Information Report (AIR), in preparation to release it for a vote by the SAE A-21 Committee. The remainder of this report consists of the proposed AIR.

Research Approach

Introduction

Models of aircraft taxi operations on the airport surface and associated fuel flow and emissions are used for several purposes, such as assessing the impacts of changes to operational procedures, airport infrastructure and fleet mixes, and conducting environmental studies. A standard method of modeling jet aircraft taxi fuel flow, for example, in the FAA's AEDT (FAA, 2022), is to assume a constant engine-specific thrust level (and resulting fuel flow rate) determined by applying a correction factor for installation effects to engine manufacturer certification data (ICAO, n.d.). However, the resulting estimate of the fuel flow rate can significantly differ from the actual characteristics during operational conditions for a given aircraft (Nikoleris et al., 2011). This difference can be due to a variety of factors, such as engine age (as the engine ages, the amount of fuel that it burns changes) and pilot techniques (such as "riding the brakes" instead of throttling down the engines when coming to a stop). The AIR analyzes operational data to develop more realistic fuel flow models for taxi operations to improve the accuracy of airport surface fuel and emissions calculations.

Current Taxi Fuel Flow Modeling

Figure 1 shows a typical fuel flow rate profile (post-pushback and engine start) during taxi operations. This profile is from a common narrow-body twin engine commercial aircraft. Although the fuel flow magnitudes vary with aircraft type, the shape is representative of most jet-powered commercial aircraft. The fuel flow rate profile can be divided into two distinct types of regions: baseline regions (two of which are identified by dashed-line ovals) and fuel flow spike regions (one of which is identified with a dotted-line oval). The baseline fuel flow regions are characterized by a nearly constant (low variation) fuel flow rate over extended time intervals under normal moving taxi conditions, and the fuel flow spike regions correspond to the periods of increased thrust needed to re-start movement after a period of being stopped.

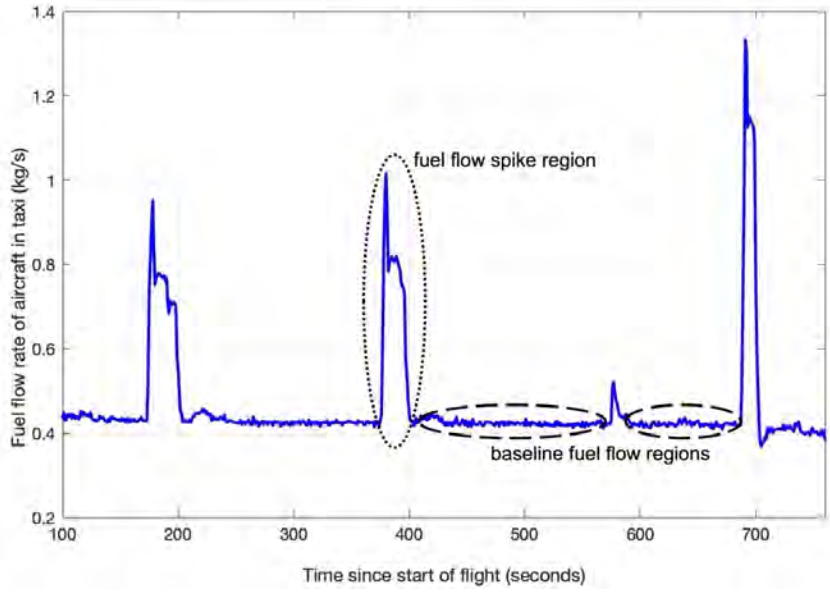

Figure 1. Typical fuel flow rate profile during taxi operations for twin-engine narrow-body commercial aircraft.

Although the spikes correspond to periods of higher thrust and higher fuel flow rates, more than 90% of the total taxi fuel consumption occurs during periods when the fuel flow rate is close to the baseline (flat) value (Chati, 2018). Therefore, the recommendations in this technical manuscript relate to the baseline taxi fuel flow rate. The spikes in fuel flow rate are important for emissions and noise calculations, and contribute to the variability in fuel burn between flights. Future studies could investigate these time periods further.

Standard fuel flow modeling approaches such as those documented in SAE AIR6183 (SAE, 2022), which have been extended for use in taxi operations in AEDT (FAA, 2022), use the Boeing Fuel Flow Method (BFFM2). The form of BFFM2 used in FAA (2022) for the taxi phase is given by:

$$\dot{m}_f = B_m \dot{m}_{f_{ICAO}} \delta \theta^{-3.8} e^{-0.2M^2} \quad (1)$$

where $\dot{m}_f$ is the fuel flow rate in kg/s at non-reference conditions, B_m is a dimensionless adjustment factor, $\dot{m}_{f_{ICAO}}$ is the fuel flow rate in reference (certification 7% idle power setting) conditions, as contained in the ICAO Aircraft Engine Emissions Databank (ICAO, n.d.), δ is the static pressure ratio (ambient to sea level), θ is the static temperature ratio (ambient to sea level), and M is the Mach number. In DuBois & Paynter (2006) and FAA (2022), an adjustment factor of 1.1 is used in the taxi mode to account for engine installation effects. As in BFFM2, this equation is normally used to correct at-altitude fuel flow to sea-level conditions and vice versa. Of note, in the taxi phase, the Mach number is close to 0, and the temperature and pressure ratios for most operations are close to 1. That is, the taxi phase fuel flow rate approximates to:

$$\dot{m}_{f_{Taxi}} \approx 1.1 \dot{m}_{f_{ICAO\ 7\%\ Setting}} \quad (2)$$

Enhanced Taxi Fuel Flow Modeling

To compare this current model to the fuel flow rates during actual operations, Chati (2018) and Clemons et al. (2018) conducted ordinary least squares (OLS) regression of baseline fuel flow rates per engine during taxi for different aircraft and engine types, to obtain a model that is consistent with BFFM2 (Equation 1). For this purpose, FDR data containing operations from a major European carrier and a major Middle Eastern carrier from 2016 were obtained (full details in Chati, 2018). Consequently, the narrow-body aircraft flights in this dataset were to or from airports primarily in Europe and the Middle East, whereas the wide-body aircraft included many flights to or from major international airports in the United States. The FDR dataset reported key aircraft and engine parameters (including fuel flow rates) as time-series data at a 1-Hz sampling rate.

The flights in the FDR data set were split into two disjoint sets, one used to build the model and the other used as the test data set. The resulting proposed enhanced models for the (anonymized) aircraft/engine types available in the dataset are shown in Table 1. The right side of Table 1 shows the resulting errors for the proposed OLS-based model compared with the estimates based on the original model (Equation 1 with $B_m = 1.1$) for the test data set. The mean percentage and absolute errors are substantially reduced with the OLS-based model. The original model is seen to be a significant overestimate relative to the values observed in operational data. Furthermore, the median value of the multiplicative constant estimated from FDR data across the aircraft/engine types is calculated to be 0.80. Of note, this proposed value represents both engine installation effects and (most importantly for this application) the actual operational power settings of aircraft during airport taxiing and idling conditions. In the SAE AIR, we also presented a validation of these findings using different data sources.

Table 1. Proposed models for mean taxi fuel flow rate built from operational FDR data and error performance relative to the existing model in AEDT (Clemons et al., 2018).

Aircraft/engine type (number of flights available for training)	**Proposed model** (θ & δ terms were close to unity and are omitted)	**Mean error (%): estimated − actual**		**Mean absolute error**	
		Proposed model	**Original model**	**Proposed model**	**Original model**
Narrow-body twin engine 1 (103)	0.81 $\dot{m}_f$	1.0	36.3	13.3	39.4
Narrow-body twin engine 2 (46)	0.80 $\dot{m}_f$	3.8	47.1	14.9	50.1
Wide-body twin engine 1 (117)	0.78 $\dot{m}_f$	−3.0	36.4	5.8	39.1
Wide-body twin engine 2 (81)	0.75 $\dot{m}_f$	−2.2	42.3	3.1	43.1
Wide-body four engine 1 (37)	1.02 $\dot{m}_f$	−0.7	7.8	9.1	12.5
Twin engine regional jet 1 (95)	0.97 $\dot{m}_f$	0.1	17.7	5.5	19.3

Summary and Recommendations

The analyses presented in this report indicate that the current commonly used baseline taxi fuel flow rate model (FAA, 2022), namely:

$$\dot{m}_{f_{Taxi}} = B_m \dot{m}_{f_{ICAO\ 7\%\ Setting}} \quad (3)$$

where $B_m = 1.1$ for the taxi mode, to represent installation effects, results in a significant overestimation of the baseline taxi fuel flow rates relative to operationally observed values. Considering the findings of the analyses of the operational datasets, the median value of the estimated multiplicative factor across all aircraft types considered was found to be 0.80, including both installation and operational factors. Therefore, standard aircraft taxi fuel flow models are recommended to be modified to use an additional taxi fuel flow rate adjustment factor $B_f = 0.80/1.1 = 0.73$, thus yielding a new taxi fuel flow rate model:

$$\dot{m}_{f_{Taxi}} = B_m B_f \dot{m}_{f_{ICAO\ 7\%\ Setting}} \quad (4)$$

where $B_m = 1.1$ accounts for installation effects as in the existing model, and the new multiplicative factor $B_f = 0.73$ accounts for operational effects, such that the product $B_m B_f = 0.80$, in agreement with the recommendations from this analysis.

Milestones

We have primarily worked on the SAE A-21 report and are providing support in the implementation of a new queuing model within AEDT. We are also preparing for the final report.

Major Accomplishments

The AIR document described in this report was recently approved by SAE Committee A21 for adoption as a new SAE standard.

Publications

None.

Outreach Efforts

None.

Awards
None.

Student Involvement
None.

Plans for Next Period
We will continue preparing for closing out this project. The Period of Performance ends on February 13, 2023.

References
Clemons, E., Reynolds, T., Badrinath, S., Chati, Y., & Balakrishnan, H. (2018, June 25). Enhancing aircraft fuel burn modeling on the airport surface. *2018 Aviation Technology, Integration, and Operations Conference*. 2018 Aviation Technology, Integration, and Operations Conference, Atlanta, Georgia. Doi: 10.2514/6.2018-3991

Chati, Y.S. (2018). *Statistical Modeling of Aircraft Engine Fuel Burn* [Ph.D. Thesis, Department of Aeronautics and Astronautics, Massachusetts Institute of Technology] https://dspace.mit.edu/handle/1721.1/115658.

FAA. (2022). *Aviation Environmental Design Tool (AEDT), Version 3e, Technical Manual.* https://aedt.faa.gov/Documents/AEDT3e_TechManual.pdf.

ICAO. (2023). *Aircraft Engine Emissions Databank*. https://www.easa.europa.eu/domains/environment/icao-aircraft-engine-emissions-databank.

Nikoleris, T., Gupta, G., & Kistler, M. (2011). Detailed estimation of fuel consumption and emissions during aircraft taxi operations at Dallas/Fort Worth International Airport. *Transportation Research Part D: Transport and Environment*, *16*(4), 302–308. Doi: 10.1016/j.trd.2011.01.007

SAE. (2022). *Procedures for the Calculation of Airplane Fuel Consumption* (Publication No. AIR6183). https://www.sae.org/standards/content/air6183/.

DuBois, D., & Paynter, G. C. (2006). *"Fuel flow method2" for estimating aircraft emissions*. 2006-01-1987. Doi: 10.4271/2006-01-1987

Project 47 Clean-Sheet Supersonic Aircraft Engine Design and Performance

Massachusetts Institute of Technology

Project Lead Investigator

Prof. Steven R. H. Barrett
Professor of Aeronautics and Astronautics
Department of Aeronautics and Astronautics
Massachusetts Institute of Technology
77 Massachusetts Avenue
Cambridge, MA 02139
617-452-2550
sbarrett@mit.edu

University Participants

Massachusetts Institute of Technology (MIT)

- P.I.: Prof. Steven R. H. Barrett
- FAA Award Number: 13-C-AJFE-MIT, Amendment Nos. 052, 059, 074, 076, 090, and 106
- Period of Performance: March 29, 2019 to August 31, 2023 (with the exception of funding and cost-share information, this report covers the period from October 1, 2021 to September 30, 2022)
- Tasks:
    1. Evaluate the impact of improved technology on relative performance benefits of clean-sheet and derivative engines
    2. Evaluate the impact of advanced take-off trajectories for supersonic transport (SST) using variable noise reduction systems (VNRS) on community noise

Project Funding Level

This project received $1,250,000 in FAA funding and $1,250,000 in matching funds. Sources of match are approximately $288,000 from MIT, plus third-party in-kind contributions of $177,000 from Byogy Renewables Inc., $634,000 from NuFuels LLC, and $151,000 from Savion Aerospace Corporation.

Investigation Team

- Prof. Steven Barrett - P.I. (Tasks 1 & 2)
- Dr. Raymond Speth - co-P.I. (Tasks 1 & 2)
- Dr. Choon Tan - co-P.I. (Tasks 1 & 2)
- Dr. Jayant Sabnis - co-investigator (Tasks 1 & 2)
- Mr. Prakash Prashanth - graduate student (Task 1)
- Mr. Laurens Voet - graduate student (Task 2)
- Mr. Wyatt Giroux - graduate student (Task 1)

Project Overview

Engines for supersonic aircraft, compared with those for subsonic aircraft, present unique challenges in terms of their fuel consumption, noise, and emissions impacts because of their unique operating conditions. The propulsion systems currently proposed by the industry are derivative engines (Figure 1) designed around the unmodified core (high-pressure compressor [HPC], combustor, and high-pressure turbine [HPT]) of existing subsonic engines, with modifications to the low-pressure spool (fan and low-pressure turbine [LPT]).

This project is aimed at evaluating the design space of "clean-sheet" engines designed specifically for use on civil supersonic aircraft, and to determine the resulting environmental performance of such engines. Unlike previous commercial supersonic engines, which were adapted from military aircraft, or planned propulsion systems derived from current commercial engines, a clean-sheet engine takes advantage of recent advances in propulsion system technology to substantially improve performance, and reduce emissions and noise footprints. This project will quantify these benefits for a range of engine designs relevant to currently proposed civil supersonic aircraft.

Specific goals of this research are as follows:

- Develop a framework for quantifying the noise and emissions footprints of propulsion systems used on civil supersonic aircraft
- Assess the difference in environmental footprints between a derived engine and a clean-sheet engine for a civil supersonic aircraft
- Assess VNRS used during noise certification of Supersonic Level 1 type aircraft and their effects on landing and take-off (LTO) emissions
- Develop a roadmap for technology development, focusing on reducing the environmental footprint associated with engines for civil supersonic aircraft

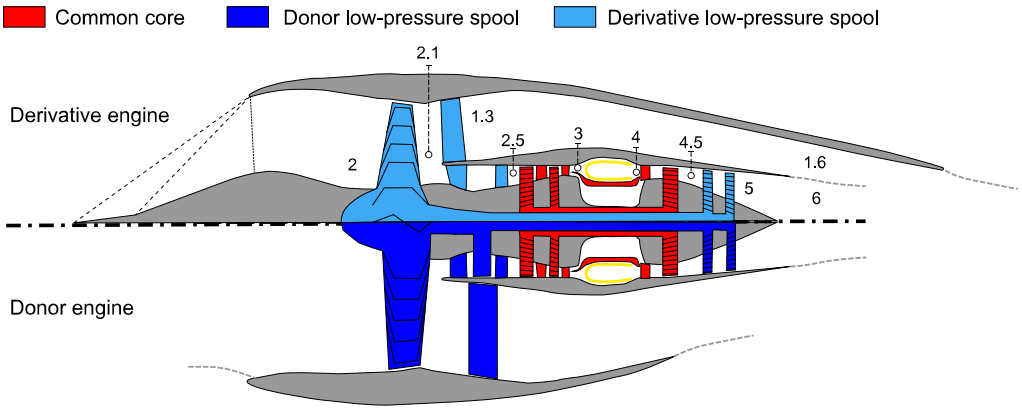

Figure 1. Engine architecture schematic. Lower half shows the subsonic donor engine. The high-pressure spool (red) core is used in the derivative engine (top half) along with modifications to the inlet, fan, and nozzle, as shown in the top half.

Task 1 - Evaluate the Impact of Improved Technology on Relative Performance Benefits of Clean-Sheet and Derivative Engines

Massachusetts Institute of Technology

Objective

The objective of this first task is to quantify the impact that improvements in technology will have on the relative performance of clean-sheet engine designs over derivative designs. Specifically, we consider the impact of technology improvements in the turbomachinery design, turbine material, cooling technology, and combustor design for low nitrogen oxide (NO_x) emissions for the Supersonic Transport Concept Aircraft (STCA) developed by NASA (Berton et al., 2019).

Research Approach

We parameterize the technology level of various components as follows:

Turbomachinery
The technology level of the turbomachinery components (fan, compressor, and turbines) is quantified by the polytropic efficiency (η_p) of the components.

Turbine material and cooling technology
The turbine material limits, such as advanced ceramic matrix composites, thermal barrier coatings, and cooling technology, are quantified by the metal temperature that the turbine vanes and blades are allowed to reach (T_{vane} and T_{blade}, respectively).

Combustor technology
The design space benefits of a clean-sheet engine design would be more readily accessible if the emissions of NO_x were reduced by using a more advanced combustor model. The combustor technology can be parameterized by using a previously developed reactor network model.

Major Accomplishments

The sensitivity of the thrust specific fuel consumption to the technology levels of the turbomachinery, turbine material, and cooling were calculated for both clean-sheet and derivative engines. Figure 2 shows that the derivative engine benefits from a 0.33% and 0.46% improvement in SFC per percentage-point improvement in the polytropic efficiency of the LPT and fan, respectively. These sensitivities are calculated for an optimal engine, sized for a fixed propulsion system requirement (on the basis of the thrust requirement of the STCA). Specifically, each point on the graph represents an engine optimized for minimum SFC with the constraints outlined in the previous section. Because the derivative engine uses the donor core, only the fan and LPT can be designed by using the improved technology.

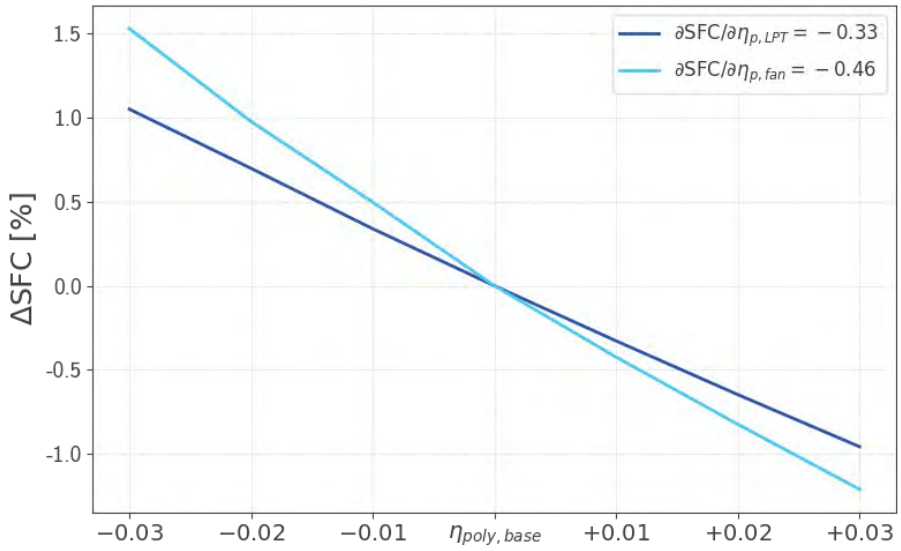

Figure 2. Sensitivity of a derivative engine SFC to the polytropic efficiency of the low-pressure spool components (LPT and fan)

The sensitivities of the clean-sheet engine are different from those of the derivative engine because the core of the engine can be redesigned to obtain an SFC optimal engine at each point. Because the high-pressure spool of the clean-sheet engine is designed, we also calculated the sensitivity of SFC to the polytropic efficiency of the HPC and HPT in addition the low-pressure spool components, as shown in Figure 3.

For a clean-sheet engine design, the pressure ratio of the engine is limited not by the material limits of the last stage of the HPC but by the imposed constraint on the NO_x emissions index, EI(NO_x). We found that a 1% increase in the allowable turbine metal temperature results in 0.25% decrease in the clean-sheet engine SFC.

The cumulative effects of improvements on each of the above engine components are shown for both the derivative and clean-sheet engine in Figure 4. Table 1 shows the assumed magnitude of improvement to the engine components. Improvements in the low-pressure spool and low-NO_x combustor designs have the largest benefit in clean-sheet engine SFC. The clean-sheet engine with advanced technology has a 4.1% lower SFC than the derivative engine with advanced low-pressure spool components.

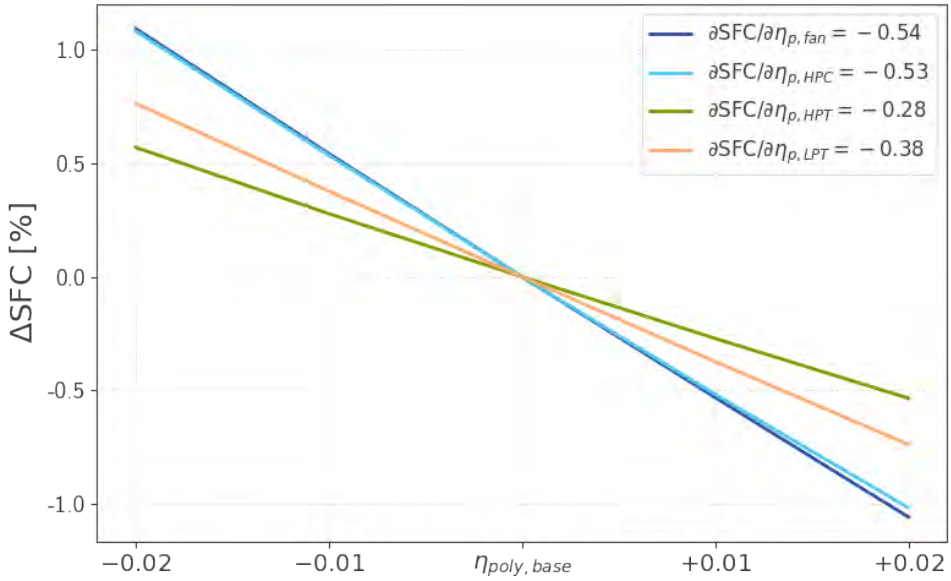

Figure 3. Sensitivity of clean-sheet engine SFC to the polytropic efficiency of the turbomachinery.

Table 1. Assumed magnitude of technology improvements for clean-sheet and derivative engines.

Components	Derivative engine	Clean-sheet engine
$\Delta\eta_p$ of low-pressure spool turbomachinery	+0.02	+0.02
$\Delta\eta_p$ of high-pressure spool turbomachinery	-	+0.01
$\Delta T_{metal,HPT}$	-	+100 K
EI(NO_x)	-	Improved low-NO_x combustor modeled on the PW1133G TALON-X combustor

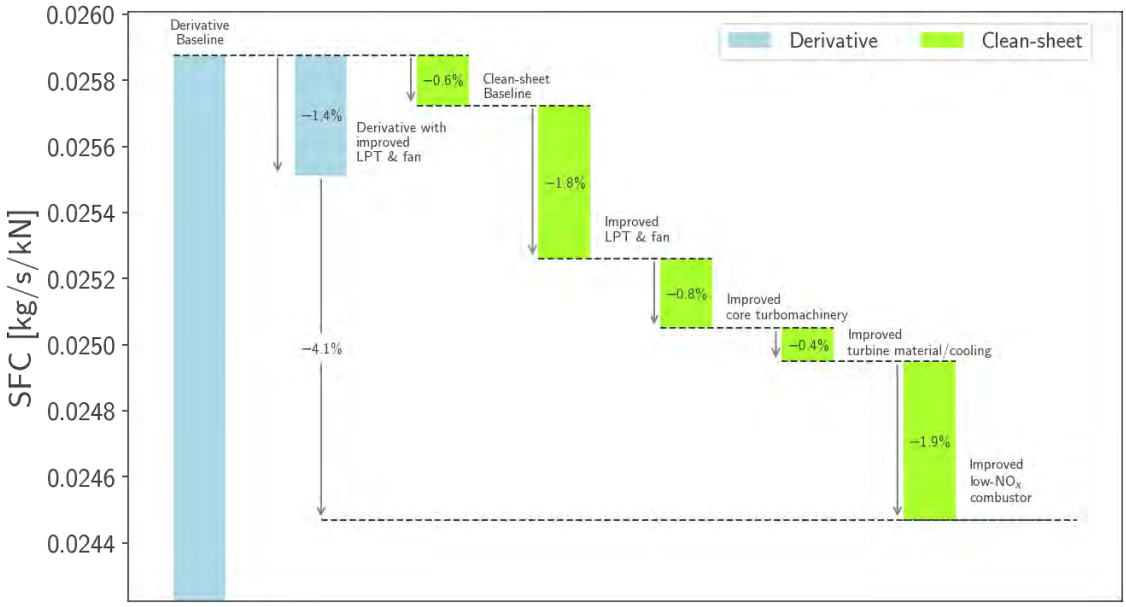

Figure 4. Impact of technology improvements on the SFC of derivative and clean-sheet engines for the STCA.

Publications
None.

Outreach Efforts
- Presentation at the ASCENT Advisory Committee Spring Meeting (April 5–7, 2022)
- Presentation at the Aviation Emissions Characterization Roadmap Annual Meeting (May 24–26, 2022)

Awards
None.

Student Involvement
This work was performed primarily by graduate research assistant Prashanth Prakash working under the supervision of Dr. Jayant Sabnis, Dr. Raymond Speth, and Dr. Choon Tan.

Plans for Next Period
In the next period, we will quantify the effects of a fan diameter constraint on the emissions and noise of SST aircraft. The results presented above focus on engines with a fixed fan diameter, prescribed for the NASA STCA. Varying the fan diameter will alter the engine design characteristics (fan pressure ratio, nacelle drag, etc.) for the same mission requirements, thereby affecting mission fuel consumption, NO_x/CO_2 emissions, and noise.

We will also assess the potential for using unconventional engine architectures to decrease the environmental impacts of SST, both in cruise and LTO. The difference between the LTO and cruise requirements of SST engines is greater than that of subsonic equivalents because of the supersonic design conditions. We will investigate the use of electrical machines (motors and generators) to be used along with variable geometry components to design “variable cycle” gas turbine engines for SST that can lead to lower noise and emissions from SST aircraft.

References

Berton, J. & Geiselhart, K. (2019). *NASA 55-tonne Supersonic Transport Concept Aeroplane (STCA) release package*. NASA GRC/NASA LaRC.

Task 2 - Evaluate the Impact of Advanced Take-off Trajectories for SST Using VNRS on Community Noise

Massachusetts Institute of Technology

Objectives

The objective of this task is to extend our evaluation of the noise impacts of advanced take-off trajectories to incorporate VNRS. These advanced take-off trajectories are designed and optimized by using the take-off certification noise level as a representative metric for noise around airports. The take-off certification noise level incorporates noise levels measured at two locations, i.e., the lateral and flyover microphones. To assess whether these advanced take-off trajectories are effective in community noise reduction, we calculate community noise contours.

Research Approach

- The pyNA aircraft noise estimation tool (Voet et al., 2021) is used to calculate the community noise contours around airports for the advanced take-off trajectories for SST using VNRS.
- The community noise contours are applied to an existing airport. In this work, the New York John F. Kennedy (JFK) airport is chosen. The departure from JFK is from runway 31L.

Major Accomplishments

Figure 5 summarizes the noise levels of the advanced take-off trajectories for the NASA STCA using VNRS when the certification noise metric is applied. Reduced cut-back altitudes (from 260 m to 35 ft) and increased take-off speeds (from 200 kts to 250 kts) enable as much as 7 EPNdB of cumulative noise reduction. When continuous thrust control (also described as programmed thrust cut-back) is used, an additional 3.6 EPNdB of cumulative noise reduction can be achieved. The inherent tradeoff between lateral and flyover noise for the discrete high-altitude and low-altitude thrust cut-back trajectories can be seen in Figure 5. At increased take-off speed, the advanced take-off trajectory with continuous thrust control avoids this tradeoff by reducing flyover noise without increasing lateral noise, with respect to those with the low-altitude cut-back.

Programmed high-lift devices are found to be ineffective in reducing take-off noise for the NASA STCA. Figure 5 shows that, even with the use of advanced take-off trajectories, the NASA STCA is unable to meet current noise limits for subsonic transport set by the International Civil Aviation Organization (ICAO) in Annex 16 Chapter 14. Additional noise reduction might be achieved by incorporating reduced thrust take-off procedures, as explored by Berton et al. (2019) and Olson (1992).

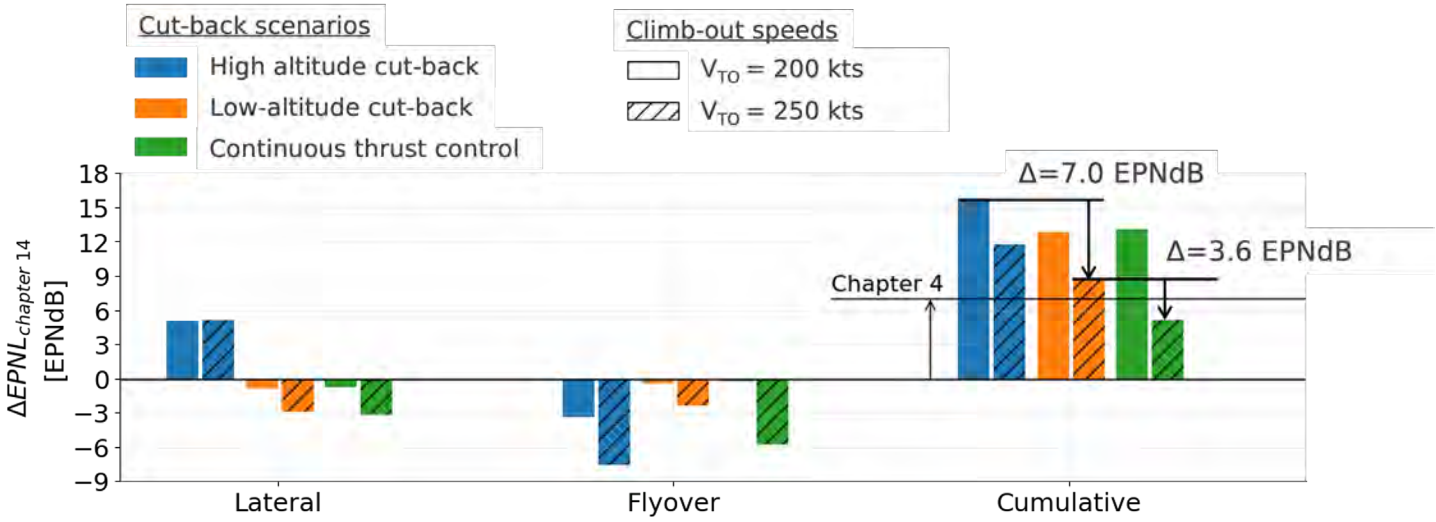

Figure 5. Comparison of the lateral, flyover, and cumulative certification noise levels of standard and advanced trajectories with the ICAO Annex 16 Chapter 14 noise limits. The Annex 16 Chapter 4 noise limits are also indicated for reference.

The impact of the advanced take-off trajectories on community noise is shown in the sound exposure level (SEL) line contours and ΔSEL color contours in Figure 6. The top left plot shows the community noise contours for the standard take-off trajectory, abiding by the current noise standards for subsonic transport in ICAO Annex 16. The noise is highest underneath the flight path on the centerline and decreases when laterally moving away in the *y*-direction. The center plot on the top row shows the ΔSEL between the high-altitude and low-altitude cut-back.

With the low-altitude cutback, the community noise contours show the tradeoff between points in the airport vicinity and downstream, indicated by the blue and red regions. This tradeoff is also captured when the certification noise metric is used. At increased take-off speeds, the same tradeoff is observed; however, the average noise is reduced because of the reduced jet shear at higher take-off speeds.

The high-altitude cut-back achieves the largest noise reduction in downstream regions, whereas the low-altitude cut-back achieves the largest noise reduction in regions in the vicinity of the airport. With continuous thrust control (at increased take-off speeds), the advanced take-off trajectory achieves noise reduction in the combined region between airport vicinity and downstream. Overall, this trajectory achieves the largest noise reduction relative to all other advanced take-off trajectories.

Figure 7 compares the community noise contours for the high-speed advanced take-off trajectories with continuous thrust control and low-altitude cut-back, i.e., the two trajectories with lowest cumulative noise levels when the certification noise metric is used. With the continuous thrust control trajectory, noise is reduced in the areas where it was already low (away from the flight path, as shown in the line contour of Figure 5), and is not reduced underneath the flight path, where the noise was the highest. These findings illustrate where the certification and community noise metrics are not aligned, and thus suggest re-examination of the certification noise metric for SST using advanced take-off trajectories.

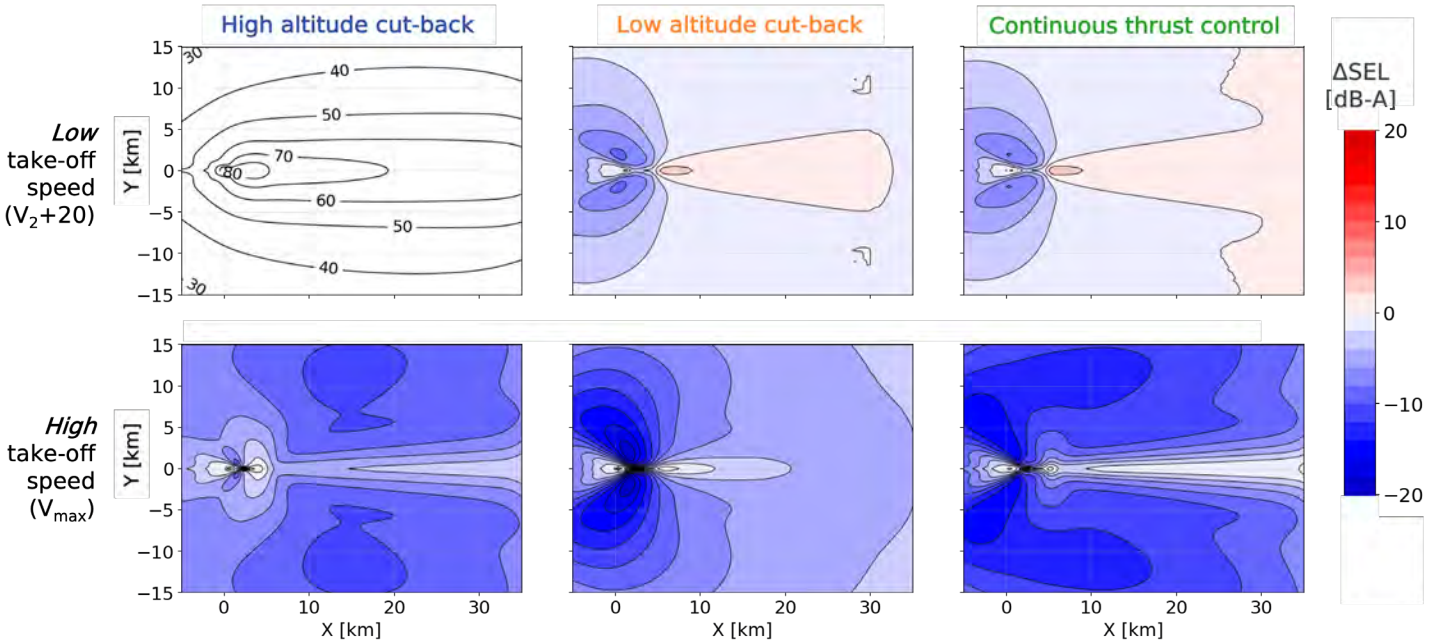

Figure 6. Top left: SEL line contours for the NASA STCA standard single thrust cut-back trajectory abiding by the noise standards for subsonic transport defined in ICAO Annex 16. Top middle and top right, bottom row: ΔSEL color contours for the NASA STCA advanced take-off trajectories. The origin is the aircraft brake release point.

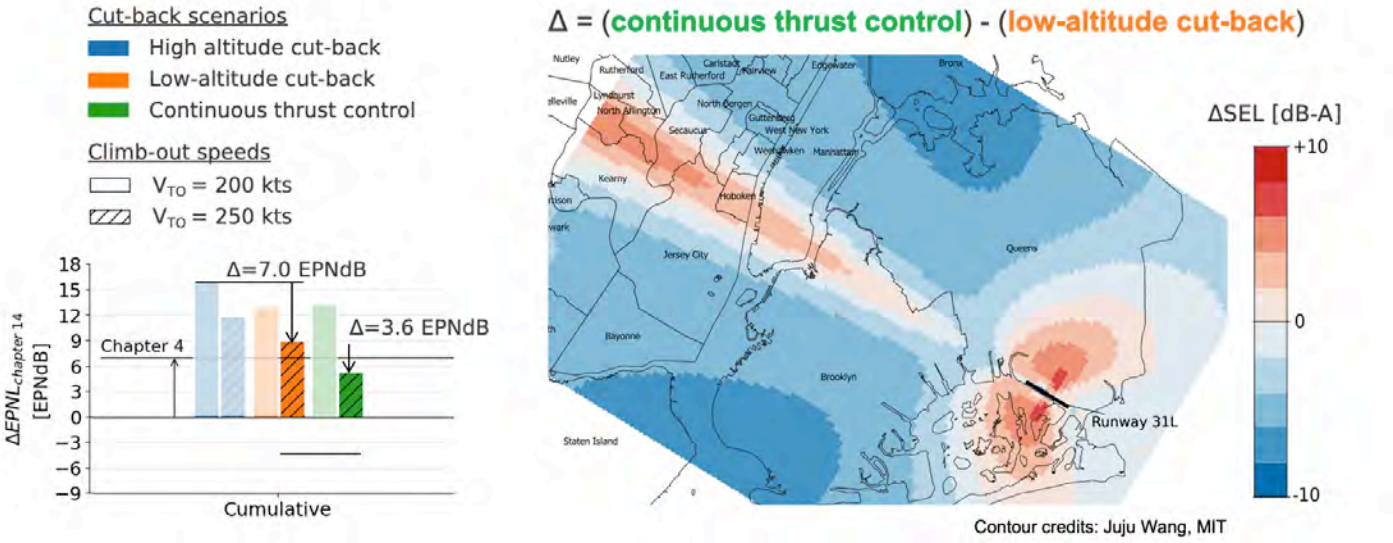

Figure 7: Left: comparison of certification cumulative noise levels between high-speed continuous thrust control and low-altitude cut-back trajectories. Right: ΔSEL color contours for high-speed continuous thrust control and low-altitude cut-back trajectories taking off from runway 31L at New York JFK airport.

Publications

Voet, L., Speth, R. L., Sabnis, J. S., Tan, C. S., & Barrett, S. R. (2022, June 14). *On the Design of Variable Noise Reduction Systems for Supersonic Transport Take-off Certification Noise Reduction*. 28th AIAA/CEAS Aeroacoustics 2022 Conference, Southampton, UK. https://doi.org/10.2514/6.2022-3052

Outreach Efforts

- Presentation at the ASCENT Advisory Committee Spring Meeting (April 5–7, 2022)
- Presentation at the Aviation Emissions Characterization Roadmap Annual Meeting (May 24–26, 2022)

Awards

None.

Student Involvement

This task was conducted primarily by Laurens Voet, a graduate research assistant working under the supervision of Dr. Jayant Sabnis, Dr. Raymond Speth, and Dr. Choon Tan.

Plans for Next Period

This task is complete.

References

Berton, J. & Geiselhart, K. (2019). *NASA 55-tonne Supersonic Transport Concept Aeroplane (STCA) release package*. NASA GRC/NASA LaRC.

Olson, E. D. (1992). *Advanced takeoff procedures for high-speed civil transport community noise reduction*. 921939. https://doi.org/10.4271/921939

Project 048 Analysis to Support the Development of an Engine nvPM Emissions Standard

Massachusetts Institute of Technology

Project Lead Investigator

Steven Barrett
Associate Professor
Department of Aeronautics & Astronautics
Massachusetts Institute of Technology
77 Massachusetts Ave
Building 33-316
Cambridge, MA 02139
617-452-2550
sbarrett@mit.edu

University Participants

Massachusetts Institute of Technology (MIT)

- P.I.: Professor Steven Barrett
- Co-P.I.: Dr. Raymond Speth
- FAA Award Number: 13-C-AJFE-MIT, Amendment Nos. 027, 036, 045, 054, 065, 069, 083, and 087
- Period of Performance: July 8, 2016 to November 30, 2022 (reporting here with the exception of funding level and cost share only for the period October 1, 2021 to September 30, 2022)
- Tasks:
    1. Evaluation of cruise emissions based on ground measurements
    2. Development and calibration of a reactor network model
    3. Identification of parameters influencing cruise emissions

Project Funding Level

This project received $950,000 in FAA funding and $950,000 in matching funds. The sources of match are approximately $214,000 from MIT, plus third-party in-kind contributions of $87,000 from University College London, $158,000 from Oliver Wyman Group, $156,000 from Byogy Renewables, Inc., $153,000 from NuFuels, LLC, and $182,000 from Savion Aerospace Corporation.

Investigation Team

- Professor Steven Barrett (MIT) serves as P.I. for Project 48, as head of the Laboratory for Aviation and the Environment. Professor Barrett coordinates internal research efforts and maintains communication among investigators in the various MIT research teams.
- Dr. Raymond Speth (MIT) serves as co-P.I. for Project 48. Dr. Speth directly advises student research in the Laboratory for Aviation and the Environment, and focuses on the assessment of fuel and propulsion system technologies targeting reduction of aviation's environmental impacts. Dr. Speth also coordinates communication with FAA counterparts.
- Dr. Jayant Sabnis (MIT) serves as co-investigator for Project 48. Dr. Sabnis co-advises student research in the Laboratory for Aviation and the Environment. His research interests include turbomachinery, propulsion systems, gas turbine engines, and propulsion system–airframe integration.
- Akshat Agarwal (MIT) was a graduate student in the Laboratory for Aviation and the Environment. Before his graduation in 2021, he was responsible for conducting cost–benefit analysis of the nonvolatile particulate matter (nvPM) emissions standard and developing methods for estimating nvPM emissions on the basis of smoke number measurements.

- Dr. Bang-Shiuh Chen (MIT) was a postdoctoral associate in the Laboratory for Aviation and the Environment. He was primarily responsible for evaluating and improving models for estimating full-flight emissions from certification measurements.
- Adrien Guenard (MIT) is a graduate student in the Laboratory for the Aviation and the Environment. His work focuses on the development of a new cruise metric for nitrogen oxide (NO_x) emissions.

Project Overview

The FAA's Office of Environment and Energy is working with the international community to implement an international aircraft engine nvPM standard for engines with rated thrust greater than 26.7 kN. The nvPM standard will influence the development of future engine technologies, thus resulting in the reduction of nvPM emissions from aircraft engines, and consequently leading to reduced human health and climate impacts from aviation. During the Committee on Aviation Environmental Projection (CAEP)/11 cycle, the FAA, alongside other national aviation authorities, developed an nvPM emissions standard for the mass and particle number emitted by aircraft engines, and this project has continued to support the FAA by providing a technical basis for the implementation of the nvPM emissions standards.

Task 1 - Evaluation of Cruise Emissions Based on Ground Measurements

Massachusetts Institute of Technology

Objective

The objective of this task was to compare cruise and ground nvPM emissions of engines present in the International Civil Aviation Organization (ICAO) Engine Emissions Databank (EEDB).

Research Approach

During the CAEP/12 cycle, the Mission Emissions Estimation Method (MEEM) was developed, thereby enabling the estimation of nvPM cruise emissions from certification data (Ahrens et al., 2022). MEEM estimates combustor temperature (T_3) and pressure (P_3) for cruise conditions. A T_3–P_3 correlation is then used to estimate cruise emissions from ground certification data. We used MEEM to estimate cruise emissions of 130 engines in the ICAO EEDB. Engines with staged combustors were excluded from the study. Cruise emissions were compared with ground certification emission data. Cruise emission rates, $E_{\mathrm{r,cruise}}$, are expressed in mg/s/kN (mass) or #/s/kN (number) according to the following equation:

$$E_{\mathrm{r,cruise}} = \frac{EI_{\mathrm{cruise}}\, W_{\mathrm{f,cruise}}}{F_{00}}$$

where EI_{cruise} is computed by using MEEM, $W_{\mathrm{f,cruise}}$ is the fuel flow at cruise condition, and F_{00} is the rated thrust. $W_{\mathrm{f,cruise}}$ is estimated by interpolating W_{f} at the four landing and takeoff (LTO) thrust setting points and evaluating the interpolation at the ground reference thrust, F_{GR}, defined in MEEM. LTO emissions are expressed by dividing the EEDB LTO metric D_{p}/F_{00}, in mg or #/kN, by the total duration of the LTO cycle, τ_{LTO} as follows:

$$E_{\mathrm{r,LTO}} = \frac{D_{\mathrm{p}}/F_{00}}{\tau_{\mathrm{LTO}}}$$

D_{p}/F_{00} data are corrected by loss factor coefficients, as described in the EEDB.

The results of this study for nvPM mass and number are presented in Figures 1 and 2. The red zones emphasize engines presenting similar LTO emissions but large differences in cruise emissions. This observation suggests that the LTO metric does not capture the full range of variation in cruise emissions.

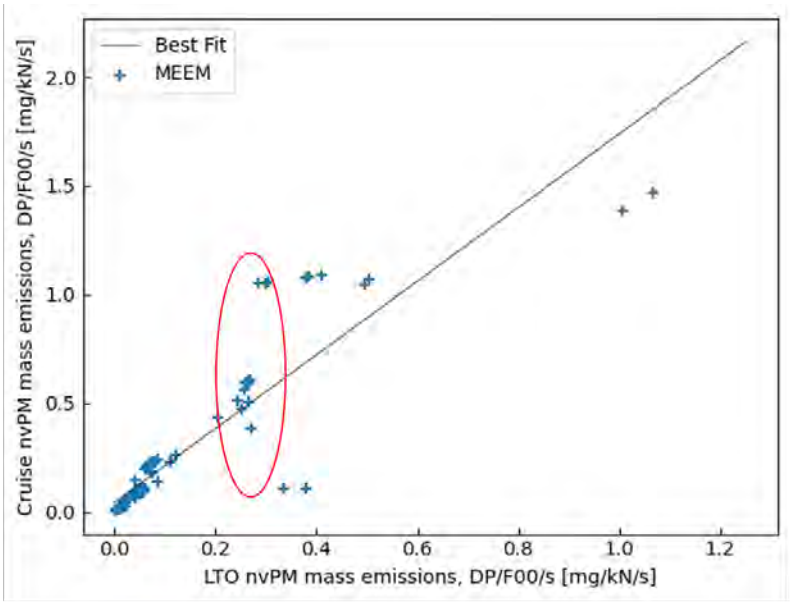

Figure 1. Cruise versus ground nvPM mass emissions.

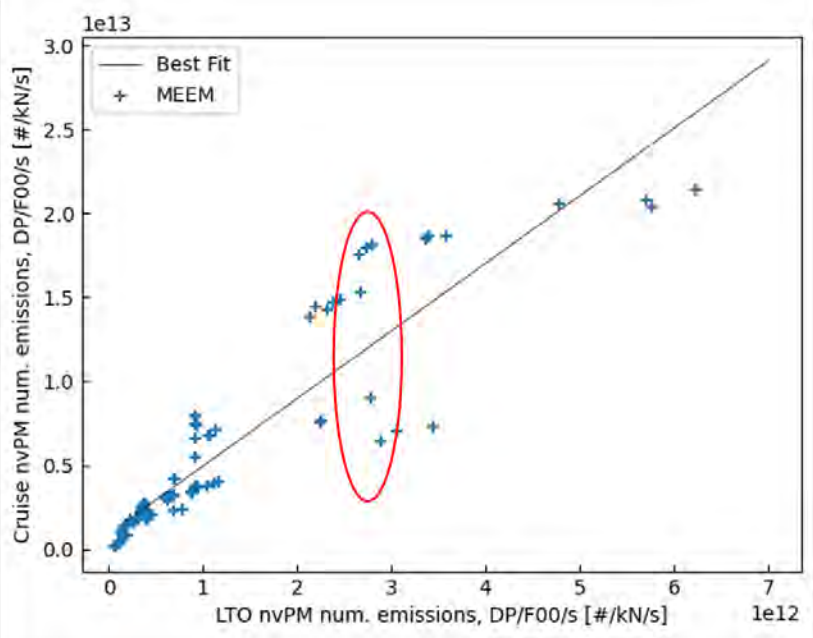

Figure 2. Cruise versus ground nvPM number emissions.

Figure 3 shows an example of an engine with high LTO emissions with respect to its cruise emissions. This engine reaches its maximum nvPM emissions index (EI) at the idle condition, thus leading to a large LTO metric. Cruise EI is then computed as the EI at ground for a thrust setting between 30% and 85% of F_{00}, corrected by T_3 and P_3. For this type of emission profile, the average cruise emission rates are lower than those for LTO. This analysis demonstrates the existence of engines with LTO emissions that are not representative of their cruise emissions.

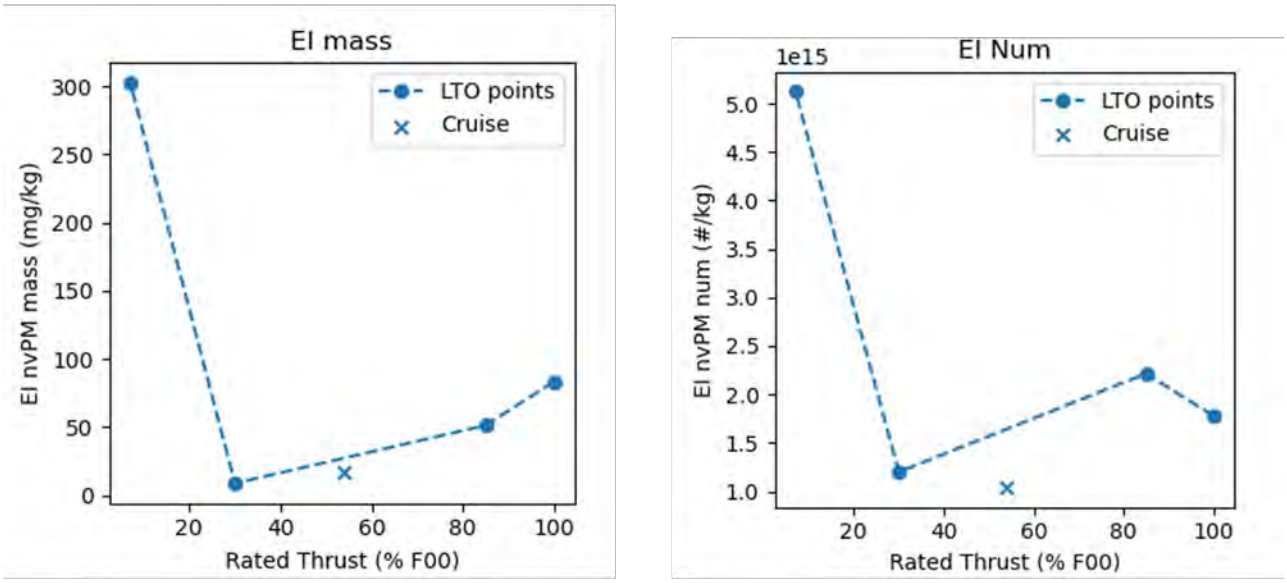

Figure 3. nvPM mass and number emission profiles for an outlier engine.

Milestone
The complete analysis was presented in a working paper for CAEP/13-WG3/3-ECTG.

Major Accomplishments
This work was presented to CAEP/13-WG3/3-ECTG and supported the development of the rationale for defining a cruise/climb nvPM emissions metric.

Publications
None.

Outreach Efforts
- Presentation to CAEP/13-WG3/3-ECTG meeting (October 17–21, 2022)
- Presentation during the ASCENT 2022 Fall Meeting (October 25–27, 2022)

Awards
None.

Student Involvement
Graduate student Adrien Guenard conducted the analyses.

Plans for Next Period
This task is complete.

References
Ahrens, D., Méry, Y., Guénard, A., & Miake-Lye, R. C. (2022, June 13-17). A New Approach to Estimate Particulate Matter Emissions from Ground Certification Data: The nvPM Mission Emissions Estimation Methodology (MEEM). *Proceedings of the ASME Turbo Expo 2022: Turbomachinery Technical Conference and Exposition. Volume 3A: Combustion, Fuels, and Emissions*. Rotterdam, Netherlands. https://doi.org/10.1115/GT2022-81277

Task 2 - Development and Calibration of a Reactor Network Model

Massachusetts Institute of Technology

Objective

This task was aimed at developing a reactor network that captures the physical phenomena relevant to emissions formation in aircraft engine combustors and can be used to estimate gaseous pollutant emissions.

Research Approach

A reactor network has been developed by using the open-source combustion software Cantera. The concept of this model is to represent the physical phenomena acting in a rich-quench-lean (RQL) combustor that are relevant to emissions formation. The primary zone is modeled as a set of perfectly stirred reactors, with equivalence ratio (ϕ) inhomogeneity represented by varying the equivalence ratio in the perfectly stirred reactors according to a normal distribution. The parameters of the normal distribution depend on the operating parameters of the engine (Saboohi et al., 2017). The secondary zone is modeled by using two plug flow reactors. These reactors model the mixing between the air coming from the primary zone and the air coming from the dilution holes and the liner cooling system. Figure 4 shows a schematic view of the combustor network model.

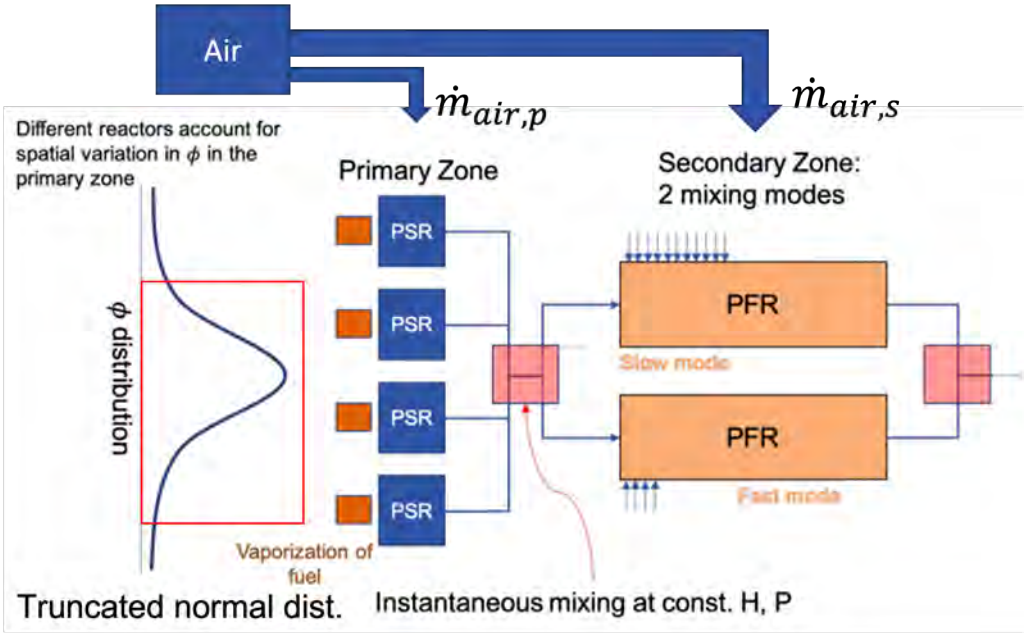

Figure 4. Architecture of the combustor reactor network model.

The air partitioning and the volume of the reactors can be adjusted to calibrate the reactor network against real RQL combustor data. Air partitioning in the model is defined by the fraction of air entering the primary zone (primary zone air fraction [PAF]) and in the secondary zone. The secondary zone is modeled by using two plug flow reactors. For each plug flow reactor, the incoming air can be separated into two categories: the air coming from the primary zone and the air coming from the dilution and cooling holes. The coefficients g and a describe the partitioning of these two air sources into each of the plug flow reactors. The reactor volumes are determined by the parameter VPZ (in m^3) for the primary zone, and L_{FM} and L_{SM} (in m) for the plug flow reactors.

To calibrate the model, CFM56-7B was chosen as a reference RQL combustor engine. The reactor network model was coupled with a Numerical Propulsion System Simulation model providing the combustor inlet conditions (T_3, P_3, W_f, and fuel air ratio).

The reactor network model was then calibrated by adjustment of the combustor parameters to match the CFM56-7B NO_x and CO emissions tabulated in the EEDB. The results of this calibration are presented in Figure 5.

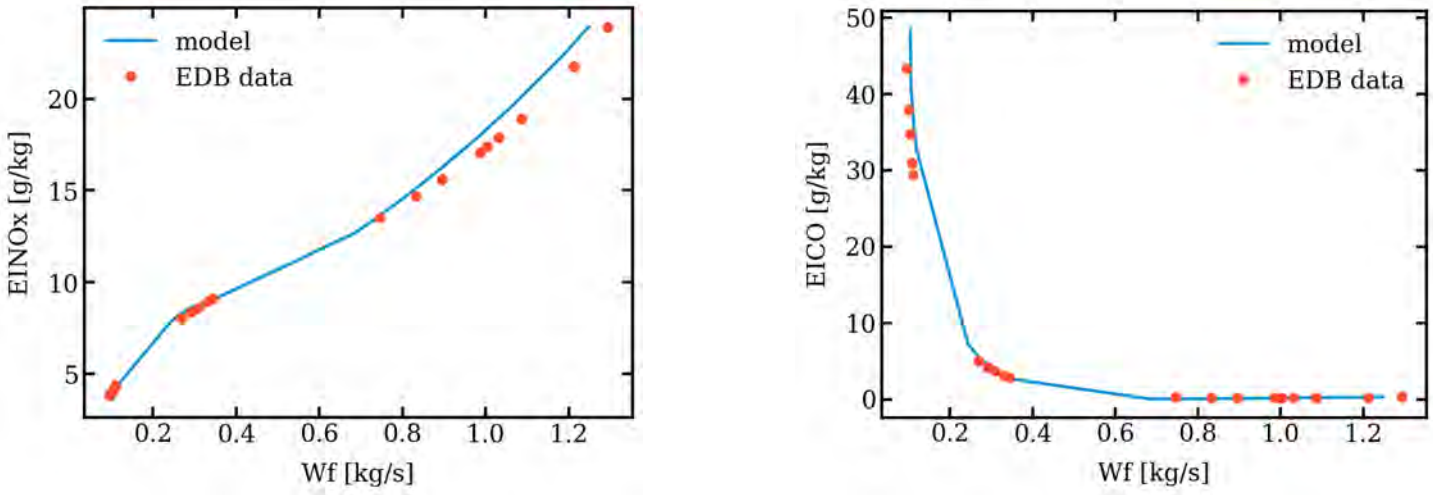

Figure 5. Calibration of NO_x and CO emissions against CFM56-7B EEDB data.

For an RQL combustor, the reactor network model can capture the physical phenomena of gaseous pollutant formation over the entire thrust range. Having demonstrated that the reactor network model is able to produce reliable results in terms of gaseous emissions, we can use the model to investigate the impacts of combustor and engine design on gaseous emissions.

Milestone
The results of this analysis were presented to FAA project managers and to the WG3 EMI ad hoc group in September 2022.

Major Accomplishments
The model developed herein was used to conduct Task 3, as described in this report.

Publications
None.

Outreach Efforts
- Presentation to CAEP/13-WG3/3-ECTG meeting (October 17–21, 2022)
- Presentation during the ASCENT 2022 Fall Meeting (October 25–27, 2022)

Awards
None.

Student Involvement
Postdoctoral associate Dr. Bang-Shiuh Chen conducted the analysis.

Plans for Next Period
This task is complete.

References
Saboohi, Z., & Ommi, F. (2017). Emission prediction in conceptual design of the aircraft engines using augmented CRN. *The Aeronautical Journal*, *121*(1241), 1005–1028. https://doi.org/10.1017/aer.2017.40

Task 3 - Identification of Parameters Influencing Cruise Emissions

Massachusetts Institute of Technology

Objective

The objective of this task was to conduct a sensitivity analysis on the combustor reactor network to identify the parameters influencing cruise emissions, particularly parameters that lead to differences in trends between cruise and LTO emissions.

Research Approach

Miller et al. (2022) compared cruise and ground NO_x emissions and presented NO_x emission profiles for 69 in-service engines. Cruise emissions were compared with ground-level emissions, as presented in Figure 6. This study sheds light on the same phenomenon observed for the nvPM emissions in Figures 2 and 3. Some engines that have similar LTO emissions exhibit large differences at cruise. An example of this phenomenon is highlighted in the red circle in Figure 7.

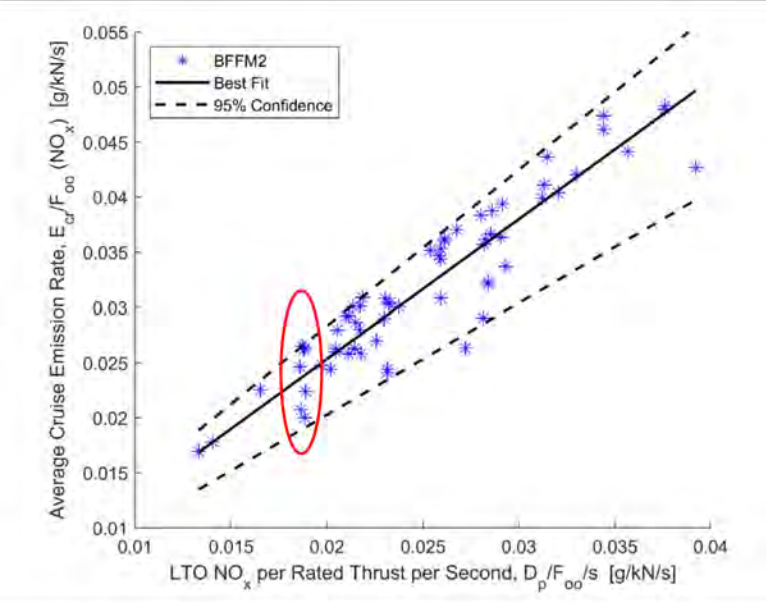

Figure 6. Cruise versus ground NO_x emissions for 69 EEDB engines. From Miller et al. (2022).

The research approach adopted for this task used the reactor network model to explore the space of ground versus cruise emissions and to identify combustor parameters explaining the existence of such vertical profiles. A CFM56-7B engine cycle was used as the basis for conducting sensitivity analysis. The Numerical Propulsion System Simulation was used to compute the combustor inlet thermodynamic conditions at all operating points. The sensitivity analysis was performed on the combustor parameters while the engine cycle parameters were held constant.

Figure 7 presents the parameters under investigation. The parameters were sampled from uniform distributions $\mathcal{U}(a_i, b_i)$, where a_i and b_i delimit the range for the parameter i. Parameter ranges were limited to designs that lead to high combustor efficiency (defined as a combustor exit temperature within 5% of the value calculated from equilibrium). After the range of each parameter was defined, NO_x emissions were computed for ground and cruise conditions. For ground emissions, the emission rate is defined as follows:

$$ER_{ground} = \frac{\sum_{i=1}^{4} W_{f,i} * EI_i * t_i}{t_{LTO}}$$

where the summation is over the four LTO points: takeoff, climb out, approach, and idle. For cruise, the emissions rate is defined as follows:

$$ER_{cruise} = \sum_{i=1}^{3} W_{f,i} * EI_i$$

where the summation is over the three cruise points used in the definition of the ICAO CO_2 metric value.

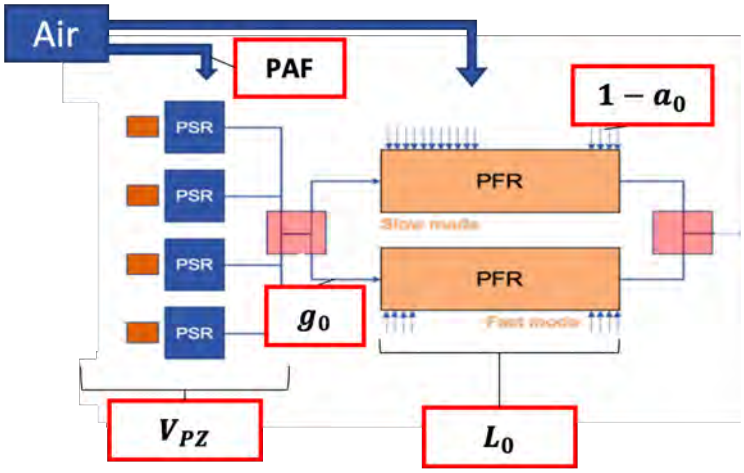

Figure 7. Combustor schematic showing parameters included in the parametric study (red boxes). PAF is the fraction of air directed into the primary zone; V_{PZ} is the volume of the primary zone; g_0 and a_0 are the fractions of air coming from the primary zone and from the dilution holes that are injected in the fast mode plug flow reactor, respectively; and L_0 is the length of the secondary zone plug flow reactor (PFR).

On the basis of these metrics, we computed sensitivity indices for ground and cruise conditions for each combustor model parameter. The sensitivity indices are calculated as follows:

$$S_i = \frac{\mathbb{V}ar_{X_i}(\mathbb{E}_{X\sim i}[Y|X_i])}{\mathbb{V}ar(Y)}$$

by using the method of Saltelli et al. (2002). Sensitivity indices vary between 0 and 1, and can be interpreted as the amount of variance in metric Y that is explained by parameter X_i. Figure 8 presents the sensitivity indices and the sampling points obtained by comparing the LTO NO_x metric to cruise emissions.

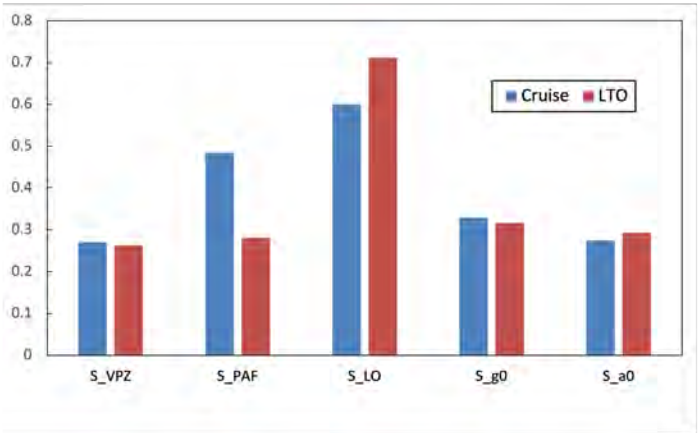

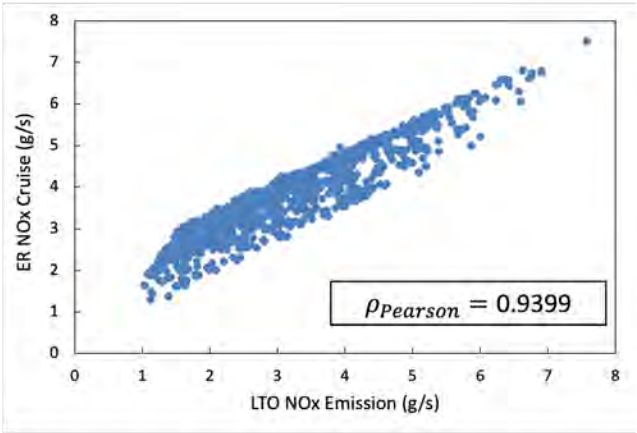

Figure 8. Sensitivity indices and sampling points for the LTO versus cruise study.

The primary zone volume, V_{PZ}, and the parameters describing the distribution of air in the secondary zone (a_0 and g_0) have similar sensitivity indices at ground and at cruise. In contrast, the sensitivity indices of the PAF and of the length of the fast mode plug flow reactor, L_0, vary between LTO and cruise. These latter two parameters can lead to combustor designs that create emission profiles such as those observed in the red circle in Figure 6.

This phenomenon is explored further in Figure 9, where V_{PZ}, a_0, and g_0 are kept constant while PAF and L_0 vary. Each point in Figure 11 represents a unique combustor configuration. Because PAF and L_0 have different effects on NO_x emissions at ground and at cruise, some combustor configurations lead to similar NO_x emissions at ground but to large differences at cruise. This sensitivity analysis study has enabled the identification of combustor parameters influencing NO_x emissions at cruise and at ground.

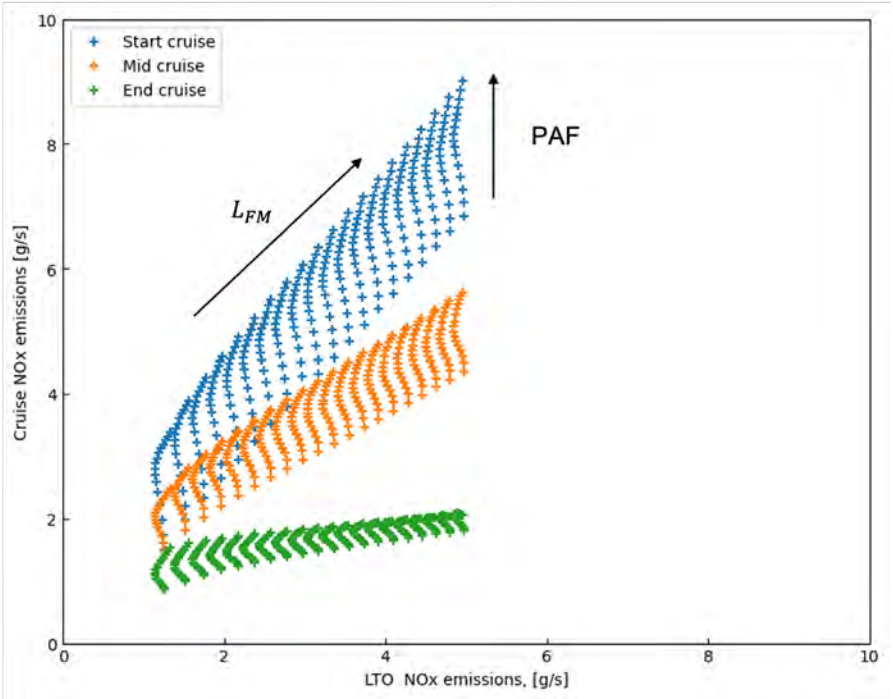

Figure 9. Parametric study varying the PAF and fast mixing zone length, L_{FM}.

Milestone
The complete analysis has been presented to the FAA.

Major Accomplishments
None.

Publications
None.

Outreach Efforts
Our results have been communicated to the FAA in regular presentations.

Awards
None.

Student Involvement

Graduate student Adrien Guenard conducted the analyses and presented the work.

Plans for Next Period

The methods and data used for this analysis will be transferred to ASCENT Project 83, where they will be used to help define new emissions metrics that are more relevant to cruise operations than the existing LTO metric.

References

Saltelli, A. (2002). Making best use of model evaluations to compute sensitivity indices. *Computer Physics Communications*, 145(2), 280-297. Doi: 10.1016/S0010-4655(02)00280-1

Project 049 Urban Air Mobility Noise Reduction Modeling

The Pennsylvania State University, Continuum Dynamics, Inc.

Project Lead Investigator

Kenneth S. Brentner
Professor of Aerospace Engineering
Department of Aerospace Engineering
The Pennsylvania State University
233 Hammond Building
University Park, PA
814-865-6433
ksbrentner@psu.edu

University Participants

The Pennsylvania State University (Penn State)

- P.I.: Kenneth S. Brentner, Professor of Aerospace Engineering
- FAA Award Number: 13-C-AJFE-PSU-049, Amendment No. 82
- Period of Performance: October 1, 2021 to September 30, 2022
- Tasks:
    12. Develop several additional notional Urban Air Mobility (UAM) and Electric Vertical Take-off and Landing (eVTOL) aircraft models for noise testing
    13. Continue validating the new flight simulation/noise prediction system
    14. Investigate test trim strategies for notional UAM/eVTOL vehicles
    15. Develop a database of noise predictions for UAM and eVTOL vehicles during the various stages of operation
    16. Begin investigation of low-noise flight operation development

Project Funding Level

The FAA provided $280,000 in funding. Continuum Dynamics, Inc. (point of contact: Dan Wachspress) provided $75,000 of cost sharing in the form of a 1-year license for the Comprehensive Hierarchical Aeromechanics Rotorcraft Model (CHARM) rotorcraft comprehensive analysis software to Penn State. Penn State also provided $18,400 in equipment cost sharing, for a total of $93,400 cost sharing.

Investigation Team

- Kenneth S. Brentner, P.I., Penn State; acoustic prediction lead (Tasks 12–16)
- Eric Greenwood, co-P.I., Penn State; acoustics prediction/analysis (Tasks 13, 14, 16)
- Joseph F. Horn, co-P.I., Penn State; flight simulation lead (Tasks 12-15)
- Daniel A. Wachspress, co-P.I., Continuum Dynamics, Inc.; rotor loads, wake integration, and CHARM coupling (Tasks 12-14, 16)
- Ze Feng (Ted) Gan, Graduate Research Assistant, Penn State; developing PSU-WOPWOP noise prediction software and performing acoustic predictions (Tasks 13 and 15)
- Bhaskar Mukherjee, Graduate Research Assistant, Penn State; software coupling, establishing new aircraft models, developing simulations for new aircraft types, performing acoustic predictions, and developing flight abatement procedures (Tasks 12–16)

Project Overview

A wide variety of unconventional configurations for UAM and eVTOL aircraft, most with many electrically driven propellers and lifting rotors, have been proposed and are currently under development by companies worldwide. These novel

configurations make up a new category of aircraft that will need to be certified, particularly for acceptable noise levels, given their urban operations. Furthermore, the noise of UAM and eVTOL vehicles is expected to be one of the factors determining community and passenger acceptance. Therefore, first-principles noise predictions of these aircraft will be important for providing the FAA with information independent from that provided by manufacturers, and before manufacturer flight test or certification noise data are available. For clarification, unmanned aerial systems (UAS, also known as drones), UAM, and eVTOL vehicles all share electric motors as the source of power to drive the rotors. In most cases, UAM are likely to use batteries, but the electrical power could come from fuel cells, gas generators, or other sources. Furthermore, although most UAS and UAM vehicles are likely to have VTOL capabilities, such capabilities are not a requirement. In this report, these UAM and eVTOL are used synonymously, whereas UAS are eVTOL drones.

In ASCENT Project 38, the helicopter noise prediction system initially developed in ASCENT Project 6 was successful in accurately predicting the noise of six helicopters (usually within sound exposure levels of 1–3 SELdBA), when the predictions were compared with results from an FAA/NASA rotorcraft noise abatement flight test performed in August and October of 2017. Sound exposure level contours from the flight test were compared with predictions for several flight procedures. The noise prediction system developed in Project 38 consisted of the PSUHeloSim flight dynamics simulation code coupled to the CHARM aeromechanics modeling software and the PSU-WOPWOP noise prediction code. This coupling with the flight simulation code was demonstrated to be important for noise prediction, which markedly improved when the simulation was modified to track the time-dependent aircraft position, velocity, and attitude flown in the individual run, rather than the nominal flight path.

To build upon the success of ASCENT Project 38, in ASCENT Project 49, we took an analogous approach of coupling a flight simulation code with CHARM and PSU-WOPWOP. The PSUHeloSim flight simulation component of the noise prediction system used in Project 38 was replaced with DEPSim, a flight simulation code designed for many electrically driven rotors and the unique control strategies to fly such vehicles effectively. Coupling of DEPSim with CHARM was performed in work outside ASCENT, but the DEPSim–CHARM coupling with PSU-WOPWOP was performed in this project.

The goal of this project is to develop a noise prediction system with the initial capability to analyze the noise from UAM and eVTOL vehicles with unique configurations under any flight conditions. This project should enable the FAA, manufacturers, and related entities to investigate how this new class of vehicles—and their noise—might be integrated into the national airspace. Emphasis is placed on modeling the unique features of UAM and eVTOL configurations not commonly seen in conventional rotorcraft, such as rotors with variable rotation speed, and complex unsteady aerodynamic interactions between the many rotors and the airframe. Because UAM vehicles will probably have lower tip speeds to achieve acceptable noise levels, broadband noise is expected to become the dominant rotor noise source; accordingly, fast, accurate modeling of rotor broadband noise is a goal of this project. Another goal is to use the noise prediction system developed in this project to provide guidance on how to fly these vehicles in a quiet manner through flight operations. Because the analysis and computations are based on fundamental physics, noise abatement procedures for novel new vehicles can be developed.

Task 12 - Develop Several Additional Notional UAM/eVTOL Aircraft Models for Noise Testing

The Pennsylvania State University

Objective

The goal of this task is to develop notional aircraft models for understanding the acoustic characteristics of different UAM/eVTOL configurations. Required data from aircraft configurations must be extracted to enable flight simulation of maneuvers via the PSUDEPSim–CHARM–PSU-WOPWOP noise prediction system.

Research Approach

Table 1 summarizes the inputs required for any aircraft to be modeled in the noise prediction system. Barring the lack of available aircraft and rotor geometries, the primary hurdle remains the aircraft controller design in PSUDEPSim. Although most of the controller design is automated within PSUDEPSim, users must provide a trim schedule (initial guesses for state of control effectors that result in trimmed flight at various steady conditions) and the gains of the control mixers, which determine how the control effectors are actuated. For example, the structure of the control mixers determines whether the rotor thrust is controlled via the variation in angular velocity, collective pitch, or both.

Table 1. Parameters required by the PSUDEPSim–CHARM–PSU-WOPWOP noise prediction system.

Tool	Required input	Status	Challenges
PSUDEPsim	• Aircraft properties: weight, inertia, fuselage properties, rotor layout with respect to aircraft center of gravity • Gains for control mixers • Trim schedules or initial guess for controller to trim the aircraft in steady state	• Gains for control mixers and control inputs for trim schedules are currently being hand-tuned	• Information on existing commercial aircraft is lacking • Hand-tuning is extremely time-intensive, and more automated methods are required
CHARM	• Detailed rotor geometry: o Hub and tip radii o Chord and twist distribution o Airfoil polars	• A simple utility has been developed to obtain CHARM-friendly input files • A library of airfoil polars for common airfoils is being built • A utility has been developed to generate airfoil polars by using XFOIL for CHARM	• Openly available rotor geometries for eVTOL/UAM are limited • Estimation is difficult, because rotors tend to have complex twist and chord distribution
PSU-WOPWOP	Distribution of thickness across blade span	• This parameter can be estimated by using OpenVSP • A utility has been developed to convert OpenVSP blade geometry to the PSU-WOPWOP grid format required for thickness noise calculations	

Milestones

- Obtained input files for CHARM describing rotor geometry and airfoil polars (C-81)
- Obtained grid geometry required for calculation of thickness noise in PSU-WOPWOP
- Developed tools for determining parameters required in building flight controllers in PSUDEPSim

Major Accomplishments

- A utility code in FORTRAN has been written to obtain input files containing rotor geometry for CHARM.
- C-81 airfoil polars used by CHARM can be compiled for different airfoils by using XFOIL.
- An external tool has been developed that converts OpenVSP files to structured grids, which serve as input to PSU-WOPWOP for calculating thickness noise.
- A subsystem based on the CHARM Rotor Module has been developed that can simulate the aerodynamic response from rotors in any aircraft configuration, according to prescribed control inputs. The goal is to create procedures wherein a user commands the aircraft to perform certain maneuvers/actions that help determine the gains along the roll, pitch, and yaw axes of the aircraft that maintain required stability margins.
- Strategies for robust trim are being developed that will help generate accurate trim schedules required in PSUDEPSim.

Publications

None.

Outreach Efforts

None.

Awards
None.

Student Involvement
Bhaskar Mukherjee, a graduate assistant working on his PhD at Penn State, is integrating new aircraft into the PSUDEPSim-CHARM-PSU-WOPWOP noise prediction system.

Plans for Next Period
The Penn State Rotor Acoustics Group is acquiring more rotor and aircraft geometries through measurements of commercial drones. An immediate next step is to integrate the Tarot X-8 drone used in flight test measurements of noise in ASCENT Project 77. The design optimization capabilities of the CHARM standalone code are being explored to generate reasonable notional rotor designs for passenger-sized eVTOL aircraft.

Task 13 - Continue Validating the New Flight Simulation/Noise Prediction System
The Pennsylvania State University

Objective
One objective of this task is to validate time-varying broadband noise predictions by using full-scale flight test data, because the broadband noise model used by the noise prediction system—the Brooks, Pope, and Marcolini (BPM) model—is typically validated in the literature by using time-averaged noise measurements of small-model-scale wind tunnel tests.

Research Approach
Time-varying broadband noise predictions were compared with flight test noise measurements for a Bell 206 helicopter (Schmitz et al., 2007), for a variety of flight path angles (level and descending flight). This data set is well suited to studying time-varying noise, because the microphones are fixed to the aircraft, such that de-Dopplerization of noise signals is not required. This data set was readily available and well understood, because one of the project investigators (Prof. Eric Greenwood) was part of the joint NASA-Army-University of Maryland team that conducted the measurements. In contrast, flight test data of UAM aircraft are not easily accessible.

For computing the aerodynamic loading needed as input for noise predictions, the aircraft was trimmed by using the PSUHeloSim flight simulation code previously developed in ASCENT Project 38. Because no pilot control commands or flight disturbances inherent to flight test were modeled, the trim state was maintained. Therefore, these cases validate only the noise prediction, not the flight dynamics or controls, which differ between helicopters and UAM aircraft. Nonetheless, the validation is valuable, because time-varying broadband noise is not yet well understood, even for helicopters in steady flight conditions, and time-varying broadband noise predictions have not been well validated in the literature. Furthermore, aerodynamic interactions can still occur in trimmed flight: for helicopters, blade-vortex interaction (BVI) is known to occur in descent, and main rotor/tail rotor (MR/TR) interactions can occur even in level flight. Aerodynamic interactions important for helicopters represent more general aerodynamic interactions expected to be important for UAM aircraft noise. For example, BVI represents a rotor interacting with its own wake, and MR/TR interactions are a type of rotor-rotor interaction.

To validate the time-varying broadband noise, comparisons of modulation depth are made between the noise predictions and flight test measurements.

Milestones
The milestones reached for this task include validation of time-varying broadband noise with flight test noise measurements, including accurate prediction of noise modulation depths and trends.

Major Accomplishments
Spectrograms are shown in Figure 1 for a microphone fixed to the aircraft, below the main rotor advancing side. The Bell 206 helicopter is in steady level flight, with a forward flight speed of 60 knots. In the self-noise predictions, the dominant feature is the main rotor modulation peak in the observer time range $0.4 < t < 0.8$ main rotor blade passage periods. Although

the main rotor self-noise levels are higher than those of the tail rotor in the predictions, the tail rotor has a higher blade passage frequency; consequently, the tail rotor noise modulation remains visible when the main rotor noise levels are low (e.g., at t = 0.1 times the main rotor blade passage period).

Despite good prediction of discrete frequency noise with respect to the flight test noise measurements, broadband noise is significantly underpredicted. This underprediction is not a uniform level offset, because tail rotor broadband noise levels are particularly underpredicted. In the measurements, main and tail rotor broadband noise have similar levels; in contrast, in the predictions, tail rotor broadband noise levels are much lower than those of the main rotor. Despite these differences, the predictions do accurately capture the modulation trends and depths, thus helping validate the noise predictions.

These results also reveal aspects in which noise predictions could be improved. For example, significant aperiodicity in tail rotor broadband noise is observed between tail rotor blade passages in the measurements. However, these aperiodicities are not in the predictions, possibly because of MR/TR interactions that were not modeled.

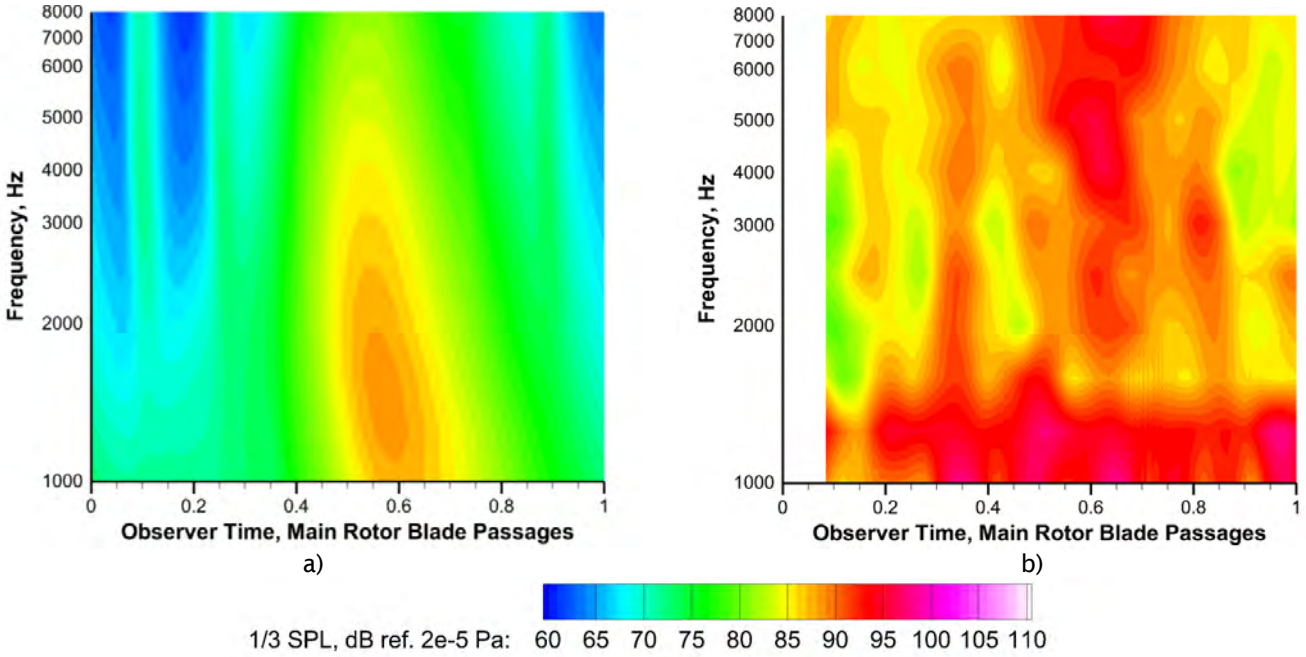

Figure 1. Spectrograms for 60-knot level forward flight. (a) Broadband self-noise predictions. (b) Flight test noise measurements.

The noise predictions in Figures 2 and 3 are shown for the same microphone as in Figure 1, but for a 60-knot, steady 7.5° descent flight condition. For this flight condition, BVI evidently occurs, as indicated by the discrete frequency noise peak seen in both the noise measurements and predictions (Figure 2). In the measurements, BVI adds broadband noise peaks at lower and higher frequencies, nearly in phase with the BVI peaks seen in the acoustic pressure time history. However, this finding is not seen in the broadband noise predictions (Figure 3), although the discrete frequency noise predictions accurately resolve the BVI peak fairly well.

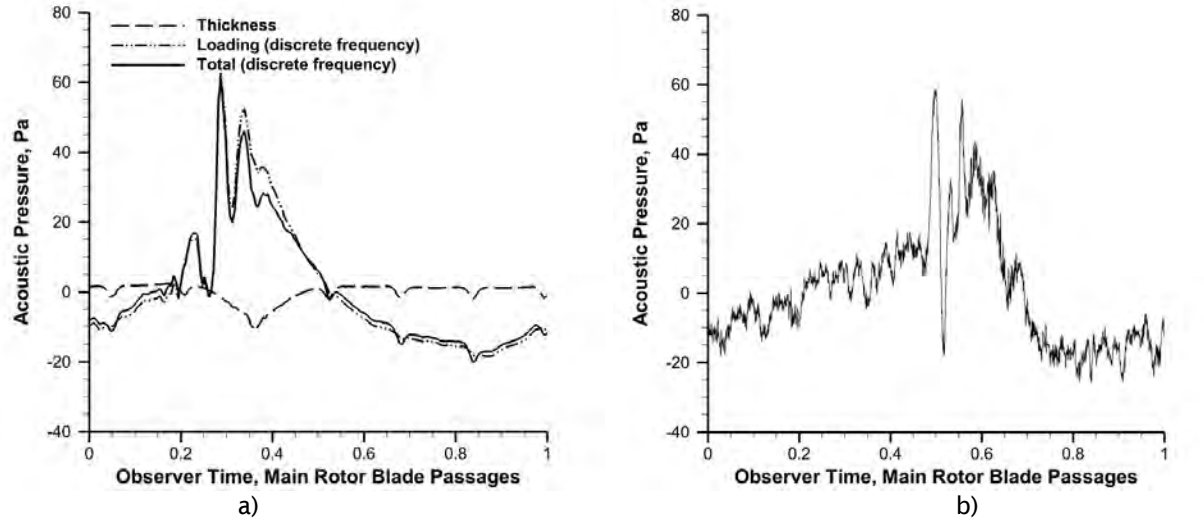

Figure 2. Acoustic pressure time histories for 60-knot, 7.5° descent. (a) Discrete frequency noise predictions. (b) Flight test noise measurements.

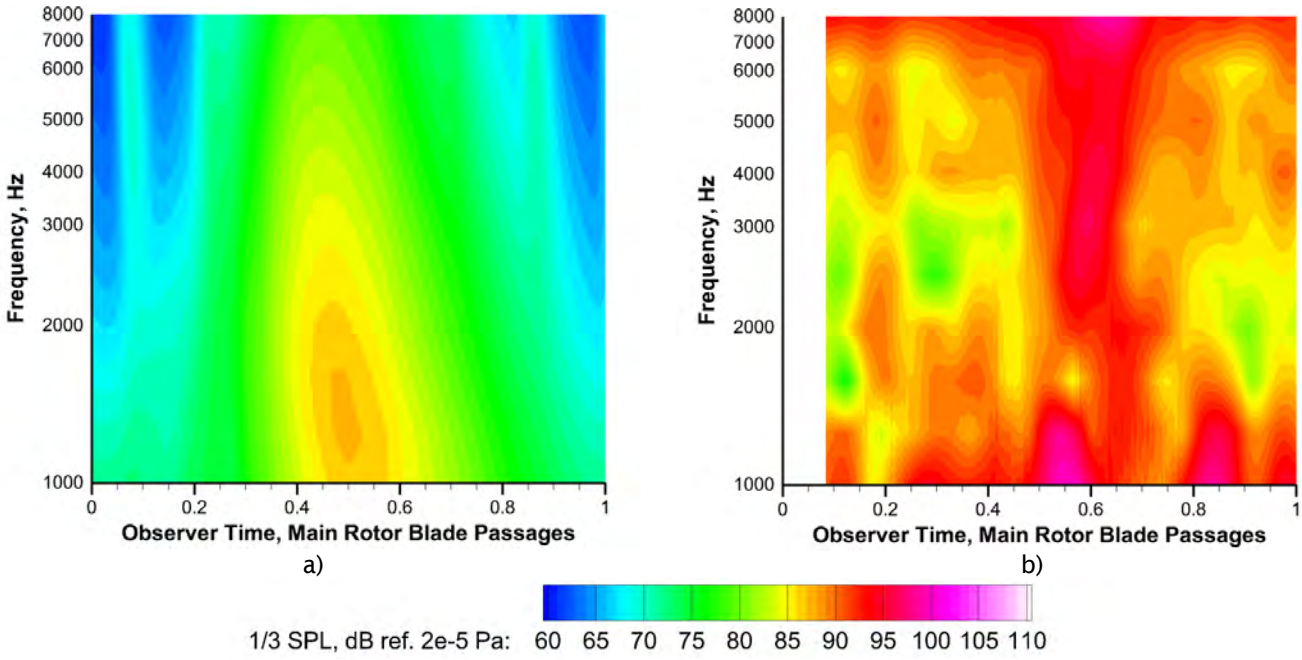

Figure 3. Spectrograms for 60-knot, 7.5° descent. (a) Broadband self-noise predictions. (b) Flight test noise measurements.

Publications

Published conference proceedings

Gan, Z.F.T., Brentner, K.S., Greenwood, E. (2022, June 14-17). *Time Variation of Helicopter Rotor Broadband Noise.* 28th AIAA/CEAS Aeroacoustics Conference, Southampton, UK.

Outreach Efforts

None.

Awards

None.

Student Involvement

Ze Feng (Ted) Gan, a graduate research assistant currently working toward his PhD degree at Penn State, performed validation of the time-varying broadband noise predictions for this task.

Plans for Next Period

The results shown above motivate refined modeling of possible sources of noise aperiodicity, particularly aerodynamic interactions. Noise caused by aerodynamic interactions will be thoroughly investigated, because it is expected to be important for the complex geometric configurations of UAM aircraft.

The underpredicted broadband noise levels previously shown suggest that modeling self-noise (broadband noise generated by turbulence that develops over the rotor blades) as the only broadband noise source may be insufficient. Therefore, we aim to model noise generated by aerodynamic interactions, such as ingestion of atmospheric or wake turbulence, in future work.

References

Schmitz, F. H., Greenwood, E., Sickenberger, R. D., Gopalan, G., Sim, B. W.-C., Conner, D. A., Moralez, E., and Decker, W. (2007). *Measurement and Characterization of Helicopter Noise in Steady-State and Maneuvering Flight.* American Helicopter Society 63rd Annual Forum & Technology Display.

Sargent, D. C. (2008) *In-Flight Array Measurements of Tail Rotor Harmonic Noise* [M. S. thesis, University of Maryland].

Task 14 - Investigate Test Trim Strategies for Notional UAM/eVTOL Vehicles

The Pennsylvania State University

Objective

The objective of this task is to explore various trim strategies for different notional UAM/eVTOL aircraft configurations. Several of these configurations tend to have more control effectors than are required for stable trimmed flight. The additional control effectors can be used to lower noise.

Research Approach

Figure 4 provides an overview of the mitigation strategies currently being explored. Notably, controller design strategies directly affect aircraft trim, particularly when additional control effectors are available. Thrust from rotors controlled via electric motors can be controlled by varying the angular velocity (variable revolutions per minute [RPM]) or collective pitch (variable pitch). These two methods of control can also be mixed to allow for more complex strategies. Aircraft trim strategies are diverse and highly correlated to the aircraft configuration being analyzed.

Current work has focused on a generic eVTOL aircraft, which is a lift plus cruise configuration (Figure 5 and Table 2). This configuration has a wing that enables redundant control in the form of the operating angle of attack controlled via the pitch of the aircraft. Control of the wing lift provides control over total rotor thrust and consequently noise. Task 9 (last year) demonstrated the impact of this strategy on deterministic noise from generic eVTOL performing a level turn maneuver. However, considering the impact of trim strategies on time variation in broadband noise is also important.

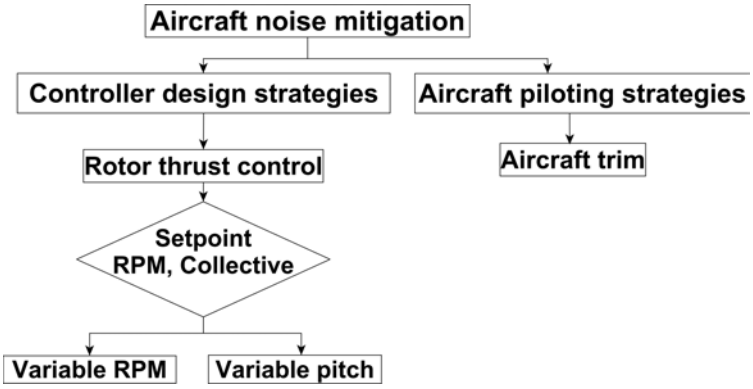

Figure 4. Overview of noise mitigation strategies.

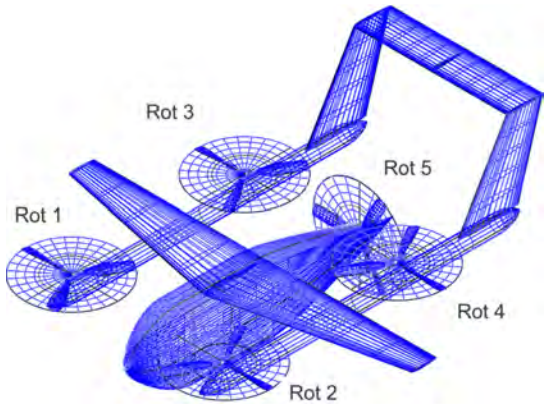

Figure 5. Generic eVTOL configuration.

Table 2. Properties of generic eVTOL aircraft.

Parameter	Generic eVTOL
Number of lift rotors	4
Number of pusher propellers	1
Gross weight	1,000 lb
Lift rotor radius	2.82 ft
Pusher prop radius	2.82 ft

Milestone

- Investigated the impact of variable RPM, variable pitch rotor thrust control strategies on broadband noise for generic eVTOL

Major Accomplishments

- Flight simulations of 10- and 50-knot level cruise were performed. The spectrogram of broadband noise for an observer in far field below the aircraft (Figure 6) revealed differences between variable pitch and variable RPM control schemes. The variable pitch scheme appeared to have higher peak noise levels in every modulation cycle, as a direct result of the lack of phase differences between rotors in the variable pitch scheme (Figure 7). This analysis opens new avenues of investigation of the effects of phase differences between rotors of an aircraft.
- Analysis of noise from turn maneuvers has revealed the effect of stall on broadband noise. The BPM model allows for separation of stall noise terms, thus helping isolate its importance. As shown in Figure 8, stall noise can add as much as 10 dBA to the total noise levels.

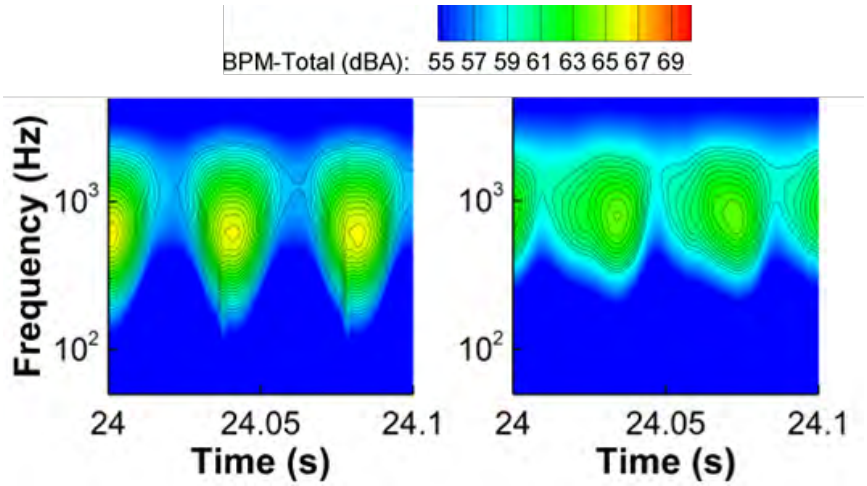

Figure 6. Spectrogram for 10-knot cruise at microphone in far field directly below the aircraft. Variable pitch (left); variable RPM (right).

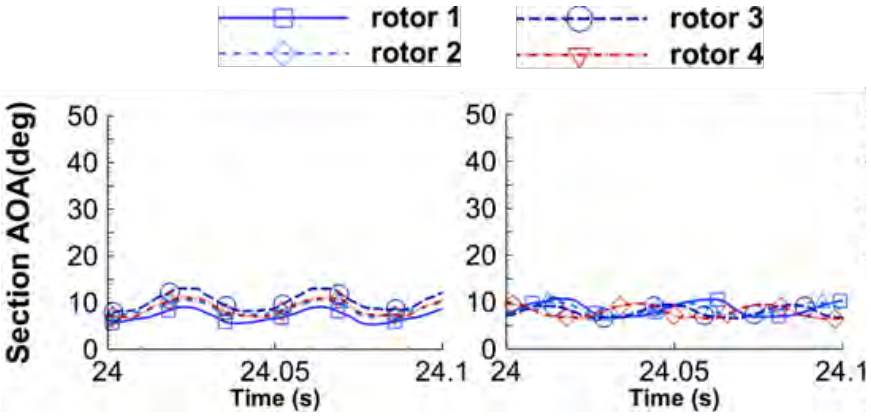

Figure 7. Variation in angle of attack at the rotor mid-section. Variable pitch (left); variable RPM (right).

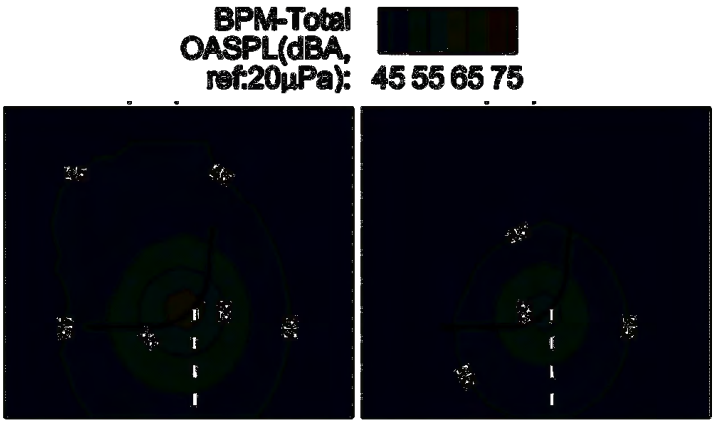

Figure 8. Broadband self-noise during a turn maneuver. Noise with stall (left); noise without stall (right).

Publications

Mukherjee, B., Brentner, K. S., Greenwood, E., Theron, J.-P., & Horn, J. F. (2022, May 10-12). *An Investigation of Piloting and Flight Control Strategies on Generic eVTOL Noise.* Vertical Flight Society's 78th Annual Forum & Technology Display, Fort Worth, TX. DOI: 10.4050/F-0078-2022-17441.

Outreach Efforts

None.

Awards

None.

Student Involvement

Bhaskar Mukherjee, a graduate assistant working on his PhD at Penn State, is investigating the impact of control schemes on eVTOL aircraft noise.

Plans for Next Period

On the basis of consistent findings from the controls and dynamics community, rotors in passenger sized eVTOL aircraft are poorly controlled via the variable RPM scheme. OEM manufacturers are highly likely to use a combination of variable pitch and variable RPM schemes. Future efforts will be directed to explore combinations of variable pitch and variable RPM further.

Task 15 - Develop a Database of Noise Predictions for UAM and eVTOL Vehicles During the Various Stages of Operation

The Pennsylvania State University

Objective

The objective of this task is to use the data generated in Tasks 13 and 14 to compile a database of vehicle models and noise predictions for various aircraft. This task will also develop and provide documentation of the "database," its contents, and how to add additional vehicle data to the database.

Research Approach

The approach to accomplishing this task is to use the noise prediction system developed in this project to make noise predictions for different aircraft under various flight conditions. Flight conditions can include flight speed, flight path angle (e.g., level vs. descending flight), maneuvers, etc. Ultimately, the initial database is envisioned to comprise a sequence of

acoustic hemisphere data for each stage of a particular flight operation for an eVTOL aircraft. The format will allow the hemisphere data to be compatible with advanced air mobility (AAM) and potentially the Aviation Environmental Design Tool. In addition to the speed and flight path angle defined by the AAM hemisphere format, the data will be extended to include other flight state data unique to eVTOL configurations and additional acoustic data that may be required to calculate noise metrics in future versions of AAM.

Milestones

The milestones reached for this task include the following:

- Prediction of time-varying broadband noise for level and descending flight
- Prediction of aircraft response to external gusts

Major Accomplishments

- The noise generated at different flight conditions (e.g., flight path angles) studied for helicopters under Task 2 provides insight into the future development of a noise database for UAM and eVTOL aircraft. Particular insight has been gained for time-varying broadband noise, as studied in Task 13, which has not been extensively studied in the literature for helicopters in steady flight conditions, let alone UAM and eVTOL aircraft in maneuvering flight. Work described in this report under Task 13 contributes to this task by studying the time-varying broadband noise of a Bell 206 in nominally steady level flight and 7.5° descent.
- The generic eVTOL aircraft has been used to investigate several maneuvers, including level cruise, steady turns, and level acceleration. Every maneuver was analyzed with the rotors controlled by either the variable RPM or the variable pitch scheme. An overview of maneuvers executed is listed in Table 3.
- Updates to the PSUDEPSim–CHARM–PSU-WOPWOP noise prediction system have enabled prediction of noise with the aircraft experiencing external gusts. A new utility has been written that enables generation of 3D grids that allow the creation of gust profiles that can vary with respect to time. Currently, step gust profiles are used in maneuvers.

Table 3. Current library of maneuvers successfully executed with generic eVTOL aircraft (Fig. 5).

Type of maneuver	Flight speed (knots)	Notes	Rotor thrust control scheme
Level cruise	10, 20, 30, 40, 50, 60	None	Variable pitch, variable RPM
Level turn	50	None	Variable pitch, variable RPM
Level acceleration	10	Accelerate to 50 knots at 0.025*g* acceleration	Variable pitch, variable RPM
External step gust	10	30 ft/s gust along the principal axes of the aircraft	Variable pitch, variable RPM

Publications

Published conference proceedings

Gan, Z.F.T., Brentner, K.S., Greenwood, E. (2022, June 14-17). *Time Variation of Helicopter Rotor Broadband Noise.* 28th AIAA/CEAS Aeroacoustics Conference, Southampton, UK.

Mukherjee, B., Brentner, K. S., Greenwood, E., Theron, J.-P., & Horn, J. F. (2022, May 10-12). *An Investigation of Piloting and Flight Control Strategies on Generic eVTOL Noise.* Vertical Flight Society's 78th Annual Forum & Technology Display, Fort Worth, TX. DOI: 10.4050/F-0078-2022-17441.

Outreach Efforts

None.

Awards

None.

Student Involvement
Ze Feng (Ted) Gan, a graduate research assistant currently working toward his PhD degree at PSU, performed time-varying broadband noise predictions for level and descending flight for this task.

Bhaskar Mukherjee, a graduate assistant working on his PhD at Penn State, is creating a database of noise predictions of eVTOL/UAM aircraft.

Plans for Next Period
- Flight test data are available for other descent angles (3˚, 6˚, 9˚, and 12˚), for which noise predictions will be made for this task and validated for Task 13.
- With the recent release of PSUDEPSim v2, the current library of noise predictions is expected to be substantially expanded to include climb and descent maneuvers.

Task 16 - Begin Investigation of Low-Noise Flight Operation Development
The Pennsylvania State University

Objective
The objective of this task is to amalgamate the findings of Tasks 13 and 14 to develop low-noise flight operational procedures.

Research Approach
Current findings from Tasks 13 and 14 have indicated that broadband noise is more dominant than deterministic noise for rotors operating at low tip Mach numbers. Stall has been shown to be a potentially significant contributor to noise. Other acoustic phenomena such as BVI, blade–wake interaction (BWI), and turbulence ingestion noise must be included in developing low-noise flight operations.

Milestones
- Developed flight control strategies that avoid blade stall
- Identified flight regimes that will result in strong BVI and BWI noise

Major Accomplishments
Preliminary changes have been made to PSUDEPSim to accommodate changes in rotor setpoint. The setpoint includes the rotor collective pitch when thrust is actuated by the variable RPM scheme, and the rotor RPM when thrust is actuated by the variable pitch scheme.

Publications
None.

Outreach Efforts
None.

Awards
None.

Student Involvement
Bhaskar Mukherjee, a graduate assistant working on his PhD at Penn State, is identifying strategies to develop low-noise flight operation strategies for eVTOL/UAM aircraft.

Plans for Next Period
Current noise prediction capabilities must be extended to include BVI, BWI, and turbulence ingestion noise. Understanding these aspects will aid in identifying further low-noise operation strategies.

Project 050 Over-Wing Engine Placement Evaluation

Georgia Institute of Technology

Project Lead Investigator

P.I.: Professor Dimitri N. Mavris
Director, Aerospace Systems Design Laboratory
School of Aerospace Engineering
Georgia Institute of Technology
404-894-1557
dimitri.mavris@ae.gatech.edu

Co-P.I.: Dr. Chung Lee
Research Engineer
Aerospace Systems Design Laboratory
School of Aerospace Engineering
Georgia Institute of Technology
404-894-0197
chung.h.lee@ae.gatech.edu

University Participants

Georgia Institute of Technology

- P.I.: Dr. Dimitri Mavris; Co-P.I.: Dr. Chung Lee
- FAA Award Number: 13-C-AJFE-GIT-057
- Period of Performance: February 5, 2020 to June 4, 2022
- Tasks relevant for this period (December 2021 to June 2022):
  1. Shape optimization of nacelle and wing
  2. Mission and trajectory analysis reformulation

Project Funding Level

Georgia Institute of Technology (Georgia Tech) was funded at $590,000 for a two-year project. Georgia Tech has agreed to a total of $590,000 in matching funds. This total includes salaries for the project director, research engineers, and graduate research assistants, as well as computing, financial, and administrative support, including meeting arrangements. The institute has also agreed to provide tuition remission for the students, paid for by state funds.

Investigation Team

Georgia Institute of Technology
P.I.: Dimitri Mavris
Co-P.I.: Chung Lee
Aerodynamics and parametric geometry: Jai Ahuja, Srujal Patel, Kenneth Decker
Multidisciplinary analysis and optimization (MDAO) methods: Christian Perron
Mission and systems integration: Evan Harrison
Graduate students: Mengzhen Chen, Sam Crawford, Marc Koerschner, Bilal Mufti, James Van der Linden, Anish Vegesna, Savri Gandhi, Samuel Moore

Project Overview

The over-wing nacelle (OWN) aircraft concept has promising environmental benefits due to the engine noise shielding provided by the wings and the potential to reduce landing gear height and therefore gear noise. However, if not optimized, this engine placement may cause penalties in fuel burn due to aerodynamic interactions between the wing and propulsor. In

this work, the team aims to develops an MDAO method for OWN aircraft. This task builds on past efforts by including noise shielding effects and analyzing multiple flight conditions to minimize fuel burn. One major challenge is the computational expense of analyses such as computational fluid dynamics (CFD). Thus, the approach relies on MDAO and efficient adaptive sampling techniques to use high-fidelity analyses where they are most needed for system analysis.

The optimization of an OWN aircraft configuration over a mission with noise constraints will enable accurate trade-offs between noise benefits and fuel burn. As a secondary benefit, the MDAO method will demonstrate efficient sampling methods for coupled, computationally intensive simulations in system analysis. These methods are useful to the FAA because many current applications require high-fidelity simulations to accurately assess physics phenomena such as noise and emissions. Both the OWN results and the MDAO techniques will enable more physics-informed decisions about the environment.

Work in 2020 focused on preliminary tasks to prepare a software tool chain and workflow for optimization, whereas efforts in 2021 focused on the execution of a full-scale MDAO process using supercomputing resources. Thus, the efforts in 2021 focused on a two-stage design process: nacelle location selection and preliminary shape optimization of the wing and nacelle. In 2022, we completed a second-stage shape optimization and implemented aero-propulsion integration with the mission and systems.

Note that the work described in this 2022 annual report only includes efforts up to June 2022. However, we discussed with FAA stakeholders a likely continuation of the project in 2023. Therefore, while finalizing a design optimization study, we also shifted our focus to laying the groundwork in aero-propulsion-mission analysis to enable sizing and mission analysis based on higher-fidelity physics data.

We deliberately assumed the same basic engine cycle and aircraft size while optimizing both over-wing and under-wing configurations. We found a 4% higher fuel flow at cruise for the OWN design. However, this preliminary result does not yet account for larger engine sizes that are possible due to engine clearance above the wing or for other mission segments such as climb. These issues will be considered in future research efforts in 2023.

Throughout the project, we emphasized two major themes in research methodology: (a) posing a more controlled comparison of OWN vs. under-wing nacelle (UWN) aircraft and (b) carefully accounting for numerical uncertainty.

A more controlled comparison of OWN and UWN aircraft is needed

Physics code uncertainty dominated the MDAO and research strategies. There can be significant discrepancies between un-calibrated CFD predictions and the flight performance of actual vehicles. Therefore, in the absence of validation data, it would be uninformative or misleading to compare the CFD-based performance of an optimized OWN with that of actual UWN vehicles. In addition to the physics discrepancy, there is an inconsistency in the MDAO problem for an OWN study with a two-year scope compared with the UWN configuration, which has been refined by the aircraft industry for around 70 years.

It is not practical for the present OWN study to include more design physics such as flight mechanics, static and dynamic structural constraints, nacelle geometry constraints due to acoustical liners and de-icing components, or pylon aero-thermo-structural mechanics. However, this can result in OWN performance that is overly optimistic due to an under-constrained problem formulation. This approach can lead to unrealistic conclusions about OWN compared with traditional UWN designs.

The goal is to provide FAA stakeholders with evidence to gauge the intrinsic aero-propulsive (dis)advantages of OWN vs. UWN designs. It is impossible to pose a perfectly controlled experiment; however, we adopted a “drag race” approach of optimizing OWN and UWN under the same MDAO formulation. This is an important decision in study methodology: it halves the computational budget needed to optimize each configuration, while leading to a more controlled comparison and more credible conclusions.

Uncertainty is a key theme

In our 2021 research, we found that careful uncertainty quantification is crucial to avoid misleading or less credible conclusions about OWN benefits. There are no relevant empirical data for direct validation or calibration of OWN or even UWN designs with powered turbofan engines. However, even controlling the numerical uncertainties due to CFD or MDA is important. Such uncertainty tracking has been incorporated into the optimization strategy itself. For example, we avoid optimization or adaptive sampling below an “uncertainty floor” of the physics code.

We found that much of the recent published literature on OWN designs relied on CFD meshes on the order of 0.8–30 million cells or nodes. Different CFD meshes and solvers have different dependences between mesh density and solution accuracy. For example, different solvers may be node-centered or cell-centered and will have different orders of formal accuracy due to computational stencils. User skill can also lead to different accuracies for similar cell counts. Nonetheless, most previous academic and industry studies have not included mesh sensitivity studies or accounted for numerical uncertainty due to the mesh, which is of critical importance. For example, there is a risk of reporting a 4% difference in fuel burn for OWN compared with UWN while the uncertainty is of a comparable order.

Careful attention to valid OWN vs. UWN comparisons and numerical uncertainty thus informs much of the detailed work in our 2022 tasks. We believe that such a research strategy will not lead to a simplistic performance comparison between the two configurations. However, it will yield more credible and complex conclusions to inform FAA stakeholders about potential environmental impacts of each configuration.

The details of the 2022 tasks are described in the following sections.

Notation and Abbreviations
α: angle of attack
C_D: drag coefficient
C_L: lift coefficient
CFD: computational fluid dynamics
L/D: lift-to-drag ratio
MDAO: multidisciplinary design analysis and optimization
O( ): order of magnitude
OWN: over-wing nacelle
UWN: under-wing nacelle

Task 1 - Shape Optimization of Nacelle and Wing

Georgia Institute of Technology

Objectives

The overall goal of this task is to design a problem architecture for MDAO to assess a single-aisle OWN transport aircraft. The MDAO process will use CFD and noise analysis codes such as NASA's Aircraft Noise Prediction Program (ANOPP), as well as weights, engine cycle, and mission analysis. The formulation was stated in the first year of the project, and it has evolved during the project according to our physics results. However, the following working MDAO problem statement was adopted:

- Minimize: fuel burn for a baseline mission
- Subject to: range and detailed side constraints
- With respect to: design variables including engine nacelle position (focusing on forward placement), nacelle and wing geometry, engine cycle, and operating condition
- Given: baseline single-aisle aircraft model and mission profile
- Returning: fuel burn

In discussion with FAA technical advisors, more emphasis is placed on aerodynamic performance optimization rather than noise, which is necessarily of lower fidelity. Thus, the single objective function of fuel burn is minimized, although noise is evaluated as a response with respect to design variables.

Research Approach

Research in previous years focused on MDAO formulation, tool-chain development, and the first-stage design process. In this first-stage design, we varied a small number of nacelle and wing shape variables and focused mainly on the nacelle location relative to the wing body in the X-Z plane (for a fixed span-wise Y location). Figure 1 shows examples of how the nacelle location was varied. The black dots show reference points fixed to the nacelle. The 3x5 grid of black dots was sampled, and detailed optimization was conducted given those nacelle locations. The blue nacelles are closest to the wing, and the grey nacelles are farthest. We selected the orange cases as final locations for a detailed second-stage optimization.

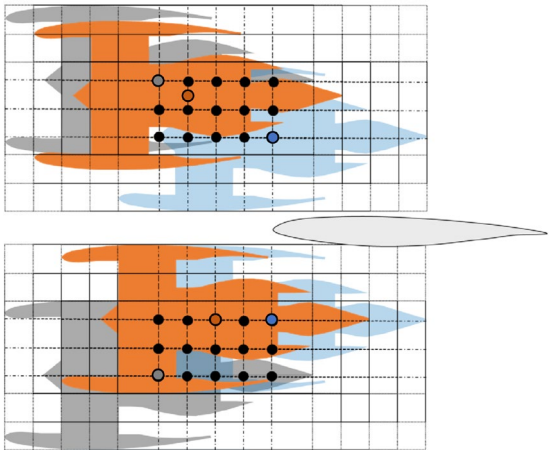

Figure 1. Orange locations are final selections for over-wing nacelle and under-wing nacelle designs.

We note that the selection of these orange cases was highly subjective, especially for the OWN case. Our 2021 work showed that fuel efficiency at cruise improves as the nacelle moves farther away from the wing. This is a consequence of the reduced MDAO problem statement, which does not include a structures/weights discipline. In a more realistic, larger-scale problem, the structural weight and drag of the pylon as well as the wing structure would penalize nacelle placements far from the wing.

There are few publicly available empirical pylon weight values; thus, we referred to physics models used in MDAO studies for order-of-magnitude estimates. For example, Gazaix and colleagues reported an optimized pylon mass of roughly 700 kg for a similar class of aircraft (Gazaix et al., 2019). Perturbing weight values in our baseline case in NASA's Flight Optimization System (FLOPS) mission analysis show order-of-magnitude sensitivities of O(1%) change in mission fuel burn due to an O(1000 lbf) aircraft weight perturbation. It is difficult to guess precisely how the pylon mass increases with nacelle distance from the wing attachment points, but it is reasonable to assume that the weight increases at least proportionally (or even more) with increases in this distance. Therefore, we roughly estimate that doubling the pylon length has an impact of O(1%) on the mission fuel burn. Consequently, we selected arbitrary intermediate nacelle locations for further refinement.

After down-selecting a nacelle location, our 2022 work focused on a more detailed shape optimization of the nacelle and wing. We used a gradient-free active subspace technique to reduce 45 wing and nacelle shape variables to 7 active modes or hybrid design variables that captured the main features of the original variables. We reported the theoretical details of this technique for canonical aerodynamic examples in a recent conference paper (Mufti et al., 2022). To optimize the active variables, we used a kriging or Gaussian process-based adaptive sampling method to minimize fuel flow rate at cruise (Mach 0.8, 39 kft). The procedure is a variant of a common expected improvement or efficient global optimization method described by Jones et al. (1998).

Note that this is a reduced/approximate version of the overall problem statement of minimizing fuel burn over an entire mission. The adaptive sampling continued until the expected improvement in fuel flow fell below the "noise floor" or the uncertainty in the coupled aero-propulsion analysis.

Results are shown in Table 1.

Table 1. Second-stage optimization results. L/D: lift-to-drag ratio; OWN: over-wing nacelle; UWN: under-wing nacelle.

Parameter	Baseline OWN	Optimized OWN	Baseline UWN	Optimized UWN
Fuel flow rate (lb/h) at cruise	2,600	2,330	2,290	2,240
L/D	19.3	21.5	20.5	21.3
Power code (throttle)	48.3	45.4	44.9	44.4
Pressure recovery	0.9965	0.9975	0.9975	0.9976

Surface pressure contours for baselines and optima for the two cases are shown in Figure 2. In both cases, there are significant shocks between the nacelle and fuselage. The shocks are slightly weakened in the optimized cases, but the differences are visually difficult to discern in the color maps. For OWN, the shock over the nacelle weakens substantially and moves aft. This trend is related to an increased maximum radius near the highlight for the optimized OWN.

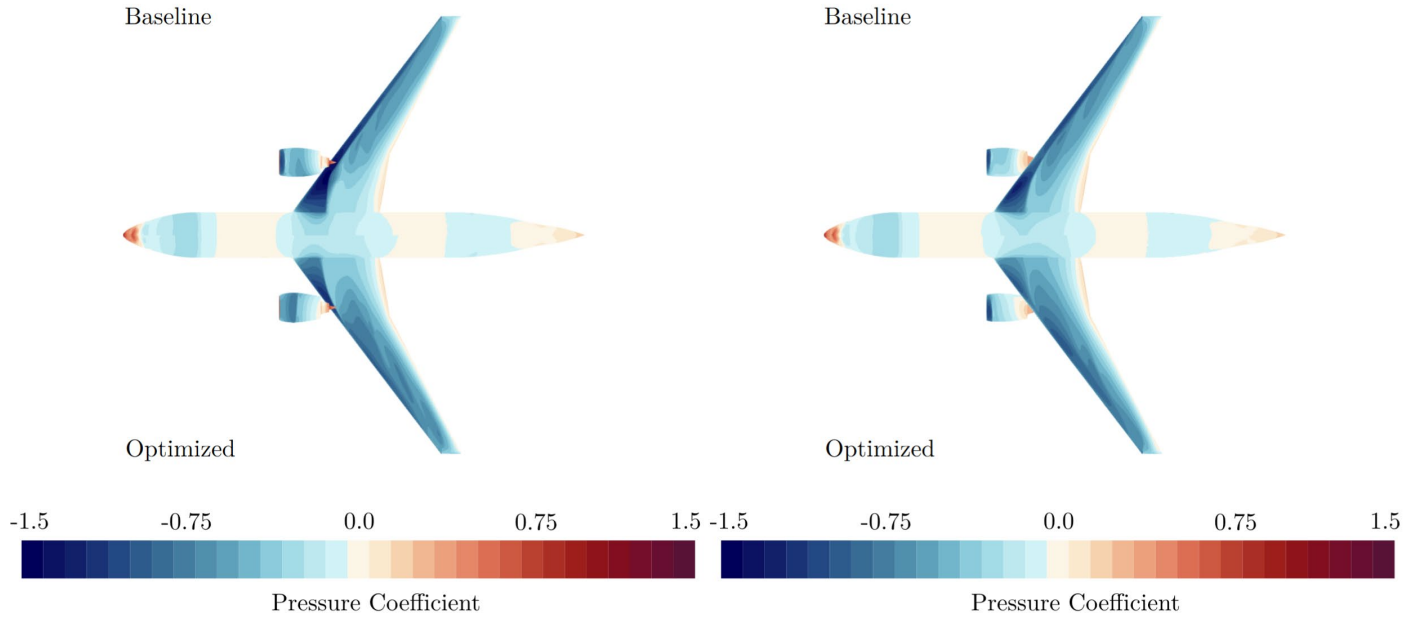

Figure 2. Pressure contours for baseline and optimum over-wing nacelle (left) and under-wing nacelle (right) designs.

This particular analysis shows an OWN design with a 4% higher fuel flow rate compared with the UWN design, but we avoid broad conclusions or generalizations from this result. This study deliberately aimed to control many factors to first compare the effect of moving an engine of fixed size between the two configurations. This effort is a precursor to our 2023 study on the effect of sizing. Furthermore, Task 2 describes work toward fuel burn prediction over an entire mission.

Milestone(s)

Include a description of any and all milestones reached in this research according to previously indicated timelines.

Major Accomplishments

- Completed optimization and comparison of OWN and UWN designs under cruise conditions for a fixed engine cycle and size
- Used final configurations to produce aero-propulsion data for use in the drag- and thrust-free mission analysis described in Task 2

Publications

Published conference proceedings

- Mufti, B., Chen, M., Perron, C., & Mavris, D. N. (2022, June 27). A multi-fidelity approximation of the active subspace method for surrogate models with high-dimensional inputs. *AIAA AVIATION 2022 Forum*. AIAA AVIATION 2022 Forum, Chicago, IL & Virtual. https://doi.org/10.2514/6.2022-3488

Outreach Efforts

- Collaborated with a NASA OWN expert during regular teleconferences with the FAA.

Awards
None.

Student Involvement
Mengzhen Chen and Bilal Mufti, continuing PhD students, contributed by testing different MDAO formulations using coupled propulsion cycle and CFD analyses.

Plans for Next Period
None.

References
Gazaix, A., Gallard, F., Ambert, V., Guénot, D., Hamadi, M., Grihon, S., Sarouille, P., Druot, T. Y., Brézillon, J., Gachelin, V., Plakoo, J., Desfachelles, N., Bartoli, N., Lefebvre, T., Gürol, S., Pauwels, B., Vanaret, C., & Lafage, R. (2019, June 17). Industrial application of an advanced bi-level mdo formulation to aircraft engine pylon optimization. *AIAA Aviation 2019 Forum*. AIAA Aviation 2019 Forum, Dallas, Texas. https://doi.org/10.2514/6.2019-3109

Jones, D. R., Schonlau, M., & Welch, W. J. (1998). Efficient Global Optimization of Expensive Black-Box Functions. *Journal of Global Optimization*, *13*(4), 455–492. https://doi.org/10.1023/A:1008306431147

Task 2 - Mission Analysis and Trajectory Optimization Setup
Georgia Institute of Technology

Objectives
In Task 1, we performed CFD-based aero-propulsion optimization for cruise conditions based only on computational limitations. We then aimed to evaluate fuel burn for OWN and UWN configurations over a mission including climb, etc. In consultation with our FAA project manager, we re-directed our objective to delve into a more fundamental reformulation of aero-propulsion-mission analysis.

Research Approach
The mission analysis task has diverged substantially from what we envisioned at the beginning of this research in 2020. Georgia Tech had previously relied heavily on its Environmental Design Space suite of mission sizing and synthesis tools built around NASA's FLOPS mission analysis and the propulsion cycle analysis based on NASA's Numerical Propulsion System Simulation (NPSS). During our research, we learned that our aero-propulsion integration physics required fundamental changes to mission analysis assumptions. This problem arose because almost all existing conceptual mission analysis codes assume relative independence between airframe aerodynamic drag polars and propulsion cycle. Such assumptions may be highly inaccurate if there is tight coupling of aero-propulsion physics in novel concepts such as those for OWN or boundary layer ingesting aircraft. Our preliminary tests suggested that fuel burn errors due to traditional mission analysis tools may be comparable or even larger than the difference between OWN and UWN results. At about the same time in 2022, we had very fruitful discussions with NASA experts who were working in a similar area. In consultation with our FAA project manager, we directed our effort toward developing novel mission analysis methods and code. Although our work is preliminary, we will continue these efforts in 2023.

In 2021, we formulated an aero-propulsion MDA approach that essentially planted a set of NPSS cycle analysis surrogate models within the CFD solver. Related to this, we adopted a drag- and thrust-free approach that accounted for integrated net forces instead of attributing forces to either the airframe or engine. Ideally, the bookkeeping of forces should not matter so long as the governing conservation laws are satisfied. However, legacy mission analysis codes treat these forces differently, and their interfaces limit the physical coupling effects that can be captured.

More specifically, codes such as FLOPS treat aerodynamic drag as a function of Mach number, altitude, and lift. The mission analysis code also uses engine decks (input tables) to capture quantities such as thrust, power code (throttle), Mach number, altitude, and fuel flow rate. However, when the airframe and engine are tightly integrated, drag actually depends on the engine inlet and outlet flow. The drag polars should depend on thrust. The engine also depends on the airframe aerodynamic field. Consider that the angle of attack affects the flowfield above the wing. With a forward-mounted OWN, the engine nozzle flow does not exhaust to free-stream conditions but rather into a high-speed/low-pressure region above the wing, as shown

in Figure 3. This flowfield can affect the propulsion operation. Even if the nozzle flow is choked, the external flowfield can influence the location and size of the sonic region as well as deflection of the exhaust plume, as shown in Figure 3. The aircraft angle of attack influences this external flowfield and therefore the engine operation. Legacy mission codes may not be able to read an engine table that explicitly captures this type of dependence.

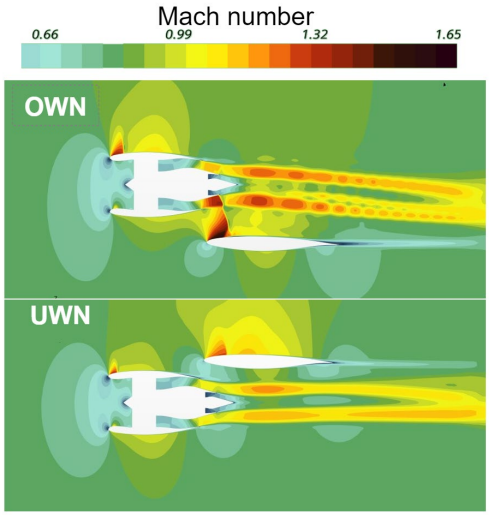

Figure 3. The external flowfield influences the engine cycle; these effects may not be captured in legacy mission analysis codes. OWN: over-wing nacelle; UWN: under-wing nacelle.

Several efforts in the field toward modern conceptual sizing and synthesis are currently underway, including LEAPS (Capristan et al., 2020), GASPy (Marfatia & Bergeson, 2021), SUAVE (MacDonald et al., 2017), TASOPT (Drela, 2016), MARLi (Druot et al., 2019), and Environmental Design Space (Nunez et al., 2021). Many of these efforts rely on traditional thrust and drag bookkeeping to account for propulsive and aerodynamic effects. The prevalence of novel aircraft concepts, which leverage coupled dynamic effects such as aero-propulsive interactions, has been found to produce considerable uncertainty within the traditional vehicle sizing and synthesis processes upon which these methods are often based. In our work, we began to reformulate the aircraft sizing and synthesis processes to leverage a more general kinematic expression of air vehicle performance.

Traditional sizing and synthesis methods within the conceptual and preliminary design phases, as presented in seminal works by Anderson (2000), Roskam (2005), and Raymer (2006), generally use an iterative approach to air vehicle design that begins with an initial vehicle layout or specification followed by disciplinary analysis. The results of these analyses are then leveraged to conduct performance analyses of the design, often as a combination of point performance measures and performance in a selected design scenario. These performance results are compared with corresponding requirements and used to iteratively modify the vehicle layout and configuration. Similar design methods, such as the energy-based constraint analysis of Mattingly et al. (2002), use a similar layout-analysis-performance design cycle that emphasizes the tuning of scaling factors within the design process. In these traditional sizing and synthesis approaches, the linkage between disciplinary analyses and vehicle-level performance is most evident through the utilized equations of motion. Most commonly, the aircraft equations of motion are posed as Eq. (1) and Eq. (2):

$$T\cos\epsilon - D - W\sin\gamma = m\frac{dV}{dt} \tag{1}$$

$$L + T\sin\epsilon - W\cos\gamma = m\frac{V^2}{r_c} \tag{2}$$

In these equations, ϵ is the engine mounting angle, γ is the aircraft flight path angle, r_c is the radius of curvature in the vertical plane, and the thrust, lift, drag, weight, and velocity are represented as $T, L, D, W,$ and V, respectively. These equations

represent two-dimensional translational motion of a point-mass system, a common representation of air vehicles in the conceptual design phase. Disciplinary analysis traditionally focuses on estimating the "forces of flight" as distinct phenomena. That is, conceptual or preliminary aircraft analysis provides estimates of lift and drag that are considered as independent from the thrust forces estimated via propulsive analysis. In later steps, performance analysis typically modifies Eq. (1) and Eq. (2) to consider particular point performance conditions or uses these equations to assess design mission performance. In these cases, estimates of the forces of flight are leveraged from upstream modeling and analysis efforts.

In the development of novel vehicle concepts and configurations, the fundamental layout-analysis-performance cycle is largely preserved. However, the nature of these concepts tends to dictate more nuanced disciplinary analysis, often characterized by the estimation of coupled dynamic effects. The transition toward design processes enriched with highly coupled analysis has been enabled by emerging MDAO methods. However, the consequence of this enrichment is a deviation from the traditional forces-of-flight formulation upon which the sizing and synthesis processes are based.

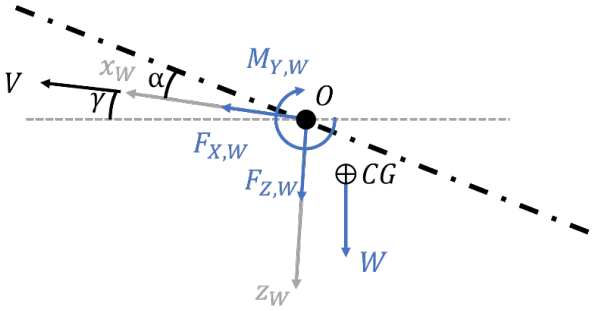

Figure 4. Point-mass representation free-body diagram.

To apply equations of motion of the form of Eq. (1) and Eq. (2) for highly coupled forces, one must implement a bookkeeping scheme that separates coupled forces into the traditional force representation. This process is likely to produce some degree of representation error, which may be on the order of 10%. While this error may often be acceptable within some aspects of conceptual design studies, it can lead to spurious conclusions when assessing the relative benefits of proposed configurations in terms of overall fuel burn.

The OWN mission and trajectory analysis addressed some of these sources of error within the design process by reformulating the basis of performance analysis to leverage a more general kinematic formulation of the equations of motion. With this approach, one can represent a wider variety of force and moment representations, which can include both traditional force-of-flight approaches or the results of highly coupled methods. Let us consider the point-mass system shown in Figure 1, which represents notional forces on a vehicle in the wind-axis reference frame along the X-Z plane. The translational equations of motion for this system are provided as Eq. (3) and Eq. (4), which pose external forces on the vehicle in general kinematic terms with no specific distinction or delineation of disciplinary forces.

$$F_{x,W} - mg\sin\gamma = m\frac{dV}{dt} \tag{3}$$

$$F_{z,W} + mg\cos\gamma = -mV\frac{d\gamma}{dt} \tag{4}$$

Because the kinematic formulation is a more general expression of rigid body equations of motion, more specific expressions of external forces can be readily incorporated in Eq. (3) and Eq. (4). For instance, traditional aerodynamic forces may be expressed as follows:

$$F_{x,aero} = -D\,, \quad F_{z,aero} = -L \tag{5}$$

Similarly, traditional propulsive forces may be expressed as follows:

$$F_{x,prop} = T\cos\epsilon\,, \quad F_{z,prop} = T\sin\epsilon \tag{6}$$

Summation of the forces expressed in Eq. (5) and Eq. (6) along each axis and substitution in Eq. (3) and Eq. (4) directly yield the traditional equations of motion expressed as Eq. (1) and Eq. (2).

In addition to supporting traditional forces of flight, a more general kinematic formulation of the equations of motion provides a convenient interface for coupled forces common to novel aircraft concepts. The resultant forces that arise from coupled analyses need only be resolved into the appropriate reference frame. Thus, this approach avoids additional representation errors that may arise from bookkeeping coupled forces in an intermediate disciplinary representation.

The benefits of utilizing a more general kinematic formulation of the equations extend beyond their utility for accommodating diverse external forces. A similar treatment of the equations of motion leveraged by Chakraborty and Mishra (2021) eschewed the traditional forces-of-flight formulation in favor of a kinematic-based expression of the equations in order to synthesize a variety of vehicles in disparate classes, including fixed-wing general aviation aircraft, electric vertical takeoff and landing vehicles, and rigid airships. These various vehicle categories share a common performance analysis formulation, which by nature enables the consideration of diverse external forces that may diverge from the traditional forces of flight.

Within an MDAO framework such as NASA's OpenMDAO, the proposed approach provides the basis for a flexible performance analysis. Kinematic equations of motion may be utilized with minimal modification to upstream analyses. For instance, the existing aerodynamic analysis, which provides estimates of lift and drag throughout the flight envelope, may be interfaced with the kinematic equations of motion by implementing Eq. (5), requiring little to no modification of existing methods or techniques.

We used OpenMDAO as well as NASA's Dymos optimal controls package to optimize trajectories for climb and cruise. In the spirit of controlled experimentation, the OWN and UWN aircraft began takeoff with the same gross weight and fuel. Note that a fully converged mission analysis for a target range would involve iterative solution of a boundary value problem, and the converged takeoff gross weight would be an output. Instead, we deliberately did not enforce this closure and simply allowed the aircraft to cruise to a fixed distance (no descent or landing modeled).

Our preliminary results reveal a need for further research. In particular, the trajectory optimization is highly under-constrained such that we find many solutions with unrealistic trajectories, including wildly oscillating throttle/power code settings or angles of attack over time. Further, if we impose physically realistic yet arbitrary constraints (such as limiting the derivatives of control variables), the resulting fuel burn is highly sensitive to our arbitrary settings. Simply put, the fuel burn for a single aircraft concept varies so greatly with these arbitrary constraints that the variation likely exceeds the difference between OWN and UWN designs. We will address this challenge in ongoing 2023 work.

Milestone(s)

Initial theory and software development

Major Accomplishments

- Theoretical development of a more general drag- and thrust-free mission and trajectory analysis method
- Initial implementation in OpenMDAO and Dymos software

Publications

None.

Outreach Efforts

Met and collaborated with the NASA GASPy and OpenMDAO development team.

Awards

None.

Student Involvement

M.S. students Anish Vegesna, Marc Koerschner, James Van der Linden, and Sam Crawford contributed to system/mission analysis formulation.

References

Capristan, F.M., Caldwell, D., Condotta, R., Petty, B. (2020). *Aircraft Analysis Using the Layered and Extensible Aircraft Performance System* (Report No. TM-2020-220558). NASA Scientific and Technical Information Program.

Marfatia, K. J., & Bergeson, J. D. (2021). *Aircraft flaps modeling in openMDAO*. https://ntrs.nasa.gov/citations/20210019908

Drela, M. (2016). *TASOPT 2.16 Transport Aircraft System Optimization*. Cambridge, MA.

MacDonald, T., Clarke, M., Botero, E. M., Vegh, J. M., & Alonso, J. J. (2017). SUAVE: an open-source environment enabling multi-fidelity vehicle optimization. In 18th AIAA/ISSMO Multidisciplinary Analysis and Optimization Conference (p. 4437).

Druot, T. Y., Belleville, M., Roches, P., Gallard, F., Peteilh, N., & Gazaix, A. (2019, June 17). A multidisciplinary airplane research integrated library with applications to partial turboelectric propulsion. *AIAA Aviation 2019 Forum*. AIAA Aviation 2019 Forum, Dallas, Texas. https://doi.org/10.2514/6.2019-3243

Salas Nunez, L., Tai, J. C., & Mavris, D. N. (2021, January 11). The environmental design space: Modeling and performance updates. *AIAA Scitech 2021 Forum*. AIAA Scitech 2021 Forum, VIRTUAL EVENT. https://doi.org/10.2514/6.2021-1422

Anderson, J. D. (2012). *Introduction to flight* (7th ed). McGraw Hill.

Roskam, J. (2005). *Airplane design*. DARcorporation.

Raymer, D. P. (2006). *Aircraft design: A conceptual approach* (4th ed). American Institute of Aeronautics and Astronautics.

Mattingly, J. D., Heiser, W. H., & Pratt, D. T. (2002). *Aircraft Engine Design* (2nd ed). American Institute of Aeronautics and Astronautics.

Chakraborty, I., & Mishra, A. A. (2021). Generalized energy-based flight vehicle sizing and performance analysis methodology. *Journal of Aircraft*, *58*(4), 762–780. https://doi.org/10.2514/1.C036101

Project 051 Combustion Concepts for Next-Generation Aircraft Engines

Massachusetts Institute of Technology

Project Lead Investigator

Steven R. H. Barrett
Professor of Aeronautics and Astronautics
Director, Laboratory for Aviation and the Environment
Massachusetts Institute of Technology
77 Massachusetts Ave, Building 33-322, Cambridge, MA 02139
617-253-2727
sbarrett@mit.edu

University Participants

Massachusetts Institute of Technology (MIT)

- P.I.: Professor Steven R. H. Barrett
- FAA Award Number: 13-C-AJFE-MIT, Amendment Nos. 061, 071, 079, and 097
- Period of Performance: February 5, 2020 to September 19, 2023 (reporting here with the exception of funding level and cost sharing only for the period October 1, 2021 to September 30, 2022)
- Tasks:
    1. Evaluate water injection to extend the operating envelope and reduce emissions
    2. Evaluate the effect of fuel stage ratio on the emissions of a lean-burn radially staged combustor

Project Funding Level

This project received $900,000 in FAA funding and $900,000 in matching funds. Sources of match are approximately $226,000 from MIT, plus third-party in-kind contributions of $674,000 from NuFuels LLC.

Investigation Team

- Professor Steven Barrett - P.I. (Tasks 1 & 2)
- Dr. Raymond Speth - co-P.I. (Tasks 1 & 2)
- Dr. Jayant Sabnis - co-investigator (Tasks 1 & 2)
- Syed Shayan Zahid - graduate student (Task 1)
- Yang Chen- graduate student (Tasks 2)

Project Overview

The objective of this project is to evaluate the impacts of novel combustion concepts on aircraft engine performance. Specifically, the performance characteristics of interest are the engine efficiency and emissions. With advances in material technology in the past 50 years, aircraft engines with higher pressure and temperature ratios have been designed to improve the engine total efficiency and reduce fuel consumption. However, the increase in combustor temperatures tends to produce higher nitrogen oxide (NO_x) emissions, which account for a substantial portion of aviation's environmental impact. Different combustor techniques have been developed to both reduce emissions and maintain high efficiencies. The novel combustion concepts currently being investigated in this project are engine water injection and lean-burn radially staged combustion. These concepts are being studied by using numerical models for aircraft mission simulation (Transport Air System Optimization [TASOPT]), engine simulation (Pycycle and Numerical Propulsion System Simulation), and combustor emissions simulation (Pycaso).

Task 1 - Evaluate Water Injection to Extend the Operating Envelope and Reduce Emissions

Massachusetts Institute of Technology

Objectives

Water injection can be used to control temperatures in the engine, thus potentially expanding the design space and enabling decreases in mission fuel burn and emissions. For this task, we evaluated the impacts of water injection at (a) the low-pressure compressor inlet, (b) the high-pressure compressor inlet, and (c) the combustor inlet. For each option, the effect of water injection on the engine cycle was evaluated to determine engine designs, which were optimized for the impacts of water injection, i.e., considering allowable limits on compressor discharge temperature and turbine inlet temperature. Water injection reduces peak temperatures and therefore NO_x formation. Simultaneously, reducing temperature in the compression process tends to improve the compressor adiabatic efficiency under the same polytropic efficiency, thereby contributing to higher engine thermal efficiency.

In the past, water injection was used primarily for thrust augmentation, at a time when emissions were not thoroughly evaluated as part of the aircraft design process. For this reason, the existing literature on the effect of water injection on emissions is sparse, thus justifying the need to conduct analyses. One drawback with water injection is the weight of water being carried. We evaluate the extent to which benefits in terms of mission fuel consumption and emissions reduction are obtainable through engine water injection, and in what range the returns become diminishing, owing to the weight of water carried on board.

Research Approach

- Perform psychrometric calculations to determine the maximum amount of water that can be vaporized at the low-pressure compressor (LPC) inlet, high-pressure compressor (HPC) inlet, and HPC outlet
- Develop a modified engine cycle model to capture the impacts of water injection into different stages of the compressor on the overall efficiency of the engine (with thrust and combustor outlet temperature kept constant while the engine is resized for different amounts of water injection)
- Use the Pycaso chemical reactor network model to analyze the impact of engine water injection on the NO_x emissions of a rich-quench-lean combustor
- Use the Breguet range equation to assess the total impacts of engine water injection on total fuel consumption and NO_x emissions for sample missions with different ranges; for different flight ranges, identify the optimal water to air ratios for either minimizing fuel consumption with a specific NO_x emissions reduction or minimizing NO_x emissions with no fuel consumption penalty
- Use the Schmidt-Appleman criterion to evaluate the impact of water injection on contrail formation
- Use a mass and energy conservation model to evaluate the droplet lifetime of water injected in LPC and HPC

Major Accomplishments

- Determined that efficiency increases for both pre-LPC and pre-HPC water injection, but decreases for post-HPC water injection, and that for the same water-to-fuel ratio, pre-LPC water injection induces a greater efficiency gain than pre-HPC injection
- Found that water injection in all three locations reduces NO_x emissions
- Determined that, owing to the weight of water carried on board, water injection is more beneficial for short-range flight in terms of the tradeoff between fuel consumption and NO_x emissions
- Found that water injection yields a significant increase in persistent contrail formation
- Estimated the droplet lifetime for water injected in LPC or HPC, which was found to be less than the residence time within the compressor stages, thus suggesting that injected water will be fully evaporated

Publications

Zahid, S. S. (2022). *Impact of Water Injection on Emissions of Nitrogen Oxides from Aircraft Engines* [Thesis, Massachusetts Institute of Technology]. https://dspace.mit.edu/handle/1721.1/144573

Outreach Efforts

Results were presented during the ASCENT Advisory Committee Meeting (October 26-28, 2021).

Awards
None.

Student Involvement
This task was conducted primarily by Syed Shayan Zahid, working under the supervision of Dr. Jayant Sabnis and Dr. Raymond Speth.

Plans for Next Period
This task has been completed.

Task 2 - Evaluate the Effect of Fuel Stage Ratio on the Emissions of a Lean-burn Radially staged Combustor
Massachusetts Institute of Technology

Objective
A lean-burn radially staged combustor contains two flame zones: a rich diffusion pilot flame and a lean partially premixed main flame. Examples of this type of combustor are the dual annular combustor, the twin annular premixed swirl (TAPS) combustor, and the TAPS-II. Further developments are expected in the future, given the potential for NO_x reduction. Previous studies have found differing results regarding how the fuel stage ratio (the ratio between the fuel mass flow rate in the main flame to the fuel mass flow rate in the pilot flame) affects NO_x emissions, and whether an optimal fuel stage ratio exists that would minimize NO_x emissions across all flight conditions. The objective of this task is to understand how the distribution of fuel between pilot and main stages affects the NO_x emissions of a radially staged combustor, and to identify an optimal control scheme for the fuel staging for this type of combustor.

Research Approach
- Create a TASOPT model approximating the performance of a 737-9 Max aircraft, and compute engine requirements for a representative mission
- Calibrate an engine cycle model by using Numerical Propulsion System Simulation to approximate the performance of a CFM LEAP-1B engine, and compute the combustor inlet conditions for the TASOPT mission
- Develop and calibrate a Pycaso chemical reactor network model to simulate the performance of a TAPS-II combustor in a CFM LEAP 1B engine, and compute the NO_x emissions under a range of conditions
- Sweep across the sea-level-static thrust condition from 4% to 100% rated thrust, and across phases of flight, including the landing and takeoff cycle, and cruise operation for a range of fuel stage ratios; compute the resulting NO_x emissions

Major Accomplishments
- Determined that, as thrust increases, and through different phases of flight, the optimal fuel stage ratio varies in a semi-discrete fashion with the following characteristics:
  - The main flame equivalence ratio corresponding to the optimal fuel stage ratio lies within a narrow range (0.4–0.47 in the current study).
  - Two optimal semi-constant fuel stage ratio modes exist during medium- to high-power operation, wherein fuel staging can be used.
- Found that the medium-power mode and the high-power mode with optimal fuel stage ratio correspond to a main-flame-dominated NO_x production mode and a pilot-flame-dominated NO_x production mode, respectively

Publications
Chen, Y. (2022). *Effects of Fuel Split Ratio on NO_x Emissions of a Lean-burn Staged Combustor* [Thesis, Massachusetts Institute of Technology]. https://dspace.mit.edu/handle/1721.1/144712

Outreach Efforts
None.

Awards
None.

Student Involvement
This task was conducted primarily by Yang Chen, working under the supervision of Dr. Jayant Sabnis and Dr. Raymond Speth.

Plans for Next Period
Uncertainties in the combustor model should be assessed by evaluating fuel stage ratio studies for different configurations of the combustor model. In addition, we plan to further investigate the narrow equivalence ratio range for the optimal main flame. The findings may lead to a general definition of the optimal fuel stage ratio control scheme for a lean-burn radially staged combustor. The results could then be used to estimate the minimum achievable cruise NO_x emissions for other combustor designs based solely on ground measurement data.

Project 052 Comparative Assessment of Electrification Strategies for Aviation

Massachusetts Institute of Technology

Project Lead Investigators

Steven R. H. Barrett
Professor of Aeronautics and Astronautics
Director, Laboratory for Aviation and the Environment
Massachusetts Institute of Technology
77 Massachusetts Ave, Building 33-207, Cambridge, MA 02139
617-452-2550
sbarrett@mit.edu

Florian Allroggen
Executive Director Aerospace Climate and Sustainability & Research Scientist
Laboratory for Aviation and the Environment
Department of Aeronautics and Astronautics
Massachusetts Institute of Technology
77 Massachusetts Ave, Building 33-115A, Cambridge, MA 02139
617-715-4472
fallrogg@mit.edu

Raymond Speth
Principal Research Scientist
Laboratory for Aviation and the Environment
Department of Aeronautics and Astronautics
Massachusetts Institute of Technology
77 Massachusetts Ave, Building 33-322, Cambridge, MA 02139
617-253-1516
speth@mit.edu

University Participants

Massachusetts Institute of Technology (MIT)

- P.I.: Professor Steven R. H. Barrett; co-P.I.s: Dr. Florian Allroggen, Dr. Raymond Speth
- FAA Award Number: 13-C-AJFE-MIT, Amendment Nos. 062, 072, 080, 093, and 098
- Period of Performance: February 5, 2020 to September 19, 2023
- Tasks:
    1. Develop a suite of roadmaps for aircraft electrification (covered in previous reporting period; not reported for this period)
    2. Develop a system-level engineering model of power conversion processes and aircraft energy requirements
    3. Develop a model for analyzing the economics and emissions of electrification strategies
    4. Analyze the system-level costs and benefits of the electrification strategies

Project Funding Level

This project received $1,060,000 in FAA funding and $1,060,000 in matching funds. Sources of match are approximately $276,000 from MIT, plus third-party in-kind contributions of $460,000 from NuFuels, LLC, $110,000 from Savion Aerospace Corporation, and $214,000 from Google, LLC. Funding is reported for the full period of performance, as noted above.

Investigation Team

P.I.:	Professor Steven Barrett (MIT) (all MIT tasks)
Co-P.I.s:	Dr. Florian Allroggen (MIT) (all MIT tasks)
	Dr. Raymond Speth (MIT) (Tasks 1, 2, and 4)
Co-investigator:	Dr. Sebastian Eastham (MIT Task 4)
Postdoctoral Associates:	Christoph Falter (all MIT tasks)
Graduate Research Assistants:	James Abel (MIT Tasks 3 and 4)
	Dun Tan (MIT Task 2 and 4)
	Prashanth Prakash (MIT Task 4)

Project Overview

The long-term goal of this project is to quantify the costs, emissions, and environmental impacts (i.e., climate and air-quality impacts) of different electrification approaches for commercial aviation. The electrification pathways include battery-electric ("all-electric") aircraft, and aircraft using drop-in sustainable aviation fuels (SAFs) made with substantial electricity input ("PtL") and liquid hydrogen (LH_2)-powered aircraft. The project helps identify the best approach for using one unit of electric energy to power aviation. For this purpose, we develop both system-level engineering and system-level economic models, which assess electricity generation, fuel production, fuel transportation and storage, aircraft energy requirements, and aircraft operations. The models analyze different electrification pathways by using what can be described as a "power station to wake" approach. They quantify differences in costs and emissions associated with each electrification approach and compare them to a set of baseline aircraft powered by petroleum-derived fuels or drop-in SAFs made from biomass or waste streams. The outputs are used in a cost–benefit analysis, which provides insights into the net benefits associated with each technology, while also considering each technology's environmental impacts.

Task 2 - Develop a System-level Engineering Model of Power Conversion Processes and Aircraft Energy Requirements

Massachusetts Institute of Technology

Objective

The goal of this task is to develop an aircraft technology model as well as a fuel production model. Jointly, these models provide a technical representation of the power conversion processes from initial power generation to propulsion on board the aircraft. During the reporting period, our analysis focused on the aircraft model. Specifically, we analyzed hydrogen-powered aircraft to understand how different fuel system configurations for LH_2-powered aircraft influence aircraft performance.

Research Approach

We designed an LH_2-powered aircraft using multi-disciplinary design and optimization based on the Transport Aircraft System Optimization (TASOPT) code. The first-principles-based approach ensures that the results for unconventional designs, such as those using a turbo-electric powertrain or cryogenic fuels, represent the physics of the system and are not derived from extrapolating historical data.

To understand how different fuel system configurations affect LH_2-powered aircraft performance, we assessed two tank designs: (a) single-walled foam insulated tanks and (b) double-walled vacuum insulated tanks. The two tank models represent a wide spectrum of potential tank designs by characterizing the respective volume, weight, and thermal requirements. The range of tank designs was then integrated into the aircraft model to investigate the impact of tank design (particularly gravimetric efficiency) on aircraft performance.

Milestone

The modeling of LH_2 narrowbody aircraft has been completed, including a sensitivity study of the impact of tank design on aircraft performance. The results have been summarized in an early manuscript draft.

Major Accomplishments

We assessed the trade-off between aircraft energy demand and tank thermal efficiency (hydrogen boiloff). As expected, single-walled insulated tanks with a higher gravimetric efficiency were found to have a lower aircraft energy demand than their heavier double-walled counterparts. However, single-walled tanks are generally associated with an increase in hydrogen boiloff because of their lower thermal efficiency. In this study we optimized short-, medium-, and long- range aircraft with a spectrum of tank designs; the results are summarized in Figure 1. Aircraft with heavier tanks (gravimetric efficiency of 27%–35%) have an energy demand 14%–49% greater than that of an aircraft with a lighter tank (gravimetric efficiency of 60%–70%). Our results are consistent with findings reported in the literature in showing that the feasibility of LH_2 aircraft is dependent on the tank architecture. Lightweight tanks are preferred because of their higher gravimetric efficiency, thereby enabling more efficient aircraft design.

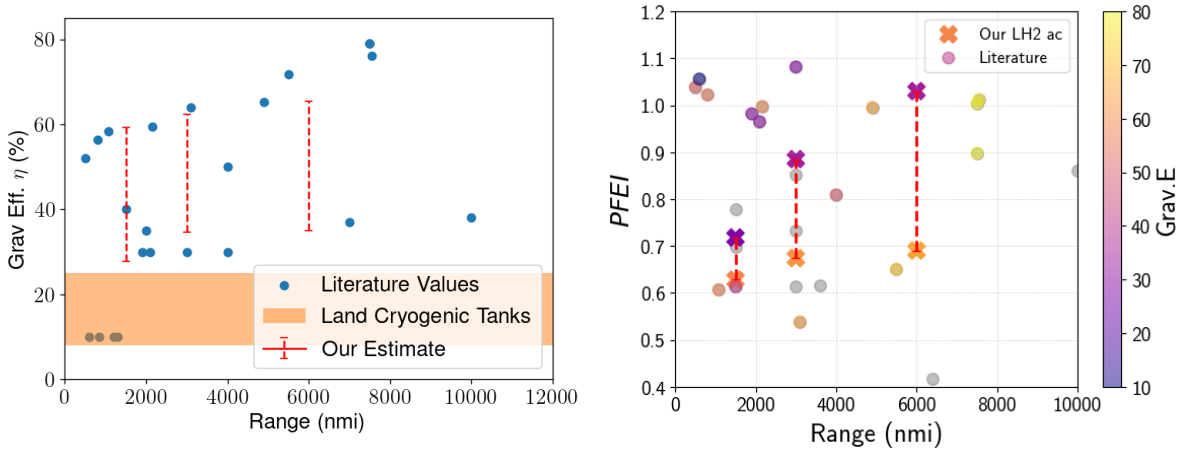

Figure 1. Gravimetric efficiency (left) and PFEI of the aircraft (right) presented in this study, plotted against existing aircraft in the literature. Gravimetric efficiency measures the ratio between the weight of fuel stored and total weight of the fuel and tank infrastructure. PFEI is the mission payload fuel energy index, which is used to measure the energy demand of the aircraft per passenger distance flown.

Publications

None.

Outreach Efforts

- Provision of insights into the aircraft model during the Spring 2022 ASCENT meeting
- Presentation to the MIT Airline Industry Consortium (Summer 2022)
- Presentation to numerous industry stakeholders and government agencies

Student Involvement

During the reporting period, the MIT graduate student involved in this task was Dun Tan.

Plans for Next Period

Over the coming year, we plan to extend the analyses to additional market segments and electrification strategies. The current aircraft implementations in TASOPT are limited to single-aisle aircraft for medium-haul routes. The team will continue to perform additional work including aircraft models with longer or shorter ranges, as well as higher or lower passenger capacity.

Task 3 - Develop a Model for Analyzing the Economics and Emissions of Electrification Strategies

Massachusetts Institute of Technology

Objective

The goal of this task is to develop a system-level analysis capability for assessing the possible electrification pathways and their deployment in various aircraft electrification scenarios. The system model focuses on fuel production, fuel distribution, airport infrastructure (covered in the previous reporting period), and aircraft operations. Outcomes of interest include the operating costs, required investments, and life-cycle greenhouse gas (GHG) emissions of the system.

During the current reporting period, our focus was on developing a model to assess potential supply chain designs for PtL fuels and LH_2 to meet aviation demands, while considering local production conditions, particularly for renewable power generation.

Research Approach

We developed a four-step modeling approach to calculate the global costs and emissions for LH_2 and PtL production, to meet aviation demand in global displacement scenarios. In the first step, we calculated the global energy demand for passenger aviation in 2019 and for a year-2050 traffic scenario. Second, we computed the fuel production strategy that meets the energy demand at each airport while minimizing fuel cost. Geographic information system data sets were used to calculate the levelized cost of renewable electricity generation (wind and solar photovoltaic) at every location. A techno-economic fuel production and energy transmission model determined the resulting fuel cost at each production site. An optimization loop linked each airport to the energy production locations that minimizes the systemwide fuel cost. Third, we calculated the cost of additional airport infrastructure for liquid hydrogen refueling operations. Finally, the system life-cycle emissions were assessed. The life-cycle analysis encompassed embedded carbon emissions associated with electricity generation, fuel production (e.g., catalyst production and capital infrastructure construction), and fuel transportation.

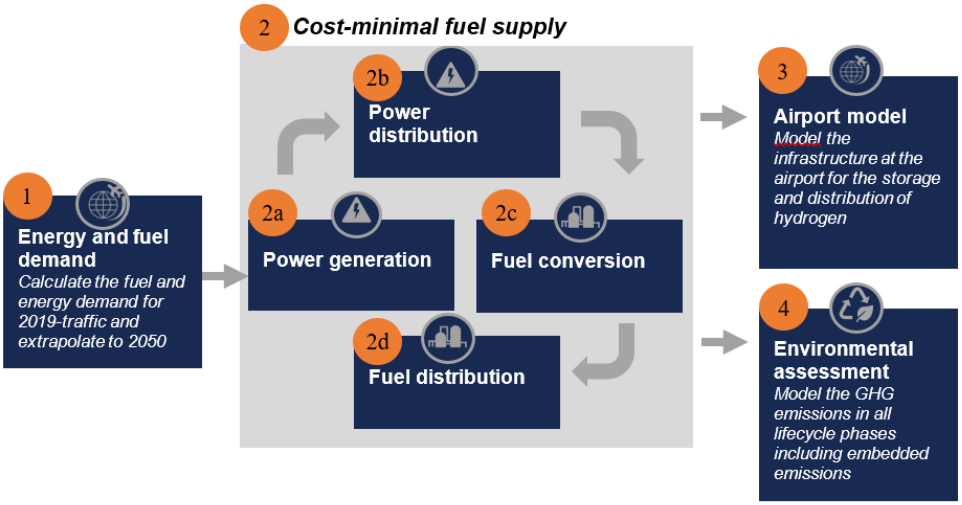

Figure 2. Summary of the fuel supply system modeling approach.

Milestones

The global model of for PtL and LH_2 supply chains has been completed. The results have been presented to several audiences (described below), and a manuscript is currently under development.

Major Accomplishments

On a per unit of energy basis, we found that the average cost of LH_2 fuel and PtL in 2050 will be approximately 2.0 and 2.8 times the average price of Jet A in 2021. The higher predicted cost of PtL than LH_2 is driven largely by the higher specific electricity demand of production for PtL (approximately 1.5× that of LH_2) and the investment cost of direct air capture.

The predicted cost of LH_2 at the airport exhibits greater regional variability than the cost of PtL, because of the relatively high cost of transporting energy in an LH_2 aviation system, owing to the fuel's physical properties (low temperature and tendency to leak). The high cost of fuel transportation also drives the model toward selecting energy generation sites close to the airport; consequently, LH_2 production systems tend to be regional. The regional renewable energy generation capacity hence greatly affects the price of LH_2. In contrast, PtL can be produced at sites of low-cost electricity generation and then transported to the airport. The distribution costs of PtL are low, thus resulting in a global fuel production system with relatively small cost variation between airports. The model further suggests that both PtL and LH_2 production would rely on wind energy, because of its relatively high-capacity factor in optimal regions.

The life-cycle GHG emissions of LH_2 and PtL production with current technology fall between 4.9 and 7.9 (median 6.1) gCO_2 eq./MJ for LH_2, and 10.2 and 12.5 (median 11.2) gCO_2 eq./MJ for PtL. Thus, the life-cycle GHG emissions are 93%–97% lower for LH_2, and 87%–93% lower for PtL, than the global average fossil Jet A life-cycle GHG emissions. The greater emissions footprint of PtL than LH_2 is due to the higher energy intensity of PtL production and the emissions from catalyst production. Variations in life-cycle emissions among production sites result from differences in the achievable capacity factor, which affects the extent of energy infrastructure required to generate the required amount of electricity.

Results and analysis of our supply chain modeling for PtL and LH_2 were included in the International Civil Aviation Organization long-term global aspirational goal report.

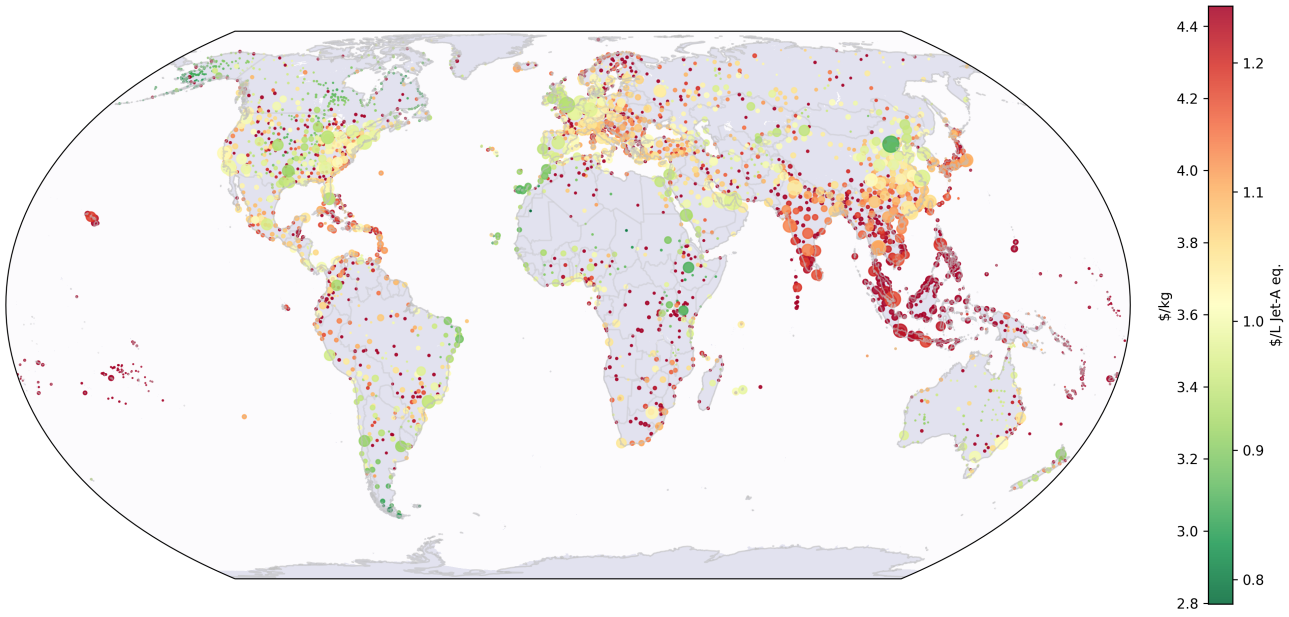

Figure 3. Map of global LH_2 fuel costs by airport in 2050. The circles represent single airports and their respective fuel demand. The marker area corresponds to fuel demand.

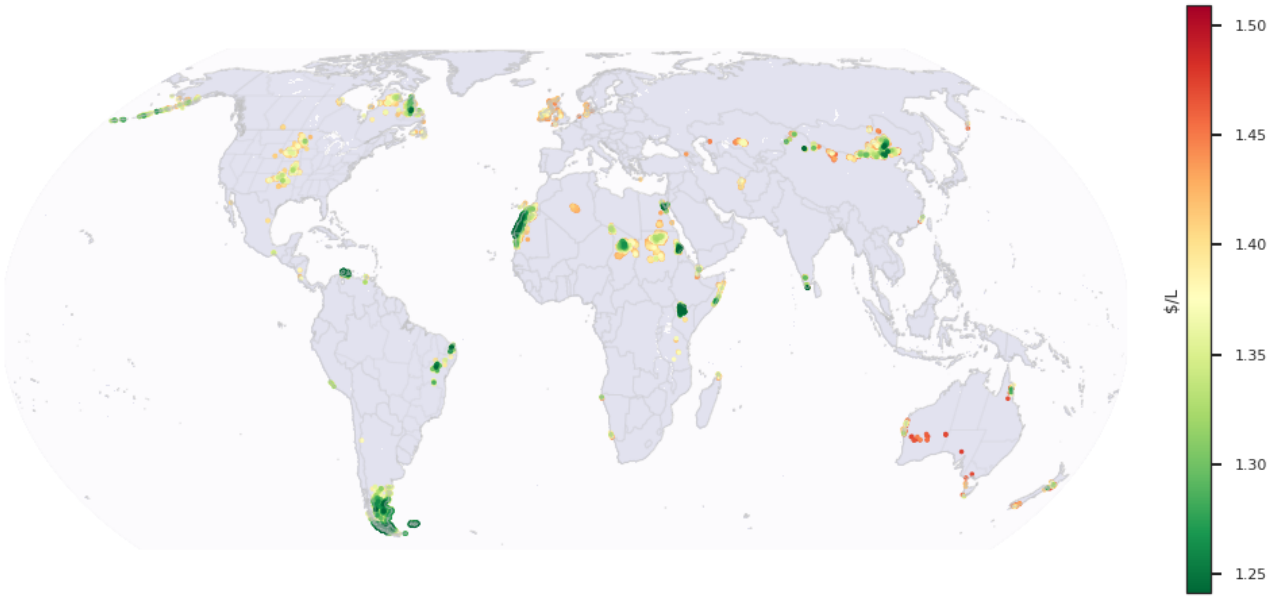

Figure 4. Map of global PtL fuel costs in 2050 by production site. The circles represent electricity generation locations.

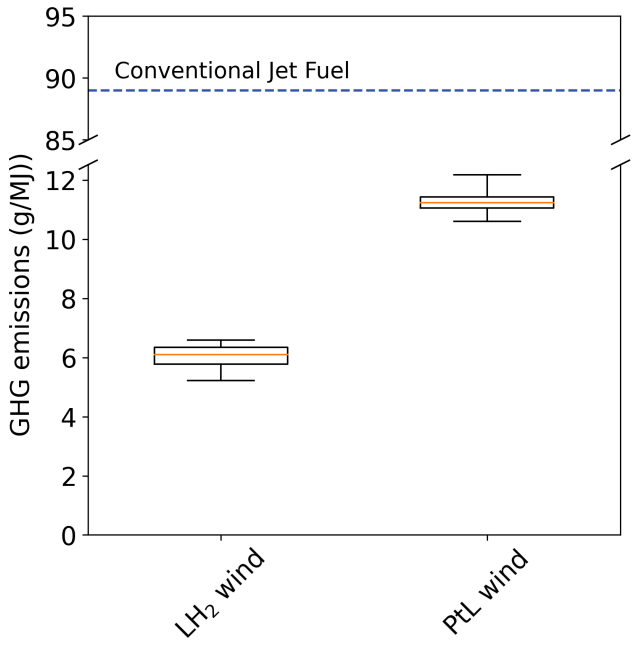

Figure 5. Life-cycle GHG emissions of LH_2 and PtL production using current technology for selected wind and photovoltaic sites. Boxes show interquartile range, and whiskers show the percentiles 0–97.5 (to exclude outliers at small remote airports). The orange line represents the GHG emissions with median production volume.

Publications

ICAO (2022). *Report on the feasibility of a long-term aspirational goal (LTAG) for international civil aviation CO_2 emission reductions*. https://www.icao.int/environmental-protection/LTAG/Pages/LTAGreport.aspx

Outreach Efforts

- Provision of insights into the aircraft model during the Fall 2021 ASCENT meeting
- Presentation to the MIT Airline Industry Consortium (Fall 2021)
- Presentations to the MIT Climate & Sustainability Consortium (January 2022)
- Presentation to the Transportation Research Board SAF Subcommittee (March 2022)
- Presentation to AEC (Spring/Summer 2022)
- Presentation to the NASA Cryogenic Hydrogen Workshop (September 2022)
- Presentation to numerous industry stakeholders and government agencies
- Results of PtL and LH_2 modeling, distributed as part of the LTAG analysis

Student Involvement

During the reporting period, the MIT graduate student involved in this task was James Abel.

Plans for Next Period

We are planning to investigate the key sensitivities that will determine whether LH_2 or PtL fuels provide a more viable strategy. Furthermore, we will assess system designs to optimize PtL and LH_2 production around intermittent electricity sources.

Task 4 - Analyze the System-LEVEL Costs and Benefits of the Electrification Strategies

Massachusetts Institute of Technology

Objective

The goal of this task is to develop a system-level analysis capability for comparing different electrification strategies while integrating the engineering and assessment models developed under Tasks 2 and 3. During the current reporting period, we worked with the ASCENT 47, 51, and 58 teams to assess whether an aviation system with near-zero environmental impact could be designed. Our focus during the current reporting period was on the single-aisle market segment, assuming an aircraft with 220 seats and a range of 3,000 nmi. We define a system with near-zero environmental impact as one that has net-zero climate impacts, including CO_2 and non-CO_2 impacts, and a greater than 95% reduction in monetized air quality impacts.

Research Approach

We developed a system-level approach (Figure 6) that models (a) fuel production pathways for SAFs (including SAFs from biomass and PtL) and LH_2, (b) the aircraft and its propulsion system, (c) contrail avoidance, and (d) environmental impacts (air quality and climate impacts).

Fuel production was assessed by using the models outlined under Task 3. We assumed renewable electricity produced from wind and solar resources to produce hydrogen via electrolysis. CO_2 used in the production of PtL fuel was assumed to be obtained via direct air capture. The aircraft and propulsion system were modeled by following the design and optimization code TASOPT, which was updated to include higher-fidelity propulsion system models in Numerical Propulsion System Simulation. Post-combustion emissions control was implemented in the aircraft system design to reduce NO_x emissions. Contrail avoidance was modeled to estimate the extent to which persistent contrail length could be reduced for each aircraft-fuel system.

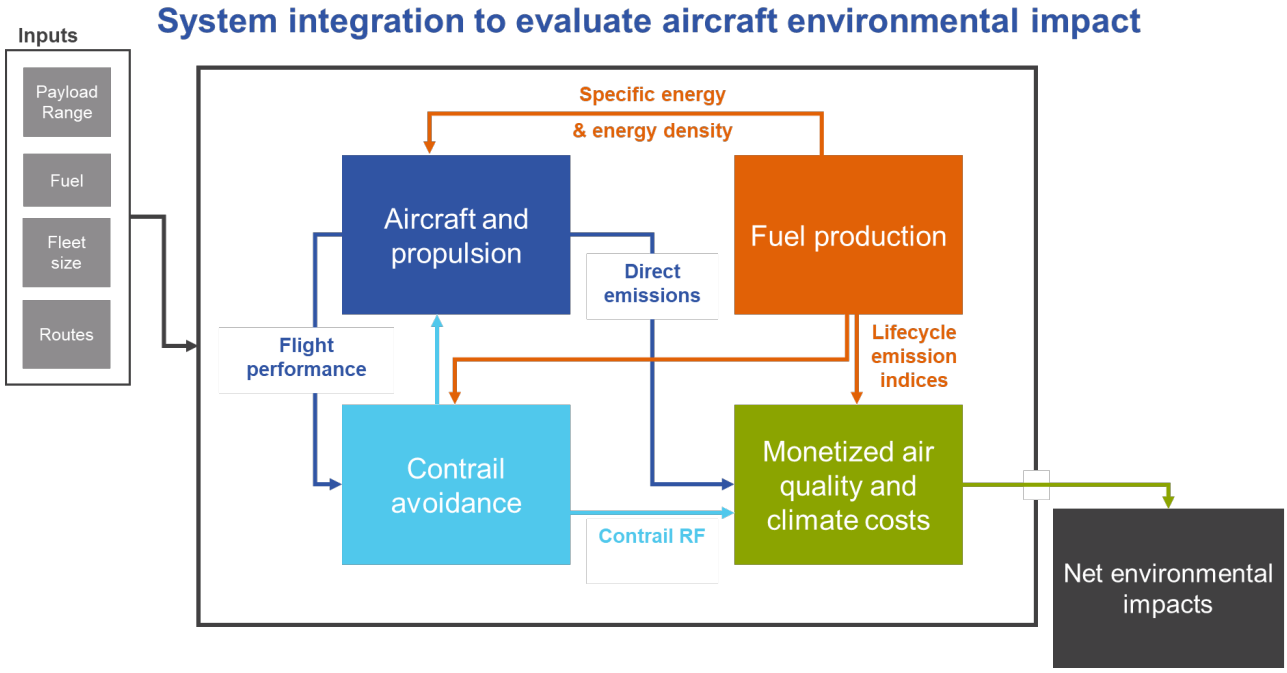

Figure 6. System integration schematic showing the interactions among the four key modeling domains.

Milestones

The model has been completed, and the results have been presented to numerous audiences (described below).

Major Accomplishments

We found that both PtL drop-in fuel and liquid hydrogen are compatible with reaching the net-zero impact goal outlined above. Figure 7 shows the total societal costs of operating (a) a conventional single-aisle aircraft system powered by fossil Jet A (with or without carbon capture and storage), and (b) the net-zero system (ZIA) relying on a biomass-derived SAF (hydroprocessed esters and fatty acids; fats, oils, and greases), PtL, or LH_2. The societal costs are defined as the sum of the monetized air quality and climate costs, the fuel costs, and the cost of atmospheric CO_2 removal (to reach net-zero climate goals in light of remaining life-cycle emissions). Although the average fuel costs associated with the transition to a zero-impact system increases by 16%–68% (depending on fuel choice), a transition to ZIA systems results in a reduction of total societal costs between 43% and 55%, depending on the fuel choice. This finding suggests that a transition to such a novel system would be beneficial to society.

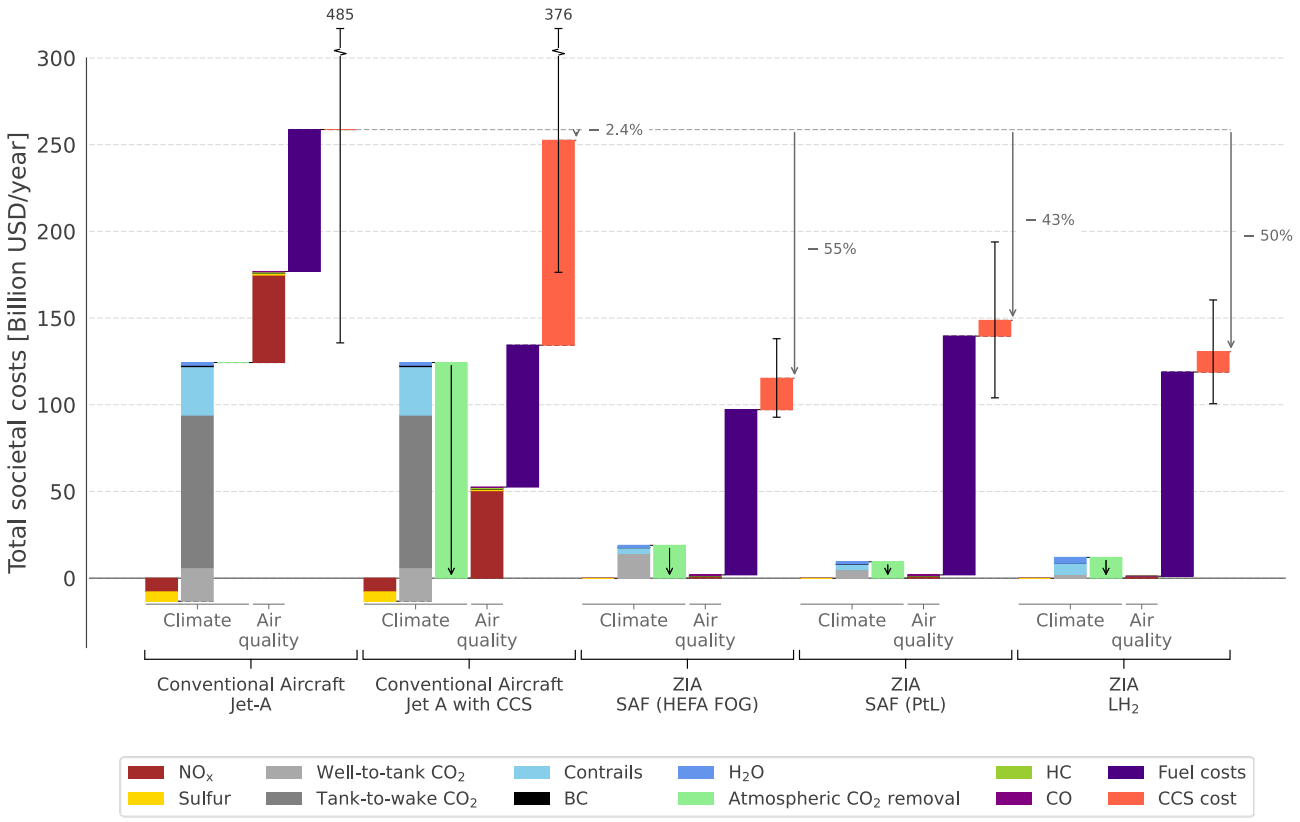

Figure 7. Total societal costs associated with the scenarios considered.

Publications
None.

Outreach Efforts
- Provision of insights into the aircraft model during the Fall 2022 ASCENT meeting
- Presentation to the MIT Airline Industry Consortium (Summer 2022)
- Presentations to the MIT Climate & Sustainability Consortium (June 2022)
- Presentations to numerous industry stakeholders and government agencies

Student Involvement
During the reporting period, the MIT graduate students involved in this task were James Abel, Dun Tan, and Prashanth Prakash.

Plans for Next Period
The next step is to evaluate how the model can be rolled out to additional market segments and electrification approaches.

Project 053 Validation of Low-Exposure Noise Modeling by Open-Source Data Management and Visualization Systems Integrated with AEDT

Stanford University

Project Lead Investigator

Juan J. Alonso
Vance D. and Arlene C. Coffman Professor
Department of Aeronautics & Astronautics
Stanford University
Stanford, CA 94305
650-723-9954
jjalonso@stanford.edu

University Participants

Stanford University

- P.I.: Prof. Juan J. Alonso
- FAA Award Number: 13-C-AJFE-SU-022
- Period of Performance: October 1, 2021 to September 30, 2022
- Tasks:
    1. Completion of an operational prototype of Metroplex Overflight Noise Analysis (MONA) including Aviation Environmental Design Tool (AEDT) integration
    2. Preliminary AEDT noise prediction assessment in day–night average sound level (DNL) 55–65 dB areas
    3. Data-science formats and scientific computing for large-scale airspace analyses
    4. Viable alternative approach routes into the San Francisco Bay Area metroplex

Project Funding Level

With the addition of $90,000 in bridge funding, Year 2 funding was stretched to cover all expenses for both Years 2 and 3 of ASCENT Project 53. Cost sharing above this amount is being provided by various sources. Mr. Thomas Rindfleisch is contributing his time without compensation, and Mr. Donald Jackson is also contributing a substantial amount of time (approximately 65% full-time equivalent) without compensation, to the project. In addition, contractor costs for the development of the MONA project website, the cost of undergraduate student support and summer interns, and some equipment purchases (and installation costs) are also being used to generate cost sharing for this project. During the first 36 months of this project, a total of more than $1.3 M of cost sharing has already been accounted for.

Investigation Team

The investigation team comprises faculty, graduate and undergraduate students, and collaborators, as listed below with their respective areas of expertise and contribution:

1. Juan J. Alonso (P.I., Stanford Aeronautics & Astronautics): overall responsibility for the project and its technical and administrative elements
2. Nick Bowman (graduate student, Stanford Computer Science): MONA project cloud infrastructure, cloud-based execution of AEDT analyses, Apache Kafka-based data collection; October 1, 2021 to September 30, 2022
3. Sanjaye Narayan (graduate student, Stanford Computer Science): flight trajectory database analysis and synthesis, AEDT infrastructure support; October 1, 2021 to September 30, 2022
4. Brian Munguía (graduate student, Stanford Aeronautics & Astronautics): AEDT, cloud-based AEDT study execution, and AEDT debugging; October 1, 2021 to September 30, 2022

5. Donald Jackson (collaborator, independent consultant): overall MONA project infrastructure (servers, databases, and hardware/software monitoring), geographic information system (GIS), web-based visualization deployment, and technical guidance; October 1, 2021 to September 30, 2022
6. Thomas Rindfleisch (collaborator, Emeritus Professor, Stanford University): noise monitoring and filtering, aircraft trajectory collection/processing, and visualization; October 1, 202 to September 30, 2022
7. Aditeya Shukla (undergraduate student, Stanford Aeronautics & Astronautics): artificial intelligence/machine learning classification of aircraft trajectories, real-time sound-level monitoring (SLM) software, artificial intelligence/machine learning noise modeling; October 1, 2021 to September 30, 2022

Project Overview

The MONA project was undertaken to provide objective real-time data, analyses, and reports to key stakeholders and policymakers, to mitigate the noise impacts of the deployment of new NextGen procedures. This system (a) collects and archives air traffic data by using a network of antennae and receivers, (b) analyzes noise impacts by using a variety of metrics, (c) visualizes the resulting large-scale data sets, and (d) uses a network of sound-level monitors to enhance the quality of noise predictions. The focus of this ASCENT project is to improve upon MONA noise predictions through tighter integration with AEDT. In particular, our work is focused on the following three tasks: (a) integration and automation of AEDT's noise analysis capabilities, (b) validation and verification (V&V) of AEDT's noise predictions in DNL 55–65 dB areas, and (c) proposal of software engineering/architectural choices for future AEDT development to enhance usability in multiple workflows, including Application Programming Interface (API) formulation, visualization interfaces, resilient data acquisition and storage, and cloud computing.

The expected benefits of this project mirror the tasks described above, including (a) an ability to automate complex noise analyses in metroplexes so that they are available nearly in real time after the preceding 24-hr period, (b) a better understanding of the accuracy of AEDT's current noise models in low-noise (DNL 55–65 dB) areas and the reasons for the discrepancies (if any) in existing predictions, and (c) recommendations to software developers regarding flexible architectures and APIs for AEDT, to make the tool more versatile and generally applicable. AEDT predictions are built around the policy context of an average annual day. Most of the V&V results produced and shared by the MONA team had focused on a cumulative daily basis, for which flight track data were directly collected. In a major accomplishment in this period of performance, we automated the analysis of every flight into San Francisco International Airport (SFO) for an entire year (July 1, 2021 to June 30, 2022); therefore, some of our preliminary results also include DNL for an actual entire year of flight operations. The focus of the work reported here is on arrivals at SFO, primarily those at runway 28L.

Background and Previous Accomplishments

The MONA project started approximately 4 years ago, with the main objective of providing objective real-time data, analyses, and reports to key stakeholders and policymakers to aid in mitigating the noise impacts of the deployment of new NextGen procedures. Since then, we have developed and deployed a system that (a) collects, archives, and makes available air traffic data by using a series of networked antennae and receivers 24/7, (b) analyzes noise impacts by using a variety of metrics (based on both a MONA-developed noise prediction tool and the noise prediction tools within AEDT), (c) visualizes the resulting large-scale data sets in a simple, user-friendly manner by using a bespoke website as well as Uber's kepler.gl (n.d.) and deck.gl (n.d.) large-scale data visualization toolboxes, and (d) has deployed a small network of low-cost, Stanford-owned, sound-level monitors scattered across the South Bay in the Bay Area, including data from the noise monitors deployed by SFO to cross-calibrate measurements by MONA and SFO monitors, collect noise measurements from a wider geographic range, and enhance noise predictions so that they exactly describe the actual noise levels experienced.

The longer-term objectives of the MONA project are to (a) ensure the V&V of all noise predictions provided (by AEDT or other tools) in both areas near the airport and other areas farther from the airport, (b) achieve full automation of complex noise analyses in regions around airports in the United States, including AEDT-based noise predictions, (c) make all results web accessible for in-depth interpretation of historical and proposed changes, (d) eventually study potential alternative traffic patterns in complex airspace to mitigate aviation environmental impacts, and (e) export the proven/validated MONA technology to other airport regions via open-source software/hardware.

At the present time (December 2022), the MONA software continues to develop and mature, to enable completion of the main research tasks in ASCENT 53. MONA has deployed a small network of Automatic Dependent Surveillance–Broadcast (ADS-B)/multilateration (MLAT) antennae, and we have developed the software necessary to merge the data streams from all these antennae, including deduplication of sightings, identification of aircraft equipment and routes flown, physical

interpolation of data missing from the joint observations, and archiving (in appropriate database formats) of the information collected for successive analysis. Moreover, substantial scrutiny has been paid to understanding the best ways to use AEDT (by understanding how to most accurately model aircraft trajectories, aircraft equipment, and aircraft noise), so that any comparisons with experimental data present the results obtained from AEDT in the best possible light.

Second, MONA has achieved a level of integration with FAA's AEDT software that enables fully automatic processing of noise exposure at arbitrary receptor locations for arrival routes into the San Francisco Bay Area airports. As a preview of the results presented in this yearly report, the level of cloud-based automation achieved by the ASCENT 53 team now allows us to process an entire year of flights (including hundreds of thousands of operations) in approximately 2.5 calendar days, thus enabling the collection and processing of unprecedented amounts of data that allow statistically significant conclusions to be drawn. Third, MONA has now fully incorporated measurements from networked sound-level monitors via the Apache Kafka system, and has developed and validated approaches for non-aircraft-noise filtering (of the raw noise data), according to digital filtering, aircraft position information, and automated identification of background noise levels that have been validated and verified. These techniques have also been markedly improved during the period of performance, with extensive help from our FAA project manager, Mr. Susumu Shirayama, who has worked side by side with our team.

Finally, although not an explicit task of ASCENT 53, we have continued our efforts to interface the above-described MONA software modules with the kepler.gl open-source visualization framework, to enable visualization and animation of aircraft positions and paths, noise predictions, various routes and procedures, etc., to better communicate the results of our work (Figure 1).

Figure 1. MONA visualization using kepler.gl (n.d.) and deck.gl (n.d.) of traffic patterns in the San Francisco Bay Area, including a 24-hr view of aircraft traffic patterns. Trajectories are colored by altitude, with purple/magenta indicating low altitudes and blue indicating high altitudes.

For the current period of performance, our main objectives can be described (from the approved proposal document) as follows:

a) Completing an operational prototype of MONA that (a) integrates ADS-B paths and possibly other FAA sources of information (such as AEDT-Optimized Threaded Track), (b) AEDT analyses, (c) noise measurements, and (d) visualization capabilities
b) Completing our assessment of the noise prediction capabilities (from experimental data) of AEDT in DNL 55–65 dB areas
c) Extending, perfecting, and evaluating the MONA prototype to a wider range of test sites and traffic types
d) Producing an analytic account of the level of accuracy to which we can measure sound levels embedded in typical background noise with a network of sound monitors
e) Correlating observed noise with specific causes relating to the aircraft state

f) Investigating the best-suited formats (including data-science-friendly formats such as Parquet for Hadoop and others) for storing flight track information (and associated metadata) and processing all information through standard data-science workflows
g) Proposing alternate approach/departure routes in and out of the San Francisco Bay Area metroplex that can reduce noise impacts while maintaining throughput, efficiency, and safety

The remainder of this report describes the progress that we have made in each of these seven elements of our research program. The report mirrors the results presented at the ASCENT Program Annual Meeting held in Alexandria, Virginia, on October 25–27, 2022.

Task 1 - Completion of an operational prototype of Metroplex Overflight Noise Analysis (MONA) including Aviation Environmental Design Tool (AEDT)

Stanford University

Objectives

In previous annual reports, we have described the incremental improvements in the various components of the MONA system, including collection and ingestion into a modern database of ADS-B and noise data; preparation of trajectory data for consumption by AEDT; automation of large numbers of analyses using AEDT; and extraction and archiving of AEDT output study data to compare predicted and experimental findings. The main accomplishment in this domain during the past year has been the increase in the functionality and maturity of our entire MONA system, thus allowing us to compare simulated and experimental noise data for an entire year of arrival flights into SFO. Such a comparison has not been achieved in any noise study in the literature to date, to our knowledge. We are now routinely able to run a simulation of an entire year of arrivals into SFO (along runways 28R/L) in approximately 2 days. Consequently, we can observe differences in the predictions from AEDT (and comparisons with experimental data) while varying many simulation parameters affecting AEDT predictions (e.g., trajectory simulation approaches, Base of Aircraft Data [BADA] 3 vs. BADA4 modeling, weather simulation data, equipment databases and matching, etc.) The MONA system is a research tool that allows us to rapidly perform studies enabling better assessment of the predictive quality of AEDT runs.

In the remainder of this section, we provide short descriptions of all elements of the currently operational MONA prototype. This description is a shortened version of the description provided in last year's report, which is provided here to contextualize the results presented in subsequent sections. Our automation method is based on our own cloud-based AEDT execution environment, which we have named remote AEDT (`raedt`), which works on Google Cloud Project instances of arbitrary size (number of processors, memory, etc.).

As a consequence of community complaints, resulting from the changes in air-traffic patterns over the San Francisco Bay Area metroplex during the past 5 years, it became increasingly clear that there is a dearth of high-quality aircraft noise data (from measurements and/or predictions), particularly in areas away from the airport boundary that have not traditionally been the main focus of noise complaints. In addition, through several community interactions, we became aware of the difficulties involved in relating potential flight route changes to noise impacts on the ground. This lack of actionable data and methods to effectively communicate with broad, and-often-non-technical, communities led us to develop the MONA system. The MONA project set out to achieve the following objectives:

- Measure and analyze ground noise data generated by aircraft overflights in complex metroplex situations
- Create, curate, and archive experimental data sets that can serve as an openly available database for V&V of improved noise prediction methods
- Fully automate noise analyses based on the AEDT without a need for user intervention
- Share key analysis results with broad communities of stakeholders through compelling interactive visualizations

The MONA system has evolved into a complex open-source project with multiple elements, which are described below.

Research Approach

Measurement and Collection of Data
To quantify and analyze the noise impact of aircraft overflights, both the trajectories of aircraft flights and the resulting ground noise must be known. To that end, MONA collects the following types of data:

- Aircraft flight profiles (via ADS-B) and speed over ground
- Sound levels
- Flight and aircraft metadata
- Air traffic routes and procedures
- Wind and weather conditions

Sensor Controller
The measurement of sound levels and reception of ADS-B transmissions require a distributed network of sensors mounted outdoors throughout the geographic region of interest, and a means to access/retrieve the data. For the MONA project, we have implemented a series of sensor controllers, incorporating a single-board computer, a global positioning system (GPS) receiver (to provide a highly accurate time pulse, as well as three-dimensional location), with both network connectivity and power via Power over Ethernet (PoE). These components are integrated within a waterproof/weatherproof enclosure, to support long-term outdoor deployment. The sensor controller runs a Network Time Protocol (NTP) daemon, configured to use the output of the integrated GPS receiver (in pulses per second), to provide a Stratum-1 time base, thereby minimizing time differences among our distributed network of sensors. We developed software to collect each sensor's output and transmit/publish the data in real time via the Internet to a centralized aggregator hosted at a data center. A single sensor controller can simultaneously support both ADS-B reception and SLM. Because of the long-term field deployment of the sensors, autonomous operation and secure remote access are essential.

Figure 2 shows our standard MONA ground station installation and a view of the sensor controller components inside their weatherproof enclosure.

Figure 2. Sensor controller rooftop deployment with ADS-B and SLM (left); sensor controller components (right).

ADS-B Receiver
The primary ADS-B receivers in the MONA network are based on the PiAware/`dump1090-fa` software by FlightAware (AeroAPI, n.d.), by using a standard RTL-SDR dongle (inside the sensor controller enclosure in Figure 2, right), connected to an ADS-B antenna affixed to the same enclosure. Every second, the JSON output of `dump1090-fa` is captured by a software daemon, and the ADS-B messages within are minimally processed and then transmitted/published to our centralized aggregator,

implemented as an Apache Kafka cluster. The collector daemon also publishes receiver metadata (including GPS location and sensor controller status) to the same aggregator.

Sound-Level Monitoring (SLM)
We use Convergence Instruments (CI) SLMs, connected via Universal Serial Bus to the sensor controller, to measure noise. Another software daemon captures the outputs of the SLM and transmits/publishes them in real time to a centralized server, again by using Apache Kafka. Recent models of the CI SLM optionally support a USB-Audio feature, providing access to the sampled audio waveform, which we selectively save/transmit to capture both noise metrics and audio recordings of aircraft overflights. The SLM collector daemon publishes SLM metadata (including SLM configuration, GPS location, and sensor controller status) to the central server.

Flight and Aircraft Metadata
Aircraft ADS-B positions alone do not provide a complete description of the flight. Important/valuable missing metadata include:

- Arrival and departure airports
- Assigned runways
- Air traffic control assigned routes and procedures
- Airframe, engine, and ownership

Arrival and departure airport information can often be obtained via external API access or inferred by comparison of the first or last known ADS-B position with airport/runway locations. Air traffic control (ATC) assigned procedures, routes, and runways can be inferred by comparison of an aircraft's trajectory to the locations (and sequences) of waypoints and runways. An area of ongoing development is the integration/incorporation of the FAA System Wide Information Management (SWIM) data feeds, to combine this rich source of metadata with ADS-B aircraft positions. SWIM messages are ingested into Kafka topics, thus providing reliable reception of these real-time data feeds. Airframe, engine, and ownership information are obtained by joining the aircraft's ICAO24 unique identifier (included in the ADS-B message) with aircraft registration datasets, including the FAA Aircraft Registry (for US aircraft), and OpenSky's Aircraft Metadata Database (for other aircraft).

Air Traffic Routes and Procedures
FAA Coded Instrument Flight Procedures (CIFP) is a definitive source of information that we download, parse, and archive monthly. The CIFP provides data on airport, runway, and waypoint locations, which we use for geospatial processing and queries. Flight procedures are converted to a directed-graph representation, and then processed with both standard and custom graph algorithms.

Wind and Weather
ADS-B messages usually provide the aircraft's ground speed but do not provide its airspeed, which is an important factor for the prediction of the resulting noise. We obtain wind speed and direction measurements from the National Oceanic and Atmospheric Administration (NOAA) High-Resolution Rapid Refresh (HRRR) dataset, and in conjunction with the ADS-B provided ground speed and heading information, we estimate the net airspeed, which is used to define the specific aircraft trajectory for noise prediction.

Data Collection, Archival Storage, Access, and Management
Real-time ADS-B messages, SLM measurements, and SWIM data feeds are received and stored by a distributed-event streaming platform implemented by using Apache Kafka (n.d.). These streams are processed and subsequently ingested into a Postgres database, augmented with both PostGIS (supporting geospatial queries) and TimescaleDB (supporting very large time-series tables). ADS-B messages from multiple receivers are deduplicated and segmented into flights, and relevant metadata are added. Trajectories are included in each flight record/row, encoded as PostGIS 4D LineStrings, thus enabling arbitrary spatiotemporal queries supporting statistical analyses on vast numbers of flights over arbitrary time periods. Our work frequently requires knowledge of the point, distance, and/or time of closest approach (PCA, DCA, or TCA) of an aircraft trajectory to a location of interest (LOI) such as the position of an SLM. PostGIS queries can dynamically compute, filter, and return these values for any stored flight trajectory and LOI combination.

Data Processing and Analysis
The raw data acquired by the MONA system must be processed before they can be input in our analyses and used to compute statistics for the information collected. This section describes some of the data analyses that we have automated in MONA. After aircraft trajectories and measured noise have been captured, stored, and made available for future use, we process, analyze, quantify, compare, categorize, and summarize the noise impacts.

Attribution of Sound Levels to Aircraft Overflights
The sound-level measurements obtained both from MONA SLMs and other providers (such as SFO's noise monitoring terminal [NMT] stations) include sampled aggregate sound pressure levels generated from every source, but only the noise resulting from aircraft overflights is relevant to our research. Several techniques for attributing sound peaks to aircraft are described in the literature. Particularly relevant examples include threshold and duration, directional and/or arrayed microphones, and spectral identification/categorization. In our experience, an effective method is Determined Aircraft Position/Location for Aircraft Noise Extraction (DA-PLANE), This algorithm involves computing the time and distance of an aircraft's closest approach to the SLM location (from ADS-B trajectory data), which gives the estimated time of the aircraft's sound peak at the SLM. Subsequently, we use time-series filtering and analysis to locate peaks above the time-varying background in the sound profile that may have been caused by aircraft overflights. These peaks are then time-matched with the closest approach data to isolate and identify the sound peaks resulting from specific aircraft. The net profile amplitudes of isolated peaks above the background are then analyzed to extract the desired noise metrics for each identified overflight event. Other implementations of this technique include those of Harding and Ferrier (2014), and Giladi (2020). In the MONA system, the maximum $LAeq_{1s}$ value and SEL metrics are extracted and stored in the database, with relations to both the flight (aircraft) and SLM (measurement) location.

Metric Computation
With aircraft trajectories encoded as geospatial datatypes and measured noise metrics attributed to specific aircraft flights and precise locations, we compute standard noise metrics such as number-above, DNL/Community Noise Exposure Limit (CNEL), time-above, and background level. Non-noise metrics, such as overflight counts per day (within a distance/range), are also computed.

Aircraft Noise Prediction
Deploying SLMs with sufficient numbers and geographic density to obtain measured noise data is not feasible throughout an entire set of geographically connected airports (cost and logistics are two major constraints). However, all air traffic can be captured via ADS-B by deploying a relatively small number of receivers over the metroplex area. Ideally, we could use the collected trajectory data to predict the noise generated by each and every aircraft on a fine-grained receptor grid to estimate noise metrics across the entire region of interest.

The FAA's AEDT is the required software application for assessment of U.S. regulatory actions related to aircraft noise and emissions. Our (aspirational) goal is to run AEDT predictions for every aircraft flight across the San Francisco Bay Area each day, then aggregate the resulting predicted noise metrics, to provide quantified noise impacts across the entire metroplex, as a function of location and time.

To this end, we have completed a software environment to:

- Automate AEDT study creation, execution, and metric result extraction
- Accurately model AEDT flight trajectories by using ADS-B data
- Evaluate and compare AEDT's noise predictions to measured noise levels, in a manner similar to that of Giladi and Menachi

More detailed descriptions of these individual tasks follow.

AEDT Automation
Current AEDT implementation and workflows are focused primarily on desktop computer applications, via its graphical user interface. This usage model does not support the automated processing of thousands of flights per day over many years. To implement an automation facility, we leveraged AEDT's use of, and reliance on, a Microsoft SQL Server database. Using AEDT's database schema documentation in conjunction with a database table "diff" tool that we developed, we gained an understanding of how to create and populate the tables necessary to describe a complete AEDT study. We then developed a software library to facilitate scripted study creation over a network connection to the SQL Server database used by AEDT.

AEDT provides a command-line utility, `RunStudy.exe`, to initiate the execution of a specified study that we can invoke over the network. An AEDT study's computed metrics are written into the SQL Server database, so that we can also access and extract these results over the network.

We created a virtual machine (VM) disk image including AEDT and all supporting packages preinstalled, which can be instantiated and run at any scale on a commercial cloud provider. We then developed a study-executor application that takes a study description as input; orchestrates and connects to an AEDT VM; creates an AEDT study by using the trajectory of the flight's database ID (provided in the study description), including altitude and speed controls to match the observed trajectory; executes the study; and extracts/stores the metric results in our database. Next, we developed a study-creation application that generates any number of study descriptions (based on SQL queries specifying any desired database column criteria) and submits each resulting study description to a job queue. Finally, we enhanced the study executor to query the job queue for a study description to process.

As a result, we can run any number of AEDT studies in parallel and are limited only by the number of AEDT VMs and study executors that we create. Both the job and extracted-metrics queues are implemented by using the Apache Kafka (n.d.) cluster.

AEDT Trajectory Modeling from ADS-B Data
AEDT is typically used to model flights from a number of specified ground track positions (without altitude). AEDT combines the specified ground track with flight performance models from the Aircraft Noise and Performance (ANP) Database and EUROCONTROL's BADA to simulate the aircraft's trajectory for its predictions. This computed, simulated trajectory may differ from the trajectory reported by ADS-B. AEDT provides additional functionality to add altitude and airspeed control codes to the ground track (Section 3.9.1, "Track Control Flights," in the AEDT3d Technical Manual), which we use to more closely model the reported trajectory.

The ADS-B trajectory processing steps that we use include the following:

- Smoothing and filtering to remove anomalies that AEDT would reject (e.g., increases in altitude during a descent).
- Line Segment Simplification (Douglas & Peucker, 1973; Ramer, 1972).
- Estimation of the aircraft's airspeed, using ADS-B provided ground speed and heading, in combination with wind speed and direction data obtained from NOAA.

Comparison of AEDT noise predictions with measured noise
Our AEDT studies specify the LAmaxand SEL noise metrics, per flight, at each receptor (SLM) location. These metric values are stored in our database, with relations to the flight and location, as we do with the measured noise peaks attributed to aircraft (described previously). With both predicted and measured noise, comparisons are made across various cohorts of flights, which can be specified by filtering, grouping, analyzing, and reporting by any available set of metadata fields (e.g., aircraft model and route). During the past year, we have spent most of our time performing AEDT-based simulations and predictions and comparing them with the experimental data that we have collected. The results obtained from these comparisons are the main content of this annual report. The ability to display the results of these comparisons is key to the understanding of both the differences between predictions and experiments, and the potential root causes of these differences.

Task 2 - Preliminary AEDT Noise Prediction Assessment in DNL 55–65 dB Areas

Stanford University

Objectives

Disclaimers
The results in this section represent our V&V efforts for AEDT conducted during the current period of performance (October 1, 2021 to September 30, 2022). These results represent our first attempt at yearly comparisons between AEDT predictions and experimental noise data. As such, and until improved results are published in a peer-reviewed journal (as of February 2023, we have completed substantially more comparisons than the work presented in this annual report) the results here

should be considered preliminary. The findings provide an indication of our main observations but lack the level of confidence required to make sufficiently strong statements. Moreover, whereas AEDT is the tool used for regulatory purposes in the United States, we have used a version of AEDT that we call AEDT-AE, which uses the collected aircraft track data, and both BADA4 performance models and altitude and speed controls, to complete the simulations. We do not claim that AEDT-AE has any regulatory value.

The noise prediction modules in AEDT, on the basis of noise-power-distance (NPD) relationships and certification data, were developed and calibrated mainly for areas close to airports with objectionable noise (> DNL 65 dB), at a constant velocity (160 knots), and for a particular aircraft high-lift system and landing gear configuration. Even including efforts such as those in ASCENT Project 43 (which reevaluated the NPD curves by using Aircraft Noise Prediction Program [ANOPP] analyses and the ability to change the aircraft configuration during arrival/departure procedures), there is evidence that the accuracy of AEDT's predictions in areas of relatively lower noise (between DNL 55 and 65 dB) may warrant review and improvement. For these reasons, in this series of tasks, we have undertaken a preliminary evaluation of the accuracy of AEDT's predictions when measured against sound level readings from two different locations in the arrival paths to SFO: one relatively close to the airport and one further away.

Our main accomplishments over the past 12 months include:

- Completion of the MONA system to archive, process, and query all measured and predicted data (described in a previous section)
- Completion of the AEDT-AE processing system: creation of single flight studies, study execution, and extraction of study results, at any desired scale
- Completion of preliminary and statistically significant comparisons of measured versus AEDT-AE-predicted noise, at two locations, for every flight, over 12 months

In our previous annual report, we described our results (circa October 2021), which were based primarily on an early prototype of MONA and all its constituent modules and, at most, 1 month (mid-July to mid-August 2021) of arrivals data over two different SLM locations. During the past 12 months, we have continued to improve the modeling capabilities and the noise processing algorithms in AEDT-AE and MONA, and we have been able to process substantially more flights (an entire year's worth) containing many more observations of all types of aircraft, under a wide variety of atmospheric and weather conditions. We consider the data set used in the preliminary results presented here to be both statistically significant and representative of the variability that would be observed over a representative period of time (1 year).

Data Set

Two common threads have emerged from recent assessments of various noise predictions in the literature. First, in all such studies, only a handful of flights have been examined, and therefore the variations in all potential input variables affecting the predictions (aircraft weight, weather patterns, high-lift system deployment, etc.) are not observed thoroughly and frequently enough to perform any significant statistical analysis. Such dearth of data also prevents detailed studies to attribute the discrepancies between measured and predicted noise levels to their actual sources, thus preventing the improvement of existing models. Secondly, the low volume of data does not allow the slicing of the datasets by aircraft class, atmospheric conditions, or even geometric position relative to the SLM locations: if the datasets are small to start with, further slicing only decreases the size of the resulting dataset leading to unconverged statistics that cannot be relied upon. The outcome of these shortcomings is that any attempt at improving current noise modeling strategies is impossible without dataset of sufficient size to provide statistical significance. For these reasons, we have focused on creating a dataset with approximately 135,000 flights (and 135,000 x 40 noise observations at PCAs; significantly more data points are available if the entire time history of the noise recordings is considered) that is described in more detail below.

Our data set for both AEDT-AE predictions and SLM measurements contains all arrivals into SFO runways 28L/R for a period of an entire year: July 1, 2021 to June 30, 2022. In this report, we focus on noise predictions and measurements at two main SLM locations: SFO-NMT-12 and SIDBY:

- SFO-NMT-12 is an SLM owned by SFO and operated for SFO by EnviroSuite; it is located close to the flight tracks for final approach into runways 28L/R, approximately 6 mi from touchdown. The measured DNL at this location is ~60 dB. This location is not quite within the DNL 65 dB area but is very close. Flights on final approach to SFO that fly by this location are normally at an altitude of approximately 1,700 ft and an airspeed of approximately 160-180 knots.

- SIDBY is a Stanford-owned SLM whose measurement accuracy has been assessed with a colocated SFO sound monitor and is located at the SIDBY waypoint. The SIDBY waypoint is overflown by aircraft following the SERFR, PIRAT, and BDEGA approach routes to SFO. SIDBY is located approximately 12 mi from touchdown at SFO runways 28L/R. Although we collect data for all aircraft overflying the SIDBY waypoint, our analysis reported here focuses on (a) all flights overflying SIDBY and (b) flights overflying SIDBY that approach SFO via the SERFR route only. We classify the data in this way to assess the impacts of various approach routes into SFO. The measured DNL at this location is ~46 dB.

A map of the area southeast of SFO is shown in Figure 3, and the locations of the two SLMs and typical approach paths into SFO are colored by flight altitude (green/blue denote high altitudes, whereas red/magenta denote altitudes close to the ground.)

Figure 3. Locations of the two SLMs (SFO-NMT-12 and SIDBY) used in this study.

The total data set contains approximately 135,000 distinct flights. Predictions / simulations use AEDT-AE and a separate study for each of these flights. As each flight is simulated, we compute and extract noise metrics at both SFO-NMT-12 and SIDBY but also (although not reported here) at approximately 35 other SLM locations for future assessments and comparisons. All aircraft types are observed in our database, although the main aircraft types are regional jets and single-aisle aircraft. We purposefully exclude general aviation (GA) aircraft from our data set, to focus on noise comparisons for the commercial fleet. In our first complete version of AEDT-AE, the nearly 135,000 studies completed with our `raedt` software required five entire days to compute by using 128 VMs on Google Cloud. At the time of writing of this report, the computational time required to perform a similar study is less than 2 days, as a result of various processing improvements.

For the SFO-NMT-12 location, the relevant statistics are as follows:

- A total of 134,178 flights were initially considered.
- Flights occurred over an entire contiguous 12-month period, under all types of weather conditions, such as rain, various humidity and temperature levels, winds, etc., thus representing the typical variations observed at SFO.
- A total of 4,057 GA flights were discarded.

- An additional 34,870 flights were discarded because the associated noise events did not meet our criteria for goodness of fit (i.e., the recorded noise events were deemed to include additional noise sources beyond aircraft noise or had been distorted by atmospheric turbulence, to the point that our confidence was lower than required).
- A total of 5,568 additional flights were left out of our data set because more than one flight was observed in the neighborhood of the PCA at the TCA.
- Finally, 3,417 overflights were discarded because they did not meet additional criteria to be counted, including altitude, distance, and heading constraints that we had imposed on all overflights.
- The remaining flights for this location, for the 12-month period starting on July 1, 2021, numbered 86,266.

For the SIDBY location, the following are the relevant statistics:

- 64,885 flights were initially considered
- 1,579 GA flights were discarded
- An additional 41,775 flights were discarded because the associated noise events did not meet our criteria for Goodness of Fit (i.e. ,the recorded noise events were deemed to include additional noise sources beyond aircraft noise or had been distorted by atmospheric conditions to the point that our confidence was lower than).
- A total of 280 additional flights were left out of our data set because more than one flight was observed in the neighborhood of the PCA at the TCA.
- Finally, 7,960 overflights were discarded because they did not meet additional criteria to be counted, including altitude, distance, and heading constraints that we had imposed on all overflights.
- The remaining flights for this location, for the 12-month period starting on July 1, 2021, numbered 21,056

Although we may run larger data sets in the future, we believe that these data sets are sufficiently large to support the preliminary conclusions presented in this report. As described earlier in this annual report, we believe that this data set is the largest of its kind; typical publications in the literature have used data sets of 10–50 individual flights.

Among the various SLMs from which we have data, these two are particularly interesting because, although they are both under arrival tracks, they are located in two areas with highly different noise levels. SFO-NMT-12 is presumably in an area for which the noise predictions of AEDT-AE are relatively accurate (near the airport), whereas SIDBY is substantially farther from the airport and is in an area that was not specifically targeted during the development of the noise prediction algorithms in AEDT-AE.

Research Approach

To accomplish the objectives of this task, we pursued a number of steps that are not described in detail here, including the following:

1. Data acquisition and archiving for noise measurements at the two locations, SFO-NMT-12 and SIDBY. We have completed the acquisition of the raw noise data (Leq samples at 1-s intervals), over a period of approximately 3 years. All these data have been curated so that they provide meaningful comparisons with AEDT predictions.
2. As a pre-processing step to the V&V portion of this work, we completed the development of a series of non-aircraft noise removal algorithms that combine filtering techniques, automatic identification of multiple aircraft peaks, automatic detection of background and peak noise levels, and real-time information regarding the position, velocity, and heading of the aircraft to maintain high levels of accuracy. We also included a goodness-of-fit measure based on a least-squares fit to a theoretical noise model. As described above, we have a very high degree of certainty that the overflights retained truly correspond to actual aircraft, without additional non-aircraft sources of noise present.

Note that the raw SLM data at multiple locations, including SFO-NMT-12 and SIDBY, are currently captured and stored in a Apache Kafka centralized DB with associated timestamps which can be retrieved by running respective SQL queries. These data come from calibrated networked Convergence Instruments (n.d.) equipment that we have installed at various locations around the San Francisco Bay Area (as described earlier in this report), which have been tested with colocated sound measurement equipment loaned by SFO and have been found to agree with that equipment to within 0.1–0.2 dB. Specifically, for SFO-NMT-12, as described above, the noise data have been provided by EnviroSuite on behalf of SFO.

The following figures are meant to provide statistically significant information but only preliminary conclusions, because we have yet to understand the reasons for the discrepancies observed. These reasons must be understood before final

conclusions are drawn from this study. The data set includes all types of aircraft, but predominantly E75L, B73X (B737-800, B737-900), and A320/A321. We have removed all general aviation flights from this data set, and we have ensured that no flights are included whose line-of-sight elevation at the PCA to a SLM is less than 40° (so that any aircraft not in proximity to the SLM are disregarded).

Preliminary Results for the SFO-NMT-12 Location

Preliminary observations resulting from processing of the data predicted and collected at the SFO-NMT-12 are presented below. Figures 4 and 5 show coarse-grained histograms (in the sense that they contain all aircraft of all types over a 12-month period) for both LAmax and SEL for all 86,266 flights considered in this study. The data have been binned in 0.5-dB intervals and represent the actual noise metric values (for each individual flight) for both AEDT-AE predictions (in orange) and SLM measurements (in light blue), after removal of background noise. The data set includes only aircraft/flights that can be modeled with BADA4. Several observations can be made from these two figures. First, the variability and multimodality of the AEDT-AE-predicted data are quite substantial and are absent in the SLM measurements, which appear to show a Gaussian-like distribution for the aircraft observed. The AEDT-AE prediction distribution is multimodal, thus indicating the provenance of each bar in the histogram from different aircraft types and classes. At this SLM location, when aircraft are on final approach to SFO runways 28L/R, little variability is attributable to differences in altitude and airspeed, or to the state of the high-lift system and undercarriage. The AEDT-AE predictions consider seasonal variations in weather that smooth out some of the peaks of the multimodal distribution. In contrast, the SLM data are heavily homogenized and show no indication of various types of aircraft.Our conjecture is that atmospheric, turbulence, and weather conditions might result in a type of mixing that leads to smoother distributions. We have been conducting finer slicing of the data set, by aircraft type, to better understand these effects. Our results will be discussed at the next ASCENT meeting. The difference in the means of the AEDT-AE and SLM distributions in LAmax is approximately 3 dB (underprediction by AEDT-AE).

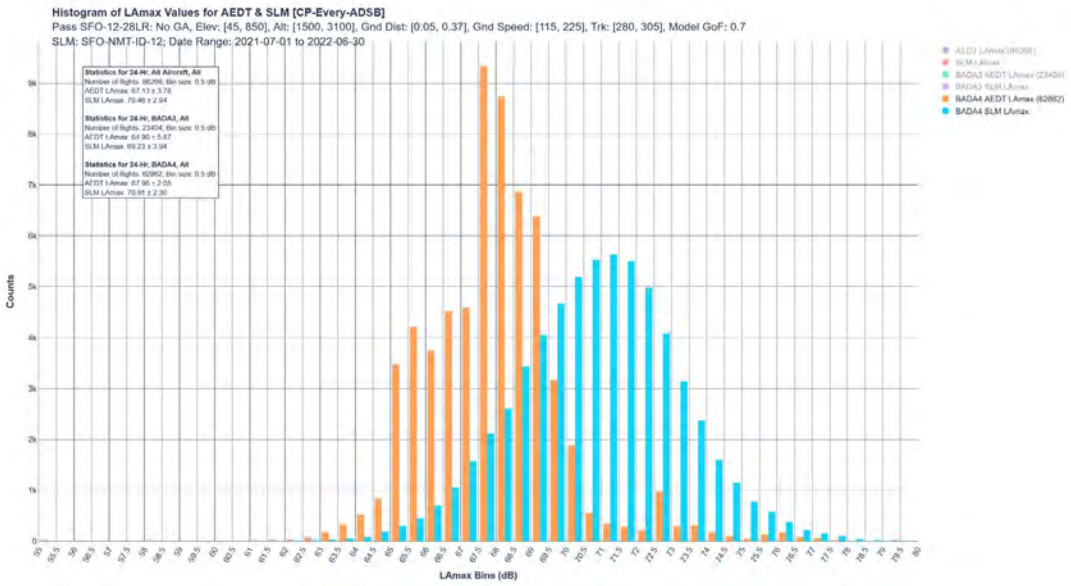

Figure 4. Histogram with the LAmax values from AEDT-AE predictions (orange) and SLM measurements (light blue) at the SFO-NMT-12 location. LAmax data are binned into 0.5-dB intervals. **Preliminary data: please do not cite or quote.**

Figure 5 shows similar results for the exact same data set, but for the SEL metric instead of LAmax. The predictions for SEL are slightly better, with a difference in the means of the predicted and measured distributions of approximately 2.6 dB (underprediction by AEDT-AE). The AEDT-AE SEL histogram appears highly similar to that for LAmax but has less accentuated multimodality. This finding makes sense, given the integrated nature of the noise metric.

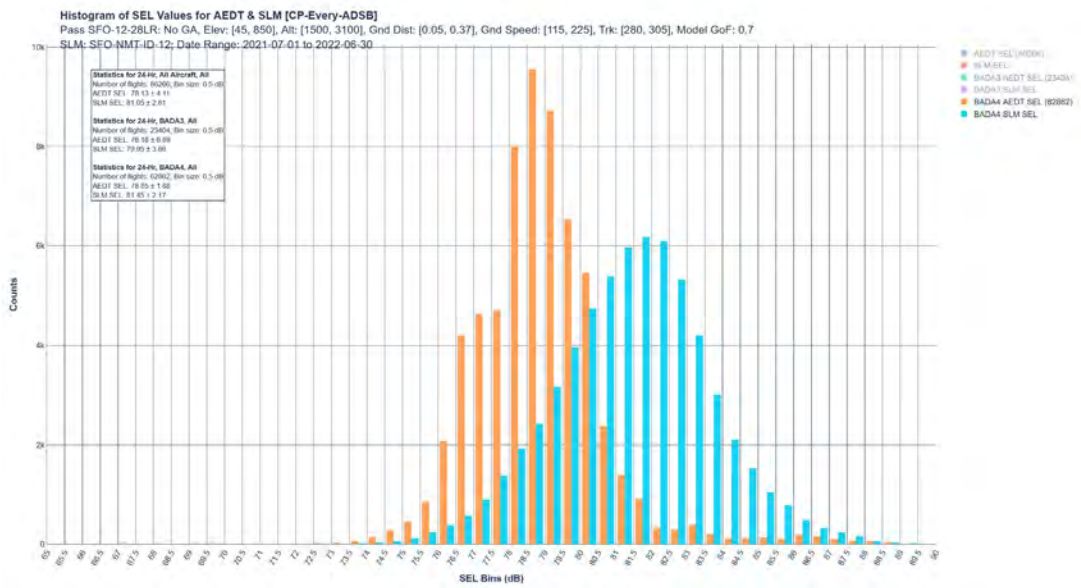

Figure 5. Histogram with the SEL values from AEDT-AE predictions (orange) and SLM measurements (light blue) at the SFO-NMT-12 location. SEL data are binned into 0.5-dB intervals. **Preliminary data: please do not cite or quote.**

Figure 6 displays the differences between the predicted (AEDT-AE) and measured (SLM) noise levels for both LAmax (in orange) and SEL (in light blue). Again, these results are for the same data set containing only BADA4 aircraft. Regardless of the metric, these preliminary results indicate a consistent underprediction of −3.0 dB (with a standard deviation of 2.3 dB) for LAmax and −2.6 dB (with a standard deviation of 2.1 dB) for SEL. These results are consistent in both trends and value with the results that we presented in last year's annual report, which were based on a far smaller data set (30 days in the summer vs. 12 months).

Finally, Figure 7 displays our calculations for the DNLs for both the predicted (AEDT-AE) and measured (SLM) noise levels. On the basis of an entire 12-month period of measurements, using AEDT-AE, we predicted a DNL at this location of 58.1 dB, as compared with the measured DNL of 60.1 dB, thus indicating an underprediction of DNL 2.0 dB. Notably, AEDT-AE is not approved for regulatory use, and these results remain preliminary. Some outliers in the plot correspond to the accounting of flights during daylight savings days and an outage for one of our ADS-B collectors. These results will later be compared with the same DNL predictions and measurements at a location farther from the airport (SIDBY). Although additional work will be conducted to further refine our estimates of the differences, we expected that AEDT-AE would do a significantly better job at a location close to the airport, but a DNL 2 dB difference in absolute value over an entire 12-month period is considered significant.

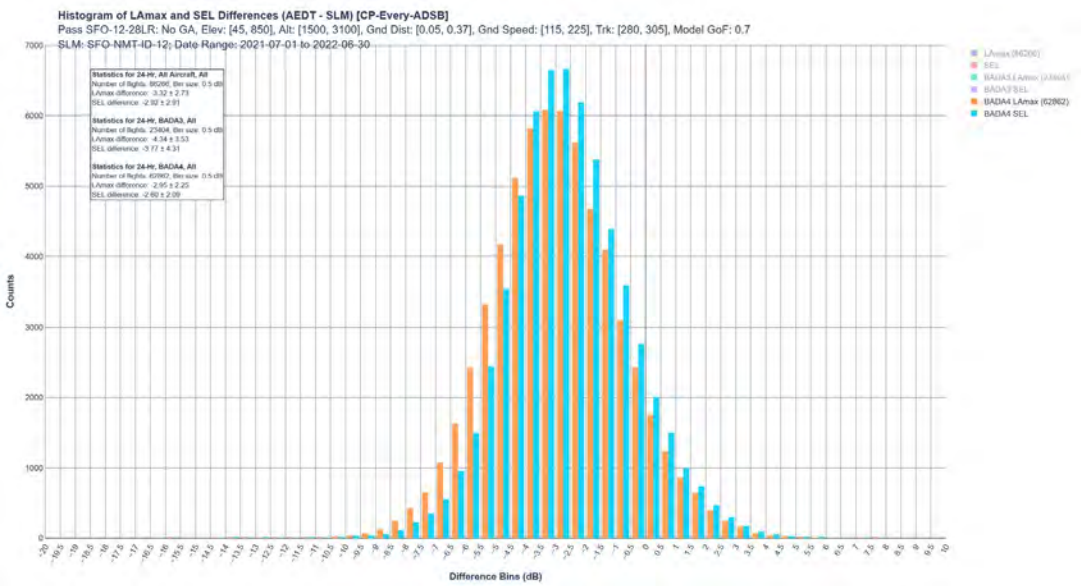

Figure 6. Histograms with the LAmax (orange) and SEL (light blue) differences between AEDT-AE predictions and SLM measurements at the SFO-NMT-12 location. A negative value indicates underprediction by AEDT-AE. Noise level difference data are binned into 0.5-dB intervals**. Preliminary data: do not cite or quote.**

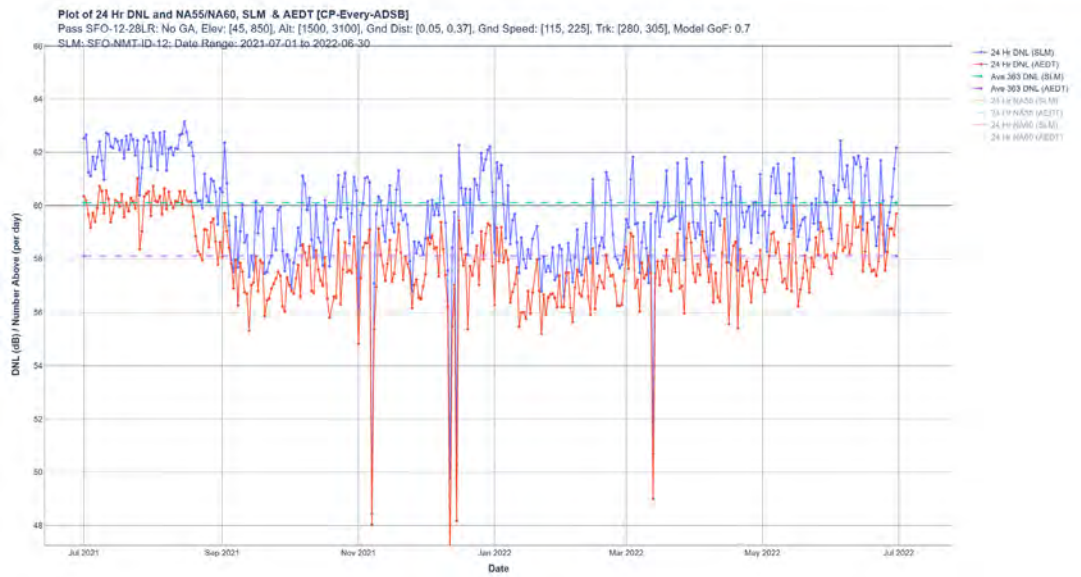

Figure 7. Daily calculated (red) and measured (blue) DNL (in dB) at the SFO-NMT-12 location. The SLM DNL is 60.1 dB, whereas the AEDT-AE-predicted DNL is 58.1 dB. **Preliminary data: do not cite or quote**.

Preliminary Results for the SIDBY Location

Preliminary observations resulting from processing of the data predicted and collected at the SIDBY SLM are presented below. Notably, the data set at SFO-NMT-12 contains additional flights, because it includes not only aircraft approaching via the SERFR, BDEGA, and PIRAT routes, but also all aircraft arriving from the east through the DYAMD route. Nonetheless, the total data set still contains 64,885 flights over the same 12-month period spanning July 1, 2021 to June 30, 2022.

Figures 8 and 9 show coarse-grained histograms (in the sense that they contain all the aircraft of all types over a 12-month period) for both LAmax and SEL for the 17,046 flights considered in this study (starting from 64,885 flights but retaining only those passing all of our quality checks). The data have been binned in 0.5-dB intervals and represent the actual noise metric values (for each individual flight) for both AEDT-AE predictions (in orange) and SLM measurements (in light blue), after removal of background noise. The data set includes only aircraft/flights that can be modeled with BADA4. Several observations can be made from these two figures, which are similar in many respects to the observations made for the SFO-NMT-12 location. First, the variability and multimodality of the AEDT-AE-predicted data remain significant, albeit somewhat reduced when compared to SFO-NMT-12, and it is absent in the SLM measurements, which appear to showcase a Gaussian-like distribution for the aircraft observed. Of note, the Gaussian-like distribution for the measured noise levels is not as smooth at what we saw at SFO-NMT-12, but the slight noisiness in the results is caused by the fact that the number of flights considered in the histograms is approximately one-quarter the number of flights used in SFO-NMT-12. The AEDT-AE prediction distribution remains multimodal, and the provenance of each bar in the histogram from different aircraft types and classes is indicated. Close examination and data analysis based on individual classes of aircraft showed that the predicted histogram peak at approximately 55 dB LAmax is a merger of both larger regional jets and single-aisle aircraft (with those aircraft contained in the 52–60 dB range), whereas the twin aisle and large twin aisle categories are seen at higher noise levels.

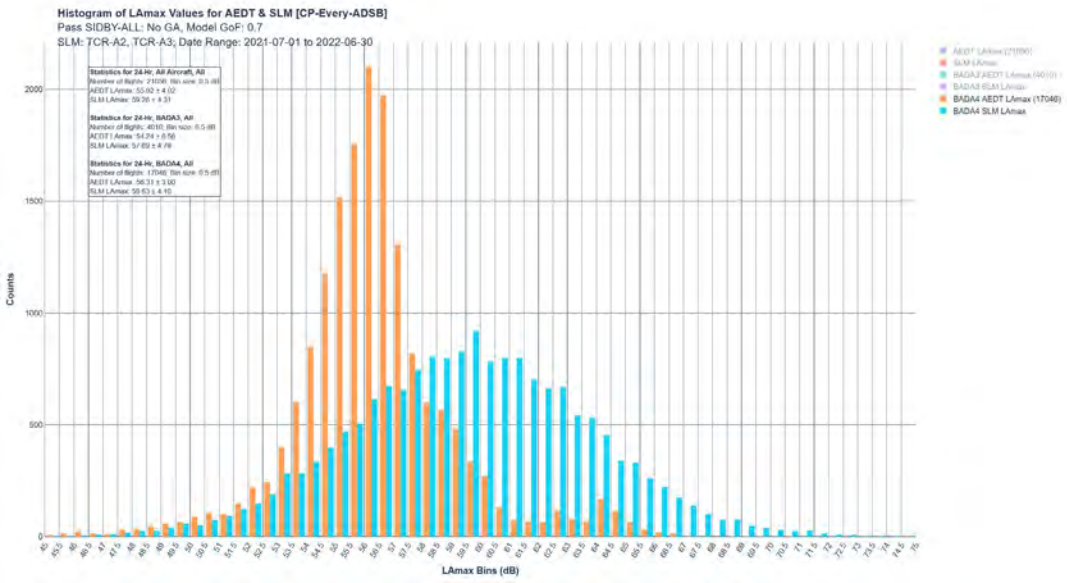

Figure 8. Histogram with the LAmax values from AEDT-AE predictions (orange) and SLM measurements (light blue) at the SIDBY location. LAmax data are binned into 0.5-dB intervals. **Preliminary data: do not cite or quote**.

At this SLM location, which has combinations of aircraft trajectories that are highly concentrated (as with those arriving along the SERFR route) and highly diffuse (as with those arriving along the BDEGA and PIRAT routes), substantial variability in altitudes, airspeeds, and distances at the PCA is observed. Therefore, the measured histogram is rather broad and has a large standard deviation. This natural variability, together with variations in atmospheric, turbulence, and weather conditions, result in a very smooth distribution of noise events. The difference in the means of the AEDT-AE and SLM distributions is approximately −3.3 dB (underprediction by AEDT-AE), with a very large standard deviation for LAmax of 3.5 dB.

Figure 9 shows similar results for the exact same data set, but for the SEL metric instead of LAmax. The predictions for SEL are significantly better, with a difference in the means of the predicted and measured distributions of approximately −1.7 dB (underprediction by AEDT-AE) and a very large standard deviation of 3.2 dB. The AEDT-AE SEL histogram is highly similar to that for LAmax but has less accentuated multimodality, given the integrated nature of the noise metric.

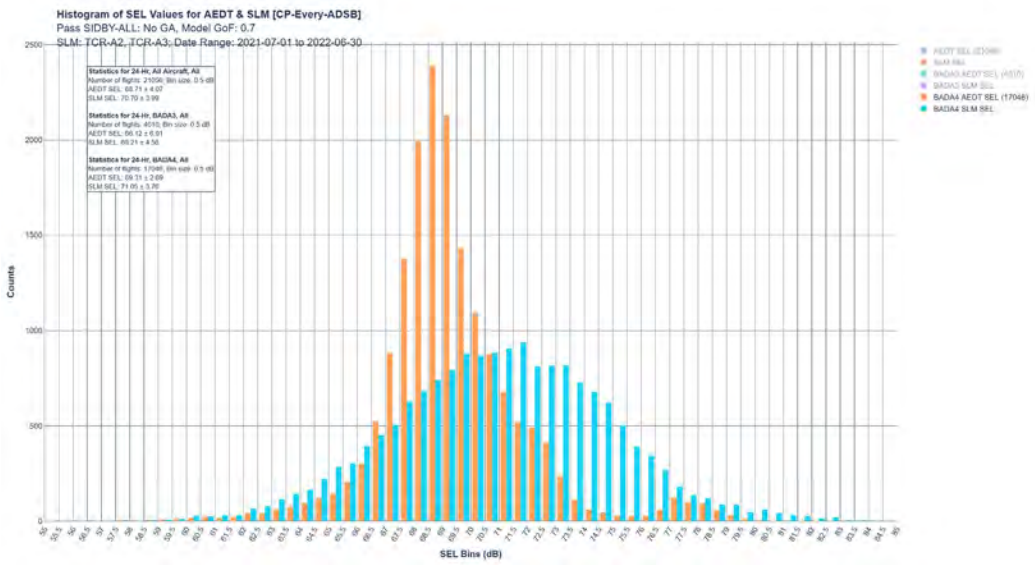

Figure 9. Histogram with the SEL values from AEDT-AE predictions (orange) and SLM measurements (light blue) at the SIDBY location. SEL data are binned into 0.5-dB intervals. **Preliminary data: do not cite or quote**.

Figure 10 displays the differences between the predicted (AEDT-AE) and measured (SLM) noise levels for both LAmax (in orange) and SEL (in light blue). Again, these results are for the same data set containing only BADA4 aircraft. Regardless of the metric, these preliminary results indicate a consistent underprediction of −3.3 dB (with a standard deviation of 3.5 dB) for LAmax and −1.7 dB (with a standard deviation of 3.2 dB) for SEL. These results are consistent, in both trends and values, with the results that we presented in last year's annual report, on the basis of a far smaller data set (30 days in the summer vs. 12 months).

Finally, Figure 11 displays our calculations for the DNLs for both the predicted (AEDT-AE) and measured (SLM) noise levels. On the basis of an entire 12-month period of measurements, using AEDT-AE, we are able to predict using AEDT-AE, a DNL at this location of 43.9 dB, as compared with the measured DNL of 46 dB. The underprediction of DNL by 2.0 dB was very similar in magnitude to the underprediction observed much closer to the airport at SFO-NMT-12. It must be noted that AEDT-AE is not approved for regulatory use and that these results are still preliminary. The outliers in the plot correspond to the accounting of flights during daylight savings days. In comparison with the same DNL predictions and measurements at the location closer to the airport (SFO-NMT-12), we do observe that AEDT-AE predictions are slightly better for SEL, but nearly identical for both LAmax and DNL. While additional work will be conducted to further refine our estimates of the differences, and as we mentioned earlier, our expectation was that AEDT-AE would do a significantly better job at a location close to the airport; however, this conjecture was not borne out by the data. We must be careful and restrict our preliminary conclusions to date to arrivals into SFO only. We expect that the predictions for departures will significantly improve, and we are currently working on those results.

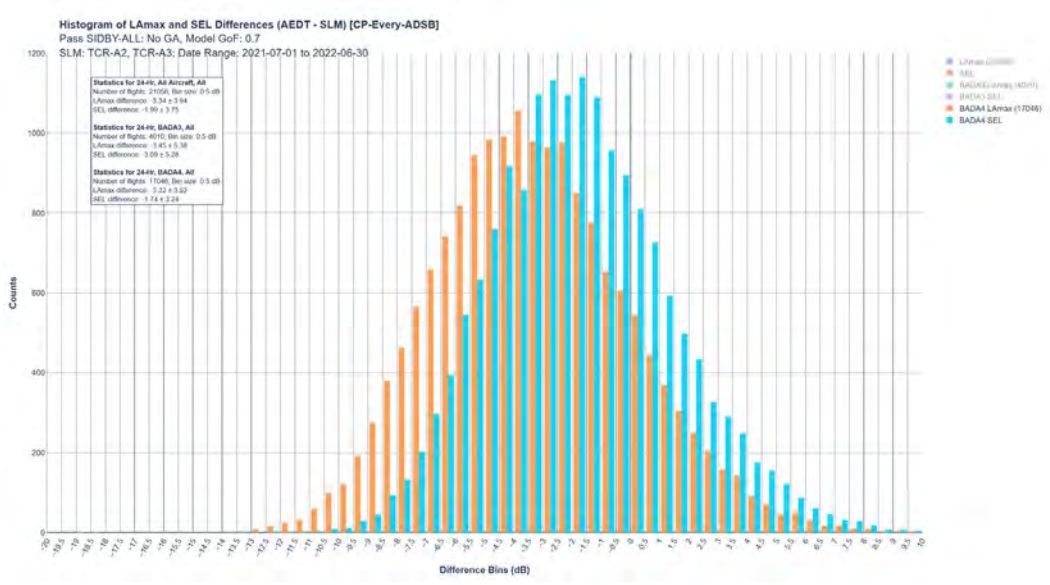

Figure 10. Histograms showing the LAmax (orange) and SEL (light blue) differences between AEDT-AE predictions and SLM measurements at the SIDBY location. A negative value indicates an underprediction by AEDT-AE. Noise level difference data are binned into 0.5-dB intervals. **Preliminary data: do not cite or quote.**

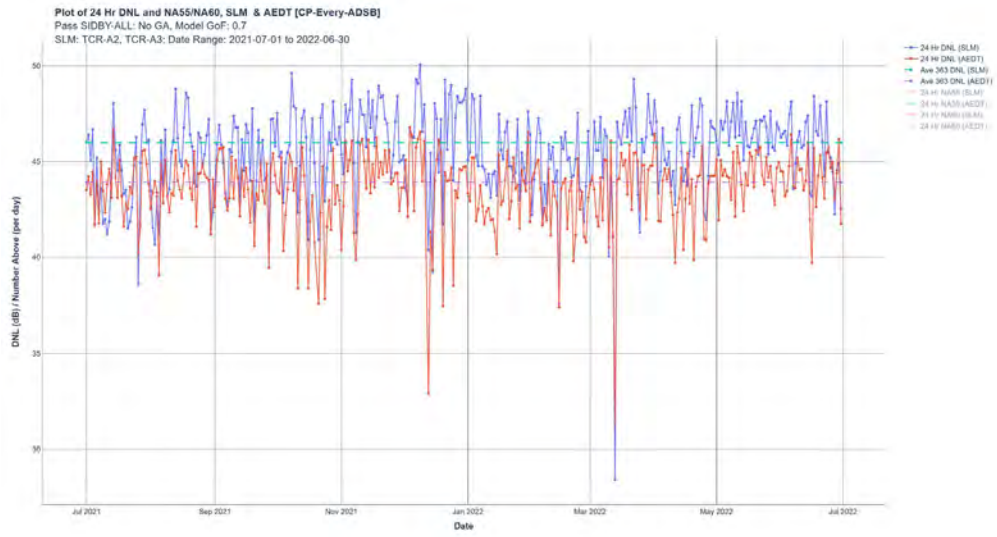

Figure 11. Daily calculated (red) and measured (blue) DNL values (in dB) at the SIDBY location. The SLM DNL value is 60.1 dB, whereas the AEDT-AE-predicted DNL value is 58.1 dB. **Preliminary data: do not cite or quote.**

Impact of Calibrated Airspeed on Noise Predictions

For aircraft noise models to provide useful information for both community impact assessments and airspace redesign, the models must faithfully represent the level of noise produced by aircraft overflights in both areas near the airport, where the noise levels can be substantial (DNL > 65 dB), and in areas farther from the airport, where the noise levels are typically lower (DNL ~50 dB). A number of recent studies, including some by the authors, have attempted to assess the accuracy of the SAE-AIR-1845 aircraft noise model used by AEDT-AE, which was originally intended for use only in the vicinity of airports. Giladi et al. (2020), for example, have conducted assessments of the predicted vs. measured noise and have found that "the AEDT

model underestimates noise levels, sometimes considerably, by 4 to 7 dB(A) in the SEL metric, even when using an accurate flight path for its input." The findings suggest that "aircraft noise model validation should be separated into four cases; takeoffs and landings, and for each operation, a different approach should be used for close and far [SLMs]." The authors further suggest that improvements in the predictive quality of the models might also "involve correction of at least the NPD tables, as well as takeoff profiles." Huyhn et al. have used techniques combining predictions from the NASA Aircraft Noise Prediction Program (ANOPP, and its most recent version ANOPP2) and measurements to assess the potential of arrival procedures flying delayed deceleration approaches to minimize the noise observed on the ground. The authors have found that "delayed deceleration approaches correlated with monitor readings with lower noise levels of an average of 3–6 dB SEL compared to early deceleration approaches across different aircraft types," in addition to observing that substantial effort and sophistication was necessary, beyond standard noise models, to match the measurement data.

The data sets collected, particularly that for SFO-NMT-12, as described earlier, allowed us to examine a key weakness of the noise model used in AEDT. This weakness is structural: the noise levels are based on NPD curves and were developed for areas of the flight paths where engine noise was the dominant noise source; however, this dominance is no longer the case in many arrivals operations. As shown in Figure 12 (adapted from AIAA 2011-2854) for aircraft in approach situations, the contributions from engine and aircraft noise can be highly similar, and therefore a noise model that does not account for both sources of noise on arrivals can underestimate the overall predicted noise levels, particularly farther from the airport, such as at the SIDBY location.

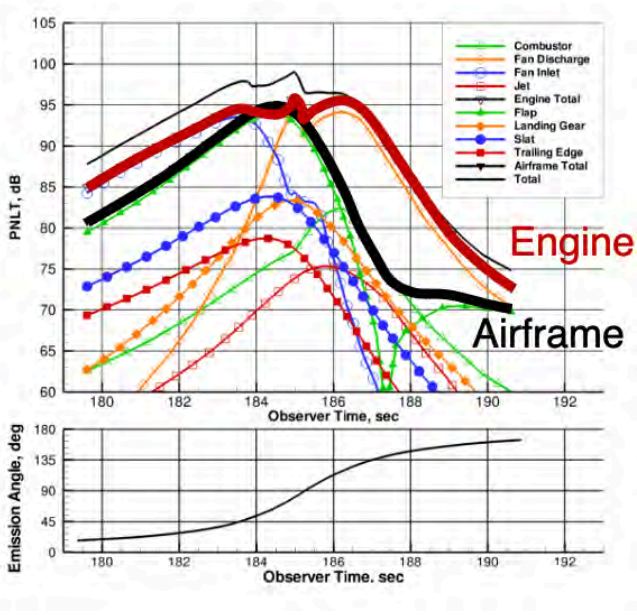

Figure 12. ANOPP2 component noise predictions for conventional aircraft in approach. Adapted from Lopes & Burley, AIAA 2011-2854, 17th AIAA/CEAS Aeroacoustics Conference.

Using the data collected at SFO-NMT-12 for approaches into SFO runway 28L alone, we plotted the predicted (AEDT-AE, in blue) and measured (SLM, in red) noise data, as a function of calibrated airspeed (CAS) from the ADS-B feed (Figure 13). We expected that the noise levels would increase with airspeed, because of the contribution from airframe noise scales with the value of the airspeed. Our expectation was indeed confirmed by the trendline from the measurements, wherein an increase of approximately 0.4 dB for every 10-knot increase in CAS was observed. The trend for the predictions from AEDT-AE was counterintuitive: the trend line predicted an average decrease of 0.3 dB for every 10-knot increase in CAS. This opposite trend in the noise levels with CAS might contribute to the overall underestimation of noise levels by AEDT-AE.

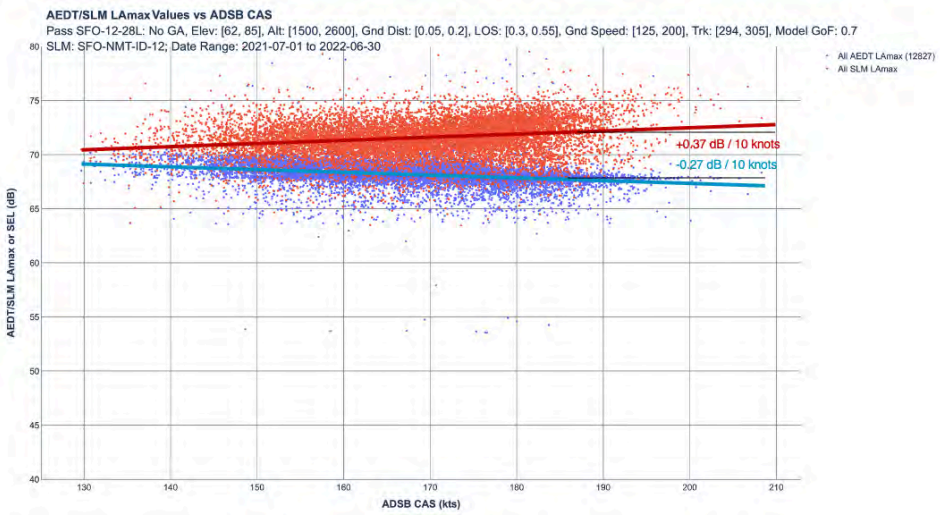

Figure 13. Predicted (AEDT-AE) in red and measured (SLM) LAmax noise levels in blue at the SFO-NMT-12 location, as a function of CAS. Only single-aisle aircraft landing at runway 28L are included in this data set of 12,827 flights.

Preliminary Conclusions

Disclaimers: The results in this section represent our conclusions resulting from the work conducted during the current period of performance (October 1, 2021 to September 30, 2022). These results represent our first attempt at yearly comparisons between AEDT predictions and experimental noise data and variations with CAS. As such, and until improved results are published in a peer-reviewed journal (as of February 2023, we have completed substantially more comparisons than presented in this annual report), the results presented here should be considered preliminary. They provide an indication of our main observations but lack the level of confidence required to make sufficiently strong statements. Moreover, while AEDT is the tool used for regulatory purposes in the United States, we used a version of AEDT that we call AEDT-AE, which uses the collected aircraft track data, BADA4 performance models, and altitude and speed controls to complete simulations (BADA, n.d.). We do not claim that AEDT-AE has any regulatory value.

Our preliminary conclusions from the work presented in this annual report on our early comparisons between AEDT-AE predictions and SLM measurements is summarized in the following statements. Additional work conducted since the beginning of October 2022 will further strengthen these conclusions, but the overall preliminary findings still stand, and minor changes have been made after additional scrutiny. The conclusions of these studies will be considered final after peer-reviewed publications become available in the summer of 2023.

- Preliminary investigations indicated an underestimation of noise predictions for individual-event sound levels on arrival operations to SFO by ~1.7–3.3 dB (mean values) for both LAmax and SEL metrics, regardless of the DNLs at the location of the noise monitoring station. We arrived at this preliminary conclusion after examining approximately 135,000 flights and devoting substantial effort to retaining only a subset of flights whose associated noise events were of the highest quality and represented aircraft activity only.
- BADA4 aircraft modeling results in significant improvement in noise predictions over BADA3 aircraft. In the work presented here, we focused on BADA4 modeling, as the only way for AEDT-AE to incorporate altitude and speed controls (instead of using standard profiles for altitude and airspeed in modeling aircraft trajectories by using BADA3). This improvement is likely to be related to the better aircraft performance model available in BADA4 (for some aircraft types only), thus leading to a better estimation of the engine noise component. Further comparisons across multiple aircraft classes (with BADA3 vs. BADA4) have recently been conducted and will be reported at a later time. The new observations strengthen this preliminary conclusion.
- The variability in the difference between measurement and prediction was high, with a standard deviation of ~3–5 dB. We believe that this important area warrants further investigation to ascertain the main causes of this high variability.

- The SAE-AIR-1845 model used in AEDT-AE does not properly account for the variation in noise resulting from changes in CAS. This aspect is a shortcoming of the noise prediction method for arrivals operations and is not meant as a criticism of the existing noise model which, in its original publication, recognized the conditions for its proper use and situations in which the model would fail to provide accurate predictions.
- The expectation of AEDT's improved accuracy in noise estimates in higher DNL noise areas did not appear to be borne out by the data in the two arrival locations examined. As our study progresses, we intend to verify this preliminary conclusion at several other locations to ascertain whether our initial observations might change. This observation has been restricted to arrivals operations, whereas we expect departure operations to yield better results.
- AEDT predictions for aggregate noise metrics (not individual flights) still show significant differences of around DNL 2.0 dB regardless of the location of the noise monitoring station and the DNL values of those locations. Our continued work to strengthen this conclusion has not yet resulted in any modifications to the statements being made in this annual report.

Major Accomplishments

- Completed a completely new infrastructure for ASCENT 53/MONA that has been shown to scale to the types of data collection and analysis expected for a complex metroplex, such as the Bay Area
- Demonstrated full automation of the AEDT analysis pipeline and of the noise prediction/measurement comparisons for arbitrarily large data sets
- Demonstrated the use of the ASCENT 53/MONA infrastructure to simulate (and compare) flights arriving at runways 28L/R at SFO over a period of 12 months (more than 135,000 individual flights); decreased the computational time required to complete such studies to approximately 2 days
- Drew preliminary conclusions from the comparisons between AEDT predictions and SLM measurements at two locations (SIDBY and SFO-NMT-12) under the arrival routes to SFO
- Concluded an investigation of the trends of AEDT-AE noise prediction methods with CAS, and reported our results.

Publications

Jackson, D. C., Rindfleisch, T. C., & Alonso, J. J. (2021). A system for measurement and analysis of aircraft noise impacts. *The 9th OpenSky Symposium*, 6. https://doi.org/10.3390/engproc2021013006

Outreach Efforts

Over the past few months, we have developed a closer relationship with SFO and the technical leads at EnviroSuite, which deploys, monitors, and makes available the noise data at approximately 40 locations in the Bay Area. We have hosted technical interactions with both groups on various topics including the filtering techniques for non-aircraft noise that we have developed in ASCENT 53. These outreach efforts have resulted in the sharing of noise data at many locations, including historical data sets, and a commitment to continue to share data as they are acquired in the future.

Awards

None.

Student Involvement

Several undergraduate and graduate students are/have been part of our team during this past year. Their names and areas of responsibility are listed at the beginning of this document. Several students graduated during the current period of performance, but we have enlisted new students to continue the work. Their contributions are acknowledged here, because the project would not have advanced to this extent without them.

Plans for Next Period

We intend to complete all three tasks in our Statement of Work as planned. In addition to the completion of all milestones, the release of appropriate parts of the ASCENT 53/MONA project and the demonstration of various capabilities through participation in aircraft noise related meetings/conferences are also envisioned. Two manuscripts detailing our efforts are under preparation and will be submitted to archival journals for review in March 2023. The expected publication is in the Fall of 2023.

References

Next generation air transportation system (Nextgen) | Federal Aviation Administration. (n.d.). Retrieved May 18, 2023, from https://www.faa.gov/nextgen

PiAware—Ads-b and MLAT receiver. (n.d.). FlightAware. Retrieved May 18, 2023, from http://flightaware.com/adsb/piaware/

Apache Kafka. (n.d.). Apache Kafka. Retrieved May 18, 2023, from https://kafka.apache.org/

Jetdev. (n.d.). *Jetvision Webshop*. Retrieved May 18, 2023, from https://webshop.jetvision.de/

Convergence Instruments. (n.d.) Sound Level Meters. Retrieved November 7, 2021, from https://dev.convergenceinstruments.com/pc/sound-level-meter-data-loggers/

AeroAPI® Flight Tracking and Flight Status api. (n.d.). FlightAware. Retrieved May 18, 2023, from http://flightaware.com/commercial/aeroapi/

FAA System Wide Information Management (SWIM). (n.d.). Retrieved November 7, 2021, from https://www.faa.gov/air_traffic/technology/swim/

FAA Aircraft Registry. (n.d.). Retrieved November 7, 2021, from https://www.faa.gov/licenses_certificates/aircraft_certification/aircraft_registry/

OpenSky Aircraft Metadata Database. (n.d.). Retrieved November 7, 2021, from https://opensky-network.org/datasets/metadata/

Coded Instrument Flight Procedures (CIFP). FAA. (n.d.). Retrieved November 7, 2021, from https://www.faa.gov/air_traffic/flight_info/aeronav/digital_products/cifp/

Benjamin, S. G., Weygandt, S. S., Brown, J. M., Hu, M., Alexander, C. R., Smirnova, T. G., Olson, J. B., James, E. P., Dowell, D. C., Grell, G. A., Lin, H., Peckham, S. E., Smith, T. L., Moninger, W. R., Kenyon, J. S., & Manikin, G. S. (2016). A north American hourly assimilation and model forecast cycle: The rapid refresh. *Monthly Weather Review*, *144*(4), 1669–1694. https://doi.org/10.1175/MWR-D-15-0242.1

Wynnyk, C. M. (2012). Wind analysis in aviation applications. *2012 IEEE/AIAA 31st Digital Avionics Systems Conference (DASC)*, 5C2-1-5C2-10. https://doi.org/10.1109/DASC.2012.6382366

Group, P. G. D. (2023, May 18). *Postgresql*. PostgreSQL. https://www.postgresql.org/

Postgis. (n.d.). PostGIS. Retrieved May 18, 2023, from https://postgis.net/

Time-series data simplified. (n.d.). Retrieved May 18, 2023, from https://www.timescale.com/

Harding, M. & Ferrier, D. (2014). *Using Post Analysis of a Noise Sample Stream in place of Noise Monitor Based Thresholds in the Detection of Aircraft Noise*. INTER-NOISE and NOISE-CON Congress and Conference Proceedings. Institute of Noise Control Engineering, Melbourne, Australia.

Giladi, R. (2020). Real-time identification of aircraft sound events. *Transportation Research Part D: Transport and Environment*, *87*, 102527. https://doi.org/10.1016/j.trd.2020.102527

H3 | H3: Hexagonal Hierarchical Geospatial Indexing System. (n.d.). Retrieved May 18, 2023, from https://h3geo.org/

FAA: FAA Aviation Environmental Design Tool (AEDT). (n.d.). Retrieved May 18, 2023, from https://aedt.faa.gov/

Giladi, R., & Menachi, E. (2020). Validating aircraft noise models. *8th OpenSky Symposium 2020*, 12. https://doi.org/10.3390/proceedings2020059012

SQL server 2019 | Microsoft. (2019). Retrieved May 18, 2023, from https://www.microsoft.com/en-us/sql-server/sql-server-2019

ANP—Eurocontrol Experimental Centre. (n.d.). Retrieved May 18, 2023, from https://www.aircraftnoisemodel.org/

Base of aircraft data (BADA). EUROCONTROL Experiemental Center. (n.d.). Retrieved May 18, 2023, from https://www.eurocontrol.int/model/bada

Douglas, D. H., & Peucker, T. K. (1973). Algorithms for the reduction of the number of points required to represent a digitized line or its caricature. *Cartographica: The International Journal for Geographic Information and Geovisualization*, *10*(2), 112–122. https://doi.org/10.3138/FM57-6770-U75U-7727

Ramer, U. (1972). An iterative procedure for the polygonal approximation of plane curves. *Computer Graphics and Image Processing*, *1*(3), 244–256. https://doi.org/10.1016/S0146-664X(72)80017-0

deck.gl: WebGL-powered Visualization Framework for Large-scale Datasets. Retrieved May 18, 2023, from https://deck.gl/

Project 054 AEDT Evaluation and Development Support

Georgia Institute of Technology

Project Lead Investigator

P.I.: Professor Dimitri N. Mavris
Director, Aerospace Systems Design Laboratory
School of Aerospace Engineering
Georgia Institute of Technology
(404) 894-1557
dimitri.mavris@ae.gatech.edu

Co-P.I.: Dr. Michelle Kirby
Chief, Civil Aviation Division
Aerospace Systems Design Laboratory
School of Aerospace Engineering
Georgia Institute of Technology
(404) 385-2780
michelle.kirby@ae.gatech.edu

University Participants

Georgia Institute of Technology

- P.I.s: Dr. Dimitri Mavris, Dr. Michelle Kirby
- FAA Award Number: 13-C-AJFE-GIT-098, 114, and 122
- Period of Performance: September 24, 2021 to September 20, 2023
- Tasks:
    1. Improved Departure Modeling
    2. Arrival Profile Modeling
    3. Full Flight Modeling
    4. System Testing and Evaluation of the FAA's Aviation Environmental Design Tool (AEDT)

Project Funding Level

Georgia Institute of Technology has received $900,000 in funding for this project. In terms of cost-share details, Georgia Tech has agreed to a total of $900,000 in matching funds. This total includes salaries for the project director, research engineers, and graduate research assistants, as well as computing, financial, and administrative support, including meeting arrangements. Georgia Tech has also agreed to provide tuition remission for the students, paid for by state funds.

Investigation Team

Prof. Dimitri Mavris, P.I., Georgia Institute of Technology, all Tasks
Dr. Michelle Kirby, Co-Investigator, Georgia Institute of Technology, all Tasks
Dr. Ameya Behere, Research Faculty, Georgia Institute of Technology, all Tasks
Dr. Tejas Puranik, Research Faculty, Georgia Institute of Technology, all Tasks
Dr. Dushhyanth Rajaram, Research Faculty, Georgia Institute of Technology, all Tasks
Mr. David Anvid, Research Faculty, Georgia Institute of Technology, all Tasks
Jirat Bhanpato, Graduate Student, Georgia Institute of Technology, Task 1 & 3
Howard Peng, Graduate Student, Georgia Institute of Technology, Task 1 & 2
Keletso Mmalane, Graduate Student, Georgia Institute of Technology, Task 2
Anushka Moharir, Graduate Student, Georgia Institute of Technology, Task 2
Hyungu Choi, Graduate Student, Georgia Institute of Technology, Task 3
Bogdan Dorca, Graduate Student, Georgia Institute of Technology, Task 4

Santusht Sairam, Graduate Student, Georgia Institute of Technology, Task 4

Project Overview

This project provides data and methods to continue to improve modeling of aircraft weight, take-off thrust, and departure and arrival procedures within the FAA's AEDT, as well as the AEDT's full flight modeling capabilities. Some of the modeling assumptions in AEDT are considered to be overly conservative and could be improved by using industry and airport flight operation data. Funding for this project will continue to support the implementation of these methods and data in AEDT4. To facilitate these efforts, the Georgia Tech team will utilize real-world flight data and noise monitoring data to improve departure, full flight, and arrival modeling.

Task 1 - Improved Departure Modeling

Georgia Institute of Technology

Objective

Prior research in ASCENT Project 45 provided recommendations for noise abatement departure procedures (NADPs) to be modeled in future versions of AEDT. Comparisons were made between NADP profiles within the NADP library to determine the differences between each profile. As a result, two profiles were found to best represent the variability among each type of NADP. This task aims to investigate the similarities between the recommended NADPs and real-world departure operations for multiple airlines and airports.

From October 2021 to September 2022, the focus of the project was to specifically investigate the effects of specific profiles and weather conditions on the differences between NADP results and real-world data. This work helped narrow down specific parameters in the process of generating noise and performance results that could lead to significant differences between AEDT calculations and corresponding real-world results.

Research Approach

Methodology

This project previously generated NADPs that could be implemented in AEDT as recommendations for minimizing the effects of noise during the take-off portion of a commercial flight. These recommendations were derived from two datasets, designated the OpenSky and Threaded Track datasets, which together cover a large number of airports and aircraft. However, while the datasets are extensive, they do not capture all variables, such as thrust data for each flight. In addition, the Threaded Track dataset, which captures many of the flights, lacks information below an altitude of 1,000 ft, representing a significant lack in data. This gap in data leads to questions about how much variability is not being captured by the data and whether that variability significantly influences the accuracy of the models generated for recommendations.

To bridge this gap, another dataset, designated Flight Operations Quality Assurance (FOQA) data, was brought for comparison with the current data. FOQA represents data on flights from KATL (Atlanta International Airport), complete with thrust data and data below 1,000 ft. In addition, we applied weather data from the Automated Surface Observing System to determine whether there are any correlations between weather and flights that could cause differences between the flight profiles and flight data.

To assess for correlations, a set of Python scripts was used to run cases and compare both performance and noise data. To provide a baseline, Boeing 737-800 and 737-900 flights from KATL were used for comparison, as these flights were included in all datasets and provide a good representation of a generic commercial aircraft. The data to be compared were separated into three categories, as shown in Table 1. In particular, the team sought to assess sound exposure level (SEL) noise contours and performance data and to identify differences resulting from weather or profile differences.

Table 1. Categories of comparison. FPP stands for Fixed-Point Profile

DEFAULT	PROCEDURAL+WEATHER	FPP+WEATHER
The current profile, as in the Aviation Environmental Design Tool, using as many defaults as possible	The current profile, but with default, averaged weather substituted for actual weather corresponding to the flight data	The data from FOQA, instead of noise abatement departure procedures (NADPs)
• Using NADP 2-11 and STANDARD profiles • Weight set to "Alternate Weight," with the load factor more indicative of real-world flights • Reduced thrust 15% (RT15) • Default, averaged weather conditions across all airports	• Using NADP 2-11 and STANDARD profiles • Weight set to "Alternate Weight," with the load factor more indicative of real-world flights • RT15 • Weather corresponding to real-world data	• Using FPP defined from FOQA data, including real-world thrust, altitude, weight, and ground speed • Weather corresponding to real-world data

Cases were then run, and flights in each of the categories were compared with each other via pairwise comparisons.

Afterwards, we closely examined the noise contours resulting from the cases. The percentage differences for the metrics of area, length, and width were calculated using the following equation:

$$\Delta\% = \frac{Case - Default}{Default}$$

Results and Discussion

Default vs. Procedural

We first compared the NADP profile itself and the NADP profile with corrected weather data. Figure 1 shows each of the performance metrics compared with the cumulative ground distance and displays how the flights are distributed in this comparison.

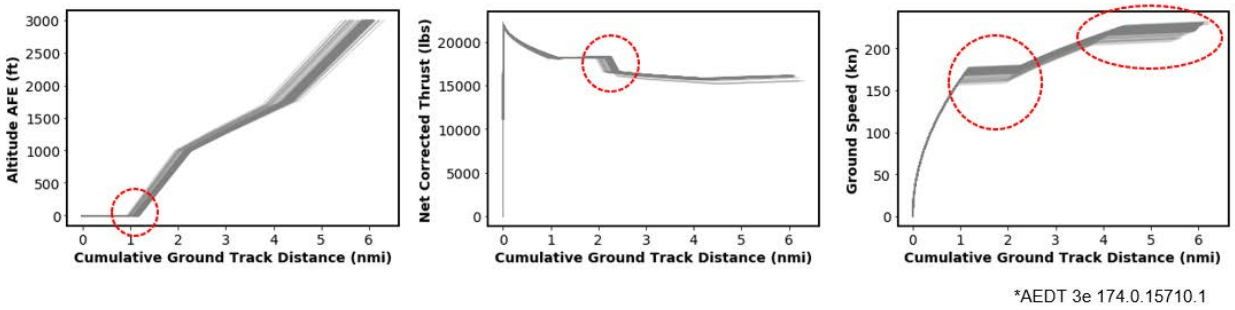

Figure 1. Plots with cumulative track distance. AFE: Above Field Elevation, nmi: nautical mile.

The differences in the metrics represent variation in the flight results solely due to differences in weather conditions. Key points in the flights are also highlighted here. The left panel shows differences in the lift-off point resulting from weather conditions. The middle panel shows the difference in the thrust cutback point, and the right panel shows the difference in ground speed. In Figure 2, the comparison between the AEDT-calculated lift-off and the actual lift-off shows that, in general, the NADP profiles underpredict where lift-off is occurring when weather conditions are utilized. Figure 2 also compares the

weights calculated by AEDT, which were used for both the default and procedural cases, compared with the third FOQA weight, demonstrating that the errors in the weights are randomly distributed.

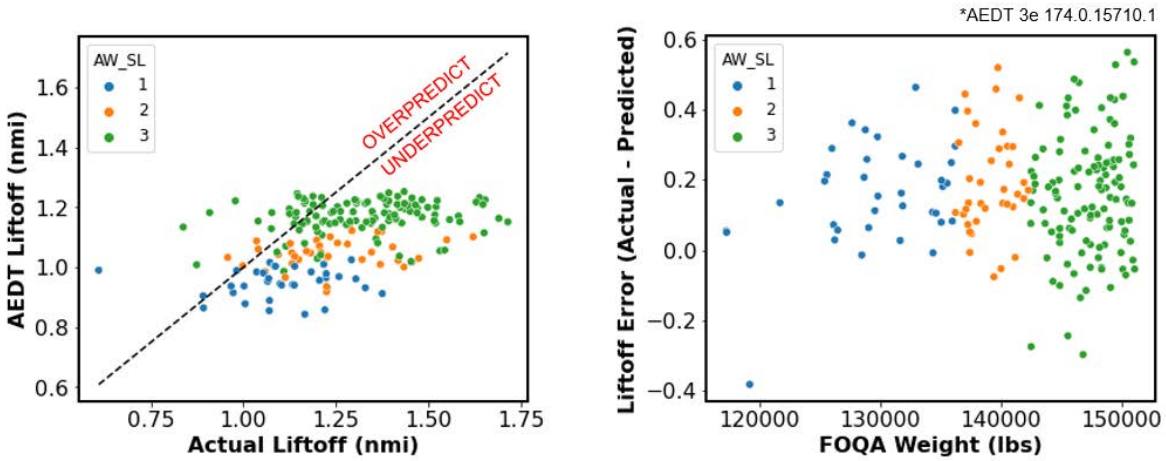

Figure 2. Comparison of Aviation Environmental Design Tool (AEDT) results and actual results. nmi: nautical mile; FOQA: Flight Operational Quality Assurance.

Procedural vs. Fixed-Point Profiles

For this comparison, the take-off distance is an important metric to assess. Figure 3 shows the difference between the take-off distance for the NADP and FOQA, with the same weather data used in both cases.

Case	TEMPERATURE (F)	DEW_P (F)	REL_HUM	WND_SPD (KTS)	Liftoff Error (nmi)
Short TO	46.40	42.80	87.194154	1.39	-0.30
Long TO	46.40	42.80	87.194154	0.00	+0.56

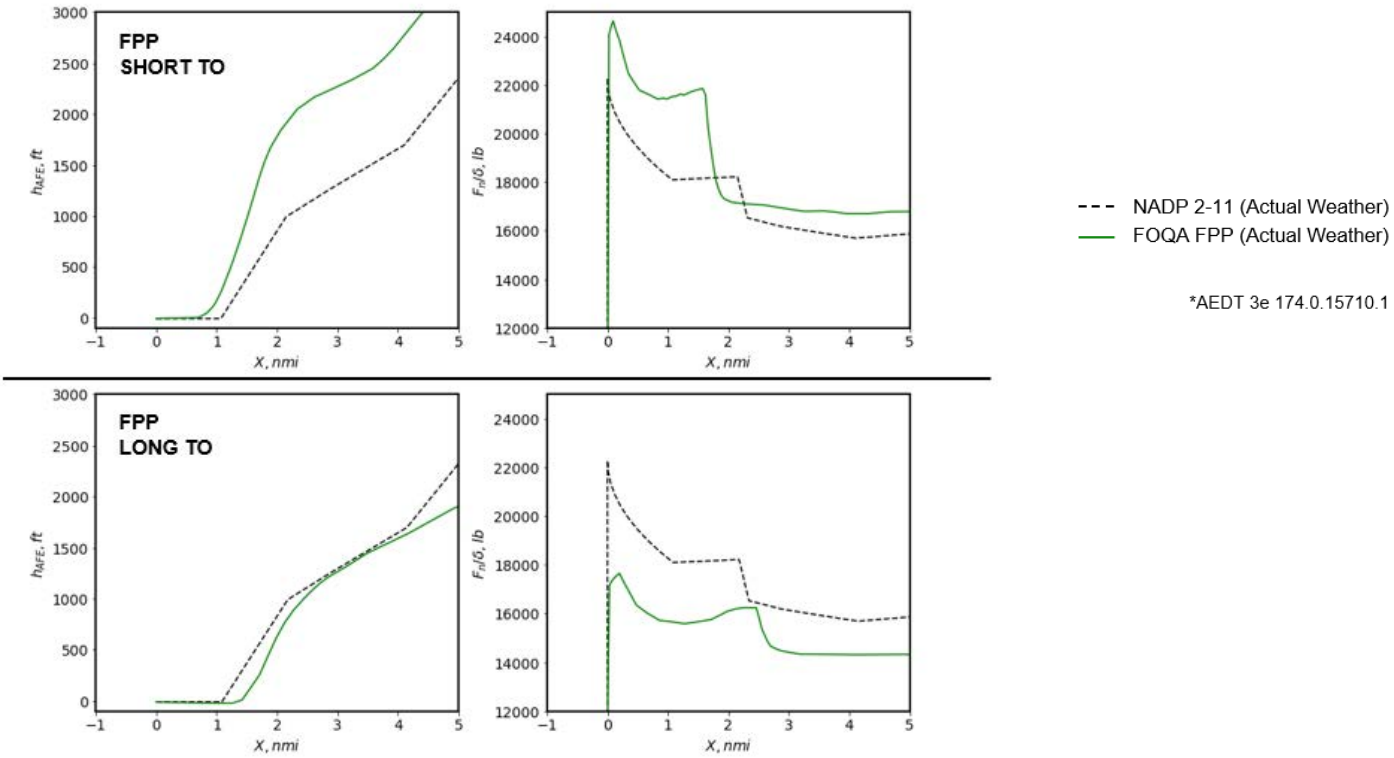

Figure 3. Effects of take-off (TO) distance. NADP: noise abatement departure procedure; nmi: nautical mile; FOQA: Flight Operational Quality Assurance; FPP: Fixed-Point Profile.

From these results, it is clear that there are significant differences between the two datasets below 1,000 ft. As shown in both the plots and the table, the NADP has the issue of underpredicting short take-off flights and overpredicting long take-off flights. The plots present the error in altitude and thrust due solely to differences in take-off. Although the plots visually show quite a bit of error, further work is needed to determine whether the magnitude of the error is sufficiently significant to warrant the creation of additional NADP profiles.

Effects on Noise

The most important parameters in this project are the noise metrics, and the results indicate a significant effect on noise. Figure 4 presents comparisons of the produced noise contours for different weather conditions modeled using the NADP 2-11 profile with alternate weights and reduced thrust 15. The heatmap displays the SEL difference (dB) between the NADP 2-11 profile modeled using the default AEDT average airport temperature and actual weather conditions.

Case	TEMPERATURE (F)	DEW_P (F)	REL_HUM	WND_SPD (KTS)
Default	63.93	52.46	66.35	6.94
Low Temperature	32.00	23.00	69.06	5.79
High Temperature	93.20	64.40	38.76	6.13

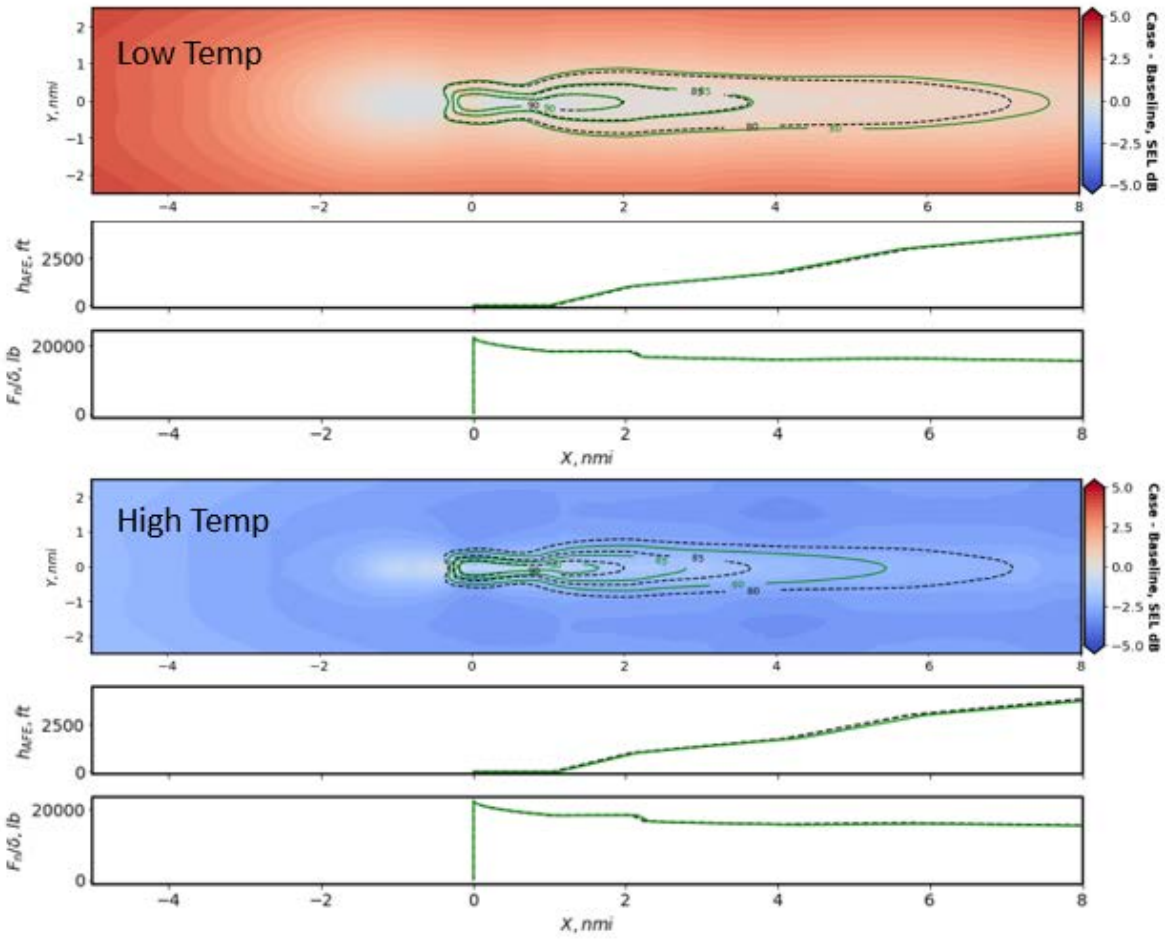

Figure 4. Noise effects due to temperature. AEDT: Aviation Environmental Design Tool; NADP: noise abatement departure procedure; SEL: sound exposure level.

When weather conditions are varied for the high-temperature case, the contour areas diminish in size. This effect may be attributed to the combined effects of temperature and humidity differences between the default weather and the actual weather used in modeling. This effect is presumably due to the atmospheric absorption and acoustic impedance adjustment, which are highly dependent on these weather parameters. Further investigation is needed before any conclusive remarks can be made.

In Figure 5, the effect of headwind on the noise contours is shown. That data indicate that the noise is not significantly affected by the headwind, as the noise contours do not visibly change for low-wind vs. high-wind conditions.

Case	TEMPERATURE (F)	DEW_P (F)	REL_HUM	WND_SPD (KTS)
Default	63.93	52.46	66.35	6.94
Low Wind	66.20	64.40	93.93	0.00
High Wind	60.80	51.80	72.22	12.99

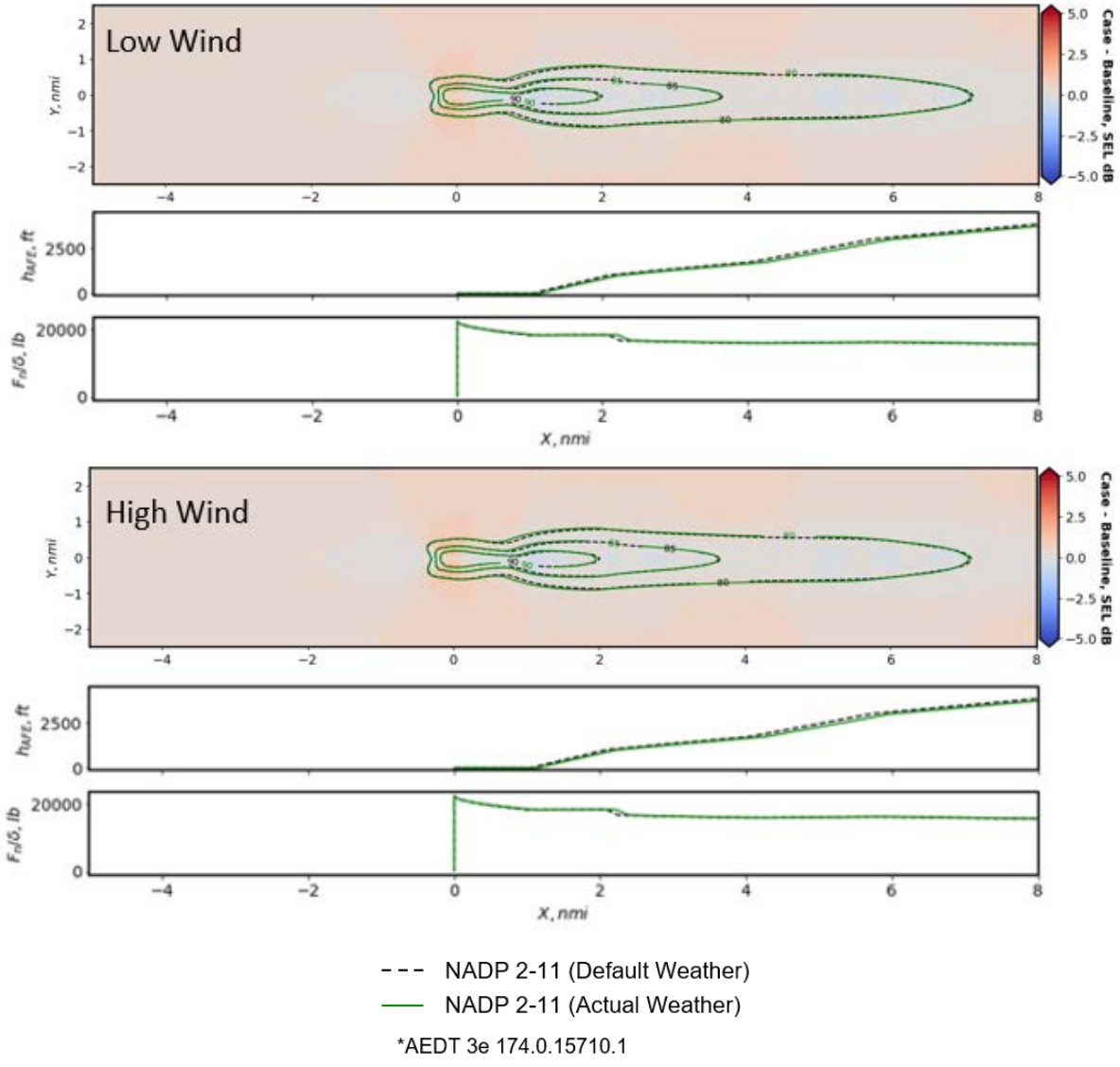

Figure 5. Noise effects due to wind. AEDT: Aviation Environmental Design Tool; NADP: noise abatement departure procedure; SEL: sound exposure level.

Another factor to consider is take-off performance, notably the thrust and lift of each flight and their effects on the noise contour. It was found that differences in thrust and lift-off significantly affect the noise contours, but there are also several additional factors, such as temperature, that have a lesser effect. In general, as the take-off distance increases, the width of the noise contour decreases and the contour length increases.

Although there are differences, it appears as though the noise contours are still constrained to a limited area around the airport for the given airport and runway. In both cases, the 90-dB contour remains isolated inside the airport and does not extend outside the airport. However, there are substantial changes for some of the 80- and 85-dB contours. It may be useful to further examine these contours in future work.

The SEL curves and contours are reasonable and indicate that the process and results for determining the SEL are suitable. Work will be continued along these lines in order to better compare the differences currently observed between real-world flights and NADP results. In particular, we plan to examine day–night average sound level contours, using AEDT to generate airport-level contours by aggregating flights from each of the three aforementioned categories and comparing them with each other and SEL results. This work will provide further details about these differences and their sources.

Milestone(s)

- None

Major Accomplishments

- Acquired relevant weather and real-flight data for comparing NADP profile results to actual flights
- Created experiment cases based on NADP profiles, real-world weather, and actual flight data and generated noise results through AEDT
- Analyzed SEL contours to determine factors for noise and performance differences between NADP profiles and real-world flights

Publications

None

Outreach Efforts

Biweekly calls
Bi-annual ASCENT meetings

Awards

None

Student Involvement

- Jirat Bhanpato and Howard Peng (Graduate Research Assistants, Georgia Institute of Technology) participated in this research.

Plans for Next Period

- Perform airport-level analyses to compare differences in performance and noise due to weather and profile differences.
- Investigate any resulting significant differences.

Task 2 - Arrival Profile Modeling

Georgia Institute of Technology

Objective

The AEDT currently models arrival profiles using specified fixed-point trajectories or manufacturer-provided procedures. In Task 2, we compare data from real-world flights to the AEDT models to make recommendations on how to improve AEDT models to better capture real-world operations.

The objective of Task 2 is to identify and develop recommendations for AEDT that will allow it to better capture aircraft behavior during arrival. The specific focuses of this task are to (a) accurately capture the arrival of aircraft at airports based on real-world data and (b) enhance the ability of AEDT to model aircraft approaches and classify them as one of several arrival profiles suggested by analyses of real-life data. The goals for this period were to perform clustering based on the optimal clustering algorithm and to verify the sensitivity of the clusters by executing arrival profile modeling in AEDT. At the end of this project, recommendations will be made regarding which AEDT arrival profiles should be integrated into the system and what information those profiles should include.

Research Approach

Methodology

In the previous year, it was determined that clustering would be the best method for accomplishing the goals of this task, as this approach reduces the number of individual arrival flights to be analyzed. A range of potential algorithms that could be used to perform clustering were identified, as shown in Table 2, each with a different mathematical approach and formulation.

Table 2. Exploring clustering algorithms.

Method	Details	Advantages	Disadvantages
K-Means	Distance-based	Fastest algorithm; tighter clusters compared with hierarchical methods	Requires knowledge of the number of clusters
K-Medoid	Distance-based	More robust to noise compared with K-Means	Assumes spherical data; requires knowledge of the number of clusters
Agglomerative	Hierarchical	Orders objects	Requires knowledge of the number of clusters
DBSCAN (Density-Based Spatial Clustering of Applications with Noise)	Reachability- and density-based	No need to pre-specify the number of clusters	Does not handle different densities well
Mean Shift	Centroid-based	No need to pre-specify the number of clusters	Cannot control the number of clusters
OPTICS (Ordering points to identify the clustering structure)	Reachability- and density-based	Handles different densities better then DBSCAN; no need to pre-specify the number of clusters	Slower than DBSCAN
BIRCH (Balanced iterative reducing and clustering using hierarchies)	Hierarchical	Faster than other hierarchal algorithms	Slower than K-Means; requires knowledge of the number of clusters

After identifying the best clustering method, trends in cluster allocation were studied. The distribution of cluster points aided in recognizing how the data can be generalized for AEDT recommendations. Eight metrics were explored for this purpose: (1) level-off height, (2) level-off length, (3) level-off distance to airport, (4) total flight distance, (5) level-off delta V, (6) longitude, (7) latitude, and (8) airport altitude. The clusters had similar behavior across these metrics and led to a reduced number of points for AEDT generalization. As shown in Figure 6, the largest level-off heights (ft, Above Ground Level (AGL))

occurred in 3 of the 20 clusters (clusters 7, 12, and 19). Clusters 0–3 and 15–17 were similar to each other, with similar trends for the level-off height, length, and distance to the airport. In Figure 7, the level-off delta V was rounded to the nearest multiple of 10 knots. Here, more differences were observed between clusters 0–2 and 15–16.

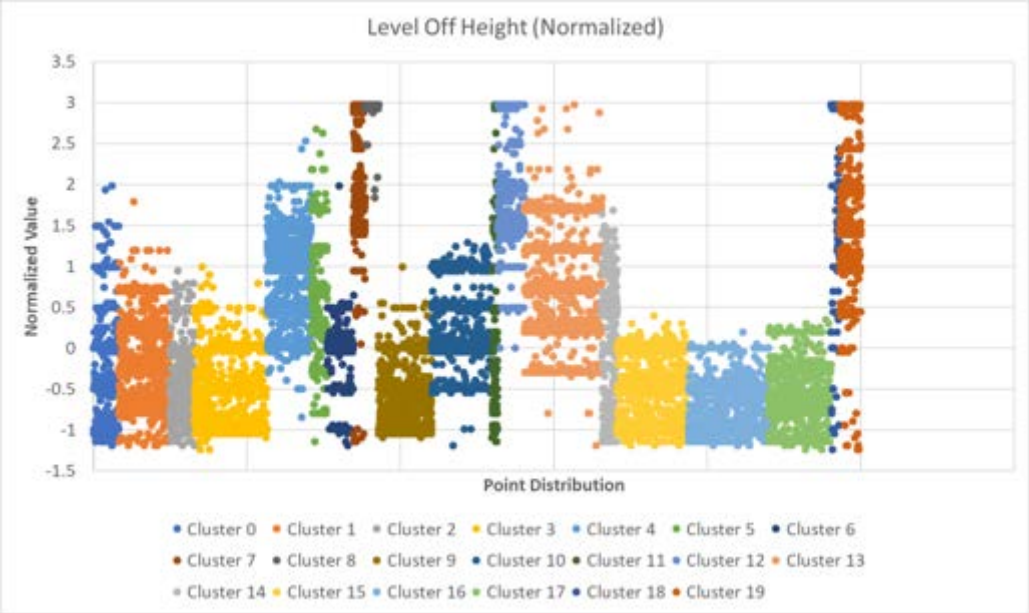

Figure 6. Point distribution of clusters for level-off height.

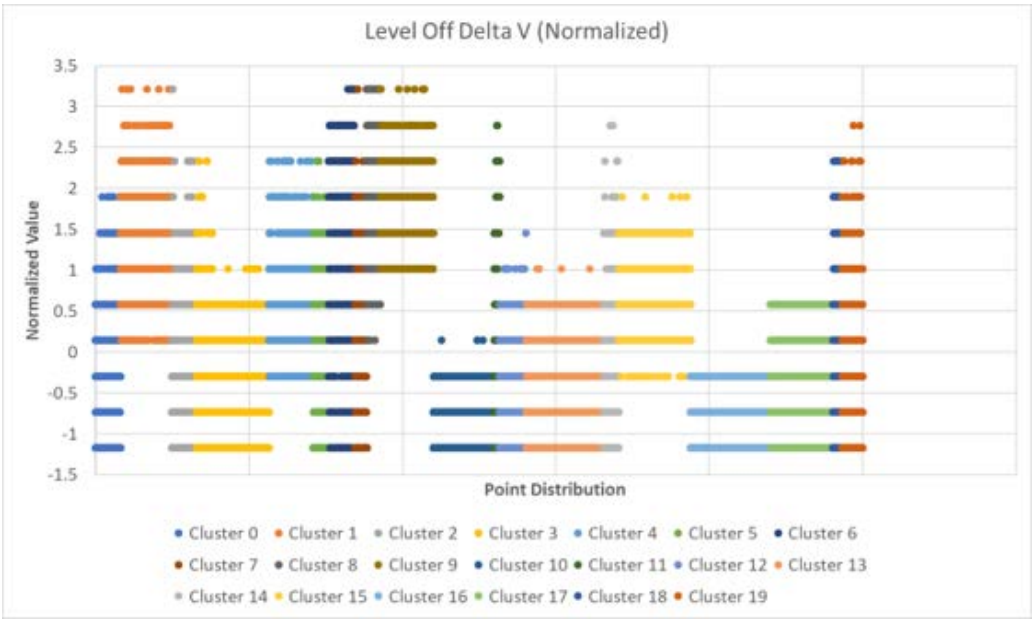

Figure 7. Point distribution of clusters for level-off delta V.

Visualizations were created to assess how the clustering is affected by geography. The goal of the visualization was to plot all clusters on a map to visually determine whether there were clear groupings of airport arrival patterns within clusters. Tableau

was used to construct the map-based visualization. To verify the sensitivity of the clusters, arrival modeling was performed with AEDT, comparing the centroid of each cluster to the default STANDARD profile. The nature of all clusters was determined by comparing the environmental metrics obtained from the results of arrival modeling. The modeling gave the range of level-off parameters, i.e., the minimum and maximum of each level-off parameter.

Table 3. Procedural definition of random flights from cluster 2 arrival operation for the Boeing 737-800 at KATL.

Step	Flap ID	Step Type	Altitude (ft)	Calibrated Airspeed (knots)	Distance (ft)	Glide Slope
1	A_00	Descend	8,400	249		3
2	A_00	Level	5,400	250	21,500	
3	A_01	Level	5,400	246	3,671	
4	A_05	Level	5,400	243	5,209	
5	A_15	Descend	5,400	240		3
6-9	Same as Default	Same as Default	Same as Default	Same as Default	Same as Default	Same as Default

Results and Discussion

K-Means and BIRCH were identified as the best clustering methods based on three quantitative scoring metrics that indicate the quality of the identified clusters: the silhouette score, Davies–Boudlin index, and Calinski–Harabasz index. The clustering score comparisons are shown in Figure 8. After the clustering methods were selected, they were implemented on a test dataset consisting of all level-offs from the three busiest airports in the full dataset to determine the primary features that significantly affect level-off parameters.

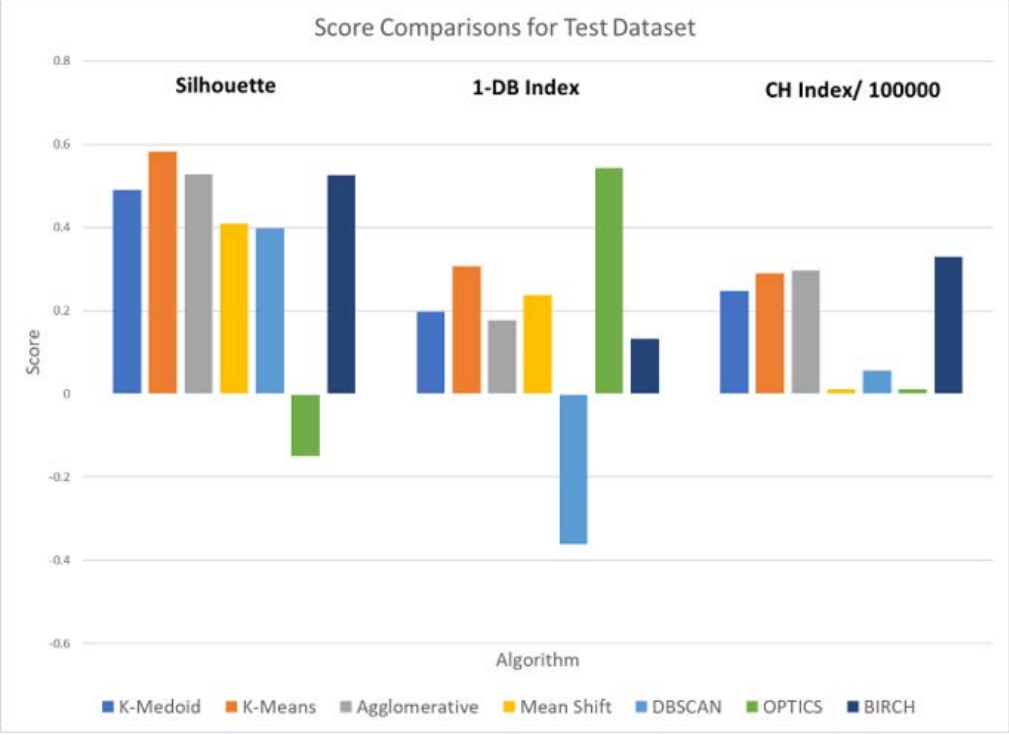

Figure 8. Score comparisons for a test dataset. CH: Calinski–Harabasz; DB: Davies–Boudlin; DBSCAN: Density-Based Spatial Clustering of Applications with Noise; OPTICS: Ordering points to identify the clustering structure; BIRCH: Balanced iterative reducing and clustering using hierarchies.

The cluster distribution was plotted against the chosen metrics for three types of datasets: test, small, and large. It was observed that the cluster distributions were similar for the test and large datasets, with a poor correlation between the metrics for small and large datasets. Figure 9 shows the cluster distribution for the BIRCH algorithm across 10 clusters for a complete dataset. The y-axis consists of the percentage for each cluster, and the x-axis gives the cluster label (0–9). The plot shows that BIRCH has one prominent cluster in which a significant number of points are distributed. Figure 10 shows the cluster distribution for the K-Means algorithm (10 clusters) applied to a complete dataset. The axis definitions are the same as those in Figure 9. The plot shows that the K-Means distribution is spread more evenly than the BIRCH distribution.

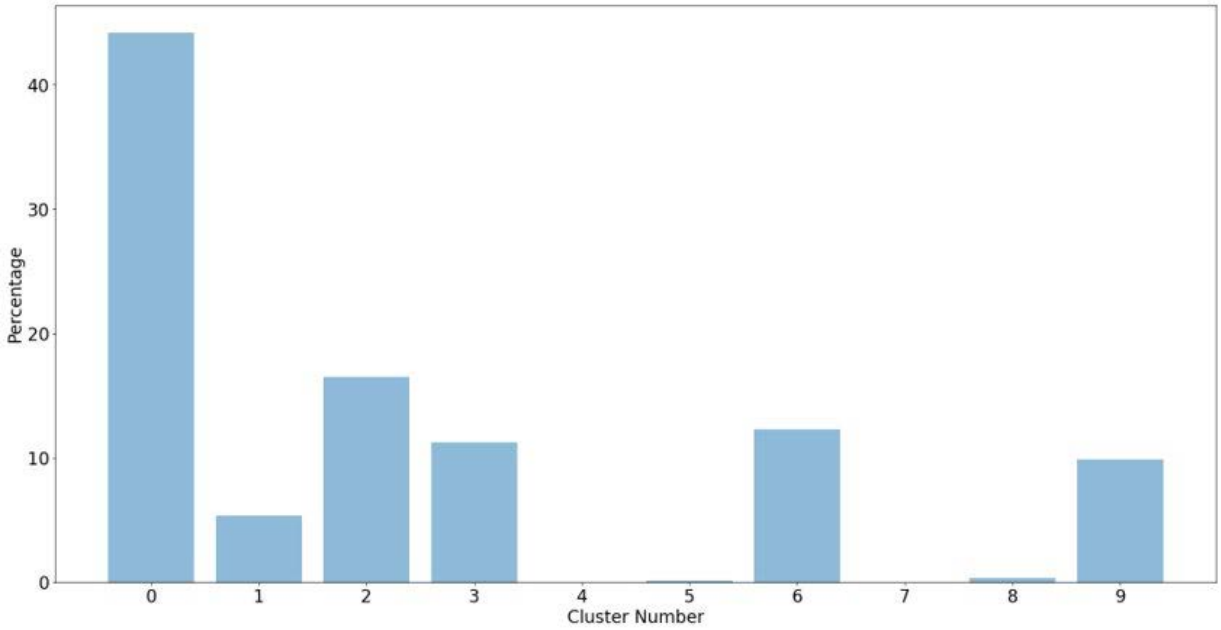

Figure 9. Cluster distribution for the BIRCH algorithm.

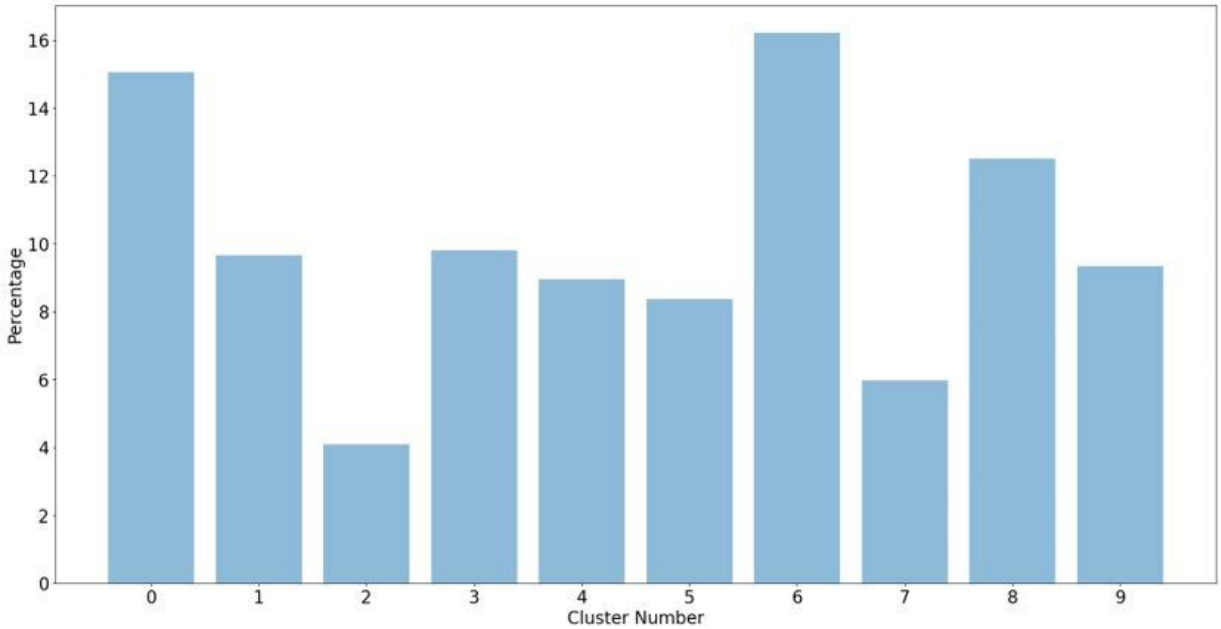

Figure 10. Cluster distribution for the K-Means algorithm.

Tableau was selected as the platform to produce data visualizations as a dashboard. The dashboard includes the locations of airports on a U.S. map, displaying cluster distributions, airport diagrams, scatter plots of level-off length vs. height, histograms for level-off fields vs. flight counts at each airport, the distribution of flights across clusters, centroids for each cluster, etc. As shown in Figure 11, data for a specific airport are filtered, and the histograms contain detailed flight counts for different metrics, which are useful for analyzing the flights arriving at an airport.

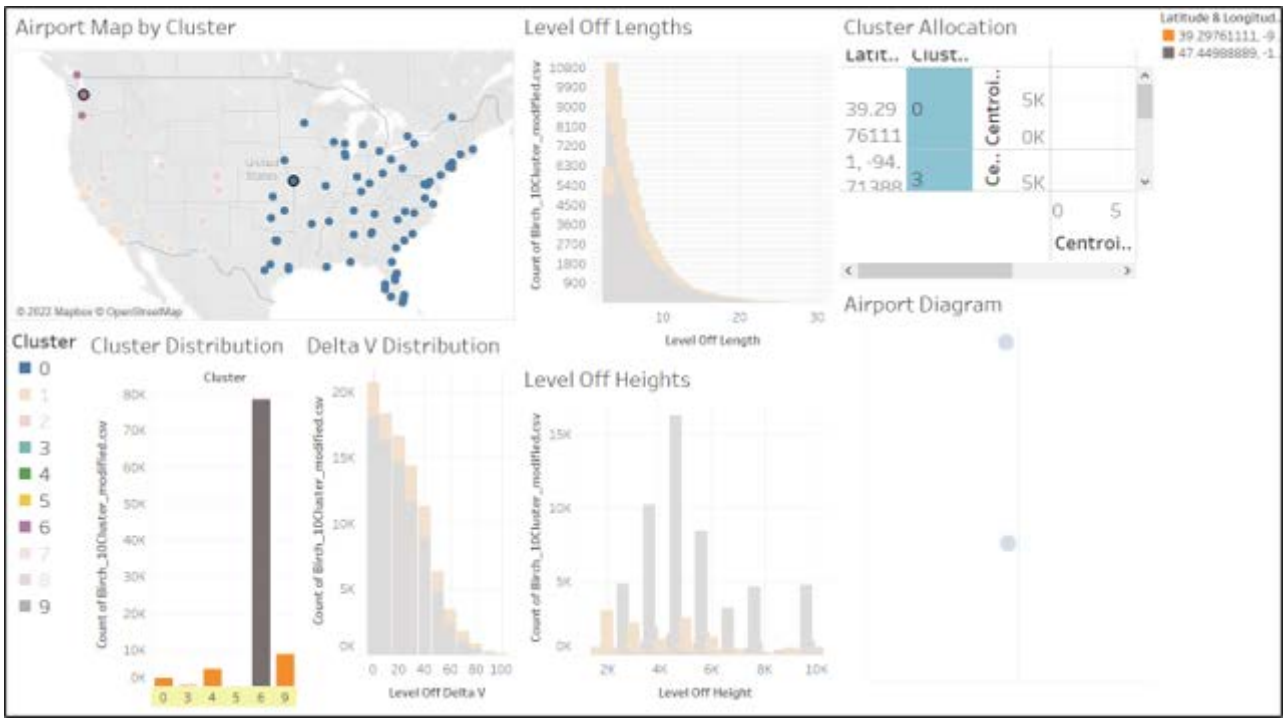

Figure 11. Tableau comparing KSEA (Seattle-Tacoma International Airport) and KMCI (Kansas City International Airport). BIRCH: Balanced iterative reducing and clustering using hierarchies

A study was designed in AEDT to understand and quantify the sensitivity of performance, noise, and emission metrics to the level-off definitions yielded by the clustering results. The default STANDARD arrival was compared with Random Flight 1 and Random Flight 2 arrivals at KATL. It was observed that Cluster 2 had a larger area for the 65-, 70-, and 75-dB contours, which was likely due to the shorter level-off lengths of Random Flight 1 and Random Flight 2.

Figure 12. Example of cluster centroid vs. randomly clustered flights.

The clustering shown here indicates reasonable allocations for the level-off data. The sensitivities also produce results that are aligned with expectations. Thus, the next steps are to assess the sensitivities in detail, confirm the results and parameters

that differentiate the clusters, and start moving the task closer to making recommendations for arrival profile implementation. In the next year, the efforts of ASCENT 43 will be merged with Task 2 of ASCENT 54. With this merge, the modeling of Noise-Power-Distance data (NPDs) for multiple speeds and configurations will also be considered within this task.

Milestones
None

Major Accomplishments
- Identified K-Means and BIRCH as the best clustering methods based on three quantitative scoring metrics
- Analyzed cluster distribution by plotting against set metrics and identified K-Means as having a uniform spread of distribution
- Created visualizations in Tableau to compare cluster parameters and geographical distribution parameters
- Determined the sensitivity of the clusters by performing arrival modeling on AEDT while maintaining the cluster centroid as the default

Publications
None

Outreach Efforts
Biweekly calls
Bi-annual ASCENT meetings

Awards
None

Student Involvement
- Keletso Mmalane and Anushka Moharir (Graduate Research Assistants, Georgia Institute of Technology) participated in this research.

Plans for Next Period
- Continue to analyze variability in environmental metrics from profiles in all clusters.
- Use percentiles of each level-off parameter for modeling instead of five randomly selected values.
- Include the modeling of speed- and configuration-dependent Noise Power Distance data (from ASCENT 43).

Task 3 - Full Flight Modeling
Georgia Institute of Technology

Objective
This task aims to improve the usability of the full flight modeling within AEDT without employing the often complicated and time-consuming process of using the sensor path functionality that is the current standard for AEDT. In the previous year, Task 3 attempted to verify the notion that the use of threaded track data as an input to AEDT full flight modeling could be validated by comparison to actual/historical flight data provided via FOQA datasets. Ideally, proper comparisons would validate the use of thread track data as a source for determining typical routing between city pairs and substantiate the associated fuel consumption models using either Base of Aircraft Data (BADA) 3 and/or BADA4 datasets. A successful validation would provide an alternative to the more laborious and time-consuming use of sensor path data.

The results of the work completed during the last year have led to a proposed re-definition of the approach that may be most appropriate for AEDT to support simplified, yet statistically valid modeling of the National Airspace System flight frequency and cumulative fuel burn/emission analysis. This approach utilized a more rudimentary method, such as the great-circle distance (GCD) + % additive correctly integrated with seasonal wind/temperature history. This analysis was enabled by the supplementary tool set PaceLab Mission Suite (PLMS). PLMS has integrated seasonal wind data that are not currently available in the AEDT system via Modern-Era Retrospective Analysis for Research and Applications version 2 (MERRA-2).

In addition, based on the results of the work completed in the past years, the Georgia Tech team recommends that a new AEDT functionality be developed to allow for the input of statistical wind histories (MERRA-2 datasets are too granular for large-scale studies). As an alternative, it is proposed that AEDT be modified to allow for fixed input wind/temperature models. According to a discussion with the Volpe development team, it may be possible to accomplish this effort by using the existing software structure. The creation of a "nominal" wind/temperature dataset as a default may provide a solution.

While each of these recommendations would need further investigation and vetting, the overall approach would allow for the use of GCD + % system modeling in a rapid and efficient manner to provide statistically valid modeling of National Airspace System route densities and cumulative emission analyses.

The report material is subdivided into the following areas with corresponding methodology, results, and discussion sections:

- Great Circle Route Planning
- Seasonal Average Wind Model

Research Approach

Investigation 1. Alternative Methodology: Great Circle Route Planning

Methodology

An alternative approach has been taken to demonstrate that a simplified route based on seasonal wind averages can provide a statistically valid prediction for time and fuel. This alternative approach was chosen because AEDT's weather data modeling hinder AEDT's time and fuel predictions when using a single notional route vs. actual flight histories. We used the PLMS tool to compare actual FOQA flight histories. The PLMS tool is a commercial tool for route and aircraft economic analysis and produces metrics such as payload capacity, maximum range, trip time, and fuel burn by flight segment. Because the aircraft performance modeling of the PLMS tool is derived from the Original Equipment Manufacturer (OEM) dataset and the wind data are based on the Boeing commercial model, the PLMS is a suitable tool for comparing real FOQA flights. As a proof of concept, we performed a sensitivity analysis between the FOQA flights and the range of GCD + % variance using the PLMS tool.

Results and Discussion

In the first step, we determined how well the predicted trip distance matches the FOQA flight histories within the cluster obtained in Investigation 2 by adding some variance to the GCD in the PLMS tool. Histograms were generated for city pairs and used to find the closest trip distance obtained using the PLMS tool with respect to the actual flight histories. We added 25 nautical miles to the analysis with the PLMS tool, considering the influence of vectoring by air traffic controllers near departure or arrival airports.

Error! Reference source not found. The histogram bin width was set to 5 nautical miles, and the results of a sensitivity analysis of trip distances for KATL-KSEA-KATL are shown in the histogram in Figure 13. The red vertical dotted line represents the median trip distance of FOQA flights within the cluster. The blue and purple vertical dotted lines show the GCD + 3% and 5% variance, respectively, as the trip distance predicted by the PLMS tool. The histogram is not a perfect bell shape, especially for KSEA-KATL, because the FOQA data do not include all flights for a given city pair over a selected time period. However, considering the limitations of the FOQA data, it is still possible to compare the trip distance representing the actual FOQA flights. As shown in Figure 13, for the histogram of KATL-KSEA-KATL, the GCD + 3% gives the trip distance closest to the median trip distance of the FOQA flights within the cluster. Moreover, the median trip distance of the FOQA flights for KSEA-KATL is larger than the median trip distance of the FOQA flights for KATL-KSEA due to wind conditions during the flight.

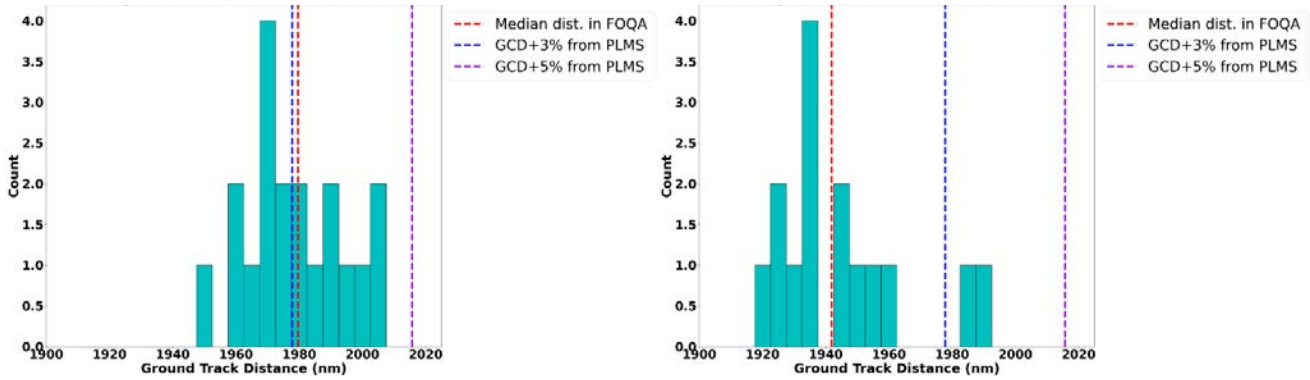

Figure 13. Histogram from a sensitivity analysis of trip distance for KATL-KSEA (left) and KSEA-KATL (right). nm: nautical mile; PLMS: PaceLab Mission Suite.

The histograms in Figure 14 display the average wind distribution for FOQA flights within the cluster. The red vertical dotted line is the median of the average wind of the FOQA flights. The blue dotted line is the wind condition with 50% reliability obtained by the PLMS tool. There is no significant difference between the red and blue dotted lines. The average wind condition is always positive for KATL-KSEA, whereas the average wind condition for KSEA-KATL is always negative except for one case. The headwind conditions during the flight for KATL-KSEA lead to a greater trip distance.

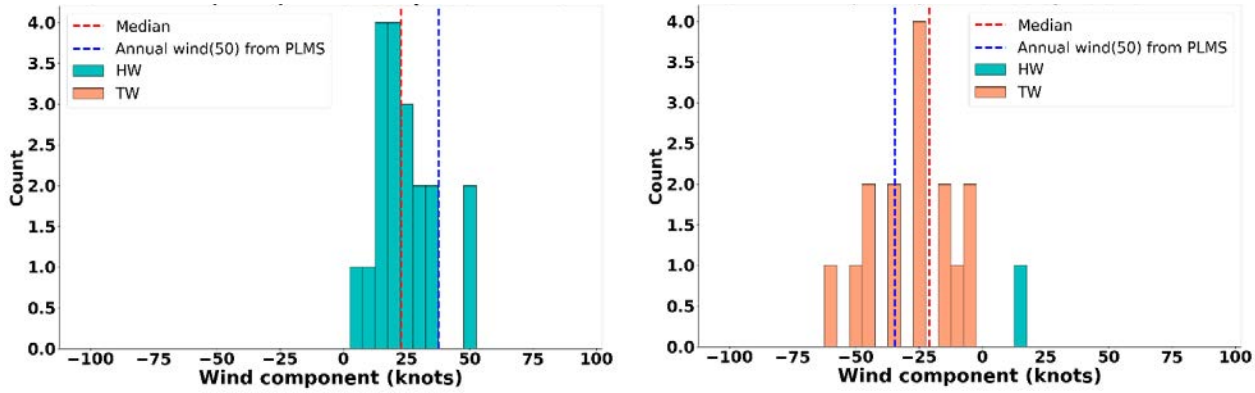

Figure 14. Histogram for sensitivity analysis of average wind conditions for KATL-KSEA (left) and KSEA-KATL (right). HW: headwind; PLMS: PLMS: PaceLab Mission Suite; TW: tailwind; FOQA: Flight Operational Quality Assurance.

Error! Reference source not found. The results of a sensitivity analysis for the trip distance between FOQA flights and the PLMS product are given in Table 4. The GCD + 3% variance shows the smallest error compared with the median trip distance of the FOQA flights for all identified city pairs. KATL-KSEA and KSLC(Salt Lake City International Airport)-KLAS(Las Vegas International Airport) have the most significant error of 1.9% for the comparison between the median trip distance of the FOQA flights and the GCD + 3% variance obtained by the PLMS tool.

Table 4. Sensitivity analysis of the trip distance between FOQA flights and the PaceLab Mission Suite tool.

City pair	Avg. Ground Track Distance (nm) within the cluster (FOQA)	Trip distance (nm) from Pace Lab			% Error		
	Median	GCD + 0%	GCD + 3%	GCD + 5%	GCD + 0%	GCD + 3%	GCD + 5%
ATL - LAS	1562.7	1517.8	1588.3	1618.1	-2.9	1.6	3.5
LAS - ATL	1567.3	1517.8	1588.3	1618.1	-3.2	1.3	3.2
ATL - MSP	838.0	787.7	836.3	852.0	-6.0	-0.2	1.7
MSP - ATL	838.5	787.7	836.3	852.0	-6.1	-0.3	1.6
ATL - SEA	1979.6	1895.9	1977.8	2015.7	-4.2	-0.1	1.8
SEA - ATL	1941.8	1895.9	1977.8	2015.7	-2.4	1.9	3.8
ATL - SLC	1450.3	1381.4	1447.9	1475.5	-4.8	-0.2	1.7
SLC - ATL	1444.4	1381.4	1447.9	1475.5	-4.4	0.2	2.2
ATL – LGA	711.1	661.6	706.4	719.7	-7.0	-0.7	1.2
LGA - ATL	695.6	661.6	706.4	719.7	-4.9	1.6	3.5
LAS - SLC	352.7	319.4	354.0	360.3	-9.4	0.4	2.2
SLC - LAS	351.5	319.4	354.0	360.3	-9.1	0.7	2.5
	347.4	319.4	354.0	360.3	-8.1	1.9	3.7

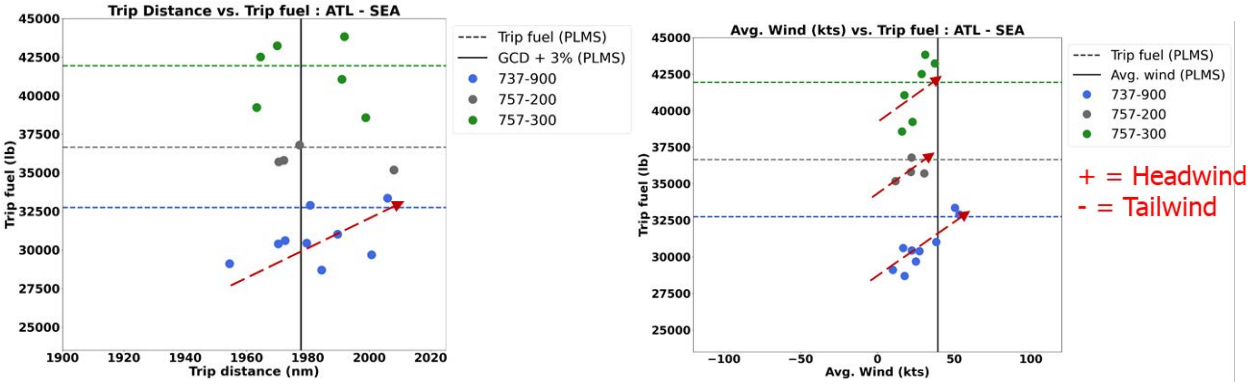

Figure 15. Comparison of the total fuel burn between FOQA flights and results obtained via the PLMS tool for KATL-KSEA. GCD: great-circle distance; PLMS: PaceLab Mission Suite.

In the previous step, the GCD + 3% variance obtained via the PLMS tool gave the closest representation of the actual FOQA flights. Therefore, the cumulative total fuel burn and wind based on the GCD + 3% variance from the PLMS tool were predicted and compared with values for actual FOQA flights. The PLMS analysis results based on GCD + 3% variance consistently correlate with actual FOQA fuel burn data and wind predictions. As shown in Figure 15, the total fuel burn data for FOQA flights are consistently scattered around an estimate of the trip fuel for each aircraft obtained via the PLMS tool, with an influence from aircraft performance and structural limits.

Investigation 2. Alternative Methodology: Seasonal Wind Model

Methodology

A direct comparison of AEDT's time and fuel predictions based on notional single routes vs. actual flight histories is hampered by AEDT's weather data modeling. A simplified route based on seasonal wind averages could enable an alternative approach to provide statistically valid predictions for time and fuel. This task aims to develop a weather model representing seasonal averages compatible with AEDT.

AEDT can use high-fidelity, airport annual average, and International Standard Atmosphere (ISA) weather data for performance modeling used for noise and emission modeling. MERRA-2 is one of the high-fidelity weather data sources that

AEDT can use. MERRA-2 covers the world and has a grid resolution of 0.5 degrees in latitude and 0.625 degrees in longitude. MERRA-2 data files are provided in netCDF-4 format. AEDT takes weather information from the MERRA-2 instantaneous weather data according to a specified location and time. From MERRA-2, seven variables are retrieved, including temperature, geopotential height, specific humidity, eastward wind, northward wind, surface pressure, and sea-level pressure.

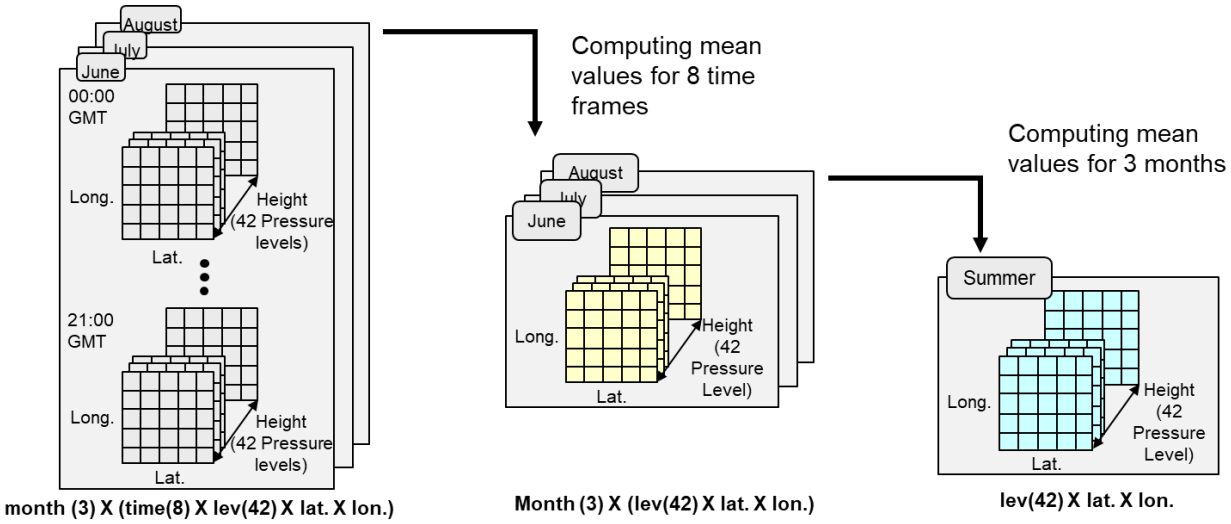

Figure 16. Procedure for data fusion (e.g., summer).

AEDT uses "inst3_3d_asm_Np" weather files for three-dimensional weather data and "inst1_2d_asm_Nx" weather files for surface (two-dimensional) weather data. However, "instU_3d_asm_Np" and "instU_2d_asm_Nx" are used to develop seasonal weather models because of the convenience and computational cost of averaging the variables through Python code. "instU_2d_asm_Nx" and "instU_3d_asm_Np" give instantaneous two- and three-dimensional monthly diurnal means in MERRA-2, respectively. "instU_3d_asm_Np" contains variables that define the dimensions of longitude, latitude, and time at 42 pressure levels. The data in "instU_3d_asm_Np" are collected every 3 hr, starting from 00:00 UTC. (i.e., 00:00, 03:00, ..., 21:00 UTC).

The procedure for developing a seasonal model is shown in Figure 16. Data from 2016 to 2020 were downloaded and divided according to the corresponding seasons as follows:

- Winter: December, January, and February
- Spring: March, April, and May
- Summer: June, July, and August
- Fall: September, October, and November

For example, let us suppose that we are creating a summer seasonal weather model. As mentioned above, each variable in the data has dimensions of time (8) x pressure level (42) x latitude x longitude. In the first step, average values are computed over the eight time frames in each data collection to create dimensions of pressure level (42) x latitude x longitude. The next step calculates the average values for the summer months of June, July, and August. All steps are implemented via Python code and use the "NC$WXEditorWPF.exe" application to ensure that the generated file format is correct. Lastly, a fuel consumption study is performed in AEDT using the FOQA trajectory input to compare the total fuel burn based on different weather data sources.

Results and Discussion

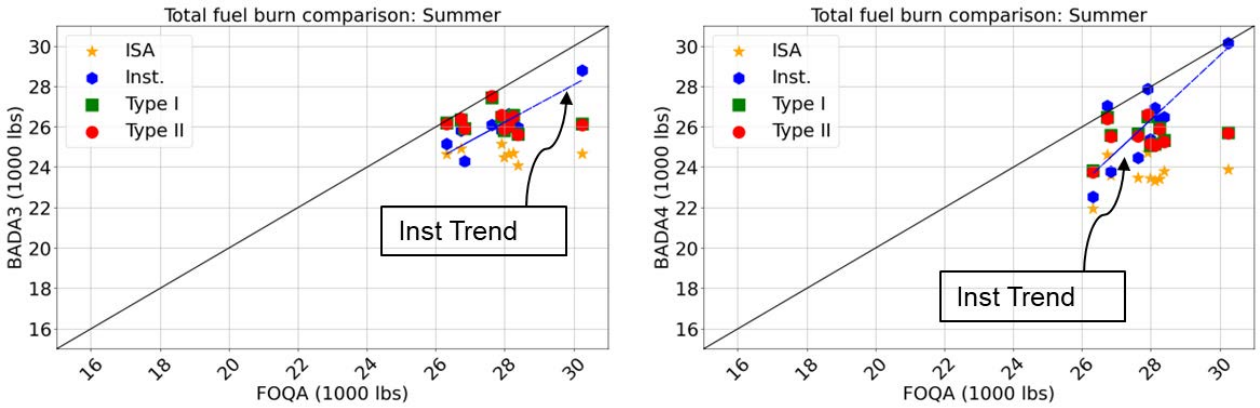

Figure 17. Total fuel burn comparison for KATL-KSEA. BADA: Base of Aircraft Data; ISA: International Standard Atmosphere; FOQA: Flight Operational Quality Assurance.

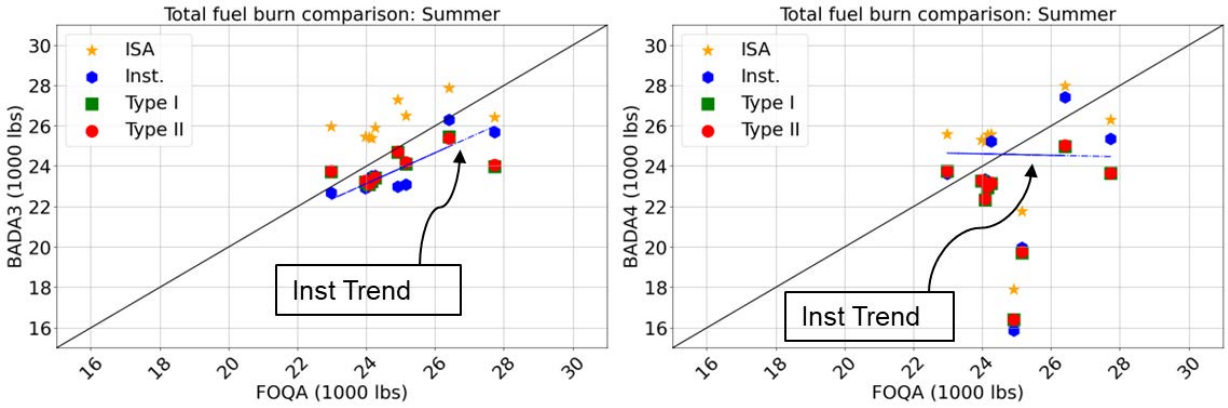

Figure 18. Total fuel burn comparison for KSEA-KATL. BADA: Base of Aircraft Data; ISA: International Standard Atmosphere, FOQA: Flight Operational Quality Assurance.

The cumulative fuel burn was compared using AEDT modeling with different weather data types. Figures 17 and 18 compare the fuel burn for KATL-KSEA and KSEA-KATL, respectively. In each figure, the left plot is the fuel burn computed by BADA3 modeling, and the right plot shows the fuel burn obtained by BADA4 modeling. The B739 airframe type was used in these comparisons. Note that only the en-route phase of the flight (FL100, >10,000 ft) is considered.

The four different weather data types compared in each figure are as follows:

1. ISA (yellow)
2. MERRA-2 instantaneous weather data (blue)
3. Type I seasonal weather data, considering the time frame, time (8) x pressure level (42) x latitude x longitude (green)
4. Type II seasonal weather data, disregarding the time frame, pressure level (42) x latitude x longitude (red)

In Figures 17 and 18, each point represents the total fuel burn for one flight. The location of each point along the x- and y-axes denotes the cumulative fuel burn for the flight in FOQA data and the AEDT model based on different weather data, respectively. The figures also show a solid black line for which the values along the horizontal and vertical axes are equal; if a data point falls on this line, the total fuel burn predicted by AEDT matches the total fuel burn reported by FOQA data.

According to Figures 17 and 18, the total fuel burn predicted using the instantaneous MERRA-2 weather data that matches the date of the FOQA flight is generally most similar to the total fuel burn obtained from FOQA data. This finding is consistent with the basic expectation that the instantaneous MERRA-2 weather data most closely track the actual values recorded in the FOQA data. The blue trend line generated from the blue dots (predicted from MERRA-2 instantaneous data) shows a slope similar to that of the solid black line, where the total fuel burn between FOQA and AEDT modeling is equal, especially for BADA3 modeling. The gap between the two lines arises because the fuel required from FOQA data may vary substantially depending on factors such as engine degradation and the status of engine maintenance.

In addition, the ISA dataset underpredicts the fuel required for westbound flights (KATL-KSEA) because it does not consider actual headwinds (i.e., higher value of equivalent static air miles). Moreover, the ISA dataset overpredicts the fuel required for eastbound flights (KSEA-KATL) because it does not take advantage of the tailwind (smaller value of equivalent static air miles). Moreover, when ISA weather data or seasonal weather models are applied, the fuel burn prediction based on BADA3 modeling is closer to the total fuel burn obtained from FOQA data than the fuel burn prediction based on BADA4 modeling.

We note that minor differences in fuel burn prediction arise when two types of seasonal weather models are used (types I and II), as shown by the green and red dots in Figures 17 and 18. Therefore, only type II models are recommended for the seasonal average weather because of the convenience in data processing.

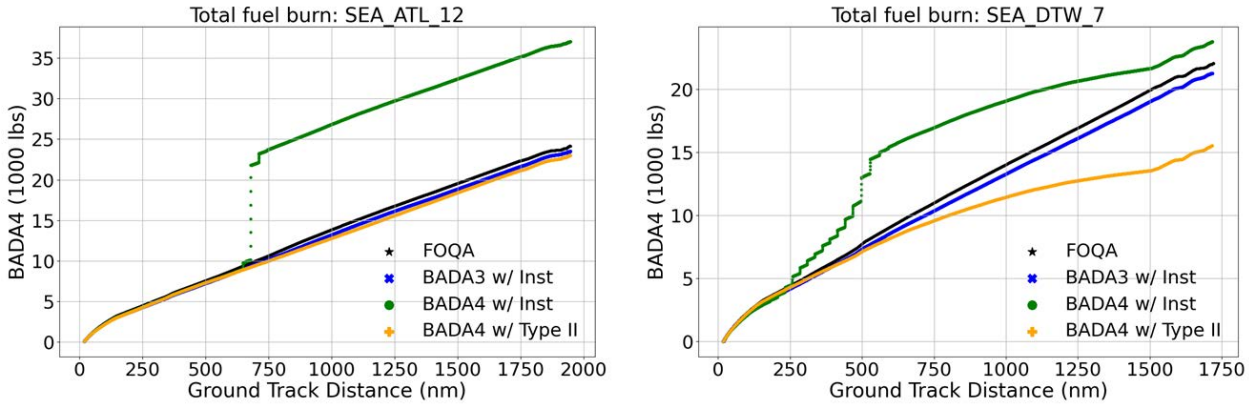

Figure 19. Total fuel burn comparison between FOQA and Aviation Environmental Design Tool modeling. BADA: Base of Aircraft Data; FOQA: Flight Operational Quality Assurance.

The total fuel burn was compared between FOQA and AEDT modeling using different weather data sources. The legend in Figure 19 is as follows.

- FOQA: Black
- BADA3 modeling with MERRA-2 instantaneous weather data: Blue
- BADA4 modeling with MERRA-2 instantaneous weather data: Green
- BADA3 modeling with type II seasonal weather data: Yellow

Numerous cases/conditions produced fuel flow discontinuities (high fuel flow over a short time period) in the AEDT output, resulting in a step function additive to the integrated fuel burn when the BADA4 model is used with MERRA-2 instantaneous weather data. This behavior was not observed when BADA3 was used with MERRA-2 instantaneous weather data. Moreover, discontinuity segments did not appear in the total fuel burn calculation for BADA4 modeling with type II seasonal weather data. Further investigation into these BADA4 discontinuities will be implemented.

Milestones

None

Major Accomplishments

- Conducted sensitivity analysis between FOQA flights and a range of GCD + % variance using a supplementary/independent route analysis tool: PLMS
  - PLMS route fuel burn analysis integrates historical seasonal wind data and applies reliability factors.
- Based on the success of the PLMS analysis, developed a weather model (i.e., wind) representing seasonal averages compatible with AEDT
  - This modeling was derived from publicly available MERRA-2 datasets.
- Generated two supplemental reports:
  - ASCENT Project 054: AEDT Evaluation and Development Support
  - ASCENT Project 054: Supplementary AEDT Functionality Analysis

Publications

None

Outreach Efforts

Biweekly calls
Bi-annual ASCENT meetings

Awards

None

Student Involvement

- Hyungu Choi and Jirat Bhanpato (Graduate Research Assistants, Georgia Institute of Technology) participated in this research.

Plans for Next Period

- Continue investigating causes of BADA4 discontinuities in the BADA4 fuel burn calculation.
- Further investigate GCD + % system modeling.
- Develop alternative aircraft routing history data sources (System Wide Information Management, OpenSky, FlightAware Research Hub) to replace consistent sourcing of FOQA data from airlines, which is problematic.

Task 4 - System Testing and Evaluation of AEDT

Georgia Institute of Technology

Objective

To provide the best possible environmental impact modeling capabilities in AEDT, the FAA Office of Environment and Energy continues to develop AEDT by improving existing modeling methods and data and adding new functionalities. The FAA Office of Environment and Energy seeks an independent effort in system testing to evaluate the accuracy, functionality, and capabilities of AEDT and to support future model development. The objective of this task is to provide the FAA with high-quality systematic testing and evaluation of the capabilities of AEDT 3 and its future releases and to identify gaps in the tools' functionality and areas for further development.

Research Approach

Within this task area, the Georgia Tech research team has been coordinating with the FAA and Volpe National Transportation Systems Center on upcoming AEDT features and testing and evaluating newly incorporated capabilities. For each AEDT release, depending on the update type, key features and functionalities are identified for capability demonstration to ensure that the implemented features are working properly. We are then either provided with or define for ourselves the scope and test cases for the system testing and evaluation effort. These cases are typically defined based on the key changes to the AEDT version from the previous releases. Due to the dynamic nature of the AEDT development process, we remain flexible in the choice of the testing and evaluation approach and the scope of our work. The best available methods and data are used to ensure accuracy in the functionalities of newly released AEDT versions. When required, uncertainty quantification

analysis is conducted to understand the sensitivities of output responses to variation in input variables and to quantify the major contributors to output uncertainties.

In the following subsections, the various features and functionalities that were tested from October 2021 to September 2022 are described. In addition, various bugs were identified, reported, and re-tested to support the AEDT development process.

AERMOD Performance Updates
AEDT's American Meteorological Society/Environmental Protection Agency regulatory model (AERMOD) module performs modeling of pollutant dispersion within short distances of industrial sources, and its integration into the software enables higher-fidelity emission analyses. This task aimed to discern the extent to which AERMOD taxes computer memory in its calculations and to identify specific computational bottlenecks in these processes.

Testing was conducted through the creation of a large-scale study featuring over 1.5 million arrival and departure operations split across Auxiliary Power Units (APUs) and Ground Support Equipment (GSEs). AERMOD's involvement in emission calculations was monitored using software designed to track memory usage at important computational junctures and compared with results from both prior tests and varying study settings.

Results demonstrated a 15% improvement in overall AERMOD efficiency relative to prior AEDT releases, but these outcomes were localized only to cases involving emission dispersion calculations (rather than inventory tabulations).

Touch-and-Go/Circuit Profile Development
This task focused on the development of touch-and-go and circuit profiles for two new aircraft in AEDT 3e, namely the 7879 and 747-400RN, using the existing approach and departure procedures as the baseline. This development was performed for both Aircraft Noise & Performance database (ANP) fixed-wing civil aircraft with defined procedural profiles, and the developed profiles were provided to the AEDT development team for integration into the FLEET database.

Profiles were created using programming scripts to copy appropriate steps from the relevant departure or arrival profile. All created profiles were tested for accuracy by modeling noise metric results over a noise grid.

Ability to Import Flight Operations from CSV Files
This feature adds the ability to import aircraft operations and tracks from CSV input files into an existing AEDT study via both the graphical user interface (GUI) and command line tool. Incorporation of this option into AEDT streamlines the process of setting up large studies by eliminating the need to directly interface with the underlying Structured Query Language (SQL) database containing operations and their properties.

We performed testing by attempting to import a series of both properly and improperly formatted aircraft and helicopter operation CSV files. Results indicated proper feature functionality, with both GUI and command line interfaces importing correct operations and rejecting improperly formatted files.

View/Edit Individual Tracks
This feature focused on testing the new track visualization updates in AEDT 3e, which allowed the user to generate the full airport layout, only the ground elements, or only selected tracks with ground elements and interact with each of these layers in the airport designer. Additionally, the user can now change the maximum number of tracks that can be displayed at one time in the AEDT settings menu.

A large study containing tens of thousands of tracks was used for testing purposes. Most of the visualization tests (e.g., generating all layout options, testing track selection availability, testing the maximum number of tracks) were successful, with the exception of a few small display issues in the AEDT user interface that were identified as bugs. Furthermore, due to machine limitations, the maximum track number setting was changed from 25,000 to 100 when the visualization was performed in the GUI. The correct warning and error messages were displayed when the user tried to visualize more tracks than the actual maximum setting.

Updated Start-of-Takeoff-Roll Noise Directivity
Updates to the International Civil Aviation Organization (ICAO) methodology for noise directivity calculations necessitated a corresponding change to AEDT's noise maps for all affected aircraft. These modifications were examined by comparing the

take-off noise contours of all airplanes in the FLEET database between a prior and current AEDT version. A full cross-examination of all AEDT aircraft demonstrated a consistent shift in noise directivity in the current release, in line with ICAO specifications. The typical extent of ICAO's alterations is apparent in Figure 20, which presents modeling results of aircraft departure from the KATL airport.

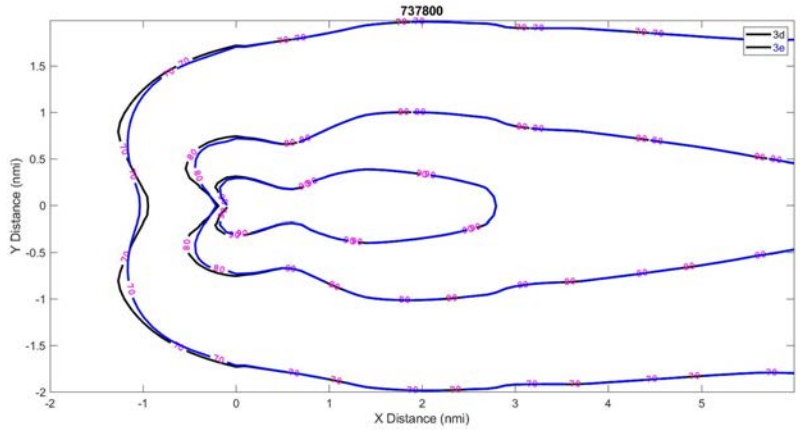

Figure 20. Previous and current 737-800 noise contours. nmi: nautical mile.

Milestones
None

Major Accomplishments
- Conducted several detailed investigations and testing efforts for system testing of new AEDT features
- Completed the first draft of a comprehensive Uncertainty Quantification report, currently being reviewed by the FAA

Publications
None

Outreach Efforts
- Bi-weekly calls
- Attendance at bi-annual ASCENT meetings
- Attendance at the American Institute of Aeronautics and Astronautics Aviation Conference and OpenSky Symposium to present conference papers

Awards
None

Student Involvement
Bogdan Dorca and Santusht Sairam (graduate research assistants, Georgia Institute of Technology) participated in this research.

Plans for Next Period
- Continue system testing efforts to support ongoing AEDT development.
- Revise the Uncertainty Quantification report draft based on FAA feedback and finalize the draft for publication.

Project 055 Noise Generation and Propagation from Advanced Combustors

Georgia Institute of Technology
Raytheon Technologies Research Center

Project Lead Investigator

Timothy Lieuwen
Professor
Daniel Guggenheim School of Aerospace Engineering
Georgia Institute of Technology
270 Ferst Drive, G3363 (M/C 0150)
Atlanta, GA 30332-0150
Phone: 404-894-3041
tim.lieuwen@aerospace.gatech.edu

University Participants

Georgia Institute of Technology

- P.I.s:
  - Timothy Lieuwen, Professor
  - Suresh Menon, Professor
  - Adam Steinberg, Professor
  - Vishal Acharya, Senior Research Engineer
  - Benjamin Emerson, Senior Research Engineer
  - David Wu, Research Engineer
- FAA Award Number: 13-C-AJFE-GIT-058
- Period of Performance: February 5, 2020 to December 31, 2023
- Tasks:
  1. **Facility Development at Georgia Institute of Technology (GT)**
     This task addresses the design of experiments that will be performed at GT. The task involves coordination between the teams to develop and define the aerodynamic design of a rich-quench-lean, quick quench, lean burn (RQL) combustor for this study. This task is led by Tim Lieuwen and Adam Steinberg, with support from Ben Emerson and David Wu.
  2. **Simulations of the GT Experiment**
     This task includes simulating the GT experiment, with a focus on the pre-combustion flow dynamics, flame dynamics, and post-combustion dynamics of pressure and entropy disturbances. This task is led by Suresh Menon.
  3. **Reduced-Order Modeling (ROM)**
     This task consists of creating a ROM framework for the unsteady response of the flame and the generation of entropy disturbances due to unsteady heat release. This task is led by Vishal Acharya.

Raytheon Technologies Research Corporation

- P.I.s:
  - Jeffrey Mendoza, Technical Fellow Acoustics
  - Duane McCormick, Principal Research Engineer
  - Julian Winkler, Staff Research Engineer
  - Lance Smith, Principal Research Engineer
- FAA Award Number: 13-C-AJFE-GIT-058 (subaward through GT)
- Period of Performance: February 5, 2020 to December 31, 2023

- Tasks:
  4. **Facility Development at Raytheon Technologies Research Corporation (RTRC)**
     This task addresses the design of experiments that will be performed at RTRC. The task involves coordination between the teams to develop and define the aerodynamic design of an RQL combustor for this study. This task is led by Jeffrey Mendoza, Lance Smith, and Duane McCormick.
  5. **Post-Combustion Modeling**
     This task consists of both post-processing and simulation efforts. First, the post-combustion simulation data from the simulation of the GT experiment are mined to investigate the dynamics of entropy fluctuations and their transport. Next, simulations are used to model noise propagation in the post-combustion architecture of the engine. The simulations are split across the different sections: nozzle, turbine, and far-field. This task is led by Jeffrey Mendoza and Julian Winkler.

Project Funding Level

FAA funding: $4,500,000 (GT – $2,500,000 and RTRC – $2,000,000)
Cost-share: $4,500,000 (GT – $2,500,000 from AE school and RTRC – $2,000,000 from company funds)
Total funding: $9,000,000

Investigation Team

Tim Lieuwen (GT): P.I. Professor Lieuwen is the lead P.I. overseeing all tasks. Specifically, he leads the GT experiments and design in Tasks 1 and 2 along with Professor Steinberg. In addition, he co-leads the modeling tasks in Task 1 for pre-combustion, flame response, and post-combustion modeling along with Dr. Acharya.
Adam Steinberg (GT): Co-P.I. Professor Steinberg manages the design of experiment diagnostics and measurements.
Suresh Menon (GT): Co-P.I. Professor Menon manages the tasks for simulations of the GT experiment.
Vishal Acharya (GT): Co-P.I. Dr. Acharya co-manages all modeling tasks for the pre-combustion, combustion, and post-combustion physics along with Professor Lieuwen. In addition, as administrative coordinator, he is responsible for general project management, such as project deliverables, group meetings, and interfacing with the FAA project manager.
Benjamin Emerson (GT): Co-P.I. Dr. Emerson is responsible for designing and maintaining experimental facilities, as well as experimental operations and management and the safety of graduate students.
David Wu (GT): Co-P.I. Mr. Wu is responsible for designing and maintaining experimental facilities, as well as experimental operations and management and the safety of graduate students.
Achyut Panchal (GT): Research Engineer. Dr. Panchal reports to Professor Menon and works on simulations of the GT experiment.
Sangjae Kim (GT): Graduate Student. Mr. Kim is working on large-eddy simulation (LES) studies for the GT rig.
Amalique Acuna (GT): Graduate Student. Mr. Acuna works on and operates the experiment at GT. Mr. Acuna has graduated.
Shivam Patel (GT): Graduate Student. Mr. Patel is funded by a NASA University Leadership Initiative contract, but he actively contributes to the maintenance, construction, and operation of the experiment at GT.
Sungyoung Ha (GT): Graduate Student. Mr. Ha is the lead experimentalist on the GT rig.
Jananee (GT): Graduate Student. Jananee is responsible for optical diagnostics on the GT rig.
Parth Patki (GT): Graduate Student. Mr. Patki works on the hydrodynamics modeling subtask (pre-combustion disturbances).
Tony John (GT): Graduate Student. Mr. John works on the entropy modeling subtask (post-combustion disturbances).
Jeffrey Mendoza (RTRC): Co-P.I. Dr. Mendoza is the leader of the RTRC team and oversees their contributions to the project. He leads the subtasks related to modeling, measurements, and simulation for post-combustion disturbances, nozzle interactions, turbine interactions, and far-field sound propagation.
Lance Smith (RTRC): Co-P.I. Dr. Smith is responsible for the design and measurements of the RTRC experiment. He works closely with the GT team to ensure similarities between both experiment setups.
Duane McCormick (RTRC): Co-P.I. Dr. McCormick responsible for the design and measurements of the RTRC experiment as well as finite-element calculations in the design process.
Jordan Snyder (RTRC): Dr. Snyder is responsible for the design, measurements, and data processing using tunable diode laser absorption spectroscopy and chemiluminescence in the RTRC combustor rig.
Julian Winkler (RTRC): Co-P.I. Dr. Winkler is responsible for the simulation tasks at RTRC and focuses on post-combustion disturbances, nozzle interactions, turbine interactions, and far-field sound propagation.
Kenji Homma (RTRC): Dr. Homma is responsible for the far-field sound propagation simulations.
Aaron Reimann (RTRC): Dr. Reimann is responsible for ROM and high-fidelity modeling of the propagation of direct and indirect noise sources through the turbine nozzle and supports the far-field sound propagation simulations.

Sudarshan Koushik (RTRC): Dr. Koushik is responsible for post-processing the GT LES simulation data to model post-combustion disturbances.

Project Overview

The objective of this project is to develop and validate physics-based design tools that can predict noise production mechanisms and their relative significance and ultimately reduce the noise output of future engines. The motivation for this project stems from recent and future advances in aircraft engine technology. High-bypass engine technology has significantly reduced the traditionally dominant engine noise sources, namely, fan and jet exhaust noise. Noise generated in the combustor has become a dominant source of engine noise for future advanced aircraft designs. In addition, as combustors evolve to increase efficiency and reduce pollutant emissions, methods for predicting and mitigating combustion noise have severely lagged, with legacy methods being insufficient to predict noise from next-generation combustors. This drawback has motivated the objective of this project, which addresses the critical need for physics-based design tools. The resultant understanding of noise generation and propagation, along with validated noise prediction tools, will enable more rapid and cost-effective designs of low-noise engines for future aircraft.

The project objectives will be achieved through a program of cooperative experiments, high-fidelity simulations, and physics-based ROM. The physical processes involved are tightly coupled and directly determine the project tasks, as shown in Figure 1.

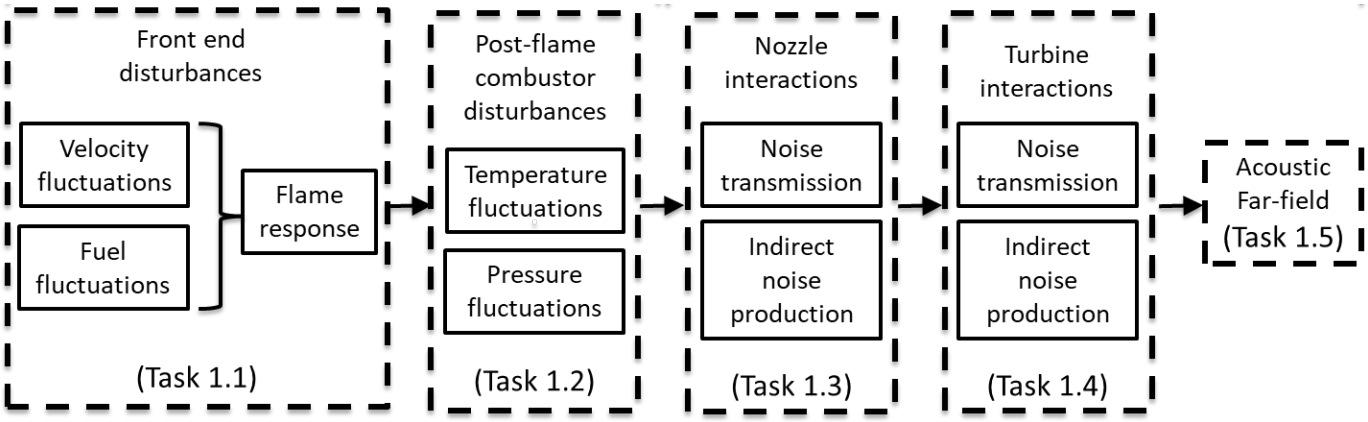

Figure 1. Physical processes and project tasks for noise generation.

The physics of noise generation begins with source disturbances upstream of the combustion zone, which involve unsteady dynamics in the flow and incoming fuel (spray), followed by the response of the combustion zone (flame) to these upstream disturbances. The fluctuations in the unsteady heat release lead to the generation of pressure and entropy fluctuations. These fluctuations propagate further downstream in the combustor, interact with the nozzle and turbine, and eventually lead to far-field sound generation. With the complex interplay of unsteady physics in the different parts of the engine, it is challenging to develop a ROM.

An important goal of this project is to generate high-quality reference data from both measurements and validated high-fidelity simulations, including measurements of the flow, spray, and flame unsteadiness in the head end of the combustor. Subsequently, the secondary combustion zone is characterized. The generation of entropy and pressure disturbances is then characterized through measurements of temperature and pressure fluctuations, followed by measurements of noise reflection and transmission through the turbine and nozzle section and sound measurements in the far-field. The measurements are accompanied by LES and finite-element simulations that are validated against the measurements. Collectively, these data are generated across a range of operating parameters and provide a source database for the modeling task.

The main goal of this project is to develop a robust design tool that can predict noise at operating points for which prior measurements/data are unavailable. To achieve this goal, two major tasks are needed. First, ROM and frameworks must be developed for different aspects of the engine architecture: flow/spray models, flame response models, entropy generation

models, entropy propagation models, nozzle interaction models, turbine interaction models, and far-field noise generation models. The ROM for each of these aspects involves simplifications and assumptions that are validated against the source database. The validation study and iterative improvement of model predictions serve as the second task to achieve this goal.

In this report, we summarize the efforts of both teams from October 2021 to September 2022. The efforts primarily include improvements to the GT rig to achieve a better match with RTRC experiments as well as RTRC rig campaigns with the Continuous Lower Energy, Emissions, and Noise (CLEEN) rig. In addition, ROM frameworks and simulations have been further advanced. A workflow has been established to transfer simulation data to ROM tasks, and different subtask benchmarking targets have been identified. Finally, task input–output relationships between the different transfer functions have been identified, as this is the first step in building the toolchain implemented in the design tool.

Task 1 - Facility Development at GT

Georgia Institute of Technology

Objective

The objective of this task was to make improvements and additional measurements with the RQL combustor designed in the previous year. The first portion of this year was dedicated to the manufacturing and assembly of new components. Once the combustor had been installed at the GT facility, diagnostic tools were installed to measure the flame and pressure dynamics. A test matrix was developed and used to enable comparison and validation of the GT and RTRC data, especially at the overlapping points of the approach condition.

Research Approach

Over the past year, the GT team has analyzed data from the prior year's testing. The team's assessment of the data has led to a re-design of the rig, a re-manufacturing and assembly of the rig, and recommissioning, shakedown, and testing with the new rig. The design activity began at the end of the previous year, and the design/build/test process was completed this year.

The previous year's data campaign identified several opportunities for improving the rig. The first opportunity related to optical access. Analysis of the chemiluminescence data showed excellent access to the quench zone, but insufficient access to the primary zone near the fuel nozzle. Therefore, one objective of the re-design was to move the optical access upstream to the dump plane. This change required a re-design of the combustor liner and windows. Figure 2 shows an example of a chemiluminescence image from last year's campaign, showing good optical access and high-quality images, but a "truncated" image for the first ¼ inch downstream of the dump plane (left side of the image).

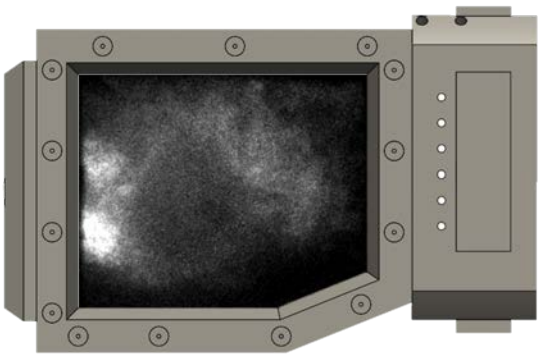

Figure 2. Chemiluminescence imaging from last year's campaign.

Another objective for the re-design was to improve leakage flows, repeatability, and the match to the RTRC rig. Data analysis showed that the GT rig had a larger air leakage from the shroud flow into the combustor. While some leakage here is integral to any combustor, a closer match was desired. Improving this leakage required a re-design of the interface between the combustor liner and the dump plane. In the original rig, this seal was obtained by integrating a knife edge seal into the combustor liner and pressing this seal into a graphite gasket upon assembly. To reduce leakage, a bolted/flanged/gasket

design was implemented. This change necessitated a re-design of the exhaust end of the combustor to facilitate assembly because the knife edge design at the upstream end of the liner allows the knife edge to thrust deeper into the graphite as the rig heats up and thermally expands (this is largely the source of the leakage). With the upstream end of the liner rigidly bolted to the dump plane, a thermal stress relief had to be accommodated on the exhaust end. This relief was provided by designing a slip fit of the exhaust pipe against the pressure vessel, which is sealed with O-rings in a piston ring arrangement. The previous sealing method and new components are illustrated in Figure 3.

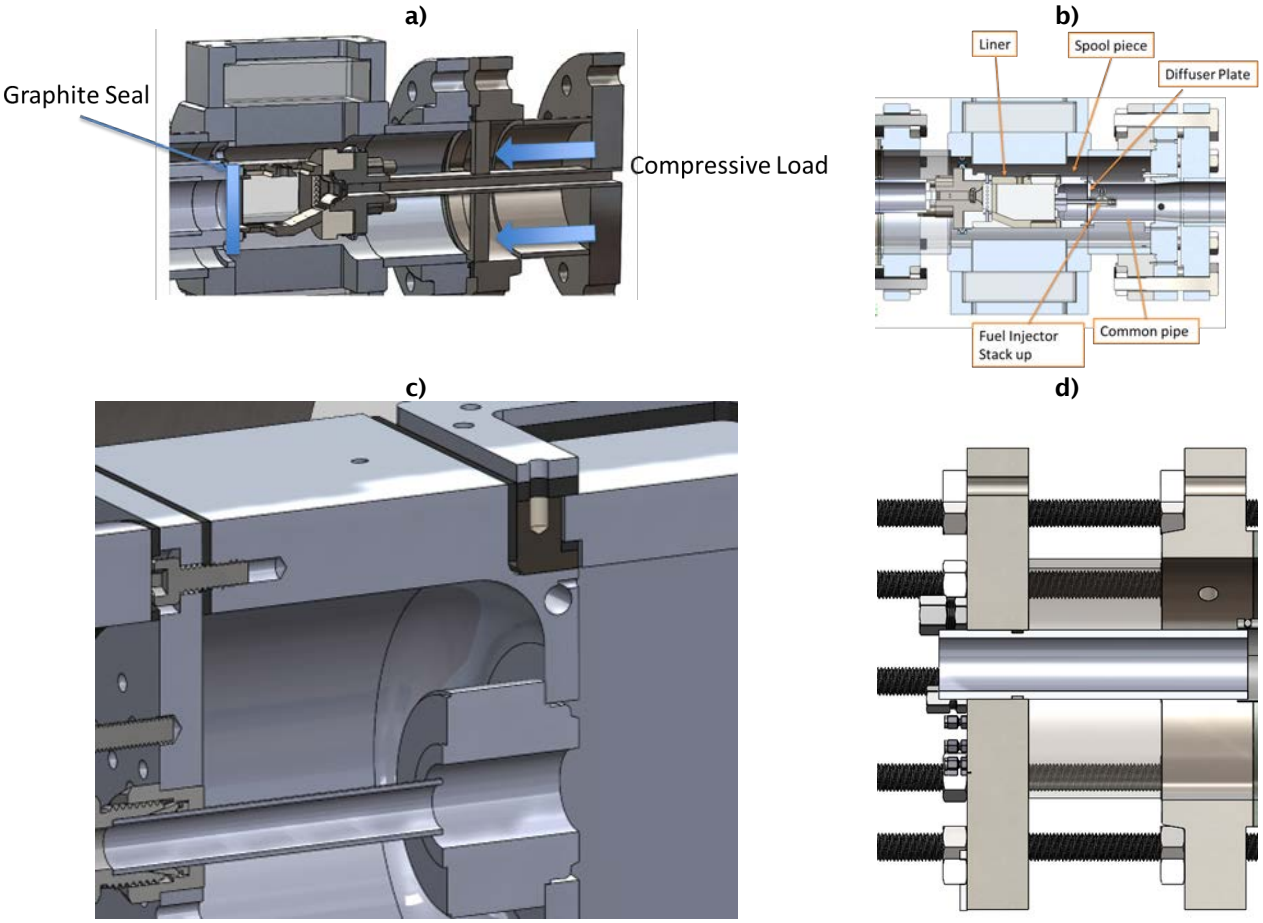

Figure 3. Combustor liner sealing methods. a) The original compressive sealing method, b) section view of the re-designed sealing assembly (flow is right to left), c) bolted spool/dump plane/liner assembly for improved sealing, and d) sliding O-ring exhaust pipe.

A second drawback of the previous rig sealing method related to the durability of the combustor. After many assembly and heating cycles, the compressive load on the combustor began to deform the combustor liner. The compressive load was produced by thermal expansion of the combustor liner, which was rigidly attached at the exhaust and had minor thermal expansion freedom with the upstream-end graphite. The liner had sufficient strength to handle this compressive load, except in the vicinity of the windows; there was insufficient material around the windows to handle this cyclic load at high temperatures, and the liner began to deform and break windows in this area (see Figure 4).

Figure 4. Liner deformation and broken windows due to compressive failure at high temperature.

Finally, with this major re-design activity, we took the opportunity to improve the manner in which the fuel injector is held in the combustor. This improvement included a mechanism to allow adjustability of the injector immersion distance and concentricity. The immersion distance is an important matching parameter for the RTRC rig; thus, better control of this parameter has immediate scientific value. Improved concentricity of the fuel injector also has an inherent impact on the comparison between the rigs. This change was accomplished with a triangular injector holder plate with adjustment hardware at the vertices of the triangle (see Figure 5).

a) b)

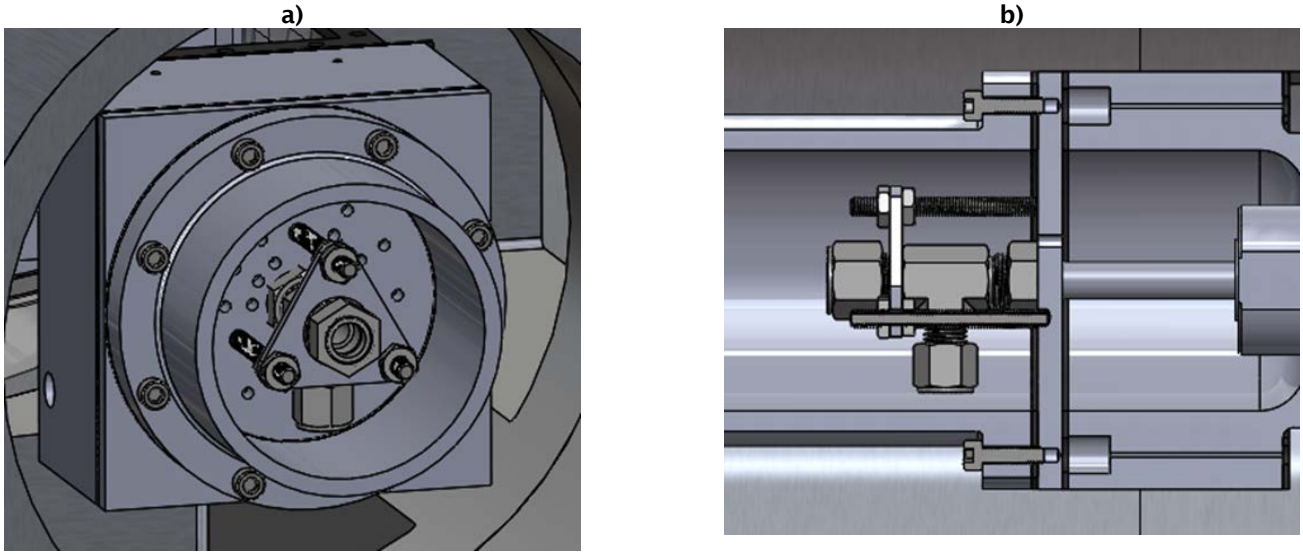

Figure 5. New adjustable fuel injector holder. a) Isometric view of the adjustable triangular holder and b) side section view that includes the fuel injector.

While the rig was being re-designed, we used this downtime to re-design the rig support structure and major plumbing and to perform a complete gutting and cleaning of the test cell. The re-designed rig support frame and plumbing result in a more compact rig that is more efficient to work around and accommodates better optical access (more room for diagnostic

equipment). The shorter run of plumbing also aids in achieving higher preheat temperatures (combustor inlet air temperature). Figure 6 shows various steps in the process of rig/plumbing re-design, test cell gutting, and build-up.

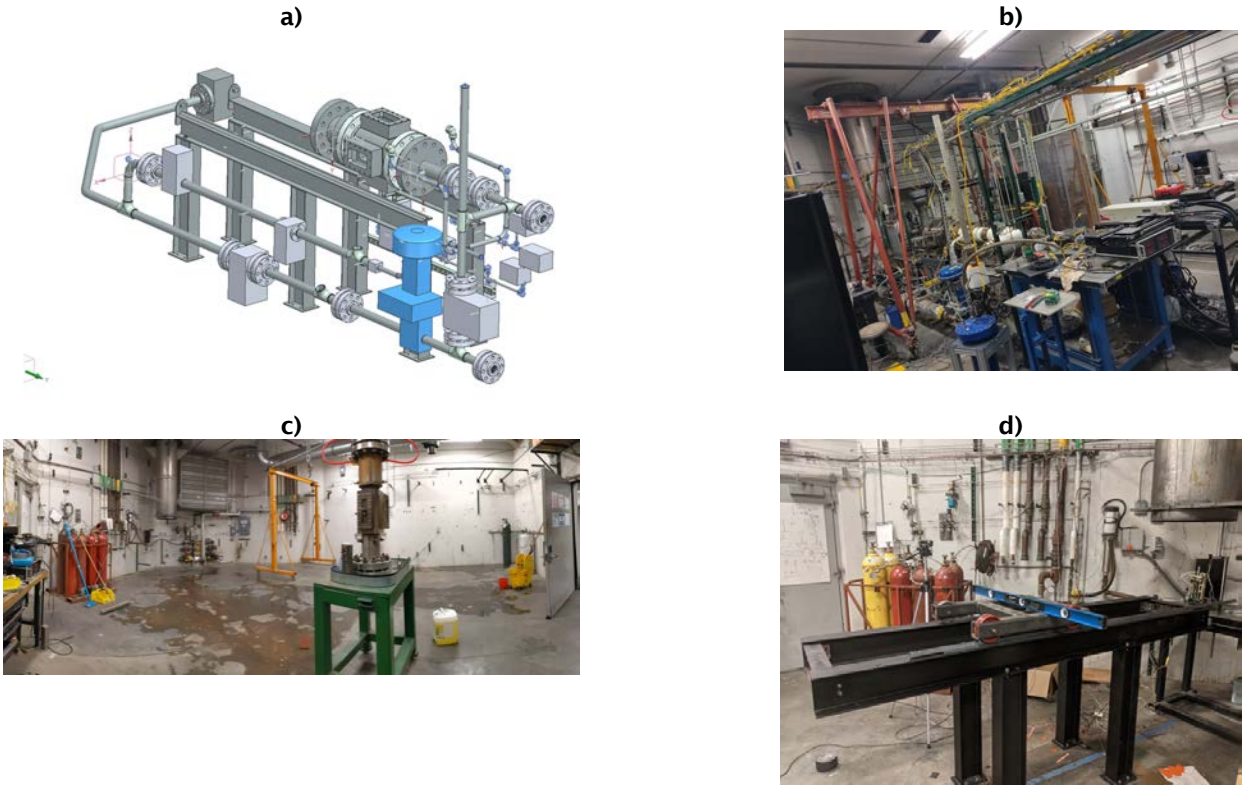

Figure 6. Rig structure, plumbing, and test cell refreshing. a) Final design for the rig support structure and plumbing layout, b) test cell before cleanout, c) gutted test cell for re-building, and d) initial build of the rig structure.

The completed re-design of the rig is shown in Figure 7. The re-designed rig was successfully constructed and assembled during this year. An initial shakedown of the new plumbing system led to fine adjustments in the various flow control orifices in the plumbing network (to achieve the right swirler/quench air split with room for control/adjustability).

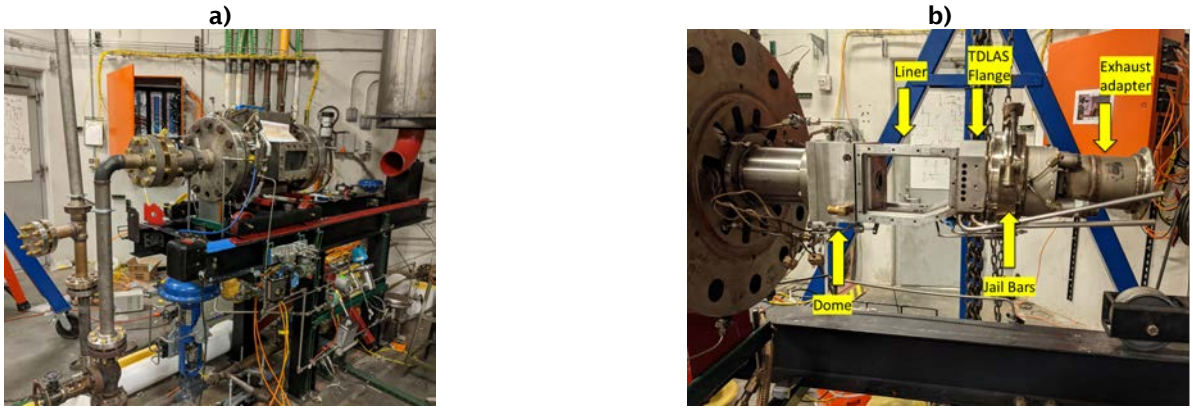

Figure 7. Completed rig re-build. a) Exterior of the rig with the pressure vessel bolted together and b) the new internal components with the pressure vessel removed. TDLAS: tunable diode laser absorption spectroscopy.

An initial reacting shakedown of the rig identified two hurdles to overcome. The first hurdle was related to the durability of the quartz windows, which were susceptible to breaking during ignition of the rig. We have temporarily overcome this drawback by finding a "softer" way to start the rig (i.e., with operational procedures). We are also working on a re-design of the window mounting mechanism to further address this issue, which remains as future work. The second hurdle was an igniter durability issue. The combustion noise of this rig tended to vibrate the igniter in a way that the electrode would advance slightly into the combustor, rendering it inoperable for subsequent ignitions. This drawback resulted in many unsuccessful tests. We re-designed the igniter from a single electrode to a double-electrode system. The greatest challenge of the double-electrode system was identifying dielectrics that allow us to connect leads to the igniter in a high-temperature environment without arcing. The new igniter has proven successful in reducing the number of failed tests. These igniter considerations are shown in Figure 8.

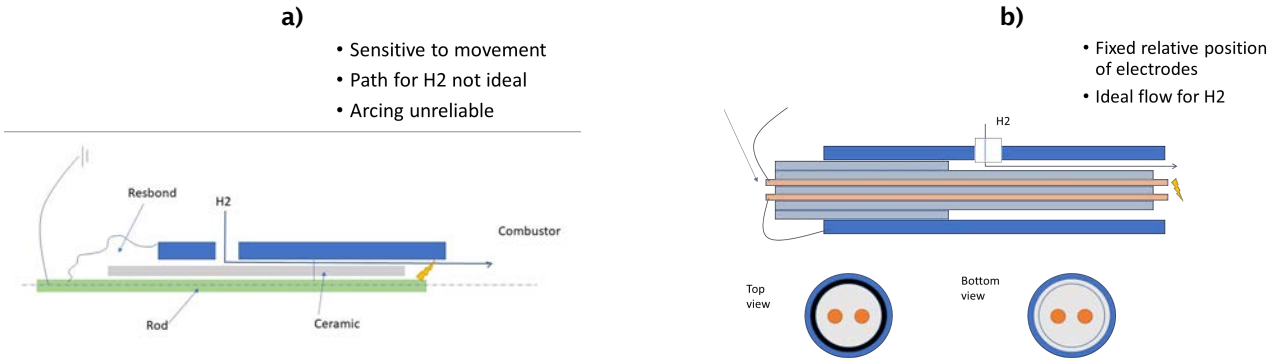

Figure 8. Schematic comparing the a) old single-electrode igniter and b) new double-electrode igniter.

Finally, we have recently begun operating the rig and have made preliminary chemiluminescence and acoustic measurements. Figure 9 shows a burn spot on our high-speed intensifier, which is partially located in our measurement region of interest. We are able to use image processing techniques to measure the unsteady heat release rate from these images; thus, this burn spot does not prevent the team from achieving their scientific goals. However, in future tests, we anticipate using a different intensifier to obtain higher-quality images. A screenshot from one of the high-speed image series is shown in Figure 9, which includes the burn spot (snowflake pattern) but otherwise exhibits excellent image quality up to the dump plane. The image shows shear-layer combustion, which was unobservable with the earlier rig.

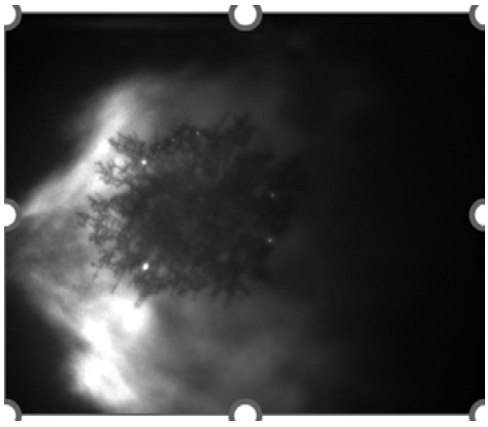

Figure 9. Screenshot of high-speed chemiluminescence imaging.

Milestones

- The GT team has completely re-designed the combustor and its structural support/plumbing layout.
- The GT team has completed a test cell cleanout and procurement, manufacturing, and assembly of a new combustor.
- The GT team has shaken down the combustor, overcome all hurdles uncovered in the shakedown, and begun testing the new combustor.

Major Accomplishments

The designed RQL combustor was manufactured and installed at the GT facility. The rig has been re-designed and rebuilt to enable higher-quality data, better durability, and improved matching to the RTRC rig.

Publications

None.

Outreach Efforts

None.

Awards

None.

Student Involvement

- **Amalique Acuna (GT):** Graduate Student. Mr. Acuna works on and operates the experiment at GT. Mr. Acuna has graduated.
- **Shivam Patel (GT):** Graduate Student. Mr. Patel is funded on a NASA ULI contract, but he actively contributes to the maintenance, construction, and operation of the experiment at GT.
- **Sungyoung Ha (GT):** Graduate Student. Mr. Ha is the lead experimentalist on the GT rig.
- **Jananee (GT):** Graduate student. Jananee is responsible for the optical diagnostics on the GT rig.
- **Archit Bapat (GT)**: Graduate student. Mr. Bapat is funded as a teaching assistant. He is assisting with the optical diagnostics on the GT rig.

Plans for Next Period

The GT rig team plans to continue the measurement campaign during the next period, with the inclusion of additional diagnostic methods throughout the process.

Task 2 - Simulations of the GT Experiment

Georgia Institute of Technology

Objective

The objective for the task this year is to use updated geometry and flow conditions and complete reactive LES studies using the GT compressible solver LESLIE. In addition, a key objective is to collect time-dependent three-dimensional (3D) snapshots of conservative variables from the LES for GT experimental conditions and transfer those findings to the RTRC and GT modeling teams. Sample post-processing scripts for computing additional variables from the 3D snapshots will also be provided.

Research Approach

Code Updates

The current version of the GT compressible solver contains three parts: CFDPreProc, LESLIE, and CFDPostProc. CFDPreProc is a pre-processor that can create a grid, set boundary conditions, etc. LESLIE is a core compressible solver that conducts multiphase reactive LES. The previous versions of LESLIE could output 3D snapshots of primitive variables, e.g., pressure, density, temperature, mass fractions; however, the simulations had to be rerun to output additional quantities such as reaction rates, heat release rate, or enthalpy. Considering the high computational cost of repeating full-scale LES, a code update was conducted as a second-year effort of this program, where the 3D snapshots outputted by the LESLIE code are now given in terms of the conservative variables that are directly solved for in our compressible framework, including the density, momentum, total energy, partial densities, etc. The primitive variables are still needed for the computation of noise-related quantities; therefore, a CFD post-processing software, CFDPostProc, was created to read the conservative variable-based 3D snapshots and compute additional primitive quantities. This code was provided to RTRC along with the 3D snapshots. The conservative variables form an exclusive and exhaustive set of variables; therefore, all other quantities can be computed from this set.

Solver Details

A fully compressible Eulerian finite-volume formulation for the gas phase and a Lagrangian formulation for the liquid phase were used in this study. An eddy-viscosity approach with a one-equation subgrid kinetic energy (k_{sgs}) model is used for the closure of gas-phase subgrid-scale fluxes. Because regions may exist in the plenum or outflow duct in which turbulence is not well established, the k_{sgs}-equation coefficients set to constant values, rather than being dynamically computed. Subgrid dispersion for spray particles is modeled using a stochastic separated flow model. Modeling of dense spray, corresponding compressible volume blockage effects, and breakup are also available, as we have previously shown, but these conditions are not considered here; instead, a dilute injection of spray is considered. Secondary breakup modeling will be included in the future.

The combustion is modeled via a finite-rate kinetics approach, using a two-step, six-species mechanism for kerosene. Subgrid closure for turbulent combustion is provided by a simplified partially stirred reactor model, where the mixing time (τ_m) is computed locally using k_{sgs} and the chemical time (τ_c) is precomputed for the operating conditions from laminar premixed flame solutions under stoichiometric conditions. Further details about our modeling approach can be found in our recent works and are not repeated here for brevity.

LESLIE is a well-established multi-block, structured, fully compressible finite-volume solver. A hybrid second-order central and third-order upwind method is used for the gas-phase evolution. A fourth-order Runge–Kutta solver is used for solving the Lagrangian equations. For computational efficiency, instead of tracking individual Lagrangian particles, the particles are grouped together in “parcels,” which are tracked in a Lagrangian manner. A particle-per-parcel value of 8 is used in this work, which has shown to provide a good balance between accuracy and efficiency for gas-turbine combustor LES.

Computational Configuration

Our previous effort focused on the LES of cold flow, using a reduced geometry without a swirler. To capture the physics of the shear flow and a swirl-stabilized spray flame, a swirler is included in the CAD geometry, as shown in Figure 10. The flow from the inlet plenum enters the combustion chamber via two concentric swirlers (one axial and one radial). After the reaction zone, three cooling jets on the top and two on the bottom are available to reduce the temperature. In addition, multiple small quench holes are present on the dome plate for reducing the wall temperature. The flow exits the outflow duct through

jail bars, which act as a nozzle that chokes.

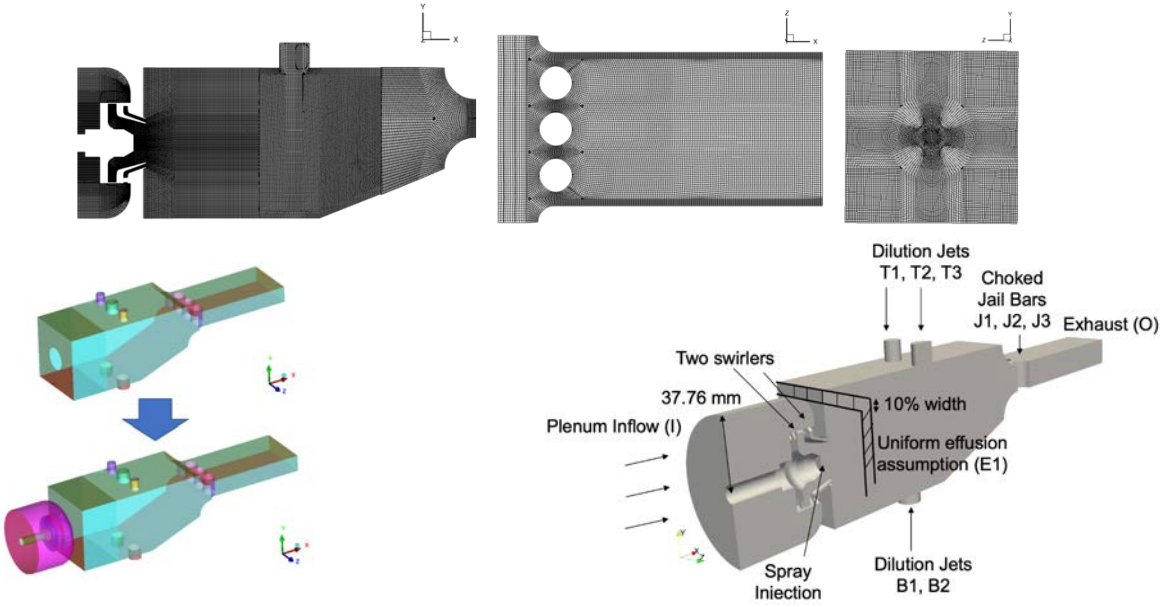

Figure 10. Revised computational domain with a swirler for LES. Top: Schematics for the new multi-block structured grid (main combustor at the center x-y plane, region behind the jail bars at the center x-z plane, and shear-layer region at the y-z plane located at one third of the axial length of the main combustor). Bottom left: Addition of a swirler to the CAD model. Bottom right: Entire computational domain with key features and corresponding boundary conditions.

The multi-block structured grid has 6.8 million cells and 4,571 blocks, and grid clustering is applied to the near region of the shear flow from the swirler and jail bars. To handle geometrical complexities, six multi-block structure grids are generated with hanging nodes, which are stitched together via an interpolation technique of the same order as the employed numerical scheme. Shear layers are resolved with 10–15 points across, and the swirlers have 10 or more points along their span, consistent with previous LES. Small quench holes on the dome plate are not resolved, but a pre-specified mass flow rate is injected through these holes using a porous boundary condition, as discussed below. To demonstrate the sufficiency of the LES grid, the turbulent kinetic energy is computed at a representative point in the shear layer, as shown in Figure 11, to capture the inertial subrange. This result has been confirmed at other points within the combustor, e.g., cooling jets, swirling shear layer, etc., but these data are not shown here for brevity.

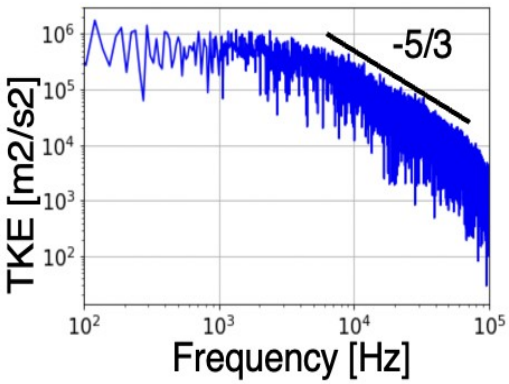

Figure 11. Turbulent kinetic energy (TKE) spectra in the shear layer show the inertial subrange captured by large-eddy simulations.

The LES solver is MPI-parallel, and the simulations are run on 1,440 cores. The flow-through time of the combustor is estimated to be 8 ms based on the entire length of the computational domain and a reference bulk velocity of 30 m/s. Initial transients are neglected for two flow-through times, and the statistics are then collected over at least six additional flow-through times. A simulation for a single flow-through time utilizes 51,840 CPU hours on GT's super-computing cluster (Partnership for an Advanced Computing Environment-Phoenix) with Intel Ivy-bridge i7 processors.

Boundary Conditions

During this period of work, the boundary conditions were revisited to be consistent with the GT experiments. All gas-phase inlet boundary conditions have now been updated to constant mass flow inlets based on experimental data inputs. The inflow boundary condition (ahead of the inlet plenum [I] and dilution holes [T1, T2, T3, B1, B2]) is modeled using a characteristic Navier–Stokes boundary condition. The mass flow rate for the main inflow (I) is set as 93.89 g/s (based on GT rig inputs). The total mass flow rates through the top (T1, T2, T3) or bottom (B1, B2) dilution holes are 117.03 g/s. The incoming air is at 673.3 K. The flow through the jail bar (J1, J2, J3) chokes and pressurizes the combustor to the nominal target. With choking, the outflow (O) is supersonic at the domain outlet. The outflow following the choked nozzle is modeled using a sponge boundary condition, but no waves are expected to travel upstream into the combustor chamber from this region because the nozzle is choked. The quench holes are not resolved; therefore, they are modeled using a porous boundary condition. The mass flow rate specified through the quench holes is 93.89 g/s.

The Lagrangian spray droplets are injected in a stochastic manner using two concentric injectors. The mass flow rate is 2.4 g/s through the primary injector and 6.89 g/s through the secondary injector. In the absence of any experimental measurements for this injector, a log-normal size distribution with a Sauter mean diameter of 30 μm is injected, similar to previous gas-turbine LESs (Patel & Menon, CF, 2008). A secondary breakup model was not considered during this period of work; however, additional simulations are planned to evaluate the effect of a secondary breakup model on the results. The primary injector is modeled as a solid cone injector with a 60^0 angle; the secondary injector surrounds the primary injector and is modeled as a hollow cone injector with 90^0 and 120^0 as the inner and outer angles, respectively. The injection temperature of the liquid fuel is 330 K, and the velocities are set as 25 m/s. This dilute injection occurs 1 mm downstream of the actual injector plate. This is an empirical injection procedure but can be improved in the future based on experimental insights.

Case Details

Even though only cold-flow and reactive simulations for the GT experimental rig conditions were proposed for Year 2, due to confusion during the grid generation near the end of Year 1, we simulated two chamber pressures during this period of work. The baseline simulation matches the experimental apparatus at GT and maintains a pressure of ~8.7 atm. Another simulation was conducted for a higher chamber pressure by increasing the diameter of the jail bars downstream, which reduces the nozzle area. In the baseline simulation, the jail bar diameter is 13.2 mm, whereas in the high-pressure simulation, the jail bar diameter is 14.2 mm. Isentropic, adiabatic zero-dimensional analysis showed the chamber pressure for the baseline and high-pressure cases to be 0.87 MPa and 1.00 MPa, respectively.

Data Output

The simulations output 3D snapshots of conservative variables, as noted above. The output frequency of these outputs is 10^4 Hz, and 500 such snapshots are outputted for each case over the span of a 50-ms simulation time. The snapshots are only collected after the initial transients for the first two flow-through times have been neglected. A single 3D snapshot is ~1 GB in size. A total of 350 corresponding snapshots were provided to RTRC for further processing and comparison against their experimental data. Additional data files can be provided as required. The CFDPostProc software and a sample script were also provided for computing primitive quantities such as pressure, temperature, density, and reaction rates from these files.

In addition to the 3D gas-phase snapshots, the Lagrangian data of the parcel are also saved at the same frequency and are available for computing the spray droplet statistics as well. This processing is currently underway, and the results will be reported during Year 3. A single droplet snapshot is ~50 MB in size.

Because the 3D gas-phase snapshots are rather large, it was not possible to collect them at a higher frequency. However, the simulation collects high-frequency data at 10^6 Hz for ~200 probe points distributed throughout the computational domain. These points are uniformly placed along the x/y/z directions within the combustor, through the nozzle, and within the exit plenum. These data can be used for accurately computing the frequency characteristics of the system.

Finally, although it is possible to compute time-averaged statistics (mean, root mean square [RMS]) using the outputted 3D snapshots, fine-grained time averaging is also conducted within the code, and the mean and RMS primitive quantities are outputted for the entire 3D domain. These quantities include the primitive variables, such as velocity, temperature, pressure, density, species mass fractions, and reaction rates. The size of a single time-averaged file is ~4 GB. These files were provided to the GT modeling team for use in ROM.

Instantaneous Results

The LES can capture 3D unsteady large-scale flow, flame, and spray structures. Instantaneous spray particles and a flame surface represented by a 2500 K temperature iso-surface are shown in Figure 12 to illustrate the LES. The flame surface is highly wrinkled because of turbulence, and the spray particles propagate downstream and vaporize in the surrounding high-temperature zone. As a result of the swirl, a low-pressure zone is created in the center, and a vortex breakdown bubble (VBB) (also known as a central toroidal recirculation zone) is formed. This behavior has been observed for many other gas-turbine combustors and is a key feature of swirling flows. For this combustor, there are two swirlers, but the observed VBB features are still qualitatively similar to past studies with a single swirler. Correspondingly, a negative velocity is observed in the center, as shown by the instantaneous axial velocity contours on the z-center slice in Figure 13a. The swirling shear layers are highly turbulent and can provide a zone for vaporization and flame stabilization. Due to the swirling jets, corner recirculation zones are also observed. The instantaneous velocity contours show the effect of the quench jets near the corners, but these jets dissipate quickly after injection. The cooling jets significantly affect the overall flow field by disrupting the continuation of the VBB, at least in the z-center slice shown here.

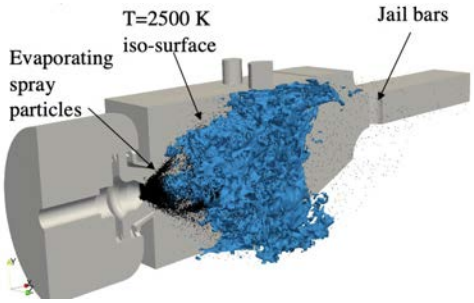

Figure 12. Three-dimensional flame (T=2500 K iso-surface) and spray (Lagrangian particles as black dots) features are visualized from large-eddy simulations for the baseline case.

The temperature contours at the same instant are shown in Figure 13b. The circulation zone of the VBB remains hot and is filled with combustion products produced by burning. Due to the high temperature, spray vaporization occurs in the surrounding regions. Fuel burning occurs in the shear layers, and the effects of large-scale turbulence on the burning fuel are clearly visible here. The cooling jets mix with the products, and highly turbulent mixing is observed. Finally, the Mach number contours on a y-slice are shown in Figure 14. As expected, the flow chokes at the nozzle created by the jail bars, and the flow converts from subsonic to supersonic. The supersonic flow after the nozzle shows a complex shock structure. All results discussed in this section are for the baseline case, i.e., a chamber pressure of ~ 8.7 atm. However, the high-pressure case (chamber pressure: ~10 atm) also shows similar results in terms of the flow field and flame stabilization.

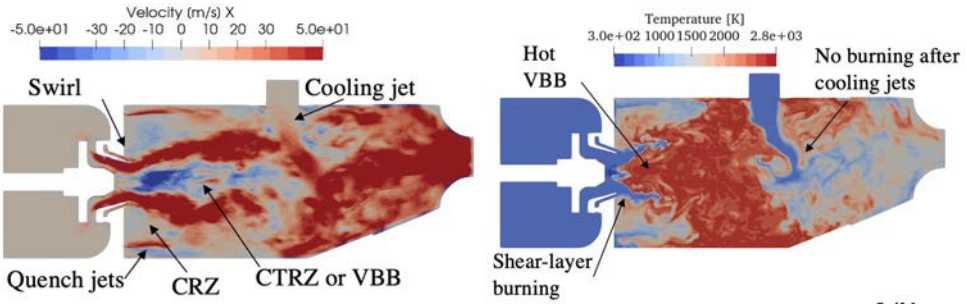

(a) Axial velocity **(b) Temperature**

Figure 13. Flow and flame structures on the center z-slice of the combustor at an instant for the baseline case. CRZ: corner recirculation zone; CTRZ: central toroidal recirculation zone; VBB: vortex breakdown bubble.

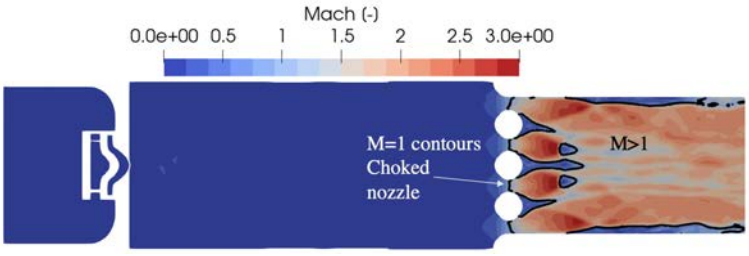

Figure 14. Instantaneous Mach number (M) contours for a y-slice of the combustor in the baseline case. The black line indicates the sonic boundary (M=1).

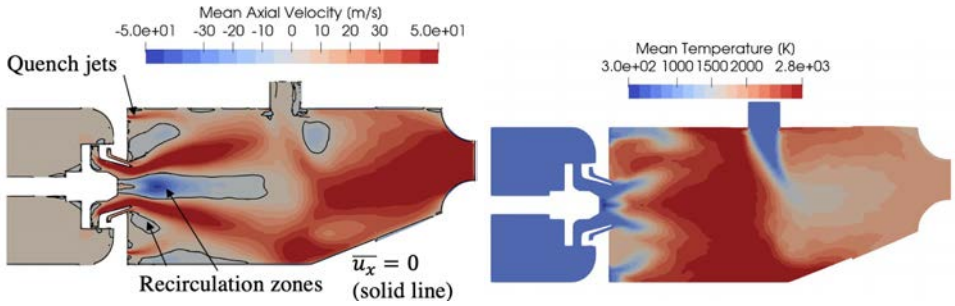

(a) Axial velocity **(b) Temperature**

Figure 15. Time-averaged flow and flame structures for the center z-slice of the combustor in the baseline case. The black lines indicate the recirculation zone boundary.

Time-Averaged Results

Time-accurate LES results were averaged over six flow-through times. The corresponding mean axial velocity and mean temperature are shown in Figure 15 for the z-center slice. The center recirculation zone boundary is clearly visible in Figure 15a, starting from the swirler and ending where the cooling jets enter. The predicted recirculation zone is narrow and long. A small region of positive velocity is observed in the center of the swirler near the injector plate, due to the injected Lagrangian particles that also transfer momentum to the gas phase via drag. A small recirculation zone is also observed right after the cooling jets, demonstrating the complex flow structures that are observed in this combustor. In the time-averaged results, the VBB shows the presence of hot products, as noted before. The cooling jets reduce the overall flow temperature by the time the flow reaches the nozzle. The effect of quench jets is also clear, as they reduce the temperature near the corners. Like earlier results, the data shown here are for the baseline case, but the high-pressure case shows similar results.

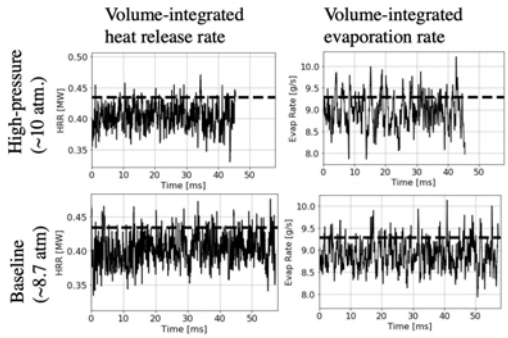

Figure 16. Time variation of the volume-integrated heat release rate (HRR) and evaporation rate within the combustor. The dashed lines show ideal values that assume 100% evaporation and burning of the injected fuel.

Dynamics and Global Quantities

Various quantities, i.e., chamber pressure, volume-integrated heat release rate, volume-integrated evaporation rate, and mass flow rates through various planes, are continuously monitored during the simulation. To obtain a global measure, the heat release rate and evaporation rate are integrated over the entire volume of the combustor. These rates are reported in Figure 16. The oscillations may be due to the turbulence or acoustics in the combustion chamber, and they can contribute to noise generation. The ideal values (shown by the dashed line in Figure 16) were computed with the assumption that all of the injected fuel vaporizes and burns. With respect to these ideal values, the efficiency of the heat release and evaporation processes are ~90% and ~95%, respectively. This behavior is similar for both pressures.

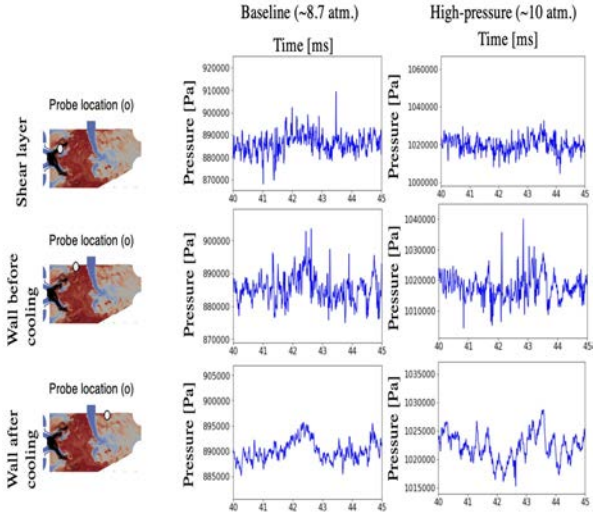

Figure 17. Pressure dynamics within the combustor at various representative points.

Next, to further elucidate the dynamics and acoustics within the system, we assessed the time variation of pressure at representative points within the combustor, as shown in Figure 17. The representative points are within the shear layer and on the top wall before and after the cooling jets. The mean pressure within the chamber is close to 8.7 atm and 10 atm for the baseline and high-pressure cases, respectively, as expected. The pressure dynamics also show visible differences between the baseline and high-pressure cases. A spectral analysis of the pressure signature shows 2350 Hz and 2700 Hz as dominant frequencies for the baseline and high-pressure cases, respectively. These data will be analyzed further to compute the reflection coefficient, transfer functions, etc.

Milestones

- Grid and boundary conditions were updated to be consistent with GT experiments.

- Reactive flow LESs were conducted for the baseline condition, which is supposed to match the GT experiments, and for a high-pressure condition that was obtained by increasing the jail bar diameter.
- Correspondingly, 350 3D snapshots from the LESs were provided to RTRC for further noise-related processing.
- A sample post-processing pipeline for processing 3D snapshots was created and provided to RTRC.
- Time-averaged data were provided to the GT ROM team.

Major Accomplishments

A new grid has been established, boundary conditions have been updated, the reacting spray flame has been stabilized at the proper location, and a statistical steady state has been established for both the baseline and high-pressure conditions. Data in the form of 3D snapshots and time-averaged data from LESs have been provided to the RTRC and GT modeling groups. In addition, sample post-processing scripts for converting the 3D files with conservative variables to primitive variables relevant to noise have also been provided.

Publications

Published Conference Proceedings

Panchal, A., & Menon, S. (2023, January 23). Large eddy simulation of combustion noise in a realistic gas turbine combustor. *AIAA SCITECH 2023 Forum*. AIAA SCITECH 2023 Forum, National Harbor, MD & Online. https://doi.org/10.2514/6.2023-1349

Outreach Efforts

None.

Awards

None.

Student Involvement

- Sangjae Kim (PhD student) focused on grid generation and initial cold-flow LESs during the start of Year 2.
- Tarun Golla (currently an undergraduate student, planning to pursue a Master's degree with a thesis) has been working on developing post-processing scripts for computing source terms pertaining to direct and indirect noise using the 3D snapshots. He will focus on evaluating the effects of using a secondary breakup model.
- Leo Kastenberg (undergraduate) worked on developing the post-processing scripts.
- Maxwell Hall (undergraduate) has been working on post-processing the high-frequency trace data.
- Nolan Amblard (undergraduate) has been working on developing scripts for principal orthogonal decomposition.

Plans for Next Period

In the next period, comparisons with data from the GT rig will be conducted in terms of acoustic data and chemiluminescence. We will also evaluate the effect of secondary breakup modeling on the LES predictions. Additionally, some post-processing tools, which are currently being tested, will be used to study both direct and indirect noise sources. Additional data over a longer time can be provided to the RTRC and GT modeling teams as needed.

Task 3 - Reduced-Order Modeling

Georgia Institute of Technology

Objective

The overarching objective of this task is to create quick-action ROMs to accurately predict different aspects of noise generation mechanisms that then collectively feed into a design tool for noise prediction. The specific objective of the GT ROM task focuses on the head-end physics in the architecture, namely, the flow and spray dynamics, flame dynamics, and generation of entropy disturbances by the flame. The spray/flow dynamics feed into the flame dynamics, which cause direct combustion noise. The flame dynamics also result in entropy disturbances, which then lead to indirect combustion noise at the nozzle. The flame response modeling and the model for the generation of entropy disturbances are provided as inputs to the post-combustion models that will be developed by RTRC. Depending on the prediction results obtained from the RTRC models, these head-end models will be iteratively refined.

Research Approach

In this reporting period, we focused on ROM tasks pertaining to hydrodynamics, flame dynamics, and entropy generation. We studied the hydrodynamics of a swirling jet using an in-house hydrodynamic stability analysis tool that captures the leading-order coherent dynamics of the flow field. The goal of the tool is to measure the flow response by studying the velocity disturbances resulting from simulated external forcing noise. The hydrodynamics will eventually result in a velocity model that is used with the flame dynamics model to generate heat release. We further studied the contributions of different chemical source terms contributing to entropy generation for a premixed flame, excluding the diffusion effects. Chemical source studies were performed for varying fuels, oxidizers, and preheating conditions.

Hydrodynamics Modeling

In this reporting period, an effort was made to develop a hydrodynamic forced response framework to measure the swirling jet global mode response to an imposed boundary forcing function. We studied swirling jets as amplifier flows, which, in the literature, are known to alter the flow response in the presence of external noise that can occur during combustion. Apart from the well-known advantages of swirling jets as canonical flow fields in combustion systems, swirling flows usually result in unsteady hydrodynamic structures that can couple with acoustics. Modeling and predicting the hydrodynamic structures can be important, especially in the presence of combustion, as these structures can interact with and perturb the flame. Hydrodynamic stability analysis has emerged as a tool for modeling the dynamics of swirling flows in recent decades. This type of analysis is particularly useful for predicting receptivity, or the range of frequencies amplified by the flow. In other words, hydrodynamics provides a transfer function from the background turbulence to large-scale vortical disturbances (which disturb the flame to produce direct noise). Additionally, hydrodynamic stability analysis is particularly valuable for parametric studies to determine the sensitivity of the flow response to major design parameters, thus providing a powerful engineering tool. Traditional global hydrodynamic stability analyses have focused on instability generated within the domain (unforced or natural hydrodynamics). Our effort has been to model how the flow response can be altered if instability is introduced at the inlet in a more global framework.

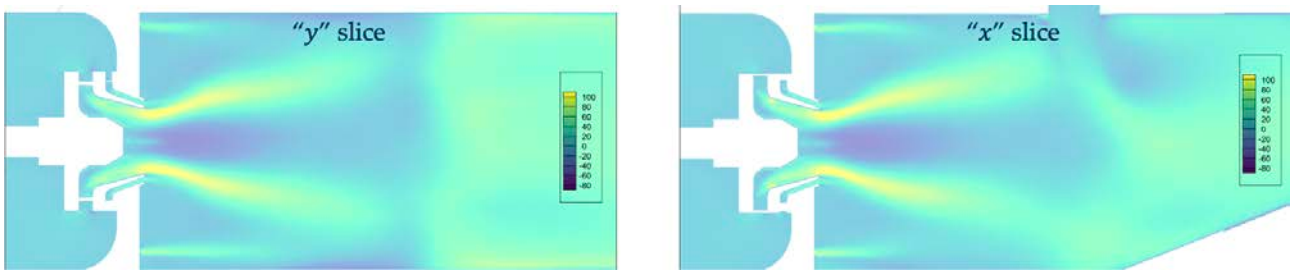

Figure 18. Schematic showing the axial velocity contours of a sliced 3D flow field in Cartesian coordinates. Courtesy of A. Panchal and S. Menon.

To study the global mode response to an imposed forcing function, we utilize the time-averaged combustor flow fields supplied as part of the LESs performed for this project. We decompose the 3D velocity fields into two 2D slices with the same axial coordinate. These slices are denoted as the x-slice and y-slice, as displayed in Figure 18. We then conduct a coordinate transform into cylindrical coordinates. Transforming the data into cylindrical coordinates gives us an advantage in establishing an axisymmetric geometry for our model.

The governing equations for this analysis include the linearized continuity and momentum equations in their incompressible form:

$$\nabla \cdot \vec{u}' = 0$$
$$\frac{\partial \vec{u}'}{\partial t} + \left(\bar{\vec{u}} \cdot \nabla\right)\vec{u}' + \left(\vec{u}' \cdot \nabla\right)\bar{\vec{u}} + \frac{\nabla p'}{\bar{\rho}} - \nu \nabla^2 \vec{u}' = 0 \qquad (1)$$

For this analysis, we use a bi-global stability analysis framework, which allows the calculated modes to vary significantly along two coordinates. Utilizing the axisymmetric configuration of the problem, the velocity and pressure disturbances are assumed to take the following harmonic form shown below. The amplitude of the mode is a function of the radial and spatial coordinates, while temporal and azimuthal periodicity is maintained by using the frequency ω and azimuthal wave number m. The azimuthal wave number, m, will capture the helical modes of swirling jets of interest.

$$g'(r,\theta,z,t) = \hat{g}(r,z)e^{-i(\omega t - m\theta)} \quad (2)$$

The assumption of a bi-global mode in the linearized governing equations results in a set of four coupled partial differential equations. We present appropriate boundary conditions for each equation in Table 1.

Table 1. Boundary conditions for each equation.

	Axis	Walls	Inlet	Outlet
Radial Velocity	$u_r' = 0$	$u_r' = 0$	$u_r' = A_0 e^{-i\omega t}$	$u_r' = 0$
Tangential Velocity	$u_t' = 0$	$u_t' = 0$	$\frac{\partial u_t'}{\partial \mathbf{n}} = 0$	$u_t' = 0$
Axial Velocity	$\frac{\partial u_z'}{\partial \mathbf{n}} = 0$	$u_z' = 0$	$\frac{\partial u_z'}{\partial \mathbf{n}} = 0$	$u_z' = 0$
Pressure	$\frac{\partial p'}{\partial \mathbf{n}} = 0$	$\frac{\partial p'}{\partial \mathbf{n}} = 0$	$\frac{\partial p'}{\partial \mathbf{n}} = 0$	$p' = 0$

At the centerline, we assume no fluctuations in radial or tangential velocity to conform with an axisymmetric flow. At the wall, all velocity disturbances must vanish. At the inlet, we impose the inhomogeneous Dirichlet boundary condition for the velocity normal to the inlet plane to simulate the external boundary forcing for this problem. For the outlet, homogenous Dirichlet boundary conditions are imposed for velocity and pressure disturbance amplitudes.

We developed a code to solve the equations using finite elements in COMSOL. To validate the code, a historical dataset with an axisymmetric base flow was used. The natural hydrodynamics was tested by an unforced global analysis. We correlated the growth rates of unstable modes with the Strouhal number (oscillatory frequencies) to validate the linear trend predicted in the literature and ensured that the code accurately captured the unstable solutions.

Flame Response Modeling

In the prior reporting periods, we presented the flame response framework for spray flames along with example flame configurations and the effect of spray parameters on mean flame shapes and dynamical flame shape characteristics. In this reporting period, we analyzed the global response of the flames using spatially integrated total unsteady heat release rate disturbances. To reiterate, the configuration used for this framework is shown in Figure 19, with fuel droplets injected in a center duct and air injected in the outer ducts. The fuel flows in the inner duct with $0 < r < R_F$, and the air/oxidizer flows in the outer ducts with $R_F < r < R$. The fuel exits the duct and enters the combustion zone as a mix of fuel gas and a spray of liquid fuel droplets, which, after evaporation and diffusive mixing, result in the spray diffusion flame being modeled.

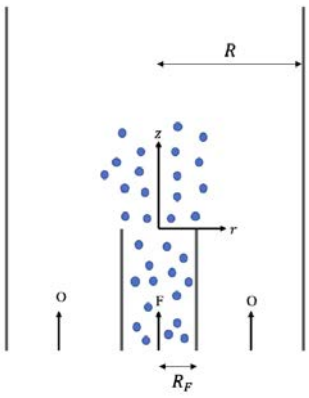

Figure 19. Schematic of the ducted spray flame configuration. Fuel droplets are injected in the center duct (shown in blue), and oxidizer gas is injected in the outer ducts.

The gaseous (Z) and droplet mixture (Z_d) fractions are one-way-coupled through vaporization of the droplet, which generates fuel gas. The steady-state mixture fractions are governed as follows:

$$u_{z,0}\frac{\partial Z_{d,0}}{\partial z}+u_{r,0}\frac{\partial Z_{d,0}}{\partial r}-\frac{1}{Pe_d}\left(\frac{\partial^2 Z_{d,0}}{\partial z^2}+\frac{\partial^2 Z_{d,0}}{\partial r^2}\right)+\Gamma_V Z_{d,0}=0 \tag{3}$$

$$u_{z,0}\frac{\partial Z_{0}}{\partial z}+u_{r,0}\frac{\partial Z_{0}}{\partial r}-\frac{1}{Pe_g}\left(\frac{\partial^2 Z_{0}}{\partial z^2}+\frac{\partial^2 Z_{0}}{\partial r^2}\right)-\Gamma_V Z_{d,0}=0 \tag{4}$$

The fluctuations in the mixture fractions are then governed by the following equations:

$$\frac{\partial Z_{d,1}}{\partial t}+u_{z,0}\frac{\partial Z_{d,1}}{\partial z}+u_{r,0}\frac{\partial Z_{d,1}}{\partial r}-\frac{1}{Pe_d}\left(\frac{\partial^2 Z_{d,1}}{\partial z^2}+\frac{\partial^2 Z_{d,1}}{\partial r^2}\right)+\Gamma_V Z_{d,1}=-\left(u_{z,1}\frac{\partial Z_{d,0}}{\partial z}+u_{r,1}\frac{\partial Z_{d,0}}{\partial r}\right) \tag{5}$$

$$\frac{\partial Z_{1}}{\partial t}+u_{z,0}\frac{\partial Z_{1}}{\partial z}+u_{r,0}\frac{\partial Z_{1}}{\partial r}-\frac{1}{Pe_g}\left(\frac{\partial^2 Z_{1}}{\partial z^2}+\frac{\partial^2 Z_{1}}{\partial r^2}\right)-\Gamma_V Z_{d,1}=-\left(u_{z,1}\frac{\partial Z_{0}}{\partial z}+u_{r,1}\frac{\partial Z_{0}}{\partial r}\right) \tag{6}$$

The boundary conditions are given by the following:

$$\begin{aligned} &0\le r\le\zeta\rightarrow\begin{cases} Z_{d,0}(r,z=0,t)=\sigma_d & Z_{d,1}(r,z=0,t)=0 \\ Z_0(r,z=0,t)=1-\sigma_d & Z_1(r,z=0,t)=0 \end{cases} \\ &\zeta<r\le 1\rightarrow\begin{cases} Z_d(r,z=0,t)=0 & Z_{d,1}(r,z=0,t)=0 \\ Z(r,z=0,t)=-\sigma_O & Z_1(r,z=0,t)=0 \end{cases} \end{aligned} \tag{7}$$

$$\begin{aligned} &\frac{\partial Z_{d,0}}{\partial r}(r=1,z,t)=0 \qquad \frac{\partial Z_{d,1}}{\partial r}(r=1,z,t)=0 \\ &\frac{\partial Z_{0}}{\partial r}(r=1,z,t)=0 \qquad \frac{\partial Z_{1}}{\partial r}(r=1,z,t)=0 \end{aligned} \tag{8}$$

The above system is solved for both the droplet and gaseous mixture fractions. The flame position fluctuation along the local normal is given by the following:

$$\xi_{1,n}(z,t)=-\frac{Z_1(r=\xi_0(z),z,t)}{\left|\nabla Z_0\right|_{(r=\xi_0(z),z)}} \tag{9}$$

The instantaneous mixture fraction and instantaneous local flame position fluctuations will be used in the expressions for the spatially integrated unsteady heat release rate fluctuations. The local heat release per unit area of the flamelet surface depends on the reactant mass burning rate (MBR), $\dot{m}''_F$, and the heat release per unit mass of reactant, h_R, expressed as follows:

$$\dot{q}(\vec{x},t)=\dot{m}''_F(\vec{x},t)\,h_R(\vec{x},t) \tag{10}$$

Note that we exclude the effect of evaporation on the heat release since it is negligible. Because the combustion reaction for the spray flame occurs in the gaseous state, the gaseous mixture fraction is the sole contributor to the reactant MBR and is defined as follows:

$$\dot{m}''_F=\frac{-(1+\varphi_{Ox})^2}{\varphi_{Ox}}\rho D\frac{\partial Z}{\partial n} \tag{11}$$

Here, n is the direction normal to the local instantaneous stoichiometric mixture fraction iso-surface. The global flame response is denoted by the spatially integrated unsteady heat release rate, which is given by the following:

$$\dot{Q}(t)=\int_A \dot{m}''_F\,h_R\,dA \tag{12}$$

Here, the integration is performed over the instantaneous iso-surface at the stoichiometric mixture fraction.

A key focus of this work is to explore the effect of the addition of spray and evaporation on changes to the mixture fraction and thus the overall heat release dynamics. From Eq. (11)–(12), we have the following relation:

$$\dot{Q}(t) = \int_0^{L_f(t)} \frac{(1+\varphi_{Ox})^2}{\varphi_{Ox}} \rho h_R D \left(\left.\frac{\partial Z(r,z,t)}{\partial z}\right|_{r=\xi(z,t)} \frac{\sin\theta}{\cos\theta} - \left.\frac{\partial Z(r,z,t)}{\partial r}\right|_{r=\xi(z,t)} \right) dz \tag{13}$$

Here, θ is the local angle of the mean flame surface with respect to the axial direction. Linearizing the mixture fraction Z, the flame position ξ, and the flame height L_f and assuming the transverse diffusion to be dominant, the above expression simplifies as follows:

$$\dot{Q}(t) = \frac{-(1+\varphi_{Ox})^2}{\varphi_{Ox}} \rho h_R D \left\{ \underbrace{\int_0^{L_{f,0}} \left.\frac{\partial Z_0}{\partial r}\right|_{r=\xi_0(z)} dz}_{\dot{Q}_0} + \underbrace{\int_0^{L_{f,0}} \left.\frac{\partial Z_1}{\partial r}\right|_{r=\xi_0(z)} dz}_{\dot{Q}_{1,MBR}(t)} + \underbrace{\int_0^{L_{f,0}} \xi_{1,n} \left.\frac{\partial}{\partial n}\left(\frac{\partial Z_0}{\partial r}\right)\right|_{r=\xi_0(z)} dz}_{\dot{Q}_{1,WA}(t)} \right\} \tag{14}$$

Note that the fluctuations in the mixture fraction contribute to the heat release dynamics in two ways:

- Direct contribution from the fluctuating mixture fraction, which is referred to as the MBR term
- Indirect contributions through fluctuations in flame position (see Eq. (9)), referred to as the weighted area (WA) term

The flame transfer function is defined as follows:

$$\hat{F} = \hat{F}_{MBR} + \hat{F}_{WA} = \frac{\hat{\dot{Q}}_{1,MBR}(\omega) + \hat{\dot{Q}}_{1,WA}(\omega)}{\dot{Q}_0} \tag{15}$$

$$\hat{F}_{MBR} = \frac{\int_0^{L_{f,0}} \left.\partial \hat{Z}_1/\partial r\right|_{r=\xi_0(z)} dz}{\int_0^{L_{f,0}} \left.\partial Z_0/\partial r\right|_{r=\xi_0(z)} dz} \tag{16}$$

$$\hat{F}_{WA} = \frac{\int_0^{L_{f,0}} \hat{\xi}_{1,n} \left.\frac{\partial}{\partial n}\left(\frac{\partial Z_0}{\partial r}\right)\right|_{r=\xi_0(z)} dz}{\int_0^{L_{f,0}} \left.\frac{\partial Z_0}{\partial r}\right|_{r=\xi_0(z)} dz} = \frac{\int_0^{L_{f,0}} \hat{\xi}_{1,n} \left[\left.\frac{\partial^2 Z_0}{\partial r \partial z}\sin\theta_0 - \frac{\partial^2 Z_0}{\partial r^2}\cos\theta_0\right]\right|_{r=\xi_0(z)} dz}{\int_0^{L_{f,0}} \left.\frac{\partial Z_0}{\partial r}\right|_{r=\xi_0(z)} dz} \tag{17}$$

Here, the local mean flame angle is denoted as θ_0 and determined from the mean flame position as follows:

$$\tan\theta_0(z) = \frac{d\xi_0(z)}{dz} \tag{18}$$

For illustration, let us consider the following flow field:

$$\begin{aligned} u_{z,0} &= 1 \qquad u_{z,1} = \cos(2\pi \mathrm{St}\left(t - k_c z\right)) \\ u_{r,0} &= u_{r,1} = 0 \end{aligned} \tag{19}$$

Here, $\mathrm{St} = fR/u_0, k_c = u_0/u_c$ are the non-dimensional frequency (Strouhal number) and a non-dimensional disturbance convection parameter. For the purpose of this illustration, we neglect axial diffusion and use the mixture fraction solutions derived in prior work (for $k_c = 0$).

In the prior reporting period, we studied the effect of the spray on the mean mixture fraction field through two main parameters for the spray: droplet loading, σ_d, and vaporization Damkohler number, Γ_V. It was shown that as the droplet loading increases (moving from a pure gaseous diffusion flame to a spray flame), the flame height also increases. Additionally, the delay in generation of fuel gas due to vaporization had important and unique impacts on the mean flame shape. Similarly, the vaporization Damkohler number was shown to affect the mean flame shape around $\Gamma_V \sim 1$ but had little

impact for large $\Gamma_V \gg 1$. We will use these findings as the basis for example calculations, as the mean flame shape is a critical parameter for combustion instability. We fixed the following parameters for these calculations: $\zeta = 0.25; Pe_d = 1000; Pe_g = 10$.

First, let us consider the effect of droplet loading on the flame response for a fixed vaporization Damkohler number, as shown in Figure 20. Here, we assume $k_c = 0$. In this figure, the different colors denote different droplet loadings, the solid line corresponds to the total flame response, the dashed line corresponds to the MBR contribution, and the dotted line corresponds to the WA contribution. Results for a pure gaseous diffusion flame (black curve, $\sigma_d = 0$) are shown for reference. Note that the MBR contribution dominates the WA contribution. For all cases, the overall FTF begins at unity and shows classical non-monotonic behavior with local minima and maxima, as expected. As the droplet loading increases, the overall flame response increases and exceeds unity for the maximum loading. This finding contrasts with observations of non-premixed flames and premixed flames, where disturbance convection is required to result in FTF amplitudes that exceed unity. Additionally, as the droplet loading increases, the contribution of the WA term increases. This trend can be attributed to the increase in local flame response fluctuations with droplet loading, which is a direct contributor to this term, as shown in Eq. (17). Note that for larger Strouhal numbers, the WA contribution exceeds the MBR contribution for the highest droplet loading. In summary, these results indicate that strong changes occur to the overall flame response as we move from a pure gaseous diffusion flame to a pure spray flame, indicating significant influences on overall combustion instability characteristics.

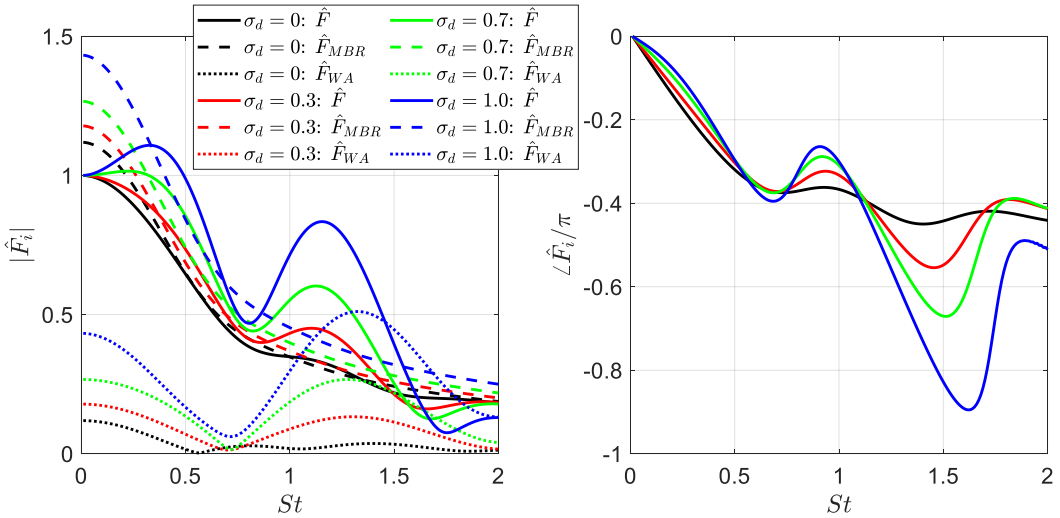

Figure 20. Variation in magnitude and phase of the overall flame response and its mass burning rate (MBR, dashed) and weighted area (WA, dotted) contributions for different droplet loadings with a fixed vaporization Damkohler number, $\Gamma_V = 10$.

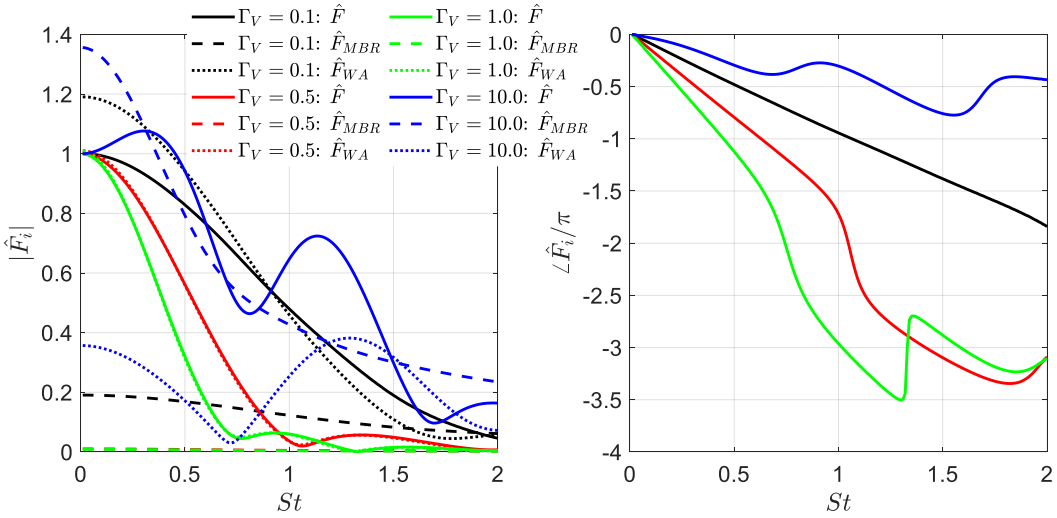

Figure 21. Variation in magnitude and phase of the overall flame response and its mass burning rate (MBR, dashed) and weighted area (WA, dotted) contributions for different vaporization Damkohler numbers with a fixed droplet loading, $\sigma_d = 0.5$.

Next, we consider the effect of the vaporization Damkohler number on the flame response for a fixed droplet loading, as shown in Figure 21 for $k_c = 0$. This parameter is a measure of the competing effect between vaporization and convection timescales. For the case corresponding to $\Gamma_V = 0.1$, the flame response shows a monotonic decrease, with the WA contribution being dominant. This finding is contrary to observations for larger values of Γ_V , where the opposite dominance is seen. As Γ_V increases, the overall flame response amplitude decreases but begins to show the classical minima and maxima. For $\Gamma_V = 1$, the MBR contribution is almost 0, and the flame response is almost entirely determined by the WA term. This result differs from findings for a pure gaseous flame, where the MBR term is typically the dominant contributor. Overall, these results show how differences in the vaporization and convective timescales affect the overall flame response and its different contributors.

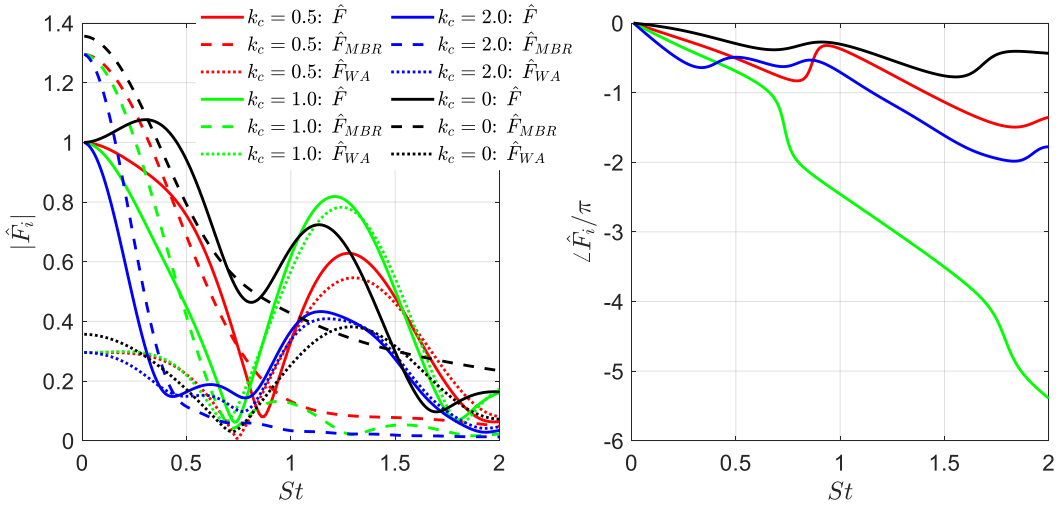

Figure 22. Variation in magnitude and phase of the overall flame response and its mass burning rate (MBR, dashed) and weighted area (WA, dotted) contributions for different disturbance convection speeds with a fixed spray flame configuration, $\sigma_d = 0.5, \Gamma_V = 10$.

Finally, we consider the effect of the disturbance convection speed on the response of a given spray flame configuration. Figure 22 shows this variation for a fixed droplet loading and vaporization Damkohler number of $\sigma_d = 0.5, \Gamma_V = 10$. The baseline case with no disturbance convection (bulk forcing) is shown by the black curves. Note that as disturbance convection is introduced and decreased (increasing k_c), the flame response decreases for low Strouhal numbers. In this low Strouhal range, the dominant contributor is the MBR term. As the Strouhal number increases, the WA term becomes the dominant contributor. Additionally, the overall flame response does not follow a monotonically decreasing "envelope"; instead, the response shows an increase in the local maxima around the unity Strouhal number region. These features are unique to the spray flame case and are typically not observed in classical premixed and gaseous diffusion flame studies. Overall, these results indicate that a typical Strouhal number scaling for spray flames cannot be deduced and that the flame response can be as significant at higher Strouhal numbers as it is at lower Strouhal numbers.

Generation of Entropy Disturbances

At the flame, where molecular transport processes are negligible compared with chemical reaction processes, the governing equation for the entropy dynamics is as follows:

$$\rho T \frac{Ds}{Dt} = -\sum_{i=1}^{N} \tilde{\mu}_i \dot{w}_i \tag{20}$$

By expanding this chemical potential term further, we obtain the following:

$$S_e = -\sum_{i=1}^{N} \tilde{\mu}_i \dot{w}_i = \underbrace{-\sum_{i=1}^{N} h_{f,i}^0 \dot{w}_i}_{S_{e,1}} \underbrace{-\sum_{i=1}^{N} \dot{w}_i \int_{T_0}^{T} c_{p,i} dT}_{S_{e,2}} + \underbrace{\sum_{i=1}^{N} T s_i \dot{w}_i}_{S_{e,3}} \tag{21}$$

Here, $S_{e,1}$ or $\dot{q}$ is the chemical heat release term. Several prior research efforts on entropy dynamics during combustion have assumed, without evidence, that only the heat release term contributes to the generation of entropy disturbances at the flame and that the other terms are negligible. The first focus of this task was to investigate the relative contributions of the heat release term compared with the entire chemical source term, S_e. $S_{e,2}$ and $S_{e,3}$ can be expanded by assuming a constant specific heat and ideal gas relations to gain more insight:

$$S_{e,2} = p\left(\frac{\dot{n}}{n}\right)\left[\left(\frac{\gamma}{\gamma - 1}\right)\frac{T_0 - T}{T}\right] \tag{22}$$

$$S_{e,3} = S_{e,3a} + S_{e,3b} + S_{e,3c} = p \ln n \left(\frac{\dot{n}}{n}\right) + T\sum_{i=1}^{N} s_i^0 \dot{w}_i - R_u T \sum_{i=1}^{N} \frac{\dot{w}_i}{MW_i} \ln n_i \tag{23}$$

To test the dominance of the heat release rate over the remaining terms, a 1D Cantera simulation was conducted for various hydrocarbon fuel combustion scenarios. The following ratios can be computed to reflect the behavior of the terms:

$$\alpha_1 = \frac{\int S_{e,1} dx}{\int S_e dx}, \alpha_2 = \frac{\int S_{e,2} dx}{\int S_e dx}, \alpha_3 = \frac{\int S_{e,3} dx}{\int S_e dx}, \alpha_{3,\text{major}} = \frac{\int S_{e,3,\text{major}} dx}{\int S_e dx} \tag{24}$$

$$S_{e,3,\text{major}} = T s_{fuel} \dot{w}_{fuel} + T s_{O_2} \dot{w}_{O_2} + T s_{CO_2} \dot{w}_{CO_2} + T s_{H_2O} \dot{w}_{H_2O}$$

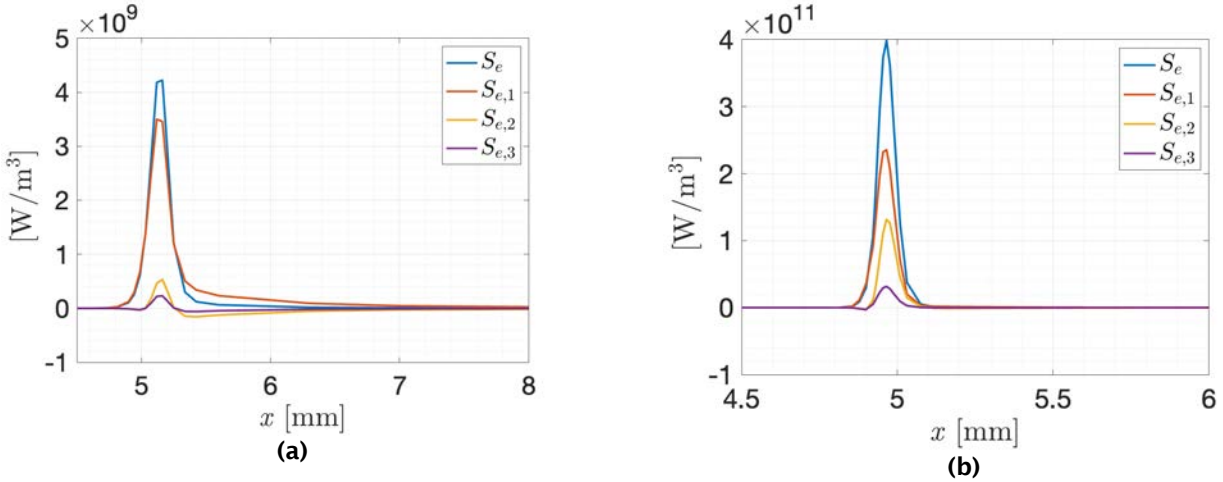

Figure 23. $S_{e,1}$, $S_{e,2}$, and $S_{e,3}$ for (a) methane–air and (b) methane–oxygen at $T_u = 500$ K, $\phi = 0.75$, and $p = 1$ atm.

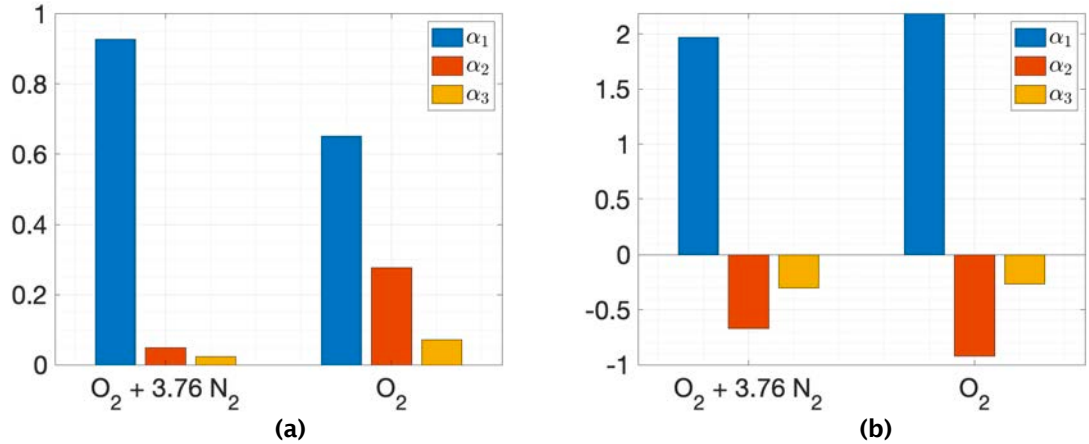

Figure 24. α_1, α_2, and α_3 for (a) methane–air and methane–oxygen; (b) hydrogen–air and hydrogen–oxygen combustion at $T_u = 500$ K, $\phi = 0.75$, and $p = 1$ atm.

Figure 23 shows flame profiles of the three terms for premixed methane–air and methane–oxygen flames at $T_u = 500$ K, $\phi = 0.75$, and $p = 1$ atm. Figure 23a clearly shows that $S_{e,1}$ is dominant for methane–air combustion, in which case the entropy production terms can be equated with the heat release rate. Figure 23b displays results for oxygen, showing that although $S_{e,2}$ and $S_{e,3}$ are smaller than $S_{e,1}$, they are not negligible. Figure 24a displays results for the same conditions used in Figure 23, but with a spatial integration. This figure shows that $S_{e,1}$ is the largest contributor and is dominant for air-fueled systems, whereas for oxygen–fuel combustion, $S_{e,2}$ and $S_{e,3}$ provide a contribution of approximately 35%. Figure 24b displays results for hydrogen–air and hydrogen–oxygen mixtures, showing that the contributions from $S_{e,2}$ and $S_{e,3}$ are less than zero. This result is expected because both terms are influenced by molar production. For complete hydrogen combustion, the ratio of product moles to reactant moles is less than unity for air and oxygen cases.

Similar analyses were conducted for a variety of hydrocarbon n-alkane fuels and jet fuels. Ratios are displayed in Figure 25 for three hydrocarbon fuels. It must be noted that dissociation has a significant influence on $S_{e,3}$ and $S_{e,2}$ due to molar production. The $|\alpha - \alpha_{\text{major}}|$ term indicates the effect of dissociation. In a similar analysis for common jet fuel, the results were comparable to those of n-dodecane for combustion in air, as shown in Figure 26.

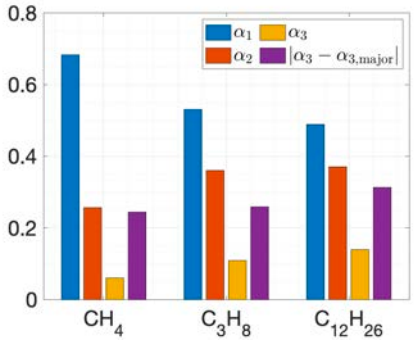

Figure 25. Flame-integrated ratios α_1, α_2, and α_3 and $\alpha_{3,\mathrm{major}}$ for three oxygen–fuel cases at $T_u = 500$ K, $\phi = 0.75$, and $p = 1$ atm.

Figure 26. Flame-integrated ratios α_1, α_2, and α_3 for jet fuel combustion at $T_u = 500$ K, $\phi = 0.75$, and $p = 1$ atm. ATJ: alternative jet fuel.

Based on the figures and analysis provided above, the exothermic heat release, $S_{e,1}$, is by far the dominant term in air-breathing systems. However, the combined influence of the $S_{e,2}$ and $S_{e,3}$ terms can sometimes exceed that of $S_{e,1}$ in pure oxygen systems. In turn, $S_{e,2}$ and $S_{e,3}$ are heavily influenced by dissociation. In other words, any effect that incites dissociation will tend to influence the contributions from $S_{e,2}$ and $S_{e,3}$ and, as a result, will reduce the relative contribution from $S_{e,1}$.

To understand the dependencies of α_1, α_2, and α_3 under different operating conditions and to study dissociation effects, results were compared over a range of pressures and adiabatic flame temperatures. Figure 27a shows the pressure dependencies of α_1, α_2, and α_3 for both methane–air and methane–oxygen mixtures, clearly showing that $S_{e,1}$ is dominant over $S_{e,2}$ and $S_{e,3}$ for methane–air combustion, but $S_{e,2}$ and $S_{e,3}$ are of much greater significance for the oxygen–fuel cases. An increase in pressure induces a monotonic increase in α_1, which can be attributed to suppressed dissociation at elevated pressures. Figure 27b shows the influence of adiabatic flame temperature (T_{ad}) on α_1. The flame temperatures were independently varied by varying the equivalence ratios ($0.45 < \phi < 0.7$) and preheat temperatures ($350 < T_u < 800$). The figure illustrates that increasing T_{ad} decreases α_1 as dissociation is promoted at higher flame temperatures. The results can be compared at an elevated pressure (which causes the flame temperature to also increase). We observed that the combined effect of increased exothermicity at higher flame temperatures and suppressed dissociation at elevated pressures increases α_1 but still with a declining trend for increasing flame temperatures. This result can be clearly discerned by comparing the triangle markers at $p = 15$ atm, which show a much greater α_1 than their circular counterparts at $p = 1$ atm.

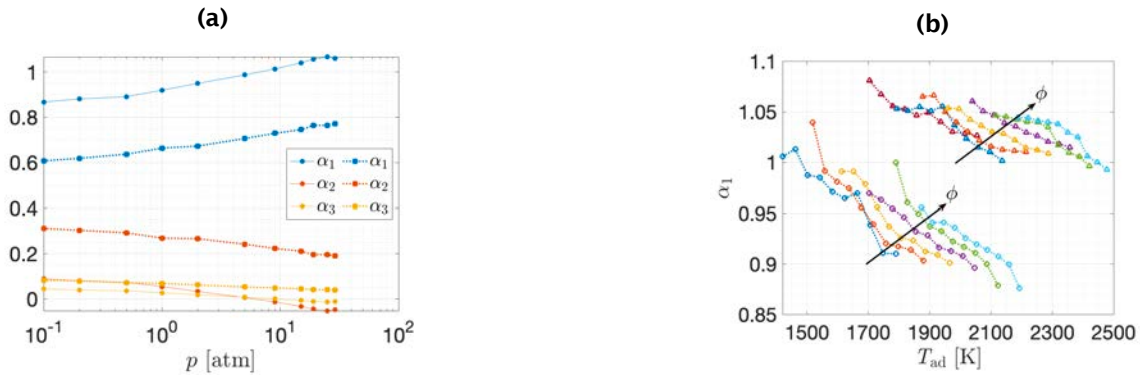

Figure 27. (a) Flame-integrated ratios α_1, α_2, and α_3 for methane–air (solid) and methane–oxygen (dotted) combustion as a function of pressure at T_u = 500 K and ϕ = 0.75. (b) Flame-integrated ratio α_1 for methane–air combustion as a function of adiabatic flame temperature and equivalence ratio at $p = 1$ atm (circles) and $p = 15$ atm (triangles).

Assuming that chemical heat release is the dominant source of entropy generation, retaining only the dominant heat release source for entropy transport results in the following:

$$\frac{D(\rho s)}{Dt} = \frac{\partial(\rho s)}{\partial t} + u\frac{\partial(\rho s)}{\partial x} = \frac{\dot{q}}{T} \tag{25}$$

$$\frac{d}{dt}\int_{V(t)}(\rho s)dV + \int_{A(t)}\rho s\left(u-u_s\right)\cdot\vec{n}dA = \int_{V(t)}\frac{\dot{q}}{T}dV \tag{26}$$

Many previous studies have assumed that the heat release primarily occurs at the burn temperature T_b. Another study was motivated by this assumption to investigate the distributed heat release effects implicitly assumed by the following approximation:

$$\int_{V(t)}\frac{\dot{q}}{T}dV \sim \frac{1}{T_b}\int_{V(t)}\dot{q}dV \tag{27}$$

The study aimed to quantify κ_b, defined as the ratio of the approximation shown in the above equation to the exact distributed heat release integral:

$$\kappa_b = \frac{\frac{1}{T_b}\int_{V(t)}\dot{q}dV}{\int_{V(t)}\frac{\dot{q}}{T}dV} \tag{28}$$

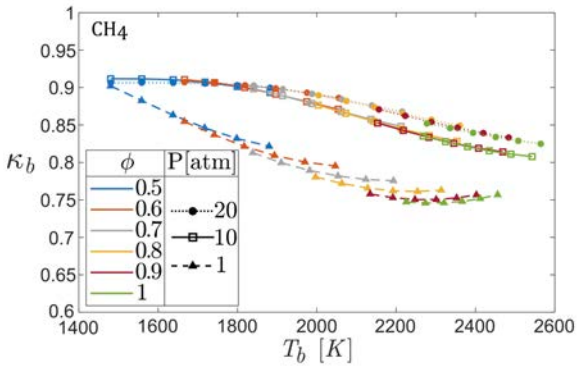

Figure 28. κ_b as a function of T_b for methane–air mixtures under various operating conditions.

For methane–air combustion, κ_b was computed for various equivalence ratios and pressures. For each pressure and equivalence ratio combination, the results were plotted against the calculated burn temperature. For this fuel–air mixture, steady-state calculations showed that κ_b ranged from 0.75 to 0.9, as shown in Figure 28. This result indicates that for these operating conditions, an error of less than 25% exists between the exact and approximate evaluations for entropy generation. Utilizing the valid assumption that heat release primarily occurs at T_b, the spatially integrated heat release divided by the adiabatic flame temperature will aid our analysis in estimating the flame-generated entropy, as discussed below.

Estimation of Flame-Generated Entropy

We have now established that for air-breathing systems under relevant operating conditions, the heat release is the major source term at the flame for entropy generation. In the previous report periods, we presented results for convectively compact flames. In this reporting period, we considered premixed and non-premixed flames perturbed by harmonic flow/mixture disturbances and compared the results for entropy fluctuations generated by these flames. We define an entropy transfer function, which is the ratio of a normalized entropy fluctuation and the normalized excitation amplitude:

$$\Im_s = \left(\hat{s}_1/\tilde{S}\right)\Big/\left(\hat{F}_1/F_0\right) \tag{29}$$

Here, $\tilde{S} = \dot{Q}_0/\rho T_b R u_{x,0}$, and $\hat{F}_1/F_0$ is the excitation amplitude normalized by its mean value. For most practical configurations, flames are convectively non-compact for a broad range of frequencies of interest; thus, these non-compactness (or, equivalently, phase cancellation) effects are significant and profound. While general results can be developed independent of flame geometry/configuration in the convectively compact case, the problem is configuration-dependent in general. We consider two model problems for premixed and non-premixed flames.

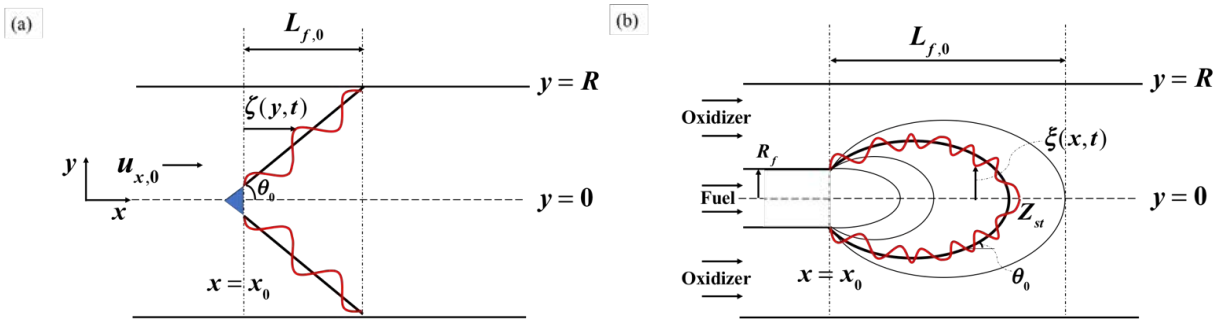

Figure 29. Schematic of (a) premixed and (b) non-premixed flame configurations.

We consider premixed (Figure 29a) and non-premixed (Figure 29b) flame configurations in this analysis. An explicit expression for the heat release rate fluctuations of a premixed and non-premixed flame can be derived. In the response to velocity fluctuations, calculations show that entropy fluctuations are not generated by a premixed flame. Note that this zero-response result also holds if the results are generalized to include the flame stretch sensitivity, which leads to burning rate fluctuations for reasons discussed later. For the non-premixed flame configuration, in the high Peclet limit, we obtain the same result, showing that velocity-driven flames may have a flame response but not an overall entropy response.

In the presence of equivalence ratio fluctuations ($\phi_1 = \varepsilon\phi_0 e^{i\omega x/u_{x,0}} e^{-i\omega t}$), the solution for entropy fluctuations from a premixed flame is given by the following:

$$\hat{s}_1 = \left(\frac{h_{R,1}}{h_{R,0}} - \frac{T_{b,1}}{T_{b,0}}\right)\frac{h_{R,0}}{T_{b,0}} e^{\frac{i\omega L_{f,0}}{u_{x,0}}} \tag{30}$$

Note that there is no term involving $S_{L,1}$, implying that flame stretch effects, which introduce flame speed fluctuations, do not contribute to the generation of entropy fluctuations. Further, we can relate the burn temperature to the heat release as follows:

$$T_b = T_u + \frac{\min(1,\phi) f_s H}{(1+\phi f_s)\bar{c}_p} \tag{31}$$

Here, ϕ is the equivalence ratio, $f_s = \left(m_f / m_{ox}\right)_{st}$ is the stoichiometric fuel–air ratio, and H is the heat released per kilogram of fuel. We can express h_R as follows:

$$h_R = \frac{\min(1,\phi) f_s H}{1 + \phi f_s} \tag{32}$$

From the above expressions, with the assumption of constant $\bar{c}_p$, perturbations in h_R and T_b can be related as follows:

$$T_{b,1} = \frac{h_{R,1}}{\bar{c}_p} \tag{33}$$

Thus, Eq. **Error! Reference source not found.** takes on the following form:

$$\hat{s}_1 = \frac{h_{R,1}}{h_{R,0}} \bar{c}_p \left(1 - \frac{T_{u,0}}{T_{b,0}}\right) \frac{T_{u,0}}{T_{b,0}} e^{\frac{i\omega L_{f,0}}{u_{x,0}}} \tag{34}$$

Then, the entropy transfer function defined as $\Im_s = \left(\hat{s}_1 / \tilde{S}\right) \Big/ \left(\hat{\phi}_1 / \phi_0\right)$, where $\tilde{S} = h_{R,0} / T_{b,0}$, is given by the following:

$$\Im_s = \frac{\partial\left(h_R / h_{R,0}\right)}{\partial\left(\phi / \phi_0\right)} \frac{T_{u,0}}{T_{b,0}} e^{\frac{i\omega L_{f,0}}{u_{x,0}}} \tag{35}$$

It is clear from the above solution that the magnitude of the entropy transfer function is independent of the Strouhal number, although the magnitude is a function of the equivalence ratio ϕ_0. This result changes when the equivalence ratio fluctuations convect at a speed different from the mean flow speed; an investigation of this scenario is ongoing. Figure 30 presents an example calculation that shows the dependence of the magnitude of the entropy transfer function on the mean equivalence ratio for a methane–air flame at standard temperature and pressure. Note that the $\frac{\partial\left(h_R / h_{R,0}\right)}{\partial\left(\phi / \phi_0\right)}$ term obtained from the empirical model has a discontinuity at $\phi_0 = 1$, which is reflected in $\left|\Im_s\right|$ at $\phi_0 = 1$. Further, it is evident from Eq. (35) that the phase varies linearly with flame Strouhal number, which is a feature of a convecting disturbance. The solutions obtained for the premixed flame indicate that the MBR fluctuations do not contribute to the generation of entropy fluctuations. Only h_R and T_b fluctuations, which occur via equivalence ratio fluctuations, contribute to the generation of entropy fluctuations.

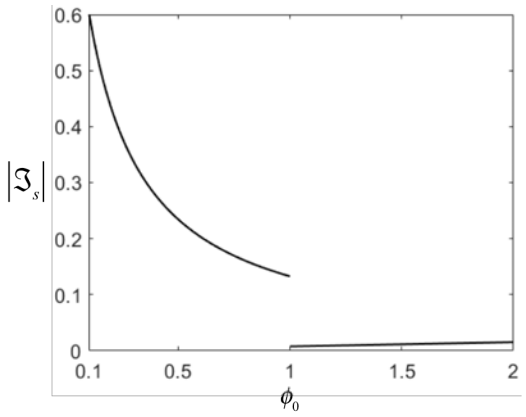

Figure 30. Magnitude of entropy fluctuations generated as a function of the mean equivalence ratio.

For non-premixed flames perturbed with inlet mass fraction fluctuations, the entropy fluctuations are as follows:

$$\bar{\hat{s}}_1 = \frac{e^{i\omega L_{f,0}/u_{x,0}}}{\rho T_{b,0} R u_{x,0}} \left(\int_0^{L_{f,0}} \left(\hat{q}_1 - \frac{\hat{T}_{b,1}}{T_{b,0}} \dot{q}_0 \right) e^{-\frac{i\omega x}{u_{x,0}}} dx \right) \tag{36}$$

When fuel and oxidizer mass fractions at the inlet are perturbed harmonically ($Y_{f,i} = Y_{f,i,0} + \hat{Y}_{f,i} e^{-i\omega t}$, $Y_{ox,i} = Y_{ox,i,0} + \hat{Y}_{ox,i} e^{-i\omega t}$), the solutions for the non-premixed problem can be derived. To analyze the response to fuel mass fraction fluctuations at the inlet ($\hat{Y}_{f,i,1} = \varepsilon Y_{f,i,0} e^{-i\omega t}$) in the absence of oxidizer mass fraction fluctuations, we can normalize the entropy generated to define the entropy transfer function. Because the mass fraction can be related to the equivalence ratio as $\phi = 1/f_s\left(Y_{f,i}/Y_{ox,i}\right)$, we have $\phi_1/\phi_0 = Y_{f,i,1}/Y_{f,i,0}$.

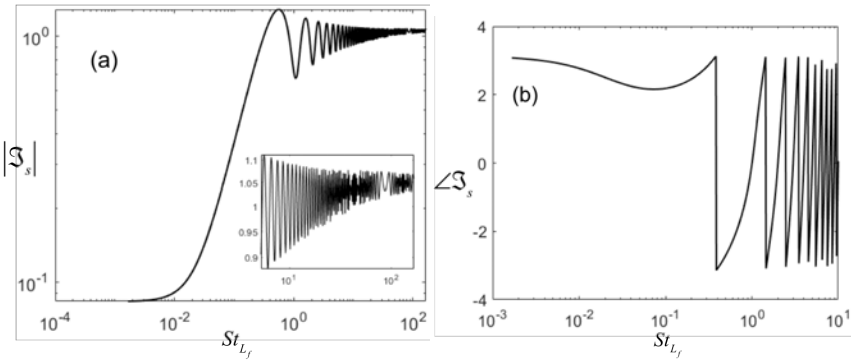

Figure 31. Strouhal number dependence of the (a) magnitude and (b) phase of the entropy transfer function for a non-premixed flame forced by fuel mass fraction fluctuations at $Pe = 50$.

Figure 31 represents the Strouhal number ($St_{L_f} = fL_{f,0}/u_{x,0}$) dependence of the magnitude and phase of the entropy transfer function ($\Im_s = \left(\hat{s}_1/\tilde{S}\right)/\left(\hat{\phi}_1/\phi_0\right)$) for a non-premixed flame perturbed by fuel mass fraction fluctuations at the inlet. We can see that the magnitude of the entropy transfer function increases with increasing frequency. This result demonstrates that mass fraction fluctuations generate significant entropy fluctuations for a non-premixed flame, especially for large Strouhal numbers. Note that the transfer function asymptotes to unity for large Strouhal numbers (see inset plot). The phase has a monotonic variation with increasing Strouhal number, which can be primarily attributed to the convection of disturbances. The results show that mixture fluctuations generate significant entropy fluctuations for premixed and non-premixed flames. Unlike velocity perturbations, mixture perturbations cause changes in the burn temperature, which lead to the generation of entropy fluctuations.

Milestones

- Illustrated how spray parameters affect the global flame response
- Confirmed that entropy generation by heat release is dominant for jet fuel combustion in premixed flames
- Demonstrated that results for entropy generation in convectively non-compact premixed and non-premixed flames showing velocity fluctuations do not lead to net entropy disturbances, but mixture perturbations result in non-zero net entropy disturbances
- Developed a bi-global hydrodynamic stability framework to study the global mode response of swirling flows to external boundary forcing
- Validated the framework by conducting a natural, or unforced, hydrodynamics study and comparing the results with published data

Major Accomplishments

The spray flame response framework was used to determine the local mixture fraction solutions, which were used to assess the global flame response. The effects of spray parameters were illustrated using an example configuration.

A framework for a low-order hydrodynamics tool that can predict flow responses in the presence of acoustic excitations has been proposed. This tool was successfully validated by performing a natural, or unforced, hydrodynamics study in COMSOL. A comparison of the study results with published historical data showed that the model can correctly predict growth rates

of unstable modes as a function of natural oscillatory frequencies. With the current validation process complete, the model can now be extended to simulate the effects of external boundary forcing.

The entropy dynamics study addressed the assumption of high-activation energy limits by analyzing the deviation of entropy from the actual entropy when using this assumption. The entropy generation from two model flame geometries for premixed and non-premixed flames showed that velocity fluctuations are not important, but mixture fluctuations are significant.

Publications

Published conference proceedings

Acharya, V. S. (2022, January 3). Global dynamics of the velocity-coupled response of spray flames. *AIAA SCITECH 2022 Forum*. AIAA SCITECH 2022 Forum, San Diego, CA & Virtual. https://doi.org/10.2514/6.2022-1856

John, T., Acharya, V., Lieuwen, T. (2022, March). Entropy transfer functions of externally forced flames. *2022 Spring Technical Meeting of the Eastern States Section of the Combustion Institute*.

Patki, P., Acharya, V., & Lieuwen, T. (2022). Entropy generation mechanisms from exothermic chemical reactions in laminar, premixed flames. *Proceedings of the Combustion Institute*, S1540748922003455. https://doi.org/10.1016/j.proci.2022.08.069

Laksana, A., Patki, P., John, T., Acharya, V., & Lieuwen, T. (2023). *Distributed Heat Release Effects on Entropy Generation by Premixed, Laminar Flames.* Under review for International Journal of Spray and Combustion Dynamics.

Outreach Efforts

None.

Awards

None.

Student Involvement

- Graduate student Parth Patki has been involved in investigating the entropy budget of the entropy dynamics equation to determine the dominant source terms for entropy disturbances.
- Graduate student Akbar Laksana explored the entropy source term approximations under high-activation energy limits and the deviations that occur when these limits are not satisfied.
- Graduate student Tony John has been involved in modeling the generation of entropy disturbances due to a heat release source term.
- Undergraduate student Michael Wise was mentored by Tony John and Vishal Acharya in studying the entropy generation from example premixed and non-premixed flames.

Plans for Next Period

In the next year, the hydrodynamics ROM component will be extended to further study the pre-combustion flow disturbances. Utilizing the validated model for the unforced, or natural, hydrodynamics study, we will extend the bi-global framework discussed above to study the flow response to external boundary forcing in the upcoming year. We will supplement the GT time-averaged LES data by post-processing it in this task and employing a multi-inflow, axisymmetric geometry. The time-averaged velocity fields will serve as the base state for our stability calculations, and the ROM will be trained to predict the leading-order coherent dynamics of the flow field. The obtained hydrodynamic eigenmode solutions will be validated based on instantaneous flow field data from LESs and/or experiments. The velocity model generated from this analysis feeds directly into the flame response model.

The spray flame response framework will be expanded to consider spray dynamics effects, droplet dynamics, and multiple injection sites. The entropy dynamics framework will consider molecular transport effects as source terms in addition to heat release for the non-premixed flame cases, which will be expanded to include spray flame cases.

The model for entropy generation at the flame will be combined with the validated flame response model to generate source entropy disturbances, which are then input into the entropy wave transport subtask by RTRC. The predictions from the RTRC model at the nozzle will be validated against measured temperature fluctuations. This work will provide iterative feedback to improvements in both the GT entropy source model and the RTRC entropy wave transport model.

Task 4 - Facility Development at RTRC

Raytheon Technologies Research Center

Objective

The objective of this task is to design an RQL combustor that closely mirrors the GT design, with a specific focus on the higher-pressure operating points that are not possible for the GT rig. Collectively, the GT and RTRC rig capabilities will encompass a broad range of operating conditions, resulting in a robust dataset for training the design tools.

Research Approach

During the current reporting period, a second test entry was conducted. Due to facility schedule constraints, reinstallation of the ASCENT rig on the HTHP centerline was not possible. Instead, testing was performed with an FAA CLEEN combustor rig that was already installed on the centerline. The ASCENT and CLEEN rigs are shown in Figure 32. There are three main differences between these two rigs: (a) The CLEEN rig has a longer distance from the bulkhead to the choke, (b) The CLEEN rig includes air-cooled liners (resulting in a more realistic aero-combustor), and (c) The CLEEN rig incorporates a variable-length side branch system for studying thermo-acoustic instability. The latter difference was undesirable; thus, a water-cooled blanking flange was design, fabricated, and installed to address the side-branch length and eliminate leaking around the plunger (which introduced undesirable low-frequency modes).

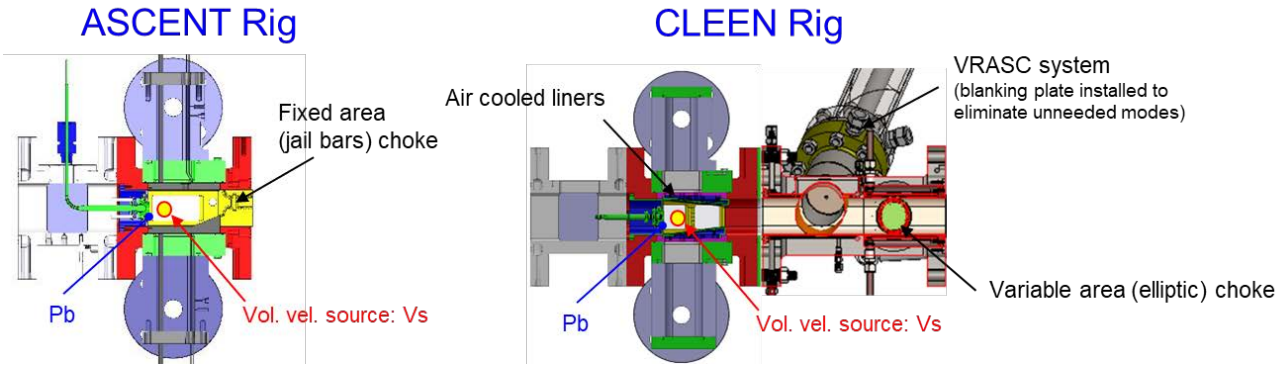

Figure 32. Comparison of ASCENT and CLEEN combustors. VRASC: variable-length side branch.

Figure 33 (left plot) shows the effect of difference #1 (longer distance) in terms of the acoustic response in the test section, which causes the quarter-wave (and higher) modes to shift into the frequency band of interest. The associated pressure node (lower response near 300 Hz) causes a dip in the dynamic pressure spectra (right plot). Because this dip is in the middle of the band of interest for combustion noise (where the typical peak is located), a correction is needed to enable, for example, assessments of legacy acoustic power scaling laws. Such corrections have been successfully developed at RTRC based on a finite-element acoustic model (matched to pressure ratio data) to provide an accurate acoustic response function to normalize the spectra (i.e., remove the mode from the spectra). This finite-element model is currently being tuned to match pressure ratio data.

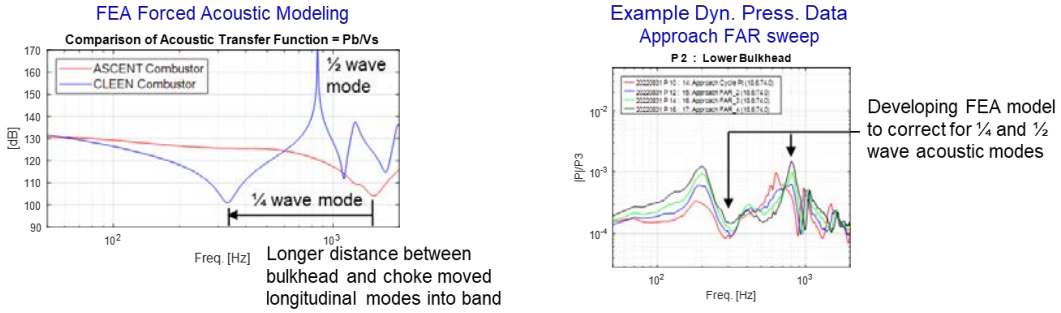

Figure 33. Acoustic response difference between the CLEEN and ASCENT combustors and example dynamic pressure spectra from the CLEEN combustor. FEA: finite-element analysis.

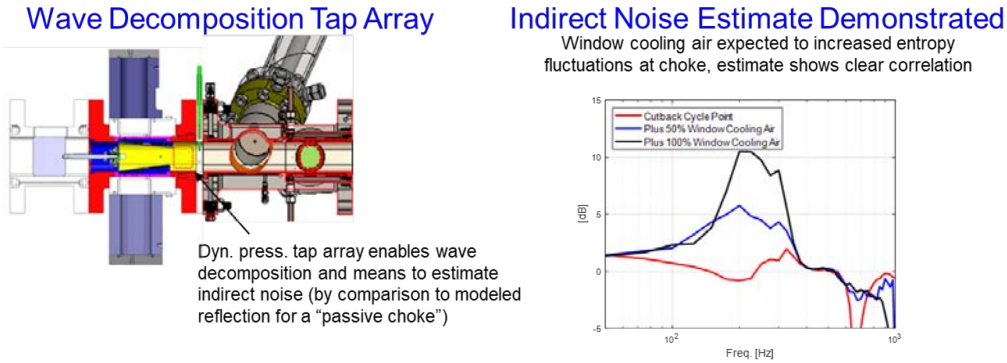

Figure 34. Dynamic pressure tap array for wave decomposition and indirect noise estimation.

Similar to the ASCENT rig, an array of four dynamic pressure taps was added to the side wall in a constant-area solid wall portion, as shown in Figure 34 (left image). The data record from this array can been processed to compute the downstream and upstream propagating waves. By comparing the computed upstream propagating wave to that computed for a "passive choke" (i.e., a choke that does not generate indirect noise) from a linearized potential solver (to account for flow acceleration), the indirect noise can be estimated. This indirect noise estimation is demonstrated in Figure 34 (right plot) for a variation in window cooling air flow rate from a nominal level to twice the nominal cooling flow. It is expected that as the cooling air increases, the indirect noise level will also increase (due to an increased level of cold spots convecting through the choke). As shown in the figure, the computed indirect noise is consistent with this expectation. Together with the temperature fluctuations to be measured in 2023 in this CLEEN combustor, these indirect noise estimates should be useful for validating a ROM of indirect noise.

Milestones

- A second RTRC experiment entry was successfully completed.
- Preliminary data from the second entry were analyzed.

Major Accomplishments

As with the previous test program (with the ASCENT combustor), extensive diagnostic measurements were obtained for four operating conditions of interest in the CLEEN rig: idle acceleration, approach, cutback, and sideline. The latter three represent conditions that are part of engine noise certification. For each operating condition, variations in the combustion parameters of FAR, inlet pressure (P_3), inlet temperature (T_3), and mass flow (i.e., flow parameter, FP_b), were evaluated, giving a total of 13 separate operating points for characterizing the effect of these parameters on combustion noise. Diagnostic data consisted of dynamic pressures at eight locations and chemiluminescence high-speed imaging (as a surrogate for the unsteady heat release field).

Publications
None.

Outreach Efforts
None.

Awards
None.

Student Involvement
None.

Plans for Next Period
During the next reporting period, extensive comparisons between the ASCENT and CLEEN combustor results will be conducted. In addition to legacy acoustic pressure scaling law assessments, direct noise (via chemiluminescence), indirect noise (via wave decomposition), and flow structure identification (via a two-point chemiluminescence correlation method) will be quantified and compared. This effort is expected to help guide the toolchain approach and validation.

Task 5 - Post-Combustion Modeling
Raytheon Technologies Research Center

Objective
The objective of this task is to develop transfer functions from the combustion zone to the nozzle, nozzle to turbine, and turbine to far-field. This task involves physics modeling of the following aspects:

- Entropy wave transport post-combustion, as unsteady heat release rate disturbances at the flame generate entropy disturbances that are then transported through the post-combustion zone
- Nozzle interactions for the dynamics of pressure disturbances through the nozzle, specifically the effect of the jail bar configuration used in both the GT and RTRC rigs
- Turbine interactions for the dynamics of pressure disturbances through the turbine
- Far-field sound propagation

Direct noise modeling will also be performed using a numerical Green's function approach with the heat release model.

Research Approach
The post-combustion-zone physics involves the effects of combustion unsteady heat release rate disturbances and post-combustion geometry on the eventual noise generation outside the engine. This modeling involves the following:

- The direct generation of combustion noise due to heat release and the interaction of these pressure disturbances with the remainder of the engine geometry, which leads to far-field noise
- Entropy disturbances generated by the flame interacting with geometric changes at the nozzle and causing pressure disturbances that then interact with the remainder of the engine geometry and lead to far-field noise

Entropy Transport Modeling
The results from the GT LESs are being studied to elucidate the entropy generation within the combustor and its transport to the combustor exit via the jail bars. Figure 35a shows the distribution of entropy perturbation within the combustor. Entropy perturbations are generated near the mixing region of the flame and the window cooling flows. There is also significant entropy perturbation in the mixing region of the dilution jets. Figure 35b shows the two-point cross-correlation of entropy perturbation between all points in the combustor with a point just upstream of the choke (shown by white dot) for a single time point. The entropy perturbation near the exit correlates well with regions associated with the window cooling flow as well as near the dilution jets. This trend suggests that the mixing of dilution jets plays a role in generating the indirect noise that exits the combustor.

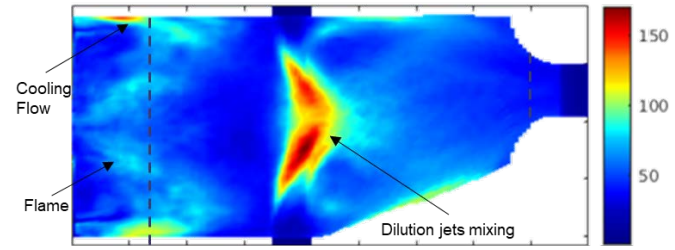

a) RMS of mass-averaged entropy perturbation

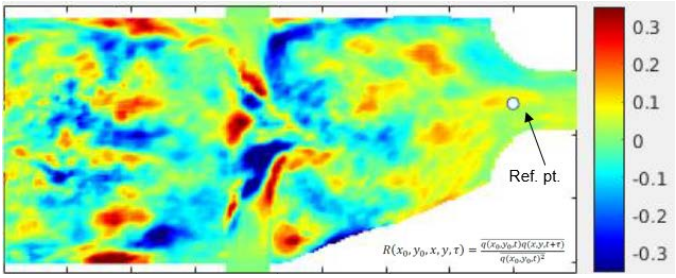

b) Two-point correlation of mass-averaged entropy with a location near the choke

Figure 35. Root mean square (RMS) of mass-averaged entropy perturbation within the combustor and two-point correlation.

The entropy transport within the combustor can be considered as a scalar transport phenomenon. The mean advection time of a scalar can be estimated from the flow streamlines, and the entropy transport can then be represented as a transfer function. The mean flow from the LES results was used to seed streamlines starting near the flame and near the top and bottom dilution jets (Figure 36a). The streamlines were seeded along a regular grid to enable the computation of the mass flow rate and convection along each stream tube. The transfer function of the entropy from the seeding location to the choke can then calculated using the equation shown in Figure 36b, which is plotted in the figure. The inputs to these transfer functions will be entropy perturbations generated at these source locations. The results suggest that the entropy convection is substantial up to a frequency of approximately 1000 Hz; beyond this point, the amplitudes decrease. Moreover, the transfer function from the dilution jets to the choke is equal to or larger in magnitude than the flame-to-choke transfer function.

Figure 36b also presents the two-point correlation between the entropy at the flame and choke obtained from the equation shown in Figure 36b. The two-point correlation obtained using the instantaneous LES time histories matches well with the transfer function calculated from the mean flow streamlines. This result is useful because it suggests that the entropy transfer function can be estimated using a Reynolds averaged Navier–Stokes computation, which can be many orders of magnitude faster than a full LES computation.

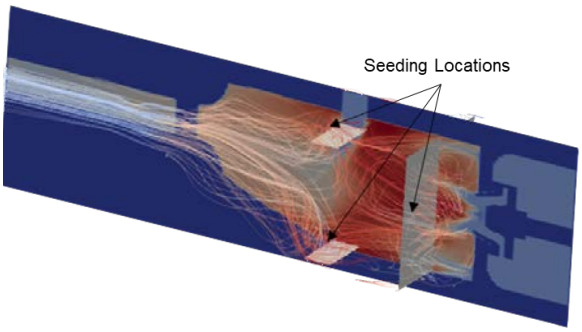

a) Seeding location for streamlines

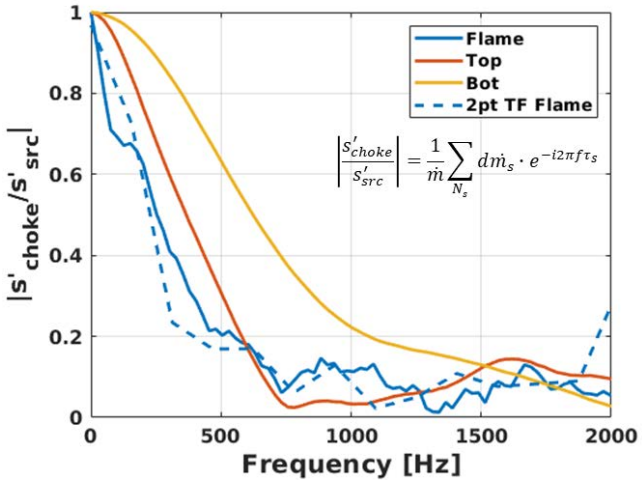

b) Entropy transfer function from the different source locations to the choke

Figure 36. Streamlines within the combustor and associated transfer functions (TFs).

Direct Noise Modeling

Direct noise modeling is performed using a numerical Green's function approach, which uses an appropriate Green's function in conjunction with either a measured or simulated/modeled unsteady heat release rate disturbance field, in order to calculate the pressure disturbance at a particular location in the combustor. While this modeling was not performed during the current reporting period, a prior workflow established by RTRC under a NASA program has been reviewed and will be leveraged for this work. This work was summarized under Task 4.

Nozzle Interaction Modeling

The goal of this task is to establish and improve a ROM for the transmission and/or generation of direct and indirect combustion noise through a nozzle or geometrical representative of the first set of turbine vanes. Within this context, simulation work on the RTRC combustor jail bar rig continued from last year. The updated computational model is shown in Figure 37. The model does not include any reacting flows; this model focuses only on matching the flow conditions of the as-tested points without combustion processes and then applying temperature forcing at the inlet to study indirect noise generation. To better represent the test rig setup, a high-fidelity lattice Boltzmann method (LBM) simulation domain was extended to incorporate more features of the test rig, compared with the efforts described in the last annual report. In particular, the dump plenum downstream of the jail bars was extended, and the numerical sponge zone damping was adjusted to further reduce reflections occurring at the domain outlet. In addition, the inlet boundary conditions were changed from total pressure conditions to static pressure and velocity conditions. This change was found to reduce reflections from the inlet.

Entropy wave forcing was achieved through time-harmonic temperature variations introduced at the domain inlet. These temperature disturbances convect with the mean flow and generate acoustic waves propagating upstream and downstream when the entropy wave passes through the accelerated flow between the jail bars, as shown in Figure 38 for a forcing frequency of 600 Hz. These simulations provide insight into the process of indirect noise generation from entropy (temperature) disturbances. The simulation results were compared with compact nozzle theory (CNT), which predicts an acoustic response that is independent of the forcing frequency. As shown in Figure 39, the simulations indicate that there is some sensitivity to spatial location in the LBM simulations, but the overall averaged transfer function across the combustion chamber is very similar to but slightly lower than the CNT prediction. The simulations were repeated for different forcing frequencies. The transfer functions from the LBM vary with frequency, while the CNT predicts a transfer function that is independent of frequency. Overall, the predicted transfer functions obtained from the CNT and LBM were found to be of the same order of magnitude. A similar type of analysis was performed for the downstream propagating acoustic waves. Comparisons with CNT results are ongoing and will be used to further assess the suitability of the CNT to accurately predict the indirect noise wave conversion process.

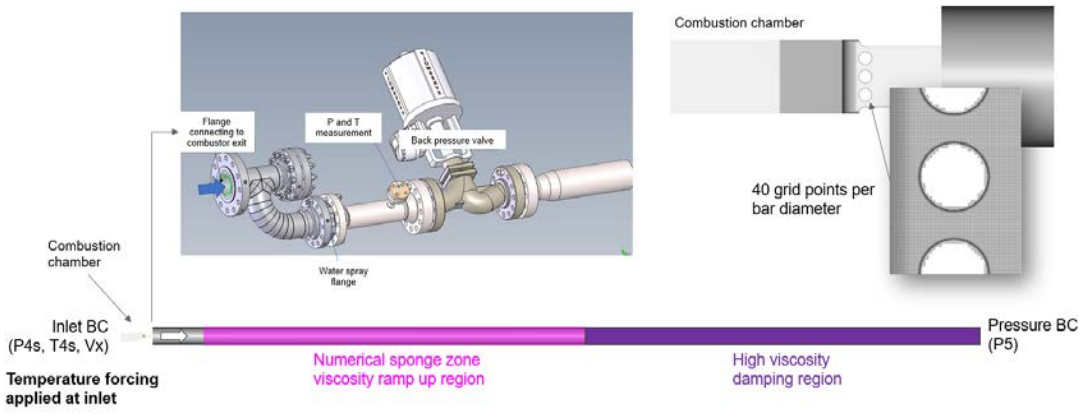

Figure 37. Extended computational domain for RTRC jail bar rig acoustic simulations.

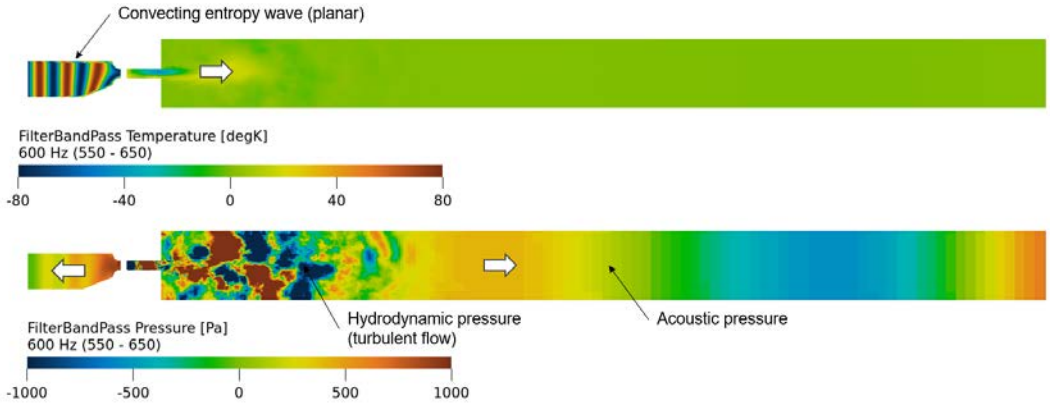

Figure 38. Entropy plane wave harmonic forcing with f = 600 Hz and resulting acoustic pressure waves propagating upstream and downstream, when the entropy wave interacts with the jail bar choke.

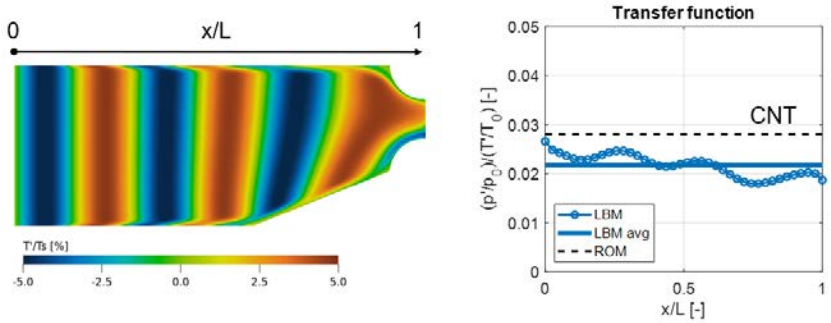

Figure 39. Transfer function predicted by the lattice Boltzmann method (LBM) for the conversion of an entropy plane wave to an upstream propagating acoustic pressure wave, compared with the reduced-order model (ROM) based on the compact nozzle theory (CNT).

Turbine Interaction Modeling

This task focuses on simulations of a high-pressure public domain turbine rig from the Polytechnic University of Milan and the German Aerospace Center to investigate direct and indirect noise propagation through a representative high-pressure turbine stage. A comprehensive set of high-fidelity LBM simulations (Figure 40) was performed in Year 1 for high-subsonic and transonic turbine flow conditions and was successfully validated against experimental data from the German Aerospace Center.

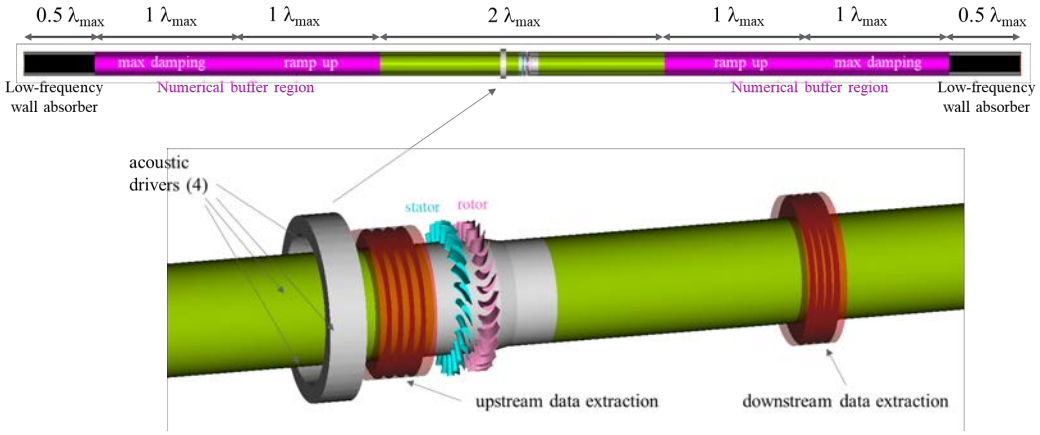

Figure 40. Simulation domain with virtual acoustic drivers for studying direct noise propagation through the turbine stage.

The sound power reflection coefficient and transmission coefficient agreed well between simulation and experiment. The remaining portion of the sound power (1-R-T, where R is the reflection and T is the transmission), which is neither reflected nor transmitted, was found to be approximately 60% of the total sound power, as shown in Figure 41. It was hypothesized that this portion of the power is related to sound dissipation caused by the conversion of acoustic energy into shed vorticity from the blade and vane trailing edges and other sharp geometrical features. A comparison to actuator disk theory (ADT) showed that the theory overpredicted the transmitted sound, as it does not account for such sound dissipation effects.

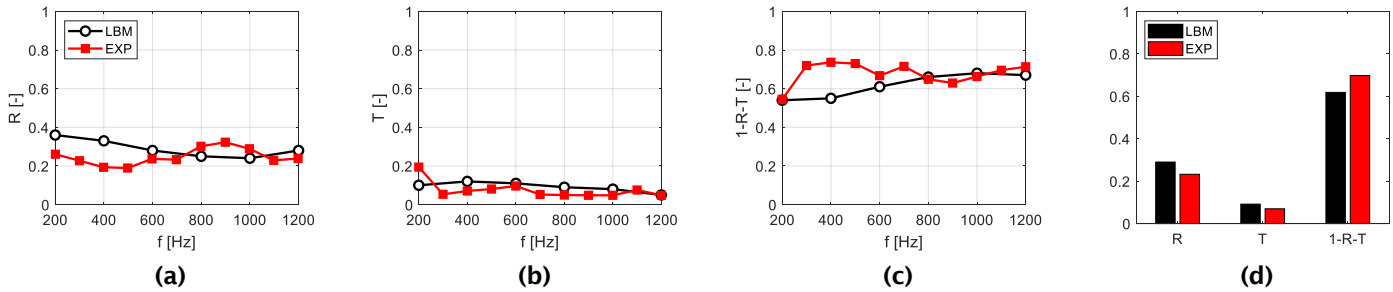

Figure 41. Sound power coefficients from lattice Boltzmann method (LBM) simulations and experiments (EXP) for the high-subsonic flow condition. (a) Reflection (R), (b) transmission (T), (c) unaccounted portion (1-R-T), and (d) frequency-averaged values.

To confirm that the sound is indeed dissipated by physical processes rather than representing simulation artifacts, a canonical simulation case was created, replacing the turbine stage with a thin slotted disk (Figure 42). An analytical model by Dowling & Hughes (1992) exists for this case, which predicts sound dissipation due to flow through the sharp-edge slots. This model was used and compared with the high-fidelity LBM simulations to demonstrate that a large amount of predicted dissipation in LBM is due to the physical process of converting acoustic energy into vortical motion. The slotted open area was chosen to match the minimum area of flow through the turbine stator. The simulations compared well with the analytical model for sound reflection over a wide Mach number range, as shown in Figure 43. The predicted sound dissipation was found to be in reasonable agreement, with the analytical model predicting slightly higher values. Overall, both the simulations and model predicted sound power dissipation at approximately 40% for the mean flow Mach numbers of interest.

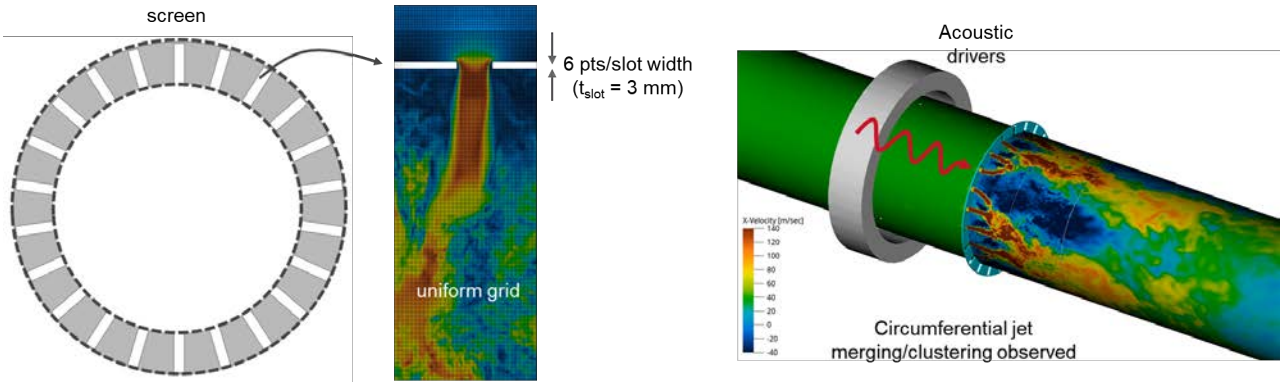

Figure 42. Simulation of acoustic dissipation, where the turbine is replaced by a thin screen with rectangular openings.

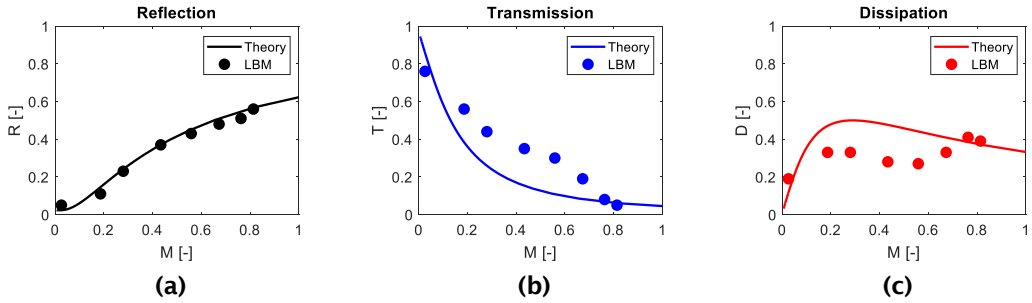

Figure 43. Sound power coefficients for sound through a slotted disk with mean flow: lattice Boltzmann method (LBM) simulations compared with the analytical solution of Dowling & Hughes. (a) Reflection (R), (b) transmission (T), (c) dissipation (D). M: Mach number.

These types of simulations were repeated with the turbine instead of the slotted disk, and the results are shown in Figure 44. Overall, the guide vanes (stator) dissipate more sound than the slotted disk for the same mean flow Mach number. The dissipated sound is slightly higher for the complete turbine stage (stator–rotor), but the trends are similar to those of the stator-alone simulations. This study helped substantiate the physical mechanisms responsible for sound dissipation in the turbine stage. This effort provides useful information for improving ADT to account for loss mechanisms and to eventually improve the predictive capability for combustion noise propagation through a turbine stage and into the far-field. Work on this ROM improvement started during this report period.

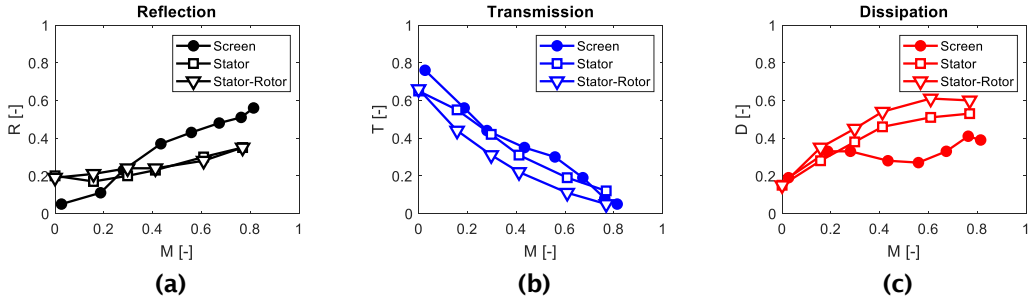

Figure 44. Sound power coefficients from lattice Boltzmann method simulations for sound passing through a slotted disk, turbine guide vane (stator), and turbine stage (stator–rotor), with mean flow. D: dissipation; M: Mach number; R: reflection; T: transmission.

Far-Field Noise Modeling

The far-field propagation modeling toolchain based on ACTRAN/DGM was developed during the last reporting period. However, some follow-up research activities were performed during the current reporting period. One such effort was a closer examination of the broadband combustion noise directivities calculated by the model toolchain. The findings from this study have been published as a conference paper. One notable aspect of this study was the comparison of the model-predicted combustion noise directivities with those of the corresponding core noise separated from engine test data obtained during the execution of the Pratt & Whitney FAA CLEEN I program. Figure 45 shows the results obtained for the sideline certification condition.

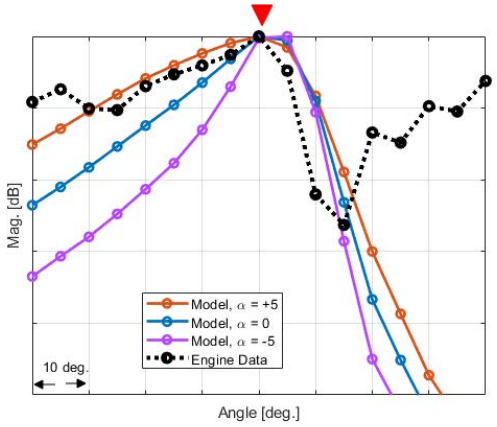

Figure 45. Comparison of model-predicted overall directivity and engine test data for the sideline condition.

Figure 45 shows multiple model-predicted directivities for a range of parameter α. This parameter, α, changes the source mode distribution by skewing the magnitude either toward higher-order modes with $\alpha > 0$ or toward lower-order modes with $\alpha < 0$. $\alpha = 0$ implies that all modes have equal magnitudes. Overall, the model-predicted results capture the measured peak noise directivity angles reasonably well. Moreover, the shape of the directivity is reasonably well captured around the peak, including the steeper magnitude roll-off toward higher angles. The model and the data diverge at off-peak angles, especially toward high angles, but this trend might be due to extraneous noise components in the data that were not completely removed by the source separation method. This finding points to a need for improved experimental noise separation techniques for identifying combustion noise components in engine tests, which is a challenge by itself due to the presence of extraneous noise sources.

Another activity that started during this period was the development of a generic far-field model that can be more easily adapted to a wide range of engines with different geometries and flow conditions. Because the current far-field propagation model uses a specific engine geometry, a new finite-element mesh model must be created in order to analyze multiple different engines. Furthermore, the mean flow fields must be analyzed by re-running the CFD for different engine conditions. The goal of this new effort is to create a more widely applicable far-field propagation model that also includes essential geometry and flow conditions as parameters that can be easily changed. Figure 46 shows a conceptual schematic of the parameterized far-field combustion noise propagation model.

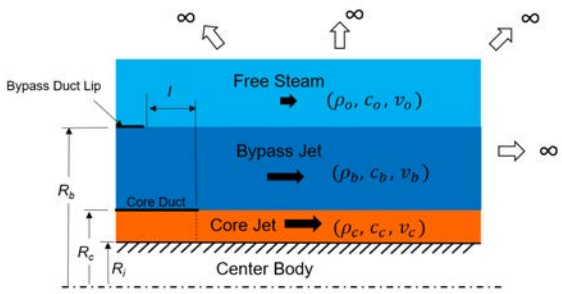

Figure 46. Conceptual schematic of a reduced-order parametric far-field combustion noise propagation model with flow conditions and geometrical parameters.

As shown in Figure 46, this model incorporates some simplifications to the aft engine geometries and the mean flow field. The mean flow field is assumed to be separated into three distinct constant flow regions, where each region is characterized by three constants (ρ, c, v), namely, the density, speed of sound, and flow velocity. The engine exhaust geometry has also been simplified such that it can be characterized by a couple geometrical parameters. This aft engine ROM concept has been devised by referencing a similar analytical model by Habard and Astley but adapted to use ACTRAN, which is our primary acoustic propagation modeling tool. The development of this parametric far-field ROM is currently ongoing.

Milestones

- Entropy wave transport: The GT LES data have been interrogated to obtain a transfer function of the entropy from the generation location (flame and dilution jets) to the choke.
- Nozzle interactions: Entropy–acoustic wave conversion in the RTRC combustor has been demonstrated and compared with the nozzle ROM.
- Turbine interactions: Simulations and comparisons with analytical models confirmed that a large amount of sound power is dissipated in the turbine stage by means of vorticity generation.

Major Accomplishments

For the entropy wave transport modeling effort, a workflow has been established to obtain LES flow data and two-point correlations as well as a transfer function based on mean streamlines for entropy transport. The analysis shows that the entropy transport to the combustor exit, and hence the indirect noise, may depend not only on the flame but also on entropy perturbations near the dilution jet and, to a smaller extent, the window cooling flow. The two-point correlation based on instantaneous LES data compares well with the mean-flow-based transfer function estimate, suggesting that this calculation can be performed via Reynolds averaged Navier–Stokes simulations for future combustor designs.

For the nozzle interaction task, the RTRC jail bar rig was simulated by high-fidelity LBM simulations with a refined domain size, grid resolution, and boundary conditions. The simulations visualized and quantified the entropy–acoustic wave conversion process in the combustor rig when entropy waves interact with the jail bar choke. Simulation results were compared with CNT results.

For the turbine interaction task, high-fidelity LBM simulations successfully demonstrated that a large amount of sound power is dissipated in the turbine stage, which is not predicted by the ADT ROM. This discrepancy presents an opportunity to refine the ROM in the future.

For the far-field propagation task, a more careful assessment of the model-predicted combustion noise directivities has been conducted, including a comparison with available engine data. The results have been summarized and published as a conference paper.

Publications

Homma, K., Reimann, A., Winkler, J., & Mendoza, J. (2022, June 14). Caa prediction of turbofan engine combustion noise directivity. *28th AIAA/CEAS Aeroacoustics 2022 Conference*. 28th AIAA/CEAS Aeroacoustics 2022 Conference, Southampton, UK. https://doi.org/10.2514/6.2022-2975

Outreach Efforts
None.

Awards
None.

Student Involvement
None.

Plans for Next Period
The LES flow field from GT will be further interrogated to obtain direct noise estimates. An approach based on proper orthogonal decomposition is currently being evaluated for the purpose of separating the important effects within the combustor that contribute to direct and indirect noise.

For the nozzle interaction task, the team will further evaluate and refine the tools and processes developed for the RTRC rig and will then apply them to the GT rig for further validation and cross-comparison.

For the turbine interaction task, the team will continue to improve the ADT to account for acoustic dissipation effects and then perform parametric studies to investigate different source types of turbine–wave interaction. This effort includes spinning wave modes and higher-order modes entering the turbine stage and different turbine designs. The results will be compared to the ADT, in order to evaluate this theory against a more diverse set of source types. Additionally, we will apply the improved ROM to a multi-stage turbine design with parameter variations to provide insight into the effects of realistic turbine design features on expected sound transmission behavior.

For the far-field noise propagation task, the team will focus on completing additional comparisons of the transfer function-based far-field ROM to the FAA CLEEN I far-field engine data. In addition, the team will continue working on the ROM as part of the integration effort for the overall combustion noise model framework that can be used to compute the propagation of combustion noise from the combustor to the far-field.

References
Dowling, A. P., & Hughes, I. J. (1992). Sound absorption by a screen with a regular array of slits. *Journal of Sound and Vibration*, *156*(3), 387–405. https://doi.org/10.1016/0022-460X(92)90735-G

Task 6 - Toolchain Development
Georgia Institute of Technology & Raytheon Technologies Research Corporation

Objective
The objective of this task is to develop a toolchain combining the ROMs developed in the previous tasks to enable the computation of far-field combustion noise. The toolchain is envisioned as a set of transfer functions that model each stage in the acoustic radiation process, as schematically illustrated in Figure 47. The GT team is currently working on the transfer function of the front-end disturbances from the fuel flow rate to the entropy and unsteady-heat release. The post-flame combustor transfer function is currently being analyzed based on the GT LES results that are currently available. The last two stages involving the turbine interactions and the far-field radiation have been completed and have been integrated into the current toolchain.

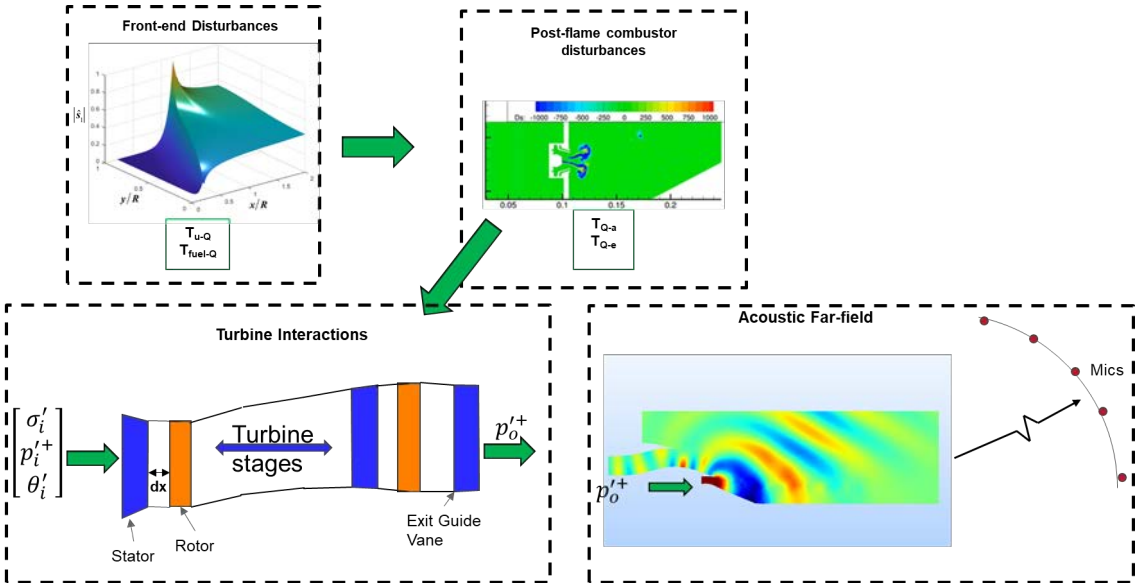

Figure 47. Schematic of the toolchain for predicting far-field combustor noise.

Research Approach

The turbine transfer function is based on the ADT by Cumpsty & Marble (1977) for a single turbine stage. The single-stage ADT is represented in a transfer function by the following equation, where σ, p^+, p^-, and ϑ, are the entropy, forward-propagating pressure, backward-propagating pressure, and vorticity waves, respectively.

$$[E_1].[M_1]\begin{bmatrix}\sigma_1'\\ p_1'^{+}\\ p_1'^{-}\\ \theta_1'\end{bmatrix} = [E_2].[M_2]\begin{bmatrix}\sigma_2'\\ p_2'^{+}\\ p_2'^{-}\\ \theta_2'\end{bmatrix} \; where\ [E]\&\,[M]\ represent\ the\ Euler\ equations\ and\ jump\ conditions\ across\ the\ stage$$

$$\left[\prod_{n=1}^{N_r-1}\left\{\left[B_1^{n+1}\right]\left[T^n\right]\left[B_2^n\right]^{-1}\right\}\right]\left[B_1^1\right].V_i^1 = \left[B_2^{N_r}\right].V_o^{N_r}\ where\ [B] = [E].[M]\ \&$$

$$[T] = \begin{bmatrix} e^{ik_x^s dx} & 0 & 0 & 0\\ 0 & e^{ik_x^+ dx} & 0 & 0\\ 0 & 0 & e^{ik_x^- dx} & 0\\ 0 & 0 & 0 & e^{ik_x^\theta dx}\end{bmatrix} \text{ is the phase delay matrix}$$

The single-stage ADT is combined with a phase-delay transfer function [T] to propagate the acoustic, entropy, and vorticity waves between consecutive stages, which are chained together to form a ROM for the whole turbine. As input, these equations take the acoustic and entropy waves exiting the combustor, and the solution is the acoustic and entropy waves exiting the multi-row turbines.

Figure 48 shows the forward-propagating acoustic and entropy waves exiting a single rotor–stator stage and results for a two-stage example with constant pressure and entropy inputs. As the number of stages increases, the relative contribution of the direct noise (blue line) decreases compared with the entropy noise (red line) at higher frequencies. Moreover, the acoustic pressure exiting the turbine for a combined input of acoustic and entropy noise (yellow line) is not directly related to the direct and entropy noise alone. This result suggests that the relative phasing between the direct and entropy noise becomes influential as the number of stages increases.

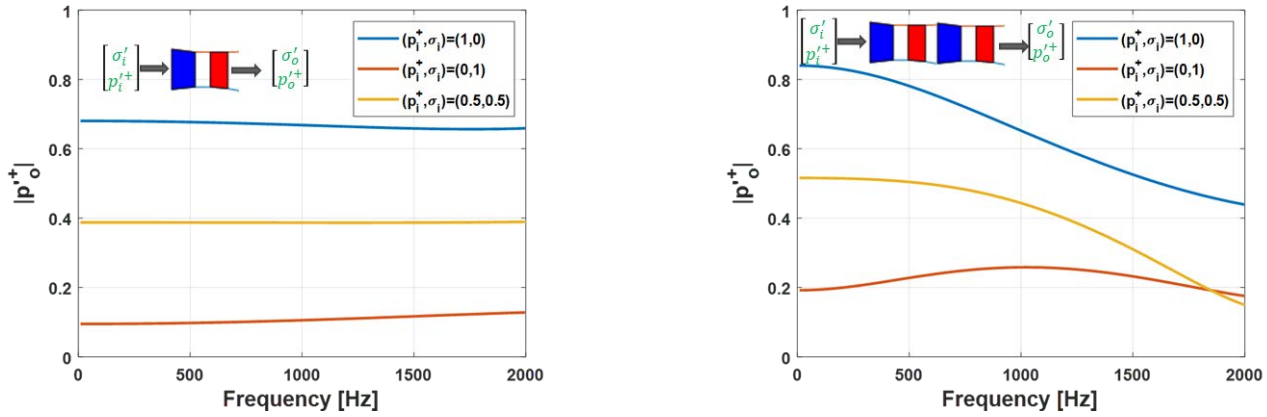

Figure 48. Propagating acoustics from a one- and two-stage turbine for constant pressure and entropy inputs.

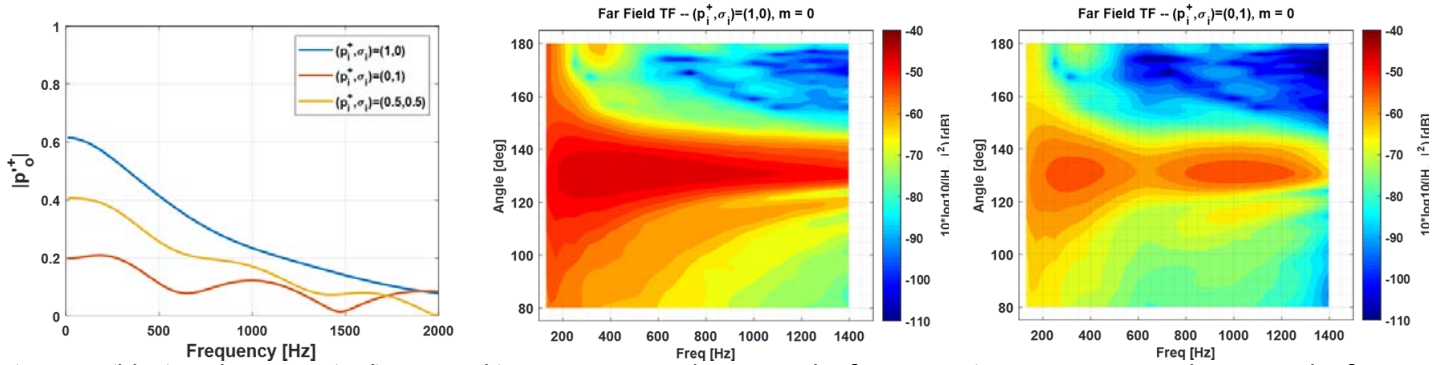

a) Direct (blue) and entropy (red) noise exiting the turbine

b) Direct noise radiation to the far-field

c) Entropy noise radiation to the far-field

Figure 49. Direct and Indirect noise radiation to the far-field from a realistic engine under approach conditions. TF: transfer function.

For a realistic multi-stage turbine under approach conditions, acoustic transfer functions were calculated for direct and indirect noise by solving the above set of equations, as presented in Figure 49. The acoustic pressure exiting the turbine is used as input to the far-field acoustic transfer function developed in Task 5 to obtain the radiated noise. Because the pressure and entropy inputs are constant as a function of frequency, the contour plots in the figure can be considered as "combustor exit-to-far-field" acoustic transfer functions for the planar mode (m=0). As expected, the direct noise transfer is more influential than the entropy noise at lower frequencies. However, at higher frequencies, the entropy noise may have a greater impact. The entropy noise transfer functions show peaks at approximately 300 Hz and 1000 Hz.

Figure 50 shows similar plots for the first azimuthal mode (m=1). The cutoff frequency for higher-order azimuthal modes is determined by the geometry of the turbine and the flow conditions, primarily at the first vane downstream of the combustor exit. For this turbine, the m=1 mode is cut off below 713 Hz, and the m=2 mode is cut off below 1437 Hz.

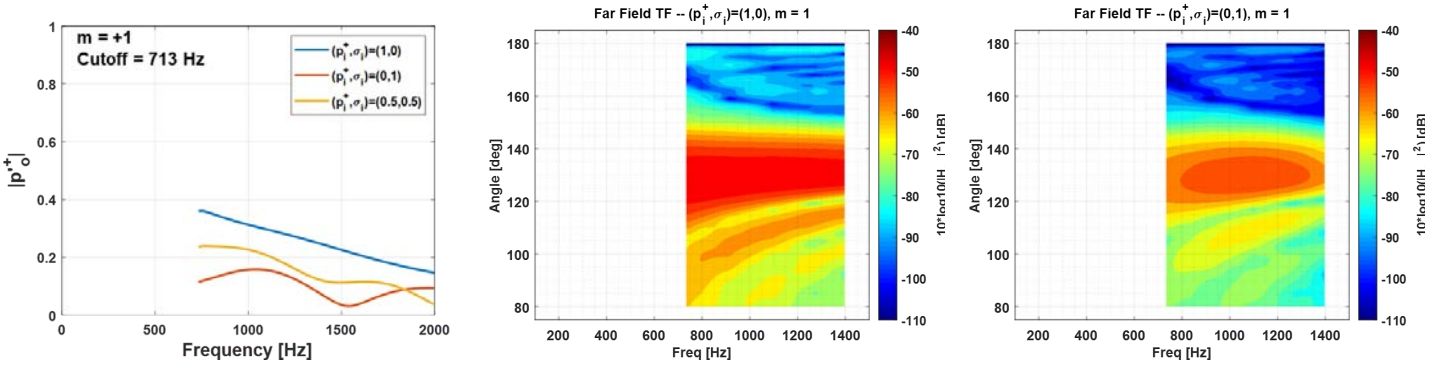

Figure 50. Direct and entropy noise radiation to the far-field for the first azimuthal mode (m=1). TF: transfer function.

Milestones

- A framework has been established for the toolchain to predict far-field combustor noise.
- The initial integration of the turbine modeling and far-field propagation tasks has been completed.

Major Accomplishments

The single-stage turbine ROM based on ADT has been combined with a phase delay transfer function between turbine rows and has been extended for realistic multi-stage turbines. The necessary inputs for this ROM are the mean flow conditions, rotor speed, and geometry for each rotor and stator row. The turbine ROM has been combined with the far-field acoustics model and has been demonstrated for a realistic engine under certain flight conditions.

Publications

None.

Outreach Efforts

None.

Awards

None.

Student Involvement

None.

Plans for Next Period

The team will continue developing the toolchain by integrating the front-end transfer function and the combustor exit transfer functions that will be developed in the previous tasks. This toolchain will then be applied to realistic engine configurations under a few key power conditions, and the results will be presented and discussed.

For the far-field noise propagation task, the team will focus on completing additional comparisons of the transfer-function-based far-field ROM to the FAA CLEEN I far-field engine data. In addition, the team will continue working on the ROM as part of the integration effort for the overall combustion noise model framework for use in computing combustion noise propagation from the combustor to the far-field.

References

Cumpsty, N., & Marble, F. (1977). The interaction of entropy fluctuations with turbine blade rows; a mechanism of turbojet engine noise. *Proceedings of the Royal Society of London. A. Mathematical and Physical Sciences*, *357*(1690), 323–344. https://doi.org/10.1098/rspa.1977.0171

Project 056 Turbine Cooling Through Additive Manufacturing

The Pennsylvania State University

Project Lead Investigator

Karen A. Thole
Distinguished Professor
Department of Mechanical Engineering
The Pennsylvania State University
NARCO Building, CATO Park, Room 148
3127 Research Drive
State College, PA. 16801
(814) 863-8944
kthole18@psu.edu

University Participants

The Pennsylvania State University (Penn State)

- P.I.s: Dr. Karen Thole, Dr. Stephen Lynch
- FAA Award Number: 13-C-AJFE-PSU-054
- Period of Performance: February 5, 2021 to August 12, 2023
- Tasks:
    1. Manufacture and test existing FAA CLEEN (Continuous Lower Energy, Emissions, and Noise) II blade designs
    2. Design new double-wall cooling technologies
    3. Manufacture and test new double-wall cooling designs for linear cascade
    4. Manufacture and test optimal double-wall cooling designs for the Steady Thermal Aero Research Turbine (START) Lab turbine

Project Funding Level

The FAA has provided $1,200,000 of funding to date. In-kind cost share of $1,500,000 has been provided to Penn State from Pratt & Whitney to cover the entire program.

Investigation Team

Name & Title	Affiliation	Role	Tasks Responsible For
Distinguished Professor Karen A. Thole	Penn State	P.I.	Management, reporting, oversight of all technical tasks
Associate Professor Stephen Lynch	Penn State	Co-P.I.	Management, reporting, oversight of Tasks 2-3
Assistant Research Professor Reid Berdanier	Penn State	Staff scientist	Tasks 1, 4
Associate Research Professor Michael Barringer	Penn State	Staff scientist	Tasks 1, 4
Scott Fishbone	Penn State	Project manager	Tasks 1, 4
Jeremiah Bunch	Penn State	Laboratory technician	Tasks 1, 4
Justin Wolff	Penn State	Graduate student	Tasks 1-4
Liam Boyd	Penn State	Graduate student	Tasks 1-4

Project Overview

Gains in cooling performance of cooled turbine airfoils have a direct impact on the efficiency and durability (lifetime) of turbine engines and are therefore the subject of much development. Today, many cooling designs for turbine airfoils use complex micro-channels placed within the wall of the airfoil to extract heat, which is otherwise known as double-wall cooling. The geometric complexities (and thus effectiveness) of the micro-channels, however, are limited by the current design space available using conventional investment casting and core tooling methods to manufacture relatively small intricate internal cooling features. This project will investigate potential thermal performance and aerodynamic efficiency improvements made possible by exploring the expanded cooling design space opportunities by directly fabricating complex cooling geometries using three-dimensional laser powder bed fusion (L-PBF), a common type of metal-based additive manufacturing (AM) method. L-PBF AM has begun to see many uses in the gas turbine industry, particularly because of the new design space enabled by this new fabrication method. However, the ability to manufacture high-efficiency intricate complex double-wall cooling airfoil design concepts is unknown. This research would generate some of the first thermal performance data at engine-relevant conditions, comparing traditional cast airfoils to advanced L-PBF AM manufactured airfoils. Understanding the potential of innovative geometric heat transfer cooling design features coupled with unique airfoil cooling configurations will serve as an important guide to future investments in advanced manufacturing and cooling design technologies.

Task 1 - Manufacture and Test Existing FAA CLEEN II Blade Designs

The Pennsylvania State University

Objective

The objective of this task is to measure the as-manufactured shape of FAA CLEEN II turbine blade airfoils using x-ray computed tomography (CT) and use that information to fabricate additively manufactured (AM) copies for direct comparison in the rotating turbine facility at Penn State. The outcomes of this effort will be (a) to provide a direct back-to-back comparison of cast versus additively manufactured airfoils; (b) learn the unknown challenges with creating double-wall designs via AM and how to translate them to cast parts for commercialization; and (c) work through the design, fabrication, and testing of additive blades that will spin at engine-relevant conditions.

Research Approach

AM Design and Printing Trials

At the end of the prior annual reporting period, a representative cast blade from Pratt & Whitney's FAA CLEEN II program was selected for replication through AM. Pratt & Whitney performed mechanical analysis, generated manufacturing drawings for the AM airfoils, and assisted with securing an AM vendor.

While AM is continually evolving as an important manufacturing technology, this project has identified the challenges of printing a turbine blade given the many features present, including the typically used ribs and pedestals, as well as the external film-cooling holes. During this past year, we have worked with over 20 vendors across the United States to assess their capabilities in terms of making an AM blade. Even after identifying the vendors with the best expertise and printing technologies, we have found that at least three test trials are needed. Such test trials are shown in Figure 1 for the National Experimental Turbine (NExT) blade (note the PW blade is proprietary). As can be seen in Figure 1, the trials become progressively better, which are dependent upon the print direction and the various process parameters. This information has been provided to the turbine community in various presentations illustrating the state of the art of AM.

A particularly important outcome from this project has been the AM learning that, as mentioned, has been shared. This learning was key to the NASA HyTEC Program, a challenging project that START is currently involved with, in which Pratt & Whitney is the prime. An advanced blade is being additively manufactured to evaluate new cooling technologies. The deadlines and ability to meet the HyTEC Program requirements would not have been possible without the support of ASCENT 056.

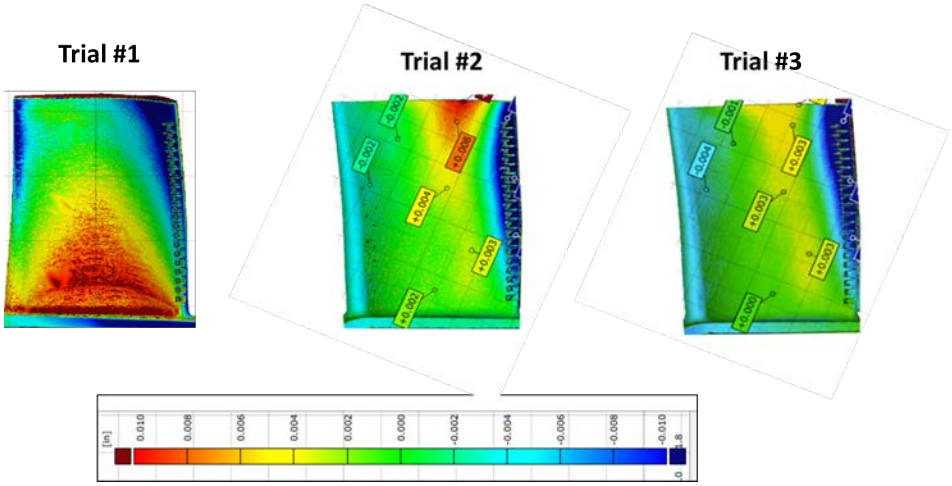

Figure 1. Illustration of a trial build of a turbine blade.

In addition, the learning that took place as a result of this past year includes the fact that replicating a cast blade through the use of AM is particularly challenging because some of the features needed for the casting process are not needed for the AM process. These features, required to hold the casting in place for example, are generally small, which is a challenge for the AM process. Further research is needed to assess the future of using AM for development of turbine parts, particularly in understanding what features are needed.

In terms of the cooling features in the FAA CLEEN II blades, we were able to demonstrate through ASCENT 056 that it was possible to drill the trailing edge slots, which cannot be easily printed, into the AM blades. This manufacturing method had not been demonstrated thus far by many vendors and, as such, is another accomplishment of this past year's work. It is not yet possible to print the film-cooling holes successfully in a cooled turbine blade at aircraft engine scale due to the hole size. As such, cooling holes were traditionally manufactured using electro-discharge machining after the blades were printed.

From demonstration trials with two vendors for Pratt & Whitney's FAA CLEEN II blades, Vertex Manufacturing was selected to move forward with fabrication of the AM airfoils. Vertex Manufacturing also completed a trial print build to ensure the production print would run smoothly. While the trailing edge did not come out as well as desired, which is also illustrated in Figure 1 with the best trial, the rest of the blade met the aerodynamic shape tolerance by +/- 0.003 inches. This approach is as good as or better than casting and is a great result for the program. Production printing commenced in May, but final machining operations for the critical attachment points (fir tree) and for film-cooling holes were delayed due to vendor backlog. In the meantime, Penn State sectioned a few blades and had a micro-CT scan done to understand internal features and how they replicated relative to the cast blade.

After a vendor delay, the blades were machined and sent to a new film-cooling hole drill vendor, Arc Drilling. They were able to successfully complete drilling the film-cooling holes for the blades and send them back to Vertex for final inspection. Arc Drilling, a company not previously known to Pratt & Whitney, was able to showcase their manufacturing abilities, opening the door to potential future projects. The completed blades arrived at Penn State in November and are now being inspected before rig testing can begin.

Task 2 - Design New Double-Wall Cooling Technologies

The Pennsylvania State University

Objective

The objective of this task is to develop novel double-wall cooling designs that feature microchannel concepts being explored in the literature and that can be achieved via additive manufacturing (AM). The designs will be generated with advice from Pratt & Whitney so that the concepts can be leveraged for commercialization. The designs will be packaged into cascade test

articles that are measured in the high-speed linear cascade at Penn State using infrared thermography in Years 2-3 of the project.

Research Approach

Design of Linear Cascade Test Articles and Infrastructure

In the previous annual reporting period, the design of the linear cascade hardware was discussed in detail. The airfoil is based on the 75% span section of the FAA CLEEN II airfoil. Seven 2-dimensional airfoils were implemented into an AM-printed cascade. Three removable center test airfoils were incorporated into the cascade hardware design to enable rapid changeout of novel cooling designs. In addition, the data reduction technique of the cascade requires an infrared (IR) camera calibration airfoil set, which has both spatial calibration markers that can be used to transform the IR image and variable internal temperature that can be used to develop a camera-observed-temperature to true-temperature mapping. This calibration airfoil and a generic microchannel cooling airfoil with appropriate coolant feeds were designed with instrumentation that is enabled by the use of AM fabrication. Figure 2 shows a schematic of the coolant routing from the base of the test airfoil insert, with flowpaths leading to the microchannels in the airfoil body and instrumentation locations at the inlet and outlet of the microchannels.

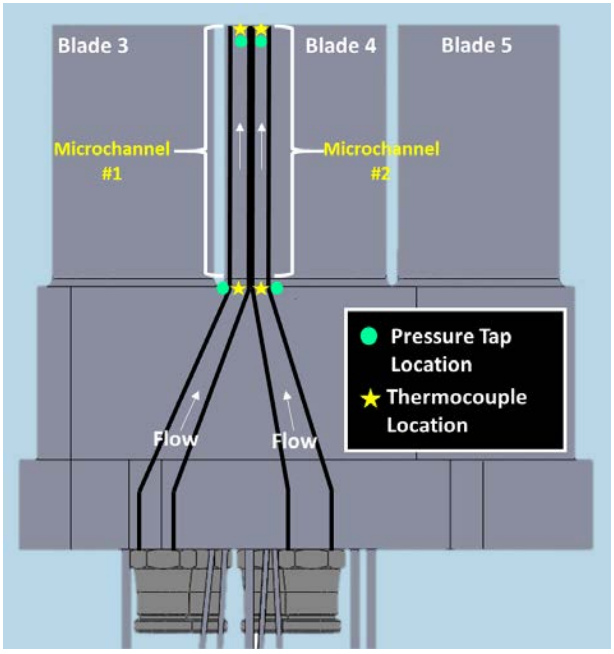

Figure 2. Design of cooling flowpath and instrumentation for microchannels in linear cascade hardware.

In the previous annual reporting period, we also described several novel microchannel cooling geometries that were developed based on concepts in the open literature, some of which have been previously demonstrated using AM. Figure 3 shows some of the designs, which were grouped by their type. Pin fin designs include a standard circular pin (manufactured in additive manufacturing (AM) by Kirsch and Thole (2017a), as well as a triangular pin design tested by Ferster et al. (2018). These are expected to have high pressure loss but also high cooling effectiveness. The second grouping is for ribs (turbulators), which do not span the entire channel but act to locally trip the flow. The discrete W shape by Wright et al. (2004) is a conventional design, but the wavy S-shaped ribs of King and Pietraszkiewicz (2018) are based on a patent and may have a similar effect as wavy channels studied by Kirsch and Thole (2017b). The channel-only configurations include the baseline empty microchannel that replicates the existing FAA CLEEN II design, as well as a wavy microchannel that is based on the findings of Kirsch and Thole (2017b).

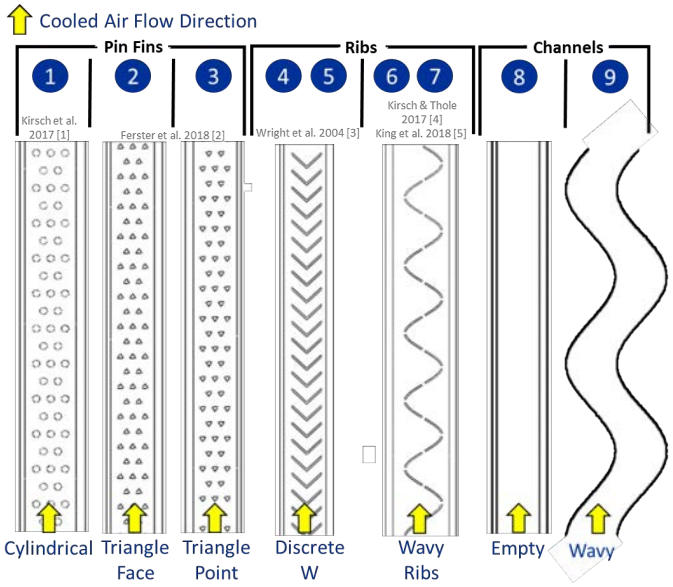

Figure 3. Novel cooling concepts packaged into the microchannels in this study.

To ensure a reasonable match between lab conditions and scaled engine conditions, the external to internal heat transfer coefficient (h) ratio and the microchannel wall Biot numbers were evaluated. The h ratio is defined as the external convection heat transfer coefficient of a particular channel over the internal heat transfer coefficient and is important to match between the cascade experiment and the engine condition for relevance of the data. Figure 4 illustrates h ratio calculations performed for an empty channel cooling design (no geometries) at a medium Mach number condition and at a variety of Reynolds number conditions. An h ratio of 1.0 is typically seen within a gas turbine engine. Channel 2a and 2b in Figure 4 generally match the h ratio of a typical engine over the range of internal channel Reynolds number conditions. Some of the other channels have higher h ratios, but at higher Reynolds number conditions, all channels come within a reasonable range of the h ratio. Channels 1 and 3 are located in a region where the external h is very high for the airfoil, so a large amount of internal cooling is needed.

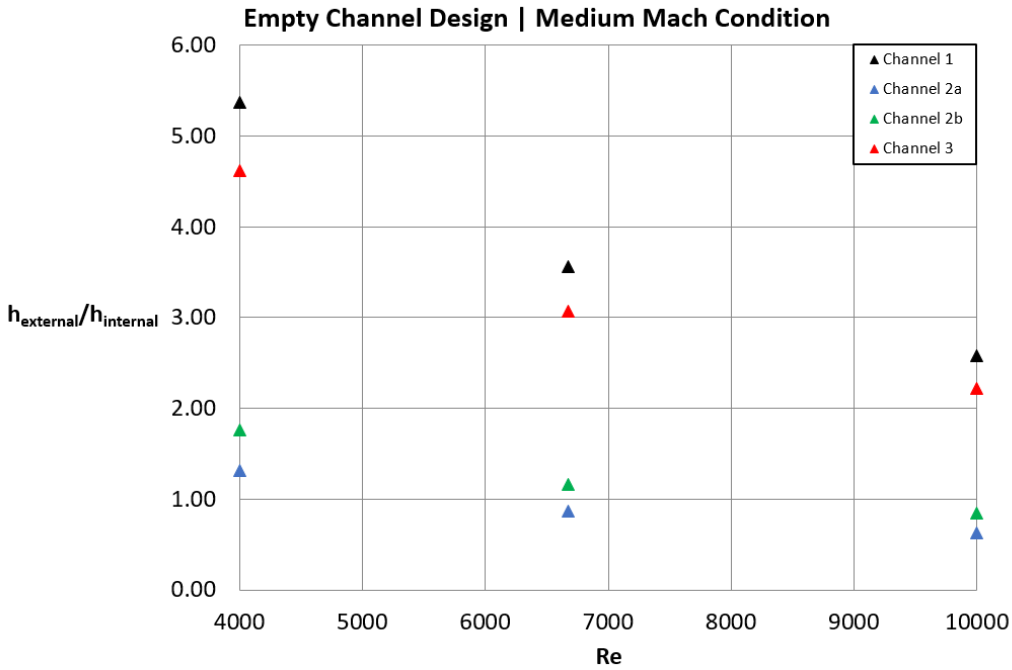

Figure 4. Plot of the external to internal convection coefficient at different internal channel Reynolds numbers.

Figure 5 provides an example of the Biot number calculations that were performed. The Biot number is another nondimensional parameter representing the ratio of external convection to conduction in the metal, and it should also be matched as closely as possible to engine conditions. The results are expressed as a scaled value, as the cascade hardware wall thickness (t) is less than that of a typical engine. Scaling the Biot number data by a wall thickness ratio, as seen in the top of Figure 5, adjusts the raw Biot number results to obtain the proper comparison to a typical engine. Figure 5 indicates that channel 1, at a high external Mach number condition, reaches a Biot number around 0.27, which is the nominal level in a gas turbine engine. The values for other cases are somewhat lower but within a range that will be reasonable for comparison to engine conditions.

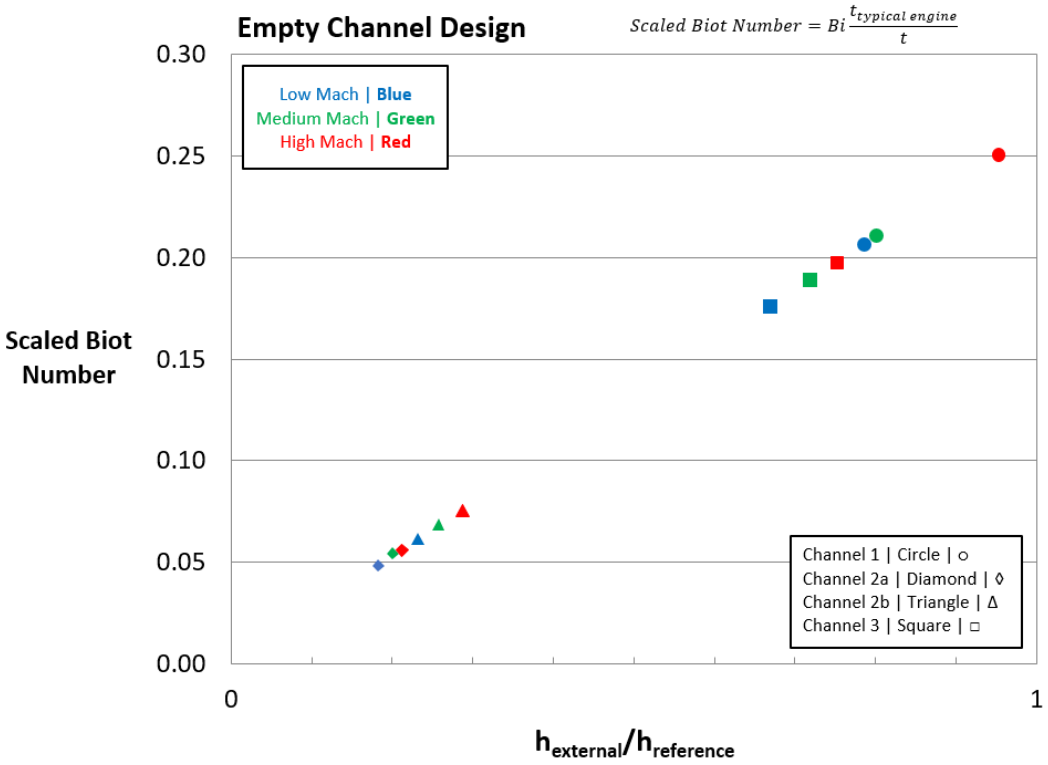

Figure 5. Plot of the scaled Biot number for each channel at different cascade Mach number conditions.

In addition to the cooled airfoil designs, the linear cascade cooling facilities have been upgraded to account for an increased number of cooling circuits and the necessary flow control. Figure 6 shows a schematic of the cooling circuits that can supply independently metered flow to four separate microchannels in the test airfoils. Note that because the cascade inlet air temperature is 100 ˚C, the cooling air is cooled using liquid nitrogen to maintain coolant-to-mainstream temperature ratios that are relevant to engine conditions.

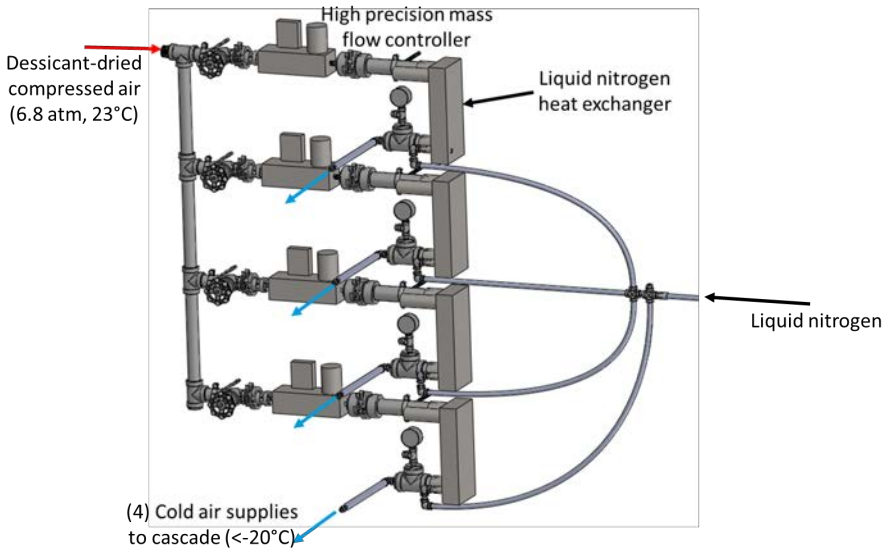

Figure 6. Upgraded cooling supply system for cascade including high precision mass flow controllers and liquid nitrogen-cooled cooling air.

Task 3 - Manufacture and Test Novel Double-Wall Cooling Designs for Linear Cascade

The Pennsylvania State University

Objective

The objective of this task is to measure the performance of the AM microchannels in the linear cascade airfoil and rank the performance of the novel geometries. This includes measuring the pressure drop and the surface temperature of the airfoils with the novel microchannel geometries. We have also developed a novel measurement technique to obtain the overall convection coefficient in the microchannels using coolant and surface temperature measurements. This technique was initially validated using conjugate computational fluid dynamics as "synthetic data," and recently we have been conducting experimental validation.

Research Approach

Fabrication of Linear Cascade Hardware

The overall cascade hardware (periodicity airfoils) and the static pressure test airfoils were initially fabricated by Keselowski Advanced Manufacturing (KAM) using L-PBF with Inconel 718 material. The vendor also applied a heat treatment for stress relief and a bead blast finish. After the hardware was received in late 2021, the condition and dimensions were thoroughly documented. The pressure tap holes were produced to satisfaction and the dimensions required for installation into the linear cascade were met. However, some post-processing on the pressure tap holes was necessary to properly fit the pressure taps; namely, the pressure tap holes were slightly undersized due to printing tolerance.

The novel microchannel test airfoils with internal geometries indicated by Figure 2 were subsequently manufactured by Vertex Manufacturing and received in late summer 2022. To date, the empty microchannel geometry has been tested as it is a validation of the novel approach to obtain internal convection coefficients. The other geometries are being instrumented and tapped for compressed air fittings. Pending results from the current study, a few other novel geometries may be built to understand interactions between augmentation features or repeatability of small internal features and the impact on performance.

Experimental Validation of Flowfield and Development of IR Camera Calibration

The flow field of the FAA CLEEN II 2D-airfoil for the linear cascade studies has also been validated by comparing surface pressures from computational fluid dynamics (CFD) predictions of the airfoil and the measured surface pressures from the linear cascade hardware. Figure 7 provides a generic example of an airfoil geometry with corresponding pressure tap locations, such as pressure side 1 (PS1) and suction side 4 (SS4). Figures 8-10 show the percent difference, Equation (1), between the CFD and cascade pressure data at selected locations around the three center airfoils (airfoils 3, 4, and 5 of seven total). The airfoil's static pressure data was collected at three exit Mach number conditions corresponding to low, normal, and high operating conditions for turbines; Figures 8-10 correspond to an exit Mach number under normal operating conditions. Each Mach number condition was tested at two separate Reynolds numbers. The figures indicate that the percent difference between expected pressure and measured pressure was within about 3%, which is well within expected variation.

$$\%\, Difference = \left|\frac{P_{Cascade} - P_{CFD}}{P_{CFD}}\right| * 100\% \qquad \text{Eq. 1}$$

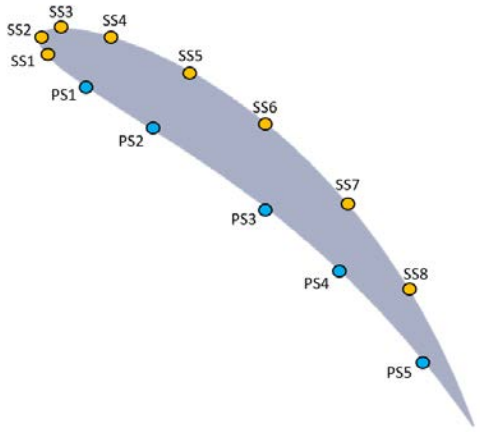

Figure 7. Generic airfoil geometry with example of static tap locations. PS, pressure side; SS, suction side.

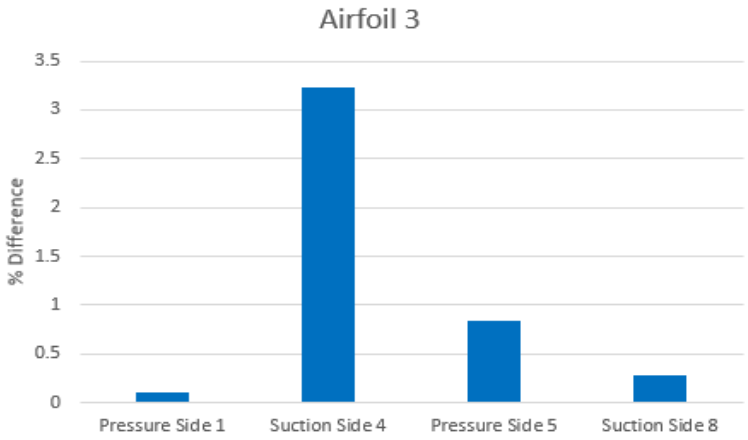

Figure 8. Percent difference between airfoil 3 computational fluid dynamics and linear cascade pressure data.

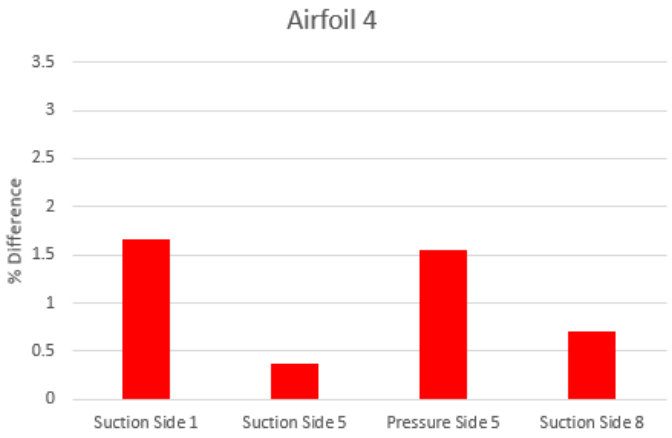

Figure 9. Percent difference between airfoil 4 computational fluid dynamics and linear cascade pressure data.

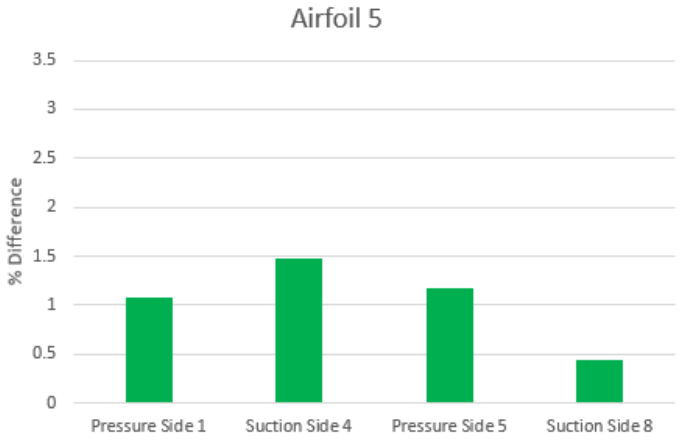

Figure 10. Percent difference between airfoil 5 computational fluid dynamics and linear cascade pressure data.

Before testing, the IR camera must be calibrated. Spatial and temperature calibrations of the IR camera were obtained to get accurate, properly positioned surface temperature results. Figure 11 depicts a de-warped calibration image of the pressure side of the blade, where the dots are the grid pattern in the airfoil surface coordinate system. As expected, the grid pattern is very regular despite the image having been taken at a steep surface angle to the airfoil. This spatial calibration is utilized to identify the physical location of a specific channel's outer wall. Temperature calibration was also performed with this same hardware (painted flat black). Thermocouples were placed on the surface of the blade at two locations that were visible in the IR camera image. Once the airfoil was heated to cascade conditions, and as the airfoil gradually cooled, data points were collected simultaneously by the thermocouples and the IR camera, as exemplified by Figure 12. Trendlines were created for all unique image locations using a linear regression analysis. The trendlines for both locations matched closely to one another, which was expected because the surfaces of interest were all painted with the same flat black paint and were not at extreme angles relative to the camera sensor. The trendline is used on experimental data to adjust the observed IR camera temperature to the real temperature (as determined by the thermocouples).

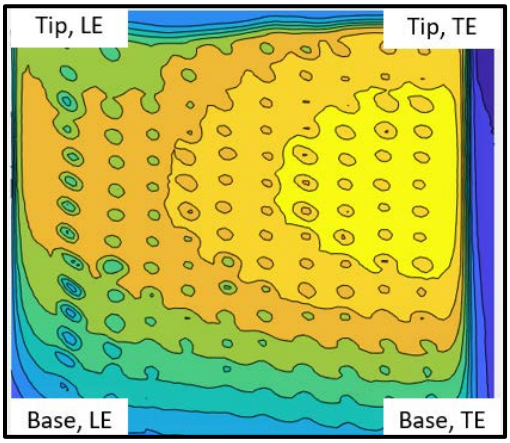

Figure 11. De-warped infrared spatial calibration image for the pressure side of the airfoil.

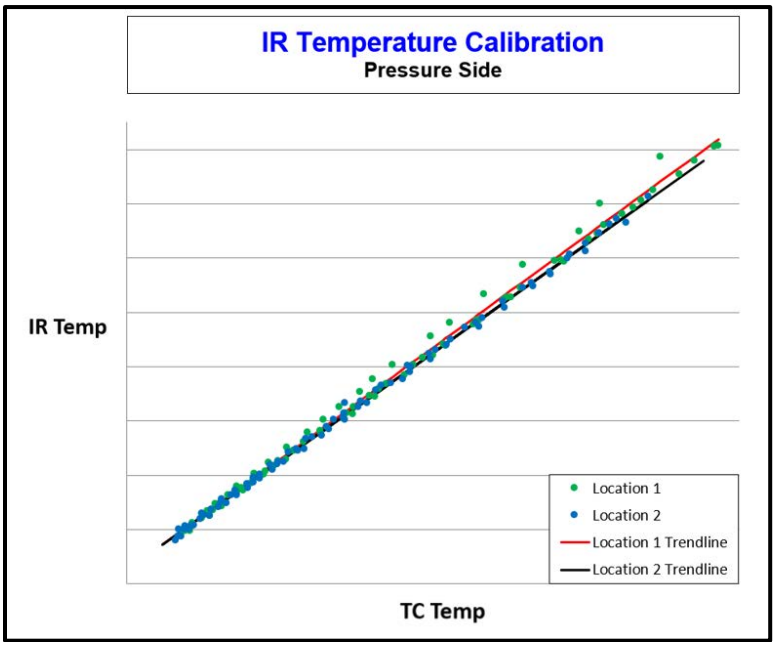

Figure 12. Infrared camera temperature calibration data and trendline information for the pressure side of the airfoil.

Development and Computational Validation of Microchannel Data Reduction Technique

A novel experimental technique was developed to measure the overall convection coefficient of a microchannel in situ, using the instrumentation embedded into the microchannels. Figure 13 indicates a set of two control volumes for microchannel 2a.

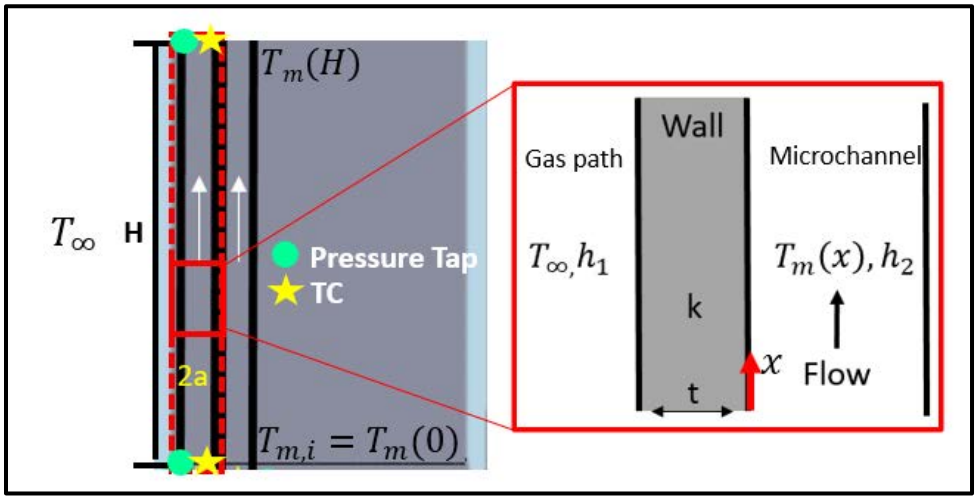

Figure 13. Two different control volumes (overall channel in dashed, local through wall in solid) for development of the data reduction method.

The overall control volume in the dashed red in Figure 13 can be used to derive Eq. (2), which is the variation of the microchannel bulk temperature $T_m(x)$ as a function of distance, for a constant external temperature (T_∞, the local total temperature of the cascade flow, which generally remains constant) outside the microchannel wall. The bulk temperature variation depends on the mass flow through the channel, the specific heat of the air in the channel (c_p), the perimeter of the microchannel, and the overall heat transfer coefficient which incorporates external convection, conduction through the microchannel wall, and internal convection:

$$\frac{T_m(x) - T_\infty}{T_{m,i} - T_\infty} = e^{\left(-\frac{Px}{\dot{m}c_p}\right)\bar{U}} \qquad \text{Eq. 2}$$

Pertinent to this study, the microchannel hardware and cascade system were designed to measure the inlet (x=0, denoted as i) and outlet (x=H) bulk temperatures as well as the cooling massflow, such that the overall convection coefficient can be solved for, as shown in Eq. (3):

$$\bar{U} = -\frac{\dot{m}c_p}{A_s} ln\left[\frac{\left(T_\infty - T_m(H)\right)}{\left(T_\infty - T_{m,i}\right)}\right] \qquad \text{Eq. 3}$$

Furthermore, from the local control volume (solid red) in Figure 13, a steady-state thermal circuit can be developed between the external gas path temperature T_∞ and the local internal channel bulk temperature $T_m(x)$. The circuit is depicted in Figure 14.

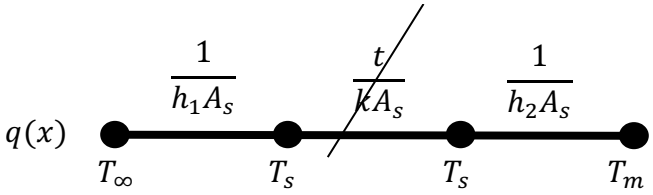

Figure 14. Thermal circuit between the external gas path and the internal bulk temperature at some location x in the microchannel.

From analysis of the heat flow in the circuit, Eq. (4) can be obtained, which relates the overall heat transfer coefficient across the circuit to the external convection coefficient via the local external surface temperature $T_s(x)$ which is measured by the IR camera in the experiment:

$$\frac{q(x)}{A_s} = q"(x) \approx \bar{U}[T_\infty - T_m(x)] = h_1[T_\infty - T_s(x)] \quad \text{Eq. 4}$$

Rearranging gives an estimate of the external convection coefficient (h_1) from the measurements and calculations in the previous equations:

$$h_1 = \bar{U}\frac{[T_\infty - T_m(x)]}{[T_\infty - T_s(x)]} \quad \text{Eq. 5}$$

where $T_m(x)$ would need to be determined by applying Eq. (2). Once the external convection is known, and with an assumption of negligible conduction through the thin microchannel wall, the average internal convection coefficient is obtained by the definition of the overall heat transfer coefficient:

$$h_2 = \frac{1}{\left(\frac{1}{\bar{U}} - \frac{1}{h_1}\right)} \quad \text{Eq. 6}$$

Key assumptions in the above methodology include (a) negligible temperature variation around the perimeter of the microchannel, (b) negligible conduction loss in the microchannel wall, and (c) negligible lateral variation in the external surface temperature. To determine if these assumptions are valid and to identify whether the proposed methodology is accurate, conjugate CFD was conducted to predict the solid and fluid temperature fields in a manner analogous to the experiment.

Figure 15 illustrates the computational domain with boundary conditions that was used to perform the CFD analysis on the empty channel cooling design. The fluid domain has periodic walls so that a single airfoil could be simulated in the ideal environment of a cascade. At the inlet, stagnation conditions were applied, and at the outlet, a static pressure was imposed such that the isentropic Mach number and exit Reynolds number were matched to the cascade test conditions. A mass flow inlet with the conditions from the experiment was imposed on the microchannel inlet, and a conjugate analysis (coupled temperatures/heat fluxes at the solid–fluid interfaces) was performed. A mesh sensitivity and iterative convergence study was performed to ensure that the baseline mesh was of sufficient quality for realistic answers.

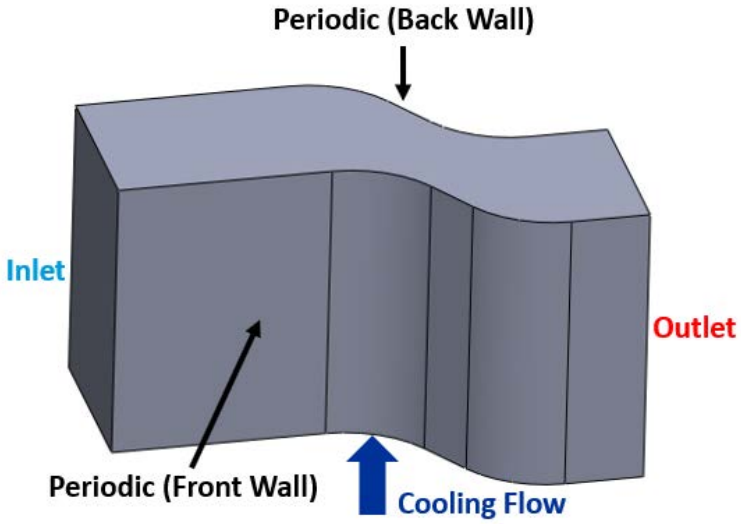

Figure 15. Computational domain and boundary conditions for the conjugate computational fluid dynamics study.

One of the assumptions of the data reduction technique was negligible conduction through the microchannel wall. Figure 16 shows a plot of channel 2a temperatures as a function of height, extracted on a line going along the microchannel midway between its left and right walls. The temperatures include the inside wall and outer wall surface temperatures as well as the bulk temperature through the channel (yellow). Clearly, there is very little difference between the inner and outer microchannel walls, and both are less than the reference temperature (the gas path temperature). Also, the methodology described in Eqs (2)-(3), whereby the overall convection coefficient is determined from inlet and outlet bulk temperatures and then used to find bulk temperature anywhere in the microchannel, compares well to the predicted bulk temperature in the CFD.

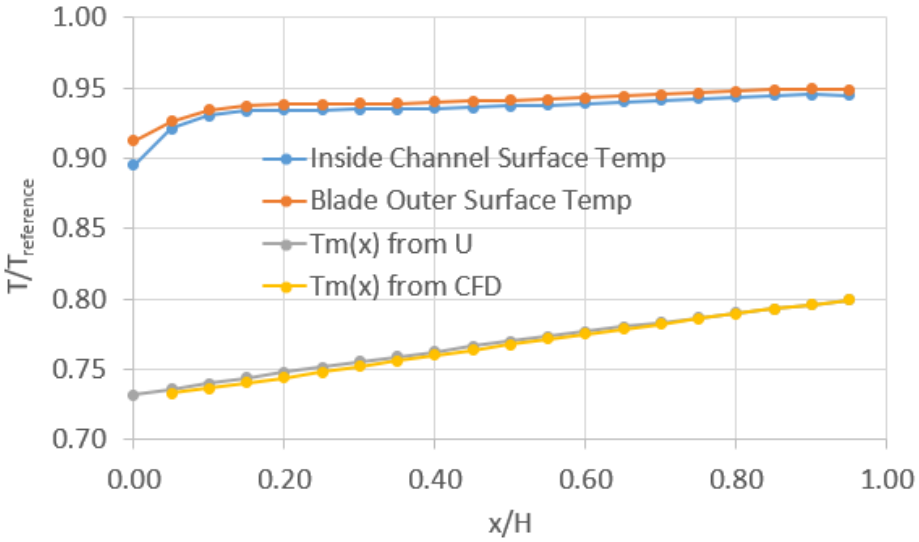

Figure 16. Surface and microchannel bulk fluid temperatures extracted from a computational fluid dynamics simulation of channel 2a.

Using the results in Figure 16 in the rest of the data reduction technique of Eqs (4)-(6), the estimated internal heat transfer coefficient was within 0.1% of the direct result from the CFD, which is excellent agreement but does not take into account inevitable experimental uncertainty, which will be addressed during the next quarter.

Another major assumption of the data reduction technique in Eqs (2)-(6) is that the temperature variation around the perimeter of the microchannel is negligible. To evaluate this, eight probes were placed around the inner surface of the microchannel (Figure 17). Each of these probes extends down the length of the channel and independently measures the temperature on the inner surface. Figure 17 plots the z position along the channel normalized by the total channel length versus the nondimensional surface temperature. Note the small scale of the graph, indicating that the variation around the perimeter of the microchannel is small.

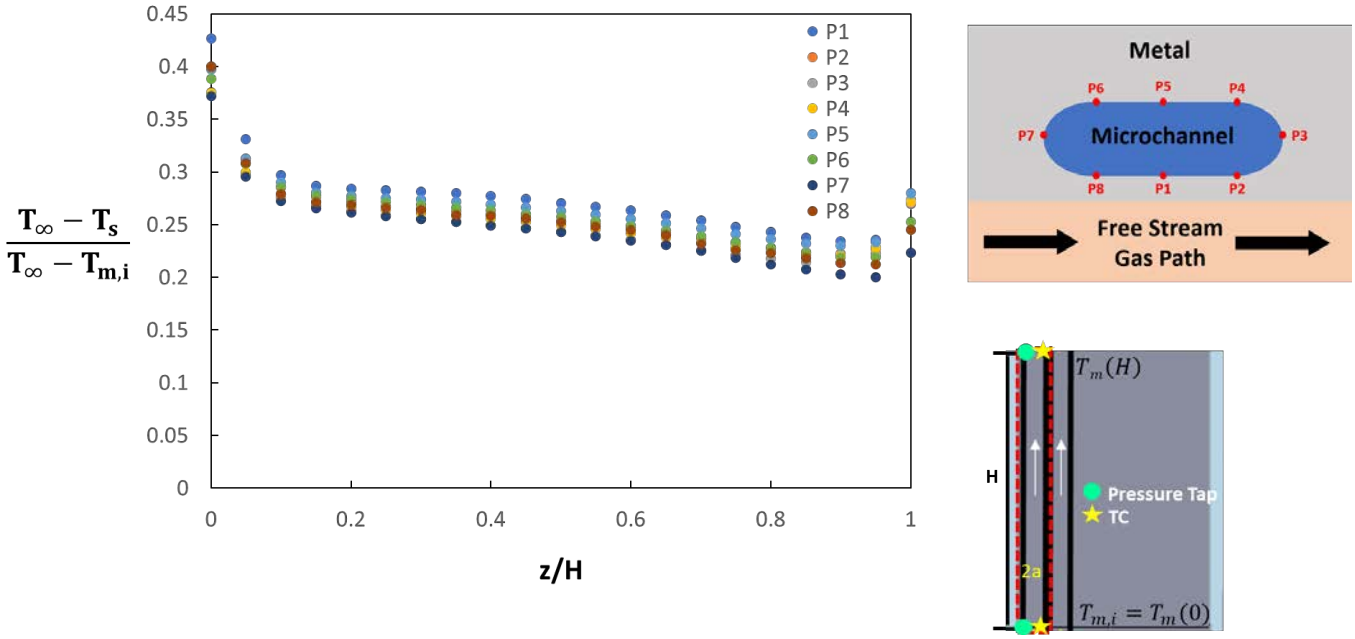

Figure 17. Probe locations around periphery of microchannel and resulting variation in local surface temperature as a function of height.

Preliminary Experimental Validation of Microchannel Data Reduction Technique

Preliminary measurements of channel pressure drop (presented as a friction factor augmentation relative to a smooth channel) were obtained for the empty microchannel geometry at a range of internal Reynolds numbers. Figure 18 presents the results for repeated trials for Channel 2b, which show very good repeatability, as well as reasonable agreement to existing literature on AM microchannels (Wildgoose et al. [6]) and the Colebrook equation using a correlation provided in Stimpson, et al. [7] for the estimated arithmetic mean roughness to hydraulic diameter (Ra/Dh; these values are still being determined exactly for this geometry). The internal convective heat transfer coefficient is being investigated currently and will be discussed in the next quarterly report.

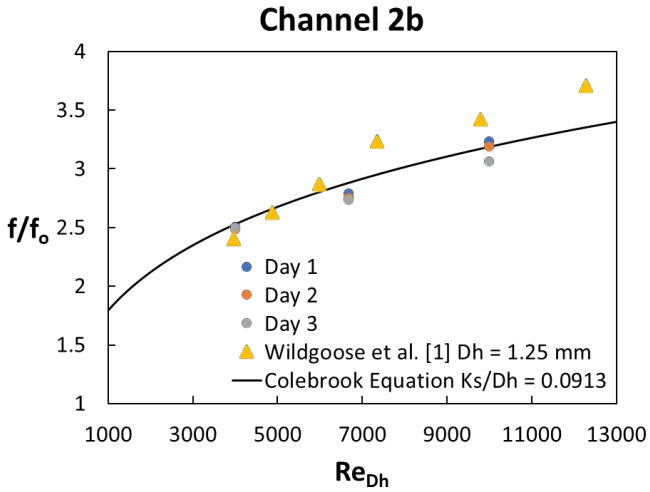

Figure 18. Friction factor augmentation for the empty microchannel in this study versus existing literature.

Milestone(s)

Milestone	Due Date	Estimated Date of Completion	Actual Completion Date	Status
Workplan	3/5/20	3/4/20	3/5/20	Completed
COE Meeting 1	4/1/20	4/1/20	4/1/20	Completed
COE Meeting 2	10/1/20	10/1/20	9/30/2020	Completed
Annual Report	2/4/21	11/15/2020	11/15/2020	Completed

Major Accomplishments

The major accomplishments for task 1 in 2022 was the trials of the cooled FAA CLEEN II blades leading to a successful completion. For task 2 it was the finalized design for novel internal cooling features and the development of a drawing package for vendors. Fabrication of the designs is considered in Task 3 but was also completed in 2022.

Publications

Wolff, J., 2022, “Development of Experimental Methodology to Determine the Heat Transfer of Additively Manufactured Airfoil Channels in a High-Speed Linear Cascade Rig”, Master’s Thesis, Additive Manufacturing and Design Program, Penn State University.

Boyd, L., 2023, “Novel Cooling Designs in Additively Manufactured Microchannels”, ASME Poster GT2023-110173, accepted.

Plans for Next Period

The plans for next period of task 1 include testing the AM CLEEN II blades in the START test turbine.

The completed blades will be inspected at Penn State and Pratt & Whitney so the impacts of AM can be overserved. The blades then will be tested in the START turbine using the recently developed IR thermography capability. The results will be compared with the original FAA CLEEN II cast airfoils to provide the first back-to-back comparison of cast versus AM.

The novel in situ internal convection coefficient technique will continue to be validated, and experimental uncertainty will be assessed and improved in Q4 2022 to Q1 2023. CT scans of the manufactured parts will be conducted and analyzed to obtain accurate values for hydraulic diameter and internal roughness, and the remaining microchannel designs will be tested in Q1-3 of 2023.

Outreach Efforts

Presented research findings were given throughout this year, as illustrated in the table below.

Event	Date	Attendees
Biweekly calls	Every 2 weeks	Pratt & Whitney (PW) aero/durability engineers
Quarterly calls with turbine OEMS	Once per month	Industry partners: Solar, Siemens, Honeywell
Center of Excellence Bi-Annual Meetings	6/6/2022 and 12/5/2022	PW aero/durability engineers and management
Center of Excellence Bi-Annual Meetings	11/8/2022	Solar turbine engineers
PSU Design for Additive Manufacturing (DFAM) Accelerator	9/27/2022	NASA, ONR, Air Force, Academia, AM Machine OEMs (EOS, Velo, GE, etc)
DOE NExT Annual Review Meeting	10/4/2022	DOE, NASA, FAA, PW, Solar, Siemens, Honeywell, Georgia Tech
NASA University Leadership Initiative Meeting	10/5/2022	DOE, NASA, FAA, PW, Mesoscribe, Howard U, Georgia Tech
Congressional Staffer Lab Tour	10/20/2022	U.S. Rep GT Thompson's legislative assistant Brian Arata
Visit from FAA Program Managers	11/30/2022	Joshua Glottmann, Levent Ileri

Presented findings on learning from AM to Solar Turbines in the November Center of Excellence on November 8, 2022, and to Pratt & Whitney at the June (June 6, 2022) and December (December 5, 2022) program reviews. Reported on manufacturing learning at a Department of Energy Review meeting at Penn State on NExT on October 5, 2022, and at a NASA University Leadership Initiative review meeting at Penn State on October 6, 2022. The DOE meeting involved industry members including Honeywell, Solar Turbines, Siemens, and Pratt & Whitney.

Mr. Scott Fishbone presented learning from the additive manufacturing of turbine blades to the 2022 DFAM Accelerator Conference on September 27, 2022, in State College, PA. Representatives from additive manufacturing machines, government agencies, and academia attended the event and were fascinated to see the amount of knowledge learned from the project.

Awards

None to report.

Student Involvement

Justin Wolff completed a master's of science degree in additive manufacturing in October 2022 from the work funded by this program. Justin has been responsible for analyzing CT scan data of the FAA CLEEN II blades, compiling a review package that was presented by him to Pratt & Whitney, researching and designing novel cooling strategies into the linear cascade hardware, performing conjugate CFD, and testing linear cascade hardware.

Liam Boyd is a new master's degree student who started on the project in summer 2022 and will complete the validation of the in situ microchannel testing methodology, as well as experimentally test the remaining microchannel geometries. Liam will also conduct analysis of CT scan data from the microchannel geometries and compare it to the design intent to understand the feature resolution of various microchannel enhancements.

References

Ferster, K. K., Kirsch, K. L., & Thole, K. A. (2018). Effects of geometry, spacing, and number of pin fins in additively Manufactured microchannel pin fin arrays. *Journal of Turbomachinery*, *140*(1), 011007. https://doi.org/10.1115/1.4038179

King, C., Pietraszkiewicz, E. F. (2018). *S-Shaped Trip Strips in Internally Cooled Components*. U.S. Patent No. 10156157.

Kirsch, K. L., & Thole, K. A. (2017). Pressure loss and heat transfer performance for additively and conventionally manufactured pin fin arrays. *International Journal of Heat and Mass Transfer*, *108*, 2502–2513. https://doi.org/10.1016/j.ijheatmasstransfer.2017.01.095

Kirsch, K. L., & Thole, K. A. (2017). Heat transfer and pressure loss measurements in additively manufactured wavy microchannels. *Journal of Turbomachinery*, *139*(1), 011007. https://doi.org/10.1115/1.4034342

Stimpson, C. K., Snyder, J. C., Thole, K. A., & Mongillo, D. (2017). Scaling roughness effects on pressure loss and heat transfer of additively manufactured channels. *Journal of Turbomachinery*, *139*(2), 021003. https://doi.org/10.1115/1.4034555

Wildgoose, A. J., Thole, K. A., Sanders, P., & Wang, L. (2021). Impact of additive manufacturing on internal cooling channels with varying diameters and build directions. *Journal of Turbomachinery*, *143*(7), 071003. https://doi.org/10.1115/1.4050336

Wright, L. M., Fu, W.-L., & Han, J.-C. (2004). Thermal performance of angled, v-shaped, and w-shaped rib turbulators in rotating rectangular cooling channels (AR=4:1). *Journal of Turbomachinery*, *126*(4), 604–614. https://doi.org/10.1115/1.1791286

Project 057 Support for Supersonic Aircraft En route Noise Efforts in ICAO CAEP

The Pennsylvania State University

Project Lead Investigator

Victor W. Sparrow
United Technologies Corporation Professor of Acoustics
Graduate Program in Acoustics
The Pennsylvania State University
201 Applied Science Bldg.
University Park, PA 16802
814-865-6364
vws1@psu.edu

University Participants

The Pennsylvania State University (Penn State)

- P.I.: Victor W. Sparrow, United Technologies Corporation Professor, Graduate Program in Acoustics
- FAA Award Number: 13-C-AJFE-PSU Amendments 55, 77, and 86
- Period of Performance: February 5, 2020 to April 13, 2023
- Tasks:
    1. Obtaining confidence in signatures, assessing metrics sensitivity, and adjusting for reference day conditions
    2. Assessing secondary sonic boom propagation

Project Funding Level

This project focuses on multiple tasks at The Pennsylvania State University and its subcontractors Queensborough Community College and Farmingdale State University. The FAA funding to Penn State from mid-2022 to 2023 was $110,000. Matching funds are expected to meet cost sharing on all tasks across 2022 and 2023. In-kind contributions have been pledged by Boom Supersonic ($150,000), Gulfstream ($100,000), and Exosonic ($110,000).

Investigation Team

- Victor W. Sparrow, P.I. (Tasks 1 and 2), Penn State
- Joshua Kapcsos, graduate research assistant (Task 1), Penn State
- Kimberly A. Riegel, co-investigator (Task 2), subrecipient to Penn State, Farmingdale State College, State University of New York
- Robert Downs, scientist (Task 2), Volpe National Transportation Systems Center
- Michael Rybalko, Joe Salamone, et al., Boom Supersonic (industrial partner)
- Brian Cook, Matthew Nickerson, Joe Gavin, and Charles Etter, Gulfstream (industrial partner)
- John Morgenstern, Exosonic (industrial partner)

Project Overview

We are on the verge of a true revolution in passenger aircraft development. Companies such as Boom Supersonic, Gulfstream Aerospace Corporation, Lockheed Martin, Exosonic, and others are reaching the point at which they can build, and deliver to users, aircraft capable of flying supersonically in an environmentally responsible way. This development will allow for decreased air transportation travel times, to the great benefit of everyone.

To introduce new supersonic aircraft, these vehicles must be certified as being sufficiently quiet to not highly annoy the public. Preparation for such a certification process has been ongoing for several years in the FAA Office of Environment and Energy (AEE). Working with its international partners in the International Civil Aviation Organizations (ICAO)'s Committee for Aviation Environmental Protection (CAEP), the FAA has been laying the groundwork for certification standards. The FAA's efforts have been supported by both universities and other government agencies. Specifically, Penn State has supported the FAA/AEE through Projects 8 and 24 in the PARTNER Center of Excellence and more recently in Projects 7, 41, and 42 of the ASCENT Center of Excellence. Summaries of these research efforts can be found on the websites provided. To date, a group of six candidate metrics for sonic boom certification have been agreed upon in CAEP's Working Group 1 (WG1; noise) Supersonic Task Group (SSTG). Multiple schemes for certification have been generated. Several schemes have been eliminated from further consideration, and others are currently being evaluated for possible implementation. Procedures have been proposed for acquiring and processing ground measurement of the sonic boom signatures, but all possibilities remain under discussion. The extent to which atmospheric conditions will affect the measurements, and the requirements and roles of numerical simulations of sonic booms propagating from the aircraft to the ground are being considered. One particularly challenging aspect is the influence of the atmosphere in distorting sonic boom signatures, owing to atmospheric turbulence, and the subsequent effects on the metric values. These are just several of the gaps that must be filled.

All these topics are being worked on, in a stepwise manner, in FAA and in WG1's SSTG. Recent efforts in ASCENT Project 41 have been aimed at supporting the FAA with technical expertise in the development of the certification procedures, as well as gaining an initial understanding of secondary sonic booms. Secondary sonic booms, also known as over-the-top sonic booms, are the sound energy that travels upward at heights above the aircraft cruise altitude and lands at distant locations. Secondary sonic booms are the reason that the Concorde was requested to transition from supersonic to subsonic speeds at substantial distances before entering the continental United States. ASCENT Project 41 ended in early 2021, and ASCENT Project 57 is now in its third year. However, much remains to be done, and efforts lasting several more years will be required to advance certification standards for supersonic aircraft.

In 2023 and beyond, continued support for supersonic aircraft noise efforts will be necessary for the FAA and its international partners to fill technical solution gaps and continue progressing toward certification procedures. Although other universities and industries will continue their focus on aircraft design and landing and takeoff studies, continued work on sonic boom issues will be essential, because these remain the greatest barrier to the use of environmentally responsible supersonic aircraft. ASCENT Project 57 will support the ongoing activities in ICAO CAEP and their WG1 (noise), with a focus on establishing supersonic aircraft en route procedures and metrics for noise certification standards, and to support the interface with the ICAO Air Navigation Commission to address related noise issues.

In the 2020–2023 project period, the emphasis will be on continuing the research support for supersonic aircraft en route procedures, including the utilization of an agreed-upon reference day atmosphere, the establishment of techniques for incorporating measurement data and simulations into a draft certification procedure, and the consideration of off-design flight speed sonic booms, such as focus booms and acceleration booms. Support will also be provided for a more comprehensive analysis of NASA's SonicBAT data set and efforts on methods to remove the effects of atmospheric turbulence on measured sonic boom waveforms to support certification. The 2020–2023 research will also need to consolidate and process the results of research in 2019–2020 on the topic of secondary sonic booms as a potential noise issue for the initial supersonic airplanes. This material will be of particular interest to ICAO's Air Navigation Commission, because it could affect the operation of supersonic aircraft in the near term.

Task 1 - Obtaining Confidence in Signatures, Assessing Metric Sensitivity, and Adjusting for Reference Day Conditions

The Pennsylvania State University

Objectives

ASCENT Project 57 is a transition from ASCENT Project 41: "Identification of Noise Acceptance Onset for Noise Certification Standards of Supersonic Airplanes." As national aviation authorities move toward developing noise certification standards for low-boom supersonic airplanes, several research gaps exist in the areas of signature fidelity, metrics, metrics' sensitivity to real-world atmospheric effects, adjustments for reference conditions, etc. The objective of this task is to support the FAA in the development of technical standards for civil supersonic aircraft under ICAO CAEP. This effort provides the FAA with

technical noise expertise regarding the development of noise certification standards for future civil supersonic passenger aircraft, primarily in the area of en route noise (sonic boom) minimization and/or abatement.

Task 1 in ASCENT Project 57 focuses on research initiatives needed to move toward the development of a low-boom supersonic en route noise certification standard. One objective was to expand the existing database of shaped sonic boom ground waveforms by continuing to simulate the effects of turbulence within various planetary boundary layer heights above the ground. Simulation parameters were verified, and a grid refinement study was conducted. Another objective was to conduct a reference day crosscheck for the new humidity profile agreed upon by CAEP's WG1.

Research Approach

Background

Propagation code KZKFourier is an augmentation of the Burgers equation into a KZKFourier propagation equation to include nonlinearity, diffraction, and absorption in directional sound beams, to simulate wind and temperature fluctuation effects of the atmospheric boundary layer according to the Ostashev and Wilson (2015) model. During the 2019–2020 academic year, PCBoom 6.7.1.1 and KZKFourier were used above and within the atmospheric boundary layer, respectively, to simulate turbulence effects of atmospheric boundary layer heights of 268.2, 411.4, and 1026.7 m, corresponding to SonicBAT Flight 5 conditions. Information regarding this endeavor appears in the 2020 report for ASCENT Project 057. After propagation of shaped boom signatures through 10 randomly generated atmospheres, the data were shared with the WG1 SSTG Procedures Subgroup (PrSG), in which zero-padding and spiking artifacts were discovered near the beginnings and ends of certain ground signatures; the plots shown in the 2020 report did not span the entire retarded time domain of the ground waveform data. These artifacts were corrected in the 2020–2021 academic year, which appears in the 2021 report for ASCENT Project 057.

Expansion of Shaped Boom Database

After correction for the artifacts in shaped boom ground signatures during the 2020–2021 academic year, NASA requested an additional 10 simulated passes of the C609 aircraft, which models the forthcoming NASA X-59 QueSST demonstrator, in the SonicBAT Flight 5 atmospheric conditions. Thus, 10 more random seeds were used to generate atmospheres in KZKFourier for each of the three boundary layer heights: 268.2, 411.5, and 1026.7 m. The expanded database was shared with the ICAO SSTG PrSG, and this expansion to 20 realizations plus the zero-turbulence condition allowed NASA to meet the required sample size for statistical tests. Each realization resulted in 100 ground waveforms at virtual microphones, for a total of 2,000 waveforms per atmospheric boundary layer (ABL) height (Figure 1).

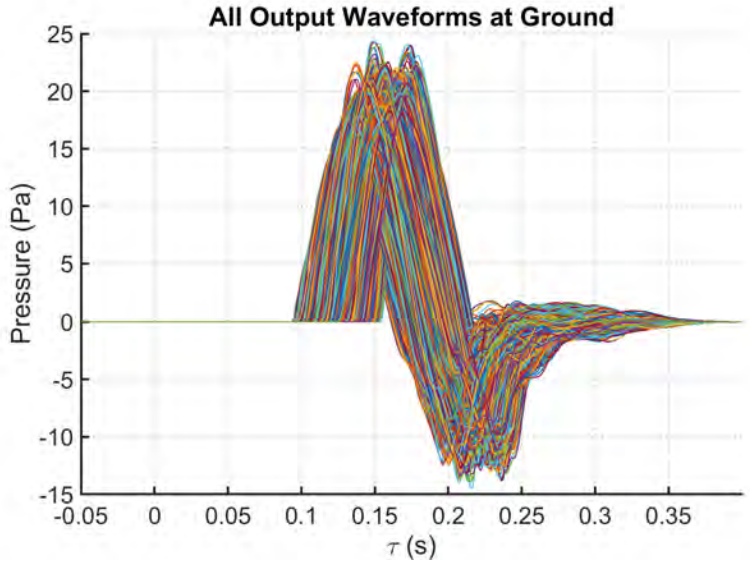

Figure 1. All 2,000 C609 ground waveforms after propagation through 20 randomly generated 1026.7-m atmospheric boundary layers.

KZKFourier Parameter Check

Penn State also investigated the capability of KZKFourier to run more extreme scenarios regarding atmospheric boundary layer height, turbulence parameters, etc. Checks included boundary layer heights of 2 km and 3 km, ambient temperature of 0 ˚C, and doubling the turbulence parameters of friction velocity, mixed-layer velocity scale, and surface-layer temperature scale with respect to the parameters of previous Penn State/JAXA databases. Individually testing the more extreme boundary layer heights, ambient temperature, and turbulence parameters gives a better idea than previous data regarding whether KZKFourier can handle some of the more extreme conditions presented in the SonicBAT report, because the previous waveform databases represented average SonicBAT conditions. Only one random seed was used for these checks.

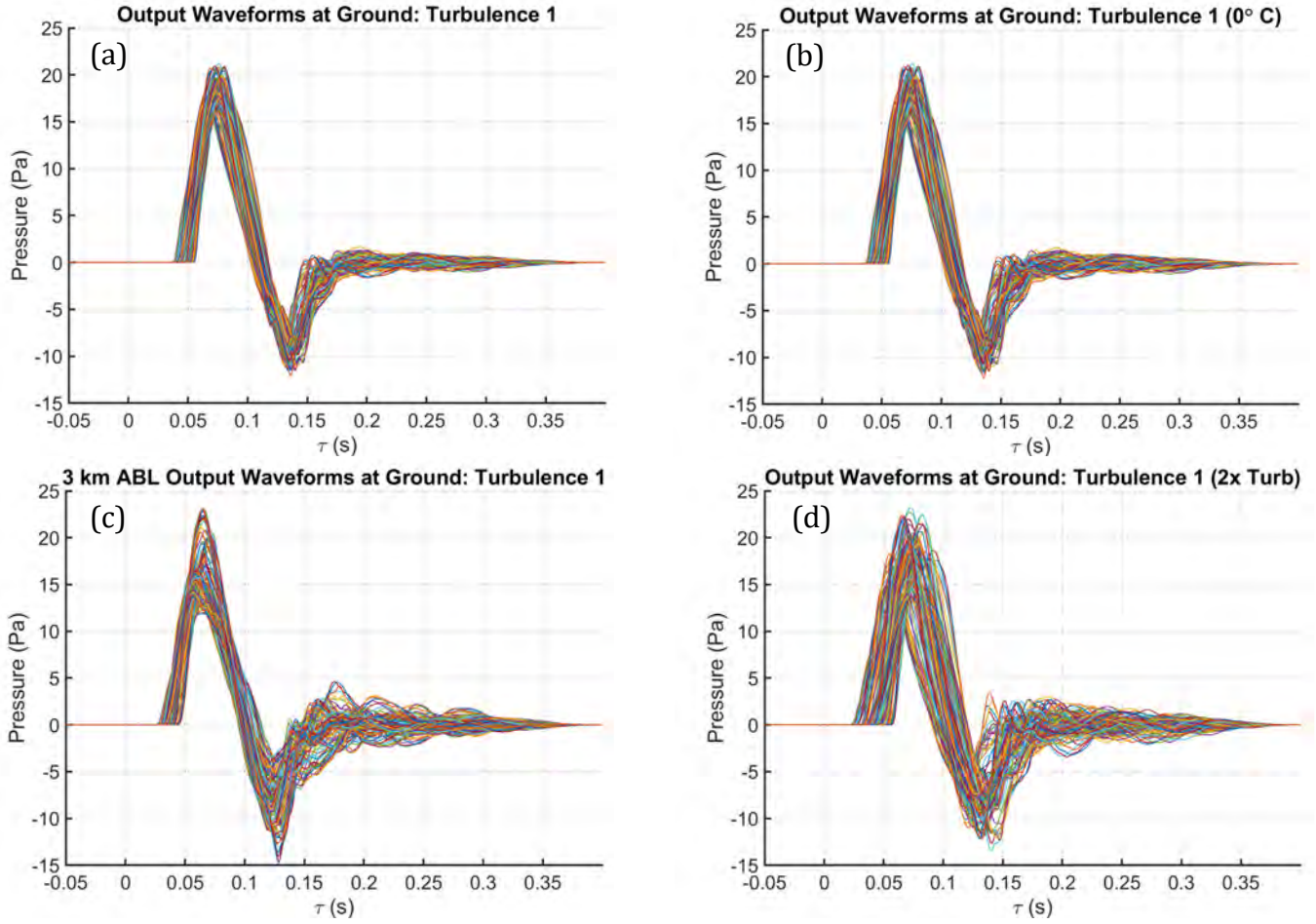

Figure 2. C609 shaped boom ground waveforms after single seed propagation through (a) original 1026.7-m ABL, (b) 0 ˚C ambient temperature, (c) 3-km ABL, and (d) doubled turbulence strength.

It was concluded that KZKFourier is capable of running simulations with freezing temperatures and atmospheric boundary layer heights of at least 3 km (Figure 2). In addition, the KZKFourier turbulence parameters of friction velocity, mixed-layer velocity scale, and surface-layer temperature scale can be doubled with respect to previous Penn State/JAXA databases only if the propagation step size is reduced. In this case, the propagation step size was halved to 0.20 m to circumvent error in KZKFourier simulation.

Grid Refinement Study

At the conclusion of the KZKFourier parameter check, SSTG PrSG members requested a grid refinement study to investigate whether the propagation code would yield the same results if the propagation step size were lowered. For this study, the

turbulence strength remained doubled, as in the above parameter check, and the grid refinement study therefore compared the necessary propagation half-step of 0.20 m to a quarter step of 0.10 m. When propagation step size was halved under doubled turbulence conditions, the differences between KZKFourier results were found to be negligible (Figure 3). However, the runtime of the quarter-step simulation was more than twice that of the half-step simulation.

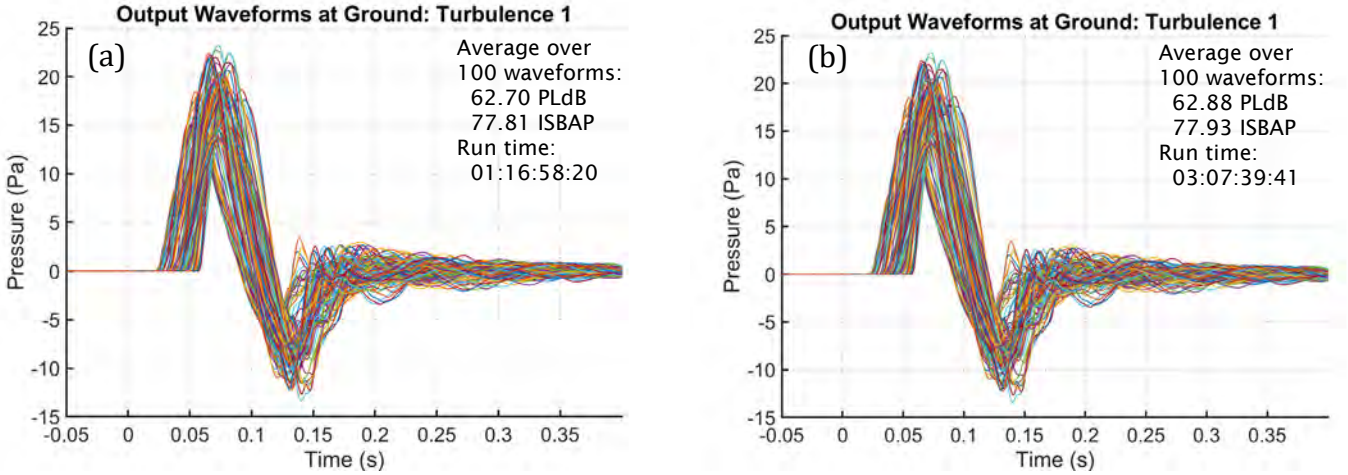

Figure 3. C609 shaped boom ground waveforms after (a) 0.20-m half-step size and (b) 0.10-m quarter-step size single random seed propagation through 1026.7-m ABL under doubled turbulence strength.

Reference Day Crosscheck

CAEP's WG1 (noise technical) agreed upon a standardized, Reference Day Atmosphere in 2021. Because members of WG1 did not have experience in using the reference day, Penn State initiated a reference day check in early 2022 to determine whether WG1 participants achieved similar results when using the new reference day atmosphere. The major difference between the new reference day and previous standard atmospheres was the humidity profile (Figure 4).

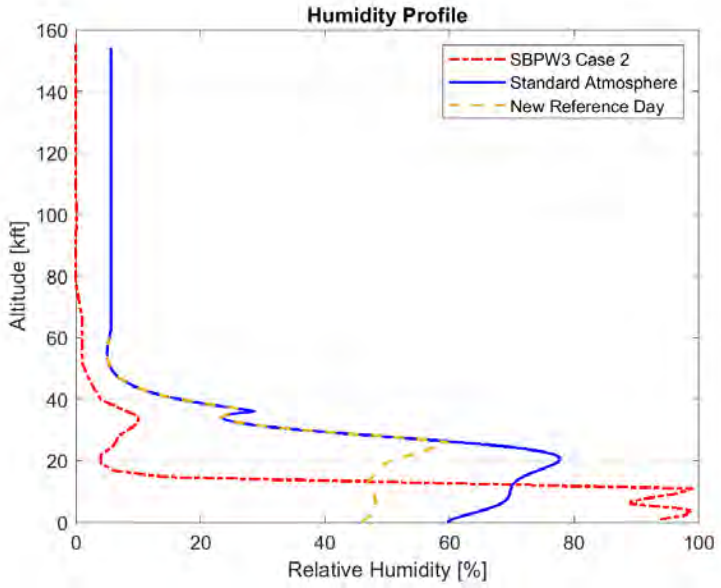

Figure 4. Humidity profiles from case 2 of the 3rd AIAA Sonic Boom Prediction Workshop (SBPW3), previous standard atmosphere, and new reference day atmosphere.

Participants inserted the new reference day atmosphere into their sonic boom codes, by using propagation case 2 from the Third AIAA Sonic Boom Prediction Workshop for all other parameters. Most participants used differing propagation codes. No-wind and windy cases were requested, and participants provided sonic boom signatures across the carpet, cutoff angles, ground intersections, propagation times, and the six sonic boom metrics under consideration by the SSTG: ASEL, BSEL, DSEL, ESEL, PL, and ISBAP. Ten international organizations participated in the reference day check, and eight of the participants submitted all materials to Penn State. Although not identical, the participants' results were in close agreement regarding ground footprints, cutoff angles, and metrics versus azimuthal angle (Figure 5). A major finding is that these international participants in WG1 now have the agreed-upon reference day atmosphere in their various sonic boom codes. The work toward en route supersonic certification schemes can now continue to develop, given that the schemes safely rely on an-agreed upon reference day atmosphere. Penn State will continue to work with participants to extend the analysis.

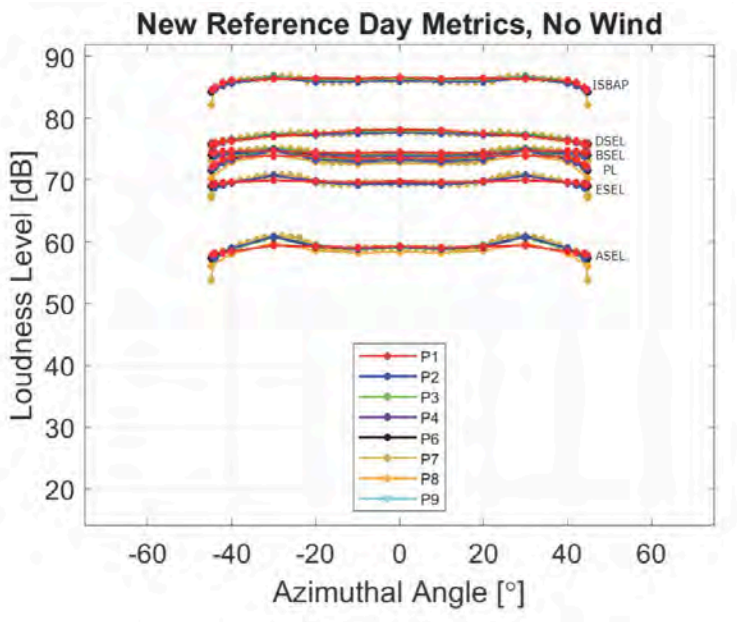

Figure 5. Sound level metrics versus azimuthal angle, calculated by eight international participants (1–4 and 6–9) for the C609 shaped boom signature propagated through the new reference day atmosphere with no wind.

Milestones

The shaped boom ground waveform database was expanded from 10 to 20 C609 passes and made available to WG1/SSTG/PrSG. Results of the KZKFourier parameter check and grid refinement study were presented to WG1/SSTG/PrSG. A new reference day crosscheck was conducted in WG1.

Major Accomplishments

The expansion of the C609 ground waveform database allowed NASA to conduct statistical tests that aid in the development of technical standards for civil supersonic aircraft and sonic boom propagation models. A result of the new reference day crosscheck is that the WG1 international participants now have the agreed-upon reference day atmosphere in their sonic boom codes. Because the results agreed closely, and the schemes were found to safely rely on the new reference day atmosphere, the work toward en-route supersonic certification schemes can continue to develop.

Publications

None.

Outreach Efforts

None.

Awards
None.

Student Involvement
Joshua Kapcsos was the Penn State graduate research assistant who worked on ASCENT Project 57 during the 2021–2022 academic year.

Plans for Next Period
Penn State will continue to work with the participants of the new reference day crosscheck to extend the analysis. KZKFourier is being extended to incorporate inhomogeneous atmospheres.

References
Ascent. (n.d.) *PARTNER: The partnership for air transportation noise and emissions reduction – ascent.* https://ascent.aero/partner/

Ascent. (n.d.) *Ascent.* https://ascent.aero/

Bradley, K. A., Hobbs, C. M., Wilmer, C. B., Sparrow, V. W., Stout, T. A., Morgenstern, J. M., Underwood, K. H., Maglieri, D. J., Cowart, R. A., Collmar, M. T., Shen, H., & Blanc-Benon, P. (2020). Sonic booms in atmospheric turbulence (SonicBAT): The influence of turbulence on shaped sonic booms (Report No. NASA/CR-2020-220509). National Aeronautics and Space Administration, Armstrong Flight Research Center, Edwards, CA.

Loubeau, A., Doebler, W., Wilson, S. R., Ballard, K., Coen, P. G., Naka, Y., Sparrow, V. W., Kapcsos, J., Page, J. A., Downs, R. S., Lemaire, S., & Liu, S. R. (2021). Developing certification procedures for quiet supersonic aircraft using shaped sonic boom predictions through atmospheric turbulence. The Journal of the Acoustical Society of America, 149(4), A102–A102. https://doi.org/10.1121/10.0004646

Maglieri, D., et al. (2014). *Sonic Boom: Six Decades of Research* (NASA/SP-2014-622). National Aeronautics and Space Administration, Langley Research Center, Hampton, VA.

Ostashev, V., & Wilson, D. (2015). *Acoustics in moving inhomogeneous media* (2nd ed.). CRC Press, Boca Raton, FL.

Stout, T. (2018). *Simulation of n-wave and shaped supersonic signature turbulent variations* [Ph.D. dissertation, Pennsylvania State University].

Task 2 - Assessing Secondary Sonic Boom Propagation
The Pennsylvania State University
Farmingdale State College, State University of New York
Volpe National Transportation Systems Center

Research Approach

Atmospheric Profile Stability
In previous work, we used monthly meteorological data to predict the behavior of secondary sonic booms. To validate the use of monthly averages, the stability of the atmospheric profiles was investigated in detail.

Monthly Extremes
To determine the variability of each month with respect to the mean values, we examined the atmospheric profiles of temperature and wind speed. The maximum and minimum, as well as the monthly average were created to show the differences between the most extreme values and the monthly means. For example, a winter month profile and a summer month profile are shown in Figure 6. The weather profiles show more variability in the winter than the summer between the monthly average and the extreme maximum and minimum profiles.

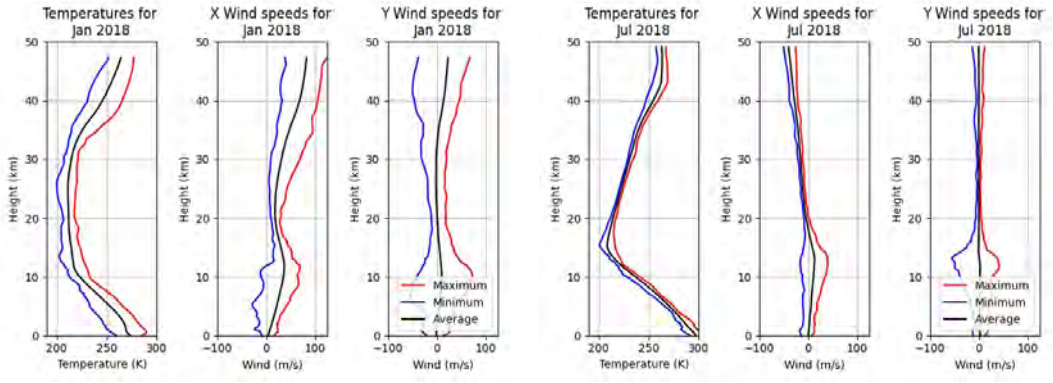

(a) (b)

Figure 6. Monthly average temperature and wind speed profiles compared with the maximum and minimum profiles for New York for (a) January and (b) July 2018.

After the atmospheric profiles for each month were created, the impacts on coastal arrivals were simulated. Specifically, the project team looked for any incidence in which the monthly average predictions varied from the extreme conditions. To create these simulations, we used PCBoom to determine the secondary sonic boom arrival locations. A Concorde aircraft was used with a trajectory simulating an approach into a New York airport, where the aircraft decelerated from Mach 2 to Mach 1.18 off the East coast of the United States. Figure 7 shows the arrival location predictions for January from the monthly mean atmospheric profile compared with the maximum and minimum atmospheric profiles. Figure 8 shows the arrival location predictions for the typical summer month of July. Although some substantial differences exist between the arrival locations, particularly in the summer months, the impact on the coastline does not change. In Figure 7, for a typical winter month, no impact on the coast is expected in the approach to the East coast of the United States. In Figure 8, for a typical summer month, for all three cases, impacts on the coastline are expected. This was the case for all months of the year except February, April, and December. In the February 2018 predictions (Figure 9), the minimum profile shows a dramatically different prediction than does the mean monthly value.

Time-of-day Atmospheric Variation

To better understand the variation, we further broke down the atmospheric profiles for the months in which the mean resulted in different predictions from the maximum and minimum profiles, to determine which factor had the largest impact. The first parameter examined was the time of day from the weather profile. Atmospheric profiles were available every 6 hours for the location off the eastern coast of the United States. We examined how the atmospheric profile varied by time of day, throughout the day. Figure 10 shows several days in the month of Februrary and the extent to which the atmospheric profiles varied throughout the day. For any given day, the differences among times of day had minimal impacts on the atmospheric profile. Consequently, variations in time of day showed no differences in the predicted arrival locations of the secondary sonic booms.

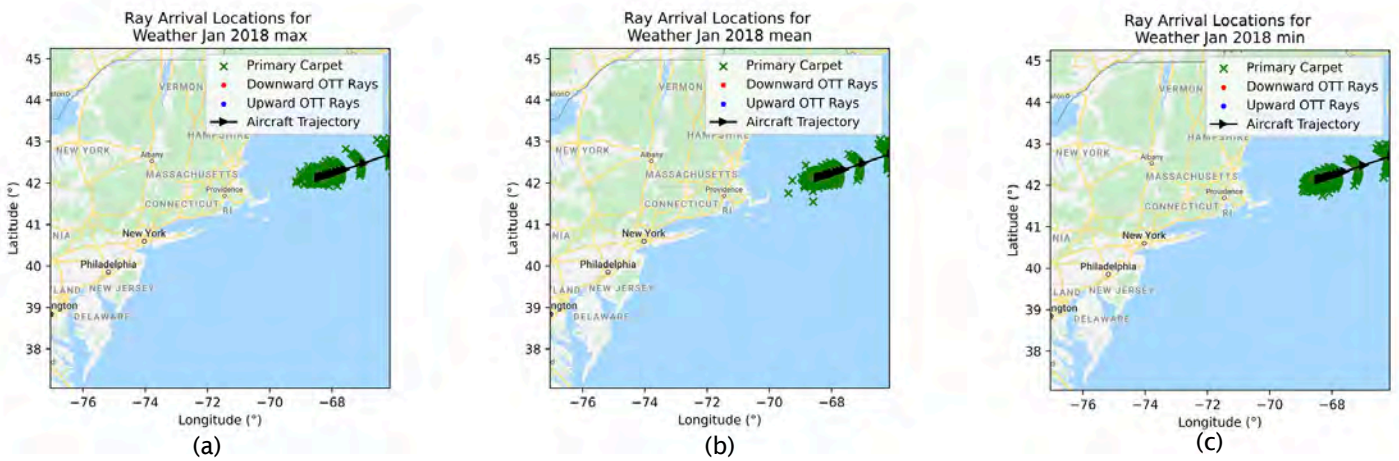

Figure 7. Simulated arrival locations for the (a) maximum, (b) mean, and (c) minimum atmospheric profiles for January 2018.

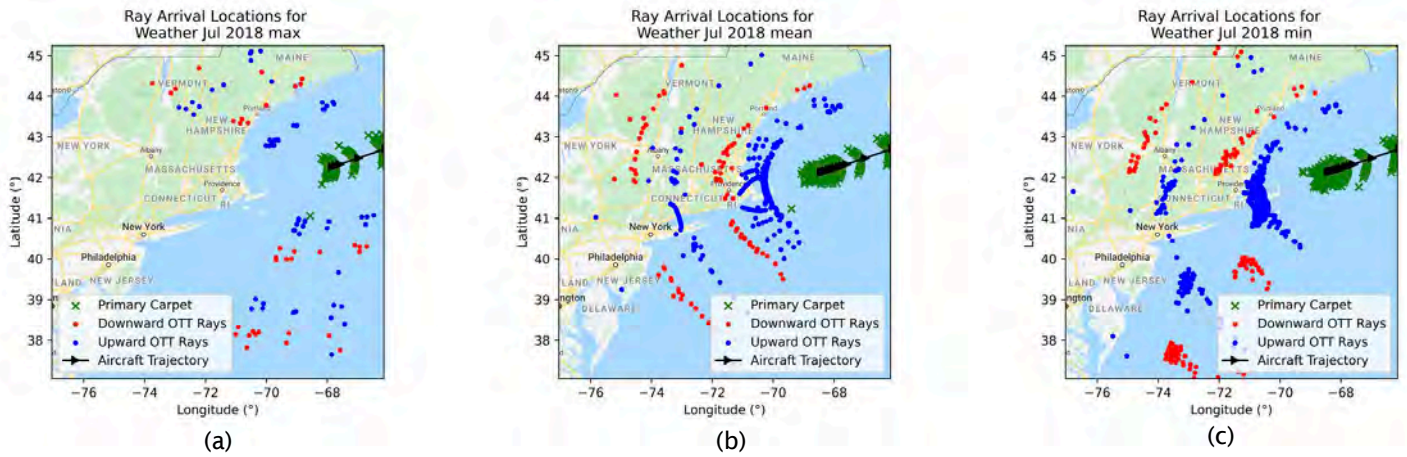

Figure 8. Simulated arrival locations for the (a) maximum, (b) mean, and (c) minimum atmospheric profiles for July 2018.

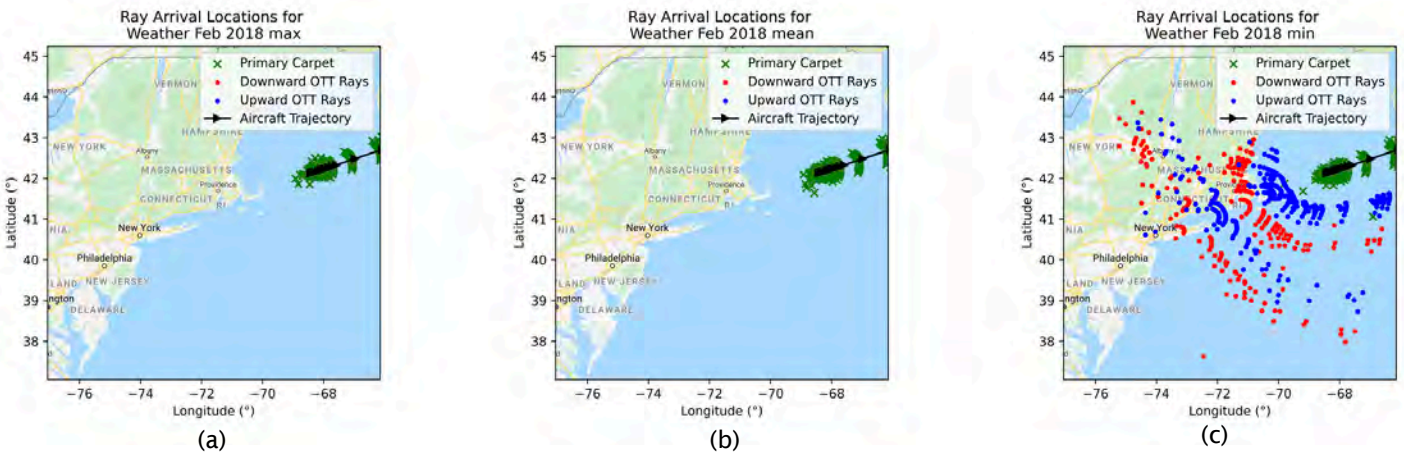

Figure 9. Simulated arrival locations for the (a) maximum, (b) mean, and (c) minimum atmospheric profiles for February 2018.

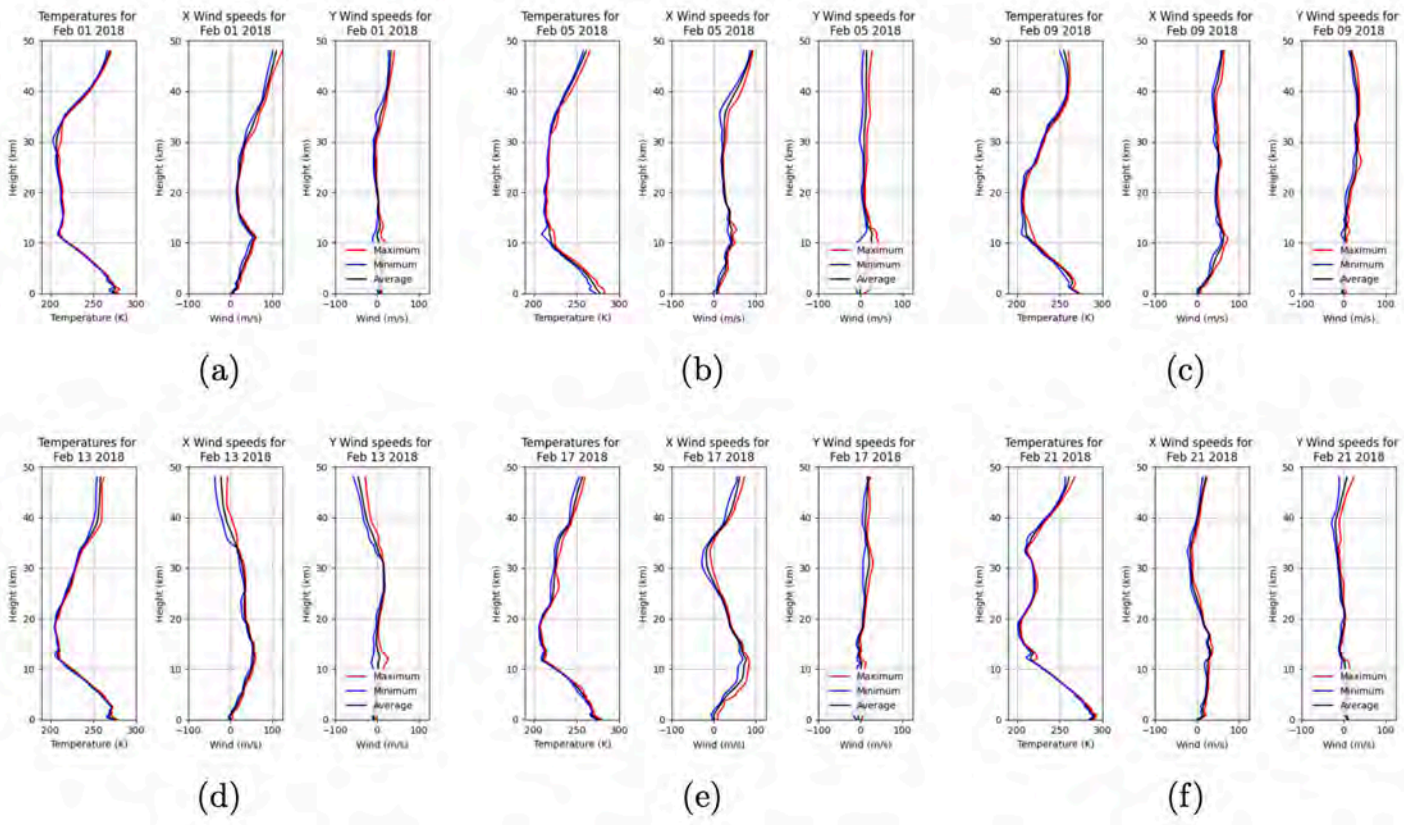

Figure 10. Variability in the atmospheric profiles across different times of day for the sample days (a) February 1, (b) February 5, (c) February 9, (d) February 13, (e) February 17, and (f) February 21 in the month of February 2018.

Daily Atmospheric Variation

The daily change throughout the month showed the greatest variation. To understand how often the daily profiles yielded different results from the monthly averages, we used the daily atmospheric profiles to predict the arrival locations of secondary sonic booms. The same arrival trajectory as in previous simulations was used. The results were then compared with monthly average simulations to determine how often the results differed. Except for February, December, and April, the daily averages agreed with the monthly averages in terms of impact on the coastline. For February, the monthly average atmospheric profile resulted in no secondary sonic boom arrivals. For the daily averages, seven days resulted in secondary sonic booms, and five of those days had impacts on the coastline. Thus, agreement was found 82% of the time. In December, the monthly atmospheric profile resulted in no secondary sonic boom arrival locations. For the daily averages, six days resulted in secondary sonic booms, and five of those days had arrivals that affected the coastline, thus resulting in agreement 84% of the time. In April, the monthly average atmospheric profile resulted in no secondary sonic boom arrival locations. For the daily averages, four days resulted in secondary sonic boom arrivals, and two of those days affected the coastline, for an agreement of 87%. All days that affected the coastline were late in the month; this finding was not unexpected, because April is a transition month between winter and summer.

Summary Regarding the Use of Monthly Average Profiles

To determine whether the monthly average atmospheric profiles are sufficient, the coastline daily atmospheric profiles were used to compare to the monthly average atmospheric profiles. Overall, the agreement between daily and monthly averages was at 96.5%. Therefore, using monthly averages is appropriate to predict the arrival locations of secondary sonic booms throughout the year.

Additional Support from Volpe National Transportation Systems Center

In support of secondary sonic boom propagation modeling, Volpe evaluated a PCBoom test case, on the basis of 1979 Concorde flights, in which caustic location did not appear coincident with crossing rays. The test case inputs were modified to use a geomode-format trajectory, because the ray tracing modes used in secondary boom modeling are not fully compatible with longlat-format trajectories. Of note, Volpe has separately developed a fix for this issue, which was delivered to NASA in July 2022. Until that modification is available in a publicly released version of PCBoom, the current recommendation is to use geomode-format trajectories for secondary boom modeling.

To investigate determination of caustic location in the secondary boom test case, PCBoom was modified to provide additional diagnostic output:

1. Ray paths for four corners of the ray tube, in local coordinates in feet and geodetic coordinates (longitude, latitude) in degrees
2. Components of the wave-normal unit vector along the primary ray

Quantities output as part of the new diagnostic file are those used internally for ray tube area calculations. The ray tube areas were verified with external calculations in MATLAB. The method implemented in PCBoom ray tube area calculation (following C. L. Thomas, "Extrapolation of Wind-Tunnel Sonic Boom Signatures Without Use of a Whitham F Function," in NASA SP-255, Third Conference on Sonic Boom Research, Schwartz, I.R., (Ed.), January 1971) was summarized in a set of supplementary slides, along with the internal details of how PCBoom selects initial points to form a ray tube. Finally, a study was conducted to examine the effect of user-selectable propagation time step in PCBoom. The results indicated that focus location can substantially vary for large time steps, as in the supplied test case. Reducing the time step to 0.5 s (PCBoom default) or less produced consistent focus locations.

In support of model validation with 1979 Concorde data, Volpe investigated a newly discovered set of detailed hard-copy tracking data from that test campaign. A catalog of the available data was produced and documented in a separate tech memo. Comparisons of the previously available data in the report by Rickley and Pierce were made. Previous re-analyses of flights from the 1979 campaign were limited by available tracking data. This newly uncovered archive may potentially be used for more accurate reproduction of aircraft conditions for many flights. Similarly, a database of trajectories for Concorde flights near the eastern U.S. coast may have other uses relevant to ASCENT Project 57.

Milestone

The use of average monthly atmospheric profiles was validated as an appropriate way to predict the impacts of secondary sonic booms on coastlines.

Major Accomplishments

ASCENT Project 57 Task 2 extended knowledge of secondary booms impacting coastlines; now the project can continue making predictions confidently using the average monthly profiles for prediction.

Publications

Peer-reviewed journal publications

Riegel, K. A., & Sparrow, V. W. (2022). Secondary sonic boom predictions for U.S. coastlines. *The Journal of the Acoustical Society of America*, *152*(5), 2816–2827. Doi: 10.1121/10.0014860

Outreach Efforts

None.

Awards

None.

Student Involvement

None.

Plans for Next Period

In Task 2, we will continue to work toward accurate acoustic signatures for secondary sonic booms; this work will be essential to assess community impact. The project team will also determine the feasibility of prediction of the impact location of secondary sonic boom rays from upcoming test flights of the X-59 Quesst aircraft.

References

Plotkin, K., Page, J., & Haering, E. (2007). *Extension of PCBoom to over-the-top booms, ellipsoidal earth, and full 3-D ray tracing* [Presentation]. 13th AIAA/CEAS Aeroacoustics Conference.

Rickley, E. & Pierce, A. (1980). *Detection and assessment of secondary sonic booms in New England* (Report No. FAA-AEE-80-22). Defense Technical Aviation Center, Fort Belvoir, VA.

Saha, S., Moorthi, S., Wu, X., Wang, J., Nadiga, S., Tripp, P., Behringer, D., Hou, Y.-T., Chuang, H., Iredell, M., Ek, M., Meng, J., Yang, R., Mendez, M. P., van den Dool, H., Zhang, Q., Wang, W., Chen, M., & Becker, E. (2014). *The NCEP Climate Forecast System Version 2*. Journal of Climate, *27*, 2185-2208. Doi: 10.1175/JCLI-D-12-00823.1

Thomas, C.L. (1970). *Extrapolation of Wind-Tunnel Sonic Boom Signatures Without Use of a Whitham F Function*. NASA SP-255, Third Conference on Sonic Boom Research.

Project 058 Improving Policy Analysis Tools to Evaluate Higher-Altitude Aircraft Operations

Massachusetts Institute of Technology

Project Lead Investigator

Steven R. H. Barrett
Professor of Aeronautics and Astronautics
Director, Laboratory for Aviation and the Environment
Massachusetts Institute of Technology
77 Massachusetts Ave, Building 33-322, Cambridge, MA 02139
617-452-2550
sbarrett@mit.edu

Sebastian D. Eastham
Research Scientist
Laboratory for Aviation and the Environment
Massachusetts Institute of Technology
77 Massachusetts Ave, Building 33-322, Cambridge, MA 02139
617-253-2170
seastham@mit.edu

University Participants

Massachusetts Institute of Technology (MIT)

- P.I.: Prof. Steven R. H. Barrett
- FAA Award Number: 13-C-AJFE-MIT, Amendment Nos. 064, 089, and 099
- Period of Performance: February 5, 2020 to September 19, 2023
- Reporting Period: October 1, 2021 to September 30, 2022
- Tasks (Note: tasks completed before this reporting period are listed as completed):
    1. Develop a set of emissions scenarios for high-altitude aviation
    2. Extend and validate MIT's existing atmospheric simulation capabilities (completed)
    3. Simulate atmospheric impacts of high-altitude emissions by using updated capabilities
    4. Calculation of atmospheric sensitivity matrices
    5. Develop and update operational tools capable of quantifying environmental impacts of aviation
    6. Regionalized contrail parameterization
    7. Investigate the dependence of aviation emissions impacts on non-aviation factors

Project Funding Level

This project received $1,150,000 in FAA funding and $1,150,000 in matching funds. Sources of match are approximately $218,000 from MIT, plus third-party in-kind contributions of $391,000 from NuFuels, LLC, $127,000 from Savion Aerospace Corporation, and $414,000 from Google, LLC.

Investigation Team

Principal Investigator:	Prof. Steven Barrett (MIT) (all tasks)
Co-Principal Investigator:	Dr. Sebastian Eastham (MIT) (all tasks)
Postdoctoral Researcher:	Dr. Sadia Afrin (MIT) (all tasks)
Graduate Research Assistants:	Lucas Jeongsuk Oh (MIT) (Tasks 1, 3, and 4)
	Joonhee Kim (MIT) (Tasks 4–6)
	Carla Grobler (MIT) (Task 7)
	Prakash Prashanth (MIT) (Task 7)

Project Overview

Companies are proposing, developing, and testing aircraft operating at higher altitudes, such as commercial supersonic aircraft and high-altitude, long-endurance unmanned aerial vehicles. These aircraft offer the potential to enable new use cases and business models in the aviation sector. However, the combustion emissions of these vehicles will have atmospheric impacts that differ from those of conventional subsonic aviation, because of the higher altitudes of emission. Emissions at higher altitudes are associated with a different chemical environment, longer emissions lifetimes, and transport of emissions over greater distances. Furthermore, new developments in emissions impact estimation have provided a more nuanced view of the environmental consequences of conventional aircraft activity, including the recognition that their climate and air quality impacts both vary depending on the prevailing conditions of the emissions and the time horizon of the assessment.

In this project, we propose to quantify the environmental consequences of such high-altitude aviation emissions. For this purpose, we will perform high-fidelity atmospheric simulations by further developing and applying the GEOS-Chem UCX tropospheric–stratospheric chemistry–transport model and its adjoint. The results will be leveraged to (a) evaluate the climate (radiative forcing; RF) effects of high-altitude aircraft emissions, and (b) estimate the sensitivity of the global ozone column and surface air quality to these emissions. Consequently, the climate, air quality, and ozone impacts for a small number of different proposed supersonic aircraft designs and performance characteristics will be quantified. We will also perform a historical assessment of the impacts of aviation emissions, quantifying how factors such as changing emissions indices and an evolving chemical background have affected—and will affect—the total impacts. On the basis of data from these simulations, a flexible, rapid approach for assessing the impacts of sub- and supersonic aircraft will be presented.

Task 1 - Develop a Set of Emissions Scenarios for High-Altitude Aviation

Massachusetts Institute of Technology

Objective

This task is aimed at developing emissions inputs that cover scenarios relevant to near-future aviation, extending impact estimation to cover a range of altitudes exceeding those of current commercial airline activities. The specific focus of the work during this period was to test and refine the developed global supersonic emissions inventories.

Research Approach

The team continued to develop a mathematical model able to produce an estimate of emissions of key chemical species (e.g., nitrogen oxides (NO_x), sulfur oxides (SO_x), water vapor, black carbon, and organic carbon) during the reporting period. In the meantime, deficiencies were found and corrected. In particular, the previously developed MIT scenarios evaluated the market too conservatively with respect to the scenario designed in ASCENT 10, thus resulting in a significant difference in the amounts of emissions by the supersonic fleet. Therefore, new emissions scenarios were developed on the basis of the assumption that the market status of the supersonic fleet is high, low, or intermediate, to strengthen the capabilities of our research. This diversification of the emissions scenarios not only allows us to predict the demand for the future supersonic fleet for each demonstrated situation, but also expands the predictability and capabilities of our tool.

The fuel burn emissions maps corresponding to each scenario are shown in Figure 1. In the MIT High case, the market need for supersonic aviation has high growth, the MIT Low case reflects low economic growth, and the MIT Mid case is intermediate between the MIT High and MIT Low cases. The difference between the MIT Low and MiT High cases is reflected in underlying market demand; however, the flight frequency does not simply increase for the same overall flight network. As the market expectation increases, flight frequency can increase but new routes can also be established for supersonic travel. The base supersonic aircraft fleet to be assessed was designed through prior research under ASCENT 58, a previous NASA-funded project, and additional information from ASCENT 47.

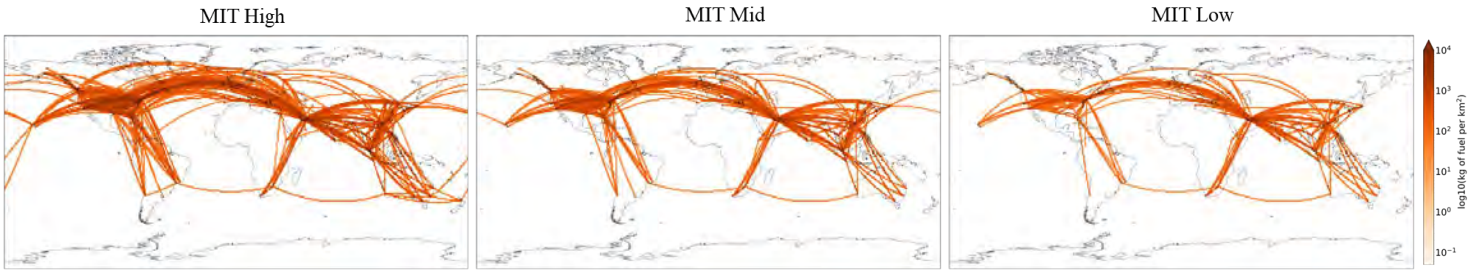

Figure 1. Emissions maps for representative supersonic aircraft developed at MIT. Left: MIT High; middle: MIT Mid; right: MIT Low.

In addition to using the emissions inventory developed by ASCENT 58, our team used an emissions scenarios from ASCENT 10. Using emissions scenarios produced in other studies helps to ensure that the model is robust. In particular, our team can verify our tools' capabilities and increase the reliability of the results through exchanges with the research group conducting environmental analysis by using the ASCENT 10 data. Therefore, we also interacted with the ASCENT 22 team in the emissions inventory we produced.

The tool developed under ASCENT 58 expects data to be converted to a common resolution. This requires solving two problems, which were explored in the process of preparing emissions data from ASCENT 10. First, a difference existed between the resolution of the tool used by ASCENT 10 and that used by our tools. The second problem was that a naïve application of segmented data (as provided by ASCENT 10) results in discontinuities in the emission grid. Therefore, we recognized a need to develop an algorithm to change any resolution to fit the dimension requirements of our tool and developed an algorithm to solve the two problems described above—the discrepancy in resolution and discontinuity.

To solve the discontinuity problem, we used a method of splitting discrete points into smaller pieces than the minimum grid size of the target resolution. This method calculated all values at designated points through 3D linear interpolation (latitude, longitude, and height) among discontinuously distributed locations along the flight path. Therefore, data arranged in tiny grids needed to be redistributed according to the targeting resolution to resolve the disparity in resolution. To this end, we cut the atmosphere in advance according to the target resolution (i.e., a large grid), then calculated the value corresponding to the target resolution grid by counting the small grid in a large grid and adding all emission elements inside it. Ultimately, we verified the law of mass conservation before and after conversion to determine whether any abnormalities were present. The changes in emissions before and after algorithm conversion are shown in Figure 2.

Figure 2. Emissions maps for representative supersonic aircraft developed by ASCENT 10 before and after conversion. Left: before the conversion; right: after the conversion.

We compared and analyzed the results developed by ASCENT 10 and ASCENT 58. When compared with ASCENT 10, ASCENT 58 has more conservative market expectations, and our team predicted that fewer supersonic fleet flights would occur in the target year. Our team also has an estimate of 2035 subsonic flights. Table 1 summarizes overall design choice and emissions characteristics under the three scenarios in ASCENT 58, one scenario provided in ASCENT 10, and the 2035 subsonic flight.

Table 1. Design information and emissions characteristics of supersonic fleets for each emissions inventory (Georgia Institute of Technology [Georgia Tech] case from ASCENT 10; MIT cases from ASCENT 58 and ASCENT 4; and subsonic 2035 case)

	Emissions cases				
	Georgia Tech	**MIT High**	**MIT Mid**	**MIT Low**	**Subsonic 2035**
Mach number	2.2	1.6	1.6	1.6	-
Passenger capacity	55	100	100	100	-
Maximum range, nmi	4,500	3,500	3,500	3,500	-
Cruise ceiling, km	21	17	17	17	12
Fuel per 100 seat-km, kg/100 seat-km	19.0	7.15	7.13	7.08	2.26
Total fuel burn, Tg	122	43.1	19.3	9.56	424
Fleet average EINO_x, g/kg-fuel	14.7	9.05	9.05	9.18	15.2
Total NO_x, Gg ($GgNO_2$ equivalent)	1800	390	175	87.8	6440
Total black carbon, Gg	6.12	1.36	0.607	0.300	34.8
Fuel sulfur content, ppm	600	600	600	600	600
Fleet average EIH_2O, kg/kg-fuel	1.231	1.231	1.231	1.231	1.231

We also conducted a detailed analysis of the information provided by ASCENT 10 and the information developed by our team. The emissions by altitude and latitude were calculated for more detailed analysis and comparison. The ASCENT 10 team projected that approximately 83% of emissions would be allocated to the northern hemisphere (NH). In contrast, our team projected that approximately 91% of emissions would occur in the NH. More specifically, we projected that 57% of emissions would occur between 30˚ and 60˚ latitude, whereas ASCENT 10 projected 38%. Because of the difference in cruise ceiling altitude, the altitude at which the greatest emissions occur is also different.

The attitude at which the greatest emissions occur is the 19–21 km band for the ASCENT 10 inventory, compared to 16-18 km for the MIT inventory (see Figure 3). This is a useful difference, as we can rigorously assess the response simulated in the ASCENT 58 tool for multiple cruise altitude scenarios.

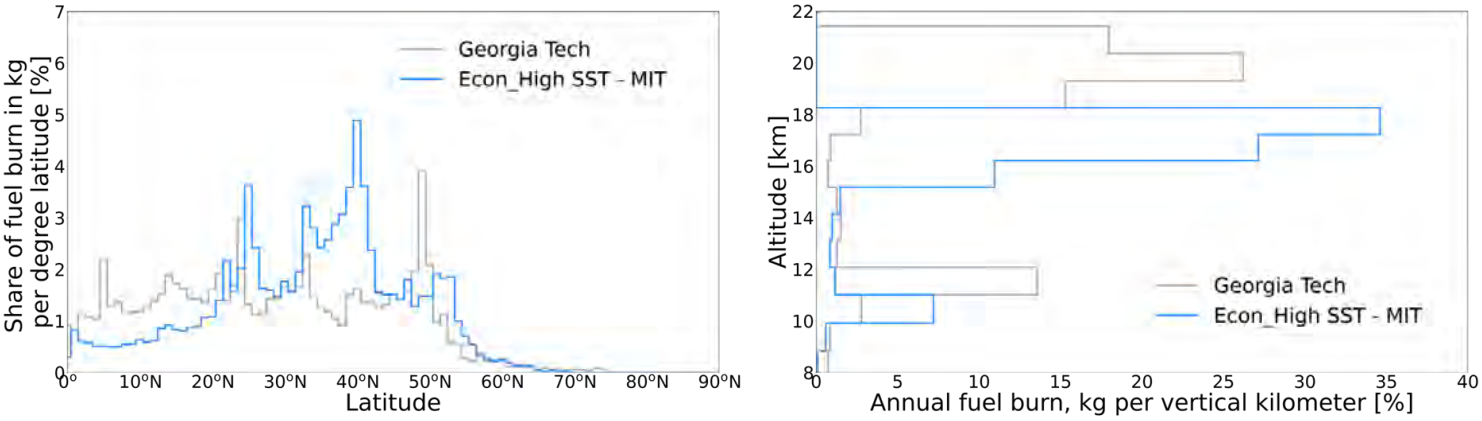

Figure 3. Share of fuel burn distribution. Left: annual fuel burn distribution by latitude; right: by altitude.

Milestones

- New emissions maps for representative supersonic aircraft were generated (Figure 1).
- The ASCENT 10 data were transformed into continuous data and modified for use in the MIT simulation tool (Figure 2).
- The characteristics of the scenarios developed by ASCENT 58 and ASCENT 10 were analyzed (Table 1 and Figure 3).

Major Accomplishments

- The team developed new emissions scenarios assuming high-activity market status.
- New developed emissions inventories were provided to ASCENT Project 22 to enable comparison of estimated impacts by using multiple models.
- The team developed an algorithm that can modify the entire dimensions and continuity of the data even if the data formats differ. The ASCENT 10 data were changed to align with those of ASCENT 58 with the algorithm (Figure 2).

Publications

None.

Outreach Efforts

Progress on all tasks was communicated during biweekly briefing calls with the FAA and reported in quarterly progress reports. ASCENT project 58 was also the subject of a report delivered to the 2022 ASCENT Fall Meeting.

Awards

None.

Student Involvement

During the reporting period of academic year (AY) 2021–2022, the MIT graduate student involved in this task was Lucas Jeongsuk Oh.

Plans for Next Period

Task 1 was largely completed in AY 2021–2022. The team will continue testing, refining, and comparing the global emissions data sets in AY 2022–2023.

Task 2 - Extend and Validate MIT's Existing Atmospheric Simulation Capabilities

Massachusetts Institute of Technology

Objective

The objective of Task 2 is to extend and validate MIT's existing atmospheric simulation capabilities, with the specific goal of ensuring that impacts on critical metrics of air quality and climate can be accurately represented. During AY 2020–2021, the team developed and tested a higher-resolution version of the GEOS-Chem UCX tropospheric–stratospheric global chemistry–transport model to capture localized effects.

Research Approach

The team is using the GEOS-Chem UCX tropospheric–stratospheric global chemistry–transport model as the central tool to quantify climate, air quality, and ozone impacts resulting from high-altitude aviation (Eastham et al., 2014). Therefore, the capabilities of this model for these purposes must be evaluated, and those capabilities must be extended where necessary. Two major subtasks have been identified: Task 2a, increasing the resolution of the model to capture localized impacts at a global resolution of 2°×2.5° or equivalent; and Task 2b, implementing a technique to estimate stratospherically adjusted RF, rather than instantaneous RF. Task 2b was largely completed in AY 2019–2020, whereas Task 2a work was completed in AY 2020–2021. Details of this task have been provided in prior annual reports.

Milestones

Task 2 was completed in AY 2020–2021.

Major Accomplishments

A manuscript was published that used the new stratospherically adjusted RF calculations to evaluate the impacts of supersonic civil aviation on the environment.

Publications

Eastham, S. D., Fritz, T., Sanz-Morère, I., Prashanth, P., Allroggen, F., Prinn, R. G., Speth, R. L., & Barrett, S. R. H. (2022). Impacts of a near-future supersonic aircraft fleet on atmospheric composition and climate. *Environmental Science: Atmospheres*, *2*(3), 388–403. Doi: 10.1039/D1EA00081K

Outreach Efforts

Progress on all tasks was communicated during biweekly briefing calls with the FAA and reported in quarterly progress reports.

Awards

None.

Student Involvement

None.

Plans for Next Period

Task 2 was completed in AY 2020–2021.

References

Eastham, S. D., Weisenstein, D. K., & Barrett, S. R. H. (2014). Development and evaluation of the unified tropospheric–stratospheric chemistry extension (Ucx) for the global chemistry-transport model GEOS-Chem. *Atmospheric Environment*, *89*, 52–63. Doi: 10.1016/j.atmosenv.2014.02.001

Task 3 - Simulate Atmospheric Impacts of High-Altitude Emissions by Using Updated Capabilities

Massachusetts Institute of Technology

Objective

The objective of this task is to estimate the atmospheric response to the representative near-future aviation scenarios described in Task 1, and to convert the raw model outputs to impacts. These simulations will calibrate the simulated impacts and the performance of the new version of the Aviation environmental Portfolio Management Tool–Impacts (APMT-IC).

Research Approach

To achieve the goal of Task 3, the team plans to conduct simulations for more than 10 years. During this reporting period, simulations for a total of 3 years were executed with further simulations ongoing.

Our team plans to ultimately include all chemical species (NO_x, SO_x, water vapor, black carbon, organic carbon, and unburned hydrocarbons) to estimate the atmospheric response to supersonic aviation. The focus thus far has been on NO_x which was identified as the priority pollutant, excluding other pollutants for the purpose of initial evaluation. We therefore simulate three years of impacts for supersonic aircraft NO_x emissions from three different fleets as previously described.

First, the baseline case underlying all simulations was set. The baseline assumed a point at which no future supersonic aviation would occur. Our team updated the subsonic aviation with the estimate for the year 2035 and included the estimation in the baseline to increase credibility. Thus, we created a test case that adds a supersonic fleet case to the baseline. In this way, we determined the degree of the environmental impact of near-future aviation scenarios by subtracting the environmental response obtained through baseline from the results obtained through the test case.

Specific outcomes investigated for each scenario are changes in the global ozone column and in surface air quality, including ozone and fine particulate matter ($PM_{2.5}$). These results were calculated at a global resolution of 2˚×2.5˚ (see Task 2) by using GEOS-Chem (including the UCX stratospheric chemistry capabilities). These outcomes were estimated by forward sensitivity analysis in Task 4. Figure 4, Figure 5, and Figure 6 show the simulation results for the third year. Each result is an environmental change caused by the supersonic fleet.

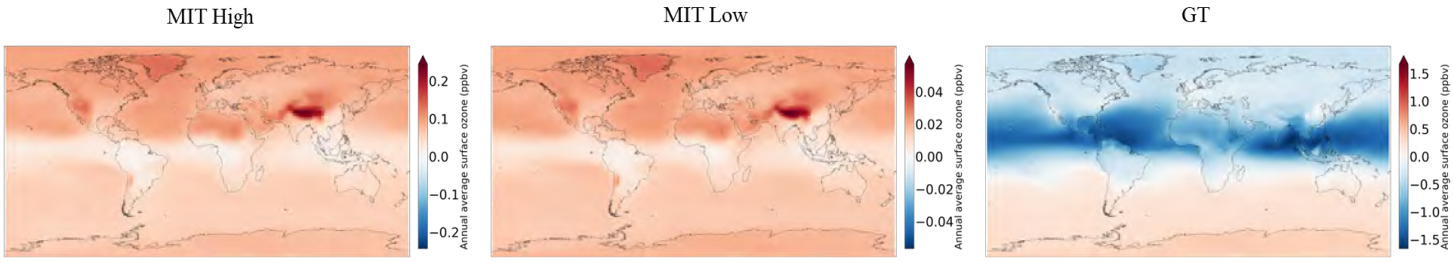

Figure 4. Changes in annual mean surface ozone concentrations due to SST emissions from three scenarios after 3 years. Left: MIT High; middle: MIT Low; right: Georgia Tech (ASCENT 10).

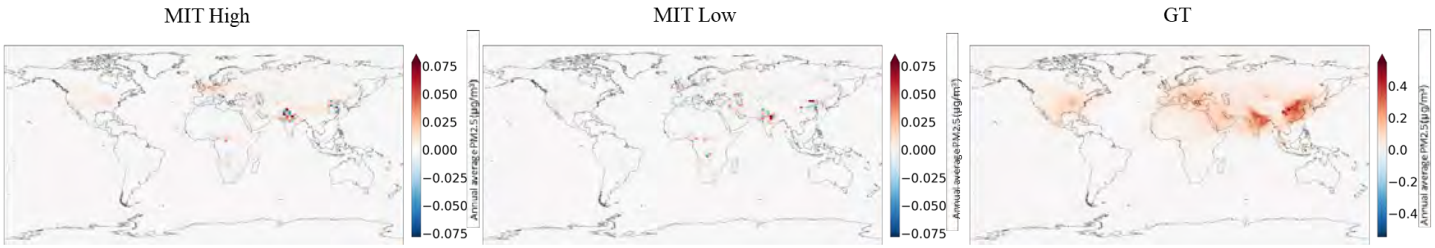

Figure 5. Changes in annual mean surface $PM_{2.5}$ concentrations due to SST emissions from three scenarios after 3 years. Left: MIT High; middle: MIT Low; right: Georgia Tech (ASCENT 10).

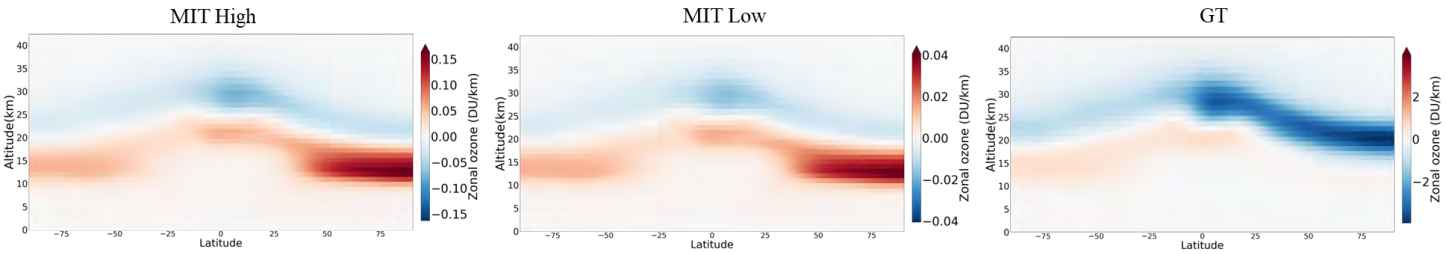

Figure 6. Changes in zonal mean ozone concentrations due to SST emissions from three scenarios after 3 years. Left: MIT High; middle: MIT Low; right: Georgia Tech (ASCENT 10). DU/km = Dobson units per vertical kilometer.

The simulated impacts of emissions differ for the different fleets. Surface ozone increases in response to the MIT cases but decreases in response to the Georgia Tech/ASCENT 10 case, because the cruise flight altitude in the case of Georgia Tech is higher than that of MIT. This is also the cause of the different pattern of ozone change (Figure 6). Meanwhile the pattern of change is nearly identical for MIT High and MIT Low, reflecting the relative linearity of the response for emissions at the same altitude. In addition, because the Georgia Tech case emits more NO_x than the MIT case, the resulting increase in $PM_{2.5}$ is greater.

Milestones

- Full forward GEOS-Chem simulations at high resolution (2°×2.5°) to quantify the climate, ozone, and air quality response to representative supersonic aircraft emissions were performed (Figure 4, Figure 5, and Figure 6).
- APMT-IC was tested by using the outputs of atmospheric responses to representative supersonic aircraft emissions.
- The climate, air quality, and ozone impact sensitivities developed in Task 4 by using GEOS-Chem simulations were calibrated with these estimates.

Major Accomplishments

- Three years of GEOS-Chem simulations using the supersonic emissions inventory developed by MIT and informed by the ASCENT Project 47 engine design were completed.
- The emissions inventory developed by the ASCENT 10 supersonic aircraft design team has also begun to be processed for simulation with GEOS-Chem.

Publications

None

Outreach Efforts

Progress on all tasks was communicated during biweekly briefing calls with the FAA and reported in quarterly progress reports.

Awards

None.

Student Involvement

During the reporting period of AY 2021–2022, the MIT graduate student involved in this task was Lucas Jeongsuk Oh.

Plans for Next Period

During the next project period, the project team will continue to conduct spin-up simulations and detailed analysis of the climate, air quality, and ozone impacts to supersonic aviation, on the basis of the data provided in Task 1. In addition, the team will continue calibrating the climate, air quality, and ozone impact sensitivities developed in Task 4 by using Task 3 GEOS-Chem simulations.

Task 4 - Calculation of Atmospheric Sensitivity Matrices

Massachusetts Institute of Technology

Objective

The objective of this task is to convert the impacts calculated under Task 3 for each scenario into sensitivities of environmental impacts with regard to key parameters. This process will enable the evaluation of local outcomes in air quality and support Task 5 in the rapid quantification of environmental impacts from any inventory with gridded emissions.

Research Approach

This task requires a set of GEOS-Chem simulations in which representative perturbations of a species are included over a predefined region. By calculating the change in environmental impact quantities (zonal mean ozone, surface particulate matter, and so on), the sensitivity of these quantities to emissions in each region can be determined. Linear combination of the sensitivities can then be performed to represent diverse emissions cases, including new altitude distributions, geographical distributions, and exhaust compositions for subsonic and supersonic aviation.

The team conducted sensitivity analysis for emissions at altitudes up to 26 km atmosphere, divided into a cruise (above 8 km) and non-cruise (under 8 km) region. Above 8 km, 40 regions are specified on the basis of latitude and altitude only. Below 8 km, we specify six regions on the basis of longitude and latitude. Each region (e.g., North America, Europe, and the Middle East) is defined as a compromise to ensure that areas where emissions from aviation are likely to grow differently are independently modeled while also minimizing the number of distinct regions (because each requires additional simulations to characterize). Detailed information on the non-cruise case is shown in Figure 7.

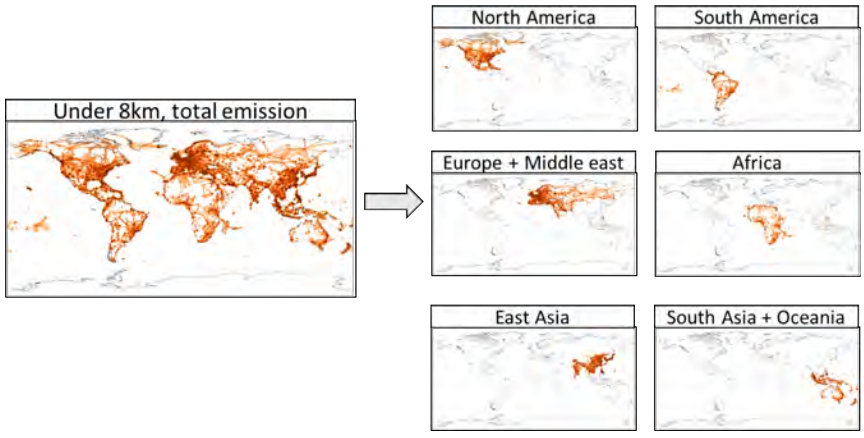

Figure 7. Illustration of the six geographical regions specified below 8 km for sensitivity analysis. The values shown in each panel are proportional to the total annual fuel burn from aviation.

Changes in model output (i.e., air quality, ozone column, RF, etc.) were taken as the sensitivity of that output to an emission anywhere within the source region. This approach is illustrated in Figure 8. By covering the full range of target altitudes, a gridded sensitivity map can be reconstructed, wherein changes in gridded outputs can be evaluated through element-wise multiplication of the sensitivities with a gridded aircraft emissions distribution (Figure 9). We have performed GEOS-Chem

simulations to quantify the climate, ozone, and air quality responses to aviation NO_x emissions for the first 5 years. Figure 10 shows these outcomes averaged over all years.

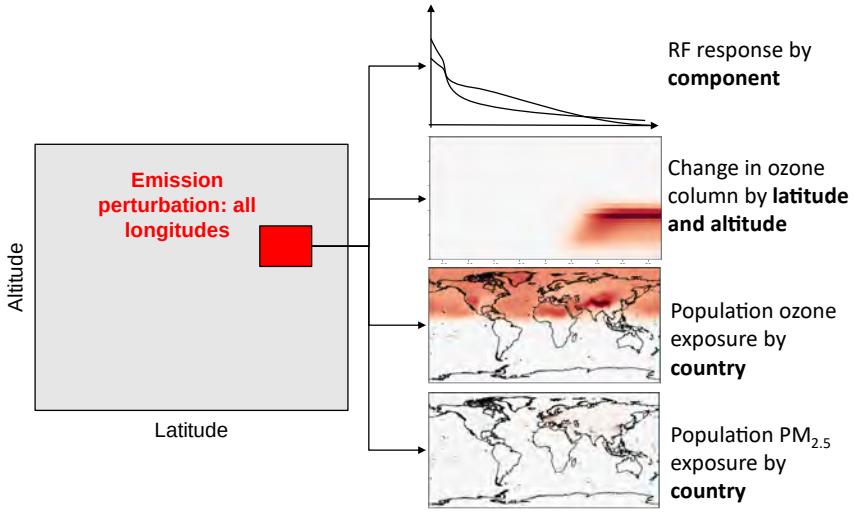

Figure 8. Approach for estimating emissions sensitivities derived from GEOS-Chem. Outputs were generated for 40 separate cruise regions and six separate non-cruise regions for 10+ years. Column ozone and air quality impacts were saved at a spatial resolution of 2˚×2.5˚. Outputs were normalized on a per-unit NO_x emissions basis.

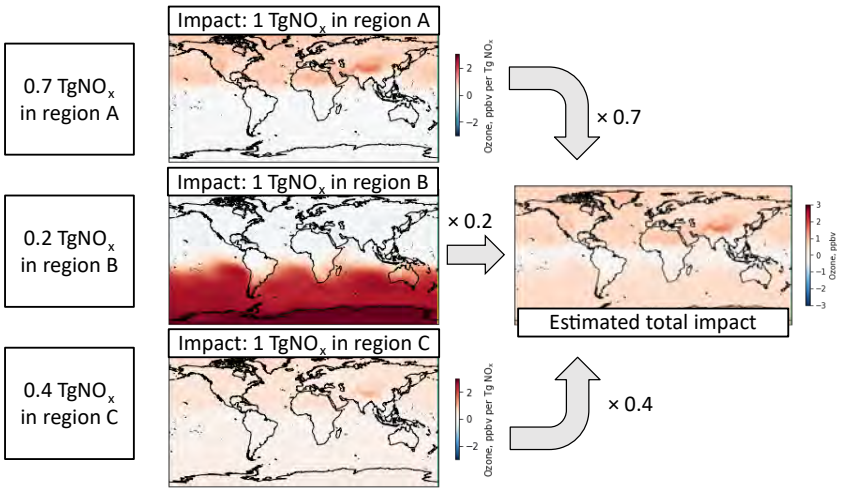

Figure 9. Example case analysis using linearized NO_x emissions sensitivities. Environmental impacts were estimated as the weighted sum of each sensitivity region's impacts, wherein the weights are the amount of NO_x in each region.

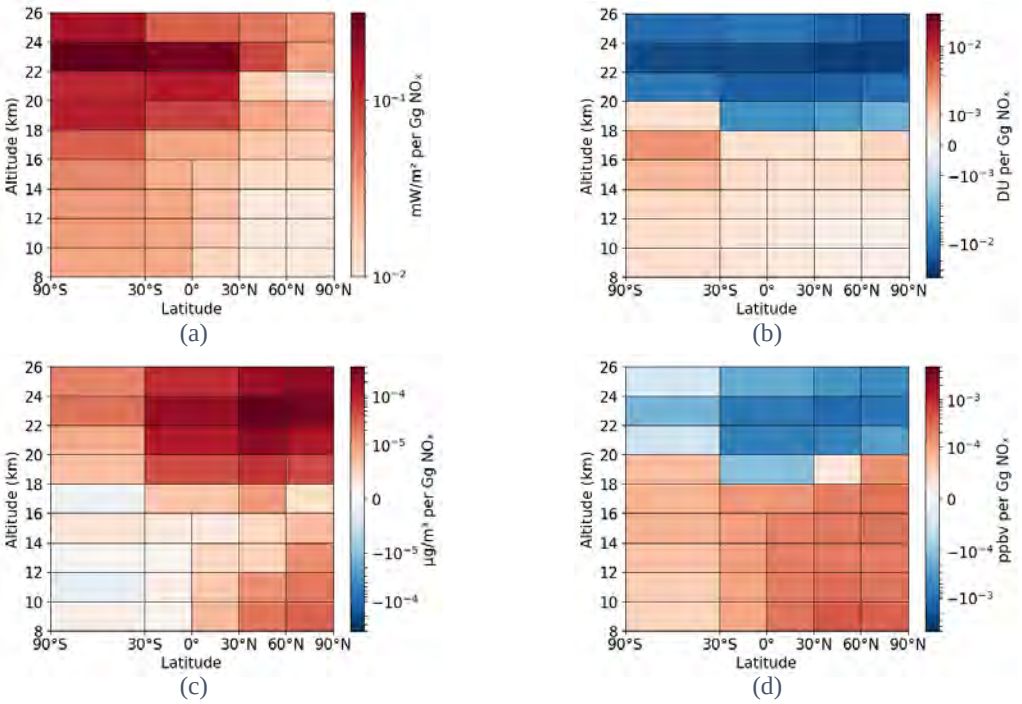

Figure 10. Spatially discretized NO_x sensitivity results averaged over the first 5 years for cruise regions: (a) radiative forcing (RF), (b) global average column O_3, (c) population-weighted average $PM_{2.5}$ exposure, and (d) population-weighted average surface O_3 exposure. The sensitivities at cruise altitudes are defined by altitude and latitude dimensions. Averaged column O_3, $PM_{2.5}$ exposure, and surface O_3 exposure impacts can be expanded into local (gridded) results.

The basic procedure for estimating total impact from a given emissions scenario is shown in Figure 9. We currently assume that the relationship between emissions and impacts is approximately linear, although this assumption may be revised for very large emission rates, on the basis of further analysis.

To test this assumption, we performed an analysis that aggressively tests the linearity assumption. Figure 11 shows how ozone in a single cell responds to increased emissions of ozone in a single region. The red line shows the estimated linear slope to be used in APMT-IC, whereas the black line shows the "true" results. We found that the linear fit performs well for emissions rates below 200 Gg NO_x/year, although deviations from the linear case were observed for very high emissions rates (above 300 Gg NO_x/year). As a reference, for ASCENT 10, the maximum NO_x emitted in each region corresponds to 360 Gg and 106 Gg for the MIT High case. Thus, the existing procedure is sufficient for evaluation of supersonic aviation up to the scale predicted by the MIT High case, but an additional set of simulations may be needed to capture the behavior of very high-uptake scenarios such as the ASCENT 10 prediction.

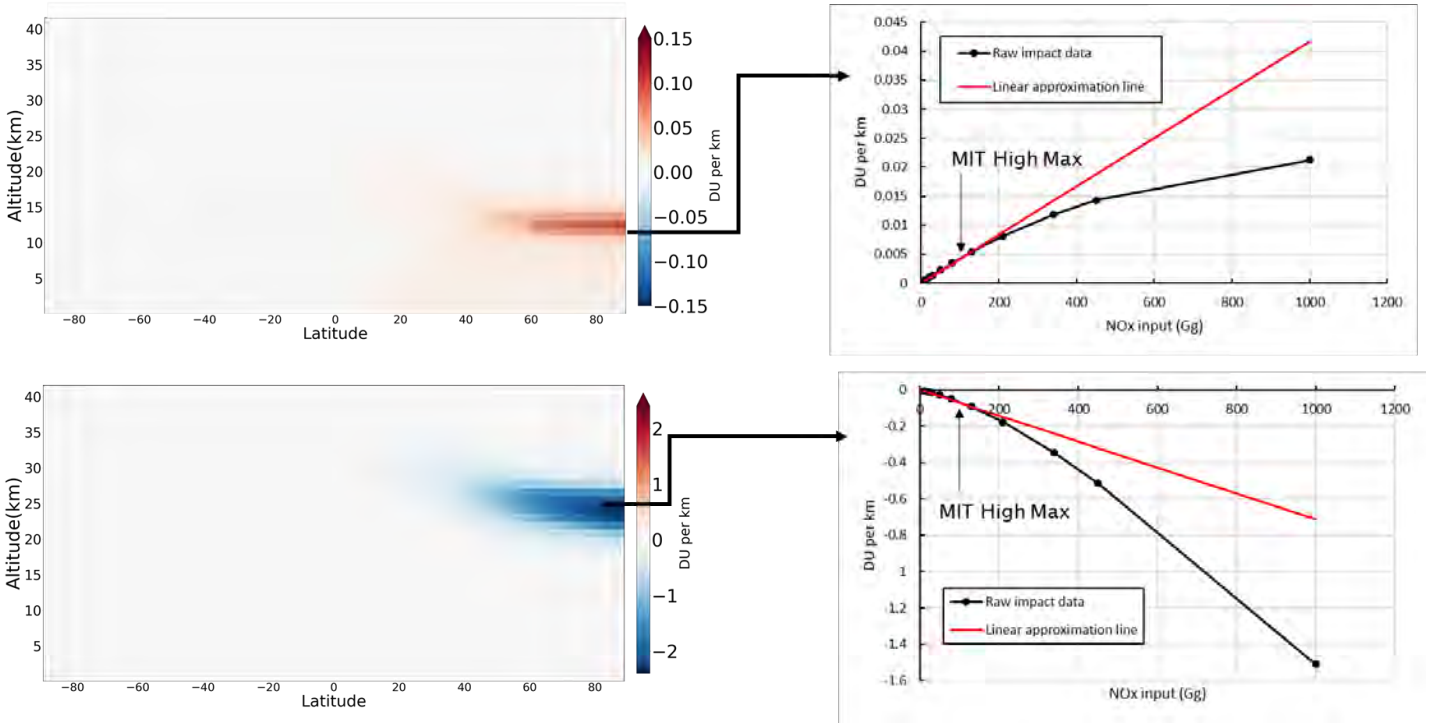

Figure 11. Response of the zonal ozone according to the amount of NO_x. Left: example cases for checking linearity (left column); right: results with linear estimation (right column).

Ultimately, our team evaluated the consistency between the sensitivity-based approach and GEOS-Chem forward model by calculating impacts for using the MIT High case from Task 1 with both methods (Figure 12 through Figure 14). Although analysis is ongoing, the results have shown good qualitative agreement to date and have been implemented in the upgraded APMT under Task 5.

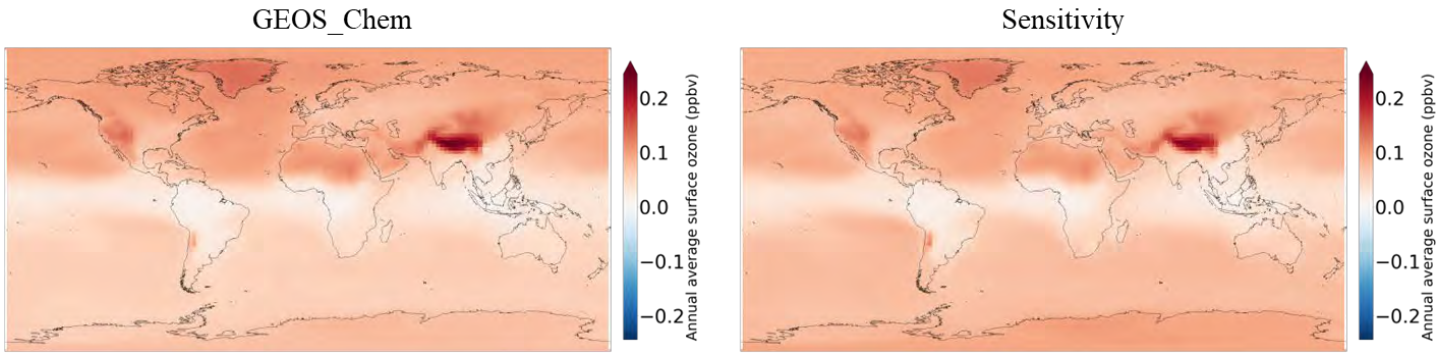

Figure 12. MIT High case third year D (test case − baseline) map for annual average surface ozone for GEOS-Chem (left) and sensitivity (right) cases; ppbv = parts per billion per volume.

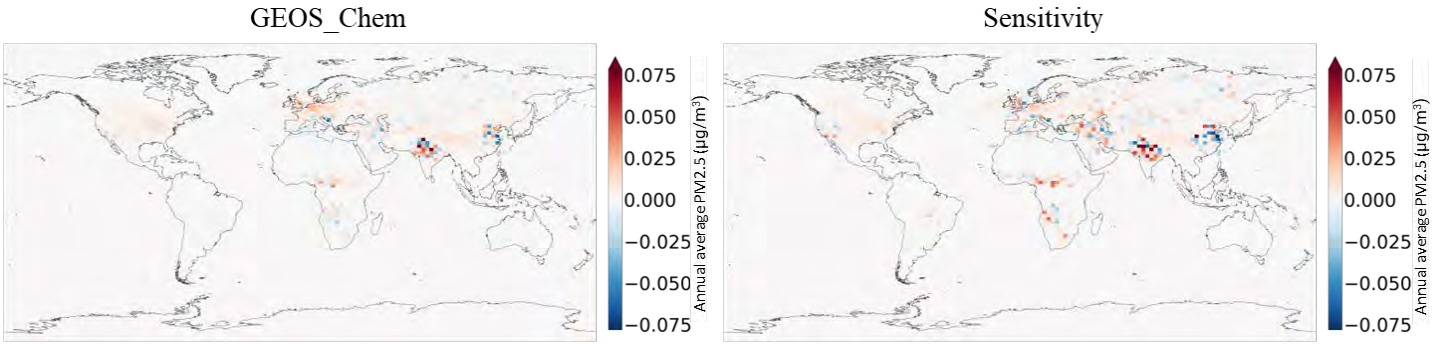

Figure 13. MIT High case third year D (SST scenarios − baseline) map for $PM_{2.5}$ for GEOS-Chem (left) and sensitivity (right) cases; mg/m^3 = micrograms per cubic meter.

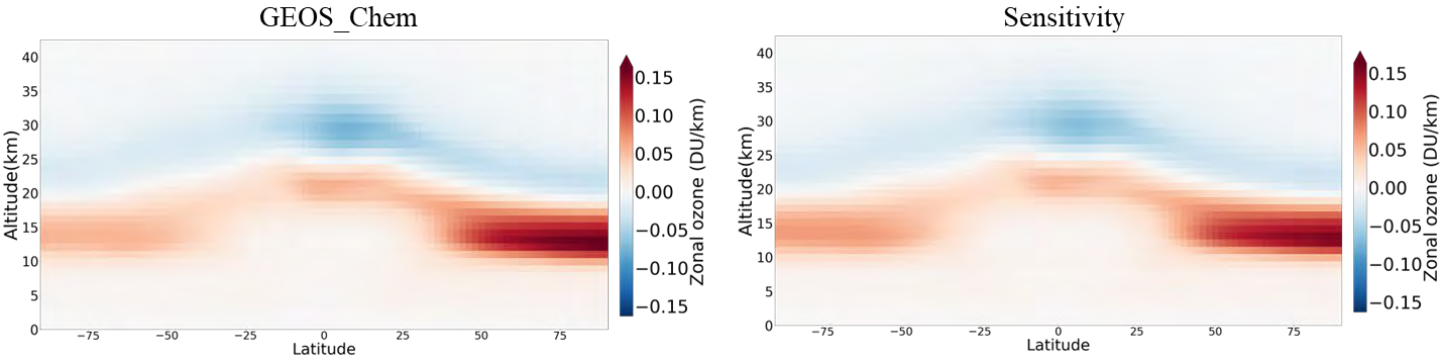

Figure 14. MIT High case third year D (SST scenarios − baseline) map for zonal ozone for GEOS-Chem (left) and sensitivity (right) cases; DU/km = Dobson units per kilometer.

Milestones

- A refined discretization of the atmosphere to distinguish between non-cruise and cruise altitudes has been established.
- Simulations in GEOS-Chem to evaluate the atmospheric responses to representative perturbations in each region for NO_x emissions have been obtained for 5 years, thus enabling an initial assessment of the accuracy of the sensitivity-based approach.

Major Accomplishments

- Estimates of impacts for the MIT SST and ASCENT 10 emissions inventories have been compared by using the linearized NO_x emissions sensitivities and full GEOS-Chem forward simulations.
- Communication with the ASCENT 22 team has begun for qualitative model intercomparison regarding the environmental impacts of supersonic aircraft emissions.

Publications

None.

Outreach Efforts

Progress on all tasks was communicated during biweekly briefing calls with the FAA and reported in quarterly progress reports.

Awards
None.

Student Involvement
For the AY 2021–2022 reporting period, graduate students Lucas Jeongsuk Oh and Joonhee Kim were involved with this task.

Plans for Next Period
During the next project period, the project team will generate gridded sensitivity data for as many as 10 years of NO_x emissions, as well as sensitivity data for H_2O, black carbon, and SO_x. Where necessary, additional simulations will be performed to refine the regions for which sensitivities are calculated. A limited set of additional "extreme case" simulations may also be performed to understand the degree of non-linearity in the response of ozone to NO_x.

Task 5 - Develop and Update Operational Tools Capable of Quantifying Environmental Impacts of Aviation
Massachusetts Institute of Technology

Objective
The objective of this task is to operationalize the results of Tasks 1–4. The eventual outcome will be a re-engineered version of APMT for climate and air quality impacts, calibrated on the basis of updated sensitivity data, and upgraded to provide monetized impacts that consider the possibility of different cruise altitudes (among other characteristics). Ozone layer impacts will also be provided in the updated model.

Research Approach
This task aims to produce a more broadly capable operational tool by reimplementing the APMT-IC structure in the Julia programming language. During AY 2021–2022, the most recent GEOS-Chem sensitivity data for NO_x emissions described in Task 4 were implemented in the updated (in development) APMT, along with the framework for other key emission species. The team also updated APMT to incorporate current scientific understanding of climate modeling from the Intergovernmental Panel on Climate Change (IPCC) Sixth Assessment Report (AR6). The high-level model overview is shown in Figure 15.

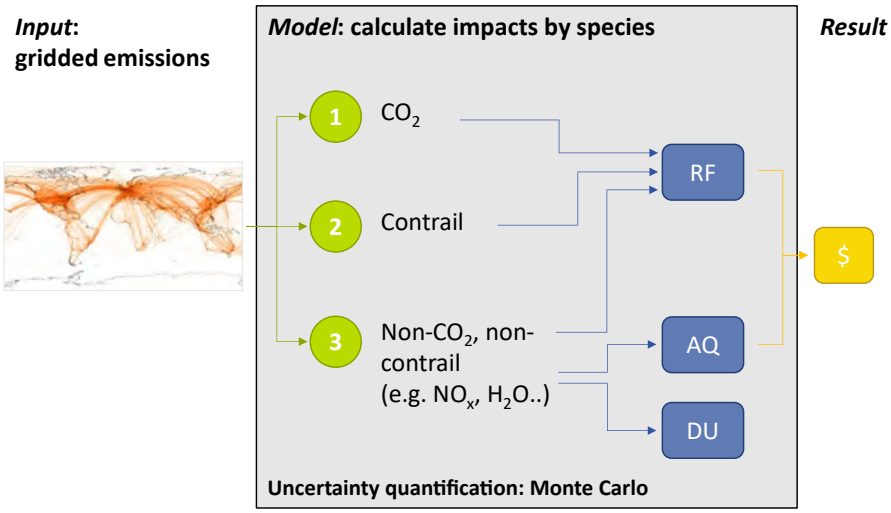

Figure 15. Model overview.

In APMT, impacts are calculated for the following groups of species: (a) CO_2, (b) contrails, and (c) non-CO_2, non-contrail, as described in detail below.

1. CO_2 is a well-mixed greenhouse gas whose impacts are insensitive to the location of emissions. Its climate sensitivities have been updated to correspond to the background CO_2 concentrations, according to the Shared

Socioeconomic Pathways (SSPs). The team calculated Impulse Response Functions (IRFs) (Joos et al., 2013) by running the Model for the Assessment of Greenhouse Gas Induced Climate Change (MAGICC6) (Meinhausen et al., 2011), as shown in Figure 16. IRFs represent the time-dependent abundance of CO_2 caused by an additional unit of emissions at the time of emission.

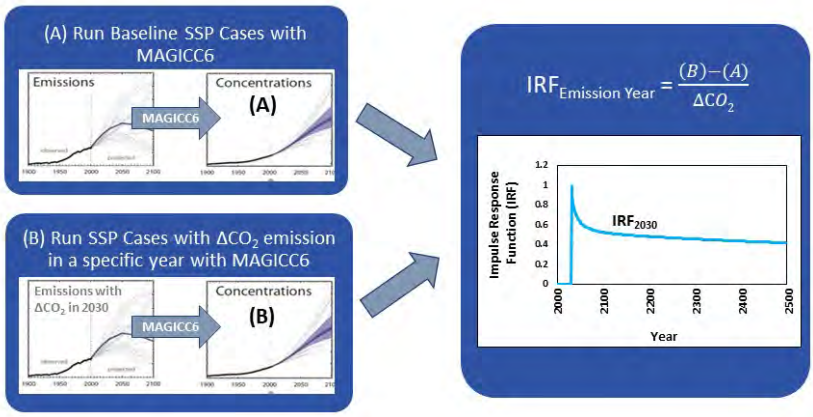

Figure 16. Schematic describing the method used to calculate CO_2 IRFs.

Figure 17 shows the IRFs for four SSP scenarios. The data in red represent MAGICC6 outputs, and the data in gray represent extrapolated data. The RF calculation for a given CO_2 concentration has also been updated to include interactions between CO_2 and N_2O, according to the most recent spectroscopic data (Etminan et al., 2016).

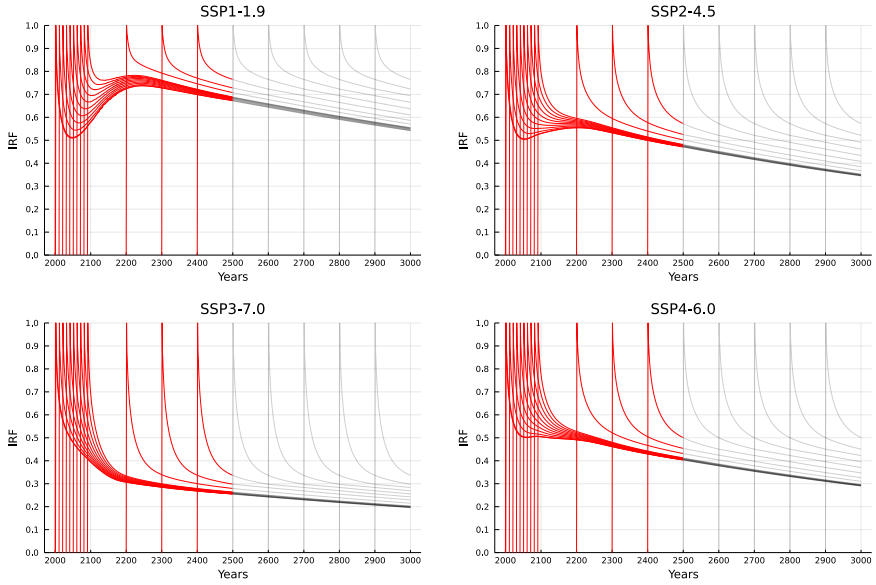

Figure 17. Updated IRFs for scenarios SSP1-1.9, SSP2-4.5, SSP3-7.0, and SSP4-6.0. The first number of the scenario labels refers to the SSP (1–5), and the second number refers to approximate global effective RF in 2100. These emissions scenarios supersede the representative concentration pathways used in previous versions of APMT-IC.

2. The climate impacts of contrails have been updated to incorporate the differential contrail forcing by region, as described in Task 6.

3. Finally, the framework for non-CO_2, non-contrail (e.g., NO_x, SO_x, black carbon, and H_2O) emissions sensitivities has been included. During AY 2021–2022, NO_x sensitivities were implemented to estimate the climate, air quality, and ozone column impacts. As described in Task 4, these sensitivities regionalize the air quality impacts to show outcomes by country for exposure to fine particulate matter ($PM_{2.5}$) and surface ozone.

In APMT, climate RF impacts are translated into temperature change and resulting damages. The background temperature change was also calibrated to updated SSP emission backgrounds by using MAGICC6 for an appropriate range of equilibrium climate sensitivity values. Figure 18 shows the distribution of the background temperature change relative to the 1850–1900 IPCC reference period for several SSP scenarios.

Health impact calculations were extended to include the Global Exposure Mortality Model concentration response function from Burnett et al. (2018) for population $PM_{2.5}$ exposure. Future projections of country-level population and gross domestic product have also been updated to correspond to the SSP scenarios.

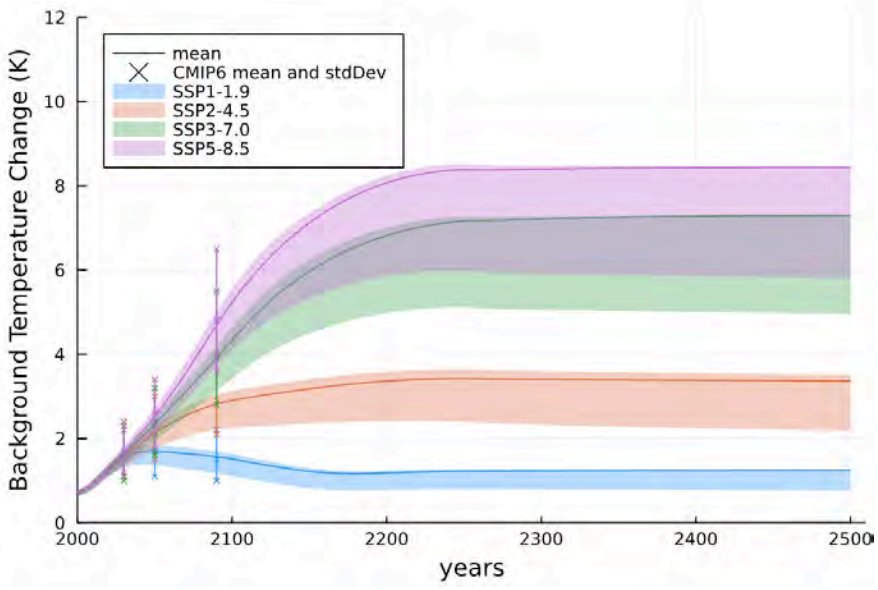

Figure 18. Updated SSP background temperature change. The shaded regions indicate percentiles 33–67, and the solid lines indicate the mean temperature change. The skewed distribution is driven by the Roe and Baker (2007) distribution used by U.S. federal agencies from the most recent social cost of carbon estimates. The CMIP6 temperature estimates (mean and 90% CI) reported in AR6 are also shown for comparison.

Milestones

- The team presented a preliminary demonstration to the FAA on how to run the updated APMT, including specifying the inputs of gridded aviation emissions and interpreting the climate and air quality impact results.
- Data for CO_2 concentrations, background temperature change, country-level gross domestic product growth, and population projections have been updated on the basis of SSP scenarios.
- The framework for emissions sensitivity has been incorporated into the model, as well as the first 5 years of NO_x sensitivity data from Task 4.

Major Accomplishments

- APMT is now capable of estimating localized air quality and column ozone impacts.
- Health impacts can be calculated in APMT by country and for multiple concentration response functions.
- AMPT also includes impact trajectories corresponding to the most recent SSP scenarios from IPCC AR6, thus ensuring policy relevance.

Publications
None.

Outreach Efforts
Progress on all tasks was communicated during biweekly briefing calls with the FAA and reported in quarterly progress reports. A poster presentation was provided on the updates to APMT and the trade-offs associated with high-altitude NO_x emissions at the Fifth International Conference on Transport, Atmosphere and Climate, 2022 (TAC-5). In addition, the previous version of APMT was used to derive climate impacts for a study focusing on identifying aviation cost and emissions pathways toward net-zero climate impacts by 2050 (Dray et al., 2022).

Awards
None.

Student Involvement
During the reporting period of AY 2021–2022, the MIT graduate student involved in this task was Joonhee Kim.

Plans for Next Period
The project team will integrate the larger set of Task 4 sensitivities into the new version of APMT, including future years for NO_x as well as other key emission species. APMT will then be used to evaluate the monetized climate and air quality damages for multiple subsonic or SST inventories. The tool will also include accessible output and visualization of outcomes.

References
Burnett, R., Chen, H., Szyszkowicz, M., Fann, N., Hubbell, B., Pope, C. A., Apte, J. S., Brauer, M., Cohen, A., Weichenthal, S., Coggins, J., Di, Q., Brunekreef, B., Frostad, J., Lim, S. S., Kan, H., Walker, K. D., Thurston, G. D., Hayes, R. B., … Spadaro, J. V. (2018). Global estimates of mortality associated with long-term exposure to outdoor fine particulate matter. *Proceedings of the National Academy of Sciences*, *115*(38), 9592–9597. Doi: 10.1073/pnas.1803222115

Dray, L., Schäfer, A. W., Grobler, C., Falter, C., Allroggen, F., Stettler, M. E. J., & Barrett, S. R. H. (2022). Cost and emissions pathways towards net-zero climate impacts in aviation. *Nature Climate Change*, *12*(10), 956–962. Doi: 10.1038/s41558-022-01485-4

Etminan, M., Myhre, G., Highwood, E. J., & Shine, K. P. (2016). Radiative forcing of carbon dioxide, methane, and nitrous oxide: A significant revision of the methane radiative forcing. *Geophysical Research Letters*, *43*(24). Doi: 10.1002/2016GL071930

Joos, F., Roth, R., Fuglestvedt, J. S., Peters, G. P., Enting, I. G., von Bloh, W., Brovkin, V., Burke, E. J., Eby, M., Edwards, N. R., Friedrich, T., Frölicher, T. L., Halloran, P. R., Holden, P. B., Jones, C., Kleinen, T., Mackenzie, F. T., Matsumoto, K., Meinshausen, M., … Weaver, A. J. (2013). Carbon dioxide and climate impulse response functions for the computation of greenhouse gas metrics: A multi-model analysis. *Atmospheric Chemistry and Physics*, *13*(5), 2793–2825. Doi: 10.5194/acp-13-2793-2013

Meinshausen, M., Raper, S. C. B., & Wigley, T. M. L. (2011). Emulating coupled atmosphere-ocean and carbon cycle models with a simpler model, MAGICC6 – Part 1: Model description and calibration. *Atmospheric Chemistry and Physics*, *11*(4), 1417–1456. Doi: 10.5194/acp-11-1417-2011

Roe, G. H., & Baker, M. B. (2007). Why is climate sensitivity so unpredictable? *Science*, *318*(5850), 629–632. Doi: 10.1126/science.1144735

Task 6 - Regionalized Parameterization of Contrails
Massachusetts Institute of Technology

Objective
This task aims to parameterize contrails, linking distance flown in a given region to the expected RF. In the existing version of APMT-IC (v24c), the total impacts of emissions are quantified per unit of additional fuel burned for the current subsonic fleet. A review by Lee et al. (2020) of aviation's impacts from 2000 to 2018 has highlighted two specific gaps in the APMT-IC framework for estimating contrail RF impacts. The first gap is the need for a more sophisticated representation of the contrail impacts from the number and distribution of flights. Owing to the complex relationship between contrail production and other engine parameters, estimating contrail impacts per unit of distance flown is a better metric than per unit of fuel burn. The second gap is that the brief, localized nature of contrails, as well as the sensitivity of contrail production to

surrounding weather conditions, leads to probable differences in the likelihood of contrail formation as a function of location. Therefore, the objective of this task is to link the distance flown in a given region to the expected RF.

Research Approach

Parameterization of contrail formation on the basis of only the quantity of fuel burned, or even total global cruise flight distance, does not consider the localized nature of the likelihood of contrail formation as a function of region or the climate impact resulting from a persistent contrail. To address these gaps, the new framework of APMT incorporates the spatial distribution of contrail RF impacts per flight distance flown from Agarwal (2021).

Figure 19 shows the distribution of the mean contrail energy forcing per distance flown in specific region for cruise altitudes between 9 and 12 km. The regions are defined as North America, contiguous United States, Western Europe, Russia, Middle East, South and East Asia, North Atlantic, South Atlantic, North Pacific, Central Pacific, and all remaining areas.

These regional distributions were obtained in Agarwal (2021) by using the central limit theorem with a sufficiently large number of samples. The mean value of the random samples in each region is normally distributed, and confidence intervals with 95% likelihood of containing the sample mean were provided. The confidence intervals representing the uncertainty from using a sampling-based approach to estimate contrail RF impacts were included in APMT. To account for the uncertainty due to uncertain contrail properties, APMT aligns with the overall contrail RF uncertainty of ±70% in Lee et al. (2020).

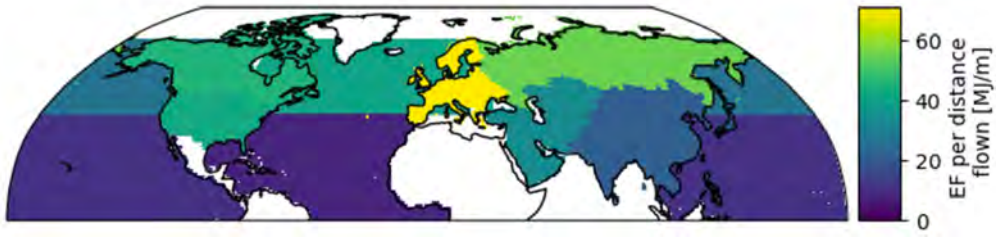

Figure 19. Spatial distribution of mean contrail energy forcing (EF) per distance flown in the Northern Hemisphere (Agarwal 2021).

Contrail impacts provided as the energy forcing (EF) per distance flown were obtained from an annual flight schedule. They were converted in APMT to the RF per distance flown by dividing the EF by the Earth's surface area and the number of seconds in a year.

$$\text{RF per distance flown} = \frac{\text{EF per distance flown}}{\text{surface area} \cdot \text{seconds per year}} = \frac{\text{J}}{\text{m flown}} \cdot \frac{1}{\text{m}^2 \cdot \text{sec}} = \frac{\text{W} \cdot \text{sec}}{\text{m flown}} \cdot \frac{1}{\text{m}^2 \cdot \text{sec}} = \frac{\text{W/m}^2}{\text{m flown}}$$

The code being developed in Julia for APMT now accepts gridded flight distances. The total contrail RF impact for a given emissions inventory was calculated as the linear sum of each region's RF per distance flown multiplied by the distance flown in that region (r_c).

$$\text{RF}_{\text{contrail}} = \sum_{r_c} (\text{RF}_{\text{contrail}} \text{ per flight km})_{r_c} \times (\text{flight km})_{r_c}$$

In IPCC's AR6, effective RF (ERF) was recommended to be used as a more useful measure of the global temperature response than the RF metric. To adjust the estimated RFs from Agarwal (2021) to ERFs, the model applies the ERF/RF ratio derived from Bickel et al. (2020), Ponater et al. (2006), and Rap et al. (2010). This ratio is modeled as an uncertain variable with a triangular distribution with a minimum value of 0.31, mode of 0.42, and maximum of 0.59 (fraction).

Milestones

- APMT has been updated to accept gridded flight distances.
- Coarsely defined regions and the expected average contrail forcing resulting from 1 km of flight in those regions, on the basis of Agarwal (2021), have been included in the model.

Major Accomplishments
The team has implemented the contrail "RF by location" sensitivities, thus resulting in the first reduced-order, flexible tool for rapid evaluation of aviation's contrail-related climate impacts.

Publications
None.

Outreach Efforts
Progress on all tasks was communicated during biweekly briefing calls with the FAA and reported in quarterly progress reports.

Awards
None.

Student Involvement
During the reporting period of AY 2021–2022, the MIT graduate student involved in this task was Joonhee Kim.

Plans for Next Period
Task 6 was largely completed in AY 2021–2022. During the next reporting period, the team plans to evaluate the altitude sensitivity of contrail impacts. The model currently does not estimate regional contrail RF for high-altitude aviation.

References
Agarwal, A. (2021). *Quantifying and reducing the uncertainties in global contrail radiative forcing* [Doctoral thesis, Massachusetts Institute of Technology]. https://dspace.mit.edu/bitstream/handle/1721.1/140372/agarwal_aa681_PhD_AeroAstro_thesis.pdf?sequence=1&isAllowed=y

Bickel, M., Ponater, M., Bock, L., Burkhardt, U., & Reineke, S. (2020). Estimating the effective radiative forcing of contrail cirrus. *Journal of Climate*, *33*(5), 1991–2005. Doi: 10.1175/JCLI-D-19-0467.1

Lee, D. S., Fahey, D. W., Skowron, A., Allen, M. R., Burkhardt, U., Chen, Q., Doherty, S. J., Freeman, S., Forster, P. M., Fuglestvedt, J., Gettelman, A., De León, R. R., Lim, L. L., Lund, M. T., Millar, R. J., Owen, B., Penner, J. E., Pitari, G., Prather, M. J., Sausen, R., & Wilcox, L. J. (2020). The contribution of global aviation to anthropogenic climate forcing for 2000 to 2018. Atmospheric Environment, 117834. Doi: 10.1016/j.atmosenv.2020.117834

Ponater, M., Pechtl, S., Sausen, R., Schumann, U., & Hüttig, G. (2006). Potential of the cryoplane technology to reduce aircraft climate impact: A state-of-the-art assessment. *Atmospheric Environment*, *40*(36), 6928–6944. Doi: 10.1016/j.atmosenv.2006.06.036

Rap, A., Forster, P. M., Haywood, J. M., Jones, A., & Boucher, O. (2010). Estimating the climate impact of linear contrails using the uk met office climate model: Climate impact of linear contrails. *Geophysical Research Letters*, *37*(20). Doi: 10.1029/2010GL045161

Task 7 - Investigate the Dependence of Aviation Emissions Impacts on Non-Aviation Factors
Massachusetts Institute of Technology

Objective
Aviation emissions since the start of the jet age have caused present-day climate impacts through CO_2 and non-CO_2 impacts (Grobler et al., 2019; Lee et al., 2020) and have also been responsible for air quality impacts over this time. These atmospheric impacts have been shown to vary by the region of emissions, emissions altitude, and season of emissions (Fichter et al., 2005; Gilmore et al., 2013). Additionally, contrail climate impacts are sensitive to particle number emissions (Bock and Burkhardt, 2016; Teoh et al 2019). The non-CO_2 climate impacts continue to propagate over years to decades through their impact on global surface temperature.

Over the past 40 years, the region, altitude, and chemical composition of aviation emissions have varied. Therefore, evaluation of present-day and future impacts from aviation requires accurate estimate of aviation's emissions over the past 40 years. Existing aviation impact assessments have relied on evaluation of specific years, and/or have scaled these impacts

by fuel and emissions, which do not capture heterogeneities in the region and altitude of emission (Lee et al., 2020). Consequently, the total cumulative temperature change and the air quality impacts attributable to aviation remain uncertain.

The objective of this task is to understand how the impacts of aviation have been driven by changes in both aviation and non-aviation factors. We first will derive a bottom-up emissions inventory for global commercial civil aviation spanning the jet age from 1980 to present day in 2019. This inventory will be the first to capture differences in region, altitude, and chemical composition of the emissions over this time span.

The results will provide insights into trends in emissions over time, such as emissions quantities by species, location, and season. As such, we will obtain insights into how changes in fleet composition as well as aircraft and engine design have changed the importance of pathways through which aviation influences the climate. Furthermore, this work will enable a future assessment of how these changes in emissions characteristics have affected the cumulative climate impact of aviation.

The second component of this research is to use atmospheric modeling to investigate the influence of both changes in aviation emissions and changes in non-aviation factors regarding environmental outcomes. This component includes both an investigation of the effects of the historical emissions described above, and an investigation of the mechanisms underlying aviation's ongoing impacts.

Research Approach

Global aviation operation data were obtained from Official Airline Guide schedule data. For 1980–2010, these data are at 5-year resolution; for 2013–2019, these data are at 1-year resolution. Aircraft performance and fuel burn were quantified with Base of Aircraft Data 3 (BADA3). Emissions species of NO_x, HC, and CO were determined from the ICAO Emissions Databank. These ground-level emissions from the ICAO Emissions Databank were extended to cruise altitude by using Boeing Fuel Flow Method 2. Non-volatile particulate mass and particle number emissions were estimated by using the SCOPE11 correlation method and, if available, direct measurements (Agarwal et al., 2019; Ahrens et al., 2022).

The preliminary derived fuel burn totals were compared with fuel burn totals from other studies in the literature, as shown in Figure 20. This figure includes the International Energy Agency (aviation fuel burn totals. This statistic represents the total annual fuel consumption of fuels meeting jet fuel specifications and may include fuel that is used in other applications, such as ground vehicles, engine testing and other uses (Olsen et al., 2013). As such, these International Energy Agency totals are considered a theoretical upper bound of aviation jet fuel usage (Olsen et al., 2013). Other aviation emissions inventories are also plotted in Figure 20, with our preliminary annual fuel burn totals matching studies with a similar scope.

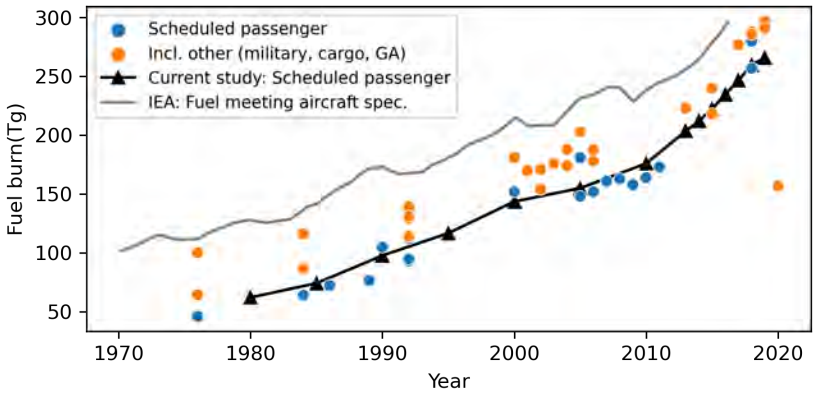

Figure 20. Comparison of our preliminary annual fuel burn totals with fuel burn totals in the literature.

These fuel burn totals were gridded into the locations where the emissions occur (Figure 21 and Figure 22). In 1980, the largest contribution of fuel burn was from North America, and by 2019 North America, Europe, and East Asia had similar contributions to total global annual fuel burn. Over this period, the emissions share in North America is halved, whereas the share in East Asia is tripled. This change in regional distribution is likely to affect the magnitude of climate and air quality impacts over time, because emissions in different regions lead to different climate impacts, sometimes differing by more than a factor 2 (Lund et al., 2017).

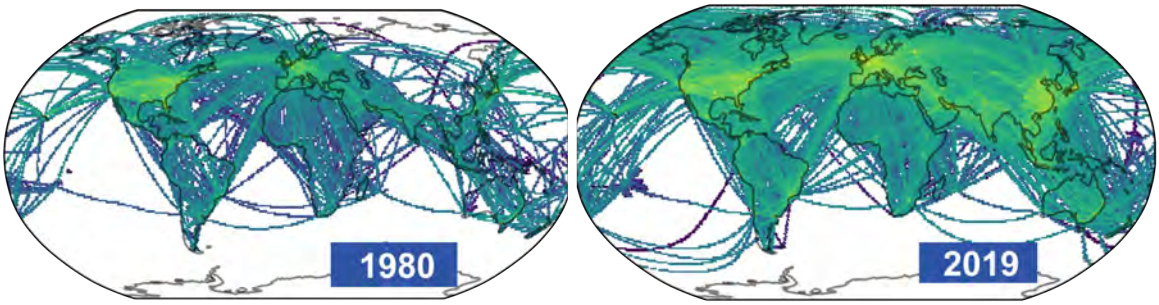

Figure 21. Preliminary locations of emissions in 1980 (left) and 2019 (right).

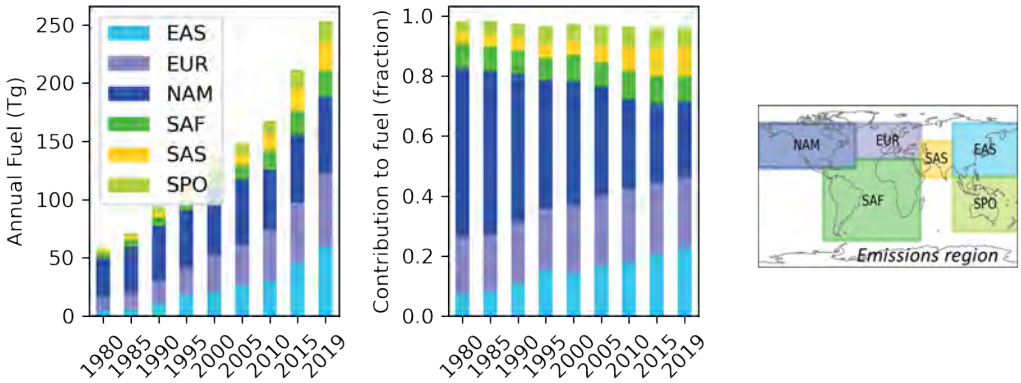

Figure 22. Evolution of regions of aviation emissions over time. Emissions outside the six indicated areas are negligible; totals can be inferred as the difference between the totals in the center lower panel and 1.0.

We also investigated the differences in the times of day when emissions occur. This aspect is important, because contrail lifetimes are typically only several hours, and their radiative impacts are sensitive to the time of day when contrails occur and persist. We consider four regions (United States, North Atlantic, Europe and Asia), and plot the fraction of fuel burn occurring in each region by the hour of the day (Figure 23). The figure also shows the local daytime/nighttime at the center of the region. In all four regions, our preliminary results indicated that the share of fuel burn occurring during the night increases, thus indicating a potential increase in contrail impacts per unit fuel burn over this period.

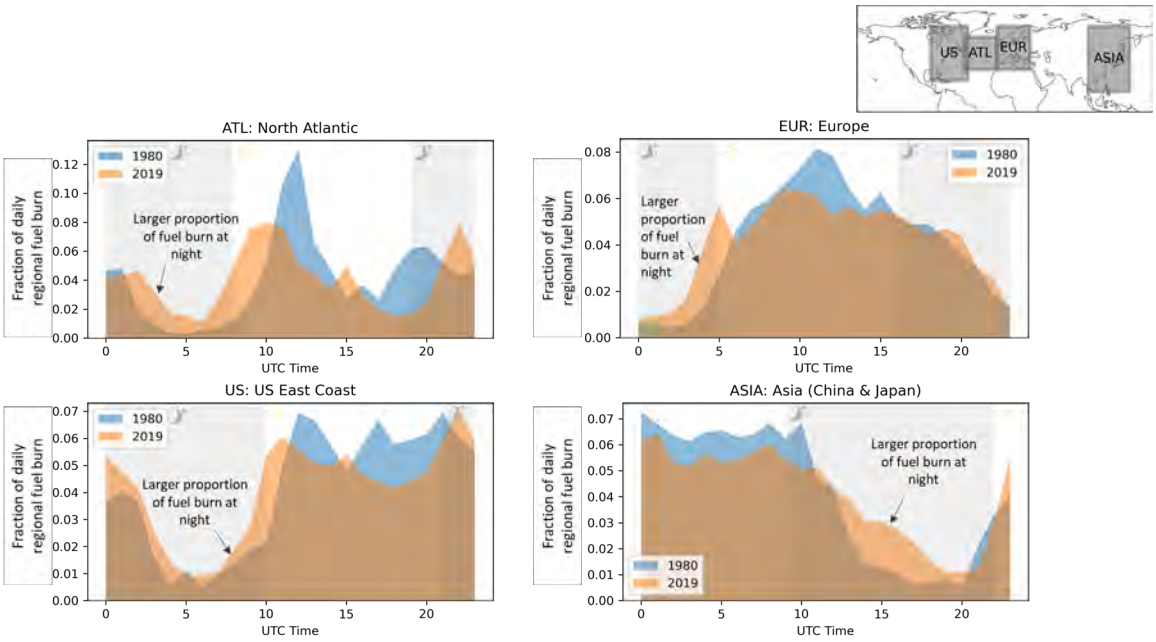

Figure 23. Difference in fuel burn by time of day between 1980 and 2019. In all regions considered, the fraction of fuel burn occurring during the night increases.

The final trend investigated involves how the emissions composition of NO_x and nonvolatile particulate matter (nvPM) changes over time. Our preliminary results showed that NO_x emissions increased by 36% over this period, and nvPM emissions decreased by 76% (Figure 24). Figure 24 also shows the distribution of emissions indices of the different engines that make up the total fleet-wide NO_x and nvPM emissions indices, thus indicating a variation among different engines of more than an order of magnitude. Therefore, these results may be sensitive to the specific aircraft-engine matchings selected in the emissions software. Consequently, further work is needed to further refine these aircraft–engine matchings in the emissions software.

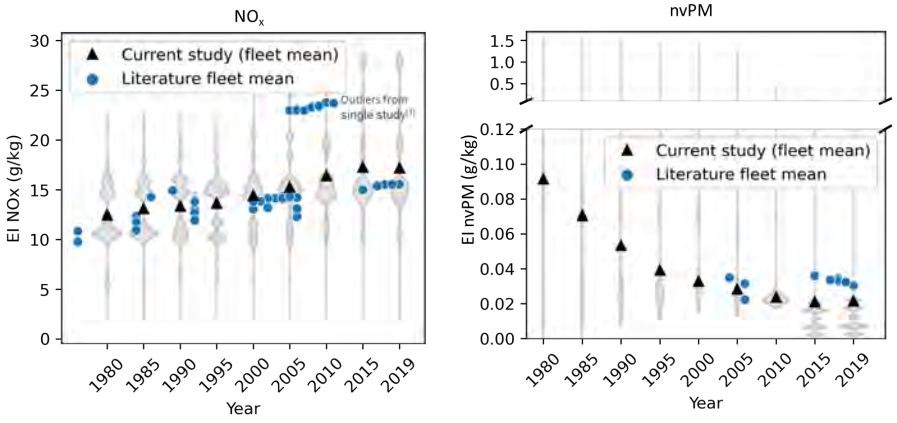

Figure 24. For NO_x, the outliers are all from the same study (Waisuik et al 2016). Note: these results are only preliminary.

Most of our investigation of the mechanisms underlying aviation's impacts, and its relationships with aviation and non-aviation factors, will be performed by using the data derived from the above work. However, we have also started performing parallel simulations to tease apart how aviation emissions alter atmospheric composition, including the role of aviation NO_x and SO_x in changing global aerosol burdens and their climate impacts. A manuscript on this work was presented at the TAC-

5 conference and published this year (Prashanth et al., 2022). By separately investigating each emissions component in simulations with the GEOS-Chem chemistry transport model, we established that aviation NO_x rather than SO_x is responsible for 72% of surface-level aerosol, but that both aviation and non-aviation SO_x significantly contribute to the overall climate impacts of aviation-attributable aerosol. This aspect is critical for understanding how different aviation emissions regulations might influence aviation's long-term environmental impacts.

Milestones

- A preliminary emissions inventory was derived by using a preliminary set of emissions schedule data.
- These emissions were compared with other inventories, and trends were investigated, including region of emissions, time of day when emissions occur, and emissions composition over time.

Major Accomplishments

A preliminary emissions inventory was derived, and trends were investigated, showing that climate and air quality impacts are likely to have varied over time. Furthermore, a manuscript was published on aviation's contribution to aerosol concentrations and the relative role of non-aviation emissions. Both sets of work were presented at an international conference in Germany in June 2022.

Publications

Grobler, C., Fritz, T., Allroggen, F., Eastham S., & Barrett, S.R. (2022). *Commercial civil aviation emissions from 1980 to the present day* [Oral presentation]. 5th International Conference on Transport, Atmosphere, and Climate (TAC-5.

Prashanth, P., Eastham, S. D., Speth, R. L., & Barrett, S. R. H. (2022). *Aerosol formation pathways from aviation emissions* [Oral presentation]. 5th International Conference on Transport, Atmosphere, and Climate (TAC-5).

Prashanth, P., Eastham, S. D., Speth, R. L., & Barrett, S. R. H. (2022). Aerosol formation pathways from aviation emissions. *Environmental Research Communications*, *4*(2), 021002. https://doi.org/10.1088/2515-7620/ac5229

Outreach Efforts

Progress on all tasks was communicated during biweekly briefing calls with the FAA and reported in quarterly progress reports. This work was also presented to the scientific community at TAC-5, in Germany, in June 2022.

Awards

None.

Student Involvement

This emissions inventory work was performed by PhD student Carla Grobler. She also presented the preliminary emissions inventory work at the TAC-5 conference in Germany. The investigation of aerosol impacts from aviation emissions was performed by Prakash Prashanth, who was also a PhD student at the time.

Plans for Next Period

During the next reporting period, the team plans to finalize the emissions inventory as follows:

- Enhance cruise altitude accuracy
- Update emissions code to use the more recent BADA 3.16 data
- Improve aircraft engine matching by using purchased fleet data or other manual methods
- Generate final gridded emissions inventory for the schedule years

References

Agarwal, A., Speth, R. L., Fritz, T. M., Jacob, S. D., Rindlisbacher, T., Iovinelli, R., Owen, B., Miake-Lye, R. C., Sabnis, J. S., & Barrett, S. R. H. (2019). Scope11 method for estimating aircraft black carbon mass and particle number emissions. *Environmental Science & Technology*, *53*(3), 1364–1373. https://doi.org/10.1021/acs.est.8b04060

Ahrens, D., Méry, Y., Guénard, A., & Miake-Lye, R. C. (2022). A new approach to estimate particulate matter emissions from ground certification data: The nvpm mission emissions estimation methodology(Meem). *Volume 3A: Combustion, Fuels, and Emissions*, V03AT04A035. https://doi.org/10.1115/GT2022-81277

Bock, L., & Burkhardt, U. (2016). Reassessing properties and radiative forcing of contrail cirrus using a climate model. *Journal of Geophysical Research: Atmospheres*, *121*(16), 9717–9736. https://doi.org/10.1002/2016JD025112

Fichter, C., Marquart, S., Sausen, R., & Lee, D. S. (2005). The impact of cruise altitude on contrails and related radiative forcing. *Meteorologische Zeitschrift*, *14*(4), 563–572. https://doi.org/10.1127/0941-2948/2005/0048

Gilmore, C. K., Barrett, S. R. H., Koo, J., & Wang, Q. (2013). Temporal and spatial variability in the aviation NO_x-related O_3 impact. *Environmental Research Letters*, *8*(3), 034027. https://doi.org/10.1088/1748-9326/8/3/034027

Grobler, C., Wolfe, P. J., Dasadhikari, K., Dedoussi, I. C., Allroggen, F., Speth, R. L., Eastham, S. D., Agarwal, A., Staples, M. D., Sabnis, J., & Barrett, S. R. H. (2019). Marginal climate and air quality costs of aviation emissions. *Environmental Research Letters*, *14*(11), 114031. https://doi.org/10.1088/1748-9326/ab4942

Lee, D. S., Fahey, D. W., Skowron, A., Allen, M. R., Burkhardt, U., Chen, Q., Doherty, S. J., Freeman, S., Forster, P. M., Fuglestvedt, J., Gettelman, A., De León, R. R., Lim, L. L., Lund, M. T., Millar, R. J., Owen, B., Penner, J. E., Pitari, G., Prather, M. J., … Wilcox, L. J. (2021). The contribution of global aviation to anthropogenic climate forcing for 2000 to 2018. *Atmospheric Environment*, *244*, 117834. https://doi.org/10.1016/j.atmosenv.2020.117834

Lund, M. T., Aamaas, B., Berntsen, T., Bock, L., Burkhardt, U., Fuglestvedt, J. S., & Shine, K. P. (2017). Emission metrics for quantifying regional climate impacts of aviation. *Earth System Dynamics*, *8*(3), 547–563. https://doi.org/10.5194/esd-8-547-2017

Olsen, S. C., Wuebbles, D. J., & Owen, B. (2013). Comparison of global 3-D aviation emissions datasets. *Atmospheric Chemistry and Physics*, *13*(1), 429–441. https://doi.org/10.5194/acp-13-429-2013

Reynolds, T. (2008, September 14). Analysis of lateral flight inefficiency in global air traffic management. *The 26th Congress of ICAS and 8th AIAA ATIO*. The 26th Congress of ICAS and 8th AIAA ATIO, Anchorage, Alaska. https://doi.org/10.2514/6.2008-8865

Teoh, R., Schumann, U., & Stettler, M. E. J. (2020). Beyond contrail avoidance: Efficacy of flight altitude changes to minimize contrail climate forcing. *Aerospace*, *7*(9), 121. https://doi.org/10.3390/aerospace7090121

Project 059(A) Jet Noise Modeling to Support Low Noise Supersonic Aircraft Technology Development

Georgia Institute of Technology

Project Lead Investigators

Dimitri Mavris
Regents Professor
School of Aerospace Engineering
Georgia Institute of Technology
Mail Stop 0150
Atlanta, GA 30332-0150
404-894-1557
dimitri.mavris@ae.gatech.edu

Jimmy Tai
Senior Research Engineer
School of Aerospace Engineering
Georgia Institute of Technology
Mail Stop 0150
Atlanta, GA 30332-0150
404-894-0197
jimmy.tai@ae.gatech.edu

University Participants

Georgia Institute of Technology (Georgia Tech)

- P.I.s: Dr. Dimitri Mavris (P.I.), Dr. Jimmy Tai (co-P.I.)
- FAA Award Number: 13-C-AJFE-GIT-070
- Period of Performance: October 1, 2021 to September 30, 2022

Project Funding Level

The project is funded at the following levels: Georgia Tech, $100,000. Cost-sharing details are below.

Georgia Tech has agreed to a total of $100,000 in matching funds. This total includes salaries for the project director, research engineers, and graduate research assistants, as well as computing, financial, and administrative support, including meeting arrangements. The institute has also agreed to provide tuition remission for the students, paid for by state funds. During the period of performance, in-kind cost sharing is also obtained for cost share.

Investigation Team

Georgia Tech

- P.I.: Dimitri Mavris
- Co-Investigator: Jimmy Tai
- Project Manager/Technical Lead: James Kenny
  - Primary technical developer, project manager, and student advisor
- Supporting Engineers: Jai Ahuja
  - Supporting technical developer, aerodynamics SME
- Students: Student technical support role involved completing various tasks to support completion of supersonic inlet code, actual tasks varied depending on timeframe support was provided

- Noah Chartier: Graduate Research Assistant, provided technical support from 2021 to 2022, co-developed majority of the inlet code with James Kenny
- Andrew Tai: Undergraduate Research Assistant, supported between late 2021 to early 2022
- Sijan Tan: Graduate Research Assistant, supported inlet code development from mid-2022 to current year

Project Overview

The original purpose of this project was to develop and assess computational tools to simulate the flow and noise of civil supersonic aircraft engines and to identify novel methods for noise reduction. In addition to noise predictions, the impact of the noise reduction methods on overall engine performance would be assessed. The predictions would include consideration of the engine inlet, engine cycle, mixers and ejectors, and unsteady jet exhaust. Accurate prediction of the engine exhaust flow would enable the noise generated by the theoretical system to be computed. Predictions were to be assessed through comparison with available experimental measurements provided by Project 59 research partners focusing on experimental methods.

In discussion with the FAA, the overall direction of the project has been changed. Instead of developing and simulating jet noise reduction technologies, Project 59A will provide benefits for addressing the supersonic jet noise problem through a different approach—considering the supersonic inlet's effects. The Project 59a team will still be supported by experimental data provided by other Project 59 technical partners, including the work jet noise experimentation, led by Dr. Krishnan Ahuja at Georgia Tech, and system operating conditions for the initial experimental geometry, which will result from discussions with other Project 59 partners.

As a result of this change, Georgia Tech's research team will now be pursuing means to identify a thrust-noise break-even relationship for arbitrary and real nozzle-based jet noise reduction technologies. Collaboration with other Project 59 partners will allow models to be developed and studies to be performed for real, experimentally developed nozzle-based jet noise reduction technologies. Additionally, the Project 59a research team will facilitate exploration of how variable geometry for supersonic inlets can potentially recover thrust lost by the aforementioned nozzle technologies.

If successful, the ASCENT Project 59a research will develop a means for performing systems-level studies for supersonic propulsion systems to identify the break-even line for any given engine assembly (engine, inlet, nozzle) whose thrust impact cost outweighs the noise reduction benefit. Additionally, low-fidelity, low-speed aerodynamics models will be implemented for the supersonic inlet, as well as new variable-geometry models, to determine whether any thrust lost by the addition of the jet noise technology can be recovered by sole use of inlet variable geometry (including the external compression inlet ramps or cone, a variable-geometry cowl lip, and potentially blow-in doors), without further manipulation of the throttle. In future work, higher-fidelity modeling capabilities will be incorporated into the zeroth-order inlet performance tool. Additionally, if the hypothesis that thrust degradations due to nozzle devices can be recovered by variable geometries in off-design configurations, then a design tool that manually achieves an optimum design will be developed from the analysis capability. Essentially, the research team will identify a way to enable rapid identification and selection of nozzle-based jet noise technologies for a given installed engine configuration, to ensure that the jet noise technology is not degrading aircraft thrust to an extent that the technology is no longer beneficial, and to determine the effectiveness of off-design variable-geometry configurations for conditions of low speed/high inlet air demand conditions.

Project Introduction

The chief objectives of this research project are twofold: first, to facilitate the capability to perform thrust-noise break-even studies for arbitrary nozzle-based jet noise technologies, and second, to develop capabilities to identify the impacts of supersonic inlet configurations and designs on thrust recovery—thus ultimately determining whether off-design supersonic inlet configurations can recover the thrust detriment from noise technologies used for jet noise regulation compliance. As a consequence of the Georgia Tech research team's departure from being coupled with Pennsylvania State University (PSU) researchers, and the modification of the overall project direction, the major project milestones for Year 2 and beyond have been modified.

Whereas Task 2.2 previously was described as "Determination of boundary conditions from 'Vision SST Engine Cycle'," the replacement task for this period was to continue improvement of Task 2.1, "Assembly of zeroth-order methods to predict inlet performance." At the initially projected due date for Task 2.1, the supersonic inlet analysis tool developed during the first year, although functional, was found to lack many capabilities necessary to analyze the installed inlet performance across the entire supersonic transport (SST) mission profile. Some of these lacking capabilities included the abilities to predict

required inlet capture area, accurately calculate internal shocks and losses for mixed compression conditions for a supersonic 2D inlet; predict and determine additive (pre-entry) drags and cowl lip suction forces; predict the location and corresponding strength of the normal shock when swallowed; and accurately predict the low-speed losses associated with conditions of low speed and high air demand conditions (i.e. takeoff). Furthermore, the team used part of Year 2 to improve the supersonic inlet analysis tool's user interface and perform debugging to achieve highly robust performance across a variety of supersonic inlet geometries and mission profiles—from external compression to mixed compression inlets, as well as from transonic design Mach numbers to low hypersonic values (1.2 to 5) and off-design cases. The tool now functions well across many conditions. Additionally, the tool was integrated (currently as a first-iteration effort) with the team's internal supersonic aircraft and engine sizing and synthesis tool (FASST, also used for ASCENT Project 10), by converting the inlet code into a rapid-running executable.
From the first year of effort, a highly functional supersonic inlet analysis tool was found to be required to perform thrust recovery analyses, in accordance with the initial goal of the project. Therefore, the focus for the first and second years was on the robust development of this capability. However, during the third and final year of this project, continued development of the supersonic inlet tool will take a secondary role, and the execution and facilitation of the jet noise reduction-break-even study tool will become the chief priority.

Because the project vision has substantially changed since the end of Year 1 (and the previous annual report, for Project 59a), the milestones below have been updated (with removal of Task 4 and "Script construction for generation of Aircraft Noise Prediction Program (ANOPP) custom jet noise source"; modification of Task 2.2, "Determination of boundary conditions from 'Vision SST Engine Cycle'"; and modification of due dates) to reflect the current glide path for task completion and deliverables for the team, and ensure project completion by the end of the final period of performance in late September, 2023.

Milestone(s)
The major milestones and planned due dates are as follows:

Task No.	Milestone	University	Planned due date
Task 1	Selection of initial geometry in coordination with other Project 59 Investigators	PSU and Georgia Tech	12/15/2020
Task 2.1	Final assembly of zero-order methods to predict inlet performance: Complete supersonic inlet analysis code and continue development	Georgia Tech	1/30/2023
Task 2.2	Determination of boundary conditions from "Vision SST Engine Cycle"—collaboration efforts: Identify engine and operating conditions for inlet studies to be performed	Georgia Tech	8/01/2023
~~Task 4~~	~~Script construction for generation of ANOPP custom jet noise source~~	~~PSU and Georgia Tech~~	~~9/1/2022~~
Task 5	Submission of interim project report	PSU and Georgia Tech	12/1/2022
Task 6	Extension of zeroth-order methods for inlet performance to include low-speed aerodynamics: Add low-speed viscous effects and ameliorating methods	Georgia Tech	4/15/2023
Task 7	Formulation and Execution of thrust-noise break-even study	Georgia Tech	8/15/2023
Task 8	Execution of the variable-geometry thrust recovery study	Georgia Tech	8/30/2023
Task 9	Submission of the final project report	Georgia Tech	9/31/2023

Major Accomplishments

The first and second years of work largely comprised creating and developing the supersonic inlet analysis code, and refining its capabilities, as described above. The first year of effort was focused primarily on the assembly of various zeroth-order methods to conduct this inlet analysis, whereas the second year of effort was focused primarily on making the tool useful and suitable for the Project 59a research goals. First-year accomplishments included the following:

- Completion of a simple parametric 2D analysis tool able to predict the following:
  - Pressure recovery between freestream and engine face
  - Oblique and normal shock predictions
  - Inlet geometry schematic for verification
  - Bleed, bypass, and spillage drags
- Validation of tool performance against several published 2D inlets
  - Good agreement with mixed compression, M_d= 5.0 inlet provided in IPAC (Inlet Performance Analysis Code) technical report, (Barnhart, 1997).
  - Good agreement with external compression, M_d= 2.3 inlet in *Fundamentals of Aircraft and Airship Design,* (Nicolai & Carichner, 2013)
  - Completed analysis and validation of Performance of Installed Propulsion Systems—Interactive (PIPSI) "R2DSST" $M_d = 2.3$ mixed compression inlet, (Kowalski & Atkins, 1979).

During the second year of the Project 59a efforts, capability gaps were closed, and several capabilities were improved:

- Many capability gaps between the Year 1 supersonic inlet analysis tool and needs were identified and improved:
- Inlet–engine airflow matching → bypass mass flow determination
- Inlet capture area sizing
- Cowl lip suction and additive drag predictions
- Nacelle wave drag predictions
- Improved mixed compression inlet performance prediction
- Improved accuracy of location and strength of internal oblique shock train
- Improved accuracy of location and strength of internal terminal normal shock
- Completed initial integration of supersonic inlet tool and supersonic engine and aircraft analysis and design tools (FASST)

Task 1 - Select Jet Nozzle Geometry

Georgia Institute of Technology and Pennsylvania State University

Objective

To unify and maximize the impact of work across relevant ASCENT projects, Georgia Tech and PSU will coordinate efforts to select an initial jet nozzle geometry. In work with Dr. Krishnan Ahuja, the experimental data from this standard geometry (gathered in ASCENT project 59) will be used to inform the work of ASCENT Project 59A. This work did not utilize the efforts of the A59a team at the Georgia Tech Aerospace Systems Design Laboratory (ASDL), but rather the nozzle and noise researchers from GT (Dr. Ahuja) and PSU.

Research Approach

The combined PSU and Georgia Tech research team will work together to identify promising geometries for use across the ASCENT projects. The selected geometry must be relevant to the project goals, and also achievable regarding experimental measurement, computational analysis, and other supporting tasks. Specific evaluation criteria may include jet velocity reduction and thrust loss.

This task was completed during the first year of work. Although the results of this effort were not used to complete the inlet analysis code, it was helpful in identifying and converging upon the ultimate objective of the project, and establishing cooperative working relationships with other Project 59a partners.

Milestones(s)

As this task was accomplished in the first year, no update is possible for the current year's report.

Major Accomplishments
None.

Publications
None.

Outreach Efforts
None.

Awards
None.

Student Involvement
None.

Plans for Next Period
None.

Task 2 - Translate Installed Cycle Performance Requirements into Boundary Conditions
Georgia Institute of Technology

Objective
Task 2 aims to leverage engine cycle modeling capabilities to determine the installed thrust for an engine of interest that is appropriate for commercial supersonic transport. The thermodynamic properties across this mixed flow turbofan engine, alongside the install thrust value, are used to characterize the mixer exit, nozzle entrance, and nozzle exit operating conditions during takeoff. Because the initial testing and high-fidelity simulations are not (yet) representative of a mixed flow turbofan, these operating conditions (i.e., total pressure, total temperature, mass flow, geometry, etc.) will inform the testing team regarding relevant testing conditions.

Research Approach (Georgia Tech)
Task 2.1: Determine Installed Thrust
To ensure that minimum thrust is lost due to implementation of potential jet noise reduction technology, the installed thrust requirement must be determined, because it is directly proportional to jet velocity. A major contributor to installed thrust is inlet performance, which is highly dependent on how the engine is integrated with the vehicle. Therefore, the primary element of Task 2 is to investigate zeroth-order methods to predict inlet performance for different inlet designs and off-design configurations.

Task 2.2: Generate Boundary Conditions
Initially, the objective of this task was for Georgia Tech to analyze the engine cycle developed by ASCENT Project 10 to estimate the best operating conditions for takeoff and landing to minimize certification noise levels. This task was updated to reflect the required boundary condition/experimental data generated by project partners, to be used in Tasks 7 and 8. Additionally, the timeline was updated to reflect when these data were required by the Project 59a research team. Some beneficial data for modeling will include mixer and nozzle conditions, i.e., total temperature, total pressure, and mass flow rate, as well as measured thrust vs. noise for each tested jet noise reduction technology or mixer type.

Task 2.1 - Zero-order Methods to Predict Inlet Performance
A major contributor to installed thrust is inlet performance, which is highly dependent on how the engine is integrated with the vehicle. To capture thrust recovery due to improved inlet performance, the Georgia Tech team must develop a means to predict inlet performance across the SST flight envelope, particularly at low-speed conditions during which jet noise is most prominent (i.e., landing and takeoff).

During the first year, the Georgia Tech team completed an initial the model development for the 2D inlet case, by developing a modular 2D supersonic inlet anlaysis tool. In addition, the team has completed an initial validation of the 2D inlet case with satisfactory preliminary results. Table 1 compares the developed tool's predicted total pressure recovery to that produced by IPAC across the mission-relevant range of freestream Mach number (Barnhart, 1997). Here, the supersonic inlet is designed for a freesteam Mach number of 5, and evaluated across a range of lower "off-design" operating freestream Mach settings. The maximum and average error values were found to be 3.69% and 0.82%, respectively, across this range.

Table 2 compares the developed tool's predicted total drag coefficient and that produced by IPAC across the mission-relevant range of freestream Mach number (Barnhart, 1997). This drag term includes the contributions of spillage, bleed, and bypass drag on the engine inlet. Again, the supersonic inlet is designed for a freesteam Mach number of 5 and is evaluated across a range of lower "off-design" operating freestream Mach settings. The maximum and average error values were found to be 9.88% and 1.19%, respectively, across this range.

{θ, ℓ}: per ramp segment
{θ, x}: per ext. cowl segment
{θ}: per int. cowl segment
cloff: engine vertical offset from local
ℓ_{th}: throat length
ℓ_{in}: total inlet length
t_c: cowl thickness (above engine face)
htr: hub to tip ratio
D_2: engine diameter
w_c: cowl width
w_{th}: throat width

Figure 1. Geometry inputs to define inlet in Year 1 supersonic inlet analysis code.

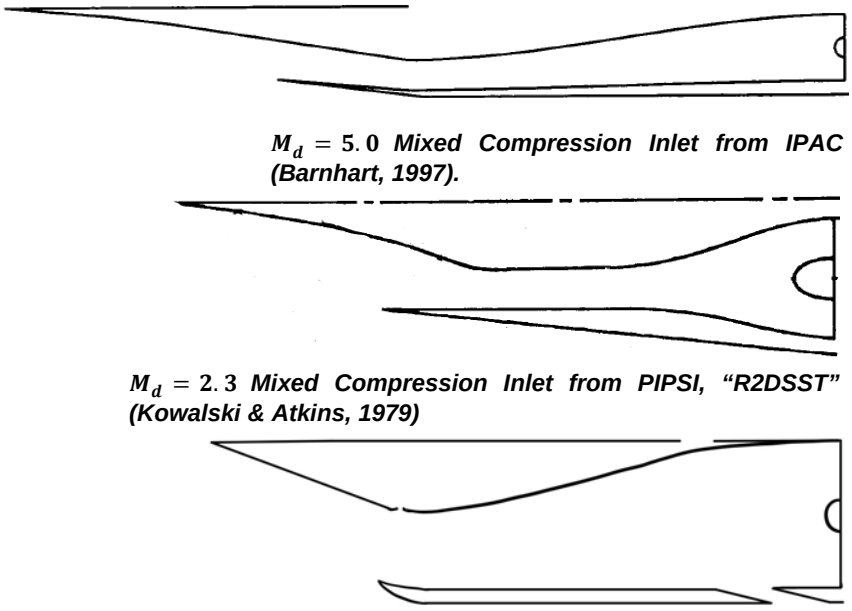

$M_d = 5.0$ Mixed Compression Inlet from IPAC (Barnhart, 1997).

$M_d = 2.3$ Mixed Compression Inlet from PIPSI, "R2DSST" (Kowalski & Atkins, 1979)

$M_d = 2.3$ External Compression Inlet from Nicolai & Carichner (2013)

Figure 2. Three 2D supersonic inlets used to validate the Year 1 inlet analysis tool; top inlet performance results are displayed below.

Table 1. Validation case: total pressure recovery.

Freestream Mach number	Modeled	Reference	Error (%)
0.01	0.9586	0.9608	−0.23
0.2	0.9586	0.9608	−0.23
0.4	0.9586	0.9608	−0.23
0.6	0.9586	0.9608	−0.23
0.8	0.9586	0.9608	−0.23
1.0	0.9586	0.9608	−0.23
1.2	0.9517	0.9539	−0.23
1.4	0.9404	0.9456	−0.55
1.6	0.9233	0.9285	−0.56
1.8	0.8767	0.8816	−0.55
2.0	0.8107	0.8153	−0.57
2.5	0.8591	0.8760	−1.97
3.0	0.7873	0.7875	−0.03
4.0	0.6618	0.6427	2.88
5.0	0.5349	0.5152	3.67

Table 2. Validation case: total drag coefficient.

Freestream Mach number	Modeled	Reference	Error (%)
0.01	0.0000	0.0000	0.00
0.2	0.0000	0.0000	0.00
0.4	0.1976	0.1799	9.88
0.6	0.3086	0.3024	2.05
0.8	0.3831	0.3811	0.53
1.0	0.4809	0.4797	0.25
1.2	0.6537	0.6617	−1.21
1.4	0.3953	0.3855	2.53
1.6	0.3264	0.3265	−0.01
1.8	0.3245	0.3250	−0.15
2.0	0.3426	0.3411	0.45
2.5	0.3007	0.3000	0.23
3.0	0.2994	0.2987	0.23
4.0	0.2315	0.2307	0.35
5.0	0.0175	0.0175	0.00

The developed inlet performance analysis tool is intended to help identify competitive supersonic inlet designs for overcoming negative performance impacts accompanying noise reduction nozzle technologies across the flight envelope, as well as identifying the resulting behaviors associated with low-speed performance and off-design ramp (and other variable geometry) configurations of the inlet. To this end, a sensitivity study was performed to evaluate inlet variable-geometry settings that may be capable of recovering thrust across off-design flight segments (takeoff, landing).

For the second year, the inlet performance tool was extended to include several capabilities for performance modeling. One simple capability added for the second year was a schematic showing the user where the external oblique shocks are located with respect to the external portion of the supersonic inlet (Figure 3). This schematic allows users of the supersonic inlet analysis script as a standalone tool (i.e., not coupled to an engine/airframe sizing and synthesis tool) to quickly identify whether an external shock system is attached to the inlet, or a detached shock system has been formed. In work for Year 3, the normal shock system, whether external or internal, will be included in the schematic. Additionally, the subsonic diffuser portion (the internal inlet section closest to the engine face) will reflect the actual curvature reflected in the model (here, it is straight, without curvature).

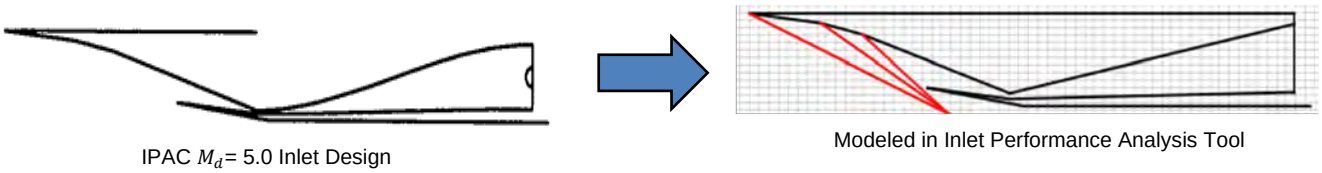

Figure 3. Inlet and shock schematic enabled in supersonic inlet tool during Year 2 work.

In addition to the modeling fidelity improvements listed in the "Major Accomplishments" section above, many more stations and the physical properties of airflow at those stations can be modeled as a consequence of the Year 2 work. Instead of simply considering the total pressure recovery and drags, as displayed for the Year 1 work in Tables 1 and 2, the work of Year 2 enabled a much closer examination of the supersonic inlet performance at each station. The performance of the inlet at each of these additional stations was compared with those from the published results of the M_d=5.0 mixed compression inlet from IPAC (shown at top in Figure 2). Detailed results for the M = 3.0 off-design case of this inlet are shown in Table 3; the design case and other off-design cases down to M = 0.01 had similar performance results with respect to the validation error. As described previously, a greater level of fidelity regarding flow station performance, as well as improvements in the accuracy of the model was achieved. Using the Year 2 inlet analysis tools, the team had found an improvement in accuracy regarding total pressure recovery (total pressure ratio across the entire inlet) as a consequence of the improvement in shock location predictions and internal reflected shock quantities.

Table 3. Validation results for IPAC M_d= 5.0 inlet and M = 3.0 off-design case.

Outputs	Local calculated	Local reference	Error (%)	Cowl lip calculated	Cowl lip reference	Error (%)	Throat calculated	Throat reference	Error (%)
Flow area (ft²)	0.6905	0.6905	0.0000	0.3953	0.3955	0.0594	0.1600	0.1598	−0.1126
Mach number	3.0000	3.0000	0.0000	2.3982	2.3990	0.0335	1.3149	1.3140	−0.0700
Static pressure (lbf/ft²)	156.7630	156.3000	−0.2962	390.6043	389.5000	−0.2835	1,960.9823	1,959.0000	−0.1012
Static temperature (R)	389.9700	390.0000	0.0077	508.6205	507.7000	−0.1813	812.6533	811.5000	−0.1421
Density (slg/ft³)	0.0002	0.0002	−0.2490	0.0004	0.0004	−0.2472	0.0016	0.0014	−13.3433
Velocity (ft/s)	2,905.4154	2,904.0000	−0.0487	2,650.0449	2,649.0000	−0.0394	1,838.3284	1,835.0000	−0.1814
Total pressure (lbf/ft²)	5,753.6784	5,743.0000	−0.1859	5,694.5814	5,684.0000	−0.1862	5,545.0869	5,534.0000	−0.2003
Total temperature (R)	1,093.6709	1,092.0000	−0.1530	1,093.6709	1,092.0000	−0.1530	1,093.6709	1,092.0000	−0.1530
Mass flow (lbm/s)	21.8556	21.8200	−0.1630	15.0913	15.0700	−0.1411	13.2882	13.2700	−0.1370
$\frac{P_{T_1}}{P_{T_L}}$	$\frac{P_{T_1}}{P_{T_{L\,REF}}}$	$\frac{P_{T_{TH}}}{P_{T_1}}$	$\frac{P_{T_{TH}}}{P_{T_{1\,REF}}}$	$\frac{P_{T_2}}{P_{T_{TH}}}$	$\frac{P_{T_2}}{P_{T_{TH\,REF}}}$	$\frac{P_{T_X}}{P_{T_Y}}$ (across normal shock)	$\frac{P_{T_X}}{P_{T_{Y\,REF}}}$ (across normal shock)	Number of internal shocks	Number of internal shocks (reference)
0.9897	0.9900	0.9737	0.9740	0.8164	0.8174	0.897	.8952	3	3

During Year 3 work, low-speed viscous loss prediction models will be integrated, as will a variable-geometry cowl lip configuration to enable the exploration of potential airflow maximization at low speeds. If time allows, the modeling of blow-in doors will also be completed toward this same end.

Milestones(s)

- Completion of the initial inlet analysis code

- Addition of additive drag prediction
- Addition of bleed and bypass drag models
- Addition of normal shock position predictions
- Addition of internal shock train predictions (starting conditions)
- Addition of angle of attack effects
- Validation against published data
- Integration with engine model

Major Accomplishments

First-year accomplishments included the following:

- Completion of a simple parametric 2D analysis tool able to predict the following:
  - Pressure recovery between freestream and engine face
  - Oblique and normal shock predictions
  - Inlet geometry schematic for verification
  - Bleed, bypass, and spillage drags
- Validation of tool performance against several published 2D inlets
  - Good agreement with mixed compression, M_d= 5.0 inlet provided in IPAC (Inlet Performance Analysis Code) technical report, (Barnhart, 1997).
  - Good agreement with external compression, M_d= 2.3 inlet in *Fundamentals of Aircraft and Airship Design,* (Nicolai & Carichner, 2013)
  - Completed analysis and validation of Performance of Installed Propulsion Systems—Interactive (PIPSI) "R2DSST" $M_d = 2.3$ mixed compression inlet, (Kowalski & Atkins, 1979).

During the second year of the Project 59a efforts, capability gaps were closed, and several capabilities were improved:

- Many capability gaps between the Year 1 supersonic inlet analysis tool and needs were identified and improved:
- Inlet–engine airflow matching → bypass mass flow determination
- Inlet capture area sizing
- Cowl lip suction and additive drag predictions
- Nacelle wave drag predictions
- Improved mixed compression inlet performance prediction
- Improved accuracy of location and strength of internal oblique shock train
- Improved accuracy of location and strength of internal terminal normal shock
- Completed initial integration of supersonic inlet tool and supersonic engine and aircraft analysis and design tools (FASST)

Publications

No manuscripts or works have been submitted for publication at this time of this report.

Outreach Efforts

None.

Awards

None.

Student Involvement

The progress of this project has been possible due to the involvement of and technical work by students. All graduate research assistants, as well as the undergraduate research assistant who worked on this task individually enabled the progress and near-completion of the inlet analysis tool, to be used in future tasks. Additionally, the project manager, James Kenny, served as a graduate research assistant during the first year of the project, and he continues to provide technical and management work towards the completion of this task.

Plans for Next Period

The next period of this task requires the final completion and validation of the zeroth-order inlet analysis tool and the finalized integration with the supersonic engine analysis and design code, FASST. Completion of both of these steps will

facilitate the completion of the following tasks.

Task 6 - Extension of Zeroth-Order Methods for Inlet Performance to Include Low-Speed Aerodynamics

Georgia Institute of Technology

Objective

To enable the completion of Tasks 7 and 8, low-speed aerodynamics modeling must be facilitated for the supersonic inlet, including the viscous effects encountered by supersonic inlets during landing and takeoff conditions. The current supersonic inlet analysis model uses a simple viscous loss relationship, which is scaled depending on the freestream air Mach number and the sharpness and radius of the inlet cowl lip, taken from the IPAC publication's equations (Barnhart, 1997). This loss cannot account for the potential improvements achieved by modulating the variable geometry of the inlet to maximize airflow, and minimize the viscous effects incurred by incoming air when pulling around the cowl lip and sidewalls.

Research Approach

Several approaches will be followed to identify computationally low-cost methods for determining low-speed aerodynamics over the supersonic inlet ramps, cowl lip, or compression center cone:

- Perform literature review to identify analytical methods for modeling low-speed viscous flow over a flat ramp with varying angles of attack or incidence
- Implement these methods within the script, and compare results for validation against published sources as well as published experimental data
- Perform flat-plate loss approximations, and compare them with experimental data and the results achieved above
- Select the method yielding the best results with reasonable computation execution time

Milestones(s)

Major milestones for this project in the second year of the project had not been accomplished at the time of initial submission of this report, with the exception of an in-depth literature review of low-fidelity approaches for low speed aerodynamics modeling. As of the time of this report, a preliminary low-speed aerodynamics model has been developed and tested, and is currently being validated by the team against experimental data.

- Literature review to understand how low-speed aerodynamics is currently modeled analytically
- Development of models for each segment of the inlet
- Integration of each part of the inlet low-speed aero model
- Validation against of overall model against published data

Major Accomplishments

Major accomplishments include completion of a lengthy literature review into the topic of low-fidelity low-speed aerodynamics modeling, and the initial development of the modeling code.

Publications

None.

Outreach Efforts

None.

Awards

None.

Student Involvement

This task has been primarily worked on by graduate research assistant, Sijan Tan.

Plans for Next Period

During the final period of the project, the low-fidelity, low-speed aerodynamics model will be fully integrated into the model and utilized to complete the final tasks of the project.

Task 7 - Execution of Thrust-Noise Breakeven Study

Georgia Institute of Technology

Objective

Because supersonic engines are likely to be throttled back at takeoff, any loss of thrust due to the implementation of noise technologies could theoretically be offset by simply pushing the throttle forward. However, doing so may reduce or completely offset any noise benefits achieved by the technology in the first place. In that case, another approach to recovering the lost thrust may be warranted. Although each technology is unique in the amount of noise reduction and thrust loss, the breakeven line (the point at which pushing the throttle forward to recover thrust completely offsets the noise benefits of the technology) can nonetheless be evaluated. The concept of this proposed study is illustrated in Figure 4.

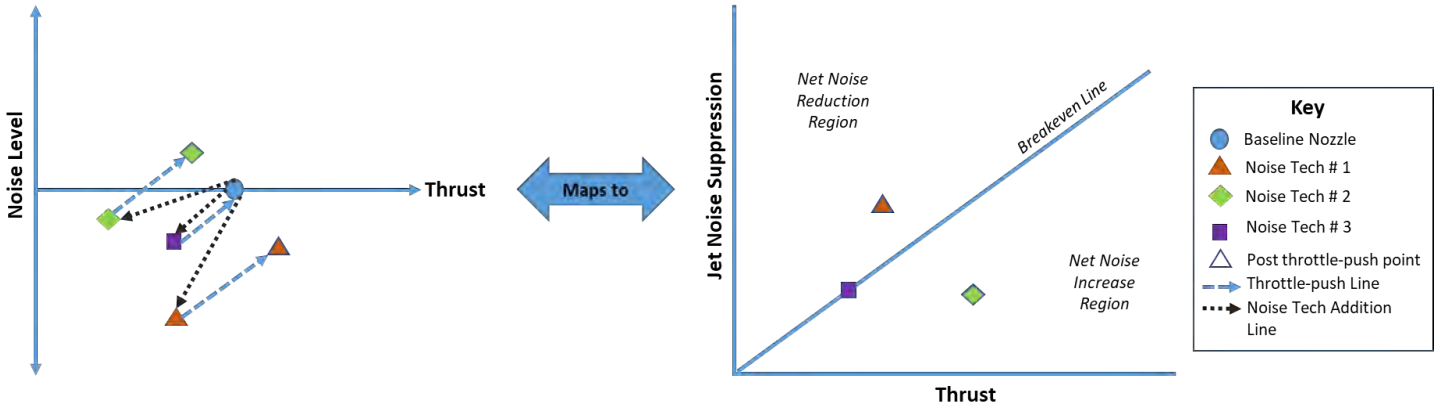

Figure 4. Thrust-noise break-even study concept.

Research Approach

To perform this study, we propose examining different levels of noise reduction through the jet suppression factors within ANOPP; thrust loss will be simulated by a reduction in the gross thrust coefficient in the engine analysis which will utilize the Numerical Propulsion System Simulation (NPSS).

The first step will be to establish a baseline with no noise technology. Second, the resulting thrust loss and noise benefit will be computed by using the jet suppression factors and gross thrust coefficient. Third, the aircraft will be flown again with an increase in throttle to offset the thrust loss, and the noise will be evaluated. For a range of jet suppression factors, the C_{fg} resulting in the noise benefit being offset will be identified to construct a break-even line (as shown in the figures). The goal is to determine the line of jet suppression and gross thrust, C_{fg}, simulating an arbitrary noise technology that, owing to a throttle push to recover lost thrust, yields no net change in noise with respect to the baseline design without noise technology. Until this study is performed, this line is unknown, so we will need to simulate multiple possible combinations of Jet suppression and C_{fg}. As can be seen on the left in Figure 4, Technology 1 yields a large initial reduction in noise (orange triangle), and the throttle push to recover thrust reduces the benefit but maintains an overall net reduction in noise. However, Technology 2 (green diamond) yields a small reduction in noise and a large reduction in thrust. Therefore, when the throttle is pushed forward, the result is a net increase in noise. Technology 3 (purple square) "breaks even" when the throttle is pushed and is therefore a point on the line. In accordance with Task 2.2 in the milestones table above, experimental thrust and noise data will be obtained from Project 59 research partners, then used in this effort to validate the approach and determine a realistic thrust-noise break-even line.

Milestones(s)
No milestones for this task have been accomplished for the current year.
- Establish baseline for noise and thrust with baseline supersonic engine with no noise technology
- Develop nozzle noise technology models and implement to determine thrust and noise effects for them
- Determine thrust-noise breakeven line

Major Accomplishments
None.

Publications
None.

Outreach Efforts
None.

Awards
None.

Student Involvement
None.

Plans for Next Period
The completion of this task will take place in the third year, and the next reporting period.

Task 8 - Execution of the Variable Geometry Thrust Recovery Study
Georgia Institute of Technology

Objective
After low-speed aerodynamics can be approximated, and additional variable-geometry configuration options are enabled (variable-geometry cowl lip (VGCL)), studies will be performed to determine whether the off-design inlet configurations can assist in overcoming the thrust losses incurred by using nozzle-based jet noise technologies. That is, the objective is to enable greater thrust at landing and takeoff conditions without requiring a higher throttle setting, thus expanding the net noise decrease region, illustrated on the right in Figure 4.

Research Approach
For this task, a sensitivity study to determine the effects of the variable geometry at low speeds will be completed first. If the variable geometries are shown to have an effect on the overall low speed installed engine performance, they will then be modulated to identify a potential thrust recovery for several arbitrary nozzle-based jet noise technologies.

Milestone(s)
- Development of the VGCL model
- Validation of VGCL model
- Completion of study to determine if VGCL can allow the installed engine to perform better than the thrust-noise breakeven line established in Task 7
- Completion of studies for several notional nozzle technologies

Major Accomplishments
None.

Publications
No literature was written or published during Years 1 or 2. However, upon the completion of the studies proposed for the Year 3 tasks, a manuscript will be written for submission to AIAA Aviation 2024.

Outreach Efforts

Research Engineer James Kenny attended, and presented progress for this project at, the 2022 ASCENT Advisory Board Meeting in Alexandria, Virginia.

Awards

None.

Student Involvement

The Georgia Tech student team currently consists of one graduate research assistant and two full-time research engineers. Over the past performance period, all members have been engaged in formulating the approach being pursued for the inlet modeling activity. Graduate research assistant Sijan Tan has worked on developing the inlet modeling tool to more accurately reflect cowl lip suction benefits at low speeds and to improve other parts of the code. Previous students on the project during the performance period include Noah Chartier, who was pivotal in creating the skeleton of the inlet code, as it currently stands, and Andrew Tai, an undergraduate researcher, who helped improve the internal shock prediction model over one semester. Research engineers James Kenny and Jai Ahuja have been engaged in improving the inlet performance analysis tool to be more robust for all desired example model inlet geometries and configurations, as well as extending the capabilities of the tool to predict shock locations, as well as improve spillage accuracy and many other capabilities.

Plans for Next Period

Georgia Tech

The Georgia Tech team plans to complete the tasks listed in Table 1 with Georgia Tech designation. Work will continue toward completion on the assembly of a zeroth-order inlet design and analysis environment, and the completion of the milestone table below:

- Complete final assembly of zeroth-order methods to predict inlet performance
- Identify potential collaboration efforts to use experimental data from other Project 59 members
- Complete and submit a Year 3 interim project report
- Extend zeroth-order methods for inlet performance to include low-speed aerodynamics
- Perform thrust–noise break-even study
- Perform variable-geometry thrust recovery study
- Submit the final project report

Table 4. Anticipated milestones for the next research period.

Milestone	Owner	Planned due date
Final assembly of zeroth-order methods to predict inlet performance	Georgia Tech	1/30/2023
Determination of boundary conditions from "Vision SST Engine Cycle"—collaboration efforts	Georgia Tech	5/31/2023
Submission of interim project report	PSU and Georgia Tech	12/1/2022
Extension of zeroth-order methods for inlet performance to include low-speed aerodynamics	Georgia Tech	4/15/2023
Execution of thrust–noise break-even **study**	Georgia Tech	7/1/2023
Execution of the variable-geometry thrust recovery study	Georgia Tech	8/1/2023
Submission of the final project report	Georgia Tech	9/31/2023

References

Barnhart, P. J. (1998). Inlet performance analysis code developed. *Research and Technology*. https://ntrs.nasa.gov/search.jsp?R=20050177169

Kowalski, E. J. (1979). Computer code for estimating installed performance of aircraft gas turbine engines. *Library of Inlet/Nozzle Configurations and Performance Maps*. https://ntrs.nasa.gov/citations/19800004788

Nicolai, L.M., & Carichner, G.E. (2013). Chapter 15, Section 7. *Fundamentals of Aircraft and Airship Design: Volume 1*. American Institute of Aeronautics and Astronautics.

Project 059(B) Jet Noise Modeling and Measurements to Support Reduced LTO Noise of Supersonic Aircraft Technology Development

Georgia Institute of Technology/Gulfstream Aerospace Corporation

Project Lead Investigator

Krishan K. Ahuja
Regents Professor
School of Aerospace Engineering
Georgia Institute of Technology
270 Ferst Drive, NW Atlanta, GA 30342-0150
404-290-9873
Krish.Ahuja@ae.gatech.edu

University Participants

Georgia Institute of Technology (Georgia Tech)

- PI: Krishan K. Ahuja, Regents Professor
- FAA Award Number: 13-C-AJFE-GIT-060
- Period of Performance: October 1, 2021 to September 30, 2022
- Tasks:
  1. Consultation with the advisory panel
  2. Defining nozzle requirements and design tests
  3. Design and fabricate a baseline mixer nozzle
  4. Test setup and experimental data acquisition
  5. Data dissemination
  6. Design and build a mixer for year 3 investigation
  7. Proposal for a follow-on effort for year 3
  8. Reporting and data dissemination

Project Funding Level

This project received $250,000 from FAA and $250,000 of cost-sharing from Gulfstream for the reporting period. (This is the same as received for the Year 1 effort.)

Investigation Team

- Dr. Krishan Ahuja, PI, Georgia Tech
- Dr. Jimmy Tai (co-PI), Georgia Tech
- Dr. Aharon Karon, co-investigator and lead experimentalist, Georgia Tech Research Institute (GTRI)
- Dr. Robert Funk, experimentalist, GTRI
- Reagan C. Mayo, graduate research assistant, GTRI
- Jackson Larisch, graduate research assistant, GTRI
- David N. Ramsey, graduate research assistant for portion of the program; subsequently a National Science Foundation Fellow working on fundamental issues related to the current project, Georgia Tech

Project Overview

The overall goal of this project is to perform cost-effective supersonic transport (SST) jet noise research/technology experiments to enable low-, medium-, and high-fidelity jet noise prediction methods. The specific objective is to design the

experiments in collaboration with industry, NASA, the Department of Defense (DOD), FAA, and modelers funded by the FAA to help develop improved jet noise prediction methods with reduced uncertainty and to enable industry to design quieter supersonic jet engines with higher confidence regarding the noise that will be generated. In collaboration with Gulfstream Aerospace Corporation (GAC), Georgia Tech's industry partner on this project, a representative baseline nozzle design will be selected for experiments at Georgia Tech. The data acquired will consist of far-field noise, high-speed flow visualization, source location, and detailed mean and unsteady flow measurements.

The experimental data acquired by Georgia Tech will be provided to key stakeholders and other computational teams funded by FAA to validate their computational simulations to confirm that jet noise predictions using semi-empirical and computational modeling approaches can be reliably used for jet noise evaluation.

This project has eight tasks, as listed below. The task titles are self-descriptive and reflect the task objectives. A short objective statement, research approach, and summary of the accomplishments to date for each task is provided after each task description. However, to put context to the tasks of the current period (Year 2), a brief summary of the tasks conducted in year 1 is provided below and we will refer to this as Task 0. To avoid confusion in the numbering of tasks for year 1 and year 2, roman numerals are used to refer to the tasks of year 1.

Task 0 - Summary of Year 1 Tasks

Georgia Institute of Technology

Objective(s)

The objectives of Year 1 tasks are outlined as subtasks listed below:

i. Form an Advisory Panel

This task has been completed.

ii. Identify a Baseline Nozzle Requirements and Design Tests

This task has been completed.

iii. Design and Fabricate a Baseline Nozzle

This task has been completed. This baseline nozzle was also used in year 2.

iv. Test Setup and Experimental Data Acquisition

The experimental facility is completely set up for the program. All acoustic measurements in the GTRI static anechoic chamber have been completed. The particle image velocimetry (PIV) data acquisition for the unheated core jet has been completed. Flow visualization for the unheated core jet has been completed. Halfway through the program, we suffered a few setbacks with respect to problems with the beamforming array as well as heat insulation of the flow diagnostic facility. The facility in the anechoic chambers was, however, OK, which allowed us to continue acquiring the acoustic data. Both setups are expected to become operational during the tenure of the current program. As improvements to the PIV post-processing scheme and schlieren photography were acquired during the 2022 reporting period, details on these will be included in the description of new results below.

v. Data Dissemination

The final model design was shared with the modeling teams in November 2021. All acoustic data, both for the unheated and heated-core conditions, have been shared with the modelers. All of the unheated core flow PIV data have also been shared with the modelers, and the flow visualization has been made available to the modelers.

vi. Assess Readiness of Design Tools for a Simple Baseline Nozzle Configuration

Whereas Task 5 just provides the data to the modelers, the objective of this task is to interact with the modelers in terms of verifying their codes with the measurements made under this project at Georgia Tech. Partners GAC and Aerospace Systems Design Lab (ASDL) will also be comparing their low-fidelity codes with our data.

vii. Proposal for a Follow-on Effort for Years 2 and 3

Proposals for both Years 2 and 3 were submitted.

viii. Reporting and Data Dissemination
All Year 1 reports (annual and quarterly) were submitted. See above or status of the data dissemination.

Research Approach
The research approach for the Year 1 effort has been described in detail in various Year 1 reports and consisted of seven technical tasks and one reporting task as summarized above under tasks with numbers in roman numerals.

Milestones
Described in Year 1 reports and consisted of completing the tasks as summarized above under tasks with numbers in roman numerals.

Major Accomplishments
These are described in various Year 1 reports and consisted of accomplishing the objectives of the tasks listed above with numbers in roman numerals. These accomplishments included building a model scale confluent nozzle, setup which was mounted in GTRI's anechoic chamber and also in a flow diagnostics facility. Considerable amount of farfield acoustic data complemented by PIV data was acquired, which was provided to the modeling team working on Project 59 for validating computational codes being developed by them. Data was acquired for a number of operating conditions and three mixing lengths. Certain conditions produced discrete tones, which were later identified to be associated with a feedback phenomenon.

Publications
None.

Outreach Efforts
None.

Awards
None.

Student Involvement
One graduate student (David Nate Ramsey) and an undergraduate student (Reagan Mayo).

Plans for Next Period
Conducting Year 2 effort described below.

Task 1 - Consultation with the Advisory Panel
Georgia Institute of Technology

Objective
The objective of this task is to receive regular feedback from industry and NASA subject matter experts in supersonic jet noise.

Research Approach
At the beginning of the Year 2 effort, a meeting was held with the whole ASCENT 59 project team and the advisory panel to discuss the direction of the research effort for the year. The project 59B team continued to discuss the project progress and direction with the advisory panel throughout the effort. Most meetings were organized and conducted by Dr. Sandy Liu of FAA.

Milestones
None. The team of modelers and experimentalists under this project were to meet during the tenure of the project on dates organized by Dr. Sandy Liu and discuss the progress and plans. The team met at least four times during the year.

Major Accomplishments
Project 59B team shared the results of the Year 2 effort with the advisory panel as well as the modelers.

Publications
None.

Outreach Efforts
None.

Awards
None.

Student Involvement
One graduate student (David Nate Ramsey) and an undergraduate student (Reagan Mayo).

Plans for Next Period
Meet on a regular basis as arranged by FAA.

Task 2 - Defining Nozzle Requirements and Design Tests
Georgia Institute of Technology

Objective
The objective of this task is to define the nozzle requirements and design the experiments.

Research Approach
During the Year 1 effort, the baseline nozzle and tests were based on a paper engine design created by the Georgia Tech ASDL guided by the ASCENT 10 project on engine cycle selection for a GT Medium SST (55-passenger class). For simplicity, it was decided that the GT nozzle model tested under this project would not have a plug. For the purpose of calculating the area of the outer (secondary flow) duct, the annular areas of the paper engine were used to calculate the area of the secondary flow duct in the model nozzle facility. The GTRI model is a 0.045 scale of the paper engine. The mixing length/exhaust nozzle exit diameter (L_e/D_e) are 0.7, 1, 2, and 3. As will be described below, during the Year 2 effort, tabs were added to the primary nozzle to increase the mixing between primary and secondary streams. The goal was to create a mixer nozzle with a simple geometry, with the goal of providing the modeling teams with a mixer nozzle that is not as geometrically complicated as a lobed mixer.

To be consistent with the Year 1 work, the same condition matrix was used for Year 2. Figure 1 shows the conditions used on a per configuration basis, as well as for each core temperature (unheated or 500˚F). As with the Year 1 experiments, these tests have been designed with variations in nozzle design and/or operating parameters in order to explore the accuracy of semi-empirical and computational tools for predicting jet noise. To better test the ability of the tabs to increase the mixing between the primary and secondary stream, most of the focus was in the L_e/D_e = 0.7 configuration, although the effects of increasing the mixing length were also explored. Additionally, the configuration of the tabs was varied.

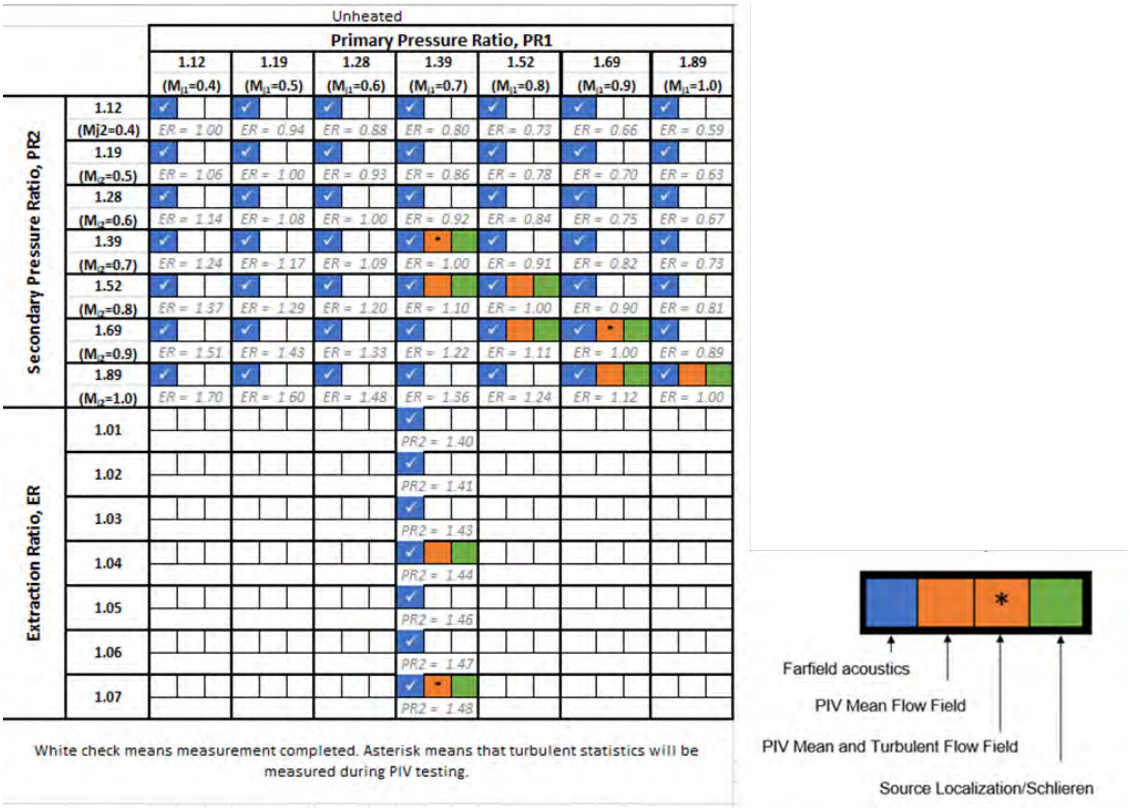

Figure 1. Test condition matrix. PIV, particle image velocimetry.

Milestones
Define the nozzle requirements and design the experiments at the start of the Year 2 effort.

Major Accomplishments
Completed defining nozzle requirements and design the experiments and selected the test matrix as outlined above.

Publications
None.

Outreach Efforts
None.

Awards
None.

Student Involvement
One graduate student (David Nate Ramsey) and an undergraduate student (Reagan Mayo).

Plans for Next Period
Plan for conducting tests with heated flow and with a Forced Mixer.

Task 3 - Design and Fabricate Baseline Mixer Nozzle

Georgia Institute of Technology

Objective

The objective of this task is to select the tab geometries that will added to the primary nozzle of the confluent nozzle.

Research Approach

For the purpose of creating a mechanical mixer nozzle with a simple geometry, tabs were added to the primary nozzle of the confluent nozzle. The baseline confluent nozzle that was used during the Year 1 effort is shown in Figure 2. The primary nozzle was transformed into a mixer nozzle by adding mechanical tabs to the nozzle exit. Two types of tabs were used for this purpose. The first are D-type tabs (referred to as "D-tabs"), which were tested by Ahuja and Brown (1989) who showed significant increases in jet mixing when installed at the exit of a single nozzle and are shown in Figure 3. The other type of tabs are delta-type tabs (referred to as "delta-tabs"), which are shown in Figure 4 and have been used in many studies (Hileman, 2003; Saiyed, 1999; Tam, 2000). Figure 5 shows where the tabs were positioned in the confluent nozzle.

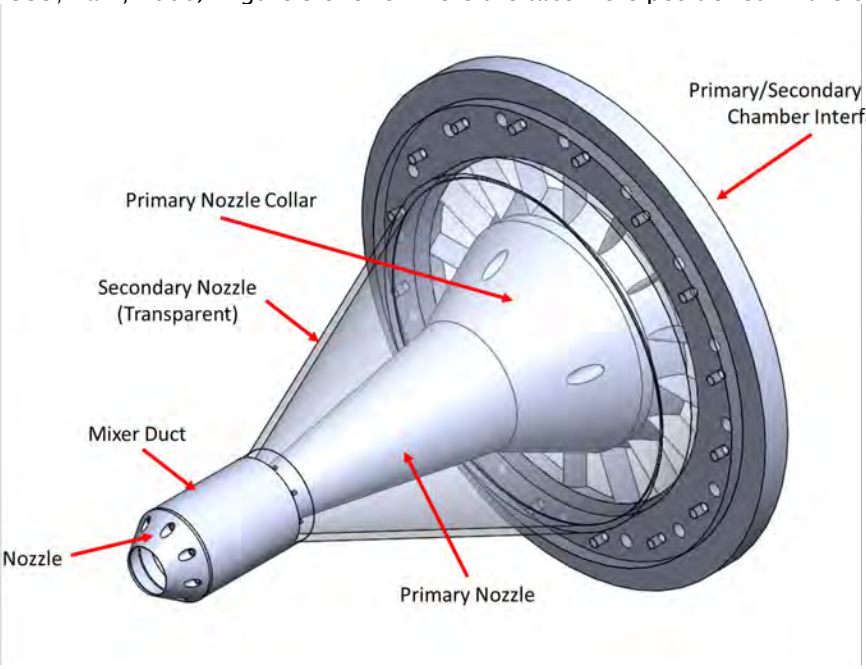

Figure 2. Experimental model design.

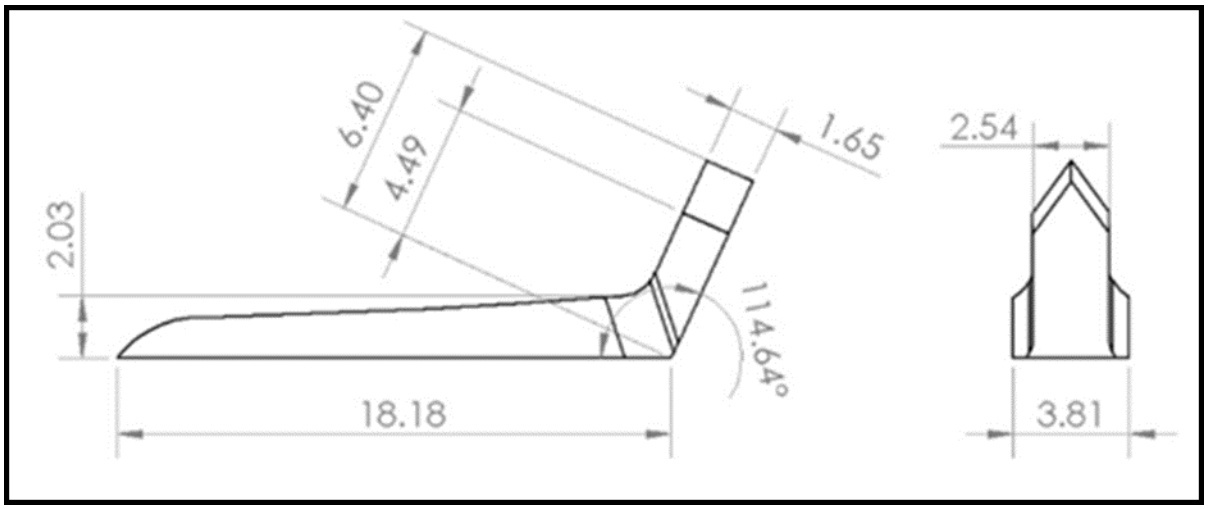

Figure 3. Design of the D-tab (dimensions in mm).

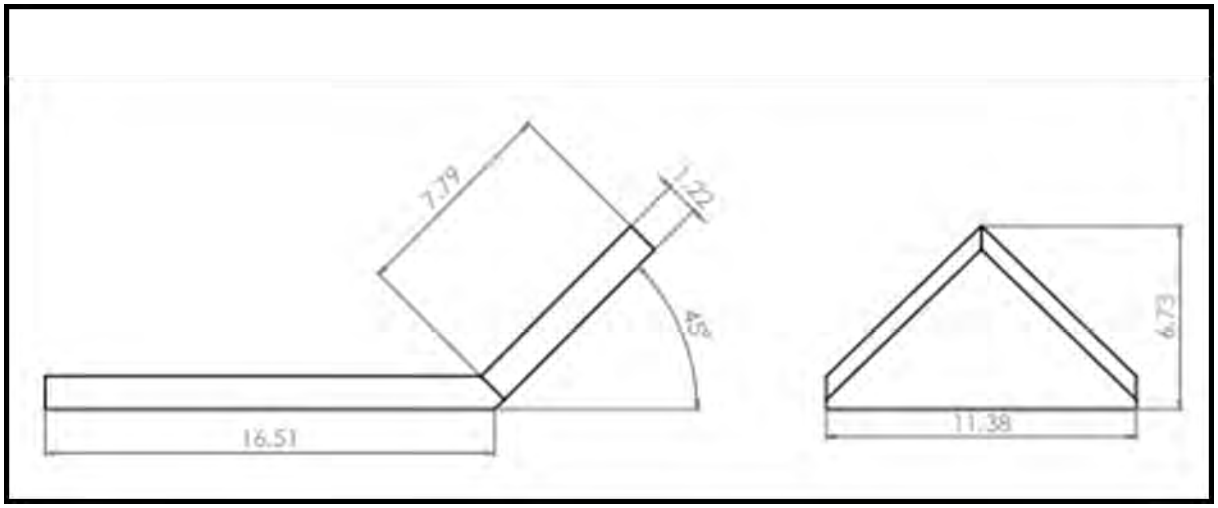

Figure 4. Design of the delta-tab (dimensions in mm).

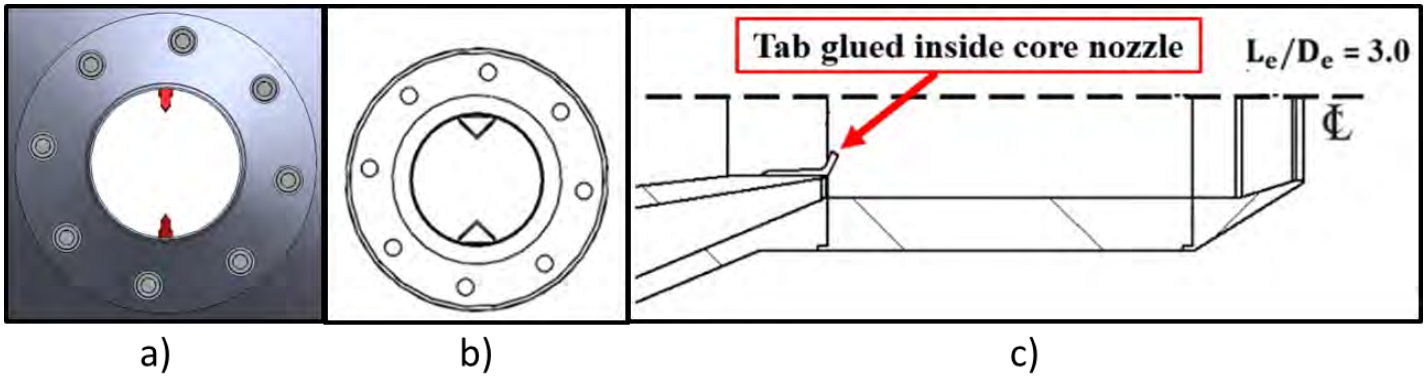

Figure 5. Tabs in the core nozzle: (a) D-tabs, (b) delta tabs, and (c) cross-sectional view of nozzle showing tab position.

Milestones
select and design a baseline mixer while waiting for our Cost-share partner Gulfstream to design and manufacture a forced multi-lobe mixer.

Major Accomplishments
Selected tabs as the baseline mixers as described above.

Publications
None.

Outreach Efforts
None.

Awards
None.

Student Involvement
Three graduate students (David Nate Ramsey, Reagan Mayo, and Jackson Larisch).

Plans for Next Period
None.

References
Ahuja, K., & Brown, W. (1989, March 13). Shear flow control by mechanical tabs. *2nd Shear Flow Conference*. 2nd Shear Flow Conference, Tempe, AZ, U.S.A. https://doi.org/10.2514/6.1989-994

Hileman, J., & Samimy, M. (2003). Effects of vortex generating tabs on noise sources in an ideally expanded Mach 1.3 jet. *International Journal of Aeroacoustics*, *2*(1), 35–63. https://doi.org/10.1260/147547203322436935

Saiyed, N., & Bridges, J. (1999, May 10). Tabs and mixers for reducing low bypass ratio jet noise. *5th AIAA/CEAS Aeroacoustics Conference and Exhibit*. 5th AIAA/CEAS Aeroacoustics Conference and Exhibit, Bellevue,WA,U.S.A. https://doi.org/10.2514/6.1999-1986

Tam, C. K. W., & Zaman, K. B. M. Q. (2000). Subsonic jet noise from nonaxisymmetric and tabbed nozzles. *AIAA Journal*, *38*(4), 592–599. https://doi.org/10.2514/2.1029

Task 4 - Test Setup and Experimental Data Acquisition

Georgia Institute of Technology

Objective

The objective of this task was to conduct the tests and acquire and analyze the data. So far, during the Year 2 effort, only acoustic measurements have been acquired. Because of a major failure in the GTRI Flow Diagnostic Facility (this was a failure that occurred after repairing another earlier failure), as reported in the quarterly progress reports, PIV data could not be obtained earlier. As noted above, extensive unheated core flow high-speed schlieren flow visualization was acquired as part of the Year 1 effort. Likewise, considerable improvements to the PIV data were made. As these two sets of data were acquired during this period of performance, these are reported in this report.

Research Approach

PIV Measurements

The PIV data were acquired in GTRI's Flow Diagnostics Facility using a double-pulsed, two-dimensional PIV system. The details of GTRI's Flow Diagnostics Facility were reported by Burrin et al. (1979) with salient details repeated here for completeness. The Flow Diagnostics Facility is a sister facility to GTRI's Anechoic Jet Facility, having identical plenum interfaces and identical plenum-to-nozzle area contraction ratios.

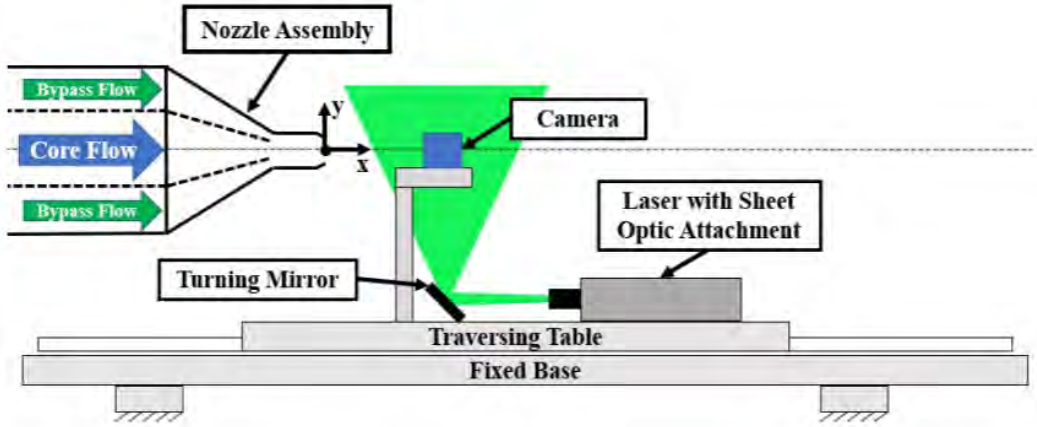

(a)

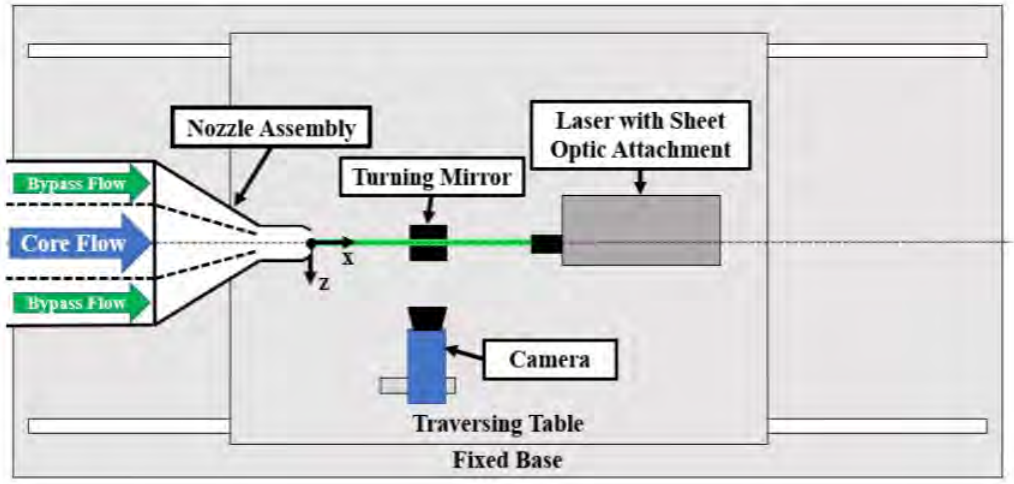

(b)

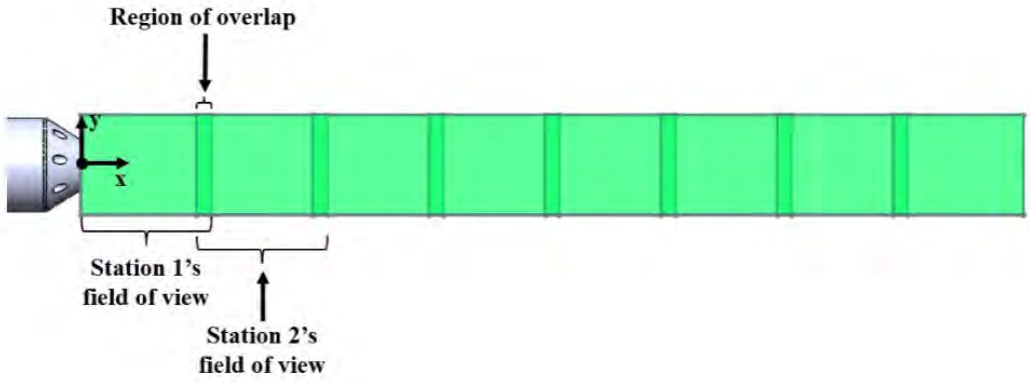

(c)

Figure 6. Particle image velocimetry (PIV) system: (a) side view, (b), top-down view, and (c) multi-station acquisition scheme.

The PIV system is shown schematically in Figure 6. Figure 6a and b show side- and top-down-view schematics of this system, respectively. Figure 6c illustrates the camera's nominal field-of-view at each of the stations along the traverse. In selecting the time delay between image pairs, an optimization routine built into the DaVis software was used. The DaVis software is the LaVision proprietary PIV software that is used for the data acquisition and post-processing. This routine recommends a time delay between image pairs based in part on the peak Q-ratio (the ratio of highest and second highest correlation peak values) for several different time delays. A low Q-ratio indicates that a particle displacement cannot be accurately predicted from the correlation plane of a given image pair in a given interrogation window.

The measured instantaneous velocity fields may contain spurious velocity vectors. Spurious vectors are characterized as having exceedingly large or small magnitude and/or erroneous direction relative to the expected velocity vector. Of course, the expected vector field is not known a priori, and criteria for identifying these spurious vectors must be employed. In this work, spurious vectors are detected and rejected at two different stages of the data processing routine. First, the instantaneous velocity fields are screened in a processing stage referred to as "vector post-processing." A filtering operation is used to detect and replace vectors that have a large deviation from their neighbors. This filtering operation is based on the framework of a dynamic mean value operator (Raffel, 2018). In particular, the filter was set to "strongly remove and iteratively replace" in the DaVis software – removing vectors that had a difference to the local mean outside of one standard deviation of the neighboring vectors before re-inserting vectors whose difference to the local mean is within two standard deviations of the neighboring vectors once the filter was applied. For vectors that failed to satisfy the criterion, the median of the neighbors was used to replace the vector. This filter was executed twice on each instantaneous velocity field. Further, a range of acceptable particle displacements was specified. Finally, any instantaneous vectors whose associated Q-ratio was less than 2.0 were deleted. The success of these vector post-processing operations in removing outliers without modifying the remainder of the velocity field is shown to be successful on a single, instantaneous velocity field in Figure 7. The top frame shows the result without the vector post-processing routine and the bottom frame shows the same field with the vector post-processing routine executed, both of which use the same color scaling shown on the far right. This vector field is a measurement across the shear layer of the jet from the core nozzle in isolation operated at $\boldsymbol{M_j}$ = 0.58, unheated, with the jet flowing from left to right in the figure. This portion of the data processing routine has remained unchanged since the first release of PIV measurements. However, refinements have been made that are outlined in the next paragraph.

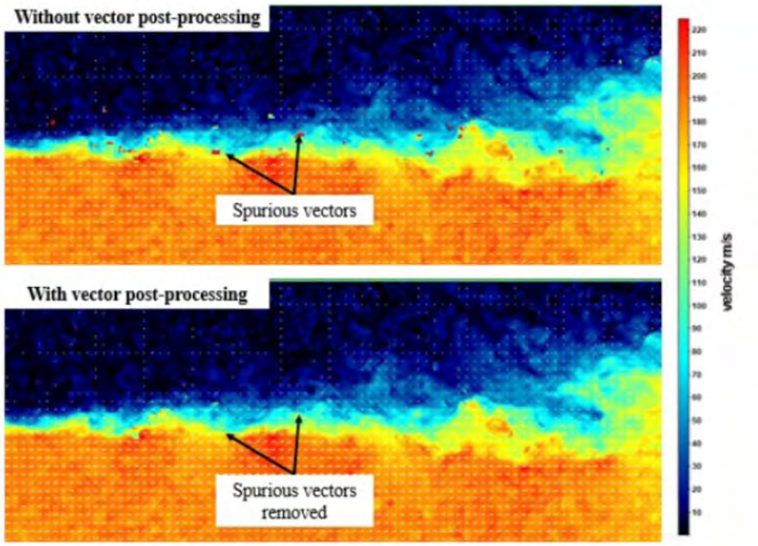

Figure 7. Success of vector post-processing in replacing spurious vectors. Both frames show the same region of shear layer of jet from single nozzle in isolation, M_j = 0.58, unheated.

The ensemble averaging of the PIV measurements now includes applying Chauvenet's criterion for spurious vector (i.e., outlier) rejection, which is believed to be an improvement over the more aggressive outlier rejection scheme used before this change. This change only has an appreciable impact on the measurements of velocity fluctuation (i.e., turbulence intensity), with relatively small changes to the mean velocity measurements. Chauvenet's criterion was reported to be used by Bridges and Wernet (2011) and is a sample size–dependent criterion that suggests thresholds outside of which values are unlikely to be sampled. If values are measured outside of these thresholds, the data are considered outliers. In each PIV interrogation window across all instantaneous velocity fields being ensemble averaged, Chauvenet's criterion is applied to each component of the measured velocity vectors. This criterion assumes that the measured velocities within each interrogation window are sampled from a Gaussian parent distribution. The reader astute in turbulent flows would likely dispute this assumption, and rightfully so. It is known that the turbulent velocities in a free shear layer are not always Gaussian distributed (as discussed in greater detail by Pope (2000)). In particular, the probability density function (PDF) of velocity at a point may have non-zero skewness, whereas a Gaussian distribution would have zero skewness. This potential criticism is acknowledged; however, a Gaussian PDF of velocities is not assumed aside from computing outlier rejection thresholds. Histograms of displacement in units of pixels, as acquired using the PIV measurement system, are presented in Figure 8. This figure shows that the use of Chauvenet's criterion correctly flags obviously spurious vectors (at the tips of the red arrows) without wrongly flagging seemingly trustworthy vectors (based on their presence in a larger distribution of data). Displaying the displacement histogram with units of pixels serves the secondary purpose of providing evidence that the PIV measurements are not affected by peak-locking effects. Were peak-locking present in the data, the displacement vectors would be biased toward integer displacement values (Raffel, 2018). Demonstrating this fact is vital to the integrity of the fluctuating velocity measurements produced, as Christensen (2004) showed that peak-locking may strongly affect second-order velocity statistics (i.e., the standard deviation of velocity reported in the present work).

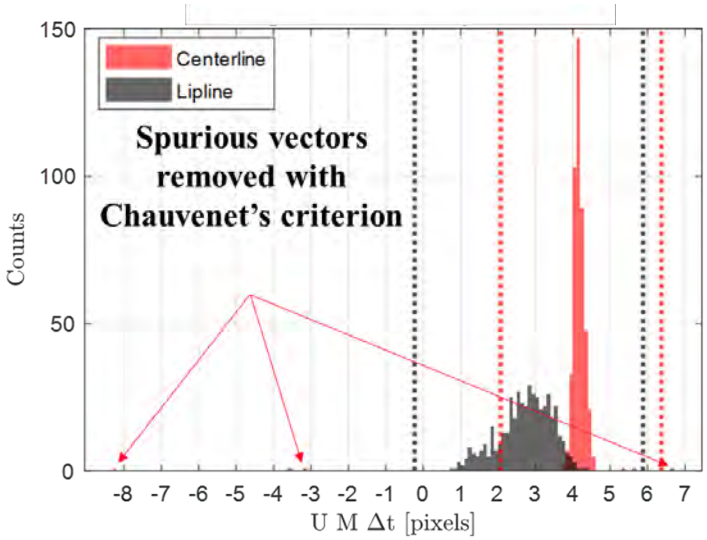

Figure 8. Histogram of axial displacement along lipline (x/D_e= 0.7, y/D_e=0.5, N=1500 image pairs) of jet from single nozzle (M_j = 0.58, unheated). Vertical lines show Chauvenet criterion boundaries.

Ahuja et al. (1982) acquired mean and unsteady velocity measurements of a jet produced by a convergent nozzle with an exit diameter of 2 inches (5.08 cm) in the GTRI Flow Diagnostics Facility using a laser Doppler velocimetry (LDV) system. As shown by Bridges and Wernet (2011), the LDV data of Ahuja et al. (1982) and several other sources of published jet flow-field measurements agree reasonably well when normalized. Thus, in the present work, agreement between flow-field measurements reported by Ahuja et al. (1982) and a validation dataset acquired using the present work's PIV system (when both are presented in normalized form) is taken to provide a high degree of confidence in the PIV measurements. This relies, of course, on the accuracy of historical datasets. The 1.6-inch nozzle used here is shown in Figure 9a and the agreement between the validation dataset is shown in Figure 9b. This agreement is even better than before Chauvenet's criterion was implemented in the data processing routine.

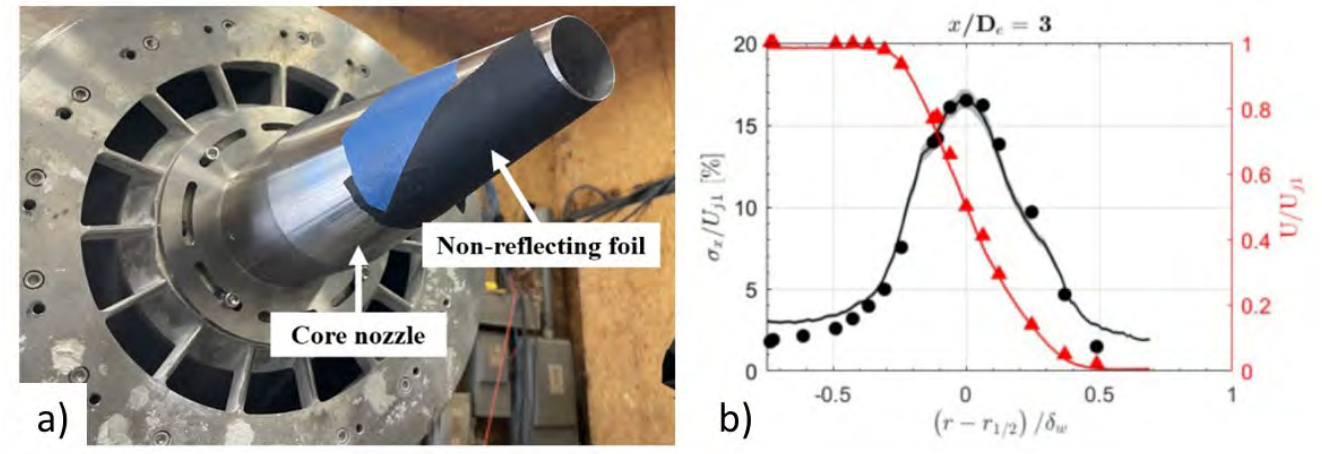

Figure 9. Validation dataset: (a) nozzle used, and (b) agreement with dataset from Ahuja et al. (1982). Curves are PIV data, and markers are historical LDV data from Ahuja et al. (1982). PIV, particle image velocimetry; LDV, laser Doppler velocimetry.

Figure 10 shows typical jet flow fields at a lower pressure ratio ($PR_1 = PR_2 = 1.39$, unheated), and Figure 11 shows what is believed to be a self-excited flow field at a high subcritical pressure ratio ($PR_1 = PR_2 = 1.69$, unheated).

Witze (1974) provided a model for the centerline velocity distribution of a compressible free jet, which was shown to agree well with experimental data. Bridges and Wernet (2011) used the potential core length obtained by the theory reported by Witze (1974) as a means to collapse PIV measurements acquired at different conditions. The "Witze model" (as it will be referred to hereafter) may be expressed as follows:

$$\bar{u}_c\left(\frac{x}{D_e}\right) = 1 - \exp\left(\frac{-1}{2\kappa\left(\frac{x}{D_e}\right)(\bar{\rho}_e)^{0.5} - X_c}\right) \tag{1}$$

$$\kappa = 0.08\left(1 - 0.16M_j\right)(\bar{\rho}_e)^{-0.22}$$

Here, $X_c = 0.70$, and the remaining parameters are defined in Witze's report. In the present work, claims about the shortening of the potential core of a jet under self-excited flow conditions are sought to be made. Using the measurements of the flow field alone, no direct evidence supporting such a claim can be found. There is no baseline, unexcited measurement that can be acquired for a self-excited condition – the excitation is always present. Were this an experiment involving a jet that was acoustically forced using a controlled sound source, measurements with and without the acoustic forcing could be acquired and compared. Instead, a different approach must be formulated using what is known about the behavior of the confluent nozzle. The self-excited condition to be characterized is the $PR_1 = PR_2 = 1.69$, unheated condition. It is known from other experiments that conditions with unity extraction ratio at lower pressures do not produce tones. Thus, if Witze's model for the centerline velocity distribution agrees well with the measurements at conditions with no tones, the model may be assumed to provide a reference for the shortening of the potential core of the jet caused by self-excitation.

The centerline mean velocity distribution of three different mixing lengths with unity extraction ratio at $PR_1 = 1.39$ are shown in Figure 12a and at $PR_1 = 1.69$ are shown in Figure 12b, along with Witze's model. It can be seen that all curves agree reasonably well with Witze's model for the lower pressure ratio, regardless of mixing length. However, the high subcritical condition shows a large departure from Witze's model, suggesting that a significant increase in mixing occurs at this condition relative to a single, unexcited jet. The farfield noise produced by the nozzle at this high subcritical pressure ratio is shown in Figure 13.

It is noted that there exists a mean axial velocity gradient close to the nozzle exit plane in Figure 12, and some explanations for this are offered. This phenomenon is believed to be a result of the contraction of the exhaust nozzle proximate to its exit plane. The contraction requires the fluid to turn radially inward near the upstream side of the exhaust nozzle and then to straighten out in a similar fashion near the exhaust nozzle exit plane. At these two locations, a force is required for the fluid to turn. Near the upstream side of the exhaust nozzle, the required force is supplied by the solid body of the nozzle. Near the exhaust nozzle exit plane, no solid body exists to supply the required force – it must instead come from the fluid itself in the form of a pressure gradient if the flow is to become approximately parallel as it exits the nozzle. The fluid near the center of the exhaust nozzle may supply the required pressure gradient if the fluid is at an elevated static pressure and thus has not yet reached its fully expanded velocity. Morris et al. (2010) measured a similar effect in the flow field produced by a single nozzle, and also attributed this effect to the nozzle's convergence at the nozzle exit plane.

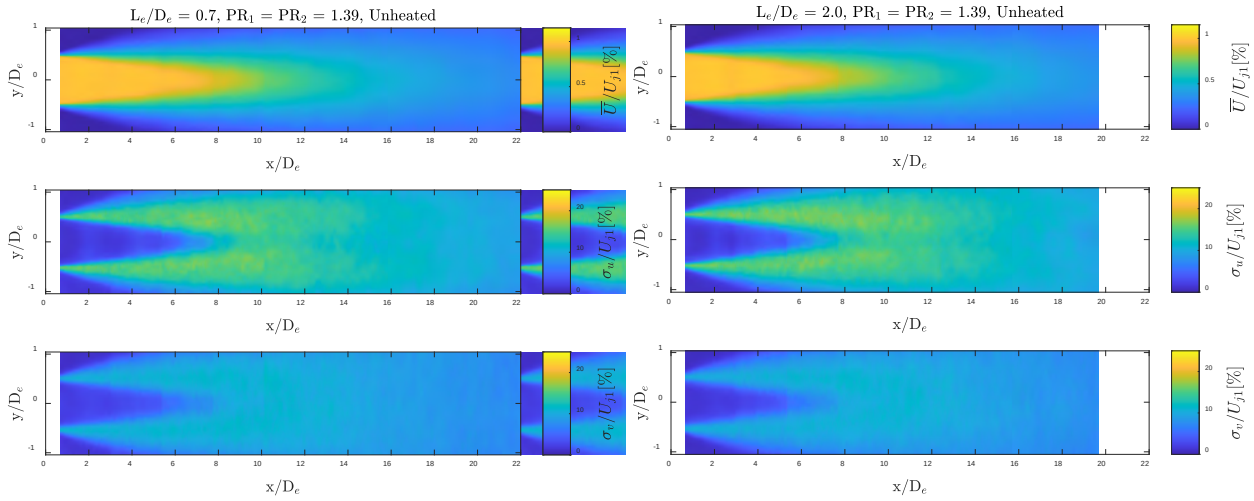

(a) **(b)**

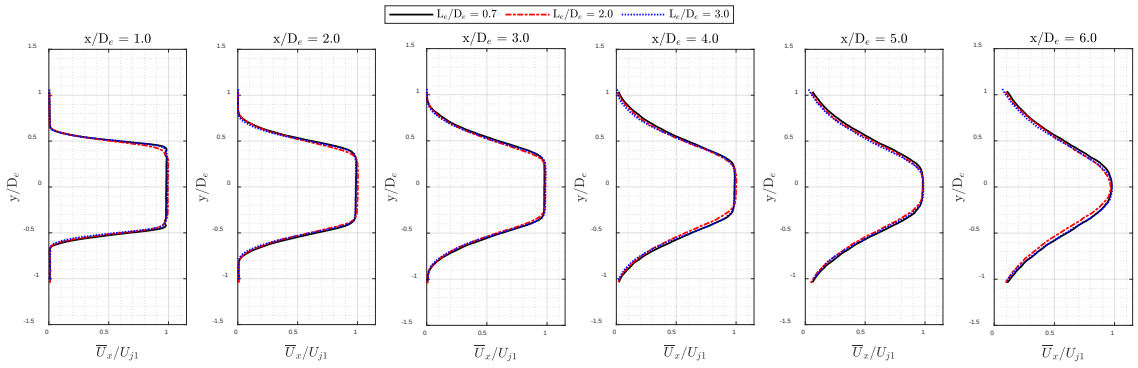

(c)

(d)

Figure 10. Typical flow field of jet from confluent nozzle ($PR_1 = PR_2 = 1.39$, unheated): (a) mean velocity, axial fluctuation intensity, and radial fluctuation intensity for $L_e/D_e = 0.7$; (b) mean velocity, axial fluctuation intensity, and radial fluctuation intensity for $L_e/D_e = 2.0$; (c) radial profiles of mean velocity near the nozzle exit for several mixing lengths; and (d) radial profiles of axial fluctuation intensity near the nozzle exit for three mixing lengths. N = 750 image pairs.

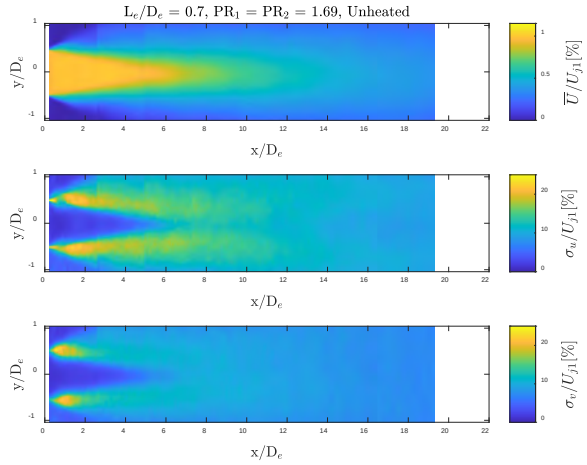

(a)

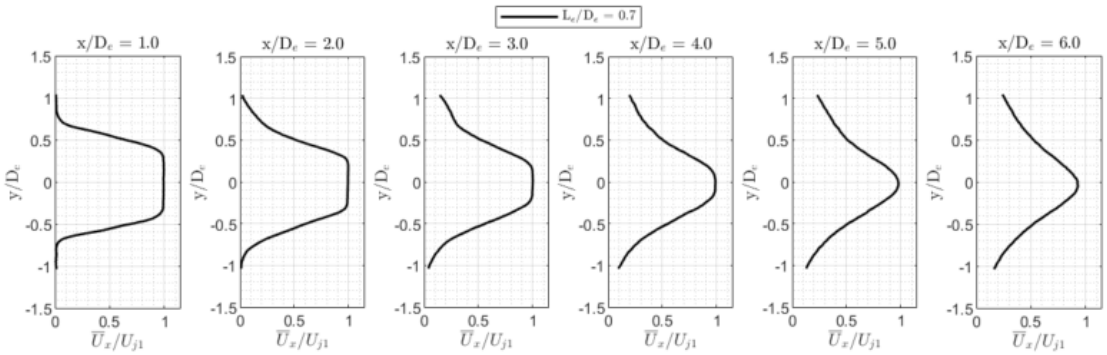

(b)

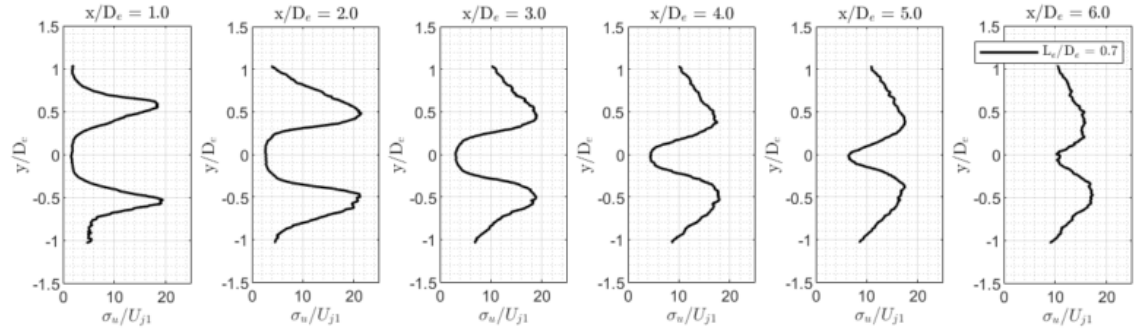

(c)

Figure 11. Self-excited flow field of jet from confluent nozzle ($PR_1 = PR_2 = 1.69$, unheated): (a) mean velocity, axial fluctuation intensity, and radial fluctuation intensity for $L_e/D_e = 0.7$; (b) radial profiles of mean velocity near nozzle exit; and (c) radial profiles of axial fluctuation intensity near nozzle exit. N = 750 image pairs.

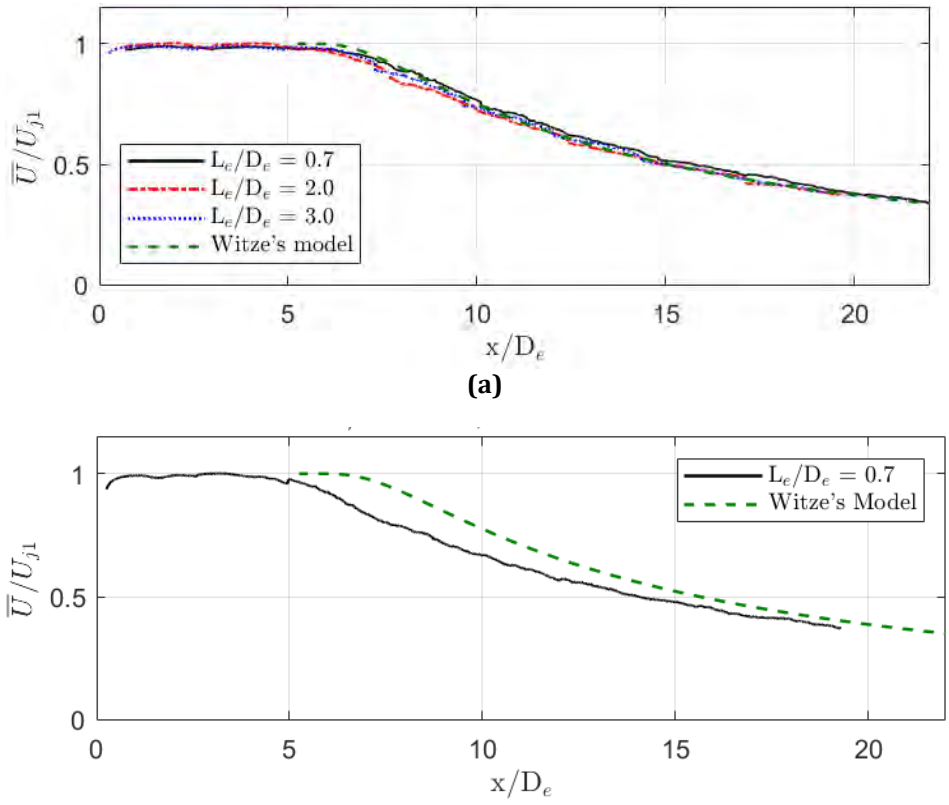

Figure 12. Centerline mean velocity distributions: (a) typical flow field including Witze's model for single jet ($PR_1 = PR_2 = 1.39$, unheated) and (b) self-excited conditions and Witze's model for single jet ($PR_1 = PR_2 = 1.69$, unheated). N = 750 image pairs.

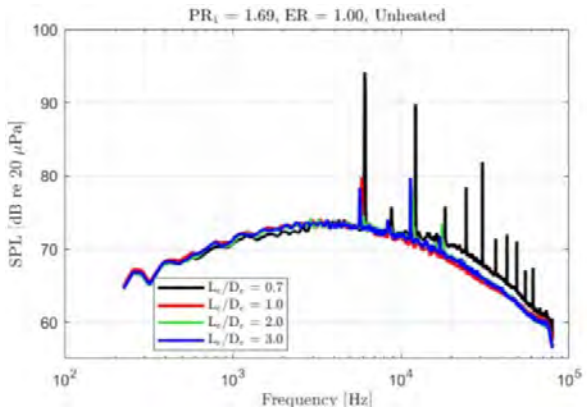

Figure 13. Lossless, fully corrected farfield jet noise spectra at high subcritical condition $PR_1 = PR_2 = 1.69$, unheated. $\theta = 90°$ (R = 84.7D_e).

High-Speed Schlieren Flow Visualization

GTRI's z-shaped schlieren setup is shown in Figure 14. An arc lamp light source emits light that follows a z-shaped path along a series of mirrors and lenses. The light source is positioned at the focal point of the first parabolic mirror, sending collimated light into the test section (the horizontal region between the two parabolic mirrors). The second parabolic mirror focuses the light rays (now refracted by density gradients within the test section) to a focal point. At the appropriate focal point, a knife-edge cutoff is positioned in one of two orientations: vertical (knife-edge normal to jet axis) or horizontal (knife-edge parallel to jet axis). These two knife-edge orientations reveal axial and transverse density gradients in the test section, respectively. The light is then passed through a pair of refocusing lenses that allow the camera to be placed far from the jet, which may be heated, in order to protect the camera. The schlieren images are captured on a Vision Research Phantom V2512 monochrome ultra-high-speed camera, with a resolution of 1,280 × 800 pixels at 25,000 frames per second and with a 1-μs exposure time. The video files being released to modeling teams will be in the .AVI format, with 100 frames total at 20 frames per second. While only short, 100-frame videos are being released, 2,500 images were recorded at each condition, and the longer duration measurements are available upon request. In the present work, only single snapshots from a few high-speed schlieren measurements are shown and discussed.

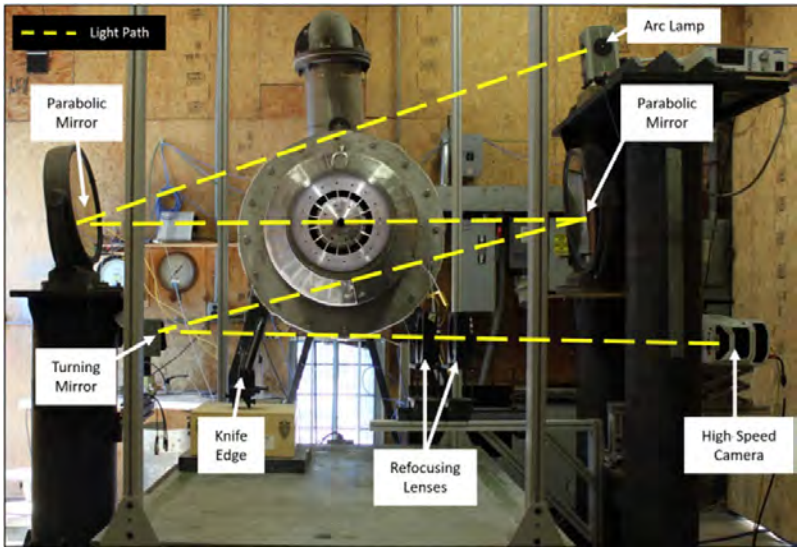

Figure 14. Georgia Tech Research Institute's z-shaped schlieren setup.

Representative schlieren snapshots are shown for the shortest mixing length (L_e/D_e = 0.7) and ER = 1.00 in Figures 15 to 17, each of which shows both transverse and axial density gradients. As the pressure ratio (and thus its Reynolds number) is increased, the turbulent density gradients become increasingly well defined. This is expected for two reasons. First, turbulent velocity fluctuations and their associated stresses on the fluid increase with Mach number. Second, the smallest scales of turbulence decrease with increasing Reynolds number ($Re = U_j D_e/\nu$). Relatively small changes are made to the apparent density gradients by increasing ER from 1.00 to 1.07 at the PR_1 = 1.39 condition, as shown in Figure 18. Similarly, little change is seen as ER is set to 1.10 (Figure 19). For the most part, the flow field at all of these conditions remains typical.

Figure 20 and Figure 21show examples of the self-excited conditions (PR_1 = 1.69, ER = 1.00) for two mixing lengths of L_e/D_e = 0.7 and 2.0, respectively. These conditions have larger jet spreading and apparent excited instability waves or coherent large-scale structures, which were absent in the flow for the other conditions. It is noted that increasing the pressures to a critical pressure ratio eliminates the tone and evidence of self-excitation (see Figure 17). It can be seen that the shortest mixing duct has greater jet spreading and stronger large-scale structures than the L_e/D_e = 2.0 mixing duct at the PR_1 = 1.69, ER = 1.00 condition.

Throughout these schlieren images, the axial density gradient near the nozzle exit plane is visible. An explanation for this effect is offered in the previous section on the PIV measurements.

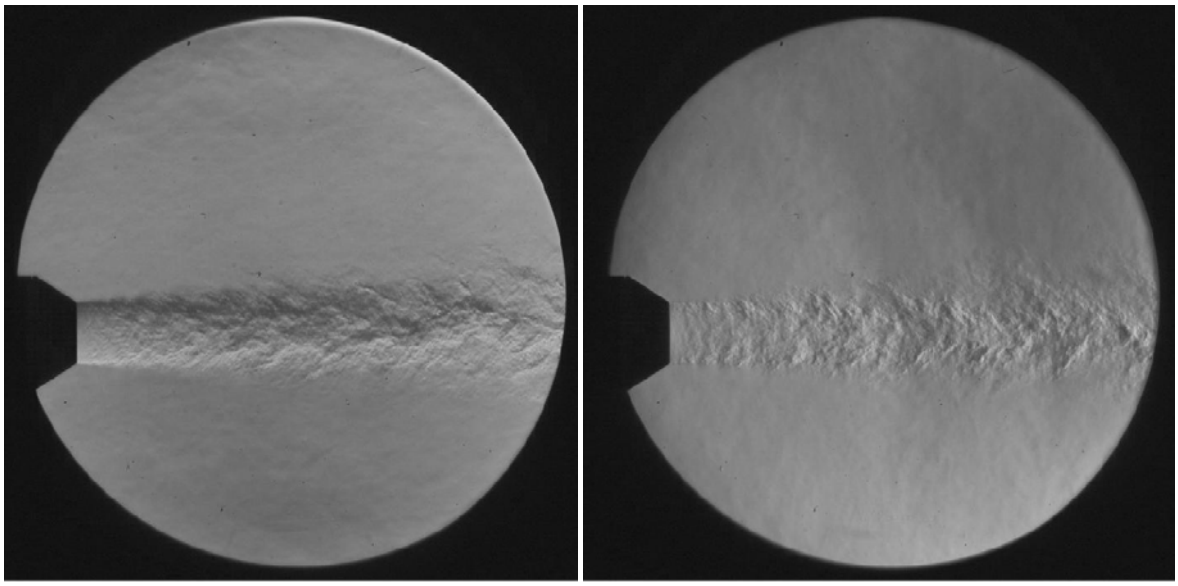

(a) **(b)**

Figure 15. Schlieren flow visualization of $L_e/D_e = 0.7$ at $PR_1 = 1.39$, $ER = 1.00$, $PR_2 = 1.39$, unheated configuration: (a) transverse density gradients, and (b) axial density gradients.

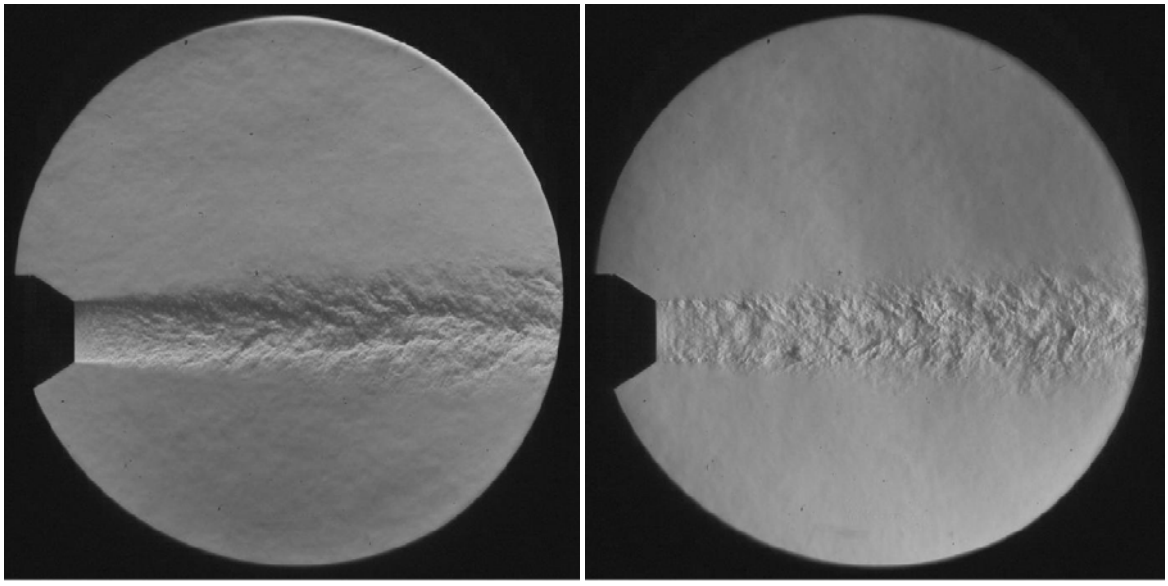

(a) **(b)**

Figure 16. Schlieren flow visualization of L_e/D_e = 0.7 at $PR_1 = 1.52$, $ER = 1.00$, $PR_2 = 1.52$ unheated configuration: (a) transverse density gradients, and (b) axial density gradients.

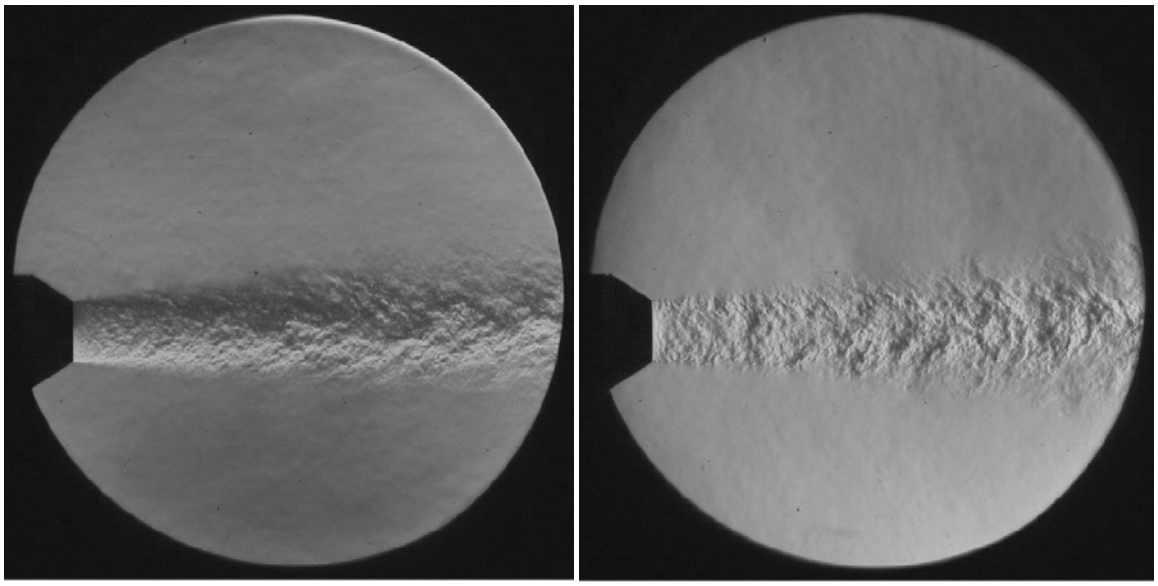

(a) **(b)**

Figure 17. Schlieren flow visualization of L_e/D_e = 0.7 at $PR_1 = 1.89, ER = 1.00, PR_2 = 1.89$, unheated configuration: (a) transverse density gradients, and (b) axial density gradients.

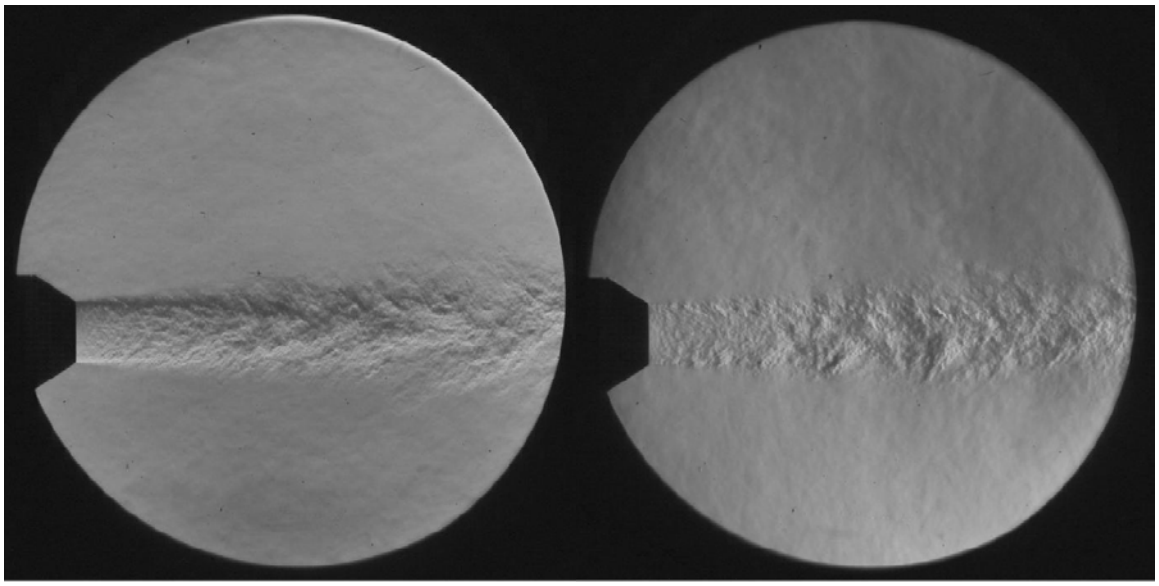

(a) **(b)**

Figure 18. Schlieren flow visualization of L_e/D_e = 0.7 at $PR_1 = 1.39$, $ER = 1.07$, $PR_2 = 1.49$, unheated configuration: (a) transverse density gradients, and (b) axial density gradients.

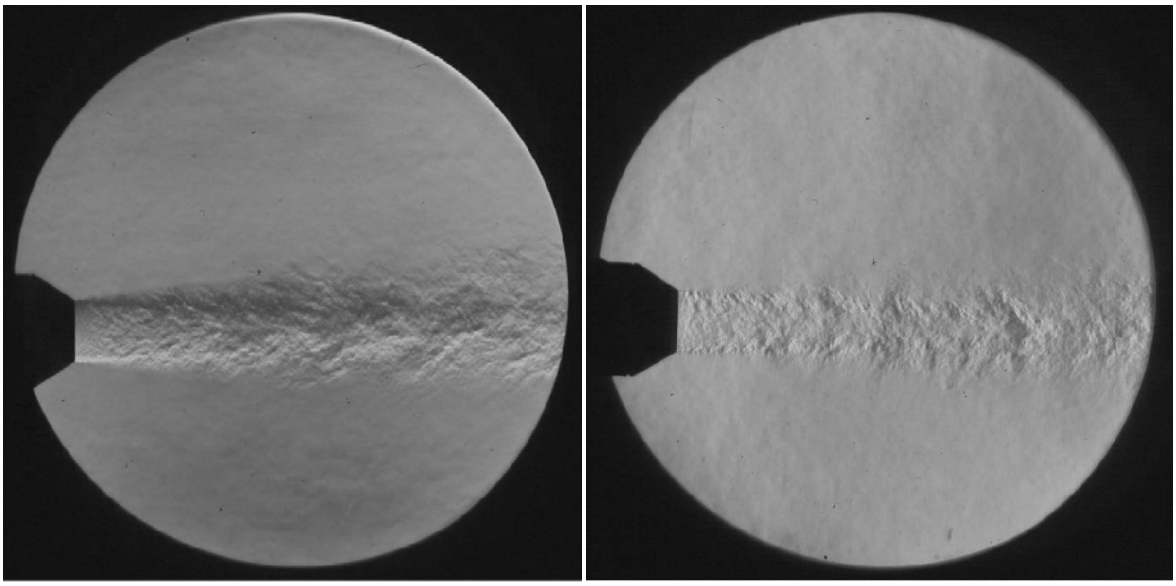

(a) **(b)**

Figure 19. Schlieren flow visualization of $L_e/D_e = 0.7$ at $PR_1 = 1.39$, ER = 1.10, PR_2=1.52 unheated configuration: (a) transverse density gradients, and (b) axial density gradients.

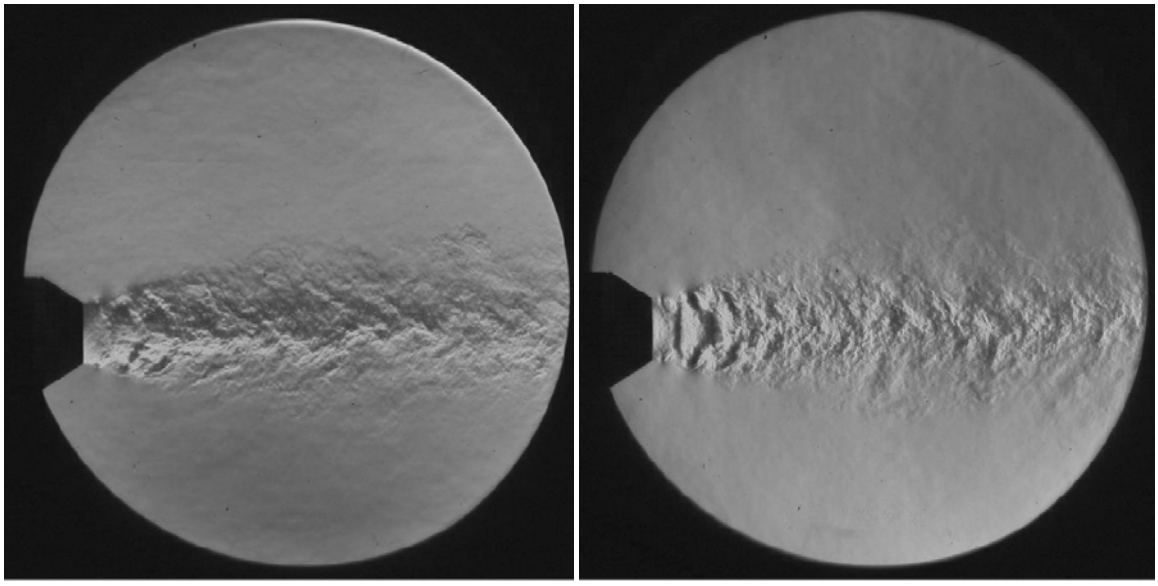

(a) **(b)**

Figure 20. Schlieren flow visualization of L_e/D_e=0.7 at $PR_1 = 1.69, ER = 1.00, PR_2 = 1.69$, unheated configuration: (a) transverse density gradients, and (b) axial density gradients.

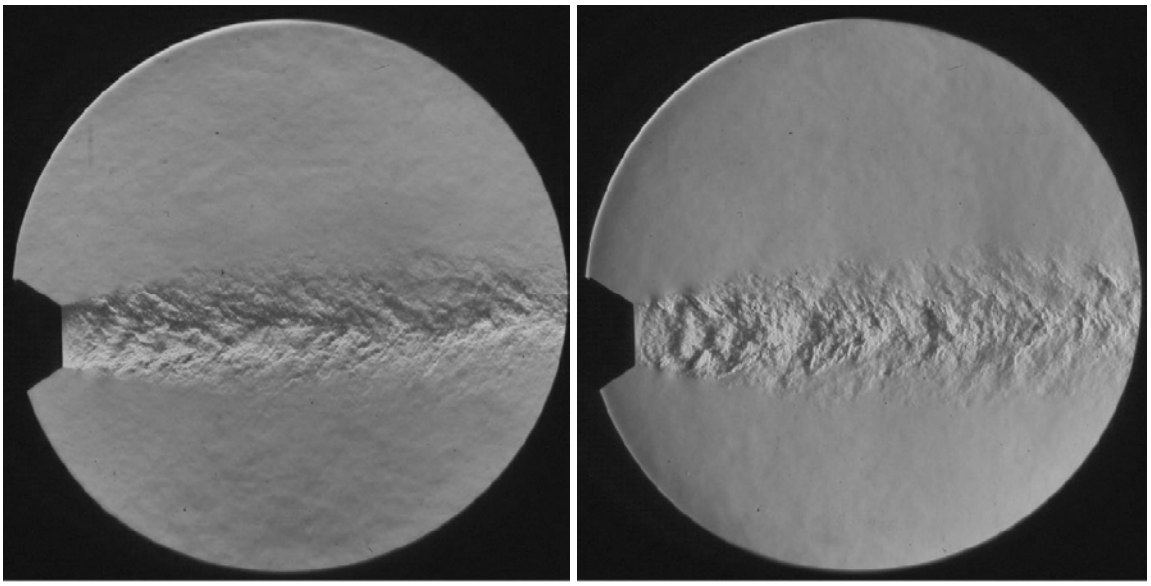

(a) **(b)**

Figure 21. Schlieren flow visualization of L_e/D_e=2.0 at $PR_1 = 1.69, ER = 1.00, PR_2 = 1.69$, unheated configuration: (a) transverse density gradients, and (b) axial density gradients.

Acoustic Measurements of Mechanical Tabs as a Forced Mixer

Facility Setup and Testing Description

The test model was mounted in the GTRI Anechoic Jet Facility for the acoustic data acquisition as seen in Figure 22. This facility is described in detail in Burrin et al. (1974), Burrin and Tanna (1979), and Ahuja (2003). Figure 23 shows the definitions of the polar (θ) and azimuthal (ϕ) angles used in positioning the microphones in the jet facility. Farfield microphones were mounted on polar arcs at angles between 30˚ and 120˚ with respect to the jet axis in 10˚ increments using the convention shown in Figure 23a. Three arcs were present during testing at azimuthal angles of 0˚, 45˚, and 90˚, as defined in Figure 23b. The jet upstream conditions were set by controlling the ratio of the total pressure to the ambient pressure (PR = p_t/p_a) for both the primary and secondary streams. Both the primary and secondary streams were varied between pressure ratios of 1.12 and 1.89. The extraction ratio (ER = p_{t2}/p_{t1}) was used as another parameter to define the secondary pressure ratio for a given primary stream pressure. Per insight and advice received from GAC and FAA, ERs between 1.00 and 1.07 are the most realistic conditions for a given PR_1 for mixed-flow conditions. In the unheated tests, the primary total temperature varied between 60˚F and 70˚F; and, during heated testing, it was set nominally to 500˚F. As a note, in this program the pressure ratio, PR, will refer to the ratio between upstream total and ambient pressures. In addition to the acoustic measurements, the primary and secondary total pressure and temperature, the primary and secondary mass flow rates (measured at the control valve), and the ambient pressure, temperature, and relative humidity were measured.

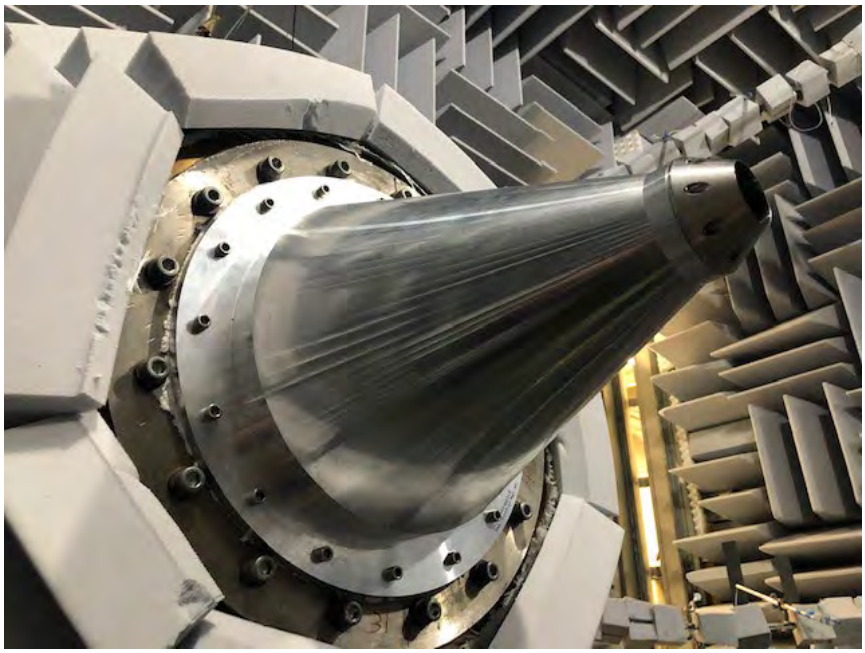

Figure 22. Project model set up in the Georgia Tech Research Institute Anechoic Jet Facility.

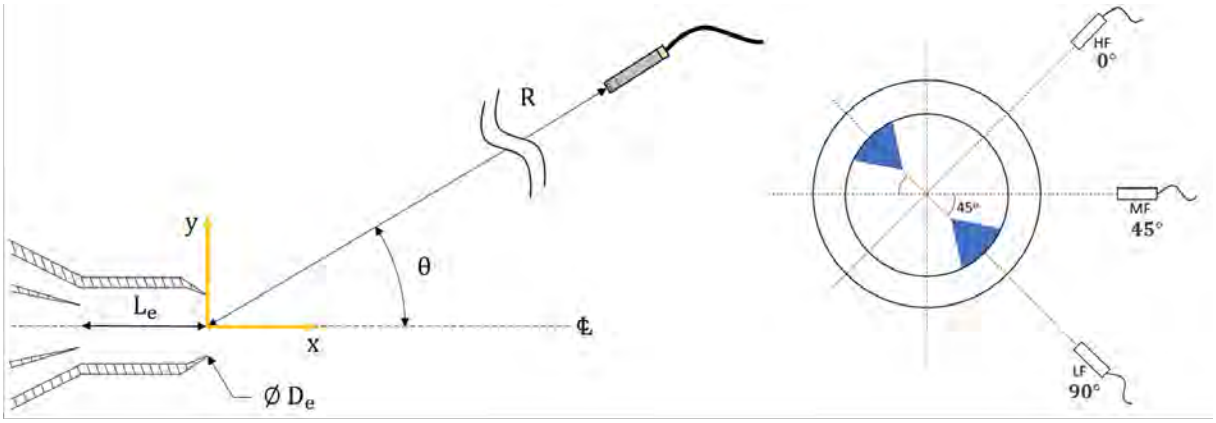

a) b)

Figure 23. Polar and azimuthal angle conventions.

The GTRI used two types of microphones that have the same performance. The first type are Bruel and Kjaer (B&K) 4939 ¼-in. free-field microphones and are attached to B&K 2669 preamplifiers. The B&K microphone-preamplifier combinations are connected to B&K 2960-A-0S4 Nexus conditioning amplifiers that, in addition to amplifying the signal, act as the microphones' 200 mV power supply. The second type of microphones are PCB Piezotronics Type 378C01 pre-polarized ¼-in. free-field microphones. These microphones utilize the IEPE capability so are powered directly from the data acquisition modules without a separate power supply. The microphone signals are sampled at 204.8 kHz using NI PXIe-4499 modules. The acoustic pressure time histories are then processed into averaged sound pressure level (SPL) spectra using a window size of 6,400 samples, 50% overlap, and a Hanning window. To render the data to lossless form for use by the modelers, the

following corrections are applied to these SPL spectra: free-field response correction, windsock correction (if necessary), atmospheric attenuation, and distance. These corrections are described in detail in Karon (2016).

Effect of the D-tabs on the Jet Noise Produced by the Confluent Nozzle

As stated above, the main focus of the Year 2 efforts is using mechanical tabs as a geometrically simple forced mixer. Mechanical, 3D-printed D-tabs were added to the interior of the core nozzle of the pre-existing confluent nozzle. Figure 24 shows this nozzle geometry, with the D-tabs installed at the core nozzle exit shown in red. In the context of a single nozzle, installing mechanical tabs near the nozzle exit plane that protrude into the jet flow is known to produce a substantial increase in mixing between the jet and the ambient relative to a tab-free nozzle (Ahuja, 1990). No prior published works have explored the use of mechanical tabs in lieu of more complex lobed mixers in an internally mixed nozzle. The findings of this research might shed light on the behavior of tabs as an alternative forced mixer geometry. Additionally, this was a good intermediate exercise while a forced mixer, described later, was being designed for the Year 3 effort.

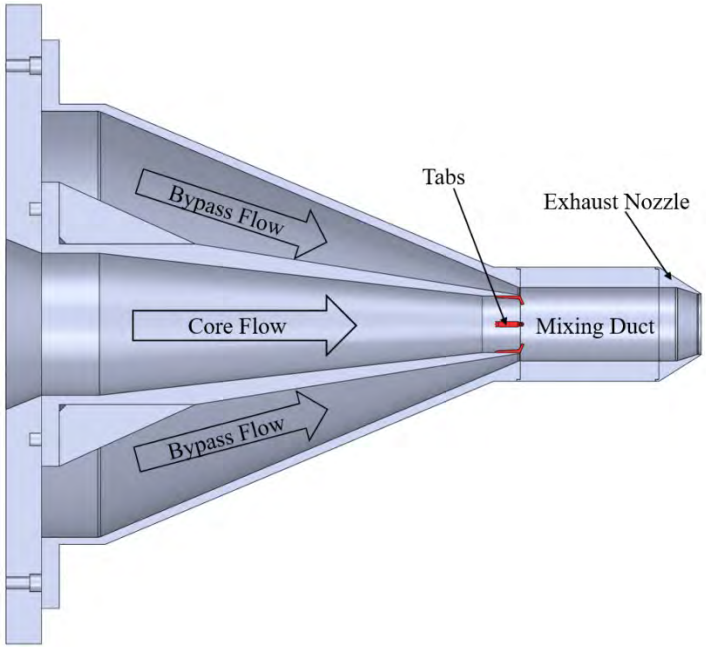

Figure 24. Cross-section of the nozzle configuration with the D-tabs installed. Tabs are shown in red.

Farfield jet noise measurement conducted with the confluent nozzle during year 1 revealed that, under certain operating conditions, the nozzle produced tonal noise (accompanied by radical changes to the resultant jet flow field). One hypothesis is that some of these tones are caused by a feedback mechanism inside the mixing duct. The first leg of this hypothetical feedback mechanism would involve the growth of a shear-layer instability (i.e., instability of the core-jet shear layer) inside the mixing duct and subsequent interaction of a large-scale coherent structure with the exhaust nozzle lip or other solid surfaces inside the nozzle. Farfield jet noise measurements acquired with the confluent nozzle equipped with tabs will shed light on the validity of this hypothesis. In short, adding tabs is likely to inhibit the growth rate of large-scale coherent structures before they may interact with the lip of the exhaust nozzle. Various configurations of the confluent nozzle equipped with tabs were tested, with the configurations shown in Figure 25. Although a wide range of conditions were tested, the following results are presented as typical results: PR_1 = 1.39 and ER = 1.0, PR_1 = 1.69 and ER = 1.0, and PR_1 = 1.39 and ER = 1.07. The tabs were tested with the confluent nozzle in both L_e/D_e = 0.7 and 3.0 configurations.

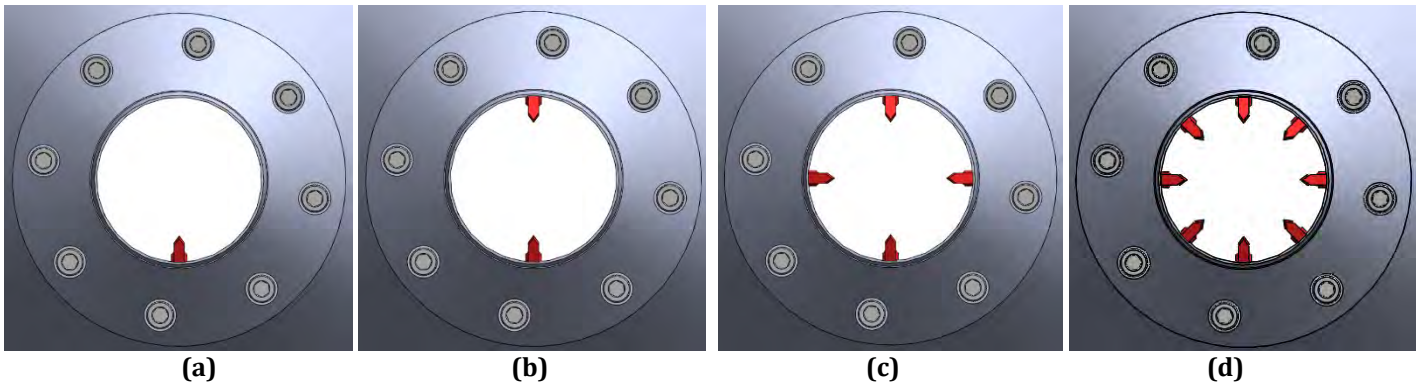

Figure 25. View looking upstream into tab-equipped internally mixed nozzle in (a) single-tab, (b) two-tab, (c) four-tab, and (d) eight-tab configurations.

Figures 26 and 27 show the effect on the jet noise produced by adding tabs to the core nozzle at the PR_1 = 1.39 and ER = 1.0, for mixing lengths L_e/D_e = 0.7 and 3.0, respectively. As shown in Figure 26, for L_e/D_e = 0.7, no tab configuration had any appreciable effect on the noise. Similarly, as shown in Figure 27, for L_e/D_e = 3.0, tabs, irrespective of the number used, had no appreciable effect at low frequencies (the left of the spectral peak), but increasing the tab number to four and then to eight seemed to increase the noise at higher frequencies. In particular, the noise at high frequencies is elevated by a maximum of 2 dB. These level increases begin at 20 kHz for the four-tab case and at 7 kHz for the eight-tab case.

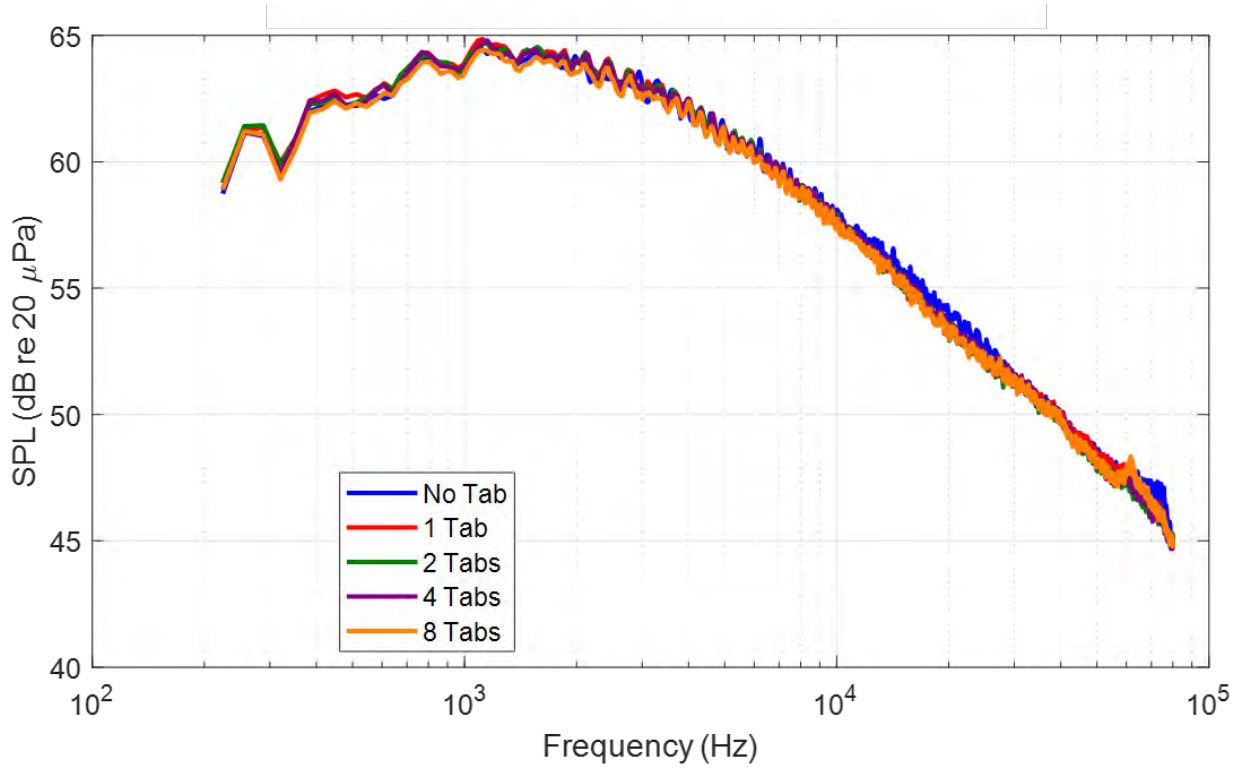

Figure 26. Effect of tabs on noise from a confluent nozzle. FAA Project Model, D_e = 1.7 in. and L_e/D_e = 0.7. PR_1 = 1.39, ER = 1.0, unheated, R = 12 ft, θ = 90°, Δf = 32 Hz, lossless.

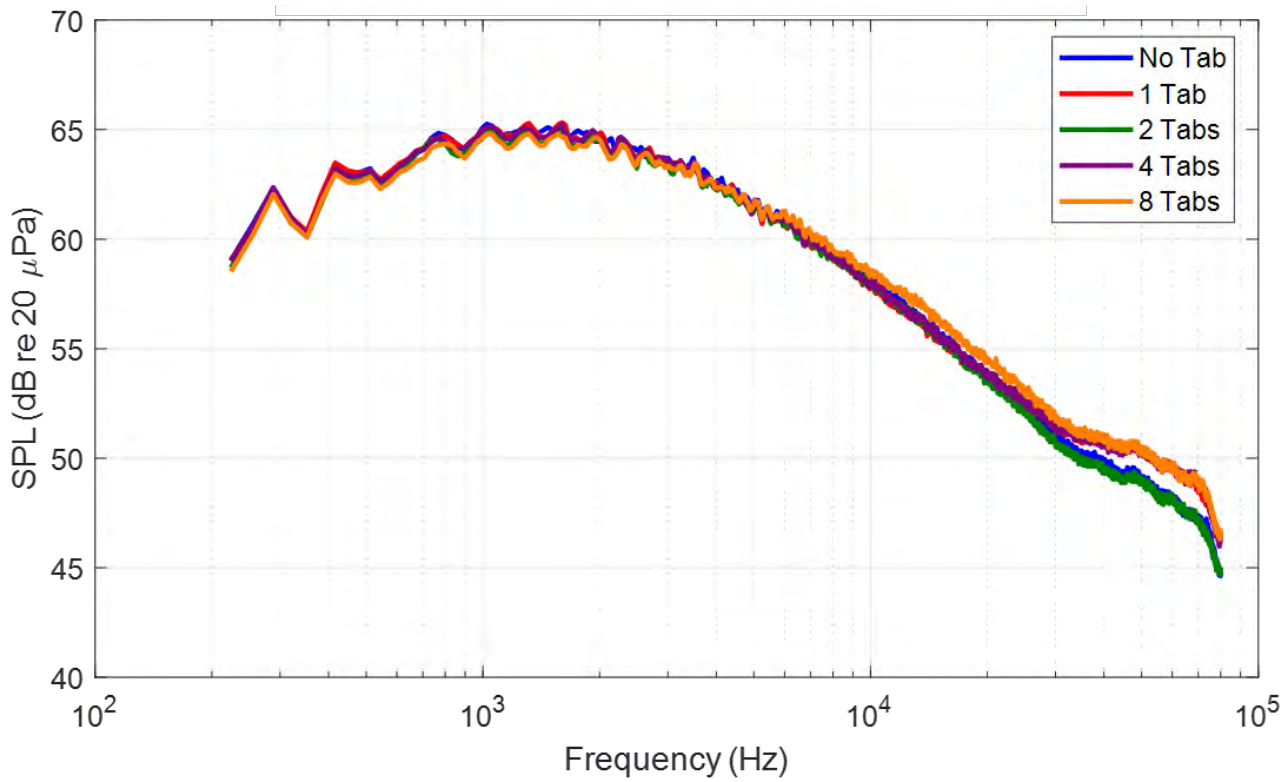

Figure 27. Effect of tabs on the noise from a confluent nozzle. FAA Project Model, D_e = 1.7 in. and L_e/D_e = 3.0. PR_1 = 1.39, ER = 1.0, unheated, R = 12 ft, θ = 90°, Δf = 32 Hz, lossless.

As has been previously presented, the confluent nozzle at the condition of PR_1 = 1.69 and ER = 1.0 produces tones that excite the jet flow. If the tone is the result of a feedback phenomenon, boundary layer perturbation via tabs is known to eliminate the tone. A well-known example is the case of suppressing screech by inserting the tip of a screw driver at the exit of a shock-containing jet. Figures 28 and 29 show the effect on the jet noise produced by adding tabs to the core nozzle at this condition, for mixing lengths L_e/D_e = 0.7 and 3.0, respectively. The tone is *not* eliminated by any of the tab configurations. Observing Figure 28, the addition of one or two tabs results in a maximum of 2 dB reduction in broadband noise over the frequency range of 1 kHz to 13 kHz, whereas the other tab configurations have no effect on the broadband noise. Looking at the effect on the tones alone, the one- and two-tab configurations cause the tone to shift to a higher frequency by 1.6 kHz and decrease in tonal amplitude by about 5 dB. The four- and eight-tab configurations cause a minor tone frequency shift of less than 200 Hz, with a 2–3 dB reduction in the tonal level.

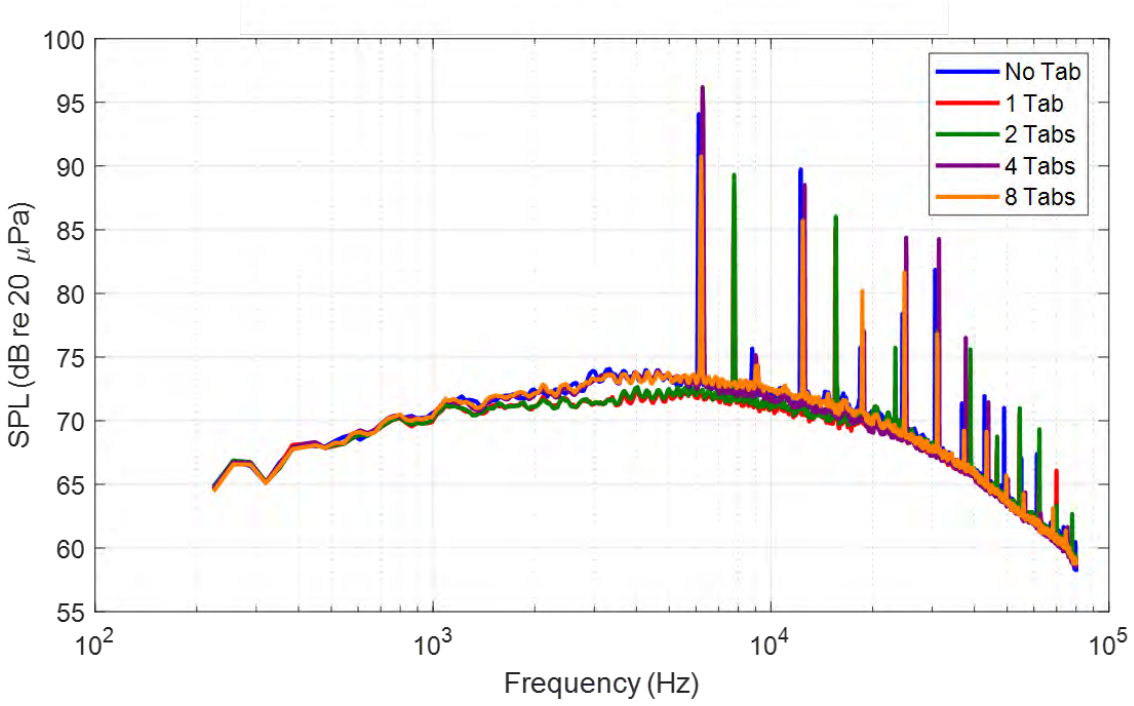

Figure 28. Effect of tabs on the noise from a confluent nozzle. FAA Project Model, D_e = 1.7 in. and L_e/D_e = 0.7. PR_1 = 1.69, ER = 1.0, unheated, R = 12 ft, θ = 90°, Δf = 32 Hz, lossless.

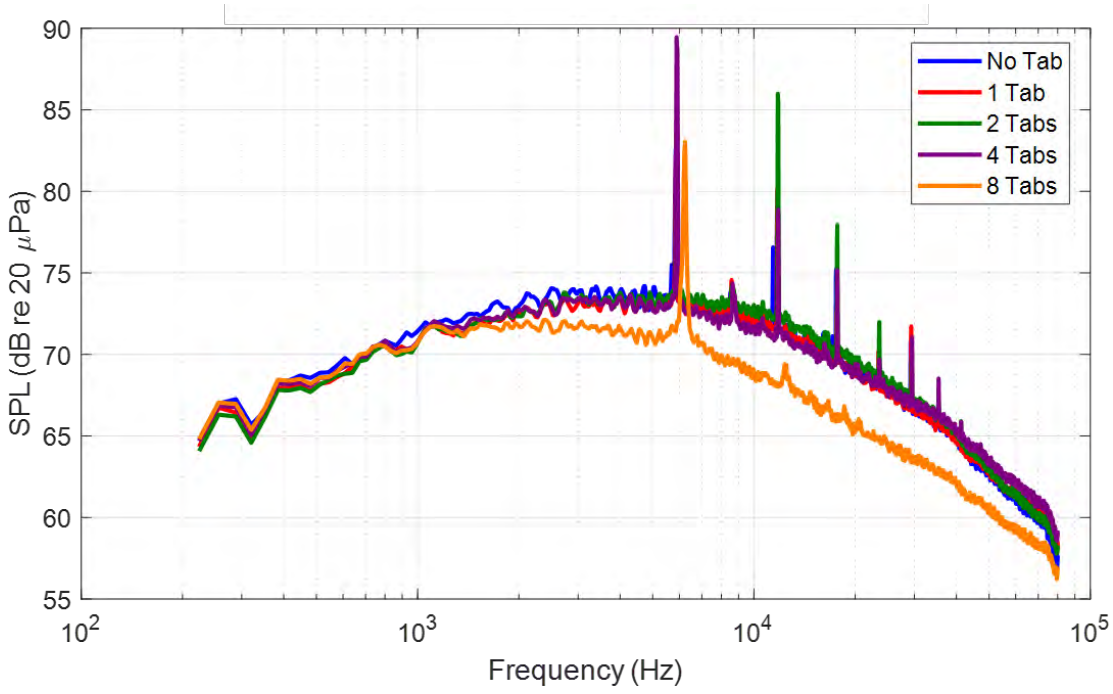

Figure 29. Effect of tabs on the noise from a confluent nozzle. FAA Project Model, D_e = 1.7 in. and L_e/D_e = 3.0. PR_1 = 1.69, ER = 1.0, unheated, R = 12 ft, θ = 90°, Δf = 32 Hz, lossless.

The effect of the tabs on L_e/D_e = 3.0 configuration differs significantly from that of the L_e/D_e = 0.7 configuration, as shown in Figure 29. It can be seen that all tab configurations except the eight-tab configuration produce essentially the same broadband noise as the no-tab configuration. The eight-tab configuration reduces the broadband noise by as much as 3 dB starting at frequencies above 2 kHz. Only one dominant tone is seen for this configuration, which has shifted to the right by about 400 Hz compared to that for the no-tab case and is also lower in amplitude. The other tab configurations produce the same tone frequency as the no-tab confirmation, but the levels of the harmonics increase with the number of tabs. No immediate explanations are available for this result.

The results shown in the last two figures were for an extraction ratio of unity. When the extraction ratio was increased to 1.07, the tones seen in the above figures mostly disappeared, as shown in Figures 30 and 31, which show the effect of the tabs on the noise produced by the confluent nozzle for PR_1 = 1.39 and ER = 1.07 for L_e/D_e = 0.7 and 3.0, respectively. For both mixing duct lengths, the tabs do not seem to make substantial difference. The exception to this is the one- and two-tab configurations, which generate a high-frequency tone for L_e/D_e = 0.7.

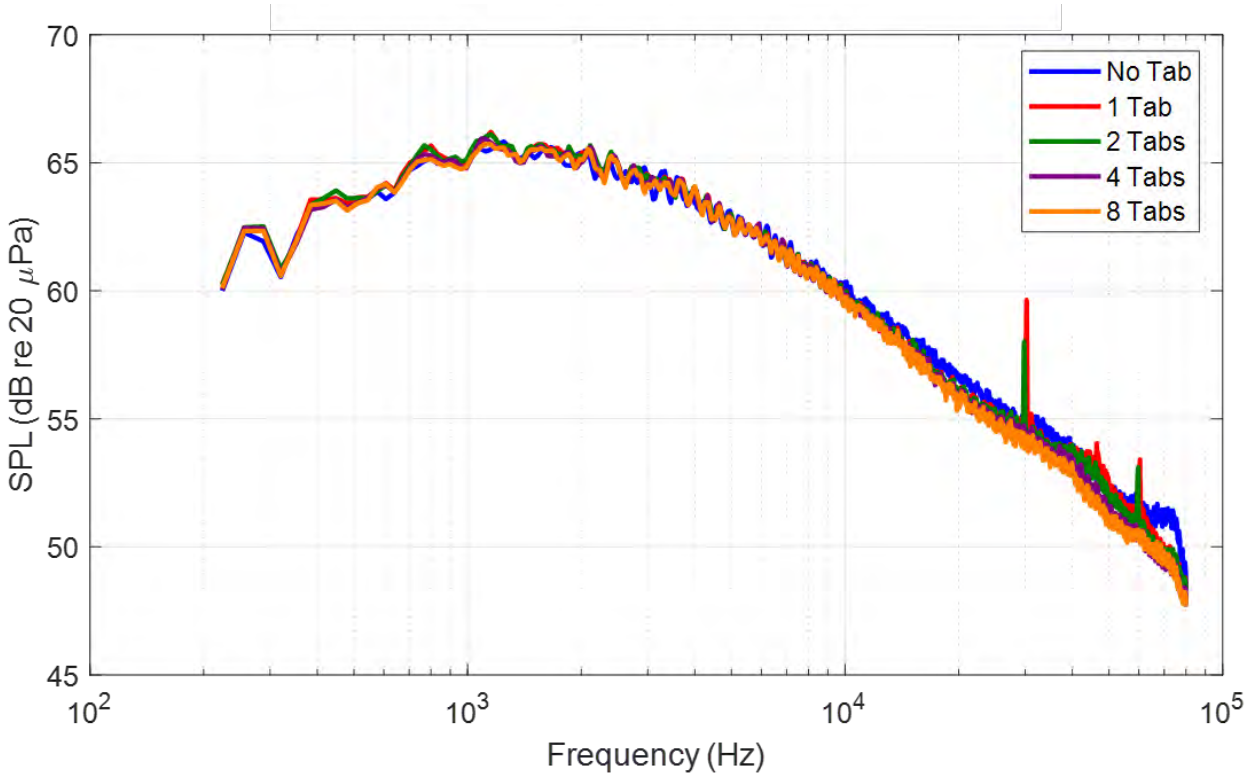

Figure 30. Effect of tabs on the noise from a confluent nozzle. FAA Project Model, D_e = 1.7 in. and L_e/D_e = 0.7. PR_1 = 1.39, ER = 1.07, unheated, R = 12 ft, θ = 90°, Δf = 32 Hz, lossless.

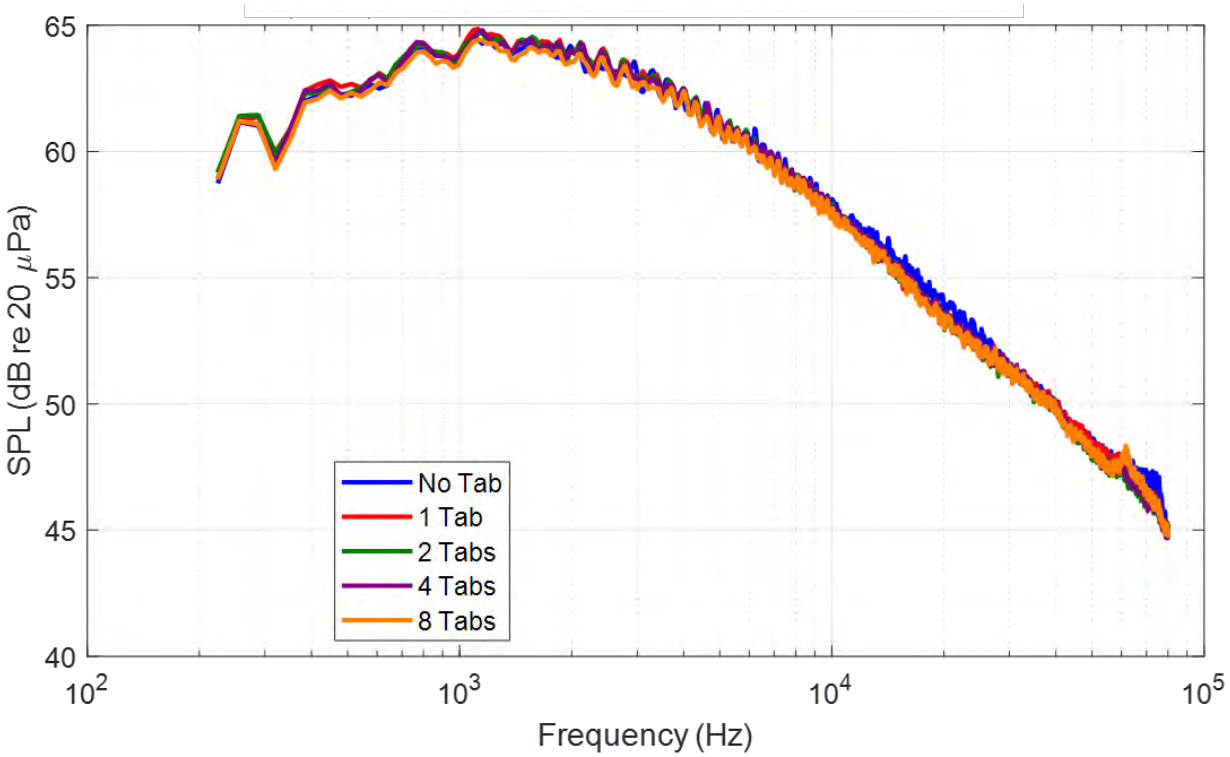

Figure 31. Effect of tabs on the noise from a confluent nozzle. FAA Project Model, D_e = 1.7 in. and L_e/D_e = 3.0. PR_1 = 1.39, ER = 1.07, unheated, R = 12 ft, θ = 90°, Δf = 32 Hz, lossless.

Effect of the Delta-Tabs on the Jet Noise Produced by the Confluent Nozzle

As described above, in addition to testing the D-tabs, delta-tabs (as shown in Figure 4) were tested for their effects on the noise produced by the confluent nozzle. For this set of testing, two tabs were installed as shown in Figure 5b. Figure 32 shows the effect of the azimuthal angle on the noise produced by the confluent nozzle with two metal delta-tabs attached to the core nozzle for the condition of PR_1 = 1.39, ER = 1.0 and at a polar angle of θ = 90°. The inset image in Figure 32 shows the orientation of the tabs with respect to the microphones for the readers' reference. As can be seen in Figure 32, at frequencies below 10 kHz, the noise without tabs and with tabs at all azimuthal angles is the same. Above 10 kHz, the tabbed nozzle case showed 3-dB increases at all azimuthal angles. At frequencies above 30 kHz, the ϕ = 90° direction seems to converge back with the no-tab case; the reason for this is not clear and would require additional analysis.

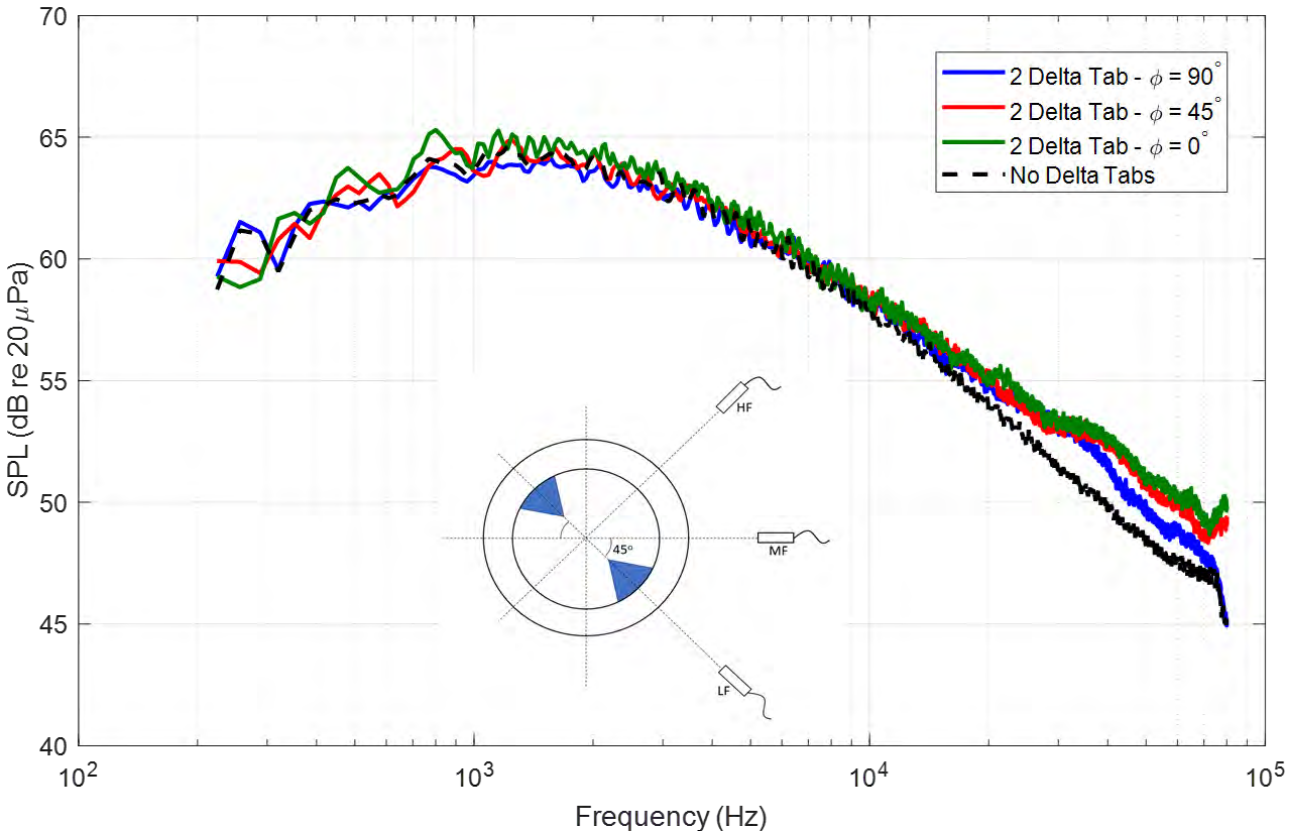

Figure 32. Effect of delta-tabs on the noise from the nozzle. D_e = 1.7 in, L_e/D_e = 0.7. PR_1 = 1.39, ER = 1.00, Tt,1 = Tt,2 = 60°F, R = 12 ft, θ = 90°, Δf = 32 Hz, lossless.

Figures 33 and 34 show the effect of the two delta-tabs on the jet noise spectra at PR_1 = 1.39, ER = 1.0, with a heated core flow ($T_{t,1} \approx 500$°F) at polar angles of 30° and 90°, respectively. As in Figure 32, Figures 33 and 34 show three azimuthal angles. In the rear-arc as shown in Figure 33, the delta-tabs create a 3-dB decrease in the peak noise at all azimuthal angles. Above 6 kHz, the delta-tabs actually increase the noise by as much as 4 dB. Additionally, at frequencies above 6 kHz, there is a difference in the azimuthal angles. Between 6 kHz and 35 kHz, the azimuthal angle aligned with tab produces up to 3 dB lower noise than the other azimuthal angles. Above, 35 kHz the azimuthal angles converge. In the sideline angle, as shown in Figure 34, at frequencies below 7 kHz, the tabs do not have any effect on the noise. Above 7 kHz, the tabs create an up to 3 dB increase in noise.

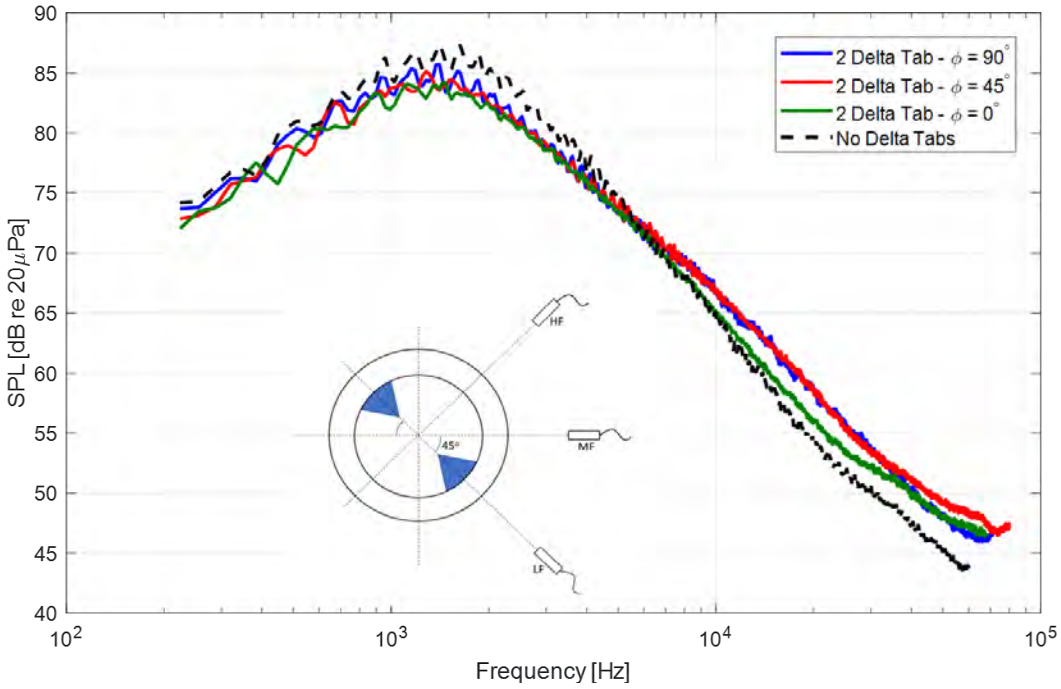

Figure 33. Effect of delta-tabs on the noise from the confluent nozzle. D_e = 1.7 in, L_e/D_e = 0.7. PR_1 = 1.39, ER = 1.00, Tt,1 = 500˚F, Tt,2 = 60˚F, R = 12 ft, θ = 30˚, Δf = 32 Hz, lossless.

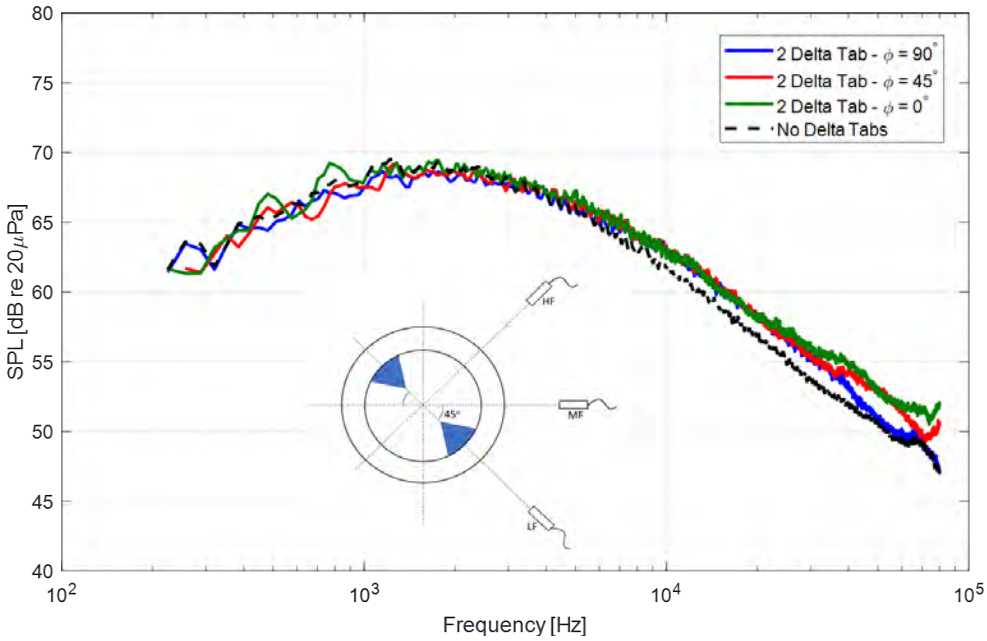

Figure 34. Effect of delta-tabs on the noise from the confluent nozzle. D_e =1.7 in, L_e/D_e = 0.7. PR_1 = 1.39, ER = 1.00, Tt,1 = 500˚F, Tt,2 = 60˚F, R = 12 ft, θ = 90˚, Δf = 32 Hz, lossless.

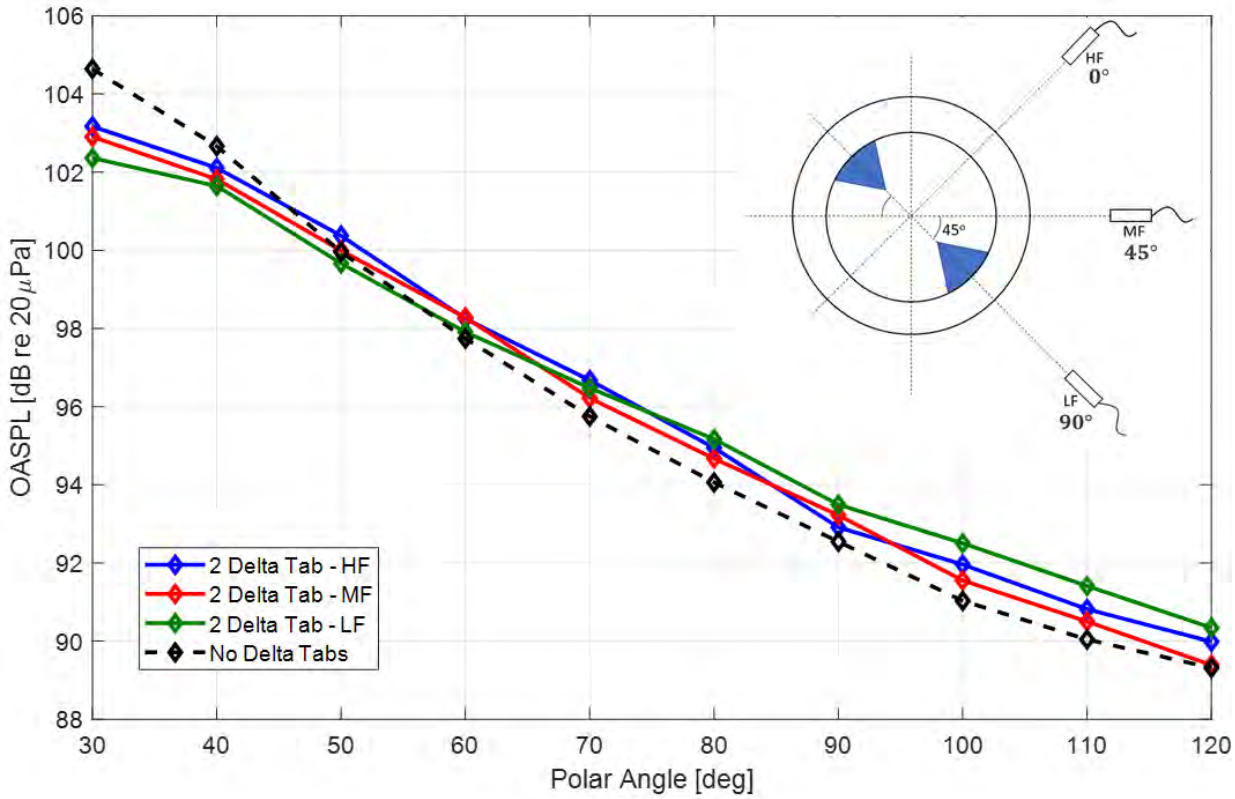

Figure 35. Effect of delta-tabs on the noise from the confluent nozzle. D_e = 1.7 in, L_e/D_e = 0.7. PR_1 = 1.39, ER = 1.00, Tt,1 = 500˚F, Tt,2 = 60˚F, R = 12 ft, Δf = 32 Hz, lossless.

At the same PR_1 = 1.39, ER = 1.00, $T_{t,1}$ = 500˚F operating condition, the effect of two delta-tabs on overall SPL (OASPL) is shown in Figure 35. At a polar angle of 30˚, where OASPL is greatest, a decrease of 1.5-2.3 dB is observed, depending on the azimuthal angle. In general, a decrease in OASPL exists at the lowest polar angles. At polar angles above 60˚, tabs always produce an increase in OASPL. Maximum OASPL increases of 0.5-1.4 dB (depending on azimuthal angle) occur at a 110˚ polar angle. Additionally, a trend of azimuthal dependency of OASPL is seen in Figure 35. When the observation angle is parallel to the line-of-symmetry of the delta-tabs, greater effects due to delta-tabs are seen relative to the other two measured azimuthal angles (both a greater OASPL reduction at smaller polar angles and greater OASPL increase at larger polar angles). Finally, the decrease in low-polar-angle OASPL and increase in high-polar-angle OASPL indicate that the delta-tabs yield enhanced interstream mixing compared to the tab-free confluent nozzle. These trends of low-polar-angle, low-frequency noise reduction at the cost of increased high-frequency noise been reportedly offered by lobed mixers as well (Mengle, 1997). The conclusion that the tabs have improved the interstream mixing between the core and bypass flows relative to the tab-free confluent nozzle is currently rooted purely in the acoustic measurements, and future work will include flow measurements of the jet plume produced by the confluent nozzle with tabs added to the core nozzle.

Similar results for chevrons were shown by Alkislar et al. (2007), where chevrons on a single nozzle enhanced mixing of jet exhaust flow and ambient air. This mixing broke up large-scale turbulent structures that propagate downstream toward low polar angles, and therefore increase small-scale turbulence that is dominant at higher polar angles. It is postulated that delta-tabs in the core nozzle are causing a similar behavior; however, flow visualization will be done to gain more information on the behavior of the jet with the implementation of the delta-tabs.

Comparison of D-Tabs and Delta-Tabs

Figures 36 and 37 show farfield jet-noise spectra acquired at polar angles of 30˚ and 90˚ (at an azimuthal angle of 45˚ from the tab, see Figure 23) with the nozzle run at the PR_1 = 1.39, ER = 1.00 operating condition. Each of these figures highlights the effects of adding either two 3-D printed delta-tabs or D-tabs to the core nozzle inside the confluent nozzle. As shown in Figure 36, the presence of either type of tab is shown to make no difference on the noise in the rear-arc. This shows that any noise produced by the tabs does not exceed contributions by the jet mixing noise. Alternatively, in the sideline, as shown in Figure 37, the D-tabs create noise reduction of up to 1 dB at the spectral peak and up to 2.5 dB at frequencies above 10 kHz, whereas the delta-tabs actually increase noise by up to 1.5 dB at frequencies above 10 kHz.

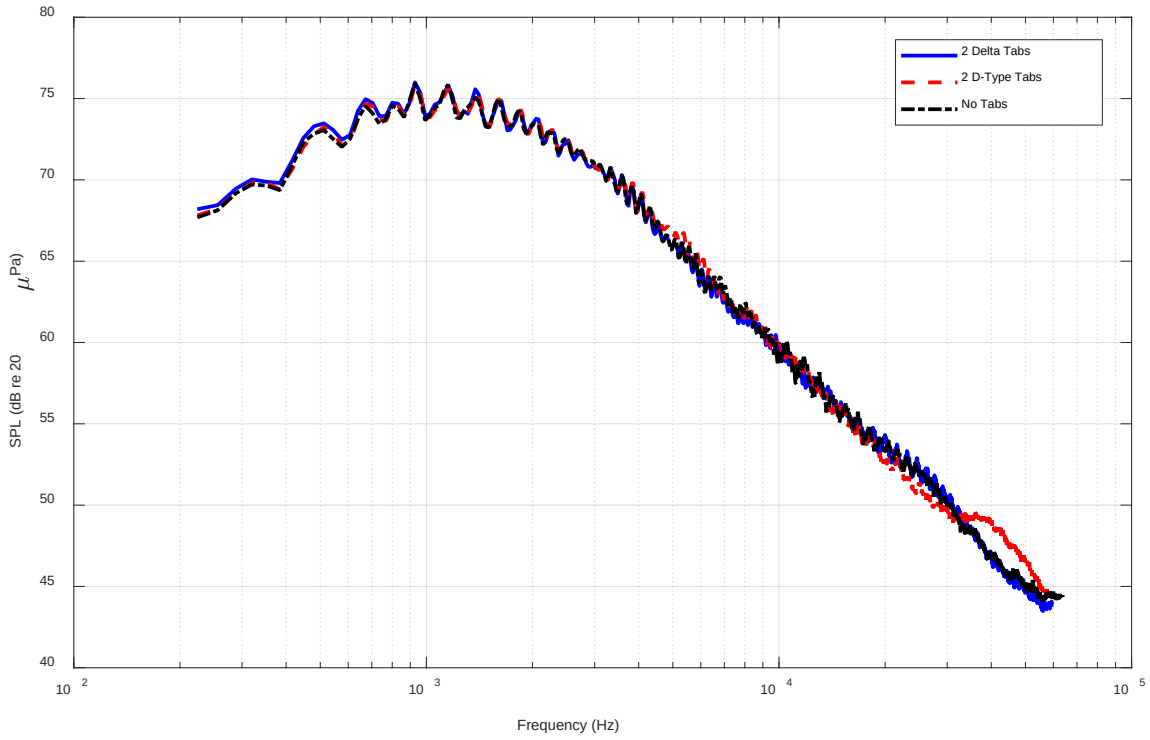

Figure 36. Jet noise generated by FAA nozzle with and without tabs in the core nozzle. D_e = 1.7 in, L_e/D_e = 0.7. PR_1 = 1.39, ER = 1.00, Tt,1 = Tt,2 = 60˚F, R = 12 ft, θ = 30˚, ϕ = 45˚, Δf = 32 Hz, lossless.

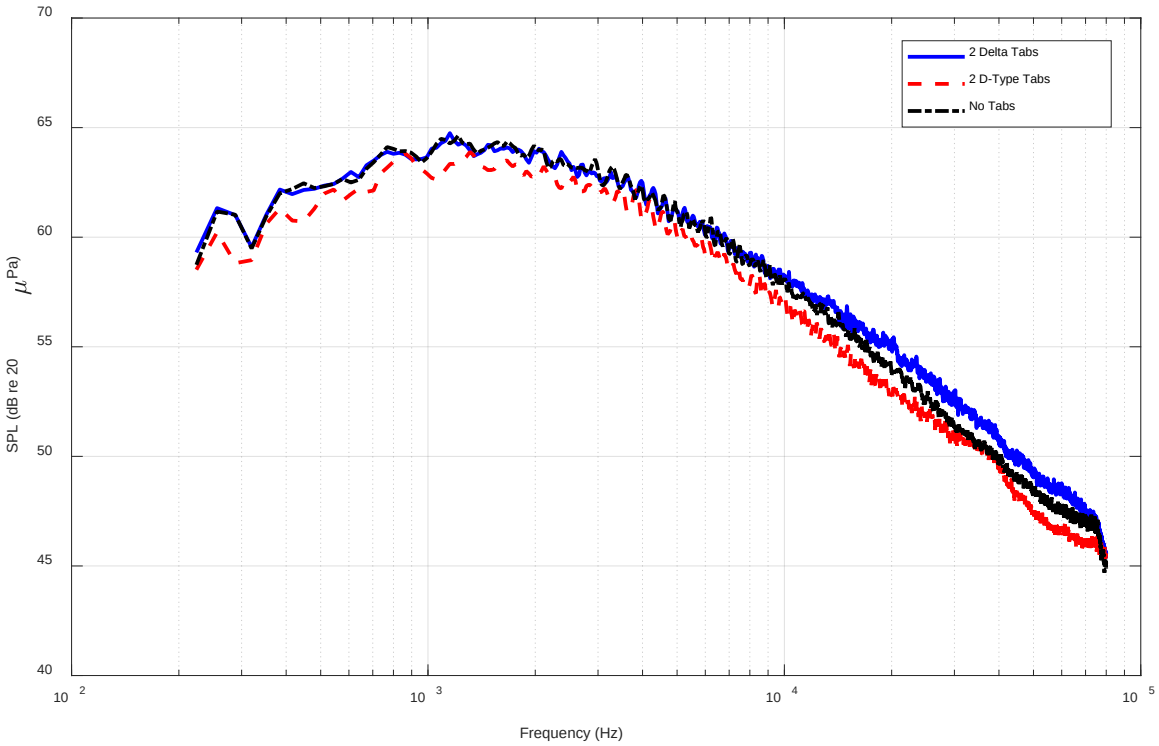

Figure 37. Jet noise generated by FAA nozzle with and without tabs in the core nozzle. D_e = 1.7 in, L_e/D_e = 0.7. PR_1 = 1.39, ER = 1.00, Tt,1 = Tt,2 = 60°F, R = 12 ft, θ = 90°, ϕ = 45°, Δf = 32 Hz, lossless.

Additional Understanding of Tones

Several publications discuss the importance of exhaust-nozzle design in the context of dual-stream, internally mixed nozzles. In particular, rapid changes in nozzle-wall angle (relative to the nozzle centerline) between the convergent and final straight sections of the final exhaust nozzle have been found to give rise to an additional noise source when forced mixers are used [19, 20]. This additional noise source was high frequency (relative to the frequency of peak jet noise), broadband in nature, directed toward θ = 70° with respect to the downstream jet axis, and appeared at high-subcritical pressure ratios. This noise source was attributed to the interaction between turbulence produced by the forced mixing of the two streams inside the nozzle and a shock near the exit plane of final exhaust nozzles with rapid changes in nozzle-wall angle. Final exhaust nozzles with more gradually contoured walls did not yield this additional noise source (Garrison, 2005). The shock near the final exhaust nozzle exit was found to terminate regions of supersonic flow that existed, despite the ideally expanded velocity of the flow being subsonic. This was hypothesized to be due to "flow turning effects" associated with the rapid change in nozzle-wall angle (Garrison, 2005). The region of supersonic flow was confined to a volume of fluid near the inner wall final exhaust nozzle, downstream of its return to straight. As noted by Garrison et al. (2005) and emphasized here, the associated additional noise source did not appear with a confluent nozzle (i.e., without a forced mixer) regardless of exhaust nozzle design. Nonetheless, the work of Garrison et al. is relevant here because they showed that final exhaust nozzles with rapid changes in nozzle-wall angle gave rise to an unfavorable flow phenomenon at high-subcritical pressure ratios.

The confluent nozzle used in the present work utilizes a final exhaust nozzle that has a rapid change in nozzle-wall angle before its final straight section – much like the nozzles studied by Garrison et al. (2005) that produced an unfavorable flow phenomenon. This, combined with the fact that the confluent nozzle produces a resonance at ER = 1.00, unheated operating conditions at high-subcritical pressure ratios (but not at lower pressure ratios), provides reason to believe that the exhaust nozzle's geometry may play a role in this resonance. This is not to say that the exhaust nozzle contains regions of supersonic flow at these operating conditions like those shown in the computational fluid dynamic predictions by Garrison et al. (2005);

however, it seems that the final exhaust nozzle is a likely region in which unfavorable flow phenomena may occur at high-subcritical pressure ratios.

To explore the hypothesis that the final exhaust nozzle geometry plays a role in setting up the resonance at PR_1 = 1.69 (M_j = 0.9), ER = 1.00, unheated operating conditions, several boundary-layer-tripping experiments were conducted, the most of which is described here. A trip ring was installed in the final exhaust nozzle's converging section as shown in Figure 38a and 38b. This trip ring was fashioned out of lock wire with a 0.5-mm diameter and was retained by four, roughly equally spaced rectangles of duct tape (approximately 0.45 mm thick). As shown by the sideline jet-noise spectra acquired with and without this trip ring in Figure 39, the addition of the trip ring suppresses the resonance entirely. The tones and the broadband amplification of jet noise associated with excitation of the jet both vanish, leaving behind a typical jet-noise spectrum (Ramsey, 2022). This is a powerful result. Regardless of the full, detailed physics underlying the confluent nozzle's resonance at this operating condition, the resonance is eliminated by a simple addition of a boundary-layer trip to the final exhaust nozzle geometry. The present resonance is therefore apparently driven by laminar boundary-layer separation (based on the success of a boundary-layer trip in suppressing it), and thus has striking similarity to the transonic resonance of the converging-diverging nozzles studied by Zaman and Dahl (1999). Yet more work is needed to obtain a rigorous understanding of the resonance in the present work. Nonetheless, some additional discussion is offered below.

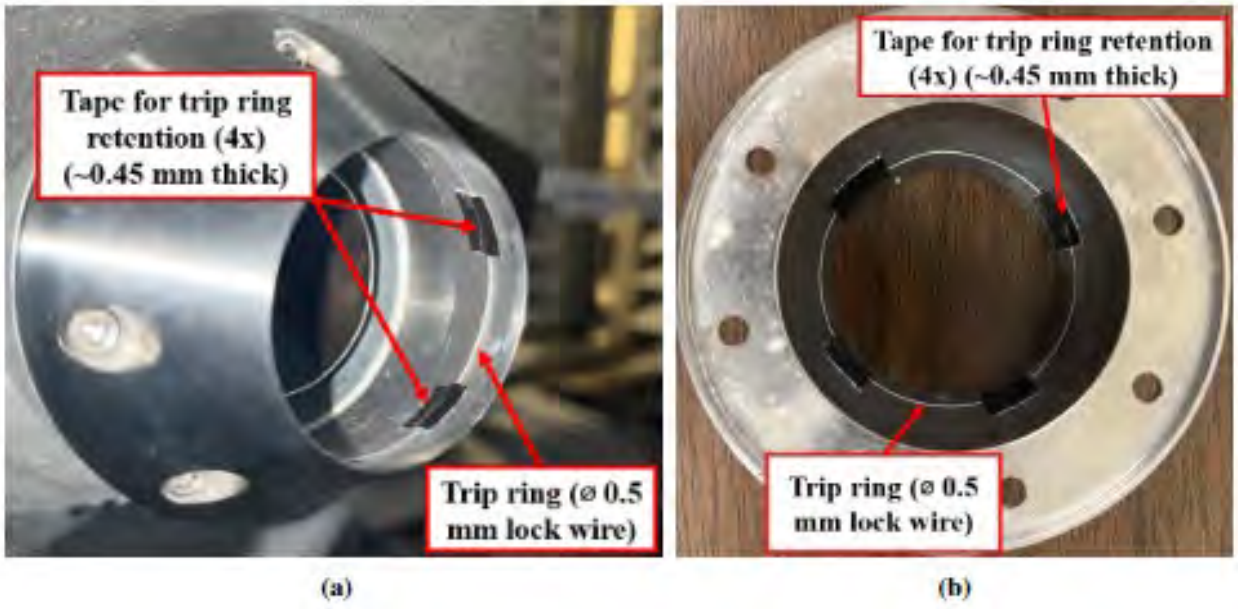

Figure 38. Boundary-layer trip configurations: (a) view from exit, and (b) view from upstream.

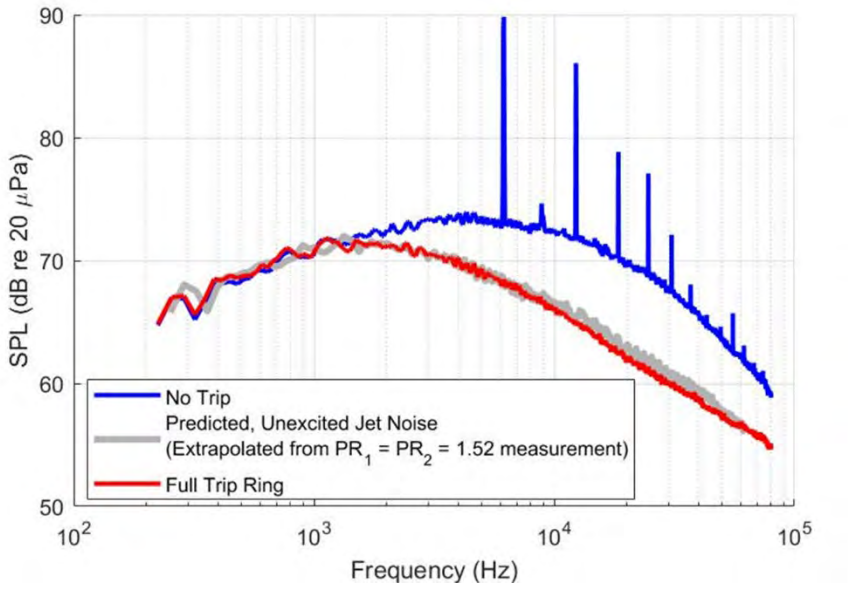

Figure 39. Effect of the boundary-layer trip ring on the noise from a confluent nozzle. FAA Project Model, D_e = 1.7 in. and L_e/D_e = 0.7. PR_1 = 1.69, ER = 1.0, unheated, R = 12 ft, θ = 90°, Δf = 32 Hz, lossless.

One possible explanation for the strength of the acoustic tones produced is that a resonant feedback loop is set up in the final straight section of the exhaust nozzle. As a hypothetical example, this feedback loop could comprise a downstream-travelling convective flow instability initiated at the exhaust nozzle's radius before the final straight section, sound generation due to this instability's interaction with the final exhaust nozzle lip, the upstream propagation of this sound, and the receptivity of the sound by a later flow instability. This is similar to the feedback considered in the study by Zaman and Dahl (1999). The existence of this feedback loop remains a hypothesis to be tested, and jet-noise measurements with fine increments in Mach-number between M_j = 0.9 and M_j = 1.0 at unheated, ER = 1.00 operating conditions with no boundary-layer trip are planned by Nate Ramsey for his PhD thesis funded by NSF. The results will be included in the FAA reporting as a value added to the program via his fundamental research. This will help elucidate the Mach-number dependence of this resonance and more clearly determine whether such a feedback loop is a plausible explanation. This focused testing is required because this ER = 1.00 resonance does not occur below $M_j \approx 0.9$ nor at M_j = 1.0, the two highest-pressure operating conditions tested as part of the larger test program. It is our hope that when the resonance is fully understood, the vanishing of the resonance at the sonic condition (M_j = 1.0) will become clear as well. This was not a feature of the resonances studied by Zaman and Dahl (1999).

It should be pointed out that because these results indicate that the tones may be a result of some feedback phenomenon associated with the flow just upstream of the final nozzle, anything done at the core nozzle may not have much impact on the tones. This indeed seems to be the case for the results shown above, where adding a smaller number of tabs did not have a major impact on tones. Where the tones were affected, that may be due to the flow arriving at the main nozzle exit being more turbulent with tabs than that without them. Additional work will be needed to understand the underlying phenomenon. It is felt that as long as we can eliminate the tones by a simple wire trip as described above, we will have high-quality data devoid of jet-noise amplification, simulating turbulent flows of a full-scale system and for validating the measurements.

Milestones

Conduct the following three sets of measurements for the baseline confluent nozzle configuration:

1. Flow visualization and PIV data for selected unheated flows for which extensive farfield acoustic data was acquired in Year 1.
2. Develop a methodology to eliminate the high-amplitude tones that were observed for certain operating test conditions in the Year 1 study.
3. Acquire acoustic data to quantify the effects of selected tab configurations on farfield jet noise.

Major Accomplishments
Met all of the above milestones.

Publications
None.

Outreach Efforts
None.

Awards
None.

Student Involvement
Three graduate students (David Nate Ramsey, Reagan Mayo, and Jackson Larisch).

Plans for Next Period
Complete heated flow data acquisition. Also, complete the design of a forced mixer.

Task 5 - Data Dissemination
Georgia Institute of Technology

Objective
The objective of this task is to maintain contact with the modelers being funded by FAA under ASCENT Project 59 and provide them with the nozzle design and both the acoustic and flow data from the current project.

Research Approach
This task involves disseminating the Year 2 data to the modelers. The modelers already have access to the data from the confluent nozzle as described in Task 0. We will release the geometries and available data from the nozzle equipped with tabs in the near future.

Milestones
Continue providing the modelers being funded by FAA under ASCENT Project 59 both the acoustic and flow data from the current project.

Major Accomplishments
All milestones met.

Publications
None.

Outreach Efforts
None.

Awards
None.

Student Involvement
Three graduate students (David Nate Ramsey, Reagan Mayo, and Jackson Larisch).

Plans for Next Period
None.

Task 6 - Design and Build a Mixer for Year 3 Investigation

Georgia Institute of Technology and Gulfstream Aerospace Corporation

Objective

The objective of this task is to design a sub-scale, realistic, internally mixed nozzle configuration with a lobed mixer for the primary nozzle.

Research Approach

A design capability has been developed for sizing, contouring, and surfacing of a forced multi-lobe mixer appropriate to medium bypass ratio turbofan engines. The process is initialized via analytic design of a confluent mixer and matching the static pressure on the mixing plane between the primary and secondary streams. The analytics can be optimized for ideal or thermally perfect (variable gamma) core flow. The confluent mixer performance is verified by CFD and confirmed to match performance characteristics in terms of bypass ratio, discharge coefficient, and velocity coefficient. Unsurprisingly, the confluent mixer offers limited thrust gain because mixing physics are limited to instability waves on the free shear layer between streams.

A lobed mixer is then designed to achieve target thrust gain characteristics for performance. The confluent mixer is treated as a neutral surface. Lobes are designed to flow hot core air into the space above the neutral surface. Gullies are designed to flow cool bypass air below the neutral surface. Scarfing and scalloping are used to enhance small-scale vortical structures on the mixing plane and realize mixing efficiencies two or three times greater than that for the confluent mixer design.

In a medium bypass ratio engine, this optimal mixing efficiency implies lobes and gullies with different penetration ratios. Design rules are developed to manage the asymmetry while still minimizing chute and mixing losses. Two-dimensional Bezier control curves are developed to meet the various design rules with three lofts specifying the (1) mixer trailing edge, (2) axial profile of the lobe, and (3) axial profile through the gully. These are intersected with the neutral surface to provide additional guide curves for construction.

A Python interface into Rhino3D is then used to loft the forced lobe mixer and complete surfacing. Geometry is exported to IGS and ready for either CFD or fabrication at a model shop. Initial design-of-experiments have been completed in RANS to check the design process and aero-thermodynamic performance. Initial proof-of-principle studies are complete, and we have initiated design of the actual mixer for the GTRI experiments.

A forced lobe mixer has been finalized for testing at GTRI. Static pressure matching at the mixing plane is achieved between streams, while ensuring good thrust gain due to mixing and protection of the nozzle inner mold line from unmixed core flow hot spot temperature distributions. A technical report is in development describing the design process and improvements that would logically lead to an optimal multidisciplinary solution.

The design has been checked for thermal distortions via a finite element analysis. Thickness distributions have been set slightly larger than implied by the geometric scale factor in order to ensure robustness and to ensure only modest deviations from the cold shape to hot shape. Actual estimates of hot shapes will be delivered to GTRI as part of the final geometry transmittal.

The 3D CAD geometry has been peer reviewed with GTRI, the FAA, and with ASCENT 59 university partners. An initial geometry has also been peer reviewed with the GAC model shop, and material has been ordered to ensure timely manufacturing. The parts will be released for manufacture as soon as an aero database has been completed and design performance has been verified across the range of intended operating conditions. Figure 40 depicts the lobed mixer.

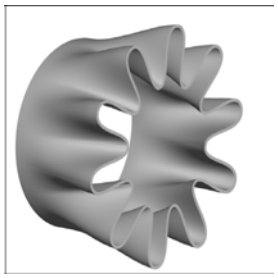

Figure 40. Depiction of the Gulfstream Aerospace Corporation (GAC)-designed lobed mixer.

Milestones
Complete the design of a sub-scale, realistic, internally mixed nozzle configuration with a lobed mixer for the primary nozzle.

Major Accomplishments
Two lobed mixers designed and will be available in Year 3 for testing.

Publications
None.

Outreach Efforts
None.

Awards
None.

Student Involvement
Three graduate students (David Nate Ramsey, Reagan Mayo, and Jackson Larisch).

Plans for Next Period
Fabricate the forced mixers for testing in Year 3. Also, acquire additional flow and acoustic data as needed to understand the observed flow/acoustic phenomenon.

Task 7 - Proposal for a Follow-on Effort for Year 3
Georgia Institute of Technology

Objective
The objective of this task is to prepare a proposal for a follow-on effort for Year 3.

Research Approach
This task involves preparing a proposal for Year 3 funding using a more complicated core nozzle. A forced lobe mixer configuration was selected. Georgia Tech's Cost-share partner Gulfstream will assist in designing and manufacturing the nozzle

Milestones
Submit a proposal to FAA to test a forced mixer that fits the existing test facility.

Major Accomplishments
The proposal was submitted in May 2022.

Publications
None.

Outreach Efforts
None.

Awards
None.

Student Involvement
Three graduate students (David Nate Ramsey, Reagan Mayo, and Jackson Larisch).

Plans for Next Period
If the project is funded, will begin testing the forced mixers.

Task 8 - Reporting and Data Dissemination
Georgia Institute of Technology

Objective
The objective of this task is reporting of the results acquired under Year 2 effort and disseminating the data to the modelers.

Research Approach
Submit all quarterly reports at the end of each quarter and the annual report at the end of the year. Prepare a quad chart for submission to the ASCENT Program as an update for the spring FAA ASCENT Advisory Committee meeting, and prepare a full progress presentation for the fall FAA ASCENT Advisory Committee meeting.

Milestones
- The experimental model was designed and fabricated.
- All acoustic measurements have been acquired.

Major Accomplishments
The experimental model was designed and fabricated. All acoustic measurements have been acquired.

Publications
Ramsey, D. N., Karon, A. Z., Funk, R., & Ahuja, K. K. (2022, June 14). Jet noise from a low-bypass confluent nozzle: Mixing length and extraction ratio effects. *28th AIAA/CEAS Aeroacoustics 2022 Conference*. 28th AIAA/CEAS Aeroacoustics 2022 Conference, Southampton, UK. https://doi.org/10.2514/6.2022-2863

Ramsey, D. N., Mayo, R., Karon, A. Z., Funk, R., & Ahuja, K. K. (2022, June 14). Self-excited jet from a low-bypass confluent nozzle at unity extraction ratio. *28th AIAA/CEAS Aeroacoustics 2022 Conference*. 28th AIAA/CEAS Aeroacoustics 2022 Conference, Southampton, UK. https://doi.org/10.2514/6.2022-2864

Outreach Efforts
None.

Awards
None.

Student Involvement
Three graduate students (David Nate Ramsey, Reagan Mayo, and Jackson Larisch).

Plans for Next Period

- Complete flow measurements
- Completed tab study
- Prepare for Year 3 efforts

References

Ahuja, K., & Brown, W. (1989, March 13). Shear flow control by mechanical tabs. *2nd Shear Flow Conference*. 2nd Shear Flow Conference, Tempe,AZ,U.S.A. https://doi.org/10.2514/6.1989-994

Hileman, J., & Samimy, M. (2003). Effects of vortex generating tabs on noise sources in an ideally expanded Mach 1.3 jet. *International Journal of Aeroacoustics*, *2*(1), 35–63. https://doi.org/10.1260/147547203322436935

Saiyed, N., & Bridges, J. (1999, May 10). Tabs and mixers for reducing low bypass ratio jet noise. *5th AIAA/CEAS Aeroacoustics Conference and Exhibit*. 5th AIAA/CEAS Aeroacoustics Conference and Exhibit, Bellevue, WA, U.S.A. https://doi.org/10.2514/6.1999-1986

Tam, C. K. W., & Zaman, K. B. M. Q. (2000). Subsonic jet noise from nonaxisymmetric and tabbed nozzles. *AIAA Journal*, *38*(4), 592–599. https://doi.org/10.2514/2.1029

Burrin, R. H., & Tanna, H. K. (1979). The Lockheed-Georgia coannular jet research facility. *The Journal of the Acoustical Society of America*, *65*(S1), S44–S44. https://doi.org/10.1121/1.2017259

Raffel, M., Willert, C. E., Scarano, F., Kähler, C. J., Wereley, S. T., & Kompenhans, J. (2018). *Particle image velocimetry: A practical guide*. Springer International Publishing. https://doi.org/10.1007/978-3-319-68852-7

Bridges, J. & Wernet, M. P. (2011). The NASA subsonic jet particle image velocimetry (PIV) dataset (NASA TM-2011-216807). https://ntrs.nasa.gov/api/citations/20110023688/downloads/20110023688.pdf

Pope, S. B. (2000). *Turbulent flows* (1st ed.). Cambridge University Press. https://doi.org/10.1017/CBO9780511840531

Christensen, K. T. (2004). The influence of peak-locking errors on turbulence statistics computed from PIV ensembles. *Experiments in Fluids*, *36*(3), 484–497. https://doi.org/10.1007/s00348-003-0754-2

Ahuja, K., Lepicovsky, J., Tam, C., Morris, P, & Burrin, R. (1982). *Tone-Excited Jet: Theory and Experiments* (NASA CR-3538). https://ntrs.nasa.gov/api/citations/19830004698/downloads/19830004698.pdf

Witze, P. O. (1974). Centerline velocity decay of compressible free jets. *AIAA Journal*, *12*(4), 417–418. https://doi.org/10.2514/3.49262

Morris, P. J., & Zaman, K. B. M. Q. (2010). Velocity measurements in jets with application to noise source modeling. *Journal of Sound and Vibration*, *329*(4), 394–414. https://doi.org/10.1016/j.jsv.2009.09.024

Burrin, R. H., Dean, P. D., & Tanna, H. K. (1974). A new anechoic facility for supersonic hot jet noise research at lockheed - georgia. *The Journal of the Acoustical Society of America*, *55*(2), 400–400. https://doi.org/10.1121/1.3437223

Ahuja, K. K. (2003). Designing clean jet-noise facilities and making accurate jet-noise measurements. *International Journal of Aeroacoustics*, *2*(3), 371–412. https://doi.org/10.1260/147547203322986188

Karon, A. (2016). *Potential factors responsible for discrepancies in jet noise measurements of different* studies [Ph.D. Dissertation, Daniel Guggenheim School of Aerospace Engineering, Georgia Institute of Technology].

Ahuja, K. (1990, October 22). An evaluation of various concepts of reducing supersonic jet noise. *13th Aeroacoustics Conference*. 13th Aeroacoustics Conference, Tallahassee, FL, U.S.A. https://doi.org/10.2514/6.1990-3982

Mengle, V., Dalton, W., Bridges, J., Boyd, K., Mengle, V., Dalton, W., Bridges, J., & Boyd, K. (1997, May 12). Noise reduction with lobed mixers—Nozzle-length and free-jet speed effects. 3rd AIAA/CEAS Aeroacoustics Conference. 3rd AIAA/CEAS Aeroacoustics Conference, Atlanta, GA, U.S.A. https://doi.org/10.2514/6.1997-1682

Alkislar, M. B., Krothapalli, A., & Butler, G. W. (2007). The effect of streamwise vortices on the aeroacoustics of a Mach 0.9 jet. Journal of Fluid Mechanics, 578, 139–169. https://doi.org/10.1017/S0022112007005022

Garrison, L., Lyrintzis, A., Blaisdell, G., & Dalton, W. (2005, May 23). Computational fluid dynamics analysis of jets with internal forced mixers. *11th AIAA/CEAS Aeroacoustics Conference*. 11th AIAA/CEAS Aeroacoustics Conference, Monterey, California. https://doi.org/10.2514/6.2005-2887

Tester, B., & Fisher, M. (2006, May 8). A contribution to the understanding and prediction of jet noise generation by forced mixers: Part III Applications. 12th AIAA/CEAS Aeroacoustics Conference (27th AIAA Aeroacoustics Conference). Cambridge, Massachusetts. https://doi.org/10.2514/6.2006-2542

Ramsey, D. N., Mayo, R., Karon, A. Z., Funk, R., & Ahuja, K. K. (2022, June 14). Self-excited jet from a low-bypass confluent nozzle at unity extraction ratio. 28th AIAA/CEAS Aeroacoustics 2022 Conference. 28th AIAA/CEAS Aeroacoustics 2022 Conference, Southampton, UK. https://doi.org/10.2514/6.2022-2864

Zaman, K., & Dahl, M. (1999, January 11). Aeroacoustic resonance with convergent-divergent nozzles. 37th Aerospace Sciences Meeting and Exhibit. 37th Aerospace Sciences Meeting and Exhibit, Reno, NV, U.S.A. https://doi.org/10.2514/6.1999-164

Project 059(C) Modeling Supersonic Jet Noise Reduction with Global Resolvent Modes

University of Illinois Urbana-Champaign

Project Lead Investigator

Daniel J. Bodony
Blue Waters Professor
Department of Aerospace Engineering
University of Illinois Urbana-Champaign
306 C Talbot Labs
104 S. Wright
Urbana, IL 61801
217-244-3844
bodony@illinois.edu

University Participants

University of Illinois Urbana-Champaign (UIUC)

- P.I.s: Dr. Daniel J. Bodony and Dr. Tim Colonius
- FAA Award Number: 13-C-AJFE-UI-031
- Period of Performance: October 1, 2021 to September 30, 2022
- Tasks:
    1. Establishment of industry-relevant low bypass ratio (BPR) engine parameters and acoustic assessment workflow with cost-sharing partner (completed)
    2. Automated Reynolds-averaged Navier–Stokes equation (RANS) predictions of jet exhaust (completed)
    3. Resolvent mode computation—primary and sensitivity (completed)
    4. Python resolvent mode interpolation tool (paused)
    5. Python optimization tool for jet noise reduction (JNR) (version 1) (completed)
    6. Application of version 1 optimization tool on Georgia Institute of Technology Research Institute (GTRI) dual-stream nozzle (in progress)
    7. Reformulation of resolvent modes by using local turbulent kinetic energy (in progress)
    8. Development and implementation of design parameter gradient direction for JNR (in progress)
    9. Application of version 2 optimization tool on GTRI dual-stream nozzle (not yet started)
    10. Application of version 1 optimization tool on Gulfstream- and Boom-relevant geometry (in progress)
    11. Collaborate with P.I.s for ASCENT Projects 10 and 47 (not yet started)

Project Funding Level

The FAA provided $199,999 in funding. In-kind cost matching agreements were established with Gulfstream ($100,000; contact person Dr. Brian Krupp [brian.krupp@gulfstream.com]) and with Boom ($50,000; contact person Dr. Joe Salamone [joe.salamone@boom.aero]).

Investigation Team

- Dr. Daniel Bodony, UIUC, P.I. (Task 1, 3, 11)
- Mr. Jay Woo, UIUC, MS (Task 2, 3, 4, 5, 6, 8, 9)
- Dr. Tim Colonius, California Institute of Technology (Caltech), co-P.I. (Task 3, 7, 11)
- Mr. Liam Heidt, Caltech, PhD student (Task 3, 7)

Project Overview

This ASCENT project leverages recent research in global-resolvent-mode-based descriptions of jet turbulence and its associated noise to develop a physics-based tool for estimating the impact of JNR strategies on the takeoff noise of civil supersonic transports. The software tool will efficiently identify promising JNR technologies and will more precisely evaluate the noise impact of parametric variation in a specific JNR approach. The tool will be compatible with the fleet-scale evaluation codes Global and Regional Environmental Analysis Tool (GREAT; Georgia Institute of Technology) and Fleet Level Environmental Evaluation Tool (FLEET; Purdue University) developed in ASCENT Project 10 and integrated into the ASCENT Project 47 "clean sheet" evaluation tool targeting civil supersonic transport.

The proposed research will create a multi-fidelity JNR tool that can operate in two modes: one mode for specific engine estimates and one mode for fleet-scale estimates:

JNR evaluation for an engine mode
According to the RANS-provided mean flow for a specific engine, the global resolvent description of wavepackets and their sensitivity to mean flow variations will be computed. The solutions will provide estimates of the low-frequency radiated noise, and the sensitivity derivatives, will estimate how the noise changes as a result of changes in the engine design, thus enabling JNR optimization.

Fleet-level estimation mode
The resolvent modes and their sensitivity derivatives for existing JNR strategies (e.g., chevrons or internal mixers) will be pre-computed for canonical jet exhaust profiles and flow conditions, compressed, and stored within an efficient data layout that can be quickly evaluated within FLEET, GREAT, and/or NASA's Aircraft Noise Prediction Program.

The Year 2 proposal was approved for funding with a period of performance of October 1, 2021 through September 30, 2022, and a budget of $199,999. The Year 2 statement of work included five tasks, listed above as Tasks 7–11, and rephrased from the prior year's annual report. The status of each task is given in parentheses.

Task 1 - Establish Industry-relevant Low-BPR Engine Parameters and Acoustic Assessment Workflow with Cost-sharing Partner [Completed]

University of Illinois at Urbana-Champaign

Objective

The objective of this task is to work with our cost-sharing partner to identify the anticipated range of characteristics of the low-BPR engines being considered for business-class civil supersonic transport. These parameters include, but are not limited to, diameter, BPR, mass flow rate, core and fan stream pressure ratios, core stream temperature ratio, thrust, nozzle configuration, plug designs, chevron designs, internal mixer designs, and afterburner design.

Research Approach

The research approach involves conducting face-to-face meetings and document exchange to obtain industry-relevant low-BPR engine parameters and acoustic assessment workflows.

Milestones

- Find new cost-sharing partner candidate
- Establish a nondisclosure agreement to initiate discussions
- Exchange low-BPR engine parameters and acoustic assessment workflow

Major Accomplishments

All milestones have been completed. A nondisclosure agreement between UIUC and Boom was signed, and subsequent discussions led to Boom's partnership with $50,000 in-kind cost sharing. The Boom commitment letter is attached. A cost-sharing agreement with Gulfstream was also established for $100,000 in-kind cost sharing. The Gulfstream letter is attached.

Publications

None.

Outreach Efforts
None.

Awards
None.

Student Involvement
None.

Plans for Next Period
Communication between UIUC and the principal contacts at Boom and Gulfstream will continue, and will focus on exchanging results, sharing data, and evaluating the UIUC-developed JNR workflow within each company's design process.

Task 2 - Automated RANS Predictions of Jet Exhaust
University of Illinois at Urbana-Champaign

Objective
The objective of this task is to develop and verify an automated toolchain for using RANS methods to predict the jet exhaust plume from candidate near-sonic multi-stream jet nozzles.

Research Approach
Achieving JNR will require changes to the engine cycle and nozzle geometries. A Python-based software infrastructure is to be developed that takes parametrically defined computer-aided-design-based descriptions of nozzle geometries, automatically generates meshes and boundary conditions for the nozzle internal flow path and the external nozzle plume, initiates an open-source RANS solver, and curates the data.

Milestones
- Additional developments in computational fluid dynamics flow path
- Verification of RANS simulation results
- Automation of Python infrastructure

Major Accomplishments
Milestone 1 has been completed and included subtasks such as adjusting the boundary conditions and increasing the computational domain of the mesh grid for each nozzle model. Post-processing calculations have also been developed to monitor properties of the nozzle exhaust and thereby characterize steady flow behavior. Milestone 2 has been completed, and included results obtained from post-processing that have been verified through comparison with a numerical solution based on quasi-1D flow theory for mixed exhaust jet nozzles. Milestone 3 has been completed and included full automation of individual computational fluid dynamics processes.

Publications
None.

Outreach Efforts
None.

Awards
None.

Student Involvement
Jay Woo was responsible for developing the Python toolchain.

Plans for Next Period
None. Task is complete.

Task 3 - Resolvent Mode Computation—Primary and Sensitivity
Caltech (lead) and University of Illinois at Urbana-Champaign

Objective
The objective of this task is to develop and verify a resolvent mode computation tool suitable for evaluating the JNR potential of candidate near-sonic multi-stream jet nozzles.

Research Approach
Achieving JNR will require changes to the engine cycle and nozzle geometries. Estimation of the JNR potential of candidate cycles and geometries will use resolvent mode descriptions of the coherent wavepacket-associated jet noise of the loudest sound sources. We denote the resolvent calculations that provide the input–gain–output modes of the resolvent operator $(i\omega - A)^{-1}$ as "primary," and we denote the changes in those modes due to changes in the jet nozzle geometry and engine cycle as "sensitivity." The resolvent operator requires knowledge of the linearized Navier–Stokes operator A generated for each nozzle and its exhaust plume, and a global mode computational infrastructure. The sensitivity of the resolvent input–gain–output modes requires knowledge of the change in A, e.g., δA, resulting from changes in the nozzle design and/or engine cycle.

Milestones
- Primary resolvent mode computation capability
- Resolvent mode training data and fitting
- Resolvent mode sensitivity computation capability

Major Accomplishments
Milestone 1 has been completed and tested on single-stream subsonic and supersonic jets. Milestone 2 has been completed by using GTRI dual stream jet data. Milestone 3 has been completed and validated by using GTRI dual stream jet data.

Publications
Pickering, E.(2021). *Resolvent Modeling of Turbulent Jets* [Doctoral thesis, California Institute of University]. doi:10.7907/szxb-f168. https://resolver.caltech.edu/CaltechTHESIS:03022021-005902351

Outreach Efforts
None.

Awards
None.

Student Involvement
Ethan Pickering was responsible for the primary resolvent mode computation and the preliminary training data and fitting tasks; he graduated and left Caltech. Liam Heidt is the current student, who learned from Ethan and now leads the global mode computation and its data-driven alignment. Jay Woo is responsible for running and applying the resolvent calculation and its sensitivity.

Plans for Next Period
None. Task is completed.

Task 4 - Python Resolvent Mode Interpolation Tool

University of Illinois at Urbana-Champaign (lead) and Caltech

Objective

The objective of this task is to develop and verify a Python-based interpolation tool for computing resolvent input-gain-output modes at nozzle geometry and/or engine cycles for which RANS data are unavailable but are near previously known input-gain-output modes from nearby nozzle geometries and/or engine cycles.

Research Approach

By using kriging interpolation methods, a response surface-based interpolation approach will be developed to estimate resolvent input-gain-output modes for estimating the radiated noise from an engine geometry/engine cycle for which previously computed RANS data, linearized operators, and resolvent data are unavailable.

Milestones

- Identify candidate interpolation methods and down-select
- Develop a Python tool to implement the interpolation method
- Verify the Python tool

Major Accomplishments

Milestone 1 has been completed: a kriging method has been chosen. Milestones 2 and 3 have not yet started.

Publications

None.

Outreach Efforts

None.

Awards

None.

Student Involvement

Jay Woo is responsible for developing the Python toolchain.

Plans for Next Period

We will begin Milestone 2.

Task 5 - Python Optimization Tool for JNR

University of Illinois at Urbana-Champaign (lead) and Caltech

Objective

The objective of this task is to develop and verify a Python-based optimization tool that searches the optimization space of the engine geometry/cycle, to identify design choices that improve JNR.

Research Approach

Using gradient-informed optimization methods, an optimization approach will be developed for estimating JNR potential from a class of candidate engine geometries/cycles by using resolvent mode predictions of jet noise based on linearized operators described by RANS predictions of the jet exhaust plume.

Milestones

- Identify candidate optimization methods and down-select
- Develop a Python tool to implement the optimization method

- Verify the Python tool

Major Accomplishments
Milestone 1 has been completed, and the conjugate gradient method was selected for the optimization. Milestones 2 and 3 are also complete.

Publications
None.

Outreach Efforts
None.

Awards
None.

Student Involvement
Jay Woo was responsible for implementing the optimization tool.

Plans for Next Period
None. Task is complete.

Task 6 - Application of Version 1 Optimization Tool on GTRI Dual-stream Nozzle
University of Illinois at Urbana-Champaign (lead) with Caltech.

Objective
The objective of this task is to apply the Python-based tool developed from Tasks 2–5 to the GTRI dual-stream nozzle with extensible mixer duct lengths, to predict the quietest configuration.

Research Approach
The automated Python toolchain, starting with the moderate mixer duct length, will be applied to predict the mixer duct length that yields the quietest configuration. The predictions will be compared with the GTRI-measured acoustic field.

Milestones
- Select the GTRI operating condition of interest
- Apply the optimization tool
- Compare the predicted quiet configuration to the measured quiet configuration

Major Accomplishments
Milestone 1 has been completed and was based on the conditions for which GTRI jet velocity PIV data and acoustic data are available. Milestone 2 has been partially applied: a user-guided optimization has been performed but the fully automated design has not. Milestone 3 has not yet been attempted.

Publications
None.

Outreach Efforts
None.

Awards
None.

Student Involvement
Jay Woo will be responsible for applying version 1 of the optimization tool to the GTRI nozzle.

Plans for Next Period
We will apply the automated Python optimization tool to Milestone 2 and compare its predictions with the GTRI data in Milestone 3.

Task 7 - Reformulation of Resolvent Modes by Using Local Turbulent Kinetic Energy
Caltech

Objective
The objective of this task is to develop a means for the resolvent gain predictions to be internally calibrated by using information from the RANS-predicted flow-fields.

Research Approach
A calibrated reconstruction of the input–output modes from the resolvent formulation is used to estimate the jet's turbulent kinetic energy, as predicted by the RANS model.

Milestones
- Finalize the calibration formulation
- Implement the calibration procedure
- Verify the calibration procedure

Major Accomplishments
Task 7 has been started. However, initial results from Caltech showed that the original formulation for calibrating the resolvent modes by using the local turbulent kinetic energy led to an ill-posed problem whose solutions were not suitable. A new formulation is being developed.

Publications
None.

Outreach Efforts
None.

Awards
None.

Student Involvement
Liam Heidt will continue to be responsible.

Plans for Next Period
We will continue Task 7 by developing the new self-calibration formulation and applying it to GTRI flow field data.

Task 8 - Development and Implementation of Design Parameter Gradient Direction for JNR

University of Illinois at Urbana-Champaign (lead) with Caltech

Objective

The objective of this task is to develop and verify an updated Python-based optimization tool based on version 1 and the self-calibration procedure developed in Task 7 that searches the optimization space of the engine geometry/cycle, to identify design choices that improve JNR.

Research Approach

Using gradient-informed optimization methods, we will develop an optimization approach for estimating JNR potential from a class of candidate engine geometries/cycles by using self-calibrated resolvent mode predictions of jet noise, on the basis of linearized operators described by RANS predictions of the jet exhaust plume.

Milestones

- Incorporate self-calibrated resolved mode implementation into the Python toolchain
- Incorporate lessons-learned updates from version 1 of the Python toolchain into version 2
- Verify implementation

Major Accomplishments

Milestone 1 will be completed pending the new formulation for self-calibration determined in Task 7. Milestone 2 is in progress; the automated Python optimization tool is being applied to the GTRI dual stream nozzle data. Milestone 3 has not yet been started.

Publications

None.

Outreach Efforts

None.

Awards

None.

Student Involvement

Jay Woo and Liam Heidt will be jointly responsible.

Plans for Next Period

We will complete Milestone 2 early in Year 3. Milestone 1 development is paused while Task 7 is being completed. Milestone 3 will begin once Milestone 1 has been completed.

Task 9 - Application of Version 2 Optimization Tool on GTRI Dual-stream Nozzle

University of Illinois at Urbana-Champaign (lead) with Caltech

Objective

The objective of this task is to apply version 2 of the Python-based tool developed in Tasks 2–5, by using self-calibration from Task 7 and implementation in Task 8, to the GTRI dual-stream nozzle with extensible mixer duct lengths, and predict the quietest configuration.

Research Approach
Apply the automated Python toolchain, starting with the moderate mixer duct length, to predict the mixer duct length that yields the quietest configuration. Predictions are compared with the GTRI-measured acoustic field.

Milestones
- Apply the optimization tool
- Compare the predicted quiet configuration to the measured quiet configuration

Major Accomplishments
Task 8 has not been started.

Publications
None.

Outreach Efforts
None.

Awards
None.

Student Involvement
Jay Woo will be responsible for applying version 2 of the optimization tool to the GTRI nozzle.

Plans for Next Period
We will begin Task 9 once Tasks 7 and 8 are complete.

Task 10 - Application of Version 1 Optimization Tool on Gulfstream- and Boom-relevant Geometry
University of Illinois at Urbana-Champaign

Objective
The objective of this task is to work with Gulfstream and Boom to apply version 1 of our optimization tool to a supersonic nozzle design of relevance to Gulfstream and Boom. Performance, successes, and failures will be documented.

Research Approach
Transition the results of version 1 of the Python optimization tool to Gulfstream and Boom for internal evaluation of the tool.

Milestones
- Develop and implement a cost-sharing agreement with appropriate intellectual-property safeguards
- Work with Gulfstream and Boom engineers to identify cases of interest
- Apply optimization code to Gulfstream and Boom cases of interest

Major Accomplishments
Milestone 1 has been completed, and the letters of support from Gulfstream and Boom are included. Milestone 2 has been completed, and the NASA Plug20 configurations of Bridges et al. (NASA TM-20210010291) were selected. Milestone 3 has not yet been started.

Publications
None.

Outreach Efforts
None.

Awards
None.

Student Involvement
Jay Woo and P.I. Daniel Bodony will be jointly responsible.

Plans for Next Period
We will begin Milestone 3 when Gulfstream provides UIUC with the Plug20 flow data computed with their RANS code(s).

Task 11 - Collaborate with P.I.s for ASCENT Projects 10 and 47
University of Illinois at Urbana-Champaign

Objective
The objective of this task is to collaborate with P.I.s on ASCENT Projects 10 and 47 to understand fleet-scale estimation needs and constraints and develop a prototype software interface that connects the engine-class tool from Task 3 to FLEET/GREAT.

Research Approach
Discuss, document, and identify implementation possibilities for connecting version 1 (or version 2) of the JNR optimization tool within their project software tools.

Milestones
- Engage P.I.s on ASCENT Projects 10 and 47 to understand their goals, data, and software ecosystems.
- Identify possible means through which ASCENT Project 59C tools could be integrated in Project 10 and 47 ecosystems.
- Re-engage project 10 and 47 P.I.s to down select the most promising integration path.

Major Accomplishments
This task has not yet been started.

Publications
None.

Outreach Efforts
None.

Awards
None.

Student Involvement
Jay Woo and P.I. Daniel Bodony will be jointly responsible.

Plans for Next Period
We will begin Task 11 in the next year.

Project 059(D) Physics-Based Analyses and Modeling for Supersonic Aircraft Exhaust Noise

Stanford University

Project Lead Investigator

Sanjiva K. Lele
Professor
Department of Aeronautics & Astronautics
Stanford University
Durand Building
496 Lomita Mall
Stanford, CA 94305
650-723-7721
lele@stanford.edu

University Participants

Stanford University

- P.I.s: Dr. Sanjiva K. Lele and Dr. Juan J. Alonso
- FAA Award Number: 13-C-AJFE-SU-024
- Period of Performance: January 1, 2022 to December 16, 2022
- Tasks:
    1. Develop and refine research plans in coordination with ASCENT Project 59 partners
    2. Large eddy simulation (LES)-based simulation, modeling, and validation of jet noise predictions
    3. Reynolds-averaged Navier–Stokes (RANS)-based simulation, modeling, and validation of jet noise predictions

Project Funding Level

This project received $200,000 per year from the FAA; in-kind matching from Stanford; and cost-share matching from Gulfstream.

Investigation Team

Dr. Sanjiva K. Lele (P.I.), Department of Aeronautics and Astronautics, Stanford University
Dr. Juan J. Alonso (P.I.), Department of Aeronautics and Astronautics, Stanford University
Gao Jun Wu, PhD student, Department of Aeronautics and Astronautics, Stanford University
Tejal Shanbhag, PhD student, Department of Aeronautics and Astronautics, Stanford University
Kristen Matsuno, PhD student, Department of Mechanical Engineering, Stanford University
Olivia Martin, PhD student, Department of Mechanical Engineering, Stanford University

Project Overview

Improved methods for prediction and reduction of noise for civil supersonic aircraft would be highly valued by the research and technology development community engaged in civil supersonic aircraft development. Beyond the aircraft and engine companies, organizations such as NASA, the FAA, and the Department of Defense research and technology community would also benefit from the improved methods and tools. Ultimately, supersonic jet noise tools with predictive capabilities can be used to design better noise mitigation systems and to provide estimates of noise for certification studies.

The project involves coordinated development of both low- and high-fidelity approaches for jet noise predictions for civil supersonic aircraft being considered in ASCENT, including the tasks listed above. High-fidelity simulations of the jet exhaust

flow and noise will be developed for a carefully selected subset of configurations and operating points being tested by the Georgia Institute of Technology (Georgia Tech) team. In parallel, RANS computations of a broader range of configurations and operating conditions relevant to civil supersonic aircraft will be performed and used to develop improved jet noise source models and more accurate far-field noise propagation kernels. The noise source and noise propagation modeling will leverage high-fidelity simulation data and ongoing Georgia Tech experiments, as well as other noise and flow measurements available in the archival literature. Our goal is to understand the predictive quality of RANS-based noise prediction approaches with improved source and/or propagation models, to enable designers to better capture the trade-offs typical in the development of full civil supersonic aircraft configurations.

Task 1 - Develop and Refine Research Plans in Coordination with ASCENT Project 59 Partners

Stanford University

Objectives

We aim to determine a plan for the simulation study that covers the range of operating conditions and possible nozzle configurations relevant to civil supersonic jet exhaust. The plan must include the current test plan from our experimental partner at Georgia Tech.

Research Approach

The planning involved discussions with Project 59 partners and reaching out to external advisors at NASA and elsewhere in academia and industry. On the basis of this exercise, a decision was made that the project should focus on axisymmetric dual-stream nozzles with an internal mixer, and the possibility of an internal and/or external nozzle plug. We also searched for nozzle configurations, and flow and noise measurement data in archival literature, which would be deemed relevant for civil supersonic aircraft and could be used in the development of noise prediction methods. Comprehensive exploration indicated that the bulk of jet noise data including studies of noise reduction concepts was in the regime of moderate-to-high BPR and thus not particularly relevant to civil supersonic aircraft. Although these findings affirmed the need for the planned laboratory measurement campaign by Project 59 partner Georgia Tech, they also highlighted the need to use the most relevant data from the published literature to kickstart the modeling and simulation efforts. Two specific data sets associated with jet noise tests at NASA Glenn Research Center were thus identified.

Georgia Tech Dual Stream Nozzle

A co-annular nozzle geometry with a variable-length mixing duct is designed and being tested extensively by the team at Georgia Tech. After discussions among the project collaborators and key stakeholders, a test matrix has been determined for the Year 1 and 2 experimental efforts. The jet Mach number for each of the two streams varies between $M_j = 0.4$ and $M_j = 1.0$, and the length of the nozzle mixing duct can be adjusted to be 0.7, 1.0, 2.0, or 3.0 times the length of the nozzle diameter, $D_e = 1.7$ inches.

Bridges and Wernet Internal Mixer

In 2004, Bridges and Wernet (NASA Glenn Research Center) reported flow and noise measurements for internally mixed two-stream nozzles with variations in the mixer duct length and mixer geometry. The operating conditions involve transonic and low-supersonic jet exhaust velocity and moderate BPR. This configuration has been used in previous RANS-based noise prediction studies by Rolls Royce and Purdue University, along with a more recent LES study. We have been in touch with Rolls Royce and NASA regarding the nozzle geometry and the measurement data. We hope that the geometry and data will become available to us in the future. This configuration is of interest to us, because it is unique in providing both jet flow measurements and far-field noise at conditions relevant to civil supersonic flights.

Recent Jet Noise Measurements at NASA Glenn Research Center

As part of NASA's Commercial Supersonic Technology Project, under the Advanced Aero Vehicle Program, Dr. James Bridges at NASA Glenn Research Center (personal communication, 2020) recently completed jet noise measurements on specially designed modular nozzle configurations at operating points selected to be relevant to commercial supersonic aircraft. He plans to make the nozzle geometry and measurement data available in the future. NASA's plans include noise predictions using a variety of computational tools. We are interested in exploring a selected subset of NASA's test matrix in our Project 59 studies. We have obtained the computer-aided-design geometry for the nozzle and have begun early efforts in geometry

cleaning and mesh generation. The mesh generation for this case is fairly challenging, because of the steep curvature and sharp edges in the mixer lobes.

Milestones
The simulation plan for Years 1–2 has been determined and followed. Our plan for Year 3, regarding nozzles with noise mitigation concepts, is being finalized, with a focus on studying the effects of mixing enhancement devices at heated jet conditions.

Major Accomplishments
A research plan regarding the nozzle geometry and flow conditions to be studied has been developed. The plan includes both the experimental study by our partner at Georgia Tech and other relevant work from NASA Glenn Research Center.

Publications
None.

Outreach Efforts
Communication with researchers at NASA Glenn Research Center has been established, and ideas for possible collaboration have been exchanged.

Awards
None.

Student Involvement
Three graduate students are involved in this part of the project. G. Wu and K. Matsuno have conducted literature research on relevant jet experiments and simulations involving similar flow conditions and nozzle mixing devices. T. Shanbhag has conducted literature reviews on acoustic modeling of jet noise. K. Matsuno completed her PhD recently. O. Martin has joined the project and is helping with the simulations of the mixer nozzle.

Plans for Next Period
We will continue to refine our research plan according to the ongoing discussions among teams of Project 59. In particular, we will select nozzle geometries with noise mitigation concepts of interest to the industrial partners for the development of next-generation supersonic civil transport aircraft.

Task 2 - LES-based Simulation, Modeling, and Validation of Jet Noise Predictions
Stanford University

Objectives
In collaboration with ASCENT partners in Project 59, we plan to develop physics-based analyses for supersonic aircraft exhaust noise. The main goals of these analyses are to develop improved jet noise prediction methods by using a multi-fidelity approach. As part of the high-fidelity approach, LES will be conducted for a carefully selected set of configurations and operating points corresponding to tests conducted by the experimental team at Georgia Tech. The LES data will provide the turbulence flow statistics and will be leveraged for acoustic source modeling.

Research Approach
In the past project year, the high-fidelity modeling efforts have focused on the dual-stream conical nozzle designed and tested by Georgia Tech. The nozzle exit diameter, D_e, is 1.7 inches, and a mixing duct with adjustable length with respect to the nozzle diameter is present. LES and far-field acoustics modeled by the permeable Ffowcs Williams and Hawkings (FW-H) formulation are obtained by using the compressible solver CharLES, developed by Cascade Technologies. Work in Year 1 has been published in a conference manuscript (Wu et al., 2022). In the manuscript, we report results at $M_j = 0.8, 0.9$ for the geometry with the shortest mixing duct, $L/D_e = 0.7$. However, the comparison of noise spectra between LES and available

measurements showed spurious numerical artifacts at high frequencies. During project Year 2, we have focused on determining the causes of such discrepancies with a mesh sensitivity study. With improved mesh resolution in the jet shear layers, errors at the high-frequency range have been reduced. Further validation of LES results has been performed with more recent experimental measurements from Georgia Tech. Turbulence statistics from the improved LES data sets are then used to support the development of RANS-based acoustic source models, as discussed in Task 3.

Progress in Jet Noise Modeling and Simulations

The nozzle geometry was designed and tested by the Project 59 partner at Georgia Tech (Figure 1). The area ratio of the secondary to the primary nozzle is 2.25. An exhaust mixing duct is attached to the end of the co-annular nozzle, and the length of the mixing duct is 0.7 D_e. LES of the jet exhaust flow and noise is conducted at $M_j = 0.8$ for both the primary conical nozzle alone and the co-annular nozzle. For the primary nozzle test case, iterative mesh refinement is performed among four different meshes. For the co-annular nozzle, a moderate mesh design is selected on the basis of the analysis of the primary nozzle test case. Table 1 provides a summary of all test cases.

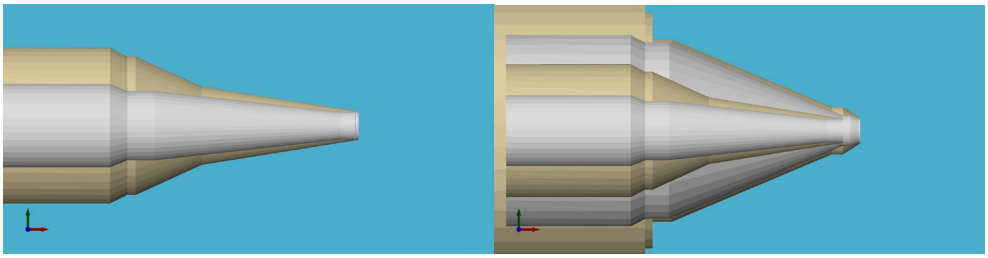

Figure 1. Left: primary nozzle. Right: co-annular nozzle designed by Georgia Tech.

Table 1. Summary of the test cases. All flow conditions are non-heated.

M_{j1}	M_{j2}	Mesh cell count in millions (mesh label)	LES simulation time $t_{sim}\, c_\infty/D_{e1}$
0.8	N/A	18 (A), 27 (B), 98 (C), 131 (D)	700
0.8	0.8	30 (coB)	900

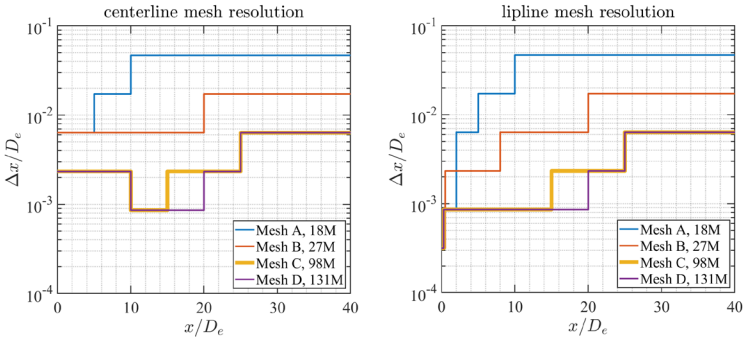

Figure 2. Mesh resolutions along the centerline (left) and the lipline (right) for the primary nozzle test case.

Figure 2 shows the mesh resolutions for the primary nozzle case along the jet centerline and the lipline. Figures 3 and 4 compare the mean streamwise velocity and turbulent kinetic energy obtained from the four meshes. As the jet plume exits

the nozzle, turbulence intensifies along the shear layers, then grows in thickness as the jet expands further downstream. Sufficiently fine mesh grids are required in regions close to the jet lipline to resolve the energetically dominant turbulent scales. The nature of the Voronoi mesh introduces non-smooth grid resolution changes in the streamwise direction. As seen in the case with mesh A, such jumps in grid resolution truncate the continuous growth of turbulence along the shear layers and predict a shorter potential core length than observed with the other three meshes. This aspect is further indicated in Figure 5, which indicates that the lipline TKE profile contains spikes at locations where the grid coarsens in mesh A. From B to C, significant improvements in TKE are observed near the end of the jet potential core, between $x/D_e = 8$ and 10. From C to D, mesh grids between $x/D_e = 15$ and *20* are further refined but result in only minor improvement. Figure 6 shows the far-field acoustic predictions together with microphone measurements. Comparison of the results from mesh A, B, and C indicates that the grid improvement in the jet shear layers successively reduces the spurious hump at high frequencies. As expected, the results from mesh C and D show no significant variation. Even with the finest mesh, the LES results still differ from the measurements in two regions. For $St < 0.1$, LESs underpredict noise by as much as 3 dB at $\theta = 60^{\circ}$; for $St > 3$, the LES spectra have a faster falloff rate than indicated by the measurements. The exact reasons for these discrepancies are currently unknown.

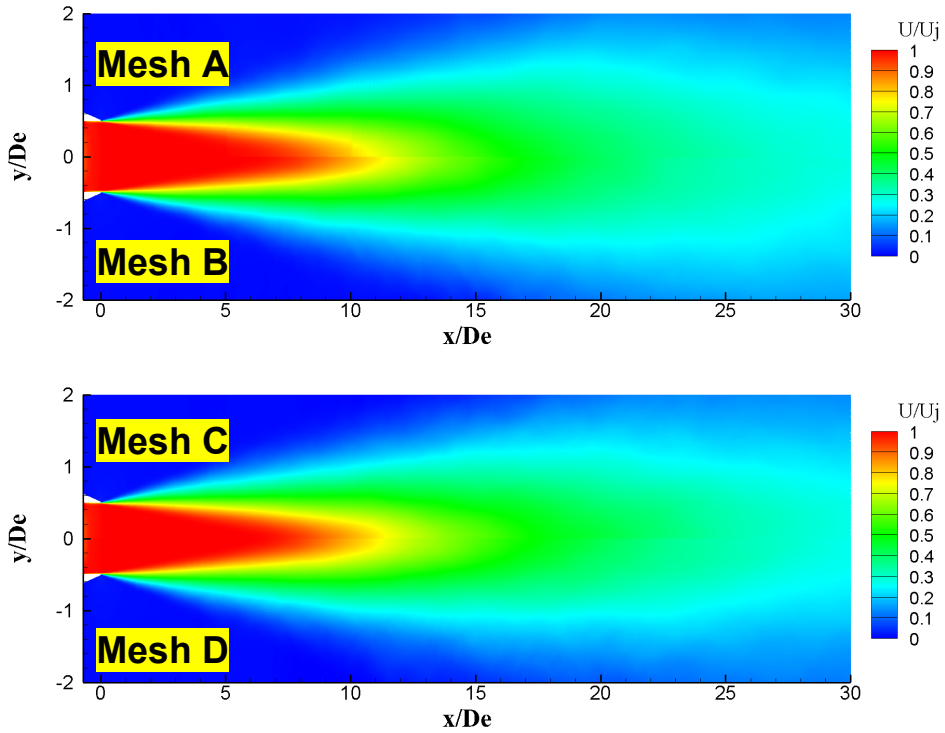

Figure 3. Comparison of mean streamwise velocity among all meshes for the primary nozzle case.

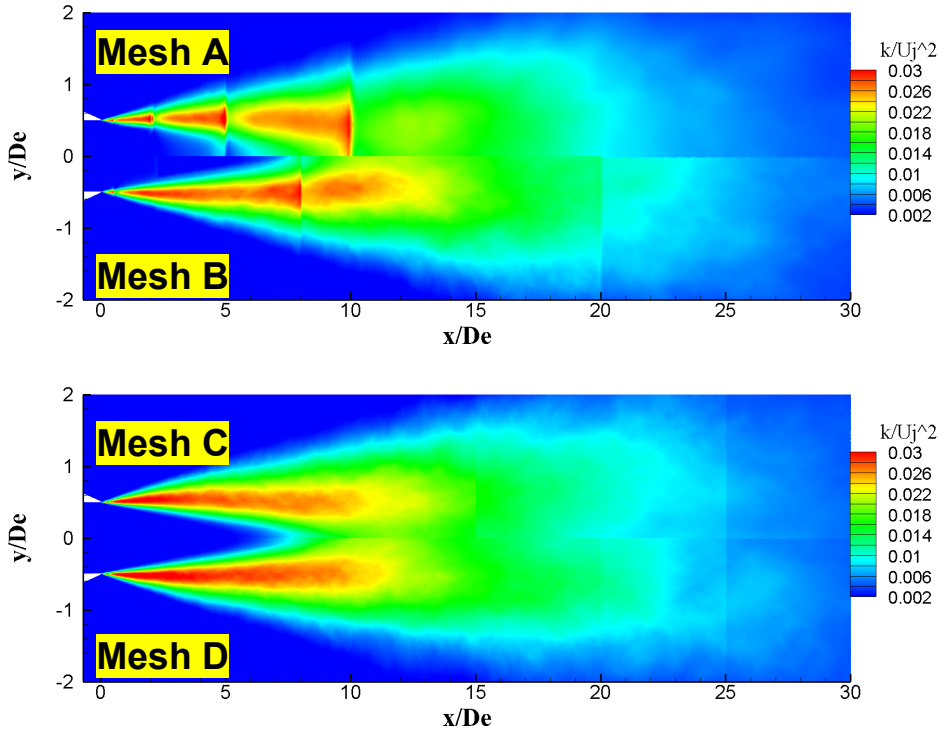

Figure 4. Comparison of mean turbulent kinetic energy among all meshes for the primary nozzle case.

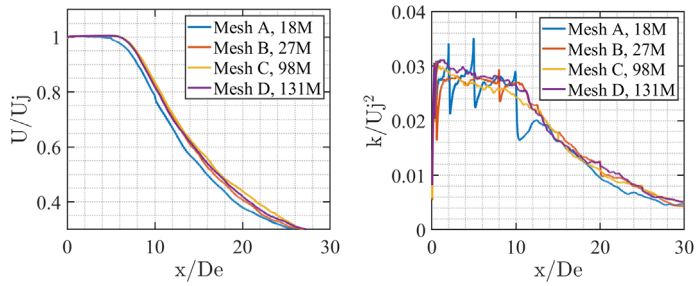

Figure 5. Comparison of mean centerline velocity (left) and lipline TKE (right) among all meshes for the primary nozzle case.

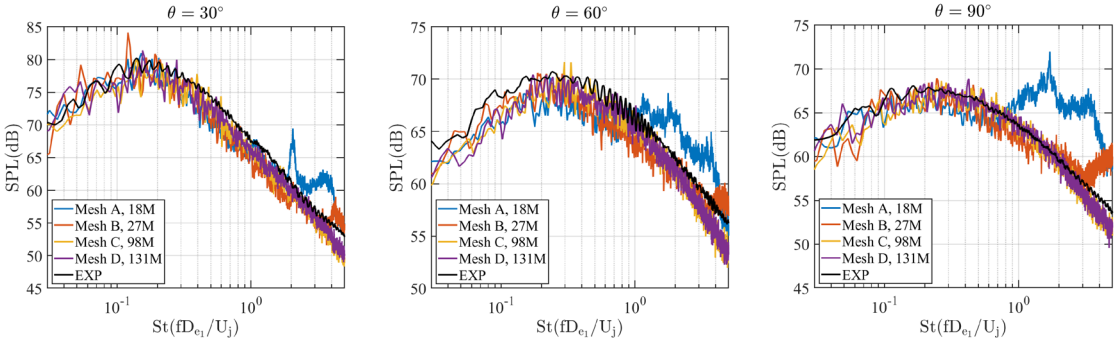

Figure 6. Comparison of acoustic spectra among all mesh cases and experiments.

On the basis of the lessons learned from the primary nozzle test case, the mesh for the co-annular nozzle test case is created such that the grids in the shear layers up to $x/D_e = 18$ are kept at $\Delta x/D_e = 0.025$, corresponding to a moderate mesh resolution similar to that of mesh B. Figures 7 and 8 compare the mean streamwise velocity between LES and PIV data. LES agrees with measurements well in terms of the overall jet spreading rate, potential core length, and the decay in the centerline jet velocity. Similarly to the primary nozzle case, the acoustic results from LES underpredict the noise at $St > 1$ (Figure 9), as expected because of the relatively modest but carefully tailored grid resolution. Near $St = 4$, the experimental data at $\theta = 30^\circ$ contain a small bump introduced by undesirable microphone vibrations (according to comments from the Georgia Tech team). This bump might further exacerbate the mismatch between LES and experimental results. The LES acoustic results can be further improved with a finer grid resolution, such as mesh C and D for the primary nozzle case.

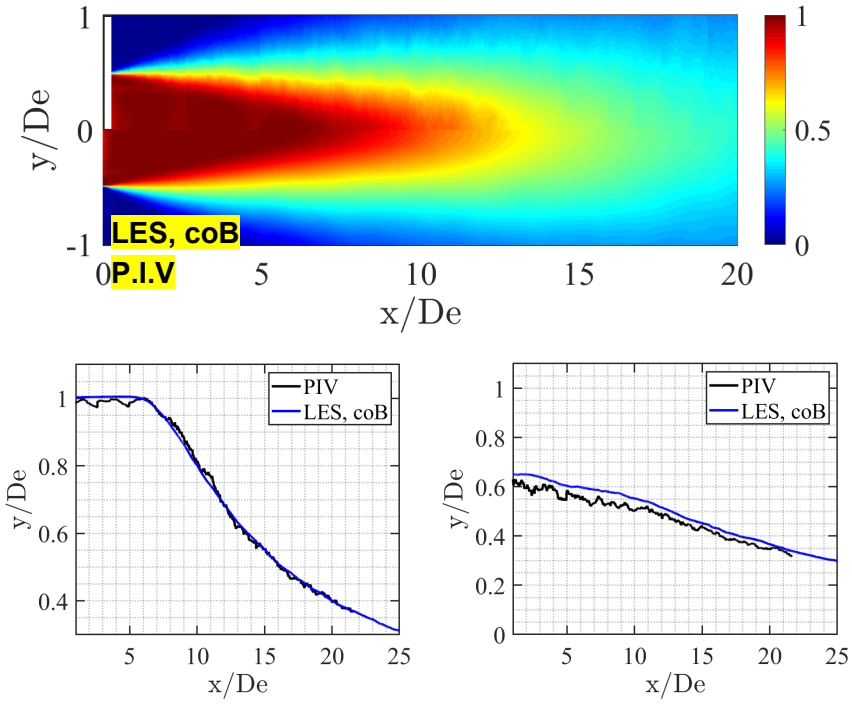

Figure 7. Comparison of mean streamwise velocity between experiments and LESs. Top: contour viewed in the midplane. Bottom left: centerline velocity profile. Bottom right: lipline velocity profile.

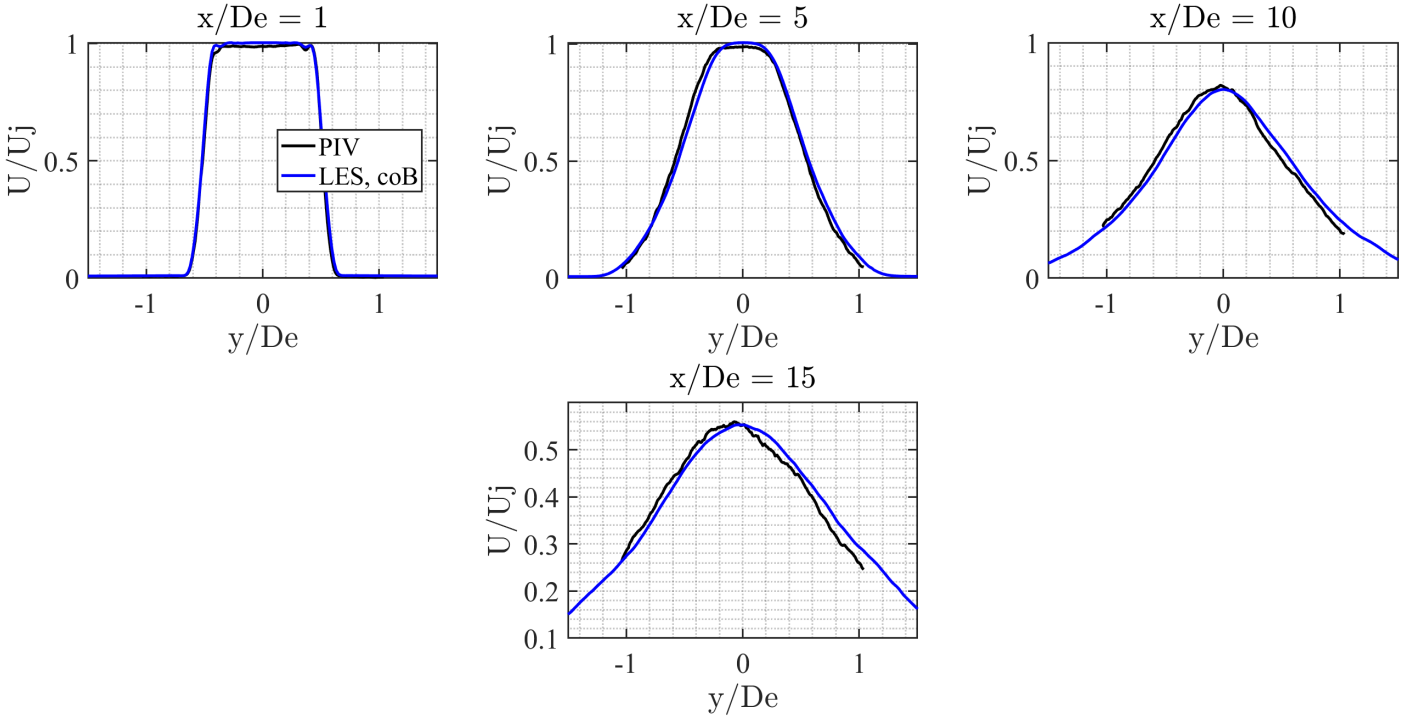

Figure 8. Radial profile comparison.

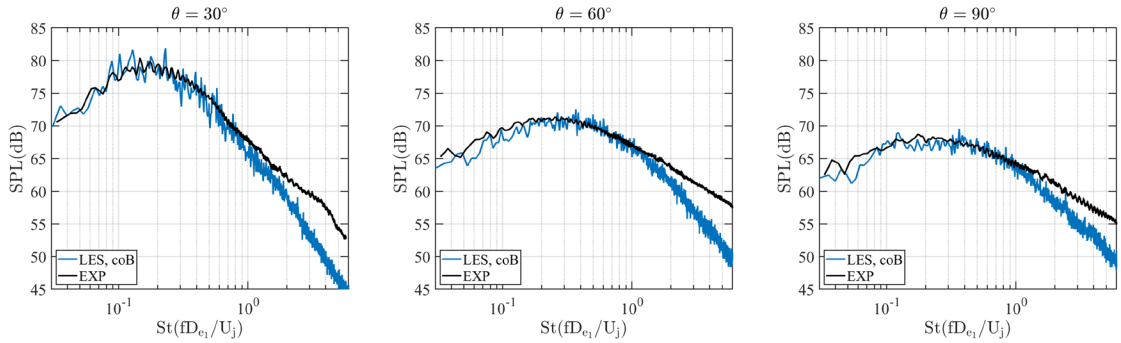

Figure 9. Comparison of acoustic spectra between LESs and experiments.

Milestones

LESs for test cases corresponding to the Georgia Tech. experimental test matrix have been significantly improved. Numerical errors due to insufficient grid resolution inside the jet shear layers have been identified and addressed.

Major Accomplishments

Over the past project year, we have made steady progress in high-fidelity simulations of jet noise, in accordance with the test plan set up by our Project 59 partners. LESs have been conducted for the Georgia Tech co-annular nozzle by using the compressible solver CharLES, developed by Cascade Technologies. The nozzle configuration with the shortest mixing duct, $L/D_e = 0.7$, is considered for two Mach numbers $M_j = 0.8$. The reason for the previously reported spurious high-frequency hump in the noise spectra has been identified through a detailed mesh sensitivity study. Because of insufficient resolution and aggressive coarsening of grids along the jet shear layers, the development of turbulent kinetic energy is inaccurately modeled, thereby resulting in the appearance of the high-frequency hump in the far-field SPL spectra. With improved grids,

the agreement between the LESs and experimental data for the mean velocity statistics is satisfactory, but discrepancies for far-field acoustics persist. Further investigation of the causes of such discrepancies is needed.

Publications

Published conference proceedings

Wu, G. J., Shanbhag, T. K., Molina, E. S., Lele, S. K., & Alonso, J. J. (2022, January 3). Numerical simulations and acoustic modeling of a co-annular nozzle with an internal mixing duct. *AIAA SCITECH 2022 Forum*. AIAA SCITECH 2022 Forum, San Diego, CA & Virtual. https://doi.org/10.2514/6.2022-2404

Outreach Efforts

Communication with Project 59 partners in ASCENT and with NASA scientists has been established. Deeper collaboration with the Georgia Tech experimenters and NASA scientists is expected as the project progresses further.

Awards

None.

Student Involvement

One graduate student, G. Wu, is involved in this project task.

Plans for Next Period

We plan to further refine the current LES results and achieve better agreement with experimental data. SPOD analysis with the LES data will be conducted to analyze the large-scale coherent structures associated with low-frequency acoustics. LES at additional flow conditions and geometries corresponding to the most recent experimental study at Georgia Tech and NASA Glenn Research Center will be performed.

Task 3 - RANS-based Simulation, Modeling and Validation of Jet Noise Predictions

Objectives

The project involves coordinated development of both low- and high-fidelity approaches for jet noise prediction. For the low-fidelity approach, RANS computations of a broader range of configurations and operating conditions relevant to civil supersonic aircraft will be performed and used to develop improved jet noise source models and more accurate far-field noise propagation kernels.

Research Approach

Ray tracing methods

In this work, we implement a RANS-based prediction method based on geometrical acoustics. Both the source model and the far-field propagation model use information obtained from a standard *k*-epsilon simulation of the jet flow. We perform all such simulations by using the open-source code SU2. The propagation model, which accounts for the effects of sound refraction, is based on a ray tracing method. This implementation makes very few simplifying assumptions regarding the flow field geometry and therefore is applicable to complicated nozzle configurations that result in inherently three-dimensional propagation effects. The highly parallel nature of the ray tracing algorithm also makes this method ideal for graphics-processing-unit implementation for accelerated analysis, optimization, and design. Our implementation of the source and propagation models as separate modules allows us to study their effects in isolation.

The presence of a moving medium and spatial gradients in the speed of sound significantly affect the refraction of sound waves reaching the far field. We account for these effects by introducing the flow factor, which represents the ratio of the pressure amplitude measured at the observer due to a particular source, with and without the jet flow being present. We make a high-frequency approximation to utilize the geometrical ray tracing method to describe wave propagation in non-uniform media. This method does not require the solution of an additional PDE over a domain extending to the far field, and it is well suited to complex and possibly asymmetric jet configurations. We follow Pierce's ray tracing formulation: a very large number of rays is launched from each acoustic source location, the path of each ray is computed by solving a governing

ODE for the velocity of a wavefront in a moving medium, and the pressure ratio along the ray tubes is subsequently computed by using the Blokhintsev invariant.

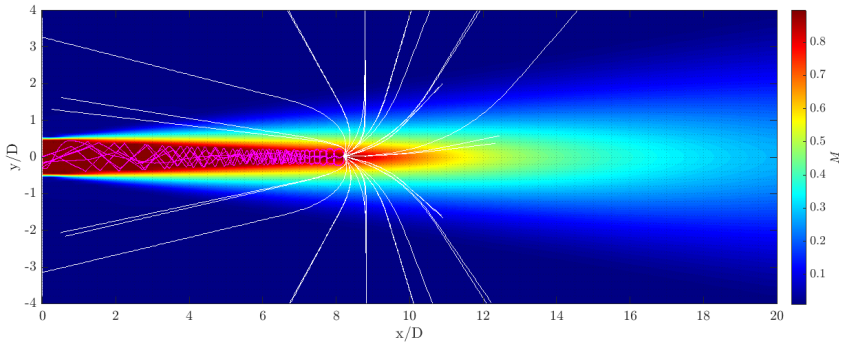

Figure 10. Ray path curvature due to flow refraction effects.

The effects of sound refraction by the jet flow can be observed in the paths taken by rays between the source locations and the far field. In the absence of any flow, and any flow gradients, each ray would follow a straight line from its source to its observer location on our chosen far-field sphere, following the angle at which it was launched. When the jet flow is included, a high degree of ray curvature exists in regions with high spatial gradients of velocity and sound speed. The flow factor is calculated by comparison of the number of rays that end at a given far-field location for the cases of no flow (straight rays) and jet flow (curved rays). Figure 10 shows the paths taken by a small number of rays being launched from an example source located close to the jet axis and to the end of the potential core. Some of the rays cross through the shear layer region, where velocity and speed-of-sound gradients along the ray paths are high. Consequently, these rays curve away from the jet axis. According to this observation, we expect that the addition of the flow factor will, in the case of acute polar observer angles, decrease the far-field SPL with respect to that obtained by using the source model alone. In contrast, in the case of obtuse polar angles, we expect to see the SPL increased by flow refraction effects. At an observer angle of 90°, the effects of refraction due to sound-flow interaction should be very small; therefore the flow factor is physically expected to be close to unity for all source locations. Notably, rays launched from this source location that fall within a critical range of launch angles remain trapped inside the jet's potential core. This behavior is physically expected: the rays undergo total internal reflection upon encountering a critically high value of local flow gradient transverse to the shear layer. The trapping of these rays and the corresponding reduction in effective acoustic propagation from inside this region to the far field leads to the conclusion that no significant concentration of true acoustic sources exists in the inviscid core. Therefore, in choosing the locations for the fictional sources in the ray tracing method, placing a very large number of sources inside this core is inefficient.

The effects of refraction on the computed far-field SPL may be studied in isolation by plotting the flow factor as a function of source location for different values of the polar observer angle. The flow factor is plotted in Figure 11 on a decibel scale for polar angles of 90° and 60° (with the azimuthal observer angle fixed at 90°) to demonstrate the net effect of ray curvature for sources in different regions of the jet plume. Positive values indicate refractive amplification, whereas negative values correspond to attenuation. For an observer located at 90°, the flow factor value is close to 1 everywhere, as expected; amplification due to refraction is negligible. However, at acute polar angles, in regions close to the nozzle exit where velocity and sound speed gradients are substantial, large shifts due to the effects of sound-flow interaction are observed. Much of the acoustic source region is attenuated, most significantly in the inviscid core, where total internal reflection is a dominating effect, as previously discussed. Moreover, the flow factor distribution is not axisymmetric, even for this axisymmetric round jet case. Sources located on the opposite side of the jet from the observer's location of interest are subjected to the greatest refraction shift. This finding is consistent with our observation of high ray curvature coincident with traversing of the shear layer. Sources located opposite from the observer must pass through these high-gradient regions twice before reaching the far field, thus resulting in a higher degree of ray scattering.

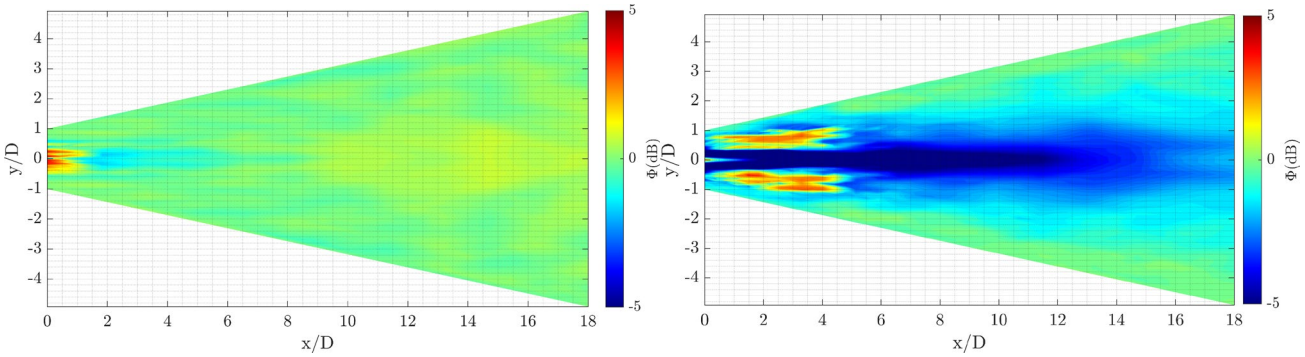

Figure 11. Flow factor for observer angles of (a) θ = 90° and (b) θ = 60°. The observer is above the plane of the figure (ϕ = 90°).

Optimization of turbulent time scales

For RANS methods to accurately model the turbulent correlation functions appearing in the source term of the Lighthill equation, a proper definition of the relevant turbulent length and time scales is required. Incorporating the inherent frequency dependence of these quantities has also been shown to be crucial for accurate acoustic prediction, particularly in the low- and high-frequency limits. Harper-Bourne (2000) originally proposed the form of the frequency dependence of length scales in low-Mach-number flows; this model was later applied by Morris and Boluriaan (2004), and implemented by Self (2004) in a statistical noise prediction framework. Self and Azarpeyvand (2009) further studied the frequency dependence of the length and time scales appearing in the source term definition of the MGBK method and proposed a new improved time scale accounting for the rate of transfer of turbulent energy between different wavenumbers.

In this work, we leverage information from LES of the jet flow emerging from a simple conical nozzle, to propose an improved form of the turbulent time scale for use in RANS-based jet noise prediction. From the unsteady LES data, the two-point velocity correlations are directly extracted for different locations in the flow field. We then apply several existing models for the characteristic turbulent scales from the literature. These models are used to compute predictions for the two-point correlation functions, which are compared with the true correlations extracted from the LES data. We derive the optimal spatially varying form of the turbulent time scale by optimizing a weight function over individual time scales that account for turbulent production, dissipation, and energy transfer within the jet. Studying the distribution of this weight function will allow us to determine which of these mechanisms dominate at different locations in the flow field. We hope that this approach will be generalizable to RANS-based acoustic prediction for other jet cases.

Figure 12 shows the fourth-order velocity fluctuation correlation computed at two different axial locations along the nozzle lipline for varying axial separations, and the corresponding Gaussian function approximations. Such function approximations have previously been used by authors to attempt to capture the effects of sound sources arising from both fine-scale turbulence and large-scale flow structures. Although the primary peak in the correlation may be well captured by a Gaussian fit, such a model form is unable to capture negative loops or secondary peaks, both of which are features associated with substantial flow inhomogeneity and are clearly present in this case. Therefore, in future work, a non-Gaussian fitting function that can capture these features may be advantageous; possible candidates include Bessel functions, exponential cosine mixtures, and Gaussian mixtures.

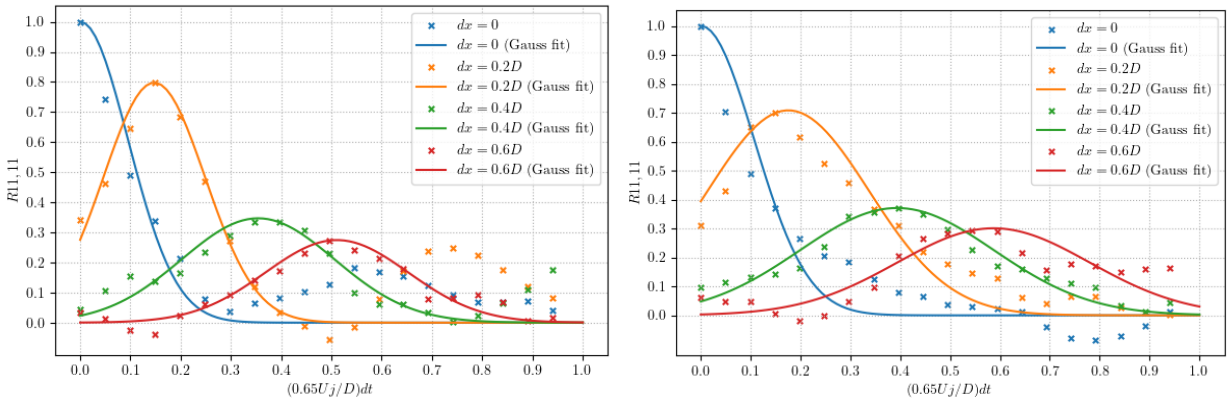

Figure 12. Gaussian fitting to the fourth-order two-point velocity correlation results, corresponding to the lipline $r/D = 0.5$ at (a) $x/D = 4$ and (b) $x/D = 6$.

In the same manner, we extract the fourth-order correlation at every point in the flow field and perform the same Gaussian fitting operation. This process allows us to obtain a spatially varying distribution of the characteristic time scale plotted in Figure 13a after averaging in the azimuthal direction and normalizing by the maximum field quantity (black dashed lines indicate the region occupied by the spreading turbulent jet). The velocity fluctuations over the potential core of the jet are correlated over quite small time scales and remain small along the jet centerline. Moving through the shear layer and the region where most acoustic sources are physically located, the time scale substantially varies; outside the spreading region of the flow, fluctuations appear to be correlated over a time period 4–5 times greater than that observed in the potential core. Figure 13b–d shows the characteristic time scales corresponding to turbulent dissipation, production, and energy transfer. By comparing these distributions against the findings in Figure 13a, we can more intuitively understand the different regions of the jet flow in which each mechanisms dominates and therefore is likely to be most influential when noise generation is computed.

In the region immediately downstream of the nozzle exit, the true distribution is best approximated by the production scale. Slightly further downstream, the dissipation and transfer scales become more relevant, capturing the contrast among short correlation scales along the core, larger scales outside of the spreading region, and a distinct pattern of short scales along the spreading region edges. Far downstream of the end of the potential core, the energy transfer scale appears to most closely resemble the true distribution, with large scales appearing relatively close to the axis. Figure 13e shows the normalized time scale distribution obtained by solving the weight optimization problem. This optimized field captures many qualitative features of the true distribution of time scales quite well.

Figure 14 shows the SPL computed by using the optimized scale distribution, compared with experimental results (experiments performed at Georgia Tech, narrow-bin SPL data obtained via private communication). The figure also shows the same spectrum computed by using the energy transfer scale proposed by Azarpeyvand and Self (2009); this scale is intended to reduce to that associated with different active turbulent mechanisms in regions of the flow where these dominate, and therefore should produce high-quality predictions across the band of relevant frequencies. The far-field spectrum computed with the optimized scales captures the overall spectrum shape very well across the full band of frequencies. A comparison of the optimized scale spectrum against the transfer scale spectrum indicates that both capture high-frequency falloff very well, and the optimized scale results in some improvement in low-frequency prediction; specifically, the flattening and overprediction observed in the transfer scale spectrum has been rectified. The transfer scale spectrum also slightly overpredicts the peak frequency of the spectrum; the optimized scale spectrum appears to do the opposite, underpredicting the peak frequency and slightly overpredicting the peak magnitude. For comparison, Figure 14 shows the same far-field SPL spectrum computed directly from LES data by using a permeable FW-H surface. The RANS-based acoustic predictions using the optimized time scale distribution produce a similar overall error compared with the experiment to FW-H. The FW-H computed spectrum better captures the overall spectrum shape but slightly underpredicts noise below $St = 0.2$, owing to insufficient simulation duration, and predicts a faster high-frequency falloff than that observed in the RANS or experimental result. The faster falloff for $St > 2$ probably results from a mismatch in jet initial shear layer turbulence from the experiment.

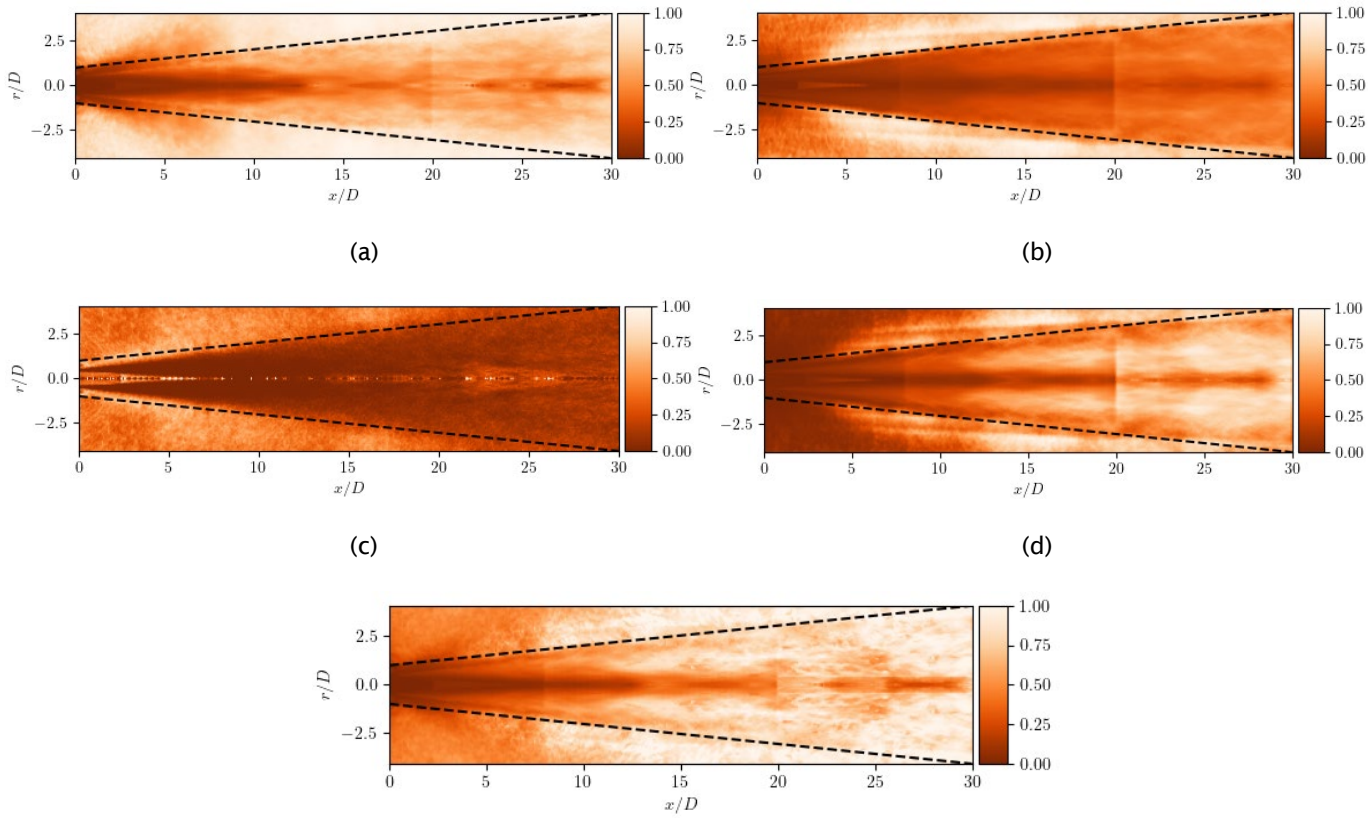

Figure 13. Spatial distribution of characteristic time scale: (a) true, computed from LES data, (b) dissipation, (c) production, (d) energy transfer and (e) optimized reconstruction.

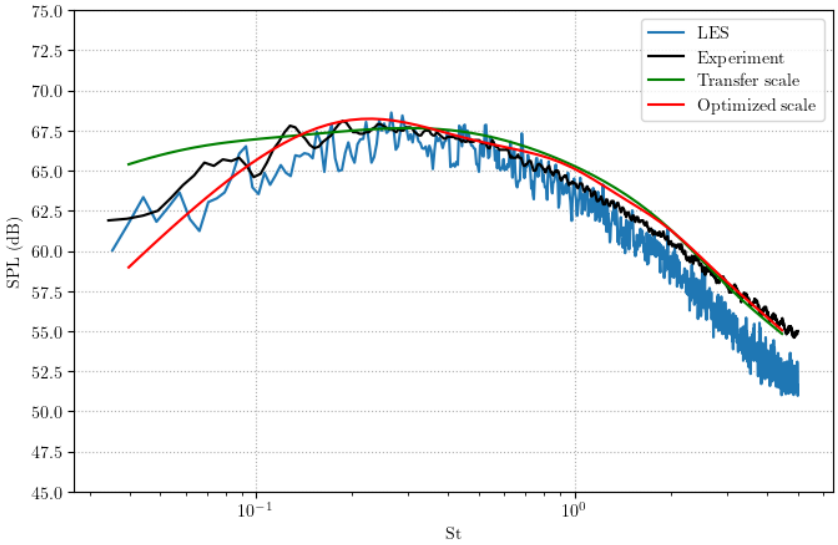

Figure 14. Far-field SPL at r = 75D, θ = 90°, computed by using LES-FW-H, energy transfer time scale, and optimized time scale, compared against experimental measurements.

Milestones

We have extended our modular implementation of the low-fidelity (RANS-based) acoustic prediction tool as described above, and tested it against experimental acoustic measurements for the Go4Hybrid round jet test case and the Georgia Tech primary nozzle test case.

Major Accomplishments

We have extended our previous source modeling implementation to include turbulent time scales based on different physical mechanisms. We have also proposed an optimization method to allow our source model to approximate the true turbulent correlations obtained from LES data. Our previous modular implementation of the low-fidelity acoustic model has been extended to include a far-field propagation tool based on the high-frequency geometrical method of ray tracing. This method is highly parallelizable and amenable to GPU implementation. We hope that this method will allow us to accelerate acoustic computation for the high-frequency part of the spectrum.

Publications

Published conference proceedings

Shanbhag, T. K., Zhou B. Y., Ilario, C. R. S., & Alonso, J. J. (2022, July). *Ray tracing methodology for jet noise prediction*. (ICCFD11-2022-1201). Eleventh International Conference on Computational Fluid Dynamics (ICCFD11).

Shanbhag, T. K., Wu, G. J., Lele, S. K., & Alonso, J. J. (2023, January 23). Optimization of turbulent time scales for jet noise prediction. *AIAA SCITECH 2023 Forum*. AIAA SCITECH 2023 Forum, National Harbor, MD & Online. https://doi.org/10.2514/6.2023-1159

Outreach Efforts

None.

Awards

None.

Student Involvement

T. Shanbhag has led the efforts with the ray tracing method for far-field propagation and optimization of time scales for improved acoustic source modeling described in the previous section.

Plans for Next Period

We will extend our work on optimized forms of the turbulent time scale in the acoustic source model, with an aim to propose a predictive form of this optimized scale that can be computed from RANS quantities alone. The source and propagation models have already been extended to automatic differentiation enabled implementations by using the Jax library. We hope to leverage this to begin to perform adjoint-based design optimization with far-field noise as an objective function to minimize.

References

Ahuja, K. K., Mavris, D. N., Tai, J., Karon, A. Z., Funk, R. B., and Ramsey, D. N. (2020. *Project 059B Jet Noise Modeling and Measurements to Support Reduced LTO Noise of Supersonic Aircraft Technology Development*. FAA ASCENT Annual Report.

Azarpeyvand, M., & Self, R. H. (2009). Improved jet noise modeling using a new time-scale. *The Journal of the Acoustical Society of America*, *126*(3), 1015–1025. https://doi.org/10.1121/1.3192221

Balsa, T. F., & Gliebe, P. R. (1977). Aerodynamics and noise of coaxial jets. *AIAA Journal*, *15*(11), 1550-1558.

Barber, T. J., Chiappetta, L. M., & Zysman, S. H. (1997). Assessment of jet noise analysis codes for multistream axisymmetric and forced mixer nozzles. *Journal of Propulsion and Power*, *13*(6), 737–744. https://doi.org/10.2514/2.5246

Blokhintzev, D. (1946). The propagation of sound in an inhomogeneous and moving medium i. *The Journal of the Acoustical Society of America*, *18*(2), 322–328. https://doi.org/10.1121/1.1916368

Brès, G. A., Ham, F. E., Nichols, J. W., & Lele, S. K. (2017). Unstructured large-eddy simulations of supersonic jets. *AIAA Journal*, *55*(4), 1164–1184. https://doi.org/10.2514/1.J055084

Brès, G. A., Bose, S. T., Emory, M., Ham, F. E., Schmidt, O. T., Rigas, G., & Colonius, T. (2018, June 25). Large-eddy simulations of co-annular turbulent jet using a Voronoi-based mesh generation framework. *2018 AIAA/CEAS Aeroacoustics Conference*. 2018 AIAA/CEAS Aeroacoustics Conference, Atlanta, Georgia. https://doi.org/10.2514/6.2018-3302

Bres, G. A., Towne, A., and Sanjiva, K. L. (2019). Investigating the effects of temperature non-uniformity on supersonic jet noise with large-eddy simulation. AIAA Paper 2019-2730.

Frendi, A., Nesman, T., & Wang, T.-S. (2002). On the effect of time scaling on the noise radiated by an engine plume. *Journal of Sound Vibration*, 256, 969–979.

Ilário, C. R. S., Azarpeyvand, M., Rosa, V., Self, R. H., & Meneghini, J. R. (2017). Prediction of jet mixing noise with Lighthill's Acoustic Analogy and geometrical acoustics. *The Journal of the Acoustical Society of America*, *141*(2), 1203–1213. https://doi.org/10.1121/1.4976076

Karon, A. Z. (2016). *Potential factors responsible for discrepancies in jet noise measurements of different studies* [Ph.D. thesis, Georgia Institute of Technology]. https://smartech.gatech.edu/handle/1853/56264?show=full

Khavaran, A., Krejsa, E., & Kim, C. (1992, January 6). Computation of supersonic jet mixing noise for an axisymmetric CD nozzle using k-epsilon turbulence model. *30th Aerospace Sciences Meeting and Exhibit*. 30th Aerospace Sciences Meeting and Exhibit, Reno,NV,U.S.A. https://doi.org/10.2514/6.1992-500

Harper-Bourne, M. (2000, June 12). Twin-jet near-field noise prediction. *6th Aeroacoustics Conference and Exhibit*. 6th Aeroacoustics Conference and Exhibit, Lahaina,HI,U.S.A. https://doi.org/10.2514/6.2000-2084

Karabasov, S. A., Afsar, M. Z., Hynes, T. P., Dowling, A. P., McMullan, W. A., Pokora, C. D., Page, G. J., & McGuirk, J. J. (2010). Jet noise: Acoustic analogy informed by large eddy simulation. *AIAA Journal*, *48*(7), 1312–1325. https://doi.org/10.2514/1.44689

Khavaran, A. (1999). Role of anisotropy in turbulent mixing noise. *AIAA Journal*, *37*(7), 832–841. https://doi.org/10.2514/2.7531

Khavaran, A., & Bridges, J. (2005). Modelling of fine-scale turbulence mixing noise. *Journal of Sound and Vibration*, *279*(3–5), 1131–1154. https://doi.org/10.1016/j.jsv.2003.11.054

Lighthill, M. J. (1952). On sound generated aerodynamically I. General theory. *Proceedings of the Royal Society of London. Series A. Mathematical and Physical Sciences*, *211*(1107), 564–587. https://doi.org/10.1098/rspa.1952.0060

Morris, P., & Boluriaan, S. (2004, May 10). The prediction of jet noise from cfd data. *10th AIAA/CEAS Aeroacoustics Conference*. 10th AIAA/CEAS Aeroacoustics Conference, Manchester, GREAT BRITAIN. https://doi.org/10.2514/6.2004-2977

Pierce, A. D. (1989). *Acoustics: An introduction to its physical principles and applications* (1989 ed). Acoustical Society of America.

Ribner, H. (1969). Quadrupole correlations governing the pattern of jet noise. *Journal of Fluid Mechanics, 38*(1), 1-24. doi:10.1017/S0022112069000012

Self, R. H. (2004). Jet noise prediction using the Lighthill acoustic analogy. *Journal of Sound and Vibration*, *275*(3–5), 757–768. https://doi.org/10.1016/j.jsv.2003.06.020

Tadmor, E. (2003). Entropy stability theory for difference approximations of nonlinear conservation laws and related time-dependent problems. *Acta Numerica, 12*, 451-512. doi:10.1017/S0962492902000156

Tam, C. K. W., & Auriault, L. (1999). Jet mixing noise from fine-scale turbulence. *AIAA Journal*, *37*(2), 145–153. https://doi.org/10.2514/2.691

Wundrow, D. W., & Khavaran, A. (2004). On the applicability of high-frequency approximations to Lilley's equation. *Journal of sound and vibration*, *272*(3-5), 793-830.

Project 059(E) Moderate-Fidelity Simulations for Efficient Modeling of Supersonic Aircraft Noise

The Pennsylvania State University

Project Lead Investigator

Philip Morris
Boeing/A.D. Welliver Professor Emeritus
Department of Aerospace Engineering
Pennsylvania State University
233C Hammond Building
University Park, PA 16802
814-863-0157
pjm@psu.edu

University Participants

Pennsylvania State University

- P.I.s: Dr. Philip Morris (P.I.), Dr. Daning Huang (co-P.I.)
- FAA Award Number: 13-C-AJFE-GIT-070
- Period of Performance: January 1, 2022 to December 31, 2022
- Tasks:
  - Perform LES for external flow on inner nozzle
  - Implement FWH surface data extraction
  - Calculate far field noise and compare with measurements
  - Develop grid and obtain RANS solution for internal flow of the dual stream nozzle.
  - Perform LES for external flow for dual stream nozzle
  - Use FWH analogy to calculate far field noise and compare with measurements.

Project Funding Level

The project is funded at the following level: FAA: $100,000. Cost sharing of $100,000 is provided by the Pennsylvania State University through salary support of the faculty P.I.

Investigation Team

Pennsylvania State University

- Principal Investigator: Dr. Philip Morris
- Co-Principal Investigator: Dr. Daning Huang
- Graduate Student: Dana Mikkelsen

Project Overview

The purpose of this project is to develop and assess efficient computational tools to simulate the flow and noise of civil supersonic aircraft engines.

The prediction of noise from supersonic jets, particularly when noise reduction devices are present, is a challenging computational task. Methods based on Reynolds-averaged Navier–Stokes (RANS) solutions are relatively inexpensive to perform and provide satisfactory predictions of the average flow field, even for quite complicated geometries. The subsequent prediction of noise on the basis of acoustic analogies is highly efficient but becomes difficult when the nozzle lacks simple axisymmetry. Methods based on large eddy simulation (LES) provide considerably more information about the unsteady flow and the noise generated. However, LES is computationally expensive, particularly when the engine geometry

is complex. This situation is encountered in the case of nozzles with noise reduction devices, such as internal mixers. Noise predictions based on LES can be made quite efficiently by using the Ffowcs Williams and Hawkings (FW-H) acoustic analogy (Farassat and Succi, 1983; Ffowcs Williams and Hawkings,1969), but long time records are required to predict the noise radiated to far-field observers, thus adding additional expense to LES.

The approach in Project 59E is a compromise between the accuracy and high computational cost of LES and the noise-prediction limitations of RANS-based simulations. The simulations conducted in the initial stage of the project use RANS, and these calculations serve as a starting point for the LES. In anticipation of the addition of internal mixers to the nozzle geometries, only RANS simulations are planned to be conducted for the internal flow; subsequently, LES, coupled with the FW-H acoustic analogy, will be used to predict the external flow and the noise generated. The RANS solution at the jet exit will be used as an initial condition for the external LES. This process will require the addition of some unsteady information, as guided by a very limited number of LESs. This approach will reduce the total computational cost by removing much of the geometric complexity and the associated grid requirements for LES of the internal flow.

The utility of this approach is that it will make LES for nozzles with noise reduction devices more accessible to more users, particularly industry engineers with very limited computational resources and time available for multiple simulations in the design process.

In addition, the LES-based predictions will be supplemented by more traditional acoustic-analogy approaches based on RANS, with an emphasis on modeling high-Strouhal-number noise radiation.

If successful, the ASCENT Project 59E research will develop methods to predict the noise generated and radiated by civil supersonic aircraft engines. The developed tools should enable airframe and engine manufacturers to assess the noise impacts of engine design changes and to determine whether the designs will meet current or anticipated noise certification requirements.

Task 1 – RANS and LES of Single and Dual Stream Nozzles

Pennsylvania State University

Objective

During the first project year, because of a change in direction from the originally proposed research, the original project 59A was split into two parts. The new project 59A, being conducted at Georgia Institute of Technology (Georgia Tech), will examine the effects of different inlets and the introduction of noise reduction devices on the performance of selected engine cycles and geometries. The new project 59E focuses on the prediction of the flow and noise from different nozzle configurations, and is the work described in the present report.

Research Approach

Grid Generation, RANS, and LES Simulations

A computational mesh of the inner nozzle of the coannular nozzle geometry being used by Georgia Tech was provided by Gulfstream. The exit diameter of the nozzle is 40.64 mm. The grid originally used a trimmed hexagonal mesh with a base size of 4 mm. A conic refinement zone of base size 1 mm encapsulated the end of the nozzle and extended 0.4 m (approximately 10 jet diameters) beyond the nozzle exit. This refinement zone was necessary to capture the eddies present in the LES. However, simulations with this grid created a longer potential core and a steeper drop-off in a baseline RANS simulation than was present in the experiments. Figure 1 shows the trimmed hexagonal mesh with Mach number contours from a RANS simulation overlaid. The nozzle pressure ratio (NPR) was 1.86.

In view of the issues with trimmed hexagonal mesh, an unstructured, adaptive polyhedral mesh was used instead. This polyhedral mesh used the same base size of 4 mm and included the same 1-mm refinement zone around the nozzle exit, extending 0.4 m downstream. A larger volumetric control of 1 cm was used farther downstream of the nozzle. Both the previous mesh and this polyhedral mesh included four prism layers along the walls of the nozzle. The adaptive polyhedral mesh underwent two mesh refinement iterations and contained 41.6 million cells, whereas the trimmed hexagonal mesh contained 43.2 million cells. Figure 2 shows the adaptive polyhedral mesh with Mach number contours from a RANS simulation overlaid. The NPR was 1.86.

Figures 3 and 4 show a comparison of the predicted centerline and lipline velocity relative to the exit velocity as a function of downstream distance and the measurements by Bridges and Wernet (2010).

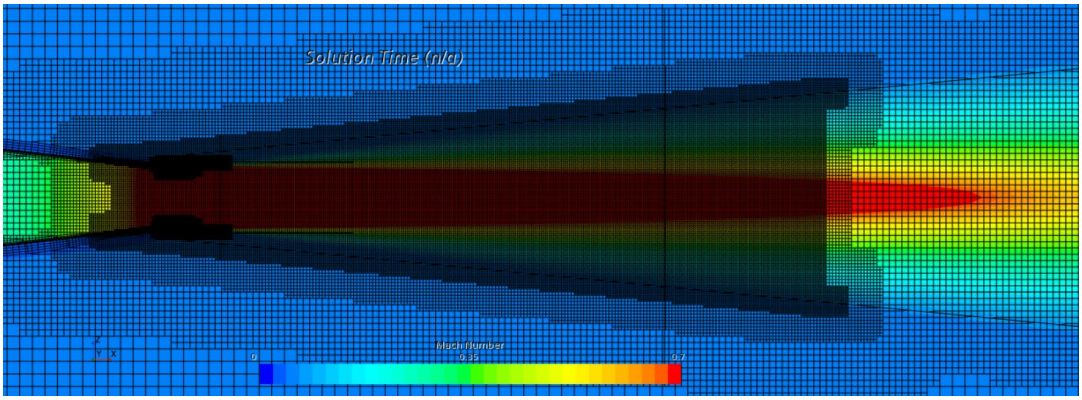

Figure 1. RANS simulation at NPR = 1.86 with the trimmed hexagonal mesh overlaid.

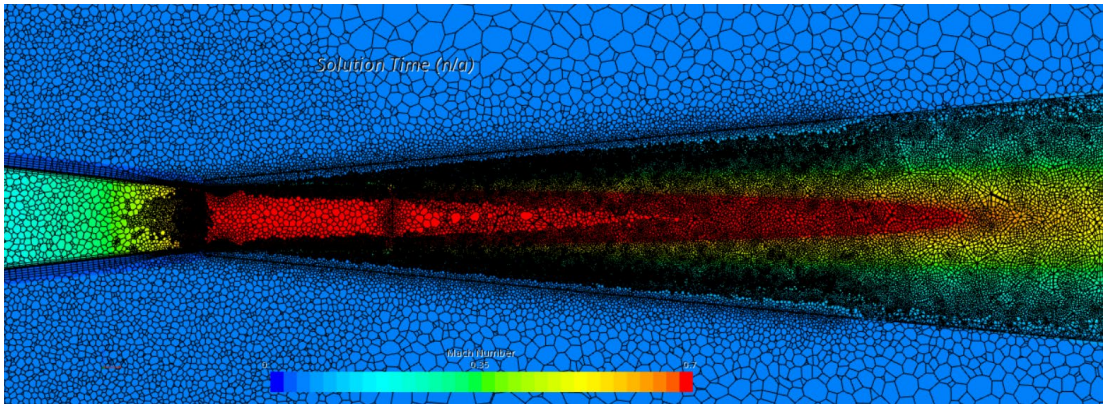

Figure 2. RANS simulation at NPR = 1.86 with the adaptive polyhedral mesh overlaid.

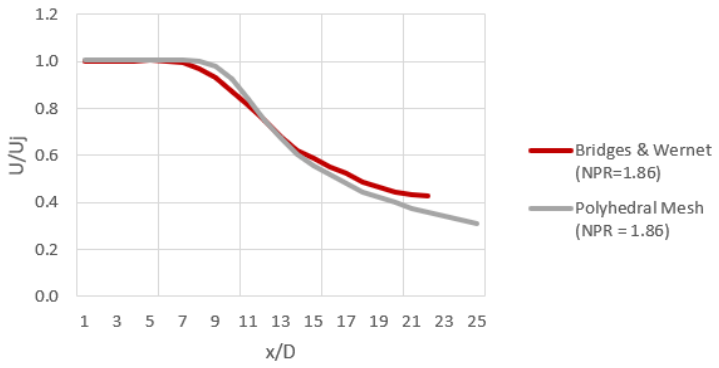

Figure 3. Comparison of experimental and simulation centerline axial mean U/U_j for the polyhedral mesh at NPR = 1.86.

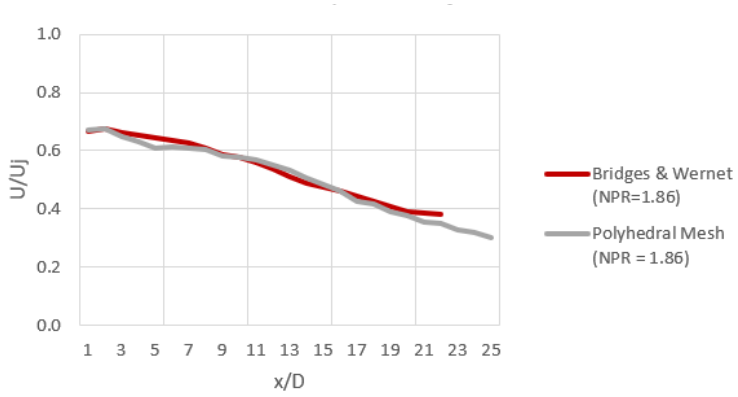

Figure 4. Comparison of experimental and simulation lipline U/U_j for the polyhedral mesh at NPR = 1.86.

The simulation with the polyhedral mesh was then run as an LES at NPR = 1.86 and Total temperature ratio, TTR = 1. It used a second-order temporal discretization with a time step of 2×10^{-6} s. Figure 1 shows instantaneous Mach number contours for NPR = 1.86 and TTR = 1.0.

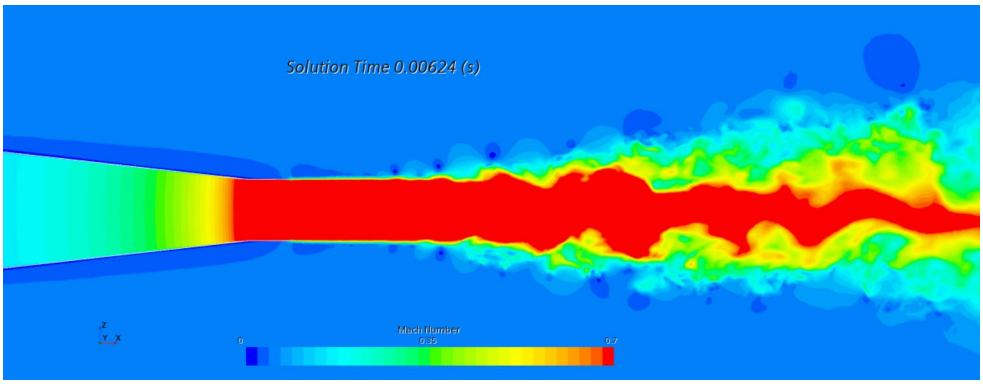

Figure 5. LES at NPR = 1.86 and TTR = 1 using the polyhedral mesh.

FW-H Data Extraction and Verification

A Python code was written for the FW-H calculations. The code performs two tasks. First, given the scattered spatiotemporal data extracted from the FW-H surface in STARCCM+, the code interpolates the data onto a multi-block structured grid, which consists of a conic surface surrounding the jet flow and a circular plane closing the cone in the downstream direction (Figure 6). To accurately interpolate the data on a curved surface, the 3D conic unstructured surface is first mapped to a 2D structured surface. The data are interpolated by cubic splines on the 2D surface, then mapped back to a 3D structure conic surface (Figure 7). Furthermore, the grid can be refined in regions where spatial variation is strong, e.g., near the nozzle.

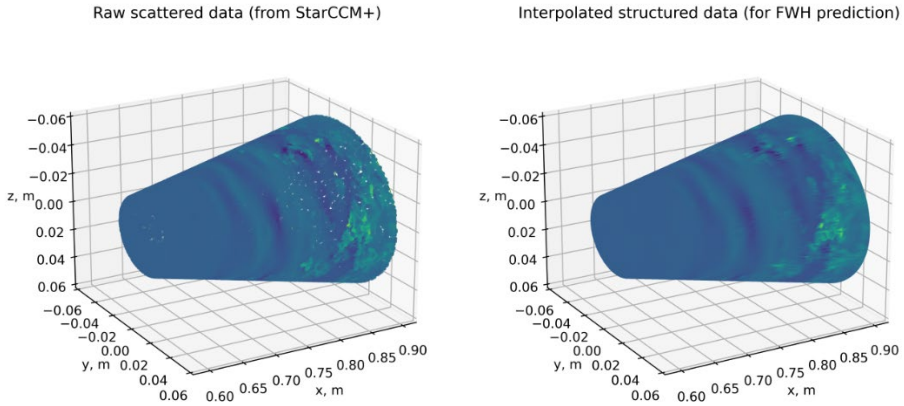

Figure 6. Illustration of the 3D FW-H surface at one time step, visualizing the density variation.

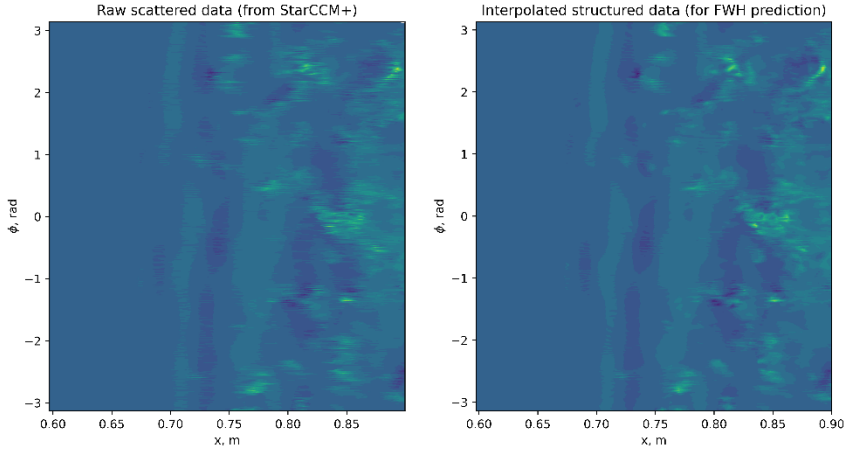

Figure 7. Illustration of the cubic interpolation on the mapped 2D structured surface.

Second, given the locations of observers, the FW-H code calculates the far-field acoustic pressure. The FW-H formulation is simplified, owing to the stationarity of the FW-H surface and the observers. Because the full LES data are currently being extracted from STARCCM+, the FW-H prediction was tested by using data synthesized from a monopole source placed at the origin (Figure 8), with multiple observer locations (Figure 9).

The FW-H prediction matches well with the analytical solutions at all observer locations, with errors less than 1.5% (Figure 10), and the error decreases as the grid is further refined. The test case verifies the correctness of FW-H code.

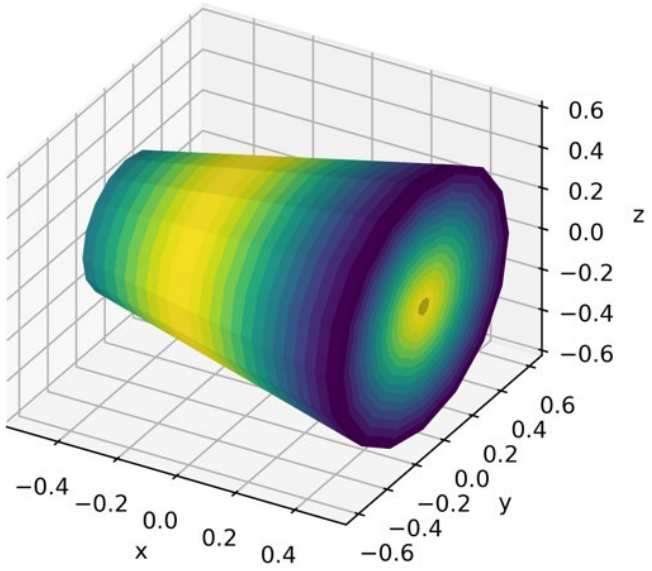

Figure 8. Pressure contours on the FW-H surface for a monopole source placed at the origin.

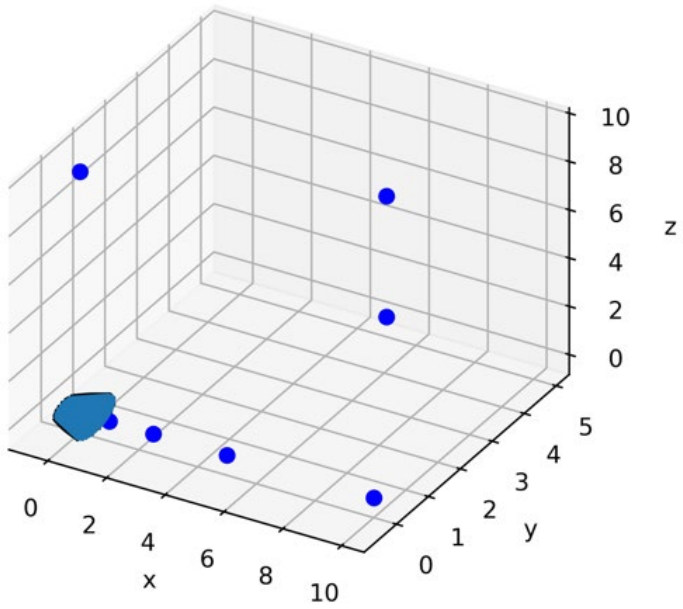

Figure 9. Observer locations (blue dots) with respect to the FW-H surface (cyan).

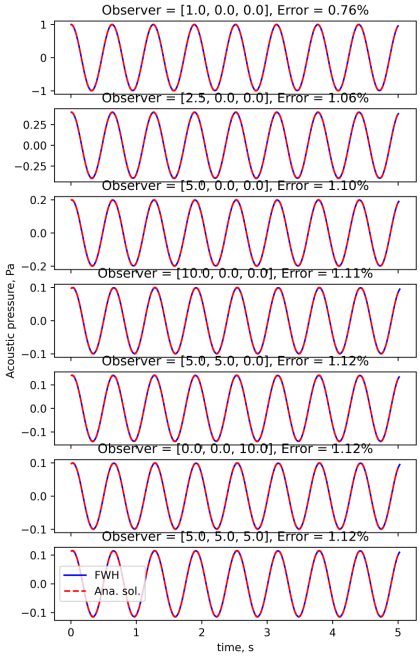

Figure 10. Comparison of FW-H predictions and analytical solutions at all observer locations.

RANS Solution for Dual-Stream Nozzle

A RANS simulation was conducted for the full dual-stream Georgia Tech nozzle geometry for an NPR of 1.39. Velocity magnitude contours are shown in Figure 11.

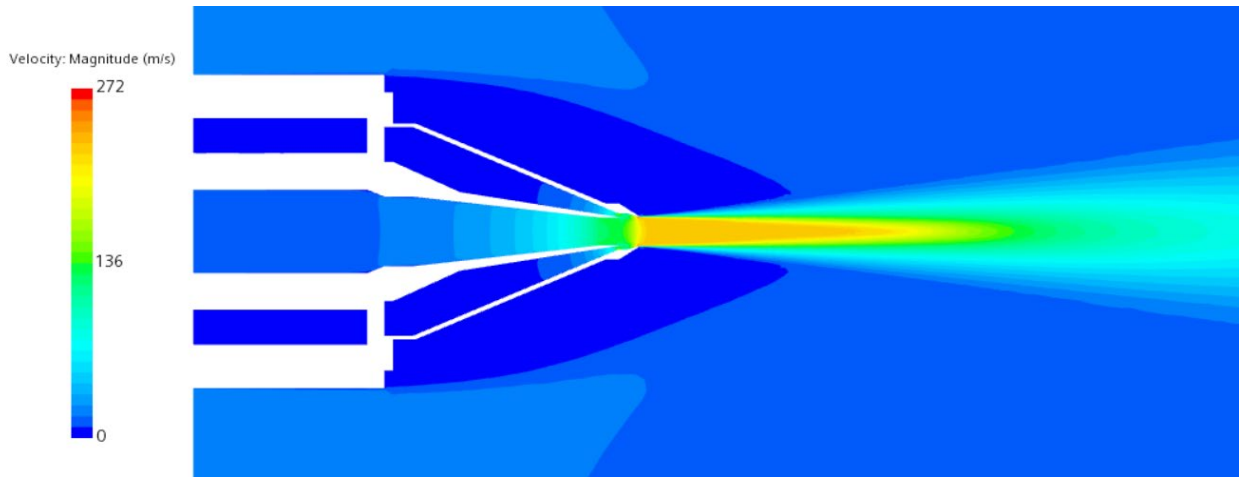

Figure 11. Velocity contours for the co-annular nozzle at NPR = 1.39 and TTR = 1.

The extracted centerline axial velocity (Figure 12) and the axial lipline velocity (Figure 13) showed good agreement with the experimental data provided by Georgia Tech for the same nozzle geometry.

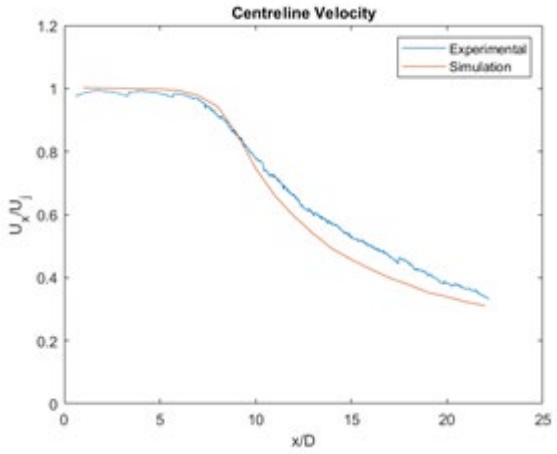

Figure 12. Comparison of centerline axial velocity at NPR = 1.39 and TTR = 1 from experiments provided by Georgia Tech and RANS simulations using STARCCM+.

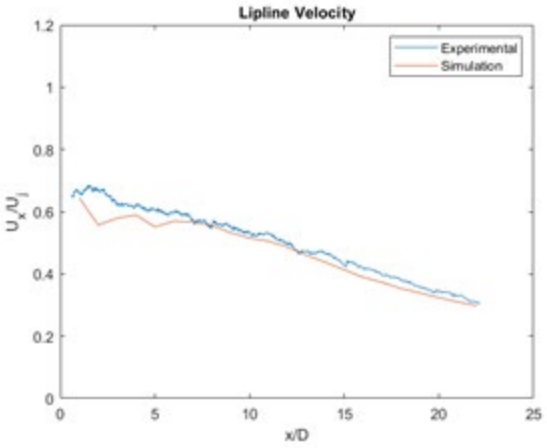

Figure 13. Comparison of lipline axial velocity at NPR = 1.39 and TTR = 1 from experiments provided by Georgia Tech and RANS simulations using STARCCM+

Acoustic Analogy for High-Strouhal-Number Predictions

The frequency range of interest for aircraft certification is 50 Hz to 10000 Hz. For full-scale engines, Strouhal numbers from 0.1 to 100 are included (Viswanathan, 2018). Quite recent LESs of subsonic jet noise by Brès et al. (2018) have indicated that LESs with 69-M control volumes and nozzle interior turbulence modeling can achieve an upper-Strouhal-number limit of 4 (additional information in Brs, et al. (2019)). This value remains well below the upper-Strouhal-number limit required for aircraft certification.

In principle, methods based on acoustic analogies have no Strouhal-number-range limit, but their accuracy depends on correct modeling of the statistical properties of the equivalent noise sources and the accurate evaluation of the sound propagation through the non-uniform jet flow. Many methods have successfully made predictions of the radiated noise at 90˚ to the jet axis.

The widely used MGBK method (for example, Khavaran, et al. (1994) and many subsequent references) uses steady CFD to provide a model for the mean flow and the turbulence scales. In a departure from the usual approach based on an acoustic analogy, Tam and Auriault (1999) have provided a physics-based model for the noise from the fine-scale turbulence. A generalized acoustic analogy was developed by Goldstein (2003), and Goldstein and Lieb (2008) have demonstrated good agreement with noise measurements for convectively subsonic flows. Subsequent extensions of Goldstein's generalized acoustic analogy (for example, by Karabasov et al. (2010)) have used complementary LESs to indicate the relative strengths of the quadrupole equivalent source terms that appear in the acoustic analogy. This last approach prompts the question of why an acoustic analogy is needed for an LES of the unsteady jet flow. In addition, if LES is used to describe source characteristic noise, both fine-scale and large-scale turbulence are included.

The aim of the present research is to develop an efficient model describing the high-frequency behavior of the radiated noise. The approach uses an acoustic analogy to predict the noise from the fine-scale turbulence, and uses LES to predict the lower frequencies (Strouhal numbers). Initially, we are using Tam and Auriault's (1999) approach. Figure 14 shows a prediction of noise at 90˚ to the jet axis by using Tam and Auriault's model (1999). The agreement with measurements by Bridges and Brown (2005) is very good, except at high frequencies.

Ongoing work involves reassessing the modeling coefficients in the Tam and Auriault model, with a goal of matching the spectral density's high-frequency behavior at all angles. The purpose is to model the fluctuations responsible for the high-frequency noise rather than the noise generated by all scales.

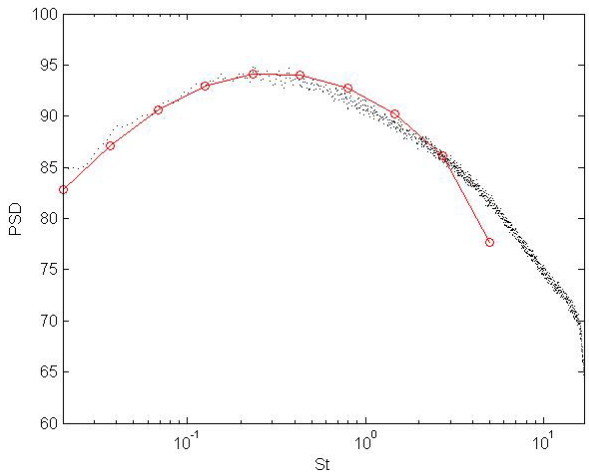

Figure 14. Comparison of predictions (red) with experimental results (black) at 90˚ to the jet axis. *Mj* = 1.0, TTR = 1.0

Major Accomplishments

The tasks for the second project year included continued RANS simulations as well as LES. The focus was initially on the Georgia Tech inner nozzle. Subsequent calculations used, or are using, a first internal mixer case. In addition, acoustic-analogy-based predictions are underway, and are aimed at predicting very high frequencies that are important for noise certification assessments. Finally, a code has been developed for far-field noise prediction using LES simulation data and verified with a synthetic benchmark problem.

Publications
None.

Outreach Efforts
ASCENT Advisory Board Meeting.

Awards
None.

Student Involvement
For the second year, the Pennsylvania State University team included one graduate research assistant. Ms. Dana Mikkelsen has been the lead on the computational fluid dynamics simulations and will continue in this role for the remainder of the project.

Plans for Next Period
During the next research period, a RANS solution will be obtained for an internal mixer nozzle (Figure 15). This solution will be compared with experimental data and will provide a baseline characterization of the flow; it will then be used as a basis of comparison for subsequent moderate-fidelity simulations.

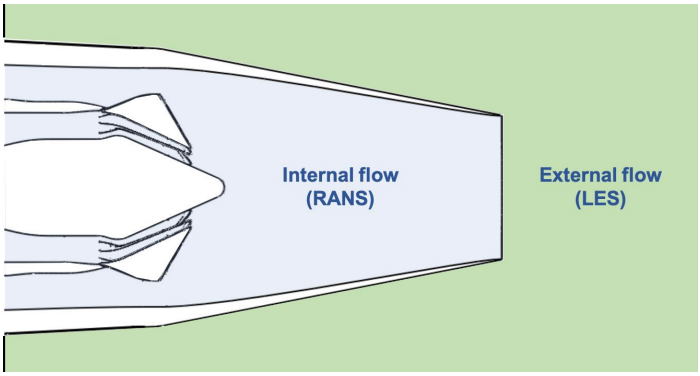

Figure 15. Sketch of the dual-stream, internally mixed plug nozzle with lobed mixer. 122Am5plnt (Bridges and Wernet, 2021).

A grid for an LES solution will then be developed, and a moderate-fidelity solution will be obtained by using the RANS solution as an initial condition at the jet exit. The LES solution will provide the unsteady flow information needed for the next task, in which the FW-H analogy will be used to calculate the far-field noise for the internal mixer nozzle.

The code detailed in an earlier section will be used to extract data from the FW-H surface in STARCCM+ and interpolate it onto a structured conical surface. The FW-H analogy will be used to calculate the far-field noise. The far-field predictions will be in the form of overall sound pressure level and power spectral densities, and these predictions will be compared with experimental data. Adjustments to parameters such as grid resolution may be made. These tasks will then be repeated for an external plug nozzle with an internal mixer (Figure 16).

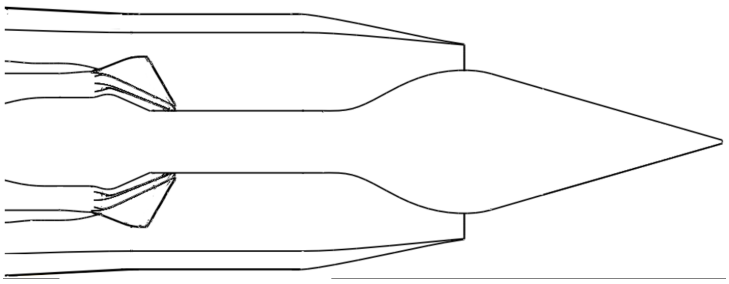

Figure 16. Sketch of external plug nozzle with short mixing duct (Bridges and Wernet, 2021).

As noted above, the Tam and Auriault method for fine-scale noise prediction will be modified, and probably extended, to enable the prediction of the high-frequency noise radiation. This approach will be applied to all geometries considered.

Table 1 shows the anticipated list of milestones for the next research period.

Table 1. Anticipated tasks and milestones for the next research period.

Task No.	Milestone	Planned due date
Task 1	Internal mixer nozzle RANS solution and comparisons with measurements completed	February 15, 2022
Task 2	Internal mixer nozzle moderate-fidelity solution completed	April 30, 2022
Task 3	Internal mixer nozzle noise predictions and comparisons with measurements completed	May 31, 2023
Task 4	Grids for moderate-fidelity simulation of external plug nozzle with internal mixer completed	June 31, 2023
Task 5	External plug nozzle moderate-fidelity solution completed	August 31, 2023
Task 6	External plug nozzle noise predictions and comparisons with measurements completed	October 31, 2023
Task 7	Extension of acoustic analogy to predict high Strouhal numbers	October 31, 2023
Task 8	Annual ASCENT report submitted	November 30, 2023

References

Farrasat, F. & Succi, G.P. (1983). The prediction of helicopter rotor discrete frequency noise. *Vertica, 7* (4), 497-507.

J. E. Ffowcs Williams, & Hawkings, D. L. (1969). Sound Generation by Turbulence and Surfaces in Arbitrary Motion. *Philosophical Transactions of the Royal Society of London. Series A, Mathematical and Physical Sciences*, *264*(1151), 321–342. http://www.jstor.org/stable/73790

Bridges, J., & Wernet, M. (2010, June 7). Establishing consensus turbulence statistics for hot subsonic jets. *16th AIAA/CEAS Aeroacoustics Conference*. 16th AIAA/CEAS Aeroacoustics Conference, Stockholm, Sweden. https://doi.org/10.2514/6.20

Viswanathan, K. (2018). Progress in prediction of jet noise and quantification of aircraft/engine noise components. *International Journal of Aeroacoustics*, *17*(4–5), 339–379. https://doi.org/10.1177/1475472X18778279

Brès, G., Jordan, P., Jaunet, V., Le Rallic, M., Cavalieri, A., Towne, A., . . . Schmidt, O. (2018). Importance of the nozzle-exit boundary-layer state in subsonic turbulent jets. *Journal of Fluid Mechanics, 851*, 83-124. doi:10.1017/jfm.2018.476

Brès, G. A., & Lele, S. K. (2019). Modelling of jet noise: A perspective from large-eddy simulations. *Philosophical Transactions of the Royal Society A: Mathematical, Physical and Engineering Sciences*, *377*(2159), 20190081. https://doi.org/10.1098/rsta.2019.0081

Khavaran, A., Krejsa, E. A., & Kim, C. M. (1994). Computation of supersonic jet mixing noise for an axisymmetric convergent-

divergent nozzle. *Journal of Aircraft*, *31*(3), 603–609. https://doi.org/10.2514/3.46537
Tam, C. K. W., & Auriault, L. (1999). Jet mixing noise from fine-scale turbulence. *AIAA Journal*, *37*(2), 145–153. https://doi.org/10.2514/2.691
Goldstein, M. E. (2003). A generalized acoustic analogy. *Journal of Fluid Mechanics*, *488*, 315–333. https://doi.org/10.1017/S0022112003004890
Goldstein, M. E., & Leib, S. J. (2008). The aeroacoustics of slowly diverging supersonic jets. *Journal of Fluid Mechanics*, *600*, 291–337. https://doi.org/10.1017/S0022112008000311
Karabasov, S. A., Afsar, M. Z., Hynes, T. P., Dowling, A. P., McMullan, W. A., Pokora, C. D., Page, G. J., & McGuirk, J. J. (2010). Jet noise: Acoustic analogy informed by large eddy simulation. *AIAA Journal*, *48*(7), 1312–1325. https://doi.org/10.2514/1.44689
Bridges, J., & Brown, C. (2005, May 23). Validation of the small hot jet acoustic rig for aeroacoustic research. *11th AIAA/CEAS Aeroacoustics Conference*. 11th AIAA/CEAS Aeroacoustics Conference, Monterey, California. https://doi.org/10.2514/6.2005-2846
Bridges, J. E., & Wernet, M. P. (2021, August 2). Noise of internally mixed exhaust systems with external plug for supersonic transport applications. *AIAA AVIATION 2021 FORUM*. AIAA AVIATION 2021 FORUM, VIRTUAL EVENT. https://doi.org/10.2514/6.2021-2218

Project 060 Analytical Methods for Expanding the AEDT Aircraft FLEET Database

Georgia Institute of Technology

Project Lead Investigator

Dimitri N. Mavris
Director, Aerospace Systems Design Laboratory
School of Aerospace Engineering
Georgia Institute of Technology
270 Ferst Drive, Mail Stop 0150
Atlanta, GA 30332-0150
404-894-1557
dimitri.mavris@ae.gatech.edu

University Participants

Georgia Institute of Technology

- P.I.: Professor Dimitri Mavris
- FAA Award Number: 13-C-AJFE-GIT-104
- Period of Performance: October 1, 2021 to September 30, 2022
- Tasks:
    1. Identification and review of aircraft not in the Aviation Environmental Design Tool (AEDT)
    2. Analytical method development

Project Funding Level

The current FAA funding for this project is $150,001 from October 1, 2021 to September 30, 2022. The Georgia Institute of Technology has agreed to a total of $150,001 in matching funds.

Investigation Team for All Tasks

- Dr. Dimitri Mavris (P.I.), Georgia Institute of Technology
- Dr. Michelle R. Kirby, Georgia Institute of Technology
- Dr. Mayank Bendarkar, Georgia Institute of Technology
- Dr. Dushhyanth Rajaram, Georgia Institute of Technology
- Dr. Ameya Behere, Georgia Institute of Technology
- Styliani I. Kampezidou (graduate student), Georgia Institute of Technology
- Cristian Puebla-Menne (graduate student), Georgia Institute of Technology

Project Overview

The AEDT relies on aircraft noise and performance (ANP) data provided by aircraft manufacturers to support the calculation of aircraft trajectories and noise at receptors by using aircraft performance information and noise-power-distance (NPD) relationships for specific aircraft/engine combinations. In the ANP/Base of Aircraft Data (BADA) workflow, ANP performance data are also used in the calculation of emissions inventories and air quality dispersion. However, not all aircraft in the fleet are represented in the ANP database. When ANP data are not available for a specific target engine/airframe combination, AEDT uses a substitute aircraft from the ANP database to model the target aircraft by closely matching the certification noise characteristics and other performance parameters. However, a problematic issue is that the best substitute according to noise criteria does not always match the best substitute for emissions criteria. In addition, substitute aircraft do not capture the environmental benefits of newer aircraft with noise and emissions reduction technologies, thus resulting in overly conservative noise and emissions estimates.

The goal of this research is to improve the accuracy of AEDT noise and emissions modeling of aircraft not currently in the ANP database. Georgia Institute of Technology will identify and review aircraft not currently modeled in the AEDT and will collect information and necessary data to better understand the characteristics of these aircraft. Various statistical analysis methods will be used to classify the aircraft as different types in terms of size, age, technologies, and other engine/airframe parameters. Quantitative and qualitative analytical methods will be identified and evaluated for each aircraft type to develop ANP and noise data for the aircraft. Validation data from real-world flight and physics-based modeling will be gathered to validate the methods. After validation, the models will be applied to develop ANP and noise data for the aircraft. Finally, recommendations and guidelines will be developed for implementing the developed data in the AEDT, to expand the AEDT Fleet database to include noise and performance data for aircraft currently not in the ANP database.

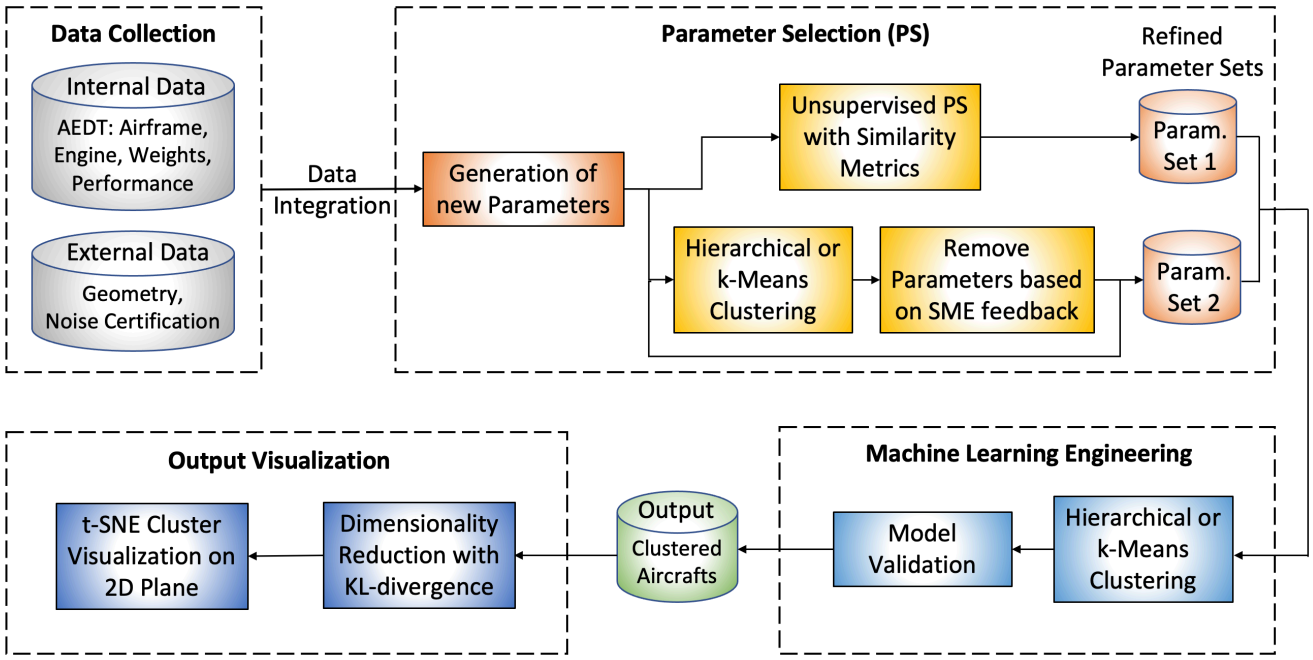

Figure 1. Overview of ASCENT Project 60 tasks and workflow.

The flowchart in Figure 1 presents an overview of the project approach. The first step is to identify the necessary aircraft parameters that will be used to better estimate the substitution aircraft. These parameters are already included in the internal data (Fleet database) or will be collected from external resources.

Task 1 - Identification and Review of Aircraft not in the AEDT

Georgia Institute of Technology

Objective

The objective of Task 1 is to identify aircraft that are not currently modeled with ANP data in the AEDT for noise and emissions modeling. In the Fleet database, specific aircraft engine/airframe combinations are defined by a series of ANP and noise coefficients that are used with the BADA and SAE-AIR-1845 algorithms to conduct performance, emissions, and noise modeling. The Fleet database contains representative aircraft for the entire fleet; some aircraft are modeled according to ANP data, whereas others are represented by a substitution aircraft. This task involves the identification of aircraft that do not have ANP data and are represented by a substitution aircraft.

Research Approach

Creating the AEDT FLEET Extension Database

Aircraft without ANP data in AEDT

The aircraft not currently modeled with ANP data are identified by reviewing the AEDT Fleet database and conducting a literature survey. The identified aircraft of interest are further investigated to identify gaps between them and the substitution aircraft in terms of performance, noise, and emissions. This step involves reviewing the existing literature on these aircraft and acquiring the information and data necessary to better determine their engine/airframe characteristics. In addition, the ANP data in the Fleet database are studied to summarize key parameters for which the analytical methods will develop ANP data. The existing ANP aircraft substitution methods and the current substitution methods implemented in AEDT are also investigated to support the development of analytical methods.

The Fleet database consists of 3,626 airframe and engine combinations; only 269 have available ANP data (native), whereas the remaining 3,357 do not (proxy). The proxy aircraft have a unique equipment ID (the primary key in the SQL database) and a default equipment ID, which is assigned as the equipment ID of the closest native aircraft, in terms of ANP similarity. Apparently, the native aircraft have a matching equipment ID and default equipment ID. This substitution enables proxy aircraft to borrow ANP data from native aircraft for the purposes of conducting environmental analyses and studies. Figure 2 below illustrates the Fleet database breakdown in terms of ANP data availability as well as the current efforts in extending the available parameters. The additional parameters collected from external resources are summarized in Table 1.

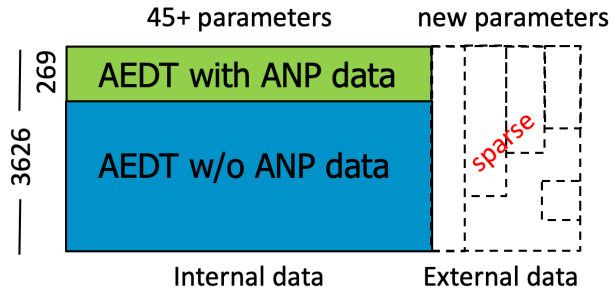

Figure 2. Fleet database breakdown with respect to ANP data availability.

Aircraft Database Literature Study

The main objective of this task is to collect data from various databases for a wide range of aircraft. This information is helpful in determining which performance, emissions, and noise parameters will be used for the substitution algorithm. In particular, we are interested in the following categories of data:

- **Airframe**: general aircraft information and classifications; example: maximum range
- **Engine**: important engine specifications; example: bypass ratio
- **Aircraft**: information on an airframe/engine combination; example: maximum takeoff weight (MTOW)
- **Aircraft geometry**: example: wing area
- **Emissions**: main emission indices; example: unadjusted fuel flow during takeoff
- **Noise certification**: example: flyover noise level

Overview of Tables Available in the Fleet database (Internal Data) and Associated IDs:

Some of the internal data collected from the Fleet database correspond to:

- FLT_EQUIPMENT (provides the AIRFRAME_ID and ENGINE_ID for each equipment EQUIP_ID)
- FLT_AIRFRAMES (contains airframe information that can be accessed by using the AIRFRAME_ID from the corresponding EQUIP_ID in the FLT_EQUIPMENT table)
- FLT_ANP_AIRPLANES
- FLT_FLEET
- FLT_ENGINES (contains information on engines and emissions that can be retrieved by using the ENGINE_ID from the corresponding EQUIP_ID in the FLT_EQUIPMENT table)
- FLT_ENGINES.MODEL
- FLT_CAT_DESIGNATIONS

- FLT_CAT_ICAO_TYPES
- FLT_BADA_ACFT
- FLT_ANP_AIRPLANE_NOISE_GROUPS
- FLT_NOISE_CERTIFICATION

The Fleet database contains 3,626 EQUIP_IDs, 848 unique AIRFRAME_IDs and 686 unique ENGINE_IDs. The FLT_NOISE_CERTIFICATION table has a total of 8,288 records (rows). Among the 3,626 equipment types, only 535 (15%) have noise certification records. All these records have a one-to-many match; i.e., for a certain equipment type, multiple matches exist in the FLT_NOISE_CERTIFICATION table. The number of matches ranges from 2 to more than 100. Efforts by the FAA to identify a unique path from EQUIPMENT_IDs to unique NOISEDB_IDs are ongoing; hence, our team will focus on collecting noise parameter values from up-to-date reliable external data sources. Regarding noise parameter values from the Fleet database, two potential routes for retrieving NOISEDB_IDs are proposed in Figure 3.

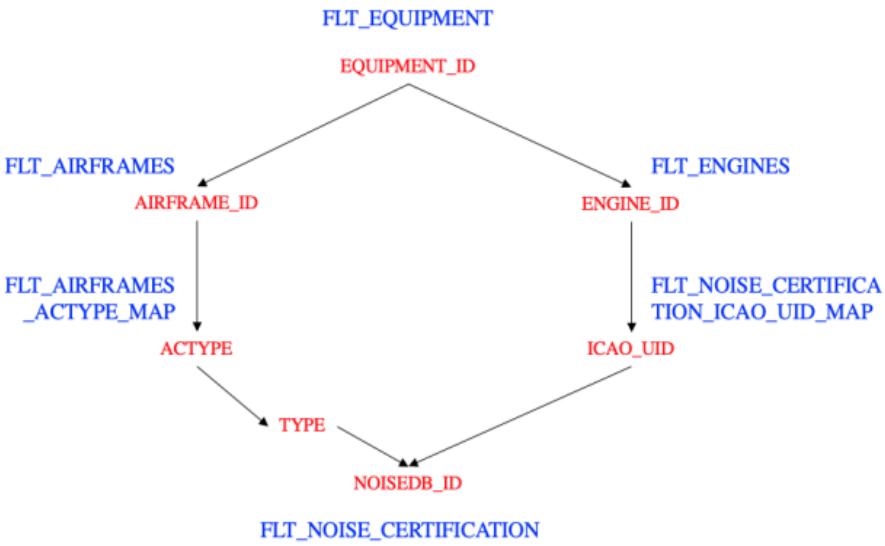

Figure 3. Two alternative Fleet database routes for identifying the one-to-many choices from EQUIPMENT_ID to NOISEDB_ID.

To create an initial database to use for the analytical methods in Task 2, we applied filtering to the original number of unique equipment IDs to establish a subset of engine/airframe combinations for which external data would be gathered. The first filter eliminated the military and cargo designation codes and small SIZE_CODE aircraft. The next filter eliminated military and general aviation, according to the AIRCRAFT_TYPE designation. This filtering reduced the unique equipment IDs to 2,443. For the remaining EQUIP_IDs, the AIRFRAME_MODEL names were grouped to determine the number of unique airframes. With an initial focus on U.S. applications of AEDT, airframe models not operated in the United States and the production status of the airframe models were eliminated. For future efforts of this research, a broader set of aircraft types can be included to extend beyond U.S. operations. These filters reduced the total airframes for which external data are required to a manageable number of 138. Notably, each airframe could have multiple engine types.

Data Sources Used

The external databases used to extend AEDT's available parameters are summarized in Table 1 below. To augment the existing ANP database for the unique engine/airframe combinations that do not have ANP data, we identified external data sources. The databases considered to populate the extended Fleet database table (Figure 2) are provided below. First, information from the internal Fleet database was used, and then, various other databases were retrieved to populate the external parameters:

- AEDT ANP (Fleet + FLEET-FULL databases): The Fleet database, the most comprehensive performance database available, contains multiple performance parameters for a wide variety of airframe/engine combinations. Although it is not publicly available, the FLEET-FULL database contains information for all registered aircraft worldwide.

Minimum and maximum values for the same airframe/engine combinations are available for certain aircraft parameters (e.g., MTOW), depending on the aircraft equipment used by an airline on board.

- Janes: This database contains aircraft information such as certification date, weight, range, production date, and status, as well as corresponding engine information (i.e., thrust, number of engines, power, and speed). This database also contains wing and fuselage dimensions, maximum payload, and number of passengers (Janes, n.d.)
- EASA Emissions Databank v28 (EASA, 2023) This Microsoft Excel-based database covers turbojet and turbofan engines for which emissions are regulated (static thrust of 27 kN or higher). It contains engine emissions for CO, nitrogen oxides (NO_x), and unburned hydrocarbons as well as several engine performance parameters, including bypass ratio and thrust-rated output
- Jet Engines: This database contains engine information only, such as thrust type, SFC type, airflow, overall pressure ratio, fan pressure ratio, bypass ratio, speed, and engine dimensions (Meier, 2021).
- Piano v2.2: This database contains aircraft and engine combination data, including wing and fuselage dimension information, weight, payload, and specific air range evaluations (Lissys Ltd., n.d.)
- European Union Aviation Safety Agency (EASA) Type Certificate Data Sheet (TCDS): This database contains aircraft-specific variants and designation of the engines certified on the aircraft, in addition to geometric and performance information. (EASA 2023).
- Bluebook: This database contains aircraft/engine combination information, such as thrust, maximum speed, recommended speed, stall speed dirty, fuel, gross weight, empty weight, range, length, height, and wingspan
- Elsevier: This database contains aircraft and engine information, including thrust, number of passengers, weight, payload, fuselage dimensions, and wing dimensions (Jenkinson, et al., 2001a; Jenkinson, et al., 2001b).
- EASA certification noise databases (EASA, 2023) https://www.easa.europa.eu/en/domains/environment/easa-certification-noise-levels. This very large Excel database consists of aircraft/engine types, effective perceived noise in decibels (EPNdB), and noise levels for lateral, flyover, and approach. EASA is a collection of four noise databases that address heavy propeller-driven airplanes, jet airplanes, light propeller-driven airplanes, and rotorcraft
- DGACv2.30: This noise certification database offered by French authorities will be used along with EASA noise certification values to collect up-to-date noise certification levels (NoisedB, 2023).
- Online photographic material: For the purposes of identifying wingtip presence, wing location, and engine location, pictures available online have been considered.

According to engineering judgement and prior research on key drivers of noise, emissions, and fuel burn, a set of parameters to define a unique engine/airframe combination were established, which include internal AEDT data and external data. The purpose of the additional parameters is to enhance the information for a particular combination, so that a better substitute aircraft can be identified to represent the environmental impact of that combination (performance, noise, and emissions). In Table 1, the first column indicates the broader parameter group; the second column provides the parameter details, which could be an existing Fleet database parameter or a newly added one; and the third column shows internal or external resources from where the parameters were collected. This ANP extension database will serve as the basis for the analytical method approach in Task 2.

Table 1. Summary of external data sources used to extend the AEDT FLEET database.

Parameter group	Collected parameters	Resources
Performance	Typical cruise speed, typical range	Jet Engines, Piano, Janes, Bluebook, public resources
Weights	Maximum payload	Piano, Janes, Elsevier
Geometry	Wingspan, wing area, fuselage height/ width/length, typical number of passengers	Piano, Janes, Bluebook, public resources
Engine	B/P ratio, pressure ratio, thrust, emissions	Jet Engines, Piano, Janes, Elsevier, International Civil Aviation Organization Engine Emissions Databank, Purdue Engineering, Campbell Hill
Noise	Flyover, lateral, approach	EASA noise database

To populate ANP database with noise data, we used two sources from EASA certification noise level database (EASA, 2023).For jet airframe/engine combinations, MAdB Jets (210408) and its updated version, MAdB Jets (20220331), were used; for propeller-driven aircraft, MAdB Heavy Prop (21325) was used. The data extracted from these sources consisted of the following information:

- Lateral noise level
- Flyover noise level
- Approach noise level

In each case, along with the noise level, the limit, the margin as well as cumulative noise values in EPNdB units were extracted. The methods used for matching comprised the following steps. In the ANP database, a total of 996 airframe/engine candidate combinations for noise data population was selected. The population procedure was started by selecting a specific airframe of interest (for example, the Airbus A321-200 Series). For that airframe, a specific engine among the different options available was selected (for example, the CFM56-5B3/2P). After the specific airframe/engine combination was defined, the exact same combination was searched and selected in EASA certification noise level database. For matching to be performed, the selected airframe/engine combination in EASA was required to be unique. To ensure this unique matching, we used a set of successive selection criteria involving the following sequence of steps:

- Use the EASA TCDS to verify that the variants existing in the EASA certification noise level database (e.g., MAdB Jets) for the airframe selected are certified.
- Use the EASA TCDS to verify that the engine emissions and thrust parameters in the ANP database are correct.
- When differences are found, they are identified and registered by matching the ANP Equipment ID and EASA Record number.
- For the certified airframe/engine combination in the EASA certification noise level database, select the MTOW.
- If no unique combination is obtained, proceed to select the maximum landing mass.
- If the combination still has more than one option, the maximum cumulative noise level can be selected.
- In cases in which more than one airframe/engine combination have the same noise values, the first entry is selected.
- Finally, if more than one combination remains after the application of the preceding criteria, the most recent modification date for the data of the remaining combinations is selected. This modification date corresponds to the most recent date when the existing values for the selected combination were entered in the database.

The rationale underlying these selection criteria is to choose the most representative noise value of the combination selected. After a unique combination is found, the corresponding noise values are transferred from the EASA database to ANP. To increase the number of combinations available for which noise values were obtained, engines with similar designation codes were selected for some airframes. In this case, the criterion for selection was a direct comparison of the main parameters (bypass ratio, overall pressure ratio, and rated thrust) of the similar engines. If the parameters were within 5% of each other, the combination was considered valid and was added to the ANP database. The application of these criteria enabled the generation of the noise values for the airframe/engine combinations used in Task 2.

Challenges in Data Integration

Multiple challenges exist in collecting data from external resources and integrating them into the extended AEDT table:

- The data quality from websites other than those of the FAA, manufacturers, or certification organizations may be questionable.
- The external data are sparse, thus generating challenges for machine learning (ML) model training.
- The integration of multiple databases can be labor-intensive, unless automation is introduced to bypass it.

After incorporation of noise parameter values for flyover, lateral and approach noise from the EASA certification noise level database, the number of available airframe and engine combinations was only 438.

Milestone(s)

Developed a framework for new external data to be used in Task 2

Major Accomplishments

Populated new extension database and created additional certification database

Publications

None

Outreach Efforts
Biweekly calls
Bi-annual ASCENT meetings

Awards
None

Student Involvement
Styliani I. Kampezidou (graduate student)
Cristian Puebla-Menne (graduate student

Plans for Next Period
Continue gathering certification data

References
Cirium. (n.d.) *Aviation Analytics.* https://www.cirium.com/
Janes | Login for world leading open source defense intelligence. (n.d.). https://customer.janes.com/janes/home
European Union Aviation Safety Agency. (2023). *ICAO Aircraft Engine Emissions Databank.* https://www.easa.europa.eu/domains/environment/icao-aircraft-engine-emissions-databank
Meier, N. (2021). *Jet Engine Specification Database.* http://www.jet-engine.net/
Lissys Ltd. (n.d.) *Piano's Aircraft Database.* https://www.lissys.uk/dbase.html
Aircraft Bluebook. (2023). *Aircraft Bluebook – Spring 2023 Vol. 23-01.* https://aircraftbluebook.com/Tools/ABB/ShowSpecifications.do
Jenkinson, L., Simpkin, P., Rhodes, D. (2001). *Civil Jet Aircraft Design: Aircraft Data A File.* https://booksite.elsevier.com/9780340741528/appendices/data-a/default.htm
Jenkinson, L., Simpkin, P., Rhodes, D. (2001). *Civil Jet Aircraft Design: Aircraft Data B File.* https://booksite.elsevier.com/9780340741528/appendices/data-b/default.htm
European Union Aviation Safety Agency. (2023). *EASA Certification Noise Levels.* https://www.easa.europa.eu/en/domains/environment/easa-certification-noise-levels
NoisedB. (2023). *Noise Certification Database Version 2.34.* https://noisedb.stac.aviation-civile.gouv.fr/bdd
Aircraft Bluebook. (2023). *Aircraft Bluebook – Spring 2023 Vol. 23-01.* https://aircraftbluebook.com/Tools/ABB/ShowSpecifications.do
European Union Aviation Safety Agency. (2023). *EASA Certification Noise Levels.* https://www.easa.europa.eu/en/domains/environment/easa-certification-noise-levels

Task 2 - Analytical Method Development
Georgia Institute of Technology

Objective
The objective of Task 2 is to develop analytical methods and solutions that can improve the modeling of aircraft types (airframe/engine combinations) that are not included in the ANP database. In this process, ML and data mining (DM) approaches are used to analyze aircraft features (both internally and externally collected), ANP data, and environmental output data, as well as to gain insights and evidence of better model substitution and approximation. The following research questions can be answered while developing these more advanced analytical methods:

- How can substitutions be better assigned for aircraft types not included in the ANP database?
- How can representative aircraft models be better chosen to develop more ANP data, with the aim of more sufficiently covering the entire population?
- Which aircraft features should be used in the identification of aircraft substitution?
- How can the current ANP data be better utilized to approximate the remaining aircraft with more flexibility?

Research Approach
The data-driven analytical methods used in this task are based primarily on ML and DM techniques. The solution for each research question consists of multiple ML/DM algorithms. In general, the analytical techniques that are useful in this project

can be classified into five categories: clustering, dimensionality reduction, regression, feature selection, and data visualization. Table 2 presents examples and objectives for all five categories.

In this project, the data collection and integration (Task 1) and analytical method development (Task 2) have been conducted in parallel. The proposed analytical approaches have been applied to selected problems. However, notably, because the master data set has not yet been finalized, as described in previous sections, the concepts of the analytical methods are demonstrated primarily through notional or incomplete data sets. The present report highlights the progress made over the past year and is not cumulative.

The method is outlined in Figure 1. It begins with a data fusion step, wherein different data sources are queried and merged with the AEDT Fleet database to create the ANP Extension database, as explained in Task 1. The resulting database contains 3,626 airframe engine combinations with 112 columns. The total number of airplanes with NO_x emission data is 2,361 which decreases to 520 when noise data are also included. Of these, 269 aircraft have data from the ANP database.

Three broad areas will be explored to synthesize ANP data for aircraft lacking these data. The first step is to explore unsupervised clustering to group similar aircraft by using the enriched data set from Task 1. Native aircraft (with ANP data) within each cluster can be considered potential substitutes for other aircraft without ANP data within each cluster. Clustering also aids in identifying outliers in the data and correcting the data entries for any potential errors.

A second approach potentially customizes ANP data by using statistical techniques and regressions to enable more flexible synthesis for ANP data rather than the currently used one-to-one substitution for aircraft without ANP data. The third approach in Figure 1 will explore hybrid models, wherein a composite model of multiple closest ANP aircraft is used to synthesize ANP data for non-native aircraft in AEDT. This approach is currently being developed and will be included in future work.

Using Clustering to Identify Representative Aircraft Model Portfolios

Groups of similar aircraft are placed in the same cluster, and dissimilar aircraft are placed in other clusters. Clustering is a typical task in unsupervised ML, and extensive methods have been reported in the literature. The choice of a specific clustering algorithm depends on the objectives of the problem. In this project, clustering can be used to achieve at least two aims. The first aim is to group similar aircraft and compare the results with the current ANP aircraft substitutions to improve the current substitution mapping and to identify gaps. Many algorithms in the literature, such as *k*-means (KM), hierarchical clustering, and DBSCAN, can all achieve this objective. The second aim is to select representative aircraft types from the population through clustering. In a basic process, all *n* aircraft are first partitioned into *k* clusters; one aircraft from each cluster is then selected to represent all aircraft in that cluster. Methods are also available for conducting clustering and representative aircraft selection simultaneously.

To categorize the airframe/engine combinations on the basis of the different parameters within the enriched data set, we use two clustering techniques: KM and agglomerative hierarchical clustering (AHC). In the present work, aircraft with similar performance, geometry, engine characteristics, noise, and emissions are grouped. The dimensionality of this task is equal to the number of parameters selected by using subject matter experts (SME) inputs, which are shown in Table 2. These parameters have been selected after multiple rounds of clustering experiments involving SME feedback. The effects of the parameters on the physics of noise propagation and their correlation with other parameters in Table 1 were considered.

Table 2. Selected SME parameters for clustering.

Group	Parameter	Units
Geometry	Wing area	ft^2
	Wing aspect ratio	
	Fuselage volume	ft^3
Performance	Gross weight	lbs
	Cruise Mach	
	Typical range	nm
	Number of passengers	
	Cruise altitude	ft
Engine	Pressure ratio	
	Total thrust	kN
	Bypass ratio	
Emissions	NO_x	gm/kg
Noise	Flyover noise	EPNdB
	Approach noise	EPNdB
	Lateral noise	EPNdB

The number of clusters is determined with the elbow method for KM clustering, wherein a suitable trade-off between error and the number of clusters is determined. Figure 4 shows the inertia (elbow) plot for selecting the number of clusters for the KM algorithm. The same number of clusters is used for AHC.

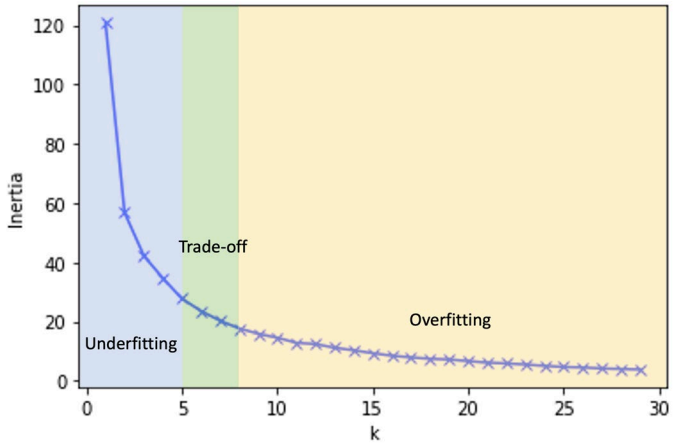

Figure 4. Inertia (elbow) plot for KM clustering.

The clusters can be visualized by using scatterplot matrices and also using *t*-distributed stochastic neighbor embedding (*t*-SNE) (Melit Devassy, 2020). *t*-SNE is very useful for visualizing data with more than three dimensions, by creating a low-dimensional embedding of the original data in two-dimensional or three-dimensional space (Maaten, 2008). The embedding is generated by minimizing the Kullback–Leibler divergence over all high-dimensional data points with a gradient descent method. *t*-SNE is an updated version of the originally proposed SNE that mitigates the crowding problem and optimization problems, by using a symmetric SNE objective function and simpler gradients as well as Student's *t* distribution instead of a Gaussian distribution to evaluate the similarity of the data points in the low-dimensional space (Hinton, 2002).

Preliminary Clustering Results:
The approximately 520 aircraft for which the ADET Fleet extension database has complete parameter data are included in the preliminary results herein. An elbow plot denoting the inertia (within cluster sum of squares) versus the number of clusters is shown in Figure 5. Approximately five to seven clusters appear to be ideal to divide the data. Although this is helpful for KM clustering, it is also used for AHC in the present work.

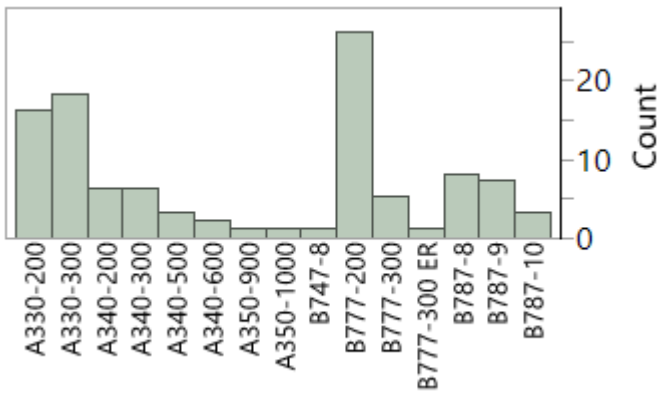

(a) Cluster 0

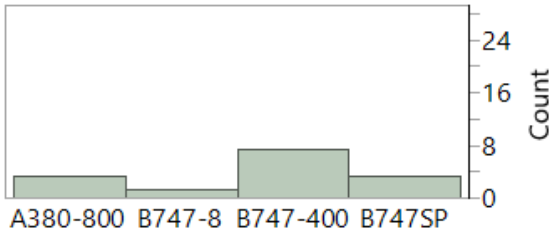

(b) Cluster 1

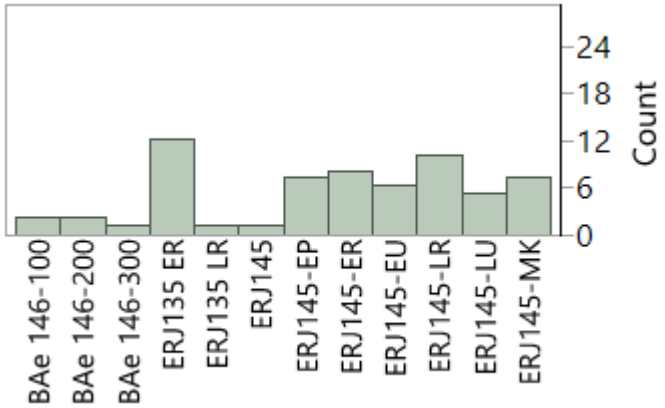

(c) Cluster 2

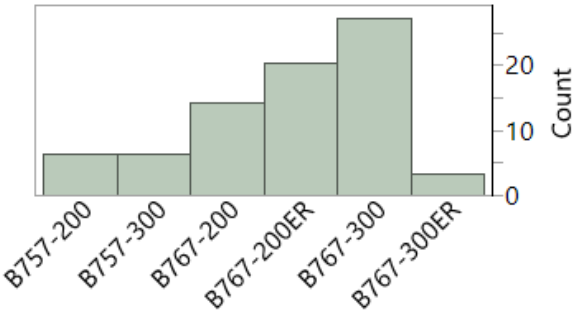

(d) Cluster 3

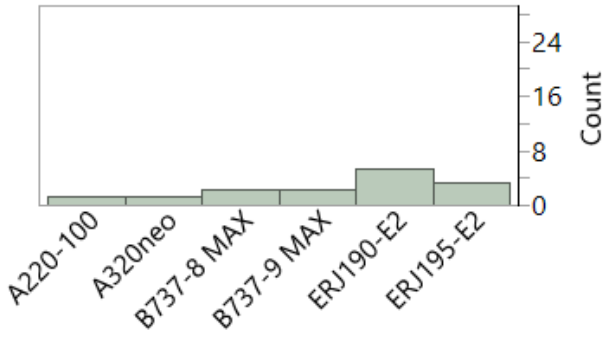

(e) Cluster 4

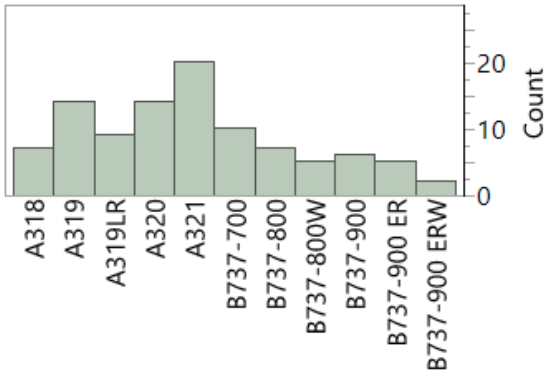

(f) Cluster 5

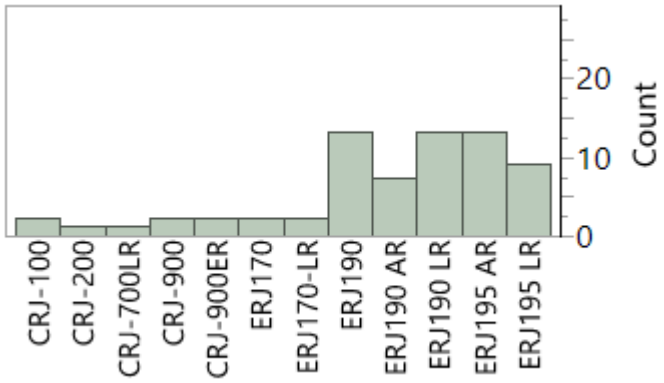

(g) Cluster 6

Figure 5. Preliminary hierarchical clustering results.

Results with AHC with seven clusters are shown in Figure 5. The efficacy of clustering is determined on the basis of SME feedback. Overall, the clusters show good agreement with real-world distinctions: larger wide-body aircraft form cluster 0, so-called "jumbo" jets form cluster 1, regional jets form clusters 2 and 6, smaller wide-body aircraft are in cluster 3, newer-generation small single-aisle aircraft are in cluster 4, and traditional small single-aisle aircraft are in cluster 5.

Visualizing the results of clustering poses a challenge, because the algorithm operates in 15 dimensions, but the results can be presented in only two. Figure 6 shows an example scatterplot matrix of NO_x and noise emissions for aircraft within cluster 1. As expected, the largest aircraft and highest thrust engines that pair with them have the highest emissions and noise signatures, and thus are at the top right of almost every plot. Clear distinctions between clusters are not expected in this figure, which shows only 4 of the 15 dimensions used for clustering.

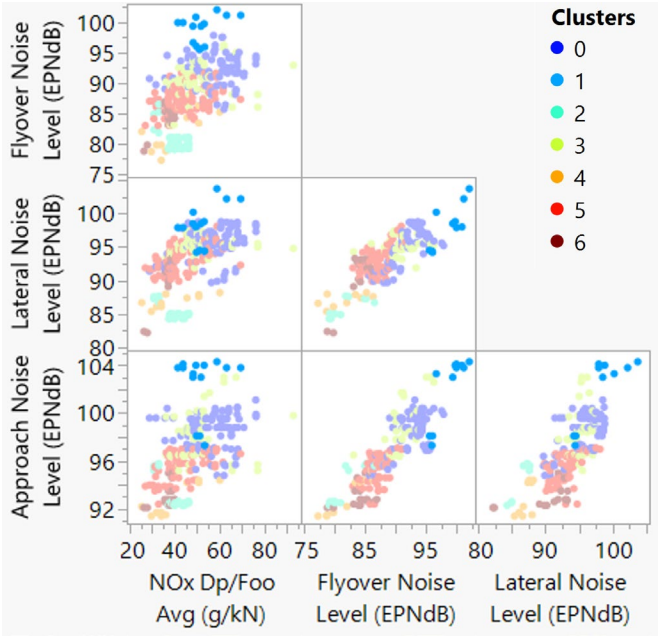

Figure 6. Scatterplot matrix of emissions and noise, with cluster 1 highlighted.

Parameter importance is difficult to gauge for unsupervised learning clustering algorithms. Therefore, to determine the importance of the parameters with the greatest effects on the clusters, we fit a supervised random forest algorithm with 100 trees to the cluster numbers while using the same 15 parameters used to cluster the aircraft. A parameter importance function of this random forest was evaluated to indicate the parameter importance of the AHC clusters (Figure 7).

	Clusters		
Predictor	Contribution	Portion	Rank ^
Wing Area (ft^2)	718.266	0.5533	1
Wing Aspect Ratio	267.938	0.2064	2
MX_GW_TKO	135.672	0.1045	3
Pressure Ratio	44.751	0.0345	4
fuselage_volume	41.153	0.0317	5
total_thrust (kN)	38.250	0.0295	6
Lateral Noise Level (EPNdB)	16.292	0.0125	7
FENV_ALT	14.392	0.0111	8
B/P Ratio	8.287	0.0064	9
CR_MACH	4.774	0.0037	10
Flyover Noise Level (EPNdB)	3.197	0.0025	11
Approach Noise Level (EPNdB)	2.542	0.0020	12
Typical Range (nmi)	2.083	0.0016	13
Pax	0.332	0.0003	14
NOx Dp/Foo Avg (g/kN)	0.286	0.0002	15

Figure 7. Parameter importance for overall clustering.

The idea underlying segregating the aircraft within the AEDT Fleet extension database into clusters is to observe whether aircraft with ANP data (native) are present in certain clusters with non-native aircraft. This process can help identify more suitable substitute ANP aircraft for airframe/engine combinations that do not have ANP data.

The present work makes two primary contributions. The first is the generation of the Fleet extension database, which enriches the AEDT Fleet database with performance, weight, emissions, and noise parameter values from openly available external data sources. The second is the exploration of various ML techniques to identify commonalities and patterns in the airframe/engine combinations. The changes to the Fleet database will be contrasted against the default AEDT mapping of different airframe/engine combinations to ANP native aircraft, thereby enabling the exploration of areas for improvement in fleet modeling of noise and emissions within AEDT, to improve its accuracy.

Major Accomplishments

The major accomplishments for this period performance include the following:

- A literature study was conducted on databases to collect performance, emission, and noise data for target aircraft.
- A new template was created for the Fleet extension database, and external data were gathered.
- External databases were gathered to augment the extension database with completion of 520 aircraft engine combinations.
- A literature survey was conducted on analytical methods in clustering, dimensionality reduction, feature selection, and data visualization.
- Unsupervised clustering was explored on the available Fleet extension database to better group similar aircraft and provide insights on the parameters driving the grouping.
- The results were postprocessed by using bar charts, scatterplot matrices, *t*-SNE, and parameter importance calculations to help better understand the trends.

Publications

None.

Outreach Efforts

Biweekly calls
Bi-annual ASCENT meetings

Awards
None.

Student Involvement
Styliani I. Kampezidou (graduate student)
Cristian Puebla-Menne (graduate student

Plans for Next Period
- Finalize the ANP extension database to include noise certification data, to serve as the basis for Task 2
- Continue to refine analytical methods on the new database, identify gaps in the approach, and implement them on the remaining engine/airframe combinations within the FLEET database
- Validate the methods in Task 2

References
Hinton, G. E., & Roweis, S. (2002). Stochastic neighbor embedding. *Advances in neural information processing systems*, *15*.
Maaten, L.V., & Hinton, G.E. (2008). Visualizing Data using t-SNE. *Journal of Machine Learning Research, 9*, 2579-2605.
Melit Devassy, B., & George, S. (2020). Dimensionality reduction and visualisation of hyperspectral ink data using t-SNE. *Forensic Science International*, *311*, 110194. https://doi.org/10.1016/j.forsciint.2020.110194

Project 061 Noise Certification Streamlining

Georgia Institute of Technology

Project Lead Investigator

Professor Dimitri N. Mavris (P.I.)
Director, Aerospace Systems Design Laboratory
School of Aerospace Engineering
Georgia Institute of Technology
Aerospace Systems Design Laboratory (ASDL)
Weber Space Science & Technology Building, Room 301A
275 Ferst Drive, NW, Atlanta, GA 30332
404-894-1557
dimitri.mavris@ae.gatech.edu

Dr. Michael Balchanos (Co-P.I.)
Research Engineer II
Aerospace Systems Design Laboratory
School of Aerospace Engineering
Georgia Institute of Technology
Aerospace Systems Design Laboratory (ASDL)
Weber Space Science & Technology Building, Room 105
275 Ferst Drive, NW, Atlanta, GA 30332
404-894-9799
michael.balchanos@asdl.gatech.edu

University Participants

Georgia Institute of Technology

- P.I.s: Dr. Dimitri Mavris, Dr. Michael Balchanos
- FAA Award Number: 13-C-AJFE-GIT-066
- Period of Performance: October 1, 2021 to September 30, 2022
- Tasks:
    1. Interview Industrial Partners on Current Noise Certification Processes
        - 1.1 FAA Noise Certification Regulation Review
        - 1.2 Industry Partner Interviews via Workshops
    2. Develop a Streamlined Noise Certification Procedure for Existing Aircraft
        - 2.1 Current Process Assessment
        - 2.2 Streamlined Process Definition
        - 2.3 Streamlined Process Assessment and Revision
    3. Develop a Flexible Noise Certification Procedure for New Aircraft
        - 3.1 Flexibility Assessment of Streamlined Process
        - 3.2 Flexible Process Definition
        - 3.3 Flexible Process Assessment and Revision
    4. Simulate Streamlined and Flexible Noise Certification Procedures
        - 4.1 Identification of a Modeling Approach
        - 4.2 Noise Certification Process Metric Definition
        - 4.3 Model Calibration
        - 4.4 Certification Process Simulation

Project Funding Level

The total amount of current funding from the FAA for ASCENT Project 061 is $250,000 for a 12-month period of performance. The Georgia Institute of Technology has agreed to a total of $83,333 in matching funds.

Investigation Team

The ASCENT Project 061 Georgia Institute of Technology (Georgia Tech) Aerospace Systems Design Laboratory (ASDL) investigation team is shown in Figure 1. Professor Dimitri Mavris is the P.I. of this project, joined by Dr. Michael Balchanos, Research Engineer II as the Co-P.I. and Project Manager. In support of the co-P.I.s, a team of three research faculty, Dr. Jimmy Tai, Senior Research Engineer, Mr. David Anvid, Senior Research Engineer, and Dr. Evan Harrison, Research Engineer II are acting as Technical Advisors on both the planning and technical development for the allocated tasks. The team is joined by five graduate student assistants, who are supporting Project 061 as they work toward their MSc and PhD degrees. All team members are affiliated with the ASDL, under the School of Aerospace Engineering at Georgia Tech.

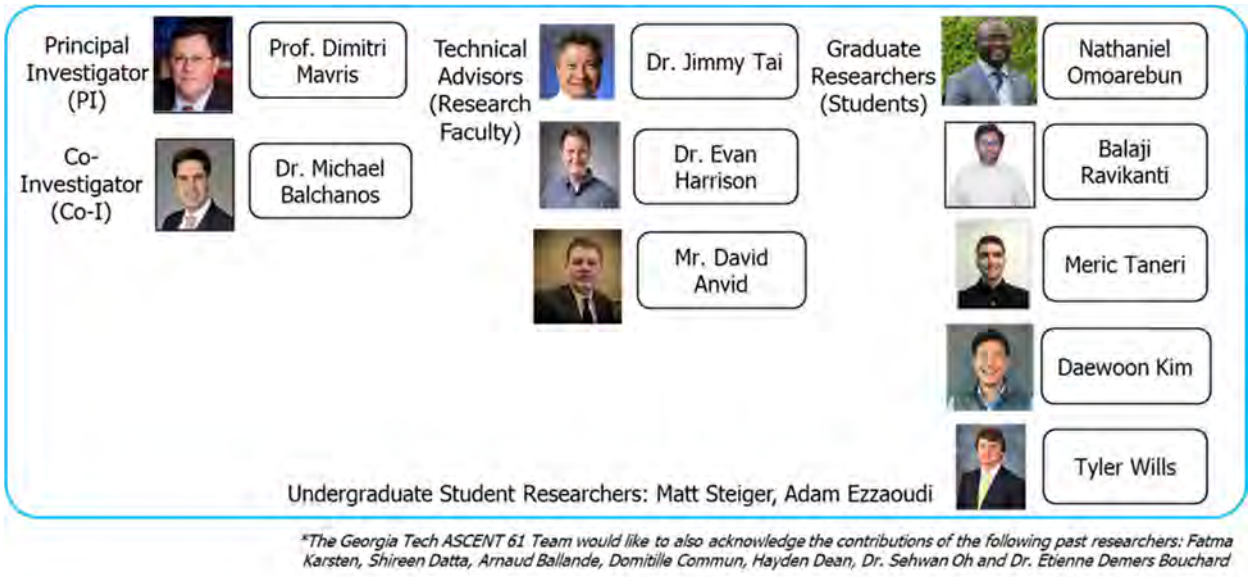

Figure 1. ASCENT Project 061 Georgia Tech ASDL team.

From the team of graduate student researchers, the following roles and responsibilities have been defined:

- **Mr. Daewoon Kim,** a second-year MSc student, is leading the team's model-based systems engineering (MBSE) efforts for representing the baseline certification process in Systems Modeling Language (SysML).
- **Mr. Nathaniel Omoarebun,** a fifth-year PhD student, is supporting the team's MBSE efforts and SysML modeling activities.
- **Mr. Balaji Ravikanti,** a second-year MSc student, is leading the team's efforts in understanding and documenting current certification procedures in SysML, as well as formulating candidate procedures for unmanned aerial system (UAS) noise certification, tied to Part 36, Appendices H and J, and recent FAA notices of proposed rulemaking (NPRMs).
- **Mr. Tyler Wills,** a second-year MSc student, is supporting the team's efforts in process improvement modeling (PIM) methods and process simulation.
- **Mr. Merc Taneri,** a second-year MSc student, is leading the team's efforts in PIM methods, stochastic process simulation (Markov chain Monte Carlo [MCMC]), and interactive visualization.

Past technical advisors who contributed to the tasks:

- **Dr. Sehwan Oh**, Postdoctoral Researcher, focused on exploring current certification regulations, understanding their structure (hierarchy, associations, etc.) linked to Task 1, and providing input on the application of discrete event and agent-based methods as part of the efforts planned for Task 4.

- **Dr. Etienne Demers Bouchard,** Postdoctoral Researcher, focused on exploring process modeling methods from the literature and formulating a canonical problem to assess the feasibility and applicability of various methods.

Former students who have contributed to the tasks:

- **Ms. Shireen Datta,** an MSc student, supported efforts in documenting current procedures and exploring regulation-driven requirements, which are now included in the verification model.
- **Ms. Fatma Karsten,** a PhD student, worked on flight testing plan implementation and an effective perceived noise level (EPNL) calculation module within the MBSE verification model.
- **Mr. Arnaud Ballande**, an MSc student, worked on a process simulation capability for evaluating equivalent procedures under the PIM task.
- **Ms. Hayden Dean,** a PhD student, was instrumental in capturing and understanding current regulations and certification procedures, as dictated by the Title 14 Subchapter C, Part 21, and Part 36, as well as Part 36 Advisory Circulars (ACs), with a particular focus on AC 36-4D and an emphasis on guidance instructions regarding flight testing for noise certification.
- **Ms. Domitille Commun,** a PhD student, worked on implementing a discrete event simulation (DES) model-based process simulation capability for the certification baseline.

Project Overview

Noise certification procedures (with their inclusion of equivalent procedures) have served aviation stakeholders (original equipment manufacturers [OEMs], regulators, operators, airports, etc.) well since the 1960s (Metzger, 1970; Ollerhead, 1968; Senzig, 2018). With new vehicle types and new technologies (including new entrants, digital technologies for airframes, propulsion, and measurements, etc.), it is necessary to critically examine the existing certification processes. Key features of current certification practices include equivalent procedures and supporting technology, which many OEMs utilize (FAA, 2023). Equivalent procedures are anticipated for both existing and new standards to further accommodate innovation in the future.

The project objective is *to examine current noise certification procedures and identify opportunities to streamline the noise certification process while recommending process updates for building the flexibility needed to accommodate all air vehicle types*. Project 061 seeks to propose quantifiable process improvements and facilitate the application of traditional systems engineering for complex systems and Model-Based Systems Engineering (MBSE), while leveraging these methods for the management of regulatory requirements. To perform the proposed research under this three-year effort, Georgia Tech has teamed with several industrial partners with extensive experience in noise certification. Each industrial partner represents different types of vehicles, such as large subsonic transports, propeller-driven small aircraft, and rotorcraft.

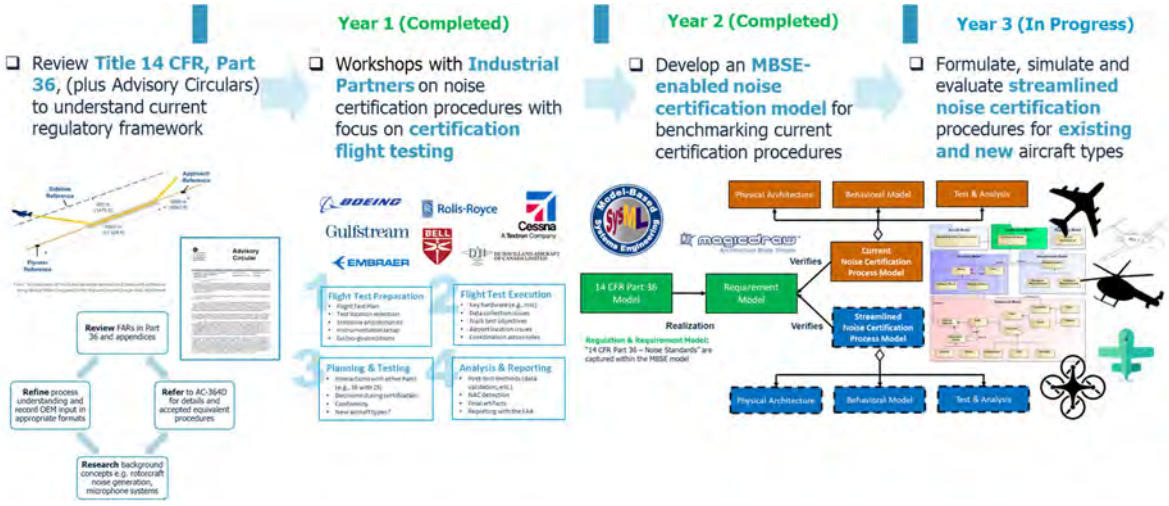

Figure 2. Roadmap toward a model-based framework for exploring current and streamlined noise certification. AC: advisory circular; CFR: Code of Federal Regulations; FAR: Federal Acquisition Regulation; MBSE: model-based systems engineering; NAC: non-acoustical change; OEM: original equipment manufacturer.

The ASCENT Project 061 team is seeking to accomplish the following goals:

- Identify opportunities for increased efficiency (by expediting steps and simplifying processes) and flexibility in current noise certification processes to accommodate multiple vehicle categories.
- Formulate and evaluate revised noise certification processes for current vehicle types and offer recommendations to the FAA (Part 36, AC 36-4D, etc.) (FAA, 2017).
- Develop process modeling methods to enable quantitative assessments of noise certification.
- Facilitate the application of traditional systems engineering processes for complex systems and MBSE, leveraging these methods for the management of regulatory requirements.
- Leverage the technical expertise acquired in investigating and modeling noise regulatory frameworks and recommend procedures for certification testing and analysis to the FAA for small propeller-driven vehicles and UASs.

Overall ASCENT 061 Roadmap and Statement of Work
An overview of the ASCENT 061 roadmap toward goals and milestones is shown in Figure 2.

The main goal is to provide recommendations to the FAA in the form of feasible equivalent procedures, supported by the latest technologies/hardware, as well as analysis techniques to support the certification of future air vehicle types. These recommendations should be accompanied by evidence that the suggested equivalent procedures are fully in compliance with Part 36 (FAA, 2017) and use case examples for future air vehicles, e.g., small propeller-driven aircraft and UASs. To implement this roadmap and achieve the targeted outcomes, the team will engage in four main tasks, along with the subtasks that have been prioritized for Year 2 of ASCENT 061. These tasks are summarized below.

Task 1: Interview Industrial Partners on Current Noise Certification Processes
- 1.1 FAA Noise Certification Regulation Review [Year 1]
- 1.2 Industry Partner Interviews via Workshops [Year 1]

Task 2: Develop a Streamlined Noise Certification Procedure for Existing Aircraft
- 2.1 Current Process Assessment [Year 1]
- 2.2 Streamlined Process Definition [Year 2]
- 2.3 Streamlined Process Assessment and Revision [Year 2]

Task 3: Develop a Flexible Noise Certification Procedure for New Aircraft
- 3.1 Flexibility Assessment of Streamlined Process [Year 2]
- 3.2 Flexible Process Definition [Year 2]
- 3.3 Flexible Process Assessment and Revision [Year 2]

Task 4: Simulate Streamlined and Flexible Noise Certification Procedures
- 4.1 Identification of a Modeling Approach [Year 1]
- 4.2 Noise Certification Process Metric Definition [Year 2]
- 4.3 Model Calibration [Year 2]
- 4.4 Certification Process Simulation [Year 2]

For the full three-year period of performance, the complete timeline for finalizing all Project 061 tasks is shown in Table 1.

Table 1. ASCENT Project 061 task planning timeline.

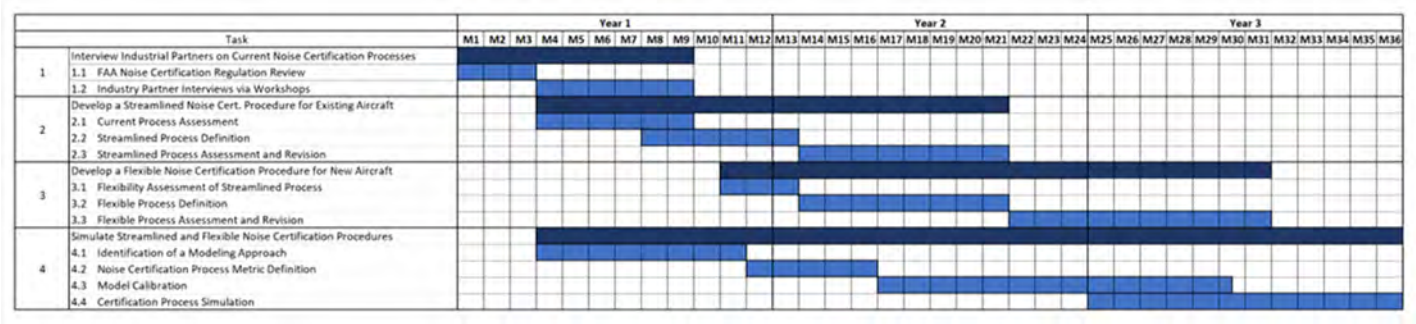

Pivoting to UAS Category (effective June 2022)

The FAA's Office of Environment and Energy (AEE) has suggested a timeframe for pivoting to UAS category certification model exploration, using the transport category certification model as a basis. The main task for the Georgia Tech team is to investigate the feasibility and applicability of current ASCENT 061 models and analysis tools for exploring procedures and flight test planning to support noise certification of small propeller-driven UASs. The primary issue with UAS certification is that the spectrum of possible and available configurations covers a large class of aerial systems with completely different characteristics, as shown in Figure 3.

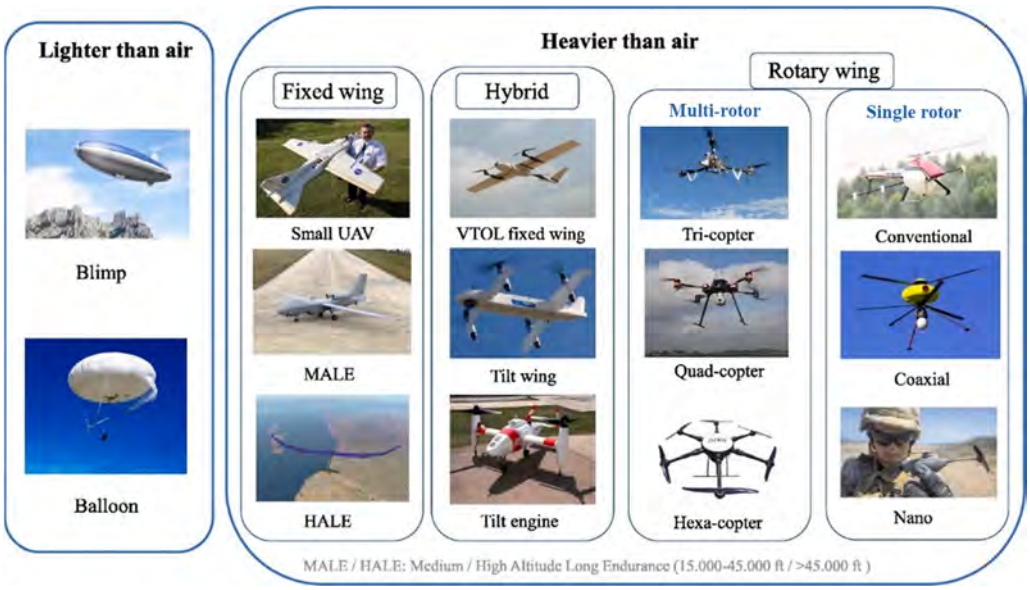

Figure 3. Overview of unmanned aerial system concepts. UAV: unmanned aerial vehicle; VTOL: vertical takeoff and landing.

It is assumed to be unlikely that UAS noise certification will be addressed as a "clean sheet of paper" process. Multiple efforts are underway to establish guidance for noise certification, similar to that for the transport category. The International Civil Aviation Organization (ICAO) is the recognized authority for developing and establishing a global baseline for noise standards and stringencies. Although rulemaking by the ICAO may lag behind the efforts of individual countries, ultimately, the harmonization of certification requirements among national airworthiness authorities (NAAs) is desirable. Several iterations of the regulatory framework may be required before this target is achieved.

The ASCENT 061 team has agreed with the FAA AEE to adjust the statement of work (SoW) in order to lay the groundwork for noise certification for the UAS category, as this initiative has been given a higher priority. Key challenges that have been identified and will be addressed by the Georgia Tech team are as follows:

- There is currently a large spectrum of UAS designs and configurations under testing for production. As the FAA is preparing to release guidance for UAS noise certification, it is important to determine whether the MBSE-enabled method developed under ASCENT 061 is sufficiently flexible to accommodate UAS testing actions and to help establish a workflow that meets current and upcoming regulations.
- As there are currently no general regulations and the application of current certification procedures is on a case-by-case basis (e.g., recently completed certification framework for the Matternet UAS), it is important to assess whether current testing procedures are effective for UASs.
- We must determine how the ASCENT 061 team can use the established framework to demonstrate its effectiveness in assisting the FAA through the assessment of NPRM plans, as these are being iterated before they become approved as part of the UAS noise certification standards.

Putting this plan forward, the suggested starting point is to perform an inventory of existing certification practices for low MTOW general aviation and propeller/rotor-driven aircraft (i.e., fixed wing and rotorcraft). Currently, the priority is to focus

on UASs before urban air mobility (UAM), as the anticipated risks are expected to be higher for the latter. In response to this pivot, the following guiding actions have been set:

- Study current certification practices for noise for small propeller-driven airplanes (Code of Federal Regulations (CFR) Title 14, Part 36, Appendix G) and light helicopters (Code of Federal Regulations (CFR) Title 14, Part 36, Appendix J).
- Perform a literature/technical review of noise source characteristics associated with propeller/rotor propulsion systems.
- Explore current practices for UAS flight testing for noise. The ASCENT 061 team has been encouraged to explore collaboration with ASCENT 077 researchers at Penn State regarding their research on "Measurements to Support Noise Certification For UAS/UAM Vehicles and Identify Noise Reduction Opportunities."
- Utilize the team's current MBSE-enabled certification framework to test current procedures for UASs and its overall flexibility to accommodate multiple aircraft categories.

As a starting point for the literature search, Appendices G and J are considered the only aircraft noise certification standards that might be applicable for noise certification of small Unmanned Aircraft Systems (sUAS) in the United States, but a number of additional standards will be reviewed and included in formulating certification practices, including the following:

- ICAO Annex 16 Volume 1 Chapters 8, 10, 11, and 13
    - These are applicable to all fixed wing, rotorcraft, and tiltrotors below a Maximum takeoff weight (MTOW) of 3,175 kg.
- NASA Ref. Publication 1258, Aeroacoustics of Flight Vehicles: Theory and Practice Volume 1 & 2, August 1991.

SoW/Task Definitions for UAS Noise Certification Research

Following the reassigned focus on UAS certification, the original task definitions that had guided the work on transport category aircraft noise certification required a review. An updated SoW has been formulated to guide the pivot toward the development of use cases that address the FAA's needs for UAS noise certification. This SoW is based on the concept that the original tasking is substantially complete; thus, a significantly revised SoW is necessary to reflect the integration of UAS certification goals with the previously developed MBSE and PIM modeling. This development will entail the generation of multiple libraries that enable flexibility of use across a broader range of UAS configurations and support traceability between regulations, requirements, and elements of the library.

The tasks under the revised SoW are defined as follows:
(Please note: This is a notional construct for this annual reporting period and will be described in more detail during future reporting. Modifications or revisions to this SoW may occur based on the research sponsor's input.)

Task 1: Develop a Traceable Structure for UAS Noise Certification Requirements (Year 2)

1.1 Document related regulations and current standards.
1.2 Generate noise certification requirements from currently known and established regulations.
1.3 Define a validation process for noise requirements.

Task 2: Develop a Library of UASs and Testing Procedures (Year 3)

2.1 Perform a technical documentation of UASs.
2.2 Conduct a technical documentation of UAS noise testing equipment.
2.3 Define UAS noise test plans.
2.4 Define possible simulation techniques.

Task 3: Develop a Noise Certification Procedure Based on Existing Practices (Years 2, 3)

3.1 Transfer noise testing plans to the MBSE model (Year 2).
3.2 Transfer noise testing data to the MBSE model (Year 3).
3.3 Develop a full noise test plan (Year 3).
3.4 Implement a validation process (Year 3).

Task 4: Develop Alternative Procedures and Assess Their Performance with Existing Tools (Year 3)

4.1 Develop alternative testing procedures using the elements library.
4.2 Transfer alternative procedures to the PIM.
4.3 Report on the performance of the alternative procedures.

Matrixing of Parallel ASCENT Project Efforts
Within the topic of UAS testing and certification for noise, there are currently three related, but unique ASCENT research efforts:

- ASCENT 77: Measurements to Support Noise Certification for UAS/UAM Vehicles and Identify Noise Reduction (Penn State University)
- ASCENT 9/94: Geospatially Driven Noise Estimation Module (Georgia Tech ASDL)
- ASCENT 061: Noise Certification Streamlining (Georgia Tech ASDL)

To preclude "mission creep" into other projects' remit and to leverage the work of the other ASCENT teams, the Project 061 team has been coordinating on a regular basis with Project 077 and Project 009/094 team members (as highlighted in Figure 4). The main collaboration areas are the following:

- ASCENT 77: Data sharing. Experimental test data provide real-world input for noise certification modeling. The results of the ASCENT 77 testing efforts provide a better understanding of the most significant parameters affecting UAS noise characteristics. The weighting of these parameters may influence modifications to the existing MBSE model.
    - Comparison of field geometry, test equipment, and basic flight profiles in addition to UAS configuration, weight, and vehicle performance
- ASCENT 09/91: Evaluation of possible vehicle operational environments and the practical impacts of noise profiles on the public. While the ASCENT 09/91 efforts do not provide direct technical data for MBSE modeling, these efforts do provide context for how noise level outputs from the certification process may be applied to an operational environment.

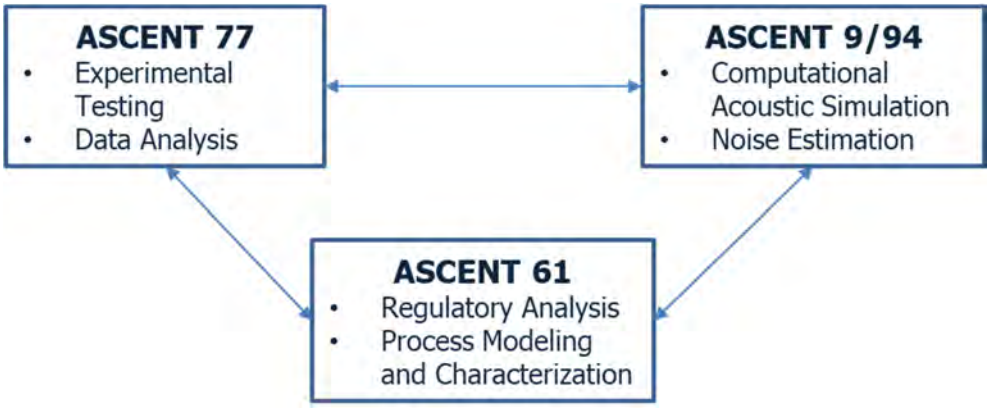

Figure 4. Coordination with parallel ASCENT work related to unmanned aerial system certification.

Summary of Major Accomplishments (to date)
Transport Category Tasks

- Completed **architecting of a noise certification modeling and assessment framework** for transport category aircraft
- Formulated use cases that are aligned with needs and recommendations provided by OEM partners, with a focus on exploring implications of alternative testing procedures on regulatory compliance and highlighting the benefits of process simplification (e.g., lateral microphone placement or removal, if trusted analysis is used)
- Achieved key improvements in a SysML-based verification model based on training materials provided by VOLPE (acoustical designated engineering representatives regarding the processes of determining EPNLs used in FAA Recurrent Seminars)
- Conducted PIM for process assessment, evaluation, and testing of equivalent procedures using Markov chains
- Provided a demonstration by assessing a simplified noise collection/analysis process, with the Waco YMF-5 propeller aircraft as an example
- Documented options for equivalent procedures in a database/library compilation
- Conceptualized and developed a visualization environment to aid as a use case demonstrator and decision support environment

UAS Category Pivot

- Completed initial steps and updated the SoW to explore the applicability of the current ASCENT 061 framework for noise certification of rotor or small propeller-driven UASs
- Performed a literature search on current noise certification practices for UASs
    - CFR Title 14 Part 36 Appendix G, J, and H **Error! Reference source not found.**
- Produced a plan to modify the ASCENT 061 MBSE noise certification framework to accommodate UAS category vehicles in order to provide oversight on Equivalent Procedures (EP) and regulatory compliance

In the following sections, key contributions are highlighted, along with detailed descriptions of technical progress, research approaches, key milestones, and accomplishments for each task.

Task 1 - Interview Industrial Partners on Current Noise Certification Processes

Georgia Institute of Technology

Objectives

In support of the main research objective of Project 061, Task 1 focuses on examining current noise certification procedures (Task 1.1) and benchmarking against current industry practices in how these procedures are adopted and implemented (Task 1.2). In particular, the subtasks are organized as follows:

Task 1.1: FAA Noise Certification Regulation Review

- Perform a thorough review of FAA noise certification regulations for large subsonic jet and transport category airplanes, as well as rotorcraft types of vehicles (14 CFR, Chapter 1, Subchapter C, Part 36, Subparts B and H). With input from the FAA, the Georgia Tech team will also explore propeller-driven small airplanes and propeller-driven commuter category airplanes.
- Include recent certification regulations for new types of aircraft (e.g., advanced air mobility), in addition to conventional configurations.
- Document existing regulatory framework for aircraft noise certification, including both specified regulatory standards and accepted means of compliance.

Task 1.2: Industrial Partner Interviews via Workshops

- Gather information through interviews and workshops on industry-applied noise certification procedures, including equivalent procedures.
- Propose workshops and invite industry partners with subject matter expertise on airframe noise certification (large transport, small propeller aircraft, and rotorcraft).
- Facilitate a dedicated workshop for each vehicle type and plan for follow-up events to iterate on feedback obtained, as well as to share lessons learned and the derived recommendations.
    - The focus of the workshop is to identify areas of opportunity to streamline the certification process for each type of vehicle and to allow subject matter experts to suggest potential solutions.

[UAS Pivot] Task 1: Develop a Traceable Structure for UAS Noise Certification Requirements (Year 2)

- Document related regulations and current standards.
- Generate noise certification requirements from currently known and established regulations.
- Define a validation process for noise requirements.

Research Approach

Task 1.1

For Task 1.1, the main goal was to review and document current noise certification procedures. The task objective was to gain an understanding of the current regulatory framework for aircraft noise certification, as required by FAA regulations and followed by OEMs to demonstrate compliance. In particular, the team conducted a thorough literature review of relevant 14 CFR parts (mainly Part 36) and associated documents where relevant (e.g., ACs such as AC 36-4D (Federal Register, 2022). With recommendations from the team's partners, this task also considered other documentation from the European Union Aviation Safety Agency (EASA), the ICAO Environmental Technical Manual, and the VOLPE website.

Along with the extensive review of Federal Acquisition Regulations (FAR) and literature on the regulatory framework, the team produced a series of views to demonstrate the flow of procedures, associations, and dependencies across regulatory items. Finally, the team obtained background information on noise generation for various aircraft categories, as well as technologies used during testing, to better understand current recommended practices and the potential for alternative equivalent procedures with the use of modern technologies and equipment. One of the benefits of this task's outcome is that team members quickly became more knowledgeable of the certification basics in preparation for Task 1.2 (industry interviews) and were able to build a comprehensive MBSE representation (in SysML) of the current framework (see Task 2.1). An overview of the methodology behind the review of FARs and literature is provided in Figure 5. Please see Appendix A of this document for a full overview and documentation produced under this exercise.

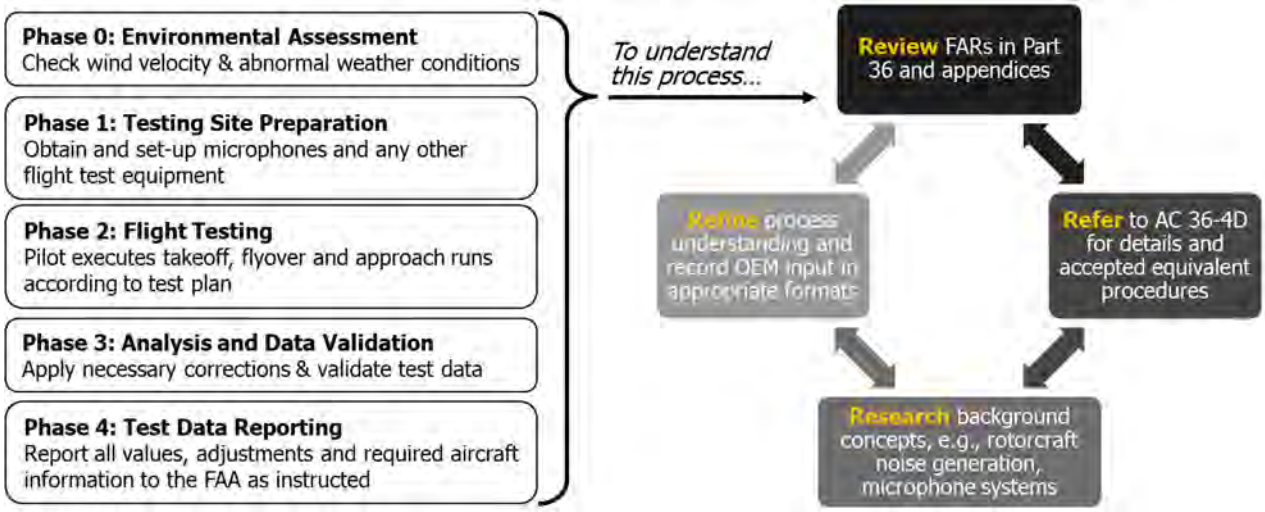

Figure 5. Noise certification regulation review (Task 1.1). AC: advisory circular; FAR: federal acquisition regulations; OEM: original equipment manufacturer.

The approach that was formulated under Task 1.1 has been applied to the [UAS Pivot] Task 1, in order for a similar database and series of views to be produced for current certification regulations.

Task 1.2

Task 1.2 aims to enhance the team's understanding of the current noise certification process through interactions with subject matter experts from various OEMs, with the objective of leveraging industry insight into practical aspects of noise certification requirements. This goal was achieved via virtual workshops, guided by questionnaires compiled by the team based on the reviews completed under Task 1.1. Based on insights and findings from documented work under Task 1.1, the team has identified topics for which more context and additional insight into ancillary/non-regulatory processes is needed, with regards to how the certification procedure is facilitated by each OEM partner. These topics are shown in Figure 6.

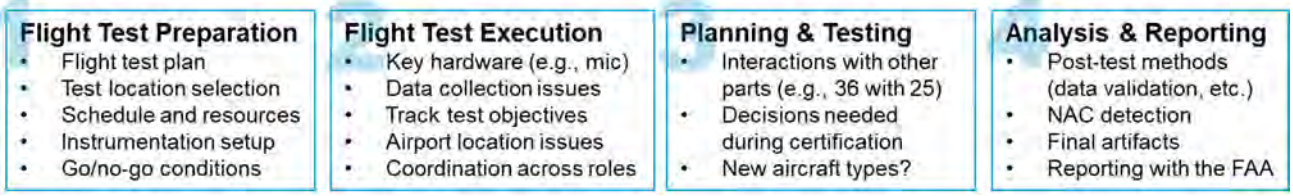

Figure 6. Workshop interview topics for transport category aircraft. NAC: non-acoustical change.

The overarching goal of these workshops was to identify common practices, checkpoints, and milestones across industry partners, while soliciting feedback on key challenges they have identified on their end, as well as what recommendation each

partner would provide and why. Such suggestions could convert to opportunities for potential process streamlining if recommended practices are out of sync with current technology. The limitation in this exercise is that no recommendations should suggest or presume any change in the regulatory side; hence, the suggestions should be concentrated on equivalent procedures, with either simplified processes or connections to modern technologies that are expected to meet the same regulations.

To facilitate a directed discussion within the workshops/interviews, the Georgia Tech team formulated questions on the discussion topics listed in Figure 6 and produced questionnaires that were then distributed to the participants prior to the respective meetings. A high-level summary of the questions is as follows:

- What is the current guidance provided by the FAA for noise certification?
- How does a company interact with the FAA to ensure that requirements and constraints related to noise regulations are satisfied and that the vehicle is compliant?

The initial workshop along with the subsequent interviews with the participants generated a wealth of information. Planning and a methodological approach are required to post-process and direct this information toward usable conclusions and insightful findings.

While the level of detail in the answers and feedback obtained varied significantly across the participants, the team was able to summarize the overall themes of the feedback provided under the defined categories. The main takeaways from the OEM feedback are the following:

- Acoustical changes/non-acoustical changes (ACs/NACs) are challenging to navigate without standardized approval procedures. More detailed feedback would be useful for OEMs to propose suitable solutions.
- Test site selection is normally restricted by sound measurement technology and requirements (e.g., the lateral microphone component) and by weather window options.
- Delays in flight testing are primarily weather-induced, but are occasionally due to communication disruptions.
- Conformity discussions can be significantly time/effort-consuming, especially for cases in which there is a need to justify changes that are unrelated to acoustics.
- Regarding interactions between Part 36 and Part 25/23, there seems to be a discontinuity between environmental and design standards, often leaving little space to apply acoustic improvements.
- There is no single standardized software for calculating EPNL values from noise data collected during flight testing; rather, each OEM's methodology and code are different.

This lack of standardization appears to be a common area of opportunity for improvements across current noise certification procedures. This observation is even more relevant for the UAS category, where regulations will be expected to cover a broader range of configurations.

[UAS Pivot] Task 1

The purpose of this task is to establish a work thread that repeats the work completed for the transport category, with the intent to document and understand the current regulatory framework for UAS noise certification. With the completion of the first phase of the literature search, the following observations have been documented:

- No clear regulatory framework
  - Study will rely on NPRMs and Appendices G, J, and H of CFR Title 14 Part 36 (FAA, 2017).
- No clear categorization of UAS configurations
  - Study will propose criteria, e.g., weight, propeller number/type/orientation, flight envelope, maximum speed, and operational altitude.
- No test data immediately available
  - Study will rely on test plan information, test-day logs, and available/sharable noise data from ASCENT 77.
- No established validation process against regulation-driven requirements
  - Study will track/ensure traceability among regulations, testing requirements, and certification procedures.

Aside from published regulatory guidance, several previous studies were available and provided a baseline for the testing procedures. These studies were the following:

- The document entitled "Noise Measurement Report: Unconventional Aircraft - Choctaw Nation of Oklahoma: July 2019," which provides an explanatory overview of the noise certification approach for UASs.
- The document entitled "Sound Exposure Level Duration Adjustments in UAS Rotorcraft Noise Certification Tests," which provides an overview of the applicability of the "duration correction" for manned helicopters on small UASs.

As a pilot exercise and with the recommendation of the FAA, the ASCENT 061 team has selected the NPRM 86 FR 48281 (FAA, 2022) to evaluate the procedure for type certification for the Matternet M2 UAS, as highlighted in Figure 7. Please note that the Matternet noise standard final rule was eventually published in September 2022.

Figure 7. NPRM 86 FR 48281* for evaluating the procedure for type certification for the Matternet M2 unmanned aerial system (FAA, 2022).

The process that the ASCENT 061 team has followed is shown in Figure 8. The first step involves exploring and gathering requirements. This information was organized under the following criteria: noise level classification, vehicle/operational classification, and noise metrics. For the testing framework, the search included flight profiles, system under test (SUT) configurations, and available measurements.

Figure 8. Process for reviewing noise certification for unmanned aerial system regulations.

In the second step, the search included the gathering of supporting data for noise measurements. A dataset was obtained from the test data and insights of the ASCENT 77 group for the Octocopter (Tarot X8) **Error! Reference source not found.**, which included data for hovering, vertical takeoff and landing, flyover, maneuvering, and approach/climb, as shown in Figure 9. The tests were conducted for varying payload weights, speeds, and weather conditions. Alternatively, data and measurements could be obtained from academic or industrial research literature (e.g., FAA UAS BEYOND program) or from trusted noise prediction models.

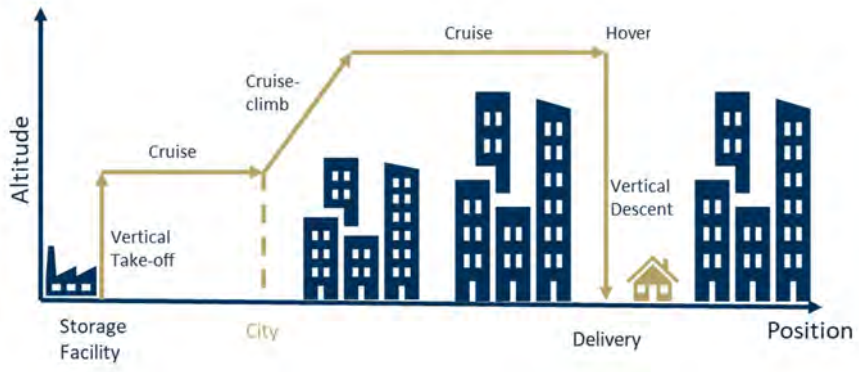

Figure 9. Typical mission profile for a delivery unmanned aerial system.

With the available data, the third step is to perform a requirement analysis, which is the basis for the regulation assessment proposed in the NPRM (FAA, 2022). This analysis will make use of the ASCENT 061 MBSE-enabled certification framework, for which regulations must be mapped to requirements, which will be subsequently implemented in SysML and tested in MagicDraw.

The U.S. Department of Defense Systems Engineering Guidebook, under section 4.2.7, defines the attributes of "Good Requirements," which are further categorized to help characterize the effectiveness of the requirements, as shown in Figure 10. The attributes pertaining to the quality and standard of writing (listed in green) are met, given that the NPRM is largely based on the existing enforced regulation.

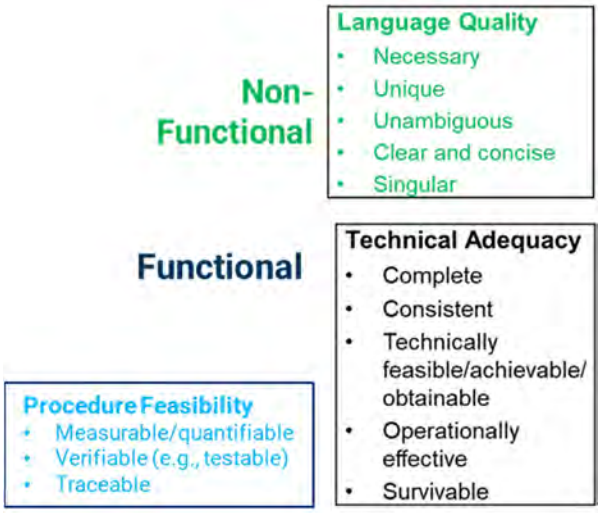

Figure 10. Criteria for analyzing certification testing requirements.

A typical mission profile is shown in Figure 9. The NPRM (86 FR 48281) presents only the noise certification basis for one new model of UAS seeking type certification, the Matternet M2 (FAA, 2022). The NPRM is traced to and draws from the best practices and proven methods of the existing enforced regulations and incorporates requirements that are verifiable in principle. Part 36 Appendix J, however, covers an alternative noise certification procedure for helicopters under Subpart H, having a maximum certified takeoff weight of not more than 7,000 lbs. V_H is defined as the airspeed in level flight obtained using the minimum specification engine power corresponding to the maximum continuous power available. V_{NE} is the never-exceed speed. A comparison table of testing requirements between the NPRM and the Part 36 Appendix J is shown in Table 2.

Table 2. Matternet M2 noise certification requirements (FAA, 2017; FAA, 2022). MTOW: maximum takeoff weight; NPRM: notice of proposed rulemaking.

Measurement Parameter	NPRM	Part 36 Appendix J	More NPRM Details
Reference Altitude	250 feet	492 feet	Test altitude may be lowered to attain acceptable signal-noise ratio and the noise data will then be mathematically adjusted to reference altitude
Reference Flight Speed (Empty Weight)	$0.9V_{NE}$ †	N/A	Two test speeds are employed because the sensitivity of noise level to weight and flight speed are unclear for MM2
Reference Flight Speed (Maximum Takeoff weight)	Maximum Performance Speed	Minimum of $0.9V_H$*; $0.9V_{NE}$; $0.45V_H$ + 65 kts; $0.45V_{NE}$ + 65 kts;	
Noise Level	78 dB	‡82+3.0[$\log_{10}$(MTOW/3125) /$\log_{10}$(2)] dB	78 = 82 + 3.7 (accounts for reduced ref altitude) – 7.7 (noise curve reduction for MM2)

Modeling the requirements relies on ontological descriptions and element stereotypes of the system under consideration and its constituent parts, along with key relationships between elements of the system. To build the model, descriptive and prescriptive versions of potential FAA certification regulations are introduced. Element relationships are used to enable a representation of model relationships, where containment is used to represent the hierarchical arrangement. Further refinement of the model was enabled by access to training material and process information provided by VOLPE. Finally, resources tied to the certification process could be traced throughout the entire model and for all exchanges that have been documented. In Figure 11, an excerpt view is shown from the full requirement model developed by the A61 team, sourced by the regulations within the NPRM (FAA, 2022) model, as well as Part 36.

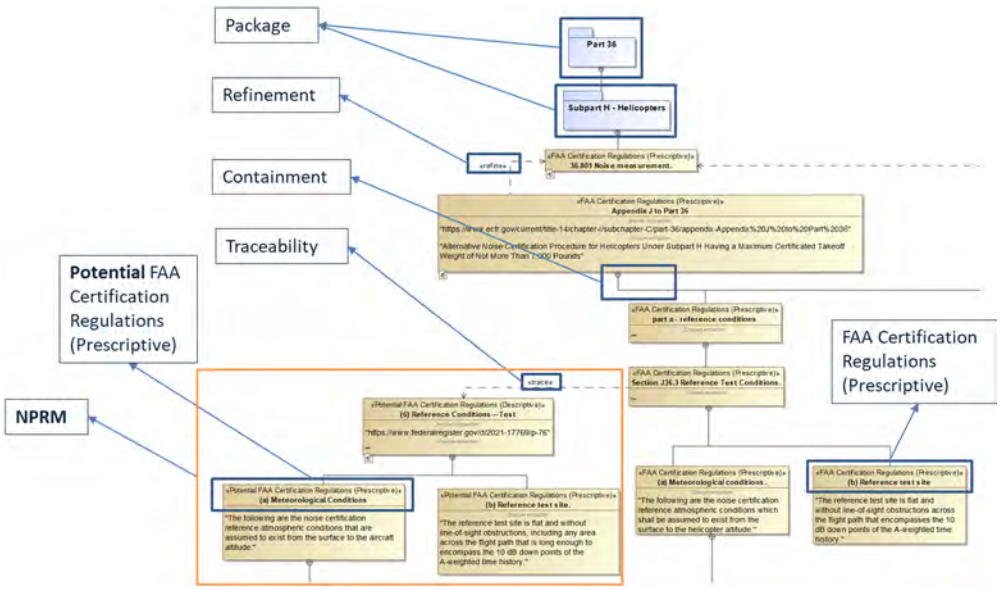

Figure 11. Regulations model for unmanned aerial systems (partial view, excerpt).

The next action in the requirement analysis phase is to assess the technical adequacy of the proposed requirements. The following criteria have been set for ensuring a consistent set of regulatory statements that are generally applicable to the noise certification of UAS category vehicles:

- Regulatory statements shall not directly contradict each other.
- No regulatory statement may entirely prevent compliance to one or more other statements.
- A technically feasible/achievable/obtainable set of regulatory statements that are generally applicable to the noise certification of UAS category vehicles shall adequately account for aspects of noise generation mechanisms that give rise to uncontrollable variations in noise radiation.

- Regulatory statements that are generally applicable to the noise certification of UAS category vehicles shall specify noise metrics and test profiles that enable applicants to determine the noisiest vehicle configurations.
- Regulatory statements shall be measurable/quantifiable, verifiable (e.g., testable), and traceable.

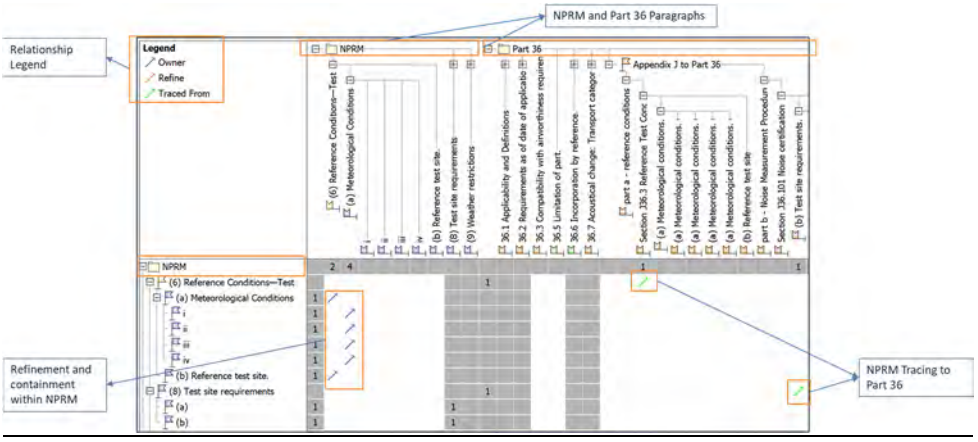

Figure 12. Dependency matrix (excerpt).

Scalability is an important factor, as regulatory statements that are generally applicable to UAS category vehicles shall encompass a broad range of operating conditions and vehicle types, which is evident from the organization of Part 36. "Weather Restrictions" pertain to testing environments imposed on different aircraft categories. For instance, multi-rotor vertical takeoff/landing aircraft conducting package deliveries in urban city centers present a particular combination of vehicle type and operational scenario that shall be analyzed, and then the approach shall be extended to other combinations. Hence, in Figure 13, the level of "completeness" for regulations refers to the coverage footprint of the unique combinations of vehicles and operations that pertain to noise generation for a particular use case.

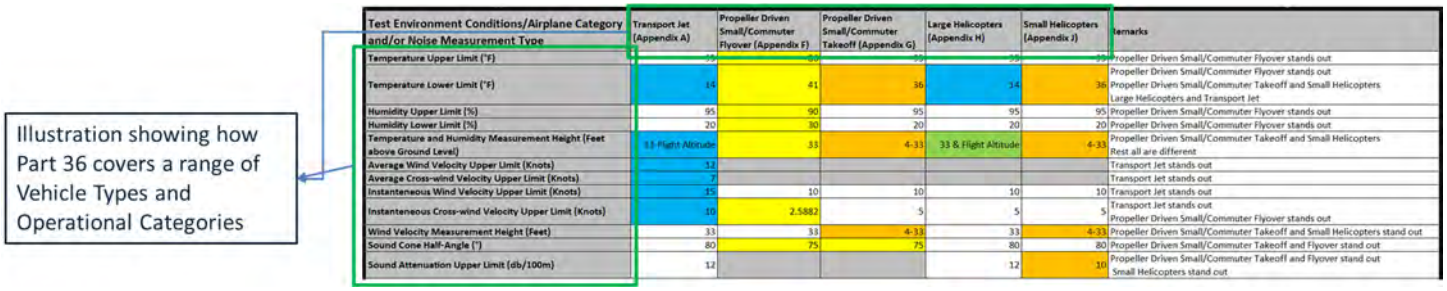

Figure 13. Vehicle types and operational categories covered by Part 36.

The certification analysis framework proposed in Figure 8 has been demonstrated end-to-end, for instance, in assessing the technical feasibility of NPRM paragraph 26(b) by leveraging the experimental test data provided by ASCENT 077. Paragraph 26(b) states that "The minimum sample size acceptable for the aircraft flyover certification measurements is six. The number of samples must be sufficient to establish statistically a 90 percent confidence limit that does not exceed ±1.5 dB(A)." Experimental test data (More, 2011) at flight speeds of 10 and 20 mph conducted over two days with varying weather conditions were considered to cover a range of natural variability. Figure 14 shows that within a wide range of sample standard deviation, as is evident from the experimental data considered, increasing the number of runs reduces the length of the confidence interval that is expected from a controlled process. It is also observed that decreasing the number of runs beyond the prescribed six runs can also result in meeting the requirement for a considerable range of sample standard deviations. Hence, the experimental data suggest that the requirement is technically feasible.

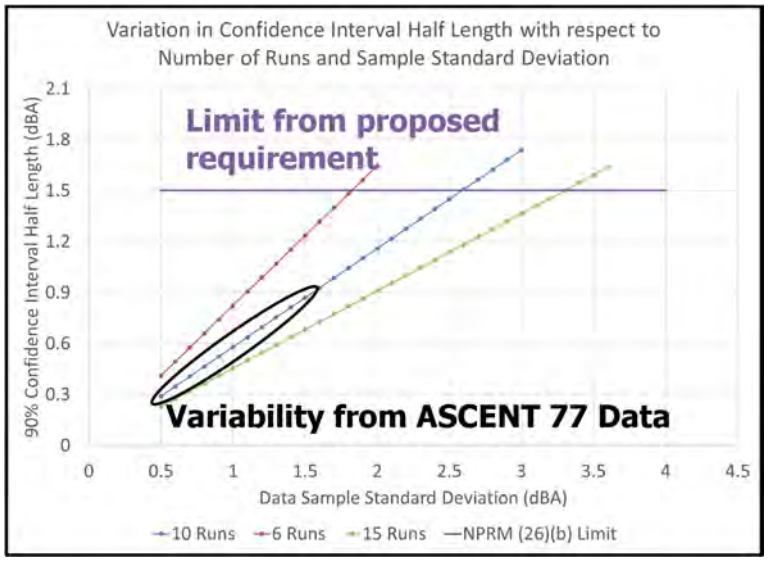

Figure 14. Technical feasibility analysis of NPRM paragraph 26(b). NPRM: notice of proposed rulemaking.

When repeated with the traceability afforded by the MBSE framework shown in Figure 11 and Figure 12, this process results in a holistic assessment of a body of regulatory statements for the attributes outlined in Figure 10.

Milestones

Between October 2021 and September 2022, the following milestones were achieved:

- Participation in Fall 2021, Spring 2022, and Fall 2022 ASCENT Advisory Committee Meetings
- Completion of Tasks 1.1 and 1.2. for the transport category
- Extension of Tasks 1.1 and 1.2 for the exploration of UAS regulations for noise
    - The findings and documentation were utilized to define a requirement model in SysML as a first step to reconfigure the MBSE framework for UAS category certification modeling.
- Completion of exploration and assessment of NPRM (86 FR 48281) (FAA, 2022) which presents only the noise certification basis for one new model of UAS seeking type certification, the Matternet M2

Major Accomplishments

For Task 1.1, the following accomplishments are reported:

- Completion of a literature review on current noise certification practices, as dictated by Title 14 Part C, Part 21 on certification procedures and Part 36 on noise regulations (including Part 36 ACs), with a particular focus on AC 36-4D **Error! Reference source not found.** and an emphasis on the instruction regarding flight testing for certification
- Summary and visual representation of the regulations and their associations (both in flow chart and SysML views)
- Identification of certain gaps in understanding the certification process, which have been documented and have enabled the production of a topic questionnaire to further support the facilitation of workshops with industry partners, as planned for Task 1.2

Task 1.1 is now completed.

For Task 1.2, the following accomplishments are reported:

- Workshops were completed for the large transport category, and feedback and input from industry partners were collected during the workshop. Additional responses and guidance were obtained through follow-up meetings during Years 1 and 2.
- Key takeaways became available, which have been shaping the research direction and clarified priorities within the problem (e.g., streamlining to be targeted not only in terms of time and cost, but also for complexity reduction and exploration of technologies to support process simplification).

Task 1.2 is now completed for transport category aircraft, and tasks will be repeated for rotorcraft and small propeller-driven air vehicles.

For the UAS-specific version of Task 1, the following accomplishments are reported:

- Performed a literature search and documented regulations and current testing standards for rotor and small propeller-driven UASs.
- Defined a traceable structure for UAS noise certification requirements, using the MBSE verification model developed for the transport category.
- Published articles with the International Council of the Aeronautical Sciences (ICAS) 2022 and the American Institute of Aeronautics and Astronautics (AIAA) SciTech 2023.

Publications

Peer-reviewed journal publications
None.

Published conference proceedings

Kim, D., Karagoz, F., Datta, S., Balchanos, M., Anvid, D., Harrison, E., & D.N. Mavris (2022). *A Model Based Systems Engineering Approach to Streamlined Noise Certification of Transport-type Aircraft.* In 33rd Congress of International Council of the Aeronautical Sciences ICAS, Stockholm, Sweden, 2022.

Kim, D., Taneri, M., Omoarebun, E.N, Wills, T., Balchanos, M., & Mavris, D. (2023). *MBSE-Enabled System Verification and Process Improvement of Transport Aircraft Certification.* Accepted and to be presented In AIAA SciTech 2023 Forum, National Harbor, MD, January 23-27, 2023.

Written reports

December 2021 ASCENT Quarterly Report, ASCENT Project 61. (2022, January 30). *Noise Certification Streamlining*. Award number 13-C-AJFE-GIT-066.

March 2022 ASCENT Quarterly Report, ASCENT Project 61. (2022, April 30) "*Noise Certification Streamlining*. Award number 13-C-AJFE-GIT-066.

June 2022 ASCENT Quarterly Report, ASCENT Project 61. (2022, July 30). "*Noise Certification Streamlining*. Award number 13-C-AJFE-GIT-066.

September 2022 ASCENT Quarterly Report, ASCENT Project 61. (2022, October 30). *Noise Certification Streamlinin*g. Award number 13-C-AJFE-GIT-066.

Annual Report (period ending September 2021), ASCENT Project 61. (2021, December 12). *Noise Certification Streamlining*", Award number 13-C-AJFE-GIT-066.

Outreach Efforts

- Completed follow-up meetings with OEM partners for feedback on the certification model through Spring 2022.
- Completed a project overview and a capability demonstration to VOLPE and requested information for model finetuning.
- Participated in conferences (ICAS and AIAA SciTech).

Awards

None.

Student Involvement

- All participating graduate students have supported Task 1 activities by contributing to the literature and background search and reviewing current regulations and FAA-instructed certification procedures.
- Recent efforts to document current regulations for UAS noise certification are currently led by Balaji Ravikanti.

Plans for Next Period

- Plan a series of workshops with partners and subject matter experts on rotorcraft and small propeller-driven air vehicles.
- Demonstrate noise certification based on NPRM 86 FR 48281.
- Demonstrate an EP assessment through certification modeling across different UAS configurations.
- Publish articles with AIAA Journal and AIAA SciTech.

Task 2 - Develop a Streamlined Noise Certification Procedure for Existing Aircraft

Georgia Institute of Technology

Objectives

Task 2.1: Current Process Assessment

- Identify which aspects of the present process would benefit from the proposed concept. As current procedures are captured and mapped against the regulatory requirements, this task seeks to enable an assessment capability for testing equivalent procedures within the overall certification model.

Task 2.2: Streamlined Process Definition

- Incorporate feedback from industry partners with identified areas of improvement over the present process to formulate a new certification process.
- Focus on the use of technology that seeks to transform the certification to a simpler process that can still demonstrate that regulatory requirements are being met.
    - Process modeling within Task 4 should also yield improvements in the cost and efficiency of the noise certification process.

Task 2.3: Streamlined Process Assessment and Revision

- Solicit feedback on the proposed process alternatives from the FAA, VOLPE, and industry partners.
- Revise the suggested process, which incorporates key aspects of the collected feedback in order to build a consensus among the research partners.

[UAS Pivot] Task 2: Develop a Library of UASs and Testing Procedures (Year 3)

2.1 Perform a technical documentation of UASs.
2.2 Conduct a technical documentation of UAS noise testing equipment.
2.3 Define UAS noise test plans.
2.4 Define possible simulation techniques.

Research Approach

Task 2.1 Current Process Assessment

Work that has been completed under Task 1 with benchmarking of current practices, as well as input from the workshops, will be compiled and used to inform a certification process model formulated in SysML (implemented in MagicDraw and Cameo Toolkit software tools). To enable reusability and flexibility for testing equivalent procedures, the MBSE-enabled platform allows the representation of systems from documents to explicit representation of systems via models; hence, it merges product information and engineering models. The platform provides a consistent system model that everyone can "view," maintaining a shared system model as the authoritative source of information, a feature that is helpful in preserving a common understanding among people with different roles and responsibilities. MBSE allows regulations and requirements to be linked to certification steps and can represent links and associations between regulations. This approach improves communication among stakeholders, complexity management, and precision of operational use cases; thus, it addresses common issues that arise during certification audits, e.g., requirement traceability, configuration management, document control, and change impact analysis. In sum, information previously captured in individual silos is now integrated together to enable greater transparency (including technical baselines, resources, workflow, etc.).

For Task 2 and particularly subtask 2.1, the goal is to assess current noise certification procedures by implementing an MBSE-enabled model. Typically, MBSE methods are used to represent a vehicle's lifecycle and enable the use of data and information as an integrated systems engineering approach. In the case of Project 061, the product is a process architecture, within which current procedures will be assessed, and equivalent procedures will be proposed, defined, implemented, and tested within this environment. The overall progression from the building blocks and subject matter expert input provided by Task 1 to the full MBSE model formulation for certification and implementation is showcased in Figure 15.

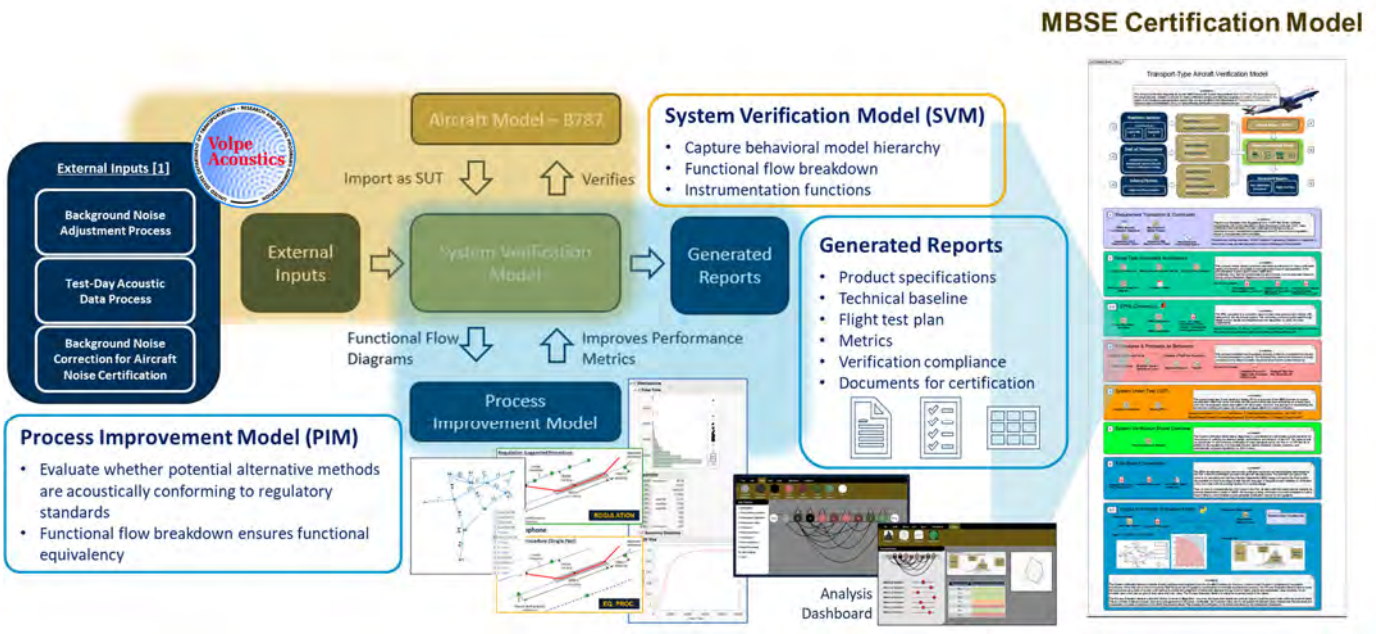

Figure 15. Model-based systems engineering (MBSE) approach for the noise certification modeling platform. SUT: system under test.

The roadmap for creating an MBSE system architecture is not unique. Several approaches have been introduced in the literature, but a commonly preferred option is the requirements–functional–logical–parametric approach (More, 2011) which maps to the traditional systems engineering "Vee" approach. A custom model development process was created to capture the functional architecture of the noise certification process, as shown in Figure 16. Marked in blue are inputs to the process that are provided by activities outside of the MBSE environment, which include an operation concept of the certification (as documented in Tasks 1.1 and 1.2), as well as requirements that represent Part 36, Appendix A and Appendix B regulations for noise. Moreover, these inputs are a placeholder for importing the validation protocol for instruments used in aircraft noise certification testing, as well as a representation for flight test plans, as adopted by airframe OEMs.

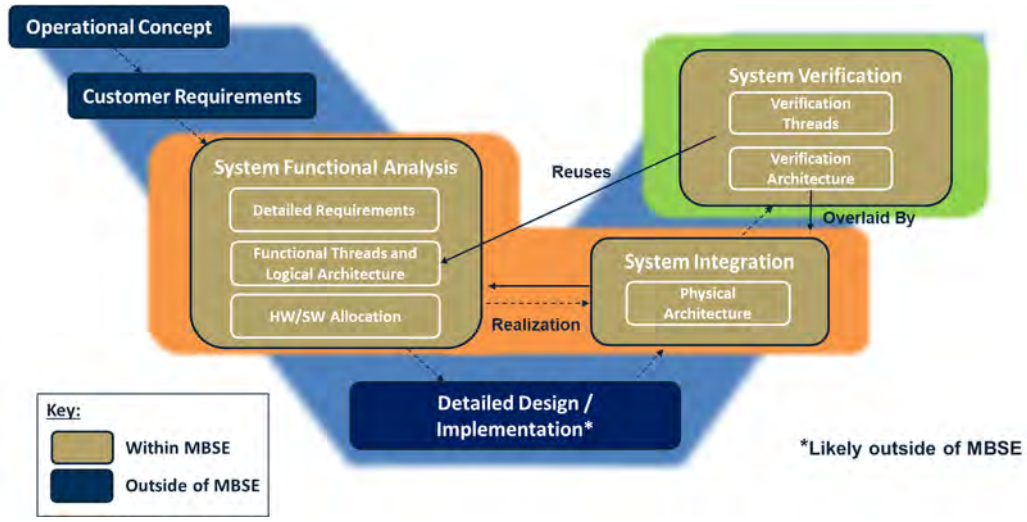

Figure 16. Model-based systems engineering (MBSE) architecture and functional model development workflow, leveraging the requirements–functional–logical–parametric approach. SW: Software; HW: Hardware.

The activities shown in gold within the process are the aspects of system modeling that are captured within the MBSE environment. As shown in the development flow, regulations and information about the certification process are captured as requirements and functional blocks within the model. A digital thread is created between the regulation, requirement, and function to build a verification thread. The form in the certification process that displays a function is also threaded by an <<allocation>> relationship to build a full digital thread from the certification standard to the form that verifies the standard.

Following the requirements–functional–logical–parametric approach, a more detailed workflow has been formulated toward implementing the verification model. This version is shown in Figure 17, where the steps for converting input information (artifacts shown in blue) toward a completed model in SysML are further explained. In the middle part of the figure, artifacts and templates provided by the OEMs used during the certification are converted into model representations in SysML. For instance, a requirement model in SysML is populated by requirements extracted from Title 14 CFR Part 36, Appendices A and B (FAA, 2017), through a process developed in-house (as discussed later in this document).

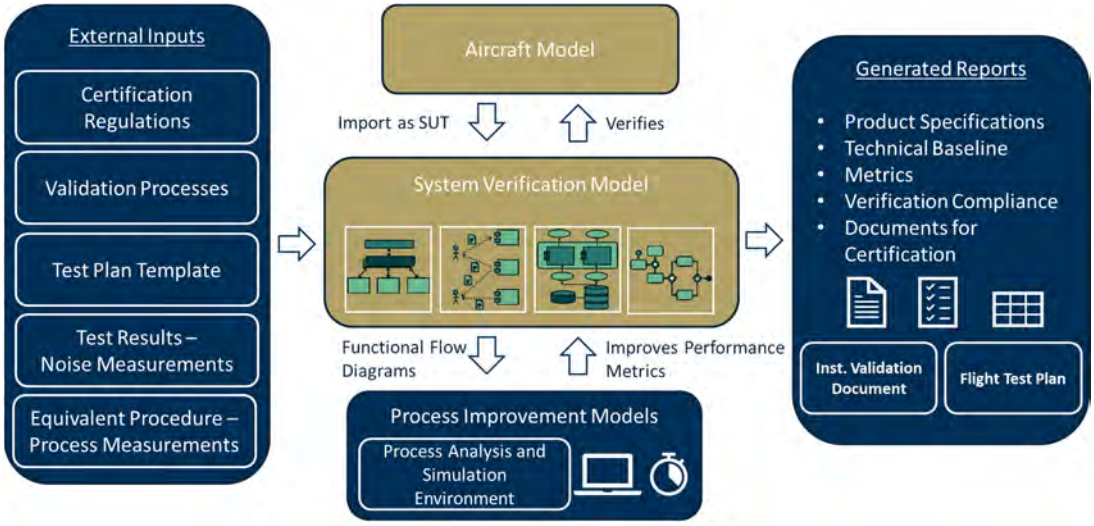

Figure 17. Model-based systems engineering (MBSE) verification model structure. SUT: system under test.

The validation process contains the steps needed to showcase that vehicle noise levels calculated from flight testing results are meeting the requirements. Part of meeting the requirements is the instrumentation setup, which is implemented as a logical architecture within the model. A library of instrument model representations is also constructed, from which alternative instrumentation lineups can be modeled. The latter feature is key, as this framework should allow for the evaluation of equivalent procedures, e.g., lateral microphone placement. Other components of the verification model are the test procedures and the test report checklist, which are prototyped as activity diagrams in SysML, as well as the vehicle configurations represented as a state machine.

Completing the verification model is any applicable regulation text in the form of a SysML verification thread. With the verification model in place, the user can import any aircraft model, perform the certification equivalent process by executing the verification model, and then generate a final report, which would contain the instrument validation document and flight test plan. It is crucial that the overall framework be implemented in a highly modular fashion in order to obtain the needed flexibility for testing equivalent procedure alternatives and for accommodating a broader range of air vehicle designs and configurations. Following the structure of the verification model shown in Figure 17, the SysML implementation is currently comprised of the following modules:

1. Requirement translation and constraints
2. Noise testing instrument architecture, e.g., EPNL conversion
3. Procedures, protocols, and behavior
4. SUT
5. System verification model overview
6. Auto-report generation and output to process evaluation model

Model Refinement with VOLPE Assistance

Modules 1–3 from the list above have been further refined with regard to definitions and representations. This refinement was enabled by documents and training modules that were received from VOLPE, including the following documents (VOLPE, 2018; VOLPE, 2003; VOLPE, 2003; FAA, n.d.; Aleksandraviciene, 2018):

- Implementation of background noise adjustment
- Background noise correction for aircraft noise certification
- Test-day processes (acoustic data, adjustments, instrumentation, etc.) in diagram format

After a thorough review of the material, the ASCENT 061 team was able to extract the needed information and apply it on certain views within the MBSE certification model. A key outcome was the generation of process flow diagrams, as shown in Figure 18, which provide the basis of the event process models needed to improve the accuracy of the PIM within the certification framework.

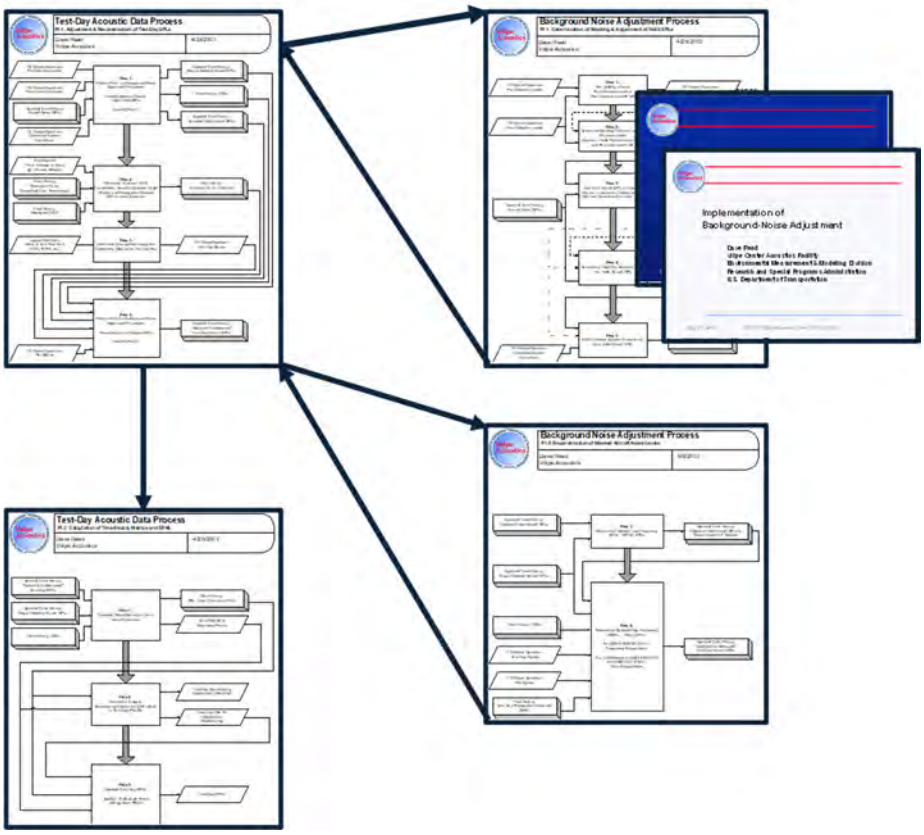

Figure 18. Use and association of content provided through documents shared by VOLPE.

Event Process Modeling

With detailed guidance from the documents listed above, event-driven processes were defined and created within the certification model. Additions include modeling of the test-day acoustic collection process and test scenario event processes (takeoff, approach, flyover). A thread that shows the various hierarchy levels of activity diagrams was established, as shown in Figure 19.

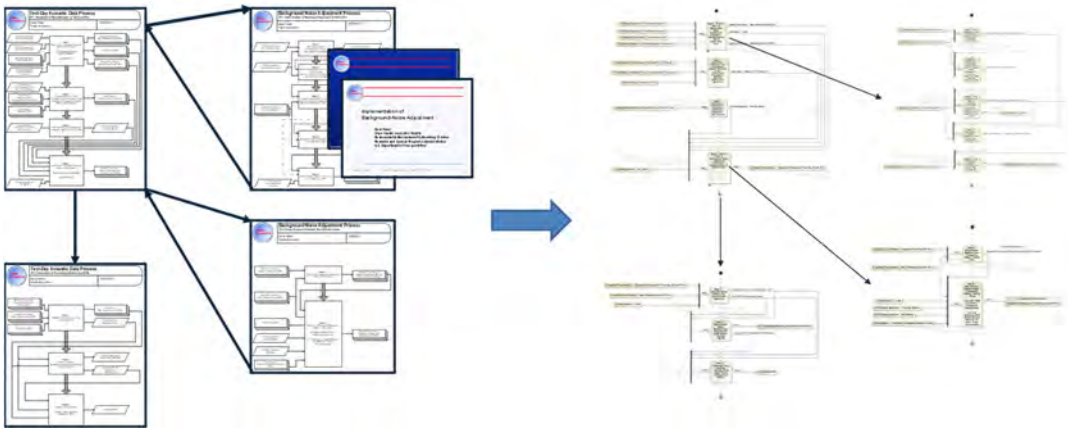

Figure 19. Definition of event processes for certification testing and conversion to SysML views.

Library Creation
A new task was identified to command the creation of libraries within the certification model, in order to allow for added flexibility and modularity, in response to Task 3 requirements. Current libraries include the aircraft library, engine library, microphone library, and data amplifier library. The SUT representation has been modified to allow for adaptability to various aircraft/engine types and configurations, including UASs.

Aircraft Testing Environment
Another finalized improvement on the certification model is the modeling of the transport aircraft test environment, including the flight test setup configuration. With input from the documents shared by VOLPE, the model was updated and refined to include the addition of various instrumentation system architectures.

Noise Calculation
Aircraft noise certification typically requires noise measurements at three reference points: flyover, lateral, and approach. Therefore, EPNL calculation was established by considering three different maximum permitted noise levels. The process was tested against a known flight dataset from an industry partner for a transport category aircraft that has been certified. The test data contain a spectral noise history of the aircraft at an unknown reference point, without the inclusion of background noise adjustment or reference condition corrections. The metrics of interest include the following:

- *Annoyance-based measure or EPNL* (in units of EPNdB). This metric accounts for subjective effects of aircraft noise on humans over the duration of the perceived noise level (PNL). Because certification-quality EPNdB cannot be directly measured, it is calculated as described in the Annex 16 standard.
- *Loudness-based measure*. For this metric, the maximum sound exposure level is calculated (in dBA units).

The available data for sound pressure levels, frequency distributions, and time variation measurements are used to evaluate levels in EPNdB units and to validate the EPNL tool in the verification model. EPNL is widely used in aircraft noise projections and is based on prior loudness models. While loudness is considered the most effective contributor to annoyance, other attributes such as sharpness, tonelessness, roughness, and fluctuation strength may also affect the annoyance perceived. FAA's EPNL metric considers intensity, tonelessness, and duration of the aircraft noise.

Before the EPNL is calculated, corrections must be applied to the measured data to account for uncertainties related to the measurement system, microphone and recording system used, background noise, actual flight path, and meteorological conditions present when the measurements were taken. A conversion process of the flight test data is required to obtain certification-quality EPNdB, as it cannot be directly measured from raw test data. The standardized conversion process is described in ICAO Annex 16, which contains the aircraft noise standards. The EPNL calculation is performed utilizing the programs written by More (2011) as per ICAO Annex 16. The steps for EPNL calculation, per the ICAO-recommended practice, are as follows:

1. Convert the sound pressure level (SPL) to the instantaneous PNL for each 0.5-s sample, by means of a noy table.

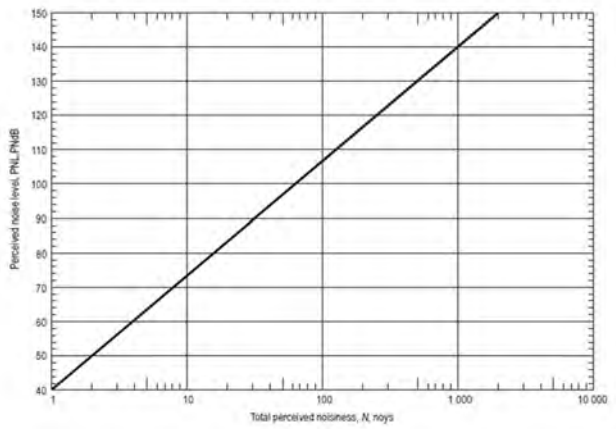

Figure 20. PNL as a function of total perceived noisiness.

2. Calculate the tone correction factor C to account for the subjective response to the presence of spectral irregularities.
3. Calculate PNLT = PNL + C, for each 0.5-s increment of time.
4. Calculate the duration correction D for the entire flight (where T = 10 s and $\Delta t = 0.5\ s$).

$$D = 10 \log \left[\left(\frac{1}{T} \right) \sum_{k=0}^{d/\Delta t} \Delta t \cdot \text{antilog} \ \frac{\text{PNLT}(k)}{10} \right] - \text{PNLTM}$$

5. Calculate EPNL = PNLTM + D, where PNLTM = max(PNLT).

The validation results are depicted in Figure 21, where the available flight test data are compared with the calculated PNL values. The results show that the PNLs calculated from the sound pressure levels align with the validation data, except for a small peak between 20 and 25 s with a difference of less than 1%. The corrected PNLs are also depicted in the figure as a reference; however, these values could not be compared against known data, as the given dataset was limited to the uncorrected values. Therefore, EPNL is calculated with both corrected and uncorrected PNL values. As the results show, the EPNL tool used in the verification model can match the validation data. For comparison, the maximum noise levels from the requirements are also provided at flyover, lateral, and approach reference points. The data used to validate our EPNL conversion tool were provided by one of our industry partners and include raw noise measurements from a previously certified transport aircraft.

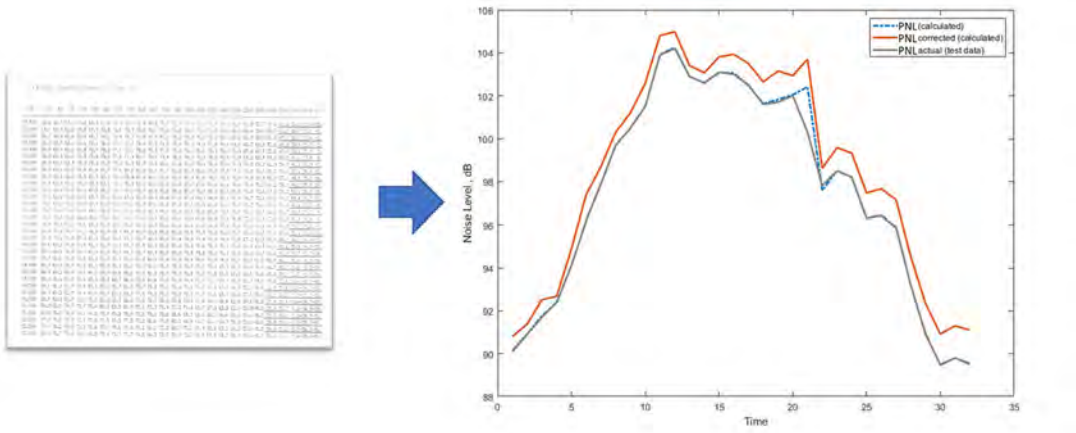

Figure 21. Validation results for the effective perceived noise level (PNL) analysis module.

Regarding the implementation of noise metric calculations, there is no option for directly performing such analyses within the SysML-based certification model. A possible solution is to create a function in MATLAB and then incorporate the analysis in the verification thread. For this purpose, a version of a software tool written in MATLAB for calculating the EPNL, based on 14 CFR Parts 36 and 91 (Konzel, 2022), was identified in the literature. Expanding on the logical architecture library, the EPNL calculation has been implemented through a block representation in the MBSE framework, as shown in Figure 22. The team completed the integration by effectively linking the EPNL calculation to the MATLAB source code of this analysis through use of the Cameo Simulation Toolkit (More, 2011).

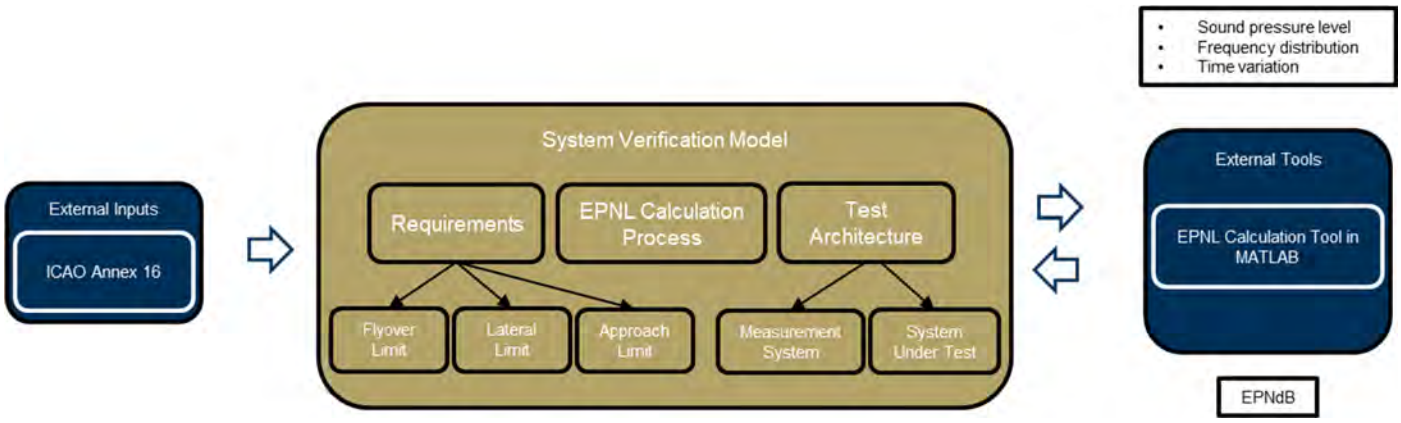

Figure 22. Integration of effective perceived noise level (EPNL) analysis in the verification thread. ICAO: International Civil Aviation Organization.

In conclusion, Task 2.1 is complete, resulting in a verification model that allows for a basic certification assessment (for the transport category). However, several improvements and additions are required before the fully planned capability is in place. Planned improvements include targeting the expansion to the UAS category, as follows:

- Repurpose the verification model for other categories, particularly for UASs.
  - This step will be further addressed by Task 3.
- Build test constraints for the SUT for UASs.
  - Import regulations from CFR Title 14 Part 36 Appendix G, J, and H and translate to verifiable requirements.
  - Define constraints with numerical/logical limits and apply to systems.
- Document the EPNL calculation process to verify noise constraints on the SUT.
  - Import raw noise testing data into the verification model (data possibly available through ASCENT 077).
  - Verify noise requirements using EPNL-converted noise data.

Task 2.2 Streamlined Process Definition

The objective for this task is to explore options for formulating streamlined certification process alternatives, driven by feedback from the OEM partners. The following target objectives for streamlining the certification process are currently being considered:

- Reduce the number of steps in the process, with an anticipated savings in time and cost. Replace steps, mostly in analysis, data preparation, and post-processing, with digital tools.
- Enhance automation on procedural tasks (e.g., data retrieval, queries, processing, and report generation).
- Implement affordable technology solutions, e.g., virtual sensing. The goal is to utilize digital tools that will allow the omission of physical instrumentation, such as lateral microphones.

A comprehensive literature search led to the identification of options for equivalent procedures, and the findings are summarized in Table 3. However, in follow-up discussions with OEM partners, it was concluded that potential improvements in noise certification procedures and testing extend beyond time and cost savings. Possible higher value-added improvements to streamline noise certification (with input kindly provided by Boeing) are as follows:

- Simplify setup requirements to facilitate more test locations/weather windows (i.e., remove 4-ft microphones for the ground plane and remove lateral locations all together).
- Evaluate NAC limits in the context of testing uncertainty.

- Address conformity issues by formulating an acoustical conformity concept.
- Expand the use of certification by analyses to expedite approval procedures within the FAA. This step would involve criteria developed for approval for acoustical analyses that define new certification noise levels (acoustical change by analysis), leading to a framework for oversight that gives FAA confidence in the manufacturer tools/methods used.

Along with the selection of the equivalent procedures of interest, based on the above feedback, the outcome of Task 2.2 is to present certain use cases for which a feasibility demonstration of an equivalent procedure would be possible. This effort would require data for calibrating the certification model against the SUT configuration and for showcasing quantifiable improvements against the process criteria listed above, while meeting the same regulatory constraints and requirements as the benchmarked certification procedure.

Table 3. Summary of options for equivalent procedures (EPs) provided by workshop/interview feedback.
(Note: This is an inclusive list of findings collected through the partners' responses and does not determine the final outcome nor any chosen direction, as these options are still under discussion between the team and project partners.)

Title/summary of EP or a grouping of EPs	Time savings	Cost savings	Providing compliance flexibility to the applicant
Flight path intercept in lieu of full takeoff/ landing profiles	Yes (by factors of 5-10)	Yes (less wear, less maintenance)	
Lateral mic placement (single or multi pair)	Possibly (multiple = better data)	Yes (single pair)	
Derivation of noise-power-distance (NPD) data (data reduction/expansion by analysis, based on few points)	Yes (several weeks)	Yes	
Approved measurements at non-reference points (adjusted data)		Possibly	Yes (in test conditions/ site selection)
Exceeding sound attenuation limits allowed in some cases			Yes (in test conditions)
Static-to-flight projections (not making a new noise-power-distance (NPD) database)	Yes (no flight test for derivations)	Yes (no flight test for derivations)	Possibly (gives a noise change range for derived versions)
Inflow control device & calibration options (for change of engine)			? (provides an option to certify engine change)
Cert by analysis noise-power-distance (NDP) data extrapolation for design changes with predictable noise effects)	Yes (no flight test for derivations)	Yes (no flight test for derivations)	

A potential use case (also endorsed by OEM partner feedback) is an alternative setup and placement of the lateral microphone. The microphone setup must abide by Regulatory Requirement B36.3, B36.4, which relates to "Measurement point(s) defined as point(s) on the line parallel to and 1476 ft (450 m) from the runway centerline, where noise level is a maximum during takeoff." The main benefit of this alternative layout is the reduction in complexity that is present due to the use of multiple microphone arrays along the lateral line, aside from direct savings in acquisition and maintenance costs and the time needed for setting up. As a drawback, however, this solution covers a smaller sound field than multiple arrays, and more test points may be needed to obtain sufficient data for compliance (accuracy, data quality). The top panel in Figure 23 displays the current microphone setup and how their locations are chosen.

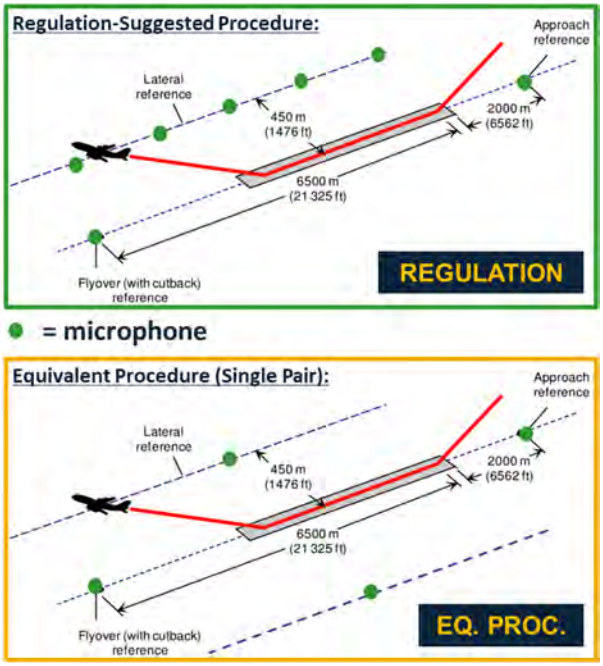

Figure 23. Equivalent procedure example: a lateral microphone setup **Error! Reference source not found.**.

For the proposed equivalent procedure, a single pair of symmetric microphone stations is considered, with a placement as shown in Figure 23. With the use of the verification thread and for a given aircraft model as the SUT, the following constraints and requirements must be met:

- Full takeoff power, configuration, and airspeed as in Regulation B36.7(b)(3-4)
- At several specified heights above a track (covering a range of 200–2000 ft)
- At right angles to and midway along the line joining the two microphone stations
- Lateral noise determination based on matching data from both lateral microphones for each fly-past
- Adjusted noise levels: symmetric OR asymmetric (one or two regression curves)
    - Usually second order; justification needed for exceptional use of third order
- Confidence interval of reported EPNL within +/- 1.5 dB (Regulation A36.5.4)
- Minimum of six runs to obtain sufficient data for compliance

Task 2.3 Streamlined Process Assessment and Revision

For this task, the objective is to further assess the feasibility of the proposed equivalent procedures and apply any revisions, per feedback from the FAA, VOLPE, and industry partners. The quantitative assessment, which will be supported under the PIM module developed under Task 4, is the main enabler for allowing an iterative process until process alternatives can meet the expectations for process streamlining and simplification.

This task is currently underway. As additional meetings with OEMs have been held, it has become evident that obtaining past test data from OEMs and/or gaining additional insight into a test baseline and testing plan would be difficult. In the interest of time and with the lack of testing data and lack of direct access to information for providing a SUT baseline, a decision has been made, with support by the FAA AEE, to immediately pivot to a UAS category SUT for the framework demonstration. As mentioned above, the existing connections and synergies with other ASCENT projects are expected to provide the resources needed to support the demonstration of this framework as a platform for evaluating equivalent procedures. An expanded breakdown of Task 2.3, specific to UASs, is provided in the next section.

[UAS Pivot] Task 2: Develop a Library of UASs and Testing Procedures

Research tasks on investigating and archiving technical documentation of UASs, as well as recommended procedures for noise testing, started in July 2022. One of the key studies that the ASCENT 061 team has started to document and that has been valuable in identifying the most important technical challenges for UAS noise testing is the document entitled “Noise

Measurement Report: Unconventional Aircraft" by the Choctaw Nation of Oklahoma (July 2019). The described practice for UAS noise testing took place on a grassland, which, taking the flight envelope into consideration, is not suitable due to the following reasons:

- Dense areas can have a different "perceived" noise.
- High altitudes and dense areas over buildings and hard surfaces can have different reflective behaviors.
- Within buildings, noise can be reflected, amplified, or attenuated.

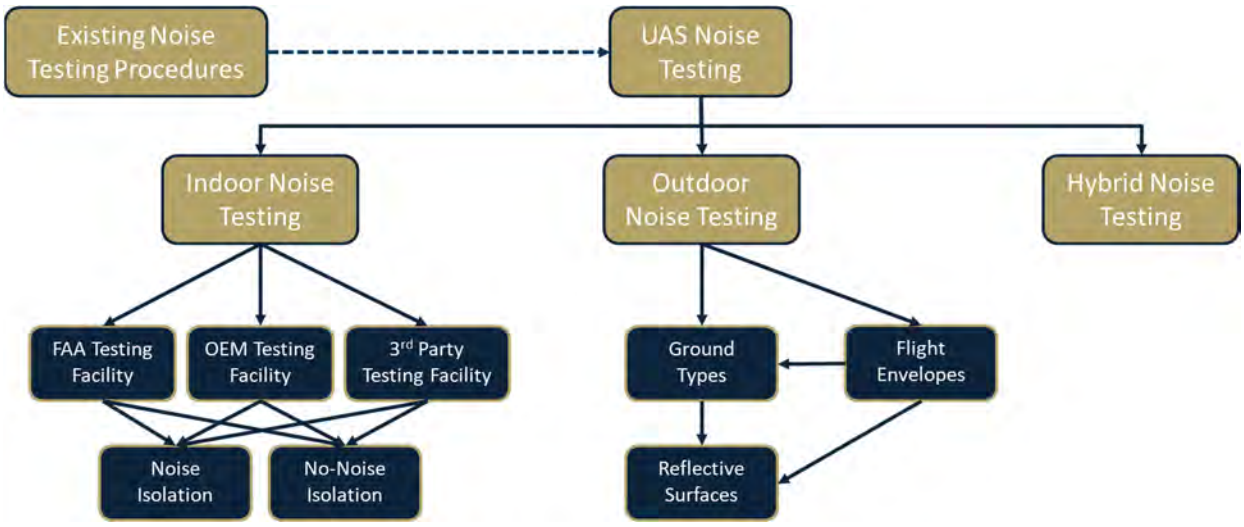

Figure 24. Alternative noise testing procedures for an unmanned aerial system (UAS). OEM: original equipment manufacturer.

Part of this grassroots effort in discovering the state of the art is the technical documentation on UAS noise testing equipment. By assessing testing procedures from a regulatory perspective, we can build some simple alternatives under the system verification model, and examples are shown in Figure 24. Finally, the UAS noise test plans must be defined and executed. Physical testing will not cease to exist, but simulation techniques are needed for testing process alternatives.

Milestones

- A first complete version of the noise certification process model has been implemented in SysML.
- Through the verification model, the applicability of MBSE methods for this problem has been demonstrated.

Major Accomplishments

- A noise certification process model represented in SysML has been completed, where equivalent procedures can be tested through a requirement verification model.
- UAS noise testing practices and processes have been documented.

Publications

None.

Outreach Efforts

- Provided a full Year 2 performance review to the FAA AEE
- Technical discussions and feedback provided by VOLPE
- Collaboration with ASCENT 077 and Dr. Eric Greenwood's research group

Awards

None.

Student Involvement

- The implementation of the verification model required significant skillset development in the use of SysML and software, which all students were successfully able to acquire.
- All students participated in the integration of all main enablers into a first complete version of the verification model.

Plans for Next Period

- Finalize the baseline model for current certification practices for UASs.
- Proceed to the next steps for MBSE framework development:
  - Model finetuning, consistent format, reusability, easy navigation setup
  - UAS configuration definitions
  - Noise testing procedures
  - Process alternatives and evaluation
- Identify use case examples to plan for demonstration, based on selected areas of improvement.
- Implement an interactive decision support tool to aid in further showcasing the capabilities of the MBSE framework through the selected use case examples.

Task 3 - Develop a Flexible Noise Certification Procedure for New Aircraft

Georgia Institute of Technology

Objectives

The focus of Task 3 is to develop an overall definition of a more flexible certification process and the evaluation criteria for determining that the procedure is more streamlined than the baseline. The pivot to a UAS focus is well aligned with the objectives of this task, where flexibility will be driven by the requirement for the MBSE model to accommodate a range of UAS configurations and payloads. Task 3 will build upon the capabilities of the integrated MBSE platform and leverage contributions from all other tasks. The following subtasks will be conducted under Task 3:

Task 3.1: Flexibility Assessment of Streamlined Process

- Evaluate the flexibility of the streamlined noise certification process for new category air vehicles.

Task 3.2: Flexible Process Definition

- Define and recommend improvements for the streamlined noise certification process to accommodate a flexible noise certification process with respect to vehicle type.

Task 3.3: Flexible Process Assessment and Revision

- Solicit feedback on the new process from the FAA and industry partners.
- Perform a revision of the suggested process by incorporating key aspects of the collected feedback in order to build a consensus among research partners.

Research Approach

Task 3.1

Task 3.1 seeks to define what is meant by a “flexible” process. One way to develop this definition to determine whether the introduction of a different vehicle configuration leads to a large number of incompatibilities with the streamlined process under evaluation. For instance, it is important to assess how the rotorcraft configuration affects the microphone technology and quantity needed and the microphone placement in the testing facility. This subtask will involve testing procedures, and a mapping of compatibilities between vehicle configurations and testing procedures will be produced. A set of criteria and evaluation metrics is needed in order to assess the combinations of vehicle configuration, testing procedures, and uncertainty factors against regulatory-derived requirements, which will be implemented within the MBSE certification framework. Hence, a proposed set of flexibility criteria for the certification process could include the following:

- Compatibility and applicability of equivalent procedures
- Complexity (e.g., if a switch to another configuration requires more steps to setup) and additional instrumentation if a vehicle is more sensitive to variations in certain factors during testing
- Sensitivity to NACs different than other categories
- Sensitivity to weather, etc.

The defined criteria will be tested and applied in the following tasks; hence this task is considered as completed.

Task 3.2

Based on the verification model available for the transport category, a first iteration of the proposed concept for evaluating a flexible certification process has been formulated, as presented in Figure 25. The original model is sufficiently flexible to accommodate a different set of regulations as one of the inputs, which, like in the transport category example, will undergo a conversion to requirements based on a digital thread and a requirement model in SysML. The fields that are currently undergoing adjustments are highlighted in orange, and the algorithm modifications for the logical conversion are in progress. Similarly, a conversion of the noise instrument validation protocol to SysML views is underway. However, the vehicle representation model (top right in Figure 25) is not process-dependent, and the interface definitions require modifications for this module to interface with the verification model.

After considering the above modifications, a UAS-specific version for the MBSE certification framework has been formulated, as showcased in Figure 26. The ASCENT 061 team has been working to convert the following information items into SysML views:

- Certification regulations: An updated requirement model has been finalized, based on guidance from Appendices H and J and with the use of the NPRM (FAA, 2022) as a template.

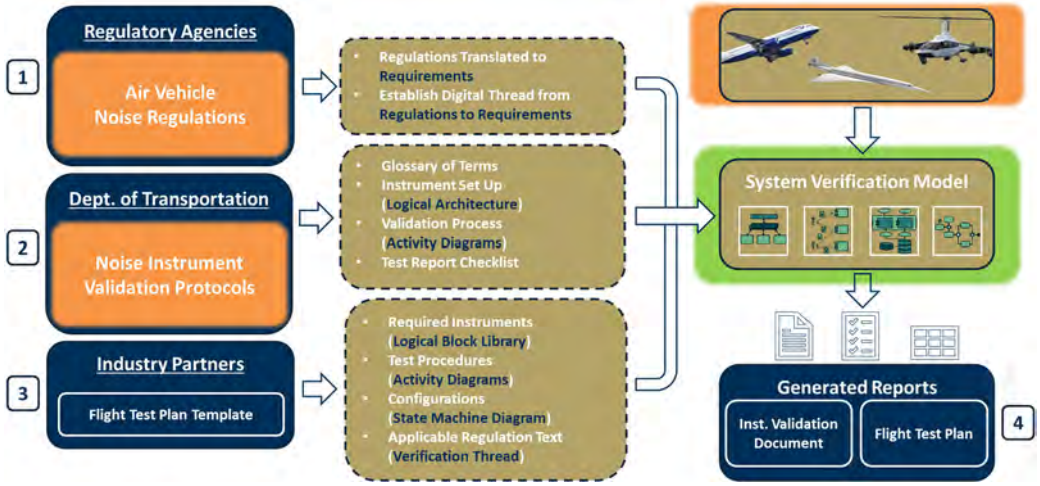

Figure 25. Verification model for multiple vehicle configurations.

- Validation processes: Validation processes are driven by current guidance from the NPRM-derived instruction for UAS certification testing.
- Test plan template: The Matternet (USDOD, 2022) example for certification testing has been used to generate a testing plan template.
- Test results and noise measurements: The ASCENT 061 team is collaborating with the ASCENT 077 team and has obtained samples of noise measurements in order to further define the analysis functions that will produce the validation metrics. These metrics will be used for validation and for assessments of the proposed streamlining improvements and equivalent procedures.
- Equivalent procedures: Utilizing the format of a database with equivalent procedures built for transport category configurations, the ASCENT 061 team will build a similar database and incorporate a modeling approach for assessing the impact of an alternative against the baseline.

Based on the workflow proposed in Figure 25, the integrated framework for flexibility assessment of the certification process is expected to be reusable for a broader set of UAS configurations, as highlighted in Figure 26.

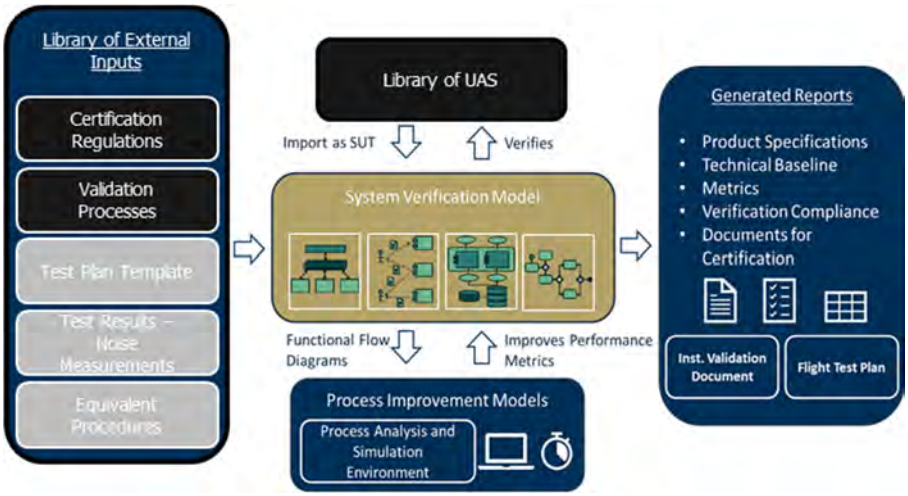

Figure 26. Model-based systems engineering certification framework version for unmanned aerial systems (UASs) to test category flexibility in equivalent certification procedures. SUT: system under test.

Task 3.3

The certification framework for UASs developed under Task 3, as well as the use of the PIM completed under Task 4, will allow for measuring process flexibility, efficiency, complexity, and other figures of merit as part of comparing alternatives to the baseline. Framing this problem as a decision-making problem, in this context, an "alternative" would be a version of the baseline certification process with a specific combination of a testing plan, instrumentation selection, and a setup for measurements and processing methods, as dictated by a possible equivalent procedure.

After the model has been calibrated with inputs and parameter definitions that will be obtained from noise testing data resulting from ASCENT Projects 077 and 094, the model will rely on statistical analysis and an identification of process bottlenecks and showstoppers. Another set of metrics of interest will target the impact quantification of process complexities and will be used to indicate gaps and further drive certification process simplification through the use of technologies and estimation methods (e.g., virtual sensing and instrumentation), where process steps could be reduced or eliminated.

As a means of facilitating a scenario-based parametric decision-making capability, the ASCENT 061 team has been developing an interactive visualization environment. Through the use of visual representations of the process and key analysis outputs, this environment serves as a user-friendly interface for requirement validation, exploration of process alternatives and their impacts, detection of process shortcomings and gaps, and ranking for the selection of test plans, instrumentation, and noise measurement data analysis against user-set criteria. The ranked alternatives are validated through an assessment of the equivalency for a procedure to standard regulatory practices. A notional representation of the final version of this environment is shown in Figure 27.

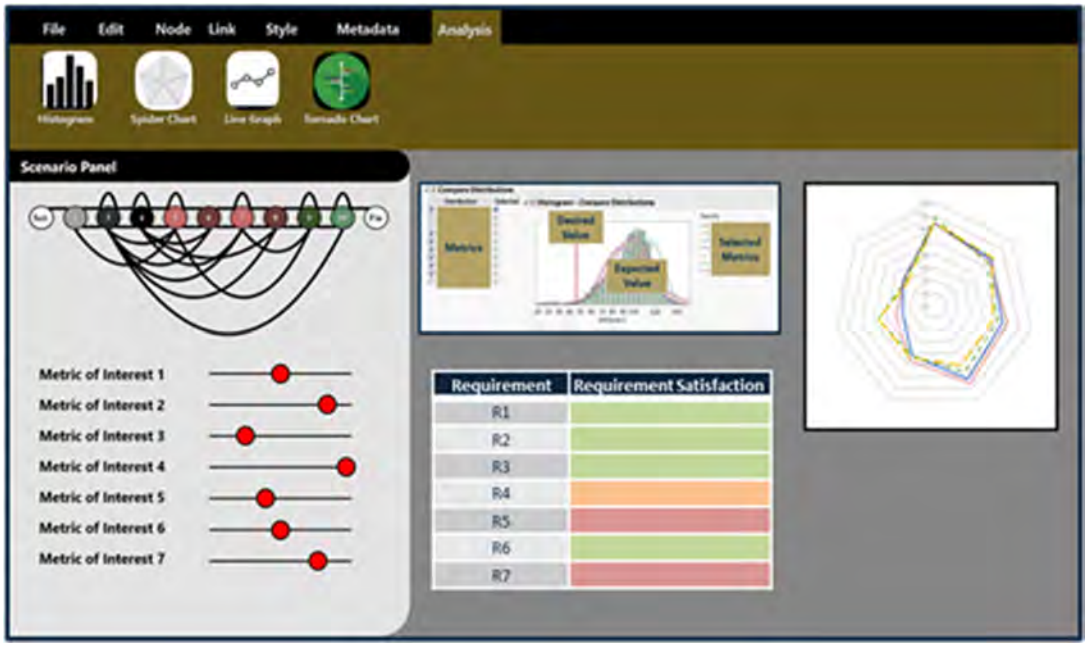

Figure 27. Graphical user interface for process specification.

As interactive dashboard development is often approached as a spiral development, the capabilities and features included in the current version are as follows:

- Left side: Here, a process alternative is represented (one at a time), including all steps of the test plan execution and the preparation and post-processing of noise data. At the lower portion of the left side of the tool, a set of slide bars allows the user to select the priorities/desirability of the evaluation criteria and metrics used (e.g., time, resources, budget, complexity, redundancy, etc.).
- Center: In this part, the focus is on data analytics supported by Monte Carlo process simulations, using probabilistic inputs. Hence, the results are typically in the form of distributions for the metrics of interest and allow for exporting means, median values, and cumulative distribution functions (CDFs) to assess whether constraints and requirements are being met. The table in the lower center portion presents an assessment check on whether requirements are being met, which is included to provide guidance toward the exploration of procedures and technologies that would help close any gaps and meet all requirements.
- Right side: For multi-variate and multi-criteria problems, a spider chart is used to compare process alternatives against multiple criteria. This chart can help to drive the evaluation of all tested process alternatives and map the strengths and weaknesses of each alternative against the prioritized evaluation criteria.

An early version of the interactive certification process exploration and selection capability, built as a minimum viable product, is presented in Figure 28. In this version, the user can prioritize the process evaluation metrics, represent the certification process alternative of interest as a graph, and then view all distributions obtained by Monte Carlo experiments, with statistical analysis results given in a radar plot for all alternative processes. The highest ranked process from the selection portion is displayed in its process diagram version and can then be compared with the baseline. If requirements are not met and certain capability gaps exist, the user can expand the space of process alternatives and repeat the analysis.

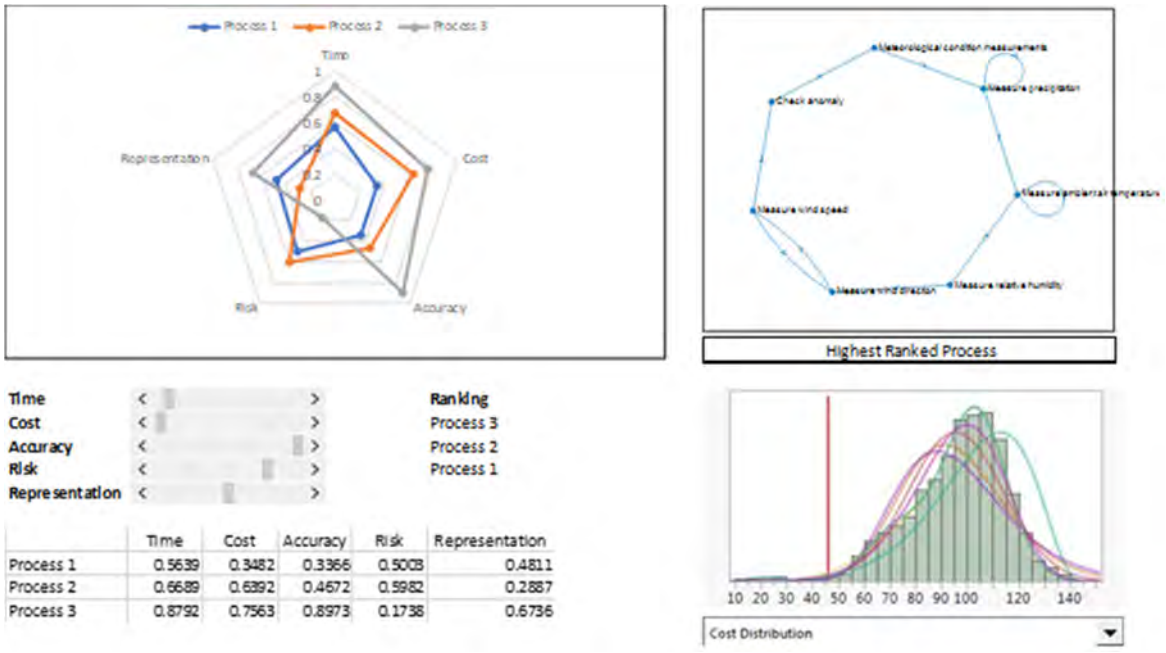

Figure 28. Early implementation of a minimum viable product for the visualization environment.

To enable the multi-criteria, parametric, and interactive capability for rapid exploration of certification alternatives, the PIM, which executes a process simulation through Markov chains and graph analysis, can allow probabilistic Monte Carlo simulations for investigating the limitations of each process alternative. This capability is primarily the focus of Task 4 and is presented in the following section of this report.

Milestones

Please see the milestones under Task 1.

Major Accomplishments

- An initial concept formulation and implementation roadmap have been completed for the MBSE framework to accommodate multiple UAS types and to allow for process effectiveness and flexibility evaluation.
- Metrics have been developed and the PIM has been integrated under a parametric interactive decision support environment. The concept has been demonstrated through a minimum viable project exercise.

Publications

None.

Awards

None.

Student Involvement

The full student team has participated in brainstorming sessions toward formulating the integrated certification process assessment framework for UASs.

Plans for Next Period

- Perform a morphological matrix exercise to explore and identify feasible certification process alternatives, based on permutations of UAS type, testing plan, testing and sensing technologies, data analysis methods, and map options for evaluation criteria.
- Finalize process evaluation metrics and incorporate them in the next iteration of the decision support tool.

- Demonstrate a simple use case, where a number of feasible alternatives lead to comparisons with the process baseline. The use case and the improvement propositions within the alternative options will be formulated with input from subject matter experts and current gaps in meeting certification targets.

References

Metzger, F. B., & Foley, W. M. (1970). *Stol aircraft noise certification-a rational approach*. SAE Transactions. 700325. https://doi.org/10.4271/700325

U.S. Department of Transportation, Federal Aviation Administration. (1969). *Federal Aviation Regulation, Part 21, Certification Procedures for Products and Ports; Part 36, Noise Standards: Aircraft Type Certification*. https://www.ecfr.gov/current/title-14/chapter-I/subchapter-C/part-36

Ollerhead, J. (1968). *Subjective Evaluation of General Aviation Aircraft Noise* (Technical Report NO-68-35).

Senzig, D.A. & Marsan, M. (2018). *UAS Noise Certification*.

FAA (2023). 14 CFR Part 36 – NOISE STANDARDS: AIRCRAFT TYPE AND AIRWORTHINESS CERTIFICATION. https://www.ecfr.gov/current/title-14/chapter-I/subchapter-C/part-36

FAA. (2017). *Advisory Circular 36-4D – Noise Standards: Aircraft Type and Airworthiness Certification*.

Federal Register. (2022). *Noise Certification Standards: Matternet Model M2 Aircraft* (NPRM 86 FR 48281). https://www.federalregister.gov/documents/2022/09/12/2022-19639/noise-certification-standards-matternet-model-m2-aircraft.

FAA. (2022). *Noise Certification Standard: Matternet Model M2 Aircraft*. https://www.regulations.gov/document/FAA-2021-0710-0016.

US Department of Defense. (2022). *Systems Engineering Guidebook Section 4.2.7.* Office of the Deputy Director for Engineering. Washington, D.C.

VOLPE Guides, "Validation Protocol for Digital Audio Recorders User in Aircraft-Noise Certification Testing" [2010].

VOLPE Guides, "Audio Recording & Analysis System Validation Checklist" [2018].

VOLPE Guides, "Test Data Acoustic Data Process" [2003].

VOLPE Guides, "Background Noise Adjustment Process" [2003].

FAA. (n.d.) *Details on FAA Noise Levels, Stages, and Phaseouts*. https://www.faa.gov/about/office_org/headquarters_offices/apl/noise_emissions/airport_aircraft_noise_issues/levels/.

Aleksandraviciene, A. (2018). *MagicGrid Book of Knowledge*. Kansas, 2018. NoMagic.

More, S. (2011). *Aircraft Noise Characteristics and Metrics* [Ph.D thesis Dissertation, Purdue University].

Konzel, N. (2022). *Ground based measurements and acoustic characterization of small multirotor aircraft* [Masters Thesis, Pennsylvania State University].

Task 4 - Simulate Streamlined and Flexible Noise Certification Procedures

Georgia Institute of Technology

Objectives

Task 4 seeks to explore options for evaluating noise certification within the MBSE certification framework. The purpose for this task is to allow a performance baseline to be established for current procedures and to allow for the evaluation and comparison of more flexible process alternatives as they are formulated within Tasks 2 and 3. The breakdown of tasks under Task 4 is as follows:

Task 4.1: Identification of a Modeling Approach

- Explore options for modeling approaches in order to simulate and evaluate the certification process within the MBSE framework.

Task 4.2: Noise Certification Process Metric Definition

- Identify a set of metrics to allow for a quantitative comparison of the current and proposed noise certification processes.

Task 4.3: Model Calibration

- Identify a benchmark for noise certification procedure simulations.
- Perform calibration of noise certification procedure simulations.

Task 4.4: Certification Process Simulation

- Execute simulations of current and proposed noise certification procedures.

The goal of Task 4 is to identify process modeling approaches for the purpose of simulating and evaluating the performance of a noise certification procedure. Task 4 delivers a solution, which, in a broader sense, is referred to as the PIM. Tasks 4.1–4.3. focus on PIM implementation, whereas Task 4.4 integrates the PIM into the current MBSE framework. The PIM must analyze the process performance and interface with the verification model for completing steps regarding requirements and compliance. The PIM must also be flexible and reusable within the verification thread and must accommodate UAS configurations. An overview of the integrated verification thread and the PIMs is shown in Figure 29.

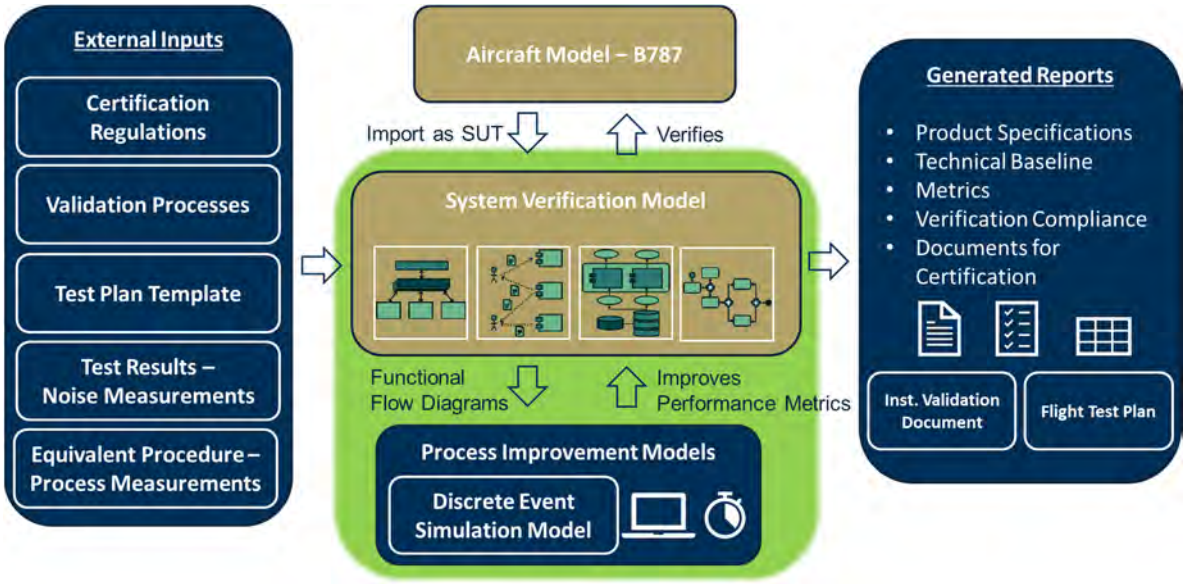

Figure 29. Integration of the process improvement model within the model-based systems engineering certification framework. SUT: system under test.

Task 4.1

The team has completed a literature review on process modeling methods to enable process simulation. These methods are listed below:

- DES, where a clock tracks the duration of the transition between model states
- Agent-based simulation methods
- System dynamics
- MCMC simulation methods

These techniques are evaluated on the basis of how well they can capture and simulate actual industry-applied procedures and their ability to interface with the verification thread. For simulating a simple process that is representative of transport category certification, the DES modeling approach appears to be the most effective. To demonstrate feasibility, a proof-of-concept version was developed using the DES method in a Python-based environment. The chosen example covered the testing process for a flyover approach, as shown in Figure 30. The objective was to demonstrate that a process model, as defined in the MBSE framework, can be simulated using DES. With the model states imported, DES can track the clock and return the time points at which each event is concluded. The DES results are then fed back as an input and update the process diagram in the verification model, which then checks the process model against requirements and compliance.

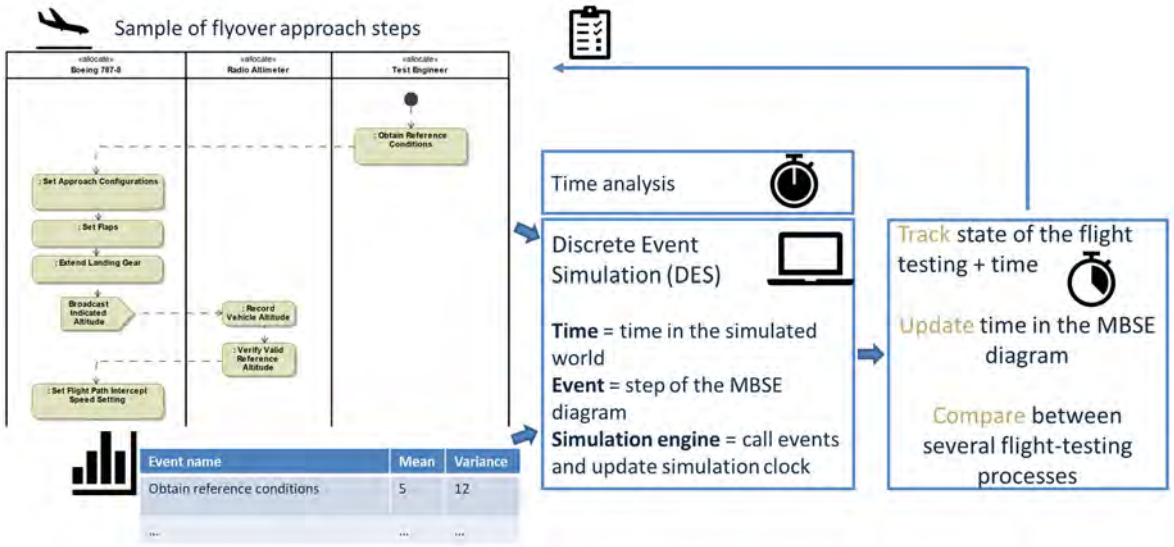

Figure 30. Discrete event simulation for a flyover approach. MBSE: model-based systems engineering.

However, because flight testing procedures are impacted by uncertainties, a different modeling approach is needed. To account for uncertainties, a probabilistic model using Markov chains has been developed to improve the accuracy of how interactions and emerging effects are captured. This approach is better suited to support use cases, with the objective of further process simplification, especially for flight testing portions, instrumentation setup, and measurement systems. This simplification could involve eliminating or replacing steps and possibly utilizing advanced data-driven or physics-based modeling approaches as a substitute.

Because of the extension of DES to Markov chain approaches and the need for large samples, the team adopted the MCMC approach, where a Markov chain model is used to run a Monte Carlo study to collect sample runs, given an input probability matrix and stakeholder value function. Each run is associated with an incurred time, cost, and accuracy penalty, and the output is provided in the form of activity diagrams and responses that are fed back to the verification model within the MBSE framework. Through the requirement model within the MBSE framework, the MCMC simulation data are imported to perform acceptance–rejection sampling, where each run (with its associated metric) is accepted or rejected by requirements/constraints within the verification model. The format of the MCMC simulation data follows the form of a step-by-step sequence (similar to a DES).

Summarizing the development of the PIM, the implementation path is shown in Figure 31, which illustrates the interface with the verification model. Using a similar flyover approach plan example, as in Figure 30, the process model informs the PIM, which converts the flyover approach test into an executable simulation model. Based on the type of requirement test selected by the user, the appropriate response values, parametric settings for baseline values (time, cost, resources, disruption risks, accuracy penalty, etc.), and distributions for Monte Carlo simulations are chosen. The Monte Carlo (MC) simulation then generates the PIM metrics and prepares the dataset for verification.

For this task, the literature search, exploration of modeling options and selection, and proof-of-concept implementation are now completed.

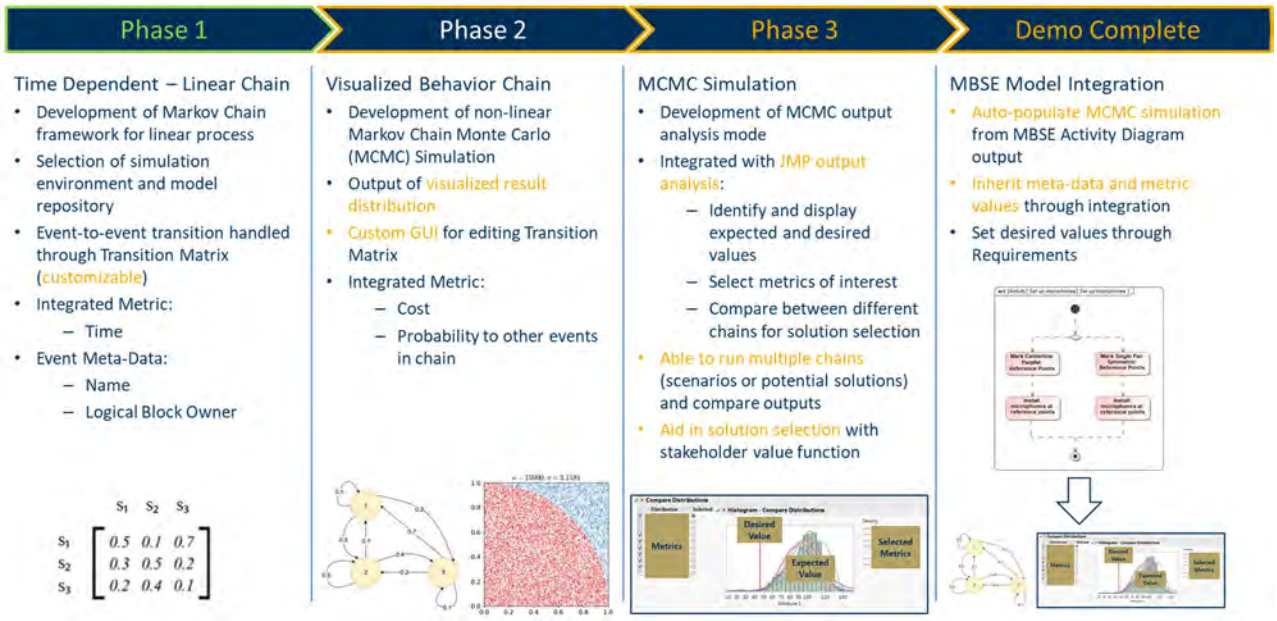

Figure 31. Functional development plan based on a process improvement model. GUI: graphical user interface; MBSE: model-based systems engineering; JMP: John's Macintosh Program.

Task 4.2

With the PIM model now available in a flexible and customizable format, Task 4.2 seeks to expand the process simulation and analysis towards metrics that will link to use case objectives and process selection of improved alternatives.

The selected metrics should allow for a quantitative comparison of current and proposed streamlined noise certification process options. The current list of identified metrics is as follows:

- Time: schedule cost incurred to complete event
- Cost: budget cost incurred to complete event
- P(Failure): probability of repeating an event or reverting to a previous event (does incur time and cost [full or partial] in each occurrence)
- P(Success): probability of moving out of the current event
- Accuracy penalty: impact on overall accuracy value for executing the event (does not incur an additional cost in each occurrence)

Depending on the requirements and acceptance–rejection distributions, changes will be proposed for the process model, (e.g., by incorporating equivalent procedures, modifying recording lineups, considering conformity models, etc.), and then, another iteration cycle will be ready for execution. The long-term benefit is that the process will evolve as a key function for testing the feasibility of equivalent procedures, all within the automation of workflows and functions enabled by the MBSE framework.

At present, currently identified metrics have been applied in a use case demonstration under Task 4.4 for the transport category. With the pivot to UAS configurations, the team is expanding on this task to identify metrics that extend beyond the efficiency-oriented focus of the original process streamlining concept, with an added focus on flexibility for a metric to accommodate alternative UAS concepts.

Task 4.3

The objective of Task 4.3 is to produce a baseline of a noise certification procedure simulation and to propose a calibration step, as process data become available from ASCENT 061 partners. The analysis workflow for the PIM module is shown in Figure 32. The goal of the workflow within the PIM is to analyze the complexity of the process and to identify potential bottlenecks by assessing time, cost, and node/step criticalities. The workflow is completed in three basic steps:

- *Definition of test data*: This step includes a test plan, setup, instrumentation and recording information, and sound pressure level measurement data.
- *Process representation as an event chain through graph modeling*: In this step, the process is converted and represented as a weighted directed graph. Each node represents a step in the process, and the edges represent transitions between steps. The progression through the steps is represented by probabilities and parameters at each step.
- *Execution of the MCMC algorithm*: The simulation starts from a node, and a "roll the dice" (generate a random number) function is performed. Depending on the outcome and the probability of each path, the algorithm selects the next node. A learning factor is utilized to update the probabilities of progressing through the steps (increased probability the second time).

Regarding the simulation outcomes, the PIM in its current form tracks time and cost metrics for each completed certification process, as well as the complexity/uncertainty-driven error propagation.

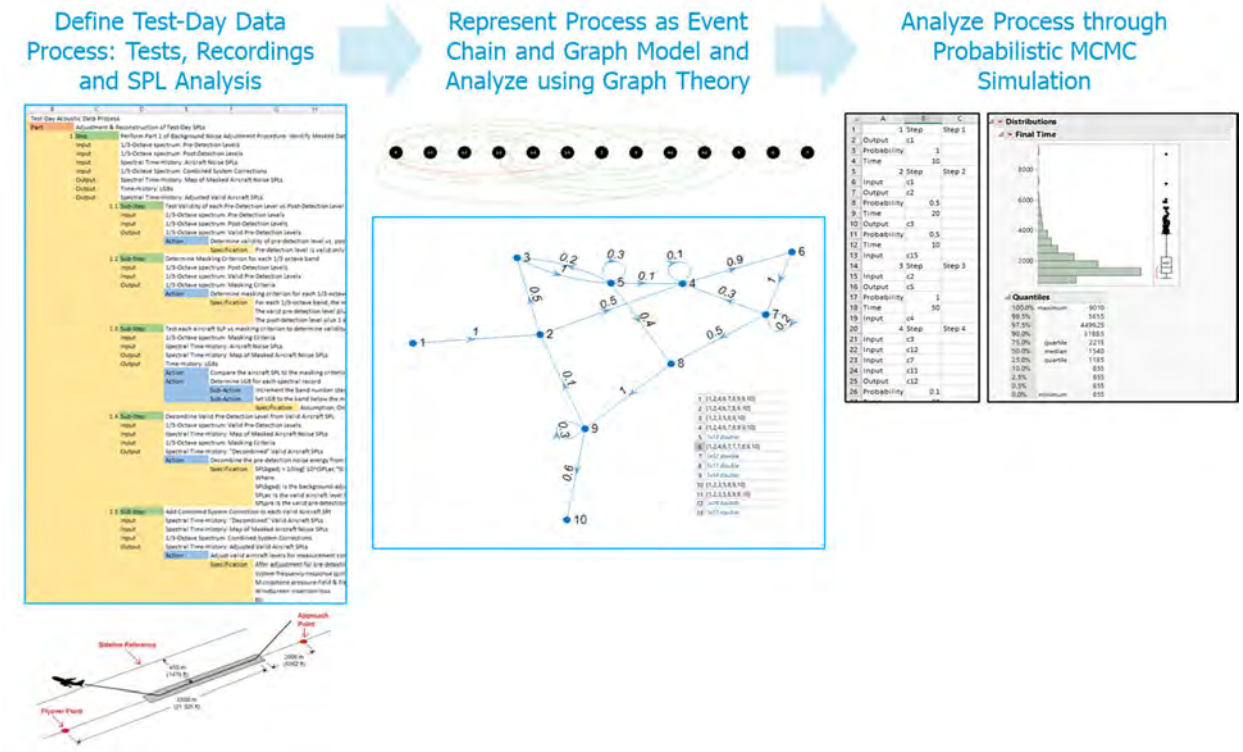

Figure 32. Analysis workflow based on the process improvement model. MCMC: Markov chain Monte Carlo; SPL: sound pressure level.

Calibration is an essential step for ensuring model accuracy and the validity of results and findings. This task requires a completed process simulation capability, which will be calibrated against a baseline that captures current certification testing plans and processing steps. The pivot to the UAS category has included plans to interface with ASCENT partners who can provide testing plans and noise datasets to be used as calibration data and overall process information. This task will be one of the key focus topics for the project's Year 3 activities. Scalability issues are bound to arise as this model is expanded to reflect the full verification thread; thus, the next step is to discuss options for data that ASCENT 061 partners could provide for further calibrating the model, according to the use cases of preference.

Task 4.4

In a proof-of-concept demonstration of the complete certification process simulation capability within the PIM, the team has been formulating use case examples based on scenarios provided by OEM partners. For these examples, simulation runs are

being executed to test modifications and proposed improvements over the baseline process. Under this task, a first demonstration of the PIM has been completed. For this example, the goal is to assess the impact of a simplified noise collection/analysis process for Waco YMF-5 propeller aircraft.

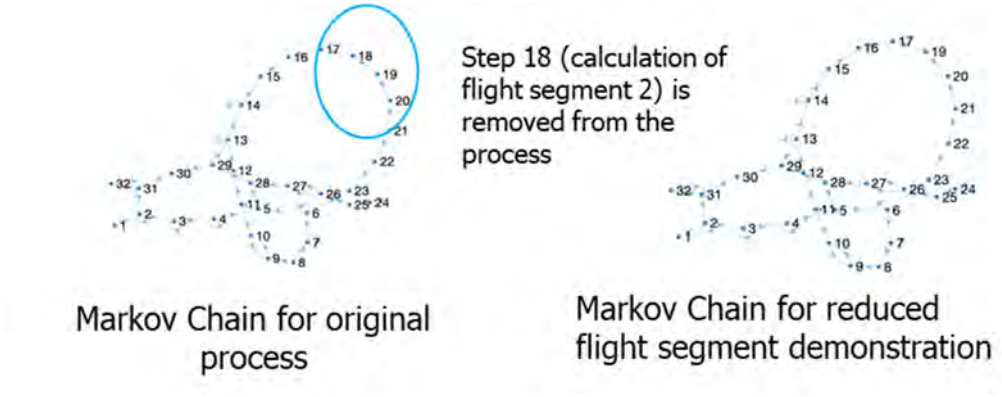

Figure 33. Process modification: Step 18 (calculation of the second flight segment) is removed from the flight-testing process.

The baseline (original) process was formulated within the PIM and executed using best estimates for times and cost. The term "best" implies that the team had to rely on rationalized assumptions that were initially formulated by input from OEM partners. As this information could be of a sensitive nature for most OEMs, the guidance was provided at a higher level, without any limitations on how this information would be distributed. Hence, for this example, a simplified process for flight segment testing is proposed, where a certain calculation is removed from the standard process. As shown in Figure 33, the simplified process removes step 18 (calculation of the second flight segment) while other steps were updated with new values to capture the updated process.

Table 4. Summary of cost ($) and time (hr) improvements.

		Mean
Original	**Cost($)**	166,770
	Time(hr)	155
Reduced Segments	**Cost($)**	140,430
	Time(hr)	151

A comparison of the two process alternatives is presented in Table 4. The results were obtained from an MCMC analysis and comparison between the baseline and simplified process. The PIM was able to quantify measurable savings in time and cost. In particular, the average process cost shows a reduction of 16%, and the average process time shows a decrease of 2%. The results are highlighted in Figure 34, where the Monte Carlo simulation data are plotted as distributions for the cost and time required for the process.

With this fundamental example showcased under this task, the groundwork is set for scaling up the PIM to more comprehensive modifications, which would also include technology impact forecasting functions. As this practice will now be exclusive to the UAS category, the team's priorities are to investigate current noise testing plans and procedures and to be in a position to propose promising equivalent procedures.

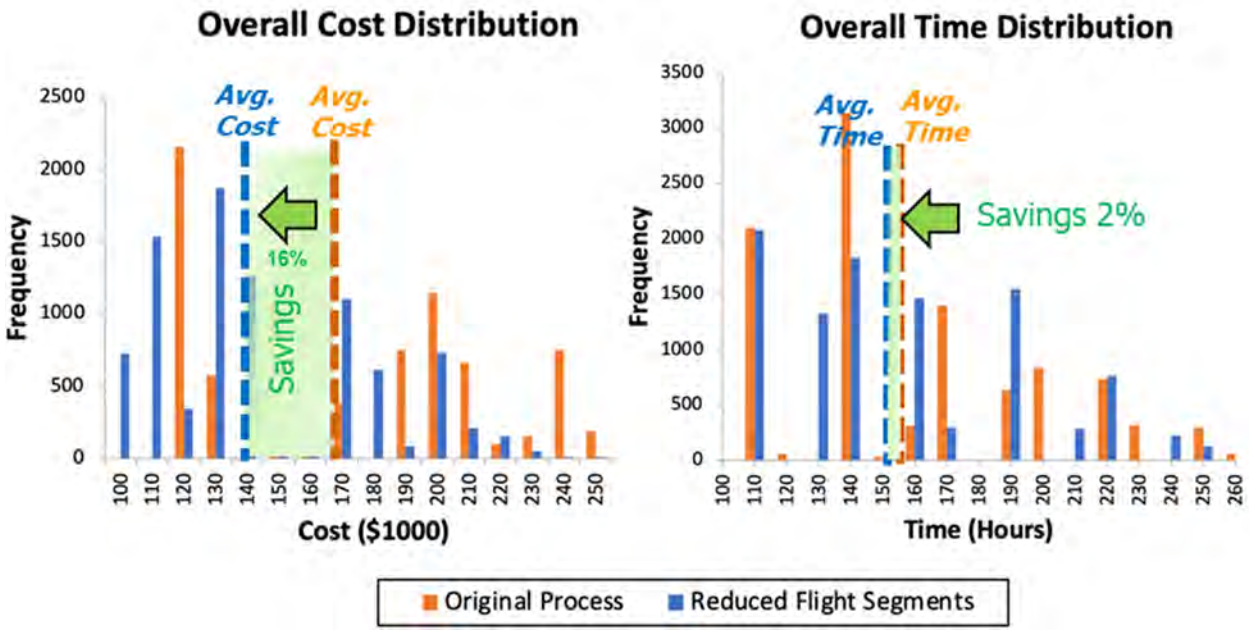

Figure 34. Execution of Markov chain-based Monte Carlo analysis and comparison between the baseline and simplified process.

Milestones

Please refer to the milestones listed under Task 1.

Major Accomplishments

- Development of a small-scale PIM using DES, as a deterministic modeling exercise
- Development of a more comprehensive stochastic model using stochastic MCMC methods, formulated in a way that enables seamless integration into the verification thread within the MBSE framework
- Definition of a starting set of metrics, as a working solution with a focus on process efficiency improvements
- Approach for integrating the PIM with the verification model within the MBSE framework
- Finalized PIM analysis workflow with the use of Monte Carlo simulation for Markov chain models of the certification testing process
- Workflow integrated with the MBSE verification model
- Proof-of-concept use case for assessing the impact of process simplification through quantifiable outcomes, which has been supported by the current working version of the MCMC-enabled PIM module

Publications

None.

Outreach Efforts

- Presentation of concepts to VOLPE partners, who provided feedback on the tools and analysis methods
- Collaboration with ASCENT 077 and 094 research groups
- Discussions with experts in the field with similar applications, e.g., process simulations for industrial systems, manufacturing, supply chains, etc.

Awards

None.

Student Involvement

While a small portion of the team has been leading the technical approach of PIM development, this task has involved the full team, as PIM integration with the MBSE model is a key enabler to be addressed early in the process.

Plans for Next Period

- Continue with the PIM development steps, toward a full verification model scale capability for the UAS category.
  - Finalize the interface with the MBSE verification model.
  - Ensure flexibility with other UAS configurations (the Matternet M2 example is the current working baseline).
  - Iterate on noise measurement data to be used for PIM improvements.
  - Integrate sound pressure level conversion to EPNL for UASs.
  - Expand on metrics that can better track process complexity and vulnerability and test against varying contingency scenarios, with the goal of ensuring that the analysis is capable of driving robust decisions.
  - Calibrate the model with input from ASCENT 077 work.
- Expand on metric definitions at a level beyond process inefficiencies (e.g., directly addressing time and costs) and consider complexities that could affect the process with bottlenecks and unnecessary use of resources (e.g., duplicate testing, time-intensive procedures, etc.). The flight-testing part of the process will be the primary focus.
- Formulate a simple certification problem for each vehicle type and use it as a pilot for comparing and selecting the appropriate method.
- Integrate results and PIM analysis in the interactive decision support tool.

References

Metzger, F. B., & Foley, W. M. (1970). *Stol aircraft noise certification-a rational approach*. SAE Transactions. 700325. https://doi.org/10.4271/700325

U.S. Department of Transportation, Federal Aviation Administration. (1969). *Federal Aviation Regulation, Part 21, Certification Procedures for Products and Ports; Part 36, Noise Standards: Aircraft Type Certification*. https://www.ecfr.gov/current/title-14/chapter-I/subchapter-C/part-36

Ollerhead, J. (1968). *Subjective Evaluation of General Aviation Aircraft Noise* (Technical Report NO-68-35).

Senzig, D.A. & Marsan, M. (2018). *UAS Noise Certification*.

FAA (2023). 14 CFR Part 36 – NOISE STANDARDS: AIRCRAFT TYPE AND AIRWORTHINESS CERTIFICATION. https://www.ecfr.gov/current/title-14/chapter-I/subchapter-C/part-36

FAA. (2017). *Advisory Circular 36-4D – Noise Standards: Aircraft Type and Airworthiness Certification*.

Federal Register. (2022). *Noise Certification Standards: Matternet Model M2 Aircraft* (NPRM 86 FR 48281). https://www.federalregister.gov/documents/2022/09/12/2022-19639/noise-certification-standards-matternet-model-m2-aircraft.

FAA. (2022). *Noise Certification Standard: Matternet Model M2 Aircraft*. https://www.regulations.gov/document/FAA-2021-0710-0016.

US Department of Defense. (2022). *Systems Engineering Guidebook Section 4.2.7.* Office of the Deputy Director for Engineering. Washington, D.C.

VOLPE Guides, "Validation Protocol for Digital Audio Recorders User in Aircraft-Noise Certification Testing" [2010].

VOLPE Guides, "Audio Recording & Analysis System Validation Checklist" [2018].

VOLPE Guides, "Test Data Acoustic Data Process" [2003].

VOLPE Guides, "Background Noise Adjustment Process" [2003].

FAA. (n.d.) *Details on FAA Noise Levels, Stages, and Phaseouts*. https://www.faa.gov/about/office_org/headquarters_offices/apl/noise_emissions/airport_aircraft_noise_issues/levels/.

Aleksandraviciene, A. (2018). *MagicGrid Book of Knowledge*. Kansas, 2018. NoMagic.

More, S. (2011). *Aircraft Noise Characteristics and Metrics* [Ph.D thesis Dissertation, Purdue University].

Konzel, N. (2022). *Ground based measurements and acoustic characterization of small multirotor aircraft* [Masters Thesis, Pennsylvania State University].

Conclusion - ASCENT 061 Year 2 Recap

The following key tasks and activities have been completed within the ASCENT 061, Year 2 performance period:

- Built a noise certification modeling and assessment framework for transport category aircraft:
  - Informed by training materials and data provided by VOLPE and OEMs
  - Completed verification model implementation using the ASCENT 061 MBSE framework

  - Completed PIM for process assessment, evaluation, and testing of equivalent procedures; expanded the current version from a deterministic DES approach to a probabilistic MCMC approach
  - Demonstrated the framework by assessing a simplified noise collection/analysis process for the Waco YMF-5 propeller aircraft
- Established a connection with VOLPE and developed a plan for regular status checks, model reviews, and auditing of findings
- Developed the first proof of concept of an interactive decision support capability for exploring and assessing equivalent procedures
- UAS pivot: Explored the applicability of the current ASCENT 061 framework for noise certification of rotor or small propeller-driven UASs
  - Performed a literature search on current noise certification practices for UASs; identified gaps and opportunities
  - Analyzed proposed noise certification guidance based on NPRM 86 FR 48281 and used this guidance as a benchmark
  - Formulated a requirement model based on current regulations and incorporated this model in the MBSE certification framework
  - Modified the ASCENT 061 MBSE noise certification framework for the UAS category to provide oversight on equivalent procedures and regulatory compliance
- Engaged in a broader outreach of ASCENT 061 to the aviation community on noise certification
  - ASCENT fall/spring meetings
  - Other groups within VOLPE
  - Boeing Commercial Aircraft Acoustics Division
- Exchanged noise measurements and knowledge with the ASCENT 77 team
- Provided annual and quarterly reports, which are available on the ASCENT Knowledge Services Network (KSN) database
- Prepared contributions and new technical capabilities that will be published in conferences and peer-reviewed journal articles:
  - Kim, D., Karagoz, F., Datta, S., Balchanos, M., Anvid, D., Harrison, E., & D.N. Mavris (2022). *A Model Based Systems Engineering Approach to Streamlined Noise Certification of Transport-type Aircraft*. In 33rd Congress of International Council of the Aeronautical Sciences ICAS, Stockholm, Sweden, 2022.
  - Kim, D., Taneri, M., Omoarebun, E.N, Wills, T., Balchanos, M., & Mavris, D. (2023). *MBSE-Enabled System Verification and Process Improvement of Transport Aircraft Certification.* Accepted and to be presented In AIAA SciTech 2023 Forum, National Harbor, MD, January 23-27, 2023.

Appendix A - Survey of Title 14, Part 21 and Part 36

FAA rules are described in the U.S. Code of Federal Regulations, Title 14 (14 CFR), Chapter 1. Aircraft certification procedures and noise standards are found in Subchapter C, Parts 21 and 36, respectively. Additional relevant sections of Subchapter C include the following:

- **Part 21 – Certification Procedures**
- Parts 23–31 – Airworthiness Standards for Aircraft
- Parts 33–35 – Airworthiness Standards for Aircraft Engines
- **Part 36 – Noise Standards**
- Part 39 – Airworthiness Directives
- Part 43 – Maintenance
- Part 45 – ID and Registration Marking
- Part 47 – Aircraft Registration
- Part 48 – Registration and Marking for Small Unmanned Aircraft
- Part 49 – Recording of Aircraft Titles and Security Documents

Benchmarking of current certification practices will be driven by Part 21, Part 36 (FAA, 2017), and AC 36-4D (procedures and steps for noise certification (Federal Register, 2022). Please note that this list of requirements is derived from the FAA standards, guidance, and practices alone. The FAA works closely with the international community to ensure that their standards align with ICAO noise regulations and can adapt to changing noise mitigation technologies (FAA, 2022). ICAO

noise regulations (Chapter 3) use FAA's FAR36 Stage 3 as a starting point. It is acknowledged that other NAAs, such as the EASA, have practices that may vary from FAA requirements.

The intent is to identify any potential gaps in the team's understanding of noise certification procedures and to detect any equivalent procedures and accepted means of compliance that should be noted. Figure A1 presents an overview of the process, which is broken down into five phases. This review covered the mapping of all detailed procedures contained in AC 36-4D on the testing practices (the "how"), whereas Part 36 focuses on the regulatory side (the "what") for compliance.

The following subsections present the team's findings and high-level process views.

Figure A1. Overview of the noise certification process as described in Parts 21 and 36 and Advisory Circular 36-4D.

Phase 0: Checking Environmental Factors
In this phase, the goal is to measure and verify that weather and testing conditions are appropriate. This step includes checking the wind velocity and assessing for abnormal meteorological conditions. One must also verify that the terrain meets the appropriate FAA specifications. In the case that a non-airport test site is sought, the test site criteria must be followed. Figure A2 provides a visual summary of the steps that must be performed before field setup occurs.

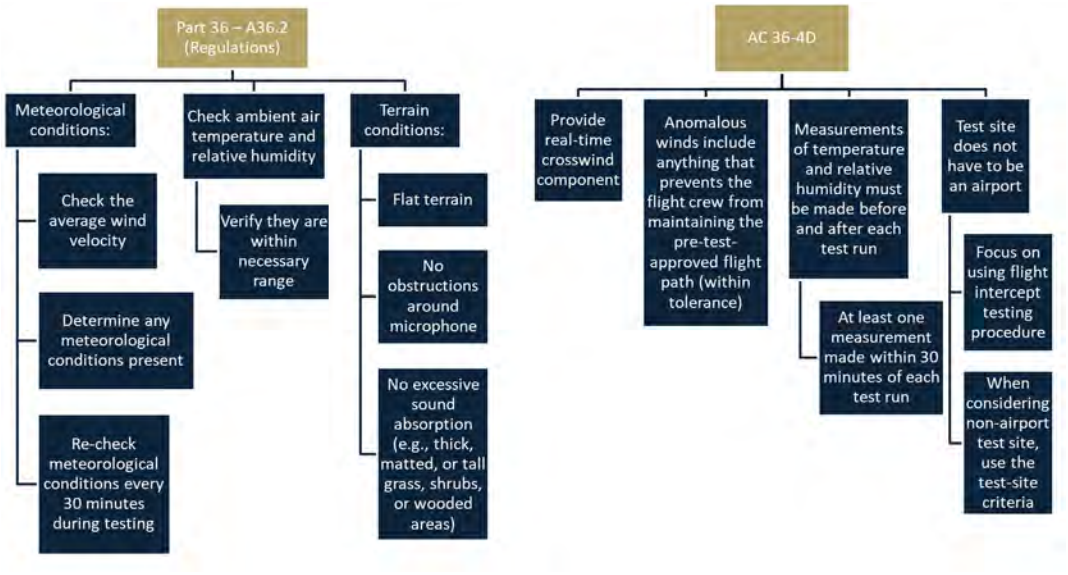

Figure A2. Phase 0: Checking environmental factors. AC: advisory circular.

Based on Phase 0 benchmarking, the team prioritized the following inquiries to the industry partners, in support of Task 1.2:

- Is an airport used for testing, or is another location typically used? If elsewhere, where are the certification procedures completed?
- How difficult is it to obtain FAA approval to conduct the test at another location besides an airport?
- If an organization has multiple certification sites, how does testing differ amongst the sites (e.g., in the number of trials needed to successfully certify)?

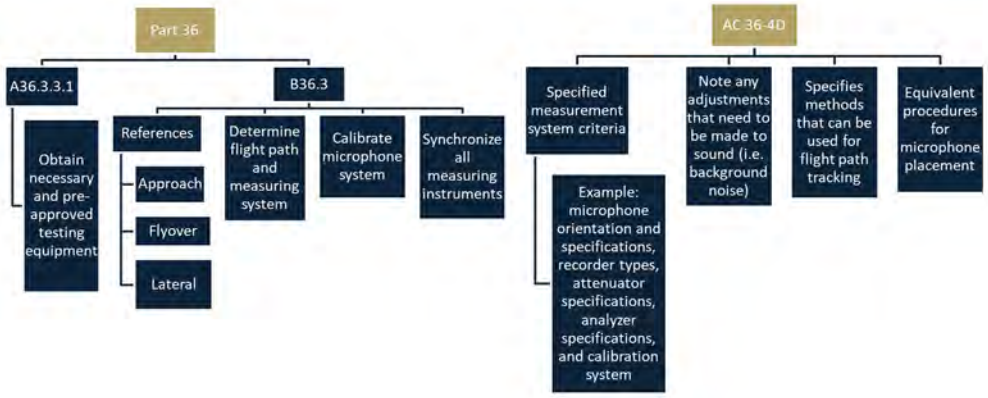

Figure A3. Phase 1: Field setup. AC: advisory circular.

Phase 1: Field Setup

For Phase 1, the field setup procedures prioritize the selection and setup of equipment, calibration, and ensuring that equivalent procedures are fully defined. Figure A3 shows the complete steps of the setup procedure. Testing equipment must be preapproved. Much of the hardware setup involves setting up approach, takeoff, and lateral microphones, which must be calibrated. There are two equivalent procedures that can be used for lateral microphone placement. Flyover and approach reference points remain the same. A flight tracking system must be determined, and all measuring instruments must be synchronized.

Based on Phase 1 benchmarking, the team has identified the following inquiries for industry partners:

- What equipment is used for certification?
- What equipment (if any) could be seen as an opportunity for upgrading or could potentially be replaced by newer technology, but is required for use by the FAA?

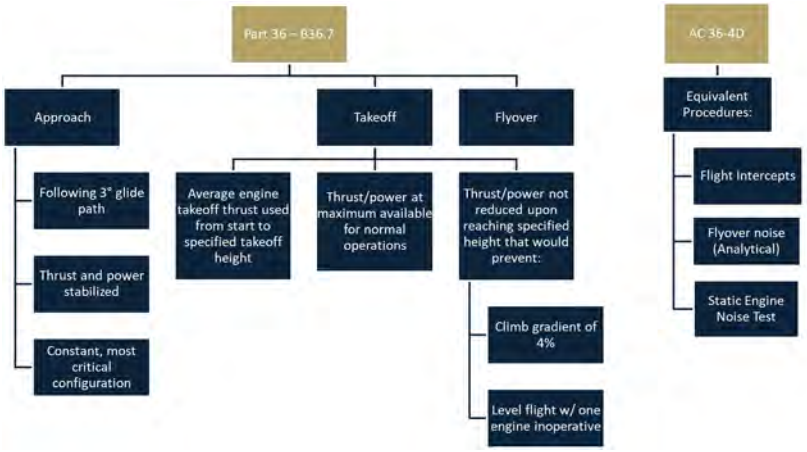

Figure A4. Phase 2: Testing. AC: advisory circular.

Phase 2: Testing
The testing procedures listed in Part 36 and AC 36-4D are outlined in Figure A4. The benchmarking exercise has also identified three equivalent testing procedures: flight intercepts, flyover noise, and static engine noise testing.

In lieu of the full takeoff and/or landing profiles described in A36.9.2.1 and A36.9.2.2 of Part 36, *flight path intercepts* can be used. This procedure eliminates the need for actual takeoffs and landings. Moreover, it leads to significant cost and operational advantages at high gross weight, while substantially reducing the test time required and site selection issues. The shorter test time also provides a high probability of stable meteorological conditions, reduced wear, reduced fuel consumption, and greater consistency in generated data.

Flyover noise levels with thrust (power) reduction may also be established without making measurements during takeoff with full thrust (power) followed by thrust (power) reduction. This can be accomplished by merging tone-corrected perceived noise level (PNLT) versus time measurements obtained during constant power operations.

Last, *static engine noise tests and projections to flight noise levels* (403.a.3) are performed when changes are made to the powerplant or when a similar powerplant is installed. This process is also performed after the initial noise certification of a "datum" airplane. This process provides sufficient additional data or source noise characteristics to allow for predictions regarding the effect of changes on airplane certification noise levels.

In summary of Phase 2, takeoff, flyover, and approach flight tests for noise certification must still be completed. Three types of equivalent procedures are recommended. When applicable, static engine noise tests are used, and flyover noise certification can be completed analytically.

As part of the team's assessment for this phase, the following inquiries were addressed to our industry partners:

- How often are equivalent procedures used instead of procedures specified in appendix A/B?
- How many tests (e.g., approach, takeoff, and flyover) are usually conducted for noise certification?

Phase 3: Analysis
Phase 3 involves the analysis for determining the EPNL. This phase involves the following steps, which are also outlined in detail in Figure A5:

- Find the perceived noise level (PNL(k)).
- Correct for spectral irregularities.

- Determine the duration correction.
- Determine the EPNL.

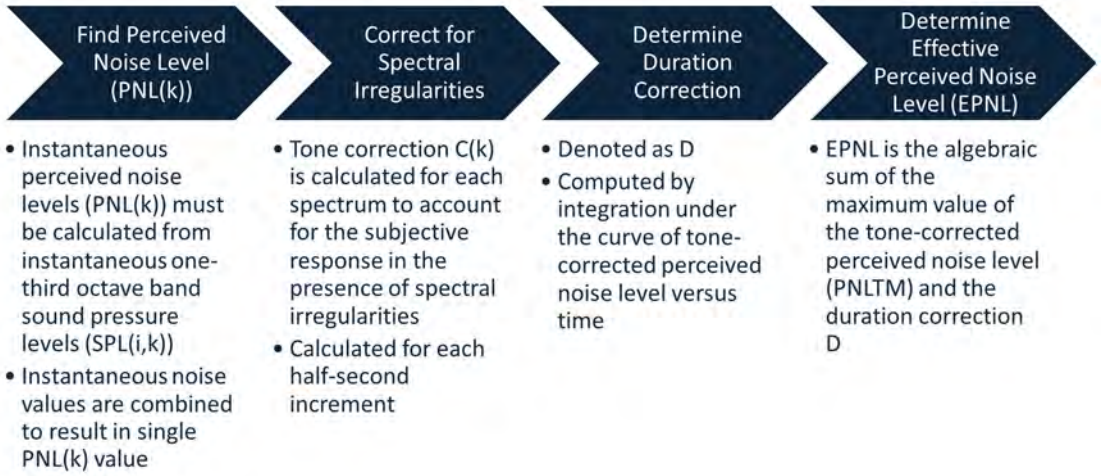

Figure A5. Phase 3: Analysis steps for calculating EPNL.

EPNdB (effective perceived noise in decibels) is a measure of human annoyance to aircraft noise, which has unique spectral characteristics and sound persistence. The EPNL (measured in EPNdB) consists of the instantaneous PNL corrected for spectral irregularities (tone correction factor) and for duration.

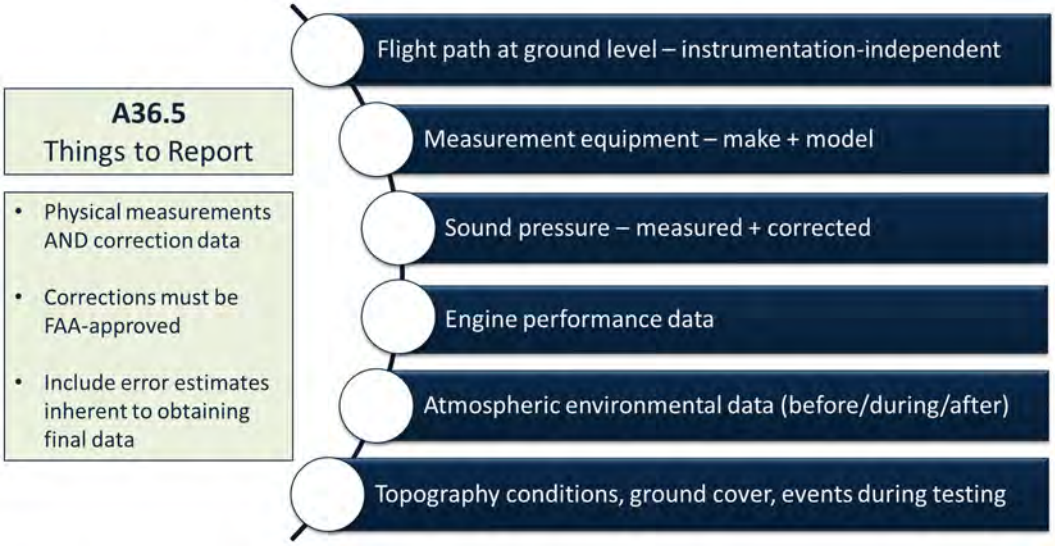

Figure A6. Phase 4: Reporting.

Phase 4: Reporting
In this phase, the goal is to ensure that the correct types of data to be recorded during analysis are selected and meet the given FAA requirements, e.g., inclusion of error estimates. This step also determines what materials must be reported for FAA inspection and approval, ranging from test data and adjustments to noise recordings and instrument calibrations. The reporting requirements based on current regulations are summarized in Figure A6.

Appendix B - Workshop Planning and Findings for the Transport Category

Task 1.1

Starting with Task 1.1, the main action pursued by the team was to review and document current noise certification procedures. The task objective is to gain an understanding of the current regulatory framework for aircraft noise certification, as required by FAA regulations and followed by OEMs to demonstrate compliance. In particular, the team conducted a thorough literature review of relevant 14 CFR parts (mainly Part 36) and associated documents where relevant (e.g., ACs such as AC 36-4D). With recommendations from the team's partners, other documentation from the EASA, the ICAO Environmental Technical Manual, and the VOLPE website were also considered.

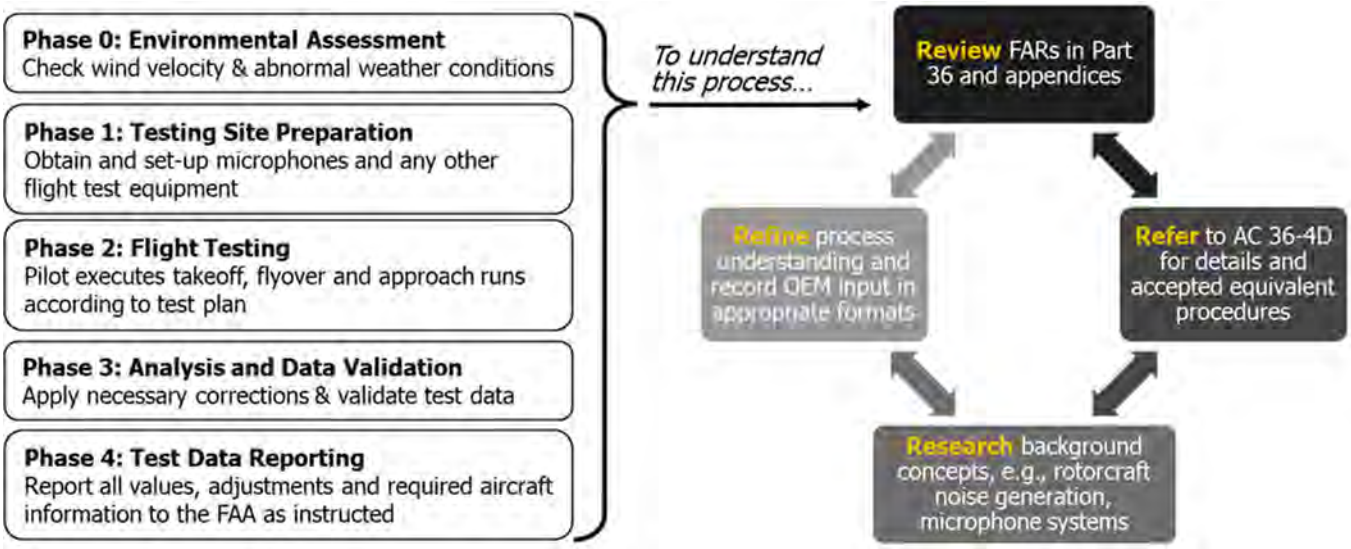

Figure B1. Noise certification regulation review (Task 1.1). AC: advisory circular; FAR: Federal Aviation Regulations; OEM: original equipment manufacturer.

As the full certification process is comprised of multiple processes and standard procedures, which are highly coupled, with recommendations by the FAA and OEM partners, the team focused on the certification flight testing phases in this exercise. Specific to flight testing phases, FARs in Part 36 and Appendix A and B have been reviewed and documented. This review included AC 36-4D for providing details on currently accepted equivalent procedures for the large transport aircraft category.

Along with an extensive review of FARs and literature on the regulatory framework, the team produced a series of views to demonstrate the flow of procedures, associations, and dependencies across regulatory items. Finally, the team obtained background information on noise generation for various aircraft categories, as well as technologies used during testing, to better understand current recommended practices and the potential for alternative equivalent procedures with the use of modern technologies and equipment. One of the benefits of this task is that team members quickly became more knowledgeable of the certification basics in preparation for Task 1.2 (industry interviews) and for building a comprehensive MBSE representation of the current framework in SysML (see Task 2.1). An overview of the methodology behind the review of FARs and literature is provided in Figure B1. Please see Appendix A of this document for a full overview and for the documentation produced under this exercise.

Task 1.2

Task 1.2 aims to enhance the team's understanding of the current noise certification process through interaction with subject matter experts from various OEMs, with the objective of leveraging industry insight into practical aspects of noise certification requirements. This step was performed via virtual workshops, guided by questionnaires compiled by the team based on the reviews completed under Task 1.1. Through insights and findings from documented work under Task 1.1, the team identified topics for which more context and additional insight into ancillary/non-regulatory processes are needed, with regard to how the certification procedure is facilitated by each OEM partner. These topics are shown in Figure B2.

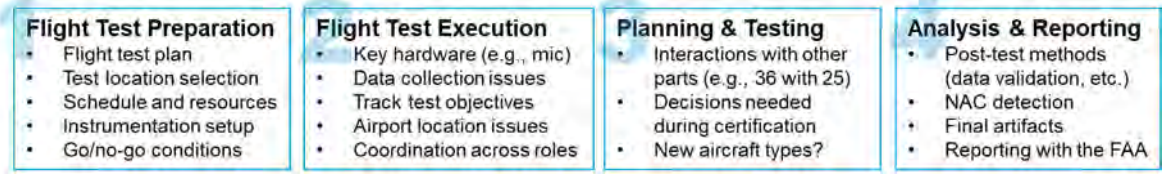

Figure B2. Workshop interview topics for transport category aircraft. NAC: non-acoustical change.

The overarching goal of these workshops is to identify common practices, checkpoints, and milestones across industry partners, while soliciting feedback on key challenges they have identified on their end, as well as what recommendation each partner would provide and why. Such suggestions could convert to opportunities for potential process streamlining, whereas other recommended practices could be out of sync with current technology. The limitation in this exercise is that no recommendations should suggest or presume any change in the regulatory side; hence, the suggestions should be concentrated on equivalent procedures, with either simplified processes or connections to modern technologies, which are still expected to meet the same regulations.

The first workshop was planned by the Georgia Tech team and was held virtually on November 5, 2020. Discussion centered on certification practices for large transport and business jet categories for aircraft, as applied by the team's industry partners (representing airframers such as Boeing, Gulfstream, and Rolls-Royce). With the forum in place and the key connection established, a series of follow-up workshops and interviews was planned, which extended from January 2021 to May 2021. In this expanded outreach, most interviews were planned with one OEM partner at a time, in order to ensure that participants would be more comfortable sharing their thoughts and expertise, without the time constraints of a high-participation event and with more flexibility in scheduling and needed follow-ups. Moreover, the list of participating partners had been expanded to include more OEMs (Embraer, Cessna, De Havilland Canada) beyond those supporting the original workshop of November 2020. VOLPE Center has also participated in shaping the team's knowledge and understanding of the recommended procedures, especially for the flight-testing portion of the process. The final set of participating OEMs who have contributed to the completion of this task is shown in Figure B3.

Figure B3. Participating partners (airframe manufacturers, VOLPE) in workshops/interviews under Task 1.2.

To facilitate a directed discussion within the workshops/interviews, the Georgia Tech team formulated questions on the discussion topics listed in Figure B4 and produced questionnaires that were distributed to the participants prior to the respective meetings. A high-level summary of the questions is as follows:

- What is the current guidance provided by the FAA for noise certification?
- How does a company interact with the FAA to ensure that requirements and constraints related to noise regulations are satisfied and that the vehicle is compliant?
- How does the company perform the testing, internal processes, etc.?

- Can you identify procedures within flight testing that should be revised or updated to reflect the capabilities of modern configurations? Are there any opportunities for improvement?
- Are existing certification procedures and methods sufficient to meet future configurations?
- Regarding certification amendments due to type design changes, if a vehicle needs to be recertified after design changes have been made, does your organization's approach change from the first round of certification?

The actual questionnaires are included in Appendix B, in the format in which they were distributed to the workshop participants.

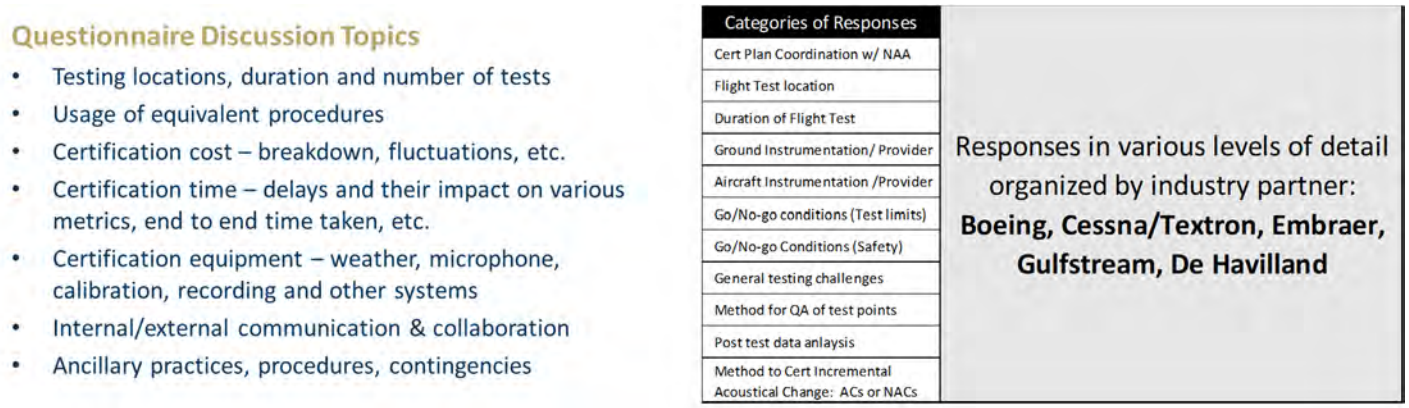

Figure B4. Post-processing of collected information and categorization. AC: acoustical change; NAA: national airworthiness authorities; NAC: non-acoustical change; QA: quality assurance.

The initial workshop and follow-up interviews with the participants generated a wealth of information. Planning and a methodological approach are required to post-process this information and to direct it to usable conclusions and insightful findings. One idea was to generate categories, under which the collected material from the questionnaire responses will be sorted and organized. For this purpose, a number of categories have been defined, as shown in Figure B4.

While the level of detail in the answers and feedback obtained varied significantly across the participants, the team was able to summarize the primary themes of the feedback under the defined categories, as shown in **Table** B1. To summarize these findings, the main takeaways from all OEM feedback are the following:

- ACs and NACs are challenging to navigate without standardized approval procedures. More detailed feedback would be useful for OEMs to propose suitable solutions.
- Test site selection is normally restricted by sound measurement technology and requirements (e.g., lateral microphone component) and by weather window options.
- Delays in flight testing are primarily weather-induced and are occasionally due to communication disruptions.
- Conformity discussions can be significantly time/effort-consuming, especially for cases in which there is a need to justify changes that are unrelated to acoustics.
- Interactions between Part 36 and Part 25/23 can be challenging, as there seems to be a discontinuity between environmental and design standards, often leaving little space to apply acoustic improvements.
- There is no single standardized software for calculating EPNL values from noise data collected during flight testing. Each OEM's methodology and code are different.

This lack of standardization appears to be a common area of opportunity for improvements across current noise certification procedures. Within the same context, some participant-recommended value-added outcomes could be explored; not all of these outcomes can necessarily be explored within the current Project 061 SoW, but some could be appropriate use case opportunities for Years 2 and 3 or beyond. Participant-recommended outcomes that could be evaluated through the use of the MBSE-enabled platform for streamlined certification are the following:

- Along with exploring improvements in time and cost, the Project 061 team could explore options to simplify testing and instrumentation setup requirements to facilitate more test locations/weather window options (i.e., which could allow 4-ft microphones to be removed for ground planes and lateral microphones to be removed all together).
- Testing uncertainty could be managed through the evaluation of NAC limits.
- Conformity issues could be addressed through the formulation of a concept that could tested and demonstrated within the MBSE-based verification framework.
- Criteria for approval for acoustical analyses could be defined to establish new certification noise levels (AC by analysis).
- As a longer-term goal, a framework for oversight could be defined to give the FAA confidence in manufacturers' tools/methods used in noise certification (e.g., with pre-defined audit guidelines/procedures).

Table B1. Summary of findings from the transport category workshop and interview feedback. AC: acoustical change; NAC: non-acoustical change.

Subject	Boeing	Cessna/Textron	Embraer	Gulfstream
Test deliverable setting	Not much deliberation	Some deliberation, approved easily	Follow exact regulation protocol	Early FAA involvement for flight planning
Test location	Airport for safety, restricted by lateral mic requirement	Low traffic, stable weather (current site in CA)	Remote location, restricted by season/weather and traffic	Based on acoustic & atmospheric environment (current sites in CA, GA)
Time spent on site	Final checks 1 month out (if new site, 2-year prep)	5-6 hours/day if stable weather	2-hour set up, 5/7-hour testing (10-day window)	1 series in 2 days, 1-hour sunrise setup, 6-day approach
Instrumentation	Highly optimized lab procedures	Consultant: 6 mics (1 central, 2 lateral + backups)	Consultant: approved Volpe list equipment (old	Pole & ground plane mics, daily setup/take-down
Go/ no-go conditions	Borderline test points discussed with Eng. Unit	Mainly weather related	Mainly weather related, occasional aircraft issue	Upper atmosphere weather/ wind issues
General testing challenges	Mainly weather, rarely from equipment or communications	Mainly weather, equipment old but reliable, crucial to maintain comms	Cell phone reliance, can lose comms airport-test site (must stop testing)	Mainly weather
Confirmation of meeting test objectives	Parameters printed to support decision, borderline points	Check raw noise level (test engineer/mic teams), verify GPS, monitor NPD trends	Consultant responsible: get approx. 60-80 test points	Get approx 40 points, sound pressure/exposure for NPD, monitor tolerances on PFD
Post test data anlaysis	3-4 months, flight & engine test combined in NPD to find uncertainties	Data check after test, 1-2 months for report & revisions before FAA (2-3 mth total)	Time consuming in-house analysis, matching results to predictions	
Acoustical Change - ACs or NACs	Game-changer = AC by analysis ; difficult to get FAA approved tools ; high scrutiny on small ACs ; have killed modifications that cause AC>0.3 dB	Game-changer = AC by analysis ; can be 3-6 month response time from FAA with no constructive feedback even with past accepted methods ; Textron proposed FAA procedure library to reduce guesswork	Nightmare to submit AC ; approval discussed with ANEC especially for newer ACs ; lack of common ground & standardisation between NAC reviewers	Tedious ; if performance changes, rely on NPD equivalence to provide basis for compliance plan/report ; if no performance change, do method analysis of noise increment

The exercise under Task 1.2 with identified findings and participant-provided recommendations has successfully established the need for a solution that allows one to explore and formulate a standardized, simplified certification procedure that is flexible to accommodate different types of air vehicles and new technologies. This procedure would require a comprehensive systems engineering process that enables connectivity throughout the certification steps and traceability of regulatory compliance. As model reusability and scalability across different categories are very important, the team has been utilizing MBSE methods to effectively "re-architect" the certification procedures in order to achieve the goals and the desired outcomes that have been identified through the feedback obtained by Task 1.2 activities.

Appendix C - Workshop Interview Questionnaires

Comprehensive Questionnaire (original version for November 2020 workshop)

SUBJECT MATTER EXPERT FEEDBACK REQUEST SHEET
Project 61: Noise Certification Streamlining – FAA ASCENT
Workshop 1 – Transport Category Aircraft
Conducted by the Georgia Institute of Technology

What is the purpose of this study and workshop?
"Noise Certification Streamlining" is Project 61 within the Center of Excellence for Alternative Jet Fuels and Environment (ASCENT), the Federal Aviation Administration Aviation Sustainability Center. The purpose of the project is to examine, and document current noise certification processes as applied by the industry and develop a more streamlined and flexible noise certification process for all applicable air vehicles. As part of this approach, the Project 61 team will seek to identify opportunities for increased efficiency and flexibility in the existing noise certification process, develop revised noise certification processes, and perform quantitative assessments. Lastly, the team will extensively apply Systems Engineering (SE) processes for complex systems, enabled by Model-Based Systems Engineering (MBSE) techniques, to facilitate certification process benchmarking and management of regulatory requirements.

The purpose of this questionnaire Is to acquire Subject Matter Experts' (SME) opinions about the future of noise certification and the related research areas that should be addressed. The Project 61 team is expected to have 5-8 participants.

Who can I contact if I have questions about the study?
If you have questions, comments, or concerns about this study, you can talk to one of the researchers. Please contact
Dr. Jimmy Tai (Email: jimmy.tai@ae.gatech.edu, Phone: (404) 894-0197),
Dr. Evan Harrison (Email: evan.harrison@asdl.gatech.edu, Phone: (706) 401-0976)
Dr. Michael Balchanos (Email: michael.balchanos@asdl.gatech.edu, Phone: (404) 894-9799).

Research Area: Noise Certification Process

Goal: Examine and understand current noise certification procedures and recommend guidelines to the FAA for a more streamlined and flexible noise certification process for all applicable air vehicles

Overview
Noise certification procedures were developed in the 1960s and many parts of the regulations may reference processes and equipment that are obsolete. Consequently, many Original Equipment Manufacturers (OEMs) utilize equivalent procedures and technology not explicitly addressed in the regulations. The objective of this research is to properly document the current noise certification procedures, examine the current process and identify areas of improvement, and develop a streamlined noise certification process for all applicable air vehicles. To perform the proposed research, Georgia Tech has teamed with several industrial partners with extensive experience in noise certification, across different classes of vehicles, ranging from large subsonic transports to business jets to rotorcraft.

The main focus for Workshop 1 will be transport category aircraft.

At present, the research team at Georgia Tech are members of two FAA Centers of Excellence: The Partnership to Enhance General Aviation Safety, Accessibility and Sustainability (PEGASAS) and the Aviation Sustainability Center (ASCENT). Through its participation in these centers, Georgia Tech has demonstrated its ability to collaborate with industry and the FAA to study various safety and certification problems and provide key understanding and insight.

Disruptors

Disruptors are defined as novel technologies or concepts of operation that are likely to disrupt the current paradigm. Based on previous benchmarking exercises and SME feedback, we have identified the following potential disruptors relevant to the current research area:

- Application of traditional Systems Engineering (SE) processes for complex systems, Model-based Systems Engineering (MBSE), and utilization these methods for the management of regulatory requirements
- Digital documentation of the noise certification process
- Modeling methods for simulating current certification process and simulation-based experimentation for testing improved and streamlined process alternatives

Are there any other disruptors or scenarios that you would include in this list?

Description of current certification practices

Noise Certification regulations contained in Title 14 of the Code of Federal Regulations Part 36 (14 CFR Part 36). Title 14 includes most of the regulations specifying the FAA's charter and regulations. Part C of Title 14 contains aircraft regulations, divided into Parts numbered 21-49 (Parts 50-59 reserved). These are the following:

- Part 21 – Certification Procedures
- Part 23-31 – Airworthiness standards for aircraft
- Part 33-35 – Airworthiness standards for aircraft engines
- Part 36-- Noise Standards
- Part 39 – Airworthiness Directives
- Part 43 – Maintenance
- Part 45 – ID and Registration Marking
- Part 47 – Aircraft Registration
- Part 48 – Registration and Marking for Small Unmanned Aircraft
- Part 49 – Recording of Aircraft Titles and Security Documents

Benchmarking of current certification practices will be driven by Part 21 (Certification Procedures) and Part 36 (Noise Standards). Please note that this list of regulatory practices is derived from the FAA methods and standards alone. They are a sub-set of the original ICAO standards. It is acknowledged that other NAAs such as EASA may have practices that may vary from FAA requirements.

What questions must be answered to describe the overall process for current noise certification practices adopted by the industry?

Q1. What is the current guidance provided by the FAA for noise certification?
- **a.** Who is currently responsible for overseeing existing noise certification procedures?

Q2. How does a company interact with the FAA to ensure that requirements for noise are satisfied and that the vehicle is compliant?
- **a.** How will these requirements change for different vehicles?
- **b.** What does a nominal testing timeline look like?
- **c.** What type of certification phases are taking place?
- **d.** What kinds of delay factors exist? How do they affect the timeline?
- **e.** What happens if you fail a noise certification demonstration?
- **f.** Does your company factor in potential noise certification failures?

Q3. How does the company perform the testing, internal processes, etc.?
- **a.** What technologies and methods are standard in support of the certification process?
- **b.** How is data being collected, managed, and facilitated?
- **c.** How is storage of the data handled?
- **d.** How are the instruments calibrated? Under what schedule?

e. What is the process for acquiring and operating the right hardware?
f. How do companies decide upon the testing conditions (e.g., weather, seasonality effects, location, etc.)?

Q4. Can you identify regulations that are obsolete and should be eliminated, as well as any opportunities for improvement?
a. Can you provide an example?

Q5. Are existing certification procedures and methods sufficient to meet future configurations?
a. Can you provide an example as it relates to transport category aircraft?
b. If not, what improvements must be made and how soon should these changes be implemented?
c. Has your organization already faced any challenges to certify newer designs with the existing certification framework? If so, what aspect of the regulations were the challenges faced in?

Q6. Certification Amendments Due to Type Design Changes – If a vehicle needs to be recertified after making design changes, does your organization's approach change from the 1st round of certification?
a. Does it take almost as much time/effort as the first time, or significantly less? If the former, why do you think there is no gain in time efficiency?
b. If your organization created any models/interpretations of the original regulations (to understand them better), are these used for certification amendments due to type design changes or do you return to the full collection of original documents?
c. Are there any instances where a type design change may require a full noise certification test?

Topic 1: Benchmarking of current practices: Transport Category Aircraft

Goal: Benchmark, evaluate and identify inefficiencies in current noise certification procedures for Transport Category Aircraft noise and provide recommendations to the FAA on streamlining certification practices.

General

Q1.1 How many tests (e.g. Approach, Takeoff, and Flyover) do you usually conduct for noise certification?
a. Are tests completed in a single day or must they be completed over multiple days?

Q1.2 Do you use an airport for testing or elsewhere?
a. If elsewhere, where do you complete the certification procedures?
b. How hard is it to get FAA approval to conduct the test at another location besides an airport?
c. If your organization has multiple certification sites, do you see a difference between them (e.g. in number of trials needed to successfully certify)?

Q1.3 How often are equivalent procedures used instead of the procedures specified in appendix A/B?
a. If you used an equivalent procedure, which procedure are you using?
b. What is the main reason for using the specified equivalent procedure?
c. Do you see a need to use more equivalent procedures for newly developed vehicles rather than the established versions that may need re-certification?
d. Are there particular sections where equivalent procedures make more sense to use rather than the originally specified procedures?

Impact Area 1: Certification Cost

Q1.4 What is the relative breakdown of cost associated with noise certification of an aircraft?
a. What percentage of the certification budget is devoted to the relative phases outlined in question 2 in the previous section?

Q1.5 What are areas in noise certification that have fluctuating costs (e.g. fuel)?
- **a.** How often do these cost fluctuations affect noise certification?
- **b.** Can you provide an example where fluctuating costs prevented the noise certification of an aircraft?
- **c.** Is there a specific configuration of aircraft that are more impacted by fluctuating costs? Why is this type of aircraft more impacted?

Impact Area 2: Certification Time

Q1.6 What sort of delays frequently occur in the certification process?
- **a.** What metrics do these delays eventually affect (e.g. revenue loss from delivery delays, unsatisfactory reports from inspectors, post-delivery issues or need to recall)?
- **b.** What role does weather/location of your facilities play in delays (if any)?

Q1.7 How much time is spent completing the certification procedure for large transport category aircraft? (e.g. hours, days, weeks, etc.)
- **a.** Are there particular sections of certification that take longer than others?

Q1.8 Where do you see an area to minimize the time taken to complete the certification process?

Q1.9 How many times a year are you conducting noise certifications?

Impact Area 3: Certification Equipment

Q1.10 What equipment does your team use for certification?
- **a.** What meteorological system is used?
- **b.** What microphones are used?
- **c.** What recording and reproducing equipment is used?
- **d.** What calibration systems are used?

Q1.11 What equipment (if any) do you see as "out of date" but are required to use by the FAA?

Q1.12 Is there a piece of equipment that you prefer to use over the specified equipment in appendix A/B?
- **a.** How long does it take for an equipment approval by the FAA?

Critical Milestones & Task Outputs

Q1.13 What process (if any) do you use to "translate" the appendix materials into requirements that are easy to check off?

Q1.14 How often is there confusion between various departments conducting noise certification?
- **a.** Do you get reports of confusion/misunderstanding from technicians or engineers who are responsible for reading the requirements from the FAA?
- **b.** Is there any confusion with the pilots who are responsible for flying the aircraft during testing?

Summary & Outcomes

Q1.15 Is there anything that is not directly specified in advisory circulations or in the FAA regulations, that is important to know when conducting transport category certification?

Topic 2: Ancillary Practices, Procedures, and Contingencies

Goal: Please describe ancillary practice or procedures that may be required to support the certification effort but do not directly demonstrate compliance to the regulations. Do these practices shorten, lengthen, or provide economic benefit to the applicant? Also, do these practices support contingency efforts if initial efforts to demonstrate compliance are not achieved?

Description

Q2.1 Has there ever been a project that was canceled because there was not a way to noise certify it with the FAA?
- **a.** If so, why couldn't it be noise certified?
- **b.** Did you seek FAA approval to certify the aircraft?

Q2.2 Are there any non-regulatory procedures (e.g., anything recorded and procedural that is not required by the FAA regulations) that your team uses to certify your aircraft?
- **a.** If so, please explain the procedure(s) in as much detail as possible.
- **b.** Do you believe your procedures are more efficient?
  - i. If so, please explain why.
  - ii. If not, please explain the motivation for using the prescribed procedures.

Deviations from Certification Requirements of Part 36:

Q2.3 What, if any, are common alternative procedures for Part 36 noise certification? For each alternative procedure, please answer each of the parts separately.
- **a.** What is the reason for the change?
- **b.** What are the potential benefits of this change from the as written standard?
- **c.** What is the process of documentation for the change?

Summary & Outcomes

Q2.4 Summary of the required outcomes for this topic area. How do the tasks from the research fill the gap described before?

<u>Simplified Questionnaire (Used on January 2021 and after)</u>

<u>Topics of discussion</u>:

- Flight Test Preparation
  - Negotiation process of Flight Test objectives (with FAA)
  - Is access to a Flight Test Plan document and/or Sample Test Card for a noise measurement test possible?
  - Selection of testing location (e.g., airport, and why?)
  - Up-front preparation steps
  - Detail of typical schedule (typical number of allotted days/hours & FTEs)
  - Set up of DAS/DAU and key instruments.
  - Go/No-go conditions
- Test Execution
  - Details of key hardware set up.
    - Microphone type selection, location.
    - Specifically, about how information is relayed.
  - General challenges during data collection
    - Physical barrier (weather, environment, etc.)
    - Common instrument issues
    - Key points of difficulty (specific data type, communication amongst teams, etc.)
  - How do the test engineers confirm test objectives were met during test?
  - Challenges of airport testing
  - Sensitivities of airport/testing site location? (e.g., data quality issues… trees, snow, freezing temperatures, moisture from humidity/rain/etc.?)
  - Coordination between roles (test pilot, ATC, ground crew, test engineers, etc.)

- Miscellaneous in planning and testing
    - [Comment from Workshop 1]: "The 'decision process for Part 36 is not as 'easy to set up' as some of the other parts. Also, Part 36 does not 'interact very well' with the other parts, e.g., 25."
        - What decisions need to be made at different points in the certification process?
        - What does your decision process look like, is it more difficult for new aircraft?
- Analysis & Reporting
    - Discuss general post-test analysis method(s).
        - How to match predicted versus actual for verification.
        - Effort length and duration
    - Discussion of final artifact from flight test
    - How is the data stored with the FAA (report/database/etc.)?
    - Analysis Methods for small items: Determination of NAC
        - Is AC 36-4D the sole source of guidance and methods for small changes?
        - What tools / methods might make NAC determinations simpler?
        - Would analysis methods that allowed cumulative changes greater than 0.30 db be beneficial? (i.e., reduced flight demonstrations)

Appendix D - Implementation of the Verification Model

In the following, we present a brief overview of how each module has been implemented and how the integration development spiral was pursued. The integration process followed the steps shown in Figure D1.

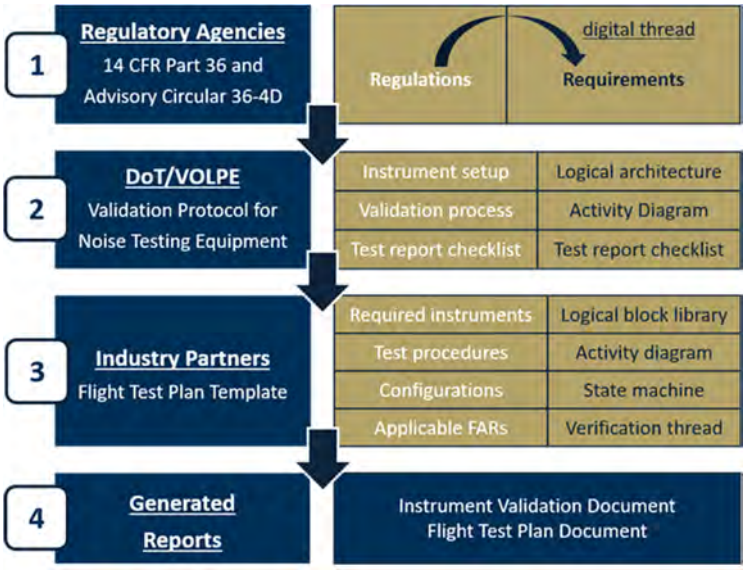

Figure D1. Verification model integration steps. CFR: Code of Federal Regulations; DoT: Department of Transportation; FAR: Federal Aviation Regulations.

Step 1 includes the conversion of regulations to requirements. In this context, a requirement normally represents a single design constraint, extracted from one or more regulations. A method of verification is required in order for this design constraint to be satisfied by the SUT. To provide this verification step, a constraint block is introduced as a verification mechanism by integrating engineering analysis into a model. In particular, with the use of a constraint block, it is possible to quantify the textual requirement using mathematical and logical expressions only, while verification simulations, which can determine whether a certain metric meets a requirement, can be enabled. Overall, the constraint block acts as an interface that links a requirement model and the logical/physical model of an SUT. Figure D2 presents an example of how a regulatory article can be imported as a requirement, linked to the verification model, and tested.

A36.3.7.4 When slow time averaging is performed in the analyzer, the response of the one-third octave band analysis system to a sudden onset or interruption of a constant sinusoidal signal at the respective one-third octave nominal mid-band frequency, must be measured at sampling instants 0.5, 1, 1.5 and 2 seconds(s) after the onset and 0.5 and 1s after interruption. The rising response must be −4 ±1 dB at 0.5s, −1.75 ±0.75 dB at 1s, −1 ±0.5 dB at 1.5s and −0.5 ±0.5 dB at 2s relative to the steady-state level. The falling response must be such that the sum of the output signal levels, relative to the initial steady-state level, and the corresponding rising response reading is −6.5 ±1 dB, at both 0.5 and 1s. At subsequent times the sum of the rising and falling responses must be −7.5 dB or less. This equates to an exponential averaging process (slow time-weighting) with a nominal 1s time constant (*i.e.*, 2s averaging time).

ID: Name	Requirement Text	Owned By	Traced To	Satisfied By
40: Sudden Onset Response Sampling Instants	The analysis system shall have a response (to the sudden onset of a constant sinusoidal signal) that is measured at sampling instants 0.5, 1, 1.5 and 2 seconds after the onset.	Measurement System Requirements	A36.3.3.1, 1D A36.3.7.1 A36.3.7.4	Sound pressure level response (Analysis System: Value Property)
41: Interruption Response Sampling Instants	The analysis system shall have a response (to the sudden interruption of a constant sinusoidal signal) that is measured at sampling instants 0.5 and 1 second after the onset	Same as ID 40	Same as ID 40	Same as ID 40
42: Rising Response Limits	The analysis system shall have a rising response that conforms to these dB values at each sampling instant (relative to the steady-state level): −4 ±1 dB at 0.5s, −1.75 ±0.75 dB at 1s, −1 ±0.5 dB at 1.5s and −0.5 ±0.5 dB at 2s.	Same as ID 40	Same as ID 40	Same as ID 40
43: Falling Response Limits	The analysis system shall have a falling response such that the sum of the output signal levels is −6.5 ±1 dB, at both 0.5 and 1s (relative to the initial steady-state level, and to the corresponding rising response)	Same as ID 40	Same as ID 40	Same as ID 40
44: Sum of Rising and Falling Response	The analysis system shall have a sum of rising and falling responses less than or equal to -7.5dB (at subsequent times).	Same as ID 40	Same as ID 40	Same as ID 40

Figure D2. Regulation to requirement: example for design constraint formulation.

Step 2 seeks to implement the validation protocol for noise testing (as dictated by VOLPE's guidance) in a logical model. This step returns the representation of the physical noise instrument architecture as a SysML logical model. The architecture description is achieved by using "blocks," essentially describing a system by reusable, modular units. These blocks contain structural and behavioral features that define relationships between parts via connectors. An example of a block, representing the microphone type used during flight testing, is shown in Figure D3. Each block is functionally verified by constraints (highlighted in blue), contains a hierarchy to define parts (highlighted in orange), and holds defined values as value properties (highlighted in green).

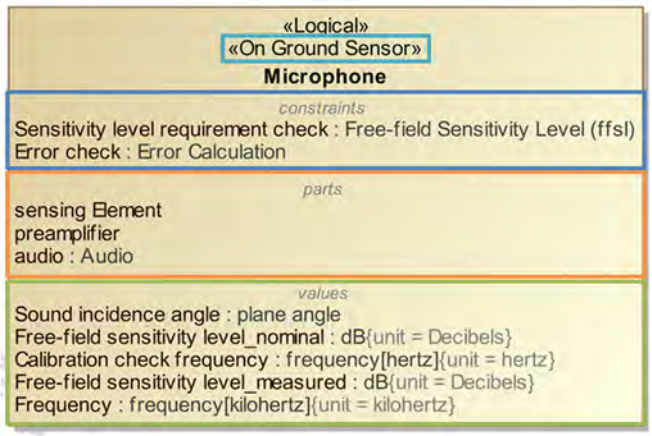

Figure D3. Example of a logical block, representing physical microphone technology.

The instrumentation architecture is further characterized by the types of sensors used, e.g., two types of sensors: <<On Ground Sensor>> (namely the microphone, as represented by the logical block in Figure D3) and <<On A/C Sensor>>. An example of a SysML logical representation of a microphone and hardware setup as part of the VOLPE validation protocol is shown in Figure D4.

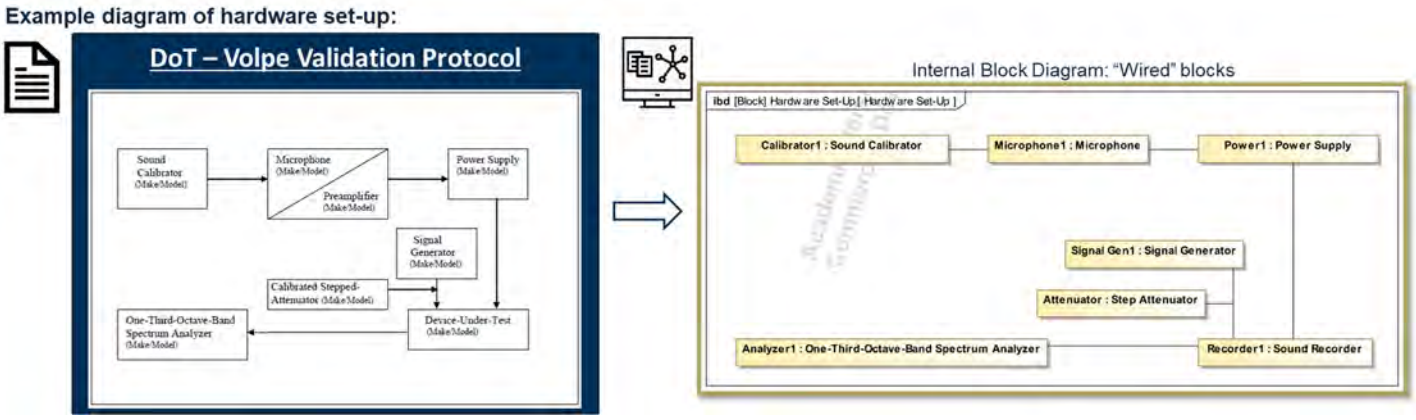

Figure C4. Example diagram of hardware setup. DoT: Department of Transportation.

The complete logical architecture representation in a SysML environment provides a unified model for all system elements (single source of truth), full transparency, and shared understanding of the system. This model is an extensible representation of the system and its components with their properties, with a clear definition of interfaces between architectural elements. This architecture is described hierarchically, with the system decomposition level being dictated by the requirements. As more architectural elements are progressively included, the model can be easily updated accordingly. An example of a complete logical hierarchical architecture is shown in Figure D5.

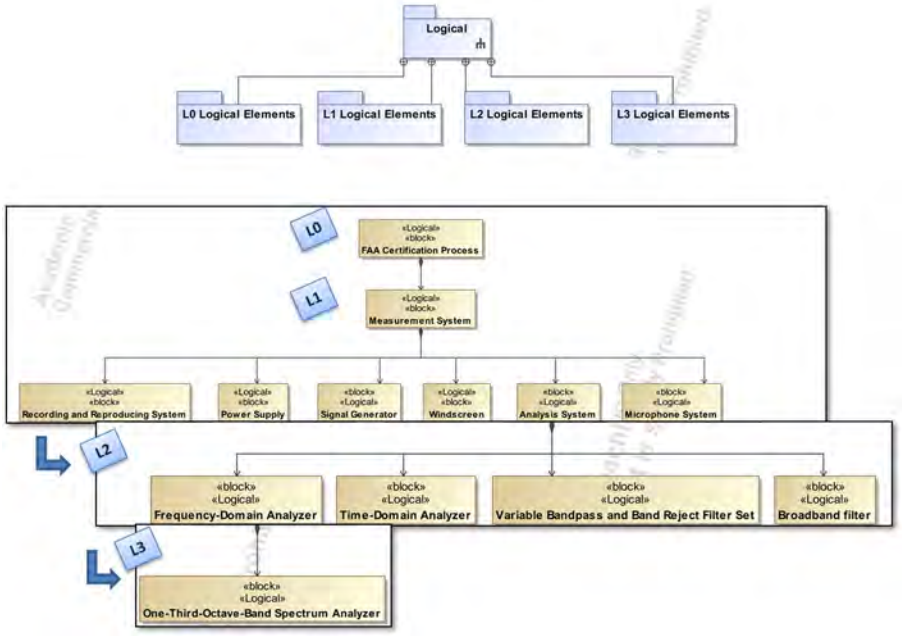

Figure D5. Logical architecture for the verification model.

The parametric construct allows for the logical architecture to be executable through simulations, which is key for performing requirement verification. This construct includes improved traceability among requirements, architecture, and verification information. The stored information in relevant blocks is used for requirement verification, with the quantitative characteristics defined as value properties for each block. This step requires validation/measurement data for an SUT, in order to create instances within the model for data representation. The requirement verification is performed by executing the logical architecture, using the Cameo Simulation Toolkit. An example of requirement verification for the microphone setup within the logical architecture in SysML is shown in Figure D6.

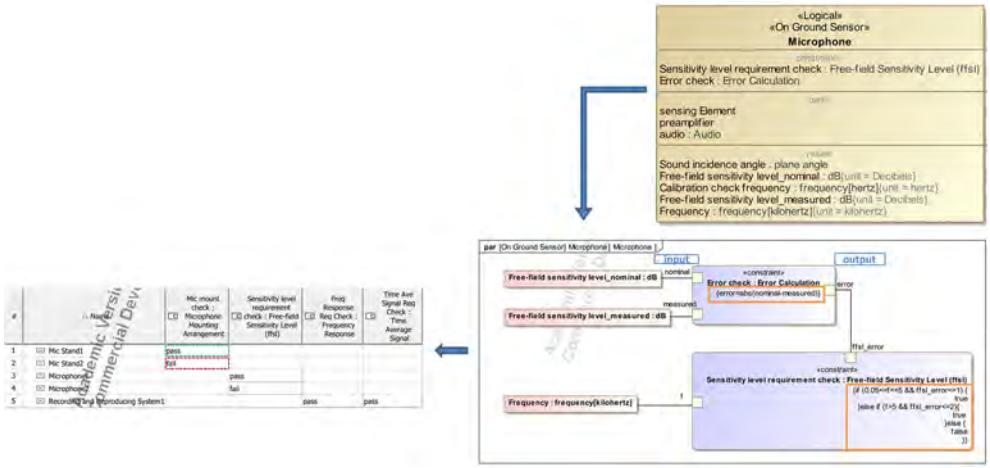

Figure D6. Requirement verification of the logical architecture: an example.

At the current state, the logical architecture model can accommodate the full aircraft noise certification test system, an example physical view, and the corresponding logical architecture implementation shown in Figure D7. The SUT that has been used for verification model development is based on a Boeing 787-8 configuration, and its logical representation in SysML is shown in Figure D8.

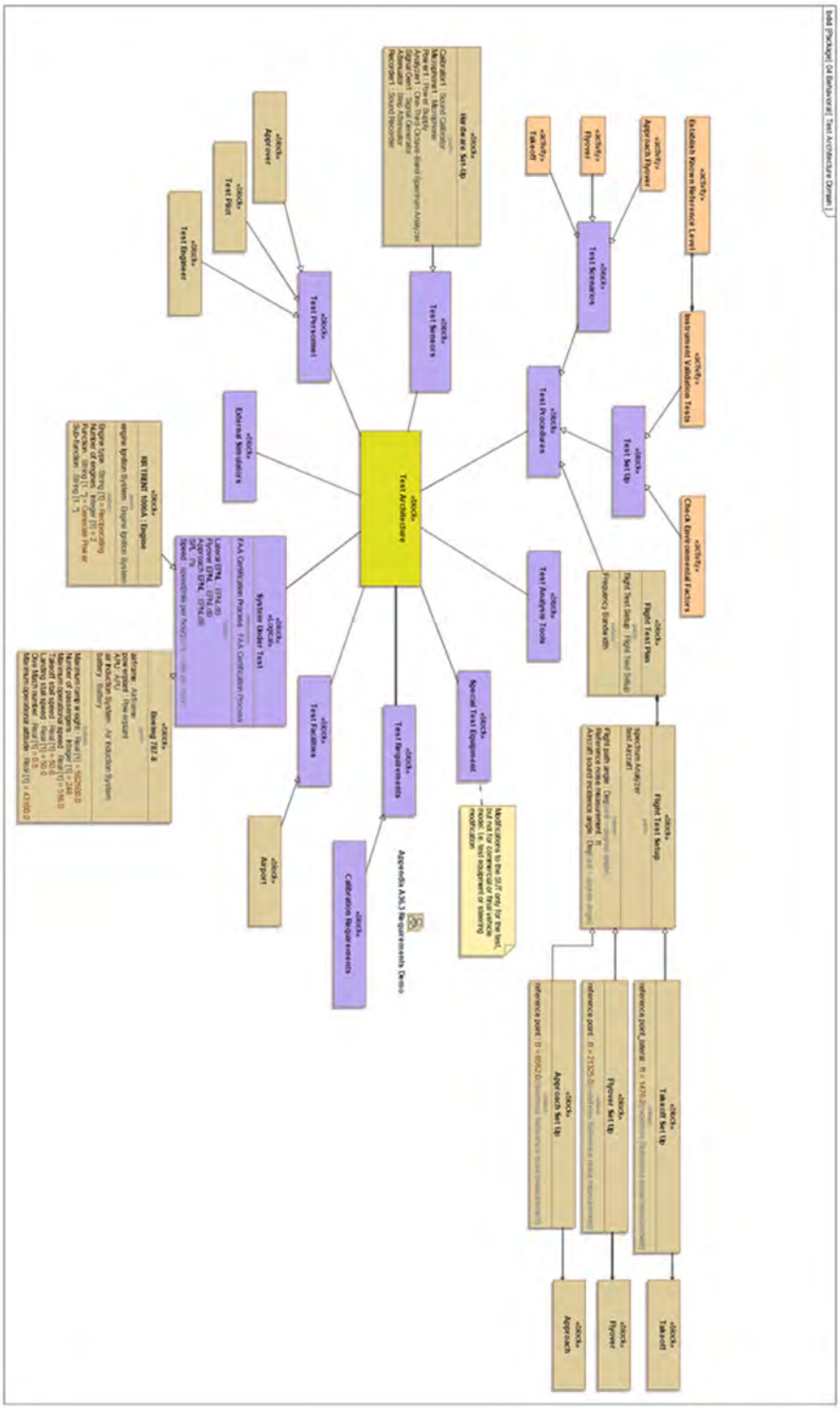

Figure D7. Flight testing architecture domain.

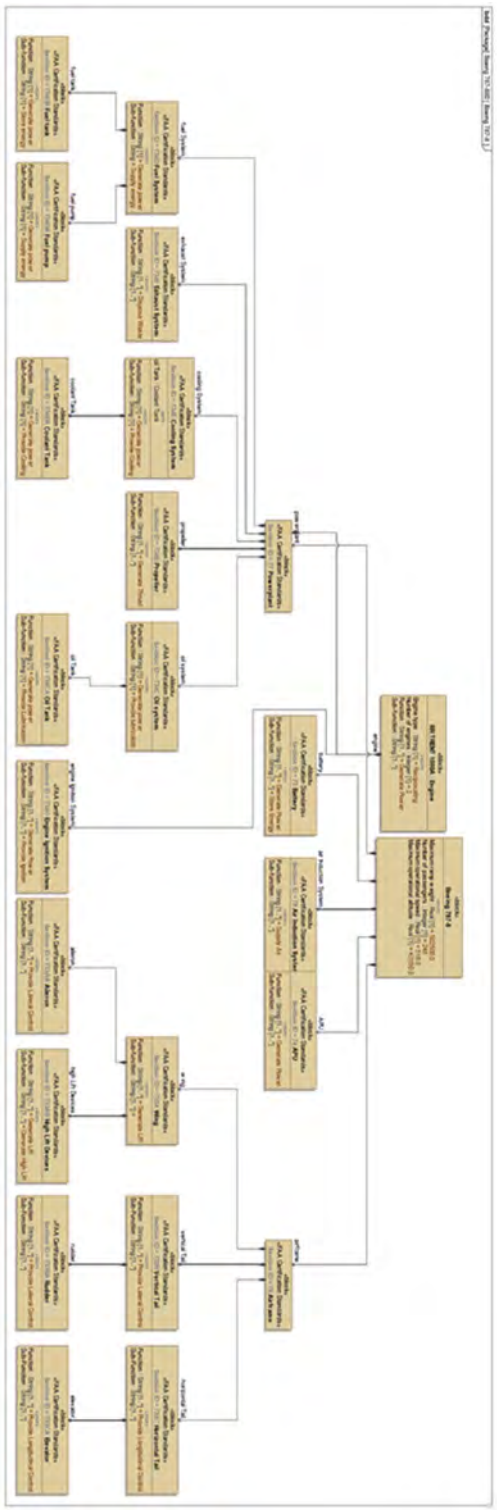

Figure D8. Aircraft model (Boeing 787-8) used as the system under test (SUT).

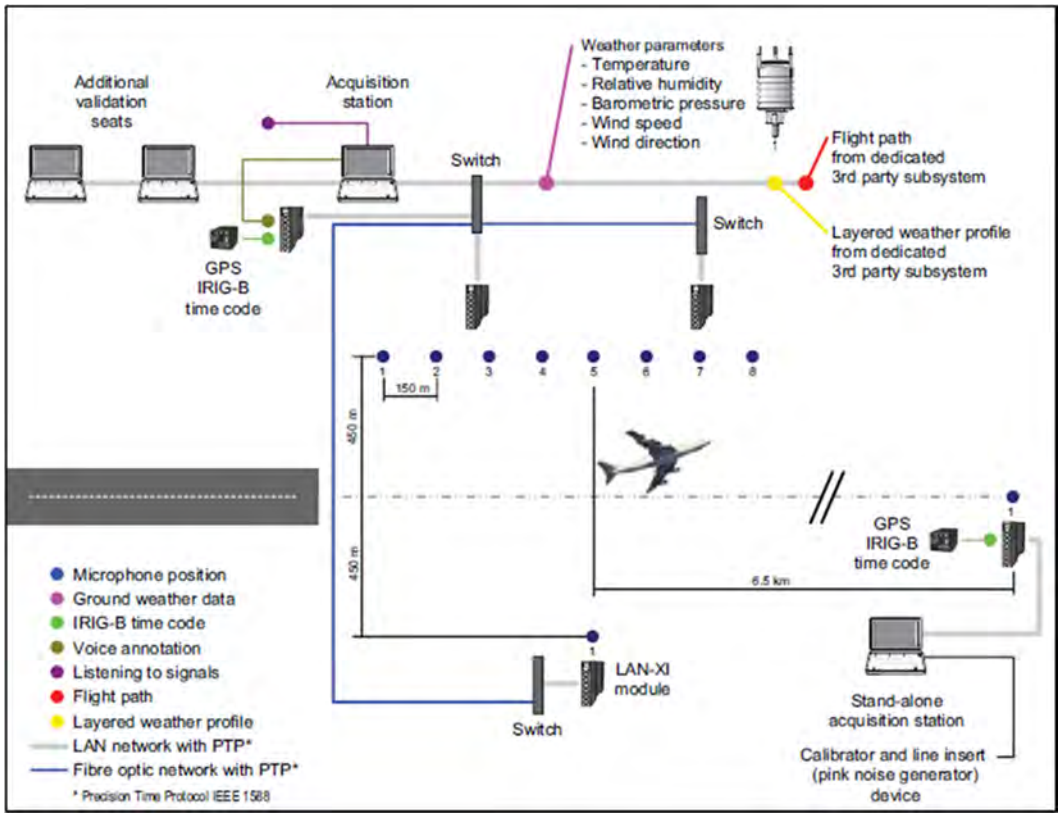

Figure D9. Schematic overview of aircraft noise certification test system by Brüel & Kjær. GPS: Global Positioning System; IRIG: Inter-Range Instrumentation Group; LAN: Local Area Network; PTP: Precision Time Protocol.

Step 3 of the verification model implementation process involves the representation of the flight test procedures as behavioral models. As test procedures are written in text (bullet points, numbered lists, etc.), functions performed by the system and the external system interfaces are not clearly defined. To model the process as behavioral diagrams, it is necessary to define functions allocated to systems and establish functional flows with defined interfaces, as shown in Figure D10.

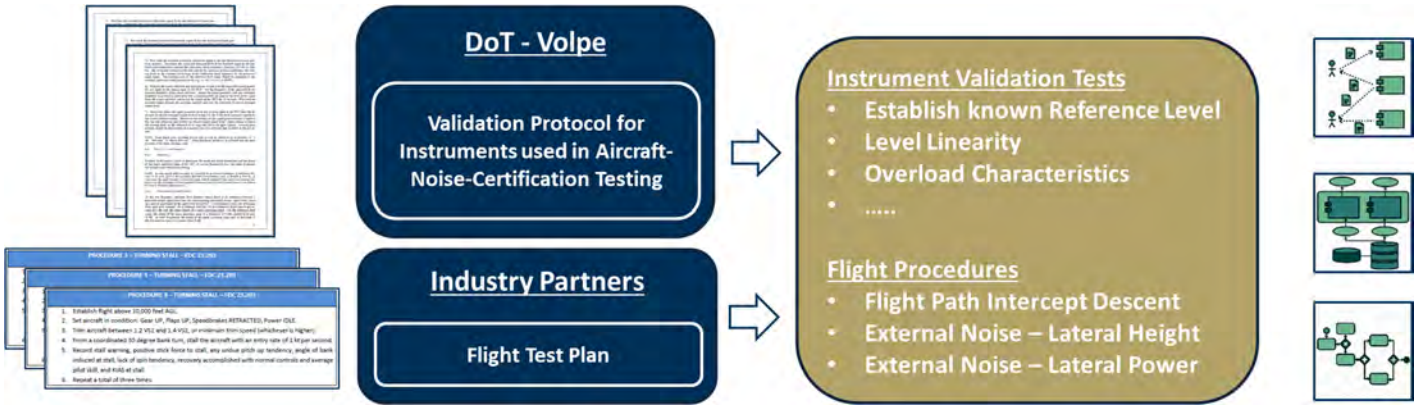

Figure D10. Process for representation of flight test procedures as behavioral models. DoT: Department of Transportation.

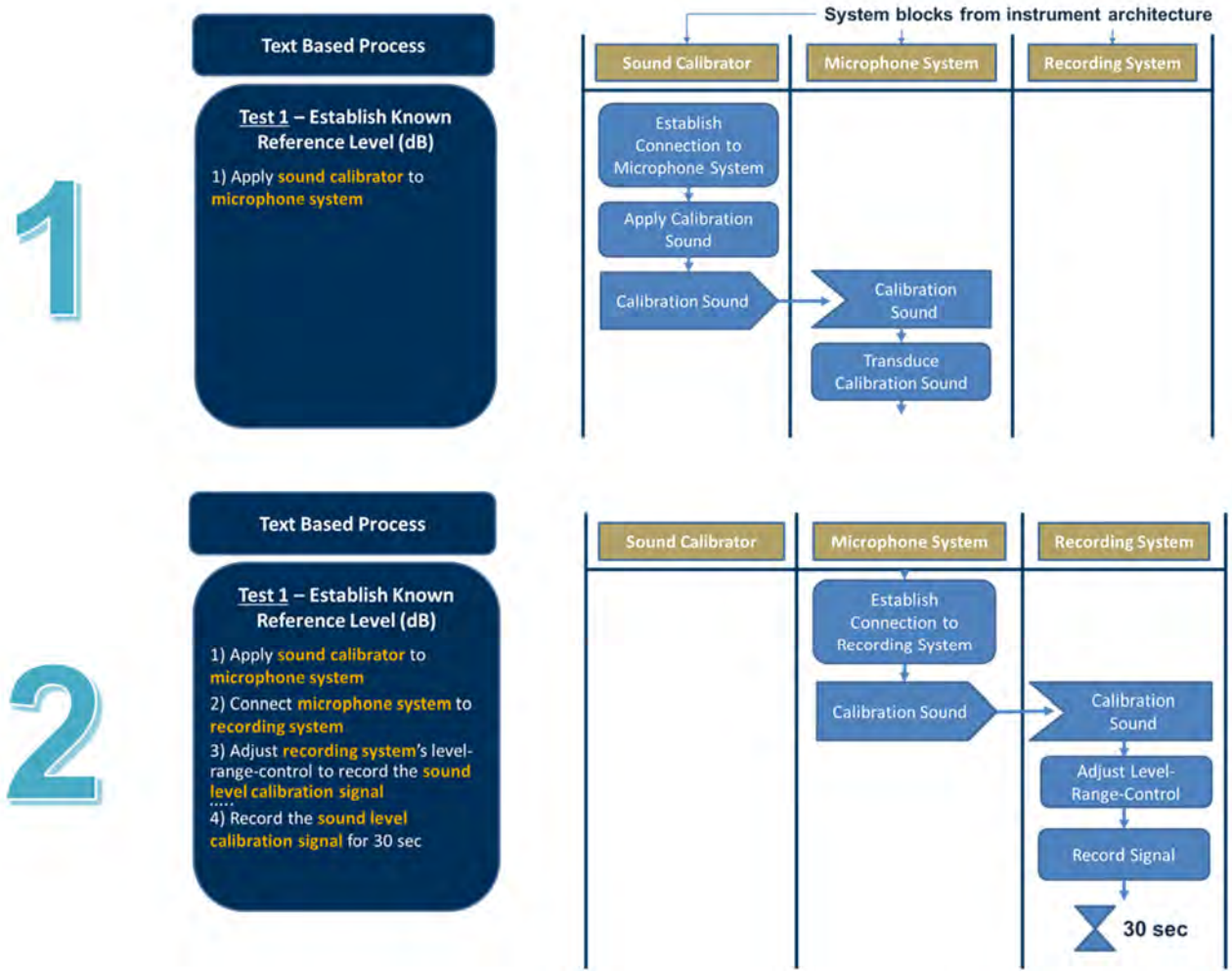

Figure D11. Text-based method for behavioral process model implementation.

To clarify and demonstrate how this process functions in practice, an example is provided in Figure D11. The purpose of the example test function is to establish a known reference noise level (in dB), with steps of the process listed in text format (indicated on the left side of the figure). Starting from phase 1 of the implementation (at the top of the figure), the first process step indicates that 1) a sound calibrator is applied to the microphone system. In the behavioral process model, this step corresponds to the use of three system blocks from the instrument architecture library, namely, the sound calibrator, the microphone system, and the recording system. In terms of process steps, a connection between the sound calibrator and the microphone system must be established, and the calibrator must then supply a calibration sound to the microphone. In the next phase of steps (phase 2 at the bottom part of the figure), there is instruction to 2) connect the microphone system to the recording system, 3) adjust the recording system's level-range control to record the sound level calibration signal, and 4) record the sound level calibration signal for 30 s. These process steps are then populated to the process model on the right side of Figure D11 and mapped accordingly to the system blocks.

Continuing this same implementation path, the completed process mode for establishing a known reference noise level is shown in Figure D12. Following similar steps, behavioral process models in SysML were formulated for the flight-testing phases of interest, which are the 1) approach flyover and 2) takeoff.

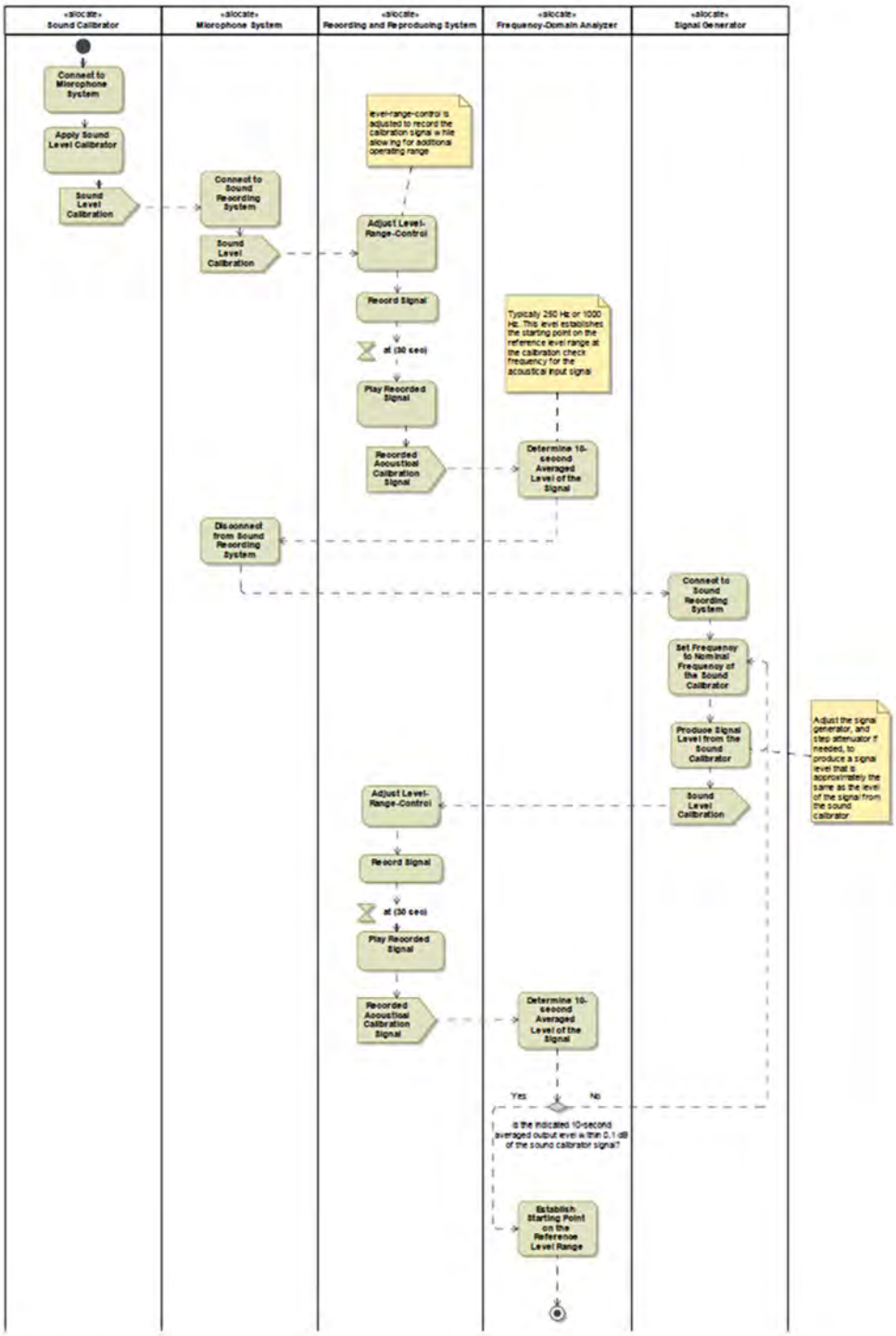

Figure D12. Process model for establishing a known reference noise level (baseline noise definition process).

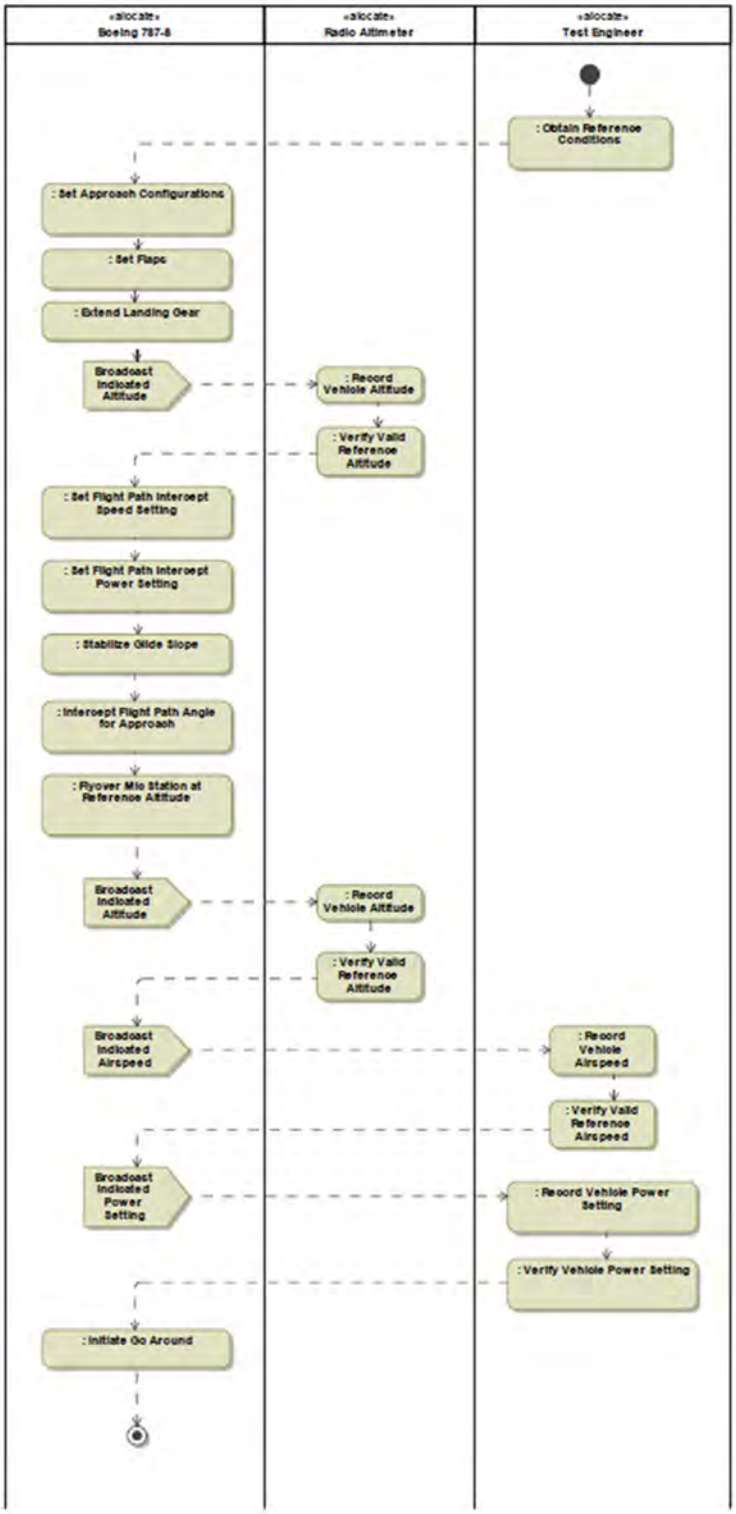

Figure D13. Behavioral process model for approach flyover.

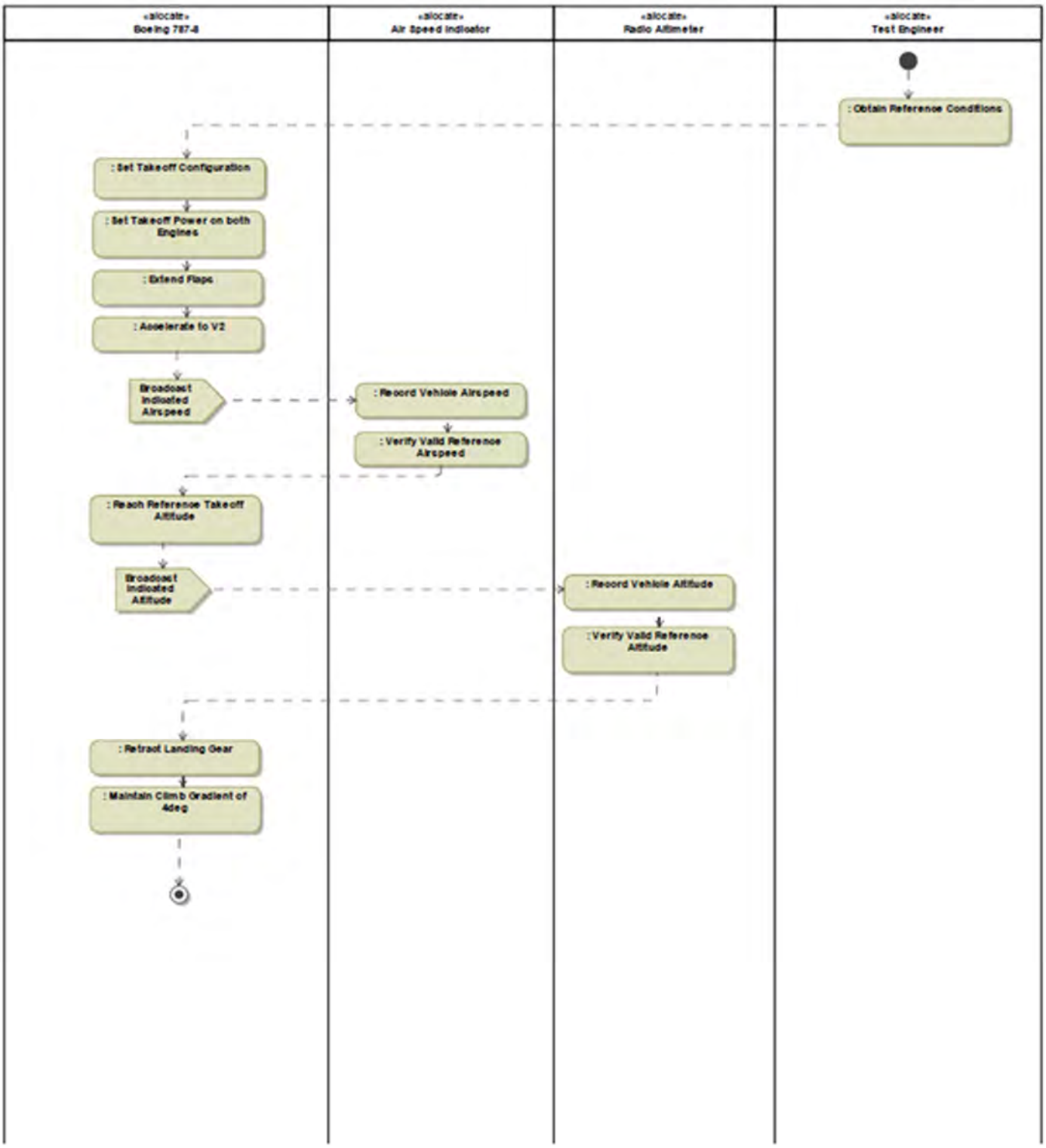

Figure D14. Behavioral process model for takeoff.

Step 4, the final integration step for the verification model, is the automated document generation. A suite of reports is generated through this function, including the following documents:

- Product specifications
- Technical baseline
- Metrics
- Verification compliance

The produced reports also include the following documents for certification:

- Instrumentation validation document
- Flight test plan

Project 062 Noise Model Validation for AEDT

Georgia Institute of Technology
The Pennsylvania State University

Project Lead Investigator

Dimitri N. Mavris
Director, Aerospace Systems Design Laboratory
School of Aerospace Engineering
Georgia Institute of Technology
Mail Stop 0150
Atlanta, GA 30332-0150
404-894-1557
dimitri.mavris@ae.gatech.edu

Victor W. Sparrow
United Technologies Corporation Professor of Acoustics
Graduate Program in Acoustics
The Pennsylvania State University
201 Applied Science Bldg.
University Park, PA 16802
814-865-6364
vws1@psu.edu

University Participants

Georgia Institute of Technology (Georgia Tech)

- P.I.s: Prof. Dimitri Mavris and Dr. Michelle Kirby
- FAA Award Number: 13-C-AJFE-GIT-106 and 13-C-AJFE-GIT-125
- Period of Performance: September 27, 2021 to September 20, 2023
- Tasks:
    1. Noise Modeling in AEDT with Automation
    2. Assessing the Use of High-Fidelity Meteorological Data in AEDT Noise Calculations

The Pennsylvania State University (PSU)

- P.I.: Prof. Victor Sparrow
- FAA Award Number: 13-C-AJFE-PSU, Amendments 59, 83, and 89
- Period of Performance: October 1, 2021 to September 20, 2023

Project Funding Level

The project is funded by the FAA at the following levels: Georgia Tech: $235,000; PSU: $140,000. Cost-sharing details are below.

Georgia Tech has agreed to a total of $235,000 in matching funds. This total includes salaries for the project director, research engineers, and graduate research assistants, as well as computing, financial, and administrative support, including meeting arrangements. Georgia Tech has also agreed to provide tuition remission for the students, paid for by state funds.

For PSU, Spire Global (http://www.spire.com/), is providing cost-sharing funds in the form of meteorological data and research support. The point of contact for this cost sharing is Ms. Ashley O'Neil (703-853-8468; ashley.oneill@spire.com). Metropolitan Washington Airports Authority is providing sound level meter data from Dulles International Airport as in-kind

cost sharing; the point of contact is Mr. Mike Jeck (703-417-1204; Michael.jeck@mwaa.com). Additional in-kind cost sharing is being provided by the PSU College of Engineering to meet the required matching of $140,000.

Investigation Team

Georgia Tech
Prof. Dimitri Mavris, P.I., Georgia Tech
Dr. Michelle Kirby, co-investigator, Georgia Tech
Dr. Mayank Bendarkar, research faculty, Georgia Tech
Sabastian Abelezele, graduate student, Georgia Tech
Amber Willitt, graduate student, Georgia Tech
Wiame Benzerhouni, graduate student, Georgia Tech

PSU
Prof. Victor Sparrow, P.I., PSU
Harshal Patankar, graduate student, PSU
Emma Shaw, graduate student, PSU

Project Overview

The focus of this project is to assess the accuracy of the Aviation Environmental Design Tool (AEDT) in estimating noise in the vicinity of airports as well as further afield. The foundation of AEDT noise modeling is based on the Integrated Noise Modeling (INM) tool, which has undergone several validation and verification efforts in the past, specifically at the Denver International Airport (DIA), and has shown continual improvements in the agreement between modeling predictions and measurement data. During the development of AEDT, multiple algorithm updates have occurred. This project seeks to quantify the new noise modeling capabilities through comparison with field measurement data from DIA and other airport monitoring systems. The research team will develop a detailed model validation plan, review the plan with the FAA for concurrence, execute the plan, and make recommendations for future AEDT development. The research, once completed, is expected to provide a noise model validation benchmark that can be used not only to respond to questions regarding AEDT noise prediction accuracy, but also to allow the tool development team to prioritize further development of modeling features and enhancements. The research team will also collaborate with PSU on the assessment of the noise propagation assumptions and the use of higher-fidelity weather data.

Task 1 – Noise Modeling in AEDT with Automation

Georgia Institute of Technology

Background and Objective

In the past decade, demand for air passenger services growth has increased, with a long-term average exceeding 5% in terms of revenue passenger miles (Juniac, 2012). To mitigate the environmental impacts of this growth in aviation, and to maximize the economic benefits that can be achieved through higher efficiency and performance, NASA's Environmentally Responsible Aviation project has suggested aggressive goals (Suder, 2012). This set of goals includes a target to reduce the noise emissions created by aviation over the 2015, 2020, and 2025 timeframes. The first step in mitigating noise emissions is having the capability to model them with a high level of accuracy. The FAA's AEDT (Federal Aviation Administration, n.d.) has among of the most advanced capabilities for both modeling aircraft operations and computing associated environmental metrics. AEDT is a software system that models aircraft performance in space and time, to estimate fuel consumption, emissions, noise, and air quality consequences. AEDT's primary objective is to facilitate the environmental review of federal actions associated with changes in airports, airspace, and other applicable aviation activities.

Several past efforts have studied the improvement of modeled procedures in AEDT or the comparison between AEDT capabilities and real-world operational data. Noise abatement departure procedures (NADPs) are commonly used to mitigate community noise either closer to the airport or further afield. Lim, et al. (2020) have provided a set of 20 NADP profiles suitable for modeling a large variety of operations that are typically observed in the real world. Behere & Lim (2020) and Behere & Isakson (2020) have focused on quantifying the impacts of such NADP profiles on noise modeling and have identified the most representative NADP profiles. AEDT has also been used in the creation of alternative rapid noise modeling tools (Levine, 2019; Monteiro, 2018), in comparing aviation environmental impact mitigation strategies (Yu, 2019), and in

various other community noise quantification studies (Yu, 2019; Salgueiro, 2021; Thomas, 2019). Other efforts have focused on using large amounts of real-world data to produce reduced-order models for rapid computation of noise impacts (Behere & Rajaram, 2021) or for estimating the impacts of average types of operations at different airports (Behere & Bhanpato, 2021).

Prior studies related to noise model validation date back to AEDT's predecessor, INM. Several prior efforts have focused on validating AEDT or INM to quantify the agreement between the model predictions and the data recorded from actual operations. Page et al. (2000) have investigated a 1997 data set from DEN to determine how INM's prediction accuracy changed with different thrust prediction methods. They have found that the manufacturers' look-up values of normalized thrust were the most accurate. They then used this information to improve the noise–power–distance (NPD) curves in INM from historical manufacturer data. Forsyth and Follet (2006) used the same 1997 DEN data to update INM's database, with an emphasis on higher altitudes. Spectral classes were created to correct the NPD information with respect to SAE AIR-1845 atmospheric absorption. In another study performed with the 1997 DEN data, Plotkin et al. (2013) studied options to further enhance the modeling capability by accounting for the effects of weather and terrain.

Since its introduction by the FAA in 2015, numerous studies have been performed on AEDT. Hobbs et al. (2017) have proposed an easily implementable method for including ground cover effects on noise propagation calculations by using algorithms originally implemented in the Advanced Acoustic Model (Page, 2000). These algorithms use optical straight-ray theory, as adapted for acoustics, to model noise propagation, in addition to the Fresnel ellipse method. This process has been found to improve noise propagation calculations with respect to empirical data, on data from Portland International Airport, San Francisco International Airport (SFO), and Oakland International Airport. Downing, et al. (2019) investigated a method for including terrain and manufactured structural effects in AEDT's noise propagation calculations in 2019. Three separate models were evaluated with respect to their ability to accurately predict how buildings and barriers affect aircraft noise: the Traffic Noise Model (TNM) (Hastings, 2019), SoundPLAN 7.4 (which uses ISO 9613-2), and the National Cooperative Highway Research Program's Reflection Screening Tool. After validation using data from Los Angeles International Airport (LAX) and Long Beach Airport, the TNM method was recommended as the best option, because its noise calculations have variability and consistency similar to those of AEDT's baseline calculations. In previous research by Gabrielian et al. (2021), an automated framework was demonstrated for validation of noise modeling capabilities within AEDT by using real-world flight and noise monitor data. In other work, the authors studied AEDT's noise prediction capability while using high-fidelity weather data (Gabrielian & Puranik, 2021).

The remainder of this report provides information on noise modeling data sources, AEDT assumptions, and automation capabilities developed for the current work. It also discusses the results generated for the bulk flight operations modeled, along with particular or aggregate insights.

Research Approach

System-level noise modeling in this report follows the procedure detailed in our previous work (Gabrielian & Puranik, 2021). Two important elements in this modeling are summarized herein for completeness: (a) the data sources used during modeling, and (b) the modeling assumptions and alternatives available for each assumption.

Data Sources Used

Several data sources with different fidelity can be used for noise modeling, ranging from simple ground-based radar observations to data fusion from multiple sensors on an aircraft itself. The two main data sets relevant to this manuscript are described below.

1. ***Flight operational quality assurance (FOQA)*** data are recorded by the airline operating the flight. The basis for the FOQA program is laid out in FAA Advisory Circular 120-82, which states: "The value of FOQA programs is the early identification of adverse safety trends that, if uncorrected, could lead to accidents" (FAA, 2004). Therefore, FOQA systems record large amounts of data at one recording per second (i.e., 1 Hz). These data have been used for several safety-related applications in prior work (Puranik, 2018; Lee, 2020). The important elements of the FOQA data in this manuscript relate to the detailed time history of parameters such as altitude, speed, thrust, weight, configuration (flaps and gear), and so on, for each flight modeled in AEDT.
2. ***Noise monitoring data*** contain five key parameters: a unique flight ID, noise monitor locations, class of noise reading, sound exposure level (SEL), and L_{max} metrics of associated noise events. The flight ID in the noise monitor data allows flights to be matched to the appropriate flight from FOQA data, thereby matching the aircraft configuration and the time of the noise event with the noise metric value. The class of the noise reading identifies

the confidence with which the noise reading has been matched with the corresponding flight ID. The highest confidence is marked as a class 1 reading. These locations (except for their altitude) are used in flight modeling discussed in subsequent sections. The noise monitor data are used as a benchmark comparison for noise results calculated by AEDT.

The framework for modeling and automation developed in this manuscript is independent of the data source used and will need to be modified only to account for the availability of parameters if other data sources are used. In this work, the data used are obtained from flight operations at SFO and noise monitoring readings obtained from the SFO airport noise program (SFO, n.d.).

Modeling Assumptions and AEDT Capabilities

Modeling in AEDT offers users multiple settings for critical assumptions related to the modeling of performance and noise. A matrix of alternatives for these options is shown in Tables 1 and 2. Although the possible options and their combinations may be large, not all listed options are compatible or included in the present work. These limitations are noted while discussing the modeling assumptions individually.

Table 1. Modeling options for departure operations.

Assumption	AEDT default	Option 2	Option 3	Option 4	Option 5
Thrust	Full	FOQA	RT05	RT10	RT15
Weight	AEDT	FOQA	Alternative weight		
Ground track	Standard	FOQA			
Procedure	Standard	FOQA	NADP1_1	NADP2_11	
Weather	Standard	FOQA	ASOS	High fidelity	
Surface	Soft	Hard			
Terrain	None	Actual			
Flaps	AEDT	FOQA			
Gear	AEDT	FOQA			
NPDs	AEDT	NPD+C			

Table 2. Modeling options for arrival operations.

Assumption	AEDT default	Option 2	Option 3	Option 4	Option 5
Thrust	Full	FOQA			
Weight	AEDT	FOQA			
Ground track	Standard	FOQA			
Procedure	Standard	FOQA			
Weather	Standard	FOQA	ASOS	High fidelity	
Surface	Soft	Hard			
Terrain	None	Actual			
Flaps	AEDT	FOQA			
Gear	AEDT	FOQA			
NPDs	AEDT	NPD + C			

SFO is selected for the present work because the research team has access to real-world noise monitoring data from that airport. For the purposes of this study, 269 departing and arriving flights at SFO have been down selected. The flights consist of Boeing 717-200; 737-800,900; 757-200,300; Airbus A319-100 and A320-200 airframes.

Several settings are available under every assumption (row) in Tables 1 and 2, which can affect the performance and noise for each flight operation. This section provides a summary of each option and how it might potentially affect the calculations. For further details, readers are referred to the AEDT technical manual (Ahearn, 2016).

1. ***Thrust settings***: The options for thrust in AEDT can be seen through some of the procedures in the FLEET database. Apart from a full thrust assumption, the true thrust value at different points along the departure or arrival is available from the FOQA data and can be used. RT15 corresponds to a 15% reduced thrust during the takeoff procedure.

Investigation of thrust settings upon takeoff and cutback in ASCENT Project 45 has identified that 15% reduced thrust is regularly used by operators in real-world scenarios. This decrease in takeoff and cutback thrust results in a 30% decrease in the area of the 80-dB SEL contour for a single-aisle aircraft (Mavris, 2018). Other options available within AEDT include 5% and 10% reduced thrust; however, these options are not studied in the present work. The final thrust option available is the actual thrust from the flight given in the FOQA data.

2. ***Procedure:*** The FLEET database has two types of profiles that can be used: procedural profiles and fixed-point profiles (FPPs). Procedural profiles define an aircraft's thrust, speed, and trajectory in a series of steps. Examples of procedural profiles include the standard profile, NADP1, and NADP2. FPPs fully define the location and state of the aircraft in the sky, as well as its state: thrust and speed. FPPs are used to model FOQA data within AEDT because they can include the speed and thrust from flight data.

3. ***Weight:*** Modified alternative weight procedures are available within AEDT that can be combined with the standard or reduced thrust procedures. FOQA weight can also be used within AEDT with FPPs. In this way, the information regarding weight, thrust, and speed can be used in one FPP for each flight modeled.

4. ***Ground track:*** The ground track comprises the latitude and longitude points on the ground of the aircraft during its flight. The default AEDT modeling for ground tracks is straight into the airport, parallel with the runway that the aircraft is using upon arrival, or straight out of the airport upon departure. These default settings are likely to result in incorrect predictions in comparison with real-world noise observations and are therefore not included in the current analysis. The FOQA ground track data, reflecting the true flight paths into or leaving airports, are used in the present work.

5. ***Weather:*** The default weather settings used in AEDT studies are located in the AIRPORT database. These settings include temperature, relative humidity, wind speed, sea-level pressure, and dew point, which affect performance and acoustic calculations. The wind direction is always assumed to be a headwind direction. Although AEDT can use high-fidelity weather data in multiple formats [21], the present work is limited to the default setting.

6. ***Surface and terrain***: The surface options within AEDT are available for propeller aircraft, including hard and soft surface options that affect the ground reflection and other properties in noise calculations. For the present work, the AEDT default value is assumed for these settings.

7. ***Flaps and landing gear:*** The flap and gear schedule for modeling in AEDT are provided with each of the procedures or the flap schedule defined in the FOQA data.

8. ***NPD curves:*** Noise calculations in AEDT rely on NPD curves derived in a process similar to that used in aircraft noise certification. Noise levels are obtained as a function of observer distance via spherical spreading through a standard atmosphere. In noise analysis, AEDT applies other correction factors to obtain the desired sound field metrics at the location of the receiver. NPD + configuration (NPD + C) curves that may enable more accurate noise prediction due to aircraft configuration and speed changes are under study (Mavris, 2019) and are not included in the present work.

Compatibility of Settings

Of the settings discussed previously, those varied in this study include the procedures and profiles, thrust, and weight. Importantly, not all these variations are compatible with one another. For example, the FOQA FPPs are incompatible with reduced thrust or alternative weight settings, because the FOQA FPPs specify the thrust at every step, and the weight at the start of the takeoff or landing segments, whereas the reduced thrust or alternative weight settings calculate these parameters with respect to the standard profile. Likewise, the FOQA thrust values cannot be used in a procedural profile because they are numerical (in pounds), whereas the procedural profiles require thrust type and step type definitions that subsequently produce their own thrust values. Consequently, a compatibility matrix is created, yielding the actual number of combinations for flights to be modeled. Arrivals have fewer combinations of modeling settings than departure profiles. The only profiles available for arrivals are the standard and FPP from the FOQA data, and one thrust setting is available.

In the present study, the combination of settings yields seven different jobs per noise metric for departures. For arrival modeling, it yields two different jobs for each noise metric. Running these cases on 129 departures and 140 arrivals requires some form of automation capability, as discussed in detail in reference (Gabrielian & Puranik, 2021a) and summarized below.

Automation Capability

An automation capability was developed to handle these combinations in a time-efficient manner. Automation is required not only for setting up the many combinations of settings within AEDT (also called pre-AEDT automation) but also for post-processing of the results generated (post-AEDT automation). The pre-AEDT automation consists of nine SQL automation scripts (Figure 1). The user specifies the profiles to be modeled (either procedural or FPP), the ground tracks, and a combination matrix. This matrix maps profile IDs and ground track IDs together with runway specifications to model the correct combinations from the matrix options in Table 1 and Table 2. These scripts work on multiple AEDT and user-created databases to set up the studies. After scripts 0a through 4b have been executed, script 5 can be executed, which gathers all the information from the previous scripts and sets up the metric results within a new AEDT study. After the user runs all studies within the AEDT graphical user interface, the results, including performance, emissions, and noise, are exported into .csv files with a batch report run tool. Each case in the combination test matrix results in four reports, which are then processed with MATLAB and Python post-processing scripts (post-AEDT automation).

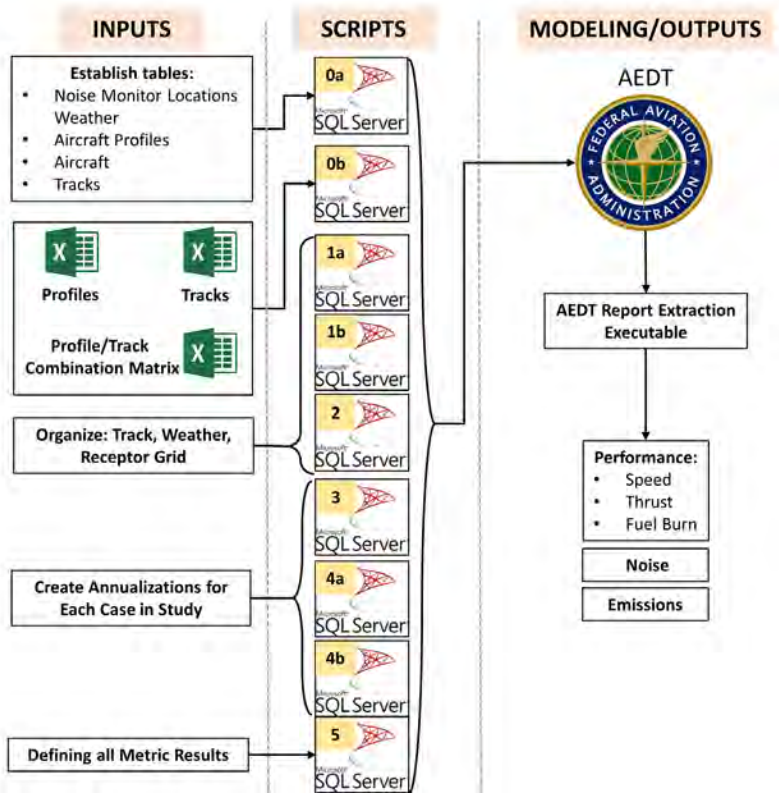

Figure 1. Noise modeling process automation steps.

Preliminary Results

The modeling framework was implemented on 129 departing and 140 arriving flights at SFO by using AEDT version 3c. In total, there are 616 (437 departures and 179 arrivals) noise events, wherein a noise event refers to a particular flight triggering a particular monitor. The number of noise events is greater than the number of flights because some flights triggered multiple monitors. The flights have been given arbitrary flight IDs (GT-xxx) to anonymize the real-world flight details. Figure 2 shows a map of the noise monitor locations in the SFO airport area along with their assigned IDs. All noise monitors triggered with the highest confidence (class 1) and mapped to the corresponding flight are used as truth values for comparing AEDT predictions. In this section, detailed results are provided for one departure and one arriving flight at SFO, followed by results on AEDT prediction accuracy on a per-noise-monitor basis.

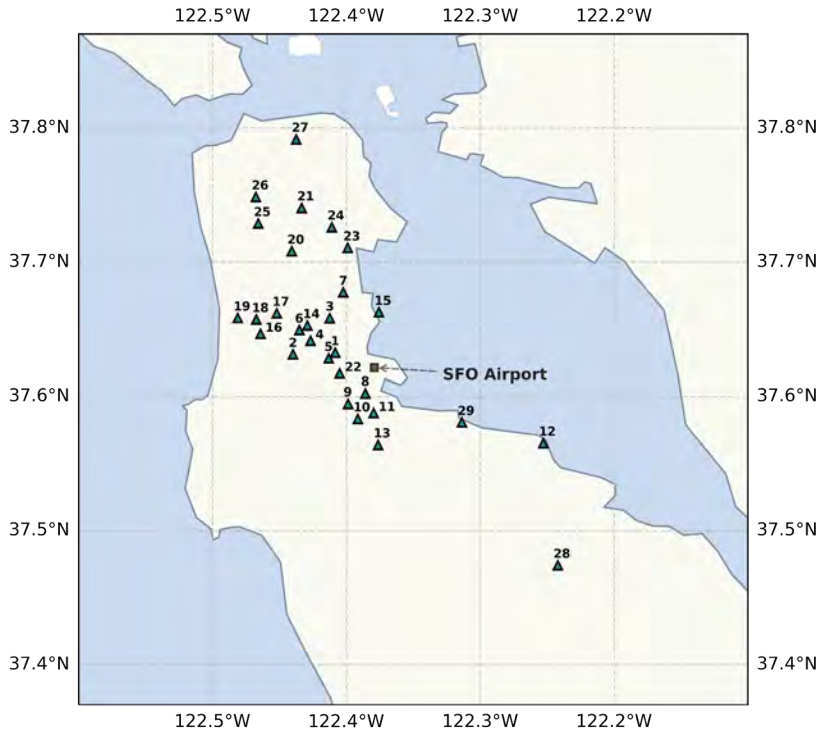

Figure 2. Locations of noise monitors around San Francisco International Airport (SFO).

Although using the FOQA flight track and trajectory are expected to result in aircraft performance and noise predictions that are closest to those measured, they are not necessarily always available to AEDT users. Therefore, investigating AEDT noise prediction accuracy under various modeling options is important from a usability perspective. The individual flight modeling results are elaborated upon in the following subsection.

Individual Flight Results

Detailed performance and noise results are available for all 269 flights, but one departure flight is reported below as an example. Table 3 provides the AEDT airport weather parameters for the two flights of interest in the present work. AEDT airport weather uses the average annual weather and therefore is the same for both flights modeled, because they operated in the same year.

Table 3. Airport weather conditions for the flights.

Weather	Temperature (°F)	Sea-level pressure (mb)	Dew point P (f)	Relative humidity (%)	Wind speed (kts)	Wind direction (°)
AEDT default	57.88	1,016.65	48.13	69.92	8.76	N/A

Flight Number GT1015

Flight GT1015 was a Boeing 737-800 with an origin–destination pair of SFO–LAX, thus making this a stage length 1 departure. The real-world flight data give the gross weight at takeoff as 145,591 lbs.

Figure 3 shows the performance plots for flight GT1015, as part of the data extracted from AEDT with the AEDT report extraction executable. The aircraft performance, on the basis of procedural profiles, shows that the alternative weight reduced thrust values for 15 profiles are shallower than the others, whereas the FOQA FPP (actual flight) is shallowest. The monitors triggered by this flight as well as the ground track are shown in Figure 4. The noise comparison for flight GT1015 in Figure 5 shows both underpredictions and overpredictions of the noise created at the noise monitor locations. An

interesting trend is observed when the noise monitor predictions are compared with the aircraft ground track and monitor locations from Figure 3. Noise values at monitors 1, 4, 6, 18, and 19 tend to be underpredicted. They also appear to be below the aircraft flight paths. Monitors 5, 14, 16, and 17 are all further from the flight's ground track and tend to be overpredicted. Although these comparisons may not provide conclusive insights alone, they can be valuable when aggregated across different flights and modeling assumptions.

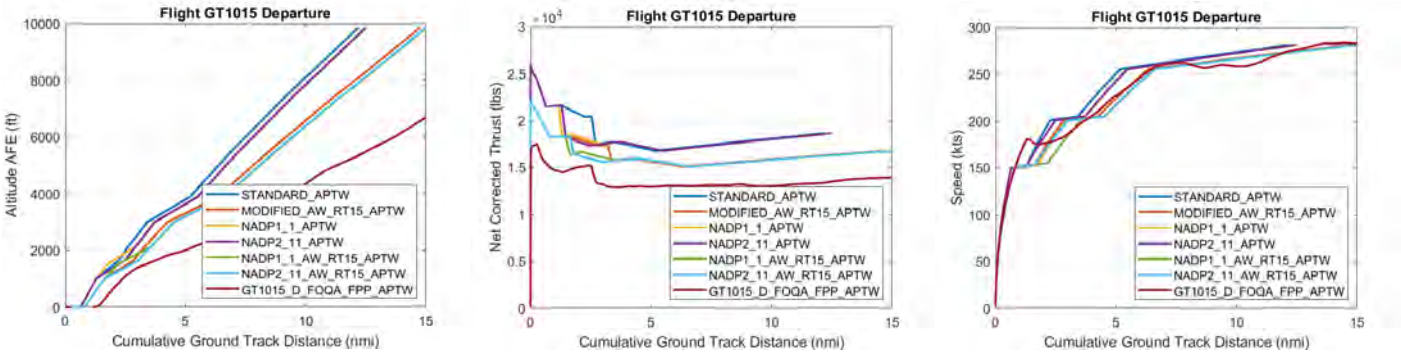

Figure 3. Altitude, thrust, and ground speed performance for flight GT1015.

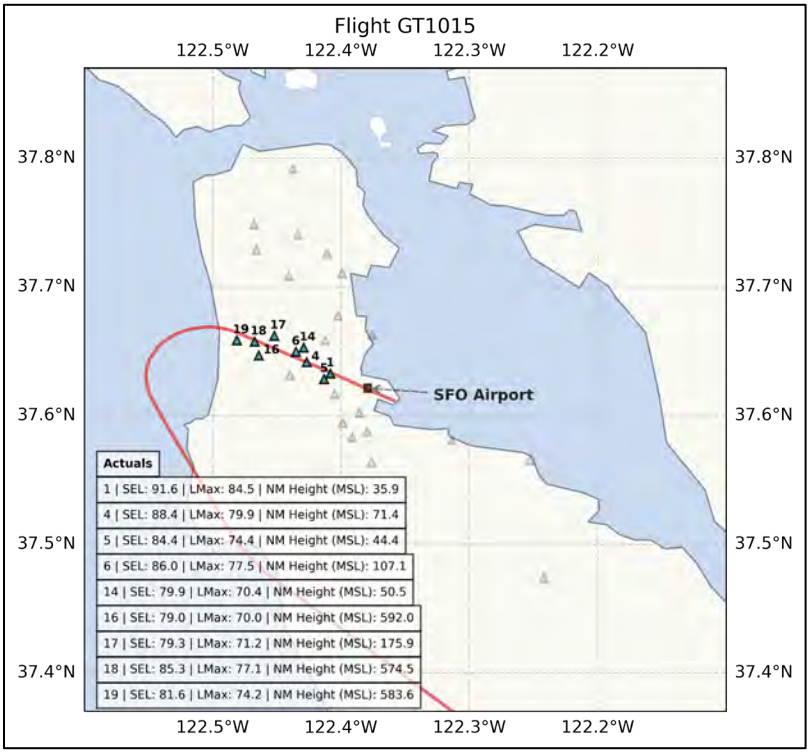

Figure 4. Trajectory and monitors triggered for flight GT1015.

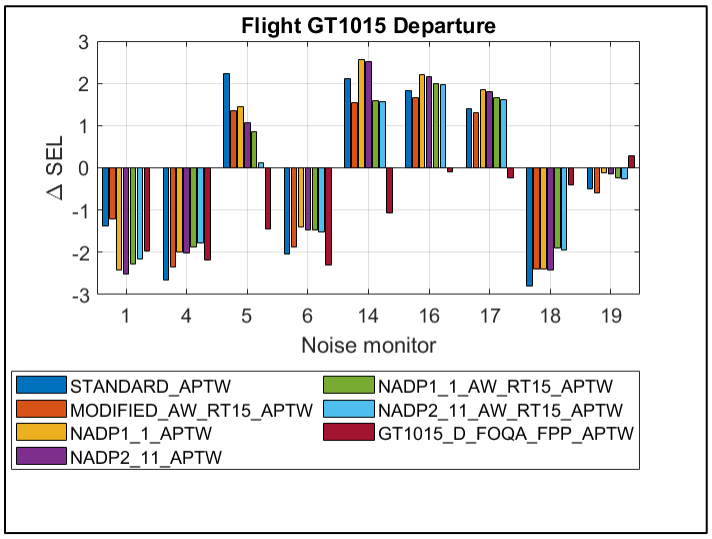

Figure 5. AEDT predicted − measured noise (dB) results for flight GT1015. SEL, sound exposure level.

Identifying Outliers

According to the results of the bulk analysis, some flights had relatively high Δ SEL (AEDT predicted − measured noise) values. Some flights with these high Δ SEL values were investigated to identify any anomalous patterns or factors. The identified anomalous patterns or factors causing the high Δ SEL can be used to easily rule out flights in future analyses, to prevent the simulation of anomalous flights whose results will eventually be discarded.

On the basis of preliminary observation of the data, several anomalous factors were identified. Results from flights that triggered monitor 8 consistently had high Δ SEL. This monitor has therefore been excluded from all further analyses and results. Some monitors had duplicate or multiple readings for the same flight for the same noise event. The Δ SEL could be high in these cases depending on the reading chosen. Therefore, the reading from the noise monitor corresponding to the point of closest slant distance for the flight that triggered it was selected. From some departure flights' tracks, we observed that some monitors located far behind the takeoff point and in the opposite direction of the flight path were triggered. Finally, some arrival flights had tracks that looped around the monitors. Some of these were arrivals that had to go-around to attempt landing a second time. After elimination of flights affected by the aforementioned anomalous factors, some flights with high Δ SEL still remained. Further analyses were conducted for these additional flights, and the SEL value measured by the noise monitor was assumed to be from a non-flight related event that could have occurred near the monitor. As stated earlier, a total of 616 noise events (437 departures and 179 arrivals) were present; after exclusion of flights affected by anomalous factors, 488 events remained (368 departures and 120 arrivals). The 269 modeled flights also reduced to 211 (97 departures and 114 arrivals).

Aggregate Flight Modeling Results

Individual flights can be analyzed to compare the performance and noise prediction accuracy of the different modeling options within AEDT, as shown previously. To obtain more meaningful inferences, we perform a statistical analysis of all 211 modeled flights in this section. To this end, a per-noise-monitor prediction capability was calculated by using the results generated for only departure flights. Instead of viewing one flight at a time, all flights that triggered a particular noise monitor are considered at each profile. The eight profiles for the departures are Alternate Weight Reduced Thrust (AW_RT15), Flight Operations Quality Assurance Fixed Point Profile (FOQA_FPP), Noise Abatement Departure Procedure Alternate Weight Reduced Thrust (NADP1_AW_RT_15), Noise Abatement Departure Procedure Alternate Weight Reduced Thrust (NADP2_AW_RT_15), NADP1, NADP2, Standard Procedure with Average Airport Weather (STD_APTW), and Standard Procedure with Automated Surface Observing System (ASOS) Airport Weather (STD_ASOS). The difference between the AEDT predictions and measured noise observations for these monitors is computed and analyzed with box plots (Figures 6–8). Ideally, these box plots would show a median of zero and a small spread, indicating minimal error between predictions of multiple operations and real-world data.

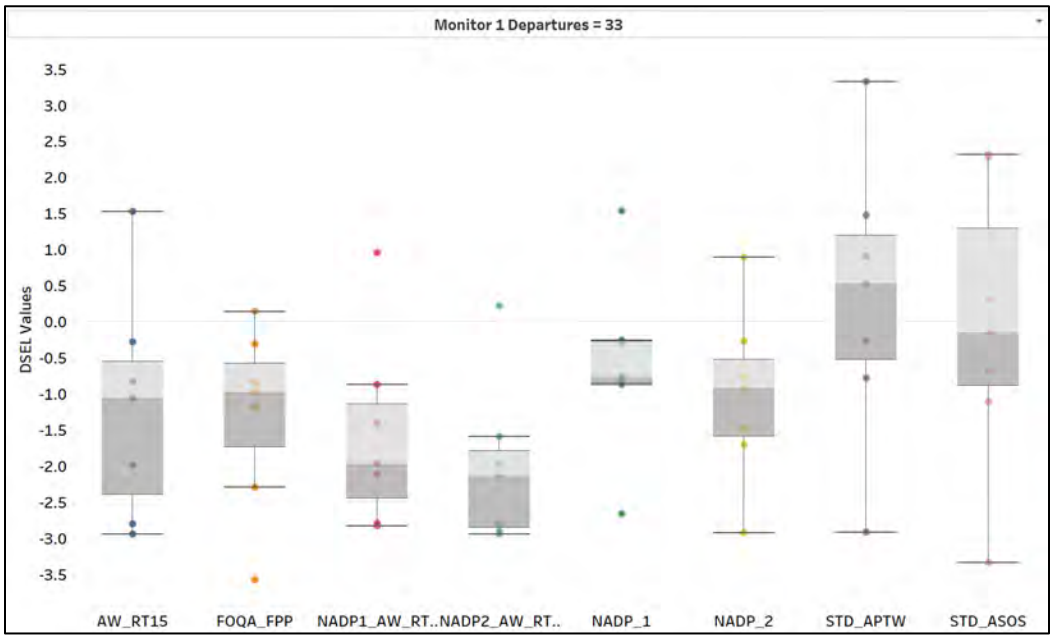

Figure 6. Predicted − measured sound exposure level (dB) noise box plot for noise monitor 1 triggered by departing flights.

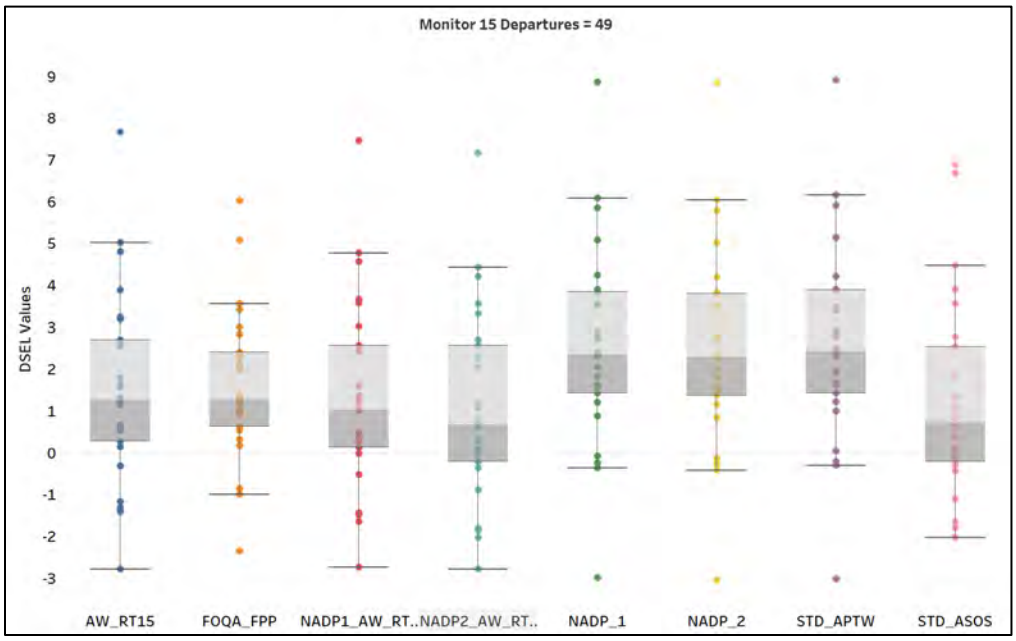

Figure 7. Predicted − measured sound exposure level (dB) noise box plot for noise monitor 15 triggered by departing flights

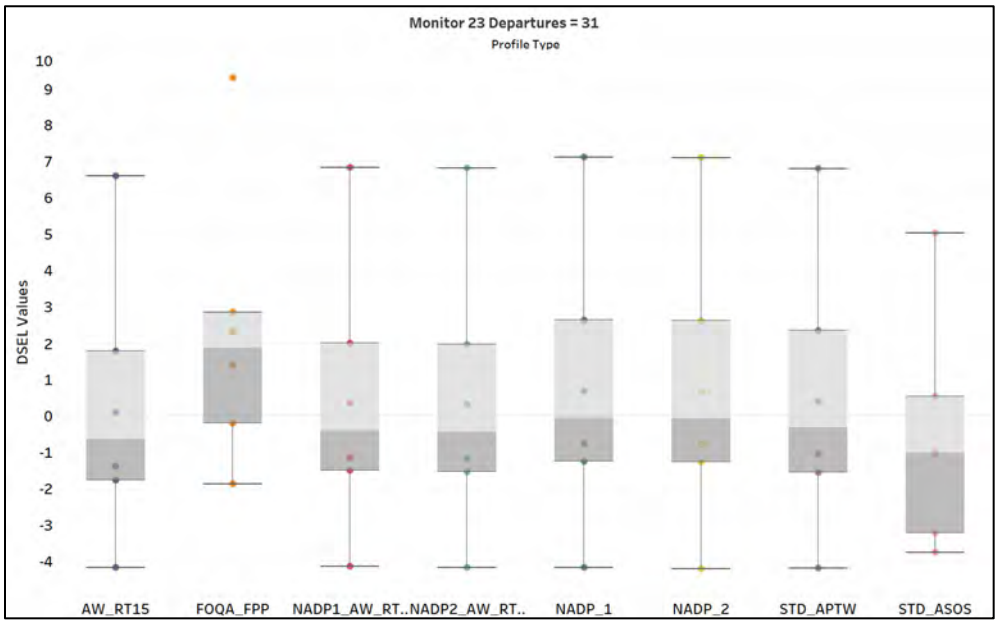

Figure 8. Predicted − measured sound exposure level (dB) noise box plot for noise monitor 23 triggered by departing flights.

The box plots shown in Figures 6–8 are generated by subtracting real-world measured SEL values from the AEDT-predicted SEL results for the 97 departures. Not all flights triggered a particular monitor with class I confidence. For instance, only 33 flights triggered monitor 1, whereas 49 flights triggered monitor 15. According to an initial analysis of all 97 departures, the FOQA_FPP profile provides the best prediction precision for all 25 monitors in the filtered data set, according to the minimal spread in the Δ SEL values and low median error. The STD_APTW and NADP profiles provide median errors closer to zero than the FOQA predictions. However, they also have some of the highest spreads between the 25% and 75% quantiles. Consequently, these three profiles perform well in predicting the average sound level over many operations but may have large errors for individual flight noise predictions. In general, a trend of slight underprediction at all monitors is seen for all profiles. However, for monitor 15, the overall trend appears to be overprediction by AEDT, and the alternative weight profiles provide results closest to the measured values. The FOQA_FPP profile again provides the lowest spread with a few outlier flights.

The box plots in Figures 6–8 are preliminary results that will be updated after bulk studies of hundreds of flights have been performed within AEDT for the different modeling assumptions. As shown, numerous outliers (|Δ SEL| > 5 dB) still exist in the Δ SEL plots, probably because of factors such as higher wind speeds, surrounding noise events, etc., that will require further investigation before the results can be finalized. The results shown here are intended to provide a sample of the statistical analysis capability currently under development at Georgia Tech and do not constitute final validation outcomes.

Preliminary Dashboard Development

A preliminary dashboard was developed as a tool to provide visual and meaningful representation of the data. To build the dashboard, the data are pre-processed, and a new Microsoft Excel spreadsheet serving as a template is constructed on the basis of four different files: monitors' location, the SFO FOQA dataframe of approach and departure, and the master results database. All these files are generated internally from AEDT. Specific tabs from the files above are pasted into a new Excel spreadsheet, and the parameters not used in building the dashboard are deleted. During pre-processing, only necessary parameters are extracted, to decrease the size of the file imported into the visualization tool and therefore shorten the processing time. The spreadsheet is imported into Tableau, each of the four tabs above is added, SFO arrivals and departure tabs are combined, and the microphone altitudes are matched with the noise and performance data by using the monitors' numbers. These noise events' data are in turn matched with the SFO dataframe data by using the unique flight ID.

To visualize the data, the generated Excel spreadsheet is imported into Tableau, and different plots are created (Figure 9). The first plot (middle top), the monitor location map, shows the exact positions of the monitors in SFO and their altitudes above sea level. Next (top right), the FOQA flight map shows the flight tracks for both departures (red) and arrivals (blue). Additionally, the performance plots (top, middle, bottom, and left) show the height above takeoff and touchdown, the ground speed, and the net average thrust for both departures (red) and arrivals (blue). These three plots do not require data manipulation, and the necessary parameters are dragged and dropped into the equivalent fields of Tableau's main window. Finally, the box plot (bottom right) shows the Δ SEL for all eight profiles. The results in Figure 9 are preliminary and are intended only to showcase the capability under development. The box plot requires pre-processing in Excel, because every row of data contains all profile types (FOQA_FPP, STD_APTW, AW_RT15, NADP1, NADP2, NADP1_AW_RT15, NADP2_AW_RT15, and STD_ASOS). The aim of the processing is to transpose profile types into multiple rows so that each data entry can be drawn as a separate curve. To ensure that the dashboard is interactive and user-friendly, all different plots are linked, and the data can be filtered out with the ground track ID, operation (departure or arrival), airframe, departure or arrival airport, noise class (overhead or sideline), whether the aircraft is flying over land or water, elevation angle, flap position, horizontal distance, and slant distance, The detailed process to create the dashboard by starting from the raw data files is explained in a separate set of internal documentation available from Georgia Tech.

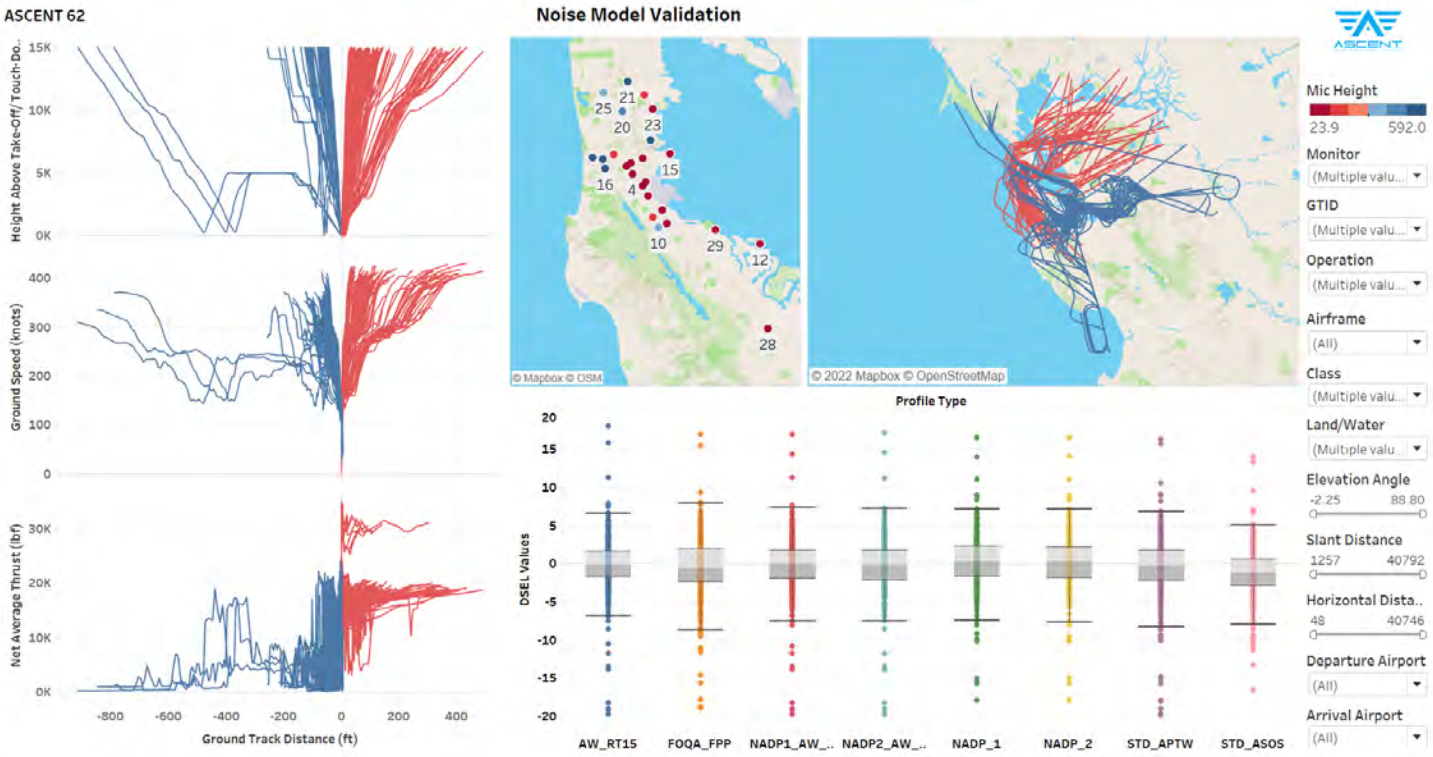

Figure 9. The final layout of the dashboard with the different visualization capabilities and filters.

Milestone(s)

None.

Major Accomplishments

Georgia Tech accomplishments

- Completed successful implementation of the AEDT automation pipeline for (a) modeling real-world flights in various settings, and (b) extracting and visualizing results from noise modeling efforts
- Successfully ran 269 flights at all identified settings from the test matrix, analyzed over 616 noise events (437 departures and 179 arrivals) to generate preliminary validation results.

Coordinated with the PSU team to provide flight data required for tasks relevant to PSU tasks

Publications

Bendarkar, M. V., Bhanpato, J., Puranik, T. G., Kirby, M., & Mavris, D. N. (2022, June 27). Comparative assessment of AEDT noise modeling assumptions using real-world data. AIAA AVIATION 2022 Forum. AIAA AVIATION 2022 Forum, Chicago, IL & Virtual. https://doi.org/10.2514/6.2022-3917

Outreach Efforts

Held biweekly calls with the FAA, the Volpe Center, and ATAC, and participated in biennial ASCENT meetings.

Awards

None.

Student Involvement

Georgia Tech

Graduate research assistants: Sabastian Abelezele, Amber Willitt, and Wiame Benzerhouni

Plans for Next Period

In the next period, Georgia Tech plans to:

- Analyze the modeled noise events to evaluate the effects of different assumptions and aircraft or ambient conditions
- Provide insights into the statistical significance of results at various noise monitoring stations
- Develop the interactive dashboard containing the modeling results with all different settings combined for performing trade-off studies
- Work with PSU, the FAA, and various noise monitoring offices and airlines to expand the validation study to different airports

References

Federal Aviation Administration. (n.d.) *Aviation Environmental Design Tool (AEDT).* https://aedt.faa.gov/

SFO. (n.d.). *Webtrak*. https://webtrak.emsbk.com/sfo13

Juniac, A. (2019). *IATA Annual Review 2018*. https://www.iata.org/publications/Documents/iata-annual-review-2018.pdf.

Suder, K. (2012, July 30). Overview of the NASA environmentally responsible aviation project's propulsion technology portfolio. *48th AIAA/ASME/SAE/ASEE Joint Propulsion Conference & Exhibit*. 48th AIAA/ASME/SAE/ASEE Joint Propulsion Conference & Exhibit, Atlanta, Georgia. https://doi.org/10.2514/6.2012-4038

Lim, D., Behere, A., Jin, Y.-C. D., Li, Y., Kirby, M., Gao, Z., & Mavris, D. N. (2020, January 6). Improved noise abatement departure procedure modeling for aviation environmental impact assessment. *AIAA Scitech 2020 Forum*. AIAA Scitech 2020 Forum, Orlando, FL. https://doi.org/10.2514/6.2020-1730

Behere, A., Lim, D., Li, Y., Jin, Y.-C. D., Gao, Z., Kirby, M., & Mavris, D. N. (2020, January 6). Sensitivity Analysis of Airport level Environmental Impacts to Aircraft thrust, weight, and departure procedures. *AIAA Scitech 2020 Forum*. AIAA Scitech 2020 Forum, Orlando, FL. https://doi.org/10.2514/6.2020-1731

Behere, A., Isakson, L., Puranik, T. G., Li, Y., Kirby, M., & Mavris, D. (2020, June 15). Aircraft landing and takeoff operations clustering for efficient environmental impact assessment. *AIAA AVIATION 2020 FORUM*. AIAA AVIATION 2020 FORUM, VIRTUAL EVENT. https://doi.org/10.2514/6.2020-2583

LeVine, M. J., Lim, D., Li, Y., Kirby, M., & Mavris, D. N. (2019). Quantification of error for rapid fleet-level noise computation model assumptions. *Journal of Aircraft*, *56*(4), 1689–1696. https://doi.org/10.2514/1.C035169

Monteiro, D. J., Prem, S., Kirby, M., & Mavris, D. N. (2018, January 8). React: A rapid environmental impact on airport community tradeoff environment. *2018 AIAA Aerospace Sciences Meeting*. 2018 AIAA Aerospace Sciences Meeting, Kissimmee, Florida. https://doi.org/10.2514/6.2018-0263

LeVine, M. J., Bernardo, J. E., Pfaender, H., Kirby, M., & Mavris, D. N. (2019). Demonstration of a framework for comparing aviation environmental impact mitigation strategies. *Journal of Aircraft*, *56*(3), 1116–1125. https://doi.org/10.2514/1.C035170

Yu, A., & Hansman, R. J. (2019, June 17). Approach for representing the aircraft noise impacts of concentrated flight tracks. *AIAA Aviation 2019 Forum*. AIAA Aviation 2019 Forum, Dallas, Texas. https://doi.org/10.2514/6.2019-3186

Salgueiro, S., Thomas, J., Li, C., & Hansman, R. J. (2021, January 11). Operational noise abatement through control of climb profile on departure. *AIAA Scitech 2021 Forum*. AIAA Scitech 2021 Forum, VIRTUAL EVENT. https://doi.org/10.2514/6.2021-0007

Thomas, J. L., & Hansman, R. J. (2019). Framework for analyzing aircraft community noise impacts of advanced operational flight procedures. *Journal of Aircraft*, *56*(4), 1407–1417. https://doi.org/10.2514/1.C035100

Behere, A., Rajaram, D., Puranik, T. G., Kirby, M., & Mavris, D. N. (2021). Reduced order modeling methods for aviation noise estimation. *Sustainability*, *13*(3), 1120. https://doi.org/10.3390/su13031120

Behere, A., Bhanpato, J., Puranik, T. G., Kirby, M., & Mavris, D. N. (2021, January 11). Data-driven approach to environmental impact assessment of real-world operations. *AIAA Scitech 2021 Forum*. AIAA Scitech 2021 Forum, VIRTUAL EVENT. https://doi.org/10.2514/6.2021-0008

Page, J. A., Hobbs, C. M., Plotkin, K. J., & Stusnick, E. (2000). *Validation of aircraft noise prediction models at low levels of exposure* (NASA/CR-2000-210112). NASA. https://ntrs.nasa.gov/api/citations/20000068518/downloads/20000068518.pdf

Forsyth, D. W. & Follet, J. I. (2006). *Improved Airport Noise Modeling for High Altitudes and Flexible Flight Operations* (NASA/CR-2006-21451) NASA.

Plotkin, K. J., Page, J. A., Gurovich, Y., Hobbs, C. M., et al. (2013). *Detailed weather and terrain analysis for aircraft noise modeling*. John A. Volpe National Transportation Systems Center (US).

Hobbs, C. M., Gurovich, Y. A., Boeker, E., Hasting, A., Rapoza, A., Page, J., Volpe, J. A., Airport Cooperative Research Program, Transportation Research Board, & National Academies of Sciences, Engineering, and Medicine. (2017). *Improving aedt noise modeling of mixed ground surfaces*. Transportation Research Board. https://doi.org/10.17226/24822

Downing, J. M., Calton, M. F., Page, J. A., & Rochat, J. L. (2019). *Improving AEDT Modeling for Aircraft Noise Reflection and Diffraction from Terrain and Manmade Structures* (Tech. Rep. ACRP 02-79).

Hastings, A. L. (2019). *Traffic Noise Model 3.0 - Technical Manual* (Tech. Rep. FHWA-HEP-20-012). U.S. Department of Transportation, Volpe National Transportation Systems Center.

Gabrielian, A. B., Puranik, T. G., Bendarkar, M. V., Kirby, M., Mavris, D., & Monteiro, D. (2021, August 2). Noise model validation using real world operations data. *AIAA AVIATION 2021 FORUM*. AIAA AVIATION 2021 FORUM, VIRTUAL EVENT. https://doi.org/10.2514/6.2021-2136

Gabrielian, A., Puranik, T., Bendarkar, M., Kirby, M., & Marvis, D. (2021). Validation of the aviation environmental design tool's noise model using high fidelity weather. *INTER-NOISE and NOISE-CON Congress and Conference Proceedings*, *263*(2), 4810–4822. https://doi.org/10.3397/IN-2021-2846

Federal Aviation Administration. 2004. *Advisory Circular, 120-82 - Flight Operational Quality Assurance*. https://www.faa.gov/regulations_policies/advisory_circulars/index.cfm/go/document.information/documentID/23227

Puranik, T. G., & Mavris, D. N. (2018). Anomaly detection in general-aviation operations using energy metrics and flight-data records. *Journal of Aerospace Information Systems*, *15*(1), 22–36. https://doi.org/10.2514/1.I010582

Lee, H., Madar, S., Sairam, S., Puranik, T. G., Payan, A. P., Kirby, M., Pinon, O. J., & Mavris, D. N. (2020). Critical parameter identification for safety events in commercial aviation using machine learning. *Aerospace*, *7*(6), 73. https://doi.org/10.3390/aerospace7060073

Ahearn, M., Boeker, E., Gorshkov, S., Hansen, A., Hwang, S., Koopmann, J., Malwitz, A., Noel, G., Reherman, C. N., Senzig,D. A., et al. (2016). *Aviation Environmental Design Tool (AEDT) Technical Manual Version 2c*. FAA.

Mavris, D., Kirby, M., Lim, D., Li, Y., Pfaender, H., Levine, M., Brooks, J., Behere, A., Gao, Z., Chan Jin, Y., & Kim, J. *Project 045 Takeoff/Climb Analysis to Support AEDT APM Development* (Tech. Rep. ACRP 02-79). ASCENT.

Mavris, D. (2019). *Project 043 Noise Power Distance Re-Evaluation.* https://s3.wp.wsu.edu/uploads/sites/2479/2020/05/ASCENT-Project-043-2019-Annual-Report.pdf, last accessed 14 June 2020.

Task 2 - Assessing the Use of High-Fidelity Meteorological Data in AEDT Noise Calculations

The Pennsylvania State University

Objective

One challenge in validating aircraft noise models is knowing the state of the atmosphere during field tests. In collaboration with the industrial partner Spire Global (http://www.spire.com/), the PSU team is providing the relevant high-fidelity meteorological data to support the AEDT noise model validation work being conducted by Georgia Tech. At present, the

AEDT noise model uses high-fidelity meteorological data only for performance calculations. For noise calculations, AEDT does not use high-fidelity meteorological data directly (for example, when calculating the Acoustic Impedance Adjustment or the Atmospheric Absorption Adjustment). As an exploratory step, PSU is investigating the possibility of incorporating high-fidelity meteorological data in AEDT noise calculations without modifying the noise model in AEDT.

Research Approach

AEDT's noise model currently assumes homogeneous weather conditions for noise calculations. The weather conditions used in noise calculations are typically ground-based measurements, such as the airport weather (typically an annual average). Although real-world weather is well known to rarely be homogeneous, the impact of meteorological inhomogeneity on AEDT's noise calculations must be investigated to determine whether it substantially improves AEDT's noise prediction capabilities. One possibility of incorporating high-fidelity weather data in AEDT's noise calculations is to explore the use of averages of meteorological variables (such as temperature and humidity) based on high-fidelity meteorological data. If this approach leads to a noticeable improvement in AEDT's noise calculations, it could enable AEDT's noise calculations to be improved without changing the existing integrated noise model in AEDT. To explore this possibility, the PSU team is working with real-world flight and noise measurement data provided by Georgia Tech for a flight departing from KSFO. The aircraft tracking data and performance results from AEDT (provided by Georgia Tech) are used by PSU in its in-house ray-tracing code to predict noise levels near the ground. A primary goal in this year's work has been to demonstrate confidence in the in-house ray-tracing code.

Aircraft trajectory and locations of noise monitors

The Georgia Tech team has provided the flight tracking data for a departing Boeing 737-800 from KSFO (anonymized flight ID: GT786D). Figure 10 shows the aircraft track associated with the flight and a color scale showing flight altitude above the mean sea level. The region marked by a dash-dotted blue line is shown in detail to draw attention to the nine noise monitoring stations around KSFO.

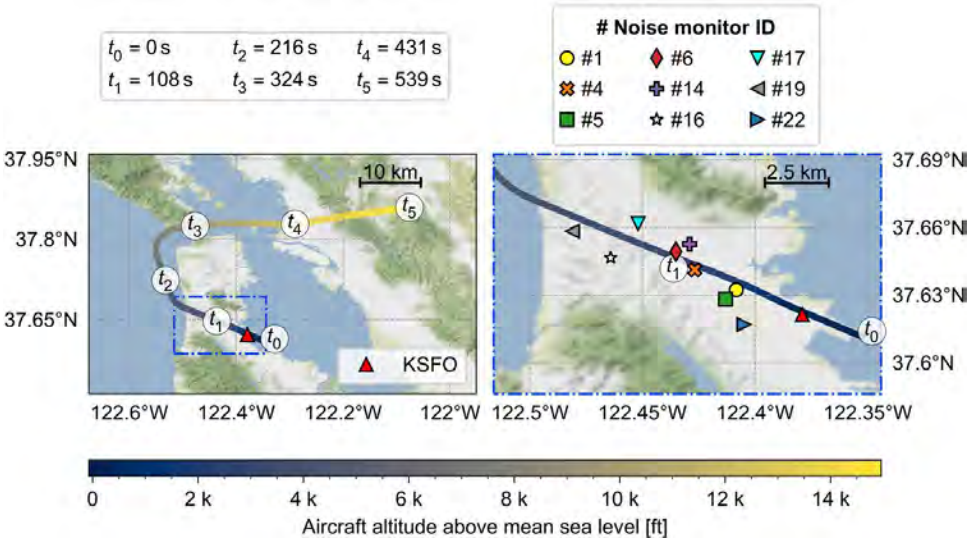

Figure 10. Aircraft trajectory and locations of the noise monitors around KSFO (anonymized flight ID: GT786D).

The noise monitor data available for this flight do not include the time history of the received noise but only the L_{Amax} (*A*-weighted maximum sound level) and the SEL (*A*-weighted sound exposure level). The data for this flight are used for conducting numerical experiments using an acoustic ray-tracing code developed in-house to predict noise levels at the noise monitor locations.

Comparison of meteorological conditions

Meteorological conditions play an important role in correctly modeling noise propagation. Specifically, the temperature and humidity conditions play a critical role, because they affect the propagation path as well as the atmospheric absorption. For the event under investigation, Figure 11 shows the relevant temperature and specific humidity profiles. In Figure 11, the inhomogeneous meteorological profiles obtained near KSFO from the Spire Global data are shown with a black line. As

indicated in Figure 10, the portion of the flight relevant for the noise measurements involves aircraft altitudes less than 2 km. Hence, an average of the Spire Global data over all heights from 0 to 2 km is an important abstraction of interest (shown with a dash-dotted blue line in Figure 11). Finally, the airport weather data for KSFO, as given in AEDT, are shown with a dashed red line in Figure 2. Clearly, the annual average airport weather (as given in AEDT) will not always accurately represent the meteorological conditions for a specific event; therefore, ideally, the inhomogeneous data shown by the black line (Spire Global data) in Figure 11 would be used. Modifying the existing integrated noise model in AEDT to include inhomogeneous meteorological data for noise calculations will be challenging. Instead, if using average weather conditions based on the inhomogeneous data (dash-dotted blue line Figure 11) satisfactorily improves the noise predictions (in comparison to annual average weather), this change in AEDT would be easier to implement. To investigate this possibility, the PSU team has set out to first try to mimic AEDT's noise model by modifying a general-purpose acoustic ray-tracing code developed in-house. If successful, the PSU team can then modify the in-house code to calculate the noise by using both the inhomogeneous meteorological data and the average weather based on the inhomogeneous data.

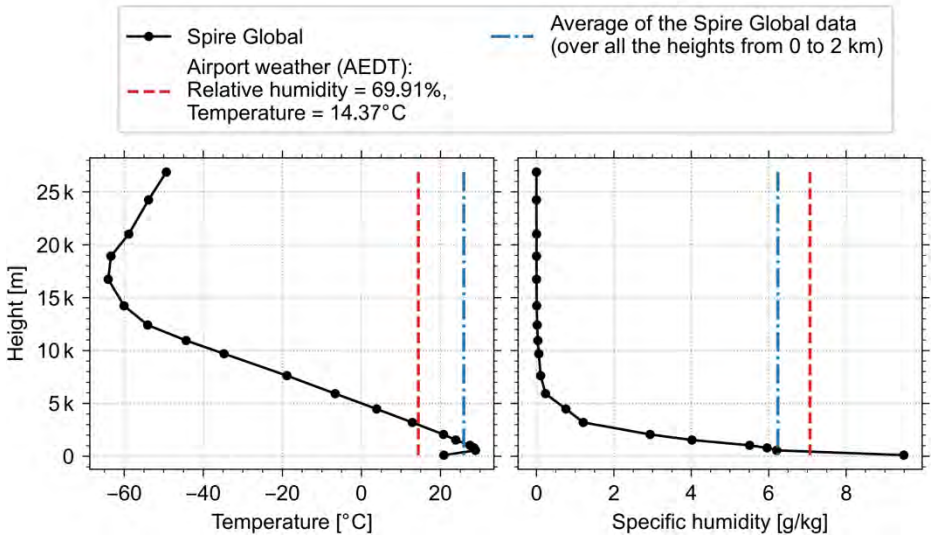

Figure 11. Comparison of the temperature and specific humidity profiles from AEDT and Spire Global data for flight GT786-D.

Attempting to reproduce AEDT's noise calculations by using PSU's in-house code

Before attempting to use meteorological data other than the airport weather in noise calculations, demonstrating confidence in the in-house code developed at PSU is crucial. This area has been a primary focus of the work performed over the past year at PSU. Apart from specifying meteorological profiles, PSU's in-house ray-tracing code requires the source levels at 1 m from the aircraft. The thrust-dependent source levels are obtained by using the time history of thrust values obtained from AEDT's performance report (provided by the Georgia Tech team). The thrust levels are used with the spectral class data and the NPD tables from AEDT to obtain the correct source levels. As noted in the AEDT 3d technical manual (Lee, 2021), the NPD data implicitly contain absorption for the reference day conditions, as specified in SAE-AIR-1845 (SAE International, 1995). The source levels used in the in-house code have been extracted by carefully removing the built-in atmospheric absorption as well as the spherical spreading assumed in the NPD data. The in-house ray-tracing code is then used to propagate the noise to the noise monitors, accounting for the aircraft trajectory and the locations of the noise monitors. Atmospheric absorption is then applied according to SAE-ARP-5534 (SAE International, 2013). The in-house code has a provision to include the effect of ground impedance as well as user-specified aircraft directivity information. Because the goal is to match AEDT's predictions, the PSU team used the Lateral Attenuation Adjustment, as defined in the AEDT 3d technical manual (Lee, 2021), to account for ground reflection, refraction, airplane shielding, and engine installation effects. During this investigation, we noted that the correct use of lateral attenuation adjustment brought the in-house predictions significantly closer to AEDT's predictions.

Preliminary results comparing AEDT and in-house code

The Georgia Tech team ran an AEDT study with the FOQA data by using the fixed-point procedural profile and the airport weather to provide noise predictions at the noise monitor locations shown in Figure 10. These results were compared with the noise predictions obtained with PSU's in-house code assuming homogeneous weather as in AEDT (dashed red line in Figure 11). Table 4 shows the difference between the in-house noise predictions and the AEDT noise predictions for the maximum *A*-weighted sound pressure level (LA_{max}) and the *A*-weighted SEL. Reassuringly, the noise prediction using PSU's in-house code, as modified to match AEDT, closely matches AEDT's prediction, with only two calculations exceeding a 1-dB difference.

Table 4. Difference between the in-house noise predictions and AEDT's noise predictions across multiple monitors.

Monitor ID	1	4	5	6	14	16	17	19
Δ LA_{max} (dBA)	−0.35	−0.32	−0.7	−0.38	−0.74	−1.24	−0.86	−0.38
Δ SEL (dBA)	0.21	1.02	−0.22	0.86	0.24	−0.35	0.07	0.57

Importantly, the in-house code performs point-to-point (propagation from a point source to a point receiver) calculations, whereas AEDT uses an integrated noise model that calculates noise metrics as an aggregate over multiple segments in flight. This distinction might explain the differences in noise predictions in Table 4. This exercise has improved the PSU team's understanding of AEDT's noise model and has supported confidence in the in-house code. In the next project period, PSU's validated in-house code will help in assessing the inclusion of high-fidelity meteorological data for noise calculations in AEDT.

Understanding AEDT's acoustic impedance and atmospheric absorption adjustments

In parallel with the above comparison between PSU's in-house code and AEDT's noise calculations, PSU is continuing efforts to gain a deeper understanding of the AEDT noise calculation. By having a clear understanding of the contributions to the AEDT noise calculation, and how each contribution is affected by high-fidelity meteorology, the project can assess the potential benefits or drawbacks of including high-fidelity data in a future release of AEDT.

When calculating noise level adjustments due to weather, AEDT defaults to single yearly averages for each airport, thus effectively treating the propagation path (atmosphere) as homogeneous, which is not necessarily a realistic assumption. PSU has been examining the use of high-fidelity weather data from Spire Global in calculating the acoustic impedance adjustment (AI_{adj}), an important contributor to the AEDT noise calculation. AI_{adj} depends on air density and the speed of sound, which can be found through the air temperature and barometric pressure given in the Spire Global data by using thermodynamics. Through processing the Spire Global data and calculating the density and sound speed, AI_{adj} is visualized in a 2D map over KSFO (assuming dry air and no wind) in Figure 12.

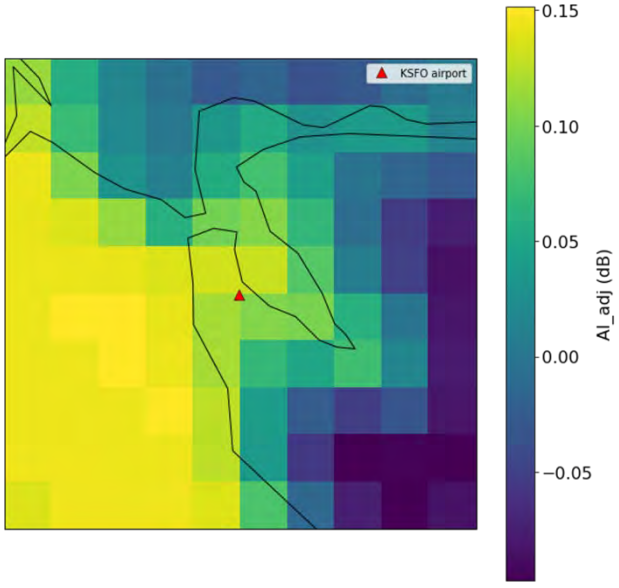

Figure 12. Top-down view of AI_{adj} in a 139 × 139 km grid around KSFO, assuming a constant height.

This visualization shows an AI_{adj} value range from approximately −0.2 dB to 0.15 dB. The variation occurs over regions that differ geographically (e.g., over the land north and south of the airport as well as the ocean to the west). The value relies on the variation in air temperature. This model accounts for only a single isobaric level at one time, but 3D models of the environment were also created, with AI_{adj} calculated by using the full set of high-fidelity weather data (Figure 13).

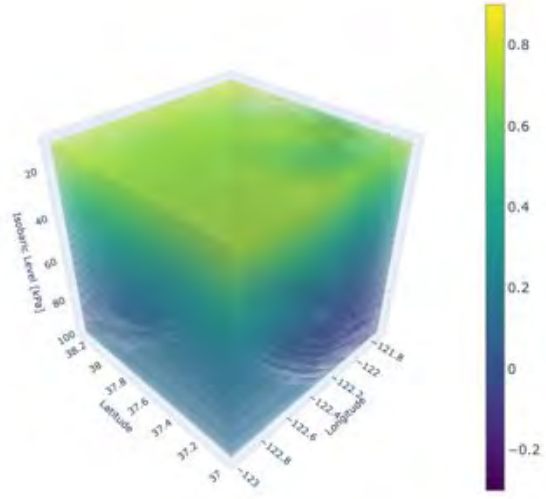

Figure 13. 3D view of AI_{adj} in the space around KSFO with the same geographic extent as in Figure 12. The elevation shown here ranges from 90 to 16,680 m (295 to 54,725 feet).

For this set, AI_{adj} ranges from approximately −0.2 dB to 0.8 dB, which is notably larger than the range in the 2D model. Because the full set of data covers a very large range of altitudes, and flight operations typically occur in only the lowest 2 km of the atmosphere, a separate model was created in which only the first 2 km of atmosphere is considered (Figure 14).

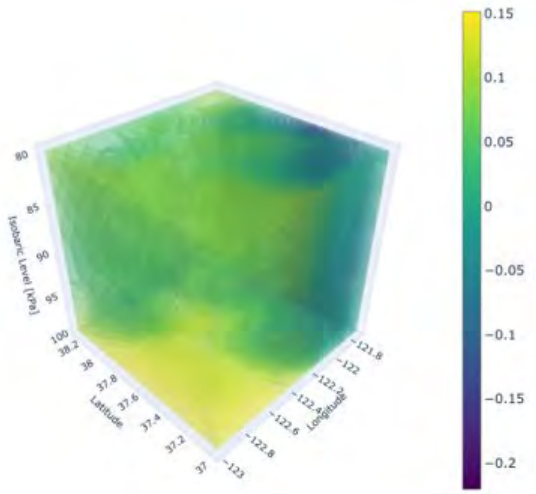

Figure 14. Three-dimensional view of AI_{adj} in the space around KSFO with the same geographic extent as in Figure 12. Of note the elevation shown here ranges from only 90 m to 2 km. The colors shown closest to the ground are identical to those in Figure 12.

The AI_{adj} value range in Figure 14 is lower than that in Figure 13, and shows the variation over space more clearly. These visualizations indicate that AI_{adj} varies considerably around KSFO . Currently, AEDT uses the value of AI_{adj} at the airport for the noise calculation. However, a flying aircraft is not always at the airport location. Hence, future work will investigate whether using a value of AI_{adj} based partially or entirely on the 3D aircraft location improves AEDT noise predictions.

Ongoing work in a preliminary stage of development is also assessing the atmospheric absorption adjustment (AA_{adj}), another contributor to AEDT's noise prediction. On the basis of previous ASCENT projects, 3D meteorology is expected to profoundly influence the calculation of atmospheric absorption, and AA_{adj} will have a larger impact on noise calculations than that seen for AI_{adj}.

PSU has also been in contact with Washington Metropolitan Airports Authority regarding the use of their noise monitor data for upcoming validation efforts in the next phase of the work.

Milestones

None.

Major Accomplishments

(The project started in July 2020)
PSU accomplishments

- PSU's in-house ray-tracing code is predicting noise near the ground within 1 dB of the predictions by AEDT, thereby suggesting the legitimacy of the in-house code. This step is important in investigating the potential use of high-fidelity weather in AEDT.

Publications

Shaw, E., & Sparrow, V. (2022). Modeling acoustic impedance and atmospheric absorption around airports using high-fidelity weather data. *NOISE-CON Congress and Conference Proceedings*, *264*(1), 104–110. https://doi.org/10.3397/NC-2022-698

Outreach Efforts
Held biweekly calls with the FAA, the Volpe Center, and ATAC, and participated in biennial ASCENT meetings.

Awards
None.

Student Involvement
PSU
Graduate research assistants: Harshal Patankar and Emma Shaw.

Plans for Next Period
In the next period, PSU plans to:

- Continue to support the Georgia Tech team, consider the differences in AEDT noise predictions with and without high-fidelity weather, and assess whether updating the atmospheric absorption and acoustic impedance adjustments with high-fidelity weather will have a noticeable effect on AEDT noise predictions
- Assess the use of averages based on the high-fidelity weather data as an input to the AEDT noise model instead of using ground-based weather measurements
- Advance understanding of the acoustic impedance and atmospheric adjustments used in AEDT noise predictions
- Continue working with the Washington Metropolitan Airports Authority and other airports, as needed, to support ongoing and future AEDT noise validation efforts in conjunction with Georgia Tech, as advised by the FAA
- Provide the relevant high-fidelity meteorological data to support the AEDT noise model validation work being conducted by Georgia Tech (using high-fidelity meteorological data obtained by PSU either through collaboration with Spire Global [www.spire.com] or from alternative sources if needed, as demonstrated in the ASCENT Project 062 annual report in 2021 (Shaw & Sparrow, 2022).

References
Lee, Cynthia, et al. (2021). *AEDT Version 3d* [Technical Manual] (No. DOT-VNTSC-FAA-21-06). United States Department of Transportation. Federal Aviation Administration.

A-21 Aircraft Noise Measure Noise Aviation Emission Modeling. (n.d.). *Procedure for the calculation of airplane noise in the vicinity of airports*. SAE International. https://doi.org/10.4271/AIR1845A

SAE International. (2013). *Committee A-21, Aircraft Noise, Application of Pure-Tone Atmospheric Absorption Losses to One-Third Octave-Band Data, Aerospace Information* (Report No. 5534).

Sparrow, E. (2021). *ASCENT Project 062 2021 Annual Report*. FAA, Washington, DC. https://s3.wp.wsu.edu/uploads/sites/2479/2022/10/ASCENT-Project-062-2021-Annual-Report.pdf.

Project 063 Parametric Noise Modeling for Boundary Layer Ingesting Propulsors

Georgia Institute of Technology

Project Lead Investigator

Professor Dimitri N. Mavris (P.I.)
Director, Aerospace Systems Design Laboratory
School of Aerospace Engineering
Georgia Institute of Technology
Phone: (404) 894-1557
Fax: (404) 894-6596
Email: dimitri.mavris@ae.gatech.edu

Dr. Jonathan Gladin (Co-P.I.)
Chief, Propulsion and Energy Division
Aerospace Systems Design Laboratory
School of Aerospace Engineering
Georgia Institute of Technology
Phone: (404) 894-5788
Fax: (404) 894-6596
Email: jgladin3@gatech.edu

University Participants

Georgia Institute of Technology (Georgia Tech)

- P.I.s: Dr. Dimitri N. Mavris, Dr. Jonathan Gladin
- FAA Award Number: 13-C-AJFE-GIT-064
- Period of Performance: October 1, 2020 to June 6, 2022
- Tasks:
    1. Literature review and problem parameterization
    2. Development of a parametric noise model
    3. Model validation exercises
    4. Tool documentation

Project Funding Level

The project funding amount is $300,000 from the FAA and a cost share match from Georgia Tech of $300,000.

Investigation Team

Dr. Jonathan Gladin – Research Engineer II – CO-P.I., Overall task lead (Tasks 1 and 4)
Dr. Miguel Walter – Research Engineer II – Technical aeroacoustics lead (Task 2 and Task 3)
Dr. Jai Ahuja - Research Engineer II – Reynolds-averaged Navier–Stokes (RANS) computational fluid dynamics (CFD) design lead (Task 2 and Task 3)
Mr. Ross Weidman – Graduate Research Assistant – Computer-aided design and geometry (Task 1)
Mr. José Zavala – Graduate Research Assistant – CFD analysis (Task 1 and Task 4)
Mr. Grant Stevenson – Graduate Research Assistant -- Aeroacoustics (Task 2, Task 3, and Task 4)

Project Overview

While the study by Clark et al. (2018) is interesting in that it represents a first-cut approach for quantifying a boundary layer ingestion (BLI) impact due to distortion based on experiments, there are several factors that may call such approaches into question. The first factor is the validity of the open-rotor experiment for predicting the sound pressure level contribution to the tonal noise impact on an embedded turbofan engine. The second factor is the fact that there are many ways to achieve BLI, and the interactions may vary significantly depending on the type and quantity of the distortion ingested and for varying fan applications such as ducted electric fans, propellers, or turbofan engines. Thus, Georgia Tech proposes to close the gap identified from this literature by developing a parametric fan noise module for a generic BLI propulsor based on the specifics of the BLI configuration and propulsor design. Parameters influencing the model would include distortion intensity, distortion type (i.e., radial vs. circumferential), frequency, multiple-per-rev, fan design parameters, location on the airplane, mounting (embedded vs. flush), and potentially other relevant physical parameters. The module will attempt to quantify the impact of BLI on turbulent ingestion and mean flow distortion noise based on lower-order methods but would seek to validate such methods against higher-fidelity approaches and any publicly available experimental data sets, such as those used in the above publication or others. The module will also seek to model the effects of ducted vs. unducted shielding of BLI noise sources so as to quantify the validity of using “equivalent” experimental data sources for BLI approximations. A validation exercise will be conducted whereby the lower-order methods are tested against higher-fidelity analyses for a D8/HWB-type ingestion configuration and compared against empirical approaches.

Task 1 – Literature Review and Problem Parameterization

Georgia Institute of Technology

Objective

The objective of this task is to research existing approaches for the quantification of noise sources related to BLI fans and to determine an appropriate modeling approach for the parametric modules. The approach should fit within the statement of work and numerical computational budget afforded to the project.

Research Approach

The approach for this task is to scan the literature associated with BLI and distortion-related noise generation for ducted fans. Each reference will be ranked by relevance and appropriateness and will be assessed as to whether it is directly applicable or usable.

Literature Review Results

A literature review on BLI, noise generation and prediction, model validation, and other related topics was conducted. The topics and research goals covered within a subset of the review are shown in Table 1. Most of the researched literature involved BLI, noise prediction, experimental validation, and numerical modeling. One limitation was the difficulty in finding literature that treated turbofans instead of open-rotor engines. The identified reports on numerical models emphasized that having well-understood correlations between the upwash of different rotor blades and the turbulence space-time correlations are critical for accurate noise estimation, partly because the widely used rapid distortion theory is less useful in cases of inhomogeneous flow distortion. In such cases, sampling the correlation function becomes essential as a substitute for the rapid distortion theory. There may also be situations in which using this correlation function as a sampling distribution shortens the computational time considerably.

Table 1. Literature review topics. BLI: boundary layer ingestion; CFD: computational fluid dynamics.

Literature	Topic Covered: BLI	Topic Covered: Inlet Distortions	Research Goal: Noise Prediction	Research Goal: Performance Prediction	Validation Method: Experimental Validation	Validation Method: CFD Validation	Results: Numerical Model Created	Topic Covered: Turbofans	Topic Covered: Open Rotor
Modelling of A Boundary Layer Ingesting Propulsor (Budziszewski, 2018)	X			X			X	X	
Predicting the Inflow Distortion Tone Noise of the NASA Glenn Advanced Noise Control Fan with a Combined Quadrupole-Dipole Model (Koch, 2012)		X	X		X		X	X	
Discretized Miller approach to assess effects on boundary layer ingestion induced distortion (Valencia, 2017)	X			X	X	X	X	X	
An Analytical Model for Predicting Rotor Broadband Noise Due to Turbulent Boundary Layer Ingestion (Karve, 2018)	X		X		X		X		X
Noise Produced by Turbulent Flow into a Rotor (Amiet, 1989)		X	X				X		X
Noise from a rotor ingesting a thick boundary layer and relation to measurements of ingested turbulence (Alexander, 2017)	X		X		X				X
Noise from a Rotor Ingesting a Planar Turbulent Boundary Layer (Alexander, 2013)	X		X		X				X
Rotor Inflow Noise Caused by a Boundary Layer: Inflow Measurements and Noise Predictions (Morton, 2012)	X		X		X				X
Enhanced Fan Noise Modeling for Turbofan Engines (Krejsa, 2014)			X		X		X	X	

Problem Parameterization and Approach

Based on the literature review results, an approach for parameterizing the problem was developed. To establish a noise module that accounts for the impact of BLI parametrically and across a range of different applications, we have chosen to develop this module using a "delta" approach. This approach will utilize a baseline non-BLI fan noise prediction from NASA's Aircraft Noise Prediction Program (ANOPP) tool and attempt to correct the noise based on a semi-empirical model that accounts for the impact of BLI on fan noise. To achieve this aim, the Georgia Tech team proposes to use computational aeroacoustics (CAA) to capture the acoustic impact of BLI parametrically, starting with one BLI configuration/architecture: a BLI tail cone thruster, similar to NASA's single-aisle turboelectric aircraft with aft boundary layer (STARC-ABL) propulsion concept. This effort will be accomplished by parametrizing the modeling approach according to Figure 1.

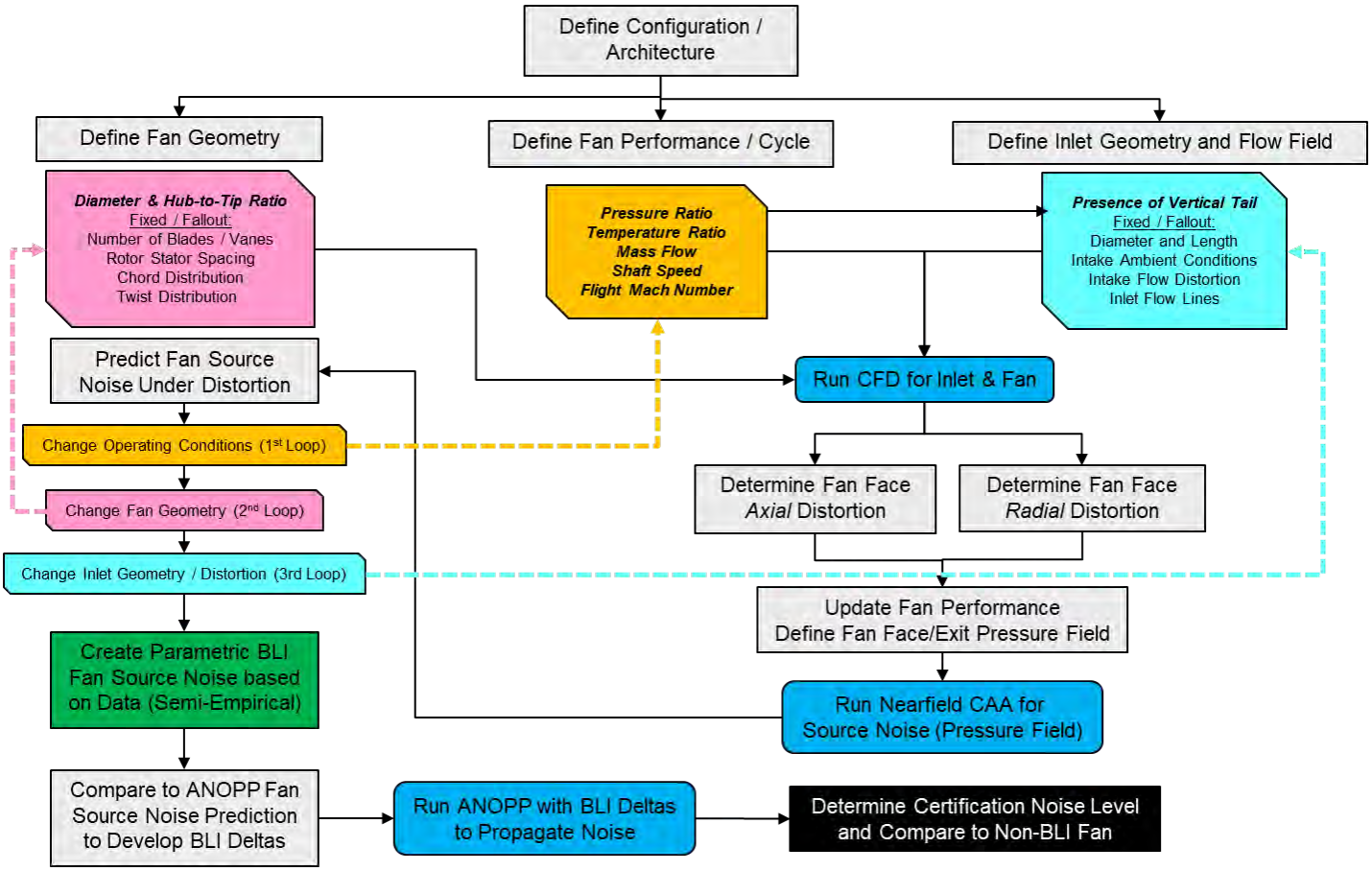

Figure 1. Proposed modeling approach to create a parametric boundary layer ingestion (BLI) noise module. ANOPP: Aircraft Noise Prediction Program; CAA: computational aeroacoustics; CFD: computational fluid dynamics.

To capture the sensitivity of the noise impact to a wide range of BLI conditions, the team will attempt to capture the acoustic impact of BLI for various fan geometries, operating conditions, and flow fields. To achieve the number of runs needed to develop such a noise model, the scope of the parameters varied under each category was limited.

Milestone

Task 1 has been completed.

Major Accomplishments

Task 1 has been completed, and an approach for defining the methodology has been determined and finalized with FAA sponsor approval.

Publications

None.

Outreach Efforts

The team retrieved source diagnostic test (SDT) geometry from NASA. The approach for noise modeling was presented to NASA acoustics engineers, who gave feedback on the approach.

Awards
None.

Student Involvement
Two graduate students were involved with this work: Ross Weidman and José Zavala. These students are graduate research assistants at Georgia Tech.

References

Alexander, W. N., Devenport, W., Morton, M., & Glegg, S. (2013, May 27). Noise from a rotor ingesting a planar turbulent boundary layer. *19th AIAA/CEAS Aeroacoustics Conference*. 19th AIAA/CEAS Aeroacoustics Conference, Berlin, Germany. https://doi.org/10.2514/6.2013-2285

Alexander, W. N., Devenport, W. J., & Glegg, S. A. L. (2017). Noise from a rotor ingesting a thick boundary layer and relation to measurements of ingested turbulence. *Journal of Sound and Vibration*, *409*, 227–240. https://doi.org/10.1016/j.jsv.2017.07.056

Amiet, R. K. (1989). *Noise produced by turbulent flow into a rotor: Theory manual for noise calculation*. https://ntrs.nasa.gov/citations/19890017312

Budziszewski, N., & Friedrichs, J. (2018). Modelling of a boundary layer ingesting propulsor. *Energies*, *11*(4), 708. https://doi.org/10.3390/en11040708

Clark, I., Thomas, R. H., & Guo, Y. (2018, June 25). Aircraft system noise assessment of the NASA D8 subsonic transport concept. *2018 AIAA/CEAS Aeroacoustics Conference*. 2018 AIAA/CEAS Aeroacoustics Conference, Atlanta, Georgia. https://doi.org/10.2514/6.2018-3124

Karve, R., Angland, D., & Nodé-Langlois, T. (2018). An analytical model for predicting rotor broadband noise due to turbulent boundary layer ingestion. *Journal of Sound and Vibration*, *436*, 62–80. https://doi.org/10.1016/j.jsv.2018.08.020

Krejsa, E. A., & Stone, J. R. (2014). *Enhanced fan noise modeling for turbofan engines*. https://ntrs.nasa.gov/citations/20150000884

Koch, L. D. (2012, September 1). *Predicting the inflow distortion tone noise of the nasa glenn advanced noise control fan with a combined quadrupole-dipole model*. 18th Aeroacoustics Conference. https://ntrs.nasa.gov/citations/20120014225

Morton, M., Devenport, W., Alexander, W., Glegg, S., & Borgoltz, A. (2012, June 4). Rotor inflow noise caused by a boundary layer: Inflow measurements and noise predictions. *18th AIAA/CEAS Aeroacoustics Conference (33rd AIAA Aeroacoustics Conference)*. Colorado Springs, CO. https://doi.org/10.2514/6.2012-2120

Valencia, E., Hidalgo, V., Nalianda, D., Laskaridis, P., & Singh, R. (2017). Discretized Miller approach to assess effects on boundary layer ingestion induced distortion. *Chinese Journal of Aeronautics*, *30*(1), 235–248. https://doi.org/10.1016/j.cja.2016.12.005

Task 2 – Development of a Parametric Noise Model
Georgia Institute of Technology

Objective
The objective of this task is to develop a parametric noise model, which will be the primary deliverable for the project. This module should be compatible with ANOPP.

Research Approach
Baseline Fan Performance Model for ANOPP

To create a baseline ANOPP noise model for the ducted SDT fan, it is necessary to model the performance of the fan over a range of flight conditions. For this purpose, a fan map was digitized from the reference material for the SDT fan, as shown in Figure 2. The data points in the plots represent data digitized from the SDT data, and the lines are the output of a computer code called "CMPGEN," a NASA code that was used to approximately match the SDT fan map. This map is used to model the fan performance during off-design conditions.

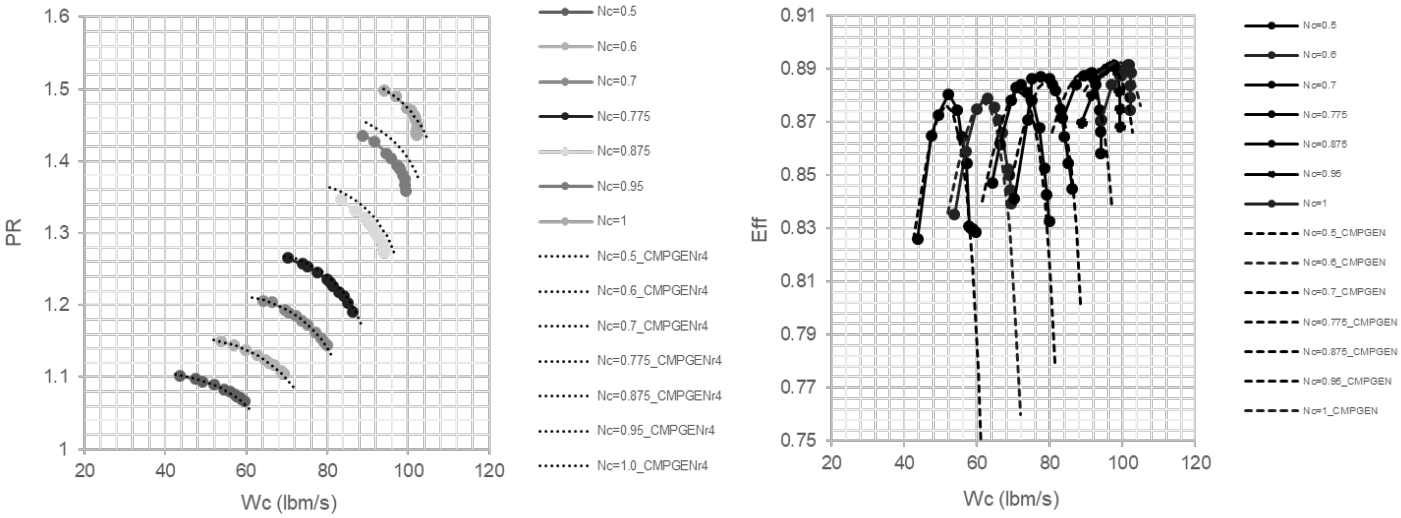

Figure 2. Source diagnostic test (SDT) fan map digitized from SDT data references. The lines represent the CMPGEN fan map performance matched to the SDT data set. PR is the total pressure ratio of the machine; Wc is the corrected air flow of the machine, Nc is the corrected rotational speed, and Eff is the adiabatic efficiency.

Next, the SDT fan needed to be scaled up to match the STARC-ABL geometry. To perform this scaling, the fan shaft power is held constant at 3,500 horsepower (hp), based on the STARC-ABL aircraft design. The aim for scaling was to create a geometrically similar fan, but at the 3,500-hp size. The scaling exercise results are shown in Table 2. The scale factors for each of the main parameters of the fan are shown in the right column. The power of 3,500 hp was used to determine the fan weight flow scale factor of 5.378. The square root of this number (2.31905) is the geometric scale factor because the corrected flow is proportional to the area, which is proportional to the radius of the fan squared. Therefore, the scale factor on the radii is 2.31905. The revolutions per minute (RPM) of the machine is also adjusted to maintain a constant tip speed for the fan, thus maintaining a roughly constant aerodynamic performance. In this process, the stage pressure ratio and corrected specific flow are held constant. A numerical propulsion system simulation (NPSS) model of the ducted fan with these specifications and the fan map above was created and was then used to produce state tables to feed into the fan noise model.

Table 2. Parameters for the source diagnostic test (SDT) and geometrically scaled SDT and scale factors derived to scale the fan. RPM: revolutions per minute.

Parameter	SDT	Scaled SDT	Scale Factor
Tip Diameter	22 in.	51.0191 in.	2.31905
Hub Diameter	6.6 in. (assuming 0.3 hub/tip ratio)	15.30573 in.	2.31905
Corrected Rotational Speed	12,657 RPM	5,457.83 RPM	1/2.31905
Corrected Tip Speed	1,215 ft/s	1,215 ft/s	1.0
Corrected Fan Weight Flow	100.5 lbs/s	540.49	5.378 (2.31905^2)
Corrected Specific Flow	41.8 lbs/s-ft^2	41.8 lbs/s-ft^2	1.0
Stage Pressure Ratio	1.47	1.47	1.0

Baseline Fan Noise Model

Before developing the parametric noise model, the team created a baseline ANOPP fan noise model using the fan performance maps and design geometry outlined in Figure 2 and Table 2, respectively. This model was used to predict the hard-wall forward and aft fan-radiated noise, with ANOPP's General Electric revised Heidmann method module, an updated formulation for improved large fan predictions. To calibrate this model, the proportional band outputs were compared with the NASA SDT fan noise levels (Woodward, 2002); this process is outlined in the model validation section of this paper. This calibration segment focused primarily on spectral noise emissions, analyzing the relationship between noise level and frequency.

Calibrating the spectral noise is a crucial preliminary step, as it ensures that the model accurately portrays the noise emitted by the fan in the forward and aft directions, on which the spatial model will rely.

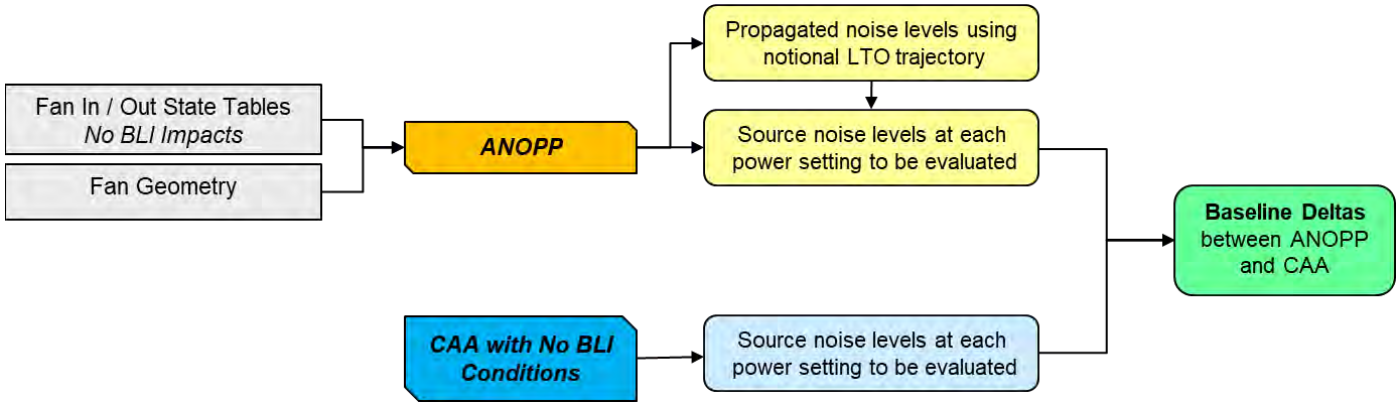

Figure 3. Modeling process to capture differences between the Aircraft Noise Prediction Program (ANOPP) and computational aeroacoustics (CAA). BLI: boundary layer ingestion; LTO: landing/takeoff.

For the baseline fan case, no additional noise sources or reflections were included. Additionally, the team did not perform modeling of acoustic liners in developing the ANOPP noise module, with the intent of solely capturing the impact of BLI and removing any acoustic liner assumptions from the ANOPP prediction.

Baseline Clean Fan Geometry with the SDT Fan

The baseline configuration chosen for the current project is based on the STARC-ABL geometry and the NASA SDT fan. The former was chosen due to the BLI effect on the rear electric propulsor, while the latter was chosen because it is a benchmark geometry for acoustic fan studies. These two geometries are integrated, with the SDT fan geometry replacing the original STARC-ABL propulsor geometry. A few modifications are needed to accomplish this integration.

The first modification concerns the NASA SDT fan. The SDT geometry is a 1/5 scaled model of a representative high-bypass turbofan, with three different vane variants. The first variant has 54 vanes, focusing on cutting-off blade passing frequency rotor–stator interaction tone. The second variant has 26 vanes cut-on for reduced broadband noise, and the third variant has 26 swept vanes for reduced noise. The SDT provided by NASA for the current project is the first variant, denoted as SDT-A hereafter. The SDT-A geometry has a flat surface at the rear because it was developed to address fan noise only and thus is not concerned with noise that would otherwise be generated from the rear part of the core. In the current project, the chosen STARC-ABL geometry utilizes an electric propulsor at the rear of the fuselage. Because the original STARC-ABL fan geometry is replaced with the SDT-A geometry, maintaining the concept of the electric propulsor, there is no core flow. Consequently, the SDT-A geometry is modified to have a plug shape at the rear so that it resembles the original STARC-ABL propulsor. The SDT-A geometry was modified by computer-aided design with a conical shape starting at the axial location of the trailing edge of the nacelle. The half-angle of the cone is 20°, and the cone vertex is smoothed out with a small spherical cap. The resulting geometry is shown in Figure 4.

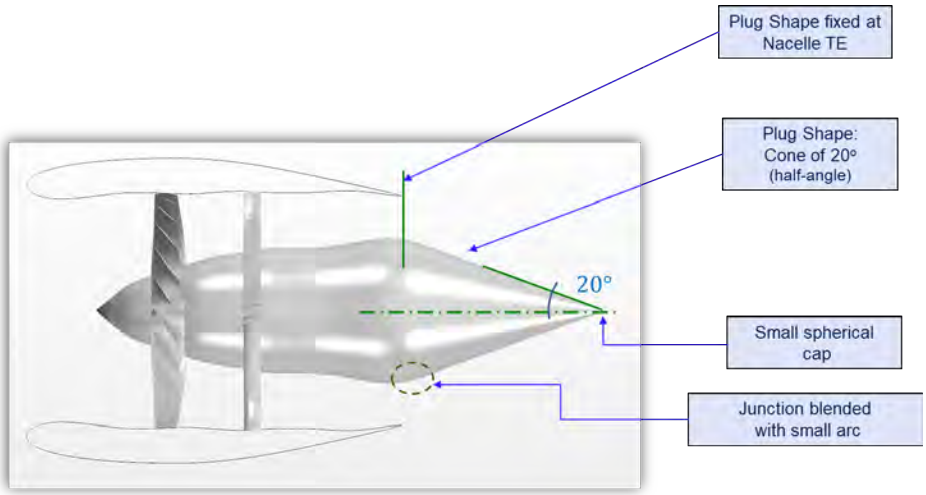

Figure 4. Modification to the SDT-A geometry. SDT: source diagnostic test; TE: trailing edge.

Integrated Geometry Design

The second modification concerns changes to the STARC-ABL fuselage in order to integrate it with the modified SDT-A geometry. This integration uses two geometrical references to replace the original electric propulsor with that of the modified SDT-A. The first reference is the distance between the nose of the fuselage and the leading edge of the nacelle, which is kept constant; the second reference is the axis of the original propulsor, which is also held constant. These geometrical references are shown in Figure 5. Next, the modified SDT-A fan geometry is scaled up by a factor of 2.7272 so that it approximately meets the dimensions at the hub of the STARC-ABL propulsor. Then, the rear part of the fuselage is modified to allow a smooth transition with the scaled and modified SDT-A geometry. All of these changes are shown in Figure 6.

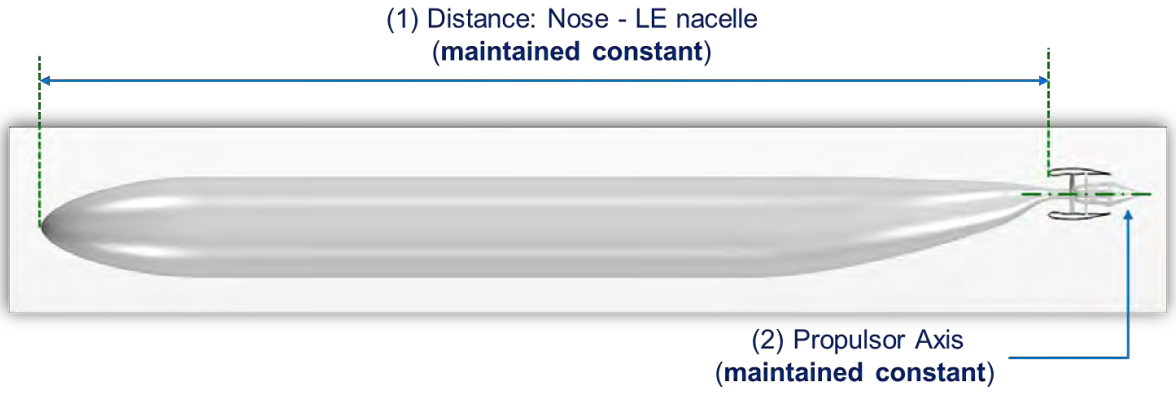

Figure 5. Geometry references for integration between STARC-ABL and modified SDT-A. LE: leading edge; SDT: source diagnostic test; STARC-ABL: single-aisle turboelectric aircraft with aft boundary layer.

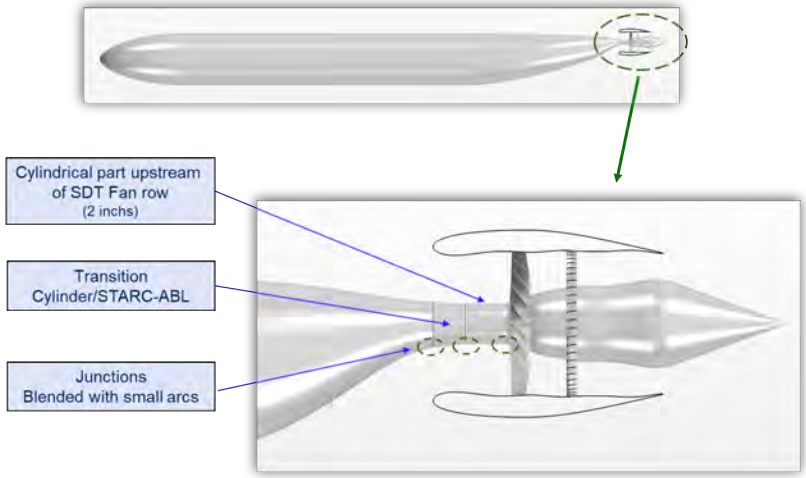

Figure 6. Modification to the fuselage for integration. SDT: source diagnostic test; STARC-ABL: single-aisle turboelectric aircraft with aft boundary layer.

The aircraft geometry considered for CFD analysis is shown in Figure 7. The vehicle is similar in size to the 737-8. Based on findings in the literature (Ahuja, et al., 2020; Kenway, et al., 2018), the vertical tail and wing wakes are expected to have non-negligible contributions to the ingested distortion and are thus included in the model.

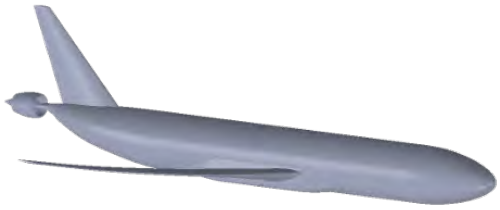

Figure 7. Boundary layer ingestion aircraft geometry model.

The nacelle is a scaled version of the SDT geometry. The inlet highlight areas and throat areas were increased further (for a fixed fan area), based on preliminary RANS CFD findings that showed a strong shock at the throat for typical cruise conditions, as shown in Figure 8. As a result of these modifications, the peak upper-throat Mach number decreased from 1.27 to 1.14, and the peak lower-throat Mach number decreased from 1.18 to 0.9.

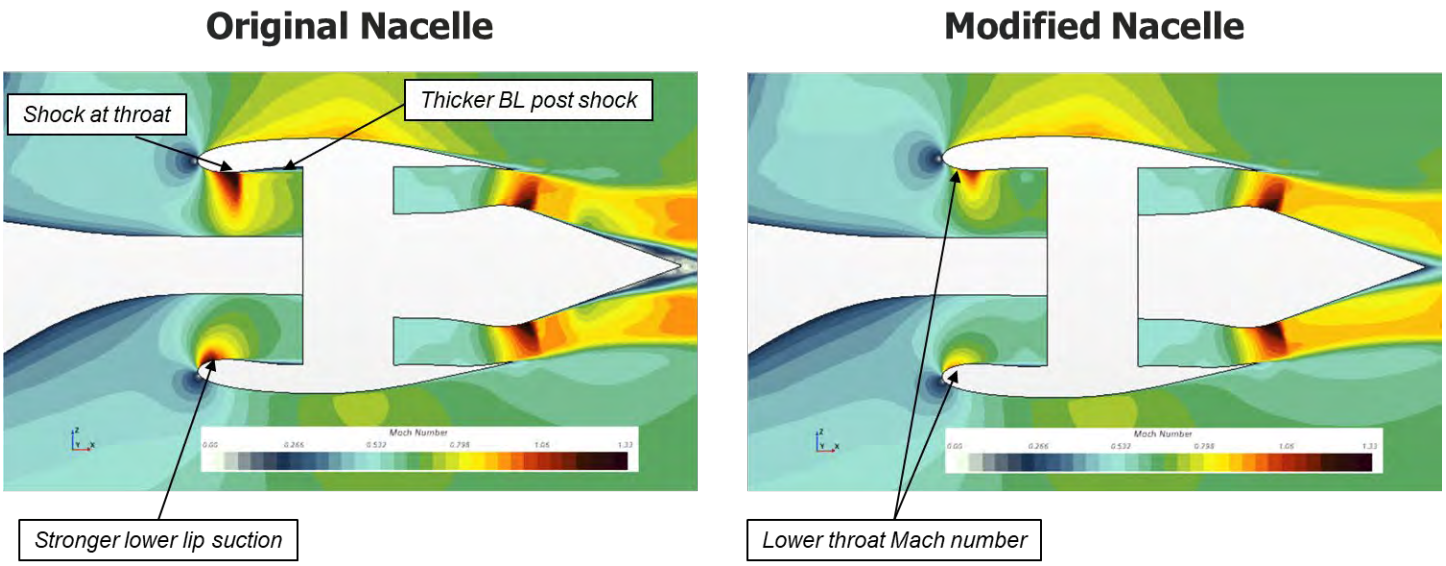

Figure 8. Comparison of original scaled source diagnostic test (SDT) inlet and modified SDT inlet performance under cruise conditions. BL: boundary layer.

RANS CFD Methodology

To determine which variables have a significant impact on inlet distortion, it was prudent to conduct preliminary CFD studies under steady-state conditions with a simplified propulsor model. As such, a one-dimensional powered boundary condition (BC) representation of the engine was considered, where the fan face was treated as a pressure outlet and the fan exit was modeled as a stagnation inlet. A target mass flow rate was specified at the fan face, with the static pressure and temperature being iteratively updated by the CFD solver to meet this requirement. At the fan exit, total pressure and temperature BCs obtained from the one-dimensional engine cycle analysis were imposed in the CFD model. While this level of fidelity for CFD analysis and propulsor modeling is not adequate for CAA, it was sufficient to gain some preliminary insight into how the ingested boundary layer is affected by certain operation and geometry parameters. In addition, the significantly lower cost of steady-state RANS modeling made it easier to conduct several studies, which could then be used to prioritize certain variables over others when the final CAA runs were conducted with a higher-fidelity model.

For the steady-state RANS cases, an unstructured Cartesian grid was developed using STAR-CCM+'s grid generation tools. Prism layers were used for near-wall refinement to capture the boundary layer. The near-wall spacing was calculated such that a wall y-plus of less than one was achieved. Volumetric refinement zones were defined over critical regions of the geometry, such as around the tail cone and engine. Standard atmospheric properties and fully turbulent conditions were assumed for this study, using the SST k-ω turbulence model. Geometric and flow symmetry around the X-Z plane (for all cases considered) allowed for half of the domain to be modeled.

Variable Sensitivity Study and Down-Selection

The primary objective of this sub-study was to determine which parameters can be varied to produce significant and meaningful changes in fan noise. In this case, the term "significant" implies that the sensitivity of noise to a parameter change must be high. The term "meaningful" implies that the change in parameter value cannot be arbitrary and should be relevant in conceptual design. At this early stage, without CAA, there is no way to directly link variable changes to fan noise. However, because there is a correlation between noise and the level of inlet distortion, it is logical to assume that significant changes in the fan face distortion profile will correlate with significant changes in fan noise. As such, the goal was to assess the sensitivity of the ingested boundary layer and corresponding distortion profile to certain variables. This study was conducted under takeoff conditions, as defined by the flight Mach number, altitude, angle of attack (AoA), and fan RPM. The RPM in this lower-fidelity CFD study was modeled by a change in target mass flow rate. Based on studies by Ahuja, et al. (2020, 2021) some variables that are typically considered in conceptual design were investigated:

- AoA
- Fan diameter
- Fuselage length

These variables have been shown to impact the ingested boundary layer characteristics. The AoA captures control surface, wing, and airframe design impacts on distortion and noise through the weight–required lift–AoA relation and has a high impact on distortion. Additionally, changing the AoA is easy in a CFD simulation, as it does not involve any geometry changes or re-meshing. Fan diameter is another key variable that impacts the level of BLI and thus fan face distortion. However, changing the fan diameter involves changing both the hub and tip diameters (to keep the same hub-to-tip ratio), which in turn requires changing the tail cone design for each particular geometry. Not only is this variable change more difficult than a simple AoA perturbation, owing to the geometry changes involved, but a one-to-one mapping between solely the fan diameter and distortion changes is not possible because of the required changes in tail cone design. However, the fan diameter represents a major parameter that varies in conceptual design and, as such, could not be ignored for this study despite the challenges. Fuselage length is a relatively easier geometry parameter to investigate and also impacts ingestion distortion through Reynolds number effects on the developing boundary layer. The following cases were considered in the study:

- AoA: baseline (8.5˚), +25%, +50%
- Fan diameter: baseline (51 in.), +10%
- Fuselage length: baseline (131 ft), +25%

The baseline case was run to obtain reference values for distortion, fan face pressure recovery, and qualitative assessments of the flow field through various scalar views. Each perturbation was then considered individually. Figures 9–12 show the fan face pressure recovery contours (ratio of fan face to freestream total pressure) for the baseline case relative to the fuselage length and AoA perturbations.

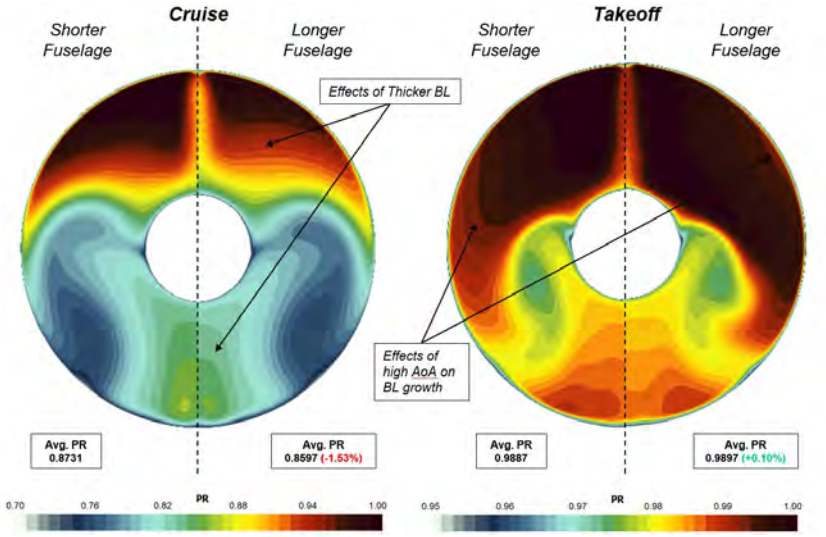

Figure 9. Impact of fuselage length on the pressure recovery (PR) contours under cruise and takeoff conditions (the shorter fuselage in this case is the baseline geometry). AoA: angle of attack; BL: boundary layer.

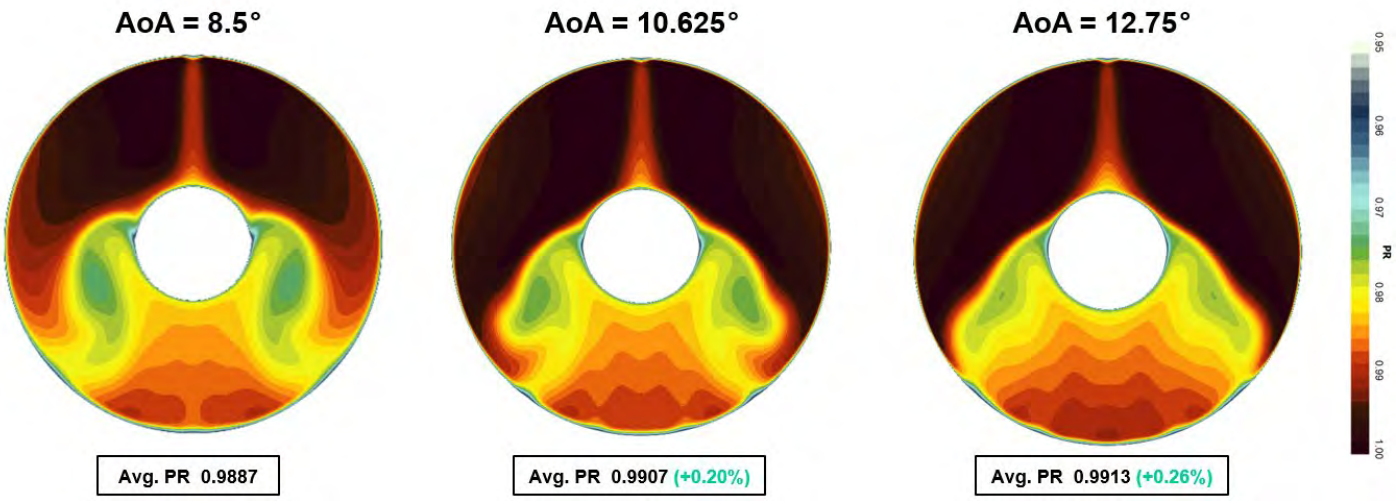

Figure 10. Impact of angle of attack (AoA) variations on fan face pressure recovery (PR) contours under takeoff conditions (baseline at 8.5°).

From Figures 9 and 10, it appears that the fuselage length perturbation under takeoff conditions qualitatively produces similar changes in fan face pressure recovery contours as the AoA variations. For all of these cases, there is a net increase in pressure recovery at the fan face due to a larger region of high total pressure flow ingested by the fan. This observation can be attributed to the differences in flow development over the fuselage, as shown in Figure 11. In this figure, the iso-contours show pressure recovery gradients. For a longer fuselage or a higher AoA, the region of pressure recovery gradients in the boundary layer and vortices is pushed outward in the Y and Z directions going along the X direction toward the nacelle. As such, the propulsor ingests a much smaller portion of this flow, resulting in an increase in fan face pressure recovery. However, from a noise perspective, these perturbations in geometry or operating conditions produce a sufficiently significant change in total pressure and thus distortion.

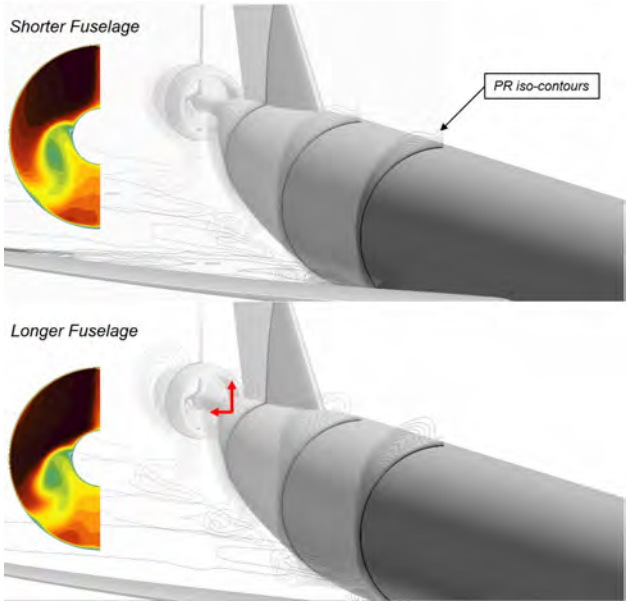

Figure 11. Differences in flow development over the fuselage under high-angle-of-attack takeoff conditions (for a fuselage length change). PR: pressure recovery.

To calculate distortion at the fan face, the aerospace recommended practice (ARP) 1420 standard was used to define the probe locations, as shown in Figure 12.

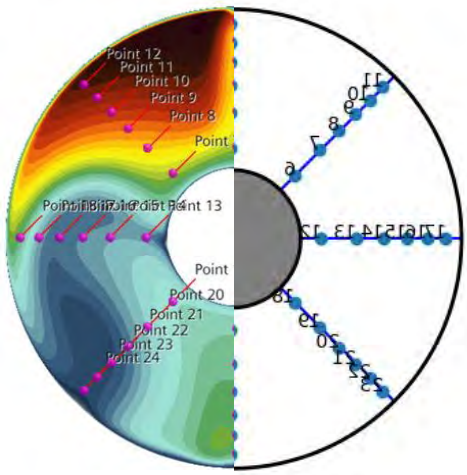

Figure 12. ARP 1420 distortion rake at the fan face.

Distortion intensities were calculated based on methods presented in work by Block (1992). Here, the authors propose representing the fan rake as individual rings of increasing radius and evaluating distortion in accordance with detected low-pressure regions. The average ring pressure was calculated, and any angular sectors with pressures lower than average were catalogued as such. Subsequently, the average low pressure for each of the low-pressure regions was calculated. Finally, the circumferential distortion intensity was obtained as the difference between the average and below-average pressures normalized by the former. If multiple low-pressure regions were found, the region showing the highest intensity was chosen.

Circumferential distortion

i	Rake ring with probes at distance R_i from the center
$Pt_i\ (\theta)$	Measured and/or interpolated rake pressure at an angle of θ degrees for the i_{th} ring
$PAV_i = \frac{1}{360} \int Pt_i\ (\theta) * d\theta$	Average pressure for ring i
$PAVLOW_i = \frac{1}{\Delta\theta_{LOW}} \int Pt_i\ (\theta_{LOW}) * d\theta_{LOW}$	Average pressure within low-pressure region for ring i
$\frac{PAV_i - PAVLOW_i}{PAV_i} * \Delta\theta_{LOW}$	Circumferential distortion for ring i

Radial distortion builds upon the aforementioned circumferential distortion. With the already calculated average ring distortions, an aggregate rake ring distortion is obtained. The radial intensity is then defined as the change between the total ring average and each ring's isolated average, normalized by the aggregate measurement.

Radial distortion

$$PFAV = \frac{1}{N}\sum_{i}^{N} PAV_i$$ Average ring distortion

$$\frac{PFAV - PAV_i}{PFAV}$$ Radial distortion for ring i

Figure 13 shows the circumferential distortion intensities while Figure 14 shows the radial distortion intensity. The baseline case is shown in dark blue. Relative to the baseline case, Figure 13 shows that AoA and fuselage length perturbations produce the largest change in circumferential distortion. However, there is no clear candidate for radial distortion, as shown in Figure 14 , where all three parameter perturbations produce peak changes in radial distortion at different locations.

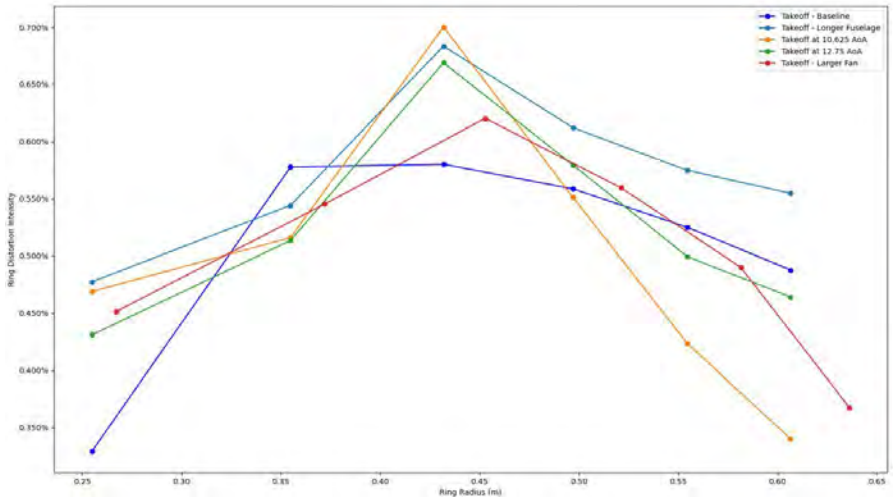

Figure 13. Circumferential distortion at takeoff for all cases. AoA: angle of attack.

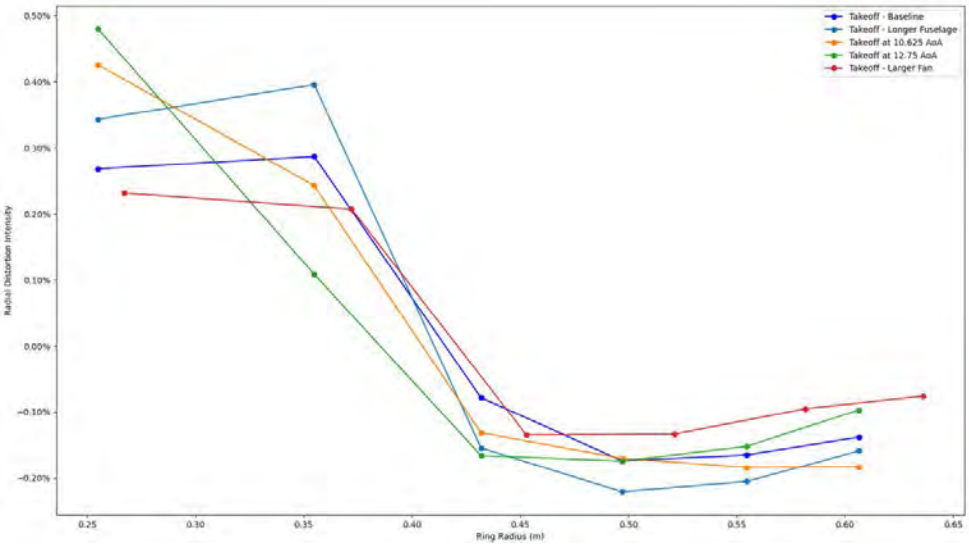

Figure 14. Radial distortion at takeoff for all cases. AoA: angle of attack.

Based on these results, the team decided to proceed with only the AoA as one of the inputs to the noise model, with the other being RPM. As such, the noise model is parametric with respect to operating conditions only and not geometry. While diameter and fuselage length also have a relatively equal claim for consideration, the increased dimensionality of the input space for the noise model would have required substantially more CAA runs, which would have exceeded the computational time and budget constraints for this project. The final sampling space for constructing the noise surrogate model is shown in Figure 15. The ranges of AoA and RPM are sufficiently large to consider takeoff, approach, and flyover, the three main noise measurement conditions. Training points are circled in red, with blue V's showing additional cases that could be run for model validation, depending on time and budget availability.

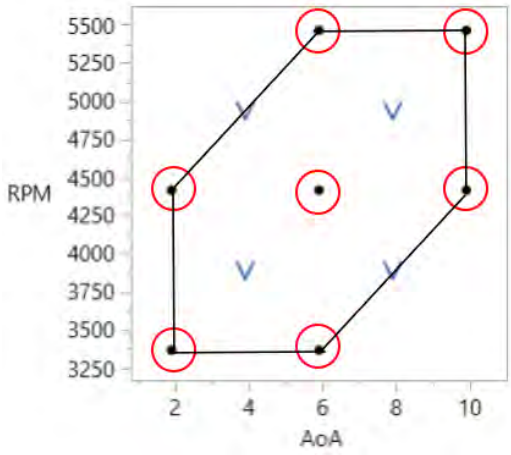

Figure 15. Revolutions per minute (RPM) and angle of attack (AoA) sampling space for parametric noise model generation.

CAA Modeling

Because the objective in the current study is to capture the effects of non-uniform flow in the boundary layers of the flow ingested by the turbofan, an unsteady aerodynamics analysis is needed. A hybrid methodology for CAA is employed in this study. This methodology consists of two main steps. The first step is related to the collection of unsteady aerodynamic flow data, while the second step involves the propagation of acoustics to the far-field.

The aeroacoustics of two configurations were studied. The first configuration focuses on the acoustics of an isolated turbofan. This configuration was examined with the purpose of **validating** our CAA approach against available experiments. The second configuration focuses on the main objective of this project: the acoustics of a BLI configuration. This configuration is denoted as the integrated configuration and comprises a generic aircraft with a tail propulsor as described above.

Unsteady Aerodynamics

Unsteady flow data were obtained by utilizing a commercial lattice Boltzmann method (LBM) solver, PowerFLOW. Unlike traditional CFD methods that solve for macroscopic fluid quantities via Navier–Stokes equations, LBM solves for microscopic particle distributions. Thus, modeling occurs at a level where the physics are more fundamental. Such solvers exhibit low dissipation properties, rendering them sound for aeroacoustic applications.

The BCs applied to all simulations in the current study are as follows: in the outer boundaries, pressure/velocity-type BCs are prescribed, whereas non-slip wall BCs are used on all solid surfaces such as those for blades, vanes, the center body, and the nacelle; the only exception here occurs in the nacelle extension of the isolated SDT simulation, which is described in more detail in the next section.

Spatial discretization is accomplished by means of variable refinement regions. Note that discretization sizes decrease by half for each variable refinement level. The smallest discretization sizes are located in regions between the tips of the blades and the nacelle. The second smallest sizes are located in regions of the leading and trailing edges of the blades and vanes, while the third smallest sizes arise in the boundary layers of the blades and vanes.

Finally, to avoid acoustic reflections from outer boundaries, a region for damping acoustic waves is used surrounding the configuration of interest. This region gradually increases the flow viscosity toward the outer boundaries, thus preventing acoustic reflections.

Far-Field Aeroacoustics

The far-field aeroacoustics are predicted by the Ffowcs Williams–Hawkings (FW-H) method. A commercial FW-H solver, Power Acoustics, is employed in this study. This solver uses unsteady flow data previously collected at a chosen surface. The chosen surface is permeable and surrounds the configuration under study. The FW-H method takes the unsteady flow data and propagates them to the far-field for specified acoustic receivers. The outcome of the FW-H solver is the acoustic pressure time history at each receiver.

Approach for Creating an Integrated ANOPP Model

After validating the ANOPP fan model, the team developed a model within the ANOPP2 framework, which includes functionality to scale two-dimensional results into a three-dimensional hemispherical surface model. This function revolves the polar arc results, shown in Figures 18 - 20, about the fan revolution axis, assuming an axial-symmetric model in this process. This assumption is valid for the designed fan model because ANOPP is a noise-source-based tool and does not include airflow interactions. Thus, the noise level difference between any of the defined points will solely be a function of distance from the noise source(s). Additionally, the lack of flow simulation prevents AoA effects from being incorporated.

To create an encompassing measurement surface, a range of directivity angles (theta; 20°–160°) and azimuthal angles (phi; -90°–90°) at a radius of 10 m was defined. This range of directivity angles was chosen to optimize the CAA model results by excluding the effects from the fuselage surface and fan-generated jet exhaust. The distance of 10 m was chosen to separate the fuselage-generated turbulent flow noise from the desired engine noise and flow effects. A microphone node resolution of 10° increments was selected to provide a good balance between computational requirements and accuracy. The resulting surface was placed below the aircraft to analyze ground-directed noise only, as shown in Figure 16. This same surface was used to generate CAA results, providing a direct comparison with the noise estimates from ANOPP.

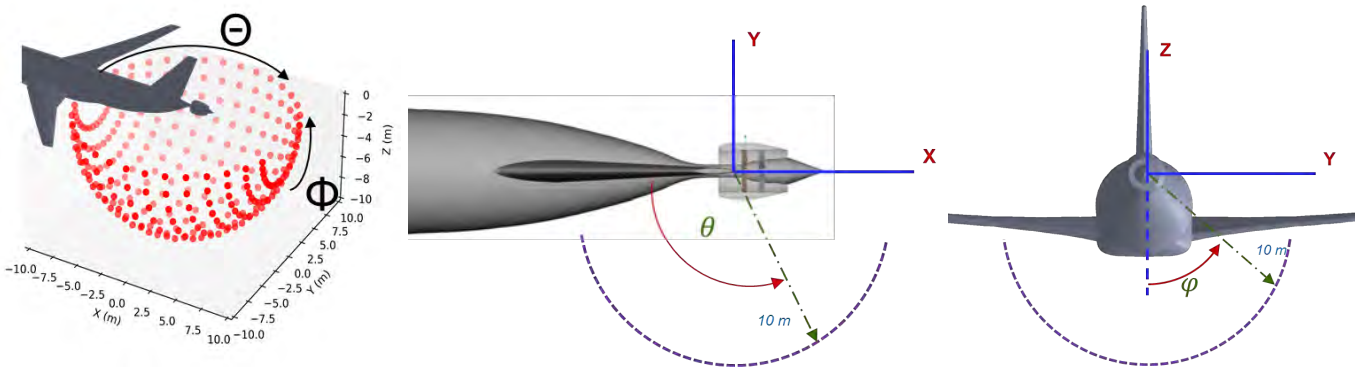

Figure 16. Noise surface example.

Because ANOPP lacks unsteady flow simulation ability and overall accuracy compared with CAA methods, the integrated ANOPP model does not estimate distorted flow effects, leaving these effects to be calculated solely by CAA. The resulting noise level surfaces are compared to calculate the impact of distorted flow due to the fuselage elements. This process was repeated for the experimental design points shown in Figure 15.

During operation, the model uses the microphone surface to calculate the resulting sound pressure level after the wave propagation and interference effects per 1/3rd octave frequency band. ANOPP then sums these band levels to calculate the overall sound pressure level (OASPL), which is useful for the final delta model to prioritize the desired spatial data over the frequency-dependent spectral data.

ANOPP Model Results

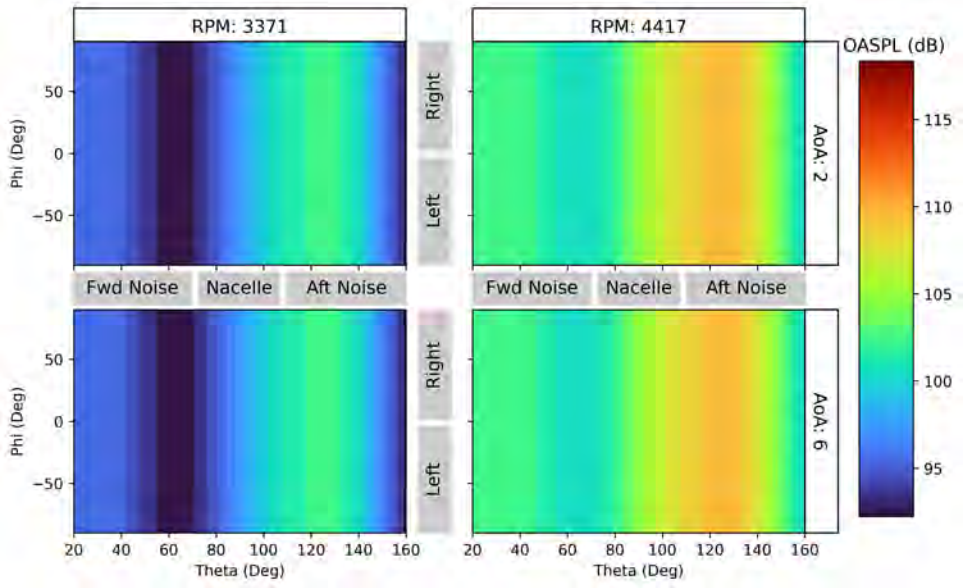

Figure 17. Spatial model results for the Aircraft Noise Prediction Program. AoA: angle of attack; OASPL: overall sound pressure level; RPM: revolutions per minute.

Figure 17 shows the interpolated results taken at each microphone for each test condition. Bands of constant values can be clearly observed, demonstrating the axially symmetric nature of the ANOPP model. These bands help identify the individual forward and aft noise sources. The noise is dominated by the aft radiated noise, with each RPM showing a clear maximum near 125°.

As previously mentioned, AoA effects are absent from these results. Because the microphone surface geometry is fixed with respect to the aircraft's body coordinates, there is no shift in minimum/maximum location. Moreover, the lack of flow simulation prevents the consideration of any fluid interactions.

Integrated CAA Setup

As previously described, the unsteady aerodynamics are modeled via an LBM solver. The unsteady aerodynamic simulations were obtained for the cases previously described in the section on variable selection, which provide AoA and RPM values for the rotor fan. Some details about the set-up of the integrated configuration are given in the following table:

Table 3. Computational aero-acoustics parameters for free-stream conditions and mesh setup.

LBM Simulation	***Value***	***Remark***
M_∞	0.23	Freestream Mach number
T_∞	285.9 K	Freestream temperature
P_∞	97,185 Pa	Freestream static pressure
Smallest spatial discretization	0.375 mm	▪ Gaps between blade tips and nacelle ▪ Leading edge and trailing edge in blades and vanes
	0.750 mm	▪ Boundary layers in blades and vanes ▪ Outer blade region
Time step	0.4791×10^{-6} s	
Mesh size	~ 1,050 million	

The far-field aeroacoustics are predicted by the FW-H solver. This solver uses unsteady flow data previously collected at a chosen surface (FW-H surface) of the permeable type, surrounding the turbofan of the integrated configuration. Moreover, the FW-H surface is an open shell at both ends, opening in the downstream and upstream ends in order to avoid contamination from the aircraft tail and turbo-machinery wakes, respectively. The FW-H method takes the unsteady flow data and propagates them to the far-field for specified acoustic receivers. For the integrated configuration, these receivers are defined on a hemisphere, oriented toward the ground with a 10-m radius. A total of 285 receivers are located on this hemisphere. The outcome of the FW-H solver is the acoustic pressure time history for each receiver. These aeroacoustic data are used for ANOPP to build the BLI noise model. Some details about the FW-H simulation are shown below:

Table 4. FW-H solver setup assumed values.

FW-H Simulation	***Value***	***Remark***
FW-H spatial discretization	6.00 mm	Permeable surface
FW-H time step	1.53×10^{-5} s	
Maximum frequency resolved	~ 5.0 kHz	
Time for collecting flow data	10 rev	Time for ten revolutions

Integrated CAA Results

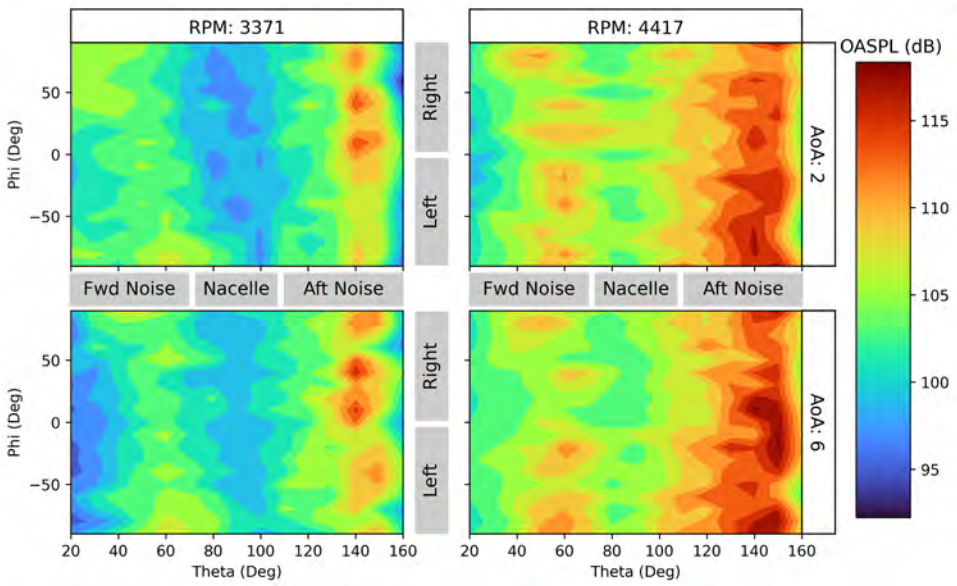

Figure 18. Integrated CAA results.

ANOPP Module Development

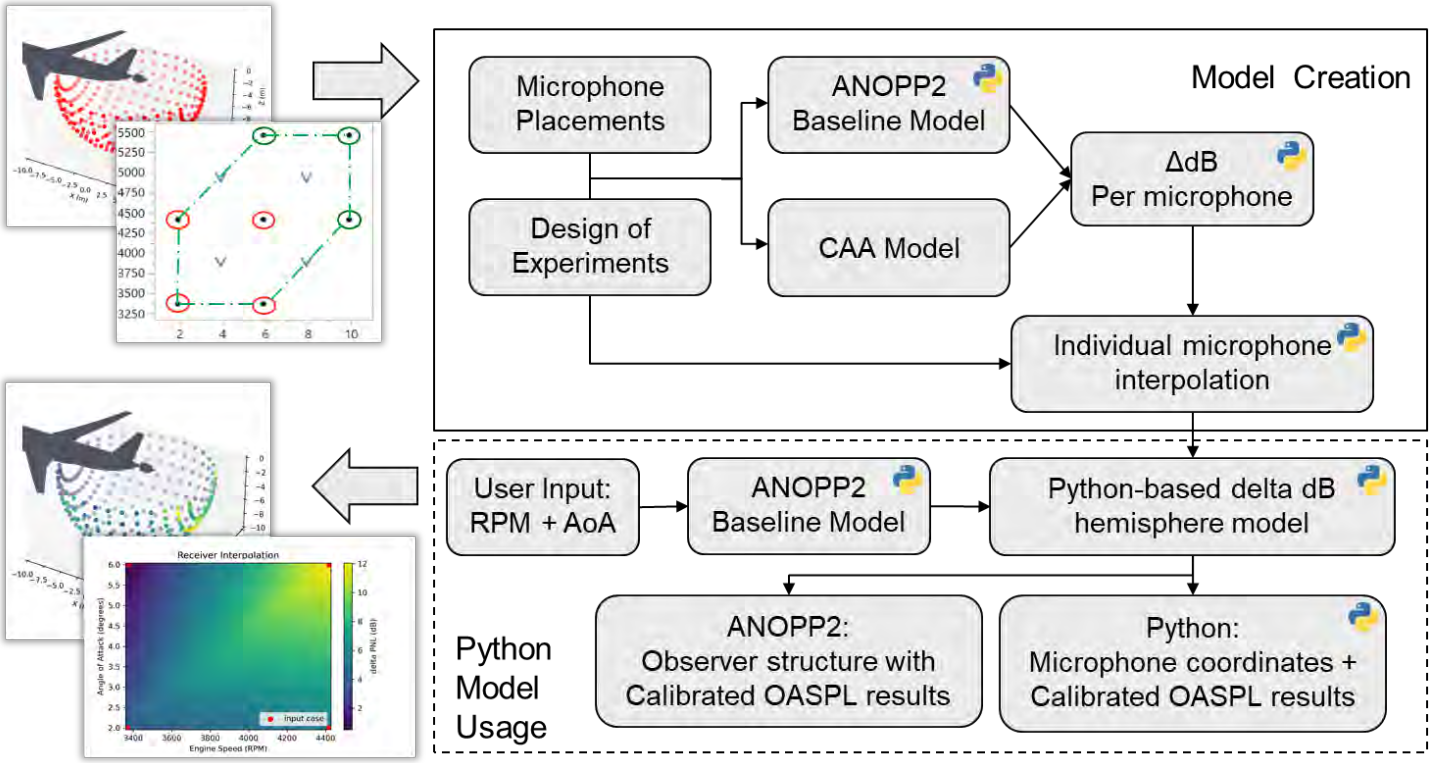

Figure 19. ANOPP model development.

Unsteady aerodynamic simulations were carried out according to the cases described in the section on variable selection.

The first step in the model extracts the pressure time history from the microphone nodes used in the CAA integrated model. For each node, the OASPL is calculated using the ANOPP2 atmospheric analysis module. This metric includes a Hanning window, followed by a transformation into a narrow band spectrum and then finally into the OASPL. These values are then used in conjunction with the OASPL outputs from the ANOPP spatial model. At each node, the ANOPP results are used as a baseline, and the difference from the actual CAA value is defined as the delta dB. A linear interpolation of each node's delta contour is generated, where RPM and AoA are inputted to estimate the delta value. Each node's interpolation is saved and reloaded when called to generate a new set of deltas for a user-input RPM and AoA.

The per-node interpolation is fit between the four cases, with each node having its bespoke fit. The average of all of these interpolations is shown in Figure 20.

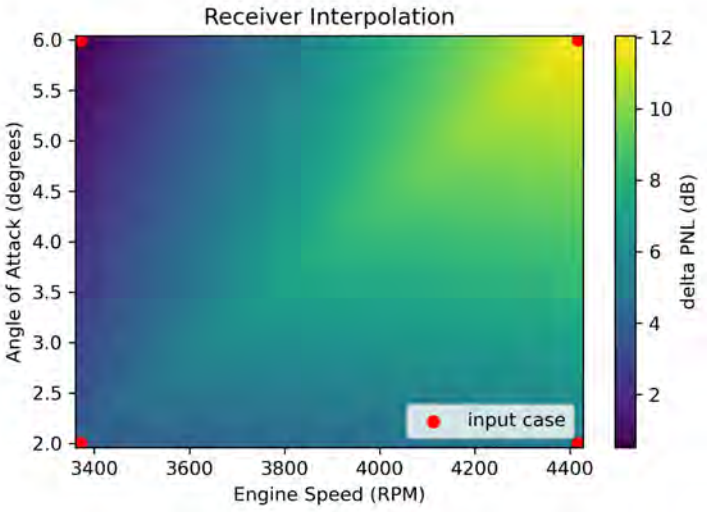

Figure 20. Average receiver interpolation. RPM: revolutions per minute. PNL: perceived noise level.

These results show that a larger correction is required as RPM increases, with the maximum average correction occurring for the case with the highest RPM and AoA. For a given RPM of 4,000 and an AoA of 4°, the interpolation models are queried and return a surface of corrected node values. A plot of this case is shown in Figure 20.

Milestones

- Baseline SDT fan performance model created
- Baseline ANOPP model created and validation exercises conducted

Major Accomplishments

- Baseline SDT fan performance model created
- Integrated BLI scaled fan performance model created
- Baseline ANOPP model created
- Baseline CFD/CAA geometry and mesh created
- Integrated, scaled CFD/CAA geometry and mesh created
- Sets of cases to be performed in CAA defined by conducting lower-fidelity RANS CFD cases to identify key sensitivities

Publications

None.

Outreach Efforts

None.

Awards

None.

Student Involvement

Two graduate students were involved with this work: Ross Weidman and José Zavala. These students are graduate research assistants in their first and second years at Georgia Tech.

References

Ahuja, J., & Mavris, D. N. (2020, January 6). Sensitivity of boundary layer ingestion effects to tube and wing airframe design features. *AIAA Scitech 2020 Forum*. AIAA Scitech 2020 Forum, Orlando, FL. https://doi.org/10.2514/6.2020-1523

Ahuja, J., & Mavris, D. N. (2021, January 11). Assessment of propulsor on-design and off-design impacts on BLI effects. *AIAA Scitech 2021 Forum*. AIAA Scitech 2021 Forum, VIRTUAL EVENT. https://doi.org/10.2514/6.2021-0605

Bloch, G. (1992). *An assessment of inlet total-pressure distortion requirements for the compressor research facility* (Publication No. WL-TR-92-2066). https://apps.dtic.mil/dtic/tr/fulltext/u2/a262299.pdf

Envia, E., Tweedt, D., Woodward, R., Elliott, D., Fite, E., Hughes, C., Podboy, G., & Sutliff, D. (2008, May 5). An assessment of current fan noise prediction capability. *14th AIAA/CEAS Aeroacoustics Conference (29th AIAA Aeroacoustics Conference)*. 14th AIAA/CEAS Aeroacoustics Conference (29th AIAA Aeroacoustics Conference), Vancouver, British Columbia, Canada. https://doi.org/10.2514/6.2008-2991

Kenway, G. K., & Kiris, C. C. (2018, January 8). Aerodynamic shape optimization of the starc-abl concept for minimal inlet distortion. *2018 AIAA/ASCE/AHS/ASC Structures, Structural Dynamics, and Materials Conference*. Kissimmee, Florida. https://doi.org/10.2514/6.2018-1912

Woodward, R., Hughes, C., Jeracki, R., & Miller, C. (2002, June 17). Fan noise source diagnostic test—Far-field acoustic

Task 3 – Model Validation Exercises

Georgia Institute of Technology

Objectives

The purpose of this task is to validate the created parametric noise models using existing data or high-fidelity simulations.

Research Approach

Baseline Validation

To validate the baseline fan noise, the predicted fan noise from the ANOPP model will be compared with published acoustic results of the SDT fan and the difference will be documented. If there is a significant difference in the ANOPP prediction and published data, a correction function in the ANOPP model can be introduced to minimize these differences. The proposed method to account for differences between the CAA results generated for the study and ANOPP is described in Section 1.2 (Figure 3). Further validation exercises may be needed depending on the results of the parametric model. The module will be used to generate both BLI and non-BLI noise results for various flight/operating conditions, which will be compared with CAA results for the corresponding conditions.

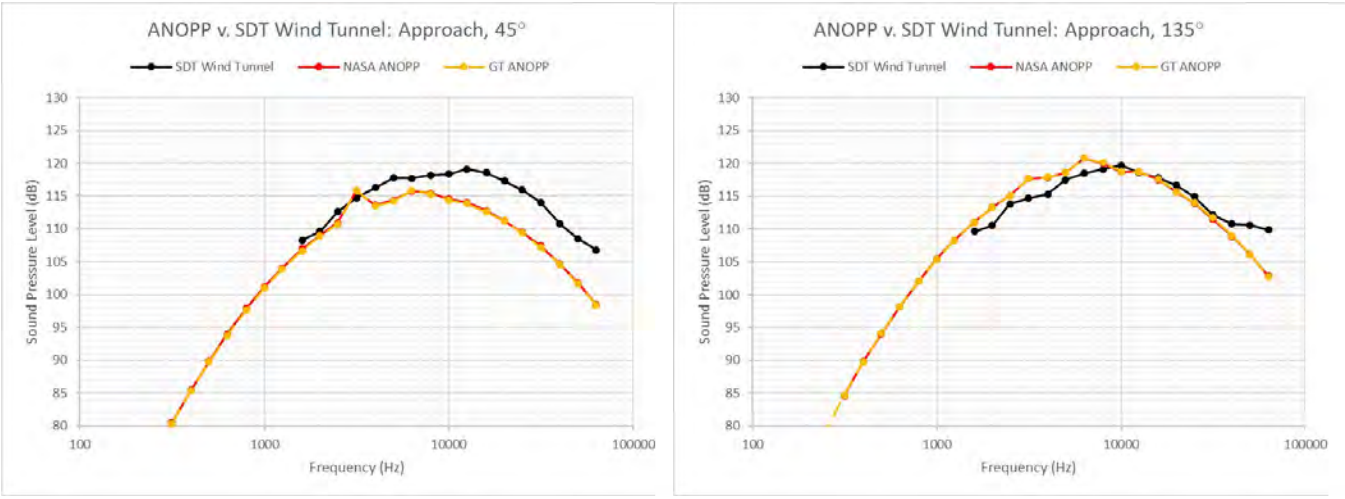

Figure 21. Comparison between the Georgia Tech (GT) Aircraft Noise Prediction Program (ANOPP), baseline NASA ANOPP, and source diagnostic test (SDT) model approaches.

Table 5. Error in the Aircraft Noise Prediction Program (ANOPP) baseline model approach. EXP: experimental; GT: Georgia Tech; RMS: root mean square; SDT: source diagnostic test.

Comparison	GT ANOPP – EXP SDT		NASA ANOPP – EXP SDT		NASA ANOPP – GT ANOPP	
Directivity Angle	45°	135°	45°	135°	45°	135°
RMS Error (dB)	4.8579	2.5529	4.7523	2.549	0.15597	0.074428

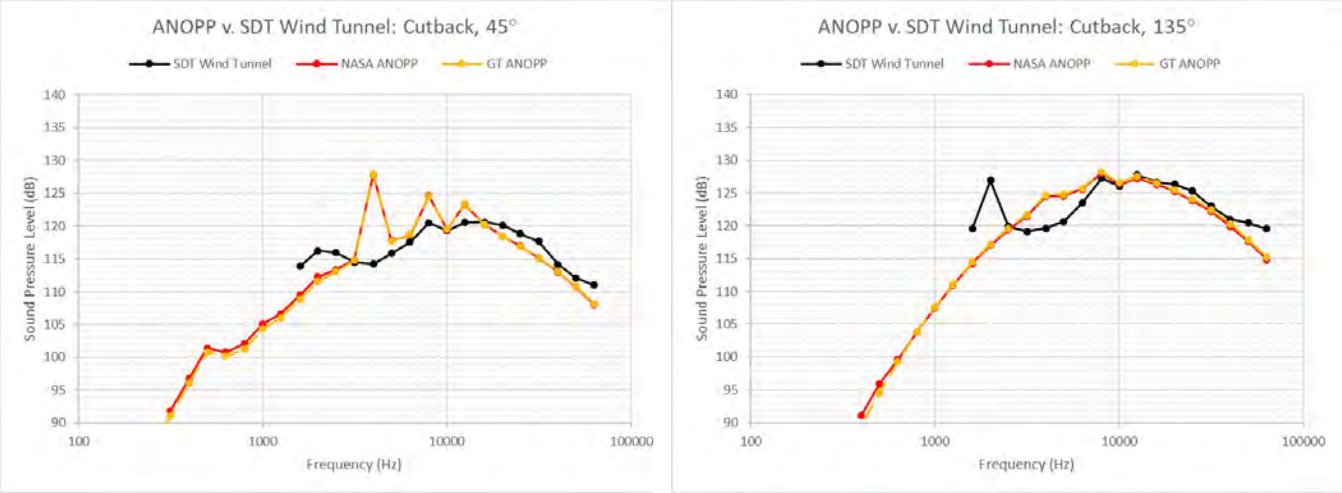

Figure 18. Cutback comparison of the Georgia Tech (GT) Aircraft Noise Prediction Program (ANOPP), baseline NASA ANOPP, and source diagnostic test (SDT) model.

Table 6. Cutback error in the Aircraft Noise Prediction Program (ANOPP) baseline model. EXP: experimental; GT: Georgia Tech; RMS: root mean square; SDT: source diagnostic test.

Comparison	GT ANOPP – EXP SDT		NASA ANOPP – EXP SDT		NASA ANOPP – GT ANOPP	
Directivity Angle	45°	135°	45°	135°	45°	135°
RMS Error (dB)	4.1761	3.4692	4.0591	3.5218	0.41517	0.47159

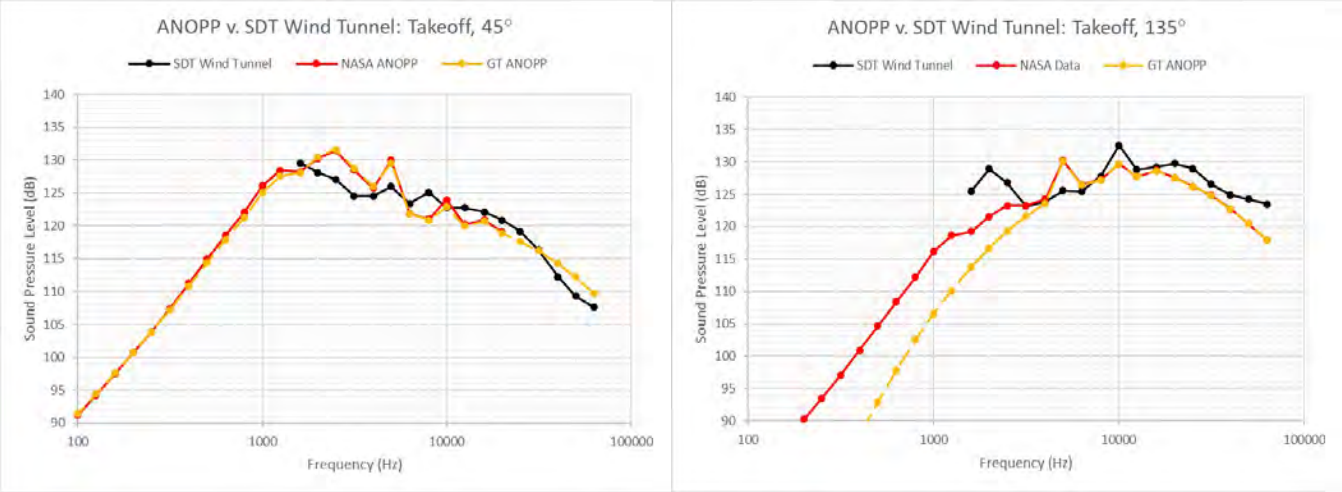

Figure 23. Takeoff comparison of the Georgia Tech (GT) Aircraft Noise Prediction Program (ANOPP), baseline NASA ANOPP, and source diagnostic test (SDT) model.

Table 7. Takeoff error in the Aircraft Noise Prediction Program (ANOPP) baseline model. EXP: experimental; GT: Georgia Tech; RMS: root mean square; SDT: source diagnostic test.

Comparison	GT ANOPP – EXP SDT		NASA ANOPP – EXP SDT		NASA ANOPP – GT ANOPP	
Directivity Angle	45°	135°	45°	135°	45°	135°
RMS Error (dB)	2.6080	5.0944	2.5755	3.4633	0.42983	8.1166

To accurately calibrate our model for each power level, the atmospheric conditions per power level used in the NASA SDT model (Envia, 2018) were copied exactly. These values are shown in Table 6.

Table 8. Atmospheric settings for the Aircraft Noise Prediction Program model. RPM: revolutions per minute.

Input Parameter	**Approach**	**Cutback**	**Takeoff**
RPM	3,371	4,417	5,463
Ambient Temperature, K	295.67	295.50	295.28
Ambient Pressure, Pa	98,440	98,300	98,250
Ambient Density, kg/m^3	1.1647	1.1647	1.1647
Freestream Mach Number	0.0	0.0	0.0

Overall, the model calibration was successful, with all but the takeoff 135° case having an RMS error margin of less than 0.5 dB when compared with the NASA ANOPP model. Because the intention was to replicate the SDT ANOPP model, and not the experimental SDT data, this calibration process was successful.

CAA Validation for the SDT Turbofan

To assess the ability of our chosen numerical approach, the team performed a validation with experimental acoustic data from a turbofan. The validation is based on SDT experiments conducted by NASA (Woodward, 2002; Heidelberg, 2022). The SDT is a General Electric-designed turbofan wind tunnel model (1/5 scale) with a rotor diameter of 22 in. The rotor consists of 22 blades, whereas the stator consists of 54 vanes. The approach condition was chosen for validation with simulation in this study. The associated conditions are shown in Table 7.

Table 9. Validation case details. RPM: revolutions per minute.

	Value	Unit	Remark
M_∞	0.10		Freestream Mach number
T_∞	288.15	Pa	Freestream temperature
P_∞	101,325	K	Freestream pressure
α_∞	0	degree	Angle of attack
Rotor speed	7,809	RPM	

In the NASA experiments, acoustic measurements were acquired from 48 sideline microphones at a distance of 89.3 in. For our validation, however, a subset of these receivers is considered. A total of 21 sideline receivers are considered, arranged as shown in Figure 24.

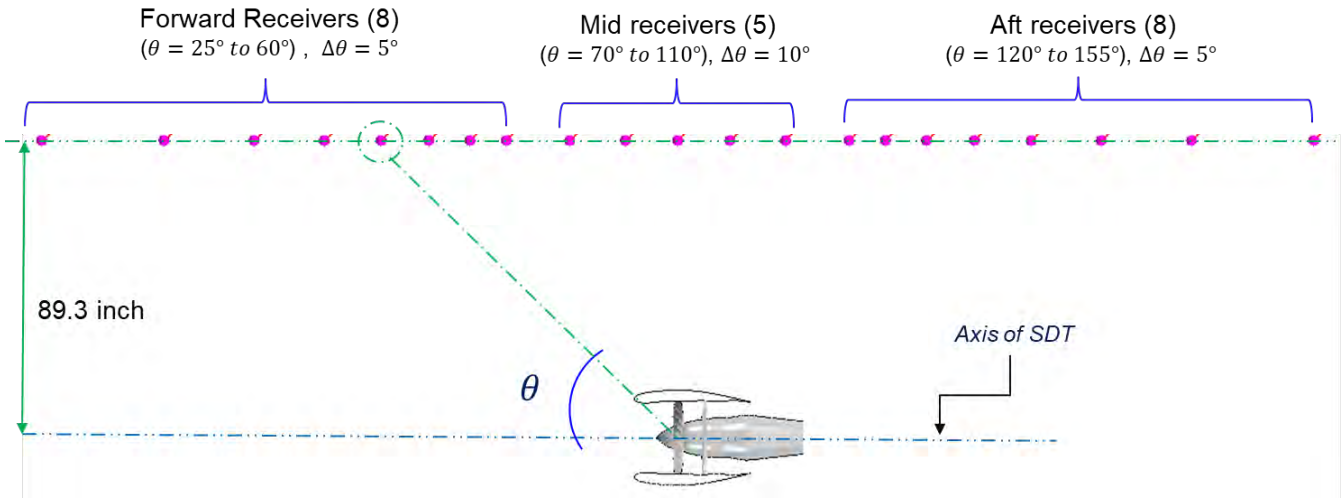

Figure 24. Arrangement of sideline receivers. SDT: source diagnostic test.

Simulation Setup

As previously described, the unsteady aerodynamics are modeled via an LBM solver. The BCs are as previously described with the exception of the extension of the center body, where slip walls are used to avoid the influence of boundary layers. Some details about the simulation set-up are shown in Table 8.

Table 10. Lattice Boltzmann method (LBM) simulation set-up.

LBM Simulation	***Value***	***Remark***
Smallest spatial discretization	0.125 mm	Gaps between blade tips and nacelle
	0.250 mm	Leading edge and trailing edge Blades and vanes
Time step	0.1626×10^{-6} s	
Mesh size	~400 million	

Aeroacoustics are predicted using the FW-H solver. This solver uses flow data recorded from the unsteady simulation at a chosen surface. The chosen surface for the current simulation is permeable, surrounding the SDT turbofan. Moreover, the FW-H surface is an open shell, with an opening in the downstream end to avoid contamination from the fan wakes. The far-

field acoustic receivers set to the FW-H solver are located as shown in 24. Some details about the FW-H simulation are shown in Table 9.

Table 11. Ffowcs Williams–Hawkings (FW-H) simulation set-up.

FWH Simulation	*Value*	*Remark*
FW-H spatial discretization	4.00 mm	Permeable surface
FW-H time step	5.2×10^{-6} s	
Maximum frequency resolved	6.4 kHz	
Period time for collection of flow data	10 rev	Time for ten revolutions

Results

Numerical predictions of sideline directivity OASPL along with experimental values are shown in Figure 25. For reference, previous LBM simulations [4] are also plotted. Our LBM simulation is capable of accurately predicting the directivity trend; however, the simulation underpredicts the OASPL, by up to 2 dB, in the most upstream receivers. Similarly, OASPL values are underpredicted in the downstream region. Nevertheless, quantification of the discrepancy, as measured by the root mean squared error between the experiment and simulation, provides an average OASPL of 1.7 dB. This average discrepancy is in agreement with previous LBM simulations (Casalino, et al., 2018), which had average discrepancies of 1.77–2.04 dB.

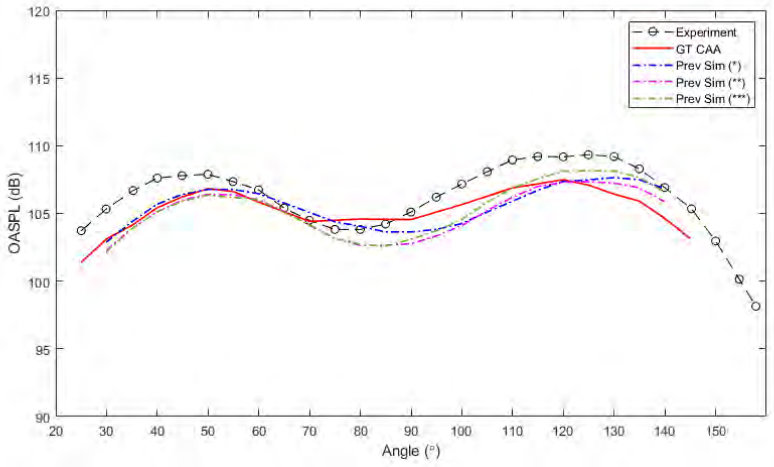

Figure 25. Comparison between numerical prediction and experiments along with previous numerical simulations. GT CAA: Georgia Tech computational aeroacoustics; OASPL: overall sound pressure level.

Milestone

Task 3 has been completed.

Major Accomplishments

The high-fidelity numerical CAA approach for the SDT turbofan under approach conditions was validated.

Publications

None.

Outreach Efforts

None.

Awards
None.

Student Involvement
Three graduate students were involved with this work: Grant Stevenson, Ross Weidman, and José Zavala. These students are graduate research assistants in their first and second years at Georgia Tech.

References
Casalino, D., Hazir, A., & Mann, A. (2018). Turbofan broadband noise prediction using the lattice boltzmann method. *AIAA Journal*, *56*(2), 609–628. https://doi.org/10.2514/1.J055674

Envia, E., Tweedt, D., Woodward, R., Elliott, D., Fite, E., Hughes, C., Podboy, G., & Sutliff, D. (2008, May 5). An assessment of current fan noise prediction capability. *14th AIAA/CEAS Aeroacoustics Conference (29th AIAA Aeroacoustics Conference)*. Vancouver, British Columbia, Canada. https://doi.org/10.2514/6.2008-2991

Heidelberg, L. (2002, June 17). Fan noise source diagnostic test—Tone modal structure results. *8th AIAA/CEAS Aeroacoustics Conference & Exhibit*. 8th AIAA/CEAS Aeroacoustics Conference & Exhibit, Breckenridge, Colorado. https://doi.org/10.2514/6.2002-2428

Woodward, R., Hughes, C., Jeracki, R., & Miller, C. (2002, June 17). Fan noise source diagnostic test—Far-field acoustic results. *8th AIAA/CEAS Aeroacoustics Conference & Exhibit*. 8th AIAA/CEAS Aeroacoustics Conference & Exhibit, Breckenridge, Colorado. https://doi.org/10.2514/6.2002-2427

Task 4 – Tool Documentation
Georgia Institute of Technology

Objective
The purpose of this task is to create documentation of the parametric noise tool created.

Research Approach
Georgia Tech will thoroughly document the tool and each of its modules, including the parameters involved, theoretical approach, algorithms utilized, output structure, and example use cases. This theory manual will be provided in addition to the validation results, which will be documented as a separate report.

The resulting tool is a combination of the ANOPP spatial model and the generated microphone interpolations. The user will input the desired AoA and RPM values and enable/disable the output result tags to generate the desired files. However, one must first initialize the model's filesystem by placing the ANOPP executable files in the script housing folder. The required files are listed under their required namespace: anopp.exe, AIC.exe, AICLIB.WRK, NPDLIB.WRK, and LIBRARY.WRK. The final preparation step is to replace the ANOPP2 application programming interface (API) location template with a reference to the true location on the user's system. Figure 26 identifies the user input locations and options within the code:

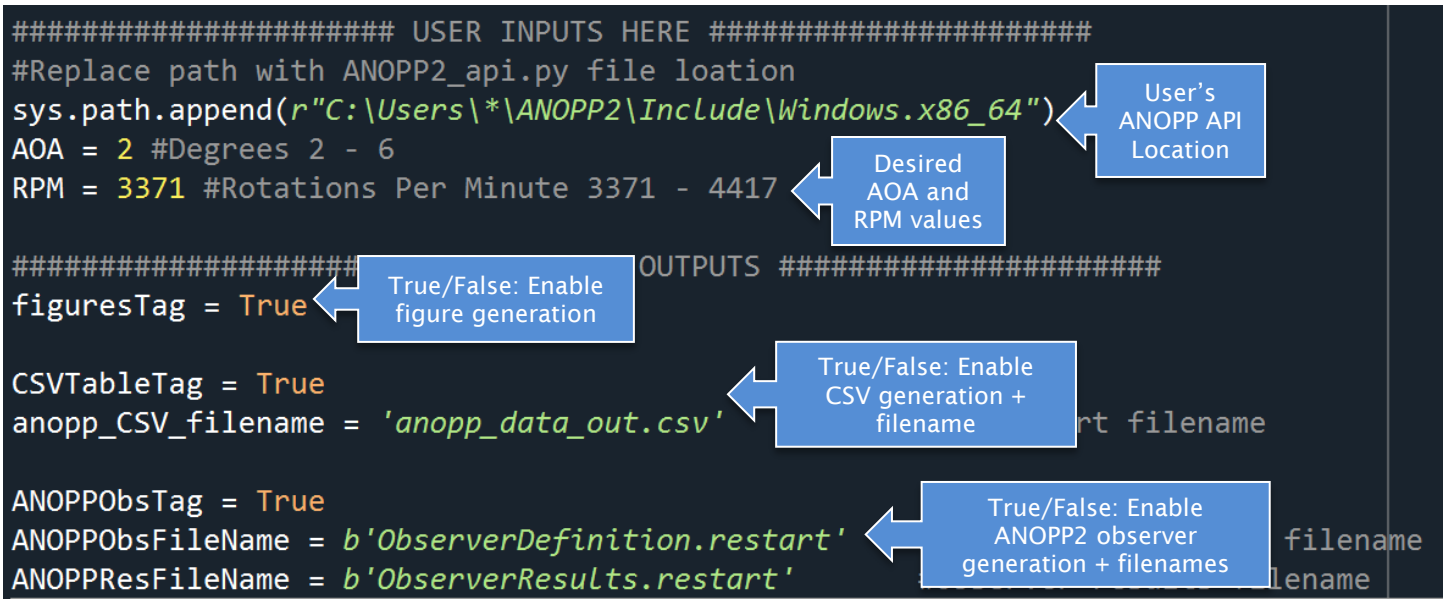

Figure 26. Description of the input file for the ANOPP2 fan noise module.

The tool will use the provided RPM value to calculate the throttle percentage to run before exporting this value to the flight plan template file. This flight path file, along with the atmosphere, observer, and propulsion configuration files will set up the remainder of the required variables. If the user desires to alter the model's parameters, these configuration files will house the majority of alteration options. An explanation of these files is beyond the scope of this tool; however, the user can refer to the ANOPP2 reference manuals for more information. ANOPP will then use AnoppSource.config as a template to build a Fortran file combining each of these mentioned components for execution. Once complete, the resulting proportional band spectrum values are added to the observer structure in the tool as a result. The tool can use this observer structure to gather the microphone positions in both spherical and Cartesian coordinate systems. More importantly, the observer structure can be used to calculate the OASPL and export those results to a Tecplot file format.

Because a Tecplot file is not directly importable into Python, the offloaded_functions.py file contains the Tecplot reader functions, a pair of programs used to read in and tabulate the data before returning the desired values in a Python-friendly Pandas data frame. The offloaded file also contains the correction code, where the interpolation functions are imported and used to calculate the delta dB required to correct the preliminary ANOPP results. This program will return the originally predicted OASPL, delta OASPL, and corrected OASPL values to the core Python script. If the user does not request any output files, the tool will complete its execution, and the user will have these three lists of OASPL values.

The three output choices, if enabled, will use the resulting data to generate plots, a comma separated variable (CSV) file, or an ANOPP2 observer definition plus an ANOPP2 observer result. The observer definition contains the nodes and their respective locations, while the observer result will contain the corrected OASPL values and the delta values used to alter the data.

Milestones
Task 4 has been completed.

Major Accomplishments
Task 4 has been completed.

Publications
None.

Outreach Efforts
None.

Awards
None.

Student Involvement
Three graduate students were involved with this work: Grant Stevenson, Ross Weidman, and José Zavala. These students are graduate research assistants in their first and seconds years at Georgia Tech.

Project 064 Alternative Design Configurations to Meet Future Demand

Georgia Institute of Technology

Project Lead Investigator

Dimitri N. Mavris
Director, Aerospace Systems Design Laboratory
School of Aerospace Engineering
Georgia Institute of Technology
Mail Stop 0150
Atlanta, GA 30332-0150
404-894-1557
dimitri.mavris@ae.gatech.edu

Michelle Kirby
Chief, Civil Aviation Division
Aerospace Systems Design Laboratory
School of Aerospace Engineering
Georgia Institute of Technology
Mail Stop 0150
Atlanta, GA 30332-0150
404-385-2780
michelle.kirby@ae.gatech.edu

University Participants

Georgia Institute of Technology (Georgia Tech)

- P.I.s: Dr. Dimitri N. Mavris (P.I.) and Dr. Michelle Kirby (co-P.I.)
- FAA Award Number: 13-C-AJFE-GIT-062
- Period of Performance: June 5, 2020 to September 24, 2023
- Tasks:
    1. Improvement of Advanced Concept Aircraft (ACA) representation in the International Civil Aviation Organization (ICAO) Committee on Aviation Environmental Protection (CAEP) Modeling and Databases Group (MDG)/Forecasting and Economic Analysis Support Group (FESG) models
    2. Alternative design approaches to meet demand
    3. Improved environmental assessment methods
    4. Exploring physics-based boundaries of the possible

Project Funding Level

The FAA provided $500,000 in funding, and Georgia Tech has agreed to a total of $500,000 in matching funds. This total includes salaries for the project director, research engineers, and graduate research assistants, as well as funds for computing, financial, and administrative support, including meeting arrangements. The institute has also agreed to provide tuition remission for the students, paid from state funds.

Investigation Team

Faculty and Research Staff
Dr. Dimitri Mavris, Georgia Tech, Principal Investigator
Dr. Michelle Kirby, Georgia Tech, Co-Principal Investigator

Dr. Jon Gladin, Georgia Tech,Technical lead Task, 1, 2, and 4

Graduate Researchers
Mr. Jimmy Tang, Georgia Tech (Task 3)
Mr. Thomas Leroy, Georgia Tech (Task 3)
Mr. Kunal Bavikar, Student Researcher, Georgia Tech (Task 1 and 4)
Ms. Emmanuella Okonkwo, Student Researcher, Georgia Tech (Task 2)
Ms. Akshiti Parashar, Student Researcher, Georgia Tech (Task 2)

Project Overview

The purpose of this ASCENT project is to improve upon the modeling approach used in the first 2 years of research and to provide insights or recommendations to the MDG regarding a more realistic approach to modeling ACA at the fleet level. In addition, the project will address alternative means of designing aircraft beyond the usual adoption of technologies with the payload and range capability of the existing fleet.

Task 1 - Improvement of ACA Representation in MDG/FESG Models

Georgia Institute of Technology

Objective

The traditional approach to modeling future aircraft types in the fleet has been to define a proxy aircraft that the new aircraft entering the fleet will replace, then establish a change in benefit. Although this process worked for evolutionary aircraft of the past, it does not work for ACAs, which may have markedly different performance behavior from that of conventional aircraft, such as different cruise altitudes and speeds, or different range capabilities for the same seat class. To model an ACA within the MDG modeling tools, manufacturers would need to provide the necessary performance, emissions, and noise coefficients defined by SAE AIR 1845 and the Base Aircraft Data (BADAv3). Prior research in this area, specifically for a blended wing body, has shown limitations in the accuracy of these tools in capturing the expected performance. The objective of Task 1 is to investigate potential opportunities for improving how ACAs are modeled within the fleet to benefit current analyses and probable future analyses.

Within Environmental Design Space (EDS), algorithms exist to create the necessary performance, emissions, and noise coefficients needed by MDG's modeling tools. Although the coefficients can be determined, how the ACA actually flies within MDG tools may not be correct, and modifications to the framework may be required. This task will investigate the shortcomings of the MDG tools for ACAs and provide recommendations to the model developers regarding means of improvement or new methods that must be developed.

Research Approach

Step 1
Identify the most likely ACA to enter the fleet in the future. This task includes the identification of the potential airframe, propulsion, energy sources, and operational improvements possible for the different seat-class aircraft over time. This step will heavily leverage work performed in years 1 and 2 in identifying relevant technologies for future vehicles but will now focus on ACAs. These technologies and concepts may include but are not limited to, blended wing bodies, truss-braced wings (TBWs), boundary layer ingestion, hybrid-electric propulsion, drop-in and non-drop-in fuels, supersonic aircraft, and cruise speed reductions.

Step 2
After the ACA is determined, develop a quantitative model within the EDS modeling framework developed by the Georgia Tech Aerospace Systems Design Laboratory

Step 3
Create the necessary performance, emissions, and noise coefficients needed by MDG's modeling tools with EDS by using the calibrated ACA model from step 2 to generate Aviation Environmental Design Tool (AEDT) coefficients and obtain noise contours.

Step 4
Analyze the results from EDS outputs; determine whether gaps exist for modeling ACA within the fleet modeling tools of MDG; and suggest potential opportunities to improve how ACA is modeled within the fleet, to benefit current analyses, as well as probable future analyses.

Milestones

- Step 1 has been completed. A TBW was selected because substantial research funds have been spent by the U.S. government to develop the theoretical and practical model of the TBW and Transonic TBW (TTBW) aircraft. For the purposes of this task, the TBW is relevant, because it is a highly efficient "new" airframe, and it has several differences in terms of mission profile with respect to a traditional tube and wing design (typically higher altitude). Although it does not use non-traditional fuel sources by definition (though it could), its configuration remains substantially different from that of the conventional tube and wing aircraft.
- Step 2 has been completed. A TBW aircraft was modeled and calibrated to match the geometry, weight, and performance of the configuration presented in the Subsonic Ultra Green Aircraft Research (SUGAR) phase 2 study by Boeing. This aircraft was selected because this TBW is expected to be deployed by the year 2035. In the process of calibrating the TBW aircraft in EDS geometric parameters, engine parameters, weight distribution, mission profile, aerodynamic parameters, and performance parameters from the SUGAR report were used as references. The following table shows the comparison between the outputs obtained from EDS and the Boeing SUGAR report.

Table 1. A comparison between outputs obtained from EDS and Boeing SUGAR report

Geometric parameters	Parameter	Units	EDS Output	SUGAR report data
Wing	Area	ft.^2	1477.1	1477.11
	Aspect Ratio		19.55	19.552
	Span	in.	2039.16	2039.301
	Taper Ratio		0.35	0.346
	Sweep 25%	deg.	12.52	12.52
Vertical Tail	Area	ft.^2	297.67	297.69
	Aspect Ratio		1	1
	Span	in.	207.043	207.043
	Taper Ratio		1	1
	Sweep 25%	deg.	41	41
Horizontal Tail	Area	ft.^2	296.25	296.24
	Aspect Ratio		5	5
	Span	in.	461.8363.	461.8363.
	Taper Ratio		0.35	0.35
	Sweep 25%	deg.	20.63	20.63
Fuselage	Width	ft.	13.88	13.875
	Depth	ft.	12.39	12.391
	Passenger Compartment length	ft.	86.54	86.541

	Units	EDS ouptput	SUGAR report data
OPERATIONAL EMPTY WEIGHT	lb.	87273	87300
Mission Fuel	lb.	31897	31900
TAKEOFF GROSS WEIGHT	lb.	149970	150000
DESIGN MISSION RANGE	Miles	4260	4260
CRUISE MACH		0.7	0.7
CRUISE L/D		25.017	25.25

- Step 3 is in process, Input files were generated to be used for AEDT environment using calibrated TBW aircraft from EDS. This was followed by modeling the TBW in AEDT and analyzing the results. A320 neo aircraft was used as reference aircraft to compare the TBW results in the AEDT framework. The results didn't quite make sense as compared to the truth model in EDS and expected trends observed from reference aircraft, so further analysis and EDS model refinement is being done currently to yield improved input files for AEDT
- Step 4 will follow in the near future.

Major Accomplishments

- Gained an improved understanding of the impact of TBW aircraft as a potential alternative design by the aircraft manufacturers
- Calibrated an EDS model of TBW aircraft (Boeing SUGAR), which can be used to understand the emissions for various mission ranges

Publications

None.

Outreach Efforts

ASCENT biannual meetings.

Awards

None.

Student Involvement

Kunal Bavikar participated in the efforts of Task 1.

Plans for Next Period

-
- Refine and improve the calibrated model to generate stable AEDT coefficients for AEDT modeling.
- Perform analysis to determine whether gaps exist for modeling ACAs within fleet modeling tools.

Task 2 - Alternative Design Approaches to Meet Demand

Georgia Institute of Technology

Objective

The objective of Task 2 is to determine the efficiency opportunity if the fleet operates with single-aisle aircraft with a design range closer to that actually flown on a day-to-day basis. That is, how would the aircraft design change if a single-aisle aircraft were sized to be optimal to fly within a continent (1,000–2,000 NM range) and at a slower Mach number (0.72 for example). To meet the longer-range requirements, a separate single-aisle design could be used for any longer ranges (closer to current single-aisle designs). Shorter ranges and lower aircraft speed requirements open the technology space to the consideration of alternative means of propulsion systems beyond the traditional turbofan engines running on conventional jet fuel. This task will use EDS to redesign a single-aisle aircraft to meet the market demand and establish a notional entry-into-service schedule for the fleet, and will determine the market-share split within the seat class for how the market share would grow with time. The outcomes will serve as the basis for the MDG fleet modeling tools to quantify the benefit at the fleet level. This task will exercise the connection with MDG tools and perhaps improve current modeling practices for goal setting or stringency analysis.

The outcomes of this task are anticipated to include quantification at the vehicle level of the benefits and interdependencies of designing an aircraft to a new paradigm, and the implications of that approach in the fleet-level environmental footprint of aviation. Applications of this task includes establishing realistic production rates for future designs, modifications to the assumed manufacturing production rates based on historical trends, changes in the market-share assumptions within a seat class or competition bin, or the non-recurring costs of developing a new aircraft (in lieu of modifying an existing product).

Research Approach

The approach for this research is to conduct the analysis as closely to the original long-term aspirational goals (LTAG) study as possible, while including the alternative approaches to meet demand in the design space. The LTAG methods include the steps shown in Figure 1.

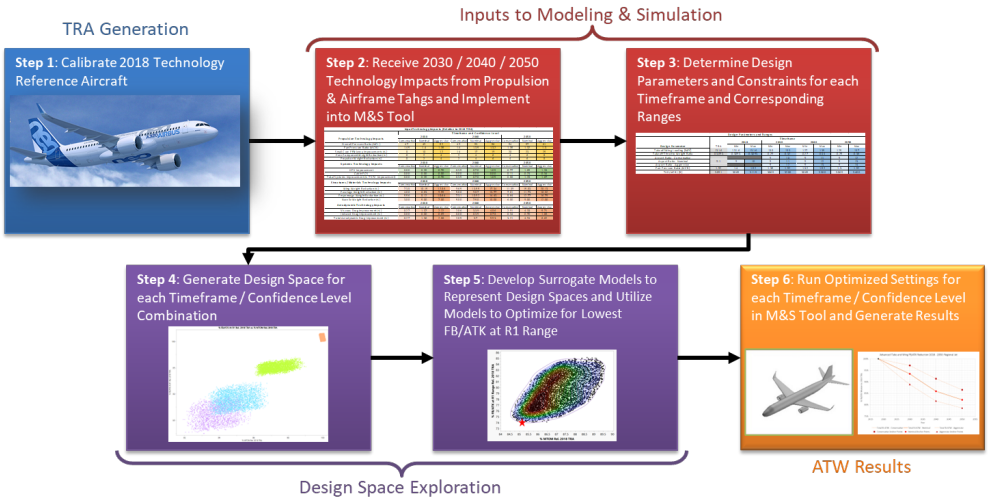

Figure 1. LTAG advanced tube and wing assessment methods.

This work is needed to adapt the methods to include alternative methods to meet demand. The test case for this work will be the narrow-body aircraft (other aircraft classes will not be assessed). The modifications to each step of the approach are as follows:

Step 1
The calibrated "2018" aircraft will continue to be the A320neo with PW1127G-JM engines. An updated version of this model will be used, which improves upon the version used in the LTAG report. However, the overall aircraft requirements, parameters, geometry, and so on will be similar. The updates made to the model are primarily to include calibration of aircraft noise, which was not considered in the LTAG study.

Step 2
The technology parameters will be kept the same for each of the unique entry into service dates (2018 and 2035). However, only moderate confidence will be considered in this case. This will reduce the number of aircraft selections that must be conducted and will help determine the difference in outputs obtained for the alternative approaches being applied for the 2035 aircraft. Furthermore, this approach will be sufficient because the final fleet-level analyses and conclusions of the LTAG were based on the moderate-confidence technology projections.

Step 3:
The design parameters for the LTAG study will be separated into fixed parameters and design variables. The fixed parameter set will be updated as follows:

- The technology impact vehicle-level results have the following design parameters fixed for technology infused vehicles:
  - Design payload and
  - Field length requirements.
- Additionally, we have:
  - Design range,
  - Design cruise Mach number,
  - Sweep, and
  - Average thickness to chord ratio.

- The additional design parameters in the second list mentioned above are proposed to be moved to the design variable category, with the exception of range.
- The range will be varied from a shorter range to the 2018 TRA design range (3360 nmi) in discrete intervals (we propose 1,360, 2,360, and 3360 nmi).
- The EDS tool will size the vehicle to maintain each payload/range capability for every point run through the simulation.
  - As the vehicle becomes lighter, the wing area and thrust required will decrease.
- Therefore, three optimizations will be performed: one time frame (2035) × one technology level × three ranges.
- An alternative approach could simply include the design range in the optimization process/clouds. Both methods can be tested with the same data set.
- Because the vehicle is evaluated at the R1 range, the R1 range will be determined by running each vehicle at constant MTOW.

To optimize the Mach number of the airplane, the wing design variables must be included in the optimization study. Initial studies have indicated that only a very minor benefit is provided by reducing the Mach number if the wing planform is fixed. Modifications to wing sweep and thickness can bring more substantial fuel burn reductions. The design variables and constraint matrix are updated as indicated in Table 2.

The design parameter ranges determined for LTAG (marked in black text) are kept consistent with those in the LTAG study. The parameters marked in red are new design parameters that are required to optimize the aircraft for a reduced Mach number.

The constraints on the engine and aircraft design are also listed below. The values in black are kept constant for the narrow body, whereas the values in red are new constraints. Because the wing design is being substantially changed in planform, sufficient fuel capacity available for storage must be ensured, to limit substantial reductions in wing sizes that would not allow the aircraft to fly at the chosen appropriate range. As the range of the aircraft is reduced, this constraint will become less active, and the design space should open up.

Table 2. LTAG advanced tube and wing assessment methods.

Design parameters and ranges			
Design parameter	**Timeframe**		
	TRA	**2035**	
		Minimum	Maximum
Takeoff wing loading (lb/ft^2)	131.6	100	140
Takeoff thrust/weight ratio	0.3093	0.28	0.38
Aspect ratio	10.95	9	11
Fan pressure ratio (Max Cruise)	1.52	1.35	1.52
T40 (Turbine Entry Temperature, deg Rankine)	3,091	3,065	3,200
Sweep	23.84	20	27
Thickness-to-chord	47.72	42	65
Cruise Mach	0.78	0.70001	0.79998

Constraints					
Constraint Parameter	Timeframe				
	2018 TRA	2018 Opt	2030	2040	2050
T3max Limit [R]	1649	1649	1800	1836	1872
Gate Constraint [ft]	110.6	118.1	118.1	118.1	118.1
Fan Diameter Constraint [ft]	6.2	6.8	6.8	6.8	6.8
Fuel Capacity [gal]	> Req.	> Req.	> Req.	> Req.	> Req.

Steps 4, 5, and 6
The process of generating data and surrogate models and applying constraints to select designs will be the same as that used during the LTAG project. The only difference is that several selection processes will need to be made for each discrete design range chosen. For each design range, four technology levels will be selected to be optimized for three design ranges selected, thus leading to 12 total optimizations performed. The objective function to be optimized in the design selection process will be, as in LTAG, a weighting of MTOW and fuel burn per available tonne kilometer (FB/ATK) at the R1 range.

Milestones

- Step 1 has been completed. The baseline 2018 calibrated model has been set for this work.
- Steps 2 and 3 have been completed. The technology parameters, design parameters, fixed parameters, and constraints have been selected to accommodate the new approaches for meeting LTAG demand.
- Step 4 is in process, and data are currently being generated for the maximum-range case.
- Steps 5 and 6 will be worked upon in the next few months.

Major Accomplishments

- The new aircraft design selection processes and design alternatives have been added to the LTAG methods.
- A model has been prepared for data collection with new parameters added into the design space.

Publications

None.

Outreach Efforts

ASCENT biannual meetings.

Awards

None.

Student Involvement

This project involves two graduate students: Emmanuella Okonkwo and Akshiti Parashar.

Plans for Next Period

In the next reporting period, this task will be completed according to the approach outlined in the approach section.

Task 3 - Improved Environmental Assessment Methods

Georgia Institute of Technology

Objective

In the first 2 years of research, MDG modeling tools were used to assess only a few future fleet scenarios, which included Advanced Tube and Wing (ATWs) and Advanced Concept Aircraft (ACA) entering the fleet. Only a small number of scenarios were considered, on the basis of the setup and execution time of the modeling tools and the human resources required to

execute them, thus representing only a subset of possibilities of how the fleet might evolve in the future. Many simplifying assumptions were also made in the modeling, such as unconstrained growth at airports. This task will investigate opportunities for how the fleet-wide modeling tools and assumptions could be sped up and improved to quantify more scenarios of the fleet evolution to provide a "what-if" capability to decision-makers. The anticipated outcomes are a set of recommendations to be provided to MDG and FESG.

Research Approach
The main approach for this task is to conduct a thorough review of the prior CAEP stringency and trend analysis assumptions used, and to evaluate the assumptions for areas of improvement, with the aim of either accelerating the analysis or simulating more real-world scenarios.

Milestones
The final milestone will be to document areas of improvement for the CAEP modeling approaches in the future.

Major Accomplishments
- Gathered an initial library of CAEP documentation back to CAEP/7
- Began reading the documentation
- Created an initial list of primary assumptions to be populated as each CAEP manuscript is read

Publications
None.

Outreach Efforts
ASCENT biannual meetings.

Awards
None.

Student Involvement
Jimmy Tang, Thomas Leroy participated in the efforts of Task 3.

Plans for Next Period
Continue reviewing prior CAEP documents, and recording assumptions and potential areas of improvement.

Task 4 - Exploring Physics-based Boundaries of the Possible
Georgia Institute of Technology

Objective
The objective of this task will be to examine the physics-based limitations of efficiency for various propulsion architectures considered for future ACA. This type of study is beneficial in that it aids the FAA in understanding the boundaries of the possible, rather than building from a baseline by applying specific individual technologies that benefit efficiency. Depending on any follow-on actions from the LTAG task group analyses, this task may also include the identification of barriers for ACA and their propulsion systems, or additional supporting analysis.

Research Approach
Step 1:
Establish a reference aircraft and corresponding engine to use as the benchmark for the task. Calibrate the selected engine in EDS using appropriate documents.

Step 2:
Conduct a literature review on the current engine design and Advancements in engine component technologies.

Step 3:
Conduct a literature review on the physical limitations in the performance of the current engine component design and use Numerical Propulsion System Simulation (NPSS) to incorporate technologies and assumptions and perform component and cyclic efficiency analysis. This step includes the following:

- Investigate the current efficiency level and predicted efficiency level for the future
- Obtain the current values for cyclic analysis of components of turbofan engine
- Investigate the predicted maximum values of cyclic parameters for the core of the engine
- Calibrate the engine to match the underlying assumptions and incorporated technologies

Step 4:
Use the calibrated base aircraft engine and apply future technology scenarios to obtain a new model to be used for applying idealized engine parameters and assumptions to obtain a futuristic idealized engine

Milestones

- Step 1 has been completed and Airbus A320 neo aircraft was selected as the baseline aircraft and it was calibrated in EDS.

- Step 2 has been completed. "ICAO -LTAG – Appendix M3 – Technology sub-group" report and "Independent expert integrated technology goals assessment and review for engines and aircraft" report were used to obtain the predicted 2050 narrow-body turbofan engine using Airbus A-320 neo as reference aircraft. This step included the study of the following aspects of engine design:
  - Ceramic matrix composite advancements and understanding the future operating temperatures
  - Advancements in turbine cooling flow
  - Clearance sensitivity for small core compressors
  - Advancements in alloys to support higher operating temperature

- Step 3 has been completed. The following assumptions based on available literature were used for cycle analysis:
  - The turbine is assumed to be made of Ceramic Matrix Composite (CMC) in order to decrease the required cooling
  - Maximum polytropic efficiency of the fan and compressor as 95%
  - Maximum polytropic efficiency of the turbine using cooling as 92%
  - Predicted future operating CMC-based turbine temperature as 1200 Celsius.

  In step 3 to understand and predict the physics-based limitation of the turbofan engine, the cycle parameters were matched to LTAG 2050 low-confidence engine cycle parameters
  - OPR – 61
  - FPR - 1.457
  - T4 max – 3413 R

  The size effects of a small core were considered and the associated penalty on compressor polytropic efficiency due to small core size was incorporated.

- Step 4 is in progress

Major Accomplishments

- Improved understanding regarding the boundaries of the possible individual technologies to benefit engine efficiency.
- Obtained upper bound of polytropic efficiency, cycle parameters, and working temperatures of various key engine components
- Created a stable baseline engine and a stable engine with 2050 timeframe technology parameters

Publications

None

Outreach Efforts

ASCENT biannual meetings.

Awards
None.

Student Involvement
Kunal Bavikar participated in the efforts of Task 4.

Plans for Next Period
- Use EDS Calibrated A320 neo aircraft as a base model and apply 2050 LTAG low-confidence engine technologies to obtain a new model
- Use the new model to apply idealized engine parameters and assumptions to obtain a new version of the A320 neo using an idealized engine based on the 2050 timeframe
- Conduct sensitivity studies based on prior subtasks within EDS

Project 065(A) Fuel Testing Approaches for Rapid Jet Fuel Prescreening

University of Dayton*

*The project will continue at Washington State University under the direction of Joshua Heyne (Joshua.heyne@wsu.edu).

Project Lead Investigator

Joshua Heyne
Associate Professor
Mechanical Engineering
University of Dayton
300 College Park, Dayton, OH 45458
937 229-5319
Jheyne1@udayton.edu

University Participants

University of Dayton

- P.I.: Joshua Heyne
- FAA Award Number: 13-C-AJFE-UD, Amendments 26, 31, 34 and 42
- Period of Performance: June 5, 2020 to September 30, 2022
- Tasks:
  1. Prescreen sustainable aviation fuels (SAFs).
  2. Develop novel testing methods for the evaluation of SAF candidates.

Project Funding Level

Amendment No. 026: $159,998 (June 5, 2020 to June 4, 2021)
Amendment No. 031: $250,000 (August 11, 2020 to August 10, 2021)
Amendment No. 034: No cost extension (August 10, 2021 to February 10, 2022)
Amendment No. 042: $195,000 (June 14, 2022 to June 13, 2023)
Cost share is from the University of Dayton, VUV Analytics, Greenfield Global, and DLR Germany.

Investigation Team

- Joshua Heyne (University of Dayton) is the P.I., coordinating all team members (both ASCENT and non-ASCENT efforts) and communicating prescreening results with SAF producers.
- Linda Shafer (University of Dayton Research Institute) is a senior research engineer responsible for two-dimensional gas chromatography (GCxGC) measurements of SAFs.
- David Bell (University of Dayton) is a Ph.D. student developing GCxGC vacuum ultraviolet (VUV) detection methods and software.
- John Feldhausen (University of Dayton) is an M.S. student developing GCxGC-VUV methods and software.
- Zhibin (Harrison) Yang (University of Dayton) is a Ph.D. student conducting Tier Alpha prediction and Tier Beta measurements.

Project Overview

This project focuses on further developing the Tier Alpha and Beta test methods, which can help minimize the fuel volume needed for testing and improve a fuel's potential for meeting ASTM approval criteria. Tier Alpha refers to low-volume analytical testing approaches (i.e., GCxGC, nuclear magnetic resonance, and infrared analytical testing). Tier Beta tests focus on directly assessing the physical and chemical properties of a fuel rather than predicting them from GCxGC methods.

Task 1 - Prescreening of Sustainable Aviation Fuels

University of Dayton

Objective

The objective of this task is to develop a tiered prescreening process for new alternative jet fuels that uses low fuel volumes and will improve a fuel's potential to meet ASTM approval criteria. This work facilitates the flow of meaningful information to fuel producers when their production processes are at a low technology readiness level while simultaneously strengthening a producer's readiness for the approval process.

Research Approach

Previous annual reports summarized significant progress toward prescreening SAF candidates. The motivation, conceptual application, detailed description, and examples of this effort were described in publications in peer-reviewed journals in the first 18 months of this project. This report documents four additional peer-reviewed journal articles, published between September 30, 2021 and October 1, 2022. Citations for the articles are listed in the *Publications* section below and are provided as Appendices 1-4:

- Paper 5-. Threshold Sooting Index of Sustainable Aviation Fuel Candidates from Composition Input Alone: Progress Toward Uncertainty Quantification
- Paper 6- Synthetic aromatic kerosene property prediction improvements with isomer specific characterization via GCxGC and vacuum ultraviolet spectroscopy
- Paper 7- Blend Prediction Model for Freeze Point of Jet Fuel Range Hydrocarbons
- Paper 8- A Dataset Comparison Method Using Noise Statistics Applied to VUV Spectrum Match Determinations

In addition to these articles, the team is currently working on documenting efforts completed between June 1, 2020 and August 30, 2022, which has advanced toward our goal of estimating the impact of fuel composition on elastomer/fuel compatibility.

Milestones

- Tier Alpha was performed a total of 99 times.
- Tier Beta was performed a total of 81 times.
- The maximum blending ratio was determined for 32 SAF candidates.
- A refinement strategy was developed for six fully synthetic SAF candidates.

Major Accomplishments

- Determined specific isomer composition down to 0.2% by mass in samples containing less than 5 µL of fuel
- Developed a numerical analysis methodology to conclusively determine whether a chromatogram peak contains more than one analyte
- Developed means to reliably estimate the sooting propensity of candidate fuels
- Developed and validated means to predict the freeze point of mixtures from first principles

Publications

Peer-reviewed Publications

Bell, D. C., Boehm, R. C., Feldhausen, J., & Heyne, J. S. (2022). A data set comparison method using noise statistics applied to vuv spectrum match determinations. *Analytical Chemistry*, *94*(43), 14861–14868. https://doi.org/10.1021/acs.analchem.2c01931

Boehm, R. C., Coburn, A. A., Yang, Z., Wanstall, C. T., & Heyne, J. S. (2022). Blend prediction model for the freeze point of jet fuel range hydrocarbons. *Energy & Fuels*, *36*(19), 12046–12053. https://doi.org/10.1021/acs.energyfuels.2c02063

Feldhausen, J., Bell, D. C., Yang, Z., Faulhaber, C., Boehm, R., & Heyne, J. (2022). Synthetic aromatic kerosene property prediction improvements with isomer specific characterization via GCxGC and vacuum ultraviolet spectroscopy. *Fuel*, *326*, 125002. https://doi.org/10.1016/j.fuel.2022.125002

Boehm, R. C., Yang, Z., & Heyne, J. S. (2022). Threshold sooting index of sustainable aviation fuel candidates from composition input alone: Progress toward uncertainty quantification. *Energy & Fuels*, *36*(4), 1916–1928. https://doi.org/10.1021/acs.energyfuels.1c03794

Boehm, R. C., Yang, Z., Bell, D. C., Feldhausen, J., & Heyne, J. S. (2022). Lower heating value of jet fuel from hydrocarbon class concentration data and thermo-chemical reference data: An uncertainty quantification. *Fuel*, *311*, 122542. https://doi.org/10.1016/j.fuel.2021.122542

Heyne, J., Bell, D., Feldhausen, J., Yang, Z., & Boehm, R. (2022). Towards fuel composition and properties from Two-dimensional gas chromatography with flame ionization and vacuum ultraviolet spectroscopy. *Fuel*, *312*, 122709. https://doi.org/10.1016/j.fuel.2021.122709

Huq, N. A., Hafenstine, G. R., Huo, X., Nguyen, H., Tifft, S. M., Conklin, D. R., Stück, D., Stunkel, J., Yang, Z., Heyne, J. S., Wiatrowski, M. R., Zhang, Y., Tao, L., Zhu, J., McEnally, C. S., Christensen, E. D., Hays, C., Van Allsburg, K. M., Unocic, K. A., … Vardon, D. R. (2021). Toward net-zero sustainable aviation fuel with wet waste-derived volatile fatty acids. *Proceedings of the National Academy of Sciences*, *118*(13), e2023008118. https://doi.org/10.1073/pnas.2023008118

Outreach Efforts

Conference presentation

American Chemical Society Fall 2021 National Meeting & Exposition in San Diego, CA

Awards

Shane Kosir

- Washington State University/Pacific Northwest National Laboratory Distinguished Graduate Research Program Recipient

Joshua Heyne

- 2022 Achievement & Leadership Award, Commercial Aviation Alternative Fuels Initiative
- 2021 Net Good Summit on sustainable travel, honored guest
- 2021 U.S. Frontiers of Engineering Symposium, National Academies of Engineering, selected participant
- 2021 Vision Award for Excellence in Scholarship, School of Engineering, University of Dayton

Student Involvement

David Bell, Ph.D. student, leads this effort.
John Feldhausen, M.S. student, participates in this effort.
Zhibin (Harrison) Yang, Ph.D. student, participates in this effort.
Shane Kosir, M.S. graduate (2021), participated in this effort.
Steven Ivec, M.S. student, participated in this effort.
Christopher Borland, M.S. student, participated in this effort.
Aaron Spelies, undergraduate student, participated in this effort.
Allison Coburn, undergraduate student, participated in this effort.
Conor Faulhaber, undergraduate student, participated in this effort.

Plans for Next Period

Finalize the publications in progress, improve Tier Alpha prediction accuracy, test dielectric constant values for various fuels, and reduce the volume required for Tier Beta measurement.

This project will continue at Washington State University with P.I. Joshua S. Heyne (Joshua.heyne@wsu.edu).

Appendix 1

Threshold Sooting Index of Sustainable Aviation Fuel Candidates from Composition Input Alone: Progress Toward Uncertainty Quantification

Paper 5: Threshold Sooting Index of Sustainable Aviation Fuel Candidates from Composition Input Alone: Progress Toward Uncertainty Quantification

1. Introduction

The aviation industry is in the process of reducing its carbon footprint. To date, six processes that convert a specified biological feedstock into a jet fuel blend stock have been incorporated into the standard specification for aviation turbine fuel containing synthesized hydrocarbons, ASTM D7566-21 [1]. In each case, the synthetic component is to be blended up to some ratio (10 to 50%) with petroleum-derived fuel to create a so-called, drop-in fuel. A drop-in fuel is one that behaves like 100% petroleum fuel within the detectability limits of the normal delivery and consumption processes that exist within the industry. For example, if an arbitrary hydrocarbon mixture were to absorb certain chemical species that have already been absorbed by certain polymeric materials (e.g. O-rings) that exist within the fuel system of an aircraft, those species could be depleted from the polymeric material, causing it to shrink and a corresponding joint that should be sealed by that polymeric material could spring a leak. That would not be acceptable, so there is a requirement for ASTM D7566 fuels to contain at least eight percent aromatics since aromatics have been identified as the class of hydrocarbons that is most involved with fuel / polymer material compatibility [2].

Aside from their relatively low hydrogen-to-carbon ratio, which may offer a small energy efficiency benefit as heat is converted to mechanical energy via compressed gas expansion through a turbine [3], the seal compatibility issue is the only one driving aromatics into fuel. As non-aromatic molecules are discovered to emulate aromatic/elastomer compatibility, such as dimethylcyclooctane perhaps, it is important to assess their impact (good or bad) on other fit-for-purpose properties [4], include smoking propensity which is added to tier a [5] by this work. Typically, aromatics have an adverse impact on aircraft energy efficiency arising from their low energy density [6] and from a combustion perspective, aromatics are believed to correlate with decreased thermal stability [7] and higher smoking propensity [8] and particulate emissions [9], while particulate emissions are believed to correlate with contrails, which may collectively have a larger impact on radiative forcing than CO2 emissions from aircraft [10]. Moreover, not all aromatics have the same impact on smoke [11,12], thermal stability, or seal swell. Similarly, not all alkanes have the same impact on smoke [13], and it follows that different fuels would have a different smoking propensity. The first revision of the standard test method for smoke point of kerosene and aviation turbine fuel, ASTM D1322 [14] was published in 1954, as it was recognized that control of this combustion-related fuel property was necessary.

Full details of ASTM D1322 are published in the standard [14], and an overview of it is provided in the experimental methods section of this paper, but for now it is important to understand some logistics. To get a single datapoint requires ~20 minutes of labor to properly prepare the lamp and take the reading. Additionally, labor time is required to get repeat points, acquire samples, manage the inventory of samples, etc. For the sake of discussion, let's say each datapoint costs two hours of labor in total. If the database contains one million hydrocarbon mixtures for which data is desired, which is the case for pre-screening of candidate high-performance fuels, the cost to acquire that data would be two million hours. To get that done in one year would require one thousand full-time employees and ~500 lamps. These are staggering numbers. Even if we used a model to reduce the number of desired datapoints from one million to one thousand, it would still require a full labor-year to get that data. It is desired therefore to use models to predict the smoke point (the result of the ASTM D1322 test) of any mixture of possible fuel constituents and to predict the smoke point of all the constituents for which data is not already available. Moreover, it is important to understand the accuracy of these models.

A method to predict the sooting tendency of mixtures based on the sooting tendencies of its constituents was introduced by Gill and Olson [15] in 1984 and has since been validated by Yan et al. [16] and Mensch et al. [17]. Their method leverages the threshold sooting index (TSI) which was introduced by Calcote and Manos [12] a year earlier as a tool to normalize smoke point data from different experiments. Equations 1 and 2 depict the blending rule and sooting index, respectively.

$$TSI_{mix} = \sum_i x_i * TSI_i \quad (1)$$

$$TSI = a + b * \left(\frac{Mw}{Sp}\right) \quad (2)$$

In these equations, x_i is the mole fraction of the ith component and TSI_i is its threshold sooting index. The determined coefficients, 'a' and 'b' are device and operator dependent, Sp is the measured smoke point, and Mw is the molecular weight of the sample molecule or mixture. While it is unclear whether Equation 2 truly puts data from different experiments into a common basis, at minimum the definition needs two anchor points to derive the device and operator dependent coefficients,

'a' and 'b'. We do not agree with Li and Sunderland [18], who argued that the dependence on molecular weight is non-physical and their approach to normalize smoke point data would be better than TSI. Additional discussion around establishing a best practice for deriving these coefficients will be presented later in this report.

Generally, the blending rule, Equation 1, can produce inaccurate predictions in two ways. The TSI corresponding to any or all the components could be inaccurate, or the neglect of potential synergistic effects could be significant relative to component uncertainty. An example of a potential synergistic effect would be compounds that produce an unusual concentration of radicals that accelerate or hinder the kinetics of combustion. Somewhat different, preferential wicking rates could alter the vapor-phase mole fractions relative to the liquid-phase mole fractions in any experiment that employs a wick, and preferential evaporation could alter this relationship in diffusion flames whether or not a wick is involved. In Figure 1, imagined data are plotted to illustrate how each of these error types influence the uncertainty in TSI_{mix} as a function of mole fraction. The example of preferential wicking or evaporation leading to a 5% off-set between the liquid and vapor phase mole fractions leads to a TSI verses mole fraction curve that is indistinguishable, without additional information, from the example of an error in the TSI of the component that is more prone to smoking. In each case, less error would result from the blending rule if the x=0 and x=1 intercepts of the best fit line through all the data were used to establish a virtual TSI of each pure component and that virtual TSI were used in the blending rule instead of the measured TSI of the pure component [19,20]. However, that approach could lead to several different virtual TSI for each molecule depending on what other molecule(s) it is mixed with. The concept of virtual TSI is not without merit, but if it is used, the virtual TSI should be derived from a global regression of a variety of mixtures and this point will be addressed more thoroughly in the methods section of this report.

In our opinion, the primary issue with Equation 1 is not with its neglect of potential differences between vapor and liquid phase mole fraction or possibly synergistic combustion kinetics [21,22], but rather with the dearth of benchmark quality data for pure components, whether directly measured or derived from regression of mixtures (virtual). To date, twelve datasets [8,13,29,30,15,17,23–28] have been published representing a total of 112 hydrocarbons. Some of these hydrocarbons are not liquids at standard temperature and pressure, some have wicking rates that are lower than their fuel consumption rate, and some are alkenes or alkynes, which are of little interest to us. Thirty-nine molecules with trusted smoke point data are saturated hydrocarbons, and twenty-six are alkylated aromatics. Of these sixty-five data points, fifty-nine can be stitched together by using TSI, Equation 3 as a tool to normalize data from three different datasets [13,17,25] into a common basis. Just twenty-five of these molecules are included within our internal database of 1,128 molecules that are to be considered as blend stock for sustainable aviation fuel. Existing data therefore represents 2.2% (25/1128) of desired data and if we include all the available, relevant data then 5% (59/1162) of the combined database could potentially serve as training data to predict the remaining 95%.

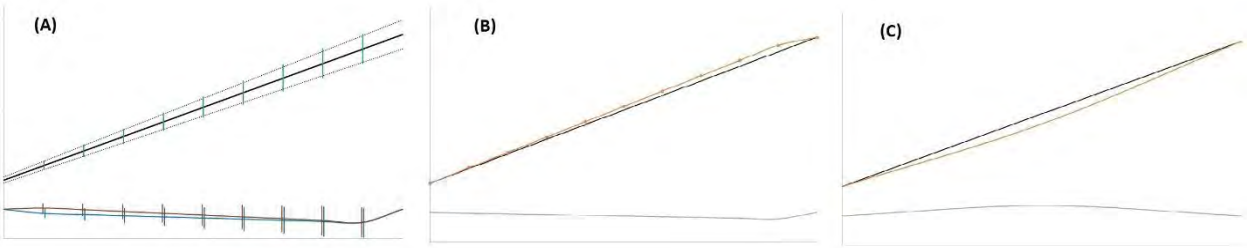

Figure 1. TSI Blending Rule Error - Shape Factors for Binary Mixtures. The horizontal axis is the liquid-phase mole fraction of component A, scale 0 to 1. The vertical axis is the threshold sooting index, scale -10 to 70. The upper curves are the TSI of the mixture, where the black line is the blending rule prediction and the the other curves represent the what actual data would look like given certain sources of error. (A) The random error at either end point is ±1 or ±5 TSI. (B) The gas phase mole fraction of component A is 5% higher than its liquid-phase mole fraction. (C) Species created through combustion of component B facilitate the combustion of soot precursors created through combustion of component A, an imagined 10% benefit for a 50/50 blend. The lower curves are the difference between the two upper curves. The vertical bars in (A) represent random error at each point.

$$100 = a * \left(\frac{142.201}{Sp(1MN)}\right) + b \quad \text{and} \quad 5 = a * \left(\frac{98.189}{Sp(MCH)}\right) + b \qquad (3)$$

Yan et al. [16] used quantitative structure-property relationships (QSPR) employing structural fragment contributions to create models [31] to estimate TSI. They executed a curve fit three times, employing a somewhat different set of dependent variables (the structural fragments) each time. They named these three sets the Joback method, modified Joback method, and SOL method. Each method employed a 5thorder polynomial (-1 to 4) to relate the TSI to a single independent variable, which was the sum of the contributions from the structural fragments. A finite segment of each polynomial was monotonic over the range of molecules used to train the model. However, for each method, the predicted TSI declines sharply as the dependent variable increases to values higher than the maximum afforded by the training set. For example, the predicted TSI of 1,3,5-tri-tert-butylbenzene is negative 31.3 while the predicted TSI of [1,4-dimethyl-1-(3-methylbutyl)pentyl]benzene is 95.8, using the so-called Jobak method. Even within the range of the correlated data, the three methods did not show qualitative agreement with each other. For example, the predicted TSI of 2,2,4,4,6,6,8-heptamethylnonane was 80.4 by the Jobak method and 14.6 by the modified Jobak method.

By delving into these issues further it was observed that the contributions from each molecular fragment, their relationships to each other, did not follow physical intuition. For example, the central carbon of neopentane should contribute more to TSI than the central carbon of isobutane, and the contribution from all fragments should be positive. In other words, it was obvious from the coefficients that the correlations were executed without logical constraints. By adding constraints onto the relationships between fragment contributions and eliminating the polynomial re-scaling, we have generated a new model to predict the TSI of arbitrary molecules that is considerably more versatile than those published by Yan [16].

Other groups have used a QSPR approach to predict [32,33] the threshold sooting index [12], yield sooting index [34], oxygen extended sooting index [32] or fuel equivalent sooting index [35]. Barrientos et al. [32] reported OESI activities for seven non-oxygenated carbon groups, three of which are related to this work. However, significant differences between their training/target datasets and our target database render those activities unsuitable for our application. Very recently, Lemaire et al. [33] reported unified index activities for twenty-nine un-oxidized carbon groups, eleven of which are relevant to this work. As that work was published after the technical aspects of this work were already complete, a comparison of the two approaches, supporting data and predictions will be made in the discussion section of this paper.

Within the experimental section of this report a basic description of the ASTM D1322 standard is provided and is followed by a discussion the additional controls (best practices) that are necessary to parlay this experiment, which was designed to inspect aviation fuel with a smoke point of 25 ± 3 mm [36], into a research tool. This is followed by a description of what has been done specifically in this work to bring three legacy datasets into a common basis with new data measured in our laboratory. The numerical methods section includes discussion around the pros and cons of using data from mixtures to help train a model to predict the TSI of molecules that will ultimately be used to help predict the TSI of different (and arbitrary) mixtures. This section also includes a detailed description of our QSPR model, the constraints that were employed for its development and justification for those constraints. The results section includes a comparison of model results with the data used to train it, as well as a check of model results against measured smoke points for two pure compounds, n-butylbenzene and dimethylcyclooctane, and one simple surrogate fuel with fully identified composition. Finally, a comparison is drawn between measured smoke points of seven complex hydrocarbon mixtures, including three conventional jet fuels, and our predicted smoke points for these mixtures. For these predictions the tier-a [5] methodology for estimating a representative property for an unknown mix of hydrocarbons with the same empirical formula was used to complement the model presented in this work. This model creates the database employed by the tier-a methodology.

2. Experimental Methods

The experimental apparatus and procedures used in this work and that of Mensch et al. are described thoroughly in ASTM D1322-19. The apparatus consists of a wick-fed lamp that can be purchased from any of a variety of suppliers (keyword search: “smoke point lamp”). A Koehler lamp was used for this work. The base of the lamp should be placed on a horizontal surface so its mounted candle section is vertical, and the flame it produces radiates vertically upward before a mounted ruler that is 5 cm in length. The flame is fully shielded on four sides. Twenty small (2.9 mm) intake holes regulate the flow of fresh air into the reaction zone and a cylindrical chimney (40 mm diameter) is positioned 5 cm above the top of the lamp to allow vitiated air to escape from the reaction zone. The fuel consumption rate is controlled by adjusting the length of wick that is exposed to air by raising or lowering the wick assembly through the candle body. The ASTM D1322 documentation also describes standardized procedures for wick preparation and defines the flame shape and tip position corresponding to the smoke point. Since 2012, revisions of the standard describe optional automation equipment, including a computer controller to adjust the length of exposed wick, and image processing software to determine the smoke point based on digitized images captured from a video camera that is mounted normal to the flame. The automation is reported to improve the reproducibility of the method by about a factor of four over the range of smoke points produced by the calibration fuels

identified in the standard. However most published smoke point data was collected prior to 2012, and the new data reported here was also collected as per the manual procedures.

While the first revision of ASTM D1322 was published in 1954, the Institution of Petroleum Technologists formed a "Standardization Sub-Committee on Tendency to Smoke" in 1931 [37]. Three years later Terry et al. [38] published details of an improved Factor lamp, which was the experimental apparatus used by Hunt [25] who published in 1953, the most extensive database of smoke point data to date. While there is a variety of small differences between this experiment and the current ASTM standard, the main features of the experiments are common and, in theory [12], their respective smoke point data, once converted to a common TSI scale should be comparable.

Olson et al. [13] had observed a local feature (a shoulder or dip) in plots of fuel consumption rate verses flame height showing up at heights corresponding to the measured smoke points, and they used this feature to define the smoke point in terms of fuel consumption rate to improve the repeatability of the measurements. The apparatus and procedures used for this experiment differ significantly from those described in ASTM D1322. Nonetheless, Olson showed good correlation (r^2 = 0.94) between their measured TSI's of 28 compounds and those reported by Calcote and Manos [12] who had compiled TSI data from 6 different sources, most extensively the data from Hunt [25].

For this work smoke points were measured for eight neat molecules, seven binary mixtures of varying composition, a six-component surrogate fuel, three conventional jet fuels and three complex mixtures under consideration as sustainable aviation fuel. While all our smoke point data is provided as supplementary material to this report, Table 1 provides a list of each molecule used, its purity and source. All measurements were taken numerous times, including at least one change of wick throughout the progression of repeat data points.

Table 1. Chemicals Used[†]

Name	Purity	Supplier
methylcyclohexane	99%	Sigma-Aldrich
1,3,5-trimethylbenene	>97%	TCI
iso-octane	>99%	Sigma-Aldrich
m-xylene	>99%	TCI
o-xylene	>98%	TCI
n-butylcyclohexane	99%	Alfa Aesar
n-octane	>99%	ACROS
toluene	99.5%	Fisher
cis-decalin	98%	TCI
1-methylnaphthalene	96%	Alfa Aesar
n-undecane	>99%	Sigma-Aldrich
hexylbenzene	98%	Alfa Aesar
iso-cetane	98%	Sigma-Aldrich
farnesane	>99%	Amyris
n-hexadecane	99%	Alfa Aesar
1,4-dimethylcyclooctane	98.5%	B.G. Harvey, NAWCWD

[†] Conventional and two of the potential sustainable jet fuel samples were provided by T. Edwards, AFRL. HEFA was provided by World Energy and SAK was provided by an anonymous supplier.

3. Numerical Methods

In previously published articles, the experiment constants labeled as 'a' and 'b' in Equation 1 have been recalculated to minimize the collective difference between ostensibly common data points between the authors' work, which is taken as the gold standard, and any previously published results to which there was value in comparing. While that is certainly one way to normalize data, it creates a different TSI units scale (analogous to Fahrenheit or Celsius temperature units scale) for every dataset and lacks any formal rigor to ensure that any of the experiments were in control i.e., properly calibrated. One step toward establishing a check on the process control is to define certain reference materials with defined TSI or smoke point values. Calcote and Manos [12] suggested pure hexane (TSI=2) and pure 1-methylnaphthalene (TSI=100) while Mensch et al. suggested pure methylcyclohexane (MCH, TSI=5) and pure 1-methylnaphthalene (1-MN, TSI=100) as reference materials, but neither imposed these constraints onto previously published datasets to which a comparison was made. Indeed, several of the earlier datasets did not include these proposed reference materials. The ASTM D1322 standard calls out iso-octane (Sp

= 42.8 mm) and six different blends of iso-octane with toluene as reference materials to be used for device calibration. While several of these reference fuels were included in this work and that of Mensch, the earlier works [13,25] included just pure iso-octane.

For inspection of aviation fuel, the iso-octane/toluene reference fuels are sufficient to establish control because they bracket the smoking propensity of any aviation fuel sample that is likely to be inspected by this method. If not, the fuel is so good or so bad that accuracy ceases to be necessary to determine whether the fuel passes inspection. However, for our purposes, many of the molecules of interest have smoke points below that of 60%v iso-octane blended with 40%v toluene, which is 14.7 mm, or above that of pure iso-octane (42.8 mm). For our purposes, additional reference materials are necessary to establish calibration throughout the entire range of smoke point or TSI values of interest. While we adopt without endorsement the convention of Mensch et al. [17] to define the TSI scale by setting its value for 1-methylnapthalene to 100 and its value for methylcyclohexane to 5, we suggest that the reference fuels of ASTM D1322 should also be used to establish control and, more importantly that another molecule or mixture with a TSI of ~60 should also be used. We suggest 1,3,5-trimethylbenzene. The advantage of MCH relative to hexane is that its flame is less susceptible to flickering noise at its smoke point because it is shorter but assigning it such a low TSI value, 5 leads to negative TSI for some normal-alkanes and lightly branched iso-alkanes, which could be confusing.

Figure 2 has been constructed to emphasize a motivation for introducing additional referee materials to establish experimental control. The filled circles shown in Figure 2 correspond to the measured data (this work) for 1-methylnaphthalene and methylcyclohexane which are connected by a solid black line. The dashed lines on either side of the solid black line correspond to plus or minus the quoted 95 percentile for smoke point repeatability, which is given by Equation 4 [14], where r is the repeatability and $\overline{Sp}$ is the average smoke point. At face value, this plot suggests that the TSI slope coefficient for our experiment could be anywhere from 2.60 to 4.95 and the intercept coefficient anywhere from -7.33 to -0.35, which is much higher than desired. Even if we are correct in our suspicion that Equation 4 is off by a factor of two, that level of uncertainty in smoke point measurement of 1-methylnaphthalene (1-MN) is still much higher than desired. Of course, one way to help reduce the repeatability uncertainty is to average over multiple readings (N) of the same experiment because the effective repeatability scales with the inverse square root of N, and we have taken ~10 repeat points for most of the data taken to support this project.

$$r = 0.0684 * (\overline{Sp} + 16) \qquad (4)$$

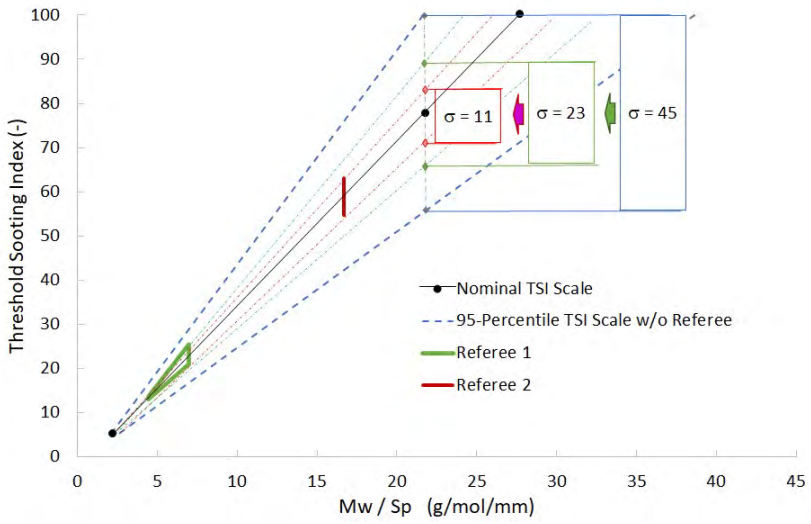

Figure 2. Impact of Reference Data Uncertainty on Experiment's TSI Scale Coefficients Nominal points are taken from this work. The horizontal line at the TSI = 100 was constructed from the nominal point and the 95-percentile repeatability quote from ASTM D1322-19.

Another way to drive sufficiently tight repeatability into the smoke point measurements of the scale-setting TSI anchor points (methylcyclohexane and especially 1-MN) is to establish TSI limits for referee fuels. The details within Figure 2 help to

illustrate how this helps. The blue, horizontal line at the top of the plot follows directly from the 95 percentile, confidence interval (Equation 4) for a single point measurement of the smoke point for 1-MN. The dashed, gray, vertical line at 22 on the horizontal axis illustrates how that random error in smoke point determination at the 1-MN anchor point is transferred into a large uncertainty (77.5 ± 22.5) in TSI for a fuel with a measured (Mw/Sp) of 22 g/mol/mm – which is within the range of data we might use to build a QSPR model. On top of that, the random error associated with smoke point measurement of the potential data point is ~ ±10 TSI. If we require the TSI of the first and fourth reference fuel blend of ASTM D1322 to be 23.2 ± 2.2 and 13.2 ± 0.3, respectively then the actual value of (Mw/Sp) of 1-MN must lie in-between the two green lines at TSI =100, and that reduces the transferred random error from the anchor point to the potential data point from ± 22.5 to ± 11.5. While the iso-octane/toluene reference fuels serve as convenient TSI referees because these data should exist for every test campaign, they do not force sufficient precision into the smoke point measurement of 1-MN. To tighten the precision further, we suggest using 1,3,5-trimethylbenzene (TSI = 58.9 ± 4.2) as a second referee. By doing that, the transferred uncertainty from the upper anchor point to the potential data point at TSI = 77.5 goes to ± 5.5. This is about half as large as the uncertainty that comes directly from the random error of smoke point measurement of the data point and contributes ± 1.2 out of the ± 11.2 overall (quadrature addition) uncertainty in the TSI of the data point, which is tolerable.

If the referee control standards are not met initially then additional repeat data points should be taken for the anchor fuels, or the referee fuels, or the apparatus correction factor should be adjusted. Before stitching any dataset into a master database of TSI values it should be put onto the same scale by adjusting its corresponding experiment TSI constants, 'a' and 'b' to satisfy Equation 3. Additionally, it should be confirmed that each of the referee criteria are met. The datasets from this work and that of Mensch meet these criteria and can be compared directly. To drive virtual compliance with these criteria for the datasets of Hunt [25] and Olson [13] a virtual data point for 1-MN was created by adjusting the reported smoke point within its repeatability window until the experiment TSI coefficients resulted in a TSI of 58.9 ± 4.2 for 1,3,5-trimethylbenzene. For the Hunt dataset the virtual smoke point of 1-MN was 4.43 mm and for the Olson dataset it was 4.60 mm, each compared to a reported smoke point of 5 mm. A summary of the recorded smoke points, virtual smoke points (where applicable), and TSI for pure toluene and each of the referee and anchor fuels is provided in Table 2, and a graphical representation of all TSI data used to support the model reported in this work is presented as Figure 3.

Table 2. Data Summary for Highlighted Fuels

Fuel	Experiment	Sp (mm)	TSI	Experiment	Sp (vSp)[1] (mm)	TSI
1-methylnaphthalene	This work	5.12	100	Olson [13]	5 (4.6)	100
Methylcyclohexane	[2] a = -3.40	43.56	5	a = -2.68	42	5
Toluene	[2] b = 3.727	7.59	41.8	b = 3.285	7	40.6
iso-octane		-	-		38	7.2
1,3,5-trimethylbenzene		7.19	58.9		6	63.1
40/60 %v toluene /iso-octane		14.88	22.4		-	-
1-methylnaphthalene	Mensch [20]	5.5	100	Hunt [25]	5 (4.43)	100
Methylcyclohexane	a = -4.75	40.8	5	a = 1.80	94	5
Toluene	b = 4.051	8.4	39.7	b = 3.059	6	48.8
iso-octane		40.0	6.8		86	5.9
1,3,5-trimethylbenzene		7.3	62.0		6	63.1
40/60 %v toluene /iso-octane		14.57	22.4		-	-

1-methylnaphthalene	Averages	4.9	100	[3] Standard Deviations	0.5	0
Methylcyclohexane		55	5		26	0
Toluene		7.2	42.7		1.0	4.1
iso-octane		55	6.6		27	0.7
1,3,5-trimethylbenzene		6.6	61.8		0.7	2.0
40/60 %v toluene /iso-octane		14.7	23.2		0.2	1.1

1. The number in paratheses corresponds to the virtual smoke point used to normalize legacy datasets.
2. 'a' and 'b' are the TSI scaling coefficients for each experiment and are defined by Equation 2.
3. Standard deviations (reproducibility) based on one value per experimental campaign.

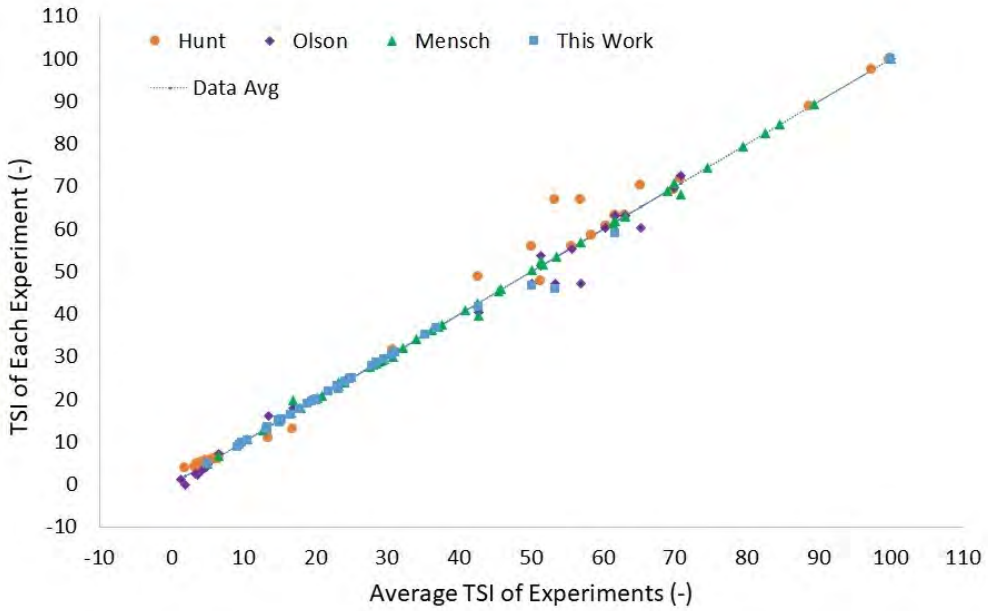

Figure 3. Full TSI Database Supporting QSPR Model Development.

The data shown in Figure 4 has been extracted from the thesis of Mensch [20] and suggests the repeatability of the experiment is an order of magnitude tighter than suggested by Equation 4. While some of this discrepancy can be attributed to signal to noise improvements afforded by taking repeat data points, we suspect there is some error in Equation 4 because we cannot believe that the same operator of the same lamp, employing similarly prepared wicks of the same material would read the flame tip position at the smoke point as 4.0 to 7.0 mm, assuming its nominal height is 5.5 mm. We think the 95 percentiles should be plus or minus one half the result of Equation 4. In the same document, the quoted reproducibility is only 37% higher than the repeatability, but we think the reproducibility, which covers differing opinions about the exact shape of the flame at its smoke point, differing intuition regarding line-of-sight being perpendicular to the ruler, lamp hardware differences (e.g. intake hole diameter), fuel purity differences, and laboratory differences (e.g. humidity, ventilation, temperature, pressure, benchtop levelness) should be substantially higher than the repeatability. If it were 2.7 times higher, that would seem about right and would be consistent with our suspicion that Equation 4 is too high by a factor of two.

The power of the TSI transformation resides in two important points. Systematic differences in smoke point data between experimental campaigns are attenuated appreciably by the transformation and the blending rule described by Equation 1

holds true [15,39]. Figure 4 provides one example comparing the result of Equation 1 with measured data and more examples (from this work) will be shown in the results section. Figure 5 provides an example of systematic error attenuation caused by the transformation of smoke point data to threshold sooting index. The data provided by Mensch is plotted along the X-axis and the Y-axis has contrived data. In one scenario the contrived smoke point data is 1 mm higher than the actual data (simulating operator reading error) and in the other scenario it is 7% higher (simulating different vent hole diameter). For that dataset, the imposed 1 mm offset in smoke point results in an average smoke point error of 11%, while the average error in TSI is 3.4%. The imposed 7% offset in smoke point results in a 1 mm smoke point difference on average and no difference at all in TSI.

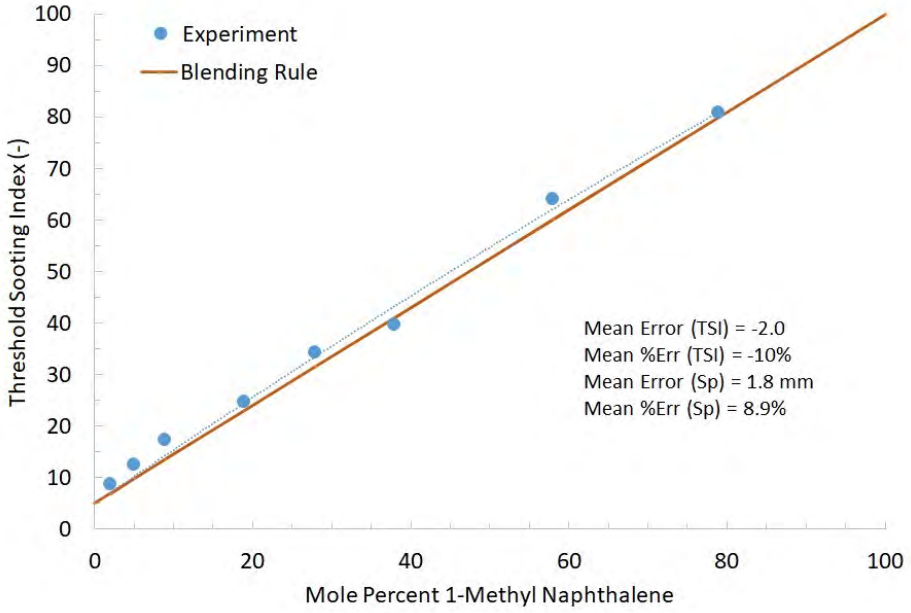

Figure 4. Evaluation of Linear Blending Rule, Equation 1 Data from Mensch [20] for binary mixtures of 1-methylnaphthalene and methylcyclohexane.

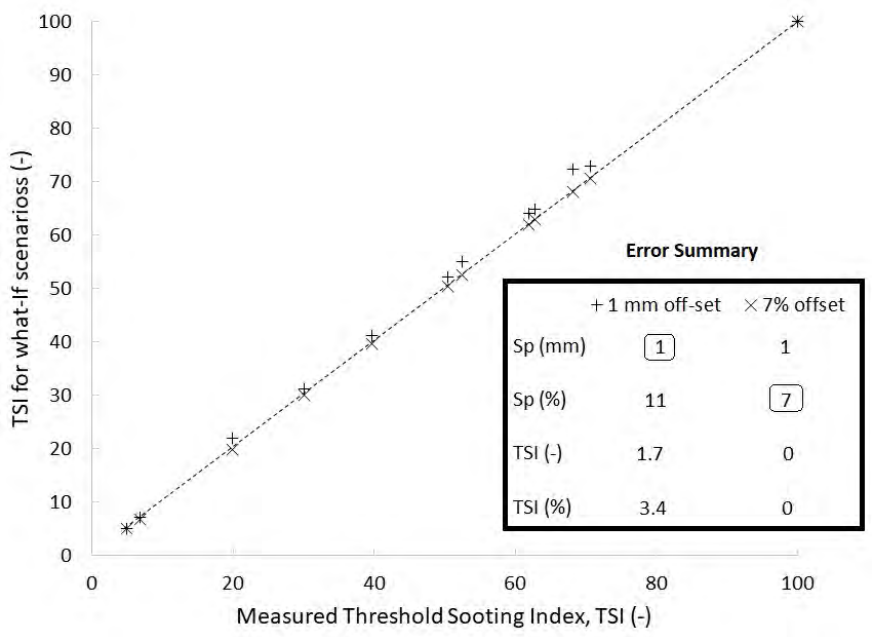

Figure 5. Partial Erasure of Systematic Differences Between Datasets Operations performed on data published by Mensch [20]. The dashed line is the original data. The + symbols are the result of adding 1 mm to each reported smoke point. The x symbols are the result of adding 7% to each reported smoke point. The arbitrary errors assigned here are larger than is possible for experiments adhering to the calibration controls described in ASTM D1322.

The linearity of the TSI blending rule, Equation 1 is particularly powerful because it opens the possibility of deriving useful smoking propensity information for materials that may not lend themselves to direct measurement. Some compounds result in a diffusion flame height that is too high (flickering) or too low (vision / optics limited) at their respective smoke points to read accurately. Some compounds are not liquids at standard ambient conditions but may exist in solution with other hydrocarbons up to some threshold concentration. Still other compounds, such as 2,6,10-trimethyldodecane (farnesane) and hexadecane cannot be evaluated as pure materials via ASTM D1322-19 because their wicking rate is less than their fuel consumption rate, under the conditions of the experiment. The wicking rate is described by the Washburn law [40], and scales inversely with dynamic viscosity and linearly with surface tension and the contact angle between the liquid and wick material. When the wicking rate is lower than the fuel consumption rate, the wick fabric starts to burn, and the apparent smoke point is lower than it would be if the wicking rate were to be increased or fuel consumption rate decreased (off-spec) by changing the conditions of the experiment. In all these cases, it is possible to measure the smoke point of a variety of mixtures that contain the problematic component (A) at some mixture fraction, and to leverage that data to determine a virtual TSI or smoke of pure A that could be used in Equation 1 for estimating the TSI (or smoke point) of some other mixture of known composition.

Another point in favor of using mixtures to derive virtual smoke points of pure molecules is that we ultimately care more about the effect that a component has on the smoke point of a mixture than what its smoke point is as a pure material. As noted in the introduction and the brief discussion around Figure 1, the TSI blending rule neglects the effects of certain physical processes such as preferential evaporation and synergistic flame chemistry that would lead to some non-linearity, but these effects are likely to show up (qualitatively) in a large variety of mixtures including the mixtures that we ultimately want a prediction for. The virtual smoke points will include some of these affects while the smoke points of pure compounds, obviously will not. The greater the variety of mixtures in the training data, the more likely it is that a derived virtual smoke point will be representative of that compound's impact in sample mixtures.

The linearity of Equation 1 also facilitates and motivates the development of linear QSPR-type models of molecules for which there is no data; pure or blended. While the uncertainty of the blending rule could be fully integrated into (i.e., transferred

to) the QSPR model uncertainty if the QSPR training dataset contained enough mixtures, for now we simply recognize that the blending rule inaccuracy is small relative to the reproducibility of the data points and is therefore neglected.

Many authors have observed the following generic trend for sooting propensity of hydrocarbons. Normal-alkanes have the lowest sooting propensity followed by iso-alkanes and cyclo-alkanes then benzene followed by alkylated aromatics and finally naphthalenes, and within each class the sooting propensity increases with carbon number. Based on these observations, the constraints documented in Table 3 are imposed on the structural fragment contributions to the threshold sooting index. The coefficient, a_0 is an unconstrained scale shift applied to all predictions. The two anchor point constraints (MCH & 1-MN) remove two degrees of freedom (d_5 and d_8), and another pair of constraints corresponding to the referee fuels are applied globally. The regression employs eight variables (six degrees of freedom) to fit the combined datasets which contains 65 molecules and 124 data points. For the model of Lemaire et al. [33], no constraints were applied and the terms we call a_0, a_5 and a_6 do not exist, but four additional terms exist that distinguish an aliphatic carbon with an aromatic group attached to if from an aliphatic carbon with only other aliphatic groups attached to it. The training database compiled by Lemaire also differs substantially from this work, as it included many oxygenated species as well as data from different types of experiments. Their so-called unified sooting index is linearly correlated with TSI. For our model, the predicted TSI for molecules is given by Equation 5 where n_i is the number of each fragment type in the molecule. By combining Equation 5 with Equation 1 the final model is derived, and it is shown in Equation 6. In this equation, the index, j refers to molecules in the mixture and i refers to fragments in the molecule and the remaining terms are as defined by Equations 1 and 5. The model of Lemaire et al. [33] has a similar form, except a_0 does not exist and their dependent variable is their unified sooting index, instead of TSI.

$$TSI = a_0 + \sum_{i=1}^{9} n_i * a_i \qquad (5)$$

$$TSI_{mix} = a_0 + \sum_i a_i * \sum_j x_j * n_{ij} \qquad (6)$$

Table 3. QSPR Fragments, Coefficients and Constraints[†]

Index	Fragment	Coefficient	Constraint	Molecules that contain the fragment (%)
1	-CH3	$a_1 = d_1$	$0 < d_1 < 1$	86%
2	-CH2-	$a_2 = a_1 + d_2$	$0 < d_2 < 1$	63%
3	>CH-	$a_3 = a_2 + d_3$	$2 < d_3 < 4$	32%
4	>C<	$a_4 = a_3 + d_4$	$0 < d_4 < 3$	8% (5 molecules)
5	-CH2- (ring)	$a_5 = (5 - d_1 - d_6 - d_0) / 6$		20%
6	>CH- (ring)	$a_6 = a_5 + d_6$	$0 < d_6 < 3$	14%
7	naphthenic[††]	$a_7 = d_7$	$0 < d_7 < 20$	6% (4 molecules)
8	=cH-(aro)	$a_8 = (100 - d_1 - d_7 - 3*d_9 - d_0) / 10$		38%
9	=c<(aro)	$a_9 = a_8 + d_9$	$0 < d_9 < 12$	37%
0	Scale shifter	$a_0 = d_0$	$-10 < d_0 < 0$	100% (65 molecules)

[†]The two constraints of the referee controls are applied globally. [††]One naphthenic fragment is assigned to a molecule if the sum of the =cH-(aro) and =c<(aro) fragments is ten.

By summing over j for each datapoint, a system of 124 equations with 'ten' unknowns is set up, where 124 is the number of data points, including mixtures and pure molecules, and the set of QSPR model coefficients $\{a_i\}$ could be determined by any multi-linear regression software package. However, for the convenience of implementing the constraints that have been discussed, the rms difference between the model and the data was minimized using the GRG nonlinear solver within Microsoft Excel™ with upper and lower bounds applied to each independent variable, d_i (see Table 3) and each referee fuel acceptability criteria. For each molecule (j) in our database, an algorithm was used to derive $\{n_{ij}\}$ based on its SMILE [41] formula and for each molecule within the training dataset the result of this algorithm was verified manually. The mole fractions were derived from measured volume fractions, molecular weights and known densities at room temperature.

4. Results

The first step toward evaluating the integrated QSPR/blending model is to compare its predictions relative to the suggested ranges for each of the referee fuels. For 1,3,5-trimethylbenzene the recommended control range is 54.7 - 63.1 TSI and our

model predicts 63.1 TSI (Lemaire's model predicts 56.1). For the 40%/60% toluene/iso-octane blend the recommended control range is 21.0-25.4 TSI and our model predicts 25.4 TSI (Lemaire's model predicts 22.2), so the model is barely in control. In the discussion to follow some of the reasons behind why the model predicts the upper limit of the referee fuels control specification will be presented, along with its implications relative to application of the model. Overall, for the coefficients listed in Table 4, the QSPR model underpredicts the average data by 0.5 TSI (mean error). Its mean absolute error is 3.6 TSI and its rms error is 4.7 TSI (the rms error of Lemaire's model is 5.6). Relative to 1162 molecules relevant to this work, an overall comparison between the predictions made by each of the QSPR models is presented in Figure 6. While the trends predicted by this work and that of Lemaire are qualitatively similar, clearly there are significant quantitative differences between all three models. Such differences could be the result of differing training data, differing model formulation or differing regression constraints or objectives. All three models predict the available data reasonably well.

Table 4. QSPR Model Coefficients.

Fragment	Coefficient
-CH3	a_1 = 0.188
-CH2-	a_2 = 1.188
>CH-	a_3 = 5.188
>C<	a_4 = 7.174
-CH2- (ring)	a_5 = 2.191
>CH- (ring)	a_6 = 3.855
naphthenic	a_7 = 6.047
=cH-(aro)	a_8 = 7.807
=c<(aro)	a_9 = 16.372
Scale shifter	a_0 = -10.00

A subset of the data and model predictions corresponding to those points with measurements from more than one research group is plotted in Figure 7. Apart from n-butylbenzene, which has a modeled TSI of 49.2 and a measurement-average TSI of 65.3, the scatter in the data looks about the same weather it is reflected about the average data or the model result. Another point that is evident from these plots that that the data of Hunt [25] (especially) and Olson [13] trend higher than the data of Mensch [17] and this work. These trends are also evident in Figure 8 which shows a comparison between our model result and all data. The model trends 3.5 TSI low compared to the data from Hunt and 3.1 TSI high compared to our data. Three data points from within the original dataset by Hunt, p-cymene, t-butylbenzene, and triethylbenzenes were excluded based on inconsistency of their recorded smoke points relative to similar molecules within the same dataset and one point, tripentylbenzenes was excluded based on its molecular weight. The next worst match (also from the Hunt dataset) corresponds to n-butylbenzene. That datapoint was retained because it was within 10 TSI of its duplicate from the Olson dataset and because there is a possibility that a special cause, not captured by this QSPR formulation, was partially responsible for its unusually high TSI measurement. The average of the reported data for n-butylbenzene is 65.3 TSI, compared to our model prediction of 49.2 and Lemaire's model prediction of 43.0.

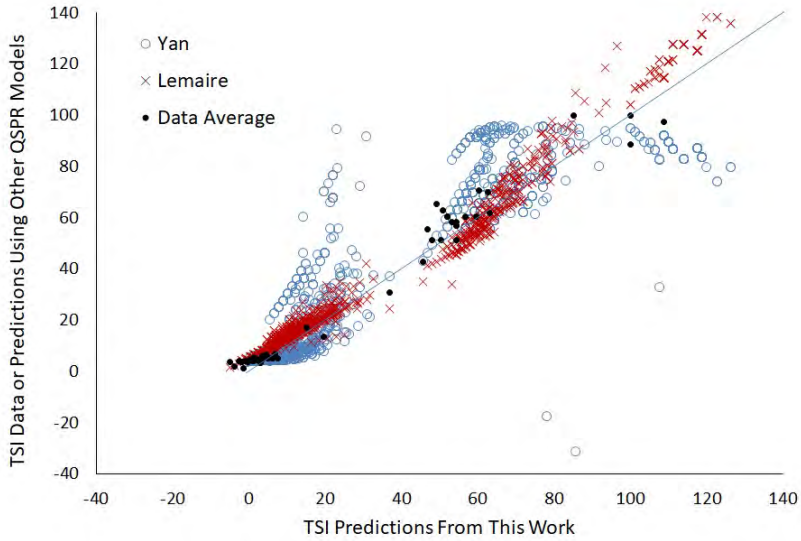

Figure 6. Comparison of QSPR Model Predictions Over The Target Database.

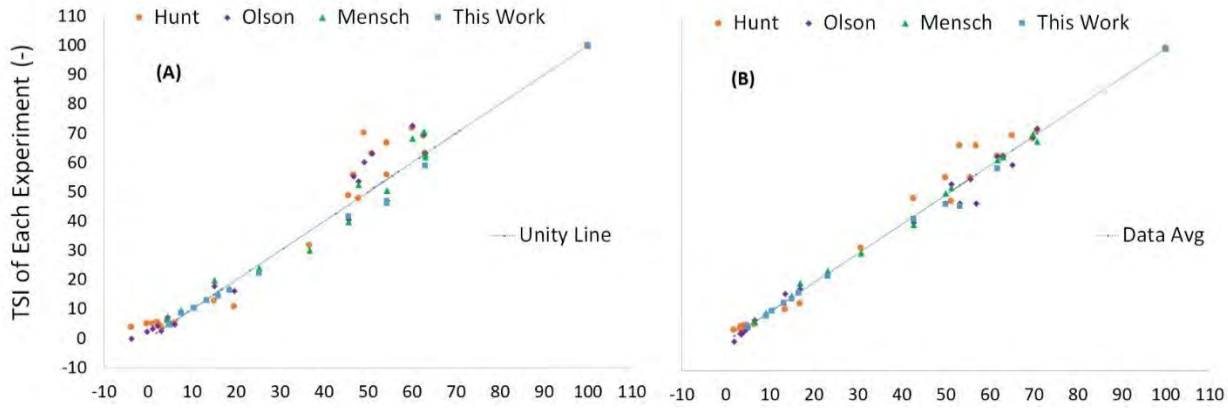

Figure 7. Model Prediction to Data in Context with Data Scatter Only points for which more than one measurement exists are presented, and the measured results are presented along the vertical axis. (A) QSPR model results are presented along the horizontal axis. (B) Average data are presented along the horizontal axis.

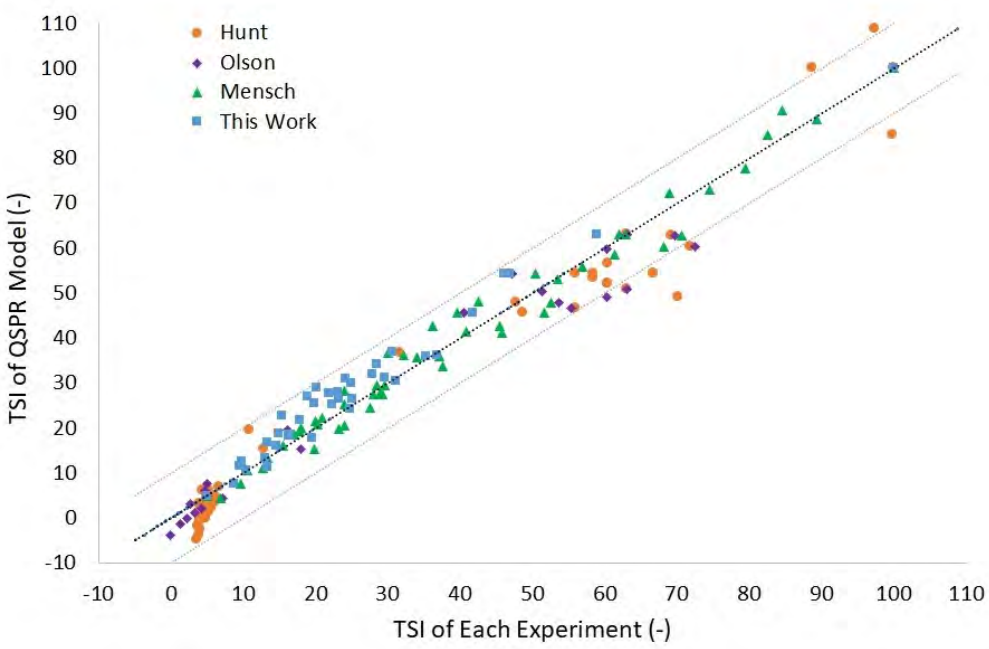

Figure 8. Model to Data Comparison All data and predictions are shown. The dashed lines correspond to the unity line and it ±10 TSI.

Although it is possible that a systematic difference in flame height readings contributes to the opposing trends (see Figure 4) of the Hunt dataset relative to this work, the more likely source is random error in the datapoint for 1-MN which is propagated via the experiment's TSI scaling coefficients, 'a' and 'b' in Equation 2, as seemingly systematic error in the remainder of the dataset (see Figure 2). For example, if the TSI scaling coefficients were derived from a smoke point for 1-MN that is 0.2 mm lower than was used for this work, the mean TSI for the Hunt dataset would drop from 35.2 to 33.9. For a systematic error in flame height reading to cause that much shift in the mean for the dataset, each of the other readings would have to be too low by 0.27 mm. This observation underscores the need for tight control around the repeatability of the upper anchor point of the TSI scale, and it also underscores a need for more benchmark quality data. Without the Hunt dataset, the coefficient for a naphthalene-like (a_7) could not be determined empirically and others would lack sufficient experimental variety to justify the regression approach.

The measured and predicted TSI of toluene and each of the toluene/iso-octane reference fuels defined in ASTM D1322 are compared in Figure 9. The blending rule, Equation 1 based on the experimentally determined TSI for toluene and iso-octane is within 1.6 TSI of the data at all points. At 25%v toluene, which strikes the fuel specification limit [1] for both smoke point and total aromatics, both models are somewhat conservative relative to the data. The QSPR model, Equation 6 is 2.0 TSI higher than the data at this important point. Above this point, its error grows more positive as driven by its error for toluene, where the QSPR model, which is a regressed model, is driven high by trying to minimize the largest mismatches to data, such as n-butylbenzene. The modeled difference between toluene and n-butylbenzene is 3 times a_2, the contribution from -CH_2- fragments, and there is a lot of data from alkanes and other alkylated benzenes that suggest a_2 is small. Therefore, the most impactful way for the regression to reduce the underprediction for n-butylbenzene is to increase a_8 or a_9 – the aromatic carbon coefficients - which drives the overprediction for toluene. At 20%v toluene, a reference fuel which matches the smoke point of average petroleum-derived jet fuel [36], both models are conservative by 1.5 TSI. At 10%v toluene, a reference fuel which matches the smoke point of best-case petroleum-derived jet fuel [25], both models are still conservative. At still lower concentration of toluene, the globally regressed QSPR model underpredicts the contribution from iso-octane, perhaps driven by a_3 or a_4, where a_4 is supported by just 5 molecules within the database that contain the >C< (chain) fragment.

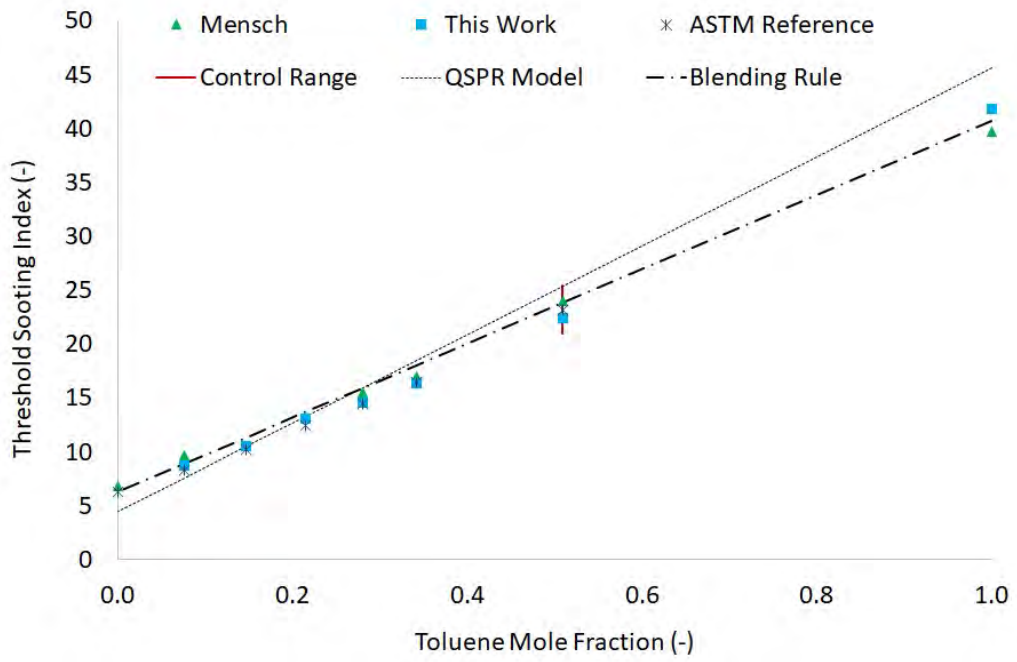

Figure 9. Measured and Predicted TSI of ASTM Reference Fuels.

In Figure 10, our QSPR model is compared with measured data for a total of five sets of binary mixtures that include toluene as one of the blended components, and in Figure 11 it is compared with three sets of measured data for binary mixtures that include iso-octane. The toluene/iso-octane blends are included in Figures 9, 10 and 11. While the data for each binary mixture lay on a straight line, confirming the validity of Equation 1, the difference between the QSPR model and the data is evident. For the iso-octane/toluene blends, the model underpredicts the data at high iso-octane concentrations but for farnesane/toluene blends the model overpredicts the data more at high farnesane concentrations than it does at high toluene concentrations (see Figure 10). Taken in isolation, this would hint at a_4 being too low and a_3 being too high since isooctane has one >C< fragment compared to none in farnesane and farnesane has three >CH- fragments compared to just one in iso-octane, but globally this is not the case. In fact, the incremental difference between a_2 and a_3 was driven to its intuitive maximum by the data regression. Turning now to the undecane/toluene and hexadecane/toluene blends shown also in Figure 10, it is evident that the model overpredicts the TSI contribution from hexadecane while its contribution from undecane matches the data quite well. Since these two molecules differ only with respect to the number of -CH2- fragments they contain, in isolation this comparison suggests the modeled contribution to TSI from the -CH2- fragment is too high. Taken globally however, the incremental difference between a_1 and a_2 also is regressed up to its intuitive upper boundary. The scale shifter coefficient, a_0 regressed to its lower intuitive limit which was imposed to restrict the number of molecules for which the predicted TSI would be less than zero. The other five regressed coefficients were near the middle of their respective intuitive ranges. While there is insufficient data to support inclusion of additional dependent variables, it may be that alkyl fragments generally contribute more to TSI when they are part of a molecule that also has an aromatic group. That said, the dataset does contain a sufficient variety of methyl-substituted molecules of the same carbon number and class to ascertain that the position of the branch along a chain or ring has immeasurable impact on its smoke point. For example, the three isomers of xylene have the same measured smoke points within a given experimental campaign.

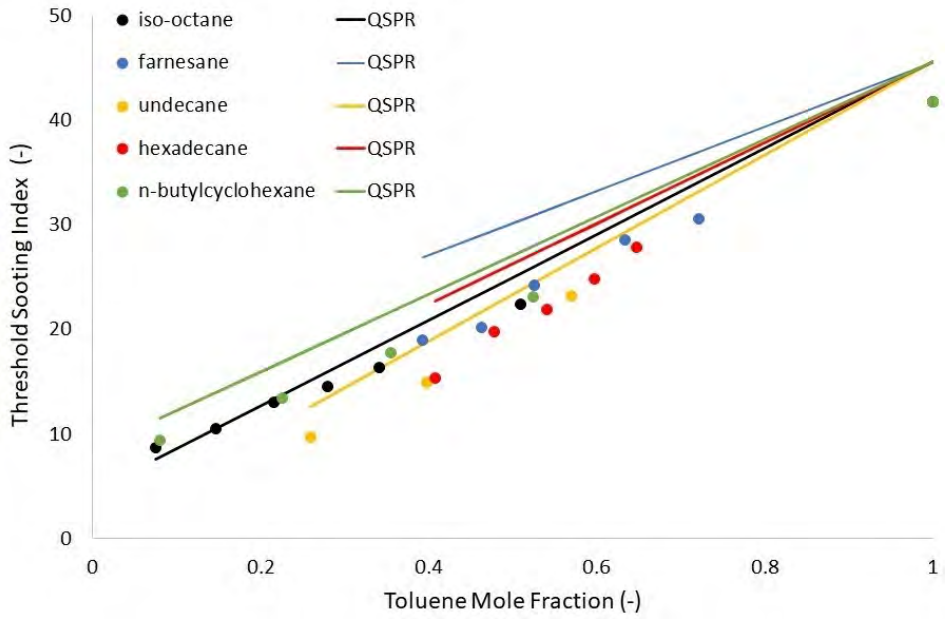

Figure 10. QSPR Model Assessment for Binary Mixtures with Toluene Filled circles represent data points. Solid lines represent model results.

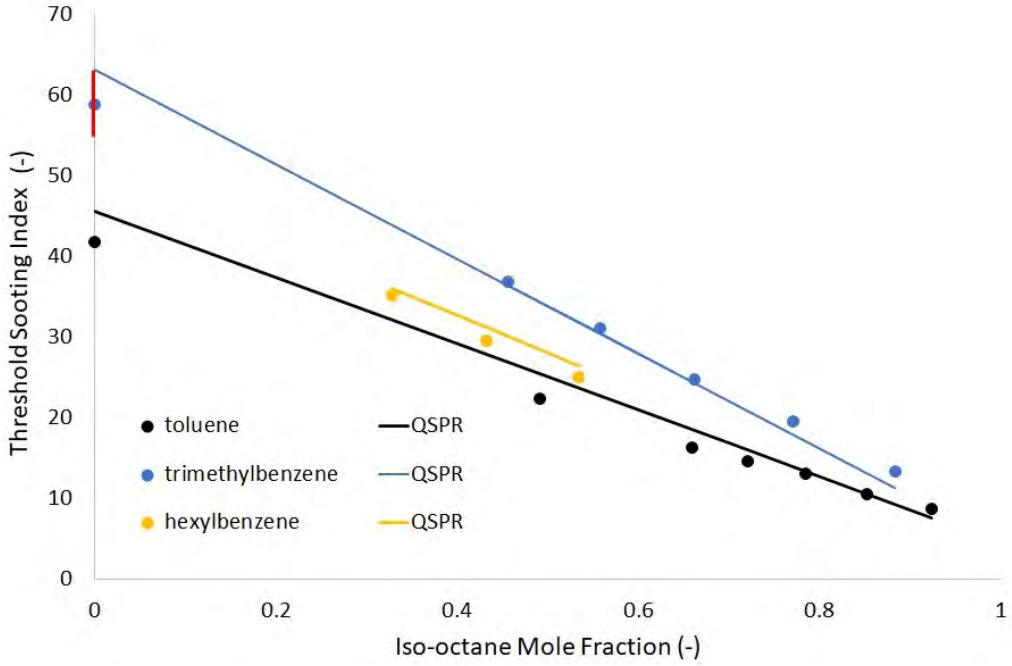

Figure 11. QSPR Model Assessment for Binary Mixtures with Iso-octane Filled circles represent data points. Solid lines represent model results.

As illustrated in Figure 11, our QSPR model matches the measurements for all mixture fractions of three sets of binary aromatic/iso-octane mixtures that were investigated. The largest difference between the model and the measurement is with respect to 100% trimethylbenzene where the model predicted a TSI of 63.1, 4.2 TSI higher than the measurement. This point also corresponds to a constraint in the regression, where the range of acceptable values for the model prediction of the TSI for trimethylbenzene is shown as a red vertical line in Figure 11. A measurement for pure iso-octane was not recorded in this work because of excess reading noise caused by flickering of the flame at its smoke point.

To validate Equation 6, measurements and predictions were made corresponding to (1) pure n-butylcyclohexane, (2) dimethylcyclooctane, and (3) a simple surrogate fuel. The results of these test cases are summarized in Table 5. The predicted TSI of n-butylcyclohexane, dimethylcyclooctane and a six-component surrogate jet fuel were 8.6, 11.2 and 17.7 TSI, respectively compared to measurements of 8.2, 10.8 and 18.5. In each case the predicted smoke point was well within the reproducibility 95-percentiles of the measurement method, which is 12.9 to 18.3 for fuel with a molecular weight of 150 g/mol and a nominal TSI of 15.2.

Another application of this model is to predict the smoke the smoke point of potential sustainable aviation fuel based on a mix of specific isomer and hydrocarbon class concentration data, as determined by GCxGC/FID-VUV measurements of samples with insufficient volume to measure smoke point directly. For this application, another, potentially large uncertainty term arises from undetermined isomer population distributions within any given class. For example, suppose we know that the mole fraction of C3-benzenes is 0.10, but we do not know how much of that is n-propylbenzene (least

Table 5. Model Validation Summary.

Fuel / Component	Mole Fraction (-)	Measured Smoke Point (mm)	Predicted Smoke Point (mm)	Measured TSI (-)	Predicted TSI (-)
n-butylcyclohexane	1.00	45.1 ± 1.3[†]	43.7	8.2	8.6
1,4-dimethylcyclooctane	1.00	36.8 ± 1.2	35.7	10.8	11.2
Surrogate 1	-	26.0 ± 1.0	27.0	18.5	17.7
n-hexylbenzene	0.076				
m-xylene	0.117				
n-octane	0.118				
iso-cetane	0.166				
n-undecane	0.273				
cis decalin	0.249				

[†]The reported uncertainty intervals are the repeatability 95 percentiles based on measurements taken for this work. 1,4-dimethylcyclooctane was not represented at any concentration within the training dataset. All other molecules were represented in the training dataset, but in different mixtures and at different concentrations.

sooting),trimethylbenzene (most sooting), or any of the other structural isomers. By assuming a uniform distribution of isomers within this class, the tier-a methodology effectively assigns a value of 56.8 TSI to this class, while the minimum TSI in this class 48.0 and the maximum is 63.1. If this class had been represented exclusively by n-propylbenzene in the real sample, our (incorrect) assumption of a uniform distribution would have introduced an error of +0.88 TSI into the prediction, and if this class had been represented exclusively by trimethylbenzene in the real sample, our assumption would have introduced an error of -0.63 TSI. The 95-percentile of the QSPR model predictions times the mole fraction for this class is ±0.89 TSI, so the isomer uncertainty term is indeed significant relative to the model uncertainty term. Moreover, if the real sample consistently favors more/less branching across all classes present then the isomer uncertainty error terms will stack up as the composition is reconstructed from the ground up in the model, while the random QSPR model errors, weighted by mole fraction, will sum in quadrature. It is therefore possible for the isomer error term to dominate, depending on the sample and how much is known about its composition. Figure 12 provides a comparison between predicted and measured smoke points of three conventional aviation fuels (labeled A-1, A-2, and A-3) and three complex mixtures that have received some attention as potential sustainable aviation fuel (labeled as C-3, C-8 and HEFA/SAK). As evident from the plot, the 95-percentile confidence intervals overlap for five of the six samples. We hypothesize that the miss for A-3 fuel is the result the real fuel having more =C<(aro) and -CH3 fragments and fewer -CH2- fragments than is predicted by our assumed uniform distribution of isomers. Work is already in progress to further utilize vacuum ultraviolet spectroscopy and calibrated time/time stencils to positively identify important isomers in samples.

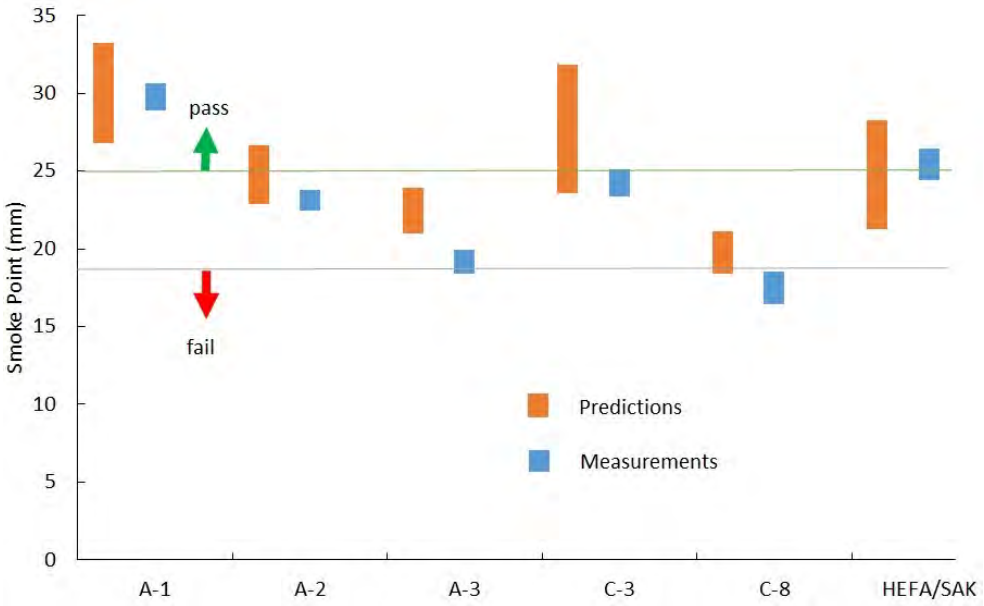

Figure 12. Predicted and Measured Smoke Points of Jet Fuels and Potential Sustainable Aviation Fuel.

5. Conclusion

A comprehensive model has been developed to the predict the threshold sooting index (TSI) of arbitrary mixtures of aliphatic and aromatic hydrocarbons of known composition. The model employs linear contributions from each of eight molecular fragments plus a global shift and a penalty factor for naphthenic compounds. It was constructed from a constrained regression over a composite database which was constructed by stitching together data from four different experimental campaigns dating back 68 years. Each of the datasets included smoke point data for 1-methylnaphthalene, methylcyclohexane, 1,3,5-trimethylbenzene, and points including toluene and iso-octane at some ratio between 0 and 1. This sub-set of data was used to established commonality of the four datasets within acceptable boundaries by using the transformation from smoke point to TSI as described by Equation 4, and verification that the TSI of two referee fuels where within acceptable limits. The TSI of trimethylbenzene was controlled to fall between 54.7 and 63.1 and the TSI of 40/60%v toluene/iso-octane, where available was verified to fall between 21.0 and 25.4. To establish conformance with these referee controls, it was necessary to fine-tune the reported smoke points of 1-methylnaphtalene in the two older datasets, within the boundaries of their respective experimental uncertainties.

Within the composite training dataset, which contained 65 molecules and 124 datapoints including simple mixtures, the model was found to match 95% of the data within 8.9 TSI. Validation of the model against n-butylcyclohexane, dimethylcyclooctane and a six-component surrogate jet fuel, resulted in predictions of 8.6, 11.2 and 17.7 TSI, respectively compared to measurements of 8.2, 10.8 and 18.5. While the agreement between model predictions and measured data for these points is as good or better than can be expected, the size of the 95-percentile band (±8.9 TSI) around the model predictions suggests there is room for improvement in the quality / consistency of the data used, or in the QSPR model, or both. While data from simple mixtures were also used to support regression to the QSPR model coefficients, the blending rule inaccuracy is less than 2 TSI, or 5% or the total uncertainty.

While the transformation of smoke point data to threshold sooting index is a powerful tool to erase constant percentage differences between smoke points measured in different experiments, and to reduce the impact of constant off-set type differences between measured smoke points, the tool is very sensitive to the precision of the smoke point measurement for 1 methylnaphthalene -- or whatever reference fuel may be chosen to set the upper range of the scale. Using the model trendline as a guide we found the data from Hunt trended 3.5 TSI higher while the data from this experiment trended 3.1 TSI lower, suggesting there are limits to the power of this data transformation and such inconsistency is likely the primary contributor to overall uncertainty in the model.

6. Acknowledgements

This research was funded by the U.S. Federal Aviation Administration Office of Environment and Energy through ASCENT, the FAA Center of Excellence for Alternative Jet Fuels and the Environment, project 065a through FAA Award Number 13-C-AJFE-UD-026, and project 066 through FAA Award Number 13-C-AJFE-UD-027, both under the supervision of Dr. Anna Oldani. Any opinions, findings, conclusions or recommendations expressed in this this material are those of the authors and do not necessarily reflect the views of the FAA.

7. References

[1] ASTM D7566 - 21 Standard Specification for Aviation Turbine Fuel Containing Synthesized Hydrocarbons, West Conshohocken, PA: ASTM International; 2021.
[2] Kosir S, Heyne J, Graham J. A machine learning framework for drop-in volume swell characteristics of sustainable aviation fuel. Fuel 2020;274:117832. https://doi.org/10.1016/j.fuel.2020.117832.
[3] Boehm RC, Scholla LC, Heyne JS. Sustainable alternative fuel effects on energy consumption of jet engines. Fuel 2021;304:121378. https://doi.org/10.1016/j.fuel.2021.121378.
[4] Colket M, Heyne J. Fuel Effects on Operability of Aircraft Gas Turbine Combustors. August. AIAA, Progress in Astronautics and Aeronautics; 2021. https://doi.org/10.2514/4.106040.
[5] Yang Z, Kosir S, Stachler R, Shafer L, Anderson C, Heyne JS. A GC × GC Tier α combustor operability prescreening method for sustainable aviation fuel candidates . Fuel 2021;292:120345. https://doi.org/10.1016/j.fuel.2021.120345.
[6] Kosir S, Stachler R, Heyne J, Hauck F. High-performance jet fuel optimization and uncertainty analysis. Fuel 2020;281:118718. https://doi.org/10.1016/j.fuel.2020.118718.
[7] DeWitt MJ, West Z, Zabarnick S, Shafer L, Striebich R, Higgins A, et al. Effect of Aromatics on the Thermal-Oxidative Stability of Synthetic Paraffinic Kerosene. Energy and Fuels 2014;28:3696–703. https://doi.org/10.1021/EF500456E.
[8] Clarke AE, Hunter TG, Garner F. The tendency to smoke of organic substances on burning. J Inst Pet 1946;32:627–42.
[9] Dodds WJ, Peters IE, Colket MB, Mellor AM. Preliminary Study of Smoke Formed in the Combustion of Various Jet Fuels. J ENERGY 1977;1:115–20. https://doi.org/10.2514/3.47933.
[10] Voigt C, Kleine J, Sauer D, Moore RH, Bräuer T, Le Clercq P, et al. Cleaner burning aviation fuels can reduce contrail cloudiness. Commun Earth Environ 2021 21 2021;2:1–10. https://doi.org/10.1038/s43247-021-00174-y.
[11] Chin JS, Lefebvre AH. Influence of Fuel Chemical Properties on Soot Emissions from Gas Turbine Combustors. Combust Sci Technol 1990;73:479–86. https://doi.org/10.1080/00102209008951664.
[12] Calcote HF, Manos DM. Effect of molecular structure on incipient soot formation. Combust Flame 1983;49:289–304. https://doi.org/10.1016/0010-2180(83)90172-4.
[13] Olson DB, Pickens JC, Gill RJ. The effects of molecular structure on soot formation II. Diffusion flames. Combust Flame 1985;62:43–60. https://doi.org/10.1016/0010-2180(85)90092-6.
[14] ASTM D1322 - 19 Standard Test Method for Smoke Point of Kerosene and Aviation Turbine Fuel, West Conshohocken, PA: ASTM International; 2019.
[15] Gill RJ, Olson DB. Estimation of Soot Thresholds for Fuel Mixtures. Combust Sci Technol 1984;40:307–15. https://doi.org/10.1080/00102208408923814.
[16] Yan S, Eddings EG, Palotas AB, Pugmire RJ, Sarofim AF. Prediction of Sooting Tendency for Hydrocarbon Liquids in Diffusion Flames. Energy and Fuels 2005;19:2408–15. https://doi.org/10.1021/EF050107D.
[17] Mensch A, Santoro RJ, Litzinger TA, Lee S-Y. Sooting characteristics of surrogates for jet fuels. Combust Flame 2010;157:1097–105. https://doi.org/10.1016/j.combustflame.2010.02.008.
[18] Li L, Sunderland PB. An Improved Method of Smoke Point Normalization. Combust Sci Technol 2012;184:829–41. https://doi.org/10.1080/00102202.2012.670333.
[19] Haas FM, Qin A, Dryer FL. "Virtual" smoke point determination of alternative aviation kerosenes by threshold sooting index (TSI) methods. 50th AIAA/ASME/SAE/ASEE Jt Propuls Conf 2014 2014. https://doi.org/10.2514/6.2014-3468.
[20] Mensch A. A Study on the Sooting Tendency of Jet Fuel Surrogates Using the Threshold Soot Index. Pennsylvania State University, 2009.
[21] Wu J, Song KH, Litzinger T, Lee SY, Santoro R, Linevsky M, et al. Reduction of PAH and soot in premixed ethylene–air flames by addition of ethanol. Combust Flame 2006;144:675–87. https://doi.org/10.1016/J.COMBUSTFLAME.2005.08.036.
[22] Wang H. Formation of nascent soot and other condensed-phase materials in flames. Proc Combust Inst 2011;33:41–67. https://doi.org/10.1016/J.PROCI.2010.09.009.

[23] Minchin S. Luminous stationary flames: The quantitative relationship between flame dimensions at the sooting point and chemical composition, with special reference to petroleum hydrocarbons. J Inst Pet Technol 1931;17:102–20.
[24] Schalla RL, McDonald GE. Variation in Smoking Tendency Among Hydrocarbons of Low Molecular Weight. Ind Eng Chem 2002;45:1497–500. https://doi.org/10.1021/IE50523A038.
[25] Hunt RA. Relation of Smoke Point to Molecular Structure. Ind Eng Chem 2002;45:602–6. https://doi.org/10.1021/IE50519A039.
[26] Van Treuren KW. Sooting Characteristics of Liquid Pool Diffusion Flames. Princeton, 1978.
[27] Schug KP, Manheimer-Timnat Y, Yaccarino P, Glassman I. Sooting Behavior of Gaseous Hydrocarbon Diffusion Flames and the Influence of Additives. Combust Flame 1980;22:235–50. https://doi.org/10.1080/00102208008952387.
[28] Tewarson A. Prediction of fire properties of materials : Part 1. Aliphatic and aromatic hydrocarbons and related polymers. NBS-GCR-86. Norwood, CA: Factory Mutual Research; 1986.
[29] Gülder ÖL. Influence of hydrocarbon fuel structural constitution and flame temperature on soot formation in laminar diffusion flames. Combust Flame 1989;78:179–94. https://doi.org/10.1016/0010-2180(89)90124-7.
[30] Ladommatos N, Rubenstein P, Bennett P. Some effects of molecular structure of single hydrocarbons on sooting tendency. Fuel 1996;75:114–24. https://doi.org/10.1016/0016-2361(94)00251-7.
[31] Poling BE, Prausnitz JM, O'Connell JP. Properties of Gases and Liquids, Fifth Edition. Fifth Edit. McGraw-Hill Education; 2001.
[32] Barrientos EJ, Lapuerta M, Boehman AL. Group additivity in soot formation for the example of C-5 oxygenated hydrocarbon fuels. Combust Flame 2013;160:1484–98. https://doi.org/10.1016/J.COMBUSTFLAME.2013.02.024.
[33] Lemaire R, Le Corre G, Nakouri M. Predicting the propensity to soot of hydrocarbons and oxygenated molecules by means of structural group contribution factors derived from the processing of unified sooting indexes. Fuel 2021;302:121104. https://doi.org/10.1016/J.FUEL.2021.121104.
[34] McEnally CS, Pfefferle LD. Improved sooting tendency measurements for aromatic hydrocarbons and their implications for naphthalene formation pathways. Combust Flame 2007;148:210–22. https://doi.org/10.1016/j.combustflame.2006.11.003.
[35] Lemaire R, Lapalme D, Seers P. Analysis of the sooting propensity of C-4 and C-5 oxygenates: Comparison of sooting indexes issued from laser-based experiments and group additivity approaches. Combust Flame 2015;162:3140–55. https://doi.org/10.1016/J.COMBUSTFLAME.2015.03.018.
[36] Martin D, Wilkins P. Petroleum Quality Information System (PQIS) 2011 Annual Report. Fort Belvoir, VA: Defense Technical Information Center; 2011.
[37] Woodrow WA. Development of Methods of Measurement of Tendency to Smoke. 1st World Pet. Congr., London, UK: OnePetro; 1933, p. WPC-244.
[38] Terry JB, Field E. . Ind Eng Chem Anal Ed 1936;8:293.
[39] Yang Y, Boehman AL, Santoro RJ. A study of jet fuel sooting tendency using the threshold sooting index (TSI) model. Combust Flame 2007;149:191–205. https://doi.org/10.1016/j.combustflame.2006.11.007.
[40] Washburn EW. The Dynamics of Capillary Flow. Phys Rev 1921;17:273. https://doi.org/10.1103/PhysRev.17.273.
[41] Weininger D. SMILES, a Chemical Language and Information System: 1: Introduction to Methodology and Encoding Rules. J Chem Inf Comput Sci 1988;28:31–6. https://doi.org/10.1021/CI00057A005.

Appendix 2

Synthetic aromatic kerosene property prediction improvements with isomer specific characterization via GCxGC and vacuum ultraviolet spectroscopy

Paper 6: Synthetic aromatic kerosene property prediction improvements with isomer specific characterization via GCxGC and vacuum ultraviolet spectroscopy

Nomenclature

A_i:	area percentage of i^{th} peak per ChromSpace
A_{class}:	area percentage of all peaks within a hydrocarbon group or class per ChromSpace
ASTM:	ASTM International
ATJ:	alcohol to jet
CI:	confidence interval
FID:	flame ionization detector
FTIR:	Fourier transform infrared spectroscopy
GC:	one-dimensional gas chromatography or gas chromatography
GC x GC:	two-dimensional gas chromatography
HEFA:	hydro processed esters fatty acids
LHV:	lower heating value or heat of combustion
m:	modulation number
MS:	mass spectroscopy
n:	representative (average) modulation
nvPM:	non-volatile particulate matter
NIST:	National Institute of Standards and Technology
NJFCP:	National Jet Fuel Combustion Program
NMR:	nuclear magnetic resonance
PIONA:	paraffins, olefins, naphthenes, and aromatics
QSPR:	quantitative structure property relationships
r^2:	correlation coefficient squared
R^2:	coefficient of determination
SAF:	sustainable aviation fuel
SAK:	synthetic aromatic kerosene
T:	temperature
TSI:	threshold sooting index
VUV:	vacuum ultraviolet light detector
Y_i:	mass percentage of i^{th} analyte
%m:	mass percentage
%v:	volume percentage
δ:	fixed time interval over which absorbance was averaged
ρ:	density
σ:	surface tension
σ_{Y_i}:	analyte quantification uncertainty
σ_z:	root property data uncertainty
σ_{isomer}:	isomeric uncertainty

1. Introduction

The reduction of anthropogenic emissions from the transportation sector has increased interest in recent years [1]. The aviation industry consumed ~400 billion liters of jet fuel globally in 2019, comprising ~10% of greenhouse gas emissions from transportation [1–3]. Current predictions show flight demand doubling from 2010 levels by 2050 [2,4], while simultaneously, airlines continue to pledge to 50% carbon reductions by 2050 [2]. Sustainable aviation fuels (SAFs) have been identified as the most viable option to achieve these desired carbon displacements [5] to address the rising airline industry and environmental goals.

On 1 December 2021, the United Airlines 737 MAX 8 aircraft flew from Chicago to Washington D.C. marking the first passenger flight, with one of two engines powered by 100% SAF [6]. The plane was propelled on a fuel blend of (1) World Energy's hydroprocessed esters fatty acids (HEFA) (ASTM D7566 A2) [7] and (2) Virent's synthetic aromatic kerosene (SAK) blended at 79 %v and 21 %v, respectively. As the name suggests, SAK is composed primarily of aromatics, which from a compositional standpoint, sharply contrasts with the composition of several other qualified SAFs. SAK is one of the only SAFs to include any aromatic component. Aromatics are associated with higher non-volatile particulate matter (nvPM) or soot

emissions, and nvPM is believed to be the primary nucleation source for aviation contrails [8]. Contrails, in turn, are suggested to be the dominant radiative forcing agent of aviation instead of CO_2 emissions alone [1]. However, not all aromatics are equivalent, with naphthalenes having higher sooting potentials [9]. Relatedly, within the SAF community, there is broad interest in compositions that can remain 'drop-in' while minimizing nvPM.

Fuels are required to have 8.4%v aromatics per ASTM D7566 to remain fungible with existing aircraft fueling infrastructure. This requirement, among others (e.g. density), often limits the amount of SAF that can be blended with petroleum-derived Jet A because SAF historically has no aromatic content. Alternative to Jet A blending, SAK provides an entirely sustainable option to achieve the aromatics requirement. The primary concern that aromatics address is material compatibility [10,11]. Aromatics offer higher density, enabling blending with lower density fuels like hydroprocessed esters fatty acids (HEFA) and Alcohol to Jet (ATJ) fuels [12], and potentially a blended dielectric constant in line with conventional fuels.

Numerous low volume (<1mL) hydrocarbon compositional analysis methods reduce SAF scale-up risks and streamline the various qualification processes [3,13–19]. Collectively, these technologies provide producers with critical property predictions that can guide feedstock-conversion engineering at earlier technology readiness levels thereby streamlining production up-scaling investment decisions. For example, a wet waste volatile fatty production process was recently guided in part by these analyses, leading to a fuel technology readiness level, in less than one year, sufficient to support ASTM D4064 testing requirements [3].

Multidimensional gas chromatography is a relatively mature technology capable of separating analytes in complex solutions and remains common in the fuel characterization community. Superposing columns with a modulator between columns affords greater separations than those afforded through single-column configurations [13,18]. Kilaz et al. provide a complete review of various analytical techniques [13], e.g., flame ionization detection (FID), mass spectroscopy (MS), Fourier transform infrared spectroscopy (FTIR), nuclear magnetic resonance (NMR), and concluded that multidimensional chromatography offers the best information to aid jet fuel composition to property relationships. These GC x GC configurations require 'stencil' calibration using MS results and reference samples. Once calibrated, stencils can determine the boundaries of various hydrocarbon classes and carbon numbers [20]. However, stencil techniques, even when coupled with MS detectors, cannot determine structural differences between most isomers [13]. For this reason, vacuum ultraviolet spectroscopy (VUV) has gained popularity in the food, forensics, environmental, and fuel research communities [18,21–24]. GC (x GC)-VUV research has demonstrated capability to identify structural and stereoisomers such as p-xylene, o-xylene, m-xylene [21], or the isomers of cis-decalin and trans-decalin [18], which were indistinguishable by MS systems.

Schug et al. explored the benchtop VUV detector in 2014 [21], suggesting its potential as a universal detector. Few species, separated from a gasoline sample, were resolved at the isomeric level in that work [21]. A later publication demonstrated the use of GC-VUV for hydrocarbon group type analysis (PIONA) of gasoline which was verified through various existing ASTM compositional methods [25]. However, in the case of a higher molecular weight jet fuel such as SAK, with higher isomerization, the second chromatographic dimension is necessary to sufficiently separate analytes as shown in this work. More recently, Wang explored a diesel fuel sample in a GCxGC-VUV configuration, but like Walsh et al. [25] , was only concerned with group type analysis between cycloalkanes and alkenes, rather than exact isomeric structures [26].

Property predictions from the compositional analysis have long been of interest within the fuel community [13,14,18,27]. Before Yang et al. [16], most fuel property predictions could be classified as 'top-down' approaches [19,28], where models are developed by regression of measured data, serving as both the independent and dependent variables. Such models risk extrapolating to non-physical results (regardless of the statistical method) and require a substantial quantity of data to quantify uncertainties [18]. Conversely, 'bottom-up' approaches [16,18,29] leverage composition data via GC x GC as one category of input, along with a library of property data corresponding to potential fuel constituents as the other category of input. These inputs are related to fuel properties by simple, and usually physically based, blending rules [16–18,30]. While the physically-based blending rules afford confidence to extrapolate to compositions beyond the historical record, all such bottom-up models afford traceability of errors, enabling a comprehensive uncertainty analysis [17,18]. The four sources of error that contribute to the uncertainty of predictions made by a bottom-up approach include the following: constituent (aka chromatogram peak, or deconvoluted peak) mass concentration measurement error, assignment of chromatogram peaks to specific isomers, isomeric properties data uncertainty, and blending rule accuracy. This work addresses the precision of the chromatogram peak assignments to specific isomers, as well as identification and deconvolution of chromatogram peaks comprised of 2 or 3 species.

Having no prior knowledge of composition or properties, a contemporary SAF candidate (Virent SAK) is investigated, starting with GCxGC/FID-VUV. Much of its composition (>71 %m) is found in coeluting peaks. Here, an isomeric identification

approach is detailed with four novel contributions: (1) definitive determination of species count (one or more than one) within any peak on the chromatogram, (2) two-dimensional VUV deconvolution with up to three analytes, (3) greater than 93%m in a real jet fuel is assigned to specific isomers, and (4) precision improvement of property predictions. Previous coelution detection methodologies leverage the completeness of reference libraries [25,26], whereas the method presented here relies solely on the measured signal. This definitive pre-processing of peaks distinguishes single elution from coelution peaks and categorizes them based on the presence of multiple unique spectra within the same peak. Finally, material compatibility and dielectric constant calculations are reported for 79/21 %v HEFA/SAK blend, further documenting the potential of SAK as a keystone blend component for potential 100% SAF.

2. Methodology

A GC x GC-FID/VUV method was employed to identify the hydrocarbon species in SAK, similar to the method used in Heyne et al. [18]. This work builds on that methodology by adding deconvolution capabilities, showing a dramatic increase in predictive accuracy due to isomeric information, and compares them to predictions done with traditional hydrocarbon group type information [16].

2.1 Reference samples

The SAK fuel sample was provided courtesy of Virent, Inc, and the HEFA fuel sample was provided by World Energy. Additional materials that composed the majority of the SAK were procured to predict SAK properties more accurately and characterize the mixture further. A summary of measured properties for each component can be found in Tables 2 and 3 in the Supplementary Material. Three reference fuels from the National Jet Fuel Combustion Program (NJFCP) [27,31,32], A-1 (POSF 10264), A-2 (POSF 10325), and A-3 (POSF 10289) were also analyzed via GC x GC-FID/MS and used as an aromatic benchmark for several temperature-independent properties.

2.2 Gas chromatography, flame ionization detector, and vacuum ultraviolet light detector

The experimental setup was arranged as GC x GC-FID/VUV, where the VUV system supported the hydrocarbon isomeric identification and the FID supported quantification. The system included two columns separated by a modulator connected to a split plate after the second column where the analytes were directed to either the FID or the VUV. The system included a SepSolve INSIGHT flow modulator and VGA-101 Vacuum Ultraviolet light detector. A graphical overview of the GC x GC-FID/VUV is displayed in Figure 1, illustrating the major components of the GC x GC-FID/VUV system.

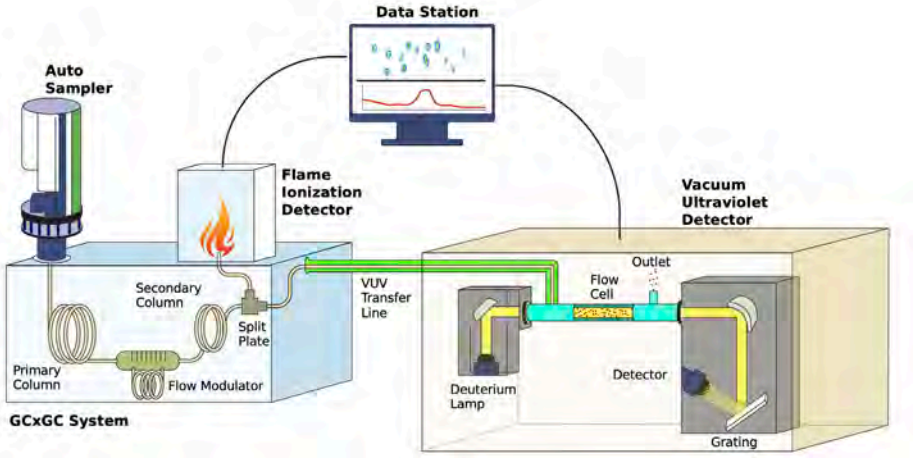

Figure 1. GC x GC-FID/VUV Test Setup Diagram

The Agilent 7693A Automatic Liquid Sampler (ALS) injected 5 μL of sample into the Agilent 8890 GC. The inlet temperature, pressure, and split ratio were maintained at 250 ˚C, 55.04 psi, and 100:1, respectively. A reverse column arrangement was chosen to achieve the desired separations for this study. Specifically, in their respective order, a Rxi-17Sil MS 60m x 0.32mm x 0.5µm and Rxi-1 15ms x 0.32mm x 0.5µm columns were utilized, both of which were manufactured by Restek. Constant flow rates for the first and second columns of 1.2 mL/min and 48 mL/min were held throughout the run with a Helium carrier

gas (grade 5.0), which passed through a Restek Triple Filter before entering the GC system. The GC oven was initialized at a temperature of 40 °C for 30 seconds, with a ramp rate of 1 °C / min until achieving a final temperature of 280 °C, where the temperature was held for 10 minutes. The GC ran for a total time of 250.5 minutes. Two modulation times and injection volumes were used. A 110-second modulation time with 5 μL injection and a 5-second modulation time with 1 μL injection was employed. The combination of long modulation times and high injection volumes enabled higher concentrations of trace analytes to be identified. While the shorter modulation time and lower injection volume facilitated deconvolution of peaks with high concentrations.

As mentioned previously and demonstrated in Figure 1, the analyte is divided at the split plate after traveling through the secondary column. One of the lines leaving the split plate junction feeds the FID where flow rates are applied to the air (ultra-zero grade) flow, H_2 (grade 6.0), and N_2 (grade 5.0) at flow rates of 400, 40, and 25 mL/min, respectively. The FID operated at a fixed temperature of 300 °C while recording data at a frequency of 50 Hz, which was processed by INSIGHT ChromSpace software (Version 1.5.1).

As illustrated in Figure 1, a second line parts from the split plate and directly connects to the VGA-101 transfer line. The sample was preferentially directed to the VUV detector relative to the FID. The length of the internal transfer line from the split plate to the VUV was shorter than the transfer line from the split plate to the FID to increase the amount of sample directed to the VUV. The transfer line from the GC to the flow cell was maintained at 250 °C. With N_2 (grade 5.0) being used as the system gas, data acquisition continuously occurred at 76.92 Hz over a wavelength range of 125 to 430 nm.

2.3 Identification and Quantification

The overall identification procedure includes the following steps: timestamp alignment between FID and VUV, removal of oversaturated VUV data, local background signal subtraction and noise reductions, coelution screening, identification of analyte(s) in the considered peak, and conversion to mass fractions. Each step of the procedure described above leveraged in-house Python (Version 3.8.5) code, which can be provided upon request.

2.4 FID and VUV Alignment

Synchronization of the FID signal to the VUV signal was completed by aligning the max signal for each peak across the experiment duration. A single offset value could be found and applied to the entire VUV dataset by minimizing the offset between the local maxima found with the separate detectors. With the offset applied, SepSolve ChromSpace FID area determinations were associated with the identified analytes and VUV data.

2.5 Analyte Identification

Pre-processing of VUV spectra included removing the full spectra at certain time stamps corresponding to cases where the absorbance at any wavelength exceeded one. Then local background subtraction and signal averaging, akin to the approach described in Lelevic et al. [33] and Heyne et al. [18], were done to attain the sample spectra used for matching against cataloged reference spectra. Single analyte identification followed the work discussed in Heyne et al. [18].

Determination of species count (one or more than one) within each peak on the chromatogram was the final pre-processing step. Prior state-of-the-art techniques [25] relied on the quality (e.g. R^2) of a multiple species match significantly exceeding that of the top single species matches in order to confirm or reject the presence of coelution. In this work, it is shown how this determination can be established prior to any matching exercise, which eliminates reliance on the completeness of spectral reference libraries. This insight is especially useful in downstream steps. For example, by demonstrating that given sample spectra originate from a single species subsequent comparison to reference spectra will either identify the most probable match or prove that the observed, sample spectra are not present in the reference library. Without first proving that sample spectra originated from a single species, any number of linear combinations of multiple spectra in the reference library could (incorrectly) meet the acceptable match criteria. Conceptually, the coelution check is done by comparing sets of spectra that are each averaged over the full width of one retention time axis (i.e. t_1 or t_2) and segments of the other retention time axis. If the spectral profile is static while sweeping through the segmented time axis, in both dimensions, the peak is comprised of a single analyte. If the normalized spectra change while traveling across the chromatogram peak, then it is known to be comprised of multiple analytes.

For chromatogram peaks shown to consist of more than one species, the sample VUV spectra at each point in time (t_1 , t_2) within that peak was matched by a linear combination of 2 or 3 reference spectra, leveraging the non-negative least-squares

optimization algorithm from Python SciPy, maximizing R^2. The decision logic around which 2 or 3 reference spectra to use as the basis functions was partially manual with the goal being to select the ones that yielded the best overall match throughout the peak. The overall concentration of each analyte was determined by summing the product of the reference spectra scale factors at each time point with the mass fraction attributed to each time point, where the integrated areas of sample VUV spectra were used to determine the mass fraction at each time point.

2.6 Quantification

Hydrocarbon type analysis was performed by generating a stencil with a method like the one described by Vozka et al. [34]. Chromatogram peak areas of each peak (A_i) were determined through the ChromSpace integration software and attributed to corresponding hydrocarbon groups (A_{class}) based on retention time, where the FID signal serves as the z-axis (or the color scale). Previous research [16–18] has leveraged the well tested hydrocarbon template from Striebich et al. for hydrocarbon group type mass fraction determinations [20], as were the mass fractions (Y_i) presented herein. To arrive at a single species mass faction, The group mass fraction per the Striebich et. al template (Y_{class}), was scaled by the area percentage of th selected peak (A_i) relative to the total area (A_{class}) of the respective hydrocarbon group. Repeatability for hydrocarbon class quantification is taken as RSD% <1.5% (n=3), as reported in a recent repeatability study [35].

$$Y_i = \frac{A_i}{A_{class}} * Y_{class} \quad (1)$$

2.7 Property Measurements

Threshold Sooting Index (TSI) values of each species identified in the report were estimated via the QSPR model of Boehm et al. [9] and the blending rule detailed in that report was used to predict the TSI of SAK. An o-ring volumetric swell study was performed with optical dilatometry techniques detailed in Faulhaber et al. [36]. Here, two acrylonitrile-butadiene o-ring materials were submerged at room temperature into separate fuel-filled vials. The first contained neat HEFA, and the second contained a 79/21 %v HEFA/SAK blend. Refractive index measurements were taken at room temperature using a Reichert TS Meter. These measurements were taken with a light emission source at 589 nm and converted into dielectric constant values for neat HEFA, SAK, and the 79/21 %v HEFA/SAK using $K=n^2$ (K is dielectric constant, n is refractive index). The accuracy of the Reichert TS Meter was +- 0.0001 nD. Other properties such as flash point, freeze point, viscosity, density, and surface tension, were experimentally determined for several of the samples using aviation fuel specification tests [7]. Both the ASTM methods names and corresponding repeatabilities and reproducibilities are listed in Table 1 of the Supplementary Material, and served to evaluate the accuracy of the predictions. [9]. All other properties required but not measured for this study were sourced by the NIST Web Thermo Tables [37].

2.8 Tier Alpha Approach for Property Predictions

The Tier Alpha approach for property predictions employs three different pieces of information: empirically derived algebraic blending rules, an extensive database of pure molecules, and the best available composition data. Where composition data is limited to hydrocarbon group level mass concentrations, a random selection of a representative member of that group is made as part of a Monte Carlo simulation that also includes uncertainties in determined mass fractions and database properties. By far, the largest source of uncertainty (precision) in these determinations has been, until recently [18], the underdetermined speciation within each of the hydrocarbon groups[17]. The coupling of VUV spectroscopy with GCxGC/FID chromatography attacks this primary source of property prediction uncertainty and now, with this work, advances in sampled VUV spectra deconvolution further attack this primary source of property prediction uncertainty. With these improvements, blending rule accuracy, rather than prediction precision may be the largest source of overall prediction uncertainty for some properties of some hydrocarbon mixtures with volatility within the jet fuel range. A flow chart describing this process is provided in Figure 2 to help conceptualize the details of this approach.

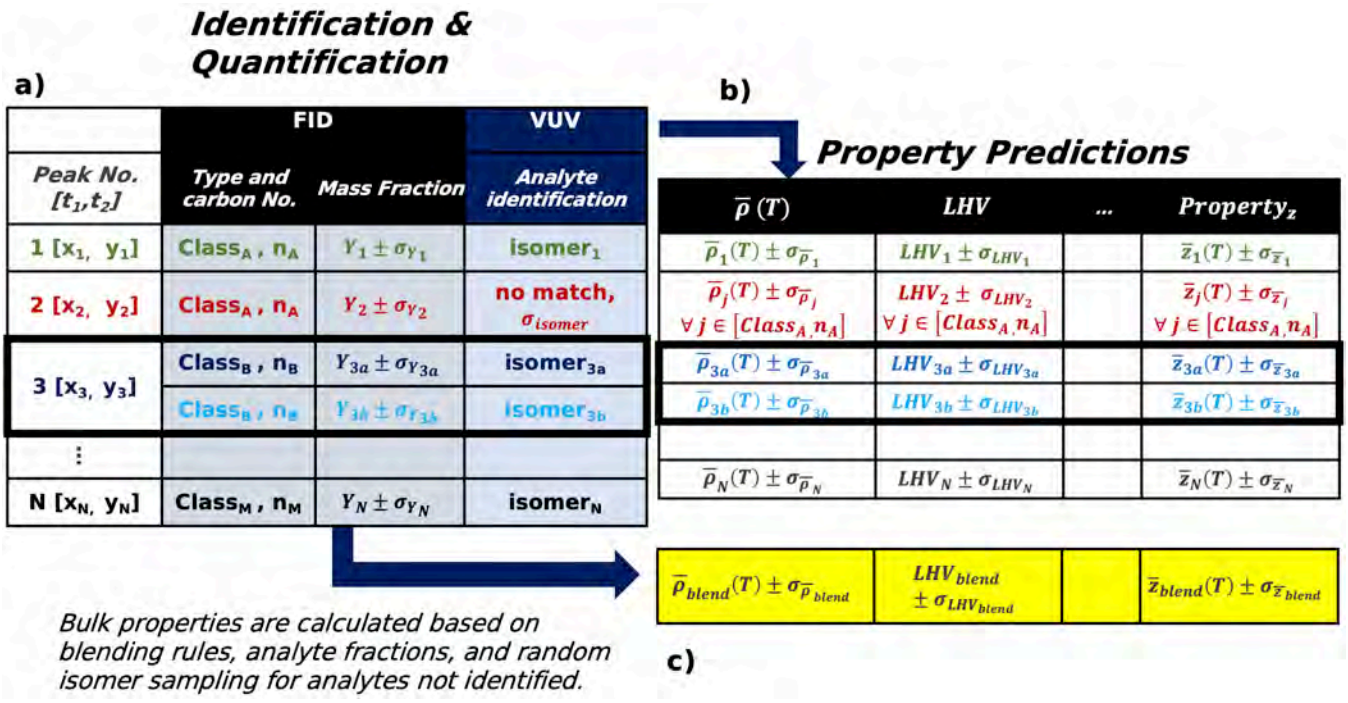

Figure 2. Illustration of the 'Tier Alpha' approach including: identification and quantification (a), component property data (b), and mixture property determinations (c). Deconvolution is depicted with a bold black outlined box.

3. Results and discussion

3.1 Identification Results

The hydrocarbon group type analysis from the GCxGC chromatograph template classifies 93.2 %m into three alkylbenzene bins; C8 (3.7%m), C9 (62.0 %m), and C10 alkylbenzenes (27.5%m). Other minor fractions are distributed across C9 (0.8 %m) and C10 cycloaromatics (1.2 %m), along with various cycloalkane and isoalkane groups, each <1.5%m, across a carbon range of C8 to C10. While that approach classifies analytes into a specific hydrocarbon group, the goal of this study is to further separate the group mass fraction into isomer-specific fractions using VUV data. Illustrated in Figure 3, the SAK chromatograph has been labeled with English letters to inform which peaks were identified through the use of the VUV detector. These English letters, summarized in Table 1, delineate 26 isomers along with their mass fractions amounting to 93.6 %m of the SAK sample. All possible isomers of C8 and C9 alkylbenzenes are identified. In contrast, C9 cycloaromatics and C10 alkylbenzenes include incomplete isomer identification due to some peaks having low signal to noise, or due to detected isomers not matching against the available reference data. All fractions from the hydrocarbon group type analysis that were not identified on the isomeric level have been summarized in Table 4 of the Supplementary Material.

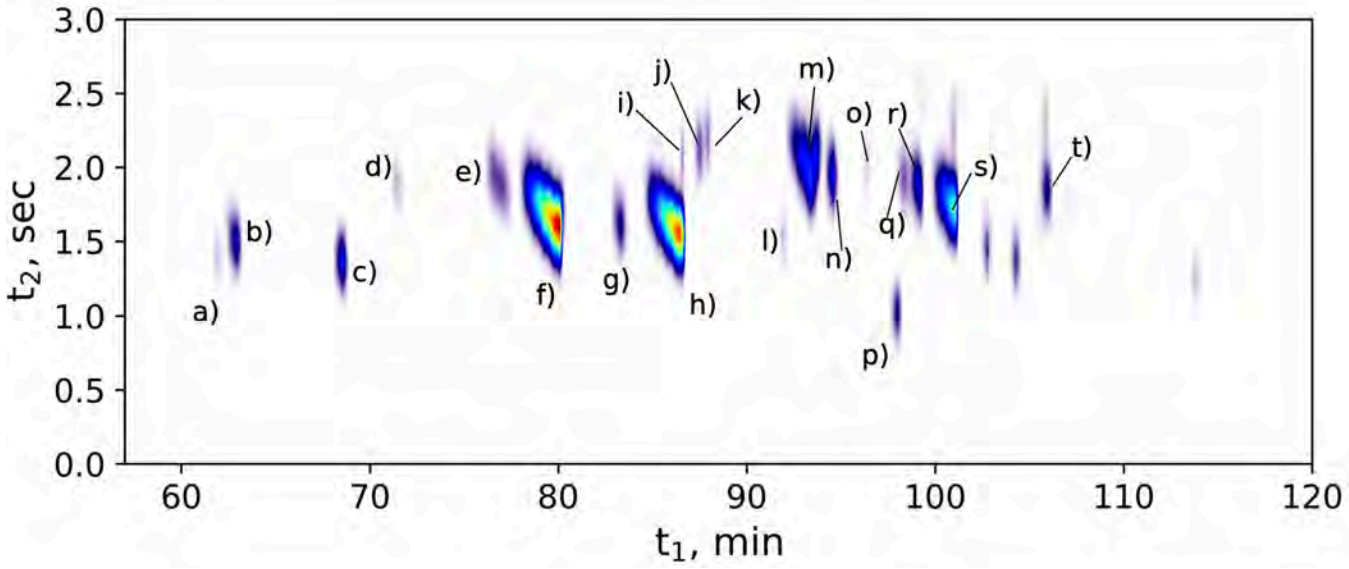

Figure 3. FID chromatograph (5 μL and 10 sec modulation time) with provided letters that correspond to identified species laid out in Table 1. The RGB color scheme is used where blue is low concentration and red is high concentration.

The two most prominent analytes present in SAK are 1-methyl-3-ethylbenzene and 1,2,4-trimethylbenzene, 20.6%m and 26.7 %m, respectively. Conversely, 1-methyl 2-n-propyl benzene (0.15 %m) and 1,3,5-trimethyl benzene (0.15 %m) are the smallest identifiable fractions. All peaks comprising at least 0.68%m of the SAK sample were identified by matching their corresponding VUV spectra with reference spectra in our library; $R^2 > 0.999$. At lower analyte concentration, the R^2 between sample and reference spectra of the same species decreases due to the low signal to noise ratio of the sample spectra. For 1-methyl 2-propylbenzene, the R^2 was 0.978.

The VUV performed excellently in the hydrocarbon group regions where the reference library was completely defined, yet limitations persist in making identifications in regions with less library coverage. This is especially true in heavy regions (>C10) where known possible isomers exponentially increases. For example, two prominent cycloaromatic peaks (lower right diagonal of the chromatogram peak 's', Fig. 3) are not identified beyond the hydrocarbon group type analysis. Conversely, all C8, C9, and C10 alkylbenzene isomer spectra are present within the reference library, which enabled comprehensive identifications. Additionally, as demonstrated by Lelevic et al., lower carbon number alkylbenzenes exhibit higher absorption (higher response factor) relative to other hydrocarbon class species. Alkanes, in contrast with low molecular weight alkyl benzenes, require higher molar concentrations for equivalent identification fidelity [38].

Table 1. Summary of the identification results organized by hydrocarbon groups. Identified species are listed along with their corresponding chromatograph peak labels in Figure 2.

Group Type	Species Name	Labels	%Mass
C9 Cycloaromatics	indane	p	0.799
C8 Alkylbenzenes	p-xylene	b*	0.384
	m-xylene	b*	1.274
	ethylbenzene	a	0.181
	o-xylene	c	1.844
C9 Alkylbenzenes	1-methyl-3-ethylbenzene	f*	20.604
	1-methyl-4-ethylbenzene	f*	10.879
	1,3,5-trimethylbenzene	f*	0.148
	1,2,4-trimethylbenzene	h*	26.686
	isopropylbenzene	d	0.275
	n-propylbenzene	e	1.92
	1-methyl-2-ethylbenzene	g	1.356
	1,2,3-trimethylbenzene	l	0.163
C10 Alkylbenzenes	sec-butylbenzene	i*	0.156
	1,3-diethylbenzene	m*	4.445
	1-methyl-3-n-propylbenzene	m*	3.213
	1-methyl-4-n-propylbenzene	m*	1.535
	1,3-dimethyl-5-ethylbenzene	n*	1.122
	1,4-diethylbenzene	n*	0.811
	1-methyl-3-isopropylbenzene	j	0.739
	1-methyl-4-isopropylbenzene	k	0.332
	1-methyl-2-n-propylbenzene	o	0.145
	1,4-dimethyl-2-ethylbenzene	q	0.678
	1,3-dimethyl-4-ethylbenzene	r	2.443
	1,2-dimethyl-4-ethylbenzene	s	10.089
	1,2,4,5-tetramethylbenzene	t	1.36

3.2 Two-Dimensional Deconvolution

Paramount to the success of identifying isomers in SAK is deconvolution capability. Coeluting species are marked with an asterisk (*) next to their peak letter label in Table 1. Collectively, 71.3 %m is contained in 6 peaks that required deconvolution, while 22.3 %m contained in 14 peaks did not require deconvolution. Nearly half of the identified isomers in this analysis required deconvolution for identification.

Figure 4 illustrates the deconvolution analysis of the largest peak in the SAK sample (labeled ‘f*’ in Table 2 and ‘f’ in Fig. 3). The bulk mass fraction of the peak is determined to be 31.6 %m of the total SAK composition. Namely, 1-methyl-3-ethylbenzene, 1-methyl-4-ethylbenzene, and 1,3,5-trimethyl benzene are found in this peak. The majority of this peak (99.54%m) is comprised of 1-methyl-3-ethylbenzene and 1-methyl-4-ethylbenzene. Also, 1,3,5-trimethyl benzene is found in

low concentrations here, 0.15%m total SAK mass or 0.46%m of the peak, respectively. Linear combinations of the scaled reference spectra for the three analytes of interest here achieve an R^2>0.999 at each timestamp reported.

The analytes at peak 'f' in Figure 2 exhibit a saturated VUV signal (absorbance exceeding 1.0) at some wavelengths, making its deconvolution less rigorous. To avoid that complication, the reduced injection volume method as described in the method section was applied. Figure 3 illustrates a blow-up of this peak after applying the reduced injection volume method. In contrast to Figure 2, the image shown in Figure 3c is from the VUV signal rather than the FID signal.

Figure 3a and 3d report the relative absorbance of 1-methyl-3-ethylbenzene and 1-methyl-4-ethylbenzene. Mathematically the absorbance signatures are dramatically different and distinguishable. The first dimension of separation, t_1, is the recorded time corresponding to modulation number, 'm', that a given analyte entered the secondary column. The second dimension, t_2, corresponds to the detection time in the VUV for a given modulation. Figure 3a illustrates the relative mass fractions of 1-methyl-3-ethylbenzene (dashed black lines) and 1-methyl-4-ethylbenzene (solid blue lines) over a given modulation index ('m'). Figure 3d compares the relative mass fractions of 1-methyl-3-ethylbenzene and 1-methyl-4-ethylbenzene for selected bins of t_2 values, with 'n' representing the first bin, and δ representing the width of each bin over t_2 for which absorbance was averaged. By parsing out the concentrations of each analyte across all of the peaks timesteps, the accuracy of the aggregate concentrations (across the whole peak) improves. Furthermore, it is possible to detect the presence minor peak concentrations, that are otherwise unidentifiable if looking at the average signal or summed signal of the entire peak, e.g., this deconvolution method reveals the presence of 1,3,5-trimethylbenzene at the low concentration of 0.15 %m.

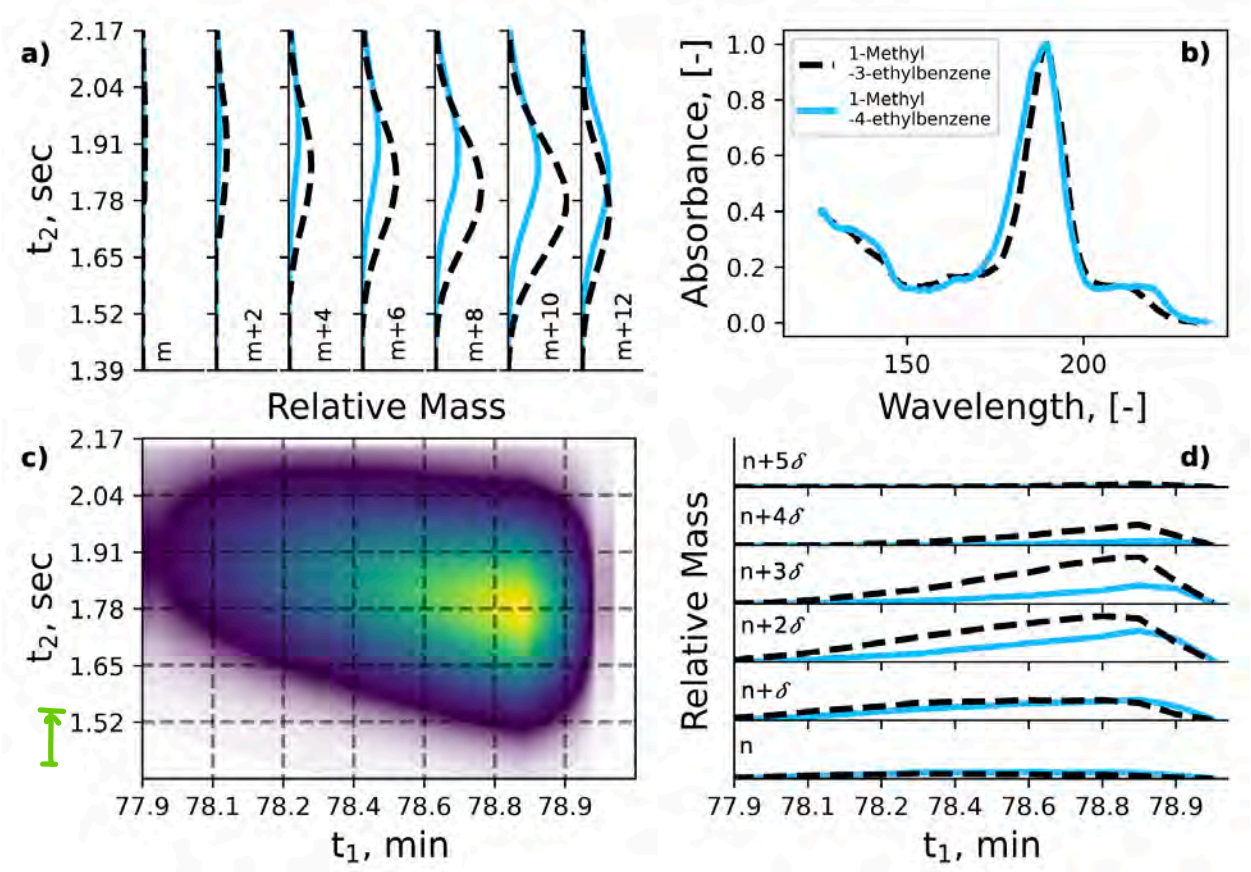

Figure 4. An illustration of the relative masses across peak 'f' (Fig. 3), determined through two-dimensional deconvolution (a and d) of 1-methyl-3-ethylbenzene (dashed black line) and 1-methyl-4-ethylbenzene (solid blue line). Subplots (c and d) depict the integrated VUV signal as a chromatographic peak and the normalized reference spectra of each species, respectively.

3.3 Fuel properties

Two sets of predictions, derived from our 'Tier Alpha' [16] methodology, are made and compared with laboratory measurements. In one set of predictions ('Tier Alpha + VUV'), the information conveyed in Table 1 is utilized in the calculations. For the other set of predictions ('Tier Alpha'), the total mass fraction of each hydrocarbon group type is randomly assigned to a specific isomer of the group in a Monte Carlo simulation. Either way, the properties of each specific component in the mixture-as-modeled are necessary input. The following mixture properties were measured and/or predicted in this work: surface tension at 22 °C, lower heating value (LHV), flash point, threshold sooting index (TSI), smoke point, freeze point, density as a function of temperature, and viscosity as a function of temperature, seal swell, and dielectric constant at 22°C.

Several temperature-independent property results are presented in Figure 5. Measurement data is represented by black-filled circles and lines. Predictions without (Table 1) isomer specificity are represented by blue open triangles and lines. Predictions that leverage the data presented in Table 1 are represented by red open circles and lines. Uncertainties for each determination are represented with 68 % confidence intervals (CI), solid lines, and 95 % CI, capped dashed lines. The accuracy of the applicable blending rule is not captured in the displayed confidence intervals. The green shaded region is derived from the aromatic fraction of the three reference fuels from the NJFCP: A-1 (POSF 10264), A-2 (POSF 10325), A-3 (POSF 10289). They are each the union of three 95% CIs as determined by the 'Tier Alpha' predictions and are intended to provide an additional context of where property values typically lie for the aromatic fraction of conventional fuels.

As evident in Figure 5, the confidence intervals (precision) of the predictions are markedly decreased when 93.6%m is attributable to specific isomers, which is not surprising since isomer uncertainty has been previously identified as the leading source of uncertainty in 'Tier Alpha' predictions when mass concentrations are lumped by hydrocarbon group [17,18]. With the improved prediction precision via specific isomer identifications, the prediction accuracy can be assessed more clearly. In these examples, however, the confidence intervals of the measurement overlap with those of both sets of predictions. Essentially no change in prediction accuracy is observed. The small shift in the prediction mean of LHV is consistent with the expectation that actual population distributions of isomers within any given hydrocarbon group are skewed toward lower heats of formation, not uniform [17]. The larger shift in the prediction mean of surface tension (σ) as well as the 4-5x improvement in the prediction precision underscores the value of the greater specificity of species identification afforded by the GCxGC/FID-VUV method relative to other separation methods where the analytes cannot be interrogated by a spectrographic method, such as VUV. The offset between the two mean surface tension predictions is due largely to the difference between the actual population distribution of C9 alkylbenzenes (accounting for 62.02 %m of the sample SAK) relative to a presumed uniform population distribution of these isomers. The mass fraction weighted average surface tension of the C9 alkylbenzenes is 0.9 mN/m less than the average surface tension of the C9 alkylbenzenes bin.

Viscosities and densities for SAK are illustrated in Figure 6 over a temperature range important to the safe operation of jet engines [27]. Specifically, Figure 6 includes SAK measurements, black circles, 'Tier Alpha' predictions without Table 1 inputs, blue lines, and 'Tier Alpha + VUV', predictions with Table 1 inputs, red lines. Uncertainty regions for each of the predicted methods are also included, where the light regions represent the 95% CIs, and the darker shaded regions represent the 68 % CIs. Device-reported uncertainties are also reported with error bars but are mostly masked due to scaling. Viscosity predictions, with Table 1 inputs, outperformed the standard 'Tier Alpha' by achieving reductions of 90% and 93% for mean error and 95 % CI, respectively. For density, mean error and 95 % CI reductions of 75 % and 89 % are observed, respectively. These accuracy and precision improvements are credited to the removal of the isomeric uncertainty gained by identifying the specific isomers that comprise more than 93%m of the SAK sample. The tier alpha method with either set of inputs, applied to viscosity, demonstrates better agreement with experimental data between 0 °C and 20 °C than they do below 0 °C. For viscosity, a portion of the error at the lower temperatures is due to error imparted through extrapolation (ASTM D341)[39] to lower temperatures than those available through NIST Thermo Tables [38]. This decrease in predictive accuracy between 0 °C and 20 °C was also observed in Heyne et al. [18]. The temperature sensitivity of density ($\Delta\rho/\Delta T$) is well captured by 'Tier Alpha + VUV' (with Table 1 inputs); deviating from the data by just 0.39%. A full tabulation of the neat material property measurements is available in Tables 2 and 3 of the Supplementary Material.

High carbon balance can be achieved with the techniques described in Section 2. The VUV absorption spectra for all known structural isomers of the major aromatic regions in this study (C8, C9 and C10 alkylbenzenes) were fully catalogued in our reference spectra library, thus eliminating concerns of encountering a false-positive match. Generally, as reference libraries become more complete at higher carbon numbers and other hydrocarbon types, the analysis demonstrated here will illuminate even more complicated and heavier fuels. To date, however, incomplete spectra libraries are relevant in instances of higher carbon numbers. For example, the two peaks to the lower right of 1,2-dimethyl-4-ethylbenzene (peak 's') in Figure 3 are unable to be resolved, likely due to incompletely catalogued VUV reference spectra for C10 cycloaromatics.

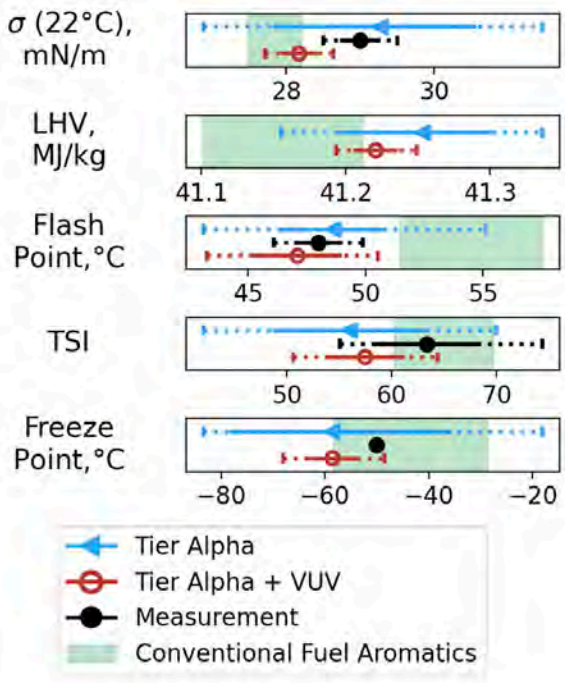

Figure 5. Comparison of predictions of 'Tier Alpha' (blue symbols and lines) to 'Tier Alpha + VUV' (red symbols and lines) in relation to nominal values determined through direct property measurement under ASTM standard methods. Conventional fuel (Jet A - only aromatic components) 95 % CI plotted as well in light green for reference.

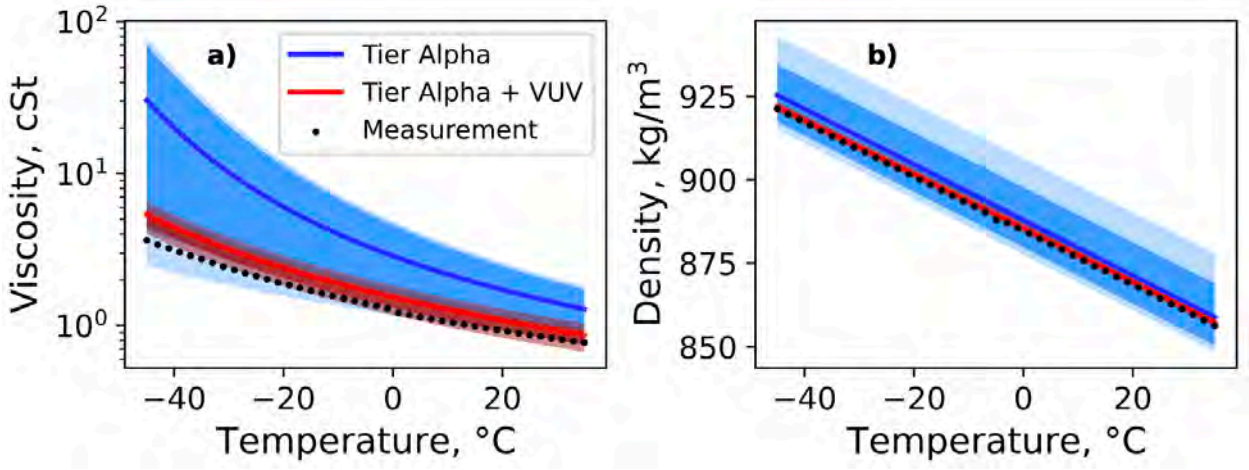

Figure 6. Predictions of viscosity and density with respect to temperature for Tier Alpha (blue line and shaded region) and Tier Alpha + VUV predictions (red line and shaded regions) in relation to measurement (black data points).

3.4 HEFA/SAK blend and HEFA properties

As mentioned in the introduction, aromatics facilitate compliance with several key properties, including material compatibility and dielectric constant. Compositions that are non-compliant with these two additional constraints, or any other fit-for-purpose or spec'd property (ASTM D7566), are not viable candidates for a 100% synthetic SAFs. Figure 7 reports the o-ring swelling, calculated dielectric constant values, and other important operability properties for a 79/21 %v HEFA/SAK blend and neat HEFA and neat SAK where available. Consistent with previous plots, the measurements, filled symbols, and uncertainties, error bars, are reported. These values are compared against a conventional fuel range (shaded green) and the specification limits, red lines, and shaded regions, described in ASTM D7566 [7] The blended HEFA/SAK composition is within the observed range of conventional fuels for each property considered in this work. Interestingly, the viscosity of the HEFA/SAK blend is significantly lower than the typical viscosities of conventional fuels. This is advantageous to engine operability as low viscosity often leads to finer and more uniformly distributed sprays at engine operating conditions that are consistent with altitude relight, ground start, and transitions in or out of flight idle [40,41]. Specifically, both the volume swell (12.3%) and predicted dielectric constant (2.096) are within the conventional fuel range.

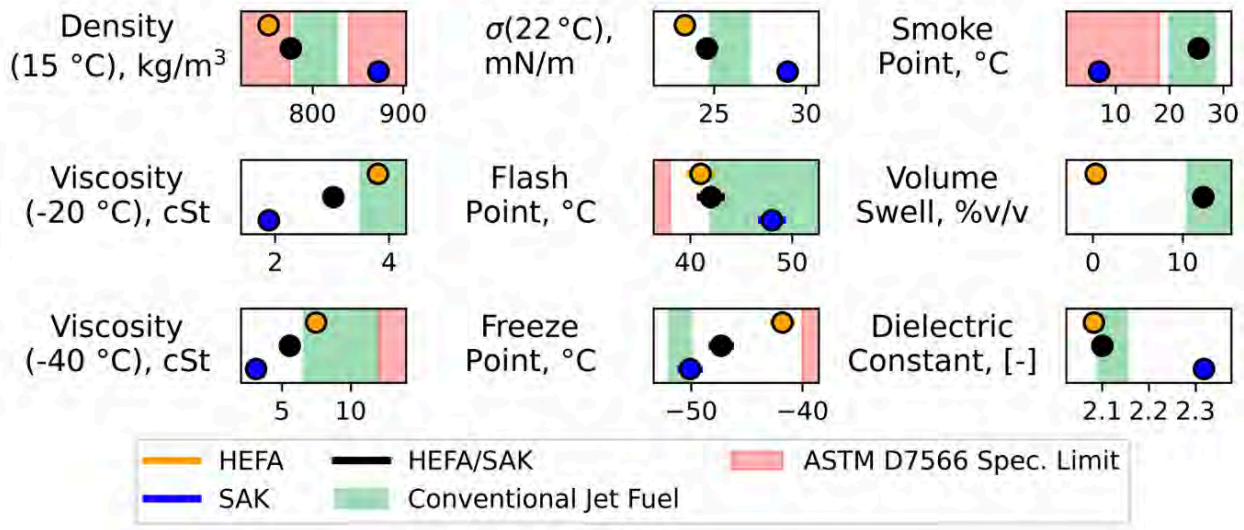

Figure 7. Selected 'fit for purpose' operability property measurements (black symbols) with measurement error (black lines), along with o-ring volume swell percentage and dielectric constant for 79/21 HEFA/SAK blend. Neat HEFA (yellow symbol and line) and neat SAK (blue symbol and line) are plotted. Conventional Jet Fuel (shaded green) and ASTM D7566 (shaded red) illustrate compliance.

4. Conclusions

A carbon balance greater than 93%m consisting of 26 separate analytes was identified in a relevant SAF (SAK) candidate. Of these, 73.1%m relied on the deconvolution method described herein. With added specific isomeric information, confidence in the property predictions improves relative to predictions predicated on conventional hydrocarbon group type analysis. Most notable, viscosity absolute error is reduced by 90% and 95-percentile confidence interval is reduced by 93%. For the properties measured, a HEFA/SAK blend illustrates a path for 100% SAF to remain drop-in for additional aviation properties (o-ring swelling and dielectric constant) while reducing nvPM with high relative aromatic contents and exhibiting other advantaged properties. Approximately 50%m of a typical conventional Jet-A is composed of in 44 peaks. Meaning the limit of detection for a VUV is not the limiting factor in using it for property evaluations. While the number of analyte spectra is the limiting bottleneck in GC x GC -VUV to property predictions, the potential for this method remains exceptionally high.

Funding

The authors would like to acknowledge funding from the U.S. Federal Aviation Administration Office of Environment and Energy through ASCENT, the FAA Center of Excellence for Alternative Jet Fuels and the Environment, project 65 through FAA Award Number 13-CAJFE-UD- 026 (PI: Dr. Joshua Heyne) under the supervision of Dr. Anna Oldani. Any opinions, findings, conclusions, or recommendations expressed in this material are those of the authors and do not necessarily reflect the views

of the FAA or other sponsors. Additional support for this paper was provided by US DOE BETO through subcontract PO 2196073.

Bibliography

[1] Lee DS, Fahey DW, Skowron A, Allen MR, Burkhardt U, Chen Q, et al. The contribution of global aviation to anthropogenic climate forcing for 2000 to 2018. Atmospheric Environment 2021;244. https://doi.org/10.1016/j.atmosenv.2020.117834.
[2] Vardon DR, Sherbacow BJ, Guan K, Heyne JS, Abdullah Z. Realizing "net-zero-carbon" sustainable aviation fuel. Joule 2022;6:16–21. https://doi.org/10.1016/j.joule.2021.12.013.
[3] Huq NA, Hafenstine GR, Huo X, Nguyen H, Tifft SM, Conklin DR, et al. Toward net-zero sustainable aviation fuel with wet waste-derived volatile fatty acids. Proc Natl Acad Sci U S A 2021;118. https://doi.org/10.1073/PNAS.2023008118/-/DCSUPPLEMENTAL.
[4] U.S. Energy Information Administration. Annual Energy Outlook 2021 2021. https:// www.eia.gov/outlooks/aeo/. (accessed January 26, 2022).
[5] de Jong S, Antonissen K, Hoefnagels R, Lonza L, Wang M, Faaij A, et al. Life-cycle analysis of greenhouse gas emissions from renewable jet fuel production. Biotechnology for Biofuels 2017;10:1–18. https://doi.org/10.1186/S13068-017-0739-7/TABLES/4.
[6] World's first passenger flight with 100% renewable fuel takes off—thanks to biotech | BIO n.d. https://www.bio.org/blogs/worlds-first-passenger-flight-100-renewable-fuel-takes-thanks-biotech (accessed May 9, 2022).
[7] Designation: D7566 − 19b Standard Specification for Aviation Turbine Fuel Containing Synthesized Hydrocarbons 1 n.d. https://doi.org/10.1520/D7566-19B.
[8] Kärcher B. Formation and radiative forcing of contrail cirrus. Nat Commun n.d.;9:1824.
[9] Boehm RC, Yang Z, Heyne JS. Threshold Sooting Index of Sustainable Aviation Fuel Candidates from Composition Input Alone: Progress toward Uncertainty Quantification. Energy & Fuels 2022:acs.energyfuels.1c03794. https://doi.org/10.1021/acs.energyfuels.1c03794.
[10] Kosir S, Heyne J, Graham J. A machine learning framework for drop-in volume swell characteristics of sustainable aviation fuel. Fuel 2020;274. https://doi.org/10.1016/j.fuel.2020.117832.
[11] Romanczyk M, Ramirez Velasco JH, Xu L, Vozka P, Dissanayake P, Wehde KE, et al. The capability of organic compounds to swell acrylonitrile butadiene O-rings and their effects on O-ring mechanical properties. Fuel 2019;238:483–92. https://doi.org/10.1016/j.fuel.2018.10.103.
[12] Edwards T. Reference jet fuels for combustion testing. AIAA SciTech Forum - 55th AIAA Aerospace Sciences Meeting 2017. https://doi.org/10.2514/6.2017-0146.
[13] Vozka P, Kilaz G. A review of aviation turbine fuel chemical composition-property relations. Fuel 2020;268. https://doi.org/10.1016/j.fuel.2020.117391.
[14] Vozka P, Modereger BA, Park AC, Zhang WTJ, Trice RW, Kenttämaa HI, et al. Jet fuel density via GC × GC-FID. Fuel 2019;235:1052–60. https://doi.org/10.1016/J.FUEL.2018.08.110.
[15] Wang Y, Ding Y, Wei W, Cao Y, Davidson DF, Hanson RK. On estimating physical and chemical properties of hydrocarbon fuels using mid-infrared FTIR spectra and regularized linear models. Fuel 2019;255. https://doi.org/10.1016/j.fuel.2019.115715.
[16] Yang Z, Kosir S, Stachler R, Shafer L, Anderson C, Heyne JS. A GC × GC Tier α combustor operability prescreening method for sustainable aviation fuel candidates. Fuel 2021;292. https://doi.org/10.1016/j.fuel.2021.120345.
[17] Boehm RC, Yang Z, Bell DC, Feldhausen J, Heyne JS. Lower heating value of jet fuel from hydrocarbon class concentration data and thermo-chemical reference data: An uncertainty quantification. Fuel 2022;311. https://doi.org/10.1016/j.fuel.2021.122542.
[18] Heyne J, Bell D, Feldhausen J, Yang Z, Boehm R. Towards fuel composition and properties from Two-dimensional gas chromatography with flame ionization and vacuum ultraviolet spectroscopy. Fuel 2022;312:122709. https://doi.org/10.1016/J.FUEL.2021.122709.
[19] Wang Y, Wei W, Zhang Y, Hanson RK. A new strategy of characterizing hydrocarbon fuels using FTIR spectra and generalized linear model with grouped-Lasso regularization. Fuel 2021;287. https://doi.org/10.1016/j.fuel.2020.119419.
[20] Striebich RC, Shafer LM, Adams RK, West ZJ, DeWitt MJ, Zabarnick S. Hydrocarbon group-type analysis of petroleum-derived and synthetic fuels using two-dimensional gas chromatography. Energy and Fuels 2014;28:5696–706. https://doi.org/10.1021/ef500813x.
[21] Schug KA, Sawicki I, Carlton DD, Fan H, McNair HM, Nimmo JP, et al. Vacuum ultraviolet detector for gas chromatography. Analytical Chemistry 2014;86:8329–35. https://doi.org/10.1021/ac5018343.

[22] Roberson ZR, Gordon HC, Goodpaster J v. Instrumental and chemometric analysis of opiates via gas chromatography–vacuum ultraviolet spectrophotometry (GC-VUV). Analytical and Bioanalytical Chemistry 2020;412:1123–8. https://doi.org/10.1007/s00216-019-02337-5.
[23] Kranenburg RF, Lukken CK, Schoenmakers PJ, van Asten AC. Spotting isomer mixtures in forensic illicit drug casework with GC–VUV using automated coelution detection and spectral deconvolution. Journal of Chromatography B: Analytical Technologies in the Biomedical and Life Sciences 2021;1173. https://doi.org/10.1016/j.jchromb.2021.122675.
[24] Skultety L, Frycak P, Qiu C, Smuts J, Shear-Laude L, Lemr K, et al. Resolution of isomeric new designer stimulants using gas chromatography – Vacuum ultraviolet spectroscopy and theoretical computations. Analytica Chimica Acta 2017;971:55–67. https://doi.org/10.1016/j.aca.2017.03.023.
[25] Walsh P, Garbalena M, Schug KA. Rapid Analysis and Time Interval Deconvolution for Comprehensive Fuel Compound Group Classification and Speciation Using Gas Chromatography-Vacuum Ultraviolet Spectroscopy. Analytical Chemistry 2016;88:11130–8. https://doi.org/10.1021/acs.analchem.6b03226.
[26] Wang FCY. Comprehensive Two-Dimensional Gas Chromatography Hyphenated with a Vacuum Ultraviolet Spectrometer to Analyze Diesel-A Three-Dimensional Separation (GC × GC × VUV) Approach. Energy and Fuels 2020;34:8012–7. https://doi.org/10.1021/acs.energyfuels.0c00688.
[27] Colket M, Heyne J, Rumizen M, Gupta M, Edwards T, Roquemore WM, et al. Overview of the national jet fuels combustion program. AIAA Journal 2017;55:1087–104. https://doi.org/10.2514/1.J055361.
[28] Berrier KL, Freye CE, Billingsley MC, Synovec RE. Predictive Modeling of Aerospace Fuel Properties Using Comprehensive Two-Dimensional Gas Chromatography with Time-Of-Flight Mass Spectrometry and Partial Least Squares Analysis. Energy and Fuels 2020;34:4084–94. https://doi.org/10.1021/ACS.ENERGYFUELS.9B04108/SUPPL_FILE/EF9B04108_SI_001.PDF.
[29] Boehm RC, Scholla LC, Heyne JS. Sustainable alternative fuel effects on energy consumption of jet engines. Fuel 2021;304. https://doi.org/10.1016/j.fuel.2021.121378.
[30] Hall C, Rauch B, Bauder U, le Clercq P, Aigner M. Predictive Capability Assessment of Probabilistic Machine Learning Models for Density Prediction of Conventional and Synthetic Jet Fuels. Energy and Fuels 2021;35:2520–30. https://doi.org/10.1021/acs.energyfuels.0c03779.
[31] Heyne JS, Colket M, Gupta M, Jardines A, Moder J, Edwards JT, et al. Year 2 of the national jet fuels combustion program: Moving towards a streamlined alternative jet fuels qualification and certification process. AIAA SciTech Forum - 55th AIAA Aerospace Sciences Meeting 2017. https://doi.org/10.2514/6.2017-0145.
[32] Heyne JS, Peiffer E, Colket M, Moder J, Edwards JT, Roquemore WM, et al. Year 3 of the national jet fuels combustion program: Practical and scientific impacts. AIAA Aerospace Sciences Meeting, 2018 2018. https://doi.org/10.2514/6.2018-1619.
[33] Lelevic A, Souchon V, Geantet C, Lorentz C, Moreaud M. Advanced data preprocessing for comprehensive two-dimensional gas chromatography with vacuum ultraviolet spectroscopy detection. Journal of Separation Science 2021;44:4141–50. https://doi.org/10.1002/jssc.202100528.
[34] Vozka P, Kilaz G. How to obtain a detailed chemical composition for middle distillates via GC × GC-FID without the need of GC × GC-TOF/MS. Fuel 2019;247:368–77. https://doi.org/10.1016/j.fuel.2019.03.009.
[35] Striebich R, Shafer L, West Z, Zabarnick S. UDR-TR-2021-159 Alternative Jet Fuel Evaluation and Specification. Dayton: 2021.
[36] Faulhaber C, Kosir ST, Borland C, Gawelek K, Boehm R, Heyne JS. Optical Dilatometry Measurements for the Quantification of Sustainable Aviation Fuel Materials Compatibility. n.d.
[37] Kroenlein K, Muzny C, Diky V, Chirico R, Magee J, Abdulagatov I, et al. NIST/TRC Web Thermo Tables (WTT) NIST Standard Reference Subscription Database 2 - Lite Edition Version 2 2011.
[38] Lelevic A, Geantet C, Moreaud M, Lorentz C, Souchon V. Quantitative Analysis of Hydrocarbons in Gas Oils by Two-Dimensional Comprehensive Gas Chromatography with Vacuum Ultraviolet Detection. Energy and Fuels 2021;35:13766–75. https://doi.org/10.1021/ACS.ENERGYFUELS.1C01910.
[39] Designation: D341 − 17 Standard Practice for Viscosity-Temperature Charts for Liquid Petroleum Products 1 n.d. https://doi.org/10.1520/D0341-17.
[40] Colket M, Heyne J. Fuel Effects on Operability of Aircraft Gas Turbine Combustors. Fuel Effects on Operability of Aircraft Gas Turbine Combustors 2021. https://doi.org/10.2514/4.106040.
[41] Hendershott T, Stouffer S, Monfort J, Diemer J, Busby K, Corporan E, et al. Ignition of conventional and alternative fuels at low temperatures in a single-cup swirl-stabilized combustor. AIAA Aerospace Sciences Meeting, 2018 2018. https://doi.org/10.2514/6.2018-1422.

Appendix 3

Blend Prediction Model for Freeze Point of Jet Fuel Range Hydrocarbons

Paper 7: Blend Prediction Model for Freeze Point of Jet Fuel Range Hydrocarbons

Nomenclature

Acronyms

ASTM	ASTM International, formerly known as American Society for Testing and Materials
DSC	Differential scanning colorimetry
SAF	Sustainable aviation fuel or fuels

Equation symbols

C_p	Constant pressure heat capacity
G	Gibbs free energy (G = H – TS)
H	Enthalpy (H = U + PV)
P	Pressure
S	Entropy
T	Temperature
N, n	Number of molecules (upper case), moles (lower case)
U	Internal energy
V	Volume fraction
x	Mole fraction
Δ	Property difference between two sets of defining environmental conditions

Subscripts

f	at the freeze point
i or j	arbitrary component of the mixture
liq	liquid
m or mix	mixture or mixing
T	total

1. Introduction

Aviation operations alone produced roughly 2% of the total carbon emissions in 2019, equating to over 900 million tons of carbon dioxide [1]. Technologies such as electric motors powered by fuel cells appear to be impossible for medium and long-haul flights and it is still unclear whether these technologies will positively impact reduction in carbon intensity [2]. A viable, short-term solution to reduce net carbon emissions are sustainable aviation fuels (SAF). SAF are derived from a renewable source and have demonstrated the ability to reduce carbon intensity to low and negative values [3]. Once a SAF is produced, it is thoroughly evaluated and endorsed by all stakeholders in an expensive and strenuous process detailed in ASTM D4054. The property and process specifications for each fuel must be approved and recorded in ASTM D7566 for quality regulation of SAF productions. Because the approval process is time and cost intensive, developing a prescreening process to identify or eliminate potential candidates is value added. Typical prescreening processes utilize very small sample volumes to measure or predict fuel properties that influence combustion figures of merit and other fit-for-purpose properties that are referred to here as key fuel properties. Recently, a prescreening method has been developed [4,5] in which the key chemical and physical properties of a potential SAF are predicted. The prescreening process provides valuable information to suppliers of possible risks to passing the evaluations of ASTM D4054. Prescreening expedites the evaluation process of alternative jet fuels by providing important feedback to potential suppliers even before a production-scale processing facility is built.

Freeze point is a key physical property of jet fuel that is essential in the prescreening process. The freeze point of jet fuel, per ASTM D1655 specification, must be below -40 °C and is typically much lower than the freeze point of several of its components. For example, n-tridecane is commonly found in both petroleum-derived jet fuel and SAF even though its freeze point is -4 °C, much higher than spec limit for the fuel. Understanding the relationship between the concentration of components in fuel and the temperature at which that component freezes out of solution is necessary toward the objective of setting concentration limits on certain components that may be introduced via SAF, for the purpose of SAF composition optimization.

The freeze point as defined by the ASTM D5972 is the temperature, upon heating, at which the last hydrocarbon crystal is detected [6]. Although the segment of the solid/liquid phase boundary that is relevant to jet fuel is analogous to the dew point curve of the liquid/vapor phase boundary, melting is used instead of freezing to measure points on this curve in order to avoid kinetic factors that create an inconsistent time lag, during heat extraction, between the conditions of thermodynamic

equilibrium and crystallization, resulting in supercooled liquid [7]. Similar kinetic factors do not exist upon melting. As defined, fuel freeze point provides an operation limit of the aircraft fuel system because fuel must remain in a liquid state to flow properly through the fuel system. If there is crystallization, the system will not operate as designed and jeopardize the operability and safety of the aircraft. Thus, an accurate knowledge of freeze point for potential SAF candidates is important.

Perhaps motivated by prior knowledge of the relatively high freeze point of n-alkanes compared to other hydrocarbons with a similar normal boiling point, early works on freeze point of various jet fuels sought to describe the relationship between n-alkanes composition variation and freeze point, with varying results. For example, Petrovic and Vitorovic determined a simple linear relationship between freeze point and the sum of the concentrations of the three longest n-alkanes present [8]. Then, Solash et al. determined a correlation between the inverse of the freeze point temperature and the logarithm of the concentration of hexadecane [9]. Affens et al. later confirmed this same behavior for several alkanes (C12-C17) with Isopar-M as well as the hexadecane in several solvents [10]. This was followed by Cookson et al. who determined a simple linear relationship (R^2 =0.91 and rmse = 1.3 ˚C) between freeze point and total n-alkane content for fuels in a relatively uniform in boiling range [11]. Differential scanning colorimetry (DSC) and cold-stage microscopy have been used by Zabarnick and others [12,13] to study phase transition behavior in jet fuels and showed that the effect of supercooling on crystallization was significant. More recently, Kuryakov and others [14–16] used a light scattering technique to detect phase transition behavior (melting, crystallization, rotator phase) in n-alkanes and showed that at low n-alkane concentrations, the sensitivity of the light scattering technique provided greater sensitivity than DSC to detect the paraffin phase transitions.

In this work, the freeze point of neat hydrocarbons as well as various blends of neat hydrocarbons with each other or with a petroleum-derived fuel are investigated. The objective of the study is to develop and validate a freeze point model for mixtures derived from first principles. The developed model is compared with existing freeze point models in the literature. The rest of the work is divided up into four sections. First, the experimental details for the freeze point measurements are provided. Second, a derivation of the freeze point model is given along with the other common models used in the literature. Next, the results of the model comparison to the experimental data are detailed. Lastly, the conclusions of the study are summarized.

2. Methodology

2.1 Experimental Setup

The Phase Technology PAC 70Xi: Cloud, Pour, and Freeze Point Analyzer was used to measure the freeze point of 55 samples as defined in ASTM D5972 [6]. The apparatus has a test resolution of 0.1 °C from -88 to 70°C and consists of a metallic sample chamber (holding 0.15 ml sample volume), a Peltier temperature controller, and a proprietary detection system based on diffusive light scattering. Upon initiation of the experiment, the sample is cooled at a rate of 15ºC/min ± 5 ºC/min until the detected opacity is above some threshold suggesting the surface of the sample is mostly solid. The system then signals the Peltier controller to warm the sample back to 20ºC at a warming rate of 10ºC/min ± 0.5 ºC/min. When the opacity returns to its original value, the apparatus will display an indicated freeze point temperature, which is -12.5 °C for the example measurement shown in Figure 1. According to the Phase Technology product brochure the reproducibility of such a measurement is ±0.8°C. Our independent evaluation of the repeatability, however, was ±10.4, motivating an alternative freeze point determination methodology. Instead of focusing on the temperature at which the opacity returns to its value at time zero, we developed a method of projecting the steepest slope on the heating side to an opacity value of zero; this point was taken as the freeze point and had an estimated repeatability 95 percentile confidence interval of ±1.5 °C. Readers interested in comparing the results of our method with those generated by the software provided by Phase Technology should contact the correspondence author. A zipped folder containing all raw data files, such as the example provided in Figure 1, is available upon request. In-between (repeat) measurements without a material change, the sample chamber is cleaned and dried using a cotton swab. In-between measurements with a material change, the sample chamber is rinsed with the new material prior to drying with a cotton swab.

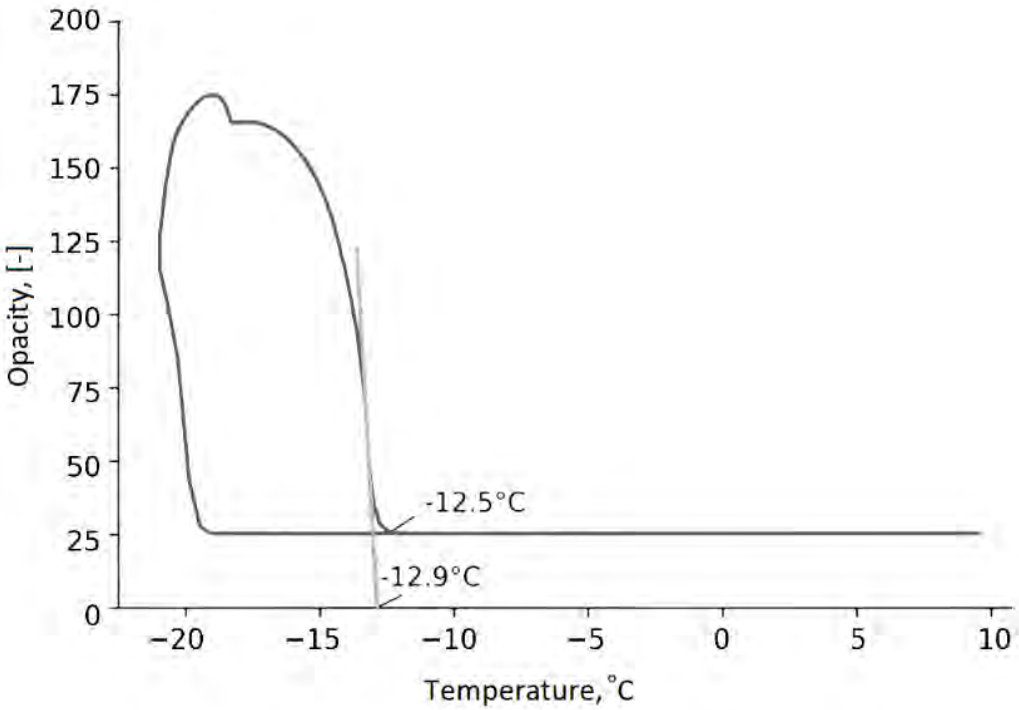

Figure 1. Representative freeze point determination by continuous opacity monitoring. The steep, straight line extending to zero opacity is an extension of the largest slope on the right side (heating) of the opacity verses temperature monitor.

2.2 Materials

Experimentally determined values were obtained from a total of seven neat liquids, 1 out-of-spec petroleum-derived fuel, and 47 binary or ternary blends of these materials for the purpose of evaluating blend freeze point prediction models. Bicyclohexyl and n-tridecane are particularly interesting because they freeze at temperatures well outside of the requirement specified in ASTM D7566 (-40 ˚C), but are known to exist at low concentration in fuels that do meet spec.[17,18] Fifteen mixtures, at various blend fractions, containing bicyclohexyl and 24 mixtures containing n-tridecane supported the primary focus of this investigation, which was to progress toward predictive capability relating to the fraction of high-freeze-point materials that a SAF may contain before it fails to meet the freeze point specification of ASTM D7566.

The supplier-reported purity and lab-measured freeze points of the neat liquids and petroleum fuel are listed in Table 1. While the reported impurities contribute to some freeze point depression of the neat liquids, three of the seven measured freeze points are higher than the values reported in the literature [19]. The primary cause of discrepancy between independent measurements is believed to be variation in sample purity rather than measurement methodology. The two neat liquids with the highest freeze points also have the highest purity, and these are the components that are most likely to freeze out of solution when they are blended with any of the other components. Relating specifically to the developed theory in later sections, accurate knowledge of the freeze point temperature and enthalpy (or entropy) of fusion of the component that is first-to-freeze (last-to-thaw) is especially important. The developed model uses this data as input and does not employ any information about the other components.

Table 1. Materials used and relevant properties.

Material	Molar Volume @ 15 ºC , (cm³/mol)	Freeze Point, (ºC) This Work / NIST	Purity as labeled
POSF 12968	187†	-34.2 / NA	NA
Bicyclohexyl	188.34	6.4 / 9.4	99%
n-Tridecane	243.87	-3.6 / -4.4	99%
Trans-decalin	154.30	-26.5 / -31.1	96.5%
1,2,3-trimethylbenzene	135.05	-29.5 / -25.3	>95%
1,2,4-trimethylbenzene	137.21	-47.5 / -44.4	98%
1,3,5-trimethylbenzene	139.11	-50.2 / -44.8	97%
Cis-1,2-dimethylcyclyhexane	140.97	-50.7 / -52	98%

† The molecular weight of sample POSF 12968 was determined from GCxGC/FID data.[18]

2.3 Blending Rules

Three blending rules are evaluated in this work. The wholly empirical model published by AlMulla et al. [20] was developed from a set of 33 data points corresponding to petroleum blends with freeze points ranging from -65 ˚C to +55 ˚C, which is substantially higher than jet fuel (-40 ˚C, maximum). This model is shown here as Equation 1 where V_i is the volume fraction of the ith component, $T_{f,i}$ is the freeze point of the ith component in Kelvin and $T_{f,m}$ is the freeze point of the mixture in Kelvin. Equation 2 is a rudimentary, volume-weighted model that seemed to capture much of the variation that had been observed in our lab prior to this study. The third model is derived from fundamental principles of thermodynamics as described next.

$$T_{f,m} = -0.639 + Ln(\sum_i V_i * (1.067)^{T_{f,i}}) \quad (1)$$

$$T_{f,m} = \sum_i V_i * T_{f,i} \quad (2)$$

For a pure solid in equilibrium with its liquid phase, the molar Gibbs free energy, G of the solid and liquid phases are equal, and the temperature is the freeze point (or melting point) regardless of the relative proportion of the liquid and solid phases in the system. The change in Gibbs free energy is nil when the proportion of the solid phase varies from 0 to 1 as enthalpy is extracted from the system while the temperature is constant. These fundamental observations, along with the definition of G, gives rise to equation 3, which is exact for pure materials, where H and S represent enthalpy and entropy, respectively and the subscript, fusion, represents the phase change.

$$T_f = \Delta H_{fusion} / \Delta S_{fusion} \quad (3)$$

For a mixture, Equation 3 can also be implemented, however, all terms refer to the freeze point, enthalpy, and entropy of fusion for the mixture and are generally unknown. To solve for these terms a Hess cycle, as illustrated in Figures 2 and 3, is constructed and analyzed. State 1 consists of two phases at a temperature equal to the freeze point of the mixture. The solid phase is assumed to consist of a single component and the liquid phase is assumed to consist of all components of the mixture except the one that freezes. State 2 also consists of two phases and differs from state 1 only with respect to system temperature which has been elevated to freeze point that the solid would have if it were isolated from the other components. To reach state 3 from state 2, the isolated solid has melted completely and the corresponding pure liquid remains isolated from the rest of the liquid components. State 4 consists of a single liquid mixture as the two isolated liquids of state 3 are mixed. Finally, to reach state 5, the liquid mixture is cooled until its temperature equals the freeze point of the mixture, the same temperature as state 1. Analogous to pure materials, states 1 and 5 represent different ends of the phase change process for which the change in G is zero. Therefore, the quantities of interest are the enthalpy and entropy differences between these two states as well as the mixture freeze point temperature. The change in enthalpy

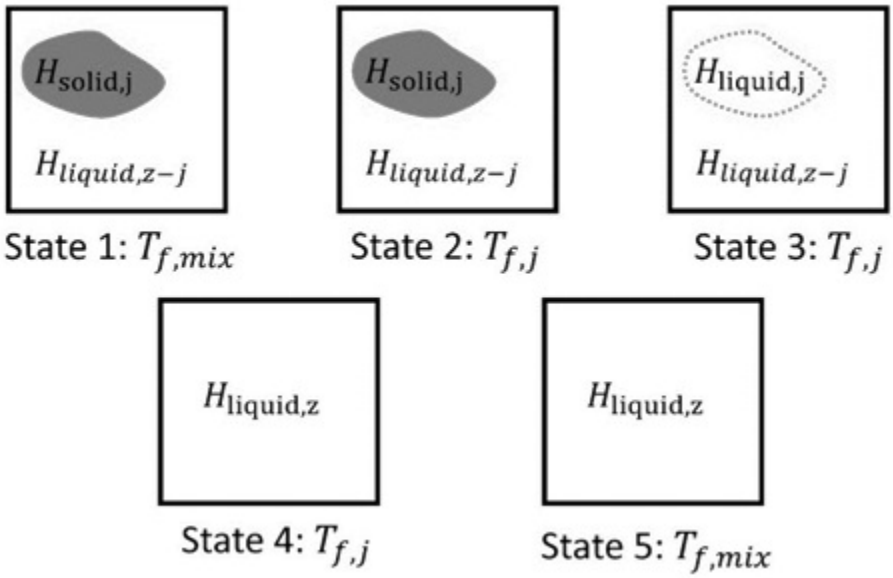

Figure 2. States of the system used in the Hess cycle. States 1 and 5 are the opposite ends of the phase transition isotherm throughout which the solid phase is in equilibrium with the mixed, liquid phase. The tracked processes are, from 1 to 5, heating, melting, mixing, cooling.

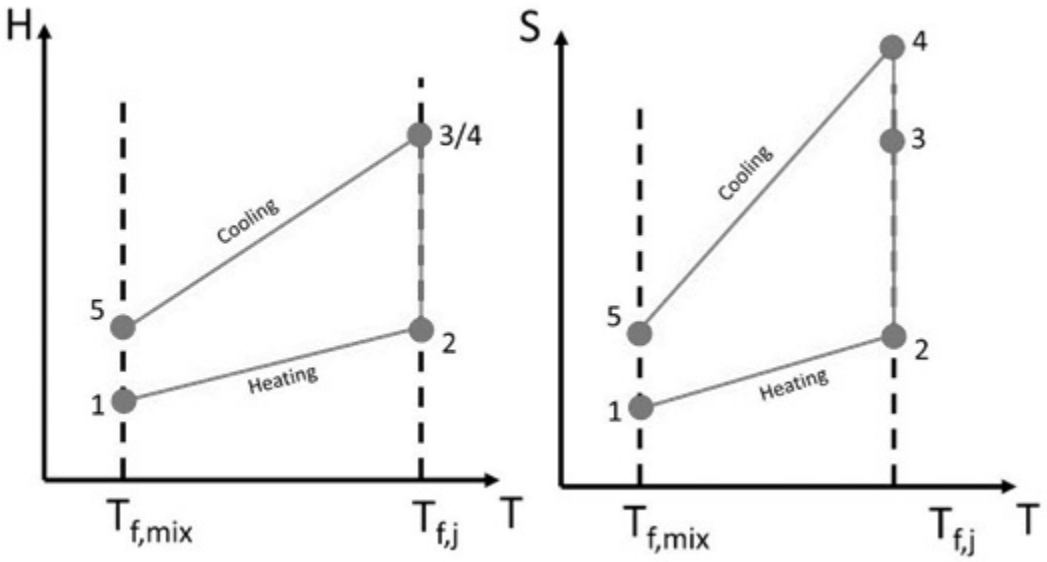

Figure 3. Enthalpy and entropy of states used in the Hess cycle.

and entropy is known or can be estimated for each leg of the Hess cycle. For one mole of component, j undergoing the phase change, Equations 5 through 14 apply, ultimately leading to Equation 4, which is the mixture analog of Equation 3. The heat capacity at constant pressure is represented by C_p in these equations.

$$T_{f,m} = \Delta H_{15}/\Delta S_{15} \quad (4)$$

$$\Delta H_{12} = C_{p,solid,j} * (T_{f,j} - T_{f,mix}) + (1/x_j - 1) * C_{p,liq,z-j} * (T_{f,j} - T_{f,mix}) \quad (5)$$

$$\Delta H_{23} = \Delta H_{fus,j} \text{ at } T = T_{f,j} \quad (6)$$

$$\Delta H_{34} = \Delta H_{mix} \quad (7)$$

$$\Delta H_{45} = (1/x_j) * C_{p,liq,z} * (T_{f,mix} - T_{f,j}) \quad (8)$$

$$\Delta H_{15} = \Delta H_{12} + \Delta H_{23} + \Delta H_{34} + \Delta H_{45} \quad (9)$$

$$\Delta S_{12} = C_{p,solid,j} * (Ln(T_{f,j}) - Ln(T_{f,mix})) + (1/x_j - 1) * C_{p,liq,z-j} * (Ln(T_{f,j}) - Ln(T_{f,mix})) \quad (10)$$

$$\Delta S_{23} = \Delta S_{fus,j} \text{ at } T = T_{f,j} \quad (11)$$

$$\Delta S_{34} = \Delta S_{mix} \quad (12)$$

$$\Delta S_{45} = (1/x_j) * C_{p,liq,z} * (Ln(T_{f,mix}) - Ln(T_{f,j})) \quad (13)$$

$$\Delta S_{15} = \Delta S_{12} + \Delta S_{23} + \Delta S_{34} + \Delta S_{45} \quad (14)$$

After expanding Equation 4, the following information is necessary to predict the freeze point of a given liquid mixture. The identity of the frozen component must be known as well as its enthalpy and entropy of fusion and the heat capacity of its solid phase. The heat capacity of the liquid mixture, with and without component j, must be estimated and the enthalpy and entropy of mixing must also be estimated. To estimate the heat capacity of the liquid mixtures, the blending rule for heat capacity [21] is used. This blending rule is reproduced here as Equation 15 where x_i is the mole fraction of the i[th]

$$C_{p,liq,z} = \sum_i x_i * C_{p,liq,i} \quad (15)$$

$$(n_T - 1) * C_{p,liq,(z-j)} - n_T * C_{p,liq,z} = -C_{p,liq,j} \quad (16)$$

component. Its application to this problem is represented by Equation 16 where n_T (or (1/xj)) is the total number of moles in the system, out of which one mole of component, j freezes. The work of Neaf [22] was leveraged to estimate the heat capacity of component, j in both the solid phase and the super-cooled liquid phase. The difference between these two estimates was scaled by x_j because in the limit of infinitesimal mole fraction, the freeze point temperature (of that component) approaches zero and the molecular-level structures of the respective phases are expected to converge. The enthalpy of mixing is estimated as zero because the changes to the internal energy (U) brought about by mixing are small relative to the changes brought about by the phase change and there is little change in volume as hydrocarbons are mixed. This approximation it written here as Equation 17, and is further justified empirically by the measurements of Lundberg [23].

$$\Delta H_{mix} = P\,\Delta V_{mix} + \Delta U_{mix} \approx P\,\Delta V_{mix} \approx 0 \quad (17)$$

The entropy of mixing is significant relative to the entropy of fusion. To estimate its magnitude, we start with the following set of approximations or assumptions, analogous to those used for gasses. We mix one mole of component, j into another liquid that contains $(n_T - 1)$ moles of molecules other than j. As a simplifying approximation, entropy is considered first on a basis of conformations and permutations of molecules rather than quantum energy levels available to the system. Moreover, the role of vacancies on the possible number of lattice conformations is, at first neglected as is the likely possibility that liquids mix on a cluster scale rather than a molecular scale. To correct for these three assumptions, an empirical scaling factor (α) is included to the computed entropy of mixing of an ideal solution. Within the ideal solution approximation, the entropy of the fluid is given by equation 18 where k is Boltzmann's constant and N is the number of molecules. This is applied to one mole of component j, $(n_T - 1)$ moles of the fluid before it is mixed with component j, and (n_T) moles of the mixed fluids, and the entropy of mixing is expressed as Equation 19, where the subscripts refer to component j (j), the final mixture (T), or the mixture without component j (T-j). By expressing the first occurrence of N_T as $(N_{T-j} + N_j)$, rearranging terms, and factoring out Avogadro's number, Equation 20 results.

$$S = k * \ln(N!) \quad (18)$$

$$\Delta S_{mixing} = k * [\, N_T \ln(N_T) - N_{T-j} \ln(N_{T-j}) - N_j \ln(N_j) \,] \quad (19)$$

$$\Delta S_{mixing} = -R * (1/X_j) * [\, (1 - X_j) * \ln(1 - X_j) + X_j * \ln(X_j) \,] \quad (20)$$

By substitution, Equation 4 can now be re-written as Equation 21, which is readily solvable by iteration: $y_n = f(y_{(n-1)})$. In this work the initial guess was determined by setting $x_i = 0$ and convergence was achieved within five iterations.

$$T_{f,mix} = \frac{\Delta H_{fusion,i} + x_i * (Cp_{sol,i} - Cp_{liq,i}) * (T_{f,i} - T_{f,mix})}{\Delta S_{fusion,i} + x_i * (Cp_{sol,i} - Cp_{liq,i}) * \ln\left(\frac{T_{f,i}}{T_{f,mix}}\right) + \alpha * \Delta S_{mixing}} \quad (21)$$

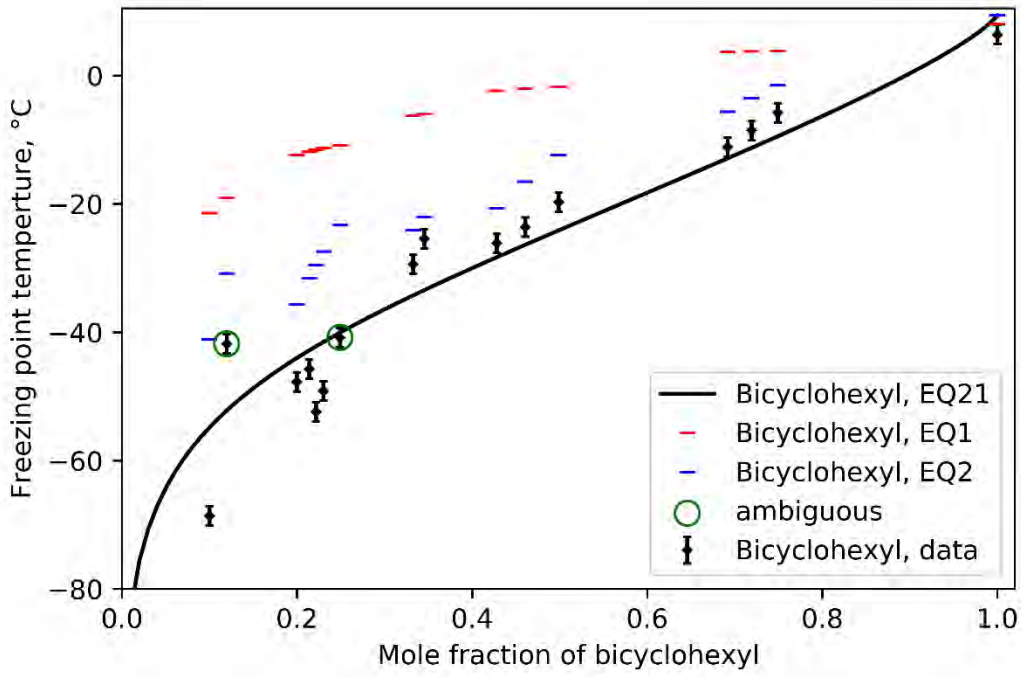

Figure 4. Measured and predicted freeze points of mixtures containing bicylcohexyl. The symbol height equals one standard deviation, measurement uncertainty. The error bar height equals two standard deviations.

3. Results and Discussion

The experimental data and model predictions are presented within three figures and one table. In Figure 4, the freeze point temperature is displayed as a function of the mole fraction of bicyclohexyl (black diamonds) because this is the component that is most likely to freeze first (or thaw last). Apart from the two (circled) data points with a declared freeze point of bicyclohexyl of -40.8 and -41.8 ˚C, there is a very high degree of confidence that the last component to melt is as labeled in the figure. Those two data points refer to mixtures that contain 75%v petroleum fuel sample POSF 12968, which has a freeze point of -34.2 ˚C when it is not diluted by other solvents. The identity of the highest-freeze-point component in those two mixtures is not known with certainty. It could be bicyclohexyl or it could be an undetermined component found in the petroleum fuel sample. Assuming, for the sake of argument, that the highest-freeze-point component originated with the petroleum blend component, it is certainly possible that diluting its concentration by a factor of 0.75 is sufficient to cause a freeze point depression of 7 ˚C.

In Figure 5, the freeze point temperature of a different subset of data is displayed as a function of the mole fraction of n-tridecane (black diamonds) because this is the components that is most likely to freeze first (or thaw last) in those mixtures. Apart from the two (circled) data points with a declared freeze point of n-tridecane of -36.6 and -32.9 ˚C, there is a very high

degree of confidence that the last component to melt is as labeled in the figure. Those two data points refer to mixtures that contain 75%v trans decalin, which has a freeze point of -26.5 ˚C when it is not diluted by other solvents. The identity of the highest-freeze-point component in these mixtures is not known with certainty. It could be n-tridecane or it could be trans decalin. Assuming, for the sake of argument, that the highest-freeze-point component is trans decalin, it is certainly possible that diluting its concentration by a factor of 0.75 is sufficient to cause a freeze point depression of 6 to 10 ˚C. Among the displayed data, seven data points have a mole fraction of n-tridecane between 0.0156 and 0.0170, mixed with a variety of solvents. The measured freeze points of these mixtures are -32.9 ± 0.8 ˚C. The predicted freeze points of tridecane, via Equation 21, in these mixtures are -18.1 ± 0.2 ˚C. In contrast, the Equations 1 and 2 prediction ranges have standard deviations of 2.2˚C and 6.0˚C, respectively. While this is a particularly conspicuous example, closer examination of all the data collected in this investigation shows little to no solvent influence on the freeze point of the highest-freeze-point component, when plotted against the mole fraction of that component. In other words, the measured data shown in Figures 4 and 5 confirm that the freeze point of component j, where j refers to either bicyclohexyl or n-tridecane in these examples, depends on the mole fraction of the highest-freeze-point component, and does not show significant variation with the identity or number of other components present in the mixture. Consistent with this observation, Equation 21 predicts no solvent influence, while Equations 1 and 2 are both influenced significantly by solvents.

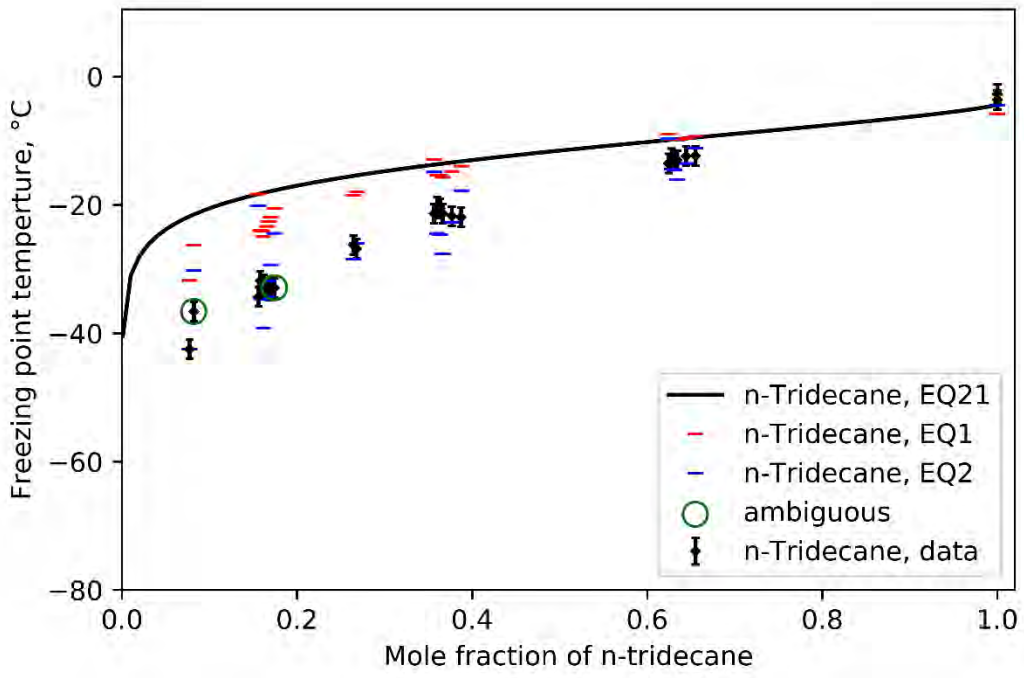

Figure 5. Measured and predicted freeze points of mixtures containing n-tridecane. The symbol height equals one standard deviation, measurement uncertainty. The error bar height equals two standard deviations.

Both sets of data show a steep decline in freeze point as the mole fraction of the highest-freeze-point component is taken below 0.25. While the model represented by Equation 21 also shows a steep roll off at low mole fraction, its knee is closer to a mole fraction of 0.10. Such an offset could be due to the assumption that the scale factor, α is independent of mole fraction and the identity of the highest-freeze-point component. We chose $\alpha = 0.25$ based on visual fit to bicyclohexyl datapoints. This selection results in a model that is conservative for both sets of data at mole fractions less than 0.25. Conservative estimates for freeze point at these low mole fractions provides a safety factor for system design. For detailed engineering work, to remove some of the conservatism, Equation 21 can be tuned to existing data by varying α; resulting in a refined design curve for the component of interest.

The modelling error is further discussed here and is summarized in Figures 6 and 7. Figure 6 is a unity plot, including the results for all three models, with filled/open symbols delineating mixtures containing bicyclohexyl or n-tridecane. The motivation for making this delineation is to underscore the observation made here that the identity of the highest-freeze-point component is particularly important to the freeze point of the mixture. The points previously identified as ambiguous in Figures 4 and 5 are included in this figure (and the next figure), which is relevant only to Equation 21 results as the predicted freeze point of bicyclohexyl (or n-tridecane) is irrelevant if that is not the highest-freeze-point component. Based on this figure alone, the superiority of Equation 21 over Equation 2 is not obvious, but clearly the extension of the wholly empirical model, Equation 1 to mixtures outside of the domain over which it was developed leads to undesirable error, especially at low freeze points.

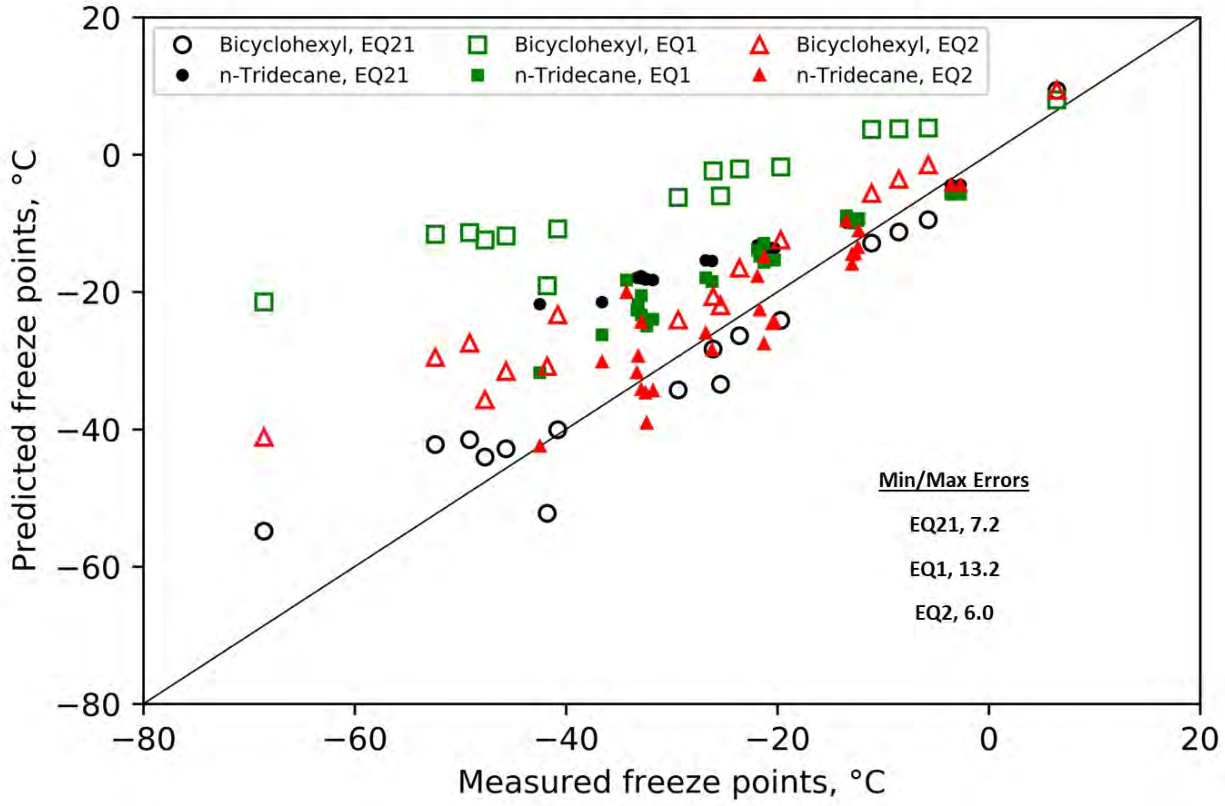

Figure 6. Unity plot assessment of modelling error.

Figure 7 shows the modeling error (prediction minus data) of each prediction method at each point, plotted as a function of the mole fraction of bicyclohexyl (open symbols) or the mole fraction of n-tridecane (filled symbols). All the models struggle to predict the freeze point of the highest-freeze-point component when it constitutes less than 25%$_{mol}$ of the mixture, which is unfortunate because real jet fuels rarely contain any component at a concentration above 25% because of volatility and freeze point restrictions[24]. (The only exception known: Annex A5 of ASTM D7566 does allow for a certain C12 isomer made from isobutanol to exist in jet fuel above this threshold.) Therefore, it is important to understand freeze point model prediction errors of relatively dilute solutes even though it is difficult to obtain a measured freeze point at lower mole fractions due to device limitations and because of competition between the various high-freeze-point components in the mixture. The results of this work indicate that the model developed here performs more consistently than the previous model. The un-tuned model (Equation 21) overpredicts by 0.7 to 20.1 °C at mole fractions between 0.065 and 0.25 (but can be tuned to match the measured data to within the 95 percent confidence interval). While the predicted temperature errors vary inversely and steeply with mole fraction in this region, the maximum observed offset in mole fraction is 0.07.

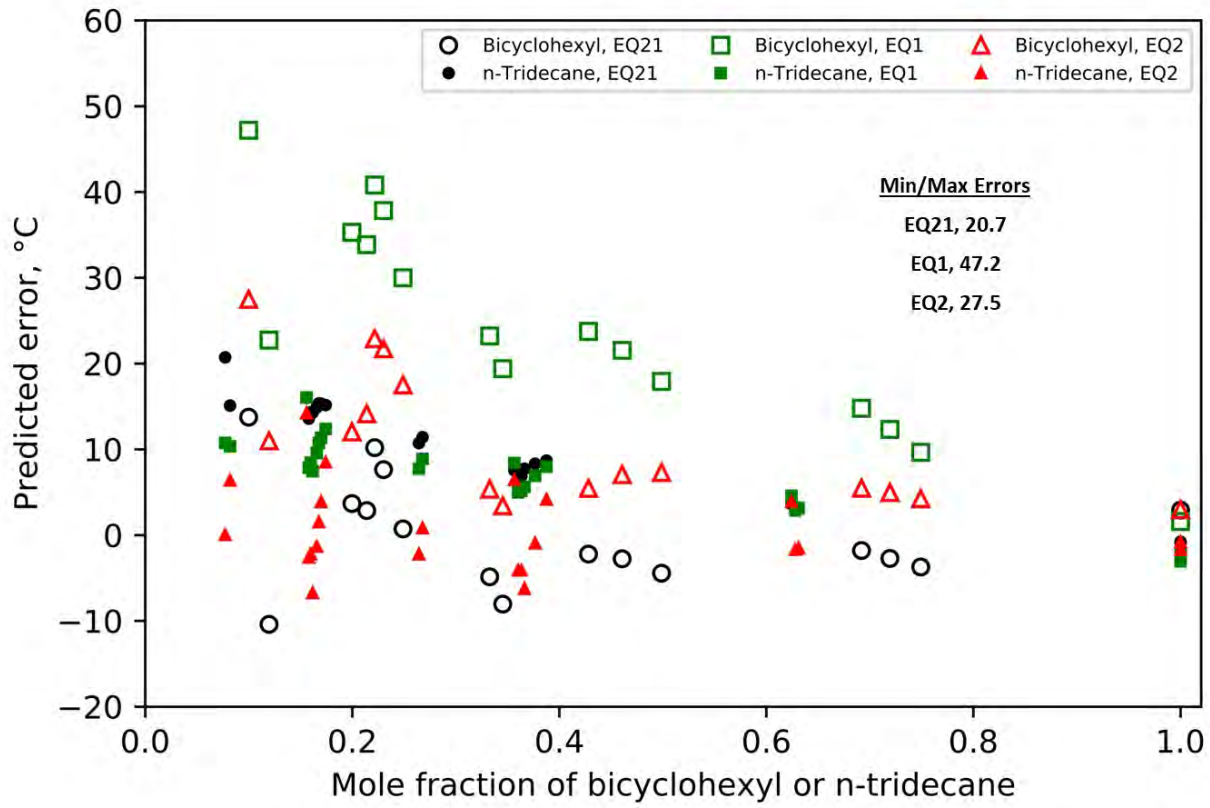

Figure 7. Modelling error as a function of high-freeze-point component mole fraction.

Quantifying allowable high-freeze-point component concentration in jet fuel is of more use to potential SAF developers. For example, the un-tuned model implies that n-tridecane can exist in jet fuel at a mole fraction up to 0.001 without risk to the freeze point specification (-40 ˚C), but the data shows that it can exist at a mole fraction up to 0.065. The un-tuned model therefore conservatively converts the specified maximum freeze point to a maximum allowed concentration of components based on risk to the to the freeze point specification. Most importantly, this model is known to be conservative. In contrast, and as seen in Figure 7, the errors stemming from the purely empirical models can be positive or negative and can have a magnitude up to 47 °C.

In problems where the composition and identity of each high-freeze-point component is known, Equation 21 is particularly convenient because it requires only two pieces of data (two of the three properties related by Equation 3) per component. In contrast, to use Equation 1 or 2, the freeze point and composition of every component is required. For example, a fuel developer may want to know how much 2-ethylnaphthalene (nBp=-7.4 ˚C) can be added to fuel (e.g., to meet the seal swell, fit-for-purpose requirement) before it presents a high risk to the freeze point specification. In this case, the evaluating engineer only needs to know, additionally, the enthalpy or entropy of fusion of 2-ethylnaphthalene and how much of this component may be already present in other blend stocks. In another potential application, a SAF developer may learn that its product freezes at, say -10 ˚C and desires to potentially alter the composition of their product to maximize the blending ratio into petroleum-derived fuel, resulting in a blended fuel with a freeze point less than -40 ˚C. The first step, in this example would be to identify each of the components in the SAF, via a technique such as GCxGC/FID-VUV[21], that present risk to the freeze point limit. The next step would be to employ the model developed here to understand how much reduction in concentration of each high-freeze-point component is necessary to drive its, as-mixed freeze point below -40 ˚C.

A potential concern with Equation 21, for species with an unusually low entropy of fusion such as trans-decalin ($\Delta S_{fusion} = 13.4$ J/mol/K), is that it may not iterate to convergence at some values of mole fraction because the denominator approaches zero. The entropy of fusion of bicyclohexyl is 24 J/mol/K, which is towards the low end of its distribution for hydrocarbons,

and for n-tridecane it is 106 J/mol/K, which is towards the high end of its distribution for hydrocarbons. The rule-of-thumb estimate for hydrocarbons provided by Walden [25] is 56.5 J/mol/K. It is this term in Equation 21 (ΔS_{fusion}) that has the biggest impact on the slopes of the freeze point verses mole fraction curves shown in Figures 4 and 5. For samples of unknown composition, application of Equation 21 is not possible but Equations 1 and 2 can be used, provided the freeze point of each component is known, even if the so-called, "component" is really a complex mixture of unknown composition instead of a neat material.

The four data points that are labeled as ambiguous in Figures 4 and 5 are provided in Table 2 along with additional data as relevant to support the point of this paragraph. All other data, including average measured freeze point and model predictions are provided in the supporting material. Table 2 contains three sets of data points. One set is comprised of three blends of 1,2-dimethylcyclohexane with petroleum fuel sample, POSF 12968 in different blend ratios. Since the measured freezing point of two of these mixtures is greater than or equal to the freeze point of neat, 1,2-dimethylcyclohexane, we know that highest-freeze-point component in these mixtures originates with POSF 12968, which has a freeze point of -34.2 C. As the fraction of POSF 12968 decreases the freeze point of the mixture decreases. At the lowest blend ratio, the freeze point of the mixture is below the freeze point of both components. The observed trend between the mole fraction of POSF 12968 and the freeze point of the mixture is consistent with those of bicyclohexyl or n-tridecane mixtures, as discussed earlier. However, the predicted freeze point of 1,2-dimethylcyclohexane is also close to the observed freeze point of the mixture. The next set of datapoints include three different mixtures comprised of 75%v POSF 12968. The observed freeze point range of these mixtures is 41.6 ± 1.2. Since we know from theory that the freeze point of any component that is mixed at 12.5% should be significantly lower than it is at 25%, we conclude that highest-freeze-point component in the mixture that contains 12.5%v of bicyclohexyl is not bicyclohexyl. The highest-freeze-point component in the mixture that contains 25%v bicyclohexyl is not clear as its observed freeze point is only 1.3 ˚C higher than the average of the other two points in this set. The last subset included in this table are mixtures that contain 75%v trans-decalin, which has a freeze point of -26.5 ˚C when not mixed. All three of the mixtures have an observed freeze point that is significantly less than that of neat trans-decalin so it cannot be immediately ruled out as the highest-freeze-point component of any of these mixtures. However, the range of observed freeze points, -39.3 to -32.9 ˚C is sufficiently high to conclude that the highest-freeze-point component in the mixture that contains 25%v n-tridecane is n-tridecane, not trans-decalin. At the other end of the range, the highest-freeze-point component in the mixture containing 25%v dimethylcyclohexane must be trans-decalin, by elimination, because the freeze point of neat 1,2-dimethylcyclohexane is lower than the observed freeze point of the mixture. Regarding the mixture that contains 12.5%v n-tridecane and 75%v trans-decalin, it is not clear which of these two materials is the highest-freeze-point component.

Table 2. Freeze point of mixtures with uncertain highest-freeze-point component with supporting data **.**

Component A Blend Ratio, %v	Component B Blend Ratio, %v	Data, ºC	EQ21, ºC	EQ1, ºC	EQ2, ºC
12DMCH [a,b] 75	POSF 12968 [b] 25	-60.3	A, -55.8 [c] B, << -34	-66.9	-71.1
12DMCH [d] 50	**POSF 12968** [e] 50	-50.5	*A, -60.2* **B, < -34**	-60.2	-64.3
12DMCH 25	**POSF 12968** 75	-42.3	*A, -66.2* **B, < -34**	-55.5	-57.5
Bicyclohexyl 25	POSF 12968 75	-40.8	A, -40.1 B, < -34	-12.4	-35.7
Bicyclohexyl	**POSF 12968**	-41.8	*A, -52.2* **B, < -34**	-22.2	-46.6

12.5 [f]	75 [f]				
12DMCH	**Trans-decalin**	-39.3	*A, << -51*	-36.6	-42.8
25	75		**B,** -33.6 [c]		
n-tridecane	*Trans-decalin*	-32.9	**A, -19.1**	-20.5	-24.4
25	75		*B,* -35.8 [c]		
n-tridecane	Trans-decalin	-36.6	A, -22.4	-26.5	-33.6
12.5 [f]	75 [f]		B, -34.8 [c]		

[a] 12DMCH is short for cis- 1,2-dimethylcyclohexane.
[b] Where neither component is italicized or bolded, it is unclear which component is the last to thaw.
[c] Used Walden's value for entropy of fusion and measured freeze points of neat material as inputs.
[d] Components identified with italics are not the last to thaw.
[e] Components identified with bold font either are or contain the highest-freeze point species.
[f] The balance of the composition is 1,2-Dimethylcyclohexane.

4. Conclusion

A new model for freeze point prediction of sustainable aviation fuel candidates is presented along with experimental measurements of several hydrocarbon blends. The model is based on first principle thermodynamics and validated with experimental freeze data. The developed model is designed to require only the following inputs: the molecular identity of the components that present risk of freezing above -40 °C, their respective mole fractions, and their repective freeze points and enthalpies and entropies of fusion as pure components. It is not necessary to know the identity or mole fractions of the light fraction, or the identity of components that are present at very low concentration. The model captures the non-linear behavior verus mole fraction for mixture freeze points, and conservatively estimates the freeze point at low mole fractions. For fractions between 0.065 and 0.25 the model is shown to overpredict the measured freeze point by 0.7 to 20.1 °C, where the larger errors correspond to low mole fraction where the change in freeze point with mole fraction is steep. The practical implication of this error is that the model underpredicts the allowable mole fraction of the high-freeze-point components. For example, the acceptable mole fraction of n-tridecane is underestimated by 0.064.

5. Supporting Information

All the freeze point data, measured and predicted, taken in support of this manuscript is provided within a single worksheet of the attached document (XLSX).

Acknowledgments

This research was funded by the U.S. Federal Aviation Administration Office of Environment and Energy through ASCENT, the FAA Center of Excellence for Alternative Jet Fuels and the Environment, project 065a through FAA Award Number 13-C-AJFE-UD-026 under the supervision of Dr. Anna Oldani. Any opinions, findings, conclusions, or recommendations expressed in this material are those of the authors and do not necessarily reflect the views of the FAA. Additional support for this paper was provided by U.S. DOE BETO through subcontract PO 2196073.

References

[1] Air Transportation Action Group: ATAG. *Aviation Beyond Borders*. Geneva, Switzerland, 2020.

[2] Air Transportation Action Group: ATAG. *Waypoint 2050*. Geneva, Switzerland, 2020.

[3] Huq, N. A., Hafenstine, G. R., Huo, X., Nguyen, H., M., Stephen, T., Conklin, D. R., Stück, D., Stunkel, J., Christensen, E. D., Cameron, Hays, Wiatrowski, M. R., Zhang, Y., Tao, L., Yang, Z., Heyne, J., Abdullah, Z., and Vardon, D. R. "Towards Net-Zero Sustainable Aviation Fuel with Wet Waste-Derived Volatile Fatty Acids." *Proceedings of the National Academies of Science*, 2021.

[4] Yang, Z., Kosir, S., Stachler, R., Shafer, L., Anderson, C., and Heyne, J. S. " A GC × GC Tier α Combustor Operability Prescreening Method for Sustainable Aviation Fuel Candidates ." *Fuel*, Vol. 292, No. September 2020, 2021, p. 120345. https://doi.org/10.1016/j.fuel.2021.120345.

[5] Heyne, J., Rauch, B., Le Clercq, P., and Colket, M. "Sustainable Aviation Fuel Prescreening Tools and Procedures." *Fuel*, Vol. 290, 2021, p. 120004. https://doi.org/https://doi.org/10.1016/j.fuel.2020.120004.

[6] ASTM. "Standard Test Method for Freezing Point of Aviation Fuels." *Manual on Hydrocarbon Analysis, 6th Edition*, 2008, pp. 342-342–4. https://doi.org/10.1520/mnl10883m.

[7] Moynihan, C., Shahriari, M., and Bardakci, T. "Thermal Analysis of Melting and Freezing of Jet and Diesel Fuels." *Thermochimica Acta*, Vol. 52, 1982, pp. 131–141.

[8] Petrovic, K., and Vitorovic, D. "A New Method for the Estimation of the Freezing Point of Jet Fuels Based on the N-Paraffin Content." *J. Inst. Petroleum*, Vol. 59, No. 565, 1973, pp. 20–26.

[9] Solash, J., Hazlett, R., Hall, J., and Nowack, C. "Relation between Fuel Properties and Chemical Composition. 1. Jet Fuels from Coal, Oil Shale and Tar Sands." *Fuel*, Vol. 57, No. 9, 1978, pp. 521–528. https://doi.org/https://doi.org/10.1016/0016-2361(78)90036-4.

[10] Affens, W., Hall, J., Holt, S., and Hazlett, R. "Effect of Composition on Freezing Points of Model Hydrocarbon Fuels." *Fuel*, Vol. 63, No. 4, 1984, pp. 543–547. https://doi.org/https://doi.org/10.1016/0016-2361(84)90294-1.

[11] Cookson, D. J., Lloyd, C. P., and Smith, B. E. "Investigation of the Chemical Basis of Kerosene (Jet Fuel) Specification Properties." *Energy and Fuels*, Vol. 1, No. 5, 1987, pp. 438–447. https://doi.org/10.1021/EF00005A011.

[12] Zabarnick, S., and Widmor, N. "Studies of Jet Fuel Freezing by Differential Scanning Calorimetry." *Energy & Fuels*, Vol. 15, No. 6, 2001, pp. 1447–1453. https://doi.org/https://doi.org/10.1021/ef010074b.

[13] Widmor, N., Ervin, J. S., Zabarnick, S., and Vangness, M. "Studies of Jet Fuel Freezing by Differential Scanning Calorimetry and Cold-Stage Microscopy." *Journal of Engineering for Gas Turbines and Power*, Vol. 125, No. 1, 2003, pp. 34–39. https://doi.org/10.1115/1.1492836.

[14] Kuryakov, V., Zaripova, Y., Varfolomeev, M., De Sanctis Lucentini, P. G., Novikov, A., Semenov, A., Stoporev, A., Gushchin, P., and Ivanov, E. "Comparison of Micro-DSC and Light Scattering Methods for Studying the Phase Behavior of n-Alkane in the Oil-in-Water Dispersion." *Journal of Thermal Analysis and Calorimetry 2020 142:5*, Vol. 142, No. 5, 2020, pp. 2035–2041. https://doi.org/10.1007/S10973-020-10001-9.

[15] Kuryakov, V. N., Ivanova, D. D., Tkachenko, A. N., and Sedenkov, P. N. "Determination of Phase Transition Temperatures (Melting, Crystallization, Rotator Phases) of n-Alkanes by the Optical Method." *IOP Conference Series: Materials Science and Engineering*, Vol. 848, No. 1, 2020, p. 012044. https://doi.org/10.1088/1757-899X/848/1/012044.

[16] Kuryakov, V. N., Kuryakov, V. N., Ivanova, D. D., Semenov, A. P., Gushchin, P. A., Ivanov, E. V., Novikov, A. A., Yusupova, T. N., Shchukin, D., and Shchukin, D. "Study of Phase Transitions in N-Tricosane/Bitumen Aqueous Dispersions by the Optical Method." *Energy and Fuels*, Vol. 34, No. 5, 2020, pp. 5168–5175. https://doi.org/10.1021/ACS.ENERGYFUELS.9B03566.

[17] Home | AJF:TD | U of I. https://altjetfuels.illinois.edu/. Accessed Jun. 5, 2021.

[18] Edwards, T. Reference Jet Fuels for Combustion Testing. 2017.

[19] Lemmon, E.W., Bell, I.H., Huber, M.L., McLinden, M. O. NIST Standard Reference Database 23: Reference Fluid Thermodynamic and Transport Properties-REFPROP.

[20] AlMulla, H. A., and Albahri, T. A. "Predicting the Properties of Petroleum Blends." *Petroleum Science and Technology*, Vol. 35, No. 8, 2017, pp. 775–782. https://doi.org/https://doi.org/10.1080/10916466.2016.1277238.

[21] Heyne, J., Bell, D., Feldhausen, J., Yang, Z., and Boehm, R. "Towards Fuel Composition and Properties from Two-Dimensional Gas Chromatography with Flame Ionization and Vacuum Ultraviolet Spectroscopy." *Fuel*, Vol. 312, 2022, p. 122709. https://doi.org/10.1016/J.FUEL.2021.122709.

[22] Naef, R. "Calculation of the Isobaric Heat Capacities of the Liquid and Solid Phase of Organic Compounds at and around 298.15 K Based on Their 'True' Molecular Volume." *Molecules 2019, Vol. 24, Page 1626*, Vol. 24, No. 8, 2019, p. 1626. https://doi.org/10.3390/MOLECULES24081626.

[23] Lundberg, G. W. "Thermodynamics of Solutions XI. Heats of Mixing of Hydrocarbons." *Journal of Chemical and Engineering Data*, Vol. 9, No. 2, 1964, pp. 193–198.

[24] Colket, M., and Heyne, J. *Fuel Effects on Operability of Aircraft Gas Turbine Combustors*. AIAA, Progress in Astronautics and Aeronautics, 2021.

[25] Walden, P. "Heat of Fusion, Specific Cohesion, and Molecular Complexity at the Melting Point." *Elektrochem*, Vol. 14, 1908, p. 713.

Appendix 4

A Dataset Comparison Method Using Noise Statistics Applied to VUV Spectrum Match Determinations

Paper 8: A Dataset Comparison Method Using Noise Statistics Applied to VUV Spectrum Match Determinations

1. Introduction

The ability to determine whether a given dataset is consistent with theory or some related dataset is critical across the sciences. Significant applications of this discipline range from criminal justice [1-3] to manufacturing process control [4,5] to name a few. In analytical chemistry, determining an analyte's identity is paramount. In this work, we show how the general notion of comparing the difference between pairs of datasets to white noise can be applied to spectral data to positively identify inconsistencies/mismatches between spectra and, in some cases, to positively identify an unknown, single molecular species.

Signature interactions (spectra) between molecules and electromagnet radiation are commonly used to identify an unknown analyte. The process includes experimentally collecting a spectrum of the unknown analyte (sample) and comparing it, one-by-one, to cataloged library of spectra of known molecules (reference) [6,7]. To score the goodness of fit between the sample spectra and an arbitrary reference spectrum, researchers typically use either the coefficient of determination (R^2), a related similarity term [8,9], or some combination of them. By summing some measure of the disparities, as done with an R^2 or mean absolute error determination, all these criteria forfeit some level of detail that may be readily detected through visual inspection. For example, common-sign disparities at consecutive wavelengths are more significant than randomly spaced disparities, and disparities in regions of low noise are more significant than disparities in regions of high noise. However, as will be discussed in this manuscript, numerical methods can illuminate the patterns which are naturally observed through visible methods, and numerical scoring facilitates automation of the match/no-match decision logic.

Electromagnetic radiation emission and absorption, mass spectrometry, nuclear magnetic resonance, characteristic chromatographic elution time, phase transition temperature, density, viscosity, refractive index, or any other observable property have been used to identify and quantify materials of interest. What began as a human-centered qualitative evaluation process has developed into the diverse field of chemometrics [10,11] where expected results, or hypotheses, are tested against measured information.

Advances in the diagnostic capabilities of spectrometers and the data processing capabilities of computers have enabled direct comparisons of reference spectra to sample spectra. For example, contemporary and widely available infrared (e.g. FTIR) and vacuum ultraviolet (VUV) light detectors can record spectra over more than a thousand wavelengths at high data acquisition frequencies.

Notably, the high acquisition rates of modern VUV detectors (77 Hz) have been capitalized in gas chromatography (GC) [12] and more recently two-dimensional gas chromatography (GC×GC).[13] In contrast to mass spectrometers, VUV detectors have the ability to discern isomeric structural differences between species [14] and show the potential to be quantitative due to the linearity of response factors.[15] The separation from GC combined with the spectral response from VUV enable isomer-specific identification potential.[12,16-22] These approaches currently 'identify' species by searching spectral libraries primarily for the highest R^2 match. This approach relies heavily on the completeness of the spectral library. The confidence in these results, although effective in simple exercises, becomes increasingly questionable as more uncertainties are included.

For the application discussed herein, high spectral and temporal resolution is needed to distinguish between structural and stereoisomers of hydrocarbons in sustainable aviation fuel (SAF) candidates. The motivation for knowing these isomers has been documented elsewhere.[19,23,24] To put it briefly here, knowing the isomeric structures minimizes the risk to candidate SAF pathways, as isomers can significantly impact aviation fuel properties.

In this work, experimental procedures and data processing are used to demonstrate that the analyte in the sample chamber and the detector noise are the only factors contributing to the observed VUV signal. The detector noise at each wavelength closely follows a Gaussian distribution and is unaffected by the presence of analyte in the detector which enables the following hypothesis: if the signal observed is not a match with reference spectra, then the residuals will have characteristics that are inconsistent with that of noise alone. For reasons that will be made clear in the methods section, the residuals are adjusted proportional to the variance of the background noise at each wavelength. The described methods are applied to three examples and discussed; a clear match and a clear mismatch with the same R^2 (0.976) and analysis of n-alkane spectra

demonstrating that unambiguous identification of analytes with spectra that are visually similar ($R^2 \geq 0.9997$) to that of several reference spectra can be accomplished. Additional examples are provided in section 2 of the supporting materials.

2. Methods

Experimental Setup. In this experiment, vacuum ultraviolet spectroscopy is coupled with comprehensive two-dimensional gas chromatography (GC×GC). A flame ionization detector is also equipped, but unused in this work. A graphical overview of the GC×GC-FID/VUV is available in the supporting materials, figure S1 illustrating the major components experimental setup. Details of this system and configuration have been described previously.[19] Key points are repeated here for convenience. A vacuum ultraviolet spectrometer (VUV Analytics, VGA-101) with an Agilent 8890 and a SepSolve GC×GC flow modulation system was used for this work. The system includes two columns with a flow modulator and a split plate connected in series after the second column. Parallel sample streams are sent to a flame ionization detector (FID) – not used for this work - and the VUV spectrometer. The columns employed were a Restek Rxi-17Sil MS (60m x 0.32mm x 0.5µm) and a Restek Rxi-1 (15m x 0.32mm x 0.5µm), respectively. The carrier gas for the separation was grade 5.0 helium, which passed through a Restek Triple Filter before entering the instrument. The carrier gas flow rate, modulation rate, oven temperature profile, sample injection volume, and duration of the experiment all contribute to the details of the separation of different species that may be in any sample. However, these items do not significantly impact the quality of spectra collected over periods during which 1 or 0 analytes flow into the VUV spectrometer. The temperature ramp rate used for the sample spectra starts at 40°C for 30 seconds, followed by a 1°C/minute ramp rate until 280°C is reached, where it remains for 10 minutes. This experimental setup uses longer than typical columns, and therefore requires a longer temperature program for optimal separations. Data is sent to the computer throughout the experiment over a range of wavelengths from 115 to 430 nm at 76.92 Hz.

Chemicals Used. Sample spectra originate from analytes that were separated using GC×GC from a petroleum-derived Jet-A fuel sample labeled as A-2 (POSF 10325) by the fuels committee of the National Jet Fuel Combustion Program [25] and Synthetic Aromatic Kerosene (SAK) by Virent.[26] Reference spectra originate from the Jet Range VUV database from VUV Analytics and supplemented with many internally measured spectra. Internally measured spectra were recorded by injecting samples of single analytes into the GC×GC system and recording the lone peak response. The spectrum for toluene was measured using a sample from Fischer Chemical (>99.5%). The spectrum for 1,3-diethylbenzene was from the VUV Analytics spectral library.

Data and Storage. Large data files are created over the course of each experiment, which last for ~250 minutes. Spectral response at ~2800 wavelengths are acquired at 76.92 Hz (F_{acq}) and typically stored at some lower frequency (F_{sto}), in this work 10 Hz, resulting in data files with sizes on the order of one gigabyte each. Absorption intensity (I) is determined by Equation 1. In this equation, "dark" is the number of counts detected when the light source is turned off and L_0 is the number of counts detected with the lamp on, immediately prior to sample injection. The subscript reflects the fact that each of these signals vary with wavelength, and L is the number of counts detected at 76.92 Hz. The stored values of I_λ are sums of Z snapshots, where Z is the ratio of the acquisition frequency to storage frequency.

$$I_\lambda = \Sigma[\log(L_{0,\lambda} - dark_\lambda) - \log(L_\lambda - dark_\lambda)]_i \quad (1)$$

The variation in light intensity as a function of wavelength is driven by the VUV light source and is significant. The intensity of light at, say 160 nm is much higher than the intensity of light at, say 300 nm, so the impact of a few random counts on I_{160} is significantly lower than the impact of the same few random counts on I_{300}. At this level of data processing the magnitude of the noise varies with wavelength. Subsequent steps are taken to remove this sensitivity. A plot showing the variability of the light source at different wavelengths is included in supporting materials, figure S2.

Spectra Acquisition. All spectra ($I_{sam,\lambda}$) are extracted from the stored data points. Raw sample intensity at each wavelength ($\overline{I_{raw,\lambda}}$) is averaged over a modulated period of time containing N_{sam} data points and bracketing the highest intensity of the analyte peak of the chromatogram. From this raw sample average, a background signal is subtracted as defined by Equation 2, where the background signal ($\overline{I_{BG,\lambda}}$) is averaged over a period of time that is at least double that used for the raw sample and throughout an elution period that is free of analyte yet closely coupled with the analyte time stamp. By doing this, any drift in mean background signal throughout an experiment is removed from the spectrum to be compared. The integration windows for the raw sample and the background are selected manually during visual inspection and the variation in rms noise introduced by the manual process is estimated to be 5% of the rms background noise.

$$I_{sam,\lambda} = \mathrm{N_{sam}} * (\overline{I_{raw,\lambda}} - \overline{I_{BG,\lambda}}) \quad (2)$$

Spectrum Scaling. Intuitively, we all make two datasets (i.e. spectra or images) size consistent to facilitate comparisons. Typically for spectra, the intensity of either the sample or the reference would be adjusted to make the mean average difference between them equal to zero. This ostensibly minimizes R^2. However, minimizing the sum of the square divided by the background variance at each wavelength (σ_λ^2) helps to deemphasize noisier portions of the spectrum in favor of regions with sharper signal. Equation 3 is provided to clarify this processing step. In this equation, a scaler, α, is varied to minimize the objective function, Q. In this context, σ_λ^2 can be determined from any set of partitions of the data where no analyte is detected, and these need not be from the same run. In practice, the intensity as defined by equation 1, meaning no additional averaging as in equation 2, is used to determine σ_λ^2. This measure of noise variance does change over time as a product of lamp decay or other factors so periodic updates to σ_λ^2 are made.

$$Q = \sum_\lambda \frac{\left(I_{sam,\lambda} - \alpha * I_{ref,\lambda}\right)^2}{\sigma_\lambda^2} \quad (3)$$

Residuals. The difference between a pair of size-consistent spectra (their residuals, r) can be more indicative of similarity between them than an overlay. In this work, the residuals are adjusted proportional to the standard deviation of the background noise (σ_λ) to remove sensitivity to wavelength, as defined by Equation 4. By doing this, the distributed characteristics (or moments) of the residual should be the same as the moments of the noise, provided the two spectra match. The value in this normalization scheme will be further highlighted later in this paper.

$$\epsilon_\lambda = \frac{I_{sam,\lambda}}{\sigma_\lambda} - \alpha * \frac{I_{ref,\lambda}}{\sigma_\lambda} \quad (4)$$

First Moment. The first moment of ϵ, the mean value ($\bar{\epsilon}$) is the sum of ϵ_λ over all wavelengths, which should be zero for matching spectra, divided by the total number of wavelengths, *N*.

$$\bar{\epsilon} = \frac{\sum \epsilon_\lambda}{N} \quad (5)$$

We recommend trimming the wavelength range of the spectrum to exclude everything except the union of ranges that are active with respect to each possible match to the sample spectrum, where 'active' implies absorption evident upon visual inspection with intensity ~2x the background noise. When a sample spectrum is compared against a reference spectrum that does not match it, the first moment will not be zero because α is determined by Equation 3 rather than minimization of the first moment. By excluding portions of the spectrum where the signal is ostensibly zero, the mean of the residual is not dampened by extraneous points and therefore easier to detect.

Second Moment. The second moment of ϵ is its variance (σ_ϵ^2) as defined in Equation 6. It depends primarily on three details of the experiments and data processing procedure: $\mathrm{N_{sam}}$, $\mathrm{N_{ref}}$, and α which are not consistent from experiment to experiment. To get around these dependencies, we recognize and exploit the fact that all these influences have the same impact on the signal variance whether or not the signal reflects an absorbance. For convenience, the tail (or inactive region) of the residual, meaning the region of wavelengths where ostensibly no absorbance occurs for either spectrum, sample or reference, is used to define the expected variance for matching spectra throughout the entire spectral range. Using the variance in the tail has the added advantage of capturing any noise existing in the reference spectrum. Spectrum splitting rather than wavelength trimming is recommended for evaluation of the variance, where the active portion of the spectral range is used to identify mismatching spectra and the inactive portion of the spectral range is used to define the expected variance.

$$\sigma_\epsilon^2 \equiv \left(\frac{1}{N}\right) * \sum_\lambda (\epsilon_\lambda - \bar{\epsilon})^2 \quad (6)$$

Third Moment. The third moment of ϵ, shown by Equation 7, is its skew (*Sk*), which should be zero provided the two spectra match one another, consistent with Gaussian noise distribution. Unlike the lower moments, inclusion of ostensibly zero signal over much of the spectrum helps to establish the shape of the distribution which in turn helps to clarify features that are introduced via mismatches in the active region of the spectrum. In the mathematical representation, when there is a mismatch, $\sigma_\epsilon$is reduced by the inclusion of the ostensibly zeroes data. Moreover, the sum is larger because it includes more terms and $\bar{\epsilon}$ is driven closer to zero and further from ϵ_λ over a preponderance of the active region of the spectrum, where that difference contributes most to *Sk*.

$$Sk = \left(\frac{1}{N * \sigma_\epsilon^3}\right) * \sum_\lambda (\epsilon_\lambda - \bar{\epsilon})^3 \quad (7)$$

Fourth Moment. The fourth moment of the distribution of ϵ, shown by Equation 8, is its kurtosis (κ). If the two spectra match one another the kurtosis of the distribution of the residual should be equal to that of a spectrum obtained from a blank run (3.0). Once again, inclusion of ostensibly zero signal in the inactive region of the spectral range helps to establish a baseline shape, which in turn helps to highlight departures (mismatches) from a normal distribution.

$$\kappa = \left(\frac{1}{\sigma_\epsilon^4}\right) * \sum_\lambda (\epsilon_\lambda - \bar{\epsilon})^4 \quad (8)$$

Quantile-Quantile (Q-Q) Plots. A plot of the quantiles of ϵ against the quantiles of a Gaussian distribution provides an alternative (or additional) measure of its distribution. The coefficient of determination (R^2) of this curve can be used to quantify the plots. For matching spectra, R^2 should be 1.0, as the noise in the measured absorption and the normalized residuals of known matches has been determined separately to be Gaussian. For mismatching spectra, the R^2 of this curve is generally much lower than the R^2 obtained by direct comparison (overlays) of the two spectra, which renders the R^2 of a Q-Q plot easier to interpret than the R^2 between two spectra (overlays).

Consecutive Signs. Random noise about a mean signal is equally likely to fall above or below the mean. The probability of C consecutive signals falling above the mean is $0.5^C \equiv p$. For a residual of two spectra comprised of N wavelengths, there are $(N + 1 - C) \equiv N'$ opportunities to achieve C consecutive signs. Generally, Equation 9 represents the probability (P) of observing exactly k occurrences of exactly C consecutive signs in a residual between two matching spectra comprised of N wavelengths. For any comparison between two spectra, it is straightforward to determine the maximum length of consecutive signs (C'), or the number of occurrences (k') of C consecutive signs. These numbers (1 & C') or (k' & C) can be inserted into equation 8, serving as one end of a summation over k, with 0 or N' serving as the other end, to get the probability that the residual in question is truly just random noise about zero, as it should be for matching spectra.

$$P_k = \left(\frac{N'!}{k! * (N' - k)!}\right) * p^k * (1 - p)^{N' - k} \quad (9)$$

Evaluation of consecutive signs provides a particularly convenient way to assess whether the process described herein results in truly random distributions when comparisons are made between spectra originating from the same exact sample or the same sample compound. It has been determined from 144 such comparisons of trimmed spectra containing 744 points each that a small bias exists, as we found 9-28 consecutive signs in the processed experimental data, compared to 7-15 consecutive signs when fully synthesized random data was used to simulate 144 residuals. While it is possible this bias could be introduced by one of the numerical processes, such as scaling for example, when compared against the number of consecutive signs found in the residuals between mismatching spectra, 68-289 consecutive signs in a field of 2448 comparisons, it is quite evident that the small bias observed in the processed experimental data is much less than the observed difference between known matches and known mismatches.

Moment Probabilities. Just as probability can be assigned to a particular determination of consecutive signs, the probability of an observed mean being part of a Gaussian distribution can be readily determined from established statistical methods. For the higher moments, however the formulae necessary to make these determinations are not generally available. To create a guide to serve a purpose like that of equation 9, random sampling from an ideal Gaussian distribution was used to create 25,000 batches of N points. The moments of each batch of N points were tallied and analyzed as a set of 25,000 items. The 95th percentile was extracted from this analysis for 30 different values of N to create the contours of the shaded regions shown in Figure 1.

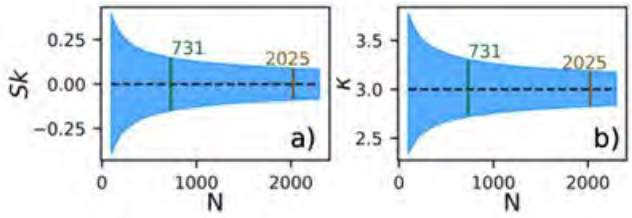

Figure 1. Random point selection simulations from a true Gaussian distribution demonstrating 95th percentile ranges of the (a) third and (b) forth moments as a function of population size. Any result within these ranges can be explained as noise alone.

A summary of the 95th percentile for each moment is provided in Table 1. When the numerical processing of experimental data comparison reveals a moment that is significantly outside of the 95th percentile of an ideal Gaussian distribution, there is a high degree of confidence that the corresponding sample and reference species are not the same. Definitive matches are harder to determine because that requires proof that only one out of all plausible matches cannot be ruled out. Because some analytes, especially those toward the lower volatility range of jet fuel may be isomers for which the reference spectra do not exist in the library there will be cases for which this process can only narrow the range of possible matches. That said, when the analyte happens to be one of the isomers for which a reference spectrum does exist, this process will identify that reference molecule as a probable match to the analyte.

3. Examples and Discussion

Background Signal. The images shown in Figure 2 were extracted from data collected at all timestamps during the first 20 minutes of an experiment, during which no analyte elutes from the chromatograph. The plotted result for each wavelength was derived by analyzing the distribution of the signals recorded at each timestamp. The skew is approximately 0.0 at all wavelengths and the kurtosis is nearly 3.0, illustrating that the background noise follows a Gaussian distribution at all

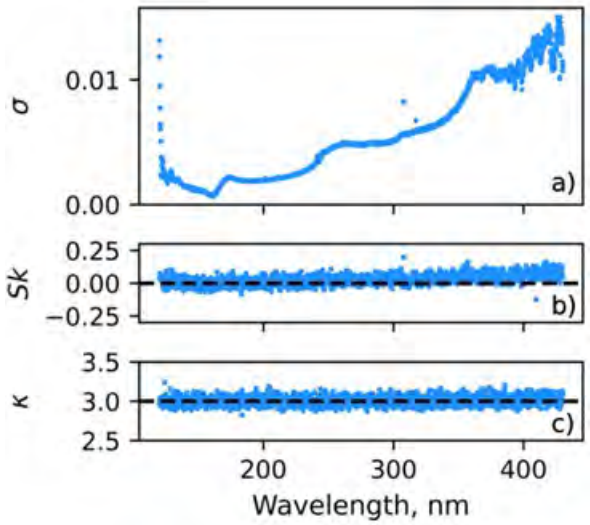

Figure 2. Statistics of VUV response with no analyte present in the detector at each independent wavelength. (a) Standard deviation, (b) skew, and (c) kurtosis at all wavelengths demonstrate an approximate Gaussian distribution with varying standard deviations. Dividing by standard deviation at each wavelength makes all measurements comparable for statistical analysis.

wavelengths. The mean background signal is also nearly zero at all wavelengths, confirming there is no change in absorption relative to time zero, and no significant change in light source intensity occurs throughout the 20-minute period selected for this background. However, the magnitude of the noise as measured by relative to its standard deviation is dependent on

the wavelength. This data is represented by the term σ_λ in Equations 3-5. By dividing each raw signal input at a given wavelength by σ_λ its standard deviation goes to one, but its skew and kurtosis remains the same, indicative of a Gaussian distribution. By normalizing the Gaussian distributions at each wavelength to the same size (via division by σ_λ) any collection of points sampled from each of the distributions, such as a single time stamp of the background noise across the spectrum, will also follow a Gaussian distribution with a standard deviation of one.

Table 1. Summary of Residual Moments Distribution Features Relevant to the Spectra Comparisons of this Work.

Moment	Mean	N	95th Percentile
$\bar{\epsilon}$	0.00	N/A	$\pm 2\sigma_\epsilon / N^{0.5}$
†	1.00	731/1294	± 0.064
Sk	0.00	2025	± 0.088
κ	3.00	2025	$2.83 - 3.19$

† The ratio of the variances between the two partitions of the spectra is expected to equal one.

Matching Spectra. Figure 3 provides an example where the measured spectrum of toluene in A-2 is compared against its reference spectrum. The chromatogram peak corresponding to the sample analyte elutes at the same time as a toluene standard which provides supporting information to the statistics-driven conclusion that the analyte is toluene. Visually, the overlay of the spectra (Figure 3a) does look like a match, but the R^2 is low because of the low signal-to-noise ratio of the sample. A scale factor (α) of 1.026 was applied to render the two spectra size consistent. Figure 3b shows the residuals or difference between the measured and reference signal. The 2σ shaded region is the expected range the data will fall in based off the background noise profile (from figure 2a). For further detail on this process, see section 1 of the supporting material. Figure 3c shows the residuals after scaling for noise, demonstrating the equivalence of noise across the spectrum. Figure 3d shows the histogram of the residuals is very similar to a Gaussian distribution with a standard deviation as suggested by the tail data. Figure 3e shows another confirmation the residuals are consistent with a Gaussian distribution, evidenced by the linearity and high R^2 in the Q-Q plot. The moments of the noise-adjusted residual distribution being consistent with random sampling from a Gaussian distribution, which is summarized in Table 1, correctly suggests that the reference spectrum is a probable match to the sample spectrum. The high degree of linearity observed in the Q-Q plot of the noise-adjusted residuals further confirms that it is Gaussian and the relatively low count of consecutive wavelengths at which the sign of the residual is unchanged is also consistent with a match. The residuals therefore exhibit characteristics that are consistent with that of noise alone and can be logically attributed to noise alone. It is worth noting however that as signal-to-noise ratio decreases, several of the suggested measures of match approach that of noise alone (a Gaussian distribution) even when the sample and reference spectra do not correspond to the same species. The correct interpretation of this note is that fewer plausible matching species can be ruled out as signal strength decreases. For the one correct match, 6 out of the 7 suggested measures are not impacted by the signal-to-noise ratio.

Clearly Mismatched Spectra. Aviation fuel and sustainable aviation fuel usually contains a significant fraction of molecules with 12 or more carbon atoms for which hundreds of isomers are possible. A complete library of reference spectra of isomers of such hydrocarbons does not yet exist. As such, it is not yet possible to determine with absolute certainty that any given sample matches one of the reference spectra that happens to exist in the library. In some cases, the overlay of the sample spectra with one or more of the available reference spectra will be visually indistinguishable. The comparison between an unknown sample separated from Virent SAK by GC×GC is one such example and is highlighted in Figure 4. Figure 4 follows the same template as Figure 3, contrasting the difference in these criterion and subplots for a non-match. In this case the elution time of the analyte suggested that the analyte was an aromatic with 10 carbons. The highest R^2 to our library was to 1,3-diethylbenzene, 0.976, which is consistent with those of known matches, like the toluene example from Figure 3. While it is already clear from a plot of the residuals in Figures 4b and 4c that the R^2 of the overlay is misleading, each of the other measures of match suggested in this work also prove, even in isolation, that this sample is not 1,3-diethylbenzene. The appropriate conclusion to draw from these results is that the sample is not a species included in our library. Such eliminations help to reduce the range of fuel properties that would otherwise be ascribed to this peak on the chromatogram for property estimations by the tier α methodology.[24]

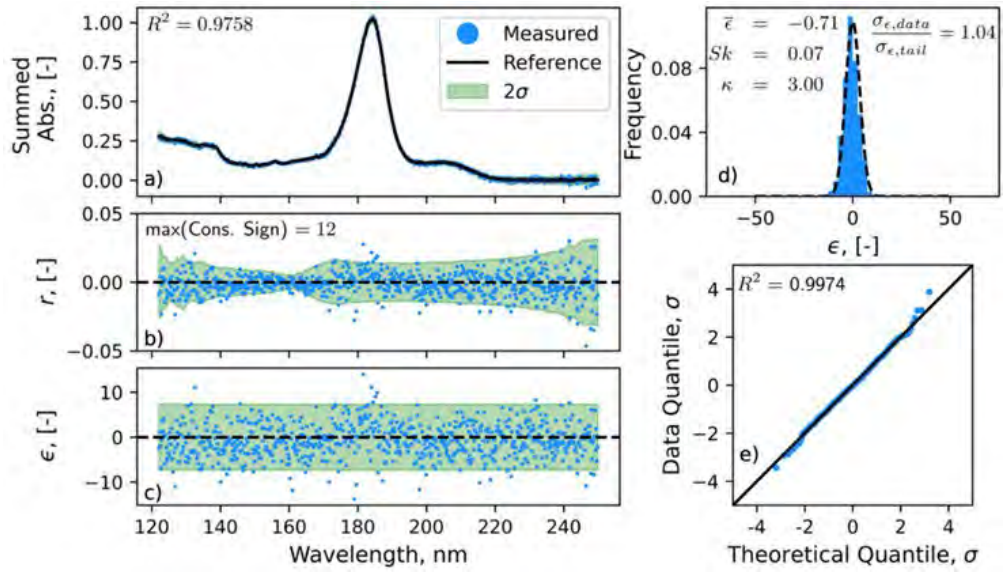

Figure 3. Example results of a definitive positive identification of toluene in petroleum derived A-2. (a) Shows the measured spectrum of a peak in A-2 and the reference spectrum for Toluene. (b) Residuals or differences between the measured and reference spectra and (c) the results after dividing through by wavelength specific σ. In both (b) and (c), the green region represents the expected 95th percentile range based on the background noise and tail data statistics. (d) The histogram of normalized residuals, ϵ, approximate a normal distribution, also evidenced in (e) a Q-Q plot of the normalized residuals showing strong linearity.

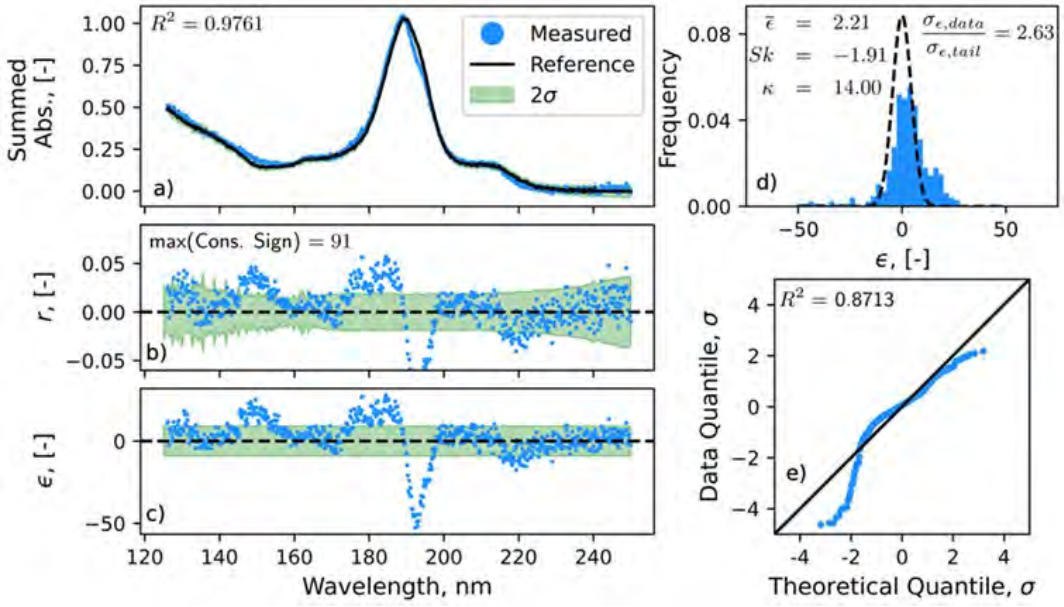

Figure 4. Example of a definitive negative identification of 1,3-diethylbenzene in Virent SAK. (a) Shows the measured spectrum of an analyte in SAK and the reference spectrum for 1,3-diethylbenzene. (b) Residuals or differences between the measured and reference spectra and (c) the results after dividing through by wavelength specific σ. In both (b) and (c), the green region represents the expected 95th percentile range based on the background noise and tail data statistics. (d) The histogram of normalized residuals does not approximate a normal distribution, also evidenced in (e) a Q-Q plot of the normalized residuals showing poor linearity.

Spectra Comparisons with High R^2. This paragraph provides a summary of comparisons between spectra of that are known to exhibit among the smallest differences in absorption known to these authors: n-undecane, n-dodecane, and n-tridecane.[20] Generally, for n-alkanes it is not unusual for the highest R^2 of a set of sample/reference spectra overlays to occur, misleadingly, between the sample, having *n* carbon atoms, and a reference, having $m \neq n$ carbon atoms. In this work, the three sample spectra were measured from analytes separated from A-2 by GC×GC and the three reference spectra were extracted from our library. An overlay plot of the three reference spectra is provided in Figure 5, while Figure 6 provides a summary of nine pairwise comparisons between three samples and three reference spectra. The lowest R^2 out of the nine comparisons is 0.9997 and visually, in Figure 5a, it is difficult to see any offsets between the lines. Figure 5b is included to highlight the area with the greatest divergence between spectra. The reference spectra were used in Figure 5 to stand-in for the sample spectra so the point could be made with one plot instead of nine. The words across the top of Figure 6 represent sample spectra and the symbols represent reference spectra, where the colors are consistent between sample and reference. For undecane and tridecane, the correct match shows a mean, standard deviation ratio, skew, kurtosis, Q-Q plot R^2, and maximum count of consecutive signs, each closest to the corresponding theoretical value for a Gaussian distribution. For dodecane the mean and the maximum count of consecutive signs are each closest to their respective theoretical values, while the other five measures do not clearly distinguish the dodecane sample from the tridecane reference. These statistics should be employed in aggregate. Each statistic should demonstrate results plausibly consistent with noise alone. The numerical result from R^2 of the spectra overlay comparison, alone would not be able to correctly determine the best match, in part because it is driven by the noise in the reference and sample spectra. In contrast, the moments of ϵ and the linearity of the Q-Q plot are not impacted the measurement noise.

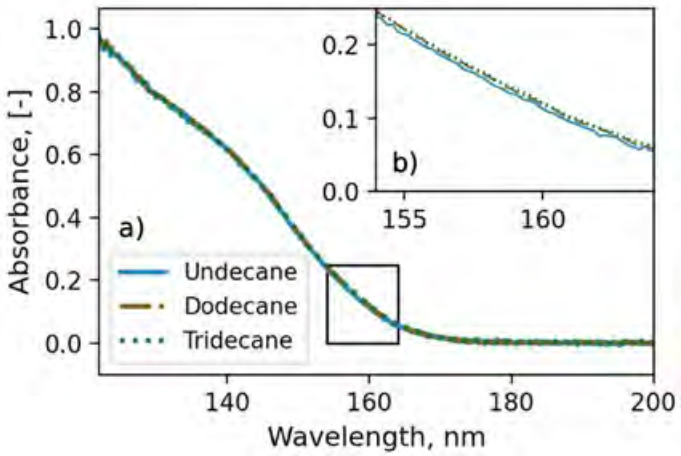

Figure 5. (a) Spectra overlay of three normal alkanes for typical wavelengths of interest and (b) magnification of the area of greatest difference in absorbance for n-undecane, n-dodecane, and n-tridecane

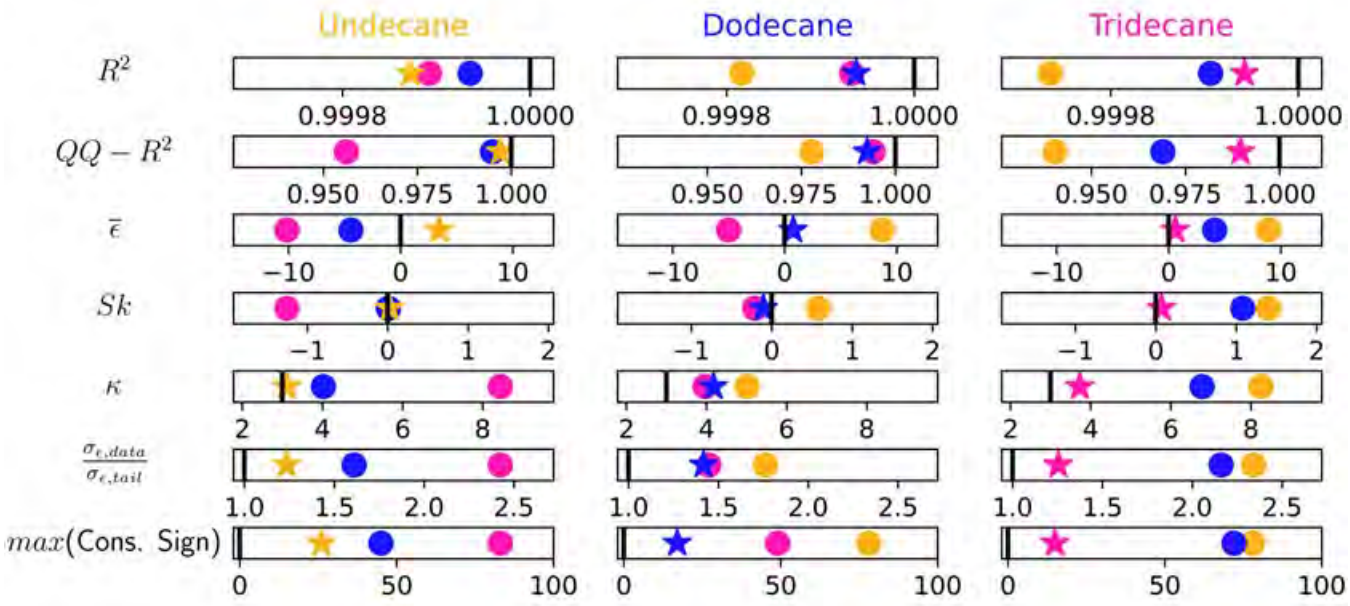

Figure 6. Scorecard of numerical analyses of residuals between measured and reference spectra of three normal alkanes. Stars rep-resent the correct match and circles represent incorrect matches. Undecane is incorrectly identified using R2 alone, but with other statistics considered the correct match can be observed. In all three examples shown, for all of the statistics, the correct match per-forms strongly, even if not always the best. The statistics should be interpreted collectively.

4. Conclusions

Six measures of the distribution of the residual between numerically adjusted spectra have been shown to be invaluable for comparing plausible matches of reference spectra to sample spectra of analytes eluted from a two-dimensional gas chromatograph. These measures include its first four moments (mean, variance, skew and kurtosis), the R^2 of a Q-Q plot with the distribution of the residual on one axis and an ideal Gaussian on the other, and the maximum count of consecutive (by wavelength) signs within the residual.

These measures, taken in combination, facilitate a logical ranking of all plausible matches, rendering positive identification of a single-component analyte possible provided a reference spectrum exists for all plausible matches. Unknown analytes, for which reference spectra are not available for all plausible matches (isomers), can be partially identified by definitive elimination of many of the otherwise plausible matches. Such eliminations help to reduce the uncertainty in fuel component property calculations. In contrast, the R^2 of the spectra overlay, by itself, is often ambiguous as many reference spectra will have an R^2 close to the maximum of the set.

Several numerical processing steps are described that remove differences in the background signal and noise characteristics at different wavelengths. Without these operations the residuals would not exhibit a distribution of values similar in shape to the noise at any wavelength. For our experiment the background noise has been shown to have a kurtosis value of three (Gaussian) at all wavelengths, and the numerically adjusted residuals of known matches have been shown to exhibit the same characteristics.

One exemplar application of the methodology is a definitive match of n-undecane, n-dodecane and n-tridecane sample spectra to their corresponding reference spectrum. While this example is impressive, the greatest power of the methodology generally is in its ability to unambiguously identify mismatches because the distributions of residuals between mismatching spectra are very clearly not Gaussian, and have a high consecutive sign count, even in cases where the R^2 between the compared spectra is ambiguous.

Supporting Information

In the supporting information there is a schematic of the GC×GC-VUV experimental setup, a figure of the VUV lamp counts vs wavelength, and there are the chromatograms of A-2 and Virent SAK. In addition, a set of comparisons between sample and reference spectra of three isomers of C_8H_{18} is provided along with a brief description.

Acknowledgements

The authors would like to acknowledge funding from the U.S. Federal Aviation Administration Office of Environment and Energy through ASCENT, the FAA Center of Excellence for Alternative Jet Fuels and the Environment, project 65 through FAA Award Number 13-CAJFE-UD-026 (PI: Dr. Joshua Heyne) under the supervision of Dr. Anna Oldani. Any opinions, findings, conclusions, or recommendations expressed in this material are those of the authors and do not necessarily reflect the views of the FAA or other sponsors. Additional support for this paper was provided by US DOE BETO through subcontract PO 2196073.

References

[1] Moses, K. R.; Higgins, P.; Mccabe, M.; Prabhakar, S.; Swann, S. Chapter: Automated Fingerprint Identification System.
[2] Uenuma, F. The First Criminal Trial That Used Fingerprints as Evidence | History| Smithsonian Magazine. *Smithsonian Magazine*. 2018.
[3] Pandey, F.; Dash, P.; Samanta, D.; Sarma, M. ASRA: Automatic Singular Value Decomposition-Based Robust Fingerprint Image Alignment. *Multimed. Tools Appl. 2021 8010* **2021**, *80* (10), 15647–15675. https://doi.org/10.1007/S11042-021-10560-5.
[4] MacCarthy, B. L.; Wasusri, T. A Review of Non-Standard Applications of Statistical Process Control (SPC) Charts. *Int. J. Qual. Reliab. Manag.* **2002**, *19* (3), 295–320. https://doi.org/10.1108/02656710210415695/FULL/PDF.
[5] Lim, S. A. H.; Antony, J.; Albliwi, S. Statistical Process Control (SPC) in the Food Industry – A Systematic Review and Future Research Agenda. *Trends Food Sci. Technol.* **2014**, *37* (2), 137–151. https://doi.org/10.1016/J.TIFS.2014.03.010.
[6] Streitwieser, A. J.; Heathcock, C. H. *Introduction to Organic Chemistry*, Second.; Macmillan Publishing Co., Inc.: New York, 1981.
[7] Atkins, P. W. *Physical Chemistry*, Third.; Freeman and Company: New York, 1986.
[8] Zachariah Samuel, A.; Mukojima, R.; Horii, S.; Ando, M.; Egashira, S.; Nakashima, T.; Iwatsuki, M.; Takeyama, H. On Selecting a Suitable Spectral Matching Method for Automated Analytical Applications of Raman Spectroscopy. *ACS Omega* **2021**, *6*, 26. https://doi.org/10.1021/acsomega.0c05041.
[9] Li, J.; Hibbert, D. B.; Fuller, S.; Vaughn, G. A Comparative Study of Point-to-Point Algorithms for Matching Spectra. *Chemom. Intell. Lab. Syst.* **2006**, *82* (1–2), 50–58. https://doi.org/10.1016/J.CHEMOLAB.2005.05.015.
[10] Brereton, R. G.; Jansen, J.; Lopes, J.; Marini, F.; Pomerantsev, A.; Rodionova, O.; Roger, J. M.; Walczak, B.; Tauler, R. Chemometrics in Analytical Chemistry—Part I: History, Experimental Design and Data Analysis Tools. *Anal. Bioanal. Chem. 2017 40925* **2017**, *409* (25), 5891–5899. https://doi.org/10.1007/S00216-017-0517-1.
[11] Keithley, R. B.; Mark Wightman, R.; Heien, M. L. Multivariate Concentration Determination Using Principal Component Regression with Residual Analysis. *TrAC Trends Anal. Chem.* **2009**, *28* (9), 1127–1136. https://doi.org/10.1016/J.TRAC.2009.07.002.
[12] A. Schug, K.; Sawicki, I.; D. Carlton, D.; Fan, H.; M. McNair, H.; P. Nimmo, J.; Kroll, P.; Smuts, J.; Walsh, P.; Harrison, D. Vacuum Ultraviolet Detector for Gas Chromatography. *Anal. Chem.* **2014**, *86* (16), 8329–8335. https://doi.org/10.1021/ac5018343.
[13] Gröger, T.; Gruber, B.; Harrison, D.; Saraji-Bozorgzad, M.; Mthembu, M.; Sutherland, A.; Zimmermann, R. A Vacuum Ultraviolet Absorption Array Spectrometer as a Selective Detector for Comprehensive Two-Dimensional Gas Chromatography: Concept and First Results. *Anal. Chem.* **2016**, *88* (6), 3031–3039. https://doi.org/10.1021/acs.analchem.5b02472.
[14] Wang, F. C. Y. Comprehensive Two-Dimensional Gas Chromatography Hyphenated with a Vacuum Ultraviolet Spectrometer to Analyze Diesel-A Three-Dimensional Separation (GC × GC × VUV) Approach. *Energy and Fuels* **2020**, *34* (7), 8012–8017. https://doi.org/10.1021/acs.energyfuels.0c00688.
[15] Lelevic, A.; Geantet, C.; Moreaud, M.; Lorentz, C.; Souchon, V. Quantitative Analysis of Hydrocarbons in Gas Oils by Two-Dimensional Comprehensive Gas Chromatography with Vacuum Ultraviolet Detection. *Energy and Fuels* **2021**, *35* (17), 13766–13775. https://doi.org/10.1021/acs.energyfuels.1c01910.
[16] Roberson, Z. R.; Goodpaster, J. V. Differentiation of Structurally Similar Phenethylamines via Gas Chromatography–Vacuum Ultraviolet Spectroscopy (GC–VUV). *Forensic Chem.* **2019**, *15*, 100172. https://doi.org/10.1016/J.FORC.2019.100172.

[17] Roberson, Z. R.; Gordon, H. C.; Goodpaster, J. V. Instrumental and Chemometric Analysis of Opiates via Gas Chromatography–Vacuum Ultraviolet Spectrophotometry (GC-VUV). *Anal. Bioanal. Chem. 2020 4125* **2020**, *412* (5), 1123–1128. https://doi.org/10.1007/S00216-019-02337-5.
[18] Leghissa, A.; Smuts, J.; Qiu, C.; Hildenbrand, Z.; Schug, K. Detection of Cannabinoids and Cannabinoid Metabolites Using Gas Chromatography with Vacuum Ultraviolet Spectroscopy. *Sep Sci plus* **2018**, *1*, 37– 42. https://doi.org/doi.org/10.1002/sscp.201700005.
[19] Heyne, J.; Bell, D.; Feldhausen, J.; Yang, Z.; Boehm, R. Towards Fuel Composition and Properties from Two-Dimensional Gas Chromatography with Flame Ionization and Vacuum Ultraviolet Spectroscopy. *Fuel* **2022**, *312*, 122709. https://doi.org/10.1016/J.FUEL.2021.122709.
[20] Anthony, I. G. M.; Brantley, M. R.; Gaw, C. A.; Floyd, A. R.; Solouki, T. Vacuum Ultraviolet Spectroscopy and Mass Spectrometry: A Tandem Detection Approach for Improved Identification of Gas Chromatography-Eluting Compounds. *Anal. Chem.* **2018**, *90* (7), 4878–4885. https://doi.org/10.1021/ACS.ANALCHEM.8B00531/SUPPL_FILE/AC8B00531_SI_001.PDF.
[21] G.M. Anthony, I.; R. Brantley, M.; R. Floyd, A.; A. Gaw, C.; Solouki, T. Improving Accuracy and Confidence of Chemical Identification by Gas Chromatography/Vacuum Ultraviolet Spectroscopy-Mass Spectrometry: Parallel Gas Chromatography, Vacuum Ultraviolet, and Mass Spectrometry Library Searches. *Anal. Chem.* **2018**, *90* (20), 12307–12313. https://doi.org/10.1021/acs.analchem.8b04028.
[22] Feldhausen, J.; Bell, D. C.; Yang, Z.; Faulhaber, C.; Boehm, R.; Heyne, J. Synthetic Aromatic Kerosene Property Prediction Improvements with Isomer Specific Characterization via GCxGC and Vacuum Ultraviolet Spectroscopy. *Fuel* **2022**, *326*, 125002. https://doi.org/10.1016/J.FUEL.2022.125002.
[23] Boehm, R. C.; Yang, Z.; Bell, D. C.; Feldhausen, J.; Heyne, J. S. Lower Heating Value of Jet Fuel from Hydrocarbon Class Concentration Data and Thermo-Chemical Reference Data: An Uncertainty Quantification. *Fuel* **2022**, *311*. https://doi.org/10.1016/j.fuel.2021.122542.
[24] Yang, Z.; Kosir, S.; Stachler, R.; Shafer, L.; Anderson, C.; Heyne, J. S. A GC × GC Tier α Combustor Operability Prescreening Method for Sustainable Aviation Fuel Candidates . *Fuel* **2021**, *292* (September 2020), 120345. https://doi.org/10.1016/j.fuel.2021.120345.
[25] Edwards, T. Reference Jet Fuels for Combustion Testing. In *AIAA SciTech Forum - 55th AIAA Aerospace Sciences Meeting*; American Institute of Aeronautics and Astronautics Inc.: Grapevine, TX, 2017; pp 1–58. https://doi.org/10.2514/6.2017-0146.
[26] Colket, M.; Heyne, J. *Fuel Effects on Operability of Aircraft Gas Turbine Combustors*, August.; AIAA, Progress in Astronautics and Aeronautics, 2021. https://doi.org/10.2514/4.106040.

Project 065(B) Fuel Testing Approaches for Rapid Jet Fuel Prescreening

University of Illinois at Urbana-Champaign

Project Lead Investigator

Tonghun Lee
Professor of Mechanical Science & Engineering
University of Illinois at Urbana-Champaign
1206 W. Green St., Urbana, IL 61801
517-290-8005
tonghun@illinois.edu

University Participants

University of Illinois at Urbana-Champaign (UIUC)

- P.I.: Professor Tonghun Lee
- FAA Award Number: 13-C-AJFE-UI-039
- Period of Performance: October 1, 2021 to September 30, 2022
- Tasks:
    1. Characterization of optimized M1 fuel nozzles under lean blowout (LBO) conditions
    2. Ignition testing and characterization of the M1 combustor by using optimized fuel nozzles

Project Funding Level

FAA funding level: $150,000
Cost sharing: 100% match provided by software license support from Converge, Inc.

Investigation Team

- Tonghun Lee, Professor, UIUC: overall research supervision
- Eric Wood (graduate student, UIUC), Caleb Trotter (undergraduate student, UIUC): experimental efforts in characterizing the M1 combustor, including laser and optical diagnostics

Project Overview

This study is aimed at introducing a new compact test rig (M1 combustor), developed with original equipment manufacturer (OEM) support within the National Jet Fuel Combustion Program (NJFCP), that can screen fundamental combustor behavior on much lower fuel volumes (approximately gallons) before tier 3 and 4 tests in the ASTM D4054 evaluation. In the NJFCP, the referee rig at the Air Force Research Laboratory (AFRL) was used as a foundational test rig for this goal. The M1 may have the potential to perform these tasks at reduced fuel volumes (approximately gallons rather than hundreds of gallons) in a simplified and open architecture that can be readily shared and operated at different locations at a fraction of the cost. Both the Army Research Laboratory (ARL) and Argonne National Laboratory (ANL) will be partners in the effort to fully characterize the M1 facility. If successful, these efforts will allow fuel providers and OEMs to conduct basic combustor tests by using an identical testing architecture and identical test conditions at multiple test locations, in contrast to the referee rig, which is housed in a secure government facility (AFRL). Tests in smaller test rigs can provide a platform for individual suppliers or researchers to independently test their new fuels, and to make predictions without requiring the use of one single facility. Over time, as test data are accumulated, the potential for test rigs such as the M1 to predict actual tier 3 and 4 performance will increase, thus potentially reducing the burden of relying on capital-intensive ASTM rig and engine tests.

Background of the M1 Combustor

Under the FAA-funded NJFCP, the referee rig combustor at AFRL was used to determine the sensitivity of combustor performance parameters, such as LBO and ignition parameters, to the chemical composition of novel fuels. The results from this investigation were instrumental in establishing a relationship between fuel chemistry and its effects on combustor performance. Professor Tonghun Lee's research group conducted a substantial portion of the laser and optical diagnostic work for the referee rig as part of the NJFCP, including quantitative-phase Doppler particle analysis, which provided key quantitative data for the simulation efforts.

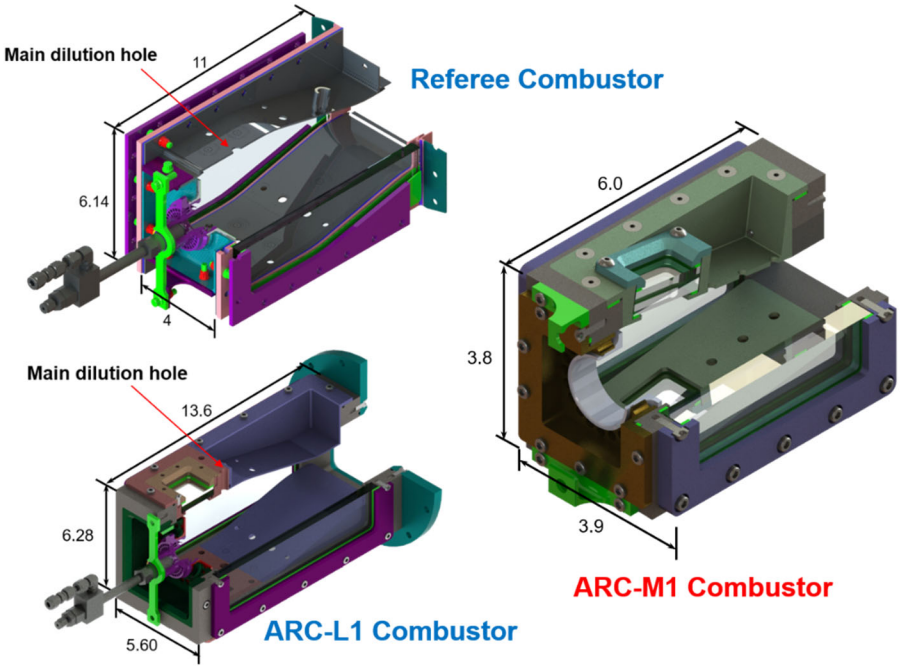

Figure 1. The referee combustor at AFRL, the ARC-L1 combustor, and the ARC-M1 combustor.

Simultaneously, the ARL team worked with NJFCP researchers to complement the referee combustor efforts by performing high-altitude relight tests at the ARL Aberdeen Proving Grounds, where a new altitude test chamber had just been commissioned. During the planning phase, ARL decided to build two new combustors to address several of the referee combustor's shortcomings related to optical access and flow split uncertainty. The first combustor would have the exact same dimensions as the referee combustor but with enhanced optical access and a less complicated liner for air cooling. A lack of vertical optical access had made velocity field measurements in the referee combustor virtually impossible, and the complicated liner had caused difficulties in accurately predicting air flux into the combustor. This new combustor would be termed Army Research Combustor-L1 (ARC-L1). Additionally, an effort was made to build a smaller combustor for more flexible testing with lower fuel and air requirements. This smaller version would be termed the ARC-M1. The main architecture proposed in this study is based on this design. Both combustors were designed by a subcommittee composed of NJFCP researchers and OEM representatives. The construction of both combustors was originally carried out by the research group of the P.I. (Tonghun Lee) at UIUC.

The referee combustor, L1, and M1 are shown in Figure 1. Continuing this heritage, ARL will be a key partner in the analysis of this combustor in terms of both numerical simulation efforts and X-ray imaging of spray break-up, which will be performed at the Advanced Photon Source of ANL. In addition to the laser and optical measurements available at UIUC, the goals include characterizing the operating characteristics of the M1 combustor in an unprecedented way to enable wide adoption in the academic/industrial community as a test platform for new fuel blends. After this characterization is complete, the basic physics, dimensions, and operational envelope of the combustor will be openly shared with the academic and commercial sectors. This work is expected to provide a common platform not only for prescreening sustainable aviation fuels (SAFs) but also for performing other sustainability-related experiments involving novel fuels in a laboratory setting.

Task 1 - Characterization of Optimized M1 Fuel Nozzles under Lean Blowout Conditions

University of Illinois at Urbana-Champaign

Objectives

In this task, LBO measurements are conducted on the ARC-M1 combustor by using four different fuels with a range of key properties to demonstrate the effects of different fuel properties on combustion behavior. This same testing matrix is completed by using multiple designs of liquid fuel spray nozzles to demonstrate the effects of the liquid fuel spray behavior on the global LBO combustion performance. Previous LBO studies on the ARC-M1 have demonstrated a strong dependence of LBO performance on parameters governing fuel atomization and vaporization, thus suggesting that these are the limiting steps in the process for burning fuel at these lean equivalence ratios. This study investigates whether that same dependence might be observed across fuel nozzles with varying atomization performance or whether other fuel properties may become more dominant for other fuel nozzles. By collecting LBO measurements at well-controlled, relevant operating conditions across multiple fuel nozzles, a more comprehensive picture can be captured of the operational regime in which the ARC-M1 combustor operates, thus providing insight into the behaviors governing gas turbine operation at these conditions. This work should aid in the integration of alternative jet fuels into fuel pipelines by providing insight into combustor operations using much lower fuel volumes than other large-scale test rigs.

Research Approach

Throughout the NJFCP, the referee combustor and several other combustors were carefully characterized under a variety of relevant operating regimes, including blowout and ignition. These studies were conducted under a range of standard operating conditions that are relevant to gas turbine operational regimes, and are likely to expose differences between fuels with varying properties. Although experiments in the referee combustor have provided valuable data regarding the fuel effects near LBO, operating the referee rig has several disadvantages. The scale of the referee combustor results in large air and fuel flow rate requirements, thus making setup and operation expensive, particularly for studies of new alternatively derived fuels, which may be difficult to manufacture. Therefore, the ability to obtain similar results from a smaller combustor with decreased fuel and air requirements would be beneficial. The M1 combustor uses substantially less air and fuel, thereby reducing the overall instrumentation expense and complexity, as well as the volume of fuel needed to conduct tests over a range of conditions. With these advantages, the M1 combustor could be used to evaluate the performance of new fuels with much less fuel, thereby decreasing the supply requirements for a potential new fuel supplier. To achieve this goal, we must ensure that the trends observed in a smaller combustor convey the physics observed in other test combustors, such as the referee combustor.

Overview of Lean Blowout Testing

Performing LBO measurements on a combustor in a reliable and repeatable manner involves careful control of all combustor operating parameters including fuel flow rate, air flow rate, air temperature, and combustor pressure. To ensure that combustor conditions are stable before LBO testing is conducted, the combustor is ignited at a fuel flow rate above the LBO point, and combustion is sustained at that flow rate until the air outlet temperature reaches a steady-state condition. After steady-state temperatures are reached, the fuel flow rate is slowly reduced until blowout occurs. For these experiments, the fuel flow rate is reduced by approximately 0.05 g/min per second. This slow ramp rate helps ensure that the combustor wall temperature does not bias the LBO point lower, owing to heat transfer from the hot combustor itself back into the flame. While the fuel flow rate is being stepped down, all other combustor properties are closely monitored to ensure that they remain within the specified parameter ranges. The specific LBO point is monitored by recording a photodiode signal at 100 kHz simultaneously with all other combustor parameters at 50 Hz. The lean blowoff point is determined for each test by finding the equivalence ratio at the point where the photodiode signal indicates that blowout occurred. An example of the fuel flow rate and photodiode signal measured during a single blowout attempt is shown in Figure 2. To decrease the effects of random variation in LBO on the reported results, each condition is tested at least 15 times. Operating conditions for these experiments (Table 1), have been chosen to facilitate comparison with previous experiments conducted in the ARC-M1 combustor and other combustors in the literature.

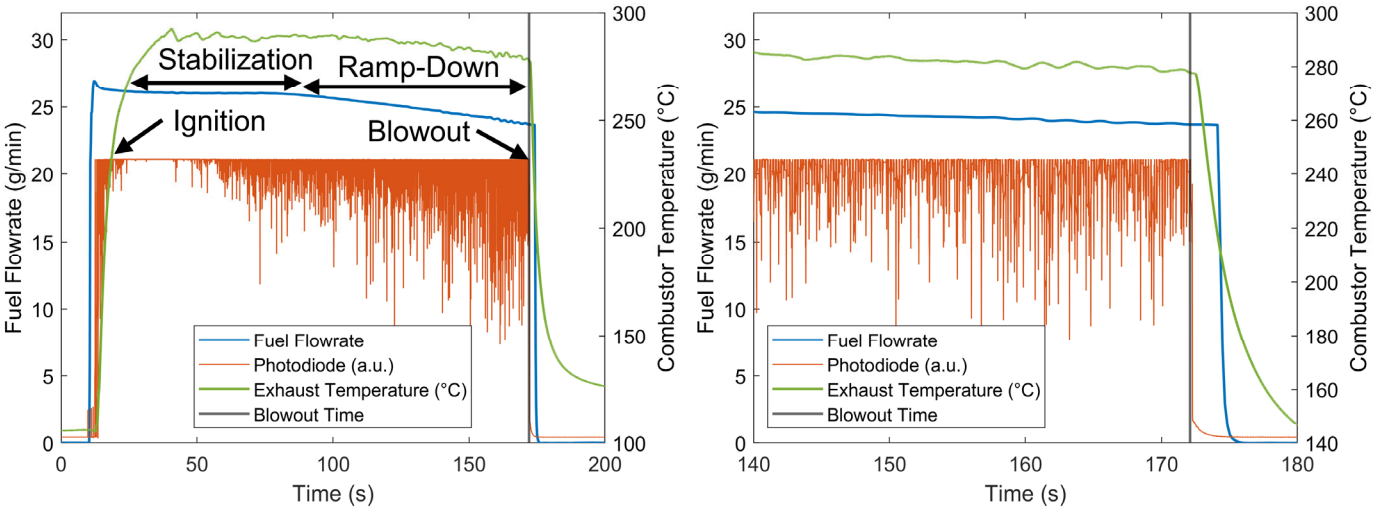

Figure 2. Example testing procedure used for lean blowout testing, showing fuel flow rate and photodiode signal during one lean blowout measurement test.

Table 1. Targeted combustor operating conditions.

Fuels	F-24, C-1, C-3, and C-5
Air preheat temperature	394 K ± 2 K
Total air flow rate	65.1 g/s ± 2%
Main air flow rate	43.4 g/s
Dilution air flow rate	10.9 g/s
Sweeping air flow rate (2×)	5.4 g/s
Combustor plenum pressure	203 kPa
Target combustor pressure drop	3%

Nozzles Evaluated in Lean Blowout Testing

The M1 combustor has been designed to allow different types of fuel spray nozzles to be installed for testing and evaluation. In these experiments, three hollow-cone fuel spray nozzles are tested to investigate the impacts of fuel spray on global combustor LBO performance. Table 2 includes a comparison between the nozzles tested as part of these experiments. An image of several of these nozzles is also shown in Figure 3. Nozzle A was previously used for extensive experiments on the M1 combustor; two additional nozzles have been chosen to enable comparisons with nozzles with better atomization than this previously tested nozzle. Fuel atomization behavior under combusting conditions in the M1 combustor was characterized previously with X-ray phase-contrast imaging, thus providing baseline information on the fuel spray dynamics in the operating combustor.

Table 2. Properties of fuel nozzles tested in these experiments.

Nozzle	Approximate minimum diameter (μm)	Approximate cone angle	Flow rate at 100 psid (L/hr)	Injection pressure at F-24 LBO (psid)
Nozzle A	344	90°	6.2	29.2
Nozzle B	150	80°	2.25	45.9
Nozzle C	150	80°	4.60	32.5

Figure 3. Nozzles tested during lean blowout testing in the M1 combustor.

Fuels for Lean Blowout Testing

In these experiments, four different fuels are tested in the M1 combustor to probe the effects of fuel properties on combustion behavior at these critical conditions. The tested fuels consist of a reference fuel, F-24 (comprising Jet A and military specific additives), and three fuels from the NJFCP with specific properties designed to probe the edges of the jet fuel operational envelope. Fuel C-1 has been developed with a low derived cetane number and a relatively flat boiling curve. Fuel C-3 has been formulated to have a high viscosity, and fuel C-5 has been developed with an extremely flat boiling curve with respect to those of other fuels. Table 3 shows selected important parameters of each fuel for comparison, demonstrating some of the key features of the fuels selected for testing.

Table 3. Comparison of key properties of the four tested fuels.

Fuel	Key features	Derived cetane number	HOC (MJ/kg)	H/C ratio	SAFR	Kinematic viscosity at 40 °C (cSt)	Surface tension (dynes/cm)
F-24	Jet A with additives	48.6	43.2	1.94	14.70	1.36	23.6
C-1	Low cetane	17.1	43.8	2.18	15.03	1.53	21.0
C-3	High viscosity	47.0	43.3	1.97	14.65	1.78	24.2
C-5	Flat boiling	39.6	43.0	1.94	14.68	0.83	22.2

Lean Blowout Performance Results

Figure 4 shows the raw results of the LBO testing on all three tested nozzles, plotted against four relevant fuel properties: 20% distillation temperature (T_{20}), 50% distillation temperature (T_{50}), derived cetane number, and kinematic viscosity. The data show the relative performance of the three tested nozzles in the combustor. Nozzle B performs "best," with the lowest LBO equivalence ratios, and nozzle A performs "worst," blowing out at substantially higher fuel flow rates and equivalence ratios than the other two nozzles. Nozzle C has equivalence ratios between those of nozzles A and B. This performance differential among nozzles is notable, because it demonstrates that small changes in the liquid fuel spray can have large effects on global combustor performance. The difference in performance between nozzle A and nozzle B on C-3 fuel is particularly notable: blowout occurs with nozzle B at a fuel flow rate and equivalence ratio nearly half that of nozzle A. These findings suggest that the combustor performance when operating on nozzle A is highly limited by the fuel spray, because simply using a better performing fuel nozzle causes a major difference in performance.

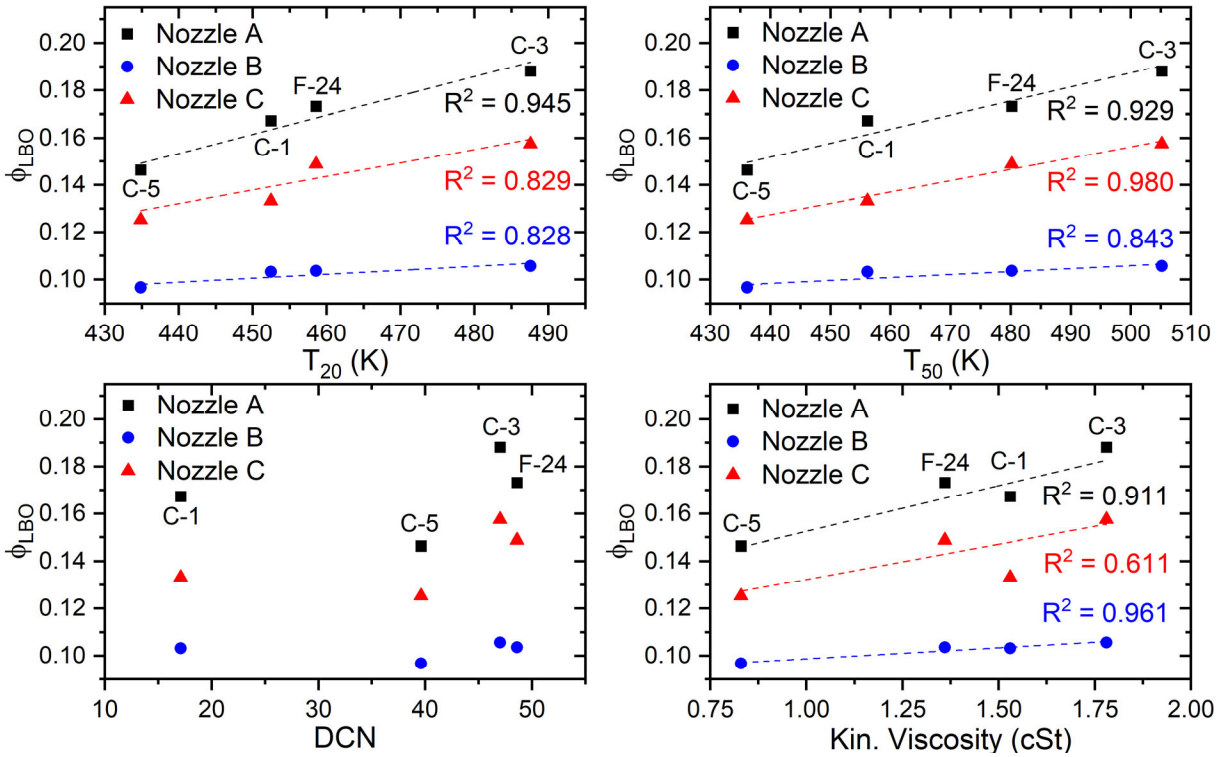

Figure 4. Absolute lean blowout equivalence ratio data from the three tested nozzles, plotted against various critical fuel properties.

Figure 5 shows the same LBO equivalence ratio results as those in in Figure 4, but the data for each nozzle are normalized by that nozzle's F-24 equivalence ratio, thereby allowing for the observation of trends in each nozzle's performance relative to its performance with the baseline jet fuel. Error bars in this plot represent two standard deviations of the LBO equivalence ratio, computed over the 15 collected trials for each test case. For all three nozzles, the relative order of LBO performance is the same: the C-5 fuel, with low viscosity and a low boiling curve, shows the most favorable performance results, followed by C-1, F-24, and the high-viscosity C-3 fuel performs worst overall. Plotting of the LBO test results against multiple fuel properties indicates that all three nozzles demonstrate that their LBO performance is strongly correlated with both the distillation curve temperatures and kinematic viscosity. None of the three tested nozzles appear to have a strong correlation between their performance and the fuel DCN, in contrast to past results on the larger referee combustor, but in line with previous test results on the ARC-M1. However, the trendlines for each tested nozzle show that nozzles A and C have very similar slopes of their correlation with these properties, whereas nozzle B has a shallower slope for all three fuel properties. These three fuel properties are highly correlated with fuel atomization and vaporization behavior, thus suggesting that the combustor has a weaker dependence on fuel atomization and vaporization behavior when operating with nozzle B, whereas the overall combustion performance of nozzles A and C has a similar dependence on atomization and vaporization.

Before conducting these experiments, we hypothesized that switching the combustor fuel nozzle from nozzle A, which has been tested extensively in the past, to the much more favorable nozzle B might result in fuel atomization and vaporization no longer being the rate-limiting step in the combustion process, and in the chemical kinetics being substantially more dominant in the global combustion performance characteristics. If this hypothesis were true, the combustion performance of nozzle B would have been in line with the results seen on the larger referee combustor, wherein a strong correlation between LBO performance and DCN was observed at comparable conditions. However, this finding was clearly not the case in our results. The smaller length scales of the ARC-M1 combustor indicate that the physical processes of atomization and vaporization are extremely dominant, such that even choosing a nozzle producing very small droplets cannot fully overcome the physically dominant behavior. To further adjust the combustor operating regime, changes to the combustor operating conditions are expected to be necessary, such as moving to more favorable higher temperature or pressure conditions.

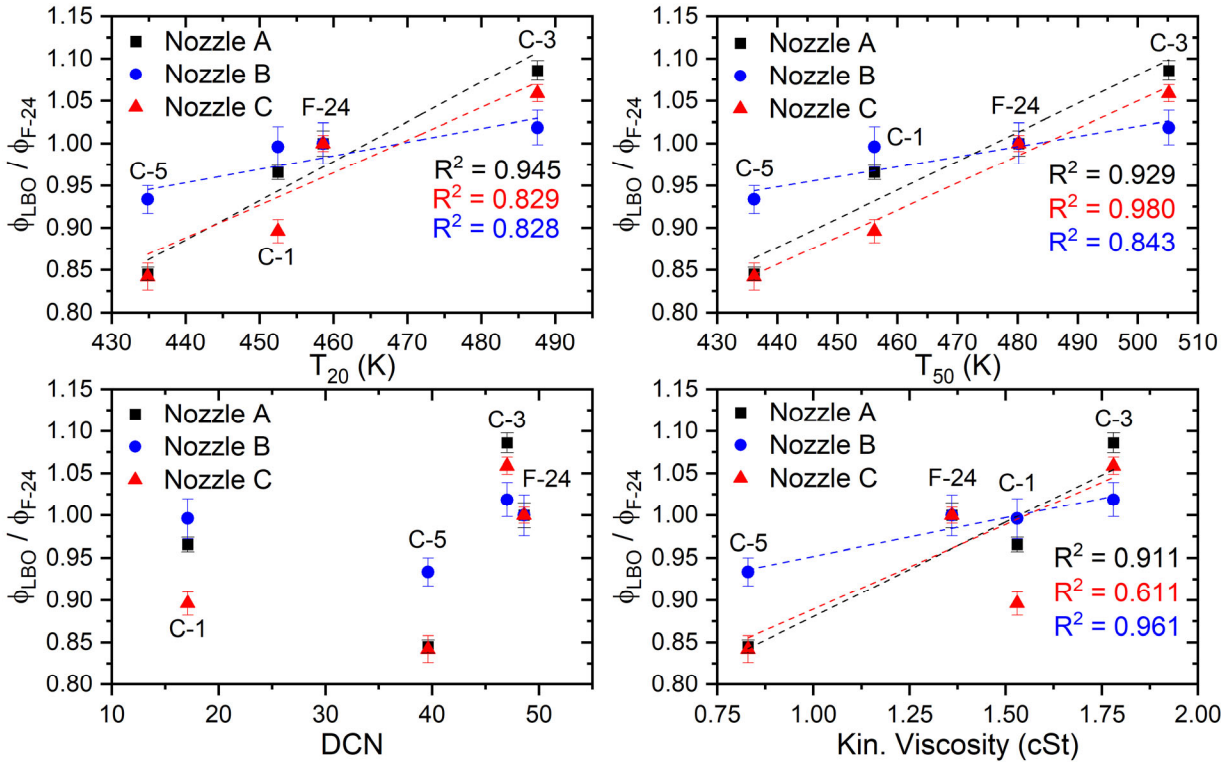

Figure 5. Lean blowout equivalence ratio data from the three tested nozzles, normalized by the lean blowout equivalence ratio for F-24 fuel. Data are plotted against multiple critical fuel properties.

Milestones

- 3 months: selection and procurement of optimized nozzles for the M1 combustor.
- 6 months: initial LBO nozzle comparison testing in the M1 combustor using one fuel.
- 9 months: full nozzle comparison LBO testing with all four fuels.
- 12 months: data analysis and identification.

Major Accomplishments

We have successfully collected LBO testing data on the M1 combustor under relevant conditions by using three different nozzles and four fuels with a wide range of liquid fuel properties. These measurements demonstrate that, by using a liquid spray nozzle with more favorable atomization performance in the M1 combustor, fuel properties related to liquid atomization and vaporization become less critical to the LBO performance of the combustor. However, owing to the small scale of this combustor, fuel atomization and vaporization remain the dominant factors, despite the more favorable atomization performance from the tested fuel spray nozzles. These measurements provide key information for identifying directions for future study to enable wider use of small-scale combustors as test platforms for SAFs.

Publications

Wood, E., Trotter, C., Lee, T., Mayhew, E., Temme, J., & Kweon, C. (2023). *Lean Blowout Dependence on Fuel Atomization in the ARC-M1 Gas Turbine Combustor.* Conference paper in preparation.

Outreach Efforts

All test data will be made accessible through https://altjetfuels.illinois.edu/.

Awards
None.

Student Involvement
This project was conducted primarily by one graduate student, Eric Wood (PhD Student), and one undergraduate student, Caleb Trotter.

Plans for Next Period
In the next period, the relationship between atomization performance from the fuel spray nozzle and global LBO performance will be investigated in greater detail by combining knowledge from this testing with high-speed X-ray spray data collected on each nozzle at ANL's Advanced Photon Source.

Task 2 - Cold-Start Ignition Testing and Characterization of the M1 Combustor by using Optimized Fuel Nozzles
University of Illinois at Urbana-Champaign

Objective
The objective of this task is to conduct cold-start ignition testing on the M1 combustor by using multiple fuel spray nozzles, to evaluate how changing fuel atomization behavior affects ignition performance. This testing builds upon previously conducted testing establishing baseline ignition performance in the combustor and the LBO testing described in Task 1.

Research Approach
To further investigate different factors' effects on ignition performance in the ARC-M1 combustor, a series of ignition tests are performed by using multiple fuel nozzles to investigate how different fuel nozzles change ignition behavior. This testing uses the combustion air and fuel supply system that has been used in several previous studies on the ARC-M1 combustor, with some modifications to expand the range of inlet conditions. This combustion system has independently controlled heated main air flow, heated dilution air flow, heated sweeping flows, and fuel flow. Main, dilution, and sweeping air flow rates are controlled with independent air mass flow controllers. The air is heated by using electrical resistance heaters, which are controlled with temperature controllers to set the air inlet temperature into the combustor. Pressurized fuel is provided by a piston accumulator pressurized with nitrogen, and a Coriolis fuel mass flow controller maintains the fuel flow rate at the desired values during testing. To achieve the sub-ambient temperature conditions necessary for these cold-start ignition measurements, a −20 ˚C capable ethylene glycol chiller is used in conjunction with a brazed plate heat exchanger to cool the incoming compressed air before the mass flow controllers. The liquid fuel is also chilled inside the piston accumulator before injection into the combustor.

Three hollow-cone fuel spray nozzles are tested in the combustor in ignition scenarios to investigate the effects of the fuel spray on these global combustor performance criteria. These nozzles are the same as those tested under LBO conditions in Task 1, and their properties are shown in Table 2. Testing is conducted at ambient pressure conditions and two different temperatures, to demonstrate how varying the inlet temperature conditions affects global combustion behavior with these different types of fuel spray nozzles. Combustor operating conditions for these experiments are shown in Table 4.

Table 4. Operating conditions for the fuel nozzle comparison cold-start ignition study.

Fuel	F-24
Air temperature	25 ˚C, −5 ˚C
Fuel temperature	25 ˚C, −5 ˚C
Total air flow rate	34.8 g/s
Combustor absolute pressure	103 kPa
Target combustor pressure drop	3%

Ignition Testing Procedures

To collect ignition probability measurements for all the above cases, the following procedure is followed. An ignition attempt is started by directing chilled fuel into the combustor without sparks for 3 s to allow the fuel flow rate to stabilize at the desired value. After this period, direct current power is supplied to the exciter, and the igniter is allowed to spark at its ~3.7-Hz frequency for up to 10 s, at which point the sparks and fuel flow are stopped. After successful ignition of the combustor, the test is considered complete, and the fuel and sparks may be stopped early. An analysis script uses the recorded photodiode signal to measure the emission from the sparks and the flame to determine which spark resulted in successful ignition. According to this process, at most one successful spark can be found in each ignition attempt. Figure 3 shows an example photodiode signal collected during an ignition attempt. After each ignition attempt, air is allowed to flow through the combustor for at least 2 minutes to clear out any remaining liquid fuel inside the combustor before the next test begins. This procedure is repeated many times at fuel flow rates across the ignition probability curve to ascertain the overall ignition behavior, ranging from no ignition cases to the maximum reasonable fuel flow rate for the testing conditions.

Ignition probability curves are determined from the recorded data sets by analysis of all tests runs and determination of the number of successful and unsuccessful sparks in each test. The actual air and fuel flow rates from each test are also calculated from the recorded data to determine the exact equivalence ratio for that test run. This data are then split into equally sized bins according to equivalence ratio, and the total number of unsuccessful and successful sparks is used to calculate the overall ignition probability in that bin. Importantly, this test procedure assumes that every spark event is independent of all others. Although this independence may not be the case because of fuel accumulation in the combustor or slight variations in flow rates throughout the test runs, every effort is made to maintain these parameters so that all test points can be considered independent.

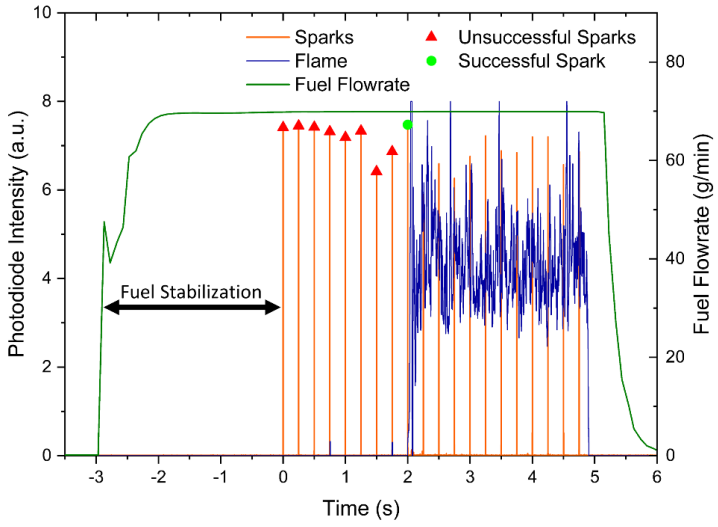

Figure 6. Ignition testing procedure for M1 combustor cold-start performance comparison evaluation.

Cold-Start Ignition Performance Results

A series of ignition tests are conducted on each of the three nozzles listed in Table 2 across the range of relevant equivalence ratios. Results for each of these three nozzles at 25 ˚C conditions are shown in Figure 7. The nozzle A results show a similar rapid transition from low to high ignition probabilities, as observed in previous M1 combustor ignition testing (using the same nozzle) at 15 ˚C conditions. Both additional nozzles tested as part of these experiments demonstrate markedly improved ignition performance over that of nozzle A, with ignition beginning to occur for both nozzles at an equivalence ratio approximately half that of nozzle A. As discussed in the introduction, gas turbine combustor ignition performance is controlled by a complex combination of factors including turbulent airflow patterns, liquid spray atomization, fuel vaporization and fuel/air mixing. These results demonstrate the complexity of the process, because a dramatic change in ignition performance is caused by simply changing the fuel spray nozzle and thus the atomization behavior. We hypothesized that both nozzles B and C provide markedly improved fuel atomization over that of the original nozzle A used for baseline testing. We expected that these nozzles would produce smaller droplets directly from the nozzle, which are easier to vaporize, thereby allowing for a flame to stabilize with less fuel in the combustor. An additional interesting factor is that, although nozzles B and C show relatively similar performance, nozzle C achieves this performance at lower fuel injection pressures than nozzle B. This finding demonstrates that although fuel pressure is a key factor in producing favorable atomization from a nozzle, it is far from the only relevant factor, and nozzle design plays the most important role in determining fuel nozzle performance.

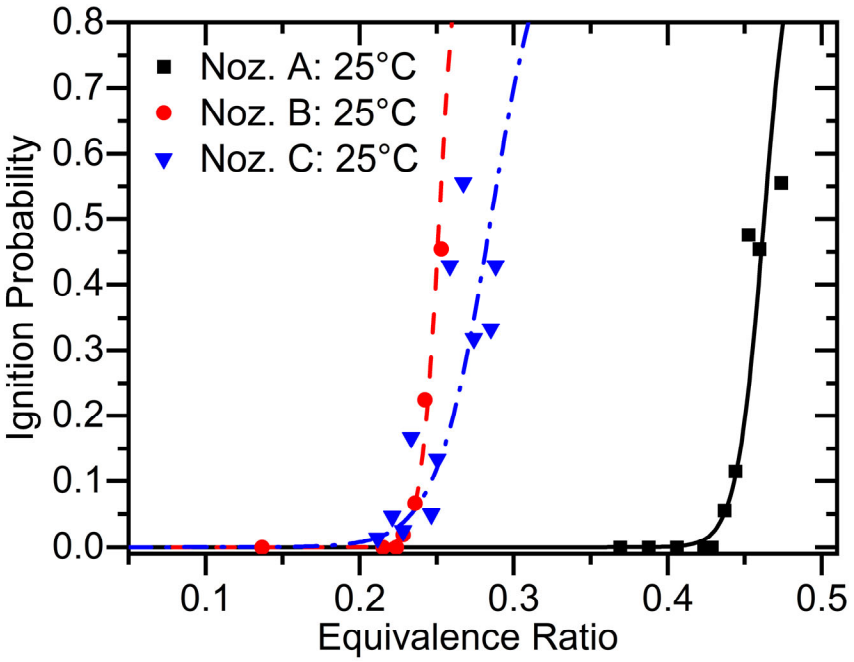

Figure 7. Comparison of ignition performance for the three tested fuel nozzles at 25 ˚C conditions.

Figure 8 shows the ignition performance results for both nozzles B and C, comparing the behavior between 25 ˚C and −5 ˚C conditions for each nozzle. As with the 25 ˚C data in Figure 6, the two nozzles appear to perform similarly at the −5 ˚C conditions, and nozzle C shows slightly poorer performance than nozzle B. Although both nozzle B (left) and nozzle C (right) begin showing ignition at approximately the same equivalence ratio, the “smaller” nozzle B ignition probability increases more rapidly than the “larger” nozzle C when moving toward higher equivalence ratios.

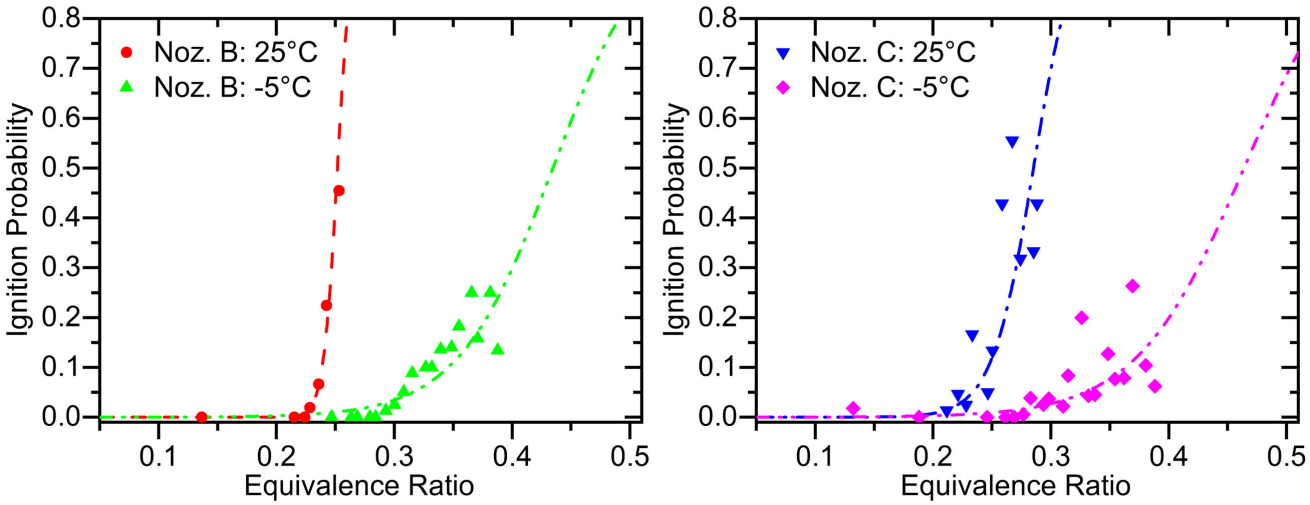

Figure 8. Comparison between ignition performance at 25 ˚C and −5 ˚C cold-start conditions for nozzle B (left) and nozzle C (right).

An interesting finding from these data, combined with data previously collected on the M1 combustor by using a high-altitude chamber, is that changing the nozzle performance and ambient temperature affect the ignition probability curves in markedly different ways. Changing between fuel nozzles with different atomization behavior appears to shift the entire ignition probability curve left or right (to lower or higher equivalence ratios), whereas moving to lower-temperature (less favorable) inlet conditions reduces the slope of the curve (ignition probability rises more slowly). These factors are important to understand as future efforts attempt to further characterize the physics controlling gas turbine ignition behavior by applying more advanced diagnostic techniques to the ARC-M1 combustor.

Milestones

- 6 months: construction of infrastructure to support cold-start ignition testing in the M1 combustor at UIUC, including chilling system for low-temperature measurements.
- 9 months: M1 combustor setup for ignition testing, shake-down, and selection of cold-start test conditions.
- 12 months: data collection for cold-start ignition performance in the M1 combustor; analysis of collected data to determine ignition probability curves and relative performance between tested nozzles.

Major Accomplishments

We have conducted cold-start ignition testing on multiple fuel nozzles in the M1 combustor to evaluate how fuel nozzles with varying atomization performance affect ignition behavior in a realistic small-scale gas turbine environment. In combination with the results shown above in Task 1, these data comprehensively demonstrate how liquid spray atomization from different fuel nozzles couples with global combustor performance in realistic LBO and ignition scenarios. These results motivate further research to determine how small-scale combustors, such as the M1 combustor, could be used to evaluate fuel effects in larger-scale combusting environments.

Publications

Wood, E. J., Motily, A., Trotter, C. J., Lee, T., Mayhew, E., Coburn, V. D., Temme, J., & Kweon, C.-B. (2022, January 3). Fuel spray and operating condition impact on ignition performance in the arc-m1 combustor. *AIAA SCITECH 2022 Forum*. AIAA SCITECH 2022 Forum, San Diego, CA & Virtual. https://doi.org/10.2514/6.2022-0364

Outreach Efforts

All test data will be made accessible through https://altjetfuels.illinois.edu/.

Awards

None.

Student Involvement

This project has been conducted primarily by two students: Eric Wood (PhD) and Caleb Trotter (undergraduate).

Plans for Next Period

Now that combustor performance has been characterized by using multiple liquid spray nozzles, the connection between droplet atomization and global performance will be investigated in greater detail with advanced diagnostics, such as high-speed X-ray imaging of droplet breakup during spark events in the operating M1 combustor. Performing these advanced diagnostics precisely during the spark event is very challenging because of the short timescales of the high-energy sparks; therefore, development of this capability will be a principal component of the upcoming work on this project.

Project 066 Evaluation of High-Thermal-Stability Fuels

University of Dayton and University of Dayton Research Institute

Project Lead Investigator

Joshua Heyne
Associate Professor
Mechanical Engineering
University of Dayton
300 College Park
Dayton, OH 45458
937-229-5319
Jheyne1@udayton.edu

University Participants

University of Dayton

- P.I.s:
  1. Joshua Heyne, Associate Professor
  2. Randall Boehm, Research Engineer
- FAA Award Number: 13-C-AJFE-UD, Amendments 27 and 30
- Period of Performance: June 1, 2020 to September 30, 2022
- Tasks:
  1. Identify/create a jet engine model including all components necessary to evaluate the impact of fuel properties.
  2. Build and apply a heat transfer model for the fuel system.
  3. Identify engine cooling trade-offs that can be leveraged to optimize engine/aircraft system efficiency.
  4. Estimate gains in fuel efficiency.
  5. Identify critical blend components and solvents to study.
  6. Create and test blends for thermal stability in jet fuel thermal oxidation testing (JFTOT) and quartz crystal microbalance testing (QCM).

Project Funding Level

FAA provided $284,997 in funding, which is allocated between amendments 27 and 30 as follows:

- 13-C-AJFE-UD-027: $184,997
- 13-C-AJFE-UD-030: $100,000

Cost sharing is provided by DLR Germany.

Investigation Team

- Joshua Heyne (University of Dayton) is the project lead investigator, responsible for building the team and coordinating team activities, driving toward the completion of major milestones.
- Randall Boehm (University of Dayton) is a research engineer with 20 years of relevant industry experience and is responsible for leading the technical efforts on this project.
- Lily Behnke (University of Dayton) is a graduate student research assistant, responsible for integration of the engine performance models (EPMs) and fuel property models with JudO, a tool developed internally to help optimize fuel composition against user-defined objectives.
- Jeffrey Spruill (General Electric [GE]-Aviation) is a product performance engineer, responsible for applying audited EPMs as necessary to judge potential drop-in fuel effects on a variety of engines for various mission points,

environmental conditions, and engine deterioration levels. Additionally, Jeff is responsible for estimating non-drop-in fuel effects arising from conceptual design changes to engine thermal management systems that lead to increased reliance on fuel as a coolant instead of compressed air.
- Gurhan Andac (GE-Aviation) is a combustion engineer, responsible for coordinating the efforts at GE in support of this project.

Project Overview

It has long been understood that increasing the reliance on jet fuel as a primary coolant for both the engine and the aircraft has significant performance and efficiency benefits relative to the use of air as a coolant (Bruening, 1999) but fuel degradation and coking at high temperatures restrict how much heat can be put into the fuel. In some military applications, the performance benefits are sufficiently large to justify the creation of specialty fuels such as JP7 and JPTS, which can tolerate much higher temperatures than petroleum-derived Jet A or Jet A1 (JP8) (Edwards, 2007). In land-based applications of gas turbines, weight is of little consequence; thus, the operations of waste heat recovery (WHR) for plant efficiency or the reduction of combustor inlet temperature for emission reductions can be accomplished by a wide variety of techniques, all of which are impractical for flight because of their impact on the mass of the power plant. Nonetheless, these applications provide some common examples of how controlling the air temperature along its flow path through the engine can have a large impact on performance, durability, and energy efficiency (Wilfert, 2007). Numerous works relating to fuel deoxygenation (Zabarnick, 2020) and other methods for decreasing coking propensity and its impacts (Mancini, 2004) have largely been motivated at the sponsorship level by these benefits.

More recently, sustainable alternative fuels (SAFs) have received much attention because they can contribute to high-priority geopolitical goals to diversify energy supply chains and reduce greenhouse gas emissions. Most of these efforts have focused on streamlining the evaluation and approval processes to use synthetic fuels at some blend ratio with petroleum-derived jet fuel to create a so-called drop-in fuel that can be used within existing infrastructure without objection from any stakeholders (Colket, 2021). Additionally, there have been discussions regarding characteristics of synthetic blend components (such as low aromatics, high specific energy, and high thermal stability) that would make these components attractive as potential specialty fuels (such as JPTS) or high-performance fuels. Kosir et al. (2020) recently published work highlighting the efficiency gain that could be realized by using fuels with high specific energy via a lower aircraft weight at take-off, resulting in less mass that must be lifted and held against the force of gravity.

The weight of fuel uplifted to an aircraft, as necessary to complete its mission, is certainly an important component to consider in assessing the integrated engine/aircraft energy demand and efficiency. The energy efficiency of the engine is also expected to be influenced by other fuel properties, including the following:

1. **Hydrogen/carbon (H/C) ratio**. Through its impact on combustor exhaust gas composition, this ratio has a small impact on the ratio of heat capacity (gamma), combustor exit temperature, and work extracted during expansion through the turbine, even when the total enthalpy created at the combustor is unchanged.
2. **Viscosity**. Viscosity impacts the heat transfer coefficients, which ultimately determine how much waste heat is recovered by the fuel (coolant) and delivered back to the engine via the combustor.
3. **Energy density**. Energy density, measured in joules per liter (J/L), impacts volumetric flow rates, which in turn impact heat transfer coefficients.
4. **Specific heat**. The specific heat influences heat transfer coefficients but, perhaps more importantly, also has a direct impact on the temperature rise in the fuel per unit of heat energy absorbed, which in turn may impact the coking rate.
5. **Coking rate**. The coking rate drives several high-level design decisions relating to the thermal management of an engine. Coking rate is also known as fuel thermal stability.

References

Bruening, G. B., & Chang, W. S. (1999). Cooled cooling air systems for turbine thermal management. *Volume 3: Heat Transfer; Electric Power; Industrial and Cogeneration*, V003T01A002. https://doi.org/10.1115/99-GT-014

Edwards, T. (2007). Advancements in gas turbine fuels from 1943 to 2005. *Journal of Engineering for Gas Turbines and Power*, *129*(1), 13–20. https://doi.org/10.1115/1.2364007

Wilfert G, Sieber J, Rolt A, Baker N, Touyeras A, & Colantuoni S. (2007). *New Environmental Friendly Aero Engine Core*

Concepts. ISABE-2007-1120. 18th Int Symp Air Breath Engines.
Zabarnick, S., West, Z. J., Arts, A., Griesenbrock, M., & Wrzesinski, P. (2020). Studies of the impact of fuel deoxygenation on the formation of autoxidative deposits. *Energy & Fuels*, *34*(11), 13814–13821. https://doi.org/10.1021/acs.energyfuels.0c02603
Mancini, A. A., Ackerman, J. F., Leamy, K. R., & Stowell, W. R. (2007). *U.S. Patent No. 7,311,979*. Washington, DC: U.S. Patent and Trademark Office.
Colket, M., Heyne, J., & Lieuwen, T. C. (Eds.). (2021). *Fuel effects on operability of aircraft gas turbine combustors*. American Institute of Aeronautics and Astronautics, Inc. https://doi.org/10.2514/4.106040
Kosir, S., Stachler, R., Heyne, J., & Hauck, F. (2020). High-performance jet fuel optimization and uncertainty analysis. *Fuel*, *281*, 118718. https://doi.org/10.1016/j.fuel.2020.118718

Task 1 - Identify/Create a Jet Engine Model Including All Components Necessary to Evaluate the Impact of Fuel Properties

University of Dayton

Objectives

This work has three primary objectives. The potential impact of fully synthetic SAFs on the specific fuel consumption (SFC) of a jet engine with no associated change in engine design or logic will be assessed in Phase 1. In Phase 2, the team will evaluate the impact of leveraging the high thermal stability of SAF candidates by increasing WHR up to a limit driven by the requirement that the fuel vapor pressure must remain below the normal working fuel pressure for all operating conditions. To achieve an increased WHR for this phase of the assessment, only straightforward, evolutionary design changes will be considered. In Phase 3, the aim is to identify and examine the coupled influence of increased WHR with optimized cooling flow schedules (Deveau, 1985).

Research Approach

At some level, one might argue that the maximum additional WHR is determined by the proposed shift in the maximum fuel temperature requirement, for instance, (160-127)*Cp, where 160 °C is the proposed temperature for high-thermal-stability fuels, 127 °C is the requirement corresponding to petroleum-derived Jet A, and Cp is the heat capacity of the proposed fuel. While this is true at some level, it provides only part of the story. For this study, a fuel system thermal model (FSTM, Figure 1) was created to simulate the heat pickup of fuel in real engines. This model allows us to quantify the influence of fuel property variations on the temperature rise and WHR within existing architectures. This model also enables evaluations of concept-level design changes that are intended to drive more heat into the fuel. A high-level EPM (Figure 2) was created to enable evaluations and comparisons of different conceptual designs that drive the same amount of total heat into the fuel (approximately 33*Cp more than baseline) but take heat from difference sources. The EPM also enables evaluations of the H/C impact on combustor exit temperature and turbine work extraction, which is usually neglected in performance models because it is thought to be a small impact and the H/C ratio of fuel onboard an aircraft is generally not known. The final component in the overall impact on system efficiency is the weight, including the difference (decrease) in fuel weight necessary to complete the same representative mission, as well as the difference (increase) in weight created by the concept-level design changes being considered.

A distribution of properties for potential SAFs is created by virtually blending individual molecules by a random association of mole fractions, whose values are also randomly determined, with specific molecules possessing known physical and chemical properties (Lemmon, 2018; Kroenlein, 2019). The fuel properties of the mixtures are derived from the mixture definition and constituent properties according to ideal mixture blending rules, which have been documented elsewhere (Flora, 2019). This trial guess at a SAF candidate is then passed through a filter to determine whether it is expected to pass ASTM D1655 and ASTM D7566 fuel specifications. If the candidate passes this filter, it is included within the distribution that is input to the FSTM and EPM as part of a simulation. See Figure 3 for a graphical representation of the fuel selection methodology. The motivation behind this approach was to maintain a physical link between different properties, as the full set of properties is derived from each fuel and the property variation is driven by fuel composition variation rather than arbitrary simulation. All liquid fuel properties include first-order temperature dependence, whereas none of the properties include pressure dependence.

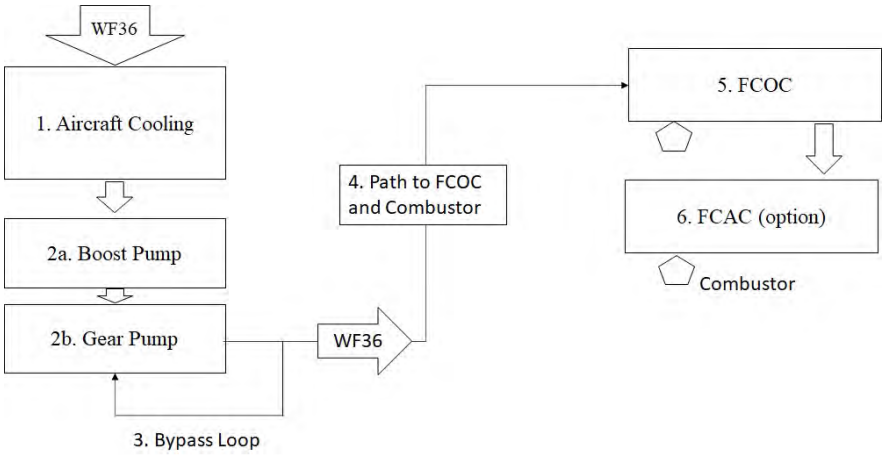

Figure 1. Block diagram of the fuel system thermal model for the pilot study (Boehm, 2021) and fuel optimization. FCAC: fuel-cooled air cooler; FCOC: fuel-cooled oil cooler; WF36: fuel flow rate to the combustor.

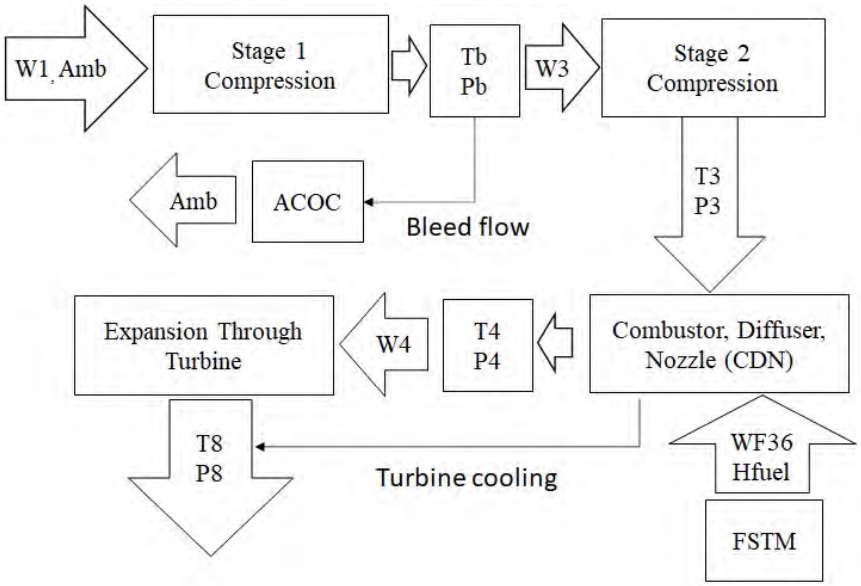

Figure 2. Block diagram of the engine performance model for the pilot study (Boehm, 2021) and fuel optimization. ACOC: air-cooled oil cooler; FSTM: fuel system thermal model; WF36: fuel flow rate to the combustor.

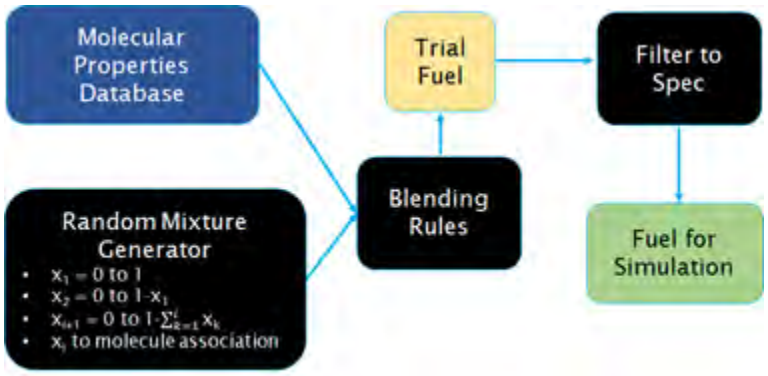

Figure 3. Fuel creation flow chart.

For bookkeeping convenience, the total enthalpy supplied to the engine per unit time (W_f * LHV) is to be conserved for all initial simulations. The net work per unit time (P_{net}) from the engine (expansion plus compression) varies in these simulations depending on fuel composition and conceptual design, in contrast to real applications, where thrust * air speed (~P_{net}) would be conserved and the fuel flow (W_f) would be changed to meet that demand. Once the initial calculation is made, the fuel flow is varied in the simulation, as it would be in a real engine, until P_{net} is equal to the value for the baseline engine model and reference fuel. The relative difference in fuel flow between the initial and final calculation represents the energy savings.

A graphical summary of the methodology is provided in Figure 4. Major inputs include the diameters and lengths of each element in the FSTM, engine operating conditions such as the pressure ratio and air flow splits at each station in the EPM, the baseline fuel-to-air ratio, and temperature boundary conditions for the FSTM. Several fuel properties are provided to the FSTM, while the EPM receives the H/C ratio and lower heating value (LHV) as input.

A validation of this model, relative to fuel property influences and cooling strategy, will be accomplished by comparison to audited performance models of jet engines produced by GE-Aviation.

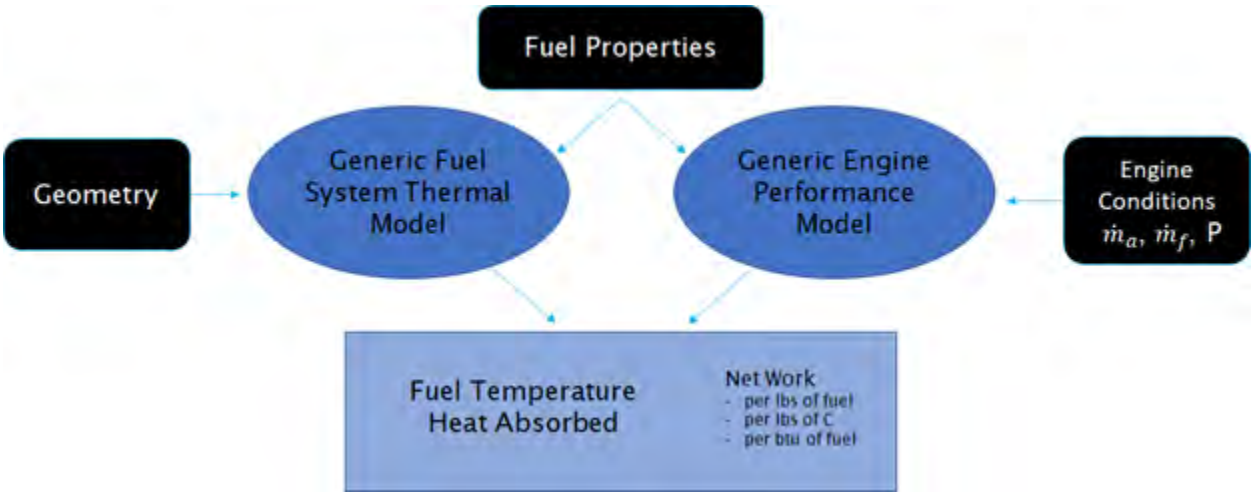

Figure 4. Flow chart of fuel effects and conceptual design evaluation.

Milestones

- The conceptual design of a model jet engine to serve as a tool for evaluating the impact of fuel property variation on jet engine fuel efficiency was completed (August 2020).

- All models used in proof-of-concept work were integrated into JudO, which has been previously used (Kosir, 2020) to optimize fuel composition against defined objectives (September 2021).
- A reference mission (December 2021) and aircraft (March 2022) were established, affording the integration of fuel effects on system-level efficiency.

Major Accomplishments

- As a major accomplishment, we constructed and verified the FSTM and EPM and their integration with Monte Carlo methods, which was necessary to complete most of the remainder of this project.
- All tools needed to assess fuel effects on SFC have been integrated into our internal code for SAF optimization (JudO).

Publications

Boehm, R. C.; Scholla, L. C.; & Heyne, J. S. (2021). Sustainable alternative fuel effects on energy consumption of jet engines. Fuel *304*, 121378. https://doi.org/10.1016/j.fuel.2021.121378

Outreach Efforts

None.

Awards

None.

Student Involvement

- Lily Behnke, M.S. student, accomplished integration/translation of the Excel-based EPM and FSTM into the Python-based JudO program and was responsible for the results shown in Figures 1–6,10, and 11.
- Jack Hoog, M.S. student, participated in the identification and selection of a reference aircraft.

Plans for Next Period

- Integrate/code the reference mission and aircraft into the optimizer to reduce the dimensionality of the optimization.

References

Boehm, R. C., Scholla, L. C., & Heyne, J. S. (2021). Sustainable alternative fuel effects on energy consumption of jet engines. *Fuel*, *304*, 121378. https://doi.org/10.1016/j.fuel.2021.121378

Lemmon, E.W., Bell, I.H., Huber, M.L., & McLinden, M.O. (2018). NIST Standard Reference Database 23: Reference Fluid Thermodynamic and Transport Properties-REFPROP, Version 10.0. *National Institute of Standards and Technology, Standard Reference Data Program*.

Kroenlein, K., Muzny, C. D., Kazakov, A. F., Diky, V., Chirico, R. D., Magee, J. W., ... & Frenkel, M. (2019). NIST Standard Reference 203: TRC Web Thermo Tables (WTT) Version 2-2012-1 Professional. *National Institute of Standards and Technology*.

Flora, G., Kosir, S. T., Behnke, L., Stachler, R. D., Heyne, J. S., Zabarnick, S., & Gupta, M. (2019, January 7). Properties calculator and optimization for drop-in alternative jet fuel blends. *AIAA Scitech 2019 Forum*. AIAA Scitech 2019 Forum, San Diego, California. https://doi.org/10.2514/6.2019-2368

Deveau, P. J., Greenberg, P. B., & Paolillo, R. E. (1985). *U.S. Patent No. 4,513,567*. Washington, DC: U.S. Patent and Trademark Office.

Kosir, S., Stachler, R., Heyne, J., & Hauck, F. (2020). High-performance jet fuel optimization and uncertainty analysis. *Fuel*, *281*, 118718. https://doi.org/10.1016/j.fuel.2020.118718

Task 2 - Build and Apply a Heat Transfer Model for the Fuel System

University of Dayton

Objective

The goal of this task was to create a model that would output heat absorption, representative of real jet engine fuel systems, based on applied boundary conditions such as fuel properties, fuel velocity and momentum, and hot-side temperatures.

Research Approach

The fuel system was broken down into elements for which the author had experience-based guidance relating to fuel inlet and outlet temperatures. In concert with experience-based guidance relating to fuel momentum and system pressure losses, the fuel system geometry, including the flow diameter and length, and hot-side boundary conditions were established for a baseline fuel flow through the modeled fuel system. This model then became the basis for assessing the impact of varying fuel properties.

In the pilot study (Boehm, 2021), Monte Carlo simulations resulted in population distributions plotted against the normalized WHR, as shown in Figure 5. In this context, the recovered waste heat is defined as the total heat absorbed by the fuel in route from the fuel tank to the combustor, which is then divided by the reference enthalpy of the fuel ($LHV*W_f$) supplied to the combustor for the initial calculation of P_{net}. The fuel flow rate at high power is approximately ten times higher than it is at low power, and the flow within the fuel system is turbulent regardless of the fuel properties. Under these circumstances, heat transfer coefficients are not very sensitive to fuel property variations, and thus, the two curves representing high-power operation are nearly vertical. At low-power operation, the flow within the fuel system starts out as laminar and transitions to turbulent as the viscosity drops with increasing fuel temperature. Under these circumstances, heat transfer coefficients are sensitive to fuel property variations, and thus, the two curves representing low-power operation show 0.2% variation in the normalized WHR.

The WHR term is not expected to have a large impact on the overall system efficiency because relatively little fuel is used at low power (top of descent) relative to take-off, climb, or long-haul cruise and because WHR is small compared with $LHV*W_f$. Nonetheless, this savings is worth optimizing because it can be potentially realized without sacrificing any other measure of fuel performance and without any change to the engine. We have already begun to optimize the fuel composition to maximize the LHV and total savings resulting from WHR, which will be discussed further under Task 4. In support of this goal, we have collected the necessary property data for thousands of molecules, which have been pruned to 1,124 molecules based on volatility, expected thermal stability, data completeness, and data consistency relative to similar molecules. We have also added the capability to predict the smoke point for each random composition.

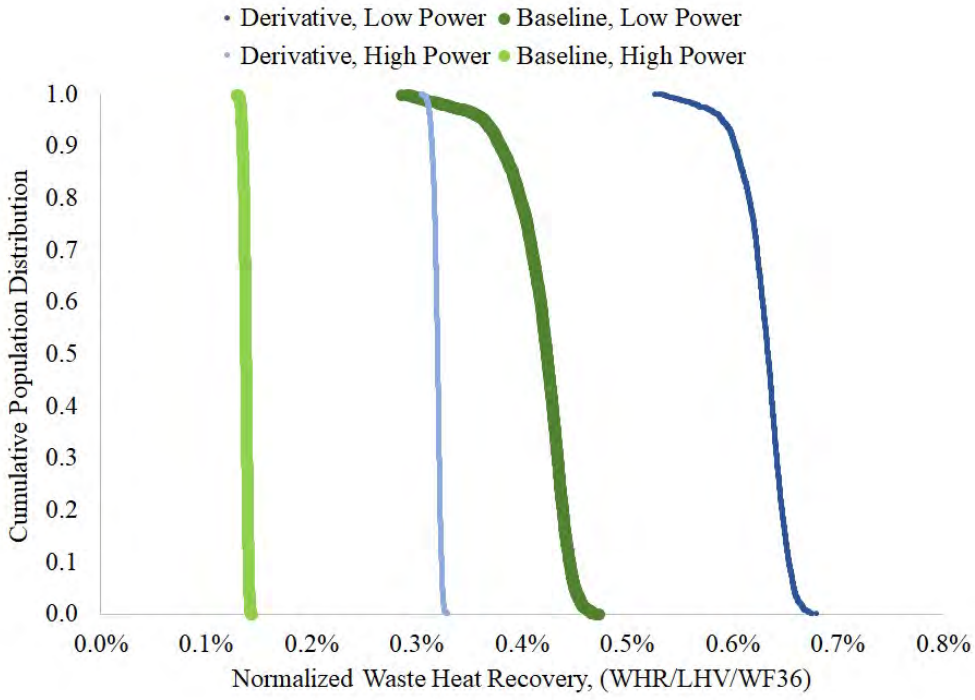

Figure 5. Impact of fuel properties on heat recovered from the engine by the fuel. LHV: lower heating value; WF36: fuel flow rate to the combustor; WHR: waste heat recovery.

Milestones

- Preliminary construction of this model, including integration with Monte Carlo methods and verification of heat transfer coefficient correlations, was completed (October 2020).
  - All models used in proof-of-concept work were integrated into JudO, which has been previously used (Kosir, 2020) to optimize fuel composition against defined objectives (September 2021).

Major Accomplishments

- As a major accomplishment, we constructed and verified the FSTM and EPM and their integration with Monte Carlo methods, which was necessary to complete most of the remainder of this project.
- All tools needed to assess fuel effects on SFC were integrated into our internal code for SAF optimization (JudO).

Publications

Boehm, R. C.; Scholla, L. C.; & Heyne, J. S. (2021). Sustainable alternative fuel effects on energy consumption of jet engines. Fuel *304*, 121378. https://doi.org/10.1016/j.fuel.2021.121378

Outreach Efforts

None.

Awards

None.

Student Involvement

- Logan Scholla, M.S. student, participated in the identification and selection of heat transfer coefficient correlations.
- Lily Behnke, M.S. student, accomplished integration/translation of the Excel-based EPM and FSTM into the Python-based JudO program and was responsible for the results shown in Figures 1–6,10, and 11.

Plans for Next Period

None.

References

Boehm, R. C., Scholla, L. C., & Heyne, J. S. (2021). Sustainable alternative fuel effects on energy consumption of jet engines. *Fuel*, *304*, 121378. https://doi.org/10.1016/j.fuel.2021.121378

Kosir, S., Stachler, R., Heyne, J., & Hauck, F. (2020). High-performance jet fuel optimization and uncertainty analysis. *Fuel*, *281*, 118718. https://doi.org/10.1016/j.fuel.2020.118718

Task 3 - Identify Engine Cooling Trade-Offs That Can Be Leveraged to Optimize Engine/Aircraft System Efficiency

University of Dayton and GE-Aviation

Objective

The goal of this task was to document ideas relating to how original equipment manufacturers (OEMs) might design an engine thermal management system to minimize air pressure losses due to cooling or to reduce the overall system weight by capitalizing on the improved thermal stability of fully synthetic SAFs. This task also focused on estimating the savings afforded by each design change concept.

Research Approach

One advantage of simplified EPMs is that they facilitate conceptual design trades. For this project, we have considered four conceptional design variations to the thermal management system that increase the reliance on fuel as a coolant. The simplest concept is to add a heat exchanger anywhere in the system, sized such that the fuel temperature at the limiting design point is increased from its current limit, taken as 127 °C, to a new higher limit, taken as 160 °C. The current limit is driven by fuel thermal stability. Once this limit is elevated via high-quality synthetic fuel, the next temperature limit is driven by elastomeric material specifications or platform/fuel volatility requirements, which coincidentally are both near 160 °C for

existing elastomeric seals and conventional jet fuels. Provided that the heat recovered by this new heat exchanger is truly waste heat and neglecting the impact of the exchanger's weight on aircraft fuel efficiency, the afforded energy savings of this configuration can be determined without an EPM or FSTM under the design-limiting operating condition, although the FSTM is necessary for other operating conditions. This simple configuration is labeled as "D" in Figure 6. In the next simplest concept, the fuel-cooled oil cooler is enlarged just enough to enable elimination of the air-cooled oil cooler (ACOC). Such a configuration would be lighter than the baseline engine, which would provide some fuel efficiency benefit at the system level, but this aspect is neglected in the calculations summarized in Figure 6. This configuration is labeled as "C" in Figure 6. The large difference between the savings at high power and the savings at low power for this configuration arises because the sink pressure (altitude-dependent ambient pressure) is unrelated to the pressure ratio achieved by the first stage of compression. The savings at the design point are driven by an input to the model, namely, the fraction of heat removed from the lube oil by air, with the remaining heat removed by fuel. Presently, there is significant uncertainty in the aero-savings estimate for this configuration; thus, work is underway at GE-Aviation to provide a better estimate by using a derivative of an audited performance model of a GE engine for a narrow-body airframe. This estimate will also include the influence of the weight savings. However, based on a simple model of the heat exchanger performance, GE has determined that complete elimination of the ACOC in this application would not be possible unless the maximum fuel temperature limit were raised by 107 °C instead of the 33 °C increase presumed for this analysis based on the fuel system material limits (e.g., elastomers) and fuel volatility. In the most involved concept, the cooled cooling air is coupled with active clearance control of the turbine airfoils. The configuration representing this concept is labeled as "E" in Figure 6. The turbine efficiency is an input to the EPM, and the difference between the savings of configuration E and that of configuration D is primarily driven by this input. The fuel savings is approximately double the increase in turbine efficiency because the Brayton cycle efficiency (i.e., overall engine efficiency) is approximately 50%. While this term is represented by the arbitrary choice of a 0.1% improvement in turbine efficiency for all operating conditions, a detailed design of an active clearance control concept is needed to estimate how airfoil clearances change with cooling airflow split variation. The airflow supplied to the regions that most need cooling (usually the mid span of the blades and vanes) can be reduced when the cooling air is cooled. This frees up air flow that can be used to cool the case (outer diameter) under operating conditions (usually high power) in which the clearance between the case and the blades is highest. To determine the impact on gap height, a detailed heat transfer analysis is required, and to gauge the impact of a gap height change on the aerodynamic efficiency of the engine, a detailed fluid dynamics calculation is needed. These analyses require a full definition of product geometry, which is obviously OEM-proprietary. Although we have requested that GE-Aviation include representative results of such a concept as part of their contribution to this project, they have not agreed to this request. Because turbine inefficiency is generally the largest source of engine inefficiency after accounting for the unavoidable heat engine (Brayton cycle) inefficiency, there is a strong possibility that cooled cooling air can be utilized most effectively by coupling it with active clearance control.

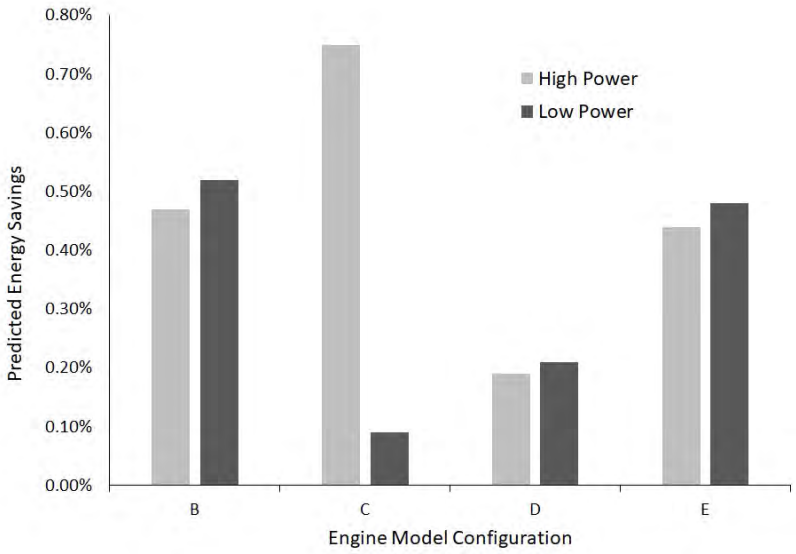

Figure 6. Summary of predicted energy savings for a variety of engine model configurations. B. Cooled cooling air with a reduced cooling flow. C. Enlarged fuel-cooled oil cooler in place of an air-cooled oil cooler. D. Cooled cooling air alone. E. Cooled cooling air and improved turbine efficiency (0.700 to 0.701).

The configuration labeled as "B" in Figure 6 is the same configuration labeled as "derivative" in Figures 5 and 7. For this configuration, the turbine cooling air flow budget is reduced such that the change in enthalpy of the cooling air is matched to that of the baseline configuration at high power. In this study, the cooling flow was reduced to 29.75% of W3, compared with 30.00% of W3 for the baseline configuration, where 30% was an input to the model. By comparing the results for configuration B with those for configuration D, we can see that the savings achieved by reducing parasitic air flows can exceed the savings obtained from improvements in WHR.

By definition, none of the thermal management system design changes considered here correspond to drop-in fuel benefits. To take advantage of the higher thermal stability of SAFs relative to conventional jet fuel and to improve SFC, some design changes are necessary. Such changes should be expected to afford an improvement of 0.5%, which compares favorably with the savings that could potentially be realized on a drop-in basis, as discussed in the next section.

As an independent effort, GE-Aviation estimated an engine efficiency benefit of 0.28% and a weight savings of 22.5 kg per engine if the ACOC is completely removed from an undisclosed engine in a narrow-body application, for each of the mission mixes shown in Table 1. These results are consistent with the earlier estimate (item C, Figure 6) made by the team at the University of Dayton.

Table 1. Time weightings of mission points used by General Electric to estimate fuel effects.

	Take-off	Climb	Cruise	Flight Idle	Ground Idle
Short Haul	5%	35%	50%	5%	5%
Long Haul	5%	30%	55%	6%	4%

Milestones

- Three potential cooling trade-offs have been identified, and the sub-models needed to execute these trade-off studies were built (November 2020).
- The simulations necessary to support the proof of concept were completed (November 2020).
- A scientific paper summarizing this progress was accepted for publication (July 2021).

Major Accomplishments

- A proof-of-concept paper was published in the journal *Fuel*.

Publications

Boehm, R. C.; Scholla, L. C.; & Heyne, J. S. (2021). Sustainable alternative fuel effects on energy consumption of jet engines. Fuel *304*, 121378. https://doi.org/10.1016/j.fuel.2021.121378

Outreach Efforts

None.

Awards

None.

Student Involvement

None.

Plans for Next Period

None.

Task 4 - Estimate Gains in Fuel Efficiency

University of Dayton and GE-Aviation

Objectives

The first goal of this task is to estimate the impact of fuel property variation on engine-level fuel consumption (SFC). The second goal is to optimize fuel composition in order to minimize the SFC while maximizing the specific energy (LHV), which could minimize aircraft fuel consumption, where the fuel LHV is factored into the mass of fuel uplifted into the aircraft.

Research Approach

To accomplish the first goal, the tools developed in Tasks 1 and 3 were used in conjunction with a Monte Carlo simulation of fuel composition derived from a database of 94 molecules, where a filter was used to eliminate random compositions that led to certain properties outside of fuel specifications or fit-for-purpose properties, as predicted via algebraic blending rules. For the second goal, we improved our approach regarding the SAF volatility requirements, added a requirement for the smoke point, and placed a limit on the number of ingredients allowed in the fuel. In addition, the database was expanded to 1,124 molecules. A small (un-converged) Monte Carlo simulation serves as a starting point for optimizing the randomly chosen mole fractions of each molecule from the master database. The engine-level fuel economy and LVH are maximized via mixed-integer distributed ant colony optimization. To arrive at a global solution set, this process is repeated multiple times until all molecules in the database have been chosen at least once by the small initializing Monte Carlo simulation.

Status

Progress toward this task was documented by a presentation given in January 2022 at the American Institute of Aeronautics and Astronautics SciTech Forum in San Diego. For convenience, this paper is included within this section of the report (see Appendix A). Another paper, sponsored in part by this project, documents the creation of a model to predict the sooting propensity of a fuel based solely on its composition. To avoid double-dipping on credit for this work, its reproduction is included with the annual report for Project 65A.

The database used to derive fuel compositions and property estimates now includes 1,124 species, and for each of these molecules, the database contains ten (meaningful) properties, of which four include their respective temperature dependence. Relative to the pilot study, the number of species was increased by a factor of 12.6, and the number of properties was increased by 30%. In addition, we now have an improved model that enables the prediction of freeze points and potentially guides us to restrict the concentration of individual species to a maximum of 10% or that enables a reasonably conservative estimation of freeze points for candidate fuels suggested by the optimizer. In the near term, we expect to add the dielectric constant and energy density to the property filter and seal swell to the list of properties to estimate for candidate fuels.

We also developed a transfer function to relate fuel weight (heating value per unit mass, LHV) to energy savings, corresponding to 0.4% savings per MJ/kg increase in LHV. This scalar is based on a rough physical model of a Boeing 737-800 aircraft and a mission consisting of climb and cruise. This scalar has been validated against an empirical model supplied by Georgia Tech, which was derived from real fuel usage and mission data for the Boeing 737-800. This transfer function will enable consolidation of the LHV and engine savings objectives into one dimension, thereby trimming the number of near-optimal compositions toward a point rather than a line. There will be fewer candidates for considering the harder-to-estimate properties such as seal swell, volatility ranges, freeze point, acquisition cost, and thermal stability.

Figures 7–10 are included in Appendix A to document the noted benefits of SAF relative to petroleum-derived fuel and the current status of progress toward composition optimization. Of note, the difference between Figure 10 in Appendix A and Figure 5 included in Task 2 is the result of several weeks of computation.

Milestones

- A database of 2,000 fully synthetic SAF candidates and a variety of reference fuels was created (November 2020).
- The number of entries in the molecular properties database was increased from 94 to over 2,000 (July 2021).
- Data consistency and completeness were verified (October 2021).
- A model was built and validated to generate smoking propensity data for all molecules in the database (October 2021).
- A peer-reviewed article covering smoking propensity models was published (January 2022).
  - All models used in proof-of-concept work were integrated into JudO, which has been previously used (Kosir, 2020) to optimize fuel composition against defined objectives (September 2021).
- A smoke point filter was added to JudO, and volatility-related predictions and filters were streamlined (August 2021).
- The first successful evolution toward optimized SAF composition was achieved (November 2021).

Major Accomplishments

- The molecular properties database was expanded ten-fold.
- A model was created to estimate the smoking propensity of potential SAF.
- We demonstrated that 100% SAF compositions meeting all considered specifications can favorably impact both fuel weight and engine efficiency.

Publications

Boehm, R. C.; Scholla, L. C.; & Heyne, J. S. (2021). Sustainable alternative fuel effects on energy consumption of jet engines. Fuel *304*, 121378. https://doi.org/10.1016/j.fuel.2021.121378

Boehm, R. C.; Yang, Z.; & Heyne, J. S. (2022). Threshold sooting index of sustainable aviation fuel candidates from composition input alone: Progress toward uncertainty quantification. Energy & Fuels. *36(4)*, p 1916. https://doi.org/10.1021/acs.energyfuels.1c03794

Behnke, L. C.; Boehm, R. C.; & Heyne, J. S. (2022). *Optimization of Sustainable Alternative Fuel Composition for Improved Energy Consumption of Jet Engines.* In AIAA Scitech 2022 Forum; p 2056. https://doi.org/10.2514/6.2022-2056

Outreach Efforts

Conference Presentation: AIAA SciTech 2022, San Diego, CA. Video: **https://doi.org/10.2514/6.2022-2056.vid**

Awards

None.

Student Involvement

- Logan Scholla, M.S. student, managed the proof-of-concept, fuel properties database, and Monte Carlo composition selection.
- Lily Behnke, M.S. student, accomplished integration/translation of the Excel-based EPM and FSTM into the Python-based
  JudO program, was responsible for the results shown in Figures 1–6,10, and 11, and participated in many discussions and decisions regarding this program.
- Jack Hoog, M.S. student, participated in this program.

Plans for Next Period

- Complete the identification of molecules that tend to improve fuel properties toward system efficiency and publish a peer-reviewed journal article on this topic.
- Complete a producibility evaluation of the identified molecules (golden molecules).
- Revise the working-level database, exclude molecules that offer no benefit, and verify the properties of golden molecules.
- Make recommendations regarding fuel quality control specifications for non-drop-in 100% SAF.
- (Boom) Complete OEM trade studies on system-level fuel economy vs. fuel temperature and effective enthalpy.

References

Kosir, S., Stachler, R., Heyne, J., & Hauck, F. (2020). High-performance jet fuel optimization and uncertainty analysis. *Fuel*, *281*, 118718. https://doi.org/10.1016/j.fuel.2020.118718

Tasks 5 & 6 - Identify, Create, and Test Blends for Thermal Stability in Jet Fuel Thermal Oxidation Testing (JFTOT) and Quartz Crystal Microbalance Testing (QCM)

Objective

The goal of these tasks is to evaluate the solutions identified by the second goal of Task 4 for thermal stability.

Research Approach

The solutions identified in the second goal of Task 4 will be analyzed to find common threads in terms of fuel properties and compositions. It is expected that a relatively small number of molecules with high concentration in several solutions will be identified, and we will discuss these molecules with experts regarding their potential impact on thermal stability. Any such molecule, judged by subject-matter experts to present an elevated risk of coking relative to isoparaffins, will be targeted for experimental evaluation of thermal stability at varying concentrations. Other factors to consider in these selections include availability of the molecule and its potential impact on seal swelling, freeze point, and distillation fraction temperature distribution. These tasks cannot be initiated until more progress is made on the fuel optimization. The current status of identifying golden molecules is presented in Figure 11.

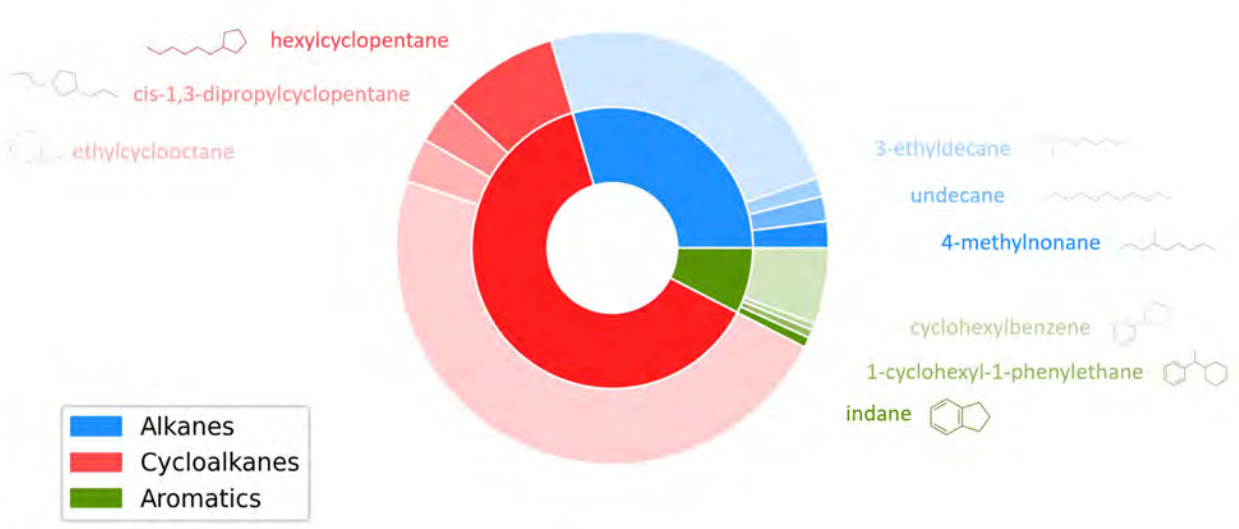

Figure 11. Average composition of 100% sustainable aviation fuel candidates (drop-in) by hydrocarbon type and most prevalent species within each type.

Student Involvement

Lily Behnke, M.S. student, participated in long-range planning for this task.

Plans for Next Period

From the pool of compositions identified in Task 4, select at least two compositions for detailed evaluation of thermal stability in blends with a variety of petroleum jet fuel samples.

Appendix A

Optimization of Sustainable Alternative Fuel Composition for Improved Energy Consumption of Jet Engines

Lily C. Behnke
Randall C. Boehm
Joshua S. Heyne
University of Dayton, Dayton, OH, 45469, USA

Abstract

As anthropometric emissions continue to rise globally, reducing emissions from combustion systems is critical to environmental preservation. It is understood that a method for decreasing emissions contributions from the aviation sector is sustainable aviation fuel (SAF). SAF adoption relies on the ability to maintain or surpass the current performance metrics of petroleum derived fuels while also complying with critical operability limitations. High thermal stability SAFs have the potential to provide value in terms of reducing maintenance cost associated with coking and the ability to drive more heat into the fuel therefore increasing energy delivered to the combustor. It was determined that SAFs composed of mostly cycloalkanes with some aromatics maximize the energy savings for both high and low power engine operating conditions. This result is likely tied to the effects of H/C ratio on turbine performance. Furthermore, this work demonstrates that at least a 0.05% savings is possible at the high power conditions from SAF mixtures that meet critical operability limits necessary for SAF approval. However, it was observed that at the low power condition identified SAF mixtures had not yet surpassed conventional petroleum fuel in terms of energy savings. This work provides preliminary results for the design of a high thermal stability SAF that will increase savings over the course of a mission requiring operation at both low and high power conditions respectively.

Nomenclature

SAF	=	sustainable aviation fuel
TSI	=	threshold sooting index
FSTM	=	fuel system thermal model
EPM	=	engine performance model
LHV	=	lower heating value

Introduction

As global carbon emissions continue to rise, current research shows that the levels of anthropogenic emissions generated by combustion systems are one of the leading contributions to global climate change (Lee, 2021). Failure to combat the damaging effects of climate change has the potential for devastating global impacts and overall societal instability. It is, therefore, critical that aviation technologies are developed to meet the rising demand for air travel in such a way that anthropogenic emissions do not proportionately increase. One technique that provides a near term solution to minimizing greenhouse gas emissions is sustainable aviation fuel (SAF). Figure 1 outlines the key performance and operability metrics for SAF approval and compatibility with modern day aircraft (Kosir, 2020). The yellow-red shading outlines properties influencing aircraft safety and operability that a SAF candidate needs to satisfy. Furthermore, properties associated with the potential for SAF performance improvements are shown with the green shading. It can be observed that total energy content and thermal stability metrics of a potential SAF are known to add value and performance benefits in addition to the environmental advantages (Flora, 2019). While the benefits of increased energy content have been previously investigated, the benefits of high thermal stability for SAFs remains largely unexplored (Kosir, 2019).

Figure 1. Key performance and operability metrics for jet fuel.

Increasing reliance on jet fuel rather than the use of air as a coolant for the engine and aircraft adds both performance and efficiency benefits (Bruening, 2014). Increased thermal stability of a fuel allows for better thermal management of the engine and, in turn, more energy delivered to the combustor and extracted by the turbine. Furthermore, increased thermal stability of SAFs enables decreases in specific fuel consumption and maintenance costs associated with coking. Coke deposits within fuel nozzles and other fuel system components on jet engines result from waste heat, which is absorbed from other engine and aircraft fluids, and trace amounts of contaminates like transition metals, sulfur, nitrogen, and dissolved oxygen. The presence of coke in the fuel nozzles precipitates maintenance by creating hot streaks or increased spread in exhaust gas temperature. This increased variation in temperature around the circumference of the combustor in turn causes increased combustor emissions and negatively impacts turbine efficiency, which drives up CO2 emissions and fuel cost (Mellor, 1990). Moreover, deposits can affect fuel spray quality, which also impacts operability and increases CO and NOx emissions. Therefore, the significance of increased thermal stability yields both performance and environmental benefits.

A previously conducted pilot study was carried out to observe the engine-level energy savings for SAF fuels for both a baseline engine configuration and a derivative engine configuration (Boehm, 2021). Monte Carlo simulations resulting in population distributions of 2500 SAFs were evaluated in terms of savings benefits for sustainable aviation fuels. The results of this simulation revealed the sensitivities of the model and which fuel properties had the largest effect on the final savings metric. While this work focused on the trends and general methodology for evaluating high thermal stability aviation fuels, there remains work to identify SAF species most suited for harnessing thermal stability benefits. This requires SAFs that are able to remain within important property limits such as viscosity, threshold sooting index (TSI), density, etc. while improving performance metrics as discussed in Fig. 1 (Yang, 2021).

The aim of this research is to utilize optimization techniques to identify SAF candidates yielding high savings and specific energy while complying with crucial operability constraints. It is anticipated that the results of this work will extend into experimental testing for further evaluations of the coking effects of favorable molecules. The results of this work will extend the current capabilities of SAF species from a performance standpoint while also leading to a greater understanding of effects that currently lead to maintenance and emissions issues in modern aircraft engines.

Methodology

Material

As previously outlined, the focus of this work is to identify SAF candidates for increased thermal stability benefits to add value from an efficiency and maintenance standpoint. Furthermore, understanding the effect that various molecules and functional groups have on savings metrics and properties of significance is valuable. For the scope of this work, a database of 1,124 SAF species with respective property data was compiled and utilized as constituents appropriate for optimization. The fuels in this database were composed of a variety of carbon types including aromatics, cycloaromatics, naphthalenes, cycloalkanes, alkanes, bicycloalkanes, and tricycloalkanes. Fuel property data for this work was obtained from the National Institute of Standards and Technology (NIST) fuel property database. Properties relevant to both ASTM D1655 and ASTM D7566 specifications as well as temperature dependent properties necessary for calculating saving benefits were obtained

(ASTMa, n.d.; ASTMb, n.d.). For each generated SAF mixture throughout the course of the optimization the mixture properties were calculated from known physical and chemical properties based on the mole fractions assigned to each of the constituents. For each theoretical SAF mixture the chemical and physical properties were derived from blending rules based on the mixture definition and constituent properties which are detailed elsewhere (Kosir, 2019).

FSTM and EPM

This work fundamentally relied on the ability to evaluate the potential efficiency and performance benefits of a fuel as a function of its fuel properties. A tailored version of a previously developed fuel system thermal model (FSTM) and engine performance model (EPM) were leveraged to quantify the thermal stability benefits of SAFs (Boehm, 2021). The FSTM quantifies the heat pick-up of a fuel by calculating the waste heat recovery and temperature rise as a function of the fuel properties. Furthermore, an EPM was also implemented to compare savings metrics through different conceptual engine design changes that vary the manner in which heat is driven into the fuel. The combination of these models along with fuel property inputs allowed for a final savings comparison to conventional petroleum derived aviation fuel. Additionally, each of these models allows for alterations to accommodate a potential design change that would drive more heat into the fuel and therefore decrease the losses from using air as a coolant. The scope of this work focused solely on the baseline configuration in order to evaluate SAF fuel candidates most suited for modern day aircraft combustion systems.

In addition to calculating fuel savings, several fuel properties including viscosity, heat capacity, thermal conductivity, and energy density influence the performance of heat exchangers, while H/C and molecular weight influence burnt gas composition which effect combustor exit temperature and turbine performance in the EPM model. The pilot study highlighted that low H/C ratio was favorable for turbine performance but also runs the risk of soot issues as a result of high TSI. Considering this key finding, this work combined an updated method for TSI mixture predictions (Boehm, 2022). As a result, a wide array of molecules were selected to appeal to the sensitivities of these models and further explore the impact of fuel properties on energy savings.

Optimization

While previous work demonstrated fuel savings benefits for both the baseline and derivative cases, it was observed that optimization would determine whether comparable savings could be realized without an engine design change. Including optimization methodology allowed for a greater consideration of SAF species and the identification of species with the greatest thermal stability benefits. Furthermore, a constrained optimization allows for the consideration of critical operability constraints that may be limiting factors for realistic savings benefits not filtered in the pilot study. A flowchart demonstrating the general optimization methodology is demonstrated in Fig 2.

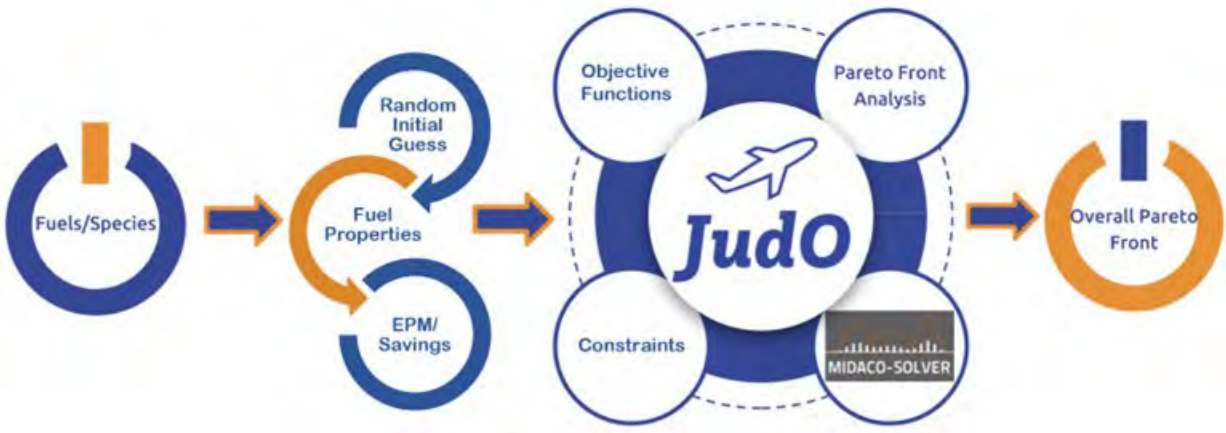

Figure 2 Optimization methodology labeled as the Jet Fuel Blend Optimizer (JudO) incorporating the FSTM and EPM.

As illustrated in Fig. 2 each optimization began with a randomly generated initial guess from the array of 1,124 SAF species which were each assigned a random mole fraction. Due to the number of species in the database, the maximum number of species for each mixture was constrained to 20 to avoid copious amounts of species being selected with nearly negligible

concentrations. Then the fuel properties required for the objective functions, constraints, and temperature dependent coefficients required for the FSTM and EPM were calculated for the randomly generated SAF mixture. These properties included, lower heating value (LHV), TSI, viscosity at -20˚C, density at 20˚C, H/C ratio, molecular weight, vapor pressure at 160˚C, T10, and temperature dependent coefficients for density, viscosity, specific heat and conductivity. As previously discussed, these properties are significant specifications required for the aviation fuel approval process. Viscosity and density are known to be key combustor figure of merit operability limits (i.e. e.g. ignition probability at cold conditions) (Colket, 2017). TSI is significant from an emissions standpoint and LHV acts as an important performance metric and weight parameter. These properties were then fed into the FSTM and EPM models for the evaluation of energy savings as a single metric. JUDO then combined the objective functions, constraints, and mixed-integer ant colony optimization (MIDACO) software with pareto front analysis to identify optimal fuel compositions for the respective objective functions (Schlueter, 2013). Specific optimization settings were chosen based on recommendations outlined elsewhere (Midaco-Solver, 2018). The respective objective functions and constraints used in this work can be seen in Table 1.

Table 1. Optimization parameters used in this study for high and low power settings.

Setting	Objective Functions	Constraints
High Power	LHV, Savings	viscosity at -20˚C (<8 cSt), density at 20˚C (< 0.84 , > 0.775 kg/m^3), TSI (< 20), T10 (< 205˚C), $\sum x_i$ = 1, Pvap at 160˚C < 1
Low Power		

The parameters outlined in Table 1. Show the objective functions and constraints used for both the high and low power scenarios that were run. The low power condition is meant to represent to the mission conditions from cruise to flight idle while the high power scenario represents conditions for takeoff and climb. Specifically, the two conditions are intended to capture the minimum and maximum fuel flow of the operating envelope. For each optimization, energy savings and LHV were maximized to simultaneously maximize the performance metrics of the SAF mixture. Furthermore, the operability limits as previously described acted as constraints.

Results and Discussion

The results presented in this section focus on the savings metrics and corresponding fuel compositions for both the high and low power baseline engine configurations. While previous work focused on outlining the methodology for obtaining the savings value, these results investigate the SAF species and functional groups best suited for simultaneous savings and LHV benefits. Each scenario utilizes “A2”, a specific sample representing average petroleum derived conventional jet fuel, as a point of comparison.

Fig. 3 shows the pareto front for the high power optimization demonstrating the trade-off between LHV and energy savings. The pink star represents the reference fuel A2 which has a savings value of zero since the FSTM and EPM are normalized to the fuel flow and mission demand for conventional petroleum jet fuel. The larger points with the color bar represent the identified SAF mixture solutions with the color bar representing the mole fraction of aromatic content present in each mixture. Strong consideration is placed on the limiting of aromatics from an emissions standpoint (i.e., smoke point), therefore the amount aromatics in a SAF mixture requires specific consideration. It can be observed that generally the solutions with higher savings values have a greater amount of aromatic content. While most of the SAF mixtures have savings values that are less than zero, there are some that yield positive savings benefits. Furthermore, there are a few solutions that provide marginal savings benefits as well as LHV improvements to A2. Furthermore, Fig. 3 illustrates a few points that stray from the general cluster of points. This is due to the fact that this is a highly constrained optimization with a large database to choose from. It is anticipated that with more computational time, which is not in the scope of this paper, coupled with an initial guess filter that requires the initial guess to pass ASTM specifications would lead to more solutions that could push the overall front outward towards higher LHV and savings metrics.

The high power pareto front shows the relative aromatic content for each optimal solution while Fig.4 further details the composition of each optimal solution as a function of savings. The composition is expressed from zero to one to demonstrate the breakdown of the mole fraction representation from each carbon group for the mixture. The brown area represents the

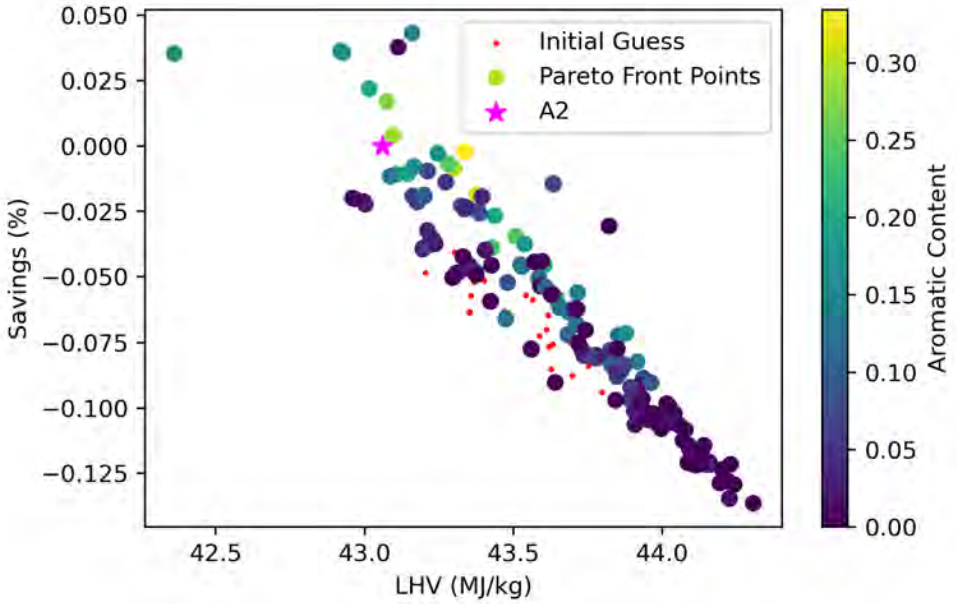

Figure 3. Pareto front solutions from the high power engine operating condition show a potential savings and LHV increase from SAF mixtures compared to standard petroleum fuel A2.

Mole fraction of the composition that is made up of alkanes while the pink represents the mole fraction of cycloalkanes in the mixture and the green represents the mole fraction of aromatics in the mixture. In this case, cycloalkanes include monocycloalkanes, bicycloalkanes, and tricycloalkanes, and aromatics include aromatics, cycloaromatics, and naphthalenes. Fig. 4 shows that generally as savings increases so does cycloalkane content and aromatic content. Conversely, as savings increases alkane content decreases. This is likely a result of the dependency of the FSTM and EPM on H/C ratio with a low H/C ratio increasing savings metrics as a result of improved turbine performance with increasing gamma (Cp/Cv). While low H/C ratio may potentially lead to sooting issues and high TSI, the incorporation of the TSI constraint within this optimization allows for solutions to be within the acceptable range. This affect also describes a potential limiting factor for mixture solutions that provide increased savings and will act as a metric for identifying favorable SAF species.

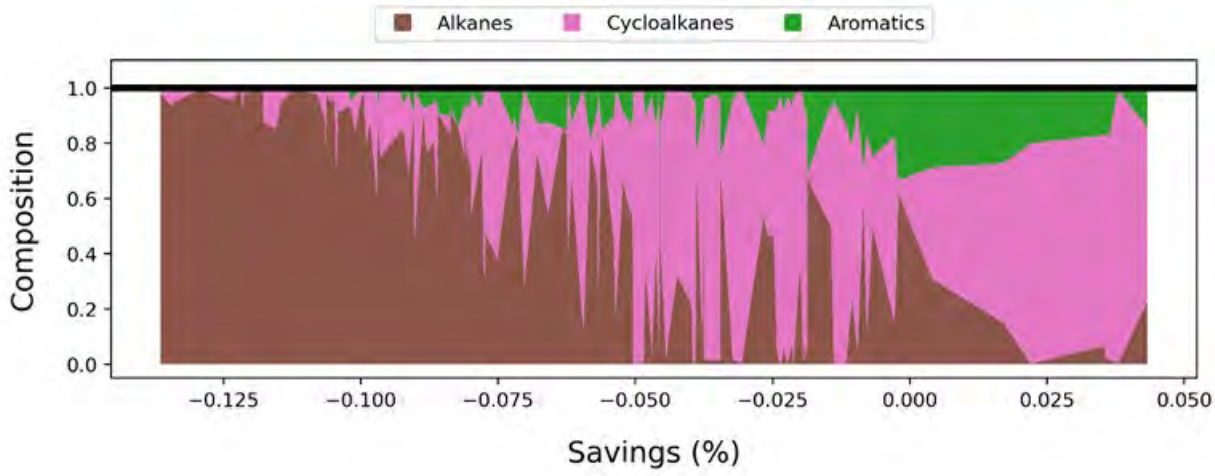

Figure 4. Graphic showing the composition of each optimal solution for high power as a function of savings. The constituents in the optimal solutions are grouped by functional group, alkanes, cycloalkanes, and aromatics.

Fig. 5 exemplifies the pareto front results for the low power setting of the EPM and FSTM. The pink star once again represents A2 while the points with the color bar are the identified pareto front points. Similar to the high power result, the color bar represents the amount of aromatic content present in each of the solution. It can be seen that generally the solutions with higher savings values contain more aromatics. Moreover, there is only one solution that offers a positive savings metric with an LHV that is slightly less than A2. This indicates that for this scenario the current pareto front has not exceeded the benefits of A2. As discussed with the high power result, it is worth noting that this is a highly constrained optimization problem. With added computational time and an initial guess filter there is room to further explore the results of this optimization.

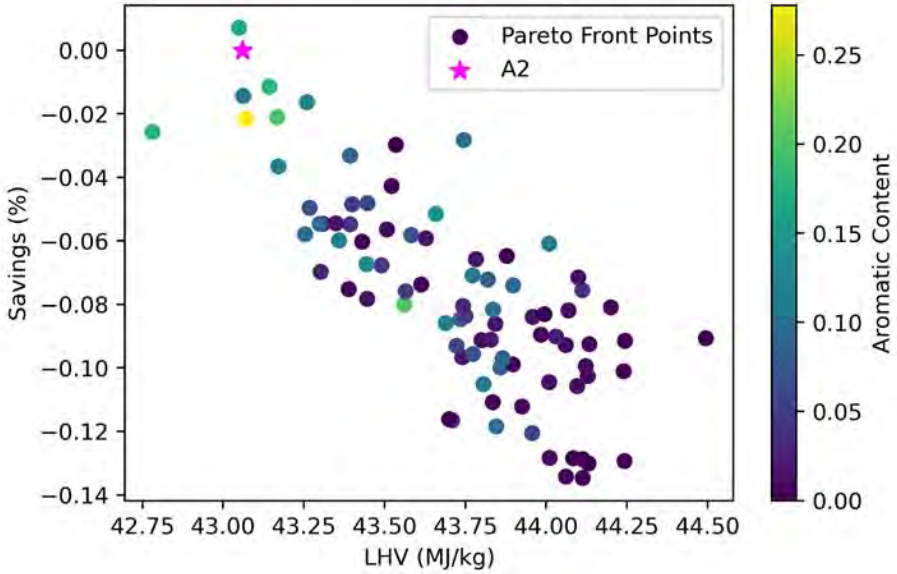

Figure 5. Pareto front solutions from the low power engine operating condition showing mostly negative savings impacts from SAF mixtures compared to standard petroleum fuel A2.

Similar to the high power result, Fig. 6 portrays the breakdown from a carbon group standpoint of the pareto front solutions for low power. Composition of the optimal solutions as a function of savings is shown with composition ranging from zero to one to show the mole fraction representation from each carbon group. At lower savings values the composition of the optimal solution is largely alkanes, while larger savings values result in higher concentrations of cycloalkanes and aromatics. Once again, cycloalkanes include monocycloalkanes, bicycloalkanes, and tricycloalkanes, and aromatics include aromatics, cycloaromatics, and naphthalenes. This result is similar to what is observed in the high-power scenario and further suggests that higher savings values could be achieved from mixtures that are higher in cycloalkanes with some aromatics.

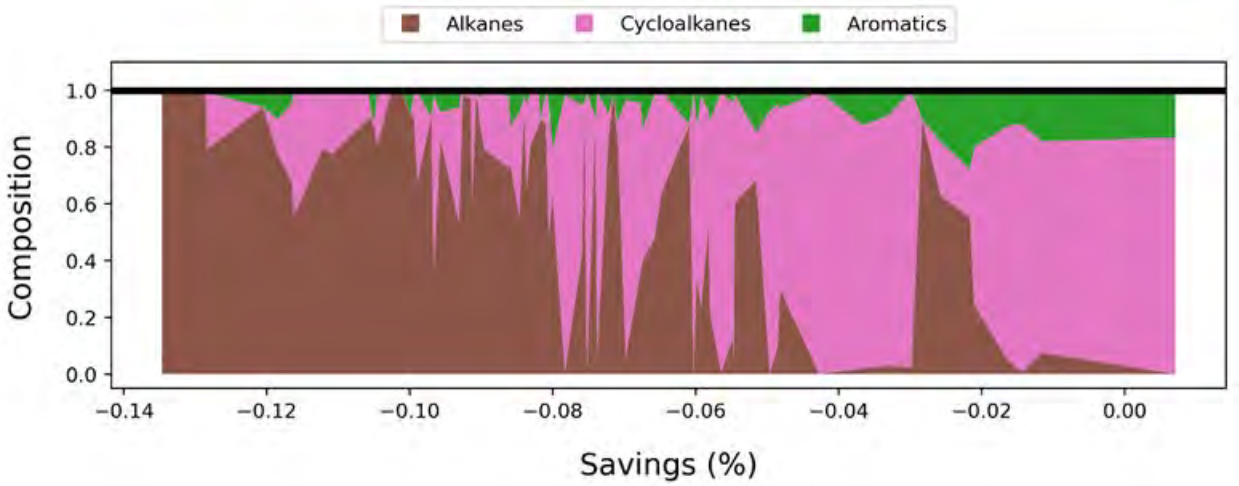

Figure 6. Graphic showing the composition of each optimal solution for low power as a function of savings. The constituents in the optimal solutions are grouped by functional group, alkanes, cycloalkanes, and aromatics.

Conclusion

This research has sought to identify SAF mixtures and carbon groups with properties providing value from an efficiency and energy content perspective. The high power model results indicate that several SAF mixtures composed of primarily cycloalkanes with a few aromatics have the potential to add energy savings from high thermal stability benefits. However, the low power result has not yet yielded a result that predicts improved savings from SAF mixtures. Despite this result, the low power results confirm the conclusion from the high power result that a greater presence of cycloalkanes with some aromatics yields higher savings metrics than mixtures of primarily alkanes. It is anticipated that with increased computational time much more of the composition space will be explored and many more solutions with both higher savings and LHV relative to A2 will be found.

In this work the low power and high power conditions were analyzed separately, however in reality each of the operating conditions would be met throughout the course of a flight. Future work will focus on combining and weighting the fuel consumed at each condition into a single savings metric. The repeating of the optimization with a combined mission savings term with added computational time allowed for exploration of optimal mixtures. Furthermore, following the combined optimization, SAF identified optimal species will be experimentally tested for thermal oxidative stability metrics.

Acknowledgments

This research was funded by the U.S. Federal Aviation Administration Office of Environment and Energy through ASCENT, the FAA Center of Excellence for Alternative Jet Fuels and the Environment, project 66 through FAA Award Number 13-C-AJFE-UD-027 under the supervision of Anna Oldani. Any opinions, findings, conclusions or recommendations expressed in this material are those of the authors and do not necessarily reflect the views of the FAA.

We would like to acknowledge Zhibin Yang, and the Heyne Energy and Appropriate Technologies lab members for their support in this research effort, of which, would not be possible without their help.

Noted Benefits of SAF

This section includes three figures (Figures 7–9) that clearly illustrate the potential benefits of 100% SAF and one figure (Figure 10) that clearly illustrates the status of the fuel optimization when work was suspended on this project. Figure 7 has been shown on multiple occasions in quarterly reports, prior annual reports, and the proof-of-concept journal article on this topic. It illustrates that fuel composition does directly impact engine efficiency at both high and low power but that increased fuel temperature (enabled via the high thermal stability of SAF) can have a much larger impact, provided that the engine design is modified to take advantage of this characteristic. Figure 8 presents the results of a commonly used test for inferring jet fuel thermal stability and the differences between petroleum jet fuel and currently approved SAF blend components. The results shown in Figure 8 justify the proposal to raise the maximum fuel temperature limit on aircraft designated for 100% SAF usage, as suggested by the results shown in Figure 7. The reduced sooting propensity of SAF relative to petroleum fuel, proven by the flame visualization shown in Figure 9, is also a direct benefit of SAF, but one that is difficult to quantify. This benefit is primarily linked to the aromatic concentration in the fuel.

The data shown In Figure 10 are sufficient to demonstrate that it is possible to simultaneously increase the specific heat (LHV) and engine operating efficiency, with the latter being primarily increased via reduced viscosity or H/C ratio. The composition of potential SAFs meeting these objective is strongly represented by cycloalkanes.

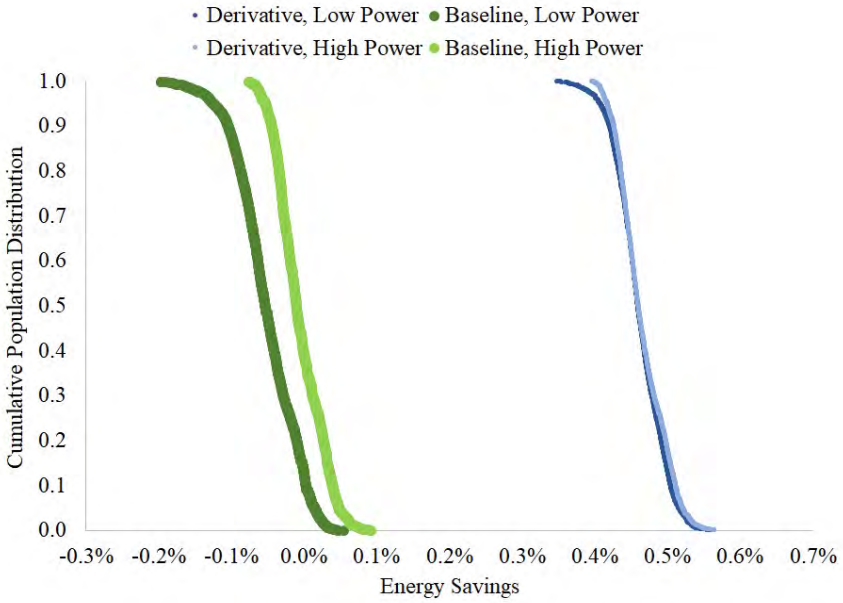

Figure 7. Impact of design and fuel property on fuel energy savings.

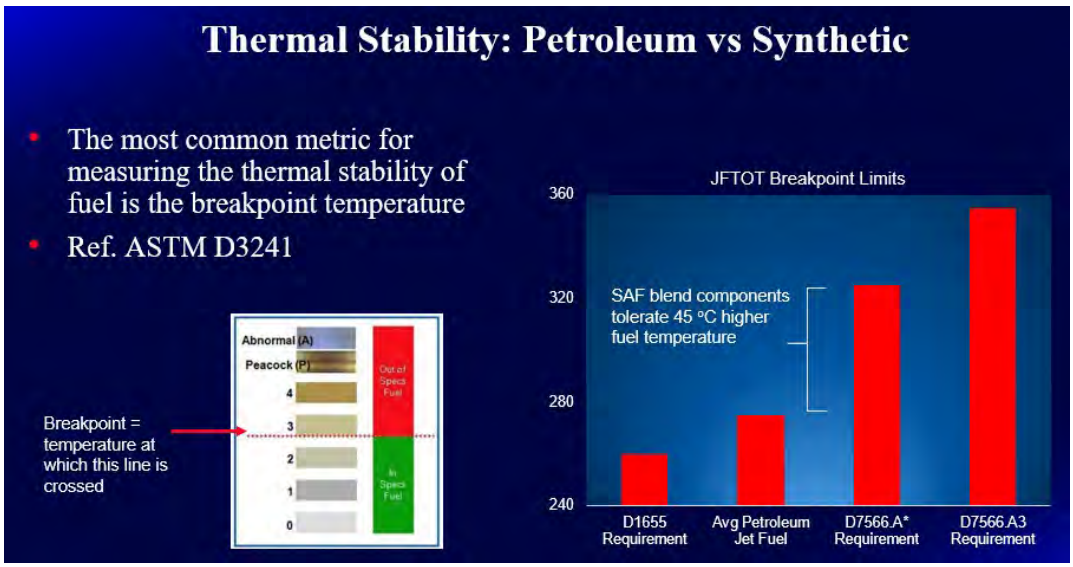

Figure 8. Comparison of fuel thermal stability between sustainable aviation fuel (SAF) and petroleum-derived fuel. ASTM: American Society for Testing and Materials; JFTOT: jet fuel thermal oxidation test.

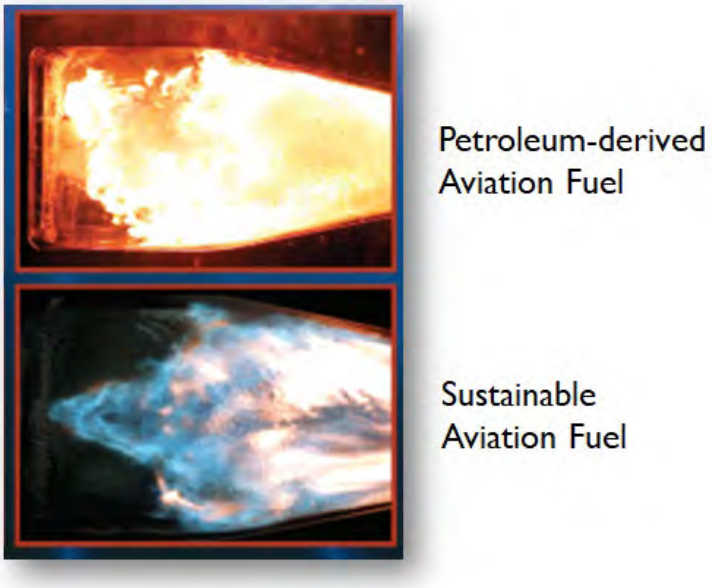

Figure 9. Comparison of flames produced by sustainable aviation fuel or petroleum-derived fuel under similar operating conditions.

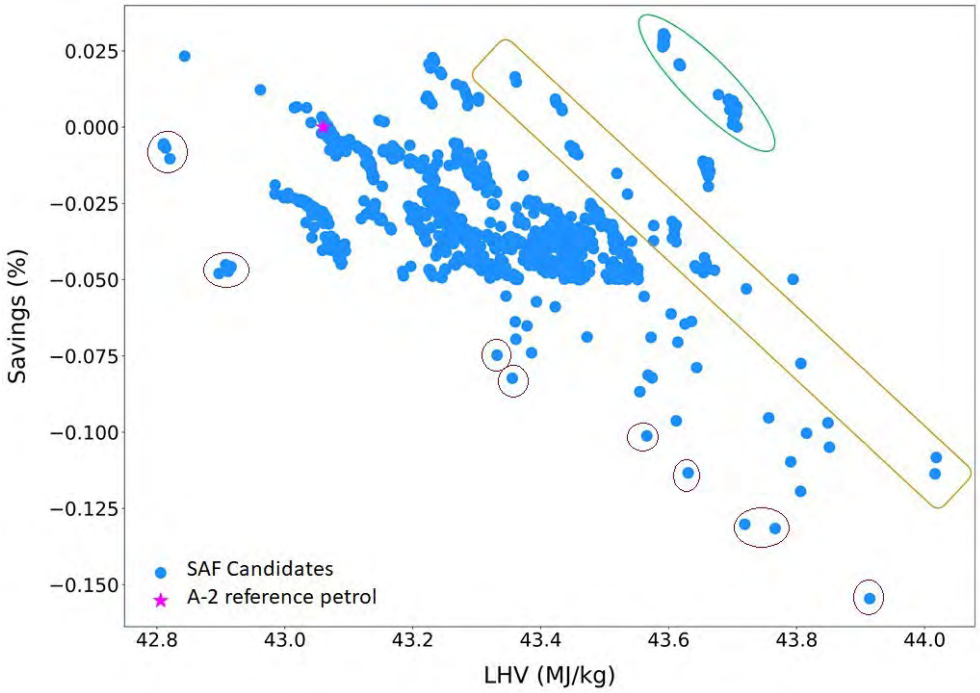

Figure 10. Lower heating value (LHV) and relative energy efficiency at low power for 100% sustainable aviation fuel (SAF) candidates (drop-in).

References

Lee, D. S., Fahey, D. W., Skowron, A., Allen, M. R., Burkhardt, U., Chen, Q., Doherty, S. J., Freeman, S., Forster, P. M., Fuglestvedt, J., Gettelman, A., De León, R. R., Lim, L. L., Lund, M. T., Millar, R. J., Owen, B., Penner, J. E., Pitari, G., Prather, M. J., … Wilcox, L. J. (2021). The contribution of global aviation to anthropogenic climate forcing for 2000 to 2018. *Atmospheric Environment*, *244*, 117834. https://doi.org/10.1016/j.atmosenv.2020.117834

Kosir, S., Heyne, J., & Graham, J. (2020). A machine learning framework for drop-in volume swell characteristics of sustainable aviation fuel. *Fuel*, *274*, 117832. https://doi.org/10.1016/j.fuel.2020.117832

Flora, G., Kosir, S. T., Behnke, L., Stachler, R. D., Heyne, J. S., Zabarnick, S., & Gupta, M. (2019, January 7). Properties calculator and optimization for drop-in alternative jet fuel blends. *AIAA Scitech 2019 Forum*. AIAA Scitech 2019 Forum, San Diego, California. https://doi.org/10.2514/6.2019-2368

Kosir, S. T., Behnke, L., Heyne, J. S., Stachler, R. D., Flora, G., Zabarnick, S., George, A., Landera, A., Bambha, R., Denney, R., & Gupta, M. (2019, January 7). Improvement in jet aircraft operation with the use of high-performance drop-in fuels. *AIAA Scitech 2019 Forum*. AIAA Scitech 2019 Forum, San Diego, California. https://doi.org/10.2514/6.2019-0993

Bruening, G. B., & Chang, W. S. (1999). Cooled cooling air systems for turbine thermal management. *Volume 3: Heat Transfer; Electric Power; Industrial and Cogeneration*, V003T01A002. https://doi.org/10.1115/99-GT-014

Mellor, A. M. (Ed.). (1990). *Design of modern turbine combustors*. Academic Press.

Boehm, R. C., Scholla, L. C., & Heyne, J. S. (2021). Sustainable alternative fuel effects on energy consumption of jet engines. *Fuel*, *304*, 121378. https://doi.org/10.1016/j.fuel.2021.121378

Yang, Z., Kosir, S., Stachler, R., Shafer, L., Anderson, C., & Heyne, J. S. (2021). A GC × GC Tier α combustor operability prescreening method for sustainable aviation fuel candidates. *Fuel*, *292*, 120345. https://doi.org/10.1016/j.fuel.2021.120345

ASTMa. *Standard specification for aviation turbine fuels*. (n.d.). Retrieved April 15, 2023, from https://www.astm.org/d1655-21b.html

ASTMb. *Standard specification for aviation turbine fuel containing synthesized hydrocarbons*. (n.d.). Retrieved April 15, 2023, from https://www.astm.org/d7566-21.html

Boehm, R. C., Yang, Z., & Heyne, J. S. (2022). Threshold sooting index of sustainable aviation fuel candidates from composition input alone: Progress toward uncertainty quantification. *Energy & Fuels*, *36*(4), 1916–1928. https://doi.org/10.1021/acs.energyfuels.1c03794

Colket, M., Heyne, J., Rumizen, M., Gupta, M., Edwards, T., Roquemore, W. M., Andac, G., Boehm, R., Lovett, J., Williams, R., Condevaux, J., Turner, D., Rizk, N., Tishkoff, J., Li, C., Moder, J., Friend, D., & Sankaran, V. (2017). Overview of the national jet fuels combustion program. *AIAA Journal*, *55*(4), 1087–1104. https://doi.org/10.2514/1.J055361

Schlueter, M., Erb, S. O., Gerdts, M., Kemble, S., & Rückmann, J.-J. (2013). MIDACO on MINLP space applications. *Advances in Space Research*, *51*(7), 1116–1131. https://doi.org/10.1016/j.asr.2012.11.006

Midaco-Solver. (2018). MIDACO User Manual. http://www.midaco-solver.com/data/other/MIDACO_User_Manual.pdf

Project 067 Impact of Fuel Heating on Combustion and Emissions

Purdue University

Project Lead Investigators

Robert P. Lucht
Ralph and Bettye Bailey Distinguished Professor of Combustion
School of Mechanical Engineering
500 Allison Road
Purdue University
West Lafayette, IN 47907-2014765-714-6020
Lucht@purdue.edu

Carson D. Slabaugh
Associate Professor
School of Aeronautics and Astronautics
500 Allison Road
Purdue University
West Lafayette, IN 47907-2014
765-494-3256
cslabau@purdue.edu

University Participants

Purdue University

- P.I.s: Dr. Robert P. Lucht and Dr. Carson D. Slabaugh
- FAA Award Number: 13-C-AJFE-PU-038
- Period of Performance: October 1, 2020 to September 30, 2022
- Task:
    1. Investigate the effects of fuel heating on combustion and emissions for aviation gas turbines

Project Funding Level

Project 67 is funded by the FAA at the level of $250,000 for the project period June 5, 2020 to June 4, 2021; an additional $250,000 for the time period from June 5, 2021 to September 30, 2022; and an additional $250,000 for the time period from October 1, 2022 to September 30, 2023. The required cost-sharing 1:1 match of $750,000 is provided by Purdue University.

Investigation Team

- The P.I. for the project is Professor Robert P. Lucht (Purdue). Professor Lucht is the major advisor of Colin McDonald (Purdue).
- The co-P.I. is Professor Carson D. Slabaugh. Professor Slabaugh (Purdue) is the major advisor of John Philo (Purdue) and Tristan Shahin (Purdue).
- The PhD graduate students are Colin McDonald, John Philo, and Tristan Shahin. The graduate students are responsible for the design of system components, such as the fuel heating system, and will be responsible for executing test operations. Research Engineer Dr. Rohan Gejji (Purdue) is also working on the project, helping the graduate students with their design projects, and supervising the test operations.

Project Overview

The goal of this project is to evaluate the effects of heating jet fuel before injection in an aviation gas turbine combustor on combustion efficiency, pollutant emissions, and dynamics. In an aircraft engine, heat that would otherwise be wasted can be directed into the fuel to increase its sensible enthalpy before injection. Thermochemistry dictates that this increase in sensible enthalpy must lead to lower fuel consumption for a given combustor exit temperature. However, the effects of elevated fuel temperature on combustion performance characteristics (such as the fuel spray pattern, spatial distribution of reaction zones, pollutant emissions, and combustion dynamics) are not yet well understood. We will perform experiments with heated fuels by using a piloted, partially premixed fuel injector located in an optically accessible combustor. This process will allow us to apply advanced laser diagnostic techniques to compare the behavior of the combustor at different fuel temperatures over a wide range of operating conditions.

The platform for the planned experiments is the Combustion Rig for Advanced Diagnostics (COMRAD). The test rig (Figure 1) is designed to operate at steady-state conditions with thermal power as high as 8 MW, inlet air pressure (P_3) as high as 4.0 MPa, and inlet air temperature (T_3) as high as 1,000 K. To facilitate operation at these conditions, the test article is made of aviation-grade alloys and is thoroughly water cooled, and the inner windows are film cooled with heated nitrogen. Before this project, extensive testing with ambient-temperature fuels was performed in this rig, with a focus on 5- and 10-kHz particle image velocimetry (PIV) measurements in the downstream boundary condition window section, and 50- and 100-kHz PIV measurements in the flame zone.

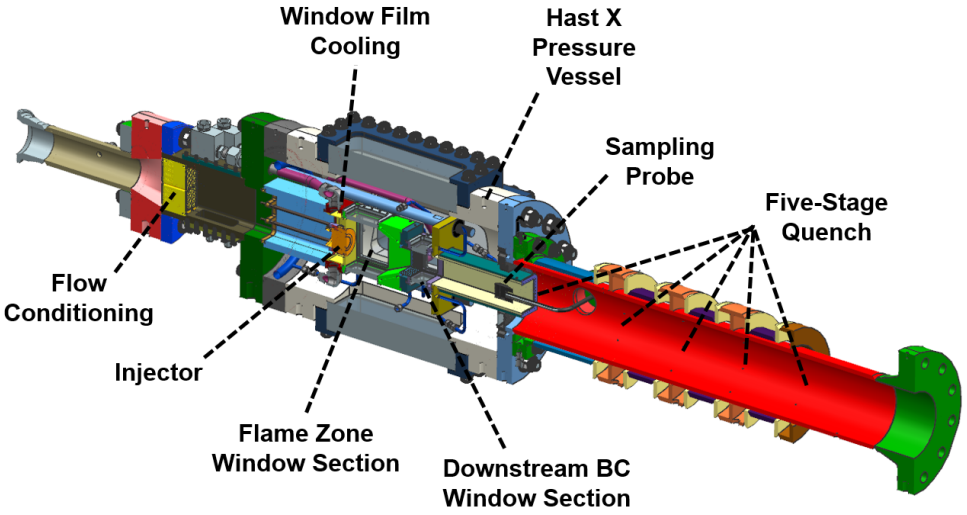

Figure 1. Schematic diagram of the Combustion Rig for Advanced Diagnostics (COMRAD).

Task 1 - Investigate the Effects of Fuel Heating on Combustion and Emissions for Aviation Gas Turbines

Purdue University

Objective

The goal of this project is to determine the effects of fuel heating on the performance of aviation gas turbines. Fuel heating can potentially lead to higher efficiency but can also lead to changes in the fuel distribution pattern and in the locations of reaction zones in the combustor. These changes may also affect pollutant emissions and combustion dynamics during engine operation. We will perform experiments using heated fuels and will measure the fuel distributions, reaction zone distributions, pollutant emissions, and combustion dynamics at a range of fuel temperatures from near room temperature to above the supercritical temperatures for hydrocarbon fuels.

Research Approach

We will perform experiments with heated fuels by using a piloted, partially premixed fuel injector located in an optically accessible combustor. This experimental system will allow us to apply advanced laser diagnostic techniques to compare the behavior of the combustor at different fuel temperatures over a wide range of operating conditions. These advanced diagnostic techniques include fuel planar laser-induced fluorescence (PLIF) imaging to monitor fuel distribution patterns, hydroxyl (OH) radical PLIF (OH PLIF) imaging to monitor reaction zones, and PIV to measure the flow fields. We will also measure emissions with probe sampling and will use pressure transducers to measure combustion dynamics.

Milestones

The milestones for the work performed in fiscal year 2022 are as follows:

1. A fuel heater capable of heating three independent circuits of jet fuel to 700 K at 4.0 MPa was developed and successfully deployed in the test cell. Measurements were collected with both the Fischer–Tropsch synthetic paraffinic kerosene fuel (FT-SPK) Shell GTL GS190 and the petroleum-based fuel Jet A.
2. A new emissions sampling probe was used to collect measurements of pollutant emissions and combustion efficiency. Emissions measurements collected with our old sampling probe were repeated for operation with the Shell GTL GS190 fuel. Measurements were also collected for operation with Jet A fuel. These measurements had not previously been collected with the old sampling probe.
3. OH PLIF measurements were successfully collected at 10 Hz to characterize the reaction zone location as a function of fuel temperature for both the Shell GTL GS190 and Jet A fuels. The data analysis of the images to obtain flame surface density maps is in progress.
4. The effect of fuel heating on combustion dynamics was investigated for both Shell GTL GS190 and Jet A fuels. A significant reduction in the combustion dynamics was observed at higher fuel temperatures. This decrease in pressure fluctuation coincided with the disappearance of droplets detectable by Mie scattering in the flow from the injector main annulus.

Major Accomplishments

In the current reporting period, we continued our investigation of the effects of injection of heated jet fuel on the combustion efficiency and emissions in a model aviation gas turbine combustor. Combustion experiments with heated fuel were performed at a range of equivalence ratios at pressures of 1.0 and 2.0 MPa. The tests focused on emission sampling, high-frequency pressure measurements, and OH PLIF measurements.

Facility Overview

COMRAD is supplied by facility fluid systems including heated air, heated nitrogen, high-pressure water, and liquid jet fuel. Two types of liquid jet fuel were used separately for this work: (a) Jet A and (b) Shell GTL GS190, an FT-SPK. The rig features a piloted swirl injector (shown schematically in Figure 2b), housed inside a duct within a large windowed pressure vessel enabling optical access to the entire flame from four sides. Figure 2a shows a diagram of the test rig. Combustion air is supplied to the test article at 755 K and up to 20 bar. After it is metered, the air passes through a flow conditioner and into the air plenum, which supplies both the pilot and main sections of the injector.

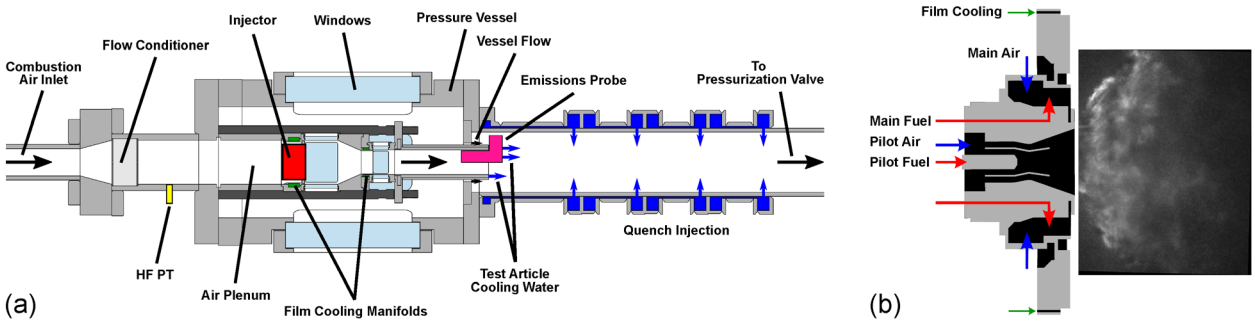

Figure 2. (a) Schematic diagram of the test rig, highlighting the primary design features. (b) Schematic diagram of the injector (inner passages are not representative of the actual injector) with a single frame of OH* chemiluminescence from a high-speed camera.

Liquid jet fuel is supplied to the injector at temperatures as high as 590 K by an 81-kW fuel heater. The fuel heater (Figure 3) comprises a stack of copper blocks with 20 cartridge heaters inserted into each block. Fuel flows in stainless steel tubes through three independent circuits, two pilot circuits, and one main circuit. The mass flow rates in each circuit are measured with Coriolis flow meters. In the fuel heater, the stainless steel tubes are clamped between each pair of copper blocks before being delivered to the test rig. The temperature of the fuel is monitored both in the fuel heater (to ensure that no phase change is encountered) and immediately upstream of the injector. Fuel passes through approximately 50 cm of trace-heated tubing from the heater to the test rig. The tubing is air-jacketed within the test rig to inhibit heat transfer from the heated air before the injector is reached. To prevent coking in the fuel lines at high fuel temperatures, the fuel tank is sparged with nitrogen for 30 minutes before use to remove dissolved oxygen, and the tank ullage is purged with nitrogen during the experiment. A dissolved-oxygen sensor (Mettler Toledo Inpro 6850i) is used to ensure that the levels of dissolved oxygen remain below 0.2% of the fully saturated level during the experiment. An inert gas purge circuit is used to avoid collection of stagnant fuel in the heater and the tubing to the experiment when fuel is not flowing to the experiment. This purge displaces the fuel to a collection tank through a bypass circuit and counter-flow heat exchanger that cools the fuel temperature to ambient temperature with water as the heat transfer medium.

Figure 3. Photograph of the assembled fuel heating system.

At the injector, fuel is injected into two co-swirling flows of air separated by a bluff body. The inner flow forms the pilot flame, and the outer flow forms the main flame, where most the fuel is burned. The fuel flow rates to the pilot and main circuits are separate, to enable independent control of the fuel/air ratio in each part of the flame. The pilot flame is operated at a higher fuel/air ratio than the main flame, thereby allowing the main flame to stabilize as the pilot products mix with the main reactants. The main reactant stream is assumed to be partially premixed when it reaches the flame, but the pilot flame is mostly non-premixed.

The flame zone is contained by a rectangular duct with a height/width ratio of approximately 1.4. Fused quartz windows are installed on each side of the duct to enable imaging of the flame, which is not presented in this work. These windows are film cooled with heated nitrogen at approximately 590 K to lessen the thermal load created by the flame. The film cooling flow rate is independently controlled but is set to a constant fraction of the combustion air flow rate. The duct then contracts vertically to a height/width ratio of approximately 0.75. Downstream of this contraction, another windowed section is present. A separate supply of heated air flows through the pressure vessel at the same pressure as the combustor, and this flow merges with the test article flow in a pipe, where water is radially injected into the flow to cool it.

An electrically actuated butterfly valve is installed at the exit of the flow path to back-pressurize the combustor. The inner duct is coated with a thermal barrier coating and cooled by internal water channels. This cooling water is directed into the flow at the exit of the inner duct.

Heated air and nitrogen sources are metered with sonic Venturi nozzles, high-pressure water is metered with cavitating Venturi nozzles, and jet fuel is metered with Coriolis flow meters. The test rig is equipped with pressure transducers (GE PMP50E6) and K-type thermocouples (Omega GKMQSS-062G) for flow metering and in several different locations throughout the flow path. These instruments are sampled at 100 Hz to monitor the operating conditions, and a National Instruments LabVIEW virtual instrument is used to display measured values and send commands to pneumatically and electrically actuated valves in the test cell. The relative uncertainties of calculated mass flow rates have been determined to be below 0.83% for gases and below 0.10% for liquid fuel according to the Kline–McClintock method, with a 95% confidence interval. A high-frequency pressure transducer (Kulite WCT312M-70BARA) is installed in the air plenum to monitor acoustic oscillations.

Emissions Sampling and OH* Imaging

An exhaust sampling probe (Figures 1 and 4), is installed at the exit of the inner duct. The sampling probe features five 0.38-mm holes on its upstream surface, which are spaced at 5%, 15%, 25%, 35%, and 45% of the channel height and centered relative to the channel width. The internal flow path of the probe is designed such that the pressure drop across the sample holes is sufficient to choke the flow through each hole, thereby ensuring a uniform sample of the exit cross-section. Similarly to the inner duct, the probe is coated with a thermal barrier coating and contains internal water cooling channels, which are directed into the flow path at the downstream surface of the probe. After exiting the probe, the emissions sample is routed out of the pressure vessel and maintained at 464 K by wrap-heated tubing as it flows to a Fourier transform infrared spectrometer (MKS Instruments MG2030). The spectrometer measures absorption spectra by using a Michelson interferometer, and the spectra are then used to calculate the mole fractions of major and minor product species, including CO_2, O_2, H_2O, CO, NO, NO_2, and unburnt hydrocarbons (UHC). After reaching steady state at under operating conditions, these spectra are acquired at 1 Hz for 20 s. In this work, average concentrations are reported, and one standard deviation is used as the uncertainty of each species concentration.

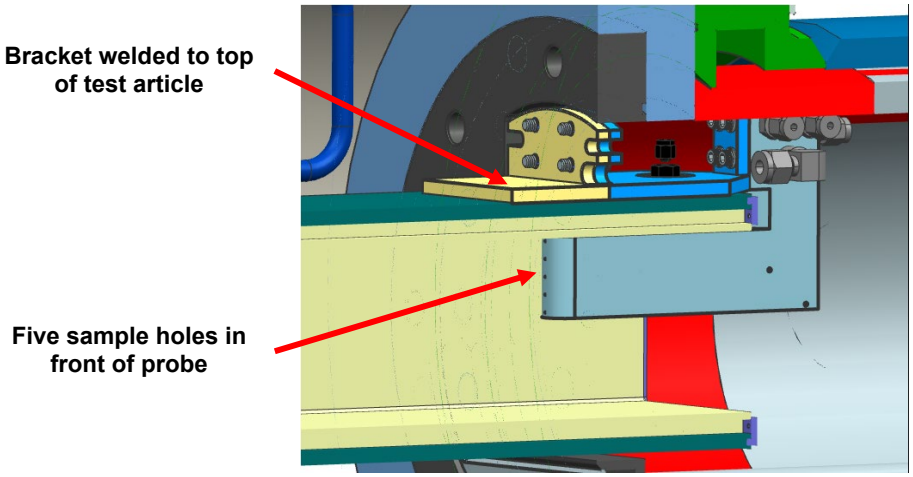

Figure 4. CAD rendering of the new emissions probe design.

Experiments with heated fuel began in March of 2021, after the fuel heater fabrication was completed. Initial measurements were performed with a probe supplied by GE, but we were concerned that the holes in that probe were too large to choke the flow. In addition, we observed that our water vapor measurements showed substantial fluctuations, thus indicating that liquid water might have been condensing in our sampling line. Consequently, we designed and fabricated the new probe described above, repeated the measurements with Shell GS 190 fuel, and performed additional measurements with Jet A fuel for a rigorous comparison of these two fuels. In general, the repeated measurements with the new probe for the Shell GS190 fuel were consistent with the measurements collected with the “old” probe, except that the water vapor measurements were much improved.

The emissions sampling and OH* chemiluminescence imaging were performed under the conditions listed in Table 1 (the asterisk indicates electronically excited OH molecules). A range of fuel–air equivalence ratios were tested for three fuel temperatures at an inlet air pressure of 1.0 MPa. Additional measurements were collected at an inlet air pressure of 2.0 MPa at the highest fuel temperature to determine the effect of increased pressure on emissions. Because the fuel heater heats the pilot and main fuel circuits independently, the fuel temperature reported herein is a mass-flow-weighted average of the fuel temperature of each circuit. The inlet air temperature and the pressure drop across the injector were held constant for all conditions.

Table 1. Test conditions. The equivalence ratio was varied within the specified range for each set of conditions.

Fuel	$\dot{m}_{air}$ [kg/s]	T_3 [K]	P_3 [bar]	ϕ_{total}	$\dot{m}_{f,pilot}/\dot{m}_{f,total}$	$T_{fuel,avg}$ [K]
Both	0.59 ± 0.01	755 ± 21	9.7 ± 0.5	0.39–0.52	0.30 ± 0.01	366 ± 2
Both	0.59 ± 0.01	755 ± 17	9.7 ± 0.5	0.37–0.52	0.30 ± 0.01	478 ± 7
Jet A	0.59 ± 0.01	755 ± 3	9.7 ± 0.6	0.37–0.51	0.30 ± 0.01	589 ± 7
FT-SPK	0.59 ± 0.01	755 ± 18	9.7 ± 0.3	0.38–0.61	0.30 ± 0.01	589 ± 13
Both	1.18 ± 0.02	755 ± 29	19.4 ± 0.6	0.37–0.51	0.30 ± 0.01	589 ± 11
Fuel	$\dot{m}_{air}$ [kg/s]	T_3 [K]	P_3 [bar]	ϕ_{total}	$\dot{m}_{f,pilot}/\dot{m}_{f,total}$	$T_{fuel,main}$ [K]
FT-SPK	0.59 ± 0.01	755 ± 14	9.7 ± 0.1	0.52 ± 0.01	0.30 ± 0.01	366–603

For both fuels, the measured values of CO and UHC followed the expected trend (Figures 5 and 6). The CO and UHC values from these figures were used to calculate combustion efficiency, which is shown for both fuels in the left panel of Figure 5. The plots of UHC show error bars representing one standard deviation of the measurement, whereas plots of other species do not show visible error bars, owing to the small magnitudes of their standard deviations. Several UHC values are below zero, but they are all within approximately one standard deviation of zero. With an increasing total equivalence ratio, both CO and UHC decrease before approaching an asymptote at zero. When the fuel injection temperature increased, the combustor generally produced less CO and UHC, thus indicating that the flame had fewer locations where the fuel was unable to burn completely.

With Jet A, compared with the FT-SPK, the combustor produced significantly more CO and UHC at low total equivalence ratios, with $T_{fuel,\,avg}$ = 366 K. As the Jet A fuel was heated to 589 K, the CO emissions by the combustor decreased until they closely matched the CO emissions with the FT-SPK fuel. With the FT-SPK fuel, very little change in CO and UHC emissions was detected with changes in the fuel temperature. The increased inlet air pressure of 18.4 bar at the fuel temperature of 589 K caused a slight decrease in CO and UHC when the Jet A fuel was used at low total equivalence ratios, but almost no change when the FT-SPK fuel was used or when the equivalence ratio was above approximately 0.44.

Nitrogen oxide (NO_x) emissions from the combustor are shown in Figure 6. With both fuels, as the total equivalence ratio was increased, the NO_x emission index increased approximately linearly between ϕ_{total} = 0.37 and ϕ_{total} = 0.52. However, two conditions were sampled at ϕ_{total} = 0.54 and ϕ_{total} = 0.60 at $T_{fuel,\,avg}$ = 589 K, and indicated that the NO_x emission index began to decrease when the total equivalence ratio was raised beyond approximately ϕ_{total} = 0.51.

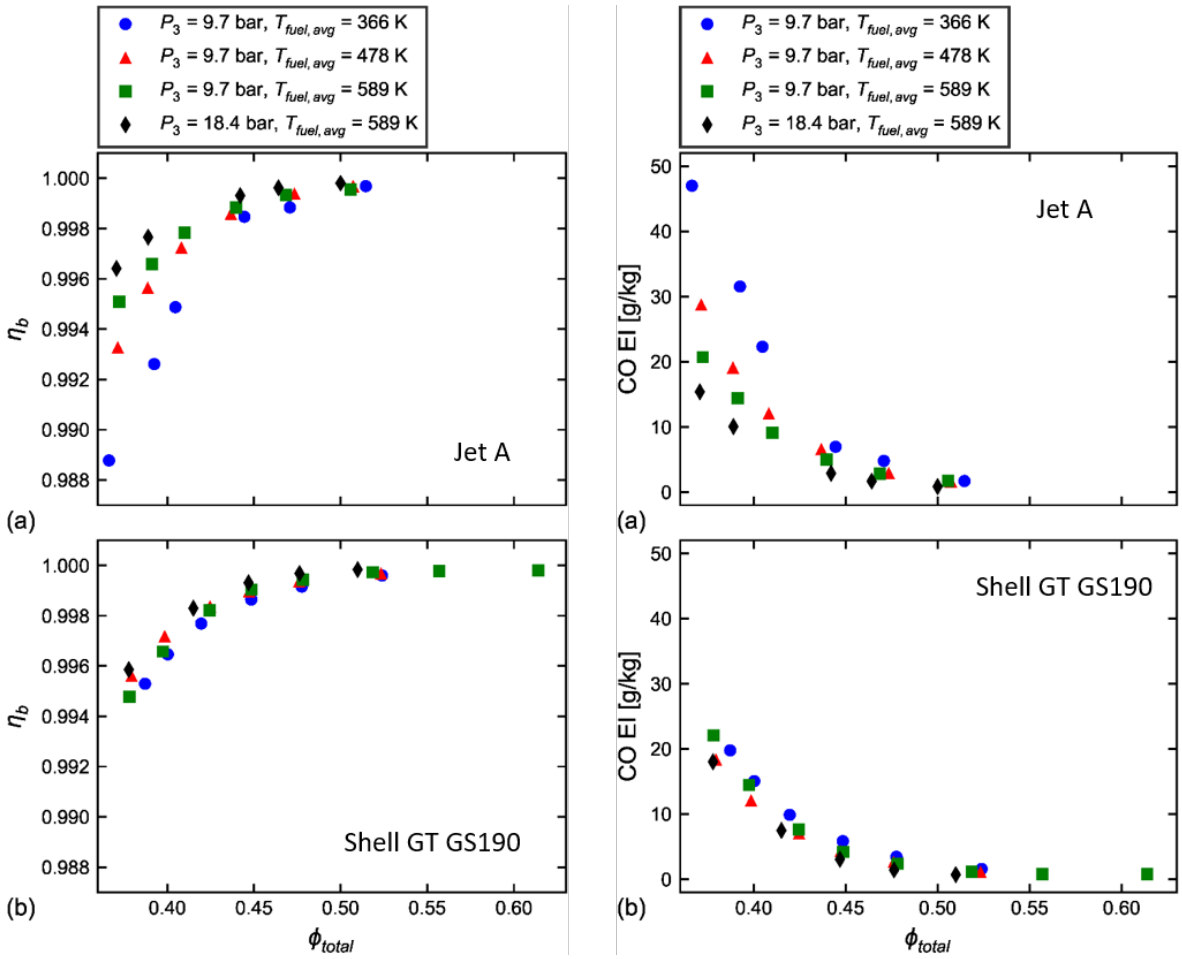

Figure 2. Comparison of combustion efficiency and CO emissions for Shell GT GS190 and Jet A fuels. Combustion efficiency (left panel) and CO emissions (right panel) were measured at a range of equivalence ratios at three fuel temperatures with P_3 = 9.7 bar and at $T_{fuel,av}$ = 589 K for P_3 = 18.4 bar.

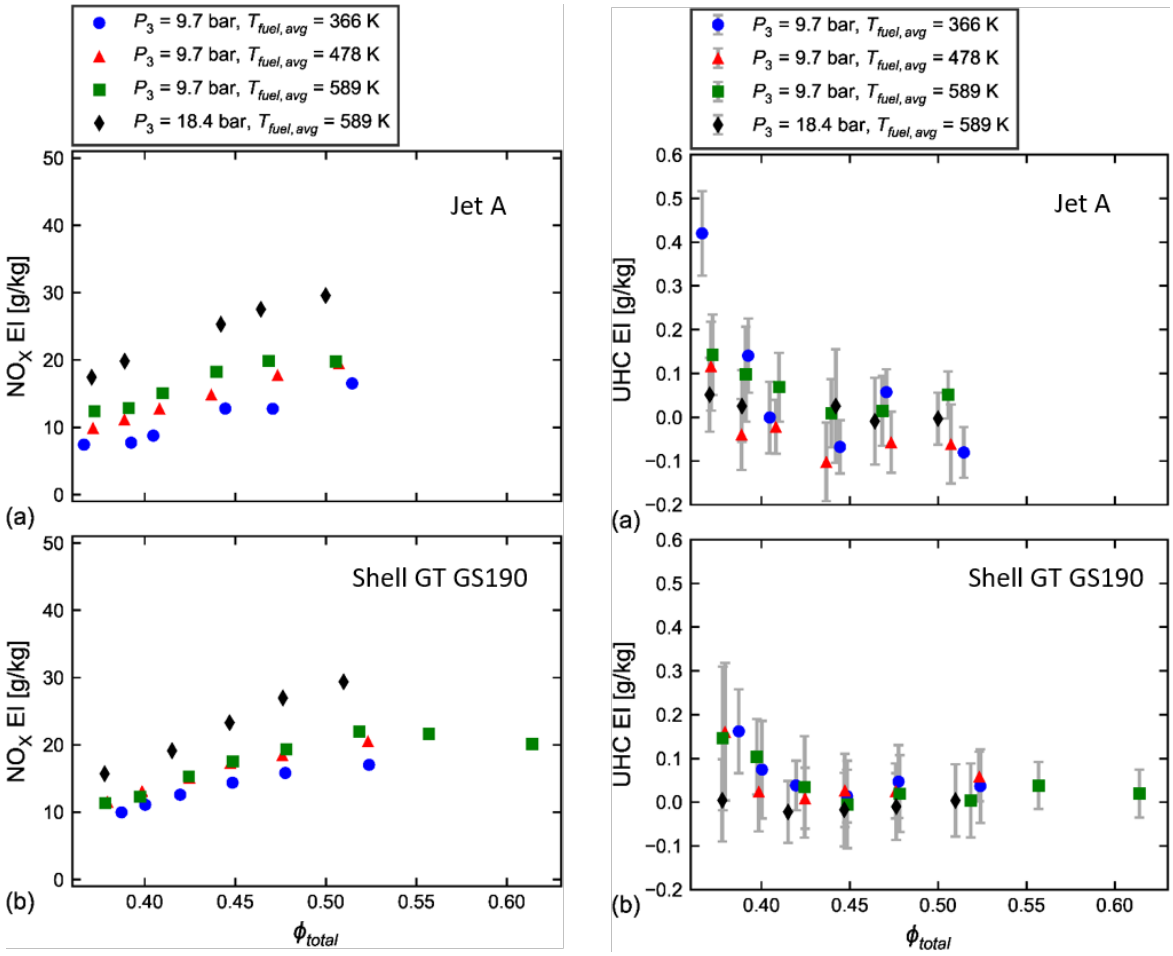

Figure 3. Comparison of NO_x and UHC emissions for Shell GT GS190 and Jet A fuels. NO_x emissions (left panel) and UHC (right panel) emissions were measured at a range of equivalence ratios at three fuel temperatures with P_3 = 9.7 bar and at $T_{fuel, avg}$ = 589 K for P_3 = 18.4 bar.

The Zeldovich mechanism is believed to be largely responsible for NO_x formation in this combustor; therefore, increases in the total equivalence ratio are expected to result in higher NO formation rates in lean regions of the flame. Because the pilot-to-total fuel split was fixed at 30%, and the air split was never varied, the pilot flame was always operated at a richer equivalence ratio than the main flame by a constant factor. Consequently, at the highest total equivalence ratio tested, ϕ_{total} = 0.60, the pilot flame was rich. In this regime, the pilot flame is cooler than its maximum temperature, and it is starved of oxygen; both these factors inhibit the forward reaction rates of the Zeldovich mechanism. At lower ϕ_{total}, unsteadiness in the pilot flowfield still creates regions in the pilot flame that are rich, thus slowing local NO_x formation. Because the main fuel flow has a longer distance to evaporate and mix with the surrounding air before burning, it is assumed to be partially premixed with the surrounding air by the time it begins to burn. Thus, the main flame has less variance in local equivalence ratio than the pilot flame.

The fuel temperature was varied at multiple total equivalence ratios between 0.37 and 0.52, and a significant effect on NO_x emissions was measured. With the Jet A fuel, the NO_x emission index increased by 16%–45% when $T_{fuel, avg}$ was raised from 366 K to 478 K, and the NO_x emission index increased by an additional 2%–25% when $T_{fuel, avg}$ was raised from 478 K to 589 K. With the FT-SPK fuel, the NO_x emissions index rose by 16%–21% when $T_{fuel, avg}$ was raised from 366 K to 478 K, but little change was seen when $T_{fuel, avg}$ was raised from 478 K to 589 K. As the fuel temperature is raised, the adiabatic flame

temperature increases very slightly. Consequently, the forward reaction rates of the Zeldovich mechanism increase, and slightly more NO is formed in both the pilot and main flames on average, but these responses do not account for the increase in NO_x observed with increasing fuel temperature. Instead, we hypothesize that changes in flame structure due to the increased fuel temperature are responsible for the increased levels of NO_x as the fuel temperature increases. For example, the density of Jet A decreases by approximately 29% as it is heated from 366 K to 589 K. For a given flow rate of fuel, the fuel jets that emit from the injector will penetrate farther when the fuel is heated, thus leading to a different fuel mixture fraction throughout the combustor. Consequently, a less uniform fuel–air mixture may be observed in the main reactant stream. A less uniform mixture will tend to produce higher levels of thermal NO_x due to the presence of pockets of gas with near-stoichiometric fuel/air ratios.

OH PLIF Imaging

OH PLIF imaging was successfully demonstrated in August 2021 at 10 Hz, thereby allowing a region approximately 40 mm in width to be captured in each frame. These experiments were continued in the fiscal year 2022 project period. For these experiments, a 532-nm pump laser beam was directed into a dye laser filled with rhodamine 590 dye. The output of the dye laser was tuned to an electronic transition in the Q branch of the OH molecule near 283 nm, thus resulting in the short-lived fluorescence (for several nanoseconds) of a fraction of these molecules as they relaxed back to their ground electronic state. With each laser shot, this fluorescence was captured by a CMOS camera (Phantom v2512) with an -image intensifier (Lambert HiCATT). Locations with high gradients in OH (particularly in the upstream part of an image), are indicative of the reaction front (or “flame surface”), where the highest levels of heat release occur.

Because of variations in intensity along the laser sheet and absorption effects, OH PLIF images cannot be treated as quantitative maps of OH concentration. Instead, these images must be processed to generate useful statistics. By converting the images into binarized maps showing which regions contain OH, quantitative information about the flame can be obtained. To do so, a robust edge detection method is required. For this project, a method known as semantic segmentation is used to separate each OH PLIF image into regions of signal and background. Semantic segmentation involves training a convolutional neural network to recognize these regions by learning from human-labeled images. To date, 176 images have been manually labeled, of which 156 were used as training images, and 20 were used as validation images. From this data set, the accuracy of this semantic segmentation model has exceeded that of most of the thresholding methods typically used by our group and others. A representative image and the detected edges are shown in Figure 7. Further refinement of the edge detection model is in progress, and the model will be applied to future OH PLIF images taken for this project. At present, too few OH PLIF experiments have been performed to draw meaningful conclusions regarding differences in the flame between conditions, but sufficient results are expected in the next year of the project.

Combustion Dynamics

Combustion dynamics was measured in the COMRAD test by using a high-frequency pressure transducer in the inlet air plenum (Figure 1). A longitudinal mode instability was observed at approximately 825 Hz in both the pressure readings and in the time-resolved OH* chemiluminescence images (Figure 8a). The comparison of the instability amplitude for both Jet A and Shell GS190 fuels as a function of fuel temperature is shown in Figure 8b. The instability amplitude decreases considerably as a function of fuel temperature for both Shell GS190 and Jet A fuels. A possible explanation for this decrease in the combustion instability amplitude is provided by Mie scattering images of droplets in exit flow from the main flow annulus. Droplets are clearly evident in the exit flow from the main annulus at fuel temperatures below 400 K but are not observed at higher temperatures (Figure 9). One potential explanation for the decrease in the combustion dynamics with increasing fuel temperatures is that the dynamics may be associated with the droplet evaporation process. Another possible explanation is that the increasing fuel temperatures may change the impedance in the main fuel circuit, thus leading to a significant decrease in dynamics. Figures 10 and 11 show phase-conditioned OH* chemiluminescence and Mie scattering images for a case with a high instability level (Figure 10) and a case with a low instability level. The instability level for a fuel temperature of 312 K (Figure 11) is markedly lower than that for a fuel temperature of 294 K (Figure 10).

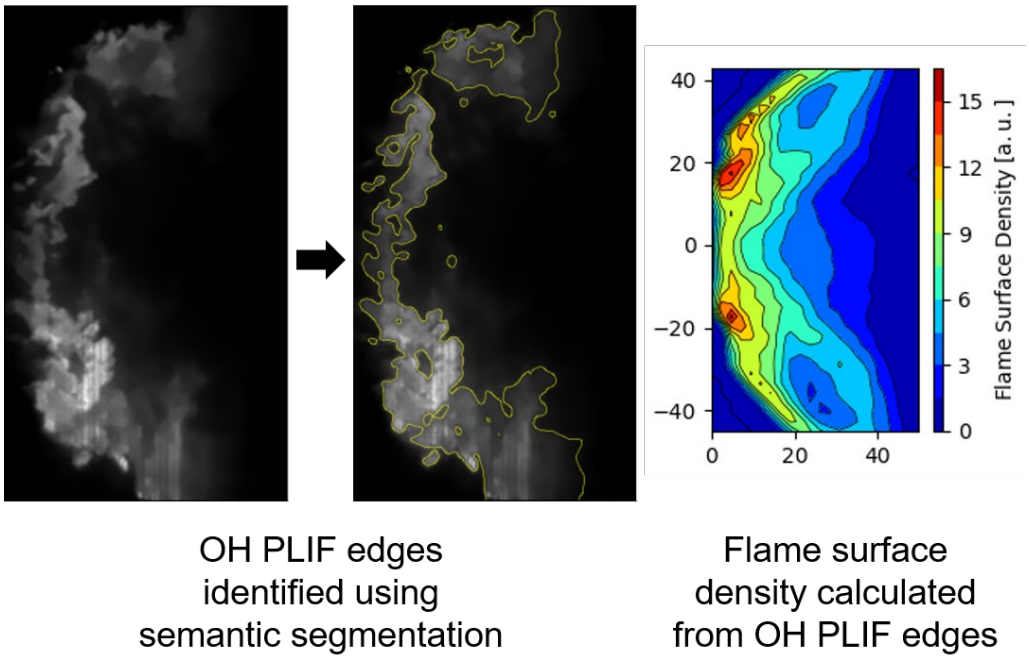

Figure 7. Representative OH PLIF image, with detected edges from the semantic segmentation model shown in yellow on duplicate images.

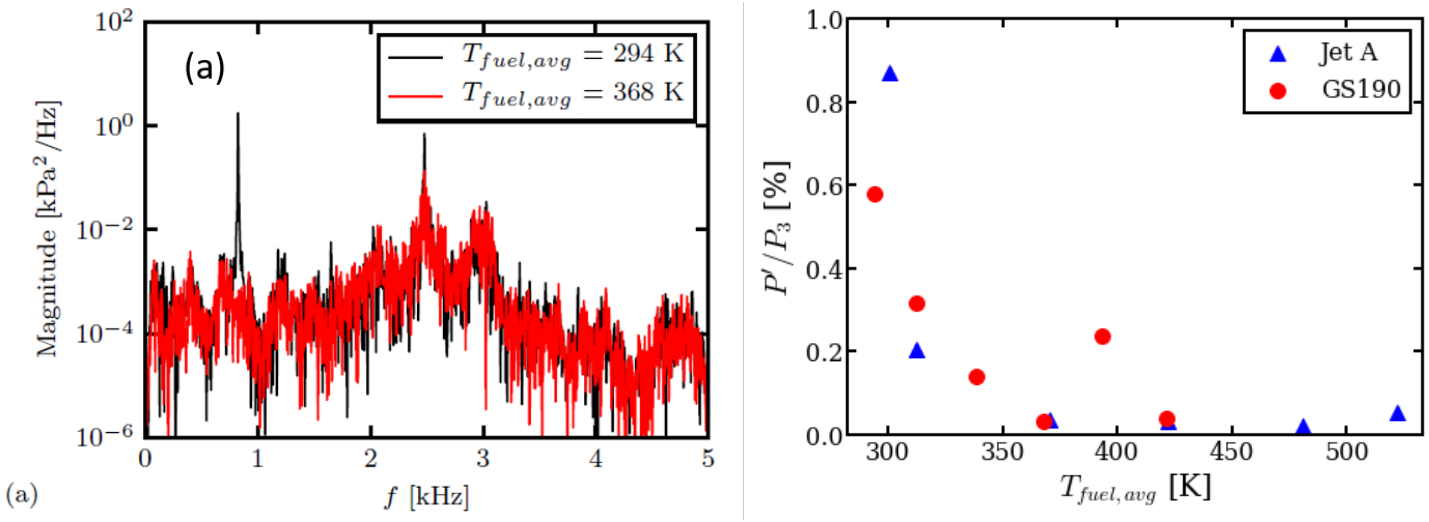

Figure 8. (a) Power spectrum of the pressure measurement in the inlet air plenum for two different fuel temperatures for Shell GS 190 fuel. (b) Comparison of the instability amplitude as a function of fuel temperature for Jet A and Shell GS190 fuels.

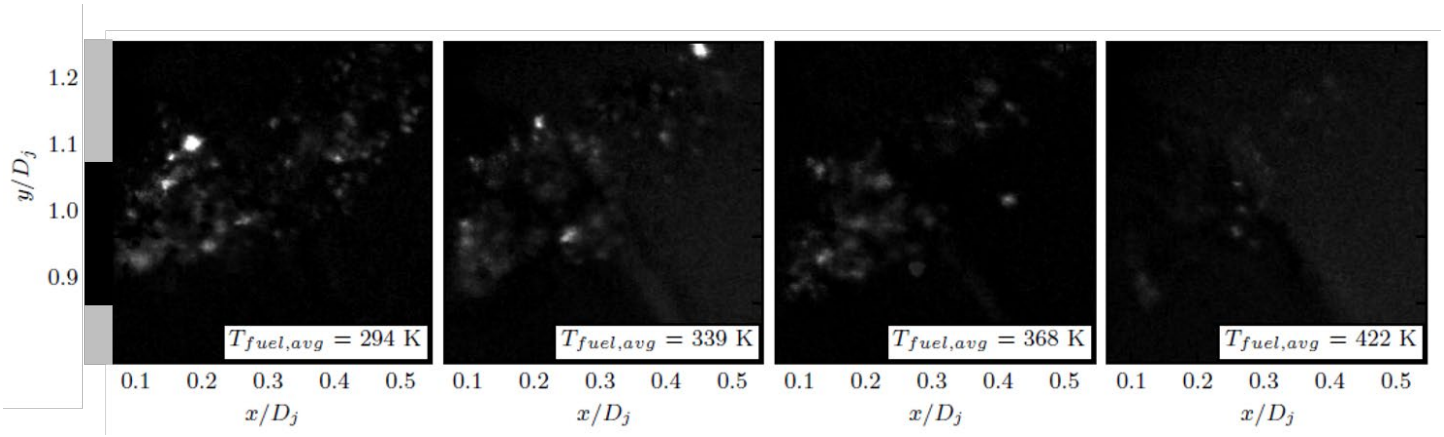

Figure 9. Mie scattering images of GS190 fuel droplets at the exit of the main annulus of the twin annular premixed swirl injector as a function of fuel temperature.

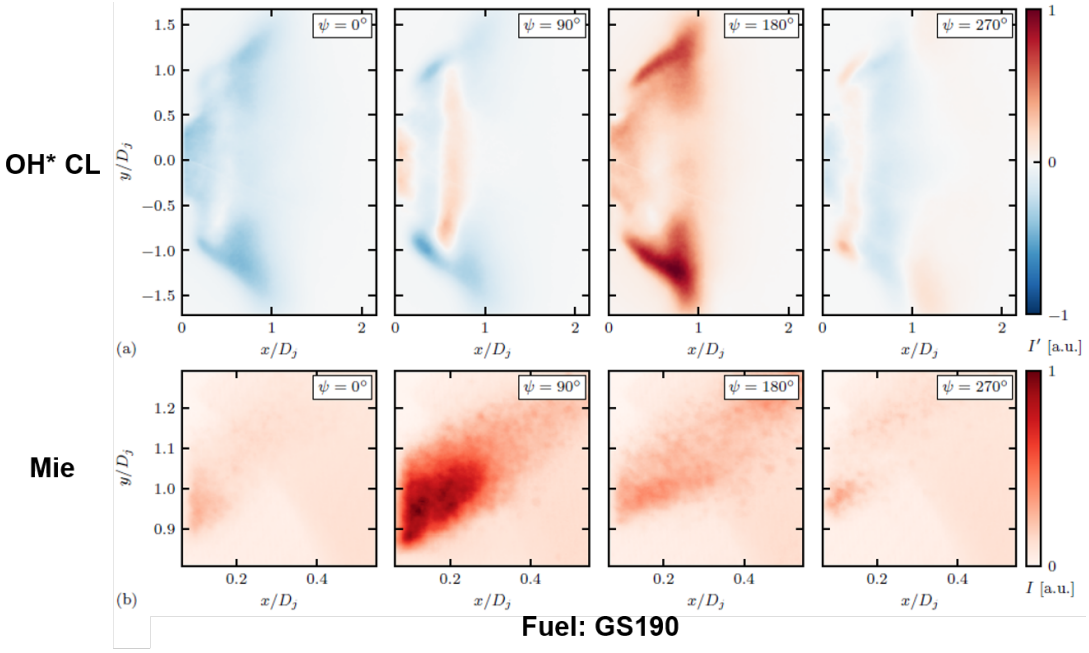

Figure 10. Phase-conditioned average OH* chemiluminescence and Mie scattering images for GS190 combustion at a fuel temperature of 294 K. The phase ψ = 0˚ corresponds to the minimum intensity level for the OH* chemiluminescence. The GS190 fuel droplets are observed at the exit of the main annulus of the twin annular premixed swirl injector as a function of fuel temperature.

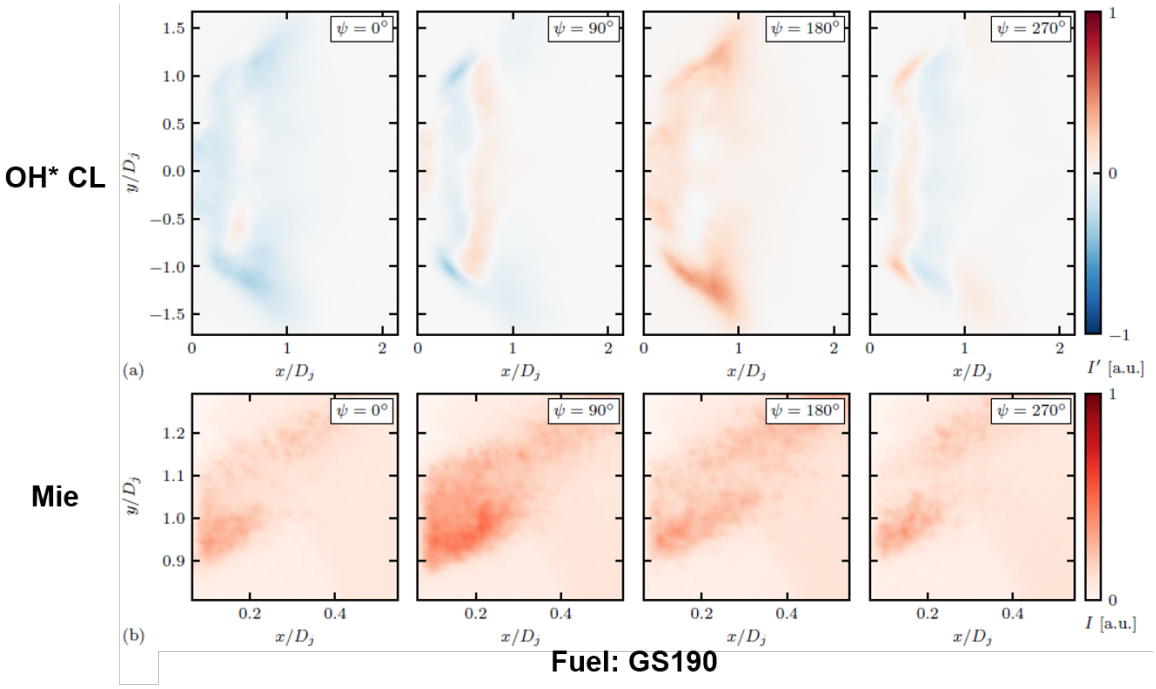

Figure 11. Phase-conditioned average OH* chemiluminescence and Mie scattering images for GS190 combustion at a fuel temperature of 312 K. The phase $\psi = 0^{\circ}$ corresponds to the minimum intensity level for the OH* chemiluminescence. The GS190 fuel droplets are observed at the exit of the main annulus of the twin annular premixed swirl injector as a function of fuel temperature.

Publications

Published conference proceedings

McDonald, C. T., Philo, J. J., Shahin, T. T., Gejji, R., Slabaugh, C. D., & Lucht, R. P. (2021, August 9). Effect of fuel temperature on emissions and structure of a swirl-stabilized flame. *AIAA Propulsion and Energy 2021 Forum*. AIAA Propulsion and Energy 2021 Forum, VIRTUAL EVENT. https://doi.org/10.2514/6.2021-3480

Journal Articles

Philo, J. J., McDonald, C. T., Shahin, T. T., Gejji, R. M., Lucht, R. P., and Slabaugh, C. D. (2022). Fuel heating effects on the flow and flame structure of a piloted swirl injector. *AIAA Journal, under review*.

McDonald, C. T., Shahin, T. T., Philo, J. J., Gejji, R. M., Fish, D. D., Slabaugh, C. D., and Lucht, R. P. (2022). Emissions Measurements in a Liquid-Fueled Aviation Gas Turbine Combustor with Heated Fuels. *ASME Journal of Engineering for Gas Turbines and Power, in preparation.*

Outreach Efforts

None.

Awards

None.

Student Involvement

Three PhD students, Colin McDonald, John Philo, and Tristan Shahin, are working on the project. The project provides outstanding research experiences for the graduate students, including the design of system components for, and the operation of, a sophisticated aviation gas turbine combustion test rig, as well as application of advanced laser diagnostic

methods for measurements in this test rig. As noted above, the graduate students have been responsible for designing system components, such as the fuel heating system, and for executing test operations.

Plans for Next Period

The focus for the third year of this project will be a detailed comparison of a selected sustainable aviation fuel (SAF) with a well-characterized petroleum-based fuel, Jet A, or fuel A2 from the National Jet Fuel Combustion Program. The SAF will be a mixture of paraffins and aromatic compounds, and the composition will be selected in consultation with other FAA ASCENT researchers and our collaborators at GE Aviation. The SAF composition is expected to be 92% FT-SPK and 8% single-ring aromatic compounds. The first stage of the comparison will involve combined physical sampling probe emission measurements and chemiluminescence emission measurements. In the next stage of the comparison, we will use high-speed PIV to measure the velocity flowfield, and both 10-Hz and 10-kHz OH PLIF to monitor the structure and dynamics of the reaction zones.

The fuel sprays will be studied in a non-reacting setting by using simultaneous fuel PLIF and Mie scattering imaging. The rig will be operated under the same conditions as those for other diagnostics, except that the fuel spray will not be ignited. The Fischer–Tropsch fuel that we have used to date in the project has no aromatic compounds and thus does not fluoresce. However, the A2 fuel and the selected SAF contain aromatic compounds; thus, both liquid fuel and fuel vapor will fluoresce. Mie scattering imaging will be performed in concert with the fuel PLIF measurements. Because Mie scattering occurs when light is scattered off droplets, the Mie scattering measurements will allow us to decouple the spray of liquid droplets from the plume of evaporated fuel that ensues.

The near-nozzle region will also be studied by using coherent anti-Stokes Raman scattering (CARS) spectroscopy of the N_2 molecule, which will provide point-wise temperature measurements. Differences in temperature throughout the flame zone at varying fuel temperature will be crucial to understanding how differences in fuel inlet temperature are manifested in chemical kinetics and consequently pollutant emissions. We had planned to use a 10-Hz Nd:YAG laser with a broadband dye laser for these measurements. However, Profs. Lucht and Slabaugh have recently been awarded funding through the Department of Defense University Research Instrumentation Program to purchase a state-of-the-art ultrafast laser system. We will use this system to perform 1-kHz femtosecond CARS temperature measurements in the reaction zone instead of 10-Hz nanosecond CARS temperature measurements. Temperature time histories will be recorded at different locations throughout the flowfield for several fuel temperatures and a range of operating conditions. The ultrafast laser system may also enable the use of CARS line imaging temperature measurements.

Project 068 Combustor Wall Cooling with Dirt Mitigation

The Pennsylvania State University

Project Lead Investigator

Karen A. Thole
Distinguished Professor
Department of Mechanical Engineering
The Pennsylvania State University
START Lab, 3127 Research Drive
State College, PA 16801
814-863-8944
kthole@psu.edu

University Participants

The Pennsylvania State University

- P.I.s: Dr. Karen Thole and Dr. Stephen Lynch
- FAA Award Number: 13-C-AJFE-PSU-057
- Period of Performance: October 1, 2021 through September 30, 2022
- Tasks:
  1. Manufacturing and testing of combustor liner cooling concepts with small coupons
  2. Testing of scaled models of optimal cooling concepts
  3. Facility planning for 1×-scale combustor simulator

Project Funding Level

For the entire 3-year effort, the ASCENT funding was $1,400,000, and matching funds of $1,400,000 were provided by Pratt & Whitney.

Investigation Team

Name	Affiliation	Role	Task responsibilities
Distinguished Professor Karen A. Thole	The Pennsylvania State University	P.I.	Management, reporting, and oversight of all technical tasks
Associate Professor Stephen Lynch	The Pennsylvania State University	Co-P.I.	Management, reporting, and oversight of Tasks 1–3
Associate Research Professor Michael Barringer	The Pennsylvania State University	Research Advisor	Task 3
Scott Fishbone	The Pennsylvania State University	Project Manager	Tasks 1–3
Brandon Fallon	The Pennsylvania State University	Graduate Student	Task 1
Kyle McFerran	The Pennsylvania State University	Graduate Student	Tasks 1 and 2
Chad Schaeffer	The Pennsylvania State University	Graduate Student	Task 3

Project Overview

A critical issue related to the operation of gas turbines in today's world is the ingestion of dirt and other fine particles that lead to dirt buildup and reduced cooling of hot section components, such as the liner walls of the combustion chamber. With rising needs to fly in dirty environments, the criticality of operations in dirty environments is increasing. Modern gas turbine

engines typically use a double-walled combustor liner with impingement and effusion cooling technologies, whereby impingement cooling enhances the backside internal cooling, and effusion cooling creates a protective film of coolant along the external liner walls. Dirt accumulation on the internal and external surfaces severely diminishes the heat transfer capability of these cooling designs. This study also investigates the development of a combustor profile simulator upstream of the Steady Thermal Aero Research Turbine (START) test turbine. Combustor profiles affect turbine performance and durability. As combustor designs evolve, particularly the liner cooling technologies, understanding the impacts on the turbine is important. This study investigates practical designs applied to combustor walls to decrease dirt accumulation, and also explores the development of a profile simulator that can replicate relevant temperature and pressure profiles upstream of a test turbine

Task 1 - Manufacturing and Testing of Liner Cooling Concepts

The Pennsylvania State University

Objective

The goal of this task is to produce an effective cooling design for combustor walls that is insensitive to dirt accumulation at existing or lower coolant flow rates. Various parameters such as dirt deposition, flow behavior, and heat transfer effectiveness will be investigated and quantified to compare the efficiency of candidate designs. Improved understanding of the underlying reasons for dirt sensitivity and deposition behavior is also being sought.

Research Approach

Background

The focus of the project is on the impacts of ingestion of dirt and other fine particulate matter in gas turbine engines. These particles are known to block the cooling holes and passages needed to effectively cool combustion chamber walls. Gas turbine engines often use double-walled combustor liners comprising impingement and effusion cooling plates (Figure 1). The impingement plate enhances backside internal cooling, and the effusion plate creates a protective film of coolant along the external liner walls. As particulate matter accumulates on these plates, the heat transfer performance severely diminishes, thus ultimately leading to component failure.

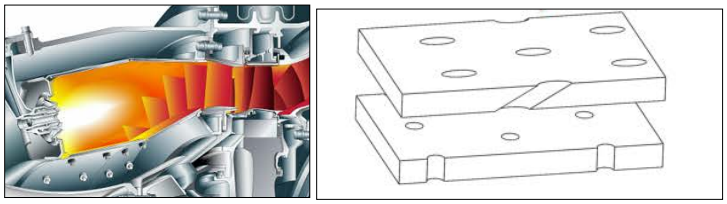

Figure 1. Schematic of double-walled combustor liner geometry.

A double-wall combustor liner consisting of an impingement, spacer, and effusion plate is shown in Figure 1. The impingement plate has straight holes resulting in high-velocity jets that impinge on the backside of the effusion plate, which is exposed to the hot main gas path. The spacer plate creates a small controllable gap between the impingement and effusion plates. The effusion plate uses cooling holes angled at 30˚ to create a film effect along the external wall exposed to the hot combustion gases. The goal of this research is to determine a double-wall design enabling favorable cooling while being exposed to a dirty cooling flow that results from the turbine engine intake during flight. To achieve this goal, the research this past year has evaluated the use of conical structures placed on the surface of the effusion plate, as denoted by red cones in Figure 2.

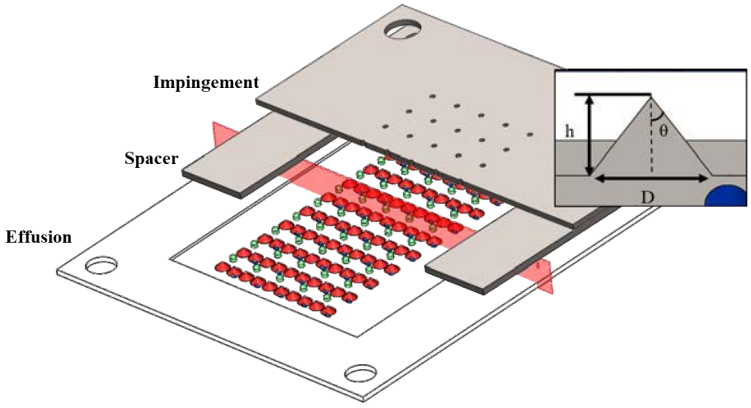

Figure 2. Schematic of the pin-cone aligned double-walled combustor liner configuration.

Table 1 details the combustor liner concepts tested during this period. All these concepts were developed by The Pennsylvania State University START Lab. These concepts consisted of a flat pin-cone aligned (PCA) baseline, PCA with variable cone heights, and PCA with variable cone diameters. Three impingement plates with a range of impingement jet diameters were also tested. All impingement and effusion plates were printed with a FormLabs Form 3 SLA 3D printer with high-temperature resin.

A schematic of the test facility used in this study is shown in Figure 3. The facility is capable of two dirt injection modes, both of which have been found to produce identical trends in performance. Consequently, a decision was made to use only slug feed injection in this quarter, to minimize the amount of testing required. In the slug feed method, dirt was split into three portions of equal mass, referred to as slugs. Each slug was sequentially placed into the slug feed chamber located upstream of the coupon. The chamber was then pressurized above the mainstream flow pressure and opened with a ball valve that injected the dirt into the system. Downstream of the location where the dirt was injected, the flow entered a clear, rectangular plenum with a splash plate at the start to ensure uniformity (Figure 3). A filter box was attached to the backside of the effusion plate to prevent dirt from scattering into the laboratory environment. At ambient conditions, each test used 2 grams of dirt at a fixed pressure ratio (PR) of 1.045, which can be determined with Equation 1.

$$\mathrm{PR} = \frac{P_{0C}}{P_{\infty}} \tag{1}$$

Table 1. Dimensions of test geometry.

	Baseline (no cone)	Cone Geometry						Impingement		
Parameter Varied	-	Height			D			Di		
h [mm]	-	0.7	1.4	2.2	1.4			1.4		
D [mm]	-	2			2	3	4	0.08		
De [mm]	1.3	1.3			1.3			1.3		
Di [mm]	1.03	1.03			1.03			1.03	1.59	2.15
θ	-	35	55	65	55	43	34	55		
S1/Di | S2/Di	6.2	6.2			6.2			6.2	4	0.1
S1/De | S2/De	5	5			5			5		
Name	Flat Baseline	PCA-SS	PCA Baseline	PCA-TS	PCA Baseline	PCA-MM	PCA-ML	PCA Baseline	PCA-625	PCA-845
Picture	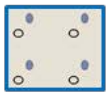	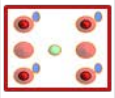	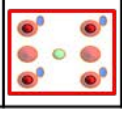	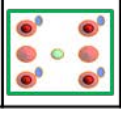	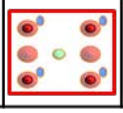	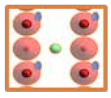	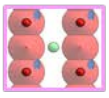	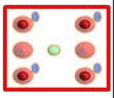	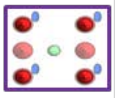	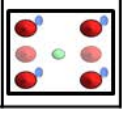

In each test, the flow rate, PR, and dirt captured were measured. These measurements were then used to calculate the capture efficiency (η_c) and flow parameter (FP) for the impingement and effusion plates. Definitions for FP and capture efficiency are shown in Equations 2 and 3. Capture efficiency is determined by subtracting the dirt mass on the effusion plate surface from the total mass of dirt that successfully passed through the coupon. Upstream dirt located on the first impingement plate, piping, and plenum is not included in the capture efficiency.

$$\mathrm{FP} = \frac{4\dot{m}\sqrt{T_{oc}R}}{\pi P_{up} N D^2} \tag{2}$$

$$\eta_c = \frac{M_{eff} - M_{cl}}{D_{int}} \times 100 \tag{3}$$

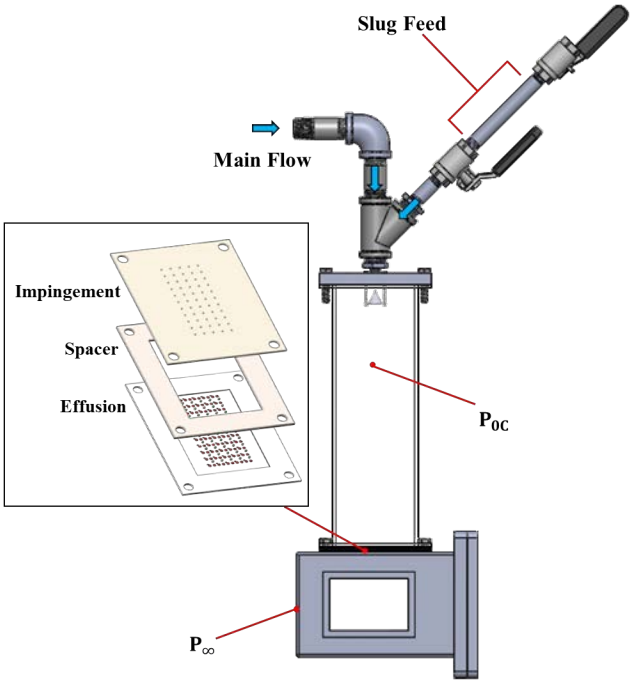

Figure 3. Diagram of the test facility used for dirt deposition studies.

Figure 4 shows the locations where dirt was deposited relative to the coupon assembly. The dirt passes through the impingement plate (blue) and impinges on the cold side of the effusion plate (red) not in contact with the hot combustion gases.

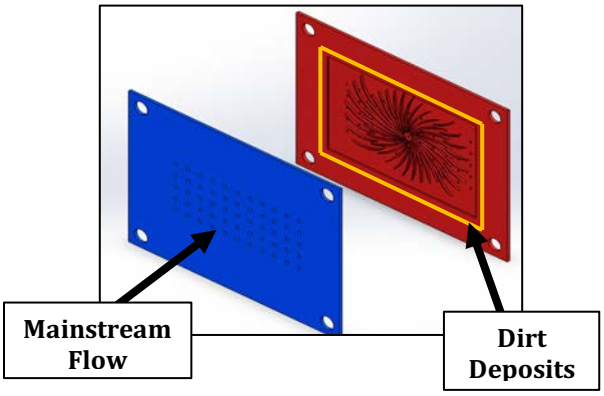

Figure 4. Dirt deposition location (orange) relative to the coupon assembly.

Results

Figure 5a–h displays the experimental dirt deposition patterns on a periodic section of the effusion plate. The colored outline surrounding each image matches that of the legend in Table 1. Dirt is represented by the white circular mounds on the effusion plate surface, which are directly aligned with the impingement jets on the opposite wall. The flat baseline effusion plate is shown in Figure 5a. The dirt deposition pattern indicated that dirt "peaks" formed uniformly in areas where the dirt-laden flow impinged on the flat surface. These dirt peaks had the highest concentrations of dirt, and the concentrations tapered off as the radial distance from the impingement site increased. Between the impingement sites, straight lines of dirt,

referred to as “ridges,” deposited at lower concentrations than those of the dirt peaks. These ridges formed in a stagnation region created by the collision of the wall jets that spread radially outward.

Similarly to that on the flat baseline effusion plate in Figure 5a, dirt deposition on the baseline pin-cone geometry in Figure 4b was concentrated in a dirt peak at the impingement site where a cone was located. Integrating the cones appeared to alter the radial dirt spread, as indicated by the absence of the dirt ridges previously observed in the flat baseline case. Furthermore, a thin ring of deposition was observed around the pins located in the four corners surrounding the impingement site, also as a result of the disrupted radial dirt spread.

When the impingement diameter increased, as in Figure 5c,d, minimal qualitative changes were seen in the dirt deposition pattern from the top-down perspective. Although not pictured, the height of the dirt peak grew, thus causing the dirt to form more loosely packed structures. These structures often broke apart and scattered across the effusion plate surface during testing, thereby explaining the increased presence of dirt clumps in Figure 5c,d.

Modifying the shape of the cone resulted in a deposition pattern similar to that of the baseline pin-cone effusion plate in Figure 5b. In Figure 5e,f, the diameter of the cones was enlarged; consequently, the radial spread of dirt increased. This amplified radial deposition indicated that dirt was more likely to deposit in areas where the flow had a non-zero velocity component directed at the wall. The height of the cone was modified in Figure 4g,h; Figure 5g corresponds to decreased height, and Figure 5h corresponds to increased height. As the height of the cone decreased and increased (Figure 5g,h, respectively), the height of the dirt peak changed, but the dirt pattern remained largely the same as that in the pin-cone baseline in Figure 5b. These findings indicated that the dirt pattern is not significantly modified as cone parameters are changed and that dirt deposits predominantly on the cones.

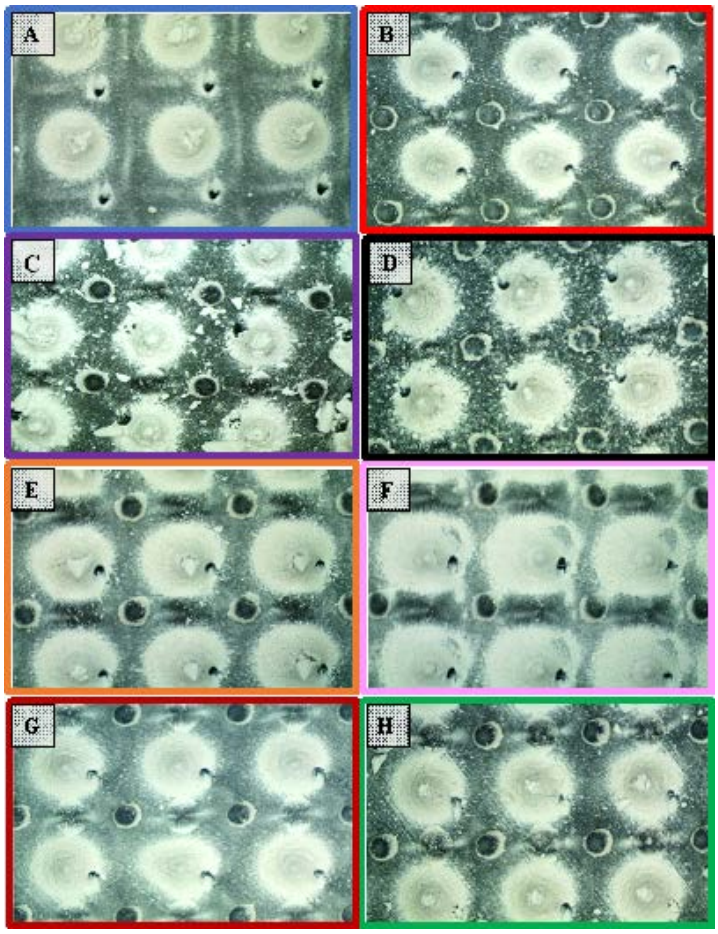

Figure 5. Post-test dirt deposition on all effusion plates. From left to right, (a) flat baseline, (b) pin-cone baseline, (c,d) effect of impingement, (e,f) effect of cone diameter, (g,h) effect of cone height.

The performance of each coupon was compared by using the capture efficiency shown in Equation 3, which quantifies the dirt adhering to the effusion plates' cooling holes and surface. High dirt capture, i.e., high capture efficiency, is not desired, because the dirt blocks film cooling holes and creates undesired thermal insulation between the liner walls. The capture efficiency of each concept is depicted in Figure 6.

The flat baseline case (Figure 5a) set the standard, with a capture efficiency of 42%. When the pins and cones were integrated onto the baseline geometry (Figure 5b), the capture efficiency decreased to 38%. As the impingement jet diameter increased to 1.6 mm (Figure 5c) and 2.2 mm (Figure 5d), further decreases of 6% and 10%, respectively, with respect to the pin-cone baseline effusion plate were seen in the capture efficiency (Figure 5b). Of note, for each of the first four geometries (Figure 5a–d), the mass flow rate was nearly constant. Because the mass flow rates were identical, the impingement velocities for the flat baseline and pin-cone baseline coupons (Figure 5a,b) were nearly the same, thereby indicating that this cone design was effective in positively modifying the near-wall flow in the regions surrounding the cone. When the jet diameter increased, the corresponding impingement velocity decreased, and the loosely packed dirt peaks shown in Figure 5c,d formed. This finding indicated that lower impingement velocities (and subsequently lower particle momentum) barred dirt particles from separating from the flow as readily, thus halting aggressive particle adhesion to the surface and decreasing the dirt capture.

For successive increases in cone diameter (Figure 5e,f), the capture efficiency increased to 45%. As discussed in the prior section, increasing the cone diameter enabled dirt to spread further radially and adhere to the larger surface area on the cones. Interestingly, when the diameter of the cone was reverted to the original value, and the height of the cone was

decreased, the capture efficiency remained at 45%. However, when the cone height increased, the capture efficiency decreased to 39%.

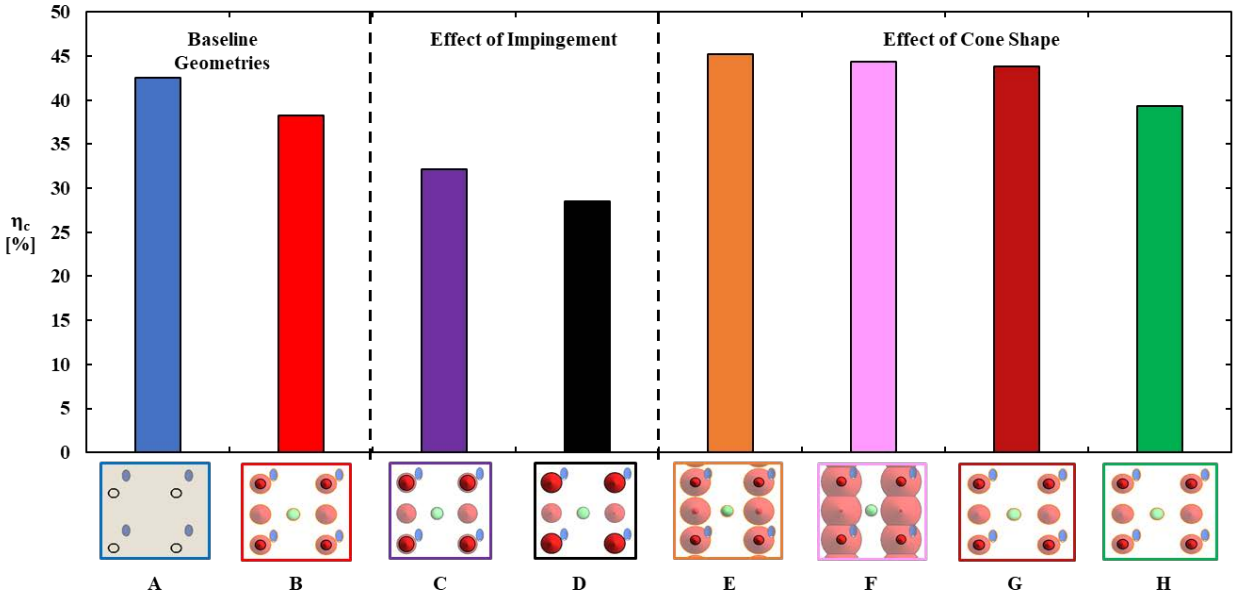

Figure 6. Capture efficiencies for all impingement and effusion plate pairs at a pressure ratio of 1.045 with 2 g of dirt.

The FP of each design was calculated and scaled to the capture efficiency (Figure 7). Data acquired in the previous quarters are also incorporated into this graph. Effusion plates tested with an impingement plate containing 1.03-mm-diameter jets are represented by circular points. The hollow cores within several of the circular points indicate that the conical structure on the effusion plate was modified. The purple diamond and black triangle denote the effusion plates that were tested with impingement plates containing jets of 1.6 mm and 2.2 mm in diameter, respectively. Of note, each coupon had a different FP despite having operated at the same PR.

The data showed a nearly linear correlation between the capture efficiency and FP, such that coupons with high FP are expected to capture more dirt. This increase in dirt capture occurred because the impingement velocity rose with increasing FP increased, thus increasing deposition in areas around the cones where flow was reoriented. The coupons with the lowest dirt capture had larger impingement jets, thus greatly reducing the FP.

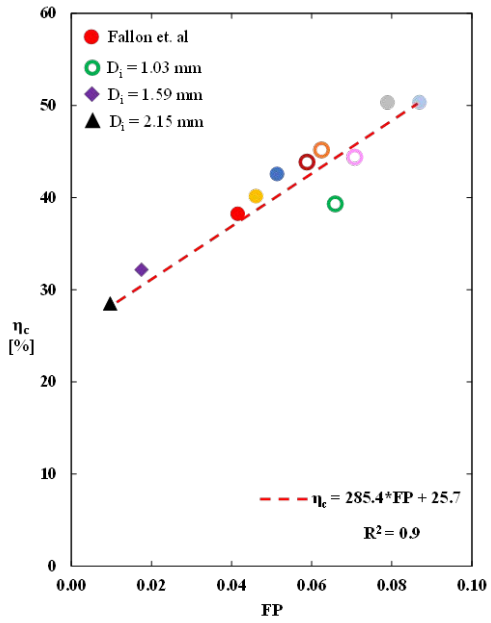

Figure 7. Capture efficiency as a function of flow parameter at a pressure ratio of 1.045 with 2 g of dirt.

Computational Predictions

To understand the flow phenomena between the impingement and effusion plates, we performed computational fluid dynamics (CFD) simulations with no particles on all geometries listed in this study. These computational studies were performed with the commercial CFD code STAR-CCM+. A steady, three-dimensional Reynolds-averaged Navier–Stokes (RANS) simulation with a shear-stress transport k-ω turbulence model was used. A stagnation pressure inlet and atmospheric pressure outlet were used as boundary conditions to replicate the PR of 1.045 used in experimental studies (Figure 8). The hexahedral meshes were achieved by using the prism layer mesher, trimmer, surface remesher, and surface wrapper models. A base cell size of 0.2 mm and four prism layers were used to construct each mesh, which contained 14.8 million cells on average. For evaluation of grid independence, the jet Reynolds number for the flat baseline coupon was compared on mesh sizes varying from 4.85 million to 10.1 million nodes. The maximum variance in jet Reynolds number did not exceed 1.2%. The solution converged after a minimum of 1,000 iterations, and the residuals were lower than 1×10^{-4}.

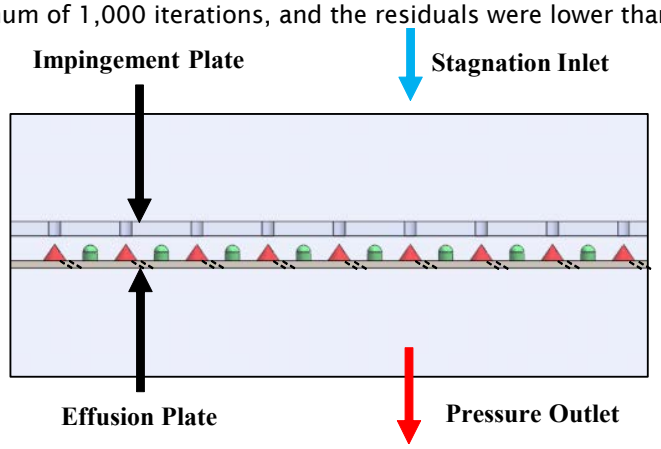

Figure 8. CFD domain detailing the position of the coupon with the prescribed boundary conditions.

The CFD-predicted flow field (Figure 8) displays the normalized velocity magnitude in the space between the impingement and effusion plates. The contours were centered on the impingement jet and run longitudinally through the cones (location denoted by the shaded red plane in Figure 2). The site of the impingement jet and the out-of-plane effusion holes is represented by dashed black lines and dashed red lines, respectively.

Figure 9a shows the flow field for the flat baseline geometry that did not contain any pin-cone structures. The velocity contour revealed that a stagnation region formed as the impingement jet impacted the effusion wall, thus causing dirt to deposit and form into a peak. As the jet transitioned from impingement flow to wall jet flow, the sharp turn in flow direction coupled with velocity fluctuations enabled more particle separation from the flow. However, after the flow transitioned to wall jet flow, dirt deposition diminished. This finding illustrated that particulate matter was more likely to separate from the flow when sudden changes in flow direction occurred. Eventually, the radially extending wall jets originating from the impingement jets collided with each other and produced a new stagnation region that created the dirt ridges in Figure 5a.

The pin-cone baseline in Figure 9b had lower dirt capture than the flat baseline geometry, thereby indicating that the cone structure and layout could be effectively used to reduce dirt deposition. The internal flow field showed that the placement of the cone directly in the impingement path caused the impingement jet to accelerate down the cone. This increase in velocity on the cone's surface increased the particles' momentum, and consequently facilitated separation of particulate matter from the flow traversing down the cone. As the impingement jet reoriented to wall jet flow, the velocity of the jet decreased, thereby hindering easy separation of particulate matter from the flow. Because the particulate matter could not readily separate from the flow, it was unable to contact and adhere to the surface; consequently, dirt capture on the flat portion of the plate decreased. The radially spreading wall jet then continued outward until it collided with other conical structures that were not aligned with the impingement jet. Small amounts of dirt deposited at the bases of these cones as the flow direction transitioned upward. However, because the flow was directed upward, away from the surface, deposition on the wall was limited to the base of the cone, thus preventing the formation of the straight dirt ridges displayed in Figure 9a.

Next, the flow-field effects of increasing the impingement jet diameter (Figure 9c,d) were investigated. Of note, increasing the jet diameter caused the impingement velocity to decrease, thereby resulting in lower particle momentum and subsequently much lower deposition on the surface. The main cause of this decreased deposition is likely to stem from this reduction in impingement velocity, which hindered the separation of particulate matter from the flow, even at the bases of the cones where the flow direction was reoriented. As discussed in the prior section, these lower impingement velocities also caused more loosely packed dirt peaks to form on the cones; these dirt peaks were often broken and scattered across the surface. We suspect that these dirt structures were often broken because they were susceptible to demolition by larger particles that might have clumped together in the mainstream flow before impinging on the surface.

The effect of the increased cone diameters on the internal flow is displayed in Figure 9e,f. Both geometries exhibited higher impingement velocities than any of the other coupons, thus increasing the inertial impaction rate and dirt capture. In addition to larger impact velocities, the larger-diameter cones prevented the flow from reorienting to wall jet flow as quickly; consequently, more dirt deposition occurred further from the impingement site. This discovery is consistent with the experimental deposition studies in Figure 5e,f, which indicated more deposition in the radial direction.

The final set of contours in Figure 9g,h evaluated the internal flow characteristics around cones of different heights. The short cone shown in Figure 9g had capture efficiencies and impingement jet velocities similar to those of the large-diameter cones. As the jet impinged on the short cone, a substantial stagnation region formed at the cone's tip, thereby resulting in dirt retention and contributing to deposition. Owing to the cone's reduced height, high-speed flows were seen near the base of the cone where flow reoriented, and consequently increased dirt deposition. When the height of the cone increased, a substantial decrease in capture efficiency was seen, to levels similar to the pin-cone baseline. The evaluation of the tall cones' flow field in Figure 9h showed that the enlarged stagnation point that formed at the tip of the cone in Figure 9e–g was eliminated and the flowfield more closely matched that of the pin-cone baseline in Figure 9b. Because of the increased height of the cone, the flow velocity decreased at a higher location on the cone's surface, thus causing less dirt separation when the flow reoriented at the cone's base. However, owing to the steepness of the cone, a larger stagnation region formed at the base of the cone where dirt could gather. Despite the marginally worse dirt capture than that observed for the pin-cone baseline coupon, higher impingement velocities were achieved by using the tall cones.

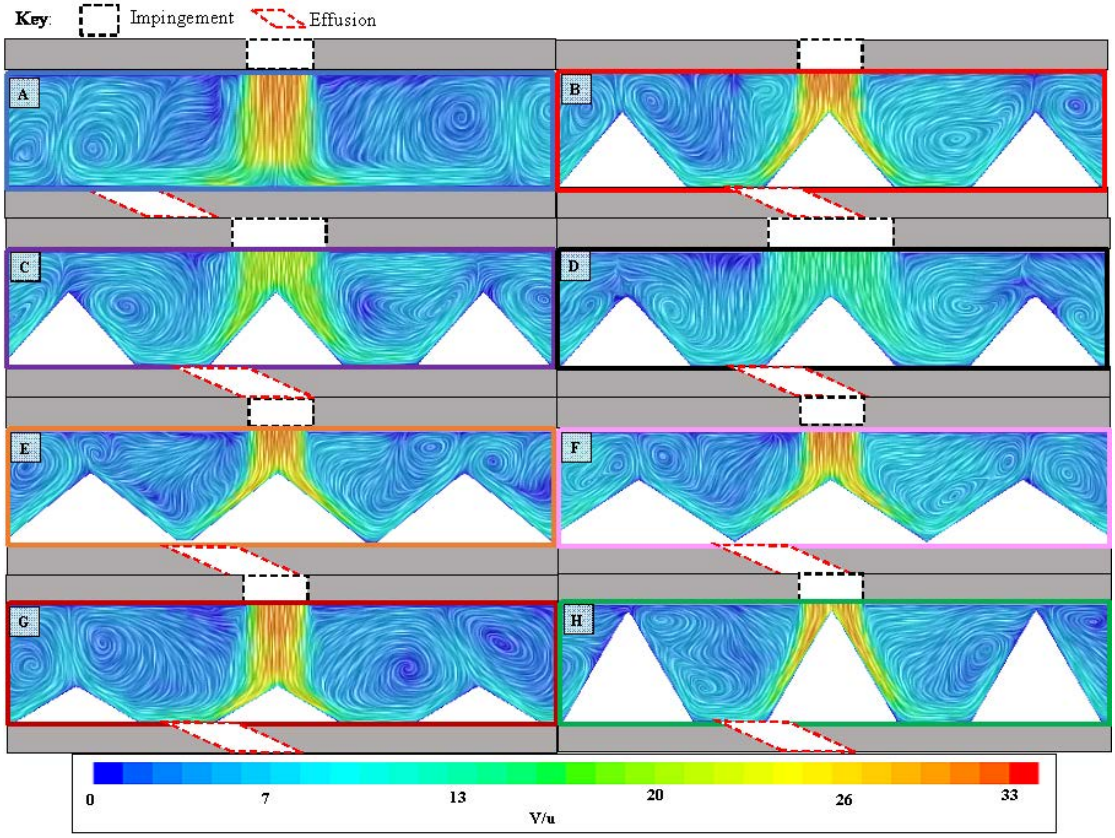

Figure 9. Computationally predicted flow field between the impingement and effusion walls. From top to bottom: (a) flat baseline, (b) pin-cone baseline, (c,d) effect of impingement, (e,f) effect of cone diameter, (g,h) effect of cone height.

Task 2 - Testing of Scaled Models of Optimal Cooling Concepts

The Pennsylvania State University

Objective

The goal of this task is to assess the impacts of dirt deposition on the heat transfer of double-wall designs, with the aim of using the designs from Task 1 to desensitize the impacts of the dirt deposition.

Research Approach

Background

To understand the durability of double-walled combustor liners with and without dirt, evaluation of the heat transfer coefficients on either side of the effusion and impingement plates is important. A new experimental method is being investigated to determine heat transfer coefficients on all walls of the double-wall design. The proposed method consists of three cases that will be used to determine h_∞, h_1, and h_2.

Figures 10–12 show the different test cases that will be simulated to determine how the convective heat transfer coefficients on each surface will be measured. Case 1 (Figure 9) will be used to calculate h_∞, the heat transfer coefficient on the hot side of the effusion plate. Similarly, Case 2 (Figure 10) shows how h_1, the heat transfer coefficient on the cold side of the effusion plate, will be deduced. Case 3 (Figure 11) shows how h_2, the heat transfer coefficient on the hot side of the impingement plate, will be evaluated. In each of these cases, differing wall boundary conditions are used.

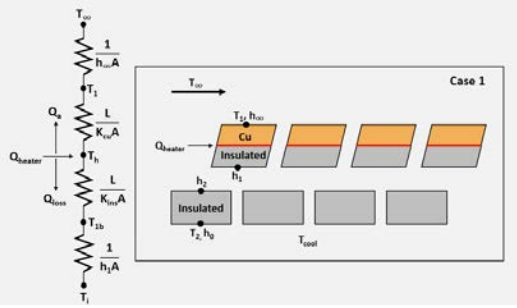

Figure 10. Case 1 illustrating the method to determine h_∞.

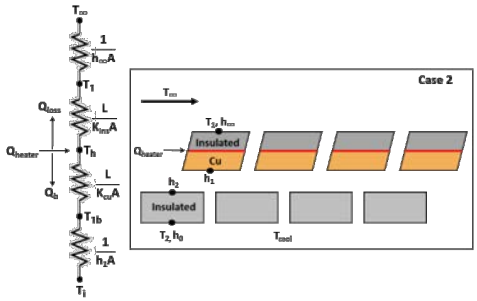

Figure 11. Case 2 illustrating the method to determine h_1.

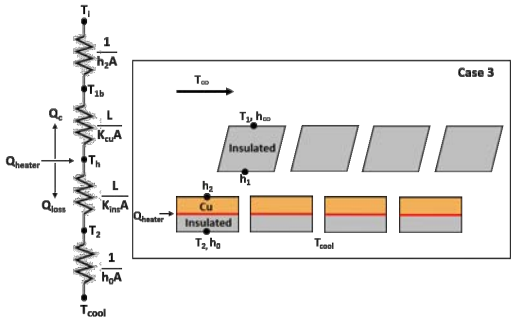

Figure 12. Case 3 illustrating the method to determine h_2.

Results

In this past year, case 1 was the focus for developing and benchmarking the testing facilities. The basis for comparison was an impingement jet study with an array of jets, similar to the double-wall design pursued by Hollworth and Berry (1978), who used arrays of impingement jets to cool a flat copper plate situated on top of an electric heater and insulation, a setup similar to our proposed heater composite. Using the results of Hollworth and Berry as an appropriate baseline for the case of no dirt, we validated the results from our testing methods.

Figure 13a,b shows the heater design as well as the results. The comparisons showed differences with respect to the literature; however, the slopes from the baseline study agreed favorably. One primary concern identified in these initial tests is that the heater power was too low, thereby causing large uncertainties in the data. Since these results were achieved, a new heater was ordered and is currently being used, with favorable results. In addition, Figure 13b shows preliminary data indicating the impact of the dirt accumulation. Lower Nusselt (Nu) numbers indicate decreased liner cooling, which in turn negatively affects the cooling and leads to higher wall temperatures.

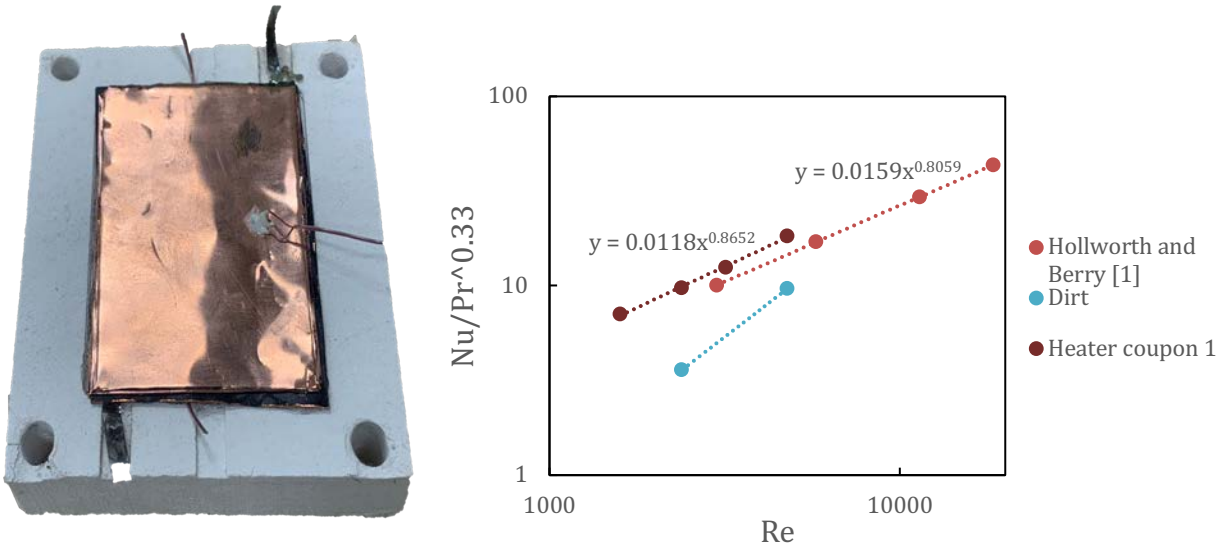

Figure 13. (a) Heater coupon 1 used for testing, and (b) nondimensionalized plot of heat transfer from heater coupon 1 compared with the literature.

Task 3 - Facility Planning for 1×-scale combustor

The Pennsylvania State University

Objective

Although this particular task is for Year 3, initial work has begun through discussions on the design requirements for the simulator. These discussions have taken place with Dr. Steve Kramer at Pratt & Whitney. The START team has identified a potential area for the simulator design. In addition, cost matching has already been provided by Pratt & Whitney to accomplish this task, should the FAA fund the third year of this project.

Background

Figure 14 illustrates the need for placing a combustor simulator upstream of the START test turbine. The data in Figure 14 show the range of nonuniformities of non-dimensional pressures (C_p) and temperatures (θ) that occur at the exit of the combustor, both of which affect turbine performance. Because various fuels will be used for combustion in the future, simulating these profiles become even more critical.

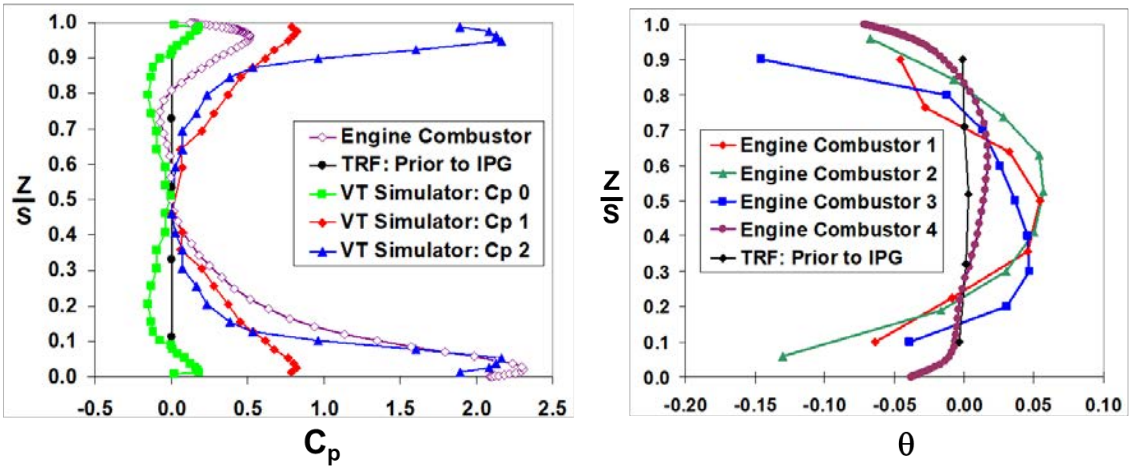

Figure 14. Combustor exit profiles from the literature indicating non-uniform pressures and temperatures (θ) (Barringer et al., 2009).

Results

A combustor simulator is to be designed and implemented in the START turbine rig, upstream of the turbine test section. The design space for the profile simulator is shown in Figure 15. The purpose of the simulator is to replicate the pressure, temperature, and elevated turbulence profiles characteristic of a modern gas turbine combustor. The simulator is a device consisting of a series of solid and perforated walls that form a central chamber, similarly to the concept of a gas turbine engine combustion chamber.

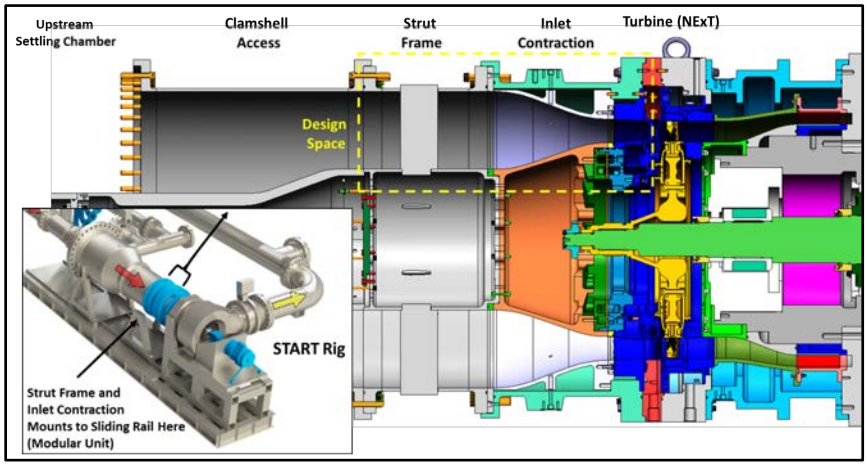

Figure 15. Design space of the combustor simulator upstream of the START test turbine inlet.

During this period, a new CAD rendering was made on the basis of an initial design concept, as well as numerous CFD simulations. A design firm (Agilis) has been working with The Pennsylvania State University to exchange feedback on design requirements to develop a preliminary design. The simulator design includes three rows of dilution holes and an effusion slot. The first row is used for turbulence generation within the flow. The second and third rows are used as profile generators. The second and third rows are used to help achieve the pressure and temperature profiles generated by modern combustors. The dilution row not in use will be plugged to prevent flow from entering or exiting through the dilution hole. All dilution holes will be fitted with removable grommets, thus allowing for quick changes in dilution hole diameters in studies on changes in momentum flux ratios within a combustor. The momentum flux ratio is a non-dimensional number describing how far a jet can penetrate into the main flow. The momentum flux ratio can be calculated with Equation 4.

$$I = \frac{\rho_{jet} V_{jet}^2}{\rho_\infty V_\infty^2} \quad (4)$$

The effusion slot will be used to further tailor the profiles desired. At this time, the effusion slot was not modeled or used in any of the preliminary CFD simulations.

The dilution hole configuration was designed to keep the dilution holes offset from each other within the same row and to keep each row staggered from the row preceding it. The first-row dilution holes have a range of 0.5–0.7 inches. The corresponding momentum flux ratio over this range of diameters is approximately $50 < I < 275$. The momentum flux ratio range is created by varying the mass flow through the first row and/or by installing differently sized grommets into the first-row dilution holes. The dilution hole pattern is shown in Figure 16.

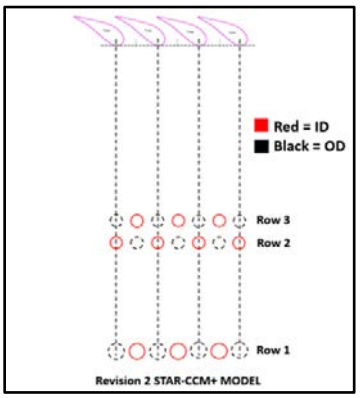

Figure 16. Revisions in dilution hole design with revision 1 (left) and revision 2 (right).

An initial design concept for the profile simulator is shown in Figure 17a. Within the model, the dilution hole pattern was designed to be integrated in the START facility. The dilution holes were modeled with the exit normal to the wall, with the 3D model shown in Figure 17b.

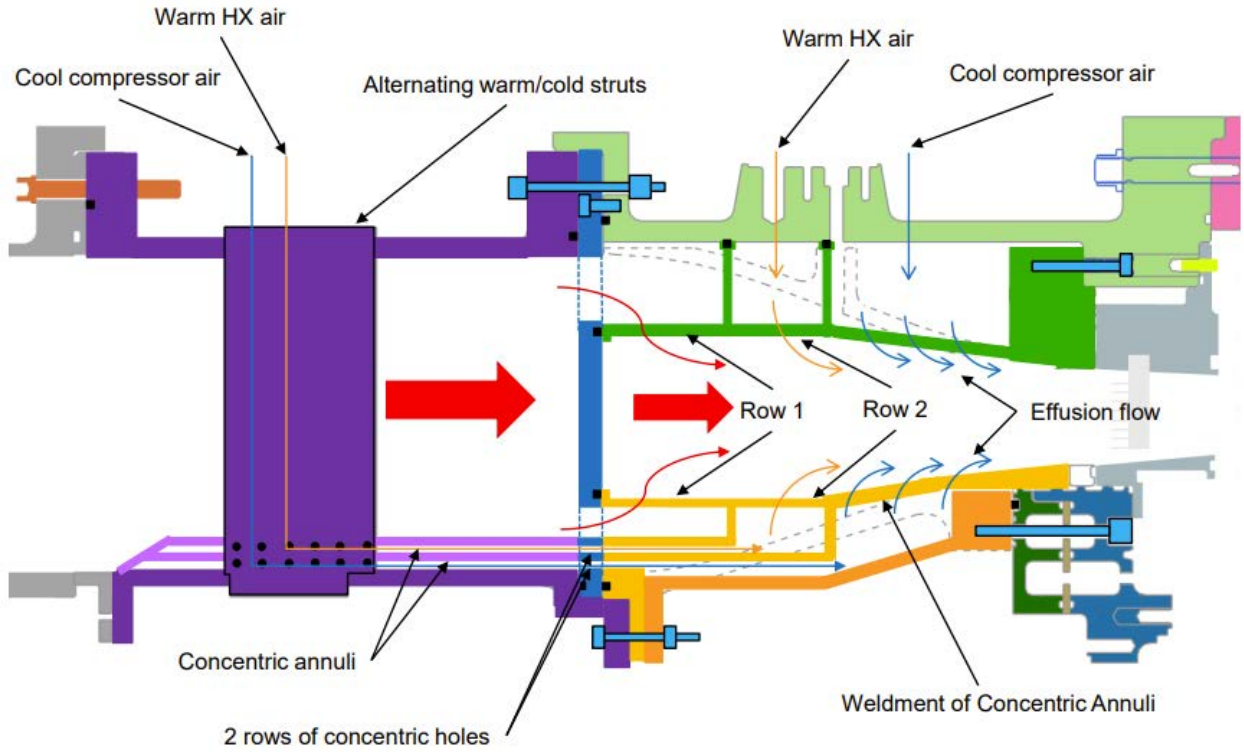

Figure 17a. Initial design concept for the combustor profile simulator.

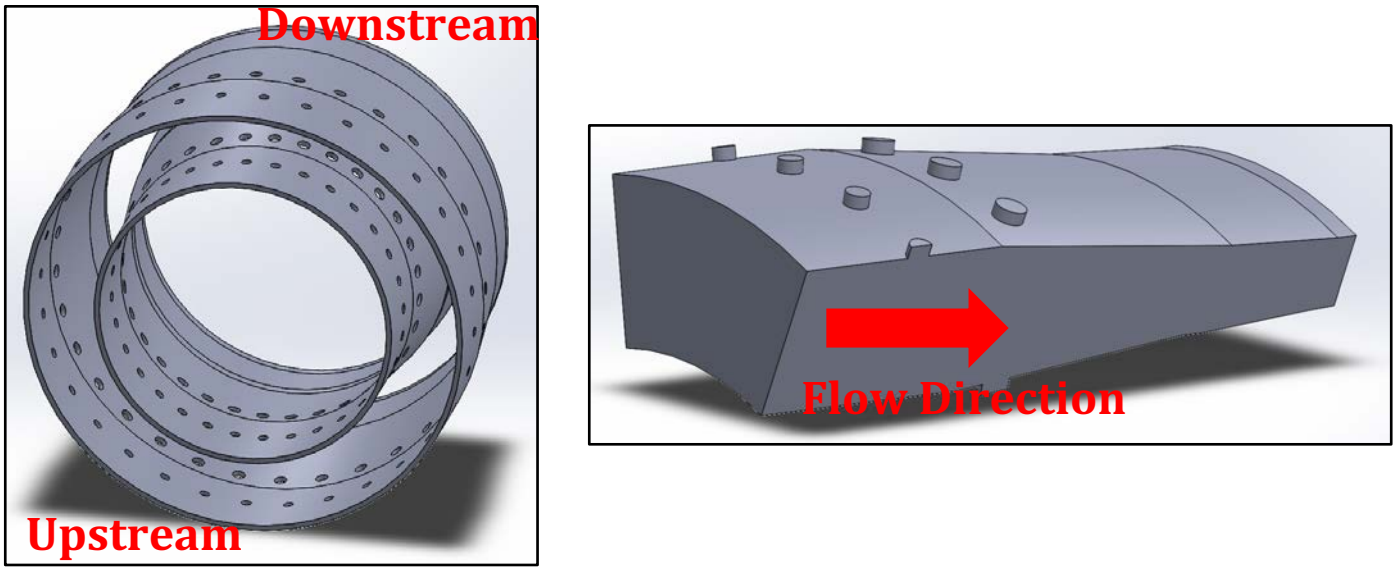

Figure 17b. Revision 3 Solidworks 3D model of real rig hardware with dilution holes.

Multiple CFD simulations were completed to determine the effects of mass flow distribution through the dilution holes, the dilution hole diameters, and other important parameters relating to combustor characteristics. The domain of the simulation began at the start of the inlet contraction section and stopped at the vane leading edge. The simulation inlets included the

main gas path inlet and the dilution holes. All inlets were mass flow inlets, and the temperature at the inlet of the main gas path matched the temperature of the first-row dilution jets. The reason for keeping the main gas path and first row dilution flow at the same temperature is to maintain the temperature required at the vane leading edge. If all dilution jet flow were kept at the compressor exit temperature of 220 ˚F, then the temperature needed at the main gas path inlet would exceed the safety temperature of the rig hardware. The outlet boundary condition was a pressure outlet, defined with the static pressure at the vane leading edge.

A variety of steady RANS simulations were completed to decrease computational time and yield initial results. On the basis of the initial RANS results, course changes can be made to achieve profiles that are close to those desired. After a desired result from a RANS simulation was achieved, a shift to multiple large eddy simulations (LES) was made. LES captures the intense mixing occurring with a jet in cross flow. According to the data collected from the LES simulations, a CFD test matrix is being created to determine the optimal simulations to run. LES has dramatically increased the computational time required; therefore, running simulations with meaningful results is very important. We have been comparing our LES simulations to our RANS results to determine how accurately the RANS is predicting our solutions. A comparison between an LES case and RANS case for a velocity contour at the mid-passage is shown in Figure 18a. The increase in resolution of the large eddies within the flow is characteristic of a LES simulation. Understanding how the model used affects the non-dimensional temperature profile is also important. A comparison between the LES- and RANS-generated non-dimensional temperature profile is shown in Figure 18b. These profiles show overall good agreement, and excellent agreement in the midspan region. The profiles begin to differ in the hub and tip regions, but do not differ by a concerning amount. Work is continuing on the overall design based on various structural and CFD simulations.

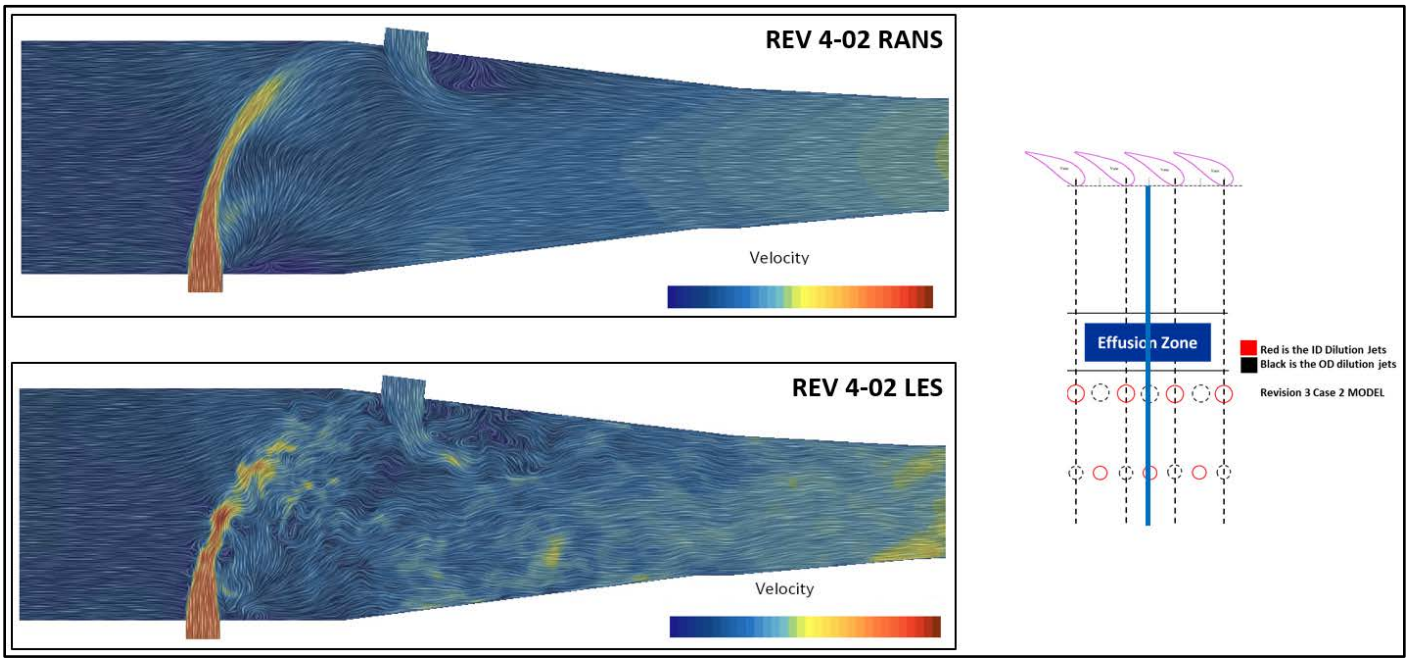

Figure 18a. REV 4-02 LES CFD simulation velocity contour compared with RANS velocity contour.

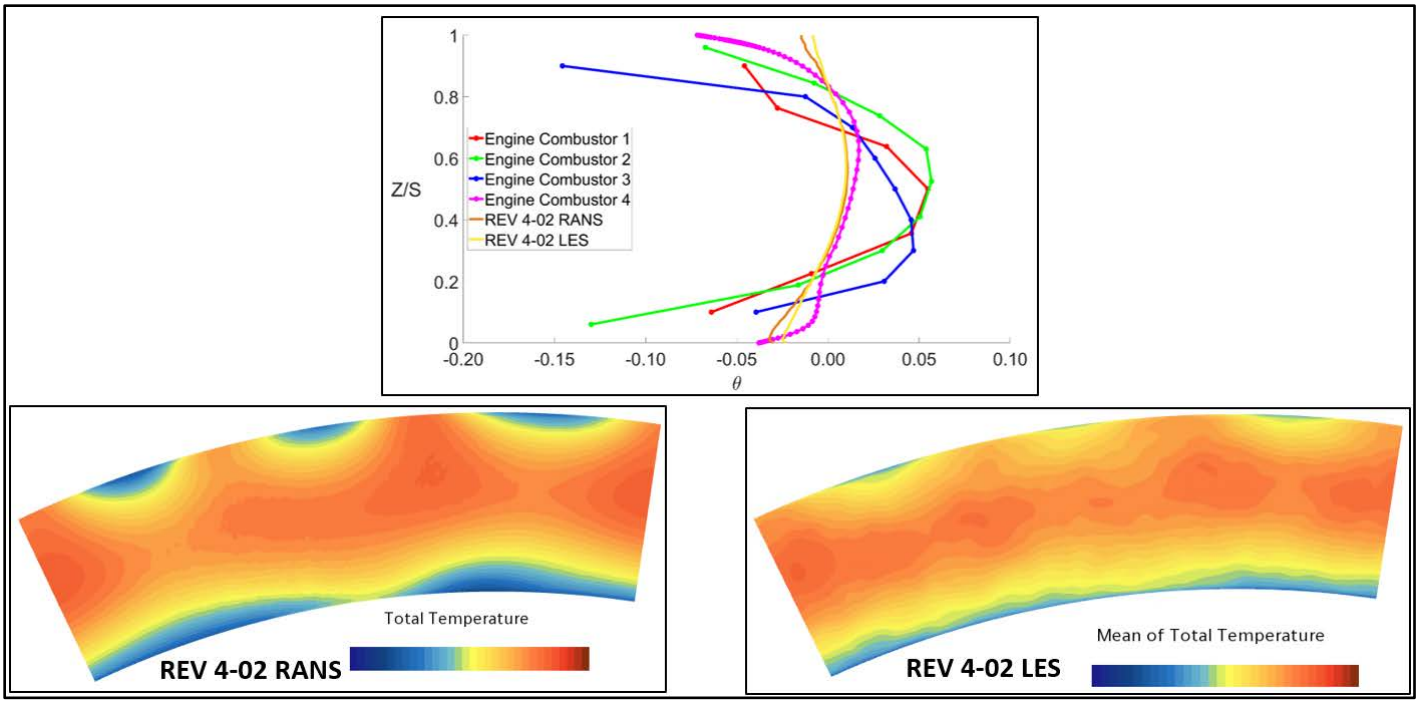

Figure 18b. REV 4-02 LES CFD simulation non-dimensional temperature profile compared with RANS.

Milestones

Milestone	Status
Workplan	Completed
COE Meeting 1	Completed
COE Meeting 2	Completed
Annual Report	Completed

Major Accomplishments

The major accomplishments for this past year include:

- Task 1- The manufacturing and testing of new combustor liner cooling concepts that capture less dirt than the traditional design.
- Task 2- The development of a method for evaluating heat transfer on combustor liners with and without dirt.
- Task 3- The design of a combustor profile simulator with accompanying computational predictions of the flowfield to meet the needs for the START facility.

Publications

McFerran, K., Fallon, B., Fox, S., Thole, K., Lynch, S., Lundgren, R., Kramer, S. *Comparison of Dirt Deposition on Double-Walled Combustor Liner Geometries.* Abstract under review for TurboExpo 2023.

Outreach Efforts

Bi-weekly presentations are given to Pratt & Whitney through this joint collaboration. Additional presentations of this combustor simulator concept have been provided to the Department of Energy, Siemens Energy, Honeywell, and Pratt & Whitney. Industry partners are very supportive of this direction and are providing guidance.

Awards
None.

Student Involvement
Brandon Fallon completed his MSME degree and is now employed by Blue Origin. Kyle McFerran has taken over the studies on liners and is focusing on the heat transfer measurements for Task 2. Sarah Fox, an undergraduate Schreyer Honors student, also successfully graduated and is now fully employed by Lockheed-Martin. Chad Schaeffer is performing the CFD simulations and assisting in the design of the combustor profile simulator. Chad also successfully passed the PhD qualifying exam in January 2022. All students are involved in weekly meetings with their advisors (Thole/Lynch) and in regular meetings with Pratt & Whitney. They regularly present their findings to Pratt & Whitney, including to a larger Pratt & Whitney audience in the biannual Center of Excellence meetings (June and November).

Plans for Next Period
During this next year, we will complete the heat transfer benchmarking and compare the various designs with and without dirt, in terms of the convective cooling (Task 2). For the profile simulator, we will complete the computational predictions as well as the design and begin the manufacturing (Task 3).

References
Hollworth, B. R., & Berry, R. D. (1978). Heat transfer from arrays of impinging jets with large jet-to-jet spacing. *Journal of Heat Transfer*, *100*(2), 352–357. https://doi.org/10.1115/1.3450808

Barringer, M. D., Thole, K. A., & Polanka, M. D. (2009). Effects of combustor exit profiles on vane aerodynamic loading and heat transfer in a high pressure turbine. *Journal of Turbomachinery*, *131*(2), 021008. https://doi.org/10.1115/1.2950051

Nomenclature
$\dot{m}$	mass flow rate through test facility
Nu	Nusselt number
P_{up}	upstream test facility pressure
P_{down}	downstream test facility pressure
Re	Reynolds number
T_{oc}	supply coolant temperature
N	number of impingement holes
D	cooling hole diameter
η_c	capture efficiency

Project 069 Transitioning a Research nvPM Mass Calibration Procedure to Operations

Missouri University of Science and Technology, Aerodyne Research Inc. and The U.S. Air Force Arnold Engineering Development Center

Project Lead Investigator

Philip D. Whitefield
Professor Emeritus of Chemistry
Department of Chemistry
Missouri University of Science and Technology
400 W 11th Street, Rolla, MO 65409
573-465-7876
pwhite@mst.edu

University Participants

Missouri University of Science and Technology (MS&T)

- P.I.: Philip D. Whitefield, Professor Emeritus of Chemistry
- FAA Award Number: 13-C-AJFE-MST, Amendments 014, 020, and 023
- Period of Performance: June 5, 2020 to January 31, 2024
- Task:
  1. Investigate the validity of the centrifugal particle mass analyzer (CPMA) mass calibration research approach for non-volatile particulate patter (nvPM) certification measurement systems

Project Funding Level

Project	Funding	Matching	Source
13-C-AJFE-MST; Amendment 014	$846,707.00	$846,707.00	EMPA letter
13-C-AJFE-MST; Amendment 020	$100,853.00	$100,853.00	FOCA letter
13-C-AJFE-MST; Amendment 023	$99,999.00	$99,999.00	GE letter

Investigation Team

- Professor Philip Whitefield, P.I., MS&T (Task 1)
- Steven Achterberg, research technician, MS&T (Task 1)
- Max Trueblood, research technician, MS&T (Task 1)
- Dr. Richard Miake-Lye, subcontractor, Aerodyne Research, Inc. (Task 1)
- Dr. Robert Howard, subcontractor, Arnold Engineering Development Center (AEDC), U.S. Air Force (Task 1)

Project Overview

This project is designed to investigate the validity of the CPMA mass calibration research approach. The assessment will extend across all nvPM mass ranges encountered during certification tests. The primary goal will be the successful transitioning of the research methods to operations. The project will begin with a laboratory assessment leading to dedicated turbine engines as the test sources at the U.S. Air Force AEDC. The challenge mass devices for calibration (micro-soot sensor [MSS], laser-induced incandescence monitor, and cavity attenuated phase shift monitor) will be provided by the North

American Reference nvPM Measurement System, together with the CPMA and other necessary instruments, such as a DMS500 particulate analyzer, and aerosol mass spectrometer.

Task 1 - Investigate the Validity of the Centrifugal Particle Mass Analyzer (CPMA) Mass Calibration Research Approach for nvPM Certification Measurement Systems

Missouri University of Science and Technology

Objectives

The objectives of this task are to acquire the components of a CPMA-based mass calibration system similar to that described in SAE E31 discussion paper DP-32 (presented by Dr. G. Smallwood) from the annual SAE E31 committee meeting on June 17–21, 2019, in Saclay, France, assemble the system, and evaluate its performance.

Research Approach

Subtask 1.1

Acquire the components of a CPMA-based mass calibration system similar to that described in SAE E31 discussion paper DP-32 (presented by Dr. G. Smallwood) from the annual committee meeting on June 17–21, 2019, in Saclay, France.

Subtask 1.2

Assemble and test the CPMA-based mass calibration system's performance at MS&T's laboratories, by using a miniature combustion aerosol standard (Minicast) as the nvPM generation source (Figure 1). Compare the laboratory performance of the MS&T CPMA-based mass calibration system with the performance of two very similar systems owned and operated by University of Alberta and the Canadian National Research Council.

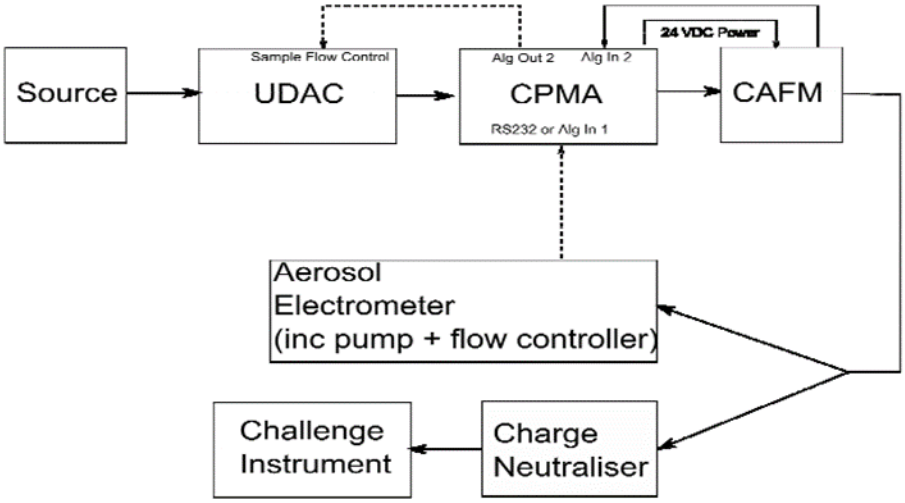

Figure 1. Schematic diagram of the CPMA-based mass calibration system.

Subtask 1.3

Investigate the validity of the CPMA mass calibration research approach across all nvPM mass ranges encountered during certification tests, to successfully transition the methods to operations

Subtask 1.3a

Deploy (transport and install) the North American Reference System, including the CPMA-based mass calibration system and ancillary diagnostic suite, with the Air Force AVL nvPM measurement system and the two Canadian CPMA systems, at engine

testing facilities at Arnold Air Force Base, Tennessee, which will include the J85 turbojet and a gas-turbine-based "start cart" as nvPM sources.

Subtask 1.3b
Evaluate the performance of the three CPMA-based mass calibration systems, surveying across all mass ranges by using the start cart as the nvPM source; compare these results with concomitant mass calibration data acquired with SAE E-31 OCEC-based mass calibration methods.

Subtask 1.3c
Demonstrate the performance with an nvPM emissions test on the J85 engine, with calibration including standard elemental carbon/organic carbon (EC/OC) analysis, as well as the CPMA-based calibration system described in document DP-32.

Subtask 1.3d
Decouple the diagnostic suites from the Arnold Air Force Base engine facilities, and transport them back to Missouri and Massachusetts.

Subtask 1.4
Analyze and interpret the data gathered in Tasks 2 and 3.

Subtask 1.5
Prepare and deliver a final report.

Milestones

- A laboratory-based assessment strategy has been developed and reviewed by the advisory team.
- Essential components for the assessment study, including a Minicast nvPM source, a sample mixing and distribution plenum, and a semi-continuous EC/OC analyzer (Sunset), have been acquired and tested. Substantial effort has been invested in assuring the performance of the analyzer, with modest success. The MS&T team has worked closely with Sunset and will send a representative to the forthcoming engine demonstration. Backup manual EC/OC sampling will be performed at the engine demonstration.
- The CPMA mass standard source has been operated in conjunction with the and MSS mass monitors.
- The MS&T CPMA-based calibration system has undergone a laboratory-based performance comparison with two Canadian CPMA-based calibration systems.
- Engine emissions testing performance has been conducted at AEDC.
- A final assessment report has been delivered.

Major Accomplishments

Essential diagnostic equipment has been acquired, and work on subtasks 2 and 3 is being pursued. Figure 2 shows a schematic diagram of the mass standard evaluation system, exploring the dynamic nvPM mass concentration range that can be used. The CPMA mass standard system has been operated in conjunction with the laser-induced incandescence monitor and MSS mass monitors. Good agreement was achieved between the standard and monitors. The relationship was found to be linear over a broad range of mass. An example calibration for the MSS+ is presented in Figure 3. The MS&T CPMA-based calibration system has undergone a laboratory-based performance comparison with two Canadian CPMA-based calibration systems, and all three systems have been found to be in excellent agreement, with <5% variation among systems.

Publications

Published conference proceedings

Whitefield, P (2022). *Transitioning a Research nvPM Mass Calibration Procedure to Operations* [Oral presentation]. ASCENT Advisory Board Meeting, Alexandria, VA.

Outreach Efforts

The CPMA-based mass calibration system has been transported to Canada for a laboratory-based intercomparison study.

Awards

None.

Student Involvement

One graduate student, Godwin Ogbuehi, and two undergraduate students have been assigned to this project.

Plans for Next Period

We plan to continue to pursue the statement of work from subtasks 2–5 as described above with a test campaign scheduled for April/May 2023. Deployment of the CPMA enhanced North American Reference System for nvPM to AEDC was scheduled for March 2022, but this activity has been delayed twice, once until October 2022 because of unforeseen contractual issues that have since been resolved, and once until April/May 2023 because of issues related to funding and AEDC facility scheduling.

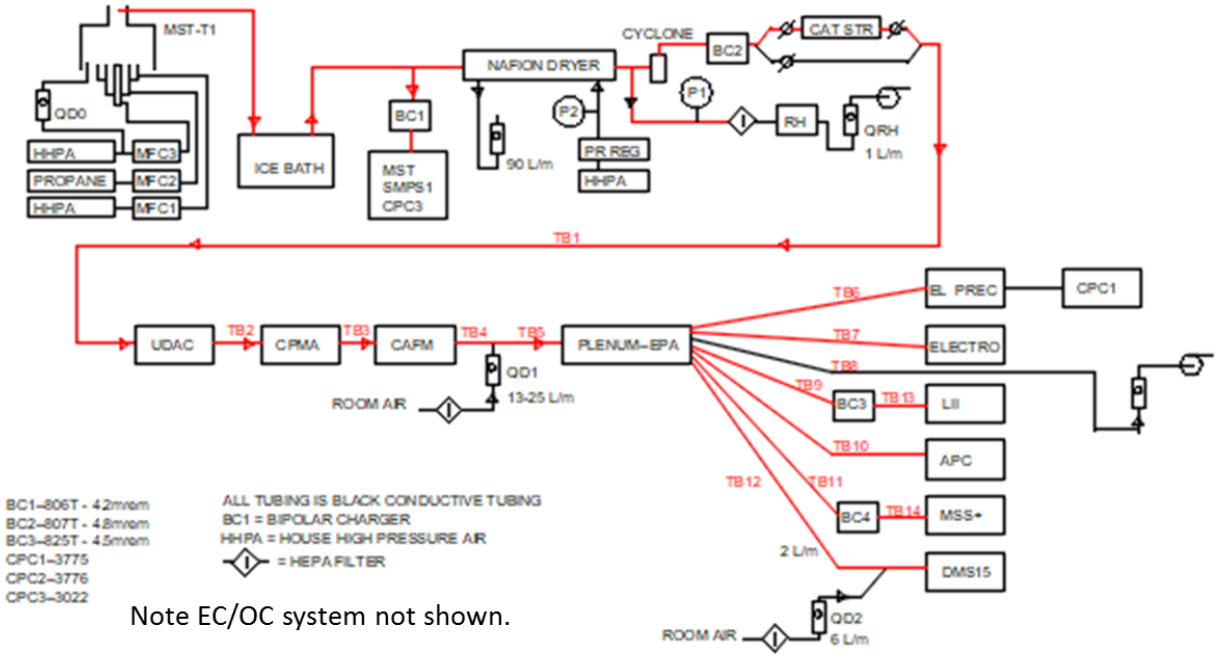

Figure 2. Schematic for mass standard assessment studies in Tasks 2 and 3.

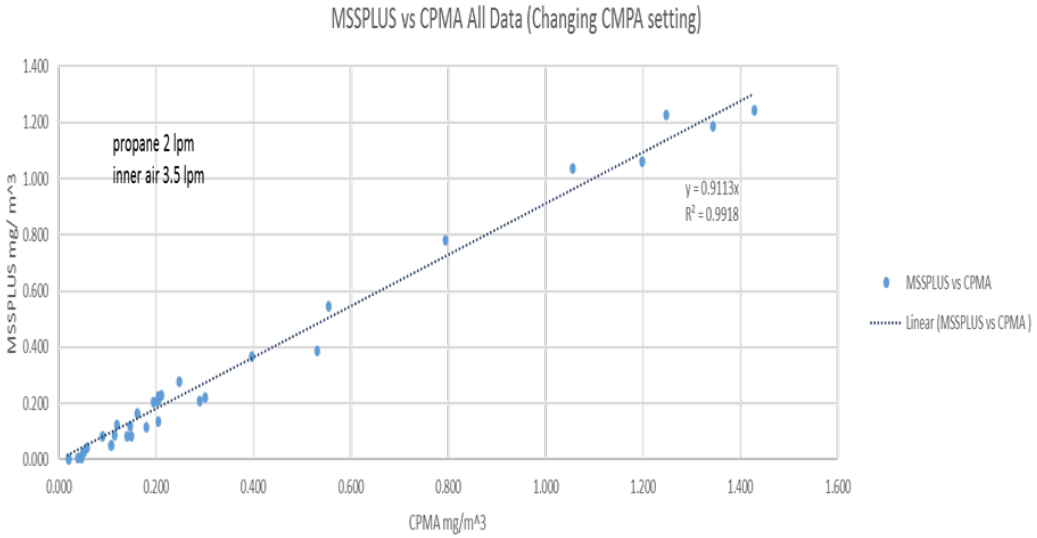

Figure 3. MSS calibration using the CPMA system.

Project 070 Reduction of nvPM Emissions from Aero-Engine Fuel Injectors

Georgia Institute of Technology

Project Lead Investigator

Wenting Sun
Associate Professor
School of Aerospace Engineering
Georgia Institute of Technology
270 Ferst Drive, Atlanta, GA 30332
404-894-0524
wenting.sun@aerospace.gatech.edu

University Participants

Georgia Institute of Technology

- P.I.: Dr. Wenting Sun
- FAA Award Number: 13-C-AJFE-GIT-080
- Period of Performance: August 11, 2021 to August 10, 2022
- Tasks:
    1. Measurement of non-volatile particulate matter (nvPM) formation and oxidation processes
    2. nvPM model development and validation
    3. Experimental facility development and operation

Project Funding Level

The total amount of funding from the FAA is $1,500,000. The funding match includes $1,350,000 from Georgia Institute of Technology and $150,000 from Honeywell.

Investigation Team

- Lead P.I. Wenting Sun, from the Georgia Institute of Technology, will oversee the entire project and coordinate among co-P.I.s. He will work with one graduate student and one research engineer in leading Task 3.
- Co-P.I.s Adam Steinberg, Ellen Yi Chen, Timothy Lieuwen, and Jechiel Jagoda, from the Georgia Institute of Technology, will work with two graduate students in leading Task 1.
- Co-P.I.s Rudy Dudebout and Fang Xu, from Honeywell, will lead Task 2.

Project Overview

Reducing nvPM from gas turbine engines is essential for improving air quality and decreasing the environmental impact of aviation. However, predicting and controlling nvPM remains a challenge because of the complicated physical and chemical processes at play. The proposed research will characterize the formation/oxidation of nvPM and optimize the design of an aeronautical gas turbine fuel injector to reduce nvPM at flight-relevant conditions. In this project, we developed a sector combustor containing three fuel injectors. The sector combustor simulates a section of the Honeywell auxiliary power unit combustor and injectors. The combustor is fabricated through 3D printing, and the fuel injectors are directly provided by Honeywell. Details of the combustor are presented in the next section. The goals of this project include the following:

1. Developing a high-pressure experimental platform suitable for combustor testing at practical conditions and allowing for academic advanced diagnostics
2. Conducting optical diagnostics to measure the nvPM volume fraction and primary particle size; hydroxyl (OH) radical distribution; and the drop features of fuel injectors
3. Developing empirical correlations describing nvPM formation/oxidation by using experimental data

4. Validating computational fluid dynamics (CFD) simulations to facilitate fuel injector design optimization

Task 1 - Measurement of nvPM Formation and Oxidation Processes

Georgia Institute of Technology

Objectives

In this task, laser-induced incandescence (LII) measurements will be performed to quantify the soot volume fraction and primary particle size; OH planar laser-induced fluorescence (PLIF) will be conducted to understand the soot oxidation process; and Mie scattering measurement will be conducted to understand the characteristics of liquid fuel sprays.

Research Approach

In the first year, the high-pressure combustor was successfully commissioned, and LII was conducted to quantify the soot volume fraction. We will conduct simultaneous OH PLIF measurements to understand the interaction between nvPM formation and oxidation. We will then conduct droplet Mie scattering analysis to characterize the fuel spray. We will also conduct sampling measurements in the combustor exhaust to analyze the exhaust composition (via gas chromatography) and nvPM composition/morphology (via X-ray photoelectron spectroscopy [XPS] and scanning electron microscopy [SEM]), thus advancing understanding of nvPM kinetics. All measurements will be performed in a model aeronautical gas turbine combustor operated with a liquid jet fuel at engine-relevant operating conditions. All subtasks under Task 1 will proceed in parallel, because the ultimate aim is to measure multiple parameters simultaneously.

In Year 2 of this project, the focus is the commissioning of a new high-pressure combustor rig and conducting preliminary optical measurements. The following sections detail the mechanism of the proposed optical diagnostics and preliminary LII results to measure the nvPM volume fraction.

Subtask 1.1 - LII Measurement

LII uses short laser pulses to heat small particles to vaporization temperatures. The light emission, or incandescence, of the nvPM is then measured to deduce the relative volume fraction and primary particle size. Two-dimensional implementations of LII are performed by shaping the laser beam into a uniform sheet and capturing the incandescence at various wavelengths on sensitive time-gated cameras. The prompt emission immediately after the arrival of the laser pulse describes the volume fraction or spatial concentration of nvPM particles. By applying sufficient laser intensity to uniformly sublimate the nvPM and calibrating these measurements against emissions from known flames, the absolute volume fractions can be determined.

For nvPM particle sizing, time-resolved LII techniques can be used to obtain the incandescence decay over time. This approach is based on small particles showing faster cooling than large particles after laser heating, owing to their larger surface-to-volume ratio. The primary particle size can be evaluated through solving energy and mass balances. For measuring the decays, which are on the order of several hundred nanoseconds in atmospheric-pressure flames, ultra-high-speed cameras are necessary.

Recently, we have successfully demonstrated a single-camera, single-laser-shot technique for collecting these measurements by capturing the decay time constants at 10 million frames per second with a 50-ns gate. At these imaging rates, the flame motion appears stationary, thereby enabling accurate pixel-by-pixel measurements of the decay time. The data from each pixel are then fitted to a model to determine the primary nvPM particle sizes for the entire scene at the moment of the measurement. The statistics for these images can then be compared with show regions of the flame where nvPM growth and nvPM oxidation typically occur.

The LII measurements described in this subtask were conducted by using the fundamental 1,064-nm output of a solid-state neodymium-doped yttrium aluminum garnet (Nd:YAG) laser operating at 5–10 kHz, to avoid exciting the OH and polycyclic aromatic hydrocarbon fluorescence. The laser beam is formed into a sheet that is then passed through the combustor. The incandescence is subsequently measured with time-gated cameras by using the appropriate filters (near 640 nm) to avoid C_2 Swan band emissions. The experimental setup for LII is presented in Figure 1. The fundamental 1,064-nm output of an Nd:YAG laser was expanded into a laser sheet by using a combination of lenses. The laser sheet passed the flames inside the combustor to excite nvPM particles, and the LII signal was then collected by a high-speed camera.

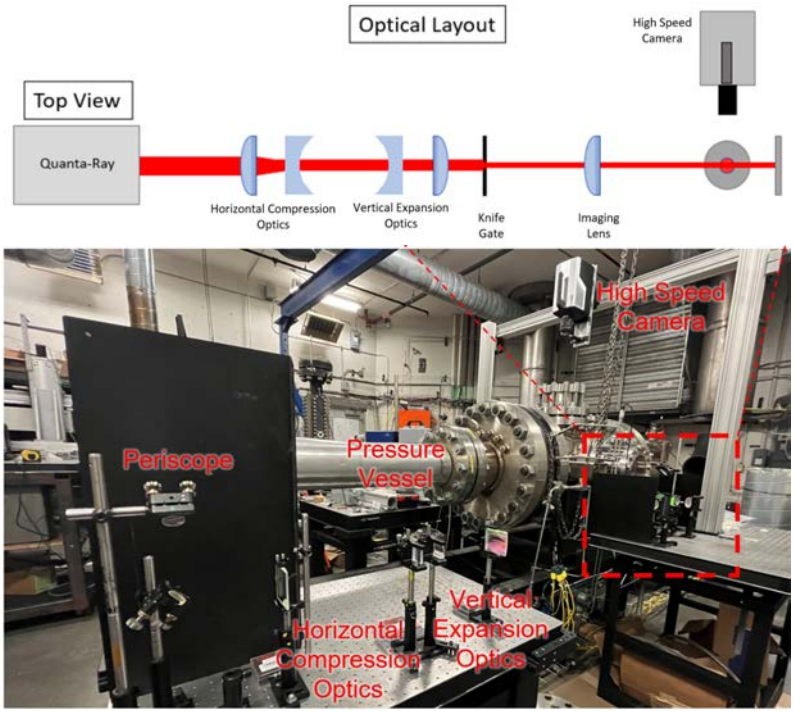

Figure 1. Experimental schematic of LII. Top: schematic. Bottom: photograph.

Figure 2 shows a photograph of the laser sheet passing the three fuel injectors inside the combustor. The laser used to excite the nvPM has 106 mJ of laser power (1,064-nm laser, 5-ns pulse length, 10-Hz repetition rate), for a fluence of 0.14 J/cm^2. An ultra-high-speed camera (Shimadzu HPV-X2) was used to capture the incandescence from above, at a capture rate of 10 MHz with an exposure of 50 ns. Figures 3–5 show the LII data indicating soot incandescence across the midline of the combustor at 100 ns, 200 ns, and 300 ns after laser excitation, respectively. Incandescence decay can be seen for this condition. The center of the middle injector is clearly seen, as well as some of the turbulent flame features. Of note, the time scale of incandescence is much shorter (ns) than that of the flow field (ms). Therefore, the measurement was taken with the flow field frozen.

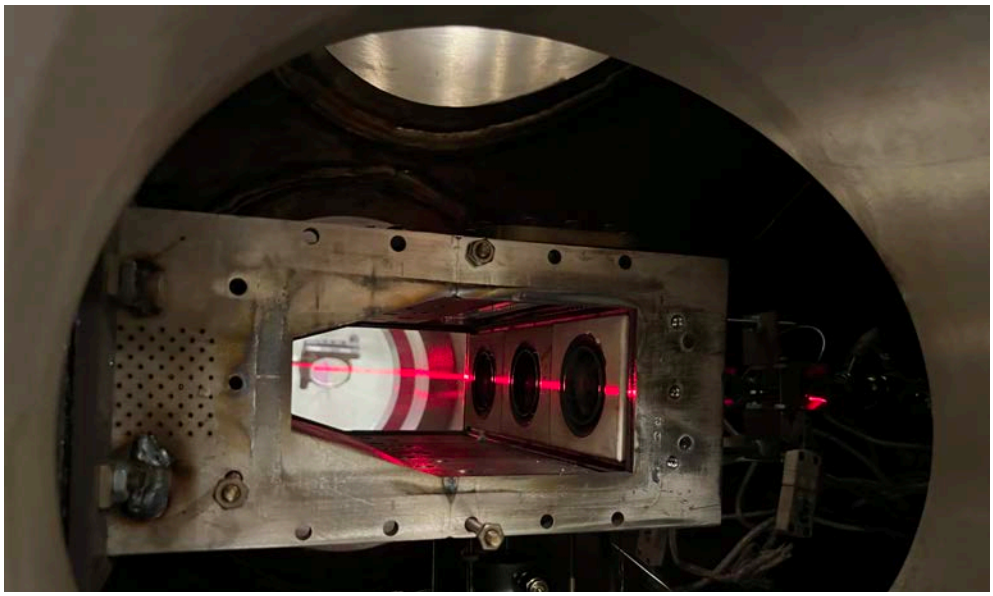

Figure 2. Direct photograph of a laser sheet passing the combustor.

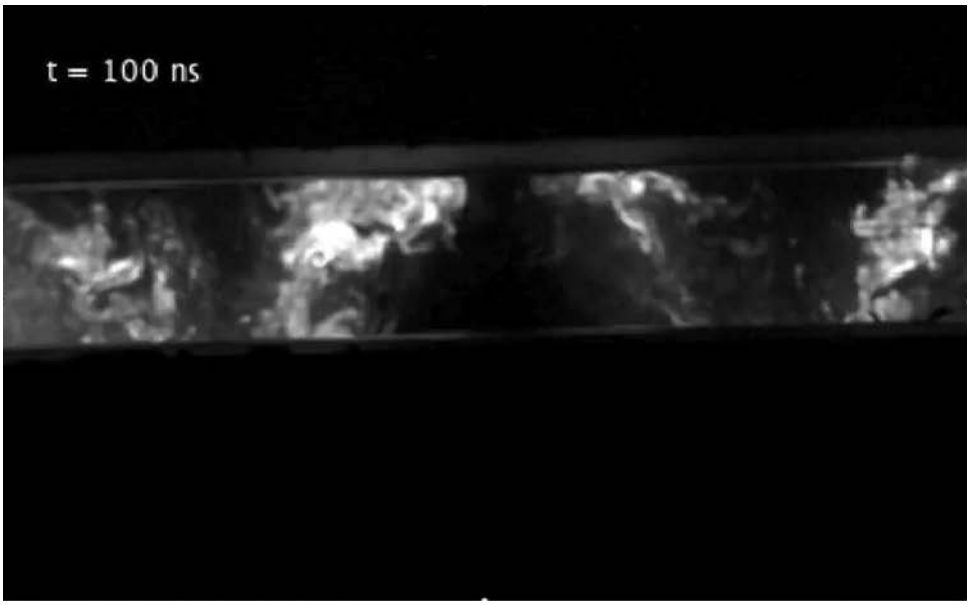

Figure 3. Time-resolved LII data showing soot incandescence across the midline of the combustor 100 ns after laser excitation.

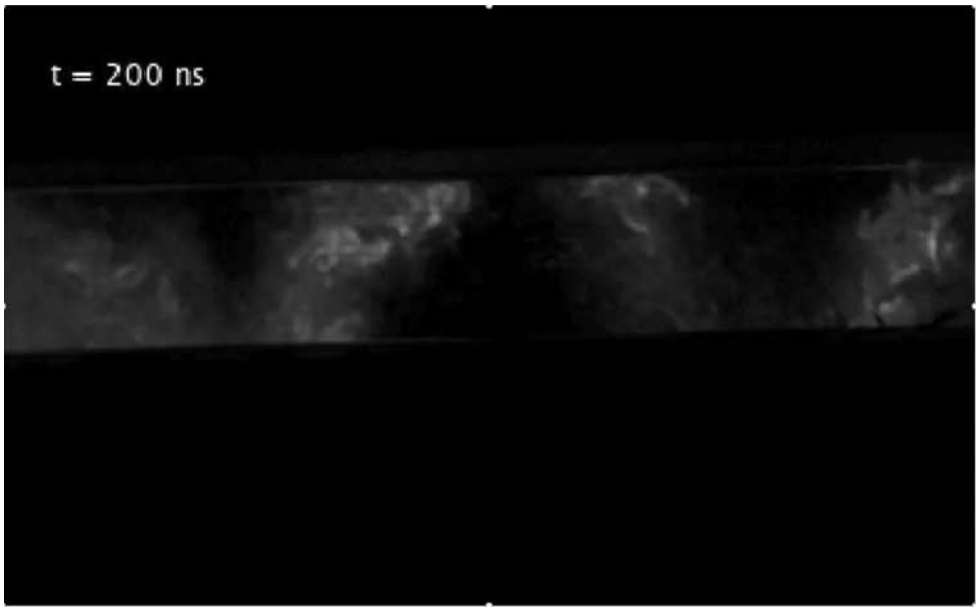

Figure 4. Time-resolved LII data showing soot incandescence across the midline of the combustor 200 ns after laser excitation.

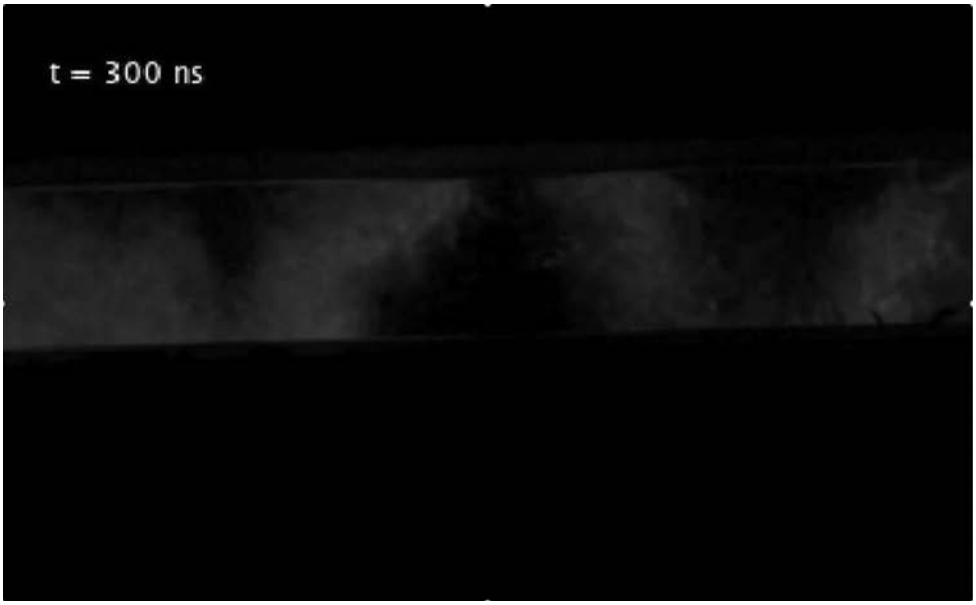

Figure 5. Time-resolved LII data showing soot incandescence across the midline of the combustor 300 ns after laser excitation.

Subtask 1.2 - OH PLIF Measurement

Oxidation through reaction with OH is expected to be a critical pathway through which nvPM is destroyed in the flame. Understanding the relative trajectories of nvPM and OH through the combustor is therefore essential to predicting the final nvPM output.

Hydroxyl radicals form during high-temperature hydrocarbon oxidation, reaching super-equilibrium concentrations near the location of maximum heat release rate, then decreasing to equilibrium concentrations in post flame region. Substantial concentrations of OH are observed in hot product gases at temperatures above ~1,500 K. Fortunately, owing to its strongly absorbing energy transitions at wavelengths that are relatively accessible to high-energy pulsed lasers, OH can be readily measured with PLIF. The main challenges in performing OH PLIF in the combustor of interest herein are laser power absorption and signal trapping through the high-density gas at 10 bar.

We will perform OH PLIF measurements simultaneously with the 2D LII measurements to understand the interaction between nvPM and OH. Measurements will be collected at a 5–10 kHz repetition rate by using the frequency-doubled output of a dye laser (rhodamine 6G), pumped by a frequency-doubled solid-state laser (Nd:YAG). More than 7 W of ultraviolet laser light can be produced by our laser system, which is sufficient to acquire signal across the combustor domain. The laser beam will be formed into a sheet, made coincident with the LII laser sheet, and transmitted through the combustor. The OH PLIF signal will be filtered through an appropriate bandpass filter (approximately 307 nm) and recorded with a high-speed intensified camera. Appropriate corrections will be made for laser power absorption, intensity variations, and detector response. The resultant data will provide time-resolved 2D images of the OH distribution, which will be correlated with the nvPM dynamics to better understand the oxidation process and how specific trajectories influence the nvPM ultimately output from the combustor.

Subtask 1.3 - Fuel Droplet Mie Scattering Measurement
An important factor controlling nvPM formation is the mixing between the fuel from the injector spray and the air in the combustor. The fuel injector spray can be characterized by measurement of the size and spatial distribution of liquid fuel droplets. Through Mie scattering imaging techniques, the spatial distribution of micro-sized fuel droplets can be determined via measurement of elastic light scattering. However, quantification of the spray properties from Mie scattering is challenging, predominantly because of multiply scattered photons, interference seed particles used for particle image velocimetry, and the relationship between scattering intensity and droplet size. Here, the objective is to obtain qualitative information on the fuel spray trajectory, including spray angle; penetration; and the relative locations of the liquid fuel, flame, and nvPM.

To study the fuel droplet distribution of different injectors at pressure in a non-reacting environment, the liquid fuel droplet distribution will be measured via Mie scattering at a 5–10 kHz repetition rate. The second harmonic of an Nd:YAG laser will be formed into a sheet and transmitted through the spray inside the experimental facility. The scattered light will be imaged at an angle perpendicular to the laser propagation by using a high-speed camera. This signal will then be separated from the particle image velocimetry seed particle scattering through adaptive threshold-based segmentation techniques.

Subtask 1.4 - Extractive Sampling Measurement
In this task, exhaust gas samples will be extracted and analyzed via gas chromatography (gas phase), XPS (solid phase), and SEM (solid phase). The gas chromatography (Inficon Fusion μGC) analysis will reveal comprehensive information on large hydrocarbons formed during the combustion of Jet A fuel, such as detailed structures of polycyclic aromatic hydrocarbons, ethylene, and other intermediate species relevant to soot formation.

The XPS and SEM analyses will provide data on nvPM composition and morphology to help understand the detailed formation mechanism of nvPM. Two possible mechanisms for nvPM formation may be detected during the combustor test. The first is due to the liquid fuel impinging on the wall, accompanied by chemical reactions at the wall. The second results from flame products such as soot or coked droplets. These two types of solid particles can be differentiated through chemical and morphology analysis. Solid particles formed due to wall wetting feature low carbon but markedly high oxygen content (e.g., 70%–80% carbon and 20% oxygen), and small amounts of hydrogen and nitrogen, because of incomplete oxidation of the fuel at low temperatures. In contrast, solid particles formed from flame products feature high carbon and low oxygen content (e.g., 98% carbon and 2% oxygen). In terms of morphology, solid particles formed due to wall wetting exhibit amorphous structures, whereas solid particles formed from flame products are spherical, with typical diameters of 4–5 micrometers. For these experiments, a water-cooled sampling probe will be used to collect samples of exhaust gas from the pressure vessel.

Milestone(s)
LII measurements of nvPM formation inside the combustor

Major Accomplishments
LII measurement demonstrating nvPM formation

Publications

R. McGrath, E. Bugay, J. Juergensmeyer, A. Zheng, D. Wu, A. Steinberg, W. Sun, E. Mazumdar, "Single-camera Time-Resolved laser-induced Incandescence Measurements in a RQL Aeroengine Combustor," the 13th U.S. National Combustion Meeting College Station, TX, 77844, March 19–22, 2023

Outreach Efforts

None

Awards

None

Student Involvement

This task involves three graduate students (Jeremiah Jeurgensmeyer, Ezekiel Bugay, and Russell McGrath).

Plans for Next Period

We will conduct simultaneous LII and OH PLIF measurements.

Task 2 - nvPM Model Development and Validation

Honeywell

This task involves the simulation of the sector combustor developed by the Georgia Institute of Technology team and comparison of the experimental measurements obtained in Task 1 with detailed numerical simulations, for the purpose of model development and validation. A numerical framework to model the gas turbine combustor system was established on the basis of Honeywell's previous experience, and detailed simulation was conducted. In this numerical framework, a commercial solver was used to obtain CFD solutions with a large eddy simulation (LES) turbulence model, by using a dynamic Smagorinsky model. The combined heat release/turbulence model consists of non-premixed diffusion flamelets generated by using a detailed Jet A kinetic model describing the formation of aromatic species up to pyrene. The simulation includes radiation with the discrete ordinate method due to H_2O, CO_2, and nvPM (weighted-sum-of-gray-gases model). The liquid fuel spray is modeled with Lagrangian tracking of droplets with stochastic secondary breakup, calibrated to experimental data. The domain is discretized by using polyhedral cells and consists of the entire geometry from the inlet of the rig to the exhaust of the combustor. The simulation is initially converged with a Reynolds-averaged Navier–Stokes (RANS) solution, then run with five flow-throughs to initialize the solution and subsequently an additional five flow-throughs to obtain statistical averages. The numerical simulation will be compared with experimental results from optical measurements (LII, OH, and Mie scattering) at different flow conditions using different fuel injectors.

In this year, comprehensive numerical simulation was conducted by the Honeywell team to aid in combustor design and understand the performance of fuel injectors. Different numerical models, including a RANS model and LES, were used for the same simulation to understand the effects and accuracy of different numerical models. RANS and LES produced different results when given the same boundary conditions and same kinetic model (Figure 6). LES had higher fidelity, although the computation time was approximately 10 times longer than that of RANS. We used LES to further simulate the combustor with different fuel injectors. Four different sets (configurations 1–4) of fuel injectors were simulated for comparison purposes. Given the amount of experimental work, we will focus on two sets of fuel injectors in the experiments and compare the results with the simulations. Numerical simulation of all these four sets of fuel injectors was conducted, and different fuel injectors showed differences in performance (Figure 7), thus indicating the effect of fuel injectors on nvPM formation.

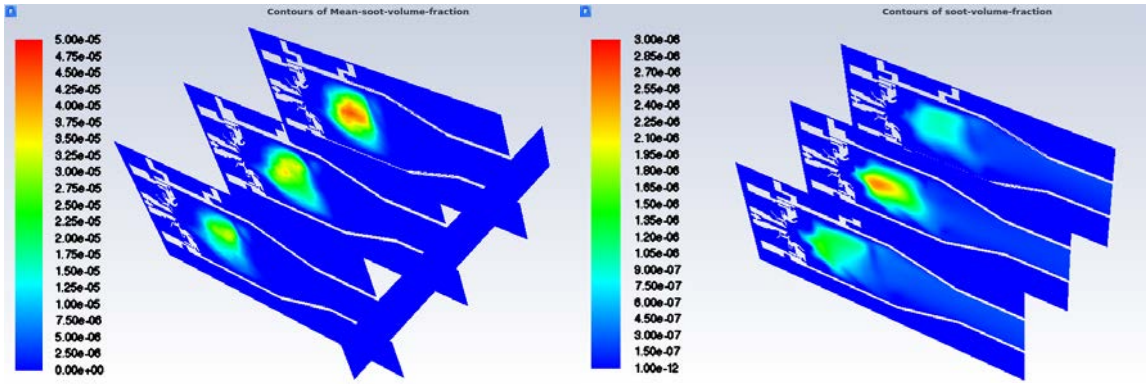

Figure 6. Predictions of mean soot volume fraction from LES (left) and RANS (right).

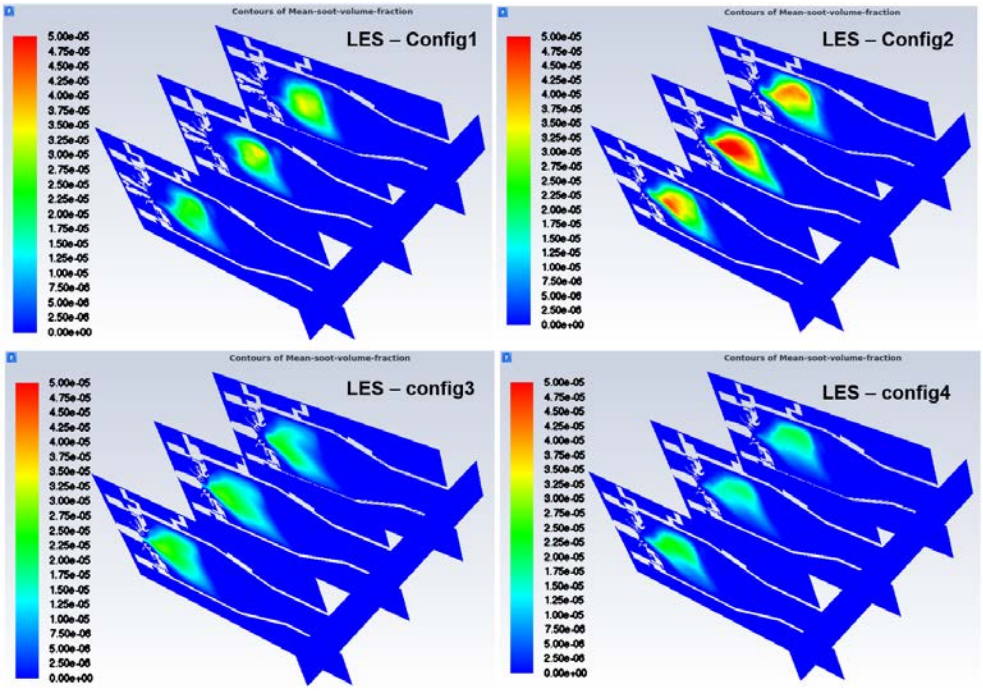

Figure 7. Predictions of mean soot volume fraction from LES for four different sets of fuel injectors.

Milestone(s)

CFD simulation of the designed combustor

Major Accomplishments

Detailed design and CFD analysis of the combustor

Publications

None

Outreach Efforts

None

Awards
None

Student Involvement
None. This task is conducted by Honeywell team.

Plans for Next Period
Detailed numerical simulation comparison with experimental data.

Task 3 - Experimental Facility Development and Operation
Georgia Institute of Technology and Honeywell

Objective(s)
The objective of this task is to develop the sector combustor with three fuel injectors and optical windows. This combustor will be operated at high-pressure and high-temperature conditions to replicate real engine conditions. This sector combustor is used as the test bed for Task 1 and Task 2.

Research Approach
In this task, we successfully designed and commissioned a high-pressure model gas turbine combustor. Such a design is challenging, because it must accommodate advanced optical measurements with practical applicability from the perspectives of both industry and academia. To achieve this goal, the Georgia Institute of Technology team and Honeywell team worked closely and designed a unique combustor with three fuel injectors. The three-fuel-injector design minimizes injector-combustor wall interaction, which is common in conventional combustor design with only one fuel injector. Our optical measurement will focus on the center fuel injector. Three large optical windows are located on the top and side walls of the combustor, thus enabling optical diagnostics. CFD was conducted to design the windows' cooling and filming features to avoid window damage and blackout by soot. The combustor is placed inside a large high-pressure vessel with adequate optical access through two 10-inch-diameter windows and one 8-inch-diameter window. This combustor enables optical access for academic study and is similar to the practical combustors in engines. Figure 8 shows a photograph of the high-pressure system and combustor frame.

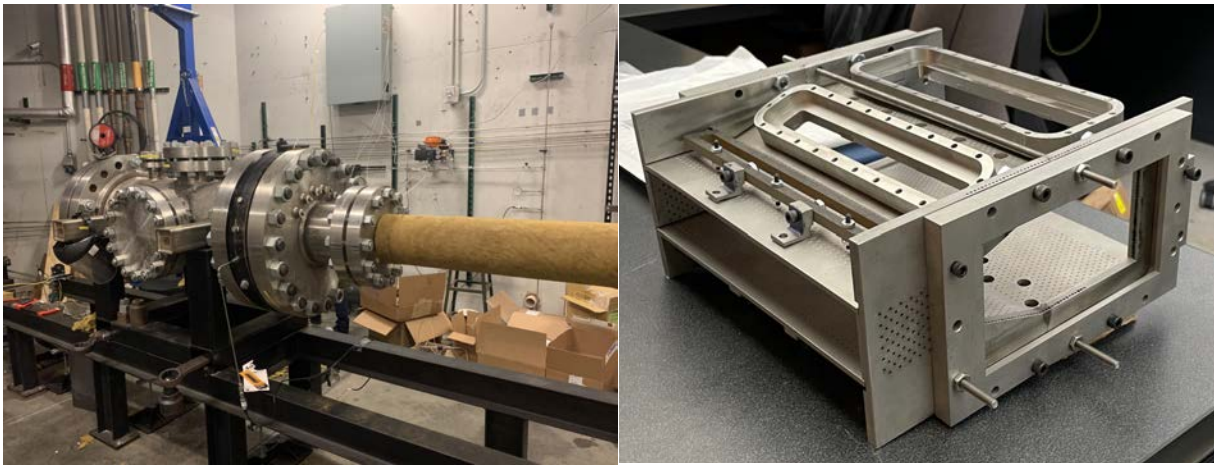

Figure 8. Photograph of the high-pressure system (left) and combustor frame (right).

Figure 9 shows the operation of the sector combustor with all three fuel injectors ignited. The fuel is Jet A with an air temperature 450 ˚F at 10 atmospheres. The yellowish rich flame front is clearly seen near the fuel injector, thus indicating nvPM formation. Moreover, the rich flame can be seen to be quenched by further air injection, and most of the nvPM is oxidized after the quenching of the rich flame. The LII diagnostic was conducted in the rich flame region.

Figure 9. Rendering of the proposed combustor with three fuel injectors.

Figure 10 shows the extinction phase of the combustor by shutting off the fuel valve. With reduced luminescence, the combustor can be seen clearly through the window. No particle deposition was observed after the operation of the combustor, thereby demonstrating the success of the combustor design. In the following year, more systematic measurements will be conducted for both Jet A and sustainable aviation fuel (SAF).

Figure 10. Side view (left) and top view (right) of the combustor during fuel shutoff.

Milestones

1. Design and fabrication of the high-pressure system
2. Design and commission of a unique combustor with three fuel injectors

Major Accomplishments

The major accomplishments of Year 2 of this project include the following:

1. Design, fabrication, and commissioning of the high-pressure rig

Publications

None

Outreach Efforts

None.

Awards

None.

Student Involvement

Project 70 involves four graduate students (Jeremiah Jeurgensmeyer, Sundar Manikandan, Ezekiel Bugay, and Russell McGrath) and two research engineers (David Wu and Subodh Adhikari).

Plans for Next Period

In the following year, our main goal is to upgrade the combustor system to allow higher fuel flow rate in the system to align the testing condition conditions with Honeywell auxiliary power unit operating conditions.

Project 071 Predictive Simulation of nvPM Emissions in Aircraft Combustors

Georgia Institute of Technology

Project Lead Investigator

Suresh Menon
Professor at School of Aerospace Engineering
Georgia Institute of Technology
270 Ferst Drive, Atlanta, GA 30332-0150
404894-9126
suresh.menon@aerospace.gatech.edu

University Participants

Georgia Institute of Technology (GT)

- P.I.: Prof. Suresh Menon
- FAA Award Number: 13-C-AJFE-GIT-067
- Period of Performance: October 1, 2021 to September 30, 2022
- Tasks:
    1. Kinetic modeling: improvements in the soot kinetic model to predict development of polycyclic aromatic hydrocarbon (PAH) pathways in representative sooting fuels
    2. Nucleation modeling: simulation of PAH rings at a range of relevant flame temperatures to identify key species contributing to the soot nucleation process.
    3. Surface growth and aggregation modeling: reaction-transport-limited growth of soot particle models for cluster–cluster aggregation
    4. (LES): coupling the multi-scale models developed in Tasks 1–3 in a method of moment within LES for soot–turbulence–chemistry interactions with application to canonical flames.

Project Funding Level

Current FAA funding is for a 3-year effort (July 2020 to September 2023), with a request of $500,000 per year from ASCENT (per year). Additional request for funding in year 3 have been submitted. Cost-sharing is provided as follows.

- GT provides cost-sharing for its share of $150,000 per year. The GT point of contact is Kevin Ellis (kevin.ellis@aerospace.gatech.edu).
- Raytheon Technologies Research Center (RTRC) provides cost-sharing of $250,000 per year. Dr. Colket is a consultant in this project with many years of experience in soot modeling. The RTRC contact is John LaSpada (LaSpadJW@RTRC.utc.com).
- The University of Michigan (UM) provides cost-sharing in the amount of $100,000 per year. The UM point of contact is Alexandra Thebaud (thealexi@umich.edu).

Investigation Team

- Prof. Suresh Menon, GT: P.I., Task 4
- Dr. Miad Yazdani, RTRC: co-P.I., Task 3
- Dr. Steve Zeppieri, RTRC: co-P.I., Task 1
- Prof. Angela Violi, UM: co-P.I., Task 2
- Dr. Meredith (Med) Colket, Consultant, RTRC: co-investigator, Task 1

Project Overview

This project is being used to establish a new multiscale approach to predict soot formation in aircraft combustors. A hierarchy of first-principles simulation methods is being used to account for the multiscale physics of the formation and transport of non-volatile particulate matter (nvPM, also called soot in the literature). The final objective is to use this multiscale approach to model the physics in LES of realistic gas turbine combustors. We target and isolate the layers of empiricisms that currently exist, for example, in particle inception models, the roles of precursor species in nucleation, the particle shape assumptions and their impact on surface growth, the sensitivity of predictions to particle size distribution, and the ad hoc coagulation/coalescence mechanisms. The team already has all modeling tools, but a systematic coupling of these tools in a multiscale, multi-physics strategy has yet to be accomplished by any research group. Hence, this study will establish new predictive ability by integrating these capabilities.

The multiscale and multi-physics layers of collaborations among the cost-sharing groups are summarized in Figures 1 and 2, and briefly described herein. The kinetics group at RTRC is conducting a study to understand the role of gas-phase kinetics in predicting important species potentially labeled as soot precursors. The information on reduced kinetics from RTRC is being used by GT and UM to evaluate LES performance and the process of nucleation. In the UM study, the propensity of gas-phase species to form dimers (considered the building blocks of soot inception) under flame conditions is being studied. Identification of soot precursors and the rates of formation of soot nuclei will be the output from these studies. This nucleation rate will be provided to GT to update the source terms associated with nucleation processes through a six-moment method of moment with interpolative coefficients (6-MOMIC) approach, and the information on the structures of these soot nuclei will be provided to RTRC for modeling of surface growth and aggregation processes. Outputs from the aggregation studies in RTRC in the form of global surface growth and aggregation models will then be fed back to GT to update the source term surface growth and aggregation models in the 6-MOMIC approach. Canonical studies are underway at GT to provide information regarding the variations in local conditions, such as pressure, temperature, and local equivalence ratios due to turbulence–chemistry interactions; this information should be useful in each stage of the abovementioned studies. LES studies at GT will also involve modeling the effects of chemistry–soot–turbulence interactions by using advanced subgrid models including the linear eddy mixing (LEM) model. As a project deliverable (at the end of this research effort), the final assessment of both the existing soot model and the improved soot model will be conducted in canonical flame configurations.

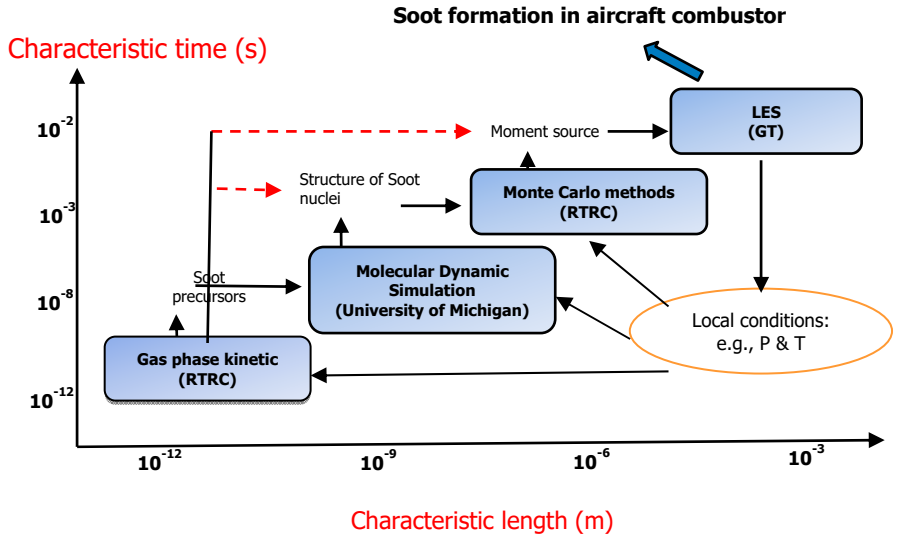

Figure 1. Multiscale collaborative efforts to improve nvPM (soot) predictions.

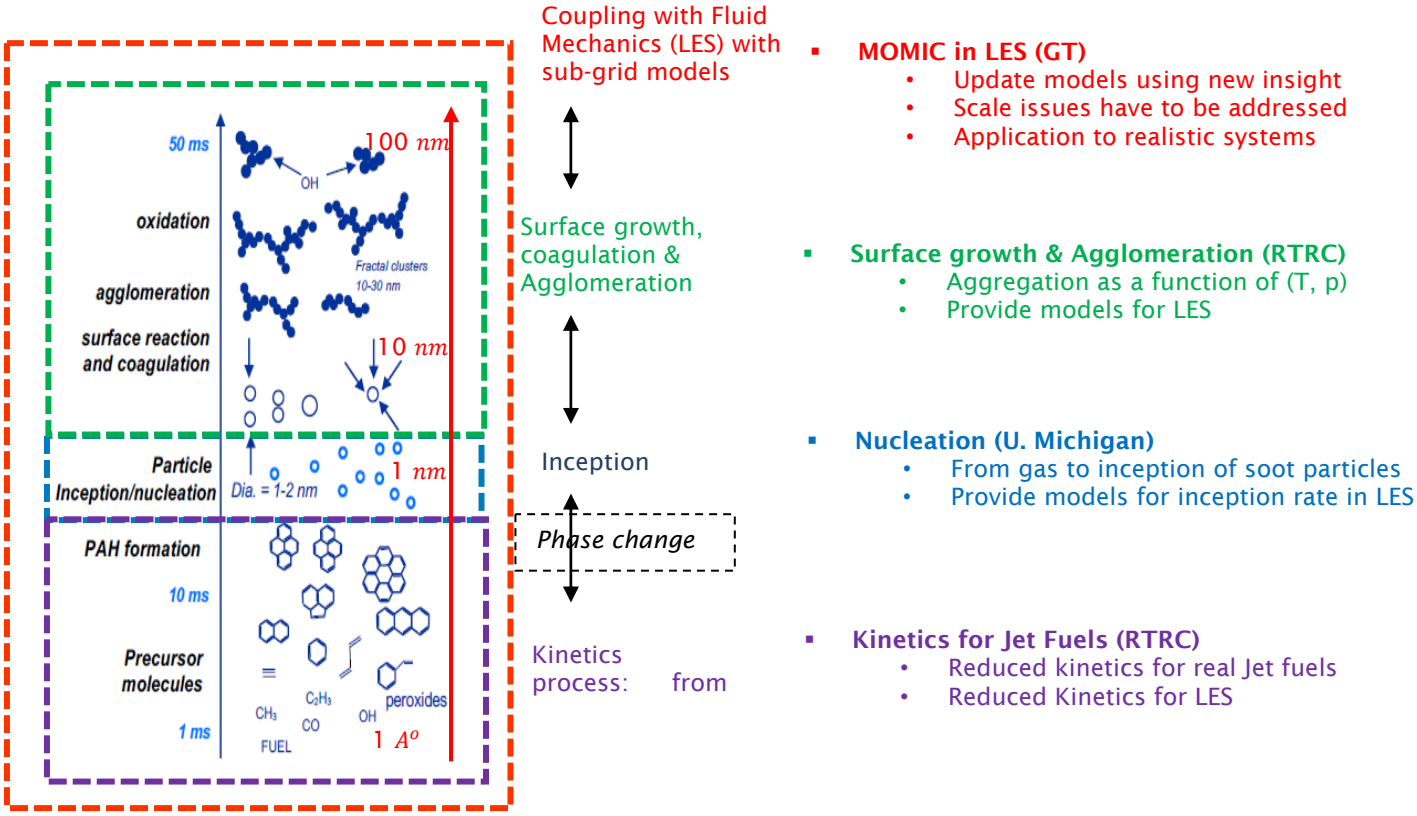

Figure 2. Multiscale collaborative efforts to improve nvPM (soot) predictions.

Task 1 - Kinetics Modeling

Raytheon Technologies Research Center

Objective

The objective of this task is to develop validated, detailed, and reduced chemical kinetic models of parent fuel decomposition and oxidation reactions, with a special focus on fuel rich chemistry, to enable the accurate evolution of PAH/soot precursor formation and incipient soot particle formation, and the evaluation and improvement of reduced-order soot formation models. Year 1 fuel activities focused on ethene, whereas the Year 2 efforts shifted the focus to Jet A fuels, which will be continued in the remainder of the project. The reduced-order kinetic model is also crucial for assessment in Rich-Burn–Quick-Quench–Lean-Burn (RQL) combustors.

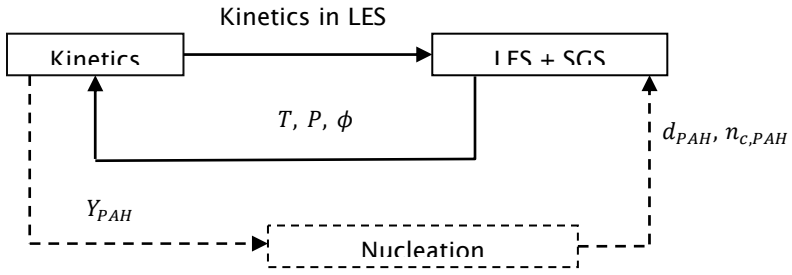

Figure 3. Coupling of LES–kinetics activities.

Research Approach

Reduced-order Model Development for use in LES

The schematic in Figure 3 shows the coupling between the LES, nucleation, and kinetic activities focused during the span of the current Year 2 of the project, where *T*, *P*, and ϕ represent the temperature, pressure, and equivalence ratio of the surrounding gas phase. These background conditions are obtained from the LES studies of canonical premixed and non-premixed configurations. Moreover, PAH represent the polycyclic aromatic hydrocarbon species considered as the soot precursors. The objective of the current kinetic efforts was focused on downselecting the detailed kinetic model of jet fuels and reducing it to a non-stiff version with finite rate expressions for precursor species production determining Y_{PAH}. This kinetic model is to be fed directly into LES studies at GT. The precursor species characteristics (n_{PAH}, d_{PAH}) concentrations will also be input to nucleation studies at UM to assess their ability to form dimers.

In Year 1, published ethene kinetics with varying details of PAH/particulate matter (PM)-related chemistry were assessed. In Year 2, the annual efforts focused on a similar approach for evaluating compact Jet A mechanisms including any PAH chemistry. Although no compact Jet A mechanism with PAH chemistry was identified, two compact mechanisms were selected for evaluation and further study: the Kollrack mechanism (Kollrack,1976) and the HyChem mechanism (Wang et. al., 2018). Essentially, both models implement semi-empirical (i.e., non-Arrhenius) reactions for Jet A. The Kollrack mechanism uses two oxidation/hydrogen abstraction reactions (O_2 and OH) as the initiation reactions. The HyChem model uses seven semi-empirical Jet A reactions: one pyrolysis and six abstraction reactions. The Kollrack mechanism uses product species yielding simple integer stoichiometric coefficients (e.g., C_2H_4 and C_2H_3); in contrast, the HyChem approach uses detailed non-integer stoichiometric coefficients for a wide product spectrum of compounds associated with the fuel decomposition (i.e., C_2H_4, C_3H_6, iC_4H_8, nC_4H_8, C_6H_6, CH_3, CH_4, H, etc.). These non-integer coefficients are derived from canonical (e.g., flow reactor, shock tube, or opposed jet) experiments involving the fuel. The subsequent chemistry involving these fuel intermediate species is the published "USC Mechanism" small-species kinetics model.

On the basis of the above methods, a third mechanism was developed under this program. Earlier analysis within this project indicated that the Wang-Frenklach mechanism (1997) showed good agreement with the results of PM-related experiments using an ethene fueled, well-stirred reactor. Accordingly, following the HyChem approach, semi-empirical Jet A reactions were developed and combined with the Wang-Frenklach ethene kinetics model. This approach provides a heuristic model that is relatively small, handles Jet A fueled systems, and affords PAH/PM-related kinetic information. In this third model, the products associated with the fuel-based reactions are those already in the Wang-Frenklach mechanism: C_2H_4, C_2H_3, C_2H_2, CH_4, CH_3, H_2, H, and C_6H_6. A summary of the above three mechanisms is provided below.

Table 1. Comparison of the number of species, reactions, and PAH chemistry in the above mechanisms.

Mechanism	Fuel Rep.	# Species	# Reactants	PAH Chemistry?
Kollrack	C12H23	21	30	No
HyChem	C11H22	44	202	No
Mod. W-F	C12H23	100	547	Yes

The figures of merit associated with these studies were ignition delay and perfectly stirred reactor (PSR) lean blow-out profiles developed within the National Jet Fuel Combustion Program for the HyChem and Kollrack models. Figure 4 shows the ignition delay times associated with stoichiometric blends of Jet A/air at 30 atm and initial temperatures of 1,000–1,600 K.

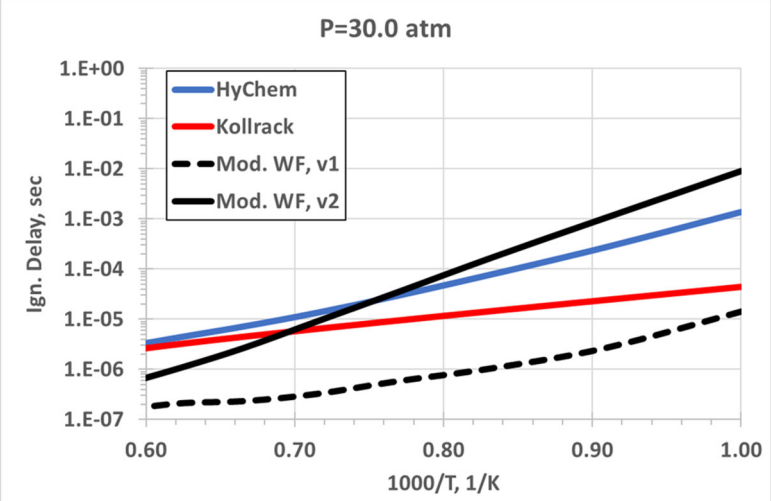

Figure 4. Comparison of ignition delay times associated with the above mechanisms at the indicated conditions.

On the basis of the assumption that the HyChem model is realistic (given that it was developed from exactly such experimental data), the version of the modified Wang-Frenklach model that included benzene as a fuel intermediate species compares well with the HyChem profiles, whereas both the Kollrack and non-benzene modified Wang-Frenklach mechanisms do not trend well with the other two mechanisms.

Similar observations are obtained from the comparisons of each mechanism's PSR lean blow-out profiles (Figure 5). The modified Wang-Frenklach mechanism that includes benzene yields a profile in excellent agreement with the HyChem model, in terms of both the reactor temperature profile and the residence time at blow-out. The modified Wang-Frenklach mechanism that does not include benzene yields a lower reactor blow-out temperature and residence time. The Kollrack mechanism temperature profile is unique and occurs at a considerably lower temperature than the other three mechanisms.

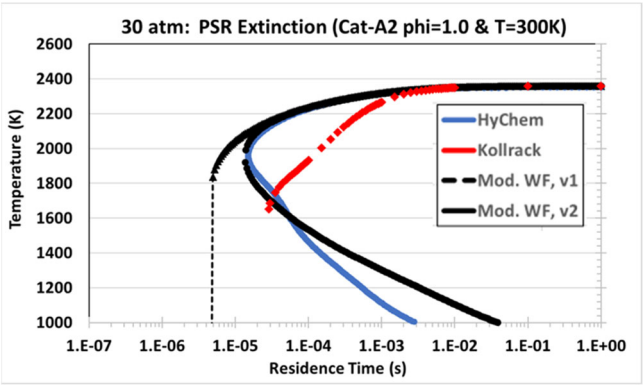

Figure 5. Comparison of PSR lean blow-out profiles associated with the above mechanisms at the indicated conditions.

The final check used the modified Wang-Frenklach mechanism in conjunction with previously developed RTRC reactor network models of RQL combustors and compared the results to experimental data (Figure 6). For a front-end equivalence ratio of approximately 2.25, the modified Wang-Frenklach mechanism predicts a combustor exit smoke number of 32.9. This value is in good agreement with the experimentally obtained smoke number values at similar operating conditions.

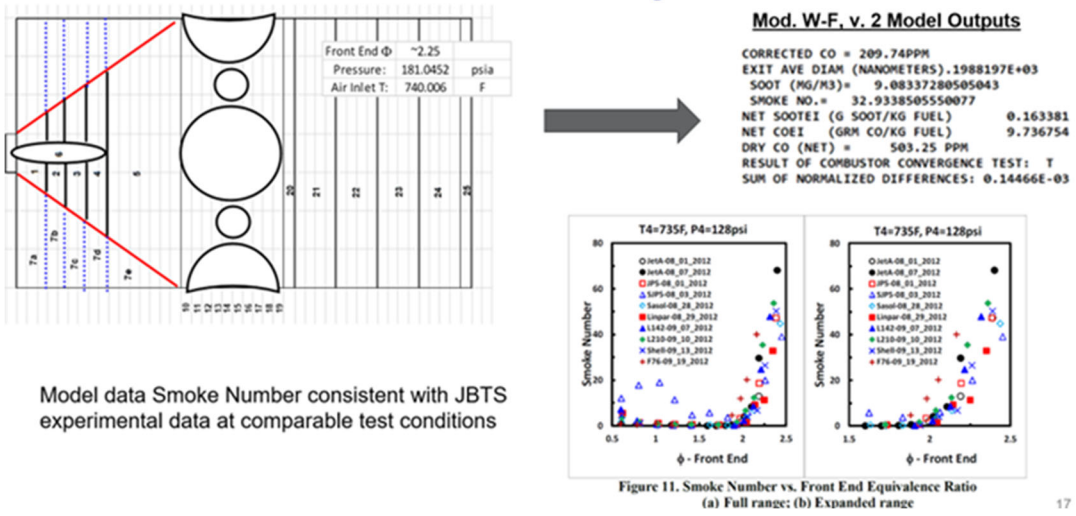

Figure 6. Comparison of combustor exit smoke number values for the indicated RQL combustor operating conditions.

The goal of this year's activities was to determine whether a suitably compact mechanism that incorporates both Jet A and PAH/PM kinetics information could be developed. On the basis of the analysis conducted to date, the construction of such a mechanism appears to be feasible, and efforts in developing such a model (e.g., extending the HyChem mechanism to include PAH chemistry, and adding additional larger intermediate chemistry reactions to the Wang–Frenklach mechanism) will be the focus of the remaining period of the project.

Milestone(s)

Milestone	Planned due date
Assessment of Jet A fuel chemistry	9/30/2022

Major Accomplishments

Framework for assessment of reduced kinetics including PAH pathways

Publications

None.

Outreach Efforts

None.

Awards

None.

Student Involvement

None.

Plans for Next Period

Future efforts will focus on developing a reduced-order Jet A fuel mechanism with validation over a wide range of conditions. The reduced kinetics will be provided to GT, and the information on the gas phase will be provided to UM for nucleation studies.

References

See Task 4 reference list.

Task 2 - Nucleation Modeling

University of Michigan

Objective

The objective of this task is to develop models for nanoparticle inception, a critical step in predicting emissions. This effort bridges the work on gas-phase chemistry (RTRC) with the model for particle growth (RTRC) and provides inputs for the MOMIC model (GT).

Research Approach

Current models for particle inception are unable to reproduce a variety of experimental data, including molecular structure. This work is aimed at developing a predictive model for particle inception that can provide accurate chemical and physical growth pathways for PAHs. Molecular dynamics (MD) simulations are used to study the collisions of PAHs and the formation of aromatic dimers leading to soot inception.

In the last annual efforts, methodology and the MD approach was established for the assessment of the dimer formation stability of different aromatic species. In the current annual effort, we continued the atomistic simulations of these species and higher PAH species, also including oxygen content. Figure 7 shows the structures of gas-phase compounds considered in this study and the results for their homo-dimerization propensity. The data points are broadly clustered in three groups. The first is composed of the compounds I.C (462 u), I.D (462 u), and I.E (460 u), which have the same mass and oxygen/carbon ratios (0.125) and are less stable than I.A (448 u) and I.B (472 u), which constitute the second group. This difference indicates that the presence of oxygen slightly destabilizes the dimers, an effect possibly caused by the increased repulsive electrostatic interactions of oxygenated molecules compared with pure aromatic hydrocarbons. The third group is formed by I.F (402 u), I.G (452 u), and I.H (502 u), which are less likely to dimerize than the other two groups. The low dimer stability of the third group may be due to the presence of a sigma bond, which introduces an internal rotatable bond that interferes with the formation of clusters.

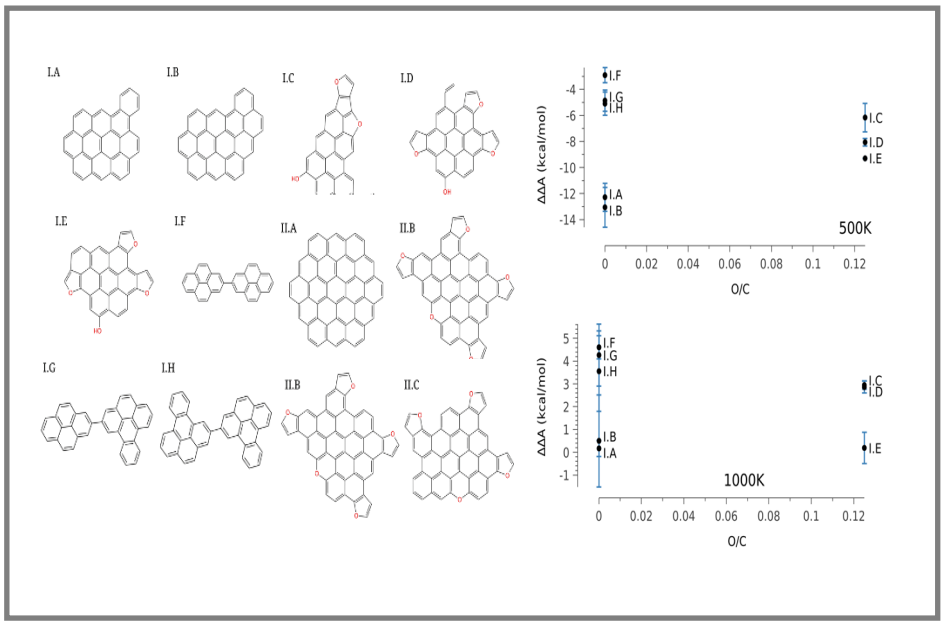

Figure 7. Structural formula of gas-phase compounds (left) and homo-dimerization propensity at 500 K and 1,000 K as a function of oxygen/carbon ratio.

Several conclusions can be drawn from this study. First, the details of the structures of the species that nucleate cannot be ignored. Mounting evidence indicates that the presence of five-membered rings, aliphatic side chains, and oxygenated

groups in soot precursors does not change the nucleation mechanism leading to soot formation. Our results pertaining to both the dimerization propensity and the change in free-energy barriers between monomers and dimers, both of which directly relates to the kinetic rates of dimerization, show otherwise. Second, the effects of shape, presence of oxygen, mass, and rotatable bonds are tightly intertwined, and have different importance as well as diverse temperature dependencies, although they are all dominated by entropic effects at high temperatures. The presence of oxygen affects the dimer propensity by reducing the molecular cohesion due to electrostatic repulsion, although, notably, the force field used in this study cannot capture the effect of molecular polarizability.

These results have been used as a first approach toward the development of predictive trends for quantifying dimer stability. Because of the presence of various intertwined dependencies, we will need a new approach to separate the contributions and their relative importance. Next, we will combine MD simulations with machine learning approaches to identify the main characteristics that drive nucleation and determine the corresponding rates.

Future work will be aimed at improving upon the relationships that we obtained by identifying additional factors influencing dimer stability. This process will involve close feedback with kinetics studies at RTRC to modify the kinetics mechanism in parallel. After the key precursors are identified, the collision rates of these dimers will be provided as inputs in the soot nucleation rates used in the LES-MOMIC code.

Milestone

Milestone	Planned due date
MD assessment of pool of PAH dimers	9/30/2022

Major Accomplishments

MD simulations for pools of PAH rings at a range of flame temperatures

Publications

None.

Outreach Efforts

None.

Awards

None.

Student Involvement

One student at UM is involved in this work.

Plans for Next Period

MD Simulations at UM

Future work will seek to improve upon the relationships that we obtained by identifying additional factors that influence dimer stability. This process will involve close feedback regarding kinetics studies at RTRC to enable modification of the kinetics mechanism in parallel. Once the key precursors are identified, the collision rates of these dimers will be used as inputs in the soot nucleation rates in the LES-MOMIC code.

References

See Task 4 reference list.

Task 3 - Surface Growth and Aggregation Modeling

Raytheon Technologies Research Center

Objective

The objective of this task is to develop a physics-based framework for the prediction of soot particle growth after the inception process. The growth consists of agglomeration due to collisions between the primary particles and surface growth as a result of direct deposition of the precursors on the aggregate. The final aggregate fractal structure and its temporal evolution as a function of local conditions are of interest. This model will provide the morphology characteristics and the growth rate of the particles, which will serve as inputs into the MOMIC formulation.

Research Approach

Soot particles from nucleation stages undergo various surface growth processes and form primary particles. These primary particles are spherical with typical diameters of 1–10 nm. The focus of this effort is to understand evolution of fractal dimension of aggregate since the formation of primary particles to final fractal aggregates through processes of surface growth and aggregation. Experimentally, the structures of these soot particles have been demonstrated to be dependent on the local conditions (e.g., local equivalence ratio). These surface growth process can occur because of heterogeneous reactions of gas-phase precursors on solid soot particle surfaces (reaction limited growth) or through the transport of soot precursors in high-speed flames (transport limited growth). Most of the current growth models account for only reaction limited growth and ignore transport limited growth as well as cluster–cluster interactions, which may be important in aggregate formation. In this work, information on background gas-phase species contributing to soot particles, the structure of the initial soot nuclei, and the local conditions is merged to understand the fundamental processes contributing to the formation of large soot aggregates.

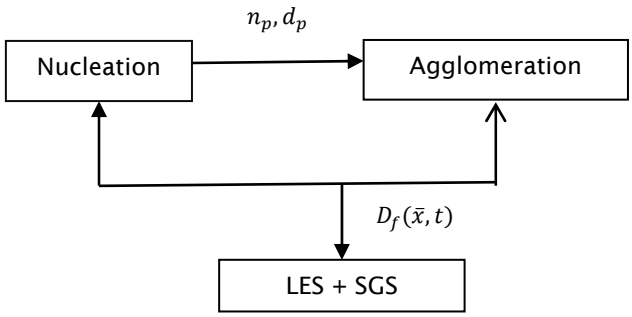

Figure 8. Post-inception growth of soot particles (LES-RTRC-UM coupling).

The coupling between the growth framework being developed at RTRC with MD simulations from UM and the LES study at GT is briefly highlighted in Figure 8. The growth module takes the number density and size distribution of incipient soot particles from nucleation as an input and tracks the growth of such particles along the statistically averaged path lines, which have varying background LES conditions in form of temperature (*T*), pressure (*P*) and local equivalence ratio (ϕ), as detailed below. The output from such studies in the form of the parametrized fractal dimension (D_f) will be fed back into the LES-MOMIC soot approach.

The developed post-inception growth model described in previous annual efforts has been shown to capture the effects of different operating conditions on the growth characteristics of the particles, including size and morphology. The parametric exercise of this model, however, may become computationally prohibitive if a range of operating parameters and combinations therein is swept over. A path line-sampling approach is proposed (schematic in Figure 10), in which the full flow-field (obtained by the LES) is represented through statically sampled path lines over which the operating conditions would be time variant. For example, the temperature and fuel/air ratio would evolve over the course of time as a particle moves from the injector toward the exit of the combustor. This time history is then provided to the growth model, wherein the variation in particle characteristics will be solved over the course of this timeframe for each individual path-line histogram (example output in Figure 9). This information is then fed back into the LES with time–space mapping through the path line coordinates and nearest-point interpolation to provide full spatial representation of growth

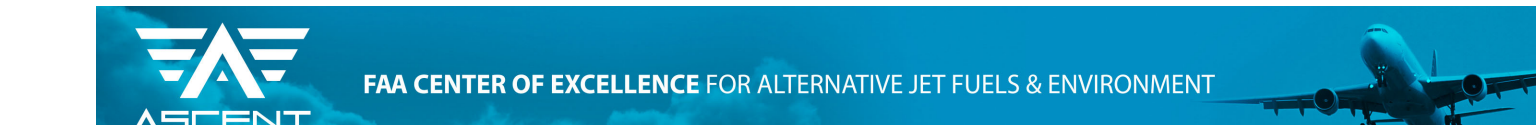

information, which is then used in the MOMIC approach. This approach effectively reduces the computational overhead of the growth model to a dozen simulations (assuming that this number of path lines is sufficient to properly sample the combustor flow field), as compared with potentially hundreds in the conventional parametric approach. Of note, this process is considered a one-way coupling approach, in which the macroscopic changes in the flow-field due to the interaction with the soot-particle transport are assumed to have negligible impact on the growth characteristics of the particles.

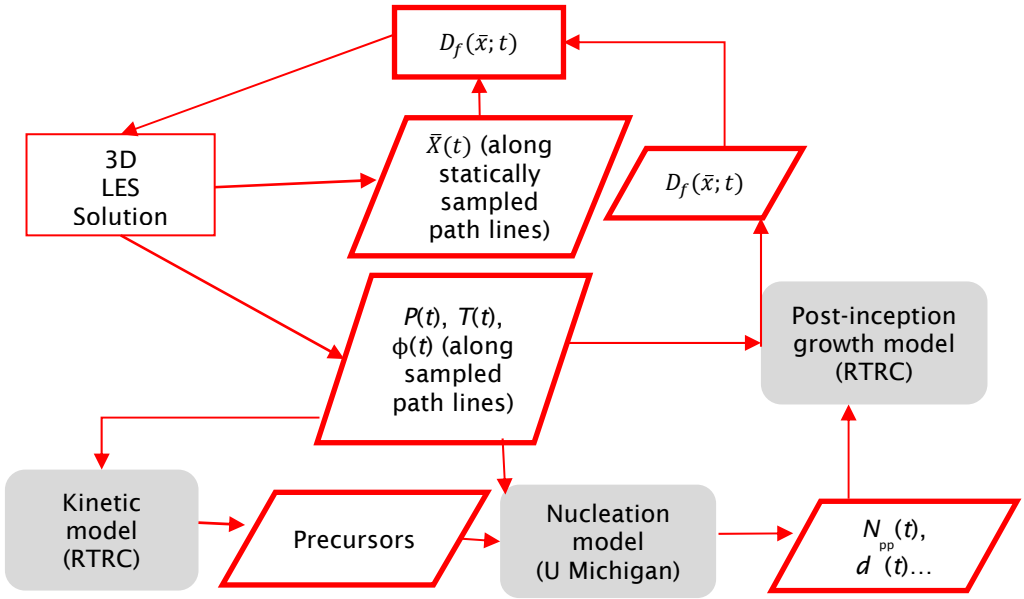

Figure 9. One-way coupled strategy for growth of soot particles.

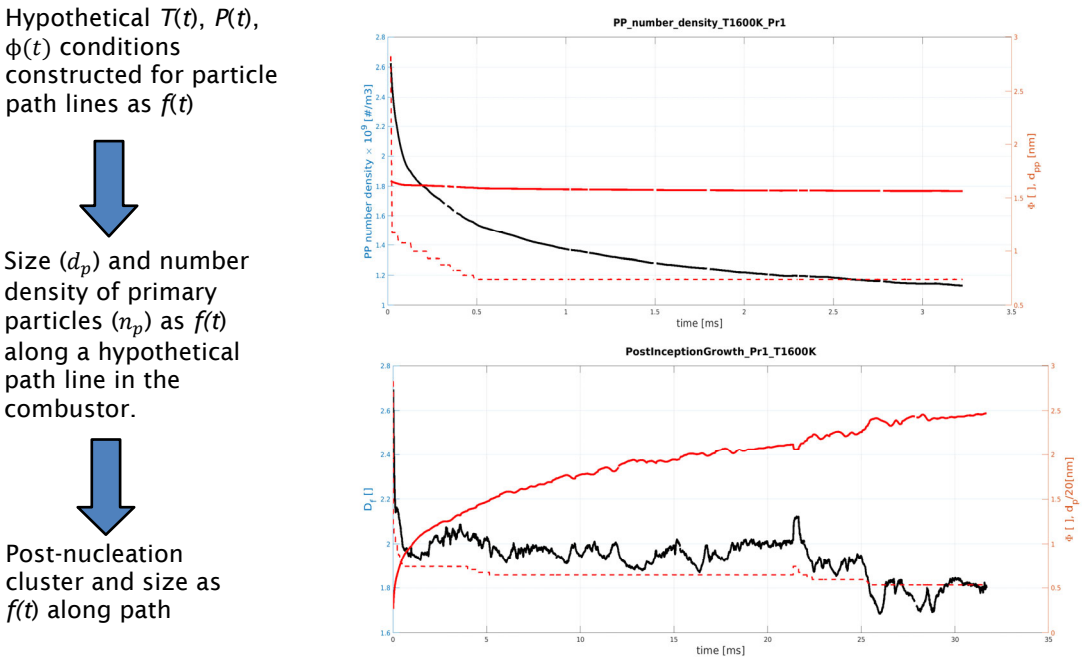

Figure 10. Demonstration of a one-way coupled strategy along the hypothetical LES path-line.

The future work for the remainder of the project uses actual LES simulated data for the premixed and non-premixed flames instead of hypothetical path lines, as demonstrated above.

Milestone(s)

Milestone	Planned due date
One way coupled MC studies of surface growth	9/30/2022

Major Accomplishments

One-way coupled demonstration of using hypothetical LES-like data for soot fractal growth.

Publications

None.

Outreach Efforts

None.

Awards

None.

Student Involvement

None.

Plans for Next Period

The future work for the remainder of the project will use actual LES simulated data for the premixed and non-premixed flames instead of hypothetical path lines, as demonstrated above.

References

See Task 4 reference list.

Task 4 - Large Eddy Simulations

Georgia Institute of Technology

Objective

The objective of this task is to develop a physics-informed LES framework to model soot formation in turbulent reacting configurations of canonical and combustors with practical relevance. The current report discusses the LES-MOMIC and LEMLES-MOMIC frameworks to address large-scale simulations of soot modeling in turbulent reacting flows. The current steps also included a collaboration with the kinetics group to include the effects of various mechanisms within the LES framework, updating the MOMIC framework to incorporate models for key PAH pathways and comparing it with the old MOMIC framework, which does not account for PAH pathways.

Research Approach

LES studies of turbulent sooting problems are very difficult because of the multiscale nature of soot inception, coagulation, and surface growth that must be modeled in a highly turbulent and reactive environment, typically in a complex combustor configuration. Most prior studies have focused on global models that approximate the small-scale physics. Consequently, many available models account for the underlying physics. In contrast, simulations require some approximations, because the computational resources will never meet the simulation requirements. In the current effort, we balance contributing to the prediction of soot formation physics in a realistic gas turbine combustor with the need to obtain high-fidelity, reliable predictions by using advanced models. To achieve this goal, we leverage our past LES capability and upgrade the models by using the results from MD and Monte Carlo (MC) studies. Soot evolution is tracked with MOMIC, wherein the first six moments of the particle size distribution function are used.

The full set of compressible reacting multispecies Navier–Stokes equations cannot be solved directly, because a direct numerical simulation is not feasible for practical applications. For LES, the large-scale flow features are resolved, and subgrid modeling is used for the smaller scales.

The LES governing equations can be written as follows:

$$\frac{\partial \bar{\rho}}{\partial t} + \frac{\partial}{\partial x_i}(\bar{\rho}\,\widetilde{u_\iota}) = 0$$

$$\frac{\partial}{\partial t}(\bar{\rho}\,\widetilde{u_\iota}) + \frac{\partial}{\partial x_j}\left(\bar{\rho}\,\widetilde{u_\iota}\,\widetilde{u_\jmath} + \bar{P}\,\delta_{ij} - \overline{\tau_{\iota\jmath}} + \tau_{ij}^{sgs}\right) = 0$$

$$\frac{\partial}{\partial t}\left(\bar{\rho}\,\tilde{E}\right) + \frac{\partial}{\partial x_j}\left[\left(\bar{\rho}\,\tilde{E} + \bar{P}\right)\widetilde{u_\iota} + \overline{q_\iota} - \widetilde{u_\jmath}\,\overline{\tau_{\iota\jmath}} + H_i^{sgs} + \sigma_i^{sgs}\right] = 0$$

$$\frac{\partial}{\partial t}\left(\bar{\rho}\,\widetilde{Y_k}\right) + \frac{\partial}{\partial x_j}\left[\bar{\rho}\,\widetilde{Y_k}\,\widetilde{u_\jmath} - \bar{\rho}\,\overline{D_k}\,\frac{\partial \widetilde{Y_k}}{\partial x_j} + \Phi_{j,k}^{sgs} + \Theta_{jk}^{sgs}\right] = \bar{\rho}\,\widetilde{\dot{w}_k}$$

$$\frac{\partial}{\partial t}\left(\bar{\rho}\,\widetilde{Y}_{soot}\right) + \frac{\partial}{\partial x_j}\left[\bar{\rho}\,\widetilde{Y}_{soot}\,\widetilde{u_\jmath} - \bar{\rho}\,\overline{D}_{soot}\,\frac{\partial\,\widetilde{Y}_{soot}}{\partial x_j} + \widetilde{V_T}_{soot}\,\widetilde{Y}_{soot} + \Phi_{j,k,soot}^{sgs} + \Theta_{jk,soot}^{sgs}\right] = \bar{\rho}\,\widetilde{\dot{w}}_{soot}$$

$$\frac{\partial}{\partial t}\left(\bar{\rho}\,\widetilde{M_k}\right) + \frac{\partial}{\partial x_j}\left[\bar{\rho}\,\widetilde{M_k}\,\widetilde{u_\jmath} - \bar{\rho}\,\overline{D}_{soot}\,\frac{\partial\,\widetilde{M_k}}{\partial x_j} + \widetilde{V_T}\,\widetilde{M_k} + \Psi_{j,k}^{sgs} + \Omega_{j,k}^{sgs}\right] = \bar{\rho}\,\widetilde{\dot{M}_k}$$

Here, $\widetilde{u_\iota}$ is the *i*-th filtered velocity, $\bar{\rho}$ is the filtered density, and $\bar{P}$ is the filtered pressure, which is computed from the filtered equation of state. $\tilde{T}$ is the filtered temperature, $\tilde{E}$ is the filtered energy, $\widetilde{Y_k}$ and $\widetilde{Y}_{soot}$ represent the filtered *k*-th gas-phase species and soot mass fraction, respectively, and $\widetilde{M_k}$ represents the *k*-th moments of the particle size distribution function. The details regarding the computations of all these quantities have been described elsewhere (El-Asrag & Menon, 2009) and hence are not discussed herein in specific detail. The filtered heat flux $\bar{q}$ can be supplied to an optically thin radiation model to include effects of radiation. The terms $\tau_{ij}^{sgs}, H_i^{sgs}, \sigma_i^{sgs}, \Phi_{j,k}^{sgs}, \Theta_{j,k}^{sgs}, \Psi_{j,k}^{sgs}$, and $\Omega_{j,k}^{sgs}$ contain the effects of the

subgrid scale on the filtered quantities. Modeling of these terms remains challenging; in addition, the closed system of equations must be solved together in three-dimensional space with temporal accuracy.

In this work, an eddy viscosity type subgrid model with constant coefficients is used to obtain the closure of subgrid momentum stresses and subgrid enthalpy flux. In the LEM formulation, the gas-phase species conservation equations are not spatially filtered as in other LES equations. Instead, the exact unfiltered equations are solved by using a two-scale, two-step Eulerian–Lagrangian approach. First, within each LES cell, the one-dimensional LEM model is used to solve for the scalar fields (species mass fraction, soot mass fraction, LEM temperature, and soot integer moments) along a notional line oriented along the maximum scalar gradient. Second, the subgrid scale fields are convected across the LES cell faces by using a Lagrangian transport approach through the splicing algorithm, which reproduces the effect of large-scale advection of the scalars by the flow field. The resulting scalar fields are then filtered in each LES cell to recover LES-resolved species mass fractions to be used in LES-resolved energy and state equations. The application of LEM for non-sooting ethylene flames was established in the Year 1 annual efforts. Its extension to a MOMIC model with PAH pathways is yet to be demonstrated.

In the current annual period, efforts were focused on incorporating the effects of aromatic precursors on various soot formation processes. The main areas of improvement involved soot nucleation physics based on PAH species, additional surface growth effects due to PAH condensations, and improvements in the structure of aggregates formed. Because Since coagulation of soot particles is already handled in detail in the old-MOMIC approach, no additional improvements are needed or currently planned.

Three variations in the MOMIC model were used:

1) In the last annual effort, the old-GT-MOMIC approach (El-Asrag & Menon, 2009) with moment source terms based on simplified soot kinetics (Leung & Lindstedt, 1991) was used to study soot formation in ethylene-air laminar as well as turbulent flames.
2) In the current annual efforts, the RTRC optimized Lindstedt soot model is implemented within the MOMIC code and is termed the RTRC-MOMIC model hereafter.
   Both MOMIC models 1 and 2 use C_2H_2-based nucleation and surface growth processes for soot particles. The coefficients are fitted to improve soot volume fraction predictions.
3) We also focused on incorporating the effects of aromatic precursors on various soot formation processes and identifying how these inputs can be obtained. This MOMIC model is noted as a new-GT-MOMIC model and is based on the Frenklach MOMIC approach (Brown et al., 1998). This model uses nucleation based on pyrene dimerization as well as a detailed mechanism of hydrogen abstraction–carbon addition for soot growth. It also uses condensation of pyrene dimers on the surfaces of soot particles.

The improvements of the new-GT-MOMIC over the old-GT-MOMIC were assessed by conducting numerical simulations at conditions prescribed in 0D PSR reactor simulations by Vaughn et. al. (1998). As shown in Figure 11, the improved MOMIC approach with additional relevant detailed of PAH species predicts a soot volume fraction closer to the experimental observations.

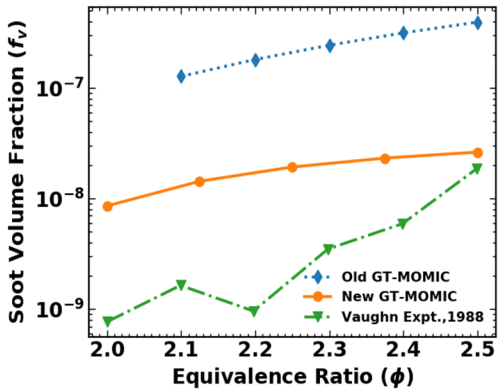

Figure 11. Comparison of old and new GT-MOMIC approaches for rich ethylene flames.

Similarly, all three models are assessed in a 0D PSR of a rich premixed ethylene mixture ($\phi = 2.5$) with P_{ref} = 1 atm, residence time of 0.005 s, and varying reactor temperature from 1,500 K to 2,000 K. The results comparing RTRC-MOMIC and old GT-MOMIC are shown in Figure 12.

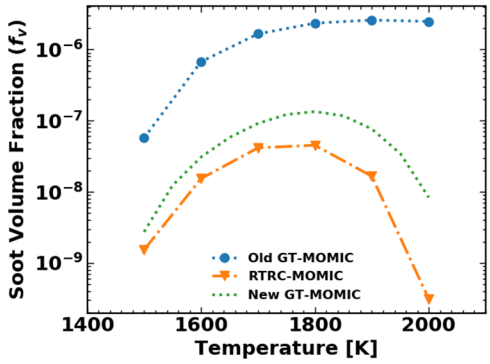

Figure 12. Soot volume fraction dependency on the temperature of the 0D PSR reactor.

As seen in Figure 12, the old GT-MOMIC model predicts higher levels of the soot volume fraction and fails to capture the bell-shaped dependency of the soot volume fraction on the reactor temperature. The RTRC-MOMIC model overcomes these shortcomings, and trends of variation of soot volume fraction with temperature match well with the predictions of the new GT-MOMIC model.

Verification of the New-GT-MOMIC Framework

The new-GT-MOMIC framework (including nucleation, surface growth, and coagulation) is now verified against the Frenklach-MOMIC approach for a range of conditions within the 0D PSR configurations. A detailed 99-species Wang-Frenklach ethylene-air mechanism (1997) is used to account for PAH species formation up to pyrene (and is assumed as the heaviest PAH species undergoing soot inception). The new-GT-MOMIC is verified with respect to the published data (Figure 13).

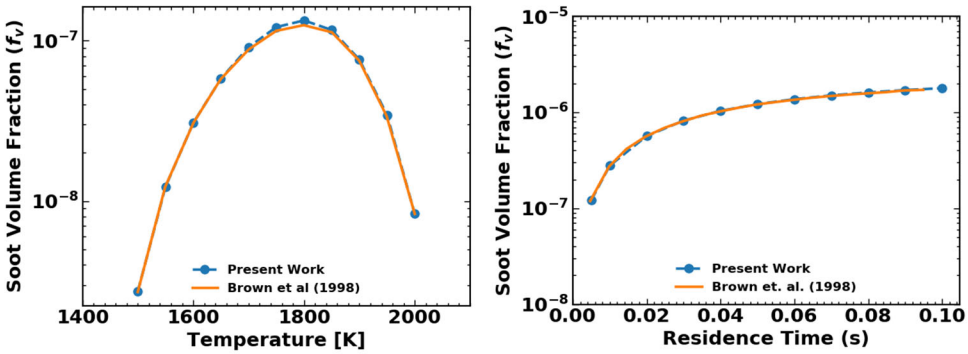

Figure 13. Comparison of the present work with 0D PSR simulations of Brown et al. (1998).

Numerical Simulations of a Premixed Flame of Jet fuels in a Turbulent Environment

The new GT-MOMIC code is coupled with the in-house compressible flow solver LESLIE to study soot formation in reacting simulations: 3D calculations of premixed flames of jet fuels with gasified Jet A fuel are performed. The fuel kinetics is based on the 62-species reduced mechanism developed by Lu and coworkers at the University of Connecticut. The proposed test intends to use the LES-MOMIC model with finite rate chemistry for a premixed flame turbulence interaction problem (El-Asrag et. al., 2007). The schematic for the configuration is shown in Figure 14a. The turbulence level is varied, so that the flame is in the distributed/broken reaction zone regime. The initial flame front is obtained from the laminar premixed flame solution and is specified at the center of the domain, with the left side denoting the reactants and the

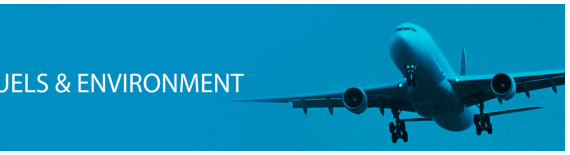

right side denoting the products. The extent of the computational domain is 15 mm × 15 mm × 15 mm in the streamwise *x*, transverse *y*, and spanwise *z* directions. The flow field is initialized by using the von Karman–Pao energy spectrum. Characteristic inflow–outflow conditions are specified in the streamwise direction and are periodic in the other two directions. The LES grid resolution chosen for the simulations is 96 × 96 × 96 LES cells, with the assumption of quasi-laminar chemistry, i.e., no closure for sub-grid turbulence–chemistry interactions is considered. Figure 14b shows the evolving color contour of soot number density in the post flame region. The initial planar flame structure appears severely wrinkled because of the presence of the background turbulence. Figure 15 shows the spatially averaged profiles of the soot mass fraction and temperature along the axial direction. These preliminary results establish the functionality of the first canonical reacting setup of jet fuels that we will be investigating in the current project. Further analysis is underway to understand how the various intermediate processes are interrelated in formation of the final soot particles.

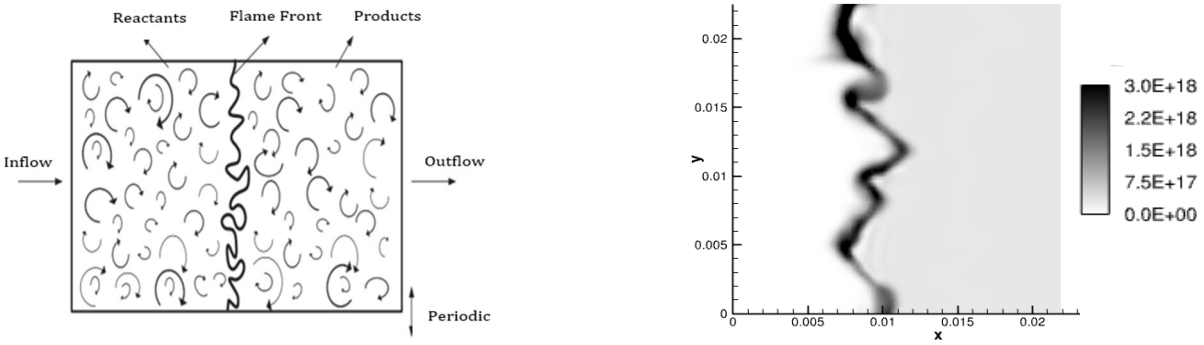

(14a) (14b)

Figure 14. Soot evolution from a rich Jet A/air flame Interacting with background turbulence. (a) Schematic of the problem statement. (b) Contours of soot number density (1/m^3) evolution from jet fuel flames.

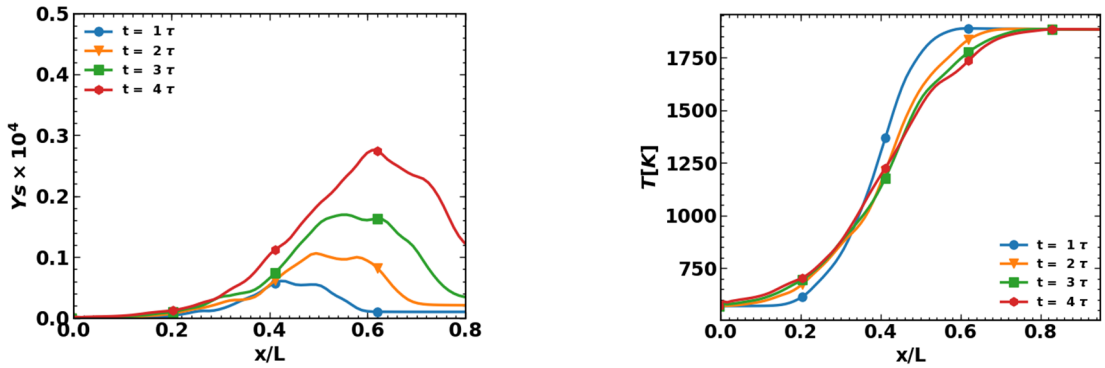

(15a) (15b)

Figure 15. Spatially averaged contour lines of soot mass fraction (a) and temperature (b) from the jet fuel flame

Numerical Simulations of Temporal Mixing Layers from Jet A Fuel

In this section, 2D calculations of a temporal mixing layer with gasified Jet A fuel are performed, thus providing an ideal non-premixed configuration for the assessment of soot models in which strong coupling between fluid dynamics and chemistry is present. The setup described herein is based on the 3D DNS calculations of an *n*-heptane–air mixture by Atilli et al. (2014). A representative two-dimensional strip (width H = 15 mm) of Jet A fuel (diluted with 85% N_2 by volume) is surrounded by air (21% O_2 and 79% N_2 in volume), as shown in Figure 16. The rectangular computational domain is approximately 94 mm long in a direction parallel (horizontal) to the fuel strip and 105 mm wide in a direction

perpendicular to the fuel strip. Both the oxidizer and the fuel strip are at atmospheric pressure. The air stream is preheated to 800 K to increase the resistance of the flame to the extinction induced by the strain. The computational domain is discretized in a uniform mesh with a total of 1,048,576 cells (1,024 × 1,024), which corresponds to the minimum grid spacing of $\Delta x = \Delta y = 91.5$ micrometers. This resolution is equivalent to the resolutions of DNS studies. Characteristic non-reflecting outflow boundary conditions are imposed in a direction perpendicular to the fuel strip (vertical), and periodic boundary conditions are applied in the other direction. The fuel strip moves to the right at a velocity of 8.74 m/s while the air co-flow moves in the opposite direction at the same speed. For initialization, the temperature and species mass fractions are taken from a flamelet and mapped from mixture fraction space onto the crosswise direction by using a mixture fraction profile:

$$z(y) = \frac{1}{2}\left[\mathrm{erf}\left(\frac{\frac{1}{2}\delta + y}{\sqrt{2\sigma_1^2}}\right) + \mathrm{erf}\left(\frac{\frac{1}{2}\delta - y}{\sqrt{2\sigma_1^2}}\right)\right]$$

Here, y represents the spatial location in a perpendicular direction, the parameter δ controls the width of the fuel strip, and the slope parameter σ_1 controls the slope of the profile. The values of these parameters were taken as 7.5 mm and 1.8. The simulations are conducted by using the 62-species reduced chemical kinetics model for Jet A fuel developed under the National Jet Fuel Combustion Program.

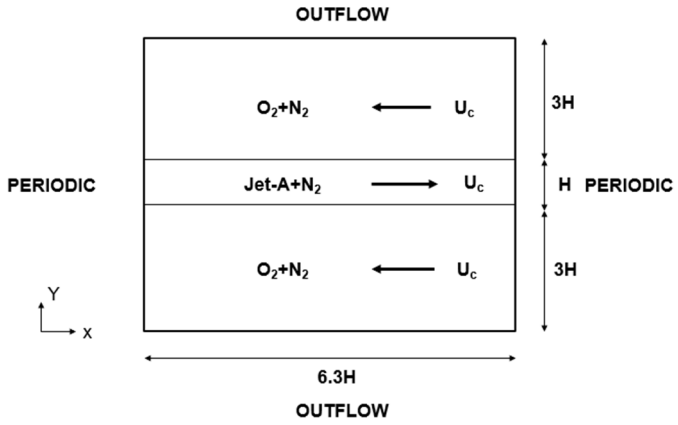

Figure 16. Schematic of the temporal mixing layer of Jet A fuel.

Figure 17 shows the time evolution contours for the Jet A fuel mass fraction at four different times (t = 5 ms, 10 ms, 15 ms, and 20 ms). The mixing layer grows with time, and the simulations are continued until the time reaches 20 ms, when large structures form. As can be seen, the growth of shear layers causes the wrinkling of the flame at the fuel/air interface. Figure 18 shows the contours of evolution of the soot precursor (pyrene), and similar evolution is plotted for the soot number density overlapped with isolines of temperature in Figure 19. The soot number density closely follows the pyrene formation zones in the non-premixed flames, as the nucleation process is assumed to occur through pyrene dimerization. Finally, Figure 20 shows the average profiles of velocity u normalized by characteristic flow velocity U_o, number density of the soot particles formed and the soot mass fraction profiles. The quantitative magnitudes of the soot mass fraction (~10^{-4}) as well as the number density (~10^{12} 1/cm^3) match well with the values obtained by Atilli et. al. (2014).

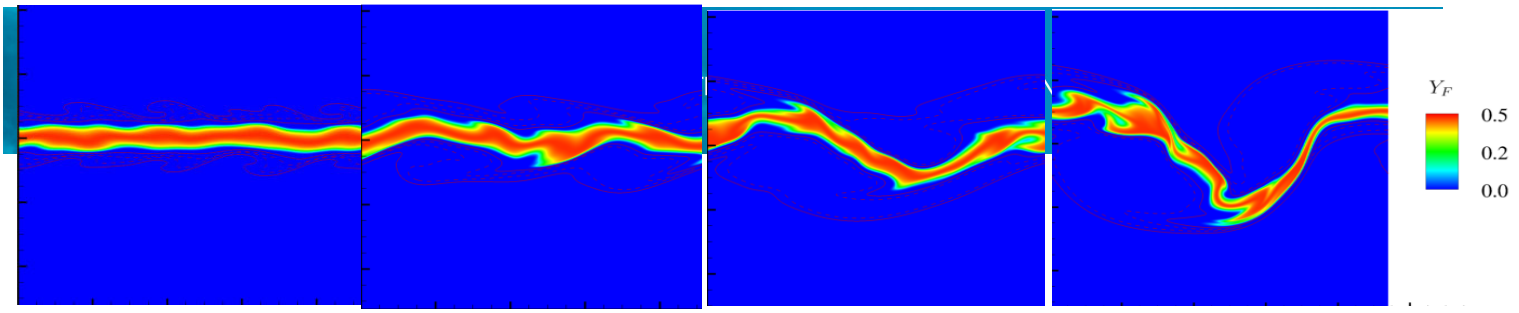

Figure 17. Contours of the Jet A fuel mass fraction overlaid with temperature isolines.

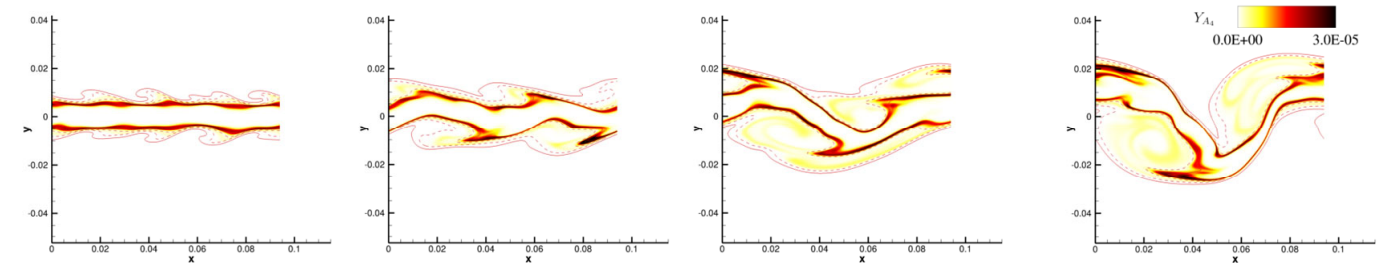

Figure 18. Contours of the pyrene mass fraction overlaid with temperature isolines.

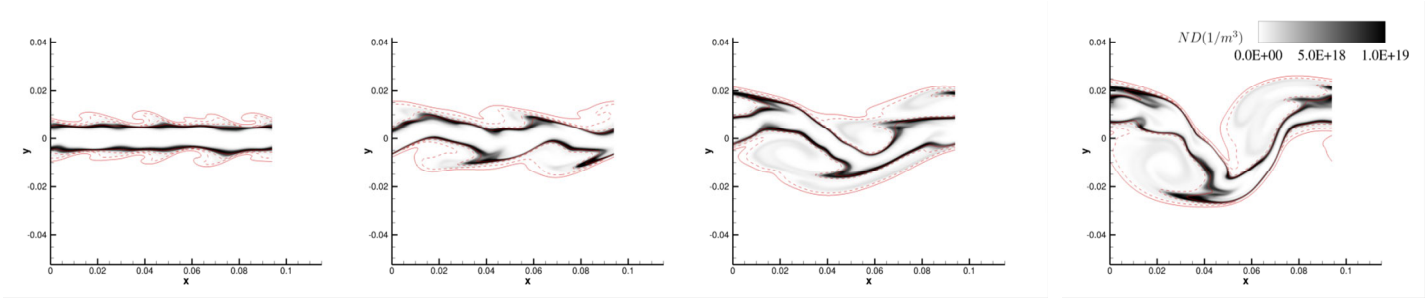

Figure 19. Contours of soot evolution overlaid with temperature isolines; T = 1,600 K (----) and T = 2,000 K (——).

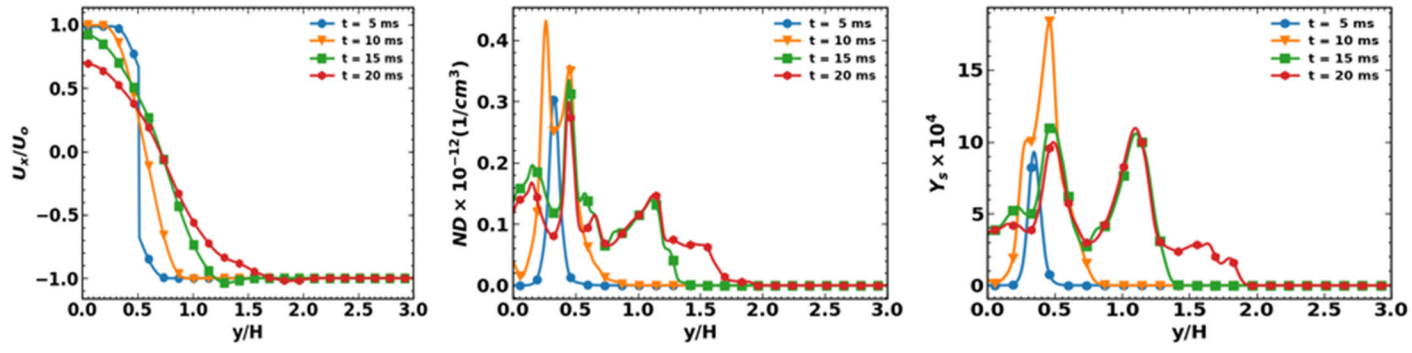

Figure 20. Spatially averaged profiles of velocity, soot number density, and soot mass fractions.

Milestones

Milestone	Planned due date
Improvement of the MOMIC model, identification of inputs and a multiscale strategy for model assessment	9/30/2022

Major Accomplishments

Improvement of the MOMIC framework with PAH pathways, verification against established data, inputs for MOMIC modeling, and simulations of canonical premixed and non-premixed configurations of Jet A fuels

Publications

None.

Outreach Efforts

None.

Awards

None.

Student Involvement

PhD student Shubham Karpe has been assisting in the development of the MOMIC framework within the LES code at GT.

Plans for Next Period

The future work at GT involves incorporating inputs from the abovementioned studies in the existing verified MOMIC framework and assessing any improvements by using the canonical configurations discussed above. The Year 3 efforts will also focus on simulating the RQL combustor rig currently being experimentally investigated under ASCENT FAA Project 70.

References

Attili, A., Bisetti, F., Mueller, M. E., & Pitsch, H. (2014). Formation, growth, and transport of soot in a three-dimensional turbulent non-premixed jet flame. *Combustion and Flame*, *161*(7), 1849–1865. https://doi.org/10.1016/j.combustflame.2014.01.008

Balthasar, M., & Frenklach, M. (2005). Monte-Carlo simulation of soot particle coagulation and aggregation: the effect of a realistic size distribution. *Proceedings of the Combustion Institute, 30*(1), 1467–1475. https://doi.org/10.1016/j.proci.2004.07.035

Chen, J.-Y. (1988). A general procedure for constructing reduced reaction mechanisms with given independent relations. *Combustion Science and Technology*, *57*(1-3), 89–94. https://doi.org/10.1080/00102208808923945

Colket, M. B., Hall, R. J., & Stouffer, S. D. (2004, June 14-17). *Modeling soot formation in a stirred reactor* [Presentation]. Proceedings of the ASME Turbo Expo 2004: Power for Land, Sea, and Air, Vienna, Austria. https://doi.org/10.1115/GT2004-54001

Glarborg, P., Kee, R. J., Grcar, J. F., & Miller, J. A. (1986). *PSE: a Fortran program for modeling well-stirred reactors* (Report No. SAND86-8209). Sandia National Laboratories, Livermore, CA.

El-Asrag, H., & Menon, S. (2009). Large eddy simulation of soot formation in a turbulent non-premixed jet flame. *Combustion and Flame, 156*(2), 385–395. https://doi.org/10.1016/j.combustflame.2008.09.003

El-Asrag, H., Lu, T., Law, C. K., & Menon, S. (2007). Simulation of soot formation in turbulent premixed flames. *Combustion and Flame, 150*(1-2), 108–126. https://doi.org/10.1016/j.combustflame.2007.01.005

Frenklach, M. (2002). Method of moments with interpolative closure. *Chemical Engineering Science, 57*(12), 2229–2239. https://doi.org/10.1016/s0009-2509(02)00113-6.

Kireeva, E. D., Popovicheva, O. B., Persiantseva, N. M., Timofeyev, M. A., & Shonija, N. K. (2009). Fractionation analysis of transport engine-generated soot particles with respect to hygroscopicity. *Journal of Atmospheric Chemistry*, *64*(2-3), 129–147. https://doi.org/10.1007/s10874-010-9173-y

Kollrack R., (1977) ASME paper 76-WA/GT-7, Dec. https://doi.org/10.1115/77-GT-5

Wang, H., Xu, R., Wang, K., Bowman, C. T., Hanson, R. K., Davidson, D. F., Brezinsky, K. and Egolfopoulos, F. N. (2018)

A physics-based approach to modeling real-fuel combustion chemistry-I. Evidence from experiments, and thermodynamic, chemical kinetic and statistical considerations *Combustion and Flame, 193:502-519* https://doi.org/10.1016/j.combustflame.2018.03.019

Leung, K. M., Lindstedt, R. P., & Jones, W. P. (1991). A simplified reaction mechanism for soot formation in nonpremixed flames. *Combustion and Flame, 87*(3-4), 289–305. https://doi.org/10.1016/0010-2180(91)90114-q

Lignell, D. O., Chen, J. H., & Smith, P. J. (2008). Three-dimensional direct numerical simulation of soot formation and transport in a temporally evolving nonpremixed ethylene jet flame. *Combustion and Flame, 155*(1-2), 316–333. https://doi.org/10.1016/j.combustflame.2008.05.020

Lu, T., & Law, C. K. (2005). *A directed relation graph method for mechanism reduction.* Proceedings of the Combustion Institute, *30*(1), 1333–1341. https://doi.org/10.1016/j.proci.2004.08.145

Mitchell, P., & Frenklach, M. (1998). Monte Carlo simulation of soot aggregation with simultaneous surface growth-why primary particles appear spherical. *Symposium (International) on Combustion, 27*(1), 1507–1514. https://doi.org/10.1016/s0082-0784(98)80558-4

Saldinger, J. C., Elvati, P., & Violi, A. (2021). Stochastic and network analysis of polycyclic aromatic growth in a coflow diffusion flame. *Physical Chemistry Chemical Physics, 23*(7), 4326–4333. https://doi.org/10.1039/d0cp03529g

Slowik, J. G., Cross, E. S., Han, J.-H., Davidovits, P., Onasch, T. B., Jayne, J. T., Williams, L. R., Canagaratna, M. R., Worsnop, D. R., Chakrabarty, R. K., Moosmüller, H., Arnott, W. P., Schwarz, J. P., Gao, R.-S., Fahey, D. W., Kok, G. L., & Petzold, A. (2007). An inter-comparison of instruments measuring black carbon content of soot particles. *Aerosol Science and Technology, 41*(3), 295–314. https://doi.org/10.1080/02786820701197078

Srinivasan, S., & Menon, S. (2015). *Soot modeling using the linear eddy model* (Report No. CCL-TR-2015-03-10)., Environmental Protection Agency.

Stouffer, S., Striebich, R. C., Frayne, C. W., & Zelina, J. (2002, July 12-17). *Combustion Particulates Mitigation Investigation Using a Well-Stirred Reactor* [Presentation]. 38th AIAA/ASME/SAE/ASEE Joint Propulsion Conference & Exhibit, Indianapolis, IN.

Sun, Y., & Beckermann, C. (2007). Sharp interface tracking using the phase-field equation. *Journal of Computational Physics, 220*(2), 626–653. https://doi.org/10.1016/j.jcp.2006.05.025

Xu, F., & Faeth, G. M. (2001). Soot formation in laminar acetylene/air diffusion flames at atmospheric pressure. *Combustion and Flame,* 125(1-2), 804–819. https://doi.org/10.1016/s0010-2180(01)00221-8

Xu, Z., & Meakin, P. (2008). Phase-field modeling of solute precipitation and dissolution. *The Journal of Chemical Physics, 129*(1), 014705. https://doi.org/10.1063/1.2948949

Project 072 Aircraft Noise Exposure and Market Outcomes in the United States

Massachusetts Institute of Technology

Project Lead Investigators

R. John Hansman
T. Wilson Professor of Aeronautics & Astronautics
Department of Aeronautics & Astronautics
Massachusetts Institute of Technology
77 Massachusetts Avenue, 33-303
Cambridge, MA 02139
617-253-2271
rjhans@mit.edu

Christopher R. Knittel
George P. Shultz Professor of Applied Economics
Sloan School of Management
Massachusetts Institute of Technology
77 Massachusetts Avenue, E62-527
Cambridge, MA 02139
617-324-0015
knittel@mit.edu

Steven R. H. Barrett
Professor of Aeronautics and Astronautics
Department of Aeronautics and Astronautics
Massachusetts Institute of Technology
77 Massachusetts Avenue, 33-207
Cambridge, MA 02139
617-452-2550
sbarrett@mit.edu

Jing Li
Assistant Professor of Applied Economics
Sloan School of Management
Massachusetts Institute of Technology
77 Massachusetts Avenue, E62
Cambridge, MA 02139
617-252-1131
lijing@mit.edu

Florian Allroggen
Executive Director Aerospace Climate & Sustainability & Research Scientist
Department of Aeronautics and Astronautics
Massachusetts Institute of Technology
77 Massachusetts Avenue, 33-115A
Cambridge, MA 02139
617-715-4472
fallrogg@mit.edu

University Participants

Massachusetts Institute of Technology

- P.I.: Professor R. John Hansman
  Co-P.I.s: Professor Christopher R. Knittel, Professor Steven Barrett, Professor Jing Li, and Dr. Florian Allroggen
- FAA Award Number: 13-C-AJFE-MIT, Amendment Nos. 075, 081, and 094
- Period of Performance: August 11, 2020 to January 13, 2023
- Tasks (tasks listed below are general project tasks; reporting includes the period from September 1, 2021 to August 31, 2022):
  1. Literature review (completed during the past reporting period)
  2. Empirical identification strategy and scope of data set
  3. Calculation of noise impact metrics
  4. Cleaning and aggregation of housing transaction data set
  5. Descriptive analysis of data set
  6. Empirical analysis (not reported; task to be worked on in the coming reporting period)

Project Funding Level

This project received $480,000 in FAA funding and $480,000 matching funds. Sources of match are approximately $133,000 from MIT, plus third-party in-kind contributions of $268,000 from NuFuels LLC, and $79,000 from Savion Aerospace Corporation.

Investigation Team

- Professor R. John Hansman, P.I., MIT (Tasks 1, 2, 3, 5, and 6)
- Professor Christopher R. Knittel, co-P.I., MIT (Tasks 1, 2, 4, 5, and 6)
- Professor Steven R.H. Barrett, co-P.I., MIT (Tasks 1, 5, and 6)
- Professor Jing Li, co-P.I., MIT (Tasks 1, 2, 4, 5, and 6)
- Dr. Florian Allroggen, co-P.I., MIT (all tasks)
- Dr. Xibo Wan, postdoctoral associate, MIT (Tasks 1, 2, 4, 5, and 6)
- Zhishen Wang, graduate student, MIT (Tasks 3 and 5)
- Kevin Zimmer, graduate student, MIT (Tasks 3 and 5)

Project Overview

As enplanements at U.S. airports have increased by almost 50% over the past two decades, the number of Americans exposed to substantial levels of aircraft noise have substantially decreased. However, considerable concerns regarding aircraft noise remain in some airport communities. This project leverages revealed-preference approaches to infer the “implicit price” of aircraft noise exposure from market outcomes in U.S. airport communities. More specifically, the research team is quantifying the capitalized disutility associated with aircraft noise exposure through analyzing the empirical relationship between aircraft noise exposure and transaction values for residential properties in communities surrounding U.S. airports. The project leverages potential changes in noise exposure associated with quasi-experimental settings, e.g., the opening of new runways or changes in arrival and departure paths, to empirically identify potential house price impacts. The results provide insights into the average impacts of noise exposure on residential property values, while also assessing dynamic adjustment processes and potential heterogeneities in revealed preferences, targeting factors, such as time, location, or noise exposure patterns.

Task 1 - Literature Review

Massachusetts Institute of Technology

Objective

The goal of this task is to review and summarize the existing body of literature in two topic areas:

- Empirical analyses of the impacts of noise exposure on residential property values
- Noise exposure metrics

Research Approach
The research team systematically reviewed and summarized the existing literature. This process entailed the following:

1. Presenting an overview of existing economic studies on the impacts of noise exposure on residential property values
2. Comparing different noise metrics and their applications, including but not limited to day–night average sound level (DNL), equivalent sound level, maximum sound levels (L_{max}), and metrics considering the frequency and amplitude of noise events

Milestone
The team completed a literature review during the past reporting period.

Major Accomplishments
An outline of findings can be found in the report for the previous reporting period.

Publications
None.

Outreach Efforts
None.

Awards
None.

Student Involvement
Zhishen Wang worked on this task.

Plans for Next Period
The team will continue to update the literature review as needed.

Task 2 - Empirical Identification Strategy and Scope of Data Set
Massachusetts Institute of Technology

Objective
The goal of this task is to describe a strategy for empirically identifying the causal impacts of aircraft noise on residential property values. This task includes identifying valid model specifications to explain variations in residential property prices as well as the most suitable noise metrics to capture noise impacts.

Research Approach
For quantifying the total noise costs (including annoyance), economists have proposed stated-preference and revealed-preference methods. Whereas stated-preference approaches use surveys to obtain estimates of the willingness to pay for noise reductions and/or for the willingness to accept aircraft noise exposure (Bristow et al., 2015), revealed-preference approaches infer the "implicit price" of noise exposure from market outcomes (Rosen, 1974). Hedonic pricing studies face a variety of challenges, including (a) omitted-variable bias, particularly due to unobserved neighborhood characteristics and to omission of the positive amenity impact of airports in surrounding communities; (b) misspecification of the functional form; and (c) stability assumptions regarding preferences among individuals across space and time (Chay & Greenstone, 2005; Kuminhoff et al., 2010; Nelson, 2004; Parmeter & Pope, 2013). To address some of these concerns, the most recent studies have relied on quasi-experimental settings that leverage changes in noise exposure, e.g., those due to flight track changes, to empirically identify the causal impacts of noise exposure on property values (Almer et al., 2017; Boes & Nüesch, 2011; Winke, 2017; Zheng et al., 2020).

For this study, the team identified experimental settings that provide exogenous variation in noise exposure to analyze the impacts of noise exposure on residential property values. Most importantly, the introduction of high-precision area navigation (RNAV) and/or performance-based navigation procedures since 2012 has led to the relocation of departure and

approach flight paths or may have concentrated noise exposure along defined flight tracks. In addition, new runway configurations, such as those at Chicago O'Hare International Airport, have led to changes in noise exposure patterns. This variation will be used in this analysis.

To identify the capitalized impact of aircraft noise on house prices, the team uses hedonic difference-in-differences designs (Kuminoff et al., 2010; Parmeter et al., 2007; Parmeter & Pope, 2013) and exploits the two sources of variation outlined above. The capitalized impact of noise exposure is estimated as the change in prices between the pre- and post-implementation periods for houses with different levels of aircraft noise exposure. The main specification is as follows:

$$lnP_{ijt} = \beta_0 + \beta_1 lnNoise_{it} + \beta_2 Z_{ijt} + \beta_3 X_{ijt} + \gamma_{jt} + \eta_m + \epsilon_{ijt} \quad (1)$$

where *i* indicates the house, *j* is the zip code where house *i* is located, and *t* is the year. The outcome of interest is the house price (in 2011), lnP_{ijt}, which is the log of the Consumer Price Index-deflated sale price for property *i* at zip code *j* in year *t*. $lnNoise_{it}$ represents the log of the noise exposure of property *i* in year *t*. To obtain unbiased estimates of noise impacts, we include (a) the vector Z_{ijt} which captures house characteristics such as property age, building area, and house condition; (b) the vector X_{ijt} of neighborhood attributes such as census-block-group-level demographics and household median income, as well as distance to local (dis)amenities (e.g., city hall, rail, road, shopping mall, and open space); and (c) zip-code-by-year fixed effects γ_{jt} and month fixed effects η_m to control for unobserved time-varying neighborhood attributes and the seasonality of housing prices. $\epsilon_{ijt}$is an idiosyncratic error term. Standard errors are clustered at the level of the fixed effect to account for remaining spatial correlation.

The coefficient of interest is β_1, which measures the percentage change in the average house price growth due to a 1% change in noise exposure. The coefficient can be interpreted as the capitalized effect of noise exposure or the marginal willingness to pay in the post-period equilibrium if the change in noise exposure is orthogonal to the initial level of the noise, house and neighborhood characteristics, and to changes in those variables. A negative coefficient indicates that prices decrease with higher noise levels.

The specification shown in Equation 1 leaves open the question of which characteristics of aircraft noise exposure affect house prices. To investigate how home buyers respond to aircraft noise in terms of level, frequency, and extreme events, we explore several metrics, such as annual DNL, the number of days in a year that households experience at least one noise event above 60-dB L_{max}, and the number of noise events above 60-dB L_{max} during the peak day. The team uses machine learning techniques (least absolute shrinkage and selection operator, or LASSO) to systematically assess these metrics and to identify the most relevant noise characteristics to capture the capitalized noise response.

Milestone

The team has refined the empirical strategy, specifically focusing on identifying different modeling strategies to capture heterogeneities among properties and neighborhoods, while leaving sufficient variation to measure the impact of aircraft noise.

Major Accomplishments

The team tested several econometric methods to reduce the bias from omitted variables. Most importantly, the results suggest limited noise change within individual census-block groups (Figure 1). Census-block-group fixed effects therefore preclude the model from identifying the noise impacts on housing price. Therefore, the team proceeded with using explicit measures such as census-block-group demographics and economic variables as well as distances to local (dis)amenities to control for neighborhood effects instead of fixed effects. In addition, the team added zip-code-by-year fixed effects and month fixed effects to control for unobserved time-varying neighborhood attributes and the seasonality of housing prices. Work on identifying the most significant noise metrics is underway.

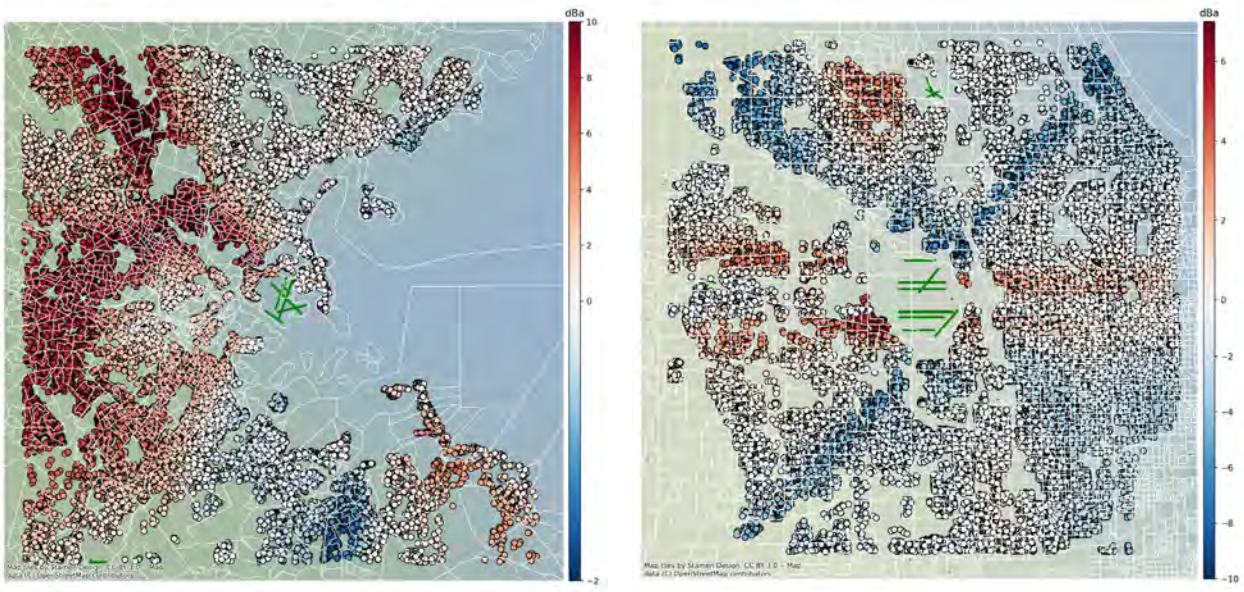

Figure 1. DNL changes over time within census-block groups in Boston (left) and Chicago (right). Noise changes are shown for residential properties in the sample, i.e., those that were sold in 2011 and 2016. White lines depict census-block-group boundaries. Limited variation in noise changes is seen within individual census-block groups. Figures are based on preliminary calculations and are subject to revision.

Publications
None.

Outreach Efforts
The team presented the approach in a presentation during the ASCENT Spring meeting in 2022 and in a project summary submitted to the ASCENT Fall meeting in 2022.

Plans for Next Period
The team will continue to refine the empirical approach.

Awards
None.

Student Involvement
None.

References
Almer, C., Boes, S., & Nüesch, S. (2017). Adjustments in the housing market after an environmental shock: evidence from a large-scale change in aircraft noise exposure. *Oxford Economic Papers*, *69*(4), 918-938. https://doi.org/10.1093/oep/gpw071

Ahlfeldt, G. M., & Maennig, W. (2013). External productivity and utility effects of city airports. *Regional Studies*, *47*(4), 508-529. https://doi.org/10.1080/00343404.2011.581652

Beimer, W., & Maennig, W. (2017). Noise effects and real estate prices: A simultaneous analysis of different noise sources. *Transportation Research Part D*, *54*, 282-286. https://doi.org/10.1016/j.trd.2017.05.010

Boes, S., & Nüesch, S. (2011). Quasi-experimental evidence on the effect of aircraft noise on apartment rents. *Journal of Urban Economics*, *69*, 196-204. 10.1016/j.jue.2010.09.007

Bristow, A. L., Wardman, M., & Chintakayala, V. R. K. (2015). International meta-analysis of stated preference studies of

transportation noise nuisance. *Transportation*, *42*(1), 71-100. https://doi.org/10.1007/s11116-014-9527-4
Chay, K. Y., & Greenstone, M. (2005). Does air quality matter? Evidence from the housing market. *Journal of Political Economy*, *113*(2), 376-424. http://dx.doi.org/10.1086/427462
Kuminghoff, N. V., Parmeter, C. F., & Pope, J. C. (2010). Which hedonic models can we trust to recover the marginal willingness to pay for environmental amenities? *Journal of Environmental Economics and Management*, *60*, 145-160. https://doi.org/10.1016/j.jeem.2010.06.001
Rosen, S. (1974). Hedonic prices and implicit markets. Product differentiation in pure competition. *Journal of Political Economy*, *82*(1), 34-55. http://dx.doi.org/10.1086/260169
Winke, T. (2017). The impact of aircraft noise on apartment prices: a differences-in-differences hedonic approach for Frankfurt, Germany. *Journal of Economic Geography*, *17*, 1283-1300. https://doi.org/10.1093/jeg/lbw040
Wolfe, P. J., Kramer, J. L., & Barrett, S. R. H. (2017). Current and future noise impacts of the U.K. hub airport. *Journal of Air Transport Management*, *58*, 91-99. https://doi.org/10.1016/j.jairtraman.2016.09.002
Zheng, X., Peng, W., & Hu, M., 2020. Airport noise and house prices: A quasi-experimental design study. *Land Use Policy*, *90*, 104287. DOI: 10.1016/j.landusepol.2019.104287
Black, S. E. (1999). Do better schools matter? Parental valuation of elementary education. *The Quarterly Journal of Economics,* 114(2), 577–599. https://doi.org/10.1162/003355399556070
Tsui, W. H. K., D. T. W. Tan, and S. Shi (2017). Impacts of airport traffic volumes on house prices of New Zealand's major regions: A panel data approach. *Urban Studies*, 54(12), 2800–2817. DOI: 10.1177/0042098016660281
Von Graevenitz, K. (2018). The amenity cost of road noise. *Journal of Environmental Economics and Management, 90*, 1–22. DOI: 10.1016/j.jeem.2018.04.006
Parmeter, C. F. and J. C. Pope (2013). *Quasi-experiments and hedonic property value methods*. In Handbook on experimental economics and the environment. Edward Elgar Publishing. https://doi.org/10.4337/9781781009079.00007
Ossokina, I. V. and G. Verweij (2015). Urban traffic externalities: Quasi-experimental evidence from housing prices. *Regional Science and Urban Economics, 55*, 1–13. https://doi.org/10.1016/j.regsciurbeco.2015.08.002

Task 3 – Calculation of Noise Metrics

Massachusetts Institute of Technology

Objective

The goal of this task is to calculate aircraft noise exposure in communities surrounding selected U.S. airports. These analyses will be used to derive noise exposure changes associated with changes in flight trajectories (e.g., owing to new runways or new procedures).

Research Approach

The MIT team uses the Aviation Environmental Design Tool (AEDT) to model noise exposure according to historical flight track data at high temporal and spatial resolution. The high-resolution approach is required, because the noise changes in performance-based navigation procedures are expected to be highly localized. One limitation of AEDT is in processing speed. Because it calculates noise for each flight track individually, a single day of flights can require hours to process. To circumvent this limitation, a fast model was developed at MIT under this project (Jansson, 2021). This model uses AEDT outputs for various aircraft types to set up a noise lookup table. Next, it uses flight track data from the Airport Surface Detection Equipment, Model X (ASDE-X) and applies the noise–power–distance curves from AEDT to obtain accurate noise data on an annual scale.

The tool is currently set up to calculate DNL and N_{above} as noise metrics. The N_{above} metric is the number of instances an overflight event is above a certain L_{max} threshold over a day. For example, an N_{60} of 25 indicates that 25 overflight events had an L_{max} of 60 dB or greater that day. We use N_{above} in addition to DNL in our assessments.

Milestone

The team set up the modeling chain and ran the model for three airports (described below). In addition to DNL metrics, analysis was conducted for N_{60}.

Major Accomplishments

The team set up the modeling chain and ran detailed noise analyses for the years 2012 and 2016 for Boston Logan, Seattle Tacoma, and Chicago O'Hare airports (results in Task 4).

Publications
None.

Outreach Efforts
The team presented the approach in a presentation during the ASCENT Spring meeting in 2022 and in a project summary submitted to the ASCENT Fall meeting in 2022.

Awards
None.

Student Involvement
Zhishen Wang and Kevin Zimmer worked on this task.

Plans for Next Period
The team will continue this task by refining the modeling approach and simulating noise exposure at additional airports.

Task 4 - Cleaning and Aggregation of the Housing Transaction Data Set
Massachusetts Institute of Technology

Objective
The goal of this task is to obtain a data set on transaction values for residential properties in the United States. The data set must capture detailed data for each transaction, including the location of the property, and the characteristics of the transaction (e.g., purchase price and closing date) and the property (e.g., lot and property sizes, and numbers of bedrooms and bathrooms).

Research Approach
The research team obtained the Zillow Transactions and Assessor Dataset (ZTRAX) and developed methods for cleaning it during previous reporting periods. Details can be found in the Year 2021 annual report.

Milestone
The team completed this task during the previous reporting period.

Major Accomplishments
An outline of the approach can be found in the report for the previous reporting period.

Publications

Outreach Efforts
The team presented the approach in a presentation during the ASCENT Spring meeting in 2022 and in a project summary submitted to the ASCENT Fall meeting in 2022.

Awards
None.

Student Involvement
None.

Plans for Next Period
The team will continue to update cleaning methods as necessary.

Task 5 - Descriptive Analysis of the Data Set

Massachusetts Institute of Technology

Objective

For a small subset of airports, the team conducts descriptive analyses of noise and residential property value data to gain insights into the validity of the data sets, as well as general noise and property value trends.

Research Approach

Descriptive analyses are conducted by analyzing data obtained under Tasks 3 and 4. During the reporting period, we focused on analyzing noise data for Boston Logan International Airport, Chicago O'Hare International Airport, and Seattle Tacoma International Airport, and on residential property values surrounding these airports. All analyses are limited to a radius of 20 nautical miles around the airports, because of range limitations for the ASDE-X data.

Milestone

Preliminary empirical analyses shown in last year's report were extended to better understand correlations between noise exposure changes and changes in property values.

Major Accomplishments

Descriptive analyses of noise trends for Chicago O'Hare International Airport

The fast noise modeling method was run for Chicago O'Hare International Airport data to create average 24-hr DNL noise plots. One run was completed for 2011, and one run was completed for 2016. This procedure allows us to compare the noise levels before and after the opening of runway 10C/28C and runway 10R/28 L in 2013 and 2015, respectively. In the preliminary results (Figure 2), we observe noise increases in the east-west direction. These noise changes track the changes in runway configuration for Chicago O'Hare International Airport.

Figure 2 also includes an analysis using the N_{above} metric with a 60-dBA threshold (N_{60}). The overall trends were found to be similar to the DNL changes. Notably, the primary changes to N_{60} occur closest to the airport.

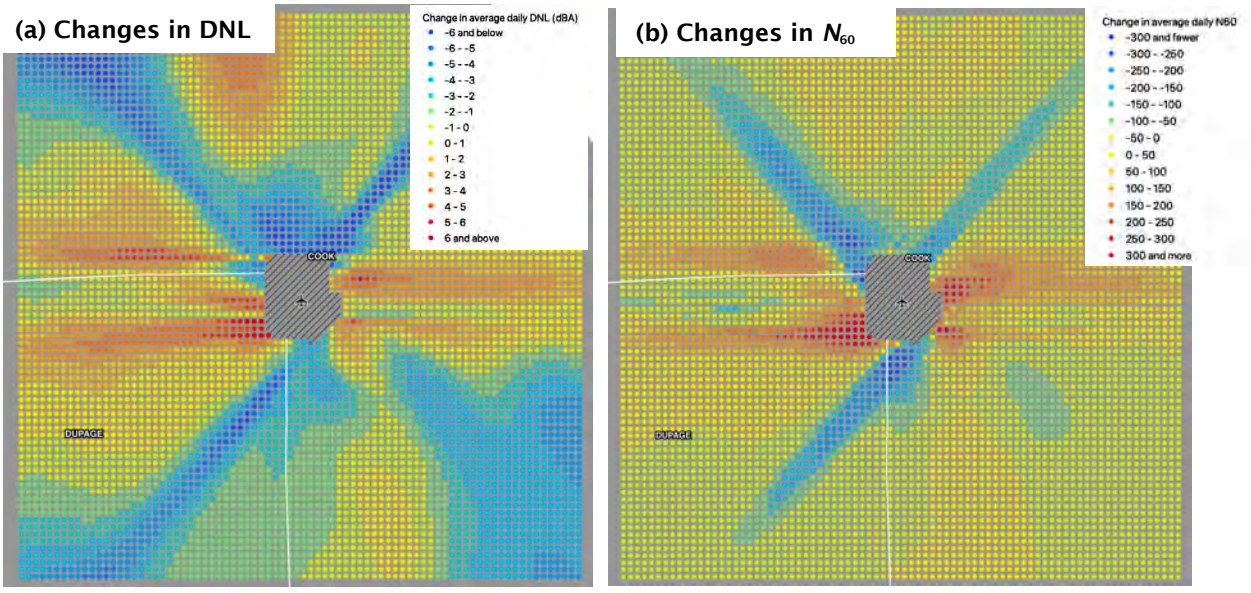

Figure 2. Preliminary calculation of changes in (a) annual average DNL (left) and (b) annual average daily N_{60} (right) between 2011 and 2016 for Chicago O'Hare International Airport. The effects of increased use of east-west runways and decreased use of northeast-southwest/northwest-southeast runways can be seen. Results shown are subject to revision.

Descriptive analyses of noise trends for Seattle Tacoma International Airport

The noise trend analysis was also run for Seattle Tacoma International Airport, which operates primarily three north-south runways. Our preliminary analysis (Figure 3) showed a general increase in daily average DNL, possibly because of an increase in operations. Near the airport, we find slight shifts in DNL, probably as a result of differences in runway use.

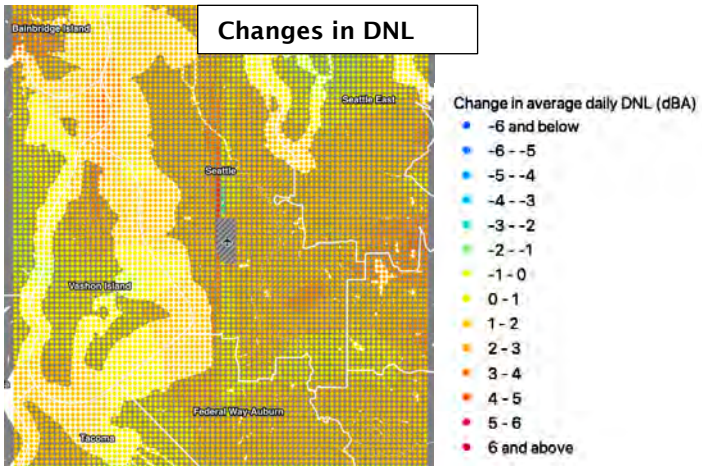

Figure 3. Preliminary calculation of changes in annual average DNL between 2011 and 2016 for Seattle Tacoma International Airport. Results shown are subject to revision.

Descriptive analyses of residential real-estate value in the Boston and Chicago areas

In 2011, the average house sold in Boston sample had a price of approximately $487,230. By 2016, the price had increased to $610,080 (Figure 4). The average house was 80 years old, with four bedrooms and two bathrooms, and 2,286 square feet of living area on a lot of 9,873 square feet. It was located in census-block groups where 23% of the neighborhood was nonwhite, 19% of the neighborhood was under 18 years of age, and the average median family income was $96,780. In contrast, the average house in the Chicago sample did not show any clear sale price trend; was 60 years old; had three bedrooms and two bathrooms; and was on a lot of 7,719 square feet. It was located in block groups where 26% of the neighborhood was nonwhite, 22% was under 18 years of age, and the average median family income was $89,010.

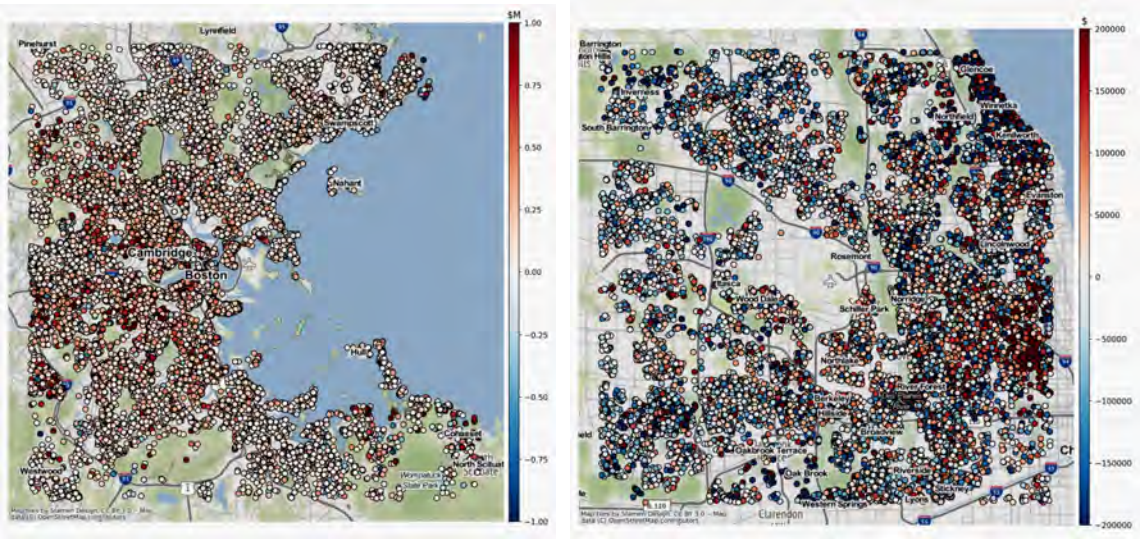

Figure 4. Changes in housing price in 2016–2019 vs. 2009–2011 in Boston (left) and Chicago (right). The property sample includes only houses sold during both the 2016–2019 and 2009–2011 period. Results are subject to revision.

Correlation between housing price and noise

To explore the correlation between housing price changes and DNL changes, the team created a set of "comparable houses" for which the housing prices fell into a particular decile bin in the Boston and Chicago samples (Table 1). For each decile, the correlation graph between changes in log housing prices and changes in log DNL was plotted (Figure 5). In Boston, houses with lower sale prices showed a positive correlation between house price changes and noise exposure changes, probably because of other underlying effects (e.g., renovations). For houses with higher sales prices, a significant correlation was not found. In Chicago, we found similar evidence of houses with lower sales prices. However, houses with higher sales price showed a negative correlation between changes in housing price and changes in DNL over our study period.

Table 4. Transaction price ranges in the residential property subsamples containing "comparable houses," as defined by sales-price deciles. Extreme values are omitted.

Housing price decile bin	Range of transaction price: Boston sample ($)	Range of transaction price: Chicago sample ($)
1	40,000–160,000	31,000–100,000
2	162,500–214,900	101,000–134,500
3	216,000–258,000	135,000–160,000
4	260,000–305,000	161,500–191,500
5	308,000–340,000	192,000–228,500
6	340,500–400,000	229,000–262,000
7	402,500–473,500	264,000–321,000
8	475,500–580,800	324,500–400,000
9	584,000–820,000	402,500–585,000
10	829,000–2,590,000	587,000–3,731,500

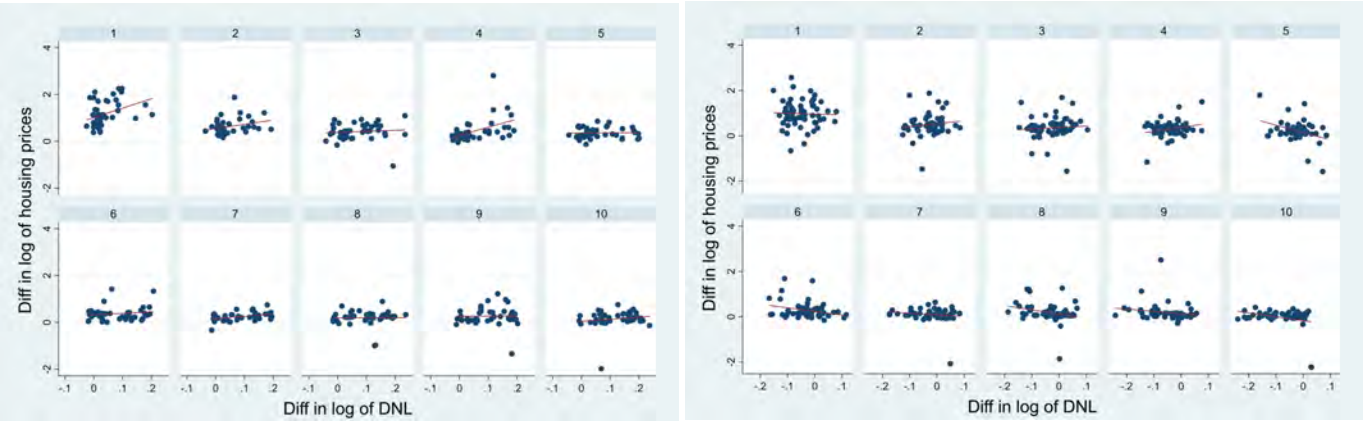

Figure 5. Housing price changes vs. DNL changes by house price group (group 1: lowest house price decile; group 10 highest house price decile) in Boston (left) and Chicago (right). Results are subject to revision.

Publications

None.

Outreach Efforts
The team presented the approach in a presentation during the ASCENT Spring meeting in 2022 and in a project summary submitted to the ASCENT Fall meeting in 2022.

Awards
None.

Student involvement
Graduate students Zhishen Wang and Kevin Zimmer worked on this task.

Plans for Next Period
The team will continue to roll out descriptive analyses to evaluate general trends and data set validity.

Project 073 Fuel Composition Impact on Combustor Durability

University of Dayton Research Institute

Project Lead Investigator

Steven Zabarnick
Division Head, Fuels and Combustion Division
University of Dayton Research Institute
300 College Park, Dayton, OH 45469-0043
937-229-3961
Steven.Zabarnick@udri.udayton.edu

University Participants

University of Dayton Research Institute

- P.I.: Steven Zabarnick, PhD
- FAA Award Number: 13-C-AJFE-UD, Amendment 029
- Period of Performance: August 11, 2020 to September 30, 2021
- Task:
    1. Perform radiation measurements of various fuel types in the referee combustor to evaluate the effect of fuel composition on combustor liner lifetime
- Period of Performance: August 10, 2021 to February 10, 2022: Amendment 036
- Period of Performance: October 1, 2021 to September 30, 2022: Amendment 040
- Period of Performance: October 1, 2022 to September 30, 2023: Amendment 044

Project Funding Level

Amendment No. 029	$299,148
Amendment No. 040	$199,865
Amendment No. 044	$200,000
Total	**$699,013**

Cost-sharing will be provided by fuel producers and engine/airframe original equipment manufacturers (OEMs). The cost-sharing will be given in fuel provided for testing and in fuel performance data provided for the evaluation.

Investigation Team

Steven Zabarnick, Project Director/P.I.
Scott Stouffer, Senior Research Engineer, Co-Investigator:
Tyler Hendershott, Research Engineer, Combustor operations
Jeff Monfort, Research Engineer, Radiation Measurements
Harry Grieselhuber, Technician, Combustor testing
Jeff Gross, Technician, Combustor testing
Graduate Student: TBD
Undergraduate Student: TBD

Project Overview

In this study, the effects of fuel chemical composition on radiative heat transfer and the resulting combustor liner lifetime will be evaluated. Alternative fuels contain ratios of hydrocarbon types that may be substantially different from those in

familiar petroleum-based fuels. In petroleum-based fuels, higher aromatic levels are known to contribute to greater particulate matter loading radiative heat transfer and reduced combustor liner lifetimes. Consequently, aromatic compounds are limited to 25 vol% in the ASTM D1655 jet fuel specification. Some candidate alternative fuels contain synthetically produced aromatic compounds and cycloparaffins, which must be evaluated for their radiative heat transfer characteristics. The measurements collected in this project will provide insights into the effects of fuel type on liner lifetime. Several fuel types will be investigated, including a synthetic aromatic kerosene, a baseline Jet A fuel, and a fuel high in cycloparaffins (e.g., Shell IH^2 fuel). Diagnostic methods to be used in the investigation include the measurement of wall and gas temperatures, and the use of infrared (IR) cameras and radiometers.

Task 1 - Perform Radiation Measurements of Various Fuel Types in the Referee Combustor to Evaluate the Effect of Fuel Composition on Combustor Liner Lifetime

University of Dayton Research Institute

Objective

The objective of this program is to provide insights into the effect of fuel type on engine combustor liner lifetime. This study will ensure that candidate drop-in fuels will perform satisfactorily in jet engines and not increase the need for engine maintenance or decrease flight safety. The findings of this study may also indicate which fuel composition changes may reduce radiative heat transfer and therefore increase combustor liner lifetime.

Research Approach

Fuel chemical composition is well known to strongly affect soot formation, smoke production, and radiative heat flux in gas turbine combustors (Chin & Lefebvre, 1990). Studies of petroleum-based fuels with varying levels of aromatic levels have indicated that these properties increase with the overall content of aromatic species. Other parameters such as hydrogen content, hydrogen/carbon (H/C) ratio, and smoke point have also been correlated with liner temperatures, but the effects of individual types of aromatic species have not been well studied. Candidate alternative fuels may meet the overall limits for aromatic species but may contain individual species or mixtures of species that are markedly different from those in petroleum-derived fuels. Radiation heat transfer to combustor liners is a major issue affecting the durability and operational envelope of gas turbine engines. Radiation can cause high heat fluxes, thus resulting in localized heating, hot spots, and high thermal gradients along and across the liner. Increases in liner temperature can decrease liner durability (Gleason & Bahr, 1980). Intense heating can cause problems with low cycle fatigue, cracking, and buckling of the liner and, in extreme cases, localized melting of the liner. The combustor walls can be convectively cooled by effusion or film cooling; however, film cooling typically imposes a cycle performance penalty, along with elevated levels of CO and unburnt hydrocarbons, particularly at low power settings. Because of concerns regarding the effects of fuel type on radiation, the radiant heat flux is considered a figure of merit by aircraft engine OEMs in the evaluation of alternative fuels for aircraft use (Boehm, 2013).

The radiation from a gas turbine flame has two main components: (a) "non-luminous" radiation from product gases, such as CO_2, H_2O, and CO, and (b) luminous radiation from non-volatile particulate matter (principally soot).

Non-luminous radiation corresponds to the infrared region and has a spectral distribution, whereas the luminous radiation is broadband, and a fraction of the radiation appears at visible wavelengths. Typically, as the pressure is increased, the luminous radiation from soot particles becomes the dominant source of heat flux to the liner walls. Whereas the convective component of the wall heat transfer depends on the fluid dynamics and gas temperature distribution near the walls, the peak radiant fluxes are related to the combinations of high-temperature gas and non-volatile particulate matter.

The emissivity of the combustion gases is typically related in an expression such as:

$$\epsilon_g = 1 - exp\left[-aPL(ql)^{0.5}T_g^{-1.5}\right]$$

where P = gas pressure in kPa
l = characteristic length factor, which is a function of combustor geometry
T_g = gas temperature in K
q = fuel-to-air ratio
L = luminosity factor

The luminosity factor is set to 1 for gaseous emissivity. For sooting flames associated with liquid aviation fuels, the luminosity is >1 and can be correlated with the fuel composition. Several relations between luminosity and fuel type have been reported in the literature (Lefebvre, 1999; Naegeli, 1980; Clark, 1982). In general, the luminosity factor has been found to decrease with increasing H/C ratio and decreasing aromatic content of the fuel. Other correlations in the literature have addressed the correlations with smoke point and naphthalene content. Although IR has been used as a diagnostic tool in basic flame experiments (Rankin, 2012), very little work using multiple radiometer and/or planar measurements of IR emissions in practical combustors has been reported in the literature. The referee rig combustor is ideal for assessing radiation heat transfer because the walls are heavily cooled—a condition that tends to suppress the convective component and thus the background radiant heating from opposing walls, so that the wall heat transfer is primarily from the flame radiation. Furthermore, provisions have been made for radiometer access to the combustor walls in the referee rig.

The referee rig combustor was developed to conduct experimental combustion research. Highlights of previous contributions to the evaluation of alternative fuels include the following:

1. Experimental measurements of lean blowout (LBO) for fuels at conditions of interest to OEMs and the National Jet Fuels Combustion Program, which have resulted in the unexpected finding of a high correlation between the derived cetane number and the LBO limit
2. Experimental measurements of boundary conditions for the combustor, including air flow splits to support numerical combustion modeling efforts
3. Development of cold air and cold fuel capabilities for the facility, to enable atmospheric cold start ignition experiments to be conducted over a range of conditions
4. Further extension of the facility's ability to allow altitude relight experiments to be conducted with a range of fuels at simulated altitudes of 25,000 ft
5. Examination of the effects of heated fuels on combustion characteristics and emissions

The work with the referee rig combustor has yielded publications that detail cold start ignition (Hendershott, 2018), ignition at elevated temperatures (Stouffer, 2017), LBO characteristics (Corporan, 2017; Esclapez, 2017; Colborn, 2020), particulate and gaseous emissions (10), acoustic response (Monfort, 2017), flow through the liner effusion passages (Erdmann, 2017; Briones, 2017), spray characteristics (Mayhew, 2017), and altitude relight ((Stouffer, 2020; Stouffer, 2021).

Milestones

The anticipated major milestones and planned due dates are as follows:

Milestone	Planned due date
Test plan provided	December 1, 2020
Initial instrumentation experiments conducted	September 2022
Detailed testing performed for a range of fuels	April 1, 2023
Final report	September 30, 2023

Major Accomplishments

Experiments during the past year involved initial evaluations of the instrumentation, including thermocouples on the combustor liners, radiometers, and visible and infrared cameras. The experiments were all conducted with the cooperation of the Air Force Research Laboratory by using the referee combustor rig. Three fuels were used for these initial experiments:

1. A2, a baseline average Jet A fuel containing 17% v/v aromatic compounds
2. Hydroprocessed esters and fatty acids (HEFA) fuel containing <0.5% v/v aromatic compounds, which has been shown to produce relatively low levels of non-volatile particulate matter in previous experiments (Corporan, 2017)
3. A highly aromatic fuel containing 30% v/v aromatic compounds, which produces high levels of non-volatile particulate matter

At the same equivalence ratio, all three fuels have similar expected heat release (within 1%), according to the heat of combustion and the stoichiometric fuel and air ratios.

Figure 1 shows the visible light images captured with a digital single-lens reflex camera for the three fuels. All images were adjusted to equivalent exposure levels and show that the visible light increases with the equivalence ratio. In general, the flame stretches further along the combustor length as the equivalence ratio is increased. The images also show that at any

equivalence ratio, the flame images show that the fuels rank as follows in brightness from highest to lowest: high-aromatic fuel, baseline A2 fuel, and HEFA fuel.

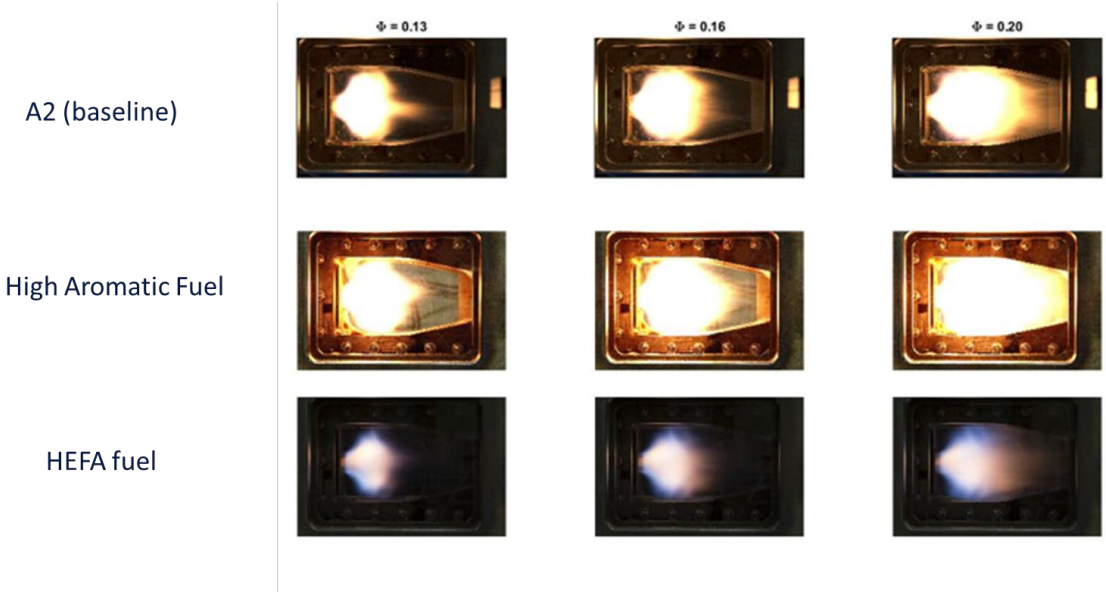

Figure 1. Visible radiation for three fuels as a function of the equivalence ratio (ϕ).

Wall temperatures and incident radiation measurements

The referee combustor was designed with a radiometer port enabling installation of a radiometer in the top combustor liner wall. The installation of the radiometer through the top liner wall required an extension to the pressure vessel to be built to allow for clearance of the cooling, and purge tubes as well as the wires. Figure 2 shows the installation of the radiometer. The radiometer was a Gardon type and was mounted near the dome region of the combustor (Figure 2C). The radiometer is cooled and measures the total radiation enclosed in a 150° cone centered at the gauge location.

Initial experiments with the radiometer indicated the following observations:

- The radiometer was sensitive to changes in the combustor operating point and fuel type over the entire range of conditions.
- The radiometer purge flow (N_2 over the radiometer surface windows) was found to have little impact on the combustor operation or the intensity of the flame.
- As the combustor pressure increased, the radiation level increased.
- As the equivalence ratio increased, the incident radiation measured at the radiometer generally increased.

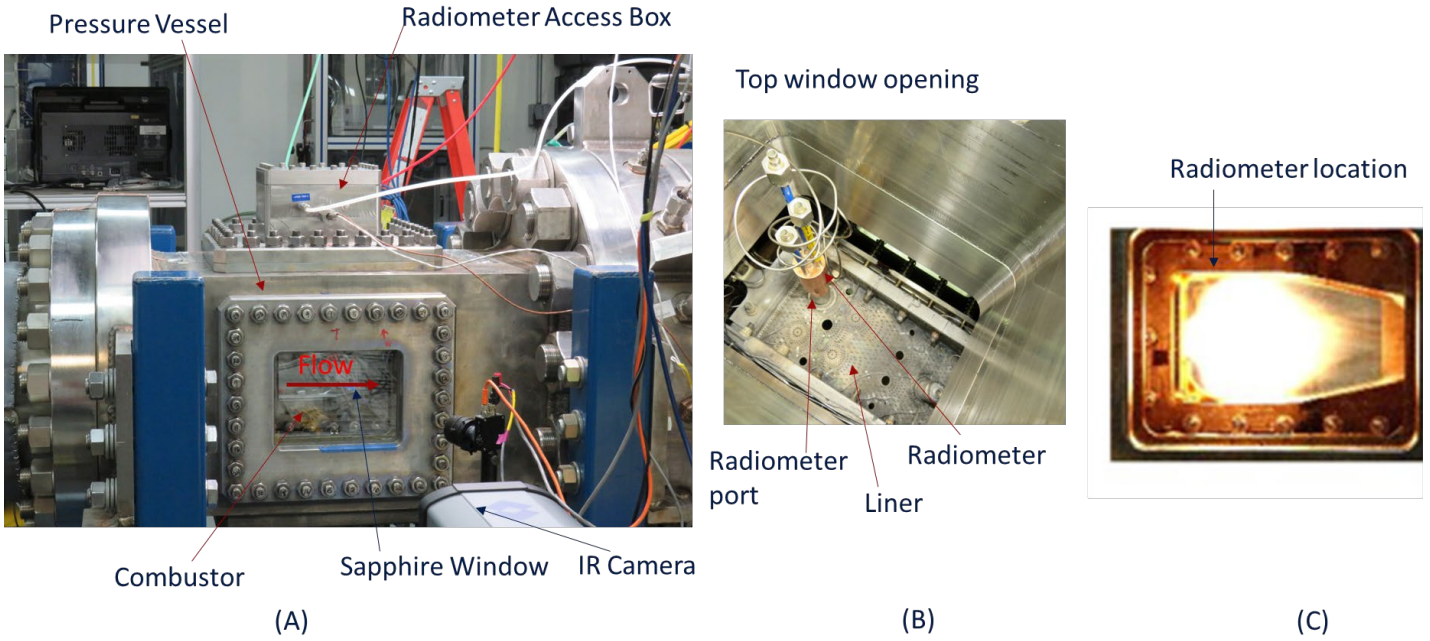

Figure 2. Experimental setup of the radiometer and IR camera. (A) Side view. (B) Top view, looking through the radiometer access box. (C) Radiometer location inside the combustor.

Figure 3 shows the radiometer output versus the equivalence ratio for the three fuels. The equivalence ratio shown is the global equivalence ratio, which is lower than the equivalence ratio in the primary zone, owing to the high levels of effusion cooling through the combustor liner, as previously discussed (Erdmann, 2017). The primary zone equivalence ratio is 5.5 times the global equivalence ratio; consequently, at the highest global equivalence ratio shown (0.24), the primary zone equivalence ratio is approximately 1.32 (fuel rich). Over most of the range of equivalence ratios, the highest radiative loading at the radiometer location is observed for the high-aromatic fuel. The results show that over most of the range, the radiative heating at the gauge location increases with the equivalence ratio. The exception to this trend occurs for the highest the equivalence ratio for the A2 fuel and the high-aromatic fuel. At this the equivalence ratio, the radiative loading at the gauge location for two fuels with the highest aromatic content is lower than that at the next highest the equivalence ratio.

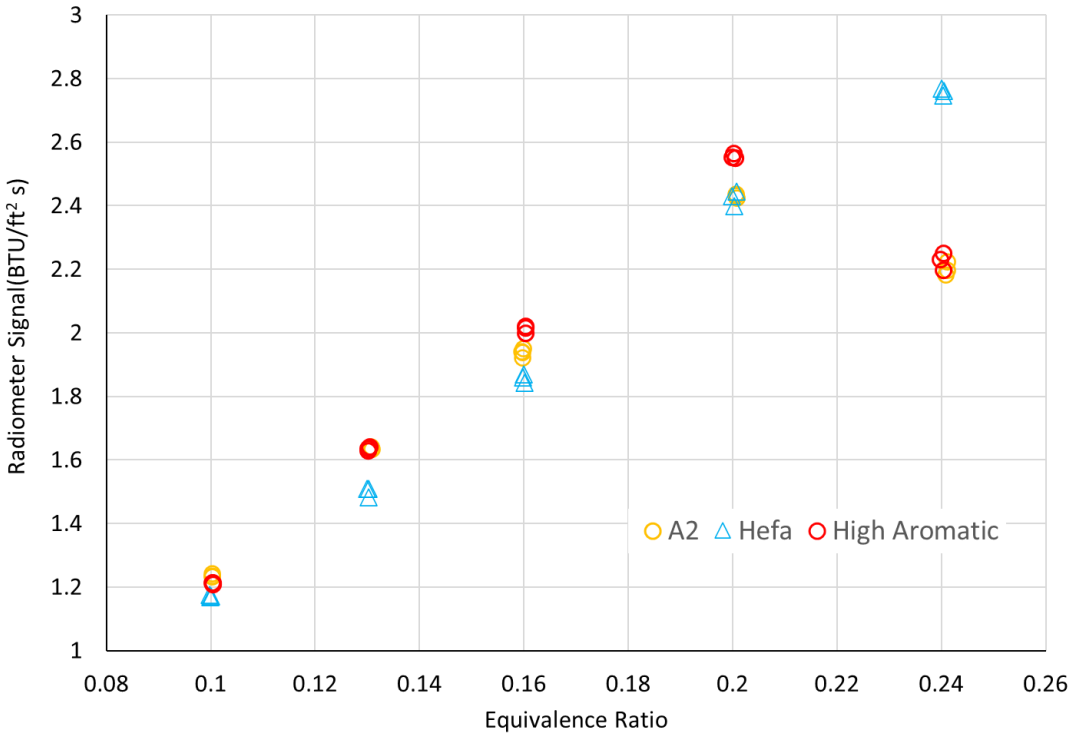

Figure 3. Radiometer signal versus equivalence ratio. Measurements were taken at T_{air} = 250 ˚F, T_{fuel} = 120 ˚F, P_{cmb} = 30 psia, and ΔP = 3%.

Thermocouples were mounted on the backside (cold side) of the combustor. The temperature rise on the backside was used as a secondary indication of total heating to the combustor walls, including both convective and radiative heat transfer. Figure 4 shows the average of the thermocouples on the upstream side of the combustor (upstream of the secondary dilution holes). Of note, the trends in this plot are consistent with those shown for the radiometer output shown in Figure 2. The wall temperatures for the A2 and the high-aromatic fuels decrease at the highest equivalence ratio, showing a trend similar to that observed for the incident radiation. This finding is believed to be due to the flame exhibiting a greater shift downstream for the A2 and the high-aromatic fuel. This trend is also shown in the infrared imaging results in Figure 5.

Figure 4. Average wall temperatures for the region upstream of the secondary dilution Jets. Measurements were taken at T_{air} = 250 ˚F, T_{fuel} = 120 ˚F, P_{cmb} = 30 psia, and ΔP = 3%.

The results indicate that the radiometer output is a measurement of the incident radiation at the gauge location. Therefore, to gain a more comprehensive picture of the radiation in the combustor, more radiometer locations are needed. In the next series of tests, the intent is to manufacture a side panel and install more radiometers in the combustor at different locations to obtain a more comprehensive picture of the incident radiation.

Infrared camera visualization experiments

At the beginning of the program, large-scale sapphire windows were purchased to allow for visualization of the IR radiation with infrared cameras in the spectral range of 1.5 to 5 μm. The intent was to obtain large-scale IR images in the combustor and also use filters to sample spectral regions that are dominated by either blackbody radiation or by radiation from major species (H_2O, CO_2, and CO). The referee rig uses two sets of windows for visualization: (a) an inner set that is associated with the combustor and is exposed to the combustion gases, and (b) an outer set that is installed in the surrounding pressure vessel. The inner windows are relatively thinner and are exposed to a large thermal gradient and a small pressure gradient, whereas the outer windows are exposed to large pressure gradients with much lower thermal gradients. The large outer windows worked well throughout the experiments, whereas the inner windows were found to be highly susceptible to thermal cracking. Efforts were made to improve the inner-window performance by allowing more room for thermal expansion. However, the cracking was determined to be due not to constrained thermal expansion but to thermal shock within 30 s of ignition.

Visualizations were conducted with a combination of quartz inner windows and sapphire outer windows. Quartz windows are robust with respect to the thermal shock, because of the low thermal expansion coefficient, but have the disadvantage of low transmission of IR radiation. This low transmission partially obscures the visualization of the radiation in the combustor by interference from the hot inner-window surface. The effect is more pronounced at wavelengths greater than 2.5 μm. The results from the visualization using this approach showed qualitative agreement with the radiometer findings. Figure 5 shows the infrared measurements using the quartz inner windows and sapphire outer windows along with a neutral-density broadband filter. The results are qualitatively in agreement with those in Figures 3 and 4 for the radiometer and wall

thermocouples. Of note, at the highest equivalence ratio, the regions with the highest signal for the A2 and the high-aromatic fuel, compared with HEFA fuel, are shifted further downstream.

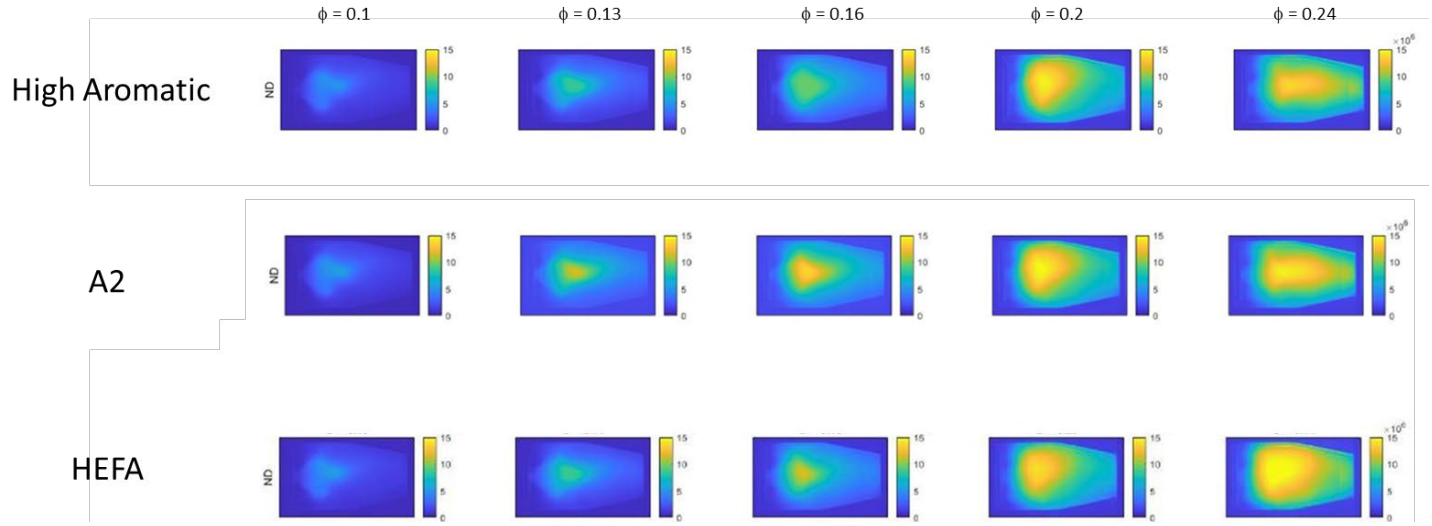

Figure 5. Infrared camera measurements for using a neutral-density filter. Measurements were taken at T_{air} = 250 ˚F, T_{fuel} = 120 ˚F, P_{cmb} = 30 psia, and ΔP = 3%.

An alternative configuration for the inner window was also considered, by using thin, round port windows installed in a metallic side window. Initial experiments used a 37-mm-diameter side window and were found to be successful over a wide range of conditions. With this configuration, we were able to measure IR radiation by using spectral filters over the spectral range of the camera in proof-of-concept experiments. This window design is being extended to more port windows for subsequent experiments.

Publications
None.

Outreach Efforts
None.

Awards
None.

Student Involvement
None.

Plans for Next Period
The plans for the next period are to build on the results of the initial experiments to add more radiometers and enable IR visualization. Sampling of the combustor exhaust will also be conducted, to measure and characterize the particulate matter number density and size distribution. This second phase of experiments will include additional fuels, such as the Shell IH^2 high-cycloparaffin fuel. Discussions are ongoing with Shell to obtain sufficient volumes of IH^2 fuel for testing.

References

.

Chin, J. S., & Lefebvre, A. H. (1990). Influence of fuel composition on flame radiation in gas turbine combustors. *Journal of Propulsion and Power*, *6*(4), 497–503. https://doi.org/10.2514/3.25462

Gleason, G.C. & Bahr, D.W. (1980). *Fuel property effects on Life Characteristics of Aircraft Turbine Engine Combustors* (Report No. 80-GT-55).

Boehm, R., Lohmueller, S., Andac, G., Aicholtz, J., Williams, R., James, S., ... & Greene, M. (2013). Development of Combustion Rules and Tools for the Characterization of Alternative Fuels, Phase 2A. *Rept. AFRL-RQ-WP-TR-2013-0223*.

Lefebvre, A.H. (1999). *Gas Turbine Combustion*. 2nd Edition, Taylor and Francis, Philadelphia.

Naegeli, D.W. & Moses, C.A. (1980). *Effects of Fuel Properties on Soot Formation in Gas Turbine Engines* (Report No. 80-GT-62).

Clark, J. A. (1982). Fuel property effects on radiation intensities in a gas turbine combustor. *AIAA Journal*, *20*(2), 274–281. https://doi.org/10.2514/3.7908

Rankin, B. A., Blunck, D. L., Katta, V. R., Stouffer, S. D., & Gore, J. P. (2012). Experimental and computational infrared imaging of bluff body stabilized laminar diffusion flames. *Combustion and Flame*, *159*(9), 2841–2843. https://doi.org/10.1016/j.combustflame.2012.03.022

Hendershott, T. H., Stouffer, S., Monfort, J. R., Diemer, J., Busby, K., Corporan, E., Wrzesinski, P., & Caswell, A. W. (2018, January 8). Ignition of conventional and alternative fuel at low temperatures in a single-cup swirl-stabilized combustor. *2018 AIAA Aerospace Sciences Meeting*. 2018 AIAA Aerospace Sciences Meeting, Kissimmee, Florida. https://doi.org/10.2514/6.2018-1422

Stouffer, S., Hendershott, T., Monfort, J. R., Diemer, J., Corporan, E., Wrzesinski, P., & Caswell, A. W. (2017, January 9). Lean blowout and ignition characteristics of conventional and surrogate fuels measured in a swirl stabilized combustor. *55th AIAA Aerospace Sciences Meeting*. 55th AIAA Aerospace Sciences Meeting, Grapevine, Texas. https://doi.org/10.2514/6.2017-1954

Corporan, E., Edwards, J. T., Stouffer, S., DeWitt, M., West, Z., Klingshirn, C., & Bruening, C. (2017, January 9). Impacts of fuel properties on combustor performance, operability and emissions characteristics. *55th AIAA Aerospace Sciences Meeting*. 55th AIAA Aerospace Sciences Meeting, Grapevine, Texas. https://doi.org/10.2514/6.2017-0380

Esclapez, L., Ma, P. C., Mayhew, E., Xu, R., Stouffer, S., Lee, T., Wang, H., & Ihme, M. (2017). Fuel effects on lean blow-out in a realistic gas turbine combustor. *Combustion and Flame*, *181*, 82–99. https://doi.org/10.1016/j.combustflame.2017.02.035

Colborn, J., Heyne, J. S., Hendershott, T. H., Stouffer, S. D., Peiffer, E., & Corporan, E. (2020, January 6). Fuel and operating condition effects on lean blowout in a swirl-stabilized single-cup combustor. *AIAA Scitech 2020 Forum*. AIAA Scite ch 2020 Forum, Orlando, FL. https://doi.org/10.2514/6.2020-1883

Mayhew, E., Mitsingas, C. M., McGann, B., Hendershott, T., Stouffer, S., Wrzesinski, P., Caswell, A. W., & Lee, T. (2017, January 9). Spray characteristics and flame structure of jet and alternative jet fuels. *55th AIAA Aerospace Sciences Meeting*. 55th AIAA Aerospace Sciences Meeting, Grapevine, Texas. https://doi.org/10.2514/6.2017-0148

Monfort, J. R., Stouffer, S., Hendershott, T., Wrzesinski, P., Foley, W., & Rein, K. D. (2017, January 9). Evaluating combustion instability in a swirl-stabilized combustor using simultaneous pressure, temperature, and chemiluminescense measurements at high repetition rates. *55th AIAA Aerospace Sciences Meeting*. 55th AIAA Aerospace Sciences Meeting, Grapevine, Texas. https://doi.org/10.2514/6.2017-1101

Erdmann, T. J., Burrus, D. L., Briones, A. M., Stouffer, S. D., Rankin, B. A., & Caswell, A. W. (2017). Experimental and computational characterization of flow rates in a multiple-passage gas turbine combustor swirler. *Volume 4B: Combustion, Fuels and Emissions*, V04BT04A076. https://doi.org/10.1115/GT2017-65252

Briones, A. M., Stouffer, S., Vogiatzis, K., & Rankin, B. A. (2017, January 9). Effects of liner cooling momentum on combustor performance. *55th AIAA Aerospace Sciences Meeting*. 55th AIAA Aerospace Sciences Meeting, Grapevine, Texas. https://doi.org/10.2514/6.2017-0781

Stouffer, S. D., Hendershott, T. H., Colborn, J., Monfort, J. R., Corporan, E., Wrzesinski, P., & Caswell, A. (2020, January 6). Fuel effects on altitude relight performance of a swirl cup combustor. *AIAA Scitech 2020 Forum*. AIAA Scitech 2020 Forum, Orlando, FL. https://doi.org/10.2514/6.2020-1882

Stouffer, S.D., Hendershott, T.H., Boehm, R., Lovett, J. (2021). Chapter 4: The Referee Rig Combustor. Fuel effects of operability of gas turbine combustors. Progress in Astronautics and Aeronautics. *AIAA 2021* https://doi-org.wrs.idm.oclc.org/10.2514/5.9781624106040.0115.0142

Project 074 Low Emissions Pre-Mixed Combustion Technology for Supersonic Civil Transport

Georgia Institute of Technology

Project Lead Investigator

Adam Steinberg
Associate Professor
School of Aerospace Engineering
Georgia Institute of Technology
620 Cherry Street
Atlanta, GA 30313
404-897-1130
adam.steinberg@gatech.edu

University Participants

Georgia Institute of Technology (GT)

- P.I.: Adam Steinberg, Associate Professor, School of Aerospace Engineering
- FAA Award Number: 13-C-AJFE-GIT-079
- Period of Performance: August 11, 2020 to September 30, 2023
  Period of Performance Covered in Report: October 1, 2021 to September 30, 2022
- Tasks:
  1. Experimental measurement of flame structure, combustion dynamics, and emissions
  2. Large eddy simulations of combustor operation and emissions
  3. Thermoacoustic modeling

Project Funding Level

FAA: $1,999,998
GT: $1,000,262
GE Research: $999,736

Investigation Team

Name	Affiliation	Role	Tasks
Adam Steinberg Associate Professor	GT	P.I.	Management, reporting, technical oversight of all tasks, oversight of optical diagnostics in Task 1
Ellen Mazumdar Assistant Professor	GT	Co-P.I.	Oversight of OH planar laser-induced fluorescence (PLIF) measurements in Task 1
Joseph Oefelein Professor	GT	Co-P.I.	Oversight of first-principles large eddy simulations (LESs) in Task 2 and overall coordination of Task 2
Jerry Seitzman Professor	GT	Co-P.I.	Oversight of gas-phase fuel/air mixing diagnostics in Task 1
Michael Benjamin Consulting Engineer	GE Aviation	Co-P.I.	Oversight of combustor design in Task 1, coordination of GT/GE LES collaboration in Task 2

Krishna Venkatesan **Principal Engineer**	GE Research	Co-P.I.	Oversight of combustor operation in Task 1 and data collection for Task 3
Oleksandr Bibik **Senior Research Scientist**	GT	Participant	Task 1
Hannah Bower **Research Engineer**	GE Research	Participant	Task 1
Fei Han **Engineering Manager**	GE Research	Participant	Task 3
John Hong **Lead Engineer**	GE Research	Participant	Task 1
Nick Magina	GE Research	Participant	Task 3
Victor Salazar **Lead Engineer**	GE Research	Participant	Task 1
R. Narasimha Chiranthan	GE Aviation	Participant	Task 2
Manampathy Giridharan	GE Aviation	Participant	Task 2
Hiranya Nath	GE Aviation	Participant	Task 2
Sriram Kalathoor **Graduate Research Assistant**	GT	Graduate Student	Task 2
Mitchell Passarelli **Graduate Research Assistant**	GT	Graduate Student	Task 1 & 3
Sundar Ram Manikandan **Graduate Research Assistant**	GT	Graduate Student	Task 1
Samuel Wonfor **Graduate Research Assistant**	GT	Graduate Student	Task 1 & 3
Andrew Zheng **Graduate Research Assistant**	GT	Graduate Student	Task 1
Neilay Amin **Research Assistant**	GT	Undergraduate Student	Task 2
Preethi Mysore **Research Assistant**	GT	Undergraduate Student	Task 2
Coleman Pethel **Research Assistant**	GT	Undergraduate Student	Task 1
Katrina Potak **Research Assistant**	GT	Undergraduate Student	Task 2
Mihir Rao **Research Assistant**	GT	Undergraduate Student	Task 1
Andrew Semelka **Research Assistant**	GT	Undergraduate Student	Task 1
Rachel Wilder **Research Assistant**	GT	Undergraduate Student	Task 2

Project Overview

Market demand for high-speed transport is expected to drive a rapid re-emergence of commercial supersonic transport (CST) aircraft over the coming decades. This impending CST revival, combined with the increasingly harmful impacts of anthropogenic climate change, mandates advancements in CST-focused environmentally compatible technologies and policies. In comparison to subsonic aircraft, engines for CST aircraft (a) operate at a significantly lower overall pressure ratio (OPR) and bypass ratio, (b) experience higher combustor inflow temperatures (T_3), lower pressures (p_3), and higher fuel/air ratios under cruising conditions, and (c) cruise at higher altitudes. The reduced OPR and bypass ratio result in increased thrust-specific fuel consumption, thus increasing fuel burn and making it fundamentally more challenging to reduce emissions. Furthermore, the combination of low OPR and high cruise T_3 and fuel/air ratio (FAR) results in complicated trade-offs between nitrous oxide (NO_x) under cruise conditions and other emissions (CO, nonvolatile particulate matter [nvPM] and unburnt hydrocarbon) at lower power.

Several recent studies have assessed potential CST fleet emissions and environmental impacts based on currently deployed rich burn–quench–lean burn combustors (typically Tech Insertion combustors) designed for subsonic transport (Berton, 2020; Speth, 2021; Hassan, 2020; Kharina, 2018). These studies demonstrate that innovations in combustor architecture will be required to meet emission and efficiency targets, helping to enable an environmentally compatible CST market. Despite the high T_3 and FAR, peak flame temperatures must be moderated to meet NO_x targets, while also maintaining efficiency and achieving low levels of CO, unburnt hydrocarbon, and nvPM. This will require increased fuel-lean pre-mixing prior to combustion.

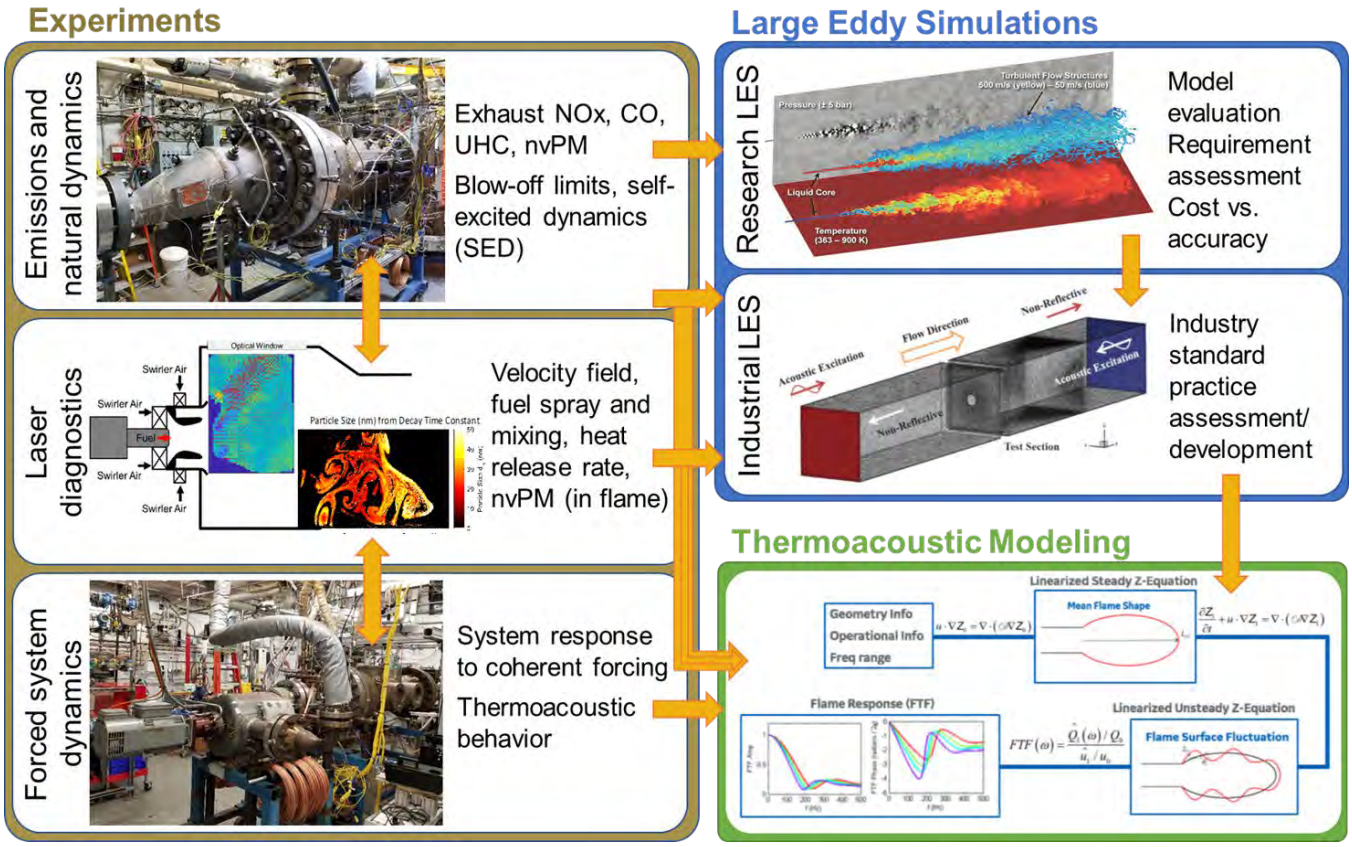

Figure 1. Project overview. FTF: flame transfer function; LES: large eddy simulation; nvPM: nonvolatile particulate matter; UHC: unburnt hydrocarbon.

Lean pre-mixed pre-vaporized (LPP) combustors are a promising path to lowering emissions from future CST engines. In LPP combustors, fuel is injected, partially pre-vaporized, and partially pre-mixed with air before the reactants enter the combustor. While the LPP concept is not new, e.g. (Niedzwiecki, 1992) achieving good vaporization and mixing in a flight-appropriate package has been challenging in the past. However, these issues can potentially be alleviated by the high T_3 in CST combustors—which results in faster vaporization—and advanced manufacturing to enable compact rapid-mixing flow elements.

Thus far, the ability of current design methodologies to predict the operability and emissions of LPP combustors under relevant conditions is unproven. Hence, there is a critical need to generate high-quality experimental data for CST combustor conditions, coupled with the development and validation of computational fluid dynamics (CFD) simulations and reduced-order thermoacoustic models. This project addresses this need through a combination of experiments, LESs, and thermoacoustic modeling, all applied in a novel LPP combustor of interest to future CST applications. Figure 1 shows the elements of this research project.

Task 1 - Experimental Measurements of Flame Structure, Combustion Dynamics, and Emissions

Georgia Institute of Technology

Objective

This task represents the experimental effort to measure the flame structure, dynamics, and emissions in a novel LPP combustor concept, designed specifically for low-emission operation under typical conditions encountered by CST engines.

Research Approach

Efforts under Task 1 over the reporting period consisted of four main activities.

1) Design, fabrication, and deployment of a new LPP combustor test article for experiments in a test cell at GE Research that is capable of acoustic forcing
2) Design, calibration, and deployment of the measurement systems
3) Experimental Campaign 2 to study the forced and self-excited dynamics of the LPP combustor using optical diagnostics from GT that were transported to GE Research and deployed in the GE test cell
    a. GT students were onsite at GE Research for a total of nearly 9 person-months over Summer 2022 to conduct this experimental campaign in collaboration with GE staff.
4) Analysis of the experimental data from Campaigns 1 and 2

Experimental Design, Fabrication, and Deployment

Considerable preliminary work was performed to enable on-schedule execution of Experimental Campaign 2. The following major elements of the test rig at GE Research were designed and fabricated:

1) Test rig spool pieces
2) Optical combustor liner
3) Water-cooled exhaust system with ports for various pressure and emission probes
4) Window blank with pressure measurement ports

Experimental Campaign 2 was undertaken at GE Research between July and September 2022 in the GEB test facility (Figure 2). The THOR rig housed at GEB contains the ASCENT test article and can handle combustion experiments for single-cup fuel nozzle configurations. Figure 3 shows details of the THOR rig vessel assembly. The THOR rig consists of an optically accessible vessel that is rated to 17.2 bar (275 psia) and 810 K (1000 ˚F), which contains several large ports that enable optical and laser access to the test section.

The test article built for Experimental Campaign 2 is shown in Figure 4. The combustor test article consists of an LPP dome, square optical liner, and constant-area tail pipe section. A constant-area hot section was chosen to eliminate any combustor back-projection uncertainties of the acoustic pressure from the downstream multi-microphones. The test article design was based on GE's existing THOR optical liner design, which was successfully employed over the last eight years for various optical and laser diagnostic efforts for aero-engine studies. The LPP dome is shown schematically in Figure 5, consisting of four bluff-body-stabilized pre-mixed flames surrounding a non-pre-mixed swirling pilot; details of the four pre-mixed flames are redacted.

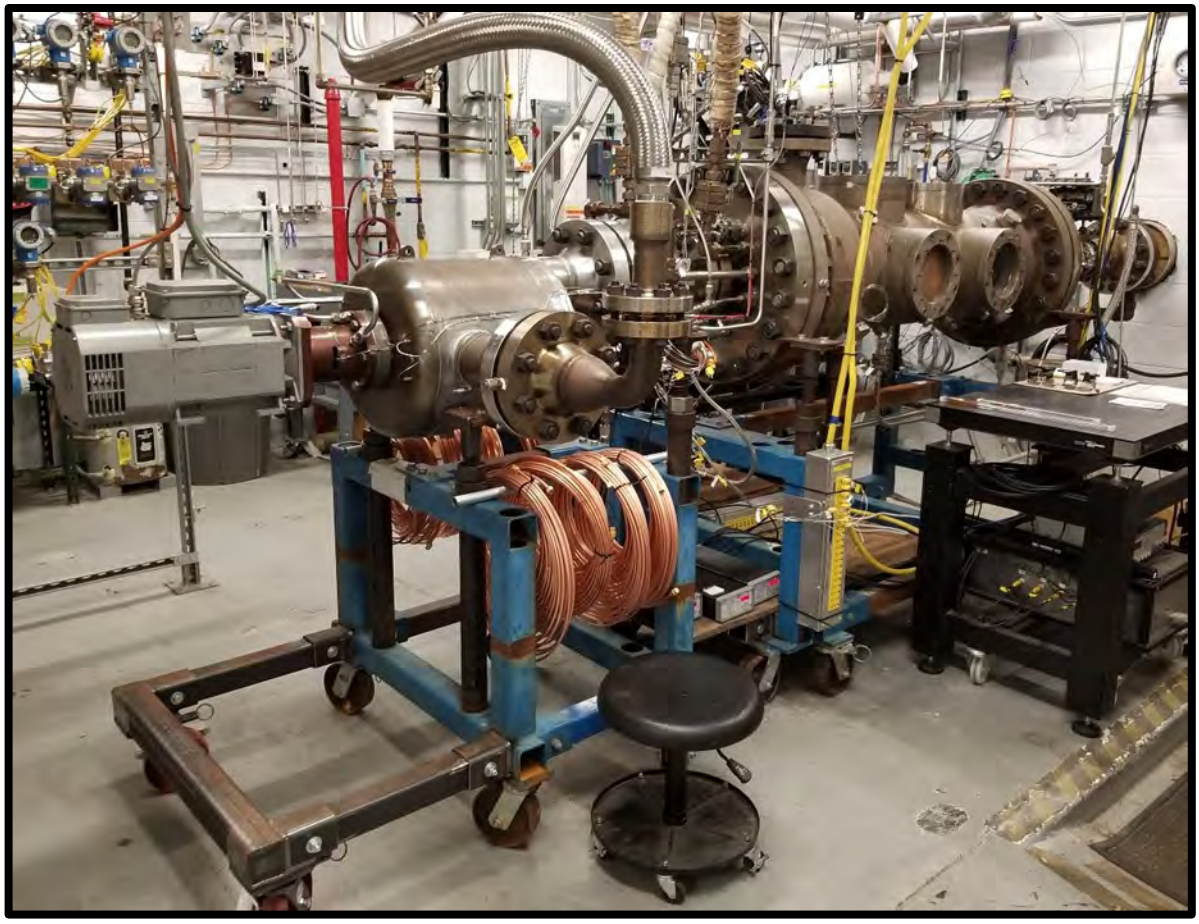

Figure 2. THOR test rig and diagnostic setup at the GEB test facility.

For the various diagnostic measurements employed in this campaign, quartz windows were employed for the side walls and the top wall of the combustor section. The combustor bottom wall was a water-cooled window-blank with ports for an ignitor and three dynamic pressure sensors. The downstream tail pipe consisted of a water-cooled constant cross-section liner with ports for dynamic pressure sensors. A water-cooled orifice plate, located at the end of the tail pipe section, provided the necessary acoustic boundary condition to suppress self-excited combustor tones. The dimensions of this orifice plate were based on the predicted rig tones and designed to withstand thermal loading.

The rig is continuously supplied with high-pressure preheated air for combustor and cooling needs. The typical combustor air flow ranges from 0.2 to 0.4 kg/s, and vessel cooling bypass air is provided at approximately 0.4 kg/s at 600 K. The test facility also features a topping heater that can potentially increase the air temperature delivered to the rig. Three liquid Jet A lines supply fuel to the combustor. One of the three fuel lines supplies the fuel to the pilot. The two other fuel lines feed the top and bottom fuel circuits for the main mixer. A torch ignitor is located inside the combustor to ignite the fuel–air mixture. All of the air, fuel, and water flows to the test rig are individually metered and controlled. Below is a list of various flows to the test rig:

1. Air flow
    a. Siren air flow into combustor
    b. Siren bypass air flow into combustor
    c. Combustor window purge air
    d. Vessel cooling bypass air

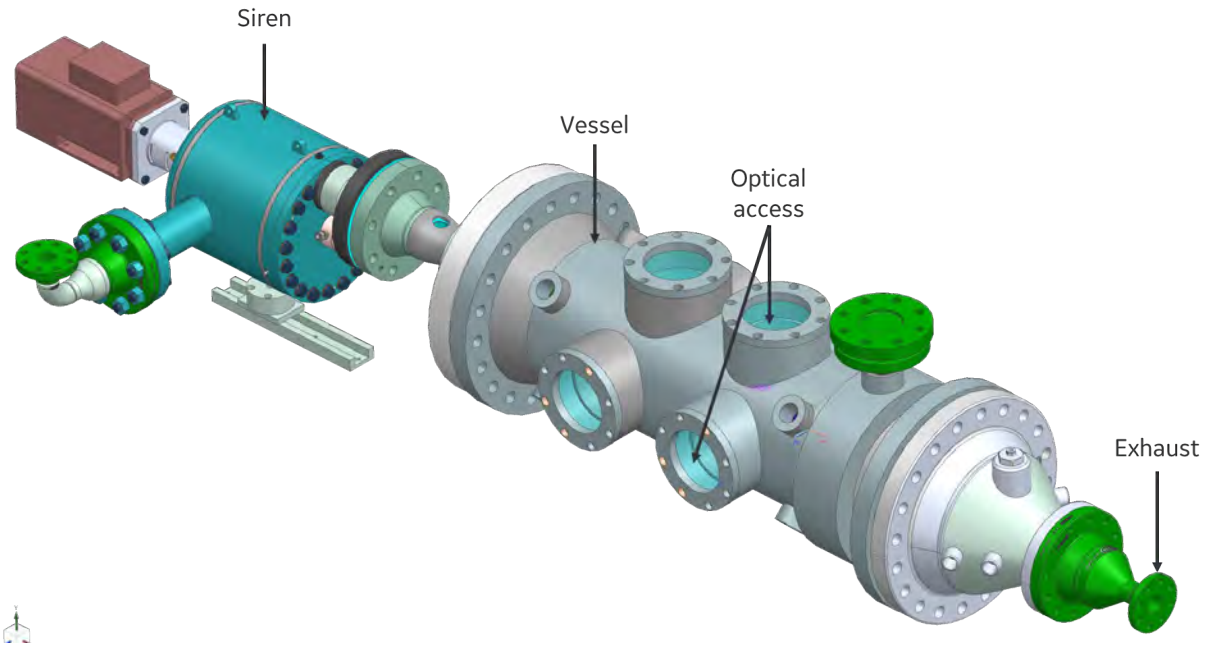

Figure 3. THOR rig siren and pressure vessel assembly employed for the ASCENT Experimental Campaign 2. The vessel features several optical ports suitable for the different diagnostics used in the campaign.

2. Fuel flow
    a. Pilot fuel
    b. Main mixer top fuel
    c. Main mixer bottom fuel
3. Water flow
    a. Siren cooling water
    b. Test article cooling water
    c. Exit orifice cooling water
    d. Pressure vessel reducer cooling water

One can control the static pressure inside the combustor test article by changing the inlet flow pressure (p_3) and the back pressure at the exit. A back pressure valve is employed at the exit of the THOR rig to set both the combustor pressure and the appropriate dome pressure drop ($\mathrm{d}p/p_3$). The THOR rig is instrumented with numerous thermocouples, pressure sensors, and flowmeters to monitor the hardware integrity and operating conditions of interest. The data generated by these sensors are read by a high-speed data acquisition and control system (National Instruments). Dynamic pressure sensors (PCB) were located axially along the mid-plane at specific locations along the test article (see Task 3) for monitoring combustion dynamics and for measuring the acoustic flame transfer function (FTF). A multi-physics model (COMSOL) was employed to fine tune the location of the dynamic sensors to encompass the frequency range of measurements for the multi-microphone method.

A major objective of Experimental Campaign 2 is to characterize the various coupling mechanisms between fluctuations in velocity ($\vec{u}'$), heat release (q'), fuel (or equivalence ratio ϕ'), and pressure (p') for the LPP combustor. Lean pre-mixed pre-vaporized systems are inherently susceptible to combustion-induced oscillations. Practical combustor systems for supersonic flight will need to achieve robust combustor performance over the entire range of supersonic cycle conditions. Understanding component performance and subsequent system interactions is key for early identification of combustion dynamic challenges and solutions.

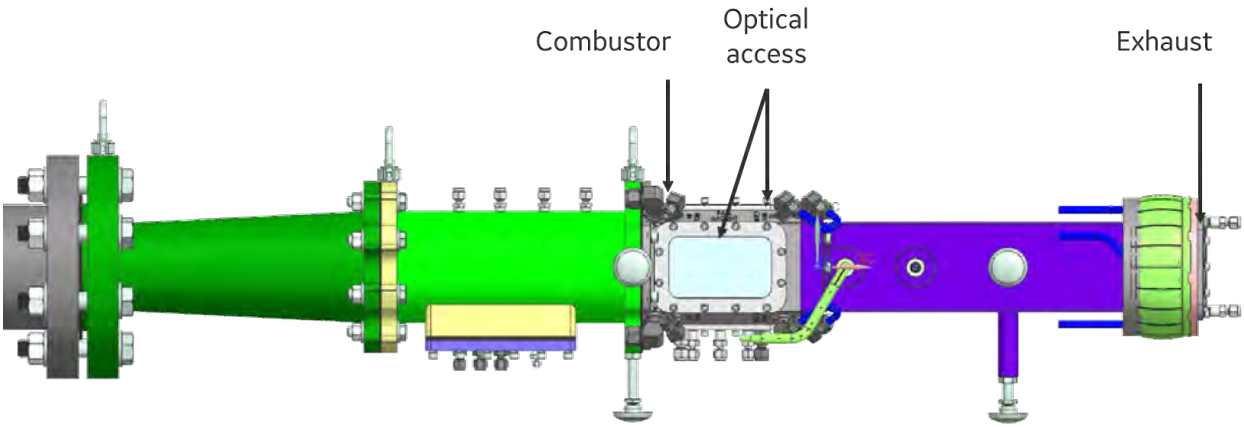

Figure 4. Test article designed for ASCENT 74 Campaign 2.

To this end, the device shown on the left of Figures 2 and 3 is a high-pressure siren that can be used to force oscillations in the air flow with different frequencies and amplitudes. FTF measurements – acquired by measuring the flame response to forcing – enable combustor dynamic performance characterization and provide important insights into the acoustic–heat release coupling. Moreover, the FTF provides key data for validating both analytical and higher-fidelity models for design tools. Hence, FTF measurements were an important focus of Experimental Campaign 2.

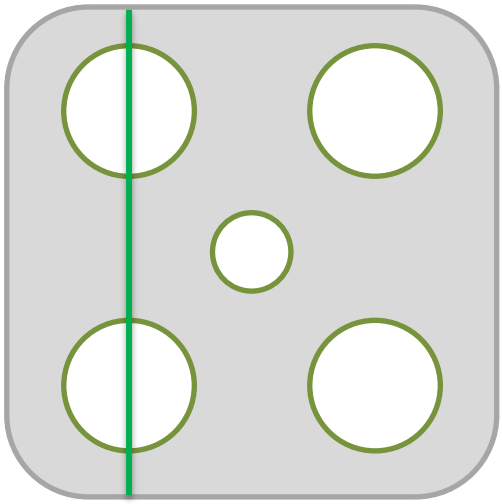

Figure 5. Combustor geometry with the laser sheet position indicated by a green line. The four corners contain the partially pre-mixed bluff-body-stabilized main flames. The bluff-body geometry has been redacted.

The siren device is employed to modulate the frequency of the air sent to the pre-mixer. By varying the rotational speed of the electric motor to the siren device, the modulation frequency can be tuned from 1 to 1050 Hz. The forcing amplitude is controlled through the split between the combustor air that flows through the siren versus through a bypass. In general, a higher mass flow through the siren results in a higher forcing amplitude. One can dynamically change the forcing amplitude by bypassing the flow to the siren and mixing the bypassed (unforced) flow with the forced flow downstream of the siren and upstream of the pre-mixer. The forcing amplitude is monitored and set by dynamic pressure sensors located upstream of the pre-mixers.

Shakedown experiments were undertaken to screen for combustion dynamics behavior, and test conditions were appropriately chosen to coincide with specific operating points of relevance from Experimental Campaign 1 during the previous reporting period. The conditions chosen for this campaign were fixed to the same combustor pressure and equivalence ratios as Campaign 1, but different air preheat temperatures were employed because high-amplitude combustion dynamics behavior was generally observed only at lower air preheat temperatures. Acoustic and optical FTFs and various optical diagnostic measurements were obtained at a fixed air mass flow rate over a range of fuel/air ratios, corresponding to thermal powers of $P_{th} = 0.32 - 0.4$ MW in the pre-mixed main flames. Table 1 provides a summary of the measurements obtained during Campaign 2. Variations in inlet air temperature also helped to ascertain the impact of fuel evaporation on the combustion behavior.

Table 1. Summary of operating conditions. CL: chemiluminescence; FTF: flame transfer function; PLIF: planar laser-induced fluorescence; SPIV: stereoscopic particle image velocimetry.

p_3 (psia)	T_3 (F)	dp/p_3 (%)	P_{th} (MW)	FTF, Acoustic	FTF, Optical	SPIV	OH PLIF	OH* CL	Fuel PLIF
115	670	3.7	0.36–0.40	Yes	No	No	Yes	Yes	Yes
115	550	3.7	0.32–0.44	Yes	Yes	Yes	No	Yes	Yes

Design, Calibration, and Deployment of Diagnostics

Measurements during Experimental Campaign 2 consisted of the following:

1) Dynamic pressure transducer measurements with which to characterize the combustor acoustics and measure FTFs (see Task 3)
2) High-speed stereoscopic particle image velocimetry (SPIV) to measure the velocity field dynamics
3) High-speed OH* chemiluminescence (CL) and OH PLIF to measure the flame dynamics
4) Aromatic PLIF at a repetition rate of 10 Hz to measure the fuel vapor distribution

In addition to these new measurements, work that started in Year 1 was completed to calibrate laser-induced incandescence (LII) measurements of nvPM for the conditions in this combustor. However, LII measurements were de-scoped from Campaign 2 in favor of more detailed flow and flame diagnostics due to the low levels of nvPM measured in Campaign 1. Moreover, based on results from the LES activities (see Task 2), the team decided to add phase Doppler particle analysis and exhaust emissions to Campaign 2, which were not in the original scope. These measurements are ongoing at the time of this report.

Deployment of these diagnostics in the GE test cell required significant optical design efforts due to space and operational constraints. For example, the GE test cell comprised different regions to contain the combustor test article and lasers/control systems. Geometric arrangements around the test article were restricted due to interferences with building infrastructure and the need for routine access to the inside of the pressure vessel. Hence, initial activities were conducted in the Ben T. Zinn Combustion Lab at GT to design the optical path, test the configurations, and de-risk the operations at GE. These efforts included optimal configurations for combining and transmitting laser beams with different wavelengths and spatial characteristics between the laser region and test article, optimal configurations for simultaneously forming multiple laser sheets through a single set of telescope optics, and optimal signal collection configurations. The resultant layouts of the laser and test article spaces are shown in Figure 6.

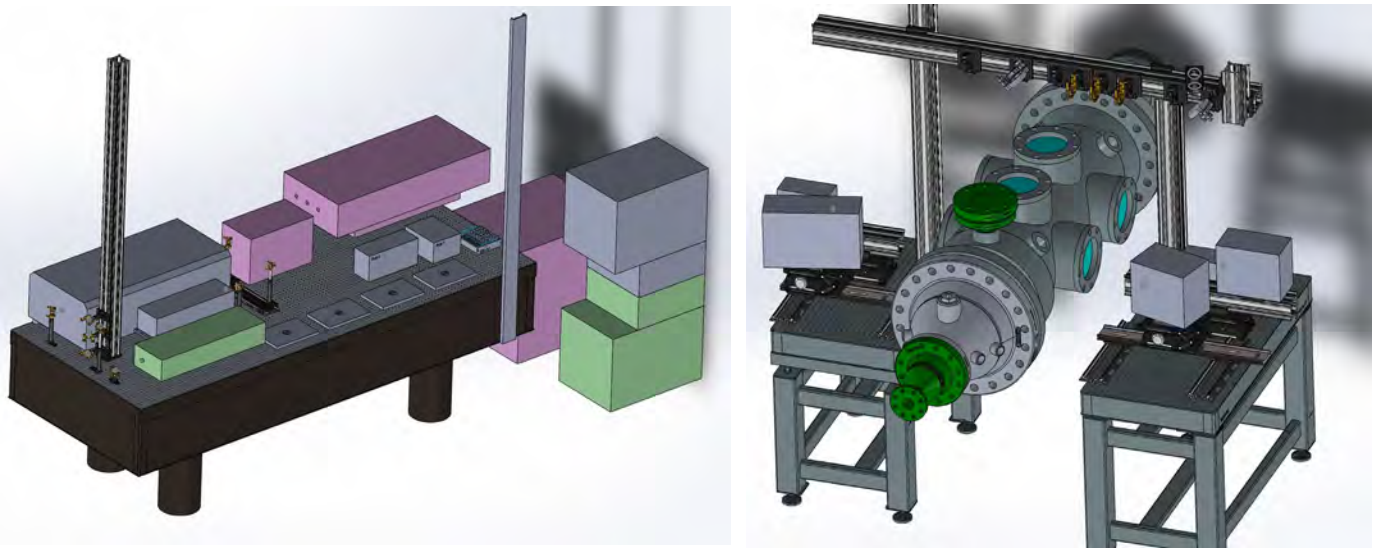

Figure 6. Optical layout in the GE test cell. Left: Laser and control room configuration. Right: Test cell configuration.

CL imaging of OH* at 308 ± 5 nm served as the metric for line-of-sight integrated heat release rate measurements. Previous experiments (Kheirkhah, 2017; Passarelli, 2019) and wide-spectrum measurements from a portable spectrometer (Ocean Optics HR2000) showed that OH* is the most appropriate indicator of heat release rate. A sample spectrum is shown in Figure 7, with the peak corresponding to OH* emissions indicated. The CL images were recorded at a Strouhal number of $St \equiv fD/U = 1.9$ by a high-speed camera (Photron SA-5) coupled to an image intensifier (Invisible Vision, gate time of 50 μs), commercial objective lens (Nikkor 105 mm UV, f/# = 11), and bandpass filter (312 ± 12.5 nm). Here, f is the recording frequency, D is the pre-mixer diameter, a**nd U is the average axial speed of the gas exiting the pre-mixer.**

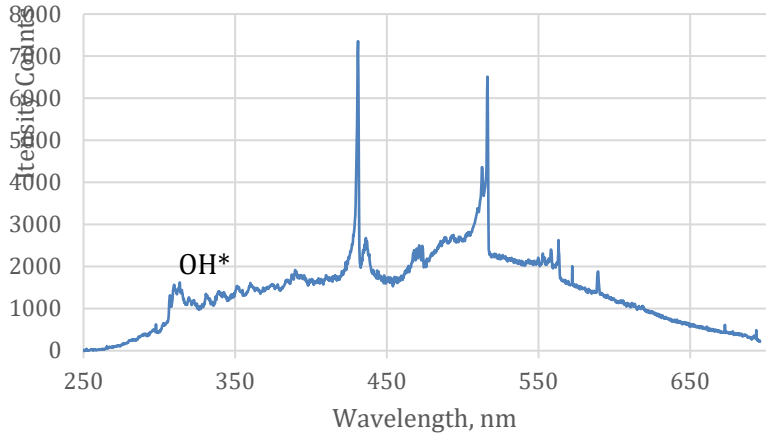

Figure 7. Sample spectrometer readings with the OH* peak indicated.

Qualitative measurements of the fuel mixing behavior were obtained via PLIF of the aromatic species naturally present in the Jet A fuel. The flow was illuminated at a repetition rate of 10 Hz using the fourth harmonic (266 nm) output of an Nd:YAG laser (Spectra Physics Quanta-Ray PRO 350). Laser-induced fluorescence was collected using an intensified camera (Andor, gate time of 100 ns) with an objective lens (Nikkor 105 mm UV, f/# = 4.5) and a two-filter setup consisting of a bandpass (340 ± 40 nm) and a steep-edge long wave pass filter (325 ± 3.5 nm). This filter setup was chosen to align with the center of the fluorescence spectrum of kerosene vapor (Orain, 2014) while simultaneously blocking the signal from OH* CL. Simultaneous shot-to-shot beam profile measurements were obtained by using a phosphorescence plate. The plate was

placed in the path of residual transmission from the 266-nm sheet through the final mirror above the combustor. This low-intensity copy of the sheet induced phosphorescence on the plate, which was then imaged with a separate camera system (FLIR Blackfly USB3). The PLIF images were processed for spatial calibration, background removal, intensifier white-field response, shot-to-shot laser sheet intensity and profile variations, and laser power absorption through the medium.

To characterize the flow field inside the combustor, a double-pulsed, two-camera SPIV setup was used at $St = 0.95$. A high-speed 532-nm Nd:YAG laser (Quantronix) illuminated the flow with pulse separation times varying between 5 and 8 μs and a laser sheet thickness of approximately 2 mm near the beam waist. Mie scattering from nominally 1-μm ZrO_2 tracer particles that were seeded was collected into the two SPIV cameras (Phantom), each equipped with bandpass filters (532 ± 2.5 nm), objective lenses (Tamron 180 mm, f/# = 5.6), and Scheimpflug adapters. While the Stokes number of the tracer particles was too high to track the small-scale features of the flow, the particles were sufficient for measuring the larger-scale, thermoacoustically coupled flow dynamics of interest here. Vector processing was performed using a multi-pass algorithm with an adaptive window shape and size and an iterative vector filter in commercial software (LaVision). Spurious vectors were identified and removed from the vector fields by a median filter outlier detection algorithm. Any remaining gaps in the gas-phase dataset were filled using gappy proper orthogonal decomposition (Saini, 2016).

The OH PLIF excitation system consisted of a frequency-doubled dye laser (Sirah), pumped by an Nd:YAG diode-pumped solid-state laser (EdgeWave). The dye laser system was tuned to excite the $Q_1(7)$ line of the A-X (1,0) transition of OH at 283.2 nm, with a pulse energy of approximately 0.5 mJ/pulse at $St = 0.95$. The OH fluorescence signal was captured by a high-speed CMOS camera (Photron) combined with an image intensifier (UVi). Note that the OH PLIF data are still being analyzed and are not discussed here.

Pressure fluctuations were measured by dynamic pressure transducers (PCB), mounted to the ends of calibrated waveguides in a semi-infinite loop configuration; see Task 3 for details of the pressure measurement locations. A data acquisition system (National Instruments) recorded the pressure and camera timing signals at a sampling rate of 100 kHz.

In addition to the diagnostic setup for Experimental Campaign 2, activities were undertaken during this performance period to analyze the LII data acquired in Campaign 1 (during the previous performance period). This activity will support future experimental campaigns involving LII measurements of nvPM, other projects within ASCENT, and the general scientific community's ability to measure nvPM in high-pressure combustors; the development and validation of methods for measuring soot particle sizes and volume fractions are essential for quantifying the nvPM created during the combustion of Jet A fuels at high pressure. Thus, we validated time-resolved LII (TiRe-LII) measurements using direct soot sampling techniques in order to enable the use of TiRe-LII for direct, non-intrusive nvPM particle sizing.

During this performance period, we focused on the development of a custom soot sampling system that uses transmission electron microscope (TEM) grids to directly sample soot from a small pre-mixed, pre-vaporized calibration burner (Manikandan, 2022). This small burner runs with Jet A fuel, a methane pilot flame, and nitrogen crossflow. The soot sampler operated inside the pressurized burner and was able to rotate TEM grids quickly through the flame to quench and capture soot particles. The grids were then analyzed in a TEM, and soot particle diameters were extracted. In these photos, several features were noted. First, the number of soot particles per agglomerate was higher (>200) than that noted in previous work with ethylene. Second, in some cases, soot restructuring was observed. This restructuring could be due to the exposure of soot particles to water, sulfuric acid, or other combustion products. Third, several mineral-like or fiber-like structures were noted and attributed to S, Fe, or Ca/P, which are commonly found in Jet A fuel (Baldelli, 2020).

While the soot samples were collected, TiRe-LII videos were also captured. For this imaging diagnostic (Chen, 2018; Passarelli, 2022) a 1,064-nm laser was shaped into a 2 x 26 mm sheet with a fluence of 0.08 J/cm^2. This beam was shaped into a top-hat profile and relay-imaged onto the combustor. The resulting incandescence signal was measured by an ultra-high-speed camera (Shimadzu, 10 million frames per second, 55-ns exposure). The decay profiles from each pixel in the image were then extracted and fitted to the LII model developed last fiscal year. This model neglects sublimation due to the low laser fluences used and includes additional terms to capture the shielding effect of large soot agglomerates.

Examples of the data captured by these two techniques are illustrated in Figure 8. For initial validation testing, fuel–air ratios ranging from 0.13 to 0.26 were tested at atmospheric pressure, 1.4 bar, and 2.8 bar. Histograms of these measurements are shown in Figure 9. The results of the two methods agree well, with the average particle size from both measurements on the order of 12–18 nm. This size range matches with prior Jet A soot sampling measurements reported in the literature (Liati, 2019). Using the validated model and TiRe-LII technique, we aim to conduct measurements inside various high-pressure turbine combustors.

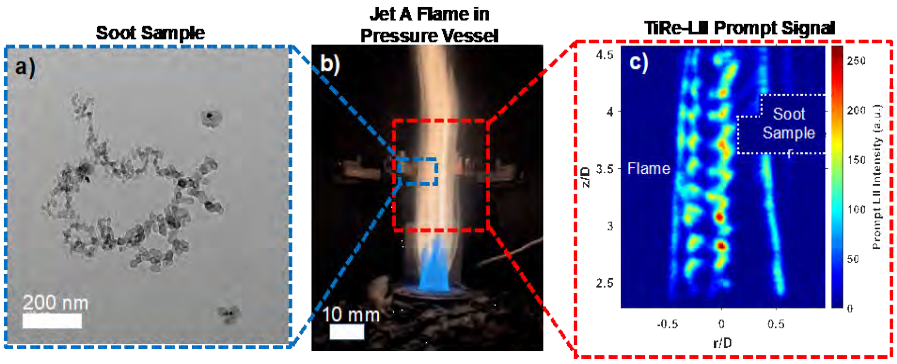

Figure 8. Validation of non-intrusive optical TiRe-LII soot particle sizing with soot sampling measurements in a Jet A flame. The soot sampling mechanism can be seen behind the flame in the center image. TiRe-LII: time-resolved laser-induced incandescence.

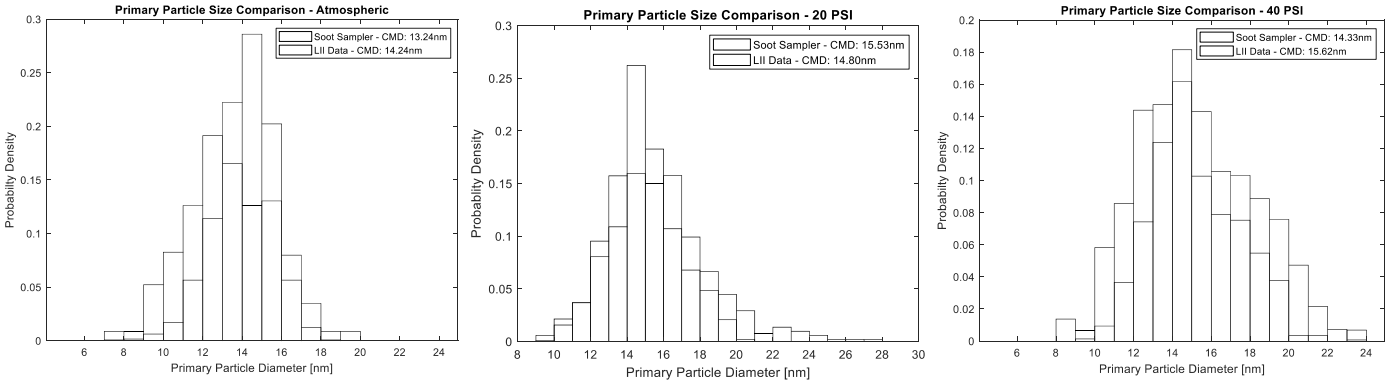

Figure 9. Comparison of soot particle mean diameter (CMD) measured from time-resolved laser-induced incandescence (TiRe-LII) measurements and direct soot sampling show good agreement for atmospheric pressure, 1.4-bar, and 2.8-bar environments.

Experimental Campaign 2

Combustor and Operating Conditions

As described above, Experimental Campaign 2 was performed at GE Research in Niskayuna, NY with the ASCENT 74 test article installed in the THOR rig (Figures 2-5). Each main flame operates under fuel-lean conditions, burning partially pre-vaporized and pre-mixed Jet A fuel. For the laser diagnostics described below, the laser sheet passed through the centers of the main flames on one side of the combustor, as indicated in Figure 5. Prior to data acquisition, the combustor was allowed to settle to steady state, as verified by an examination of static pressure, thermocouple, and mass flow rate measurements.

Data Analysis and Results

Analysis of data from Campaign 2 is ongoing; sample results are presented here. Thus far, the majority of the combustor dynamics analysis has employed spectral proper orthogonal decomposition (SPOD) and phase conditioning. SPOD, which can be applied to any of the high-speed data (OH*, SPIV, etc.), is a modification to classical POD (Sirovich, 1987), wherein a sliding lowpass filter is applied along the diagonals of the correlation matrix before the temporal coefficients are calculated via eigenvalue decomposition (Sieber, 2016). This filtering operation effectively constrains the resulting modes to distinct frequency bands. Unlike traditional filtering operations, such as bandpass filtering the data or phase-averaging the POD modes, the filter in SPOD does not cause any loss of information: the energy outside of the frequency band for a given mode

is redistributed to other modes. SPOD is also more robust to nonstationarity in the data than other spectral decomposition techniques, such as dynamic mode decomposition (DMD (Schmid, 2010; Tu, 2013; Jovanovic, 2014; Roy, 2017), which can experience severe mode splitting. Sieber *et al.* drew a connection between DMD and SPOD, stating that SPOD is similar to a temporally sliding DMD (Sieber, 2016). Figure 10 illustrates the general procedure used to identify and extract the dynamics at the dominant frequencies in the data.

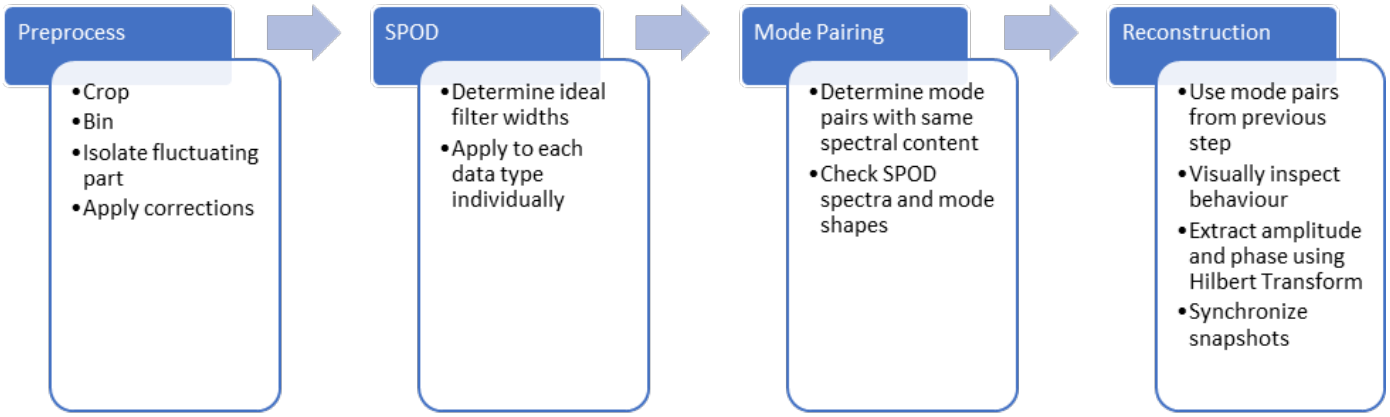

Figure 10. General mode isolation procedure. SPOD: spectral proper orthogonal decomposition.

SPOD is applied following fairly standard data preprocessing. Based on the work by Sieber *et al.* (2017), a Gaussian finite impulse response filter whose standard deviation yields the same cut-off frequency as a box filter with half the length was implemented for SPOD. The third step of this procedure uses the automatic pairing algorithm developed by Sieber *et al.* (2016). This algorithm computes the harmonic correlation or spectral coherence between each mode pair to detect modes with the same spectral signature, but offset by π/2 in phase. As with classical POD, the appearance of modes with similar energy and spectral content but lagging by π/2 radians indicates the presence of coherent oscillatory structures in the data. Thus, the SPOD modes with the strongest harmonic correlation are paired to identify such coherent structures. These mode pairs are then used in the final step to reconstruct the coherent dynamics they represent.

To select the filter widths, the SPOD spectra and spectral content of the modes were examined for filter widths varying from 0 (POD) to the full length of the dataset (effectively a discrete Fourier transform). The ideal filter width is one that yields the fewest modes (or highest energy per mode) with the least amount of mode blending (when one mode contains information at several frequencies).

In addition to SPOD, phase-conditioned mean fields were computed. For this step, the phase "clock" is computed as the complex phase angle of the Hilbert transform of the combustor pressure signal. During data acquisition, a signal from each optical measurement is acquired, indicating the time of each optical frame, which can then be cross-referenced against the phase of the clock. The clock signal and corresponding optical measurements were divided into eight equal phase bins; phase-correlated mean fields for each phase angle were computed from the optical measurements in each bin.

The mean fuel PLIF signal for cases with $P_{th} = 0.40$ MW at different forcing frequencies is shown in Figure 11. Frequencies were normalized to the Strouhal number, $St = fD/U$, as described above. No significant qualitative differences in mean fuel distribution were observed across the different forcing frequencies, indicating no bifurcation in overall flame or flow structure as the system is forced. This observation also held for different thermal powers, corresponding to a leaner FAR.

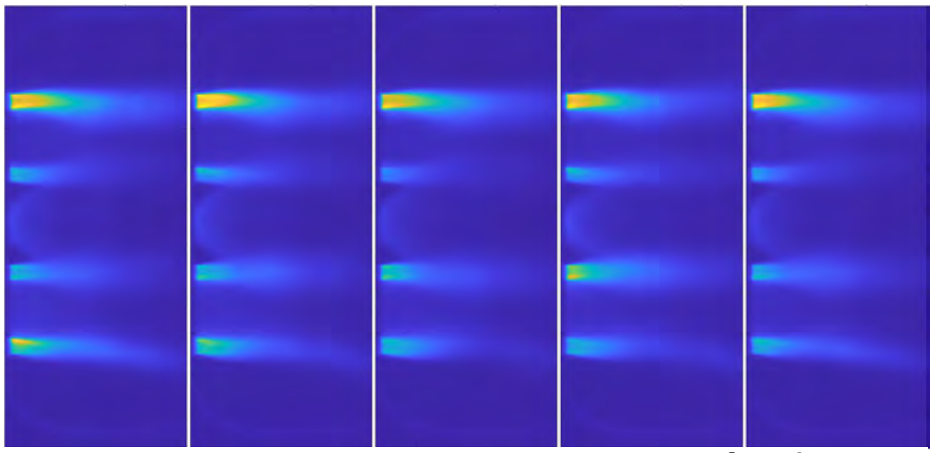

$St = 0.056$ $St = 0.094$ $St = 0.13$ $St = 0.17$ Unforced

Figure 11. Mean fuel planar laser-induced fluorescence fields for $P_{th} = 0.40$ MW at different forcing frequencies.

As will be discussed below, the combustor shows the strongest response to forcing at $St \approx 0.13$. Figure 12 shows mean fuel PLIF fields for $St \approx 0.13$ forcing cases, across different thermal powers. As the FAR decreases, unburnt fuel is measured in the recirculation zones behind the combustor bluff bodies and farther downstream. This observation is indicative of local extinction along the inner shear layer between the reactants and the recirculation zone, allowing mixing of unburnt reactants. This trend is also indicative of a more axially distributed heat release. The phase-conditioned mean fuel PLIF fields at different phases of the pressure cycle (not shown here) did not demonstrate any coherent oscillations in the fuel flow for any combination of thermal power and forcing frequency. Hence, heat release oscillations at the flame do not appear to be due to an oscillating equivalence ratio; rather, heat release oscillations are anticipated to arise from velocity coupling. Thus, a detailed analysis of the velocity dynamics is needed.

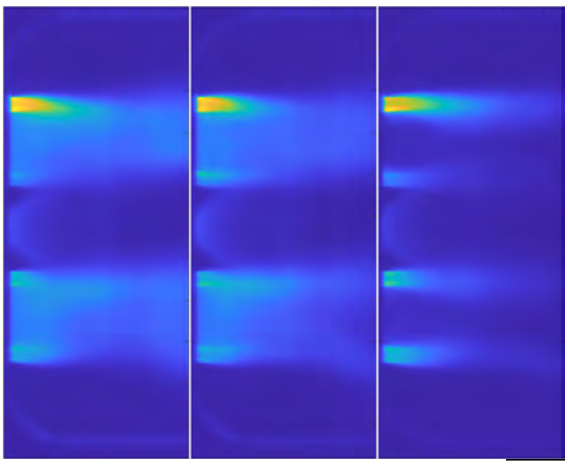

$P_{th} = 0.32$ MW $P_{th} = 0.36$ MW $P_{th} = 0.40$ MW

Figure 12. Mean fuel planar laser-induced fluorescence fields at different FAR values for $St = 0.13$.

Figure 13 shows the mean velocity fields for different forcing frequencies and without forcing at $P_{th} = 0.36$ MW. The vector arrows show in the in-plane velocity, while the background colormap indicates the out-of-plane velocity. All absolute velocity scales have been removed for proprietary reasons. Similar to the fuel PLIF fields, there are no major qualitative changes in the velocity field as the system is forced. The largest difference is that the unforced case has a slightly higher swirl velocity in the downstream region compared with the forced cases. No major changes in mean flow structure have been observed at the different thermal powers in any of the data processed thus far.

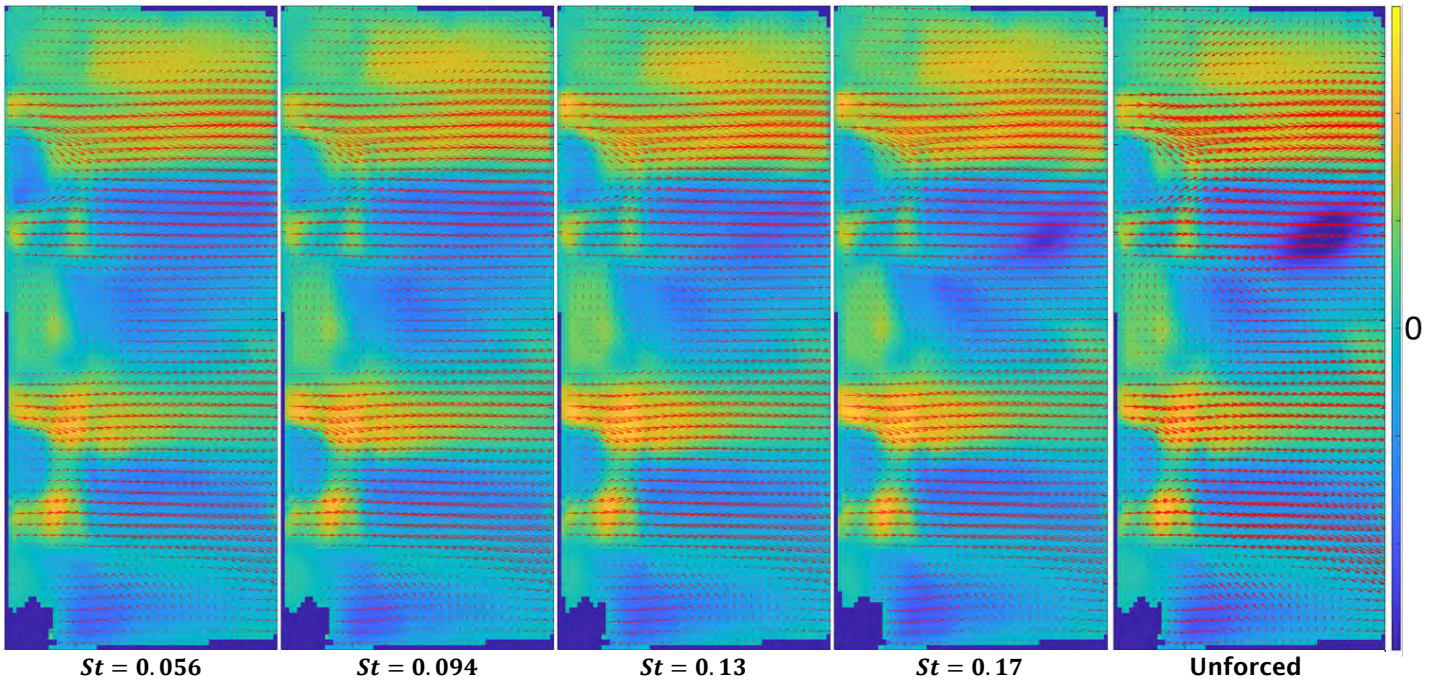

Figure 13. Mean velocity fields for $P_{th} = 0.40$ MW. Vector arrows are the in-plane velocity, and the background is the out-of-plane velocity, with blue and yellow indicating positive and negative velocities, respectively.

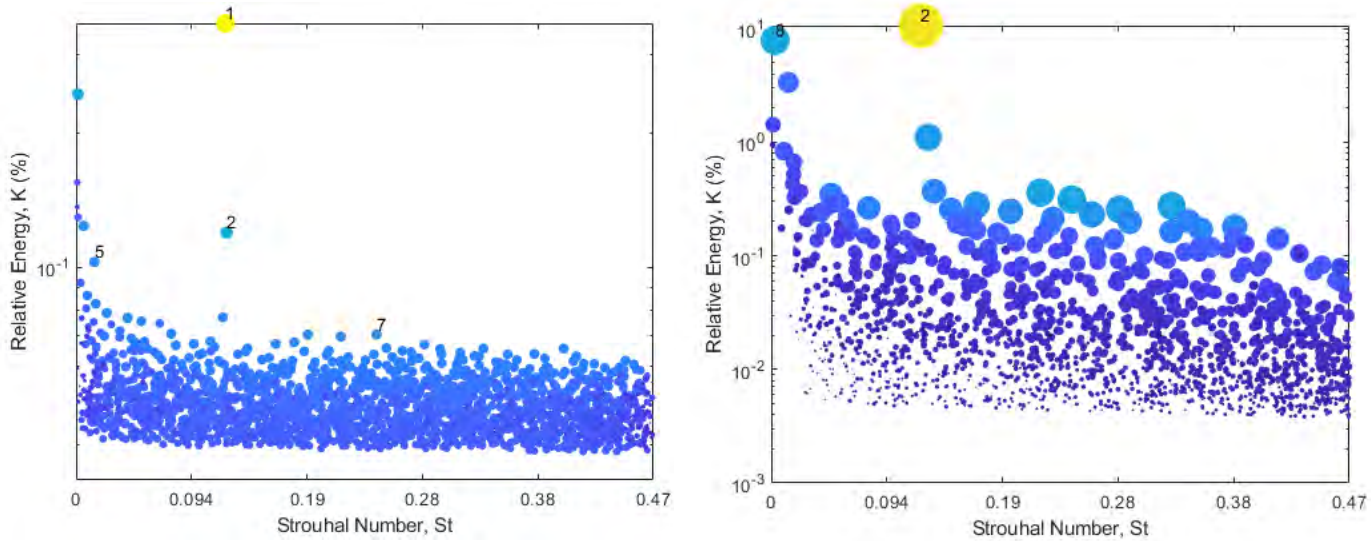

Figure 14. Spectral proper orthogonal decomposition spectrum of stereoscopic particle image velocimetry (left) and OH* chemiluminescence (right) data at $P_{th} = 0.40$ MW without forcing.

To investigate the self-excited and forced velocity field dynamics, SPOD was applied to the SPIV and OH* CL data. The SPOD spectra for the unforced $P_{th} = 0.40$ MW case are shown in Figure 14. Each dot in the SPOD spectrum represents a coherent pair of basis modes. The vertical position of the dot represents its relative contribution to the flow (in the sense of velocity fluctuation magnitudes), and the size/color of the dot represents the relative spectral coherence of the modes making up the pair; high-energy coherent mode pairs are indicated by large dots with a high vertical position.

The dominant feature of the SPOD spectra are the high-energy, coherent velocity oscillations at $St = 0.12$. This frequency corresponds well to the value of $St \approx 0.13$ used in the forced studies and exhibits a strong response to forcing. It is noted that the OH* CL signal also exhibits dynamics at $St \approx 1$, which is not shown on these plots for clarity. These high-frequency dynamics may be the subject of future study.

Figure 15 shows a time sequence of velocity field reconstructions from the dominant $St = 0.12$ SPOD mode pair in the SPIV data over a typical oscillation cycle. The field of view encompasses only the top half of the combustor for clarity, and the shown velocities represent fluctuations at $St = 0.12$ around the mean field. Periodic vortex shedding from the dome face occurs, predominantly in the outer shear layer between the main inflow and the combustor walls. Preliminary observations indicate that this vortex expands and interacts strongly with the more downstream regions of the flame toward the right side of the field of view. Ongoing analysis is coupling the SPOD-reconstructed velocity and heat release dynamics to elucidate their interaction and validate modeling.

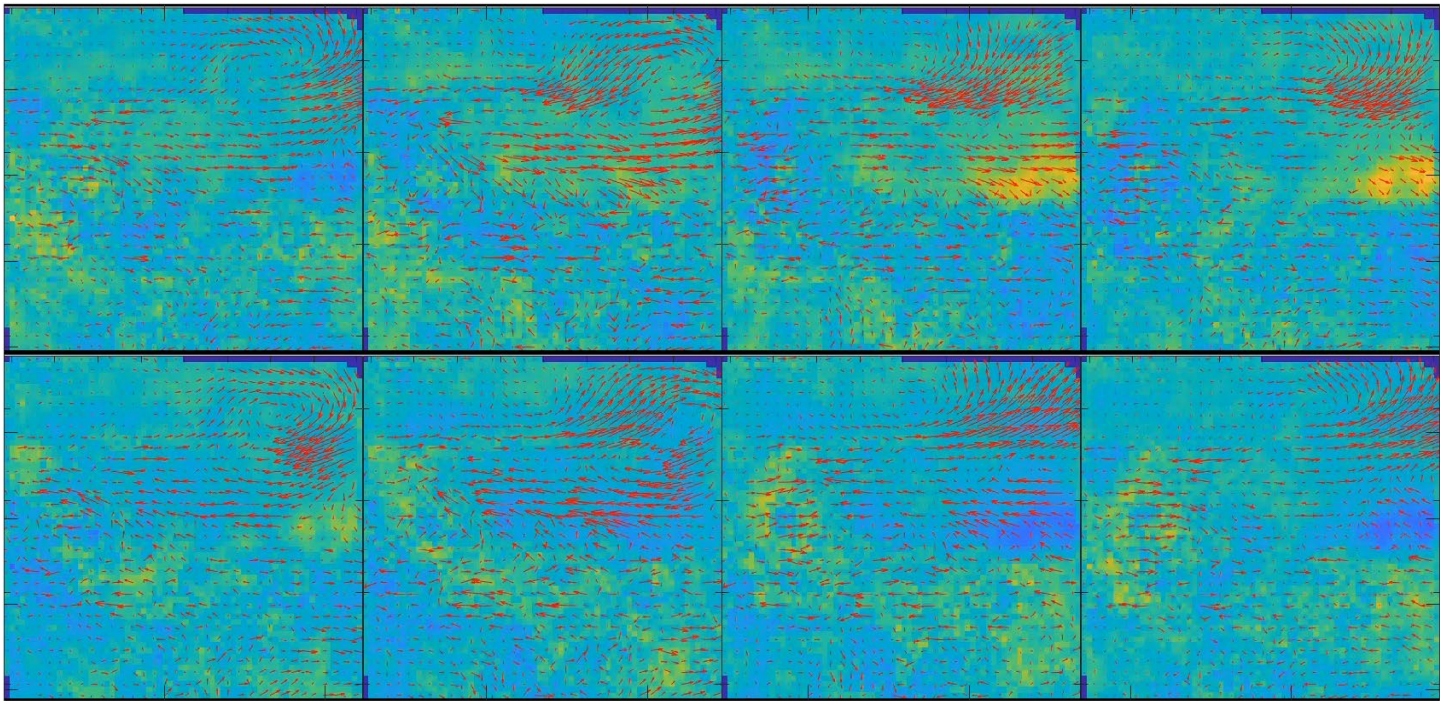

Figure 15. SPOD-reconstructed velocity field dynamics over one oscillation at $\boldsymbol{St = 0.12}$ for an unforced case at $\boldsymbol{P_{th} = 0.40}$ **MW**. The field of view has been cropped to highlight the upper half of the combustor. Vector arrows are the in-plane velocity, and the background is the out-of-plane velocity, with blue and yellow indicating positive and negative velocities, respectively. SPOD: spectral proper orthogonal decomposition.

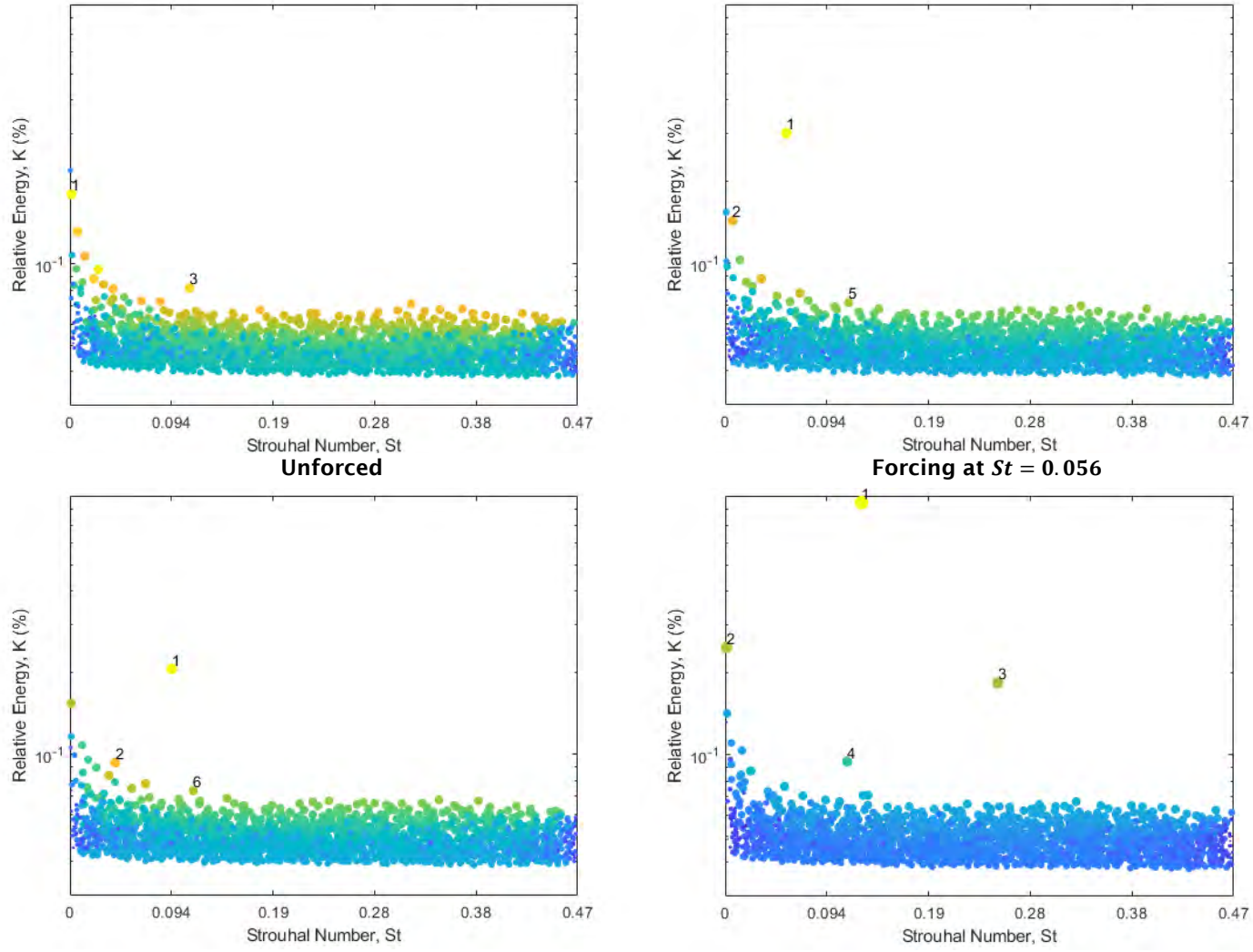

Figure 16. Spectral proper orthogonal decomposition spectra from stereoscopic particle image velocimetry measurements at $P_{th} = 0.36$ MW.

Figure 16 shows SPOD spectra from the SPIV data for the unforced case and with forcing at $St = 0.056, 0.094,$ and 0.13 for $P_{th} = 0.36$ MW. The OH* CL spectra are similar and are not included here for brevity. Interestingly, this leaner case does not exhibit the strong self-excited dynamics at $St = 0.12$ observed for the $P_{th} = 0.40$ data. Instead, a signficantly weaker self-excited oscillation occurs at approximately $St = 0.11$. The magnitude of the velocity response to forcing is relatively unchanged between $St = 0.056$ and 0.094, but increases by a factor of approximately five at $St = 0.12$, aligning well with the FTF measurements and analysis in Task 3. Ongoing analysis is investigating the forced velocity dynamics for cases exhibiting stronger self-excited oscillations at $P_{th} = 0.4$ MW.

Milestones

- Campaign 2 test rig design (complete)
- Measurement system design (complete)
- Campaign 2 test rig fabrication (complete)
- Experimental Campaign 2 (complete)

- Data processing from Campaign 1 (complete)
- Data processing from Campaign 2 (on schedule for completion in Q2 2023, 50% complete)

Major Accomplishments

- Design, fabrication, deployment, and operation of a novel LPP combustor
- Advancement of various optical diagnostics for high-pressure gas turbine conditions
- Optical measurements providing insights into combustion dynamics in the LPP combustor

Publications

Published conference proceedings

Passarelli, M. L., Wonfor, S. E., Zheng, A. X., Manikandan, S. R., Mazumdar, Y. C., Seitzman, J. M., Steinberg, A. M., Bower, H., Hong, J., Venkatesan, K., & Benjamin, M. (2022, January 3). Experimental characterization of a lean prevaporized premixed combustor for supersonic transport applications. *AIAA SCITECH 2022 Forum*. AIAA SCITECH 2022 Forum, San Diego, CA & Virtual. https://doi.org/10.2514/6.2022-2347

Passarelli, M. L., Wonfor, S. E., Zheng, A. X., Mazumdar, Y. C., Seitzman, J. M., Steinberg, A. M., Salazar, V., Venkatesan, K., & Benjamin, M. (2023, January 23). Forced and unforced dynamics of a lean premixed prevaporized combustor for civil supersonic transport. *AIAA SCITECH 2023 Forum*. AIAA SCITECH 2023 Forum, National Harbor, MD & Online. https://doi.org/10.2514/6.2023-0920

Zheng, A. X., Manikandan, S., Wonfor, S. E., Steinberg, A. M., & Mazumdar, Y. C. (2023, January 23). Planar time-resolved laser-induced incandescence for particulate emissions in premixed flames at elevated pressures. *AIAA SCITECH 2023 Forum*. AIAA SCITECH 2023 Forum, National Harbor, MD & Online. https://doi.org/10.2514/6.2023-2435

Outreach Efforts

Eight semesters of undergraduate research-for-credit have been associated with this project.

Awards

None.

Student Involvement

- Mitchell Passarelli (PhD Candidate), GT: Mie scattering and OH* CL measurements
- Samuel Wonfor (PhD Candidate), GT: fuel PLIF measurements
- Andrew Zheng (PhD Candidate), GT: TiRe-LII processing of OH PLIF measurements
- Sundar Ram Manikandan (MS Candidate), GT: thermophoretic nvPM sampling system
- Coleman Pethel, Mihir Rao, Andrew Semelka (BS Students), GT: assistance in data processing, calibration burner, diagnostics design, etc.

Plans for Next Period

- Complete processing of data from Campaign 2 (Q2 2023)
- Complete Campaign 3 test rig design, fabrication, and assembly (Q2 2023)
- Perform Experimental Campaign 3 (Q2–3 2023)
- Analyze data from Campaign 3 (Q3–4 2023)

References

Berton, J. J., Huff, D. L., Geiselhart, K., & Seidel, J. (2020, January 6). Supersonic technology concept aeroplanes for environmental studies. *AIAA Scitech 2020 Forum*. AIAA Scitech 2020 Forum, Orlando, FL. https://doi.org/10.2514/6.2020-0263

Speth, R. L., Eastham, S. D., Fritz, T. M., Sanz-Morere, I., Agarwal, A., Prashanth, P., Allroggen, F., & Barrett, S. R. H. (2021). *Global environmental impact of supersonic cruise aircraft in the stratosphere.* https://ntrs.nasa.gov/citations/20205009400

Hassan, M., Pfaender, H., & Mavris, D. (2020, June 15). Design tools for conceptual analysis of future commercial supersonic aircraft. *AIAA AVIATION 2020 FORUM*. AIAA AVIATION 2020 FORUM, VIRTUAL EVENT. https://doi.org/10.2514/6.2020-2620

Kharina, A., MacDonald, T., Rutherford, D. Environmental performance of emergic supersonic transport aircraft. (2018). *International Council on Clean Transportation.*

Niedzwiecki, R. W. (1992). Low emissions combustor technology for high-speed civil transport engines. *NASA. Langley*

Research Center, First Annual High-Speed Research Workshop, Part 2. https://ntrs.nasa.gov/citations/19940028975

Kheirkhah, S., Cirtwill, J. D. M., Saini, P., Venkatesan, K., & Steinberg, A. M. (2017). Dynamics and mechanisms of pressure, heat release rate, and fuel spray coupling during intermittent thermoacoustic oscillations in a model aeronautical combustor at elevated pressure. *Combustion and Flame*, *185*, 319–334. https://doi.org/10.1016/j.combustflame.2017.07.017

Passarelli, M. L., Wabel, T. M., Venkatesan, K., Cross, A., & Steinberg, A. M. (2019, August 19). Experimental analysis of thermoacoustic oscillations in a model aeronautical gas turbine combustor at realistic conditions. *AIAA Propulsion and Energy 2019 Forum*. AIAA Propulsion and Energy 2019 Forum, Indianapolis, IN. https://doi.org/10.2514/6.2019-3949

Orain, M., Baranger, P., Ledier, C., Apeloig, J., & Grisch, F. (2014). Fluorescence spectroscopy of kerosene vapour at high temperatures and pressures: Potential for gas turbines measurements. *Applied Physics B*, *116*(3), 729–745. https://doi.org/10.1007/s00340-013-5756-z

Saini, P., Arndt, C. M., & Steinberg, A. M. (2016). Development and evaluation of gappy-POD as a data reconstruction technique for noisy PIV measurements in gas turbine combustors. *Experiments in Fluids*, *57*(7), 122. https://doi.org/10.1007/s00348-016-2208-7

Manikandan, S.R. (2022). *Experimental characterization of NVPM in a laminar premixed jet flame at elevated pressure using thermophoretic sampling and transmission electron microscopy* [Master's thesis, Georgia Institute of Technology].

Baldelli, A., Trivanovic, U., Corbin, J. C., Lobo, P., Gagné, S., Miller, J. W., Kirchen, P., & Rogak, S. (2020). Typical and atypical morphology of non-volatile particles from a diesel and natural gas marine engine. *Aerosol and Air Quality Research*, *20*(4), 730–740. https://doi.org/10.4209/aaqr.2020.01.0006

Chen, Y., Cenker, E., Richardson, D. R., Kearney, S. P., Halls, B. R., Skeen, S. A., Shaddix, C. R., & Guildenbecher, D. R. (2018). Single-camera, single-shot, time-resolved laser-induced incandescence decay imaging. *Optics Letters*, *43*(21), 5363. https://doi.org/10.1364/OL.43.005363

Passarelli, M. L., Wonfor, S. E., Zheng, A. X., Manikandan, S. R., Mazumdar, Y. C., Seitzman, J. M., Steinberg, A. M., Bower, H., Hong, J., Venkatesan, K., & Benjamin, M. (2022, January 3). Experimental characterization of a lean prevaporized premixed combustor for supersonic transport applications. *AIAA SCITECH 2022 Forum*. AIAA SCITECH 2022 Forum, San Diego, CA & Virtual. https://doi.org/10.2514/6.2022-2347

Passarelli, M. L., Wonfor, S. E., Zheng, A. X., Manikandan, S. R., Mazumdar, Y. C., Seitzman, J. M., Steinberg, A. M., Bower, H., Hong, J., Venkatesan, K., & Benjamin, M. (2022, January 3). Experimental characterization of a lean prevaporized premixed combustor for supersonic transport applications. *AIAA SCITECH 2022 Forum*. AIAA SCITECH 2022 Forum, San Diego, CA & Virtual. https://doi.org/10.2514/6.2022-2347

Sirovich, L. (1987). Turbulence and the Dynamics of Coherent Structures Part I: Coherent Structures. *Quarterly of Applied Mathematics, 45*(3), 561-571.

Sieber, M., Paschereit, C. O., & Oberleithner, K. (2016). Spectral proper orthogonal decomposition. *Journal of Fluid Mechanics*, *792*, 798–828. https://doi.org/10.1017/jfm.2016.103

Schmid, P.J. (2010). Dynamic mode decomposition of numerical and experimental data. *Journal of Fluid Mechanics, 656*, 5-28. doi:10.1017/S0022112010001217

Tu, J.H. (2013). *Dynamic Mode Decomposition: Theory and Applications* [Doctor of Philosophy thesis, Princeton University]. https://cwrowley.princeton.edu/theses/tu.pdf

Jovanović, M. R., Schmid, P. J., & Nichols, J. W. (2014). Sparsity-promoting dynamic mode decomposition. *Physics of Fluids*, *26*(2), 024103. https://doi.org/10.1063/1.4863670

Roy, S., Yi, T., Jiang, N., Gunaratne, G. H., Chterev, I., Emerson, B., Lieuwen, T., Caswell, A. W., & Gord, J. R. (2017). Dynamics of robust structures in turbulent swirling reacting flows. *Journal of Fluid Mechanics*, *816*, 554–585. https://doi.org/10.1017/jfm.2017.71

Sieber, M., Oliver Paschereit, C., & Oberleithner, K. (2017). Advanced identification of coherent structures in swirl-stabilized combustors. *Journal of Engineering for Gas Turbines and Power*, *139*(2), 021503. https://doi.org/10.1115/1.4034261

Task 2 - Large Eddy Simulations of Combustor Operation and Emissions

Georgia Institute of Technology

Objectives

Simulations of advanced propulsion and power systems require a multiscale physics treatment, in turn requiring trade-offs between cost and accuracy. Achieving the optimal balance is complicated due to the nonlinear nature of turbulent reacting flows, which involve multiphase mixtures, highly nonlinear chemical kinetics, multiscale velocity and mixing processes, turbulence–chemistry interactions, compressibility effects (density changes induced by changes in pressure), and variable inertia effects (density changes induced by changes in composition or heat addition). Coupling between processes occurs over a wide range of time and length scales, many being smaller than can be resolved in a numerically feasible manner. Further complications arise when liquid or solid phases are present due to the introduction of dynamically evolving interface boundaries and the resultant complex exchange processes.

The overarching objective of this task is to provide quantitative insights into the accuracy of select calculations and to assess critical trade-offs between cost and accuracy. One set of calculations is performed using preferred engineering LES solvers, with the goal of minimizing cost for a targeted accuracy, as required by industry. A companion set of high-resolution LES calculations are performed using a research solver, the RAPTOR code at GT (Oefelein, 2006; Oefelein, 2018), to provide detailed information beyond that available from the experiments alone. Complementary information from the first-principles LESs and experimentally measured data provides a unique opportunity for elucidating the central physics of turbulent combustion processes in realistic parameter spaces and for making clear assessments of how a given combination of affordable engineering-based models perform. After achieving an adequate level of validation, results from the high-resolution LES calculations will provide fundamental information that cannot be measured directly and that is relevant to the development of lower-order engineering models. Thus, a strong link between theory, experiments, and relevant applications is established. The ultimate objectives of this task are to (a) assess the model fidelity/attributes required to accurately simulate the operability and emissions and (b) assess the trade-offs between accuracy and cost.

Research Approach

The GE combustor operates with liquid Jet A (CAT-A2) fuel delivered through upstream atomizers into bluff-body-stabilized pre-mixers, as well as through a central swirling pilot. Over the initial stages of the project, the GE and GT simulation teams worked toward the development of a common computational domain that enabled detailed treatment and analysis of the rig boundary conditions and operating conditions while also working around proprietary aspects of the GE hardware. A set of calculations in Fluent were performed by GE via standard practice in a computational domain that included the upstream plenum, upstream proprietary liquid-fuel/air injection system, combustion chamber, and exhaust, as shown in Figure 17.

In contrast, due to the proprietary nature of the injection system, the GT LES computational domain begins at the burner inlet planes beginning upstream of the dome that houses the bluff-body-stabilized pre-mixers, as shown in Figure 18. The domain includes all flow features of the pilot and pre-mixers as well as fine features such as wall and dome cooling holes. The major goals of this effort are to (a) establish good correspondence between the GE and GT simulation efforts, (b) establish

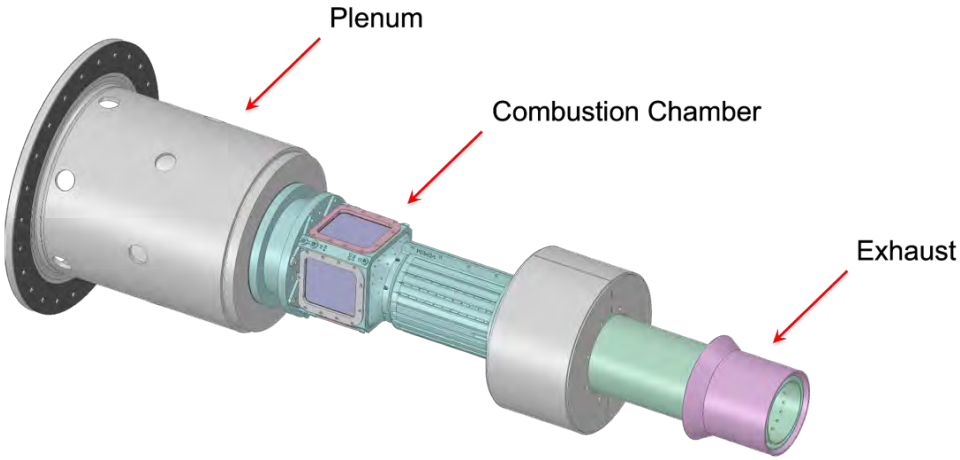

Figure 17. Extended computational domain used for the GE Fluent calculations.

advanced methodologies for the treatment of boundary conditions in "industrial-grade" rigs such as this, and (c) quantify and enable detailed analyses of the impact of both the inner combustion characteristics and the actual physical boundary conditions on the overall operating characteristics of the combustor.

Simulations performed by GT and GE are specifically designed to be complementary, not redundant. GT is performing high-resolution first-principles LESs designed to provide additional levels of information that are directly relevant to assessing, understanding, and improving the current state-of-the-art models being used, with an emphasis on accuracy over cost. The GE Fluent calculations are designed to apply "best-practices" engineering CFD to first establish the benchmark accuracy of the current models used for the conditions of interest here and then systematically assess where improvements can be made. Collectively, the combination of GT and GE calculations enables an advanced engineering workflow to systematically improve the accuracy and confidence of CFD design methodology while minimizing cost.

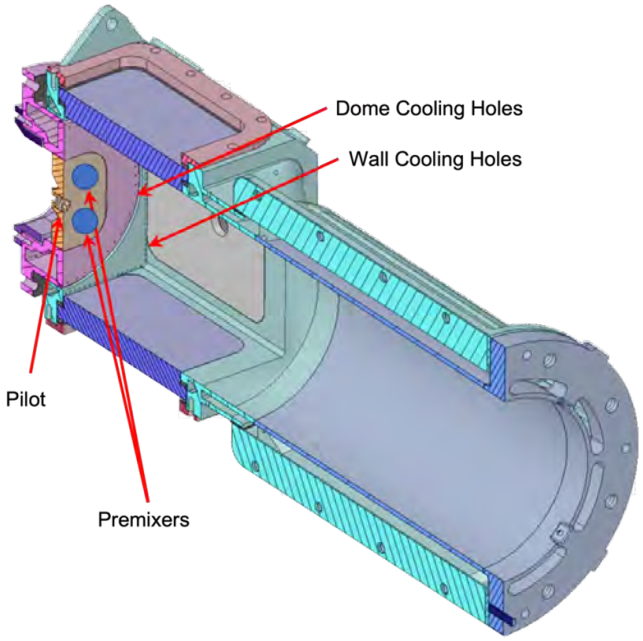

Figure 18. Computational domain used for the large eddy simulation calculations by GT.

Four high-quality production-level grids were designed for the high-resolution LESs performed at GT. The basic topology, which is shown in Figure 19, is identical to the geometry shown in Figure 18. A series of simulations using RAPTOR LES were performed to establish a foundation for comparisons between the codes. Grids composed of 30, 60, 120, and 240 million cells corresponding to the topology shown in Figure 19, were used to obtain detailed solutions at these different resolutions.

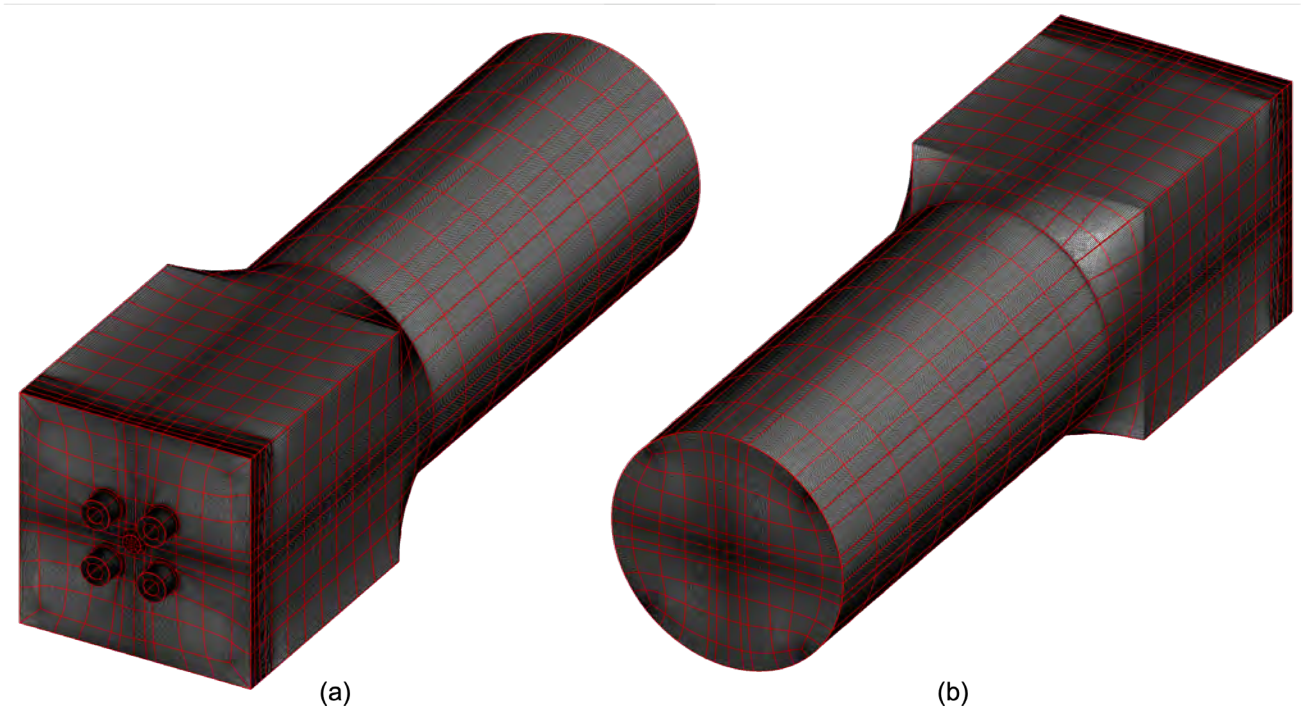

Figure 19. Grid topology used for the RAPTOR large eddy simulation calculations. Grids composed of 30, 60, 120, and 240 million cells were used to assess model performance as a function of resolution.

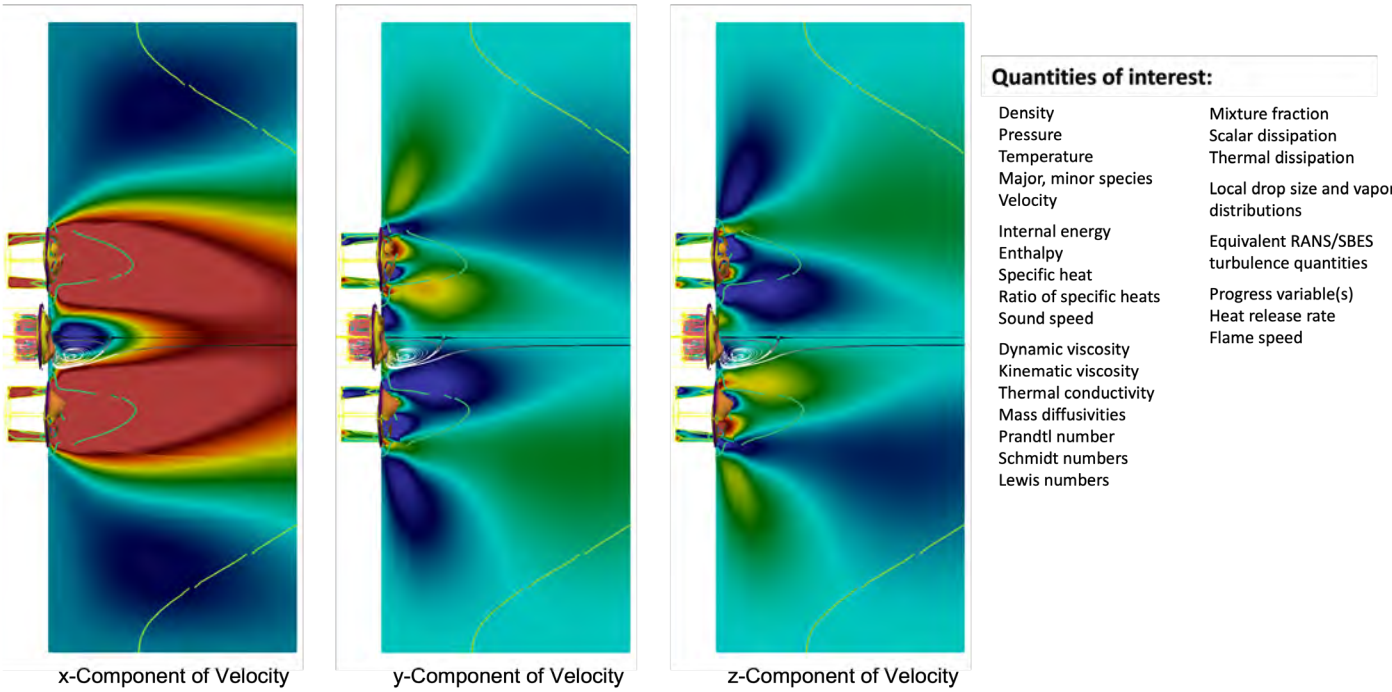

Figure 20. Representative time-averaged velocity from the RAPTOR large eddy simulation code. Quantities of interest being extracted from the simulation include those listed on the right.

Figures 20 and 21 show representative time averages and instantaneous results from the RAPTOR LES code. These results

were obtained by using the detailed treatment of boundary conditions established in Year 1. Time-dependent turbulent inflow profiles are constructed using the synthetic eddy method (Jarrin, 2009). A modified compressible formulation of the synthetic eddy method is employed to provide time-evolving turbulent inflow conditions to capture the physical nonuniformities that are present across the pre-mixer inlet planes. The inputs used to construct the signals are the nonuniform mean velocity profiles, Reynolds stress tensor, and integral scale distributions extracted directly from the GE Fluent calculations, which effectively establish a one-to-one correspondence between the codes and thus minimize uncertainties in the results due to differences in boundary conditions when comparing the interior field quantities of interest. Specific quantities of interest are also listed in Figure 21.

Having established baseline datasets from each of the codes, attention has now focused on joint comparisons between the quantities of interest listed in Figure 21. These data are being extracted from key cross-sectional planes such as those shown in Figure 22. Flow entering the combustion chamber involves a complex combination of turbulent gas-phase fluid dynamics and liquid-fuel spray dynamics. The pre-mixers inject partially pre-mixed gas laden with liquid-fuel drops. The pilot radially injects swirling air flow onto the liquid-fuel jet. The gas-phase flow velocity and liquid-fuel drop size and velocity distributions are found to be nonuniform both within and between the pre-mixers. In addition, the mass flow of air through the dome and wall cooling holes accounts for 40% of the total mass flow, and flow across the wall cooling holes is also nonuniform. Thus, there are many challenges in isolating the effectiveness of the different sub-models used in the simulations.

To isolate different effects, the GT LES is performed over a range of resolutions to quantify the fidelity with which different processes can be represented, either instantaneously or statistically. Figure 23 shows an example in a canonical non-pre-mixed flame that demonstrates this progression. At the finest level of resolution, the simulations emulate structures that are comparable to corresponding Raman–Rayleigh imaging using the exact same color scales and contour thresholds (i.e., the data are processed identically in the same manner). As the local spatial and corresponding temporal resolutions are reduced (which significantly decreases the calculation cost), the simulation can no longer emulate the actual turbulent flame structure. Instead, the simulation can only represent these dynamics from a statistical perspective. The major question then becomes to what degree are the sub-models (either LES or RANS) able to correctly represent the bulk effect of the unresolved processes as a function of these statistical quantities of interest. The progression of GT LES cases is designed to provide the quantitative data required to answer this question by reconstructing modeled terms in the engineering-based GE calculations and comparing them with corresponding reconstructions from the first-principles GT LES. These comparisons will be conducted as part of the tasks performed in Year 3.

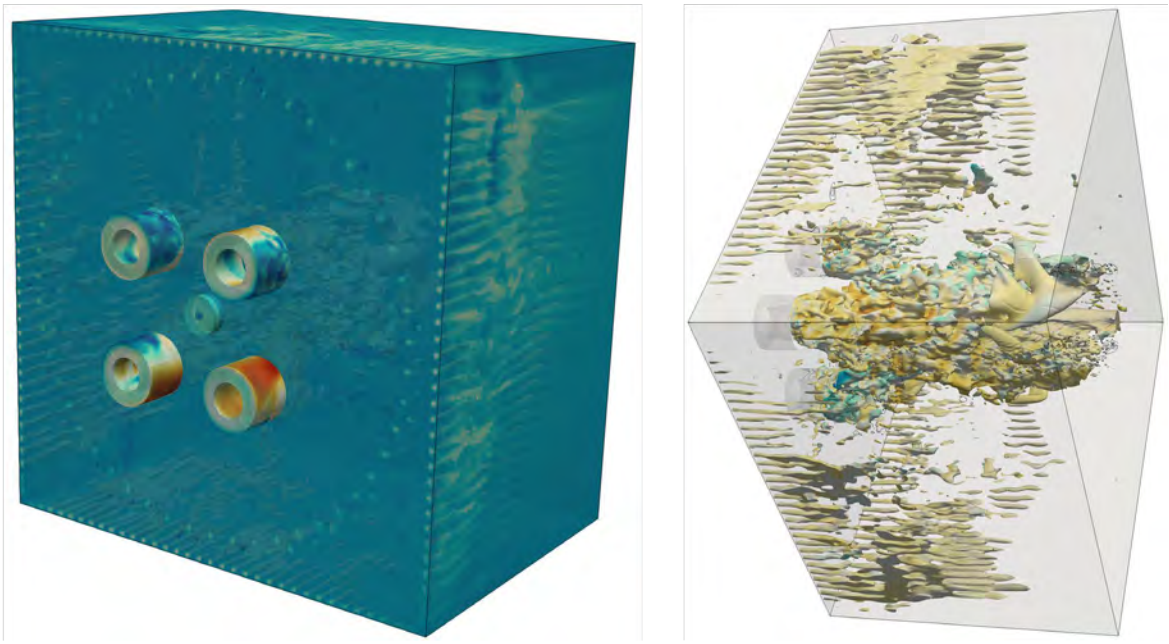

Figure 21. Representative instantaneous fields of temperature and velocity from the RAPTOR large eddy simulation code.

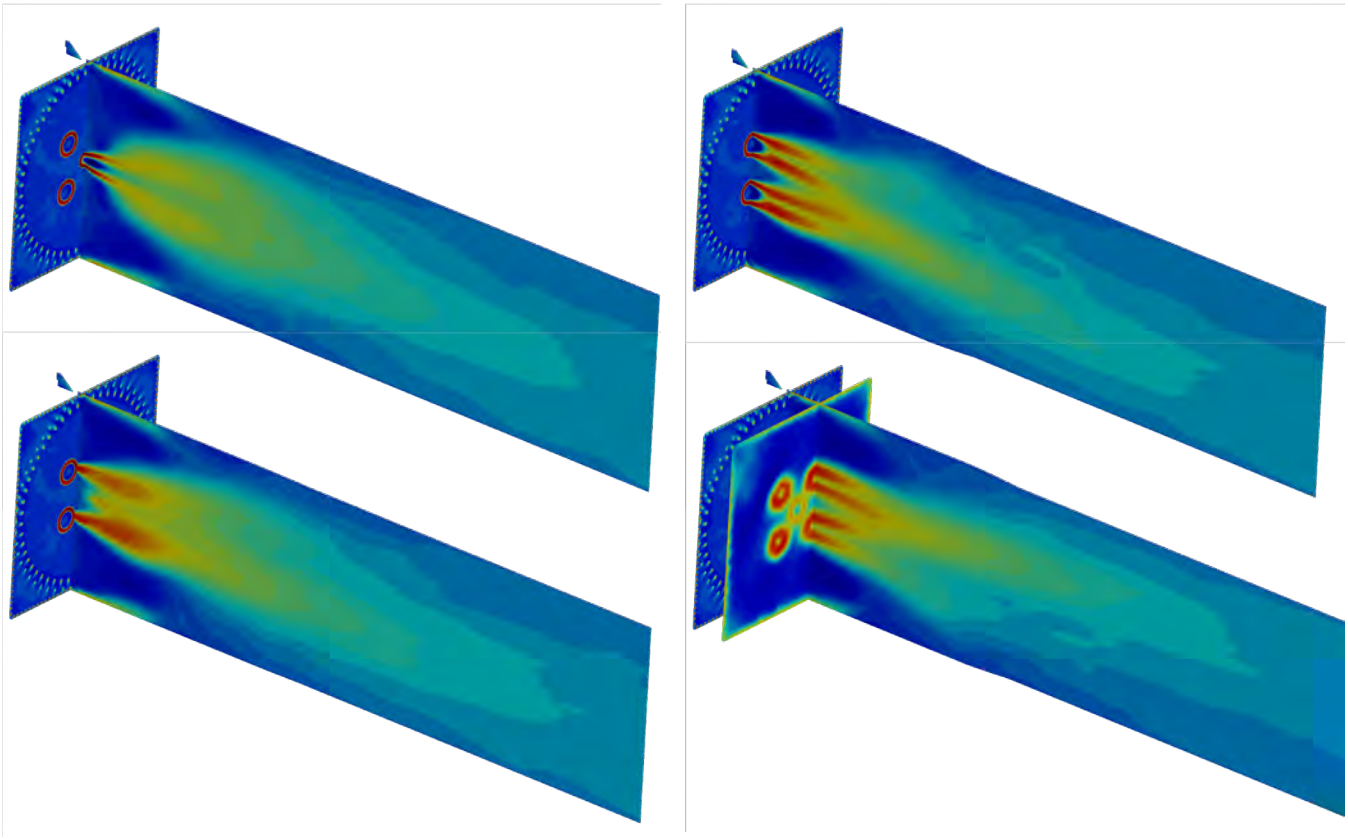

Figure 22. Representative cross-sectional planes of interest for detailed comparisons between GT large eddy simulations, GE Fluent calculations, and measured data. Corresponding line plots within each of these planes will also be extracted to further illuminate key quantitative details.

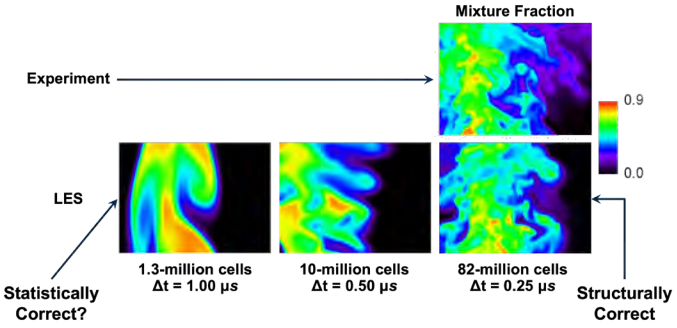

Figure 23. Analysis of a canonical non-pre-mixed flame that demonstrates how simulations at different levels of fidelity represent turbulent structures. At the finest level of resolution, the simulations emulate actual physical structures that are comparable to corresponding Raman–Rayleigh imaging (top right) using the exact same color scales and contour thresholds. LES: large eddy simulation.

In addition to the analysis of gas-phase quantities, recent observations between the experimental results and GE CFD calculations have suggested a discrepancy in the amount of liquid-fuel drops entering the chamber. Imaging within the test article suggests that most of the fuel is fully vaporized as it enters the chamber from the exit planes of the four pre-mixers. Conversely, the CFD predictions indicate a much higher level of liquid-fuel drops entering the chamber. This discrepancy

suggests that inaccuracies may be present in the spray injection models used. Specifically, a typical approximation employed to make the engineering CFD calculations affordable for design is the so-called "parcel method," where groups of drops are represented by a single "parcel" that is injected and tracked. This approach eliminates the need to track millions of physical drops in a simulation at the expense of fidelity in the time-dependent dispersion, mass exchange, and energy exchange characteristics of the spray. To assess the accuracy of the parcel method, a set of simulations are being performed with RAPTOR LES that eliminate the use of parcels and track physical drops using the same injection conditions. This effort will provide detailed quantitative guidelines regarding the maximum number of drops a given parcel can represent in these types of flow configurations. Figure 24 shows representative spray distributions produced using RAPTOR LES. The results are then processed to determine the degree to which GE simulations using parcels with different number densities reproduce the same local distributions in drop size, mass, and temperature.

Tasks performed to date have provided the foundational workflow and data required to enable one-to-one comparisons between the GE CFD and GT LES results, with an emphasis on understanding the accuracy of the engineering models being used in the GE calculations. In addition, this effort has enabled comparisons between the measured and modeled results. Studies planned as part of Year 3 tasks include analyses of (a) sub-model accuracy and performance in a complex geometric environment, (b) turbulent velocity and scalar mixing, (c) turbulent mixed-mode combustion, (d) finite-rate chemical kinetics and combustion dynamics, and (e) engineering model performance and best practices for model implementation.

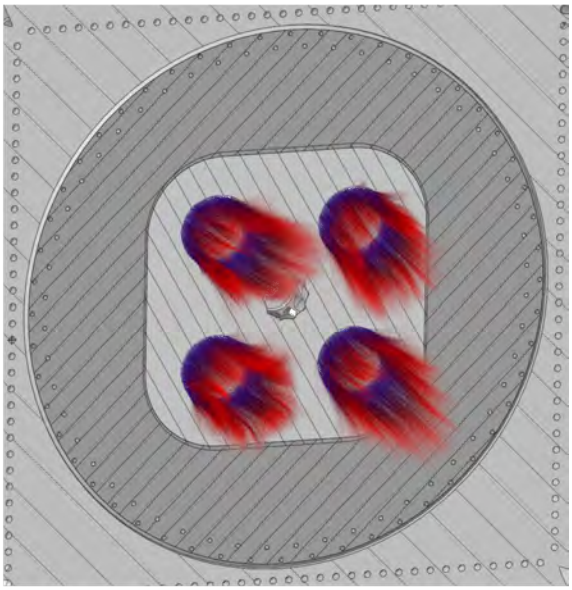

Figure 24. Representative spray distributions produced using RAPTOR large eddy simulations.

Milestones

- Detailed flow field characterization of test article 1 using RAPTOR LES (complete)
- Baseline comparisons of RAPTOR LES with engineering LES of test article 1 (complete)
- Parametric analysis of boundary condition sensitivity (complete)
- Code-to-code comparisons and analysis (test article 1 in progress, 80% complete)

Major Accomplishments

- Fluent LES simulations of the LPP combustor
- Established workflow to align space- and time-dependent boundary conditions between GE Fluent and GT RAPTOR

Publications

None.

Outreach Efforts

Four semesters of undergraduate research-for-credit have been associated with this project.

Awards
None.

Student Involvement
- Sriram Kalathoor (Graduate Research Assistant, PhD Candidate), GT: baseline calculations with RAPTOR code.
- Neilay Amin, Preethi Mysore, Katrina Potak, and Rachel Wilder (BS Students), GT: assistance in setting up grids, boundary conditions, and computational runs

Plans for Next Period
- Apply workflow and data analysis techniques developed to test article 2 (Q3 2023)
- Perform a detailed comparison of RAPTOR LES, Fluent LES, and experimental measurements of test article 2 (Q3–4 2023)

References
Oefelein, J. C. (2006). Large eddy simulation of turbulent combustion processes in propulsion and power systems. *Progress in Aerospace Sciences*, *42*(1), 2–37. https://doi.org/10.1016/j.paerosci.2006.02.001

Oefelein, J. C., & Sankaran, R. (2017). Large eddy simulation of reacting flow physics and combustion. In T. P. Straatsma, K. B. Antypas, & T. J. Williams (Eds.), *Exascale Scientific Applications* (1st ed., pp. 231–256). Chapman and Hall/CRC. https://doi.org/10.1201/b21930-11

Jarrin, N., Prosser, R., Uribe, J.-C., Benhamadouche, S., & Laurence, D. (2009). Reconstruction of turbulent fluctuations for hybrid RANS/LES simulations using a Synthetic-Eddy Method. *International Journal of Heat and Fluid Flow*, *30*(3), 435–442. https://doi.org/10.1016/j.ijheatfluidflow.2009.02.016

Task 3 - Thermoacoustic Modeling
Georgia Institute of Technology

Objectives
Lean pre-mixed combustors are susceptible to thermoacoustic instabilities, which increase emissions, decrease efficiency, reduce combustor life, and produce high-amplitude tonal noise. These instabilities occur in “islands” of the operating space that should be avoided during operation. Due to the wide range of potential operating conditions, it is not tractable to perform LESs or experiments across all relevant conditions to assess instabilities; instead, reduced-order modeling tools (i.e., thermoacoustic solvers) must be used. However, these tools have not been validated for the conditions and configurations of relevance for lean pre-mixed supersonic engine combustors. This task will develop, assess, and validate GE thermoacoustic solvers in this situation.

Research Approach
A layout of the geometry for the FTF measurements is shown in Figure 25, and a detailed description of the FTF measurements in the THOR rig can be found in Venkatesan *et al.* (2022). For compact flames with a flame length much shorter than the acoustic wavelength, the acoustic velocity at the flame base, the acoustic velocity at the same location and under the same operating condition but non-reacting, and the flame heat release oscillation are described as follows:

$$u'_{hot(1)} = u'_{cold(1)} + \bar{u}_1 \left(\frac{\bar{T}_{hot}}{\bar{T}_{cold}} - 1\right)\frac{Q'}{\bar{Q}} \quad (1)$$

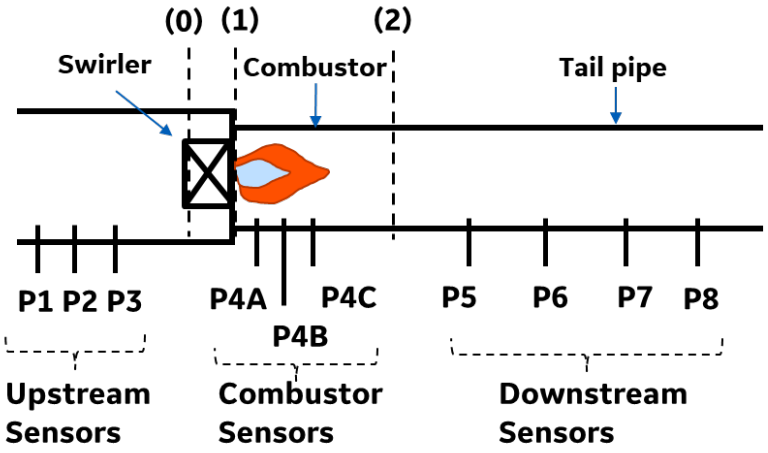

Figure 25. Illustration of the combustor, flame zone, and dynamic pressure sensors.

where $u'_{hot(1)}$ is the acoustic velocity at Location (1) for the reacting condition, $u'_{cold(1)}$ is the acoustic velocity at Location (1) for the non-reacting condition, $\overline{u_1}$ is the mean flow velocity at Location (1), Q' is the flame fluctuating heat release, ($\bar{Q}$) is the mean heat release, $\bar{T}_{hot}$ is the temperature in the combustor for the reacting condition, and $\bar{T}_{cold}$ is the temperature in the combustor for the non-reacting condition [2]. The FTF can then be written as follows:

$$FTF = \frac{\frac{Q'}{\bar{Q}}}{\frac{u'}{\bar{u}}} = \left(\frac{u'_{hot(1)}}{u'_{cold(1)}} - 1\right) / \left(\frac{\bar{T}_{hot}}{\bar{T}_{cold}} - 1\right) \quad (2)$$

During the measurements for a given operating condition, transfer functions between acoustic pressures at sensors P2–P8 with reference to P1 were obtained first for the non-reacting condition (also referred to as the cold or no-flame condition) and then for the reacting condition (also referred to as the hot or flame condition). The transfer functions were then processed to obtain acoustic velocities at the flame base, i.e., $u'_{cold(1)}$ and $u'_{hot(1)}$. Once the acoustic velocities are obtained, the FTF can be determined using Equation (2).

The air temperature in the tail pipe section is lower than the air temperature in the combustor for reacting conditions due to mixing with the window cooling flow and heat absorbed at the wall. To account for the effects of cooling air influx and non-uniform temperatures, two three-dimensional acoustic models were built using the finite-element solver COMSOL: one for the non-reacting condition and one for the reacting condition. The transfer matrix (TM) from the acoustic pressure and velocity at Location (2) to the acoustic pressure and velocity at Location (1) was then calculated using the acoustic models, with one TM calculated for the non-reacting condition and one TM for the reacting condition.

The measured acoustic pressure transfer functions from P5–P8 with reference to P1 were processed using the conventional multi-microphone technique (Polifke, 2001; Paschereit, 2002) to obtain the acoustic pressures and velocity at Location (2). The TMs were then used to determine the acoustic pressure and velocity at Location (1) as follows:

$$\begin{pmatrix} p' \\ u' \end{pmatrix}_1 = \begin{bmatrix} T_{11} & T_{12} \\ T_{21} & T_{22} \end{bmatrix} \begin{pmatrix} p' \\ u' \end{pmatrix}_2 \quad (3)$$

Once the acoustic velocities at Location (1) were obtained for both the non-reacting and reacting conditions, the FTF could be determined using Equation (2).

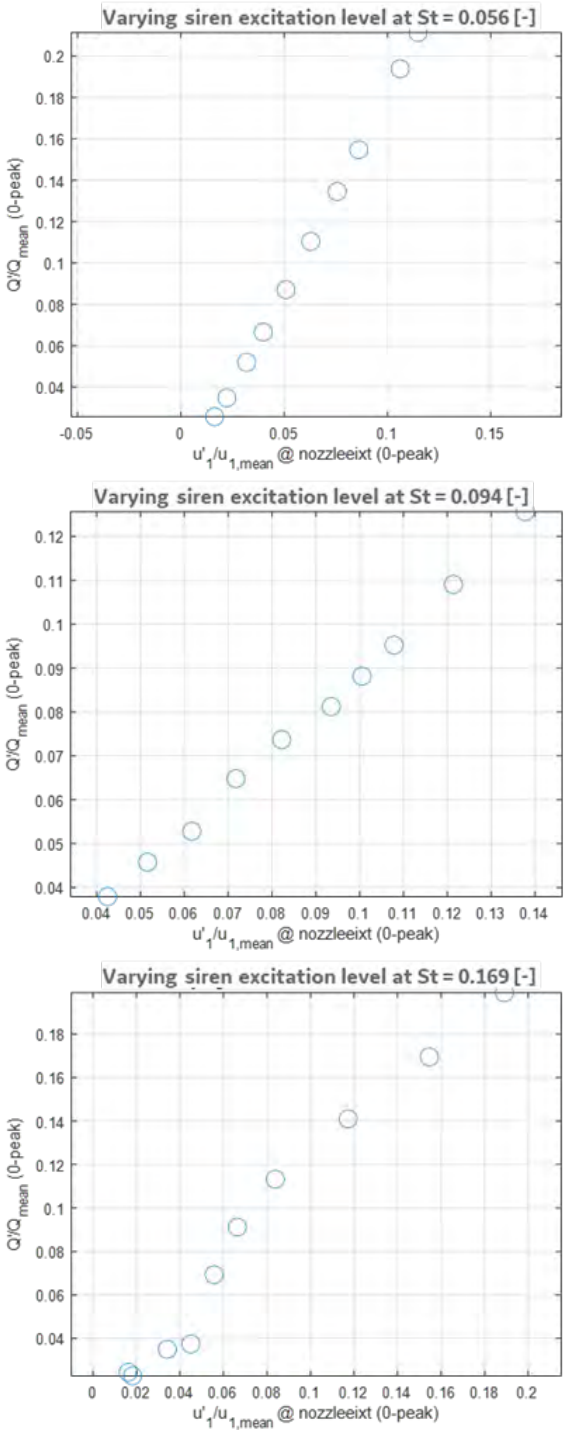

Figure 26. Linearity study at three Strouhal numbers. These frequencies spanned the full range of frequencies of interest.

Three pressure sensors (P1, P2, P3) were located upstream of the swirler. The inlet geometry upstream of the swirler can be considered uniform, as the cross-sectional area of the swirler was significantly smaller in comparison to the inlet plenum. The acoustic pressure and velocity immediately upstream of the swirler at Location (0) can be determined from the measured acoustic pressures at sensors P1–P3 using the conventional multi-microphone method. Combining the acoustic pressure and velocity at Location (0) and the acoustic pressure at Location (1), one can then obtain the swirler impedance as follows:

$$Z_{sw} = \frac{p'_{cold(0)} - p'_{cold(1)}}{u'_{cold(0)}\,\rho_{cold}\,c_{cold}\left(\frac{Area_{Comb}}{Area_{Swirler}}\right)} \tag{4}$$

where $p'_{cold(0)}$ and $u'_{cold(0)}$ are the acoustic pressure and velocity, respectively, immediately upstream of the swirler at Location (0), $p'_{cold(1)}$ is the acoustic pressure immediately downstream of the swirler at Location (1), and ρ_{cold} and c_{cold} are the mean air density and sound speed, respectively. Note that only acoustic pressures measured under non-reacting condition are needed to determine the swirler impedance. The acoustics of swirlers or burners are typically characterized by a TM that relates the acoustic pressure and velocity upstream of a swirler to the acoustic pressure and velocity downstream of the swirler (Paschereit, 2002). In this case, the axial dimension of the swirler is only approximately one tenth of the acoustic wavelength, even at 1000 Hz. Hence, the acoustic velocities upstream and downstream of the swirler were assumed to be equal, and the swirler could be characterized by the swirler impedance.

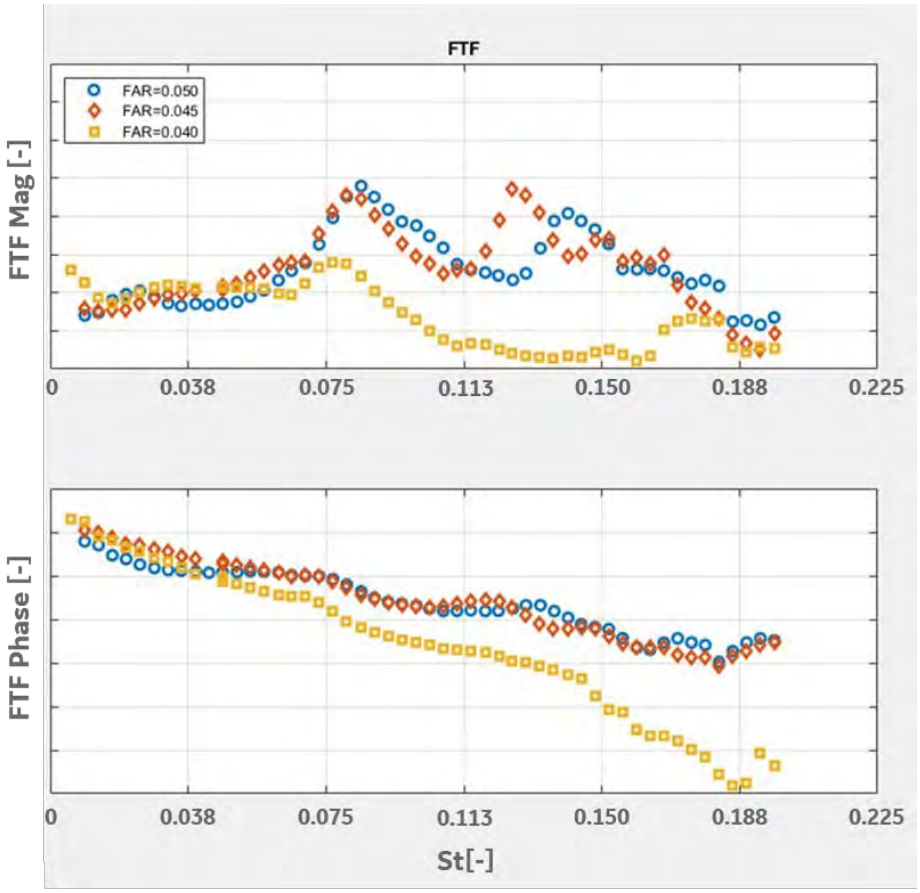

Figure 27. Acoustic flame transfer function (FTF) measurement for three different FARs.

It is well known that FTFs exhibit nonlinear behavior if the flame inlet air flow velocity perturbations become too large. In the current study, the FTFs were measured at different levels of inlet air perturbations to ascertain nonlinear behaviors. This linearity study was performed at a fixed combustor operating pressure, temperature, and equivalence ratio. The flame heat

release oscillation levels and the FTFs at the siren excitation frequency for $St = 0.056, 0.094,$ and 0.17 are shown in Figure 26 for varying levels of excitation.

In general, the flame heat release oscillation magnitude was observed to increase linearly with the flame base velocity excitation level. The deviation from linearity at very low excitation levels in Figure 26 is likely due to a higher background noise relative to the signal. However, the FTF magnitudes are observed to be linear at higher excitation levels. These results suggest that for the current measurements, the flame dynamics are in the linear regime and the FTFs obtained are linear.

Measurements of linear FTFs were undertaken for the range of operating conditions listed in Table 1. Specifically, the impact of the combustor inlet air temperature and thermal power on the FTF were each studied independently while the other operating parameters were held constant. Figure 27 shows the FTFs for three FARs (FAR1 > FAR2 > FAR3). The FTFs are observed to be strongly dependent on frequency and fuel-air ratio. The magnitudes of FTFs at the higher operating FAR are much higher across the entire frequency range, except for a narrow frequency band from $St = 0.028 - 0.056$. It is well known that liquid-fuel spray physics is highly dependent on the combustor operating FAR and temperature. High-speed CL images and flame videos of the combustor flame show changes in flame shape with changing FAR. The changes in flame shape and subsequent heat release are expected to impact the FTF response and will be the subject of detailed investigations and analyses moving forward.

Milestones

- ASCENT 74 test article designed for accurate FTF measurements
- Experimental Campaign 2 measurements of FTF performed

Major Accomplishments

- Acoustic and optical FTFs measured in the ASCENT 74 LPP combustor

Publications

Published conference proceedings

Venkatesan, K. (2022). Acoustic and Optical Flame Transfer Function Measurements in a High-Pressure Lean-Burn Aero-Engine Combustor Fueled with Jet A. ASME Turbo Expo.

Outreach Efforts

None.

Awards

None.

Student Involvement

- Mitchell Passarelli (PhD Candidate), GT: Mie scattering and OH* CL measurements
- Samuel Wonfor (PhD Candidate), GT: fuel PLIF measurements

Plans for Next Period

- Compare FTFs with analytical predictions and CFD
- Perform detailed comparisons of optical versus acoustic FTF methods

References

Venkatesan, K., Cross, A., & Han, F. (2022). Acoustic flame transfer function measurements in a liquid fueled high pressure aero-engine combustor. *Volume 3A: Combustion, Fuels, and Emissions*, V03AT04A049. https://doi.org/10.1115/GT2022-81769

Polifke, W., Paschereit, C. O., & Paschereit, K. (2001). Constructive and destructive interference of acoustic and entropy waves in a premixed combustor with a choked exit. *The International Journal of Acoustics and Vibration*, *6*(3). https://doi.org/10.20855/ijav.2001.6.382

Paschereit, C. O., Schuermans, B., Polifke, W., & Mattson, O. (2002). Measurement of transfer matrices and source terms of premixed flames. *Journal of Engineering for Gas Turbines and Power*, *124*(2), 239–247. https://doi.org/10.1115/1.1383255

Project 075 Improved Engine Fan Broadband Noise Prediction Capabilities

Boston University & Raytheon Technologies Research Center

Project Lead Investigator

Sheryl Grace
Associate Professor
Mechanical Engineering
Boston University
110 Cummington Mall, Boston, MA 02215
617-353-7364
sgrace@bu.edu

University Participants

Boston University

- P.I.: Sheryl Grace – Associate Professor, Mechanical Engineering
- FAA Award Number: 13-C-AJFE-BU Amendment 022
- Period of Performance: October 30, 2021 to November 1, 2022
- Tasks:
    1. Fan-wake surrogate model creation
    2. Improvement of the low-order model
    3. Rig test preparation

Project Funding Level

Year 2 funding:
FAA: $300,000: $115,000 to Boston University (BU), $185,000 to Raytheon Technologies Research Center (RTRC)
Match:$300,000: $115,000 from BU (data sets, faculty time, graduate student stipend)
$185,000 from RTRC (personnel time)

Investigation Team

Sheryl Grace, BU: Principal InvestigatorP.I. Tasks 1, 2, and 3
Noah Li, BU: PhD student. Tasks 1 and 2
Franky Zhang, BU: MS student. Task 1
Berkely Watchmann, BU: Undergraduate student. Task 1
Max Pounanov, BU: Undergraduate student. Task 1
Jeff Mendoza, RTRC: Co-principal investigator/P.I. Tasks 1, 2, and 3
Craig Aaron Reimann, RTRC: Staff scientist. Tasks 2 and 3
Julian Winkler, RTRC: Staff scientist. Tasks 1, 2, and 3
Dmytro Voytovych, RTRC: Staff scientist. Task 1
Kin Gwn Lore, RTRC: Staff scientist. Task 1
Michael Joly, RTRC: Staff scientist. Task 1

Project Overview

The noise signature of contemporary turbofan engines is dominated by fan noise, both tonal and broadband. Accepted methods for predicting the tone noise have existed for many years. Furthermore, engine designers have methods for controlling or treating tonal noise. However, this is not the case for broadband noise. Thus, it is clear that further reductions in engine noise will require accurate prediction methods for broadband noise to enable design decisions. Interaction noise

from the fan stage is a dominant broadband mechanism in modern high-bypass engines and is created by the interaction of turbulence in the fan wakes with the fan exit guide vanes. This project will leverage prior development of low-order models for the prediction of fan broadband interaction noise. Gaps in the low-order approach will be addressed based on knowledge gained from computation and experimentation. In particular, a method for determining the inflow into the stator via a machine learning (ML) algorithm will be developed. The low-order method will also be validated against full-scale rig data, and appropriate development will be undertaken based on the findings.

Task 1 - Fan-Wake Surrogate Model Creation

BU & RTRC

Objective

The goal of this task is to build a surrogate model using performance-level unsteady Reynolds-averaged Navier–Stokes data to specify the mean flow, turbulent kinetic energy, and turbulent length scale at locations along the helical fan-wake path.

Research Approach

Subtasks 1.1 and 1.2: Autoencoder and decoder development

The development of a multi-output ML method was the main focus of Year 2. Specifically, the decoder part of a convolution neural network (CNN) is now being used for learning the wake flow parameters of interest. Only the decoder is being used because of the mismatch between the input data type and the desired output. The input data consist of rotor geometry information from hub to tip, fan speed, engine mass flow, and basic performance-level flow information such as flow angles into and out of the fan. The output data consist of the flow variable of interest on a passage at an axial position downstream of the fan, as shown in the lower half of Figure 1.

Several findings led to the current state of the ML algorithm. First, the team determined that in order to gain high accuracy for the mean flow, it is necessary to learn the full averaged value from hub to tip and the wake deficit separately. The full average is simply a single data set from hub to tip and, as such, lends itself to a single-output type of analysis. Therefore, a deep neural network is used for learning the average value of the mean flow. A CNN is then used to learn the deficit. Second, it was found that learning the turbulence kinetic energy and turbulence dissipation parameter (k and e or w, from the computational fluid dynamics [CFD] turbulence model) separately and then creating the length scale from the learned values produced errors that led to inaccurate acoustic predictions. Hence, a new method for obtaining the length scale was devised. This method defines the length scale at every value on the CFD grid and interpolates the length scale directly onto the ML grid; then, the length scale is learned directly via a CNN.

TensorFlow is used for the CNN. In Year 2, the original R codes were ported to Python. The use of Python makes these codes more accessible to mechanical engineering students, who are often familiar with Python but not R. All of the results associated with ML performed via the method described above were reported in a conference paper (Li, 2022; Huang, 2022) and in an extended abstract submitted for Aeroacoustics 2022. These papers are attached as an appendix to this report.

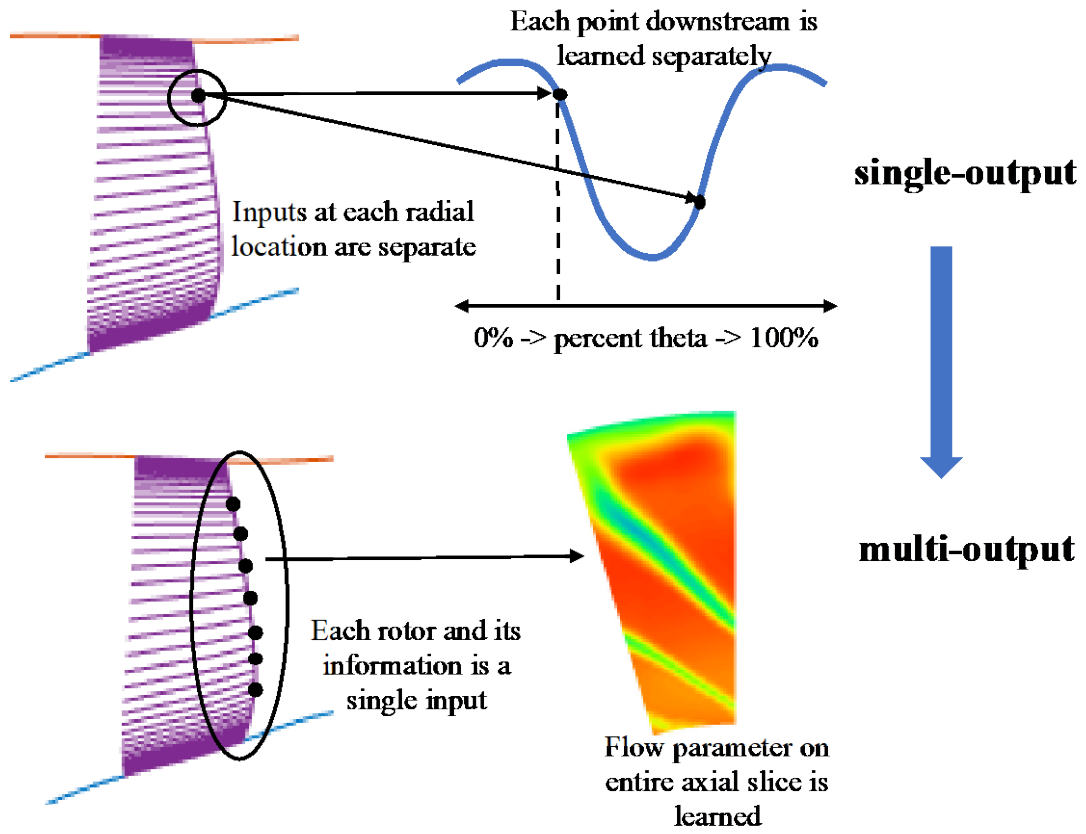

Figure 1. Single- vs. multi-output machine learning concept. The multi-output method does not require rectification of the wakes (centering) before the wakes are learned.

Subtask 1.3: Identification and creation of training data

Subtask 1.3a: Collection of existing training data: BU and RTRC worked to collect relevant existing fan-wake data sets.

Subtask 1.3b: Creation of additional training data: RTRC took the lead on developing new fans, and BU provided analyses in order to determine whether the fans were acceptable.

Throughout Year 2, a 264-case database derived from the four geometries related to the source diagnostic test (SDT) fan blade (i.e., cold [CAD], approach hot, cutback hot, and takeoff hot) was updated and improved. Closer analysis of the wake flow led to improvements in the setup of the CFD simulation.

During Year 2, much effort was spent in iterating on a method to create new fan geometries. RTRC used AxStream to create a derivative of the SDT fan blade that provided smoother variations of the geometry parameters from hub to tip. The performance metrics were similar to those of the SDT, with the new fan achieving a similar efficiency but being slightly more loaded, as shown in Figures 2 and 3. Once the baseline case was fully analyzed, slight modifications to the trailing edge thickness were made to create other geometries. It was expected that a four-fold increase in trailing edge thickness would change the wake, but it did not. Hence, for Year 3, other modifications such as increased lean, change in stagger, etc. will be pursued.

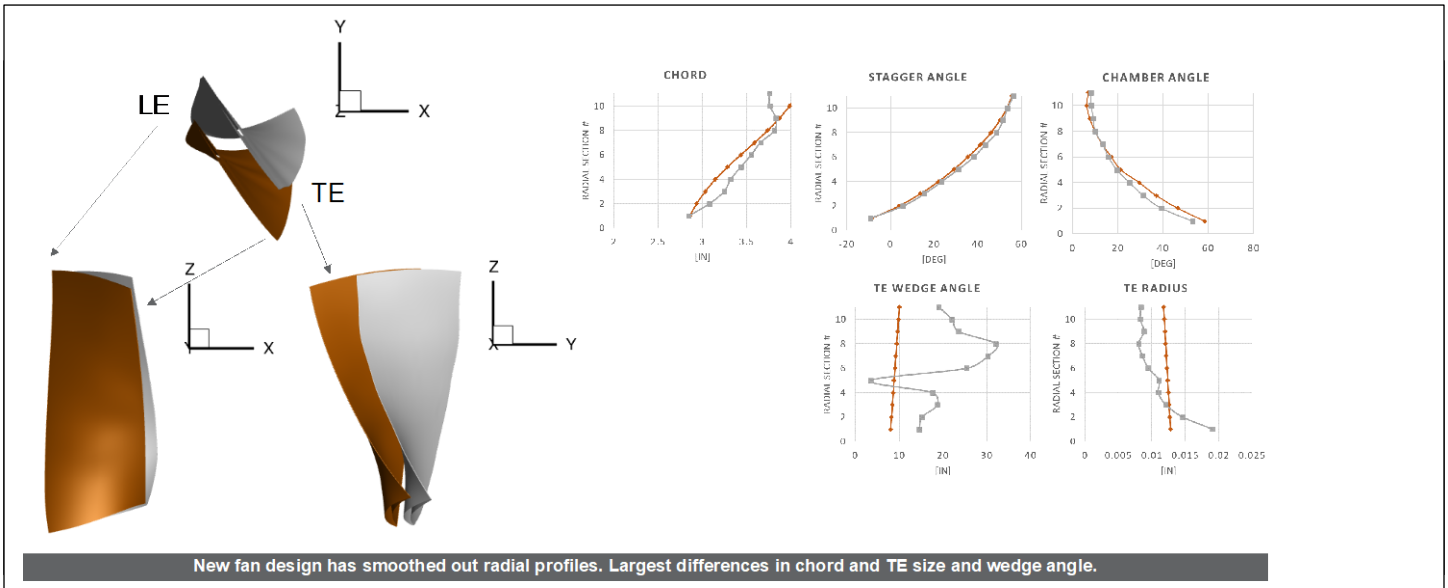

Figure 2. New baseline fan blade vs. the source diagnostic test fan blade. LE: leading edge; TE: trailing edge.

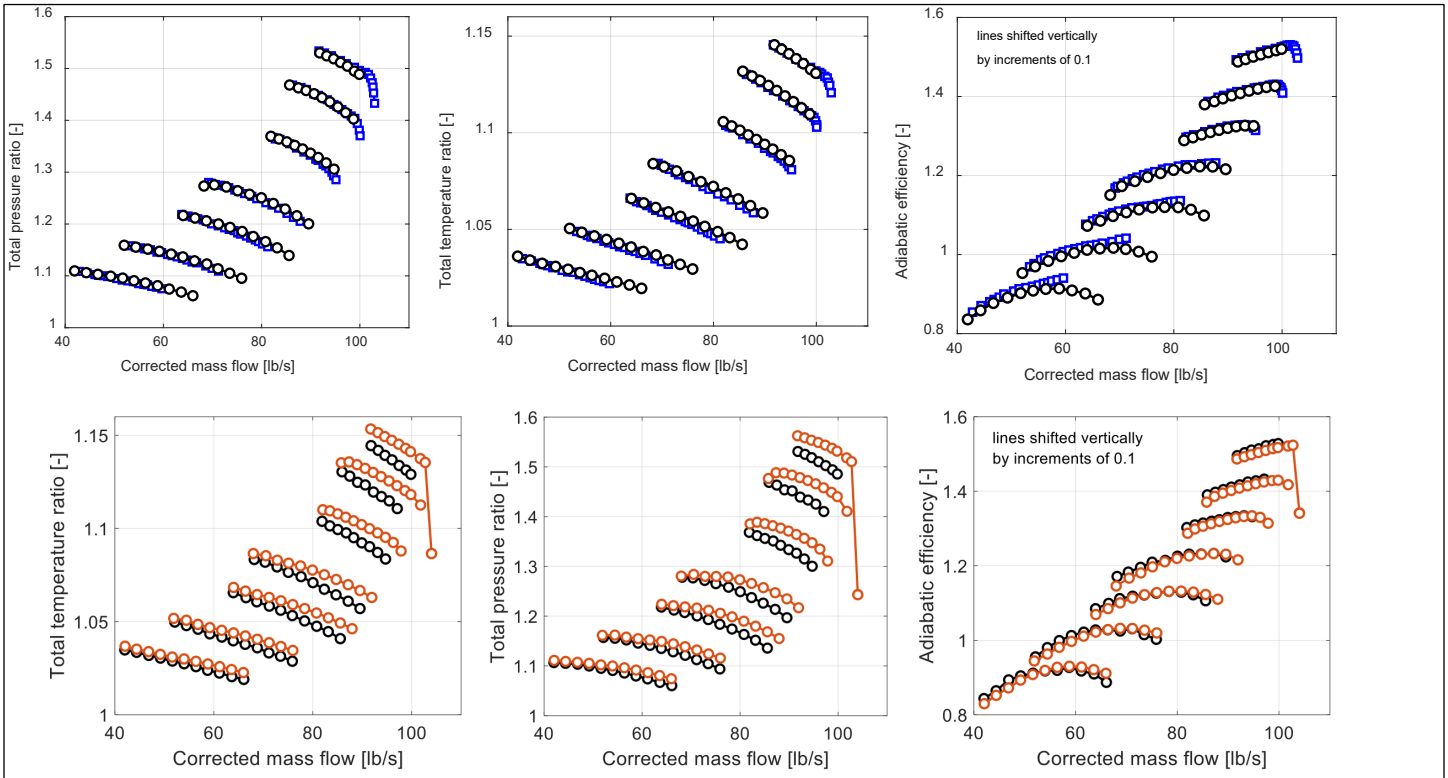

Figure 3. (Top) Performance curves for the source diagnostic test (SDT) cold (CAD) geometry. Blue: experimental data digitized from NASA TM 2013-214029. Black: computational fluid dynamics results. (Bottom) Performance curves for the new fan (orange) and SDT cutback hot geometry (black).

Subtask 1.4: Application of the surrogate model to relevant fan geometries

The deep neural network/CNN ML predictions were tested in many ways. First, the learning results were adjusted to test for robustness of the method given the original 264 fan cases. Typical 80% training and 20% test runs were performed. Next, full fan speeds were excluded from the training data and used only for testing. In all cases, the method was found to be robust. In Year 2, the ML parameters were used with the low-order acoustic method to predict the final expected power level in the bypass duct for the SDT cases. The results are described in the submitted extended abstract (Li, 2022) and show that the method is viable. A more demanding test for the method will be performed in Year 3, when very different fan geometries are introduced into the database.

Milestones

The milestones set out for Task 1 in Year 2 included the following:

- ML surrogate model refinement and validation
  - As described above, the ML model was modified and tested.
- Validation of the full cycle of ML for wake parameters
- Use of wake parameters as input to the low-order model
- Comparison of predicted sound power level against experimental results and predictions when the input is taken directly from CFD data

Major Accomplishments

- Creation of a CNN decoder method for multi-output learning
- Finalization of the CFD simulation method; 264 cases recomputed using a new grid, etc.

- Development of a new baseline fan geometry and two associated blades with larger trailing edge thickness
- Full analysis of the new fan geometry
- Creation of speed line data for the new fan geometry
- Development of a method for extracting necessary ML input data from AxStream
- First attempt to add new fan cases to the database and perform ML

Publications

Published conference proceedings

Li, N., Watchmann, B., Ramsarran, T., Winkler, J., Reimann, A., Voytovych, D., Mendoza, J., & Grace, S. M. (2022, June 14). Fan-stage broadband interaction noise trends. *28th AIAA/CEAS Aeroacoustics 2022 Conference*. 28th AIAA/CEAS Aeroacoustics 2022 Conference, Southampton, UK. https://doi.org/10.2514/6.2022-2884

Huang, Z., Shen, H., Kung, K., Carvalho, L., Thai, A., Watchmann, B., Ramsarran, T., Winkler, J., Reimann, A., Joly, M., Lore, K. G., Mendoza, J., & Grace, S. M. (2022, June 14). Fan wake prediction via machine learning. *28th AIAA/CEAS Aeroacoustics 2022 Conference*. 28th AIAA/CEAS Aeroacoustics 2022 Conference, Southampton, UK. https://doi.org/10.2514/6.2022-2883

Li, N., Zhang, Y., Winkler, C., Reimann, A., Voytovych, D., Mendoza, J., & Grace, S. (2022). Development of fully low-order prediction of fan broadband interaction noise via integration of machine learning. Submitted to 2023 AIAA Aviation-Aeroacoustics Conference.

Outreach Efforts

None.

Awards

None.

Student Involvement

In Year 2, two undergraduate students, one PhD student, and one MS student contributed to this project.

Plans for Next Period

The milestone that has been set for Year 3 of this project is ML surrogate model refinement and validation. In Year 3, the ML development focus will involve exercising the ML on a much larger database that includes more varied fan geometries. Necessary adjustments will be made to the method depending on the outcomes.

Task 2 - Improvement of the Low-Order Model

BU & RTRC

Objectives

The existing low-order methods are regularly applied to the SDT cases and, as such, have been well validated against this test, which represents one scaled fan and multiple fan exit guide vanes. The newly developed low-order method must now be validated against full-scale test data. The low-order method might also require reformulation to account for other real-flow effects.

Research Approach

Subtask 2.1: Ability to predict full-scale results

The low-order method will be applied to a full-scale geometry with available validation data. Due to the difference in the frequency range of interest for the full-scale case compared with the scaled fans, it is expected that the low-order method will require grid adjustments and integral extent adjustments. Such improvements to the low-order method will be completed as part of this task.

A non-disclosure agreement between BU, RTRC, and P&W to transfer data and information from the Continuous Lower Energy, Emissions, and Noise (CLEEN) I project is now in place. RTRC has organized the rig-scale information for CLEEN I and has begun CFD simulations to determine the type of input that is required for the low-order model. Further analyses of available data for the full rig validation are being completed by RTRC.

The low-order method has been scrutinized, and some slight modifications have been made. These modifications primarily pertain to methods for estimating duct parameters that may not be readily available if a fan-alone simulation (or ML) is used to obtain the inputs. The definition of the length scale based of Reynolds-averaged Navier–Stokes data was adjusted after much investigation into options in the literature and tests for how/when averaging should be applied during the process of preparing the CFD data as usable input data. The graduate student involved in this project is now very adept at utilizing the low-order code.

Subtask: 2.2: Inclusion of tip flow impact on the low-order model

RTRC produced CFD data for the SDT geometries with varying tip gaps, and a total of 48 cases were run. The data were used to obtain acoustic outcomes, and comparisons were made with past acoustic measurements. The low-order model shows slightly higher sensitivity to the tip flow compared with experimental measurements. However, the influence of realistic tip gaps on the broadband noise is quite small overall, and as such, it appears as though the method is basically robust to this parameter. Some related results are shown in Figures 4 and 5. Three speeds close to the original SDT values were considered, and the tip gap was varied from the nominal value of 0.002” to 0.001” and 0.003”. The input quantities measured just upstream of the exit guide vane are shown in Figure 4 for the three cases: approach (61.7% speed), 59 lbm/s; cutback (87.5% speed), 83.7 lbm/s; takeoff (100% speed), 96.9 lbm/s.

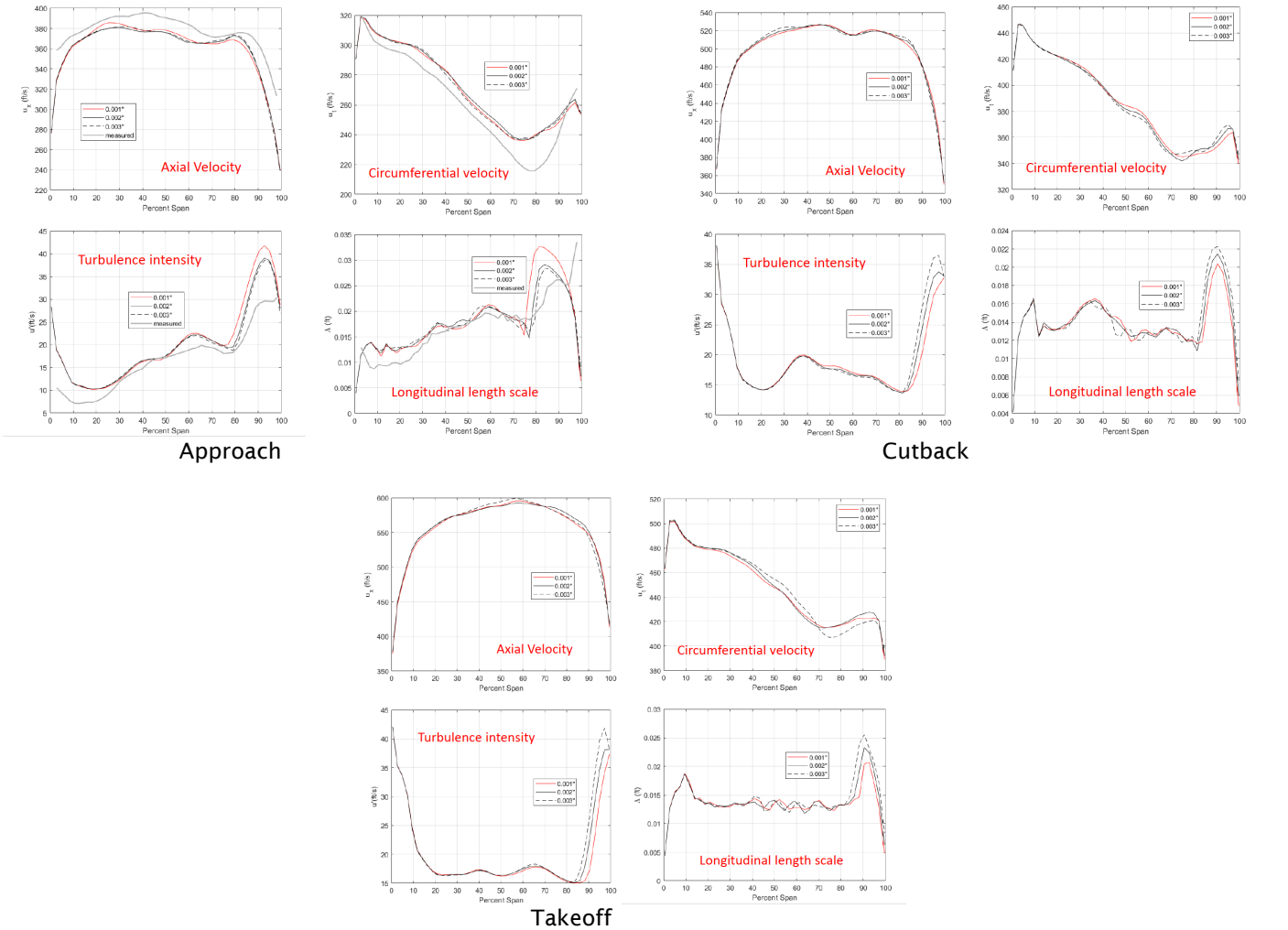

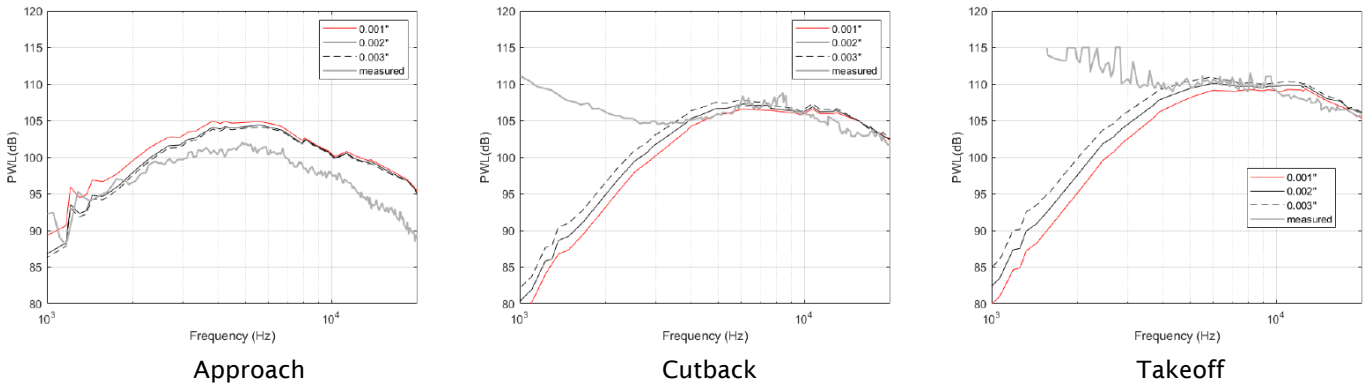

Figure 4. (Top) Comparison of low-order acoustic model input values from computational fluid dynamics Reynolds-averaged Navier–Stokes results for different fan geometries with different tip gaps. Experimental results are shown as a gray solid line when available. (Bottom) Acoustic predictions based on the different inputs.

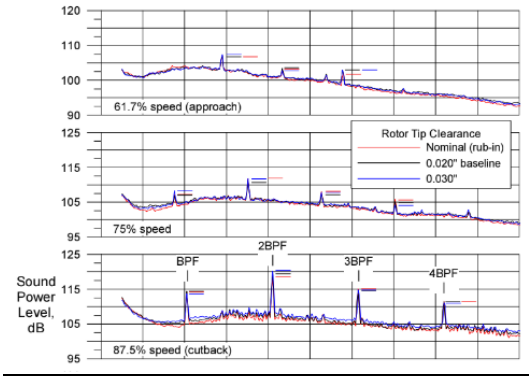

Figure 5. Measured results for the source diagnostic test fan with different tip clearances. From CITATION?

Subtask 2.3: Inclusion of inflow distortion impact on the low-order model
Two points of progress have been made on this subtask. First, some relevant data for benchmarking have been identified. Second, modification of the low-order method to make a very crude allowance for inflow asymmetry has been attempted.

A publication by Damiano's group at Delft describes the results of full fan-stage VLES lattice Boltzmann method simulations with and without inflow distortion (Romani, 2020). From this paper, examples of the flow values given for the region upstream of the exit guide vane that are relevant to application of the low-order method to the problem are shown in Figure 6.

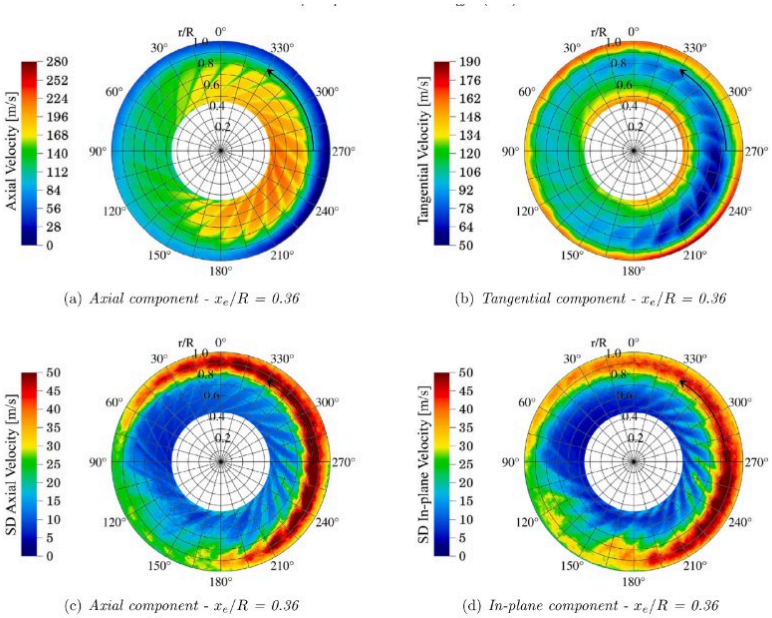

(a) *Axial component - $x_e/R = 0.36$*
(b) *Tangential component - $x_e/R = 0.36$*
(c) *Axial component - $x_e/R = 0.36$*
(d) *In-plane component - $x_e/R = 0.36$*

Figure 6. Interstage flow values from the source diagnostic test fan stage with distorted inflow (Romani et al., 2020).

The low-order model has been modified so that the exit guide vane disk analysis can be performed in chunks. This effort requires the suspension of cascade assumptions of infinite repetition. For this reason, the method is only approximate. However, different regions of the fan are solved using different inflow specifications for the cascade response part of the model. The unsteady response on the full set of vanes is then stitched together. The Green's function method can be used to integrate the vane response and obtain the duct values. We are currently in discussion with Damiano Casalino to obtain the pertinent data shown in Figure 6. In Year 3, we will assess whether this simplified model can provide insight into the trend in acoustic modifications due to inflow distortion.

Milestones

The milestones set out for Task 2 in Year 2 included the following:

- Validate low-order model on the new geometry and test rig-scale vs. full-scale applicability (to be continued in Year 3)
- Assess the impact of tip flow on the low-order model
- Assess the impact of inflow distortion on the low-order model

As described above, the tip flow study indicated that the low-order method can provide insights into the influence of the tip gap on noise; however, the trends are slightly stronger than those observed experimentally. The effect of realistic tip-gap changes is so small that this has been deemed a negligible effect. Progress was made on the inclusion of inflow distortion in the low-order model, but no results have yet been benchmarked.

Major Accomplishments

- The low-order code and pre- and post-processing codes have been updated.
- A non-disclosure agreement is in place for the transfer of CLEEN 1 data required for low-order acoustic simulations.
- CFD analysis in support of the CLEEN 1 acoustic simulation has been started.
- The effect of tip-gap differences on SDT-related noise has been analyzed and deemed negligible.
- A relevant benchmark case for the effect of inflow asymmetry on noise has been identified.
- A very low-order method for potentially handling the asymmetry has been devised and will be tested in Year 3.

Publications

Published conference proceedings

Li, N., Watchmann, B., Ramsarran, T., Winkler, J., Reimann, A., Voytovych, D., Mendoza, J., & Grace, S. M. (2022, June 14). Fan-stage broadband interaction noise trends. *28th AIAA/CEAS Aeroacoustics 2022 Conference*. 28th AIAA/CEAS Aeroacoustics 2022 Conference, Southampton, UK. https://doi.org/10.2514/6.2022-2884

Outreach Efforts

None.

Awards

None.

Student Involvement

One BU PhD student has worked on the low-order model. He has updated the code, and the pre- and post-processing methods.

Plans for Next Period

The milestones that have been set out for Year 3 related to this task include final improvements to the low-order model. The milestone of completing a full-scale validation test of the low-order method will also be continued in Year 3.

References

Romani, G., Ye, Q., Avallone, F., Ragni, D., & Casalino, D. (2020). Numerical analysis of fan noise for the NOVA boundary-layer ingestion configuration. *Aerospace Science and Technology*, *96*, 105532. https://doi.org/10.1016/j.ast.2019.105532

Task 3 - Rig Test Preparation

BU & RTRC

Objective

Experiments in the RTRC Acoustic Research Tunnel will be used to (a) investigate the effect of the downstream pylon and (b) validate noise outcomes due to fan geometry changes predicted by the low-order method in this work.

Research Approach

In developing the Year 3 proposal, RTRC and BU established plans for experiments that will leverage an existing fan rig at RTRC. The team will ensure that at least the approach rotor speed will be obtainable based on the rig electric motor constraints, as mentioned above. The process for determining the basic fan rig and a basic test plan were developed. The initial rig will include pylons similar to the CLEEN 1 design. After obtaining aerodynamic and aeroacoustic measurements for the initial setup, the downstream pylon will be removed in order to assess its impact on noise. Then, at least two other fan designs informed by the differences seen in the computational predictions of the noise will be 3D-printed and tested. The fan design will be similar to that of CLEEN 1 but on a smaller scale.

Milestone

The milestones set out for Task 3 in Year 2 included the development of a Year 3 rig test plan. As described above, this milestone was completed in support of the Year 3 proposal.

Major Accomplishments

The rig test plan has been completed.

Publications

None.

Outreach Efforts

None.

Awards

None.

Student Involvement

None.

Plans for Next Period

The milestones that have been set out for Year 3 related to this task include the following:

- Establish a final rig design
- Test the rig shakedown
- Complete rig testing

Project 076 Improved Open Rotor Noise Prediction Capabilities

Georgia Institute of Technology

Project Lead Investigator

Professor Dimitri N. Mavris (P.I.)
Director, Aerospace Systems Design Laboratory
School of Aerospace Engineering, Georgia Institute of Technology
404-894-1557
dimitri.mavris@ae.gatech.edu

Dr. Jimmy Tai (Co-P.I.)
Division Chief, Propulsion & Energy
Aerospace Systems Design Laboratory
School of Aerospace Engineering, Georgia Institute of Technology
404-894-0197
jimmy.tai@ae.gatech.edu

University Participants

Georgia Institute of Technology

- P.I.s: Dr. Dimitri N. Mavris, Dr. Jimmy Tai
- FAA Award Number: 13-C-AJFE-GIT-078
- Period of Performance: October 1, 2021 to September 30, 2022
- Task:
  - Task 3: Computational aeroacoustics (CAA) case set-up and validation

Project Funding Level

The project funding is $300,000 per year from the FAA. The cost share match amount is $300,000 per year. The sources of matching are cash and in-kind cost-share from our industry partner (GE).

Investigation Team

Dr. Dimitri Mavris, Professor, Georgia Institute of Technology (Georgia Tech) (P.I.)
Dr. Jimmy Tai, Senior Research Engineer, Georgia Tech (Co-P.I.)
Dr. Miguel Walter, Research Engineer II, Georgia Tech
Mr. Brenton Willier, Graduate Student, Georgia Tech
Mr. Grant Stevenson, Graduate Student, Georgia Tech

Project Overview

The contra-rotating open rotor (CROR) system has promising environmental benefits due to its ultra-high bypass ratio and high propulsive efficiency. The reduced fuel burn and emissions of the CROR compared with an equivalent-thrust turbofan make it a viable, economic, and environmentally friendly propulsion alternative to traditional ducted systems. However, in the absence of a noise-conditioning duct, noise penalties may arise from aerodynamic interactions within the CROR system as well as between the system and surrounding installation components such as the engine pylon. If such a system configuration is not optimized, the added effect of flow asymmetry on the aerodynamic interactions could potentially result in severe noise penalties, making the CROR system infeasible for use in the aircraft industry. In the proposed work, the team will perform a sensitivity study on the design parameters of a CROR-pylon configuration. This study will leverage knowledge from past efforts with this type of configuration in order to narrow down the space of design parameters. High-fidelity CAA

analyses will be performed to analyze the effect of each of the chosen parameters on noise. This research is intended to provide both the FAA and industry with key insights necessary for design optimization of the CROR system in the future.

Task 3 - CAA validation

Georgia Institute of Technology

Objectives

The majority of the work in Year 2 was re-directed by FAA supervision toward an extensive validation campaign of numerical simulations against experimental data. Thus, this task is focused on validating predictions from high-fidelity simulations against available experimental data from an open rotor configuration in order to evaluate discrepancies between numerical simulations and experiments. These efforts will provide evidence of the adequacy of the numerical approach for open rotor design.

Research Approach

The validation approach consists of two parts. The first part is concerned with aerodynamic calibration of simulations against experimental values for an F31/A31 open rotor. Under low Mach conditions, loading noise is the most relevant component. Therefore, loading is enforced by matching the time-averaged thrust. The calibration process results in blade pitch settings that minimize discrepancies between experimental and simulated thrusts. The second part concerns acoustic validation of the F31/A31 open rotor, which is achieved by employing calibrated pitch settings.

A hybrid approach for CAA is adopted in this work. High-fidelity simulations are the focal point of the study, and thus, such simulations are employed. The unsteady aerodynamic flow-field is simulated using a lattice Boltzmann method (LBM) solver, while far-field aeroacoustics are predicted by a Ffowcs Williams–Hawkings (FW-H) solver.

Methodology

Validation cases and experimental data

This study employs data from NASA experiments (Elliott, 2011; Sree, 2015; Stephens, 2014) or a wind tunnel open rotor model based on GE design F31/A31 blades. The validation cases are those from low-regime F31/A31 experiments, specifically for the nominal take-off (NTO) pitch setting and without the pylon geometry. The experimental NTO cases (Sree, 2015; Stephens, 2014) as a function of varying operational parameters are illustrated in Figure 1, shown as gray symbols, along with the cases chosen for validation, shown as red and blue symbols. The validation cases are chosen at rotor speeds spanning the upper half range (RPMc = 5,550.5–6,432.0). The experimental data used in the current study come from two sources: a) NASA experiments on the F31/A31 open rotor geometry and b) GE Aerospace data on the same F31/A31 experiments. The former source of data is exclusively employed for acoustic validations, while the latter is for aerodynamic calibration and comparisons. These data were shared by GE Aerospace as an industrial partner in the FAA ASCENT A76 project and are proprietary; consequently, the data are not shown here.

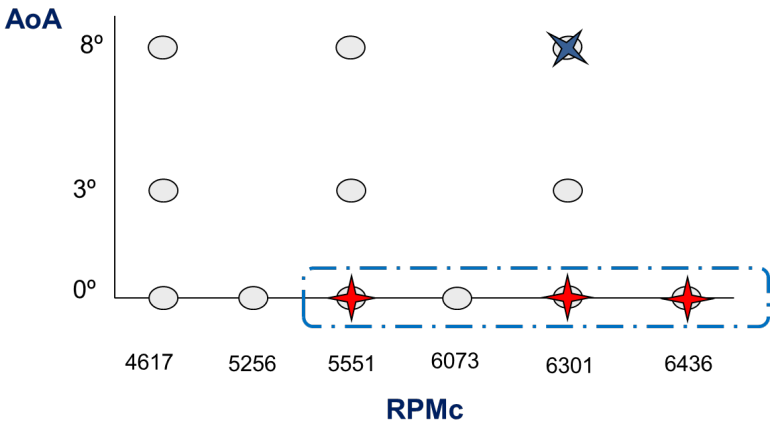

Figure 1. Validation cases as function of and corrected rotor speed (RPMc) and angle of attack (AoA)

The team employed acoustic data from NASA experiments for F31/A31(Elliott, 2011; Sree, 2015; Stephens, 2014). Three data sets are provided in the supplemental information of the NASA report (Stephens, 2014) in the form of power spectral density (PSD). These data sets are described in Table 1.

Table 1. Description of NASA acoustic data.

Data Set	Description	Remark
11	As-measured spectral data	
21	Microphone-corrected spectra	Includes corrections due to microphone and bullet-nose sensitivity and directivity
41	1-ft lossless spectra	Losses due to atmospheric attenuation are restored as gains

From the above data sets, set 41 includes all of the needed corrections, except for wind tunnel background corrections. Therefore, the fully corrected data are based on data set 41. This data set is then corrected for the background wind tunnel based on RDG 802 (set 41), which contains spectral data for the wind tunnel and model without blades (Stephens, 2014). The procedure for obtaining the fully corrected data set is as follows:

- Set 41 is converted to the sound pressure level (SPL) from PSD:

$$SPL = PSD + 10\,log_{10}(\Delta f)$$

- Set 41 in SPL is scaled back to the sideline location.
- Fully corrected data are obtained by removing the wind background noise:

$$SPL^{*} = 10\,log_{10}\left[10^{SPL/10} - 10^{SPL_{WT}}\right]$$

Two additional corrections (Rizzi, 2016) are introduced:

- The first correction ensures that the wind tunnel background does not exceed the microphone SPL to avoid invalidating the above calculation.

- The second correction rectifies low-frequency noise associated with the wind tunnel. Below 700 Hz, noise is removed by replacing that portion of data with a parabolic function with 10-dB attenuation, relative to the 700-Hz level, at 100 Hz.

Calibration in aerodynamics

Aerodynamic calibration is considered prior to acoustic validation. For low Mach conditions, loading noise is the most relevant component. Because this type of noise is thrust-dependent, enforcing a loading equality constraint is viewed as a necessary requirement for acoustic validation. Here, loading is enforced by matching the time-averaged thrust. However, it is acknowledged that this time-averaged measure might not be sufficient, as other factors may also play a role. Note that there is no attempt to directly bring CAA predictions close to experimental values; rather, CAA predictions are evaluated given that a loading metric has been met.

Pitch settings for thrust matching are calibrated by minimizing a cost function, L, consisting of the thrust discrepancy between simulations and experiments according to the following equation:

$$\boldsymbol{\zeta}^* = arg_{\zeta} \min L$$

The cost function, $L = \| \boldsymbol{w}^t \ \boldsymbol{\Delta} \|_2$, is an equally weighted l-2 norm measure of individual rotor discrepancy between the simulation thrust prediction T^{sim} and experimental thrust T^{exp}:

$$\Delta = \begin{bmatrix} \left(T_f^{sim}(\zeta) - T_f^{exp} \right) / T_f^{exp} \\ \left(T_a^{sim}(\zeta) - T_a^{exp} \right) / T_a^{exp} \end{bmatrix}$$

The calibration parameters, $\zeta = [\beta_f, \beta_a]$, contain the pitch angles of the forward and aft rotors. Such parameters vary around the nominal pitch setting:

$$[\ \beta_f^n, \beta_a^n\ ] = [\ 40.1\ °, 40.8°\ ]$$

The simulation values used to calculate discrepancies are approximated via linear regression models, fitted from training data stemming from LBM simulations. These training data consist of the forward and aft thrust from simulations for different pitch settings, which are varied around the nominal pitch setting. Note that the employed linear models are considered appropriate, as departures from the nominal pitch settings are expected to be small. A total of eighteen simulations (six per calibration case, RPMc = 4,620.0; 5,550.5; 6,432.0) were carried out. Simulations were conducted with discretization sizes of approximately 160 million voxels. Note that the resulting resolution is coarser than that used for aeroacoustics predictions; however, it is considered a suitable compromise between computational cost and accuracy based on resolution studies, which show variation within only 1% in thrust predictions between simulations at different resolutions.

Validation in acoustics

Acoustic validations are performed using the calibrated pitch blade settings obtained via the above procedure. An additional validation case at the nominal pitch setting is included as well in order to compare the numerical prediction against the calibrated case. This additional validation case is chosen at the lowest rotor speed among the considered cases, as shown in Figure 1. This case will also serve as a reference to highlight the effects of calibration on the acoustical results. The remaining validation cases for the calibrated parameters are performed next.

The rotor speed range in the present acoustic validations targets the upper half of the rotor speed span of the F31/A31 experiments. International Civil Aviation Organization certification limits the effective perceived noise level – a human-hearing-weighted and time-averaged metric of overall sound level - of each aircraft. This process examines three flight conditions (takeoff, flyover, and approach) and compares the resulting effective perceived noise level against a maximum value. Because the takeoff and flyover flight regimes are dominated by engine noise, as opposed to approach and airframe noise, these flight rotor speeds will continue to be the focus of this study. The calibration and validation cases addressed in the current study are a subset of the NASA experiments (Elliott, 2011; Sree, 2015) at the NTO pitch settings, as shown in Figure 1.

The frequency range is an important aspect to consider in this study. The ideal frequency range to be addressed in the current study should cover the entire high-annoyance portion (i.e., human-hearing constraint) at 10 kHz. This value applies to the full-scale model, whereas in the wind tunnel model, this threshold increases to 50 kHz, based on a scale factor of 5 with respect to the full-scale model (Stephens, 2014). Simulations in the current study attempt to address at least part of the high-annoyance portion. Consequently, most overall noise metrics will be computed in the range of 0.5–50 kHz for consistency with experiments.

Numerical Simulations

Simulations in the current study rely on a hybrid strategy for CAA analysis. The unsteady aerodynamics flow-field is simulated by means of an LBM solver. During the runtime of the aerodynamic solver, flow-field data are collected at specified surfaces. These data are then used as input to a far-field acoustics solver. An acoustic solver based on the FW-H equations is then employed for predicting far-field acoustics. Both aerodynamics and acoustics methods are described in more detail below.

Geometry employed in simulations
The geometry of interest is an open rotor based on the sub-scale model corresponding to the GE design F31/A31 blade set. The geometry details are provided in Table 2:

Table 2. Sub-scale F31/A31 open rotor.

	Number and type of blades	Diameter
Front rotor	12 / F31	0.66 m
Aft rotor	10 / A31	0.63 m

The geometry includes the nacelle as well as the rotating hub for both front and aft rotors. Nevertheless, the simulated geometry does not include the blade-to-blade angle variation from assembly present in the experiment (Sree, 2015), as such information is not available. The geometry in the simulations also differs from the actual experiment in that the aft extension of the nacelle downstream of the aft rotor is purely cylindrical instead having a varying sectional radius as in the actual geometry. Moreover, the geometry used in our simulations does not include gaps in junctions such as those found between the nacelle and rotating hubs and between the blades and hubs.

The utilized F31/A31 blade shape corresponds to the maximum-climb flight condition. The geometry was provided with blade pitch settings of 60.5°/59.0°. Thus, any blade pitch setting addressed in the current study is determined from the aforementioned forward and aft pitch angles. Moreover, the blade shapes are fixed according to the maximum-climb flight condition regardless of the operational parameters of the simulated cases. As previously reported (Falissard, 2018), blade deformations due to the operating point influence aerodynamics and acoustics performance. The balance between aerodynamic, centrifugal, and Coriolis forces results in blade deformation, especially on the outward half span of the blades. Larger deformations are observed for the cruise condition, followed by the take-off and approach conditions. Differences in shape between non-running and running blades exhibited differences of approximately 5% in thrust coefficient predictions. Thus, the study found that accounting for blade deformations improves simulation predictions. Ideally, each operating condition in the simulations should use the corresponding deflected shape. Unfortunately, a lack of information on blade shapes prevented accounting for such effects. Therefore, the only available shape (i.e., at maximum climb) is employed in the present study.

Unsteady aerodynamics
The unsteady aerodynamic flow-field is obtained by employing a commercial LBM solver, PowerFLOW. Unlike traditional fluid mechanics solvers, which are based on a continuity assumption via the Navier–Stokes equations and solve for macroscopic quantities, the LBM solves for the Boltzmann equations by tracking the evolution of microscopic particle distributions in the fluid. Thus, modeling occurs at a mesoscopic scale, corresponding to simplified microscopic behavior, where the physics are more fundamental. Such modeling results in low dispersion and dissipation properties, which is highly desirable for aeroacoustics purposes.

Turbulence modeling is achieved by means of a very large eddy simulation. To reduce the spatial resolution requirement in near-wall regions, a hybrid wall treatment model is chosen. This modeling is based on the standard log law of the wall and includes a laminar sub-layer model accounting for the effects of favorable and adverse pressure gradients.

The boundary conditions are defined as follows: in the outer boundaries, pressure/velocity boundary conditions are prescribed, whereas non-slip wall boundary conditions are prescribed on surfaces of both rotors and the nacelle. In the nacelle extension, however, slip wall boundary conditions are prescribed in order to avoid the influence of boundary layers in those locations. The boundary values ($V_\infty, T_\infty, p_\infty$) and rotor speed in the current simulations are set to those of the wind tunnel conditions and rotor speed measured in the F31/A31 experiments, ,respectively; however, their values are not provided here owing to proprietary restrictions.

Spatial discretization is achieved via variable refinement (VR) regions. The spatial resolution increases two-fold with each VR level. The highest resolution is used at the leading and trailing edges of the blades, whereas the second highest resolution is applied at the tip of the blades, specifically in the volumetric regions at the tips, in order to resolve the tip vortex. Details regarding the employed VR levels are shown in Table 1. The highest resolution is 0.125 mm, whereas the solver time step is approximately 3.7×10^{-7} s. The typical discretization size for simulations in the current study is approximately 900 million voxels. This size is the upper limit that can be computationally afforded in the current study,

Table 3. Lattice Boltzmann method (LBM) simulation set-up. LE: leading edge; TE: trailing edge.

LBM Simulation	***Value***	***Remark***
Smallest spatial discretization	0.125 mm	At blade LE, TE, and tips
Time step	0.370 μs	
Mesh size	900 million voxels	Typical discretization

Aeroacoustics

The far-field aeroacoustics are predicted by employing a commercial FW-H solver, PowerAcoustics. Moreover, to prevent acoustic reflections from the outer boundaries, a sponge region surrounding the open rotor geometry toward the outer boundaries is considered. In this region, the fluid kinematic viscosity is progressively increased so that outgoing acoustic waves are dissipated.

As input, the FW-H solver takes flow data collected at certain surfaces. These surfaces can be either permeable or impermeable. Employing permeable FW-H surfaces for addressing, even partially, the high-annoyance portion of noise spectra would require such a high spatial resolution that the simulations would be intractable for the current study. Thus, impermeable FW-H surfaces are employed instead. These surfaces are defined at both rotor surfaces, including not only the blades but also the rotating hub part.

Flow data are recorded at the aforementioned impermeable FW-H surfaces for collection time periods of 12–16 rotor revolutions at a rate of approximately 190 kHz. Spectral data are obtained by applying a Fourier transformation to the resulting data from the acoustic solver. The employed window width is 50%, and a parabolic Welch windowing function with 50% overlapping is applied to the acoustic data.

Acoustical data are obtained at the sideline receivers as described for previous experiments (Sree, 2015); these receivers are located at a distance, d, of 5 ft from the rotor. This set consists of 18 receivers, spanning from approximately 17.5 ^{o} to 140^{o}, and is uniquely used for calculating discrepancy measures for comparison with experimental results. Likewise, a second set is also defined, consisting of sideline receivers located at the same distance d, but with a higher spatial resolution of 2.5^{o} separation and spanning a larger range of angles, 15 ^{o}–160 ^{o}. The receiver arrangement is illustrated in Figure 2.

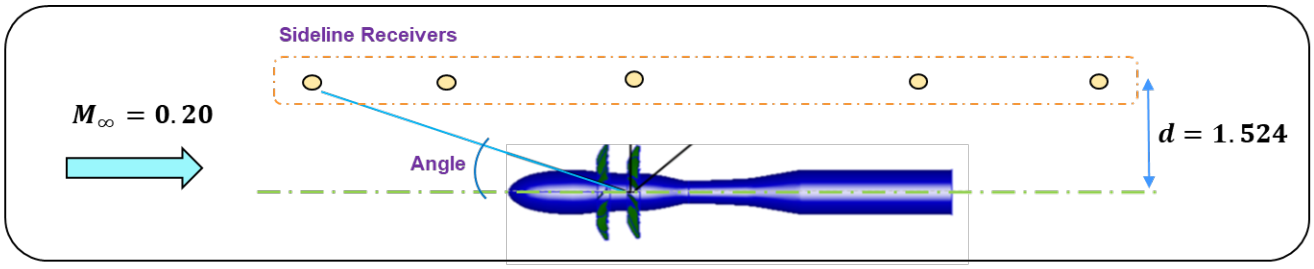

Figure 2. Receiver arrangement for the F31/A31 experiments (figure adapted from Nark et al. [6]).

Results

Calibration in aerodynamics

Results from the aerodynamics calibration are shown in Table 4 as angular departures ($\delta\beta$) from the NTO pitch setting, such that $\beta^* = \beta^n + \delta\beta^*$, where β^n is the NTO angle. Note that for all rotor speeds investigated in this study, the resulting pitch angles increase slightly over the nominal angle due to thrust underprediction at the nominal angles. Moreover, after calibration, the aerodynamics are re-calculated at higher-resolution LBM simulations, which is needed for aeroacoustics. Hence, the resulting thrust may vary slightly; however, the discrepancy for each individual rotor is within 1%, which is in accordance with the experimental uncertainty (Stephens, 2014). In addition, the calibrated pitch at RPMc = 6,250.5 is taken to be the same as that for the highest rotor speed because the predicted thrust is found within the acceptable threshold for calibration, which is verified by the calculated thrust discrepancy, as shown in Figure 3 (right).

Table 4. Resulting calibrated pitch setting.

RPMc	$\delta\beta_f^*$	$\delta\beta_a^*$	*Remark*
5,550.5	+ 0.288°	+ 0.709°	
6,250.5	+ 0.460°	+ 0.428°	Same as that for the highest rotor speed
6,432.0	+ 0.460°	+ 0.428°	

Comparisons of thrust between LBM predictions, previous simulations (Nark, 2016) and experimental measurements are shown in Figure 3. All solvers can well predict thrust trends with rotor speed, as shown on the left; however, for the nominal pitch setting, all of the solvers exhibit some degree of discrepancy from experimental measurements, as shown on the right. LBM simulations for the calibrated pitch setting exhibit the smallest discrepancy due to the thrust-matching process. At nominal pitch settings, there are apparent variations in predictions among solvers: corresponding LBM simulations underpredict the thrust at all rotor speeds, whereas predictions from a previous study (Nark, 2016) mostly overpredict the thrust. Discrepancy levels are smaller for the OVERFLOW solver, whereas the FUN3D solver and LBM simulations exhibit comparable magnitudes of discrepancy.

Torque ratio predictions from LBM simulations and previous studies (Nark, 2016) are compared with NASA experimental results in Figure 4. For the nominal pitch setting, none of the solvers accurately capture the trends, as shown on the left. Indeed, all solvers predict monotonically decreasing trends with rotor speed, while the NASA experiments exhibit a nearly flat trend. In contrast, the LBM simulations with calibrated pitch settings produce not only qualitatively better trends but also closer values. Discrepancies in torque ratio, shown on the right, exhibit a significant departure from the experimental results at the lowest rotor speed for all simulations with the nominal pitch setting; however, these discrepancies decrease with increasing rotor speed.

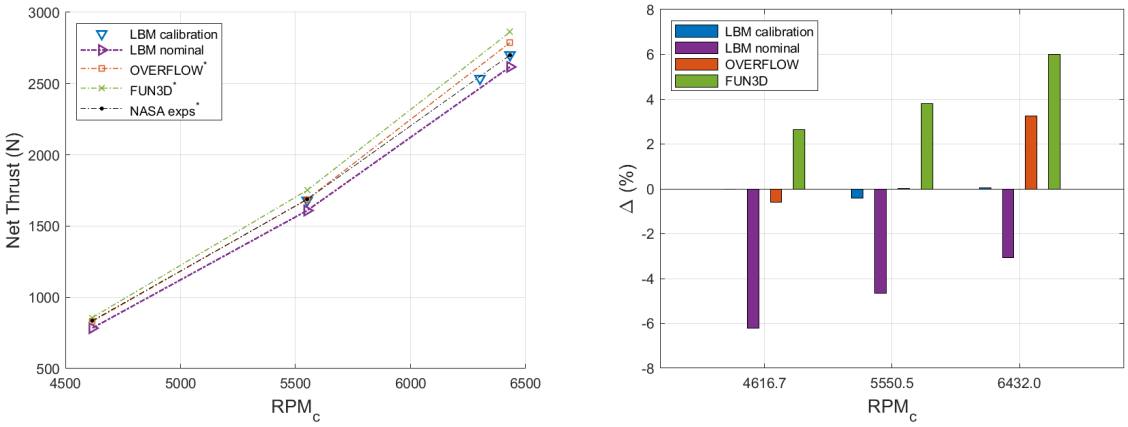

Figure 3. Thrust comparison: simulated and experimental thrust (left) and discrepancy with experimental results (right). LBM: lattice Boltzmann method.

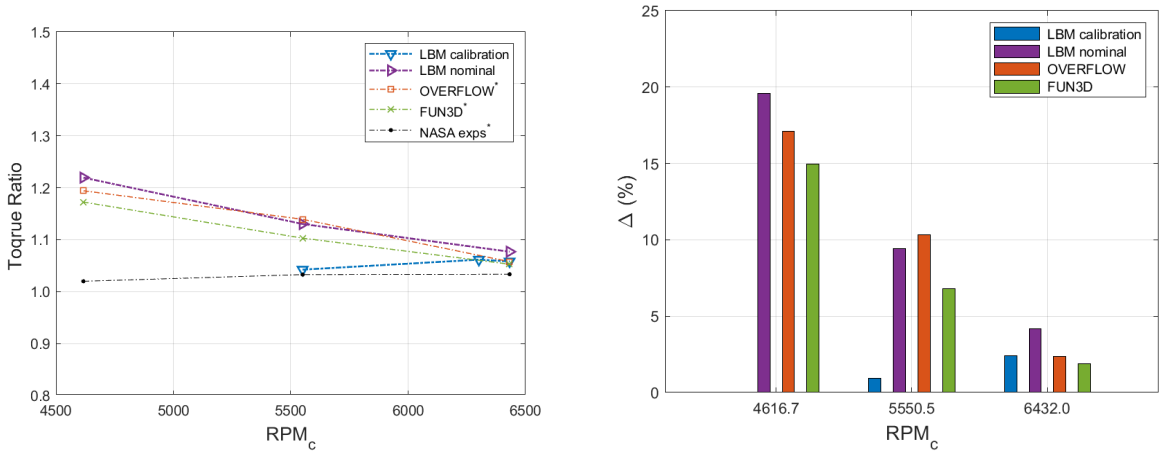

Figure 4. Torque ratio comparison: simulated and experimental torque ratio (left) and discrepancy with experimental results (right). LBM: lattice Boltzmann method.

Validation in acoustics

The effect of calibrating pitch settings on overall noise metrics is shown in Figure 5. Overall SPL (OASPL) directivities from simulations using both calibrated and nominal pitch settings along with that of NASA experiments are shown on the left, while respective average discrepancies are shown on the right. The predictions are from intermediate-resolution simulations of approximately 600 million voxels. There is a notable variation in agreement between simulations and experiments along directivity angles. Small differences are found for intermediate angles of 25°–80°, whereas the differences increase for smaller and larger forward and aft angles, respectively. Moreover, no observable differences in directivity were found between predictions for the nominal and calibrated pitch settings. Indeed, in terms of overall noise metrics, small changes in discrepancy were found between the calibrated and nominal pitch settings, at 0.05 dB for OASPL and 0.29 dB for the overall power level (OPWL).

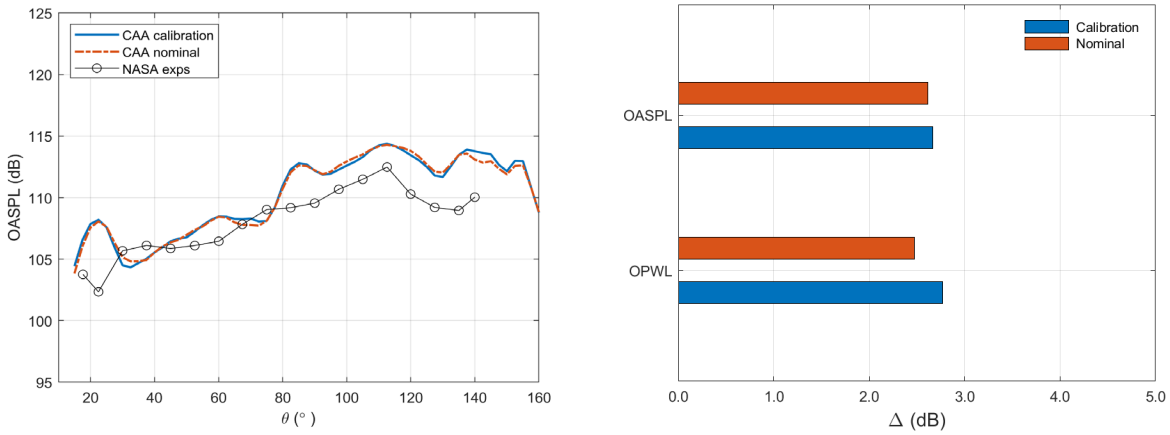

Figure 5. Comparison between nominal and calibrated pitch settings: OASPL directivity (left) and discrepancy (right). CAA: computational aeroacoustics; OASPL: overall sound pressure level; OWPL: overall power level.

The OASPL directivity for different rotor speeds and the corresponding averaged discrepancies for all calibrated pitch settings are shown in Figures 6 and 7. The OASPL associated with the directivity curves clearly increases with increasing rotor speed, as expected. Note that small changes in OASPL values are observed at most directivity angles for the two highest rotor speeds due to their proximity in RPMc. Moreover, a closer agreement in trends and values can be seen for the two highest rotor speeds, especially for directivity angles of 20°–100°. To illustrate the effect of different corrections in the experimental measurements, discrepancies are calculated with respect to all relevant sets of the experimental data, as previously described. Note that partial correction in experimental data could lead to discrepancy variations of 0.2–0.5 dB. Nevertheless, the actual discrepancy is measured with respect to the fully corrected data (blue bar). Values of approximately 1.5 dB are found for the two highest rotor speeds, whereas the discrepancy is larger for the lowest rotor speed, at approximately 2.5 dB.

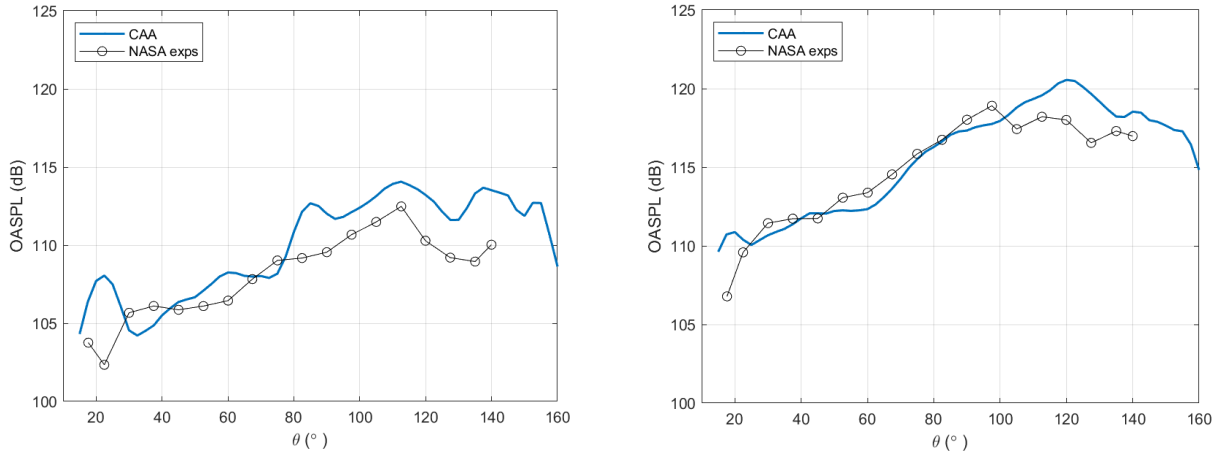

Figure 6. OASPL directivity: 5,550.5 RPMc (left) and 6,301.4 RPMc (right). CAA: computational aeroacoustics; OASPL: overall sound pressure level.

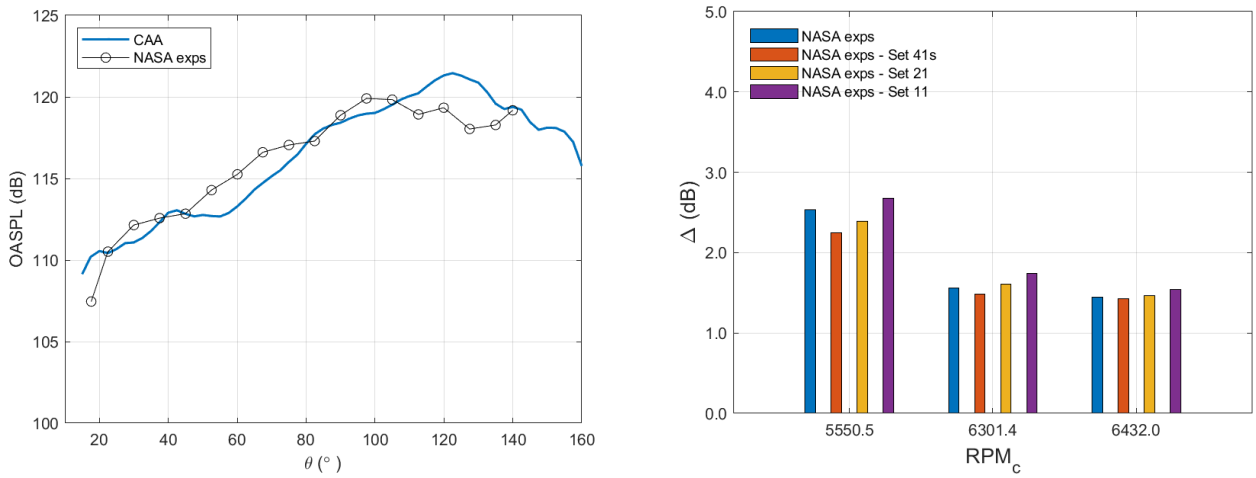

Figure 7. OASPL directivity at 6,432 RPMc (left) and discrepancy (right). CAA: computational aeroacoustics.

Acoustic energy generated by the open fan configuration is calculated from the OPWL. This quantity is calculated by integrating the source power level spectrum for frequencies from 0.5 to 50 kHz. The power level spectrum is obtained by assuming axisymmetry with respect to the propulsor axis, $\psi \in [0, 2\pi]$, and is calculated by using only the same receiver locations used in the experiments. The sideline acoustics data are mapped onto a constant radius, equal to the sideline distance *d*, by assuming spherical spreading (Stephens, 2014). Comparisons of OPWL calculated from simulations and that of experiments are shown in Figure 8. The OPWL trends with corrected rotor speed are in qualitative agreement with the experimental trends, as shown on the left. Closer agreement is found above 6,000 RPMc, whereas the agreement decreases at lower speeds. Numerical predictions are closer to the experimental values at the two highest rotor speeds, with an average discrepancy of less than 1 dB, whereas larger values of 2.5 dB are found at the lowest rotor speed, as shown on the right.

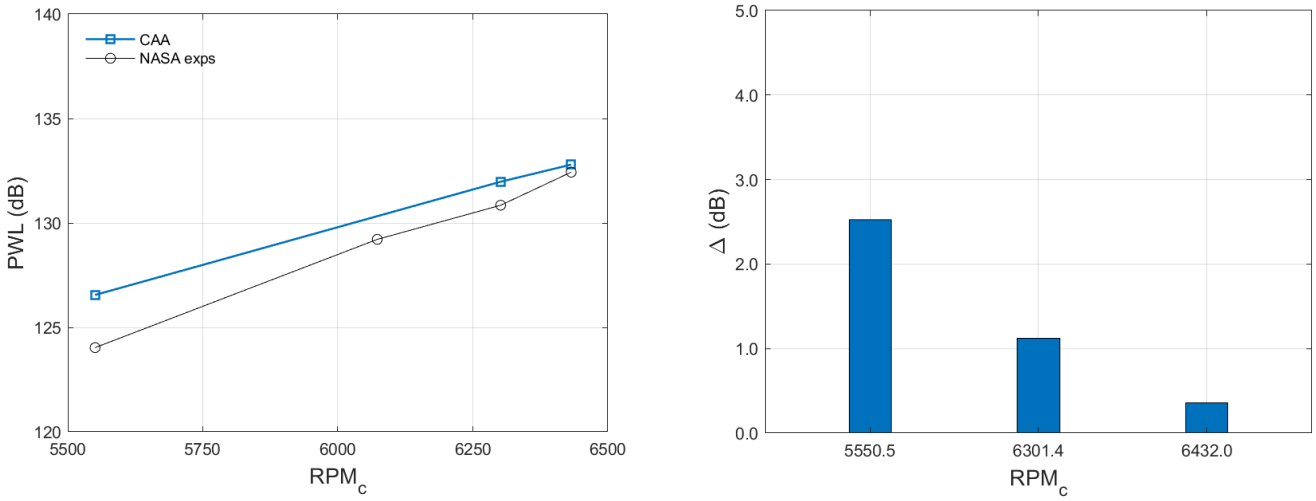

Figure 8. Overall power level (PWL) for calibrated cases. CAA: computational aeroacoustics.

Considerations

The results reported in this document should be viewed in light of the following considerations:

1. Lack of knowledge regarding actual geometry

- Variability in installation of the F31/A31 wind tunnel model, such as blade pitch variation, could lead to angular variations of up to 0.1° from blade to blade.
- Blade deformation may arise from rotation, as blades deform differently at each rotor speed.

2. Simulation aspects
   - The FW-H solver with impermeable surfaces does not account for convection effects (Cerizza, 2022).
   - Impermeable surfaces may not account for very near effects in the flow-field.

Note that each of the above considerations can influence the simulation predictions and hence may result in discrepancies, although the magnitude of these discrepancies is unknown. Installation variability has been argued to result in discrepancies in both aerodynamics and acoustics (Nark, 2016; Envia, 2012). Moreover, neglecting deformations due to operating conditions has also been found to result in aerodynamic and acoustic discrepancies (Falissard, 2018).

Aspects related to simulations are currently being addressed by the authors and will be reported in future work. However, aspects related to a lack of knowledge in geometry are intrinsic to experiments and thus unavoidable in simulations unless provided as part of the outcome from experiments.

Milestones
None.

Major Accomplishments
Extended validation has been completed for all cases at a zero angle of attack.

Publications
"Aerodynamic Calibration for Aeroacoustics Validation of an Open Fan Configuration," to appear on AIAA SciTech 2023.

Outreach Efforts
None.

Awards
None.

Student Involvement
For this task, Brenton Willier (continuing PhD student) and Grant Stevenson (continuing MS student) worked on geometry preparation for numerical analysis and acoustic data analysis.

Plans for Next Period
Future work will focus on completing the remaining validation cases. These remaining cases include a case with a non-zero angle of attack and a case with the nominal pitch setting.

References
Elliott, D. (2011, June 5). Initial investigation of the acoustics of a counter rotating open rotor model with historical baseline blades in a low-speed wind tunnel. *17th AIAA/CEAS Aeroacoustics Conference (32nd AIAA Aeroacoustics Conference)*. 17th AIAA/CEAS Aeroacoustics Conference (32nd AIAA Aeroacoustics Conference), Portland, Oregon. https://doi.org/10.2514/6.2011-2760

Sree, D. (2015). *Far-field acoustic power level and performance analyses of F31/A31 open rotor model at simulated scaled takeoff, nominal takeoff, and approach conditions* (Report No. 2015-218716). NASA. https://ntrs.nasa.gov/citations/20150008245

Stephens, D. B. (2014). *Data Summary Report for the Open Rotor Propulsion Rig Equipped with F31/A31 Rotor Blades* (Report No. 2014-216676). NASA .

Rizzi, S. A., Stephens, D. B., Berton, J. J., Van Zante, D. E., Wojno, J. P., & Goerig, T. W. (2016). Auralization of flyover noise from open-rotor engines using model-scale test data. *Journal of Aircraft*, *53*(1), 117–128. https://doi.org/10.2514/1.C033223

Falissard, F., Chelius, A., Boisard, R., Gaveriaux, R., Canard-Caruana, S., Delattre, G., Gardarein, P., & Mauffrey, Y. (2017, June 5). Influence of blade deformations on open-rotor low-speed and high-speed aerodynamics and aeroacoustics. *23rd AIAA/CEAS Aeroacoustics Conference*. 23rd AIAA/CEAS Aeroacoustics Conference, Denver, Colorado. https://doi.org/10.2514/6.2017-3869

Nark, D. M., Jones, W., Boyd, D., & Zawodny, N. (2016, January 4). Isolated open rotor noise prediction assessment using the F31A31 historical blade set. *54th AIAA Aerospace Sciences Meeting*. 54th AIAA Aerospace Sciences Meeting, San Diego, California, USA. https://doi.org/10.2514/6.2016-1271

Envia, E. (2012). *Open Rotor Aeroacoustic Modeling* (Report No. 2012-217740). NASA.

Cerizza, D. (2022). *DS Simulia corporation*. Private Communication.

Project 077 Measurements to Support Noise Certification for UAS and UAM Vehicles and Identify Noise Reduction Opportunities

The Pennsylvania State University

Project Lead Investigator

Eric Greenwood
Assistant Professor of Aerospace Engineering
Department of Aerospace Engineering
The Pennsylvania State University
229 Hammond Building
University Park, PA
(814) 863-9712
eric.greenwood@psu.edu

University Participants

The Pennsylvania State University

- P.I.: Eric Greenwood, Assistant Professor of Aerospace Engineering
- FAA Award Number: 13-C-AJFE-PSU-067
- Period of Performance: October 1, 2021 to September 30, 2022
- Tasks:
    1. Computational Modeling of Unmanned Aircraft System (UAS) and Urban Air Mobility (UAM) Configurations
    2. Development of a Source Separation Process (SSP) for Distributed Propulsion Vehicles
    3. Development and Testing of a Reconfigurable Multirotor UAS Vehicle
    4. UAS Noise Measurement and Analysis of Variability
    5. UAM Noise Measurements

Project Funding Level

$500,000 awarded by FAA. $495,933 cost share from Beta Technologies for labor, flight test support, and technical data.

Investigation Team

- Eric Greenwood, P.I., The Pennsylvania State University (Tasks 1—5)
- Kenneth S. Brentner, Co-P.I., (Task 4, Task 5)
- Eric N. Johnson, Co-P.I., The Pennsylvania State University (Task 3)
- Joel Rachaprolu, Graduate Research Assistant, The Pennsylvania State University (Task 2)
- N. Blaise Konzel, Graduate Research Assistant, The Pennsylvania State University (Task 1)
- Keon Wong Hur, Graduate Research Assistant, The Pennsylvania State University (Task 4)
- Vítor T. Valente, Graduate Research Assistant, The Pennsylvania State University (Task 3)
- Sebastian Lopez, Graduate Research Assistant, The Pennsylvania State University (Task 5)
- Rupak Chaudhary, Graduate Research Assistant, The Pennsylvania State University (Task 4, Task 5)

Project Overview

Measurement techniques for conventional propeller-driven aircraft and rotorcraft are well established. These techniques typically assume that the acoustic state of the vehicle does not change over the duration of a steady-state pass over a microphone or microphone array. UAS and UAM platforms violate the steadiness assumption employed in the measurement and modeling of conventional aircraft noise. Rotor or propeller states, such as the rotational speed or blade pitch angle, will vary continuously and independently as the vehicle control system responds to atmospheric perturbations. Many of these vehicles employ distributed propulsion systems, in which the rotors or propellers are not locked in phase. When multiple rotors or propellers operate at similar blade passing frequencies, coherent addition of the tonal noise will result in lobes of acoustic radiation that are tightly focused in certain directions. As the phase relationships between the rotors change over time, the directionality of these lobes will vary. Consequently, the noise cannot be modeled as a single stationary source, and no two flight passes will result in the same noise radiation pattern on the ground. Moreover, because numerous possible combinations of control inputs can result in the same flight condition, there is no longer a unique mapping of the overall flight condition of the vehicle to a corresponding acoustic state. This project aims to develop noise measurement techniques and data analysis methods that can reduce this variability, thereby allowing repeatable characterization of UAS and UAM noise.

Task 1 - Computational Modeling of UAS and UAM Configurations

The Pennsylvania State University

Objective

The goal of this task is to develop computational models of UAS and UAM aircraft to provide a simulated environment in which various noise measurement configurations and data processing methods can be rapidly investigated ahead of acoustic flight testing. During the reporting period, this task was focused on establishing criteria for far-field acoustic measurements of small multicopter UASs.

Research Approach

A computational investigation was conducted to determine the distance of the acoustic far-field for the Tarot X8 octocopter in a hovering flight condition. The far-field distance was found by comparing the sound pressure level (SPL) computed by PSU-WOPWOP—which includes all near-field acoustic terms—to propagation from a compact source by spherical spreading, i.e., the 1/r law. For this research, the far-field distance is defined as the point at which the PSU-WOPWOP prediction diverges from 1/r scaling of the farthest predicted SPL by 0.3 dB. An example of determining the far-field distance for this vehicle is shown in Figure 1. A logarithmically spaced array of observers is placed along a line extending from the center of the aircraft at an azimuth angle of $\psi = 180^{\circ}$ and elevation angle of $\theta = -60^{\circ}$. In this figure, the predicted SPL is plotted in blue against a logarithmic scale of the distance in single rotor diameters, D. The red dashed line plots the far-field SPL from the farthest observer corrected back to closer distances according to spherical spreading. The two lines begin to diverge in the near-field; the last point at which these lines diverge by less than 0.3 dB is shown by a yellow circle, representing the far-field distance along this ray. Because the observers are located at discrete distances from the center of the vehicle, the divergence from spherical spreading at this location may be less than 0.3 dB in some directions. Figure 2 plots the difference between the predicted and scaled levels, showing how the change in levels begins to increase rapidly as the observer enters the near-field at approximately 5 D.

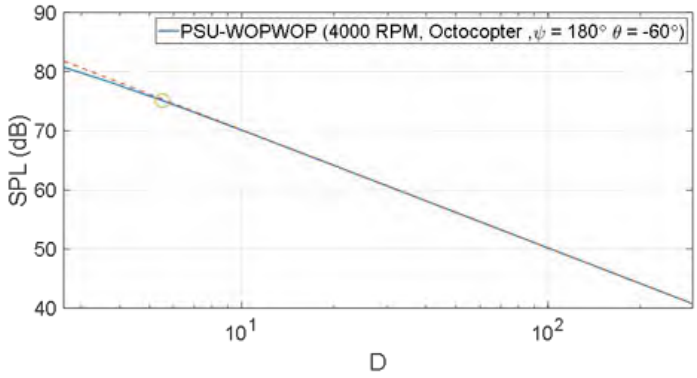

Figure 1. Variation in predicted and *1/r*-scaled noise levels with increasing distance. SPL: sound pressure level.

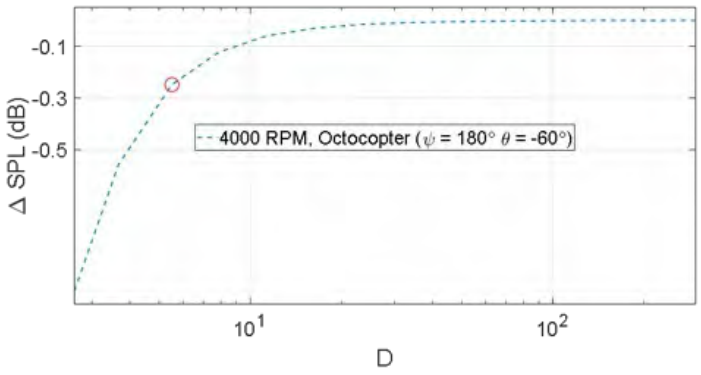

Figure 2. Difference between predicted and *1/r*-scaled noise levels with increasing distance. SPL: sound pressure level.

Milestone

The milestone for this task is to develop a computational approach to establish the distance at which microphones must be placed from multirotor UAS and UAM aircraft to ensure that measurements are made in the acoustic far-field of the aircraft.

Major Accomplishments

The process described above was repeated for a wide range of azimuth and elevation angles about the center of the aircraft to examine the variation in the far-field distance as the emission angle varies. These data are plotted on a hemisphere, using a stereographic projection of the hemisphere, as shown in Figure 3. The azimuth angle, ψ, is plotted azimuthally from 0˚ at the tail of the aircraft to 180˚ at the nose, and the elevation angle, θ, is plotted radially, with 0˚ representing noise radiated in the plane of the rotors at the edge of the plot and -90˚ representing the noise radiated directly below the vehicle, shown in the center of the plot. The direction used to generate Figures 1 and 2 is shown in blue in Figure 3 for reference. Several parametric studies were conducted using this method to investigate the parameters that affect the far-field distance for small multirotor UASs.

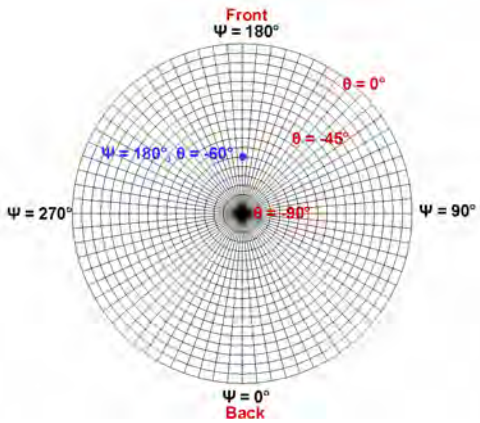

Figure 3. Acoustic hemisphere coordinate system, shown using a stereographic projection. The observer direction used in Figures 1 and 2, located at azimuth $\psi = 180°$ and elevation $\theta = -90°$, is marked in blue.

Far-Field for Different Rotor Noise Sources

PSU-WOPWOP allows the contribution of different generating mechanisms (i.e., noise sources) to be evaluated separately; these include rotational noise sources, thickness and steady loading noise, and broadband airfoil self-noise, caused by turbulent pressure fluctuations on the rotor blades. The far-field distance was determined for each of these noise source mechanisms individually, as well as for the combination of all noise sources. Figure 4 plots stereographic far-field distance hemispheres for both a single rotor and the complete octocopter configuration for thickness, loading, and broadband noise sources. Figure 5 plots the far-field distance for complete prediction including all noise sources.

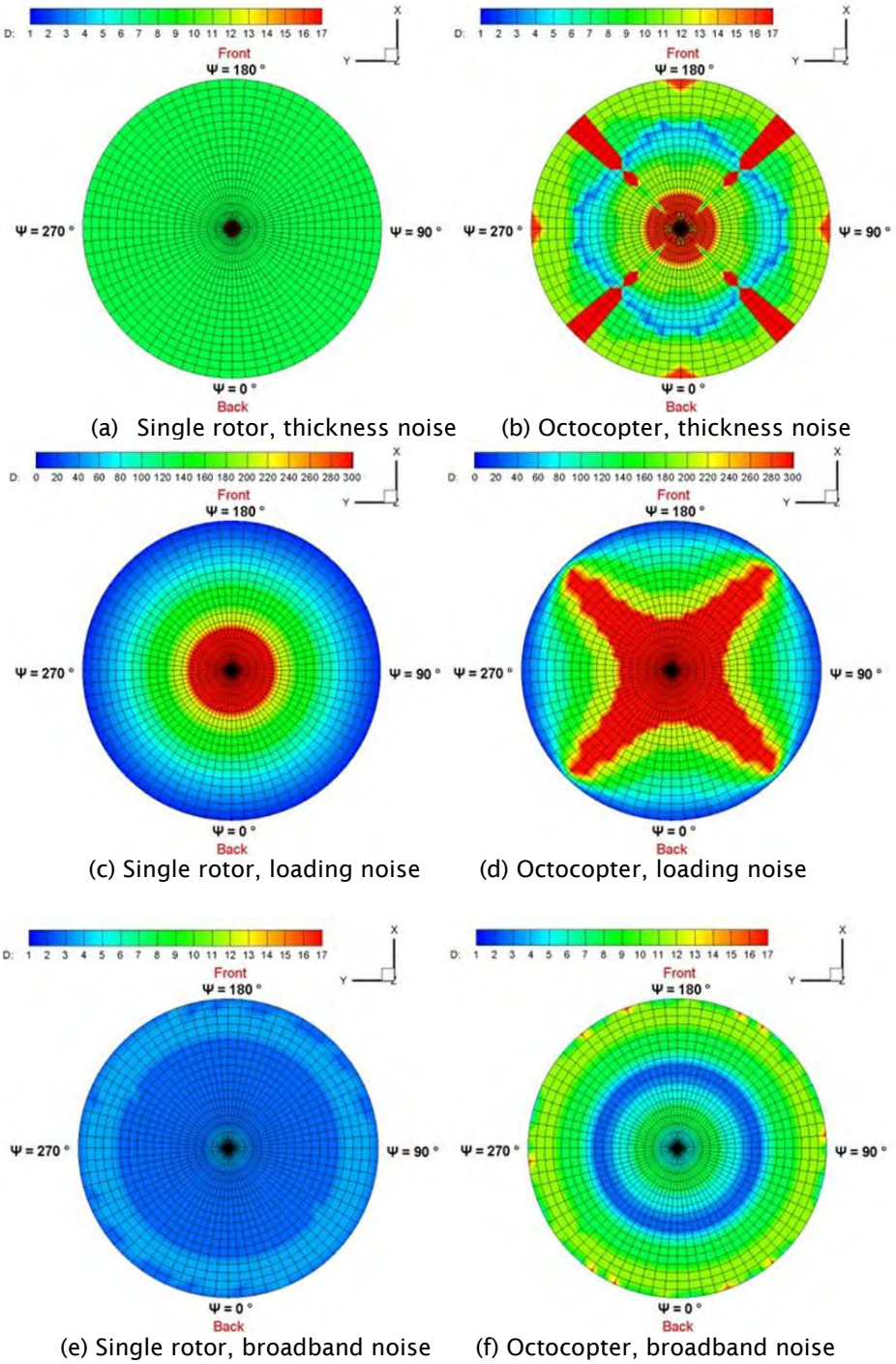

(a) Single rotor, thickness noise (b) Octocopter, thickness noise

(c) Single rotor, loading noise (d) Octocopter, loading noise

(e) Single rotor, broadband noise (f) Octocopter, broadband noise

Figure 4. Variation in computed far-field distance by noise source mechanism.

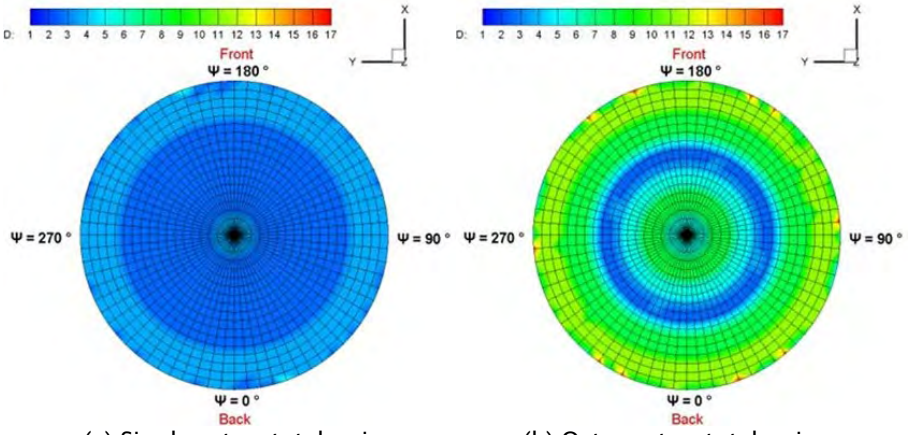

(a) Single rotor, total noise (b) Octocopter, total noise

Figure 5. Computed far-field distance for the combined total of all noise source mechanisms.

For the single isolated rotor, the far-field distance is axisymmetric for all noise sources. The predicted far-field distance is also constant across all elevations for the thickness noise source, i.e., from $\theta = 0°$ shown at the edges to $\theta = -90°$ at the center of the plot. There is a large variation in far-field distance with elevation angle for loading noise, with the distance tending to increase as the observer moves farther out of the plane of the rotors. For broadband noise, the far-field distance tends to reach a maximum distance at an intermediate elevation angle, approximately 20˚ below the plane of the rotor. Because broadband noise dominates the radiated acoustics for this low-tip-speed rotor (i.e., a tip Mach number of 0.23), the far-field distance for all rotors combined is in close agreement with that of the broadband noise sources alone. Similar results are obtained for the octocopter configuration, except that acoustic interference between the rotors results in an azimuthal variation in the calculated far-field distance for the discrete-frequency (i.e., tonal) noise sources. Four "lobes" of increased far-field distance are observed for the octocopter configuration, where a constant rotation rate of 4,000 RPM is maintained by each rotor.

Table 1 lists the minimum, maximum, and average far-field distances across all emission angles shown on the hemisphere for each noise source and configuration. Very large far-field distances (up to nearly 300 *D*) were computed for loading noise sources. The far-field distance computed for thickness noise is significantly lower, ranging from approximately 8 diameters for a single rotor to approximately 11 diameters for the complete octocopter configuration. The broadband noise has the shortest predicted far-field distances, averaging 3 diameters for a single rotor and approximately 7 diameters for the complete configuration.

Table 1. Minimum, maximum, and average far-field distance for each noise source. D: rotor diameter.

	Minimum/Maximum (D)	Average (D)
Thickness		
Single Rotor	7.9/7.9	7.9
Octocopter	3.7/16.3	10.7
Loading		
Single Rotor	7.9/296.3	170.0
Octocopter	11.3/296.3	215.3
Broadband		
Single Rotor	2.6/3.7	3.0
Octocopter	2.6/11.3	6.9
Total		
Single Rotor	2.6/3.7	3.0
Octocopter	2.6/11.3	6.9

Number of Rotors

Another study was conducted to investigate the effect of changing the number of rotors on the far-field distance of the vehicle. The total noise generated by all sources is used, which is again dominated by broadband noise for this configuration. In addition to the single and octocopter configurations studied in the previous section, a quadcopter and hexacopter configuration are also included. Far-field distance spheres are plotted in Figure 6, and the maximum, minimum, and average values across all directions are tabulated in Table 2. The directionality characteristics are similar for all configurations, as the noise is dominated by the broadband source terms. The computed far-field distance increases as the number of rotors increases, even though the rotor-to-rotor distance remains constant for all configurations.

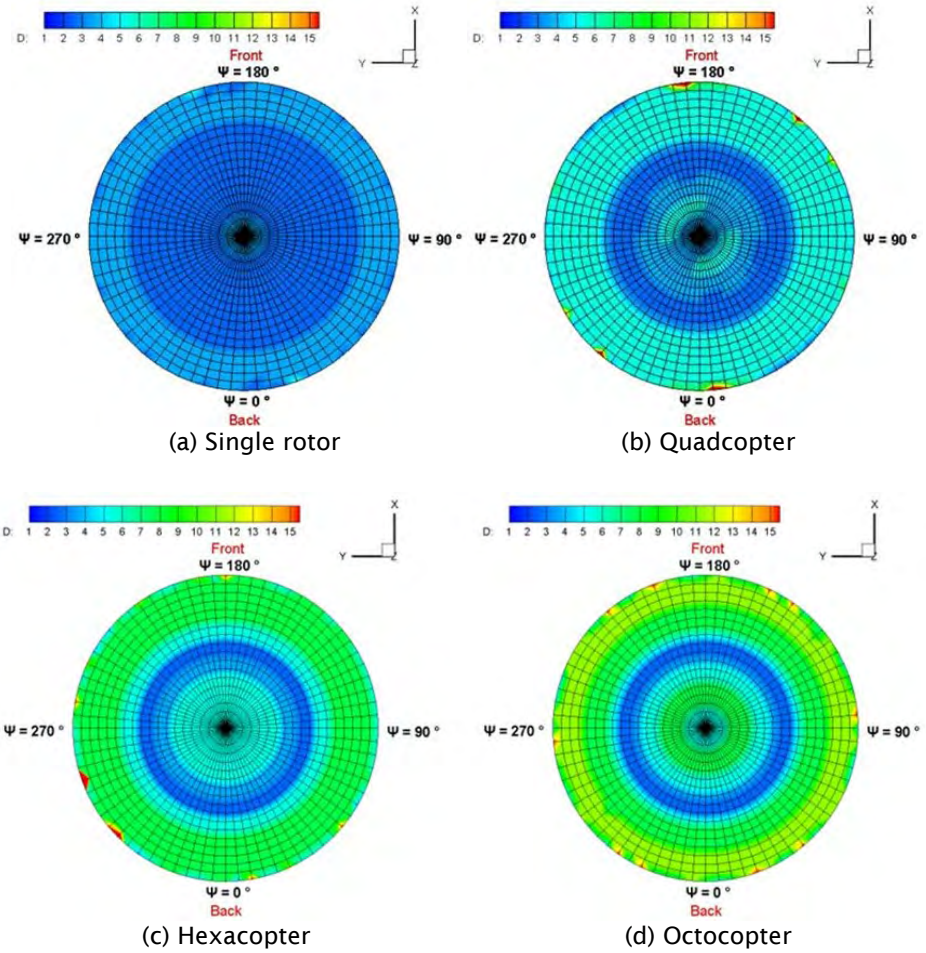

(a) Single rotor (b) Quadcopter

(c) Hexacopter (d) Octocopter

Figure 6. Variation in far-field distance with the number of rotors.

Table 2. Minimum, maximum, and average far-field distance as the number of rotors is varied. D: rotor diameter.

Number of Rotors	Minimum/Maximum (D)	Average (D)
1	2.6/3.7	3.0
4	2.6/5.5	4.2
6	2.6/7.9	5.7
8	2.6/11.3	6.9

Publications

Hur, K., Zachos, D., Brentner, K., & Greenwood, E. (2023, January). *Determining the Acoustic Far-field for Multirotor Aircraft* [Abstract]. 10th Biennial Autonomous VTOL Technical Meeting & 10th Annual eVTOL Symposium, Mesa, AZ.

Outreach Efforts

The investigation team holds monthly meetings with an external advisory board consisting of a dozen interested parties from government and industry.

Awards

None.

Student Involvement

M.S. student Keon Wong Hur is primarily responsible for the development of UAS noise predictions. Specifically, the far-field distance studies were conducted to generalize the definition of the far-field distance of UAS and UAM aircraft. This information will be utilized to inform the design of future UAS and UAM noise measurements. Ph.D. student Rupak Chaudhary has started working with higher-fidelity modeling using the Penn State Noise Prediction System (DEPSim/CHARM/PSU-WOPWOP). These predictions will include the flight dynamics of the vehicle based on the DEPSim multirotor flight simulation code, including the variation in RPM required to track a trajectory. The resulting acoustic predictions will be compared with experimental data from both outdoor acoustic flight test measurements and laboratory experiments conducted under controlled conditions.

Plans for Next Period

The higher-fidelity Penn State Noise Prediction System will be used to develop a more realistic model of multirotor aircraft noise generation, including rotor–rotor aerodynamic interactions and unsteady flight. This system will be used to elucidate the variability of multirotor aircraft noise and to design and validate experimental approaches intended to reduce the variability in experimental characterization of multirotor aircraft noise.

Task 2 - Development of an SSP for Distributed Propulsion Vehicles

The Pennsylvania State University

Objective

The objective of this task is to develop a process for separating the noise generated by rotors or propellers at non-constant, but potentially similar, RPM values from flyover measurements of UAS and UAM vehicles.

Research Approach

The SSP developed in this task is mainly a two-step process that combines a time-domain de-Dopplerization procedure and Vold–Kalman (V-K) order tracking filter. The flowchart in Figure 7 outlines the steps of the SSP. This approach will de-Dopplerize ground-based acoustic measurements and separate the individual rotor noise components with the capability to extract time-varying impulsive noise. Performing this source separation in the specified time domain will enable the application of a wide range of post-processing techniques in both the time and frequency domains. Moreover, the need to characterize the acoustic directivity of these aircraft demands that the processed data be projected onto an acoustic hemisphere to illustrate the noise radiation patterns.

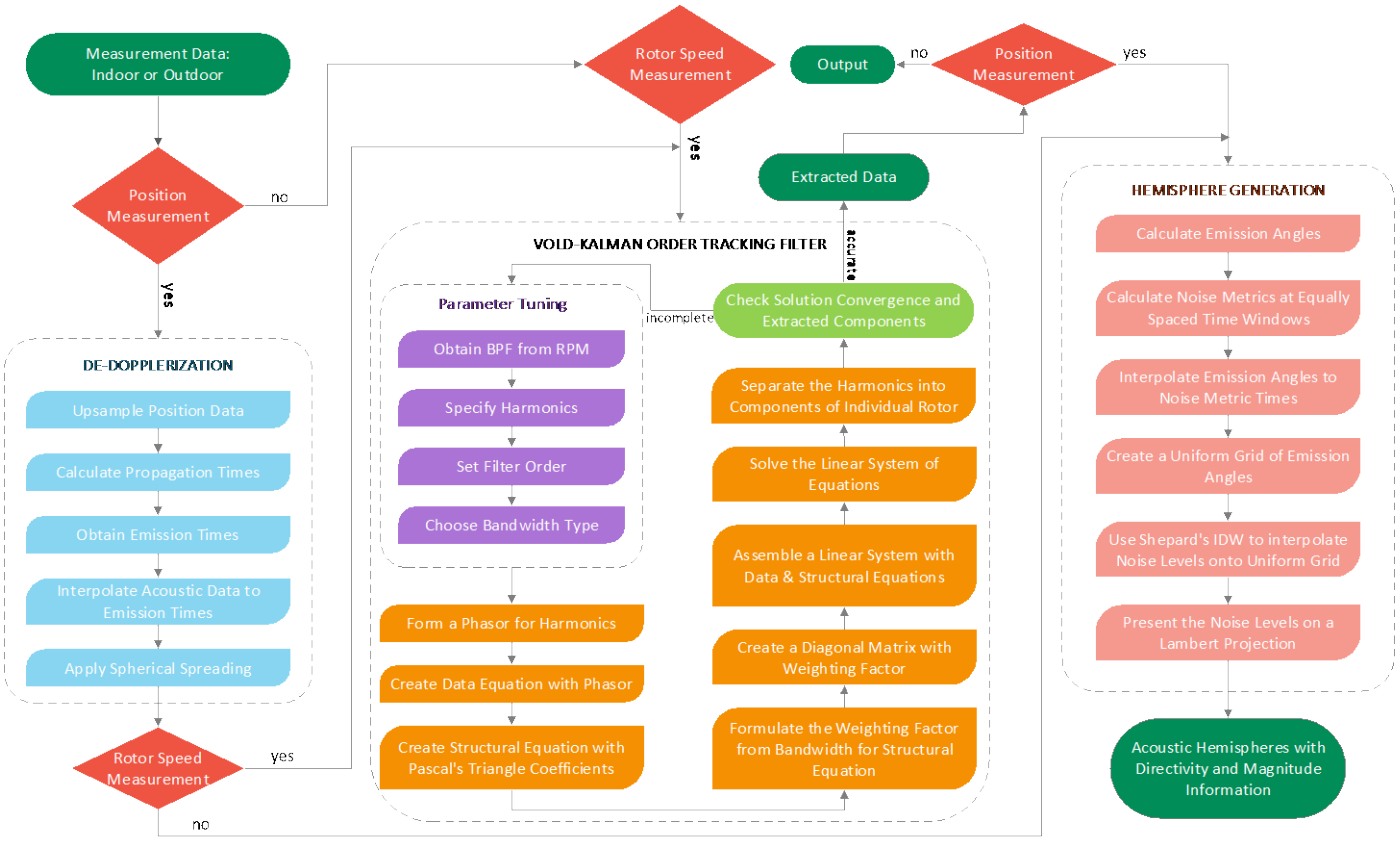

Figure 7. Flowchart of the system architecture of the source separation process. BPF: blade passing frequency. IDW: inverse distance weighting.

Each step of the SSP was verified on computational and experimental/flight test data to assess the performance. Acoustic analysis with the SSP components was also performed, in which individual steps of the SSP were isolated and applied to different data sets. The V-K filtering technique was applied to anechoic wind tunnel acoustic measurements from a coaxial rotor. De-Dopplerization and acoustic hemisphere generation steps were applied to acoustic flyover measurements of the Tarot X8 multirotor aircraft. Once both the de-Dopplerization and order tracking filter procedures were verified, a combination of two steps was used to analyze Bell 430 helicopter flight test data.

Milestones

The milestones for this task consist of (a) developing an SSP for stationary acoustic measurements, (b) implementing a de-Dopplerization approach to covert non-stationary measurements to a stationary frame, (c) applying the process to simulated and measured data to evaluate the effectiveness of the separation, and (d) applying the process to multirotor aircraft acoustic measurements to extract acoustic components for each rotor.

Major Accomplishments

The effectiveness of the developed SSP approach was tested with three data sets: anechoic wind tunnel measurements of a coaxial rotor setup, acoustic measurements of a Tarot X8 multirotor UAS aircraft, and acoustic flight test measurements of a Bell 430 helicopter. Some results are presented below to highlight the capabilities and limitations of the SSP.

Acoustic Measurements of a Coaxial Setup in an Anechoic Wind Tunnel

This data set was used because the rotors were operating at close and crossing rotor speeds, which is similar to rotor speeds observed in multirotor vehicles. The experimental setup included a test stand that held the motors in a coaxial configuration.

A combination of 1/2" and 1/4" Bruel & Kjaer microphones mounted on a curved linear microphone array were used to collect acoustic measurements. The rotor stand included a tachometer along with other instrumentation for performance measurements. The tachometer measured the rotor RPM with high resolution at 131 kHz. The acoustic data were also sampled at 131 kHz; in this way, the acoustic signals were synchronized with the RPM measurement for both rotors to apply the source separation. The experimental setup is shown in Figure 8.

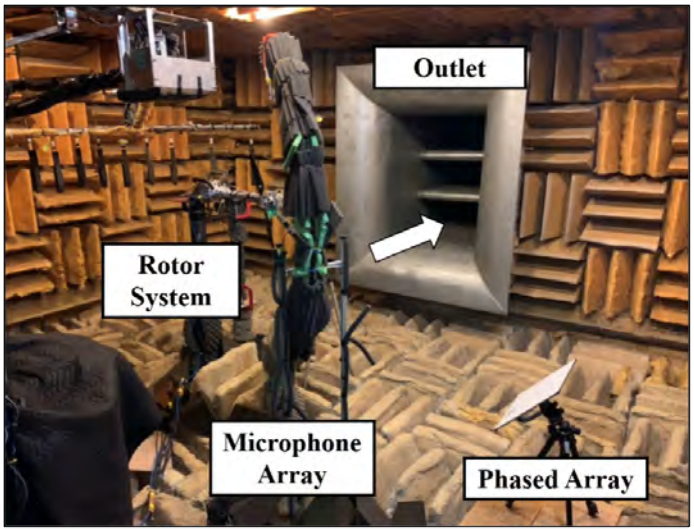

Figure 8. Experimental setup of a coaxial rotor on a test stand in the Penn State anechoic wind tunnel.

The close and crossing rotor rotational speeds of the top and bottom rotors of the coaxial setup are shown in Figure 9. The top and bottom rotor noise components were extracted via the V-K filter of the SSP. Figure 10 presents results in the frequency domain for a time point of 20 s and an elevation angle of -30°. The Original signal is the original acoustic signal measurement from the experiment. The Rotor 1 and Rotor 2 components are the extracted harmonic components of the top and bottom rotors obtained by the V-K filter of the SSP. The Residual component is the leftover component after the extracted Rotor 1 and Rotor 2 components are removed from the original signal. The Residual component is primarily comprised of broadband noise.

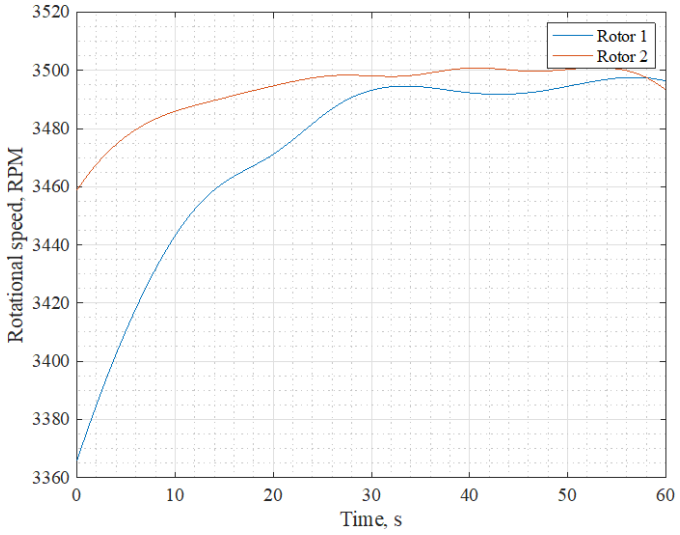

Figure 9. Time variation of rotor speeds for the coaxial rotor experiment.

The signal was initially subjected to a high-pass filter to remove any shaft-order tones caused by imbalances in the test stand; thus, there is negligible acoustic energy below 100 Hz. The V-K filter was then applied to extract the rotor tones from the original signal. The results of the extraction are displayed in Figure 10, which shows that the magnitude and frequency of the extracted rotor 1 and rotor 2 signals correspond to the harmonic peaks from the original signal, indicating a clean extraction of rotor harmonic components in the frequency domain.

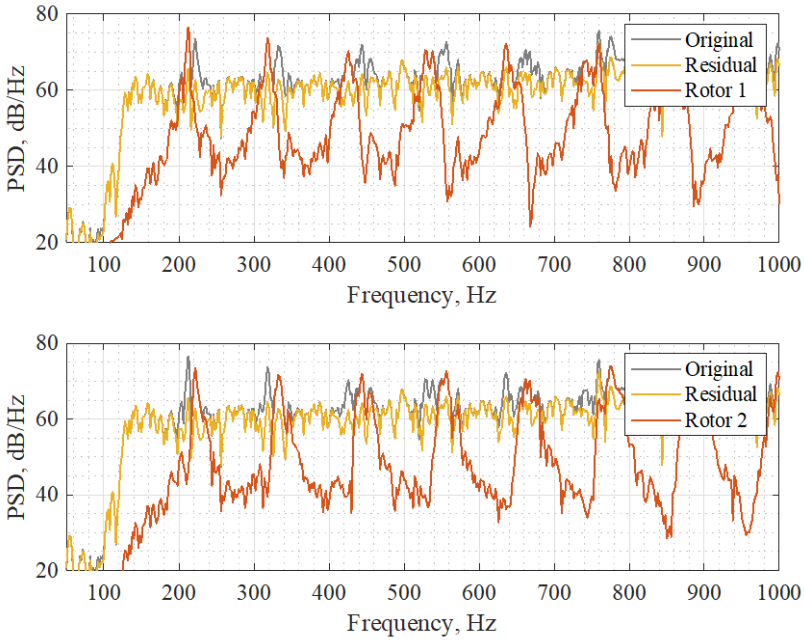

Figure 10. Spectra of original, residual, and extracted rotor signals for the edgewise forward flight case at a time point of 20 s. PSD: power spectral density.

Acoustic Flight Test Measurements of the Bell 430 Helicopter

The SSP was then applied to measured acoustic flight test data for an instrumented Bell 430 helicopter collected by NASA, Bell, and the U.S. Army. The instrumentation for the flight test included a main rotor shaft encoder, which allowed an accurate measurement of the main rotor rotational speed (RPM). The gear ratio was used to infer the tail rotor RPM from the main rotor RPM measurement, and these RPM readings were used to obtain the blade passage frequencies for both rotors. Using onboard differential global positioning system (DGPS) tracking data, the propagation times were calculated, the acoustic measurements were de-Dopplerized, and the V-K filter was used to extract the first 20 harmonics of the main rotor and the first 10 harmonics of the tail rotor.

The SSP was first applied to steady-state cases to examine the performance with acoustic flyover measurements. For the steady-state cases, the acoustic state of the aircraft is straightforward, and the noise sources do not change rapidly over time. The extracted measurements of the main rotor and tail rotor were used to produce acoustic hemispheres to investigate the directivity of the rotors. The hemispheres for a level-flight case are shown in Figure 11, with the main rotor hemisphere on the left and the tail rotor hemisphere on the right.

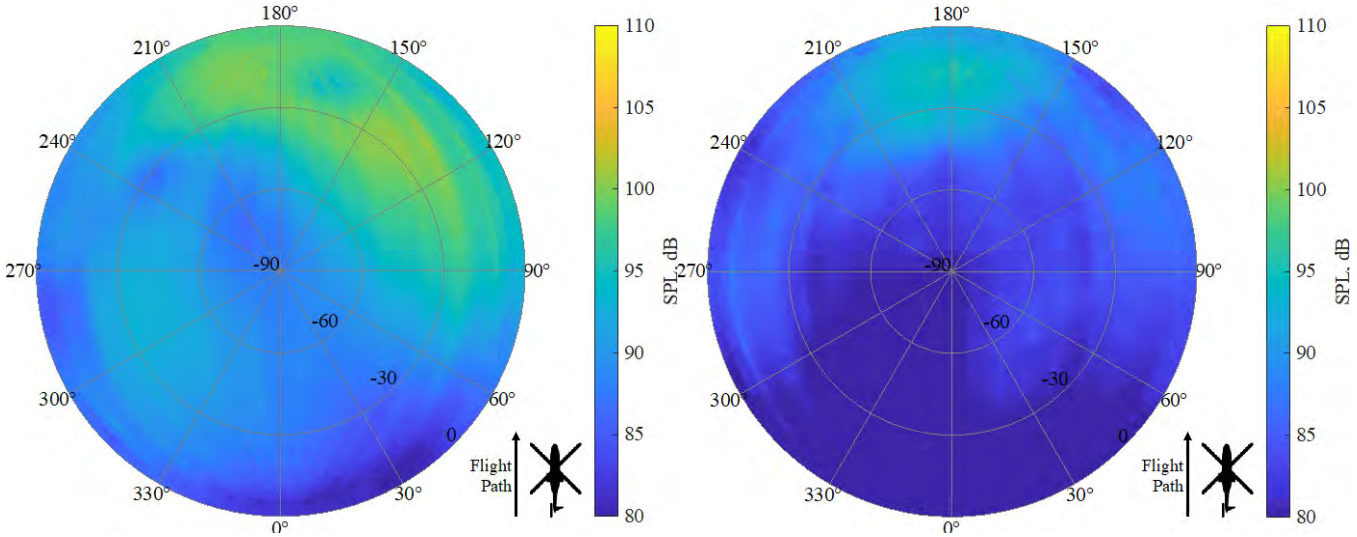

Figure 11. Acoustic hemispheres of the separated main rotor (left) and tail rotor (right) for an 80-kt level-flight condition. SPL: sound pressure level.

Both hemispheres shown in Figure 11 present noise levels normalized to a distance of 100 ft from the aircraft. In the main rotor hemisphere, higher main rotor noise levels can be seen both toward the advancing side of the rotor and directly in front of the aircraft. As shown in the tail rotor hemisphere plot, the noise of the tail rotor reaches a maximum level directly ahead of the helicopter, at an azimuth angle of 180˚. The hemispheres for the main rotor and tail rotor agree with the directivity patterns expected from theoretical predictions.

The SSP was then applied to maneuvers to investigate the effectiveness of its application to non-steady-state conditions. A microphone is selected, and the noise characteristics of the helicopter throughout the maneuver are analyzed while measurements are obtained at the observer microphone location. In this case, the condition was a cyclic pitch-up condition initiated at an indicated airspeed of 60 kt. Figure 12 presents a composite plot showing the extracted SPL time histories, observer measurement location, and acoustic pressure time series for selected observer locations during the maneuver.

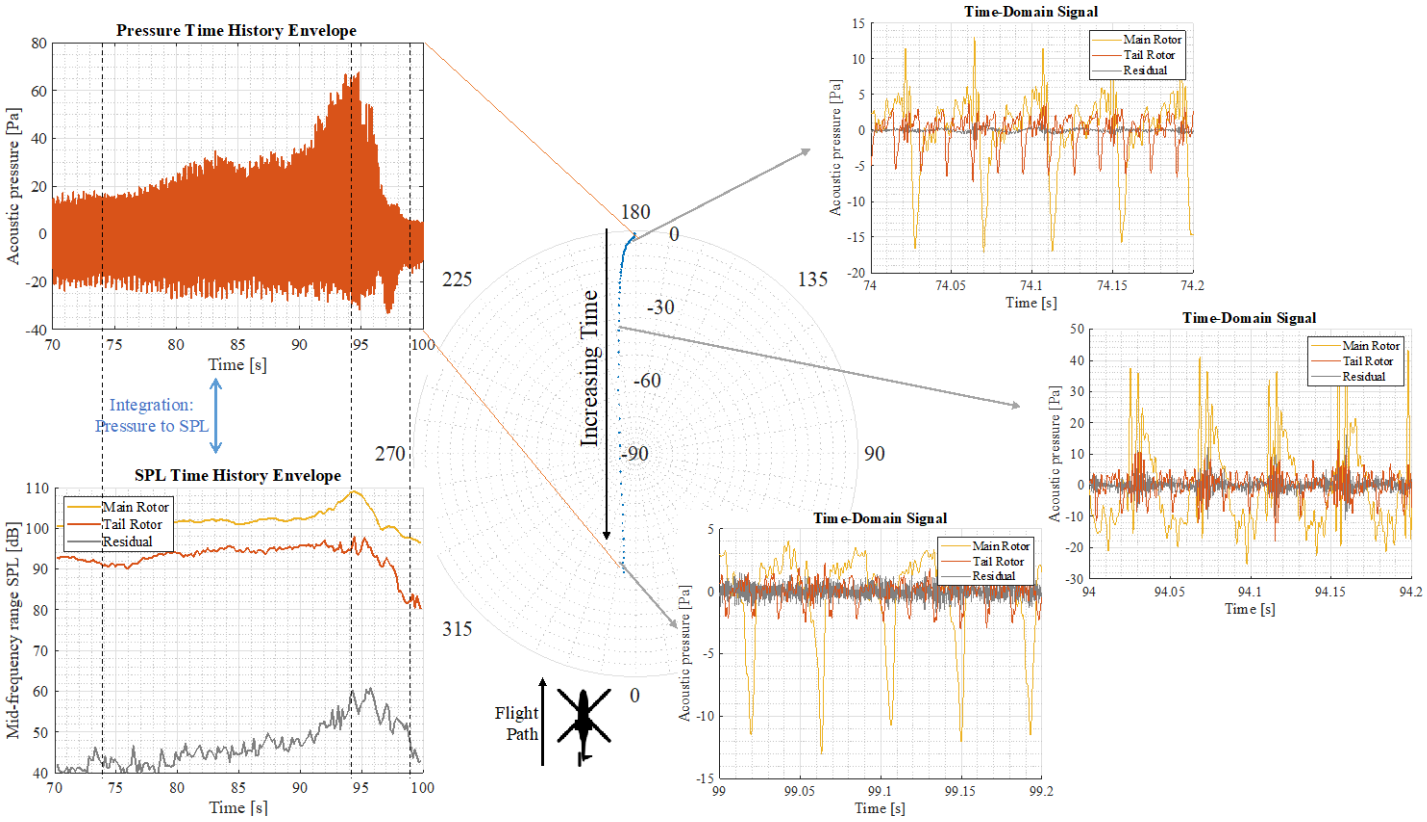

Figure 12. Acoustic pressure time series and mid-frequency SPL (sound pressure level) time history for the extracted signals along a microphone track with the extracted signals on a hemisphere for a cyclic pitch-up maneuver flight condition.

The presented SPL plots are integrated over a mid-frequency range of 90–470 Hz, which lies between the 4th and 20th harmonic of the main rotor blade passing frequency, to emphasize the blade—vortex interaction (BVI) noise in the extracted signals. The tonal components of both rotors are significantly higher than the residual component. The extracted signal of the main rotor is presented along with the extracted tail rotor signal at three time instants to highlight the different noise sources that are involved during a maneuver. The tail rotor noise is relatively constant throughout the maneuver. The waveforms show characteristic negative peaks associated with the tail rotor thickness noise, which are not expected to vary much with changes in the rotor operating condition.

Acoustic Flight Test Measurements of the Tarot X8 Multirotor UAS

Flight test measurements of the Tarot X8 octocopter were performed at the Mid-State Regional Airport (KPSB) in Philipsburg, PA, as described in more detail in Task 4. Although this aircraft did not have the instrumentation required to measure the rotor speed, an accurate measurement of the aircraft position data was used to apply some components of the SSP. First, the de-Dopplerization step of the SSP was applied, and then, the acoustic measurements were de-propagated to generate acoustic hemispheres.

Figure 13 presents the acoustic hemisphere with the overall SPL (OASPL) metric for a flyover at an altitude of 50 ft and a speed of 10 mph. Figure 14 presents the acoustic hemisphere for the same flyover at an altitude of 50 ft and a speed of 10 mph, but with an A-weighted SPL. The noise hemispheres for both metrics have similar noise “hotspots” under the aircraft. However, there is a difference in the noise levels of the OASPL hemisphere, where the levels are higher in directions closer to the plane of the horizon.

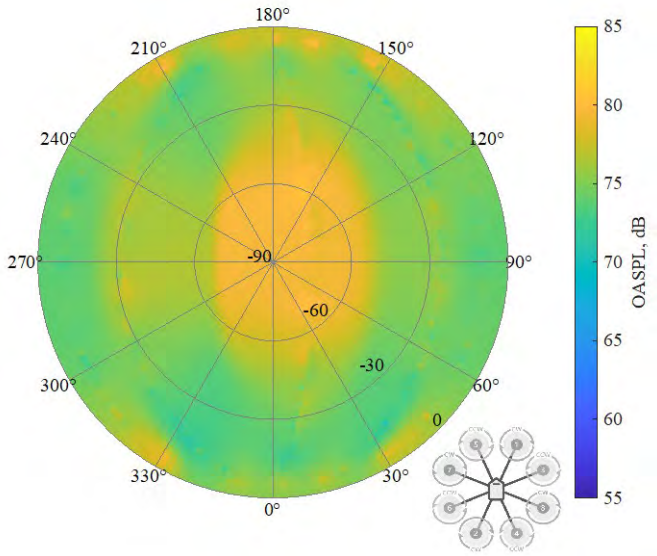

Figure 13. Acoustic hemisphere for level-flight flyover conditions at 50 ft and 10 mph, shown as the unweighted overall sound pressure level (OASPL), dB.

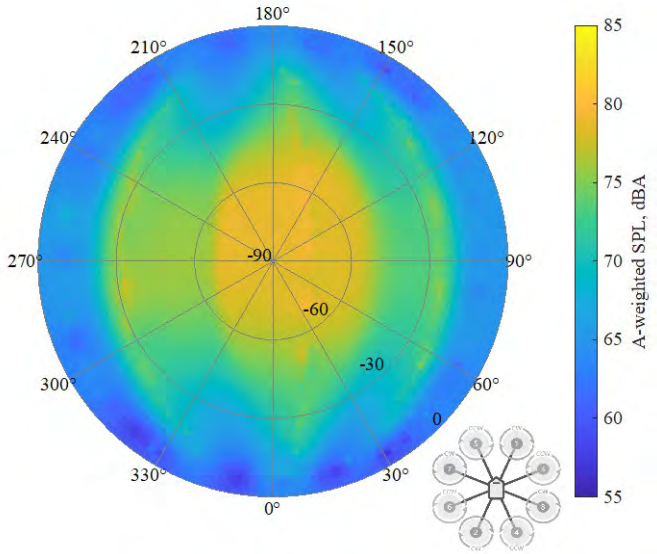

Figure 14. Acoustic hemisphere for level-flight flyover conditions at 50 ft and 10 mph, shown as the A-weighted sound pressure level (SPL), dBA.

In the OASPL metric hemisphere, there are "lobes" of acoustic energy in the plane of the horizon toward the forward and aft directions at azimuth angles of 30˚, 150˚, 180˚, 210˚, and 330˚. These observer locations are closer to the horizon of the aircraft, i.e., they are measured at distances further from the aircraft. This variability may be related to acoustic interference of the rotational noise sources (thickness and loading noise) generated by the vehicle, which radiated most prominently in the plane of the rotors. These variations are less prominent in the A-weighted noise hemisphere, which de-emphasizes the lower harmonic tones and is largely determined by the higher-frequency unsteady loading and broadband noise sources.

Publications

Rachaprolu, J., & Greenwood, E. (2022, May). *Helicopter Noise Source Separation using an Order Tracking Filter.* Vertical Flight Society Forum 78.

Rachaprolu, J. (2022, November). *Development of a Source Separation Process for Multirotor Aeroacoustic Analysis* [Master's thesis, The Pennsylvania State University].

Outreach Efforts

The investigation team holds monthly meetings with an external advisory board consisting of a dozen interested parties from government and industry. The SSP developed under this task has been provided to Blue Ridge Research and Consulting, who intend to use the method to isolate noise generated by a multirotor vehicle in hovering and low-speed flight. Posters presenting this method have been shown at the Penn State Center for Acoustics and Vibration Workshop (October 2021) and at the Vertical Flight Society Forum 78 (May 2022).

Awards

Best Poster Award, Center for Acoustics and Vibration Workshop, October 2021.
Best Paper Award, Acoustics Session, Vertical Flight Society Forum 78, May 2022.

Student Involvement

M.S. Student Joel Rachaprolu developed and tested the SSP on computational data and extended the application of the process to helicopter flight test data and baseline UAS measurement data. Rachaprolu is currently working on implementing the SSP on multirotor UAS aircraft with encoded motors.

Plans for Next Period

This task has been completed. However, this process has not yet been applied to multirotor UAS aircraft. Once the SSP is applied to a multirotor UAS with accurate measurements of rotor phase and/or RPM, a more accurate mathematical solution for the filter can be implemented to improve the resolution of the extracted signals. While the hardware for measuring rotor RPM has been validated in the laboratory and installed on the research UAS developed in Task 3, software still needs to be developed to enable recording of the RPM onboard the aircraft.

Task 3 - Development and Testing of a Reconfigurable Multirotor UAS Vehicle

The Pennsylvania State University

Objective

The objective of this task is to design and develop a multirotor UAS vehicle that can be easily reconfigured to explore the acoustic effects of different UAS vehicle configurations and their influence on the noise measurement and data processing approaches developed in this project.

Research Approach

Both small- and large-sized reconfigurable multirotor UAS aircraft were designed, with a smaller vehicle serving as a testbed for design concepts that were later integrated into the larger and more capable aircraft. Developmental ground and flight testing was performed prior to flights for acoustic data collection. These initial tests have focused on the hexacopter configuration to ensure a higher level of redundancy during initial testing. Onboard instrumentation includes a real-time kinematic DGPS and an inertial measurement unit. This sensor suite also allows a time-accurate position and state estimate that can be correlated to the acoustic measurements.

Milestones

The milestones for this task consist of (a) the identification of acoustically significant configuration changes to be made on the vehicle, (b) initial design of the vehicle and selection of sensors, (c) control system design, and (d) ground and flight testing.

Major Accomplishments

Following initial testing, both vehicles went through a second design iteration based on lessons learned.

Small Reconfigurable UAS

The size of the aircraft was increased to approximately 530 mm, measured from tip to tip of the motor mounts. The new frame retains the capability to handle three motor arm configurations: hexacopter, quadcopter, and tricopter. Carbon fiber was used for the main body, arms, and motor mounts. These configuration changes allow the use of a higher-accuracy real-time kinetic DGPS on the small UAS and support additional onboard research instrumentation. This change also extends the limit on propeller size to 8 inches.

Large Reconfigurable UAS

The size of the large UAS was increased to approximately 1,650 mm from tip to tip of the motor mounts. The reconfigurable characteristics remain unchanged from the original design. An additional level was added to the main body to support additional avionics, including a weather station for airspeed and atmospheric condition measurements during flight. When fully assembled with batteries, the weight of the empty aircraft is 40 lb, which is below the Part 107 limit of 55 lb; however, higher gross weights may be flown with an approved waiver. The maximum propeller size was increased to 32 inches for the hexacopter configuration. Light-emitting diode strips were installed below the arms to indicate the orientation of the vehicle while in flight.

Flight Testing and Acoustic Measurement

After the redesign process, the large UAS was used for acoustic measurements over four different test days and across several different flight conditions, including hover, forward flight, and ascent–descent maneuvers. Photographs of the large UAS in the field are shown in Figure 15. More detailed information regarding these test conditions and preliminary results can be found in the description of Task 4 in this document.

Figure 15. Photographs of the large reconfigurable unmanned aircraft system at Mid-State Regional Airport on the ground (left) and in the air (right).

Publications

Valente, V., Johnson, E., & Greenwood, E. (2022, September). *Implementation of a phase synchronization algorithm for multirotor UAVs*. 2022 IEEE/AIAA 41st Digital Avionics Systems Conference (DASC), Portsmouth, VA.

Valente, V., Johnson, E., & Greenwood, E. (2023, May). *An Experimental Investigation of eVTOL Flight State Variance on Noise.* Abstract submitted to the Vertical Flight Society Forum 79, West Palm Beach, FL, May 2023.

Outreach Efforts
The investigation team holds monthly meetings with an external advisory board consisting of a dozen interested parties from government and industry. Technical data regarding the reconfigurable multirotor UAS have been shared with investigators from the Georgia Institute of Technology, the University of Salford, Texas A&M University, and the NASA Langley Research Center. Discussions are ongoing about potential opportunities for collaboration.

Awards
None.

Student Involvement
Ph.D. student Vítor T. Valente was primarily responsible for the design, assembly, and configuration of both UASs. He also served as the safety pilot for the UASs during flight testing procedures.

Plans for Next Period
Plans for the following term include acoustic characterization of the small version of the reconfigurable multirotor UAS inside Penn State's flow-through anechoic chamber. These efforts will include noise measurements made while the aircraft applies a synchrophasing algorithm to steer and reduce the radiated tonal noise. Based on the results of this initial investigation, low-noise control algorithms for outdoor free flight will be developed, and outdoor testing and acoustic measurements will be made. For the large UAS, the team plans to continue collecting acoustic data for different conditions and configurations.

Task 4 - UAS Noise Measurement and Analysis
The Pennsylvania State University

Objective
The objective of this task is to conduct an acoustic flight test campaign to collect noise measurements for a variety of UAS vehicles under a variety of operating conditions and configurations.

Research Approach
Acoustic measurements of a flying UAS were conducted at the Mid-State Regional Airport, surrounded by the Moshannon State Forest and Black Moshannon State Park near Philipsburg, PA. Research noise measurements were made for the Tarot X8 octocopter UAS and the large reconfigurable research UAS described in Task 3. Each vehicle was flown through a range of operating conditions, including hover, forward flight at several speeds, climb, and descent. Flyover testing was conducted at several altitudes, from near ground level to 400 ft above ground level (AGL), in order to evaluate the ability to scale UAS noise measurements made at one flight altitude relative to another, given the relatively low noise levels of small UASs. Acoustic measurements were made with Penn State's networked, battery-powered, and field-deployable acoustic data acquisition system capable of sampling at up to 125 kHz at 24-bit resolution with subsample accurate GPS time synchronization across all nodes. A microphone array was designed to capture both spatial and temporal variations in the radiated noise. Weather instrumentation was also deployed, including measurements of wind speed, direction, temperature, pressure, and humidity.

Milestones
The milestones for this task consist of (a) collecting a baseline acoustic, performance, and meteorological data set of UAS noise measurements and (b) analyzing the data to quantify and understand the variability of UAS noise.

Major Accomplishments
Tarot X8 Acoustic Variability Study
Building on the noise measurement approach developed in the previous year of this project, a more extensive data set was collected for the Tarot X8 octocopter, as shown in Figure 16. To assess the noise variability, repeated flyover measurements were conducted for the same nominal flight condition. Acoustic data were collected using a distributed array of microphones, as shown in Figure 17. This array features two lines of microphones perpendicular to the flight track, to capture noise across a range of sideline angles at two different instances in time, as well as a smaller subarray of microphones parallel to the flight track, to capture noise at the same emission angle at four different times during each flyover. Two different microphone installation types were employed, as shown in Figure 18. Inverted ground-plane microphones were located at all

measurement positions. Elevated tripod-mounted microphones were collocated with ground-plane microphones at one centerline and one sideline location.

Figure 16. Tarot X8 octocopter.

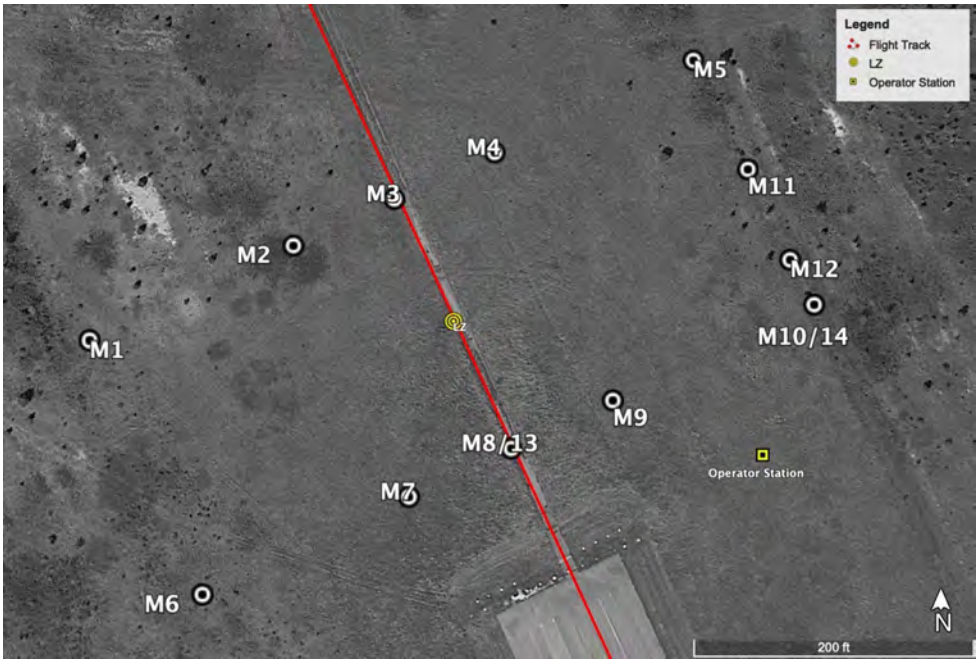

Figure 17. Acoustic array for the unmanned aircraft system at the approach end of Runway 16 at Mid-State Regional Airport. LZ: Landing Zone.

Figure 18. Inverted ground-plane (left) and elevated (right) microphone installations.

Flyover noise measurements were conducted at a range of altitudes and speeds. For each test point, the vehicle would fly along the flight path in both the "nominal" and "opposing" directions. Numerous repeated test points were collected for each flyover condition. For example, 20 repeated test points were collected for flyover conditions with a flight speed of 20 mph at 50-ft altitude AGL. Figure 19 presents the mean A-weighted SPL time history measured at the centerline microphone location for all 20-mph, 50-ft-AGL flyover flight conditions (solid black line). The grey envelope surrounding the mean represents the variation across the entire set of flight conditions. The variation in SPL ranges from 3 dB at the point where the aircraft overflies the microphone to as high as 8 dB when the vehicle is farther from the microphone. Similar trends are observed for other flight conditions and observer locations, with the greatest variability found for observers far from the aircraft and at emission angles near the plane of the rotors. Integration of the SPL into the sound exposure level (SEL) showed SEL variations ranging from 4 to 7 dBA, with the greatest variations observed for the microphones farthest from the flight track.

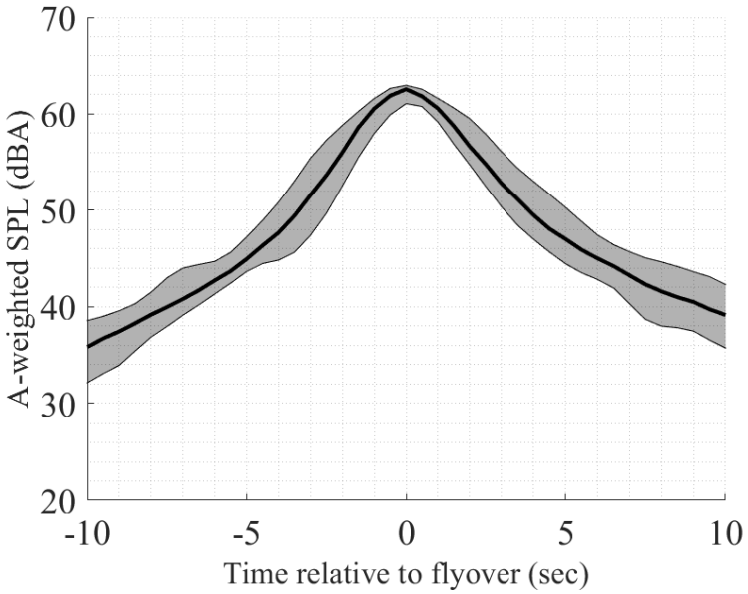

Figure 19. Variation in A-weighted sound pressure level (SPL) time histories for 20-mph level-flight flyover conditions at 50 ft above ground level over centerline microphone M3.

A linear, equally spaced microphone array consisting of microphones M10, M12, M11, and M5, which run parallel to the vehicle flight path, was designed to gather noise data for the same flight condition and emission distance at four different instances in time for each run. The schematic in Figure 20 shows how repeated measurements are made at the same angle at different points in time during each flyover. The variation in measured SPL at different time points during a single run is termed the intra-run variability. An analysis was conducted to compare the degree of intra-run variability with the inter-run variability measured at the same microphone across repeated runs for the same flight condition.

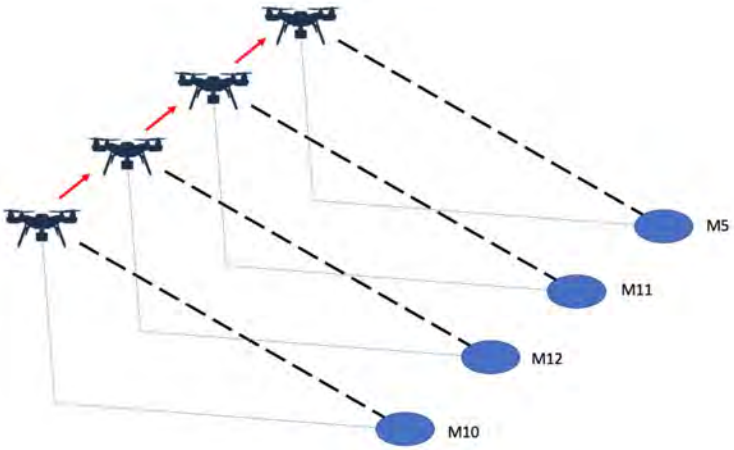

Figure 20. Schematic showing the process of measuring intra-run variability using the sideline microphone array.

Table 3 shows the variation in the peak SPL for 20-mph, 50-ft-AGL flyovers across different runs and sideline array locations. For convenience, entries in the table are color-coded based on the SPL magnitude, with the highest levels coded red and the lowest coded green. For each run number, associated with both a nominal upwind and opposing flight path heading, values are tabulated separately for each direction. No clear trends or biases appear across microphone locations or flight path directions. The bottom row of the table summarizes the mean SPL for each location, along with the minimum and maximum

levels and the corresponding range of levels, representing the inter-run variability. Likewise, the rightmost column provides the same statistics across all microphone locations for each run, representing the intra-run variability.

Overall, the mean SPL for all cases shown in Table 3 was 38.9 dB, with a minimum of 35.8 dB and a maximum of 42.8 dB. Significantly, the range between the minimum and maximum measured values tended to be less within one run (as measured using different microphones) than for the same microphone across all runs. Within a run, the range of SPL variation was 2.2 dB for a single microphone averaged across all runs, whereas the SPL variation averaged across the four microphones and across all runs was 5.0 dB. Consequently, while intra-run variations are significant, they do not entirely explain the variation observed between repeated runs of the same flight condition. This result implies that variability in the flight state during a run has a smaller effect on the variation of noise levels than changes in noise occurring over a longer time scale, e.g., due to changes in ambient atmospheric conditions.

Table 3. Comparison of inter- and intra-run variations in A-weighted sound pressure level. FPH: flight path heading.

	Run	M10	M12	M11	M5	Mean	Range
Nominal FPH	19	39.3	39.1	37.8	39.9	39.0	2.1
	20	37.6	38.2	37.9	38.3	38.0	0.7
	21	38.7	38.1	35.8	38.1	37.7	2.8
	22	38.3	38.4	36.6	39.4	38.2	2.8
	23	39.0	37.4	37.0	39.2	38.1	2.2
	24	38.1	38.0	36.9	39.7	38.2	2.8
	25	39.6	38.9	38.2	39.8	39.1	1.6
	9	38.0	40.4	36.8	37.6	38.2	3.6
	12	38.3	40.7	38.2	40.2	39.3	2.4
Opposite FPH	19	39.2	38.0	36.5	38.4	38.0	2.7
	20	38.7	38.1	37.6	39.0	38.4	1.4
	21	38.8	38.5	37.7	39.6	38.6	1.8
	22	38.5	38.7	39.1	40.6	39.2	2.2
	23	39.4	38.5	38.2	39.9	39.0	1.7
	24	40.8	38.9	38.3	39.2	39.3	2.5
	25	41.2	41.3	39.7	40.9	40.8	1.6
	9	41.3	39.7	39.0	41.8	40.4	2.7
	12	42.8	42.3	41.3	41.1	41.9	1.7
	Mean	39.3	39.1	37.9	39.6		
	Range	5.3	5.0	5.5	4.2		

Another analysis was conducted to investigate the variation in integrated SEL as the flyover altitude of the aircraft was varied. Data for nominal 20-mph flyovers conducted at flight altitudes of 50, 100, and 250 ft are plotted in Figure 21. Figure 21 also presents several curves intended to correct the data back to a 50-ft flyover altitude with the following equation:

$$L_{AE} = \bar{L}_{AE\,50} + C \log_{10} \frac{H}{50}$$

where L_{AE} is the corrected A-weighted SEL, $\bar{L}_{AE\,50}$ is the average SEL for the 50-ft flyover flight condition, H is the flyover altitude of the measured data, and C is a coefficient controlling the scaling of noise from one altitude to another. FAR Part 36 Appendix J provides a flyover altitude correction for helicopters, where $C = 12.5$ dB based on experimental measurements. The theoretical correction for an omnidirectional source flying at constant speed corresponds to $C = 10.0$ dB. A best fit of the measured data available for the Tarot X8 in this flight condition yields $C = 8.9$ dB. However, it should be noted that limited data are available at the highest altitude, where the signal-to-noise ratio is only 15 dBA. Additionally, the high degree of variability in the source noise may significantly affect the best-fit curve. Additional data across a wider range of altitudes should be collected to establish the appropriate altitude correction factor for small multirotor UASs.

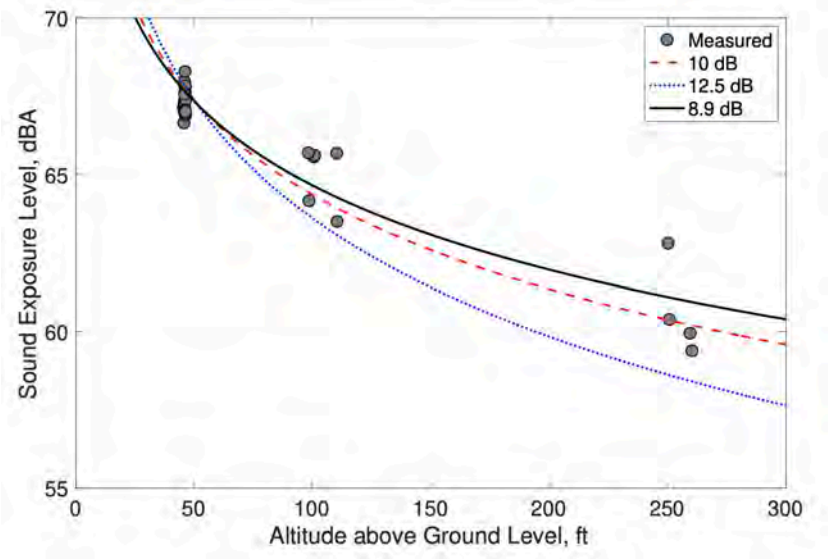

Figure 21. Sound exposure level as a function of altitude.

More detailed analyses of the Tarot X8 acoustic measurements are provided in the publications associated with this task, including spectral variations over time in forward flight and hover, a comparison of noise measurements obtained with different microphone installations, and a detailed analysis of directivity variations across repeated flyover conditions.

Large Reconfigurable UAS

Acoustic, weather, and flight state data for over 120 individual test points have been collected for the large reconfigurable UAS during the reporting period, covering a wide variety of vehicle configurations and operating conditions, as listed in Table 4. A photograph of the large reconfigurable UAS on its approach to landing is shown in Figure 22.

Table 4. Test points collected for the large reconfigurable unmanned aircraft system (UAS).

Reconfigurable UAV							
09-02-2022		**09-09-2022**		**09-24-2022**		**10/24/2022**	
Hover	13	Hover	6	Hover	0	Hover	69
Flyover	4	Flyover	9	Flyover	21	Flyover	0
Descent/Ascent	0	Descent/Ascent	3	Descent/Ascent	0	Descent/Ascent	0

Figure 22. Full-size reconfigurable unmanned aircraft system (hexacopter configuration) in the landing procedure after one mission.

Vehicle state data and local ambient weather data have been collected and correlated to the acoustic data for each test point using GPS time. A preliminary analysis of the acoustic data collected during these tests has been performed. Figure 23 shows a spectrogram of the noise measured for the large UAS in hover at 50-ft altitude AGL at microphone M8, located 200 ft from the hover test point. The rotor tones can be seen to vary significantly in frequency and magnitude as the rotor RPM values are adjusted to maintain a stable hover flight condition.

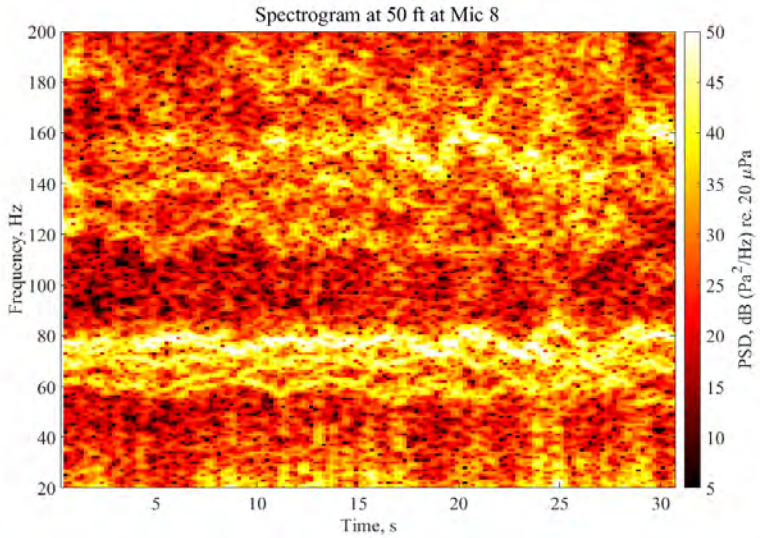

Figure 23. Spectrogram of a hover flight condition at 50 ft above ground level for the full-size reconfigurable unmanned aircraft system. PSD: power spectral density.

The relationship between the vehicle state and noise variation is currently being investigated. Figure 24 presents the vehicle pitch and roll attitude time histories against the A-weighted SPL for the same recording. It can be seen that the large increase in SPL occurring at approximately 25 s corresponds to a change in the roll attitude of the aircraft.

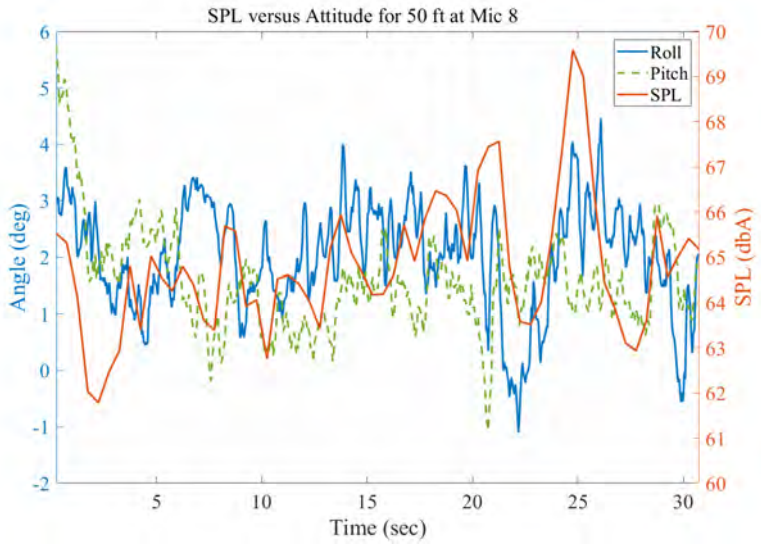

Figure 24. Sound pressure level (SPL) time histories and attitude of the vehicle (roll and pitch) for the hover condition at 50 ft.

Further data analysis will be conducted to identify other states that could be related to this change and the magnitude and causes of variability in the measured acoustic data. Data for both the Tarot X8 and large reconfigurable UAS are being organized and packaged to simplify the collected noise, weather, and vehicle data into a streamlined database that can be used by the FAA and subsequently the broader research community.

Publications

Konzel, N.B., and Greenwood, E. (2022, May). *Ground-based Acoustic Measurements of Small Multirotor Aircraft.* Vertical Flight Society Forum 78, Ft. Worth, TX.

Greenwood, E., and Konzel, N.B. (2022, June). *Measurement and Characterization of Multirotor Unmanned Aerial System Noise.* NOISE-CON 2022, Lexington, KY.

Outreach Efforts

The investigation team holds monthly meetings with an external advisory board consisting of a dozen interested parties from government and industry. Discussions have been held with the investigation team for ASCENT Project 61 to validate streamlined procedures for UAS noise data collection and analysis. Data collected for UAS under this task may also be provided to collaborators at the University of Salford and the NASA Langley Research Center to enable psychoacoustic evaluations of UAS noise using their auralization and human subject testing capabilities.

Awards

None.

Student Involvement

Ph.D. student Vítor T. Valente and M.S. students N. Blaise Konzel, Joel Rachaprolu, and Sebastian Lopez conducted acoustic flight testing of the Tarot X8 and large reconfigurable UAS. Vítor T. Valente was responsible for the operation and analysis of data collected for the large reconfigurable UAS. N. Blaise Konzel conducted the analysis of acoustic variability for the Tarot X8.

Plans for Next Period

Analysis of data collected during the current reporting period will continue in the next period. These efforts will include the processing of all UAS flyover data into acoustic hemispheres, with an emphasis on characterizing the statistical variability of noise levels emitted over all frequencies and directions. The variation in acoustic characteristics with changes in nominal flight condition will be investigated, including changes in flight speed and flight path angle (i.e., climb and descent). Additionally, a more detailed comparison of differences between data measured using inverted ground-plane and elevated microphones will be conducted, including the changes in spectral quantities and the effect on integrated noise metrics such as the SEL and effective perceived noise level.

The test team will continue to collect data for a wide range of UAS configurations and operating conditions. New array designs will be investigated to help decouple the variations in noise over time from the variations with emission angle. The measured flight state of the reconfigurable UAS will be correlated to measured acoustic data, with the aim of identifying the cause of UAS noise variability and establishing limits on acceptable flight state variation for repeated acoustic characterizations of multirotor aircraft. Additional data will be collected on the variation in noise with flight altitude, including very low altitudes where the microphone may be in the acoustic near-field of the aircraft.

Task 5 - UAM Noise Measurements

The Pennsylvania State University

Objective

The objective of this task is to conduct an acoustic characterization of Beta Technologies' UAM aircraft.

Research Approach

Test plans were developed to characterize the noise of the ALIA-250 UAM in forward flight and vertical flight operating modes. Plans were also developed for the ALIA-40d subscale model in transition and the prop truck test rig in hover and low-speed forward flight conditions.

Milestone

The milestone for this task consists of collecting a baseline acoustic, performance, and meteorological data set of UAM noise measurements across several operating modes.

Major Accomplishments

Noise measurements of the ALIA-250 UAM aircraft were conducted by the Penn State test team in August 2022, as shown in Figure 25. Data were collected for the aircraft in a conventional takeoff and landing configuration for flyover flight conditions at several altitudes and airspeeds, as well as during takeoff and approach. Six repeated test points were collected for each flyover flight condition, allowing the variability in noise to be assessed. Over 40 individual test points were collected over multiple days of testing. A limited data set was also collected for the prop truck test rig at several RPM values and low-speed forward flight conditions. Aircraft availability and weather prevented full-scale vertical flight and subscale flight noise measurements from being conducted during the current reporting period.

Figure 25. Noise measurement of the ALIA-250 in flyover by the Penn State team.

Publications
None.

Outreach Efforts
The investigation team holds monthly meetings with an external advisory board consisting of a dozen interested parties from government and industry.

Awards
None.

Student Involvement
M.S. student N. Blaise Konzel developed the test plans. Ph.D. student Vítor T. Valente and M.S. student Joel Rachaprolu conducted the field measurements with BETA Technologies in Plattsburgh, NY.

Plans for Next Period
Noise measurements will be conducted for the full-scale vertical flight and the subscale aircraft in transition in the next reporting period. These data will be analyzed to assess the acoustic characteristics, including noise variability, of UAM aircraft.

Project 078 Contrail Avoidance Decision Support and Evaluation

Massachusetts Institute of Technology

Project Lead Investigator

P.I.: Steven R. H. Barrett
Professor of Aeronautics and Astronautics
Director, Laboratory for Aviation and the Environment
Massachusetts Institute of Technology
77 Massachusetts Ave, Building 33-207, Cambridge, MA 02139
617-253-2727
sbarrett@mit.edu

University Participants

Massachusetts Institute of Technology

- P.I.: Prof. Steven R. H. Barrett
- FAA Award Number: 13-C-AJFE-MIT, Amendment Nos. 086 and 100
- Period of Performance: October 1, 2021 to September 19, 2023
- Reporting Period: October 1, 2021 to September 30, 2022
- Tasks:
    1. Contrail Forecast Module
    2. Contrail Identification Module
    3. Contrail Radiation Module
    4. Trajectory Planning Module

Project Funding Level

This project received $1,100,000 in FAA funding and $1,100,000 in matching funds. Sources of matching are approximately $168,000 from Massachusetts Institute of Technology (MIT), plus third-party in-kind contributions of $469,000 from Savion Aerospace Corp. and $463,000 from Google, LLC.

Investigation Team

Principal Investigator:	Prof. Steven Barrett (MIT) (all tasks)
Co-Investigators:	Dr. Sebastian Eastham (MIT) (all tasks)
	Dr. Florian Allroggen (MIT) (all tasks)
	Dr. Raymond Speth (MIT) (all tasks)
	Dr. Jayant Sabnis (MIT) (all tasks)
Graduate Research Assistants:	Jad Elmourad (MIT) (Tasks 3-4)
	Vincent Meijer (MIT) (Tasks 1-2)
	Louis Robion (MIT) (Tasks 1-2)

Project Overview

Contrails are white, line-shaped ice clouds that form behind aircraft. Contrails and subsequent contrail cirrus are thought to account for approximately one half of the climate warming attributable to aviation. Contrail avoidance through vertical and horizontal flight path changes is estimated to cause fuel burn penalties of a few percent. Thus, contrail avoidance is a potentially cost-effective way to mitigate the climate impacts of aviation. However, contrail avoidance has not been demonstrated at scale, and a comprehensive toolset to support this approach has not been developed. The goal of this project is to create a contrail avoidance decision support and evaluation tool that can be utilized to optimize and evaluate

the benefits, costs, and practicality of contrail avoidance. In addition, subject to agreement with industry partners, we will seek to test contrail avoidance in a way that has no implications for air traffic control or safety.

This project aims to satisfy four specific objectives: (a) develop the capabilities necessary to predict the formation and impacts of contrails from a given flight, (b) evaluate the financial costs and environmental benefits of deviating from a given path to avoid a contrail, including uncertainty, (c) integrate these capabilities into an operational tool that can provide near-real-time estimates of the costs and benefits of a contrail avoidance action, informed by automated, coordinated observational analysis and modeling, and (d) evaluate the effectiveness of these tools in a safe, scientifically sound real-world experiment.

The objectives outlined above will be met through a work program that comprises the following tasks:

1. Contrail Forecast Module
2. Contrail Identification Module
3. Contrail Radiation Module
4. Trajectory Planning Module

The following tasks will be included under future periods of performance (not funded through the current submission) and will provide an outlook for follow-on work in future project years.

5. Cost–Benefit Evaluation Module
6. Airline Integration
7. Experiment Evaluation Module

The remainder of this document presents a description of the first four tasks, including research progress and next steps.

Task 1 - Contrail Forecast Module

Massachusetts Institute of Technology

Objective

The goal of Task 1 is to develop a contrail forecast module that predicts the likelihood of persistent contrail-forming conditions one day ahead, in the hours before the flight, and in real time during a flight. This module is intended to allow airlines to decide ahead of time whether flights may wish to use contrail avoidance, to file flight plans accounting for the best estimated cruise altitude, and to adjust in real time (subject to pilot workload and air traffic control constraints).

Research Approach

Prediction will be performed using a combination of U.S. agency meteorological forecasts and observational data, including prior satellite observations of contrails from earlier flights. We will begin by using meteorological data from the NASA Global Modeling and Assimilation Office Goddard Earth Observing System (GEOS) Forecast Product, which has a moderate resolution (0.25° latitude by 0.3125° longitude globally) and provides new 5- and 10-day forecasts each day (Rienecker et al., 2008). As the project progresses, we will evaluate regional products such as the National Oceanic and Atmospheric Administration High-Resolution Rapid Refresh (HRRR) system to provide greater resolution over the United States.

Evaluating existing forecasts

We evaluated the capability of existing numerical weather prediction (NWP) models to forecast persistent contrail formation areas (PCFAs). This evaluation was achieved by transforming the meteorological variables provided by these NWP models into a Boolean grid marking PCFAs. PCFA calculation relied on the Schmidt–Appleman criterion for contrail formation and the ice supersaturation criterion for contrail persistence. Together, we term these conditions "persistent contrail conditions" (PCCs). Additionally, we used a satellite-based contrail detection algorithm to evaluate the ground-truth PCFAs. By randomly sampling points on the grid and comparing these two sets of PCFAs, we evaluated the capability of NWP models to forecast PCFAs.

We used two metrics – precision and recall – which vary between 0 and 1, with 1 indicating optimal performance for a metric. Precision indicates the ratio of true positives to the sum of true positives and false positives. In other words, precision

indicates the number of times that the NWP model correctly forecasts a PCFA divided by the total number of times that the NWP model forecasts a PCFA. Recall indicates the ratio of true positives to the sum of true positives and false negatives. In other words, recall indicates the number of ground-truth PCFAs that the NWP model was able to forecast divided by the total number of ground-truth PCFAs (i.e., including those that the NWP model did not forecast).

We applied this procedure to the NWP product HRRR provided by the National Oceanic and Atmospheric Administration. The HRRR has 3-km resolution and is updated hourly. We found that the performance was low, with a precision mean below 1% and a recall mean below 50% (see Figure 1.1).

Furthermore, an evaluation of ECMWF Reanalysis v5 (ERA5) wind data was conducted because wind velocities and uncertainty play an important role for both contrail nowcasting and contrail-to-flight attribution (as discussed below). The wind uncertainty was quantified by comparing ERA5 values with Aircraft Meteorological Data Relay (AMDAR)-reported values. The results showed that ERA5 and AMDAR horizontal winds agreed within a root mean square error (RMSE) of less than 3 m/s (see Figure 1.2), which is expected given that these measurements are assimilated. We switched from modeling the wind uncertainty as a Gaussian distribution with constant standard deviation to using a standard deviation that is a linear function of the wind speed as shown below.

$$\sigma_{ERA5} = \alpha|u_{ERA5}| + \beta$$

where σ_{ERA5} is the standard deviation of the wind, u_{ERA5} is the wind velocity, and α and β are parameters determined by model fits to the data. We modeled the eastward and northward components of the wind independently. The resulting values for α and β are shown in Table 1.1.

Table 1.1. Values for the wind uncertainty model parameters.

Wind component	α [-]	β [m/s]
Eastward	0.0106	1.7
Northward	0.0878	1.15

We also assessed the performance of multiple techniques for wind data interpolation by artificially “coarsening” the ERA5 grid and comparing the interpolated wind values with those at the grid points that were removed. We found that bicubic interpolation in the horizontal, quadratic interpolation in the vertical, and linear interpolation in the temporal dimension performed best. The results of this evaluation will form part of the basis for incorporating uncertainty into PCFA forecasts, a key component of final tool development.

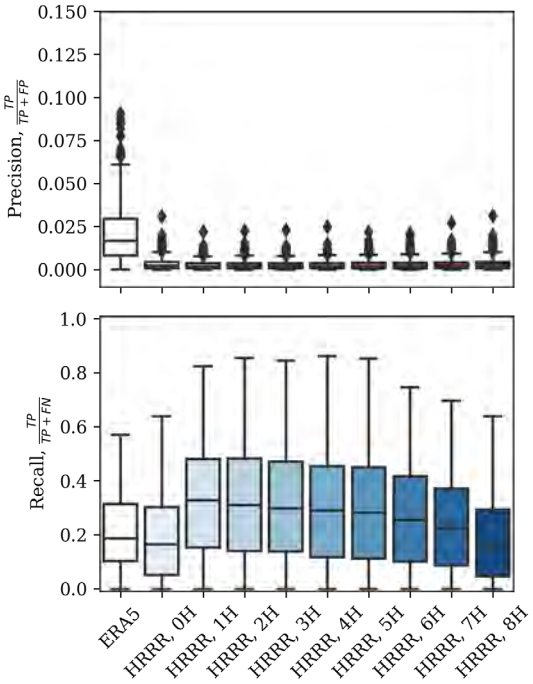

Figure 1.1. Preliminary estimate of the performance of the ECMWF Reanalysis v5 (ERA5) reanalysis and High-Resolution Rapid Refresh (HRRR) forecast, measured by recall (top) and precision (bottom), as a function of forecast lead time. The data represent 1,000 randomly sampled time points in 2018 and 2019. FN: false negative; FP: false positive; TP: true positive.

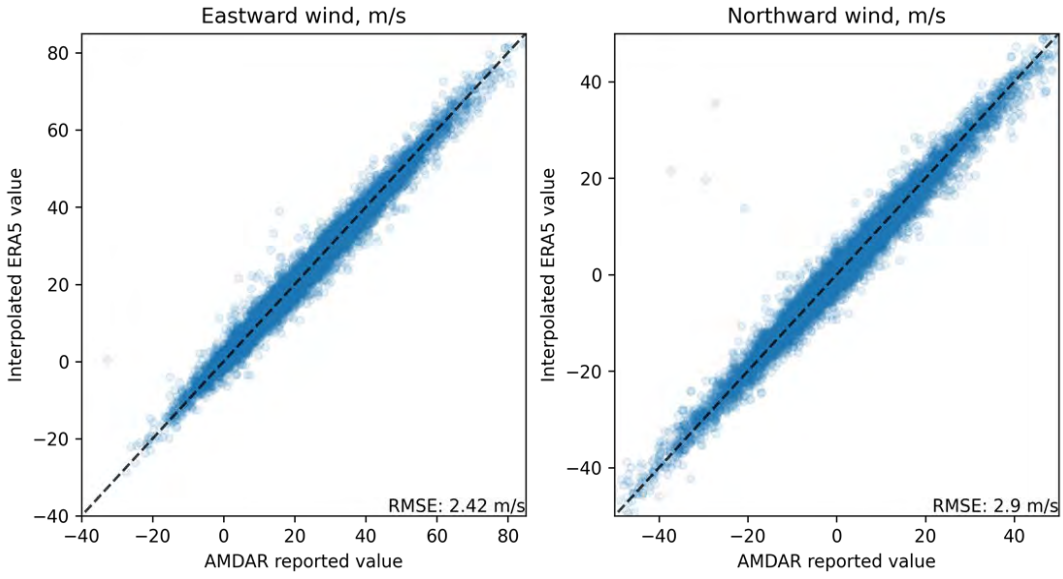

Figure 1.2. Comparison between ERA5 and Aircraft Meteorological Data Relay (AMDAR) horizontal winds. RMSE: root mean square error.

Development of contrail nowcasting

Because our metrics indicated that NWP data alone are not sufficient to accurately forecast PCFAs, we investigated nowcasting, which is an approach that uses recent contrail observations to forecast PCFAs. For example, if contrails were detected in region X, the nowcasting approach would forecast a PCFA in region X, at least for short lead times. The nowcasting approach can also include wind data to forecast the advection of the PCFA (see Figure 1.3). Because of this feature, the above-mentioned quantification of the ERA5 wind uncertainty was useful. The nowcasting approach relies heavily on the contrail identification module (see Task 2).

We investigated two approaches to nowcasting: Eulerian persistence and Lagrangian persistence (see Figure 1.3). In the Eulerian persistence approach, we assume that the region in which contrails are detected will continue to be a PCFA for the near-term future. In the Lagrangian persistence approach, the PCFAs move horizontally with the wind.

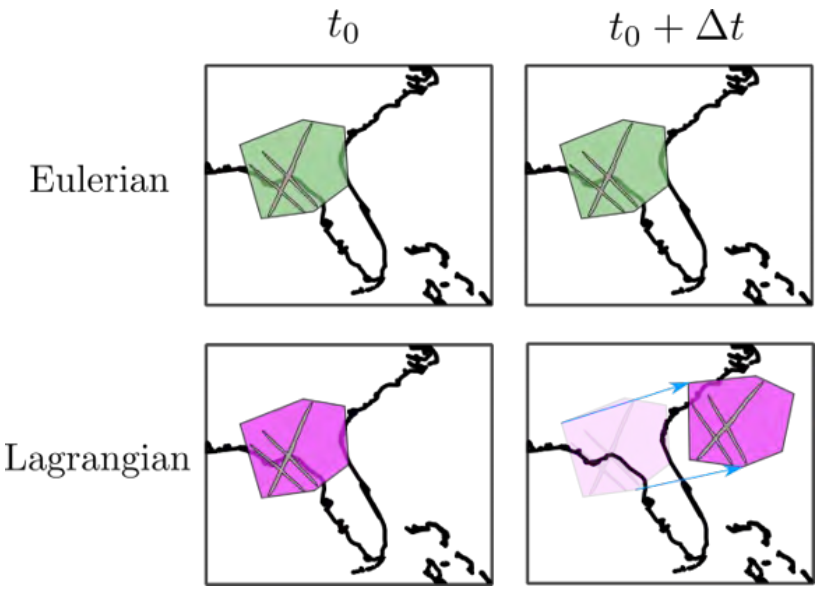

Figure 1.3. Schematic of two approaches to nowcasting: Eulerian and Lagrangian. The gray lines represent contrail detections whereas the regions in solid green and magenta indicate the location of persistent contrail formation areas that would be estimated by the nowcasting approach.

The performance of these two nowcasting approaches was compared with that of the two NWP-based models: ERA5 and HRRR. The result for the recall metric is shown in Figure 1.4. Compared with Figure 1.1, which shows a preliminary estimation of the HRR performance, Figure 1.4 only quantifies the recall metric because an accurate estimation of the precision metric depends on work being developed under Task 2, namely combining contrail observations with flight track data. As shown in Figure 1.4, and by definition, the nowcasting approaches initially have 100% recall. The plot shows that even though the performance of the nowcasting approaches deteriorates quickly with increased lead time, the nowcasting approaches are still better for lead times up to 2 h. The ERA5 performance is independent of the lead time (single reanalysis) whereas the HRRR performance improves with lead time (differences in assimilated data).

The superior performance of the Eulerian approach compared with the Lagrangian approach reflects three factors. Firstly, we know from visual analysis of contrail observations that PCFAs do not move at the same speed as the contrails themselves. Because contrails are advected by the wind, the PFCAs move at a separate speed, likely related to the factors that give rise to PCFAs in the first place. Secondly, we know that the wind data are imperfect, meaning that advection of the PCFAs based on wind data will also suffer from accumulating error. Finally, the definition of a PCFA based on observations is itself uncertain (see Task 2), which may introduce different biases for the two approaches.

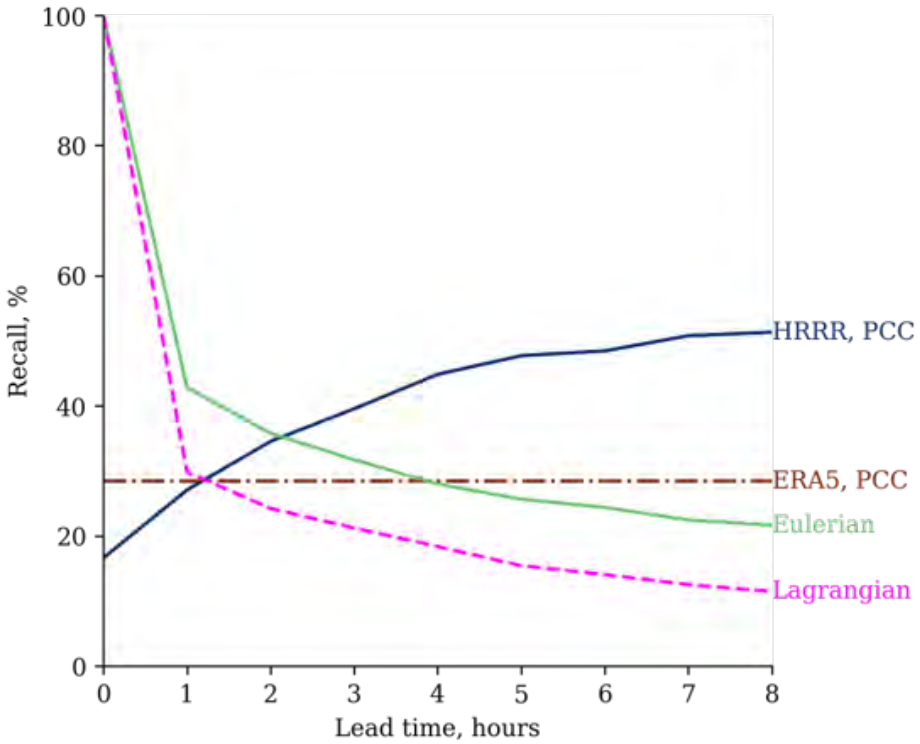

Figure 1.4. Evaluating the performance of various forecasting approaches as a function of lead time. HRRR: High-Resolution Rapid Refresh; PCC: persistent contrail condition; ERA5: ECMWF Reanalysis v5.

Based on this assessment, future tool development is focused on contrail nowcasting, with the goal of further leveraging observations rather than relying on NWP models.

Milestone

Milestone 1: Concept demonstration and first implementation of a contrail forecasting functionality for the FAA [*complete*].

Major Accomplishments

- Evaluated existing NWP models on their ability to predict contrail-forming regions
- Quantified errors in ERA5 wind velocity and wind shear data that could compromise flight attribution and nowcasting components
- Evaluated the performance of simple nowcasting approaches, comparing them with other NWP models

Publications

None.

Outreach Efforts

An oral presentation was given by Vincent Meijer at the 5th International Conference on Transport, Atmosphere and Climate in Munich, Germany, hosted by the German Aerospace Center.

Authors: Vincent R. Meijer, Sebastian D. Eastham, Steven R. H. Barrett
Title: Using satellite-based observations of contrails to inform contrail avoidance strategies
One-sentence summary: Comparison of satellite-based observations of contrails with numerical weather prediction data indicates that forecasts of persistent contrails are lacking. Short-term approaches that utilize observational data of contrails are shown to outperform numerical weather prediction models.
Date: June 29, 2022
Publication status: N/A

Awards
None.

Student Involvement
The research for this task was primarily conducted by Vincent Meijer with assistance from Louis Robion, both graduate research assistants at MIT. The communication of this research to the FAA was primarily conducted by Jad Elmourad, a graduate research assistant at MIT.

Plans for Next Period
- Develop and evaluate a nowcast of contrail-forming regions based on current inferred conditions, projected winds, and a physics-based understanding of contrail-forming regions.
- Use the improved contrail height estimates (see Task 2) to extend the nowcast of contrail observations from 2D to 3D.
- Evaluate the accuracy of forecasts in predicting contrail formation using the new approach developed under the contrail identification module.

References
Rienecker, M. M., Suarez, M. J., Todling, R., Bacmeister, J., Takacs, L., Liu, H. C., & Nielsen, J. E. (2008). The GEOS‐5 Data Assimilation System: Documentation of versions 5.0. 1 and 5.1. 0, and 5.2. 0 (NASA Tech. Rep. Series on Global Modeling and Data Assimilation, NASA/TM‐2008-104606, Vol. 27, 92 p.). *Greenbelt, MD: NASA Goddard Space Flight Center*.

Task 2 - Contrail Identification Module
Massachusetts Institute of Technology

Objective
The objective of Task 2 is to develop a real-time contrail identification module that locates contrails both horizontally and vertically. This module will be necessary to evaluate whether contrail avoidance has been successful. Furthermore, this module will enable contrail forecasting approaches that are based on contrail detections and that might prove to be more reliable for shorter lead times than approaches based on numerical weather forecasts. The initial version will use Geostationary Operational Environmental Satellite (GOES) observations combined with a deep learning approach developed by MIT (under NASA sponsorship) to identify contrails from space. Future developments could include other satellite products, ground observations, and other observations.

Research Approach
We started with a contrail detection algorithm based on satellite imagery from GOES-16. This algorithm was then used to develop a probabilistic estimate of the contrail-forming regions using a kernel density estimation (KDE) approach, building on prior NASA-funded work. Flight data were then integrated into the model to improve our estimates. These steps allowed the contrails to be located horizontally. Next, we initiated the development of a contrail height estimation algorithm. A validation dataset of contrail locations was created to improve the performance of the algorithms. Furthermore, we have started integrating temporal data into the contrail detection algorithm. This integration improves the temporal consistency of the contrail detections (i.e., a given contrail is detected in every frame of a series of images) and may allow contrails to be detected earlier. This latter piece of information would significantly improve our ability to determine which flight created the detected contrail and to therefore verify the success of contrail avoidance actions.

Probabilistic approach using KDE
The initial implementation of a contrail identification module, developed under prior NASA funding, relied on binary PCFAs. This implementation was achieved by mapping satellite-observed contrails onto a grid, estimating the region bounded by the observed contrails on the grid, and then transforming the grid into a set of polygons based on the density of contrail observations. However, we discovered two issues with this approach. First, contrail detections were not temporally consistent, which led to polygons that frequently changed shape. Second, this approach did not account for uncertainty in the detections and did not make use of prior knowledge about the shape of PCFA regions. For these reasons, we moved toward a probabilistic approach.

Instead of a binary map of PCFAs, we now use a contrail detection mask to generate a KDE. The idea behind this KDE is that each contrail "induces" its own probability distribution (the kernel) and that the distributions of multiple contrails may interact. One such example is the case of two contrails (see Figure 2.1), where the PCFA probability between the two contrails increases as they approach each other. The kernel is parametrized as a multivariate Gaussian distribution. These parameters can be used to encode prior knowledge on PCFAs. For example, using three different parameters, the shape of the induced KDE can be stretched along the contrail length, perpendicular to the contrail length, or in proportion to the contrail length.

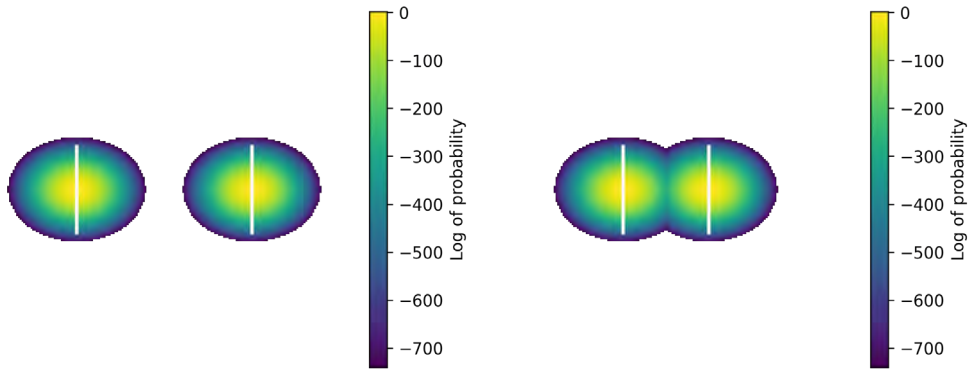

Figure 2.1. Example of kernel density estimates from contrail detections. The white lines represent contrail detections, and the colormap represents the probability of the detection being a persistent contrail formation area. The left plot shows two contrails that are far from each other. The right plot shows the interaction of two contrails close to each other.

Integration of flight data

Contrail detections provide information about contrail locations; however, for a location without any contrail detections, there are multiple possible scenarios. One possibility is that the region is not a contrail-forming region whereas the other possibility is that no flights have passed through that region. Without integrating flight data into our model, we are not able to differentiate between these two scenarios. Therefore, we investigated the integration of flight data to improve the probabilistic estimate of PCFA locations.

The advection of flight data was implemented in order to match flight locations at the time that a contrail is detected from the satellite. The advection of flight data uses ERA5 wind data, leveraging the ERA5 wind uncertainty model developed under Task 1 (discussed above).

The flight density data and probabilistic contrail detections can be combined by using Bayes' rule to improve our estimate of contrail regions. An example is shown in Figure 2.2. This approach provides the desired behavior in three ways. First, regions with contrail detections have a high probability of being a PCFA. Second, regions with no contrail detections but with high flight density have a low probability of being a PCFA. Finally, regions with no contrail detections and low flight density have an intermediate probability of being a PCFA. In the last case, the probability should revert to the climatological mean for PCFAs. This approach has shown promise but is still under development.

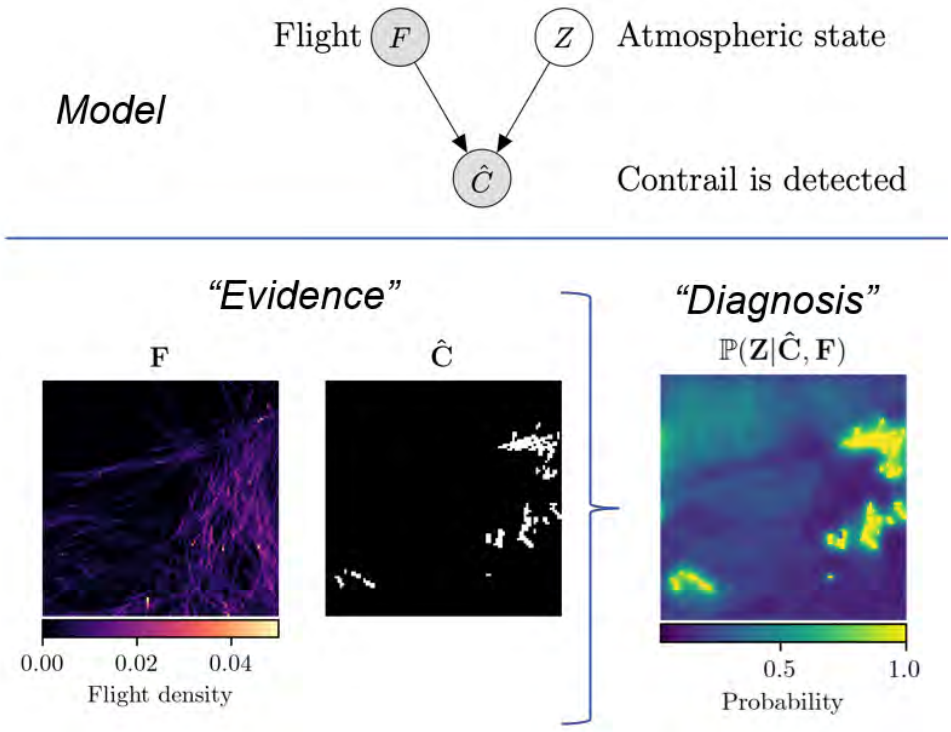

Figure 2.2. Example of applying Bayes' rule to derive the persistent contrail formation area (PCFA) probability by combining contrail detections with flight data. The three plots are maps of the same region, located within the contiguous United States (CONUS). The left plot represents flight density, the middle plot represents the contrail detections (with a threshold), and the right plot represents the estimated probability of a location being a PCFA.

Creation of a collocated contrail dataset

Under a prior grant, we developed an automated collocation procedure consisting of contrails detected and matched on both GOES Advanced Baseline Imager and NASA Cloud-Aerosol Lidar with Orthogonal Polarization (CALIOP) instruments. This procedure was applied to all 2018, 2019, 2020, and 2021 CALIOP overpasses, resulting in a validation dataset of approximately 3,200 contrail cross-sections. This dataset is the foundation of our validation efforts, as it provides a ground-truth dataset of contrail observations including longitude, latitude, altitude, time, width, and depth.

Development of a height estimation algorithm

Using the validation dataset described above, we performed a quantitative evaluation of state-of-the-art height estimation approaches. One such approach has been developed for cirrus clouds (Kox et al., 2012; Strandgren et al., 2017), but we found that it does not perform as well on contrails. We found that the RMSE in estimated contrail altitude was 3.3 km, approximately four-fold larger on the contrail-only dataset than the cirrus data test set. This precludes accurate identification of PCFA altitude, as PCFAs are thought to be on the order of only 500-1,000 m in vertical extent. As a result, we initiated the development of a height estimation algorithm targeted at contrails.

We explored two different machine-learning-based models: random forests and neural networks. We found that by training an algorithm directly on the contrail dataset, we were able to reduce the RMSE by a factor of 4–5 compared with the algorithm trained on the cirrus dataset, yielding the current RMSE of approximately 600 m. Work is ongoing to further reduce this error and to broaden our validation dataset. We are also expanding the contrail height estimation algorithm so that it outputs additional metrics related to the estimation uncertainty. An example from the algorithm's test set is shown in Figure 2.3.

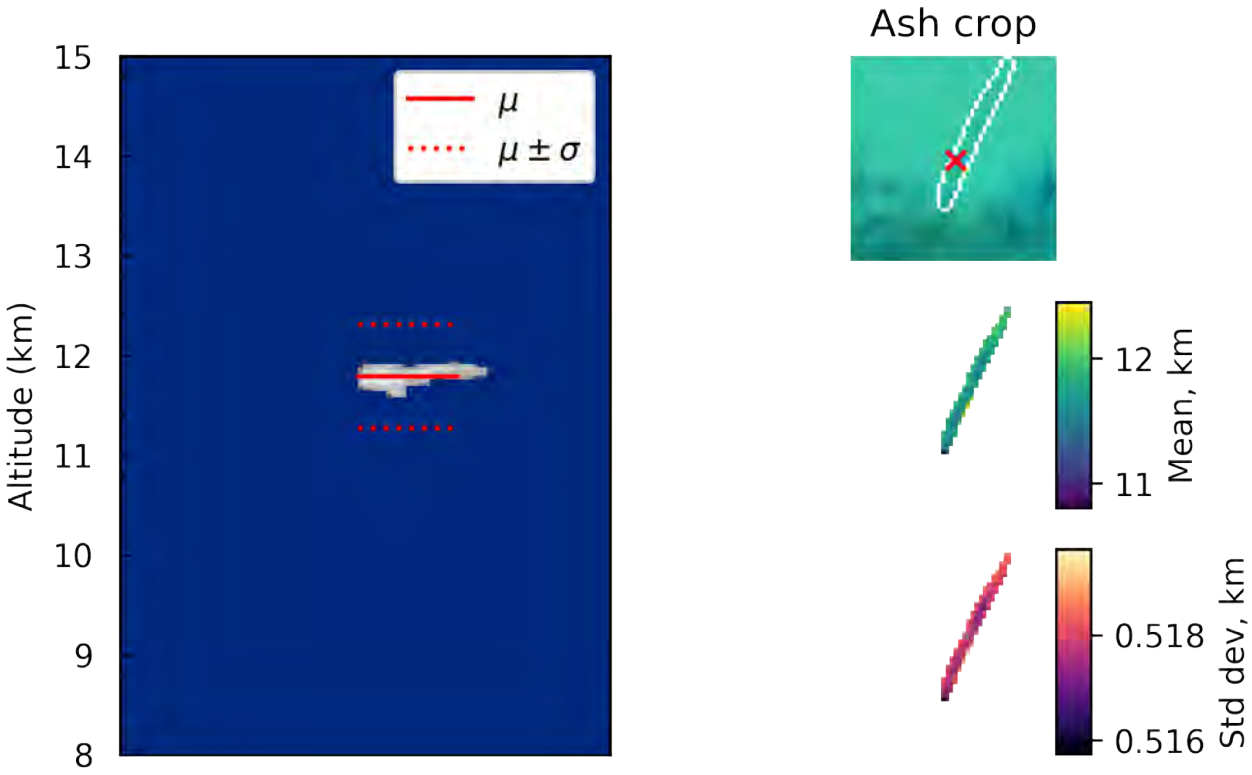

Figure 2.3. Example of contrail height estimation. The plot on the left shows a contrail cross-section observed by the Cloud–Aerosol Lidar with Orthogonal Polarization (CALIOP) instrument. The solid red line represents the mean height of the contrail estimated by the height estimation algorithm. The dashed red lines represent the mean ± one standard deviation. The top right image shows the boundary of the contrail detected on the Geostationary Operational Environmental Satellite (GOES) Advanced Baseline Imager. The "x" represents the GOES pixel that was collocated with the CALIOP data. The lower right figure shows the pixel-wise output of the height estimation algorithm; specifically, the mean height and standard deviation of the contrail are shown.

Integration of temporal data in contrail detections

Contrail detection masks produced by the detection algorithm are computed independently, meaning that a mask at time t+Δt does not use information provided by the detection mask at time t. For a sequence of consecutive GOES-16 images, this approach sometimes leads to temporal inconsistencies, where a contrail can be detected at t, not detected at t+5 min, and detected again at t+10 min. This motivated work under our NASA Atmospheric Composition Modeling and Analysis Program (ACMAP) grant to improve detections, which we are now leveraging, improving, and operationalizing in this work.

To increase the robustness of our contrail detections, in our NASA-funded ACMAP work, we began to implement a Kalman filtering approach to smooth the detection signal. This approach relies on our knowledge of advection, which governs the movement of contrails, and our observations, which correspond to the detection masks produced by the detection algorithm. By combining this information, we seek to construct a contrail detection signal that is more consistent in time than the detections alone.

We selected this approach because it is physics-based and does not require additional training data, as required by a machine learning model. A machine learning model would need to be trained with a large number of sequences of consecutive GOES images in which contrails are manually labeled. Creating a sufficiently large dataset to train such an algorithm would be difficult and very time-consuming. Having temporally robust consistent contrail detections may also enable us to identify new contrails on GOES images, which would facilitate the validation of a contrail avoidance strategy by simplifying the attribution of new contrails to the flights that produced them.

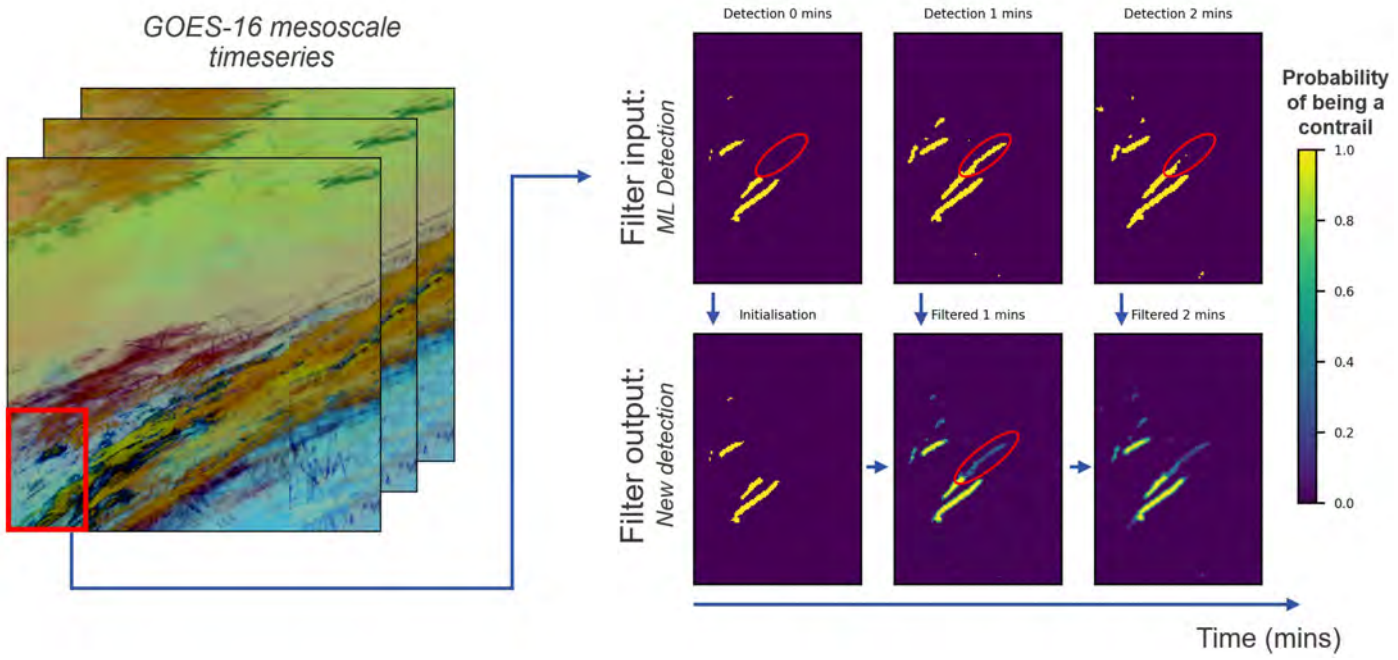

Figure 2.4. Example output of the prototype Kalman filter. Given a time series of Geostationary Operational Environmental Satellite 16 (GOES-16) mesoscale images, we can detect contrails using the machine learning detection algorithm. These contrail detection masks are then used as "observations" to compute filtered detections. Left plot: Sequence of ash transforms of GOES-16 images. Right plot: Diagram of the Kalman filter pipeline with contrail detection masks. Machine learning detections (top row) are used as an input to the filter. At each timestep, the filter computes a prediction of the next state based on the previous filtered output and combines it with the current machine learning detection. This produces a new "filtered detection." The red ovals on the top row highlight a clear false positive detection at T = 1 min. The red oval on the bottom row shows that the filtered product assigns a low probability of those pixels being contrails, effectively smoothing the detection signal. ML: machine learning.

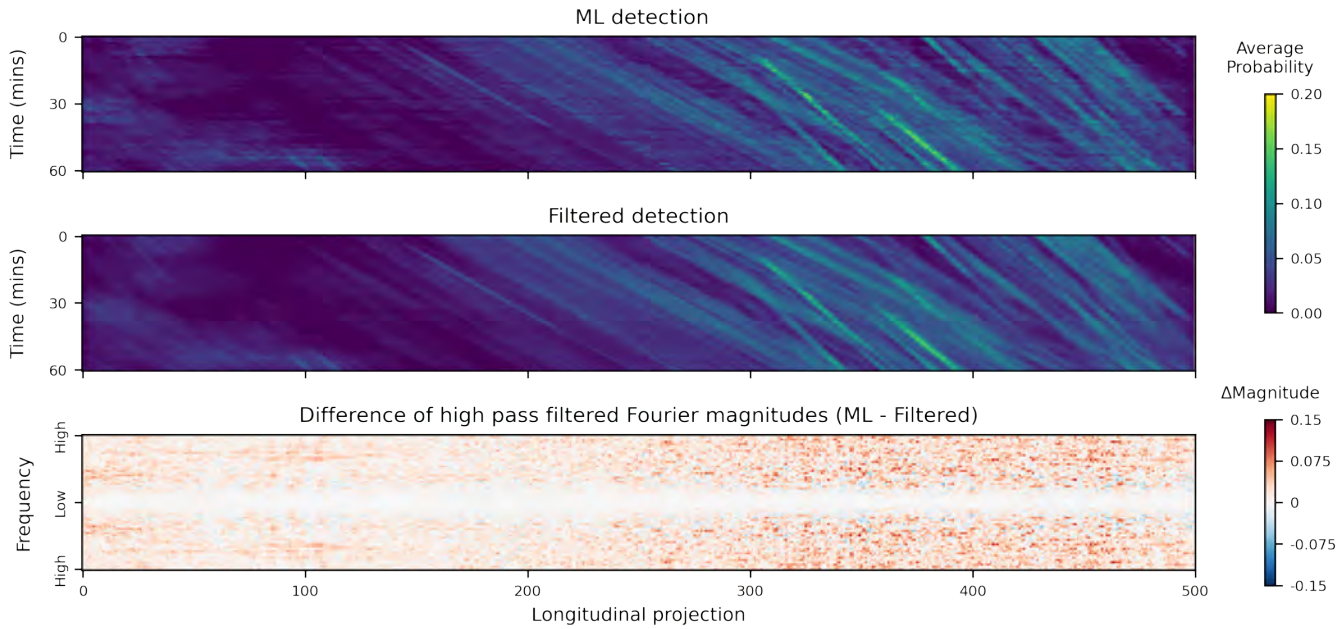

Figure 2.5. Two Hovmöller diagrams of a 60-min series of contrail detections and their Fourier transforms. The detection mask at each timestep is averaged along the vertical axis, and these data are then concatenated to present a time series of the average probability in that direction. We then compute the Fourier transform of each time series for both the machine learning detection and the filtered detections. By taking their difference in magnitude, we find that the machine learning detection time series contain substantially more high-frequency components than their filtered counterpart, showing the smoothing provided by the Kalman filter. ML: machine learning.

The final product of our ACMAP work was a prototype Kalman filter that was capable of smoothing detections, but that had not yet been validated against observations, tuned to improve performance, or leveraged to provide operational benefits. The work under ASCENT 78 aims to address these issues.

Creation of a contrail-labeled GOES mesoscale sequence

To evaluate the performance of the Kalman filtering approach, we started labeling a 2-h-long sequence of GOES mesoscale images. This GOES product provides images every minute and will allow us to compare a ground-truth sequence of contrail labels with those produced by the detection algorithm and Kalman filter.

This labeled sequence will first be used to tune and quantify the performance of the filter. For this step, we are currently exploring methods relying on Lagrangian advection of air parcels and wind data from numerical prediction models. Along the trajectory of an air parcel, the manual labels and filtered detections indicate whether a point is part of a contrail. We then compare the detection series of the filtered output and of the labels for that air parcel. We can tune and quantify the performance of the filter based on the similarity of the two series.

For operational use, if the filtered detection were consistent in time, the tracking of individual contrails would be easier. Tracking contrails over time would allow us to identify when a contrail has formed, which would facilitate matching the contrails to the aircraft that produced them, as it narrows the time window for potential “source” flights. To validate tracking and attribution algorithms, we expect to continue using the labeled sequence of contrails.

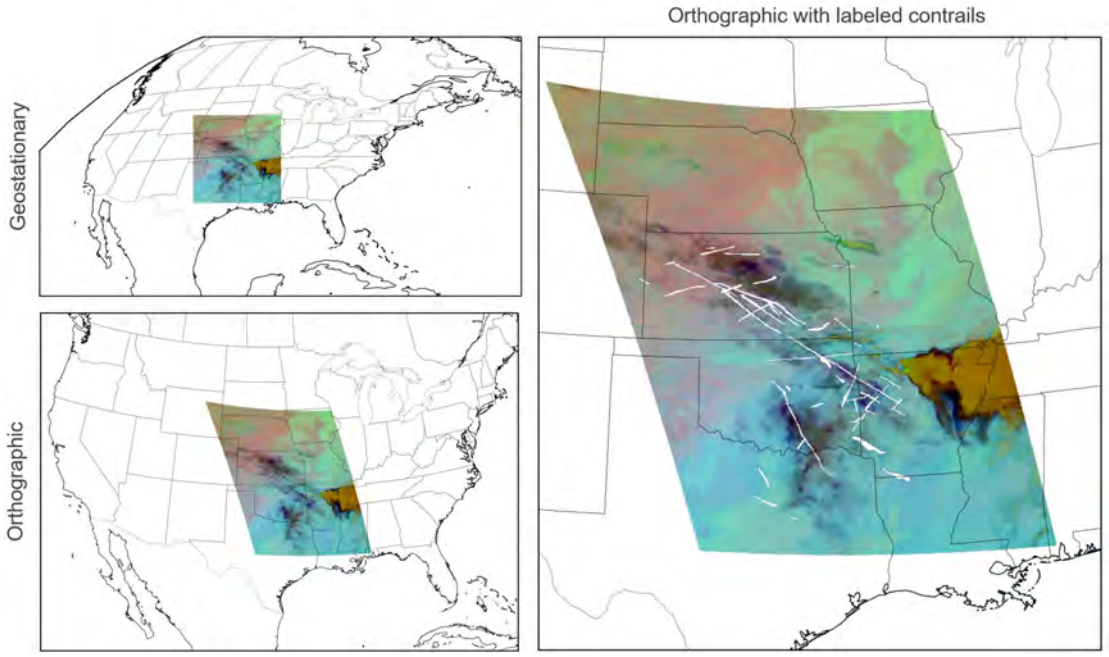

Figure 2.6. Ash transform of a Geostationary Operational Environmental Satellite 16 (GOES-16) mesoscale image on 2022-04-21 at 08:00 UTC. The geostationary image shows what is directly captured by GOES. We reproject the image to an orthographic projection centered on the contiguous United States to manually label the contrails (shown in white on the right plot). The time series is labeled from 08:00 to 10:00 UTC on 2022-04-21. This time series identifies over 100 contrails, which can each be tracked individually on the dataset.

Milestone

Milestone 2: Demonstrate first implementation of a contrail identification module to the FAA [*completed*].

Major Accomplishments

- Developed a KDE approach to extend contrail detections into an estimate of regional contrail formation likelihood
- Developed an approach to combine advected flight track data and contrail observations in order to evaluate the accuracy of contrail-forming region forecasts
- Created a validation dataset for contrail heights by collocating contrails detected by the GOES Advanced Baseline Imager and CALIOP instruments
- Evaluated the accuracy of the current state-of-the-art approach to contrail height estimation
- Began development of an improved height estimation approach including an uncertainty metric
- Developed a preliminary dataset of manually labeled contrails on a *sequence* of GOES images
- Began ground-truth evaluation of our Kalman filtering algorithm to enable more accurate filter tuning

Publications

None.

Outreach Efforts

An oral presentation was given by Vincent Meijer at the 5th International Conference on Transport, Atmosphere and Climate conference in Munich, Germany, hosted by the German Aerospace Center.

Authors: Vincent R. Meijer, Sebastian D. Eastham, Steven R. H. Barrett
Title: Using satellite-based observations of contrails to inform contrail avoidance strategies

One-sentence summary: Comparison of satellite-based observations of contrails with numerical weather prediction data indicates that forecasts of persistent contrails are lacking. Short-term approaches that utilize observational data of contrails are shown to outperform numerical weather prediction models.
Date: June 29, 2022
Publication status: N/A

Awards
None.

Student Involvement
The research for this task was primarily conducted by Vincent Meijer and Louis Robion, graduate research assistants at MIT. The communication of this research to the FAA was primarily conducted by Jad Elmourad, a graduate research assistant at MIT.

Plans for Next Period
- Extend KDE and flight density construction from 2D to 3D.
- Investigate the usage of larger-scale NWP variables to improve the contrail height estimation.
- Complete the development of a filtering method to ensure more accurate contrail detections, including operationalization.
- Finalize and deploy a contrail height estimation technique including an evaluation of accuracy and uncertainty.

References
Kox, S., Bugliaro, L., & Ostler, A. (2014). Retrieval of cirrus cloud optical thickness and top altitude from geostationary remote sensing. *Atmospheric Measurement Techniques*, *7*(10), 3233–3246. https://doi.org/10.5194/amt-7-3233-2014

Strandgren, J., Bugliaro, L., Sehnke, F., & Schröder, L. (2017). Cirrus cloud retrieval with MSG/SEVIRI using artificial neural networks. *Atmospheric Measurement Techniques*, *10*(9), 3547–3573. https://doi.org/10.5194/amt-10-3547-2017

Task 3 - Contrail Radiation Module
Massachusetts Institute of Technology

Objective
The objective of Task 3 is to develop a contrail radiation module. This module will evaluate the warming of individual contrails (both existing and counter-factual) by incorporating information on surface albedo, cloud cover, and other factors. The contrail radiation module enables us to assess the contrail impact of flight trajectories. Eventually, when integrated with the other modules, this module will allow us to extract climate-optimal contrail avoidance strategies.

Research Approach
In this task, we will develop two main capabilities: (a) simulating contrail formation, persistence, and evolution and (b), evaluating the radiative forcing impact of contrails. This module will initially be built on MIT's Aircraft Plume Chemistry, Emissions, and Microphysics Model (APCEMM) (Fritz et al., 2020) and the Contrail Evolution and Radiation Model (Caiazzo et al., 2017) and will incorporate recent advances in contrail radiative modeling (Sanz-Morère et al., 2020; Sanz-Morère et al., 2021). The radiative forcing impact evaluation will be built using Atmospheric Radiation Measurement's Rapid Radiative Transfer Model (RRTM) (Mlawer et al., 1995). Later versions will be calibrated and iteratively improved using measured contrail radiative effects from satellite observations, enabling improved cost–benefit assessments.

Overview
The flow chart in Figure 3.1 gives an overview of the various steps involved in the contrail radiation module, starting from a given trajectory and ending with the contrail climate impact of that trajectory.

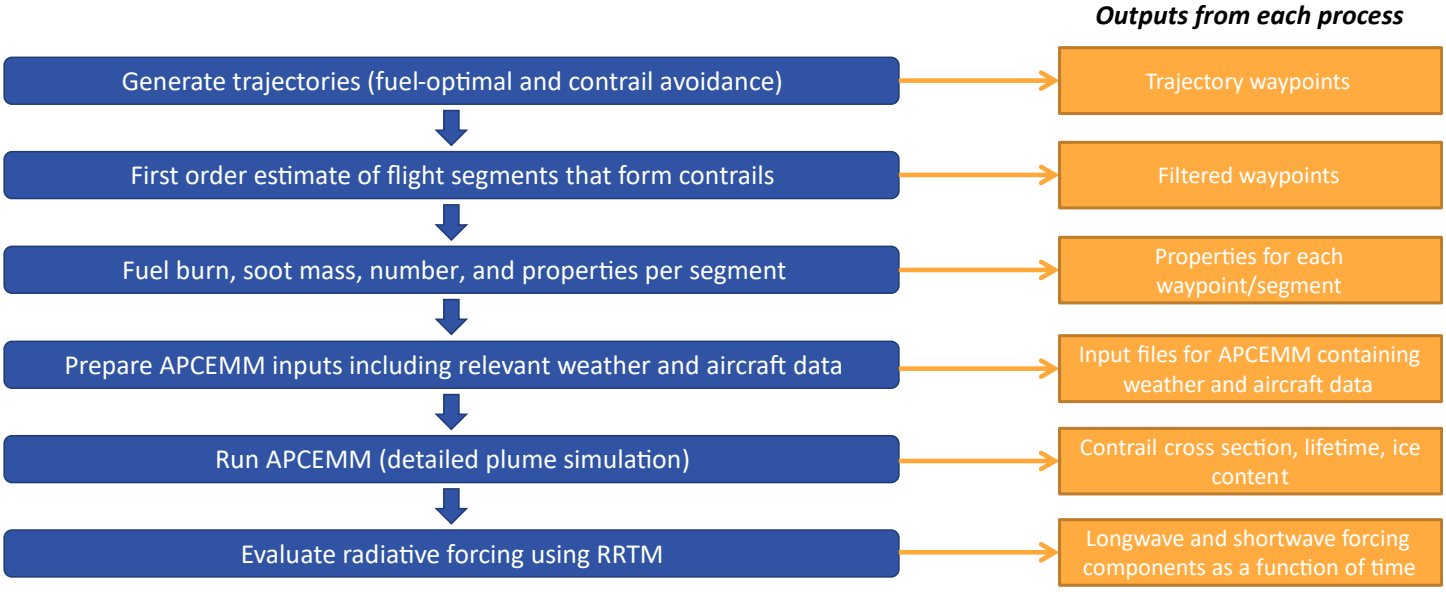

Figure 3.1. Overview of contrail radiation module: steps and outputs. APCEMM: Aircraft Plume Chemistry, Emissions, and Microphysics Model; RRTM: Rapid Radiative Transfer Model.

The contrail radiation module starts with an aircraft trajectory, which can be obtained from the trajectory planning module (see Task 4). This trajectory goes through a first-pass filter that estimates which segments of the flight will form persistent contrails according to the Schmidt–Appleman criterion and ice supersaturation criterion. For those segments, the fuel burn, soot mass, soot number, and other properties are obtained. Subsequently, the input files for APCEMM are prepared, which includes fetching the relevant weather and aircraft data. Then, the contrail plume is simulated by running APCEMM. The simulation outputs a time series of various plume properties, such as ice aerosol volume, particle number, surface area, horizontally and vertically integrated optical depths, etc. These outputs are then used to evaluate the time series' radiative forcing of the contrail using the RRTM.

Develop capabilities to simulate contrail formation, persistence, and evolution
The approach here was to embed APCEMM into a flexible "on-demand" tool to simulate contrails resulting from observed or anticipated flights.

The major modifications made to APCEMM during the implementation were related to the weather data. Because weather data are used across different modules (and tasks), the choice of weather data must be consistent across the modules. ERA5 from the European Centre for Medium-Range Weather Forecasts (ECMWF) was used in all of the other modules (contrail forecasting, contrail identification, and trajectory planning). However, the Modern Era Retrospective for Research and Analysis 2 (MERRA-2) product from NASA's Global Modeling and Assimilation Office was used in the initial implementation of the contrail radiation module. We then switched to ERA5, directly using the same meteorological variables from ECMWF when readily available and inferring those which were not readily available.

Table 3.1. Variables retrieved for use in the Aircraft Plume Chemistry, Emissions, and Microphysics Model (APCEMM) and Rapid Radiative Transfer Model (RRTM).

Variable	Unit	Used in
Eastward wind	m/s	APCEMM
Northward wind	m/s	APCEMM
Pressure	Pa	APCEMM / RRTM
Specific humidity	kg/kg	APCEMM / RRTM
Air temperature	K	APCEMM / RRTM
Geopotential	m^2/s^2	APCEMM / RRTM
Tropopause pressure	Pa	RRTM
Surface albedo for near infrared, diffuse	-	RRTM
Surface albedo for near infrared, direct	-	RRTM
Surface albedo for visible, diffuse	-	RRTM
Surface albedo for visible, direct	-	RRTM
Surface emissivity	-	RRTM
Fraction of cloud cover	-	RRTM
Specific cloud ice water content	kg/kg	RRTM
Specific cloud liquid water content	kg/kg	RRTM
Specific rain water content	kg/kg	RRTM
Specific ice water content	kg/kg	RRTM

Develop capabilities to evaluate the radiative forcing impact of contrails

We implemented a high-speed radiative impact estimation approach based on the results from APCEMM simulations, using the RRTM. We used 16 wavelength bands for the surface emissivity values that are part of the longwave forcing calculation.

Case study: Applying the contrail radiation module

We applied the full contrail radiation module to a set of simulated trajectories in order to verify that the components of the pipeline are well integrated. An example flight with its resulting contrail climate impact is shown in Figure 3.2, and an example of the more detailed outputs of the contrail radiation module are shown in Figure 3.3.

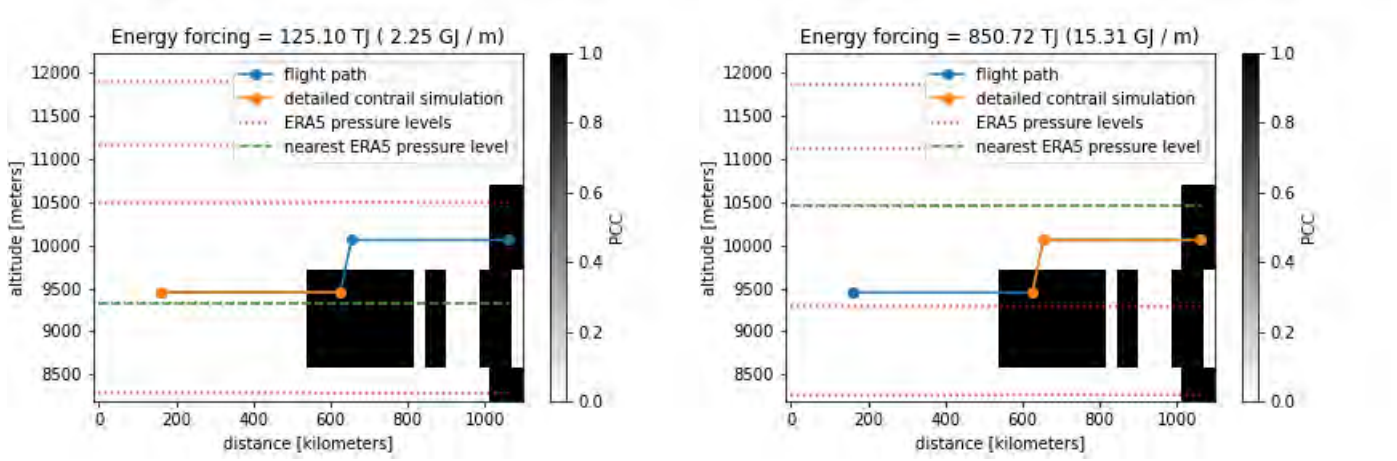

Figure 3.2. Example of applying the contrail radiation module to a flight trajectory. The trajectory is split into two parts (left and right). In each plot, the solid black region represents persistent contrail formation areas (PCFAs) (here, only a binary persistent contrail condition [PCC] map is considered), the blue line represents the flight trajectory, the orange line represents the section of the flight trajectory that is being considered, the dashed red lines represent the ECMWF Renalysis v5 (ERA5) pressure levels at which weather data are provided, and the green dashed line highlights the ERA5 pressure level that is nearest to the flight section under consideration. In the title of each subplot, the contrail energy forcing per contrail length is given as well as the total contrail energy forcing per flight segment.

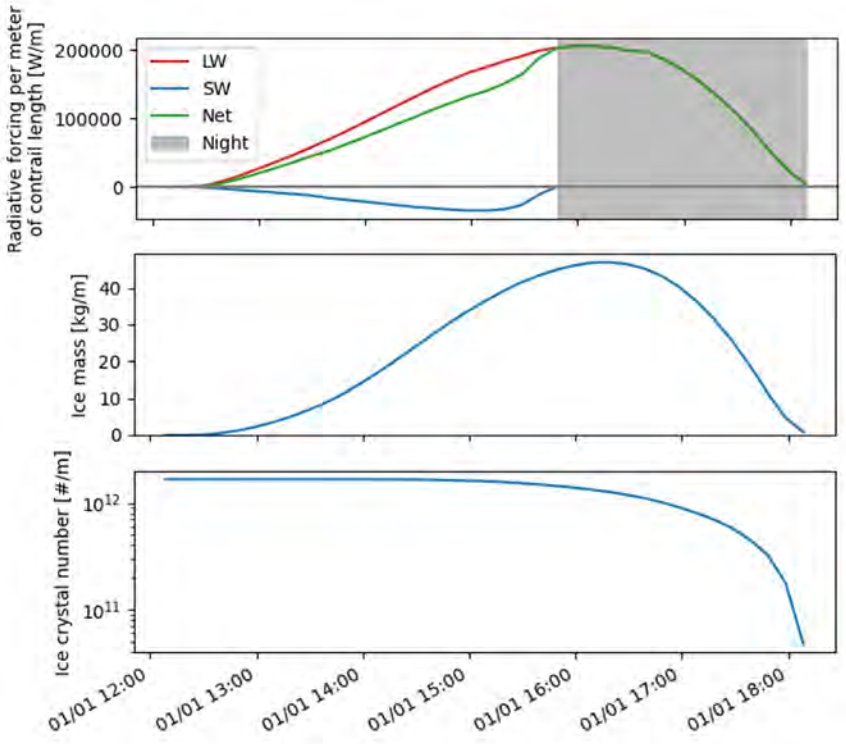

Figure 3.3. Example output from applying the contrail radiation module to one point along a flight trajectory. The top plot shows the radiative forcing impact of the contrail, separated into its warming longwave (LW) and cooling shortwave (SW) components. The x-axis is time. The middle plot shows the evolution of the contrail ice mass, and the bottom plot shows that of the contrail ice crystal number. All values are given per unit contrail distance.

Milestone

Milestone 3: Demonstrate a first implementation of the contrail radiation module to the FAA [*completed*].

Major Accomplishments

- Developed a pipeline to simulate contrail formation and evolution along projected flight tracks using an intermediate-fidelity contrail model (APCEMM)
- Integrated a radiative transfer model to run on the results from the APCEMM simulation
- Modified APCEMM and radiative impact estimation approach to use different meteorological data (ECMWF forecast instead of MERRA-2 reanalysis)
- Applied the entire contrail radiation pipeline (contrail plume simulation and radiative impact estimation) on a set of simulated trajectories output by the trajectory module
- Performed preliminary comparisons of the outputs of the contrail radiation module with other literature studies and models

These accomplishments will enable further development of the contrail radiation module in order to obtain a faster working module based on the heuristic approach described below.

Publications

None.

Outreach Efforts
None.

Awards
None.

Student Involvement
This task was primarily conducted by Jad Elmourad, a graduate research assistant at MIT.

Plans for Next Period
Heuristic approach

Applying the contrail radiation module to a set of trajectories made it clear that there is a large computational cost for running the plume simulation using APCEMM and the radiative forcing calculation using RRTM. In order to align with this project's goal of enabling near-real-time decision-making, we decided to pursue the development of a faster simulation approach that would not largely compromise accuracy. This approach will be based on *heuristics* derived from more detailed calculations, i.e., using the capabilities developed above.

References
Fritz, T. M., Eastham, S. D., Speth, R. L., & Barrett, S. R. H. (2020). The role of plume-scale processes in long-term impacts of aircraft emissions. *Atmospheric Chemistry and Physics*, *20*(9), 5697–5727. https://doi.org/10.5194/acp-20-5697-2020

Caiazzo, F., Agarwal, A., Speth, R. L., & Barrett, S. R. H. (2017). Impact of biofuels on contrail warming. *Environmental Research Letters*, *12*(11), 114013. https://doi.org/10.1088/1748-9326/aa893b

Sanz-Morère, I., Eastham, S. D., Allroggen, F., Speth, R. L., & Barrett, S. R. H. (2020). *Effect of contrail overlap on radiative impact attributable to aviation contrails* [Preprint]. Radiation/Atmospheric Modelling/Troposphere/Physics (physical properties and processes). https://doi.org/10.5194/acp-2020-181

Sanz-Morère, I., Eastham, S. D., Allroggen, F., Speth, R. L., & Barrett, S. R. H. (2021). Impacts of multi-layer overlap on contrail radiative forcing. *Atmospheric Chemistry and Physics*, *21*(3), 1649–1681. https://doi.org/10.5194/acp-21-1649-2021

Mlawer, E.J., Taubman, S.J., Clough, S.A. (1995). *RRTM: a rapid radiative transfer model* (Report No. PL-TR-96-2080, 278). Proceedings of the 18th Annual Conference on Atmospheric Tramission Models.

Task 4 - Trajectory Planning Module
Massachusetts Institute of Technology

Objective
The objective of Task 4 is to develop a trajectory planning module that will forecast fuel burn and emissions as a function of the spectrum of potential flight paths that will be taken. The initial version will consider conventional fuel, CO_2 emissions, and vertical altitude deviations, but each of these categories can be expanded in the future. The module will initially focus on one common aircraft type.

Research Approach
Development of trajectory optimization

As input, the trajectory optimization module will take an origin–destination pair, departure time, weather data, and airplane performance data. The module will then output a set of trajectories based on varying degrees of contrail avoidance. For each route, it will output the fuel burn, distance traveled through contrail-forming regions, and flight time.

ERA5 weather data from ECMWF will be used in the initial development; these data will primarily include temperature, relative humidity, and wind velocity. The former two meteorological variables have been used to determine the regions that form

persistent contrails; however, in the future, this submodule could be replaced with the contrail forecasting module (see Task 1).

MIT's Transport Aircraft System OPTimization (TASOPT) tool (Drela, 2011) was used to determine airplane and engine performance metrics such as fuel flow rates during climb and cruise, climb and descend rates, air–fuel ratios, true airspeed, and exhaust gas temperatures. A single aircraft type was used, with its performance metrics calculated for different operating conditions. The operating conditions were specified by the altitude and aircraft gross weight.

The optimization followed a graph-based approach in which a uniform-cost search algorithm was implemented. The airspace at cruise between the origin–destination airports was mapped onto a 2D grid. One dimension was the altitude, and the other dimension was the distance traveled along the lateral track. In this initial development phase, the lateral track of the aircraft was fixed to the great circle route; however, future implementations could expand this approach to allow for horizontal deviations.

The initial formulation of the cost function was a weighted sum of fuel burn and contrail length, as shown below.

$$J = C \times \theta + \mathrm{F} \times (1 - \theta)$$

where J is the cost function, C is the contrail length, F is the fuel burn, and θ is the tradeoff parameter that determines the degree of contrail avoidance.

$\theta = 0$: gives the baseline case, in which the flight is optimized for fuel burn
$\theta = 1$: gives the maximum contrail avoidance case

The parameter θ can be varied between 0 and 1 in order to simulate different degrees of contrail avoidance.

Application
We applied the trajectory planning module to a large set of global flights in order to assess the fuel burn penalty associated with contrail avoidance (targeted at contrail length minimization). We sampled 100,000 random flights from the 2019 flight schedule operated by a narrow-body aircraft fleet. The aircraft performance model was based on a single-aisle aircraft approximating the Boeing 737 MAX 9.

The results are shown in Figure 4.1. We found that 98% of contrail length can be avoided by exclusively using vertical re-routing. Furthermore, contrail avoidance costs an additional 0.3% in fuel on average, when considered from a fleet-wide perspective, and 1% in fuel if only the contrail-forming flights are considered.

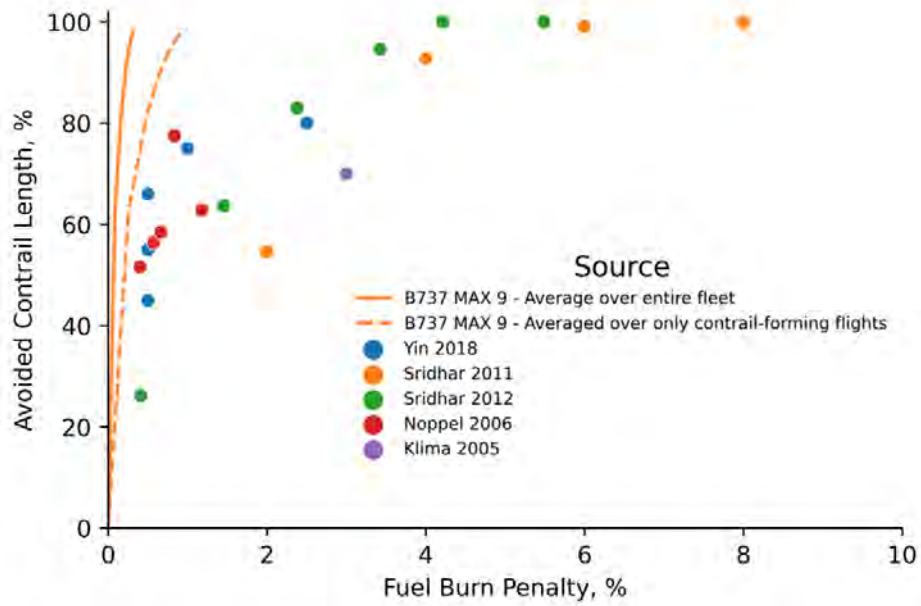

Figure 4.1. Tradeoff between avoided contrail length and fuel burn penalty for a Boeing 737 MAX 9 for a full year of global operations. The results are presented for two cases: for the entire fleet (solid line) and for only contrail-forming flights (dashed line). Results from other studies are included for comparison, even though the studies differ in their approach (type of deviation, fuel model, weather data, region, routes, and scale).

Furthermore, we studied the impact of constraining the maximum fuel penalty per flight. We found that limiting the maximum fuel penalty per flight to 5% did not significantly affect the amount of contrail reduction obtained. Imposing this limit reduced the avoided contrail length by 0.9% and the fleet-wide fuel burn penalty by <0.1%. However, this step ensures that no single flight is encouraged to make large deviations, reducing the possibility of a large inadvertent penalty. This is particularly important given the level of uncertainty in PCFA predictions.

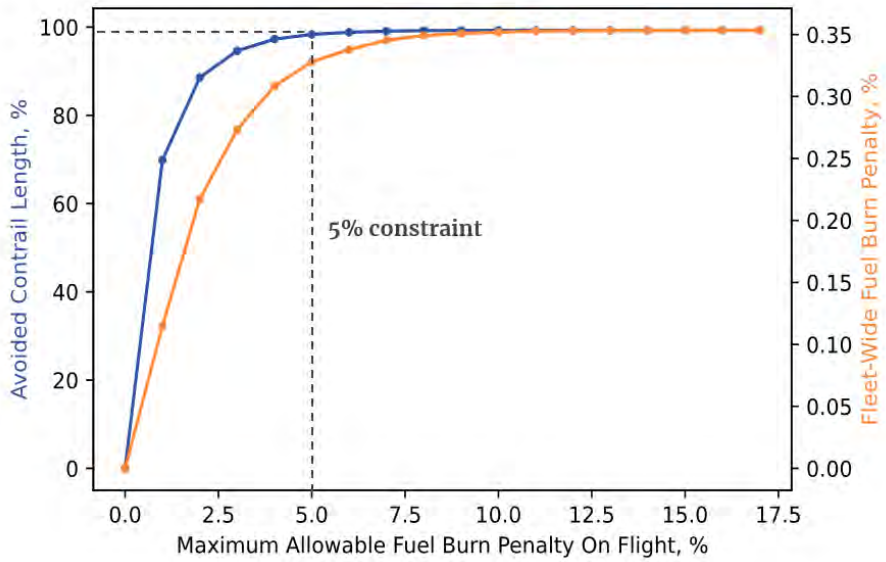

Figure 4.2. Impact of constraining the maximum fuel penalty per flight. The x-axis shows the fuel penalty constraint that was applied. The left axis and blue line show the percentage of contrail length avoided. The right axis and orange line show the fleet-wide fuel burn penalty.

At this stage, the trajectory planning module is focused on contrail length minimization. However, we intend to integrate this module with the contrail radiation module to develop the capability for trajectory optimization focused on climate impact (contrail and CO_2 energy forcing). For this purpose, we will combine both the current trajectory planning and contrail radiation modules in an optimization loop with multiple hierarchical levels. The trajectory planning component will generate trajectories and determine the order for exploring possible trajectories according to the best-known contrail impacts at the time. These trajectories will then be passed to the contrail radiation component, which will refine the estimates of the contrail impacts and send them back to the trajectory planning component. This procedure will loop until certain convergence criteria are reached.

Milestone

Milestone 4: Demonstrate the first implementation of a trajectory optimization module to the FAA [*completed*].

Major Accomplishments

- Developed a trajectory model to simulate flights with differing degrees of contrail avoidance
- Performed preliminary estimates of the fuel burn penalty associated with limited vertical deviations using weather data

Publications

None.

Outreach Efforts

A poster presentation on ASCENT 78 was delivered to the 5th International Conference on Transport, Atmosphere and Climate conference in Munich, Germany, hosted by the German Aerospace Center.

Authors: Jad Elmourad, Sebastian D. Eastham, Raymond L. Speth, Florian Allroggen, Steven R. H. Barrett
Title: Flight Level Optimization for Contrail Avoidance
One-sentence summary: Preliminary results regarding the contrail–CO_2 tradeoffs associated with contrail avoidance.
Date: June 27–30, 2022
Publication status: N/A (poster presentation)

FAA support was acknowledged.

Awards

None.

Student Involvement

This task was primarily conducted by Jad Elmourad, a graduate research assistant at MIT.

Plans for Next Period

- Integrate the contrail forecasting module after it is completed to replace the current calculation of PCCs.
- Extend the module to incorporate lateral deviations.
- Integrate this module with the contrail radiation module in order to directly optimize for climate impact.

References

Drela, M. (2011). *Development of the D8 Transport Configuration*. 29th AIAA Applied Aerodynamics Conference. Honolulu, HI.

Greitzer, E. M., Bonnefoy, P., De la Rosa Blanco, E., Dorbian, C., Drela, M., Hall, D., Hansman, R., Hileman, J., Liebeck, R., Lovegren, J., Mody, P., Pertuze, J., Sato, S., & Spokovsky, Z., Tan, C. (2010). *N + 3 Aircraft Concept Designs and Trade Studies, Final Report Volume 1* (Report No. 2010-216794/VOL1). NASA Technical Reports 2, 216794.

Project 079 Novel Noise Liner Development Enabled by Advanced Manufacturing

The Pennsylvania State University

Project Lead Investigator

Timothy W. Simpson
Paul Morrow Professor of Engineering Design & Manufacturing
Department of Mechanical Engineering
The Pennsylvania State University
University Park, PA 16803
814-863-7136
tws8@psu.edu

University Participants

The Pennsylvania State University

- P.I.: Timothy W. Simpson, Paul Morrow Professor of Engineering Design & Manufacturing
- FAA Award Number: 13-C-AJFE-PSU-079
- Period of Performance: October 1, 2021 to September 30, 2022 (no cost extension to December 31, 2022)
- Tasks:
    1. Preliminary design and acoustic analysis of novel liners for testing
    2. Detailed design and additive fabrication of novel liner solutions
    3. Acoustic evaluation of additively manufactured novel liners

Project Funding Level

$300,000 from FAA; $300,000 match from The Pennsylvania State University ($100,000) and Raytheon Technologies Research Center ($200,000)

Investigation Team

The Pennsylvania State University (PSU):

- Tim Simpson, P.I., responsible for project management, task coordination, and student advising
- Allison Beese, co-P.I., responsible for supporting Task 1 and student advising
- Eric Greenwood, co-P.I., responsible for supporting Task 3 and student advising
- Jay D. Martin, co-P.I., responsible for supporting Task 2 and student co-advising
- Andy Swanson, graduate student (MS), responsible for work on Tasks 1–3
- Michael Geuy, graduate student (PhD), responsible for work on Tasks 1–3

Raytheon Technologies Research Center (RTRC):

- Jeff Mendoza, P.I., responsible for project coordination and management at RTRC
- Julian Winkler, co-P.I., responsible for acoustic analysis and evaluation as part of Tasks 1–3
- Aaron Reimann, co-P.I., responsible for acoustic analysis and evaluation as part of Tasks 1–3
- Kenji Homma, co-P.I., responsible for acoustic analysis and evaluation as part of Tasks 1–3
- Paul Braunwart, co-P.I., responsible for acoustic analysis and evaluation as part of Tasks 1–3

Project Overview

PSU and its Applied Research Laboratory in collaboration with its industrial partner, RTRC, and government collaborator, NASA Langley Research Center (LaRC), are helping the FAA develop and advance innovative engine acoustic liner technology to meet the demands of low noise for future aircraft. The team is developing and demonstrating a methodology to design

and manufacture novel lattice structures that enhance noise attenuation in aircraft engines. Analysis and experimental testing are applied to understand the effect of geometry and feature size of the lattices to control noise while ensuring the manufacturability of these complex structures in different materials. Advanced manufacturing technologies are used to enable rapid design–build–test cycles for design development, including assessments of structural integrity and acoustic performance. Promising engine liner designs and their performance will be documented and archived for the FAA to aid future advancements in aircraft engine noise reduction.

The overall project approach includes the following steps:

1. Establish a set of acoustic requirements for future aircraft engine designs.
2. Design and analyze lattice-based acoustic liners using advanced software tools.
3. Perform rapid, iterative prototyping and testing to identify promising designs and materials.
4. Conduct detailed assessments of manufacturability.
5. Perform acoustic and structural evaluations of novel liners in collaboration with NASA LaRC.
6. Document results and archive data for the FAA.

This project will be accomplished through the three tasks described below.

Task 1 - Preliminary Design and Acoustic Analysis of Novel Liners

PSU and RTRC contributed to this task.

Objective

The goal of Task 1 is to develop and demonstrate a methodology for rapid design, analysis, fabrication, and testing of novel structures that can enhance noise attenuation in aircraft engines.

Research Approach

Design framework

The team prototyped a digital workflow to design, analyze, fabricate, and test acoustic liner geometries in Year 1 by using the different additive manufacturing (AM) capabilities available at PSU's Center for Innovative Materials Processing through Direct Digital Deposition and leveraging the liner acoustic performance prediction capabilities developed at RTRC. The rapid acoustic liner development methodology is illustrated in Figure 1, color-coded based on who is primarily responsible for each aspect of the framework. As indicated, the PSU and RTRC teams are working together to generate solid models of acoustic liners, which are then exported for analysis and manufacturing. PSU (in blue) selects a suitable AM process and material, plans and fabricates the liner, and then post-processes the liner prior to inspection. In parallel, RTRC (in salmon) performs simulations at varying levels of fidelity based on the level of analysis desired. Reduced-order models give rapid, but less accurate results, while finite element (FE) methods and the lattice Boltzmann method (LBM) provide increased accuracy at higher computational cost. Metrics of interest are predicted and then compared with appropriate test results from normal impedance tube (NIT) testing (at PSU, RTRC, and NASA LaRC) and grazing flow impedance tube (GFIT) testing (at RTRC and NASA LaRC). Results are then collected, stored, and reviewed by all to identify the next design iteration.

The multi-fidelity approach developed and used at RTRC to expedite acoustic analysis is shown in Figure 2. This approach consists of a mix of mid- and high-fidelity approaches to predict advanced liner acoustic performance on a component basis (i.e., single liner sub-element) or within a system (such as a duct or engine nacelle). The primary design path that was used for Task 1 is highlighted in Figure 2 (a dashed black line encircles the design path) and consists of a two-step approach. In the first step, FE simulations of novel liner topologies are performed to predict the acoustic impedance, using a virtual NIT. In the second step, the acoustic impedance is used as a boundary condition in a virtual representation of the NASA GFIT facility for a 16-inch-long liner section. The NASA GFIT facility geometry was selected, as this experimental facility will be used to validate acoustic liner performance in the presence of a grazing flow and sound source. Note that any duct geometry with known source and flow conditions can be utilized within this workflow. The insertion loss (sound power reduction due to the liner) is determined from this simulation as the primary metric to assess liner performance and to down-select concepts for testing at NASA, to be performed in Task 3. This design path was used in Task 2 for refined analysis of advanced liner concepts and concept screening. In Task 1, and as further described below, initial screening of novel acoustic liner concepts was performed by using the high-fidelity LBM-based NIT simulation setup shown in Figure 2. This approach has the advantage that it does not rely on any liner acoustic models, but instead, the exact liner geometry is considered in the analysis and the acoustic performance is determined by using the equivalence of simulating the full Navier–Stokes fluid flow equations. This

approach allows us to study the effect of small geometry details on acoustic losses and is suitable for studying novel structures for which the acoustic performance is unknown and for which the acoustic loss mechanisms must be accurately predicted. This approach is more computationally intensive and is therefore not well-suited for design studies, but is more appropriate for exploratory studies. Hence, this approach is used in Task 1, followed by the design approach outlined above for Task 2.

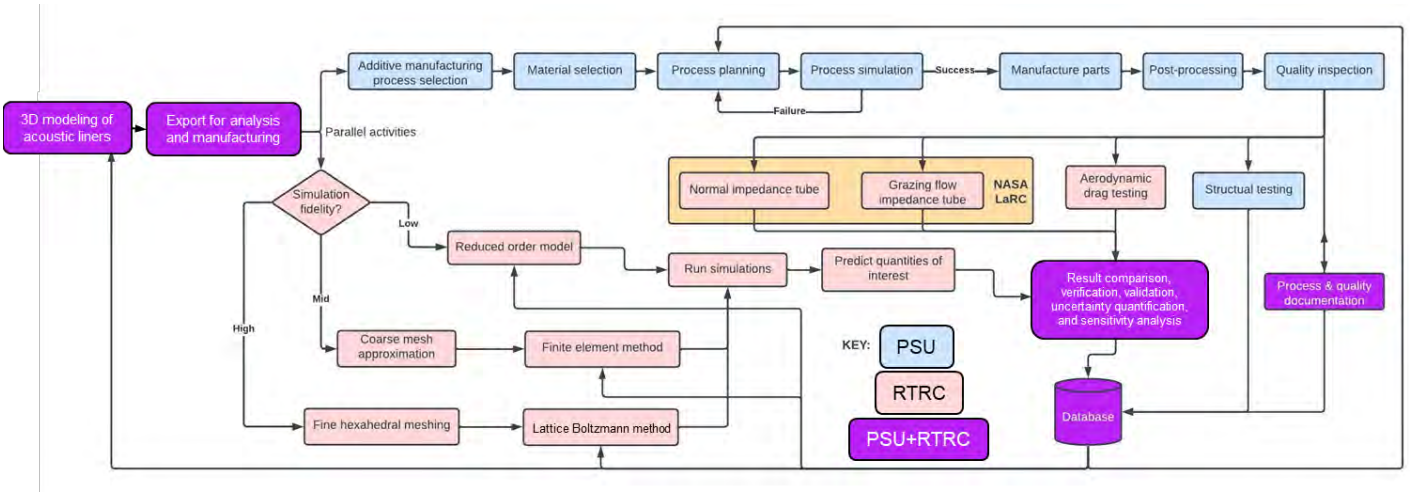

Figure 1. Rapid acoustic liner development methodology. LaRC: Langley Research Center; PSU: The Pennsylvania State University; RTRC: Raytheon Technologies Research Center.

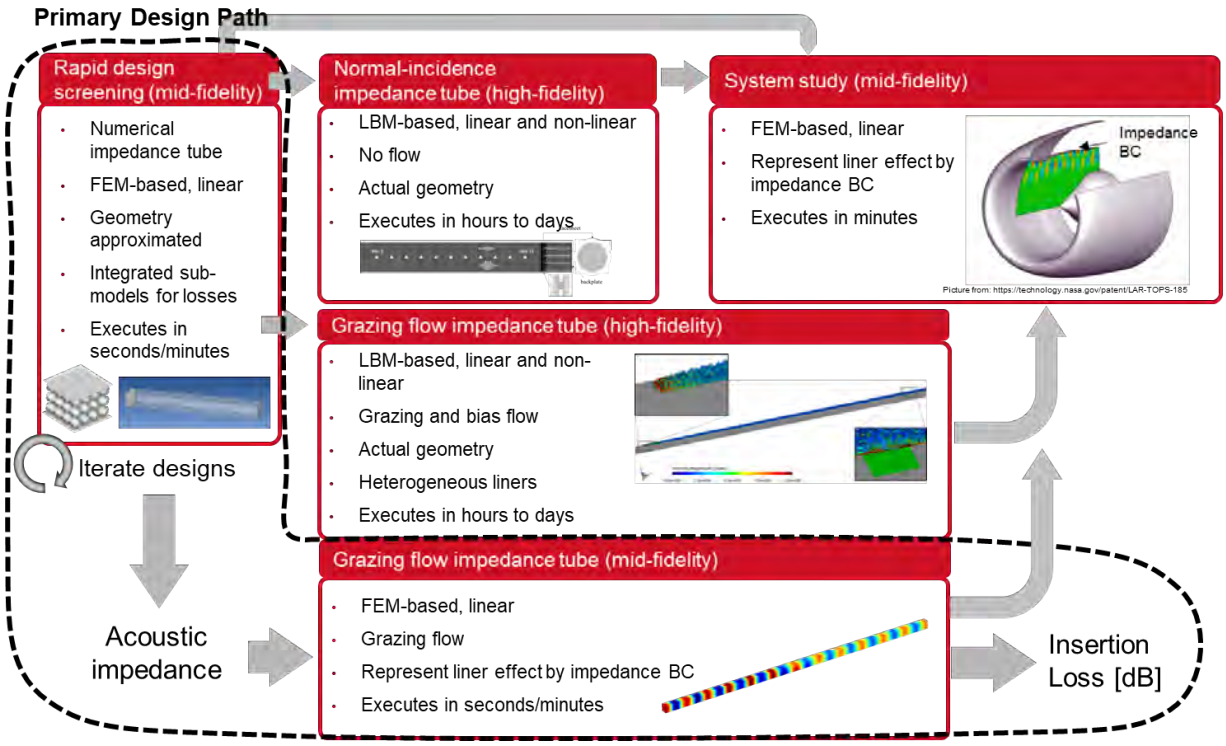

Figure 2. Multi-fidelity modeling and analysis capabilities used for complex acoustic liner design screening. BC: boundary condition; FEM: finite element method; LBM: lattice Boltzmann method.

Reference liner definition and experiments

To validate current prediction models and to establish a baseline for manufacturing and RTRC/PSU test-facility cross-comparisons, a set of single-degree-of-freedom (SDOF) liners was chosen from the literature (Howerton, 2017). The design and performance details of those liners were provided by NASA LaRC. PSU fabricated round and square samples of the AE01 liner, as shown in Figure 3. These test specimens were produced using a Formlabs Form3L SLA resin printer in Grey Pro resin with a layer height of 50 μm and a zero inclination angle, arranged so as to avoid the laser seamline, which causes degradation of small geometries. The specimens were then cleaned per the manufacturer's instructions but were not subject to any additional post-processing. These samples were then tested in the NITs at RTRC and PSU. Additional details on the equipment and methods used during NIT testing can be found in the description of Task 3.

(a) RTRC NIT sample 1 (D = 100 mm)

(b) RTRC NIT sample 2 (D = 29 mm)

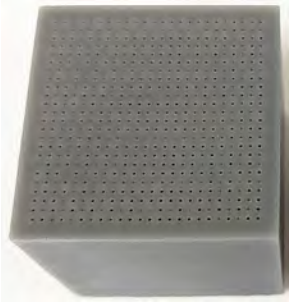

(c) PSU and LaRC NIT sample (L = 50.8 mm)

Figure 3. Initial 3D-printed polymer samples for normal impedance tube (NIT) testing at The Pennsylvania State University (PSU) and Raytheon Technologies Research Center (RTRC). LaRC: Langley Research Center.

Table 1. Corresponding dimensions of initial 3D-printed test samples.

Sample Type	Facesheet Thickness	Facesheet Hole Diameter	Percent Open Area	Liner Core Depth	Outside Core Wall Thickness
LxL square	0.762 mm	0.762 mm	10.18%	51.9 mm	2.5 mm
D=29 mm	0.762 mm	0.762 mm	10.08%	51.9 mm	2.5 mm
D=100 mm	0.762 mm	0.762 mm	10.02%	51.9 mm	2.5 mm

RTRC performed predictions of the liner sample using the high-fidelity LBM simulation approach discussed above and compared those predictions with impedance tube test data. Two different types of simulations were performed: simulations with the as-designed liner and simulations with the as-printed liner. The as-printed geometry was obtained from an x-ray computed tomography (CT) scan via geometry recreation. The as-printed liner was found to deviate slightly from the as-designed liner, as shown in Figure 4. The orifice shapes were rounded compared with the sharp-edged design, and the effective hole diameter and facesheet thickness deviated as well, due to underexposure of the material and shrinkage during post-processing. These differences had a noticeable impact on the acoustic performance, as shown in Figure 4, where the as-designed predictions deviate from the test data. The test data in this figure were obtained from the 29-mm-diameter RTRC NIT.

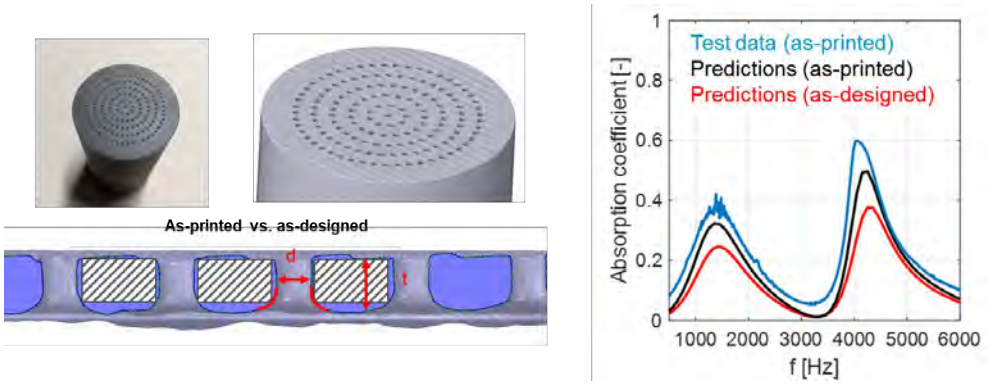

Figure 4. Difference between as-designed and as-printed liner geometry and resulting acoustic performance.

Repeating the simulations with the as-printed geometry 5howed a much closer agreement with the test data, largely closing the "modeling gap." Thus, whereas the as-printed designs deviate from the as-designed liner, it is possible to account for such deviations in the design and manufacturing processes once a quantitative relationship has been established. In addition, this comparison demonstrates how the high-fidelity LBM simulation tool can capture these effects and can ultimately be used to improve the mid-fidelity design tools. The overall agreement between predictions and test data was found to be satisfactory, thus providing the confidence needed to move to the next step of studying more advanced liner concepts with novel backing structures using the high-fidelity LBM approach.

Based on the deviations and defects observed in the first set of AE01 liner samples, adjustments were made to the process settings and materials to minimize future issues. To validate the new manufacturing approach, another set of AE01 liner samples was manufactured and inspected by optical profilometry (OP), which is a rapid, nondestructive, noncontact surface measurement technique (see Figure 5). The primary data outputs of OP include dimensions, surface roughness, and high-resolution images. If needed, these data can be leveraged for additional process improvement or for calculating design correction values.

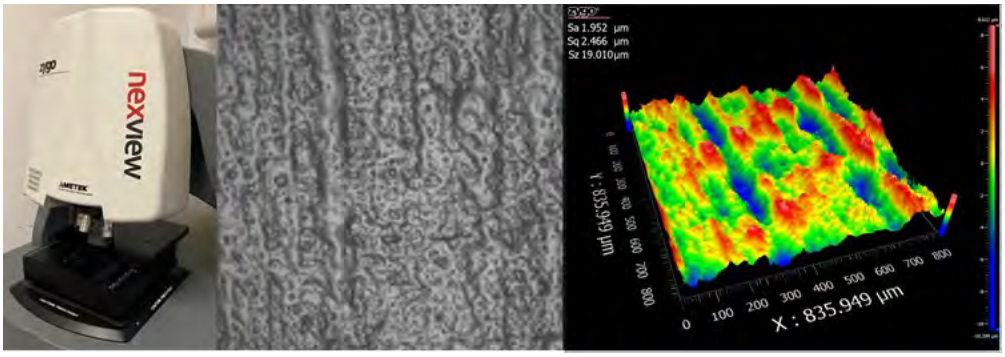

Figure 5. AE01 images and surface roughness measurements acquired with the Zygo Nexview optical profilometry instrument.

To determine whether the new process settings addressed the issue of facesheet hole shrinkage, high-resolution OP images were analyzed with ImageJ, an open-source image-processing software from the National Institutes of Health. Using the particle analysis module, an average hole diameter deviation was determined for each facesheet hole using a co-centric ellipse-fitting approach. Most deviation values fell within the expected tolerance of ±30 µm. The resulting distribution is shown in Figure 6. Significant outliers were typically a result of misalignment between the facesheet holes and the honeycomb core underneath. Ultimately, we determined that it was acceptable to proceed with this manufacturing configuration without using design correction values.

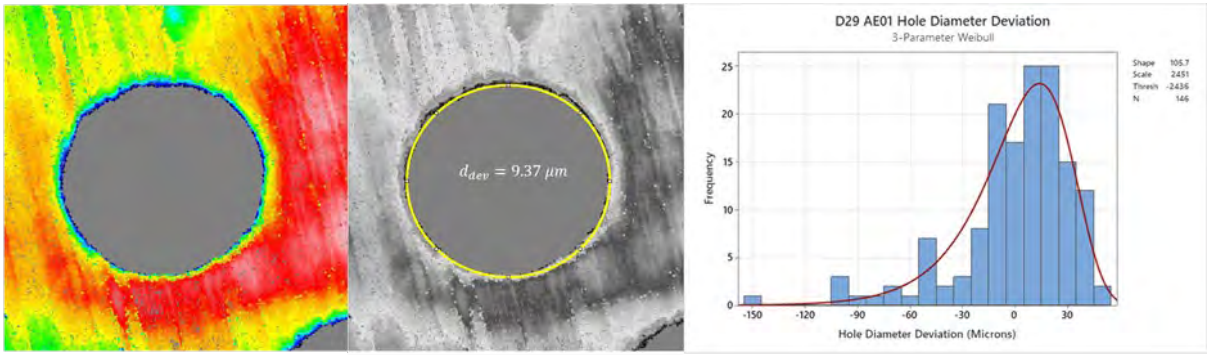

Figure 6. Distribution of facesheet hole diameter deviation.

Evaluation of novel liner backing structures

Triply periodic minimal surfaces (TPMSs) are mathematically well-defined periodic non-self-intersecting surfaces that partition the available volume into two intertwined congruent labyrinth structures. The surfaces represent highly flexible, adaptable, and versatile building blocks for generating more complex structures for material design. Because of the well-defined mathematical nature of these surfaces, one has extensive control over the structures that can be built by manipulating the equations and combining different surfaces. A selection of candidate TPMSs was considered in Task 1, and their potential as novel acoustic liner backing structures was evaluated. MATLAB and the computer-aided design (CAD) software package nTopology were used for geometry generation. The TPMS-based lattice structures shown in Figure 7 were screened for acoustic performance in the absence of grazing flow. The normal incidence acoustic absorption was determined for the structures themselves and in combination with a facesheet.

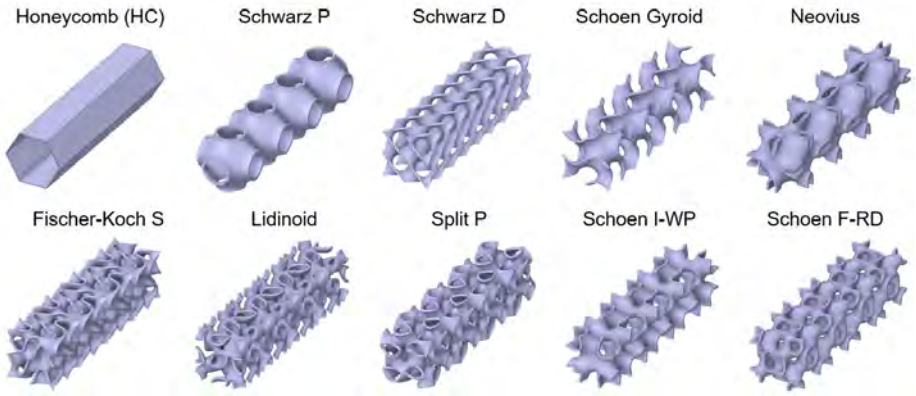

Figure 7. Selected triply periodic minimal surfaces used for performance studies of novel acoustic liners.

In practice, all liners will most likely need a facesheet; otherwise, the drag from flow over the liner would become prohibitvely large. The facesheet also adds further design parameters for tuning the liner acoustic performance, including the facesheet thickness, hole size and distribution (and alignment with the underlying core structure), and total percent open area (POA). The AE01 reference liner facesheet was chosen in conjuction with the TPMS cores. Figure 8 shows simulation results for four of the nine studied surfaces.

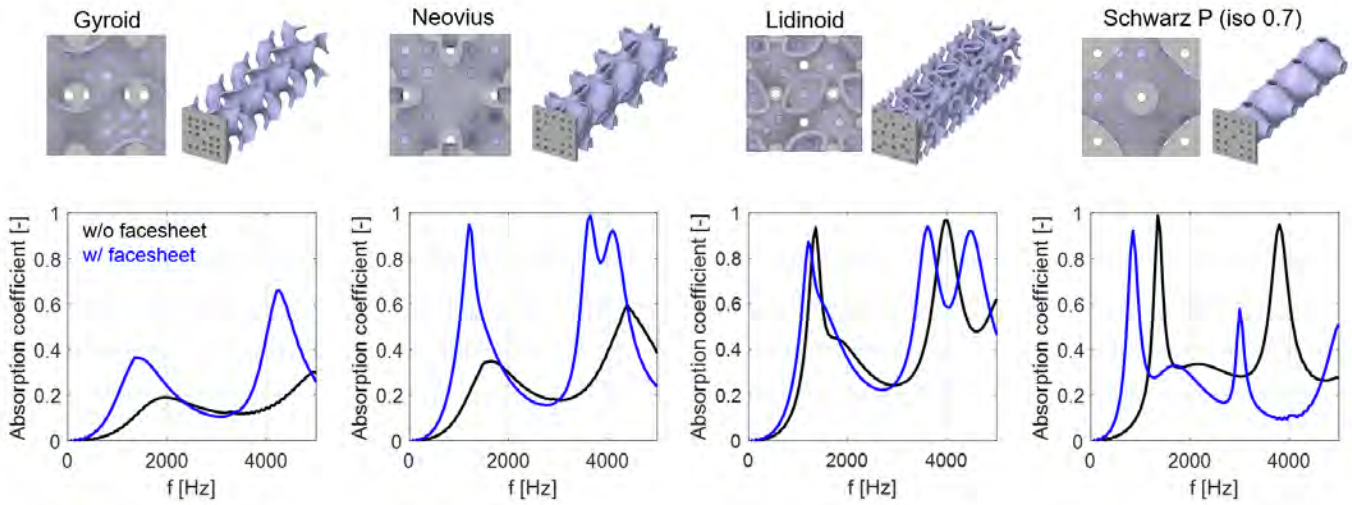

Figure 8. Predicted acoustic performance of advanced liner cores with and without the AE01reference liner facesheet.

As expected, the facesheet can have a pronounced impact on acoustic performance and must therefore be included in the analysis. However, even without a facesheet, all of the TPMS cores show pronounced acoustic absorption behavior in two separate frequency regions. These regions are related to the two different parallel paths of the acoustic wave as it passess through each TPMS: in all TPMS structures considered, the available volume is partitioned into two seperate regions. Some TPMS geometries inherently show a stronger response than others. For example, the Gyroid structure without a facesheet has a rather broadband response and low acoustic absorption, whereas the Lidinoid or Schwarz P surfaces have very pronounced and sharp peaks with high acoustic absorption, even in the absense of a facesheet. This trend is related to the underlying geometry, which consists of regions of large volume connected to neighboring regions through narrow constrictions. The Schwarz P structure is the simplest, with large volumes connected to its neighbors through narrow necks along all Cartesian directions, whereas the lidinoid structure has smaller volumes connected to each other through off-axis narrow constrictions. From a fluid mechanics perspective, these surfaces act as coupled Helmholtz resonators. Therefore, through geometry design changes, it should be possible to tune the resonance frequencies so that a desired acoustic absorption behavior (peak absorption and target frequency range) can be obtained.

To further illustrate the acoustic design choices, Figure 9 compares the acoustic performance of the Lidinoid, Neovius, and Schwarz P surfaces with a perforated facesheet. Although the underlying geometry is very different in all three cases and the internal acoustic response appears different (as shown in the contour plots), the overall acoustic performance in terms of absorption behavior is very similar for all three surfaces. This finding illustrates that different TPMS-based liners can be used to achieve the same acoustic performance. While, in principle, it is possible to proceed with designs of all of the TPMS-based liner candidates, it appears that the Schwarz P structure is geometrically the simplest of all of the surfaces while having sufficient degrees of freedom for design tuning through bulb volume and neck length and size. However, the other surfaces offer similar abilities for design tuning. Additional information is needed to down-select a suitable TPMS candidate for the advanced liner design to be performed under Task 2. For this purpose, additional requirements must be considered, related to the weight of the acoustic liner.

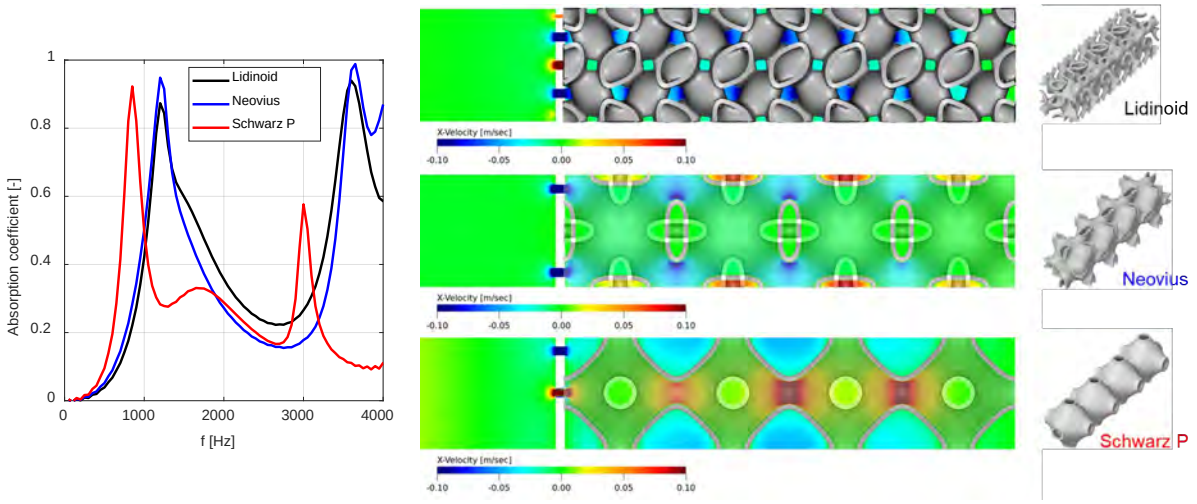

Figure 9. Predicted normal incidence acoustic absorption for advanced liners with selected triply periodic minimal surface cores.

In addition to assessing the acoustic performance of TPMS-based liners, the team performed a weight impact study, in which the surface area per unit volume was computed for each TPMS under consideration (a selection of TPMS candidates is shown in Figure 7) and compared with that of a standard honeycomb core. The goal was to obtain an advanced liner that performs better than a SDOF liner with a honeycomb core, with a reduced footprint and comparable or reduced weight. The results for a few select TPMS structures are shown in Figure 10.

The contour maps in Figure 10 show ratios of wall thickness (with respect to the honeycomb) on the horizontal axis and ratios of liner volume on the vertical axis. The contours show the weight impact relative to a honeycomb core. Contour regions in blue indicate a weight reduction compared with a standard honeycomb liner, and contours in red show a weight increase. The yellow circle shows the reference location for a liner with equal wall thickness and liner volume (depth) compared with a SDOF honeycomb core liner. For both Schwarz P and Neovius surfaces, the respective contour plots show a potential weight reduction, while the liner with a Lidinoid core would result in a weight increase. Similar maps were created for other TPMSs.

Based on these results, it was found that the Schwarz P surface provides the best surface candidate for novel liner cores, as it has the lowest surface area of all surfaces studied. In combination with its acoustic performance, the Schwarz P surface was identified as the leading candidate, as it has the lowest surface area of all TPMSs, while providing sufficient degrees of freedom to tune the structure for acoustic performance, as noted previously. Thus, we decided to proceed with Schwarz-P-based liner designs for refined analysis under Task 2.

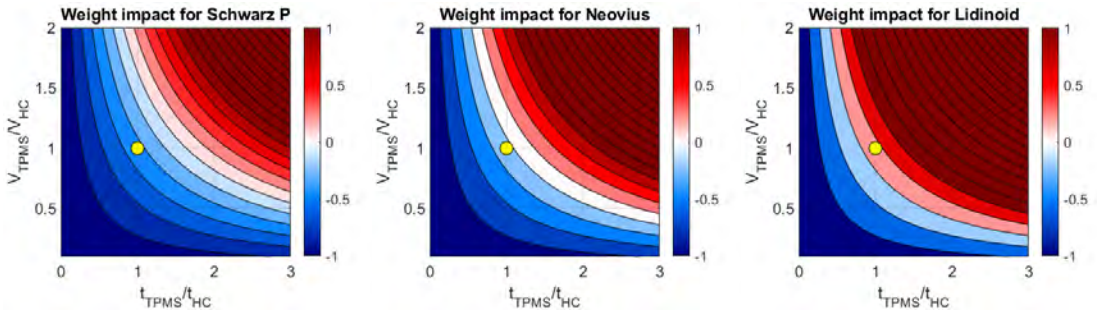

Figure 10. Weight impact maps for selected triply periodic minimal surfaces (TPMSs). HC: honeycomb core.

Milestone(s)

1. Demonstrated acoustic liner design and analysis using multi-fidelity modeling framework.
2. Fabricated baseline acoustic liners and TPMS-based lattice structures for experimental testing.
3. Identified Schwarz P lattice structure as best candidate for novel liner cores

Major Accomplishments

1. Designed and analyzed lattice-based acoustic liners using advanced software tools.
2. Performed rapid, iterative prototyping and testing to identify a promising acoustic liner design.
3. Conducted preliminary assessment of manufacturability variation within 3D printed test samples.

Publications

We plan to prepare 2–3 conference publications once experimental evaluation is complete. These publications will focus on the rapid design and analysis framework using 3D printing and modeling, analysis, and comparison with NIT test results. We will target both American Institute of Aeronautics and Astronautics (AIAA) technical conferences and AM conferences; accepted conference papers will be revised, updated, and submitted to journals as appropriate.

Outreach Efforts

None.

Awards

None.

Student Involvement

Two graduate students are involved in this research: (1) Andy Swanson, a graduate student working toward his MS in PSU's Additive Manufacturing & Design Graduate Program, and (2) Michael Geuy, a graduate student working toward his PhD in Mechanical Engineering. Andy is focusing on the rapid design and analysis framework; Michael is focusing on fabrication and manufacturing analysis.

Plans for Next Period

By the end of Year 1, the proposed framework will have been verified and validated using both 3D-printed baseline geometries and more complex liner designs derived from promising TPMS structures. Year 2 will focus on expanding the development methodology to include detailed manufacturability assessments of 3D-printed liner structures and detailed assessments of aerodynamic performance (targeting low drag).

Reference

Howerton, B. M. & Jones, M. G. (2017, June 5). A conventional liner acoustic/drag interaction benchmark database. *23rd AIAA/CEAS Aeroacoustics Conference.* 23rd AIAA/CEAS Aeroacoustics Conference, Denver, CO. https://doi.org/10.2514/6.2017-4190

Task 2 - Detailed Design and Additive Fabrication of Novel Liner Solutions

PSU and RTRC contributed to this task.

Objective

The goal of this task is to finalize the design and to additively manufacture novel acoustic liner solutions for testing and evaluation of a few select concepts.

Research Approach

The liner design approach employed in this study consisted of two steps, as described in Task 1 (see Figure 1). The first step is the prediction of the acoustic impedance based on a virtual NIT through FE modeling. In the second step, the predicted acoustic impedance is applied as an acoustic boundary condition representing the liner in a virtual grazing flow test model (which emulates NASA's grazing flow test setup) to predict the insertion loss and to down-select leading concepts for acoustic testing. The following sections explain this two-step process in more detail.

Prediction of normal incident liner impedance

Figure 11 shows the virtual NIT setup based on ACTRAN, a general-purpose acoustic modeling FE software.

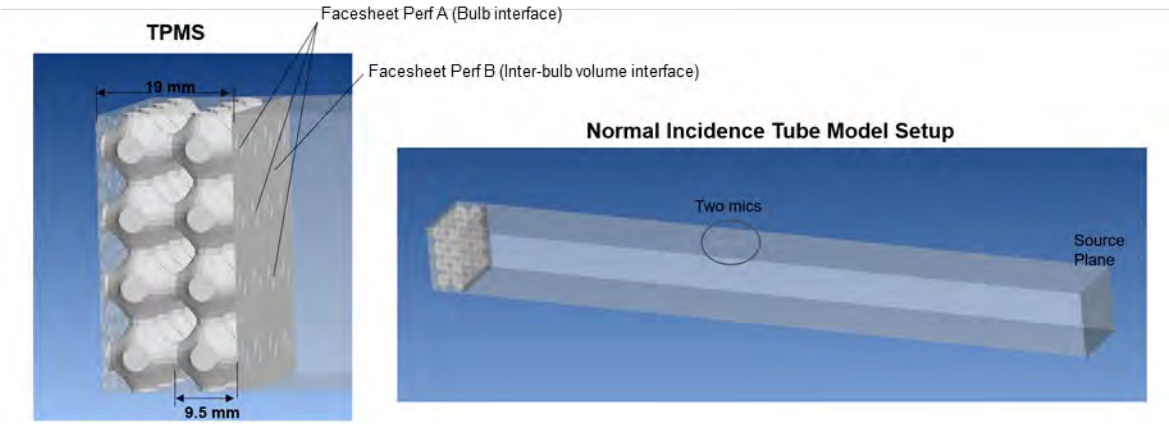

Figure 11. Liner acoustic impedance prediction based on a virtual impedance tube model setup in ACTRAN. The liner coupon model is based on a Schwarz P triply periodic minimal surface design with two bulb layers with front perforated sheets incorporating the transfer acoustic impedance calculated from a semi-analytical perforate model from the literature.

The model simulates a waveguide tube with an acoustic excitation source (i.e., a speaker) located at one end and an acoustic liner model situated at the other end. Two virtual microphones are used to measure the incident and reflected sound waves, which in turn are used to calculate the absorption coefficient and the acoustic impedance of the liner. The liner in Figure 11 is based on the Schwarz P TPMS geometry with a perforated facesheet located at the front of the liner.

In this model, the geometry of the Schwarz P TPMS is modeled with an FE mesh, while the front perforated facesheet is represented by the pre-calculated equivalent transfer impedance, based on an industry-standard semi-analytical perforate model, the Goodrich model (Yu, et al., 2008). The Goodrich model takes into account the effect of grazing flow across the perforated facesheet. Figure 12 shows the effect of the grazing flow on the liner acoustic impedance and the absorption coefficient for a Mach number, M, range of 0 (no flow) to 0.5 for an advanced acoustic liner with a Schwarz P TPMS core.

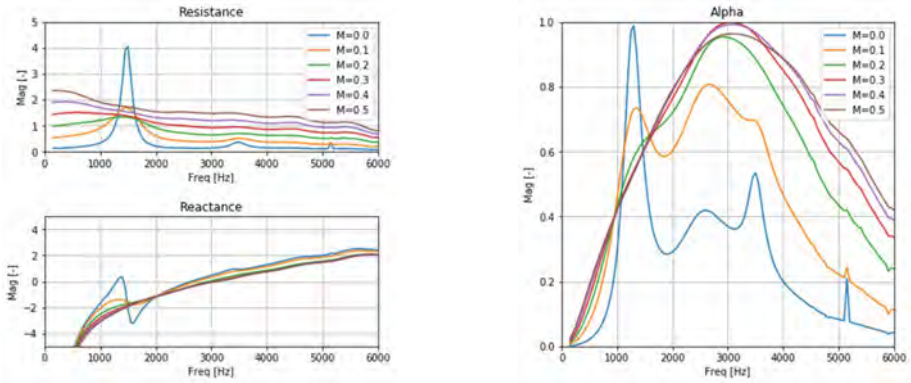

(a) Acoustic impedence (b) Normal sound absorption

Figure 12. Predicted effect of grazing flow on a Schwarz P triply periodic minimal surface liner before redesign for a grazing flow fat M = 0–0.5.

As shown in Figure 12(a), the presence of grazing flow significantly alters the acoustic performance, particularly the acoustic resistance, which tends to increase with flow Mach number. The absorption plot in Figure 12(b) shows that the absorption performance at relatively low Mach numbers (M < 0.1) consists of multiple absorption peaks, starting with a prominent peak

at approximately 1200 Hz. At higher Mach numbers (M > 0.2), these multi-peak characteristics disappear, and instead, the absorption is dominated by a single peak at a relatively high frequency of 3000 Hz. Further studies revealed that this result was due to reduced participation of the resonances associated with the Schwarz P bulb cavities caused by an excessive flow-induced resistance increase for the front perforated facesheet facing the bulb cavities. This prompted a redesign of the geometry parameters (hole diameter [d] and POA) of the bulb entrance perforated facesheet. Figure 13(a) shows the flow-dependent acoustic resistance term (labeled "Zgraz" in the figure) as a function of the two performance parameters. As shown in the figure, this flow-dependent resistance can be further reduced by increasing the POA while reducing the hole diameter, d.

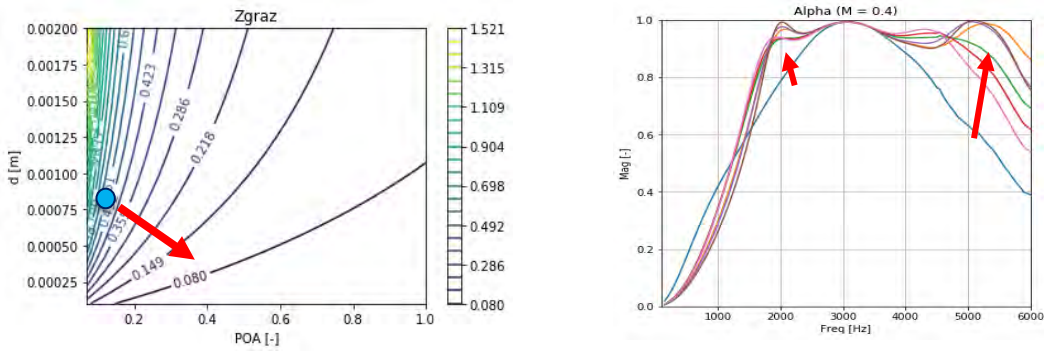

(a) (b)

Figure 13. Tuning the triply periodic minimal surface liner design parameters for a higher-Mach-number flow. (a) Flow-dependent acoustic resistance term (Zgraz) as a function of bulb entrance perforate diameter, d, and percent open area, POA. (b) Liner absorption with retuned bulb perforated facesheet parameters (absorption before retuning is shown by the blue curve).

Figure 13(b) shows the absorption performance of the Schwarz P TPMS liner at M = 0.4 for several different designs of the bulb entrance perforated facesheet. As shown in the figure, by retuning the bulb entrance perforated facesheet parameters, one can adjust the acoustic resistance and recover the bulb resonance contributions, thus achieving the desired multiple-resonance-peak absorption characteristics (which broadens the frequency bandwidth).

This investigation was critical to the design and study of advanced Schwarz-P-based liners. Numerous designs were investigated, targeting low-frequency tonal noise control (relevant to blade-pass frequencies and higher harmonics) as well as broadband performance. For each advanced liner design candidate, the acoustic impedance was determined via the simulation approach described above and then further analyzed in a virtual grazing flow simulation before the concepts were down-selected for printing and testing, as described next.

Prediction of grazing flow test insertion loss

The virtual impedance tube model in the previous step provides a means for screening multiple designs of Schwarz P TPMS-based liners. The next step is to predict the performance of the candidate designs in a grazing flow test setup that is closer to a realistic engine nacelle liner application. Figure 14 shows the ACTRAN simulation model that emulates NASA's grazing flow test setup.

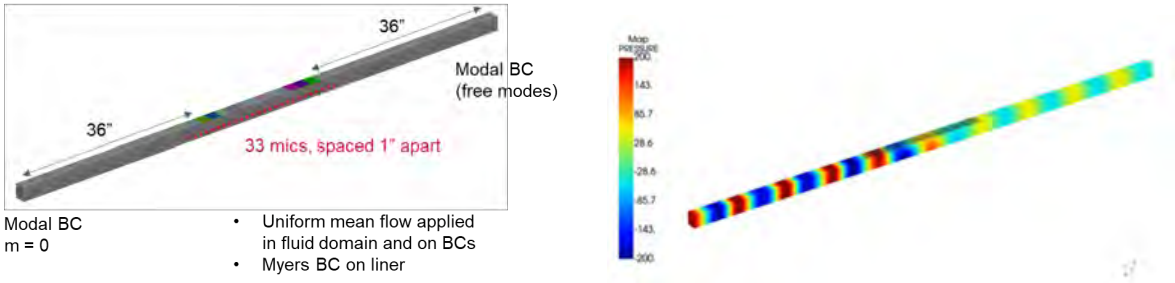

(a) Model setup

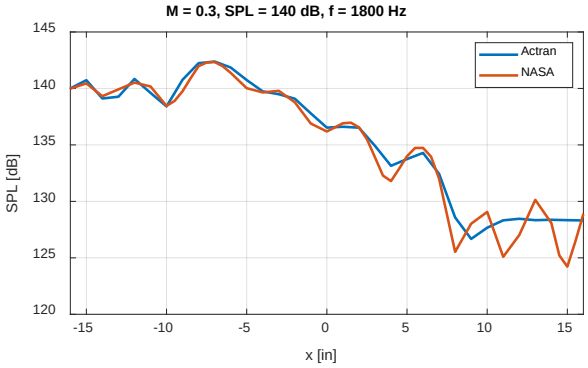

(b) Sound pressure level (SPL) as a function of axial position

Figure 14. Grazing flow test model for predicting liner attenuation performance. (a) The virtual glazing flow test model setup and (b) model vs. NASA test data for a reference single-degree-of-freedom liner. BC: boundary condition.

Unlike the NIT, which measures the acoustic liner performance for sound incident on the liner at a normal angle, the grazing flow setup measures the liner performance with respect to the sound propagating across the liner surface in the presence of air flow at engine-relevant Mach numbers. The grazing flow test tube model image shows the sound-propagating tube with a liner section in the middle, which is represented as a boundary condition with its frequency-dependent liner acoustic impedance values (obtained from the NIT model of the earlier step). This model was first validated with published attenuation performance data for SDOF liners. Figure 14(b) shows that the model-predicted sound pressure level (SPL) attenuation as a function of axial location compares well with that of the NASA data. Thus, the setup can be used reliably to study advanced liner performance.

Figure 15 shows the model-predicted insertion loss performance of two Schwarz P liner designs (three bulb layers, total depth of 1 inch) that were down-selected for the planned grazing flow testing at the NASA facility.

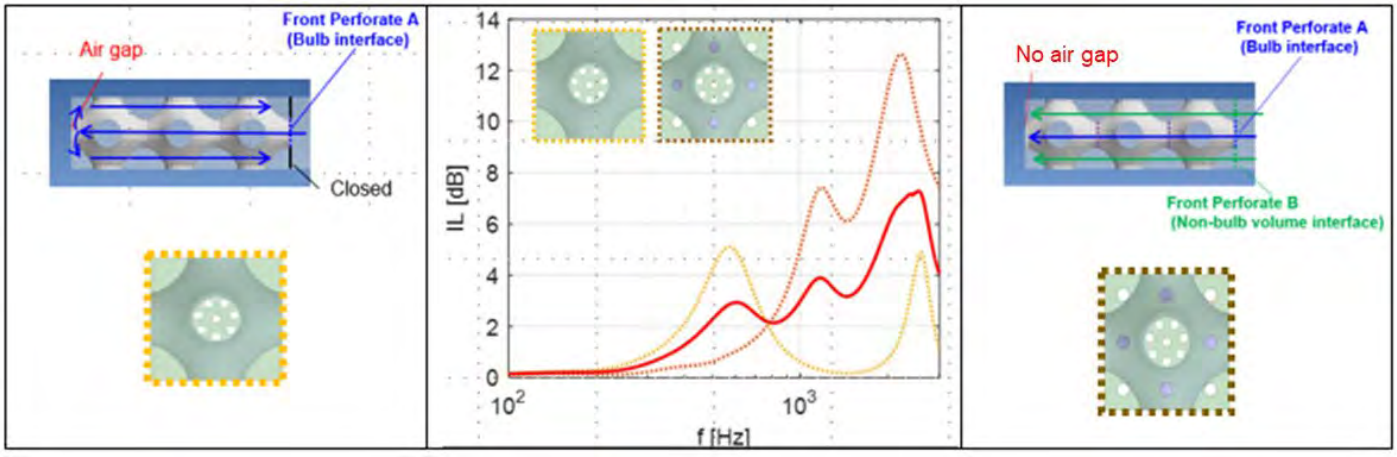

Figure 15. Predicted insertion loss (IL) performance of Schwartz P triply periodic minimal surface liner designs for planned grazing flow impedance testing at the NASA facility.

There are two variations of the Schwarz P TPMS-based liner designs with different target frequency ranges. One design targets 1–3 kHz while the other design targets the low-frequency range near 600 Hz. These liners have been designed specifically for testing with NASA's grazing flow test facility, which covers the frequency range of 400–3000 Hz.

Milestone(s)

1. Detailed acoustic evaluation of acoustic liner designs based on Schwarz P triply periodic minimal surface.
2. Identified two variations of Schwarz P lattice structure for noise attenuation in two different frequency ranges.

Major Accomplishments

1. Analyzed geometric variations of Schwarz P triply periodic minimal surface to optimize acoustic attenuation.
2. Predicted insertion loss of Schwarz P acoustic liner for grazing flow impedance testing.

Publications

We plan to prepare 1-2 conference publications once experimental evaluation is complete. These publications will discuss fine-tuning of the Schwarz P liner designs and modeling, analysis, and comparison with GFIT test results. We will target American Institute of Aeronautics and Astronautics (AIAA) technical conferences; accepted conference papers will be revised, updated, and submitted to journals as appropriate.

Outreach Efforts

None.

Awards

None.

Student Involvement

None.

Plans for Next Period

Year 2 will fabricate acoustic liner samples for grazing flow impedance testing and compare experimental results to predicted values. Analysis and simulation models will be refined and updated as needed.

Reference

Yu J, Ruiz, M. & Kwan, H.W. (2008, May) Validation of Goodrich Perforate Liner Impedance Model Using NASA Langley Test Data, *14th AIAA/CEAS Aeroacoustics Conference*, Vancouver, British Columbia Canada, AIAA-2008-2930.

Task 3 - Acoustic Evaluation of Additively Manufactured Novel Liners

Objective

The goal of Task 3 is to perform an acoustic evaluation of the additively manufactured novel liner designs generated in Tasks 1 and 2, leveraging multiple experimental testing capabilities at PSU, RTRC, and NASA LaRC.

Research Approach

Currently, two different experimental methods are being employed to evaluate the acoustic performance of different liner concepts, as shown in the development methodology in Figure 1: NIT and GFIT testing. A summary of the acoustic testing capabilities available at PSU, RTRC, and NASA LaRC for experimental evaluation is given in Table 2. Images of the NITs and GFIT facilities listed in Table 2 are shown in Figures 16 and 20, respectively.

Table 2. Summary of capabilities available at The Pennsylvania State University (PSU), Raytheon Technologies Research Center (RTRC), and NASA Langley Research Center (LaRC) for experimental testing. GFIT: grazing flow impedance tube; NIT: normal impedance tube; SPL: sound pressure level.

Acoustic Testing Capabilities Summary		Location	Sample Dimensions	Source Type(s)	Frequency Range	Maximum SPL	Centerline Mach Number
NIT	Brüel & Kjær Impedance Tube Kit Type 4206 (Large Sample Config)	RTRC	Diameter = 100 mm Height ≤ 400 mm	Broadband	500 Hz to 6.4 kHz	140 dB	0.0
	Brüel & Kjær Impedance Tube Kit Type 4206 (Small Sample Config)		Diameter = 29 mm Height ≤ 200 mm		50 Hz to 1.6 kHz		0.0
	In-House-Developed NASA Langley Specification Impedance Tube	PSU	Length = 2 in Width = 2 in Height ≤ 8.5 in	Stepped Sine Swept Sine Broadband	377 Hz to 3.4 kHz	146 dB (Broadband)	0.0
	Six-Driver High-Intensity Impedance Tube	NASA LaRC	Length = 2 in Width = 2 in Height ≤ 24 in	Stepped Sine Swept Sine Broadband	400 Hz to 3.0 kHz	155 dB (Stepped Sine) 145 dB (Swept Sine) 140 dB (Broadband)	0.0
GFIT	In-House-Developed Grazing Flow Impedance Tube	RTRC	Length = 2 in Width = 16.375 in Height ≤ 5 in	Stepped Sine Broadband	500 Hz to 6.5 kHz	160 dB	0.0–0.65
	In-House-Developed Grazing Flow Impedance Tube	NASA LaRC	Length = 2 in Width = 2–24 in Height ≤ 3 in	Stepped Sine Broadband	400 Hz to 3.0 kHz	155 dB (Stepped Sine) 145 dB (Swept Sine)	0.0–0.6

As previously mentioned, testing with NITs was primarily used to inform computational modeling and to screen out design concepts. While many different NIT configurations exist, the NITs used in this project (see Figure 16) have been configured to perform measurements using the two-microphone method from ASTM standard E1050-19. This standard calls for one or more sound sources (loudspeakers/compression drivers) to be fixed to one end of the NIT waveguide and for the sample of interest to be placed at the other end. The source then generates sound waves that travel down the tube toward the sample. By measuring the acoustic pressure over time with two stationary microphones, one can calculate the sample's absorption coefficient and acoustic impedance as a function of frequency using the signal processing algorithm explained in the ASTM testing standard. Typically, several measurements are made for a single sample to ensure consistency. In addition, the sound source type and SPL levels are varied so that non-linear effects can be evaluated.

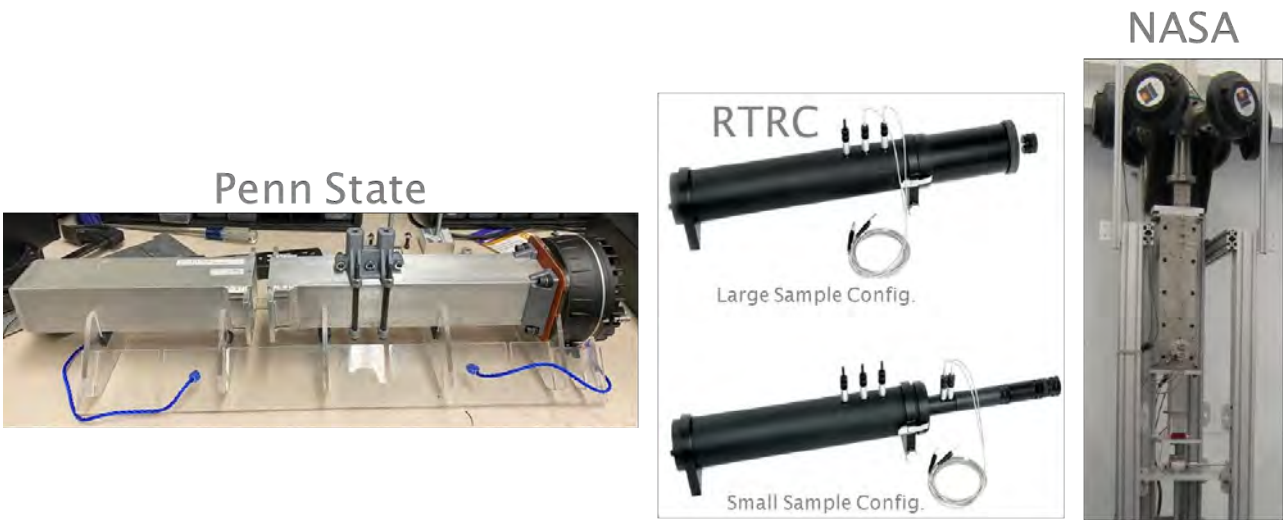

Figure 16. Normal impedance tubes found at The Pennsylvania State University, Raytheon Technologies Research Center (RTRC), and NASA Langley Research Center.

A few actions must be carried out before and during testing to ensure the quality of the NIT measurements. One of the most important preliminary steps is calibrating both microphones using an acoustic sound calibration device. Calibration ensures that the microphones are working correctly and making accurate measurements. Another important initial step is to validate the NIT measurements by testing a sample with a known absorption coefficient and comparing that with the observed results. For example, as shown in Figure 17, the PSU NIT was validated by testing a one-inch-thick Hushcloth foam sample and comparing the measured absorption coefficient with data provided by the manufacturer. When testing the samples, it is important to ensure that the sample and tube interfaces fit together correctly so that leakage does not affect the results. Petroleum jelly can be used to seal any gaps that remain after sample placement. Finally, one must also verify the software used to process the data by testing it on datasets with known solutions.

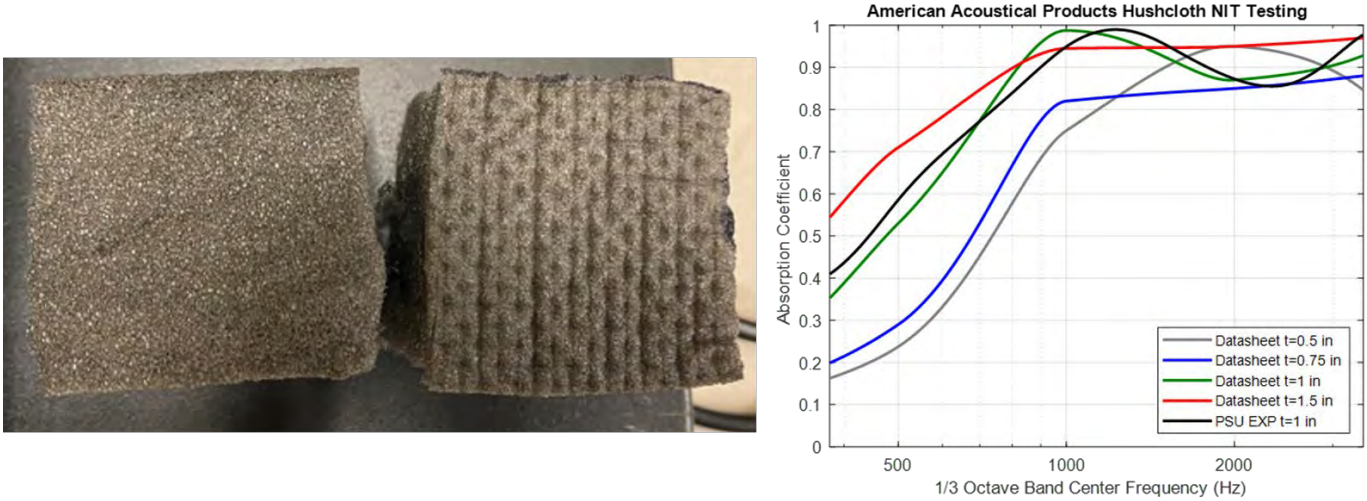

Figure 17. Validation of the normal impedance tube (NIT) at The Pennsylvania State University with Hushcloth foam (comparing black and green curves).

One of the most significant advantages of using a NIT to evaluate samples is speed, which makes this approach an ideal method for testing AM liner samples because of how rapidly prototypes can be produced. This synergy was leveraged at the beginning of the project to test the eight different AM design concepts shown in Figure 18. These designs included several

TPMS-based liners, a stochastic Voronoi foam lattice, an internal labyrinth, and a honeycomb to serve as a baseline. In addition to the different geometries, each design was printed out of thermoplastic polyurethane (TPU) and polylactic acid (PLA) polymers, soft and hard materials, respectively, to determine whether the material had any effect. In total, it took only a few hours to test and process the data from all 16 samples.

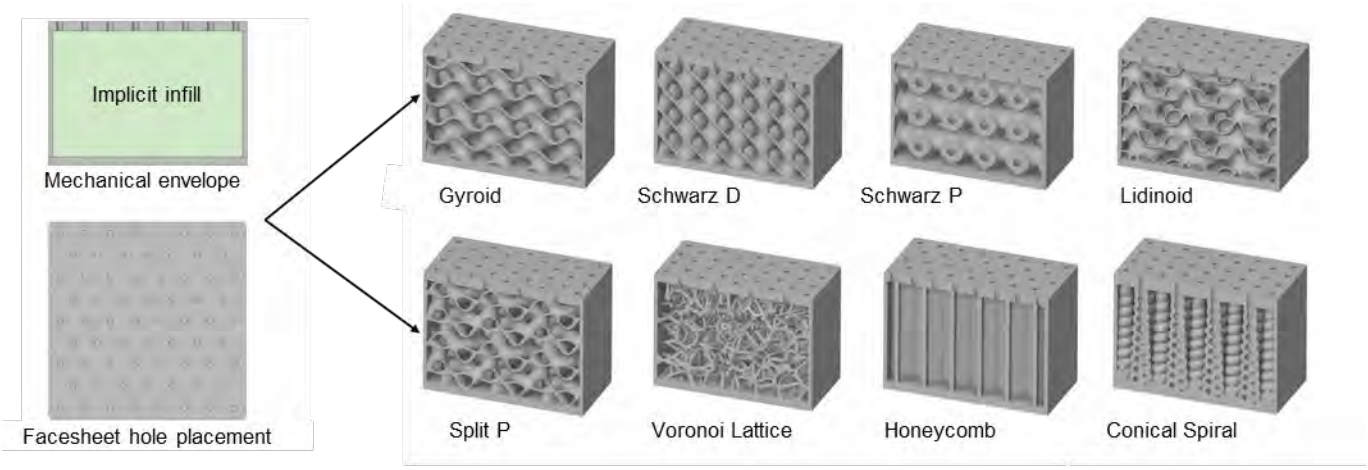

Figure 18. Eight additively manufactured acoustic liner designs evaluated with a normal impedance tube.

The absorption coefficients for the eight different designs and both materials are plotted in Figure 19. In general, the soft TPU and hard PLA performed similarly. However, in some cases, such as the Gyroid design, it is hypothesized that the soft TPU material would allow the facesheet to vibrate, adding to the overall absorption. These results also provided insights into what structures should be further investigated. In particular, the Schwarz P and Lidinoid TPMS surfaces were identified as having potential owing to their dual-degree-of-freedom absorption behavior.

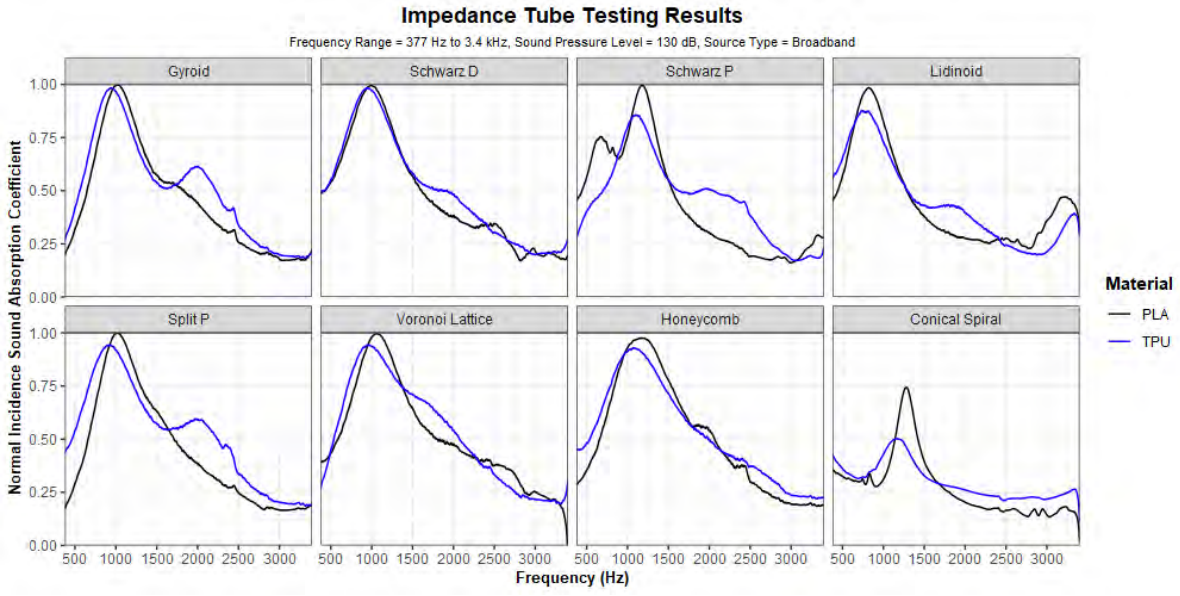

Figure 19. Absorption coefficients of the initial liner designs.

One of the downsides of evaluating liners with NITs is that flow effects are not considered. This presents an issue because, as found in Task 2, a liner's acoustic behavior strongly depends on the grazing flow it experiences. Therefore, when grazing flow effects need to be experimentally evaluated, one of the GFITs shown in Figure 20 is used. By combining acoustic sound

sources, a wind tunnel, and several microphone arrays in a single environment, key aeroacoustic performance metrics, such as drag force, acoustic impedance, and insertion losses, can be determined.

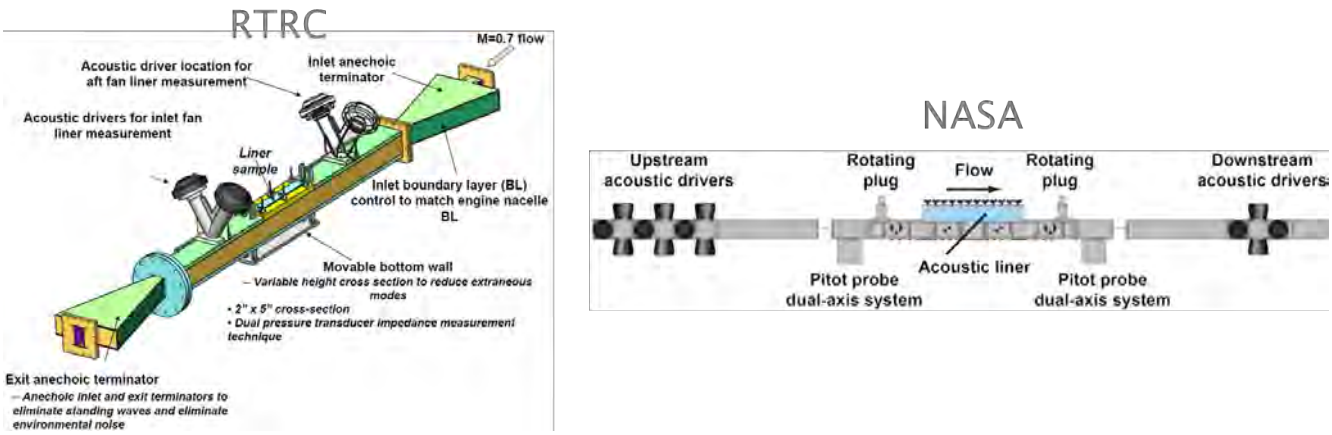

Figure 20. Grazing flow test facilities at RTRC and NASA Langley Research Center.

We are currently in the process of finalizing test samples for GFIT testing. The as-printed geometries will be measured and characterized prior to testing at RTRC. Samples will then be sent to NASA LaRC for testing in their grazing flow facility for comparison. These efforts will be a significant milestone for the project once testing is completed.

Milestone(s)

1. Compiled list of NIT and GFIT experimental facilities at PSU, RTRC, and NASA LaRC.
2. Verified baseline acoustic performance of NIT facilities at PSU and RTRC.

Major Accomplishments

1. Validated NIT evaluation capabilities at PSU and RTRC with baseline testing.
2. Performed experimental testing of multiple TPMS-based acoustic liner designs in PSU NIT facility.

Publications

We plan to prepare 2–3 conference publications once experimental testing is complete.

Outreach Efforts

None.

Awards

None.

Student Involvement

Two graduate students are involved in this research: (1) Andy Swanson, a graduate student working toward his MS in PSU's Additive Manufacturing & Design Graduate Program, and (2) Michael Geuy, a graduate student working toward his PhD in Mechanical Engineering. Andy is focusing on the rapid design and analysis framework; Michael is focusing on fabrication and manufacturing analysis.

Plans for Next Period

Additional testing of acoustic performance and material evaluation for successful manufacturing of the proposed liner concepts and a far-field noise impact study of these novel liner designs will be conducted in Year 2 to assess their merits compared with conventional and other reference liner solutions. The focus in Year 2 will also shift to acoustic liner design for a specific section of the engine, expanding from component-level tradeoffs (e.g., weight, acoustic performance, structural integrity) to subsystem-level tradeoff studies (e.g., weight, cost, drag).

Project 080 Hydrogen and Power-to-Liquid Concepts for Sustainable Aviation Fuel Production

Washington State University
Massachusetts Institute of Technology

Project Lead Investigator

Manuel Garcia-Perez
Professor and Chair
Biological Systems Engineering Department
Washington State University
LJ Smith, Room 205, PO Box 646120, Pullman, WA 99164-6120
509-335-7758
mgarcia-perez@wsu.edu

Michael P. Wolcott
Regents Professor
Department of Civil & Environmental Engineering
Washington State University
PO Box 642910, Pullman, WA 99164-2910
509-335-6392
wolcott@wsu.edu

Steven R. H. Barrett
Professor of Aeronautics and Astronautics
Director, Laboratory for Aviation and the Environment
Massachusetts Institute of Technology
77 Massachusetts Ave, Building 33-322, Cambridge, MA 02139
617-253-2727
sbarrett@mit.edu

Florian Allroggen
Executive Director Aerospace Climate and Sustainability
Laboratory for Aviation and the Environment
Massachusetts Institute of Technology
77 Massachusetts Ave, Building 33-115A, Cambridge, MA 02139
617-751-4472
fallrogg@mit.edu

University Participants

Washington State University (WSU)

- P.I.s: Manuel Garcia-Perez, Michael P. Wolcott
- FAA Award Number: 13-C-AJFE-WaSU-031
- Period of Performance: October 1, 2021 to September 30, 2022
- Tasks:
  1. Evaluate the strengths and weaknesses of hydrogen production and power-to-liquid (PtL) concepts.
  2. Assess how hydrogen production and PtL production can be integrated with existing production and distribution infrastructure (existing infrastructure and sustainable aviation fuel [SAF] technologies) to produce fuels with lower carbon intensity.

3. Synthesize the information and obtain rules on combining carbon, hydrogen, and energy sources with different conversion technologies to improve environmental impacts and costs.

Massachusetts Institute of Technology

- P.I.: Professor Steven R. H. Barrett
- FAA Award Number: 13-C-AJFE-MIT, Amendment Nos. 091 and 101
- Period of Performance: October 1, 2021 to September 19, 2023
- Tasks during current reporting period (October 1, 2021 to September 30, 2022):
    1. Develop methods for assessing the economic and environmental impacts of promising SAF production pathways.
    2. Apply models to analyze the economic and environmental footprint of SAF production pathways.
    3. Analyze the prospects of direct air capture (DAC) of atmospheric CO_2 to provide a carbon source for SAF production.

Project Funding Level

Washington State University

$450,000 in FAA funding and $450,000 in matching funds. State-committed graduate school contributions for Ph.D. students. Faculty time for Michael Wolcott, Manuel Garcia-Perez, Xiao Zhang, and Su Ha contribute to the cost share. WSU funding is reported for the reporting period.

Massachusetts Institute of Technology

$450,000 in FAA funding and $450,000 in matching funds. Sources of matching are approximately $136,000 from MIT, plus third-party in-kind contributions of $101,000 from Savion Aerospace Corporation and $213,000 from NuFuels, LLC. MIT funding is reported for the period of performance indicated above.

Investigation Team

P.I.s:	Manuel Garcia-Perez, WSU (Tasks 1, 2, 3, and 6) Michael Wolcott, WSU (Tasks 1, 2, 3, and 6) Steven Barrett, MIT (Tasks 4, 5, 6, and 7)
Co-P.I.s:	Xiao Zhang, WSU (Tasks 1, 2, 3, and 6) Su Ha, WSU (Tasks 1, 2, 3, and 6) Jonathan Male, WSU (Tasks 1, 2, 3, and 6) Florian Allroggen, MIT (Tasks 4, 5, 6, and 7)
Research Staff:	Christoph Falter, MIT, Postdoctoral Associate (Tasks 4 and 5) Aidan Garcia, WSU, Research Associate (Tasks 2, 3, and 6) Kristin Brandt, WSU, Staff Engineer (Tasks 1, 2, 3, and 6)
Graduate Research Assistants:	Valentina Sierra, WSU (Tasks 1 and 2) Tae Joong Park, MIT (Tasks 4 and 5) Tara Housen, MIT (Task 7)

Collaborating Researchers

- Corinne Drennan, Pacific Northwest National Laboratory (PNNL)

Project Overview

The aviation industry is under pressure to reduce its greenhouse gas (GHG) emissions. SAFs are considered the most promising approach for achieving the sector's GHG emission targets. To date, no comprehensive assessment exists for analyzing how different carbon, hydrogen, and energy sources can be combined with different conversion processes to produce SAF with high GHG emission reductions and low costs. The goals of this project are (a) to evaluate the strengths and weaknesses of hydrogen production and PtL concepts, (b) to assess the state of the art for the integration of hydrogen production, different carbon sources (including atmospheric CO_2 capture), and PtL production with existing infrastructure (SAF production and industries), (c) to analyze the cost and environmental impacts of these production pathways, and (d) to

synthesize this information and obtain rules on how to best combine carbon, hydrogen, and energy sources with different conversion technologies to improve environmental impacts and costs. This research will enable the identification of new pathways to optimize SAF production for maximum GHG reductions with minimal fuel costs.

Approved SAF pathways commonly use photosynthesis-derived carbon from sugars, lignocellulosic materials, or lipids. Some SAF technologies that are currently being investigated include those based on hydro-processed ester and fatty acid synthetic paraffinic kerosene (HEFA-SPK), Fischer–Tropsch synthetic paraffinic kerosene (FT-SPK), Fischer–Tropsch synthetic kerosene with aromatics (FT-SKA), synthesized iso-paraffins (SIP), Virent's BioForming synthesized aromatic kerosene, hydrodeoxygenation synthesized kerosene, catalytic hydro-thermolysis, alcohol-to-jet (ATJ) fuel, hydropyrolysis (Shell IH2), fast pyrolysis, and hydro-processed depolymerized cellulosic jet fuel. The jet fuels produced from seven paths (FT-SPK, HEFA-SPK, SIP, FT-SKA, ATJ, catalytic hydro-thermolysis, and HEFA) and by co-processing lipids and FT biocrude in refineries are now approved by the American Society for Testing Materials for use in commercial aircraft. Although these processes can result in substantial GHG reductions, their production costs are still substantially higher than those of conventional jet fuels derived from petroleum distillation ($0.88–$3.86 per liter) (Tanzil et al., 2021).

Previous studies (Tanzil et al., 2021) have shown that the quality of the carbon source determines the yield of SAF. For example, although lignocellulosic materials are 10 times cheaper than lipids (on a mass basis), the quality of the carbon source makes fuels derived from triglycerides much cheaper (2–5 times) than those derived from cellulose, hemicellulose, or lignin. Carbon in organic matrices containing a higher content of oxygen, nitrogen, and sulfur is more challenging to convert to jet fuel because of the penalties associated with the removal of oxygen, nitrogen, and sulfur, which typically consumes hydrogen. These contaminants can reduce the time between regeneration and the overall lifetime of the hydrotreating catalyst. Carbon in polymeric molecules is also more challenging to convert to jet fuel because it requires costly molecular weight reduction technologies and often lacks selectivity to the targeted jet fuel cut. Carbon in the form of aliphatic molecules can be more easily converted to jet fuel than carbon as aromatics. Carbon sources such as CO_2, biomass, coal, petroleum, and municipal solid waste (MSW) must be thoroughly investigated as feedstocks for SAF production. Because carbon is the highest-weight element in jet fuel production, high fuel yields can only be achieved in processes with high carbon conversion efficiencies.

Most technologies that produce SAF require high amounts of hydrogen, with 1 equivalent of hydrogen per fuel molecule on the low end (ATJ) and 6–8 moles of hydrogen per fuel molecule on the high end. Although hydrogen can currently be produced by many pathways using low-carbon-intensity electrons produced by wind and solar farms, current hydrogen production is mainly based on steam methane reforming (SMR), which is associated with significant CO_2 emissions. Commonly considered paths for hydrogen production include (a) steam and dry reforming of hydrocarbons, (b) water electrolysis, (c) plasma arc decomposition, (d) water thermolysis, (e) thermochemical water splitting, (f) thermochemical conversion of biomass (biomass gasification and biofuel reforming), (g) photovoltaic electrolysis, photocatalysis, and photochemical methods, (h) dark fermentation, (i) high-temperature electrolysis, (j) hybrid thermochemical cycles, (k) coal and petroleum gasification, (l) MSW gasification, (m) fossil fuel reforming, (n) biophotolysis and photo-fermentation, (o) artificial photosynthesis, and (p) photo-electrolysis (Dincer & Acar, 2015). One goal of this project is to evaluate the strengths and weaknesses of hydrogen production concepts, determine how they can be integrated with existing infrastructure to produce cheap green hydrogen, and identify the potential impact of these technologies in producing SAF.

In some biomass and waste conversion processes, carbon dioxide and methane are produced as a side product or as the starting material. To meet the specifications for liquid SAF, hydrogen will be needed to hydrogenate alkenes and hydrotreat oxygenates. Utilizing waste carbon oxides and methane can increase the amount of carbon obtained from resources in the SAF while reducing emissions. This can be done in conjunction with hydrogen production with a lower carbon intensity. A systematic analysis will examine the trade-offs between enhanced carbon utilization, the effects of increased amounts of renewable energy, the need for stability in the grid and energy storage, access to lower-carbon-intensity hydrogen against positive impacts on environmental indicators, the cost impact of such changes, and technology uncertainty in emerging science and engineering.

Over the past decade, significant progress has been made in assessing the economic and environmental properties of SAF. This work includes studies that have fostered our understanding of lifecycle analysis (LCA) in general (e.g., Stratton et al., 2010). In addition, work has focused on the economic and environmental properties of specific pathways, including jet fuel produced from HEFA (Stratton et al., 2011; Pearlson et al., 2013; Olcay et al., 2013; Seber et al., 2014), from FT pathways (Stratton et al., 2011; Suresh, 2016; Suresh, 2018), and from biomass-derived sugars using a variety of chemical and biological techniques (Bond et al., 2014; Staples et al., 2014; Winchester et al., 2015). Most recently, Monte Carlo approaches

have been systematically introduced for quantifying uncertainty and stochasticity in LCA and techno-economic analysis (TEA) (Bann et al., 2017; Suresh, 2016; Yao et al., 2017; Suresh, 2018; Oriakhi, 2020).

References

Bann, S. J., Malina, R., Staples, M. D., Suresh, P., Pearlson, M., Tyner, W. E., Hileman, J. I., & Barrett, S. (2017). The costs of production of alternative jet fuel: A harmonized stochastic assessment. *Bioresource Technology*, *227*, 179–187. https://doi.org/10.1016/j.biortech.2016.12.032

Bond, J. Q., Upadhye, A. A., Olcay, H., Tompsett, G. A., Jae, J., Xing, R., Alonso, D. M., Wang, D., Zhang, T., Kumar, R., Foster, A., Sen, S. M., Maravelias, C. T., Malina, R., Barrett, S. R. H., Lobo, R., Wyman, C. E., Dumesic, J. A., & Huber, G. W. (2014). Production of renewable jet fuel range alkanes and commodity chemicals from integrated catalytic processing of biomass. *Energy Environ. Sci.*, *7*(4), 1500–1523. https://doi.org/10.1039/C3EE43846E

Dincer, I., & Acar, C. (2015). Review and evaluation of hydrogen production methods for better sustainability. *International Journal of Hydrogen Energy*, *40*(34), 11094–11111. https://doi.org/10.1016/j.ijhydene.2014.12.035

ICAO.(2021). *CORSIA supporting document - CORSIA Eligible Fuels – Life Cycle Assessment Methodology*. https://www.icao.int/environmental-protection/CORSIA/Documents/CORSIA_Supporting_Document_CORSIA%20Eligible%20Fuels_LCA_Methodology_V3.pdf

Olcay, H., Seber, G., Malina, R. (2013). *Life Cycle Analysis for Fully-Synthetic Jet Fuel Production, MIT Support for Honeywell Continuous Lower Energy*. Emissions and Noise (CLEEN) Technologies Development, Report to the FAA.

Oriakhi, U.M. (2020). *A stochastic life cycle and greenhouse gas abatement cost assessment of renewable drop-in fuels* [Master's Thesis, Massachusetts Institute of Technology].

Pearlson, M., Wollersheim, C., & Hileman, J. (2013). A techno-economic review of hydroprocessed renewable esters and fatty acids for jet fuel production. *Biofuels, Bioproducts and Biorefining*, *7*(1), 89–96. https://doi.org/10.1002/bbb.1378

Seber, G., Malina, R., Pearlson, M. N., Olcay, H., Hileman, J. I., & Barrett, S. R. H. (2014). Environmental and economic assessment of producing hydroprocessed jet and diesel fuel from waste oils and tallow. *Biomass and Bioenergy*, *67*, 108–118. https://doi.org/10.1016/j.biombioe.2014.04.024

Staples, M. D., Malina, R., Olcay, H., Pearlson, M. N., Hileman, J. I., Boies, A., & Barrett, S. R. H. (2014). Lifecycle greenhouse gas footprint and minimum selling price of renewable diesel and jet fuel from fermentation and advanced fermentation production technologies. *Energy Environ. Sci.*, *7*(5), 1545–1554. https://doi.org/10.1039/C3EE43655A

Stratton, R; Wong, H; Hileman, J. (2020). *Life Cycle Greenhouse Gas Emissions from Alternative Jet Fuels* (PARTNER-COE-2010-001). Partnership for AiR Transportation Noise and Emissions Reduction (PARTNER).

Stratton, R. W., Wong, H. M., & Hileman, J. I. (2011). Quantifying variability in life cycle greenhouse gas inventories of alternative middle distillate transportation fuels. *Environmental Science & Technology*, *45*(10), 4637–4644. https://doi.org/10.1021/es102597f

Suresh, P., Malina, R., Staples, M. D., Lizin, S., Olcay, H., Blazy, D., Pearlson, M. N., & Barrett, S. R. H. (2018). Life cycle greenhouse gas emissions and costs of production of diesel and jet fuel from municipal solid waste. *Environmental Science & Technology*, *52*(21), 12055–12065. https://doi.org/10.1021/acs.est.7b04277

Suresh, P. (2016). *Environmental and economic assessment of alternative jet fuel derived from municipal solid waste* [Master's Thesis, Massachusetts Institute of Technology].

Tanzil, A. H., Brandt, K., Wolcott, M., Zhang, X., & Garcia-Perez, M. (2021). Strategic assessment of sustainable aviation fuel production technologies: Yield improvement and cost reduction opportunities. *Biomass and Bioenergy*, *145*, 105942. https://doi.org/10.1016/j.biombioe.2020.105942

Winchester, N., Malina, R., Staples, M. D., & Barrett, S. R. H. (2015). The impact of advanced biofuels on aviation emissions and operations in the U.S. *Energy Economics*, *49*, 482–491. https://doi.org/10.1016/j.eneco.2015.03.024

Yao, G., Staples, M. D., Malina, R., & Tyner, W. E. (2017). Stochastic techno-economic analysis of alcohol-to-jet fuel production. *Biotechnology for Biofuels*, *10*(1), 18. https://doi.org/10.1186/s13068-017-0702-7

Task 1 - Evaluate the Strengths and Weaknesses of Hydrogen and PtL Concepts in the United States

Washington State University

Objectives

The objective of Task 1 is to perform a literature review and develop design cases for hydrogen and PtL concepts.

Research Approach

In this task, we will identify areas that require more research and development to reduce technology uncertainty. Specifically, we analyze six technologies for hydrogen production: (a) steam reforming, (b) dry reforming, (c) water electrolysis, (d) gasification of carbonaceous materials (biomass, coal, bitumen, and MSW) (with steam and CO_2), (e) thermal decomposition of hydrocarbons (methane pyrolysis with capture and use of solid carbon), and (f) fossil fuel reforming. This task is being conducted by WSU and PNNL and started during Year 1. The main goal of this task is to build design cases for each of these hydrogen production technologies (mass and energy balances and TEAs) and identify the strengths and weaknesses of each technology studied. A team of hydrogen production experts from WSU and PNNL meets weekly with a Ph.D. student and post-doctoral associate from WSU to guide them in the literature review and in the creation of a road map for constructing design cases and identifying the opportunities and challenges for each of the technologies studied.

Milestones

In this first year, we started to work in two main areas: (a) a literature review of hydrogen production technologies within the context of SAF production and (b) mass and energy balances and TEAs of standalone hydrogen production technologies. We have written the first draft of a literature review for hydrogen production within the context of SAF technologies. Several standardized TEAs of hydrogen production technologies have been developed. We have calculated the minimum selling price and GHG footprint for each hydrogen production technology. The standardized TEAs are now available for team members to use.

Major Accomplishments

We have completed the first draft of a literature review on the TEAs of hydrogen production technologies (slow and high-pressure gasification, steam reforming, partial oxidation, autothermal oxidation, methane pyrolysis, and low- and high-temperature water electrolysis) and have identified several promising pathways in which hydrogen production technologies are integrated with gasification. We have also developed standardized design cases to estimate hydrogen production costs for each of the technologies studied.

Publications

Sierra V, Wolcott M, Zhang X, Ha S, Male J, Garcia A, Brand K, Garcia-Perez M, Drennan C, Holladay J: Emerging and Commercial Hydrogen Production Technologies for SAF Manufacturing: A comparative Literature Review. *Under internal review.*

Garcia-Perez, M., Garcia, A., Wolcott, M. (2022, October 24-27). *Production of cheap Sustainable Aviation Fuels (SAFs): Balancing Economic and Environmental Advantages.* Sustainable Energy for a Sustainable Future, San Pedro, San Jose.

Outreach Efforts

We presented our preliminary results at the ASCENT meeting on April 5–6, 2022, at the November 25–26, 2022 meeting, and at the Civil Aviation Alternative Fuels Initiative meeting on June 1–3, 2022 in Washington, DC.

Student Involvement

Valentina Sierra is working on the literature of hydrogen production technologies and the role hydrogen has on SAF production.

Plans for Next Period

We plan to submit the revised literature review and improve the design cases. In the next year, we will continue with our biweekly meetings with the panel of experts from PNNL to identify the strengths and weaknesses of new concepts for SAF production. We will discuss the integration of hydrogen production and PtL concepts with biomass-based SAF production

technologies. Our graduate student and research associate make presentations every 15 days and, based on recommendations from the panel of experts, work for 15 days on a new presentation.

Task 2 - Assess how Hydrogen Production and PtL Production can be Integrated with Existing Production and Distribution Infrastructure (Existing Infrastructure and SAF Technologies) to Produce Fuels with Lower Carbon Intensity

Washington State University

Objective

The goal of Task 2 is to estimate cost reduction opportunities that would arise if emerging hydrogen production technologies were co-located with SAF production technologies and existing infrastructure.

Research Approach

For SAF technologies, we study how hydrogen is used in hydrotreatment steps. We conduct weekly meetings with WSU, PNNL experts, and our Ph.D. students to identify hydrogen production opportunities in existing industries (petroleum refineries, dams, metallurgical industry, etc.). Our main goal is to estimate cost reduction opportunities that would arise if some of the emerging hydrogen production technologies were co-located with some of these industries. In a separate subtask, we will evaluate the impact of each of the emerging hydrogen production technologies on existing or emerging SAF technologies, including those based on (a) HEFA, (b) Virent's BioForming synthesized aromatic kerosene, (c) ATJ fuel, (d) natural sugar to hydrocarbon (SIP), (e) fast pyrolysis and the GFT process, and (f) selective carbonization/CO_2 gasification/steam reforming/FT processes. For each case, we will consider lignocellulose or lipids as feedstocks. Hydrogen utilization for SAF production typically occurs in a hydrotreatment step that varies depending on the technology (Tanzil et al., 2021; Han et al., 2019). This step can proceed from a simple hydrogenation, hydrodeoxygenation, hydro-cracking, or all of them together, depending on the technology (Han et al., 2019). Especially troublesome is the hydrotreatment of oligomers and materials with a high tendency to form coke (Han et al., 2019). In this task, we will develop detailed phenomenological mathematical models for the hydrotreatment step of the HEFA and fast pyrolysis pathways, which the team will then use to study potential strategies to reduce hydrogen consumption during SAF production (Chen et al., 2019; Plazas-Gonzalez et al., 2018). This type of model requires a detailed description of the chemical composition of the feedstock, the reaction mechanism, and associated kinetics (Guitierrez-Antonio et al., 2018; Talib-Jarullah, 2011; Boesen et al., 2017; Jenistova et al., 2017; Tieuli et al., 2019; Hechemi and Murzin, 2018). The modeling work will complement studies in batch and continuous hydrotreatment reactors with different catalysts to validate the mathematical model. This work will be expanded in Year 3 to cover other technologies. This work is not funded as part of the current proposal. The task will start in the next reporting period.

Milestone

This task started in January 2023.

Major Accomplishments

This task started in January 2023.

Publications

None.

Outreach Efforts

None.

Awards

None.

Student Involvement

A new student (Anika Afrin) has been hired to work on this task. She began her graduate studies on January 1, 2022.

Plans for Next Period

In the next year, we will review the different hydrotreatment technologies associated with producing SAFs and the mathematical models used to describe the operation of these reactors.

References

Boesen, R.R. (2010). *Investigation and Modelling of Diesel Hydrotreating Reactions* [PhD Thesis]. Technical University of Denmark. https://backend.orbit.dtu.dk/ws/portalfiles/portal/6470295/Thesis+Rasmus+R.+Boesen+2010+final.pdf

Chen, Z., Feng, S., Zhang, L., Shi, Q., Xu, Z., Zhao, S., & Xu, C. (2019). Molecular-level kinetic modelling of fluid catalytic Cracking slurry oil hydrotreating. *Chemical Engineering Science*, *195*, 619–630. https://doi.org/10.1016/j.ces.2018.10.007

Gutiérrez-Antonio, C., Soria Ornelas, M. L., Gómez-Castro, F. I., & Hernández, S. (2018). Intensification of the hydrotreating process to produce renewable aviation fuel through reactive distillation. *Chemical Engineering and Processing - Process Intensification*, *124*, 122–130. https://doi.org/10.1016/j.cep.2017.12.009

Han, Y., Gholizadeh, M., Tran, C.-C., Kaliaguine, S., Li, C.-Z., Olarte, M., & Garcia-Perez, M. (2019). Hydrotreatment of pyrolysis bio-oil: A review. *Fuel Processing Technology*, *195*, 106140. https://doi.org/10.1016/j.fuproc.2019.106140

Hachemi, I., & Murzin, D. Yu. (2018). Kinetic modeling of fatty acid methyl esters and triglycerides hydrodeoxygenation over nickel and palladium catalysts. *Chemical Engineering Journal*, *334*, 2201–2207. https://doi.org/10.1016/j.cej.2017.11.153

Jeništová, K., Hachemi, I., Mäki-Arvela, P., Kumar, N., Peurla, M., Čapek, L., Wärnå, J., & Murzin, D. Yu. (2017). Hydrodeoxygenation of stearic acid and tall oil fatty acids over Ni-alumina catalysts: Influence of reaction parameters and kinetic modelling. *Chemical Engineering Journal*, *316*, 401–409. https://doi.org/10.1016/j.cej.2017.01.117

Plazas-González, M., Guerrero-Fajardo, C. A., & Sodré, J. R. (2018). Modelling and simulation of hydrotreating of palm oil components to obtain green diesel. *Journal of Cleaner Production*, *184*, 301–308. https://doi.org/10.1016/j.jclepro.2018.02.275

Stratton, R; Wong, H; Hileman, J. (2020). *Life Cycle Greenhouse Gas Emissions from Alternative Jet Fuels* (PARTNER-COE-2010-001). Partnership for AiR Transportation Noise and Emissions Reduction (PARTNER).

Stratton, R. W., Wong, H. M., & Hileman, J. I. (2011). Quantifying variability in life cycle greenhouse gas inventories of alternative middle distillate transportation fuels. *Environmental Science & Technology*, *45*(10), 4637–4644. https://doi.org/10.1021/es102597f

Talib Jarullah, A. (2011). *Kinetic Parameters Estimating Hydrotreating reactions in Trickle Bed Reactor (TBR) via Pilot Plant Experiments; Optimal Design and Operation of an Industrial TBR with Heat Integration and Economic Evaluation* [Ph.D. dissertation, School of Engineering, Design, and Technology].

Tanzil, A. H., Brandt, K., Wolcott, M., Zhang, X., & Garcia-Perez, M. (2021). Strategic assessment of sustainable aviation fuel production technologies: Yield improvement and cost reduction opportunities. *Biomass and Bioenergy*, *145*, 105942. https://doi.org/10.1016/j.biombioe.2020.105942

Tieuli, S., Mäki-Arvela, P., Peurla, M., Eränen, K., Wärnå, J., Cruciani, G., Menegazzo, F., Murzin, D. Yu., & Signoretto, M. (2019). Hydrodeoxygenation of isoeugenol over Ni-SBA-15: Kinetics and modelling. *Applied Catalysis A: General*, *580*, 1–10. https://doi.org/10.1016/j.apcata.2019.04.028

Task 3 - Integration of Alternative Hydrogen and Carbon Sources into Fuel Conversion Pathways

Washington State University

Objective

The objective of Task 3 is to identify new pathways to optimize SAF production for maximum GHG reductions with minimal fuel costs.

Research Approach

This task is being conducted in two steps. As the first step, the WSU–PNNL panel of experts is meeting weekly with the Ph.D. student to discuss the potential for combining the SAF pathways studied under Task 2 with alternative carbon sources (MSW,

sludges from wastewater treatment plants, CO_2). In the second step, we will evaluate the potential integration of these technologies with the new hydrogen production technologies discussed in Task 1. We will use the information collected to propose design and synthesis rules (diagrams) to help visualize how the source of carbon, hydrogen, and available energy and the type of conversion technology impact main environmental and economic sustainability indicators. We aim to use this exercise to identify better paths for SAF production.

Milestones

We are following a holistic path to identify desired production pathways. First, we correlated the minimum fuel selling price from 50 SAF TEAs with a straightforward model proposed by Lange et al. (2016). The model estimates the production SAF cost of product yield, feedstock, and other supplied costs, including Low Carbon Fuel Standards (LCFS) and Renewable Identification Number (RIN) support. Our analysis estimated an average production cost of $272/ton of feedstock processed, which is consistent for the chemical industry. We then developed three purely stoichiometric mass balances to estimate the effect of deoxygenation method (oxygen removal as O_2, H_2O, or CO_2) on production cost. Although water deoxygenation proved to be most advantageous, all idealized models proved viable, ruling out stoichiometry alone as a limiting factor in fuel production. These simple models were also used to study the effect of oxygen addition, plastics, and carbon sequestration on the overall performance of these ideal technologies. In this way, the combustion requirements of gasification were also ruled out as a limiting factor. The team has begun to analyze biomass gasification technologies. We have concluded that existing technologies for the conversion of biomass into syngas are limited by very low carbon conversion efficiencies. To achieve carbon conversion efficiencies close to 100%, the introduction of outside hydrogen and energy is necessary. Additionally, close to one third of the syngas energy is lost when biomass is converted to SAF, presenting a limitation that must be addressed. Our group is working on the development of new technologies to address these issues.

Major Accomplishments

We have learned that the most critical factor governing production cost is fuel yield, which is directly related to carbon conversion efficiency. However, to maximize carbon conversion efficiency, it is critical to remove oxygen in the form of water by reacting it with hydrogen, which requires the introduction of hydrogen from outside the system. Currently, gasification is the leading technology for producing syngas as an intermediate. Current gasification systems must be optimized for maximum carbon conversion efficiency. An overall mass and energy balance shows that typical gasification systems are oxygen-, energy-, and hydrogen-deficient and that current designs sacrifice carbon efficiency to address the lack of energy and hydrogen. This issue can be addressed by augmenting hydrogen and energy from outside the system. Furthermore, the CO in syngas affords a C/O ratio that is much higher than the C/O ratio of biomass. Consequently, oxygen needs to be added to the system. Syngas also has an energy content higher than that of the fuel produced; therefore, nearly one third of the system's energy is released as heat. Heat integration is critical to maximizing the economic viability of technologies producing syngas as an intermediate. Because hydrogen must be produced externally to maximize fuel production yields, hydrogen production technologies and their potential synergisms with SAF production must be carefully studied to develop optimized systems. We have produced an Excel-based model that accounts for both stoichiometric and thermodynamic constraints in fuel production from biomass. This tool has not been utilized but could theoretically be updated and deployed for the testing of basic process optimization. We have placed our extended Lange model into a Python module that allows the calculation of economics for simple stoichiometric processes. We can easily extend this model to accept generalized user inputs, if needed for public outreach.

Publications

None.

Outreach Efforts

We have biweekly meetings with our panel of experts and have been advancing in progress toward the goals of this task. We have completed a literature review of hydrogen production technologies, their TEAs, and the synthesis of new SAF production pathways. Our project was presented at the Spring ASCENT meeting (April 5–7, 2022) and at the Civil Aviation Alternative Fuels Initiative meeting in Washington, DC (June 1–3, 2022). We also presented our work at the October 2022 Fuel Task Group meeting in Alexandria, VA.

Student Involvement

Valentina Sierra (student), Anika Afrin (student), Aidan Garcia (research associate) and Robert Macias (research associated).

Plans for Next Period

In this quarter, we hope to have enough information to complete TEAs of new SAF production concepts integrating biomass gasification with existing hydrogen production pathways. We plan to develop design cases for novel selective gasification processes.

References

Lange JP (2016). Catalysis for bio-refineries-performance criteria for industrial operation. *Catalysis Science and Technology* 6(13), 4759-4767

Task 4 - Develop Methods for Assessing the Economic and Environmental Impacts of the Most Promising Fuel Production Pathways

Massachusetts Institute of Technology

Objectives

Under Task 4, the MIT team aims to define a method for assessing the economic and environmental impacts of promising fuel production pathways, including those identified by the WSU team under Tasks 1–3. For this purpose, the team develops TEA and LCA models. The TEA model calculates the minimum selling price of a specific fuel, and the LCA model computes its lifecycle GHG emissions. Because the exact process layout and process characteristics (e.g., mass and energy balances, CapEx, OpEx) of novel fuel production pathways are subject to uncertainty, the modeling chain must be stochastic. This approach allows the uncertainty to be represented in input parameters, which will be propagated through the model to obtain insights into the range of economic and environmental impacts associated with fuels from novel fuel production pathways.

Research Approach

The models leverage prior work on stochastic techno-economic and lifecycle GHG emission assessments of SAF (e.g., Bann et al., 2017; Suresh et al., 2016; Oriakhi, 2020). These models will be adjusted to assess future fuel production pathways with novel layouts and increased uncertainties. In building the stochastic models, careful consideration is given to categorizing inputs as uncertain instead of variable. An uncertain variable is one for which available data are sparse or there is little understanding of what contributes to a spread in values. An uncertain variable is also an input that a biofuel facility cannot intentionally control. Priority was placed on analyzing uncertainty and including it in a Monte Carlo analysis. Variability refers to inherent heterogeneity in the outcomes for a specific variable. Variable outcomes can be intentionally controlled, e.g., by choosing a production location. Variable inputs are chosen for sensitivity studies, e.g., to assess the impact of the carbon intensity of electricity on the lifecycle emissions of a fuel. Figure 1 summarizes the categorization of inputs.

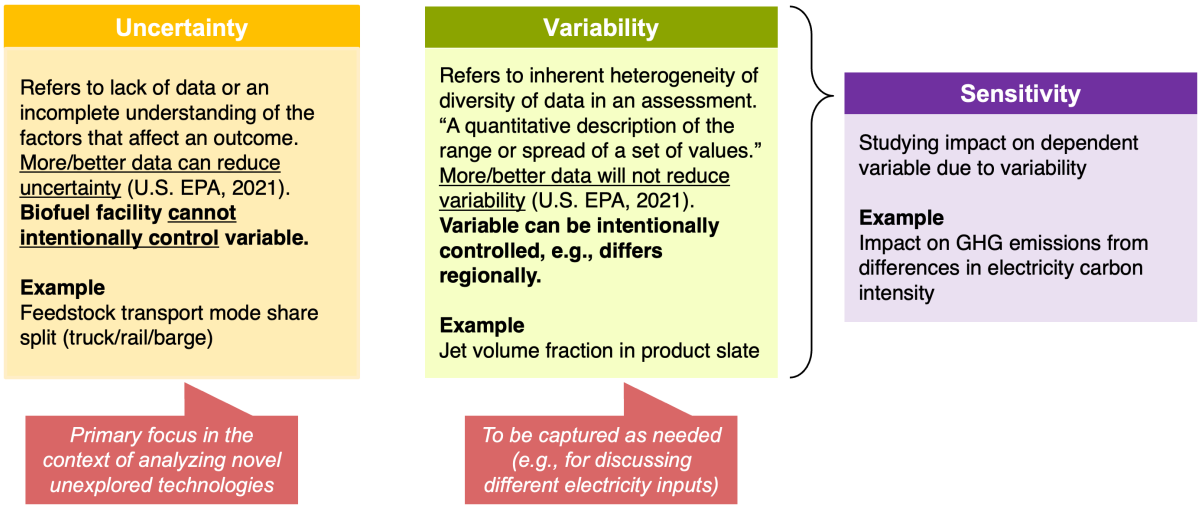

Figure 1. Input categorization as uncertainty, variability, and sensitivity. GFG: greenhouse gas.

Uncertain inputs are modeled as distributions for modeling. The LCA method follows the energy allocation method (Elgowainy et al., 2012). The TEA is implemented on the basis of the discounted cash flow rate of return (Pearlson et al., 2013). In the Monte Carlo analysis, random draws of uncertain variables are typically repeated 1,000 times. The number of runs is increased if the variance is determined to be higher than desired. This process is repeated for sensitivity studies as required.

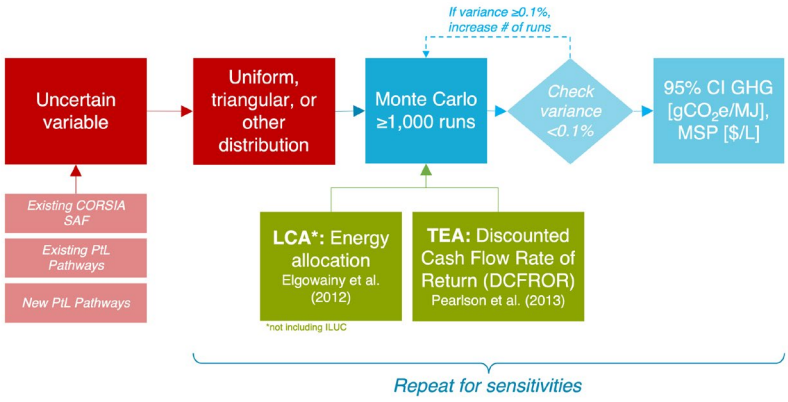

Figure 2. Modeling approach for Monte Carlo analysis for fuel lifecycle analysis (LCA) and techno-economic analysis (TEA). CI: carbon intensity; CORSIA: Carbon Offsetting and Reduction Scheme for International Aviation; GHG: greenhouse gas; PtL: power to liquid; SAF: sustainable aviation fuel.

Milestone

The MIT team presented the initial modeling approach to the FAA and other stakeholders.

Major Accomplishments

The MIT team developed a first draft of the model structure, which can be applied to existing fuel pathways. This step will provide the basis for further model development, validation, and application.

Publications
None.

Outreach Efforts
- The team provided insights into the modeling approach during the Fall 2021 and Spring 2022 ASCENT meetings.
- The team presented this work to the Fuels Task Group in October 2022.

Student Involvement
During the reporting period, Tae Joong Park (MIT graduate student) was working this task.

Plans for Next Period
The team will continue to refine the method while rolling it out to numerous pathways (Task 5).

References
Bann, S. J., Malina, R., Staples, M. D., Suresh, P., Pearlson, M., Tyner, W. E., Hileman, J. I., & Barrett, S. (2017). The costs of production of alternative jet fuel: A harmonized stochastic assessment. *Bioresource Technology*, *227*, 179–187. https://doi.org/10.1016/j.biortech.2016.12.032

Elgowainy, A. et al. (2012) *Life Cycle Analysis of Alternative Aviation Fuels in GREET.* Argonne National Laboratory, Argonne, IL, USA.

Oriakhi, U.M. (2020). *A stochastic life cycle and greenhouse gas abatement cost assessment of renewable drop-in fuels.* [Master's Thesis, Massachusetts Institute of Technology].

Pearlson, M., Wollersheim, C., & Hileman, J. (2013). A techno-economic review of hydroprocessed renewable esters and fatty acids for jet fuel production. *Biofuels, Bioproducts and Biorefining*, *7*(1), 89–96. https://doi.org/10.1002/bbb.1378

Task 5 - Apply Models to Analyze the Economic and Environmental Footprint of SAF Production Pathways
Massachusetts Institute of Technology

Objective
Under Task 5, the MIT team aims to apply the models developed under Task 4 to provide harmonized assessments of the minimum selling price and lifecycle GHG emissions of different SAF pathways. During the reporting period, the team applied the modeling chain to analyze the economic and environmental implications of using renewable electricity and hydrogen from different sources in selected CORSIA (Carbon Offsetting and Reduction Scheme for International Aviation)-eligible SAF pathways.

Research Approach
For the current reporting period, the MIT team analyzed the HEFA process with used cooking oil (UCO) feedstock. Existing literature sources (e.g., Seber et al., 2014; Lopez et al., 2010; Capaz et al., 2020; ICAO 2022) were used to populate distributions for uncertain parameters. Such uncertain parameters included transport distances for raw grease collection, rendered oil transport, natural gas and electricity use for UCO rendering and for fuel production, and process yields. Uniform distributions were fit to data whenever only low and high values were available. Triangular distributions were fit to inputs when a mean value and low and high values were available.

The Monte Carlo results shown in Figure 3 indicate that the uncertainty band (5^{th} to 95^{th} percentile spread) for the HEFA UCO base case (using hydrogen from SMR; gray line) is approximately 1.5 g CO_2e/MJ per unit SAF for U.S. grid electricity from the GREET 2019 model (Argonne National Laboratory, 2022). The team studied the sensitivity of the result with respect to electricity carbon intensity and found that the uncertainty band remains relatively small (gray line). This result arises because electricity accounts for ~5% of direct process energy in the HEFA process and the uncertainty in the electricity input is small. If the process is reconfigured to use hydrogen from electrolysis instead of SMR (green line), the sensitivity in fuel carbon intensity to the electricity carbon intensity increases significantly. For electricity inputs with a carbon intensity lower than 165 g CO_2e/kWh, the team found that the hydrogen supply from electrolysis produces a lower fuel carbon intensity than

when hydrogen from SMR is used. Electricity from solar power, wind, natural gas with carbon capture and sequestration, hydropower, and combined cycle combustion of willow are examples of electricity energy sources that would result in carbon savings.

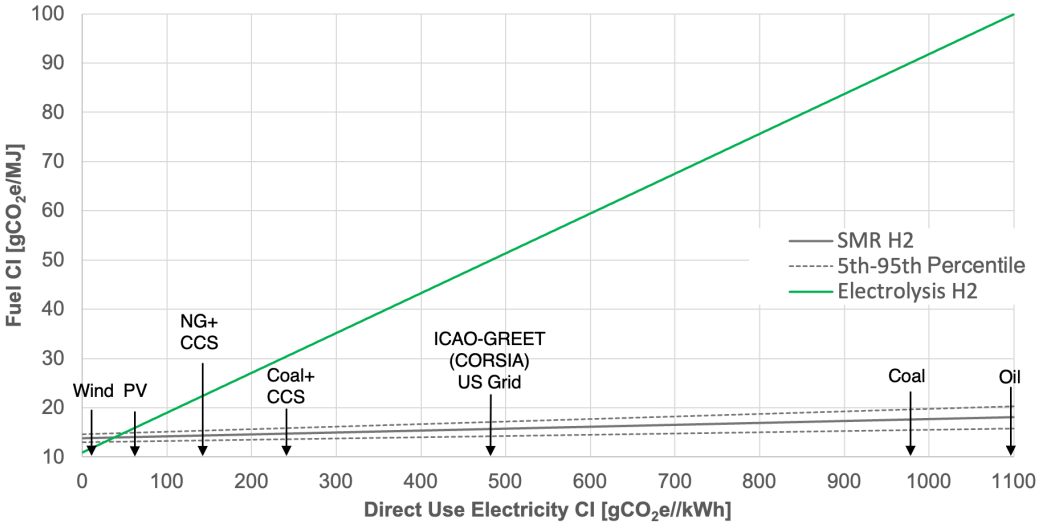

Figure 3. Sensitivity of carbon intensity (CI) for hydro-processed ester and fatty acid from used cooking oil fuel to the electricity CI for H_2 from steam methane reforming (SMR) and electrolysis. CCS: carbon capture and sequestration; NG: natural gas; PV: photovoltaic.

Milestone
The MIT team presented the initial modeling approach to the FAA and other stakeholders.

Major Accomplishments
The MIT team presented initial model results, which will provide the basis for further modification of the model.

Publications
None.

Outreach Efforts
- The team provided insights into the modeling approach during the Fall 2021 and Spring 2022 ASCENT meetings.
- The team presented this work to the Fuels Task Group in October 2022.

Student Involvement
During the reporting period, Tae Joong Park (MIT graduate student) worked this task.

Plans for Next Period
The team aims to roll out the model for additional CORSIA-eligible pathways. In addition, the team intends to start analyses on novel fuel pathways.

References
Capaz, R. S., Posada, J. A., Osseweijer, P., & Seabra, J. E. A. (2021). The carbon footprint of alternative jet fuels produced in Brazil: exploring different approaches. *Resources, Conservation and Recycling*, *166*, 105260. https://doi.org/10.1016/j.resconrec.2020.105260

Argonne National Laboratory. (2022*). Energy Systems and Infrastructure Analysis – GREET Aviation Module.* https://greet.es.anl.gov/greet_aviation

ICAO., (2022B). *CORSIA Eligible Fuels – Life Cycle Assessment Methodology (CORSIA Supporting Document)*. ICAO, Montreal, Canada. https://www.icao.int/environmental-protection/CORSIA/Documents/CORSIA_Eligible_Fuels/CORSIA_Supporting_Document_CORSIA%20Eligible%20Fuels_LCA_Methodology_V5.pdf

López, D. E., Mullins, J. C., & Bruce, D. A. (2010). Energy life cycle assessment for the production of biodiesel from rendered lipids in the United States. *Industrial & Engineering Chemistry Research*, *49*(5), 2419–2432. https://doi.org/10.1021/ie900884x

Seber, G., Malina, R., Pearlson, M.N., Olcay, H., Hileman, J.I., Barrett, S.R.H., 2014. Environmental and economic assessment of producing hydroprocessed jet and diesel fuel from waste oils and tallow. Biomass and Bioenergy 67, 108–118. doi:10.1016/j.biombioe.2014.04.024

Task 7 - Analyze the Prospects of DAC of Atmospheric CO_2 to Provide a Carbon Source for SAF Production

Massachusetts Institute of Technology

Objectives

Under Task 7, the MIT team aims to analyze proposed technological approaches for DAC as well as their readiness, scalability, and economic performance. Past and potential future trajectories of DAC technologies will be analyzed to define scenarios of how DAC could evolve to provide a potential carbon source for SAF production. In addition, the opportunity space for implementing different DAC technologies with conversion processes will be analyzed.

The initial step under this task was to provide an overview of the existing production technologies.

Research Approach

The team has focused on identifying different DAC technologies, their readiness, and potential development trajectories. This effort includes first-order stochastic assessments of economic performance for a range of technology scenarios. In addition to literature studies and detailed analyses of the different process steps, the team is conducting expert interviews.

Milestone

The MIT team ramped up work under this task in Fall 2022.

Publications

None.

Outreach Efforts

None.

Student Involvement

During the reporting period, Tara Housen (MIT graduate student) worked this task.

Plans for Next Period

The team will continue analyses of DAC processes, as described above.

Project 081 Measurement and Prediction of Non-Volatile Particulate Matter Size and Number Emissions from Sustainable and Conventional Aviation Fuels

Missouri University of Science and Technology, Aerodyne Research, and General Electric

Project Lead Investigator

Philip D. Whitefield
Professor Emeritus of Chemistry
Department of Chemistry
Missouri University of Science and Technology
400 W 11th Street, Rolla, MO 65409
573-465-7876
pwhite@mst.edu

University Participants

Missouri University of Science and Technology (MS&T)

- P.I.: Philip D. Whitefield, Professor Emeritus of Chemistry
- FAA Award Number: 13-C-AJFE-MST, Amendments 021 and 024
- Period of Performance: June 14, 2022 to June 30, 2024
- Tasks:
    1. Non-volatile particulate matter (nvPM) emission characterization from a designated combustor burning Jet A fuel and three sustainable aviation fuel (SAF) candidates
        - 1a: Develop a test matrix for combustor measurements and design an extractive sampling system.
        - 1b: Prepare an enhanced North American Reference System (NARS) apparatus for nvPM for deployment and fabricate a sampling system.
        - 1c: Deploy the NARS apparatus and support team to the General Electric (GE) designated test cell to set up the sampling system and execute the test matrix.
        - 1d: Tear down the testing facility and return the NARS apparatus to the operations base.
        - 1e: Conduct data reduction, analysis, and reporting, with the goal of providing a unique SAF emission database for the designated annular combustor.
    2. nvPM emission characterization from a designated engine operating on the same class of combustor studied in Task 1, also burning Jet A fuel and three SAF candidates
        - 2a: Develop a test matrix for engine measurements and design an extractive sampling system.
        - 2b: Prepare the enhanced NARS apparatus for deployment and fabricate a sampling system.
        - 2c: Deploy the NARS apparatus and support team to the GE designated test cell to set up the sampling system and execute the test matrix.
        - 2d: Tear down the testing facility and return the NARS apparatus to the operations base.
        - 2e: Conduct data reduction, analysis, and reporting, with the goal of providing a unique SAF emission database for the designated annular combustor/engine combination.

Project Funding Level

PROJECT	FUNDING	MATCHING	SOURCE
13-C-AJFE-MST, Amendment 021	$650,230.00	$650,230.00	FOCA Letter
13-C-AJFE-MST, Amendment 024	$1,399,770.00	$1,399,770.00	FOCA Letter GE Letter

Investigation Team

Philip Whitefield (MS&T): P.I. (responsible for all tasks)
Steven Achterberg (MS&T): Co-P.I. and lead technical support (responsible for all tasks)
William Satterfield (MS&T): Electronics and measurement specialist (support all tasks)
Richard Miake-Lye (Aerodyne Research Incorporated): Subcontractor and co-P.I. (responsible for all tasks)
Frank Bachman (GE): Subcontractor and co-P.I. (responsible for all tasks)
Joseph Zelina (GE): Subcontractor and co-P.I. (responsible for all tasks)

Project Overview

The team will make high-priority nvPM size-, number-, and mass-related measurements on both an annular combustor rig and a gas turbine engine, both independently scheduled for test cell activities, both utilizing the same combustor, and both burning conventional and alternative fuels. These studies are scheduled to take place in 2023/24 in two four-week test campaigns preceded by test design, planning, and preparation and followed by data analysis and interpretation.

Task 1 - Annular Combustor Emission Measurements with Jet A Fuel and Three Candidate SAFs

Missouri University of Science and Technology

Objectives

These efforts will focus on the following tasks:

- Performance evaluation of nvPM size diagnostics
- Performance assessment of a novel nvPM mass calibration standard
- Potential synthesis of a transfer function from combustor to full engine based on nvPM characteristics
    - In this task, the annular combustor emission characteristics will be acquired.
- Quantification of the effects of ambient conditions on combustor nvPM emissions
- Quantification of the influence of fuel composition on the emissions

Research Approach

Current nvPM certification requirements for aviation engines involve the direct measurement of mass and number concentration at the exit plane of the engine. For aviation engine manufacturers to design engines with minimal nvPM emissions, it is critical for the manufacturers to understand the nvPM behavior from its source, the combustor, to the current certification measurement plane, the engine exit. It is also valuable to understand the impact on nvPM generation when SAFs are utilized, as opposed to traditional JP fuels. To facilitate a complete understanding of the potential changes in the characteristics of nvPM passing through the aviation engine from its source to the ultimate measuring plane, as well as a better understanding of particulate losses through the engine and measuring systems, it is critical to fully characterize the nvPM size distribution throughout the engine flow path to which the particulates are exposed – from the combustor exit plane to the engine exit plane.

This project provides a unique opportunity to measure nvPM size distributions at both the combustor exhaust plane and engine exit plane for a modern aviation turbofan engine via a wide range of available nvPM size measurement systems, including a TSI scanning mobility particle sizer, Cambustion DMS500 fast particle sizer, and TSI engine exhaust particle sizer. This project allows such measurements to be performed with traditional Jet A fuel as well as several candidate SAFs. In addition, the composition of the volatile components of the measured particulate matter (PM) and their relation to the non-volatile component will be measured using the Aerodyne aerosol mass spectrometer, in combination with cavity attenuation phase shift (CAPS) black carbon measurements of extinction. The CAPS measurements can also be compared with the other nvPM mass measurements such as laser-induced incandescence and micro-soot sensor measurements.

The combustor component tests offer a unique opportunity to explore the influence of ambient effects on nvPM emissions. Because the combustor inlet conditions, including T_3, p_3, and fuel–air ratio, can be controlled independently in the combustor rig in a more systematic manner than in an engine, conditions can be chosen such that the independent effects of these variables on the nvPM emission levels and properties can be ascertained. These measurements will be of particular value for developing corrections for the effects of ambient conditions, a high priority for improving nvPM regulatory requirements by the International Civil Aviation Organization's Committee on Aviation Environmental Protection. While some recent progress

has been made on developing ambient condition corrections, data from a modern, advanced technology combustor type will enable significant advances in this area. The combustor component tests will be accompanied by corresponding measurements on a modern aviation engine incorporating an identical-design combustor.

This project represents a unique opportunity to explore the impact of the engine flow path on nvPM characteristics, from the combustor exit plane to the engine exhaust plane. This project also allows for an exploration of the characteristics of a transfer function for nvPM from the combustor exit plane to the engine exit plane. These efforts will provide valuable information regarding the influence of SAFs on nvPM characteristics in an aviation engine.

In addition to the test campaign described above, in which Jet A fuel will be employed, the tests will investigate the impact on particulate concentrations and size distributions due to SAFs relative to traditional aviation fuels, e.g., Jet A fuel.

Given the availability of a desired or specific SAF, the impact of alternative fuel will be investigated during the component test and engine portion of the project. Additional alternative fuel testing could be realized at a very fundamental level via a relatively limited scope test plan characterizing only the four landing and take-off (LTO) T3 test conditions for the component combustor. If more fidelity on the impact of SAFs is desired, the scope of the limited fundamental test plan can be systematically expanded in a modular fashion to include, for example, the four LTO test conditions as well as additional test points representing each nominal LTO point plus, or minus, excursions in T3 in predetermined increments for as many increments as desired. This approach provides maximum flexibility and expandability to accommodate available resources and fuel quantities while maximizing potential benefits and learning from the activity.

The nvPM characterization will be achieved by using an expanded aerospace recommended practice. The Aircraft Exhaust Emissions Measurement Committee (E-31) of the Society of Automotive Engineers has published Aerospace Recommended Practice (ARP) 6320, detailing a sampling system for measuring nvPM from aircraft engines (E-31P Particulate Matter Committee, n.d.). The system is designed to operate in parallel with existing International Civil Aviation Organization Annex 16-compliant combustion gas sampling systems used for emission certification of aircraft engines captured by conventional (Annex 16) gas sampling rakes. The certification measurements of nvPM emissions will be performed using this nvPM sampling system defined by the Society of Automotive Engineers.

MS&T owns and operates an ARP6320-compliant NARS for measuring nvPM emissions from the exhaust of aircraft engines. The nvPM system consists of three sections, i.e., collection, transfer, and measurement sections, connected in series (Figure 1). A description of each section is provided below.

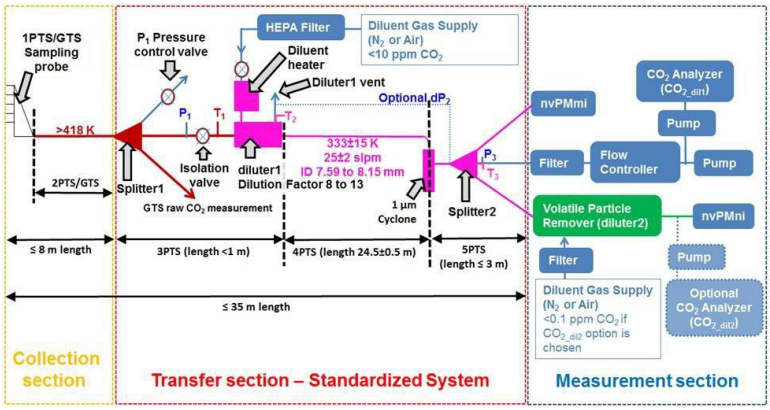

Figure 1. Components of an Aerospace Recommended Practice 6320 non-volatile particular matter system (North American Reference System).

Collection section
The collection section consists of a probe rake system and up to 8 m of a stainless sample line heated to 160 ˚C.

Transfer section
The transfer section consists of a three-way sample splitter, a PM sample eductor/dilutor, flow controllers, and sample line heater controllers. The first sub-component of the transfer section is a three-way sample splitter that divides the total exhaust gas sample from the rake into three flow streams. The first flow stream is the required flow of exhaust for the Annex 16 combustion gas sample. The second stream is the PM sample, and the third flow stream is an excess flow dump line controlled by a pressure relief valve. The PM sample is diluted by a factor of 8–13 with dry nitrogen (heated to 60 °C) by means of an eductor/dilutor. The diluted PM sample has a flow rate of 25 ± 2 SLPM and is transferred by an electrically heated, temperature-controlled conductive, grounded, carbon-loaded polytetrafluoroethylene PM sample transfer line 25 m in length, maintained at 60 °C to a 1-µm cyclone and then a second three-way splitter to direct the sample to the number and mass measurement devices in the measurement system.

Measurement section
The measurement section consists of a volatile particle remover and a particle number measurement device, a mass measurement device, and a mass flow controller, pump, and CO_2 detector as specified by ARP6320. The NARS is enhanced relative to the certification requirements in that three distinct mass measurement systems are deployed (laser-induced incandescence, micro-soot sensor, and CAPS) to provide redundant nvPM mass measurements. An additional instrument for obtaining size-dependent measurements of particle composition is also included (aerosol mass spectrometer). The additional measurements are compatible with the certification requirements because the extra flows needed for the additional measurements are drawn from the make-up flow (central leg of Figure 1) and do not affect any of the required measurements, while providing valuable additional data.

Milestones

- Test articles have been identified.
- Testing dates have been identified.
- Fuel candidates have been identified and procured.
- Combustor testing has been completed.
- Analyses have been reported.

Major Accomplishments

- This project was awarded in part in June 2022 and September 2022.
- A preliminary test plan is under development.
- SAF candidates are currently being identified.

Publications

Whitefield, P. (2022, Oct. 26). *ASCENT 81 Measurement and Prediction of nvPM Size and Number Emissions from Sustainable and Conventional Aviation Fuels* [Oral presentation]. ASCENT Advisory Board Meeting, Alexandra, VA.

Outreach Efforts

None.

Awards

None.

Student Involvement

None.

Plans for Next Period

- Test articles and testing opportunities will be identified.
- SAF candidates will be identified, procured, and delivered to test cell locations in the Cincinnati area.
- The enhanced NARS facility will be prepared for deployment and subsequently deployed.
- The designated annular combustor emission characteristics will be determined during two test campaigns.
- The raw data acquired during testing will be analyzed, interpreted, and reported.

References

E-31P Particulate Matter Committee. (n.d.). *Procedure for the continuous sampling and measurement of non-volatile particulate matter emissions from aircraft turbine engines*. SAE International. https://doi.org/10.4271/ARP6320

Task 2 - Engine Emission Measurements with Jet A Fuel and Three Candidate SAFs

Missouri University of Science and Technology

Objectives

These efforts will focus on the following tasks:

- Performance evaluation of nvPM size diagnostics
- Performance assessment of a novel nvPM mass calibration standard
- Potential synthesis of a transfer function from combustor to full engine based on nvPM characteristics
    - In this task, the full engine emission characteristics will be acquired.
- Quantification of the effects of ambient conditions on full-engine nvPM emissions
- Quantification of the influence of fuel composition on full-engine emissions

Research Approach

See the research approach described for Task 1. A research approach similar to that described in Task 1 will be employed in Task 2, focusing on engine emissions.

Milestones

- Test articles have been identified.
- Testing dates have been identified.
- Fuel candidates have been identified and procured.
- Engine testing has been completed.
- Analyses have been reported.

Major Accomplishments

- This project was awarded in part in June 2022 and September 2022.
- A preliminary test plan is under development.
- SAF candidates are currently being identified.

Publications

Whitefield, P. (2022, Oct. 26). *ASCENT 81 Measurement and Prediction of nvPM Size and Number Emissions from Sustainable and Conventional Aviation Fuels* [Oral presentation]. ASCENT Advisory Board Meeting, Alexandra, VA.

Outreach Efforts

None.

Awards

None.

Student Involvement

None.

Plans for Next Period

- Test articles and testing opportunities will be identified.
- SAF candidates will be identified, procured, and delivered to test cell locations in the Cincinnati area.
- The enhanced NARS facility will be prepared for deployment and subsequently deployed.
- The designated annular combustor engine combination emission characteristics will be determined during two test campaigns.

- The raw data acquired during testing will be analyzed, interpreted, and reported.

References

E-31P Particulate Matter Committee. (n.d.). *Procedure for the continuous sampling and measurement of non-volatile particulate matter emissions from aircraft turbine engines*. SAE International. https://doi.org/10.4271/ARP6320

Project 082(A) Modeling of the Committee on Aviation Environmental Protection Stringency Analysis

Georgia Institute of Technology

Project Lead Investigator

P.I.: Professor Dimitri N. Mavris
Director, Aerospace Systems Design Laboratory
School of Aerospace Engineering
Georgia Institute of Technology
404-894-1557
dimitri.mavris@ae.gatech.edu

Co-P.I.: Dr. Michelle Kirby
Chief, Civil Aviation Division
Aerospace Systems Design Laboratory
School of Aerospace Engineering
Georgia Institute of Technology
404-385-2780
michelle.kirby@ae.gatech.edu

University Participants

Georgia Institute of Technology

- P.I.s: Dr. Dimitri N. Mavris, Dr. Michelle Kirby
- FAA Award Number: 13-C-AJFE-GIT-117
- Period of Performance: June 14, 2022 to September 30, 2022
- Task:
    1. Dual Stringency Analysis Support

Project Funding Level

The FAA provided $300,000 in funding, and the Georgia Institute of Technology (Georgia Tech) has agreed to a total of $300,000 in matching funds. This total includes salaries for the project director, research engineers, and graduate research assistants, as well as funds for computing, financial, and administrative support, including meeting arrangements. Georgia Tech has also agreed to provide tuition remission for the students, paid from state funds.

Investigation Team

Faculty and Research Staff

Professor. Dimitri Mavris, Georgia Tech), Principal Investigator, (Task 1
Dr. Michelle Kirby, Georgia Tech, Co-Principal investigator (Task 1),
Dr. Jimmy Tai, Georgia Tech, Senior Research Engineer (Task 1)
Dr. Burak Bagdatli, Georgia Tech, Research Engineer, (Task 1)
Dr. Holger Pfaender, Georgia Tech, Research Engineer, (Task 1)
Dr. Elena Garcia, Georgia Tech, Senior Research Engineer, (Task 1)
Mr. David Anvid, Georgia Tech, Research Engineer, (Task 1)
Mr. Brennan Stewart, Georgia Tech, Research Engineer, (Task 1)

Graduate Researchers

Ms. Melek Ozcan, Georgia Tech (Task 1)
Mr. Zelin He, Georgia Tech (Task 1)

Mr. Antoine Marin, Georgia Tech (Task 1)
Mr. David Mothershed, Georgia Tech (Task 1)
Mr. Gabriel Fronk, Georgia Tech (Task 1)
Mr. Andy Tan, Georgia Tech (Task 1)
Ms. Niharika Akula, Georgia Tech (Task 1)
Mr. Jayaprakash Kambhampaty, Georgia Tech (Task 1)
Mr. Kumanan Srinivasan, Georgia Tech (Task 1)

Project Overview

This project will provide technical support to the FAA for the assessment of the 13th cycle of the Committee on Aviation Environmental Protection (CAEP/13) stringency analysis, including cost estimations of various stringency options. Prior CAEP stringency analysis included a cost-benefit assessment of different scenarios based on outdated information and relied on industry subject matter input. This project will enhance and update the assumptions based on a quantitative assessment of technological benefits and the costs associated with achieving those benefits. The end result will provide the FAA with a data-driven process for decision-making, including the interdependencies between CO_2 and noise as well as the costs associated with their mitigation.

Task 1 – Dual Stringency Analysis Support

Georgia Institute of Technology

Objectives

The purpose of this ASCENT project is to support the FAA in conducting a cost-benefit stringency analysis for CAEP/13 while considering the interdependencies between CO_2 and noise. While analyses of this type have been previously conducted, this project seeks to update the assumptions and modeling capabilities to provide a data-driven decision-making process for the FAA. This research will use the Aircraft Noise Design Effects Study (ANDES)conducted in 1994 by industry as a starting point to assess the costs associated with design trades for reducing aircraft noise to be more representative of current technology, manufacturing techniques, and operational behavior. The Georgia Tech team will assist the broader U.S. Research Team to accomplish the goals of the dual-stringency analysis.

Research Approach

In support of the broader research team, the Georgia Tech team has focused on three main research thrusts:

- Updating the non-recurring cost (NRC) function
- Updating the technology responses possible for various stringency options
- Providing broad technical support for the CAEP working groups

Methodology and Implementation

Each research thrust is an independent effort and thus has different approaches and results, as described below.

Non-Recurring Cost Function Development

For the sample problem, cost elements and approaches will be leveraged from previous CAEP analyses. Therefore, the Georgia Tech team reviewed the NRC models used in CAEP/9, CAEP/10, and CAEP/12 to gain insight into the rationale and assumptions made while these NRC models were being developed and to identify what changes are necessary for the integrated stringency analysis.

As part of the CAEP/9 assessment of noise stringency scenarios, CAEP developed and used methodologies for estimating NRC, including non-recurring aircraft owner/operator (N-R AO/O) and non-recurring manufacturer (N-R M) costs.

The CAEP/9 NRC methodology estimates N-R AO/O costs, which include the loss in fleet value incurred by aircraft operators for aircraft that will not meet noise stringency values. This estimation applies the assumption that a new noise stringency standard would reduce the market value of existing aircraft that need modifications to comply with the new standard. According to the CAEP/9 NRC analysis, the economic impact could follow two scenarios. In the first scenario, the resulting lower costs of non-compliant aircraft that need modifications would benefit other operators that would be able to purchase aircraft at a lower cost, therefore counterbalancing the loss in value to the selling operators. The second scenario covers a potential outcome with a net financial loss because the market for purchasing these aircraft would be smaller than the overall

fleet of non-compliant aircraft. This loss in fleet value was calculated for aircraft that would not meet the noise stringency values and with delivery dates between the base year and the noise stringency date (2007–2019). The Aircraft Noise Design Effects Study (ANDES) model used to estimate the noise reduction technology (NRT) response was also used to estimate the loss in fleet value. The estimation is limited to a 2-dB NRT response. The costs of retrofits were calculated using the NRT-less fuel curve (with a maximum change of 0.6% in direct operating costs).

The CAEP/9 NRC methodology also comprises N-R M costs. These costs include the additional economic impacts on manufacturers to follow a new noise stringency standard. These costs were calculated by estimating the costs to manufacture and replace failing aircraft. The costs include the cost of aircraft replacement as well as the cost to write-off new aircraft and engine programs with no previous investments. Both costs were calculated using parametric models developed by NASA, i.e., the Airframe Cost Model and the Aircraft Turbine Engine Cost Model.

As noted in CAEP/9, "there were different perspectives regarding whether non-recurring costs should be factored into the global cost effects, the non-recurring cost values were considered to be part of a range from zero to the values calculated; and, the cost-effectiveness results were presented with and without each component of the non-recurring costs."

As part of the CAEP/10 CO_2 standard development and stringency analyses, the International Coordinating Council of Aerospace Industries Associations (ICCAIA) developed a methodology for estimating NRCs representing the investments that the original equipment manufacturers (OEMs) of the airframe and engine would need to make to modify or develop an aircraft that would ultimately meet a stringency option, i.e., engineering, staff, flight testing, and tool costs. The NRC model was a function of an aircraft size parameter (maximum take-off weight [MTOW]) and a technology-level parameter (metric value [MV] improvement). The methodology relied on publicly available airplane development cost information and expert engineering judgment. The cost function was calibrated to yield NRC estimates across a wide range of airplane sizes and MV improvements, with the following form:

$$NRC\ (10^9\$) = \left(\underbrace{(Ae^{Bx} + C)}_{\text{Reference Airframe NRC}} + \underbrace{\left(Ae^{B(0.9)} + C\right) f_{(\Delta MV)} \frac{2}{\#\ Engines}}_{\text{Reference Engine NRC}} \right) \underbrace{\left(\frac{MTOW}{MTOW_{ref}} \right)^{D}}_{\text{Aircraft Size Scaling}}$$

The exponential function coefficients A, B, and C were derived by calibrating the curve to cost data for a reference aircraft, which was chosen as the Bombardier CSeries; therefore, $MTOW_{ref} = 144{,}000\ lb\ (65{,}317\ kg)$. The MTOW power coefficient D was derived through the regression of airframe NRCs estimated using the NASA Airframe Cost Model.

ΔMV represents the percentage CO_2 MV improvement of an aircraft with respect to its predecessor. Because the maximum MV improvements for smaller aircraft are limited compared with those of larger aircraft, the upper bound of MV improvement is defined as a function of MTOW. Figure 1 shows that the upper bound of the MV improvement for aircraft with an MTOW of less than 90,000 lb (40,823 kg) was defined to be linearly decreasing with decreasing MTOW whereas that of heavier aircraft was defined to be constant at 20%.

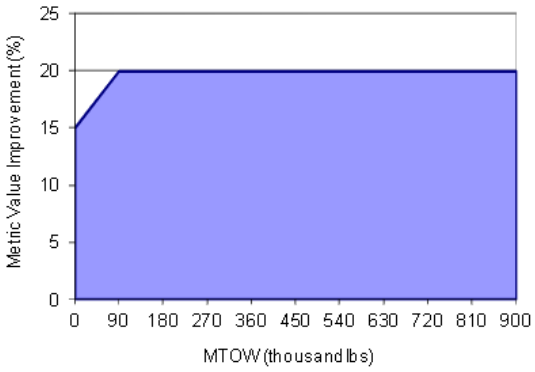

Figure 1. Boundaries of metric value improvement. MTOW: maximum take-off weight.

Because the boundaries of MV improvements vary with MTOM, the cost surface is driven by a normalized MV improvement, x:

$$x = \frac{Absolute\ MV\ Improvement - MV\ Improvement\ Lower\ Bound}{MV\ Improvement\ Upper\ Bound - MV\ Improvement\ Lower\ Bound}$$

The engine NRC was captured as a factor of the airframe NRC of a typical new aircraft with an assumed normalized MV improvement of 0.9. The factor was based on two different analyses: new engine programs (MV improvement above 8%) and performance improvement packages (PIPs) (MV improvement below 4%). For new engine program costs, the ratio of engine list price to aircraft list price was assumed to represent the ratio of engine development cost to airframe development cost. A statistical analysis of select engine list prices and corresponding aircraft list prices suggested that the engine development costs corresponded to 15% of aircraft development costs. The ratio of engine development costs to airframe development costs for A350 and a hypothetical new 737-sized aircraft was found to be approximately 15%. Similarly, PIP NRCs were derived using a ratio of PIP list price to engine list price for similar thrust classes. This review resulted in a PIP to new engine price ratio of approximately 10%–25%. A constant value of 20% was adopted, which means that PIP programs represent an additional 3% of the airframe NRC. Figure 2 shows the piecewise linear function of the factor for engine NRC with respect to MV improvement.

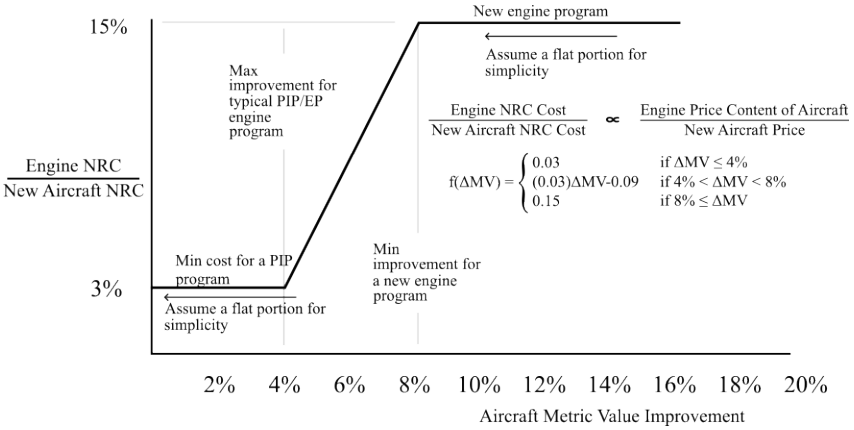

Figure 2. Profile of the engine non-recurring cost (NRC) factor. PIP: performance improvement package; EP: enhanced performance.

Table 1 presents the NRC coefficients developed to fit the airframe portion of the cost surface to publicly available data gathered on airframe development costs.

Table 1. Non-recurring cost coefficients for Method A (model from the International Coordinating Council of Aerospace Industries Associations).

	A	B	C	D
Value	0.18591	3.26306	-0.13592	0.69700

This model, also called Method A, was created to measure the relative positioning of different options. The results closely match the validation data for mid-to-large MV improvements and overestimate the NRC costs for small MV improvements. U.S. Environmental Protection Agency (EPA) and the consulting company ICF hired by EPA vocalized the need for a revised NRC equation to better account for NRCs for small values of ΔMV. ICF found data on incremental technologies such as the 767-300 winglet and GE90-115B PIP. Table 2 shows the adjusted NRC coefficients obtained after including data for small ΔMV values, using the same reference aircraft.

Table 2. Non-recurring cost coefficients for Method B (EPA/ICF model).

	A	B	C	D
Value	0.091366197	3.995	-0.028828006	0.5576

The main strength of the EPA/ICF model, also called Method B, is that it provides data points for an area in which most aircraft respond. However, the model does not scale well for large ΔMV improvements. An NRC Small Group was formed to review and understand the differences in the data and approaches as well as to develop a hybrid NRC surface equation denoted as Method A-B. Samples from Method A for mid-to-high ΔMVs and samples from Method B for low ΔMV values were gathered to remedy the limitations of both methods. Then, these samples were regressed to generate a new NRC surface. In Method A-B, the maximum take-off mass (MTOM) scaling factor D and $f_{(\Delta MV)}$ were changed to sigmoid functions to lower the engine cost component for small ΔMVs and to account for incremental improvements. The final NRC formulation of CAEP/10 is shown in Table 3 and Figure 3.

Table 3. Non-recurring cost coefficients for Method A-B.

	A	B	C
Value	0.188902	3.247077	-0.142274

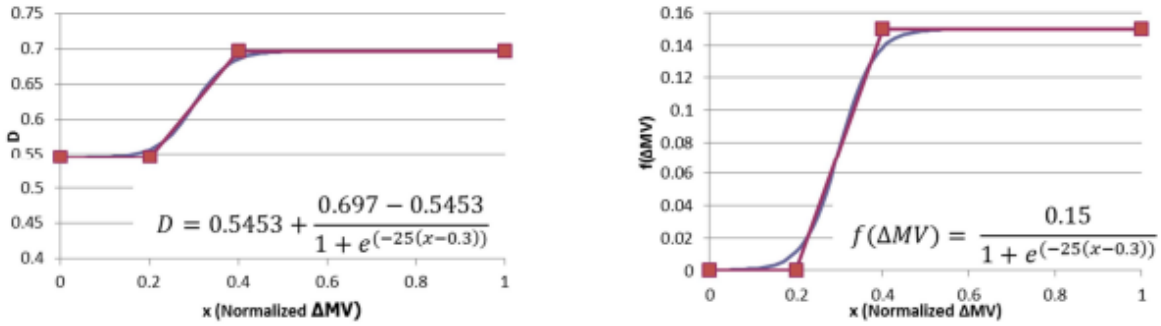

Figure 3. Coefficient D (left) and $f_{(\Delta MV)}$ (right) for Method A-B.

The Georgia Tech team used the CAEP/10 NRC functions as a starting point for the development of NRC estimates resulting from CO_2 technology response, for which it is important to avoid double counting costs resulting from a response to a CO_2 stringency and a noise stringency. A similar approach can be utilized to establish a new relationship that accounts for both changes in CO_2 MV and noise by considering the terms in the equation below to be a function of both metrics, in lieu of only CO_2.

$$NRC = \left(\left(Ae^{Bx} + C\right) + \left(Ae^{B(0.9)} + C\right) f_{(x)} \frac{2}{\#\ Engines} \right) \left(\frac{MTOW}{MTOW_{ref}} \right)^{D}$$

The necessary modifications were identified as regression coefficients (shown in blue in the equation above [A, B, and C]) and the normalized improvement variable x to include both noise and CO_2 impacts. D has a functional form and does not need to be updated. The cost data (contained in Figure 5) behind the equation were investigated for usability to create a new equation. Twenty-one aircraft programs were provided that defined a change in CO_2 MV and a publicly sourced reported airframe NRC for a given MTOM. Each entry was either a derivative aircraft of a family or a new design. Use of these data for the purpose of the CAEP/13 sample problem requires a reference aircraft that establishes the benefits in CO_2 MV.

It is assumed that a manufacturer will launch a program with the primary objective of reducing fuel burn, hence costs, to drive the market attractiveness of a new product and will use noise as a design constraint. Historically, new entrants to the market have been step changes from their predecessor in terms of fuel burn (surrogate for operating costs), and small changes in either noise or NO_x emissions are driven by meeting new regulations through PIPs or hush kits.

Each aircraft program was researched to determine a notional reference aircraft and also the specific aircraft that the program referred to instead of just "CSeries." The generality of the aircraft program description required subject matter judgement to determine what the aircraft program implied and also to identify the reference aircraft for the quoted CO_2 MV improvement. CAEP/10 analysis provided an MTOM for the program that would allow for the potential identification of a similar aircraft entry within the noise limit.

The identification of the two aircraft needed to establish the change in cumulative noise was based on expert opinions from the U.S. Research Team. Input is welcomed from the respective working group membership for modifications as needed or additional data that could be used for the regression analysis.

Of the 21 aircraft programs provided, 15 were identified to establish the change in cumulative noise associated with the given program, as depicted in Figure 4 and Figure 5. Columns shaded in tan are replications of the data contained previously. Columns shaded in yellow are the assumptions associated with the identification of the specific aircraft for the program, the MTOM assumed for a given aircraft to determine the appropriate entry in the noise limit, and the reference aircraft upon which the original CO_2 MV change was based. In some instances, the original MTOM was modified slightly to match the assumed program-specific aircraft in the noise database, as highlighted in red font. In some instances, the reference aircraft MTOM was similar to that of the program aircraft to establish the cumulative noise benefit. In other cases, an extrapolation of the cumulative noise as a function of MTOM was utilized. This approach provided the cumulative noise benefit with the CO_2 MV improvement to use as the data basis of the new regression.

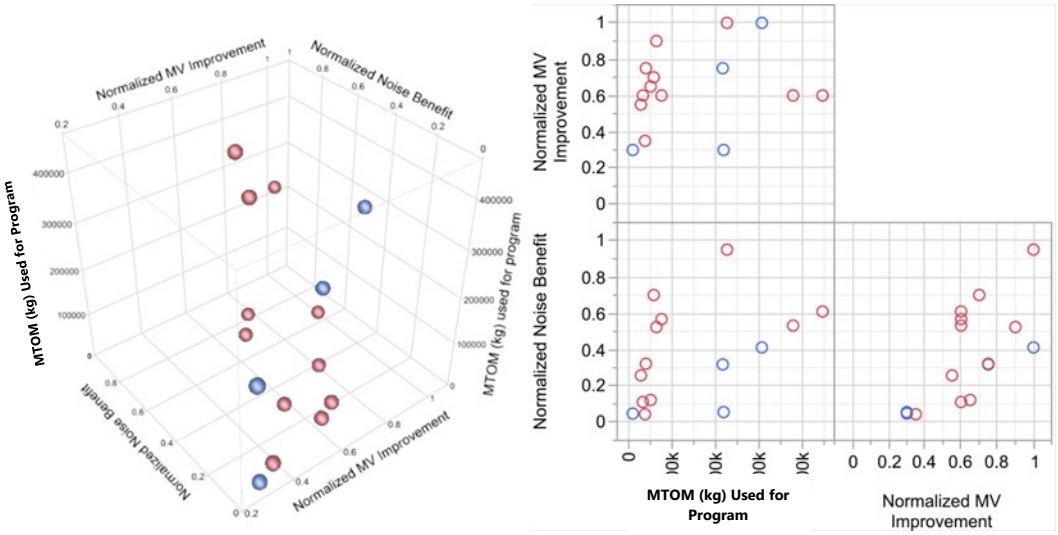

Figure 4. Aircraft program non-recurring cost data for regression analysis. MTOM: maximum take-off mass; MV: metric value.

Program	Family	MV Improvement (%)	Reported Airframe NRC (Billion 2010 USD)	Program-Specific Aircraft	MTOM (kg) Used for Program	Program Aircraft Noise Source ID	Reference Aircraft	Reference Aircraft MTOM (kg)	Reference Aircraft Noise Source ID	Noise Benefit (EPNdB)
Cseries	New	18	3.305	A220-100	65318	NdB # 6165	CRJ-900	36,400 to 38329	Extrapolated from all CRJ900 in Noise dB	13.1
787-8	New	20	10.388	B787-8	227872	NdB #11442	B767-300ER	130,952 to 186,880	Extrapolated from all B767-300ER in Noise dB	23.8
A320 neo	A320 Derivative	12	1.228	A320-2xxN	77112	NdB # 13374	A320ceo		NdB # 2023	14.2
A330/A340	New	15	5.892	A330-322	218000	NdB # 4817	A300-B4-622R	140,000 to 171,000	Extrapolated from all B4-622R in Noise dB	8.0
A330-200	A330-300 Derivative	6	0.755	A330-203	220000	NdB # 4598	A330-300	218,000	NdB # 5268	1.4
A340-500/600	A340-300 Redesign	12	4.028	A350-542	379899	NdB # 6040	A340-300	253,500 to 276,500	Extrapolated from all A330-313 in Noise dB	13.3
CRJ-700	CRJ-200 Derivative	11	1.012	CRJ-200	34010	NdB # 11641	CRJ-200	21,523 to 24,040	Extrapolated from all CRJ-100/200 in Noise dB	2.8
Global 7000/8000	Significant derivative of the 6000 with a new transonic wing	13	1.322	Global 7500	52095	NdB # 11553	Global 6000	42,411 to 45,132	Extrapolated from all Globall 6000/Express in Noise dB	3.1
Dash 8-400	Dash 8 derivative	10	0.571	Dash 8-4xx ER	29574	NdB # 11919	Dash 7	18,643 to 19,504	Extrapolated from all Dash 8-300 in Noise dB	6.5
Gulfstream V	New	15	1.293	GV	41050	NdB # 13210	Gulfstream IV	32,160 to 33,838	Extrapolated from all GIV-SP and GIV-X in Noise dB	8.1
CRJ-200	CRJ-100 derivative	5	0.436	CRJ-100/200	10905	NdB #11610	CRJ-100	24,040	NdB #11639	1.2
CRJ-1000	CRJ-900 Derivative	7	0.303	CL-600-2E25	38995	NdB #11709	CRJ-900	38,329	Extrapolated from all CRJ900 in Noise dB	1.1
747-8	747-400 Derivative	12	4	B747-8	447695	NdB #10132	B747-400	272,156 to 276,482	Extrapolated from all B747-400 in Noise dB	15.3
A350	New	20	14.166	A350-1041	307994	NdB #13393	A340-541	380,000	NdB #6040	10.3
E2 Family	E170/E190 Derivative	14	1.605	A195-E2	59200	NdB #12429	EMB-195	48,790 to 50,790	Extrapolated from all A190-100LR in Noise dB	17.5

Figure 5. Aircraft program non-recurring cost (NRC) data for regression analysis. MTOM: maximum take-off mass; MV: metric value.

A number of different functional forms were explored utilizing a non-linear regression based on the original form of the CAEP/10 NRC. The form that provided reasonable accuracy is based on normalizing the change in CO_2 MV and cumulative noise to define a new relationship for f(ΔMV), as shown below, assuming a simple weighted additive relationship between noise and CO_2 MV benefits. The term x_{CO2} was maintained from the original definition from CAEP/10, as was the coefficient D, so as to maintain the MTOM scaling effects on NRC. The normalized change in cumulative noise (x_{dB}) was normalized in a similar fashion as x_{CO2}, with the upper limit defined as 25 dB and the lower bound assumed to be zero.

$$x = \left[E x_{CO_2} + (1 - E) x_{dB}\right]$$

Of the 15 data points, 11 were utilized for model training and 4 were used as validation points. A Gauss–Newton optimizer was used to adjust A, B, C, and E until the error for the reported NRC was minimized. For the optimization problem, E was bound between 0 and 1, guaranteeing that the combined improvement variable would remain between 0 and 1, similar to the original NRC equation. The optimization results are given in Table 4 to six significant figures.

Table 4. Optimization results for the non-recurring cost equation coefficients obtained by using data from aircraft databases.

Coefficient	Value
A	0.345581
B	3.02511
C	-0.298953
E	1.00000

The regression results had reasonable error; however, because E was exactly equal to 1.0, the resulting equation ignores the impact of noise improvements on NRC. The main reason behind the optimizer's selection of 1.0 for E is the high correlation between CO_2 and noise in the data. As discussed previously, the main driver behind a program's launch is to reduce fuel burn, thus reducing the CO_2, which is also the main driver behind costs. Because noise is highly correlated with CO_2, its cost

impact is confounded with CO_2 and is already accounted for in the CO_2 term. To combat this problem, the term E in the optimization problem can be constrained to a smaller range.

An additional problem is that there are no data points in the small CO_2 improvement region ($x_{CO2} \leq 0.2$). This lack of data can lead to inaccuracies in the regression equation for small improvements as a response to a stringency option. By using models, more data points were generated to populate regions of lower CO_2 improvement. The models were used in previous work and were deemed appropriate for this effort. A relationship was built from the existing correlation between CO_2 and noise, as shown in Figure 6. While MTOM and CO_2 were sampled using the models, the synthetic data had the appropriate noise improvement, given by the equation shown in Figure 6.

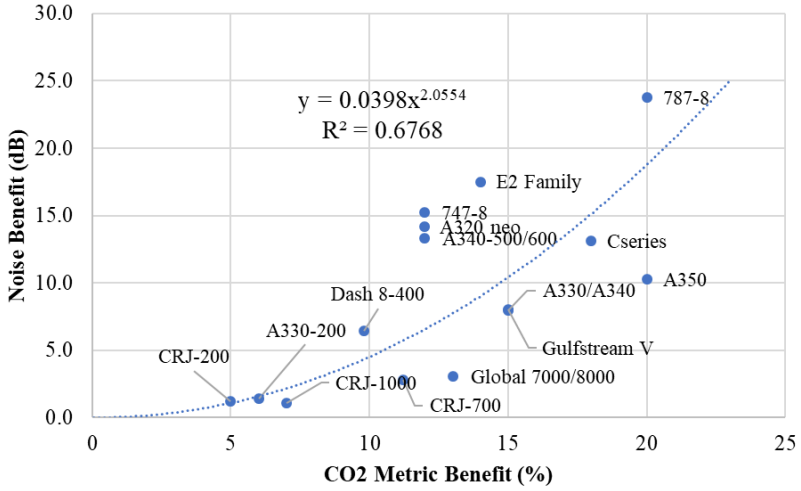

Figure 6. Noise improvement relationship based on CO_2 values for synthetic data generation.

With additional data generated and a new constraint for the parameter E (0.1–0.9), the optimization was rerun with 168 training points and 56 validation points. The results are given in Table 5. Unsurprisingly, E is still maximized within the allowed range and is driven to the upper limit of 0.9. The upper limit can be adjusted based on further discussions and expert input. The trends that can be generated from these equations are shown in Figure 7 and Figure 8. The contours on the sheet shown in Figure 8 represent increments of 5 billion 2010 USD. The equation is guaranteed to return positive values for x_{dB}, $x_{CO2} \in [0, 1]$, and MTOM ≥ 0 kg. Within the parameter space for MTOM ≤ 450,000 kg, the predicted NRC is less than 17 billion 2010 USD.

Table 5. Optimization results for the non-recurring cost equation coefficients including synthetic data.

Coefficient	Value
A	0.871231
B	2.137834
C	-0.656189
E	0.900000

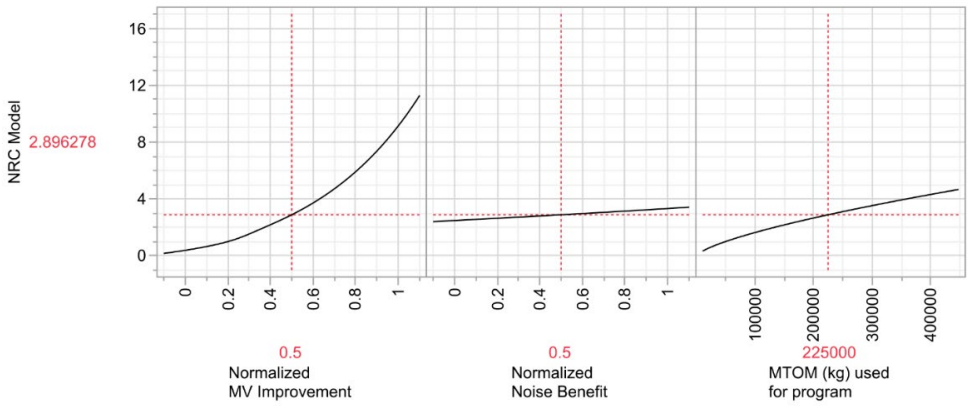

Figure 7. Visualization of the trends resulting from the non-recurring cost (NRC) function. MTOM: maximum take-off mass; MV: metric value.

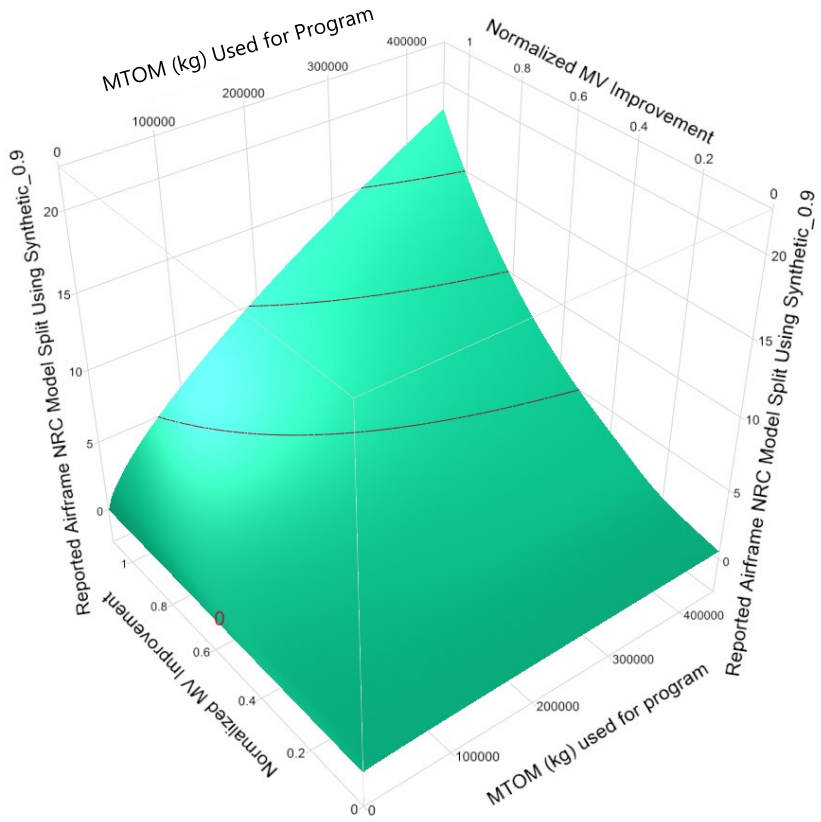

Figure 8. Ilustration of the non-recurring cost (NRC) function. MTOM: maximum take-off mass; MV: metric value.

Based on this approach, a reasonable accuracy was obtained for the majority of the aircraft program NRCs, as depicted in Figure 9, with the exception of the CRJ-200. The percent error of the predicted versus reported NRC is depicted in Figure 10. In general, the error of the regression has an interquartile range of 37%, which may be reasonable. The resulting function

tends to slightly overpredict the cost in the low-cost region. If this overprediction is unacceptable for use in the sample problem, modifications can be made to include additional data in the regression, modify the training and validation data, or change the functional form based on subject matter input. In the interim, this combined NRC curve can serve as the basis for the CAEP/13 sample problem and can be updated with further data or subject matter expert input from the working groups. The equations and regression coefficients are given in Figure 11.

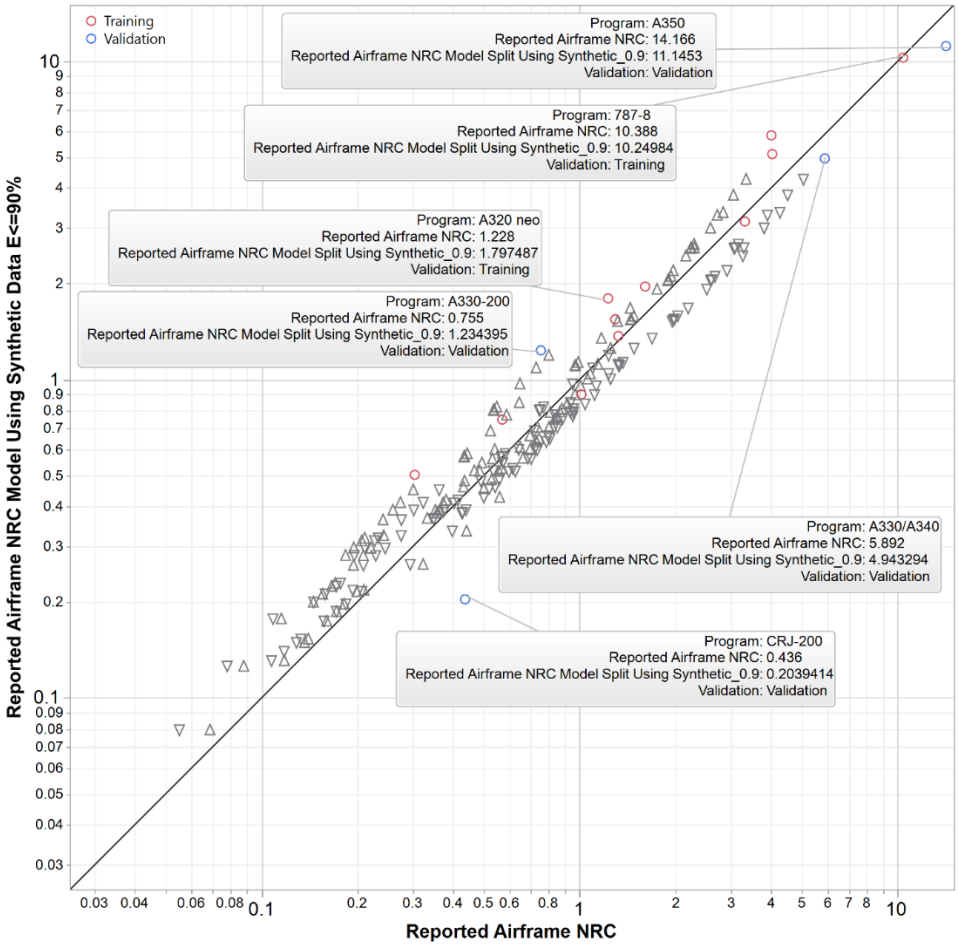

Figure 9. Accuracy of combined non-recurring cost (NRC) relationship with reported NRC.

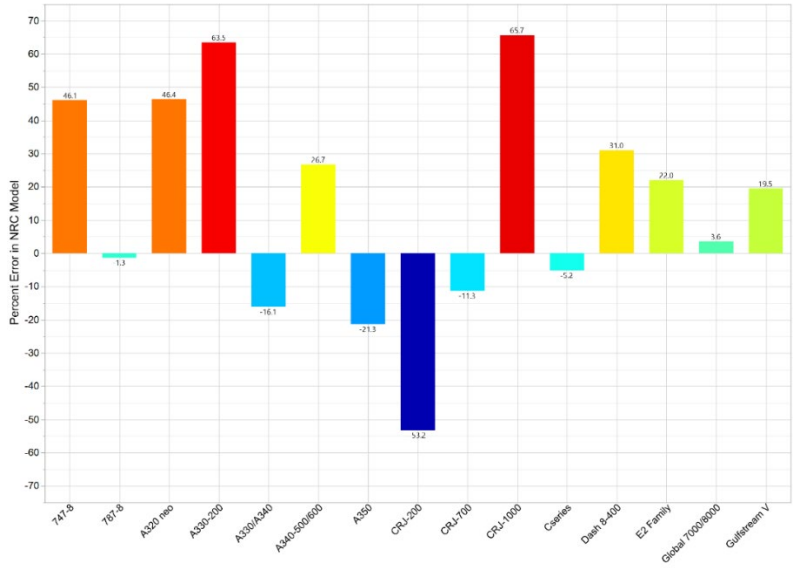

Figure 10. Percent error of combined non-recurring cost (NRC) relationship with reported NRC.

$$\mathrm{NRC} = \left[\left(Ae^{(Bx)} + C\right) + \left(Ae^{(0.9B)} + C\right) f(x) \frac{2}{n_{\mathrm{eng}}}\right] \left(\frac{\mathrm{MTOW}}{\mathrm{MTOW}_{\mathrm{ref}}}\right)^{D}$$

$$f(x) = \frac{0.15}{1 + e^{7.5-25x}}$$

$$x = \left[E x_{\mathrm{CO}_2} + (1 - E)\, x_{\mathrm{dB}}\right]$$

$$A = 0.871231$$

$$B = 2.137834$$

$$C = -0.656189$$

$$D = 0.5453 + \frac{0.697 - 0.5453}{1 + e^{7.5-25x}}$$

$$E = 0.900000$$

Figure 11. Non-recurring cost equation.

Figure 12 shows the outcome of the initial implementation of the dual CO_2- and noise-driven NRC function based on the sample problem implementation and based on the underlying sample problem growth and replacement database. While the sample problem does not focus on results (i.e., numbers), the trends in NRC across the 10×10 matrix of stringency options appear to be consistent with trends in technology responses (i.e., fixes). Each bar graph represents the total NRC from all aircraft families that require a fix for a given combination of stringency options.

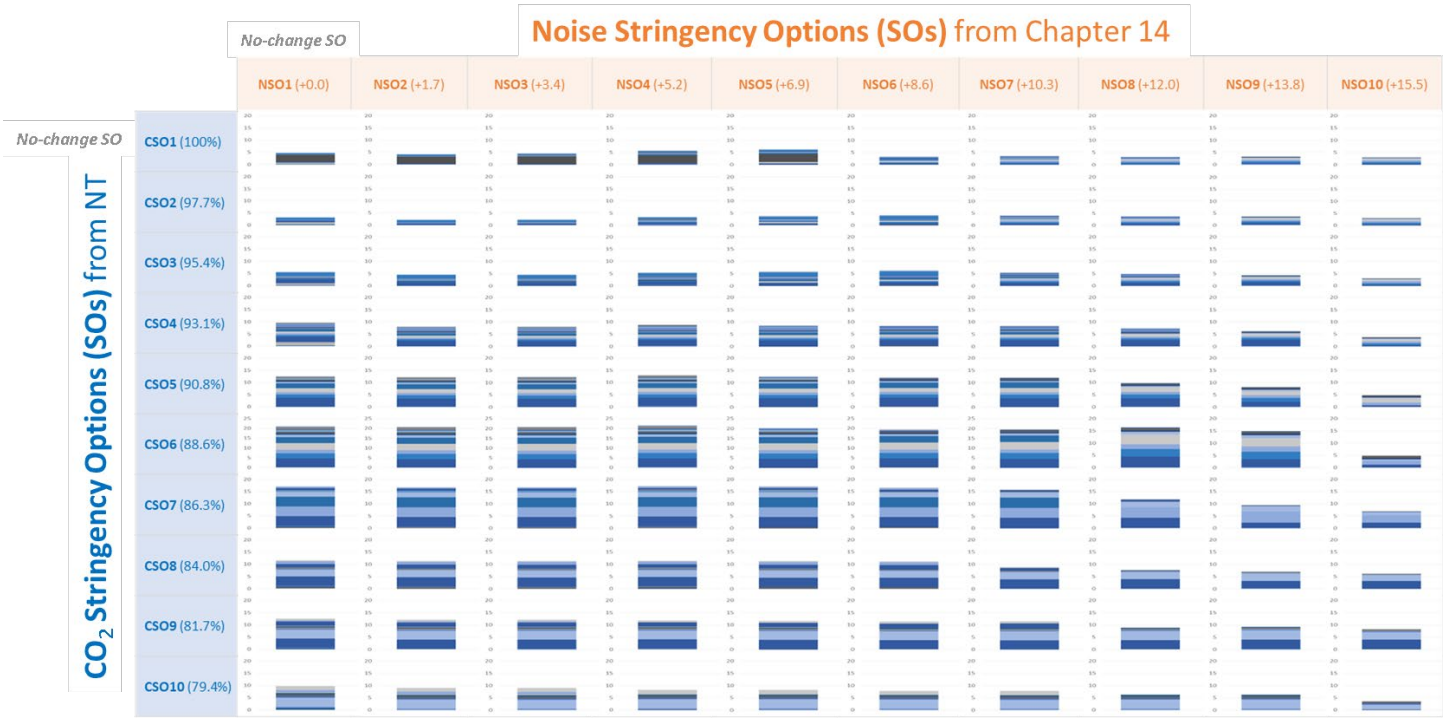

Figure 12. Summary of non-recurring costs driven by CO_2 and noise technology responses based on the Sample Problem (SP) Growth and Replacement Database (GRdb) [GRdb13 v1.5]. NT: new type.

As part of CAEP/13, a set of approaches and methodologies was developed by the cost estimation ad hoc group, aiming toward the estimation of costs (investments) associated with aircraft technology scenarios. A summary of the NRC methodology, assumptions, and data sources is shown in Figure 13.

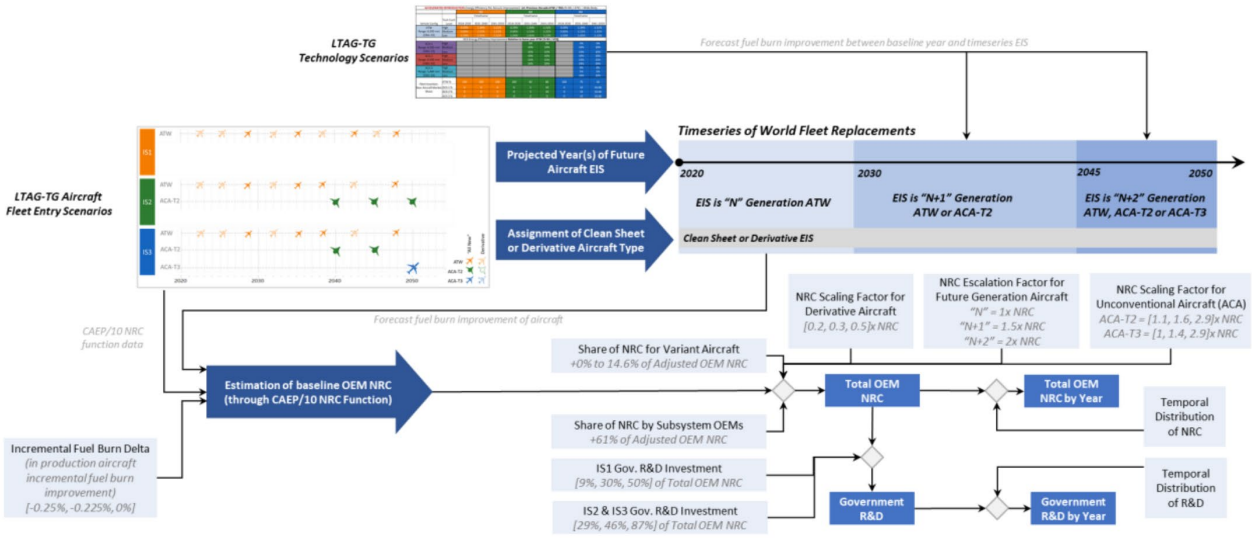

Figure 13. Summary of methodology, assumptions, and data sources for non-recurring cost (NRC) from CAEP/12. CAEP: Committee on Aviation Environmental Protection; LTAG: long-term aspiration goal; OEM: original equipment manufacturer; R&D: research and development; TG: task group; EIS: entry into service; ATW: advanced tube and wing; ACA: advanced concept aircraft.

The Georgia Tech team investigated the methodology evolved for derivative aircraft NRC, as it could be employed in CAEP/13. The cost estimation ad hoc group leveraged and modified the CAEP/10 function through scaling and/or escalation factors based on the technology scenarios. The Georgia Tech team focused on calculations for derivative aircraft only, as this is applicable to CAEP/13 integrated stringency analysis. The scaling factor for derivative aircraft was approximately 20%–50% of that of the current generation of clean sheet designs, as shown in Figure 14. Therefore, the cost estimation ad hoc group used an average scaling factor of 0.3.

Clean Sheet A/C	Derivative A/C	Clean Sheet NRC/kg	Derivative NRC/kg	Derivative Scaling Factor
A380	B747-8	$38 K	$10 K	0.27
A350	A340-500	$62 K	$12 K	0.20
*Notional Clean Sheet B737**	B737 Max	$70 K*	$35 K	0.5
*Notional Clean Sheet A320**	A320 Neo	$70 K*	$19 K	0.27
			Average:	**0.31**

**average NRC/kg for Gen 6 aircraft as there was no legacy data for a narrow-body Gen 6 vehicle*

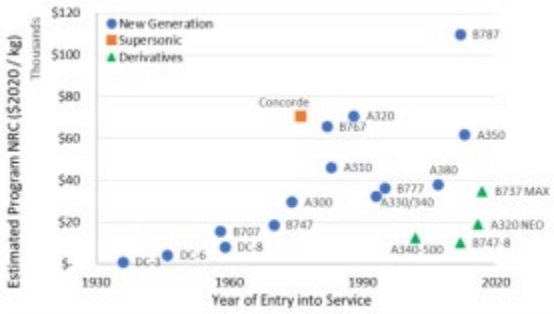

Figure 14. Non-recurring cost (NRC) for derivative aircraft from CAEP/12. CAEP: Committee on Aviation Environmental Protection. A/C: aircraft.

Sample Problem Technology Response

The Georgia Tech Aerospace Systems Design Laboratory has used an approach similar to that of the CAEP's Independent Expert Integrated Review and Long-Term Aspiration Goal (LTAG) studies in lieu of specific technology modeling. These two studies considered technologies as "bundles" of improvements in key disciplinary areas on the airframe and engine. As an example, specific composite materials were not modeled, but structural weight improvements were. A stringency analysis requires that technologies be at a Technology Readiness Level (TRL) of 8 in a given year, which will limit the scope of applicability of the possible technology "bundles" based on the year of application of the stringency. The outcome of the subtask is a set of technology assumptions to be used in modeling for the interdependency trades in the sample problem and full analysis to provide a Pareto front of the maximum available technology response for a given aircraft class.

The methodology for determining the impact of technology responses is represented in Figure 15. The system-level model calibration for the technology reference aircraft (TRA) vehicle is described in Sections A and B below. Section B provides more detail on the calibration of the acoustic properties of the technology reference aircraft (TRA) vehicle from certification databases. Section C describes how technology responses are applied to the vehicle model in a design space exploration. Section D outlines some of the optimization process for analyzing the design space and also presents preliminary results of generating Pareto fronts from the data. These sections specifically detail the wide-body twin-aisle aircraft (A330-941neo); however, the methodology is applicable to all other aircraft classes being considered in this investigation.

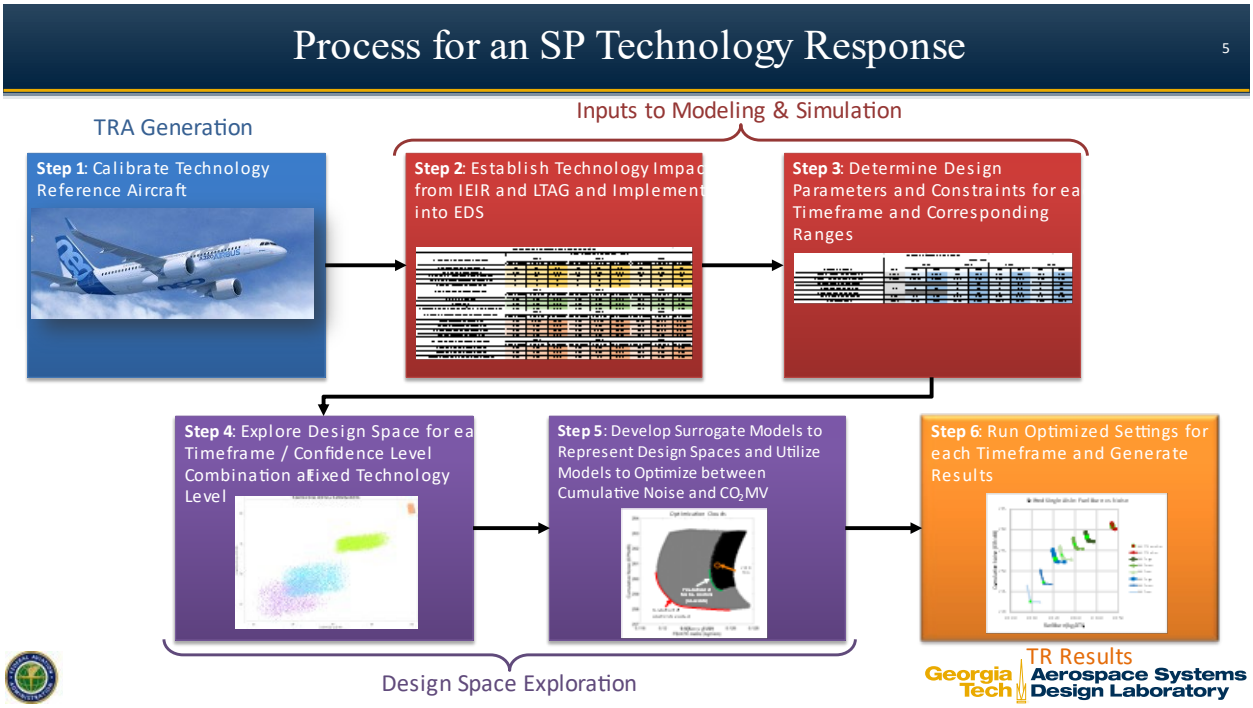

Figure 15. Process for determining a technology response (TR). IEIR: Independent Expert Integrated Review; LTAG: Long-Term Aspiration Goal; MV: metric value; TRA: technology reference aircraft; EDS: Environmental Design Space.

Vehicle Model Calibration

The creation of a vehicle model for the A330-941neo starts with data for the geometry and the engine of the vehicle. For the notional A330neo model, a notional Rolls-Royce Trent7000 engine was developed and calibrated previous to this project. The geometric data, taken from 3D-view drawings published by Airbus, include information on the control surfaces of the airplane. Various measurements of the airframe are taken, for example, the height of the tail and the chord length of the leading-edge slats. After all of the dimensions of the airplane are measured, including lifting surfaces, these values are used in various calculations to be implemented in the Flight Optimization System (FLOPS) model. FLOPS uses the input vehicle data to output a vehicle that best fulfills the mission parameters (i.e., range or desired take-off gross weight).

The specific weight variant modeled in this project is the WV901, as designated in the Airport Planning Manual (Airbus, 2021). Previous work by the Aerospace Systems Design Laboratory has defined component weights as percentages of the operational empty weight (OEW), as shown in Table 6. These percentages are based on a statistical approach for historical values of each component of the wide-body class aircraft. From these percentages, target component weights are defined and calibrated for the correct OEW (found in the Airport Planning Manual) of the specified weight variant of the A330-941neo using the wide-body class percentages for calibration of an A350 vehicle. This principle applies to the A330neo as well, as listed in Table 7. The component weight calibration is performed by iteratively varying weight factors in FLOPS (utilizing a Newton–Raphson approach) in order to reach the desired OEW. Once this process is complete, the airframe model, together with correct engine cycle parameters, is implemented in the Environmental Design Space (EDS) to form a baseline model.

Table 6. A350-XWB mass and balance summary.

MASS AND BALANCE SUMMARY	Target Wref (%)	GT-A350 Wref (%)
WING	21.668	21.778
HORIZONTAL TAIL	2.046	2.066
VERTICAL TAIL	0.841	0.849
VERTICAL FIN	0	0
CANARD	0	0
FUSELAGE	19.605	19.455
LANDING GEAR	6.779	6.765
NACELLE + PYLON	1.634	1.855
STRUCTURES TOTAL	(52.574)	(52.767)
ENGINES	14.363	14.398
THRUST REVERSERS	0	0
MISCELLANEOUS SYSTEMS	0	0
FUEL SYSTEM - TANKS AND PLUMBING	0.298	0.299
PROPULSION TOTAL	(14.661)	(14.697)
SURFACE CONTROL	1.721	1.724
AUXILIARY POWER	0.523	0.519
INSTRUMENTS	0	0
HYDRAULICS	1.411	1.404
ELECTRICAL + INSTRUMENTS	0.978	0.970
AVIONICS	1.019	1.012
FURNISHINGS + MISC. EQUIPMENT	19.805	19.654
AIR CONDITIONING + ANTI-ICING	0.972	0.965
ANTI-ICING	0	0
SYSTEMS AND EQUIPMENT TOTAL	(26.431)	(26.247)
OPERATIONAL ITEMS TOTAL	(6.334)	(6.289)
OPERATING WEIGHT EMPTY	100	100

Table 7. Calibrated mass summary for A330-941neo WV901.

MASS AND BALANCE SUMMARY	PERCENT WREF	POUNDS
WING	12.24	65528.
HORIZONTAL TAIL	1.32	7087.
VERTICAL TAIL	0.65	3499.
VERTICAL FIN	0.00	0.
CANARD	0.00	0.
FUSELAGE	11.09	59383.
LANDING GEAR	3.96	21184.
NACELLE (AIR INDUCTION)	1.09	5860.
STRUCTURE TOTAL	(30.35)	(162541.)
ENGINES	5.20	27869.
THRUST REVERSERS	0.00	0.
MISCELLANEOUS SYSTEMS	0.00	0.
FUEL SYSTEM-TANKS AND PLUMBING	0.35	1881.
PROPULSION TOTAL	(5.56)	(29750.)
SURFACE CONTROLS	1.14	6120.
AUXILIARY POWER	0.48	2552.
INSTRUMENTS	0.00	0.
HYDRAULICS	0.97	5196.
ELECTRICAL	0.73	3907.
AVIONICS	0.75	4029.
FURNISHINGS AND EQUIPMENT	11.20	59979.
AIR CONDITIONING	0.73	3889.
ANTI-ICING	0.00	0.
SYSTEMS AND EQUIPMENT TOTAL	(16.00)	(85672.)
WEIGHT EMPTY	51.91	277963.
CREW AND BAGGAGE-FLIGHT, 2	0.08	450.
-CABIN, 8	0.25	1330.
UNUSABLE FUEL	0.04	219.
ENGINE OIL	0.04	236.
PASSENGER SERVICE	2.32	12418.
CARGO CONTAINERS	0.97	5214.
OPERATING WEIGHT	55.62	297831.
PASSENGERS, 300	10.08	54000.
PASSENGER BAGGAGE	1.68	9000.
CARGO	0.00	0.
ZERO FUEL WEIGHT	67.38	360831.
MISSION FUEL	32.62	174672.
RAMP (GROSS) WEIGHT	100.00	535502.

Vehicle Acoustic Calibration

Noise produced by the vehicle is calibrated to known data taken from European Union Aviation Safety Agency (EASA) and International Civil Aviation Organization (ICAO) databases for airframe- and engine-related noise (European Union Aviation Safety Agency, 2022; (Eurocontrol Experimental Center, 2020). The noise data are implemented in EDS via several variable parameters that represent the noise produced by the engine (combustor, turbine, fan, and jet sources) and the airframe (including the tail, flaps, slats, and landing gear). Each variable contains information on noise perceived at each of the three observer positions as a result of the respective noise source (i.e., approach, cutback/flyover, and sideline). Once a baseline is determined, the flight trajectory and drag coefficients for take-off and landing are adjusted to find the best fit of noise for the model.

Noise modeling of the vehicle begins with a collection of certification data. EASA publicly shares its noise certification data for various types of aircraft (European Union Aviation Safety Agency, 2022). This certification is dependent on meeting limits on the effective perceived noise in decibels (EPNdB) for cutback, approach, and sideline observer positions of airplane

operations during take-off and landing. These three data points do not provide enough information to rigorously model various operational scenarios. Thus, the certification data are supplemented with noise power distance (NPD) data to further constrain the model. These NPD curves consider various acoustic metrics (including EPNdB and sound exposure level) taken from positions at various intervals in the sideline position relative to the runway for both take-off and landing and at various thrust settings. However, the ICAO database of NPD data is only updated every two years (Eurocontrol Experimental Center, 2020). Because the A330-941neo was recently certified, it is not included in the NPD database. Fortunately, ICAO prescribes methods for substituting a proxy vehicle in the database and for adjusting NPD curves for a missing vehicle using differences in the two vehicles' certification noise data (ICAO, 2018).

To calibrate the acoustic model, noise suppression factors are first altered with the goal of meeting both reported EPNdB and sound exposure levels of the NPD curves. If this is not possible, then only one of the metrics is chosen. These suppression factors are EDS variables that represent noise from specific components of the vehicle at a specific observation point. For example, the various approach noise suppression factors (note all of the variables ending with the suffix -AP) being optimized to match the NPD curves are depicted in Figure 16. It is easier to optimize the suppression factors grouped by their affected observer position. Figure 16 shows the desired values for the suppression factors of engine combustor noise, aft fan noise, inlet fan noise, jet noise, leading-edge slat noise, landing gear noise, trailing-edge flap noise, and engine turbine noise in that order. Once optimized via this method, the suppression factors are frozen for further trade studies.

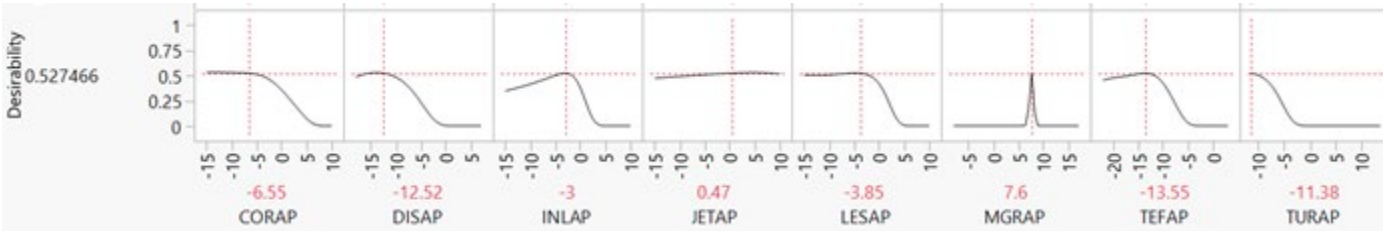

Figure 16. Optimization of approach noise suppression factors. CORAP: Suppression Factor on Core (Combustor) Noise; DISAP: Suppression Factor on Fan Discharge Noise; INLAP: Suppression Factor on Inlet Noise; JETAP: Suppression Factor on Jet Noise; LESAP: Suppression Factor on Leading Edge Slats Noise; MGRAP: Suppression Factor on Main Landing Gear Noise; TEFAP: Suppression Factor on Trailing Edge Flap Noise; TURAP: Suppression Factor on Turbine Noise

Next, a landing/take off (LTO) trade study is performed to match the vehicle certification noise found from the EASA database. The LTO study utilizes detailed FLOPS LTO results from the vehicle model, which are then used in the NASA Aircraft Noise Prediction Program (ANOPP) code to calculate the noise emission from the vehicle. Four parameters are varied in this trade study; the ranges over which these parameters were varied are listed in Table 8. The first two variables are scaling factors that scale the drag coefficients for LTO. The other two variables relate to the operation of the vehicle: the flight path angle and the altitude at which a transition from maintaining the initial constant flight path angle to maintaining a constant velocity occurs (the ANOPP variable corresponding to this altitude is known as HSTOP). A design of experiments is run with roughly 600 cases that span the design space of this study. Of those cases, the case that best matches the published certification noise for the A330-941neo is selected. Once this design point is verified, the selected design parameters are included in the EDS baseline model. The overall noise calibration method is as follows, as illustrated in Figure 17:

1. Determine target values for certification noise from the EASA database and for NPD data points using the ICAO-defined substitution method from the NPD database.
2. Optimize suppression factors to match NPD data points.
3. Freeze suppression factors.
4. Perform an LTO study to find a combination of parameters to meet target certification noise points.

Table 8. Landing/take-off study variables and design ranges.

Variable	Take-Off Drag Scaling Factor	Landing Drag Scaling Factor	Flight Path Angle (degrees)	HSTOP (feet)
Design Range	0.5–1.2	0.5–1.2	3.0–9.0	300–1,000

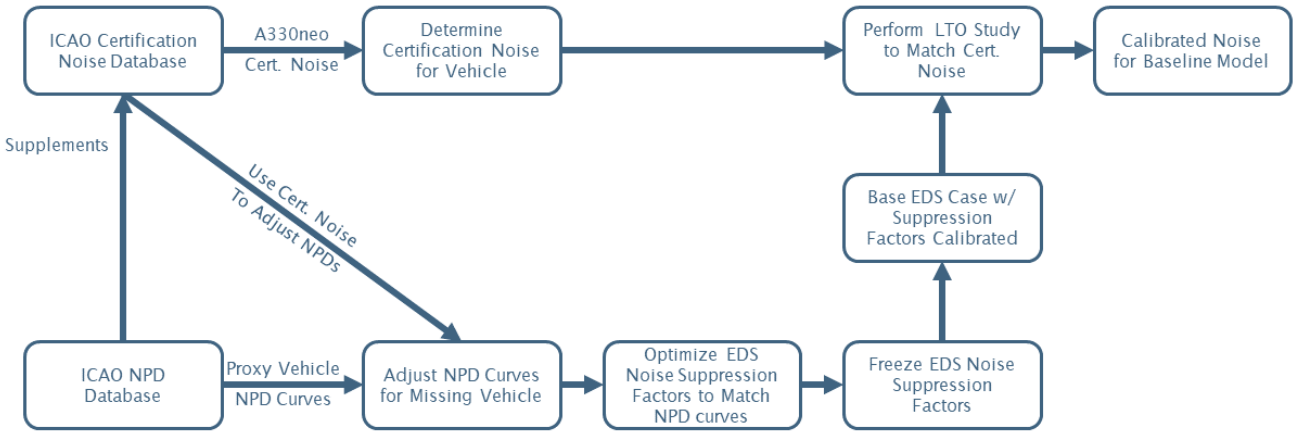

Figure 17. Calibration of the noise model. ICAO: International Civil Aviation Organization; LTO: landing/take-off; NPD: noise power distance; EDS: Environmental Design Space.

Design of Experiment Generation

With the baseline model calibrated to match publicly available data for the A330-941neo, the baseline can be adjusted to simulate technology infusion. One possible method for analyzing how current vehicles could meet future dual-stringency limits would be to predict what specific technologies might be applied by industry to their designs and then to model the impacts of those technologies on performance. However, this would require proprietary information from the company designing and manufacturing the aircraft and engine. Clearly, this approach is not feasible for the scope of this study.

Instead, the baseline is varied by applying k-factors that represent technology buckets, where a vehicle can make technology improvements in a certain aspect, such as the wing drag coefficient, without specifying what specific technology is utilized to achieve the improvement. In this fashion, the technology response is measured for various k-factors in mission parameters, and a wider design space is available.

Using these technology buckets provides a parametric approach for capturing stringency responses; however, this method results in a very large design space that can become computationally expensive to explore. An appropriate design of experiments enables efficient exploration of the technology space with maximum knowledge gained. Specifically, the baseline case is taken along with edge cases at the extremes of the k-factor ranges. The design of experiments is then filled in with uniformly random points. The 13 key metrics, which are measured outputs of the technology space exploration, are listed in Table 9. For this technology space exploration, there are 53 varied parameters.

Table 9. Key metrics for technology space exploration. CAEP: Committee on Aviation Environmental Protection; MTOW: maximum take-off weight; BPR: Bypass Ratio.

Key Metrics	
Wing Span	Cutback Noise
Approach Noise	Sideline Noise
Cumulative Noise	Noise BPR
CO_2 Metric	MTOW
Max T3	Fan Diameter
Noise Margin relative to CAEP Ch. 14	Fuel Burn per Available Ton Kilometer

Results

Because the design of experiments is somewhat computationally expensive, surrogate models are created that relate the 53 varied parameters to the 13 key metric outputs. Of the 13 key metrics, the two metrics of most interest are the cumulative noise and CO_2 metric, as these are the metrics related to the dual stringency. This approach of creating surrogate models enables further study and additional insight for the future without the need for another design of experiments. These surrogates are neural network algorithms consisting of either a single hidden layer neural network with 10 neurons or a dual hidden layer in which each layer has 10 neurons. The structure of the neural networks is driven by the complexity of correctly matching the surrogate results to the actual data. The surrogate models for these metrics are reliable: the cumulative noise surrogate has an R^2 score (correlation score) for training/validation of 0.9818/0.9810, and the CO_2 metric surrogate has an R^2 score of 0.9972/0.9970. For reference, these scores are indicative of the other metrics as well. From these neural networks, the dependence of the key metric in question on the various input parameters can be clearly seen by using prediction profile plots.

A few of the varied parameters and their impact on the CO_2 metric for the notional A330neo model are depicted in Figure 18. In this example, the aspect ratio and overall drag of the vehicle are shown to have the most impact among these parameters on the resulting CO_2 metric, with an increased aspect ratio resulting in improved carbon emissions and an increased drag having a negative impact. The fan pressure ratio and fuselage weight both cause a slight increase in the CO_2 metric whereas the weight of the engine burner (Burner_s_Wt) has no impact on the CO_2 metric. Figure 19 shows actual-by-predicted plots for the data sets of the two dual-stringency metrics. Both the R^2 score and the actual-by-predicted plots illustrate that the surrogates provide reliable stand-ins for in-depth system-level calculations without requiring high levels of computational power.

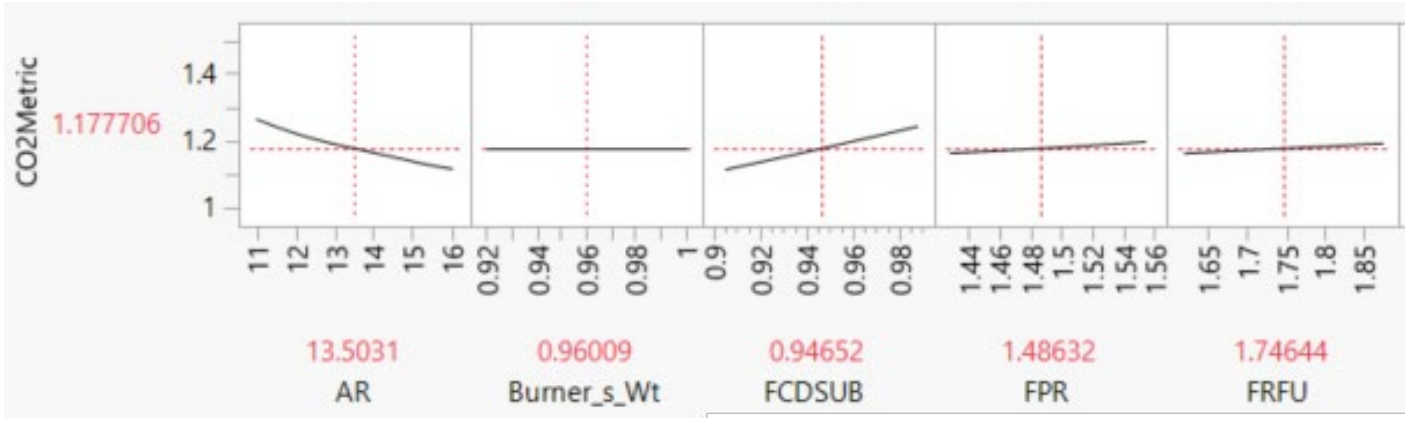

Figure 18. Snapshot of the prediction profile for the CO_2 metric, illustrating various effects of inputs to output. AR: aspect ratio; Burner_s_Wt: weight of the engine burner; FCDSUB: overall drag of the vehicle; FPR: fan pressure ratio; FRFU: weight of the fuselage.

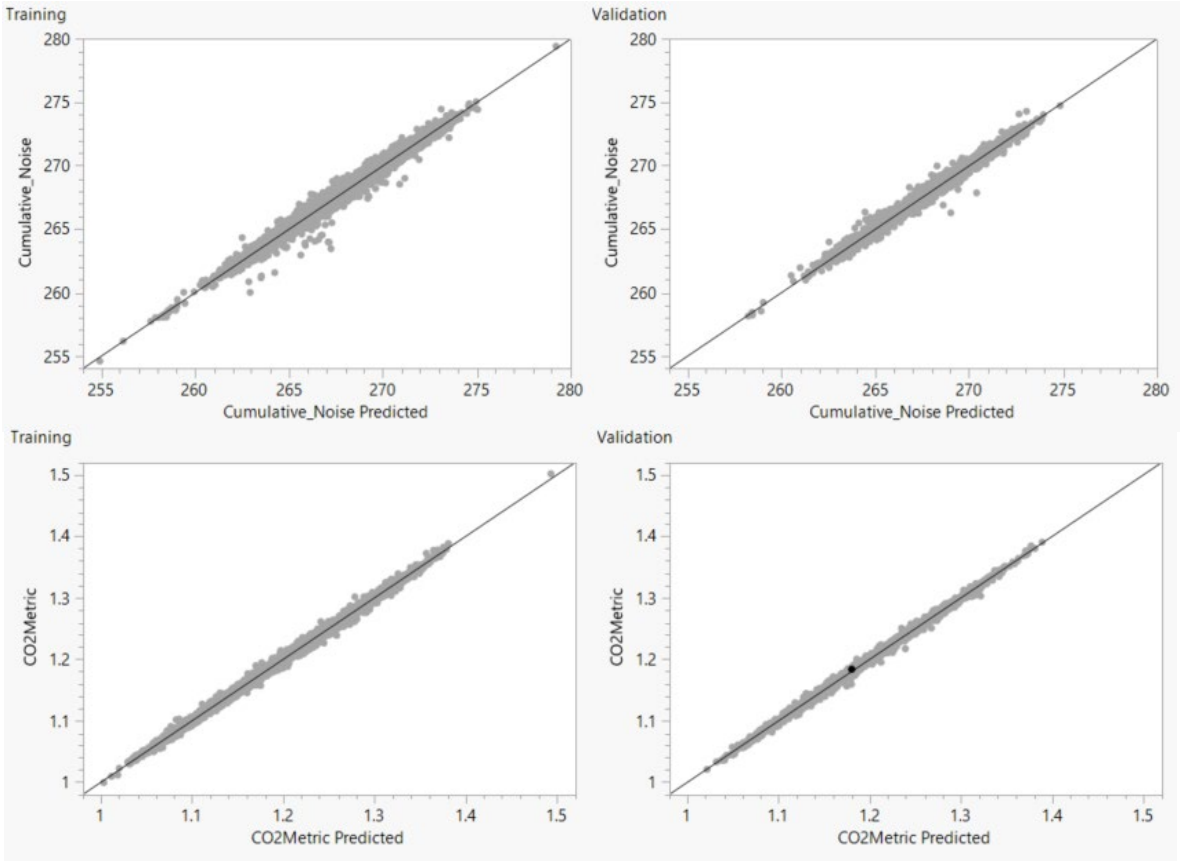

Figure 19. Actual-by-predicted plots for cumulative noise (top) and the CO_2 metric (bottom), with training set results on the left and validation sets on the right.

After the surrogates are generated, Pareto optimization occurs, which is performed for several timeframes of interest with increasing technology impacts over further timeframes. The 2030 timeframe is discussed further. Pareto optimization is an algorithm that considers two or more metrics, defines a "best-in-class" for each metric, and then performs trade-offs on the priority of each metric to draw a curved line between the two best-in-class points. Preliminary findings of the resulting Pareto front for the dual-stringency metrics of cumulative noise and the CO_2 metric are depicted in Figure 20. These graphs assume a high confidence level of technology infusion (a conservative estimation) and fix many varied parameters for the 2030 technology level. The only varied parameters that are not fixed are the design variables of fan pressure ratio, overall top-of-climb pressure ratio, aspect ratio, thrust-to-weight ratio, and wing loading. These design variables are varied and optimized. At a high level, the optimization method is as follows. Several million points are generated via random sampling within the ranges of the design space, shown in the cloud on the left. The colored points forming the Pareto front with different importance weightings assigned to the dual-stringency metrics, shown in both plots, are found by a particle swarming optimization approach. Additionally, the full Pareto front in the right plot is generated by a genetic algorithm process.

In this preliminary case, the total difference in cumulative noise between ends of the Pareto front is only approximately 0.8 EPNdB. The result of having less than 1 EPNdB in trade-offs for this study suggests that further considerations should be made for the Pareto optimization process. Improvements to this optimization are currently being investigated and should show improvement in the design space trade-off for dual stringency. Similar preliminary trade-offs have been generated for other vehicle classes, including business jets, regional jets, and narrow-body/single-aisle jets.

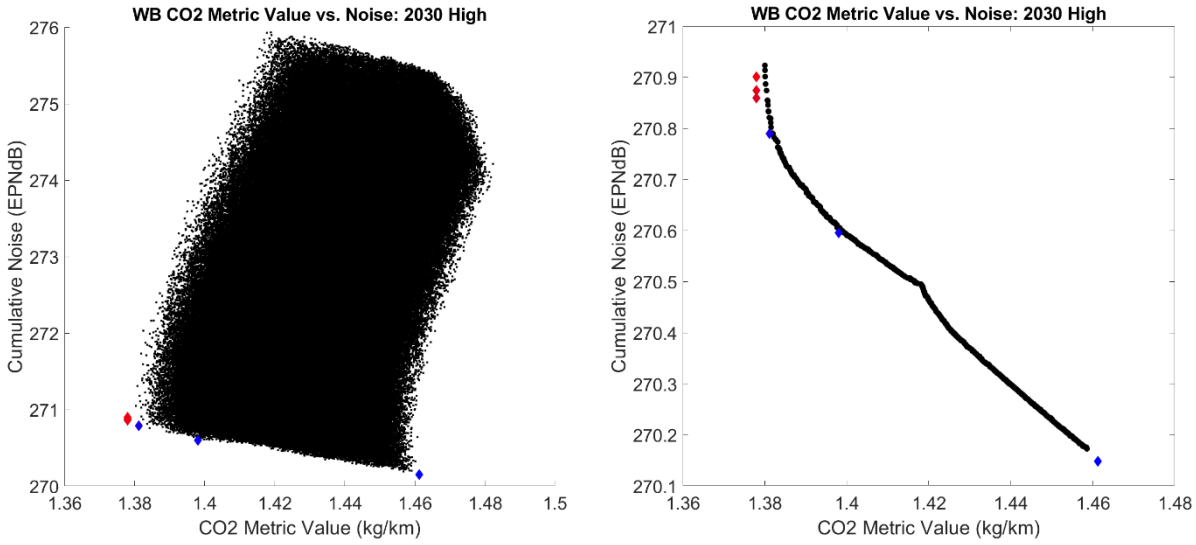

Figure 20. Wide-body (WB) Pareto fronts for 2030 (preliminary results). EPNdB: effective perceived noise in decibels.

CAEP Working Group and Industry Collaboration
The research team participated in numerous CAEP working groups including the WG1 (noise), WG3 (emissions), and MDG and FESG (modeling) working groups. Working with the broader U.S. Research Team, the Georgia Tech team developed a methodology to address the dual-stringency analysis sample problem, including assessments of current noise margins (NMs) of the in-production fleet, development of technology response methodology, contributions to the growth and replacement database, and development of an initial NRC function.

Milestones

- Develop an initial version of the NRC function for use in the Sample Problem (SP).
- Develop notional technology responses across seat classes for use in the sample problem.
- Contribute to the CAEP technical working groups.

Major Accomplishments

NRC Function

- Reviewed and reported previous CAEP work on NRC modeling
- Developed an approach to include both CO_2 and noise MV improvements in the NRC function
- Arranged meetings to coordinate with ICCAIA members in order to improve the NRC model and search for data

Technology Response for the Sample Problem

- Developed initial technology responses available across four vehicle classes

CAEP Working Group and Industry Collaboration

- Contributed to the work plan of each of the CAEP working groups

Publications

None.

Outreach Efforts

Outreach efforts included bi-annual ASCENT meetings, various CAEP working group meetings and calls, and weekly U.S. Research Team meetings.

Awards
None.

Student Involvement
Melek Ozcan, Antoine Marin, Zelin Hu, David Mothershed, Gabriel Fronk, Andy Tan, Niharika Akula, Jayaprakash Kambhampaty, and Kumanan Srinivasan (graduate research assistants, Georgia Tech) participated in the efforts of Task 1.

Plans for Next Period
NRC Function
- Engage more stakeholders in our search for data.
- Continue collaboration with the NRC ad hoc group to improve the NRC model.
- Incorporate feedback and data received.

Technology Response for the Sample Problem
- Provide further updates to technology responses as needed.
- Conduct sanity checks of industry-provided interdependencies to the sample problem.
- Modify Pareto fronts based on year of applicability if needed.

CAEP Working Group and Industry Collaboration
- Continue to support the broad technical needs of the U.S. Research Team and CAEP working groups.

Data Anonymization
Concerns regarding divulging any sensitive information from OEMs must be addressed through an anonymization process for the different working groups. Specifically, NMs, CO_2 MVs, and MTOMs must be carefully processed or even eventually removed from charts and tables, in order to prevent any of these parameters from being derived or linked between each other.

Several techniques will be investigated to provide anonymized data for NMs and CO_2 MVs that can still be handled to perform calculations and other analytic tasks needed for quantitative analysis, while preventing any sensitive OEM data from being related to a specific aircraft. Promising techniques include homomorphic encryption schemes, in which specific mathematical operations can be performed with encrypted values and the results can be decrypted to yield the correct answers. This approach could be used to enable calculations with sensitive values, with the results being made available. Another related technique is deterministic encryption, which, similar to a hash function, gives the same output values for the same input values. This method enables limited comparisons of encrypted values. However, care must be taken with specific comparisons due to the possibility of data leaking. This is also true if the data are displayed as charts or tables. Specific techniques must be applied to each case, according to the choice of representation:

- Charts: The simple moving average method, centroid method, or noise perturbation can be helpful by blurring real data points in switching from discrete to continuous representations while smoothing extreme values (simple moving average), by representing the mean of k neighbors of a value instead of that value (centroid method), or by adding noise to data sets (noise perturbation), where the noise is a random variable with a known distribution (Gaussian, uniform, etc.).

- Tables: Blurring of aircraft identification information such as NMs or CO_2 MVs can be achieved by grouping the values into wider bins, for instance, based on the first two digits of the growth and replacement database identification number or intervals for NMs and CO_2 MVs.

References
Airbus. (2021). *A330 Aircraft Characteristics – Airport and Maintenance Planning*. AIRBUS S.A.S.

European Union Aviation Safety Agency. (2022). *EASA Certification Noise Levels*. https://www.easa.europa.eu/en/domains/environment/easa-certification-noise-levels

Eurocontrol Experimental Center. (2020). *Aircraft Noise and Performance (ANP) Database: An international data resource for aircraft noise modellers*. https://www.aircraftnoisemodel.org

International Civil Aviation Organization. (2018). Recommended Method for Computing Noise Contours Around Airports (Report No. 9911). ICAO.

Project 082(B) Integrated Noise and CO_2 Standard Setting Analysis

Massachusetts Institute of Technology

Project Lead Investigator

Raymond Speth
Principal Research Scientist
Department of Aeronautics & Astronautics
Massachusetts Institute of Technology
77 Massachusetts Ave, Building 33-316, Cambridge, MA 02139
617-253-1516
speth@mit.edu

University Participants

Massachusetts Institute of Technology (MIT)

- P.I.: Dr. Raymond Speth
- FAA Award Number: 13-C-AJFE-MIT, Amendment Nos. 095 and 102
- Period of Performance: June 14, 2022 to September 19, 2023 (reporting here with the exception of funding level and cost share only for the period of June 14, 2022 to September 30, 2022)
- Tasks:
    1. Data anonymization
    2. Development of an aircraft conceptual design tool

Project Funding Level

$900,000 in FAA funding and $900,000 in matching funds. Sources of matching are approximately $94,000 from MIT, plus third-party in-kind contributions of $274,000 from Savion Aerospace Corp. and $532,000 from NuFuels, LLC.

Investigation Team

- Dr. Raymond Speth (MIT) serves as the P.I. for the A82B project. Dr. Speth advises student and postdoctoral researchers in the Laboratory for Aviation and the Environment (LAE) focused on reducing aviation's environmental impacts using fuels, propulsion technology, and policy. Dr. Speth also coordinates communication with FAA counterparts.
- Prof. Steven Barrett (MIT) serves as co-P.I. for the A82B project as the director of LAE. Prof. Barrett coordinates internal research efforts and maintains communication between investigators in the various MIT research teams.
- Dr. Jayant Sabnis (MIT) co-advises student research in LAE. His research expertise includes turbomachinery, propulsion systems, gas turbine engines, and propulsion system–airframe integration.
- Jonas J. Gonzalez (MIT) is a PhD student in LAE focusing on assessing the impacts of new aircraft technologies on certification and community noise exposure.
- Prakash Prashanth (MIT) is a PhD student in LAE focusing on the role of new airframe and engine technologies in reducing climate and air quality impacts of aviation.
- Dr. Sicheng He (MIT) is a postdoctoral associate in LAE focusing on aircraft design optimization and development of integrated software tools for modeling aircraft and environmental impacts.

Project Overview

To evaluate the economic reasonableness of proposed aircraft environmental standards, the International Civil Aviation Organization's (ICAO) Committee on Aviation Environmental Protection (CAEP) requires tools for assessing the impact of technologies and design changes intended to control aircraft noise and emissions and for evaluating the costs of implementing such changes to aircraft and engine designs. Existing methods used to support decision-making in previous CAEP noise stringencies do not represent modern aircraft and propulsion designs and technologies. The goal of this project is to develop new tools that address the shortcomings of the previous methods in support of CAEP/13 stringency analyses.

Task 1 - Data Anonymization

Massachusetts Institute of Technology

Objective

The requirement to protect sensitive original equipment manufacturer (OEM) data in the current CAEP/13 cycle necessitates a new approach to the management of data in the CAEP standard-setting process. Any data presented to the full CAEP working groups (WGs) must be anonymized to satisfy these needs. The goal of this task is to identify approaches that can provide the WGs and CAEP Steering Group with anonymized information that can be used to define, evaluate, and select stringency options for dual CO_2 and noise standards without divulging sensitive OEM data.

Research Approach

In general, data can be anonymized via data suppression, swapping, distortion, or generalization. Because the anonymized data must be used by WGs and the Steering Group to define, evaluate, and choose stringency options, data suppression (where data is simply withheld) cannot be used as an anonymization technique for the variables of interest – CO_2 metric value, certification noise value, and maximum take-off mass (MTOM). Data swapping (e.g., where aircraft names are swapped randomly and can only be identified with a swapping key) does not provide the requisite anonymity and similarly cannot be used because OEMs can infer information about their competition by eliminating their own aircraft in the resulting data outputs. While data distortion can be used in principle, it directly affects the interpretation of the anonymized data and is therefore not preferable.

Here, we adopt a combination of data generalization and selective data suppression such that the anonymized data retains undistorted values, but each data point is anonymous. The CO_2 metric value and certification noise are anonymized by only showing the value relative to the CAEP/10 standard and margin from current noise standards and suppressing the metric value and certification noise values. The MTOM is anonymized by aggregation, either on an MTOM basis or via aircraft class definitions. This approach allows observers to understand how different stringency options affect different types of aircraft (e.g., regional jets versus twin-aisle aircraft) without revealing sensitive data about individual aircraft.

Milestone

The proposed data anonymization framework has been presented to members of the CAEP WGs.

Major Accomplishments

A proposed anonymization framework has been developed, along with tools for generating data visualizations that inform decision-making while preserving anonymity.

Publications

None.

Outreach Efforts

- Progress on method development was discussed with FAA project managers during regular teleconferences.
- The proposed anonymization method was presented to CAEP WG members to collect feedback.

Awards

None.

Student Involvement
Graduate students Prakash Prashanth and Jonas Gonzalez conducted the analyses and presented this work.

Plans for Next Period
Additional feedback on the anonymization approach will be collected and used to refine the process. The tools developed will be used to process OEM-provided data as part of the stringency-setting process.

References
None.

Task 2 - Development of an Aircraft Conceptual Design Tool
Massachusetts Institute of Technology

Objective
The goal of this task is to enhance the capability of our Julia-based aircraft conceptual design software, TASOPT.jl, to incorporate new disciplines and components, including noise analysis, cost analysis, and optimization. By exploiting the interaction of different disciplines and exploring many design variables, the tool can be used to automatically find optimal designs within a design space in which human intuition is not reliable. The improved tool will enable us to model the effects of specific airframe and engine technologies on CO_2 emissions and noise levels.

Research Approach
Recent development of TASOPT.jl has focused on three specific areas: (1) modularizing the code, (2) incorporating a computationally efficient engine model implemented in Julia, and (3) adding algorithmic differentiation and optimization capabilities.

The starting version of TASOPT.jl was developed based on an older Fortran 77 program with an obsolete programming structure that limits the ability to implement new capabilities and does not provide the flexibility needed to model a variety of technologies that could be implemented to reduce CO_2 and/or noise. To address this concern, we are modularizing the software into functional components, such as structures, aerodynamics, and propulsion. We are also adopting a modern data structure inspired by the state-of-the-art general Python-based multidisciplinary design and optimization package OpenMDAO. The new data structures will facilitate design analysis and optimization by distinguishing the design variables and state variables (or output) and by making it possible to dynamically add or remove variables from the system. As an example, the extended design structure matrix for the engine module is shown in Figure 1, depicting the information flow in the system. From this, the engine data structure shown in Figure 2 is defined.

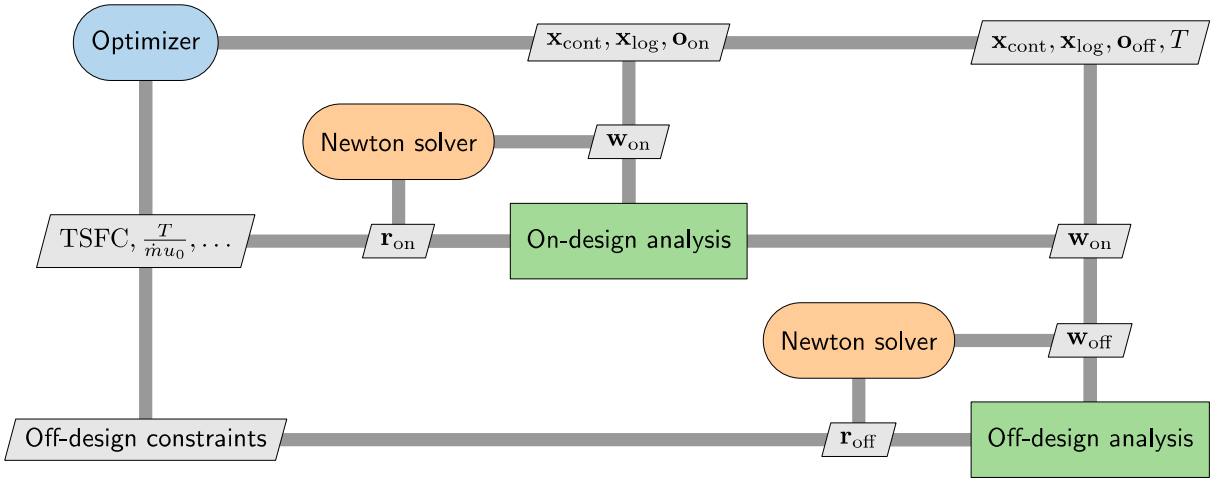

Figure 1. Extended design structure matrix for the engine module. TSFC is the thrust-specific fuel consumption.

Design variable, x		Operation condition		State variable		Off-design input
Continuous, x_{cont}	Logic, x_{log}	On-design o_{on}	Off-design o_{off}	On-design w_{on}	Off-design w_{off}	T

Figure 2: The data structure for the engine model, developed based on the extended design structure matrix (see Figure 1).

Currently, one computational bottleneck is the Numerical Propulsion Simulation System (NPSS)-based engine model, which accounts for the majority of the computational time. To reduce this cost and enable future optimizations that cannot be implemented with a black-box model such as NPSS, we have directly implemented a simplified engine model in TASOPT.jl. This simplified engine model replaces the complex equilibrium calculations used by NPSS with an approximation based on complete combustion.

Optimization is an essential part of this project because it can be used to identify the lowest CO_2 emissions and noise achievable by applying different airframe and engine technologies. However, the current optimization algorithm adopted by TASOPT.jl is the gradient-free Nelder−Mead method. Such methods scale poorly for systems with a large number of design variables. Further, this method lacks any intrinsic handling of constraints, requiring the constraints to be implemented inexactly as penalties in the objective function. In contrast, gradient-based methods using analytic derivatives computed by the adjoint method or reverse algorithmic differentiation can efficiently solve large-scale design optimization problems, and the constraints can be accurately satisfied. To enable the use of a gradient-based optimizer with TASOPT.jl, we are leveraging the Julia-based algorithmic differentiation tool, Zygote.jl. We are currently adapting the code to be able to correspond to the structure required by this tool.

Milestones

- Software modularization has been completed.
- A stand-alone version of the computationally efficient engine model has been completed, using new data structures.

Major Accomplishments

None.

Publications
None.

Outreach Efforts
Progress on method development was communicated to FAA project managers during regular teleconferences.

Awards
None.

Student Involvement
Graduate student Prakash Prashanth led the implementation of code modularization. Postdoctoral associate Sicheng He was responsible for implementing the new engine model and data structure organization.

Plans for Next Period
- Finish implementing the new data structures in the remaining model components.
- Apply algorithmic differentiation to the remainder of the model components.
- Link TASOPT.jl to PyNA, our tool for modeling aircraft noise.

References
None.

Publications Index

Project 001

Eight graduate students and 4 undergraduate students involved.

Publications

- Anderson, B. J., Mueller, D. W., Hoard, S. A., Sanders, C. M., & Rijkhoff, S. A. M. (2022). Social science applications in sustainable aviation biofuels research: Opportunities, challenges, and advancements. *Frontiers in Energy Research*, *9*, 771849. doi: 10.3389/fenrg.2021.771849
- Boglioli, M., Mueller, D. W., Strauss, S., Hoard, S., Beeton, T. A., & Budowle, R. (2022). Searching for culture in "cultural capital": The case for a mixed methods approach to production facility siting. *Frontiers in Energy Research*, *9*, 772316. doi: 10.3389/fenrg.2021.772316
- Brandt, K., Camenzind, D., Zhu, J. Y., Latta, G., Gao, J., & Wolcott, M. (2022). Methodology for quantifying the impact of repurposing existing manufacturing facilities: Case study using pulp and paper facilities for sustainable aviation fuel production. *Biofuels, Bioproducts and Biorefining*, *16*(5), 1227–1239. https://doi.org/10.1002/bbb.2369
- Brandt, K. L., Martinez-Valencia, L., & Wolcott, M. P. (2022). Cumulative impact of federal and state policy on minimum selling price of sustainable aviation fuel. *Frontiers in Energy Research*, *10*, 828789. Doi: 10.3389/fenrg.2022.828789
- Burton, C., English, R., Menard, J., & Wilson, B. (2022). The Economic Impact of a Renewable Biofuels/Energy Industry Supply Chain Using the Renewable Energy Economic Analysis Layers Modeling System, *Frontiers in Energy Research*, *10*:3389. doi: 10.3389/fenrg.2022.780795
- Busch, J., Amarjargal, O., Taheripour, F., Austin, K. G., Siregar, R. N., Koenig, K., & Hertel, T. W. (2022). Effects of demand-side restrictions on high-deforestation palm oil in Europe on deforestation and emissions in Indonesia. *Environmental Research Letters*, *17*(1), 014035. doi:10.1088/1748-9326/ac435e
- Ma, F., Lee, J. Y., Camenzind, D., & Wolcott, M. (2022). Probabilistic Wildfire risk assessment methodology and evaluation of a supply chain network. *International Journal of Disaster Risk Reduction*, *82*, 103340. Doi: 10.1016/j.ijdrr.2022.103340
- Malina, R., Prussi, M. & Taheripour, F. (2022). *Method for establishing lifecycle greenhouse gas emission factors for sustainable aviation fuels*. In 2022 Environmental Report: Innovation for a Green Transition, International Civil Aviation Organization, Montreal QC, Canada.
- Martinez-Valencia, L., Peterson, S. Brandt, K., King, A., Garcia-Perez, M., & Wolcott, M. Impact of services on the supply chain configuration of sustainable aviation fuel: The case of CO_{2e} emission reduction in the U.S. (*Submitted to Journal of Cleaner Production*)
- Taheripour, F., Sajedinia, E., & Karami, O. (2022). Oilseed Cover Crops for Sustainable Aviation Fuels Production and Reduction in Greenhouse Gas Emissions Through Land Use Savings. *Frontiers in Energy Research*, 9(790421), 10. doi: 10.3389/fenrg.2021.790421
- Taheripour, F., Kwon, H., Mueller, S., Emery, I., Karami, O., & Sajedinia, E. (2022). Biofuels induced land use change emissions: The role of implemented emissions factors in assessing terrestrial carbon fluxes. *Global Trade Analysis Project 25th Annual Conference and 2022 AAEA Annual Meeting.*
- Tanzil, A. H., Brandt, K., Zhang, X., Wolcott, M., Silva Lora, E. E., Stockle, C., & Garcia-Perez, M. (2022). Evaluation of bio-refinery alternatives to produce sustainable aviation fuels in a sugarcane mill. *Fuel*, *321*, 123992. doi: 10.1016/j.fuel.2022.123992

Reports

Six harmonized TEAs have been posted on the WSU Research Repository for public use.

- Brandt, K; Tanzil, AH; Martinez-Valencia, L; Garcia-Perez, M; & Wolcott, MP; Pyrolysis techno-economic analysis, v. 2.1. Washington State University (2022)
- Brandt, K; & Wolcott, MP; Fischer Tropsch feedstock pre-processing techno-economic analysis, v. 2.1. Washington State University (2022)

- Brandt, K; Tanzil, AH; Martinez-Valencia, L; Garcia-Perez, M; & Wolcott, MP; Fischer Tropsch techno-economic analysis, v. 2.1. Washington State University (2022)
- Brandt, K; Tanzil, AH; Martinez-Valencia, L; Garcia-Perez, M; & Wolcott, MP; Hydroprocessed esters and fatty acids techno-economic analysis, v. 2.1. Washington State University (2022)
- Brandt, K; Geleynse, S; Martinez-Valencia, L; Zhang, X; Garcia-Perez, & M; Wolcott, MP; Alcohol to jet techno-economic analysis, v. 2.1. Washington State University (2022)
- Brandt, K; Eswaran, S; Subramaniam, S; Zhang, X; & Wolcott, MP; Catalytic hydrothermolysis techno-economic analysis, v. 2.1. Washington State University (2022)
- Chan, S., Ogoshi, R. & Turn, S. Feedstocks for sustainable jet fuel production: An assessment of land suitability in Hawaii. A draft report has been prepared and a draft manuscript is under preparation for publication.
- CAEP/12-FTG/11-WP/05. Summary of the work on the core LCA group since FTG/03, October 2021.
- CAEP/13-FTG/01-WP/04: Core LCA approach for the tasks of the CAEP/13 cycle, May 2022.
- CAEP/13-FTG/02-WP/03: Summary of the progress of the core LCA subgroup on Task S.06 and S.17, October 2022.
- CAEP/13-FTG/02-WP/04: Proposed path forward on CORSIA Eligible Fuels (CEF) Using Significant Electricity Inputs, October 2022.
- CAEP/13-FTG/02-WP/14: Actual Value Method for CORSIA Eligible Fuels (CEF) Using Significant Electricity Inputs, October 2022.
- CAEP/13-FTG/02-FL/02: Core LCA Pathway Discussions, October 2022.
- CAEP/13-FTG/02-FL/03: Flowchart threshold, October 2022.
- ICAO (2022). *Report on the feasibility of a long-term aspirational goal (LTAG) for international civil aviation CO2 emission reductions*. https://www.icao.int/environmental-protection/LTAG/Pages/LTAGreport.aspx
- International Civil Aviation Organization. (2022). CORSIA methodology for calculating actual life cycle emissions values, Section 8: CORSIA methodology for calculating direct land use change emissions values. https://www.icao.int/environmental-protection/CORSIA/Documents/CORSIA_Eligible_Fuels/ICAO%20document%2007%20-%20Methodology%20for%20Actual%20Life%20Cycle%20Emissions%20-%20June%202022.pdf
- CAEP/12-FTG/11-WP/06 – "Revisions to methodology on Low Land Use Change (LUC) Risk Practices based on pilot applications", October 2021, Virtual.
- CAEP/12-FTG/11-WP/09 – "Direct Land Use Change Emissions Methodology", October 2021, Virtual.
- CAEP/12-FTG/11-WP/10 – "ILUC default values", October 2021, Virtual.
- CAEP/12-FTG/11-IP/04 – "Foregone carbon sequestration accounting for Direct Land Use Change", October 2021, Virtual.
- CAEP/12-FTG/11-IP/05 – "Updating the GTAP-BIO data base form 2011 reference year to 2014 reference year", October 2021, Virtual.
- CAEP/12-FTG/11-FL/05 – "Proposal for carinata and camelina oil HEFA pathway characterization", October 2021, Virtual.
- CAEP/13-FTG/01-WP/06 – "Approach to ILUC-Related CAEP/13 Work Plan Items", May 2022, Virtual.

Presentations

- Fowler, L.B. (June 2022). Legal and Regulatory Drivers of Sustainable Aviation Fuel. Global Council for Science and the Environment.
- Fowler, L.B. (Oct. 2022). Briefing to Volvo Corporation on Opportunities Related to the Renewable Fuel Standard and SAF.
- Ma, F., & Lee, J.Y. (2022). "Probabilistic wildfire risk assessment for a supply chain system." *Proceedings of the 13th International Conference on Structural Safety and Reliability*, Shanghai, China, September 2022.
- Taheripour F., Kwon H., Mueller S., Emery I., Karami O., & Sajedinia E. (2022). Biofuels induced land use change emissions: The role of implemented emissions factors in assessing terrestrial carbon fluxes. Presented at GTAP 25th Annual Conference and 2022 AAEA Annual Meeting.
- Turn, S. "Comprehensive Characterization of Kuikui Nuts for Bioenergy Production in Hawaii" was presented orally at the 2022 Fall American Chemical Society National Meeting & Exposition, Chicago, IL, August 21-25, 2022
- Turn, S., Participated in the Asia Pacific Economic Cooperation event, "Energy Transition toward Carbon Neutrality, APEC BCG Economy Thailand 2022: Tech to Biz" in Bangkok, making a presentation entitled, "*US Initiatives on Sustainable Aviation Fuel*."
- Wolcott, M., & Brandt, K. SAF Grand Challenge A Path to 3-billion Gallons by 2030. SAF Summit & CAAFI Biennial General Meeting. June 2, 2022.

- Zhao, J., & Lee, J.Y. (2022a). "Multi-component resilience assessment framework for transportation systems." *Proceedings of the 13th International Conference on Structural Safety and Reliability*, Shanghai, China, September.
- Zhao, J., & Lee, J.Y. (2022b). "Effect of connected and autonomous vehicles on supply chain performance." *Transportation Research Record*. https://doi.org/10.1177/03611981221115425.

Project 002

Four undergraduate students involved.

Presentations

- ASCENT Project 002: to characterize the non-volatile Particulate Matter (nvPM) emissions and develop predictive emission functions for a series of conventional and synthetic alternative jet fuels. Presented at the Coordinating Research Council (CRC) Aviation Meeting Properties and Emissions" session May 5, 2022.

Project 003

Three graduate students involved.

Publications

- Simon, M. C., Hart, J. E., Levy, J. I., VoPham, T., Malwitz, A., Nguyen. D.D., Bozigar, M., Cupples, L.A., James, P., Laden, F., & Peters, J.L. (2022). Sociodemographic patterns of exposure to civil aircraft noise in the United States. *Environmental Health Perspectives*, 130(2) https://doi.org/10.1289/EHP9307
- Nguyen, Daniel. (2022). Aircraft noise exposure trends and impact on cardiovascular health in the United States. PhD dissertation, Environmental Health, Boston University.

Presentations

- Bozigar M, Laden F, Hart JE, Redline S, Huang T, Nelson EJ, Grady ST, Levy JI, & Peters JL. (2022). Associations between aircraft noise exposure and adiposity in the U.S.-based prospective Nurses' Health Studies" presented at International Society for Environmental Epidemiology (ISEE) Conference, September 18-21.
- Grady ST, Hart JE, Laden L, Nguyen DD, Bozigar M, Nelson E, Levy JI, & Peters JL. (2022). Associations between Residential Exposure to Aircraft Noise, Cardiovascular Disease, and All-Cause Mortality in the Nurses' Health Studies. Presented at ISEE Conference, September 18-22.
- Peters JL, Grady ST, Nguyen DD, Hart JE, Whitsel EA, Stewart JD, Laden F, & Levy JI. (2022). Long-term aircraft noise exposure and incident cardiovascular disease in national US cohort studies. Presented at Inter-Noise 2022, Glasgow, Scotland, August 21-24.
- Peters, J.L., D. D. Nguyen, S. T. Grady, J. E. Hart, E. A. Whitsel, J. D. Stewart, J. I. Levy. (2022). Long-Term Aircraft Noise Exposure and Incident Hypertension in National US Cohort Studies. Presented at 182nd Meeting of the Acoustical Society of America (ASA), Denver, C), May 23-27.

Project 009

Six graduate students involved.

Project 010

Twelve graduate students involved.

Publications

- Baltman, E., Tai, J. C., Ahuja, J., Stewart, B., Perron, C., De Azevedo, J., Vlady, T. R., & Mavris, D. N. (2022). A Methodology for Determining the Interdependence of Fuel Burn and LTO Noise of a Commercial Supersonic Transport. AIAA AVIATION 2022 Forum, 1–16. https://doi.org/10.2514/6.2022-4110
- Jain, S., H. Chao, M. Mane, W. A. Crossley and D. A. DeLaurentis. (2021). Estimating the Reduction in Future Fleet-Level CO2 Emissions From Sustainable Aviation Fuel, Frontiers in Energy Research, Nov 2021, doi: 10.3389/fenrg.2021.771705
- Yang, B., M. Mane & W. A. Crossley. (2022). An Approach to Evaluate Fleet Level CO2 Impact of Introducing Liquid Hydrogen Aircraft to a Worldwide Network. AIAA 2022-3313. AIAA AVIATION 2022 Forum, June 27-July 1, Chicago, IL & Virtual. https://doi.org/10.2514/6.2022-3313

Presentations

- Baltman, E., Tai, J. C., Ahuja, J., Stewart, B., Perron, C., De Azevedo, J., Vlady, T. R., & Mavris, D. N. (2022). A Methodology for Determining the Interdependence of Fuel Burn and LTO Noise of a Commercial Supersonic Transport. AIAA AVIATION 2022 Forum.
- Yang, B., M. Mane & W. A. Crossley. (2022). An Approach to Evaluate Fleet Level CO2 Impact of Introducing Liquid Hydrogen Aircraft to a Worldwide Network. Presented at AIAA AVIATION 2022 Forum, June 27-July 1, Chicago, IL & Virtual.

Project 018

One graduate student and three undergraduate students involved.

Publications

- Mueller, S.C., Hudda, N., Levy, J.I., Durant, J.L., Patil, P., Lee, N.F., Weiss, I., Tatro, T., Duhl, T., & Lane, K. (2022). Changes in ultrafine particle concentrations near a major airport following reduced transportation activity during the COVID-19 pandemic. *Environmental Science & Technology Letters 9(9)*, 706–711. https://doi.10.1021/acs.estlett.2c00322

Presentations

- Patil, P., Mueller, S., Hudda, N., Durant, J., Levy, J. I., & Lane, K. J. (2022). *Combining multi-site UFP concentration models using stacking and location weighting*. [Meeting presentation.] 2022 Joint Statistical Meetings, Washington, DC, United States.

Project 019

Two graduate students involved.

Publications

- Pandey, G., Venkatram, A., & Arunachalam, S. (2022). Evaluating AERMOD with measurements from a major U.S. airport located on a shoreline. *Atmospheric Environment, 294, 119506*. Doi: 10.1016/j.atmosenv.2022.119506

Presentations

- Presented the ADM work in multiple avenues including the AEC Roadmap meeting held in Washington, D.C. (May 2022) and the 21st HARMO conference held in Aveiro, Portugal (September 2022).

Project 022

No students involved.

Publications

- Wuebbles, D. J. (2022). The future of travel and tourism in the changing climate. *International Affairs Forum, 14(1)*, 18–13.
- Zhang, J., Wuebbles, D., Kinnison, D., Pfaender, J. H., Tilmes, S., & Davis, N. (2022). Potential impacts on ozone and climate from a proposed fleet of supersonic aircraft. [Manuscript submitted for publication.] *Earth's Future*.

Reports

- Hauglustaine, D. R., Miake-Lye, C., Arunachalam, S., Barrett, S. R. H., Fahey, D. W., Fuglestvedt, J. S., Madden, P., Skowron, A., van Velthoven, P., & Wuebbles, D. J. (2022). *Assessment of the impact of airport emissions on local levels of NO_x and human health; impacts of cruise emissions of NO_x on human health; impacts of cruise NO_x on climate*. International Civil Aviation Organization (ICAO). The United Nations, Montreal.
- Jacob, S. D., Lee, D. S., Wuebbles, D. J., Fuglesvedt, J. S., Johansson, D., Fahey, D. W., Hauglustaine, D., Sausen, R., van Velthoven, P. J. F., & Barrett, S. R. H. (2022). *Allowed emission of carbon dioxide for limiting global mean temperature increases to 1.5 or 2˚C.* International Civil Aviation Organization (ICAO). The United Nations, Montreal.
- Wuebbles, D. J., Baughcum, S., Barrett, S., Catalano, F., Fahey, D. W., Madden, P., Rhodes, D., Skowron, A., & Sparrow, V. (2022). *Understanding the potential environmental impacts from supersonic aircraft: An update*. International Civil Aviation Organization (ICAO). The United Nations, Montreal.

Presentations

- Hauglustaine, D. R., Miake-Lye, C., Arunachalam, S., Barrett, S. R. H., Fahey, D. W., Fuglestvedt, J. S., Madden, P., Skowron, A., van Velthoven, P., & Wuebbles, D. J. (2022). *Assessment of the impact of airport emissions on local levels of NO_x and human health; impacts of cruise emissions of NO_x on human health; impacts of cruise NO_x on climate*. International Civil Aviation Organization (ICAO). The United Nations, Montreal.
- Jacob, S. D., Lee, D. S., Wuebbles, D. J., Fuglesvedt, J. S., Johansson, D., Fahey, D. W., Hauglustaine, D., Sausen, R., van Velthoven, P. J. F., & Barrett, S. R. H. (2022). *Allowed emission of carbon dioxide for limiting global mean temperature increases to 1.5 or 2˚C.* International Civil Aviation Organization (ICAO). The United Nations, Montreal.
- Wuebbles, D. J., Baughcum, S., Barrett, S., Catalano, F., Fahey, D. W., Madden, P., Rhodes, D., Skowron, A., & Sparrow, V. (2022). *Understanding the potential environmental impacts from supersonic aircraft: An update*. International Civil Aviation Organization (ICAO). The United Nations, Montreal.

Project 023

Four graduate students involved.

Project 025

One graduate student involved.

Publications

- Boddapati, V., Ferris, A. M., & Hanson, R. K. (2022). On the use of extended-wavelength FTIR spectra for the prediction of combustion properties of jet fuels and their constituent species, *Proceedings of the Combustion Institute 39*. https://doi.org/10.1016/j.proci.2022.08.041

Presentations

- Boddapati, V., Ferris, A. M., & Hanson, R. K. (2022). On the use of extended-wavelength FTIR spectra for the prediction of combustion properties of jet fuels and their constituent species, 39th International Symposium on Combustion (July 24-29, 2022) in Vancouver, British Columbia.

Project 031

No students involved.

Reports

- (2022). *Evaluation of Global Bioenergies' isobutene derived synthetic paraffinic kerosene (IBN-SPK).* (Research Report D02 - WK71952).
- (2022). *Evaluation of alcohol-to-jet synthetic kerosene with aromatics (ATJ-SKA) fuels and blends.* (Research Report).

Project 033

Two graduate students involved.

- Database made accessible through https://altjetfuels.illinois.edu/

Publications

- Oldani, A. L., Solecki, A. E., & Lee, T. (2022). Evaluation of physicochemical variability of sustainable aviation fuels. *Frontiers in Energy Research*, *10*, 1052267. doi: 10.3389/fenrg.2022.1052267
- Oh, J., Oldani, A., Lee, T., & Shafer, L. (2022, January 3). Deep neural networks for assessing sustainable jet fuels from two-dimensional gas chromatography. *Aerospace Research Central, AIAA 2022-0228*. doi: 10.2514/6.2022-0228

Project 37

Six graduate students currently involved.

Project 038

Two graduate students involved.

Publications

- Weist, L. (2022). *Helicopter Noise Modeling with Varying Fidelity Prediction Systems* [Master's thesis, The Pennsylvania State University].
- Zachos, D. R., Weist, L., Brentner, K. S., & Greenwood, E. (2022). *Variation in Helicopter Noise During Approach Maneuvers.* Paper presented at 78th Vertical Flight Society Annual Forum and Technology Display, FORUM 2022, Fort Worth, Texas, United States.
- Zachos, D. R. (2022). Noise Prediction of Rotorcraft Acoustics for a Conceptual eVTOL Design and Conventional Helicopters. M. S Thesis, The Pennsylvania State University.

Presentations

- Zachos, D. R., Weist, L., Brentner, K. S., & Greenwood, E. (2022). *Variation in Helicopter Noise During Approach Maneuvers.* Presented at 78th Vertical Flight Society Annual Forum and Technology Display, FORUM 2022, Fort Worth, Texas, United States.

Project 043

One graduate student involved.

Project 044

Three graduate students involved.

Publications

- Huynh, J., Mahseredjian, A., & Hansman, R. J. (2022). Delayed Deceleration Approach Noise Impact and Modeling Validation. *Journal of Aircraft*, *59*(5), 127-136. https://doi.org/10.2514/1.C036631
- Mahseredjian, A., Huynh, J., & Hansman, R. J. (2022). *Analysis of community departure noise exposure variation using airport noise monitor networks and operational ADS-B data*. Inter-Noise 2022, Glasgow, Scotland.
- Mahseredjian, A., Huynh, J., & Hansman, R. J. (2022). *A Data-Driven Approach to Departure and Arrival Noise Abatement Flight Procedure Development* [S. M. thesis, Massachusetts Institute of Technology]. DSpace@MIT. https://hdl.handle.net/1721.1/144311
- Salgueiro, S., Huynh, J., Li., C. & Hansman, R. J. (2022). *Aircraft Takeoff and Landing Weight Estimation from Surveillance Data*. AIAA Scitech 2022 Forum, San Diego, CA. https://doi.org/ 10.2514/6.2022-1307.

Presentations

- Mahseredjian, A., Huynh, J., & Hansman, R. J. (2022). *Analysis of community departure noise exposure variation using airport noise monitor networks and operational ADS-B data* [Presentation]. Inter-Noise 2022, Glasgow, Scotland.
- Salgueiro, S., Huynh, J., Li., C. & Hansman, R. J. (2022). *Aircraft Takeoff and Landing Weight Estimation from Surveillance Data* [Presentation]. AIAA Scitech 2022 Forum, San Diego, CA.

Project 046

No students involved.

Project 047

Three graduate students involved.

Publications

- Voet, L., Speth, R. L., Sabnis, J. S., Tan, C. S., & Barrett, S. R. (2022, June 14). *On the Design of Variable Noise Reduction Systems for Supersonic Transport Take-off Certification Noise Reduction*. 28th AIAA/CEAS Aeroacoustics 2022 Conference, Southampton, UK. https://doi.org/10.2514/6.2022-3052

Presentations

- Voet, L., Speth, R. L., Sabnis, J. S., Tan, C. S., & Barrett, S. R. (2022, June 14). *On the Design of Variable Noise Reduction Systems for Supersonic Transport Take-off Certification Noise Reduction*. 28th AIAA/CEAS Aeroacoustics 2022 Conference, Southampton, UK.
- Presentation at the Aviation Emissions Characterization Roadmap Annual Meeting (24-26 May 2022)

Project 048

One graduate student involved.

Presentations

- Presentation to CAEP/13-WG3/3-ECTG meeting (17-21 October 2022)

Project 049

Two graduate students involved.

Publications

Published conference proceedings

- Mukherjee, B., Brentner, K. S., Greenwood, E., Theron, J.-P., & Horn, J. F. (2022, May 10-12). *An Investigation of Piloting and Flight Control Strategies on Generic eVTOL Noise.* Vertical Flight Society's 78th Annual Forum & Technology Display, Fort Worth, TX. DOI: 10.4050/F-0078-2022-17441.
- Gan, Z.F.T., Brentner, K.S., & Greenwood, E. (2022). Time Variation of Helicopter Rotor Broadband Noise. AIAA-2022-2914. 28th AIAA/CEAS Aeroacoustics Conference, Southampton, UK.

Presentations

- Mukherjee, B., Brentner, K. S., Greenwood, E., Theron, J.-P., & Horn, J. F. (2022). *An Investigation of Piloting and Flight Control Strategies on Generic eVTOL Noise*, Vertical Flight Society's 78th Annual Forum & Technology Display, Fort Wort, TX, May 10–12, 2022.
- Gan, Z.F.T., Brentner, K.S., & Greenwood, E. (2022, June 14-17). *Time Variation of Helicopter Rotor Broadband Noise*. 28th AIAA/CEAS Aeroacoustics Conference, Southampton, UK.

Project 050

Eight graduate students involved.

Publications

- Mufti, B., Chen, M., Perron, C., & Mavris, D. N. (2022, June 27). A multi-fidelity approximation of the active subspace method for surrogate models with high-dimensional inputs. *AIAA AVIATION 2022 Forum*. AIAA AVIATION 2022 Forum, Chicago, IL & Virtual. https://doi.org/10.2514/6.2022-3488

Presentations

- Mufti, B., Chen, M., Perron, C., & Mavris, D. N. (2022, June 27). A multi-fidelity approximation of the active subspace method for surrogate models with high-dimensional inputs. *AIAA AVIATION 2022 Forum*. AIAA AVIATION 2022 Forum, Chicago, IL & Virtual.

Project 051

Two graduate students involved.

Publications

- Chen, Y. (2022). Effects of Fuel Split Ratio on NO_x Emissions of a Lean-burn Staged Combustor [Thesis, Massachusetts Institute of Technology]. https://dspace.mit.edu/handle/1721.1/144712
- Zahid, S. S. (2022). Impact of Water Injection on Emissions of Nitrogen Oxides from Aircraft Engines [Thesis, Massachusetts Institute of Technology]. https://dspace.mit.edu/handle/1721.1/144573

Project 052

Three graduate students involved.

Reports

- ICAO (2022). Report on the feasibility of a long-term aspirational goal (LTAG) for international civil aviation CO_2 emission reductions. Available online at https://www.icao.int/environmental-protection/LTAG/Pages/LTAGreport.aspx

Project 053

Three graduate students and one undergraduate student involved.

Project 054

Seven graduate students involved.

Project 055

Seven graduate students and four undergraduate students involved.

Publications

- Acharya, V. S. (2022). Global dynamics of the velocity-coupled response of spray flames. AIAA SCITECH 2022 Forum, San Diego, CA & Virtual. https://doi.org/10.2514/6.2022-1856
- Homma, K., Reimann, A., Winkler, J., & Mendoza, J. (2022). CAA prediction of turbofan engine combustion noise directivity. 28th AIAA/CEAS Aeroacoustics 2022 Conference, Southampton, UK. https://doi.org/10.2514/6.2022-2975
- Panchal, A., & Menon, S. (2023). Large eddy simulation of combustion noise in a realistic gas turbine combustor. AIAA SCITECH 2023 Forum, National Harbor, MD & Online. https://doi.org/10.2514/6.2023-1349
- Patki, P., Acharya, V., & Lieuwen, T. (2022). Entropy generation mechanisms from exothermic chemical reactions in laminar, premixed flames. *Proceedings of the Combustion Institute*, S1540748922003455. https://doi.org/10.1016/j.proci.2022.08.069
- Laksana, A., Patki, P., John, T., Acharya, V., & Lieuwen, T. "Distributed Heat Release Effects on Entropy Generation by Premixed, Laminar Flames", under review for International Journal of Spray and Combustion Dynamics.

Presentations

- Acharya, V. S. (2022, January 3). Global dynamics of the velocity-coupled response of spray flames. AIAA SCITECH 2022 Forum, San Diego, CA & Virtual.
- Homma, K., Reimann, A., Winkler, J., & Mendoza, J. (2022, June 14). CAA prediction of turbofan engine combustion noise directivity. 28th AIAA/CEAS Aeroacoustics 2022 Conference, Southampton, UK.
- John, T., Acharya, V., & Lieuwen, T. (2022, March). Entropy transfer functions of externally forced flames. *2022 Spring Technical Meeting of the Eastern States Section of the Combustion Institute*.
- Panchal, A., & Menon, S. (2023, January 23). Large eddy simulation of combustion noise in a realistic gas turbine combustor. AIAA SCITECH 2023 Forum, National Harbor, MD & Online.

Project 056

Two graduate students involved.

Publications

- Wolff, J., (2022). Development of Experimental Methodology to Determine the Heat Transfer of Additively Manufactured Airfoil Channels in a High-Speed Linear Cascade Rig. Master's Thesis, Additive Manufacturing and Design Program, Penn State University.

Presentations

- Boyd, L., (2023).Novel Cooling Designs in Additively Manufactured Microchannels, ASME Poster GT2023-110173, accepted.

Project 057

One graduate student involved.

Publications

- Riegel, K.A. & Sparrow, V.W. (2022). Secondary sonic boom predictions for U.S. coastlines. The Journal of the Acoustical Society of America, 152, 2816-2827. https://doi.org/10.1121/10.0014860

Project 058

Four graduate students involved.

Publications

- Eastham, S. D., Fritz, T., Sanz-Morère, I., Prashanth, P., Allroggen, F., Prinn, R. G., Speth, R. L., & Barrett, S. R. H. (2022). Impacts of a near-future supersonic aircraft fleet on atmospheric composition and climate. *Environmental Science: Atmospheres*, *2*(3), 388–403. Doi: 10.1039/D1EA00081K
- Prashanth, P., Eastham, S. D., Speth, R. L., & Barrett, S. R. H. (2022). Aerosol formation pathways from aviation emissions. *Environmental Research Communications*, *4*(2), 021002. https://doi.org/10.1088/2515-7620/ac5229

Presentations

- Grobler, C., Fritz, T., Allroggen, F., Eastham S., & Barrett, S.R. (2022). *Commercial civil aviation emissions from 1980 to the present day* [Oral presentation]. 5th International Conference on Transport, Atmosphere, and Climate (TAC-5.
- Prashanth, P., Eastham, S. D., Speth, R. L., & Barrett, S. R. H. (2022). *Aerosol formation pathways from aviation emissions* [Oral presentation]. 5th International Conference on Transport, Atmosphere, and Climate (TAC-5).
- Poster presentation on the updates to APMT and the tradeoffs associated with high-altitude NO_x emissions at TAC-5 (the 5th International Conference on Transport, Atmosphere and Climate, 2022).

Project 059

Thirteen graduate students involved.

Publications

- Ramsey, D. N., Karon, A. Z., Funk, R., & Ahuja, K. K. (2022, June 14). Jet noise from a low-bypass confluent nozzle: Mixing length and extraction ratio effects. *28th AIAA/CEAS Aeroacoustics 2022 Conference*. 28th AIAA/CEAS Aeroacoustics 2022 Conference, Southampton, UK. https://doi.org/10.2514/6.2022-2863
- Ramsey, D. N., Mayo, R., Karon, A. Z., Funk, R., & Ahuja, K. K. (2022, June 14). Self-excited jet from a low-bypass confluent nozzle at unity extraction ratio. *28th AIAA/CEAS Aeroacoustics 2022 Conference*. 28th AIAA/CEAS Aeroacoustics 2022 Conference, Southampton, UK. https://doi.org/10.2514/6.2022-2864
- Shanbhag, T. K., Zhou B. Y., Ilario, C. R. S., & Alonso, J. J. (2022, July). *Ray tracing methodology for jet noise prediction*. (ICCFD11-2022-1201). Eleventh International Conference on Computational Fluid Dynamics (ICCFD11).
- Shanbhag, T. K., Wu, G. J., Lele, S. K., & Alonso, J. J. (2023, January 23). Optimization of turbulent time scales for jet noise prediction. *AIAA SCITECH 2023 Forum*. AIAA SCITECH 2023 Forum, National Harbor, MD & Online. https://doi.org/10.2514/6.2023-1159
- Wu, G. J., Shanbhag, T. K., Molina, E. S., Lele, S. K., & Alonso, J. J. (2022, January 3). Numerical simulations and acoustic modeling of a co-annular nozzle with an internal mixing duct. *AIAA SCITECH 2022 Forum*. AIAA SCITECH 2022 Forum, San Diego, CA & Virtual. https://doi.org/10.2514/6.2022-2404

Presentations

- Ramsey, D. N., Karon, A. Z., Funk, R., & Ahuja, K. K. (2022, June 14). Jet noise from a low-bypass confluent nozzle: Mixing length and extraction ratio effects. *28th AIAA/CEAS Aeroacoustics 2022 Conference*. 28th AIAA/CEAS Aeroacoustics 2022 Conference, Southampton, UK.
- Ramsey, D. N., Mayo, R., Karon, A. Z., Funk, R., & Ahuja, K. K. (2022, June 14). Self-excited jet from a low-bypass confluent nozzle at unity extraction ratio. *28th AIAA/CEAS Aeroacoustics 2022 Conference*. 28th AIAA/CEAS Aeroacoustics 2022 Conference, Southampton, UK.
- Shanbhag, T. K., Zhou B. Y., Ilario, C. R. S., & Alonso, J. J. (2022, July). *Ray tracing methodology for jet noise prediction*. (ICCFD11-2022-1201). Eleventh International Conference on Computational Fluid Dynamics (ICCFD11).
- Shanbhag, T. K., Wu, G. J., Lele, S. K., & Alonso, J. J. (2023, January 23). Optimization of turbulent time scales for jet noise prediction. *AIAA SCITECH 2023 Forum*. AIAA SCITECH 2023 Forum, National Harbor, MD & Online.
- Wu, G. J., Shanbhag, T. K., Molina, E. S., Lele, S. K., & Alonso, J. J. (2022, January 3). Numerical simulations and acoustic modeling of a co-annular nozzle with an internal mixing duct. *AIAA SCITECH 2022 Forum*. AIAA SCITECH 2022 Forum, San Diego, CA & Virtual.

Project 060

Two graduate students involved.

Project 061

Five graduate students and two undergraduate students involved.

Publications

- Kim, D., Karagoz, F., Datta, S., Balchanos, M., Anvid, D., Harrison, E., & Mavris, D.N. (2022). A Model Based Systems Engineering Approach to Streamlined Noise Certification of Transport-type Aircraft. In 33rd Congress of International Council of the Aeronautical Sciences ICAS, Stockholm, Sweden.
- Kim, D., Taneri, M., Omoarebun, E.N, Wills, T., Balchanos, M., & Mavris, D. (2023). MBSE-Enabled System Verification and Process Improvement of Transport Aircraft Certification. Accepted and to be presented In AIAA SciTech 2023 Forum, National Harbor, MD, January 23-27, 2023.

Presentations

- Kim, D., Karagoz, F., Datta, S., Balchanos, M., Anvid, D., Harrison, E., & Mavris, D.N. (2022). A Model Based Systems Engineering Approach to Streamlined Noise Certification of Transport-type Aircraft. Presented at 33rd Congress of International Council of the Aeronautical Sciences ICAS, Stockholm, Sweden.
- Kim, D., Taneri, M., Omoarebun, E.N, Wills, T., Balchanos, M., & Mavris, D. (2023). MBSE-Enabled System Verification and Process Improvement of Transport Aircraft Certification. Accepted and to be presented In AIAA SciTech 2023 Forum, National Harbor, MD, January 23-27, 2023.

Project 062

Five graduate students involved.

Publications

- Bendarkar, M. V., Bhanpato, J., Puranik, T. G., Kirby, M., & Mavris, D. N. (2022, June 27). Comparative assessment of AEDT noise modeling assumptions using real-world data. AIAA AVIATION 2022 Forum. AIAA AVIATION 2022 Forum, Chicago, IL & Virtual. https://doi.org/10.2514/6.2022-3917
- Shaw, E., & Sparrow, V. (2022). Modeling acoustic impedance and atmospheric absorption around airports using high-fidelity weather data. *NOISE-CON Congress and Conference Proceedings*, *264*(1), 104–110. https://doi.org/10.3397/NC-2022-698

Presentations

- Bendarkar, M. V., Bhanpato, J., Puranik, T. G., Kirby, M., & Mavris, D. N. (2022, June 27). Comparative assessment of AEDT noise modeling assumptions using real-world data. AIAA AVIATION 2022 Forum. AIAA AVIATION 2022 Forum, Chicago, IL & Virtual.
- Shaw, E., & Sparrow, V. (2022). Modeling acoustic impedance and atmospheric absorption around airports using high-fidelity weather data. Presented at Noise-Con 2022, 13-15 June 2022, Lexington, KY.

Project 063

Three graduate students involved.

Project 064

Five graduate students involved.

Project 065

Six graduate students and four undergraduate students involved.

Publications

- Bell, D. C., Boehm, R. C., Feldhausen, J., & Heyne, J. S. (2022). A data set comparison method using noise statistics applied to vuv spectrum match determinations. *Analytical Chemistry*, *94*(43), 14861–14868. https://doi.org/10.1021/acs.analchem.2c01931
- Boehm, R. C., Coburn, A. A., Yang, Z., Wanstall, C. T., & Heyne, J. S. (2022). Blend prediction model for the freeze point of jet fuel range hydrocarbons. *Energy & Fuels*, *36*(19), 12046–12053. https://doi.org/10.1021/acs.energyfuels.2c02063
- Feldhausen, J., Bell, D. C., Yang, Z., Faulhaber, C., Boehm, R., & Heyne, J. (2022). Synthetic aromatic kerosene property prediction improvements with isomer specific characterization via GCxGC and vacuum ultraviolet spectroscopy. *Fuel*, *326*, 125002. https://doi.org/10.1016/j.fuel.2022.125002
- Boehm, R. C., Yang, Z., & Heyne, J. S. (2022). Threshold sooting index of sustainable aviation fuel candidates from composition input alone: Progress toward uncertainty quantification. *Energy & Fuels*, *36*(4), 1916–1928. https://doi.org/10.1021/acs.energyfuels.1c03794
- Boehm, R. C., Yang, Z., Bell, D. C., Feldhausen, J., & Heyne, J. S. (2022). Lower heating value of jet fuel from hydrocarbon class concentration data and thermo-chemical reference data: An uncertainty quantification. *Fuel*, *311*, 122542. https://doi.org/10.1016/j.fuel.2021.122542
- Heyne, J., Bell, D., Feldhausen, J., Yang, Z., & Boehm, R. (2022). Towards fuel composition and properties from Two-dimensional gas chromatography with flame ionization and vacuum ultraviolet spectroscopy. *Fuel*, *312*, 122709. https://doi.org/10.1016/j.fuel.2021.122709
- Wood, E. J., Motily, A., Trotter, C. J., Lee, T., Mayhew, E., Coburn, V. D., Temme, J., & Kweon, C.-B. (2022, January 3). Fuel spray and operating condition impact on ignition performance in the arc-m1 combustor. *AIAA SCITECH 2022 Forum*. AIAA SCITECH 2022 Forum, San Diego, CA & Virtual. https://doi.org/10.2514/6.2022-0364
- Wood, E., Trotter, C., Lee, T., Mayhew, E., Temme, J., & Kweon, C. (2023). Lean Blowout Dependence on Fuel Atomization in the ARC-M1 Gas Turbine Combustor. Conference paper in preparation.

Presentations

- Wood, E., Motily, A., Trotter, C., Lee, T., Mayhew, E., Coburn, V., Temme, J., & Kweon, C. (2022). Fuel spray and operating condition impact on ignition performance in the ARC-M1 combustor. Presented at AIAA SCITECH 2022 Forum, January 3-7, San Diego, CA & Virtual.

Project 066

Three graduate students involved.

Publications

- Boehm, R. C.; Yang, Z.; & Heyne, J. S. (2022). Threshold sooting index of sustainable aviation fuel candidates from composition input alone: Progress toward uncertainty quantification. Energy & Fuels. 36(4), 1916. https://doi.org/10.1021/acs.energyfuels.1c03794
- Behnke, L. C.; Boehm, R. C.; & Heyne, J. S. (2022). Optimization of Sustainable Alternative Fuel Composition for Improved Energy Consumption of Jet Engines. In AIAA Scitech 2022 Forum; p 2056. https://doi.org/10.2514/6.2022-2056

Presentations

- Behnke, L. C.; Boehm, R. C.; & Heyne, J. S. (2022). Optimization of Sustainable Alternative Fuel Composition for Improved Energy Consumption of Jet Engines. Presented at AIAA SCITECH 2022 Forum, January 3-7, San Diego, CA & Virtual.

Project 067

Three graduate students involved.

Publications

- Philo, J. J., McDonald, C. T., Shahin, T. T., Gejji, R. M., Lucht, R. P., & Slabaugh, C. D. (2022). Fuel heating effects on the flow and flame structure of a piloted swirl injector. AIAA Journal, under review.
- McDonald, C. T., Shahin, T. T., Philo, J. J., Gejji, R. M., Fish, D. D., Slabaugh, C. D., & Lucht, R. P. (2022). Emissions Measurements in a Liquid-Fueled Aviation Gas Turbine Combustor with Heated Fuels. ASME Journal of Engineering for Gas Turbines and Power, in preparation.

Project 068

Two graduate students involved.

Publications

- McFerran, K., Fallon, B., Fox, S., Thole, K., Lynch, S., Lundgren, R., & Kramer, S. *Comparison of Dirt Deposition on Double-Walled Combustor Liner Geometries*. Abstract under review for TurboExpo 2023

Project 069

One graduate student and two undergraduate students involved.

Project 070

Four graduate students involved.

Publications

- McGrath, R., E. Bugay, J. Juergensmeyer, A. Zheng, D. Wu, A. Steinberg, W. Sun, & E. Mazumdar. (2023). Single-camera Time-Resolved laser-induced Incandescence Measurements in a RQL Aeroengine Combustor. 13th U.S. National Combustion Meeting College Station, TX, 77844, March 19–22.

Presentations

- McGrath, R., E. Bugay, J. Juergensmeyer, A. Zheng, D. Wu, A. Steinberg, W. Sun, & E. Mazumdar. (2023). Single-camera Time-Resolved laser-induced Incandescence Measurements in a RQL Aeroengine Combustor. Presented at the 13th U.S. National Combustion Meeting College Station, TX, 77844, March 19–22.

Project 071

Two graduate students involved.

Project 072

Two graduate students involved.

Project 073

Graduate student and undergraduate student: TBD

Project 074

Five graduate students and seven undergraduate students involved.

Publications

- Passarelli, M. L., Wonfor, S. E., Zheng, A. X., Manikandan, S. R., Mazumdar, Y. C., Seitzman, J. M., Steinberg, A. M., Bower, H., Hong, J., Venkatesan, K., & Benjamin, M. (2022, January 3). Experimental characterization of a lean prevaporized premixed combustor for supersonic transport applications. *AIAA SCITECH 2022 Forum*. AIAA SCITECH 2022 Forum, San Diego, CA & Virtual. https://doi.org/10.2514/6.2022-2347
- Passarelli, M. L., Wonfor, S. E., Zheng, A. X., Mazumdar, Y. C., Seitzman, J. M., Steinberg, A. M., Salazar, V., Venkatesan, K., & Benjamin, M. (2023, January 23). Forced and unforced dynamics of a lean premixed prevaporized combustor for civil supersonic transport. *AIAA SCITECH 2023 Forum*. AIAA SCITECH 2023 Forum, National Harbor, MD & Online. https://doi.org/10.2514/6.2023-0920
- Zheng, A. X., Manikandan, S., Wonfor, S. E., Steinberg, A. M., & Mazumdar, Y. C. (2023, January 23). Planar time-resolved laser-induced incandescence for particulate emissions in premixed flames at elevated pressures. *AIAA SCITECH 2023 Forum*. AIAA SCITECH 2023 Forum, National Harbor, MD & Online. https://doi.org/10.2514/6.2023-2435
- Venkatesan, K. (2022). Acoustic and Optical Flame Transfer Function Measurements in a High-Pressure Lean-Burn Aero-Engine Combustor Fueled with Jet A. ASME Turbo Expo

Presentations

- Passarelli, M. L., Wonfor, S. E., Zheng, A. X., Manikandan, S. R., Mazumdar, Y. C., Seitzman, J. M., Steinberg, A. M., Bower, H., Hong, J., Venkatesan, K., & Benjamin, M. (2022, January 3). Experimental characterization of a lean prevaporized premixed combustor for supersonic transport applications. *AIAA SCITECH 2022 Forum*. AIAA SCITECH 2022 Forum, San Diego, CA & Virtual.
- Passarelli, M. L., Wonfor, S. E., Zheng, A. X., Mazumdar, Y. C., Seitzman, J. M., Steinberg, A. M., Salazar, V., Venkatesan, K., & Benjamin, M. (2023, January 23). Forced and unforced dynamics of a lean premixed prevaporized combustor for civil supersonic transport. *AIAA SCITECH 2023 Forum*. AIAA SCITECH 2023 Forum, National Harbor, MD & Online.
- Zheng, A. X., Manikandan, S., Wonfor, S. E., Steinberg, A. M., & Mazumdar, Y. C. (2023, January 23). Planar time-resolved laser-induced incandescence for particulate emissions in premixed flames at elevated pressures. *AIAA SCITECH 2023 Forum*. AIAA SCITECH 2023 Forum, National Harbor, MD & Online.

- Venkatesan, K. (2022). Acoustic and Optical Flame Transfer Function Measurements in a High-Pressure Lean-Burn Aero-Engine Combustor Fueled with Jet A. ASME Turbo Expo

Project 075

Two graduate students and two undergraduate students involved.

Publications

- Li, N., Watchmann, B., Ramsarran, T., Winkler, J., Reimann, A., Voytovych, D., Mendoza, J., & Grace, S. M. (2022, June 14). Fan-stage broadband interaction noise trends. *28th AIAA/CEAS Aeroacoustics 2022 Conference*. 28th AIAA/CEAS Aeroacoustics 2022 Conference, Southampton, UK. https://doi.org/10.2514/6.2022-2884
- Huang, Z., Shen, H., Kung, K., Carvalho, L., Thai, A., Watchmann, B., Ramsarran, T., Winkler, J., Reimann, A., Joly, M., Lore, K. G., Mendoza, J., & Grace, S. M. (2022, June 14). Fan wake prediction via machine learning. *28th AIAA/CEAS Aeroacoustics 2022 Conference*. 28th AIAA/CEAS Aeroacoustics 2022 Conference, Southampton, UK. https://doi.org/10.2514/6.2022-2883

Presentations

- Li, N., Watchmann, B., Ramsarran, T., Winkler, J., Reimann, A., Voytovych, D., Mendoza, J., & Grace, S. M. (2022, June 14). Fan-stage broadband interaction noise trends. *28th AIAA/CEAS Aeroacoustics 2022 Conference*. 28th AIAA/CEAS Aeroacoustics 2022 Conference, Southampton, UK.
- Huang, Z., Shen, H., Kung, K., Carvalho, L., Thai, A., Watchmann, B., Ramsarran, T., Winkler, J., Reimann, A., Joly, M., Lore, K. G., Mendoza, J., & Grace, S. M. (2022, June 14). Fan wake prediction via machine learning. *28th AIAA/CEAS Aeroacoustics 2022 Conference*. 28th AIAA/CEAS Aeroacoustics 2022 Conference, Southampton, UK.
- Nuo Li, Yifan Zhang, Julian Winkler, C. Aaron Reimann, Dmytro Voytovych, Jeff Mendoza, and Sheryl M. Grace. (2023). Development of fully low-order prediction of fan broadband interaction noise via integration of machine learning, submitted to 2023 AIAA Aviation-Aeroacoustics.

Project 076

Two graduate students involved.

Presentations

- Aerodynamic Calibration for Aeroacoustics Validation of an Open Fan Configuration, to appear on AIAA SciTech 2023

Project 077

Six graduate students involved.

Publications

- Greenwood, E., and Konzel, N.B. (2022, June). *Measurement and Characterization of Multirotor Unmanned Aerial System Noise.* NOISE-CON 2022, Lexington, KY.
- Konzel, N.B., and Greenwood, E. (2022, May). *Ground-based Acoustic Measurements of Small Multirotor Aircraft.* Vertical Flight Society Forum 78, Ft. Worth, TX.
- Rachaprolu, J., & Greenwood, E. (2022, May). *Helicopter Noise Source Separation using an Order Tracking Filter.* Vertical Flight Society Forum 78.
- Rachaprolu, J. (2022, November). *Development of a Source Separation Process for Multirotor Aeroacoustic Analysis* [Master's thesis, The Pennsylvania State University]
- Valente, V., Johnson, E., & Greenwood, E. (2022, September). *Implementation of a phase synchronization algorithm for multirotor UAVs*. 2022 IEEE/AIAA 41st Digital Avionics Systems Conference (DASC), Portsmouth, VA.

Presentations

- Greenwood, E., and Konzel, N.B. (2022, June). *Measurement and Characterization of Multirotor Unmanned Aerial System Noise.* Presented at NOISE-CON 2022, Lexington, KY, June.
- Hur, K.W., Zachos, D.R., Brentner, K.S., and Greenwood, E., "Determining the Acoustic Far-field for Multirotor Aircraft," abstract accepted for the 10th Biennial Autonomous VTOL Technical Meeting & 10th Annual eVTOL Symposium, Mesa, AZ, January 2023.
- Konzel, N.B., and Greenwood, E. (2022, May). *Ground-based Acoustic Measurements of Small Multirotor Aircraft.* Vertical Flight Society Forum 78, Ft. Worth, TX.
- Rachaprolu, J., & Greenwood, E. (2022, May). *Helicopter Noise Source Separation using an Order Tracking Filter.* Vertical Flight Society Forum 78.
- Valente, V., Johnson, E., & Greenwood, E. (2022, September). *Implementation of a phase synchronization algorithm for multirotor UAVs*. Presented at IEEE/AIAA 41st Digital Avionics Systems Conference (DASC), Portsmouth, VA.
- Valente, V.T., Johnson, E.N., and Greenwood, E., "An Experimental Investigation of eVTOL Flight State Variance on Noise," abstract submitted to the Vertical Flight Society Forum 79, West Palm Beach, FL, May 2023.

Project 078

Three graduate students involved.

Presentations

- Vincent R. Meijer, Sebastian D. Eastham, and Steven R.H. Barrett. (2022). Using satellite-based observations of contrails to inform contrail avoidance strategies. Presented at 5th International Conference on Transport, Atmosphere and Climate (TAC-5), Munich, Germany, June 29.
- Jad Elmourad, Sebastian D Eastham, Raymond L Speth, Florian Allroggen, and Steven R H Barrett. (2022). Flight Level Optimization for Contrail Avoidance. Poster presented at 5th International Conference on Transport, Atmosphere and Climate (TAC-5), Munich, Germany, June 27.

Project 079

Two graduate students involved.

Project 080

Three graduate students involved.

Publications

- Sierra V, Wolcott M, Zhang X, Ha S, Male J, Garcia A, Brand K, Garcia-Perez M, Drennan C, Holladay. Emerging and Commercial Hydrogen Production Technologies for SAF Manufacturing: A comparative Literature Review. *Under internal review*.

Presentations

- Garcia-Perez M, Garcia A, and Wolcott M. (2022) Production of cheap Sustainable Aviation Fuels (SAFs): Balancing Economic and Environmental Advantages. Sustainable Energy for a Sustainable Future, San Pedro, San Jose, October 24-27.
- Presented preliminary results at the CAAFI meeting on June (1-3, 2022) in Washington, DC.
- Presentation to the Fuels Task Group in October 2022.

Project 081

No graduate students involved to date.

Project 082

Eleven graduate students involved.

Project Funding Allocations by Federal Fiscal Year

Breakout by Project

Project		Funding Based on award date									
		2014	2015	2016	2017	2018	2019	2020	2021	2022	Total
001	Alternative Jet Fuel Supply Chain Analysis	$1,599,943	$1,425,000	$1,498,749	$1,855,461	$1,102,865	$1,034,039	$3,214,455	$1,412,313	$1,569,136	$14,711,961
002	Ambient Conditions Corrections for Non-Volatile PM Emissions Measurements	$2,800,000	$750,000	-$147,766	$725,500	-	$1,217,221	-	$521,246	-	$5,866,201
003	Cardiovascular Disease and Aircraft Noise Exposure	$200,000	$200,000	$200,000	$340,000	-	$1,729,286	-	-	-	$2,669,286
004	Estimate of Noise Level Reduction	$150,000	-	-	-	-$8,845	-	-	-	-	$141,155
005	Noise Emission and Propagation Modeling	$212,000	$200,000	-	-	-	-	-	-	-	$412,000
006	Rotorcraft Noise Abatement Operating Conditions Modeling	$250,326	-	-	-	-	-	-	-	-	$250,326
007	Civil, Supersonic Over Flight, Sonic Boom (Noise) Standards Development	$100,000	$200,000	-	-	-	-	-	-	-	$300,000
008	Noise Outreach	$ 30,000	$ 50,000	$ 75,000	$ 25,000	-	$ 30,000	-	-	-	$210,000
009	Geospatially Driven Noise Estimation Module	-	-	-	-	-	-	$250,000	$249,999	-	$499,999

Project		Funding Based on award date									
		2014	2015	2016	2017	2018	2019	2020	2021	2022	Total
010	Aircraft Technology Modeling and Assessment	$549,979	$550,000	$310,000	$669,567	$764,185	-	$2,747,116	$700,000	-	$6,290,847
011	Rapid Fleet-wide Environmental Assessment Capability	$600,000	$270,000	$299,999	-	-	-	-	-	-	$1,169,999
012	Aircraft Design and Performance Assessment Tool Enhancement	$ 90,000	-	-	-	-	-	-	-	-	$90,000
013	Micro-Physical Modeling & Analysis of ACCESS 2 Aviation Exhaust Observations	$200,000	-	-	-	-	-	-	-	-	$200,000
014	Analysis to Support the Development of an Aircraft CO2 Standard	$520,000	-	-	-	-	-	-	-	-	$520,000
017	Pilot Study on Aircraft Noise and Sleep Disturbance	$154,000	$343,498	$266,001	$134,924	-	-	-	-	-	$898,423
018	Health Impacts Quantification for Aviation Air Quality Tools	$150,000	$150,000	$200,000	$270,000	-	-	$1,299,991	$599,371	$549,921	$3,219,283
019	Development of Aviation Air Quality Tools for Airport-Specific Impact Assessment: Air Quality Modeling	$320,614	$369,996	-	$625,378	-	$300,000	$569,000	$650,000	-	$2,834,988

Project		Funding Based on award date									
		2014	2015	2016	2017	2018	2019	2020	2021	2022	Total
020	Development of NAS wide and Global Rapid Aviation Air Quality	$150,000	$200,000	$250,000	$250,000	-	-	-	-	-	$850,000
021	Improving Climate Policy Analysis Tools	$150,000	$150,000	$150,000	$150,000	-	-	-	-	-	$600,000
022	Evaluation of FAA Climate Tools	$150,000	$30,000	$ 75,000	$100,000	-	-	$200,000	$150,000	$199,999	$704,999
023	Analytical Approach for Quantifying Noise from Advanced Operational Procedures	-	$286,711	$250,000	$250,000	-	$250,000	$500,000	-	-	$1,536,711
024	Emissions Data Analysis for CLEEN, ACCESS, and Other Recent Tests	$244,975	-	$ 75,000	-	-	-	-	-	-	$319,975
025	National Jet Fuels Combustion Program – Area #1: Chemical Kinetics Combustion Experiments	-	$615,000	$210,000	$200,000	$ 2,556	$110,000	$300,000	$200,000	$200,000	$1,837,556
026	National Jet Fuels Combustion Program – Area #2: Chemical Kinetics Model Development and Evaluation	-	$200,000	-	-	-$ 2,556	-	-	-	-	$197,444
027	National Jet Fuels Combustion Program – Area #3: Advanced Combustion Tests	-	$1,010,000	$580,000	$265,000	-	$ 30,000	-	-	-	$1,885,000

Project		Funding Based on award date									
		2014	2015	2016	2017	2018	2019	2020	2021	2022	Total
028	National Jet Fuels Combustion Program – Area #4: Combustion Model Development and Evaluation	-	$470,000	$ 55,000	-	-	-	-	-	-	$525,000
029	National Jet Fuels Combustion Program – Area #5: Atomization Tests and Models	-	$640,000	$360,000	$150,000	-	$120,000	-	-	-	$1,270,000
030	National Jet Fuels Combustion Program – Area #6: Referee Swirl-Stabilized Combustor Evaluation/Support	-	$349,949	-	-	-	-	-	-	-	$349,949
031	Alternative Jet Fuels Test and Evaluation	-	$489,619	$744,891	$999,512	$183,019	-	$2,976,134	$499,784	$1,499,940	$7,392,899
032	Worldwide LCA of GHG Emissions from Petroleum Jet Fuel	-	$150,000	-	-	-	-	-	-		$150,000
033	Alternative Fuels Test Database Library	-	$199,624	$119,794	$165,000	-	$163,584	$330,000	$150,000	$150,000	$1,278,002
034	National Jet Fuels Combustion Program – Area #7: Overall Program Integration and Analysis	-	$234,999	$635,365	$192,997	$374,978	-	$582,983	-	-	$2,021,322
035	Airline Flight Data Examination to Improve flight Performance Modeling	-	$150,001	-	-	-	-	-	-	-	$150,001
036	Parametric Uncertainty Assessment for AEDT2b	-	$ 65,000	$175,000	$380,000	-	$300,000	-	-	-	$920,000

Project		Funding Based on award date									
		2014	2015	2016	2017	2018	2019	2020	2021	2022	Total
037	CLEEN II Technology Modeling and Assessment	-	$200,000	$150,000	$170,000	-	$170,000	$490,000	-	$250,000	$1,430,000
038	Rotorcraft Noise Abatement Procedures Development	-	$150,000	$150,000	$150,000	$150,000	-	$300,000	$150,000	-	$1,050,000
039	Naphthalene Removal Assessment	-	-	$200,000	$290,000	-	$350,000	-	-	-	$840,000
040	Quantifying Uncertainties in Predicting Aircraft Noise in Real-world Situations	-	-	$218,426	$200,000	-	$255,000	-		-	$673,426
041	Identification of Noise Acceptance Onset for Noise Certification Standards of Supersonic Airplane	-	-	$160,000	$221,000	-	$390,000	-	-	-	$771,000
042	Acoustical Model of Mach Cut-off	-	-	$255,000	$150,000	$170,000	-	-$120	-	-	$574,880
043	Noise Power Distance Re-Evaluation	-	-	$150,000	$ 75,000	-	$220,000	$400,000	-	-	$845,000
044	Aircraft Noise Abatement Procedure Modeling and Validation	-	-	-	-	$350,000	-	$370,000	-	-	$720,000
045	Takeoff/Climb Analysis to Support AEDT APM Development	-	-	$250,000	$ 75,000	$ 8,845	$175,000	-	-	-	$508,845
046	Surface Analysis to Support AEDT APM Development	-	-	$ 75,000	$ 75,000	$ 75,000	-	$400,000	-	$75,000	$700,000

Project		Funding Based on award date									
		2014	2015	2016	2017	2018	2019	2020	2021	2022	Total
047	Clean Sheet Supersonic Engine Design and Performance	-	-	-	-	-	$250,000	$800,000	$200,000	-	$1,250,000
048	Analysis to Support the Development of an Engine nvPM Emissions Standards	-	-	$150,000	$200,000	-	$200,000	$200,000	$200,000	-	$950,000
049	Urban Air Mobility Noise Reduction Modeling	-	-	-	-	-	-	$560,000	$280,000	-	$840,000
050	Over-Wing Engine Placement Evaluation	-	-	-	-	-	-	$590,000	-	-	$590,000
051	Combustion Concepts for Next-Generation Aircraft Engines	-	-	-	-	-	-	$600,000	-	$300,000	$900,000
052	Comparative Assessment of Electrification Strategies for Aviation	-	-	-	-	-	-	$600,000	-	$460,000	$1,060,000
053	Validation of Low Exposure Noise Modeling by Open Source Data Management and Visualization Systems Integrated with AEDT	-	-	-	-	-	-	$569,903	-	$90,000	$659,903
054	AEDT Evaluation and Development Support	-	-	-	-	-	-	$1,400,000	-	$900,000	$2,300,000
055	Noise Generation and Propagation from Advanced Combustors	-	-	-	-	-	-	$2,999,984	-	$500,000	$3,499,984

Project		Funding Based on award date									
		2014	2015	2016	2017	2018	2019	2020	2021	2022	Total
056	Turbine Cooling through Additive Manufacturing	-	-	-	-	-	-	$800,000	-	$400,000	$1,200,000
057	Support for Supersonic Aircraft En-route Noise Efforts in ICAO CAEP	-	-	-	-	-	-	$420,000	-	$110,000	$530,000
058	Improving Policy Analysis Tools to Evaluate Higher-Altitude Aircraft Operations	-	-	-	-	-	-	$500,000	$150,000	$500,000	$1,150,000
059	Modeling and Measurements of Supersonic Civil Transport Jet Noise	-	-	-	-	-	-	$849,956	$849,999	-	$1,699,955
060	Analytical Methods for Expanding the AEDT Aircraft Fleet Database	-	-	-	-	-	-	$150,000	$150,001	$150,000	$450,001
061	Noise Certification Streamlining	-	-	-	-	-	-	$250,000	$250,000	$250,000	$750,000
062	Noise Model Validation for AEDT	-	-	-	-	-	-	$350,000	$375,000	$375,000	$1,100,000
063	Parametric Noise Modeling for Boundary Layer Ingesting Propulsors	-	-	-	-	-	-	$300,000	-	-	$300,000
064	Alternative Design Configurations to Meet Future Demand	-	-	-	-	-	-	$250,000	$1,199,999	$500,000	$1,949,999
065	Fuel Testing Approaches for Rapid Jet Fuel Prescreening	-	-	-	-	-	-	$559,998	$150,000	$345,000	$1,054,998

Project		Funding Based on award date									
		2014	2015	2016	2017	2018	2019	2020	2021	2022	Total
066	Evaluation of High Thermal Stability Fuels	-	-	-	-	-	-	$284,997	$100,000	-	$384,997
067	Impact of Fuel Heating on Combustion and Emissions	-	-	-	-	-	-	$250,000	$250,000	$250,000	$750,000
068	Combustor Wall Cooling with Dirt Mitigation	-	-	-	-	-	-	$150,000	$150,000	-	$300,000
069	Transitioning a Research nvPM Mass Calibration Procedure to Operations	-	-	-	-	-	-	$846,707	$100,853	$99,999	$1,047,559
070	Reduction of nvPM Emissions from Aero-engine Fuel Injectors	-	-	-	-	-	-	$500,000	$500,000	$500,000	$1,500,000
071	Predictive Simulation of nvPM Emissions in Aircraft Combustors	-	-	-	-	-	-	$500,000	$500,000	-	$1,00,000
072	Aircraft Noise Exposure and Market Outcomes in the United States	-	-	-	-	-	-	$380,000	-	$100,000	$480,000
073	Fuel Composition Impact on Combustor Durability	-	-	-	-	-	-	$299,148	$199,865	$200,000	$699,013
074	Low Emissions Pre-Mixed Combustion Technology for Supersonic Civil Transport	-	-	-	-	-	-	$1,000,000	$999,995	-	$1,999,995
075	Improved Engine Fan Broadband Noise Prediction Capabilities	-	-	-	-	-	-	$300,000	$300,000	-	$600,000

Project		Funding Based on award date									
		2014	2015	2016	2017	2018	2019	2020	2021	2022	Total
076	Improved Open Rotor Noise Prediction Capabilities	-	-	-	-	-	-	$300,000	$300,00	-	$600,000
077	Measurements to Support Noise Certification for UAS/UAM Vehicles and Identify Noise Reduction	-	-	-	-	-	-	$500,000	$500,000	-	$1,00,000
078	Contrail Avoidance Decision Support & Evaluation	-	-	-	-	-	-	-	$550,000	$550,000	$1,100,000
079	Novel Noise Liner Development Enabled by Advanced Manufacturing	-	-	-	-	-	-	-	$299,867	-	$299,867
080	Hydrogen Production Alternatives for Sustainable Aviation Fuel (SAF) Production	-	-	-	-	-	-	-	$600,000	$758,026	$1,358,026
081	Measurement and Prediction of nvPM size and number emissions from sustainable and convention al aviation fuels	-	-	-	-	-	-	-	-	$2,050,000	$2,050,000
082	CAEP Stringency Analysis Modeling	-	-	-	-	-	-	-	-	$1,890,000	$1,890,000

Project		Funding Based on award date									
		2014	2015	2016	2017	2018	2019	2020	2021	2022	Total
083	NOx Cruise/Climb Metric System Development	-	-	-	-	-	-	-	-	$250,000	$250,000

Breakout by University*

	Funding Based on award year										
University	2013	2014	2015	2016	2017	2018	2019	2020	2021	2022	Total
Boston University	$5,000	$350,000	$350,000	$400,000	$610,000	-	$1,729,286	$1,599,962	$899,371	$549,921	$6,493,541
Georgia Institute of Technology	$5,000	$1,310,000	$1,975,001	$1,434,999	$1,468,500	$650,000	$895,000	$12,264,984	$5,434,994	$4,275,000	$29,713,478
Massachusetts Institute of Technology	$10,000	$1,153,927	$1,169,073	$1,855,000	$1,690,000	$1,000,000	$1,050,000	$5,250,000	$1,700,000	$3,885,000	$18,763,000
Missouri University of Science and Technology	$5,000	$2,800,000	$750,000	-$147,766	$725,500	-	$1,217,221	$846,707	$622,099	$2,149,999	$8,968,760
Oregon State University	$5,000	-	$160,000	$80,000	$59,000	-	-	-	-	-	$304,000
Pennsylvania State University	$5,000	$862,301	$766,711	$958,426	$890,424	$320,000	$797,623	$2,945,000	$1,619,867	$750,000	$9,915,352
Purdue University	$5,000	$389,979	$1,030,000	$763,750	$747,067	$114,185	$605,000	$1,220,116	$600,000	600,000	$6,075,097
Stanford University	$5,000	$380,000	$1,155,000	$345,000	$200,000	-	$110,000	$1,069,903	$400,000	$290,000	$3,954,903
University of Dayton	$5,000	-	$906,196	$1,349,087	$1,192,509	$574,944	-	$4,553,260	$799,649	$1,894,940	$11,275,585
University of Hawaii	$10,000	-	$75,000	$100,000	$125,000	-	$200,000	$200,000	$100,00	-	$810,000
University of Illinois	$5,000	$349,943	$553,000	$375,000	$265,000	-	$130,000	$879,956	$649,999	$499,999	$3,707,897
University of North Carolina	$5,000	$320,614	$369,996	-	$625,378	-	$300,000	$569,000	$650,000	-	$2,839,988
University of Pennsylvania	$5,000	$154,000	$343,498	$266,001	$134,924	-	-	-	-	-	$903,423

	Funding Based on award year										
University	**2013**	**2014**	**2015**	**2016**	**2017**	**2018**	**2019**	**2020**	**2021**	**2022**	**Total**
University of Tennessee	$5,000	$200,000	$100,000	$100,000	$225,000	-	$260,000	$500,000	$100,000	$200,000	$1,690,000
University of Washington	$5,000	$60,000	$29,997	$15,000	-	-	-	-$120.15	-	-	$109,877
Washington State University	$20,000	$974,228	$864,968	$725,961	$796,039	$510,918	$390,911	$1,910,374	$862,313	$927,162	$7,982,874

Breakout by State*

	Funding Based on award year										
State	2013	2014	2015	2016	2017	2018	2019	2020	2021	2022	Total
California	$5,000	$380,000	$1,155,000	$345,000	$200,000	-	$110,000	$1,069,903	$400,000	$290,000	$3,954,903
Georgia	$5,000	$1,310,000	$1,975,001	$1,434,999	$1,468,500	$650,000	$895,000	$12,264,984	$5,434,994	$4,275,000	$29,713,478
Hawaii	$10,000	-	$75,000	$100,000	$125,000	-	$200,000	$200,000	$100,000	-	$810,000
Illinois	$5,000	$349,943	$553,000	$375,000	$265,000	-	$130,000	$879,956	$649,999	$499,999	$3,707,897
Indiana	$5,000	$389,979	$1,030,000	$763,750	$747,067	$114,185	$605,000	$1,220,116	$600,000	600,000	$6,075,097
Massachusetts	$15,000	$1,503,927	$1,529,073	$2,255,000	$2,300,000	$1,000,000	$2,779,286	$6,849,963	$2,599,371	$4,434,921	$25,256,541
Missouri	$5,000	$2,800,000	$750,000	-$147,766	$725,500	-	$1,217,221	$846,707	$622,099	$2,149,999	$8,968,760
North Carolina	$5,000	$320,614	$369,996	-	$625,378	-	$300,000	$569,000	$650,000	-	$2,839,988
Ohio	$5,000	-	$906,196	$1,349,087	$1,192,509	$574,944	-	$4,553,260	$799,649	$1,894,940	$11,275,585
Oregon	$5,000	-	$160,000	$80,000	$59,000	-	-	-	-	-	$304,000
Pennsylvania	$10,000	$1,016,301	$1,110,209	$1,224,427	$1,025,348	$320,000	$797,623	$2,945,000	$1,619,867	$750,000	$10,818,775
Tennessee	$5,000	$200,000	$100,000	$100,000	$225,000	-	$260,000	$500,000	$100,000	$200,000	$1,690,000
Washington	$25,000	$1,034,228	$894,965	$740,961	$796,039	$510,918	$390,911	$1,910,254	$862,313	$927,162	$8,092,751

*Totals include administrative funds not associated with specific NFOs